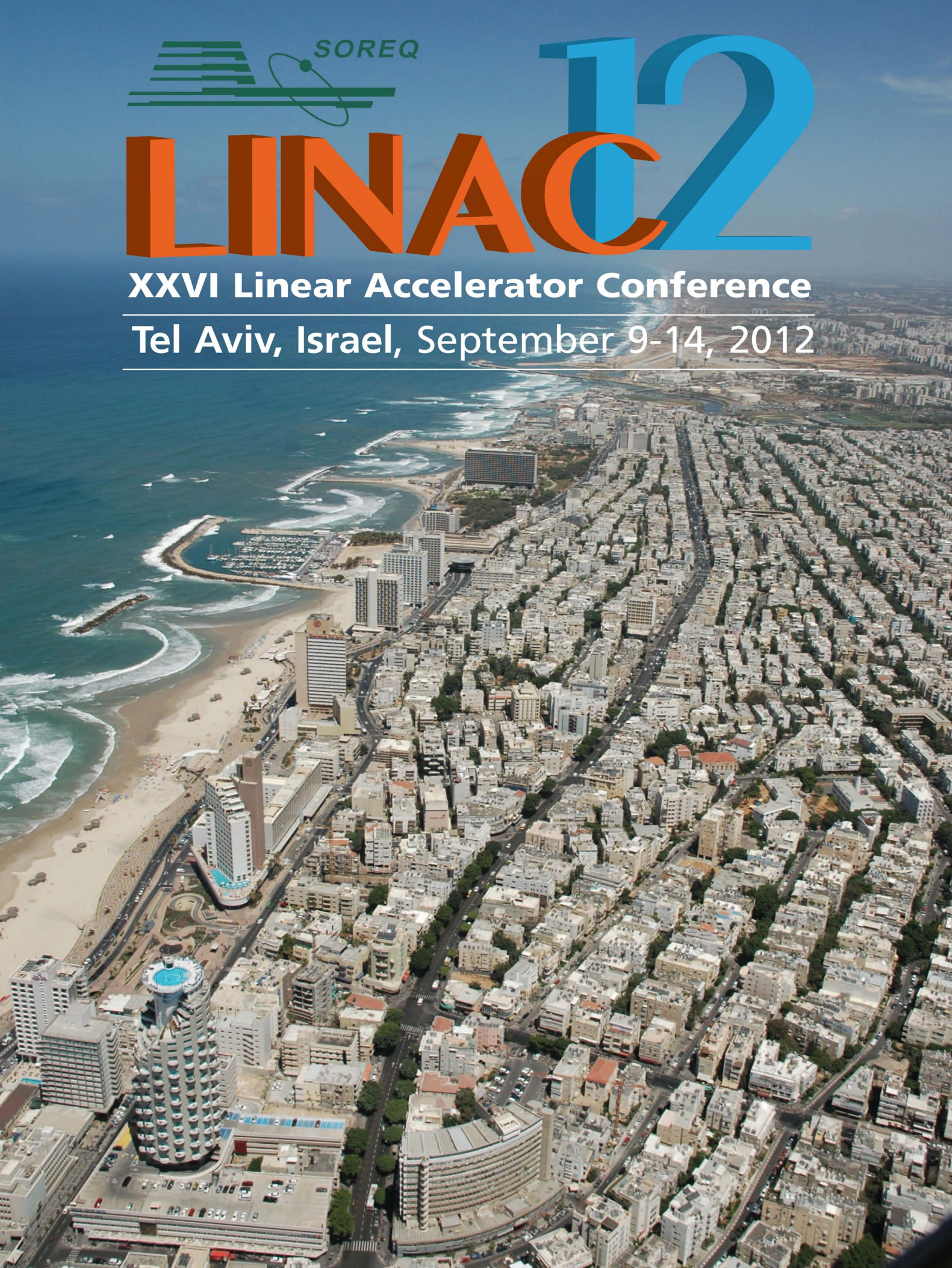
SOREQ
LINAC12
XXVI Linear Accelerator Conference
Tel Aviv, Israel, September 9-14, 2012

Contents

Preface i
Contents iii

Papers ix
SUPB001 – Analyzing Surface Roughness Dependence of Linear RF Losses 1
SUPB003 – Feasibility Study of Short Pulse Mode Operation for Multi-turn ERL Light Source 4
SUPB004 – Linac Optics Design for Multi-turn ERL Light Source 7
SUPB006 – Study of Beam-Based Alignment for Shanghai Soft X-Ray FEL Facility 10
SUPB007 – On-Line Dispersion Free Steering for the Main Linac of CLIC 13
SUPB008 – Specifications of the Distributed Timing System for the CLIC Main Linac 16
SUPB009 – Linear Accelerator based on Parallel Coupled Accelerating Structure 19
SUPB010 – Measurements of a Reduced Energy Spread of a Recirculating Linac by Non-Isochronous Beam Dynamics 22
SUPB011 – Computational Model Analysis for Experimental Observation of Optical Current Noise Suppression Below the Shot-noise Limit 25
SUPB012 – Status of CH Cavity and Solenoid Design of the 17 MeV Injector for MYRRHA 29
SUPB013 – The Beam Commissioning Plan of Injector II in C-ADS 32
SUPB014 – RF Setup of the MedAustron RFQ 35
SUPB015 – Production and Quality Control of the First Modules of the IFMIF-EVEDA RFQ 38
SUPB016 – RFQ With Improved Energy Gain 41
SUPB017 – Tuning Studies on 4-rod-RFQs 44
SUPB018 – Studies of Parasitic Cavity Modes for Proposed ESS Linac Lattices 47
SUPB019 – The Multipacting Simulation for the New-Shaped QWR using TRACK3P 50
SUPB020 – Structural Analysis of the New-Shaped QWR for HIAF in IMP 53
SUPB022 – First Measurements on the 325 MHz Superconducting CH Cavity 56
SUPB023 – Status of the Superconducting CW Demonstrator for GSI 59
SUPB024 – Development of Permanent Magnet Focusing System for Klystrons 62
SUPB025 – Development of Superconducting Radio-Frequency (SRF) Deflecting Mode Cavities and Associated Waveguide Dampers for the APS Upgrade Short Pulse X-Ray Project 65
SUPB026 – Multipacting Analysis of High-velocity Superconducting Spoke Resonators 68
SUPB027 – Mechanical Study of the First Superconducting Half-wave Resonator for Injector II of CADS Project 71
SUPB028 – The Superconducting CH Cavity Development in IMP* 74
SUPB029 – Impact of Trapped Flux and Systematic Flux Expulsion in Superconducting Niobium 77
SUPB031 – The Nonresonant Perturbation Theory Based Field Measurement and Tuning of a Linac Accelerating Structure 80
SUPB032 – The C-band RF Pulse Compression for Soft XFEL at SINAP 83
SUPB035 – RF Photoinjector and Radiating Structure for High-power THz Radiation Source 86
SUPB037 – The Development of Timing Control System for RFQ 89
SUPB038 – Multipole Field Effects for the Superconducting Parallel-Bar Deflecting/Crabbing Cavities 92
SUPB039 – Compact Superconducting Crabbing and Deflecting Cavities 95
MO1A01 – Operational Experience and Future Goals of the SARAF Linac at SOREQ 100
MO1A02 – Status of the European XFEL – Constructing the 17.5 GeV Superconducting Linear Accelerator 105
MO1A03 – SRF Linac Technology Development at Fermilab 110
MO2A02 – Increased Understanding of Beam Losses from the SNS Linac Proton Experiment 115
MO3A01 – Development of H-mode Linacs for the FAIR Project 120
MO3A02 – Commissioning of a New Injector for the RIKEN RI-Beam Factory 125
MO3A03 – FRANZ – Accelerator Test Bench and Neutron Source 130
MO3A04 – Accelerator/Decelerator of Slow Neutrons 133
MOPLB01 – Emittance Control for Different FACET Beam Setups in the SLAC Linac 138
MOPLB02 – Positron Injector Linac Upgrade for SuperKEKB 141
MOPLB03 – Advances in Beam Tests of Dielectric Based Accelerating Structures 144
MOPLB04 – A 10 MeV L-band Linac for Irradiation Applications in China 147
MOPLB05 – Applications of Compact Dielectric-Based Accelerators 150
MOPLB06 – Fermilab 1.3 GHz Superconducting RF Cavity and Cryomodule Program for Future Linacs 153

MOPLB07 – Non-destructive Inspections for SC Cavities . . . 156
MOPLB08 – Normal Conducting Deflecting Cavity Development at the Cockcroft Institute . . . 159
MOPLB09 – Status of the C-Band RF System for the SPARC-LAB High Brightness Photoinjector . . . 162
MOPLB10 – FRIB Technology Demonstration Cryomodule Test . . . 165
MOPLB11 – The Upgraded Argonne Wakefield Accelerator Facility (AWA): a Test-Bed for the Development of High Gradient Accelerating Structures and Wakefield Measurements . . . 168
MOPLB12 – X-Ray Local Energy Spectrum Measurement on Tsinghua Thomson Scattering X-Ray Source (TTX) . . . 171
MOPB001 – Emittance Control for Different FACET Beam Setups in the SLAC Linac . . . 174
MOPB002 – Positron Injector Linac Upgrade for SuperKEKB . . . 177
MOPB003 – Recent Improvements to the Control of the CTF3 High-Current Drive Beam . . . 180
MOPB004 – Design and Operation of a Compact 1 MeV X-band Linac . . . 183
MOPB005 – High Gradient Operation of 8 GeV C-Band Accelerator in SACLA . . . 186
MOPB007 – Study of Microbunching Instabilitity in the Linac of the Shanghai Soft X-Ray Free Electron Laser Facility . . . 189
MOPB011 – Photoinjector of the EBTF/CLARA Facility at Daresbury . . . 192
MOPB012 – First RF Measurement Results for the European XFEL SC Cavity Production . . . 195
MOPB013 – Experimental Results on the PHIL Photo-injector Test Stand at LAL . . . 198
MOPB014 – Electron Model of a Dogbone RLA with Multi-Pass Arcs . . . 201
MOPB016 – In-situ Measurement of Beam-induced Fields in the S-band Accelerating Structures of the Diamond Light Source linac . . . 204
MOPB017 – Integration of the European XFEL Accelerating Modules . . . 207
MOPB018 – Analyzing Surface Roughness Dependence of Linear RF Losses . . . 210
MOPB020 – LLRF System Improvement for HLS Linac Upgrade . . . 213
MOPB021 – Bunch-by-bunch Phase Modulation for Linac Beam-loading Compensation . . . 216
MOPB022 – RF Characteristic Studies on the Whole Accelerating Structure for the BEPCII Linear Accelerator . . . 219
MOPB023 – Progress on the Design and Construction of the 100 MeV / 100 kW Electron Linac for the NSC KIPT Neutron Source . . . 222
MOPB024 – Beam Dynamics Simulation and Optimization for 10 MeV Superconducting e-Linac Injector for VECC-RIB Facility . . . 225
MOPB025 – 1ms Multi-bunch Electron Beam Acceleration by a Normal Conducting RF Gun and Superconducting Accelerator . . . 228
MOPB026 – TRIUMF/VECC e-Linac Injector Beam Test . . . 231
MOPB029 – Commissioning of the X-Band Test Area at SLAC . . . 234
MOPB030 – Performance of First C100 Cryomodules for the CEBAF 12 GeV Upgrade Project . . . 237
MOPB031 – Vibration Response Testing of the CEBAF 12 GeV Upgrade Cryomodules . . . 240
MOPB032 – Stabilization of the Beam Intensity in the Linac at the CTF3 CLIC Test Facility . . . 243
MOPB033 – High Power Coupler Test for TRIUMF E-linac SC Cavities . . . 246
MOPB034 – Novel Technique of Suppressing TBBU in High-energy ERLs . . . 249
MOPB035 – The Linear Accelerating Structure Development for HLS Upgrade . . . 252
MOPB036 – Feasibility Study of Short Pulse Mode Operation for Multi-turn ERL Light Source . . . 255
MOPB037 – Linac Optics Design for Multi-turn ERL Light Source . . . 258
MOPB038 – Single Shot Bunch-by-Bunch Beam Emittance Measurement of the SPring-8 Linac . . . 261
MOPB041 – Advances in Beam Tests of Dielectric Based Accelerating Structures . . . 264
MOPB042 – On-line Dispersion Free Steering for the Main Linac of CLIC . . . 267
MOPB043 – Detailed Analysis of the Long-Range Wakefield in the Baseline Design of the CLIC Main Linac 270
MOPB045 – Specifications of the Distributed Timing System for the CLIC Main Linac . . . 273
MOPB046 – A 10 MeV L-band Linac for Irradiation Applications in China . . . 276
MOPB047 – Applications of Compact Dielectric Based Accelerators . . . 279
MOPB048 – Linear Accelerator Based on Parallel Coupled Accelerating Structure . . . 282
MOPB049 – Design of Compact C-Band Standing-Wave Accelerator for Medical Radiotherapy . . . 285
MOPB051 – Changing Attitude to Radiation Hazards and Consequent Opportunities for LINAC Applications 288
MOPB052 – Fermilab 1.3 GHz Superconducting RF Cavity and Cryomodule Program for Future Linacs . 291
MOPB053 – Non-destructive Inspections for SC Cavities . . . 294
MOPB054 – Test Results of Tesla-style Cryomodules at Fermilab . . . 297

MOPB055 – Development of Superconducting Radio-Frequency (SRF) Deflecting Mode Cavities and Associated Waveguide Dampers for the APS Upgrade Short Pulse X-Ray Project . . . 300
MOPB056 – Multipacting Analysis of High-Velocity Superconducting Spoke Resonators . . . 303
MOPB057 – Mechanical Study of the First Superconducting Half-wave Resonator for Injector II of CADS Project . . . 306
MOPB059 – The Superconducting CH Cavity Development in IMP* . . . 309
MOPB060 – RF Surface Impedance Characterization of Potential New Materials for SRF-based Accelerators . . . 312
MOPB061 – The New 2nd Generation SRF R&D Facility at Jefferson Lab: TEDF . . . 315
MOPB062 – A New Internal Optical Profilometry System for Characterization of RF Cavity Surfaces – CYCLOPS . . . 318
MOPB063 – Superconducting RF Linac for eRHIC . . . 321
MOPB064 – Developing of Superconducting RF Guns at BNL . . . 324
MOPB065 – Impact of Trapped Magnetic Flux and Systematic Flux Expulsion in Superconducting Niobium 327
MOPB066 – Alternative Approaches for HOM-Damped Cavities . . . 330
MOPB067 – Results and Performance Simulations of the Main Linac Design for B*ERL*inPro . . . 333
MOPB069 – Study of HPR Created Oxide Layer at Nb Surfaces . . . 336
MOPB070 – Quality Control of Cleanroom Processing Procedures of SRF Cavities for Mass Production . 339
MOPB071 – Process Developments for Superconducting RF Low Beta Resonators for the ReA3 LINAC and Facility for Rare Isotope Beams . . . 342
MOPB072 – Multipole Expansion of the Fields in Superconducting High-Velocity Spoke Cavities . . . 345
MOPB073 – Cold Testing of Superconducting 72 MHz Quarter-wave Cavities for ATLAS . . . 348
MOPB074 – Thermo-Mechanical Simulations of the Frequency Tuning Plunger for the IFMIF Half-Wave Resonator . . . 351
MOPB077 – Lorentz Force Detuning Compensation Studies for Long Pulses in ILC type SRF Cavities . . 354
MOPB079 – Normal Conducting Deflecting Cavity Development at the Cockcroft Institute . . . 357
MOPB080 – Status of the C-Band RF System for the SPARC-LAB High Brightness Photoinjector . . . 360
MOPB081 – Travelling Wave Accelerating Structures with a Large Phase Advance . . . 363
MOPB082 – RF Parameters of the TE - Type Deflecting Structure for S-Band Frequency Range . . . 366
MOPB083 – Operational experience with the FERMI@Elettra S-band RF System . . . 369
MOPB084 – Design of a C-band Disk-loaded Type Accelerating Structure for a Higher Pulse Repetition Rate in the SACLA Accelerator. . . . 372
MOPB086 – The Nonresonant Perturbation Theory Based Field Measurement and Tuning of a Linac Accelerating Structure . . . 375
MOPB087 – S-Band Loads for SLAC Linac . . . 378
MOPB088 – Fabrication Tests for IMP 162.5 MHz RFQ . . . 381
MOPB089 – X-Ray Local Energy Spectrum Measurement at Tsinghua Thomson Scattering X-Ray Source (TTX) . . . 383
MOPB090 – FRIB Technology Demonstration Cryomodule Test . . . 386
MOPB091 – The Injector Cryomodule for the ARIEL e-Linac at TRIUMF . . . 389
MOPB093 – The Upgraded Argonne Wakefield Accelerator Facility (AWA): a Test-Bed for the Development of High Gradient Accelerating Structures and Wakefield Measurements . . . 392
MOPB094 – Simulation Study on the Longitudinal Bunch Shape Measurement by RF Chopper at J-PARC Linac . . . 395
MOPB095 – Design of MEBT for the Project X Injector Experiment at Fermilab . . . 398
MOPB096 – Beam Loss Mitigation in J-PARC Linac after the Tohoku Earthquake . . . 401
MOPB098 – Planning for Experimental Demonstration of Transverse Emittance Transfer at the GSI UNILAC through Eigen-Emittance Shaping . . . 404
TU1A01 – Status of the IFMIF-EVEDA 9 MeV 125 mA Deuteron Linac . . . 407
TU1A03 – Chinese ADS Project and Proton Accelerator Development . . . 412
TU1A04 – FRIB Accelerator Status and Challenges . . . 417
TU1A05 – Status and Commissioning Plan of the PEFP 100-MeV Linear Accelerator . . . 422
TU2A02 – Overview of SACLA Machine Status . . . 427
TU2A03 – LCLS Operation Experience and LCLS-II Design . . . 432
TU2A04 – High Current ERL at BNL . . . 437
TUPLB01 – The Swiss FEL RF Gun: RF Design and Thermal Analysis . . . 442

TUPLB02 – Deflecting Structures with Minimized Level of Aberrations . . . 445
TUPLB04 – Results of Testing of Multi-beam Klystrons for the European XFEL . . . 448
TUPLB05 – Computational Model Analysis for Experimental Observation of Optical Current Noise Suppression below the Shot-Noise Limit . . . 451
TUPLB06 – Status of the Rare Isotope Science Project in Korea . . . 455
TUPLB07 – Reduced-beta Cavities for High-intensity Compact Accelerators . . . 458
TUPLB08 – R&D Towards CW Ion Linacs at ANL . . . 461
TUPLB09 – Design and Beam Test of Six-electrode BPMs for Second-order Moment Measurement . . . 464
TUPLB10 – Non-destructive Real-time Monitor to Measure 3D-bunch Charge Distribution with Arrival Timing to Maximize 3D Overlapping for HHG-seeded EUV-FEL . . . 467
TUPLB12 – Development of Permanent Magnet Focusing System for Klystrons . . . 470
TUPB001 – The Fine Structure of the Zone of Particle Interaction with a Finite Length Periodic Structure . . . 473
TUPB002 – Deflecting Structures with Minimized Level of Aberrations . . . 476
TUPB004 – Results of Testing of Multi-beam Klystrons for the European XFEL . . . 479
TUPB005 – Computational Model Analysis for Experimental Observation of Optical Current Noise Suppression Below the Shot-noise Limit . . . 482
TUPB006 – Stability Performance of the Injector for SACLA/XFEL at SPring-8 . . . 486
TUPB008 – Major Trends in Linac Design for X-ray FELs . . . 489
TUPB009 – C-Band Accelerating Structure Development and Tests for the SwissFEL . . . 492
TUPB010 – The Swiss FEL RF Gun: RF Design and Thermal Analysis . . . 495
TUPB011 – The Swiss FEL S-Band Accelerating Structure: RF Design . . . 498
TUPB012 – The Swiss FEL C-Band Accelerating Structure: RF Design and Thermal Analysis . . . 501
TUPB013 – Update on the Commissioning Effort at the SwissFEL Injector Test Facility . . . 504
TUPB014 – Comparative Design of Single Pass, Photo-cathode RF-LINAC FEL for the THz Frequency Range: Self Amplification vs. Enhanced Super-radiance . . . 507
TUPB015 – Warm Beamlines and Infrastructure in the European XFEL . . . 510
TUPB018 – Study of Beam-Based Alignment for Shanghai Soft X-Ray FEL Facility . . . 513
TUPB019 – Second CW and LP Operation Test of XFEL Prototype Cryomodule . . . 516
TUPB020 – Status of the European XFEL 3.9 GHz system . . . 519
TUPB021 – Study of Plasma Effect in Longitudinal Space Charge Induced Microbunching Instability . . . 522
TUPB022 – A Passive Linearizer for Bunch Compression . . . 525
TUPB023 – The Optimization of RF Deflector Input Power Coupler . . . 528
TUPB026 – Measurements of a Reduced Energy Spread of a Recirculating Linac by Non-isochronous Beam Dynamics . . . 531
TUPB028 – Status of the Rare Isotope Science Project in Korea . . . 534
TUPB029 – Beam Intensity and Energy Control for the SPIRAL2 Facility . . . 537
TUPB030 – Overview of the Superconducting Linacs of the Rare Isotope Science Project . . . 540
TUPB031 – Beam Envelope Analysis and Simulation . . . 543
TUPB032 – Beam Dynamics of the Linac ALPI-PIAVE in View of Possible Upgrades Scenario for the SPES Project. . . . 546
TUPB033 – Piezoelectric Actuator Based Phase Locking System for IUAC Linac . . . 549
TUPB034 – A Helium Injector for Coupled RFQ and SFRFQ Cavity Project at Peking University . . . 552
TUPB035 – A New Design of the RFQ Channel for GSI HITRAP Facility . . . 555
TUPB036 – Design of Re-Buncher Cavity for Heavy-ion LINAC in IMP . . . 558
TUPB039 – Conceptual Design of Superconducting Heavy Ion Linear Injector for HIAF . . . 561
TUPB040 – Status of the Linac SRF Acquisition for FRIB . . . 564
TUPB041 – Scattering of H^- Stripped Electrons from SEM Grids and Wire Scanners at the CERN LINAC4 . . . 567
TUPB042 – Progress on RFQIII Fabrication in J-PARC Linac . . . 570
TUPB043 – One Design of Heavy Ion Linac Injector for CSRm . . . 573
TUPB044 – Cryogenic System for the ADS Injector II in IMP, CAS . . . 576
TUPB046 – R&D Towards CW Ion Linacs at ANL . . . 579
TUPB047 – Status of the Superconducting RF Activities for the HIE ISOLDE Project . . . 582
TUPB048 – Discussion of the Optimisation of a Linac Lattice to Minimise Disruption by a Class of Parasitic Modes . . . 585
TUPB049 – Superconducting Low Beta Niobium Resonator for Heavy Ions . . . 588
TUPB052 – Studies of Parasitic Cavity Modes for Proposed ESS Linac Lattices . . . 591

TUPB053 – Main Coupler Design for Project X . . . 594
TUPB054 – Coherent Effects of High Current Beam in Project-X Linac . . . 597
TUPB055 – R&D of IMP Superconducting HWR for China ADS . . . 600
TUPB056 – The Multipacting Simulation for the New-shaped QWR using TRACK3P . . . 603
TUPB057 – Structural Analysis of the New-Shaped QWR for HIAF in IMP . . . 606
TUPB058 – An Analytical Cavity Model for Fast Linac-Beam Tuning . . . 609
TUPB060 – Multipacting Suppression Modeling for Half Wave Resonator and RF Coupler* . . . 612
TUPB061 – ADRC Control for Beam Loading and Microphonics . . . 615
TUPB062 – Longitudinal Dynamic Analysis for the Project X 3-8 GeV Pulsed Linac . . . 618
TUPB066 – Reduced-beta Cavities for High-intensity Compact Accelerators . . . 621
TUPB067 – Development of a Superconducting Half-Wave Resonator for PXIE . . . 624
TUPB068 – Cryomodule Designs for Superconducting Half-Wave Resonators . . . 627
TUPB069 – BEAMDULAC-SCL Code for Complex Approach of Beam Dynamic Investigation in SC LINAC 630
TUPB070 – Development of Proton Therapy at the SC Linac with BEAMDULAC-SCL Code . . . 633
TUPB071 – First Measurements on the 325 MHz Superconducting CH Cavity . . . 636
TUPB072 – Status of the Superconducting CW Demonstrator for GSI . . . 639
TUPB073 – Design and Simulation of a Test Model for a Tri-Spoke Cavity at RIKEN . . . 642
TUPB074 – Superconducting CW Heavy Ion Linac at GSI . . . 645
TUPB075 – Beam Dynamics Design of China ADS Proton Linac . . . 648
TUPB077 – Thorium Energy . . . 651
TUPB079 – Design and Beam Test of Six-Electrode BPMs for Second-Order Moment Measurement . . . 654
TUPB080 – Non-destructive Real-time Monitor to Measure 3D Bunch Charge Distribution with Arrival Timing to Maximize 3D Overlapping for HHG-Seeded EUV-FEL . . . 657
TUPB081 – Beam Diagnostics Development for Triumf E-Linac . . . 660
TUPB082 – Beam Loss Track Measurements by a Fast Trigger Scheme in J-PARC Linac . . . 663
TUPB084 – High Dynamic-Range High Speed Linac Current Measurements . . . 666
TUPB090 – Development of Permanent Magnet Focusing System for Klystrons . . . 669
TUPB091 – 176 MHz Solid State Microwave Generator Design . . . 672
TUPB092 – High Power Amplifier Systems for SARAF Phase II . . . 675
TUPB093 – Compact 4 kW Variable RF Power Coupler for FRIB Quarter-wave Cavities . . . 678
TUPB094 – High Power Tests of TRASCO RFQ Couplers . . . 681
TUPB095 – Design of Coupler for Direct Coupled Amplifier to Drift Tube Linac Cavities of the Injector RILAC2 for RIKEN RI Beam Factory . . . 684
TUPB097 – The C-band RF Pulse Compression for Soft XFEL at SINAP . . . 687
TUPB099 – Input Coupler of the J-PARC DTL . . . 690
TUPB100 – Recovery and Status Report of DTL/SDTL for the J-PARC After Earthquake . . . 693
TUPB101 – Beam Loss Occurred at DTL Cavity in J-PARC Linac . . . 696
TUPB102 – Design and Performances of Phase Monitor in J-PARC Linac . . . 699
TUPB103 – CSNS DTL Prototyping and RF Tuning . . . 702
TUPB104 – Study of the Beam Dynamics in the RISP Driver Linac . . . 705
TUPB107 – Amplitude and Phase Control of the Accelerating Field in the ESS Spoke Cavity . . . 708
TUPB108 – Uppsala High Power Test Stand for ESS Spoke Cavities . . . 711
WE1A01 – ERL-Based Light Source Challenges . . . 714
WE1A02 – Status and Future of the CLIC Study . . . 719
WE1A03 – Application of X-band Linacs . . . 724
WE1A04 – The ARIEL Superconducting Electron Linac . . . 729
WE1A05 – Linac-Based Laser Compton Scattering X-Ray and Gamma-Ray Sources . . . 734
WE2A01 – RF Power Production at the Two Beam Test Stand at CERN . . . 738
WE2A02 – Solid State Marx Modulators for Emerging Applications . . . 743
TH1A01 – Results Achieved by the S1-Global Collaboration for ILC . . . 748
TH1A02 – Compact Superconducting Crabbing and Deflecting Cavities . . . 753
TH1A03 – Superconducting Spoke Cavities for Electron and High-Velocity Proton Linacs . . . 758
TH1A04 – Superconducting Linac and Associated Developments at IUAC Delhi . . . 763
TH2A01 – The ESS Linac Design . . . 768
TH2A02 – SPIRAL2 Accelerator Construction Progress . . . 773
TH2A03 – Design and Construction of the Linac4 Accelerating Structures . . . 778

TH2A004 – Computational Model Analysis for Experimental Observation of Optical Current Noise Suppression Below the Shot-noise Limit . . . 783
TH3A01 – Status of ILC . . . 787
TH3A02 – The 12 GeV Energy Upgrade at Jefferson Laboratory . . . 792
TH3A03 – ERL-Based Lepton-Hadron Colliders: eRHIC and LHeC . . . 797
TH3A04 – Plasmas, Dielectrics and the Ultrafast: First Science and Operational Experience at FACET . . . 802
THPLB01 – Linac Construction for China Spallation Neutron Source . . . 807
THPLB02 – Performance of Ferrite Vector Modulators in the LLRF system of the Fermilab HINS 6-Cavity Test . . . 810
THPLB03 – Front-End Linac Design and Beam Dynamics Simulations for MYRRHA . . . 813
THPLB04 – Preliminary Study of Proton Beam Transport in a 10 MeV Dielectric Wall Accelerator . . . 816
THPLB05 – R&D Activities on High Intensity Superconducting Proton Linac at RRCAT . . . 819
THPLB06 – The New Option for a Front End of Ion Linac . . . 822
THPLB07 – Experience with a 4-Rod CW Radio Frequency Quadrupole . . . 825
THPLB08 – High-Power RF Conditioning of the TRASCO RFQ . . . 828
THPLB09 – Status of E-XFEL String and Cryomodule Assembly at CEA-Saclay . . . 831
THPLB11 – Experimental and Simulation Study of the Long-path-length Dynamics of a Space-charge-dominated Bunch . . . 834
THPLB12 – Photoinjector SRF Cavity Development for B*ERL*inPro . . . 837
THPB002 – Preliminary Study of Proton Beam Transport in a 10 MeV Dielectric Wall Accelerator . . . 840
THPB003 – R&D Activities on High Intensity Superconducting Proton Linac at RRCAT . . . 843
THPB004 – Current Status of the RAL Front End Test Stand (FETS) Project . . . 846
THPB005 – Front-End Linac Design and Beam Dynamics Simulations for MYRRHA . . . 849
THPB006 – Post Acceleration of Laser-generated Proton Bunches by a CH-DTL . . . 852
THPB007 – A Pulsed Linac Front-end for ADS Applications . . . 855
THPB008 – A Coupled RFQ-IH Cavity for the Neutron Source FRANZ . . . 858
THPB009 – Status of CH Cavity and Solenoid Design of the 17 MeV Injector for MYRRHA . . . 861
THPB010 – Progress in the Construction of Linac4 at CERN . . . 864
THPB011 – Linac4 45 keV Proton Beam Measurements . . . 867
THPB012 – High Resolution Emittance Measurements at SNS Front End . . . 870
THPB013 – Diagnostics Tools for Beam Halo Investigation in SNS Linac . . . 873
THPB014 – Lattice Design and Beam Dynamics Studies for Project X . . . 876
THPB015 – Performance of Ferrite Vector Modulators in the LLRF system of the Fermilab HINS 6-Cavity Test . . . 879
THPB016 – Concept: Low Energy, Low Intensity NF from ProjectX . . . 882
THPB017 – A Concept: 8GeV CW Linac, Staged Approach . . . 885
THPB020 – Annular-ring Coupled Structure for the Energy Upgrade of the J-PARC Linac . . . 888
THPB021 – Recovery Efforts from the Tohoku Earthquake and Energy Upgrade Preparation of the Beam Transport from the J-PARC Linac to the 3-GeV Synchrotron . . . 891
THPB022 – Beam Phase Measurement for PEFP Linear Accelerator . . . 894
THPB023 – Linac Construction for China Spallation Neutron Source . . . 897
THPB024 – Main Linac Physics Design Study of the C-ADS Project . . . 900
THPB025 – 325 MHz CW Room Temperature High Power Bunching Cavity for the China ADS MEBT1 . . . 903
THPB026 – The Beam Commissioning Plan of Injector II in C-ADS . . . 906
THPB027 – Progress of one of 10 MeV superconducting proton linear Injectors for C-ADS . . . 909
THPB028 – The ESS Low Energy Beam Transport Line Design . . . 912
THPB029 – The ESS RFQ Beam Dynamics Design . . . 915
THPB030 – DTL Design for ESS . . . 918
THPB031 – Status Report on the French High-intensity Proton Injector Project at SACLAY (IPHI) . . . 921
THPB032 – Beam Dynamics Design Aspects for a Proposed 800 MeV H^- ISIS Linac . . . 924
THPB034 – Status of the FAIR 70 MeV Proton Linac . . . 927
THPB035 – Experience with a 4-Rod CW Radio Frequency Quadrupole . . . 930
THPB036 – The New Option for a Front End of Ion Linac . . . 933
THPB037 – Iron Beam Acceleration with DPIS . . . 936
THPB038 – Assembly and RF Tuning of the Linac4 RFQ at CERN . . . 939
THPB039 – Design of a Four-Vane RFQ for China ADS Project . . . 942

THPB040 – High-Power RF Conditioning of the TRASCO RFQ . . . 945
THPB042 – Production and Quality Control of the First Modules of the IFMIF-EVEDA RFQ . . . 948
THPB043 – The RFQ injector for the Radioactive Ion Beam of SPES Project . . . 951
THPB044 – Plans for an Integrated Front-End Test Stand at the Spallation Neutron Source . . . 954
THPB046 – RF Setup of the MedAustron RFQ . . . 957
THPB047 – Test RFQ for the MAX Project . . . 960
THPB049 – Tuning Studies on 4-Rod-RFQs . . . 963
THPB050 – RFQ With Improved Energy Gain . . . 966
THPB051 – Improvements at the BNL 200 MeV Linac . . . 969
THPB052 – Recent Progress with the J-PARC RFQs . . . 972
THPB055 – Numerical Simulations of ProjectX/PXIE RFQ . . . 975
THPB061 – Experimental and Simulation Study of the Long-path-length Dynamics of a Space-charge-dominated Bunch . . . 978
THPB062 – Multipole Field Effects for the Superconducting Parallel-Bar/RF-Dipole Deflecting/Crabbing Cavities . . . 981
THPB063 – Simulated Performance of the CARIBU EBIS Charge Breeder Transport Line . . . 984
THPB064 – Beam Dynamics Tools for Linacs Design . . . 987
THPB065 – Status of the Beam Dynamics Code DYNAC . . . 990
THPB066 – Photoinjector SRF Cavity Development for B*ERL*inPro . . . 993
THPB068 – First Observation of Photoemission Enhancement from Copper Cathode Illuminated by Z-Polarized Laser Pulse . . . 996
THPB069 – Beam Dynamics Studies for SRF Photoinjectors . . . 999
THPB073 – Initial RF Tests of the Diamond S-Band Photocathode Gun . . . 1002
THPB074 – RF Photoinjector and Radiating Structure for High-power THz Radiation Source . . . 1005
THPB076 – Design Issues of the Proton Source for the ESS Facility . . . 1008
THPB079 – Development of a Superconducting Focusing Solenoid for CADS . . . 1011
THPB081 – The Development of Timing Control System for RFQ . . . 1014
THPB083 – Status of E-XFEL String and Cryomodule Assembly at CEA-Saclay . . . 1017
THPB084 – A Low-Level RF Control System for a Quarter-Wave Resonator . . . 1020
THPB085 – LLRF Automation for the 9mA ILC Tests at FLASH . . . 1023
THPB086 – Precision Regulation of RF Fields with MIMO Controllers and Cavity-based Notch Filters . . . 1026
THPB089 – Magnetic Characterization of the Phase Shifter Prototypes Built by CIEMAT for E-XFEL . . . 1029
THPB091 – Machine Protection Issues and Solutions for Linear Accelerator Complexes . . . 1032
THPB092 – Recent Improvements in SPring-8 Linac for Early Recovery from Beam Interruption . . . 1035
THPB094 – Performance of Beam Chopper at SARAF via RF Deflector Before the RFQ . . . 1038
THPB095 – Designing of a Phase-mask-type Laser Driven Dielectric Accelerator for Radiobiology . . . 1041
THPB096 – High-power Sources of RF Radiation Driven by Periodic Laser Pulses . . . 1044
THPB097 – FRIB Front End Design Status . . . 1047
FR1A01 – Heavy Ion Strippers . . . 1050
FR1A02 – Light Ion ECR Sources State of the Art for Linacs . . . 1055
FR1A04 – In Flight Ion Separation using a Linac Chain . . . 1059
FR1A05 – SARAF Phase II P/D 40 MeV Linac Design Studies . . . 1064
FR2A01 – Recovery of the J-PARC Linac from the Earthquake . . . 1069

Appendices **1075**
List of Authors . . . 1075
Institutes List . . . 1089

ANALYZING SURFACE ROUGHNESS DEPENDENCE OF LINEAR RF LOSSES *

C. Xu[1,2#], M. J. Kelley[1,2], C. E. Reece[1]
[1]Thomas Jefferson National Accelerator Facility, Newport News, VA 23606
[2]College of William and Mary, Williamsburg, VA 23187

Abstract

Topographic structure on Superconductivity Radio Frequency (SRF) surfaces can contribute additional cavity RF losses describable in terms of surface RF reflectivity and absorption indices of wave scattering theory. At isotropic homogeneous extent, Power Spectrum Density (PSD) of roughness is introduced and quantifies the random surface topographic structure. PSD obtained from different surface treatments of niobium, such as Buffered Chemical Polishing (BCP), Electropolishing (EP), Nano-Mechanical Polishing (NMP) and Barrel Centrifugal Polishing (CBP) are compared. A perturbation model is utilized to calculate the additional rough surface RF losses based on PSD statistical analysis. This model will not consider that superconductor becomes normal conducting at fields higher than transition field. One can calculate the RF power dissipation ratio between rough surface and ideal smooth surface within this field range from linear loss mechanisms.

INTRODUCTION

RF loss induced by roughness is considered in many RF components, such as micro strip transmission line, wave guide and RF resonator. It can be understood as the RF electromagnetic field penetrates the surface and there the induced current will pass and cause RF loss. [1] However, in a RF wave view, the incident wave is reflected, scattered and absorbed by the rough surface. Inside of a resonator, the reflected, scattered wave contributes to standing wave field, while the absorbed RF wave is attributed to the RF surface loss. These two perspectives may both be used to describe the same RF loss.

In a resonator, only several specific RF standing wave modes can exist to meet the boundary condition which is the resonator geometry. The electric and magnetic field at one location is combination a of EM components of those plane waves. Within the resonator, E and M are separated in space and interchange their energy over a distance. Thus the peak E and M field are always not the same location. With special EM setup, TE, TM, TEM are used to describe the EM field direction, if presumed direction is beam axis. In some sense, it is very tedious and difficult to expand the field into plane wave expansion. If so, the incident direction should also be from all directions. Therefore, a RF loss calculation method is required and independent of direction. It also covers all frequencies or wavelengths.

METHODOLOGY

A rough surface will cost more RF loss. [2] One simple reason is that the surface current have more current path. In another word, the RF wave as more radiation absorption surface. This RF loss will contribute into power consumption and aggravate the quality factor.

If we consider a 2D random rough surface Z= f(x) in Fig.1. We can expand the magnetic field into Fourier series as in x and z direction. [3]

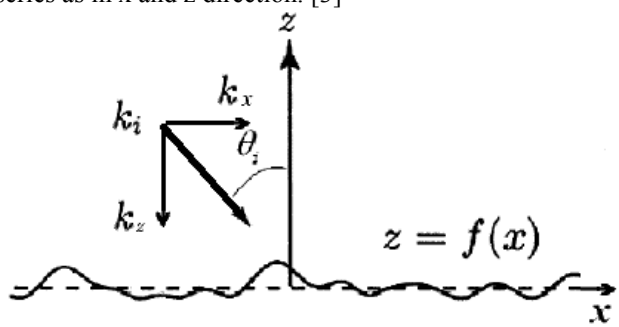

Figure 1: A plane wave incident impinging on a rough surface with incident angle θ_i.

$$\psi(x,z) = \int_{-\infty}^{\infty} dk_x \exp(-jk_x x + jk_{1z} z)\,\tilde{\psi}(k_x)$$

Where $k_{1z} = \sqrt{k_1^2 - k_x^2}$ and $k_1 = \frac{1-j}{\delta}$. Here δ is the skin depth $\delta = \sqrt{\frac{2}{\omega\mu\sigma}}$ and σ is the superconducting conductivity. The physics behind this equation is that the total magnetic field is combination of field component at each spatial wavelength. In another word, the total magnetic field can be expanded into magnetic contribution from each wavelength in spatial frequency.

If we use a second order small perturbation methods, setting

$$\tilde{\psi}(k_x) = \tilde{\psi}^{(0)}(k_x) + \tilde{\psi}^{(1)}(k_x) + \tilde{\psi}^{(2)}(k_x)$$

In first approximation, a fixed constant magnetic field H_0 is applied on the surface. Thus, the equation above becomes:

$$H_0 = \int_{-\infty}^{\infty} dk_x \exp(-jk_x x + jk_{1z} f(x))\,\tilde{\psi}(k_x)$$

Basically, we have done a Fourier transform to redistribute the magnetic field into each surface spatial wavelength in x direction.

By balancing this equation to second order, we obtain:

*Work supported by Jefferson Science Associates. xuchen@jlab.org

Copyright © 2012 by the respective authors — cc Creative Commons Attribution 3.0 (CC BY 3.0)

$$\tilde{\psi}^{(0)}(k_x) = H_0\delta(k_x)$$
$$\tilde{\psi}^{(1)}(k_x) = -jk_1H_0F(k_x)$$
$$\tilde{\psi}^{(2)}(k_x) = H_0\int_{-\infty}^{\infty}dk_x'F(k_x-k_x')F(k_x')\left(-k_1k_{1z}'+\frac{k_1^2}{2}\right)$$

For now, we have calculated the RF magnetic field on this given surface. The power absorbed by the conductor, for a given width w in y direction and length L in x direction, can be calculated from the Poynting vector.

$$P_a = \frac{w}{2\sigma}\mathrm{Re}\int ds\frac{\partial\psi}{\partial n}\psi^*$$

We simplify the results:

$$\langle P_a\rangle = \frac{wL}{2\sigma\delta}|H_0|^2\left\{1+\frac{2h^2}{\delta^2}\left[1-\frac{\delta}{h^2}\int_{-\infty}^{\infty}dk_xW(k_x)\mathrm{Re}\sqrt{k_1^2-k_x^2}\right]\right\}$$

In order to get rid of the external field, we normalize the power dissipation with that of a smooth surface.

$$\frac{\langle P_a\rangle}{P_{a,\mathrm{smooth}}} = 1+\frac{2h^2}{\delta^2}-\frac{4\pi}{\delta}\int_0^{\infty}dk_\rho\left\{k_\rho W_{2D}(k_\rho)\mathrm{Re}\sqrt{\frac{-2j}{\delta^2}-k_\rho^2}\right\}$$

$W_{2D}(k_\rho)$ is the 2D PSD from an isotropic surface.

Researcher have combined TM and TE wave mode into this equation into a 2D problem. They also avoid the assumption that surface field is a constant.

One should note:

1. The RMS and decay parameters (penetration depth) ratio, h/δ, is critical for characterizing the increased losses.

2. Third term reduces to h^2/δ^2, when the k_ρ is small. The second/third term have net contribution if $1/\delta$ and k_ρ are comparable.

3. Generally, higher $W_{2D}(k_\rho)$ brings additional loss.

APPLICATION TO SRF SURFACES

To obtain more accurate RF loss ratio, one needs to extend the PSD into as broad a frequency range as possible. Since all characterization method shave cut-off frequencies, one can at most get an extended PSD. The recent extended frequency range is 1/1.2 cm^{-1}–1/10 nm^{-1}, over 6 decades, with white light interferometry and atomic force microscopy. Because the magnetic field is expanded into horizontal spatial wavelength, the PSD frequency should cover the RF wavelength and beyond. Though an approximation methods is introduced by using Inverse Abel transforms to extend limited range, but obtaining 1D PSD with wider frequency range could improve later calculation accuracy.

$$<W(k_\rho)^{2D}>=-\tfrac{1}{\pi}\times\int_{k_\rho}^{\infty}\frac{dk_\rho}{\sqrt{k_x^{\,2}-k_\rho^{\,2}}}\frac{d}{dk_x}<W(k_x)^{1D}>$$

$$<W(k_x)^{1D}>=2\times\int_{k_x}^{\infty}\frac{k_\rho dk_\rho}{\sqrt{k_\rho^{\,2}-k_x^{\,2}}}<W(k_\rho)^{2D}>$$

This transformation also permits the transformation of the high-frequency behavior of the spectra of one dimensionality to be transformed into the high-frequency behavior of the other without knowledge of their low-frequency behavior.

We investigate SRF surfaces with current polishing methods and materials polished are large/fine/single grain Nb sheets. Buffered chemical polishing, electropolishing and mechanical centrifugal barrel polishing samples are characterized by Atomic Force Microscopy (AFM) and White light interferometry (WLI). Note that these two characterizations have different lateral resolutions and scan scopes which determine the spectral frequency ranges.

1D averaged PSD is calculated by following the routine introduced previously. [4] Such routine includes proper detrending, windowing and averaging.

In this study, the R_q and PSD are used to derive power ratio. Rq value from 4 different locations on each sample is averaged and summarised in Table 1.

Table 1: Averaged R_q with AFM and WLI

Samples	Single crystal		"Standard" fine-grained			
Treatment	After30 µm BCP	Nano polished	+100 µm BCP	+50 µm EP	Centrifugal Barrel Polishing (CBP)	
					Fine Grain	Large Grain
Atomic force microscopy ~5×5µm						
R_q(nm)	1.99	2.84	4.89	4.40	2.76	1.20
Atomic force microscopy ~100×100µm						
R_q(nm)	7.05	13.5	392.90	74.30	70.8	7.71
White light interferometry ~234×312µm (20x magnification)						
R_q (nm)	35.7	1.63	1500.4	291.7	151.8	13.5
White light interferometry ~930×1244µm(5x magnification)						
R_q (nm)	391	5.24	2008.5	642.8	335.5	49.0

One can generalize that Rq value decrease from BCP>EP>CBP Large grain> CBP Fine grain> Single crystal>Nanopolishing samples.

Averaged 1D PSD from AFM/WLI are combined in Fig.2.

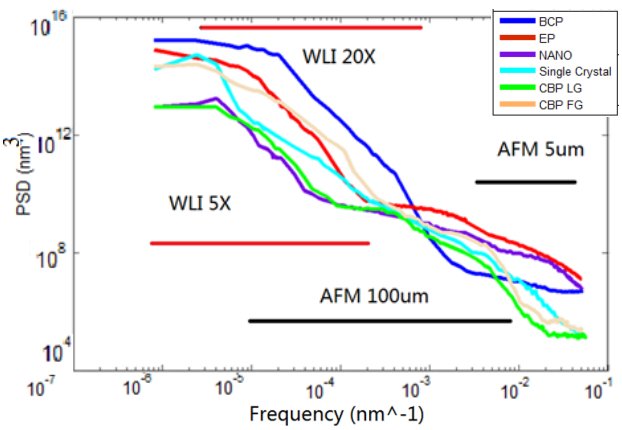

Figure 2: Joint 1D PSD models from AFM/WLI are shown and the characterization frequency domains are indicated.

Copyright © 2012 by the respective authors — cc Creative Commons Attribution 3.0 (CC BY 3.0)

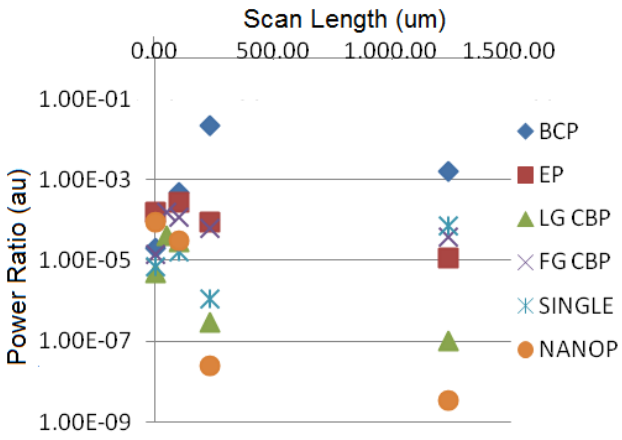

Figure 3: Power Ratio calculated from 1D PSD.

The power ratio is shown in Fig.3 and by inverse Abel transform, the 2D PSD are shown in Fig.4.

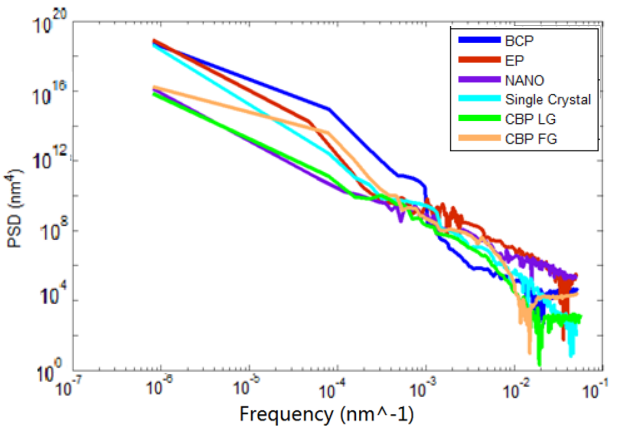

Figure 4: 2D PSD calculated from various surfaces. Power ratio index are illustrated in Fig.5.

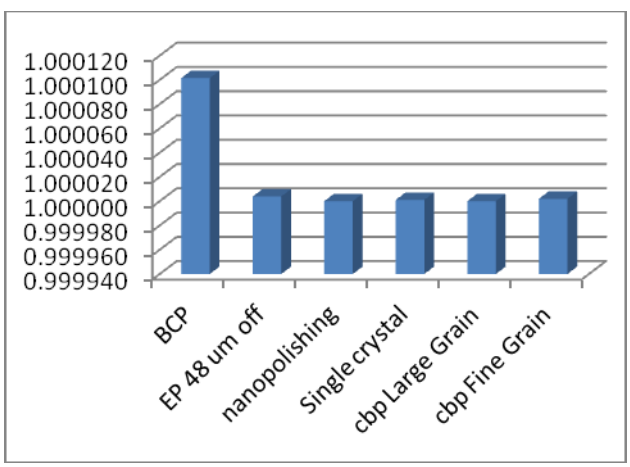

Figure 5: Power Ratio from 2D isotropic PSD.

BCP surface show higher ratio, but other surfaces suggest almost the same close to 1.

DISCUSSION

One can see from power ratio equation that the last term is an integration of 2d PSD.

$$\frac{\langle P_{a,\mathrm{rough}}\rangle}{P_{a,\mathrm{smooth}}} = 1 + \frac{2h^2}{\delta^2} - \frac{4\pi}{\delta}\int_0^\infty dk_\rho \left\{ k_\rho W_{2D}(k_\rho)\,\mathrm{Re}\sqrt{\frac{-2j}{\delta^2} - k_\rho^2} \right\}$$

Without the Re(…), the integrand is simply the square of RMS height. One can infer that if the k_ρ is small enough compared with $2/\delta$, then the Re(…) term reduced into $1/\delta$. In that limit the second and third terms cancel each other. The total power ratio becomes one. This gives substantiates the interpretation that features at larger wavelength have less RF power loss than the small high frequency features. Another understanding is that only features with lateral extent comparable to the penetration length give a significant effect on the additional power loss ratio. Applying this analysis to variously prepared niobium surfaces typical of those in SRF cavities, we find that linear RF losses depend negligibly on roughness for any of the characteristic surfaces considered. On the other hand, SRF materials are particularly susceptible to non-linear and temperature-dependent losses. The non-linear losses are reflected in the observed Q drop with increasing surface magnetic field. We are examining the influence of topography on such losses separately [5].

CONCLUSION

Spectral study suggested that surface roughness doesn't contribute much in the linear RF loss, because current practical surface a smooth enough at a wavelength closed to penetration depth.

ACKNOWLEDGMENT

Authored by Jefferson Science Associates, LLC under U.S. DOE Contract No. DE-AC05-06OR23177. The U.S. Government retains a non-exclusive, paid-up, irrevocable, world-wide license to publish or reproduce this manuscript for U.S. Government purposes.

REFERENCES

[1] H. Padamsee. RF Superconductivity. 1nd Edition (Wiley - VCH, New York 2011).
[2] L. Tsang. Scattering of Electromagnetic Waves, Theories and Applications. (John Wiley & Sons, Seattle 2004).
[3] Xiaoxiong Gu, Leung Tsang and Henning Braunisch. IEEE Microwave And Wireless Components Letters, Vol. 17, No. 7, July 2007 pp486
[4] Chen Xu, Hui Tian, Charles E. Reece and Michael J. Kelley. PRST-AB. 14, (2011) pp.123501.
[5] Chen. Xu, *et al.* in *Proc. Int. Part. Accel. Conf. 2012*, (2012). New Orleans, Louisiana: p. 2188-2190.

Copyright © 2012 by the respective authors — cc Creative Commons Attribution 3.0 (CC BY 3.0)

FEASIBILITY STUDY OF SHORT PULSE MODE OPERATION FOR MULTI-TURN ERL LIGHT SOURCE*

T. Atkinson†, A. V. Bondarenko, A. N. Matveenko, Y. Petenev,
Helmholtz-Zentrum Berlin für Materialien und Energie GmbH (HZB), Germany.

Abstract

The optic and simulation group at HZB are designing a light source based on the emerging Energy Recovery Linac superconducting technology, the Femto-Science-Factory (FSF) will provide its users with ultra-bright photons of angstrom wavelength at 6 GeV. The FSF is intended to be a multi-user facility and offer a wide variety of operation modes. A low emittance $\sim 0.1\,\mu$m rad mode will operate in conjunction with a short-pulse ~10 fs mode.

INTRODUCTION

This paper continues on from a recent introductory study[1] and highlights the physical limitations when trying to offer interchangeable modes and preserve beam quality. The paper concentrates on the short bunch mode, introducing the multi stage compression schemes in a general manner and presents the first results of the start-to-end beam simulations.

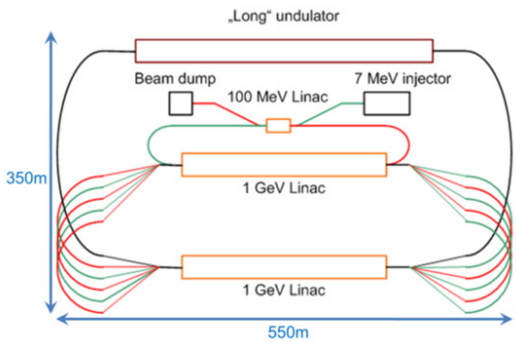

Figure 1: Schematic of the FSF Multi-Turn ERL.

The main design parameters of the FSF are listed in Table 1 and Fig. 1 shows the layout of the light source.

A SRF injector based on the design parameters of the BERLinPro[2] project delivers the 100 MeV electron beam into the main accelerator. Here two 1 GeV linacs are continually traversed until 6 GeV beam energy is reached. Each Arc contains straight sections for undulators and the final energy Arc permits a long straight section for 5000 period undulators.

The beam quality delivered to the long undulators and hence the photon brilliance attainable depends on the machine operating mode.

Table 1: Main design parameters of FSF

Parameter	High Brilliance Mode	Short Bunch Mode
Energy (GeV)	6	6
Charge (pC)	15	4
Bunch Length (fs)	>200	~10
<B> (ph/s/mm^2/mrad^2/0.1%)	10^{22}	10^{21}
B_{peak} (ph/s/mm^2/mrad^2/0.1%)	10^{26}	10^{26}

SHORT BUNCH MODE

Single pass machines do not suffer the same fate as storage rings as equilibrium is never reached. A design based on linear uncoupled optic, helps address a proof-of-principle for the short pulse mode, which is later then tested using a realistic input beam distribution from the BERLinPro injector project.

Compression in the Injector

Producing a femto-second pulse of low energy spread starts at the Gun, Table 2. Here the longitudinal electron beam properties are restricted by the photo-injector laser pulse and the superconducting RF acceleration. The primary subtle compression in the Merger between the Booster and linac minimizes transverse emittance growth.

Table 2: Injector ASTRA[3] simulations

Component	Bunch Length (mm)	Emittance (keV mm)	Energy (MeV)
Gun	0.7	0.3	1.8
Booster	1.0	2	6.6
Linac	0.45	2.2	50

The injector Arc is then used to prepare the beam for the main accelerator. The combination of a second linac to increase the beam energy to 100 MeV and the R_{56} in the Arc compress the beam to $\sigma_t \sim 660\,fs$ with a correlated energy spread of $\Delta E/E \sim 1.5 \cdot 10^{-4}$.

*Work supported by German Bundesministerium für Bildung und Forschung, Land Berlin, and grants of Helmholtz Association VH NG 636 and HRJRG-214.

† terry.atkinson@helmholtz-berlin.de

Copyright © 2012 by the respective authors — cc Creative Commons Attribution 3.0 (CC BY 3.0)

Telescopic Compression

The main acceleration stage uses a scheme based on telescopic compression. In this regime the combination of the linac chirps and the R_{56} in the Arcs are described as a simple focusing (F) and defocussing (f) lens, Eq. 1. The shortest pulse achievable from a multi-turn isochronous structure is with full compression in the final arc. This is however at the expense of a correlated energy spread, blue in Fig. 2.

$$\begin{pmatrix} z \\ \Delta E/E \end{pmatrix}_1 = \begin{pmatrix} f/F & F-f \\ 0 & F/f \end{pmatrix} \begin{pmatrix} z \\ \Delta E/E \end{pmatrix}_0 \quad (1)$$

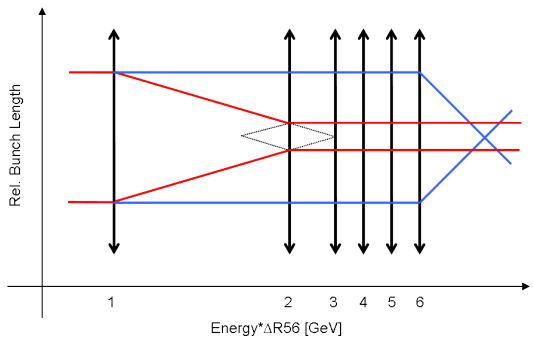

Figure 2: Telescopic bunch compression to preserve energy spread.

In order to remove the correlated energy spread and still produce a short pulse consider an alternative solution based on a telescopic lattice, red in Fig. 2. Implementing the first two arcs as achromats and accelerating either side of on-crest in each linac, the two "lenses" can share the same focal plane, just like in a telescope, to maximize the magnification and recover the energy correlation properties of the injector.

The minimal bunch length of the final beam into the long undulators is restricted by the requirement of an rms energy spread given by $\Delta E/E \sim 1/\text{UndulatorPeriods} \sim 10^{-4}$, to be $\sigma_t \sim 10\,fs$ when implementing purely linear optic.

Simulation Codes

Starting from previous calculations using ASTRA[4] up until the 50 MeV injector linac exit, the beam distribution was converted and tracked onwards through the FSF using Elegant[5].

Short Bunch Simulations

The first 50 m shown in Fig. 3 is the initial bunch compression in the injector Arc to prepare the beam for the first 1 GeV FSF linac of phase $\phi_1 = +8^\circ$ off crest . What follows this a step like bunch compression in the first Arc with $R_{56} = 20\,cm$ till the second 1 GeV linac at $\phi_2 = -20^\circ$ (placed at $s \sim 500\,m$). The second Arc of $R_{56} = 5\,cm$

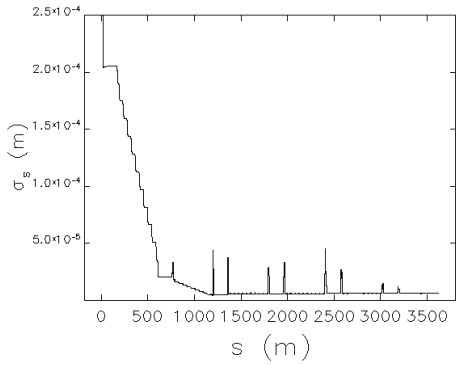

Figure 3: Bunch length variations in the FSF.

then completes the full bunch compression. These longitudinal bunch parameters are then preserved in the remaining isochronous Arcs, with some "spiking" shown due the vertical spreaders.

With the present optic a bunch length $\sigma_t \sim 20\,fs$ and energy spread $\Delta E/E \sim 1 \cdot 10^{-4}$ is achievable at the long undulator entrance Fig. 4.

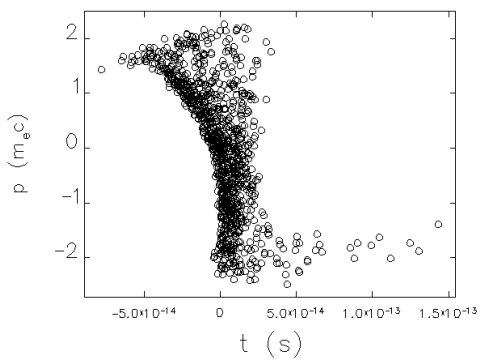

Figure 4: Phase space at long undulator entrance.

Large cumulative distortions due to radiation effects are not envisaged in this two stage process to achieve full compression as the energy after the first main linac is 1 GeV and the bunch charge is reduced for the short pulse mode.

LONGITUDINAL EMITTANCE

The longitudinal emittance can be described as an ellipse occupying a density of particles in $(c\Delta t, \delta)$ phase space. The non-linear properties of RF curvature acceleration can alter the phase distributions varying the normalized emittance.

2nd Order Aberrations

An emittance compensation scheme using higher order magnetic terms created in the Arcs is described here.

Copyright © 2012 by the respective authors — cc Creative Commons Attribution 3.0 (CC BY 3.0)

Using the linacs relative energy Eq. 2 and the Arcs bunch length Eq. 3 variations respectively one can calculate the emittance variation across the two stages as follows.

$$
\begin{aligned}
&LINAC \\
\delta_1 &= \delta_0 + R_{65} c\Delta t_0 + T_{655}(c\Delta t_0)^2 \quad (2)\\
c\Delta t_1 &= c\Delta t_0
\end{aligned}
$$

$$
\begin{aligned}
&+ARC \\
\delta_2 &= \delta_1 \\
c\Delta t_2 &= c\Delta t_1 + R_{56}\delta_1 + T_{566}\delta_1^2 \quad (3)
\end{aligned}
$$

Keeping only second order terms, assuming $\delta_0 = 0$ and substituting Eq. 2 and Eq. 3 the emittance can be approximated as Eq. 4

$$
\begin{aligned}
\epsilon^2 &= <(c\Delta t_2)^2><\delta_2^2> - <(c\Delta t_2\delta_2>^2 \quad (4)\\
\epsilon^2 &\simeq <(c\Delta t_0)^4><(c\Delta t_0)^2>\left(T_{566}R_{65}^3 - T_{655}\right)^2
\end{aligned}
$$

Emittance Correction

One can interpret Eq. 4 as a useful tool to control the normalized emittance. The accelerating phase determines both the R_{65} and T_{655} terms and sextupoles in the Arc can adjust T_{566} to compensate for them.

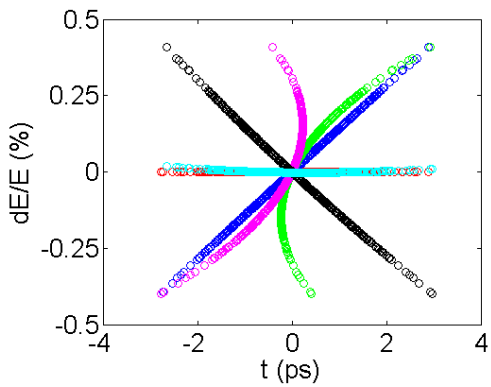

Figure 5: Correction of the 2nd order aberrations.

Fig. 5 demonstrates this concept, showing anticlockwise the variation of the beam phase space from an uncorrelated low emittance flat beam (red) through a non-linear RF chirp (blue). Then the introduction of first and second order magnetic correction, rotating and deforming the phase space (green - magenta - black) before finally a second linac is used to approximately recover the original distribution (cyan).

Emittance Correction Simulations

This scheme was adapted for the two stage telescopic bunch compression in the FSF machine simulations Fig. 6. The second order terms from the off-crest RF acceleration for the short bunch mode were optimized so that they would be fully compensated for by the T_{566} term created in the dipoles in the achromat Arcs.

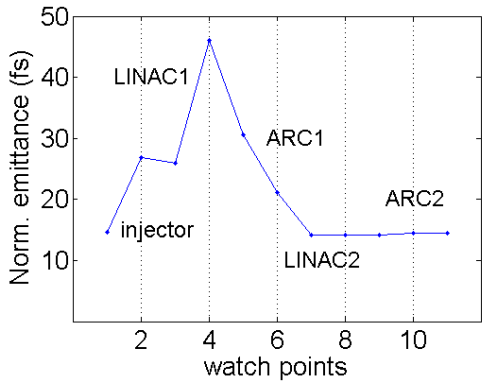

Figure 6: Recovering the injector properties.

Additional correction using sextupoles will be considered for future calculations as an essential tool for the recovery of the injectors longitudinal beam properties.

CONCLUSION

A two stage linear bunch compression scheme for the FSF light source has been presented and simulated using realistic beam parameters from the BERLinPro injector. A compensation scheme to recover the normalized emittance of the injector has been proposed.

REFERENCES

[1] Y. Petenev et al., "Feasibility Study of an ERL-Based GeV-scale Multi-turn Light Source", IPAC2012, New Orleans, USA.

[2] T. Kamps, et al., Journal of Physics: Conference Series 298 (2011) 012009.

[3] ASTRA code, A Space Charge Tracking Algorithm, http://tesla.desy.de/ meykopff/ 2012.

[4] J. Knobloch et al., Status of the BERLinPro Energy Recovery Linac Project, IPAC 2012, New Orleans, July 2012.

[5] M. Borland, "elegant: A Flexible SDDS-Compliant Code for Accelerator Simulation," Advanced Photon Source LS-287, September 2000.

Copyright © 2012 by the respective authors — cc Creative Commons Attribution 3.0 (CC BY 3.0)

LINAC OPTICS DESIGN FOR MULTI-TURN ERL LIGHT SOURCE*

Y. Petenev#, T. Atkinson, A.V. Bondarenko, A.N. Matveenko, HZB, Berlin, Germany.

Abstract

The optics simulation group at HZB is designing a multi-turn energy recovery linac-based light source. Using the superconducting Linac technology, the Femto-Science-Factory (FSF) will provide its users with ultra-bright photon beams of angstrom wavelength at 6 GeV. The FSF is intended to be a multi-user facility and offer a variety of operation modes. In this paper a design of transverse optic of the beam motion in the Linacs is presented. An important point in the optics design was minimization of the beta-functions in the linac at all beam passes to suppress beam break-up (BBU) instability.

INTRODUCTION

In this document we present a design of a Linac optics for a new 3 pass ERL-based LS with 6 GeV maximum energy of electron beam. This future facility is named Femto-Science Factory (FSF) [1].

The schematic layout of the facility is presented in Fig. 1. A beam is created in 1.3 GHz SRF gun with photo cathode. We consider an SRF injector with similar parameters to the B*ERL*inPro injector under development at HZB [2, 3]. Then it passes a 100 MeV Linac and is accelerated to 6 GeV after passing 3 times through each of two 1 GeV main Linac's. In the arcs between the acceleration stages it is assumed to have undulators with 1000 periods. In the long straight section (see Fig.1) a long undulator with 5000 periods is assumed. The main design parameters of FSF are presented in Table 1.

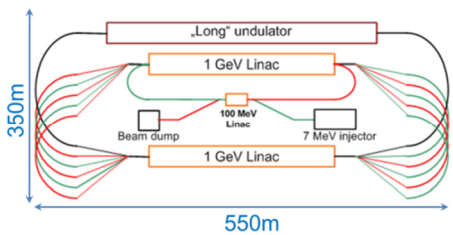

Figure 1: The scheme of FSF.

One potential weakness of the ERLs is transverse beam breakup instability, which may severely limit a beam current. If an electron bunch passes through an accelerating cavity it interacts with dipole modes (e.g. TM_{110}) in the cavity. First, it exchanges energy with the mode; second, it is deflected by the electro-magnetic field of the mode. After recirculation the deflected bunch interacts with the same mode in the cavity again which constitutes the feedback. If net energy transfer from the beam to the mode is larger than energy loss due to the mode damping the beam becomes unstable.

The actuality of this problem was recognized in early experiments with the recirculating SRF accelerators at Stanford [4] and Illinois [5], where threshold current of this instability was occurring at few microamperes of the average beam current. In the works of Rand and Smith in [6] dipole high order modes were identified as a driver of this instability. In late of the 80's the detailed theoretical model and simulation programs had been developed [7, 8]. Nowadays the interest to this problem was renewed. The requirements for more detailed theory and simulation programs [9-11] are given by the needs of high current (~100 mA) ERLs.

The threshold current for the transverse beam breakup may be estimated for the case of a single cavity and single mode for a multipass ERL in the form as [11]:

$$I_{th} \approx I_0 \frac{\lambda\!\!\!^{-2}}{Q_a L_{eff} \sqrt{\sum_{m=1}^{2N-1} \sum_{n=m+1}^{2N} \frac{\beta_m \beta_n}{\gamma_m \gamma_n}}}, \qquad (1)$$

where I_0- Alfven current, Q_a is the quality factor of HOM, $\lambda\!\!\!^{-} = \lambda/2\pi$, λ is the wavelength corresponding to the resonant frequency of the TM_{110} mode, γ_m is the relativistic factor at the m-th pass through the cavity, β_m – is the Twiss parameter, L_{eff} – is the effective length of the cavity, N is the number of passes during acceleration. It should be noted that (1) gives more realistic estimation of the BBU threshold current than a similar expression in [9] with a 1/N(2N-1) dependence on the number of passes. This is the result of an assumption in [9] of integer tunes in every turn of the ERL.

Table 1: Main Design Parameters of FSF

Parameter	High brilliance mode	Short bunch mode
E, GeV	6	6
<I>, mA	20	5
Q, pC	15	4
τ, fs	200-1000	~10
<B>, ph/s/mm2/mrad2/0.1%	$8 \cdot 10^{22}$	$\sim 4 \cdot 10^{21}$
B_{peak}, ph/s/mm2/mrad2/0.1%	10^{26}	$\sim 10^{26}$

Eq. 1 shows that it is preferable to have low β-functions at low energies. Therefore, the design was optimised to minimize beta functions of the beam in the Linac to increase the threshold current of BBU instability from one

* Work supported by German Bundesministerium für Bildung und Forschung, Land Berlin, and grants of Helmholtz Association VH-NG-636 and HRJRG-214.

#yuriy.petenev@helmholtz-berlin.de

Copyright © 2012 by the respective authors — cc Creative Commons Attribution 3.0 (CC BY 3.0)

point of view and to decrease the beats of the beta functions in the spreaders from another.

As it was shown in [1], for a scheme of FSF, presented in Fig. 1, BBU instability will develop in the 1st cavity of the 1st 1 GeV linac.

In this paper we analyze the influence of the energy gain in the preinjection linac (100 MeV) and two main linacs (1 GeV) on the BBU threshold and propose an optimized solution.

Preinjection Linac Pattern

In this part we would like to discuss BBU instability in the preinjection linac, which is coming after the merger section. In Fig. 1 it is suggested to have a 100 MeV linac. Therefore we have acceleration from 7 to 107 MeV, or deceleration for the same amount of energy. Therefore it is required to have one cryomodule with an acceleration gradient of the cavities of G = 15.5 MeV/m.

Now we would like to analyse model with a linac consisting of two cryomodules with acceleration up to 250 MeV and with a triplet of quadrupole magnets in between them, which role is to change the sign of the twiss parameter α of the beam. Let us find the initial injection twiss parameters to have the equal threshold currents for the entrance and for the middle of the linac. To find that we will use eq. 1 and a model of the linac with one dipole HOM, which we locate at different positions in the linac. In this case we assume that the 1st cryomodule is a long cavity with a transfer matrix M given by [12]:

$$\begin{pmatrix} \cos(\alpha)-\sqrt{2}\sin(\alpha) & \frac{\sqrt{8}\gamma_0 L\sin(\alpha)}{\Delta\gamma} \\ -\frac{3}{\sqrt{8}}\frac{\Delta\gamma\sin(\alpha)}{L\gamma_1} & \left(\cos(\alpha)+\sqrt{2}\sin(\alpha)\right)\frac{\gamma_0}{\gamma_1} \end{pmatrix}, \quad (2)$$

where $\alpha = \frac{1}{\sqrt{8}}\ln\left(\gamma_1/\gamma_0\right)$, $\gamma_{1(0)}$ is the final(initial) normalized energy of the particle, L – the length of the cavity (cryomodule). Also we assume that there is a symmetrical β-functions on acceleration and deceleration in the linac.

Therefore we can transfer the beta function through the 1st cryomodule as:

$$\beta_1 = \frac{\gamma_1}{\gamma_0}\left(\beta_0 m_{11}^2 - 2\alpha_0 m_{11}m_{12} + \frac{1+\alpha_0^2}{\beta_0}m_{12}^2\right), \quad (3)$$

The RF focusing in the second cryomodule is quite weak and we represent it with a cavity without RF focusing for simplicity. So the beta function at the end of the linac might be found as:

$$\beta_2 = \frac{\gamma_2}{\gamma_1}\left(\beta_1 - 2\alpha_1 L + \frac{1+\alpha_1^2}{\beta_1}L^2\right), \quad (4)$$

The minimum of the $\beta_2 = 2L^2/\beta_1$ is given, when

$$\alpha_1 = \frac{\beta_1}{L}, \quad (5)$$

Now we can proceed with an equation for the thresholds:

$$\sqrt{\frac{\beta_0\beta_2}{\gamma_0\gamma_2}} = \frac{2\beta_1}{\gamma_2-\gamma_0}, \quad (6)$$

To find the solution we will vary the initial twiss parameters and look for a maximum value of the thresholds. The numerical solution is presented in Fig. 2.

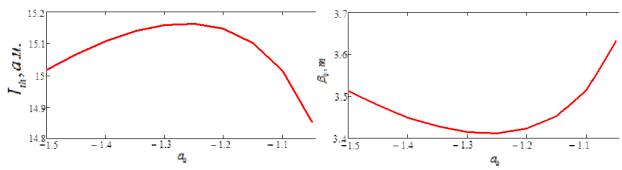

Figure 2: Threshold current, calculated using eq. 1 (without constants, which are the same for all cavities) and initial twiss parameters for preinjection Linac, consisting of two long cavities with a triplet in between.

One can see from Fig. 2 that the maximum threshold current is achieved at $\alpha_0 \sim$ -1.26 and $\beta_0 \sim 3.41$.

Different Acceleration Pattern

In this paragraph we would like to discuss an improvement of the present scheme of FSF, where we have 100 MeV preinjection and then two 1 GeV Linacs (Fig. 1), for the scheme, presented in Fig. 3.

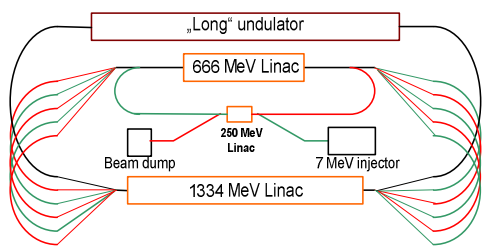

Figure 3: The improved acceleration scheme of FSF.

One of the motivations of this improvement was BBU instability. The new scheme gives roughly 1.7 times better threshold current for the 1-st cavity in the 1-st linac see Table 2, where the instability develops in the first scheme.

The easiest way to see the reason of rebalancing of the energies in the two main linacs is to analyse the eq. 1, specifically the square root in the denominator. We would

Copyright © 2012 by the respective authors — cc Creative Commons Attribution 3.0 (CC BY 3.0)

like to find a balance between the energy gains in two main linacs to have equal threshold currents for them. To do that, we will analyse a model with linacs, when a focusing from a triplets is neglected for the second and the third passes. In this model with the injection energy of about 250 MeV the transverse focusing inside the cavities can be neglected. So, we assume that the beta functions of a beam at the exit and at the entrance to the linac are about the length of the linac for the second and the third passes and for the end of the linacs at the first pass and it is about the length of the one cryomodule [1] at the entrance for the first pass.

Let's introduce G as a gradient of the cavities in MeV/m, $L= 2000$ [MeV] $/G$ is a length of the cavity structure, required to accelerate to the final energy of 2 GeV, x is the length of the first linac and, therefore, L-x is the length of the 2-nd. Now we can find energies $\gamma_{1(2),n}$ for each pass and as we said before $\beta_{1,1(6)} = \beta_{2,1(6)} \sim 12.57$ m and $\beta_{1,n} = x$ or $\beta_{2,n} = L$-x for the first and the second linac respectively and for n=2..5.

We can proceed with the following equation:

$$\sqrt{\sum_{m=1}^{2N-1}\sum_{n=m+1}^{2N}\frac{\beta_{1,n}\beta_{1,m}}{\gamma_{1m}(x)\gamma_{1n}(x)}} = \sqrt{\sum_{m=1}^{2N-1}\sum_{n=m+1}^{2N}\frac{\beta_{2,n}\beta_{2,m}}{\gamma_{2m}(x)\gamma_{2n}(x)}}, \quad (7)$$

when the threshold currents have the same values for the 1-st and last cavities in both linacs. This equation can be solved numerically and gives the result that x ~ L/3 with injection energy – $\gamma_{1,1} = 480$. This explains why we propose a new acceleration pattern in Fig. 3.

Now we proceed with a modeling of the linac optics in Elegant program [13]. Optics for all three passes through the first 666 MeV linac is presented in Fig. 4.

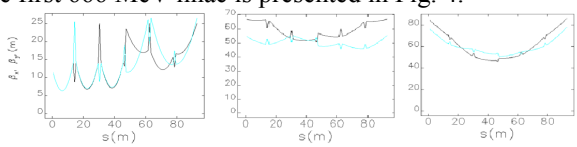

Figure 4: Optics design of the first 666 MeV linac. 3 passes with 250, 2.250 and 4.250 GeV beam injection energy from left to right correspondingly.

Also the optics was designed for the second 1334 MeV Linac and it is presented in Fig. 5.

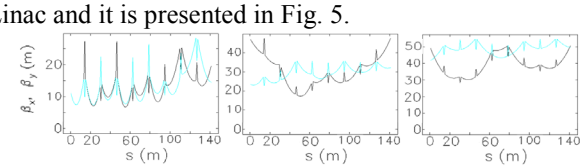

Figure 5: Optics design of the second 1334 MeV linac. 3 passes with 916, 2916 and 4916 MeV beam injection energy from left to right correspondingly.

The threshold currents for the schemes of FSF in Figs. 1 and 3 are presented in Table 2. For the estimations we used the following equation (which is a combination of eq. 1 and [9]):

$$I_{th} = \frac{2c^2}{e\omega\left(\frac{R}{Q}\right)_d Q_d}\frac{1}{\sqrt{\sum_{m=1}^{5}\sum_{n=m+1}^{6}\frac{\beta_m\beta_n}{\gamma_m\gamma_n}}}, \quad (8)$$

and we took a mode with $(R/Q)_d \cdot Q_d = 6\cdot10^5$ Ω, $\omega = 2\pi\cdot2\cdot10^9$ Hz.

Table 2: Threshold Currents for Different Schemes

Linac scheme	I_{th}, A		
	Preinjector	1st Linac	2nd Linac
0.100 + 1 + 1GeV	1.26	0.88	3.73
250 + 666 + 1334MeV	1.21	1.46	3.58

One can see from the Table 2 that the value of threshold current for the 1st main linac was improved. It was also slightly decreased for the 2nd linac and for the preinjection.

CONCLUSION

In the new proposed scheme BBU instability will develop in the preinjection Linac. In the future work we should find a way how to increase the thresholds in the preinjection linac and in the 1st by decreasing the threshold current value in the 2nd linac.

REFERENCES

[1] Y. Petenev et al., "Feasibility Study of an ERL-Based GeV scale Multi-turn Light Source", IPAC2012, New Orleans, USA.
[2] T. Kamps, et al., Journal of Physics: Conference Series 298 (2011) 012009.
[3] A.N. Matveenko, et al., "Status of the B*ERL*inPro optics design", Proc. of IPAC'11, pp.1500-1502;
[4] Claude M. Lyneis, Michael S. McAshan, Roy E. Rand, H. Alan Schwettman, Todd I. Smith and John P. Turneaure, The Stanford Superconducting Recyclotron, IEEE Transactions on Nuclear Science, Vol. NS-26, No. 3, June 1979.
[5] P.Axel, L.S.Cardman, H.D.Graef, A.O.Hanson, R.A.Hoffswell, D.Jamnik, D.C.Sutton, R.H.Taylor, and L.M.Young, Operating Experience with MUSL-2, IEEE Transactions on Nuclear Science, Vol. NS-26, No. 3, June 1979.
[6] R.E. Rand and T.I. Smith, Beam optical control of beam breakup in a recirculating electron accelerator, Particle accelerators, Vol. 11, pp. 1-13 (1980).
[7] J.J. Bisognano, R.L. Gluckstern, in Proceedings of the 1987 Particle Accelerator Conference, Washington, DC (IEEE Catalog No. 87CH2387-9), pp. 1078-1080.
[8] G.A. Krafft, J.J. Bisognano, in Proceedings of the 1987 Particle Accelerator Conference, Washington, DC (IEEE Catalog No. 87CH2387-9), pp. 1356-1358.
[9] G.H. Hoffstaetter, I.V. Bazarov, „Beam-breakup instability theory for the energy recovery linacs", Phys. Rev. ST AB 7, 054401 (2004).
[10] E. Pozdeyev, et al., "Multipass beam breakup in energy recovery linacs", NIM A 557 (2006) 176-188.
[11] N.A. Vinokurov et al., Proc. of SPIE Vol. 2988, p. 221 (1997).
[12] J. Rosenzweig, L. Serafini. "Transverse particle motion in radio-frequency linear accelerators". Phys. Rev., E49 (1994), p. 1601.
[13] M. Borland, "Elegant: A Flexible SDDS-Compliant Code for Accelerator Simulation," APS LS-287, 2000.

Copyright © 2012 by the respective authors — cc Creative Commons Attribution 3.0 (CC BY 3.0)

STUDY OF BEAM-BASED ALIGNMENT FOR SHANGHAI SOFT X-RAY FEL FACILITY

Duan Gu#, D.Z.Huang, Meng Zhang, Qiang Gu, M.H.Zhao
Shanghai Institute of Applied Physics, Shanghai 201800, China

Abstract

In linear accelerators, dispersion and transverse wake-field from alignment errors will lead to a significant emittance growth. The performance of the Free Electron Laser (FEL) process imposes stringent demands on the transverse trajectory, dispersion and emittance of the electron beam. So finding an effective Beam-Based Alignment(BBA) procedure is crucial for the success of Shanghai X-Ray FEL facility. This paper presents the preliminary study of different BBA method performances in SXFEL Linac. In addition, a MATLAB based simulation including quadrupole misalignment, dipole field errors and beam position monitor errors have been used to predict the orbit and emittance growth along the beamline and the required corrector current. Comparison with other codes is also presented.

INTRUDUCTION

As a critical development step towards constructing a hard X-ray FEL in China, a soft X-ray FEL facility (SXFEL) was proposed and will be constructed to verify the cascaded HGHG scheme and carry out the research on key technologies for X-Ray FEL. The SXFEL facility will be working at 9 nm soft X-ray band which consists of a 130MeV photo cathode injector, a main linac accelerating the beam to an energy of 840MeV, an undulator section with two stages of HGHG scheme and a diagnostic beamline. The local energy spread is 0.1%-0.15%, the peak current is about 600A and the normalized emittance is 2 mm·mrad[1].

In FEL facilities, misalignments between Quadrupoles and Beam Position Monitors(BPM) cause an increase of the transverse beam size and emittance which turns into an increase of normalized emittance. To keep the normalized emittance due to misalignment below 2 mm·rad, the average Quad-BPM misalignment in the linac must be smaller than 100um.

The traditional optical alignment can no longer meet such strict requirements, but a lot of analytical and numerical studies have been done and proved that Beam-Based Alignment technology can simultaneously eliminate the misalignment and dispersion in linac and undulator section, which obviously will leads to a much smaller emittance growth and transverse beam size. With the method above, a software based on MATLAB has been designed and simulation results have been compared with other software.

guduan@sinap.ac.cn

BBA TECHNOLOGY OVERVIEW

Over past decade, a number of different realizations have been developed to measure the offset of magnetic center of quadrupole magnet[2][4]. Most techniques are based on a common approach, which is to change the quadrupole strength and measure the resulting deflection.

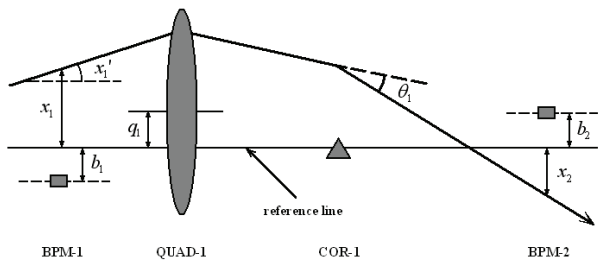

Figure 1: Common approach of BBA.

With respect to the reference line, m_i is the BPM reading at BPM-i. According to Linear optics theory (regardless wakefield effect and Quad-tilt), the transverse misalignment of upstream Quadrupole can be calculated using orbit response matrices, corrector values and inject parameters:

$$m_i = x_i - b_i = (x_i)_1 - b_i$$

$$x_i = R^{(B_1:i)}x_1 + \sum_j^{N_{Ci}} R^{(C_j:i)}c_j + \sum_j^{N_{Qi}} R^{(Q_j:i)}(I - R^{(Q_j)})q_j \quad (1)$$

Where b_i is BPM reading error due to off-axis between electronic center and geometric center. R is the 2×2 transport matrix form BPM-1 or corrector c_j or Q_j to BPM-i.

x_1 is initial incoming parameters, the unknown c_j the corrector strength and Q_j is Quadrupole misalignments, which are defined as:

$$x_1 = \begin{bmatrix} x_1 \\ x_1' \end{bmatrix};\ c_j = \begin{bmatrix} 0 \\ \theta_j \end{bmatrix};\ q_j = \begin{bmatrix} q_j \\ 0 \end{bmatrix} \quad (2)$$

Further more, we can simultaneously correct both orbit and dispersion using so called “Dispersion Free Steering” method. The optimal settings are calculated using the orbit and dispersion response matrices, which are defined as the shift of the orbit or dispersion due to corrector strength change:

$$R_{i,j} = \frac{\Delta x_i}{\Delta \theta_j}\ ;\quad D_{i,j} = \frac{\Delta d_i}{\Delta \theta_j} \quad (3)$$

Copyright © 2012 by the respective authors — cc Creative Commons Attribution 3.0 (CC BY 3.0)

Where Δx_i and Δd_i is the change of the orbit and dispersion in the BPM-i, and $\Delta\theta_j$ is the change of the strength of corrector-j. The basic aim is to find a setting of $\Delta\theta_j$ which induces orbit and dispersion that minizes in a least squares sense the final orbit and dispersion:

$$(1-w^2)\| x_{meaus}+O\Delta\theta\|^2+w^2\| d_{meaus}+D\Delta\theta\|^2=\min \quad (4)$$

More details about the algorithm procedure and successful correction results can be found at [3].

SIMULATION ON SXFEL LINAC

Soruces of the emittance growth and misalignment in the LINAC of FEL facilities has already been well-studied[2][6]. Usually it consists of field errors and stray magnet fields in the beam line as well as dispersion created upstream of the BPM, for instance, misalignment of Quadrupole, Dipole, Accelerator modules and even BPMs themselves. The Errors and launch parameters used in simulation are shown in Table 1.

Table 1: SXFEL linac Simulation Parameters

Parameter	Δx, Δy/μm (+/-)	Δθ/μrad (+/-)
DIPOLE	150	10
QUAD	150	10
ACC.MODULE	100	--
BPM	150	--
Launching error	100	150

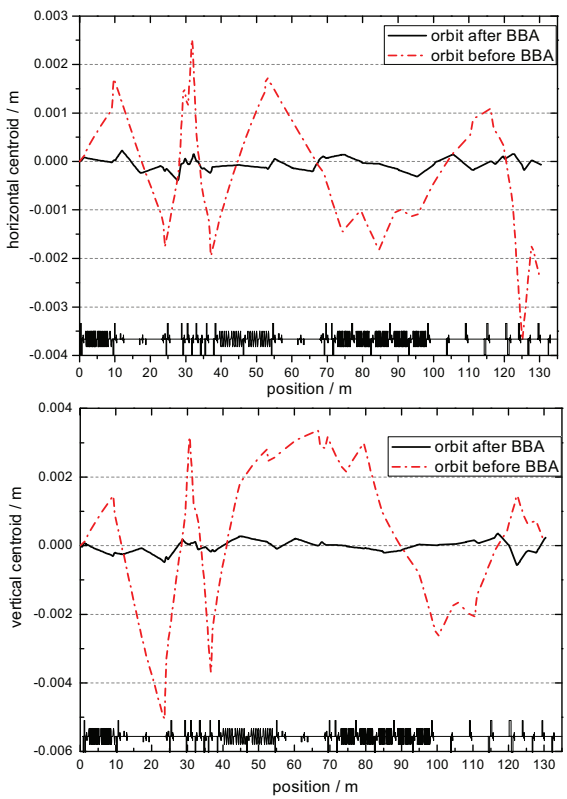

Figure 2: Comparison of orbit before and after correction.

SXFEL linac BBA simulations have been done using Elegant [7] as shown in Figure 2. After applying magnet errors and launch parameters in Table 1, we can get the correct result with Global correction method. As one can see in Figure 2, the deviation can be very large. When the electron beam travels across chicanes, the deviation will be notable increase due to the magnet effects, so these errors must be controlled in a reasonable region during BBA procedure.

In simulation results one can see that after 1st correction, the transverse orbit deviation is decline from 10^{-3}m to 10^{-4}m. Meanwhile the Smoothness of orbit and RMS orbit deviation can meet design requirement for SXFEL linac. Naturally, the impact of these errors on orbit kick and dispersion generation depend on the actual operating conditions of the accelerator, so the orbit must be measured and controlled frequently.

Further more, transverse wakefield effects caused by structure misalignment in accelerate modules is also an important factor which should be considered, as it can lead to a significant emittance growth[8]. By doing simulations, the emittance growth before and after correction are shown in Figure 3. As one can see, after BBA the final emittance growth can be controlled within 5%, and in vertical plane the correct result is much better.

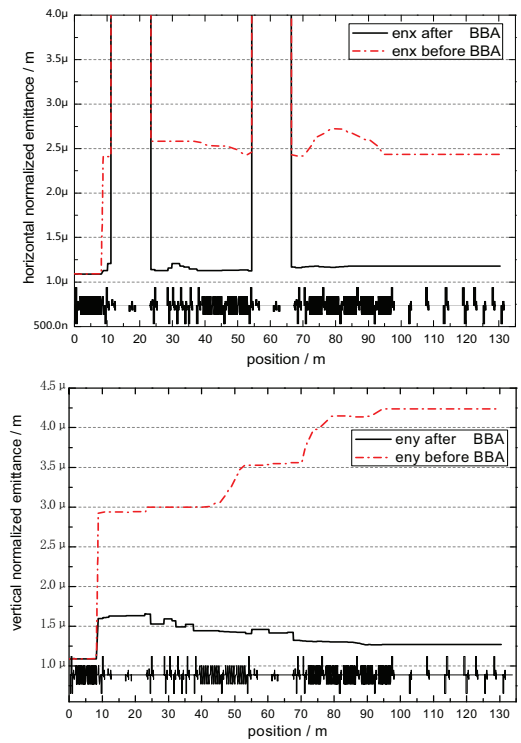

Figure 3: Comparison of emittance growth before and after correction.

CONTROL SOFTWARE DESIGN AND DEVELOPMENT

To assist the design and measurement, an automated control software based on MATLAB has been designed

Copyright © 2012 by the respective authors — cc Creative Commons Attribution 3.0 (CC BY 3.0)

with interfaces to EPICS. This software aims to connecting BBA methods and bottom devices, so we can seem it as a middle level application.

After setting launch parameters and using the BBA method above, the final offset could be determined. The flow diagram of the simulation code is shown in Figure 4.

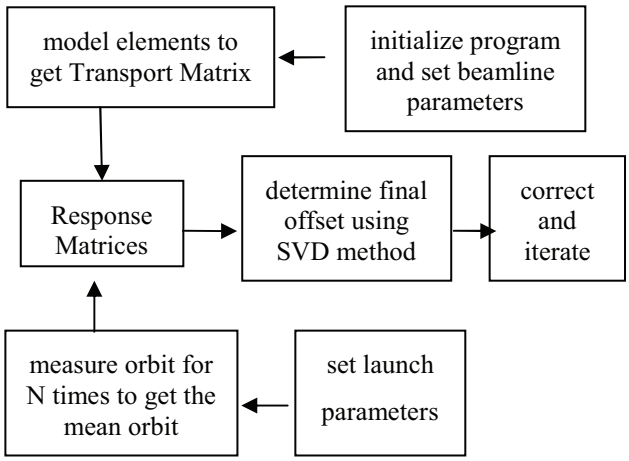

Figure 4: Flow diagram of the control program.

The response matrices are calculated from the quadrupole currents and the estimated energy along the machine. In this case, energy uncertainties such as magnets field errors and calibration errors are not take into account in this preliminary study.

After applying magnet errors and launch parameters in Table 1, we can get the correct result with Global correction method within the Matlab application. The correction results are shown in Figure 5.

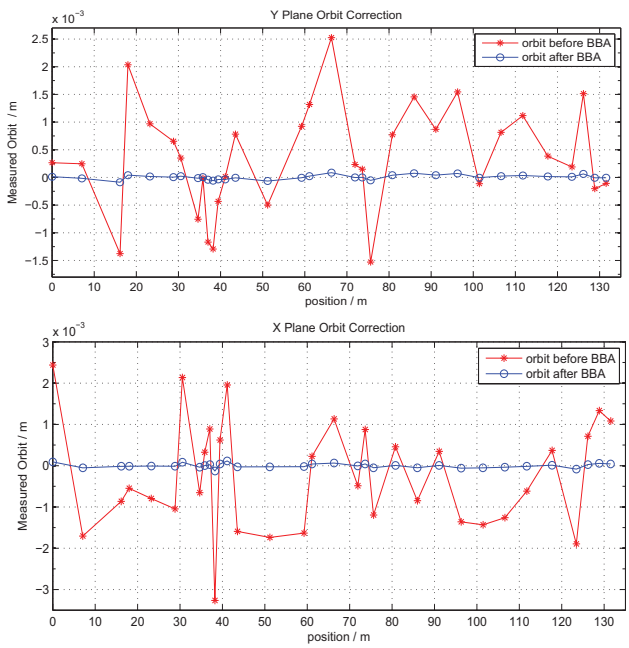

Figure 5: Simulation results from MATLAB BBA codes.

CONCLUSIONS

Preliminary design and simulations of the SXFEL Beam-based Alignment procedure have been presented in this paper, including brief introductions to main linac alignment method, beam dynamics simulations with nominal parameters, and orbit sensitivity studies. Simulations show SXFEL linac beam qualities are well within the capabilities of Beam-based Alignment technology. Further study is on the way to optimize and properly implement this technology into the SXFEL facility.

REFERENCES

[1] W.H. Huang et al, Design and Beam Dynamics Simulation for the Photoinjector of Shanghai Soft X−ray Free Electron laser Test Facility. Proceedings of FEL2011, Shanghai, China.

[2] Tor Raubenheimer, Peter Tenenbaum. Brief Review of Linear Collider Beam-Based Alignment for Linacs. LCC-0129 SLAC-TN-03-071,2004.

[3] E. Prat et al, “Measurement and Correction of Dispersion in the VUV-FEL”, EPAC’06, Edinburgh, June 2006, p. 1951..

[4] SUN Bao-gen, HE Duo-hui, LU Ping. Development of beam-based alignment system using a switchable shunt resistor for HLS. High Power Laser and Particle Beams, 2001, V13(06): 0-0).

[5] Tenenbaum P，Hendrickson L，Raubenheimer T O. Developments in beam-based alignment and steering of the Next Linear Collider main Linac. Proceedings of the 2001 Particle Accelerator Conference 2001:3837,2001.

[6] Emma P. Beam based alignment of sector-1 of the SLC Linac.EPAC-1625-1627,1992.

[7] Borland M. Elegant: A Flexible SDDS-Compliant Code for Accelerator Simulation. Advanced Photon Source LS-287,2000.

[8] John Irwin, Chun-xi Wang, Karl Bane. Transverse wakefield effect measurement via Model-independent Analysis.SLAC-PUB-7917,1979.

Copyright © 2012 by the respective authors — cc Creative Commons Attribution 3.0 (CC BY 3.0)

ON-LINE DISPERSION FREE STEERING FOR THE MAIN LINAC OF CLIC

J. Pfingstner*, D. Schulte, CERN, Geneva, Switzerland

Abstract

For future linear colliders as well as for light sources, ground motion effects are a severe problem for the accelerator performance. After a few minutes, orbit feedback systems are not sufficient to mitigate all ground motion effects and additional long term methods will have to be deployed. In this paper, the long term ground motion effects in the main linac of the Compact Linear Collider (CLIC) are analysed via simulation studies. The primary growth of the projected emittance is identified to originate from chromatic dilutions due to dispersive beam orbits. To counter this effect, an on-line identification algorithm is applied to measure the dispersion parasitically. This dispersion estimate is used to correct the beam orbit with an iterative dispersion free steering algorithm. The presented results are not only of interest for the CLIC project, but for all linacs in which the dispersive orbit has to be corrected over time.

INTRODUCTION

Linear colliders and light sources often require very small beam emittances and beam sizes to reach their goals. This fact makes these machines inherently sensitive to ground motion effects. For short time scales orbit feedbacks can be used to mitigate these effects by steering the beam with the help of beam positioning monitors (BPMs) (see [1] for the CLIC case). For longer time scales, this steering is not sufficient to preserve the beam quality as can be seen in Fig. 1. To be able to operate CLIC over longer time periods, it is essential to correct this remaining emittance growth. The development of such an algorithm is the topic of this paper.

The main reason for the remaining emittance growth is that the BPM positions itself will drift from their original position, which results in a dispersive beam orbit. The according chromatic dilutions decrease the beam quality over time. In the literature, a technique named dispersion free steering (DFS) can be found, which has been developed to correct similar chromatic dilutions (see [3] and [4]). In this paper we modify and extent this basic DFS method, such that it can be used to correct long term ground motion effects in an on-line mode. On-line means in this case that the DFS correction is applied during the normal accelerator operation in a parasitic way, without stopping the physics program. The methode will be explained an evaluated on the example of CLIC, but can be easily utilised for other accelerators.

* juergen.pfingstner@cern.ch

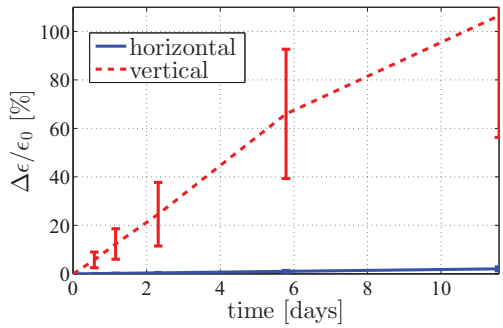

Figure 1: Simulations of the relative emittance growth over long time scales with orbit feedback in the main linac of CLIC. The used ground motion is generates according to the ATL law [2] with a constant A of $0.5\times10^{-6}\,\mu m^2/m/s$, which is the baseline for CLIC. The results have been averaged over 10 random samples of ground motion. For the initial horizontal and vertical emittance 600 nm and 10 nm have been used. The action of the orbit feedback was assumed to be perfect and therefore simulated by applying one-to-one steering without BPM noise, which is an optimistic approximation. It can be seen that already after 1 day the emittance has increased by about 10%.

ON-LINE DFS ALGORITHM

In this section, we will first introduce the basic DFS algorithm. After that the modifications necessary to apply this algorithm in an on-line mode will be discussed.

Basic DFS Algorithm

The DFS algorithm consists of two steps. In the first, the dispersion $\boldsymbol{\eta}$ at the BPMs is measured by varying the beam energy. This energy change can be created by changing the acceleration gradient, scaling the magnet strength and/or changing the initial beam energy. In the second step, corrector actuations $\boldsymbol{\theta}$ are calculated such that at the same time the measured dispersion $\boldsymbol{\eta}$ as well as the beam orbit $\boldsymbol{b}$ are corrected. Such actuations can be calculated by solving the following system of equations for $\boldsymbol{\theta}$ (see [5] for more details)

$$-\begin{bmatrix} \boldsymbol{b}-\boldsymbol{b_0} \\ \omega(\boldsymbol{\eta}-\boldsymbol{\eta_0}) \\ \boldsymbol{0} \end{bmatrix} = \begin{bmatrix} \boldsymbol{R} \\ \omega\boldsymbol{D} \\ \beta\boldsymbol{I} \end{bmatrix} \boldsymbol{\theta}, \qquad (1)$$

where $\boldsymbol{b}_0$ and $\boldsymbol{\eta}_0$ are the reference beam orbit and target dispersion respectively. The third set of equations in Eq. (1) with the unity matrix $\boldsymbol{I}$ on the right side is used to damp too high corrector actuations. The weights ω and β can be

Copyright © 2012 by the respective authors — cc Creative Commons Attribution 3.0 (CC BY 3.0)

chosen to minimise the emittance, which is easiest done in simulation via a parameter scan. The matrices $\boldsymbol{R}$ and $\boldsymbol{D}$ are the orbit and dispersion response matrix.

To increase the robustness, this DFS algorithm is usually applied sequentially to overlapping sections of the accelerator. In the case of CLIC, the main linac is partitioned into 36 fully overlapping sections each consiting of about 28 FODO cells. Note that after the correction of one section, the dispersion of the sections downstream has changed as well. It is therefore necessary to re-measure the dispersion after each DFS correction of one section.

Problem of Low Energy Variations

The primary difference between the basic and the on-line DFS algorithm is that the dispersion cannot be measured straight forward. In the basic method, a large energy deviation will be used to create large dispersive offsets in the BPMs to increase the measurement accuracy. This is however not possible for an on-line algorithm, since only tiny energy variations can be tolerated due to the energy acceptance of the final focus system of CLIC. For the simulations in this paper an energy variation of only 0.5 per mill is used.

Two main problems arise from these small induced energy variations. First of all, the induced orbit variations will be small and the necessary accuracy of the dispersion measurement has to be recovered by combining many measured orbit samples in a stochastic way to filter the noise. This dispersion estimation will be discussed in the next section. The second problem due to the small energy variations comes from the fact that the used energy deviations are so small that they are in the order of the beam energy spread, which is strongly influenced by wakefields. Therefore, changes of wakefields due to the change of beam orbits or cavity positions start to influence the dispersion measurement. This problem can be resolved by an initial cavity alignment (see [6]) before the on-line DFS, which reduces the wakefield effects for the current beam orbit. It is also beneficial to perform a cavity alignment after each full DFS correction of the linac.

Dispersion Estimation

The dispersion is measured in this paper by changing the acceleration gradient, which can be accomplished for the main linac of CLIC by a modulation of the beam intensity of the drive beam. Additionally, the initial beam energy is varied with the help of a bunch compressor. Since the induced energy variations have to be small, the individual dispersion measurements will be disturbed strongly by the influence of BPM noise and the usual jitter of the initial beam energy and the accelerating gradients. Therefore, the dispersion is determined by using many measurements and combining them to a least squares (LS) estimate to ensure the necessary accuracy. Instead of determining the LS estimate via the usual calculation of the pseudo-inverse, a very efficient recursive version of the algorithm can be derived, if the induced energy variations are chosen to be the sequence $\{-\Delta E, +\Delta E, -\Delta E, +\Delta E, \dots\}$. In this case the LS estimate of the dispersion η_N at a BPM at time step $N \in 2\mathbb{N}$ can be written as

$$\begin{aligned} \eta_N &= \left(\boldsymbol{E}^T\boldsymbol{E}\right)^{-1}\boldsymbol{E}^T\boldsymbol{b} = \frac{T_N}{N\Delta E} \quad \text{with} \\ \boldsymbol{E} &= \begin{bmatrix} -\Delta E \\ +\Delta E \\ \vdots \\ -\Delta E \\ +\Delta E \end{bmatrix} \quad \text{and} \quad T_N = \sum_{i=1}^{N}(-1)^i b_i, \end{aligned} \tag{2}$$

where $\boldsymbol{b} \in \mathbb{R}^N$ is the vector of previous BPM measurements. The so obtained estimate η_N can subsequently be used to calculate corrections θ for the next accelerator section according to Eq. (1). The question how many samples N have to be used to create an accurate enough estimate will be answered in the results section of this paper.

Integration of On-Line DFS and Orbit Feedback

When using the on-line DFS algorithm in combination with the orbit feedback, the interaction of the two subsystems has to be considered. At the dispersion estimation the beam energy changes induced by the on-line DFS will create orbit offsets that will couple to the action of the orbit feedback. By choosing the excitation to be a constant value with alternating signs, the induced disturbances are of the highest resolvable frequency of the orbit controller. Due to its design, the orbit controller frequency response demagnifies this frequency component strongly and the orbit feedback will couple only very weakly to the induced orbit offsets.

Another modification to the basic DFS algorithm is necessary, since the orbit controller will react on the changed beam orbits due to the on-line DFS corrections. The orbit feedback would aim to steer the beam back on its previous orbit. Therefore, the BPM centres of the corrected section have to be shifted electronically to the new reference orbit after the DFS correction.

If a section would be DFS corrected without considering the beam orbit in the rest of the downstream linac, the beam would be steered far from its reference orbit. This would lead to an unacceptable emittance growth. Also the orbit feedback would react strongly on the large offsets, which would also decrease the accuracy of the next dispersion estimate. Therefore, the expected beam orbit change $\hat{\boldsymbol{b}}$ in the BPMs after the current section has to be corrected with the correctors after the current section. Simulation showed that it is sufficient to use only the correctors of the next section, which reduced the necessary calculation time of the performed all-to-all steering. The according corrector actuations $\hat{\theta}$ can be calculated by solving

$$-\begin{bmatrix} \hat{\boldsymbol{b}} \\ \boldsymbol{0} \end{bmatrix} = \begin{bmatrix} \hat{\boldsymbol{R}} \\ \beta_0 \boldsymbol{I} \end{bmatrix} \hat{\theta}, \tag{3}$$

where β_0 is a damping factor for the corrector actuations.

Copyright © 2012 by the respective authors — cc Creative Commons Attribution 3.0 (CC BY 3.0)

RESULTS

To test the on-line DFS algorithm proposed, it was integrated in the simulation framework described in [1], which include the beam tracking in the main linac of CLIC, ground motion generation and the action of the orbit controller. The algorithm was tested on a beamline that was misaligned with about 11 days of ATL ground motion, followed by a one-to-one steering.

To determine how many samples are needed to estimate the dispersion sufficiently well, a simplified procedure was used. Instead of using full-scale simulations, the real dispersion was determined in simulations and corrupted with artificial BPM noise. The influence of the BPM resolution on the on-line DFS correction result is shown in Fig. 2. The effective BPM resolution in the estimate has to be about 5 nm to not worsen the average on-line DFS correction by more than 2%. Assuming a BPM resolution of 100 nm, the noise has to be reduced by a factor of 20. Since the averaging reduces the remaining noise by the factor $1/\sqrt{N}$, where N is the number of used samples, N has to be 400, which corresponds to 8 s of CLIC operation. Considering further that this procedure is repeated for 36 linac sections over two iterations, the full correction time needed is about 10 minutes not including the time needed for the cavity alignment. Additionally to the influence of noise, also the DFS algorithm itself cannot correct the chromatic dilutions fully. With perfectly known dispersion, the initial vertical emittance growth of 107.6% was reduced to 2.5% on average.

The long time periods necessary for the averaging cannot be simulated directly in reasonable time. We therefore only performed full-scale simulations with an N of 100, which corresponds to a real-time operation of about 2 minutes. Different imperfections were applied and on average the emittance growth could be reduced after two iterations to 2.8% with no imperfections, 3.7% with orbit feedback turned on and 10.4% with realistic BPM resolution.

The results for one particular ground motion sample are shown in Fig. 3. It can be observed that at the corrections of the final sections the emittance grows for a short time period. We believe that this behaviour is due to a worse steering and an improvement is subject to future work. Simulations were also performed including short-term ground motion (model B [1]) in combination with the orbit feedback for the dispersion estimation. The observed effect due to the ground motion was seen to be negligible. Another tested imperfection is the jitter of the acceleration gradients. Also here no significant degradation was observed for the maximal specification of 0.5%.

CONCLUSIONS

In this paper an on-line DFS algorithm was presented. Simulation results show that it is capable of correcting dispersive beam orbits due to long term ground motion misalignments efficiently. Two iterations of the algorithm have found to be enough to reduce the according beam emittance growth very efficiently, which takes for CLIC about 10 min. Since the time constant of the correction is much smaller than the emittance growth, there is no need to run the algorithm continuously. The mutual interaction of the algorithm with the orbit feedback was found to be small. Also the influence of ground motion and decelerator gradient jitter can be neglected. The presented algorithm is therefore an essential contribution for the successful operation of CLIC over longer time periods.

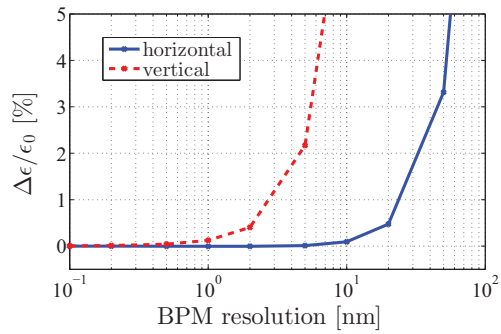

Figure 2: Relative emittance growth due to BPM resolution when using on-line DFS averaged over 20 random samples.

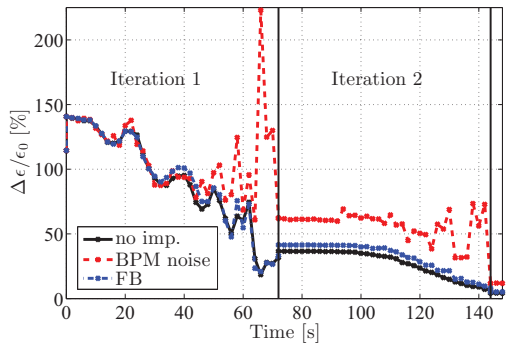

Figure 3: Relative vertical emittance during two iterations of the on-line DFS correction for one particular sample of ground motion. No imperfections are applied for the black curve (4% emittance growth). For the blue curve, the orbit feedback is turned on during the dispersion estimation. The mutual influence of the two subsystems is seen to be small (5% emittance growth). For the red curve a BPM resolution of 100 nm is used (12% emittance growth).

REFERENCES

[1] J. Snuverink et al., In Proc. of the IPAC11, TUPC023, 2011.

[2] V. Shiltsev, Phys. Rev. Spec. Top., 13:094801, 2010.

[3] T.O. Raubenheimer and R.D. Ruth, Nucl. Instrum. A 302(2), 191-208, 1991.

[4] D. Schulte, In Proc. of the PAC05, 1251-1253, 2005.

[5] A. Latina and P. Raimondi, In Proc. of the LINAC10, MOP026, 2010.

[6] N. Leros and D. Schulte, In Proc. of the EPAC02, 461-463, 2002.

Copyright © 2012 by the respective authors — cc Creative Commons Attribution 3.0 (CC BY 3.0)

SPECIFICATIONS OF THE DISTRIBUTED TIMING SYSTEM FOR THE CLIC MAIN LINAC

A. Gerbershagen, A. Andersson, D. Schulte, CERN, Geneva, Switzerland
P. N. Burrows, JAI, University of Oxford, Oxford, UK
F. Ömer Ilday, Bilkent University, Ankara, Turkey

Abstract

The longitudinal phase stability of the CLIC main and drive beams is a crucial element of the CLIC design. In order to measure and control the phase a distributed phase monitoring system has been proposed. The system measures the beam phase every 900 m. The relative phase between the measurement points is synchronized with an external reference system via a chain of reference lines. This paper presents the simulations of error propagation in the proposed distributed monitoring system and the impact on the drive and main beam phase errors and the luminosity. Based on the results the error tolerances for the proposed system are detailed.

INTRODUCTION

The Compact Linear Collider (CLIC) is a proposed 3 TeV center-of-mass energy e^+e^- collider. It is designed to extract the RF energy from high-current low-energy drive beams and use this energy for acceleration of the low-current high-energy main beams that are brought into collision.

Since the main beam acceleration is performed by the RF power extracted from the drive beam, the stability of the relative phasing of the drive and main beams is crucial for the preservation of CLIC's luminosity. A relative phase error of 0.2° @ 12 GHz between the drive and the main beam will cause a luminosity loss of 1% if the error is coherent between the 24 decelerator segments. The same luminosity loss can be caused by an incoherent error of 0.8°. [1]
Additionally to these requirements on the relative drive beam - main beam phase, the phase tolerance between the two main beams at the interaction point (IP) has been set to 0.6° @ 12 GHz [2]. Hence, in order to align the main beam phase a global phase reference over 50 km is needed.

The stated tolerance requirements have to be met on the timescale of ≈50 ns, since this is the beam loading time of the main beam accelerating structures and errors on the shorter time scale will be (at least partially) filtered out by the structures.

PROPOSED DISTRIBUTED TIMING SYSTEMS

The distributed timing system is required to establish the correct beam phase at each turn-around of the linac. This allows to measure and correct the main and drive beam phases along the main linac. There are two approaches for the design of such a system.

The first approach (A) is to use the outgoing main beams to transmit the phase information to a number of local oscillators (Fig. 1, top). These can maintain the phase accurately enough until the main beam returns on the way to the interaction point. This system requires accurate phasing between the outgoing main beams at the first booster linac near the interaction point (Fig. 2).
In the other approach (B) the master clock near the interaction point (IP) would define the nominal phase and distribute it as a signal cascade from one 900 m long decelerator segment to another (Fig. 1, bottom). This system would establish the relative phase of the local timing clocks by an optical connection independently of the beams.

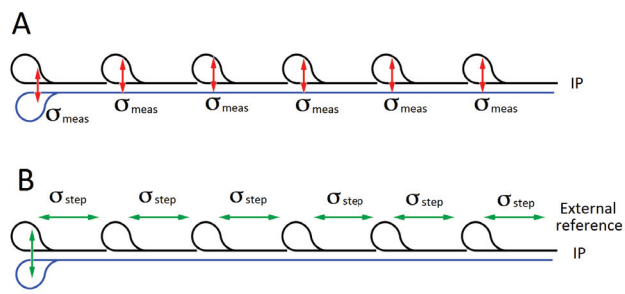

Figure 1: Phase signal propagation for the reference based on the main beam (A) and chained distribution of master clock signal (B).

Approach A has the advantage of having a relatively small error between the main and the drive beams, since the phase measurement at each drive beam decelerator is performed locally and hence no additional error is introduced during the distribution process (see Fig. 3, left). Approach B allows the correction of the main beam at its final turn-around, giving the possibility to reduce the jitter between the e^+ and e^- main beams (Fig. 3, right). However, if the drive beam correction signal is transported from the master clock via the distribution system, the noise introduced by this system would reduce the effectiveness of the phase correction. In the final CLIC design these approaches could be potentially combined.

The proposed timing distribution system is based on state of the art technology for signal distribution via optical fibers tested at XFEL (DESY, Hamburg) [3], [4]. This system is proven to provide <10 fs stability over the distance of several kilometers.
The following analysis determines the specifications of the

Copyright © 2012 by the respective authors — cc Creative Commons Attribution 3.0 (CC BY 3.0)

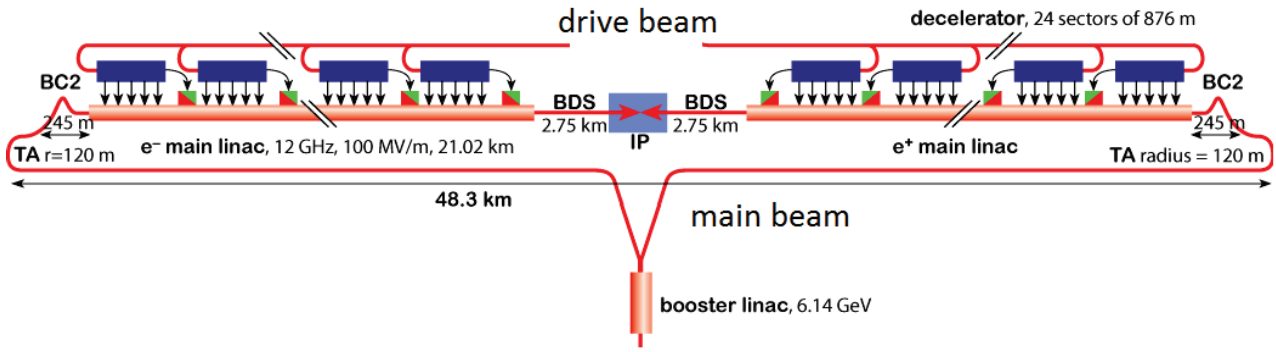

Figure 2: CLIC layout at 3 TeV.

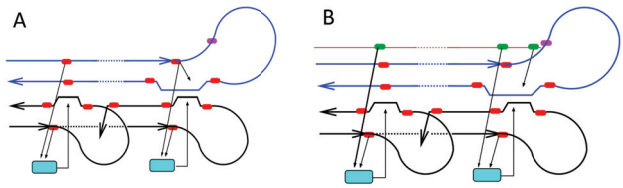

Figure 3: Phase correction system based on the main beam phase measurement (A) and on the external master clock (B) [2].

second approach (distributed timing system) and sets the requirements for the tolerances of this system.

ANALYSIS OF SPECIFICATIONS FOR THE DISTRIBUTED TIMING SYSTEM

Principle of time distribution and phase correction

As shown in Fig. 3 B, the signal from the master clock is used as the synchronization signal for the local oscillators. The master clock itself has a particular noise spectrum [5]. The impact of the noise on the local oscillators can be reduced by integrating the signal over the time intervals longer than the beam propagation time through the machine (≈ 0.2 ms).
The correction of the main beam is performed at the final turnaround with help of a kicker chicane, which can change the path length of the main beam bunches and hence their longitudinal position. The drive beam phase is also corrected via a chicane to the nominal value defined by the master clock at the turnarounds at each of the 24 decelerator modules.

The phase measurements on the main and drive beam after the chicanes ensure that the provided correction had the right value. If it is not the case, this could mean that the path length of the beams in the chicane is not as predicted, the chicane has the wrong R_{56} value or that the waveguide length has changed (e.g. due to temperature variation). To correct for these changes, a pulse-to-pulse feedback system can be introduced. Provided the changes are slow enough, the measured value of the correction error can be used to adjust the relative definitions of the monitors' nominal phase. The new definitions will ensure that the correction for the next pulse will set the drive beam bunches closer to their nominal position relatively to the main beam bunches. Hence, high stability of the local oscillator clocks must be ensured on a timescale of 20 ms, which is the pulse-to-pulse interval of CLIC.

In order to calculate the phase tolerance for signal transfer between the two subsequent decelerators, σ_{step}, (Fig. 1, B), one must calculate the impact of this error on the total phase error. We will assume a random walk of the phase error, which starts from the master clock at the IP and propagates along the machine step by step from one drive beam decelerator segment to another.

e^+ and e^- main beams phase tolerance

For the incoming main beams the relative phase tolerance at the IP is $0.6°$ @ 12 GHz $\hat{=}$ 42 μm $\hat{=}$ 140 fs [2] which corresponds to 1% of luminosity loss. Hence, one must assure that the total phase error introduced by the distributed timing system σ_{dts} is below $(140\text{ fs})/\sqrt{2}$ for each of the main beams.
Additionally to the 24 decelerator modules, each about 900 m long, we must consider that the beam delivery system of each main beam is about 2.75 km long [8]. To simplify the calculation it will be assumed that the distributed timing system for the main beam is 27, instead of 24, sectors long, hence about 2.7 km longer. One can consider the errors at each of the segments as linearly independent. Hence, the tolerance for the phase error introduced in each segment is given by

$$\sigma_{step,mm,1\%} = \frac{140\ fs}{\sqrt{27}\times\sqrt{2}} = 19.05\ fs \hat{=} 5.72\ \mu m. \quad (1)$$

The stated correction system error would cause a luminosity loss of 1%. However, in reality the largest part of the tolerance budget will be reserved for the beam itself and not for the reference jitter. Hence, the calculation only determines the upper limit for the distribution error but not

Copyright © 2012 by the respective authors — cc Creative Commons Attribution 3.0 (CC BY 3.0)

the effective system requirement, which will depend on the expected beam phase jitter. Defining the distribution system requirement to causing max. 0.1% luminosity loss, one obtains $\sigma_{step} = 5.72\ \mu m/\sqrt{10} = 1.81\ \mu m$
An advantage of the distributed timing system is that it allows to loosen the phase tolerances on the outgoing main beam by a factor of 7, since the phase correction at the final turnaround of the main beam can reduce the phase error [1], [7]. Also, the phase correction can compensate for the change in the main beam path length, given the path length change is slow enough ($\ll 20\ ms$ pulse interval).

Main beam - drive beam phase tolerance

The error σ_{step} causing 1% luminosity loss can be calculated from the main beam - drive beam relative phase error tolerance. The total error σ_{tot} introduced by the phase correction system at each decelerator must be below 0.8° @ 12 GHz for uncorrelated errors.

We assume a random walk of the distribution error segment by segment. The impact of each error is given by $\sum_{j=1}^{i} \sigma_{step}$ with i being the number of the segment counted from the IP. The total error introduced by the distributed timing system σ_{dts} is given by the sum of the errors in all segments. One should also consider that the main beam bunches are positioned at 30° of the RF wave in the four segments nearest to the IP and at 8° in other 20 segments. Hence σ_{dts} is given by

$$\sigma_{dts}^2 = \sum_{i=1}^{4}\left(\sum_{j=1}^{i}(\sigma_{step}\times\sin 30°)\right)^2 + \sum_{i=5}^{24}\left(\sum_{j=1}^{4}(\sigma_{step}\times\sin 30°)+\sum_{j=5}^{i}(\sigma_{step}\times\sin 8°)\right)^2$$

Normalising σ_{dts}^2 by the RMS value of the stated sine functions and calculating the sums, one obtains

$$\sigma_{step,md,1\%} = 0.059° \triangleq 4.12\ \mu m \qquad (2)$$

This value is of the same order of magnitude as the tolerance given by the main beam - main beam phase error consideration ($\sigma_{step,mm,1\%} = 5.72\ \mu m$) calculated in the previous sub-section. Defining as above the maximal 0.1% luminosity loss as a specification of the distribution system, the requirement for the reference stability will be $4.12\mu m/\sqrt{10} = 1.30\ \mu m$.

The 1% luminosity loss from the reference jitter has been calculated independently for main beam - main beam and main beam - drive beam phase error tolerances. In reality the same reference jitter σ_{step} would cause a luminosity loss via both channels,

$$\Delta\mathcal{L}_{total} = \Delta\mathcal{L}_{md} + \Delta\mathcal{L}_{mm} = 1\% \times \left(\left(\frac{\sigma_{step}}{\sigma_{step,md,1\%}}\right)^2 + \left(\frac{\sigma_{step}}{\sigma_{step,mm,1\%}}\right)^2\right)^2$$

Solving this equation for $\Delta\mathcal{L}_{total} = 1\%$ yields $\sigma_{step} = 3.34\ \mu m$. However, $\Delta\mathcal{L}_{total} = 0.1\%$ defines the specification of $\sigma_{step} = 1.06\ \mu m$ average error introduced by the distributed timing system at each decelerator segment.

CONCLUSIONS AND OUTLOOK

The phase jitter of the distributed timing system at each decelerator segment is calculated to be 3.34 μm for 1% luminosity loss from both the main to main and main to drive beam tolerances.This value is met by demonstrated performances [3], [4], which proves the feasibility of the distributed timing system. However, ideally the specification would be tighter - 0.1% luminosity loss, which requires a distribution system stability of 1.06 μm per segment. Hence, it has to be investigated whether the noise can be significantly reduced.

The demonstrated performance of the signal distribution includes the transformation of the optical signal into electrical and vice versa. One solution could be chaining the distribution by splitting the optical signal at each decelerator, using one part of the signal as a reference and amplifying the other part and sending it to the next decelerator. This would help to avoid transformation noise and might allow to reach the specified target. A dedicated approach would be needed to prove this concept experimentally.

It will be also necessary to demonstrate the reliability of the signal distribution technology to operate unattended in the tunnel.

REFERENCES

[1] D. Schulte et al., "Status of the CLIC Phase and Amplitude Stabilisation Concept", Proceedings of Linear Accelerator Conference LINAC2010, Tsukuba, Japan MOP024

[2] D. Schulte, First CLIC Phase Stability Meeting, November 24, 2011, http://indico.cern.ch/conferenceDisplay.py?confId=164428.

[3] F. Ömer Ilday, "Long-distance optical stabilization with femtosecond resolution", CLIC09 Workshop

[4] M. Felber, "Achievements and challenges during the first implementation phase of an engineered version in the accelerator", CLIC09 Workshop

[5] CLIC Conceptual Design Report, chapter 5.14, "Fine time generation and distribution"

[6] A. Andersson, "Phase reference system", CLIC collaboration meeting, May 10, 2012

[7] F. Stulle, "Beam phase and energy tolerances in the CLIC RTML", CLIC - Note - 874

[8] CLIC Parameter Table, http://clic-meeting.web.cern.ch/clic-meeting/clictable2010.html

Copyright © 2012 by the respective authors — cc Creative Commons Attribution 3.0 (CC BY 3.0)

LINEAR ACCELERATOR BASED ON PARALLEL COUPLED ACCELERATING STRUCTURE*

Yu. Chernousov, V. Ivannicov, I. Shebolaev, ICKC, Novosibirsk, RUSSIA
A. Levichev, V. Pavlov, A. Barnyakov, BINP, Novosibirsk, RUSSIA.

Abstract

Linear accelerator based on parallel coupled accelerating structure and RF-controlled electron gun is developed and produced. The structure consists of five accelerating cavities. The RF power feeding of accelerating cavities is provided by common exciting cavity which is performed from rectangular waveguide loaded by reactive pins. Operating frequency is 2450 MHz. RF-controlled Electron gun is made on the basis of RF triode. Linear accelerator was tested with different working regimes. The obtained results are following:

- energy is up to 4 MeV, accelerating current is up to 300 mA with pulse duration of 2.5 ns on the half of the width,
- energy is up to 2.5 MeV, accelerating current is up to 100 mA with pulse duration of 5 μs,
- energy is up to 2.5 MeV, accelerating current is up to 120 mA with pulse duration of 5 μs and beam capture of 100%.

The descriptions of the accelerator elements are given in the report. The features of the parallel coupled accelerating structure are discussed. The results of the measuring accelerator's parameters are presented.

INTRODUCTION

Compact linear electron accelerators have wide scientific and industrial applications. The more often linacs are used with energy up to 10 MeV, average beam power up to several kilowatts. In present there are two type of accelerating structures with travelling wave and standing wave. But all of these structures have sequential RF power feeding of the accelerating cells. This is cause of some problems. To supply the accelerating structure total RF power has to go from the first accelerating cell. As the power is attenuated along these structures the initial value of the power must be very high, therefore, there are breakdowns and thermal surface damage in the first accelerating cell. When the breakdown is happened in one of the accelerating cell the operating RF pulse is terminated because of all storage energy of the structure is dissipated in it. Developing of *accelerating structure with given distribution of the power along the cavities is very difficult task. Also there is problem of high order modes, vacuum pumping and etc.

The linear electron accelerator based on new type accelerating structure is developed and produced by Budker Institute of Nuclear Physics of SB RAS, Institute of Chemical Kinetics and Combustion of SB RAS and Institute of Catalysis of SB RAS [1]. The main elements of accelerator are parallel coupled accelerating structure, injector, waveguide track with vacuum RF window, focusing system and klystron KIU-111. The klystron's frequency is 2450 MHz, average power is 5 kW with pulse power of 5 MW [2]. The main goal of our efforts is to test new ideas and devices which are used in the accelerator. The mass of these elements are used in such accelerator for the first time and have some advantages.

PARALLEL COUPLED ACCELERTING STRUCTURE

The scheme of parallel coupled accelerating structure is shown in the Fig. 1 and Fig. 2. RF power from a klystron feeds the exciting cavity (1) through inductive coupling window (7). The exciting cavity supplies the accelerating cavities (2). The RF connection of the exciting cavity with the accelerating cavities is provided by magnetic field through coupling slots (5). The focusing alternative magnetic field is created along the beam axis by periodic permanent magnets (3) with radial magnetization inserted in the iron yoke (4). This kind of focusing provides large enough magnetic field while keeping the weight of the focusing system considerably small. The cupper pins (6) are used to tune the exciting cavity (1) at the resonance frequency.

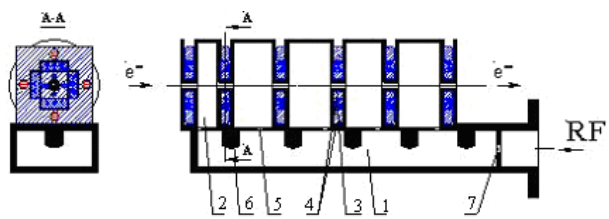

Figure 1: Scheme of the parallel coupled accelerating structure.

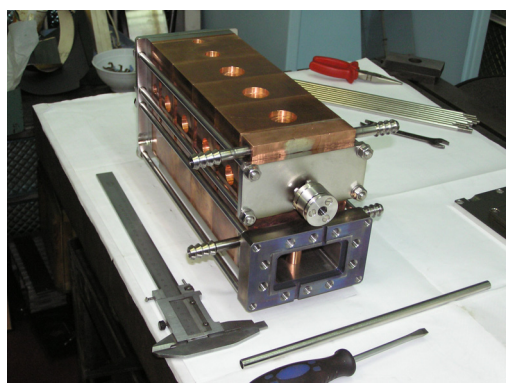

Figure 2: Parallel coupled accelerating structure.

* Work is supported by the Ministry of Education and Science of the Russian Federation, grants N 14.740.11.0836

Copyright © 2012 by the respective authors — cc Creative Commons Attribution 3.0 (CC BY 3.0)

Due to the scheme of RF power supplying this accelerating structure has some advantages versus structures with sequential power feeding. There is no need to have a high power in the first accelerating cavity. So the overvoltage and breakdown problems, thermal surface damage near the coupling slots are absent. The design of parallel coupled accelerating structure allows us to create compact periodic permanent magnet focusing system based on the permanent magnets with radial magnetization (see Fig. 1). The accelerating cavities are not connected with each other by electric field therefore aperture of the drift tubes between cavities is limited only by the beam focusing. By changing the coupling factor between exciting and accelerating cavities it is possible to make the free power distribution along the structure. If breakdown is happened in one of the accelerating cavities the storage energy only this cavity is dissipated, and only in this cavity. So the working RF pulse is not terminated but only amplitude of reflected signal is slightly changed, as it is presented on the Fig. 3.

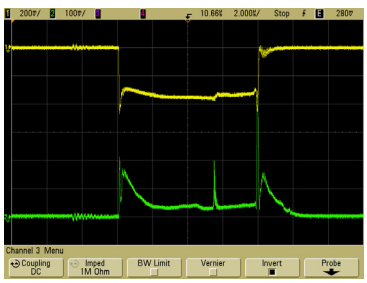

Figure 3: Breakdown in one of the accelerating cavities: 1 - signal from klystron; 2 - reflected signal from accelerating structure.

The accelerating structure can be used as for high average current with high average power as for short nano- and picoseconds duration current pulses with high amplitudes.

INJECTOR

Injector is the electron gun with DC voltage of 50 kV and pulse current up to 1 A. It is based on RF triode GS-34 and shown on the Fig. 4.

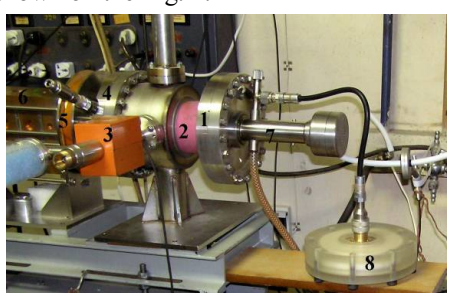

Figure 4: Injector: 1- cathode-grid unit, 2 – ceramics, 3 – vacuum pump, 4 – bunching cavity, 5 – matching solenoid, 6 - accelerating structure, 7 – coaxial cavity for RF beam control, 8 – antenna type RF lead.

Injector can work with following regimes: short pulses with duration of about nanoseconds, long pulses with duration of microseconds and long pulses with RF control for a beam π-chopper. Under using RF control the beam is modulated by coaxial cavity on bunches with length equaled to half wavelength of RF field. Due to this feature, the beam capture can be achieved up to 100%.

The cathode-grid unit 1 (see Fig. 4) is under potential of -50 kV. So, to feed the coaxial cavity 7 the antenna-type coaxial lead (8) was developed and produced. It is shown on the Fig. 5. The antenna-type lead consists of two symmetrical parts of coaxial half-wave resonator. The resonator is cut along perpendicular to the longitudinal axis plane of symmetry. The solid dielectric disk is located between the halves.

The Fig. 6 shows the measured bandpass characteristics. The reflection coefficient S_{11} at the operating frequency is 0.098 and the transmission coefficient S_{21} is 0.976. Bandwidth at the attenuation level of -3 dB is more than 1800 MHz (73%).

Figure 5: Antenna type RF lead.

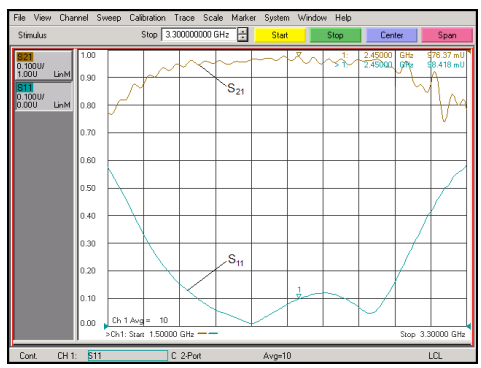

Figure 6: The transmission S_{21} and reflection S_{11} coefficients of the lead.

ACCELERATOR MEASUREMENTS

Accelerator was tested under three regimes.

The first regime is characterized by short beam pulse with duration of 2.5 ns on the half of width (see Fig. 7). The beam energy is about 4 MeV, beam current amplitude is about 300 mA. The Fig. 8 shows the cross section of the beam profile.

Copyright © 2012 by the respective authors — cc Creative Commons Attribution 3.0 (CC BY 3.0)

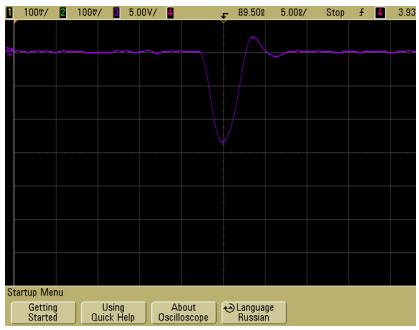

Figure 7: Oscilloscope of the accelerated beam current with duration of 2.5 ns (100 mA per cell).

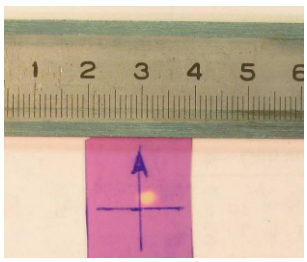

Figure 8: Cross section of the beam profile with pulse duration of 2.5 ns.

In the second regime the beam duration is 4 μs, energy is 2.5 MeV, beam capture is about 50%. Oscilloscope of the beam current and cross section of the beam profile are shown on the Fig. 10 and Fig. 11 correspondingly.

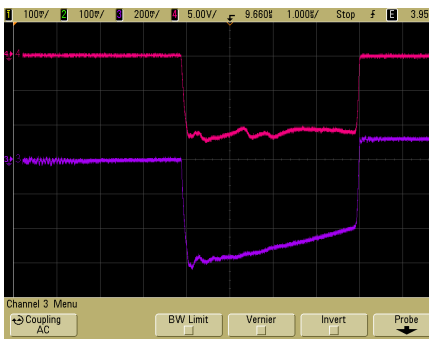

Figure 9: Oscilloscope of the accelerated beam current with duration of 4 μs: 3 – emission beam current (180 mA per cell), 4 – beam current in the end of accelerating structure (100 mA per cell).

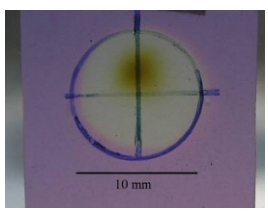

Figure 10: Cross section of the beam profile with pulse duration of 4 μs.

In the third regime the injector operated with RF control. The energy is equaled to 2.5 MeV. The feature of this regime is beam capture of 100%. Oscilloscope of the beam current and cross section of the beam profile are shown on the Fig. 12 and Fig. 13 correspondingly

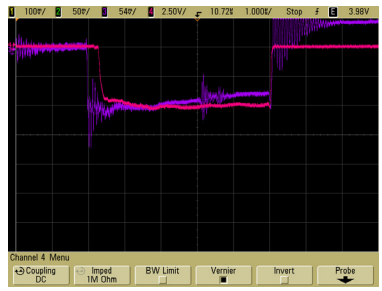

Figure 12: Oscilloscope of the accelerated beam current with RF control: 3 – emission beam current (50 mA per cell), 4 – beam current in the end of accelerating structure (50 mA per cell).

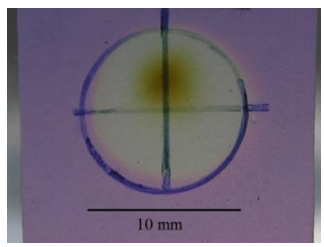

Figure 13: Cross section of the beam profile with RF control.

CONCLUSION

Linear electron accelerator based on parallel coupled accelerating structure and injector with RF control for a beam π-chopper is made, tested and measured. The beam energy is 2.5-4 MeV with total power of 2.4 MW, accelerated beam current is 100-300 mA. These values depend on the beam loading effect. The durations of the beam pulse were changed from 2.5 ns to 5 μs. With RF control the beam capture was achieved 100%. The diameter of cross section of the beam profile was about 3 mm. The beam loading effect is studying.

REFERENCES

[1] A.E. Levichev, V.M. Pavlov and et al., "Characteristics of the Parallel Coupled Accelerating Structure", IPAC'10, Kyoto, June 2010, THPEA040, p. 3765 (2010); http://www.JACoW.org.

[2] I.A. Frejdovich, P.V. Nevsky et al., JACoW, "Multy-beam klystrons with reverse permanent magnet focusing system as the universal RF power sources for the compact electron accelerators", RUPAC'06, Novosibirsk, September 2006, TUHO08, p. 100 (2006); http://www.JACoW.org.

Copyright © 2012 by the respective authors — cc Creative Commons Attribution 3.0 (CC BY 3.0)

MEASUREMENTS OF A REDUCED ENERGY SPREAD OF A RECIRCULATING LINAC BY NON-ISOCHRONOUS BEAM DYNAMICS*

F. Hug#, C. Burandt, M. Konrad, N. Pietralla, TU Darmstadt, Darmstadt, Germany
R. Eichhorn, Cornell University, Ithaca, NY, USA

Abstract

The Superconducting Linear Accelerator S-DALINAC at the University of Darmstadt (Germany) is a recirculating linac with two recirculations providing beams for measurements in nuclear physics at small momentum transfers. For these experiments an energy spread of better than 10^{-4} (rms) is needed. Currently acceleration in the linac section is done on crest of the accelerating field. The recirculation path is operated achromatic and isochronous. In this recirculation scheme the energy spread of the resulting beam in the ideal case is determined by the electron bunch length. Taking into account the stability of the RF system the energy spread increases drastically to more than 10^{-3} (rms**).**

We will present a new non-isochronous recirculation scheme which helps cancelling out these errors coming from the RF-jitters. This scheme uses longitudinal dispersion in the recirculation paths and an acceleration off-crest on a certain phase with respect to the maximum. We will present results of the commissioning of the new system including measurements of the longitudinal dispersion in the recirculation arcs as well as measurements of the resulting energy spread using an electron spectrometer.

INTRODUCTION

Operating since 1987 the Superconducting DArmstadt LINear Accelerator (S-DALINAC) is used as a source for nuclear- and astrophysical experiments at the university of Darmstadt [1]. It can accelerate beams of either unpolarized or polarized electrons [2] to beam energies of 1 up to 130 MeV with beam currents from several pA up to 60 µA. The layout of the S-DALINAC is shown in Fig. 1.

Acceleration in the injector and main linac is done by superconducting elliptical cavities with a quality factor of $Q_0 \approx 10^9$. These cavities are operating at a frequency of 3 GHz with a maximum accelerating gradient of 5 MV/m.

The main linac consists of 8 standard 20-cell cavities and can provide an energy gain of 40 MeV. By recirculating the beam two times the maximum energy of 130 MeV can be achieved. In the adjacent experimental hall this beam can be used for different experiments such as electron scattering in two electron spectrometers or experiments with tagged photons. For these experiments an energy spread of $\pm 1 \cdot 10^{-4}$ is required.

* Work supported by DFG through SFB 634
# hug@ikp.tu-darmstadt.de

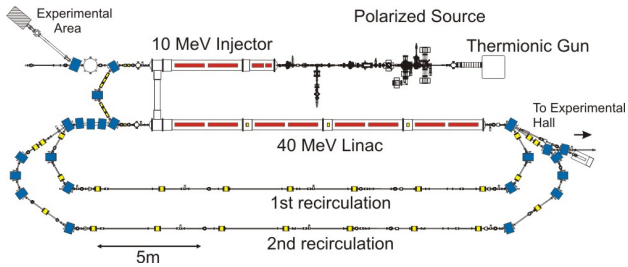

Figure 1: Floor plan of the S-DALINAC.

LONGITUDINAL BEAM DYNAMICS

The S-DALINAC is designed to use an isochronous recirculation scheme originally. On a isochronous working point the electrons are accelerated in the maximum of the accelerating field (on crest) in every turn and the bunch length is kept constantly small ($\pm$ 1°) using achromatic and isochronous recirculation paths. Isochronicity is a property of beam optics and can be described as $\mathrm{d}l/\mathrm{d}E = 0$ meaning that the length of the flight path of all electrons is independent from their energy. Acceleration on crest of the RF-field is the common mode for linear accelerators. Usually amplitude and phase jitters of the cavities are not correlated and the resulting energy spread is mainly determined by the short bunch length. In a recirculating linac the errors can add up coherently throughout the linac passages in a way that every electron sees the same errors in all passes through the linac due to the large time constant of field variations in the superconducting cavities compared to the short time of flight of the ultra relativistic electrons through the linac.

A way to overcome these correlated errors is changing the longitudinal working point to a non-isochronous one. This is the common operation mode for synchrotrons or microtrons In a non-isochronous recirculation scheme the recirculation paths provide a longitudinal dispersion $\mathrm{d}l/\mathrm{d}E = D_L \neq 0$ while the accelerating field is operated at a certain synchrotron phase $\Phi_S \neq 0$ (on edge). The electrons then perform synchrotron oscillations in the longitudinal phase space. Compared to synchrotrons a quite large phase advance per turn is needed to cancel out the RF jitters. In fact a half or full integer number of synchrotron oscillations leads to the best energy resolution of the extracted beam in a way that the resulting energy spread at extraction is only determined by the energy spread at injection while the errors caused by the RF jitters of the main linac are cancelled out. [3,4]

The usability of such a non-isochronous recirculation scheme at the S-DALINAC has been verified already by numerical simulations (see Fig. 2). The new longitudinal

Copyright © 2012 by the respective authors — cc Creative Commons Attribution 3.0 (CC BY 3.0)

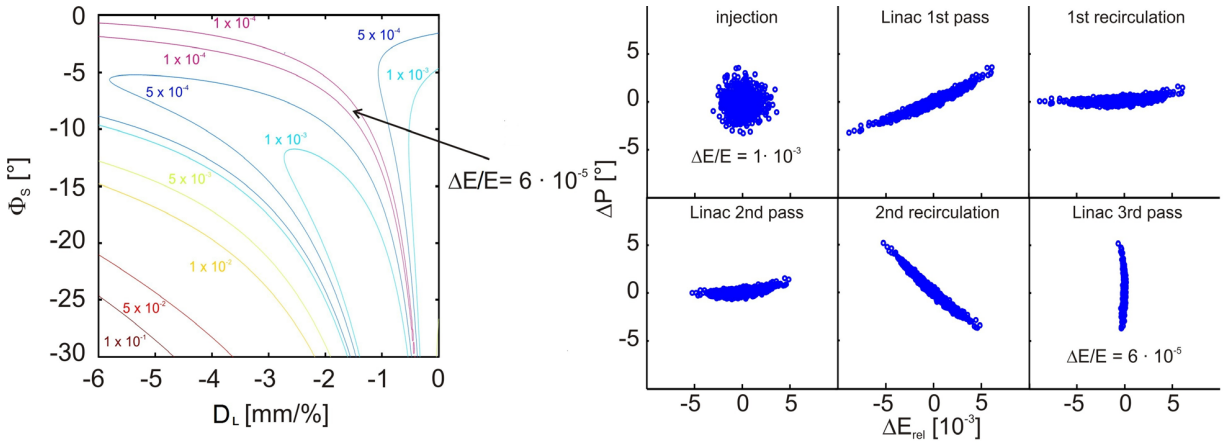

Figure 2: Hillplot of the resulting energy spread at extraction for different sets of longitudinal dispersion and synchrotron phase (left). Beside the isochronous point exist areas of reduced energy spread. The minimum has been determined to D_L = -1.5 mm/% and Φ_S = -9.5° On the right side a bunch of 5000 particle has been tracked through the linac using the optimized parameters. The particles perform a half oscillation in longitudinal phase space ending up on a reduced energy spread.

working point has been determined to D_L = -1.5 mm/% and Φ_S = -9.5° and would lead to a reduction of the energy spread to $\Delta E/E = 6.03 \cdot 10^{-5}$ which satisfies the requirements mentioned above very well. (for more details see [5,6,7])

LATTICE OPTIMIZATION

In order to tune the S-DALINAC to different non-isochronous working points in future optimizations at the recirculation paths had to be carried out. In particular the quadrupole lattice of the recirculation arcs needed to be reviewed to change the value of D_L easily while the transverse dispersion D and the transverse angular dispersion D' both equal zero at the end of every recirculation arc. The result of these optimizations are lattices for both arcs in which D_L can be manipulated easily by changing only the quadrupole gradients in the arcs. Keeping these gradients on a fixed ratio in addition D and D' remain at zero at the end of every arc like required. (for more details on this topic see [7,8])

MEASUREMENT OF LONGITUDINAL DISPERSION

The idea of adapting the concept of non-isochronous recirculation for the S-DALINAC was presented many years before [5], while the realisation, especially tuning the machine to the new longitudinal working point, needed some time. One reason was a lack of beam diagnostics developed meanwhile and described in the section below.

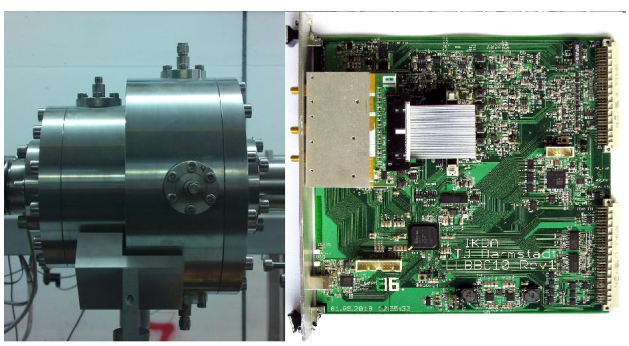

Figure 3: Measurement setup consisting of rf monitor (left) and rf board with FPGA board (right).

For the measurement of the longitudinal dispersion of the recirculation arcs RF monitors located at the beginning of the straight sections behind the last dipoles has been used. Usually, these intensity monitors, which are pillbox cavities at a 3 GHz resonant frequency (see Fig. 3 left), are used for non-destructive measurement of the beam current during operation. The passing cw beam excites an oscillation and the RF signals can be coupled out. Matter of interest is the detection of the phase of the 3 GHz oscillation excited by the beam. This can be done by mixing the RF signal of the monitor with the local oscillator frequency of the RF control system. This down conversion to the base band [9] is done on a RF board (see Fig. 3 right) leading to I/Q values describing the relative oscillation phase of the RF monitor. The I/Q values are converted into real phase values on a FPGA board then. This board is also used for setting amplifications and offsets of the measurement. The hardware is mainly part of the new developed digital LLRF system of the S-DALINAC with minor modifications due to the weak signals coming out of the RF monitors [8,9,10].

To determine D_L out of the phase values the time of flight method is used. For every quadrupole setting, corresponding to a certain dispersion D_L the energy of the beam is changed and the phase on the RF monitor is measured. If $D_L \neq 0$ the time of flight in the arc changes with respect to the beam energy and so does the phase. The results of the measurements on both recirculations is shown in Fig. 4.It can be seen that the measurement fits very well with the simulation results and that D_L can be changed over a large interval including the envisaged value of D_L = -1.5 mm/%.

Copyright © 2012 by the respective authors — cc Creative Commons Attribution 3.0 (CC BY 3.0)

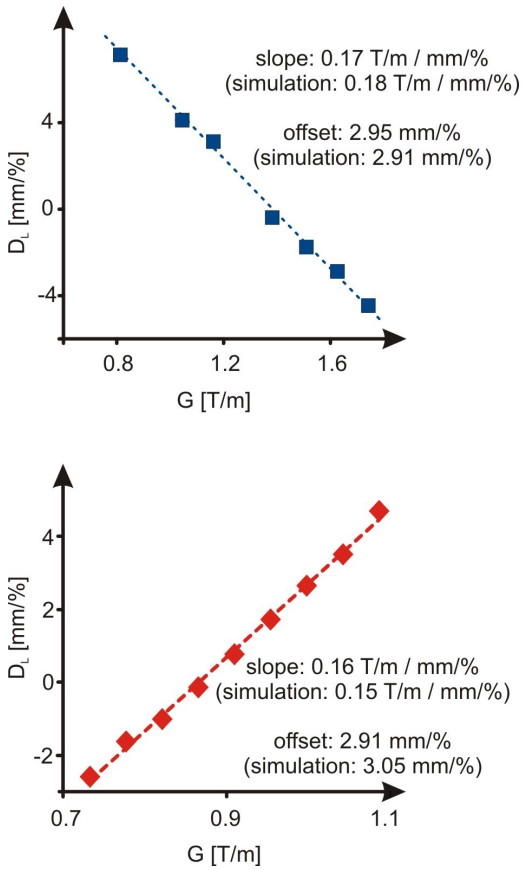

Figure 4: Measured values of D_L in the first recirculation (top) and second recirculation (bottom) for different quadrupole gradients in the arc.

MEASUREMENT OF THE ENERGY SPREAD

Having set up a detection system for D_L and characterized the recirculation arcs allowed to tune the accelerator to its new non-isochronous working point. In order to check the energy resolution of the beam an electron scattering experiment on a thin gold target has been performed. The obtained data is shown in Fig. 5. The energy spread could be reduced from ΔE = 120 keV in the isochronous mode to ΔE = 30 keV in the non-isochronous mode. Both spectra have been measured for about 30 min, which is a typical time between two saves of experimental runs for nuclear physics experiments. After this first proof of principle the following beam time has been successfully performed in the non-isochronous mode.

SUMMARY AND OUTLOOK

Using a new non-isochronous recirculation scheme for the S-DALINAC the energy spread of the electron beam could be reduced significantly. Nevertheless additional experiments are planned to check the effect of different longitudinal working points on the energy spread and compare the data with simulations shown in Fig. 2.

In addition the concept of using a non-isochronous working point to reduce the energy spread of multi-pass linacs might be interesting to overcome beam break-up limits in high current linacs or ERLs as the bunchlength during acceleration is naturally longer which generally leads to weaker excitations of HOMs [11].

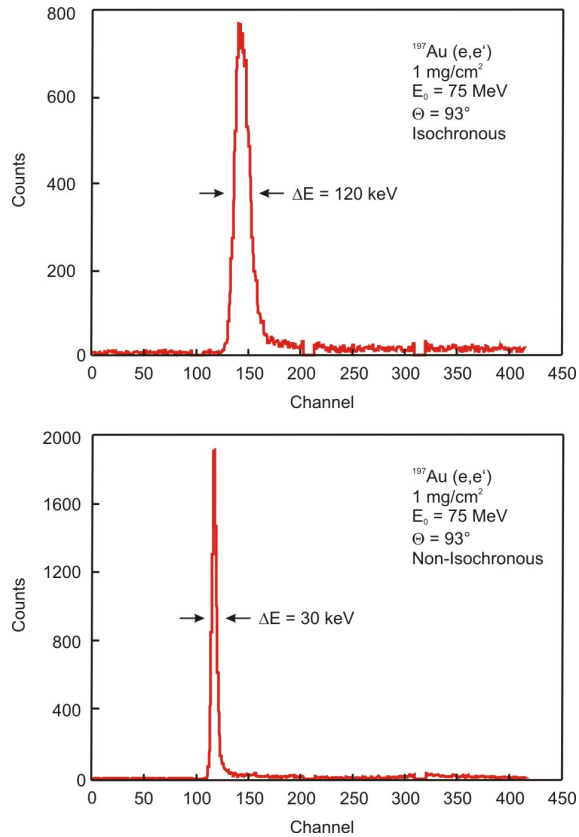

Figure 5: Energy spread of the beam obtained by elastic scattering on a thin gold target. Top: isochronous acceleration. Bottom: Non-isochronous recirculation.

REFERENCES

[1] A. Richter., EPAC '96, Sitges (1996) 110.
[2] C. Eckardt et al., IPAC '10, Kyoto (2010) 4083.
[3] H. Herminghaus, NIM A305 (1991) 1.
[4] H. Herminghaus, NIM A314 (1992) 209.
[5] R. Eichhorn et al., LINAC '06, Knoxville, Tennessee (2006) 73.
[6] F. Hug et al., IPAC '10, Kyoto (2010) 4470.
[7] R. Eichhorn et al., LINAC '10, Tsukuba, Japan (2010) 64.
[8] F. Hug et al., DITANET Conference, Seville, Spain (2011) in press.
[9] A. Araz et al., Phys. Rev. ST Accel. Beams 13, 082801 (2010).
[10] Konrad et al., Phys. Rev. ST Accel. Beams 15, 052802 (2012).
[11] J-L. Biarrotte, PAC '01, Chicago, Illinois (2001) 1098.

Copyright © 2012 by the respective authors — cc Creative Commons Attribution 3.0 (CC BY 3.0)

COMPUTATIONAL MODEL ANALYSIS FOR EXPERIMENTAL OBSERVATION OF OPTICAL CURRENT NOISE SUPPRESSION BELOW THE SHOT-NOISE LIMIT

A. Nause, E. Gover, Tel Aviv University, Israel

Abstract

In this paper we present simulation analysis of experimental results which demonstrate noise suppression in the optical regime, for a relativistic e-beam, below the classical shot-noise limit. Shot-noise is a noise resulting from the granular nature of the space-charge in an e-beam. It is linear to the beam current due to its Poissonic distribution in the emission process. Plasma oscillations driven by collective Coulomb interaction during beam drift between the electrons of a cold intense beam are the source of the effect of current noise suppression. The effect was experimentally demonstrated [1] by measuring Optical Transition Radiation (OTR) power per unit e-beam pulse charge. The interpretation of these results is that the beam charge homogenizes due to the collective interaction (sub-Poissonian distribution) and therefore the spontaneous radiation emission from such a beam would also be suppressed (Dicke's subradiance [2]). Analysis of the experimental results using GPT simulations will demonstrate the suppression effect. For the simulation results we used a full 3D GPT model of the ATF section in which the experiment took place at.

INTRODUCTION

Shot-noise is a noise resulting from the granular nature of the space-charge in an e-beam. The discreteness of the particles and the randomness of electrons emission from the cathode causes time dependent fluctuations of the charge and current density at any cross section along the beam transport line. This noise was first reported in 1918 by Schottky who made experiments in vacuum tubes.

Noise is best characterized in terms of the Fourier transform of the time-varying fluctuations in electric current, namely, by its spectral density. Gover and Dyunin showed in a 1D model [3] that it is possible to observe and control optical frequency energy and current (shot noise) fluctuations in a dense relativistic charged particles beam. GPT simulations were used to demonstrate this effect for a real-like beam starting from Shot-noise [4]. Moreover, at certain conditions, when the dominant noise in the beam is current shot noise (density fluctuations), it is possible to reduce significantly the beam noise by virtue of a collective interaction process along an interaction length corresponding to a quarter period longitudinal plasma oscillation in the beam. This means that the charge distribution in the beam can be homogenized in this process.

First experimental observation of this phenomenon using OTR from a metallic foil was presented last year [1]. Noise suppression using a dispersive section (dog-leg bend) was demonstrated in SLAC [5]. TR is proportional to the current-noise amplitude [6], and therefore can be used in order to estimate the suppression in the current noise. In this paper we press analysis of the experimental results and demonstrate this effect using full 3D GPT simulations that were carried out for this purpose.

1D Model of Noise Dynamics in Charged Electron Beams

In electron-beam transport under appreciable space-charge conditions, the microdynamic noise evolution process may be viewed as the stochastic oscillations of Langmuir plasma waves [3]. In the linear regime, the evolution of longitudinal current and velocity modulations of a beam of average current I_b, velocity βc and energy $E = (\gamma - 1)mc^2$, can be described in the laboratory frame by [7]:

$$\frac{d}{d\phi_p}\breve{i}(z,\omega) = -\frac{i}{W(z)\breve{v}(z,\omega)} \quad (1)$$

$$\frac{d}{d\phi_p}\breve{v}(z,\omega) = -iW(z)\breve{i}(z,\omega) \quad (2)$$

where $\breve{i}(\omega) = \breve{I}(\omega)e^{i\omega z/\beta c}$, $\breve{v}(\omega) = \breve{V}(\omega)e^{i\omega z/\beta c}$. $\breve{I}(\omega)$, $\breve{V}(\omega)$ are the respective Fourier components of the beam current and kinetic-voltage modulations. The kinetic-voltage modulation is related to energy and longitudinal velocity modulations: $\breve{V}(\omega) = -(mc^2/e)\breve{\gamma} = -(mc^2/e)\gamma^3\beta\breve{\beta}$, $\phi_p(z) = \int_0^z \theta_{pr}(z')dz'$ is the accumulated plasma phase, $W(z) = r_p^2/(\omega A_e \theta_{pr}\epsilon_0)$ is the beam wave-impedance. A_e is the effective beam cross-section area, $\theta_{pr} = r_p\omega_{pl}/\beta c$ is the plasma wavenumber of the Langmuir mode, $r_p < 1$ is the plasma reduction factor, $\omega_{pl} = \omega_{po}/\gamma^{3/2}$ is the longitudinal plasma frequency in the laboratory frame. The single-frequency Langmuir plasma wave model expressions [3] can be solved straightforwardly in the case of uniform drift transport. After employing an averaging process, this results in a simple expression for the spectral parameters of stochastic current and velocity fluctuations (noise) in the beam assuming that they are initially uncorrelated[]:

$$\breve{i}(L,\omega) = \cos\phi_p(L)\breve{i}(0,\omega) + (\sin\phi_p(L)/W_d)\breve{v}(0,\omega) \quad (3)$$

where $\phi_p = \theta_{pr}z$, $\theta_{pr} = r_p\frac{\omega_p'}{v_0}$, $\omega_p' = (\frac{e^2 n_0}{m\epsilon_0\gamma^3})$, $W_d = \sqrt{\mu_0/\epsilon_0}/k\theta_{pr}A_e$.

The beam current noise evolution is affected by the initial axial velocity noise through the parameter

$$N^2 = \overline{|\breve{v}(0,\omega)|^2}/W^2\overline{|\breve{i}(0,\omega)|^2} = (\omega/c\beta k_D)^2 \quad (4)$$

Copyright © 2012 by the respective authors — cc Creative Commons Attribution 3.0 (CC BY 3.0)

where $k_D = \omega_{pl}/c\sigma_\beta$ is the Debye wavenumber and $c\sigma_\beta$ is the axial velocity spread. Equation (4) suggests that current noise suppression is possible if the beam is initially cold $N^2 < 1$, and if plasma phase accumulation of $\phi_p(L) \sim \pi/2$ is feasible.

NOISE SUPPRESSION EXPERIMENT

The noise suppression demonstration experiment was conducted on the 70 MeV RF-LINAC of ATF/BNL (figure 1). The OTR measurements were carried out at a fixed point (CTR-1) 6.5 m away from the LINAC exit. Keeping the beam spot sizes on viewer YAG4 wide in all experiments made it possible to measure similar OTR image patterns on the CCD screen in all experiments (see figure 3). The measured signal S_{OTR} was the integrated charge accumulated in all of the pixels of a CCD (charge-coupled device) camera exposed to the OTR emission on the incidence of single electron-beam pulse on the screen. The measured data of $S_{OTR} = Q_b$ in CTR-0 and CTR-1 are shown in figure 2 as a function of the varied bunch charge Q_b in the range 200 to 500 pC. The pulse duration in all experiments remained approximately the same (5 pS) corresponding to an average current of 40 to 100A (figure 4). In a shot-noise-dominated beam, in the absence of collective microdynamics, the current noise and consequently S_{OTR} are proportional to I_b. Our measured data of $S_{OTR} = Q_b$ in CTR-0 lie approximately on a horizontal line, confirming the absence of collective microbunching and current-velocity noise correlation or noise suppression before this point. On the other hand, the data measured on CTR-1 exhibit a systematic drop as a function of charge (200 to 500 pC) for all beam energies (50 to 70 MeV). As the measurement conditions at the two measurement positions and at different beam energies could not be made identical, the absolute suppression level between the two points could not be determined. However, the normalized data of all measurements of noise per unit charge depicted in figure 2 show the scaling with charge for all beam energies. This demonstrates attainment of 20 to 30% relative noise suppression, and confirms the predicted effect of collective microdynamic noise suppression process in the drift section.

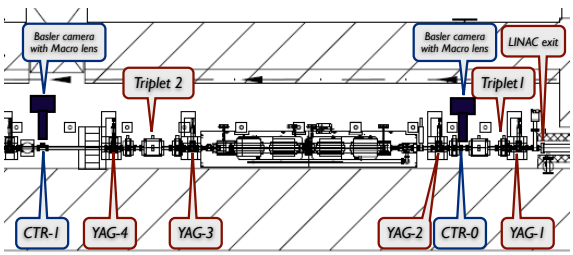

Figure 1: The ATF electron-beam transport set-up is shown from the injector RF-LINAC exit to the OTR viewer site (CTR-1).

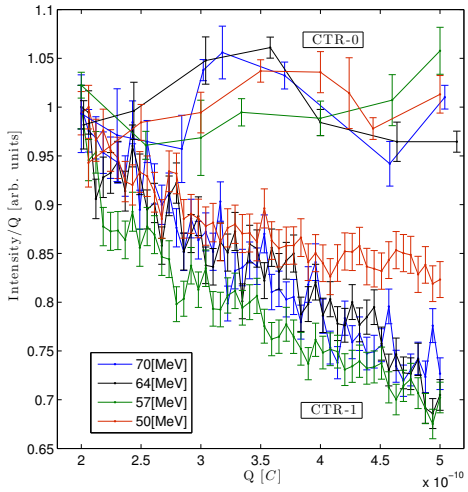

Figure 2: Integrated OTR intensity measurement signals divided by the electron pulse charge. The CTR-1 data correspond to OTR measurement from a screen, intercepting the electron beam 6.5m away from the LINAC exit. The curve's negative slope indicates relative current shot-noise suppression of 20-30% as the beam charge varies from 0.2 to 0.5 nC at different beam energies (50-70 MeV). The CTR-0 data correspond to OTR measurement right after the LINAC exit. Used for reference, its horizontal slope (linear scaling of S_{OTR} with beam charge) indicates that there was no charge suppression before the collective microdynamic process in the subsequent drift section. The error of the camera integrated signal measurement, 3%, was determined from the variance in the value of the signal due to pulse-to-pulse variation, measured repeatedly while keeping all beam control parameters fixed. The charge measurement error is 1%.

COMPUTATIONAL MODEL OF COLLECTIVE MICRODYNAMICS IN VARYING CROSS-SECTION BEAM TRANSPORT

At the exit of the Linac, the beam is current-noise dominated, and $N^2 \ll 1$. However, due to finite emittance, the axial velocity spread becomes significant as the beam is focused and consequently N^2 (Eq (4)) is no longer negligible. Furthermore, at tight focusing the uniform beam expression (Eq. (3)) cannot be used and in order to calculate the noise suppression, one should solve differential equations for variable beam parameters. In this section we show through a model case computational solution of equations (1) and (2), that the axially varying beam cross section and the excess axial velocity spread due to angular spread can account for a substantial moderation of the noise suppression effect that was realized in the experiment. This example also explains some parameter scaling features of the measurement data.

We turn the generic coupled current and ripple voltage

Copyright © 2012 by the respective authors — cc Creative Commons Attribution 3.0 (CC BY 3.0)

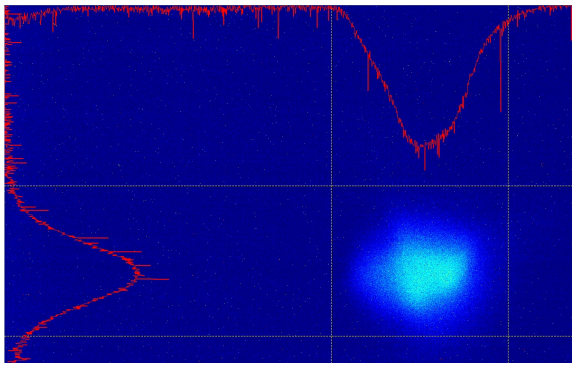

Figure 3: OTR image and axis intensity profiles. Photographed from CTR-1 with a macro lens of 1:1 magnification.

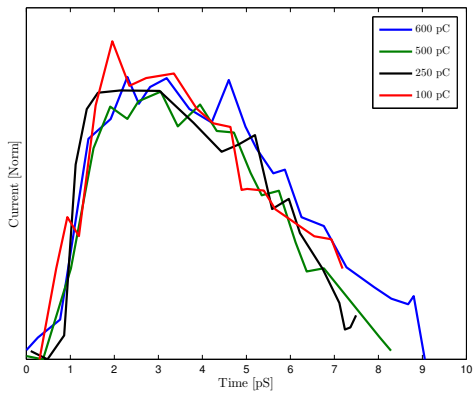

Figure 4: Temporal pulse profile of the e-beam bunch at different bunch charge levels. Pulse duration was approximately 5 pS for all experiments.

equations (1) and (2) into explicit equations in z by substituting $\frac{d}{d\phi_p} = \left(\frac{d\phi_p}{dz}\right)^{-1}\frac{d}{dz} = \frac{1}{\phi_{pr}(z)}\frac{d}{dz}$ and $W(z) = r_p^2/\omega\epsilon_0 A_e(z)\theta_p(z)$:

$$\frac{d}{dz}\breve{i}(z,\omega) = -i\omega\epsilon_0 A_e(z)\theta_p^2(z)\breve{v}(z,\omega) \tag{5}$$

$$\frac{d}{dz}\breve{v}(z,\omega) = -\frac{ir_p^2}{\omega\epsilon_0 A_e(z)}\breve{i}(z,\omega) \tag{6}$$

where $\theta_p^2(z) = eZ_0 I_0/mc^2 A_e(z)\gamma_0^3\beta_0^3$.

This set of equations can be solved explicitly numerically if $A_e(z) = 2\pi\sigma_x(z)\sigma_y(z)$ is given, and the initial conditions $\breve{i}(0,\omega), \breve{v}(0,\omega)$ are specified, and the solution at the end of the drift section L is a linear combination of the initial conditions: $\breve{i}(L,\omega) = A(L)\breve{i}(0,\omega) + B(L)\breve{v}(0,\omega)$. Assuming that the current modulation noise and the focusing enhanced velocity noise are uncorrelated at $z = 0$, we set

$$\overline{|\breve{i}(L,\omega)|^2} = |A(L)|^2\overline{|\breve{i}(0,\omega)|^2} + |B(L)|^2\overline{|\breve{v}(0,\omega)|^2} \tag{7}$$

$$\overline{|\breve{i}(0,\omega)|^2} = eI_b \tag{8}$$

$$\overline{|\breve{v}(L,\omega)|^2} = \left(\frac{mc^2}{e}\gamma_0\beta_0\right)^2\frac{e}{I_0}\sigma_{\beta z}^2 \tag{9}$$

To compute the noise evolution for the parameters of the reported experiment it is necessary to estimate the cross section dimensions $\sigma_x(z), \sigma_y(z)$ along the interaction length. This was done based on the measurements on screens YAG-1 to YAG-4, the recorded quad excitation parameters, and performing full 3-D simulation (with space-charge) using GPT.

The beam axial velocity spread due to energy spread ($\Delta E \simeq 3KeV$) is small, and its effect on the initial velocity noise is negligible. We assume that the initial velocity noise is determined by the standard deviation of the axial velocity spread (equation (9)), which was calculated for each quad setting from the angular spread standard deviations due to the focusing and emittance ($\epsilon_x, \epsilon_y \sim 2-5\mu m$):

$$\sigma_{\beta z} = \frac{1}{4}(\sigma_{\beta x}^2 + \sigma_{\beta y}^2) \tag{10}$$

The coefficients $A(z = L), B(z = L)$ were computed by

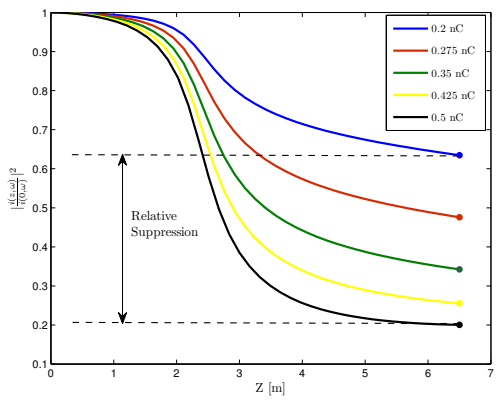

Figure 5: Noise suppression along the collective interaction region as calculated from solution of the coupled differential equations with $\sigma_x(z)$, $\sigma_y(z)$ of 70 MeV.

iterative integration of the coupled linear differential equations (5 and 6) with the initial conditions ((9)). In Figures 5 and 6 we display the results of the model computation of the variable parameters differential equations. The curves show the noise suppression as function of length and of the beam current for the two extreme energy cases E=50 MeV, 70 MeV. The relative suppression factor in the range Q_b=0.2-0.5nC at the drift section exit $L = 6.5m$ is displayed in Fig.() for the two beam-energy examples. Figure 7 can only be regarded as a model explanation for the reduced relative noise suppression effect observed in the experiment. As mentioned, there can be additional factors

Copyright © 2012 by the respective authors — cc Creative Commons Attribution 3.0 (CC BY 3.0)

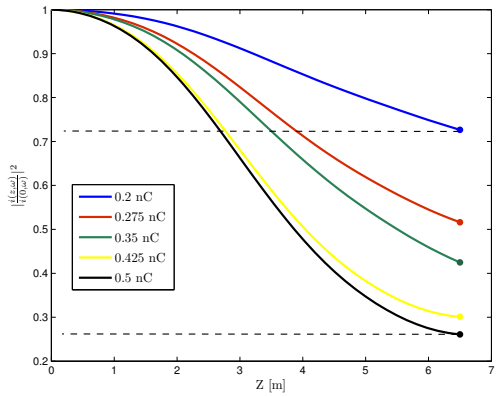

Figure 6: Noise suppression along the collective interaction region as calculated from solution of the coupled differential equations with $\sigma_x(z)$, $\sigma_y(z)$ of 50 MeV.

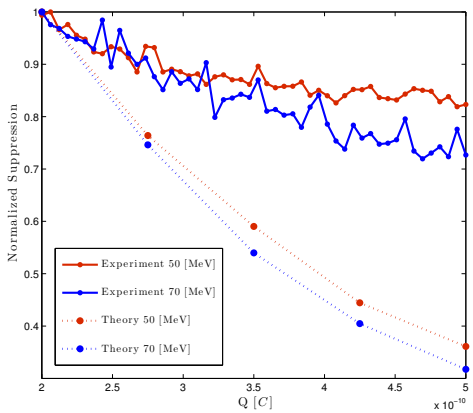

Figure 7: Relative noise suppression rate computed from Eq. 5 and 6 for E=50 MeV, 70 MeV compared to the experimental suppression results.

affecting the suppression rate. It is noted that the computed curves display significantly larger relative suppression in the range Q_b=0.2-0.5nC than the experimental curves, but in either case there is only little dependence on the acceleration energy. In the simple uniform beam model one would expect dependence of the noise suppression factor on the beam energy due to the $3/2$ power dependence of the plasma frequency on γ, which corresponds to smaller plasma phase accumulation at higher beam energy. However, the beam envelope had to be varied in the experiment in different beam energies, and one must keep in mind, that at the higher energy the beam focuses into a tighter waist due to the reduced space charge effect. This tends then to increase the plasma frequency at the waist, where most of the microdynamic process takes place.

This observation is consistent with the point of view that the beam envelope expansion and the beam charge homogenization process are in essence the same process of excess charge beam expansion when viewed in the beam rest frame (independent of the acceleration energy). This is consistent with the plasma phase accumulation theorem of constant plasma phase accumulation in a space charge dominated beam waist [3]. This provides qualitative physical explanation for the weak dependence of the relative noise suppression on the beam energy in the 50-70 MeV range, as depicted in both the experimental (figure 2) and model calculation (figure 7) curves.

REFERENCES

[1] A. Gover, A. Nause, E. Dyunin, Beating the shot-noise limit, Nature Physics, doi:10.1038/nphys2443.

[2] Dicke, R. H., "Coherence in Spontaneous Radiation Processes", Phys. Rev. 93 99–110 (1954).

[3] A. Gover, E. Dyunin, Collective-Interaction Control and Reduction of Optical Frequency Shot Noise in Charged-Particle Beams, Phys. Rev. Lett. 102, 15 (2009).

[4] A. Nause, E. Dyunin, "Optical frequency shot-noise suppression in electron beams: Three-dimensional analysis", Journal of App. Phys. 107, 103101 (2010).

[5] D. Ratner et el, "Observation of Shot Noise Suppression at Optical Wavelengths in a Relativistic Electron Beam", Phys. Rev Lett. 109, 3 (2012).

[6] Loos, H. and et al, "Observation of coherent optical transition radiation in the LCLS linac", Proceedings of the 2008 Free-Electron Laser Conference (Gyeongju, Korea).

[7] A. Gover, T. Duchovni, E. Dyunin, A.Nause, "Collective microdynamics and noise suppression in dispersive electron beam transport", Physics of Plasmas 18 123102, (2011).

Copyright © 2012 by the respective authors — cc Creative Commons Attribution 3.0 (CC BY 3.0)

STATUS OF CH CAVITY AND SOLENOID DESIGN OF THE 17 MeV INJECTOR FOR MYRRHA*

D. Mäder†, H. Klein, H. Podlech, U. Ratzinger,
C. Zhang, IAP, Goethe-Universität, Frankfurt am Main, Germany

Abstract

The multifunctional subcritical reactor MYRRHA (**M**ulti-purpose h**y**brid **r**esearch **r**eactor for **h**igh-tech **a**pplications) will be an accelerator driven system (ADS) located in Mol (Belgium). The first accelerating section up to 17 MeV is operated at 176 MHz and consists of a 4-rod-RFQ followed by two room temperature CH cavities with intertank quadrupole triplet focusing and four superconducting CH structures with intertank solenoids. Each room temperature CH cavity provides about 1 MV effective voltage gain using less than 30 kW of RF power. The superconducting resonators have been optimized for electric peak fields below 30 MV/m and magnetic peak fields below 30 mT. For save operation of the superconducting resonators the magnetic field of the intertank solenoids has to be shielded towards the CH cavity walls. Different coil geometries have been compared to find the ideal solenoid layout.

INTRODUCTION

Transmutation of long-lived radioactive waste and advanced technologies for future power generation will be investigated with the MYRRHA ADS [1]. The IAP of Frankfurt University is responsible for the development of the 17 MeV injector, a 13 meter long front end of the 600 MeV MYRRHA linac. To achieve the extremely high reliability of the beam supply for the reactor, two injectors will be driven at the same time. With this parallel redundancy the beam can be provided even during a failure of one injector. Because of thermal stress in the reactor not more than 11 beam trips of $t > 3s$ per year are allowed. The following accelerating structures up to 60 MeV are using the concept of serial redundancy [2].

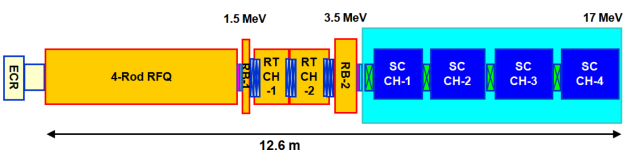

Figure 1: Overview of the MYRRHA injector.

A 4-rod-RFQ will bunch and accelerate the proton beam up to 1.5 MeV [3]. After a five gap CH rebuncher the proton bunches will be accelerated to 3.5 MeV with room temperature CH structures. Quadrupol triplets for focusing and phase probes for diagnostics are placed between the structures. 3 MV/m will be provided by the superconducing accelerators. Four bulk niobium CH cavities are assembled together with four 4.5 Tesla solenoids with coils made of NbTi in one cryomodule [Figure 1].

CH CAVITY DESIGN

Crossbar H-mode (CH) cavities are excellent candidates for acceleration of ions in the low and medium energy range. These resonators driven in the TE_{211}-Mode will be used for all accelerating and rebunching cavities after the 4-rod-RFQ from 1.5 to 17 MeV.

Room temperature CH cavities

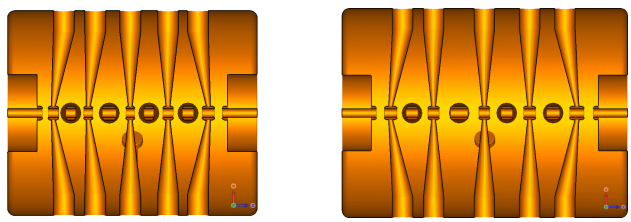

Figure 2: Scheme of the two room temperature CH structures.

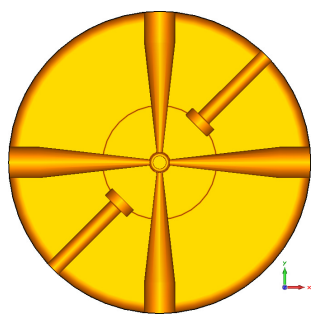

Figure 3: The diagonal tuners act mainly capacatively and provide a total frequency shift of 1 MHz.

CH-1 consists of three and CH-2 of two inclined stems [Figure 2]. Together with the extra volume around the vaults the inclination of the stems increases the induction on the outer stems. This flattens the gap voltage distribution and consequently the thermal load on the stems. The vaults at the resonator ends create additional space outside the cavity and are used for the quadrupole triplet lenses.

Each CH structure is tuned by two mainly capacitively acting tuners that provide a total frequency shift of 1 MHz.

* Work supported by the EU, FP7 MAX contract number 269565
† d.maeder@iap.uni-frankfurt.de

Copyright © 2012 by the respective authors — cc Creative Commons Attribution 3.0 (CC BY 3.0)

The tuners are mounted on the cavity wall under 45 degree to the horizontal plane [Figure 3].

Table 1: Parameter list of the room temperature CH-1 and CH-2 of MAX.

Parameter	RT CH-1	RT CH-2
Frequency [MHz]	176	176
Q-Factor (85% MWS)	14539	14964
P_{sim} [kW]	16.5	18.5
P_{real} (85% MWS) [kW]	19.4	21.8
$Z_a(\beta\lambda - def.)$ [MΩ/m]	113.5	100.6
U_0 [MV]	1.26	1.37
U_a [MV]	1.03	1.14
β_{avg}	0.066	0.077
No. of Gaps	10	10
Energy Range [MeV]	1.5 – 2.5	2.5 – 3.5
$E_a(\beta\lambda - def.)$ [MV/m]	1.8	1.6
L [mm]	715.2	833.6
$L(\beta\lambda - def.)$ [mm]	568.7	699.3
Diameter [mm]	584	608
Aperture [mm]	25	25

Superconducting CH cavities

One cryo-module will contain all cold parts of the injector. For manufacturing and transportation reasons the superconducting CH structures are not longer than 1.2 m. For this reason the number of gaps decreases with higher β_{avg} from 10 to 7.

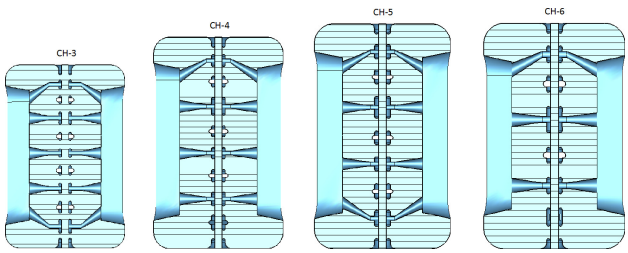

Figure 4: The four superconducting CH cavities in scale relatively to each other.

All superconducting cavities will be made of bulk Niobium and are optimised for an acceleration gradient between 3.5 and 3.9 MV/m and for a flat electric peak field distribution along the gaps. Low electric peak surface fields below 30 MV/m minimise the risk of quenching and ensure a safe operation [Table 2].

SC SOLENOID DESIGN

Superconducting solenoids driven at a maximum magnetic field of 4.5 T are used in the cold part of the injector for transversal focusing. The current densitiy of 300 A/mm^2 in the main coil is ten times smaller than the critical current density, where the solenoid is quenching [4].

Four superconducting solenoids of the same type will be placed between the accelerating cavities. The main coil

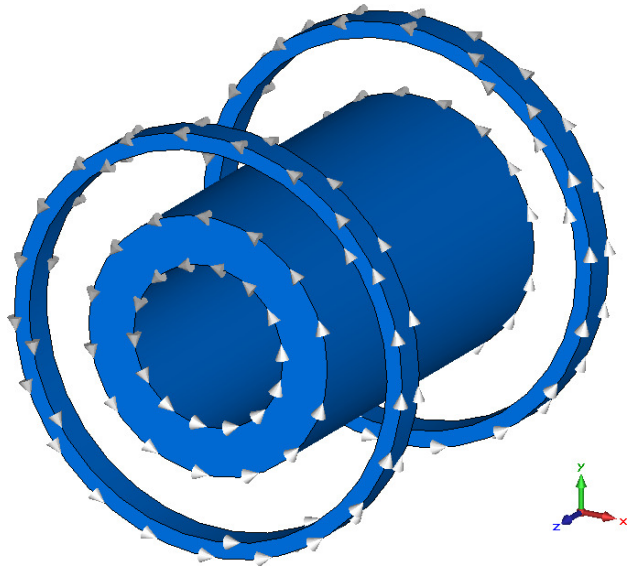

Figure 5: Main and bucking coils of the superconducting solenoid.

of the solenoid is 120 mm long and has 4300 windings of Niobium-Titanium in a copper matrix. To avoid quenching of the neighbouring accelerators the magnetic field of the solenoid has to be reduced. Two bucking coils with 420 windings at the ends of the main coil [Figure 5] minimise the fringe field [Figure 6 and 7]. All multi-filamentary superconducting wires in the solenoid can carry a total current of 120 A.

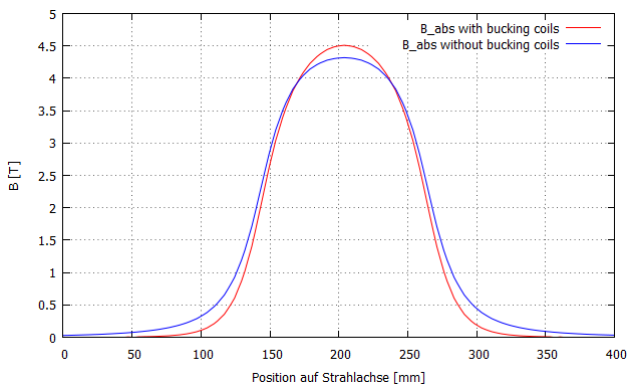

Figure 6: A solenoid with bucking coils has a lower fringe field in comparison with a simple solenoid. Both solenoids are normalized to the same focusing strength.

OUTLOOK

The new tuning concept of superconducting CH structures with static and dynamic tuners on the girders between the stems will be applied for the four sc injector cavities for MAX after a successful demonstration of this concept with a 325 MHz cavity at IAP [5].

The effects of the solenoids fringe field on the CH cavity are under investigation. Further simulations to shield the magnetic flux are necessary.

Copyright © 2012 by the respective authors — cc Creative Commons Attribution 3.0 (CC BY 3.0)

Table 2: Parameter list of the superconducting CH-3 to CH-6 of MAX.

Parameter	SC CH-3	SC CH-4	SC CH-5	SC CH-6
Frequency [MHz]	176	176	176	176
U_0 [MV]	4.25	4.72	4.93	4.78
U_a [MV]	3.50	3.98	4.18	4.09
β_{avg}	0.102	0.131	0.157	0.178
No. of Gaps	10	9	8	7
Energy Range [MeV]	3.5 – 6.7	6.7 – 10.4	10.4 – 14.2	14.2 – 17
$E_a(\beta\lambda - def.)$ [MV/m]	3.9	3.7	3.6	3.5
Geometry Factor [Ω]	62.6	67.6	70.2	73.2
$R_0/Q_0[\Omega]$	2216	2165	1817	1577
$R_0R_S[\Omega^2]$	138849	146345	127558	115473
E_{max} [MV/m]	29.27	28.06	30.59	28.92
$B_{max}[mT]$	27.8	29.7	35.27	31.35
E_{max}/E_a	7.5	7.6	8.5	8.3
L [mm]	915.9	1075.3	1129.0	1126.9
L $\beta\lambda - def.$ [mm]	901.1	1071.1	1162.1	1178.8
Diameter [mm]	600	650	684	708
Aperture [mm]	30	30	40	40

Additional measurements with a test solenoid close to a CH structure at 4.2K will be performed together with GSI in the demonstrator experiment [6]. A main focus in this layout is to put on high safety margins to reach the specified reliability.

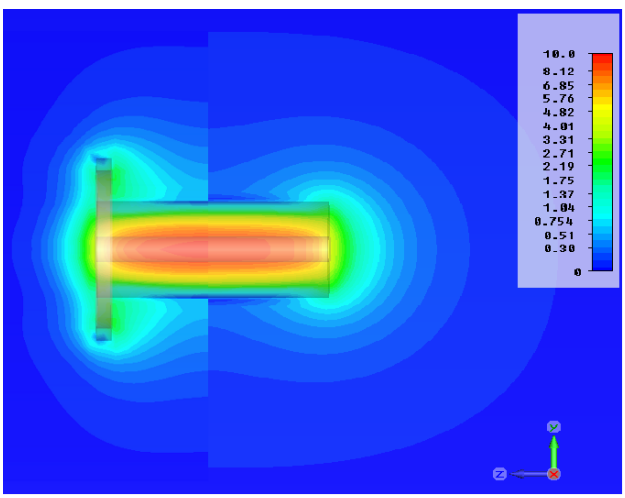

Figure 7: In this graphic two pictures with the magentic flux of a solenoid are merged. On the left side the solenoid with bucking coils is shown. The simple solenoid without bucking coils on the right side creates more spacious magnetic flux. The coloured scale is normalized to the highest field level of the left solenoid (4.5T). Both solenoids would have the same focusing strength, so the simple solenoid would have a less peak field (compare with figure 5).

ACKNOWLEDGEMENTS

This work has been supported by the EU (FP7 MAX contract number 269565).

REFERENCES

[1] J.-L. Biarrotte, A.C. Mueller, H. Klein, P. Pierini, D. Vandeplassche, "Accelerator reference design for the MYRRHA European ADS demonstrator", LINAC2010, Tsukuba, Japan, September 2010, p. 440-442

[2] D. Vandeplassche, J.-L. Biarrotte, H. Klein, H. Podlech, "The MYRRHA Linear Accelerator", IPAC2011, San Sebastian, Spain, September 2011, p. 2718-2720

[3] M. Vossberg, H. Klein, H. Podlech, A. Schempp, A. Bechtold, "4-rod-RFQ for MYRRHA", this proceedings, Paper ID:THPB047.

[4] A. Chao, "Handbook of Accelerator Physics and Engineering", World Scientific Publishing Co Pte Ltd, 1999

[5] M. Busch, F. Dziuba, H. Podlech, U. Ratzinger, W. Barth, S. Mickat, M.Amberg , M. Pekeler , "First Measurements on the 325 MHz Superconducting CH-Cavity", this proceedings, Paper ID: TUPB071

[6] F. Dziuba, M. Amberg, K. Aulenbacher, W. Barth, M. Busch, H. Podlech, U. Ratzinger, S. Mickat, "Status of the Superconducting cw Demonstrator for GSI", this proceedings, Paper ID: TUPB072

Copyright © 2012 by the respective authors — cc Creative Commons Attribution 3.0 (CC BY 3.0)

THE BEAM COMMISSIONING PLAN OF INJECTOR II IN C-ADS*

Z.J. Wang, Y. He, H. Jia, S.H. Liu, C. Li, X.B. Xu, B. Zhang,
W. Wu, H.W. Zhao IMP, Lanzhou,730000,China

Abstract

The design work of the Injector II, which is 10 MeV proton linac, in C-ADS project is being finished and some key hard wares are being fabricated. Now it is necessary to definite the operation mode of beam commissioning, including the selection of the beam current, pulse length and repetition frequency. Also the beam commissions plan should be specified. The beam commissions procedures is simulated with t-mode code GPT [1]. In this paper, the general beam commissioning plan of Injector II in C-ADS and simulation results of commissions procedures are presented.

INTRODUCTION

Nuclear energy as a kind of clean energy will be widely used in Chinese energy program in the future. But one of the serious problems is how to handle radioactive waste produced by nuclear plants. ADS, which is the effective tool for transmuting the long-lived transuranic radionuclides into shorter-lived radionuclides, is being studied in the Chinese Academy of Sciences. The road map of the project is shown in Fig. 1.

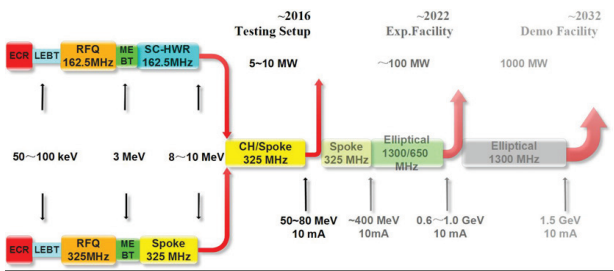

Figure 1: The roadmap of China CAS.

The linac will accelerate the proton with beam current 10mA to about 1.5GeV to produce high flux neutrons for transmutation of nuclear waste.

To ensure technical feasibility in the low energy section, two injectors for the superconduction linac are studded during the first step. One of the injectors, that is Injector II, is been designed and fabricated at Institute of Modern Physics of the Chinese Academy of Sciences.Injector II as part of the ADS is being designed and built at IMP. Injector II is composed of Low Energy Beam transport Line(LEBT), Radio Frequency Quadrupole(RFQ), Medium Energy Beam transport Line(MEBT) and the SC accelerating section. The layout of Injector II is shown in Fig. 2.The LEBT will match the proton beam with 0.035MeV from the ECR source to the RFQ by two solenoids. The RFQ will accelerate and focus the beam from 0.035 MeV to 2.1 MeV simultaneously. The MEBT has two main functions, which are to match the proton beam from the RFQ to the superconducting accelerating section and to place some on line beam diagnostics devices. The superconducting accelerating section will accelerate proton from 2.1 MeV to 10 MeV with 16 superconducting half wave resonator(HWR) cavities. .

The basic parameters of Injector II are listed in Table. 1.

Table 1: The basic parameters of injector II.

Parameters	Value
Particle type	Proton
Operation frequency(MHz)	162.5
Operation mode	CW
Input beam energy(MeV)	0.035
Output beam energy(MeV)	10
Beam current(mA)	10

In this paper, the general beam commissioning plan of Injector II in C-ADS and simulation results of commissions procedures are presented.

THE BEAM DYNAMICS OF INJECTOR II

The MEBT and superconducting section are simulated by TRACK code. The particles distribution out from the RFQ [2] are transported as the initial distribution of the downstream lianc.

The results of the simulation with three-D field map are shown in Fig. 3. The RMS envelopes in both transverse and longitudinal direction are smooth and periodic in the superconducting section. This depicts that there is good matching between MEBT and the superconducting section.

COMMISSIONS BEAMS OF INJECTOR II

The commissions beams will be chopped for the commissioning of RFQ at first stage, then we plan to use unchopped beam for the bulk of the superconducting section commissioning studies. The beam will be consistent with the beam-handing capabilities of the beam diagnostics system in use at the time.

Beam current

The 0.5mA peak current beam will be chosen to be as the initial commissioning study. The reason is we want to reduce the space charge effect as weak as possible to simply the initial commissioning. At the same time the low limitation of measurement dynamics range of the beam diagnostics device should be considered. Also the low current is

* Supported by the National Natural Science Foundation of China (Grant No.11079001)

Copyright © 2012 by the respective authors — cc Creative Commons Attribution 3.0 (CC BY 3.0)

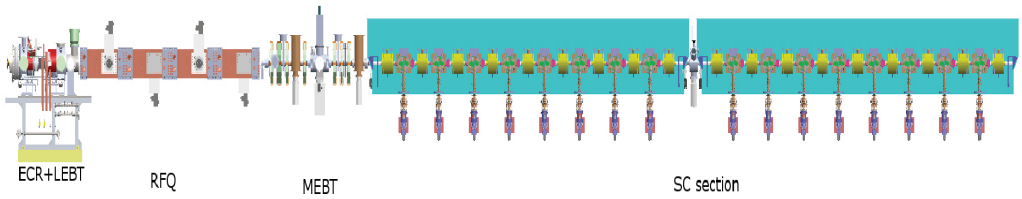

Figure 2: The layout of C-ADS Injector II .

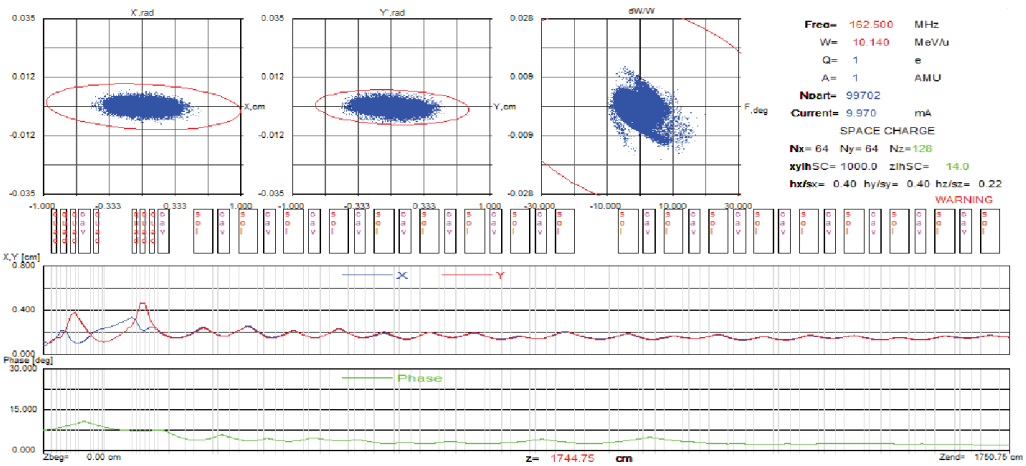

Figure 3: The simulation results of MEBT and the superconducting section.

chosen to minimize dose and activation during initial commissioning. Once the initial linac setup is done, we will increase the current to 1mA, 5mA and finally 10mA.

Pulse length

The pulse length will be set by two factors. One is the limitation of the diagnostics system. The other factor is the machine protect. At the beam commissions stage, the beam will lost on the accelerator element probably. To determine the pulse length, the time dominant code GPT is used to simulated the beam loss in superducting section, which is shown in Fig. 4. . In the Fig.4, the beam loss power distribution is shown supposing the first cavity is broken down. The maximum beam power is 1100W/m. To prevent the quench of superconducting cavity caused by lost beam, the pulse length of commissions at 10mA should be less than 100us.

Repetition rate

The beam commissioning of RFQ will be carried out at repetition rate equal or less that the repetition rate of RFQ RF power supply. Because the energy out from RFQ is 2.1MeV, the radiation activation will be not an issue. For the commissioning of superconducting section, low repetition rate 1Hz will be as initial commissioning beam. ”Beam on demand” mode will be used whenever possible and appropriate in order to minimize activation and thermal damage of the hardware by high energy and high power beam.

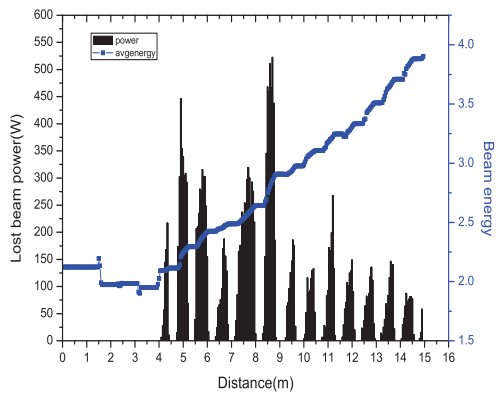

Figure 4: The lost beam power distribution when the first cavity breaks down at 10mA.

THE BEAM COMMISSIONS PLAN OF THE INJECTOR II

In InjectorII, two key sections are RFQ and superducting section. In this paper, the beam commissions plans about this two section are stated. The goal of beam commissions is CW mode at 100KW beam power. An beam dumper will be installed at the end of adjustable HEBT, which will deliver beam with different energy to the beam dumper at different stage.

Copyright © 2012 by the respective authors — cc Creative Commons Attribution 3.0 (CC BY 3.0)

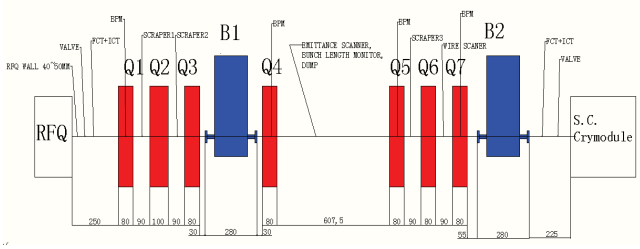

Figure 5: Layout of beam diagnostics in MEBT.

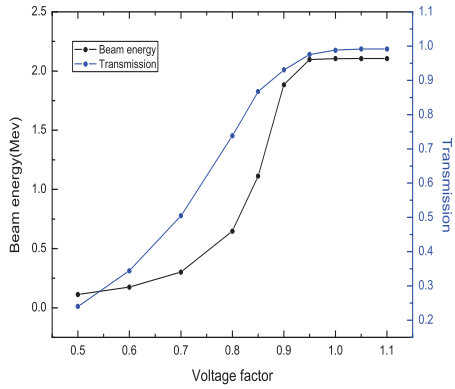

Figure 6: The relation of cavity voltage factor with beam power and transmission.

RFQ and MEBT

The RFQ section will be installed with MEBT at the same time. There are kinds of diagnostics equipments installed at MEBT as shown in Fig. 5. As shown in Fig.5, two sets ICT and FCT are located at the entrance and exit of MEBT to measure the transmission of the RFQ. Also there are other diagnostics equipments to measure the information of beam out from the RFQ, such as emittance, beam halo.

The InjectorII RFQ is designed to accelerated proton beam to 2.1MeV with code PARMTEQ-M [3]. The beam dynamics of RFQ is benchmarked with code TRACK. One of the importance processes of beam commissioning of RFQ is finding the RF operation point by comparing the calculation and experimental results of beam transmission. The simulation results for the beam transmission is given in Fig. 6.

The blue line means the beam transmission rate as a function of the voltage factor, and the black line means output energy evolution with voltage factor. The rehalation can give us an guide in the real beam commissioning experiment.

The superconducting section

For the superconducting section, there are 16 focusing period and one BPM in each period. The BPMs can be used in both transverse orbit correction and RF operation point setting. The RF operation point setting is an main process

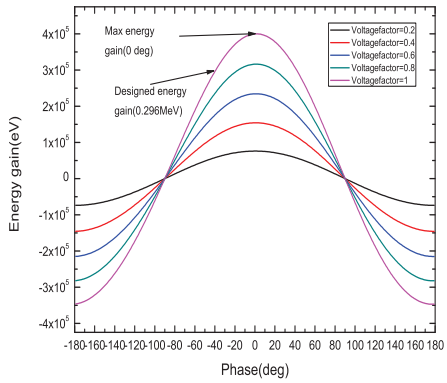

Figure 7: The energy gain of first cavity varying with voltage factor.

in beam commissioning. In the tuning of superconducting cavity, first step is to find the synchronous phase. This can be performed by rotating the phase at low accelerating voltage(150-200KV). Two BPMs down stream are used to find the maximum energy increase, which is correspond to zero degree, and then setting the phase to the designed synchronous phase. Second step is to set the amplitude of field, which can be determined by the beam energy out from the cavity. The beam energy variation with the phase is plotted in the Fig. 7. As shown in Fig.7, maximum energy gain correspond to zero degree, the synchronous phase can be find through this way.

SUMMARY

The installation of Injector II of CADS project will start at the beginning of 2013. the commissioning consists of two main stages, RFQ and superconducting section, is scheduled for 2013. The beam commissioning goal is the proton beam power of 100KW for CW 10MeV out from Injector II. The commissioning beam will begin with peak current 0.5mA, pulse length 100us and repetition rate 1Hz.

REFERENCES

[1] http://www.pulsar.nl/gpt/

[2] P.N. Ostroumov, V.N. Aseev, B. Mustapha, TRACK - a Code for Beam Dynamics Simulation in Accelerators and Transport Lines with 3D Electric and Magnetic Fields, 2007. http://www.phy.anl.gov/atlas/TRACK/Trackv37/Manuals/tv37_man_index.html

[3] K. R. Crandall et al., RFQ Design Codes, Los Alamos National Laboratory report LA-UR-96-1836

Copyright © 2012 by the respective authors — cc Creative Commons Attribution 3.0 (CC BY 3.0)

RF SETUP OF THE MedAustron RFQ*

B. Koubek, J. Schmidt, A. Schempp, IAP, Goethe University, Frankfurt am Main, Germany
J. Haeuser, Kress GmbH, Biebergemuend, Germany

Abstract

A Radio Frequency Quadrupole (RFQ) was built for the injector of the cancer treatment facility MedAuston in Austria [1]. For the RF design simulations were performed using CST Microwave Studio® and the structure was manufactured by Firma Kress in Biebergemuend, Germany. The simulations and the RF setup of the delivered RFQ are presented in this paper.

INTRODUCTION

The 216.8 MHz MedAustron RFQ was designed to accelerate protons and carbon ions from 8 keV to 400 keV [2] on an electrode length of 1.25 m. It is a state of the art 4-Rod RFQ with quite slim electrodes and newly developed connections of the stems to the electrodes. Usually clamps were used to fix the electrodes to the stems (see Fig. 2). The accuracy of the machining allows us to remove the clamps. Simulations have shown that these new connections are causing less capacitance and hence less disturbing electric field than the clamps.
Fig. 1 shows the RFQ during its preparation at the Institute of Applied Physics (IAP) in Frankfurt am Main. More details about the RFQ basic design parameter can be found in Table 1.

Table 1: Design Parameters of the MedAustron RFQ

Parameter	Value	
Frequency	216.612	MHz
Input Energy	8	keV
Output Energy	400	keV
Beam Current (max)	4	mA
Aperture (min)	2	mm
Modulation Factor (max)	2	
Electrode Length	1250	mm
Intervane Voltage	70	kV
RF Cells	15	
Beam Height in Tank	19.5	mm
Stem Thickness	20	mm
Stem Distance	68	mm
Tank Length	1233	mm
Wall Thickness	40	mm

SIMULATIONS

Simulations have been performed using CST Microwave Studio® for the RF design. During this process two different shapes of the backside of the electrodes have been investigated. One is a broad and the other one a more narrow socket of the electrodes backside. A top view of the two different shapes is shown in Fig. 2.

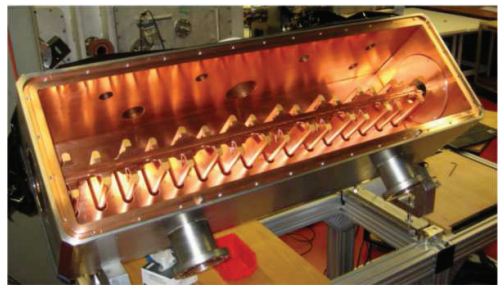

Figure 1: RFQ during preparation at IAP.

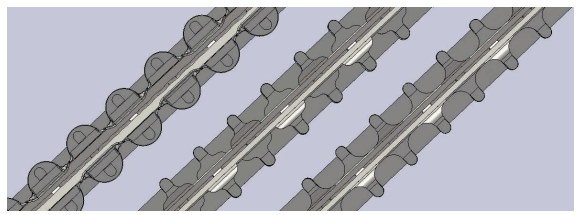

Figure 2: Former clamps (left), new broad (middle) and narrow (right) sockets.

Both shapes are rising the resonance frequency due to less capacitance compared to the old design with clamps. The broad shape increases frequency about one MHz more than the slim one, it shows less inductance and provides a fast and homogenous charge distribution on the electrode tips. Further informations about the RF characteristics of the connections of the electrodes can be found in [3].

MEASUREMENTS AND TUNING

Geometric Measurements

The accuracy of the machining and assembling of the single parts have been checked with a 3-D measurement device. The angle and the distance of the stems, the angle of the electrodes to each other and the position of the beam axis relatively to the reference surfaces have been measured. The measurements have met our expectations. Also no significant longitudinal electrode shift could be measured. Fig. 3 shows the measurement of the angle of the electrodes to each other and the longitudinal shift of the electrodes.

* Work supported by BMBF

Copyright © 2012 by the respective authors — cc Creative Commons Attribution 3.0 (CC BY 3.0)

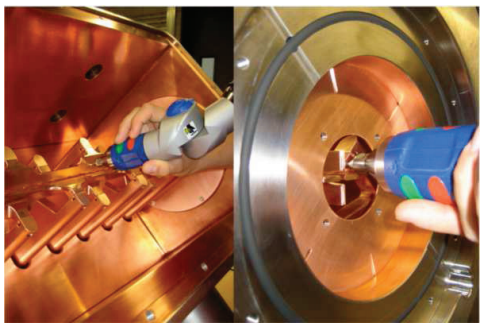

Figure 3: Measurements of the angle and the longitudinal shift of the electrodes using a 3-D measurement device.

RF SETUP

The frequency and flatness tuning have been executed in one procedure. First without the piston tuner to analyse the RF behavior of the RFQ. Later the final tuning was made with the inserted piston tuner on its zero position.
After investigation of the single influence of the tuning blocks, the piston tuner and the input power coupler on frequency and flatness, all the parts together have been adjusted and tuned. The tuning blocks have been fixed with silver screws on individual distance parts made of copper. The whole procedure is very similar to the tuning of the FNAL RFQ described in [4].

Flatness

For operation a homogenous longitudinal voltage distribution (flatness) of the electrodes is required according to the beam dynamics design. By changing the height of the tuning blocks the frequency of the RFQ and the local eigenfrequency of a single cell can be adjusted. Hence an uneven voltage distribution, caused by the modulation of the electrodes or inaccuracies by manufacturing of the RFQ, can be adjusted. The typical banana shaped flatness of the untuned MedAustron RFQ is shown in Fig. 4. It has an unflatness of about ±10 %.

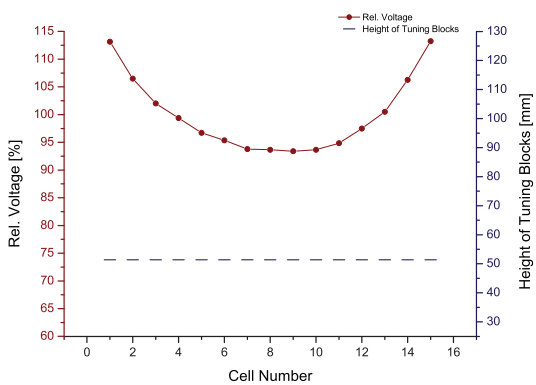

Figure 4: Untuned flatness with equal heights of the tuning blocks.

The flatness tuning is an iterative process to get an equal voltage distribution along the electrodes [5]. Each RF-cell is detuned using a perturbation capacitor (see Fig. 5). From the detuned RF-cell one can calculate the longitudinal voltage distribution of the electrodes. After this a next guess of the tuning block distribution can be made to improve the flatness.

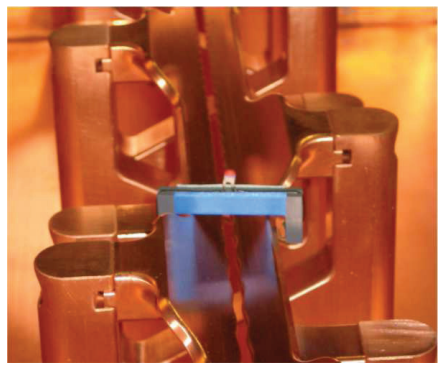

Figure 5: Pertubation capacitor used to detune each cell of the RFQ.

Piston Tuner

The frequency of the RFQ can change under operation due to several reasons. To correct the frequency a piston tuner is used. It has an influence on the resonance frequency by suppressing the magnetic field [6], but it is changing the flatness as well. If the flatness is not adjusted with an inserted tuner it may decrease of about ± 0.8 %. The piston tuner is placed in the middle of the cavity, its influence on the frequency is shown in Fig. 6.

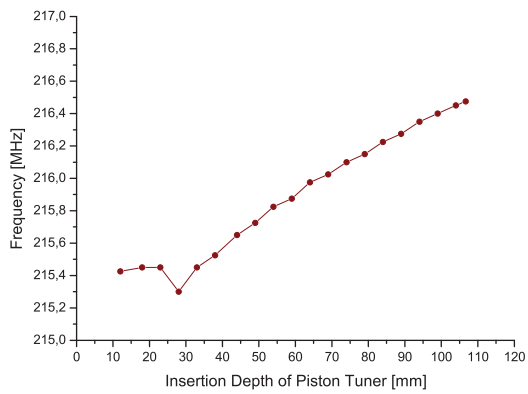

Figure 6: Frequency shift due to the piston tuner.

One can see that the insertion depth of the piston tuner has an almost linear influence on the resonance frequency of the RFQ. Before it enters the RF-cell between the stems it has only weak influence on the frequency. Then there is a small region where it disturbs the resonance of

Copyright © 2012 by the respective authors — cc Creative Commons Attribution 3.0 (CC BY 3.0)

the structure. This means one has to regard a minimum insertion depth of the piston tuner. When it enters the RF-cell between the stems it rises the frequency with its depth with an approximately linear behavior.

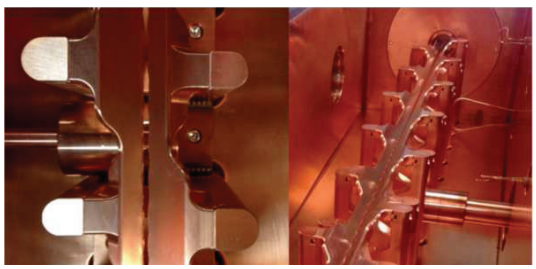

Figure 7: Top and side view of the piston tuner.

RESULTS

After the tuning process the resonance frequency was adjusted to 216.6 MHz with a deviation of the longitudinal voltage distribution of ± 1.7 %. This flatness with its distribution of the tuning blocks is shown in Fig. 8.

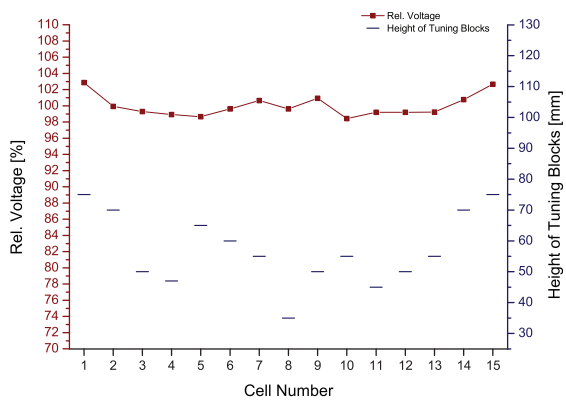

Figure 8: Final flatness and distribution of the tuning blocks.

Finally the piston tuner has been set to be able to adjust the frequency from minimum of 216.4 MHz to maximum 216.9 MHz. This values might rise about 0.1 MHz under vacuum. The overall shift of the piston tuner is about 0.5 MHz. The power coupler has a reflection of -27 dB.
The shuntipedance measured with an perturbation capacitor was 92 kΩm. The RF parameter of the MedAustron RFQ are summerized in Table 2. Overall the tuning process took several weeks and has led to quite satisfactoring results.

Table 2: RF Parameters of the MedAustron RFQ

Parameter	Value	
Frequency	216.612	MHz
Quality Factor Q_0	3600	
Voltage Distribution	± 1.7	%
Shunt Impedance	92.57	kΩm
Reflection Power Coupler	-27	dB
Transmission Pickup 1	-40	dB
Transmission Pickup 2	-39	dB
Transmission Pickup 3	20	dB

OUTLOOK

The MedAustron RFQ has been delivered at the end of July 2012. The ion source, the low energy beam transfer line and the RFQ will be commissioned at the Injector Test Stand (ITS) at CERN [7]. The test stand provides the possibility to prepare the LEBT independently from civil engineering in Austria. As soon as the building is ready the LEBT can move to Wiener Neusadt for commissioning and start of operation [8].

REFERENCES

[1] U. Dorda, A. Fabich, F. Osmic, M. Benedikt, "STATUS OF THE MEDAUSTRON ION BEAM THERAPY CENTRE", IPAC2012, New Orleans, Louisiana, USA

[2] Michael Bededikt, Johannes Gutleber, Marcus Palm, Werner Pirkl, Ulrich Dorda, Adrian Fabich, "OVERVIEW OF THE MedAustron DESIGN AND TECHNOLOGY CHOICES", IPAC2010, Kyoto, Japan

[3] B. Koubek, J. Schmidt, A. Schempp, L. Groening, "RF-DESIGN OF A 325 MHz 4-ROD RFQ", IPAC'11, San Sebastin, Spain

[4] J. Schmidt, B. Koubek, A. Schempp, "TUNING OF THE NEW 4-ROD RFQ FOR FNAL", PAC 2011, NYC, USA

[5] J. Schmidt, B. Koubek, A. Schempp, "TUNING STUDIES ON 4-ROD-RFQs", PAC 2011, NYC, USA

[6] A. Schempp, L. Brendel, B. Hofmann, H. Liebermann, "Tuner Design for High Power 4-Rod-RFQs", LINAC 2004, Luebeck, Germany

[7] F. Osmic, M. Feurstein, A. Gyorgy, A. Kerschbaum, M. Repovz, S. Schwarz, G. Burtin, "OVERVIEW OF THE BEAM DIAGNOSTICS IN THE MEDAUSTRON ACCELERATOR: DESIGN CHOICES AND TEST BEAM COMMISSIONING", IPAC2012, New Orleans, Louisiana, USA

[8] Adrian Fabich on behalf of Michael Benedikt, "MedAustron - the Austrian Ion Therapy and Research Center", CAS lecture 1st June 2012, Senec, Slovakia

Copyright © 2012 by the respective authors — cc Creative Commons Attribution 3.0 (CC BY 3.0)

PRODUCTION AND QUALITY CONTROL OF THE FIRST MODULES OF IFMIF-EVEDA RFQ

F. Scantamburlo, A. Pepato, R. Dima, INFN/PD, Padova, Italy,
C. Roncolato INFN/L.N.L., Legnaro, Italy

Abstract

The IFMIF/EVEDA RFQ, designed to accelerate a 125mA D+ beam from 0.1 MeV to 5 MeV at a frequency of 175 MHz, consists of 18 modules with length of ~550 mm each. The production of the modules has been started and 2 prototype modules plus module 16 have undergone all the production steps, including precision milling and brazing. The progress of the construction and especially the fine tuning of the design and engineering phase are reported.

BRAZING PROCEDURE MODIFICATIONS

Once completed the 2 steps brazing of the 1st module prototype, the acquisition of a continuous active scanning measuring machine (Zeiss Accura) allowed a deep and extensive investigation of the internal geometry of the cavity. A wide series of transversal and longitudinal scanning were then performed. The more detailed and reliable measurements showed a lack of symmetry induced by gravitation effect during the 1st step brazing [1]. The final geometry of the cavity resulted still within the acceptable tolerances range for a single module, but not for the complete line, figures 1 and 2. A vertical brazing assembly, which permitted instead a possibility of a single brazing step, has been developed, figure 3. In this respect, the groove geometry, layout and tooling had to be redesigned. We introduced extensive US scanning (destructive test) and inspection (non-destructive) for the qualification of the brazed surfaces (Cu-Cu and Cu-st. steel).

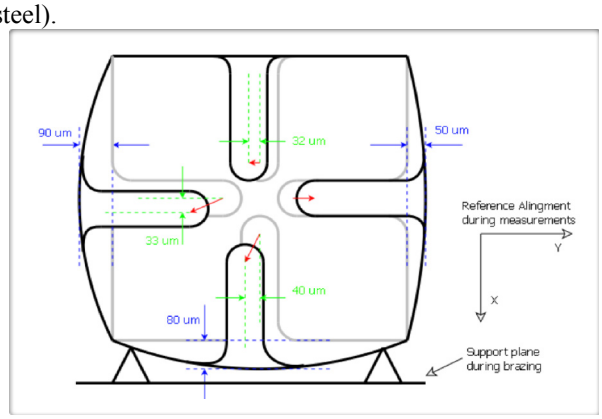

Figure 1: Scheme of the deformation of the cavity of the module 1 prototype after the second brazing

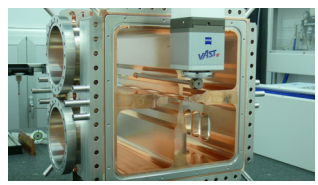

Pole	ΔX [μm]	ΔY [μm]	ΔR_0 [μm]
1	-40	-80	89.44
2	50	0	50.00
3	-32	0	32.00
4	-90	-33	95.86
	mean ΔR_0 [μm]		66.83
	$\partial f/\partial R_0$	[kHz/ μm]	7.60
	Δf	[kHz]	507.87

Figure 2: Module 1 prototype during CMM survey (left) and displacements of the tips (right).

R & D FOR SINGLE BRAZING STEP

With a single brazing step, the number of thermal cycles, reducing the mechanical properties of copper (1 annealing step + 1 final brazing step), is minimized.

The overall precision of the final geometry is optimized.

The cost and the timing of the modules production are also optimized.

Some basic tests on specimens having the same groove design, in order to compare vertical to horizontal brazing, have been performed.

Then two almost full scale tests have been performed finalizing an updated tooling set.

A complete inspection by US scan on slices of the brazed surfaces has been done (destructive). The grooves result always completely empty and no significant voids were detected on the brazing planes, figure 4.

Following these results, the production of the final modules started with SuperModule III-HE section. We adopted the vertical brazing approach but still with 2 brazing steps, until all details were well stated.

We completed the production of the module 16 (April '12), the second prototype module (July '12) and the 1st brazing step of module 17 (July '12).

The 1st single brazing step will be adopted on module 15 by October '12.

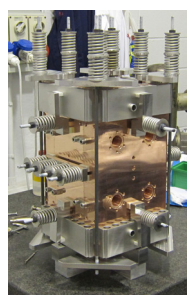

Figure 3: Full scale single brazing test

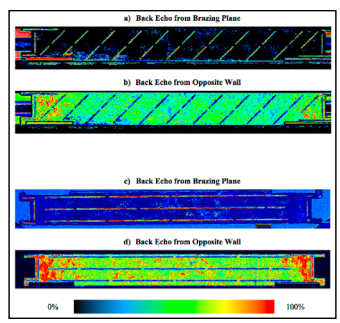

Figure 4: US inspection of two different brazing grooves design

Copyright © 2012 by the respective authors — cc Creative Commons Attribution 3.0 (CC BY 3.0)

THE MODULE 16'S PRODUCTION

The Quality Assurance of the Mechanical Machining

The continuous feedback between the mechanical machining and the measurement results was essential to guarantee the tight design tolerances.

The continuous active scanning survey of the tip geometry is mandatory to check the real geometry with adequate accuracy. The traditional point to point survey measurement (standard approach on CMM's) was attempted, but it failed.

The effectiveness of the active scanning control was essential to adjust and refine the CAM programs and the tooling fine tuning.

A standard procedure for the accurate control of each machining step of all the components and of the assembled module has been established:

- survey and qualification of each component, figure 5 and 6;
- survey and qualification of the dry-assembly of the module before the machining of the common reference planes;
- survey and qualification of the module after each brazing step;
- survey and qualification of the final module compared with the RF measurement.

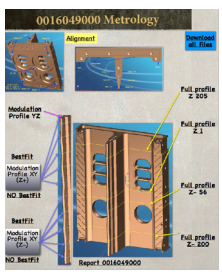

Figure 5: Inspected elements for the qualification of each CuC2 component of the cavity

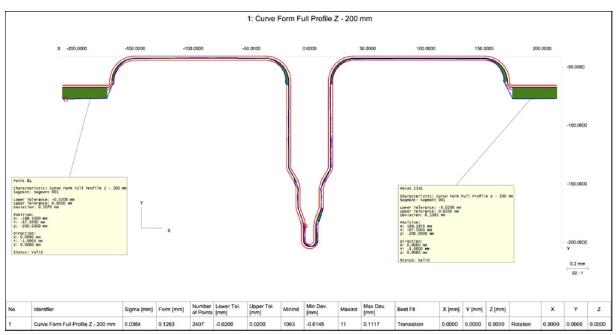

Figure 6: Example of measure of a profile by means active continuous scanning.

The Brazing Procedure, Module Dry Assembly

All the components are aligned to the nominal position and double checked, geometrically and RF.

The assembly is then machined to refine the common planes for the placement of the brazing tooling, figure 7.

The components are then dismantled, chemically cleaned, reassembled in a clean environment by means of the tooling, figure 8.

In this step the 2 sealing st. steel front rings have been mounted in order to provide a relevant constraint, embedding a smooth relative movement of components during the thermal cycle, that could cause an excessive flow down of the brazing material, figure 9.

Figure 7: Module 16 dry assembled before the machining of the common planes

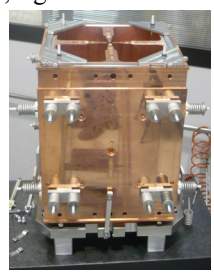

Figure 8: Module 16 assembled with the brazing tooling

The Brazing Procedure, 1st Step

We used Palcusil 10† as brazing material (optimal wetting of the surfaces while allowing for more brazing cycles repairs).

The optical inspection of the brazing joints showed an uniform distribution of the brazing material both on copper-copper and copper-st.steel.

The vacuum tightness of the cavity and of the cooling ducts was well below the specifications (1x10-9 mbar/sec*l).

Nonetheless a relative displacement between the "Ts" and the "Es" profiles was found.

This effect is explained by the relevant different expansion between CuC2 and AISI316LN.

The st. steel ring was not brazed in the first step of the first prototype module. Besides this the structural schemes are slightly different since on the first case the components are separated while in the other they are strictly joined.

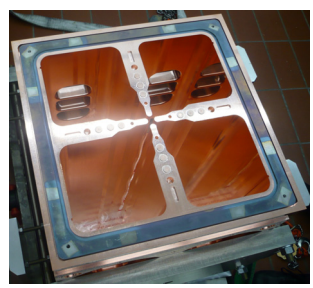

Figure 9: Module 16 after the 1st brazing step.

The Brazing Procedure, 2nd Step

The brazing material used is Cusil‡. During this step all the remaining st. steel components are brazed, figure 10. We encountered 2 problems.

† Palcusil 10 Composition: 59% Ag, 31 % Cu, 10% Pd; liquidus: 854 °C, solidus: 824 °C.

‡ Cusil Composition: 72% Ag, 28% Cu; liquidus : liquidus: 780 °C, solidus: 780 °C.

Copyright © 2012 by the respective authors — cc Creative Commons Attribution 3.0 (CC BY 3.0)

The junctions between the end side flanges and the copper were just partially brazed (as verified by US inspection).

The dimensional check of the cavity showed unexpected deformations.

The reasons:

- we discovered that the heat treatment of the end side flanges was not done following our specifications (the cooling step was too fast thus resulting on an ineffective annealing process);
- again the relevant different expansion between CuC2 and AISI316LN.

Since the brazed connection was too poor, a 3rd brazing step (using Incusil 10*) was performed to join the copper and the st. steel end side flanges by means of a series of pins, figure 11.

Beside all these problems the module 16 fulfills the specifications in terms of geometrical tolerances and vacuum tightness.

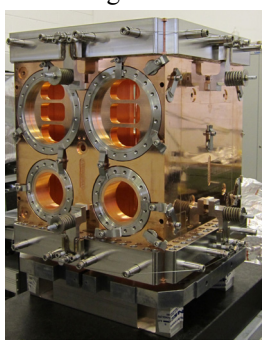

Figure 10: Module 16 before the 2nd brazing step

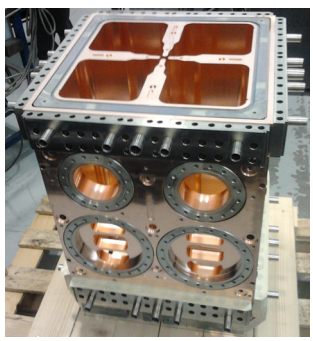

Figure 11: Module 16 after the 3rd repair brazing

Improvements - the results

Keeping in mind the problems found on module 16, a wide range of data for the thermal behaviour of copper and AISI316 were registered in the technical literature [2, 3].

We decided to perform some test with the peculiar material and dimensions to determine the overall relative expansion during our typical brazing cycles.

The tests results were better approximated by the material data as reported in reference [3]. Consequently our design was modified as follows:

- the sealing st. steel ring: any contact between copper and ring on the "Ts" sides (gap about 0.3 - 0.5 mm) was embedded, while the nominal coupling brazing tolerance on the "Es" sides was maintained to ensure a relevant coupling pressure all along the thermal cycle (accepting the residual local deformation at the joint level), figure 12;
- the end side flanges: some almost passing through incisions were introduced, softening the end side flanges stiffness, while ensuring a continuous brazing surface. The local expansion of the cavity was limited to a value around 0.01 mm, figure 13.

All these modifications were introduced and verified on the 1st brazing step of module 17 (sealing st. steel rings) and on the 2nd brazing step of the second prototype module (the incision solution was tested just at one side in order to see the differences).

We developed a more compact and effective constraint fixation made by TZM springs.

This allows for an easier positioning while increasing the contact pressure at high temperature. A more distributed number of constraints are now available.

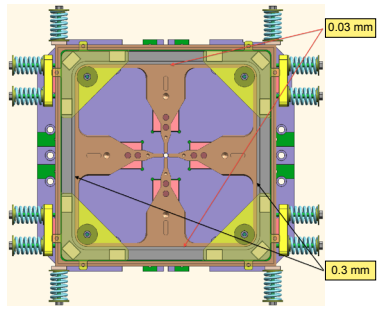

Figure 12: New design of the coupling between copper and sealing st. steel ring avoiding contact with the "Ts"

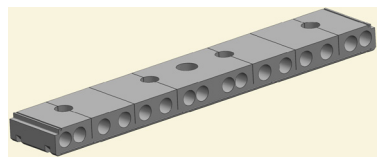

Figure 13: New design of the end side flanges with the incision to reduce the stiffness

WHAT NEXT

The single brazing method will be applied for the first time on the module 15 (October '12).

We assigned a new contract for the production of SuperModule I and the production will start soon.

The production of SuperModule II will be done within INFN. The machining of components is already started.

AKNOWLEDGEMENT

The authors wish to thank the CINEL Scientific Instruments S.r.l. for the active sustaining during R&D phase

REFERENCES

[1] Engineering Design and First Prototype Tests of the IFMIF-EVEDA RFQ, A. Pepato et al, IPAC 2010, Kyoto, Japan.

[2] Thermal expansion of some common LINAC materials, R. Valdiviez, D. Schrage, et al., Linac 2002, Gyeongju, Korea.

[3] N. C. Anderson, Lectures in Ceramic Metal Joining, Amsterdam, 1996.

* Incusil 10 Composition: 63% Ag, 27% Cu, 10% Sn; liquidus : liquidus: 730 °C, solidus: 685 °C

Copyright © 2012 by the respective authors — cc Creative Commons Attribution 3.0 (CC BY 3.0)

RFQ WITH IMPROVRED ENERGY GAIN

A.S. Plastun, NRNU (MEPhI), Moscow, Russia
A.A. Kolomiets, ITEP, Moscow, Russia

Abstract

RFQ structure is practically only one choice for using in front ends of ion linacs for acceleration up to energy about 3 MeV. This limit is due to its relatively low acceleration efficiency. However it isn't intrinsic feature of RFQ principle. It is defined only by vane geometry of conventional RFQ structure with sinusoidal modulation of vanes. The paper presents results of analysis RFQ with modified vane geometries that allow to reach acceleration efficiency compared with IH DTL structures. RFQ with modified vanes was used for design second section of heavy ion injector of TWAC for acceleration of ions with Z/A=0.33 up to 5 MeV/u.

INTRODUCTION

An RFQ output energy doesn't usually exceed several MeV. Using conventional RFQ structure for acceleration of particles for higher energies is impractical because RFQ energy gain decreases rapidly with energy at constant modulation.

Many DTL structures were proposed for beam acceleration following RFQ that use magnetic or radio frequency focusing. The structures are well studied, they can provide good accelerating efficiency and are realized in a number of linacs. In the framework of heavy ion injector development for TWAC facility [1] several designs of second section based on these structures have been studied. In addition it was considered option that uses conventional RFQ with relatively minor modification of RFQ electrodes and resonant structure.

81 MHz RFQ – front end of TWAC injector has been recently successfully commissioned [2]. It is designed to accelerate beam from laser ion source with Z/A = 0.33 up to energy 1.57 MeV/u.

This paper presents result of study of TWAC injector second section design based on modified RFQ. The main goal of the modification was to provide maximum energy gain at focusing sufficient for acceleration beam with current 30 mA up to 5 MeV/u.

ENERGY GAIN IN RFQ

Vanes with Sinusoidal Modulation

The energy gain of a particle in RFQ is

$$\Delta W = e\frac{Z}{A}UT\cos\varphi_S, \qquad (1)$$

e - electron charge, Z - charge number of the particle, A - mass number of the particle, U - voltage between adjacent vanes, T - accelerating efficiency, φ_s - phase of RF field, when synchronous particle is in a maximum of accelerating field.

Voltage U is usually chosen taking into account many different considerations. However it has to be as high as possible to increase energy gain. Its maximum value in this case is fully defined by acceptable surface electric field $E_{s\ lim}$. Most accurately voltage can be found by numerical simulation for real vane geometry and expressed as

$$U = U_{sim}\frac{E_{s\,\mathrm{lim}}}{E_{s\,sim}}, \qquad (2)$$

Here U_{sim} is voltage between vanes in computer model and $E_{s\ sim}$ is maximum field at vane surface obtained from simulation result.

Figure 1 shows results of field simulation in RFQ cell with code OPERA 3D. Simulated cell length $L_c = \beta\lambda/2$ corresponds particle energy at TWAC RFQ output. Curve 1 presents maximum field at vane surface calculated for sinusoidal modulation in $1 \le m \le 5$ range. Aperture for all modulations was constant a = 8 mm, that is average distance from axis to vane was changed as $R_0 = a(m+1)/2$. Simulation results show that for surface field limit $E_{s\ lim}$ = 250 kV/cm (about 2 Kilpatrick units for frequency f = 81 MHz) maximum voltage can reach according formula (2) $U \cong 500$ kV.

Accelerating efficiency T was calculated from simulated distribution of longitudinal field component E_z on axis. T factor for cell with sinusoidal modulation of vanes is limited by value $T \cong 0.7$. It means that the maximum effective accelerating gain per cell with studied parameters doesn't exceed $UT \cong 350$ kV.

Curve 1 shows that there is no sense to increase modulation factor more than $m = 4 \div 5$ because maximum field $E_{s\ sim}$ reduces very slowly for higher m while focusing efficiency rapidly decreases. Figure 2 shows transverse phase advance calculated with the following expression [3]:

$$\sigma^2 = \frac{2}{\pi^2}K^4 + \frac{\pi eUT}{W_{kin}}\sin\varphi,$$

$$K^2 = \frac{Z}{A}\frac{e\overline{G}}{4W_0}\lambda^2.$$

Here $\overline{G}$ is mean value of simulated transverse field gradient along RFQ cell, W_0 - rest mass of proton, λ - wavelength of RF field. Estimation shows that transverse motion is very close to stability border at $m \cong 4$. It defines limiting capability of conventional RFQ with sinusoidal modulation for higher energy gain acceleration.

It is possible to improve accelerating efficiency using trapezoidal modulation proposed in [4]. Cell with this modulation type is shown in Figure 3. The trapezoidal

Copyright © 2012 by the respective authors — cc Creative Commons Attribution 3.0 (CC BY 3.0)

modulation allows 15 ÷ 20% higher accelerating efficiency T due to better of longitudinal field component distribution along axis. It is important that this distribution is kept constant along the RFQ so T rises with particle energy at constant voltage.

However maximum surface field for this modulation type in general is close to the value for sinusoidal modulation.

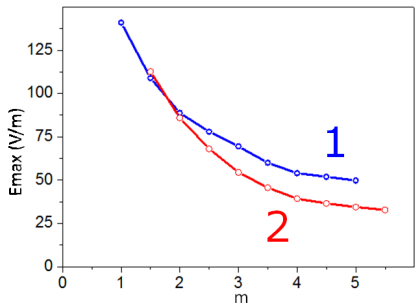

Figure 1: Calculated maximum surface electric field. Curve 1 corresponds to conventional RFQ with sinusoidal modulation, curve 2 – to RFQ with modified vanes.

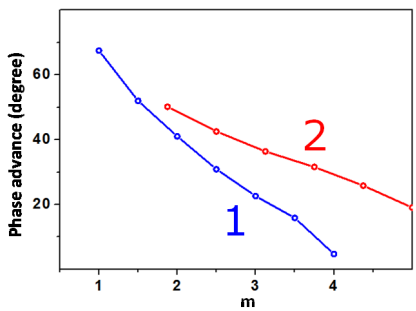

Figure 2: Calculated transverse phase advance. Curve 1 corresponds to RFQ with sinusoidal modulation, curve 2 – to RFQ with improved vanes.

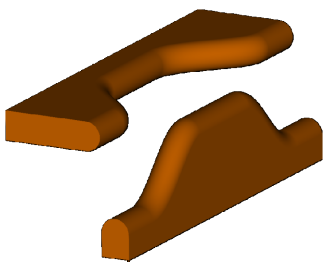

Figure 3: Adjacent vanes with trapezoidal modulation.

Improved Vanes

Whereas trapezoidal modulation considerably improves accelerating efficiency the higher voltage U is required for further energy gain increase. It can be provided if vane geometry allows reducing maximum surface field. Maximum field is reached at vane cross section with exact quadrupole symmetry for RFQ cells with conventional modulation and with parameters corresponding TWAC RFQ output. It was proposed to change vane profile at this cross section to increase distance between adjacent vanes. This can be achieved by transformation of the trapezoidal profile to almost "rectangular" one. Distribution of longitudinal component of field along axis is formed for this profile by "gap" between "rectangles" of adjacent vanes. Vane tips near axis are flat and have about the same curvature radius R_e as the vanes with conventional modulation.

Removing part of vane near axis decreases focusing efficiency. To compensate it more thick flat vanes with curved unmodulated pole are placed at distance from axis $R_q >> a$. Curvature radius of this part of vane is $R_{eq} \cong R_q$. 3D view of improved vanes is shown in Figure 4.

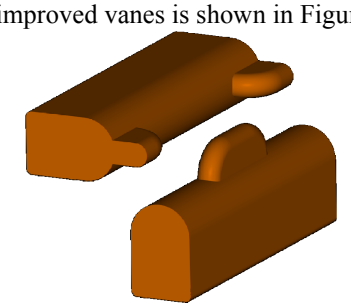

Figure 4: Adjacent vanes with improved profile.

Basic parameters of the improved geometry are shown more detailed in Figure 5. The parameters were optimized to minimize surface field, equalize it on vane surface and to increase focusing efficiency in comparison with conventional vanes with equal modulation.

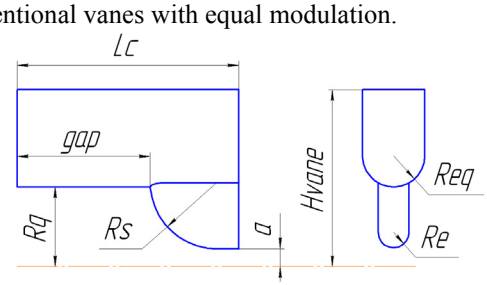

Figure 5: Basic dimensions of improved vanes.

Table 1 allows comparing field simulation results for sinusoidal and improved profiles. The same values for aperture a = 8 mm, cell length L_c = 100 mm, vane tip curvature radius R_e = 5.6 mm and modulation factor m = 4 were used for both cases of simulation.

Table 1: Field Simulation Results

Parameter	Sinus.	Impr.
Limit surface electric field E_{lim}, kV/cm	250	250
Maximum surface electric field $E_{s.max}$ @ 1V intervane voltage, V/cm	0.54	0.39
Voltage U, kV	463	636
Acceleration rate UT, kV	324	513
Transverse phase advance μ, deg	5	26

BEAM DYNAMICS SIMULATION

Improved vane profile was used to design RFQ with parameters corresponds the second section of TWAC injector for detailed computer simulation of beam

Copyright © 2012 by the respective authors — cc Creative Commons Attribution 3.0 (CC BY 3.0)

dynamics. RFQ was designed using 3D field maps calculated by OPERA code. Basic parameters of the RFQ are shown in Table 2.

Table 2: Basic Parameters of Improved RFQ

Operating frequency, MHz	81.36
Z/A of ions	0.33
Input ion energy, MeV/u	1.57
Output energy, MeV/u	5.0
Transverse emittance, norm, π mm·mrad	1.5
Maximum surface field, kV/cm	250.
Voltage, kV	685.
Electrode modulation	4.5
Cell number	20
Total length, m	3.0

Code TRANSIT written in ITEP has been used for the beam dynamics simulation. Longitudinal and transverse field components along section calculated by OPERA 3D code that was used in TRANSIT are shown in Figure 6.

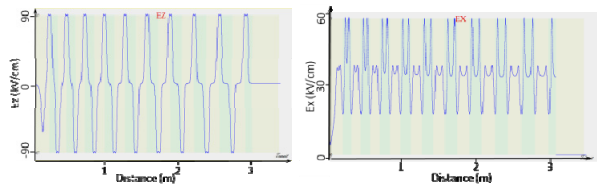

Figure 6: Longitudinal field component on axis (a) and transverse field component at r = 5 mm (b).

Figure 7 shows calculated transverse envelopes that confirm stable transverse particle motion along the section. Simulated envelope size shows that RFQ with improved vanes provides required transverse acceptance.

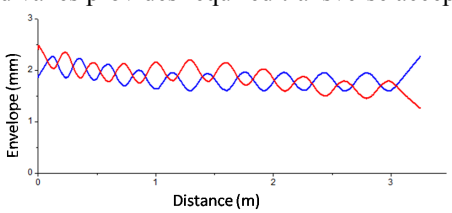

Figure 7: Transverse envelopes calculated with TRANSIT code.

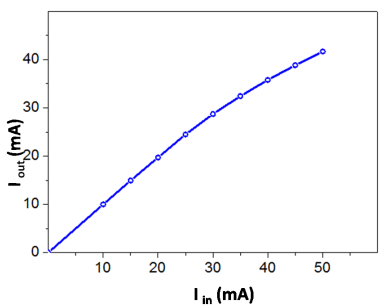

Figure 8: Calculated beam current at RFQ output in dependence on input one.

Simulation results in Figure 8 show that RFQ with improved vanes provides close to 100% beam transmission in required beam current range $0 \le I \le 30$ mA. It is important to say that in spite of complicated vane profile field has good linearity in working area that is evidenced by absence of growth of transverse and longitudinal emittances.

Table 3: Beam Transmission Parameters

Transmission, % (I = 0 / 30 mA)	100 / 98.6
Transverse rms envelope, mm (I = 0 / 30 mA)	2.0 / 3.1
Transverse emittance growth (I = 0 / 30 mA)	1.0 / 1.2
Longitudinal emittance growth (I = 0 / 30 mA)	1.0 / 1.1

CONCLUSION

RFQ structure with improved vane profile is proposed for acceleration following conventional RFQ. Computer simulation showed that new vane profile allows ≈ 30% lower maximum surface field at modulation factor m = 3÷5 comparing with conventional vanes. Accelerating efficiency of new profile is the same as provided by vanes with trapezoidal modulation.

3 m length RFQ has been designed for injector of TWAC facility. It provides about than 3.5 MeV energy gain. Computer simulations confirmed that the structure is capable to accelerate ion beam with current I = 30 mA with transmission about 100% and with only small transverse and longitudinal emittances growth.

ACKNOWLEDGMENT

Authors thank Tatyana Tretiakova for work on adjustment of her codes for RFQ with new vane profile design and beam dynamics simulation.

REFERENCES

[1] N.N.Alexeev, P.N.Alekseev, V.A.Andreev, A.N.Balabaev, V.I.Nikolaev,A.S.Ryabtsev, Yu.A.Satov, V.A.Schegolev, B.Yu.Sharkov, A.V.Shumshurov, V.P. Zavodov, "ITEP-TWAC PROGRESS REPORT", Proceedings of IPAC-2011, p.2193, San Sebastian, Spain

[2] V. Andreev, N.N. Alexeev, A.Kolomiets, V. Koshelev, B. Kondratyev, A. Kozodaev, V. Kuzmichev, Y. Orlov, V. Stolbunov, T. Tretyakova, "FIRST BEAM TEST OF 81.5 MHZ RFQ FOR ITEP-TWAC", Proceedings of IPAC-2011, p.2622, San Sebastian, Spain

[3] I.M. Kapchinskiy, "THEORY OF RESONANCE LINEAR ACCELERATORS", Harwood academic publishers, 1985

[4] O.K. Belyaev, O.V. Ershov, I.G. Maltsev, V.B. Stepanov, S.A. Strekalovskikh, V.A. Teplyakov, A.V. Zherebtsov, "IHEP EXPERIENCE ON CREATION AND OPERATION OF RFQS", Proceedings of the 20th Linac Conference, page 259, Monterey, California.

Copyright © 2012 by the respective authors — cc Creative Commons Attribution 3.0 (CC BY 3.0)

TUNING STUDIES ON 4-ROD RFQs *

J. Schmidt, B. Koubek, A. Schempp, B. Klump, IAP, Univ. Frankfurt, Germany

Abstract

A NI LabVIEW based Tuning Software has been developed to structure the tuning process of 4-rod Radio Frequency Quadrupole s (RFQs). Its results are compared to measurement data of 4-rod RFQs in different frequency ranges. For the optimization of RFQ design parameters, a certain voltage distribution along the electrodes of an RFQ is assumed. Therefore an accurate tuning of the voltage distribution is very important for the beam dynamic properties of an RFQ. A variation can lead to particle losses and reduced beam quality especially at higher frequencies. Our electrode design usually implies a constant longitudinal voltage distribution. For its adjustment tuning plates are used between the stems of the 4-rod-RFQ. These predictions are based, in contrast to other simulations, on measurements to define the characteristics of the RFQ as it was build - not depending on assumptions of the design. This will lead to a totally new structured process of tuning 4-rod-RFQs in a broad range of frequencies by using the predictions of a software. The results of these studies are presented in this paper.

RESONANT CIRCUITS

A simplified model of the 4-rod RFQ resonator is a chain of LC-oscillators where each RF cell has its own resonance frequency. In these RF cells the stems represent the inductance, while the electrodes form the capacitive part of the circuit. A more detailed model is described in [1].

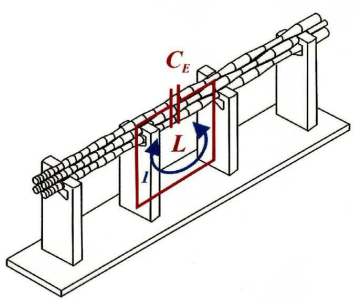

Figure 1: LC Resonator as Equivalent Circuit of a 4-Rod RFQ.

To tune this system, the resonance of each RF cell has to be tuned with tuning plates. They short cut the current path between the stems, to change the inductance of the RF cell. The longitudinal voltage distribution, the so called flatness, is a fundamental parameter in the particle dynamic design of an RFQ. Usually a constant longitudinal voltage along the electrodes is the basis of our design, but other distributions are possible as well [2].

Following the particle dynamics the longitudinal voltage distribution has to be arranged. It is measured using the capacitve perturbation method. A perturbation capacitor sits on a pair of electrodes of one RF cell to cause a frequency shift due to Thomsons law. The resulting frequency shift of the cell is proportional to its voltage (see Eq. 1).

$$U \propto \Delta f_0 = \frac{1}{\sqrt{LC}} - \frac{1}{\sqrt{L(C+\Delta C)}} \qquad (1)$$

THE VOLTAGE TUNING PROCESS

The process of adjusting the flatness is an iterative process of shifting the tuning plates and try to find a set of heights, which results in the desired distribution and total resonance frequency. This process can take some time, especially working on long RFQ structures with a lot of RF cells [3].

Due to several reasons like the changing modulation or differences in the manufacturing, the RFQ has deviations in its characteristics along the electrodes profile [4]. This leads to a different impact of the tuning plates depending on their position in the RFQ.

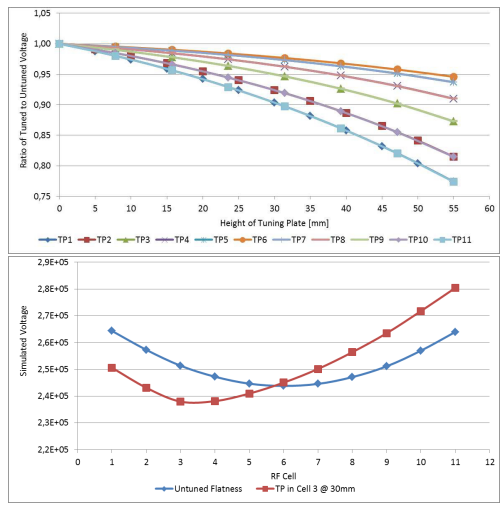

Figure 2: The voltage in z=k from raising tuning plates in all cells (upper graph) and the longitudinal change with a tuning plate in cell k=3 (lower graph).

Raising a tuning plate in cell k $\in [1, n]$ decreases the voltage in cell k and its neighboring cells k$\pm$i with i$<$i$_0$, while the voltage raises in cells k$\pm$i with i$\geq$i$_0$. This behavior is shown in Fig. 2

* Work supported by BMBF

Copyright © 2012 by the respective authors — cc Creative Commons Attribution 3.0 (CC BY 3.0)

In order to quantify this behavior effect functions EC were introduced [5], describing the shift in flatness caused by a change in the position of the tuning plate of each RF cell k. They correspond to the ratio between the tuned and the untuned flatness.

$$U_t(z,h) = U_u(z) + EC(z,h) \times U_U(z) \qquad (2)$$

The single tuning plates all have an individual effect on the RFQ EC_k(z,h). Their superposition describes the total effect of a tuning plate setting with different heights h_k.

$$U_t(z,h) = U_u(z) \times \prod_{k=1}^{n} [EC_k(z,h_k) + 1] \qquad (3)$$

To find the ration $EC_k(z,h_k)$ measurements and simulations of the flatness depending on the longitudinal position z in the RFQ and the heights of the tuning plates have been performed with the aim to find a possibility to split EC(z,h) into two separated functions, one for each k depending just on the z-position and one on the height being valid for all k.

$$EC_k(z,h_k) = EC(h_k) \cdot EC_k(z) \qquad (4)$$

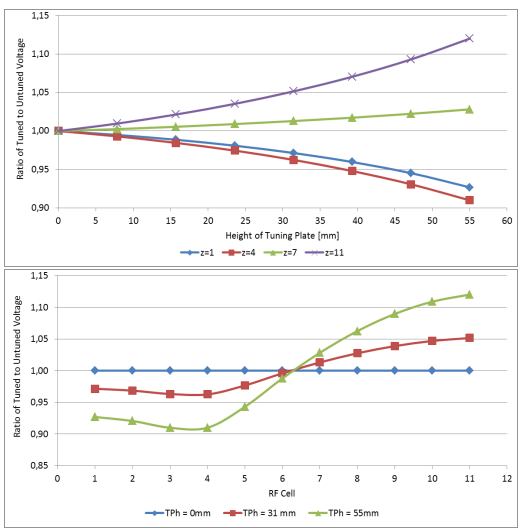

Figure 3: The ratio of the tuned and untuned flatness for a tuning plate in cell k=3 with the height at different z-positions (upper graph) and the corresponding longitudinal change at different heights (lower graph).

STATUS OF THE TUNING PROGRAM

As presented at PAC11 in New York [6] a software has been developed to predict the resulting flatness of an arbitrary tuning plate distribution, which is working well for 4-rod RFQs at 100 MHz. In this version of the program a linear approximation EC(h)=h has been used for the influence of the tuning plates height. Its results in comparison with measurements are presented in Fig. 4

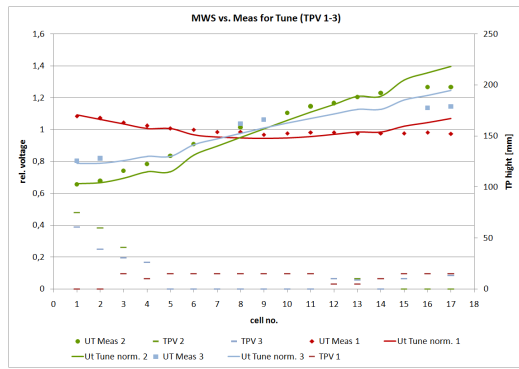

Figure 4: Results of the RFQ tuning program in comparison with three sets of measurements on a 17-cell 100 MHz RFQ [6].

This approximation turns out to be too rough for RFQs with higher frequencies around 200 MHz. Looking at Fig. 3 a square tendency with a - depending on the longitudinal position of measurement z - negative or positive gradient is visible.
To represent this behavior a higher order polynomial fit of the measurement points with different heights was implemented into the software. A comparison of the measured flatness and the simulated predictions with the corresponding tuning plate distribution with a linear and polynomial assumption is shown in Fig. 5.

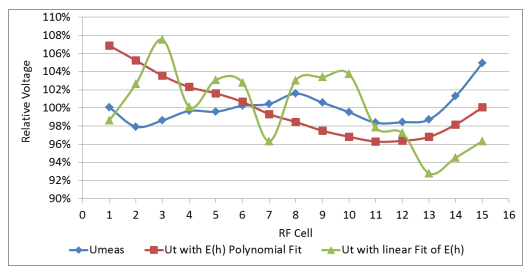

Figure 5: Comparison of the flatness prediction from the RFQ tuning program with linear and polynomial fit in comparison with its corresponding measurement on a 15-cell 200 MHz RFQ.

The measured distribution shows a x^6-like behavior, which is not included in the simulated ones. Even though the fitted version corresponds to the measurement much better, than the linear approximation, it is unfortunately not in a range to work with.

CONCLUSION AND OUTLOOK

Going from 100 to 200 MHz 4-rod RFQs the dependency of the voltage shift to the height of the tuning plate can not be approximated with a linear function anymore. A polynomial fit has been implemented to the simulation software. The results are much better, but are not precise enough to replace the manual iterative process. Other fitting methods have to be tested. Eventually the splitting of

Copyright © 2012 by the respective authors — cc Creative Commons Attribution 3.0 (CC BY 3.0)

the longitudinal and height dependency can not be separated as supposed up to now, because their coupling becomes much stronger in high frequency systems. Fig. 6 shows the change in the data sets due to the scaling process for a raising tuning plate in the middle of a 15-cell RFQ. The symmetric increase and decrease of the voltage around the cell of the tuning plate is pictured in the upper graph. This difference disappears with the scaling to h^2 completely. In the scaled case in the lower graph all curves overlap each other and values of the voltage ratios compared to points at higher tuning plate positions gets much smaller.

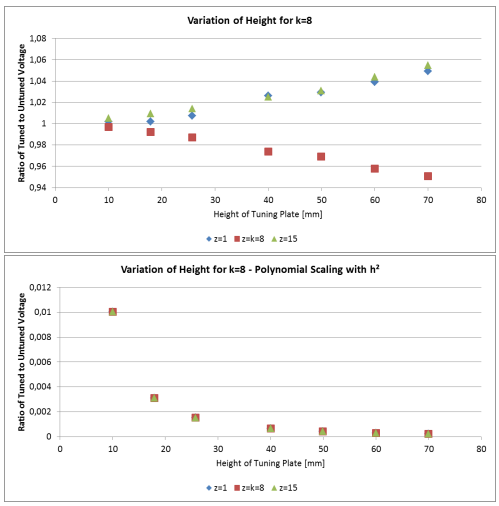

Figure 6: The ratio of the tuned and untuned flatness for a tuning plate in cell k=8 - the middle of the RFQ - with the height at different z-positions before the scaling (upper graph) and the corresponding data after applying a scaling with h^2 (lower graph).

Outlook

The vanishing of the differences in the height dependency at varying z-positions will be analyzed further. It may be an indicator of a strong coupling between the height and z-position dependency. If it is not possible to split them, there need to be another method to make the theory of the effect functions useable.

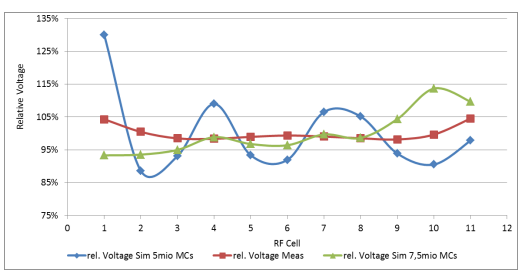

Figure 7: Results of flatness simulations of a 11-cell 200 MHz RFQ with 5 mio. and 7.5 mio. mesh cells in comparison with the corresponding measurement.

In parallel to the development of the simulation software for 4-rod RFQs the simulation of these systems using CST Microwave Studio ® is about to improve, too. As shown in the graph in Fig.7 there is a strong dependency of the flatness simulation results to the meshing of the RFQ.
Both simulation approaches will be followed further, to find a way of predicting the flatness of 4-rod RFQs. At the moment the iterative process is still needed to find the appropriate set up of the tuning plates.

REFERENCES

[1] J.X. Fang and A. Schempp, "Equivalent Circuit of a 4-ROD-RFQ", EPAC 1992, Berlin, Germany.

[2] A. Schempp, "Design of Compact RFQs', LINAC 1996, Geneva, Switzerland.

[3] T. Sieber, "Entwicklung von 4-Rod- und IH- Radio-Frequenz-Quadrupol (RFQ)-Beschleunigern fuer radioaktive Ionenstrahlen bei REX-ISOLDE und MAFF", PhD Thesis, 2001, Munich, Germany.

[4] J. Schmidt, B. Koubek, A. Schempp "Simulations of the Influence of 4-rod RFQ Elements on its Voltage Distribution", IPAC 2012, New Orleans, LA, USA.

[5] P. Fischer, "Ein Hochleistungs-RFQ-Beschleuniger fuer Deuteronen", PhD Thesis, 2007, Frankfurt, Germany.

[6] J. Schmidt, B. Koubek, A. Schempp, "Tuning Studies on 4-rod-RFQs, PAC 2011, New York City, NY, USA.

[7] A. Schempp, "Overview of Recent RFQ Projects", LINAC 2008, Victoria, BC, Canada.

[8] P. Fischer and A. Schempp, "Tuning of a 4-rod CW-Mode RFQ Accelerator", EPAC 2006, Edinburgh, Scotland.

[9] P. Fischer and A. Schempp, "Tuning CW 4-rod RFQ", LINAC 2006, Knoxville, Tennessee, USA.

Copyright © 2012 by the respective authors — cc Creative Commons Attribution 3.0 (CC BY 3.0)

STUDIES OF PARASITIC CAVITY MODES FOR PROPOSED ESS LINAC LATTICES

R. Ainsworth*, Royal Holloway University of London, UK
S. Molloy, European Spallation Source AB, Lund, Sweden

Abstract

The European Spallation Source (ESS) planned for construction in Lund, Sweden, will be the worlds most intense source of pulsed neutrons. The neutrons will be generated by the collision of a 2.5 GeV proton beam with a heavy-metal target. The superconducting section of the proton linac is split into three different types of cavities, and a question for the lattice designers is at which points in the beamline these splits should occur. This note studies various proposed designs for the ESS lattice from the point of view of the effect on the beam dynamics of the parasitic cavity modes lying close in frequency to the fundamental accelerating mode. Each linac design is characterised by the initial kinetic energy of the beam, as well as by the velocity of the beam at each of the points at which the cavity style changes. The scale of the phase-space disruption of the proton pulse is discussed, and some general conclusions for lattice designers are stated.

INTRODUCTION

The European Spallation Source is a facilty, currently in its design phase [1], for the generation of intense pulses of neutrons for studies in applied science. The neutrons are generated through the spallation process when a 5 MW (average) proton pulse is made to impact a heavy metal target.

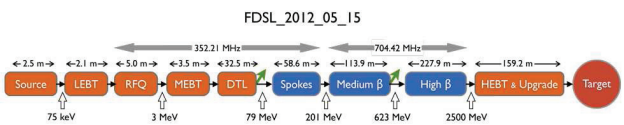

Figure 1: Block diagram of the ESS linac.

	Value	Unit
Final kinetic energy	2.5	GeV
Macropulse current	50	mA
Macropulse repetition rate	14	Hz
Bunch frequency	352.21	MHz

Table 1: Main ESS linac parameters.

A cartoon of the ESS linac is shown in Figure 1, and the main parameters of the proton beam are given in Table 1.

This note concerns the beam dynamics within the superconducting sections of the machine:

Spokes: Two–spoke cavities operating at 352.21 MHz. This section accelerates the beam from the exit of the DTL at 79 MeV to 201 MeV.

Medium β: Five–cell elliptical cavities operating at 704.42 MHz. The geometrical beta of this section is still under discussion, but is likely to be set at a value close to, $\beta_g = 0.65$. In this section, the beam is accelerated from 201 MeV to 623 MeV.

High β: Five–cell elliptical cavities operating at 704.42 MHz. As with the previous section, the geometrical beta is still under discussion, but the likely value is close to, $\beta_g = 0.92$. This section accelerates the beam to its final energy of 2.5 GeV

Given the high intensity of the beam, one major concern is that strong resonances will be excited in the superconducting cavities that will then act to disrupt subsequent bunches. In particular parasitic modes that lie close in frequency to that of the accelerating mode. They are of concern due to there small frequency spread and high R/Q relative to the accelerating mode. If they are found to be a problem, the geometric beta of the cavity may need to be altered or the velocity partitioning between the cavity families may need to be shifted.

LINACS

For the studies into Same Order Modes (SOMs), that is, modes that are part of the same passband as the fundamental accelerating mode, four linacs are investigated as shown in Table 2 where cavities per family denotes the number of cavities in the spoke, medium β and high β sections.

Linacs	Cavities per family	Energy In [MeV]
HS_2011_11_23	36-64-12	50
FD_SL_2012_04_13	32-60-120	79
FD_SSCL_2012_04_16	32-52-128	80
FD_SL_2012_05_15	28- 60-120	79

Table 2: Linacs investigated for SOM simulations.

* rob.ainsworth.2009@live.rhul.ac.uk

Copyright © 2012 by the respective authors — cc Creative Commons Attribution 3.0 (CC BY 3.0)

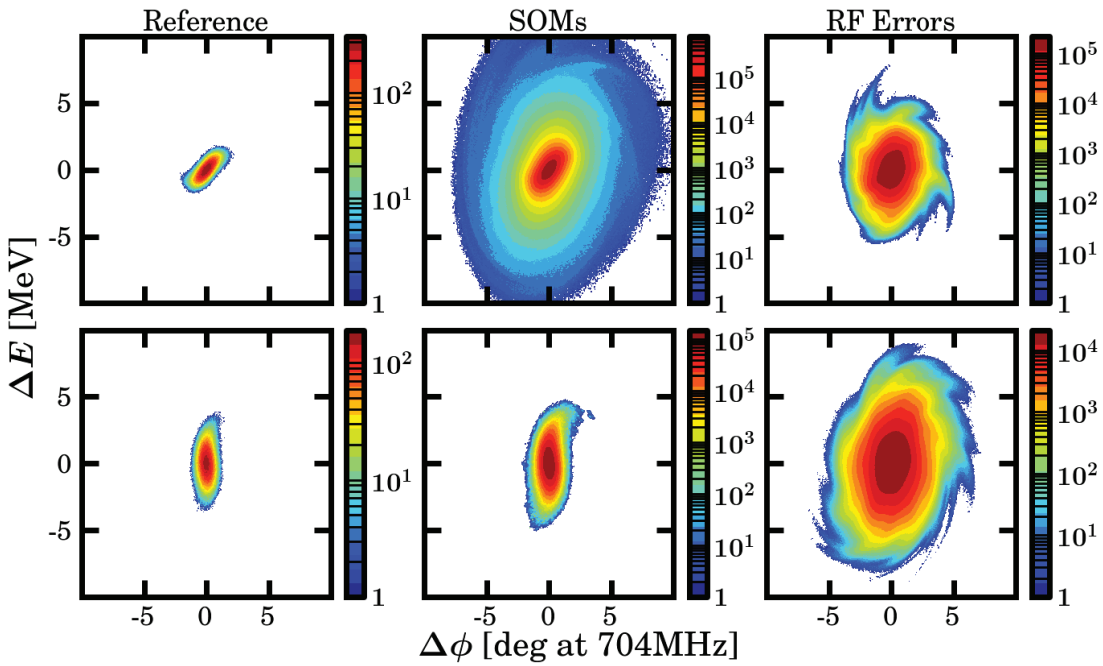

Figure 3: The Pulse phase space distribution at the end of the linac due to different effects.

SIMULATIONS

To explore the effect of these modes, a pulse train of one million point-like bunches was tracked through the superconducting section of the linac. Each bunch adds to the induced fields, these act on subsequent bunches through a kick-drift-kick model [2], and the resulting bunch energy and time errors are calculated.

For each cavity family, the SOM with the highest R/Q is used for simulations. For the spokes, the second mode is used and for the ellipticals, the $4\pi/5$ mode is used. The R/Q that will be seen in each cavity for the whole HS_2011_11_23 linac is shown in Figure 2. Of particular concern are the regions at the beginning of the spoke and medium beta sections where the R/Q of the SOMs are larger than that of the accelerating mode.

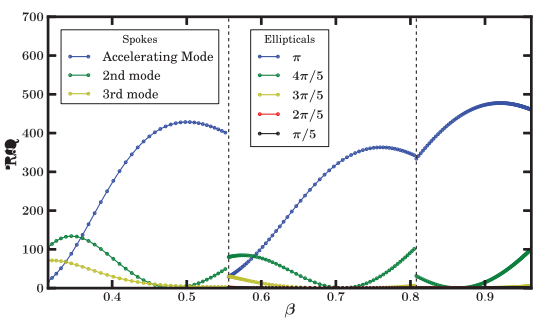

Figure 2: The R/Q for each cavity as a function of particles velocity.

The simulation is performed 1000 times using a different seed for the random number generator to set the frequencies of the SOMs. All other parameters are left constant. In addition, a charge scatter of 1% was also used [3].

Jitter from the RF system will also lead to energy and phase errors. Uniformly distributed errors of $1\%, 1^\circ$ are used in each linac with the exception of the HS_2011_11_23 linac which uses errors of $0.5\%, 0.5^\circ$. Each linac is simulated 1000 times with a different set of uniformly distributed random errors each time. The growth due to RF errors will be used as the acceptable limit in order to gauge the effect of the SOMs.

FREQUENCY SPREAD

The frequency spread of the SOMs will have a large effect on their influence. A smaller frequency spread will result in a larger coherence resulting in a larger influence on the beam. Therefore, it is important to use an reasonable value. In the late 1980's, Ron Sundelin performed a series of studies measuring the distribution of resonant frequencies of SCRF cavities [4]. The frequency spread based on empirical results is given by

$$\sigma = 1.09 \times 10^{-3} \cdot |f_n - f_0|. \quad (1)$$

This means that for the elliptical cavities where the $4\pi/5$ mode is only ~ 1 MHz away from the accelerating mode, the frequency spread will be ~ 1 kHz.

Copyright © 2012 by the respective authors — cc Creative Commons Attribution 3.0 (CC BY 3.0)

GROWTH

To quantify the growth, the area, ϵ, of the phase space created all the bunches are compared where the area is given by

$$\epsilon = \pi\sqrt{\langle\Delta E^2\rangle\langle\Delta\phi^2\rangle - \langle\Delta E\Delta\phi\rangle^2}, \qquad (2)$$

where ΔE and $\Delta\phi$ are the energy and phase error of the bunch with respect to the synchronous bunch. The growth ϵ_{RF}/ϵ is used to determine the effects of the RF and set the tolerable growth due to SOMs.

RESULTS

Figure 3 shows the effect of these modes on the pulse phase space of two linacs with different velocity partitioning over the three cavity families. The first column shows the phase space distribution with no external effects such as SOMs or RF errors acting providing a reference distribution to compare to. The middle column shows the case where a SOM is present in each cavity. The last column shows the case when RF errors are applied to the linac in form of amplitude and phase errors. The growth due RF errors is used as an acceptable limit It can be seen that the linac of the top row, which represents an earlier ESS layout, is susceptible to these modes. The bottom row, corresponding to the May 2012 linac layout, shows significantly better performance.

Table 3 shows the growth in due to SOMs and RF errors for each of the linacs simulated. It can be seen that all linacs due except the HS_2011_11_23 linac show negligible growth due to SOMs. It is thought that increasing the Energy input to the spoke section from 50 MeV to 79 MeV was the main reason the effect of SOMs was less in the other linacs. This is because at 79 MeV, the R/Q of the SOMs no longer crossed the accelerating mode in the spoke section.

SOMs	Average Growth	Max Growth
HS_2011_11_23	3.1	56.6
FD_SL_2012_04_13	1.02	1.2
FD_SSCL_2012_04_16	1.01	1.5
FD_SL_2012_05_15	1.02	1.47
RF Errors	Average Growth	Growth
HS_2011_11_23	3.3	13
FD_SL_2012_04_13	4.24	16.2
FD_SSCL_2012_04_16	3.9	14.5
FD_SL_2012_05_15	3.7	16.6

Table 3: Growth in each linac due to SOMs and RF errors.

CURRENT AND DAMPING SCAN

The final investigation was to vary the current, Ib and Q_{ex} for the simulations involving the May Baseline linac FD_SL_2012_05_15. The current was varied from the nominal current of 50 mA to a relatively high current of 150 mA in order to determine a threshold if there is one and how close the nominal current is to the threshold. The Q_{ex} is also varied from 10^4 to 10^9, previous simulations used a relatively high value of 10^8 as the actual value will not be known however it is expected to be similar to that of the fundamental mode which has a $Q_{ex} \sim 10^6$. The results are shown in Figure 4 where the dashed line represents the growth due to RF errors. At the nominal current, negligible growth is observed and it is not until 90 mA where the growth starts to exceed that of RF errors. Losses are also seen at this current for $Q_{ex} > 10^7$.

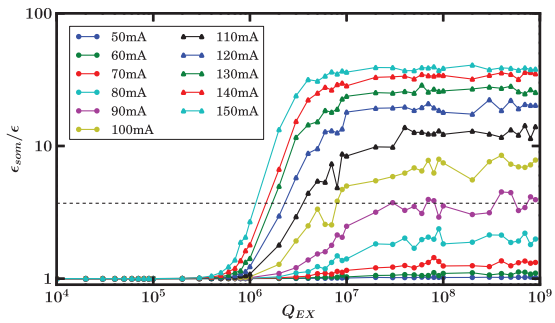

Figure 4: The average longitudinal phase space increase for 100 linacs at varying currents and Qex of the SOMs.

SUMMARY

The influence of parasitic modes in the ESS linac have been investigated with emphasis on modes that lie in the same passband as the fundamental mode. It has been shown that although it is possible to design a linac susceptible to modes in the fundamental passband, the current baseline is not affected at the nominal current and should operate up to currents on 100 mA if upgrades are desired in the future. Therefore, no change is needed to the velocity partitioning of the linac nor the geometric beta of the cavities.

ACKNOWLEDGEMENTS

The authors would like to thank Marcel Schuh for his help in benchmarking the code used in the above simulations.

REFERENCES

[1] H. Danared, " Design of the ESS Accelerator", THPPP071, IPAC12.

[2] M. Schuh et al., Phys. Rev. ST Accel. Beams 14 (2011) 051001.

[3] J. Tuckmantel et al., Phys. Rev. ST Accel. Beams 13 (2011) 021001.

[4] S. Molloy, Note, ESS Doc 92-V2.

Copyright © 2012 by the respective authors — cc Creative Commons Attribution 3.0 (CC BY 3.0)

THE MULTIPACTING SIMULATION FOR THE NEW-SHAPED QWR USING TRACK3P*

C. Zhang#, S. He, Y. He, S. Huang, Y. Huang, T. JiangR. Wang, M. Xu, Y. Yang, W. Yue, S.H. Zhang, S. Zhang, H. Zhao
Institute of Modern Physics, Lanzhou, Gansu 730000, China

Abstract

In order to improve the electro-magnetic performance of the quarter wave resonator, a new-shaped cavity with an elliptical cylinder outer conductor has been proposed [1]. This novel cavity design can provide much lower peak surface magnetic field and much higher R_a/Q_0 and G. The multipacting simulation has been done for this new QWR cavity using ACE3P/TRACK3P code, in this paper the simulation results will be presented and analyzed.

INTRODUCTION

In the Heavy Ion Accelerating Facility (HIAF) of IMP, superconducting quarter wave resonators (QWRs) with frequency of 81.25 MHz and β of 0.041, 0.085 will be applied to accelerate the ion beams from 0.3 MeV/u to 17 MeV/u. Because of the extremely high design voltage for the β =0.085 QWR cavity, an elliptical cylinder outer conductor shape has been proposed for it (see Fig. 1).

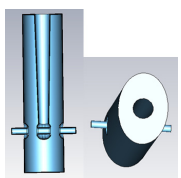

Figure 1: The elliptical cylinder outer conductor QWR model for multipacting simulation.

MULTIPACTING SIMULATION

Parallel codes Omega3P and Track3P which are developed at SLAC have been used, to obtain the field maps and then to analyse the multipacting barriers [2, 3]. When doing the multipacting simulation, one half of the QWR cavity was used taking advantage of the symmetry. Seed particles were initiated on all the RF surfaces. The accelerating gradient was scanned up to 6 MV/m firstly to locate the multipacting band, and then much finer scan interval was used in order to study the multipacting band in detail. 2 eV was used as the initial energy for primary and secondary emissions to study its effect on multipacting and typical niobium secondary electron yield *(SEY) was applied to estimate the multipacting strength* (see Fig. 2). At each field level, 50 RF cycles were used as total running time to obtain resonant trajectories.

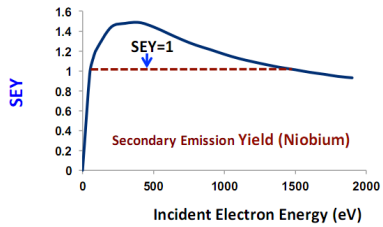

Figure 2: Secondary electron yield (SEY) for Niobium on the dependence of impact energy. The impact energy range relevant to the peak SEY is 150~700 eV. Resonant electrons with impact energies in this range are most dangerous to lead to hard multipacting.

MULTIPACTING SIMULATION RESULTS

Multipacting band at low field level

The distribution of resonant particles identified by Track3P presented the multipacting bands occurred at low field levels, Figure 3, 4 show the expanded plot around this multipacting band and impact positions.

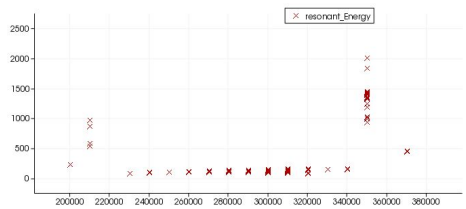

Figure 3: Impact energy vs. accelerating gradient at low field level.

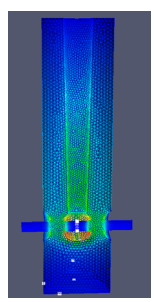

Figure 4: Impact positions at all field levels.

There are two multipacting bands, one at field levels of 0.2 ~0.34 MV/m with impact energies 80~160 eV in the beampipe region (see Fig. 5, 6); the other at around the accelerating gradient of 0.35 MV/m with impact energies 700~2000 eV in the bottom part of the cavity. In consideration of the peak SEY energy for Nb (see Fig. 2), such two bands are expected to be a soft barrier.

* Work supported by 91026001 Nature Science Foundation
# claire335@gmail.com

Copyright © 2012 by the respective authors — cc Creative Commons Attribution 3.0 (CC BY 3.0)

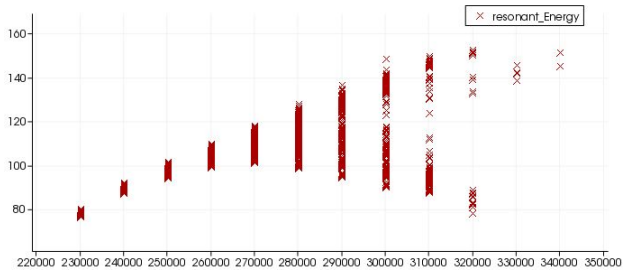

Figure 5: Impact energy vs. accelerating gradient of 0.2~0.34 MV/m.

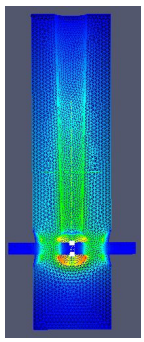

Figure 6: The beampipe impact positions for the accelerating gradient of 0.2~0.34 MV/m.

Rounding effects on Multipacting

Since it is a common method of reducing the B_{peak} near the short plate location by rounding the joints between the short plate and the inner and outer conductors, here let's see what this procedure will bring to the multipacting activities in the cavity. In order to check how the rounding will affect the multipacting status, the simulation will be done for the three situations-(a) rounding only the inner conductor joint, (b) rounding only the outer conductor joint (see Fig. 7) and (c) rounding both joints, separately.

As for the first two cases, the multipacting occurrences are very similar to that of the flat short plate QWR, both in the impact energy span (see Fig. 8, 9) and in the impact positions (see Fig. 10, 11).

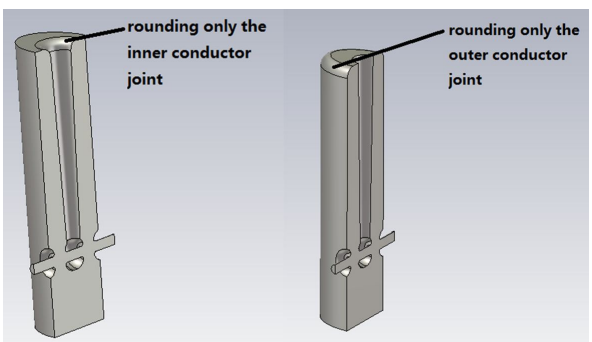

Figure 7: Rounding only one joint between the short plate and the inner or the outer conductor.

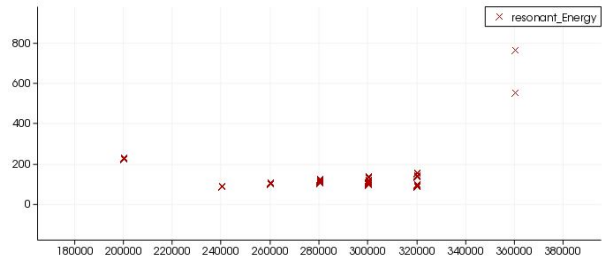

Figure 8: Resonant particle distribution for the case of just rounding the inner conductor joint.

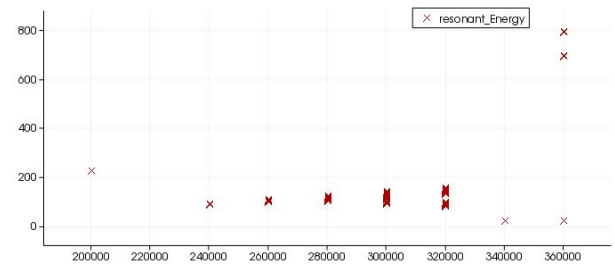

Figure 9: Resonant particle distribution for the case of just rounding the outer conductor joint.

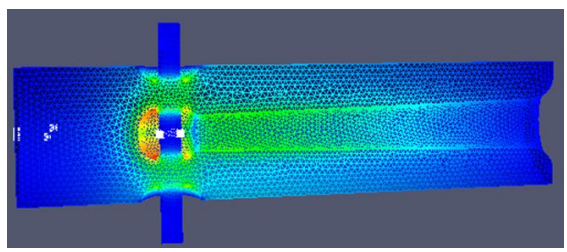

Figure 10: Impact positions for the case of just rounding the inner conductor joint.

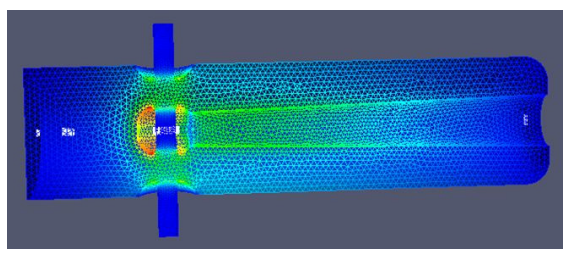

Figure 11: Impact positions for the case of just rounding the outer conductor joint.

However, the multipacting resonances are very critical for the third situation (see Fig. 12). Firstly, the resonant trajectories are expanded to the short plate region and the middle outer conductor (see Fig. 13); and secondly, the impact energies have spread around the peak of the SEY curve (see Fig. 14, 2). As a result, the attempting to lower the Bpeak by rounding both the joints can incur a very serious multipacting in the cavity. The final electro-magnetic design choose not to round the either of the joints speciously since the elliptical cylinder outer conductor cavity shape can offer low enough B_{peak}.

Copyright © 2012 by the respective authors — cc Creative Commons Attribution 3.0 (CC BY 3.0)

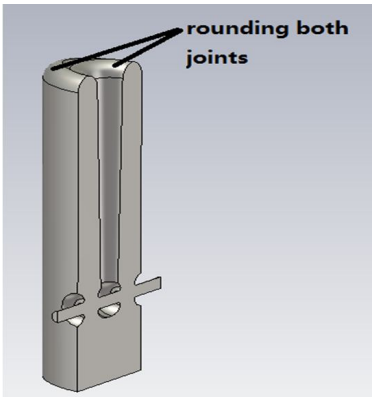

Figure 12: Rounding both joints between the short plate and the inner and the outer conductor.

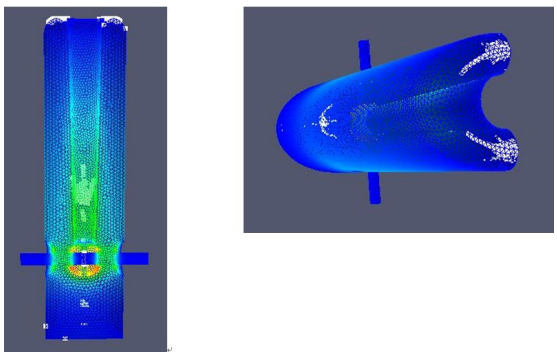

Figure 13: Impact positions for the case of rounding both joints.

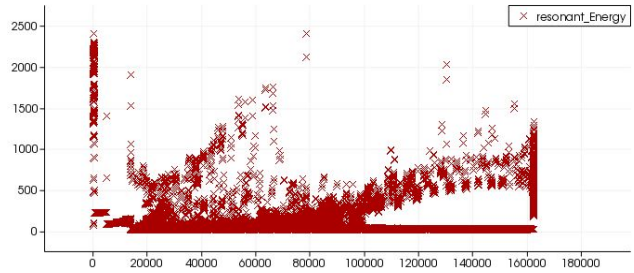

Figure 14: Resonant particle distribution for the case of rounding two joints.

SUMMARY

Track3P was used to analyze the multipacting bands in the elliptical cylinder outer conductor shaped QWR cavity. Only multipacting bands at low field levels were found and the impact energy distributions showed that no hard multipacting bands exist in the cavity. However, rounding the joints between the short plate and both the inner and outer conductors will cause more multipacting bands. The fabrication and test of the prototype cavity is in need in order to see if the experimental data will be in agreement with the simulation results.

REFERENCES

[1] C. Zhang et al, "Electro-magnetic optimization of a quarter-wave resonator.", Proc. SRF 2011, Chicago, USA, 2011.

[2] K. Ko, et al, "Advances in Parallel Computing Codes for Accelerator Science and Development", Proc. LINAC2010, Tsukuba, Japan, 2010.

[3] Lixin Ge et al, "Multipacting simulation and analysis for the FRIB Half Wave resonator using Track3P", Proc. LINAC2010, Tsukuba, Japan, 2010.

Copyright © 2012 by the respective authors — cc Creative Commons Attribution 3.0 (CC BY 3.0)

STRUCTURAL ANALYSIS OF THE NEW-SHAPED QWR FOR HIAF IN IMP*

C. Zhang#, S. He, R. Wang, M. Xu, W. Yue, S. Zhang, S. Huang, Y. Yang, Y. Huang
T. Jiang, S. Zhang, Y. He, H. Zhao
Institute of Modern Physics, Lanzhou, Gansu 730000, China

Abstract

Since the QWR cavity is very successful for the operation with frequency of 48 to 160 MHz and beta value of 0.001 to 0.2, a new-shaped QWR is being designed for the low energy superconducting section of HIAF in the Institute of Modern Physics [1]. The cavity will work at 81.25 MHz and beta of 0.085，with an elliptical cylinder outer conductor to better its electro-magnetic performance and keep limited accelerating space. Structural design is an important aspect of the overall cavity implementation, and in order to minimize the frequency shift of the cavity due to the helium bath pressure fluctuations, the Lorentz force and microphonics excitation, stiffening elements have to be applied. In this paper, structural analyses of the new-shaped QWR are presented and stiffening methods are explored.

INTRODUCTION

A stable resonant frequency for the superconducting cavity is desired, because excessive frequency fluctuations require extra power to control the RF amplitude and phase. The reasons that lead to frequency fluctuations include the fluctuations in the liquid helium pressure, Lorentz force detuning, mechanical vibration modes and the etching effect from the cavity surface treatment. Since the operating temperature for the QWR cavities is 4.5 K, the helium pressure stability will be determined by the extent to which the cryogenic plant can be controlled. The stiffening measures were intended primarily to reduce the pressure sensitivity.

MECHANICAL SIMULATION

When the EM design has been completed, the mechanical performance of the cavity should be evaluated. We tried to figure out the cavity's helium pressure sensitivity, severity of Lorentz Force Detuning plus the vibration frequency of mechanical modes, and further, to minimize the instabilities using different stiffening measures. Simulations and optimizations have been done by the 3D Multiphysics solver ANSYS-APDL [2]. In the simulation, niobium sheet of 3 mm thickness was firstly used, with the mechanical properties of Young modulus of 105000 N/mm2, Poisson ratio of 0.38 （see Fig. 1）.

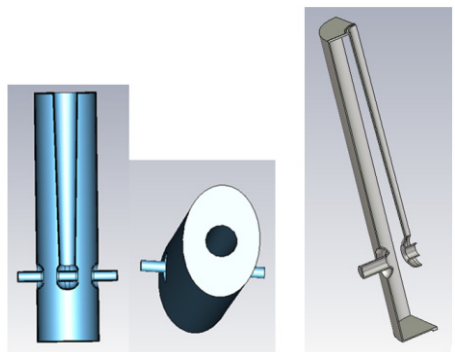

Figure 1: Mechanical model of the elliptical cylinder outer conductor QWR for the structural analysis.

Etching Effects

Surface processing is very important in order to achieve good performance of the superconducting cavity. Either the BCP or the EP is to etch proper thickness of the inner surface, which will change the frequency. According to Slater's perturbation theory, a small deformation in the cavity boundary will lead to a frequency shift.

Using the ANSYS-APDL code, the change in the frequency because of the etching can be calculated. Firstly, you have to get the electro-magnetic field distribution, and then the frequency change caused by the cavity wall's deformation can be obtained. The simulation results show that 1 μm etching thickness will lead to 27Hz increase in the frequency.

Lorentz Force Detuning

The Lorentz force on the cavity surface results from the interaction of the surface electromagnetic fields with the induced surface currents, which will exert pressure to the cavity wall, and the resulting cavity shape deformation ΔV will cause the change in the resonant frequency. The frequency shift caused by Lorentz force is often quantified by K_L which is defined as: $K_L=\Delta f/(E_{acc})^2$.

If the cavity works at the continuous wave mode, then the frequency change will be invariant, it is the static Lorentz force detuning; otherwise, when the cavity works at the pulsed wave mode, the dynamic Lorentz force detuning will be caused. In this paper, only the static situation was considered and 2.5 MV accelerating voltage was to be scaled for the naked cavity whose

*Work supported by 91026001 Nature Science Foundation
#claire335@gmail.com

Copyright © 2012 by the respective authors — cc Creative Commons Attribution 3.0 (CC BY 3.0)

beam port is fixed. The simulation result gives the K_L with the value of -0.34 Hz/(MV/m)2 (see Fig. 2).

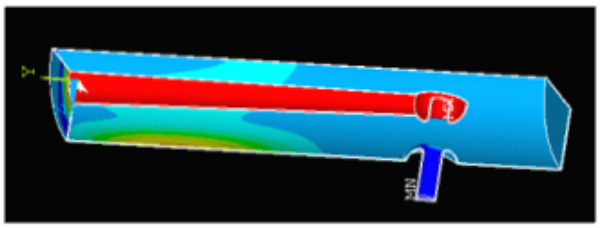

Figure 2: Deformation of the elliptical cylinder outer conductor QWR caused by Lorentz force.

Mechanical Vibration Modes

Mechanical wave in the environment can be transmitted to the cavity by various mediums, and the cavity can resonate mechanically at certain frequencies. Firstly, the naked cavity was simulated for its three lowest modes and results are shown as following, with the vibration frequency of 11 Hz, 13 Hz and 20 Hz, respectively (see Fig. 3).

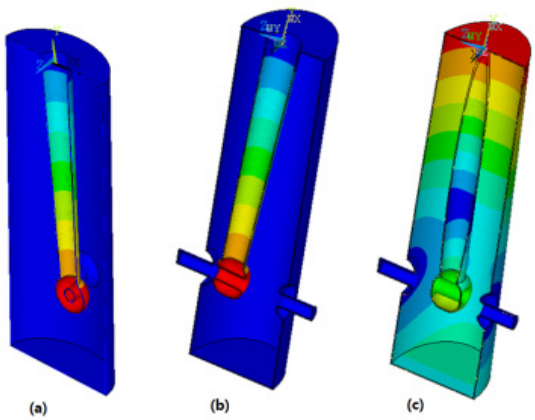

Figure 3: The lowest three vibration modes for the new-shaped naked QWR cavity.

Secondly, stiffening elements were added. A stiffening ring was added on the shorting plate and fixed in the simulation, and in order to reflect more accurately the influence of the tuner, the tuner button was fixed too (see Fig. 4-up). Different radius rings were tested to find out the strengthening effect (see Fig. 4-down). Obviously, the smallest radius ring with 60 mm can increase the mechanical frequency the highest. The vibration mode for the 60 mm stiffened-ring QWR is illustrated in Fig. 5.

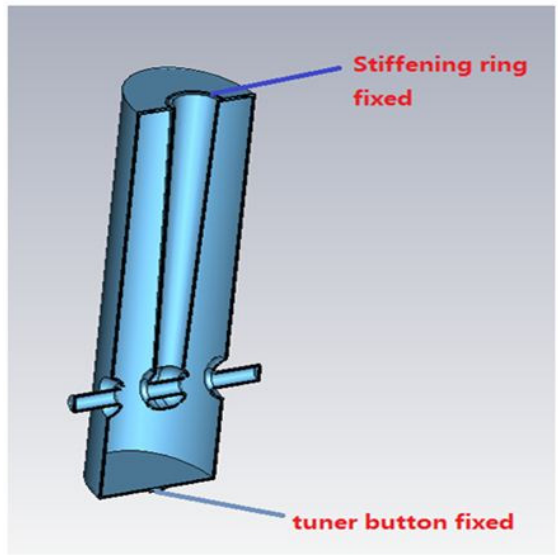

Figure 4: Stiffening ring on the short plate (up); the lowest three vibration modes frequency on the dependence of the radius of stiffening ring (down).

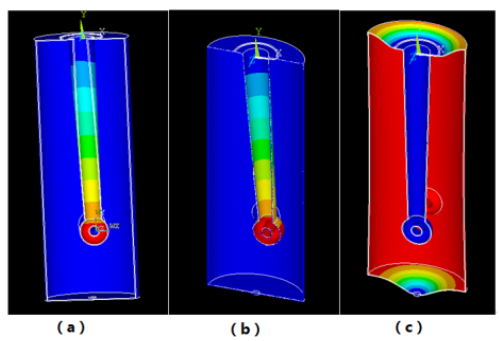

Figure 5: The lowest three vibration modes for stiffened-ring with radius 60mm QWR cavity.

Copyright © 2012 by the respective authors — cc Creative Commons Attribution 3.0 (CC BY 3.0)

Helium Pressure Detuning

In operation, the superconducting quarter wave resonator cavity with frequency of 81.25 MHz works at 4.3K, at which temperature the liquid helium's pressure fluctuates momently. The optimization goal of the mechanical design should be to minimize the cavity's pressure sensitivity. Mechanical simulations were done to quantify the displacements and the resulting frequency vibration from a constant pressure outside the cavity wall [3].

Firstly, the model we used is the one which have the stiffening ring with radius of 60mm and found that the max displacement appeared on the outer conductor corresponding to longer axis of the elliptical cylinder (see Fig. 6).; then we added two supporting rods on the shorting plate attempting to decrease the deformation caused by squeezing on the cavity wall, but the efficacy is not so good (see Fig. 7); later, thicker material (4mm) was used for the cavity wall and the simulation results showed the max displacement was reduced more than in a factor of 2 (see Fig. 8).

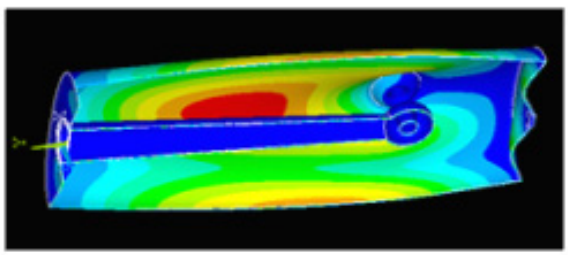

Figure 6: Deformation of ring-stiffened QWR caused by the external pressure, the frequency shift Δf due to the change in ambient pressure ΔP: df/dP~-37 Hz/mbar.

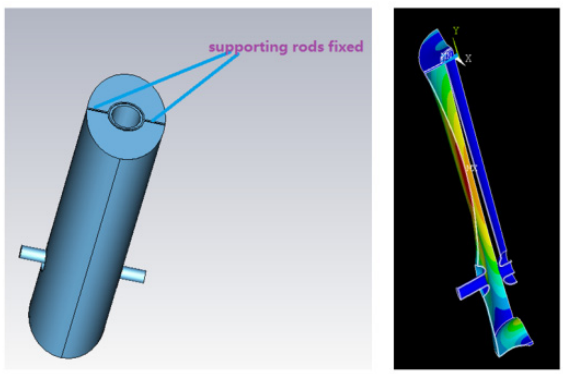

Figure7: Supporting rods on the short plate (left); deformation of ring-and-supporting-rods-stiffened QWR by external pressure: df/dP~-29 Hz/mbar.

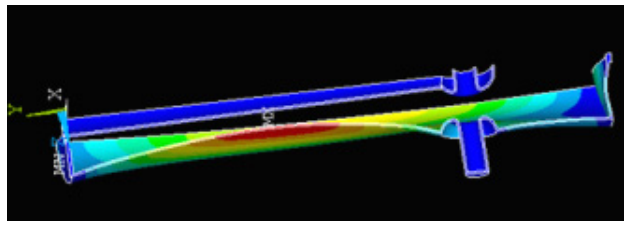

Figure 8: Deformation of ring-and-supporting-rods –stiffened-and-thickened QWR by external pressure: df/dP~-11 Hz/mbar.

CONCLUSIONS

Numerical models have been used to predict the stability of the elliptical cylinder outer conductor quarter wave resonator and relevant stiffening elements have been explored. Major flaws have been encountered in the mechanical models due to the outer conductor's elliptical cylinder shape. Better stiffening measures should be kept searching. In the next stage, the cavity with helium vessel need to be simulated and the fabrication of prototype should be carried out to verify experimentally the mechanical performance.

REFERENCES

[1] C. Zhang et al, "Electro-magnetic optimization of a quarter-wave resonator.", Proc. SRF 2011, Chicago, USA, 2011.

[2] ANSYS, Inc., Canonsburg, Pennsylvania, USA. www.ansys.com.

[3] Zaplatin E., et. al., "Structural Analyses of MSU Quarter-Wave Resonators", in Proceedings SRF 2009: 14th International Conference on RF Superconductivity: Berlin, Germany, Helmholz-Zentrum Berlin, Berlin, Germany, 2009, p.560-563.

Copyright © 2012 by the respective authors — cc Creative Commons Attribution 3.0 (CC BY 3.0)

FIRST MEASUREMENTS ON THE 325 MHz SUPERCONDUCTING CH CAVITY*

M. Busch†,[1], F. Dziuba[1], H. Podlech[1], U. Ratzinger[1], W. Barth[2,3], S. Mickat[2,3], M. Amberg[3], M. Pekeler[4]
[1]IAP Frankfurt University, 60438 Frankfurt am Main, Germany
[2]GSI Helmholtzzentrum, 64291 Darmstadt, Germany
[3]Helmholtz-Institut Mainz (HIM), 55099 Mainz, Germany
[4]RI Research Instruments, Bergisch Gladbach, Germany

Abstract

At the Institute for Applied Physics (IAP), Frankfurt University, a superconducting 325 MHz CH-Cavity has been designed and built. This 7-cell cavity has a geometrical β of 0.16 corresponding to a beam energy of 11.4 AMeV. The design gradient is 5 MV/m. Novel features of this resonator are a compact design, low peak fields, easy surface processing and power coupling. Furthermore a new tuning system based on bellow tuners inside the resonator will control the frequency during operation. After successful rf tests in Frankfurt the cavity will be tested with a 10 mA, 11.4 AMeV beam delivered by the GSI UNILAC. In this paper first measurements and corresponding simulations will be presented.

CAVITY LAYOUT

Worldwide there is a growing interest in applications demanding high beam power and quality (e.g. MYRRHA (**M**ulti Purpose H**Y**brid **R**esearch **R**eactor for **H**igh-Tech **A**pplications) [1]). The superconducting CH-cavity is an appropiate structure for these specifications being characterized by a small number of drift spaces between adjacent cavities compared to conventional low-β ion linacs [2]. Applying KONUS beam dynamics, which decreases the transverse rf defocusing and allows the development of long lens free sections, this results in high real estate gradients with moderate electric and magnetic peak fields. In the past a 19-cell, superconducting 360 MHz CH-prototype has been developed and successfully tested [3]. For future operations a new design proposal for high power applications has been investigated. Presently a new cavity operating at 325.224 MHz, consisting of 7 cells, β = 0.16 and an effective length of 505 mm (see table 1) is undergoing first measurements. Referring to the previous structure this cavity utilizes some novel features (see fig. 1):

- inclined end stems
- additional flanges at the end caps for cleaning procedures
- two bellow tuners inside the cavity
- two ports for large power couplers through the girders

* Work supported by GSI, BMBF Contr. No. 06FY7102, 06FY9089I
† busch@iap.uni-frankfurt.de

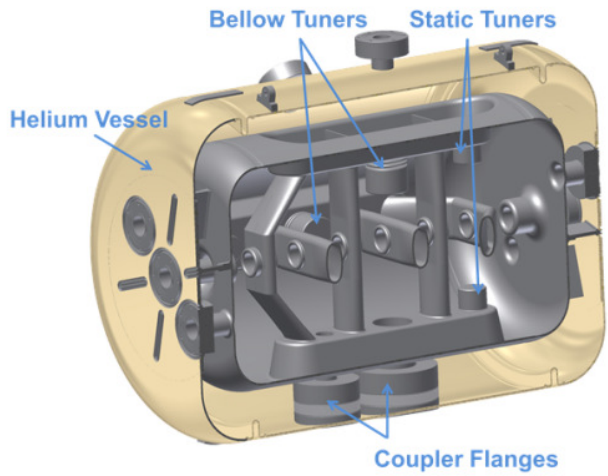

Figure 1: Layout of the superconducting 7-cell CH-Cavity (325.224 MHz, β = 0.16)[4].

Table 1: Specifications of the 325 MHz CH-Cavity.

β	0.16
frequency [MHz]	325.224
no. of cells	7
length ($\beta\lambda$-def.) [mm]	505
diameter [mm]	352
E_a [MV/m]	5
E_p/E_a	5
B_p/E_a [mT/(MV/m)]	13
G [Ω]	64
R_a/Q_0	1248
R_aR_s [$k\Omega^2$]	80

SCOPE FOR THE DYNAMIC BELLOW TUNERS

Rf, mechanical properties as well as Multipacting studies of the novel bellow tuner system can be reviewed in [5],[6], [7].

Copyright © 2012 by the respective authors — cc Creative Commons Attribution 3.0 (CC BY 3.0)

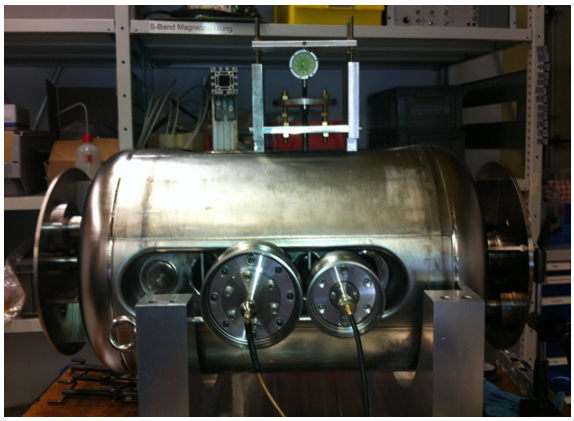

Figure 2: Setup for the test of the dynamic bellow tuners.

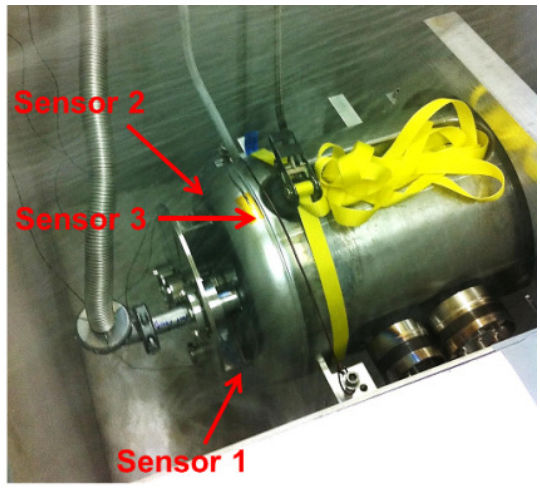

Figure 4: Setup for the preliminary cold test. Thermal sensors on top, alongside and bottom of the end cap.

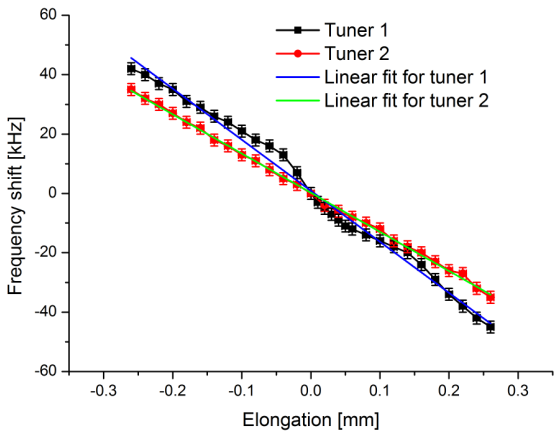

Figure 3: Frequency shift caused by elongation of tuner 1 and tuner 2.

First mechanical and rf tests regarding the scope of the dynamic bellow tuners have been performed at RI (Research Instruments GmbH [8]). The measuring configuration consisted of a framework housing a probe indicator and three spindles applying force via a metal plate on the rod of the tuners in each case (see fig. 2). Proceeding at room temperature the mechanical range of the bellow tuners was limited to $\Delta x = -0.3\ mm..0.3\ mm$ preventively. The measured frequency shift averaged $\Delta f = -172\ kHz/mm$ for tuner 1 and $\Delta f = -132\ kHz/mm$ for tuner 2. The simulated shift for the tuners is ($\Delta f = -150\ kHz/mm$) (see fig. 3).

PRELIMINARY COLD TEST

Prior to the final assembly of the cavity a preliminary cold test was arranged cooling down the cavity to LN_2 temperature. For this purpose the structure has been evacuated and inserted into an insulated metal box (see fig. 4). Three thermal sensors were attached to the top, alongside and bottom of the end caps. The cavity was leak-proof and the last remaining tuner hole was sealed with a Viton plug. This setup allowed a measurement down to an average temperature of roughly -120 °C (see fig. 5). Showing good agreement to the expected shrinkage the frequency shift at LHe should total up to 450 kHz corresponding to a shrinkage of 0.14 %.

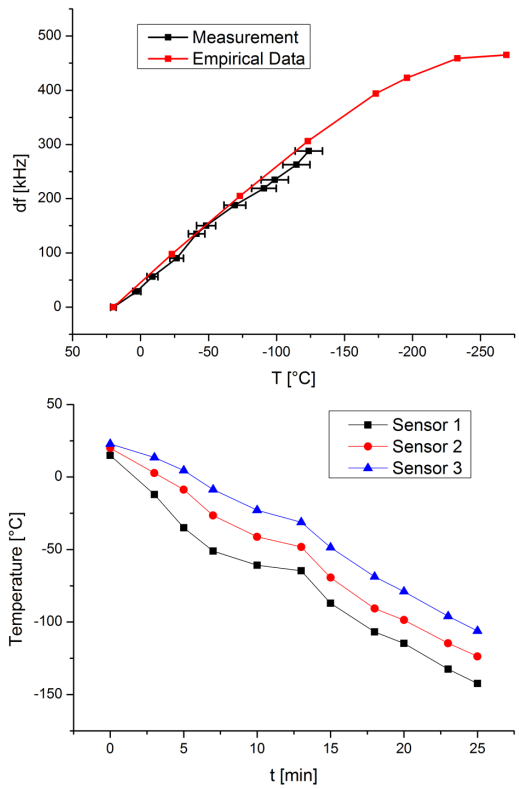

Figure 5: Top: Measured and expected frequency shift due to thermal shrinkage (Empirical data taken from: A.F. Clark, Materials at Low Temperatures). Bottom: Temperature behaviour for all three sensors.

Copyright © 2012 by the respective authors — cc Creative Commons Attribution 3.0 (CC BY 3.0)

PRESSURE SENSITIVITY

Furthermore pressure sensitivity measurements have been performed. Therefore three probe indicators were positioned on both end caps and on one cavity quarter shell (see fig. 6) to measure the deformation at the according spots. Then the cavity has been evacuated with a rotary vane pump down to 100 mbar and 1 mbar in another measurement, respectively. The frequency shift according to the measurements added up to ≈190 kHz and ≈180 kHz, respectively. According to simulations the shift is 205 kHz. The deformation on the cavity quarter shell was 0.22 mm at 100 mbar residual pressure while the simulated reference value amounts to 0.19 mm (see fig. 7).

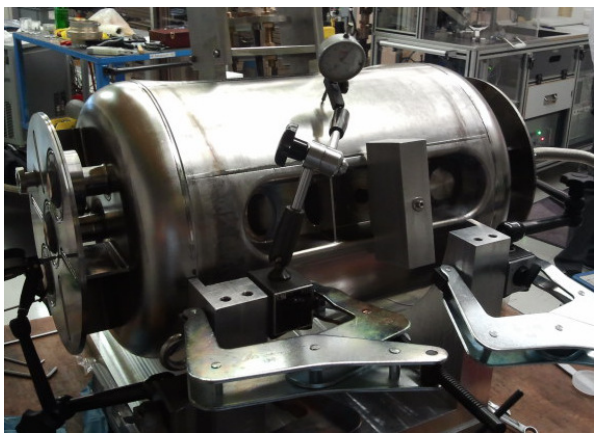

Figure 6: Setup for pressure sensitivity measurement.

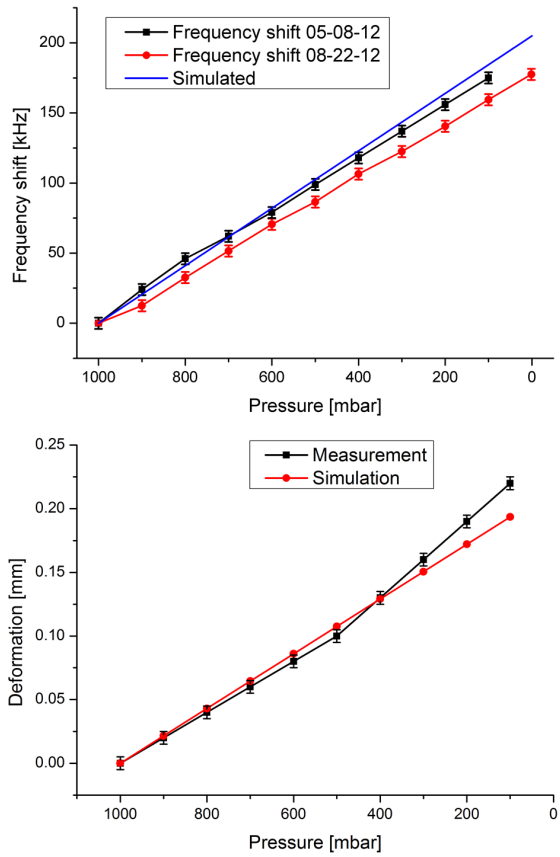

Figure 7: Top: Frequency shift due to evacuation. Bottom: Deformation of the cavity quarter shell versus residual pressure.

ACKNOWLEDGEMENT

This work has been supported by Gesellschaft für Schwerionenforschung (GSI), BMBF contr. No. 06F134I and EU contr. No 516520-FI6W. We acknowledge also the support of the European Community-Research Infrastructure Activity under the FP6 Structuring the European Research Area program (CARE, contract number RII3-CT- 2003-506395). This work was (financially) supported by BMBF 06FY161I, 06FY7102 and by the Helmholtz-InternationalCenter for FAIR within the framework of the LOEWE program (Landesoffensive zur Entwicklung Wissenschaftlich-Ökonomischer Exzellenz) launched by the State of Hesse. We'd like to thank our contact persons and the staff at RI for the close collaboration and the kind assistance for the measurements during this project.

REFERENCES

[1] H. Podlech, M. Amberg, H. Klein, D. Mder, U. Ratzinger, A. Schempp, R. Tiede, M. Vossberg, C. Zhang "General Layout of the 17 MeV Injector for MYRRHA", Proceedings of IPAC 2011, San Sebastian, Spain, p. 2574-2576 .

[2] H. Podlech, A. Bechtold, H. Liebermann, M. Busch, G. Clemente, H. Klein, U. Ratzinger, R. Tiede, C. Zhang Development of Room Temperature and Superconducting CH-Structures for High Power Applications, Proc. of the HPPA5 workshop, Mol, Belgium, 2007, p. 115-124.

[3] H. Podlech, U. Ratzinger, H. Klein, C. Commenda, H. Liebermann, A. Sauer, "Superconducting CH-Structure", Phys. Rev. STAB 10, 080101, 2007.

[4] CST Microwave Studio, http://www.cst.com.

[5] M. Busch, H. Podlech, M. Amberg, F. Dziuba, U. Ratzinger, "Superconducting CH-Cavity development", Proceedings of IPAC 2010, Kyoto, Japan, p. 753-755.

[6] M. Amberg, W. Barth, S. Mickat, M. Busch, F. Dziuba, H. Podlech, U. Ratzinger, K. Aulenbacher, "Structural Mechanical Analysis of Superconducting CH-Cavities", Proceedings of SRF 2011, Chicago, USA, p. 162-164.

[7] M. Busch, F. Dziuba, H. Podlech, U. Ratzinger, W. Barth, S. Mickat, M. Amberg, K. Aulenbacher, "Status of the 325 MHz sc CH-Cavity at IAP Frankfurt", Proceedings of IPAC 2011, San Sebastian, Spain, p. 265-267.

[8] RI, Research Instruments GmbH, Bergisch Gladbach, Germany, http://www.research-instruments.de

Copyright © 2012 by the respective authors — cc Creative Commons Attribution 3.0 (CC BY 3.0)

STATUS OF THE SUPERCONDUCTING CW DEMONSTRATOR FOR GSI*

F. Dziuba†,[1], M. Amberg[1,3], K. Aulenbacher[3,4], W. Barth[2,3], M. Busch[1], H. Podlech[1], U. Ratzinger[1], S. Mickat[2,3]

[1]IAP University of Frankfurt, 60438 Frankfurt am Main, Germany
[2]GSI Helmholtzzentrum, 64291 Darmstadt, Germany
[3]Helmholtz Institut Mainz (HIM), 55099 Mainz, Germany
[4]KPH Mainz University, 55128 Mainz, Germany

Abstract

Since the existing UNILAC at GSI will be used as an injector for the FAIR facility a new superconducting (sc) continuous wave (cw) LINAC is highly requested by a broad community of future users to fulfill the requirements of nuclear chemistry, especially in the research field of Super Heavy Elements (SHE). This LINAC is under design in collaboration with the Institute for Applied Physics (IAP) of Frankfurt University, GSI and the Helmholtz Institut Mainz (HIM). It will consist of 9 sc Crossbar-H-mode (CH) [1] cavities operated at 217 MHz which provide an energy up to 7.3 AMeV. Currently, a prototype of the cw LINAC is under development. This demonstrator comprises the first sc CH cavity of the LINAC embedded between two sc solenoids mounted in a horizontal cryomodule. One important milestone of the project will be a full performance test of the demonstrator by injecting and accelerating a beam from the GSI High Charge State Injector (HLI) in 2014. The status of the demonstrator is presented.

THE SUPERCONDUCTING CW LINAC DEMONSTRATOR

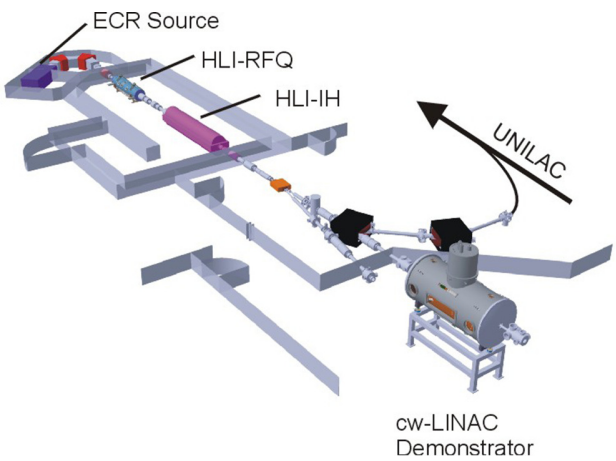

Figure 1: Demonstrator setup with the High Charge Injector at GSI.

The demonstrator will be the first section of the new sc cw LINAC at GSI. It will be operated at 217 MHz which is the second harmonic of the existing 1.4 AMeV GSI HLI. A test of the sc 217 MHz CH cavity, which is the key component of the project, under real operational conditions is the main aim of the demonstrator [2, 3]. It is planned to run a full performance test by injecting and accelerating a beam from the HLI in 2014. Figure 1 shows the cw demonstrator setup and the HLI.

STATUS OF THE SC 217 MHZ CH CAVITY

The sc 217 MHz CH cavity for the cw LINAC demonstrator (see fig. 2) will consist of 15 accelerating cells at a total length of 690 mm while the maximum gradient is 5.1 MV/m. Furthermore, the cavity is designed with the special EQUUS (EQUidistant mUlti-gap Structure) beam dynamics [4].

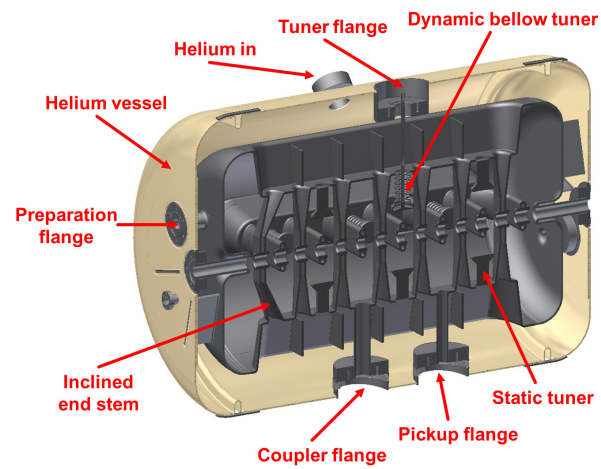

Figure 2: Side view of the sc 217 MHz CH cavity for the cw demonstrator at GSI.

The rf design of the cavity is finished. All main parameters of the cavity are shown in table 1. In June 2012 the production of the cavity has started at Research Instruments (RI) GmbH, Bergisch Gladbach, Germany. It is scheduled to be delivered to the IAP in 2013.

The cavity will be equipped with all necessary auxiliaries like a 10 kW cw power coupler, a titanium helium

* Work supported by HIM, GSI, BMBF Contr. No. 06FY7102
† dziuba@iap.uni-frankfurt.de

Copyright © 2012 by the respective authors — cc Creative Commons Attribution 3.0 (CC BY 3.0)

Table 1: Main parameters of the 217 MHz CH-cavity

β		0.059
Frequency	MHz	216.816
Accelerating cells		15
Total length	mm	690
Cavity diameter	mm	410
Cell length	mm	40.8
Accelerating gradient	MV/m	5.1
U_a ($\beta\lambda$ definition)	MV	3.12
E_p/E_a		6.4
B_p/E_a	mT/(MV/m)	5.4
R_a/Q_0	Ω	3320

vessel, several preparation flanges and a frequency tuning system. Since matching the design frequency during the fabrication and the operation process of a sc CH cavity is a serious challenge, the tuning will be done by capacitive static and dynamic tuners positioned between the stems.

Nine static tuners will be adapted accordingly during the fabrication to hit the design frequency. At a maximum height of 65 mm the frequency shift range of the static tuners is 3.6 MHz. Additionally, three slow bellow tuners (see fig. 3), driven by stepping motors control the frequency of the cavity during operation. They will readjust frequency changes and pressure effects at 4.2 K. Furthermore, two of these bellow tuners are connected to fast reacting piezo elements to compensate limitations like microphonics and Lorentz-Force-Detuning (one in operation, one in spare). The expected frequency shift range for one fast tuner during operation is ± 50 Hz/μm.

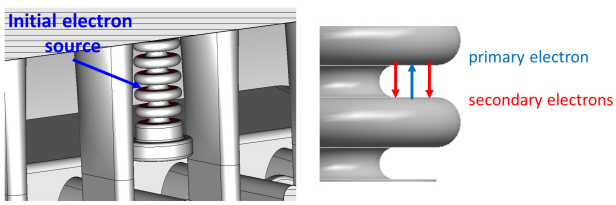

Figure 3: Final design of the 6-cell bellow tuner with the initial electron sources for the multipacting analyses.

To determine the geometry of the bellow tuners several mechanical, rf and multipacting simulations have been performed with ANSYS Workbench, CST MICROWAVE STUDIO and CST PARTICLE STUDIO. The gaps of the bellows are critical spots for multipacting. Figure 3 shows the final geometry of the 6-cell bellow tuner with a gap width of 3.5 mm and the initial electron sources for the multipacting analyses. For the simulations 12000 initial particles were chosen while the energy of the initial electrons has been varied from 2 to 5 eV with an kinetic spread of 50%. The simulated secondary emission yield (SEY)

$$\langle \mathrm{SEY} \rangle = \frac{\text{Total number of secondaries}}{\text{Total number of hits}}$$

for different accelerating gradients is shown in figure 4 as an example for an initial electron energy of 3 eV. As all simulations show, the effect of multipacting does not appear in the tuner gaps.

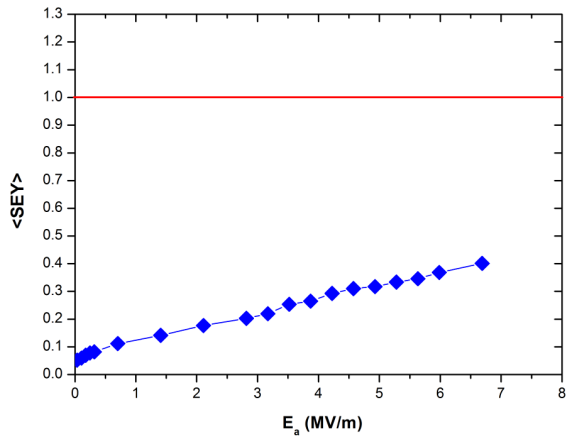

Figure 4: Simulated secondary emission yield for different accelerating gradients at an initial electron energy of 3 eV.

THE HORIZONTAL CRYOSTAT

For the planned beam tests at the GSI HLI a new horizontal cryostat is needed which houses the two sc solenoids and the sc CH cavity (see fig. 5). The final design phase of the cryostat is in progress at the moment. It is going to be built by Cryogenic Limited, London, United Kingdom and scheduled to be delivered in 2014. In comparison to a first concept study [5] the material of the vacuum vessel was changed from stainless steel to aluminum due to cost-efficient production.

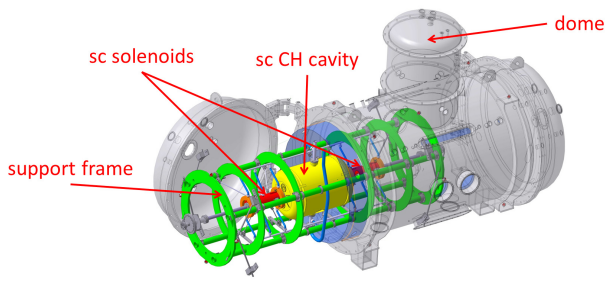

Figure 5: Layout of the horizontal cryostat close to the final design. In the center of the support frame the cavity (yellow) is embedded by two sc solenoids (red).

The main design criteria for the new cryostat are:

- modular design, universally usable - tests of various types of solenoids and CH cavities with different lengths and diameters
- various flanges for assembling options
- a dome for electrical supplies with a reservoir for cryogenic liquids
- a measuring system to control the positions of the cold masses on the beam axis

Copyright © 2012 by the respective authors — cc Creative Commons Attribution 3.0 (CC BY 3.0)

Furthermore, the LHe reservoir will have a flow rate of 100 l/h while the estimated losses of the cryostat are roughly 2 l/h.

Table 2: Design parameters of the cryostat

Inner length	mm	2200
Inner diameter	mm	1120
Material tank		Aluminum
Insulating vacuum	mbar	$< 1 \cdot 10^{-5}$
Max. system pressure	bar	< 0.5
Operating temperature	K	4.2
Temperature thermal shield	K	77
Max. static losses (stand by)	W	< 10

To investigate the behavior of the cryostat's support frame under a cryogenic environment, first thermal and mechanical simulations have been performed with CST MPHYSICS STUDIO. Therefore, three different temperature sources were added to a simple model of the cryostat and the cavity to run the stationary solver (see fig. 6). Figure 6 shows the 3D temperature distribution of the support frame with the suspension rods. Heat transfer caused by radiation was not considered in the simulations as well as insulating materials. The outer suspension rods of the support frame were fixed during the simulations. As the contour plots of figure 7 show, the total displacement in x and y direction is roughly 3 mm while in z direction a displacement of 10 mm appears.

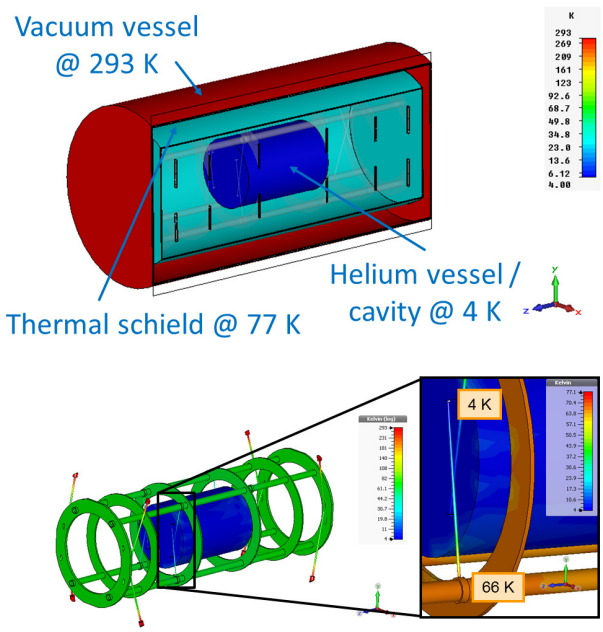

Figure 6: Temperature sources for the thermal stationary solver (top) and 3D temperature distribution of the support frame (bottom).

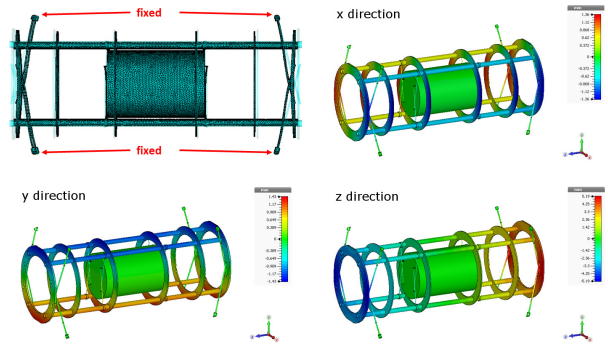

Figure 7: Deformed mesh of the support frame (scaling factor 10) and total displacement in x,y,z direction.

SUMMARY & OUTLOOK

First preparations were done to set up the cw LINAC demonstrator at the GSI HLI. A 3000 l LHe-tank as well as a helium recovery system have been delivered to GSI.

The rf design of the sc 217 MHz CH cavity is completed and its fabrication has started in June 2012 at RI. At present, the final design phase of the horizontal cryostat is in progress. The cryostat as well as the sc solenoids have been ordered from Cryogenic Limited.

The delivery of all main components is expected in 2013/14. After the assembling under clean room conditions and first rf test at the IAP, a full performance test with beam at the HLI is foreseen in 2014. Successful tests of the demonstrator are a fundamental step on the way to the proposed sc cw LINAC.

ACKNOWLEDGMENT

This work has been supported by Helmholtz-Institut Mainz (HIM) and Gesellschaft für Schwerionenforschung (GSI). This work was (financially) supported by BMBF Contr. No. 06FY7102 and by the HelmholtzInternational-Center for FAIR within the framework of the LOEWE program (Landesoffensive zur Entwicklung Wissenschaftlich-Ökonomischer Exzellenz) launched by the State of Hesse.

REFERENCES

[1] H. Podlech et al., Superconducting CH structure, Phys. Rev. STAB 10, 080101 (2007).

[2] S. Mickat et al., The sc cw-LINAC-Demonstrator - SRF Technology finds the way to GSI, in Proc. of SRF2011 (to be published), Chicago, USA (2011).

[3] F. Dziuba et al., Development of superconducting crossbar-H-mode cavities for proton and ion accelerators, Phys. Rev. STAB 13, 041302 (2010).

[4] S. Minaev et al., A Superconducting Energy Variable Heavy Ion Linac with Constant Beta, Multi-Cell Cavities of CH-Type, Phys. Rev. STAB 12, 120101 (2009).

[5] V. Gettmann et al., The sc cw-LINAC Demonstrator - an R&D project for SRF technology, in Proc. of SRF2011, Chicago, USA (2011).

Copyright © 2012 by the respective authors — cc Creative Commons Attribution 3.0 (CC BY 3.0)

DEVELOPMENT OF PERMANENT MAGNET FOCUSING SYSTEM FOR KLYSTRONS

Y. Fuwa, Y. Iwashita, H. Tongu, Institute for Chemical Research, Kyoto University, Kyoto, Japan
S. Fukuda, S. Michizono, High Energy Accelerator Research Organization, Ibaraki, Japan

Abstract

A permanent magnet focusing system for klystrons is under development to improve reliability of RF supply system and reduce power consumption. To save production cost, anisotropic ferrite magnets are used in this system. A test model has been fabricated and the power test of a 750 kW klystron with this focusing magnet is carried out. 60 % of the nominal output power has been achieved at a preliminary power test so far.

INTRODUCTION

Distributed Klystron Scheme (DKS) is proposed as one of the RF supply scheme for International Linear Collider (ILC) to reduce the cost and the down time by raising the reliability [1]. Because thousands of relatively small modulating anode (MA) klystrons ware required in DRFS scheme, the failure rate of each component must be reduced. Especially thousands units of electromagnet for klystron beam focusing would cause maintenance problems. Replacing the electromagnets by permanent magnets can eliminate their power supplies and cooling system. Hence the failure rate of the RF supply system can be reduced and cut down the operation cost. A klystron beam focusing system with ferrite magnets is under development is described.

FABRICATION OF FOCUSING MAGNET

Magnetic Materials

There have been precedents for electron beam focusing in klystrons with permanent magnets such as ALNICO, the rare earth (RE) [2,3,4]. Figure 1 shows the B-H curves for these magnet materials and anisotropic ferrite magnets. ALNICO magnets, which have high remanence, shows less coercivity and easily demagnetize. Although RE magnets such as NdFeB has high remanence and coercivity, they are rather expensive and have the resource problem. The anisotropic ferrite magnets have less remanence but higher coercivity than ALNICO. The required magnetic field for beam focusing in klystrons is less than 1 kGauss, therefore the remanence of the anisotropic ferrite magnets is enough high. And the material costs are not expensive, because anisotropic ferrite magnets are composed of iron oxide.

Magnet Field Distributions

Periodic Permanent Magnet (PPM) focusing scheme has relatively well-known magnetic field distribution. In a focusing system with permanent magnet, the alternating magnetic field can be easily generated because an integrated value of magnetic field vector along closed

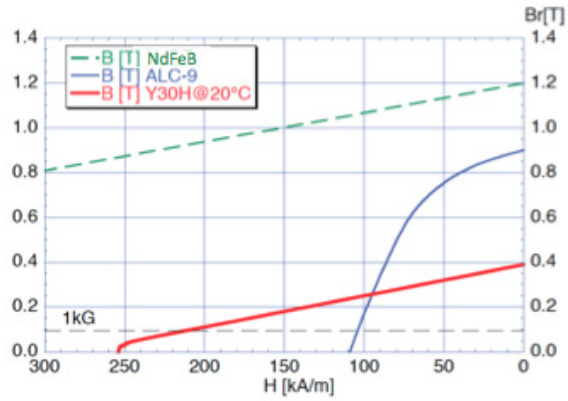

Figure 1: B-H curves of rare earth, ALNICO and ferrite magnets.

curve or infinitely-long axis is zero by the Ampere's law. However, periodicity cause stop bands. For pulse operations, the operating point always crosses such region during pulse rising time and the beam loss causes wall heating and prevents stable operation.

For safe operation, unidirectional magnetic field distribution is applied. Because the required magnet field is not high, anisotropic ferrite magnets can be used. RADIA 4.29[5,6] is used for the magnetic field design. Applied design is shown in Figure 2. Magnets shown in Figure 2 are categorized into two groups. The one group consists of magnets surrounding the klystron body

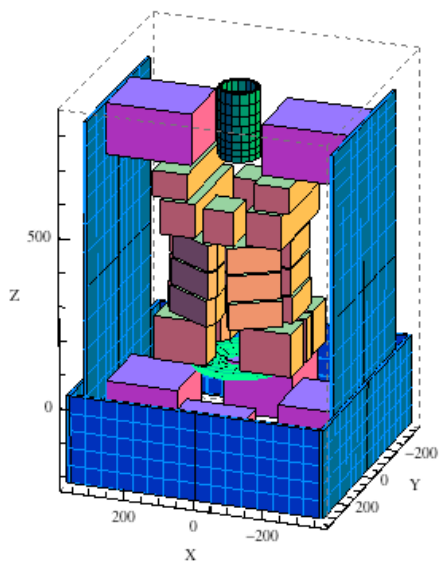

Figure 2: Layout of magnet and iron yoke.

Copyright © 2012 by the respective authors — cc Creative Commons Attribution 3.0 (CC BY 3.0)

(yellowish ones in Fig. 2), whose easy axes are parallel to the klystron beam axis. The other group consists of the bottom and the top large magnet bricks (purplish ones in Fig. 2) to form the magnetic field around the cathode and the collector area. Their easy axis is perpendicular to the klystron axis. All magnets are retractable for the insertion of the klystron. Klystrons are usually inserted from the top of the focusing magnets and thus the minimum aperture of the magnets must be larger than most fat part of the klystron such as ceramic insulator. The retractable magnets can open their aperture at the klystron installation time and close at the operation. (see Figure 3). This retracting mechanism can also be used for the field adjustment.

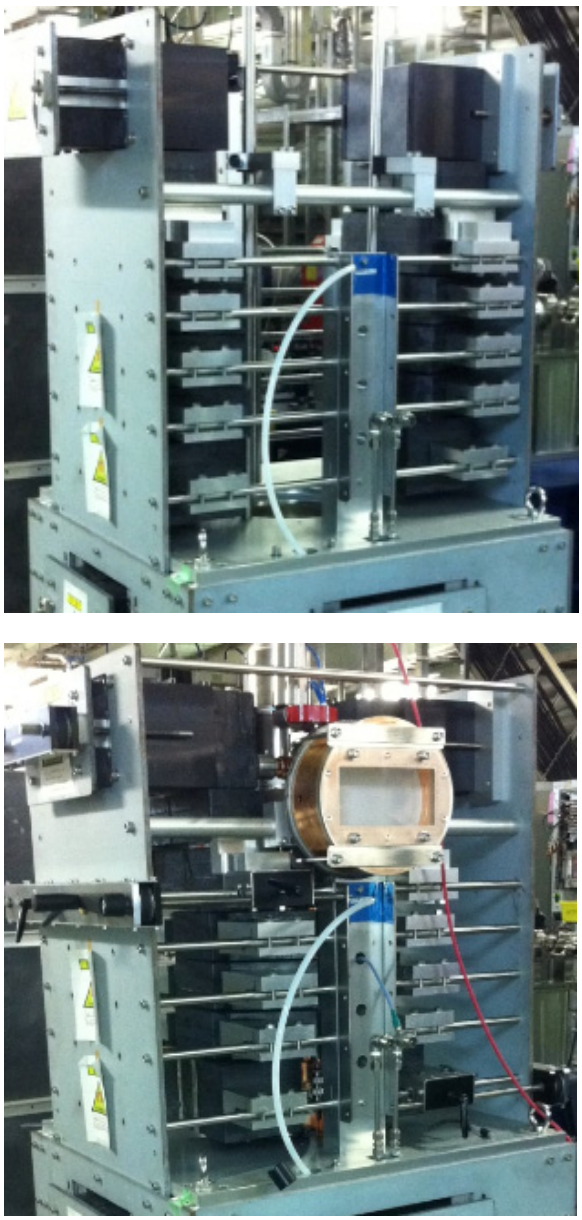

Figure 3: The magnets have larger aperture than the klystron body before the klystron installation (upper). After the klystron installation, the magnets are brought close to the klystron (lower).

KLYSTRON POWER TEST

To evaluate performance of the fabricated focusing magnet, a power test with real klystron (Toshiba E37501) is carried out. Figure 4 shows the E 37501 and Table 1 shows its nominal specification. The magnet field distribution, which is measured, adjusted is applied for power test. Figure 5 shows the longitudinal magnetic field. The blue line shows measured magnetic field generated by permanent magnets and the red line shows that by the electromagnet. The beam transport simulation has been performed by DGUN[7] using measured longitudinal magnetic field. The result of the simulation shows that the beam can pass through the klystron body without loss in the DC state (see Figure 6). Figure 7 shows transverse magnetic field components. The transverse magnetic field components are adjusted less than 10 Gauss by moving magnet's position. In the power test, the klystron was operated with 1 Hz repetition rate and the RF pulse duration was 1 ms so as not to damage the klystron body by unexpected beam loss. The result of the preliminary power test where the klystron cathode voltage is from 45 kV to 65 kV is shown in Figure 8. In Figure 8, red plots are the output maximum output power with our permanent magnets and blue plots are the max output power with an electromagnet measured by Toshiba. About sixty percent of the nominal output power at Toshiba is attained by the permanent

Figure 4: The klystron using in power test (Toshiba E37501).

Table 1: Specification of E37501

frequency	1.3 GHz
Max Output Power	750 kW
Max Efficiency	55 %
Max Gain	43 dB
Max Pulse Length	1.5 msec
Max Repetition Rate	5 Hz
Max Beam Voltage	66 kV
Max Beam Current	50 A

Copyright © 2012 by the respective authors — cc Creative Commons Attribution 3.0 (CC BY 3.0)

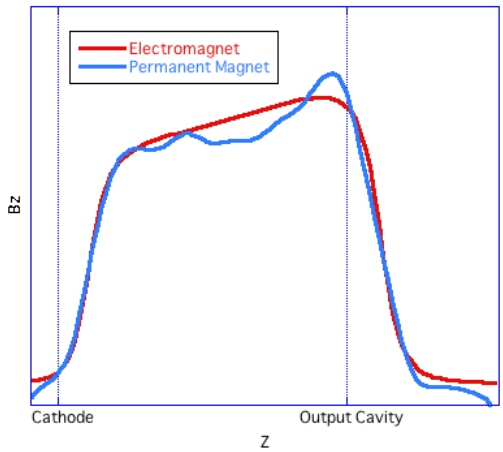

Figure 5: The longitudinal magnetic fields.

Figure 6: The result of DGUN simulation with the measured longitudinal magnetic field.

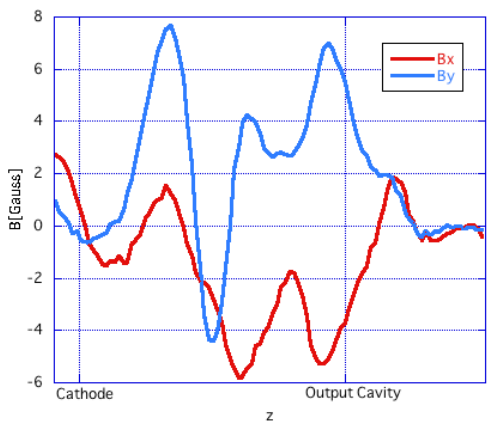

Figure 7: The measured transverse magnetic fields.

magnets in this early stage experiment. And the energy efficiency is about 33 % for our permanent magnets. This low output power and efficiency are supposed to be caused by the not optimized magnetic field in the cathode area. Figure 9 shows the calculated magnetic field in the cathode area. Although the magnetic field near the axis looks good, that on the outskirts may not be optimum, which results in beam mismatch.

Electric discharges occurred frequently in the operation and prevent stable operation. The electric discharges seem to be caused by the shape of the oil tank; the oil tank has a smaller diameter than that for the electromagnet focusing in order to reduce the distance from the magnets to the axis. This problem will be fixed by a remodeling of the tank. Further study will be continued for a better performance through magnetic field adjustment and so on.

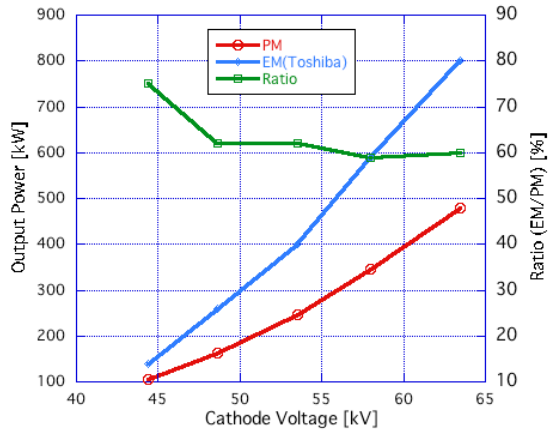

Figure 8: The preliminary result of the klystron power test.

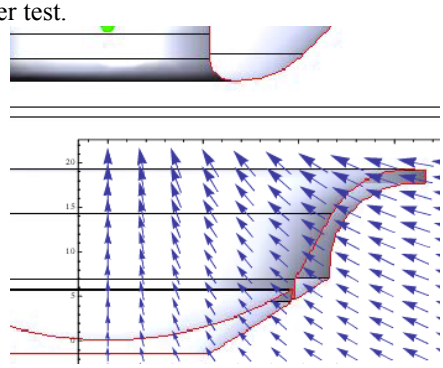

Figure 9: The calculated magnetic field in the cathode area

REFERENCES

[1] S. Fukuda, Distributed RF Scheme (DRFS) – Newly Proposed HLRF Scheme for ILC, LINAC2010, Tsukuba, pp.112-114, 2010.

[2] Jane V. Lebacqz, Status Report on Klystron Improvements, IEEE, Trans., NS-22, 3 pp.1324-1327, June1975.

[3] Fukuda, S., Shidara, T., Saito. Y., Hanaki, H., Nakao, K., Homma. H., Anami, S., Tanaka, J., PERFORMANCE OF HIGH POWER S BAND KLYSTRONS FOCUSED WITH PERMANENT MAGNET, 198624009 KEK-86-9, Feb. 1987.

[4] S. Masumoto, et al., STUDY OF PPM-FOCUSED X-BAND PLUSE KLYSTRON, Proc. of LINAC 2006, Knoxville, pp.628-630.

[5] P. Elleaume, O. Chubar, J. Chavanne, Computing 3D Magnetic Field from Inserted Devices, proc. of the PAC97, May 1997, p.3509-3511.

[6] O. Chubar , P. Elleaume, J. Chavanne, A 3D Magnetostatics Computer Code For Insertion Devices, SRI97 Conf. Aug. 1997, J. Synchrotron Rad. (1998). 5, 481-484.

[7] A. Larionov, K. Ouglekov, "DGUN-code for simulation of intensive axial-symmetric eletron beams", 6th ICAP, TU Darmstadt, Germany, 2000, p. 17.

Copyright © 2012 by the respective authors — cc Creative Commons Attribution 3.0 (CC BY 3.0)

DEVELOPMENT OF SUPERCONDUCTING RADIO-FREQUENCY DEFLECTING MODE CAVITIES AND ASSOCIATED WAVEGUIDE DAMPERS FOR THE APS UPGRADE SHORT PULSE X-RAY PROJECT*

J. Holzbauer†, A. Nassiri, G. Waldschmidt, G. Wu
Argonne National Laboratory, Argonne, IL 60439, U.S.A.

Abstract

The Advanced Photon Source Upgrade (APS-U) is a Department of Energy (DoE) funded project to increase the available x-ray beam brightness and add capability to enhance time-resolved experiments on few-ps-scale at APS. A centerpiece of the upgrade is the generation of short pulse x-rays (SPXs) for pump-probe time-resolved capability using SRF deflecting cavities [1]. The SPX project is designed to produce 1-2ps x-ray pulses for some users compared to the standard 100ps pulses currently produced. SPX calls for using superconducting rf (SRF) deflecting cavities to give the electrons a correlation between longitudinal position in the bunch and vertical momentum [2]. The light produced by this bunch can be passed through a slit to produce a pulse of light much shorter than the bunch length at reduced flux. The ongoing work of designing these cavities and associated technologies will be presented. This includes the design and prototyping of higher- (HOM) and lower-order mode (LOM) couplers and dampers as well as the fundamental power coupler (FPC). This work will be given in the context of SPX0, a demonstration cryomodule with two deflecting cavities to be installed in APS in early 2014.

INTRODUCTION

The SPX project calls for the use of an RF deflecting-mode cavity to chirp electron bunches, giving the electrons a correlation between their longitudinal position in the bunch and their vertical momentum. Synchrotron light produced from this bunch can then be passed through a physical slit to create a shorter light pulse at the proportional sacrifice of total flux. This scheme was first proposed by Zholents [1]; the scheme can be seen in Figure 1.

A significant amount of design work has gone into the RF cavities required for this project, details of which can be found in [2, 3, 4, 5, 6, 7]. This cavity application has many specific challenges including the need to heavily damp all non-operational modes to preserve beam quality for other APS users.

CAVITY DESIGN

The current design is a squashed elliptical dipole-mode cavity with a Y-shaped end group and an on-cell damping

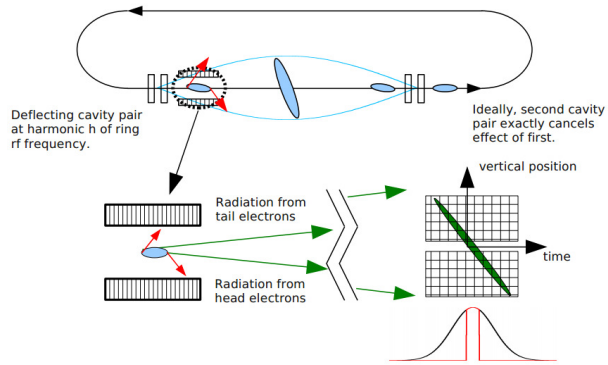

Figure 1: Schematic of Zholent's short pulse x-ray generation scheme. Image credit to [3].

port which can all be seen in Figure 2. Two of the waveguides from the Y end group will be used for damping of higher-order modes (HOMs) while the third will be primarily used as the forward power coupler. The on-cell damper is used primarily to damp the fundamental mode, called the lower-order mode (LOM). A list of the cavity parameters can be seen in Table 1.

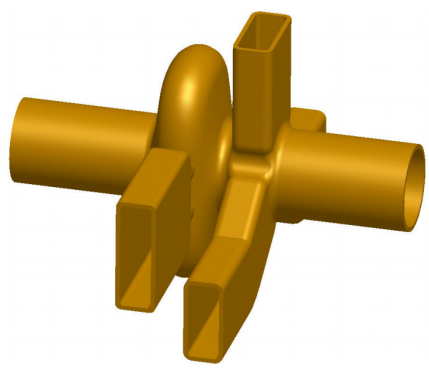

Figure 2: Schematic of a deflecting mode cavity for SPX. The LOM waveguide can be seen on-cell with the Y-end group (HOM dampers and FPC) to the right. Image credit to [3].

At this point, it is expected to use a BCP etching during cavity processing. Given the cavity parameters and this processing technique, 120 mT is the maximum expected reliable peak magnetic field. Given this and the requirement that each deflecting section have a total of 2 MV of

* Work supported by the U.S. Department of Energy, Office of Science, under Contract No. DE-AC02-06CH11357
† jholzbauer@aps.anl.gov

Copyright © 2012 by the respective authors — cc Creative Commons Attribution 3.0 (CC BY 3.0)

Table 1: Electromagnetic figures of merit

Parameter	Value
Frequency	2815 MHz
Q_0	10^9
Deflecting Voltage (V_t)	0.5 MV
Peak Surface Electric Field	41 MV/m
Peak Surface Magnetic Field	100 mT
Stored Energy	0.38 J
P_{loss} $Q_0 = 10^9$	7 W
(R/Q)'	18.6 Ω
Operational Temperature	2K

deflecting voltage to achieve 2-ps x-ray pulses [3], each cavity will be run at 0.5 MV deflecting voltage or 100 mT. In order to increase the operational margin, the possibility of electropolishing these cavities is being investigated.

HIGHER-ORDER MODE DAMPING

Because of the tight beam requirements, strong damping of non-operating modes was a focus of the overall cavity design. The squashed elliptical cavity geometry is meant to break the degeneracy of the dipole modes, increasing the frequency of the undesired dipole polarization as was done at KEK in the design of a similar deflecting mode cavity [8]. Significant work has been put into modeling of the cavities' broadband impedances [4], as well as the design of the HOM waveguides and dampers [7]. While the HOM waveguide design has been investigated in concept [9], their detailed design and packaging had not been considered until recently.

HOM Transitional Waveguide

Design of the SPX prototype cryomodule (SPX0) is well underway at JLab. Because of the broadband HOM damping requirements, it was decided to not use a window for the HOM dampers. This meant that all components of the HOM dampers would have to be assembled on the cold mass and had to fit inside the space frame for assembly. This is further complicated by the attachment of the tuner to the cavity very near to one of the HOM waveguide ports, making the HOM transitional waveguide (the waveguide running from the cavity to the damper itself) a very complex shape. This shape can be seen in Figures 3 and 4.

Despite these logistical requirements, the broadband transmission of this waveguide must not be compromised. The sizing of the HOM waveguide leading out of the cavity was chosen to have it's cutoff frequency between the operational frequency (2.815 GHz) and the first higher-order mode (estimated at 2.94 GHz). The waveguide must connect this custom sized waveguide to the HOM dampers which are based on WG340 waveguide. The placement and geometry of this taper was carefully considered to both give adequate attenuation of the operational mode and decent broadband transmission of HOM power.

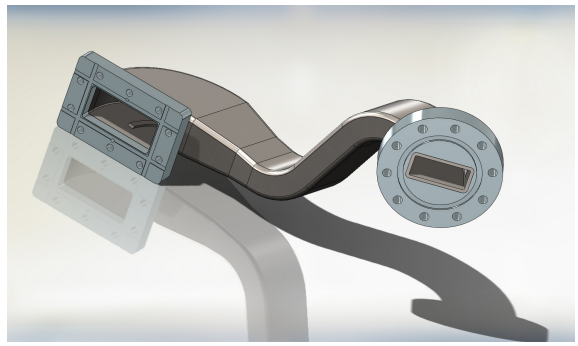

Figure 3: HOM Transitional Waveguide. Flange on the left connects to the cavity while the flange on the left connects to the damper assembly.

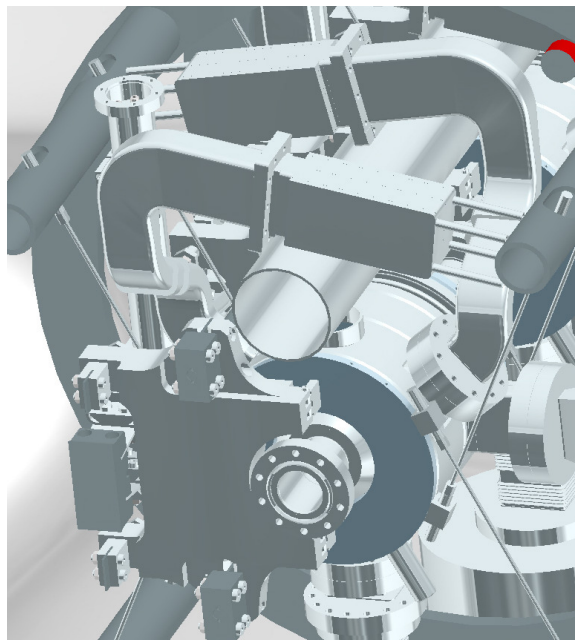

Figure 4: Section view of the SPX0 cryomodule space-frame mock-up. Cavity in helium vessel can be seen at the bottom of the image with tuner attached on the right side of the vessel. The HOM transitional waveguides and dampers can be seen crossing at the top of the image.

Given the space available, it was not possible to make the taper gradual enough to provide adequate broadband transmission because the first HOM (2.94 GHz) was still relatively close to cutoff. A ridge was added to this taper to improve transmission through the transition. The ridge was run through the taper on the wide wall and extended both toward the cavity into the S-Bend section and away from the cavity into the final, large radius bend. While this ridge improved transmission at 2.94 GHz, it also reduced transmission at some higher frequencies (3.0 GHz and 3.2 GHz) due to reflections off of the beginning of the ridge. The length of these ridge extensions was optimized to give the best broadband performance, the results of which can be see in Figure 5. The length of the ridge extension into

Copyright © 2012 by the respective authors — cc Creative Commons Attribution 3.0 (CC BY 3.0)

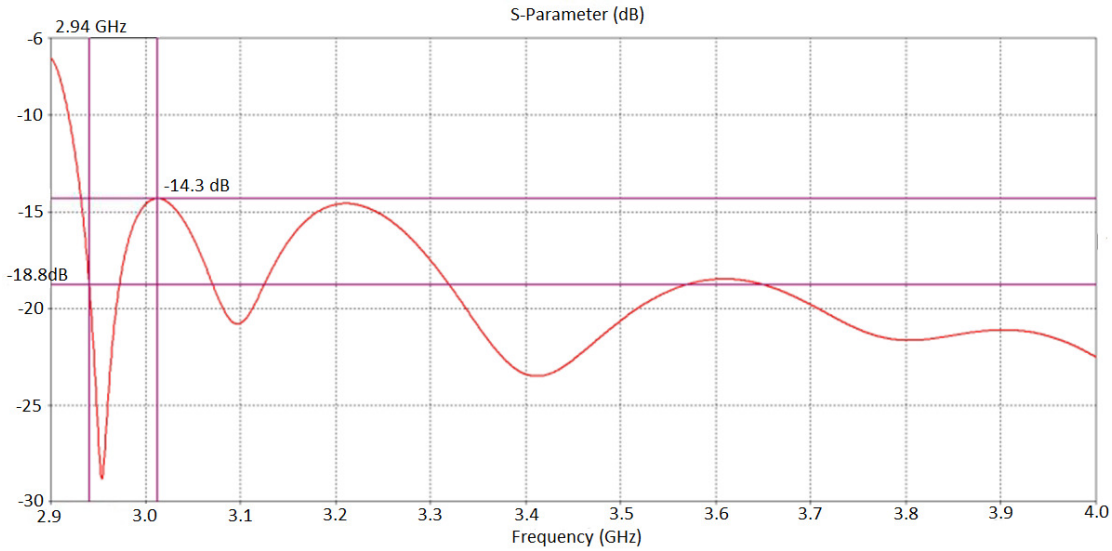

Figure 5: S11 parameter for the HOM Transitional Waveguide with optimized ridge. Reflection at the first HOM (2.94 GHz) is better than -18dB while the additional reflection cause by the ridge at 3.0 and 3.2 GHz is kept better than -14dB.

the S-Bend had the largest effect on performance. Longer ridges improved transmission at the first HOM frequency (2.94 GHz) but reduced performance at the higher frequencies. Without a ridge, S11 at 2.94 GHz was roughly -7dB, an unacceptably high reflection. Unfortunately, any reasonable ridge created the reflection at the higher frequencies which cannot be completely suppressed.

It is desired to keep the evanscant power from the operational mode reaching the HOM damper to below 10 W at full field to reduce total load on the damper. Simulations indicate that this traveling wave power should be 4.5 W, an acceptable number.

Waveguide Fabrication

When fabricated, the waveguide must be both mechancially robust and an adequate thermal barrier to keep the 2K heat load low. The HOM damper is water-cooled at room temperature outside the thermal shield and separated from the HOM transitional waveguide by a bellows, providing thermal resistance. The damper-end flange of this waveguide is expected to be strapped to the 80K cooling circuit. With a 1/8" wall of stainless steel and 10 microns of copper plating to improve RF performance, it is expected that this waveguide will contribute about 1.4 W (dynamic) to the 2 K heat load. Most of this comes from the evanescent fields in the beginning of the waveguide. Several fabrication methods are being considered for this complex geometry including fabrication from stainless steel sheet in parts, forming, and solid casting.

CONCLUSIONS

A credible design has been advanced for the HOM transitional waveguide. Prototyping is expected to begin in the coming months to validate the design and chosen fabrication process. SPX0 will provide an excellent test bed for this design and its interface with the cavity and HOM dampers. Results from this testing will be used to improved this design if necessary for the final SPX cryomodules.

REFERENCES

[1] A. Zholents et al., NIM A 425, 385 (1999).

[2] A. Nassiri et al., "Status of the Short-Pulse X-Ray Project at the Advanced Photon Source, IPAC 2012, New Orleans, LA, May 2012.

[3] Advanced Photon Source Upgrade Project - Conceptual Design Report, May 2011, http://www.aps.anl.gov/Upgrade/Documents/CDR/.

[4] H. Wang et. al., "Design, Prototype and Measurement of a Single-Cell Deflecting Cavity for the Advanced Photon Source", presented at the 2009 Particle Accelerator Conference, Vancouver, BC, Canada, May 2009, WE5PFP059.

[5] H. Wang et. al., "Crab Cavity and Cryomodule Prototype Development for the Advanced Photon Source", presented at the 2011 Particle Accelerator Conference, New York, NY, USA, March 2011, WEOCS7.

[6] G. Waldschmidt et. al., "Status of RF Deflecting Cavity Design for the Generation of Short X-Ray Pulses in the Advanced Photon Source Storage Ring", presented at the European Particle Accelerator Conference, Edinburgh, Scotland, June 2006, THPLS076.

[7] G. Waldschmidt et. al., "Superconducting Cavity Design for Short-Pulse X-Rays at the Advanced Photon Source", presented at the 2011 Particle Accelerator Conference, New York, NY, USA, March 2011, THP212.

[8] K. Hosoyama et. al., "Crab Cavity Development", presented at the 2005 Superconducting RF Workshop, Ithaca, NY, USA, June 2005, ThA09.

[9] L. Xiao et. al., "Higher Order Modes Damping Analysis for the SPX Deflecting Cavity Cryomodule", Proceedings of IPAC2012, New Orleans, Louisana, USA, pp 2414 - 2416.

Copyright © 2012 by the respective authors — cc Creative Commons Attribution 3.0 (CC BY 3.0)

MULTIPACTING ANALYSIS OF HIGH-VELOCITY SUPERCONDUCTING SPOKE RESONANTORS*

C. S. Hopper† and J. R. Delayen
Center for Accelerator Science, Department of Physics,
Old Dominion University, Norfolk, VA, 23529, USA and
Thomas Jefferson National Accelerator Facility, Newport News, VA 23606, USA

Abstract

Some of the advantages of superconducting spoke cavities are currently being investigated for the high-velocity regime. When determining a final, optimized geometry, one must consider the possible limiting effects multipacting could have on the cavity. We report on the results of analytical calculations and numerical simulations of multipacting electrons in superconducting spoke cavities and methods for reducing their impact.

INTRODUCTION

Superconducting multi-spoke cavities for frequencies of 325, 352, 500, and 700 MHz and velocities of β_0 = 0.82 and 1 have been designed and optimized [1, 2, 3] for a variety of possible applications. These applications include, but are not limited to, compact machines such as future light sources and high-energy proton or ion linacs. Here we focus on what regions of these resonators are most susceptible to multipacting events.

When the internal surface of a rf cavity is exposed to the high fields maintained in a superconducting cavity, electrons (known as primary electrons) can be emitted from the metal. The kinetic energy and trajectory of these electrons is determined by the electromagnetic fields, and in many cases, they will come in contact with another part of the surface with a certain amount of impact energy. If this energy falls within the secondary emission yield (SEY) range, then additional electrons, known as secondary electrons, will be ejected [4]. Figure 1 shows a generic SEY curve. The parameters E^I_{oc}, and E^{II}_{oc} are known as the crossover energies for which δ = 1. E_{om} marks the electron energy for which δ is maximum. These parameters can vary greatly between materials. Even for a given material, these parameters can vary widely based on both the bulk properties and surface condition.

For well prepared niobium cavities, the crossover energies are around 150 eV and 1050 eV, while E_{om} is around 375 eV [5]. We have presented preliminary results for crossover energies of 150 eV and 2000 eV previously [2]. When secondary electrons are in resonant trajectories, and each impact energy is in the range for which $\delta > 1$, then a cascade can occur generating excessive heat, thus leading to thermal breakdown. These regions are commonly called barriers, and they are classified as either "soft" or "hard." Soft barriers are those that can be conditioned through and thereby passed. It is believed conditioning occurs because multipacting electrons actually clean the surface to a point where the secondary emission yield is below unity [7]. Hard barriers are those which persist resulting in a limited achievable gradient and quenching.

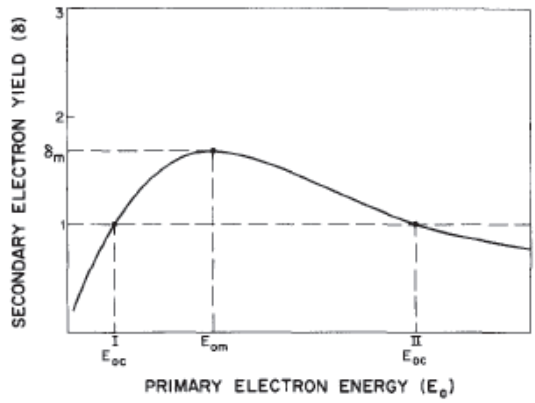

Figure 1: Definition of secondary-electron yield-curve parameters [6]

By improving the quality of the surface, the soft barriers on the gradient can be eliminated. On the other hand, hard barriers can only be overcome by changing the cavity geometry in such a way as to avoid resonant trajectories all together.

Multipacting is also characterized, most commonly, as either one-point or two-point. One-point multipacting occurs when the time of flight of the electron between two impacts is an integer number of rf cycles and that the electron's impact site is approximately the same as it's ejection site. This condition can be described in terms of the cyclotron and rf frequencies as [8],

$$\frac{f}{n} = \frac{eB}{2\pi m} \tag{1}$$

In the case of two-point multipacting, the time of flight is an odd number of half rf cycles and the impact site is not the same as the ejection site. The former condition can be described with the same parameters as (1) [9],

$$\frac{2f}{2n-1} = \frac{eB}{2\pi m} \tag{2}$$

* Work supported by U.S. DOE Award No. DE-SC0004094
† chopp002@odu.edu, chrsthop@jlbab.org

Copyright © 2012 by the respective authors — cc Creative Commons Attribution 3.0 (CC BY 3.0)

MULTIPACTING ANALYSIS

In order to analyze the multipacting conditions in our optimized multi-spoke cavities, the 3D parallel tracking code Track3P contained in the ACE3P code suite developed by SLAC was used [10]. The cavity was divided into three regions as seen in figure 2. The regions labeled 1 and 3 include the end caps, half of one spoke, and the outer conductor enclosing the end accelerating gaps. The region labeled 2 includes half of each spoke and the outer conductor enclosing the middle accelerating gap. Due to the symmetry, regions 1 and 3 give similar enough results that we will only discuss 1 and 2.

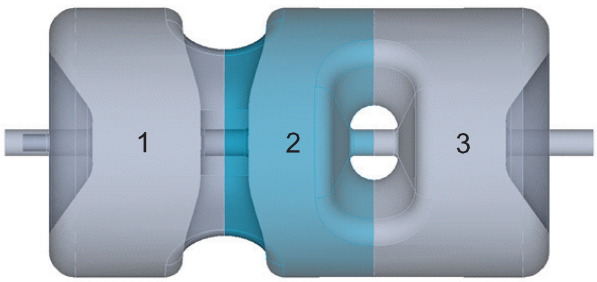

Figure 2: 325 MHz, β_0 = 0.82 cavity divided into three regions for multipacting analysis.

End cells

Figure 3 shows the resonant electrons surviving 50 rf cycles in region 1, along with their impact energies.

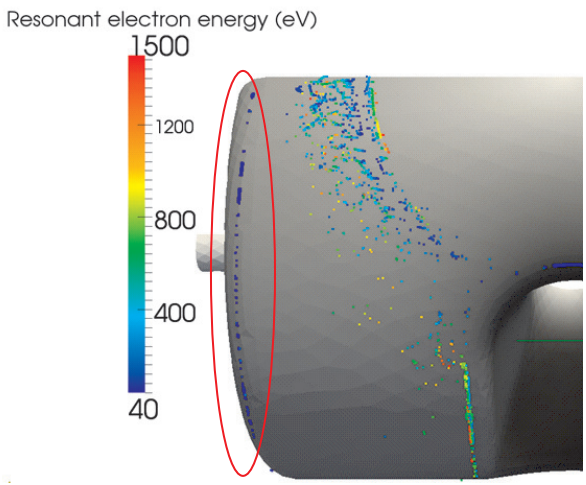

Figure 3: Resonant electrons and their impact energies surviving after 50 rf cycles as simulated by Track3P.

Figure 5 shows a plot of the resonant energies shown in figure 3. Upon inspection of figure 5, there are two observations to take note of. First, it appears that there are possible hard barriers between around 0.4 - 2 eV. Secondly, there are stable multipacting electrons at high field gradients. These electrons are found to be two-point, first order, and reside in the end cap area identified in figure 3. An example of these particle's trajectory is shown in figure 4.

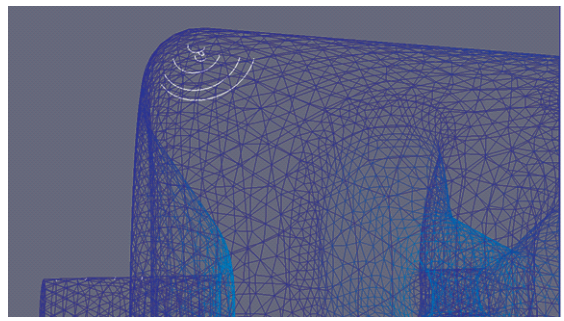

Figure 4: Two-point resonant electron trajectories in the end cap of the cavity.

The question of whether hard barriers exist has recently been tested on a similar cavity operating at 700 MHz, β_0 = 1. The cavity was designed and built in a collaboration between ODU and Niowave [3]. Multipacting analysis of that cavity showed a similar potential for hard barriers at low field gradients, but recent tests at 4.2 K have shown this not to be the case.

To address the question of soft barriers at high field gradient, the inset of figure 5 shows the multipacting electron energies present at 6 MV/m - 10 MV/m for this region of the end cap. The plots are for two different rounding radii at the outer edge, and the picture is of the end cap itself. A more subtle rounding (shown in black) has electrons with resonant impact energies of up to about 250 eV, although most fall below 150 eV. On the other hand, a larger rounding radius (shown in red), results in virtually all of the electron energies being below 100 eV.

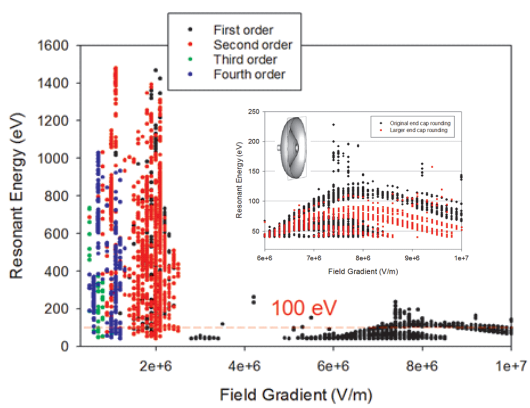

Figure 5: Resonant electron impact energy in region 1 for gradients up to 10 MV/m. The inset shows the impact energies for stable multipacting electrons for two different end cap outer rounding radii.

Copyright © 2012 by the respective authors — cc Creative Commons Attribution 3.0 (CC BY 3.0)

Center cell

The main regions of stable multipacting electron trajectories in the center accelerating gap are shown in figure 6. The low energy electrons (dark blue in color) are, as in the end caps, the ones that are still present even at high gradients. The energy of these electrons is shown in figure 7, and is similar, but slightly less than that of their counterparts at the end caps. These are also two-point, first order electrons which get trapped in the curvature where the spoke base meets the cylindrical outer conductor. As such, varying the curvature in this region can effect the electron's trajectory and impact energy. The inset of figure 7 is an example of this. For a smaller rounding radius (shown in black), there are a number of resonant electrons with energies between 100 and 120 eV for a field gradient of 7-9 MV/m. By increasing the rounding radius (shown in red), the maximum impact energy is now below 100 eV.

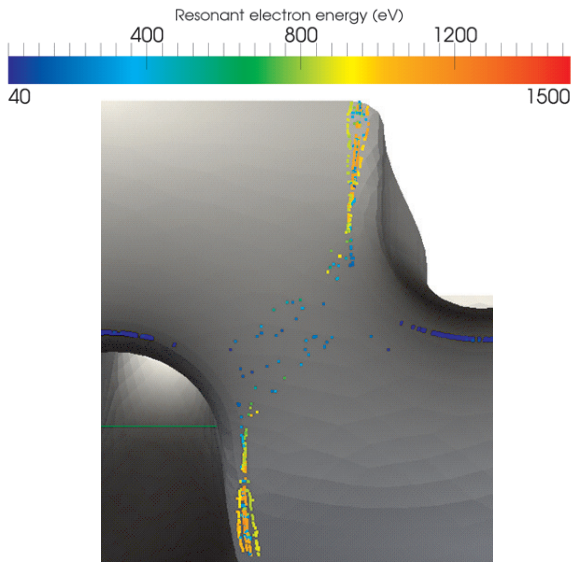

Figure 6: Resonant electrons and their impact energies surviving after 50 rf cycles as simulated by Track3P.

CONCLUSION

Multipacting simulations for multi-spoke cavities show that there is a potential for hard barriers at low field gradients and stable multipactors at high field gradients. However, recent prototype tests of an ODU designed, Niowave fabricated two-spoke cavity operating at 700 MHz has shown that these potential barriers should be able to be processed through.

Additionally, the soft barriers present at high gradients can be minimized by slightly altering the geometry in specific areas of the cavity. Both the end cap and spoke base rounding radius can be increased to a point where the stable, two-point, first order multipactors in these regions are likely to be conditioned away. Experiments at high gradients will have to be done in the future to verify this.

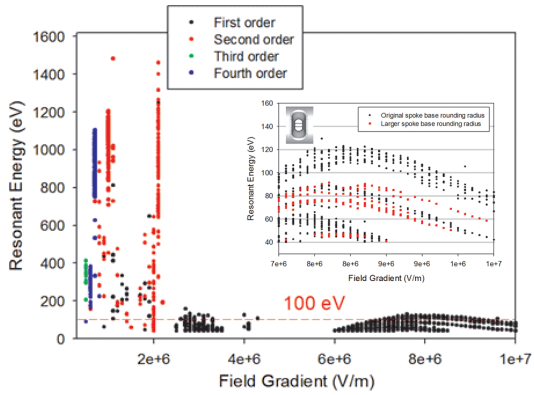

Figure 7: Resonant electron impact energy in region 2 for gradients up to 10 MV/m. The inset shows the impact energies for stable multipacting electrons for two different rounding radii where the spoke base meets the outer conductor.

ACKNOWLEDGMENT

We would like to thank Cho-Kuen Ng and Lixin Ge of SLAC for their helpful discussions on the Track3P code. We also thank Rocio Olave for her multipacting analysis of the 700 MHz cavity.

REFERENCES

[1] C. S. Hopper and J. R. Delayen, "Design of Superconducting Spoke Cavities for High-Velocity Applications," SRF2011, Chicago, July 2011.

[2] C.S. Hopper and J.R. Delayen, "Develpment of spoke cavities for high-velocity applications," Proc. of IPAC2012, New Orleans, LA, WEPPC103.

[3] D. Gorelov, C.H. Boulware, T. Grimm, J.R. Delayen, C.S. Hopper, R.G. Olave, S.U. De Silva, "Development of Superconducting 500 MHz Multi-spoke Cavity for Electron Linacs," Proc. IPAC2012, New Orleans, LA, WEPPC084.

[4] H. Padamsee and A. Joshi, J. Appl. Phys. 50 (1979) 1112.

[5] H. Padamsee, J. Knobloch and T. Hayes, "RF Superconductivity for Accelerators," John Wiley & Sons (1998).

[6] G. F. Dionne, "Origin of secondary-electron-emission yield-curve parameters," J. Appl. Phys. 46, 3347 (1975); doi: 10.1063/1.322061.

[7] F. L. Krawczyk, "Status of multipacting simulation capabilities for SCRF applications," Proc. 10th Workshop on RF Superconductivity, Tsukuba, Japan, 2001.

[8] P. Fernandes, R. Parodi and G. Bienvenu, "An Investigation on the Field Emitted Electrons in Travelling Wave Accelerating Structures," NIM A, 320 (1992) 1-8.

[9] P. Fabbricatore, G. Gemme, R. Musenich, R. Parodi and S. Pittaluga, "Experimental Evidence of MP Discharges in Spherical Cavities at 3 GHz," Proceeding of the 7^{th} Workshop on RF Superconductivity, Gif sur Yvette (1995).

[10] K. Ko et al, Advances in Parallel Electromagnetic Codes for Accelerator Science and Development, LINAC2010, Tsukuba, Japan.

Copyright © 2012 by the respective authors — cc Creative Commons Attribution 3.0 (CC BY 3.0)

MECHANICAL STUDY OF FIRST SUPERCONDUCTING HALF-WAVE RESONATOR FOR INJECTOR II OF CADS PROJECT*

Shoubo He#, Yuan He, Weiming Yue, Shenghu Zhang, Ruoxu Wang, Cong Zhang, Mengxin Xu, Fengfeng Wang, Shichun Huang, Yuzhang Yang, Shengxue Zhang, Hongwei Zhao
Institute of Modern Physics, Chinese Academy of Sciences, Lanzhou, Gansu 730000, China

Abstract

Within the framework of the China Accelerator Driven Sub-critical System (CADS) project, institute of modern physics (IMP) has proposed a 162.5MHz half-wave resonator (HWR) Superconducting cavity for low energy section (β=0.09) of high power proton linear accelerators. For the geometrical design of superconducting cavities structure mechanical simulations are essential to predict mechanical eigenmodes and the deformation of the cavity walls due to bath pressure effects and the cavity cool-down. Additionally, tuning analysis has been investigated to control the frequency against microphonics and Lorentz force detuning. Therefore, several RF, static structure, thermal and modal analyses with three-dimensional code Traditional ANSYS have been performed [1]. In this paper, we will present some results about mechanical analysis of the first superconducting HWR cavity in order to further optimization in the near future.

INTRODUCTION

The cavity geometry has been optimized to reach the design frequency 162.5MHz and β=0.09 and also we want to minimize value of peak electrical and magnetic field on the cavity surface relative to the accelerating electrical field on the cavity axes (Bpk/Eacc and Epk/Eacc) [2]. So the fabrication technology and resonator structural properties including cooling down, vacuum, etching and so on, also should be taken into account at the beginning of design. SC HWR cavities are highly sensitive to mechanical deformations due to the small loaded bandwidth of some SCRF applications. So accordingly for HWR the stability of the cavity structure against any external distortions is the primer design goal. In order to improve df/dP for a low Beta HWR cavity, the typical approach is to add some stiffening ribs on the cavity, but it will not be discussed in this paper. Here, we will investigate this type of structure and then we will improve it in the future. Primarily structural analysis was completed to determine the locations of the model that were beyond yield strength.

Since CADS accelerator will work in CW regime, the main goal of our cavity structural design is a minimization of the resonant frequency dependence on the external pressure fluctuations. The general basics of the cavity structural design are to avoid using the plane surfaces as illustrated in Figure 1. Besides, four access ports at each cavity (two at the bottom, two at the top) guarantee draining off of the chemical etching and easy access to the inner surfaces during the high pressure water rinsing (HPR).

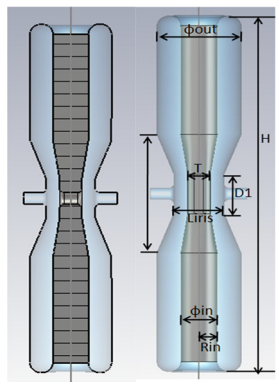

Figure 1: The cross section of HWR cavity with the main geometric parameters: Liris-iris to iris length, T-inner conductor thickness, D1-cavity diameter.

Table 1: Some Properties of HWR Cavity

Para.	Frequency	β	Diamater	Uacc	Epeak	Bpeak
Value	162.5	0.093	40	0.78	25	50
Unit	MHz	---	mm	MV	MV/m	mT

STRUCTURAL ANALYSIS

Injector II of CADS is composed by an ECR ion source, LEBT, RFQ and superconducting accelerating section. And in superconducting accelerating section, there are two cryomodules and each cryomodule is composed of 8 superconducting Half-Wave-resonator cavities and 9 superconducting solenoids. The proton beam will be accelerated from 2.1 MeV to 10MeV. Before structure analysis the geometry of HWR cavity was taken from a sat. model that was generated in software CST Microwave Studio and represented one cavity structure. The ANSYS RF results were compared to CST and to HFSS models of the same cavity for final verification. And the difference among these code result is only about 0.065%.

During mechanical analysis of HWR cavity, the variation of RF Eigen frequency was calculated, including pressure sensitivity, Lorentz force detuning, tuning sensitivity and resonant vibration and etc.. The

*This work is Supported by the National Natural Science Foundation of China (Grant Agreement 91026001)
#heshoubo@gmail.com

Copyright © 2012 by the respective authors — cc Creative Commons Attribution 3.0 (CC BY 3.0)

relationship between changes in RF frequency and mechanical deformations is given by the Slater Perturbation Theorem as the following equation 1, where E_0 and H_0 are the unperturbed electric and magnetic fields respectively, U_0 is the stored energy, f0 is the original cavity frequency, and Δf is the frequency shift:

$$\frac{\Delta f}{f_0} = \frac{\int_{\Delta v} (\mu_0 \left|\vec{H}_0(\vec{x})\right|^2 - \varepsilon_0 \left|\vec{E}_0(\vec{x})\right|^2) d^3x}{4 \cdot U_0} \quad (1)$$

PRESSURE SENSITIVITY

A sequential coupled field analysis RF-Structural-RF is used to predict the frequency shift due to cavity deformations under external pressure using codes ANSYS. As the cavity stiffening environment is hard to determine when cavity design, it is necessary to provide this research under two cavity beam port boundary conditions: fully fixed and completely free. The same meshed model was used for all types of simulations and that is very important as we can evaluate the frequency shift at the same scale.

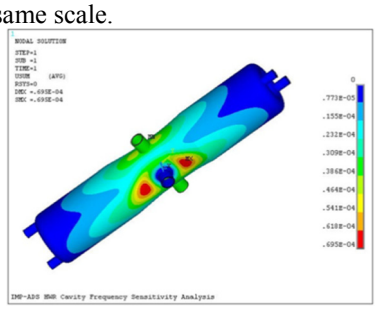

Figure 2: Structural analyses results of HWR with beam pipes fixed (cavity deformation).

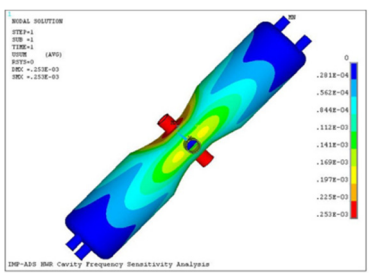

Figure 3: Structural analyses results of HWR with beam pipes free (cavity deformation).

Table 2: Pressure Sensitivity under 1 Atm

Boundary	Displacement	Stress	Δf	df/dp
fix	0.0695	5.786	17.892	23.54
free	0.252	19.066	110.773	145.6
Unit	mm	ksi	kHz	Hz/torr

From the above results we can see that the main frequency shift is caused by the beam port displacements. Although in this analysis the cavity has been simulated without helium vessel. While the helium vessel adds rigidity to the beam ports and in other words it is equivalent approximately to the fully constrained conditions. Whatever the different boundary condition, the cavity seems to be too soft so we need add some ribs on it for strength the cavity. And recently we just explore how to add these stiffening ribs.

Lorentz Force Detuning (LFD)

Since the superconducting HWR cavity will work in cw mode, so it will be static Lorentz force on the cavity walls. The pressure results in a deformation of the SC HWR cavity walls with changing the cavity volume by ΔV. And it creates the frequency shifts, which may be approximated as a perturbation using Slater's Theorem[3]. This shift is usually quantified by KL which is defined as

$$K_L = \frac{\Delta f}{(E_{acc})^2} \quad (2)$$

The numerical coupled analysis for LFD effect has been done and also an initial simulation of the cavity under beam pipes full constrain can be showed. From this formula, we can see that the frequency shift is proportional to the accelerating gradient. With the increase of accelerating gradient, the resonant frequency also decreases. Figure 4 shows the deformation of the cavity with LFD effect .

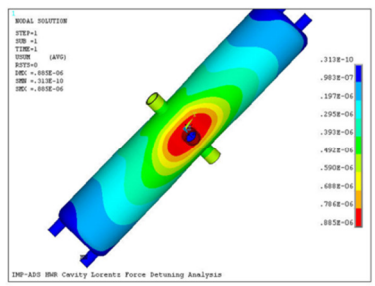

Figure 4: Deformation of the cavity wall (fix boundary condition)

From the above simulation the final fitting curve of the Δ f and E_{acc} is

$$\Delta f = -4.657 E_{acc}^2 - k \quad (3)$$

Finally according to the equation 2, the obtained Lorentz force detuning coefficient K_L is -4.657Hz/(MV/m)^2.

Modal Analysis

Generally speaking, it is difficult to eliminate vibrations in cavities because the situation around the cavity and the helium vessel is extremely complicated. In practice the structural modal analysis need to be provided with helium vessel fixed at the supports and tuner fixed by the tuner stem. While here the results is obtained from naked HWR cavity. And then we have the lowest frequency of modal analysis is 188Hz, which is far from the dangerous frequency obviously. Certainly it is need to

Copyright © 2012 by the respective authors — cc Creative Commons Attribution 3.0 (CC BY 3.0)

be further tested for all the accelerator with helium vessel, coupler, tuner and cryomudule etc. to verify the analysis.

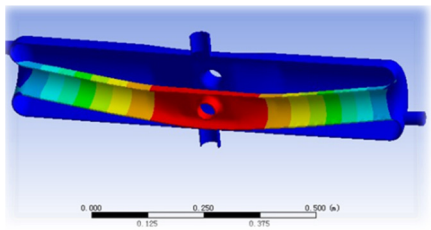

Figure 5: One of Model analyses results of HWR cavity with cleaning pipes free (cavity deformation).

Tuning Sensitivity

The role of the tuner is to ensure that the cavity resonance frequency will match the desired accelerator operating frequency. Tuners are generally made an active part of a complete RF control system which fulfills several functions. It stabilizes the frequency, amplitude, and phase variations induced by sources such as the RF drive, beam current variations, LFD, and microphonics. The usual tuning method for SC cavities is to change the length of the cells by mechanical adjustment of the overall length of the cavity. This method will not only bring in new HOM, but also not cause a big change for previous HOM[4].

The main factors that may be needed at the design of tuner are as follows:

- The tuning sensitivity of HWR cavity is 180KHz/mm;
- The spring constant of the HWR cavity is 2.2KN/mm;
- The limited space available (tuning range) is about 2mm.

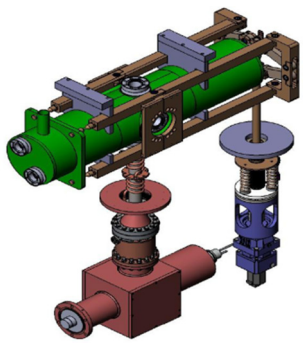

Figure 6: The IMP mechanical tuner: tuner(dark gray), helium vessel (green), and coupler (red).

Considering the fabrication tolerances for the cavity, the tuner may be able to retune the cavity over a range of 150 kHz cantered on the nominal operating frequency of 162.5 MHz.

Figure 7: Mechanical Tuner of HWR cavity test with copper HWR prototype .

CONCLUSION

We Mechanical analysis has been developed for 162.5 MHz SRF HWR cavities for the proposed CADS at IMP. The design of the tuner has been described and results of the static performance of the first copper HWR prototype have been got recently. In view of the mechanical results we find obviously that the SRF HWR cavity is much too sensitivity. So Some stiffening ribs must be added on the cavity wall. Besides, the coupled field analysis is in progress with more realistic boundary conditions ,including helium vessel.

ACKNOWLEDGMENT

We would like to thank Prof. Haipeng Wang and Dr. Gary Cheng of JLAB for the idea of simulations and helpful discussions.

REFERENCES

[1] ANSYS, Inc., Canonsburg, Pennsylvania, USA. www.ansys.com
[2] E. Zaplatin, IFMIF-EVEDA SC β=0.094 HALF-WAVE RESONATOR STUDY, SRF2009, THPPO015
[3] J.C. Slater, “Microwave Electronics,” D. Van Nostrand Co., Princeton, N.J., 1950, p8.
[4] H. Padamsee et al. RF Superconductivity for Accelerator, John Wiley & Sons, 1998.

Copyright © 2012 by the respective authors — cc Creative Commons Attribution 3.0 (CC BY 3.0)

THE SUPERCONDUCTING CH CAVITY DEVELOPING IN IMP*

M.X.XU#, Y.He, S,H.Zhang, Z.J.Wang, R.X.Wang, SH.B.He, W.M.Yue, C.Zhang, SH.CH.Huang, Y.ZH.Yang, SH.X.Zhang, T.C.Jiang, Y.L.Huang, H.W.Zhao, J.W.Xia, IMP, Lanzhou, Gansu 730000,China

Abstract

The Cross-Bar H-type (CH) cavity is a multi-gap drift tube structure operated in the H21 mode [1]. The Institute of Modern Physics (IMP) has been doing research and development on this type of superconducting CH cavity which can work at the C-ADS (accelerator driver sub-critical system of China). A new geometry CH cavity has been proposed which have smaller radius. It's suitable in fabrication, and it's can reduce cost too .Detailed numerical simulations with CST MicroWave Studio have been performed. An overall surface reduction of 30% against the old structure seems feasible. A copper model CH cavity is being fabrication for validating the simulations and the procedure of fabricating niobium cavity.

INTRODUCTION

C-ADS project with ambitious requirement regarding beam power and quality need new superconducting linac development. Superconducting Crossbar-H-Mode (CH)-cavities have two important features meet with the requirements of C-ADS. Superconducting CH cavity have high real estate gradients compared to conventional low-beta ion linacs, this feature will reduce the amount of cavity prominent. For the cross bar structure, CH cavities are more rigidly. This feature satisfy the harsh requirements of C-ADS about reliable. As this reasons, superconducting CH cavities have been choose as a backup cavity type for the C-ADS(see Fig.1). With respect to C-ADS actual application, one prototype of superconducting CH cavity (f=162.5MHz, beta=0.067, 6 cells) is presently being development in IMP.

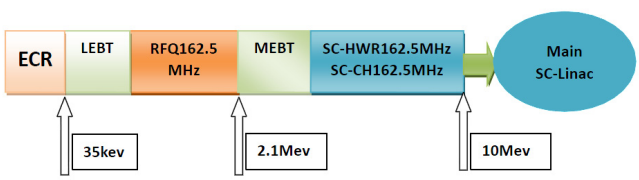

Figure 1: Layout of Injector-II for C-ADS.

*Work supported by 91026001 Nature Science Foundation of China

#xumx@impcas.ac.cn

NEW SHAPE SUPERCONDUCTING CH CAVITY

The superconducting CH cavity has electric and magnetic field structure similar with combine the 4-vane RFQ and DTL's. We can use a semi-analytical approach to estimate basic parameters like frequency. The parameter Rt and r1 are represent the radius of CH cavity and the tube radius of CH cavity respectively. Using this equivalent, we can get the resonance frequency with the radius Rt as following [1]:

$$\omega \approx c\left(\frac{0.73}{Rt^2\left(\frac{25}{144}+\frac{25}{72}Ln\left(\frac{Rt}{r1}\right)-0.2\right)}\right)^{1/2} \quad (1)$$

In case of the superconducting CH cavity of IMP, the frequency is 162.5MHz, r1 was 0.03m. Using the formula (1) can give radius Rt of the CH cavity is 0.29 meter. We have using the software CST to simulation. The radius of CH cavity is 0.32 meter [2].

The superconducting CH cavity is a complex cavity. With the radius of 0.32 meter, there are big surface. This means a large amount of high pure niobium needs and a more chance to come across defects. As in superconducting cavity, perfect surface is important for the cavity quality [3]. This size of CH cavity is not easy to protect from defects and contaminates or not suitable in the vacuum chamber of electric beam welding machine.

We try to cut a part of the girder called undercut [4] (see Fig.2).This undercut will increase inductance in the end of cavity, as this will increase the length of current flow. Increased inductance will lower the resonance frequency that we can get a smaller cavity structure in the same frequency (see Fig.3).

When we change the size of undercut in the girder of CH cavity, the radius will reduce with the width of girder liner. At most, we can reduce the radius of cavity by 20% (see Fig.4). As the radius reducing, the surfaces of the cavity reduce by 30% (see Fig.5).

Copyright © 2012 by the respective authors — cc Creative Commons Attribution 3.0 (CC BY 3.0)

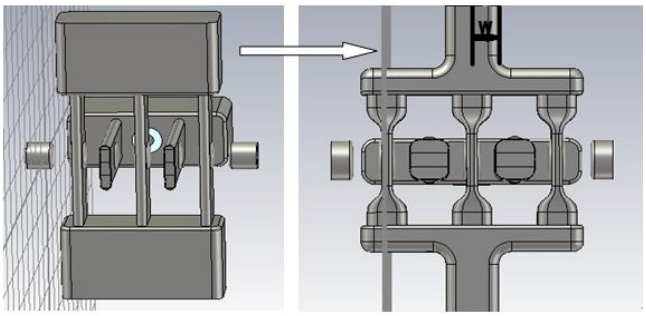

Figure 2: The copper CH cavity structure (left) and the CH cavity of use undercut in girder (right).

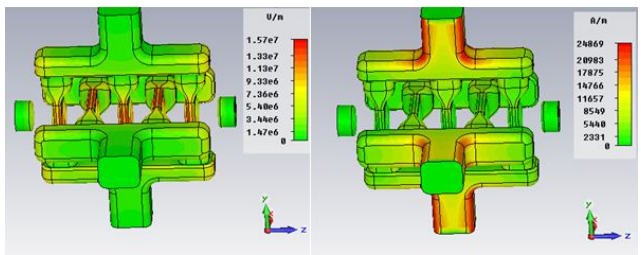

Figure 3: The electric field of use undercut CH cavity (left) and the magnet field of use undercut CH cavity.

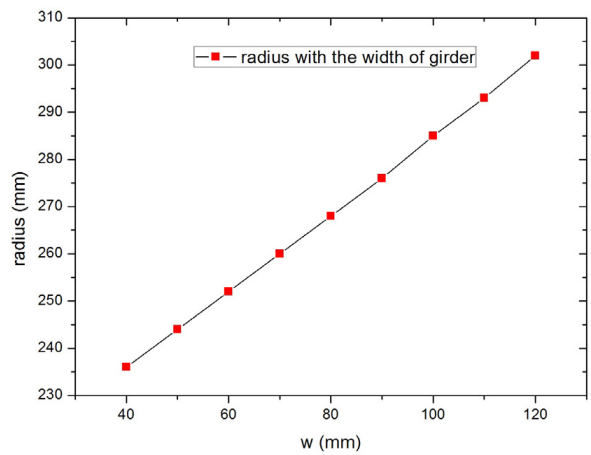

Figure 4: The radius of CH cavity with the width of girder.

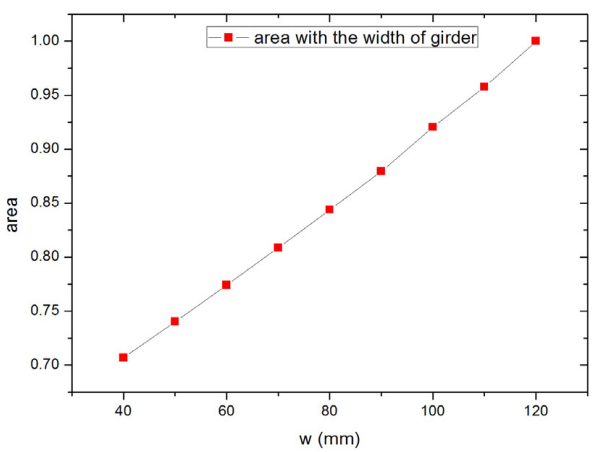

Figure 5: The surface of CH cavity with the width of girder.

This reduction has such advantages: as the cavity size became smaller, deep drawing dies became smaller too. It's easy to hand; the last electron beam welding joint have smaller length, less risk to burn a hole, easy to change position at the EBW; smaller use of high purity niobium, lower cost; less chance to come across defect in surface [4].

Field distribution variation with different undercut girder

The usage of undercut girder leads to a more homogeneous field distribution along the beam axis because the volume for the magnetic field is increased (see Fig.6).

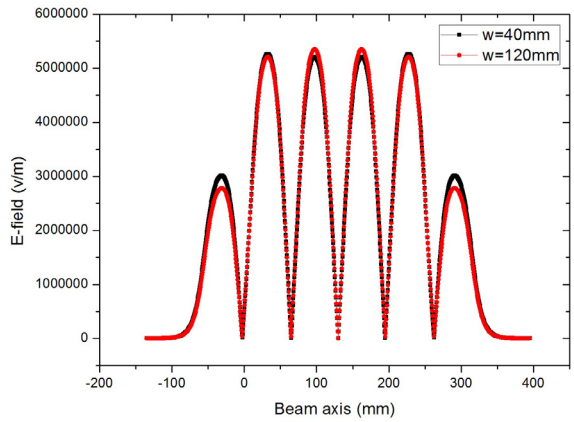

Figure 6: Field distribution of CH cavity with the different width of girder.

Frequency variation with different undercut girder

The frequency tuning is by compress and pulling the two side of cavity along beam axis. Different undercut girder influence the F/l (see Fig.7).

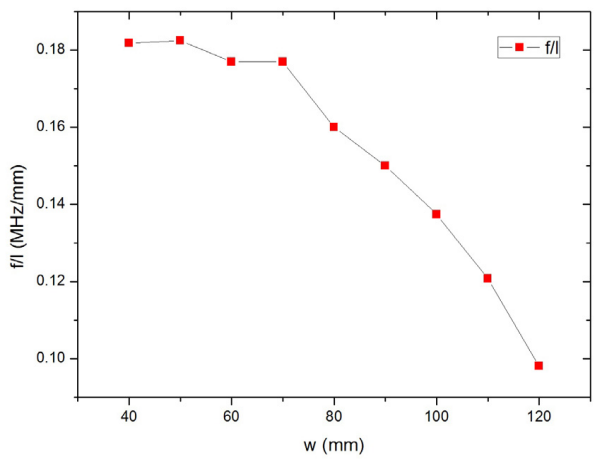

Figure 7: F/l of CH cavity with the different width of girder.

Copyright © 2012 by the respective authors — cc Creative Commons Attribution 3.0 (CC BY 3.0)

Copper prototype CH cavity fabrication

A copper prototype CH cavity has been built (see Fig.8) to validate the electromagnetic simulations, such as frequency (see Table1), field distribution along the beam axis, coupler size and position, tuning ability. And the CH cavity structure is complicate, need to check the design of dies and the path of electron beam weld in the fabrication.

Table 1: The EM parameters of the copper CH cavity

Parameter	Value	Unit
Frequency	162.5	MHz
Beta	0.067	
Ra/Q0	670	Ω
G	47	Ω
Epeak /Eacc	5.3	
Bpeak /Eacc	6.37	mT/ MV/m

OUTLOOK

We have design a superconducting CH cavity with smaller size. The future optimization will focus on lower the E_{peak} /E_{acc} and B_{peak} /E_{acc} , that it should be possible to reach higher effective voltages . The normal copper CH cavity will be finish at the end of 2012.

Figure 8: Parts of copper CH cavity.

REFERENCES

[1] H. Podlech, “New cavity shape developments for low beta applications”, Paper THOAAU06, Proc. of SRF2009, Berlin, Germany.
[1] http://www.cst-china.cn/
[3] Panamsee H, Knobloch J, Hays T. RF superconductivity for accelerators [M]. New York: John Wiley & Sons, 1998
[4] U. Ratzinger, H-type Linac structure, CERN Accelerator School,Lufthansa Training Center, Germany, 8 – 16 May 2000.

Copyright © 2012 by the respective authors — cc Creative Commons Attribution 3.0 (CC BY 3.0)

IMPACT OF TRAPPED FLUX AND SYSTEMATIC FLUX EXPULSION IN SUPERCONDUCTING NIOBIUM

J. Vogt, O. Kugeler, J. Knobloch, Helmholtz-Zentrum für Materialien und Energie (HZB)

Abstract

The intrinsic quality factor Q_0 of superconducting cavities is known to depend on various factors like niobium material properties, treatment history and magnetic shielding. To study trapped flux in Niobium we constructed a test stand at Horizontal Bi-Cavity Test Facility (HoBiCaT) at HZB using niobium rods equipped with thermal, electrical and magnetic diagnostics. The focus in this study was on the behaviour of the trapped flux when the sample is slowly warmed up towards the critical temperature T_c. Besides the (incomplete) Meissner effect we observed additional flux expulsion starting at ≈0.1K below T_c. The reduced level of trapped flux is maintained when the sample is cooled down again and can even be improved by repeating the procedure. Possible explanations for the effect are discussed.

INTRODUCTION

We already reported on the impact of temperature gradients during the cool-down on the obtained Q_0 [1]. In the quest for minimization of RF losses in SRF cavities the impact of trapped vortices is one main topic. The vortices have a normal conducting core with a surface resistance about 6 orders above that of superconducting Niobium. This surface fraction is proportional to the trapped magnetic flux. The surface resistance was determined to be 2.2nΩ per μT for a 1.5GHz cavity [2]. A crucial step in avoiding trapped flux is an improved understanding of flux trapping behaviour of Niobium.

The energetically most favourable state of bulk Niobium at 1.8K (4.2K) is the Meissner phase, in which all magnetic field present in the normal conducting state is expelled. However, expulsion of flux can be incomplete, yielding a remaining magnetization of the material even after removing the external field source. The dynamics of this trapped flux is still not well understood. One approach was the investigation of flux that is permitted to penetrate a marginal type II superconductor in the mixed state. Here, the flux tubes form a lattice and several studies [3, 4] indicate a phase transition from localized (solid, fixed regular lattice) flux tubes towards moveable (liquid) flux tubes when the superconductor exceeds certain temperature / magnetic field combinations as indicated by the black dotted "melting line" in Figure 1.

The behavior of flux that is trapped in the Meissner state is uncertain. A continuation of the melting line in this phase is conceivable, so that flux lines in the check region (Figure 1) may be able to exit the Niobium below T_c. In our study, we examine the properties of the trapped magnetic flux in the Meissner phase when the rod is slowly warmed up.

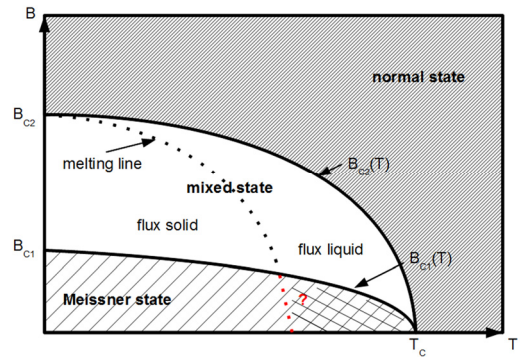

Figure 1: Magnetic phase diagram of marginal Type II superconductor [5]. The added red dotted line indicates a possible extension of the liquid/solid flux interface into the Meissner state. The size of the check region is exaggerated.

EXPERIMENTAL SETUP

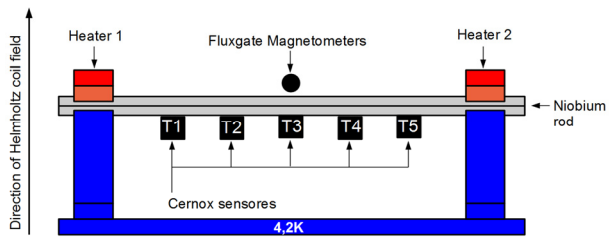

Figure 2: Experimental setup

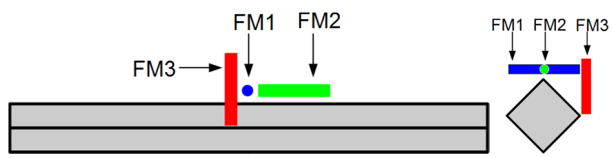

Figure 3: Positions of fluxgate magnetometers (FM): Longitudinal view (left) and cross section (right) of FM1 (black), FM2 (green) and FM3 (red)

For the experiments, a RRR=300 niobium rod (8.4x8.4x300mm) was positioned inside HoBiCaT [6]. It was conduction cooled through the posts to 4.2K. In order to reduce heat transfer into the Helium, heat conductivity was reduced by introducing a kapton foil between rod and support stands. Both ends of the rod were equipped with a resistive heater. They could be individually regulated to control the temperature of the rod with 10mK accuracy. Five Cernox temperature sensors with mK resolution and three fluxgate magnetometers with 1nT resolution (Bartington Mag-01H), one for each spatial direction,

Copyright © 2012 by the respective authors — cc Creative Commons Attribution 3.0 (CC BY 3.0)

were attached along the rod. A Helmholtz coil (HC) for the generation of a vertical magnetic field up to ±300µT enclosed the whole construction. The setup and the positions of the instruments are displayed in Figures 2 and 3.

MANIPULATION OF TRAPPED FLUX

In each of the performed experiments a magnetic field is applied using the HC while the Nb rod is cooled through T_c. Afterwards, the rod is smoothly warmed by manually adjusting the two heaters and the change in the magnetic field is observed by three fluxgate magnetometers (FM). Precise temperature control was exercised to ensure that at no time T exceeded T_c.

Manipulation without applied field

In the first set of experiments the HC is turned off after the rod has reached the minimum temperature. Hence, the signal registered subsequently by the FMs roughly corresponds to the frozen flux inside the rod. Referring to Figure 4, this is position (A).

When the rod is warmed up again, the magnetisation observed by the FMs stays constant until a temperature of T≈9.1K (<T_c) is reached. At this point the amount of trapped flux suddenly starts to drop (B) until a minimum level is reached (C). When the warming is stopped during the decrease and the rod is cooled, the level of trapped flux at the instance of stopping remains - even upon subsequent cooling.

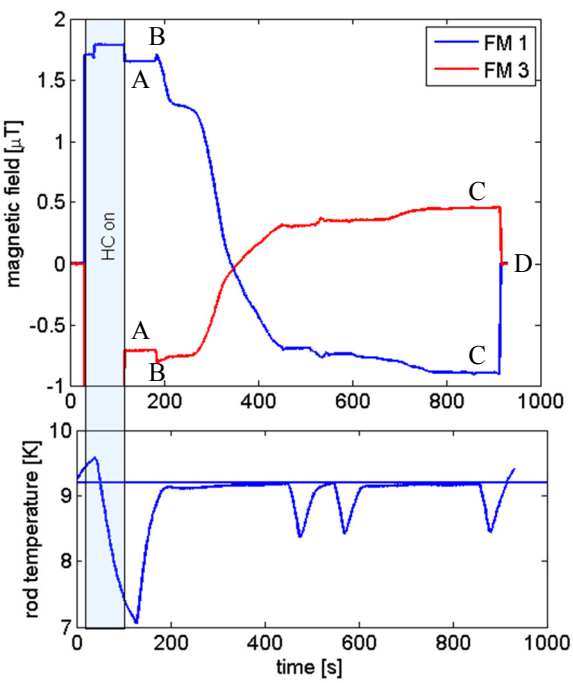

Figure 4: Behaviour of trapped flux and temperature when a HC field of 33µT is applied and trapped: Initially trapped flux (A), minimal trapped flux (C) and level of flux ambient in HoBiCaT ≈3µT (D). This value has been subtracted from all data points.

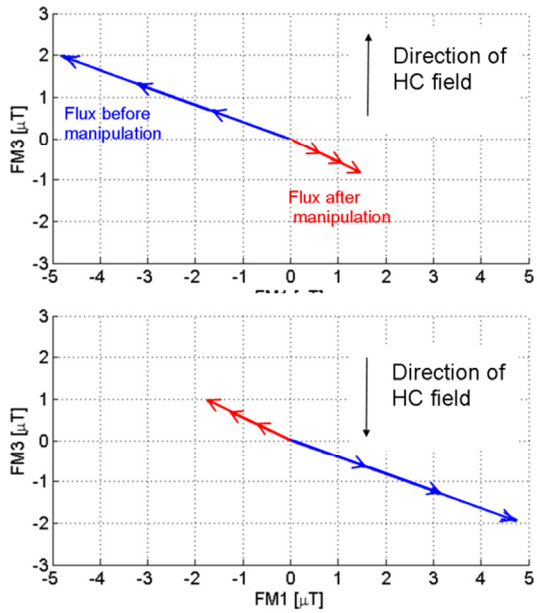

Figure 5: Trapping for HC fields: 33µT, 65µT, 97µT (above) and -32µT, -66µT, -98µT (below). The initially trapped field is blue and the field after additional expulsion is red.

The signals obtained by FM1 and FM3 are displayed in Figure 4. For better visualization their values can be combined to a vector indicating the spatial orientation of the trapped flux, see Figure 5. The signal of FM2 is more than one order of magnitude smaller than the signals of FM1 and FM3 due to the orientation of HC and rod and therefore is not displayed here.

The change in the trapped flux indicates that the warming enables the trapped flux lines to move. A possible explanation could be that the thermal energy exceeds the pinning potential and the pinning potential barrier does not hinder the movement of flux lines anymore ("liquid flux state"). Driving force for the movement could be the strive for approaching the energetically most favourable state – the complete Meissner state – given by a minimum of sc/nc interface area. Not all flux is expelled because different pinning centres have different pinning potentials [7] and not all of them can be exceeded by the thermal activation. Also the driving force reduces, the less flux remains in the sample. We observe:

(1) A redistribution of flux lines (here even change in sign due to geometry) and
(2) A reduction of the absolute amount of frozen flux

The latter is evident from the shortening of the vectors in Figure 5. Table 1 displays the values of the initially trapped field and the minimal trapped field in the end of the procedure for different HC fields. We achieved an expulsion of up to 75%.

Copyright © 2012 by the respective authors — cc Creative Commons Attribution 3.0 (CC BY 3.0)

Table 1: Magnetic field before and after expulsion

B_{HC} [μT]	$\lvert B_{trapped}\rvert$ [μT]	$\lvert B_{minimised}\rvert$ [μT]	Expulsion [%]
33	1.98	0.50	75
65	3.91	1.19	70
97	5.84	1.88	68
-32	1.87	0.88	53
-66	3.80	1.57	59
-98	5.73	2.26	61

Manipulation with applied field

These investigations raise the question how the flux tubes behave when an external field is not turned off during warm up as opposed to the above experiment, where an external field was trapped but only the ambient field remained during warm up.

Figure 6 displays a typically obtained signal of FM1. In the beginning the rod is normal conducting (A). It is cooled below T_c where flux is expelled by Meissner effect (B). The magnetic field probe measures an increase in the field density outside the rod. Afterwards the rod is slowly warmed using the heaters. Starting at a temperature of (9.08±0.01)K we observe a sudden decrease in expelled flux (C) which coincides with the onset of Paramagnetic Meissner Effect (PME) reported by Thompson [8]. The onset temperature does not depend on the applied field strength in the range of ±300μT tested here. The PME is a phenomenon observed in some high temperature superconductors and in Niobium. These materials exhibit a paramagnetic phase between the perfect diamagnetic behaviour in the Meissner state and the normal conducting state. Note the difference to classical frozen flux which is a topological coexistence of normal conducting and Meissner-like areas.

When the rod is warmed up further, a second effect occurs. When T_c is approached an additional expulsion of flux is evident (D) resulting in a lower level of residual frozen flux (i.e. a higher level of expelled flux). Subsequent repetition of cooling and heating leads to a minimized level of trapped flux (E) and each time we observe the PME. Further repetition leads only to the jumps in magnetisation due to PME but no further change in the level of trapped flux.

A possible explanation for this systematic flux expulsion could be an increased mobility of flux lines in a temperature regime close to T_c consistent with the data obtained in the first set of experiments.

In this set of experiments, HC fields of up to ±300μT were applied leading to expulsion pattern that were all similar to Figure 6. Hence, systematic flux expulsion works under these conditions.

CONCLUSION

The amount of trapped magnetic flux can be manipulated and systematically minimized while the material remains superconducting. The complete Meissner state is thus being approached.

If one could apply such a procedure to SRF cavities, this effect could lead to higher Q_0 values and operation close to the BCS-limit. In addition, the major impact of the cooling dynamics in the temperature range between 9.08K and T_c on the flux trapping behaviour could explain the impact of temperature gradients during the cool-down on the obtained Q_0 values as described in [1].

ACKNOWLEDGMENT

We would like to thank A. Frahm for the design of the testing apparatus and S. Klauke and M. Schuster for help with setting up the experiment.

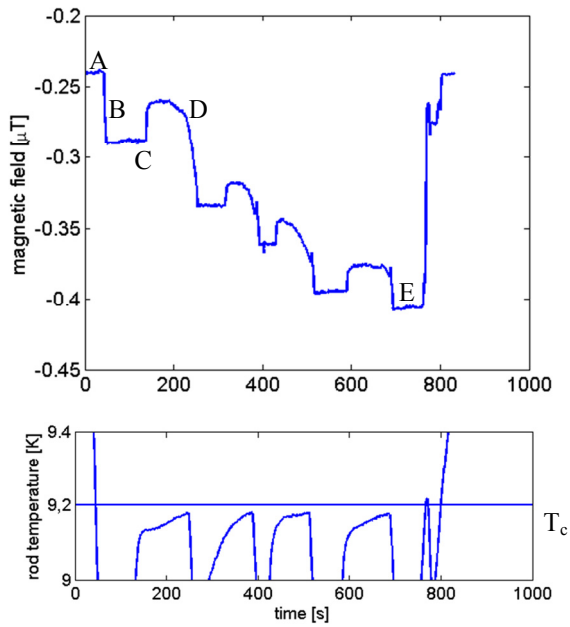

Figure 6: Behaviour of trapped flux (FM1) and temperature upon heating in ambient field (background field trapped and partially expelled)

REFERENCES

[1] O. Kugeler, J. Vogt, J. Knobloch, S. Aull, "Impact of Trapped Magnetic Flux and Thermal Gradients on the SRF Cavity Quality Factor", *Proc. 5th IPAC2012*, New Orleans (2012), p. 2203.
[2] P. Kneisel and B. Lewis, Tech. Rep. Tech. Note 94–028, Continuous Electron Beam Accelerator Facility, 1994
[3] J.W. Lynn, N. Rosov, T.E. Grigereit, H. Zhang, T.W. Clinton, Phys. Rev. Lett. 72, 1994
[4] J. Kierfeld, Phys. Rev. B 69, 2004
[5] C. Poole,"Handbook of Superconductivity", 2000
[6] O. Kugeler, A. Neumann, W. Anders, and J. Knobloch, Review of scientific instruments, vol. 81, Jul. 2010, p. 074701.
[7] W. Buckel, R. Kleiner, "Superconductivity", 2004
[8] D.J. Thompson, M.S.M. Minhaj, L.E.Wenger and J.T. Chen, Phys. Rev. Lett. 75, 1995

Copyright © 2012 by the respective authors — cc Creative Commons Attribution 3.0 (CC BY 3.0)

THE NONRESONANT PERTURBATION THEORY BASED FIELD MEASUREMENT AND TUNING OF A LINAC ACCELERATING STRUCTURE *

W. C. Fang#, Q. Gu, Z. T. Zhao, SINAP, Shanghai, China
D. C. Tong, THU, Beijing, China

Abstract

Assisted by the bead pull technique, nonresonant perturbation theory is applied for measuring and tuning the field of the linac accelerating structure. The method is capable of making non-touching amplitude and phase measurements, real time mismatch feedback and field tuning. Some key considerations of the measurement system and of a C-band traveling-wave structure are discussed, and the bead pull measurement and the tuning of the C-band traveling-wave linac accelerating structure are presented at last.

INTRUDUCTION

The Shanghai soft X-ray Free Electron Laser test facility(SXFEL)is presently being planned and designed at the Shanghai Institute of Applied Physics, CAS [1]. This facility will be located close to the Shanghai Synchrotron Radiation Facility, which is the first 3rd generation light source in mainland China [2]and it requires a compact linac with a high gradient accelerating structure and high beam quality. As a key R&D item, a room temperature C-band (5712 MHz) accelerating structure has been developed [3, 4]. For fabricating the C-band structure with high performance, the bead pull measurement system based on nonresonant perturbation theory has been developed.

There are several methods for RF structure measurement or tuning, such as the resonant perturbation method [5] and the phase shift method, however several limitations appear when they are applied to a traveling-wave accelerating structure. The resonant perturbation method picks up the amplitude of the electromagnetic field, therefore it is limited in the measurement of the standing-wave accelerating structure and the phase shift method only shows the phase information in the RF structure. For the accurate and fast tuning of a traveling-wave linac RF structure, nonresonant perturbation theory is the preferable method, which can measure the electromagnetic field distribution with both amplitude and phase, and this method is capable of making non-touch measurement, which can maintain the clean inner surface of the accelerating structure and reduce its RF breakdown rate. Furthermore, this method is also very effective in performing an accurate and fast real-time tuning of the accelerating structure, which is economical for mass fabrication of accelerating structures.

In this paper we present a cold test application of nonresonant perturbation theory on a linac RF structure [6]. This method based on the bead pull technique can pick up the amplitude and phase distribution of a linac structure, particularly for a traveling-wave structure, and is a preferable and efficient method for accelerating structure cold testing and tuning. In the following we describe firstly the theory of nonresonant perturbation and the tuning procedure and then discuss the key considerations of our measurement system with the bead pull technique. At the end we give several experimental results of our newly developed C-band traveling-wave accelerating structure tuning, which verify the feasibility of this method.

*Work supported by SINAP project
#fangwencheng@sinap.ac.cn

NONRESONANT PERTURBATION THEORY AND TUNING PRINCIPLE

According to nonresonant perturbation theory, the variation of the reflection coefficient in the input port is measured with and without a perturbation bead, which is placed at different points along a line to pick up the amplitude and phase distribution of the electromagnetic field strength, a schematic drawing is shown in Figure 1. Based on the results and post-processing, RF tuning is processed with accurate and fast real-time feedback.

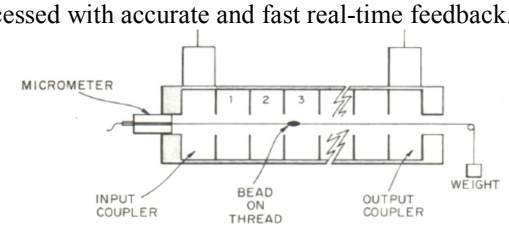

Figure 1: The field measurement based on nonresonant perturbation theory.

Nonresonant Perturbation Theory and Field Measurement

In nonresonant perturbation theory, the desired field strength is calculated as the following [6]:

$$2P_i(\Gamma_p - \Gamma_a) = -j\omega[k_e E_a^2 - k_m H_a^2] \quad (1)$$

For an accelerating structure, the TM mode is used for beam acceleration and the crucial longitudinal electrical field Ez is the unique field component on axis, thus the first equation of equation (1) is used for field measurement, and is renamed as equation(2) with reflected coefficient S11 of the Network Analyzer:

$$\Delta S11 = \Gamma_p - \Gamma_a = S11_P - S11_a = -\frac{j\omega k_e}{P_i} E_a^2 \quad (2)$$

whereS11p and S11a are acquired from the Network Analyzer, respectively corresponding to Γp and Γa in equation (1) above. In equation (2), Ea is complex data, its amplitude is the square root of the amplitude of ΔS11, and its phase is half of the phase ofΔS11. As the

Copyright © 2012 by the respective authors — cc Creative Commons Attribution 3.0 (CC BY 3.0)

bead goes through the RF structure, the distribution of Ez on axis can be measured step by step.

Tuning Principle

With the bead pull measurement, the amplitudes and phases of the field can be measured, and after post-processing the local reflected coefficient can be calculated for the later tuning procedure. For the accelerating structure, the field of the center of the ith cell can be expressed by $E_i e^{j\varphi_i}$, which is the superposition of forward and backward waves $a_n e^{j(-2\pi/3(i-n)+\psi_n)}$ and $b_n e^{j(2\pi/3(i-n)+\phi_n)}$, where the center cell is the nth cell of the three cells in Figure 2.

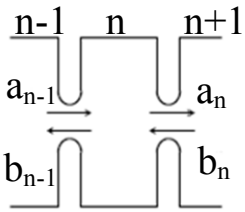

Figure 2: Forward and backward wave of nth cell.

It is supposed that the amplitudes in three adjacent cells are the same, according to [7],

$$a_n e^{j\psi_n} = E_{n-1} e^{j(\varphi_{n-1}-\pi/2)} + E_n e^{j(\varphi_{n-1}-\pi/6)}/\sqrt{3}$$
$$b_n e^{j\phi_n} = E_{n-1} e^{j(\varphi_{n-1}+\pi/2)} + E_n e^{j(\varphi_{n-1}+\pi/6)}/\sqrt{3} \quad (3)$$
$$b_{n+1} e^{j\phi_{n+1}} = E_n e^{j(\varphi_n+\pi/2)} + E_{n+1} e^{j(\varphi_{n+1}+\pi/6)}/\sqrt{3}$$

Based on equations (3), the local reflected coefficient of the nth cell is derived as equation (4)

$$\Gamma_{local,n} = \frac{b_n e^{j\phi_n} - b_{n+1} e^{j(\phi_{n+1}-2\pi/3)}}{a_n e^{j\psi_n}} = A + jB \quad (4)$$

where A and B represent the real and imaginary parts of the reflection respectively.

According to the conclusion in [8], the real part of the reflection coefficient in equation (4) is small and neglected relative to the imaginary part. The left imaginary part is dominated by the frequency detuning of each cell, which is shown in Equation (5).

$$\Gamma_{local} \approx -j\frac{2\beta Q_0 \Delta F}{(\beta+1)^2 + Q_0'^2(\Delta F)^2} \approx j\frac{Q_0 \Delta f_0}{f_0} \quad (5)$$

where f_0 is the eigenfrequency, $\Delta f_0 = f_0 - f$, and $Q_0' = c\varphi/vg$ is the eigen-parameter of each cell. In Equation (5), it is easy to find that the reflection coefficient Γ_{local} is more or less than zero respectively when f_0 is detuned above or below the operating frequency f. Based on this principle, every cell can be tuned independently according to the sign of Γ_{local}.

According to equation (5), in equation (4) A is neglected and B presents the frequency detuning. If B is more than zero, the frequency is more than the design value, and to the contrary, frequency is a little less. This is the rule for the automatic tuning process, and the process is not stopped until B reaches zero.

In equation (4), the left side represents the local reflection$\Gamma_{local,n}$of the nth cell, however in the automatic tuning process, only reflection coefficient Γ_{port} of the input port can be measured, which is the sum of the local reflection coefficients of all cells including coupling cells and periodic cells. Because of the attenuation and reflection of each cell, these reflections are added with different weight, and this is expressed as equation (6),

$$\Gamma_{port} = \sum_1^n C_n \Gamma_{local,n} \quad (6)$$

For a traveling-wave accelerating structure, the attenuated power for the nth cell is [9]

$$\left(\frac{dP}{dl}\right)_n = -2\alpha_n P \quad (7)$$

whereα_n is the attenuation factor of the nth cell and P is the power flow of the nth cell, and equation (7)can be solved as

$$P_n = P_0 e^{-2\sum_1^n \alpha_n} = P_0 e^{-2\tau_n} \quad (8)$$

so that the weight from attenuation can be expressed as

$$\Gamma_{port} = \sum_1^n e^{-2\tau_n} \Gamma_{local,n} \quad (9)$$

In equation (9), the global attenuation for all cells from the input waveguide should be added, and equation (9) is revised as

$$\Delta\Gamma_{port} = |S11| e^{-2\tau_n} \Delta\Gamma_{local,n} \quad (10)$$

where|S11|is the global attenuation factor from the input waveguide, which is equal to the reflection coefficient of the input port when detuning the input coupling cell.

Besides the effect of attenuation, the reflection of each cell also occupies some part of the weight C_n in equation (6),however the reflection of each cell is random. So the reflection of each cell cannot be derived analytically, however it can be calculated by the post-processing of the forward and backward waves in equation (3).

For a constant impedance traveling-wave accelerating structure, equation (10) is modified as

$$\Delta\Gamma_{port} = |S11| \left(\frac{a_n}{a_1}\right)^2 \Delta\Gamma_{local,n} \quad (11)$$

wherea_n is the same as that in equation (3), and $\left(\frac{a_n}{a_1}\right)^2$ includes both the attenuation factor in equation (10) and the reflection from each cell. The square represents the integrated effect of both forward and backward waves.

For a constant gradient traveling-wave accelerating structure, equation (10) is modified as

$$\Delta\Gamma_{port} = |S11| \left(\frac{a_n}{a_1}\right)^2 e^{-2\tau_n} \Delta\Gamma_{local,n} \quad (12)$$

where $\left(\frac{a_n}{a_1}\right)^2$ only represents the reflection factor, and $e^{-2\tau_n}$ is the attenuated factor, which can be calculated from design parameters.

TUNING EXPERIMENTS

Based on the design in [3], the 1.1m C-band traveling accelerating structure has successfully accomplished cold RF testing and tuning, which is shown in Figure 3. It is necessary to point out that a constant impedance structure is adopted for the 1.1m C-band structure at last, which is different from the preliminary one, for simplifying the fabrication process. The 1.1m C-band structure is tested vertically so that the pull-bead can be placed into the structure easily without touching the inner surface of the structure.

Copyright © 2012 by the respective authors — cc Creative Commons Attribution 3.0 (CC BY 3.0)

Figure 3: Vertical cold RF test for the 1.1m C-band traveling accelerating structure.

Before any tuning, the field distribution on axis is measured, which is shown in Figure 4 left. In Figure 4 left, the field distribution including amplitude and phase is very confused, and it predicts that there are complicated standing waves on axis in the accelerating structure. After the analysis by LABVIEW code in Figure4 right, apparently there are three peaks around the 15th, 22th and 50th cells and it is detuned severely. Similarly, the phase advance per cell has large fluctuation, which is expected to be about 120 degrees. Based on this severe detuning of the C-band accelerating structure, several tuning iterations are proceeded necessarily.

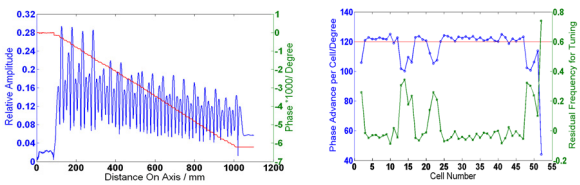

Figure 4: The field distribution and analysis before tuning

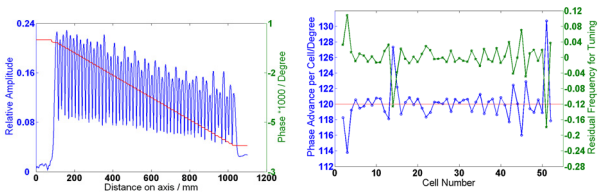

Figure: 5 The field distribution after 1st tuning.

After the first tuning phase, the field distribution and post-processing analysis are shown in Figure 5. In Figure 5 left the amplitude and phase on axis are distributed more smoothly with respect to that before tuning. In Figure 5 right, the phase advance mainly fluctuates between 118 and 122 degrees, and the amplitude of the residual frequency tuning per cell is mainly less than 0.05, which is within the permitted tolerance. However there is some slight detuning among cells, and after four water tubes are brazed, the last tuning phase eliminates the residual detuning finally.

After the final whole-structure tuning, the accelerating structure is almost matched, and the results are shown in Figure 6. According to the design target, the standing-wave ratio on axis is below 1.1 and the amplitude of phase advance fluctuation per cell is 2 degrees, corresponding to the baseline of 120 degrees per cell. In Figure 6 left, the field amplitudes in the center of cells are attenuated exponentially and the standing-wave ratio (SWR) on axis of the accelerating structure is below 1.1.In Figure 6 right, the phase advance per cell fluctuates between 118 and 122 degrees, and correspondingly the residual frequency detuning of all cells is from -0.04 to 0.04, which stays in the range of tolerance from -0.05 to 0.05. However on the both ends of accelerating structure in Figure 6 right, three cells on the each end are detuned out of the range above, which is used for the tuning of couplers.

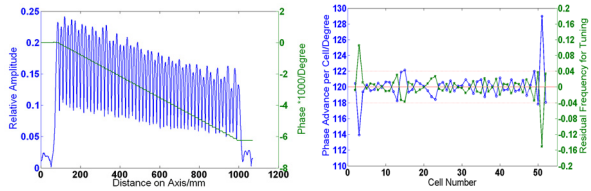

Figure 6: The field distribution after final tuning phase.

CONCLUSION

The nonresonant perturbation theory based on the bead pull measurement technique is an effective means for measuring and tuning a high gradient accelerating structure. The measurement system has been setup and successfully used in the R&D of a 1m long C-band traveling-wave accelerating structure for SXFEL. Now this prototype structure is ready for a high power RF test and since a 1.8 m long C-band constant gradient structure is under development, this measurement system becomes an indispensable tool in the accelerating structure developments.

ACKNOWLEDGEMENTS

We would like to thank Dr. Juwen Wang of SLAC for his helpful suggestion and useful discussion on the development of the measurement system, and appreciate our SINAP colleagues who join in the discussion on the nonresonant perturbation theory.

REFERENCES

[1] C. Feng et al., ChineseSci Bull, 2010, Vol.55 No.3: 221-227.
[2] M. H. Jiang et al., ChineseSci Bull, 2009, Vol54 No.22: 4171-4181.
[3] W. C. Fang et al., Chinese Sci Bull, 2011, Vol.56 No.1: 18–23.
[4] W. C. Fang et al., Chinese Sci Bull, 2011,56(32): 3420-3425.
[5] L. C. Maier et al., Journal of Applid Physics, 1952, 23(1) : 68-77.
[6] C. W. Steele, IEEE Trans.on microwave theory and techniques, 1966, MIT-14(2) : 70-74.
[7] T. Khabiboulline et al., PAC95, Dallas, TX , USA, 1995, Vol 3: 1666 – 1668.
[8] J. R. Shi et al., LINAC10, Japan, 2010, 97–99.
[9] C.G. Yao. Electron Linear Accelerator (in Chinese). Beijing: Science Press, Beijing, China, 1986,143-150.

Copyright © 2012 by the respective authors — cc Creative Commons Attribution 3.0 (CC BY 3.0)

THE C-BAND RF PULSE COMPRESSION FOR SOFT XFEL AT SINAP

W.C. Wang, Z.T. Zhao, Q. Gu, SINAP, Shanghai, China

Abstract

A compact soft X-ray free electron laser facility is presently being constructed at Shanghai Institute of Applied Physics Chinese Academy of Science (SINAP) in 2012 and will be accomplished in 2014. This facility will be located to the shanghai synchrotron radiation facility (SSRF) which is a third generation light source in china. It requires a compact linac with a high-gradient accelerating structure for a limited overall length less than 230m.The c-band technology which is already used in KEK/Spring-8 linear accelerator is a good compromise for this compact facility and a c-and traveling-wave accelerating structure was already fabricated and tested at SINAP[1], and a c-band pulse compression will be required. There are some reasons, why RF pulse compression devices are quite useful to be applied in RF power supply of the soft XFEL. For it can enhance the peak RF power by expense of RF pulse length, so it will not increase the average power and at the same time reduce the total number of the klystron, it also increases the gradient of the accelerating structure, so we need the c-band pulse compressor. AND a SLED type RF pulse compression scheme is proposed for the C-band RF system of the soft XFEL and this scheme uses TE0.1.15 mode energy storage cavity for high Q-energy storage.

The C-band pulse compression under development at SINAP has a high power gain about 3.1 and it is designed to compress the pulse width from 2.5μs to 0.5μs and multiply the input RF power of 50MW to generate 160MW peak RF power, and the coupling coefficient will be 8.5. It has three components: 3-dB coupler, mode convertors and the resonant cavities. In this paper C-band pulse compression and some components for the c-band pulse compression will be described.

INTRODUCTION

The future c-band accelerator structure of SXFEL is supposed to operate at high acceleration gradient about 40MeV per meter, this requires very high peak RF power about 160MW at frequencies 5712MHz. So as to reduce the total number of the klystron and enhance the peak RF power, the RF pulse compression is needed.

RF pulse compression is one of the methods to compress the RF pulse length and at the same time increase the peak RF power that klystron deliver. RF pulse compression is based on the principle that the RF pulse is stored in a resonance cavity or a delay line and emitted within a short time to create the short RF pulse with high peak power and then deliver it into accelerating section. At present, several RF pulse compressions systems have been already utilized successfully in the s-band or c-band linear accelerator, such RF pulse compression, the SLAC Energy Double (SLED) was the first, it was successfully applied in SLC operation, and now SLED-I，SLED-II，SLED-III（coupled cavities），BPC，DLDS and VPM（BOC）were already developed.

BPC，SLED-II and DLDS use the delay line as the energy storage cavity, have the flat output, high power gain and high efficiency, but the delay line is long and not economical. SLED-III（coupled cavities）use coupled cavities as the energy storage cavity, reduce the length of the delay line, but the output power irregular. It is applied a complex amplitude modulation on the input RF power, it is hard to control the accuracy and the stable. SLED-I has the simple structure and work stable, but it has the low power gain and less efficiency and a decaying exponential output pulse shape, so the technology AM-PM is applied for the flat output pulse shape.

In the soft XFEL, the design goal of the pulse compression is to compress the pulse width from 2.5μs to 0.5μs and to multiply the input RF power of 50MW to generate 160MW peak RF power. To satisfy this requirement for the soft XFEL, we adopted a SLED type pulse compression as the c-band pulse compressor. This scheme use TE0.1.15 mode for the storage cavity to compress an RF pulse into a short square high peak-power pulse for the course of R＆D study of the soft XFEL. Figure 1 shows the schematic diagram. This scheme consists of one 3-db coupler, two mode convertors, and a pair of high-Q resonant cavities.

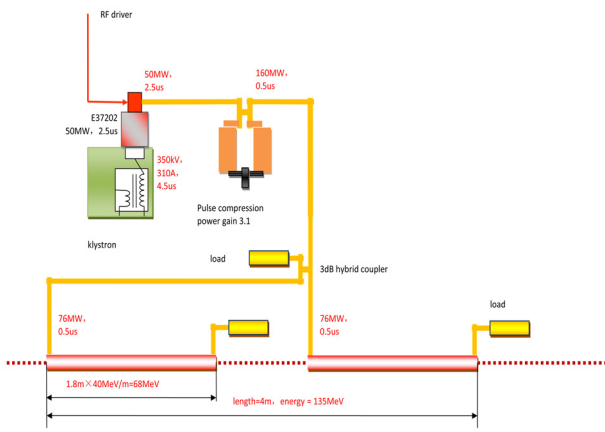

Figure1: C-band 50WM RF Scheme.

C-BAND PULSE COMPRESSOR

C-band Pulse Compressor

For the SLED type RF pulse compression, the expression of the power for the resonant cavity is[2]

$$T_C \frac{dE_e}{dt} + E_e = -\alpha E_K \quad (1)$$

Copyright © 2012 by the respective authors — cc Creative Commons Attribution 3.0 (CC BY 3.0)

where $\alpha = 2\beta/(1+\beta)$, $T_c = \frac{2Q_L}{\omega}$, Ee: emitted wave from the coupling aperture, EK: reverse wave that is equal in magnitude to the incident wave Ei from the klystron.

The expression of the energy multiplication factor Vmax is

$$V_{max} = \gamma * e^{-\frac{T_a}{T_c}}[1-(1+g)^{1+v}] * [g*(1+v)]^{-1}\text{-}(\alpha-1) \quad (2)$$

where $\gamma = \alpha(2-e^{-T_1})$, $T_a = (L/gv_{g0})\ln[1/(1-g)]$ is the filling time for the structure.

g is the gradient of group velocity along accelerating structure, v=Ta/TC[ln(1-g)]-1.

Q value of the TE_{0115}mode[3]

TE_{0115}mode was chosen as the resonant cavity mode and the Q factor can be expressed as:

$$Q_0 = \frac{\lambda*[\upsilon_{mn}^2+(p\pi R/l)^2]^{\frac{3}{2}}}{2\pi\delta\left[2p^2\pi^2\frac{R^3}{l^3}+\upsilon_{mn}^2\right]} \quad (3)$$

Optimize the cavity diameter：

The relation among resonant frequency, mode and geometry dimensions can be expressed as:

$$\left(\frac{f_0 D}{c}\right)^2 = \left(\frac{\nu_{mn}}{\pi}\right)^2 + \left(\frac{pD}{2l}\right)^2 \quad (p \neq 0) \quad (4)$$

Considering the resonant frequency, the cost, unloaded Q value, it is suitable to choose the resonant cavity length is 429.18mm and the diameter is 152.6mm. And a tuner also is designed at the end of the each resonant cavities, it used to tune the frequency.

Table 1: Parameters of the pulse compression cavity

Operation frequency	5712MHz
mode	TE0.1.15
Cavity diameter	152.6mm
Cavity length	429.18mm
Iris diameter	48mm
Cavity length	15mm
Quality factor	181710
Power gain	3.1
Coupling coefficient	8.5

The results of simulation by CST are shown in Fig. 2.

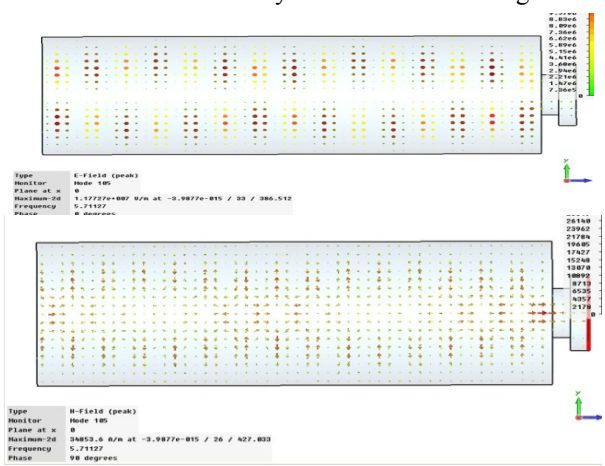

Figure 2: The cavity mode simulated by CST.

COMPONENTS FOR THE C-BAND PULSE COMPRESSION

3-dB Coupler Hybrid

3-dB coupler hybrid is an essential element to direct the flow of RF power for the RF pulse compression system. In the cavity type compressor, through this coupler an output RF power of the klystron is guided to two over coupled cavities, and waves from the each cavity are combined so as to add and transmitted to the accelerating structure. The value of the coupling depends on the width and the length of the coupling region. For 3-dB coupling, they were designed 76mm and 60mm, respectively.

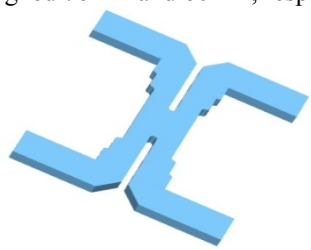

Figure 3: The 3-db hybrid coupling.

The distance of the coupling section L is a function of the width 2a as followings,

$$L = \frac{1}{4\left(\frac{1}{\lambda_{g10}}-\frac{1}{\lambda_{g20}}\right)} \quad (5)$$

Where $\lambda_{g10} = \frac{\lambda}{\sqrt{1-(\frac{\lambda}{4a})^2}}$; $\lambda_{g20} = \frac{\lambda}{\sqrt{1-(\frac{\lambda}{2a})^2}}$

Here we used a ladder type hybrid which has excellent divided ratio, phase condition, broad frequency response characteristics and the coupling is 3dB.

Table 2: Parameters of the 3-db coupler

Coupling region width	76mm
Coupling region length	60mm
First ladder length	176mm
First ladder depth	6.2mm
Second ladder length	124mm
Second ladder depth	13mm
Simulation coupling	S_{21},S_{31}=-3dB; S_{11},S_{41}<-30dB

The results of simulation by CST are shown in Fig. 4.

Mode Converter

Many modes are concentrated around the target TE0.1.nmode in the high-Q cavity of the RF Pulse Compressor. The high purity of the cylindrical TE_{01}mode must be needed to produce the designed Q-value and efficiency. Thus the many unnecessary modes can reduce the high Q-value and the efficiency if we directly connect the rectangular waveguide to the TE_{01}nmode cavity, so that a mode converter is applied between the 3-db coupler and the cavity to reduce unnecessary modes. The mode converter is shown in Fig. 5.

Copyright © 2012 by the respective authors — cc Creative Commons Attribution 3.0 (CC BY 3.0)

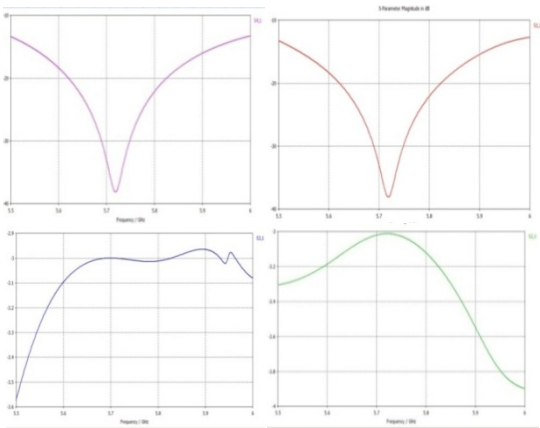

Figure 4: The simulation of the 3-db hybrid coupling.

The simulated S-parameters of the mode converter shows that the transmission coefficients of the other inconvenient modes become lower that 0.1 as S_{11}.

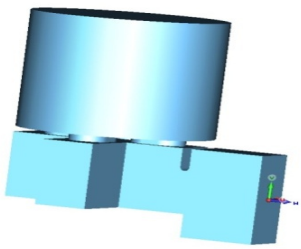

Figure 5: Mode convertor

Table 3: Parameters of the Mode Convertor

Rectangular:	BJ48, l=31.25mm
Cross rectangular:	l=80mm h=35mm
Cylindrical:	R=40mm,l=65mm
Coupling hole: Coupling height	h=4mm,a=22.18mm,b=16mm
Simulation	S_{11}<-30dB; S_{21}=0dB

The results of simulation by CST are shown in Fig. 6.

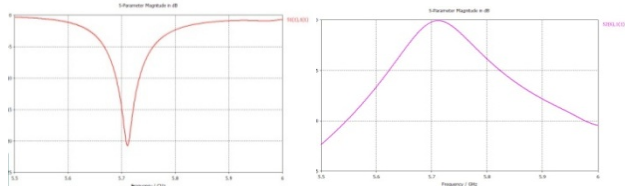

Figure 6: The simulation of the mode convertor.

CONCLUSION

In this paper we designed c-band pulse compression use TE_{0115} mode for the soft the SINAP SXFEL, and it will be fabricated in the future. And also some components for the c-band pulse compression are also designed. The low mode RF pulse comression cavity is fabricated in the SINAP.

REFERENCES

[1] Fang W C, Gu Q, Tong D C et al., Design optimization of a c-band traveling-wave accelerating structure for a compact X-ray free electron laser facility, Chinese Sci. Bull, 2011,56(32):3420-3425

[2] Z.D. Farkas, H.A. Hogg, G.A. Loew and P.B.Wilson, SLED:A METHOD OF DOUBLING SLAC's ENERGY, SLAC-pub-1453, June 1974

[3] XIAO Ou-Zheng, ZHAO Feng-Li, HE Xiang, Design and simulation of a c-band pulse compressor, CPC,2012,36(4):360-363

[4] Mitsuhiro Yoshida, Ph.D Thesis, The Research and Development of High Power C-band RF Pulse Compression System using Thermally Stable High-Q Cavity

Copyright © 2012 by the respective authors — cc Creative Commons Attribution 3.0 (CC BY 3.0)

RF PHOTOINJECTOR AND RADIATING STRUCTURE FOR HIGH-POWER THz RADIATION SOURCE

S.M. Polozov, T.V. Bondarenko,
National Research Nuclear University (MEPhI), Moscow, Russia.
Yu.A. Bashmakov, Lebedev Physical Institute of RAS (LPI), Moscow, Russia

Abstract

Sources of high-power electromagnetic radiation in THz band are becoming promising as a new method of a low activation introscopy. Research and development of accelerating RF photoinjector and radiating system for THz radiation source are reported. The photoinjector is based on disk loaded waveguide (DLW). Two different designs of accelerating structure were modelled: widespread 1.6 cell of DLW structure and travelling wave resonator structure (TWR). The resonant models of these structures and the structures with power ports were designed. Electrodynamics characteristics and electric field distribution for all models were acquired. Results of picoseconds photoelectron beam dynamics in simulated structures are reported. Designs of decelerating structures exciting Cherenkov radiation are based on corrugated metal channel or metal channel coated with dielectric. Analysis of radiation intensity and frequency band are presented.

INTRODUCTION

THz radiation is nowadays becoming promising in solving such vital problems as national security, biomedicine and in manufacturing processes control. In national security issue THz radiation can be used in introscopy systems. The definition of the weapons, explosives, drags and fissionable materials is the main aim of introscopy. The introscopy of cargo transport is much more complicated objective then passenger introscopy issue. The gamma, electron or neutron facilities are used in introscopy system including cargo introscopy at present. The compact electron or ion gun or accelerator is the basic element of such facilities. The main difficulty is the fact that it is necessary to use an electron linear accelerator (LINAC) which can derive the beam with 3-5 times energy variation. LINACs of this type are utterly complex facilities. All of gamma, electron or neutron facilities have a number of disadvantages as needs of environmental shielding and cargo activation.

High-power THz radiation source based on photoinjector and decelerating capillary channel is now one of the most discussable compact facilities providing monochromatic THz radiation of power high enough to be used for cargo introscopy [1].

Facility is based on two main parts: accelerating structure and decelerating radiating channel. Capillary is placed right after the accelerating structures and is made of copper with either dielectric coated inner surface or corrugated surface.

ACCELERATING STRUCTURES

1.6 cell DLW structure

Accelerating structure consists of two accelerators connected sequentially: 1.6 cell DLW and 9 cell TWR structure.First part of facility accelerating system is 1.6 cell standing wave accelerating structure (figure 1). This accelerating structure by itself comes artlessly as a photoinjector part of the accelerating system.

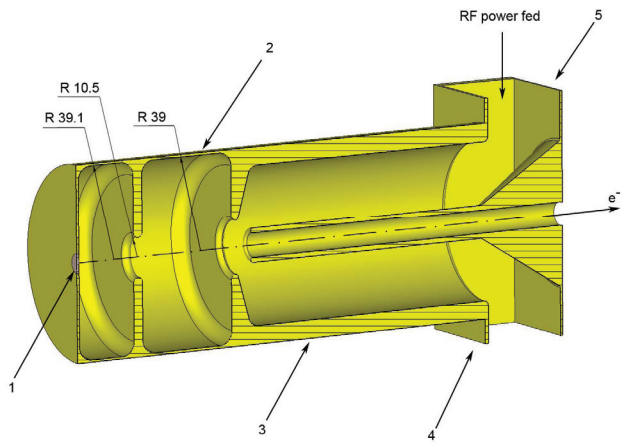

Figure 1. 1.6 accelerating structure: 1 – photocathode, 2 - resonator, 3 – coaxial wave type transformer, 4 – vacuum port, 5 – power input.

This accelerating structure operates on π mode and S-band frequency 2856 MHz (λ=105 mm). Resonant frequency of the structure was tuned to the desired value by means of cell radius variation. Iris profile was made with rounding to eliminate the possibility of breakdown. First cell length is 0.6 of full-sized cell to obtain maximum field amplitude in the center of the photocathode arranged in the cell's sidewall. Performance of the structures was also increased by rounding of shells edges. The rounding radius value was chosen to provide the highest possible shunt impedance and Q-factor.

Structure RF power input in organized by S-band standard rectangular waveguide with the coaxial coupler. RF power is fed into the structure through only one of the connected waveguides; another is used for structure field symmetry and will be applied for vacuum and other accompanying connections. This scheme provides high level of field symmetry in the system that leads to better quality of the accelerated beam.

This type of wave transformer differs from recently used RF power inputs in photoinjectors like ones in BNL Guns [2]. That type was exploiting the scheme of power

Copyright © 2012 by the respective authors — cc Creative Commons Attribution 3.0 (CC BY 3.0)

input through the coupling diaphragm directly into the full-sized cell of the structure in this wise fill cell was a wave transformer.

TWR structure

Travelling wave resonator is a type of ordinary linear accelerator structure with some additions. Basically the accelerating wave propagating in acceleration structure is travelling wave type but the trait that makes this system a resonator is energy recuperation coming out of interlocking RF power input with output and feeding power with directional coupler (figure 2). If the length of the TWR circuit is devisable to the generator wavelength, the magnitude of electromagnetic fields in TWR reaches its maximum and magnitude of the wave incoming to the load from the ring turns to minimum [3].

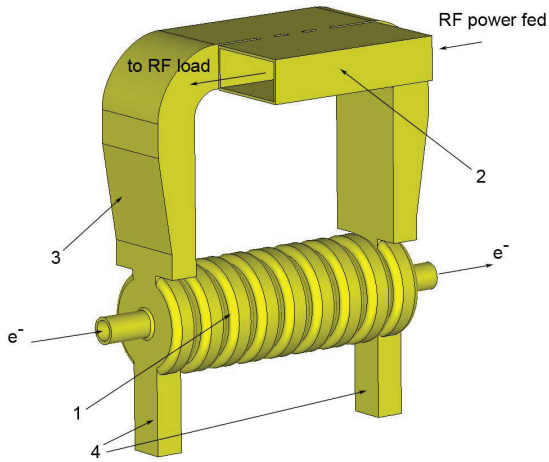

Figure 2. Travelling wave resonator structure: 1 – accelerating structure, 2 – directional coupler, 3 – TWR ring, 4 – vacuum ports.

TWR is based on 9 cell travelling wave S-band structure with $\pi/2$ operating mode. The optimal operation regime of the structure is critical mode. In this regime part of RF power is fed into the accelerating system through the directional coupler and fills in the power resistance losses in the resonators sidewalls. In this case the part of power that is not branched into the TWR ring is summed with the one from generator in the opposite phase and gives the minimal magnitude signal coming to the load. Two main parameters determining efficiency of TWR are the circuit power attenuation factor and the directivity factor of the directional coupler.

Directional coupler with narrow or wide side coupling represents the connection of two waveguides by coupling windows with space shift of quarter wavelength between the windows irradiating in the opposite directions of jointed waveguide. Directional coupler computation included receiving of required transfer coefficient in the forward direction of jointed waveguide C and simultaneously keeping transfer coefficient in the opposite direction of jointed waveguide $|\Gamma|$ below the certain level.

Three coupling window model was applied to provide high directivity level of directional coupler. Enlarging the number of coupling windows doesn't improve the directivity coefficient.

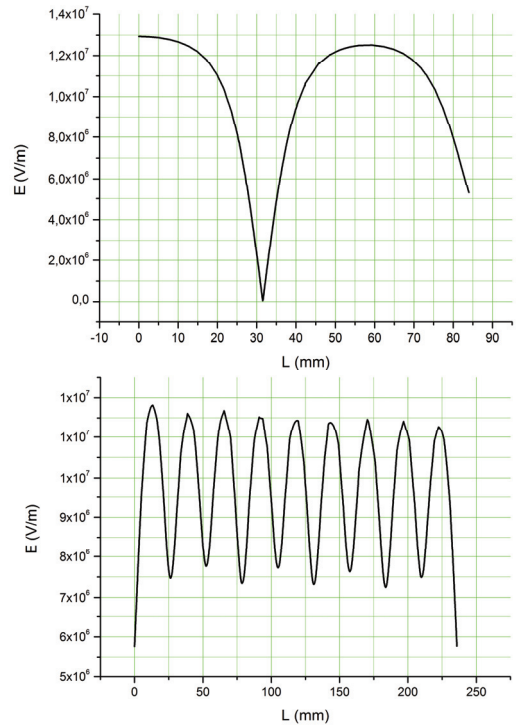

Figure 3. Electrical field magnitude plots at 1 MW power fed for 1.6 cell structure (upper) and for TWR structure (lower)

Taking into account part of the signal branching in the opposite direction and intensity attenuation factor, expression for the magnitude of electrical field spreading in TWR storage ring for critical mode can be written as:

$$A_{TWR} = \pm j \frac{1}{\sqrt{1-e^{-2\alpha_T}}} \frac{C-|\Gamma|}{C} A_{input}, \qquad (1)$$

here A_{TWR} - TWR circuit electrical field intensity magnitude, α_T - TWR ring signal intensity attenuation factor, A_{input} – RF generator signal intensity magnitude.

In considered case transition coefficient of directional coupler C=3.9% that equals to TWR ring decay coefficient at the 14 mm coupling window width, sidewall width between waveguides is 4 mm. Sidewalls width doesn't have much impact on directivity coefficient but ought to be wide enough to provide coupler ruggedness. Transfer coefficient in the opposite direction of TWR ring equals Γ=-48dB. Thus directivity coefficient of directional coupler is D=23dB. Using the formula (1) power in TWR multiplies 9 times vs. input power level.

BEAM DYNAMICS

Beam dynamics simulation in designed accelerating structures was done using BEAMDULAC-BL code

Copyright © 2012 by the respective authors — cc Creative Commons Attribution 3.0 (CC BY 3.0)

designed in laboratory DINUS of NRNU MEPhI [4]. The simulation was done with the following beam parameters: injection energy W_{inj}=5 eV, feeding RF power P=2.5MW, beam pulse current I=5 A, beam pulse charge Q=1 nC. Photoelectron beam initial radius is r=200 μm that corresponds to the laser spot of the same size focused on the cathode surface. This beam parameters values are similar to most of photoinjectors. The first accelerating section is fed by 1.5 MW and the second by 1 MW power.

The results of photoinjector beam dynamics investigation shows that at this value of RF power fed beam bunch can be accelerated to the energy of 1 MeV. The further acceleration of the beam in TWR section resulted in 5 MeV beam energy that meet the requirements for the beam in THz generation process.

Pencil-shaped and high brightness beam is necessary for Cherenkov THz generator to achieve that beam size preservation can be realized in accelerator using longitudinal magnet field focusing.

CHAPILLARY CHANNEL

Two types of channels could be used for generation of Cherenkov radiation: the conducting (metal) capillary coated by dielectric inside (see Fig. 4a) and the corrugated channel or grating surface also (Fig. 4b). The inner channel radius $d/2$ should be comparable to the wavelength, i.e. should be about 0.1 – 1 mm. The structure period t (the distance between of diaphragms) in the second case should also be comparable to the wavelength.

The main idea of using the capillary channel as a source for radiation lies in a principle of Cherenkov radiation. The phase velocity of the wave propagating inside the capillary channel is less than the electron beam velocity. So the beam propagating in such structure would induce the radiation with the frequency dependent on the channel dimensions.

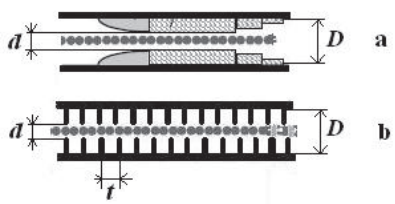

Figure 4. The conducting (metal) capillary coated inside by dielectric (a) and the corrugated channel or grating surface (b).

Different approaches can be estimated for achieving the induced power in the accelerated structures. One of the ideas is based on using the form-factor concept [5]. The decelerating structure parameters such as shunt impedance, Q-factor and group velocity are numerically investigated in terms of TM01 wave excited inside of the capillary. Then radiated power can be founded using the formula for the case of short burst mode when pulse repetition time is much longer than the beam length:

$$P = \frac{\omega}{4}\frac{r}{Q}\left|v_{group}\right| \cdot \left|\frac{q\Phi}{1-\beta_{group}/\beta}\right|^2, \qquad (2)$$

where ω - radiation resonant frequency, r – channel shunt impedance, Q – channel quality factor, q – bunch charge Φ - bunch form-factor, v_{group}, β_{group} - absolute and relative group velocity of the channel. For considered capillary channels Q is about 2000, β_{group} - 0.8 and r is around $3 \cdot 10^4$.

Another concept was discussed by Bolotovsky [6]. In this concept beam energy loss for the Cherenkov radiation is described by the force acting on the moving charge by the induced fields. Electron beam is presented as a point charge because beam sizes are smaller than induced radiation wavelength. The corrugated channel in this concept is presented as a small disk loaded. This method doesn't take in the account beam form factor.

Both cases show alike results for power radiated by the beam propagating in the channels. The goal was to achieve the radiation with 1 THz frequency. Channel length for both designs was 2 cm. Dielectric channel dimensions are: 300 μm channel radius and 30 μm teflon thickness. In case of corrugated channel transverse sizes appears to be smaller: 100 μm cell radius, 80 um diaphragm radius. For the stated above beam parameters the radiated power appears to be around 50 kW in the case of dielectric coated channel and 20 kW in case of corrugated channel in case of 1 nC beam charge and 5 MeV beam energy.

CONCLUSION

RF photoinjector and decelerating system were investigated for high-power THz generator. RF photoinjecr is based on two accelerating sections: 1.6 cell standing wave structure with coaxial power input and travelling wave section based on travelling wave resonator. Both are fed by S-band 2.5 MW magnetron. First is used to emit photoelectrons and to accelerate bunch to 1 MeV. Second is used for further acceleration to 5 MeV.

Decelerating channel can be based on two main concepts: corrugated metal channel and dielectric covered channel. Both are applicable for achieving high radiation power rates.

REFERENCES

[1] Yu.A. Bashmakov, T.V. Bondarenko, S.M. Polozov, et al., Problems of Atomic Science and Technology. Series: Nuclear Physics Investigations, 3 (79), 2012, p. 53-57.
[2] D. T. Palmer, R.H. Miller, X.J. Wang, et al., SLAC–PUB–7420, May 1997.
[3] J. L. Altman, Microwave circuits, Van Nostrand Co., 1964.
[4] T.V. Bondarenko, E.S. Masunov, S.M. Polozov, et al., Proceedings of IPAC 2011, MOPS037.
[5] A.V. Smirnov, Nuclear Instruments and Methods in Physics Research A 480 (2002), 387–397.
[6] K.A. Trukhanov, V.V. Poliektov, V.I. Shvedunov, Proceedings of RuPAC'04, p. 106.

Copyright © 2012 by the respective authors — cc Creative Commons Attribution 3.0 (CC BY 3.0)

THE DEVELOPMENT OF TIMING CONTROL SYSTEM FOR RFQ

J. Bai, L. Zeng, S. Xiao, T. Xu
Institute of High Energy Physics, CAS, Beijing, 100049, P.R China

Abstract

In order to meet the need of RFQ accelerator, Timing extension hardware based on VME configuration has been developed. In the future, it will be used in the diagnostics system of CSNS. This paper introduces the function of Timing extension hardware, EPICS driver for Timing extension hardware and MEDM operator interface.

BACKGROUND

The core research of intense-proton beam accelerator is mainly concentrated in the field of beam loss control. Based on the intense-beam RFQ accelerator [1] which accelerates proton beam of 46mA pulse current to 35MeV at more than 7% duty factor, a beam line has been built. In order to do beam loss control experiment, many devices have been developed, one of which is Timing extension hardware. Timing extension hardware, as an important device in the running of RFQ accelerator, provides high accuracy and high stability timing trigger signals for the whole system. In the future, it will be used in the CSNS (Chinese Spallation Neutron Source).CSNS adopts EPICS [2] (Experimental Physics and Industrial Control System) as its software environment. So it is necessary to develop EPICS driver [3] for timing extension hardware.

INTRODUCTION OF TIMING EXTENSION HARDWARE

Timing extension hardware uses VME bus of A24 nonpriviledged data access address modifier [6]. It is listed below as fig. 1. Since A24 space is of predicable size 16MB, default window encompassing the full space is always provided. The A24 window is for VME bus address from 0x000000 to 0xffffff, which is usually mapped by VxWorks subroutine sysBusToLocalAdrs to local memory from 0xfa000000 to 0xfaffffff [6].

```
#define VME_AM_STD_USR_DATA     0x39    /* A24, nonpriviledged data access*/
```

Figure 1: Address Modifiers of A24 nonpriviledged data access

Timing extension hardware based on VME configuration is not only consistent with RFQ requirement, it but also avoids the disadvantage of original timing control system, achieving parameters remedy on line. When operators need to remedy parameters of original timing control system, they have to stop the accelerator and calculate the parameters according to the request of experiments, and then use dip switch to change the parameters. The whole process will last almost two hours and affect the efficiency, stability and continuity. Besides, Timing extension hardware based on VME architecture achieves utility of the same hardware to perform different functions by using reconfiguration of the FPGA, which enhances the flexibility of timing extension hardware.

Timing extension hardware has two types of functions [4]. One is providing primary timing signals for RFQ and secondary timing signals which divide frequency of primary timing signals for beam commissioning and RF system. The other is providing delaying or broadening timing signals according to the needs of various devices. In fact, the principle of these two functions is calculating clock signals. For example, primary timing outputs a timing pulse when it calculates the clock signal to the certain amount. Broadening hardware is triggered by timing signal and starts counting program. It will output a TTL pulse with the width of 3us when counting program reaches to the setting value.

Fig. 2 shows timing signals of RFQ, and the timing extension hardware is shown in Fig. 3.

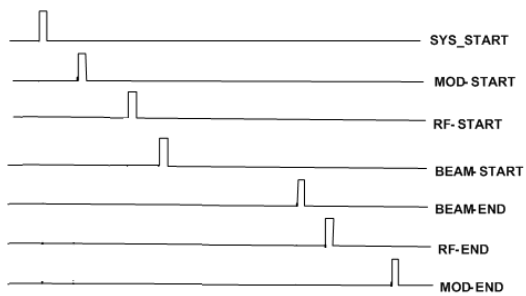

Figure 2: Timing signals of RFQ

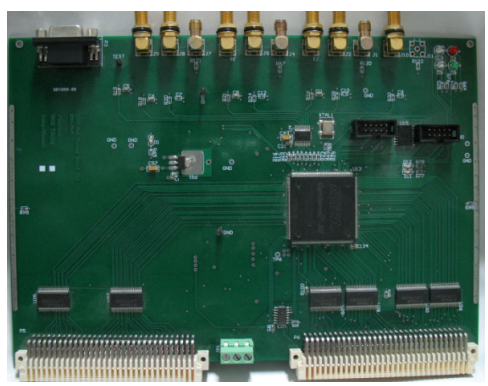

Figure 3: The timing extension hardware

Copyright © 2012 by the respective authors — cc Creative Commons Attribution 3.0 (CC BY 3.0)

Table 1: Timing control system records access registers step by step

Function	db	dbd	Device support	Driver support
Set primary timing/secondary timing value	Time:$(CARD): $(CHAN): TimingValue:set	device(ao,VME_IO, devAoTime, "Time")	devAoTime{ ….. Write_ao, ……}	Write_Val
Set delay/ broaden value	DelayOrBroaden:$(CARD):$(CHAN):Value:set			
Chose clock signal from internal or external	Time:$(CARD):ClockSignal:set	device(bo,VME_IO, devBoTime, "Time")	devBoTime{ ….. Write_bo ……}	Write_CSR
Chose logic of primary timing/secondary timing	Time:$(CARD): $(CHAN):TimingLogic:set			
Chose logic of delay/broaden	DelayOrBroaden:$(CARD):$(CHAN):Logic:set			
Chose delay or broaden	DelayOrBroaden:$(CARD):$(CHAN):Select:set			
Read timing register of card	Time:$(CARD):CSR:read	device(mbbiDirect,VME_IO, devMbbiDirectTime, "Time")	devMbbiDirectTime { ….. Read_ mbbiDirect ……}	Read_CSR
Read delay/broaden register of card	DelayOr Broaden:$(CARD):CSR:read			
Read actual primary timing/secondary timing value	Time:$(CARD): $(CHAN): TimingValue:read	device(ai,VME_IO, devAiTime, "Time")	devAiTime{ ….. Read_ai, ……}	Read_Val
Read actual delay/ broaden value	DelayOrBroaden:$(CARD): $(CHAN): Value:read			

DTYP

DTYP

DTYP

DTYP

EPICS DRIVER FOR TIMING CONTROL SYSTEM

The functions of timing extension hardware achieve by single read or write register [5]. Table 1 is provided to give an outline about how records access registers step by step.

OPERATOR INTERFACE

The operator interface which is under development makes use of MEDM [7] (Motif Editor and Display Manager). With the interface of Timing control system, operator can chose system clock, logic of primary timing and secondary timing, delay or broaden of every channel and logic of every channel. Besides, primary timing, secondary timing, delay or broaden time of each channel can be set through the Interface. Fig. 4 is the operator Interface for Timing control system.

According to the control of interface, timing extension hardware can work normally.

ACKNOWLEDGEMENTS

The authors would like to thank the CSNS Control Group, Accelerator Center, Institute of High Energy Physics, CAS to provide the EPICS platform to work on and technical support.

REFERENCES

[1] Shinian Fu, Xialing Guan. Development of High Intensity RFQ Proton Accelerator. Beijing: Atomic Energy Science and Technology 2009:1-6

[2] Argonne National Laboratory. Experimental Physics and Industrial Control System. [Online]Available: http://www.aps.anl.gov/epics/

[3] Martin R. Kraimer. IOC Application Developer Guide[M]. 1998:1-180

[4] Shuai Xiao. Lei Zeng. Xian Guo. Taoguang Xu. Timing control system of Intense-beam proton accelerator[C]. Beijing：Nuclear Electronics &Detection Technology 2011：1-7

[5] PSI. Writing EPICS Drivers

[6] WindRiver. WTN-56 Going out on the VME bus

[7] Kenneth Evans, Jr. MEDM Reference Manual: http://www.aps.anl.gov/epics/EpicsDocumentation/ExtensionsManuals/MEDM/MEDM.html

Copyright © 2012 by the respective authors — cc Creative Commons Attribution 3.0 (CC BY 3.0)

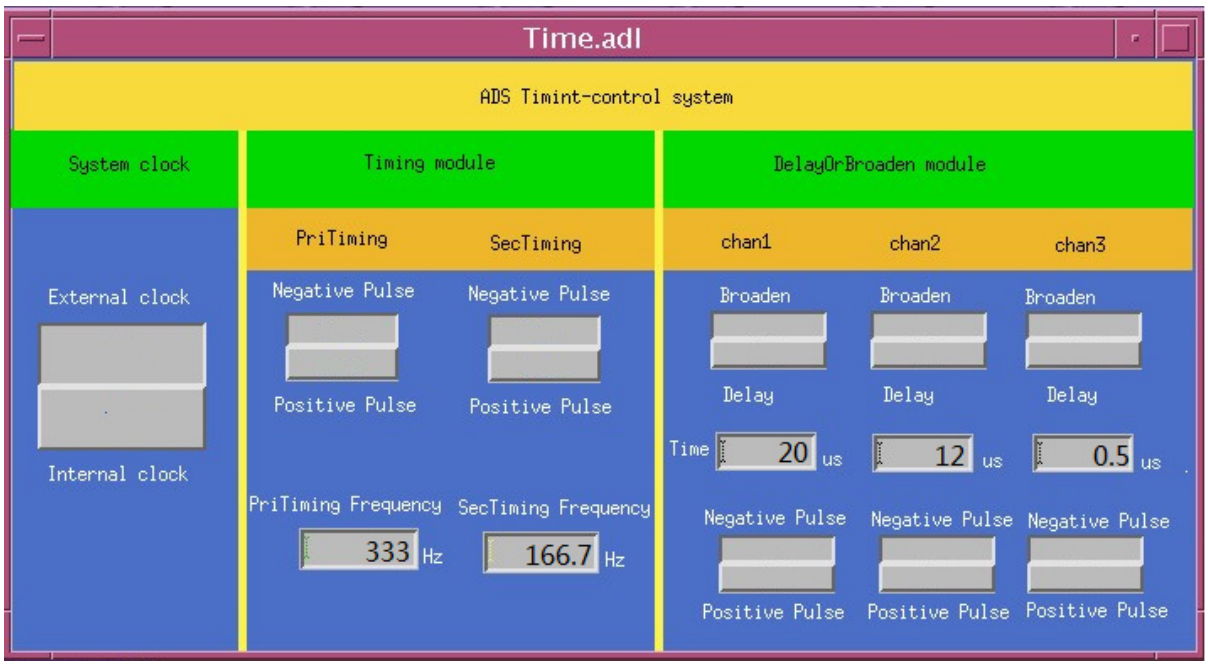

Figure 4: The operator interface

Copyright © 2012 by the respective authors — cc Creative Commons Attribution 3.0 (CC BY 3.0)

MULTIPOLE FIELD EFFECTS FOR THE SUPERCONDUTING PARALLEL-BAR/RF-DIPOLE DEFLECTING/CRABBING CAVITIES*

S. U. De Silva[1,2#], J. R. Delayen[1,2],
[1]Center for Accelerator Science, Old Dominion University, Norfolk, VA 23529, USA.
[2]Thomas Jefferson National Accelerator Facility, Newport News, VA 23606, USA.

Abstract

The superconducting parallel-bar deflecting/crabbing cavity is currently being considered as one of the design options in rf separation for the Jefferson Lab 12 GeV upgrade and for the crabbing cavity for the proposed LHC luminosity upgrade. The knowledge of multipole field effects is important for accurate beam dynamics study of rf structures. The multipole components can be accurately determined numerically using the electromagnetic surface field data in the rf structure. This paper discusses the detailed analysis of those components for the fundamental deflecting/crabbing mode and higher order modes in the parallel-bar deflecting/crabbing cavity.

INTRODUCTION

The parallel-bar/rf-dipole deflecting/crabbing cavity has been optimized from a rectangular-shaped design with cylindrical-shaped parallel bars into a design with a cylindrical-shaped outer conductor with trapezoidal-shaped parallel bars [1,2], named the rf-dipole cavity. The improved rf-dipole deflecting/crabbing cavity design operating in TE_{11}-like mode has attractive properties with low and balanced surface fields, high shunt impedance and well separated higher order modes (HOMs). The deflecting/crabbing mode is the lowest mode in the rf-dipole design.

Currently the rf-dipole design is being considered as one of the rf separator options for the Jefferson Lab 12 GeV upgrade and as one of the crabbing cavity options for proposed LHC luminosity upgrade operating at 499 MHz and 400 MHz respectively. A 750 MHz design is also being considered as a crabbing cavity for the proposed medium energy electron-ion collider (MEIC) at Jefferson Lab [3]. The first prototypes of the cylindrical-shaped 499 MHz and 400 MHz rf-dipole cavities (Fig. 1 (A) and (B)) are being fabricated and are in preparation for rf testing [4].

The 400 MHz crabbing cavity design was further modified into a square-shaped outer conductor (Fig. 1(C)) with fixed transverse dimensions of <295 mm, to meet the dimensional constraints of the LHC crabbing system. The design was further improved by curving the bar geometry at the beam aperture (Fig. 1(D)) to reduce the transverse field variation across the beam aperture.

*Authored by Jefferson Science Associates, LLC under U.S. DOE Contract No. DE-AC05-06OR23177. The U.S. Government retains a non-exclusive, paid-up, irrevocable, world-wide license to publish or reproduce this manuscript for U.S. Government purposes.
Part of this work was done in collaboration with and supported by Niowave Inc. under the DOE STTR program.
#sdesilva@jlab.org

Copyright © 2012 by the respective authors — cc Creative Commons Attribution 3.0 (CC BY 3.0)

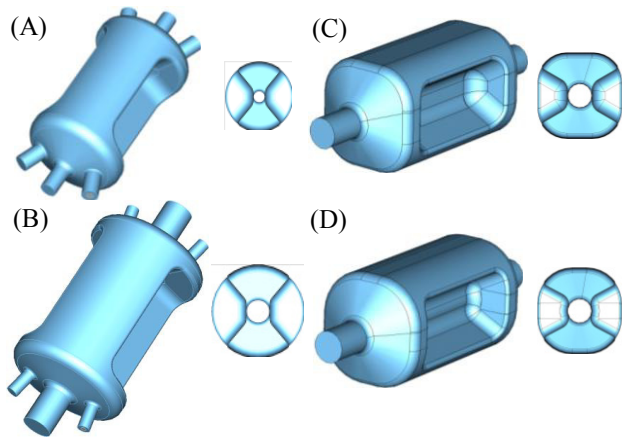

Figure 1: RF-dipole geometries and cross sections of (A) 499 MHz design, (B) cylindrical-shaped 400 MHz design, (C) square-shaped 400 MHz design and (D) square-shaped 400 MHz design with curved inner bar surfaces.

MULTIPOLE FIELD ANALYSIS

In the rf-dipole design, the field varies across the beam aperture off the beam axis generating a non-uniform transverse deflection. The field variation in x and y directions are shown in Fig. 2, for all the rf-dipole designs mentioned in Fig. 1.

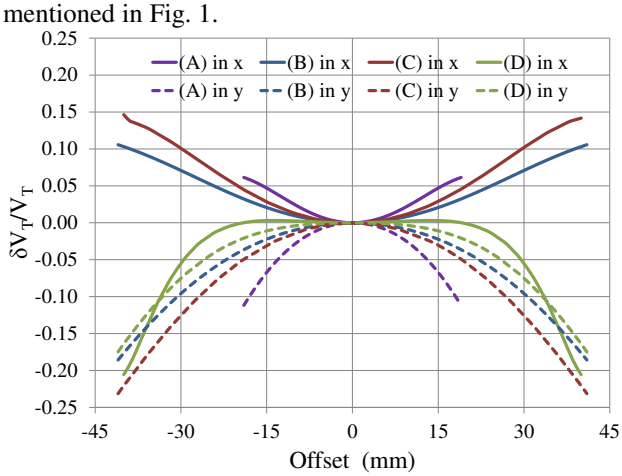

Figure 2: Normalized transverse voltage in x and y directions for designs (A), (B), (C) and (D) in Fig. 1.

The non-uniform transverse fields can generate higher orders of transverse momentum apart from the first order transverse momentum that corresponds to the deflecting or crabbing voltage. These higher order transverse multipole components may lead to perturbations in the beam. This paper presents the higher order multipole components present in the rf-dipole cavity and supressing of those components by modifying the geometry.

Calculation of Multipole Components

The fields in magnets are often expressed in terms of multipole components. The standard representation of multipole fields [5] can be expressed as,

$$B(r,\phi) = B_{ref}\sum_{n=1}^{\infty} a_n + ib_n \left(\frac{r}{r_{ref}}\right)^{n-1} e^{i(n-1)\phi} \quad (1)$$

where B_{ref} is the reference magnetic field at a given radius of r_{ref}.

Similarly, close to the beam axis, the electro-magnetic fields in an rf cavity within the beam aperture can be represented as given in Eq. 2. The symmetry in the rf-dipole cavities doesn't produce any skew components; therefore the fields can be represented as in Eq. 3.

$$E_z(r,\phi,z) = \sum_{n=0}^{\infty} E_z^{(n)}(z) r^n e^{jn\phi} \quad (2)$$

$$E_z(r,\phi,z) = \sum_{n=0}^{\infty} E_z^{(n)}(z) r^n \cos(n\phi) \quad (3)$$

The multipole field components $E_z^{(n)}(z)$ along the beam line can be obtained by using the Fourier series expansion of $E_z(r,\phi,z)$ as shown in Eq. 4.

$$E_z^{(n)}(z) = \frac{1}{r^n}\int_0^{2\pi} E_z(r,\phi,z)\cos(n\phi)\,d\phi \quad (4)$$

In rf cavities with time dependent rf fields, the higher order multipole components with time dependence can be given by $E_{acc}^{(n)}(z) = E_z^{(n)}(z)e^{j\omega t}$.

The higher order multipole components can be determined using the method given by A. Grudiev in Ref. [6]. The transverse momentum imparted by the higher order multipole field components (n>0) can be determined using the Panofsky Wenzel Theorem,

$$\begin{aligned} p_t^{(n)}(z) &= \frac{1}{c} r^{n-1}\int_{-\infty}^{\infty} F_t^{(n)} dz = -j\frac{q}{\omega}\int_{-\infty}^{\infty} \nabla_t E_z^{(n)}(z) e^{j\omega t} dz \\ &= -j\frac{q}{\omega} n r^{n-1}\int_{-\infty}^{\infty} E_{acc}^{(n)}(z) dz \end{aligned} \quad (5)$$

or by using the Lorentz Force,

$$\begin{aligned} p_t^{(n)}(z) &= \frac{1}{c} r^{n-1}\int_{-\infty}^{\infty} F_t^{(n)} dz \\ &= \frac{q}{c} r^{n-1}\int_{-\infty}^{\infty}\left[E_t^{(n)}(z)e^{j\omega t} + cB_t^{(n)}(z)e^{j\omega t}\right] dz \end{aligned} \quad (6)$$

The multipole components (b_n) are defined using the standard definition for magnets [6] as,

$$\begin{aligned} B^{(n)}(z) &= \frac{1}{qc} F_t^{(n)}(z) = j\frac{n}{\omega} E_{acc}^{(n)}(z) \left[T/m^{n-1}\right] \\ b_n &= \int_{-\infty}^{\infty} B^{(n)}(z) dz \left[T/m^{n-2}\right] \end{aligned} \quad (7)$$

These coefficients (b_n) can be used to determine the effect of higher order multipole components on beam perturbations [6].

Multipole Components for the RF-Dipole Cavity

The rf-dipole cavity has zero on axis longitudinal electric field, where the transverse deflection is given by both transverse electric and magnetic fields. The higher order multipole components can be determined using both the methods given in Eqs. 5 and 6. The $E_z(r,\phi,z)$ field data are obtained for each rf-dipole geometry using CST Microwave Studio, at three different radii within the beam aperture. A finer mesh as shown in Fig. 3 is used especially at smaller radii with a fixed number of points at each concentric cylinder.

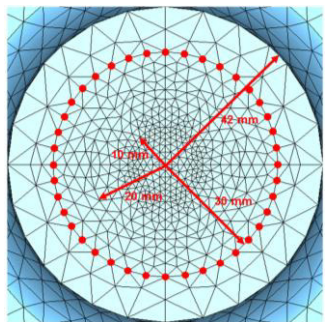

Figure 3: $E_z^{(n)}(z)$ of n = 1, 3 and 5 at r_0 = 1 cm, 2 cm and 3 cm for the cylindrical-shaped 400 MHz rf-dipole cavity.

The Fourier-decomposed field components of $E_z^{(n)}(z)$, $E_x^{(n)}(z)$ and $H_y^{(n)}(z)$ calculated using a MatLAB code at radii of 1 cm, 2 cm and 3 cm normalized to a transverse voltage (V_t) of 1 V are shown in Fig. 4, 5 and 6 for the cylindrical-shaped 400 MHz crabbing cavity. At radii closer to the beam axis the field data has higher noise content. Also, as the order increases, the noise content increases and becomes dominant over the field content. The rf-dipole cavity has components of order 2n for n = 1, 2, 3, etc. In the rf-dipole cavity the $E_z^{(n)}(z)\sin(\omega t)$ components corresponds to that of deflecting cavities and $E_z^{(n)}(z)\cos(\omega t)$ corresponds to the components related to crabbing cavities with a synchronous phase of $\phi_s = 90^0$. The higher order multipole components (b_n) can be determined by either using the Panofsky-Wenzel Theorem (Eq. 5) or using Lorentz Force (Eq. 6).

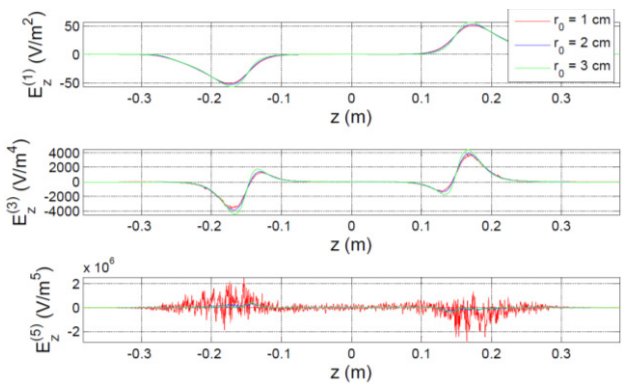

Figure 4: $E_z^{(n)}(z)$ of n = 1, 3 and 5 at r_0 = 1 cm, 2 cm and 3 cm for the cylindrical-shaped 400 MHz rf-dipole cavity.

Copyright © 2012 by the respective authors — cc Creative Commons Attribution 3.0 (CC BY 3.0)

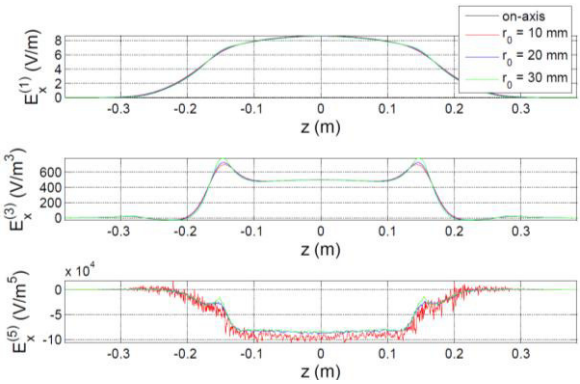

Figure 5: $E_x^{(n)}(z)$ of n = 1, 3 and 5 at r_0 = 1 cm, 2 cm and 3 cm for the cylindrical-shaped 400 MHz rf-dipole cavity.

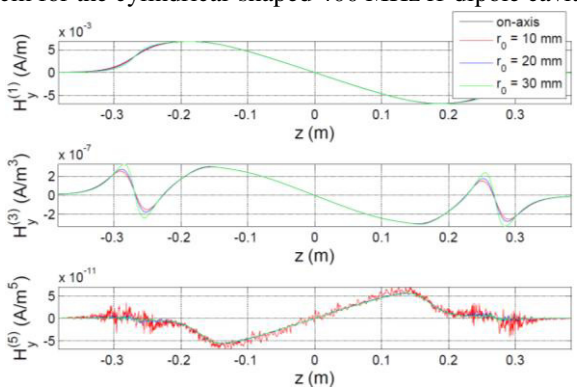

Figure 6: $H_y^{(n)}(z)$ of n = 1, 3 and 5 at r_0 = 1 cm, 2 cm and 3 cm for the cylindrical-shaped 400 MHz rf-dipole cavity.

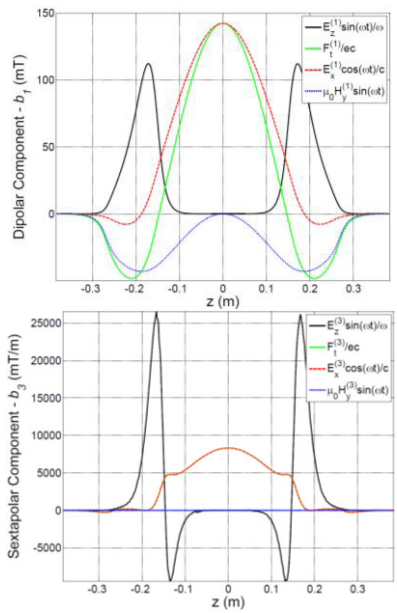

Figure 7: Dipolar and sextapolar field components of the 400 MHz cylindrical-shaped rf-dipole cavity.

The field components of the first two non-zero multipole components are shown in Fig. 7. The components $F_t^{(1)}/c$ and $E_{acc}^{(1)}(z)/\omega = E_z^{(n)}(z)\sin(\omega t)/\omega$ has different dependence on z, however gives the same b_1 when integrated along z, that corresponds to the transverse voltage given by the rf-dipole cavity.

The higher order multipole components of the fundamental deflecting/crabbing mode are shown in Table 1, for the four rf-dipole designs shown in Fig. 1. As seen by the field profiles the b_n for n = 0, 2, 4, 6… are zero. All the higher order multipole components are normalized to a transverse voltage (V_t) of 1.0 MV. Comparing the 400 MHz crabbing cavities of cylindrical-shaped outer conductor, the 400 MHz cavity with a square shaped outer conductor has higher multipole components. The square-shaped 400 MHz rf-dipole cavity with curved bar surfaces has reduced b_3 and b_5, but has higher b_7 compared to the other 400 MHz designs.

Table 1: Multipole components for the rf-dipole cavity designs shown in Fig. 1.

	(A)	(B)	(C)	(D)	Units
V_z	0.0	0.0	0.0	0.0	MV
V_t	1.0	1.0	1.0	1.0	MV
b_1	3.3	3.3	3.3	3.3	mT m
b_2	0.0	0.0	0.0	0.0	mT
b_3	8.3×10^2	3.0×10^2	4.1×10^2	1.0×10^2	mT/m
b_4	0.0	0.0	0.0	0.0	mT/m^2
b_5	$-5..8\times10^5$	-4.6×10^4	-4.1×10^4	-2.2×10^4	mT/m^3
b_6	0.0	0.0	0.0	0.0	mT/m^4
b_7	-7.1×10^8	-1.03×10^7	-2.0×10^7	-6.9×10^7	mT/m^5

CONCLUSION

The higher order multipole components were calculated for the rf-dipole cavity designs of different geometries. The modified square-shaped 400 MHz cavity with curved bar surfaces has improved lower order multipole components. The values of the multipole components are comparable to standard magnets in a beam line. The rf-dipole geometry requires further optimization in suppressing the dominant multipole components, and therefore needs to be considered as a design optimization parameter.

REFERENCES

[1] J.R. Delayen and S.U. De Silva, in Proceedings of the 15th International Conference on RF Superconductivity, Chicago, Illinois (2011), p. 219.
[2] S.U. De Silva and J.R. Delayen, in Proceedings of the 15th International Conference on RF Superconductivity, Chicago, Illinois (2011), p. 135.
[3] A. Castilla et.al., in Proceedings of the 3rd International Particle Accelerator Conference, New Orleans, Louisiana (2012), p. 2447.
[4] S.U. De Silva and J.R. Delayen, in Proceedings of the 3rd International Particle Accelerator Conference, New Orleans, Louisiana (2012), p. 2453.
[5] A.W. Chao and M. Tigner, "Handbook of Accelerator Physics and Engineering", (World Scientific Publishing Co. Pte. Ltd), 1999.
[6] J. Barranco Garcíaorelov et.al., in Proceedings of the 3rd International Particle Accelerator Conference, New Orleans, Louisiana (2012), p. 1873.

Copyright © 2012 by the respective authors — cc Creative Commons Attribution 3.0 (CC BY 3.0)

COMPACT SUPERCONDUCTING CRABBING AND DEFLECTING CAVITIES*

S. U. De Silva[1,2#]
[1]Center for Accelerator Science, Old Dominion University, Norfolk, VA 23529, USA.
[2]Thomas Jefferson National Accelerator Facility, Newport News, VA 23606, USA.

Abstract

Recently, new geometries for superconducting crabbing and deflecting cavities have been developed that have significantly improved properties over those of the standard TM_{110} cavities. They are smaller, have low surface fields, high shunt impedance and, more importantly for some of them, no lower-order-mode with a well-separated fundamental mode. This talk will present the status of the development of these cavities.

INTRODUCTION

Primarily the crabbing and deflecting structures are used to restore luminosity in particle colliders or in separating a single beam into multiple beams. The crabbing concept was initially proposed by R.B. Palmer for collider rings [1] and was later proven for linear colliders [2] as well. The applications of crabbing and deflecting cavities are not limited to the above-mentioned applications but also can be used in many applications for beam diagnostics, emittance exchange, in generating compressed x-ray beams etc. Some of the potential applications at present are the deflecting cavity needed for the Jefferson Lab 12 GeV upgrade [3] to separate the maximum energy beam into the three experimental halls and the deflecting cavity system required for the multi experimental project under Project-X [4]. One of the crabbing applications is the LHC luminosity upgrade that requires a crabbing system for vertical and horizontal crossing at the integrations regions of IP_1 and IP_5 [5].

The stringent dimensional constraints set by these current applications especially operating at low frequencies demands the design and development of compact crabbing and deflecting cavities. Compared to the crabbing and deflecting cavities operating in TM_{110} these compact designs that has been developed have improved properties with low surface fields, high shunt impedance. Most of the designs have no lower order modes (LOMs) with a widely separated higher order mode (HOM) spectrum.

The First Superconducting Deflecting Cavity

The early research in superconducting crabbing and deflecting structures was done in 1970s where the first superconducting rf deflecting cavity as shown in Fig. 1

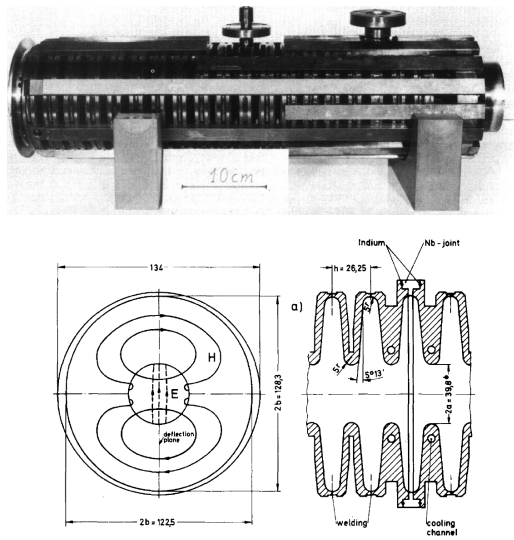

Figure 1: 19-cell end section of the 2.865 GHz rf separator cavity (top) and bi-periodic TM_{110} operating mode (bottom).

was designed and developed in KfK, Karlsruhe in collaboration with CERN [6]. The 2.865 GHz, 104-cell cylindrical-shaped standing wave rf particle separator shown in Fig. 1 installed at CERN in 1977 was capable of delivering a deflection in the vertical plane. The rf separator driven at 1.8 K, in a bi-periodic TM_{110}-type mode (Fig. 1) was in operation until 1981.

The First Superconducting Crabbing Cavity

The first crabbing cavity system was developed and installed in 2007 at KEK [7] for the KEKB electron-positron collider. The crabbing cavity shown in Fig. 2, operating in TM_{110} mode at 508.9 MHz was the only crabbing cavity system that has been in operation in a particle collider until 2010 after the installation in 2007.

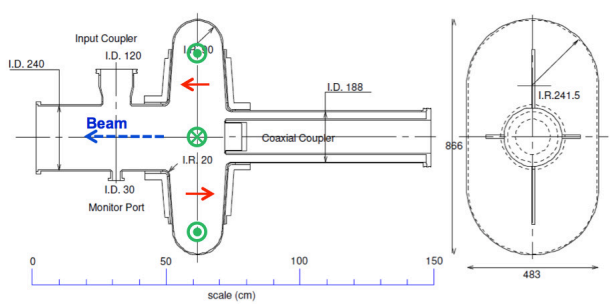

Figure 2: Superconducting 508.9 MHz KEK crabbing cavity.

*Authored by Jefferson Science Associates, LLC under U.S. DOE Contract No. DE-AC05-06OR23177. The U.S. Government retains a non-exclusive, paid-up, irrevocable, world-wide license to publish or reproduce this manuscript for U.S. Government purposes.
Part of this work was done in collaboration with and supported by Niowave Inc. under the DOE STTR program.
#sdesilva@jlab.org

Copyright © 2012 by the respective authors — cc Creative Commons Attribution 3.0 (CC BY 3.0)

The KEK crabbing cavity has a squashed elliptical geometry in order to separate the two polarizations of the TM_{110} mode. Since the TM_{110} mode is not the lowest mode in the cavity the crabbing cavity system has larger dimensions to that of a TM_{010} mode of the same frequency and was also required to have a complex higher order mode (HOM) damping scheme in order to damp the lower order mode (LOM) and near by HOMs that were close to the operating crabbing mode. The properties of the KEK crabbing cavity are listed in Table 1. The squashed elliptical geometry at 508.9 MHz operating frequency has higher surface magnetic fields with low shunt impedance.

COMPACT CAVITY DESIGNS

The standard crabbing and deflecting cavities with elliptical geometries operate in TM_{110} mode, which is not the lowest mode in these geometries. Also the squashed elliptical have very large structures at low frequencies. The current compact designs operate in TE or TEM like modes, where the deflection is given by either the electric field or by both the electric and magnetic fields. Some of those compact superconducting crabbing and deflecting cavity designs are

- 4-Rod Cavity by University of Lancaster and Jefferson Lab
- Quarter-Wave Cavity by Brookhaven National Laboratory
- Parallel-Bar Cavity/RF-Dipole Cavity by Old Dominion University and SLAC Accelerator National Laboratory

4-Rod Cavity - U. of Lancaster/Jefferson Lab

The 400 MHz superconducting 4-rod crabbing cavity [8] is an adaptation of the 499 MHz normal conducting rf separator designed by C. Leemann and C.G. Yao at Jefferson Lab for separating the 6 GeV beam into the three experimental halls in the beam switchyard area [8]. The rf separator is a two cell design as shown in Fig. 3, with each cell of ~λ/2 length and diameter.

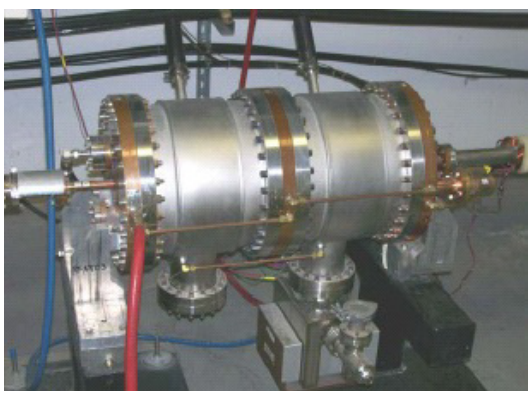

Figure 3: Normal conducting 499 MHz 4-rod rf separator cavity at Jefferson Lab.

The normal conducting 4-rod cavity has a rod configuration that gives 4 fundamental modes, with the electric field configuration shown in Fig. 4. The top left field configuration corresponds to the accelerating mode, which is the lowest mode in the design. The next mode is the deflecting/crabbing mode with the field configuration shown in bottom left of Fig. 4 with the magnetic field circulating around the rods near the end plates. In this geometry both electric and magnetic fields contribute to the net deflection.

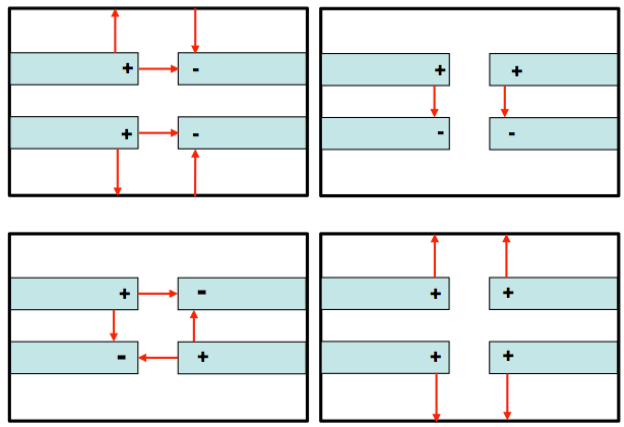

Figure 4: Electric field configuration of the 4 fundamental modes in the 4-rod geometry.

The superconducting 4-rod cavity design (Fig. 5) [9] adapted from the normal conducting design has improved bar geometry and outer conductor that gives a compact design with low surface electric and magnetic fields. The rods are further curved to suppress the higher order multipole components in the cavity.

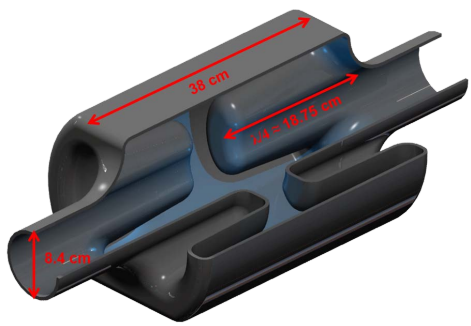

Figure 5: Superconducting 400 MHz 4-rod cavity design from University of Lancaster/Jefferson Lab.

The properties of the superconducting 4-rod cavity are shown in Table 1. This design has very high transverse [*R*/*Q*] therefore high shunt impedance compared to other compact crabbing and deflecting cavities. However the LOM at 375 MHz present close to the fundamental operating mode and the low separation between the operating mode and the next HOM as shown in the HOM spectrum in Fig. 6 require a complex damping scheme in order to damp these modes. The compact crabbing and deflecting structures have a HOM configuration with modes giving a net deflection in horizontal direction or in vertical direction and accelerating modes as shown in Fig. 6. Additionally in the 4-rod cavity there are no hybrid modes present in the geometry.

Copyright © 2012 by the respective authors — cc Creative Commons Attribution 3.0 (CC BY 3.0)

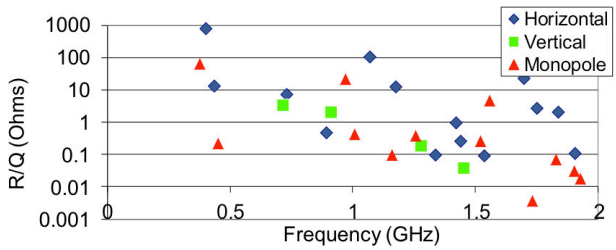

Figure 6: HOM spectrum of the 4-rod crabbing cavity.

Quarter-Wave Cavity - BNL

The standard quarter-wave cavity is modified into a crabbing and deflecting cavity utilizing the strong reentrant shape that gives a TEM field configuration near the outer conductor [10]. However the quarter-wave cavities have a strong on axis longitudinal electric field component that gives rise to an accelerating mode, present within the fundamental deflecting/crabbing mode. The quarter-wave design is modified with a pedestal at the bottom of the cavity to suppress the accelerating field component as shown in Fig. 7 [11]. The length of the longer pedestal at the top of cavity controls the frequency of the design. As shown in Fig. 7 the quarter-wave geometry at 400 MHz is optimized to reduce the surface fields and minimize the longitudinal accelerating component present in the cavity.

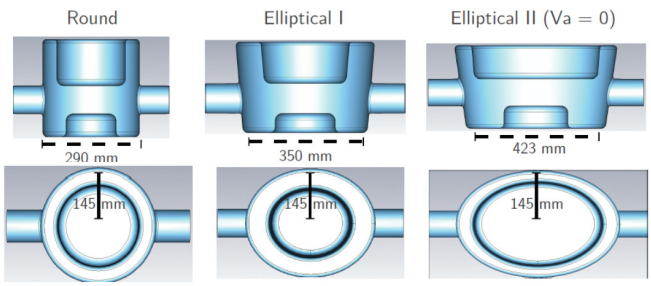

Figure 7: Superconducting 400 MHz quarter-wave deflecting/crabbing cavity by BNL.

The electric and magnetic field content of the quarter-wave crabbing cavity is shown in Fig. 8.

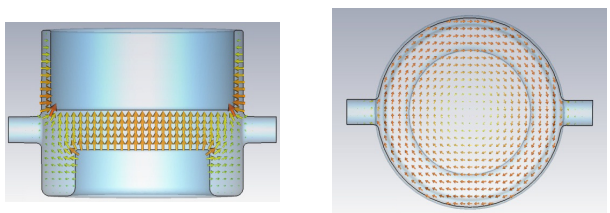

Figure 8: Electric field (left) and magnetic field (right) content of the 181 MHz quarter-wave crabbing cavity designed for eRHIC [11].

The quarter-wave cavity has two design options with the initial asymmetric geometry and a symmetric geometry to completely eliminate the longitudinal accelerating component as shown in Fig. 9. Compared to the asymmetric cavity the symmetric cavity doesn't have a longitudinal electric field component, however has a reduced mode separation between the fundamental deflecting/crabbing mode and the next HOM. The properties of the asymmetric and symmetric quarter-wave cavities are shown in Table 1. The symmetric design has improved surface fields and transverse [R/Q] however has smaller shunt impedance due to the decreased geometrical factor.

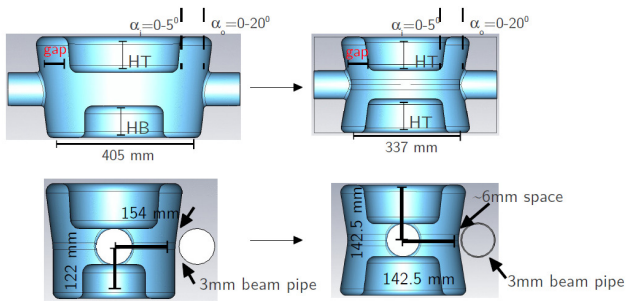

Figure 9: Asymmetric and symmetric 400 MHz quarter-wave crabbing cavities.

The HOM spectrum [8] of the asymmetric quarter-wave cavity is shown in Fig. 10, with a similar mode configuration described in the 4-rod cavity. However the asymmetric cavity also has hybrid modes present in the geometry. One of the attractive features in this design is the absence of any lower order modes.

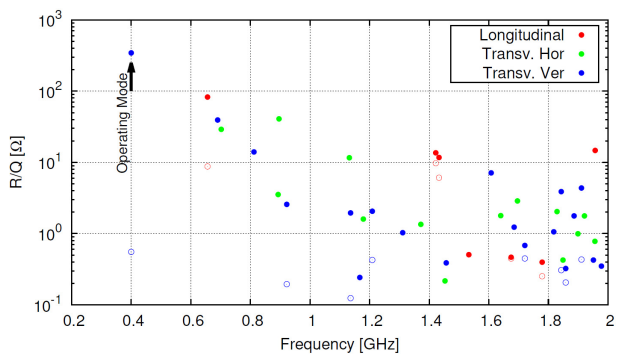

Figure 10: HOM spectrum of the asymmetric quarter-wave crabbing cavity [12].

Parallel-Bar and RF-Dipole Cavity - ODU/SLAC

The parallel-bar cavity [13] with a rectangular outer conductor with cylindrical-shaped bars operating in a TEM-like mode is being evolved into a cylindrical-shaped design with trapezoidal-shaped bar geometry [14] (Fig. 11). The latter design named rf-dipole cavity operates in a TE_{11}-like mode, where the main contribution to the net deflection is given by the transverse electric field.

A similar design was proposed by Zenghai Li at SLAC named the ridged waveguide cavity as shown in Fig. 12 [11] operates in TE_{11}-like mode. Currently ODU and SLAC are collaborating on designing a 400 MHz compact crabbing cavity. Currently the rf-dipole cavity is considered as the 499 MHz rf separator for the Jefferson Lab 12 GeV upgrade, as one of the crabbing cavity

Copyright © 2012 by the respective authors — cc Creative Commons Attribution 3.0 (CC BY 3.0)

Table 1: Properties of superconducting crabbing and deflecting cavities.

Parameter	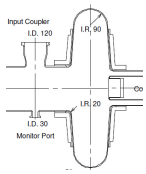 KEK Cavity	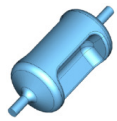 RF-Dipole Cavity	RF-Dipole Cavity	4-Rod Cavity	Asymmetric ¼-Wave Cavity	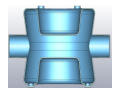 Symmetric ¼-Wave Cavity	Units
Frequency	508.9	499.0	400.0	400.0	400.0	400.0	MHz
Aperture diameter (d)	100.0	40.0	84.0	84.0	84.0	84.0	mm
d/(λ/2)	0.34	0.13	0.22	0.22	0.22	0.22	
LOM	410.0	None	None	375.2	None	None	MHz
Nearest HOM	630.0	777.0	589.5	436.6	657.0	577.8	MHz
Peak electric field (E_P^*)	4.24	2.86	3.9	4.0	5.38	4.04	MV/m
Peak magnetic field (B_P^*)	12.23	4.38	7.13	7.56	7.6	7.2	mT
B_P^* / E_P^*	2.88	1.53	1.83	1.89	1.42	1.77	mT/(MV/m)
$[R/Q]_T$	48.9	982.5	287.2	915.0	344.0	401.1	Ω
Geometrical factor	227.0	105.9	138.7	62.8	131.0	82.4	Ω
$R_T R_S$	1.1×10^4	1.0×10^5	4.0×10^4	5.7×10^4	4.5×10^4	3.3×10^4	Ω^2

At E_T^* = 1 MV/m

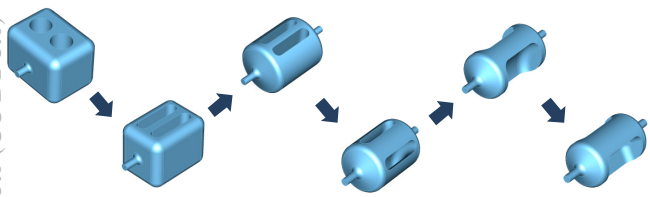

Figure 11: Design evolution of the parallel-bar cavity into the rf-dipole cavity.

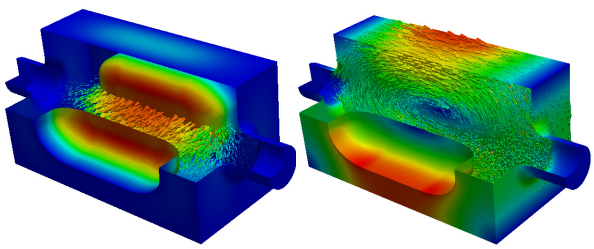

Figure 12: Ridged waveguide cavity by SLAC.

options for the LHC luminosity upgrade operating at 400 MHz, and as the 750 MHz crabbing cavity for the medium energy electron ion collider (MEIC). The field profile of the rf-dipole cavity is shown in Fig. 13.

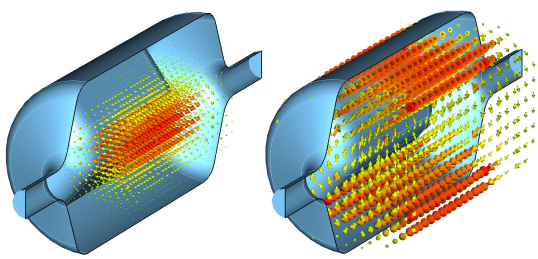

Figure 13: Electric field (left) and magnetic field (right) content in the 499 MHz rf-dipole cavity.

The properties of the 499 MHz and 400 MHz rf-dipole cavities are given in Table 1. The inner bar height and the angle of the trapezoidal shaped bars connecting to the outer conductor allows the rf-dipole design to have both reduced surface electric and magnetic fields. Therefore an rf-dipole cavity can be designed at a given design frequency and beam aperture, with a balanced ratio of peak surface magnetic field to the peak surface electric field as required by the application.

The HOM spectrum of the rf-dipole cavity is shown in Fig. 14. The rf-dipole cavity has no low order modes and the HOMs are well separated.

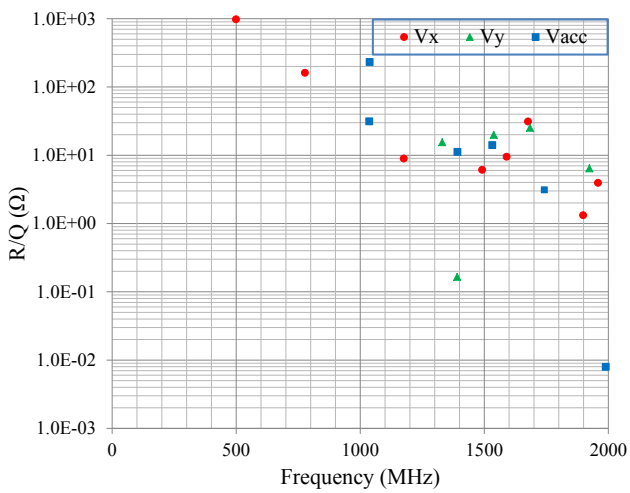

Figure 14: HOM spectrum of the 499 MHz rf-dipole cavity.

The rf-dipole design can be reduced into a more compact design with fixed transverse dimensions with a square-shaped outer conductor as shown in Fig. 15 where

Copyright © 2012 by the respective authors — cc Creative Commons Attribution 3.0 (CC BY 3.0)

the frequency of the design is controlled by the curvature of the edges of the cavity. The rf-dipole design is further modified with curved trapezoidal-shaped bar geometry to suppress the higher order multipole components.

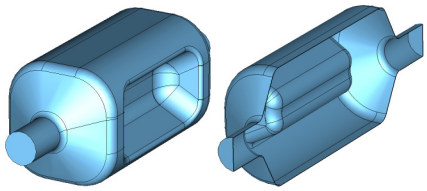

Figure 15: Square-shaped rf-dipole cavity with flat trapezoidal-shaped bar geometry (left) and with curved bar geometry (right).

CAVITY FABRICATION

First prototypes of some of the compact deflecting and crabbing cavities have already being fabricated. Fig. 16 shows the fabricated cavity designs. The prototypes of the 400 MHz 4-rod cavity, the 400MHz and 750 MHz rf-dipole cavities are fabricated at Niowave Inc. and the 499 MHz rf-dipole cavity is currently being fabricated at Jefferson Lab.

Figure 16: Prototype of the 400 MHz 4-rod cavity (top left), 400 MHz (top right), 400 MHz (bottom left) and 750 MHz (bottom right) rf-dipole cavities.

CONCLUSIONS

The development of compact deflecting/crabbing cavities was in response to the strict dimensional requirements in some current applications. All these compact designs have attractive properties in meeting the requirements. The low and balanced surface fields and high shunt impedance in these compact superconducting crabbing and deflecting cavities make them very attractive designs compared to the standard cavities operating in TM_{110} mode. The absence of lower order modes and wide separation in the higher order modes in most of the designs reduces the lower and higher mode damping complexity.

The 4-rod cavity design uses coaxial type couplers in damping the LOM and HOMs. The quarter-wave cavity design uses magnetic loop type couplers placed at the bottom of the cavity to damp the HOMs. The rf-dipole cavity is considering both the options of using the waveguide or a coaxial high-pass filter type coupling in damping the HOMs. Further studies are done on these compact cavities on addressing the important rf-related issues such as multipacting, mechanical analysis, field non-uniformity etc. The fabricated prototypes are in preparation for rf testing.

REFERENCES

[1] R. B. Palmer, "Energy Scaling, Crab Crossing and the Pair Problem", Tech. Rep. SLAC-PUB-4707 (SLAC, 1988).

[2] K. Oide and K. Yokoya, Phys. Rev. A 40, 315 (1989).

[3] J.R. Delayen et al., "Options for an 11 GeV RF Beam Separator foe the Jefferson Lab CEBAF Upgrade", Proc. of the Particle Accelerator Conference, Vancouver, BC, Canada, p. 1644, (2009).

[4] V. Yakovlev and M. Champion, "A Beam Splitter for the Project-X", LHC- CC11, (2011).

[5] R. Calaga, in Proceedings of the 2011 Conference on RF Superconductivity, Chicago, Illinois, (2011) p. 988.

[6] A. Citron et al., NIM 164, 31-55, (1979).

[7] K. Hosoyama et al, "Crab Cavity for KEKB", Proc. of the 7th Workshop on RF Superconductivity, p.547 (1998).

[8] C. Leemann and C.G. Yao, "A Highly Effective Deflecting Structure", Proc. of the 1990 Linear Accelerator Conference, p.232-234, (1991).

[9] B. Hall, "LHC-4R Crab Cavity", EUCARD SRF Annual Review, March 2012.

[10] E. Haebel, "Superconducting Cavities and Minimum RF Power Schemes for LHC", CERN/EF/RF 84-4.

[11] Q. Wu et al., "Novel Deflecting Cavity Design for eRHIC", Proc. of the15th International Conference on RF Superconductivity, p.707, (2011).

[12] R. Calaga et al., "HOM Damping and Multipacting Analysis of the Quarter-Wave Crab Cavity", Proc. of the 3rd International Particle Accelerator Conference, p. 2260, (2012).

[13] J. R. Delayen and H. Wang, Phys. Rev. ST Accel. Beams 12, 062002 (2009).

[14] J. R. Delayen, S.U. De Silva, "Designs of Superconducting Parallel-Bar Deflecting Cavities for Deflecting/Crabbing Applications", Proc. of the15th International Conference on RF Superconductivity, p.219, (2011).

[15] Z. Li and L. Ge, "Compact Crab Cavity Design and Modeling Using Parallel Code ACE3P", LHC-CC11, (2012).

Copyright © 2012 by the respective authors — cc Creative Commons Attribution 3.0 (CC BY 3.0)

OPERATIONAL EXPERIENCE AND FUTURE GOALS OF THE SARAF PROTON / DEUTERON LINAC

D. Berkovits#, L. Weissman, A. Arenshtam, Y. Ben Aliz, Y. Buzaglo, O. Dudovich, Y. Eisen, I. Eliyahu, G. Feinberg, I. Fishman, I. Gavish, I. Gertz, A. Grin, S. Halfon, D. Har-Even, Y. Haruvy, T. Hirsh, D. Hirschmann, Z. Horvitz, B. Kaizer, D. Kijel, A. Kreisel, G. Lempert, Y. Luner, I. Mardor, A. Perry, E. Reinfeld, J. Rodnizki, G. Shimel, A. Shor, I. Silverman, E. Zemach
Soreq NRC Yavne 81800, Israel

Abstract

The Soreq Applied Research Accelerator Facility (SARAF) is built as a user facility. An intense fast neutrons source, a thermal neutrons source and apparatuses for production of isotopes for basic and applied research will be available at the end of construction, foreseen in several years. SARAF is based on a high intensity CW proton / deuteron RF superconducting linear accelerator. Several novel technologies are used in order to build this demanding linac. To reduce technological risks, the construction was divided in two Phases. Phase-I was constructed in order to test and characterize the novel technologies and is in routine operation since 2010. SARAF phase-I, with its single 6 half-wave resonators separated vacuum cryomodule, is the first high current, superconducting low-beta linac in operation and it is presently delivering CW mA proton beams for target developments. Phase-II of this linac will allow acceleration up to 40 MeV and 5 mA CW proton and deuteron beams. Phase-II is now under conceptual redesign. The project status, the operational experience and the future goals of SARAF are described and discussed in this paper.

INTRUDUCTION

System Requirements

The goals of the Soreq Applied Research Accelerator Facility (SARAF) are: 1) to enlarge the experimental nuclear science infrastructure and promote research in Israel, 2) to develop and produce radioisotopes for bio-medical applications and 3) to modernize the source of neutrons at Soreq and extend neutron based research and applications [1,2]. SARAF, when it fulfils its goals, is intended to replace the aging research reactor in Soreq. These goals define the requirements from the accelerator. The requirements were optimized to fulfil all of the above goals, within domestic cost constraints. Production of isotopes for radiopharmaceuticals is mainly done by tens of MeV protons, so this is a basic requirement. Variable energy protons allow optimizing the production yield, while minimizing parasitic isotopes production. Deuterons have two main advantages in isotopes production; the production yield in the (d,2n) reaction is significantly higher than the (p,n) reaction for several targets with mass higher than 100 a.m.u [3]. In addition, at tens of MeV, the neutron yield of deuterons is significantly higher than of protons bombarding the same target [4].

Although linac based neutrons sources are usually based on high energy proton based spallation reactions [5], for tens of MeVs projectiles the neutron yield of deuterons on light element targets is higher by more than a factor of 3 with respect to spallation.

For example, while using a beryllium target, deuterons of 2 mA at 40 MeV, or 5 mA at 25 MeV, are enough to generate a thermal neutron flux that is equivalent to the flux available at the image plane of the neutron radiography apparatus at the Soreq IRR1 5 MW reactor [6].

Tens of MeV deuterons on light element targets generate fast neutrons with a forward flux and neutron energy peaked around the beam energy divided by 2.5 [4]. Such a spectrum is ideal to produce isotopes using (n,2n), (n,p), (n,α) and (n,f) reactions and therefore open new and interesting opportunities for basic and applied research. These reactions are the basis for niche intense radioactive beams at SARAF Phase-II [7,8]. For these reactions, the total amount of fast neutrons is two orders of magnitudes lower than in the spallation reaction. However, the neutron flux in the relevant range for these reactions (5-25 MeV) is higher by an order of magnitude (Fig. 1). The sources of this advantage are the low energy deuteron range in the target, which is shorter than spallation protons by an order of magnitude and the forward peaked structure of the stripping reaction.

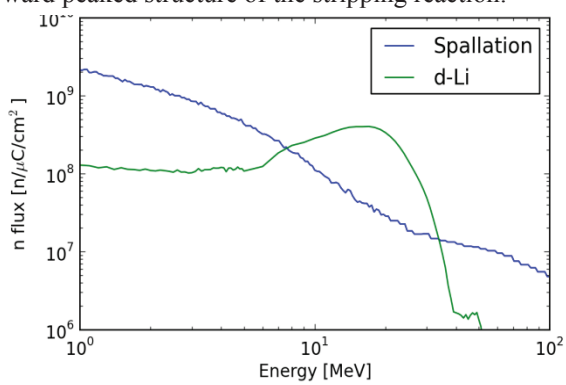

Figure 1: Forward neutron spectra comparison between 40 MeV deuterons on lithium (SARAF/IFMIF [9] like) and spallation 1400 MeV protons on tungsten (ISOLDE) [10]. The spectra were measured and simulated 8 cm downstream the targets at zero degrees.

berkova@soreq.gov.il

Copyright © 2012 by the respective authors — cc Creative Commons Attribution 3.0 (CC BY 3.0)

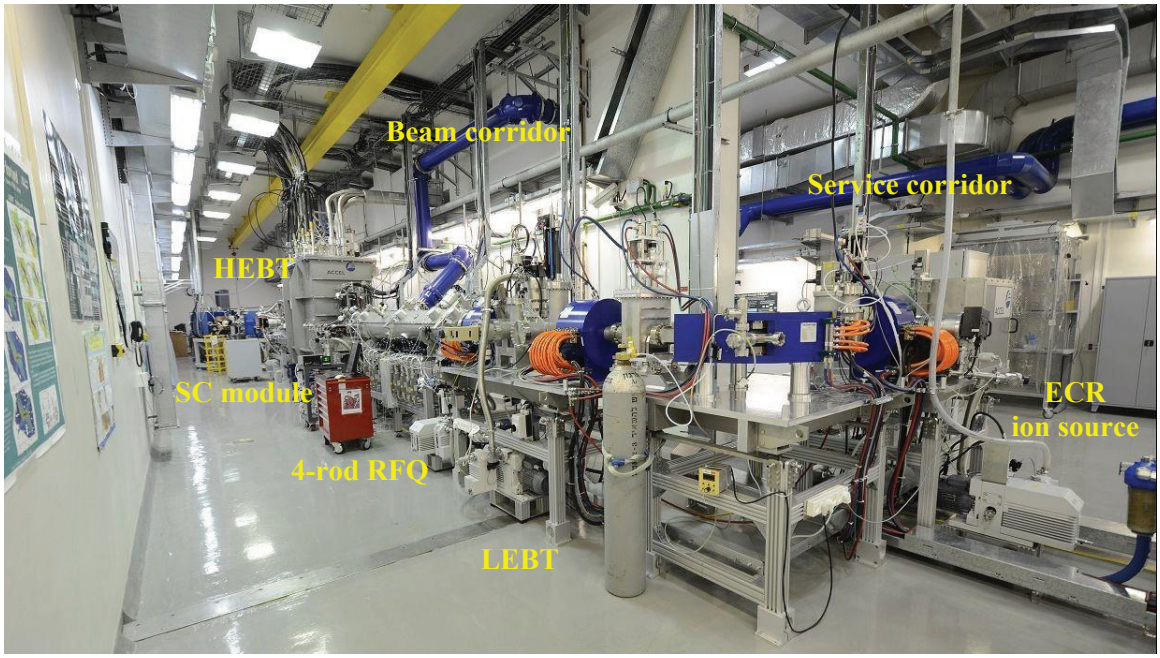

Figure 2: Phase-I 4 MeV protons and 5 MeV deuterons linac in the 4.5 m W, 5 m H and 25 m long beam corridor.

The range of tens of MeVs protons or deuterons in matter is several millimetres, so the power density developed in a tens-of-kW irradiation target is signify-cantly higher than in a MW spallation target. This requires development of new types of targets, based on both solid [11, 12] and liquid metal [13, 14], and force the linac to deliver CW beams in order to avoid a high thermal load in the targets. It also requires developing special beam and target diagnostics and a procedure to slowly ramp the beam intensity on the targets.

System Specifications

The beam specifications that cover all the above requirements are summarized in Table 1.

Table 1: SARAF Linac Top-level-requirements

Parameter	Value	Comment
Ion Species	Protons/Deuterons	$M/q \leq 2$
Energy Range	5 – 40 MeV	Variable energy
Current Range	0.04 – 5 mA	CW (and pulsed)
Operation	6000 hours/year	
Maintenance	Hands-On	Low beam loss

The demands for variable energy, proton and deuteron currents in the mA range and low beam loss that meets the definition of a hands-on maintenance are met only by a superconducting RF linear accelerator. Independently phased cavities are needed in order to allow variable energy at the exit of the linac and efficient acceleration of more than one ion species. Superconducting cavities are needed for large beam apertures that moderate beam loss.

Phase-I of the SARAF linac (Fig. 2) is composed of a 20 keV/u, 7 mA, 0.2 π mm mrad norm. rms emittance ECR ion source + LEBT [15], a 176 MHz, 4 m long, 250 kW, 4-rod RFQ [16,17,18], a 65 cm long MEBT and a 4.5 K 2.5 m long superconducting module housing 6 β_0=0.09 bulk Nb HWRs, 0.85 MV each and 3 6T solenoids in separated vacuum [19, 20, 21, 22]. The Phase-I linac routinely accelerates 1 mA CW protons up to 4 MeV and 10% duty factor deuterons up to 5 MeV. The design and commissioning of the acceleration components and the operation of the entire machine [23, 24] and the 13 m long HEBT line [25] were published in recent years. The next section describes in detail additional beam tuning issues and technical challenges.

BEAM OPERATION

Several beam-on-target experiments were performed last year with proton and deuteron beams of various energies and intensities. Proton beams at the highest available energy of ~3.9 MeV were mainly used for the tests of thin (~25μm) foil targets cooled by liquid metal [11, 12]. The thin foil targets are delicate and there were several incidents of targets being damaged. Following the insight gained from the first experiments, numerous improvements of the target arrangement and beam diagnostics quality were implemented. Initial tuning is performed a 10^{-4} duty cycle pulsed beam on a quartz viewer. Next, the duty cycle is increased to 10^{-2} and the beam position is verified on a thin Tantalum foil. Then, the first solenoid at the LEBT is defocused and the LEBT aperture is closed in order to moderate the CW beam current. The CW beam intensity is ramped up by two orders of magnitude by refocusing this solenoid and reopening the aperture. We found that it is important to ramp the beam intensity without moving its centre on target and without changing the beam distribution shape. To first order, such a ramping procedure does not change the beam distribution on the target. The target surface temperature is tracked using a pyrometer and an infrared (IR) camera. It was found that, in these targets, the

Copyright © 2012 by the respective authors — cc Creative Commons Attribution 3.0 (CC BY 3.0)

transverse spatial variation of the temperature is in the order of a square mm, so the beam tune and temperature measurements are performed with mm resolutions.

For 1 mA beam tests, we use beam dump that consists of a 250 micron Tungsten sheet fused to a water cooled cooper plate. A tungsten beam dump is chosen for Phase-I since up to 10 MeV, no activation is induced and moderated neutron radiation is expected. After a few irradiation hours of a 3 MeV 1 mA proton beam, the tungsten surface blisters (Fig. 3). The protons beam (hydrogen) implementation depth is ~30 μm inside the tungsten. The hydrogen pressure blows up the tungsten surface and a hydrogen pressure peak is measured in a nearby residual gas analyser (RGA).

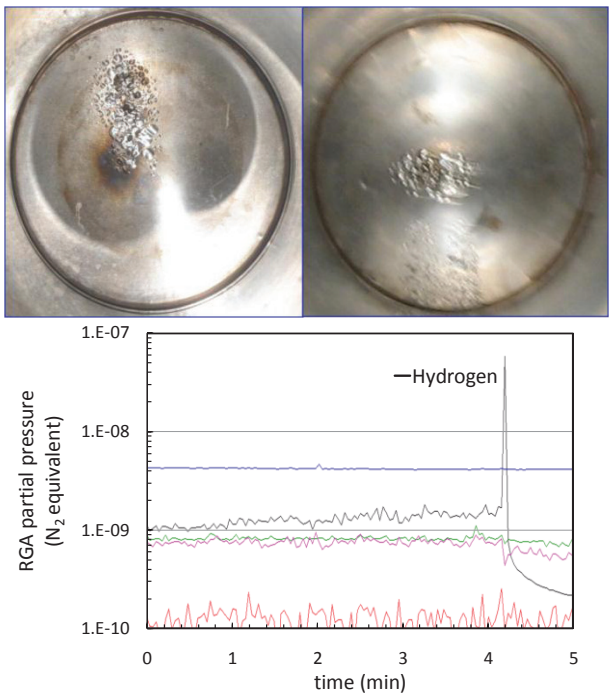

Figure 3: Top - Two 150 mm diameter Tungsten beam dumps after 8 hours of irradiation by 1 mA CW protons at 3 MeV. Bottom - Hydrogen blistering is well presented and detected using a residual gas analyser.

BEAM CURRENT TECNICAL LIMITATIONS

There were, and still are, a few technical issues that limit the beam current below the design value of 2 mA. The cavity sensitivity to helium pressure, calculated to be 16 Hz/mbar, was measured to be 56 Hz/mbar [20]. Three sub-components; the RF coupler, the RF amplifier and the tuner are affected.

Piezo Tuners Upgrade

The cryogenic system ±1.5 mbar pressure variation is manifested by frequency detuning that easily exceeds the cavities loaded bandwidth of 130 Hz. This detuning brings forth challenging demands on the cavities' tuners. The tuners include a coarse tuning stepper motor and a fine tuning piezo electric actuator (Pst150 [26]). In 2009, a dramatic reduction of the actuators range was observed, leading to the replacement of the actuators by modified ones [22]. In 2011 the piezo actuators suffered again from significant reduction of the tuning ranges (Fig. 4). During the winter maintenance period, the tuners were replaced by high voltage piezo actuators (Pst1000 [26]), which operate at 800 V and have superior mechanical strength. A smaller deterioration slope of the tuning range has been observed (Fig. 4) after this modification.

RF High Power Amplifiers (HPA) Upgrade

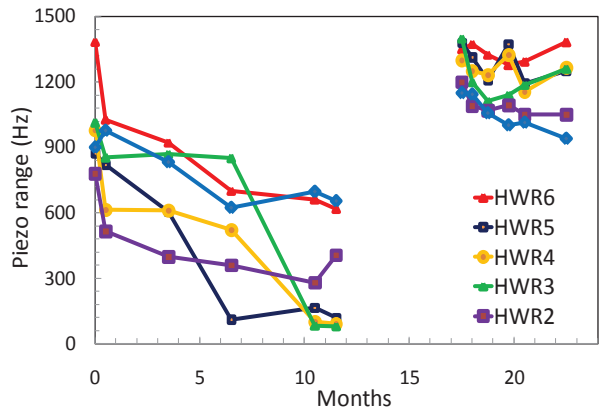

Figure 4: Piezo fast tuners dynamic range since January 2011. At the end of 2011 the piezo actuators were upgraded from low voltage to high voltage.

When the cavity is detuned, the LLRF control system [27] draws extra power from the HPA, in order to keep the cavity at its nominal accelerating voltage. Most of this power is reflected. In order to accelerate a 2 mA beam with maximal energy gain of 0.845 MV, we need 4 kW HPAs. In 2011, the original 2 kW solid state HPAs [28] were replaced by 4 kW HPAs designed and manufactured at SoreqNRC [29]. The operation of the cavities with the new power amplifiers has proven to be more stable.

RF Coupler Warming

After improving the tuners and RF amplifiers, warming of the RF couplers (Fig. 5) has become the main limiting factor in operating the linac at high fields. The capacitive coupler was designed for 4 kW [19]. The coupler enters the cryomodule from the top flange and turns to a middle plane HWR port (Figs. 6-7). The couplers warming phenomena has been recognized already at the commissioning stage [18]. A cooling copper strip line was added between the cold window and the 70 K thermal shield. This helped but not solved the problem. Thus, we are compelled to reduce the field in the 2nd, 3rd and 6th cavities in order to keep the external coupler's temperature below 120 K during long operation (Fig. 5). It is noteworthy that no significant warming is observed at the 5th cavity coupler. This cavity could be operated at a nominal voltage value, just before onset of X-ray emission. In the near future we plan to improve the

Copyright © 2012 by the respective authors — cc Creative Commons Attribution 3.0 (CC BY 3.0)

couplers cooling, by replacing the copper strip with a more massive one.

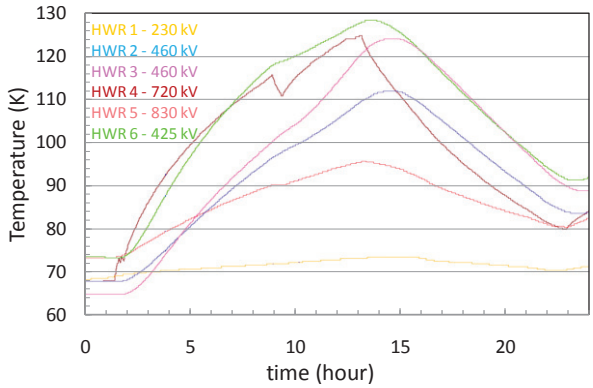

Figure 5: Couplers temperature, measured in the vicinity of the cold window, during beam operation. The RF voltage was turned on at 1h, closed at 9h for 20 min and turned off again at 13h. Beam intensity was ramped between 1h and 13h to 0.2 mA.

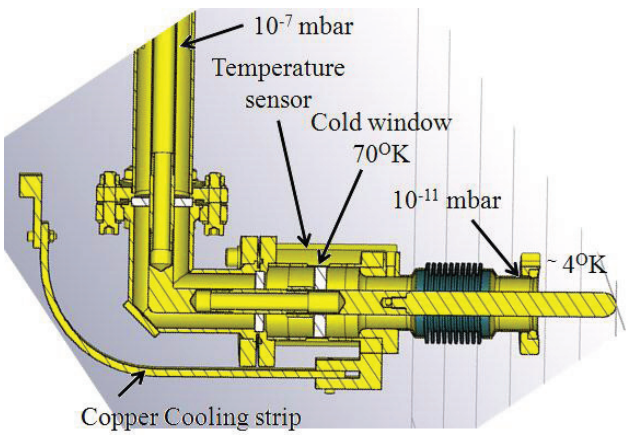

Figure 6: Drawing of the 4 kW RF coupler elbow section around the 70 K window.

At a later stage we will try adding He gas cooling around the window [30]. The cavity sensitivity to vibrations and pressure causes extra reflected power that can heat the coupler. Multipacting can also heat the coupler. A common method of suppressing multipacting is to apply a DC voltage to the coupler inner conductor. Solving the couplers warming problem will allow comfortable operation of the PSM at beam energies of 4.5 and 5.5 MeV for protons and deuterons, respectively, and an increase of the CW beam current to 2 mA.

Figure 7: Coupler elbow section (Fig. 6) photo with the cooling strip connected to the 70 K thermal shield.

PHASE-II RE-DESIGN

The goal of Phase-II is to complete the existing linac to 40 MeV and 5 mA. Novel technologies were explored for the completion of the linac. The main question was whether QWR dipole steering compensation methods are robust enough and can safely lead to a hands-on maintenance QWR proton linac. It was shown, by the Argonne National Laboratory (ANL) Linac Development department, that by using the drift tube face tilting correction method, cold BPM diagnostics and steerer correction after each QWR, the dipole steering is reduced to a negligible value [31]. The comparison between the 176 MHz HWR option and a 109 MHz QWR option showed only slight differences between the options, so for SARAF we opted for a 176 MHz HWR linac, since it enables a smoother transition from Phase-I.

A new conceptual design of a 176 MHz HWR linac was performed by the ANL group for SARAF. All Phase-I limits were addressed and solutions were found.

A MEBT that includes 2 re-bunchers was designed. Extensive simulations proved that it is possible to match proton and deuteron beams into the SC linac at beam currents from 0 to 5 mA, with no need to modify the linac tune design [31].

Varying the depth of the flat dish located in the opposite side to the RF coupler port found to be a good way for minimizating the cavity frequency sensitivity to fluctuations of the helium pressure in the novel design for Phase-II: . The results of sensitivity analyses showed that the flat dish reduces the sensitivity to 2 Hz/mbar in the low beta cavities [32] and 3.5 Hz/mbar for the high beta cavities. This is an improvement of an order of magnitude with respect to the existing Phase-I HWRs.

The HWR internal conductor was designed in a donut shape, in order to reduce the quadrupole effect and to minimize emittance growth [33].

A short 15 kW coupler was designed [34]. It enters the cryomodule from the bottom in order to keep the coupler environment clean throughout the operation life cycle. This forces the orientation of the cavities to be horizontal. A DC bias to the inner conductor is planned, to minimize multipacting, if needed. The simulated total heat load of this coupler at 4.2 K is 1.6 W.

For such a heavy loaded cavity, a dedicated fast tuner is not needed. A pneumatically actuated mechanical tuner, which compresses the cavity along the beam axis, is attached to the SS flanges outside of the helium vessel. The design of the pneumatic tuner is based upon the tuner design used since 2009 in the ANL ATLAS energy upgrade cryomodule. This tuner dynamic range at 2000 lb is 90 kHz, enough to replace both the slow step motor mechanical tuner and the dynamic piezo tuner [32].

Copyright © 2012 by the respective authors — cc Creative Commons Attribution 3.0 (CC BY 3.0)

The cryomodules that were designed for SARAF by ANL are based on the ANL experience gained in ANL in recent ATLAS upgrade projects. Special care is taken to simplify assembly, maintenance, alignment, resonator cleanliness, operating and auxiliaries system interfacing, without interfering with beam dynamics optimization [35]. The low (high) β module is 4.8 m (4.6 m) long and hosts 7 HWRs and 7 (4) solenoids. Each SC solenoid unit includes X-Y steerers and a cold BPM. The modules design fits into the existing SARAF beam corridor and leaves enough space to insert and extract modules alongside the linac.

REFERENCE

[1] Haim Watzman, NATURE 410 (2001) 399.

[2] A. Nagler, I. Mardor, D. Berkovits, K. Dunkel, M. Pekeler, C. Piel, P. vom Stein, H. Vogel."Status of the SARAF Project". Proceedings of LINAC 2006, Knoxville, August 21-25 (2006)168-170.

[3] A. Hermanne, F. Tárkányi and S. Takács, "Production of medically relevant radionuclides with medium energy deuterons", Nuclear Data for Science and Technology (2007) 1355-1358; http://nd2007.edpsciences.org

[4] M. A. Lone, A. J. Ferguson and B. C. Robertson, "Characteristics of neutrons from Be targets bombarded with protons, deuterons and alpha particles", Nuclear Instruments and Methods in Physics Research 189 (1981) 515–523.

[5] K. van der Meer *et al.,* "Spallation yields of neutrons produced in thick lead/bismuth targets by protons at incident energies of 420 and 590 MeV", Nuclear Instruments and Methods in Physics Research B 217 (2004) 202–220.

[6] K. Lavie, M.Sc. thesis Ben-Gurion University 2005.

[7] S. Vaintraub *et al.*, "A novel method for fundamental interaction studies with an electrostatic ion beam trap", J. of Physics Conf. Ser. 267 (2011) 012013.

[8] T. Hirsh *et al,*. "Towards an intense radioactive ^{8}Li beam at SARAF Phase-I", J. of Phys. Conf. Ser. 337 (2012) 012010.

[9] M. Hagiwara et al. Fus. Sci. Tech., 48 (2005).

[10] T. Stora *et al.* "A high intensity ^{6}He beam for the β-beam neutrino oscillation facility", EPL 98 (2012) 32001-p6.

[11] I. Silverman *et al.*,"Production of Palladium-103 from a thin rhodium foil target - Improved cooling concept", Nucl. Instr. Meth. B 261 (2007) 747.

[12] I. Silverman *et al.* PATENT WO/2006/035424 (2006).

[13] G. Feinberg *et al.,* "LiLiT - a Liquid-Lithium Target as an Intense Neutron Source for Nuclear Astrophysics at SARAF", Nucl. Phys. A827 (2009) 590c.

[14] S. Halfon *et al.* "High-power liquid-lithium target prototype for accelerator-based boron neutron capture therapy", App. Rad. And Isotopes 69 (2011) 1654-1656.

[15] K. Dunkel, F. Kremer and C. Piel, "Performence of the SARAF Ion Source", Proceedings of PAC07, Albuquerque (2007) 1407-1409.

[16] P. Fischer and A. Schempp, "Tuning of a 4-Rod CW-Mode RFQ Accelerator", Proceedings of EPAC 2006, Edinburgh (2006) 1583-1585.

[17] C. Piel, K. Dunkel, M. Pekeler, H. Vogel, P. vom Stein, "Beam Operation of the SARAF Light Ion Injector", Proceedings of PAC07, Albuquerque (2007) 1410-1412.

[18] C. Piel, K. Dunkel, F. Kremer, M. Pekeler, P. vom Stein, D. Berkovits and I. Mardor, "Phase-1 Commissioning Status of the 40 MeV Proton/Deuteron Accelerator SARAF", Proceedings of EPAC08, Genoa (2008) 3452-3454.

[19] M. Pekeler, K. Dunkel, R. Henneborn, C. Piel, M. Poier, P. vom Stein, H. Vogel, "Design of a Superconducting Half Wave Resonator Module for Proton/Deuteron Acceleration", Proceedings of the SRF03, Lübeck (2003) 124-127.

[20] M. Pekeler, S. Bauer, K. Dunkel, C. Piel, H. Vogel, P. vom Stein and V. Zvyagintsev, "Performance of a Prototype 176 MHz Beta=0.09 Half-Wave Resonator for the SARAF LINAC", Proceedings of the SRF, Ithaca (2005) 331-333.

[21] M. Pekeler, K. Dunkel, C. Piel and P. vom Stein "Development of a Superconducting RF Module for Acceleration of Protons and Deuterons at Very Low Energy", LINAC06, Knoxville (2006) 321-323.

[22] A. Perry, D. Berkovits, I. Gertz, I. Mardor, J. Rodnizki, L. Weissman, K. Dunkel, M. Pekeler, C. Piel, P. vom Stein, D. Trompetter and B. Aminov, "SARAF Superconducting Module Commissioning Status", Proceedings of SRF2009, Berlin (2009) 263-267.

[23] I. Mardor *et al.,* "The Status of the SARAF CW 40 MeV Proton/Deuteron Accelerator", PAC'09, Vancouver (2009) 4981-4983.

[24] L. Weissman *et al.,* "The status of SARAF linac project", Proceedings of LINAC10, Tsukuba (2010) 679-683.

[25] L. Weissman *et al.,*"The status of SARAF Phase-I linac", Proceedings of RUPAC12, Saint Petersburg (2012) 103-105.

[26] http://www.piezomechanik.com

[27] M. Pekeler, C. Piel, B. Aminov, A. Borisov, S. Kolesov and H. Piel, "Development of Low Level RF Control Systems for Superconducting Heavy Ion Linear Accelerators, Electron Synchrotrons and Storage Rings", Proceedings of PAC05, Knoxville (2005) pp.1-3.

[28] C. Piel, B. Aminov, A. Borisov, S. Kolesov, H. Piel, "Development of a Solid State RF Amplifier in the KW Regime for Application with Low Beta Superconducting RF Cavities", Proceedings of 2005 Particle Accelerator Conference, Knoxville (2005) pp.1-3.

[29] I. Fishman, I. Gertz, B. Kaizer and D. Har-Even, "High power amplifiers system for SARAF Phase II", these LINAC12 proceedings, TUP092.

[30] A. Facco, F. Scarpa, P. Modanese and Ma Yanyun, "Status of the ALPI Low-Beta Section Upgrade", Proceedings of LINAC2010, Tsukuba (2010) 181-183.

[31] P.N. Ostroumov, Z.A. Conway, M.P. Kelly, A.A. Kolomiets, S.V. Kutsaev and B. Mustapha, J. Rodnizki, "SARAF Phase II p/d 40 MeV linac design studies", these LINAC12 proceedings, FR1A05.

[32] P.N. Ostroumov, B. Mustapha, Z.A. Conway, R.L. Fischer, S. Gerbick, M. Kedzie, M.P. Kelly, I.V. Gonin, S. Nagaitsev, "Development of a Half-Wave Resonator For Project X", Proceedings of IPAC2012, New Orleans (2012) 2295-2297.

[33] B. Mustapha Z. A. Conway, P. N. Ostroumov, "A Ring-shaped Center Conductor Geometry for a Half-wave Resonator", IPAC12 New Orleans (2012) 2289-2291.

[34] S.V. Kutsaev, M.P. Kelly, P.N. Ostroumov, "Electromagnetic Design of 15 kW CW RF Input Coupler", Proceedings of IPAC2012, New Orleans (2012) 2286-2288.

[35] Z.A. Conway, G.L. Cherry, R.L. Fischer, S.M. Gerbick, M.J. Kedzie, M.P. Kelly, S.H. Kim, J.W. Morgan, P.N. Ostroumov and K.W. Shepard, "Cryomodule Designs for Superconducting Half-Wave Resonators", these LINAC12 proceedings, TUPB067.

Copyright © 2012 by the respective authors — cc Creative Commons Attribution 3.0 (CC BY 3.0)

STATUS OF THE EUROPEAN XFEL – CONSTRUCTING THE 17.5 GeV SUPERCONDUCTING LINEAR ACCELERATOR

W. Decking, DESY, Hamburg, Germany
for the European XFEL Accelerator Construction Consortium*

Abstract

The European XFEL is presently under construction in Hamburg, Germany. It consists of a 1.2 km long superconducting linac serving an about 3 km long electron beam transport system [1]. Three undulator systems of up to 200 m length each produce hard and soft x-rays via the self-amplified spontaneous emission (SASE) process. We will present the status of the civil construction and the accelerator components. The production of the 100 superconducting accelerator modules is distributed between industries and a collaboration of accelerator laboratories. We describe the carefully orchestrated production sequence, quality assurance measures and risk mitigation mechanisms. The last module is scheduled to be installed in the accelerator in spring 2015 and commissioning with beam will start in summer of that year.

OVERVIEW

The European XFEL is being constructed as an European Research Infrastructure under the participation of 12 European countries. The construction of the electron accelerator is entrusted to a consortium of 16 laboratories led by DESY, Hamburg. The laboratories contribute to the accelerator 'in-kind', i.e. by delivering sub-systems and parts under their own responsibility.

The facility will provide hard and soft X-rays for a wide range of scientific applications. In its initial stage it will host three independent photon beam lines serving two experiments each. Final extension will show three experiments for each of the five independent photon beam lines.

The European XFEL employs superconducting accelerator technology, leading to unique features compared to other X-ray FELs being constructed or in operation worldwide. It is capable of accelerating up to 27000 bunches per second, distributed into 10 pulses of 600 µs length. Bunches can be injected into two separate electron beam lines hosting two resp. up to three undulators in a row. Flexible bunch patterns and plans to provide individual bunch properties will make the European XFEL a true multi-user facility.

Progress in the electron gun development for the European XFEL and the success of LCLS led to a redefinition of the expected accelerator performance. The final energy of 17.5 GeV, together with the long undulators and the anticipated low emittance beams out of a photo-cathode gun will allow reaching photon wavelength as short as 0.5 nm [2].

The installed linac and its infrastructure bear the possibility to be converted into a CW (or quasi-CW) accelerator in the future with the potential to reach up to 6 GeV final energy (for an update on the R&D towards this option see [3]).

Table 1 gives an overview of the main parameters of the facility.

Table 1: European XFEL Parameters

Quantity	Value
maximum electron energy	17.5 GeV
macro pulse repetition rate	10 Hz
RF pulse length (flat top)	600 µs
bunch repetition frequency within pulse	4.5 MHz
bunch charge	0.02 – 1 nC
electron bunch length after compression (FWHM)	2 – 180 fs
beam power	500 kW
# of modules containing eight 9-cell superconducting 1.3 GHz cavities	101
accelerating gradient for 17.5 GeV	23.6 MV/m
# of 10 MW multi-beam klystrons	27
average klystron power for 0.03 mA beam current at 17.5 GeV	5.2 MW
photon wavelength	0.05 – 4 nm

A normal-conducting photo-cathode RF gun produces high brightness electron beams. The injector building allows the later installation of a second, completely independent injector. The main linear accelerator is sectioned into three units with 4, 12 and 84 modules each, intercepted by normal conducting bunch compressor and diagnostic sections. A collimation and beam distribution section follows the linac, where the beam can be fed into the two separate undulator beam-lines and/or a commissioning and pulse-picker dump. Each beam-line is terminated by a solid state beam dump capable of accepting up to 300 kW of continuous beam power. The SASE photon beam is delivered through up to 800 m long photon beam lines to the experimental hall. See Fig. 1 for a bird's eye view of the facility.

* BINP Novosibirsk, CEA Saclay, CIEMAT Madrid, CNRS Orsay, DESY Hamburg&Zeuthen, IFJ-PAN Krakow, IHEP Protvino, INFN Milano, INR Troitsk, NCBJ Swierk, NIIEFA St. Petersburg, PSI Villigen, SU Stockholm, UPM Madrid, UU Uppsala, WUT Wroclaw

Copyright © 2012 by the respective authors — cc Creative Commons Attribution 3.0 (CC BY 3.0)

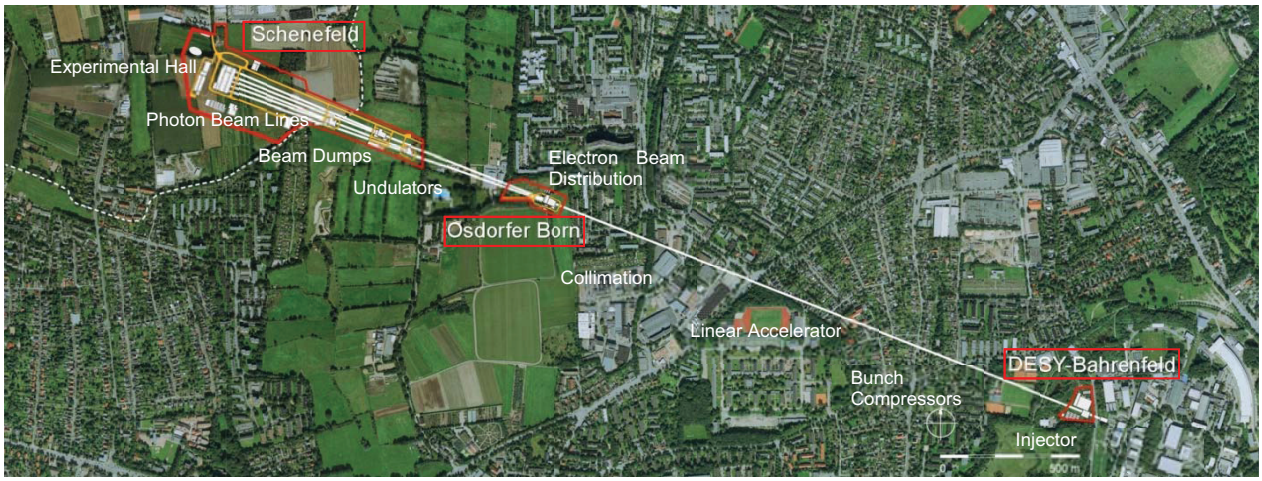

Figure 1: Bird eye's view of the European XFEL site showing the location of the three surface areas and the tunnel routing below the cities of Hamburg and Schenefeld.

STATUS

Civil Construction

The European XFEL requires a large amount of civil construction at three construction sites: on the DESY campus the injector building, modulator hall and accelerator module test facility (AMTF), the large experimental hall, tunnel separation shafts, dump shafts, office buildings and infrastructure buildings on the future XFEL experimental campus at Schenefeld 3.3 km to the west of DESY and a tunnel separation shaft and surface infrastructure buildings in between (see Fig. 1). About 5.8 km of underground tunnel connect these construction sites and fan out on the Schenefeld campus. They will host the accelerator and up to 5 independent photon beam lines and were constructed with the help of two tunnel boring machines. Work started in July 2010 and finished in June 2012, well within schedule (see Fig. 2).

Figure 2: View of the completed accelerator tunnel.

About 150000 m^3 of underground buildings had to be excavated and built. Most of the tunnel connection underground halls are finished, while the experimental hall is projected to be delivered in 2013.

Finally 12000 m^2 of surface buildings have to be erected. Most of the surface buildings on the DESY campus are about ready with the AMTF already close to start operation, the surface buildings on the other sites are only just being started. Their completion is of utmost importance for the machine installation, as they host the access devices like cranes and elevators and also mayor parts of the infrastructure.

Infrastructure Installation

With the hand-over of the main accelerator tunnel the installation of the technical infrastructure into the accelerator tunnel has begun. It will last until 2013 before first accelerator components can be delivered into the tunnel. In parallel infrastructure installation takes place in the other tunnels, shafts and buildings as they become available [4]. Planning of the infrastructure for the accelerator and the future experimental campus is a major task for DESY.

Accelerator Components

Apart from the superconducting accelerator about 3 km of so-called 'warm' beam lines have to be installed.

The photo-cathode gun will be of the same type as already in operation at the FLASH facility, DESY Hamburg, and the Photo-Injector Test Stand Zeuthen (PITZ), DESY Zeuthen. The gun body foreseen for the European XFEL is manufactured and will be conditioned and characterized at PITZ in the coming 9 months. The photo-cathode laser will be supplied by the Max Born Institute under the responsibility of DESY. It uses Yb:Yag lasing material and a pulse stacking system to provide a > 20 ps flat top with a steep rise and fall time.

The warm electron beam vacuum system is constructed by BINP and DESY. Up to a distance of 30 meters from the superconducting accelerator the vacuum system has to be particle free to avoid contamination of the cold modules in case of a vacuum leak in the warm vacuum. The undulator vacuum chambers, made of aluminium with stringent specifications on the surface roughness and

Copyright © 2012 by the respective authors — cc Creative Commons Attribution 3.0 (CC BY 3.0)

oxide layer to minimize resistive wall wake fields, pose an additional challenge.

Normal conducting magnets are produced by BINP and Efremov Institute. A total of more than 700 electro-magnets have to be delivered. The more than 120 undulator quadrupoles used for the focussing lattice in the undulator section are already on site, while the first batch of magnets that will be installed in the injector is due in autumn this year.

Beam instrumentation consisting of beam position and charge monitors, transverse beam profile monitors and various devices to measure longitudinal bunch properties are provided by DESY, PSI and INR. Most diagnostic devices have been developed and tested at FLASH and are now in the final engineering phase or already in series production.

A synchronisation system allows the measurement of beam arrival at certain stations up to 10 fs accuracy. Lasers and other devices can be locked to this system to allow synchronised pump-probe experiments [5].

The three undulator systems use moveable gap undulators of 5 m length and a period length of 40 resp. 68 mm. The contract for 91 undulators is awarded and first prototypes are on site for establishment of the fine tuning procedures.

SUPERCONDUCTING ACCELERATOR

Cavity Fabrication

The performance goal for the 800 9-cell cavities is an accelerating gradient of 23.6 MV/m at $Q_0=1\times10^{10}$.

The cavities are manufactured in industry according to the procedure previously developed at DESY (build to print). The performance is not guaranteed by the producers, in case of low performance the cavities will be re-treated at DESY. Nb sheets and parts are supplied to the producers via DESY.

The Nb sheets and tubes are produced by four different companies which have been pre-qualified for production of the required high purity sheets. All parts are individually quality controlled at DESY through an eddy current scan and tactile 3d dimension measurements before they are delivered to the cavity manufacturers.

Production of the cavities has been contracted to two companies. Both companies have erected the necessary infrastructure for the mechanical fabrication and the proper surface treatment of the cavities. After deep drawing the half cells are e-beam welded into dump bells and finally into 9-cell cavities. RF measurements and quality inspections are performed at each production step. All documentation is stored in the XFEL project EDM system by the contracting companies. The companies have also access to selected relevant information.

The surface treatment consists of an approx. 100 µm electro-polishing, ethanol rinsing, outside chemical polishing and high temperature annealing prior to cavity tuning. The cavity tuning is performed at the companies with special equipment that was developed and manufactured at DESY. After tuning the final surface treatment is either performed with another electro-polishing step or a 10 µm chemical polishing prior to the welding into the Titanium Helium vessel. Finally the cavities are dressed with auxiliary parts and higher-order mode couplers and shipped to DESY for acceptance test.

The complete procedure and infrastructure at the companies is qualified with reference cavities and pre-series cavities. First measurements of the reference cavities (production at companies and surface treatment and RF test at DESY) show performance above specification [6]. The surface treatment is established at the companies in a step-wise procedure, with the RF performance being tested after each treatment step.

Each of the 800 cavities is acceptance tested with a CW power test in a vertical cryostat. The tests are performed in a dedicated section of the AMTF hall. One vertical cryostat is already delivered to AMTF, while the 2nd is expected in November 2012. The infrastructure for vertical cavity testing is supposed to be fully operational by end of this year.

After reception and initial inspection the cavities are installed four each into an insert that allows parallel cool down and testing. The complete procedure of assembly, cool down, testing, warm up and disassembly will take about one week. The testing is performed by a team of specialist from IFJ Krakow. Presently the training and development of all steps is performed at the existing DESY infrastructure.

Accepted cavities will then be shipped to CEA Saclay for string assembly. A limited number of non-conforming cavities can be re-treated at the DESY infrastructure.

Module Assembly

The module assembly integrates all individual parts of a super-conducting module [7]:

- The power couplers are procured and warm conditioned by LAL Orsay. The copper plating of coupler parts turned out to be more challenging than anticipated and the involved parties work hard on the solution of the remaining problems.
- The cavity tuners are delivered by DESY.
- The cold vacuum pieces like bellows and intersections are made available by BINP Novosibirsk and DESY.
- The cold quadrupole package, consisting of a super-conducting quadrupole/steerer package delivered by CIEMAT Madrid to DESY, where the magnets are tested and equipped with a vacuum insert for rf-shielding.
- Beam position monitors both from DESY (button type) and CEA Saclay (re-entrant cavity type). The BPMs are connected to the quadrupole in the clean room at DESY and the complete unit is integrated into the cavity string.
- Cold masses from INFN Milano and DESY.

Module assembly starts with the assembly of the cold coupler parts to the individual cavities in an ISO4 clean room. Eight cavities are then connected together with the

Copyright © 2012 by the respective authors — cc Creative Commons Attribution 3.0 (CC BY 3.0)

quadrupole package into one cavity string, again under ISO4 clean room conditions. The cavities in the string are then equipped with tuners and magnetic shielding. The 2K He pipe is welded together and the complete string is connected to the He return pipe (cold mass), see Fig. 3. The cold mass is responsible for the mechanical rigidity of the system. All components are carefully aligned to each other and insulation shields and superinsulation are installed. Finally the cavity string/cold mass assembly is inserted into the cryostat. The warm parts of the couplers are installed and the coupler vacuum system is connected. The string is aligned within the cryostat and the complete assembly is prepared for transportation by assembly of end-caps, nitrogen filling of the cavities and assembly of surveillance instrumentation.

The string and module assembly is performed at CEA Saclay. Dedicated infra-structure has been set up during the past years, consisting of clean rooms, assembly halls, offices and ware houses [8]. Assembly of one module per week is foreseen. All critical parts of the infrastructure are laid out redundant to allow for maintenance, correction of non-conforming assembly steps or eventually a higher assembly rate.

Figure 3: Assembly of the cold mass at CEA Saclay.

Commissioning of the infrastructure and training of CEA staff has been performed since 2010 through the assembly and disassembly of XFEL prototype modules. The final assembly of 103 modules (3 pre-series and 100 series modules) is done by an industrial operator under the supervision of CEA staff. The respective company has been selected and the contract signed, training will start in autumn this year on the pre-series modules.

An assembly rate of one module/week requires careful planning of all logistics. On one hand a sufficient supply of sub-components has to be available on site, while on the other hand storage space is limited and the production of sub-components is just ramped up in time to match the assembly schedule. At least weekly video conference meetings of all involved parties are necessary despite the careful planning involving modern project planning tools.

After assembly the modules are transported by truck to DESY. A special shock absorbing frame is used to avoid misalignment and damage to the module. Shock-meters are in operation during the transport to record any unusual acceleration. The road transport has been tested with an assembled and tested module and no performance degradation has been observed.

Each of the 103 modules is tested at DESY at the AMTF. Three individual test stands (see Fig. 4) allow a through put of 1 tested module per week. The complete procedure of installation on the test bench, cool-down, testing, warm-up and disassembly is estimated to take about 2 weeks. The task is performed by the same specialist team responsible for the testing of the modules.

Figure 4: View of the module test stand in the AMTF.

Conforming modules can be stored partially on the DESY site for later installation. A small percentage of non-conforming modules could be disassembled and repaired in the DESY infrastructure.

RF System

An RF system unit consists of a 10 MW multi-beam klystron, pulse transformer, modulator and the wave-guide distribution to the individual input couplers. Contracts for all components are placed with industry.

The modulators will be placed outside of the tunnel in a dedicated hall on the DESY site. The pulse is fed into the tunnel with up to 2 km long pulse cables. These cables will be installed in the lower section of the tunnel below the floor slabs that form the transport way in the tunnel. Most of the cables are delivered and their installation into the tunnel will start this year before the floor slabs will be put finally into place.

Except for the injector and the photocathode gun one klystron feeds 4 modules (32 cavities in total). The pulse transformer and klystron are placed in the tunnel below the modules. This requires the klystron to be oriented horizontally. Prototypes of the multi-beam klystrons are in operation at the FLASH facility and show good performance [9].

The LLRF system for regulation of the RF has been developed at FLASH during the past years. In its final version it is based on the MicroTCA industrial standard. In-loop and outer-loop performance measurements show an RMS amplitude and phase regulation of $\Delta A/A = 5 \times 10{-}5$ and $\Delta\Phi = 0.009\circ$, resulting in an expected beam energy stability lower than 0.005% [10], [11].

Copyright © 2012 by the respective authors — cc Creative Commons Attribution 3.0 (CC BY 3.0)

Development of this system has greatly benefited from activities in the framework of the ILC R&D [12].

Accelerator Installation

The complete accelerator will be installed into the approximately 5.4 m diameter underground tunnel. The modules are suspended from the ceiling. This allows installing rf components and electronics easily accessible below the modules.

Module installation takes place in batches of 12 modules. These modules form one cryo-string. Each string is connected by string connection boxes. Some pre-sorting of modules is possible, with best performing module preferably at the beginning of the linac. Within a cryo-string, four modules with similar performance will be fed by one klystron.

Cooling is supplied by the existing cryo-plant that was previously used for the HERA accelerator. This plant is being refurbished to cope with the next 20 years of operation and the required 2K Helium production. Cryogenic components like transfer lines, valve boxes, connection boxes and test-cryostats are developed by BINP Novosibirsk, DESY, IHEP Protvino and WUT Wroclaw.

SUMMARY

Construction of the European XFEL is well under way with the goal of first beam in the accelerator by mid of 2015. Most of the underground civil construction is finished and the surface buildings are on schedule. Infrastructure installation has started and the procurement of accelerator components is well under way. One of the biggest challenges is the timely production of 101 super conducting accelerator modules. The production sequence has been set up and full rate series production is expected in one year.

Commissioning of the European XFEL starts with the injector in mid-2014. This includes the RF gun, one 1.3 GHz module, a third harmonic system [13], the laser heater and a section that allows bunch slice diagnostics. During the one year commissioning of the injector the remaining linac can be installed in parallel. Cool down of the main linac can only start when the complete linear accelerator is installed in mid-2015. First lasing can be expected by end of 2015.

REFERENCES

[1] M. Altarelli et al., "The European X-ray Free Electron Laser Technical Design Report", Hamburg, July 2007, DESY 2006-097.

[2] E.A. Schneidmiller, M.V. Yurkov., "Photon beam properties at the European XFEL", Hamburg, September 2011, DESY 2011-152.

[3] J. Sekutowicz, "Second CW and LP Operation Test of XFEL Prototype Cryomodule", TUPB019, these proceedings.

[4] M. Huening, "Warm Beamlines and Infrastructure in the European XFEL", TUPB015, these proceedings.

[5] H. Schlarb, "Synchronization of Accelerator Sub-systems with Ultimate Precision", TU3A01, these proceedings.

[6] A. Sulimov, "First RF Measurement Results for the European XFEL SC Cavity Production", MOPB012, these proceedings.

[7] E. Vogel, "Integration of the European XFEL Accelerating Modules", MOPB017, these proceedings.

[8] C. Madec, "Status of E-XFEL String and Cryomodule Assembly at CEA-Saclay", THPLB09, these proceedings.

[9] V. Vogel, "Results of Testing of Multi-beam Klystrons for the European XFEL", TUPLB04, these proceedings.

[10] C. Schmidt, "Precision Regulation of RF Fields with MIMO Controllers and Cavity-based Notch Filters", THPB086, these proceedings.

[11] J. Branlard et al., "The European XFEL LLRF System", IPAC'12, New Orleans, May 2012, MOOAC01, p. 55 (2012); http://www.JACoW.org

[12] J. Branlard, "LLRF Automation for the 9mA ILC Tests at FLASH", THPB085, these proceedings.

[13] E. Vogel, "Status of the European XFEL 3.9 GHz system", TUPB020, these proceedings.

Copyright © 2012 by the respective authors — cc Creative Commons Attribution 3.0 (CC BY 3.0)

SRF LINAC TECHNOLOGY DEVELOPMENT AT FERMILAB*

Vyacheslav Yakovlev# and Camille Ginsburg, Fermilab, Batavia, IL 60510, USA

Abstract

Superconducting linear accelerators are being developed for different applications: for fundamental research at the high-energy and high-intensity frontiers, in nuclear physics, for spallation neutron sources, for synchrotron radiation sources, etc. The linac applications dictate the requirements for the superconducting acceleration system, and, thus, for SRF technology. Fermilab is currently involved in two projects: ILC and Project X, both based on SRF technology. For high-intensity frontier investigations, Project X – a multi-experiment facility – is being developed based by a wide collaboration of US National and Indian Laboratories. In the CW H^- linac several families of SC cavities are used: half-wave resonators (162.5 MHz); single-spoke cavities, SSR1 and SSR2 (325 MHz); elliptical 5-cell beta=0.61 and beta=0.9 cavities (650 MHz). The pulsed 3-8 GeV linac is based on 9-cell 1.3 GHz cavities. In this paper the basic requirements for the CW superconducting Project X linac are considered as well as its specific technology challenges.

INTRODUCTION

The application of SRF technology to electron and hadron linacs has a long – almost 50 years long – and successful history. Superconducting RF cavities are now widely used and are planned to be used in linear accelerators for different applications, for example: (i) high-energy physics (SPL [1], ILC [2]) and the high-intensity frontier (Project X [3]); (ii) new X-ray free electron lasers (XFEL [4], NGLS [5], Cornell ERL [6]), (iii) spallation neutron sources (SNS [7], ESS [8]), (iv) nuclear physics and rare isotope production (ATLAS [9], ISAC-II [10], CEBAF [11], SARAF [12], SPIRAL –II [13]), (v) ADS accelerators (MYRRHA [14], Indian ADS [15], China ADS [16]). The recent progress in development of superconducting acceleration cavities was achieved substantially in connection with the ILC project, see Fig 1, where a sketch of the ILC is presented. For such a long machine, high acceleration gradient is essential: 35 MeV/m with a duty factor of 0.5%. The 9-cell ILC cavity (see Fig. 2) operates at 1.3 GHz. The ILC collaboration [2], which includes Fermilab, achieved impressive results in the development of cavity processing (which includes electro-polishing and 120°C baking, see Fig. 3) and clean assembly techniques. These developments allowed the achievement of cavity gradients at quite high and gradually increasing production yields, see Fig. 4 [17]. At Fermilab, the work on building ILC-type cavities and cryo-modules is continuing.

*Operated by Fermi Research Alliance, LLC, under Contract DE-AC02-07CH11359 with the U.S. DOE

#yakovlev@fnal.gov

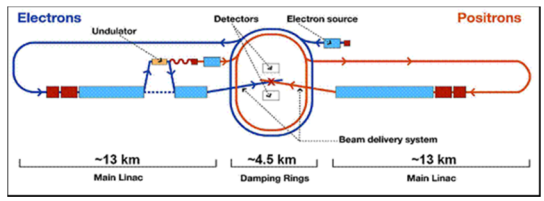

Figure 1: The ILC project sketch (2007 Reference Design).

The new large accelerator facility which is under development at Fermilab, Project X [18], is based on a CW H^- superconducting linac, which has requirements very different from what is suitable for ILC, creating new problems and new challenges.

Figure 2: Photo of the ILC 1.3 GHz 9-cell SC cavity [Fermilab Visual Media Services].

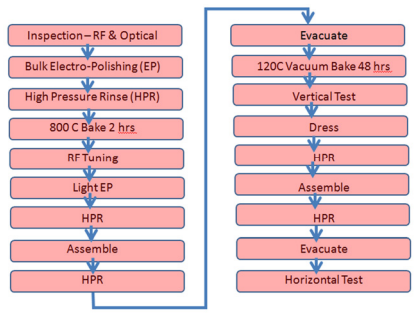

Figure 3: ILC Cavity Processing Basic Recipe.

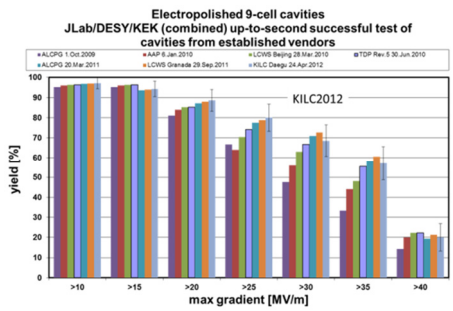

Figure 4: ILC gradient yield. ILC cavities reach 35 MV/m in vertical test more than half the time after one or two processing cycles.

DISCUSSION

Project-X, a multi-MW proton source, is under development at Fermilab. The Project X configuration is shown in Fig. 5. It enables a world-leading program in neutrino physics, and a broad suite of rare decay experiments. The facility is based on 3-GeV 1-mA CW

Copyright © 2012 by the respective authors — cc Creative Commons Attribution 3.0 (CC BY 3.0)

superconducting linac [19]. In the second stage, about 5-9% of the H^- beam is accelerated up to 8 GeV in a SRF pulsed linac to the Recycler/Main Injector. The beam from the CW linac is directed to the 8 GeV linac for further acceleration in the Main Injector up to 120 GeV, for the long baseline neutrino program.

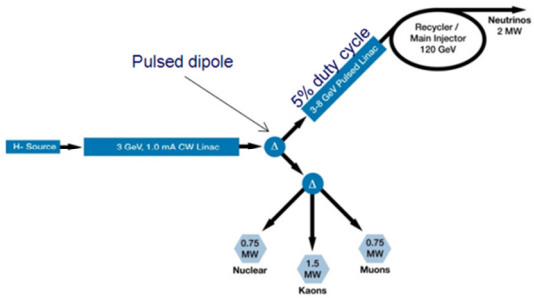

Figure 5: Project X configuration.

The 3-GeV CW linac of the Project X, see Fig. 6, contains (i) a front end with a room-temperature injection system having an H^- source, a Low-Energy Transport Line (LEBT), a 162.5 MHz RFQ, a Medium-Energy Transport Line (MEBT) with a beam chopper, (ii) a low-energy section based on 162.5 MHz Half-Wave Resonators (HWR) and 325 MHz Single-Spoke Resonators (SSR), and (iii) a high-energy section based on 650 MHz 5-cell elliptical cavities. The accelerator details for each SRF section are summarized in Table 1.

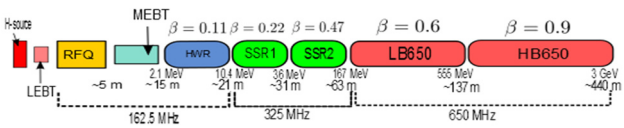

Figure 6: 3-GeV CW linac of the Project X.

Table 1: Accelerator details of the linac sections. CM: Cryomodule; D: Doublet, S: Solenoid, R: Resonator, R^n: n-Resonators Sequence.

Section	f[MHz]	Cav/mag/CML_{CM}[m]		Cell
HWR	162.5	8/8/1	5.26	S-R
SSR1	325	16/8/2	4.76	R-S-R
SSR2	325	36/20/4	7.77	$S\text{-}R^2$
LB650	650	42/17/7	7.1	R^3-D
HB650	650	152/19/19	11.21	$D\text{-}R^8$

The cavity design parameters for the low-energy sections and high-energy sections are shown in Tables 2 and 3, respectively. The HWR cryo-modules are developed by ANL [20]. The layout of the HWR cavity is shown in Fig. 6. SSR1 cavities [21], see Fig. 7, are designed by Fermilab and have been built by Zanon and Roark/Niowave. Two of them have been processed and tested showing performance consistent with design parameters. The helium vessel and tuners (coarse and fine) are also designed. The SSR2 cavity design is in progress [22]. Fermilab designed two 5-cell 650 MHz elliptical cavities for the high-energy section, at beta=0.61 (LE650) and beta=0.90 (HE650) [23]. JLAB has also developed a version of the LE650 cavity [24] with increased aperture, 100 mm versus 88 mm for FNAL design. JLAB has built and tested two single-cell cavities, see Fig. 9. One of them, #2, met Project X specifications (Q_0=2e10 at the nominal gradient).

Table 2: Cavity design parameters for the Project X low-energy section

Section	beta	Aper-ture, mm	Gain MeV	E_{peak} MV/m	B_{peak} mT	R/Q Ohm	G Ohm
HWR	0.11	33	1.8	40	62	225	48
SSR1	0.21	30	2.0	28	70	242	84
SSR2	0.47	40	3.3	32	60	292	109

Table 3: Cavity design parameters for the 5-cell elliptical cavities of the Project X high-energy section (FNAL design)

Section	beta	Grad MeV/m	Gain MeV	E_{peak} MV/m	B_{peak} mT	R/Q Ohm	G Ohm
LE650	0.61	16.6	11.7	37.5	70	378	191
HE650	0.90	17	17.7	34	61.5	638	255

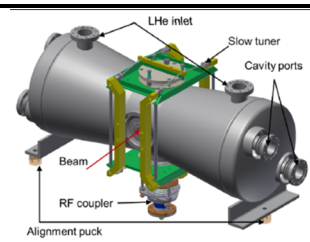

Figure 7: 3D model of HWR cavity (ANL)

Figure 8: SSR1 cavity, bare (left) and dressed (right).

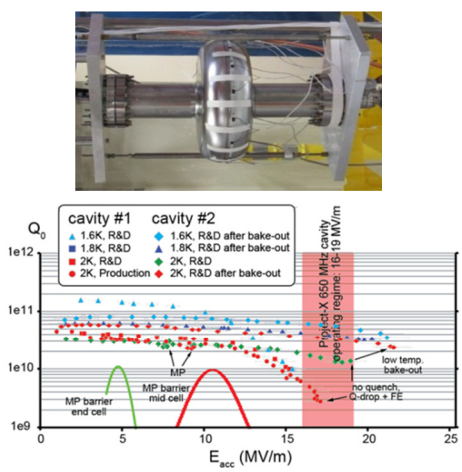

Figure 9: JLAB LE650 1-cell cavity and test results.

Copyright © 2012 by the respective authors — cc Creative Commons Attribution 3.0 (CC BY 3.0)

A HE650 single-cell cavity was designed by Fermilab, and six were built by AES, see Fig. 10. The tests are expected in October. A 3D model of the HE650 5-cell cavity is shown in Fig. 11.

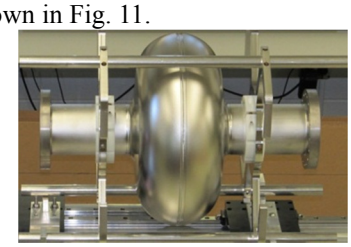

Figure 10: HE650 single-cell cavity.

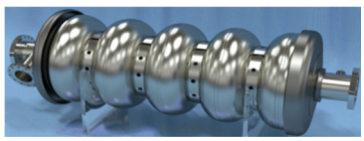

Figure 11: 3D model of HE650 5-cell cavity.

Cryo-modules for the HWR, SSR1 and high-beta 650 MHz cavities, see Fig. 12, are being designed [22,23].

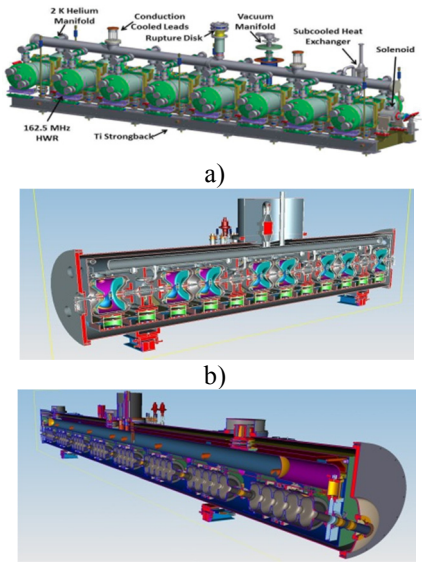

a)

b)

c)

Figure 12: Cryo-module design for a) HWR (ANL), b) SSR1 (FNAL) and c) HE650 MHz (FNAL).

The cryo-modules of Project X have substantial operational differences compared to the ILC: 100% and 0.5 % duty cycle, respectively, and thus, a big difference in RF load: ~200 W/CM at 17 MeV/m and ~5 W/CM at 35 MeV/m, respectively. Thus, achieving high gradients is not an issue for the Project X cavities, but low RF load, or high Q_0, is. RF load in the CW regime determines the power consumption of the cryogenic system, which, in turn, determines (i) the capital cost of the cryogenic system (cost of a cryogenic system is proportional to (RF load)$^{0.6}$ $\propto Q_0^{-0.6}$ for big machines [25]) and thus the cost of the entire project (cost of the cryogenic system is about 15% of the cost of a big machine); and (ii) operation cost, which is proportional to RF load, or Q_0^{-1} . Note that higher Q_0 also allows somewhat higher gradient, which may reduce the linac civil construction costs. The influence of RF load on the capital and operational cost of the Project X cryogenic system was analysed in [26]. The RF load was estimated using the averaged data on BCS resistance (the total surface resistance which determines Q_0 is the sum of residual resistance and BCS resistance) for ILC cavities [27] and Halbritter's model [28] for its gradient dependence (parameter γ=1 was taken based on these data). The cryogenic efficiency, i.e., the coefficient of performance (COP), was taken to be 890 W/W at 1.9 K, which corresponds to a modern level of cryogenic techniques [26]. In Fig. 13 a normalized capital cost of a cryogenic plant is shown versus the cavity operating temperature for two values of surface residual resistance, 5 nOhm and 10 nOhm. One can see that reduction of the residual resistance by a factor two decreases the cost by 30%. Note that the plant cost is about 75% of the total cost of the cryogenic system.

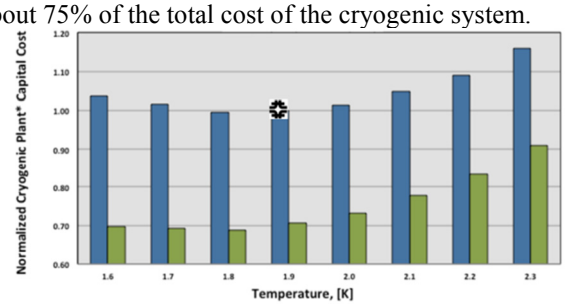

Figure 13: Normalized cryogenic plant cost versus operating temperature for different residual resistances: 10 nOhm (blue) and 5 nOhm (green).

Different approaches to reduce Q_0 are under development now. One of them is cavity processing in a nitrogen atmosphere, which creates a bulk layer of NbN on the cavity surface. NbN is a superconductor having a critical temperature of up to 16K compared to 9.2K for Nb, which gives the potential for lower surface resistance. The very first experiment [29] demonstrated the record $Q_0 \approx 7.5e10$ at 2K for a large-grain 1.3 GHz single – cell cavity (Fig 14). Another approach is hydrofluoric acid (HF) rinse of a cavity, with which one experiment [30] demonstrated a 35% increase in Q_0 at B_{peak} =70 mT for a 1.3 GHz fine-grain cavity, see Fig. 15. High-temperature baking (1400° C) is a third approach, which demonstrates Q_0~4.5e10 at B_{peak} =90 mT [31] also for 1.3 GHz, see Fig. 16. B_{peak}/E_{acc} =4.26 mT/MeV/m for all three of these cavities. Note that a Q_0 increase is demanded for any large CW superconducting accelerator, such as NGLS or ADS accelerators.

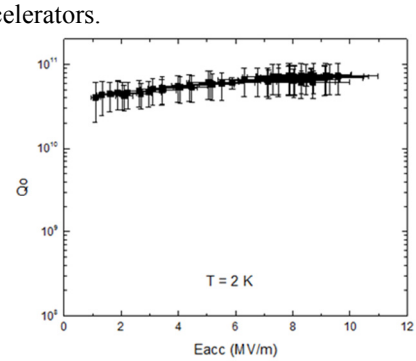

Figure 14: Q_0 versus E_{acc} for a NbN experiment.

Copyright © 2012 by the respective authors — cc Creative Commons Attribution 3.0 (CC BY 3.0)

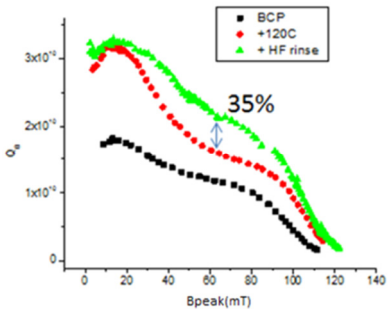

Figure 15: Q_0 versus B_{peak} for HF treatment.

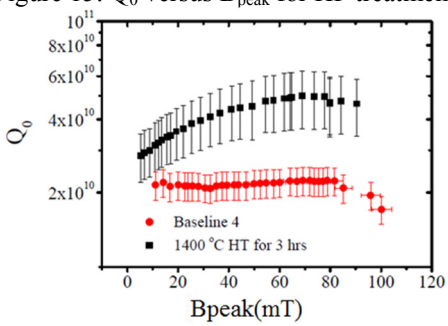

Figure 16: Q_0 versus B_{peak} for high-temperature baking.

Another critical issue for Project X and other large SC accelerators with modest beam current, e.g., NGLS, is small beam loading. Optimal coupling to the planned 1mA beam current at Project X would require relatively narrow cavity bandwidths. SC RF cavities are made from Nb sheet and the walls of the cavities are deliberately kept thin to maximize heat transfer to the surrounding superfluid helium bath. The thin walls of the cavities and the narrow operating bandwidths make them susceptible to detuning due to variations of the helium bath pressure or to mechanical vibrations (microphonics). Typically, the main source of vibration is helium pressure fluctuations [32]. As the cavities detune, additional RF power is required to maintain the accelerating gradient. If sufficient reserve RF power is not available to maintain the gradient, the beam can be lost. Sufficient reserve RF power must be provided to compensate for the peak detuning levels expected, not just for the average detuning. For narrow bandwidth cavities, providing sufficient reserve RF power can significantly increase both the acquisition cost and the operational cost of the machine. For the high-energy part of Project X, the bandwidth is about 23 Hz. In this case, a maximal detuning of 20 Hz requires an RF power overhead of 43% [33].

Microphonics can be mitigated by using the following approaches, or a combination of them: (i) providing sufficient reserve of RF power to compensate detuning; (ii) reducing the sensitivity of the cavity resonant frequency *f* to the helium bath pressure (*P)* fluctuation (*df/dP*), i.e., passive damping; (iii) actively damping microphonics using a fast tuner controlled by feedback from measurements of the cavity resonant frequency; (iv) decreasing the helium bath pressure fluctuations. To minimize *df/dP*, a number of approaches are used. A "self-compensating" scheme [34] was suggested for a triple spoke cavity, see Fig. 17. In this case, the cavity and helium vessel geometry are optimized such that a change in the stored energy of the electric field in the cavity is close to the change of stored energy of the magnetic field. Another approach is mechanical coupling of the cavity and the helium vessel, which improves the system stiffness [21], see Fig. 18. A third approach [35] exploits the idea of using a special element coupled to the cavity and separated from the helium vessel by a bellows which stretches the cavity in case of excess pressure, compensating the frequency changes caused by the cavity walls being squeezed. In SSR1 we use all these approaches to reduce *df/dP* to an acceptable level [21]. Active damping of microphonics for high – Q0 cavities was pioneered at Cornell [36]. Active piezo feedback reduces the microphonics amplitude by 70 %, see Fig. 19, and allows cavity operation with loaded Q up to 1e8. At Fermilab, an active microphonics compensation system was successfully developed and tested [37] for the SSR1 cavity at 4 K. The system allows a reduction in the r.m.s. detuning to 0.45 Hz, and peak detuning to 1.46 Hz, see Fig, 20. The system provides a very narrow peak without any evidence of long tails, which could cause rare trips. (Note that the Project X requirement is < 1 trip in 500 hours.) This approach for microphonics compensation satisfies Project X requirements, and may be useful for other large CW accelerators.

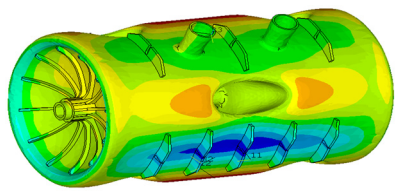

Figure 17: Self-compensating scheme for a triple-spoke cavity. Final adjustment of *df/dP* is reached by cutting the stiffening ribs on the He vessel walls.

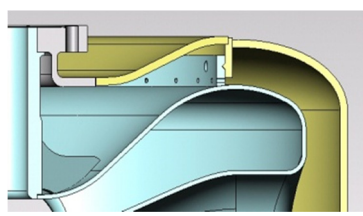

Figure 18: Mechanical coupling of the cavity and He vessel in order to improve the system stiffness.

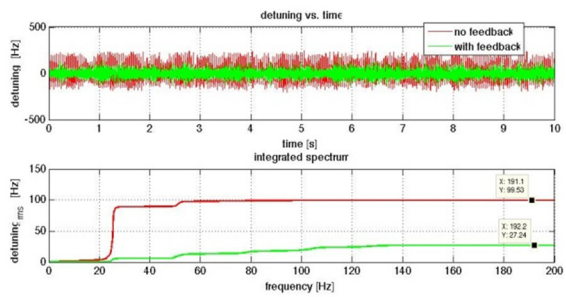

Figure 19. Active microphonics compensation in the Cornell ERL injector.

Copyright © 2012 by the respective authors — cc Creative Commons Attribution 3.0 (CC BY 3.0)

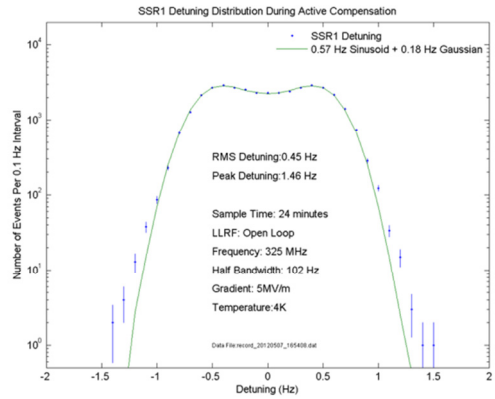

Figure 20: SSR1 active microphonics control.

CONCLUSIONS

Fermilab is proceeding with SRF activity connected to ILC and Project X. SRF for ILC is well-developed, and the international team has made good progress in achieving high accelerating gradient. New large CW linacs such as Project X, NGLS, ADS projects, ERL's, etc., need not high gradient, but high Q_0 at modest gradient. New SC material research concentrates on the achievement of high Q_0. Another critical issue for new CW projects is microphonics. Dedicated research is ongoing to develop both passive and active means for microphonics compensation suitable for large SC linacs with low beam loading.

ACKNOWLEDGMENTS

Many thanks to colleagues, from whom we have obtained the information for this presentation: Zachary Conway and Peter Ostroumov (ANL), Matthias Liepe (Cornell), Anna Grassellino, Timergali Khabiboulline, Arkadiy Klebaner, Yuriy Pischalnikov, Allan Rowe, Warren Schappert and Nikolai Solyak (FNAL), and Evgeny Zaplatin (Jülich).

REFERENCES

[1] R. Garoby, "SPL at CERN," SRF 2009, Berlin, Germany, September 20-25, 2009.
[2] ILC Reference Design Report http://www.linearcollider.org/about/Publications/Reference-Design-Report
[3] Project X Reference Design Report, http://projectx-docdb.fnal.gov/cgi-in/RetrieveFile?docid=776;filename=RDR-v0.9.pdf;version=1
[4] The Technical Design Report of the European XFEL http://xfel.desy.de/technical_information/tdr/tdr/
[5] J. N. Corlett et al., "A Next Generation Light Source Facility at LBNL",PAC 2011, New York, New York, March 20 - April 1, 2011.
[6] G. H. Hoffstaetter, S. Gruner, and M. Tigner, eds.,Cornell ERL Project Definition Design Report (2011) http://erl.chess.cornell.edu/PDDR
[7] S. Henderson, "Status of the Spallation Neutron Source: Machine and Science," PAC 2007, Albuquerque, New Mexico, USA, June 25-29, 2007.
[8] ESS Conceptual Design Report https://maiserxx.esss.lu.se/press/documents/CDR_final_120206.pdf
[9] P. N. Ostroumov et al., "ATLAS Upgrade," PAC 2011, New York, New York, March 20 - April 1, 2011.
[10] R. E. Laxdal et al., "ISAC-II: Status of the 20 MV Upgrade", SRF2009, Berlin, Germany, September 20-25, 2009.
[11] J. Preble, "CEBAF Energy Upgrade Program Including Re-work of CEBAF Cavities," SRF 2007, Beijing, China, October 14-19, 2007.
[12] L. Weissman et al., "The Status of the SARAF Linac Project," LINAC 2010, Tsukuba, Japan, September 12-17, 2010.
[13] SPIRAL-2 Project Scientific Objectives and Technical Reports, http://www.ganil.fr/research/developments/spiral2
[14] D. Vandeplassche et al., "The MYRRHA Linear Accelerator," IPAC 2011, San Sebastian, September 4-9, 2011.
[15] P. Singh, "SRF Accelerator for Indian ADS Program: Present & Future Prospects", SRF 2011, Chicago, 2011.
[16] S. Fu et al., "Proton Linac for ADS Application in China", LINAC 2010, Tsukuba, Japan, September 12-17, 2010.
[17] C.M. Ginsburg et al., KILC 2012, April, 24,2012
[18] S. Nagaitsev and S. Henderson, “Status of Fermilab Project X,” Linac 2012, Tel-Aviv, September 10-14, 2012
[19] J.-F. Ostiguy et al., “Status of the Project-X CW Linac Design,” IPAC2012, New Orleans, May 20-25, 2012.
[20] Z. Conway et al., “Development of a Superconducting Half-Wave Resonator for PXIE,” LINAC 2012, Tel-Aviv, September 10-14, 2012.
[21] L. Ristori et al., “Design of SSR1 Single Spoke Resonators for PXIE,” IPAC2012, New Orleans, May 20-25, 2012.
[22] P. Berrutti et al., “Optimization of the Geometric Beta for the SSR2 Cavities of the Project X,” IPAC2012, New Orleans, May 20-25, 2012.
[23] V. Yakovlev et al., “Concept EM Design of the 650 MHz Cavities for the Project X,” PAC2011, New York, March 28, 2011.
[24] F. Marhauser et al., ”Design, Fabrication and Testing of Medium-beta 650 MHz SRF Cavity Prototype for Project X,” IPAC11, San Sebastian, Spain. 2011.
[25] S. Claudet et al., LHC Project Report 317, 1 December 1999, Geneva.
[26] A. Klebaner et al., “Project X Cryo System Operating Temperature Analysis,”Project X Collaboration Meeting, April 12-14, 2011, Oak Ridge.
[27] C. M. Ginsburg et al., FERMILAB-CONF-08-348-TD, http://www.slac.stanford.edu/spires/find/hep/www?r=FERMILAB-CONF-08-348-TD,
[28] J. Halbritter, RF residual losses, high electric and magnetic in superconducting cavities, Eds. L Cifarelli and L. Maritato. World Scientific, 1999.
[29] A. Grassellino et al., “High Q Studies for Nb Cavities: Heat Treatments and NbN R&D at FNAL,” LINAC 2012, Tel-Aviv, September 10-14, 2012.
[30] A. Romanenko, TTC Meeting, Beijing, 2011.
[31] Dhakal et al., IPAC2012, New Orleans, May 20-25, 2012.
[32] M. Liepe, ProjectX Collaboration meeting, Fermilab, 2011.
[33] W. Schappert et al., “Microphonics control for Project X,” PAC2011, New York, March 28, 2011.
[34] Z.A. Conway et al., “Electro-Mechanical Properties Of Spoke-Loaded Superconducting Cavities,” SRF-07, Beijing 2007.
[35] E. Zaplatin, PAC 2011, New York, TUP031.
[36] M. Liepe et al., “Pushing the Limits: RF Field Control at High Loaded Q,” PAC2005, Knoxville, May 16-20, 2005.
[37] Yu. Pischalnikov and W. Schappert, “SSR1 Active Microphonics Control,” Fermilab TD/T&I, June 04 2012.

Copyright © 2012 by the respective authors — cc Creative Commons Attribution 3.0 (CC BY 3.0)

INCREASED UNDERSTANDING OF BEAM LOSSES FROM THE SNS LINAC PROTON EXPERIMENT *

J. Galambos#, A. Aleksandrov, M. Plum, A. Shishlo, ORNL, Oak Ridge, TN 37831, USA,
E. Laface, ESS, Lund Sweden, V. Lebedev, FNAL, Batavia, IL 60510, USA

Abstract

Beam loss is a major concern for high power hadron accelerators such as the Spallation Neutron Source (SNS). An unexpected beam loss in the SNS superconducting linac (SCL) was observed during the power ramp up and early operation. Intra-beam-stripping (IBSt) loss, in which interactions between H^- particles within the accelerated bunch strip the outermost electron, was recently identified as a possible cause of the beam loss. Results from a set of experiments using proton beam acceleration in the SNS linac support IBSt as the primary beam loss mechanism in the SNS SCL.

SNS BEAM LOSS EXPECTATIONS

The SNS accelerator consists of an RFQ (output energy of 2.5 MeV), a Drift Tube Linac (output energy of 85 MeV, a Coupled Cavity structure (output energy of 186 MeV) and an elliptical cell superconducting cavity structure with design output energy of 1 GeV. The SNS linac accelerates a 1 msec pulse H^- beam, which is subsequently captured in a storage ring to produce a sub μs intense pulsed neutron source.

A major advantage of superconducting RF linacs for H^- and proton acceleration is the inherently large beam aperture, which greatly alleviates the issue of beam loss relative to copper accelerating structures. During the design stage of SNS the multi-particle beam simulations indicated no beam loss in the superconducting linac (SCL) region [1,2]. Nonetheless, there was a reluctance to assume no superconducting linac beam loss and a minimal loss in this area was allocated in the beam loss budget [3], attributed to gas stripping in the warm sections between cryomodules.

OBSERVED SCL BEAM LOSS

Loss History

Early in the power ramp-up phase of the SNS operation, unexpected residual activation was measured along the SNS superconducting linac, in the warm sections between the cryomodules. The warm sections are the limiting aperture restrictions in the SCL, so it is not surprising that the observed beam loss is located in these regions. The build-up of measured residual activation over the period of the SNS power ramp-up and initial operation is shown in Fig. 1, where the the average warm section residual activation levels are superimposed on the operational beam power level. Initially, the loss detectors did not register the beam loss causing this activation, but they were moved closer to the beam pipe in the warm sections, and subsequently did detect the beam loss. Beam loss is rather uniformly distributed along the SCL.

Beam Loss Magnitude

Based on the measured residual activation levels, the beam loss can be expected to be < ~1 W/warm-section, which corresponds to < 10^{-4} fractional beam loss throughout the SCL at 1 MW. Quantifying beam loss fractions at this level is difficult. One method of producing very small fractional controllable beam spills in the SNS SCL is with a laser profile device [4]. The short pulse laser strips the outermost H^- electron from about 10^{-6} of a nominal beam pulse, creating H^0 that is subsequently lost downstream. By comparing the additional beam loss signal produced by the known amount of beam lost from the laser pulse to the measured beam loss during production, we estimate the fractional beam loss during neutron production in the SNS SCL to be a few $\times 10^{-5}$.

Possible Loss Causes

Initially, causes of the unexpected beam loss were suggested to be poor matching (transverse or longitudinal); beam halo from the ion source, or produced during acceleration; and residual gas stripping. Longitudinal tails were considered a likely loss contributor because of the sensitivity of SCL beam loss to the longitudinal setup of the upstream warm linac. Different longitudinal tunes were applied in the SCL, trading final energy for increased acceptance, but minimal impact was observed on the baseline SCL beam-loss level. The transverse match is a natural suspect, however adjustments of matching quadrupoles at the linac lattice transitions generally affect beam loss at local loss points, as opposed to the observed uniform beam loss through the SCL. Additionally, for the design transverse optics, beam mis-steering does not affect beam loss, indicating the presence of additional aperture available for the transverse tune. Finally, residual gas stripping in the upstream warm linac was addressed by measuring the change in beam loss with deteriorated warm linac vacuum to determine the impact from gas stripping and extrapolating back to ideal vacuum conditions. This indicated that gas stripping was not a major contributor to the SCL beam loss. The measured vacuum level in the warm sections between superconducting RF cryomodules is much lower than the design assumptions, and is too low to contribute to significant gas stripping beam loss.

jdg@ornl.gov

Copyright © 2012 by the respective authors — cc Creative Commons Attribution 3.0 (CC BY 3.0)

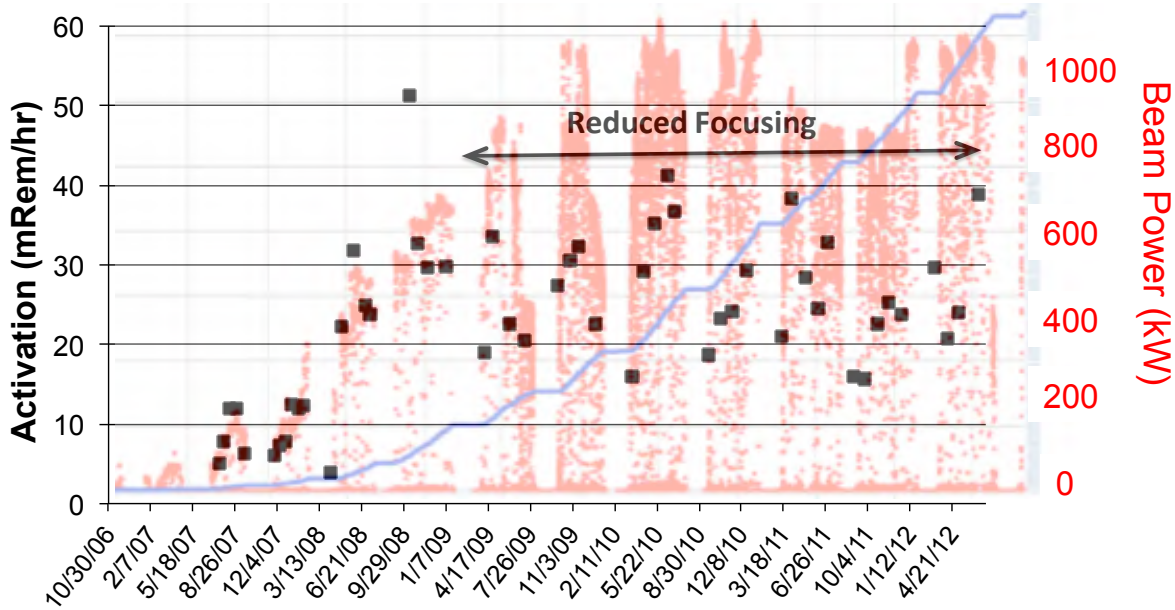

Figure 1: History of the SNS residual activation along the SCL (black marks) since initial operations, superimposed on the operational beam power level (red background). Activation levels are the average hot-spot measurement in the warm sections along the SCL, at 30 cm taken about 24 hours after the end of a run.

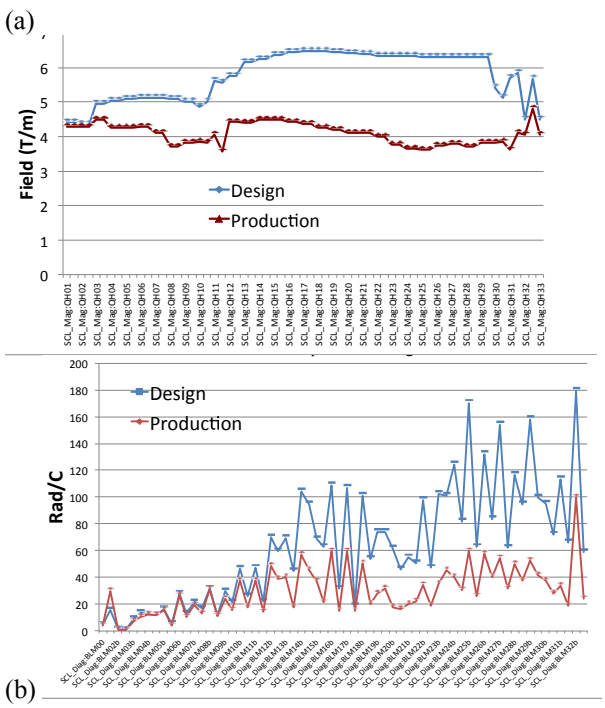

Figure 2: (a) Comparison of transverse field levels for design and production optics, (b) Measured beam loss distributions along the SCL for design and production optics. Beam loss is normalized to the transmitted charge.

Reduced Focusing Operation

A key feature of the SCL activation build-up, shown in Fig. 1, is a roll-over at the onset of reduced focusing operation. In early 2009, empirical observations revealed reduced beam loss with lower transverse focusing in the SCL. Initially modest quadrupole field level reductions were applied, but eventually the applied field level was reduced up to 40%, beyond which losses began to increase. Reducing the applied focusing strength was the primary contribution to the activation buildup "roll-over" in early 2009. Fig. 2 shows the transverse focusing field along the SCL for both the design level, and the empirically derived minimal loss condition (referred to as "production" optics here). Also shown in Fig. 2 is the measured beam loss distribution along the SCL for the design and production lattice optics. There is a systematic reduction of beam loss along most of the SCL with the reduction of the applied field. This was the single largest observed influence on loss reduction. While it initially seemed counter-intuitive that increasing the beam size would reduce beam loss, this observation proved to be a valuable insight into an unforeseen beam loss mechanism in H^- linacs.

INTRA-BEAM STRIPPING

Intra-Beam Stripping (IBSt) refers to the stripping of the outer electron from an H^- ion in an accelerated beam due Coulomb collisions with other H^- ions in the beam. This loss mechanism was examined at CERN over 20 years ago [5], but had not been considered in the SNS design. V. Lebedev first proposed this process as a loss mechanism for H^- linacs [6], and in particular for the SNS. The loss rate is proportional to the beam density squared and the cross-section for stripping. For the centre-of-mass relative velocities of the H^- particles in the bunch along the SNS SCL linac, the cross section is fairly constant [6].

Copyright © 2012 by the respective authors — cc Creative Commons Attribution 3.0 (CC BY 3.0)

PROTON BEAM AT SNS

A direct test of the IBSt loss mechanism hypothesis is to replace the H^- beam with a comparable proton beam. A set of experiments to this effect has been described in refs. [7, 8]. A simple way to produce a proton beam at SNS is to insert a thin foil into the beam to convert the H^- to H^+. The Medium Beam Energy Transport (MEBT) between the RFQ and Drift Tube Linac (DTL) is a convenient location for this purpose for the following reasons:

1. There is an available actuator for foil attachment near the start of the MEBT.
2. There are 10 independent quadrupole power supplies that can be adjusted to rematch the resultant proton beam into the downstream permanent magnet DTL.
3. Following the rematch, the beam transport through the linac is the same for H^- and protons.
4. Commercially available foils are suitable for this energy range (2.5 MeV).

Creating the Proton Beam

A 5 μg/cm^2 thick foil was chosen, which strips nearly all the beam (> 99.9%, and the un-stripped beam is lost soon afterwards in the MEBT). Foil scattering is estimated to produce minimal energy loss compared to the inherent beam energy spread, and a transverse emittance growth of only 10-20%. One limitation of the foil is beam heating. To avoid foil damage, we limit the beam pulse length to 50 μs, compared to production pulse lengths of 850 μs. The foil is 16 mm diameter, quite large compared to the RMS beam size of 1.5 - 2 mm.

Machine Setup for Protons

The foil is inserted just after the first quadrupole in the MEBT, leaving 9 additional adjustable quadrupole power supplies available to match the proton beam into the downstream DTL. The matching scheme swaps the H^- and proton horizontal and vertical Twiss parameters at the DTL entrance, while minimizing the beam size in the MEBT. The RF phases throughout the linac are adjusted by 180 degrees to provide the same longitudinal focusing and acceleration for protons as for H^-. The focusing elements in the coupled cavity linac (CCL) and SCL are left the same for the proton and H^- beams, with the exception of minor adjustments for loss tuning at the lattice transitions between the CCL and SCL.

Measured beam profiles at end of the SCL are compared for the proton and H^- beams in Fig. 3. The horizontal and vertical planes are swapped, as expected, and the general shape of the profiles is similar, indicating that the transport of the protons beam is comparable to that of the H^-. The Twiss parameters at the end of the SCL are also measured using a set of four profile measurement devices at the start of the transport section that directly follows the SCL. These parameters, shown in Table 1, indicate that the horizontal and vertical planes are effectively swapped between the two beams, as expected.

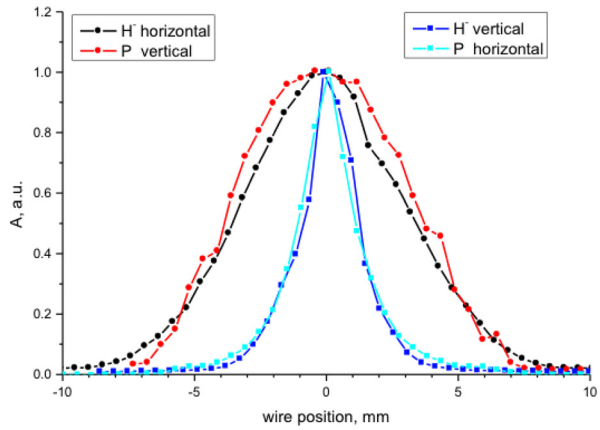

Figure 3: Measured beam profiles at the end of the SCL

Table 1: Twiss Parameters at the SCL Exit (from Ref. [7])

	Proton vertical	**H⁻ horizontal**
ε_{norm} (π-mm-mrad)	0.47	0.55
α	-2.0	-2.2
β	10.3	12.9
	Proton horizontal	**H⁻ vertical**
ε_{norm} (π-mm-mrad)	0.71	0.80
α	1.8	2.4
β	10.0	11.9

Proton Beam Transmission

For H^- beams, the transmission from the MEBT through the SCL is better than the accuracy of the current measurement (> 99%). However, for the proton beam, the transmission varies from 98% at nominal current to 86% at reduced beam intensity, with losses occurring primarily in the MEBT. This is due to the fact that the MEBT optics are intensity dependent (due to space charge), but are not adjusted with current here. Because the proton beam size is larger than the H^- (in the upstream MEBT near the foil), it is more sensitive to transmission loss.

Copyright © 2012 by the respective authors — cc Creative Commons Attribution 3.0 (CC BY 3.0)

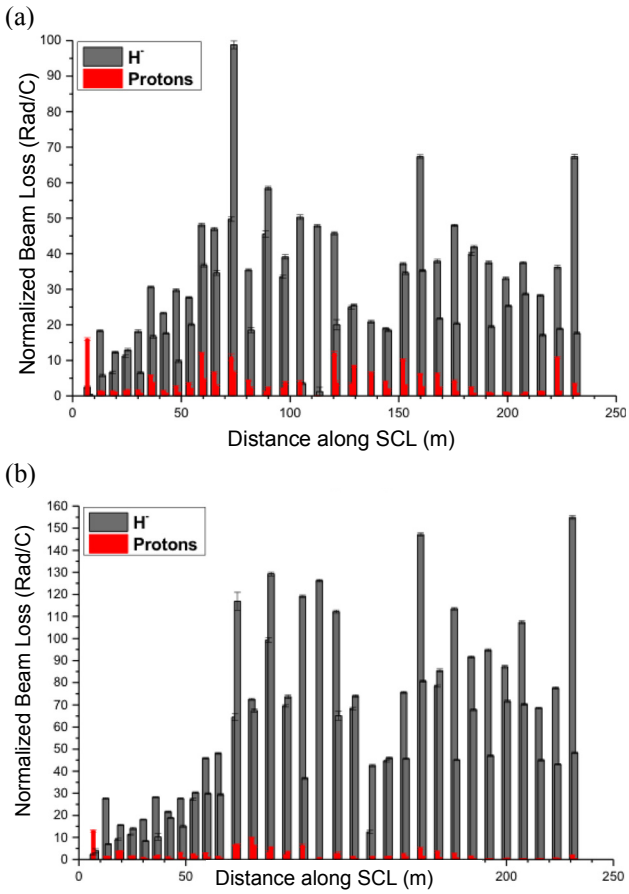

Figure 4: Beam loss along the SCL for the case of 30 mA, for proton and H^-; (a) for production optics, and (b) for design optics. Reproduced from References 7 and 8.

PROTON-H^- BEAM LOSS COMPARISON

Beam loss is primarily detected in the SNS SCL by ion chamber beam loss monitors (BLMs) [9], distributed 2 per warm section between cryomodules. Figure 4 shows a comparison of the measured beam loss along the SCL for the case of an H^- and a proton beam, with a 30 mA current. Beam loss shown here is normalized to the transmitted charge, and the values represent an average over 20 pulses, although the pulse-to-pulse variation is small. Both the H^- and proton beam cases are for 45 μs pulse lengths. Minor adjustments of the proton beam setup were performed to minimize loss (adjustments of linac RF phases by 1-2 degrees and lattice matching quadrupoles up to a few percent), as was also done for the H^- beam.

There is a dramatic reduction in beam loss throughout the SCL for the proton beam case. Many BLM readings are near the limit of detectable beam loss for the proton beam case. The BLM response for equivalent proton and H^- beam loss was verified to be the same by inserting intercepting devices into the beam directly upstream and downstream of the SCL. The much reduced beam loss throughout the SCL for protons, for a beam with similar properties as the H^- beam, signifies a beam loss mechanism unique to the H^- beam.

Loss Dependence on Intensity

It is interesting to examine the dependence of the beam loss on the beam intensity. The IBSt loss rate scales with the square of the beam density or, for constant bunch length and transverse beam size, with the square of beam current. The measured beam loss normalized to the transmitted charge (shown in Fig. 5) should vary linearly with the beam current for IBSt. Fig. 5 shows the beam loss for protons and for H^- vs. beam current. In this case each loss measurement shown in Figure 5 is the average of all BLMs along the SCL. Measurements are shown for both the design optics (strong focusing) and for the production optics (weak focusing).

For both the strong and weak focusing cases the H^- normalized beam loss varies close to linear with beam current, consistent with IBSt expectations. Also the strong focusing case (design optics) shows a higher loss rate than the weak focusing case (production optics) at all intensities, consistent with IBSt expectations. For the proton beam cases, there is no meaningful variation of the normalized beam loss with beam intensity, as expected without the possibility of IBSt mechanism (the slight decrease in normalized beam loss with intensity may be an artifact of the background subtraction method used in the BLM signal processing). There is also no meaningful difference in the normalized beam loss between the weak and strong focusing cases for the proton beam, also consistent with the lack of an IBSt loss mechanism. The slight fall-off from a linear dependence of the H^- loss vs. beam current at high values is not understood. It may be due to a dilution of the beam density due to increasing space charge forces.

SUMMARY

A series of beam measurements using a proton beam at the SNS accelerator shows much-reduced beam loss compared to an equivalent H^- beam. The H^- beam loss scaling with both intensity and focusing strength and the lack of an observable effect of the proton beam loss rate on intensity or focusing strength are all consistent with expectations of the IBSt beam loss mechanism. This loss mechanism should be considered for all future H^- linac designs. Evidence for IBSt has also been found at LANSCE [10].

For SNS, we expect to be able to tolerate the present beam loss rate with beam powers of up to 2-3 MW, without incurring the penalty of high radiation areas throughout the linac. However, efforts are aimed to reduce existing halo and operate with even larger beam sizes in an effort to further minimize IBSt effects.

Copyright © 2012 by the respective authors — cc Creative Commons Attribution 3.0 (CC BY 3.0)

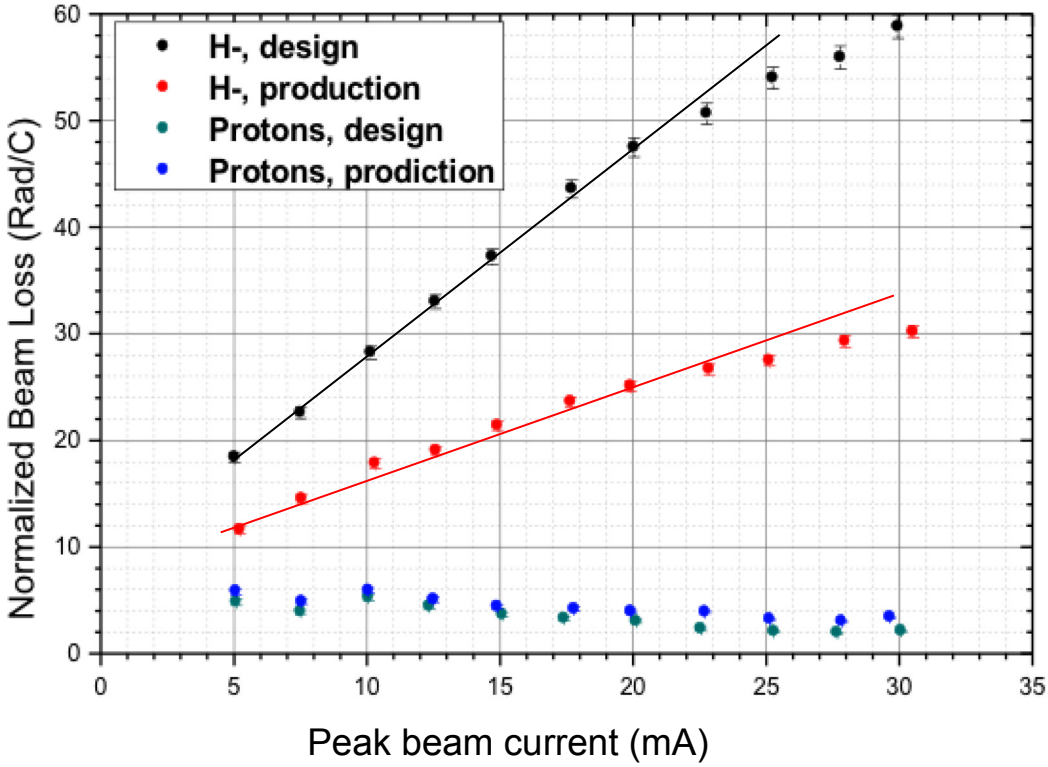

Figure 5: Beam loss vs. beam current for protons and H beams, for the cases of strong focusing (design optics) and weak focusing (production optics). The straight curves along the H^- loss measurements indicate the expected dependence from IBSt. Reproduced from Reference 8.

ACKNOWLEDGMENT

The authors are grateful to members of the SNS beam instrumentation and accelerator physics teams for useful discussions and in assistance in preparing equipment for the work described here. The work was performed at the Spallation Neutron Source accelerator at Oak Ridge National Laboratory (ORNL). ORNL/SNS is managed by UT-Battelle, LLC, for the U.S. Department of Energy under Contract No. DE-AC05-00OR22725.

REFERENCES

[1] S. Nath, et al., "Particle Beam Behavior in the SNS Linac with Simulated and Reconstructed Beams", Proceedings of the 2003 Particle Accelerator Conference, p. 1515 (2003);

[2] J. Stovall, et al, "Superconducting Linac for SNS", XX International Linac Conference, Monterey, California, p. 605 (2000); http://accelconf.web.cern.ch/AccelConf/l00/papers/TUD22.pdf

[3] N. Catalan-Lasheras, et al., "Accelerator Physics Model of Expected Beam Loss along the SNS Accelerator Facility during Normal Operation", SNS/AP Technical Note 07, 2001

[4] Y. Liu, et al., "Laser based diagnostics for measuring H- parameters", Proceedings of 2011 Particle Accelerator Conference, New York, NY, USA, p. 1433 (2011);

[5] M. Chanel, et. al., Physics letters B, 192 , n. 3,4, p.475.

[6] V. Lebedev et al., "Intrabeam stripping in H^- linacs," in Proceedings of LINAC 2010 conference, pp. 929-231;http://accelconf.web.cern.ch/AccelConf/LINAC2010/papers/thp080.pdf

[7] A. Shishlo et al., "The First Observation of Intra Beam Stripping of Negative Hydrogen in a Superconducting Linear Accelerator," Phys. Rev. Lett. 108, 114801 (2012).

[8] A. Shishlo, et. al, "H^- and Proton Beam Loss Comparison at SNS Superconducting Linac", Proceedings of IPAC2012, New Orleans, Louisiana, USA, (2012) p. 1014;

[9] A. Zhukov, et al., "SNS BLM System Evolution: Detectors, Electrons, Software", Proceedings of the 2009 PAC, Vancouver, BC, Canada, p. 4853 (2009)

[10] L. Rybarcyk et al., "H^- Beam Loss and Evidence for Intrabeam Stripping in the LANSCE Linac," IPAC2012, New Orleans, Louisiana, USA, p. 3892 (2012).

Copyright © 2012 by the respective authors — cc Creative Commons Attribution 3.0 (CC BY 3.0)

DEVELOPMENT OF H-MODE LINACS FOR THE FAIR PROJECT*

G. Clemente†, W. Barth, L. Groening, S. Mickat, B. Schlitt, W. Vinzenz, GSI, Darmstadt, Germany
U.Ratzinger, H.Podlech, R.Brodhage, M.Busch, F.Dziuba,
Goethe University, Frankfurt am Main, Germany

Abstract

H-mode cavities offer outstanding shunt impedances at low beam energies and enable the acceleration of intense protons and ion beams. Crossed-bar H-cavities extend these properties to energies even beyond 100 MeV. Thus, the designs of the new injector linacs for FAIR, i.e. a 70 MeV, 70 mA proton driver for pbar-production and a cw intermediate mass, superconducting ion linac are based on these novel cavities. Several prototypes (normal and superconducting) have been built and successfully tested. Moreover, designs for a replacement of the 90 MV Alvarez section of the GSI - Unilac will be discussed to improve the capabilities as the future FAIR heavy ion injector.

INTRODUCTION

The scientific program of FAIR requires the construction of a new 70 MeV, 325 MHz proton injector [1] for the SIS18. This machine will provide at least 35 mA of protons at a repetition rate of 4 Hz.

Beside the new proton linac, FAIR also requires a massive upgrade of the GSI UNILAC linear accelerator [2].

The UNILAC started operation in 1975 and it is one of the eldest DTL still active. Almost 40 years of high duty factor operation (up to 25 %) led to the increasing number of failures occurred in the last years. That represents a strong reliability issue for the new FAIR facility.

Additionally, the Alvarez-DTL is equipped with DC quadrupoles, which is a disadvantage for short pulse operation and limits the machine flexibility in case of the multibeam operation (different ion beam with specific magnetic rigidities and beam currents). That constraint, together with the challenging requirements of 15 mA of U^{28+}, favours the replacement of the existing DTL section by a new high energy linac with short beam pulses at low repetition rate (HE-Linac).

The linac upgrade program will be completed by a new superconducting cw heavy-ion linac [3] with an adjustable energy from 3.5 to 7.3 AMeV for the super heavy elements program (SHE-Linac).

The choice of the RF cavity type represents the most critical key for such a massive upgrade. The experience with high current operation at the HSI and HLI led to the natural decision to base the UNILAC replacement on IH-DTL cavities. On the other hand, the successful R&D performed at the Frankfurt University on room temperature [4] and superconducting CH-DTL [5] justifies the use of that kind of structures for the new proton linac and for the cw SHE linac.

* Work supported by HicforFAIR and BMBF
† g.clemente@gsi.de

H-MODE CAVITIES

H-Mode cavities are characterized by a slim tube geometry resulting in a high shunt impedance and a uniform power loss distribution (see Fig.1). Beam dynamics is designed according to an asynchronous injection energy lattice like the KONUS [6] or the EQUUS [3]. Alternatively an APF [7] lattice can be used.

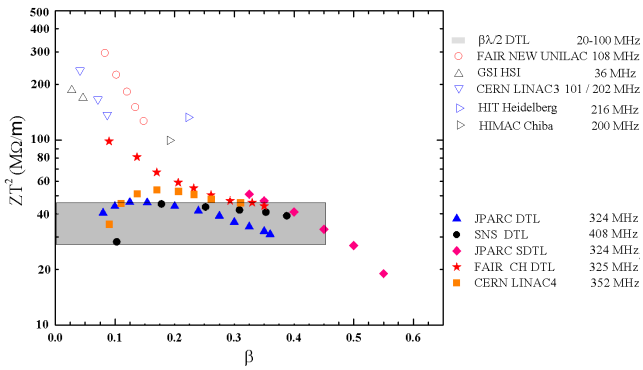

Figure 1: Effective shunt impedance of several ion and proton accelerators as function of the velocity profile.

The IH-DTL, exited in the $TE_{11(0)}$ mode is by far the most efficient RF structure in the β range from 0.01 to 0.2. For $\beta \leq 0.1$ it is competitive with superconducting structures, concerning the plug power demand, even at cw operation. Several IH-DTL are routinely in operation and this structure has established as standard solution for heavy ion in the frequency range between 30 and 200 MHz.

The CH-structure, exited in the $H_{21(0)}$ mode has a larger diameter for a given frequency compared with the IH-structure. Cavities with frequencies from 150 MHz to 3 GHz can be realized, making the CH-structure feasible for proton and ion acceleration up to 100 AMeV. Additionally, the crossbar geometry is so robust to ensure the mechanical stability required for superconducting operation. At present, the s.c CH-DTL is the only multi gap superconducting structure available at low energy.

THE CH-DTL FOR FAIR

The FAIR requirement of a dedicated proton injector pushed an intensive R&D activity in order to explore the capabilities of the room temperature CH-DTL. In 2006 a first test model was successfully built at the University of Frankfurt and later copper plated at the galvanic workshop of GSI. This 340 MHz cavity comprises eight equidistant cells of length $\beta\lambda/2$=45 mm, and was used to test all fabrication steps including welding, copper plating and designing of an efficient cooling system. Moreover, a tuning strat-

Copyright © 2012 by the respective authors — cc Creative Commons Attribution 3.0 (CC BY 3.0)

egy based on exchangeable drift tubes was adopted, and a new geometry based on larger half drift tube was developed to tune the end cells (see Fig.2). This cavity was successfully tested with a 2 kW, cw amplifier.

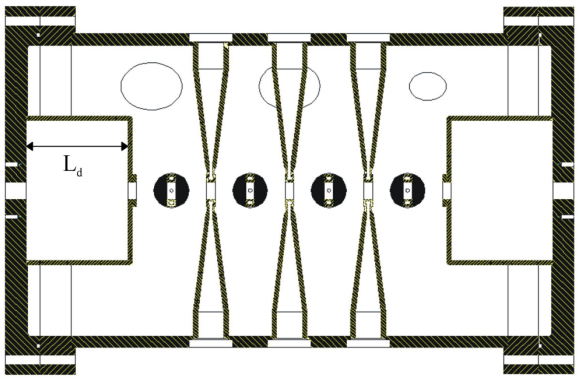

Figure 2: The geometry of the first room temperature CH-DTL.

Later on, the 3 MW 324 MHz klystron developed for JPARC opened new perspectives for the optimization of the CH-DTL. At low energy, the KONUS beam dynamics requires short sections in contrast with the high shunt impedance which favours longer cavities . To overcome this problem a coupling scheme to match one klystron to two CH sections have been developed [8].

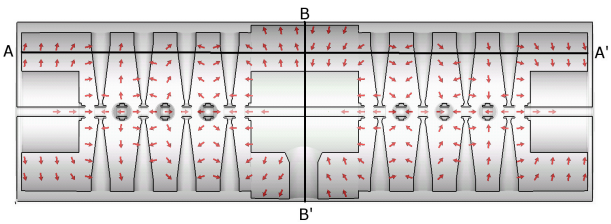

Figure 3: The electric field on the axis of a coupled CH-DTL.

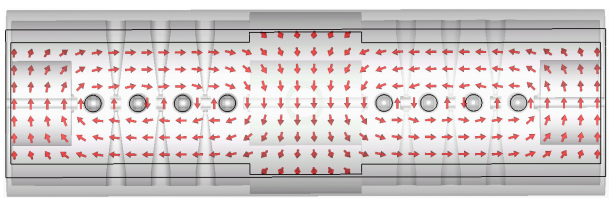

Figure 4: The magnetic field orientation inside a coupled CH. Field is shown in the plane A-A' of Fig.3.

The coupled structure consists of two CH-DTL connected through a single cell resonator. This intertank section oscillates in the Alvarez mode and the large drift tube houses an electromagnetic quadrupole triplet. The radius of the single cell resonator has to be adjusted so that the resonance frequency of this unit matches the adjacent CH cavities. RF simulations have proven that an effective coupling is achieved with this geometry. Fig. 3 and 4 show the distribution of the electric and magnetic field along the coupled structure. In particular, Fig.5 shows how the coupling cell oscillates in a TM mode like the standard DTL.

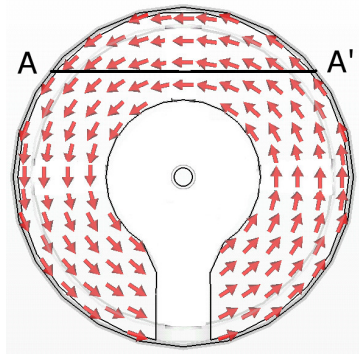

Figure 5: The magnetic field orientation inside the coupling cell. Field is shown along plane B-B' of Fig.3

Successful RF measurements on the scaled model of the second cavity of the FAIR proton injector was the milestone for the construction of the full scale prototype [9].

The main parameter of this structure are listed in Tab.1

Table 1: Main Properties of the second resonator of the FAIR Proton Linac. * indicates that calculation have been performed with a 15% reduced σ.

Energy Range (MeV)	11.7-24.4
RF frequency (MHz)	325.2
Effective Voltage (MV)	13.5
Beam Aperture (mm)	20
Magnet Aperture (mm)	30
Length (m)	2.7
RF Losses*	1.34

The cavity was delivered at the university of Frankfurt in late 2011. In a first step dummy stems and exchangeable drift tube made of Aluminum were mounted inside the cavity. Seventeen provisional tuners were installed along the structure, six in the fist CH, one in the intertank section and ten in the second CH, respectively.

First frequency measurements were in good agreement with simulations. The experimental value of 323.7 MHz is very close to the expected one of 324.4 MHz. The cavity was designed at a lower value with respect the operational frequency of 325.2 MHz to take into account the inductive effect of the tuners.

A measured field distribution along the beam axis is shown in Fig.8 while, Figs.9 and 10 compare the measured voltage with the reference one calculated with LORASR.

At present, stainless steel stems are ready for being welded inside the cavity. Copper plating will be performed in early 2013. The prototype will be then tested with a 3 MW klystron in the dedicated test bench recently built at GSI.

Copyright © 2012 by the respective authors — cc Creative Commons Attribution 3.0 (CC BY 3.0)

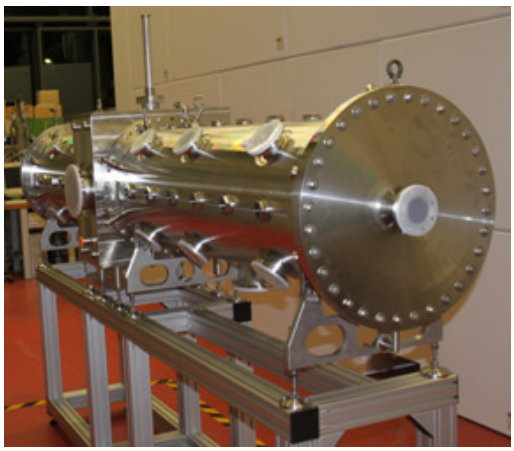

Figure 6: The second resonator of the FAIR proton linac.

Figure 7: The dummy drift tubes.

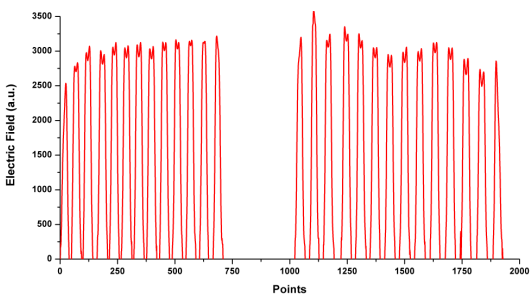

Figure 8: The measured field distribution on the axis.

The Proton Linac

The design of the FAIR proton injector is sketched in Fig.12: up to 100 mA of proton will be extracted from an ECR ion source at 95 keV. The beam is first accelerated by an RFQ to the energy of 3 MeV. After a matching section, the beam enters the first part of the drift tube linac, composed of three pairs of coupled CH-DTLs. At the energy of 37 MeV a 1.6 meter long dedicated diagnostic section is installed.

At that energy, space charge effects are reduced and the KONUS offers the possibility to build long lens free sections. For that reason, the high energy section is based on standard lens free CH cavities with slightly larger beam

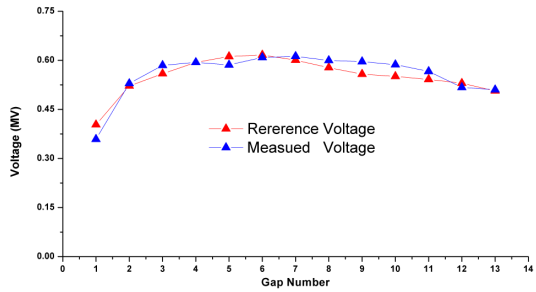

Figure 9: The voltage distribution in the first CH section.

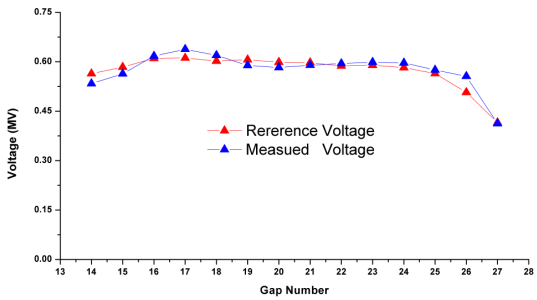

Figure 10: The voltage distribution in the second CH section.

aperture at each cavity ends. In this way the number of quadrupole triplets is reduced and the mechanical and RF design is simplified. Electromagnetic 3D simulations showed that three CH-DTL made of 21 gaps each could cover the energy range from 37 to 70 MeV within an rf power demand around 1 MW per individual cavity.

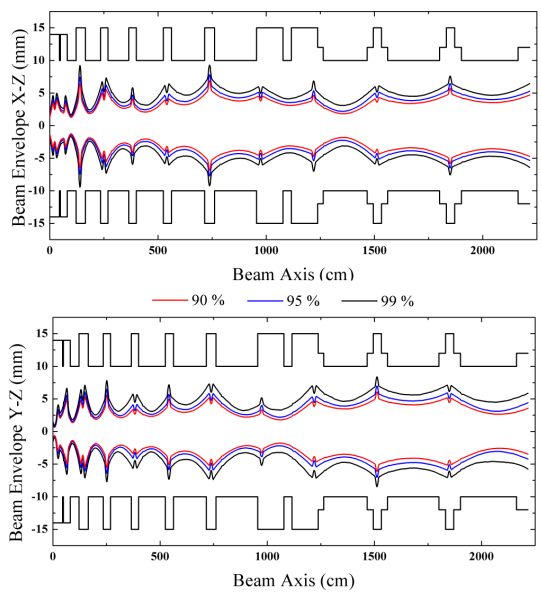

Figure 11: Beam envelope for the FAIR proton linac when 70 mA are injected in the DTL section.

The linac was designed assuming an RFQ output current ranging from 45 to 70 mA using the LORASR code. The

Copyright © 2012 by the respective authors — cc Creative Commons Attribution 3.0 (CC BY 3.0)

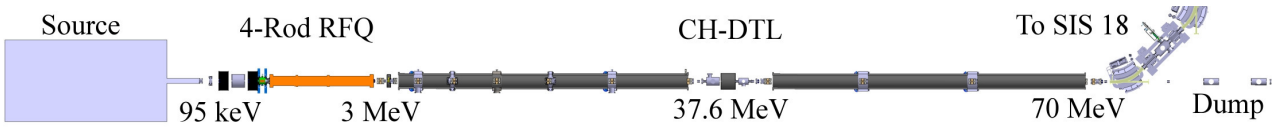

Figure 12: The schematic view of the FAIR proton linac.

Table 2: Beam Evolution of the FAIR proton injector at 70 mA

RFQ Output 95% ϵ X-X', norm. (mm mrad)	1.22
RFQ Output 95% ϵ Y-Y', norm. (mm mrad)	1.14
RFQ Output 95% ϵ ΔW-Φ (keV ns)	9.01
DTL Output 95% ϵ, norm. X-X'(mm mrad)	2.35
DTL Output 95% ϵ, norm. Y-Y' (mm mrad)	2.68
DTL Output 95% ϵ ΔW-Φ (KeV ns)	17

beam envelopes, shown in Fig.11, for the design current of 70 mA shows a large safety margin against beam losses.

Fig.13 presents the emittance including the current stated along the abscissa at the injection point. The red curve is the upper limit for the emittance that the injector, at given current, must provide. This limit is obtained from the foreseen multi-turn scenario and it depends mainly on several synchrotron parameters, such as circumference, injection energy, acceptance and filling factor. For a proper injection the linac emittance must remain below the straight line. This brilliance analysis shows that the best window for an effective injection would be around 55 mA.

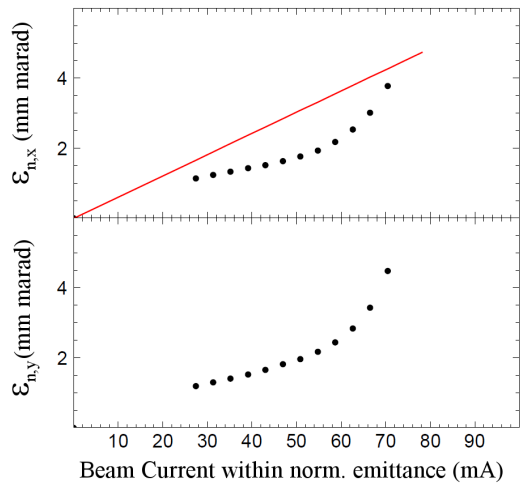

Figure 13: Brilliance analysis at the end of the proton linac in comparison with the synchrotron acceptance.

Finally, Tab.2 shows the beam evolution to the final energy of 70 MeV.

THE CW SHE LINAC

All chemical elements from 107 to 112 have been discovered at GSI.

Table 3: Main parameter of the s.c. cw SHE LINAC

A/q	6
Frequency (MHz)	217
Max. Beam Current (mA)	1
Injection Energy (AMeV)	1.4
Output Energy (AMeV)	3.5-7.3
Length (m)	13

To keep the Super Heavy Element (SHE) program at a competitive level an upgrade of the High Charge Injector (HLI) is ongoing, including a new 28 GHz ECR source and a new cw four-rod RFQ [10].At present, behind the new RFQ the existing IH-DTL injects a 1.4 AMeV beam inside the Alvarez DTL section of the UNILAC.

As the UNILAC should be operated as injector for FAIR, a strong limitation of the beam time for the SHE program is expected. To offer and adequate beam time for the nuclear chemistry program a dedicated linac is request by many scientific users. The design of a low energy cw linac would considerably profit from a multigap superconducting structure. At present, the CH-DTL is the only multigap structure which can be operated as superconducting DTL.

For that reason, a collaboration between GSI, IAP Frankfurt and HIM Mainz worked out a conceptual design based on s.c CH-DTL.

That new linac consists of nine superconducting CH-cavities operated at 217 MHz. The first three cavities accepts the beam from the HLI and perform the first stage of acceleration to 3.5 AMeV. At this point, the energy variable part begins and the final energy can be adjusted up to 7.3 AMeV within an energy spread of $\pm$ 3 AkeV. Beam focusing is provided by seven superconducting solenoids. The general parameters are listed in Table 3.

The demonstrator

The so called *Demonstrator* project includes the construction of the first s.c CH cavity with the s.c. solenois at the cavity ends, and the assembly of the components in the cryostat. A full performance beam test is foreseen at the HLI within 2014 at earliest [11].

The s.c. 217 MHz CH-structure [12] consists of 15 equidistant gaps for a gradient of 5.1 MV/m. The structure, shown in Fig.14, has inner total length is 0.69 m. Optimized field distribution is shown in Fig.15

Nine static tuners, one slow and two fast bellow tuners, will be mounted to ensure the proper frequency matching.

Further rf, mechanical and multipacting simulations are

Copyright © 2012 by the respective authors — cc Creative Commons Attribution 3.0 (CC BY 3.0)

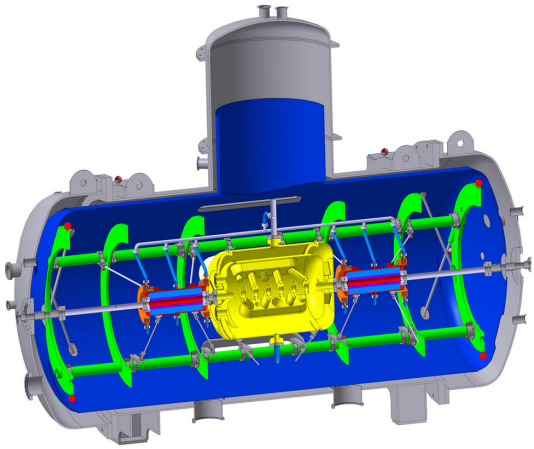

Figure 14: The demonstrator project.

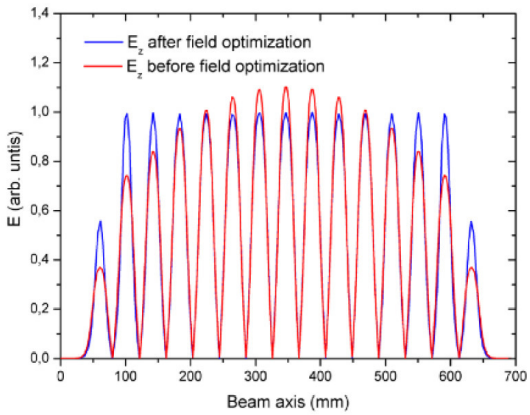

Figure 15: Field distribution of the demonstrator CH-DTL.

in progress at the moment to determine the final geometry of the dynamic bellow tuners.

THE HE LINAC

A new High Energy Linac (HE-LINAC) is presently under discussion at GSI. This new machine has to replace the 90 MV DTL section of the UNILAC.

A first proposal [13] was to increase the prestripper energy to 3 AMeV with 3 IH-DTL. The higher energy would allow generation of U^{37+} which would be further accelerated to 11 AMeV by another 4 IH-DTL.

Recently a less ambitious solution, consisting in the replacement of the Alvarez DTL, is under investigation. Six IH cavities would cover the energy up to 11.4 AMeV in approximatly 25 meter including a new matching section behind the charge separator.

This solution is more cost effective compared to the previous one, and will leave plenty of space available for a future linac upgrade. At the energy of 11.4 the frequency can be raised to 325 MHz and CH cavities could be used to increase the energy. Additionally, alternative solutions to the present gas stripper, like a C-foil or a plasma stripper are under investigation in order to generate higher charge states.

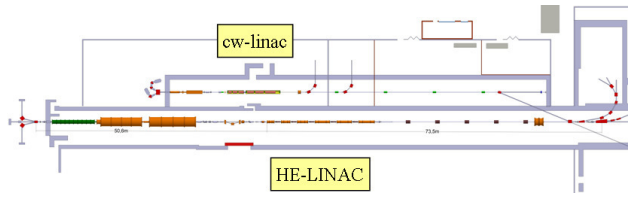

Figure 16: The proposed upgrade of the UNILAC insludig the new HE and SHE linac.

ACKNOWLEDGMENT

The authors would like to express their gratidute to the collegues of the mechanical workshop of IAP Frankfurt and of the galvanic laboratory of GSI. This work has been supported by the Federal German Ministry for Education and Research BMBF-06FY9089I and by HICforFAIR within the LOEWE funding program of the State of Hesse.

REFERENCES

[1] L. Groening et al., “Status of the FAIR Proton Linac” This Proccedings, THPB034.

[2] W. Barth et al, ”The injector system of the FAIR project”, LINAC08, Victoria, BC, Canada, MO204, p.35 (2008)

[3] S.Minaev et al., “Superconducting, energy variable heavy ion linac with constant beta, multicell cavities of CH-type” Phys. Rev. ST Accel. Beams 12, 120101 (2009).

[4] G.Clemente t al., “Development of room temperature crossbar-H-mode cavities for proton and ion acceleration in the low to medium beta range” Phys. Rev. ST Accel. Beams 14, 110101 (2011).”

[5] H.Podlech et Al, ”Superconducting CH structure” Phys. Rev. ST Accel. Beams 10, 080101 (2007).

[6] U. Ratzinger and R. Tiede, ”Status of the HUF RF linac study based on H-mode cavities”, Nucl. Inst. and Meth. in Physics Research A, 415, 1998.

[7] Y.Ywata at al, ”ALTERNATING-PHASE-FOCUSED IH-DTL FOR HEAVY-ION MEDICAL ACCELERATORS”, EPAC06, Edimburgh, UK, WEPCH169, 2328

[8] U.Ratzinger at al, ”A 70-MeV proton linac for the FAIR facility based on CH cavities”, PAC05, Knoxville, TN, USA, TH1004, 526

[9] R.Brodhage at al, ”First Coupled CH Power Cavity for the FAIR Proton Injector”, IPAC11, San Sebastian, Spain, WEPS036, 2565

[10] P. Gerhard et al, this proceedings THPB035

[11] W. Barth et al., “Superconducting CW Heavy Ion Linac at GSI” This Proccedings, TUPB074.

[12] F.Dziuba et al., “Development of superconducting crossbar-H-mode cavities for proton and ion accelerators” Phys. Rev. ST Accel. Beams 13, 041302, 2010

[13] B.Schlitt et al, “Design studies for a new heavy ion injector linac for FAIR” HIAT’11, Chicago,IL, WEC05

Copyright © 2012 by the respective authors — cc Creative Commons Attribution 3.0 (CC BY 3.0)

COMMISSIONING OF A NEW INJECTOR FOR THE RIKEN RI-BEAM FACTORY

N. Sakamoto[a*], M. Fujimaki[a], Y. Higurashi[a], H. Hasebe[a], O. Kamigaito[a],
R. Koyama[b], H. Okuno[a], K. Suda[a], T. Watanabe[a], and K. Yamada[a]
a) RIKEN Nishina Center, Wako, Saitama, Japan
b) Sumitomo Accelerator Service Ltd., Shinagawa, Tokyo, Japan

Abstract

A new injector for the RIKEN RI-Beam Factory (RIBF) was fully commissioned in October 2011. The injector accelerates ions of $m/q = 6.8$ up to 670 keV/u. To save cost and space, a direct coupling scheme was adopted for RF coupling between the DTL cavity and amplifier, based on an elaborate design with the Microwave Studio software package. The new injector has been successfully commissioned and worked very stably for beam service time, increasing the uranium beam intensity by an order of magnitude. Moreover, it is now possible to independently operate the RIBF and GARIS facilities for super-heavy element synthesis.

INTRODUCTION

Role of new injector

Since 2008, the accelerator complex at the RIKEN RI-Beam Factory (RIBF) has provided various heavy ion beams according to the programs of the RIBF experiments. The developed beams so far are polarized- and unpolarized-deuteron, ^{4}He, ^{14}N, ^{18}O, ^{48}Ca, ^{70}Zn, ^{124}Xe and ^{238}U. Among them the experiments of the new RI production require intense beams. Initial experiment using the uranium beams was carried out in November 2008, at 0.4 pnA. This intensity is insufficient for radio isotope production experiments at the RIBF. Our final goal is to realize a 1 pμA beam current for each ion.

The new injector project started because the main injector, the RIKEN Heavy Ion Linear Accelerator (RILAC) [1], was tasked with super-heavy elements (SHE) search [2]. This was a problem because the RIBF experiments could not be performed when SHE search experiments were performed. Also, the beam currents for uranium and xenon beams were unsatisfactory. Therefore we designed and built a new injector, the RIKEN Heavy Ion Linear Accelerator (RILAC2), dedicated for the acceleration of intense uranium and xenon beams to energies of 670 keV/u, which is the injection energy of the RIKEN Ring Cyclotron (RRC) [3].

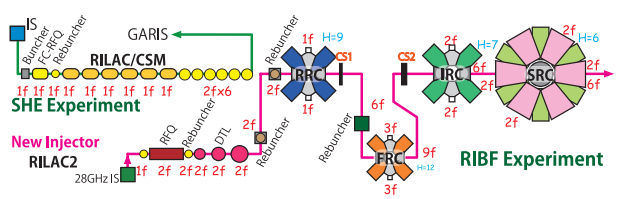

Figure 1: RIBF accelerator complex.

Xe and U acceleration by cyclotron cascades

In RIBF, Xe and U beams are accelerated by cyclotron cascades of RRC, the fixed frequency ring cyclotron (fRC) [4], the intermediate-stage ring cyclotron (IRC) [5], and the world first separate-sector superconducting ring cyclotron (SRC) [6]. In this scheme shown in Fig. 1, the intense $^{238}U^{35+}$ beams from the ion source can be accelerated by the RRC without charge stripping, before injection to the RRC. Using the stripper after the RRC, the charge state is converted to 71+ at an energy of 10.75 MeV/u for injection into the fRC. Then $^{238}U^{71+}$ beams are accelerated using the fRC with velocity gain of about 2 to suit the injection energy of the IRC. Before injection to the IRC, the charge state is converted to 86+.

For uranium, the first stripper (CS1) utilizes a 0.3 mg/cm^2 carbon foil and the stripping efficiency is about 18%. The second stripper (CS2) utilizes 17$\sim$19 mg/cm^2 carbon foil, and the stripping efficiency is about 33%. Owing to the heat load by the intense beams, these efficiency values go down with increased beam dose.

To maximize the average current, the stripper foils are changed frequently, typically 2 or 3 times/day. To increase the beam current, the stripper foil lifetime must be extended.

Injection to RRC

The beams from the RILAC2 are injected into the RRC. Layout of the key devices of the RRC is shown in Fig. 2. The function of the isochronous cyclotron is to increase the velocity of ions by the ratio of the extraction radius to the injection radius. The velocity gain of the RRC is four and the energy of the extracted beams is 10.75 MeV/u. In the case of $^{238}U^{35+}$ acceleration, the magnetic rigidity is 3.2 T·m, which is 91% of the maximum value of the RRC. The operating dee-voltage of the resonator is about 60 kV. The resonators of double-gap type with a dee angle of 23.5° provide 230 kV/turn acceleration voltage with a harmonic number of 9, resulting the total number of revolutions of 325. The gap between turns at the extraction radius is only 5.5 mm, excluding the effect of betatron motion. Therefore beam loss during cyclotron acceleration is prone to occur in the electrostatic deflection channel (EDC). Acceleration

* nsakamot@ribf.riken.jp

Copyright © 2012 by the respective authors — cc Creative Commons Attribution 3.0 (CC BY 3.0)

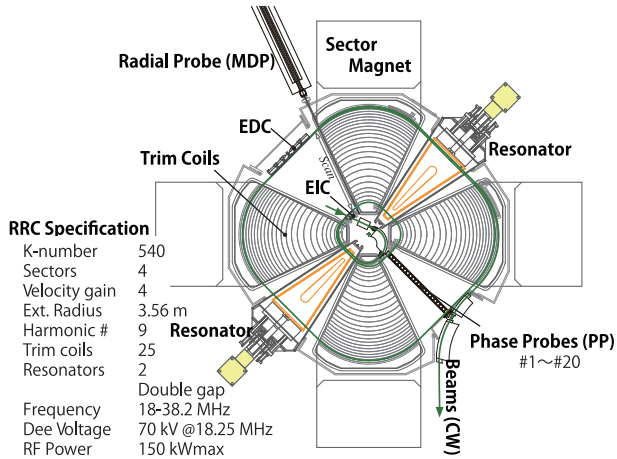

Figure 2: Layout of RRC showing injection and extraction orbits and diagnostic devices of radial-probes and 20 set of phase-probes.

voltage error is required to be within $\pm 0.1\%$ amplitude and $\pm 0.1^\circ$ phase, because unstable acceleration voltage causes fluctuations in the beam orbit and size [7]. As an injector of cyclotrons, stability of the RILAC2 RF system is required so that the injection timing of the beams remains within the acceptance of the cyclotron RF.

NEW INJECTOR RILAC2

Overview

As RILAC2 was to be installed in the remaining space of the AVF cyclotron hall, a compact design was needed. The picture after installation is shown in Fig. 3a.

The RILAC2 consists of a superconducting ECR ion source (SC-ECRIS), low-energy beam transport line (LEBT), prebuncher (BUN), RF quadrupole linac (RFQ), rebuncher, drift tube linac (DTL), and high-energy beam transport line (HEBT). Figure 5 shows a schematic of the RILAC2. While the prebuncher is operated at the fundamental frequency of 18.25 MHz, RFQ and DTL cavities

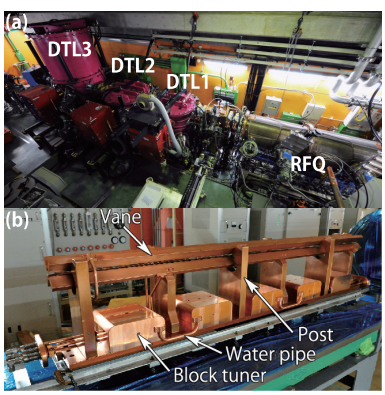

Figure 3: Pictures of RILAC2. (a)The RILAC2 accelerators installed in the AVF hall.(b)Resonator of RFQ showing the tuner blocks for frequency modification.

are operated at the second harmonic.

Superconducting ECR ion source

A new SC-ECRIS was designed and constructed to provide uranium beams 100 times more intense than those from the RIKEN 18-GHz ECRIS at RILAC [8]. Owing to the set of six solenoid coils, the plasma volume is as large as 1100 cm^3 and it is able to produce various magnetic field distribution on axis, which is both of classical B_{min} and so-called "flat B_{min}" [9]. Beam commissioning was performed in 2008 using a 18 GHz microwave power source. Last year, a new 28 GHz gyrotron power source was introduced, aiming for much higher intensity. The achieved intensities for $^{124}Xe^{25+}$ and $^{238}U^{35+}$ are 250 eμA and 60 eμA, respectively. The value 60 eμA is 30-fold that of the 18-GHz ECRIS.

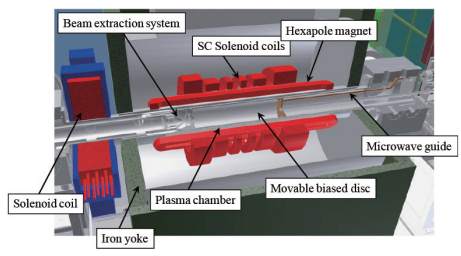

Figure 4: Cut view of SC-ECR.

RFQ Linac and Drift Tube Linac

Table 5 summarizes the design parameters of the RFQ linac and the DTL.

The RFQ linac is based on the four-rod structure. The cavity was originally developed by Nissin Electric Co., Ltd. [10]. While the original cavity had a resonant frequency of 33.8 MHz and accelerated m/q = 16 ions up to 84 keV/u in continuous wave (CW) mode, this was later modified to have a resonant frequency of 36.5 MHz and to accelerate m/q = 6.8 ions up to 100 keV/u [11]. The modification was made by adding tuner blocks between the posts which support the vanes (Fig.3b). The wall loss of the tuner blocks was estimated as 2 kW in total with the designed inter-vane voltage of 42 kV. The unloaded Q value was about 80% of ideal. The main amplifier is based on the tetrode (EIMAC 4CW50,000E) which is basically the same as that for the RILAC injector RFQ [12]. The RF power is fed through a capacitive coupler which matches the input impedance of the cavity to 50 Ω. The maximum output power is 40 kW. Owing to its relatively low frequency, the RFQ has a large focusing strength (B) of 6.8 with 42 kV inter-vane voltage, which is provided with only 18 kW RF power. The maximum modulation (m) is 2.35.

The main accelerator part of the RILAC2 is a drift tube linac (DTL) with newly designed cavities. These cavities operate in CW mode as same as RFQ. As minimization of the installation space was required, the cavities were based

Copyright © 2012 by the respective authors — cc Creative Commons Attribution 3.0 (CC BY 3.0)

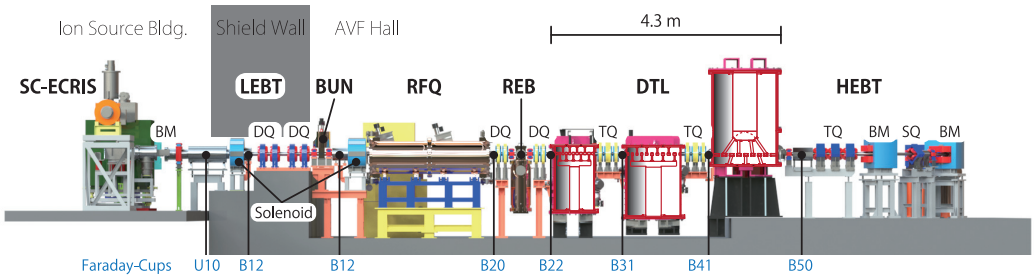

Figure 5: Side view of RILAC2 (DQ: Doublet Q lens; TQ: Triplet Q lens; SL: Solenoid magnet).

Table 1: Design parameters of RFQ and DTL.

	RFQ	DTL1	DTL2	DTL3
Frequency (MHz)	36.5	←	←	←
Duty (%)	100	←	←	←
m/q	6.8	←	←	←
E_{input} (keV/u)	3.28	100	220	450
E_{output} (keV/u)	100	220	450	670
Aperture (mm)	8*	17.5	17.5	17.5
Gap Number	-	10	10	8
Voltage(kV)	42	110	210	260
ϕ_{sync} (deg.)	-29.6**	-25	-25	-25
$P_{wall\ loss}$ (kW)	18	7	13	20

* Mean aperture (r_o), **Final synchronous phase.

the quarter-wavelength structure with a resonant frequency of 36.5 MHz, twice the 18.25 MHz beam frequency. The DTL cavities are directly coupled to amplifiers without using long coaxial lines, further compacting the DTL structure. The DTL cavities were carefully designed to accommodate the significant frequency change due to direct coupling of the tetrode (EIMAC 4CW50,000E) [13]. The coupling was designed by using Micro Wave Studio (MWS) under the following assumptions: that the Q of the actual cavity is 78% of ideal; that the resonant frequency of the cavity itself as obtained from the calculation using MWS is 75 kHz less than that of the actual cavity; that the capacitance of the tetrode is 55 pF; and that the load resistance of the tetrode is ∼700 Ω.

Low-power tests were carried out with the actual DTL cavity coupled with the amplifier (Fig. 6). In the case of DTL3, the resonant frequency of the cavity was about 0.1% higher than that of the calculation by MWS package. The unloaded Q value was 78% of ideal. The position and the size of the coupling disk of the coupler were determined by measuring $|S_{11}|$ using a network analyzer. Afterward, the coupler position was finely tuned by performing high-power tests.

When the first excitation of the DTL3 cavity by pulsed-power from the amplifier, the RF power was completely reflected due to multipactoring. After 24 hour conditioning with pulsed-power, it was observed that the pickup signal of the cavity was gradually developed. Subsequently, we

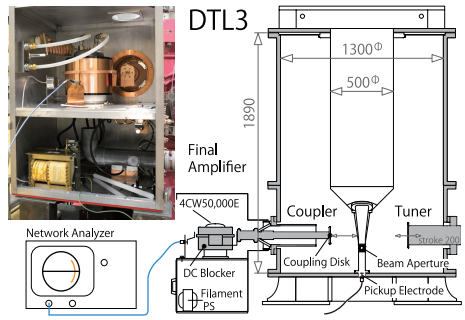

Figure 6: Setup of low-power test showing amplifier is directly coupled to DTL cavity through a capacitive coupler.

changed the conditioning power mode to CW operation, in which a large ratio of the reflection was allowed, and the gap voltage increased up to 35 kV in the first 15 minutes overcoming of levels of multipactoring.

Long-term test was performed measuring the amplitudes and the phases of the cavities continuously using commercially available RF lock-in amplifiers (SR844). The monitor system [14] is useful for determining whether the RF-feedback system works normally or not. The low-level circuit, which consists of auto-gain control and phase-lock, is based on analog feedback. The long-term stability of the amplitude and the phase of the RFQ and DTL cavities are $|\Delta V/V| \leq 0.1\%$ and $\Delta\phi \sim 0.1°$, respectively (Fig. 7).

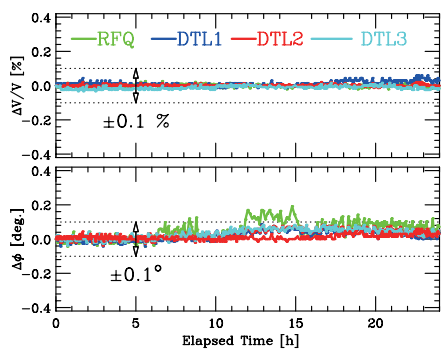

Figure 7: Amplitude and phase errors over 24 h.

.

Copyright © 2012 by the respective authors — cc Creative Commons Attribution 3.0 (CC BY 3.0)

BEAM COMMISSIONING

Acceleration test

Since the first beam of ^{124}Xe was successfully accelerated on Dec. 12, 2010, production of ^{124}Xe and ^{238}U beams has been repeatedly performed. Beam tuning was made starting with design parameters and fine adjustment was performed to maximize the beam transmission efficiency. As a result of the work described in Ref. [15], the transmission efficiency of RILAC2 has recently improved to 70∼80% (Fig. 8a). The beam energy was tuned by changing voltages and phases in the RILAC2 RF systems to 670 keV/u, as confirmed by the TOF method.

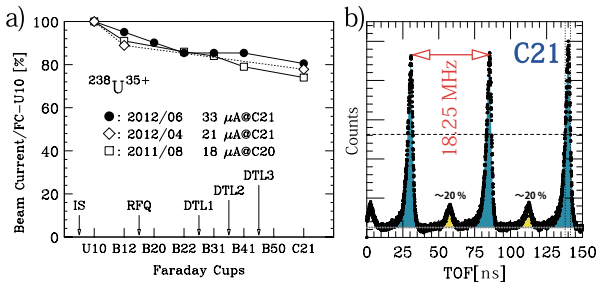

Figure 8: a) Ratio of beam current, as measured by Faraday cups, to IS. b) TOF spectrum at C21.

As shown in Fig. 8b, a prebuncher converts DC beams to bunched beams with frequency 18.25 MHz. Bunching efficiency is typically 80%, the remainder (denoted by yellow hatch in Fig. 8b) lost at RRC injection. In the case of ^{238}U^{35+}, if 75% of the 60 eμA beams from the ion source are accelerated by RILAC2 and RRC transmission efficiency of 80% is achieved, the beam current at the RRC is about 1 pμA, which corresponds to 2.6 kW. Because the cooling of the EDC stands less than 300 W, the extraction efficiency better than 90% is desirable.

The intensity and TOF timing of the beams are continuously monitored by detecting a signal from pickup electrodes induced by bunched beams. Figure 9 shows changes in the PP-S71 pickup signal over 24 hours. The longitudinal acceptance of the RRC is about ±3° in the RF phase. The corresponding timing is ±0.2 ns. Owing to stable operation of the RF system of the RILAC2 and the double rebuncher system (B7 and S6) downstream of the RILAC2, beam intensity and injection timing were stable enough for injection to the RRC (see Fig. 10). .

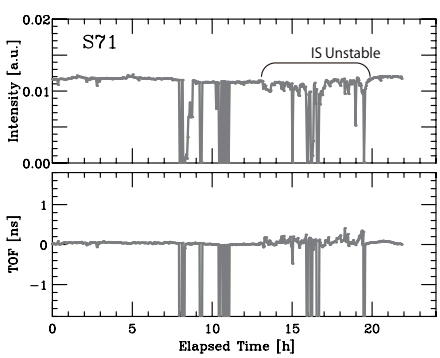

Figure 9: Measured intensity and timing at S71.

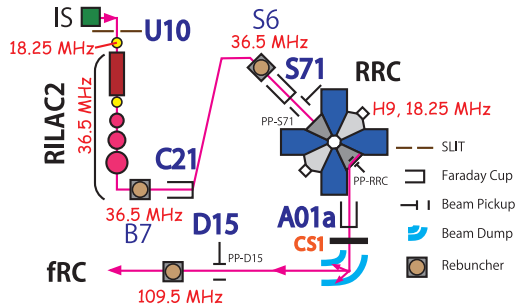

Figure 10: Schematic layout of acceleration with RRC.

Commissioning to RIBF

To date, RILAC2 has provided ^{238}U and ^{124}Xe beams for nuclear physics experiments at the RIBF, as listed in Table 2. During beam service time, RILAC2 operation has been very stable and the break time resulting from the rf down time of RILAC2 was less than 0.3% of the total scheduled beam service time. Nonetheless, maximizing the beam current on target requires elaborate tuning, and transmission efficiency of the RRC was as low as 50∼60%, as obtained from the ratio of measured current of A01a to that of S71.

Due to bunching efficiency, 20% of beams are lost at RRC injection. To extract the accelerating beams with 100% efficiency, beam-turns must be separated at EDC. The turn-pattern of beams circulating in the cyclotron is measured using a differential probe. Figure 11 shows data measured during ^{124}Xe beam service time in 2012. The turn separation at the extraction radius was particularly poor. Experimentally, the turn pattern was measured by cutting the beam at the exit of IS in horizontal and vertical directions, using a set of slits at U10 (Fig.11b). Nonetheless, the separation obtained remains imperfect.

The poor turn separation is partly due to the low voltage of the acceleration cavity. It is difficult to increase the voltage because the 18.25 MHz operation frequency is the lower limit of the cavity, and the tuners are very close to the dee electrode. The turn separation cannot be obtained if the beam's longitudinal emittance from RILAC2 does not match the acceptance of RRC. This problem has not yet been solved.

Table 2: Beam production for RIBF using RILAC2.

Nuclei	Beam Service Time	RRC out	SRC out
^{238}U	17/10/11∼ 07/12/11	0.3 pμA	3.5 pnA
^{124}Xe	11/12/11∼ 18/12/11	0.7 pμA	15 pnA
^{124}Xe	16/06/12∼ 05/07/12	1 pμA	24 pnA

RRC out:FC-A01a, SRC out:FC-G01.

Copyright © 2012 by the respective authors — cc Creative Commons Attribution 3.0 (CC BY 3.0)

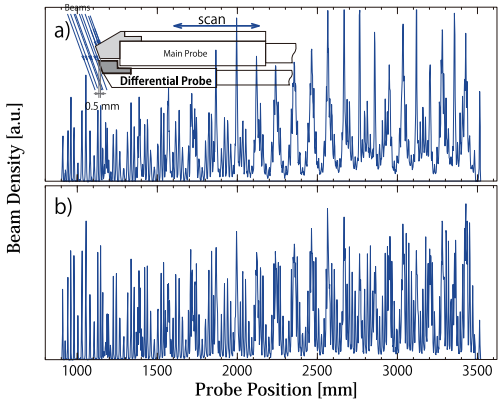

Figure 11: Turn pattern of the circulating beams in RRC. a) U10 slits were set ±5 mm in horizontal and vertical directions. b) ±1 mm and ±2 mm in horizontal and vertical directions, respectively.

Lifetime of charge strippers

Although the transmission efficiency of the RRC remains unsatisfactory, the beam current from the RRC has been greatly improved. As already reported in Ref. [16], the lifetime of the carbon stripper foil was as short as 0.5 days with 4 eμA beams during beam service time in December 2009. Exchanging the stripper foils requires several hours, and due to differences in their thickness, the RF-phase of following accelerators must be retuned. Since the beam intensity at FC-A01 was expected to exceed 10 eμA last year, we have developed carbon nanotube/sputter-deposited carbon (CNT-SDC) foil on a rotating cylinder system [17]. Its rotational speed was 0.05 revolutions per minute. It worked very well over the beam service time in December 2011, the lifetime being 4∼5 days with the maximum beam current of 3.5 pnA at the SRC. This intensity was 4-fold than in December 2009.

For ^{124}Xe acceleration, it is necessary to strip the charge from 19+ to 46+ using a fixed carbon foil. The beam intensity on the stripper foil in June 2012 was about 18 eμA. The frequency of the foil exchange was 3 times/day. Due to the heat load of energy loss at the foil, the foil became significantly thinner within a few hours. The intensity and the timing of the stripped ^{124}Xe beams observed at D15, which is located about 34 m downstream from the stripper, were gradually decreased and advanced as shown in Fig. 12. The beam intensity at the SRC was 24 pnA to the maximum.

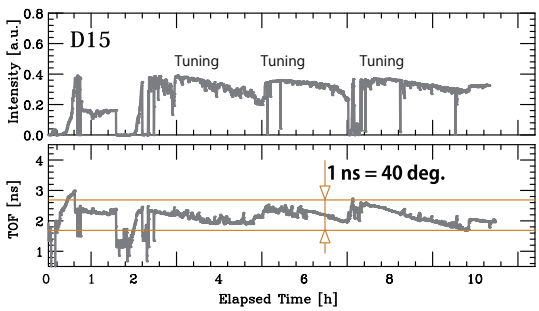

Figure 12: Intensity and timing change at D15.

SUMMARY AND PLANS

In December 2011, ^{238}U beams were successfully provided from RILAC2 and accelerated to 345 MeV/u for a beam service time of 50 days. The reliability fo the rf part of the RILAC2 was more than 97.7% during the beam service time listed in Table 2. Because it is no longer realistic to use carbon foils, we are now preparing a gas stripper system with He [18] for the beam service time scheduled this fall. The gas stripper system with N_2 is also useful for Xe acceleration. In addition, the beam chamber of the analyzing magnet downstream from the charge stripper (see Fig. 10) has been equipped with a beam dump, allowing it to withstand a 10 kW beam load.

ACKNOWLEDGEMENT

The authors thank the staff of Sumitomo Heavy Industries Ltd. for their contributions towards construction of the RILAC2. The authors also thank the operators of the Sumitomo Accelerator Service Ltd. for their cooperation in beam commissioning.

REFERENCES

[1] M. Odera et al., Nucl. Instrum. and Methods A227(1984)P187.
[2] K. Morita et al., J. Phys. Soc. Jpn. 78, 064201(2009).
[3] Y. Yano, CYCLOTRONS'92, Vancouver, p102(1992).
[4] T. Mitsumoto et al., CYCLOTRONS'04, Tokyo, p384(2004).
[5] J. Ohnishi et al., CYCLOTRONS'04., Tokyo, p197(2004).
[6] H. Okuno et al., CYCLOTRONS'04, Tokyo, p373(2004).
[7] W. Joho, "Tolerances for the SIN RING-CYCLOTRON", SIN REPORT TM-11-4(1968).
[8] T. Nakagawa et al., J. Phys. Coc. Jpn. 78, 064201(2009).
[9] G. D. Alton and D. N. Smithe, Rev. Sci. Instrum. **65**, 775(1994).
[10] H. Fujisawa, Nucl. Instrum. and Methods A345(1994)23.
[11] K. Yamada et al., IPAC'10, Kyoto, MOPD046, p.789(2010);K. yamada et al., LINAC'10, Tsukuba, TUP070, p.572(2010).
[12] O. Kamigaito et al., Rev. Sci. Instrum. **70**, 4523(1999).
[13] K. Suda, "Coupling of amplifier to drift tube linac cavities of the injector RILAC2 for RIKEN RI Beam Factory", these proceedings.
[14] R. Koyama et al., EPAC'08, Genoa, p1173(2008).
[15] K. Yamada et al., IPAC'12, New Orleans, TUOBA02, in print.
[16] O. Kamigaito et al., Cyclotrons'10, Lanzhou, TUM2CIO01.
[17] H. Hasebe et al., 26th World Conference of the International Nuclear Target Development Society, Mainz, Aug. 2012.
[18] H. Imao et al., 26th World Conference of the International Nuclear Target Development Society, Mainz, Aug. 2012.

Copyright © 2012 by the respective authors — cc Creative Commons Attribution 3.0 (CC BY 3.0)

FRANZ – ACCELERATOR TEST BENCH AND NEUTRON SOURCE

O. Meusel, L.P. Chau, M. Heilmann, H. Podlech, U. Ratzinger, K. Volk, C. Wiesner
IAP, University Frankfurt/Main, Germany

Abstract

Accelerator based neutron sources are used for different kinds of research programs in nuclear astrophysics, material science and for the development of next generation nuclear power plants. The challenge of existing and planned neutron sources is to provide highly brilliant ion beams with high reliability.

The Frankfurt neutron source FRANZ is not only a neutron source but also a test bench for novel accelerator and diagnostic concepts for intense ion beams. The experiment consists of a compact linear accelerator for the acceleration of an intense proton beam to 2MeV producing neutrons via the ^{7}Li(p,n) reaction. The final beam intensity will be 200mA. Therefore the space charge and space charge compensation effects can be studied with high statistical significance along the accelerator.

The hot filament-driven gas discharge ion source already delivers 240mA beam current with a proton fraction of 92%. The low energy beam transport LEBT section is equipped with four solenoids matching the beam into a chopper system and into a RFQ-IH combination already under construction. Coupling of the RFQ accelerator stage and the IH drift tube cavity offers the possibility to use only one power amplifier as a driver for both of these resonators and reduces investment costs. The compact design of the low-β accelerator stage is optimized for high beam intensities to overcome the expected strong space charge forces in this accelerator test bench.

The presentation will give a brief overview of the FRANZ accelerator and discusses the beam dynamics, comparing numerical and experimental results.

INTRODUCTION

To advance the development of accelerator technology a dedicated test bench was needed. Different work groups are now able to test their devices under realistic conditions with respect to the interplay of each of the accelerator components. The main focus of the planned experiments is to reach the intensity and power limits for conventional RF accelerator technics. The question of these limits is highly relevant for several future accelerator projects and the basis of next generation accelerator concepts.

It is planned to use a proton beam with beam energies of 2MeV with energy variation of about ± 0.2MeV. These parameters enable various experiments by the use of thermal neutrons produced by the ^{7}Li(p,n) reaction at the end of the accelerator test bench. Therefore an astrophysical research program was launched for the measurement of neutron caption cross sections relevant for nucleo synthesis [1].

Figure 1 shows the scheme of the experimental setup of the FRANZ facility. It consists of a high voltage terminal faciliating ion source operation, a low energy beam transport section including a chopper system, the main accelerator, a bunch compressor and target stations. Two operation modi for the experiments will be available. The compressor mode will deliver a 1ns beam pulse with a repetition rate of 250 kHz and an estimated peak beam current of 9.6A. The activation mode uses a cw beam to produce a continuous neutron flux. Because of the average power density the proton beam in activation mode is limited to a current of about 8 mA for the use of solid targets and up to 30 mA for liquid metal targets.

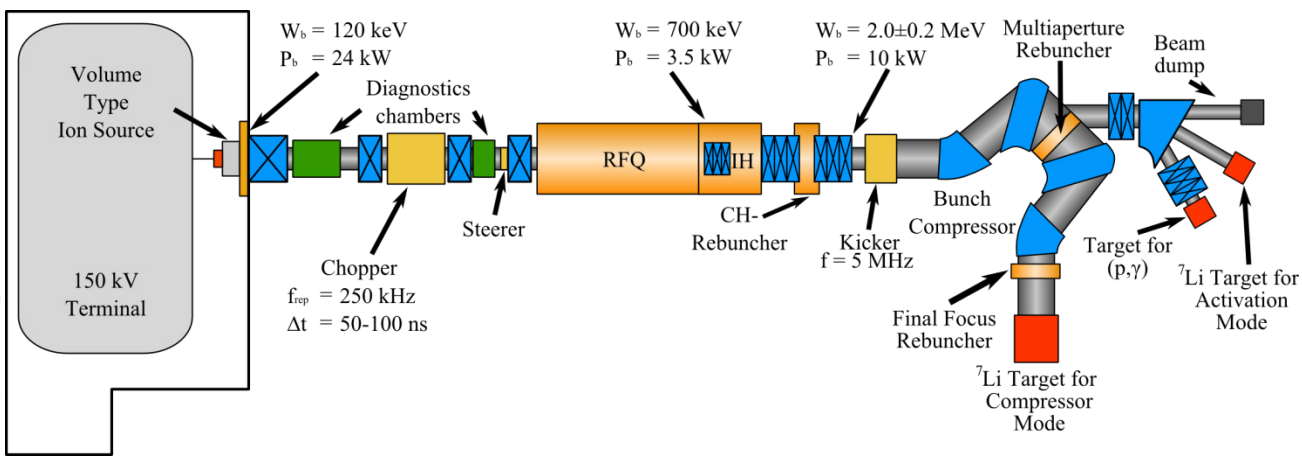

Figure 1: Experimental setup of the FRANZ facility. The accelerator test bench and neutron source consist of a 2MeV proton accelerator equipped with bunch compressor and several target stations.

Copyright © 2012 by the respective authors — cc Creative Commons Attribution 3.0 (CC BY 3.0)

ION SOURCE

A volume type ion source was chosen for FRANZ to extract the proton beam from a hot filament driven gas discharge plasma [2]. Figure 2 shows the design of the ion source. The life time of the filament is limited to about one month of operation. On the other hand the plasma temperature of a gas discharge at moderate arc power as well as the confining magnetic field is very low compared with other source types e.g. ECR sources. Therefore the beam emittance is small and gives the possibility to investigate causes of emittance growth during beam transport and acceleration along the whole test bench.

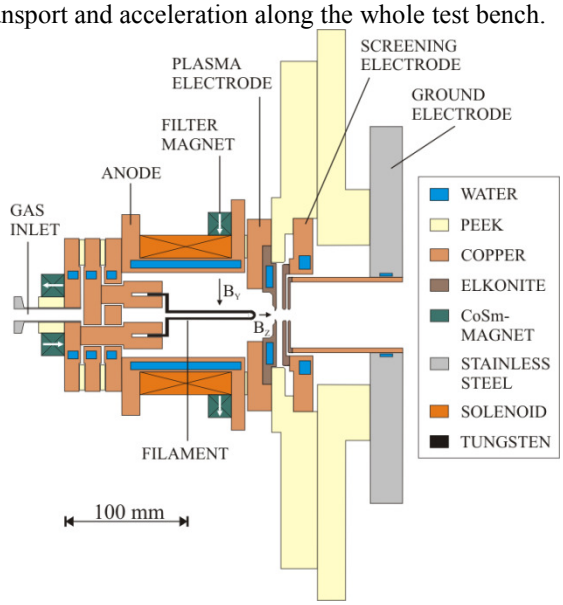

Figure 2: Crossectional view of the volume type ion source under construction.

Numerical simulations using of the IGUN code [3] show that for the planned beam intensities a triode extraction system keeps quite well the beam emittance during the extraction phase when compared with other extraction schemes [4]. The simulations for the extraction and beam transport were performed for multi species beam with measured fractions H^+ = 91%, H_2^+ = 7%, H_3^+ = 2%.

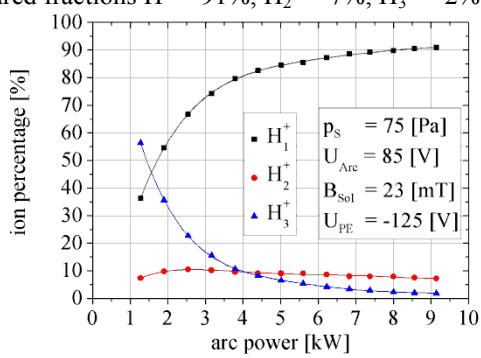

Figure 3: Measured beam composition as a function of the arc power.

The chosen aspect ratio of S = 0.61, an emission area of 0.5 cm^2 and an extraction field strength of 6.2 kV/mm result in a simulated beam radius of r_{beam} = 5.5 mm, ε_{rms} = 0.085 π mm mrad and a divergence angle of r' = 84.5 mrad. The measured total beam current was 261mA.

LEBT SECTION WITH CHOPPER

The LEBT section consists of 4 solenoids for beam focussing and includes partial of space charge compensation due to residual gas ionisation. Figure 4 shows a scheme of the planned LEBT. The first and second solenoid will be used for separation of ion species and to match the proton beam into the chopper system. Downstream of the chopper two solenoids will focus the beam into the acceptance of the RFQ. Two pumping and diagnostic tanks will be used for several non interceptive diagnostics e.g. optical beam profile measurement and beam potential measurements using a residual gas ion energy analyzer.

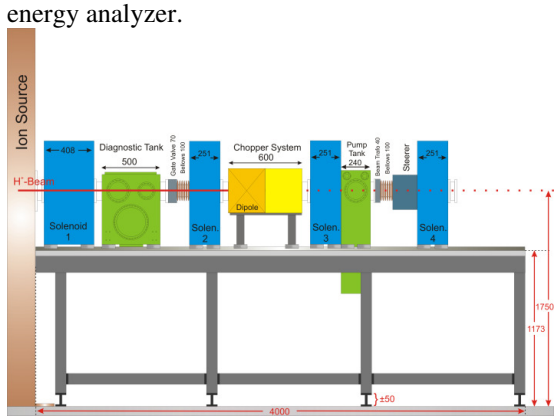

Figure 4: Scheme of the LEBT section with four solenoids and the chopper device.

The chopper system consisting of a pulsed Wien filter combined with a massless septum provide the 100 ns proton beam pulses. Figure 5 shows the arrangement of the chopper system.

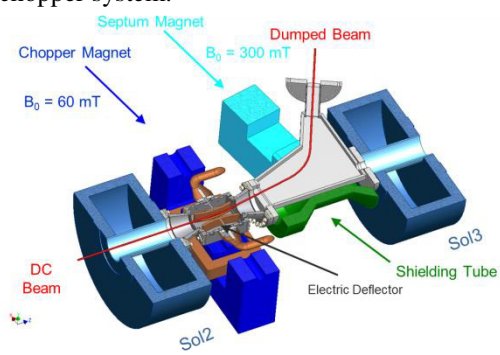

Figure 5: Cross sectional view of the chopper system consisting of a pulsed ExB filter, a septum magnet with magnetic shielding tube and an apertur.

A fast electric kicker compensates the magnetic force of the static chopper magnet with a repetition rate of 250 kHz. The massless septum consisting of a septum magnet and a shielding tube provides the post separation and a pulse with a flat top of at least 50 ns. Numerical simulation of the ExB chopper system shows an influence of secondary electrons. The high production rate of

Copyright © 2012 by the respective authors — cc Creative Commons Attribution 3.0 (CC BY 3.0)

electrons in the chopper system gives the possibility for partial space charge compensation of short beam pulses. Preliminary studies result in approximately 30% of space charge compensation by the use of a these device. For the electric deflector the secondary electrons bear the risk of sparking and sputtering from the electrodes. Therefore the shortening tubes will be used as screening electrodes. Beam transport and chopping leads into an emittance growth by a factor of 4. It seems possible to reduce this value further by optimization of beam transport with respect to the filling degree of the solenoids and a detailed description of space charge compensation. Pulsed beam with proton densities of $n_p = 8.2 \times 10^{14}$ m^{-3}, generalized perveance of $K = 3.1 \times 10^{-3}$ will be injected in the coupled RFQ-IH accelerator.

COUPLED RFQ-IH DTL

In order to minimize installation costs and to use one compact common rf amplifier a coupling of the RFQ and IH-DTL is planned [4]. Figure 6 shows a crossectional view of the coupled accelerator stages. Both of the cavities can also be used separately. The RFQ is 1.75 m long and needs an input power of 150 kW. Numerical simulations using the PARMTEQM code show a beam transmission of 95% with acceptable emittance growth at the design current I = 200 mA for an electrode voltage of about 75 kV. Output energy of the RFQ will be 0.7 MeV. The IH-DTL will boost the proton beam to its final beam energy of 2 MeV. The power consumption of the IH cavity is in a range of about 45 kW to establish a gap voltage of 300 kV. Due to the fact that a RFQ acts like a buncher, the incoming proton beam will also be compressed longitudinally. Beam transport simulation show the micro bunch phase width is in the range of 60 degree. The average bunch current increases up to 1.2A and the resulting compression ratio is $\eta = 6$.

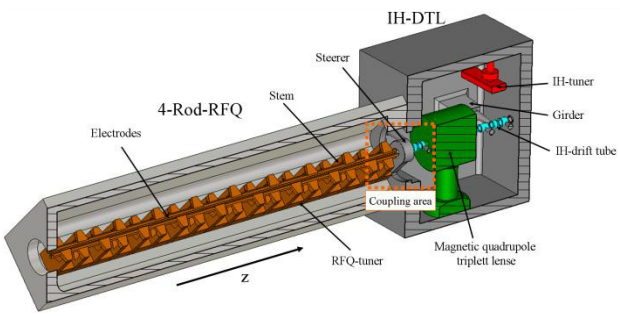

Figure 6: Cross sectional view of the coupled RFQ-IH accelerator.

BUNCH COMPRESSOR

By applying the bunch compressor concept of the Mobley type for high current beams a split magnetic dipole array include edge focusing was chosen. The periodic deflection by the RF kicker at one focus of the bending system guides up to 9 bunches on different paths to the final focus, where the neutron production target is located. As shown in figure 7 two rebuncher cavities are needed to focus the beam longitudinally.

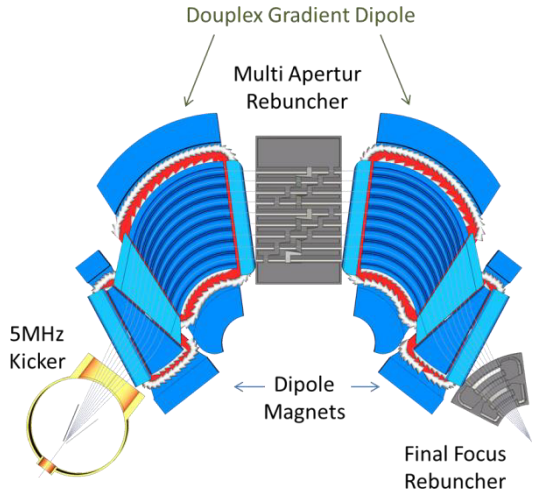

Figure 7: Scheme of the Mobley type bunch compressor.

By choosing adequate parameters all 9 bunches will overlap at the target and produce a 1.1 ns proton pulse with a proton density of $n_p = 8.2 \cdot 10^{14}$ m^{-3}. Space charge forces become dominant, the generalized perveance is $K = 2.2 \cdot 10^{-3}$. Figure 9 shows the bunch current as a function of time, the peak current is 9.6 A. The compression ratio downstream of the whole proton injector is of $\eta = 48$.

CONCLUSIONS

In a first step the beam current will be limited up to 50mA. Detailed multi particle transport simulations show that the activation mode using a 30 mA cw beam will be limited by the rf power consumption, target power deposition and radiation safety. The compression ratio of the compressor mode is 48. The resulting proton density and space charge force leads into increasing beam spot sizes and pulse duration at the ^{7}Li(p,n) target. Right after the first measurement period an intensity upgrade on 150mA and later on 200mA is planned.

REFERENCES

[1] R. Reifarth et al., “Opportunities for Nuclear Astrophysics at FRANZ”, Publications of The Astronomical Society of Australia - PUBL ASTRON SOC AUSTRALIA , vol. 26, no. 3, 2009
[2] K. Volk and W. Schweizer private communication
[3] C. Wiesner et al., "A 250 kHz Chopper for Low Energy High Intensity Proton Beams", Proc. of the Eur. Part. Acc. Conf., Genua (2008).
[4] L. P. Chau et al., “Bunch Compressor for Intense Proton Beams”, Publications of The Astronomical Society of Australia - PUBL ASTRON SOC AUSTRALIA , vol. 26, no. 3, 2009

Copyright © 2012 by the respective authors — cc Creative Commons Attribution 3.0 (CC BY 3.0)

ACCELERATOR/DECELERATOR OF SLOW NEUTRONS

M. Kitaguchi, KURRI, Osaka, Japan
Y. Arimoto, KEK, Ibaraki, Japan
P. Geltenbort, ILL, Grenoble, France
S. Imajo, Y. Iwashita, Kyoto University, Kyoto, Japan
Y. Seki, RIKEN, Saitama, Japan
H. M. Shimizu, Nagoya University, Aichi, Japan
T. Yoshioka, Kyushu University, Fukuoka, Japan

Abstract

An accelerator/decelerator for slow neutron beams has been demonstrated. The energy of a neutron can be increased or decreased by flipping the neutron spin (directly coupled to magnetic dipole moment) in magnetic field. This device is a combination of a gradient magnetic field and an RF magnetic field. Test experiments were performed by using very slow neutrons at High-Flux Reactor at Institut Laue-Langevin. Acceleration and deceleration for focusing of neutrons at the detector position was observed. Focusing neutrons enables us to transport the neutrons while maintaining density from source to experimental position. This will be a powerful technique for measurement of the permanent electric dipole moment of neutrons, which require a high density of neutrons.

INTRODUCTION

Particle accelerators have continually evolved since their invention, and nowadays are applied not only in physics experiments but also in various fields such as medical science. The properties of the beam should be optimized for each use by accelerating, decelerating, focusing and/or defocusing. Recently the neutron beam becomes important as a probe for new science including particle physics with extremely high precision. Although the ray of neutrons has been handled by some optical devices, for example, mirrors and lenses, it is impossible to control the velocity by the electric field used in an ordinary accelerator because the neutron is an electrically neutral particle. A neutron accelerator which manipulates the velocity has the advantage that experiments can be performed with high precision.

One of the most useful applications of the neutron accelerator is space-time focusing. In the case of pulsed neutrons, during transport of the neutrons to the experimental area, the neutron pulses spatially spread as some neutrons travel faster whereas some travel slower. The density decreases according to the velocity spread of the neutron pulse. When fast neutrons are magnetically decelerated and/or slow neutrons are accelerated properly in the middle of the transport, these neutrons can reach the experimental area at the same time (Fig. 1) [1, 2, 3, 4]. The density can be kept from the source to the arrival position by focusing. This enables us to utilize instantaneous-intense pulsed neutrons in order to suppress the systematic errors for some experiments which require dense neutrons, for example, search for neutron electric dipole moment (nEDM) to reveal the origin of matter in the universe. Although experimental searches have been pursued in the world [5, 6, 7, 8, 9], the nEDM has not yet been observed. The present upper limit is $|d_n| < 2.9 \times 10^{-26} e\mathrm{cm}$ (90% C.L.) [9], which is very close to the predictions of some physics beyond the standard model of particle physics, for example, supersymmetry. Using the space-time focusing and high power pulsed neutron source, we can improve experimental sensitivity by one or two orders of magnitude to search for nEDM.

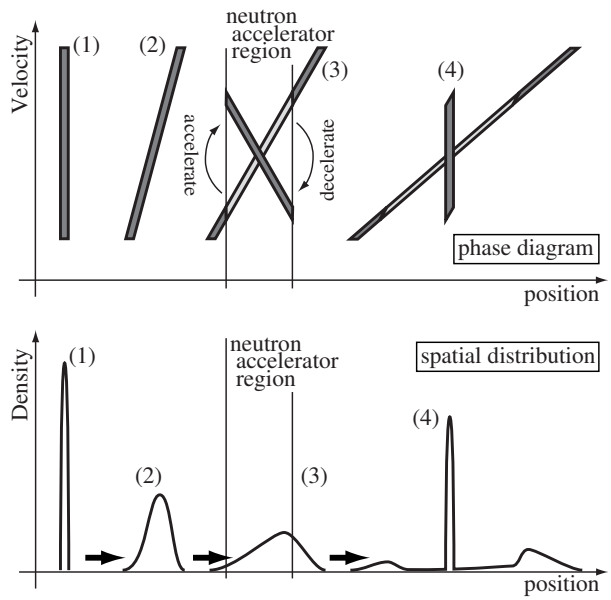

Figure 1: Concept of space-time focusing by using neutron accelerator. (1) Neutrons are generated as a pulse. (2) Neutrons spread spatially during transport. (3) Neutrons are accelerated/decelerated properly. (4) Some neutrons are focused at the experimental position. This figure illustrates the behavior of polarized neutrons.

Copyright © 2012 by the respective authors — cc Creative Commons Attribution 3.0 (CC BY 3.0)

NEUTRON ACCELERATOR FOR FOCUSING

For the acceleration/deceleration of neutrons, we can utilize flipping of neutron spin in magnetic field. Although this change is too small to be used for the focusing of fast neutrons, it is enough to realize the focusing with very slow neutrons. Such slow neutrons which have the kinetic energy of less than about 200 neV, called as ultracold neutrons (UCNs), are used in nEDM experiments. In this demonstration, we use adiabatic fast passage method (AFP), which is one of the spin flippers [12]. When a neutron passes through an RF magnetic field in the surrounding static field with smooth gradient, the neutron's spin flips with energy gain or loss corresponding to spin polarization. The change of the neutron kinetic energy is written as $2\mu B$, where B is the magnetic field at the spin flip position and μ is magnetic dipole moment of neutron. After the magnetic field, the velocity becomes into $\sqrt{v^2 \pm 2\mu B/m}$ from the incident velocity of v, where m is neutron mass and $\pm$ is represented gain and loss of the energy. In the case of deceleration, the time of flight of a neutron with the initial velocity v is written as

$$T = \int_0^{L_f} \sqrt{\frac{m}{2(E_0 - \mu B(z))}}\, dz + \int_{L_f}^{L} \sqrt{\frac{m}{2(E_0 - 2\mu B(L_f) + \mu B(z))}}\, dz, \quad (1)$$

where L_f is spin flip position, L is detector position and $E_0 = mv^2/2$ is initial kinetic energy of the neutron. When we select L_f for each velocity of the neutron properly, the time of flight can be kept constant. Because the spin flip occurs under the resonance condition, which is written as

$$\hbar\omega = 2\mu B(L_f), \quad (2)$$

where ω is the frequency of RF field, changing the frequency can be utilized to select the spin flip position (Fig. 2). There is a time lag for arriving at the spin flip position for each velocity, therefore, the frequency is represented as a function of time $\omega(t)$, which can be calculated the equations above numerically when T and $B(z)$ are given. The AFP spin flipper with time-changing RF frequency is required for focusing of neutrons.

We made the prototype of the magnetic accelerator in order to demonstrate the space-time focusing. A closeup view of the accelerator system is shown in Fig. 3. This consists of a compact static magnet to generate the gradient field with 1 T at the maximum and an RF coil to generate the resonance RF field. The change of neutron kinetic energy corresponding to 1 T is 120 neV, The magnet has anisotropic inter-poles in order to generate a homogeneous gradient of the magnetic field along the direction of neutron beam (Fig. 4) [13, 14]. The strength of the field decrease from 1 T to 0.5 T in 20 cm. The RF coil is an one-turn coil with length of 20 cm, which covers the gradient of the static field (Fig. 5). The RF frequency can be

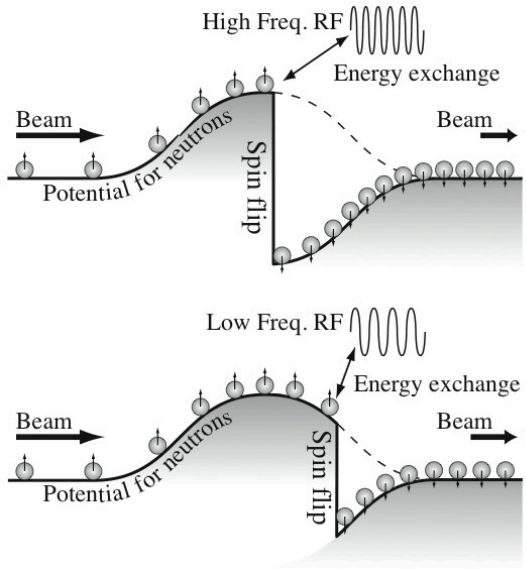

Figure 2: Control of deceleration by using AFP spin flipper with variable frequency RF. Top and bottom shows large and small deceleration respectively.

modulated automatically from 30 MHz to 15 MHz by using electric circuits with variable capacitors and a signal generator (Fig. 6). The control of the capacitors selects the spin flip position L_f, which can be synchronized with the neutron pulse. The RF power is supplied by a wideband amplifier with 1 kW output.

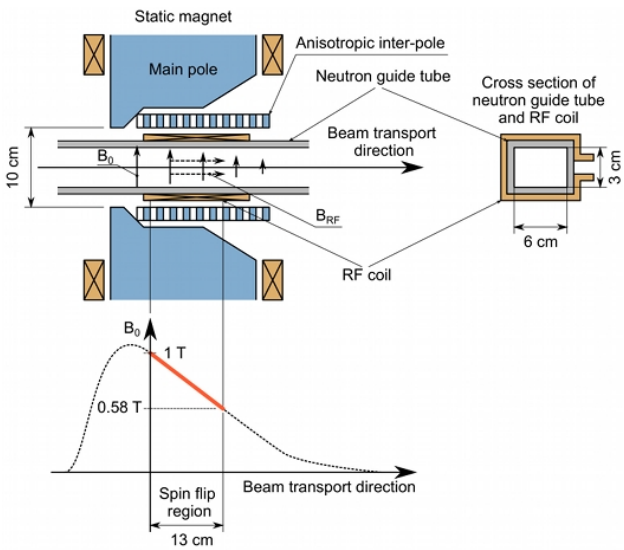

Figure 3: Closeup view of the magnetic accelerator system together with the illustration of the magnetic field gradient in the beam transport direction.

Copyright © 2012 by the respective authors — cc Creative Commons Attribution 3.0 (CC BY 3.0)

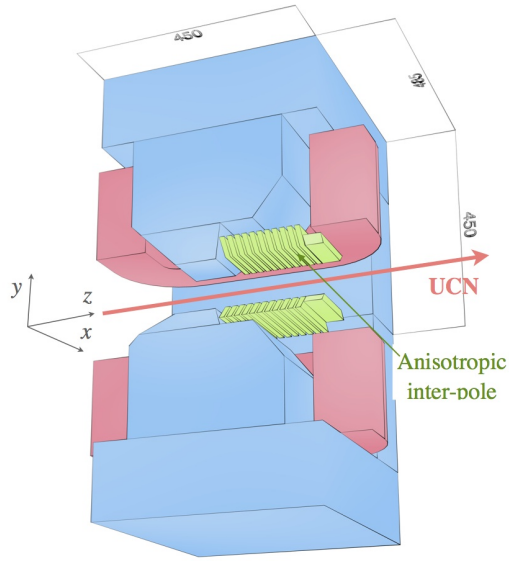

Figure 4: Magnet with anisotropic inter-poles.

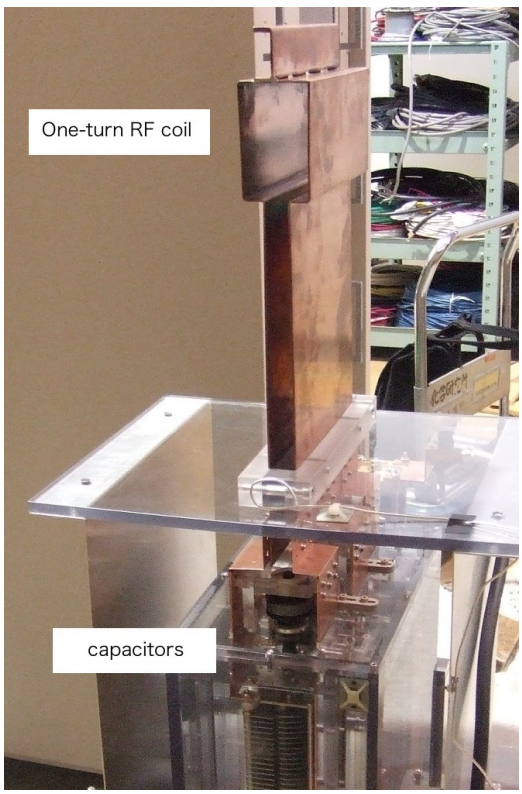

Figure 5: One-turn coil for RF and capacitors.

EXPERIMENTS AND RESULTS

The space-time focusing experiment was performed at the PF2 TES beam line in the High Flux Reactor at Institut Laue Langevin. The whole experimental setup is shown in Fig. 7. Very slow neutrons including UCNs were provided

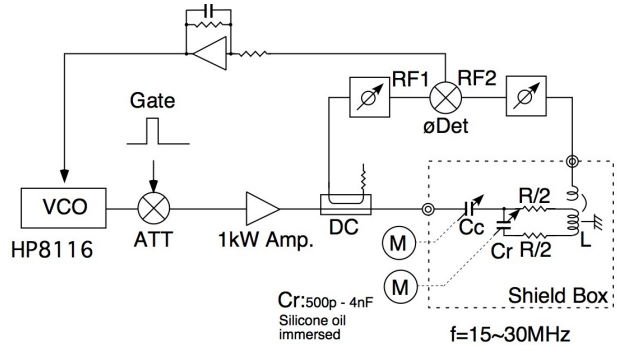

Figure 6: Electric circuit to match the resonance condition of RF.

from the turbine, which decelerates the neutrons from the reactor by using continuous reflections off rotating mirrors [15]. A mechanical shutter is used to supply pulsed neutrons. The shutter opened for 20 ms once every 2 s. A neutron-absorbing cadmium pipe is inserted just before the shutter in order to reduce the number of reflections by limiting the neutron divergence. A neutron detector, which is a ^{3}He gas detector, is set at 5.6 m downstream from the shutter. The neutrons were transported with reflections off the mirror inside the guide tube. The size of the guide is 6 cm in vertical and 3 cm in horizontal. The guide consists of assembled glass plates with nickel coating, which has high reflectivity for neutrons. Since we are going to accelerate/decelerate neutron velocity only in the transport direction, non-specular reflection at the guide surface should be suppressed as much as possible. The glass plates were polished and aligned parallel enough to keep the velocity in the transport direction. The measurements of the neutron velocity distribution through the guide tube were consistent with the simulations without non-specular reflections at the surfaces. The static magnet and RF coil were arranged midway between the shutter and the detector. The RF coil was wound to the guide tube.

We measured the TOF spectrum of the neutrons through this setup for two cases. The RF was ON and OFF. The

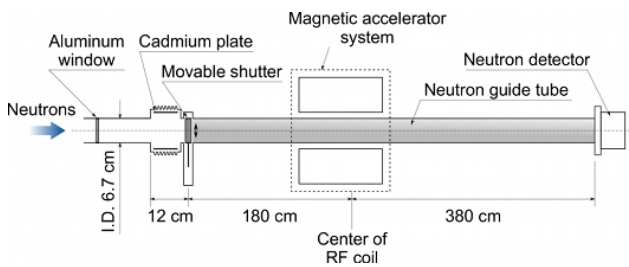

Figure 7: Experimental setup. Neutron accelerator is installed in the middle of the guide tube. The RF and data acquisition systems are synchronized with the shutter operation.

Copyright © 2012 by the respective authors — cc Creative Commons Attribution 3.0 (CC BY 3.0)

static magnetic field is constantly applied throughout the experiments. In the case of RF-OFF, the spins of the neutrons are not flipped and the net velocities are not changed before and after the static magnet. In the case of RF-ON, the RF field is applied only when neutrons with velocity from 5.7 m/s to 5.0 m/s reach the accelerator position. This caused the partial change of the shape of the TOF spectrum, which enables us to compare the case of RF-ON to that of RF-OFF easily. In the arrival time-lag of 80 ms between the neutrons of the velocity range, the frequency of the RF is swept from 28.6 MHz to 17.5 MHz, which are corresponding to 120 neV and 70 neV of the energy exchange respectively. For this demonstration, the variable capacitor were moved with the constant speed as the approximation of the frequency function $\omega(t)$. The measurement time was about 4 h for both cases. The measured TOF spectra are shown in Fig. 8. The top and bottom histograms represent the cases of RF OFF and ON, respectively. The lines show the Monte Carlo simulations with and without focusing. The non-specular reflections at the guide surfaces are not considered in these simulations. For RF-ON case, the line is calculated with spin flip efficiency of 0.5. Both of the observed histograms are in good agreement with the simulations. The ratio of these two histograms is shown in Fig. 9. The decelerated neutrons focused at the time between 1.2 s and 1.4 s can be seen. The loss of constant energy makes only defused spectrum and can not make the excess indicated in the figure.

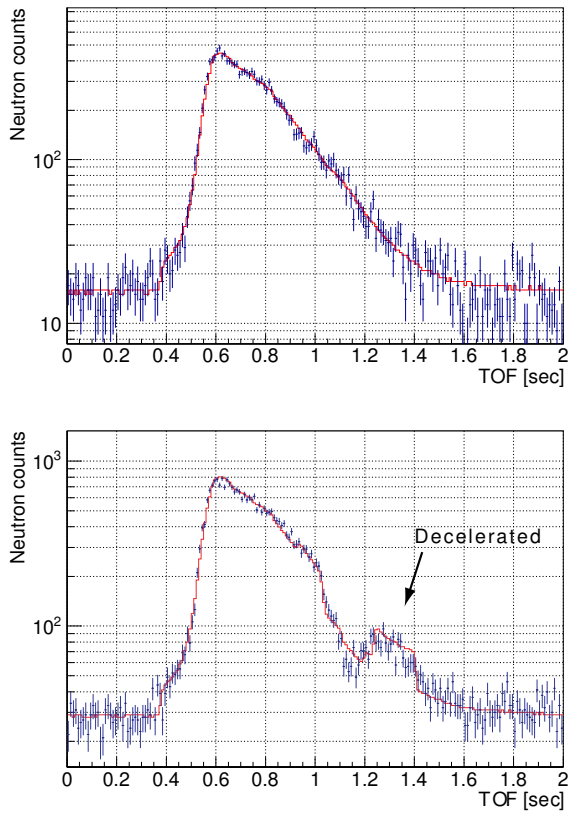

Figure 8: Neutron TOF spectra. Top and bottom show the case of RF OFF and ON respectively. Lines show the simulations.

CONCLUSION

We have successfully developed the accelerator/decelerator for slow neutrons and demonstrated neutron space-time focusing for transport of UCNs with keeping density. The results are in good agreement with simple simulations with controlling the velocities of neutrons [16]. The efficiency of the spin flip was low, however, this can be improved with the amplitude of the RF field.

This result shows the feasibility of neutron accelerator for effective transport of UCNs for various experiments. The neutrons can be gathered only in the experimental area at the focus time. When a shutter at the entrance of the experimental area closes just after the injection of the focused pulse, the UCNs can be localized only in the experimental area with high density without spreading in the guide tubes. The combination of this device and a highly-instantaneously-intense pulsed source, for example, SNS and J-PARC, enable us to utilize neutrons most effectively. It should be mentioned that the excitation current of our magnet and its stray field is constant during the experiment in contrast to the method mentioned in reference [3]. This is fairly advantageous to nEDM experiments, which requires an extremely precise magnetic field control. The constant excitation of the magnet eases a quick modulation of the accelerating energy. In addition, since this device can manipulate the longitudinal phase space distribution of the neutrons flexibly, it can adjust not only the time

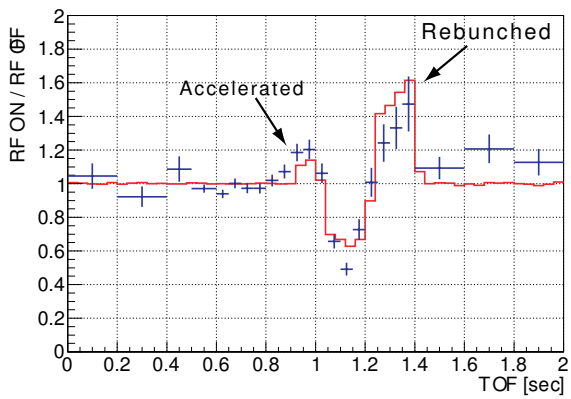

Figure 9: The ratio of these two TOF histograms. Line shows the simulation with focusing.

Copyright © 2012 by the respective authors — cc Creative Commons Attribution 3.0 (CC BY 3.0)

structure but also the energy distribution, suggested in reference [1, 2]. These features widen the application of this system. We are now planning the new nEDM experiment using this focusing technique at J-PARC [17].

ACKNOWLEDGMENT

We would like to thank T. Brenner for the intensive and helpful assistance during the experiment. This work is supported by the Grants-in-Aid for Scientific Research of the Ministry of Education of Japanese Government under the Program No. 19GS0210, No. 23244047, the Quantum Beam Fundamentals Development Program of the MEXT, and Yamada Science Foundation.

REFERENCES

[1] J. Summhammer, L. Niel, and H. Rauch, Z. Phys. B62, 269 (1986).

[2] L. Niel and H. Rauch, Z. Physik B74, 133 (1989).

[3] A. I. Frank. and R. Gähler, Phys. At. Nucl. **63**, 545 (2000).

[4] H. M. Shimizu, Y. Iwashita, M. Kitaguchi, K. Mishima, and T. Yoshioka, Nucl. Instr. and Meth. **A 634**, 55-27 (2011).

[5] J. Simith, E. M. Purcell and N. F. Ramsey, Phys. Rev. **108**, 120-122 (1957).

[6] W. B. Dress, P. D. Miller, J. M. Pendlebury, P. Perrin, and N. F. Ramsey, Phys. Rev. D **15**, 9-21 (1977).

[7] K. F. Smith, et al., Phys. Lett. B **234**, 191-196 (1990).

[8] I. S. Altarev et al., Phys. Lett. B **276**, 242 (1992).

[9] C. A. Baker, et al., Phys. Rev. Lett. **97**, 131801 (2006).

[10] B. Alefeld, G. Badurek, and H. Rauch, Z.Physik B41, 231 (1981).

[11] H. Weinfurter, et. al., Z.Physik B72, 195 (1988).

[12] A. Abragam, *Principles of Nuclear Magnetism*, Oxford University Press, Oxford (1961).

[13] Y. Arimoto, et al., Physica Procedia **17**, 20-29 (2011).

[14] Y. Arimoto et al., IEEE Trans. Appl. Supercond. **22** 4500704 (2012).

[15] A. Steyerl et al., Phys. Lett. A **116**, 347 (1986).

[16] Y. Arimoto, et. al., Phys. Rev. A **86**, 023843 (2012).

[17] Proposal to J-PARC, http://j-parc.jp/jhf-np/pac_1001/pdf/KEK_J-PARC-PAC2009-11.pdf

Copyright © 2012 by the respective authors — cc Creative Commons Attribution 3.0 (CC BY 3.0)

EMITTANCE CONTROL FOR DIFFERENT FACET BEAM SETUPS IN THE SLAC LINAC*

F.-J. Decker, W. Colocho, N. Lipkowitz, Y. Nosochkov, J. Sheppard, H. Smith, Y. Sun, M.-H. Wang, G.R. White, U. Wienands, M. Woodley, G. Yocky, SLAC, Menlo Park, CA 94025, USA

Abstract

The linac beam at SLAC requires different setups for different users at the FACET (Facility for Advanced aCcelerator Experimental Tests) area, like highly compressed, intense bunches, or lower charge, long bunches. These require typically a lengthy tuning effort since with an energy-time correlation (or "chirp") the bunch transverse wakefield kicks can be compensated with dispersive trajectory oscillations and vice versa. Lowering the charge or changing the bunch length will destroy this delicate balance. Besides the typical steering to minimize BPMs (Beam Position Monitors) with correctors, we applied different techniques to try to localize beam disturbances like dispersion with phase changes, RF-kicks and RF quadrupole fields turning a klystron off and on, or varying the phase, and finally wakefield kicks with different beam intensities. It is also important to quantify BPM to quadrupole offsets with "bowtie" plots and that the correctors give the expected kicks with orbit response matrix measurements.

INTRODUCTION

Good transverse beam emittances at different places along the SLAC Linac get typically achieved in the following way. The beam gets steered relatively flat (< 0.5 mm) using BPMs (Beam Position Monitors) and then with a lengthy tuning scheme, linac oscillations or bumps are introduced which minimize the emittance measured with wire scanners. Over the years this process typically achieved small emittance growth numbers of 50 to 100% over the initial values of 30 and 2.5 mm-mrad for x and y, so 50 by 5 mm-mrad was expected for the FACET beam in Sector 20.

Typically twice that amount and often more was only achieved. There are a few explanations (excuses) which could cause this. The typical beam rate was 10 Hz, so tuning was three times slower than at 30 Hz. The FACET chicane needed special attention, so linac tuning was cut short. And the final spot sizes after the chicane and final focus were about the same, like 30 μm, even if the emittance just in front of the chicane changed by a factor of three (300 → 100 mm-mrad in x), discouraging further linac tuning.

Additionally, frequent user requested beam changes in current and bunch length made it necessary to tune the beam emittances up again, which would make it even trickier for smaller emittances. It is assumed that the main root cause for this is that after just steering flat the initial emittance is as high as 1200 mm-mrad, and the subsequent tuning cancels this with equally large corrections. When these cancelations are not local, or are charge / bunch length dependant, small say 10% variations will create 10% of 1200 mm-mrad = 120 mm-mrad.

So the goal is to localize and reduce emittance increasing effects. For that we try to find and categorize all possible mechanisms, like dispersion, wakefield, RF-kicks, and develop procedures like special steering methods and component alignment.

Goal: Get Linac closer to good emittances with BPMs etc. so the tuning part is less.

1. BPMs
2. Correctors
3. Quads (old BBA: straight orbit)
4. BPM-to-Quad: bowtie plot or Quad change
5. Corrector strength (LOCO, R12 meas.)
6. Lattice (Quad) strength: Oscillation data
7. RF-kicks: a) sin-cos, b) dipole-quadrupole-lens
8. Measure dispersion
9. Measure with different charge (wakefield)
10. Measure with different bunch lengths
11. Others

The different methods (numbers in ( ) below) and their relevance are discussed in the following sections.

STEERING TECHNIQUES

Steering the beam to the center of a BPM (1) gets the beam down the linac relatively fast, but usually ends up with big beam emittances. Additionally we can look at the corrector (2) values along z and check for certain patterns, e.g. stronger values with + – + might indicate a BPM with a big unreal offset. With our "SVD Steering" we can adjust a gain parameter to prefer BPMs (gain high) or correctors (gain low), but this method just supports what is believed more correct.

The next step is also using the quadrupole (3) strengths in a way to get a straight trajectory. When a BPM reading is say Δx =1 mm and the corrector strength is cor = 0.03 kG-m, the two can be compared by dividing cor by the quadrupole strength Q = 20 kG: cor/Q = 1.5 mm. So the beam gets more bend up by the corrector than the $Q\Delta x$ bends it down (focussing magnet). Figure 1 shows an example where the orbit was steered flat (below 0.3 mm) but its corresponding cor/Q-values are up to 1.3 mm. This led to a global alignment of the Linac of up to 7 mm [1]. Equalizing the two locally will give a straight non-bend beam orbit and therefore no dispersion is generated. But an offset in a BPM might indicate also an offset in the RF nearby structure, causing wakefield kicks.

*Work supported by U.S. Department of Energy, Contract DE-AC02-76SF00515.

Copyright © 2012 by the respective authors — cc Creative Commons Attribution 3.0 (CC BY 3.0)

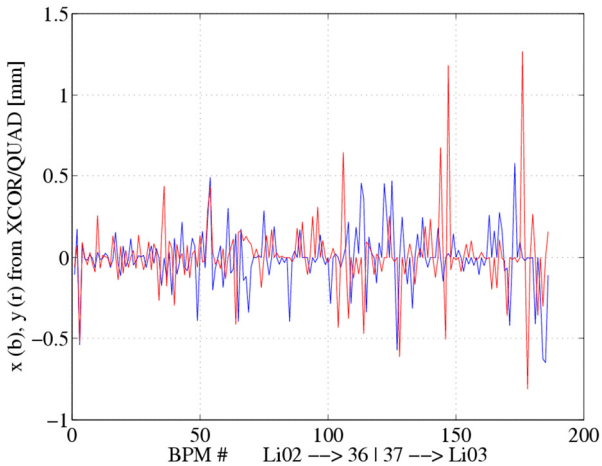

Figure 1: The absolute orbit is steered flat, but the corresponding corrector/quadrupole values for x (blue) and y (red) indicate big bending around 145.

BEAM BASED ALIGNMENT

Besides the global alignment of the Linac using optical targets inside the accelerator supporting light-pipe, there are several methods using the beam to find misalignments and then fix them. The last paragraph indicates already one such approach. Instead of steering so that $\Delta x = cor/Q$ we can align the quadrupole and accelerator locally by moving it in the $+x$ direction by Δx and putting the corrector to zero. This was done in a few places and needs to be done at all locations. But before doing this we need to be sure that the values of Δx, *cor*, Q are correct.

The BPM reading Δx can have an offset x_{off} with respect to the quadrupole and this can be measured with the beam by the bowtie-scan method (4). By varying one corrector in front of the quadrupole and measuring the effect of a downstream BPM for two different quadrupole settings versus the BPM inside the quadrupole you get a bowtie-like plot where the center of the bowtie gives the BPM offset x_{off}. This method is very lengthy requiring a few setting for each quadrupole setting and again for the other plane y. A faster but not as precise method is using just the difference orbit for the two different quadrupole settings and using the focussing model (R12s) to determine the kicks in x and y at the same time. This method should be about ten times faster and will allow us to get the BPM offsets for all BPMs in quadrupoles.

Checking the corrector strengths (5) is next and done typically by varying a corrector over a certain range that the beam is not lost and then the response matrices R12s from the corrector (point 1) to downstream BPMs (points 2) are compared to the expected from the model. When everything is aligned the exact values are not too critical since the correctors are close to zero, but to get there and for steering and for making closed three-corrector bumps (see below) it is helpful to have the right values.

The lattice or quadrupole strength (6) can be check with oscillation data, where two correctors in x, x' and two in y, y' generate oscillations which then can be fitted with expected behaviour calculated with the model. Figure 2

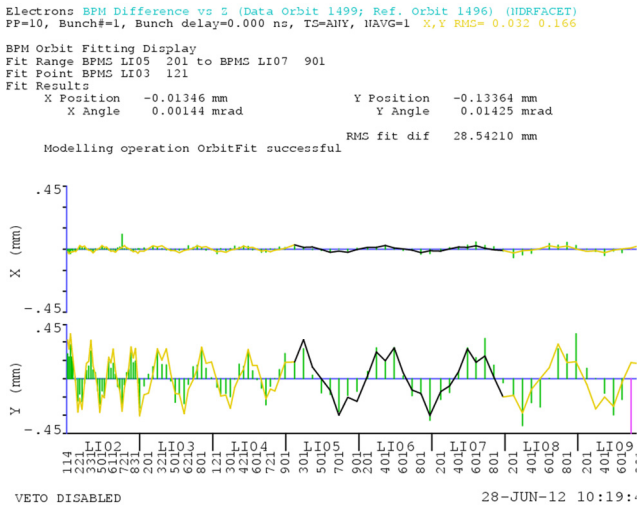

Figure 2: Oscillation data in y, at Li07 501 there seems to be an additional kick pointing to a weaker quadrupole.

shows an example where there seems to be a 15% weaker quadrupole at Li07 501. A wider grid scan can point out nonlinearities, while a few more corrector settings can trace out the design matched beam ellipse in phase space which then can be checked down the linac. With this method (at LCLS) sudden mismatches, coupling and 3% BPM scale errors were found.

RF KICKS

All the above mentioned steering and compensation techniques get messed up by RF kicks (7), and their behaviour is quite interesting. There can be sin and cos terms, an x and x' part, dipole-, quadrupole-, or lens-type kicks, even 2nd harmonic part was observed (Fig. 3).

To distinguish whether it is an angle or position effect two (nearly) closed bumps were made, one with the maximum at the beginning of the accelerator structure and one at the end (Fig. 4).

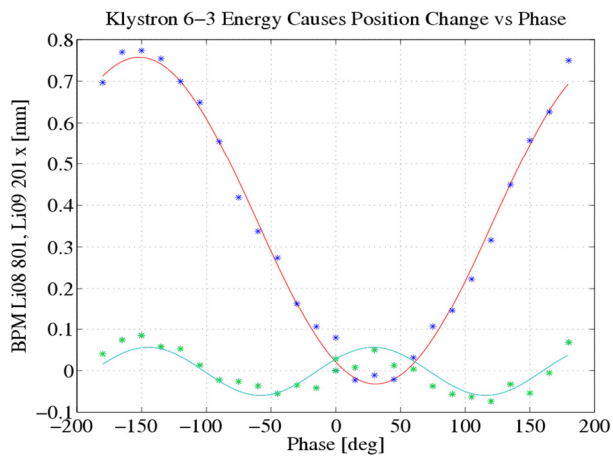

Figure 3: The phase of klystron 6-3 was varied and the resulting downstream orbit observed. At BPM Li09 201 it was up to 800 µm and in phase with acceleration, two BPMs earlier, near the zero-crossing, a 100 µm 2nd harmonic-like effect was seen.

Copyright © 2012 by the respective authors — cc Creative Commons Attribution 3.0 (CC BY 3.0)

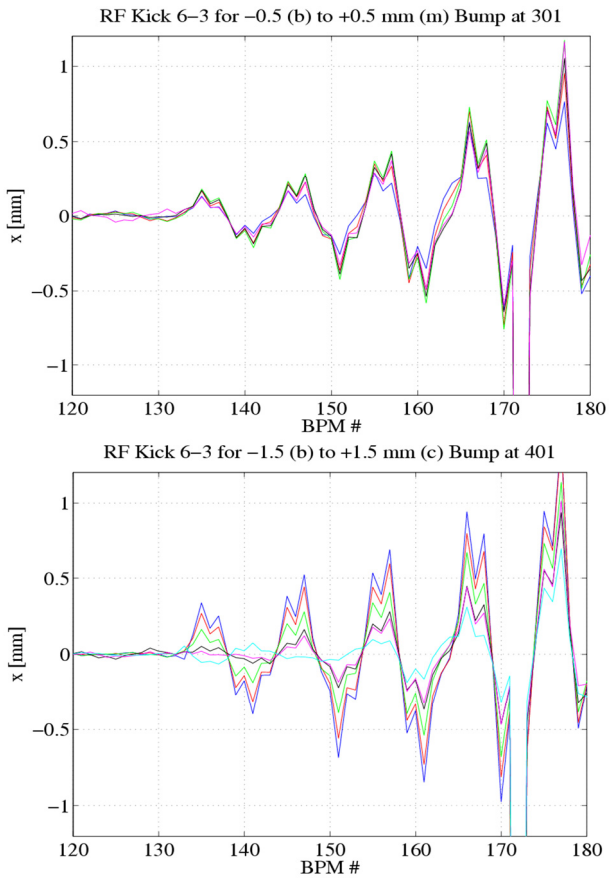

Figure 4: The RF kick of klystron 6-3 (between BPM # 132 and 133) is barely influenced by a bump with the maximum at its front at 301 (top), while at its end at 401 a +1 mm bump cancels the RF kick (bottom). Further downstream seems to be more and more dispersion.

MEASUREMENT FOR SETUP CHANGES

When the beam parameters like charge, bunch length, energy profile change the beam emittances are typically negatively influenced. By localizing and fixing the before mentioned effects as local as possible emittance growth should be minimized. Checking how much dispersion (8) the beam has at a certain point seems to be easy. The energy gets changed by ΔE and with the measured transverse position x: $x = \eta_x \cdot \Delta E/E$ the dispersion η_x is defined. The problem with the linac is that there are many ways to change the energy and on top of that there can be a change due to RF kicks when a klystron is turned off. We typically want to know how the head and the tail of a bunch having different energy due to an energy chirp might behave differently. To check that, we vary the injection phase into the linac by ±1° and then we look at the difference orbit. Since the average chirp phase before the chicane in Sector 10 is about –24° the energy change at the chicane should be about ΔE = 7.8 GeV · (cos(23°)–cos(25°)) = 111 MeV or 1.23% at 9 GeV. Any resulting orbit change in the linac is like dispersion and can be reduced with bumps or dispersion free steering methods.

The beam charge (9) and the bunch length (10) are parameters often asked by the FACET user to be changed. By dithering the damping ring capture phase the throughput and so the number of particles down the linac was varied from 2E10 to 1E10. The resulting orbit changes hint where wakefields might be an issue and where observed early in the linac (Li03). The amplitude of the RTL (Ring-To-Linac) bunch compressor can be adjusted similarly quickly to vary the bunch length, but this fast method wasn't tried yet.

To be more complete other methods and effects (11) should be mentioned too. A) There were the ballistic data measurements, were all quadrupoles, correctors and klystrons are turned off in a sector or two and the BPMs analysed before beam losses occurred. B) Hysteresis in the correctors makes the results questionable. C) Similar to the LCLS undulator where different energies are used to align the undulator, we can scale the quadrupoles and correctors while the actual energy profile and RF kicks stay fixed. With positrons which are bend magnetically in the opposite directions, while the RF kicks are typically the same (dipole kicks) the different effects can be better separated [3]. D) Electronic noise from klystrons causes a different reading for the BPMs in a nearby crate whether the klystron is on beam time or on standby.

Finally two more things should be mentioned. We changed the basic setup of the linac in two ways to make it less susceptible to dispersion. First a "staggered" chirp was introduced, which slowly increases the energy versus z correlation, and 2nd a lower 76 deg per cell lattice was used to be less susceptible to the necessary energy spread.

SUMMARY

The beam emittance control for FACET is basically done by tuning, starting at very high values (sometimes 250 times higher). This paper discusses more than twelve possible approaches to reduce the initial value locally as good as possible, so that any longitudinal or intensity changes are not coupled into the transverse dimensions.

ACKNOWLEDGMENT

The FACET team wants to thank the many support groups which make the four months short FACET runs possible, and especially the operations group for their interest and dedication to improve the beam conditions.

REFERENCES

[1] F.-J. Decker et al., "Intensity Effects of the FACET Beam in the SLAC Linac," IPAC12, New Orleans, May 2012, WEPPR040.

[2] F.-J. Decker et al., "Characterization and Reduction of Transverse RF Kicks in the LCLS Linac," PAC09, Vancouver, BC, Canada, WE5RF039.

[3] C. Adolphsen et al., "Beam-Based Alignment Technique for the SLC Linac," PAC'89, Chicago, March 1989, p. 977.

Copyright © 2012 by the respective authors — cc Creative Commons Attribution 3.0 (CC BY 3.0)

POSITRON INJECTOR LINAC UPGRADE FOR SUPERKEKB

T. Kamitani*, M. Akemoto, Y. Arakida, D. Arakawa, A. Enomoto, S. Fukuda, K. Furukawa, Y. Higashi, T. Higo, H. Honma, N. Iida, M. Ikeda, E. Kadokura, K. Kakihara, H. Katagiri, M. Kurashina, H. Matsushita, S. Matsumoto, T. Matsumoto, S. Michizono, K. Mikawa, T. Miura, F. Miyahara, T. Mori, H. Nakajima, K. Nakao, T. Natsui, S. Ohsawa, Y. Ogawa, M. Satoh, T. Shidara, A. Shirakawa, T. Suwada, H. Sugimoto, T. Takatomi, T. Takenaka, Y. Yano, K. Yokoyama, M. Yoshida, L. Zang, X. Zhou, KEK, Tsukuba, Japan
D. Satoh, Graduate School of Science and Engineering, Tokyo Inst. of Technology, Tokyo, Japan

Abstract

This paper reports on a present status of a positron injector linac upgrade for SuperKEKB. A development status of a flux concentrator for positron focusing is shown. An influence of offset layout of the flux concentrator and the target on a positron yield is described. Positron capture by L-band and large aperture S-band accelerating structures are compared in a viewpoint of satellite bunch elimination. Beam optical design compatible to electrons and positrons of different beam energies is discussed.

INTRODUCTION

The KEKB-factory is now under an upgrade to SuperKEKB for a forty times higher luminosity [1]. The injector linac is required to supply beams of higher charge and smaller emittance as shown in Table 1.

Table 1: Linac Beam Specifications

	KEKB (e^-/e^+)	SuperKEKB (e^-/e^+)
Injection Energy (GeV)	8.0 / 3.5	7.0 / 4.0
Bunch Intensity (nC)	1.0 / 1.0	5.0 / 4.0
Number of Bunch /pulse	2 / 2	2 / 2
Emittance (μm)	300 / 2100	$20 / 92_{[H]}:7_{[V]}$

To generate low emittance electron beams of 5 nC bunch intensity for injection, a photo-cathode RF gun is introduced [2] to replace the existing thermionic gun and the RF bunching section. The electron beams are accelerated up to 7.0 GeV over the entire linac and injected into the HER. Electron beams of 10 nC for positron production will also be generated with the RF gun. In a case high intensity operation of the RF gun is not stable, the thermionic gun is also used and the beams from these two guns are switched. To generate low emittance positron beams, a damping ring (DR) of 136 m circumference is introduced at a side of the linac and connected at the beam switch-yard No.2 (SY2). Beams generated in a positron capture section (PCS) are accelerated up to 1.1 GeV and injected into the DR. Positrons are extracted after 40 ms from the DR, injected back to the linac and accelerated up to 4.0 GeV for injection to the LER. Energy gain of the positrons from existing six accelerator modules (typically 160 MeV per each module) from the PCS to the SY2 is not sufficient for this 1.1 GeV injection to the DR. The PCS is relocated 40 m upstream to have a sufficient energy margin for the DR. To increase positron beam intensity four times as much, capture efficiency is enhanced in two aspects. At first, an existing 2-T pulsed coil of short field length (45 mm) right behind a positron production target, is replaced with a flux concentrator (FC) type of 5-T pulsed solenoid of long field length (200 mm). An adiabatic matching characteristics of a solenoidal field distribution with a FC, gives wider energy acceptance for positrons. As a second aspect, existing S-band accelerating structures with conventional aperture (21 mm in diameter) used in a solenoidal field of the PCS are replaced with large aperture S-band (LAS) structures (30 mm) or L-band structures (35 mm) to enlarge transverse phase space acceptance. Total length of the PCS is extended from 8 m to 16 m to boost positron beam energy from the PCS from 80 to 120 MeV. This increase of the beam energy at a transition from solenoidal to quadrupole focusing region is effective in reducing beam loss around an optical matching section.

In December of 2013, we will start a preliminary positron beam commissioning of the injector linac within limited operation parameters. A beam commissioning with the DR will be started in February of 2015. Development, fabrication and installation of the components are ongoing to be in time for the schedule.

In the following sections, as topics of significance in the positron injector linac upgrade, flux concentrator development, target protection and offset positron production, large aperture accelerating structures development, satellite bunch elimination and electron/positron compatible optics design are described .

FLUX CONCENTRATOR DEVELOPMENT

Flux concentrator is a pulsed solenoid composed of a primary coil and a copper cylinder with a conical hole inside. Induced eddy current flows through a thin slit to a inner surface and generates a strong field of several Tesla. Achievable field strength is mainly determined by a hole diameter and a primary pulsed current. They are constrained from a required aperture size, a power supply capacity and break-

* E-mail: <takuya.kamitani@kek.jp>

Copyright © 2012 by the respective authors — cc Creative Commons Attribution 3.0 (CC BY 3.0)

down limit. We have been collaborating with BINP, SLAC, Frascati and IHEP on the FC development for KEKB linac upgrade. We have performed a high power operation test of a BINP-type FC at KEK and experienced a breakdown problem. The prototype is disassembled and under careful inspection at BINP. For a coming preliminary positron beam commissioning in December of 2013, we will use a more conventional FC, two type are considered as candidates. One is a spiral slit FC based on the SLAC design. Frascati and IHEP also have been using this type of FC. The other type is a simple straight slit FC. A peak longitudinal field strength at a same current is lower with the SLAC type, but a contribution of a transverse field component which is not axial-symmetric is also smaller. Considering an effect of target offset from a field center described later, evaluation of positron capture efficiency by a particle tracking using detailed 3D field distribution is ongoing. Since the FC is installed right behind the target and its radio-activation level will be very high and a replacement work will not be easy. Thus, an engineering design to avoid mechanical failure or water and vacuum leakage problems is critically important. Decision of installation model among the candidates will be made soon with a comparison in the capture efficiency performance and engineering design consideration.

POSITRON PRODUCTION TARGET

We have used 14 mm thick (4.0 radiation lengths) amorphous tungsten and later 10 mm thick crystal tungsten for the positron production target. In the beam commissioning for SuperKEKB, an amorphous tungsten will be used to avoid precise axis alignment mechanism. For a pulse-by-pulse switching of electron and positron injections, a small hole for electron beam passage is bored a few mm apart from a center of the target. To optimized a positron yield, the target was placed on a common central axis of the pulsed coil and the DC solenoids in the KEKB linac. Thus, electron beam entered into solenoid field at a few mm offset from the axis and traveled through an excursion orbit by a fringe field. It becomes a problem at SuperKEKB, since an electron beam for injection have a small emittance as 20 μm. Emittance growth in this excursion orbit is not acceptable and a hole for electron passage should be centered on the axis of the DC solenoids. An aperture diameter of the FC is only 7 mm in the present design and the tungsten target of 4 mm diameter and the hole of 2 mm diameter should be well contained in the aperture. As a consequence, center axis of the FC has 2 mm offset from the beam line and target center has 1.5 mm offset from the FC center. We expected the offsets degrade the positron yield 20 to 30 % by a preliminary simulation study. More detailed study on this offset effect is to be done by the tracking simulation.

LARGE APERTURE CAPTURE SECTION

To enlarge a transverse phase space acceptance of the PCS, accelerating structures with larger aperture will be used. As a first candidate, we started R and D for L-band structure which had an appropriate field strength and an aperture diameter as described in Table 2. A first prototype L-band structure has been fabricated and under a high-power RF processing in a test stand. Since a large outer dimension of an RF coupler of the structure gives strong impact on a DC solenoid design, an L-band structure of slimmer body is in consideration by installing a dummy load inside the structure in a collinear geometry. In a selection of the L-band frequency, we cannot use simple half frequency (1428 MHz) of the S-band because it is not compatible with 2 bunch operation with 96 ns interval which was defined from phase synchronization constraint of the linac and the storage rings. Instead, we adopted 1298 MHz which is 5/11 of the S-band frequency. This co-prime frequency relationship was found to be useful in elimination of satellite bunch particles as described later.

The other candidate is a large aperture S-band (LAS) structure as described in Table 2. It has a larger aperture diameter (30 mm) compared with conventional S-band structures (21 mm). The LAS has a very large group velocity and a field strength is relatively low, however operation with a pulse compression by the SLED gives comparable field strength. The LAS structures are used not only in the PCS, but in subsequent two accelerator modules of quadrupole focusing region to improve transverse acceptance as described in the next section.

Table 2: Specifications of Large Aperture Structures

	L-band	LAS
RF frequency (MHz)	1298.182	2856.000
number of cells	24 + 2	57 + 2
accel. length (mm)	2001	2064
disk aperture 2a (mm)	39.4 $\rightarrow$ 35.0	31.9 $\rightarrow$ 30.0
group veloc. v_g/c (%)	0.61 $\rightarrow$ 0.39	4.2 $\rightarrow$ 3.5
shunt imp. r_0 (MΩ/m)	45.7 $\rightarrow$ 47.6	46.1 $\rightarrow$ 48.4
filling time T_f (μs)	1.360	0.180
accel. field (MV/m)	12.2@15MW	6.93@10MW
same with SLED	–	16.42

Positrons emerged from the target have wide range of energy due to a cascade shower process and long bunch tail due to path differences in spiral orbits. Simulation studies show that a positron capture in decelerating phase and a formation of a main bunch by RF phase slip is useful to reduce particles at tails of an energy distribution [3]. However, particles which are not captured in the main bunch, experience further phase slips. They can be captured in subsequent phase positions and form satellite bunches. They can have comparable beam energy as those in the main bunch and will not be eliminated by an energy collimation. A fraction of satellite particles go out of RF buckets are lost at the DR injection. Due to a civil engineering constraint, a beam loss at DR is strictly limited to be below 0.2 % of a design beam intensity (4 nC x 2 bunch). Thus, elimination of satellite particles in the linac is a critical issue for a DR

Copyright © 2012 by the respective authors — cc Creative Commons Attribution 3.0 (CC BY 3.0)

operation.

In a case we use six 2-m long L-band structures in the PCS, satellite bunches are formed in L-band wave-length intervals. Due to the co-prime relationship to the S-band wave-length, satellite bunches are accelerated or decelerated in abnormal phases in the downstream S-band linac modules and are eliminated in the linac or in an energy collimation. It is shown that a beam loss at DR injection will be suppressed to be an allowable level 0.05% [3]. In a case of a hybrid of two L-band and four LAS structures, the loss becomes 0.2%, but still acceptable. To suppress an initial construction cost by avoiding L-band component construction, it is recommended to start a beam commissioning with a configuration of all LAS structures in the PCS. In this case, the loss becomes 0.4% and further improvement is necessary. A preliminary simulation study indicates that raising S-band deceleration field around 20 MV/m can reduce satellites. More detailed study will be done soon.

POSITRON/ELECTRON COMPATIBLE OPTICS

By using accelerating structures with larger aperture, a transverse acceptance of the PCS which corresponds to an RMS emittance is enlarged from 2000 μm to 4000 μm. As described in the previous section, the PCS is relocated to a 40 m upstream position and a beam energy from this section is raised from 80 MeV to 120 MeV. As a consequence of these changes, a quadrupole focusing system after the PCS till the SY2 needs an upgrade and an addition and rearrangement of quadrupole and steering magnets will be made. In the two accelerator modules after the PCS, LAS structures of 30 mm aperture diameter are used to enlarge the transverse acceptance and quadrupoles are installed in 70 cm interval outside of the structures. In the subsequent three modules, ordinary S-band structures of 20 mm aperture are used and quadrupoles are placed in the same interval. In the subsequent four modules, quadrupole triplets are placed between the S-band structure and the interval changes from 3m to 5m according to the beam energy.

In this region between the positron production target and the SY2 before the DR, both of low energy, huge emittance positrons and high energy, low emittance electrons pass through the same quadrupole focusing system. Almost all quadrupoles in this region are DC magnets. To avoid a beam loss of the positrons, focusing strengths are optimized for them. Thus, electrons are focused in a ready-made quadrupole fields which are weak for the energy of electrons. Slight optimization to moderate electron beam size is performed within a range in which the positron optics is not significantly modified. Fig. 1 shows beam size of the positrons and the electrons.

Even with this compromised optics for the electrons, the beam sizes are kept sufficiently small. For independent orbit control of the positrons and the electrons, 12 pulsed steering magnet pairs are installed in addition to existing DC steerings. Orbit correction performance and emittance growth with this limited number of steerings should be checked by simulations and underway.

In the region after the DR till the end of the linac, both of the electrons and the positrons have low emittance and not precisely same but high energy. Quadrupole triplets and steerings are placed in 20 m interval. Total number of magnets are not so large for this region and there are no quadrupoles outside the structure, hence we decide all the quadrupoles and steerings here to be pulsed magnets. It will be useful for a precise independent matching to the storage rings and for an independent orbit control to suppress emittance growths for positrons and electrons.

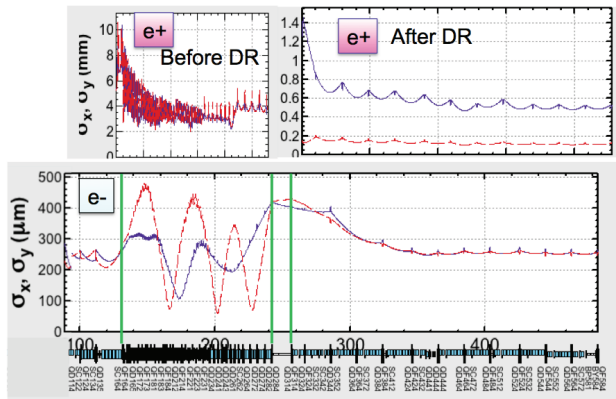

Figure 1: Positron/electron beam optics design.

SUMMARY

The KEKB positron injector linac is under an upgrade for SuperKEKB. Two types of flux concentrator in different slit geometry are in comparison by simulations and a prototype fabrication. An influence of an offset layout of the FC and the target is discussed. As accelerating structures to be used in the capture section, L-band and large aperture S-band structures are compared in a viewpoint of satellite bunch elimination. Performance of a compatible optics for electrons and positrons of different beam energies with DC quadrupoles is studied. A preliminary positron beam commissioning of the injector linac will be started in December of 2013.

REFERENCES

[1] T. Abe et al., "Belle II Technical Design Report, Chapter.2 SuperKEKB", KEK Report 2010-1, p. 19, http://www-superkekb.kek.jp/documents/B2TDR.pdf

[2] M. Yoshida, N. Iida, Y. Ogawa, M. Sato, L. Zang "SuperKEKB Injector Upgrade for High Charge and Low Emittance Electron Beam", IPAC'12, New Orleans, USA, May 2012, TUPPD035

[3] N. Iida, H. Ikeda, T. Kamitani, M. Kikuchi, K. Oide, D. Zhou "Beam Dynamics in Positron Injector Systems for the Next Generation B-factories", IPAC'11, San Sebastian, Spain, September 2011, THYA01

Copyright © 2012 by the respective authors — cc Creative Commons Attribution 3.0 (CC BY 3.0)

ADVANCES IN BEAM TESTS OF DIELECTRIC BASED ACCELERATING STRUCTURES*

S. P. Antipov[1,2], C. Jing[1,2], A. Kanareykin[1,#], J.E. Butler[1], V.Yakimenko[3], W. Gai[2]
[1]Euclid Techlabs LLC, Solon, OH, USA,
[2]Argonne National Laboratory, Argonne, IL, USA
[3]Brookhaven National Laboratory, Upton, NY, USA

Abstract

Diamond is being evaluated as a dielectric material for dielectric loaded accelerating structures. It has a very low microwave loss tangent, high thermal conductivity, and supports high RF breakdown fields. We report on progress in our recent beam tests of the diamond based accelerating structures of the Ka-band and THz frequency ranges. Wakefield breakdown test of a diamond-loaded accelerating structure has been carried out at the ANL/AWA accelerator. The high charge beam from the AWA linac (~70 nC, σ_z ~ 2 mm) was passed through a rectangular diamond loaded resonator and induce an intense wakefield. A groove is cut on the diamond to enhance the field. Electric fields up to 300 MV/m has been generated on the diamond surface to attempt to initiate breakdown. Wakefield effects in a 250 GHz planar diamond accelerating structure has been observed at BNL/ATF accelerator as well. We have directly measured the mm-wave wake fields induced by subpicosecond, intense relativistic electron bunches in a diamond loaded accelerating structure via the dielectric wake-field acceleration mechanism. A surface analysis of the diamond has been performed before and after the beam test.

INTRODUCTION

Diamond has been proposed as a dielectric material for dielectric loaded accelerating (DLA) structures [1-3]. Dielectric Loaded Accelerator structures using ceramics or other materials and excited by a high current electron beam or an external high frequency high power RF source have been under extensive study for many years [4-7]. Low loss microwave ceramics, fused silica, and CVD polycrystalline and single crystal diamonds [11] have been considered as materials for dielectric based accelerating structures to study of the physical limitations encountered in developing field strengths > 100 MV/m at microwave [4-6] and > GV/m at THz frequencies in a dielectric based wakefield accelerator [6,7,11,12]. THz radiation has been generated recently by a short ~10 GV/m pulse within a 100 μm diameter quartz fiber [7]. A planar diamond-based DLA structure was proposed recently by Omega-P, Inc., where the dielectric loading of this structure was to be made of diamond slabs fabricated using CVD (chemical vapor deposition) technology [2].

Our choice of CVD (Chemical Vapor Deposition) diamond as a loading material will allow demonstration of high accelerating gradients; up to 0.5-1.0 GV/m as long as the diamond surface can sustain a 0.5-1.0 GV/m short pulse (~ 10 ns) rf field without breaking down. Diamond has the lowest coefficient of thermal expansion, highest thermal conductivity (2×10^3 Wm^{-1} K^{-1}) and extremely low loss tangent ($<10^{-4}$) at Ka-W frequency bands. Secondary emission from the CVD diamond surface can be dramatically suppressed by diamond surface dehydrogenation or oxygen termination [3,6,8-12]. The CVD process technology is rapidly developing, making the CVD diamond fabrication process fast and inexpensive. Given these remarkable properties, diamond should find numerous applications in advanced accelerator technology [3]. Planar diamonds are available commercially in various grades including single crystal diamonds. The goal of this research is to perform a wakefield acceleration experiment using a diamond loaded structure and to test diamond for breakdown.

Euclid Techlabs had performed two wakefield experiments with diamond loaded accelerating structures: a 25 GHz structure at the Argonne Wakefield Accelerator of ANL and a 250 GHz structure at the Accelerator Test facility of BNL [9].

BEAM EXPERIMENTS WITH THE DIAMOND BASED DLA STRUCTURES

Significant progress has been made in the development and testing of high gradient dielectric accelerating structures (DLA) [1]. As various engineering challenges (breakdown, dielectric losses, efficient RF coupling) have been overcome, the technology of high gradient RF or wakefield driven dielectric loaded structures appears increasingly attractive as a viable option for high energy accelerators. Typical DLA considered in experiments is a cylindrical, dielectric tube with an axial vacuum channel inserted into a conductive sleeve or a rectangular waveguide loaded with planar dielectric pieces. In this paper we will focus on the latter structure. The dielectric constant, thickness of dielectric and the size of a vacuum gap are chosen to adjust the phase velocity of the fundamental mode at certain frequency to the beam velocity ~ c. In the application to particle acceleration, the dominant TM_{01} mode is of main interest.

*Work supported by the Department of Energy SBIR program.
#alexkan@euclidtechlabs.com

Copyright © 2012 by the respective authors — cc Creative Commons Attribution 3.0 (CC BY 3.0)

We report here the results of a wakefield breakdown test of single crystal diamond-loaded rectangular accelerating structure [10]. The high charge beam from the AWA linac (~70 nC, σ_z = 2 - 2.5 mm) was transported through a rectangular diamond - loaded resonator and induced an intense wakefield [12]. A deep (200 μm) and narrow (20 μm) groove is cut on the diamond surface to enhance the field (by approximately a factor of ε). Electric fields at least of 300 MV/m were present on the diamond surface in the groove (decay time ~ 35 ns). A surface analysis of the diamond was performed before and after the beam test. No breakdown-type damage was observed on scanning electron microscopy images [10].

Structure design was presented earlier in [10], Fig.1. Parameters of the structure were determined via parametric simulations with constraint on the thickness of commercially available diamond plates, and the minimal gap size was determined by beam dynamics [11].

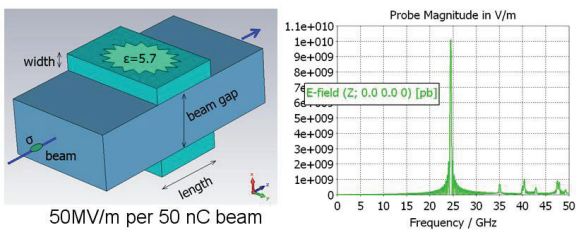

Figure 1: Left: geometry of the diamond resonator: length = 4mm, width = 1.2mm, beam gap = 4mm and overall width = 8mm. Right: spectrum of the wakefield (simulation).

To achieve stronger fields on the surface of the diamond two small 20 and 25 micron – wide, 220 micron deep grooves were laser cut on the diamond surface transverse to the beam propagation direction. There is a large field enhancement in these grooves: the field at the entrance to the groove is higher by a factor of ~ ε (5.7) than it would be in its absence [10] – a five time field enhancement because of the boundary conditions for the electric field at the surface of dielectric. For deep and narrow scratches (aspect ratio of 10 and higher) such enhancement is practically ε. As the groove becomes wider and shallower the field enhancement drops.

Diamond laser cutting is not a trivial procedure. Multistage cleaning was used to get rid of partial conductivity from carbon deposits. Special technology has been used that allowed removing practically all remaining carbon. SEM measurement confirmed that the laser cutting was successful as well as that target values of groove widths were achieved [11], Fig. 2.

In the experiment we manage to transport 72 nC charge through the structure, which corresponded to at least 300 MV/m on the surface of the groove. The bunch length measurement was not available, so for this estimate we used maximum value of 2.5mm. Shorter bunch length yields higher gradient.

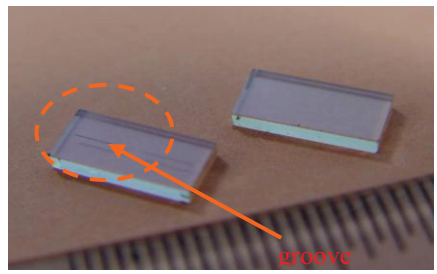

Figure 2: Field Enhancement groove machined in a planar diamond sample.

We used scanning electron microscopy to analyze the condition of the diamond surface before and after the experiment. Besides the presence of lint the surface did not undergo noticeable changes, Fig.3.

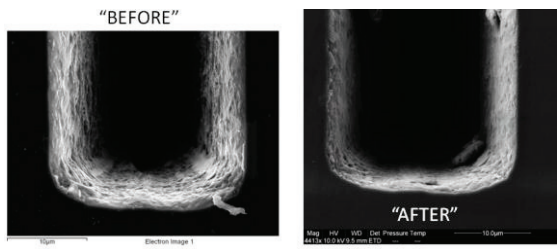

Figure 3: SEM measurement of the groove: right – before, left – after the test.

WAKEFIELD ACCELERATION IN A 250 GHZ DIAMOND STRUCTURE

Recently, we have directly measured THz wakefield acceleration/deceleration in a diamond loaded dielectric accelerating structure.

Proof of principle experiments at BNL/ATF [9] have studied wakefields in diamond structures in the 250 GHz regime. It should be noted especially that in this experiment diamond was for the first time used as a loading material for a wakefield dielectric based accelerating structure [9]. Fields produced by a leading (drive) beam were used to accelerate a trailing (witness) electron bunch, which followed the drive bunch at a variable distance. The energy gain of a witness bunch as a function of its separation from the drive bunch describes the time structure of the generated wakefield. By sweeping the separation between the drive beam and the witness beam and energy measurements of the witness beam a 0.25 THz frequency wakefield was directly sampled at the scale of about one wavelength [9,13].

The general experimental methodology is the following: a pair of beams is generated: - a high charge drive beam, followed by a smaller witness beam at a variable distance *d*. The drive beam generates a wake there and the witness beam is accelerated or decelerated depending on the delay between the two beams. We record the witness beam energy change, ΔE as a function of *d*.

Copyright © 2012 by the respective authors — cc Creative Commons Attribution 3.0 (CC BY 3.0)

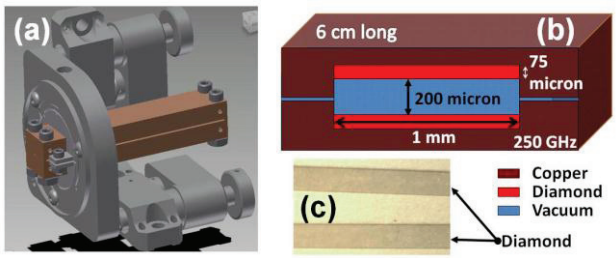

Figure 4: (a) 250 GHz structure mounted on a positioning holder; b) structure dimensions; c) photo of diamond after the experiment exhibiting no visible damage.

In the experiment we used 75 micron thick polycrystalline diamond plates loaded in a 6 cm long waveguide, Fig.4. The beam gap was 200 microns. This structure yields a wakefield dominated by a TM_{11} – like mode with 1200 micron wavelength (0.25 THz). The ATF drive beam is very short and also excites higher order modes, hence the wake is not a pure sine wave [9].

The subpicosecond drive and witness beams are produced by the technique described in [9]. A beam accelerated off-crest hence having a linear energy chirp (the head of the beam having lower energy than the tail) passes through a a dispersionless translating section. A mask is placed between the dogleg dipoles where the beam transverse size is dominated by the correlated energy spread. After the second dipole magnet the transverse pattern introduced by the mask becomes the longitudinal charge density distribution. In our case the mask was motorized and allowed creation of a drive beam followed by a witness beam at a variable delay [9].

Calibration is done via coherent transition radiation (CTR) interferometry. We fitted the recorded transverse profile by a gaussian distribution with σ_x = 50 μm, σ_y = 350 μm. The longitudinal wakefield produced by a beam with this current distribution was numerically calculated and compared with the experimental results.

The relative change in witness beam energy depending on the drive – witness separation is measured on the spectrometer. Compared to the beam energy, when it does not go through the structure, we observe energy gain and loss in the interval from -0.6 to +0.65 MeV for the witness beam following a drive beam through the DLA structure. This yields a 10.8 MV/m gradient for a 6 cm structure. The measurement accuracy was limited by the spectrometer resolution (σ = 0.028 MeV), estimated using the sharpest features obtained on the spectrometer by measuring the FWHM (full width half maximum) and dividing it by 2.355 to obtain the equivalent Gaussian width. Fig. 5 shows the measured energy change (diamonds) as a function of drive – witness separation with error bars. The shape of the experimentally mapped wake (diamonds) agrees well with the theoretical (scaled) prediction (circles) based on the wakefield (solid line) calculated for the drive beam current distribution (dashed line).

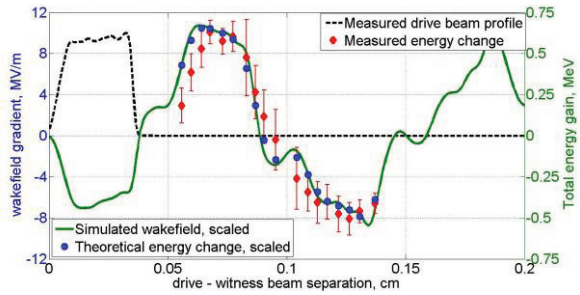

Figure 5: Energy gain of the witness beam as a function of separation from the drive beam.

SUMMARY

The emphasis of this paper is to present progress on development and fabrication of new types of diamond waveguides to be used for high gradient dielectric accelerating structures. We reported the results from development of a diamond DLA of GHz frequency range and wakefield tests of diamond-loaded rectangular accelerating structures at THz frequencies. We have directly measured THz wakefield acceleration and deceleration in a diamond loaded dielectric accelerating structure in an experiment where diamond was used for the first time in a wakefield dielectric based accelerating structure. In the 25 GHz frequency range, we achieved field levels on the order of 300 MV/m (35 ns pulse) in the structure using the 72 nC, 15 MeV beam at the Argonne Wakefield Accelerator Facility. Single crystal diamond plates produced by chemical vapor deposition (CVD) were used in the structure. A surface analysis of the diamond has been performed before and after the beam tests.

REFERENCES

[1] D. Whittum, SLAC-PUB-7910, July 1998.
[2] C. Wang, V.P. Yakovlev et al. PAC'05, 1282 (2005)
[3] A.Kanareykin et al. Proc. EPAC'06, 2460, (2006).
[4] W. Gai, AIP Conf. Proc.1086, 3, (2009).
[5] W. Gai et al. Phys. Rev. Lett. 61, 2756 (1988).
[6] A.Kanareykin. Journal of Physics, Conf. Ser., 236, p.012032, (2010).
[7] M. C. Thompson et al. AIP Conf. Proc. 877, 903 (2006).
[8] P Schoessow et al. AIP Conf. Proc. 1086, 398 (2009)
[9] S.Antipov et al. Appl. Phys. Lett. 100, 132910 (2012).
[10] S.Antipov et al. Proceedings IPAC'12, p. p.2813.
[11] A.Kanareykin. AIP Conference Proceedings, v. 1299, p. 286, 2010.
[12] S.Antipov et al. AIP Conference Proceedings, v. 1299, p. 359, 2010.
[13] S.Antipov et al. Phys. Rev. Lett. 108, 144801 (2012).

Copyright © 2012 by the respective authors — cc Creative Commons Attribution 3.0 (CC BY 3.0)

A 10 MeV L-BAND LINAC FOR THE IRRADIATION APPLICATIONS IN CHINA

G.# Pei, Y. Chi, R. Shi, Z. Zhou, Q. Yuan, F. Zhao, D. He, X. Yang, C. Yu, M. Dai, J. Liu, Y. Feng, X. Li, X. He, X. Wang, Z. Zhu, E. Tang, H. Huang, J. Zhao, C. Ma,
Institute of High Energy Physics, IHEP, Beijing, P. O. Box 918, 100049, China
Z. Li, X. Zhang, Wuxi EL PONT Radiation Technology, Ltd, No 8 Weiye Road,
Qianqiaopeijianyuan District, Wuxi, 214151, Jiangsu, China

Abstract

The electron linear accelerator has wide applications, and the demands for the irradiation applications are keeping growing in China. A high beam power 10 MeV L-band Linac has been developed recently as a joint venture of Institute of High Energy Physics (IHEP) and Wuxi EL-PONT Company in China. The Thales TH2104U klystron, 2 A thermionic electron gun and 3 m long L-band disk-loaded constant impedance RF structure were adopted. A stable electron beam of 10 MeV / 40 kW has been obtained in the last April. In this paper the detailed design issues and beam commissioning results are reported.

INTRODUCTION

IHEP in China has very rich experience in the electron linac design and development. When requested to transfer the technology to industry, many S-band electron linacs have been developed for medical and irradiation applications. For the S-band irradiation linac, the beam power is limited to be ~20 kW because of the RF structure heating/cooling issues. Due to the scaling law of $P \sim f^1$ between the RF power consumption of the accelerating structure and the frequency, L-band structure [1][2] is usually adopted for the nature extending to much higher beam power up to ~100 kW level. For any high beam power machines the power efficiency is a concern. According to Eq. (1), the maximum conversion efficiency η_{max} of the RF power to the beam power dependents only on the attenuation factor τ[3], and smaller τ is preferred.

$$\eta_{\max} = \frac{1}{2}\left[\frac{\left(1-e^{-2\tau}\right)^2}{\left(1-e^{-2\tau}\right)-2\tau e^{-2\tau}}\right] \quad (1)$$

However, there is a compromise among power efficiency, power dissipation as well as heating, peak beam current and beam energy. It is known that τ is independent of frequency, and for SLAC type 3m long disk-loaded TW structure τ is ~0.57. Suppose a 3 m long L-band structure of 34 cavities is used, τ can be roughly estimated to be 0.57*34/86=0.225. With SUPERFISH simulation and cold test, τ is shown[4] to be 0.22, which is in good agreement with the simple scaling. By putting 0.22 into Eq. (1) one can get an efficiency η_{max} of 90%, which is very excellent. In this condition, the beam current is ~900 mA according to Eq. (2).

$$i_{\eta_{\max}} = \left(\frac{P_T}{rl}\right)^{1/2}\left[\frac{\left(1-e^{-2\tau}\right)^{3/2}}{\left(1-e^{-2\tau}\right)-2\tau e^{-2\tau}}\right] \quad (2)$$

Table 1 shows the design parameters for the 10 MeV / 40 kW L-band linac. The linac is a machine with very heavy beam loading; the beam energy range of 8 to 12 MeV can be easily controlled by simply adjusting the gun bias voltage (i.e. the gun emitting beam current), but above 10 MeV is not recommended for prevention of the neutron production.

Table 1: Design parameters for the 10MeV L-band linac

Beam energy (MeV)	10
Beam power (kW)	40
RF frequency (GHz)	1.3
Peak beam current (mA)	530
Duty cycle (%)	0.75
Klysron peak power (MW)	10

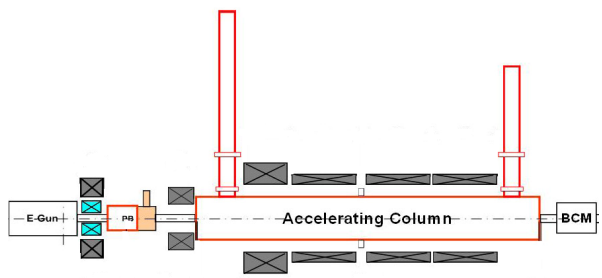

Figure 1: The schematic of the L-band linac.

DETAILED DESIGN AND SIMULATION

Figure 1 shows the schematic of the high power 10 MeV L-band linac, which mainly consists of an electron gun, an RF power source and an accelerating column. The electron gun is the 80 kV BEPC type [5] gun with 2 A Y646B cathode grid assembly. The gun system is separated from the other subsystems, which makes it easy for maintenance. The gun emitting current and the beam energy are adjustable. The RF power source is a 10 MW Thales TH2104U klystron with 130 kW average power, and the modulator was designed to make it work at 100 kW. Fig. 2 shows the Thales TH2104U klystron and its parameters.

*Work supported by the joint venture foundation of IHEP and the Wuxi EL-PONT Company in China.
#peigx@ihep.ac.cn

Copyright © 2012 by the respective authors — cc Creative Commons Attribution 3.0 (CC BY 3.0)

Frequency	1300	MHz
Output power	10	MW
Gain	> 47	%
Pulse width	> 55	μs
Duty cycle	> 1.1	%
Output average power	> 130	kW
Efficiency	45	%
Beam voltage	167	kV
Beam current	136	A

Figure 2: Thales TH2104U klystron and its parameters.

With 10 MW TH2104U klystron and a 3 m long L-band RF structure, a 10 MeV / 40 kW electron beam with a beam current of 530 mA as listed in Table 1 can be obtained. Except for the klystron, the RF structure is a key issue for the high power electron linac. The simple constant impedance structure with the cell dimension scaled from the 3 m long SLAC type disk-loaded TW structure was used, but the first 6 cells are β changed for the beam bunching requirement. Simulations with the EGUN and PARMELA codes have been conducted [6], and the simulation results were confirmed by measuring the beam performance in later commissioning. Even without the pre-buncher, a proper beam with more than 40% transmission efficiency was obtained, which is also confirmed with the machine commissioning. Fig. 3 shows the simulated beam energy spread and beam size, which are good enough for an irradiation machine.

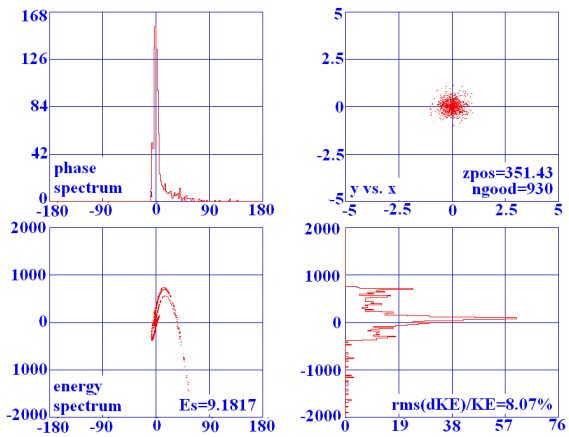

Figure 3: The simulated beam phase space.

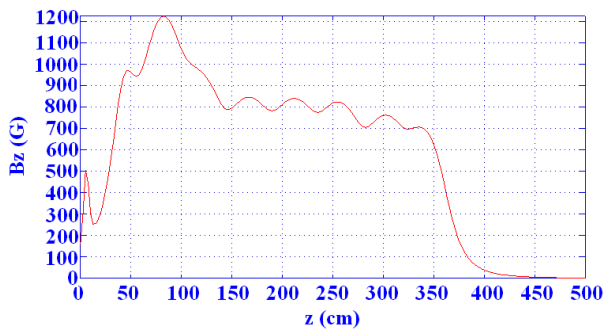

Figure 4: The solenoid magnetic field distribution along the 10 MeV / 40 kW linac.

Fig. 4 shows the designed solenoid magnetic field distribution along the whole linac. As the RF structure heating is a concern for the design of the high power electron linac, the structure iris temperature rise and its deformation were also simulated [7] and shown in Fig. 5, which indicates the maximum temperature of 62 °C under the design parameters and a tolerable deformation of ~17 μm. The cooling system is a simple water jacket around the accelerating column; A special cooling design is required if even higher beam power up to 100 kW is needed.

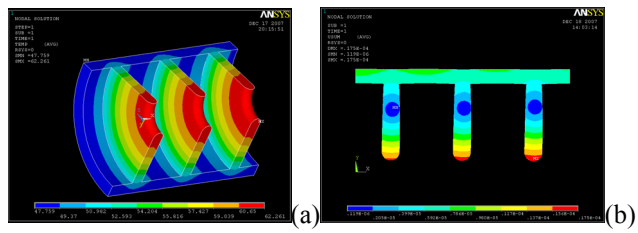

Figure 5: ANSYS results for the structure heating under the design parameters: (a) the iris temperature rise; (b) the structure deformation.

COMMISSIONING AND BEAM TEST

The machine was installed at EL PONT Company in 2009; the machine processing and commissioning were started right after the entire subsystems ready. The first beam was obtained on November 3rd, 2010. Fig. 6 is the picture of the whole linac, and Fig. 7 shows the modulator.

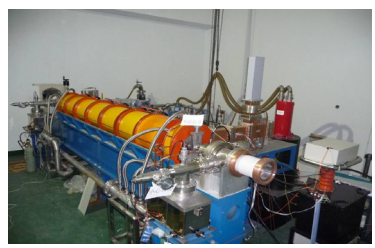

Figure 6: Picture of the L-band linac.

Figure 7: Pictures of the modulator.

Table 2 shows the milestones of the high power L-band electron linac development and commissioning progress. Almost two years were taken to get the first beam, and the main time consuming task is the klystron purchase, which takes one year and a half with almost 6 months delay. From the first beam @ 5Hz to the 40kW stable beam almost half year was taken to reach the design goal. During the high power processing process, many lessons have been learnt, such as beam instability, beam duct heating and degassing, beam loss and so on.

Copyright © 2012 by the respective authors — cc Creative Commons Attribution 3.0 (CC BY 3.0)

Fig. 8 is the beam testing results with the beam energy of 11.2MeV at 600mA beam current shown in (a) and the beam current profile measured with BCT shown in (b), which is better than the design prediction.

Table 2: Milestones of the L-band linac development

Date	Activity
October, 2007	Proposal and design
Auguest, 2008	Manufacture, purchase
September, 2009	Assembly at EL PONT
November 3rd, 2010	First beam
November 6th, 2010	Beam at 5 Hz
March 31st, 2011	30 kW
April 24th, 2011	40 kW

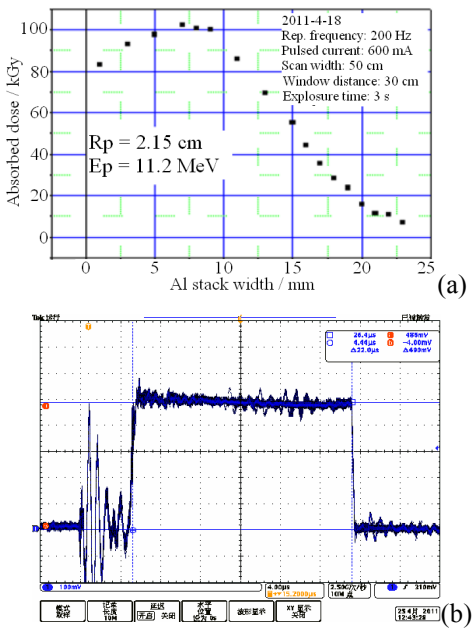

Figure 8: The beam testing results. Time-scale is 4 μs/division.

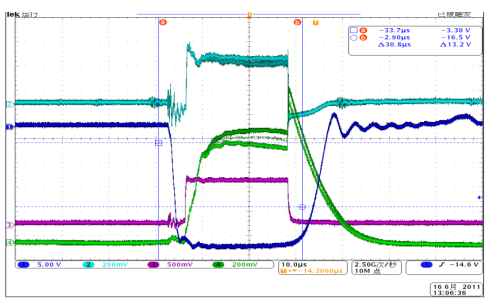

Figure 9: Machine status: blue line is the modulator high voltage waveform, turquoise the beam current from BCT, pink forward RF, and green reflected RF. Time-scale is 10 μs/division.

Many problems have been encountered during the beam testing and the machine commissioning; in particular the beam instability has very strong impact on the beam quality, the beam duct heating and the vacuum degradation, so systematic investigations were conducted for more than two months. Finally the RF driven source problem was found by monitoring the voltage standing-wave ratio (VSWR) as shown in Fig. 9, in which channel (1) in blue is the modulator high voltage waveform, channel (2) in turquoise the electron beam current from BCT, channel (3) in pink the forward RF, and channel (4) in green the reflected RF. It can be seen that the beam instability is correlated with the reflected RF (not the arcing but the VSWR change), which means the frequency is not correct even the indicator still shows 1300 MHz. After the problem was fixed, the beam instability was gone. In addition, the bunching effect of the pre-buncher was found not so strong, and taking out it would make the machine architecture much simpler.

SUMMARY

The high power 10MeV L-band electron linac is the first 40 kW irradiation linac developed and constructed in China. The first beam was obtained on November 3rd, 2010, which confirmed the design and the simulation predictions. After a few months machine processing, the designed beam parameters were achieved on April 24th, 2011. The formal beam testing was conducted by the National Institute of Metrology on December 26th, 2011, and the testing beam current is 720 mA with energy of 9.9 MeV. If the machine works at a duty cycle of 0.7% as already processed, the beam power can reach 50 kW. The conversion efficiency η from the RF power to the beam power is ~72%, a little bit lower than the theoretical prediction, which is partially because the RF power into the accelerating structure is lower than 10 MW, and/or the beam loss. Nonetheless, 72% is not bad. Now the machine has been put into operation at EL PONT Company.

ACKNOWLEGEMENT

The high beam power 10 kW / 40 MeV electron linac facility is a joint venture of IHEP and EL-PONT Company in China. Many works not mentioned here were accomplished by EL-PONT, such as infrastructure, power supply, cooling system, beam scan or deliver system and so on. Many thanks to all EL-PONT staffs for their contributions to the machine design, development, commissioning and operation.

REFERENCES

[1] J. Labrie et al., “AECL IMPELA Electron Beam Industrial Irradiations”, NIM in Physics Research, B40/41 (1989) 1153-1157.
[2] B. Park et al., “Intense L-band Electron Linac for Industrial Applications”, Proceedings of LINAC 2006, Knoxville, Tennessee, USA.
[3] The Stanford Two-Mile Accelerator, ed. by R.B. Neal, W.A. Benjamin, New York, 1968.
[4] Q. Yuan et al., private communication.
[5] 2.2/2.8GeV BEPC Injector Design (internal report, in Chinese), 1989.
[6] R. Shi, Y. Luo, private communication.
[7] H. Liu, private communication.

Copyright © 2012 by the respective authors — cc Creative Commons Attribution 3.0 (CC BY 3.0)

APPLICATIONS OF COMPACT DIELECTRIC BASED ACCELERATORS*

C. Jing#, S. Antipov, P. Schoessow, and A. Kanareykin, Euclid Techlabs LLC, Solon, OH, USA
J.G. Power, M. Conde, and W. Gai, ANL, IL, USA

Abstract

Important progress on the development of dielectric based accelerators has been made both experimentally and theoretically in the past few years. One advantage of dielectric accelerators over their metallic counterparts is their compact size, which make them attractive for industrial or medical applications. In this article, we discuss the design of dielectric based accelerators focusing on those technologies relevant toward these needs.

DIELECTRIC LOADED ACCELERATOR

The first studies of using RF driven dielectric-loaded circular waveguide for particle acceleration can be traced back to the early 1950's [1]. In recent years, because of its geometrical simplicity and availability of low loss dielectrics, theoretical and experimental investigations on dielectric based accelerators have been intensively revived. Among them, externally powered Dielectric-Loaded Accelerators (DLA), dielectric wakefield accelerators, and dielectric laser accelerators have attracted the most attention. In this paper, we concentrate on externally powered DLA technologies and possible application.

DLA structures can be made as simple as a dielectric tube surrounded by a conducting cylinder. Most of them use uniform, linear ceramic tubes so that they work as constant impedance accelerating structures. The TM_{01} mode (traveling wave accelerator) or TM_{01n} mode (standing wave) are the fundamental accelerating modes. Unlike conventional metallic accelerating structures, DLA structures do not require any structure periodicity to slow the phase velocity of the guided wave below the speed of light. For a given radius, the phase velocity of each guided wave mode in a DLA structure is governed by the dielectric constant of the material and its wall thickness. In general, for the same a/λ, where a is the radius of the beam opening and λ is the wavelength, the DLA structure can be made much smaller than a disk-loaded accelerating structure due to the high dielectric constant of the material used. This small size may be favored for applications with tight space requirements. It also facilitates the use of quadrupole lenses or a permanent solenoid around the structure to prevent the beam from breaking up in the case of high current beam acceleration. For example, for an X-band structure, given $a/\lambda=0.156$, the diameter of a cell of a 120-degree traveling wave disk-loaded accelerating structure is larger than 2 cm, but the outer diameter of the dielectric tube in a DLA structure is only 1 cm if the dielectric constant of the tube is 20.

However, the choice of dielectric constant should be considered as far more complicated than the requirement of a reduced transverse dimension. It is strongly linked with other accelerating parameters as well. A very good estimate of the group velocity of a traveling wave DLA structure is given by $V_g/c \approx 1/\varepsilon_r$ (where c is the speed of light and ε_r is the relative dielectric constant of the loaded material) when a/λ is less than 15%. The quality factor of a DLA structure can be roughly estimated as $Q \approx 5.22\times10^4/\{\sqrt{[f<GHz>\times(\varepsilon_r-1)]}+5.22\times10^4\times\tan\delta\}$, where f is the frequency of the TM01 mode in units of GHz and $\tan\delta$ is the loss tangent of the loaded material.

PARAMETER CHOICE

DLA structures are generally preferred for use in a short structure powered by short, high frequency RF pulses, which reduces the probability of RF breakdown but needs a short filling time to achieve a high RF-to-beam efficiency [2]. Consider the rough design of an X-band travelling wave DLA structure. From the group velocity estimate, we choose $\varepsilon_r=10$ for a structure with $V_g=10\%$ c. Then Q can be estimated to be 3400. Since the size of the beam opening (2a) is independent of Q but tightly related to the R/Q (figure of merit of an accelerating structure) and shunt impedance R (they both increase as the beam opening decreases), we can choose a as small as the beam emittance allows to obtain both a large R/Q and R. Meanwhile the filling time (defined as L/V_g, where L is the length of the structure) remains short since the group velocity is unrelated to the beam opening. It should be pointed out that a/λ of DLA structures cannot be chosen too small since it will increase the wakefield and thus the risk of beam break-up.

Transverse wakefield damping in DLA structures has been well studied [3]. Its implementation is rather simple: an axially slotted copper jacket filled with RF absorber or metallized strips on the outer surface of the dielectric tube surrounded with RF absorber. The low Q of the DLA structures also helps the damping of long range wakefields.

Figure 1 shows a few parameters of X-band (11.7GHz) travelling wave DLA structures. Three different dielectric constants are used in the plots, representing three commonly used low loss materials: Alumina ($\varepsilon_r=10$, $\tan\delta=1\times10^{-4}$), MgCaTiO ($\varepsilon_r=20$, $\tan\delta=1\times10^{-4}$) and Quartz ($\varepsilon_r=3.8$, $\tan\delta=6\times10^{-5}$). Figure 1(a) clearly shows that the group velocity is bounded by the reciprocal of the dielectric constant as the beam opening decreases. The quality factor of a DLA structure is the combined contribution of metal wall losses and dielectric losses, but

*Work supported by the Department of Energy SBIR program.
#jingchg@hep.anl.gov

Copyright © 2012 by the respective authors — cc Creative Commons Attribution 3.0 (CC BY 3.0)

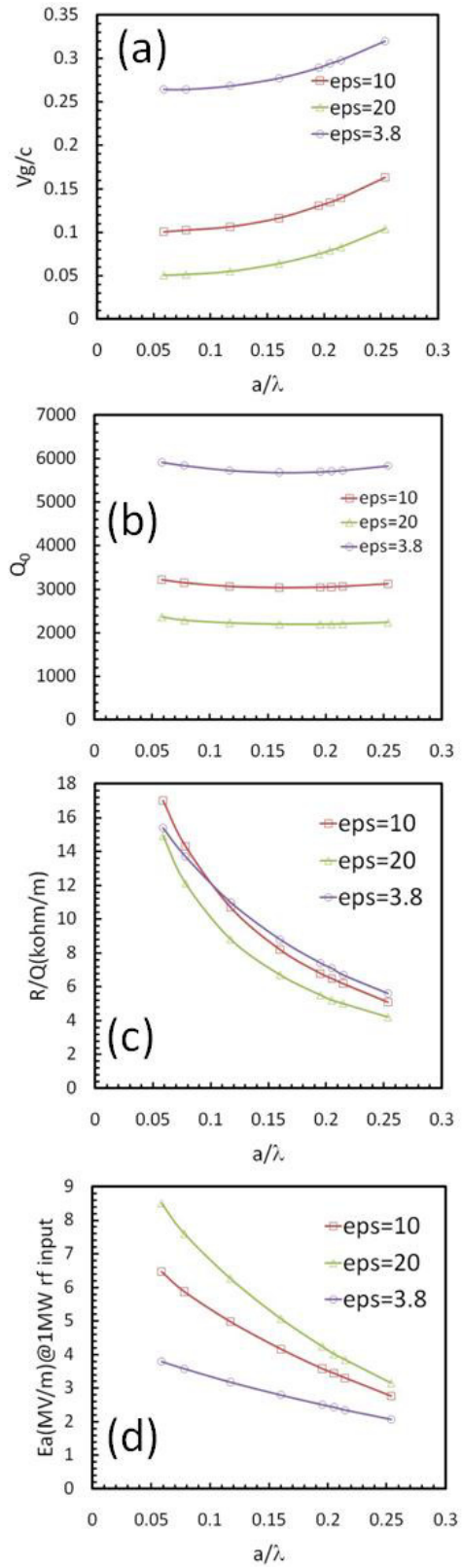

Figure 1: Dependence of parameters in DLA structures on the scaling parameter a/λ: (a) group velocity; (b) quality factor; (c) R/Q; (d) accelerating gradient.

it remains nearly constant across different size of beam channel (Fig. 1b).

From Fig. 1(c) and 1(d) we can see that the R/Q values for different dielectrics can approach or cross each other for small beam channels but the gradient in a higher ε_r DLA structure is always higher. This is because of the strong dependence of the gradient E_a on the group velocity, $E_a^2=[R/Q]\times 2\pi f\times P/V_g$, where P is the input RF power. Again, the low V_g leads to a long RF filling time which then requires a longer RF pulse to power the structure and accelerate the beam. The strong pulse length dependence of the RF breakdown rate will limit the accelerating gradient. However, in an application that does not need to operate with the gradient at a high risk level, a high dielectric constant material should be preferred since it will provide a higher gradient for a given RF power.

MULTIPACTOR

One principal effect that has limited further advances in DLA technology in the past is the problem of multipactor. The fraction of the power absorbed at saturation in the DLA structure was found to increase with the incident power, with as high as 30% of the incident power per unit length being absorbed if the dielectric material has a high Secondary Electron Yield (SEY). A thin film TiN coating, which reduces SEY, can reduce the multipactor loss below 10%. Using geometric factors, particularly the introduction of surface grooves to reduce the multipactor in DLA structures is also under investigation. However, lessons from other work show that one challenge to the success of this approach is the strong dependence upon a few critical dimensions of the groove design, which leads to a very tight machining tolerance and in turn increases the fabrication difficulties and costs.

In fact, the most effective approach to completely terminate multipactor is to use an external solenoid field. Analytical models, numerical simulations, and practical example in other applications have successfully demonstrated its effectiveness [4, 5]. In DLA structures, an external DC magnetic field in the longitudinal direction can continuously reduce the period for secondary electrons hopping on the dielectric surface (and thus spoil the resonance condition) when the ratio of the gyro-frequency to RF frequency is in the range of 0.7 to 1 (The gyro-frequency, Ω, is a plasma parameter; for electrons it is defined as $\Omega=eB/m_ec=1.76\times10^7B$ rad/s, where B is the magnetic field component perpendicular to the electron motion plane). It is equivalent to a solenoid field range from 2.8 kG to 4 kG for an X-band DLA structure. This approach is more attractive than other techniques since it can maintain all the advantages of regular DLA structures, and it is independent of the accelerator parameters other than the operating frequency.

TUNING

The need for frequency tuning (or phase velocity adjustment) of any accelerating structure arises from the fact that the phase velocity of the assembled accelerating

Copyright © 2012 by the respective authors — cc Creative Commons Attribution 3.0 (CC BY 3.0)

structure will, in general, differ from the design phase velocity due to various sources of error. In a DLA structure, these errors can be caused by machining tolerances of the dielectric dimensions, thermal expansion of the structure, dielectric constant heterogeneity, etc. The common way of tuning all-metal structures is using temperature variation or slight mechanical deformation of the accelerating structure walls. The DLA structure does not admit this possibility because the ceramic loading is usually made of a brittle microwave thermostabilized ceramic that does not allow any noticeable mechanical adjustment of its geometrical parameters. At the same time, the permittivity of BST ($Ba_xSr_{1-x}TiO_3$) ferroelectric has a strong temperature dependence. If a thin, low loss ferroelectric layer having relatively high dielectric constant (ε_r>100, tanδ<5×10^{-3}) is introduced, the DLA structure can be easily tuned by controlling its temperature. Introducing a relatively thin ferroelectric layer does not change the basic accelerating structure parameters significantly but it makes the overall average permittivity of the dielectric loaded resonator tunable in the range from tens of kHz to tens of MHz depending on the thickness of ferroelectric material [6].

RF COUPLING

Besides the dielectric loaded section, a DLA structure requires a RF coupler to feed in the high power RF signal. A well designed coupler should possess a high mode conversion efficiency (e.g. TE_{10} mode in rectangular waveguide to TM_{01} mode in DLA structure), and be less susceptible to high power breakdown. Figure 2 show three coupling schemes commonly used in DLA structures. In Fig. 2(a), the metallic RF coupler is separated from the DLA section. The tapered dielectric matching section is a part of the DLA structure that matches the impedance of the TM_{01} mode between the empty and dielectric-loaded waveguide. This coupling method can reach a very broad bandwidth at a cost of the extra length of the dielectric taper. It is worth pointing out the importance of fabricating the entire dielectric tube in a single piece. Any micro gap caused by a dielectric joint is subject to RF breakdown due to the strong field enhancement. Figure 2(b) shows a coaxial type coupling, where the impedance matching is accomplished in the coupler section so that the DLA section remains a simple straight tube. This design is very effective and compact, but the beam hole in the inner conductor of coaxial coupler may limit its usefulness in high gradient applications (i.e. where a/λ is small). Figure 3(b) shows a variation of the side coupling configuration, which is simple in fabrication but generally exhibits a smaller bandwidth than the axial coupling.

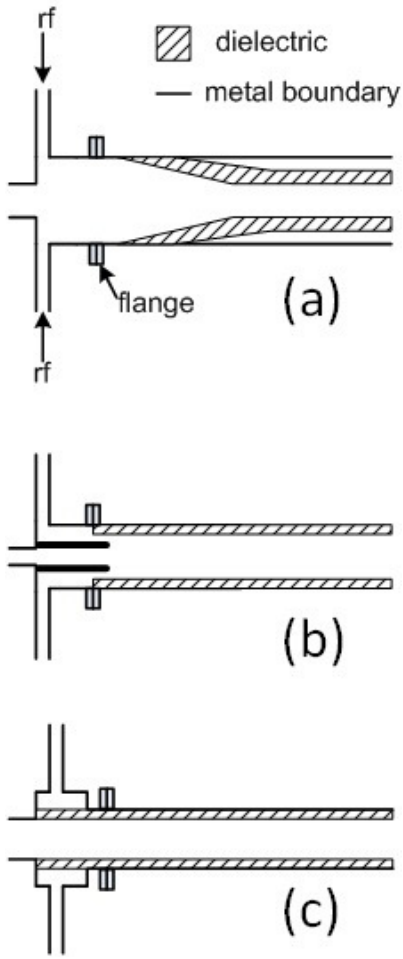

Figure 2: Three commonly used RF coupling schemes in DLA structures; (a) mode launcher; (b) coaxial coupler; (c) side coupling.

REMARKS

DLA technologies have seen significant progress for a decade. At present, it is possible to build and use a practical DLA structure. We expect that its compactness and low cost will eventually make it broadly useful in many applications.

REFERENCES

[1] G. Flesher and G. Cohn, AIEE Trans. 70 (1951): 887-893.
[2] C. Jing, et al, Proc. PAC11, NY, (2011): 2279-2281.
[3] W. Gai and C-H Ho, J. App. Phy. 70, (1991): 3955-3957.
[4] C. Chang, et al, J. Appl. Phys. 110, 063304 (2011).
[5] C-Y Yao, ANL, private communication.
[6] C. Jing, et al, Phy. Rev. Lett. 106, 164802 (2011),

Copyright © 2012 by the respective authors — cc Creative Commons Attribution 3.0 (CC BY 3.0)

FERMILAB 1.3 GHz SUPERCONDUCTING RF CAVITY AND CRYOMODULE PROGRAM FOR FUTURE LINACS*

C.M. Ginsburg#, Fermilab, Batavia, IL 60510, USA

Abstract

The proposed Project X accelerator and the International Linear Collider are based on superconducting RF technology. As a critical part of this effort, Fermilab has developed an extensive program in 1.3 GHz SRF cavity and cryomodule development. This program includes cavity inspection, surface processing, clean assembly, low-power bare cavity tests and pulsed high-power dressed cavity tests. Well performing cavities have been assembled into cryomodules for pulsed high-power tests and will be tested with beam. In addition, peripheral hardware such as tuners and couplers are under development. The current status and accomplishments of the Fermilab 1.3 GHz activity will be described, as well as the R&D program to extend the existing SRF pulsed operational experience into the CW regime.

INTRODUCTION

Work by the International Linear Collider (ILC) [1,2] community, which includes Fermilab, has motivated substantial world-wide infrastructure development and cavity performance progress. At Fermilab, this has translated to a very large commitment of resources for infrastructure and personnel development. The developed capability has led to the possibility to use the 1.3 GHz infrastructure for development of Project X [3,4], although the performance requirements are somewhat different [5]. The Project X 3 GeV CW linac requires high Q_0 at gradients (E_{acc}) in the range $15<E_{acc}<20$ MV/m; 1.3 GHz cavities can be used to investigate high Q_0. In addition, the Project X 3-8 GeV pulsed section operates at 1.3 GHz and requires ILC-like cavities with E_{acc}~25 MV/m. The status of Fermilab 1.3 GHz infrastructure, accomplishments and plans are described.

INFRASTRUCTURE

The cavities are fundamentally of the Tesla design [6], made of high RRR niobium with an elliptical cell shape, for superconducting operation at 2K. Cavity qualification has been described in detail elsewhere [7] and includes cavity inspection, surface processing, clean assembly, and one or more cryogenic qualification tests which typically include performance diagnostics. Cavities which reach the performance requirement in vertical (bare) qualification test, typically $E_{acc}>35$ MV/m, are dressed and horizontally tested. Cavities which reach the performance specification in horizontal (dressed) qualification test, also typically $E_{acc}>35$ MV/m, are assembled into cryomodules.

The joint ANL/FNAL facility is the primary infrastructure [7] for surface processing of 1.3 GHz cavities, and includes electropolishing (EP). New infrastructure at Fermilab includes two high temperature furnaces for hydrogen degassing, see Fig.1. In addition, a centrifugal barrel polishing (CBP) machine for 1-cell and 9-cell 1.3 GHz cavities has been introduced for R&D and may be used for production cavity preparation in the future, see Fig.2. CBP may be used in place of the standard bulk electropolishing step, to reduce acid use. CBP has been demonstrated to be a useful repair technique [8], and may have other benefits as well, such as reducing cavity performance sensitivity to minor manufacturing or material defects; these studies are not yet complete. A new R&D surface processing facility [9] is now fully operational for the full suite of standard EP processing for 1-cell 1.3 GHz cavities. The R&D EP tool is shown in Fig.3.

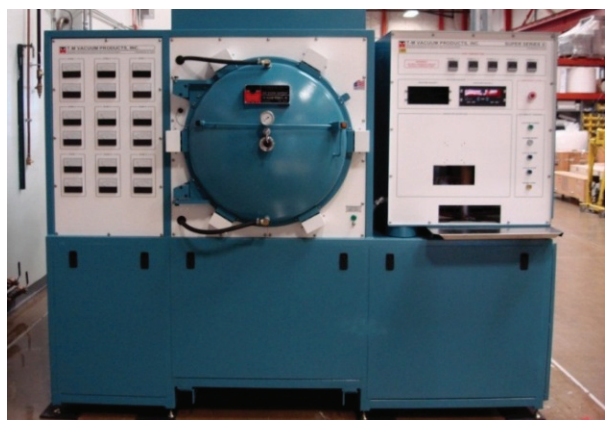

Figure 1: One of the two new vacuum furnaces.

Figure 2: Centrifugal barrel polishing machine.

*Operated by Fermi Research Alliance, LLC, under Contract DE-AC02-07CH11359 with the U.S. DOE
#ginsburg@fnal.gov

Copyright © 2012 by the respective authors — cc Creative Commons Attribution 3.0 (CC BY 3.0)

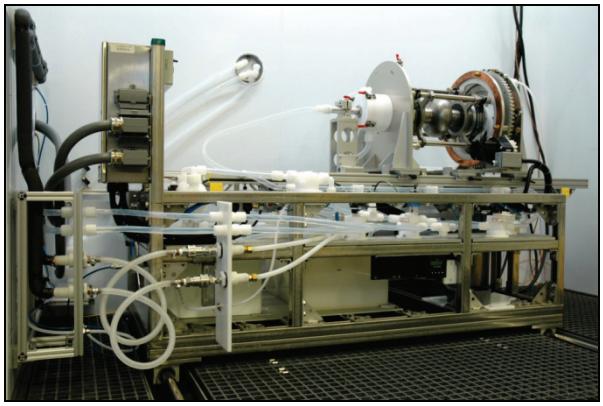

Figure 3: R&D EP tool.

ILC AND CONSIDERATIONS FOR CW

ILC R&D contributed substantially to cavity gradient performance. A worldwide effort by participating laboratories, including Fermilab, to optimize cavity processing and to develop new cavity vendors for high gradient cavities was implemented. As part of this work, a systematic analysis of cavity vertical test data was performed [10]. The data set is comprised of cavities fabricated by established vendors (ACCEL/RI, AES, MHI, Zanon), and processed by established laboratory surface processing (JLab, DESY, KEK), including electropolishing. If a cavity does not reach 35 MV/m after the initial EP processing stage, we assume it would be re-processed. Standard 2nd pass processes may include EP, HPR, or 120C bake, and are selected based on 1st pass performance at the discretion of the laboratory. There are 51 cavities in the 1st pass plot, and 35 in the 2nd pass plot. The difference in number of cavities reflects the fact that the 2nd pass may not have take place yet, or may have been done with a non-standard process. The gradient distribution of cavities which are not included in the 2nd pass yield is the same as those which are included. The ILC gradient yields, representing percentage of cavities reaching either 25 MV/m (blue points) or 35 MV/m (red points) are shown in Fig.4. ILC cavities reach 35 MV/m more than half the time after one or two EP processing cycles. For Project X, the gradient yield at 25 MV/m is of interest. In 1st pass, (69±6)% of all 51 cavities achieve >25 MV/m; and (86±13)% of 7 cavities achieve >25 MV/m considering only cavity tests taking place in 2012. In 2nd pass, (80±7)% of all 35 cavities achieve >25 MV/m; and (92±7)% of 13 cavities achieve >25 MV/m considering only cavity tests taking place in 2010-2012.

Ongoing efforts to improve cavity performance yields, either 1st pass or 2nd pass, include applying localized grinding (pioneered by KEK) to performance-limiting defects, and CBP. Many (~12) cavity repairs have been achieved through these two methods; however, at this time, cavity performance after these repairs has not been included in yield plots.

Two approaches for Q_0 optimization for Project X are being pursued at Fermilab now: venting cavities after hydrogen degassing in a nitrogen atmosphere [11], and using a hydrofluoric acid rinse as the final processing step [12]. Both approaches show promising results.

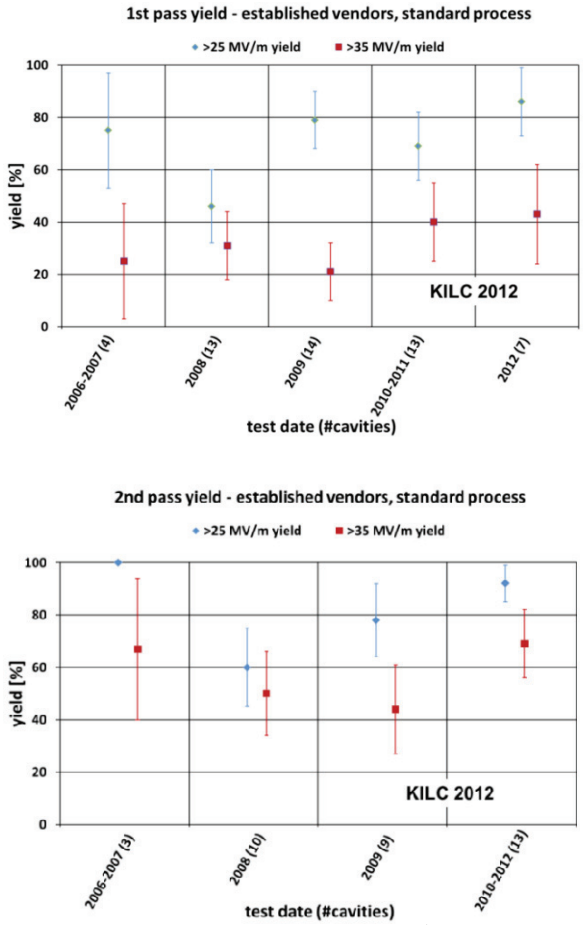

Figure 4: ILC cavity gradient yields: 1st pass (top) and 2nd pass (bottom), as a function of time. Blue points are >25 MV/m yield and red points are >35 MV/m yield.

ACCOMPLISHMENTS

Fermilab provides stewardship for 80 9-cell cavities for the ILC/Americas region. The status of these cavities is shown in Table 1. The bare cavities are processed and tested in strong collaboration with JLab, Cornell and ANL; see Fig.5 for vertical test performance.

Table 1: 9-cell Cavity Status August 31, 2012

ordered	80
received	69
processed	47
vertically tested	47
dressed	22
horizontally tested	19
CM2 installed	8

Copyright © 2012 by the respective authors — cc Creative Commons Attribution 3.0 (CC BY 3.0)

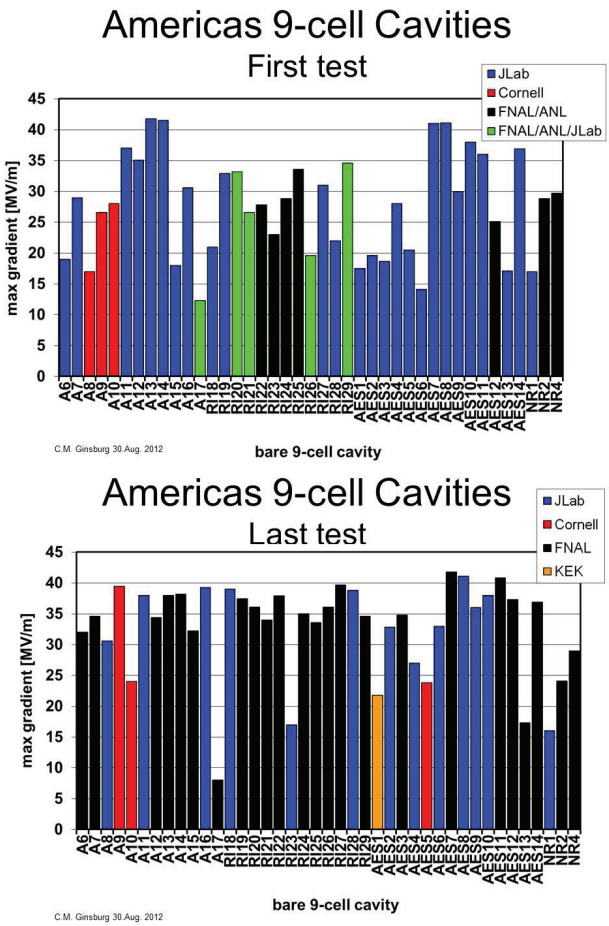

Figure 5: Gradient performance of all Americas cavities in first test (top) and last test (bottom). The test location is designated by the histogram bar color. An overall improvement is seen after additional process and test.

Two 1.3 GHz cryomodules have been assembled at Fermilab: CM1 and CM2. CM1 was built from a DESY "kit" containing parts from DESY and INFN, including surface processed, dressed, tested cavities. The magnet position is occupied by a "dummy" magnet. CM1 has been tested cold with excellent results [13]. CM2 is an 8-cavity string with a quadrupole package. CM2 is comprised of cavities which were surface processed and reached 35 MV/m in vertical test at JLab. These cavities were dressed and horizontally tested at Fermilab, then assembled into CM2. The summary of final cavity performance before CM2 assembly [14] is shown in Fig.6. CM2 will be tested at NML first without beam and then with beam within a year. All components are available for the assembly of CM3, which is expected to proceed within about a year.

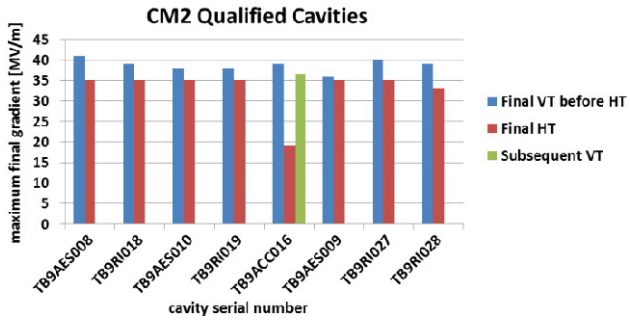

Figure 6: Gradient performance of CM2 cavities in vertical (blue) and horizontal tests (red). In one case, a subsequent dressed-cavity vertical test was performed after failed horizontal test.

ACKNOWLEDGMENTS

Material and information for this paper was provided by M. P. Kelly (ANL), R. Geng (JLab), A. Yamamoto (KEK), T. Arkan, M.S. Champion, L.D. Cooley, C. Cooper, E. Harms, A. Hocker, T. Khabiboulline, J.P. Ozelis, T. Peterson, A. Romanenko, A. Rowe, D. Sergatskov, A. Sukhanov, and V. Yakovlev (FNAL). I am grateful for their assistance. I thank my past and present colleagues in the ILC database group for providing their respective laboratories' data which were used in Figs.4-6: S. Aderhold (DESY), Z. Conway, F. Furuta (Cornell), R. Geng (JLab), Y. Yamamoto (KEK), and thank the DESY/ILC database group for their technical support. I thank the Fermilab technical staff for their hard work on cavities and cryomodules.

REFERENCES

[1] ILC Reference Design Report http://www.linearcollider.org/about/Publications/Reference-Design-Report
[2] A. Yamamoto, LINAC12, Tel-Aviv, TH3A01.
[3] Project X Reference Design Report, http://projectx-docdb.fnal.gov/cgi-bin/ShowDocument?docid=776
[4] S. Henderson, LINAC12, Tel-Aviv, TU1A01.
[5] V. Yakovlev and C.M. Ginsburg, LINAC12, Tel-Aviv, MO1A03.
[6] B. Aune et al., "The superconducting TESLA cavities," Phys. Rev. STAB **3**,092001 (2000).
[7] C.M. Ginsburg et al., LINAC10, Victoria, BC, Canada, 2010, THP026, and references therein.
[8] C. Cooper, SRF11, Chicago, WEIOA02, and references therein.
[9] C. Cooper et al., SRF2011, Chicago, TUPO025.
[10] C.M. Ginsburg et al., KILC12, Daegu, S. Korea, http://ilcagenda.linearcollider.org/contributionDisplay.py?contribId=85&sessionId=36&confId=5414
[11] A.Grassellino et al., LINAC12, Tel-Aviv, MOPB078.
[12] A. Romanenko, TTC Meeting, Beijing, 2011.
[13] E.R. Harms et al., LINAC12, Tel-Aviv, MOPB054.
[14] A. Hocker et al., IPAC12, New Orleans, WEPPC049.

Copyright © 2012 by the respective authors — cc Creative Commons Attribution 3.0 (CC BY 3.0)

NON-DESTRUCTIVE INSPECTIONS FOR SC CAVITIES

Y. Iwashita, Y. Fuwa, M. Hashida, K. Otani, S. Sakabe, S. Tokita, H. Tongu,
Kyoto University, Uji, Kyoto, JAPAN
H. Hayano, K. Watanabe, Y. Yamamoto, KEK, Ibaraki, JAPAN

Abstract

Starting from the high-resolution camera for inspection of the cavity inner surface – so-called Kyoto Camera, high resolution T-map, X-map and eddy current scanner have been developed. R&D for radiography techniques is also going on to detect small voids inside the Nb EBW seam, where the target resolution is 0.1 mm. Some radiography tests with X-rays induced from an ultra short pulse intense laser were carried out. The local treatment technique on the found defects is also realized by the Micro-Grinder.

INTRODUCTION

Non-destructive Inspections play important roles in improving yield on production of high performance SC Cavities. Starting from the high-resolution camera for inspection of the cavity inner surface [1], high-resolution T-map, X-map and eddy current scanner [2,3,4,5,6] have been developed. We are also investigating radiography to detect small voids inside the Nb EBW seam, where the target resolution is 0.1 mm. We are carrying out radiography tests with X-rays induced by irradiations of an ultra short pulse intense laser on a target metal sheet. Defects found by the inspection technique can be locally treated by the Micro-Grinder.

CAVITY CAMERA UPDATE

In order to inspect the SPL cavity at CERN, whose frequency is about a half of ILC cavity and the diameter is about twice larger, the illumination system has been enhanced to illuminate the wider surface area (see Fig. 1). Although the iris diameter is about twice larger than that of ILC's, the bore diameter at the flange position is limited (just below ø80mm). This limits the camera cylinder diameter is ø70mm. Fig. 2 shows the modification on the illumination system to illuminate the wider area with enough strength. While the former system used two LED's for each strip, the new system uses 14 LED chips on a line and two lines consist one strip. Thus 28 LED chips are used for a strip. Furthermore, the LED chip has three LED's in a package. This illumination system should provide enough light for the wider cavity surface area. Because of the larger cavity size, the working distance is longer than former model and a bigger lens system is adopted. Fig. 3 shows the overview of this system. The illumination plate on the cylinder is shown in Fig. 4. The camera cylinder can be rotated to see the annular area in a cavity without movement of the cavity, while the cavity table can rotate the cavity if it does not wear its He jacket around. The table has a function to move the cavity in its axial direction.

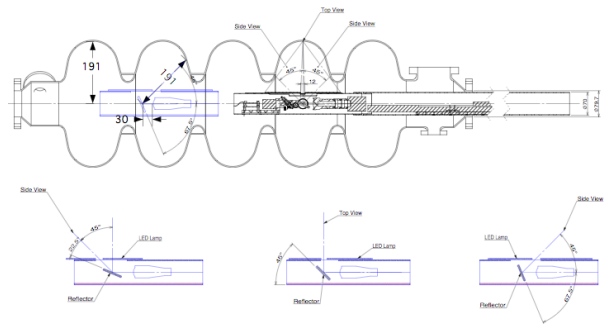

Figure 1: CavCam3 in SPL cavity.

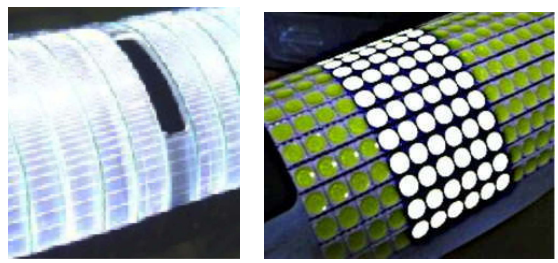

Figure 2: Enhanced illumination for wider surface area (Armadillo Illumination). 28 LED chips (right) instead of 2 LED's per strip (left) are installed.

Figure 3: Latest CavCam-3 for SPL cavity at CERN.

Figure 4: All the LED's are lighten. A diffusing panel will be install on the LED's to form the light strip. 14 chips/line x 2 lines/strip x 10 strips/side x 2 sides = 560 chips are used.

Copyright © 2012 by the respective authors — cc Creative Commons Attribution 3.0 (CC BY 3.0)

HIGH DENSITY T-MAP & X-MAP

The high density Temperature mapping system (T-map) and X-ray mapping system are under development. These systems utilize multiplexing technique to reduce the number of lines from the sensors to the measurement circuits. The temperature sensors are put on a Nb cavity surface during the vertical test to detect the temperature rise from the quench phenomena due to a defect on the inner surface, if any. Since one temperature sensor / cm^2 is assumed for the surface density, 1024 sensors will be installed on a cell and about nine thousands of sensors will be need to be connected to the measurement circuit. The number of lines needed for these connections is reduced by multiplexing the analog signals in the cryogenic area. The reduced lines include the three power supply lines (0V, ±5V), one clock line, one reset line, and two signal lines for each type of system (t-map and X-map) as shown in Fig. 5. T-sensors are installed on the inner side and X-sensors are located on the other side. T-sensors contact on the cavity surface (see Fig. 6). As shown in Fig. 7 the leaves can be instantly attached on a cell, which helps to reduce the installation time for a vertical test.

A dedicated X-map system for installation under the stiffener ring is also developed (see Fig. 8). Only X-sensors are installed on the PCB, which can slide into the space under the stiffener ring as shown in Fig. 9.

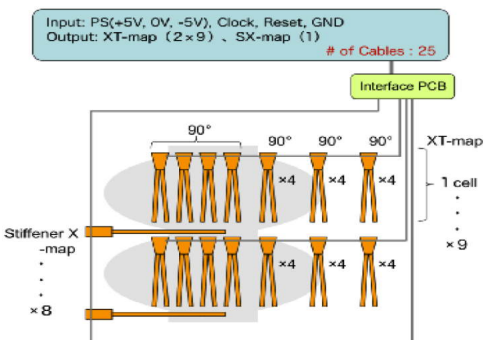

Figure 5: The inter-connection for the XT-map system.

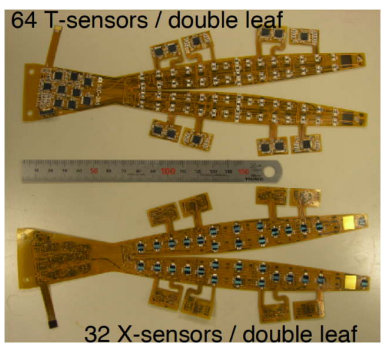

Figure 6: Leaf shaped flexible PCB.

HIGH RESOLUTION EDDY CURRENT SCAN

A Nb sheet before the press to form the cup will be inspected by a Eddy current scan [7]. Using a multi-frequency Eddy current probing system, a small void just under the surface, which may appear after surface treatments such as electropolishing (EP), would be detected. The depth information would be obtained from the three different frequency data simultaneously acquired during the measurement. The detected hole size is currently ø100µm x 50µm depth (see Fig. 10).

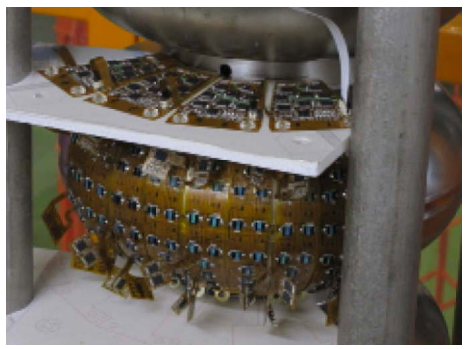

Figure 7: Installed XT-map leaves on a cell.

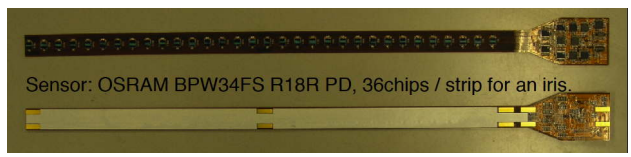

Figure 8: Stiffener X-map.

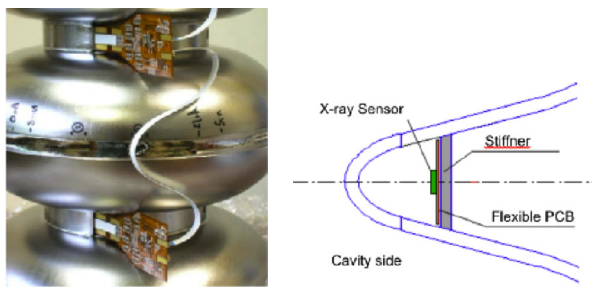

Figure 9: Installed stiffener X-map ribbons. The ribbons go under the stiffer ring.

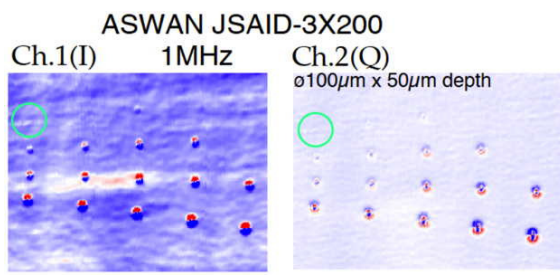

Figure 10: The high resolution eddy current scanner can detect the drilled holes on the Nb sheet down to ø100µm x 50 µm depth.

RADIOGRAPHY EFFORT

In order to inspect the EBW seam especially for possibly buried defects under the surface, various radiography techniques have been investigated such as

Copyright © 2012 by the respective authors — cc Creative Commons Attribution 3.0 (CC BY 3.0)

X-ray CT, and neutron CT. Since Nb has larger atomic number, high energy X-rays tend to be preferred for a better transmission. The contrast, however, becomes worse for high energy X-rays. Although the phase contrast techniques should have better contrast even in this case, it is not a handy way. After some trials, laser induced X-ray radiograph is under investigation (see Fig. 11). Fig. 12 shows the obtained radiography images for targets of Zr and Ag, where Zr is supposed to be better because of the X-ray energy just below the K absorption edge of the Nb. Further study is needed for better visibility and practical applications.

LOCAL REPAIR TECHNIQUE

Using the inspection devices, defects on the surfaces can be identified and analyzed. For those defects judged as harmful, the local repair technique should be applied. The micro-grinder can be inserted into the cavity, while the grinding head is retracted (see Fig. 13)[8]. After its positioning, some amount of water is applied to the area and the head with abrasives can start to grind. The grinding time can be limited by a timer up to 99 minutes. Additional EP and following processes are applied to the treated cavity to bring the cavity back to the line. Several cavities have been already repaired and show satisfactory results (see Fig. 14).

REFERENCES

[1] Y. Iwashita, Y. Tajima, H. Hayano, Development of High Resolution Camera for Observations of Superconducting Cavities, Phys. Rev. ST Accel. Beams, 11, [093501-1]-[093501-6], 2008

[2] A. Brinkmann, W.Singer, Nondestructive Testing of Niobium Sheets for Srf Cavities Using Eddy-Current and Squid Flaw Detection, Proc. LINAC08, Victoria, BC, Canada, pp.800-801

[3] L. Cooley, C. Antoine, G. Wu, D. Sergatskov, H. Jiang, R. Schuessler, O. Frianeza, Fermilab QA and QC activities, FNAL slides for TTC meeting Jan 2008

[4] Balle, Ch., Casas-Cubillos, J. et al, Influence of Thermal Cycling on Cryogenics Thermometers in Advances in Cryogenic Engineering 45B, Plenum, New York, 1999, pp. 1817.

[5] H. Tongu, et al., Multipoint T-maps for Vertical Test of the Superconducting Accelerator Tubes, Proc. of the 6th Annual Meeting of Particle Accelerator Society of Japan, (2009) 409-411.

[6] A. Canabal, et al., Development of a Temperature Mapping System for 1.3-Ghz 9-Cell Srf Cavities, Proc. PAC07 2406 - 2408 (2007).

[7] Updates on R&D of Non-destructive Inspection Systems for SRF Cavities, Y. Iwashita, H. Tongu, H. Hayano, T. Saeki, K. Watanabe, to be appeared as Proc. of SRF11, July 2011, Chicago.

[8] K. Watanabe, H. Hayano, E. Kako, S. Noguchi, T. Shishido, Y. Yamamoto, Y. Iwashita, Repair Techniques of Superconducting Cavity for Improvement Cavity Performance at KEK-STF, Proc. IPAC10, Kyoto, 2010

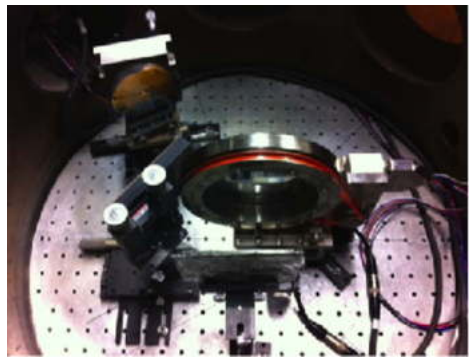

Figure 11: Layout for the laser induced X-ray radiography experiment. Various target materials can be irradiated by the laser to generate X-rays.

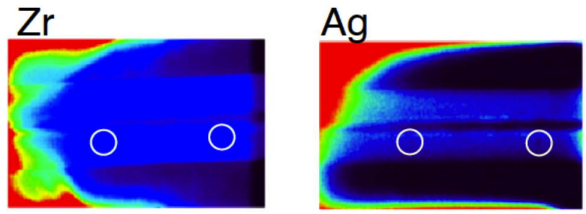

Figure 12: Obtained radiography images for targets of Zr and Ag. Both target materials give better visibility for the defects (sputter balls on the surface).

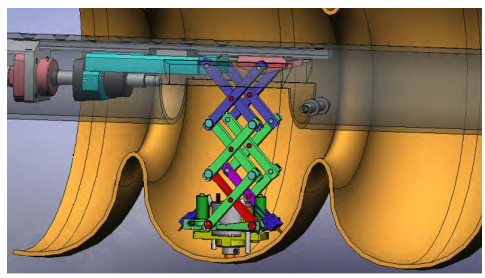

Figure 13: The grinding head assembly that has a tiny monitoring camera protrudes by a motor control towards the area to be treated.

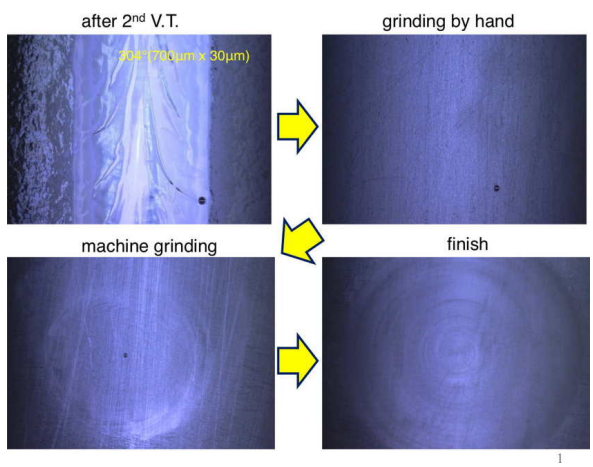

Figure 14: The progresses on the local grinding effect. The defect detected by the optical inspection was removed by the treatment.

Copyright © 2012 by the respective authors — cc Creative Commons Attribution 3.0 (CC BY 3.0)

NORMAL CONDUCTING DEFLECTING CAVITY DEVELOPMENT AT THE COCKCROFT INSTITUTE

G. Burt, P. K. Ambattu, A. C. Dexter, B. Woolley, C. Lingwood, Cockcroft Institute, Lancaster, UK
S. Buckley, P. Goudket, C. Hill, P. A. McIntosh, J. Mackenzie, A. Wheelhouse,
STFC, Daresbury, UK
V. Dolgashev SLAC, USA
A. Grudiev, CERN, Geneva, Switzerland
R M. Jones, UMAN, Manchester, UK

Two normal conducting deflecting structures are currently being developed at the Cockcroft Institute, one as a crab cavity for CERN linear collider CLIC and one for bunch slice diagnostics on low energy electron beams for Electron Beam Test Facility EBTF at Daresbury. Each has its own challenges that need overcome. For CLIC the phase and amplitude tolerances are very stringent and hence beamloading effects and wakefields must be minimised. Significant work has been undertook to understand the effect of the couplers on beamloading and the effect of the couplers on the wakefields. For EBTF the difficulty is avoiding the large beam offset caused by the cavities internal deflecting voltage at the low beam energy. Prototypes for both cavities have been manufactured and results will be presented.

INTRODUCTION

Transverse deflecting cavities are required for many applications on accelerators, including crab cavities, bunch separators, emittance exchange and for bunch length diagnostics. These cavities usually operate in a TM_{110}-like mode. The Cockcroft Institute in the UK is participating in the design of several deflectors for a range of applications including crab cavities for ILC [1], CLIC [2] and LHC [3] and a bunch length diagnostic for EBTF [4]. In this paper we concentrate on the normal conducting rf deflectors for CLIC and EBTF.

CLIC CRAB CAVITY

CLIC requires a crab cavity to rotate the bunches prior to the interaction point (IP) to achieve an effective head-on collision. As the bunch size at the IP is very small (~5 nm) the luminosity is very sensitive to the crab cavities RF phase and amplitude. This means that the beamloading must be minimised and correction applied. The beamloading is dependent on the longitudinal electric field experienced by the bunch. In crab cavities the longitudinal electric field is zero on axis but has a linear variation as the bunch goes off axis. This means the beamloading could be positive or negative depending on the beam offset. As the bunch train for CLIC is short (~200 ns), the beamloading cannot be compensated for in a single bunch train, the feedback would occur over several trains. Unless the jitter on the beam offset is much less than the bunch size the compensation will not be successful, hence the beamloading must be minimised instead [5]. In order to reduce the effect of beamloading the cavity is designed with a large power flow so that any power induced by beamloading is smaller in comparison. This is achieved by using a high group velocity travelling wave structure.

Another issue affecting beamloading is the perturbation of the input and output couplers. Couplers break the symmetry of the cavity and can give rise to monopole components to the deflecting field. A dual feed coupler keeps the symmetry of the structure and avoids monopole components but is more complex coupling arrangement requiring splitters. A single feed is the simpler coupling arrangement however this gives the end cells a large monopole component of the rf field. We have investigated methods of single feed coupling without inducing monopole component.

Single-feed Couplers

In order to minimise the monopole component of rf field in the end cells while using a single-feed coupler a number of options were investigated. Initially cancelling the monopole kick from the two end cells was studied. Consider particle moving at the speed of light. If the cell is rotated the monopole component has the sign of the real part of the voltage flipped. Hence if the input and output couplers are mounted on opposite side the real parts should cancel. If the lengths of the cells are adjusted so that the voltage is entirely real then the entire monopole component is cancelled. This however is not sufficient in travelling wave deflecting structures as the power put into the output cell will be extracted through the output coupler while the power in the input cell will travel down the structure. Hence it is necessary to cancel the beamloading in each cell individually.

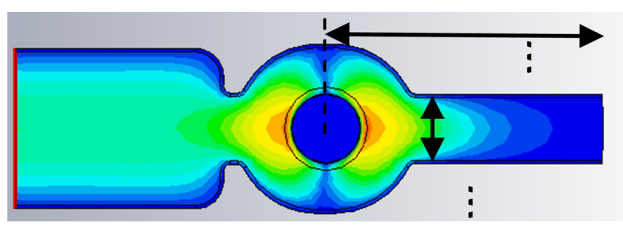

Figure 1: Dummy waveguide and input coupler on the CLIC crab cavity

In order to restore the symmetry of the cell a dummy waveguide opposite the coupler was studied. Using a

Copyright © 2012 by the respective authors — cc Creative Commons Attribution 3.0 (CC BY 3.0)

dummy waveguide was found to significantly reduce the monopole component but not reduce it to zero. The real part is reduced to zero, but the imaginary component is not and hence gives the minimum voltage. The reason for this is because there must be a power flow across the cell, from the coupler to the dummy waveguide. This means that there cannot be a full standing wave in the cavity and there must be a travelling wave component.

Another method of symmetrising the cell is to couple from the side with a TE_{02} mode coupler. This allows an equal power flow to each side hence avoiding a monopole component. However the cavity is now vertically asymmetric and hence there is a small vertical kick. However this symmetry can be recovered by adding a dummy waveguide. The TE02 mode splitter must carefully be designed to avoid excitation of a TE01 mode which gives rise to a monopole component to the fields.

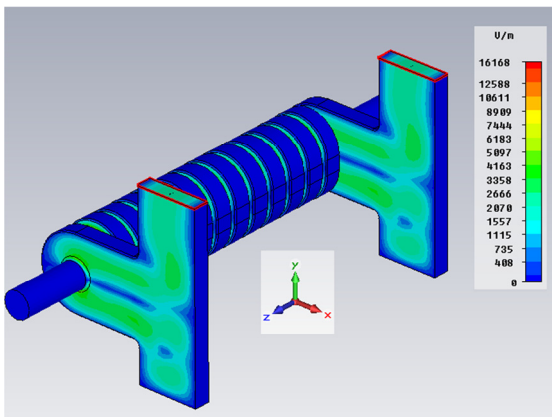

Figure 2: TE_{02} mode coupler

Wakefield Damping

As the cavity is close to the final focus magnets, where the beta function is large, it is very sensitive to transverse wakefields. It is necessary to damp any long-range wakefields within a few bunches to avoid large transverse offsets at the IP. The vertical wakefield is the most sensitive, due to the small vertical beam size, and is dominated by the opposite polarisation of the crabbing mode, known as the same order mode (SOM). As the wake is dominated by a single mode it is proposed to have this modes frequency at the zero-crossing, where the mode frequency is a half integer harmonic of the beam frequency. This means that each bunch induces a voltage 180 degrees out of phase with the previous bunch hence cancelling each other. For CLIC it is proposed that the cell has an elliptical cross-section such that the crabbing mode is at 11.99 GHz while the SOM is at 12.98 GHz. However the SOM still requires significant damping due to the very tight tolerances on vertical kicks. Choke damping and waveguide damping were both considered. Choke cavities are difficult for deflecting cavities as the choke must be polarised to damp one polarisation but not the other. Options are to use an elliptical cavity, an elliptical choke or a slotted choke [6]. The slotted choke achieved the best performance; however widening the slot to achieve better damping also reduces the Q of the crabbing mode which could be problematic due to enhanced heating. For this reason a waveguide damper was chosen for CLIC, as shown in Fig.3, as a waveguide coupler shows strong damping of the SOM without affecting the crabbing mode.

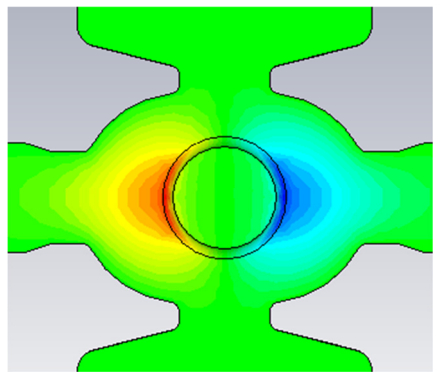

Figure 3: Damped elliptical cell of the CLIC crab cavity

Cavity Prototype

Two prototype cavities have been manufactured. One has been made by Shakespeare Engineering, a UK company, to be tested at SLAC and the other has been made at VDL, to be tested at CERN. The CERN cavity has had the parts machined and is due to be brazed soon. The SLAC cavity, shown in Fig. 4, has been fully manufactured and is currently undergoing tests at Cockcroft before shipping to SLAC.

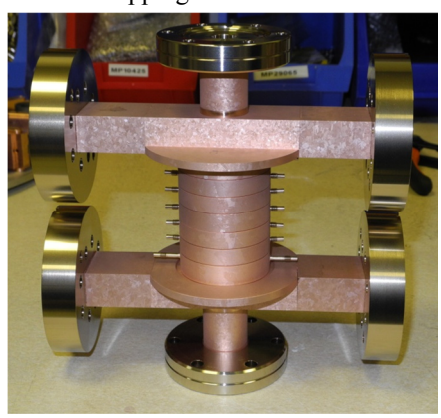

Figure 4: CLIC crab cavity prototype manufactured by Shakespeare Engineering.

EBTF TRANSVERSE DEFLECTING CAVITY

The Electron Beam Test Facility (EBTF) at Daresbury Laboratory will deliver low energy (5/6 MeV) short bunches (down to 40fs RMS) to a number of industrial experimental stations and for fundamental scientific research. In order to measure the longitudinal profile of the bunch an S-band transverse deflecting cavity will be inserted into the beamline. A transverse kick of around 5 MV is required, hence a 9 cell design has been chosen. The design of the transverse deflecting cavity has been influenced by the competing demands of high RF efficiency [7] and minimising the equal and opposite

Copyright © 2012 by the respective authors — cc Creative Commons Attribution 3.0 (CC BY 3.0)

unwanted transverse kick at the entrance and exit of the cavity which causes the low energy electrons to be displaced while traversing the cavity [8]. The coupler has a dummy waveguide to minimise the on-axis longitudinal electric field.

Minimising transverse offset

As a transverse deflecting cavity has a finite size the beam experiences a range of phases as it crosses the cavity. This means for a zero-crossing it experiences a finite force, initially in one direction and then in the other such that the net transverse momentum at the centre of the bunch is the same at the start and end of the cavity. However this does result in a transverse offset as the beam travels transversely inside the cavity. It was found that due to the beampipe the electrical centre of the end cell was not at the geometric centre. This resulted in an uneven kick producing a net transverse momentum when leaving this cell, which wasn't removed until experiencing the opposite force at the other end cell. This gave a much larger transverse offset in the cavity, of 4 mm, due to the low energy of the bunch. As the beam was offset the beamloading was much higher which significantly altered the beam energy. For ultra-relativistic beam this offset is small and typically ignored. For low energy beam of EBTF is could not be ignored and has to be minimized.

In order to counteract this effect the end cells were made much shorter such that transverse kick in the end cells for a zero-crossing particle was minimised. The final cavity is shown in Fig. 5. The particle tracking simulations in GPT [9] show the transverse offset inside the cavity is minimised, shown in Fig. 6.

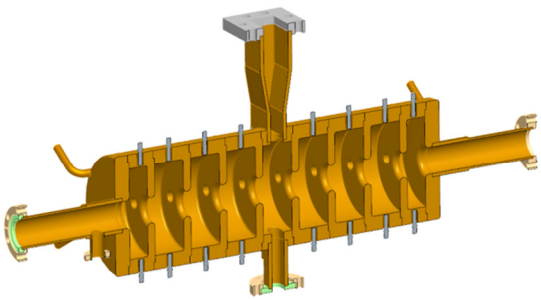

Figure 5: EBTF Transverse deflecting cavity with shortened endcells.

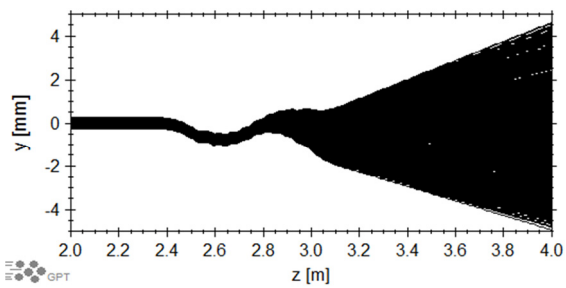

Figure 6: GPT tracking simulation of EBTF transverse motion.

Prototype Cavity

A 3-cell prototype has been produced by Research Instruments (shown in Fig. 7), to verify brazing procedure, and a contract has been placed with them for a full 9-cell structure.

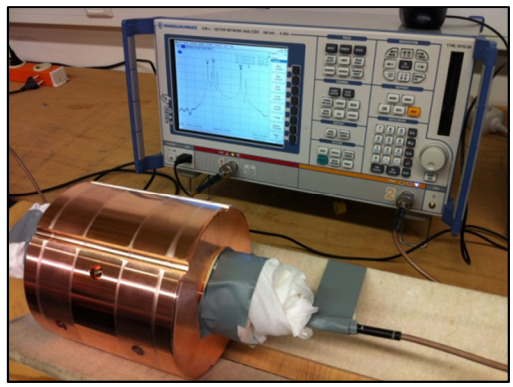

Figure 7: 3-cell prototype of the EBTF Transverse deflecting cavity.

SUMMARY

The Cockcroft Institute has a proven track record of designing deflecting cavities for numerous applications. High power testing is expected to be done on both cavities in the next few months.

ACKNOWLEDGEMENTS

This work has been supported by STFC via the Cockcroft Institute core grant and the EU through the EUCARD grant.

REFERENCES

[1] C. Adolphsen1 et. Al, Design of the ILC Crab Cavity System, EUROTeV-report-2007-010, 2007

[2] P.K. Ambattu, G. Burt, et al, An asymmetric crab cavity design for the CLIC, IPAC 2011

[3] R. Calaga, LHC Luminosity Upgrade Using Deflecting/Crabbing Cavities, ICFA DMC, Cockcroft Institute, September 2010

[4] P.A. McIntosh et al, A New Electron Beam Test Facility (EBTF) at Daresbury Laboratory for Industrial Accelerator System Development, IPAC 2012

[5] A. Dexter et.al, CLIC Crab Cavity Design Optimisation for Maximum Luminosity, Nucl. Instr. and Meth. A (2011)

[6] P.K. Ambattu et.al, Analysis and control of wakefields in X-band crab cavities for Compact Linear Collider, Nucl. Instr. and Meth. A (2011)

[7] G. Burt et al, A transverse deflecting cavity for the measurement of short low energy bunches at EBTF, IPAC 2012

[8] John Power , REPORT ON THE 2 CELL CAVITY SIMULATIONS WITH THE HALF – FULL – HALF GEOMETRY, ANL-AAI-TN-2007-003, 2007

[9] M.J. de Loos, S.B. van der Geer, General Particle Tracer,http://www.pulsar.nl/gpt

Copyright © 2012 by the respective authors — cc Creative Commons Attribution 3.0 (CC BY 3.0)

STATUS OF THE C-BAND RF SYSTEM FOR THE SPARC-LAB HIGH BRIGHTNESS PHOTOINJECTOR

R. Boni, D. Alesini, M. Bellaveglia, G. Di Pirro, M. Ferrario, A. Gallo, B. Spataro,
INFN-LNF, Frascati, Italy
A. Mostacci, L. Palumbo, ULRS, Rome, Italy

Abstract

The high brightness photo-injector in operation at the SPARC-LAB facility of the INFN-LNF, Italy, consists of a 150 MeV S-band electron accelerator aiming to explore the physics of low emittance high peak current electron beams and the related technology. Velocity bunching techniques, SASE and Seeded FEL experiments have been carried out successfully. To increase the beam energy so improving the performances of the experiments, it was decided to replace one S-band travelling wave accelerating cavity, with two C-band cavities that allow to reach higher energy gain per meter. The new C-band system is in advanced development phase and will be in operation early in 2013. The main technical issues of the C-band system and the R&D activities carried out till now are illustrated in detail in this paper.

THE SPARC-LAB AT FRASCATI LNF

The SPARC-LAB is a research facility of the INFN Frascati Laboratory (LNF) whose purpose is to conduct advanced research in the field of high brightness, low emittance electron beams [1]. The facility, able to operate also in the velocity bunching configuration, feeds six 2m. long undulators and integrates the 150 MeV S-band photo-injector with a 220 Terawatt, Ti:Sa ultrashort laser system. FEL radiation in the SASE, Seeded and HHG modes have been performed from 500 nm down to 40 nm wavelength. The photo-injector SPARC, a single bunch electron accelerator, consists of a laser driven RF Gun followed by three traveling wave (TW), constant gradient, $2\pi/3$ accelerating cavities, with the first two immersed in a solenoidal field to keep down the beam emittance growth. A second beam line has been also installed and is now hosting a narrow band THz radiation source.

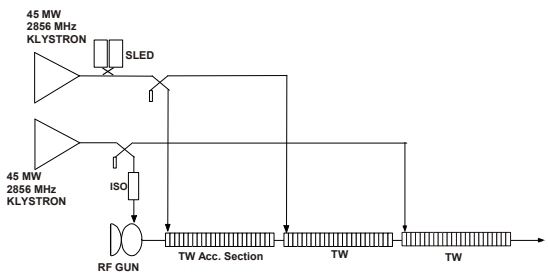

Figure 1: the SPARC photoinjector present layout

To improve the performances of the experiments and recuperate the energy that is lost in the velocity bunching configuration. it was decided to increase the beam energy by replacing the third S-band section with two, 1.4 m. long, C-band TW accelerating structures that allow to operate at higher gradient. The choice of a higher frequency, e.g. the X-band, was also considered but then discarded because more expensive and technically more challenging.

THE C-BAND RF SYSTEM

The C-band technology is relatively new in linear accelerators compared to the standard and widely used S-band systems. Nevertheless it can be considered sufficiently mature since it is already employed in other accelerator laboratories like the Spring8 (JP) and the PSI FEL (CH) facilities.

R&D of the accelerating structure

The third S-band accelerating section, that is a 3 m. long SLAC-type unit, shown in Fig.1will be replaced with two, 1.4 m., C-band sections supplied with a 50 MW, 5712 MHz Toshiba klystron through a SKIP-type pulse-compressor [2]. In order to ease design and construction, the C-band sections are constant impedance (CI) structures with large (14 mm) iris diameter to minimize the surface electric field on the iris edges and improve the pumping speed. Also, the group velocity increases and this reduces the filling time. It must be remarked that the typical exponential decay of the input compressed pulse is partially compensated by the RF losses of the CI structure, resulting in a quasi-constant field amplitude along the section. Input and output waveguides are coupled to the beam-pipe instead of to the end-cells. A 50 cm long prototype was designed at LNF and built by a local firm. Brazing and vacuum test have been made at LNF [3].

The prototype, shown in figure 2, has been power tested at KEK, in the frame of a collaboration established ad hoc with the INFN.

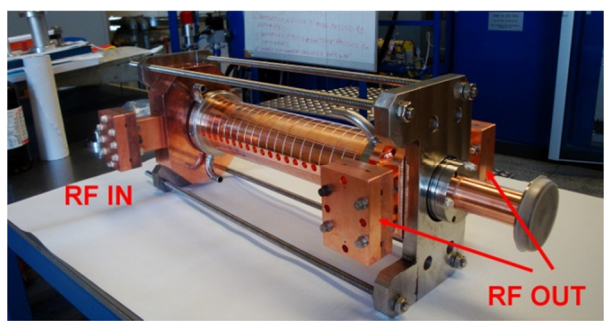

Figure 2: The C-band prototype tested at KEK.

The KEK RF station consists of a 50 MW - 2.5μsec Toshiba E37202 klystron, followed by a pulse

Copyright © 2012 by the respective authors — cc Creative Commons Attribution 3.0 (CC BY 3.0)

compressor. The results of the power tests, reported in detail in the ref. [4], was very successful and well beyond our expectations. The C-band prototype was tested up to 110 MW peak - 200 nsec - 50 Hz to a maximum average gradient of 55 MV/m, with a breakdown rate of the order of 10^{-6} bpp/min after about 300 hours of RF conditioning. A picture of the prototype is shown in figure 2.

Following the positive results of the KEK power test, we started the construction of two 1.4 m accelerating sections. The next figure 3, shows the concept of the beam-pipe coupling. This type of coupling allows the first RF cell to be mechanically unperturbed, i.e. there are no slots on the cell outer wall that normally cause heating and degrade the performances.

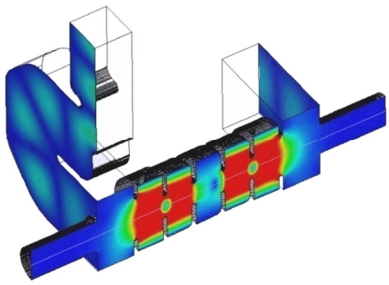

Figure 3: The waveguide beam-pipe coupling

Further, the symmetric coupling guarantees low quadrupole components on the longitudinal axis [3]. The same concept of beam-pipe coupling is applied at the accelerating section output, with two opposite flanges without combiner. So we use 2 loads per section but the power dissipated by each load is halved.

The actual accelerating structures consist of 71 cells and are 1.4 m. long, to leave 20 cm for the insertion of a pumping unit in the 3 m. left available by the 3rd S-band section. The new C-band sections have been manufactured The cells and the waveguide couplers have been machined by a local firm; then, low power test and brazing of two halves have been made at LNF where a vacuum furnace of 80 cm of internal height is available. After joining mechanically the two halves, the first C-band section was tuned at LNF by adjusting the plungers on each cell wall. The last brazing will be made shortly by a local firm, where a 2 m. long vacuum furnace is available. The C-band actual section in shown in the next figure 4. The figures 5 and 6 show the low power measurements made in laboratory with the bead perturbation technique. The following table 1 shows the main specifications of the C-band accelerating structures.

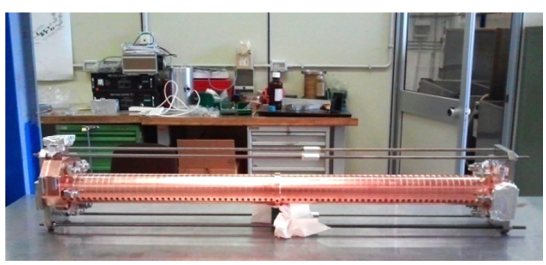

Figure 4: The two halves of one C-band section before the final brazing

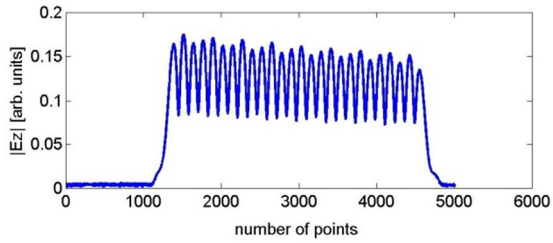

Figure 5: RF field profile of half C-band section

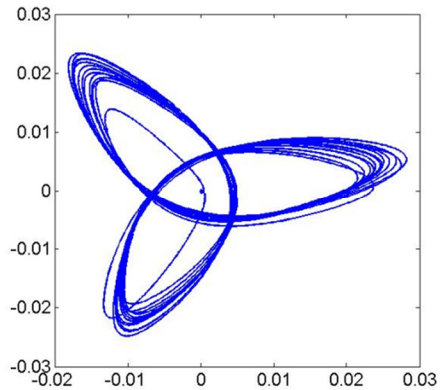

Figure 6: Phase advance per cell in the polar plane

Table 1: C-band structures main parameters

Frequency (MHz)	5712
type	TW, CI
structure	Disk loaded
Phase advance per cell	2π/3
n. of cells	71
Coupling type	beam-pipe
Iris radius (mm)	7.0
Group velocity/c	0.0283
Shunt impedance (MΩ/m)	82.9
Surf. peak E field/Acc. field	2.17
Filling time (nsec)	150
Total length with couplers (cm)	140

The RF power needed to produce the accelerating field is about 60% of input power. The residual 40% will be dissipated by two RF water-loads, supplied by CML-Engineering, connected to the output coupling ports of the accelerating sections.

The power transmission system

The layout of the complete C-band system is presented in figure 7. The RF power will be distributed to the accelerating structures by means of a network of rectangular WR187 waveguides (WG) made of OFHC copper. The total WG length from the klystron to the

Copyright © 2012 by the respective authors — cc Creative Commons Attribution 3.0 (CC BY 3.0)

accelerating sections is about 10 m. and the RF losses are of the order of 10% since the attenuation is 0.035 dB/m.

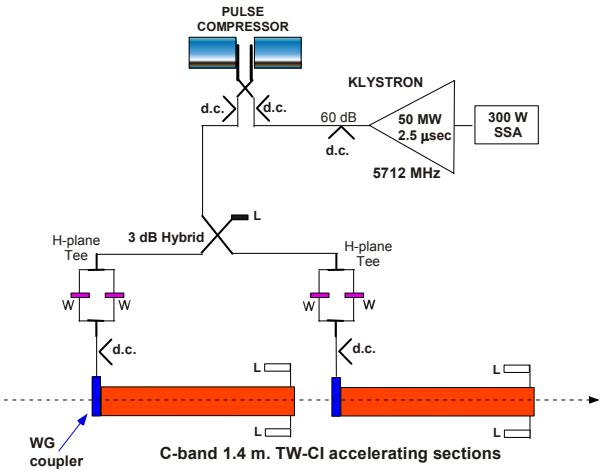

Figure 7: Layout of the SPARC C-band system

The C-band pulse compressor (PC) is under construction by the Division of Technology Development of the IHEP, Beijing, China. It is a double slot coupled cylindrical resonator system that follows the concept of the model "SKIP" developed by KEK. The PC output power is divided in two by a 3 dB hybrid junction and then delivered to the accelerating sections through two RF windows. The RF is split and recombined with two H-plane Tees. In this way the peak power through each RF window is halved as we are not sure of the actual capacity of them to handle power levels in excess of 100 MW peak.

The H-plane Tee s11 is -20 dB and the phase unbalance between outputs is about 1°. They have been designed and brazed at LNF. The machining was made by the local firm Comeb.

The RF Power Station

The RF power station consists of the Toshiba klystron E37202 driven by a solid state 400 W amplifier supplied by MitecTelecom. The pulsed klystron modulator is also a full solid state system made by Scandinova. The table 2 lists the main parameters of the RF power station. The klystron have been successfully RF tested on a dummy load up to 40 MW – 2 µsec – 10 Hz. The klystron RF conditioning is still ongoing.

Table 2: C-band power station main parameters

Frequency (MHz)	5712
Max klystron power (MW)	50
RF pulse width (µsec)	2.5
Klystron input RF power (W)	300
Klystron beam voltage (kV)	350
Max RF pulse rep. rate (Hz)	10

The Low Level RF System

The control of the C-band accelerating structures will be achieved by a digital low level RF (LLRF) system where all RF signals are down-converted to intermediate frequencies which are then digitized and processed with powerful digital processing platforms. The drive signal is finally up-converted to control the RF high power chain The schematic layout of the digital control system is shown in the figure 8.

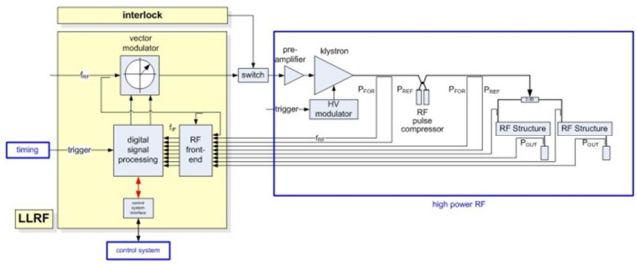

Fig. 8: Schematic layout of the digital LLRF system.

A processing board based on VME64x is under development by the PSI laboratory (CH) in collaboration with INFN. It includes a multi-core PowerPC processor and a high performance field programmable gate array Xilinx Virtex-6 on the main board and provides a variety of I/O interfaces. The goal of the digital signal processing is to implement all static algorithms like the digital down-conversion from intermediate frequency to base-band, filtering, I/Q to amplitude/phase conversions and averaging calculations in firmware in the FPGA while using the PowerPC for more sophisticated high level applications like pulse-to-pulse feedback algorithms.

REFERENCES

[1] M. Ferrario et al., "Recent Results at the SPARC_LAB Facility", IPAC11, S. Sebastian, Spain.
[2] T. Sugimura et al., "SKIP, A Pulse Compressor for SuperKEKB", Proc. of Linac2004 Conference.
[3] D. Alesini et al., SPARC-RF-11-002, LNF Techn. Note.
[4] D. Alesini et al., " Design, Fabrication and Power Test of a C-band Acc. Structure", IPAC 11, S. Sebastian, Spain.

Copyright © 2012 by the respective authors — cc Creative Commons Attribution 3.0 (CC BY 3.0)

FRIB TECHNOLOGY DEMONSTRATION CRYOMODULE TEST*

J. T. Popielarski*, E. C. Bernard, S. Bricker, C. Compton, S. Chouhan, A. Facco#, A. Fila, L. Harle, M. Hodek, L. Hodges, S. Jones, M. Klaus†, M. Leitner, D. Miller, S. Miller, D. Morris, J. P. Ozelis, R. Oweiss, L. Popielarski, K. Saito, N. Usher, J. Weisend, Yan Zhang, Z. Zheng, S. Zhao
FRIB, East Lansing, Michigan, USA
#INFN/LNL, Legnaro (PD), Italy, † Technische Universität Dresden, Dresden, Germany

Abstract

A Technology Demonstration Cryomodule (TDCM) has been developed for a systems test of technology being developed for FRIB. The TDCM consists of two half wave resonators (HWRs) which have been designed for an optimum velocity of beta=v/c=0.53 and a resonant frequency of 322 MHz. The resonators operate at 2 K. A superconducting 9T solenoid is placed in close proximity to one of the installed HWRs. The 9T solenoid operates at 4 K. A complete systems test of the cavities, magnets, and all ancillary components is presented in this paper.

INTRODUCTION

The SRF Department at Michigan State University had developed and tested four cryomodules prior to the first demonstration cryomodule for FRIB. Two of the cryomodules are working reliably in the ReA3 linac at MSU [1]. The TDCM, shown in figure 1, is the first cryomodule that demonstrates FRIB specific technology and encourages a transition to large scale engineering and quality assurance methods [2].

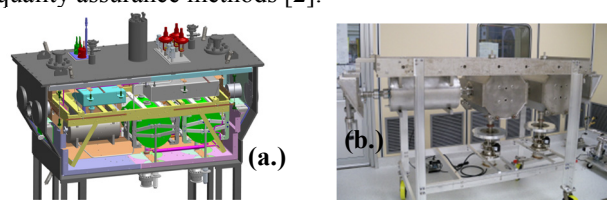

Figure 1: (a.) Rendering of TDCM in cryostat (b.) Cold mass assembly in cleanroom.

In developing the FRIB TDCM, a baseline cryomodule production method evolved for FRIB. The technical and schedule related setbacks encountered during the TDCM campaign eventually yielded reliable fabrication, processing, and certification techniques. SRF-related infrastructure and utility usage required for the TDCM assisted in finalizing planning for a new SRF high bay which will support FRIB cavity processing, vertical testing, cold mass assembly, and cryomodule bunker tests.

TDCM RELEVANCE TO FRIB

The TDCM is a developmental snapshot, and much of the technology improved as more detailed engineering analysis and sub component testing programs provided opportunities for design optimization [3- 5]. Some of the key differences are: a "bottom-up" style from the "top-down" TDCM style [4]; the rail system, support system, heat and magnetic shields assemblies were simplified; Improvements to alignment methods; an internal heat exchanger replaces the external heat exchanger; the 4K thermal intercepts will be parallel circuits as opposed the series connection in the TDCM.

With much of the cryogenic circuitry and alignment systems optimized in the baseline design before TDCM testing took place, alignment and continuous 2K operation aspects were not tested. The plumbing of the RF coupler 4K intercepts [6] required steady flow in the static state required continuous overfilling of the 4K header to ensure the couplers stayed cooled during RF conditioning.

TDCM DEVELOPMENT

Individual tests or more detailed engineering analyses conducted on the cavities, couplers, tuners, and cryogenic circuits used in the TDCM led to design optimizations and improved processing [7- 9].

Initial dunk tests showed low field emission onset values and thermal breakdown below the operating gradient; FRIB processing optimization for the HWR began during the TDCM campaign. The TDCM cavities were field emission-free [10] prior to the installation of the helium vessels.

Initial tests still showed signs of multipacting in the cavity. Repeated measurements on several cavities show a recurring barrier at 2 MV/m E_{acc}. This barrier self-conditioned as the RF power was raised, and in most tests only observed during initial 4K measurements.

During the initial dunk tests, it was discovered Q_0 was lower after a thermal cycle with no change otherwise. A closer investigation for Q-disease showed a strong reduction in the Q_0 after a 15 hour soak at 100K. The cavities were sent to JLAB for a furnace treatment to remove hydrogen from the bulk. Subsequent 'Q-soaks' and thermal cycles showed no signs of degradation. A 600°C furnace treatment was added to the baseline processing plan and a furnace has been installed at MSU [9].

After being jacketed with a helium vessel, the 1st cavity was certified using the vertical cryostat configuration [5], and no field emission was observed. This helium vessel design utilized a titanium bellows at the beamport to reduce the tuning force required for the scissor-jack tuner.

*This material is based upon work supported by the U.S. Department of Energy Office of Science under Cooperative Agreement DE-SC0000661.
#popielar@frib.msu.edu

Copyright © 2012 by the respective authors — cc Creative Commons Attribution 3.0 (CC BY 3.0)

After this cavity had been installed on the TDCM cold mass, the next jacketed cavity developed a large leak from the helium to insulating space found at the titanium bellows. The bellows were removed from the already certified cavity, requiring additional machining and welding.

TDCM TESTING

RF Amplitude and Phase Control

The resonators in the FRIB linac will operate with a very narrow BW for amplitude and phase control. For the HWR, the 30 Hz RF bandwidth available for control presents a technical challenge and increasing the RF BW has a very large impact on cost. The low level RF controller was developed at MSU and employs an ADRC algorithm [11] which is required to ensure a dynamic stability within 2% (peak-to-peak) amplitude and 2 degrees (peak-to-peak) phase. The resonators do not have fast tuning implemented to cancel microphonics. Measurements were done using a fast (1.6 kHz) data acquisition of the RF signals. The results are shown in figure 2, where the measured cavity and amplitude stability is within the limits of the measurement uncertainty. During the measurements, the cavity field was kept just below a multipacting barrier in the cavity and with the slow tuning feedback to the scissor-jack mechanical tuner turned off.

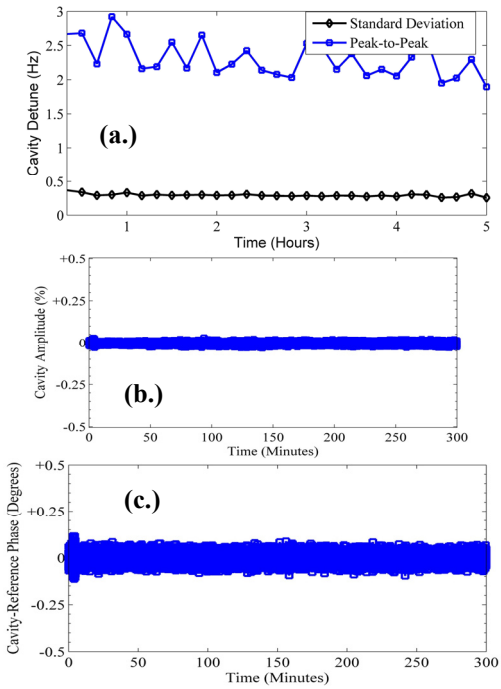

Figure 2: (a) Closed loop detuning, calculated from the forward phase changes while regulating with the cavity amplitude and phase (b, c) well within the design specification.

The 'cavity detune' (Δf) in Figure 2a is inferred from the changes in the forward phase ($\Delta\varphi_f$) and is calculated from $\Delta f = BW \times \Delta\varphi_f$. The closed loop detune inferred from the measurement agreed well with some shorter duration open loop measurements done a 2K. A slow drift of 8 Hz over five hours was measured, justifying the necessity of a slow tuner. During this measurement, the bath pressure was well regulated (less than 0.7 Torr peak-to-peak).

The next round of measurements was performed using the feedback to the slow tuner. The measured amplitude and phase stability was higher (1.4%, 0.6°, peak-to-peak), but still within the FRIB specification. It was noticed that the tuner drive was constantly moving, which created a mechanical oscillation at 110 Hz, causing a closed loop detune of 24 Hz peak-to-peak.

RF Couplers

The RF couplers had been conditioned for multipacting barriers prior to the installation into the cold mass [6]. The multipacting that was conditioned had returned after installation to and cooling of the TDCM, with similar onset levels. Coupler conditioning did not completely remove the multipacting from the coupler above 2 kW after 10 hours of RF pulses. The multipacting was suppressed by applying an external magnetic field through a coil winding around the coupler. Figure 3 shows a plot the current on the probe near the ceramic disk; 6.8 kW peak power was achieved with 4.5 kW average forward power while driving 1 MHz off-resonance. A detailed multipacting analysis [12] shows that the location of the two-point multipacting in the coaxial line depends strongly on the boundary condition at the cavity port. With the rf system 'detuned' from the cavity, the boundary condition at the coupler port is that of a short circuit, and a single two-point multipacting node exists at the voltage peak, which is approximately half way between the coupler port and the ceramic disk. However, when driving the cavity on resonance, two voltage peaks exist on the transmission line. The magnetic field suppression did not suppress the multipacting when locked to the cavity resonance.

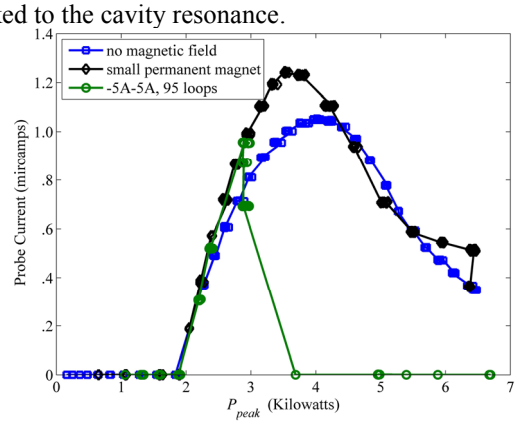

Figure 3: Multipacting suppression in the FPC while driving from the cavity off-resonance.

Tuners

The bellows used to reduce the force required to tune the cavity was replaced with a rigid connection to the helium vessel. A measurement of the tuning ratio of

Copyright © 2012 by the respective authors — cc Creative Commons Attribution 3.0 (CC BY 3.0)

360:1 greatly exceeds the expected 8:1 ratio showing that the scissor-jack mechanism was not performing as expected. This resulted in a reduced tuning sensitivity of the actuator controller (from 1.8 Hz/step to 0.03 Hz/step), which may explain the mechanical effects on the performance of the LLRF with the tuner engaged. Additional testing will be performed on an alternate tuning concept which utilizes a pneumatic drive.

Cryostat

Static load measurements on the TDCM cryostat were performed by recording liquid level as a function of time using the level sensor to infer the evaporation rate. This rate was calibrated by using a gas meter to measure the mass flow of the helium gas at room temperature. The mass flow measurement and nominal liquid volume boil-off from the header dimensions had roughly good agreement. Neither the level vs time nor the gas meter methods were calibrated with a known heat source. An evaporation rate of 2.85 W to the 2K header and 4.0 Watts to the 4K header was measured and repeated four times, with a spread of 0.22 W peak to peak.

Cavity Dynamic Load

The cavity dynamic loads, measured the same as the static load measurements described above, could not be accurately measured below the multipacting barriers (1.67 MV/m E_{acc}), since the resolution of this type of measurement is ~0.5 W. This resolution exceeds the heat load measured in the last Dewar test (0.10 Watts at 1.67 MV/m). With helium processing, a reasonable field level (4 MV/m) was reached. The dynamic load of 1.5W @ 4 MV/m yields a Q_0 of 1.2E10. This measurement was done in the last hours of the TDCM test. The load from the RF coupler at this field (850W forward power) was negligible considering a load measurement done with 4.5 kW forward power off resonance was less than the measurement resolution.

Magnets & Magnetic Field Interactions

The Earth's magnetic field is shielded from the cavities with a global mu-metal shield. Measurements on the shield showed an attenuation factor of at least 25 was achieved; however accurate measurements of the residual magnetic fields with the cold mass installed were not performed. Prior to energizing the magnets, the low field Q_0 (@1.67 MV/m) showed the possibility of high residual magnetic fields trapping fluxes up to 200 mG, but the Q drop at this field could also be explained as either measurement error or multipacting.

The 9T solenoid has a fringe field such that the flux at the nearest cavity surface is 250 Gauss. The revised FRIB specification for this fringe-field is 650 Gauss. The magnet was powered to full field; the cavities were warmed up to 30 K, and then re-cooled. The dynamic loads were measured again at 2K. The difference in the dynamic loads was less than the 0.5 W measurement resolution. A magnetic field cancellation procedure was performed by varying the power supply current, I, in a decreasing and alternating manner, e.g. a series,$\{(-0.9)^n I\}_{n=0}^{40}$ which took 5 hours to complete. The dynamic load measurement performed after this degaussing and further RF conditioning yielded a quality factor close to that measured in the vertical test.

TDCM Outlook and Future Tests

The TDCM test ended abruptly after taking only limited dynamic load data due to an unexpected cryoplant failure. A suspected helium leak in the transfer line that supplied the TDCM required mass flow rates of 3-5 g/s to maintain level in the liquid helium levels, though static load measurements indicate only 0.5 g/s is required. Therefore, running the TDCM test in parallel to NSCL experimental programs in impossible due to the unavailability of this LHe supply rate.

Though the TDCM completed a successful first round of testing in mid-2012, additional testing will be done by end of 2012. The next round of testing will focus primarily on the high power RF conditioning that commenced in the later stages of the TDCM measurements.

A new transfer line is being procured and installed to supply the TDCM from a refrigerator that is separate from the NSCL experimental program. While the transfer line is being built, the cryostat is being opened up to make some adjustments. Magnetic material found on the internal scissor jack tuning mechanisms is being removed. The RF couplers are undergoing an in-situ bake (~100-120C, 72 hours) in an effort to reduce the multipacting intensity. Additional measurement equipment will be installed to determine the dynamic load of the couplers to the intercepts and the remnant fields from the 9T solenoid before and after degaussing steps.

ACKNOWLEDGMENTS

The authors would like to thank Greg Velianoff, Jon Wlodarczak, Tom Russo, John Brandon, Mike Holcomb, and Jie Wei for their help in late night and evening shifts during RF conditioning; JLab for degassing the HWR's installed in the TDCM; Peter Kneisel, Curtis Crawford, and Bob Laxdal for their advice given regularly in weekly teleconference.

REFERENCES

[1] D. Leitner et al., Proc. of SRF 2011, pp. 674.
[2] M. Leitner et al., Proc. of SRF 2011, pp. 56.
[3] S. Miller, et al., Proc. of SRF 2011, pp. 213.
[4] M. Johnson et al., IPAC 2012, to be published.
[5] A. Facco, et al, IPAC 2012, to be published.
[6] J. Popielarski, et al, Proc. of SRF 2011, pp. 353.
[7] L. Popielarski, et al, Proc. of SRF 2011, pp. 526.
[8] R. Oweiss, these proceedings.
[9] L. Popielarski, these proceedings.
[10] J. Popielarski, IPAC 2012, to be published.
[11] J. Vincent, et al, Nuclear Instruments Methods in Physics Research A 643 (2011) pp. 11.
[12] Z. Zheng, et al, these proceedings.

Copyright © 2012 by the respective authors — cc Creative Commons Attribution 3.0 (CC BY 3.0)

THE UPGRADED ARGONNE WAKEFIELD ACCELERATOR FACILITY (AWA): A TEST-BED FOR THE DEVELOPMENT OF HIGH GRADIENT ACCELERATING STRUCTURES AND WAKEFIELD MEASUREMENTS*

M.E. Conde#, D.S. Doran, W. Gai, R. Konecny, W. Liu, J.G. Power, Z. Yusof,
ANL, Argonne, IL 60439, U.S.A.
S. Antipov, C. Jing, Euclid Techlabs LLC, Solon OH 44139, U.S.A.
E. Wisniewski, IIT, Chicago IL 60616, U.S.A.

Abstract

Electron beam driven wakefield acceleration is a bona fide path to reach high gradient acceleration of electrons and positrons. With the goal of demonstrating the feasibility of this concept with realistic parameters, well beyond a proof-of-principle scenario, the AWA Facility is currently undergoing a major upgrade that will enable it to achieve accelerating gradients of hundreds of MV/m and energy gains on the order of 100 MeV per structure. A key aspect of the studies and experiments carried out at the AWA facility is the use of relatively short RF pulses (15 – 25 ns), which is believed to mitigate the risk of breakdown and structure damage. The upgraded facility will utilize long trains of high charge electron bunches to drive wakefields in the microwave range of frequencies (8 to 26 GHz), generating RF pulses with GW power levels.

AWA FACILITY

The mission of the Argonne Wakefield Accelerator Facility (AWA) is to develop technology for future accelerator facilities. The AWA facility has been used to study and develop new types of accelerating structures based on electron beam driven wakefields. In order to carry out these studies, the facility employs a photocathode RF gun capable of generating electron beams with high bunch charges and short bunch lengths. This high intensity beam is used to excite wakefields in the structures under investigation.

The facility is also used to investigate the generation and propagation of high brightness electron beams, and to develop novel electron beam diagnostics.

The AWA high intensity electron beam is generated by a photocathode RF gun, operating at 1.3 GHz. This one-and-a-half cell gun typically runs with 12 MW of input power, which generates an 80 MV/m electric field on its Magnesium photocathode surface. A 1.3 GHz linac structure increases the electron beam energy, from the 8 MeV produced by the RF gun, to 15 MeV. The linac is an iris loaded standing-wave structure operating in the $\pi/2$ mode with an average accelerating gradient of 7 MV/m; it has large diameter irises to minimize the undesirable wakefields generated by the passage of high charge electron bunches.

The charge of the electron bunches can be easily varied from 1 to 100 nC, with bunch lengths of 2 – 2.5 mm rms, and normalized emittances of 3 to 100 π mm mrad.

The AWA laser system consists of a Spectra Physics Tsunami oscillator followed by a Spitfire regenerative amplifier and two Ti:Sapphire amplifiers (TSA 50). It produces 1.5 mJ pulses at 248 nm, with a pulse length of 2 to 8 ps FWHM and a repetition rate of up to 10 pps. A final KrF Excimer amplifier is optionally used to increase the energy per pulse to 15 mJ.

The generation of electron bunch trains (presently up to 16 bunches) requires each laser pulse to be divided by means of beam splitters into a laser pulse train. The charge in each electron bunch is determined by the energy in each laser pulse and the quantum efficiency of the photocathode material. Typically, single bunches of 100 nC can be produced (with a maximum of 150 nC occasionally reached).

WAKEFIELD ACCELERATION

The use of electron beam driven wakefields to achieve high gradient acceleration has received considerable attention. It offers the advantage of using a relativistic beam to transport the energy to the accelerating structures, decreasing the difficulties of generating and distributing RF power by conventional means; wakefields naturally constitute RF pulses that are of short duration and high peak intensity [1].

Research at the AWA facility has been exploring various types of wakefield structures, including photonic band gap structures, metallic iris loaded structures, and also more exotic schemes using metamaterials. The main focus of the facility, however, has clearly been the development of dielectric loaded structures. They offer the advantage of simple geometry and easy fabrication with accelerating properties that compare favourably with conventional iris loaded metallic structures: the axial electric field is uniform across the transverse cross section of cylindrical structures, and the uniform cross section of the structures presents no geometric features to cause field enhancement. The damping of the undesirable deflecting dipole modes seems to be more easily accomplished in dielectric loaded structures as well; planned experiments will explore the use of longitudinal slots on the metallic outer shell of dielectric structures, as a possible scheme to damp dipole modes. Dielectric structures also hold the promise of withstanding higher electric fields without material breakdown. A significant advantage offered by wakefield structures, in comparison

*Work supported by the U.S. Department of Energy under contract No. DE-AC02-06CH11357.
#conde@anl.gov

Copyright © 2012 by the respective authors — cc Creative Commons Attribution 3.0 (CC BY 3.0)

with other wakefield schemes, is the ability to accelerate positron bunches or electron bunches in basically identical fashion.

AWA FACILITY UPGRADES

The AWA Facility has several major upgrades presently underway, which will considerably enhance its capabilities.

A new one-and-a-half cell RF gun (Fig.1) has been commissioned, and it will replace the existing RF gun as the source of drive bunches. The new RF gun operates with a Cesium Telluride photocathode, and thus, due to the higher quantum efficiency of Cs_2Te, it will be able to generate longer bunch trains with high charge per bunch. We plan to generate trains with up to 32 electron bunches, each separated by one L-band RF period, and with up to 100 nC per bunch. (It should be noted that the two upper limits, i.e. 32 bunches and 100 nC per bunch, cannot be reached simultaneously, since this would load the accelerating fields in the RF gun to an unacceptable level.) These longer bunch trains will, of course, generate longer RF pulses when traversing the wakefield structures.

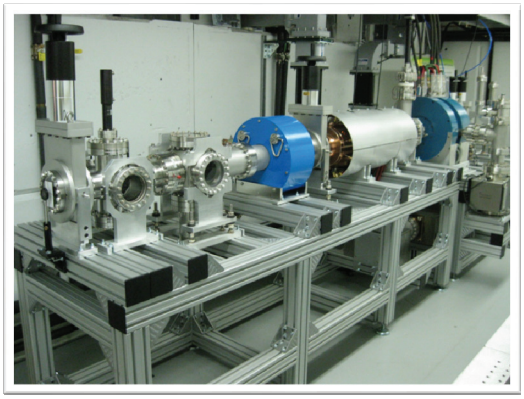

Figure 1: The new AWA RF gun (between the blue solenoids), followed by the first one of the six new linac tanks, another focusing solenoid, and two vacuum crosses for laser beam input and beam profile measurements (YAG screen). A combination of ICT and FCT (Integrating Current Transformer and Fast Current Transformer made by Bergoz) is installed in between the two crosses.

Three additional L-band RF power stations, consisting of one 30 MW Litton klystron and two 25 MW Thales klystrons, and their respective modulators, will power six new linac tanks in the drive beamline. These new klystrons have been commissioned to full power.

The new linacs [2] will be seven-cell standing-wave π mode structures, designed to operate with 10 MW of input power and 11.2 MeV energy gain. Thus, the operation of the six new linac tanks will increase the energy of the beam produced by the drive gun from 8 MeV to 75 MeV. This will, of course, allow significantly more energy to be extracted from the drive beam as it drives wakefields in the structures under test. The higher beam energy also implies a smaller physical transverse emittance of the bunches, facilitating their propagation through smaller aperture wakefield structures, and generating even higher wakefield amplitudes.

The fabrication of the first one of the six new linac tanks has been completed, and good field flatness across the cells has been achieved (Fig.2). It has been installed just downstream of the new RF gun (Fig.1). The fabrication of the remaining five linac tanks is under way, and their final brazing cycles are scheduled for October of 2012.

The commissioning of the new drive gun will free up the existing gun, which will then be used to generate a witness beam to probe the wakefields produced by the drive bunches.

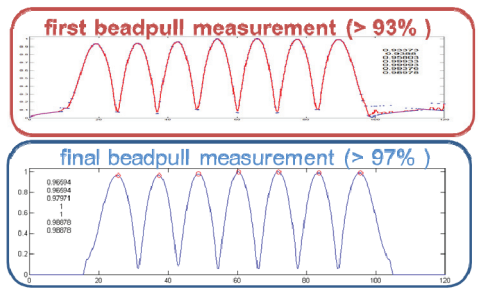

Figure 2: Bead-pulling RF measurement of first linac tank, showing good field balance across the cells.

A new beamline switchyard (Fig. 3) will be constructed to allow concomitant experiments: (a) collinear wakefield acceleration; (b) RF power generation and two beam acceleration; (c) phase space manipulation (emittance exchange, etc); (d) high brightness beam generation; (e) beam diagnostic development. This flexible beamline switchyard will allow a quicker and more efficient transition among several concurrent experimental setups.

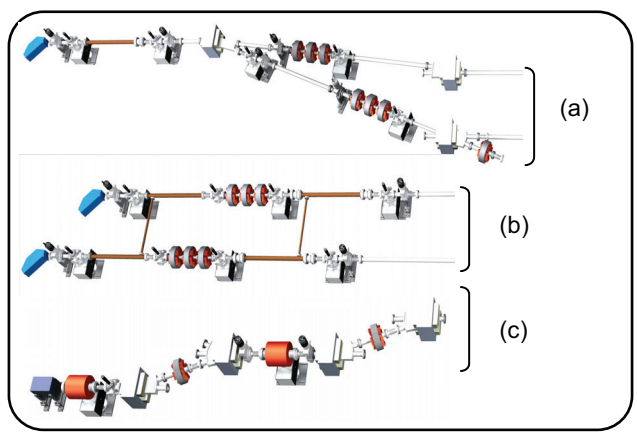

Figure 3: Different legs of the new AWA beamline switchyard will be dedicated to specific types of experiments: (a) collinear wakefield acceleration; (b) two-beam-acceleration and RF power generation; (c) phase space manipulation (emittance exchange) and beam diagnostic development.

Copyright © 2012 by the respective authors — cc Creative Commons Attribution 3.0 (CC BY 3.0)

In order to house the upgraded AWA Facility, the present bunker has been extended beyond the perimeter of the existing building, into a new annex. Figure 4 shows the interior and the roof of the expanded bunker.

(a)

(b)

Figure 4: The expanded AWA bunker: (a) plentiful interior space is now available for the installation of the new linac tanks and new beamline switchyard; (b) new RF power circulators and waveguides have been installed on the roof of the expanded bunker, ready to connect the new klystrons to the new linac tanks.

CONCLUDING REMARKS

In the past few years AWA has demonstrated high gradient fields (100 MV/m) in dielectric based wakefield structures [3]. Generation and extraction of RF power using beam driven dielectric structures has also been demonstrated [4 - 6]. Several experiments exploring new designs and new features of dielectric based wakefield structures will be conducted in the near future.

Concomitantly, AWA is undergoing upgrades that will enhance its capabilities. These upgrades will allow the generation of longer bunch trains with high charge per bunch. The higher beam energy will make it possible to excite high gradient wakefields in longer accelerating structures, thus generating hundreds of MV/m over meter scale structures. The second RF gun will provide "witness" bunches to probe the wakefields, demonstrating high gradient acceleration.

Once the upgrades are completed, the goal is to achieve accelerating gradients on the order of 0.5 GV/m in structures with approximately 3 mm apertures. The generation and extraction of RF pulses with power levels on the order of GW shall also be demonstrated. As an example, Table 1 shows the main parameters of a pair of structures that will be tested as soon as the upgraded AWA Facility becomes available. The actual hardware is seen in Fig. 5.

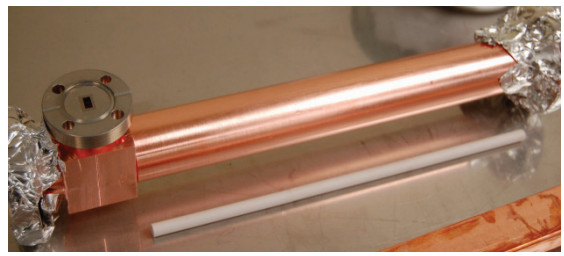

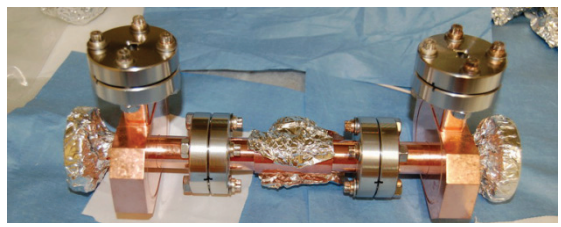

Figure 5: 26 GHz power extractor and accelerating structure.

Table 1: 26 GHz TBA Structures

Decelerating structure	**Accelerating structure**
ID / OD / length (mm) 7.0 / 9.068 / 300	ID / OD / length (mm) 3.0 / 5.025 / 300
Dielectric constant 6.64	Dielectric constant 9.70
Group velocity 0.254 c	Group velocity 0.111 c
R/Q 9.79 kΩ/m	R/Q 21.98 kΩ/m
RF Power (50 nC) 1.33 GW	R_{sh} 50.44 MΩ/m
Peak gradient 167 MV/m	E_0 (1.26 GW) 316 MV/m
Energy loss 20.5 MeV	E_{loaded} (1.26 GW) **267 MV/m**

REFERENCES

[1] W.Gai et al, "Short-pulse dielectric two-beam acceleration," J. Plasma Physics, p. 1, Feb. 2012.

[2] J.G. Power et al, "Upgrade of the Drive Linac for the AWA Facility Dielectric Two-Beam Accelerator," in proceedings of IPAC 2010, Kyoto, May 2010.

[3] M. Conde et al., "High Gradient Excitation and RF Power Generation using Dielectric Loaded Wakefield Structures," in proceedings of LINAC'08, Victoria, September 2008.

[4] F. Gao et al., "Design and Testing of a 7.8 GHz Power Extractor Using a Cylindrical Dielectric-loaded Waveguide," Physical Review ST Accel. Beams 11, 041301(2008).

[5] F. Gao et al., "Multi-Nanosecond High Power Pulse Generation at 7.8GHz with a Dielectric-loaded Power Extractor," IEEE Transactions on Nuclear Science **56** (3), p. 1492 – 1497, (2009).

[6] C. Jing et al., "The First Experiment of a 26 GHz Dielectric Based Wakefield Power Extractor," in proceedings of IPAC 2010, Kyoto, May 2010.

Copyright © 2012 by the respective authors — cc Creative Commons Attribution 3.0 (CC BY 3.0)

X-RAY LOCAL ENERGY SPECTRUM MEASUREMENT AT TSINGHUA THOMSON SCATTERING X-RAY SOURCE (TTX)*

Y.-C. Du#, Z. Zhang, L.-X. Yan , J.-F. Hua, H. Zha , W.-H. Huang , C.-X. Tang
Accelerator laboratory, department of engineering physics, Tsinghua University, Beijing, China
Key laboratory of Particle & Radiation Imaging (Tsinghua University), Ministry of Education, Beijing, 100084, China
Key laboratory of High Energy Radiation Imaging Fundamental Science for National Defense, Beijing, 100084, China

Abstract

Thomson scattering X-ray source, in which the TW laser pulse is scattered by the relativistic electron beam, can provide ultra short, monochromatic, high flux, tunable polarized hard X-ray pulse which is can widely used in physical, chemical and biological process research, ultra-fast phase contrast imaging, and so on. Since the pulse duration of X-ray is as short as picosecond and the flux in one pulse is high, it is difficult to measure the x-ray spectrum with traditional spectra measurement methods. In this paper, we introduce an iterative statistical algorithm (Expectation-Maximization) to reconstruct the spectra from the attenuation data, and the results of the X-ray spectrum measurement experiment on Tsinghua Thomson scattering is also presented.

INTRODUCTION

Thomson Scattering sources (also called Inverse Compton Scattering), which can be bright X-ray sources typically produce photons, have attracted a lot of interest as the technologies for producing low-emittance high-brightness relativistic electron sources and ultra-short high-power lasers have progressed. The X-rays that are generated by the interactions between laser and electron, exhibit high directivity, and have a polarized tunable quasi-monochromatic spectrum. The knowledge of the spectrum of an X-ray source is a key point for the development of any kind of application, for example in imaging both contrast and absorbed dose strongly depend on energy. However, direct methods performing a standard spectrometric measurement based on single photon energy measurement to detect the X-ray spectrum of Thomson Scattering sources have always been considered troublesome to implement because the beam is too intense to cause pulse pile up problems. Thomson Scattering source can produce up to 10^8 photons, bunched in 10ps long pulse [1]. An alternative way to measure the spectrum might request the measurement to be integral-type, which will not be affected by the high rate of incidence of photons. The analysis of attenuation data (transmission curves), which can provide some information about the spectral distribution of an X-ray source, as not affected by the rate of incidence of photons, is a good candidate to measure the X-ray spectrum of the Thomson Scattering X-ray source. Although there are several problems with this method, such as low accuracy, non-unique solution to ill-condition system and instability with different measurement error [2], this method can still give good estimation and reconstruction of spectra with some improvements based on the property of the measured spectra.

In this article, we introduce an iterative statistical algorithm (Expectation-Maximization) [3] to reconstruct the spectra from the attenuation data on simulated measurement. Results show that this method can give good approximations for the mean energy of the spectra, while it is not sensitive to the specific spectral distribution and the energy broadening. In order to reconstruct the shape of the spectra, especially the energy broadening, we present a new method based on the Expectation-Maximization algorithm. An preliminary experiment is also carried out on Tsinghua Thomson scattering X-ray source, the measured maximum X-ray energy is about 53keV, which is agreed well with the simulations.

OVERVIEW OF TTX

The scheme of TTX is shown in figure 1. This machine includes a 50MeV electron linac based on the photocathode RF gun and a Ti: Sapphire TW laser system. The laser system generates both the 266nm UV pulse for photocathode and the 800nm IR pulse for scattering interaction. The two pulses are derived from one 79.3MHz Ti:Sapphire oscillator in order to reduce the time jitter between the electron beam and the IR pulse. The linac system consists of a BNL/KEK/SHI type 1.6 cell S-band photocathode RF gun, a 3m S-band SLAC type travelling wave accelerating section, generates 40~50MeV ultra-short high brightness electron pulse for scattering interaction. The laser system is synchronized with the RF system through a timing circuit, with a timing jitter no greater than 0.5ps. The parameters of electron and laser were listed in the table 1.

In previous experiment, we succeed to generate and detect the X-ray signal with head-on colliding mode. The results from the MCP and X-ray CCD are shown in figure 2.

*Work supported by work is supported by NSFC under Grant Nos. 10735050, 10805031, 10975088 and 10875070 and by the 973 Program under Grant No. 2007CB815102.
dych@mail.tsinghua.edu.cn

Copyright © 2012 by the respective authors — cc Creative Commons Attribution 3.0 (CC BY 3.0)

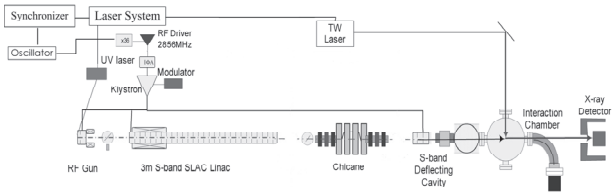

Figure 1: scheme of TTX.

Table 1: Parameters of Laser and Electron Beam

Electron		
Charge	200	pC
Energy	47	MeV
rms emittance	3	mm mrad
Bunch length	3	Ps
Beam size at interaction position	50	Um
Arriving time jitter	~500	Fs
Laser		
Wavelength	800	Nm
Pulse duration	60	Fs
Energy	<300	mJ
Beam size	~100	Um

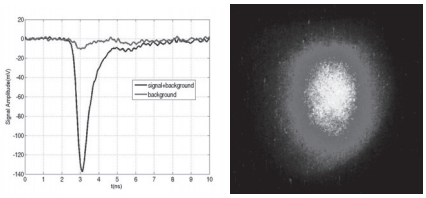

(a) (b)

Figure 2: typical X-ray signal and background from the MCP detector(a) and X-ray CCD.

LOCAL ENERGY SPECTRUM MEASUREMENT

X-Ray Spectrum Measurement from the Analysis of Attenuation Data

The relative transmission function $T(x)$ responding to an attenuator of thickness x is related with the spectrum of an X-ray beam in the following way[1]:

$$T(x)=\frac{S(x)}{S(0)}=\int_0^{E_{\max}} e^{-\mu(E)x}F(E)dE \qquad (1)$$

where $S(x)$ is the signal measured with an absorber of thickness x, and $S(0)$ is the signal measured without any absorber. $\mu(E)$ is the total attenuation coefficient of the attenuator in which are included both photoelectric and Compton effects for photons of energy E. $F(E)=\phi(E)\bullet C(E)$, where $\phi(E)$ represent the spectrum distribution of photons and $C(E)$ represent the energy response determined by the way to measure the signal $S(x)$. $E_{\max}$ is the maximum energy of the spectrum.

When we treat the problem from its numerical point of view by discretizing the integral, the Eq.(1) turns out a linear system of the form

$$T=A\bullet F \qquad (2)$$

where $T\in R^M$ represent the attenuation curve as a function of the attenuator and $F\in R^N$ is the discretized spectrum. Generally, the linear system described by Eq.(1) translates, after the disctretization, into an ill-conditioning linear system in Eq.(2). Here the Expectation-Maximization (EM) algorithm is used to obtain an approximation to the exact solution of the system Eq.(2)[2]. Expectation -Maximization algorithm is an iterative statistical algorithm with the form [3][4]:

$$F_n^{(k+1)}=F_n^{(k)}f_n,\quad f_n=\frac{\sum_m A_{nm}{}^t\dfrac{T_m}{\sum_{n'}A_{mn'}F_{n'}^{(k)}}}{\sum_m A_{nm}{}^t} \qquad (3)$$

Numerical Simulation

A Monte Carlo numerical simulation experiment is carried out to verify the method first. During the simulation process, Monte Carlo method is used to simulate the Thomson Scattering and calculate the attenuation curve through silicon with different thickness to justify the reliability and feasibility of this method. Figure 3 shows the results for the reconstruction of local spectra for different two points in the X-ray spot.

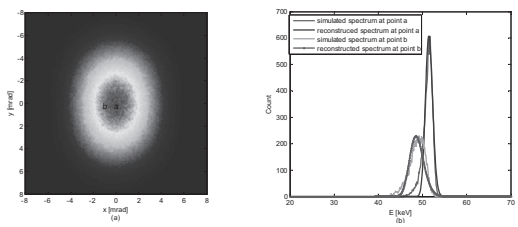

Figure 3: (a) X-ray profile simulated by CAIN and the two points selected to reconstruct local spectra. (b) Simulated and reconstructed spectra at two different points with 0.5 mrad collecting angles and 5% Gaussian random error.

It can be observed that the EM method performs well to reconstruct the local spectra of Thomson Scattering source. However, as the collecting angles increase, the X-ray spectra are not close to Gaussian distribution any more. To solve this problem, we propose an assumption that according to the spectral distribution features of Thomson Scattering, as the collecting angles increase, the right half of spectra remains almost unchanged. So we

Copyright © 2012 by the respective authors — cc Creative Commons Attribution 3.0 (CC BY 3.0)

can treat the right-half spectra of the small collecting angles given by EM algorithm as the right half for spectra of other angles within a certain range. Then we can reconstruct the spectra with the attenuation data more accurately as under this assumption, the mean energy will have direct and close relationship with the shape of spectra. Fig.4 shows the reconstruction result (top) and the simulation result (bottom) for Thomson Scattering spectra within the collecting angle range from 0.5mrad to 5mrad.

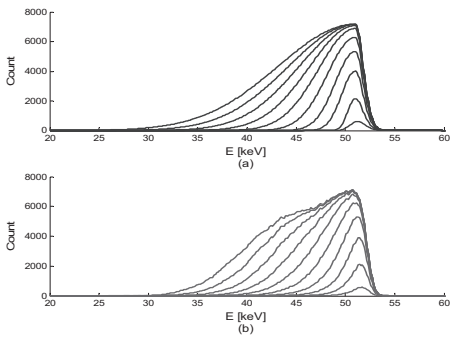

Figure 4: (a): Representative reconstruction results of spectra for collecting angles ranging from 0.5 mrad to 5 mrad with an equal interval of 0.5 mrad (b): The simulated spectra for the Thomson Scattering source with collecting angles of the same range with CAIN.

Experiment Results

A preliminary experiment is carried out on TTX to measure the X-ray spectrum. The scheme of the experiment is shown in figure 5. The silicon wafers with different thickness are used as attenuator, a CsI screen and CCD camera are used as the X-ray intensity monitor.

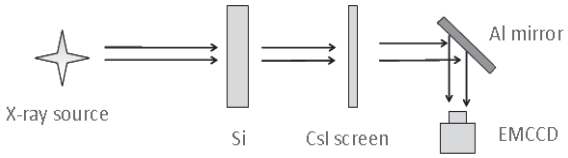

Figure 5: The scheme of the X-ray spectrum measurement.

The typical X-ray profile with attenuators is shown in figure 6. The sheltered part is used to obtain the attenuation curve and the unsheltered part is used to X-ray intensity normalization to cancel the jitter influence. The attenuation curves for point a, b, and c, the reconstructed X-ray spectrum from the attenuation curves are also shown in figure 6. The maximum X-ray energy at the center of profile is 53keV, which is agreed well with the theory expectation and simulations.

In Thomson scattering X-ray source, the X-ray energy is a function of scattered angle. In figure 7, the mean energy of the X-ray as a function of scattered angle is shown and compared with the theory and simulation expectations. The measured results are a little different to the theory curve but agreed well with the simulation results, since in theory curve the emittance effect of the electron beam is not included.

Reconstruction spectra results from measured attenuation for collecting angles ranging from 0.5mrad to 5mrad with an equal interval of 0.5mrad are shown in figure 8:The deposition efficiency of CsI screen is considered.

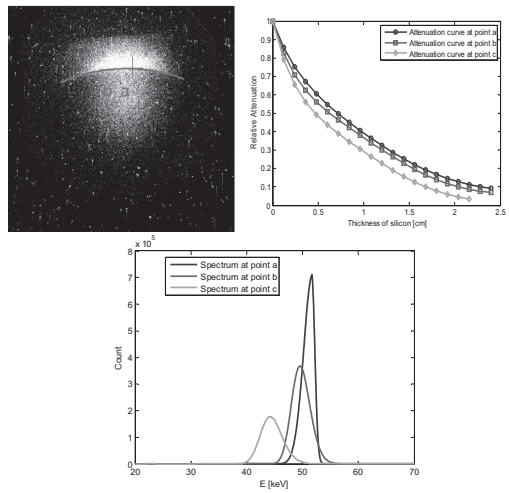

Figure 6: (top left)X-ray profile measured by EMCCD sheltered by 1.5cm silicon. (top right) Attenuation curves at points a, b, and c. (bottom) The reconstructed local X-ray spectrum from the attenuation curves.

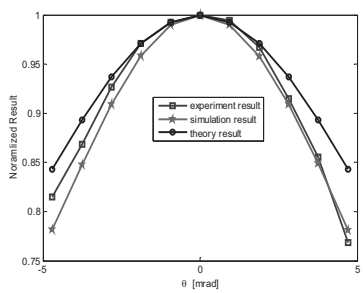

Figure 7: Mean energy along the line b-a-c in the profile, and compared with theory and simulation.

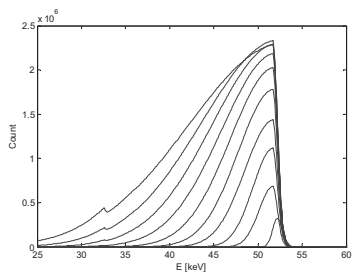

Figure 8: The x-ray spectrum with different collecting angle.

REFERENCE

[1] Emil Y. Sidky et al., "A robust method of x-ray source spectrum estimation from transmission measurement", Journal of Applied Physics 97, 124701(2005)
[2] Marian Manciu et al., Journal of X-ray Science and Technology 17 (2009) 85-99.
[3] Marco Endrizzi et al., , NIM A, 608(2009) S78-S82.
[4] Li Zhang et al., 2007 IEEE Nuclear Science Symposium Conference Record, 3089-3093, 2007.

Copyright © 2012 by the respective authors — cc Creative Commons Attribution 3.0 (CC BY 3.0)

EMITTANCE CONTROL FOR DIFFERENT FACET BEAM SETUPS IN THE SLAC LINAC*

F.-J. Decker, W. Colocho, N. Lipkowitz, Y. Nosochkov, J. Sheppard, H. Smith, Y. Sun, M.-H. Wang, G.R. White, U. Wienands, M. Woodley, G. Yocky, SLAC, Menlo Park, CA 94025, USA

Abstract

The linac beam at SLAC requires different setups for different users at the FACET (Facility for Advanced aCcelerator Experimental Tests) area, like highly compressed, intense bunches, or lower charge, long bunches. These require typically a lengthy tuning effort since with an energy-time correlation (or "chirp") the bunch transverse wakefield kicks can be compensated with dispersive trajectory oscillations and vice versa. Lowering the charge or changing the bunch length will destroy this delicate balance. Besides the typical steering to minimize BPMs (Beam Position Monitors) with correctors, we applied different techniques to try to localize beam disturbances like dispersion with phase changes, RF-kicks and RF quadrupole fields turning a klystron off and on, or varying the phase, and finally wakefield kicks with different beam intensities. It is also important to quantify BPM to quadrupole offsets with "bowtie" plots and that the correctors give the expected kicks with orbit response matrix measurements.

INTRODUCTION

Good transverse beam emittances at different places along the SLAC Linac get typically achieved in the following way. The beam gets steered relatively flat (< 0.5 mm) using BPMs (Beam Position Monitors) and then with a lengthy tuning scheme, linac oscillations or bumps are introduced which minimize the emittance measured with wire scanners. Over the years this process typically achieved small emittance growth numbers of 50 to 100% over the initial values of 30 and 2.5 mm-mrad for x and y, so 50 by 5 mm-mrad was expected for the FACET beam in Sector 20.

Typically twice that amount and often more was only achieved. There are a few explanations (excuses) which could cause this. The typical beam rate was 10 Hz, so tuning was three times slower than at 30 Hz. The FACET chicane needed special attention, so linac tuning was cut short. And the final spot sizes after the chicane and final focus were about the same, like 30 μm, even if the emittance just in front of the chicane changed by a factor of three (300 → 100 mm-mrad in x), discouraging further linac tuning.

Additionally, frequent user requested beam changes in current and bunch length made it necessary to tune the beam emittances up again, which would make it even trickier for smaller emittances. It is assumed that the main root cause for this is that after just steering flat the initial emittance is as high as 1200 mm-mrad, and the subsequent tuning cancels this with equally large corrections. When these cancelations are not local, or are charge / bunch length dependant, small say 10% variations will create 10% of 1200 mm-mrad = 120 mm-mrad.

So the goal is to localize and reduce emittance increasing effects. For that we try to find and categorize all possible mechanisms, like dispersion, wakefield, RF-kicks, and develop procedures like special steering methods and component alignment.

Goal: Get Linac closer to good emittances with BPMs etc. so the tuning part is less.

1. BPMs
2. Correctors
3. Quads (old BBA: straight orbit)
4. BPM-to-Quad: bowtie plot or Quad change
5. Corrector strength (LOCO, R12 meas.)
6. Lattice (Quad) strength: Oscillation data
7. RF-kicks: a) sin-cos, b) dipole-quadrupole-lens
8. Measure dispersion
9. Measure with different charge (wakefield)
10. Measure with different bunch lengths
11. Others

The different methods (numbers in ( ) below) and their relevance are discussed in the following sections.

STEERING TECHNIQUES

Steering the beam to the center of a BPM (1) gets the beam down the linac relatively fast, but usually ends up with big beam emittances. Additionally we can look at the corrector (2) values along z and check for certain patterns, e.g. stronger values with + – + might indicate a BPM with a big unreal offset. With our "SVD Steering" we can adjust a gain parameter to prefer BPMs (gain high) or correctors (gain low), but this method just supports what is believed more correct.

The next step is also using the quadrupole (3) strengths in a way to get a straight trajectory. When a BPM reading is say Δx =1 mm and the corrector strength is cor = 0.03 kG-m, the two can be compared by dividing cor by the quadrupole strength Q = 20 kG: cor/Q = 1.5 mm. So the beam gets more bend up by the corrector than the $Q\Delta x$ bends it down (focussing magnet). Figure 1 shows an example where the orbit was steered flat (below 0.3 mm) but its corresponding cor/Q-values are up to 1.3 mm. This led to a global alignment of the Linac of up to 7 mm [1]. Equalizing the two locally will give a straight non-bend beam orbit and therefore no dispersion is generated. But an offset in a BPM might indicate also an offset in the RF nearby structure, causing wakefield kicks.

*Work supported by U.S. Department of Energy, Contract DE-AC02-76SF00515.

Copyright © 2012 by the respective authors — cc Creative Commons Attribution 3.0 (CC BY 3.0)

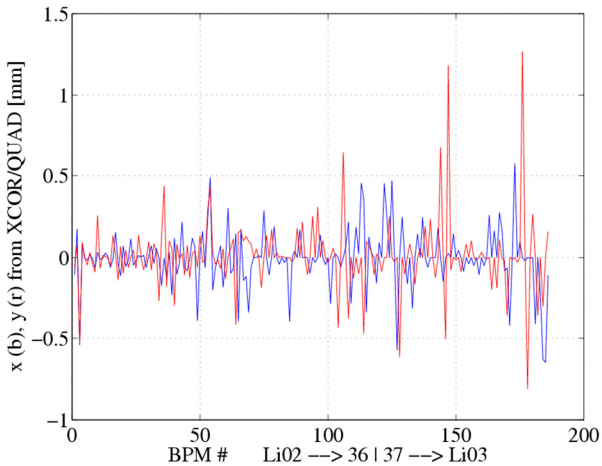

Figure 1: The absolute orbit is steered flat, but the corresponding corrector/quadrupole values for x (blue) and y (red) indicate big bending around 145.

BEAM BASED ALIGNMENT

Besides the global alignment of the Linac using optical targets inside the accelerator supporting light-pipe, there are several methods using the beam to find misalignments and then fix them. The last paragraph indicates already one such approach. Instead of steering so that $\Delta x = cor/Q$ we can align the quadrupole and accelerator locally by moving it in the $+x$ direction by Δx and putting the corrector to zero. This was done in a few places and needs to be done at all locations. But before doing this we need to be sure that the values of Δx, *cor*, Q are correct.

The BPM reading Δx can have an offset x_{off} with respect to the quadrupole and this can be measured with the beam by the bowtie-scan method (4). By varying one corrector in front of the quadrupole and measuring the effect of a downstream BPM for two different quadrupole settings versus the BPM inside the quadrupole you get a bowtie-like plot where the center of the bowtie gives the BPM offset x_{off}. This method is very lengthy requiring a few setting for each quadrupole setting and again for the other plane y. A faster but not as precise method is using just the difference orbit for the two different quadrupole settings and using the focussing model (R12s) to determine the kicks in x and y at the same time. This method should be about ten times faster and will allow us to get the BPM offsets for all BPMs in quadrupoles.

Checking the corrector strengths (5) is next and done typically by varying a corrector over a certain range that the beam is not lost and then the response matrices R12s from the corrector (point 1) to downstream BPMs (points 2) are compared to the expected from the model. When everything is aligned the exact values are not too critical since the correctors are close to zero, but to get there and for steering and for making closed three-corrector bumps (see below) it is helpful to have the right values.

The lattice or quadrupole strength (6) can be check with oscillation data, where two correctors in x, x' and two in y, y' generate oscillations which then can be fitted with expected behaviour calculated with the model. Figure 2

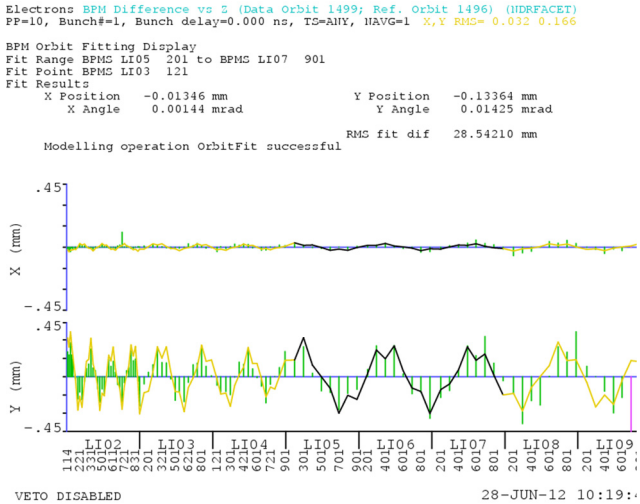

Figure 2: Oscillation data in y, at Li07 501 there seems to be an additional kick pointing to a weaker quadrupole.

shows an example where there seems to be a 15% weaker quadrupole at Li07 501. A wider grid scan can point out nonlinearities, while a few more corrector settings can trace out the design matched beam ellipse in phase space which then can be checked down the linac. With this method (at LCLS) sudden mismatches, coupling and 3% BPM scale errors were found.

RF KICKS

All the above mentioned steering and compensation techniques get messed up by RF kicks (7), and their behaviour is quite interesting. There can be sin and cos terms, an x and x' part, dipole-, quadrupole-, or lens-type kicks, even 2nd harmonic part was observed (Fig. 3).

To distinguish whether it is an angle or position effect two (nearly) closed bumps were made, one with the maximum at the beginning of the accelerator structure and one at the end (Fig. 4).

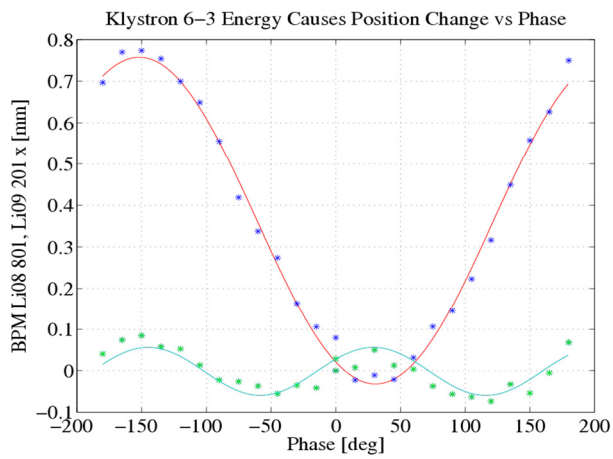

Figure 3: The phase of klystron 6-3 was varied and the resulting downstream orbit observed. At BPM Li09 201 it was up to 800 µm and in phase with acceleration, two BPMs earlier, near the zero-crossing, a 100 µm 2nd harmonic-like effect was seen.

Copyright © 2012 by the respective authors — cc Creative Commons Attribution 3.0 (CC BY 3.0)

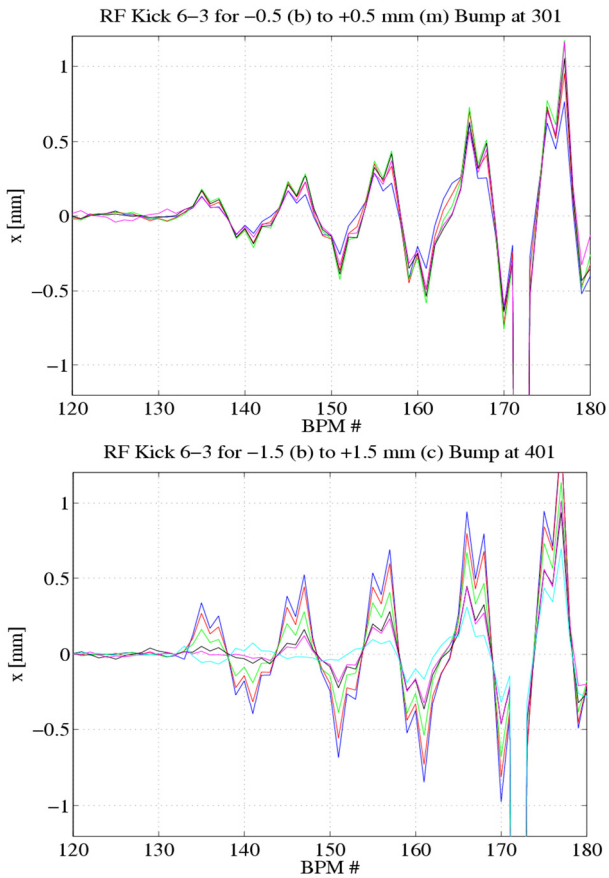

Figure 4: The RF kick of klystron 6-3 (between BPM # 132 and 133) is barely influenced by a bump with the maximum at its front at 301 (top), while at its end at 401 a +1 mm bump cancels the RF kick (bottom). Further downstream seems to be more and more dispersion.

MEASUREMENT FOR SETUP CHANGES

When the beam parameters like charge, bunch length, energy profile change the beam emittances are typically negatively influenced. By localizing and fixing the before mentioned effects as local as possible emittance growth should be minimized. Checking how much dispersion (8) the beam has at a certain point seems to be easy. The energy gets changed by ΔE and with the measured transverse position x: $x = \eta_x \cdot \Delta E/E$ the dispersion η_x is defined. The problem with the linac is that there are many ways to change the energy and on top of that there can be a change due to RF kicks when a klystron is turned off. We typically want to know how the head and the tail of a bunch having different energy due to an energy chirp might behave differently. To check that, we vary the injection phase into the linac by ±1° and then we look at the difference orbit. Since the average chirp phase before the chicane in Sector 10 is about –24° the energy change at the chicane should be about ΔE = 7.8 GeV · (cos(23°)–cos(25°)) = 111 MeV or 1.23% at 9 GeV. Any resulting orbit change in the linac is like dispersion and can be reduced with bumps or dispersion free steering methods.

The beam charge (9) and the bunch length (10) are parameters often asked by the FACET user to be changed. By dithering the damping ring capture phase the throughput and so the number of particles down the linac was varied from 2E10 to 1E10. The resulting orbit changes hint where wakefields might be an issue and where observed early in the linac (Li03). The amplitude of the RTL (Ring-To-Linac) bunch compressor can be adjusted similarly quickly to vary the bunch length, but this fast method wasn't tried yet.

To be more complete other methods and effects (11) should be mentioned too. A) There were the ballistic data measurements, were all quadrupoles, correctors and klystrons are turned off in a sector or two and the BPMs analysed before beam losses occurred. B) Hysteresis in the correctors makes the results questionable. C) Similar to the LCLS undulator where different energies are used to align the undulator, we can scale the quadrupoles and correctors while the actual energy profile and RF kicks stay fixed. With positrons which are bend magnetically in the opposite directions, while the RF kicks are typically the same (dipole kicks) the different effects can be better separated [3]. D) Electronic noise from klystrons causes a different reading for the BPMs in a nearby crate whether the klystron is on beam time or on standby.

Finally two more things should be mentioned. We changed the basic setup of the linac in two ways to make it less susceptible to dispersion. First a "staggered" chirp was introduced, which slowly increases the energy versus z correlation, and 2nd a lower 76 deg per cell lattice was used to be less susceptible to the necessary energy spread.

SUMMARY

The beam emittance control for FACET is basically done by tuning, starting at very high values (sometimes 250 times higher). This paper discusses more than twelve possible approaches to reduce the initial value locally as good as possible, so that any longitudinal or intensity changes are not coupled into the transverse dimensions.

ACKNOWLEDGMENT

The FACET team wants to thank the many support groups which make the four months short FACET runs possible, and especially the operations group for their interest and dedication to improve the beam conditions.

REFERENCES

[1] F.-J. Decker et al., "Intensity Effects of the FACET Beam in the SLAC Linac," IPAC12, New Orleans, May 2012, WEPPR040.

[2] F.-J. Decker et al., "Characterization and Reduction of Transverse RF Kicks in the LCLS Linac," PAC09, Vancouver, BC, Canada, WE5RF039.

[3] C. Adolphsen et al., "Beam-Based Alignment Technique for the SLC Linac," PAC'89, Chicago, March 1989, p. 977.

Copyright © 2012 by the respective authors — cc Creative Commons Attribution 3.0 (CC BY 3.0)

POSITRON INJECTOR LINAC UPGRADE FOR SUPERKEKB

T. Kamitani*, M. Akemoto, Y. Arakida, D. Arakawa, A. Enomoto, S. Fukuda, K. Furukawa, Y. Higashi, T. Higo, H. Honma, N. Iida, M. Ikeda, E. Kadokura, K. Kakihara, H. Katagiri, M. Kurashina, H. Matsushita, S. Matsumoto, T. Matsumoto, S. Michizono, K. Mikawa, T. Miura, F. Miyahara, T. Mori, H. Nakajima, K. Nakao, T. Natsui, S. Ohsawa, Y. Ogawa, M. Satoh, T. Shidara, A. Shirakawa, T. Suwada, H. Sugimoto, T. Takatomi, T. Takenaka, Y. Yano, K. Yokoyama, M. Yoshida, L. Zang, X. Zhou, KEK, Tsukuba, Japan
D. Satoh, Graduate School of Science and Engineering, Tokyo Inst. of Technology, Tokyo, Japan

Abstract

This paper reports on a present status of a positron injector linac upgrade for SuperKEKB. A development status of a flux concentrator for positron focusing is shown. An influence of offset layout of the flux concentrator and the target on a positron yield is described. Positron capture by L-band and large aperture S-band accelerating structures are compared in a viewpoint of satellite bunch elimination. Beam optical design compatible to electrons and positrons of different beam energies is discussed.

INTRODUCTION

The KEKB-factory is now under an upgrade to SuperKEKB for a forty times higher luminosity [1]. The injector linac is required to supply beams of higher charge and smaller emittance as shown in Table 1.

Table 1: Linac Beam Specifications

	KEKB (e^-/e^+)	SuperKEKB (e^-/e^+)
Injection Energy (GeV)	8.0 / 3.5	7.0 / 4.0
Bunch Intensity (nC)	1.0 / 1.0	5.0 / 4.0
Number of Bunch /pulse	2 / 2	2 / 2
Emittance (μm)	300 / 2100	$20 / 92_{[H]}{:}7_{[V]}$

To generate low emittance electron beams of 5 nC bunch intensity for injection, a photo-cathode RF gun is introduced [2] to replace the existing thermionic gun and the RF bunching section. The electron beams are accelerated up to 7.0 GeV over the entire linac and injected into the HER. Electron beams of 10 nC for positron production will also be generated with the RF gun. In a case high intensity operation of the RF gun is not stable, the thermionic gun is also used and the beams from these two guns are switched. To generate low emittance positron beams, a damping ring (DR) of 136 m circumference is introduced at a side of the linac and connected at the beam switch-yard No.2 (SY2). Beams generated in a positron capture section (PCS) are accelerated up to 1.1 GeV and injected into the DR. Positrons are extracted after 40 ms from the DR, injected back to the linac and accelerated up to 4.0 GeV for injection to the LER. Energy gain of the positrons from existing six accelerator modules (typically 160 MeV per each module) from the PCS to the SY2 is not sufficient for this 1.1 GeV injection to the DR. The PCS is relocated 40 m upstream to have a sufficient energy margin for the DR. To increase positron beam intensity four times as much, capture efficiency is enhanced in two aspects. At first, an existing 2-T pulsed coil of short field length (45 mm) right behind a positron production target, is replaced with a flux concentrator (FC) type of 5-T pulsed solenoid of long field length (200 mm). An adiabatic matching characteristics of a solenoidal field distribution with a FC, gives wider energy acceptance for positrons. As a second aspect, existing S-band accelerating structures with conventional aperture (21 mm in diameter) used in a solenoidal field of the PCS are replaced with large aperture S-band (LAS) structures (30 mm) or L-band structures (35 mm) to enlarge transverse phase space acceptance. Total length of the PCS is extended from 8 m to 16 m to boost positron beam energy from the PCS from 80 to 120 MeV. This increase of the beam energy at a transition from solenoidal to quadrupole focusing region is effective in reducing beam loss around an optical matching section.

In December of 2013, we will start a preliminary positron beam commissioning of the injector linac within limited operation parameters. A beam commissioning with the DR will be started in February of 2015. Development, fabrication and installation of the components are ongoing to be in time for the schedule.

In the following sections, as topics of significance in the positron injector linac upgrade, flux concentrator development, target protection and offset positron production, large aperture accelerating structures development, satellite bunch elimination and electron/positron compatible optics design are described .

FLUX CONCENTRATOR DEVELOPMENT

Flux concentrator is a pulsed solenoid composed of a primary coil and a copper cylinder with a conical hole inside. Induced eddy current flows through a thin slit to a inner surface and generates a strong field of several Tesla. Achievable field strength is mainly determined by a hole diameter and a primary pulsed current. They are constrained from a required aperture size, a power supply capacity and break-

* E-mail: <takuya.kamitani@kek.jp>

Copyright © 2012 by the respective authors — cc Creative Commons Attribution 3.0 (CC BY 3.0)

down limit. We have been collaborating with BINP, SLAC, Frascati and IHEP on the FC development for KEKB linac upgrade. We have performed a high power operation test of a BINP-type FC at KEK and experienced a breakdown problem. The prototype is disassembled and under careful inspection at BINP. For a coming preliminary positron beam commissioning in December of 2013, we will use a more conventional FC, two type are considered as candidates. One is a spiral slit FC based on the SLAC design. Frascati and IHEP also have been using this type of FC. The other type is a simple straight slit FC. A peak longitudinal field strength at a same current is lower with the SLAC type, but a contribution of a transverse field component which is not axial-symmetric is also smaller. Considering an effect of target offset from a field center described later, evaluation of positron capture efficiency by a particle tracking using detailed 3D field distribution is ongoing. Since the FC is installed right behind the target and its radio-activation level will be very high and a replacement work will not be easy. Thus, an engineering design to avoid mechanical failure or water and vacuum leakage problems is critically important. Decision of installation model among the candidates will be made soon with a comparison in the capture efficiency performance and engineering design consideration.

POSITRON PRODUCTION TARGET

We have used 14 mm thick (4.0 radiation lengths) amorphous tungsten and later 10 mm thick crystal tungsten for the positron production target. In the beam commissioning for SuperKEKB, an amorphous tungsten will be used to avoid precise axis alignment mechanism. For a pulse-by-pulse switching of electron and positron injections, a small hole for electron beam passage is bored a few mm apart from a center of the target. To optimized a positron yield, the target was placed on a common central axis of the pulsed coil and the DC solenoids in the KEKB linac. Thus, electron beam entered into solenoid field at a few mm offset from the axis and traveled through an excursion orbit by a fringe field. It becomes a problem at SuperKEKB, since an electron beam for injection have a small emittance as 20 μm. Emittance growth in this excursion orbit is not acceptable and a hole for electron passage should be centered on the axis of the DC solenoids. An aperture diameter of the FC is only 7 mm in the present design and the tungsten target of 4 mm diameter and the hole of 2 mm diameter should be well contained in the aperture. As a consequence, center axis of the FC has 2 mm offset from the beam line and target center has 1.5 mm offset from the FC center. We expected the offsets degrade the positron yield 20 to 30 % by a preliminary simulation study. More detailed study on this offset effect is to be done by the tracking simulation.

LARGE APERTURE CAPTURE SECTION

To enlarge a transverse phase space acceptance of the PCS, accelerating structures with larger aperture will be used. As a first candidate, we started R and D for L-band structure which had an appropriate field strength and an aperture diameter as described in Table 2. A first prototype L-band structure has been fabricated and under a high-power RF processing in a test stand. Since a large outer dimension of an RF coupler of the structure gives strong impact on a DC solenoid design, an L-band structure of slimmer body is in consideration by installing a dummy load inside the structure in a collinear geometry. In a selection of the L-band frequency, we cannot use simple half frequency (1428 MHz) of the S-band because it is not compatible with 2 bunch operation with 96 ns interval which was defined from phase synchronization constraint of the linac and the storage rings. Instead, we adopted 1298 MHz which is 5/11 of the S-band frequency. This co-prime frequency relationship was found to be useful in elimination of satellite bunch particles as described later.

The other candidate is a large aperture S-band (LAS) structure as described in Table 2. It has a larger aperture diameter (30 mm) compared with conventional S-band structures (21 mm). The LAS has a very large group velocity and a field strength is relatively low, however operation with a pulse compression by the SLED gives comparable field strength. The LAS structures are used not only in the PCS, but in subsequent two accelerator modules of quadrupole focusing region to improve transverse acceptance as described in the next section.

Table 2: Specifications of Large Aperture Structures

	L-band	LAS
RF frequency (MHz)	1298.182	2856.000
number of cells	24 + 2	57 + 2
accel. length (mm)	2001	2064
disk aperture 2a (mm)	39.4 $\rightarrow$ 35.0	31.9 $\rightarrow$ 30.0
group veloc. v_g/c (%)	0.61 $\rightarrow$ 0.39	4.2 $\rightarrow$ 3.5
shunt imp. r_0 (MΩ/m)	45.7 $\rightarrow$ 47.6	46.1 $\rightarrow$ 48.4
filling time T_f (μs)	1.360	0.180
accel. field (MV/m)	12.2@15MW	6.93@10MW
same with SLED	–	16.42

Positrons emerged from the target have wide range of energy due to a cascade shower process and long bunch tail due to path differences in spiral orbits. Simulation studies show that a positron capture in decelerating phase and a formation of a main bunch by RF phase slip is useful to reduce particles at tails of an energy distribution [3]. However, particles which are not captured in the main bunch, experience further phase slips. They can be captured in subsequent phase positions and form satellite bunches. They can have comparable beam energy as those in the main bunch and will not be eliminated by an energy collimation. A fraction of satellite particles go out of RF buckets are lost at the DR injection. Due to a civil engineering constraint, a beam loss at DR is strictly limited to be below 0.2 % of a design beam intensity (4 nC x 2 bunch). Thus, elimination of satellite particles in the linac is a critical issue for a DR

Copyright © 2012 by the respective authors — cc Creative Commons Attribution 3.0 (CC BY 3.0)

operation.

In a case we use six 2-m long L-band structures in the PCS, satellite bunches are formed in L-band wave-length intervals. Due to the co-prime relationship to the S-band wave-length, satellite bunches are accelerated or decelerated in abnormal phases in the downstream S-band linac modules and are eliminated in the linac or in an energy collimation. It is shown that a beam loss at DR injection will be suppressed to be an allowable level 0.05% [3]. In a case of a hybrid of two L-band and four LAS structures, the loss becomes 0.2%, but still acceptable. To suppress an initial construction cost by avoiding L-band component construction, it is recommended to start a beam commissioning with a configuration of all LAS structures in the PCS. In this case, the loss becomes 0.4% and further improvement is necessary. A preliminary simulation study indicates that raising S-band deceleration field around 20 MV/m can reduce satellites. More detailed study will be done soon.

POSITRON/ELECTRON COMPATIBLE OPTICS

By using accelerating structures with larger aperture, a transverse acceptance of the PCS which corresponds to an RMS emittance is enlarged from 2000 μm to 4000 μm. As described in the previous section, the PCS is relocated to a 40 m upstream position and a beam energy from this section is raised from 80 MeV to 120 MeV. As a consequence of these changes, a quadrupole focusing system after the PCS till the SY2 needs an upgrade and an addition and rearrangement of quadrupole and steering magnets will be made. In the two accelerator modules after the PCS, LAS structures of 30 mm aperture diameter are used to enlarge the transverse acceptance and quadrupoles are installed in 70 cm interval outside of the structures. In the subsequent three modules, ordinary S-band structures of 20 mm aperture are used and quadrupoles are placed in the same interval. In the subsequent four modules, quadrupole triplets are placed between the S-band structure and the interval changes from 3m to 5m according to the beam energy.

In this region between the positron production target and the SY2 before the DR, both of low energy, huge emittance positrons and high energy, low emittance electrons pass through the same quadrupole focusing system. Almost all quadrupoles in this region are DC magnets. To avoid a beam loss of the positrons, focusing strengths are optimized for them. Thus, electrons are focused in a ready-made quadrupole fields which are weak for the energy of electrons. Slight optimization to moderate electron beam size is performed within a range in which the positron optics is not significantly modified. Fig. 1 shows beam size of the positrons and the electrons.

Even with this compromised optics for the electrons, the beam sizes are kept sufficiently small. For independent orbit control of the positrons and the electrons, 12 pulsed steering magnet pairs are installed in addition to existing DC steerings. Orbit correction performance and emittance growth with this limited number of steerings should be checked by simulations and underway.

In the region after the DR till the end of the linac, both of the electrons and the positrons have low emittance and not precisely same but high energy. Quadrupole triplets and steerings are placed in 20 m interval. Total number of magnets are not so large for this region and there are no quadrupoles outside the structure, hence we decide all the quadrupoles and steerings here to be pulsed magnets. It will be useful for a precise independent matching to the storage rings and for an independent orbit control to suppress emittance growths for positrons and electrons.

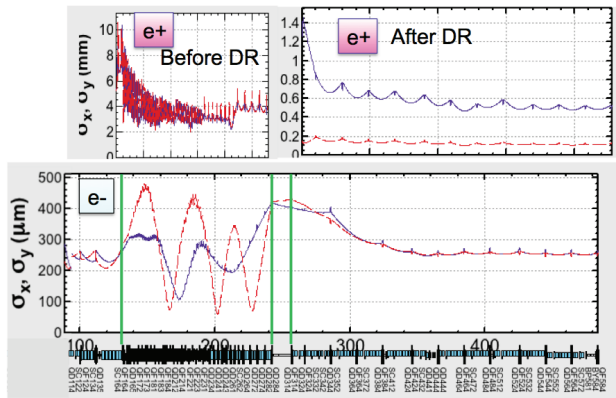

Figure 1: Positron/electron beam optics design.

SUMMARY

The KEKB positron injector linac is under an upgrade for SuperKEKB. Two types of flux concentrator in different slit geometry are in comparison by simulations and a prototype fabrication. An influence of an offset layout of the FC and the target is discussed. As accelerating structures to be used in the capture section, L-band and large aperture S-band structures are compared in a viewpoint of satellite bunch elimination. Performance of a compatible optics for electrons and positrons of different beam energies with DC quadrupoles is studied. A preliminary positron beam commissioning of the injector linac will be started in December of 2013.

REFERENCES

[1] T. Abe et al., "Belle II Technical Design Report, Chapter.2 SuperKEKB", KEK Report 2010-1, p. 19, http://www-superkekb.kek.jp/documents/B2TDR.pdf

[2] M. Yoshida, N. Iida, Y. Ogawa, M. Sato, L. Zang "SuperKEKB Injector Upgrade for High Charge and Low Emittance Electron Beam", IPAC'12, New Orleans, USA, May 2012, TUPPD035

[3] N. Iida, H. Ikeda, T. Kamitani, M. Kikuchi, K. Oide, D. Zhou "Beam Dynamics in Positron Injector Systems for the Next Generation B-factories", IPAC'11, San Sebastian, Spain, September 2011, THYA01

Copyright © 2012 by the respective authors — cc Creative Commons Attribution 3.0 (CC BY 3.0)

RECENT IMPROVEMENTS TO THE CONTROL OF THE CTF3 HIGH-CURRENT DRIVE BEAM

B. Constance, R. Corsini, D. Gamba, P. K. Skowroński, CERN, Geneva, Switzerland

Abstract

In order to demonstrate the feasibility of the CLIC multi-TeV linear collider option, the drive beam complex at the CLIC Test Facility (CTF3) at CERN is providing high-current electron pulses for a number of related experiments. By means of a system of electron pulse compression and bunch frequency multiplication, a fully loaded, 120 MeV linac is used to generate 140 ns electron pulses of around 28 Amperes. Subsequent deceleration of this high-current drive beam demonstrates principles behind the CLIC acceleration scheme, and produces 12 GHz RF power for experimental purposes. As the facility has progressed toward routine operation, a number of studies aimed at improving the drive beam performance have been carried out. Additional feedbacks, automated steering programs, and improved control of optics and dispersion have contributed to a more stable, reproducible drive beam with consequent benefits for the experiments.

INTRODUCTION

The Compact Linear Collider [1] (CLIC) is a leading contender for the next generation of high energy lepton colliders. As an essential precursor to proceeding with such a facility, the CLIC Test Facility (CTF3) at CERN has been built to demonstrate many of the technologies required for stable drive beam generation and RF power production. The complex consists of a 120 MeV e^- linac, a chicane for bunch length control, a 42 m Delay Loop (DL), an 84 m Combiner Ring (CR) and finally the CLIC Experimental Area (CLEX). A thermionic gun produces 4 Amp pulses of 1.4 us, typically at a repetition rate of 0.83 or 1.67 Hz. A sub-harmonic buncher operating at 1.5 GHz, followed by a 3 GHz buncher, generates a beam bunched at half the acceleration frequency. Since energy efficiency is key to the CLIC design, the 3 GHz CTF3 linac operates in a fully loaded configuration. In order to maximise the RF power available, 5.5 us pulses from the klystrons are compressed to around 1.4 us using resonant cavities, increasing peak power by a factor of two to over 30 MW.

As laid out in the CLIC design, at CTF3 a system of bunch frequency multiplication and pulse compression is used to generate a high-current drive beam. Injection into the DL and CR is achieved using transverse deflecting RF cavities. By coding the beam phase with a series of 180° phase shifts, 140 ns sections of the pulse may be alternately injected or allowed to bypass the DL. On exiting the DL, the delayed sections interleave with those sections bypassing. This results in a train of four 140 ns sub-pulses, separated by 140 ns, with a current of some 8 Amps and a 3 GHz bunch frequency. These four sub-pulses are then stacked in the CR before extraction to CLEX, where the final 12 GHz pulse is 140 ns long. The combined current is typically around 28 Amps before transport, since some fraction of the charge is lost to satellite bunches in the unused RF buckets.

In CLEX, the combined pulse may be directed to one of two experimental beamlines. The Test Beam Line (TBL) contains at present 12 Power Extraction and Transfer Structures (PETS), with 16 expected by end of the 2012, and is used primarily for studies into the phase and amplitude stability of the produced 12 GHz RF power and the transport of the decelerated drive beam [2]. The second beamline serves the Two-Beam Test Stand (TBTS), an experiment which is also provided a probe e^- beam by the CALIFES accelerator. The probe beam fills the role of the CLIC main beam, allowing for two-beam acceleration studies [3].

OPTICAL MODEL VERIFICATION

Control of the transverse linear optics at CTF3 is achieved using a MAD-X model of the machine. Optical transition radiation screens at key points in the lattice allow measurements of the beam emittance and Twiss parameters using standard quadrupole scan techniques. Based on these measurements, quadrupole currents are rematched using the model predictions to ensure the correct beam parameters at critical locations. Of course, the success of this method depends on the validity of the model.

Discrepancies between the predicted and measured optical functions at some screens inspired a campaign to verify the MAD-X model using beam-based optics measurements. The horizontal and vertical planes were assumed to be uncoupled and treated independently. Using a pair of calibrated dipole corrector magnets separated by a drift length, a series of beam orbits may be injected into the lattice with arbitrary positions and angles. The series of orbits can be chosen in such a way that they map out, or paint, the matched phase space ellipse expected at the location of the second corrector. In effect, each orbit behaves as a macroparticle on the matched ellipse. The orbits evolve as they propagate through the lattice in a way governed by the linear transport matrix, and thus so too does the ellipse they describe. By spacing the orbits at regular intervals covering the full phase space, and observing how the ellipse has changed at some downstream position, information is obtained about all four elements of the two-dimensional transfer matrix.

Copyright © 2012 by the respective authors — cc Creative Commons Attribution 3.0 (CC BY 3.0)

To reconstruct the ellipse at a downstream point requires a measurement of both the position and angle at this point. At CTF3, the Beam Position Monitors (BPMs) available give only position information, and therefore measurements from two adjacent BPMs are combined to calculate the orbit angles. For this step it is necessary to assume the MAD-X model between the two BPMs is correct.

For practical measurements, it is advantageous to take pairs of orbits on the ellipse separated by a 180° phase advance and use them to form a difference orbit. In this way slow drifts of the beam will be canceled. In addition, mean difference orbits over a number of pulses may be taken. To further reduce sensitivity to jitter and drifts, several similar ellipses of different areas or psuedo-emittances may be painted. Then, a fit can be made between the difference orbits at a given phase over all ellipses and a single, normalised ellipse generated.

To extract the transfer matrix from an ellipse reconstructed at some point s in the lattice, each set of N orbits is formed into a matrix $\mathbf{x}(s)$:

$$\mathbf{x}(s) = \begin{pmatrix} x_1(s), & x_2(s), & \dots & x_N(s) \\ x_1'(s), & x_2'(s), & \dots & x_N'(s) \end{pmatrix} \quad (1)$$

Then, letting s_B denote the location of the reconstruction BPM and s_K the location of the kicker:

$$\mathbf{x}(s_B) - \mathbf{M}\mathbf{x}(s_K) = 0 \quad (2)$$

Which may be solved numerically for the transfer matrix $\mathbf{M}$. Here, the equation was solved using a non-linear fitting routine implemented in MATLAB [4] with the symplectic constraint imposed in addition.

As reconstruction of the ellipse requires an assumption of the transfer matrix between BPMs, it is necessary to require consistency over multiple measurements to be certain of a measured transfer matrix's veracity. Take the situation in figure 1. In the first step, matrix $\mathbf{M_1}$ is measured assuming $\mathbf{N_1}$ to be correct. In the second step, $\mathbf{M_2}$ is measured assuming $\mathbf{N_2}$. If both $\mathbf{M_1}$ and $\mathbf{M_2}$ are consistent with MAD-X, then since $\mathbf{M_2} = \mathbf{N_1}\mathbf{M_1}$ the original assumption of $\mathbf{N_1}$ is upheld. It is possible to proceed pairwise through all BPMs in the lattice in this manner.

After making measurements of various sections of CTF3, the MAD-X model was found to accurately represent the lattice in most cases. One notable exception was

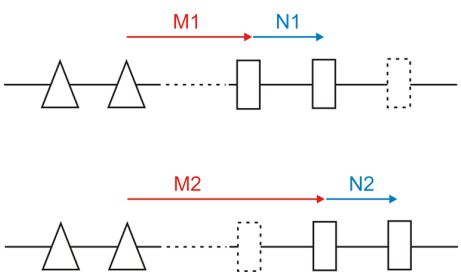

Figure 1: Procedure for measurement of the transfer matrix $\mathbf{M_1}$ between the second corrector magnet and first BPM.

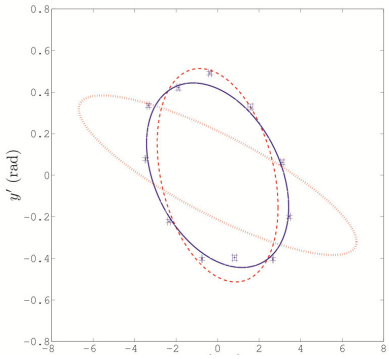

Figure 2: Reconstructed vertical ellipse at the DL BPM named BPI0358. Data points show the difference orbits. The solid blue ellipse is generated by the symplectic fit to the data, and is compared to the MAD-X prediction before (dotted red) and after (dashed red) optimisation of the main dipole FINT property.

the DL, where good agreement was obtained in the horizontal but a discrepancy was clear in the vertical. This suggested an error in the modeling of the main dipole fringe fields. By using an iterative procedure again developed in MATLAB, it was possible to fit the dipole field integral (FINT property in MAD-X) to provide the best possible match with the measurements. At each step in the iteration, the new model matrices must of course be used to reconstruct the ellipses.

In figure 2 an example of a reconstructed ellipse is shown, along with the MAD-X prediction before and after optimising the field integral. Figure 3 shows the four measured matrix elements throughout the DL lattice, again with the MAD-X predictions. In addition, a direct measurement of R_{11} and R_{12} was made by injecting a cosine- and sine-like orbit respectively, and is included for comparison. The missing measurements in the centre of the DL are due to faulty BPMs, and the matrices are given with respect to the DL injection point.

ONLINE DISPERSION MEASUREMENT

By taking advantage of CTF3's RF pulse compression system, a simple method to monitor dispersion during tuning is in use. A programed phase ramp ensures a flat top to the compressed RF pulses. By appropriate modification of the phase ramp, a step in the RF may be introduced such that the second half of the pulse has around 2 MW (∼10%) lower power than the first half. During tuning, this is done with the RF from the klystron that drives the final two cavities. Online orbit display software is then used to display the mean orbits of the first and second half of the beam pulse, along with a difference between the two. This difference is proportional to the dispersion function.

In figure 4, the orbits of the beginning and end of the pulse are shown along the linac, bypassing the DL and in the TL1 transfer line leading toward the CR, as is the difference between them. In the second plot a quadrupole in the

Copyright © 2012 by the respective authors — cc Creative Commons Attribution 3.0 (CC BY 3.0)

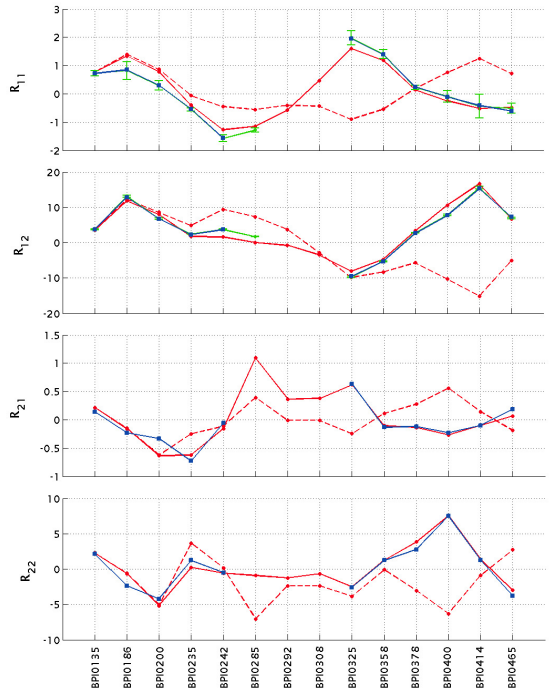

Figure 3: Vertical transport matrices for the DL. Matrices from MAD-X before (dashed red circles) and after (solid red circles) optimisation of the main dipole FINT are compared with the measured matrices extracted from reconstructed ellipses (solid blue squares) and direct measurements of R_{11} and R_{12} (green error bars).

dispersive region of the chicane, between the BPMs 0242 and 0258, has been used to minimise the downstream dispersion.

AUTOMATIC ORBIT CLOSURE

Closure of the CR orbit and of the orbit exiting the DL are very important to the generation of a well-combined beam, since different sub-pulses of the beam take different paths through the machine and are stored in the CR for different numbers of turns. To aid in operation, automatic

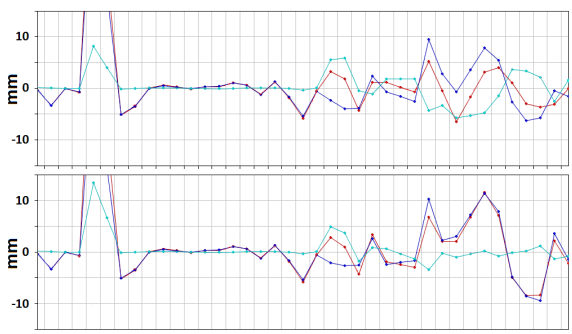

Figure 4: Horizontal orbit in the linac and TL1 before (top) and after (bottom) dispersion correction. The blue and red orbits have high and low energy respectively, and cyan shows the difference between the two.

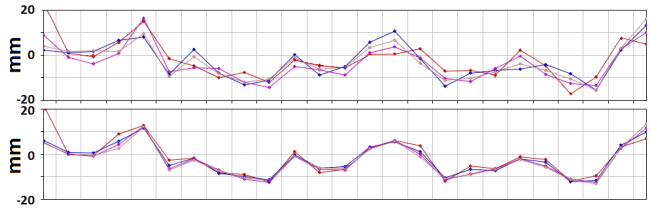

Figure 5: Horizontal orbit in the CR before (top) and after (bottom) automatic steering to inject onto the closed orbit. Each trace shows one of the four turns.

software has been developed to steer the beam in the DL out onto the same trajectory as the bypassing sub-pulses. Similarly, software is used to steer the beam onto the closed orbit of the CR. Based on measured response matrices, the system is automatic and can operate as a slow feedback to counter beam drift.

In figure 5, the horizontal orbits of four turns in the CR are shown. The 4 Amp pulse has been shortened to prevent combination. The second plot shows the effects of automatically steering the beam onto the closed orbit, which had previously been found by storing the beam for around ten turns and allowing the orbit oscillations to damp. The apparent residual difference between the turns in some BPMs is an artifact due to a droop of the BPM signal baselines. Well behaved BPMs such as 0650 and 0695 show the true orbit difference.

CONCLUSION

Beam-based measurements of the linear optics have been performed, and an error in the MAD-X model of the DL corrected. Ensuring the delayed sub-pulses and sub-pulses which bypass the DL are optically matched leads to easier transport of the combined pulse. The use of online dispersion monitoring and automatic steering has allowed for a faster and more precise setup of the beam, improving reproducibility. Coupled with recent improvements in dynamic control of CTF3, such as feedbacks which have improved the stability of the compressed RF pulses [5, 6], these developments have led to a more stable environment for research.

REFERENCES

[1] G. Guignard (Ed.), "A 3 TeV e+e- linear collider based on CLIC technology,", CERN 2000-008, 2000.

[2] E. Adli et al., "Commissioning status of the decelerator test beam line in CTF3," MOP018, LINAC2010.

[3] W. Farabolini et al., "Two beam test stand experiments in the CLEX CTF3 facility," MOOCA02, IPAC2011.

[4] MathWorks, `http://www.mathworks.com/`

[5] A. Dubrovskiy and F. Tecker, "RF pulse compression stabilization at the CTF3 CLIC test facility," THPEA043, IPAC2010.

[6] T. Persson and P. K. Skowronski, "Beam stability at CTF3," TUPPR032, IPAC2012.

Copyright © 2012 by the respective authors — cc Creative Commons Attribution 3.0 (CC BY 3.0)

DESIGN AND OPERATION OF A COMPACT 1 MeV X-BAND LINAC

G. Burt, P.K. Ambattu, C. Lingwood, T. Abram, Cockcroft Institute, Lancaster University, UK
I. Burrows, P. Corlett, A. Goulden, T. Hartnett, P. Hindley, P.A. McIntosh, K. Middleman,
Y. Saveliev, R. Smith, C. White, STFC, Daresbury Laboratories, UK

Abstract

A compact 1 MeV linac has been produced at the Cockcroft Institute using X-band RF technology. The linac is powered by a high power X-band magnetron and has a 17 keV 200 mA thermionic gun with a focus electrode for pulsing. A bi-periodic structure with on-axis coupling is used to minimise the radial size of the linac and to reduce the surface electric fields.

INTRODUCTION

Small, low-energy linacs are required by industry for the production of X-rays to be utilised in security applications and for non-destructive testing. Mobile cargo scanning systems used in the security industry typically use S-band (3 GHz) RF linacs to accelerate electrons produced from a pulsed electron gun to the required energy (typically 1-5 MeV depending on the type and thickness of the material to be scanned) [1]. Typically all the power supplies, control electronics and water cooling are placed on the back of a truck along with a robotic arm which will have the linac cavity, electron gun and target attached, along with a substantial amount of lead shielding. For mobile security applications the weight of the linac is critical to the mobility of the linac. Using higher frequency linacs reduces the cavity radius and hence the weight of the lead shielding required. For this reason an ultra-compact 9.3 GHz, 1 MeV linac has been designed at the Cockcroft Institute.

LINAC DESIGN

The linac is to be driven from a 1 MW e2v magnetron. As magnetrons are not very frequency stable the structure must be tolerant to changes in frequency. This is made more difficult by the requirement to have a small iris to have the maximum possible R/Q. In order to increase stability the structure was chosen to work in a $\pi/2$ mode. As every 2nd cell is empty there are two options to keep the R/Q high, to use a side coupled structure or an on-axis coupled bi-periodic structure. As we also want to keep the structure diameter small it was decided to use the latter. The structure is electrically coupled through the iris, this doesn't have as much coupling as magnetic coupling through slots in the wall, but is simpler to manufacture and operate. A 5 mm iris diameter was chosen to give sufficient coupling between the cells.

Although the electron gun is pulsed it has a pulse width that is several thousand RF periods hence it is necessary to bunch the electron beam within the linac cavity before acceleration. The electron beam is injected into the cavity from the gun at a relatively low energy (17 keV) and the electron velocity will not become close to the speed of light until after several cells of the cavity. This requires the length of each cell to be carefully optimised using beam dynamics codes to track each electron through the cavity such that the synchronous phase varies along the structure. As the electron velocity is dependent on the accelerating gradient, the electric field amplitude must be chosen before optimising the cavity. A peak accelerating gradient of 30 MV/m was chosen as a compromise between structure length and peak surface electric field, and this resulted in a structure with 8 accelerating cells.

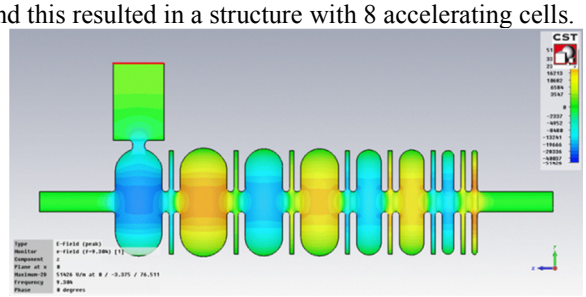

Figure 1: Compact Linac Cavity modelled in CST [4].

Particle tracking including space charge has been performed in ASTRA[2] as well as full PIC simulations in VORPAL [3], shown in Figure 2 and 3. It is observed that space charge forces are quite large in the front end of the linac where the cavity field is very low, resulting in particles spreading and hitting the cavity walls. This however is not expected to cause much heating or radiation as the impact energy is low. As the particles travel further downstream, they get bunched and transversely focused and at the exit of the linac reach 1 MeV and 50 to70 mA on average which is sufficient to produce the desired range of X-ray dose for many applications.

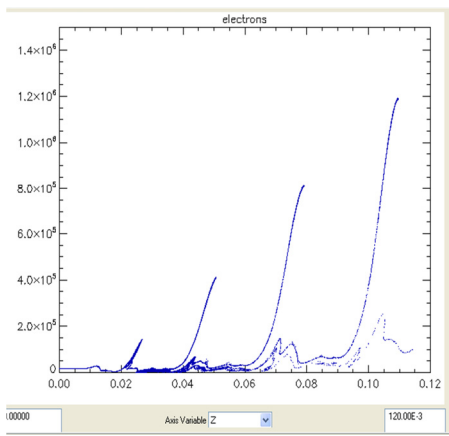

Figure 2: Electron energy, in eV, as a function of longitudinal position in the linac, in metres.

Copyright © 2012 by the respective authors — cc Creative Commons Attribution 3.0 (CC BY 3.0)

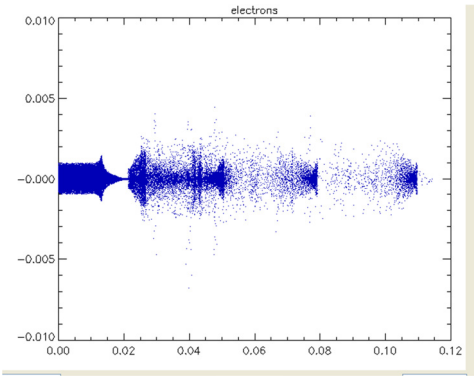

Figure 3: Electron horizontal offset plotted against longitudinal position in metres.

After optimising the basic cell shape and the length of each cell, it is necessary to model the full cavity in an RF simulation code, design an RF waveguide input coupler and to adjust the cell dimensions to account for the perturbation due to the ohmic losses. This was performed in CST Microwave Studio [4].

CAVITY MANUFACTURE

The linac cavity has been manufactured by Shakespeare Engineering, a UK precision Engineering company. The cavities were delivered to Daresbury Laboratories for final tuning and RF measurement. The cavity frequencies were measured using a vector network analyser and a resonant perturbation technique is employed to measure the field profile of the cavity. Both processes are performed in a clean laminar flow environment.

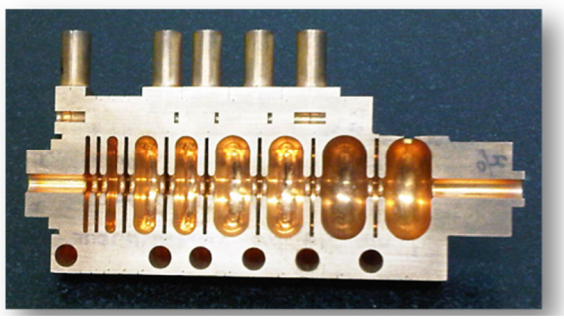

Figure 4: Cross-section of the manufactured cavity.

It was found that the manufacturing tolerances on the cavity manufacture had not been met resulting in the field only being present in some of the cells. This was confirmed by cutting a cavity in half with wire EDM, as shown in Figure 4. A new cavity is currently being manufactured to resolve some of the issues in the first cavity.

The cavity was then connected to the electron gun and pumped down. The installed cavity is shown in Figure 5.

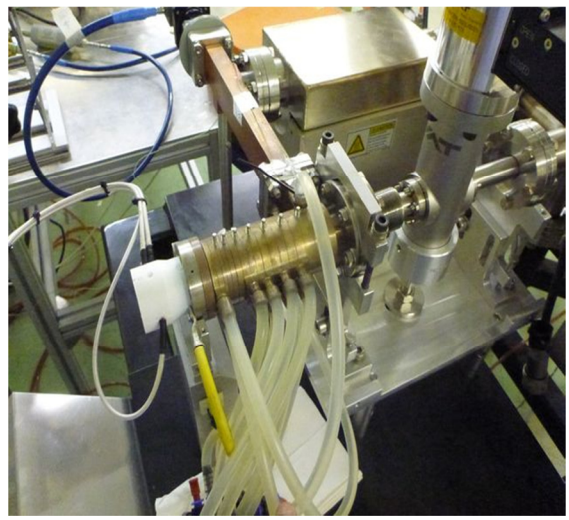

Figure 5: Compact linac cavity and gun installed.

DIAGNOSTICS LINE

In order to accurately measure the energy, current and spot size of the accelerated electron bunch a diagnostics line was constructed at the end of the linac. Integrating current transformers were placed on the cathode supply of the electron gun and in between the linac and the tungsten target for the measurement of beam current. A movable stepper drive section allowed the tungsten target to be removed from the beamline and replaced with either a straight section or a slit.

To measure the beam energy an ex-SRS dipole magnet was placed to deflect the beam down an angled beamline terminated in a Faraday Cup. The electrons energy can be calculated from the magnetic field required to deflect the beam to the Faraday cup. The magnet had previously been calibrated by the magnet group in ASTeC Department, STFC and hence the magnetic field could reliably be worked out from the magnet supply current.

In addition a radiation monitor was used to measure the X-ray production when the target is placed in the beamline.

The full diagnostics line is shown in Figure. 6.

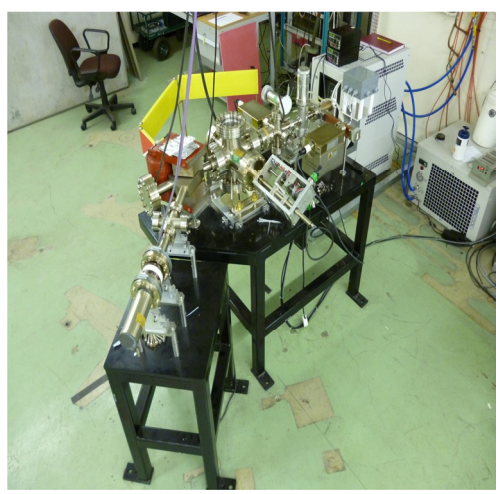

Figure 6: Compact linac Diagnostics Line.

Copyright © 2012 by the respective authors — cc Creative Commons Attribution 3.0 (CC BY 3.0)

LINAC TESTING

The linac was fully assembled in July 2011, and commissioning started with testing of the electron gun. The electron gun was found to produce 160 mA as measured by an ICT on the cathode input.

A 1.3 MW, e2v magnetron and modulator is used as the RF power source. The cavity was then tested at high power, and was found to operate well up to an input power of 800 kW, well above the design power of 450 kW. However as the field profile is not as expected it is difficult to work out what gradient this is.

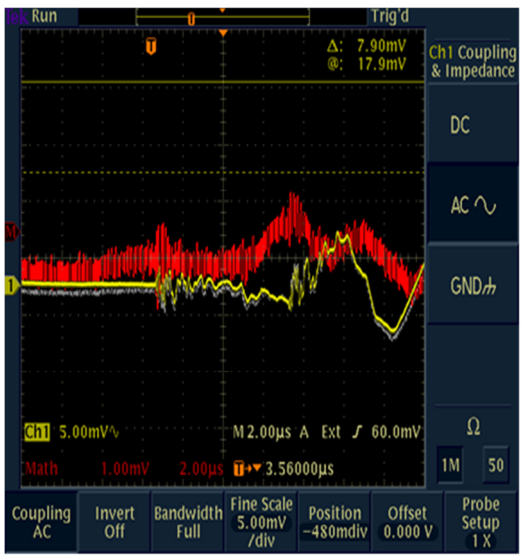

Figure 7: Faraday cup signal after the spectrometer magnet at 610 keV.

The electrons were then injected into the cavity. As there is no field in the first few cells the beam is not effectively bunched, hence a higher power is required to reach high energy. With an input power of 800 kW the maximum electron energy was measured on the spectrometer to be 610 keV. However it should be noted that due to the lack of bunching some electrons may reach a higher energy but with too low a current to be measured on the Faraday Cup. The signal from the Faraday cup is shown in Figure 7.

CONCLUSION

A compact linac has been designed and tested. Due to the cavity manufacture not meeting the design tolerances the field profile was far from ideal and field was only measured in the last 5 cells. This resulted in a lack of bunching and a lower beam energy at the output of 610 keV. A new cavity that better matches the design specification is currently being manufactured by Shakespeare Engineering and commissioning is expected to restart in the near future.

ACKNOWLEDGEMENTS

This work has been supported by STFC via the Cockcroft Institute core grant and STFC through the PNPAS program.

REFERENCES

[1] D.H. Whitten et al," State of the Art in Medical and Industrial Linear-Accelerator Systems", IVEC, 2008.
[2] ASTRA, A Space Charge Tracking Algorithm, http://www.desy.de/~mpyflo/.
[3] VORPAL, TechX Corp., http://www.txcorp.com/
[4] CST Microwave Studio, CST GmbH, Germany, http://www.cst.com/

Copyright © 2012 by the respective authors — cc Creative Commons Attribution 3.0 (CC BY 3.0)

HIGH GRADIENT OPERATION OF 8-GeV C-BAND ACCELERATOR IN SACLA

T. Inagaki#, T. Sakurai, C. Kondo, Y. Otake, RIKEN SPring-8 Center, Hyogo, 679-5148, Japan.

Abstract

In X-ray free electron laser facility, SACLA, C-band high gradient accelerator was employed in order to shorten the 8-GeV accelerator length. In total, 64 klystrons, 64 RF pulse compressors, and 128 accelerating structures are used in SACLA. Since the C-band accelerator generates high acceleration gradient (nominal 35 MV/m), associated with a high RF breakdown rate, reliability of the high power RF components and the reduction of the trip rate less than several trips per an hour are the key issues for the stable operation. At beginning of beam commissioning in 2011, the trip rate of the C-band accelerator was still high. Major causes of the trips were an RF breakdown in an accelerator cavity and an abnormal discharge in a thyratron tube. After the RF conditioning time of 700 hours, the RF breakdown rate was reduced to be 1/10 comparing with the beginning stage of the RF conditioning. Concerning the thyratron discharge, we confirmed most of the discharges do not influenced to the next pulse generated by a klystron modulator and it can be excluded from the trip items of an interlock system. We currently operate the accelerator with the beam energy as much as 8.5 GeV, and the acceleration gradient of 38 MV/m in average, with an acceptable trip rate of of once per 20-30 minutes, which provides stable laser for XFEL user experiments. Availability of the C-band high gradient accelerator for compact accelerator is confirmed.

INTRODUCTION

SACLA (SPring-8 Angstrom Compact Free Electron Laser) [1] is a unique X-ray free electron laser (XFEL) facility, aiming to generate an X-ray laser with a compact electron accelerator and an in-vacuum undulator. The compactness is important to be able to construct within an available space in the SPring-8 campus, and for lower construction costs. In order to shorten the 8 GeV accelerator length, a C-band (5712 MHz) accelerator is employed. A higher frequency is chosen to produces a higher acceleration gradient. The nominal acceleration gradient is about 35 MV/m, which is twice higher than that of conventional S-band accelerators.

Figure 1 shows the configuration of the SACLA accelerator. For the energy from 400 MeV to 1.4 GeV, 12 C-band acceleration units accelerate an electron beam at -48 degree off crest phase, which provides an energy chirp for the following bunch compression chicane BC3. After BC3, the 52 C-band acceleration units accelerate the beam up to the target energy around 5 GeV to 8 GeV, dependent on a laser wavelength.

Since SACLA is the single-pass FEL facility, if only one unit out of 64 makes a trip (interlocked failure), it surely changes the beam energy and makes a serious influence to the laser properties. For example, when each unit makes one trip per 3 days on average, the beam trip is almost hourly occurred in total. Therefore reduction of the trip rate is the crucial point for stable laser provision.

The beam commissioning was started in March 2011 and the first lasing at a 0.12 nm wavelength was achieved in June [1]. At that time the trip rate was high due to the insufficient conditioning time for RF components [2]. Major causes of these trips were RF breakdown (arcing) in cavities and abnormal discharge (pre-trigger) of thyratrons. Then we lowered the beam energy to 7 GeV, and a pulse repetition rate up to 10 pps, because the beam energy and the repetition rate were not so important for immediate beam commissioning. Instead, a high beam energy of over 8 GeV and low trip rate were required for user runs. Hence we spent much effort to reduce the trip rate. Careful RF conditioning effectively reduced the number of the RF breakdowns. Since March 2012, the SACLA accelerator is stably operated for the user experiments with the energy up to 8.5 GeV and the acceleration gradient of 38 MV/m in 10 pps.

C-BAND ACCELERATOR SYSTEM

Figure 2 shows the configuration of the C-band accelerator system. Two 1.8 m long accelerating structures are connected to a 50 MW pulse klystron with

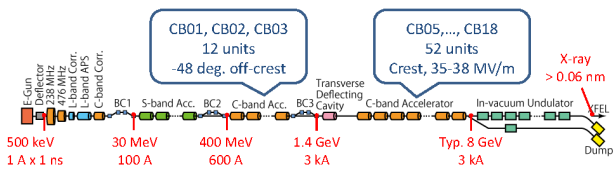

Figure 1: Configuration of the SACLA accelerator.

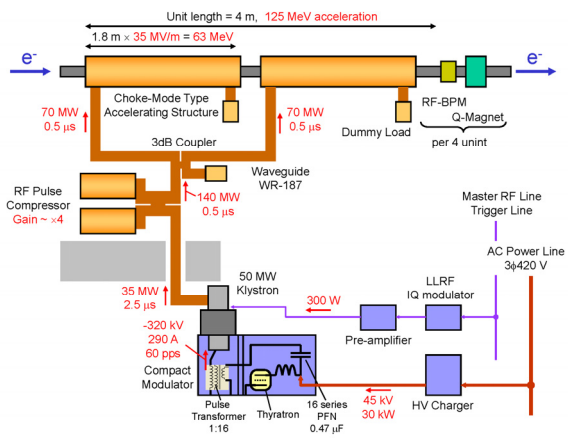

Figure 2: Configuration of the C-band accelerator system. Typical parameters for nominal operation are noted in red.

#inagaki@spring8.or.jp

Copyright © 2012 by the respective authors — cc Creative Commons Attribution 3.0 (CC BY 3.0)

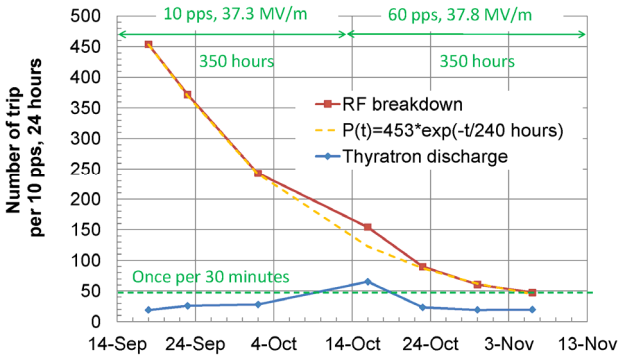

Figure 3: Number of the total trips of the 64 C-band acceleration units during the RF conditioning., due to the RF breakdown (red) and the thyratron's discharge (blue). The yellow dashed line is the exponentially fitted curve of the RF breakdown rate.

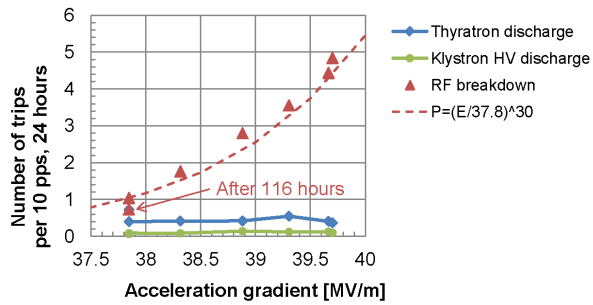

Figure 4: Trip rate of each C-band acceleration units, as the function of the acceleration gradient.

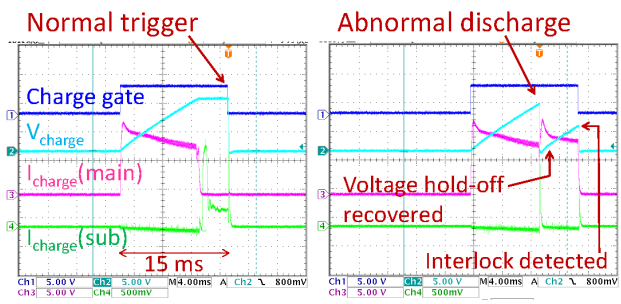

Figure 5: Typical waveforms of the charging cycle (left), and the waveforms of the abnormal discharge during the charging period (right). The charging voltage (V_{charge}) of the PFN capacitors was set at 45kV and the repetition rate was 10 pps in both waveforms.

an RF pulse compressor (SLED) system. For the nominal operation the output power of the klystron is about 35-40 MW with 2.5 μs pulse width. The RF power is once stored to two high Q cavities of the SLED. When an RF phase is inversed by a phase switch keying (PSK) using an in-phase and quadrature (IQ) modulator [3] at 2 μs point of the pulse, the stored RF power is extracted from the SLED cavities .The RF power is about 200 MW in peak, and 140 MW on average for the 300 ns filling time of the accelerating structure [2]. The RF power is fed into two accelerating structures (R_{sh}~54MΩ/m and τ~0.53) to obtain a nominal acceleration gradient of 35 MV/m. Even though we designed the cavity wall thickness of 4 mm and round off the corner of iris with a radius of 2 mm, the maximum surface electrical field is about 100 MV/m. In order to sustain such a high RF field, the structure is made of pure oxygen-free-copper with HIP treatment, carefully machined and brazed with clean environment [4].

The klystron is driven by a compact 110-MW high-voltage pulse modulator, which equips a conventional line-type pulse forming network (PFN) circuit and a thyratron tube [5]. Capacitors constituting the PFN are charged by an inverter-type highly-precion HV charger. The charged voltage is precisely regulated within about 10 ppm (rms), which stabilizes the RF output phase and amplitude of the klystron within 100 ppm and 0.2 degree, respectively.

REDUCTION OF TRIP RATE

RF Conditioning

RF conditioning is the process to obtain a higher RF field in the cavity, which clean the cavity surface and reduce the number of the RF breakdown. By the summer of 2011, we performed the RF conditioning of more than 1,000 hours and realized to operate at an acceleration gradient of 35 MV/m [2]. In order to raise the acceleration gradient up to 38 MV/m, we performed the additional RF conditioning during the night time. Figure 3 shows the progress of trip rate reduction. The RF breakdown rate P(t) is exponentially decreased with a elapsed time. The time constant of decrease of the RF breakdown rate is 240 hours. After an RF conditioning time of 2 months (700 hours), the RF breakdown rate was decreased to be 1/10 and it showed proved the possibility to obtain a high-energy electron beam up to 8.5 GeV.

In order to investigate the availability of further high acceleration gradient, we gradually raised the RF power and measured the trip rate. Figure 4 shows the trip rate depending on the acceleration gradient. We found the RF breakdown rate is proportional to the 30th power of the acceleration gradient (red dashed line in Figure 4). After a measurement time of 116 hours at a maximum acceleration gradient of 39.3 MV/m, the RF breakdown rate decreased to be 2/3 of the initial rate at the acceleration gradient of 37.8 MV/m. It proved the potential to obtain a higher acceleration gradient by further RF conditioning.

Thyratron Abnormal Discharge

Our thyratron is e2v CX-1836, which equips three control grids and is filled with deuterium gas. Figure 5 shows the waveform of a charging cycle. In normal operation, the thyratron is triggered after charging period of 15 ms. But it occasionally discharged during the charging period, without a trigger pulse. Then the interlock system detects insufficiency of a charging voltage and halts the next charging. This discharge phenomenon is known as the "pre-trigger" of the thyratron, but the rate of it is much higher than that of our

Copyright © 2012 by the respective authors — cc Creative Commons Attribution 3.0 (CC BY 3.0)

expectation. The rate seems independently of the charging voltage (see Figure 4), and was not reduced during the conditioning (see Figure 3). Therefore, it becomes a dominant reason of the interruption of the accelerator operation, especially at low energy (< 8 GeV). In normal operation, the thyratorn conducts huge current (~5 kA) by generating plasma of the deuterium gas. After PFN capacitors are fully discharged, the plasma density drops within the nominal recovery time (~20 μs) and the connection is closed [6]. We suppose the same recovery occur after the abnormal discharge. In the left figure of Figure 5, the charging voltage was raised again after the abnormal discharge occurred. It means the withstanding voltage is surely recovered and we need not to halt the next HV pulse.

We modified the interlock system not to halt the operation by the single discharge event. When the second discharge occurred within one minutes, the interlock system halts the next charging for the machine protection. In June 2012, we tentatively modified 25 units. The trip rate of the modified unit is drastically reduced to be roughly 1/3 of the previous halt rate. The remaining 39 units were modified in this summer shut down period.

PRESENT OPERATIONAL STATUS

Thanks to these improvements, we have operated SACLA with beam energy of up to 8.5 GeV. So far the C-band accelerator has operated about 10,000 hours, without any serious troubles of high power RF components of 64 units.

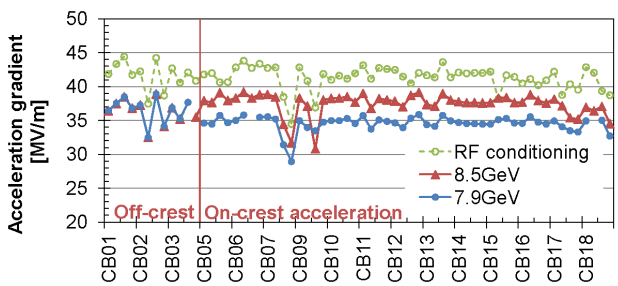

Figure 6: Typical acceleration gradients at each C-band unit in the cases of 8.5 GeV (red) and 7.9 GeV (blue). Maximum acceleration gradient values of individual RF units in the RF conditioning are also displayed (green).

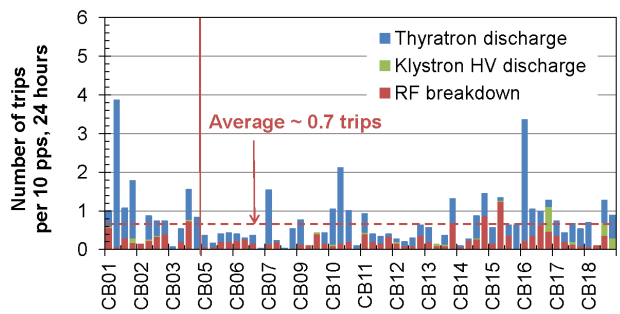

Figure 7: Trip rate of each C-band unit in July 2012. The acceleration gradient was set about 35 MV/m (7.9 GeV case of Figure 6).

Figure 6 shows the acceleration gradient of each C-band acceleration unit in two sets of typical beam energy. The averaged electrical gradient is about 38 MV/m and 35 MV/m for 8.5 GeV and 7.9 GeV, respectively. We have several standby units as a backup for troubles.

Figure 7 shows the trip rate of each unit in July. In average, the number of trips per one unit in 24 hours is 0.7 events and 1.1 events for 7.9 GeV and 8.5 GeV cases, respectively. The trip rate of the SACLA accelerator is the sum of the trip rate of the 64 units, which is once per 30 minutes for the 7.9 GeV case and once per 20 minutes for the 8.5 GeV case in 10 pps. These trip rates are still not sufficiently low to our requirement but an acceptable level for the user experiments. The trips are still dominantly caused by the thyratron discharges (65%). Since we modified the interlock systems of 39 units in this summer, we expect the trip rate will be highly reduced and we will increase the repetition rate to 20 pps or more.

SUMMARY

Since the C-band accelerator of SACLA generates high acceleration gradient as high as 35-38 MV/m, reliability of high power RF components and reduction of a trip rate are the key issues. The trip is dominantly due to an RF breakdown and an abnormal discharge of a thyratron tube. In order to reduce the number of RF breakdown, we performed an RF conditioning time of 700 hours. The RF breakdown rate was reduced to be 1/10 at an acceleration gradient of 38 MV/m. In order to reduce the number of a machine trip due to thyratron discharge, we modified the function of an interlock system. Thanks to these improvements, the trip rate was decreased and we were able to raise the beam energy. SACLA is currently operated at a beam energy of up to 8.5 GeV and an acceleration gradient of 38 MV/m, with an acceptable trip rate of once per 20-30 minutes in 10 pps. We confirmed the validity of the C-band high gradient acceleration for compact and stable XFEL facility.

REFERENCES

[1] H. Tanaka and M. Yabashi, et. al., "A compact X-ray free-electron laser emitting in the sub-angstrom region", nature photonics 2012.141, (2012).
[2] T. Inagaki, et. al., "Operational status of C-band high gradient accelerator for XFEL/Spring-8", Proc. of IPAC11, (2011).
[3] H. Maesaka, et. al., "Recent progress of the rf and timing system of XFEL/SPRING-8", Proc. Of ICALEPCS09 (2009).
[4] K. Okihira, et., al., "Mass production report of C-band choke mode accelerating structure and RF pulse compressor", Proc. Of IPAC11, (2011)
[5] T. Inagaki, et. al., "Compact 110 MW Modulator for C-band High Gradient Accelerator", Proc. of IPMHVC2012 (2012).
[6] Datasheet of e2v CX-1836 and technical notes published by e2v Technologies Limited.

Copyright © 2012 by the respective authors — cc Creative Commons Attribution 3.0 (CC BY 3.0)

STUDY OF MICROBUNCHING INSTABLITY IN THE LINAC OF THE SHANGHAI SOFT X-RAY FEL FACILITY*

Dazhang Huang#, Qiang Gu†, Meng Zhang, SINAP, Shanghai, China

Abstract

The microbunching instability (μBI) in the LINAC of a FEL facility has always been an issue which may degrade the electron beam quality. As the result, the whole facility may not be working properly. Therefore, learning how to control and reduce the instability is the key to the success of a FEL project. Shanghai soft X-ray FEL project (SXFEL) has been proposed and the feasibility study is finished. Once it is built, it will be the first X-ray FEL facility in China. In this article, detailed study will be given based on the design parameters of the facility to gain better understanding and control over the possible microbunching instability in SXFEL, which is critical to the success of the FEL project.

INTRODUCTION

The proposed Shanghai soft X-ray FEL facility is planned to be built in a few years. It will be a cascading HGHG FEL facility which will be working at 9 nm soft X-ray band. The electron beam energy of it at the exit of the LINAC will be around 840 MeV, the peak current will be around 600 A. The normalized emittance of the electron beam at the LINAC exit will be 2.0 – 2.5 mm.mrad.

Both the analytical and numerical studies show that μBI- induced growth of the global/slice energy spread in the LINAC is not ignorable; it also reduces the smoothness of the longitudinal beam current profile. Therefore, without proper control, the instability will be a serious problem and may impair the FEL process thereafter.

One way to control the instability is to increase the uncorrelated energy spread of the beam, which can be done by a laser heater [2][8], and it will also be implemented in SXFEL.

COMPUTATION AND ANALYSIS OF THE INSTABILITY

The basic principle of the microbunching instability in the LINAC of a FEL device has already been well-studied [1][2][3]. It is similar to the amplification mechanism in a klystron amplifier. The initial density modulation or white noise can be transferred into energy modulation by the impedances when the beam is being accelerated including the longitudinal space charge (LSC), coherent synchrotron radiation (CSR) and the structural impedance. When the beam is passing through the dispersive section such as the bunch compressor (chicane), the energy modulation will be turned back into the much stronger density modulation, in such a way that the microbunching instability is developed. Moreover, the CSR effect in the dispersive section will also form a positive feedback to enhance the instability. More dispersive sections in the LINAC will have more serious μBI problem. Figure 1 is the schematic description of the instability process.

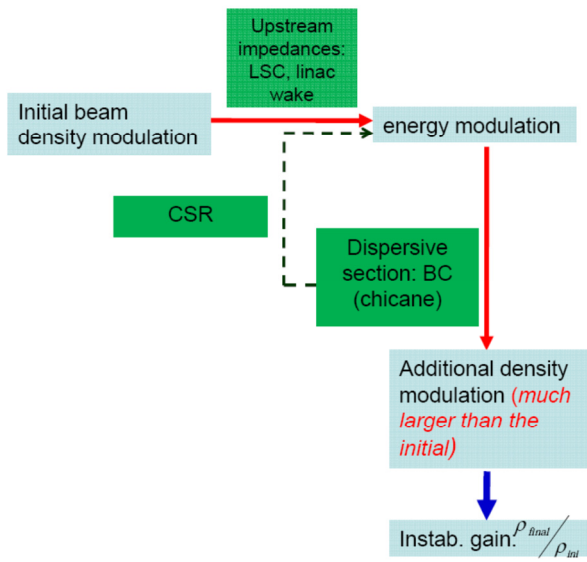

Figure 1: The microbunching instability process.

As discussed above, in the LINAC, the microbunching instability is mainly driven by the LSC, CSR and structural impedances. Since the structural impedance is more complicated and its effect on the instability is not as significant as the other two, in this article, we will be focusing on the microbunching instability introduced by the LSC and the CSR impedance.

The basic layout of the SXFEL LINAC is the following:

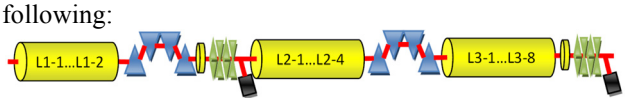

Figure 2: The layout of the SXFEL LINAC.

The SXFEL LINAC includes both S-band and C-band accelerating structures, one X-band structure to suppress the non-linear higher order mode (HOM), and two chicane-type bunch compressors (BC1 & BC2). Since there are two bunch compressors, the microbunching instability in the SXFEL LINAC is not negligible. The computation and simulation in the following is based on the design parameters of the LINAC, and the beam parameters out of the injector tracked by PARMELA [4]. Those parameters are listed in table 1.

*Work supported by National Science Foundation of China (NSFC). Project No. 11275253
huangdazhang@sinap.ac.cn
† guqiang@sinap.ac.cn

Copyright © 2012 by the respective authors — cc Creative Commons Attribution 3.0 (CC BY 3.0)

Microbunching Instability Driven by the Longitudinal Space Charge (LSC) Impedance

In general, the microbunching instability driven by the longitudinal impedance has already been studied in details [1]. The gain of the instability is computed by [1]:

$$G = Ck|R_{56}|\frac{I_0}{\gamma_0 I_A}\frac{|Z(k)|}{Z_0}\exp\left(-\frac{1}{2}C^2k^2R_{56}^2\frac{\sigma_\gamma^2}{\gamma_0^2}\right) \quad (1)$$

Where

$$C = 1/(1+hR_{56})$$

is the compressing factor. For the longitudinal space charge, the impedance takes the form [5][6]:

$$Z_{LSC}(k) = \frac{iZ_0}{\pi k r_b^2}\left[1 - \frac{kr_b}{\gamma}K_1\left(\frac{kr_b}{\gamma}\right)\right] \approx \begin{cases} \frac{iZ_0}{\pi k r_b^2}, & \frac{kr_b}{\gamma} \gg 1, \\ \frac{iZ_0 k}{4\pi\gamma^2}(1 + 2\ln\frac{\gamma}{r_b k}), & \frac{kr_b}{\gamma} \ll 1, \end{cases} \quad (2)$$

Table 1: Main beam parameters used in the μBI calculation for SXFEL (obtained from Elegant [10] simulation)

Parameter	Value
Electron energy before BC1 (MeV)	208.4
Uncorrelated energy spread before BC1 (keV)	7.67
Electron energy before BC2 (MeV)	425.1
Uncorrelated energy spread before BC2 (keV)	51.1
Compression ratio (BC1×BC2)	5×2
Peak current before BC1 (A)	60
Beam radius before BC1 (mm)	0.40
Beam radius before BC2 (mm)	0.26

The instability gain as a function of the initial modulation wavelength introduced by the LSC at the exit of SXFEL LINAC is shown in Figure 3 below. The gains in the 1st and 2nd bunch compressors are illustrated separately.

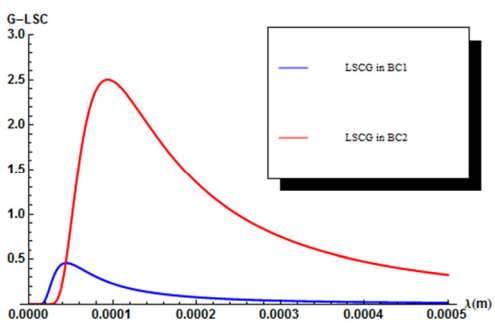

Figure 3: (color): The microbunching instability gain driven by the longitudinal space charge impedance as a function of modulation wavelength in the 1st (blue) and 2nd bunch compressors (red).

Microbunching Instability Driven by the Coherent Synchrotron Radiation (CSR) Impedance

As we already know, the electron beam in a bunch compressor can generate coherent synchrotron radiation (CSR). It can also be a source of modulation of the beam density at wavelengths small compared to the bunch length [3]. In other words, the microbunching instability can be produced from white noise due to the CSR effect in a bunch compressor.

The gain of the CSR-driven microbunching instability in a bunch compressor has already been well defined [2]. Assume a beam uniform in z and Gaussian in transverse and energy variables, the total gain induced by the CSR effect can be expressed as [2]:

$$G_f \approx \left|\exp\left[-\frac{\bar{\sigma}_\delta^2}{2(1+hR_{56})^2}\right] + A\bar{I}_f\left[\left(F_0(\bar{\sigma}_x) + \frac{1-e^{-\bar{\sigma}_x^2}}{2\bar{\sigma}_x^2}\right)\exp\left(-\frac{\bar{\sigma}_\delta^2}{2(1+hR_{56})^2}\right) + F_1(hR_{56},\bar{\sigma}_x,\alpha_0,\phi,\bar{\sigma}_\delta)\right] + A^2\bar{I}_f^2F_0(\bar{\sigma}_x)F_2(hR_{56},\bar{\sigma}_x,\alpha_0,\phi,\bar{\sigma}_\delta)\right| \quad (3)$$

According to reference [2], the first term on the right side of Eq. (3) represents the loss of microbunching in the limit of vanishing current, the second term is the one-stage microbunching amplification at low current, and the last term corresponds to the two-stage amplification at high current.

The computed microbunching instability gain driven by the CSR impedance as a function of modulation wavelength in SXFEL is shown in Figure 4. Again, the gains in the 1st and 2nd bunch compressors are illustrated separately.

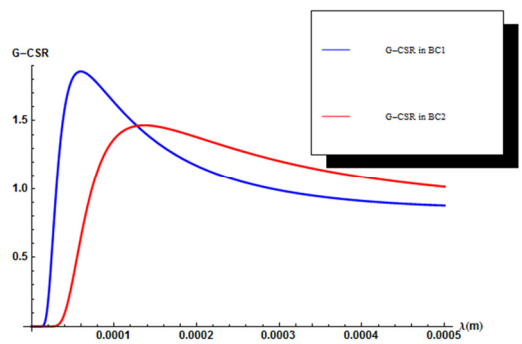

Figure 4: (color): The microbunching instability gain driven by the CSR impedance as a function of modulation wavelength in the 1st (blue) and 2nd bunch compressors (red).

Total Growth Rate of Microbunching Instability in SXFEL LINAC and Analysis

The total gain/growth rate of the instability in the SXFEL LINAC computed by analytical equations and by ImpactZ [7] is shown in Figure 5. Both the analytical solution and ImpactZ simulation peaks around ~ 100 um,

The amplitude of the two peaks looks different. It may be because of the small difference between the input parameters in the analytical computation and those in the simulation. For an example, the gain is very sensitive to

Copyright © 2012 by the respective authors — cc Creative Commons Attribution 3.0 (CC BY 3.0)

the slice (uncorrelated) energy spread and R_{56} in the chicane, etc. Figure 6 below show the peak gain as a function of the relative uncorrelated energy spread of the beam before BC1. Moreover, it may be due to the excessive suppression of noises - It is known that the beam input in the simulation includes both the numerical and physical noises; it is possible that some of the "real" physical noises are incidentally smoothed out as well while we do numerical smoothing to the input beam profile.

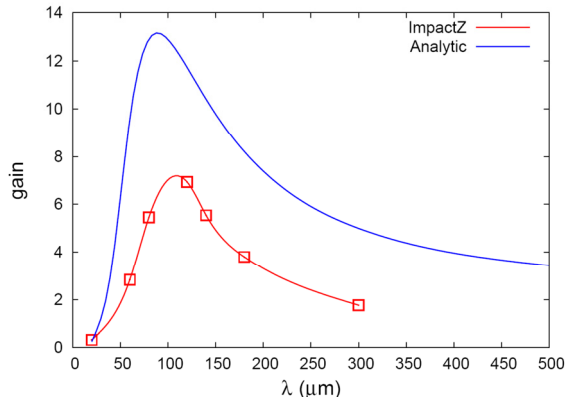

Figure 5: (color): The total μBI gain at the exit of SXFEL LINAC as a function of the modulation wavelength computed by analytical equations (blue) and ImpactZ [7] simulation (red) based on the current machine parameters.

As one can see in Figure 6, as the slice (uncorrelated) energy spread of the beam rises, the peak gain of the instability starts to fall very rapidly. It is indeed consistent with the theoretical expectation. It also tells us that in reality the gain may be very different from what we have calculated because of the possible variations of the "real" uncorrelated energy spread. Therefore, the laser heater [2] [8] is introduced to increase the uncorrelated energy spread of the beam by laser-beam interaction, in such a way to control the growth of the instability. Although the design is still not fully completed, the ongoing numerical simulation shows that it is able to reduce the gain significantly [9].

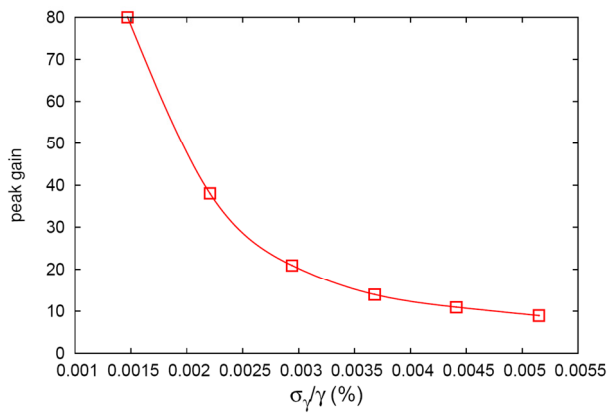

Figure 6: The peak gain computed as a function of the relative uncorrelated energy spread before the 1st chicane.

CONCLUSIONS

Microbunching instability is an important issue in the LINAC of a FEL facility. If the gain of the instability is too large, the quality of the electron beam will be destroyed and is harmful to the whole FEL device.

Both the analytical computation and numerical simulation show that the microbunching instability in SXFEL is not negligible, and the LSC impedance induced growth is larger than that driven by the CSR impedance. Moreover, the gain is very sensitive to some critical beam and lattice parameters such as the energy spread and the R_{56} in the chicanes, etc.

As a matter of fact, a laser heater is needed to suppress the instability. Further study is on the way to optimize and properly implement the laser heater into the SXFEL lattice.

REFERENCES

[1] E. L. Saldin et.al., NIMA 483 (2002) 516 – 520
[2] Zhirong Huang and Kwang-Je Kim, Phys. Rev. ST-AB, vol. 5, 074401 (2002).
[3] S. Heifets et.al., Phys. Rev. ST-AB, vol. 5, 064401 (2002).
[4] Lloyd Young and James Billen, PAC03-Proceedings, Portland, USA, 2003
[5] J. Rosenzweig, et.al., DESY Report No. TESLA-FEL-96-15, 1996
[6] Z. Huang and T. Shaftan, FEL03- Proceedings, Tsukuba, Japan, 2003
[7] Ji Qiang, et. al, Journal of Computational Physics 163, 434-451 (2000)
[8] SPARX technical design report, v2.00, July 2009
[9] Feasibility study report of SXFEL, Nov. 28th, 2011
[10] M. Borland, Advanced Photon Source LS-287, September 2000.

Copyright © 2012 by the respective authors — cc Creative Commons Attribution 3.0 (CC BY 3.0)

PHOTOINJECTOR OF THE EBTF/CLARA FACILITY AT DARESBURY

B.L. Militsyn*, D. Angal-Kalinin, N. Bliss, C. Hill, S.P. Jamison, J.K. Jones, J.W. McKenzie, K.J. Middleman, M.D. Roper, B.J.A. Shepherd, R.J. Smith, R. Valizadeh, A.E. Wheelhouse, STFC ASTeC, Daresbury Laboratory, Warrington, WA4 4AD, UK

Abstract

A photoinjector designed for Electron Beam Test Facility (EBTF) and Compact Linear Accelerator for Research and Applications (CLARA), a proposed FEL test facility is described. The photoinjector is based on a 2.5 cell S-band photocathode RF gun operating with a copper photocathode which is driven by a third harmonic of Ti: Sapphire laser (266 nm) installed in dedicated thermally stabilized room. The injector will be operated with laser pulses with energy of up to 2 mJ, a pulse duration of 80 fs RMS and initially a repetition rate of 10 Hz, with the aim of increasing this eventually to 400 Hz. At a field gradient of 100 MV/m provided by a 10 MW klystron, the gun is expected to deliver beam pulses with energy of up to 6 MeV. Bunch length and emittance of electron bunches essentially depend on the bunch charge and vary from 0.1 ps at 20 pC to 5 ps at 200 pC and from 0.2 to 2 mm·mrad respectively. Additional compression of the electron bunches required for CLARA will be provided with a velocity bunching scheme and a dedicated chicane.

INTRODUCTION

The Electron Beam Test Facility (EBTF) is a 6 MeV electron accelerator designed to provide low emittance, short pulse beams to two user stations [1-2]. It will also act as the front end for the proposed CLARA accelerator [3-4]. Initially, the beam for EBTF will be delivered by a 2.5-cell, S-band, normal-conducting, RF gun originally designed for the ALPHA-X project [5].

The front end of EBTF (Fig. 1) has been designed as a photoinjector diagnostics suite to fully characterise 6D phase space of bunches. A variety of YAG screens and slits will be used to characterise the beam transversely. Longitudinal characterisation of the beam will be provided with energy spectrometer comprising a dipole magnet and a YAG screen. Bunch length will be measured using a Transverse Deflecting Cavity (TDC) [7] to streak the longitudinal position of the particles onto the transverse plane, thus making it viewable on the YAG screen. Furthermore, if the streak is performed in the vertical plane as planned, then passing the beam around the horizontal spectrometer will make the longitudinal phase-space directly viewable on the screen. Combining the TDC with the transverse beam diagnostics will allow time-sliced emittance measurements to be made. For better thermal stability the injector is mounted on an artificial granite support.

PHOTOINJECTOR BEAM DYNAMICS

The EBTF photoinjector has been modelled both in ASTRA and GPT. The simulations presented are at the maximum bunch charge of 250 pC to show the effects of space charge. For the simulations, an intrinsic emittance of 0.9 mm·mrad per mm RMS beam size is used [6]. The simulations presented here are based on the factory measured laser pulse length of 80 fs RMS. An optimisation of the photoinjector beam line was performed looking at the beam parameters at 1, 3, and 10 m from the photocathode to observe their evolution, as shown in Fig. 2. It was found that energy spread is highly sensitive to solenoid strength due to space charge. The energy spread could be controlled by operating further off-crest in the gun, at a phase of -35° from that of maximum energy gain.

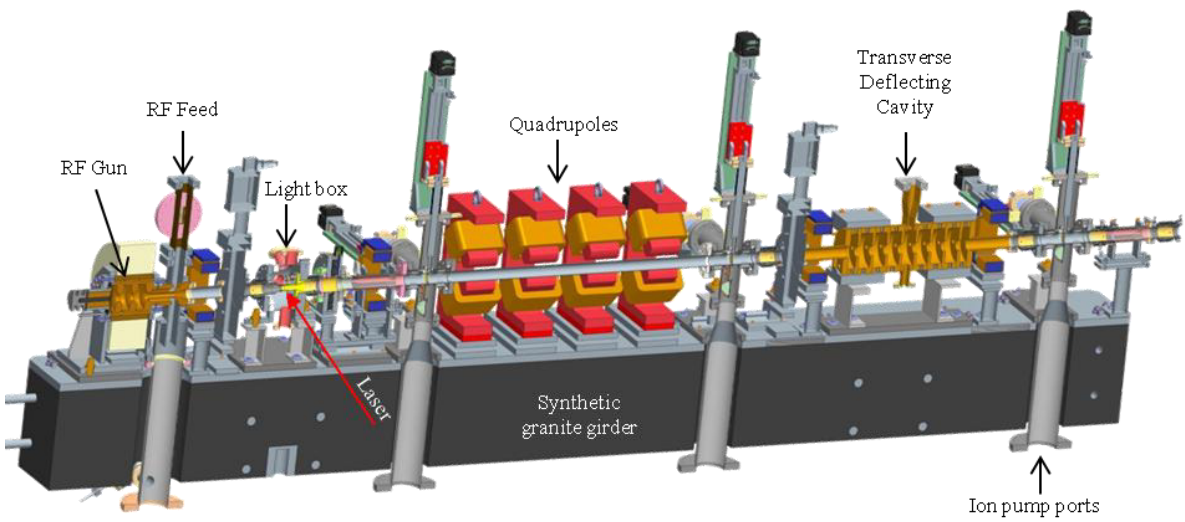

Figure 1: CAD drawing of the EBTF photoinjector

*boris.militsyn@stfc.ac.uk

Copyright © 2012 by the respective authors — cc Creative Commons Attribution 3.0 (CC BY 3.0)

To use the TDC for the bunch length diagnostic, four quadrupoles are located before it and are used to minimise the beam size in the streak plane, whilst keeping both transverse beam sizes relatively constant, as shown in Fig. 3. Minimising the transverse beam size reduces the energy spread increase when passing through the TDC, because longitudinal electric field, zero on axis of the TDC, increases linearly with distance from the axis. Since the TDC also gives, due to imperfectly matched electric and magnetic fields, an offset to the beam as well as a streak, , corrector coils are used either side of the cavity to keep the beam on axis. Fig. 4 shows the optimised particle trajectories from the cathode through the TDC to the screen.

PHOTOINJECTOR RF SYSTEM

To provide the required 6 MeV beam energy for the EBTF RF gun a K2 ScandiNova klystron modulator capable of providing 250 kV, 150 A pulses of up to 3 µs at a repetition rate between 1–400 Hz, has been procured and recently commissioned.

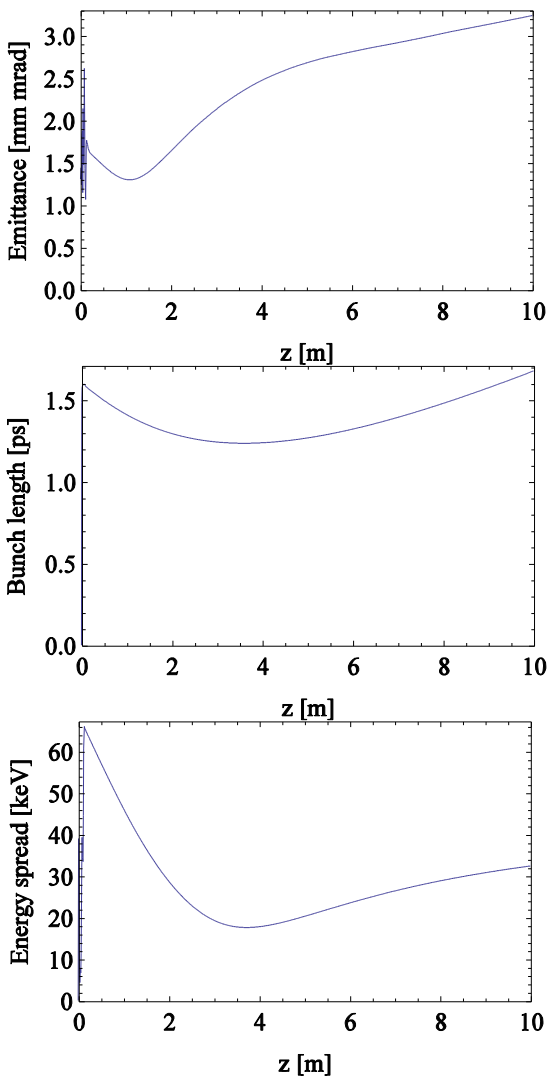

Figure 2: Evolution of beam parameters up to 10 m.

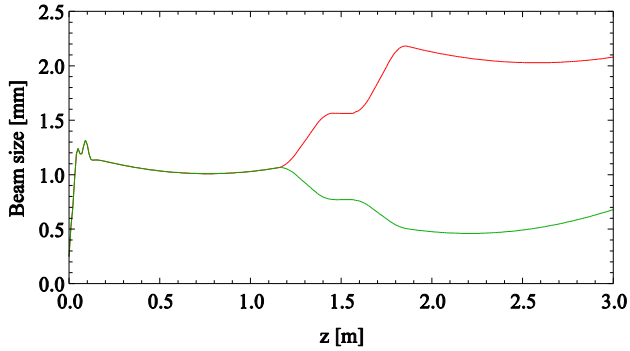

Figure 3: Horizontal (red) and vertical (green) beamsizes through the transverse deflecting cavity.

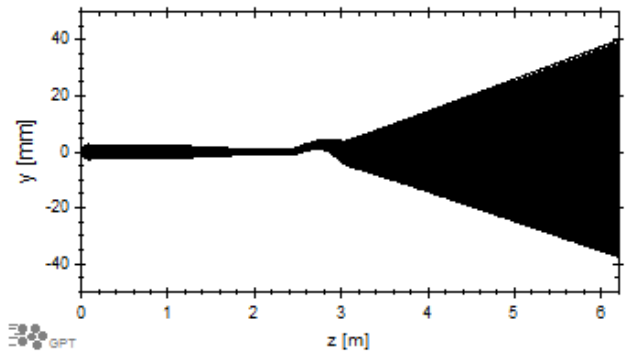

Figure 4: Vertical trajectories with the transverse deflecting cavity providing a streak.

The modulator is used to power a Thales TH2157 klystron capable of providing a peak RF output power of 10 MW at 2998.5 MHz and will be operated at a repetition rate of 10 Hz for the EBTF RF gun. For a 3 µs pulse width the modulator is designed to maintain a voltage stability of ±0.1 % with a 1 µs peak voltage top flatness of ±0.1 %. During the modulators acceptance tests jitter measurements were performed; the pulse to pulse jitter was ±1.3 ns and the pulse width jitter was ±2.7 ns.

The low level RF (LLRF) system for EBTF will consist of an ultra-stable and low noise master oscillator produced by RALAB AG, which will output locked frequencies to drive the laser and RF system. Reference distribution between the oscillator and the RF system at a frequency of 2998.5 MHz will be via temperature stabilised dielectric cables (LCF38-50J). To minimise the effect of temperature change during operation, these cables will be held at 24±0.1°C, a region where they are particularly stable.

The LLRF control of phase and amplitude for the RF gun will be via an in house built digital LLRF control system using heated and temperature stabilised RF front ends, a LLRF 4 FPGA control card [9] and a remote calibration system which will measure and correct for errors on a slow control loop as environmental factors change. Thus it will be possible to correct for pulse to pulse errors using this system and expect to achieve 0.1% amplitude and 0.1° phase stability and be able to compensate for environment changes on the machine over the period of the

Copyright © 2012 by the respective authors — cc Creative Commons Attribution 3.0 (CC BY 3.0)

day. Additionally the temperature of the RF gun will be stabilised to ±0.1°C to ensure that it is maintained at its operating frequency.

PHOTOCATHODE AND DRIVE LASER

The photocathode is a polycrystalline, oxygen-free, copper disc (Fig. 5), polished to 1µm roughness. It forms an integrated part of the 2.5-cell gun cavity and is placed at the back wall of the first half-cell. Prior to installation the cathode is degreased by washing in acetone, ethanol and finally in de-ionized water (>10 MΩ). Carbon contamination is then removed from the surface by ozone cleaning. The gun is pumped down and baked to 150°C in order to achieve pressure in the region of 10^{-10} mbar. The emission area of the photocathode plate is locally baked to a temperature of 200°C to remove oxide.

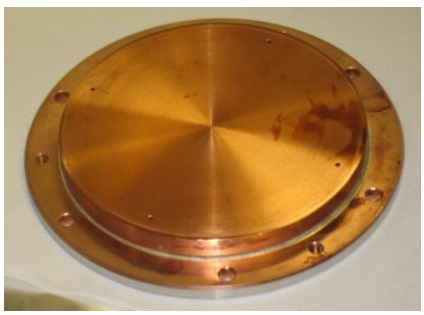

Figure 5: The photocathode of the EBTF gun.

Future developments will look at the use of higher quantum efficiency photocathode materials like single-crystal copper and other metals such as Mg, Pb, and Nb. For Cu and Nb, high-purity metal discs of 10 mm diameter and 2 mm thickness will be inserted into the cavity wall, whilst Mg will be directly deposited onto the wall surface.

The photocathode will be driven by a frequency-tripled Ti:Sapphire laser system with a repetition rate of up to 400 Hz. The pulse energy at 266 nm is 2 mJ and the pulse duration is 80 fs RMS, giving a peak power of ~10 GW. As generated, 99% of the pulse energy is contained within a beam diameter of 20 mm and so the beam intensity is ~2 GW/cm^2. The intention is to focus the UV beam to a spot size of ~1 mm FWHM on the cathode, which will increase the beam intensity to nearly 1 TW/cm^2. Significant difficulties in the transport of the full beam power will be encountered and early operation will be likely at reduced power.

To prevent beam disruption through non-linear effects, as much of the ~14 m long transport path as possible will be in vacuo and no refractive optics will be used; all beam focusing will be done with mirrors. One air to vacuum window will be required in the laser room at the entrance to the vacuum system and this will be made from calcium fluoride to prevent two-photon absorption (TPA). The laser transport vacuum will be isolated from the gun vacuum by differential pumping so that no window will be required where the beam intensity is at its highest.

The very high beam intensity also leads to a high risk of damage to the optics. All but the final mirror will have a standard ultra-fast, multi-layer dielectric coating with a high damage threshold. The final mirror sits in the gun vacuum and has a simple protected aluminium coating on a copper substrate to prevent damage from accumulated electrical charge. The photon damage threshold of this mirror will be found experimentally.

CONCLUSION

EBTF photoinjector is being installed presently at Daresbury laboratory (Fig. 6).The first commissioning stage is scheduled to begin around November-December 2012.

Figure 6: EBTF photoinjector in the assembling stage.

ACKNOWLEDGMENT

The authors would like to acknowledge the EBTF design team, the ALPHA-X collaboration and Strathclyde University.

REFERENCES

[1] P. McIntosh et al., Proc. of IPAC'12, New Orleans, USA, May 2012, p. 4076(2012)
[2] D. Angal-Kalinin et al., Proc. of IPAC'12, New Orleans, USA, May 2012, p. 646(2012)
[3] J. Clarke et al., Proc. of IPAC'12, New Orleans, USA, May 2012, p. 1750(2012)
[4] N.R. Thompson et al., Proc. of FEL'2012, Nara, Japan , August 2012, WEPD44
[5] J. Rodier et al., Proc. of EPAC'2006, Edinburg, UK, June 2006, p. 1277(2006)
[6] Y. Ding et al., PRL **102**, 254801(2009)
[7] G. Burt et al., Proc. of IPAC'12, New Orleans, USA, May 2012, p. 3335(2012)
[8] R. Akre et al., Proc. of PAC'2001, Chicago, USA, June 2001, p. 2353(2001)
[9] L. Doolittle et al., Proc. of LINAC'06, Knoxville, Tennessee, USA, p. 568(2006)

Copyright © 2012 by the respective authors — cc Creative Commons Attribution 3.0 (CC BY 3.0)

FIRST RF MEASUREMENT RESULTS FOR THE EUROPEAN XFEL SC CAVITY PRODUCTION

A. Sulimov, P. Borowiec, V. Gubarev, J. Iversen, D. Kostin, G. Kreps, K. Krzysik, A. Matheisen, W.-D. Moeller, D. Reschke, W. Singer, DESY, Notkestrasse 85, 22603 Hamburg, Germany

Abstract

The first reference cavities (RCV) for the European XFEL Project are being tested within the collaboration of Research Instruments (RI), E. ZANON, IFJ-PAN and DESY:

- production and warm RF measurements of cavities and their components at RI and ZANON;
- surface preparation at DESY;
- cold RF tests at DESY by IFJ-PAN.

Purpose of the RCV is to establish a stable cavity fabrication and qualification of the surface preparation infrastructure at industry.

All necessary RF measurements were done, starting with mechanical fabrication in 2011, till the tuning and cold cavity RF tests in 2012.

We present the first results of RF measurements within RCV production for the European XFEL.

INTRODUCTION

For the first time the superconducting (SC) cavities for the XFEL are not only fabricated by industry, but also the full preparation "ready for cold RF test".

Before starting the (pre-)serial production each supplier of XFEL SC cavities (RI and ZANON) has produced 4 dummy (DCV) and 4 reference (RCV) cavities to qualify the new equipment and check the sequence of the fabrication process.

The main aspects of the RF measurements procedure for the European XFEL were described in [1].

These measurements allow checking the RF quality of the cavity (tuning, cold RF tests) and help to predict the mechanical parameters (length after tuning or deformation during transportation).

PRODUCTION OF PARTS

The main ideas of cavity parts (dumb-bells (DB) and end-groups (EG)) control are quick tests of their shapes before final cutting and checking the correspondence of the pi-mode frequency to part's length after trimming.

Only extensive 3D shape measurements can give the final results of the cell shape status, but RF measurements can give a prognosis for a series of 32 DB in one hour. The necessary field distribution for the fundamental mode can be obtained relatively easy by cavity tuning even for a wrong shape, but the behaviour of the higher order modes (HOM) spectrum is not predictable in this case. So a wrong shape is more critical and dangerous for HOM and beam dynamics.

The results of final RF measurements, when the parts are ready to be welded together in a cavity, are collected in the XFEL database [2].

Some examples of statistical values are shown in figure 1: the correspondence of pi-mode frequency to the length for DB (a) and EG (c). As a DB consists of two half-cells the symmetry of their volumes is additionally checked (b). These values are limited by ±0.1. In case a DB is out of tolerance, it has to be checked mechanically and additionally compensated or reshaped.

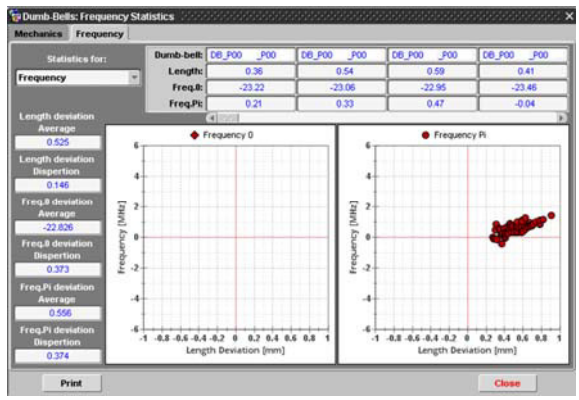

(a)

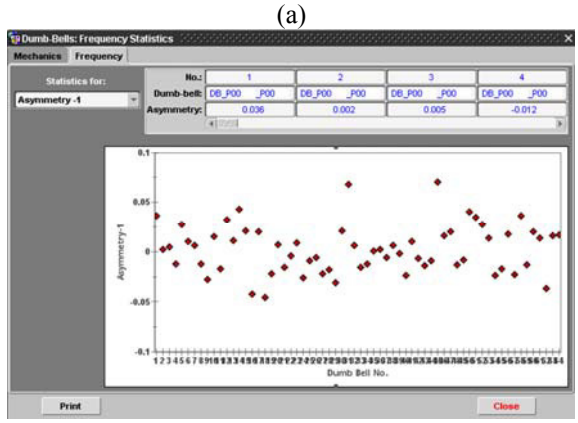

(b)

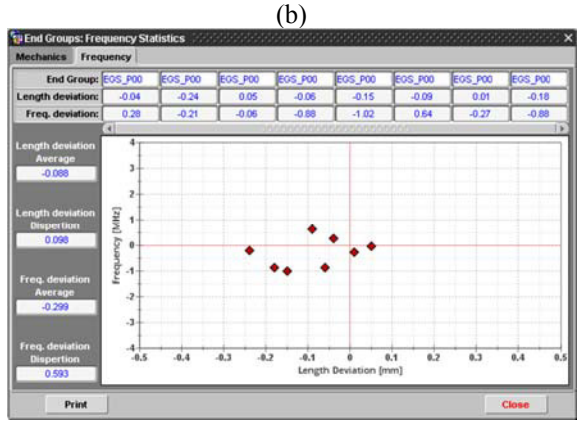

(c)

Figure 1: Statistical data for dumb-bells (a, b) and end-groups (c) are in tolerance.

Copyright © 2012 by the respective authors — cc Creative Commons Attribution 3.0 (CC BY 3.0)

CAVITY FABRICATION

To guarantee that the cavity length after tuning will be in tolerance of ± 3 mm, we make a prediction of this value twice: before and after cavity welding.

This prediction is based on the known length, pi-mode frequency of cavity parts, the amount of chemical treatment before and after welding, shrinkage of welding seams and other mechanical factors.

To compare these predictions with real values the data were collected in table 1. One can see the good accordance of predicted length deviation (first two columns). Only for cavities CAV00503 and CAV00506 the differences are a little higher and reach about 1 mm. It can be explained by the reduction of real shrinkage during cavity welding of about 0.08 mm per weld.

The difference between predicted and real values could partly be due to the different amount of chemical treatment before tuning: about 130 µm for cavities CAV00001-004, and about 180 µm for others. The influence of other factors is being analyzed.

Table 1: Length deviation relative to planned value

Cavity	dL, mm		
	predicted before welding	predicted after welding	real value
001	1.64	1.65	0.93
002	1.08	0.41	-0.45
003	3.18	3.20	2.60
004	3.03	3.07	2.18
500	0.00	0.11	2.43
502	0.02	0.16	1.09
503	0.50	1.45	3.41
506	0.49	1.12	3.10

After the cavity welding the results of all warm (at room temperature) RF measurements are collected in the XFEL database [3] as presented in figure 2. These data are accessible to the public.

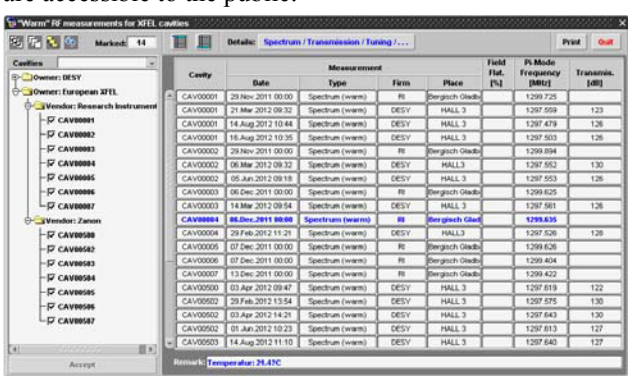

Figure 2: Presentation of warm RF measurements in XFEL database.

TUNING

The reference cavities were tuned once before the cold RF test. Results of these tuning procedures are summarised in table 2. The pi-mode frequencies for cavities CAV00001-004 are higher (about 1297.60 MHz) than for others (about 1297.44 MHz) because of the difference in planned additional chemical treatment: 40 µm and 10 µm correspondingly.

Table 2: Parameters after tuning

Cavity	Length, mm	Pi-mode frequency, MHz	Field flatness, %
001	1282.34	1297.623	99
002	1280.95	1297.644	97
003	1284.00	1297.585	98
004	1283.58	1297.545	99
500	1283.83	1297.411	99
502	1282.49	1297.419	98
503	1284.81	1297.458	97
506	1284.50	1297.459	98

As all tuning procedures for the reference cavities were done at DESY, no data transfer to the XFEL database was foreseen. An example of results' presentation is shown in figure 3 for cavity AC153. This cavity should be mounted into XFEL Module XM-3.

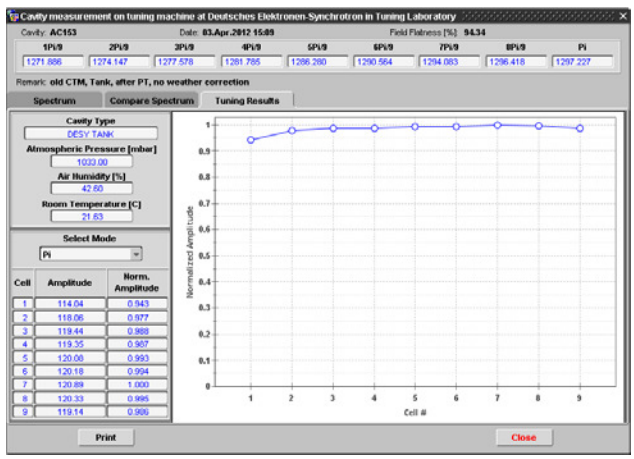

(a)

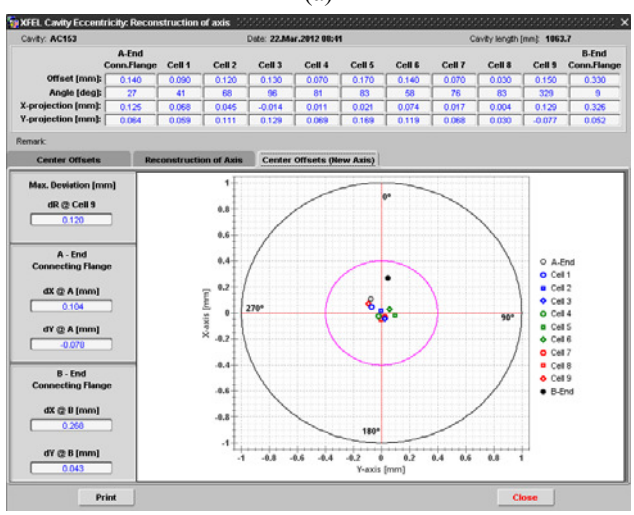

(b)

Figure 3: Tuning results: (a) - RF measurements, (b) - eccentricity

Copyright © 2012 by the respective authors — cc Creative Commons Attribution 3.0 (CC BY 3.0)

TRANSPORTATION

Each cavity has a long way from the manufacturers (RI or ZANON) to DESY for the cold RF test, then to CEA (Saclay, France) to be assembled inside the accelerating module and finally back to DESY for the module RF test and installation into the XFEL tunnel.

Comparison of cavity's spectra before and after transportation helps to control the absence of cavity deformation. Results and analysis of spectra comparison can be done automatically in the XFEL cavity database by choosing two spectra for a cavity. The Root mean-square error for the relative spectrum (RS) (1) multiplied by the operational frequency 1.3 GHz (MSE) helps us to estimate a possible deformation (cell's detuning) of a cavity.

$$RS = \{R_i\} = \{F_i/f_i - F_N/f_N\}, \quad (1)$$

where i = 1…9, $\{F_i\}$ and $\{f_i\}$ – two spectra.

As an example for cavity CAV00002, the value of MSE is only 4 kHz. The exceeding of the 10 kHz limit for MSE means that the cavity's field flatness could be lower than the critical 90%. In this case additional measurements and investigation of transportation errors have to be done.

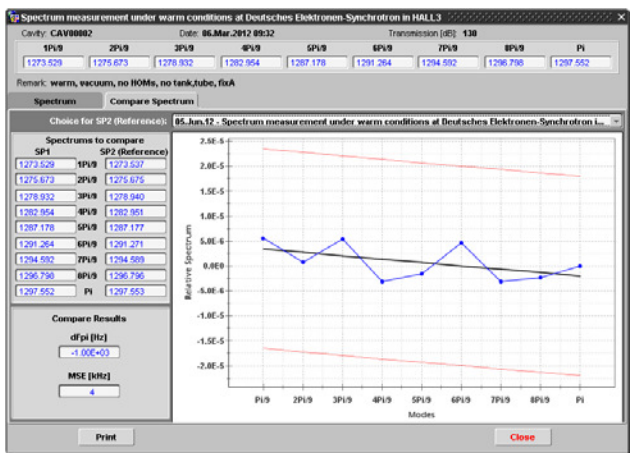

Figure 4: Comparison of two spectra (two columns at the left panel) for CAV00002. RS – blue broken line.

COLD RF TESTS

As a final quality check of the cavity a CW RF cold test is done after all preparation steps are finished. RCV were tested in LHe at 2K without cavity tank and HOM couplers feedthroughs in order to get a first performance evaluation. Later, during XFEL cavity production, cavities will be tested with all auxiliaries.

Results of the first cold RF tests (see figure 5) after the cavities' tuning and final chemical treatment at DESY of all reference cavities show the correspondence with the XFEL operation specification ($E_{acc} \geq 23.6$ MV/m with a Q-value $Q_0 \geq 10^{10}$ and radiation X-ray < 10^{-2} mGy/min).

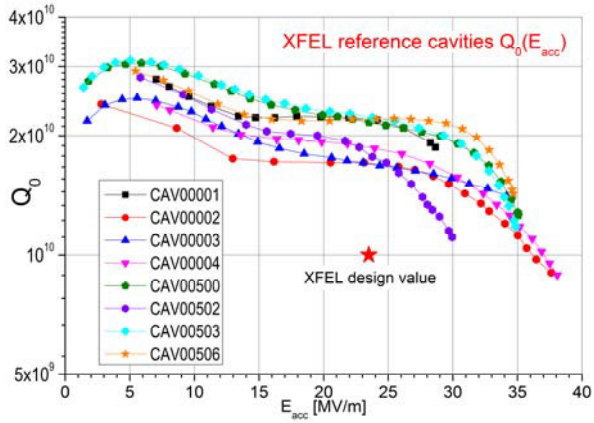

(a)

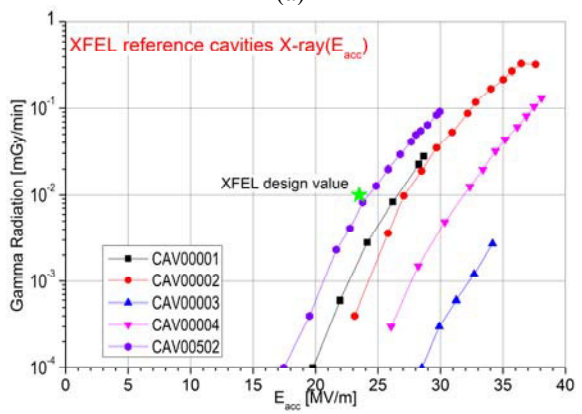

(b)

Figure 5: Cold RF test results: after surface preparation at DESY: (a) – $Q_0(E_{acc})$, (b) – X-ray(E_{acc}).

SUMMARY

The fabrication of 8 reference cavities by RI and ZANON allows us not only a test of the quality of the companies' infrastructure, but also of the communication between the members of the European XFEL Project.

The results of all measurements reflect the high quality of the so far produced cavities, which have reached accelerating gradients from 28 to 38 MV/m.

This presentation also shows the diversity of XFEL database abilities, such as collecting of all data, their presentation and automatic calculations.

ACKNOWLEDGMENTS

We would like to thank all participating colleagues from E. ZANON, Research Instruments, IFJ-PAN and DESY, whose enthusiastic effort allows us to push forward the work on cavities for the European XFEL Project.

REFERENCES

[1] A. Sulimov et al., "Description and First Experience with the RF Measurement Procedure for the European XFEL SC Cavity Production", 2nd IPAC'11, San Sebastian, Spain, 2011, pp. 277-279.
[2] http://xfel.desy.de/cavity_database/
[3] http://xfel.desy.de/cavity_database/rf_measurements/

Copyright © 2012 by the respective authors — cc Creative Commons Attribution 3.0 (CC BY 3.0)

EXPERIMENTAL RESULTS ON THE PHIL PHOTO-INJECTOR TEST STAND AT LAL

R. Roux, F. Blot, J. Brossard, C. Bruni, S. Cavalier, J.-N. Cayla, V. Chaumat, A. Gonnin, M. El Khaldi, P. Lepercq, E. Ngo Mandag, B. Mercier, H. Monard, C. Prevost, V. Soskov, A. Variola,
LAL, Université Paris-Sud, CNRS/IN2P3 Orsay, France

Abstract

The PHIL accelerator is in operation since November 2009. Its main goals are the R&D on photo-injectors and to provide electron beam to users. We report on the experimental characterization of the electron beam produced by a 3 GHz 2,5 cells RadioFrequency (RF) gun and operation with a Magnesium photo-cathode.

INTRODUCTION

The PHIL beamline [1,2] is rather simple : the photo-injector at 3 GHz called AlphaX [3] equipped with a couple of solenoids, a pair of steerers, a third solenoid to transport and focus the electron beam and a dipole to analyse the beam energy. The main diagnostics are Integrated Current Transformers (ICT) from the Bergoz Company to measure the charge and YAG screens coupled with a CCD camera to measure the transverse profile of the beam. Main parameters of the electron beam are summarized in table 1.

Table 1: PHIL Electron Beam Parameters, with Cu Photo-Cathode Except Few Runs with Mg*.

Energy (MeV)	< 5
Charge (nC), single pulse	0.01-0.4; 1*
Energy spread (%)	< 1
Emittance (πmmmrad)	< 5
Repetition rate (Hz)	5

COMMISSIONING

The RF gun has been commissioned several times rather easily. Generally it took a day to reach 5.5 MW with a RF pulse duration of 2.5 µs which is equivalent to an accelerating field of 70 MV/m. The RF commissioning has been repeated several times due to some changes of photo-cathode; we tried raw copper, copper polished with diamond paper and magnesium photo-cathodes. The commissioning took place smoothly thanks to the elliptical shape of the irises between the cells. It leads to a ratio of the surface electrical to the accelerating field close to one, thus reducing breakdown hazards.

Dark Current

The dark current or charge has been measured as a function of the accelerating field for raw copper and hand polished photo-cathodes. It was not possible to compare with the optically polished photo-cathode because of a breakdown in the RF circulator which did not allow us to increase the electrical field above 40 MV/m.

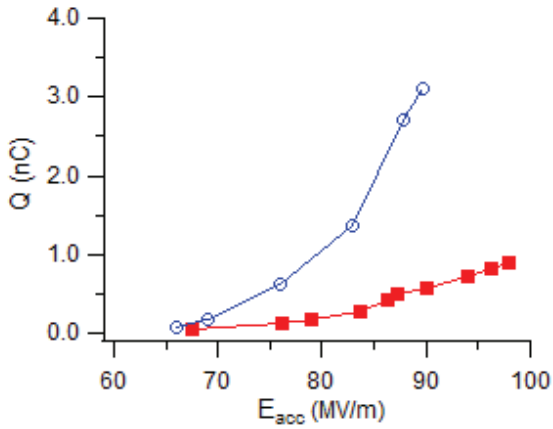

Figure 1: dark charge produced by field emission in the gun for raw copper (round points) and hand polished copper (square points) photo-cathodes.

The reduction of dark current due to the use of a polished photo-cathode is spectacular. At 90 MV/m, the dark charge with polished photo-cathode is 5.5 times lower than in the raw copper case. However, the analysis of these results according to the Fowler-Norhdeim formula [4] showed that the field amplification factor, β, has the same order of magnitude, around 100. The lower charge with the polished copper comes actually from a reduction of the emission area.

BEAM PERFORMANCES

To compare performances of different photo-injectors and also for user experiment, it is important to characterize the electron beam as a function of parameters as the relative phase between the RF and the laser, the accelerating gradient, the energy and spot size of the laser.

Dephasing Curve

The best performances of the electron beam are obtained when the electron beam is accelerated near the crest of the RF wave. However there is a range around the optimum phase on which the gun can be operated. Measurements of the beam charge as a function of the relative phase between the laser and the RF is shown in figure 2.

Copyright © 2012 by the respective authors — cc Creative Commons Attribution 3.0 (CC BY 3.0)

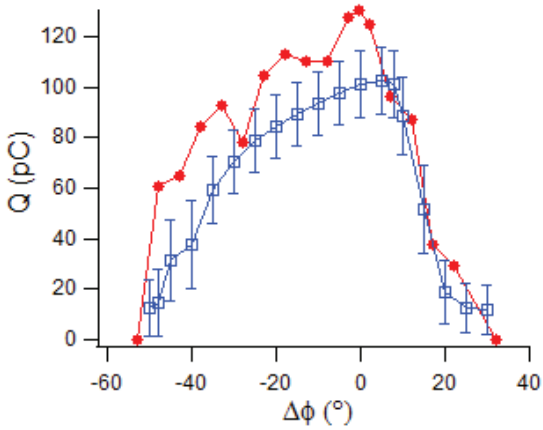

Figure 2: beam charge as a function of the relative phase between the RF and the laser for 56 MV/m, blue curve with squares and 92 MV/m, red curve with circles.

Behaviour is similar as observed in other experiments [5]. The width of the dephasing curve increases versus the accelerating gradient. Below the phase corresponding to the maximum charge, there is a slow increase due to the Schottky effect related to the increase of the accelerating gradient. On the right side of the curves, the slope is very abrupt; in less than 10° the charge can decrease by 50 %. It means that the beam performances are very sensitive to the phase. Besides there is evidence of a slow drift of the phase which is being investigated.

Transverse Dimensions and Emittance

Transverse dimensions of the electron beam are measured through the fluorescence light emitted by the beam into YAG:Ce screen. This light is then transported by a metallic mirror, an achromatic lens to a CCD camera. Four monitors are installed, the first at around 2 meters away from the photo-cathode, the second is placed just after a focusing coil in the middle of the beamline (3.5 m from the photo-cathode), the third is at the end of the straight line and the last on the deviated line after the dipole for the beam energy measurement.

Example of typical measurements is shown in figure 3.

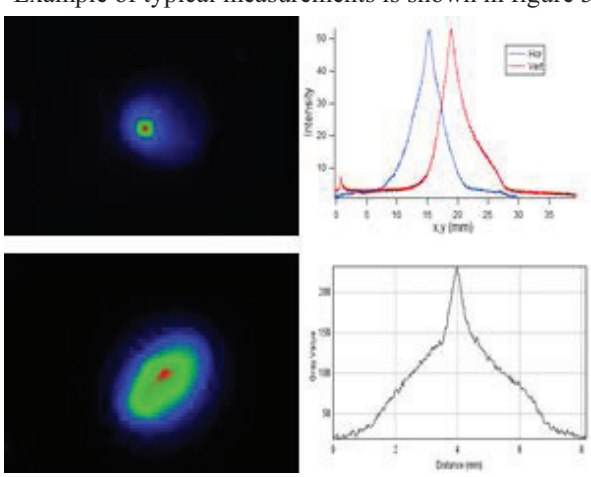

Figure 3: YAG screen images; top, 1st screen with the 1st focusing coil at 90 A; down, 2nd screen with 99 A and the 2nd focusing coil at 29 A; Q = 180 pC, E_{acc} = 63 MV/m.

The difference between both images is clear: on the first screen, the beam appears mostly round although with a vertical width 12 % larger than the horizontal one. On the second screen, it is elliptical tilted at roughly 45°; the width along the big axis is 51 % larger than on the other axis. The profile on the first screen is probably due to the laser which has a vertical width also 5 % larger than the horizontal one. However it is not enough to explain the huge ellipticity of the electron beam measured on the second screen. It looks like the action of a quadrupole or it would mean that the vertical emittance of the beam is 50 % larger than in the other direction. Both hypothesis do not seem compatible with our set-up, this problem is still under investigation. In addition there are also some problems of halo and parasitic images that we are striving to understand.

In spite of these problems, we used a solenoid scan to measure the emittance. A direct measurement with a mask made of vertical and horizontal slits is foreseen in 2013, technical drawings are under way. The principle of the measurement with the solenoid is similar to the one with the quadrupole. One measures the beam transverse dimensions as a function of the magnetic force and, knowing the coil transfer matrix, it is possible to deduce the beam matrix at the entrance of the coil. Such measurement is shown in figure 4.

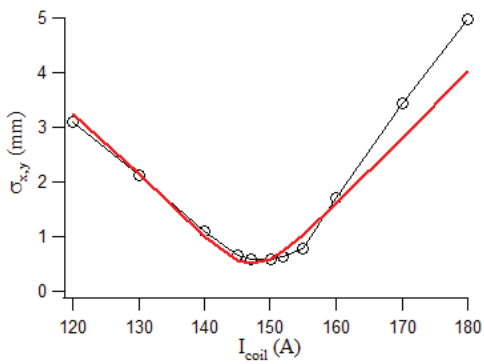

Figure 4: rms beam size, black curve with round points; least square fit restricted to [130, 160] A, red curve; Q = 150 pC, E_{acc} = 80 MV/m.

Some reasonable assumptions have been made to simplify the analysis: the beam is round and no coupling terms between the X and Y directions in the input beam matrix. So, only 3 parameters of the beam matrix must be found: σ_{11}, σ_{12} and σ_{22}. The fit was restricted to the current range [130 A; 160 A] because on the whole range of current it converged to a solution giving an imaginary emittance. So, the result of the fit is a normalized emittance of 4.6 πmmmrad. With the parameters of the experiment, PARMELA simulation gives an emittance of 2.6 πmmmrad at the entrance of the coil. The discrepancy between the simulation and the experiment can have multiple origins: problems with the images, magnetic errors, RF phase error and the fact that this method based on the transport matrix formalism neglects the space charge force. In the simulation, the emittance increases by

Copyright © 2012 by the respective authors — cc Creative Commons Attribution 3.0 (CC BY 3.0)

30 %, between the position of the YAG screen and entrance of the solenoid, due to the space charge.

Energy spread

The energy spectrum of the electron beam is measured thanks to a dipole recycled from the TTF accelerator. It is a 60° bend with 70 cm of curvature radius. The YAG screen used to measure the beam is close to the focal plane of the dipole, at 13 cm, which means there is a small contribution of the transverse dimension on the measurement. We performed a measurement of the energy spread as a function of the RF phase, shown in figure 5.

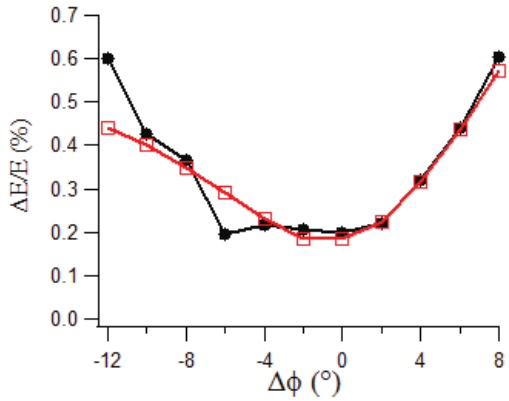

Figure 5: rms energy spread as a function of the RF phase with Q = 100 pC and E_{acc} = 54 MV/m; measurements, black curve with rounds; PARMELA simulations, red curve with squares.

The minimum energy spread is roughly 0.2 %. PARMELA simulations have been performed with the experimental parameters. The agreement with the measurements is quite satisfying. It means also that the contribution of the emittance in the measurement is negligible as we had assumed.

MAGNESIUM PHOTO-CATHODE

Several experiments have been performed elsewhere with magnesium (Mg) photo-cathode to produce higher charge [6]. The advantage of such materials is the relative easiness and low cost to carry out compared to cesium telluride for instance. We used a disk of pure Mg of 10 mm diameter and 2 mm thickness and press fitted in the centre of the copper end plate of the RF gun without baking or cleaning. The RF commissioning was 3 times longer than with the simple copper plate. The first beam with this photo-cathode produced very low charge, 80 pC at the maximum but it was expected. To have access to the good properties of pure Mg, one has to remove the oxide layer on the surface. The simplest way to do it is to focus the laser down to 0.1 mm; to scan the photo-cathode in presence of a RF field of 50 MV/m and to make explode the top oxide layer. After having performed this procedure, we measured the charge as a function of the laser energy, see figure 6.

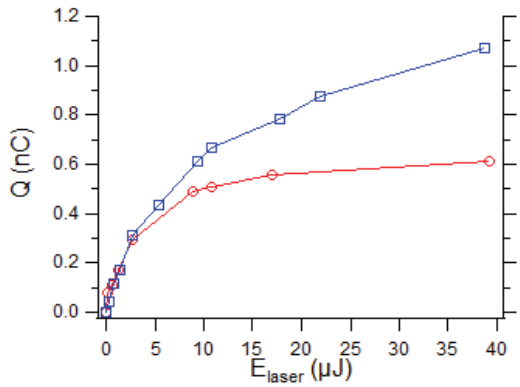

Figure 6: beam charge measured with an ICT as a function of the laser energy deposited on the Mg photo-cathode for 2 accelerating gradients; 45 MV/m, red curve with circles; 62 MV/m, blue curve with squares.

The laser cleaning led to a dramatic increase of the extracted charge, up to 1.1 nC with an accelerating field of 62 MV/m while it was only 80 pC before. Actually, we are limited by the space charge force which prevents the electrons to go out. As one can see, increasing the accelerating gradient allows one to extract more charge. The linear part of the curves, below 5 μJ, means a yield of 0.11 nC/μJ. If we could operate the gun at 90 MV/m, we could produce 4.4 nC with the maximum laser energy.

CONCLUSION

Experimental characterisation of the alphaX photo-injector has been performed. Charge, emittance and energy spread have been measured and are in good agreement with the simulations. Obtaining of high charge with magnesium photo-cathode has been demonstrated. Next step will be to operate at high gradient routinely in order to improve beam quality and higher charge. We plan also to test other RF guns and to perform user experiments.

REFERENCES

[1] R. Roux *et al.*, "PHIL: a Test Beamline at LAL" EPAC'08, Genoa, Italy, June 2008, WEPP078, p. 2698 (2008); http://www.JACoW.org

[2] J. Brossard *et al.*, "Low Energy Beam Measurements Using PHIL Accelerator at LAL, Comparison with PARMELA Simulations" PAC'11, New-York, March 2011, WEP210, p. 1885 (2011); http://www.JACoW.org

[3] T. Garvey *et al.*, "Construction of the ALPHA-X photo-injector cavity", EPAC'06, Edimburgh, June 2006, TUPCH113,p.1277 (2006); http://www.JACoW.org.

[4] G. Gatti *et al*, "Power test of a PLD film MG photocathode in a RF gun", PAC'07, Albuquerque, USA, June 2007, TUPMN037, p. 995 (2007); http://www.JACoW.org

[5] X. J. Wang, "Challenges of operating a photo-cathode RF gun injector", Chicago, USA, August 1998, TH4043, p. 866, http://www.JACoW.org

[6] T. Srinivasan-Rao *et al*, "Performance of magnesium cathode in the S-band RF gun", PAC97, Vancouver, Canada, May 1997, 3W020, p. 2790; http://www.JACoW.org

Copyright © 2012 by the respective authors — cc Creative Commons Attribution 3.0 (CC BY 3.0)

ELECTRON MODEL OF A DOGBONE RLA WITH MULTI-PASS ARCS *

S.A. Bogacz#, G.A. Krafft, V.S. Morozov, Y.R. Roblin, Jefferson Lab, Newport News, VA, USA
K.B. Beard, Muons, Inc., Batavia, IL, USA

Abstract

The design of a dogbone Recirculated Linear Accelerator, RLA, with linear-field multi-pass arcs was earlier developed [1] for accelerating muons in a Neutrino Factory and a Muon Collider. It allows for efficient use of expensive RF while the multi-pass arc design based on linear combined-function magnets exhibits a number of advantages over separate-arc or pulsed-arc designs. Such an RLA may have applications going beyond muon acceleration. This paper describes a possible straightforward test of this concept by scaling a GeV scale muon design for electrons. Scaling muon momenta by the muon-to-electron mass ratio leads to a scheme, in which a 4.5 MeV electron beam is injected at the middle of a 3 MeV/pass linac with two double-pass return arcs and is accelerated to 18 MeV in 4.5 passes. All spatial dimensions including the orbit distortion are scaled by a factor of 7.5, which arises from scaling the 200 MHz muon RF to the frequency readily available at CEBAF: 1.5 GHz. The footprint of a complete RLA fits in an area of 25 by 7 m. The scheme utilizes only fixed magnetic fields including injection and extraction. The hardware requirements are not very demanding, making it straightforward to implement.

MUON RLA WITH TWO-PASS ARCS

A schematic layout of a dog-bone-shaped muon RLA, proposed for future Neutrino Factory [2] is illustrated in the top portion of Fig. 1. Reusing the same linac for multiple (4.5) beam passes provides for a more compact accelerator design and leads to significant cost savings. In the conventional scheme with separate return arcs [4], different energy beams coming out of the linac are separated and directed into appropriate arcs for recirculation. Therefore, each pass through the linac would require a separate fixed-energy arc, increasing the complexity of the RLA. We propose a novel return-arc optics design based on linear combined-function magnets with variable dipole and quadrupole field components, which allows two consecutive passes with very different energies to be transported through the same string of magnets [6].

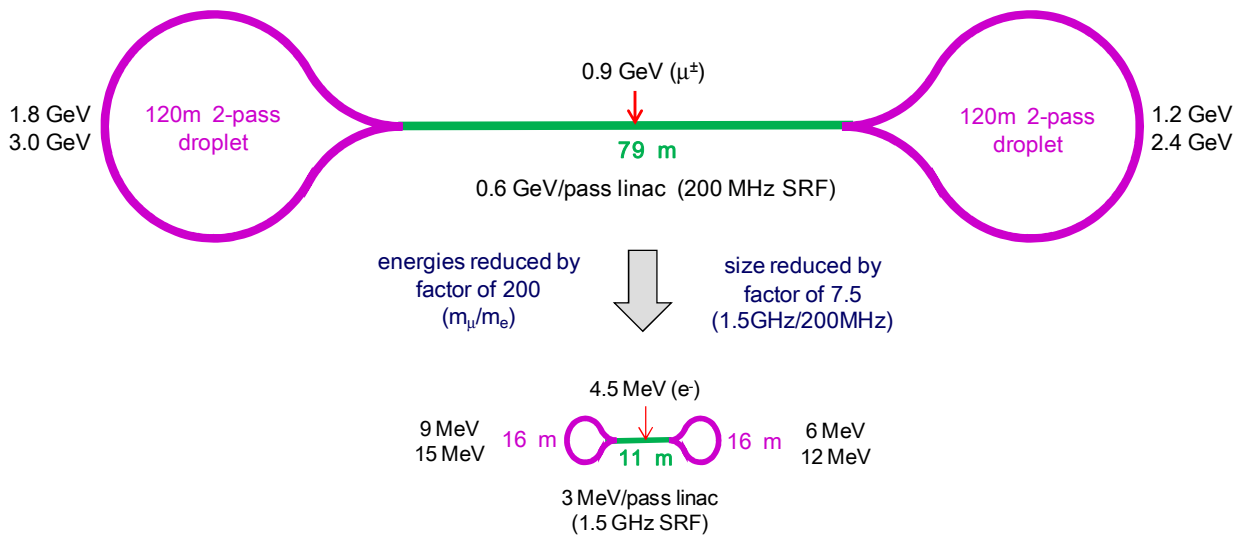

Figure 1: Schematic layout of a GeV-scale muon RLA with two-pass return arcs. A path to an 'electron model' is outlined: scaling 3.6 GeV muon RLA to 18 MeV model and replacing 200 MHz RF with a 1.5 GHz CEBAF cavity

* Supported in part by US DOE STTR Grant DE-FG02-08ER86351.
Notice: Authored by Jefferson Science Associates, LLC under U.S. DOE Contract No. DE-AC05-06OR23177. The U.S. Government retains a non-exclusive, paid-up, irrevocable, world-wide license to publish or reproduce this manuscript for U.S. Government purposes.
bogacz@jlab.org

Copyright © 2012 by the respective authors — cc Creative Commons Attribution 3.0 (CC BY 3.0)

SCALED DOWN ELECTRON MODEL

Here, we propose a straightforward test of this concept by scaling the above GeV-scale muon RLA design for electrons. Scaling muon momenta by the muon-to-electron mass ratio (~ 200) yields a scheme, in which a 4.5 MeV electron beam is injected into the middle of a 3 MeV/pass linac with two double-pass return arcs and then is accelerated to 18 MeV in 4.5 passes.

The second scaling, would involve replacing the original low frequency (200 MHz) RF, required to accommodate inherently long muon bunches, with readily available high frequency CEBAF RF (1.5 GHz). All spatial dimensions including the orbit distortion would then scale down by the ratio of the two frequencies (factor of 7.5). As a consequence, the scaled down electron model would fit in a modest test cave of 25 by 7 meters.

For the remainder of this paper, we will describe the principle of multi-pass arc architecture, a possible magnet design and field requirements, as well as a complete conceptual RLA design.

MULTI-PASS ARC OPTICS

Design Concept

The droplet arc design consists of super cells, which are required to satisfy the following basic conditions at two discrete energies (6 and 12 MeV):

- Each super cell exhibits periodic solutions for the orbit and the Twiss functions.
- At the beginning and at the end of each super cell, the periodic orbit offset, dispersion and their slopes are all zero.

The first condition ensures that the super cells bending in the same direction are optically matched while the second one provides optical matching of the cells bending in the opposite directions. The second condition also implies that the beam is centered in the linac and that the linac is dispersion free.

Linear Optics

Optics solution satisfying the above conditions can be obtained using only same-direction bends, which significantly shortens the arc (by almost a factor of 3) compared to the conventional linear NS-FFAG lattice [3], which involves alternating the 'outward-inward-outward' bends in the underlying triplet structure. We make the bending angle of each combined function magnet variable with a constraint that the bending angles of all magnets in a super cell must add up to the required fixed total bend. Such a solution combines compactness of the design with all the advantages of a linear NS-FFAG [5], namely, large dynamic aperture and momentum acceptance essential for large-emittance muon beams, and no need for a complicated compensation of non-linear effects, simpler combined-function magnet design with only dipole and quadrupole field components. We use the maximum possible bend of 60° per super cell to accommodate the largest possible number of magnets in the super cell and therefore to have the largest number of free parameters for optics tuning. The extra free parameters were used to control the maximum values of the orbit deviation, and beta functions and dispersion. Figure 2 shows solutions for the periodic orbit and dispersion of the outward-bending super cell at 6 and 12 MeV/c, respectively. An inward-bending super cell is identical to the outward-bending cell except that its bends are reversed. The super cell consists of 24 combined function magnets with dipole and quadrupole field components. The magnets are 6.5 cm long and are separated by 3 cm gaps. The total arc length is 16 m. In terms of magnetic field requirements, the maximum needed dipole field is about 650 Gauss while the maximum quadrupole gradient is about 850 Gauss/cm.

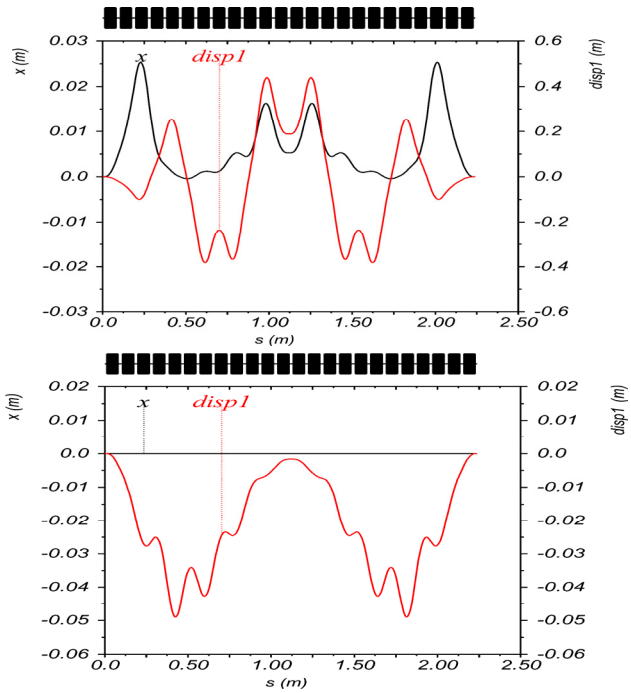

Figure 2: 6 MeV (top) and 12 MeV (bottom) periodic orbits and dispersions of the outward bending super cell.

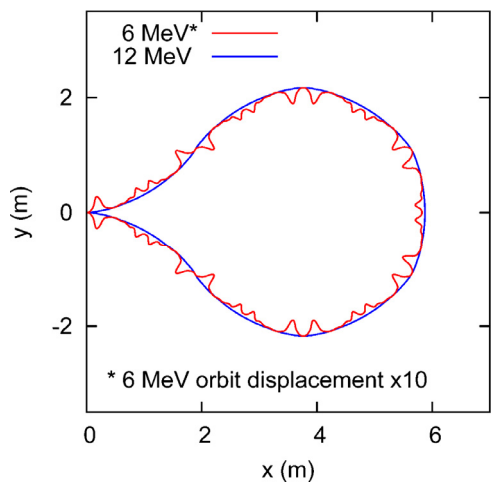

Figure 3: Layout of the 6 and 12 MeV reference orbits.

Copyright © 2012 by the respective authors — cc Creative Commons Attribution 3.0 (CC BY 3.0)

Figure 3 illustrates geometric layouts of the 6 and 12 MeV closed periodic orbits. Note that because of the varying bending angles, the arc is not perfectly circular. The largest orbit separation occurs only in a small number of magnets and is caused by the necessity to spread/recombine the different momenta orbits at the beginning of the arc.

ARC TO MULTI-PASS LINAC MATCHING

As a proof-of-principle, one can design a multi-pass linac with energy gain of 3 MeV per pass, which is matched by-design to previously described two-pass arcs for both passes simultaneously. As described in [4] the above multi-pass linac optics can be accomplished by appropriately 'tailored' focusing profile along the linac - the strengths of individual linac's fixed-field quadrupoles. Here, they are treated as free parameters used to control the beta functions at linac's ends for all consecutive passes. The proof-of-principle solution [6] was designed by modifying the so-called bi-sected linac profile [4], where the quadrupole strengths increase linearly (in a mirror-symmetric fission) from the linac's center toward the ends.

MAGNET DESIGN AND FIELD QUALITY

Design Choice

Each of 7 super-periods required to complete the droplet arc is configured with 24 individual combined function magnets: 6.5 cm in length and with 5 cm of the horizontal aperture. These magnets will be mounted on a rectangular vacuum chamber; 2.3 meter long and shaped into a 60^0 arc. As for the magnet design, a combined function Panofsky quadrupole with integral dipole windings, similar to Jlab's FEL design [7], provides a very attractive solution for an independent electrical control of both the magnetic field and its gradient.

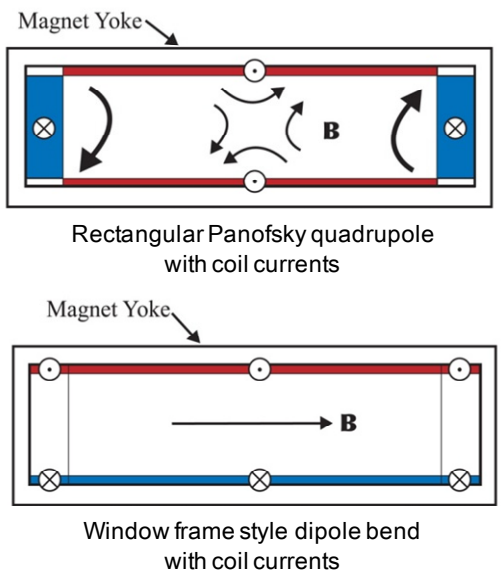

Figure 4: Quadrupole and Dipole Current Flows [7].

Relatively weak magnets, satisfying our strength requirements, can be built 'flattened' with no compromise to their field gradient uniformity and have a window frame-like yoke that, at full quadrupole current, is not near saturation [7]. Superposition of a dipole onto the Panofsky quad adds current to one of the four coils and subtracts it from its opposing coil. This is accomplished by adding variable current coils to the vacant corners of the original Panofsky design as illustrated in Fig. 4.

Field Quality Requirements – Error Sensitivity

The two-pass arc optics, illustrated in Fig. 2, was checked for error sensitivity. We launched a mini Monte Carlo simulation by creating 25 virtual arc lattices with statistically distributed magnet mis-alignment (200 μm, rms, displacement error) as well as magnet mis-powering (with 10^{-4} relative field error, rms) for both the dipole and quadrulpole components. Using pairs of horizontal and vertical correctors placed after each magnet the resulting orbit deviation was steered back to to the design orbit within 20 μm level, which corresponds to the accuracy of the orbit measurement (BPM accuracy).

CONCLUSIONS

We propose a straightforward test of a GeV scale muon RLA by scaling the muon design for electrons (via the muon-to-electron mass ratio). Presented 'electron model' features: a 4.5 MeV electron beam injected at the middle of a 3 MeV/pass linac combined with two double-pass return arcs. The beam is accelerated to 18 MeV in 4.5 passes. All spatial dimensions of the full scale RLA are shortened by a factor of 7.5, as a consequence of using a readily available 1.5 GHz CEBAF cavity, rather than the original 200 MHz RF. The footprint of a complete RLA 'demo' fits in an area of 25 by 7 m. The scheme utilizes only fixed magnetic fields including injection and extraction. Engineering design and fabrication of linear-field combined-function magnets does not seem to present a challenge [7].

REFERENCES

[1] S.A. Bogacz, Nucl. Phys. B Proc. Suppl., **149**, p. 309, 2005.
[2] Design Report, IDS-NF-020, http://www.ids-nf.org
[3] G.M. Wang et al., "Multipass arc lattice design for recirculating linac muon accelerators", in Proc. PAC'09, Vancouver, BC, p. 2736.
[4] S.A. Bogacz et al., "Recirculating linear accelerators for future muon facilities"IPAC'10, Kyoto, p. 3602.
[5] V.S. Morozov et al., "Matched optics of muon RLA and non-scaling FFAG arcs", in Proc. PAC'11, New York, NY, p. 163.
[6] V.S. Morozov et al., "Multi-pass muon RLA return arcs based on linear combined-function", in Proc. IPAC'11, San Sebastian, p. 2784.
[7] G.H. Biallas et al., "Combined Panofsky Quadrupole & Corrector Dipole" in Proc. PAC'07, Albuquerque, NM, p. 602.

Copyright © 2012 by the respective authors — cc Creative Commons Attribution 3.0 (CC BY 3.0)

IN-SITU MEASUREMENT OF BEAM-INDUCED FIELDS IN THE S-BAND ACCELERATING STRUCTURES OF THE DIAMOND LIGHT SOURCE LINAC

C. Christou
Diamond Light Source, Oxfordshire, UK

Abstract

Higher order modes induced by beam in the accelerating structures of the Diamond Light Source pre-injector linac have been directly measured using directional couplers in the high-power waveguide network. These modes are compared with an electromagnetic simulation of the structures and the use of the higher order modes for alignment of the beam to the structure is investigated.

DETECTION OF INDUCED FIELDS

Much work has been done on the analysis of wake fields using dedicated test accelerators, particularly at the ASSET facility in SLAC [1, 2] and the SBTF at DESY [3]. Extension of the method to a low-energy device in a user facility with minimal disturbance to the installed hardware offers scope for cost-effective physics studies and diagnostic development. In the work presented here, wake fields and structure higher order modes are studied in the Diamond Light Source pre-injector linac. This device uses two 5.2 m DESY linac II-type accelerating structures to generate a 100 MeV electron beam suitable for injection into the booster synchrotron [4]: the layout of the linac is shown in Figure 1. The structures are normal-conducting constant gradient designs, operating in the $2\pi/3$ mode at 3 GHz. Each structure is independently powered by a TH2100 klystron amplifier which provides a 5 µs pulse of around 20 MW five times per second in normal operation.

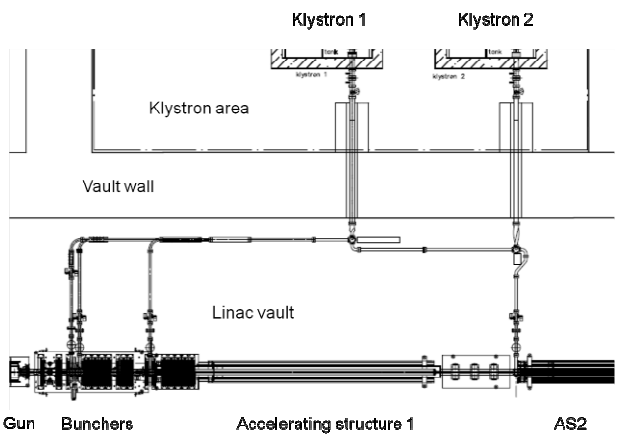

Figure 1: The Diamond linac

Directional couplers, manufactured by Spinner, are mounted in the waveguide network at the exits of the klystrons and at the windows of the accelerating structures. These couplers measure forward and reverse power and monitor operation and protect the klystrons. If either one of the klystrons is left unpowered, the beam can drift through the accelerating structure and the directional coupler can be used as a monitor of the beam-induced wake fields in the structure.

Signals were discernible on an Agilent DS091304A 13 GHz-bandwidth oscilloscope for beam drifting through bunchers and through both accelerating structures in single-bunch mode and in multibunch mode. The most intense signals were obtained for high charge (1 nC) single bunches drifting through the second accelerating structure at 47 MeV (corresponding to the standard operating gradient of the first accelerating structure) with good temporal bunching; Figure 2 shows an oscilloscope trace recorded for these parameters.

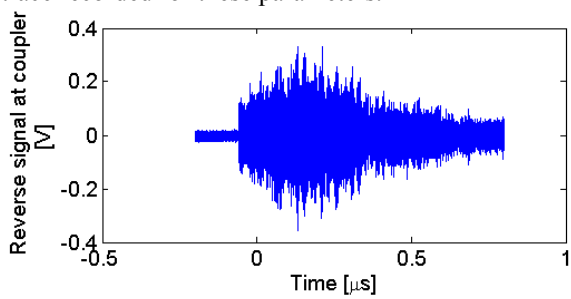

Figure 2: Passage of single bunch detected at the directional coupler in the non-powered RF line

There is rich spectral content to this induced signal, as can be seen in Figure 3. Two measurements are shown in this figure, recorded with and without beam in the structure, establishing that the most intense peaks in the spectrum are the third and fourth harmonics of the 3 GHz RF power fed to the first accelerating structure. The fundamental 3 GHz signal is not transmitted from structure to structure.

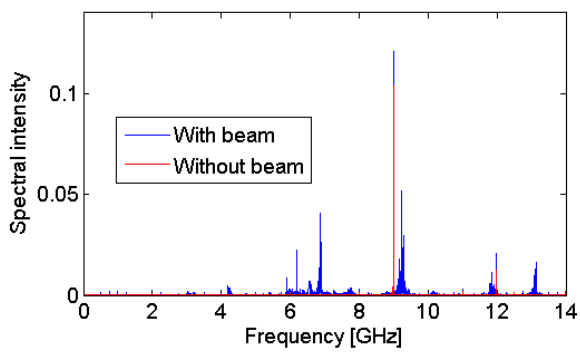

Figure 3: Frequency content of induced pulse

Copyright © 2012 by the respective authors — cc Creative Commons Attribution 3.0 (CC BY 3.0)

The wake can also be differentiated from the RF noise by making a small change to either the master oscillator frequency or the cavity temperature and observing that the RF signals shift only with frequency and the wake signals shift with only temperature, as shown in Figure 4.

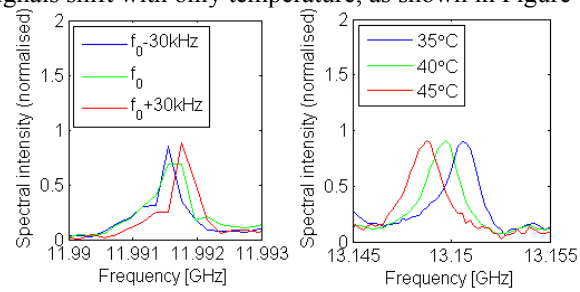

Figure 4: Effects of RF frequency and structure temperature change. The fourth harmonic of the RF frequency changes with frequency (left) and the wake-induced signal changes with cavity temperature (right).

STIMULATION OF HIGHER ORDER MODES

The trajectory of the beam in the accelerating structures can be controlled by steerer magnets located upstream of both structures. Scanning the current of the final vertical steerer before the second accelerating structure and recording the spectrum at each current gives the plot shown in Figure 5.

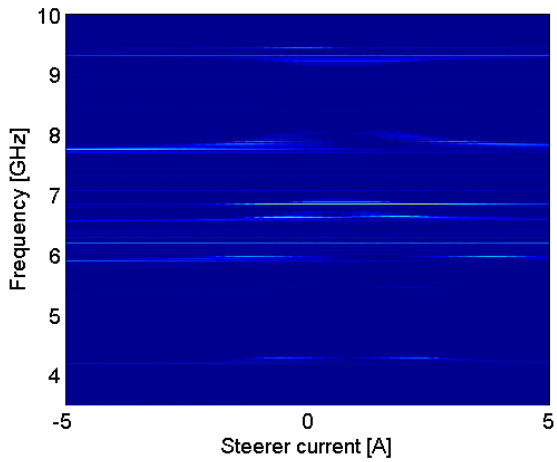

Figure 5: Frequency spectra explored by scanning steerer

Several points are immediately apparent from this plot, firstly that the frequency spectrum consists of bands rather than lines, and that these bands shift in frequency as the steer is applied. This effect arises from the constant-gradient design of the structure, requiring a tapering of cell dimensions along the structure to compensate for the loss in RF power as the pulse propagates along the structure: although the fundamental accelerating mode remains constant along the structure, the higher order modes are free to drift. Secondly, the monopole and multipole modes are easily distinguished, as the higher order azimuthal modes have a null on axis and so are absent from the spectrum when the beam is well aligned, with steerer current of approximately 1 A in this case, and grow as the beam leaves the axis.

The most intense modes are given in Table 1: this gives the lower and upper frequency limits of each band, and identifies each mode as a monopole or multipole mode.

Table 1: Classification of intense modes

Mode type	From [GHz]	To [GHz]
Multipole	4.19	4.35
Multipole	5.38	5.50
Multipole	5.90	5.98
Multipole	6.57	6.72
Monopole	6.78	6.92
Multipole	7.69	8.05
Monopole	9.13	9.32
Multipole	9.43	6.46
Monopole	11.78	11.98
Monopole	13.04	13.13

IDENTIFICATION OF MODES

Categorisation of all wake field modes is numerically intensive as the observed signal arises from a system of 156 coupled oscillating cells, each of different dimension, with TM, TE, TEM and hybrid modes all possible. To reduce the complexity of the calculation, CST Microwave Studio was used to model cells at the entrance, middle and exit of the linac; in each case studying resonant modes of the single cell, and coupling in structures of two, three and six cells of the same type. Dispersion curves in each case were then calculated by interpolating between the calculated modes for each cell type, and the behaviour of the cells was assumed to vary smoothly along the structure.

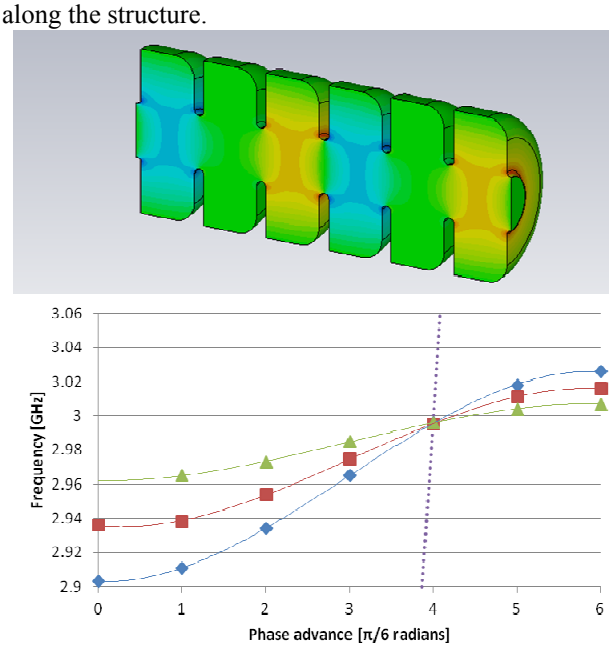

Figure 6: Simulation of accelerating mode

The validity of this approach is demonstrated in Figure 6, in which the TM01 accelerating mode is calculated for the three cells at the beginning (blue), middle (red) and

Copyright © 2012 by the respective authors — cc Creative Commons Attribution 3.0 (CC BY 3.0)

end (green) of the structure, and is shown to intersect with the $v = c$ light line (dotted), representing the relativistic electron bunch, at a phase advance of 4π over the 6 cells of the model, that is $2\pi/3$ radians per cell, near 3 GHz.

The first intense mode observed is a TM11-like mode shown at the top of Figure 7. This is a dipole mode, and so the spectrum shows a null for well steered beam. The dispersion curve intersects the light line from 4.15 GHz to 4.42 GHz, with the modes up to 4.35 GHz exiting via the first cell, and modes above that trapped and invisible. Agreement with the observed spectrum is good.

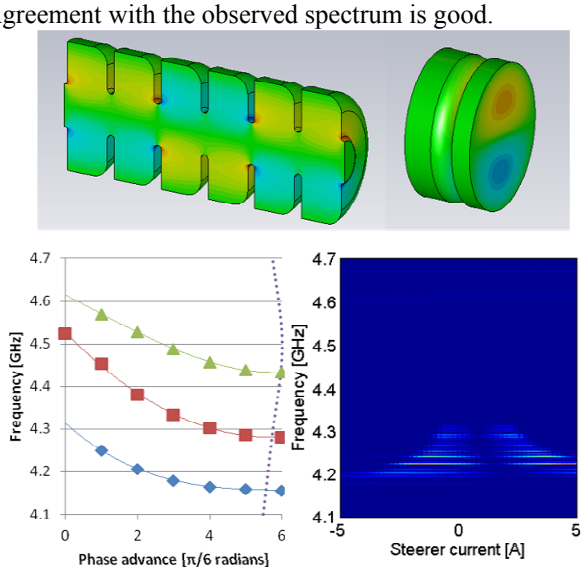

Figure 7: Simulation, dispersion curve and measurement of TM11-like mode

This approach was repeated for all modes up to the second monopole TM02 mode near 7 GHz. Results are shown in Figure 8; agreement with the model is good.

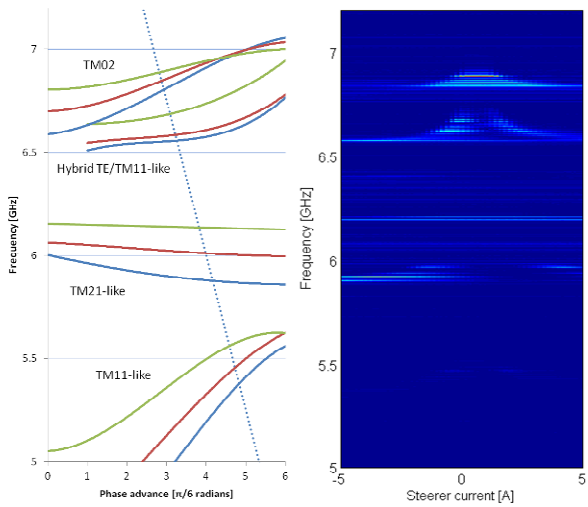

Figure 8: Scaling of dipole mode intensity in the buncher

The most intense spectral features can be clearly identified; although categorisation is difficult because of mode hybridisation and the degeneration of the simple pillbox modes in the shaped cell (for example the branches of the TM11-like mode at 4.3 and 5.5 GHz).

INDUCED FIELDS AS A DIAGNOSTIC

The trajectory-dependence of the dipole mode intensities allow the accelerating structures to be used as cavity BPMs. The absence of dipole modes in a well aligned beam is clear, leading to the possibility of an automatic multi-steerer alignment routine for the linac. A simple proof-of-principle experiment was carried out in which two steerers were scanned at the entrance to the second structure, and the ratio of the total integrated intensities of the hybrid dipole mode and monopole mode between 6.5 and 7.0 GeV was used as a measure of beam alignment. This ratio is plotted in Figure 9. The optimal position is clear, even without the ability to discriminate between horizontal and vertical position.

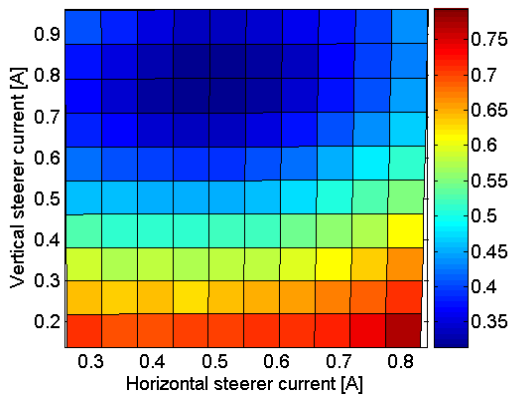

Figure 9: Optimisation of beam steer through the accelerating structure. The colour indicates the ratio of dipole to monopole intensity.

CONCLUSIONS

The directional couplers installed on the Diamond linac have been used to measure higher order modes in the structures, and CST Microwave Studio models have been used to unambiguously identify the spectral content. This simple measurement offers the opportunity to study accelerating structures in situ, and to optimise linac performance by using the accelerating structures as cavity BPMs. Use of the structures as both accelerators and position monitors offers a potential reduction in accelerator complexity and total length in future linacs.

ACKNOWLEDGEMENTS

Accelerating structure cell dimensions were kindly provided by RI Research Instruments GmbH.

REFERENCES

[1] C.Adolphsen et al., Phys. Rev. Lett. **74**, 2475 (1995).
[2] M. Siedel et al, PAC 1997 p. 434.
[3] M. Schmitz, PAC 1997 p. 569.
[4] C. Christou et al., EPAC 2006, p. 3185.

Copyright © 2012 by the respective authors — cc Creative Commons Attribution 3.0 (CC BY 3.0)

INTEGRATION OF THE EUROPEAN XFEL ACCELERATING MODULES

E. Vogel, S. Barbanotti, J. Branlard, H. Brueck, S. Choroba, L. Hagge, K. Jensch, D. Kaefer, V. Katalev, D. Kostin, L. Lilje, A. Matheisen, W.-D. Moeller, D. Noelle, B. Petersen, J. Prenting, D. Reschke, H. Schlarb, M. Schmoekel, J. Sekutowicz, W. Singer, H. Weise, DESY, Hamburg, Germany,
S. Berry, C. Madec, O. Napoly, B. Visentin, CEA, Saclay, France,
P. Borowiec, J. Swierblewski, HNINP, Kraków, Poland, A. Bosotti, P. Michelato, INFN, Milan, Italy,
W. Kaabi, LAL, Orsay, France, E. Plawski, NCBJ, Świerk, Poland, F. Toral, CIEMAT, Madrid, Spain

Abstract

The production of the 103 superconducting accelerating modules for the European XFEL is an international effort. Institutes and companies from seven different countries (China, France, Germany, Italy, Poland, Russia and Spain), organized in 12 different work packages contribute with parts, capacity for work and facilities to the production of the modules. Currently the series production of the individual parts started or is approaching. Personnel is trained for the assembly and testing of parts and as well for the complete modules. Here we present an overview and the status of all these activities.

INTRODUCTION

In the early 1990s the Tera Electronvolt Superconducting Linear Accelerator (TESLA) collaboration started working on the development of a pioneering superconducting accelerator technology [1]. The concept has proved so successful that it was also chosen for the European XFEL [2].

Each superconducting accelerating module for the European XFEL consists of several parts provided by different work packages (WPs). The core parts are the superconducting 1.3 GHz nine-cell cavities provided by WP04. They are used for beam acceleration. For beam focusing and steering each module contains a superconducting quadruple magnet from WP-11. A beam position monitor produced by WP-17 is attached to the magnet. The rf power is fed into the cavities via power couplers delivered by WP-05. The frequency tuners from WP-07 are used for keeping the cavities on resonance. Bellows connecting the individual cavities are part of the WP-08, the 'cold vacuum', likewise the coupler vacuum system. WP-06 organizes the Higher Order Mode (HOM) and pick up (PU) antennas. All these parts are installed inside the cryostat. The cryostat is also called 'cold mass' and part of the WP-03.

The final assembly is done in the responsibility of WP-09 (string assembly) and WP-03 (module assembly) at CEA, Saclay and the final module operation test is performed by WP-10 at the Accelerator Module Test Facility (AMTF) at DESY, Hamburg. Proper rf control in the later accelerator will base on properties measured during the modules tests. This item is the task of WP-02. Before transportation into the XFEL tunnel for installation, each module receives a waveguide system tailored by WP-01 to the cavity performances.

Providing infrastructure and support needed for parts tracking, quality control and nonconformity handling for all these activities is the task of the WP-40.

SUPERCONDUCTING CAVITIES

More than 800 superconducting TESLA type cavities [3] will be used for the European XFEL. They are mechanically manufactured and surface treated [4] by the two companies Ettore Zanon (EZ) and Research Instruments (RI) and delivered to DESY ready for vertical testing in the AMTF by a Polish team from IFJ-PAN, Krakow. Always eight cavities with similar performance will be put together and shipped to CEA for the string and module assembly.

Both companies manufactured reference cavities which have been surface treated at DESY and vertically tested. These cavities showed promising maximum gradients above 28 MV/m. They are used for the qualification of the companies' infrastructure created for the cavity treatment (clean room, degreasing and ultrasonic cleaning, HPR, (electro) chemical surface treatment, annealing furnaces, slow venting slow pumping systems etc.). The commissioning of the infrastructure is ongoing. The series delivery to DESY will start in November (RI) and in December (EZ).

COLD MAGNETS

The accelerating modules of the XFEL linac will be equipped with one combined superconducting magnet [5] per module, which consists of a main superferric quadrupole for focusing and two nested corrector dipoles for beam steering. The magnet series production is being done under the supervision of CIEMAT in Spain: ANTEC produces the magnets while Trinos Vacuum Projects takes care of the helium vessel, assembly and tests (electrical, pressure and vacuum). The magnetic measurements are done at DESY as a common German and Polish in-kind contribution. The conduction cooled current leads are produced at CECOM in Italy under DESY supervision while the copper coating of the beam pipe is being done by Galvano-T in Germany.

The three pre-series units have been successfully produced and tested. Green light has been given to series production in June, 2012.

Copyright © 2012 by the respective authors — cc Creative Commons Attribution 3.0 (CC BY 3.0)

POWER COUPLERS

LAL Orsay contributes to the XFEL project with the delivery of 800 power couplers [6, 7] to CEA for the assembly of 100 accelerator modules. The tasks consist of the industrial monitoring and coupler quality control at the production sites and the rf conditioning and testing at the LAL campus [8].

A 70 m^2 clean room used for the coupler preparation at LAL is under construction. The 5 MW power rf station has been installed for the conditioning of 8 couplers simultaneously. The industrial production by Thales and RI is in the last process validation phase and the mass production start is scheduled for the end of the year.

FREQUENCY TUNERS

The goal of the XFEL cold tuning system [2] is the adjustment of the cavity frequencies to the accelerator rf frequeny with a resolution better than 1 Hz. The XFEL slow tuner is based on the TTF/SACLAY tuner [9]. This tuner design is working in the TTF Linac since 1997 with high reliability. In addition, the tuning system will also compensate Lorentz Force De-tuning (static and dynamic) using piezoelectric actuators [3].

All the orders for the tuner parts have been made and the fabrication is in good progress. The drive units and piezo systems will be checked by industry prior to delivery. The first full tuner systems are available at CEA. An automatic system has been developed to verify the correct tuner installation during the string and module assembly.

BEAM POSITION MONITORS

Beam steering through the linac requires proper information on the beam position. It is provided by one beam position monitor (BPM) per module. Two different types are used, 1/3 will be re-entrant and 2/3 button BPMs [10]. Both types have different advantages and disadvantages.

The ramp up of the BPM series production is in time with the magnets arriving DESY and the last one will be produced and available mid-2013. The individual production rates of both BPM types are under investigation.

BEAM AND COUPLER VACUUM

The cavities are connected via Copper coated bellows without RF-shields. A novel sealing system has been developed [11]. It consists of rigid Nb-Ti flanges EB welded to the Niobium cavities and massive aluminum rings as gaskets. The bellows are being fabricated by BINP, Novosibirsk and delivered to CEA after particle cleaning at DESY [12].

The production of these units has been started. The first components have been delivered for the installation into the pre-series modules.

The rf power input coupler has two ceramic windows [6]. This design enables the complete closure of the cavity in the clean-room by mounting the coupler up to the first window, thus preventing any contamination during further assembly of the module. Between the two windows a common vacuum for all eight couplers is established by a sputter ion pump and a Titanium sublimation pump (TSP).

The coupler pump line systems are fabricated at BINP. After particle-cleaning at DESY, the items are delivered to CEA. The TSP and the sputter ion pumps are purchased by DESY and delivered to CEA. The delivery of the components started.

HOM AND PU ANTENNAS

HOMs are excited by beam and can spoil the beam quality [13]. Therefore, every cavity contains two HOM couplers, one at each end, to filter these modes and couple them out via coaxial antennas and cables transferring them to loads, located outside the module [14]. In addition, each cavity is equipped with a PU antenna taking a small portion of the rf power for the rf control electronics regulating amplitude and phase of the accelerating rf mode.

NCBJ (former INS-Swierk) provides, as in-kind contribution, 1616 HOM and 808 PU antennas and all cables and feed-throughs for their output lines. More than 200 sets are already on stock. They will be followed by 105 sets delivered every 3 months.

CRYOSTATS

The TESLA cryostat technology [15] incorporates the string of accelerating cavities and a cold focusing magnet together with all cryogenic process lines avoiding separate cryo-lines. Cryogenic boxes at the beginning and the end of a chain of several modules are used for the helium supply. This leads to a compact arrangement of the accelerating cavities and comparatively low cryogenic losses and is well suited for longer linacs like the XFEL.

The cryostats for the XFEL [16] are provided by IHEP, Beijing and EZ. The cryostat delivery from EZ to CEA already started with a rate of two per month. The IHEP cryostats will first arrive at DESY before being transported to CEA. IHEP starts the cryostat delivery in October.

STRING AND MODULE ASSEMBLY

An assembly infrastructure, called the 'XFEL Village', has been set up at CEA and is used by an industrial operator for the integration of the accelerator modules under CEA supervision. Two lines of seven workstations, designed to produce one module per week, will gradually integrate the different components of the module over seven weeks. Work will begin in the 112 m^2 ISO4 clean room with the assembly of the cold coupler parts to the cavities, and then the cavities and quadrupole package in a string. After string roll-out, five workstations are designed for cryostat integration, cavity alignment, ISO5 assembly of power coupler parts [17] and final inspection and shipment.

Copyright © 2012 by the respective authors — cc Creative Commons Attribution 3.0 (CC BY 3.0)

The industrial operator contract has been awarded to the company ALSYOM. The transfer of knowledge will occur through the assembly of three pre-series modules until March 2013 when ramping up the assembly rate will start with the series modules.

MODULE OPERATION TESTS

After transportation [18], the accelerator modules will be received at the AMTF by the Polish team from IFJ-PAN, Kraków. The team performs the complete test cycle starting with the entrance inspection and installation of each module at one of the three module test stands operating in parallel. The functional test includes the cool down to 2 K, the measurements of the cryogenic losses and the rf operation of all cavities to determine all required parameters like the maximum cavity gradients and the levels where field emission starts [19, 20]. After warm up the modules are handover to the next work package for wave guide installation.

The training of IFJ-PAN personnel for the assembly and testing of the modules is actually done at DESY's Cryomodule Test Bench (CMTB) and is well advanced, likewise the software and testing procedures developed by the team.

RF CONTROL TESTS

Stable rf field provided by the digital rf control is essential for the XFEL electron beam quality. Good knowledge of parameters permits the adjustment of the rf control for optimal performance. At the AMTF the subsequent parameters will be determined: the individual cavity quench voltage, the range and characteristic of the cavity slow tuning motors, the performance of the piezo actuators and sensors, the sensitivity to microphonics, the identification of other fundamental modes, the performance and characteristics of the cavity loaded Q versus the coupler motor position and the Lorentz force detuning compensation. Finally, nominal module operation will be established. A full description of the LLRF tests is given in [21].

WAVE GUIDE INSTALLATION

The variation of the cavity performance of each module will be accommodated by tailoring the rf power distribution via the wave guide system [22]. By doing so, the average accelerating voltage provided by each module is optimized. The wave guide systems will be assembled and tested in a separate infrastructure in the AMTF hall and also attached in the AMTF to the modules before the installation in the XFEL tunnel.

INFORMATION AND PROCESS SUPPORT

Module integration needs reliable procedures for gathering, processing and archiving the complete mandatory fabrication information. A solution has been established based on the concepts of tracking and tracing [23] and with the help of a central collaboration and documentation platform, the DESY Engineering Data Management System [24].

SUMMARY AND OUTLOOK

The work on the XFEL accelerating modules enters now the phase when all the series productions of the different components need to start to supply the final assembly at CEA with sufficient parts. Deviations of some components and infrastructure installations from the original schedule are addressed together with corrective measures. Furthermore, the preparation phase for the module series assembly started and the training of the personnel performing the module operation tests is well advanced. In all, quite some international machinery starts working for the production of the XFEL accelerating modules.

ACKNOWLEDGEMENTS

The authors acknowledge the significant contributions from numerous colleagues at all institutes joining the consortium for the construction of the European XFEL cold linac. Many people from industry are contributing to this effort as well.

REFERENCES

[1] TESLA - Collaboration, TESLA 1993-01
[2] The TDR of the European XFEL, Ch. 4: XFEL accelerator
[3] L. Lilje et al., Nucl. Instr. Meth. A524 (2004)
[4] D. Reschke, SRF2011, MOIOA01
[5] F. Toral et al., IEEE Trans. Appl. SC, Vol. 19, p. 1136 (2009)
[6] B. Dwersteg et al., SRF2001, PT001
[7] D. Kostin, W.–D. Möller, LINAC 2004, MOP49
[8] S. Prat, W.-D. Möller, D. Kostin, SRF2007, TH202
[9] P. Leconte et al., TESLA 1993-29
[10] B. Keil et al., IPAC'10, MOPE064
[11] K. Zapfe-Düren et al., SRF'97, C06
[12] K. Zapfe et al., SRF2003, TUP50
[13] J. Sekutowicz, EuCARD-BOO-2009-005
[14] J. Sekutowicz, SRF'93, SRF93G04; TESLA 1994-07
[15] C. Pagani, CEC1999, THA005
[16] B. Petersen, EPAC2008, WEIM03
[17] C. Madec, LINAC 2012, THPB083 (this conference)
[18] S. Barbanotti et al., PAC'09, TU6RFP050
[19] D. Kostin et al., SRF2009, TUPPO005
[20] D. Kostin et al., SRF2011, MOPO010
[21] J. Branlard et al., IPAC'12, THEPPB014
[22] V. Katalev, S. Choroba, PAC'07, MOPAN015
[23] L. Hagge et al., IPAC 2012, WEPPC004
[24] L. Hagge et al., IPAC 2011, THPC080

Copyright © 2012 by the respective authors — cc Creative Commons Attribution 3.0 (CC BY 3.0)

ANALYZING SURFACE ROUGHNESS DEPENDENCE OF LINEAR RF LOSSES *

C. Xu[1,2#], M. J. Kelley[1,2], C. E. Reece[1]
[1]Thomas Jefferson National Accelerator Facility, Newport News, VA 23606
[2]College of William and Mary, Williamsburg, VA 23187

Abstract

Topographic structure on Superconductivity Radio Frequency (SRF) surfaces can contribute additional cavity RF losses describable in terms of surface RF reflectivity and absorption indices of wave scattering theory. At isotropic homogeneous extent, Power Spectrum Density (PSD) of roughness is introduced and quantifies the random surface topographic structure. PSD obtained from different surface treatments of niobium, such as Buffered Chemical Polishing (BCP), Electropolishing (EP), Nano-Mechanical Polishing (NMP) and Barrel Centrifugal Polishing (CBP) are compared. A perturbation model is utilized to calculate the additional rough surface RF losses based on PSD statistical analysis. This model will not consider that superconductor becomes normal conducting at fields higher than transition field. One can calculate the RF power dissipation ratio between rough surface and ideal smooth surface within this field range from linear loss mechanisms.

INTRODUCTION

RF loss induced by roughness is considered in many RF components, such as micro strip transmission line, wave guide and RF resonator. It can be understood as the RF electromagnetic field penetrates the surface and there the induced current will pass and cause RF loss. [1] However, in a RF wave view, the incident wave is reflected, scattered and absorbed by the rough surface. Inside of a resonator, the reflected, scattered wave contributes to standing wave field, while the absorbed RF wave is attributed to the RF surface loss. These two perspectives may both be used to describe the same RF loss.

In a resonator, only several specific RF standing wave modes can exist to meet the boundary condition which is the resonator geometry. The electric and magnetic field at one location is combination a of EM components of those plane waves. Within the resonator, E and M are separated in space and interchange their energy over a distance. Thus the peak E and M field are always not the same location. With special EM setup, TE, TM, TEM are used to describe the EM field direction, if presumed direction is beam axis. In some sense, it is very tedious and difficult to expand the field into plane wave expansion. If so, the incident direction should also be from all directions. Therefore, a RF loss calculation method is required and independent of direction. It also covers all frequencies or wavelengths.

METHODOLOGY

A rough surface will cost more RF loss. [2] One simple reason is that the surface current have more current path. In another word, the RF wave as more radiation absorption surface. This RF loss will contribute into power consumption and aggravate the quality factor.

If we consider a 2D random rough surface Z= f(x) in Fig.1. We can expand the magnetic field into Fourier series as in x and z direction. [3]

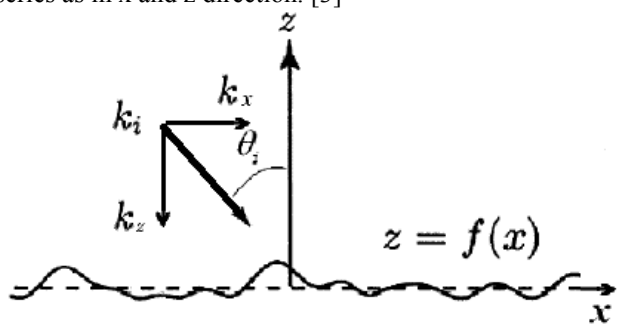

Figure 1: A plane wave incident impinging on a rough surface with incident angle θ_i.

$$\psi(x,z) = \int_{-\infty}^{\infty} dk_x \exp(-jk_x x + jk_{1z} z)\,\tilde{\psi}(k_x)$$

Where $k_{1z} = \sqrt{k_1^2 - k_x^2}$ and $k_1 = \frac{1-j}{\delta}$. Here δ is the skin depth $\delta = \sqrt{\frac{2}{\omega\mu\sigma}}$ and σ is the superconducting conductivity. The physics behind this equation is that the total magnetic field is combination of field component at each spatial wavelength. In another word, the total magnetic field can be expanded into magnetic contribution from each wavelength in spatial frequency.

If we use a second order small perturbation methods, setting

$$\tilde{\psi}(k_x) = \tilde{\psi}^{(0)}(k_x) + \tilde{\psi}^{(1)}(k_x) + \tilde{\psi}^{(2)}(k_x)$$

In first approximation, a fixed constant magnetic field H_0 is applied on the surface. Thus, the equation above becomes:

$$H_0 = \int_{-\infty}^{\infty} dk_x \exp(-jk_x x + jk_{1z} f(x))\,\tilde{\psi}(k_x)$$

Basically, we have done a Fourier transform to redistribute the magnetic field into each surface spatial wavelength in x direction.

By balancing this equation to second order, we obtain:

*Work supported by Jefferson Science Associates. xuchen@jlab.org

Copyright © 2012 by the respective authors — cc Creative Commons Attribution 3.0 (CC BY 3.0)

$$\tilde{\psi}^{(0)}(k_x) = H_0\delta(k_x)$$
$$\tilde{\psi}^{(1)}(k_x) = -jk_1H_0F(k_x)$$
$$\tilde{\psi}^{(2)}(k_x) = H_0\int_{-\infty}^{\infty}dk_x'F(k_x-k_x')F(k_x')\left(-k_1k_{1z}'+\frac{k_1^2}{2}\right)$$

For now, we have calculated the RF magnetic field on this given surface. The power absorbed by the conductor, for a given width w in y direction and length L in x direction, can be calculated from the Poynting vector.

$$P_a = \frac{w}{2\sigma}\mathrm{Re}\int ds\frac{\partial\psi}{\partial n}\psi^*$$

We simplify the results:

$$\langle P_a\rangle = \frac{wL}{2\sigma\delta}|H_0|^2\left\{1+\frac{2h^2}{\delta^2}\left[1-\frac{\delta}{h^2}\int_{-\infty}^{\infty}dk_xW(k_x)\mathrm{Re}\sqrt{k_1^2-k_x^2}\right]\right\}$$

In order to get rid of the external field, we normalize the power dissipation with that of a smooth surface.

$$\frac{\langle P_a\rangle}{P_{a,\mathrm{smooth}}} = 1+\frac{2h^2}{\delta^2}-\frac{4\pi}{\delta}\int_0^{\infty}dk_\rho\left\{k_\rho W_{2D}(k_\rho)\mathrm{Re}\sqrt{\frac{-2j}{\delta^2}-k_\rho^2}\right\}$$

$W_{2D}(k_\rho)$ is the 2D PSD from an isotropic surface.

Researcher have combined TM and TE wave mode into this equation into a 2D problem. They also avoid the assumption that surface field is a constant.

One should note:

1. The RMS and decay parameters (penetration depth) ratio, h/δ, is critical for characterizing the increased losses.

2. Third term reduces to h^2/δ^2, when the k_ρ is small. The second/third term have net contribution if $1/\delta$ and k_ρ are comparable.

3. Generally, higher $W_{2D}(k_\rho)$ brings additional loss.

APPLICATION TO SRF SURFACES

To obtain more accurate RF loss ratio, one needs to extend the PSD into as broad a frequency range as possible. Since all characterization method shave cut-off frequencies, one can at most get an extended PSD. The recent extended frequency range is 1/1.2 cm^{-1}–1/10 nm^{-1}, over 6 decades, with white light interferometry and atomic force microscopy. Because the magnetic field is expanded into horizontal spatial wavelength, the PSD frequency should cover the RF wavelength and beyond. Though an approximation methods is introduced by using Inverse Abel transforms to extend limited range, but obtaining 1D PSD with wider frequency range could improve later calculation accuracy.

$$<W(k_\rho)^{2D}>=-\frac{1}{\pi}\times\int_{k_\rho}^{\infty}\frac{dk_\rho}{\sqrt{k_x^2-k_\rho^2}}\frac{d}{dk_x}<W(k_x)^{1D}>$$

$$<W(k_x)^{1D}>=2\times\int_{k_x}^{\infty}\frac{k_\rho dk_\rho}{\sqrt{k_\rho^2-k_x^2}}<W(k_\rho)^{2D}>$$

This transformation also permits the transformation of the high-frequency behavior of the spectra of one dimensionality to be transformed into the high-frequency behavior of the other without knowledge of their low-frequency behavior.

We investigate SRF surfaces with current polishing methods and materials polished are large/fine/single grain Nb sheets. Buffered chemical polishing, electropolishing and mechanical centrifugal barrel polishing samples are characterized by Atomic Force Microscopy (AFM) and White light interferometry (WLI). Note that these two characterizations have different lateral resolutions and scan scopes which determine the spectral frequency ranges.

1D averaged PSD is calculated by following the routine introduced previously. [4] Such routine includes proper detrending, windowing and averaging.

In this study, the R_q and PSD are used to derive power ratio. Rq value from 4 different locations on each sample is averaged and summarised in Table 1.

Table 1: Averaged R_q with AFM and WLI

Samples	Single crystal		"Standard" fine-grained			
Treatment	After30 µm BCP	Nano polished	+100 µm BCP	+50 µm EP	Centrifugal Barrel Polishing (CBP)	
					Fine Grain	Large Grain
Atomic force microscopy ~5×5µm						
R_q(nm)	1.99	2.84	4.89	4.40	2.76	1.20
Atomic force microscopy ~100×100µm						
R_q(nm)	7.05	13.5	392.90	74.30	70.8	7.71
White light interferometry ~234×312µm (20x magnification)						
R_q (nm)	35.7	1.63	1500.4	291.7	151.8	13.5
White light interferometry ~930×1244µm(5x magnification)						
R_q (nm)	391	5.24	2008.5	642.8	335.5	49.0

One can generalize that Rq value decrease from BCP>EP>CBP Large grain> CBP Fine grain> Single crystal>Nanopolishing samples.

Averaged 1D PSD from AFM/WLI are combined in Fig.2.

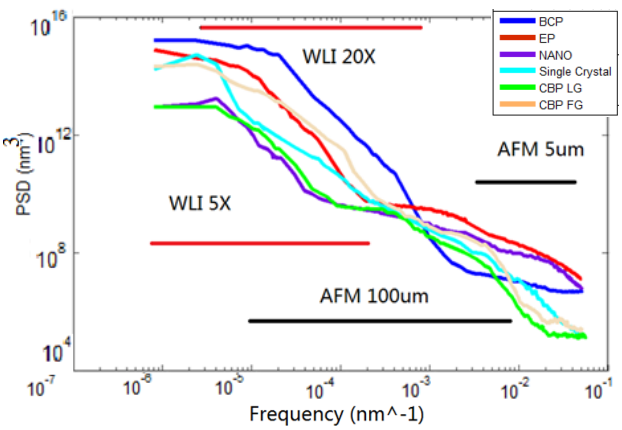

Figure 2: Joint 1D PSD models from AFM/WLI are shown and the characterization frequency domains are indicated.

Copyright © 2012 by the respective authors — cc Creative Commons Attribution 3.0 (CC BY 3.0)

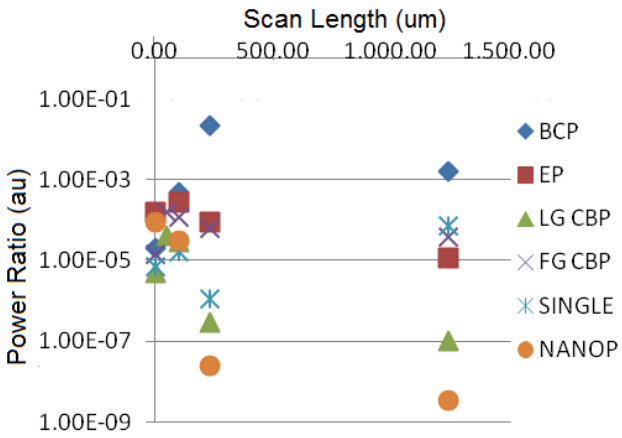

Figure 3: Power Ratio calculated from 1D PSD.

The power ratio is shown in Fig.3 and by inverse Abel transform, the 2D PSD are shown in Fig.4.

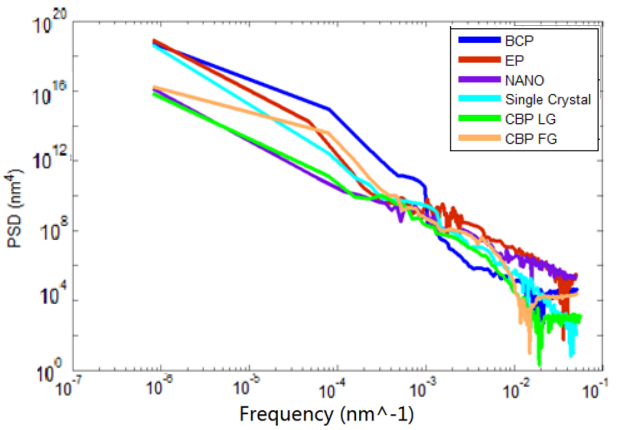

Figure 4: 2D PSD calculated from various surfaces.

Power ratio index are illustrated in Fig.5.

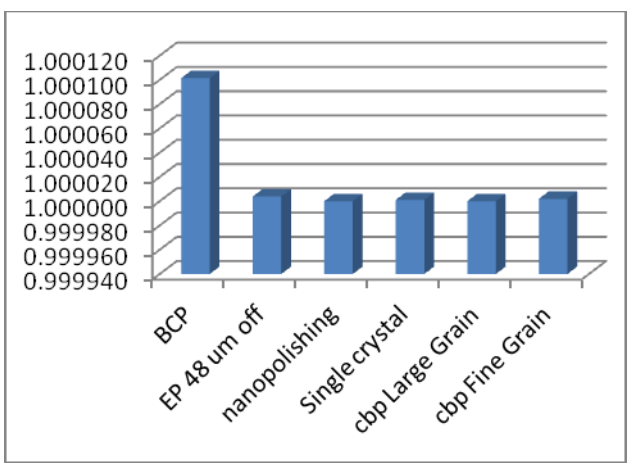

Figure 5: Power Ratio from 2D isotropic PSD.

BCP surface show higher ratio, but other surfaces suggest almost the same close to 1.

DISCUSSION

One can see from power ratio equation that the last term is an integration of 2d PSD.

$$\frac{\langle P_{a,\mathrm{rough}}\rangle}{P_{a,\mathrm{smooth}}} = 1 + \frac{2h^2}{\delta^2} - \frac{4\pi}{\delta}\int_0^\infty dk_\rho \left\{ k_\rho W_{2D}(k_\rho)\,\mathrm{Re}\sqrt{\frac{-2j}{\delta^2} - k_\rho^2} \right\}$$

Without the Re(…), the integrand is simply the square of RMS height. One can infer that if the k_ρ is small enough compared with $2/\delta$, then the Re(…) term reduced into $1/\delta$. In that limit the second and third terms cancel each other. The total power ratio becomes one. This gives substantiates the interpretation that features at larger wavelength have less RF power loss than the small high frequency features. Another understanding is that only features with lateral extent comparable to the penetration length give a significant effect on the additional power loss ratio. Applying this analysis to variously prepared niobium surfaces typical of those in SRF cavities, we find that linear RF losses depend negligibly on roughness for any of the characteristic surfaces considered. On the other hand, SRF materials are particularly susceptible to non-linear and temperature-dependent losses. The non-linear losses are reflected in the observed Q drop with increasing surface magnetic field. We are examining the influence of topography on such losses separately [5].

CONCLUSION

Spectral study suggested that surface roughness doesn't contribute much in the linear RF loss, because current practical surface a smooth enough at a wavelength closed to penetration depth.

ACKNOWLEDGMENT

Authored by Jefferson Science Associates, LLC under U.S. DOE Contract No. DE-AC05-06OR23177. The U.S. Government retains a non-exclusive, paid-up, irrevocable, world-wide license to publish or reproduce this manuscript for U.S. Government purposes.

REFERENCES

[1] H. Padamsee. RF Superconductivity. 1nd Edition (Wiley - VCH, New York 2011).
[2] L. Tsang. Scattering of Electromagnetic Waves, Theories and Applications. (John Wiley & Sons, Seattle 2004).
[3] Xiaoxiong Gu, Leung Tsang and Henning Braunisch. IEEE Microwave And Wireless Components Letters, Vol. 17, No. 7, July 2007 pp486
[4] Chen Xu, Hui Tian, Charles E. Reece and Michael J. Kelley. PRST-AB. 14, (2011) pp.123501.
[5] Chen. Xu, *et al.* in *Proc. Int. Part. Accel. Conf. 2012*, (2012). New Orleans, Louisiana: p. 2188-2190.

Copyright © 2012 by the respective authors — cc Creative Commons Attribution 3.0 (CC BY 3.0)

LLRF SYSTEM IMPROVEMENT FOR HLS LINAC UPGRADE*

G. Huang, H. Lin, Y. Liu, W. Zhou, K. Jin, D. Jia,
NSRL USTC Anhui Hefei 230029 P. R. China

Abstract

The linac beam energy will be upgraded from 200MeV to 800MeV, in order to realize the full-energy injection of storage ring at Hefei Light Source. This paper introduces the improvement of linac LLRF system, which is composed of phase reference and driver signal transmission and distribution, phase stability system, phase reversal device for SLED. The LLRF prototype has been constructed, and the test results are described in the paper.

800MEV LINAC INTRODUCTION

The layout of 800MeV linac is shown in Figure 1, and the parameters in Table 1.

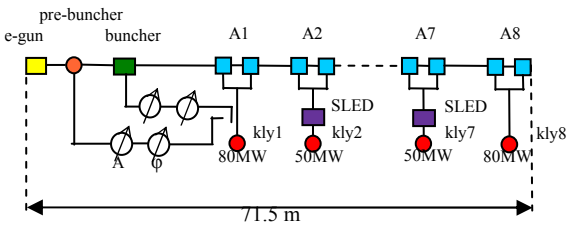

Figure 1: 800MeV Linac layout

Table 1: Linac parameters

	200 MeV	800 MeV
Beam current	50mA	1 A
Beam pulse	0.1-1μs	1 ns
Repetition /Hz	0.5	1
Energy spread	0.8%	0.5%
RF freq. / MHz	2856	2856
Acc. section	4	8
klystron	5 (20MW)	6 (50MW) +2 (80MW)
SLED	0	6

The 800MeV Linac is composed of injector (prebuncher, buncher) and eight accelerating sections. the prebuncher is a single resonant cavity, and the buncher is a 1-meter travelling wave accelerating construct. Each accelerating section contains two 3-meter constant gradient travelling wave accelerators. The design energy of linac is 1GeV, one accelerating section may stand by when linac beam energy is 800MeV.

PHASE REVERSAL DEVICE FOR SLED

Six SLEDs will be installed in RF stations from the 2nd to 7th. The SLED parameters are listed in table 2, and the test result of the SLED prototype is shown in Figure 2.

Table 2: Parameters of SLED

Freq. /MHz	2856
Q_0	~100000
β	5
Insert Loss /dB	0.2
Tuning range /kHz	± 500
Pulse time /μs	4
Power Gain /dB	7
VSWR	1.05

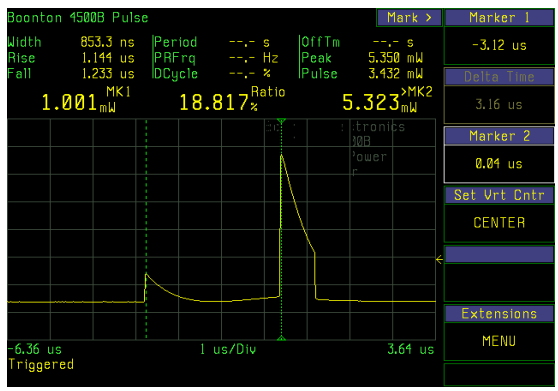

Figure 2: SLED RF output profile

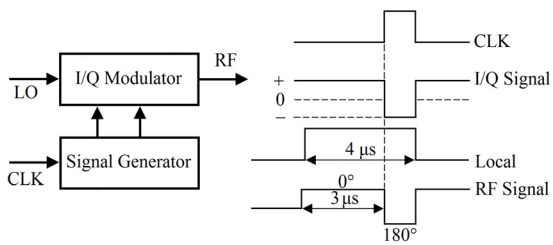

Figure 3: Schematics of the 180° phase reversal system

Table 3: Parameters of IDOH-01-45

Carrier (LO) Freq. /MHz	2000−4000
RF Freq. /MHz	LO ± 100
I & Q Freq. /MHz	DC-100
Conv. Loss /dB	10
Amplitude Balance /dB	1.0
Max. Phase Balance /°	8.0
Isolation /dB	30
VSWR min.	1.5:1

The phase reversal device for SLED showed in figure 3 is consist of fast pulse signal generator and I/Q modulator. The I/Q Modulator is the IDOH-01-45 manufactured by Pulsar Microwave company, and the parameters are

*Work supported by NFSC-CAS(11079034)
grhuang@ustc.edu.cn

Copyright © 2012 by the respective authors — cc Creative Commons Attribution 3.0 (CC BY 3.0)

shown in table 3. The I/Q pulse voltage signals is generated by Agilent 33250A , which voltage resolution is 0.1 mV. The voltage applied to the I/Q port of Modulator is about ±500 mV, so the voltage accuracy could be 0.02%.

Figure 4 shows the stability and accuracy test for phase reversal device. In 2700 seconds, the average reversal phase is 180.5°, phase error (rms) is less than 1°, and maximum phase deviation is 1.5°.

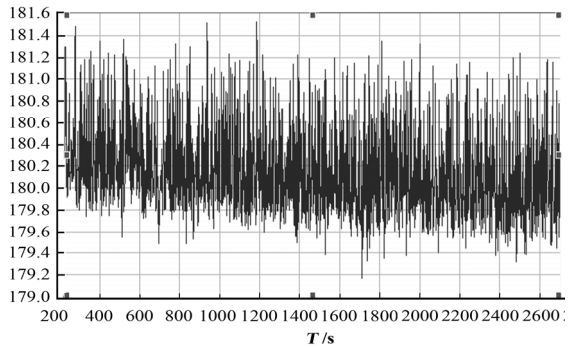

Figure 4: Phase reversal system test results

LINAC RF PHASE STABILITY

The most of new accelerator and upgrade of old one tend to select the digital LLRF system for phase stability [1-4]. But limited by budget, a simple analogy LLRF system is used for HLS 800MeV linac phase measure and control [5]. The analogy system is good enough if the linac is only used as an injector. The design requirements for stability of accelerating phase is ± 1°.

The RF phase stability system contains I/Q demodulator, data acquisition equipment, electronic phase shifter (EPS). The data acquisition equipment is Pico4424 virtual oscilloscope, I/Q demodulator is IDOH-01-458, the type of electronic phase shifter is S7-H67-444A (Pulsar Microwave Company), whose voltage set range is 0-10 V, corresponding phase shift is 360°. The control voltage comes from one 16 bits DAC PCI board.

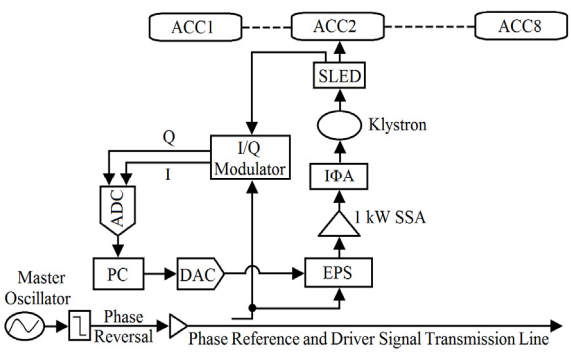

Figure 5: Diagram of phase stability system

The resolution of Pico4424 virtual oscilloscope is 16 bit， and the minimum resolution voltage is 0.03 mV under the voltage range set at 500 mV. When the LO signal of IDOH-01-458 set to 10 dBmW, RF signal is about 0 dBmW, the voltage rang of I/Q output signal is about ± 200 mV. The phase of RF signal changes 0.1°, I/Q voltage vary at least 0.2 mV, which is larger than Pico4424 resolution. Therefore the phase measuring resolution can reach 0.1°.

In the laboratory environment (room temperature stable, no external noise interference), we made a phase stability system prototype on the table test, test device is shown in Figure 7. The RF output of EPS connects to the RF signal input of I/Q modulator, to form the feedback loop. Figure 8 is open loop phase measuring results. The test lasted 2100 second, the rms error of phase measurement is less than 0.1°, which shows that the phase measurement resolution is ±0.1°. The maximum phase deviation is ±0.15 °, it means the measuring precision can reach ± 0.2°. Figure 9 shows the phase closed loop test, the phase feedback control accuracy is set to ± 0.5°. In order to avoid feedback overshoot even or self-excited, each feedback turn adjusts 30 ~ 90% of phase deviation. Setting up different target phase by control program, the loop response to different phase deviation 1°, 2°, 5°, 10°, and 20° has been examined. The loop feedback is stable without overshoot under any phase deviation.

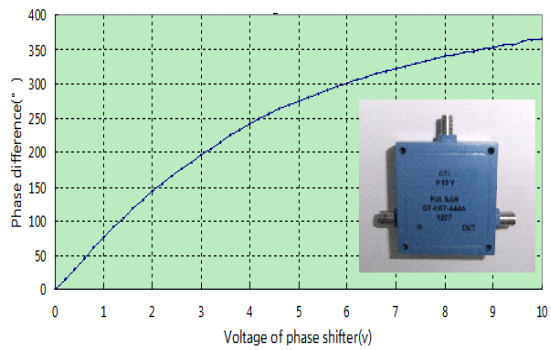

Figure 6: Phase shift *vs* control voltage

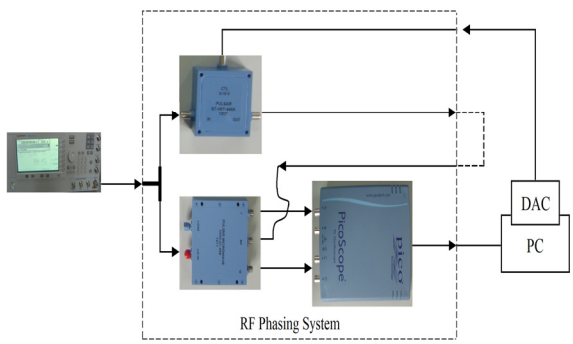

Figure 7: Self-test for RF phase stability system

Copyright © 2012 by the respective authors — cc Creative Commons Attribution 3.0 (CC BY 3.0)

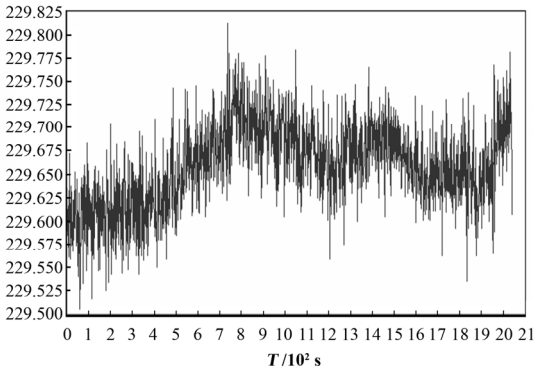

Figure 8: Phase measurement resolution

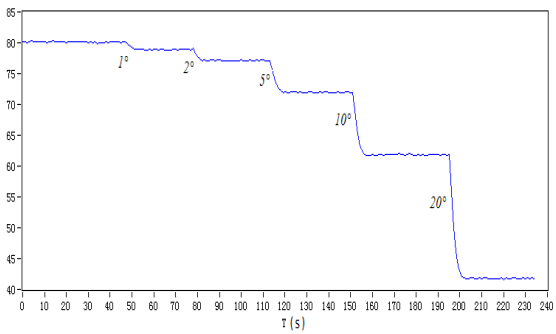

Figure 9: Loop response to different phase deviation

We tested the phase stability system in the No.1 RF station of 200MeV Linac. As shown in Figure 10, the loop is set to open before 1700 second, the RF phase drifted 1.3°. After then the loop is closed, the stable phase set at 87°, and the closed-loop control accuracy is ± 0.5° in the first 3000s, after that is ± 0.3 °. The result shows that the phase error can be controlled in ± 0.5°, but failed in ± 0.3°, since the online phase noise is ± 0.3° (Figure 11). Therefore the online closed-loop phase stability is ± 0.5 °.

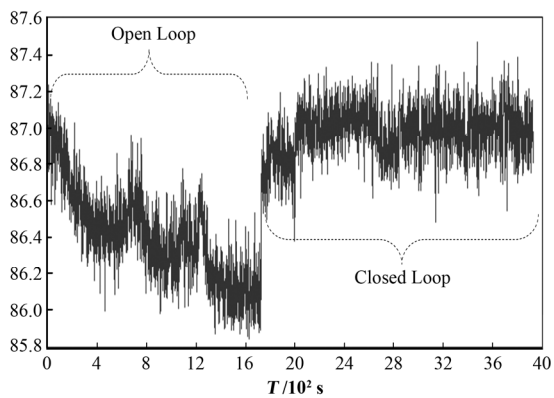

Figure 10: RF stability system online experiment

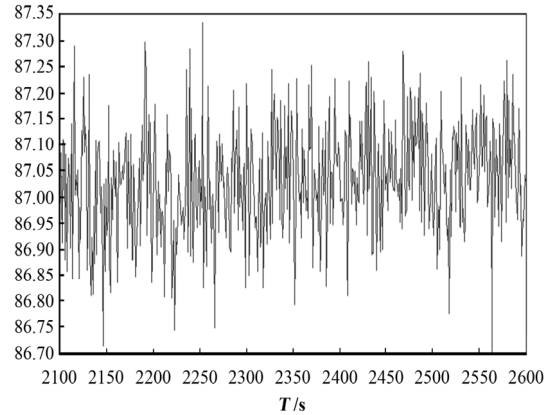

Figure 11: Background noise of online measurement

REFERENCES

[1] C. X. Yin, D. K. Liu, L.Y. Yu, "Digital phase control system for SSRF linac", Proceedings of ICALEPCS07, Knoxville, Tennessee, USA.

[2] T. Plawski, J. Delayen, C. Hovater, T. Powers. "Low level rf system for Jefferson lab cryomodule test", Proceedings of the 2003 Particle Accelerator Conference.

[3] H. Klingbeil et al., "New digital low-level rf system for heavy-ion synchrotrons", Physical review special topics - accelerators and beams 14, 102802 (2011).

[4] M. Pekeler, B. Aminov, A. Borisov, S. Kolesov, H. Piel. "Development of low level rf control systems for superconducting heavy ion linear accelerators", PAC' 05.

[5] M. Hou, Z. Geng, "Construction of the Phasing System for BEPC Linac", High energy physics and nuclear physics(Chinese), Vol. 31, No. 4, Apr., 2007.

Copyright © 2012 by the respective authors — cc Creative Commons Attribution 3.0 (CC BY 3.0)

BUNCH-BY-BUNCH PHASE MODULATION FOR LINAC BEAM LOADING COMPENSATION*

G. Huang, Y. Liu, H. Lin, W. Zhou, K. Jin, D. Jia,
NSRL USTC Anhui Hefei 230029 P. R. China

Abstract

If the linac is loaded by a high intensity, long pulse multi-bunch beam, the energy of the beam drops with time during the pulse within the accelerating structure filling time [1, 2]. The bunch phase modulation method is introduced to compensate the beam loading effect. In this method the bunch phase in the RF accelerating field is changed bunch-by-bunch, the bunch energy gain in the RF filed gradually grows up, which cancels out the drop due to beam loading. The relationship between the beam phase distribution and the linac parameters is calculated in this paper.

BEAM LOADING EFFECT

When a bunch train passes through a travelling wave accelerating structure, the loaded accelerating fields U_{acc} is defined by [3].

$$U_{acc}(t) = U_{rf}(t)\cdot\cos\varphi - U_b(t) \quad (1)$$

Where U_{rf} is the accelerating voltage conducted by input RF power(unloaded accelerating voltage), φ is the bunch phase in RF filed, U_b is the beam loading voltage,

There are two kinds of travelling-wave accelerating structure–constant impedance and constant gradient, normally used in linac. In case of constant impedance structure, the U_{rf} and U_b is expressed by

$$U_b(t) = \begin{cases} I\cdot R_M[(L-z-\frac{1}{\alpha})(1-e^{-\alpha z})+z] & t<T_F \\ I\cdot R_M\cdot L(1-\frac{1-e^{-\tau}}{\tau}) & t\geq T_F \end{cases} \quad (2)$$

$$U_{rf}(t) = \begin{cases} \sqrt{2\alpha P_0 R_M}\cdot L(\frac{1-e^{-\alpha\cdot v_g\cdot\tau}}{\tau}) & t<T_F \\ \sqrt{2\alpha P_0 R_M}\cdot L(\frac{1-e^{-\tau}}{\tau}) & t\geq T_F \end{cases} \quad (3)$$

$$z = v_g\cdot t \qquad \tau = \alpha L$$

Where I is beam current, TF is the filling time, RM is shunt impedance per length, L is the length of accelerating structure, α is attenuation coefficient, P_0 is RF input power, vg is group velocity.

U_b is the sum of each bunch induced voltage U_i. The attenuation and superposition of bunch induced voltage is shown in Figure 2.

$$U_b = \sum_{i=1}^{n} U_i \quad (4)$$

*Work supported by NFSC-CAS(11079034)
grhuang@ustc.edu.cn

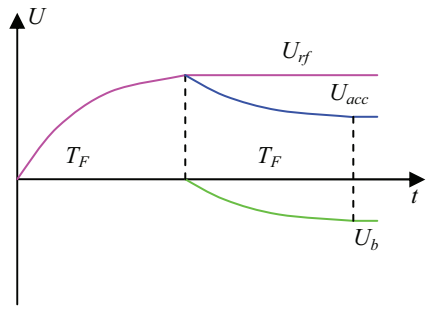

Figure 1: Transient beam loading effect.

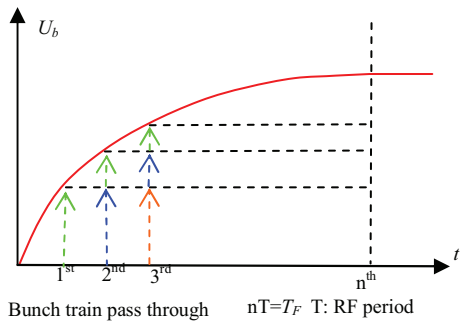

Figure 2: Attenuation and superposition of bunch induced voltage.

Some methods are used to compensate the transient beam loading. For a short pulse beam, the beam is injected before RF power is filled up (early injection method) [4]. In case of long pulse beam, the amplitude or phase of RF power is ramped to keep the U_{acc} constant during the filling time of beam injection [5, 6].

PRINCIPLE OF PHASE MODULATION METHOD

We propose the bunch phase modulation method to compensate the transient beam loading. The idea is that the bunch phase (φ) in the RF accelerating filed is changed bunch-by-bunch, therefore the bunch energy gain in the RF filed gradually changes. If the trends of the gain change is exactly contrast of the rise up of beam loading, all bunches will obtain the same energy.

Since the bunch phase shifts continuously, the beam loading is the vector superposition of all bunch's induced voltage, which is shown in Figure 4.

Copyright © 2012 by the respective authors — cc Creative Commons Attribution 3.0 (CC BY 3.0)

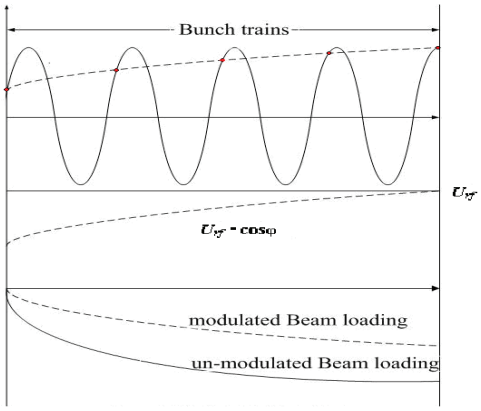

Figure 3: Principle of bunch phase modulation.

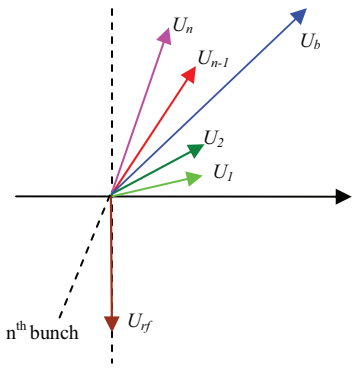

Figure 4: Vector diagram of phase modulated bunch.

CALCULATION OF THE BUNCH PHASE DISTRIBUTION

In order to calculation the beam loading of multi–bunch with different phase, we define

$$u_n = U_b(nT) - U_b((n-1)T) \tag{5}$$

Where T is RF period time.

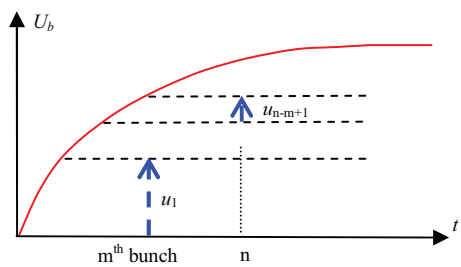

Figure 5: Bunch induced field attenuating with time.

When a bunch passes through the accelerating structure, its induced voltage in the structure is u_1, and then attenuates to u_n after nT times. So that at the moment when the nth bunch enter the accelerating structure, the voltage of the mth bunch is

$$u_n^m = u_{n-m+1} \tag{6}$$

All bunches will obtain the same energy gain U_{const}.

For the No.1 bunch with phase φ_1

$$U_{const} = U_{rf}\cos\varphi_1 - u_1$$

and the No.2

$$U_{const} = U_{rf}\cos\varphi_2 - u_1 - u_2\cos(\varphi_1 - \varphi_2)$$

Therefore the No. n

$$U_{const} = U_{rf}\cdot\cos(\varphi_n) - \sum_{i=1}^{n} u_n^i \cdot \cos(\varphi_i - \varphi_n) \tag{7}$$

A MATLAB code is programmed to find out the optimum phase distribution, the parameters of constant impedance accelerating structure listed in Table 1 come from the HLS (Hefei Light Source) 200 MeV Linac. The beam pulse length is assumed as the filling time (TF), the relative bunch amount is 2370. The calculating result is shown in Fig. 6-8.

Table 1: Accelerator Parameters

L /m	3
T_F/μs	0.83
α	0.177
Freq. /MHz	2856
R_M / MΩ/m	60
U_{rf} /MV	30MV

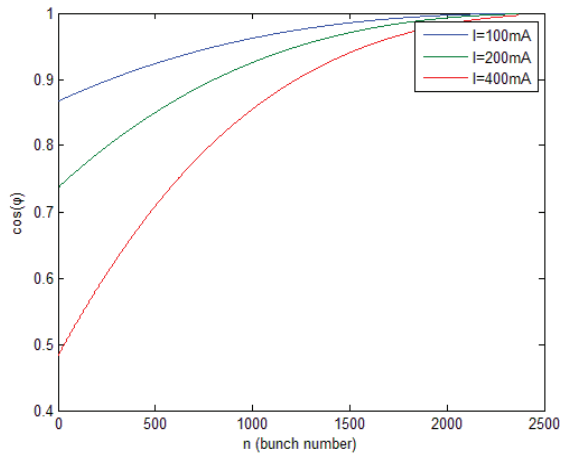

Figure 6: cosφ *vs* n

In Figure 8 the blue line (100mA modulated) is nearly coincident with the red one (100mA un-modulated). It shows that when the beam intensity is lower, the phase difference between bunches is so small that the vector superposition is similar to the direct superposition. In this case the bunch phase can simply calculated by

$$\cos\varphi_n = \frac{U_{rf} - U_b(T_F)}{U_{rf} - U_b(nT)} \tag{8}$$

Copyright © 2012 by the respective authors — cc Creative Commons Attribution 3.0 (CC BY 3.0)

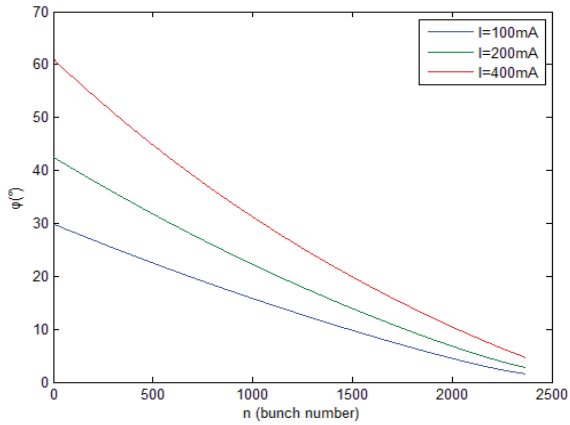

Figure7: bunch phase distribution.

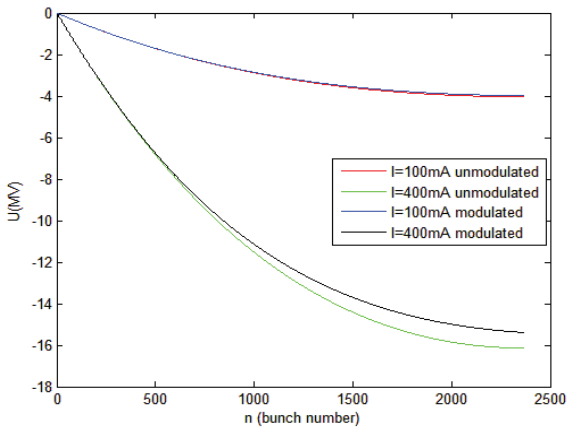

Figure 8: modulated and un-modulated beam loading.

CONCLUSIONS

The bunch by bunch phase modulation is a very interesting method to compensate the transient beam loading. The advantage of this method is that the compensation is global. If all of the accelerating sections in a linac adopt the identical structure, their beam loading will be compensated simultaneously. It would be a simple and cheap resolution for the larger linac such as linear collider. But how to realize the bunch phase modulation is a very complicated problem. At present we are developing a bunching system with the low-Q and wide-band cavity, the rf phase modulated signal can apply fast on it, the bunch phase will be modulated in the bunching procession.

REFERENCES

[1] S.H. Kim, et al., "Transient beam loading compensation in L-band travelling wave accelerating structure with intense electron beam", LINAC2010.

[2] C. Adolphsen, et al., "Beam Loading Compensation in the NLCTA", PAC97, Vancouver, BC, Canada.

[3] C. Nantista, C. Adolphsen, Calculating RF Profiles for Beam Loading Compensation of Arbitrary Current Profiles, NLC-note #25, 1997

[4] Z. Li, et al., "A combined ΔT +ΔF beam loading compensation scheme for power saving", PAC99.

[5] Z.D. Farkas and P.B. Wilson. Ramping Profile for Exact Beam Loading Energy Compensation in the NLC Detuned Structure, NLC-Note #4, SLAC, 1994.

[6] M. Satoh, et al., "Beam test of initial beam loading compensation for electron linacs", Proc. EPAC02, Paris, France, June 3-7, 2002.

Copyright © 2012 by the respective authors — cc Creative Commons Attribution 3.0 (CC BY 3.0)

RF CHARACTERISTIC STUDIES ON THE WHOLE ACCELERATING STRUCTURE FOR THE BEPCII LINEAR ACCELERATOR

S. Pei#, J. Zhang, M. Hou, X. Li, IHEP, Beijing 100049, P. R. China
B. Wang, SINAP, Shanghai 201800, P. R. China

Abstract

An accelerating structure is one device to boost the particle energy. 2856 MHz 3 m long travelling wave disk-loaded accelerating structure is applied in BEPCII linac, its RF characteristics are mainly determined by the 84 regular cells located between the input and output couplers. Input and output couplers need to be included when the whole structure RF characteristics are simulated before fabrication; otherwise it would be difficult to obtain the travelling wave fields excited in the whole structure. If the real 3D couplers are modelled during the design process, a large amount of computer resources and time need to be used. However, if the redesigned azimuth symmetric coupler is used to replace the real 3D one during the simulation process, much less computer resources and time are required. With this method proposed here, the simulation results agree well with the theoretically calculated and experimentally measured ones.

INTRODUCTION

The travelling wave (TW) disk-loaded accelerating structure is one of the key components in normal conducting (NC) linear accelerators, such as the BEPC and BEPCII linacs [1, 2], and has been studied for many years. Usually after the dimensions of each cell and the two couplers are finalized, the structure is fabricated and tuned, and then the whole structure RF characteristics are measured by using a vector network analyzer. Before the fabrication, the whole structure RF characteristics are less simulated. This is because of the structural scale (couples of meters long and centimeters in diameter at S-band) and also the personal computer capability limitations.

Because the RF characteristics of the TW structures with several tens of cells are mainly decided by the regular cells, one method to use redesigned power couplers with azimuth symmetry to replace the original 3D waveguide ones in finite element analysis (FEA) can be used. Then the whole structure RF characteristics, such as the electric field amplitude distribution along the structure's axis and the VSWR curve, can be analyzed by using the multi-physics software package ANSYS [3] with much less computer resources required.

In BEPC and BEPCII linear accelerators, 56 units of 3 m long constant gradient disk-loaded accelerating structure are employed. Table 1 shows the main specifications. Fig. 1 shows the schematic of the input/output coupler. To balance the electromagnetic field asymmetry existed in this kind of single feed input/output coupler, appropriate eccentricity offset is applied. If this real coupler shape shown in Fig. 1 is used to simulate the whole structure RF characteristics, at least 1/2 model (180^{o} azimuth angle) needs to be created, which is impossible to do with only one PC.

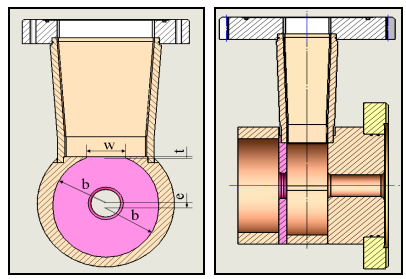

Figure 1: Schematic of the input/output coupler for the accelerating structure of the BEPCII linac. *b*—radius; *e*—eccentricity offset; *w*—coupling aperture width; *t*—coupling aperture thickness.

Table 1: Main Specifications of the TW Structure for BEPCII Linac

Parameters	Units	Values
Operating frequency	MHz	2856
Operating temperature	°C	45.0±0.1
Number of cells		84 regular cells 2 coupler cells
Section length	mm	3009 (86 cells)
Phase advance per cell		2π/3
Cell length	mm	34.99
Disk thickness	mm	5.84
Iris diameter (2*a*)	mm	26.231–19.243
Cell diameter (2*b*)	mm	83.460–81.781
Shunt impedance (r_0)	MΩ/m	54.6–63.9
Q factor		13990–13836
Group velocity	v_g/c	0.0208–0.0070
Filling time	ns	830
Attenuation coefficient	Np	0.57

ANSYS SIMULATION METHODOLOGY

The high frequency modal and harmonic solver modules in ANSYS can be used to perform the numerical finite element analysis on the whole structure RF characteristics. By using one program for all of the simulations any problems of meshing inconsistency between different types of software were eliminated.

#peisl@mail.ihep.ac.cn

Copyright © 2012 by the respective authors — cc Creative Commons Attribution 3.0 (CC BY 3.0)

A complete RF analysis on the whole TW disk-loaded structure requires 3 steps, as outlined below. Currently, the ANSYS high frequency modal and harmonic solver modules have the limitation that only 3D elements can be used. To minimize the CPU time and memory use, an axis-symmetric 3D model with a 1° azimuth angle (1/360 model) can be created to carry out the analysis. Otherwise, the azimuth angle of the model needs to be adjusted correspondingly.

1) With an HF119 high frequency tetrahedral element, modal analysis was performed in the vacuum part of each accelerating cell, the cell diameter 2*b* was varied to tune the 2π/3 mode resonating at the nominal operating frequency (2856MHz for the BEPCII linac) by fixing the iris diameter 2*a*.

2) By using the obtained dimensions of the first/last cells in Step 1, the redesigned axis-symmetric vacuum models of the input/output coupler as shown in Fig. 2 can be defined. To minimize the reflection coefficient at the input/output coupler port to the level of 10^{-2} to 10^{-3}, all of the dimensions shown in Fig. 2 except those related with the middle two cells can be adjusted. Once a flat electric field amplitude distribution along the redesigned coupler's axis is obtained and the phase difference between the middle two cells is ~120° (2π/3), the coupler's dimension can be finalized.

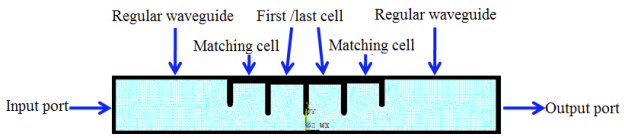

Figure 2: Schematic of the redesigned input/output couplers with azimuth symmetry.

3) Now the vacuum part of the whole structure can be modeled with the obtained cell and coupler dimensions from Steps 1 and 2. Harmonic analysis was carried out by defining the two redesigned couplers in Step 2 as input and output ports, respectively. Impedance boundary condition of copper was applied to the other outer boundary surfaces. Using the built-in macro 'SPARM' and 'HFPOWER', the scattering (*S*) parameters and the total time averaged losses can be calculated. If a harmonic response over a frequency range is performed, the *S* parameters at each frequency step for each port will be calculated, the structure's bandwidth (VSWR≤1.2) can then be known by checking the S11/VSWR data.

It is worth to point out that the mesh size consistency in all of the above analysis steps is the key for acquiring the correct simulation results. Only in Steps 1 and 2, the corresponding model dimensions need to be adjusted.

THE BEPCII LINAC STRUCTURE

By using the structural dimensions listed in [1] and the method proposed in last section, the whole structure RF characteristics on the accelerating structure of the BEPCII linac were studied.

Figure 3 shows the ANSYS model and meshing of the 43rd accelerating cell. Fig. 4 shows the corresponding electromagnetic field distributions of the 2π/3 mode operating at 2856MHz.

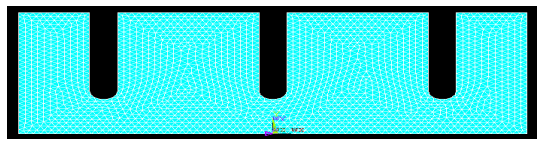

Figure 3: ANSYS model and meshing of the 43rd accelerating cell.

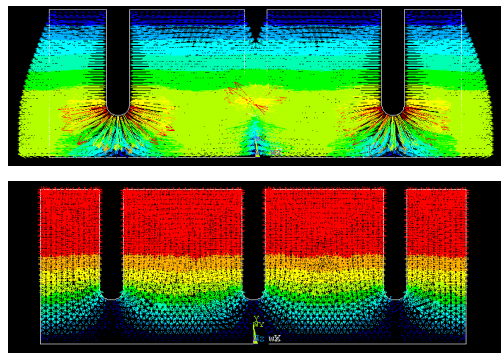

Figure 4: Electromagnetic field distributions of the 2856MHz 2π/3 mode in the 43th accelerating cell

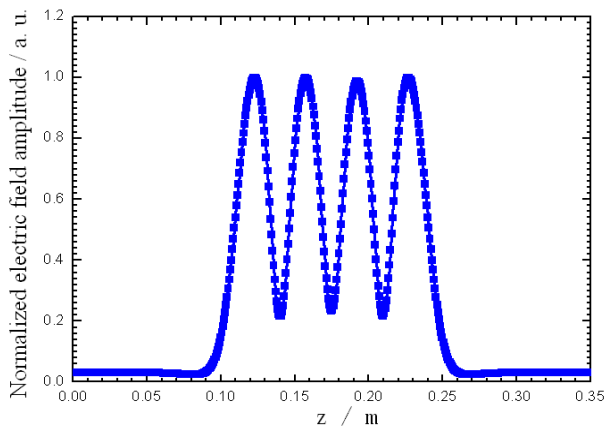

Figure 5: On-axis electric field amplitude distribution in the redesigned input coupler with azimuth symmetry.

Figure 5 shows the on-axis electric field amplitude distribution in the redesigned input coupler with azimuth symmetry of the accelerating structure for the BEPCII linac. This coupler includes two matching cells and two regular accelerating cells; the calculated phase shift between the middle two accelerating cells is ~119.4°. Correspondingly, the dimensions of the output coupler can be obtained with the same method.

The 1/360 model of the accelerating structure for the BEPCII linac is shown in Fig. 6. By appropriately defining the input and output ports in ANSYS, the amplitude distribution of the electric field along the whole structure's axis of the BEPCII linac accelerating structure can be obtained, which is shown in Fig. 7.

Copyright © 2012 by the respective authors — cc Creative Commons Attribution 3.0 (CC BY 3.0)

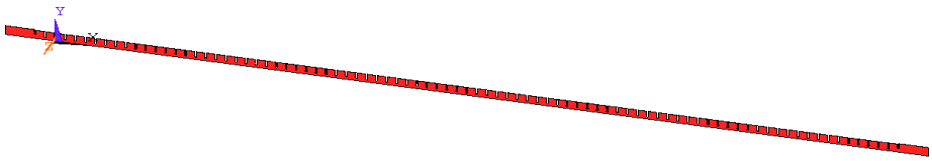

Figure 6: The 1/360 model of the accelerating structure for the BEPCII linac (total 84 regular cells and 2 coupler cells).

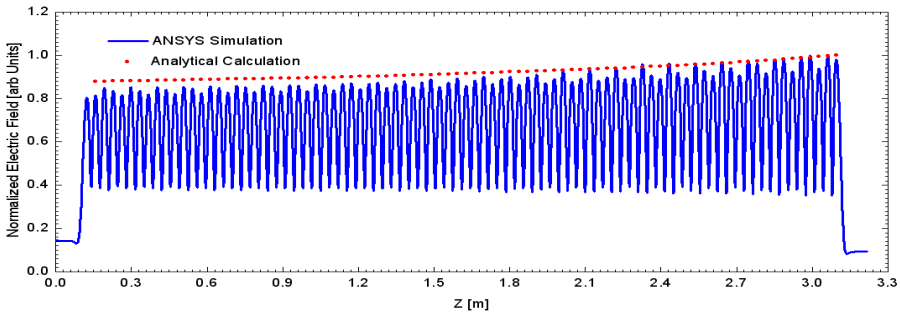

Figure 7: The electric field amplitude distribution along the structure's axis of the BEPCII linac accelerating structure.

In Fig. 7, one can see that there are 86 peaks for the ANSYS simulation result. The 1st and 86th peaks correspond to the matching cells of the input and output couplers, respectively. The middle 84 peaks correspond to the 84 regular accelerating cells. The ANSYS simulation result is consistent with the analytical one, which can be calculated with the analytical formulae listed in [4] after obtaining each cell's RF parameters such as the frequency, the quality factor Q, the shunt impedance R and the group velocity v_g. Usually, the former three ones can be calculated with SUPERFISH [5], and the last one with MAFIA [6].

With –34 dB reflection coefficient at the input port, the ANSYS simulated power attenuation coefficient to the output port is 0.56 Np (~4.85 dB), which is very close to the experimentally measured (0.57 Np) and the analytically calculated (0.54 Np) ones. By using the averaged value of the ANSYS calculated quality factor Q, which is ~13750, the corresponding filling time can be estimated to be 856 ns, which is only 26 ns longer than the experimentally measured value of 830 ns.

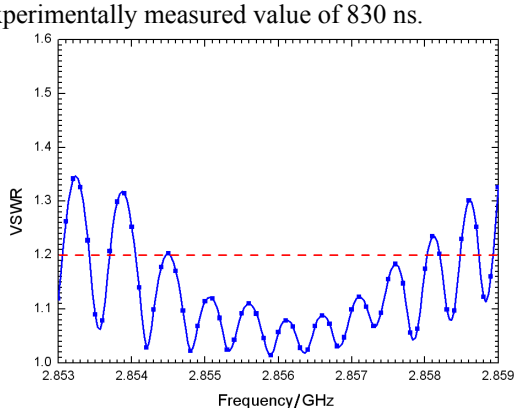

Figure 8: The ANSYS simulated VSWR curve.

Figures 8 and 9 show the ANSYS simulated and the experimentally measured VSWR curves, respectively. It can be clearly seen that the simulated frequency bandwidth is 2858.05–2854.5=3.55 MHz, while the measured one is 2858.3–2853.6=4.7 MHz. In Fig. 8, the VSWR at 2854.5 MHz is exactly 1.2, if it is not considered to be the lower limit of the bandwidth, then the ANSYS simulated bandwidth would be 2858.05–2854.05=4 MHz. Consequently, the difference of the bandwidth results between ANSYS and experiment would go from 1.15 MHz to 0.7 MHz.

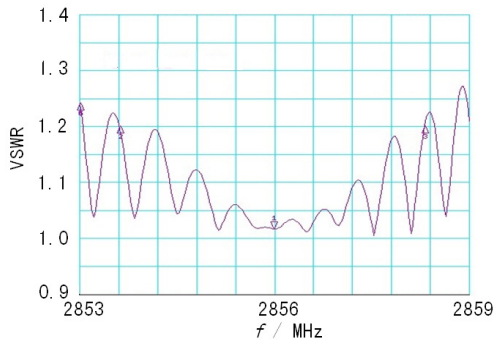

Figure 9: The experimentally measured VSWR curve.

CONCLUSION

By replacing the real 3D waveguide coupler with an axis-symmetric on-axis coupled one in ANSYS, the whole structure RF characteristics on the TW disk-loaded accelerating structure can be done with much less computer time and memory. The consistency between the simulation and experimental results of the BEPCII linac accelerating structure shows the validity of the method proposed in this paper.

REFERENCES

[1] The BEPC R&D Report, Part I, Injector, 1989.
[2] G. Pei et al., Preliminary Design Report of BEPCII Linac, IHEP-BEPCII-SB-03, 2002.6.
[3] ANSYS is a Trademark of SAS Inc., www.ansys.com.
[4] C. Yao, Electron Linear Accelerator, Beijing: Science Press, 1986, P. R. China.
[5] J. H. Billen et al., Possion Superfish: LA-UR-96-1834.
[6] The MAFIA Collaboration, MAFIA User Manual (Version 4.106), Germany: CST Inc., 2000.

Copyright © 2012 by the respective authors — cc Creative Commons Attribution 3.0 (CC BY 3.0)

PROGRESS ON THE DESIGN AND CONSTRUCTION OF THE 100 MeV / 100 kW ELECTRON LINAC FOR THE NSC KIPT NEUTRON SOURCE

S. Pei#, Y. Chi, G. Pei, S. Wang, J. Cao, M. Hou, W. Liu, Z. Zhou, F. Zhao, R. Liu, X. Kong, J. Zhao, C. Deng, H. Song, J. Liu, J. Yue, Q. Yang, D. He, K. Lv, X. He, Q. Le, X. Li, L. Wang, X. Wang, H. Ma, H. Guo, B. Deng, J. Zhang, J. Zhao, C. Ma, IHEP, Beijing, China
A. Zelinsky, M. Ayzatskiy, V. Kushnir, V. Mytrochenko, I. Karnaukhov, KIPT, Kharkov, Ukraine
Y. Gohar, ANL, Illinois, USA

Abstract

IHEP in China is designing and constructing a 100 MeV / 100 kW electron linac for NSC KIPT, which will be used as the driver of a neutron source based on a subcritical assembly. Recently, the physical design has been finalized. The chicane scheme instead of the RF chopper one has been selected. The mechanical design is on-going and will be finished in the very near future. The injector part of the machine has been installed in the experimental hall #2 of IHEP and is being commissioned and tested. The progress on the machine design and construction are reported, initial testing and commissioning results of the injector are also presented.

INTRODUCTION

One 100 MeV / 100 kW electron linac in NSC KIPT is being constructed, which will be used to drive a neutron source based on a subcritical assembly. This neutron source is a joint project between ANL (USA) and NSC KIPT (Ukraine), and IHEP in China is responsible for the linac (including the transport line to the target) design and construction. Due to the high average beam power of 100 kW and the low beam loss of ~3 kW (including intended and unintended) along the entire linac, the whole machine is being designed and constructed elaborately. Table 1 shows the main parameters of the NSC KIPT linac.

Table 1: Main Parameters of the NSC KIPT Linac

Parameters	Values	Units
RF frequency	2856	MHz
Beam energy / power	100 / 100	MeV / kW
Beam current (max.)	0.6	A
Energy spread (p-to-p)	±4	%
Emittance	5×10^{-7}	m-rad
Beam pulse length	2.7	μs
RF pulse length	3	μs
Pulse repetition rate	625	Hz
Klystron	6×30MW / 50kW	Units
Accelerating structures	10×1.336m	Units
Gun high voltage	~120	kV
Nominal gun beam current	~1–1.2	A

#peisl@mail.ihep.ac.cn

The beam energy spread at the linac exit has been changed to ±4% for peak-to-peak rather than 1% for 1σ [1] [2]. This is determined by the energy spread acceptance of the beam transport line with 90° bending angle located at the linac end. With ±4% peak-to-peak energy spread, the beam power losses along the transport line can be reduced to less than 1 kW with ±0.2 mm alignment error, ±2° phasing jitter, ±0.15% modulator voltage jitter, ±0.5% gun high voltage jitter and ±1% RF pulse flatness.

Figure 1 shows the mechanical layout of the linac including the beam transport line. The klystron gallery is located at the downstairs of the accelerator tunnel.

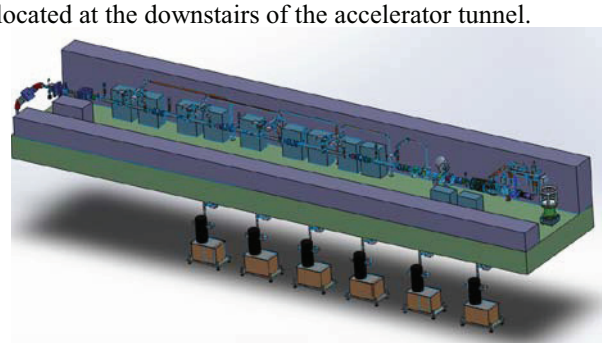

Figure 1: Mechanical layout of the linac including the beam transport line.

INJECTOR DESIGN AND TEST

To get a clean bunch without any satellite electrons in each RF period downstream the chicane system, the phases of all the RF structures (the prebuncher, the buncher and the 1st accelerating structure A0) and the solenoid field distribution in the injector are re-optimized. Finally one can obtain the phase and energy spectrums as shown in Fig. 2, which are appropriate for the beam collimation process with the chicane system to eliminate all particles with very large energy and phase spreads relative the reference particle located at the 0° phase. By this way, the beam power losses along the transport line can be minimized to the largest extent.

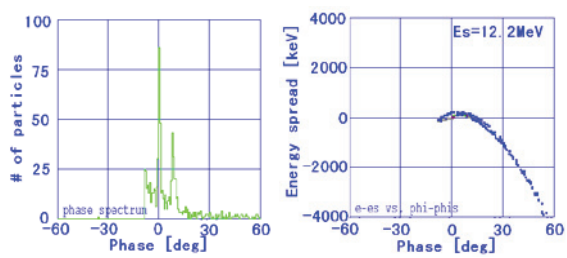

Figure 2: Phase and energy spectrums at the injector exit.

Copyright © 2012 by the respective authors — cc Creative Commons Attribution 3.0 (CC BY 3.0)

Fig. 3 shows the absolute energy spread distribution along the linac with all error and jitter effects considered.

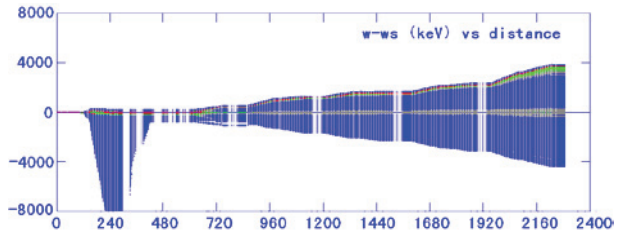

Figure 3: Absolute energy spread distribution along the linac with all error and jitter effects considered (unit: cm).

The injector part has been installed in the experimental hall #2 of IHEP, which is shown in Fig. 4. The commissioning and testing were started two months ago. For beam pulse length of 2.7 μs, the maximum current obtained at the injector exit is ~2 A, which is limited by the electron gun emission capability. No BBU effect in the injector was observed, which means the threshold current of the accelerating structure is higher than 2 A. Many effective measures are adopted in the linac design to cure the BBU effect as described in [1].

Figure 4: Injector testing facility installed in IHEP.

Fig. 5 shows the signals of BCT1 (gun exit) and ACCT1 (A0 exit, upstream the 37.5° energy analyzing magnet used temporarily for injector test). Here the beam current indicated by the ACCT1 signal is ~770 mA. The bunching efficiency is not known yet because the BCT1 is not calibrated; however, the estimated value is ~70% according to the gun current calibration before installation. The waveforms' swing up and down along the pulse is because of the interference from the old grounding system of hall #2, which was constructed more than 20 years ago.

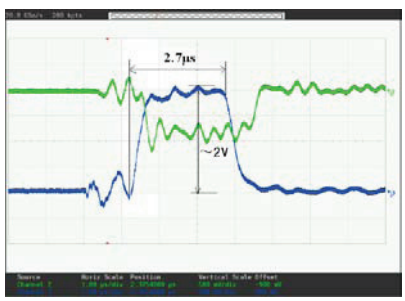

Figure 5: Signals of BCT1 and ACCT1.

Figure 6 shows the corresponding beam profile (downstream the analyzing magnet) at the energy and energy spread measurement line. It can be seen there is no high energy tails, but only low energy ones, which is consistent with the simulated energy spectrum in Fig. 2. The low energy tails will be collimated by the collimator located between the bending magnets CB2 and CB3 of the chicane system, and then a clean beam of ~600 mA without satellite electrons in each bunch can be obtained.

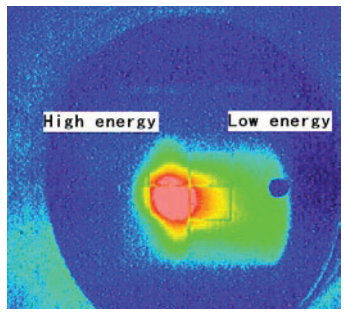

Figure 6: Beam profile at the energy measurement line.

CHICANE SYSTEM DESIGN

The chicane system is located downstream the injector but upstream the 2nd accelerating structure A1. There are 4 bends in the chicane system， mechanical layout of which is shown in Fig. 7. The bending magnets CB1 and CB4 are sectors, while CB2 and CB3 are rectangles. The 1st bending magnet CB1 was specially designed to have two functions. One is for the nominal beam collimation process with a bending angle of 10°; another is to be used as an energy analyzing magnet (AM) with 45° bending angle for measuring the beam energy and energy spread of the electron beam at the injector exit, then the RF phases seen by the beam in the prebuncher, the buncher and the 1st accelerating structure A0 can be optimized in real operation. The vacuum chambers for CB1, AM and CB2 are integrated together for saving space. Similarly, the chambers for CB3 and CB4 are also integrated.

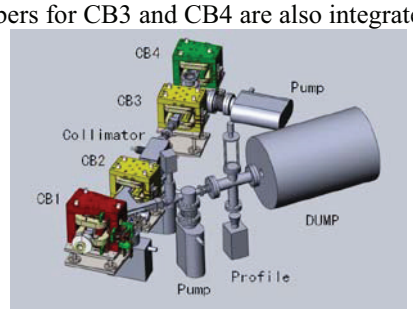

Figure 7: Layout of the Chicane system.

MAIN SYSTEMS AND COMPONENTS

Based on the decision to adopt the chicane scheme instead of the RF chopper one because of technology difficulty caused by the high beam current, construction and commissioning of all main systems are on-going.

The electron gun with Y824 cathode assembly has been in normal operation with high voltage (HV) of 120 kV (conditioned to 135 kV) for couples of months in the injector testing facility. The emitted current exceeded the design requirement of 2A. Fig. 8 shows the gun system setup in the tunnel.

Copyright © 2012 by the respective authors — cc Creative Commons Attribution 3.0 (CC BY 3.0)

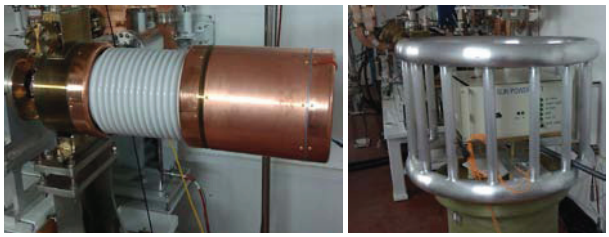

Figure 8: The electron main body and the HV station.

Figure 9 shows the modulator and the Toshiba E37311 klystron. ~400 Hz rep. rate (less than the design goal of 625 Hz) with 3μs RF pulse width has been reached because of the electrical capability of the experimental hall. Higher rate to 625 Hz will be conditioned after the electrical network upgrade. Fig. 10 shows the klystron output at 100 Hz. 30 MW peak power has been obtained.

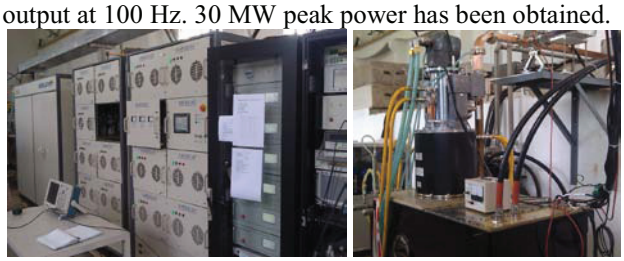

Figure 9: The modulator and Toshiba E37311 klystron.

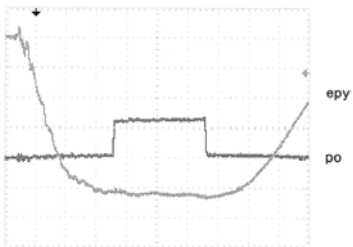

Figure 10: The klystron output at 100 Hz.

Most of the beam instrumentation devices are being fabricated and tested. Fig. 11 shows the ACCT with electromagnetic shielding and the BPM.

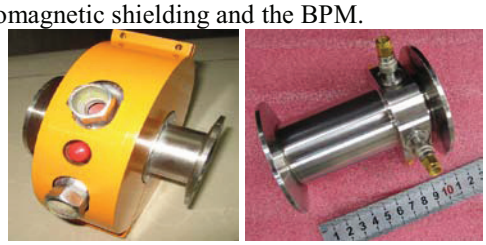

Figure 11: ACCT and BPM

The 1st accelerating structure A0 has been installed in the injector testing facility and is running well at couples of Hz rep. frequency. In the near future, it will be tested to run at 625 Hz with the nominal input power. If the result is positive, another 9 structure will be fabricated.

The LLRF system is being tested in this month. As shown in Fig. 12, the klystron drive waveform is optimized to obtain the desired pulse shape with minimized fluctuation. The testing of the firmware for digital signal processing including feed-forward and feedback control algorithms has been finished.

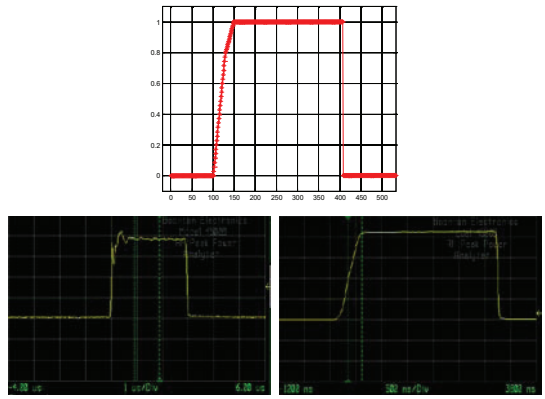

Figure 12: The klystron drive (upper), amplifier output before (lower left) and after (lower right) optimization.

The control system is based on EPICS, which includes all front-end controller, driver and operator screen as shown in Fig. 13. Currently, the design has been finished; most components are in the purchasing and tuning stage. The injector control system is being in operation stably.

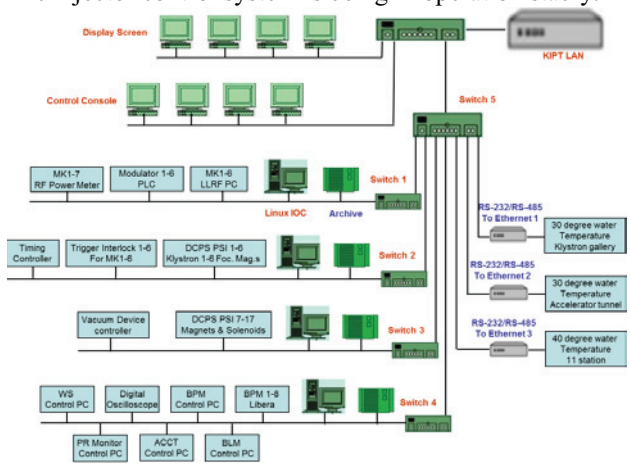

Figure 13: The control system architecture.

The water cooling system is designed to be composed by 3 subsystems: 1) first loop of 30 (max.) ±1°C for the tunnel devices; 2) first loop of 30 (max.) ±1°C for the klystrons gallery devices; 3) 40±0.2°C constant temperature system for the accelerator. The prototype is in well operation for the injector testing facility.

SUMMARY

The design and construction scheme of the 100 MeV / 100 kW linac for NSC KIPT neutron source has been finalized. The injector testing facility is being in operation to test the related systems / components. Currently, the testing results are acceptable. However, further work still need to be done to improve the machine performance including test of the beam loading compensation online.

REFERENCES

[1] S. Pei et al., MOPS033, Proceedings of IPAC2011, San Sebastian, Spain.
[2] Y. Chi et al., TUPC034, Proceedings of IPAC2011, San Sebastian, Spain.

Copyright © 2012 by the respective authors — cc Creative Commons Attribution 3.0 (CC BY 3.0)

BEAM DYNAMICS SIMULATION AND OPTIMIZATION FOR 10 MeV SUPERCONDUCTING E-LINAC INJECTOR FOR VECC-RIB FACILITY

S.Dechoudhury#, Vaishali Naik, Alok Chakrabarti, DAE/VECC, Kolkata, India
Gabriel Goh, SFU, Burnbay, British Columbia, Canada
Friedhelm Ames, Richard Baartman, Yu-Chiu Chao, Robert Edward Laxdal,
Marco Marchetto, Lia Merminga, Fang Yan, TRIUMF, British Columbia, Canada

Abstract

In the first phase of ongoing collaboration between VECC (India) and TRIUMF (Canada) a 10 MeV superconducting (SC) electron linac injector will be installed at VECC. This will constitute a 100 keV DC thermionic gun with grid delivering pulsed electron beam at 650 MHz. Owing to low beam energy from the gun, a capture cryomodule (CCM) consisting of two beta=1, 1.3 GHz single cell elliptical cavities will be installed for pre-acceleration of electron beam to around before it enters an Injector Cryomodule (ICM). The ICM consists of one 9-cell beta=1 elliptical cavity that will provide acceleration to 10 MeV. The present paper depicts the beam dynamics simulation and optimization of different parameters for the injector with a realistic simulated beam emittance from the electron gun.

INTRODUCTION

The proposed electron linac would eventually accelerate 10mA CW electron beam (16 pC/bunch) to 50 MeV with 1.3 GHz superconducting RF cavities. The e-Linac consist of a thermionic gun with 650MHz RF modulated grid followed by a buncher and the two cryomodules. The injector cryomodule (ICM) consisting of a single 9-cell 1.3 GHz niobium cavity followed by an accelerator cryomodule (ACM) having two 9-cell cavities [1]. Systematic optimization of the beam line with wide range of objectives and constraints has been carried out for this e-Linac. The TRIUMF machine would also be used in ERL or RLA mode [3]. Keeping this in mind, option of accelerating high brightness beam of 100pC/bunch charge with better longitudinal beam quality has been kept in the base-line design considering a 300 keV thermionic gun [2].

However, for the VECC facility a 100 keV electron gun would be developed for initial tests of the injector [1] because the present site has several limitations. The ICM would be identical to the TRIUMF machine and would be built and tested at TRIUMF and will be shipped to VECC. Since the 100 keV beam with a $\beta \approx 0.55$ is ill suited to be directly injected into the ICM, some pre-acceleration of the beam to an energy $\geq$ 300 keV will be needed. To achieve this, a capture cryo-module having two independently phased β =1 single cell cavities will be added before the Injector Cryo Module (ICM). The beam dynamics optimization of the 10 MeV injector for the VECC e-Linac facility will be presented.

sdc@vecc.gov.in

ELECTRON GUN SIMULATION

The electron gun consists of a cathode with a grid placed 150 micron away from the electron emitting surface, on which the modulating voltage would be applied. First the electrostatic field between electron emitting surface and grid and finally up-to anode was simulated using SIMION [4]. The electric field distribution thus generated was then used in GPT [5] for estimating the longitudinal and transverse emittance of 100keV electron beam. GPT simulation was done for different geometries essentially varying the cathode angle and cathode-anode distance. An optimum gap of 9.5 cm was chosen between the anode and cathode for good beam quality and a robust solution [6].The conduction angle of the gun was varied in order to estimate the beam structure both longitudinally and transversely for $\pm 16^0$ and $\pm 20^0$ beam.

For both the cases the bunch charge was 16pC which yields 10mA average current for conduction angle of $\pm 20^0$. Two factors are expected to influence transverse emittance growth - temperature of electron emitting surface (1400 K~ 0.13eV) and influence of grid due to the lens action of the micro holes in the mesh. It can be seen analytically that grid induced emittance dominates over the thermal effect. The "*Reiser model*" [7] for grid induced emittance cannot be used since the angle is not << 1. The analytically calculated grid effect was therefore included in the simulation.

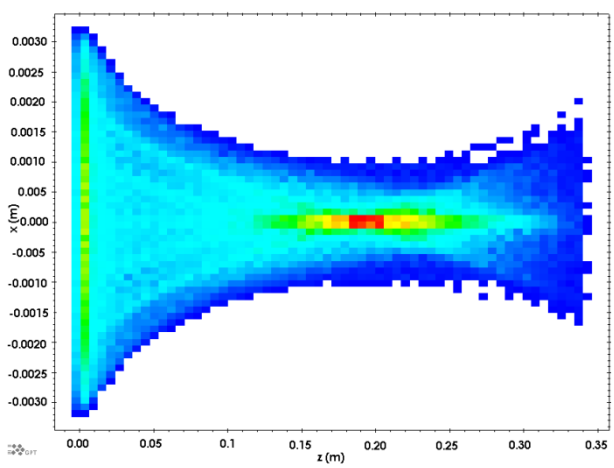

Figure 1: GPT simulated density distribution of 100 keV electron beam with 16pC, conduction angle of $\pm 20^0$

Copyright © 2012 by the respective authors — cc Creative Commons Attribution 3.0 (CC BY 3.0)

The normalized emittance of electron beam was taken to be 19 mm mrad (4 times RMS emmittance) assuming a transverse spread same as that of the longitudinal energy spread [8]. GPT simulated beam for 16 pC, ± 20^0 conduction angle, cathode-anode distance of 9.5cm is shown in Figure 1. Maximum electron density at the axis occurs at a distance of 200 mm from the electron emitting surface. The simulated parameters for the 100 keV electron beam for ±16^0 and ± 20^0 conduction angles are listed in Table 1.

Table1: Parmeters of 100 keV electron beam (simulation)

Conduction Angle	±16^0	± 20^0
εn,rms (X) π mm mrad	5.02	4.85
εn,rms (Y) π mm mrad	5.01	4.84
εn,rms (long.) π keV mm	0.92	1.694
Bunch Charge (pC)	15.5	16

BEAM LINE CONFIGURATION

The 100 keV electron beam simulated from GPT with realistic features was used for optimization of the base-line configuration for the VECC injector. The beam tracking was carried out in ASTRA [9], where the input fields for elliptical cavities, buncher and solenoids was created using SUPERFISH [10]. In order to test for robustness of the baseline configuration, multivariate optimization technique involving genetic algorithm was utilized as described in reference [2]. In continuation with work carried out earlier, the base line configuration starts with a 1.3 GHz normal conducting buncher after the gun. Earlier it was already established that compared to 650 MHz buncher, the present buncher perform better in terms of bunching the beam without substantial tail longitudinally.

In the next stage two β = 1 single cell elliptical cavities were used. The acceleration is achieved in the first single cell cavity whereas the second cavity essentially only bunches the beam. The additional bunching in the capture section comes with the cost of transverse defocusing. The required transverse focusing is achieved with a solenoid placed between the CCM and ICM. A 10mm virtual aperture is defined through the cavities and any solution where the electron hits this aperture is discarded. This in other words takes care of electron hitting the superconducting cavity. Layout of the proposed beam-line is shown in Figure 2. The last solenoid is redundant for 10 MeV case but would be needed if we would like to further enhance the energy to 30 MeV in subsequent two 9-cell cavities. Also at 10 MeV the last solenoid would be needed as a part of diagnostic equipment.

A genetic algorithm was used to find the above optimized layout by using variables as field strength of solenoids, electric field and phases of cavities to achieve particular sets of constraints and objectives. This algorithm was useful to search for robust solutions against near singularities in the modeling process. Distances have been kept considering required space for hardware as well as space constraints in mind. The solution sets for which the objectives of minimizing EmitX and energy width ΔE (rms) and constraint of achieving final energy greater than 10 MeV with ±16^0 GPT simulated beam were achieved are shown in Figure 3 and the same for ±20^0 case are shown in Figure 4.

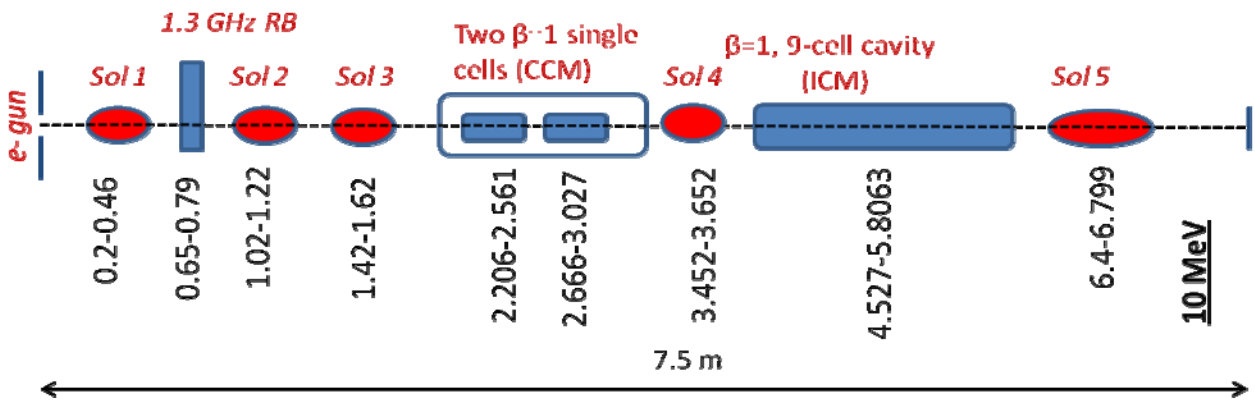

Figure 2. Layout of 10 MeV injector for VECC e-Linac

Copyright © 2012 by the respective authors — cc Creative Commons Attribution 3.0 (CC BY 3.0)

The optimized beam dynamics parameters for one of the solution with $\pm16^0$ GPT simulated beam are shown in Figure 5. The first single cell cavity accelerates the 100 keV electron beam to 600 to 800 keV while the second cavity acts as mainly as a buncher with energy at its exit of around 1 MeV. The required solenoid fields are in the range of 300 to 400 Gauss. The required acceleration gradient E_{acc} in the first and second capture cavity is around 4.5 MV/m and 0.5 MV/m respectively. The rms bunch width at 10 MeV for most of the solution is less than 6mm going down to as low as 1-2mm, while transverse and longitudinal emittance are found to be within acceptable limits.

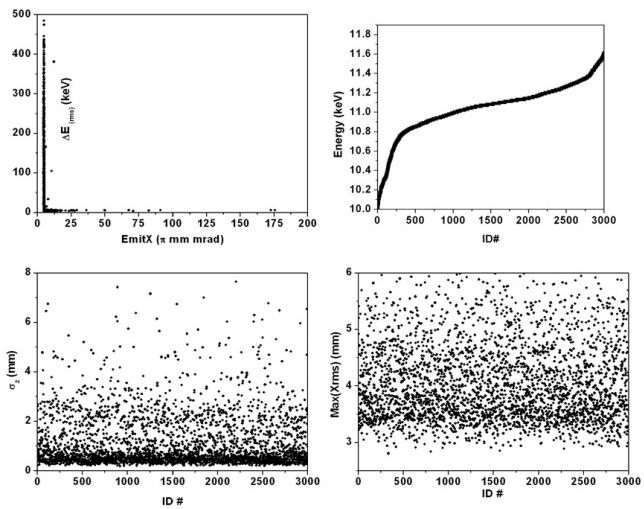

Figure 3. Solution sets with $\pm16^0$ GPT simulated beam

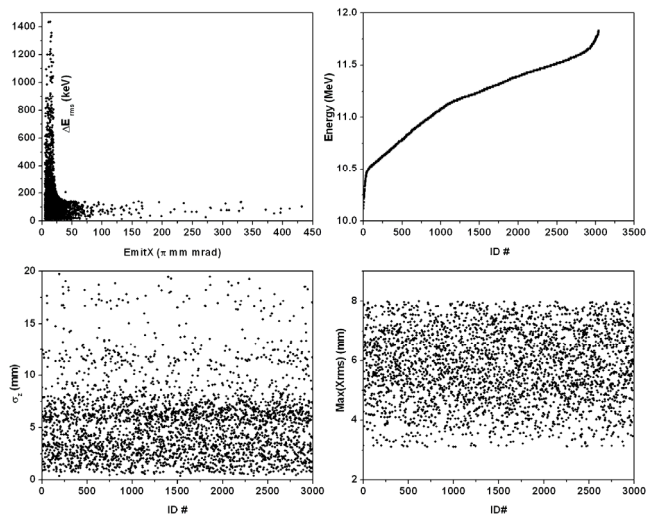

Figure 4. Solution sets with $\pm20^0$ GPT simulated beam

For most of the solutions the maximum value of Xrms is less than 6-8mm. The beam does not develop appreciable longitudinal tail. As far as acceleration upto 10 MeV, both $\pm16^0$ and $\pm20^0$ perform in similar fashion in terms of longitudinal and transverse beam quality. Just out of academic interest, optimisation was extended upto 50 MeV with both type of GPT simulated beam. $\pm16^0$ beam does not develop appreciable longitudinal tail thus not creating problem when accelerated to 50 MeV. This is not the case with 20 degree beam which is although comparable to 16 degree beam upto 30 MeV. But it seems to perform inferior in terms of number of solutions and also in terms of value of end parameters at 50 MeV. This is due to increase in number of particles in tail part of longitudinal structure of beam.

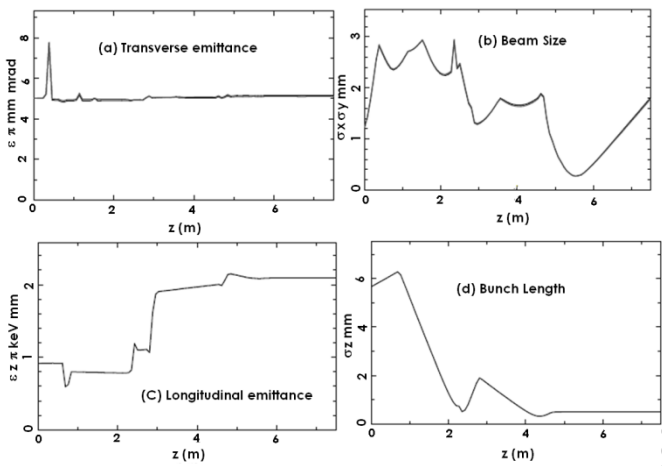

Figure 5. Optimised beam dynamics parameters with $\pm16^0$ beam;(a) transverse emittance, (b) beam size, (c) longitudinal emittance, (d) bunch length variation along the length.

REFERENCES

[1] V. Naik et al., "VECC-TRIUMF injector for E Linac project", LINAC 10, TH202, p. 727 (2010)
[2] Y.C.Chao et al., "TRIUMF-VECC Electron Linac Beam Dynamics Optimisation", ICAP 09, THPSC012, p. 277 (2009)
[3] Lia Merminga et al., "ARIEL: TRIUMF's Advanced RarE Isotope Laboratory", IPAC 11, WEOBA01, p. 1917 (2011)
[4] SIMION 8, //www.simion.com
[5] GPT, //www.pulsar.nl/gpt
[6] Y.C.Chao, //http: elinac.triumf.ca
[7] M.Reiser, "Theory & Design of charged particle beams", Wiley-VCH
[8] R. Baartman, //http:elinac.triumf.ca
[9] http://tesla.desy.de/~lfroheli/astra
[10] http://laacg1.lanl.gov

Copyright © 2012 by the respective authors — cc Creative Commons Attribution 3.0 (CC BY 3.0)

1 ms MULTI-BUNCH ELECTRON BEAM ACCELERATION BY A NORMAL CONDUCTING RF GUN AND SUPERCONDUCTING ACCELERATOR*

M. Kuriki†, H. Iijima, S. Hosoda, HU/AdSM, Higashi-Hiroshima, Japan
K. Kawase, G. Isoyama, R. Kato, ISIR, Osaka, Japan
K. Watanabe, H. Hayano, J. Urakawa,KEK, Tsukuba, Japan
A. Kuramoto, Sokendai, Hayama, Japan
S. Kashiwagi, Tohoku U., Sendai, Japan
K. Sakaue,RISE, Tokyo, Japan

Abstract

KEK-STF (Superconducting Test Facility) has been constructed to establish super-conducting accelerator technology for ILC (International Linear Collider). This facility is also used to demonstrate a high-brightness quasi-monochromatic X-ray generation by inverse laser Compton scattering. For the both purposes, high intensity electron beam in multi-bunch and long macro-pulse formats is important. The beam commissioning has been started since February 2012. 1 ms macro pulse train is successfully generated and 40 MeV acceleration was confirmed. We report the progress of the beam commissioning including the basic beam properties.

INTRODUCTION

Aim of KEK-STF(Superconducting Test Facility)is establish the super-conducting accelerator technology for ILC(International Linear Collider) which is a future project of high-energy physics. In STF, a beam acceleration test will be performed with parameters almost equivalent to those in the real ILC, 8.7 mA average current in 0.9 ms length macro-pulse. In super-conducting accelerator, the input RF power and phase should be well controlled by monitoring RF field of the cavity for stable beam acceleration which can be examined only with a real beam. In ILC beam format, the 3.2 nC bunch is repeated with 369 ns spacing up to 0.9 ms. Total number of bunch is 2625 in a macro pulse. We call this operation mode as ILC mode.

Another purpose of STF is MEXT Quantum Beam project, generating high brightness and quasi-monochromatic X-ray by inverse Compton Scattering[1]. In this case, 62 pC bunch is repeated each 6.15 ns up to 1 ms macro pulse. We call this mode as Q-beam mode.

These high-average and long macro pulse beam formats are generated by a normal conducting 1.3 GHz photo-cathode RF gun. It was originally developed by DESY for FLASH/XFEL[2]. The Gun cavity fabricated by FNAL was installed at KEK-STF. The design peak field of the gun is 50 MV/m at 4.5 MW RF power. Cs_2Te photo-cathode is employed for beam generation. It is prepared as thin-film by evaporation on Mo cathode block in a vacuum chamber (preparation chamber)[3].

* Work supported by Quantum Beam Project of MEXT, Japan.
† mkuriki@hiroshima-u.ac.jp

By switching laser systems, the macro pulse in ILC mode and Q-beam mode are produced with this RF gun system. A laser system for ILC mode was developed as a collaborative work between KEK, Hiroshima Univ., IAP, and JINR in Russia in 2010[4][5]. This system is based on 3 MHz Yb fiber oscillator. The pulse train is amplified by Nd:YLF laser pumped by flash lump. 266 nm UV pulse train up to 0.9 ms was obtained as 4th harmonics of the fundamental mode. Another laser system based on 162.5 MHz mode-lock oscillator with MOPA system was developed for Q-beam mode[6]. UV laser pulse train was obtained as FHG by LBO and BBO. Typical UV laser energy per bunch is 500nJ or less.

The STF beam line setup for Q-Beam mode is schematically shown in Fig. 1. The beam properties are observed by various beam monitors set in the beam line, FC(Faraday Cup), ICT(Integrated Current Transformer), BPM(Beam Position Monitor), etc. SC accelerator boost up the beam energy up to 40 MeV. The beam size at IP (Interaction Point) for laser-Compton scattering after acceleration is designed to be 10μm[7].

In this article, we report successful generation and acceleration of 1 ms macro pulse by this photo-cathode RF gun and super-conducting accelerator.

STF INJECTOR

The injector is based on 1.3 GHz L-band normal conducting RF gun originally developed by DESY for FLASH/XFEL[2]. The design peak field is 47 MV/m with 4.0 MW input RF power. To generate 1 ms long macro pulse with RF gun, suppressing dark-current, i.e. field-emission from the cavity wall, is an important issue. The dark-current should be well below the average beam current in the macro pulse for a stable operation and clear X-ray signal detection from the laser-Compton scattering. The gun cavity conditioning was performed with nominal high power RF processing and ethanol rinse. The detail of the conditioning was explained elsewhere[8][9][3].

The cavity processing was performed in three stages. Between the first and second stages, ethanol rinse for the cavity was performed. The summary of the cavity conditioning was given in Fig.2; The dark current is shown as a function of accelerating field. The dark current was decreased roughly more than an order of magnitude by the

Copyright © 2012 by the respective authors — cc Creative Commons Attribution 3.0 (CC BY 3.0)

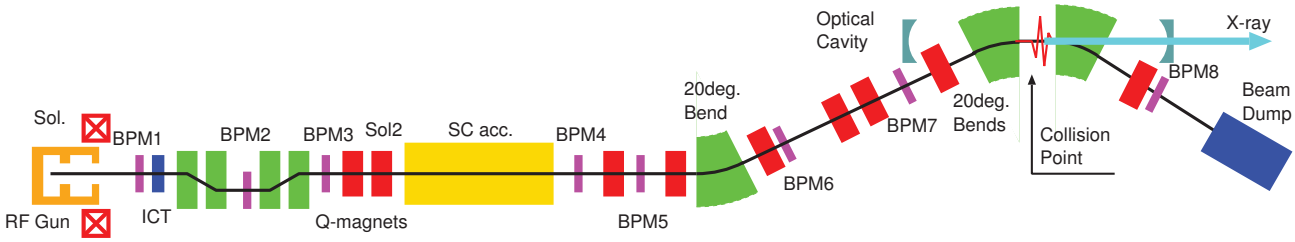

Figure 1: Schematic view of STF beam line. Beam current and position are measured by ICT(Integrated current Transformer) and BPM (Beam Position Monitor). After acceleration by a couple of SC cavities, the beam is focused on IP (Interaction Point) down to 10μm for efficient laser Compton scattering.

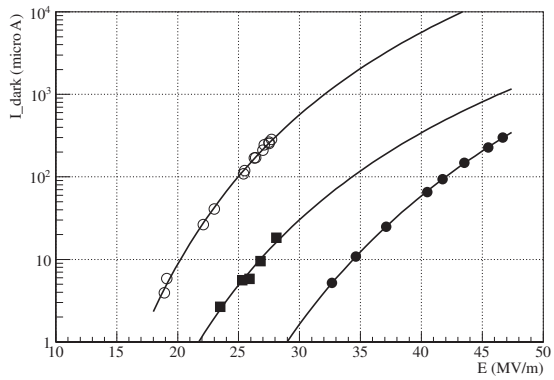

Figure 2: Dark current as a function of field, after first processing(open circle), second processing (filled square) and third processing (filled circle). Lines are expected dark current based on Fowler-Nordheim theorem.

ethanol treatment. Further reduction was observed by high power RF processing. Lines in Fig. 2 show the expectations according to Fowler-Nordheim theorem[10] assuming 4.7 eV work-function of Cu as cavity material. The expectation at 40.2 MV/m was 5.9 mA for first processing, 0.36 mA for second processing, and 0.062 mA for third processing which corresponds to 0.6% of the beam current. The dark current was suppressed by two orders of magnitude by the cavity conditioning.

The laser system for Q-beam mode was developed by Waseda Univ. and KEK for the Quantum Beam mode[6]. IR pulse train is generated by $\mathrm{Nd:YVO_4}$ mode lock oscillator in 162.5 MHz. The pulse train is amplified by a couple of two path Nd:YLF amplifiers. The CW IR pulse train is then clipped by Pockels cell to form the macro pulse structure, i.e. 1 ms pulse train in 5 Hz. The IR laser energy 17μJ / bunch is achieved. UV pulse train is generated by conversion from IR to UV with non-linear crystals, LBO for SHG and BBO for FHG, respectively. Finally, more than $500nJ$/bunch UV laser is obtained.

Cs_2Te cathode was made on Mo plug by evaporation in another vacuum chamber (preparation chamber) connected to the RF gun cavity. After the evaporation, the cathode plug is transferred and inserted to the gun cavity from backside without breaking vacuum. QE (Quantum Efficiency) of Cs_2Te was measured in preparation chamber by UV light from Xe lump and was typically more than 5% at the

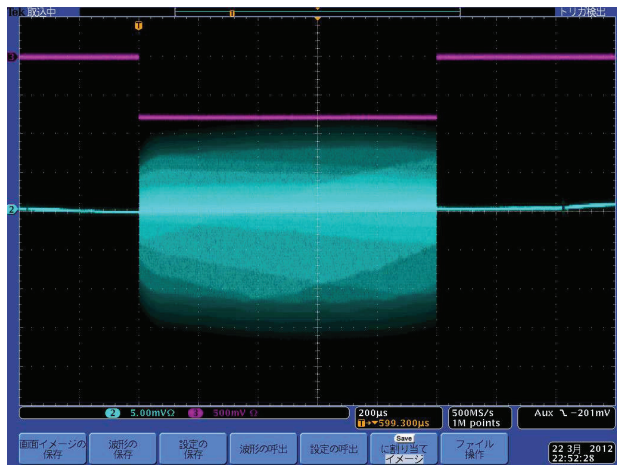

Figure 3: Beam temporal profile taken by BPM2 sum signal.

evaporation, but it was rapidly decreased down to less than 1%. QE in real operation is enhanced by the strong surface field in RF Gun giving more than 2 % QE[11].

1 ms BEAM GENERATION

1 ms beam generation test has been started since February 2012. Up to this period, 4.0 MW RF was successfully fed into the RF gun cavity, but the commissioning was performed with 2.0 MW RF for lower trip rate. Starting from 40μs, 1 ms pulse generation from the RF gun was examined. During the experiment, the field in the cavity was typically 33 MV/m. Detail of the tuning was given in Ref.[11]. After the basic beam tuning, number of bunches was gradually increased. After several iterations of the tuning and the bunch number increments, 1 ms macro pulse generation was achieved. Figure 3 shows the temporal profile of the 1 ms macro pulse. The shaded area shows sum of BPM signals which consist in 162450 bunches, but it is a shaded area due to limited resolution. Square pulse shown above it is the gate signal for laser pulse and has 1 ms duration. The bunch intensity was slightly less than 60 pC measured by ICT output. According to these measurements, it was confirmed that the multi-bunch electron beam with 1 ms pulse duration and very close to 10 mA average current was successfully generated by the photo-cathode RF gun.

Copyright © 2012 by the respective authors — cc Creative Commons Attribution 3.0 (CC BY 3.0)

1 ms BEAM ACCELERATION

The beam is accelerated by the SC accelerator. It consists from a couple of 1.3 GHz 9 cells cavities made from Nb with its length 1 m. These cavities are installed in a super-fluid He cooled cryomodule operated in 2 K. The acceleration field is 14.5 and 24.0 MV/m for each cavities[7], respectively. After the injector tuning, the acceleration test was performed with a shorter pulse length. The horizontal beam orbit after the first bending magnet was observed at BPM6 by scanning RF phase of the SC accelerator. The result is shown in Fig. 4. A clear dependence of the horizontal beam position on the RF phase was observed. According to a beam optics design, the crest beam position corresponds to 40.2 MeV/c[12]. The beam acceleration more than 40 MeV was confirmed.

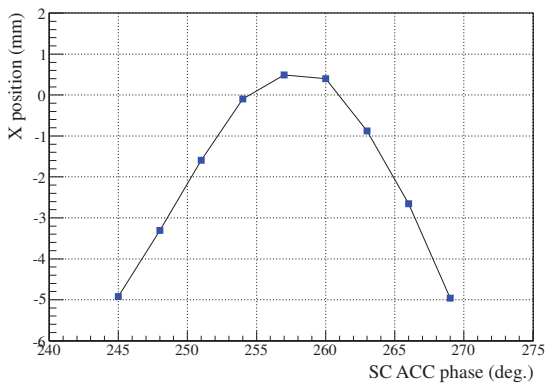

Figure 4: The horizontal beam position by BPM6 is plotted as a function of RF phase of SC accelerator. The maximum position corresponds to 40.2 MeV/c[12].

The final goal of Quantum Beam experiment at STF is demonstrating a high flux quasi-monochromatic X-ray generation by laser-Compton scattering with a compact system. The target value is more than $1.0 \times 10^{10} Photon/sec/1\%BW$. To realize this number, not only amount, but also quality like low-emittance and small spot size at IP are important. The design beam emittance at IP is $0.5\pi\mathrm{mm.mrad}$ and the beam size is $10\mu\mathrm{m}$ in rms for efficient X-ray generation. The bunch length is 12 ps and the bunch charge is 60 pC. The laser pulse stored in the optical cavity has the same 12 ps bunch length with 50 mJ energy per bunch.

The beam size and beam emittance was measured with tungsten wire scanner $10\mu\mathrm{m}$ in radius. This scanner is set at IP on a retractable mount. The emittance was qualified with Q-scan method in horizontal and vertical directions, respectively. The results were 0.82 and 1.34 $\pi\mathrm{mm.mrad}$ for horizontal and vertical directions, respectively. The bunch charge was 35 pC which is almost one half of the designed value. The RF power for RF gun was 3.5 MW giving 40 MV/m peak field . The field gradient of SC accelerator was 14.5 and 24.0 MV/m giving 40.2 MeV beam energy. The measured beam emittance is still twice bigger than the designed value. The beam size was measured directly with the same wire scanner. The results were 36.2 and 36.1 $\mu\mathrm{m}$ in horizontal and vertical directions, respectively. These numbers are still more than three times larger than the designed value, 10 $\mu\mathrm{m}$.

The both beam emittance and beam size are way from the designed numbers. It means that the emittance tuning and the beam optics tuning have to be carefully done. For example, the beam size at cathode should be optimized to minimize the emittance growth by the space charge effect. Solenoid strength should be adjusted for the emittance compensation at the given bunch charge and size. The beta matching should be made at the exit of SC accelerator including the focusing effect.

Although we have demonstrated the quantitative design parameters of the beam, e.g. bunch charge, average current, macro pulse length, and energy, these numbers were achieved not at once. Up to now, the maximum intensity of 1 ms pulse accelerated up to 40 MeV was 6.5 mA corresponding to 40 pC bunch charge. Demonstrating the beam satisfying the all requirements at once is another important mile-stone.

SUMMARY AND FUTURE PROSPECT

At KEK-STF, the beam test to generate 1 ms and 10 mA pulse was successfully carried out. The basic beam parameters such as beam current, macro pulse length meet the requirements. The beam was accelerated by SC accelerator and more than 40 MeV energy was confirmed, but the intensity was 60% of the designed value. The beam emittance was measured as 0.8 and 1.3 $\pi\mathrm{mm.mrad}$ for horizontal and vertical axes, respectively. The beam size at IP was 36 $\mu\mathrm{m}$ which is more than three times larger than the designed value. For efficient X-ray generation, these properties should be improved by progress of the beam and optics tuning.

REFERENCES

[1] http://kocbeam.kek.jp/project/index.html

[2] B. Dwersteg, et al., NIM A 393(1997)p93-95.

[3] H. Sugiyama et al.,Proc. of PESP2010 (2010).

[4] M. Kuriki et al., Proc. of IPAC2010(2010) THPEC024.

[5] A. Potemkin et al., Quant. Elec. 40(2010)1123-1130.

[6] K. Sakaue, 9th RF Gun WS (http://kocbeam.kek.jp/rfgws9/) (2012) in Japanese.

[7] K. Watanabe, et al., J. Particle Accel. Society of Japan, Vol.9(2),p82-91(2012) *in Japanese*.

[8] M. Kuriki et al., Proc. of IPAC2011(2011) MOPC014.

[9] Y. Takahashi, et al., Proc. of 7th annual meeting of PASJ(2010)471-474.

[10] J. W. Wang, PhD Thesis, Stanford U. (1989) p.104.

[11] M. Kuriki et al., Proc of IPAC 2012(2012) TUPPD034.

[12] M.Fukuda, STF techical note (2012) (in Japanese).

Copyright © 2012 by the respective authors — cc Creative Commons Attribution 3.0 (CC BY 3.0)

TRIUMF/VECC E-LINAC INJECTOR BEAM TEST

R.E. Laxdal, F. Ames, Y.C. Chao, K. Fong, C. Gong, A. Laxdal, M. Marchetto, W.R. Rawnsley, S. Saminathan, V. Verzilov, Q. Zheng, V. Zvyagintsev, TRIUMF, Vancouver, Canada
J. Abernathy, D. Karlen, D. Storey, U. of Victoria, Victoria, Canada
V. Naik, A. Chakrabarti, VECC, Kolkata, India

Abstract

TRIUMF is collaborating with VECC on the design of a 10 MeV injector cryomodule to be used as a front end for a high intensity electron linac. A electron gun and low energy beam transport (LEBT) have been installed in a test area to act as the injector for the cryomodule test. The LEBT includes a wide variety of diagnostics to fully characterize the beam from the gun. A series of beam tests are being conducted during the stage installation. The test configuration details and results of beam tests will be presented.

INTRODUCTION

TRIUMF is now preparing a new high intensity (10mA) 50MeV superconducting electron linear accelerator [1], e-Linac, as a key element of the ARIEL project. In brief the e-Linac consists of five 1.3GHz nine-cell niobium cavities each providing 10MV acceleration with two 50kW power couplers supplying the required beam loaded rf power. The five cavities are housed in three cryomodules, with a single cavity in an injector cryomodule, EINJ, and two identical accelerating cryomodules EACA and EACB with two cavities in each module.

TRIUMF began developing EINJ in 2010 in collaboration with the VECC laboratory in Kolkata. As part of the collaboration two EINJs will be fabricated and beam tested at TRIUMF. One EINJ will be shipped and installed at VECC and the second will be installed in the e-Linac. The initial EINJ is presently in fabrication [2].

A beam test area is being installed in the ISAC-II building to eventually test the two injector cryomodules with beam. The site utilizes the existing ISAC-II cryogenics infrastructure and enables testing of the cryomodules well before the expected availability of the e-Linac cryogenics in 2014. The schedule calls for accelerated beam tests in early 2013. Moreover, the injector test facility provides an ideal proving ground for e-linac design and operation strategies. It duplicates the front-end of the e-linac up to the exit of the injector cryomodule with enhanced diagnostics capability for benchmarking both the performance of the gun but also of the various diagnostics themselves. In addition the test installation allows early demonstration and troubleshooting of various e-Linac sub-systems including MPS, controls, beam modes, safety, LLRF, HPRF, cryogenics and important feedback on beam quality, halo formation and high intensity operation. Commissioning this facility began Nov 2011.

INJECTOR LAYOUT

The test layout, shown in Fig. 1 includes an electron gun, a low energy beam transport (LEBT) complete with a beam diagnostics leg, the EINJ cryomodule, a medium energy beam transport and diagnostic end station (MEBT) and beam dump. Two guns are envisaged. In the first phase (present) a 100kV thermionic gun with rf modulated gridded cathode bias is utilized. The cathode rf drive is at 650MHz providing rf bunches for one of every two accelerating buckets. This will soon be replaced by a 300kV gun also with rf modulated gridded cathode bias at 650MHz. The higher energy is needed to achieve efficient capture in the EINJ while the 100kV gun is perfectly sufficient to characterize the rf modulation and commission the LEBT and diagnostics. In both cases the specified peak current is 10mA, with a bunch length of $\leq \pm 20^0$ of 650 MHz (170 ps), a bunch charge of 15.3 pC, an energy spread of $\leq \pm 1$ keV and a transverse emittance of ≤ 30 μm normalized to a 2σ x 2σ cylindrical beam.The rf modulation can also be pulsed to provide a macro duty cycle varying from 0.1% to 99.9% duty cycle at various macro periods.

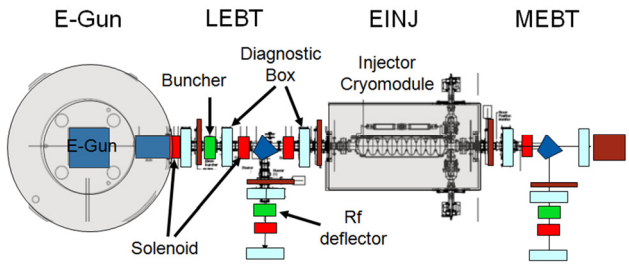

Figure. 1: TRIUMF/VECC beam test configuration.

The LEBT straight section is designed to prepare the beam for acceleration. Three solenoids are used to provide transverse matching and transportation. An initial solenoid provides a waist at the buncher while the two downstream solenoids match the beam to the cryomodule. A 1.3GHz room temperature buncher provides longitudinal matching to the EINJ. An analyzing diagnostic line includes a 90^0 bending spectrometer, diagnostic boxes and a 1.3GHz rf deflector for bunch length measurements.

DIAGNOSTICS

The diagnostics used in the LEBT are shown in Fig. 2. The diagnostics fit in multi-port custom chambers machined out of solid stainless steel bulk material. The

Copyright © 2012 by the respective authors — cc Creative Commons Attribution 3.0 (CC BY 3.0)

diagnostic chamber has eight transverse ports, four on the horizontal and vertical axis and four on the 45 degree axis. Two ports are occupied with an ion pump and turbo-pump roughing system respectively leaving six available for diagnostics.

The diagnostics comprise devices for a wide range of beam intensities. More details can be found in [3]. A standard water cooled Faraday cup (FC) can dissipate beam powers up to 200W. A high power Faraday cup (HPFC) is designed to take the full 1kW and is positioned at the end of the beamline. A high power slit (HP-Slit or Linear profile monitor (LPM)), shown in Fig. 3, consists of a water cooled copper plate with two 1mm slits cut at 45 degrees to the plate and 90 degrees from each other.

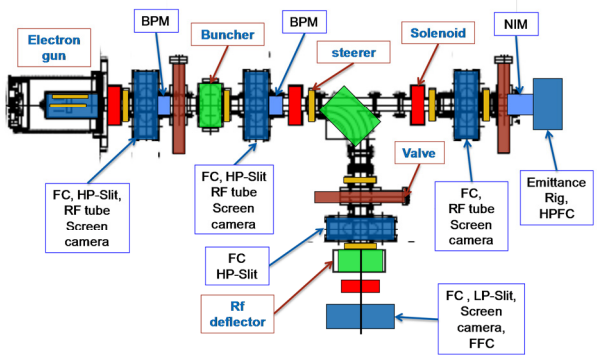

Figure 2: LEBT beam diagnostics, optical elements and rf devices.

The HP-Slit can absorb about 200W. An identical low power device, LP-Slit, has no water cooling provision and can dissipate a few watts only. The slit device is positioned on a 45 degree diagnostic port and when scanned in front of a Faraday cup gives beam x and y profile information. The device also doubles as an emittance defining slit when fixed in the beam. In longitudinal analysis mode the HP-slit in the box upstream of the analyzing dipole is used as an object slit and the HP-slit in the box upstream of the rf deflector is used to select an energy slice. The rf deflector is then used to analyze the time width of the selected beam. The slit plate also has a 2mm collimator to be used in a fixed mode to define the beam shape.

Several scintillator screens are used in the line. Each monitor includes two or three targets, optics and a camera. Possible target options are a 0.5 mm thick piece of gold-plated Yttrium Aluminium Garnet (YAG) scintillators, Chromox scintillators and a calibration target. An Optical Transition Radiation (OTR) screen is available for the MEBT. The screens can only dissipate a few Watts of beam power. A third type of profile device is the Allison type high power emittance scanner [4]. The device is designed to take up to 1kW with power densities up to 20W/mm^2. In brief the device consists of a front plate that selects a slice of the beam and a set of steering plates that scan the beamlet across a back slit to a Faraday cup to define the beam divergence. Quadrant button-type BPMs are also used for non-intercepting beam position information.

In the time domain an intercepting 50Ω co-axial fast Faraday cup (FFC) is used to measure bunch characteristics with a lower limit resolution of ~100ps. A non-intercepting monitor (NIM) capacitive pickup is used to record beam phase information. Higher resolution timing information is available from an rf deflector.

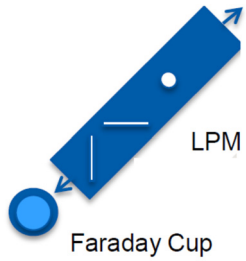

Figure 3: The LPM scanning slit profile monitor and collimator.

RF DEVICES

There are two rf devices installed in the LEBT; a 1.3GHz buncher operating in TM010 mode and a 1.3GHz deflecting cavity operating in a TM110-like mode.

Buncher

The bunching cavity is manufactured by Niowave and is identical to cavities designed and fabricated for the EMMA FFAG project at Daresbury [5]. Beam dynamics set the maximum required peak electric field on axis to 0.5MV/m and this corresponds to an integrated voltage defined by $V_0 = \int E_z dz = 30\,\mathrm{kV}$ based on a field profile from CST. The effective voltage of the cavity for β=1 φ=0 particle is normalized by T_0≅0.78 to V_{acc}=23.4kV. The measured shunt impedance, $R_{sh}=V^2/2P$, of the buncher cavity is 3.3MΩ. This converts to a linac shunt impedance ($R=2R_{sh}T_0^2$) of R=4.0MΩ for Q_0=20000 and R/Q=200Ω. The normalized transit time factors ($T_n=T/T_0$) at 100keV and 300keV are 0.64 and 0.89 respectively.

Deflector Cavity

The deflector cavity is designed after a Cornell deflecting cavity [6] but with simplifications to ease manufacturing. A TM110 pillbox vertically deflecting mode cavity is modified with entrance and exit nose cones that generate a concentrated magnetic deflecting field at entrance and exit and provide an on-axis vertical dipole field (Fig. 4) to enhance the effective perpendicular shunt impedance given by $R_\perp = \frac{(V_\perp)^2}{P} = \frac{(V_\perp)^2 Q}{\omega U}$ where $V_\perp$ is the effective perpendicular voltage gain from the magnetic and electric dipole components, Q is the quality factor of the mode and U is the stored energy. The vertical deflection is given by $y' = \frac{dy}{dz} = \frac{1}{\beta^2}\frac{V_\perp}{E}$ where E is the total energy of the electron. For β=1 CST gives $\frac{R_\perp}{Q} = 940\Omega$ while at β=0.78 (300keV) and β=0.55

Copyright © 2012 by the respective authors — cc Creative Commons Attribution 3.0 (CC BY 3.0)

(100keV) $\frac{R_\perp}{Q} = 480\Omega$ and $\frac{R_\perp}{Q} = 160\Omega$ respectively with an expected Q of 10000.

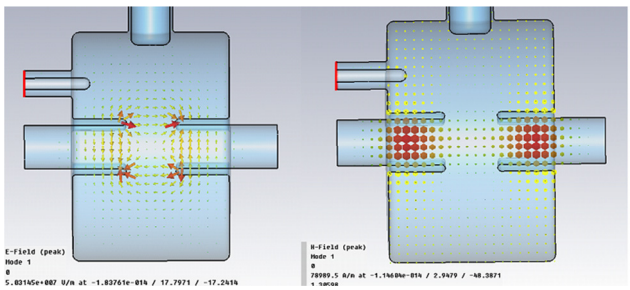

Figure 4: Electric and magnetic components of deflector field.

INSTALLATION AND BEAM TESTS

The equipment is being installed in stages. Presently the 100kV gun, complete LEBT and analyzing station are installed. The EINJ is in fabrication [2] and the MEBT station has components both in fabrication and in final design including a 30kW beam dump. The equipment is pre-cleaned in ultrasound and assembled in a clean room as major sub-assemblies. Each sub-assembly is then transported to the test area and installed into the system. When joining the new equipment to the existing equipment the open volume is slightly pressurized with filtered N_2 to reduce the risk of particulate contamination. The sealed line is evacuated and baked at ~150C for 48 hours. Typical vacuum is in the low 10^{-9} Torr range.

A series of beam tests have been organized with the installed equipment. These tests are designed to measure the properties of the beam but most importantly to establish techniques and procedures, qualify and characterize diagnostics and troubleshoot and evaluate sub-systems all well in advance of the e-Linac final installation. Initial beam tuning confirms the beam dynamics modeling for the solenoid and correctors. The emittance scanner has been characterized over a wide range of beam intensities with emittances recorded for peak power densities up to 100W/mm^2[4]. Measurements demonstrate an emittance of 90% of the beam within 30µm. The horizontal beam emittance as a function of bunch charge selected from the 100kV gun is shown in Fig. 5.

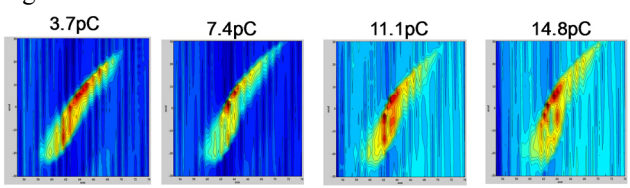

Figure 5: Horizontal emittance scan at various bunch charge settings.

The gun rf has been successfully used to provide a variable duty factor beam to adjust the beam intensity for different tuning regimes near the peak bunch charge. Typical low intensity operation is at 1kHz repetition rate with 1µsec macro-pulses (0.1% duty) with 10µA average beam current. All diagnostics including LPMs, FCs, FFCs and NIM have been characterized with beam and function as designed. The BPM and electronics have been characterized by scanning the beam with steering correctors. Both Chromox and YAG screens have been characterized. Charging up of YAG screens has been mitigated by depositing a thin gold coating on the surface.

The two rf devices are installed and commissioned. The measured installed Q of the buncher is 18500. The measured values on deflector transverse shunt impedance is $\frac{R_\perp}{Q} = 400\Omega$ for β=0.78 with a measured Q of 5400. The shunt impedance is slightly down from initial estimates due to a slight difference in actual nose positions compared to that of the simulations. The Q of the deflector was 8700 during the bench test before final cleaning so we suspect some surface pollution. Both buncher and deflector have been phase locked to the gun rf and first beam tests have been completed. The buncher effective voltage has been verified in beam based TOF tests. Fig. 6 shows the first demonstration of rf deflection of the beam on a scintillator screen. Future tests will involve characterizing the longitudinal emittance at various gun conditions.

The 300kV gun is being prepared for installation starting in Oct. 2012. The EINJ is in fabrication for installation and accelerated beam tests in early 2013.

Figure 6: Beam on a scintillator screen with rf deflector off and with rf deflector on at 0 degrees.

REFERENCES

[1] S. Koscielniak, et al., `ARIEL Superconducting Electron Linac', these proceedings.
[2] R.E. Laxdal, et al., `The Injector Cryomodule for the ARIEL e-Linac at TRIUMF', these proceedings.
[3] V. Verzilov, et al., `Beam Diagnostics Development for TRIUMF e-Linac', these proceedings.
[4] A. Laxdal *et al*: "High Power Allison Scanner for Electrons", TUCP04, proc. BIW 2012, Jefferson Laboratory, Newport News VA.
[5] C.D. Beard, et al., `EMMA RF Cavity Design and Prototype Testing at Daresbury', Proceedings of EPC08, Genoa 2008.
[6] S. Belomestnykh, et al., `Deflecting Cavity for Beam Diagnostics in ERL Injector', Proceedings of PAC07, Albuquerque, 2007.

Copyright © 2012 by the respective authors — cc Creative Commons Attribution 3.0 (CC BY 3.0)

COMMISSIONING OF THE X-BAND TEST AREA AT SLAC[#]

C.G. Limborg-Deprey*, C. Adolphsen, M. Dunning, S. Gilevich, C. Hast, K. Jobe, D. McCormick, A. Miahnahri, T. Raubenheimer, A.E. Vlieks, S. Weathersby, and D. Walz, SLAC, Menlo Park, California, R. Marsh, LLNL, Livermore, California, USA

Abstract

The X-Band Test Area (XTA) was installed in the NLCTA tunnel at SLAC over the spring and summer of 2012. The first gun to be tested is an upgraded version of a 5.5 cell, 200 MV/m peak field X-band gun designed at SLAC in 2003 for a Compton scattering experiment run in ASTA [1]. The first photo-electron beam was generated at the end of July. We report on the results of the first eleven days of commissioning.

X-BAND TEST AREA

The X-Band Test Area (XTA) is a gun test facility located in the SLAC NLCTA tunnel that uses exclusively X-Band technology. In its initial configuration, a 5.5 cell photo-rf gun is followed by a 1-m long accelerator structure (denoted T105) that had been built for NLC rf breakdown studies. Both are driven by a single klystron whose power is compressed (x4 in magnitude) with a SLED-II system. A combination of high power phase shifters and 3 dB hybrids allows the phase and amplitude of the gun and accelerator to be controlled independently.

Simulations [2] have shown that such a photoinjector has great potential to be a compact driver for X-ray FELs [3], for a compact Compton-generated photon source [4] and for Ultra-Fast Electron Diffraction. The main challenges of this technology were expected to be alignment and high dark current levels. Early operation of the facility indicates that these issues are manageable. Detailed tuning and full beam characterization will continue this year.

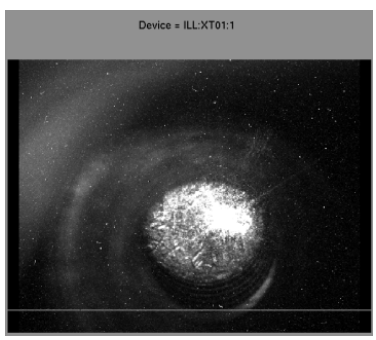

Figure 1: Green alignment laser striking the cathode.

LASER SYSTEM

Photo-Injector Laser

A Spectra Physics Tsunami oscillator locked at 79.3 MHz to the rf master clock provides a 305 mW, 65 nm bandwidth seed to a Coherent Elite regenerative Ti:Sapphire amplifier. The regenerative amplifier produces 600Hz, 3.5 mJ pulses of IR. This amplifier is shared with another experiment so pulses are sent to the XTA line at 300 Hz. The stretched IR pulses are transported through 26 m of vacuum pipe via relay imaging, yielding 2.6 mJ of IR at the XTA laser table. The IR is then compressed to 70 fs pulses of 1.7 mJ each. A non-linear tripling of the frequency with two 0.3 mm thick BBO crystals yields 120 uJ UV pulses. Finer tuning should provide a higher conversion efficiency, up to 10%, which this is not required initially.

Alignment Laser

A green laser was used to align the optics to the cathode – the image of this laser on the cathode is shown in Fig. 1. This procedure had to be implemented for two reasons: the rf gun does not have a removable cathode and the laser injection chamber was installed after the gun had already been positioned. The UV pulse follows the path defined by the green laser. A leakage of 10% before entering the injection chamber is sent to a virtual cathode camera as shown in Fig. 2.

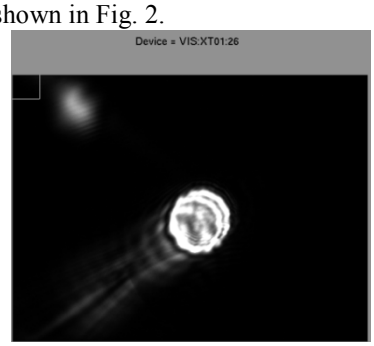

Figure 2: Virtual cathode image (4x6 mm): the main spot is the non-attenuated UV and the upper left spot is the green laser attenuated with filters.

Injection Chamber

The gun irises are 4 mm in radius which translates into a laser half-opening angular aperture of 45 mrad from the last adjustable mirror. Optimum emittance compensation requires having the first accelerator positioned as close as possible to the gun exit. However the injection mirror, which is located in between, has to be far enough away from the cathode to allow a reasonable beam stay-clear. As a compromise, the ~ 45 degree injection mirror was located 53 cm from the cathode plane. It is a 12.7 mm diameter Al substrate mirror with a UV protected Al coating. An extraction mirror for viewing the cathode is located symmetrically opposite of the injection mirror with a 7 mm gap between them. The injection chamber also accommodates a YAG screen combined with a

Work supported by the U.S. Department of Energy under contract DE-AC02-76SF00515.

*corresponding author: limborg@slac.stanford.edu

Copyright © 2012 by the respective authors — cc Creative Commons Attribution 3.0 (CC BY 3.0)

Faraday cup. A shadow of the two mirrors is visible on the dark current imaged on the YAG screen as shown in Fig. 3.

X-BAND GUN

After transport to the XTA area from the SLED II compression system, the rf is split via a 6 dB H-plane hybrid. A quarter of the power feeds the gun and three quarters feeds the T105 accelerator. The gun power is split, sent through the two phase shifters and recombined. Each phase shifter has a 110-deg range and the relative phase can be adjusted remotely to vary the combined power from zero to 100% of the input power. The linac line is also equipped with a 110-deg phase shifter to adjust the relative gun-to-linac phase (although this can also be done by changing the gun shifters in common). With 76 MW from the SLED II system and the 20% attenuation that occurs during transport, the gun input power is 15.2 MW, which should produce a cathode peak field of 186 MV/m after 200 ns.

Gun Exit Energy

The bunch energy was measured by recording the beam excursion on a YAG screen as a function of corrector strength (see Fig. 3). A bunch energy of 6.85 MeV +/- 0.15 MeV was observed with 76 MW from SLED II. Both vertical and horizontal measurements are consistent. This beam energy corresponds to a cathode peak voltage of at least 180 MV/m and depends on the rf-to-beam phase at the cathode (see Fig. 4), which was not known for this experiment.

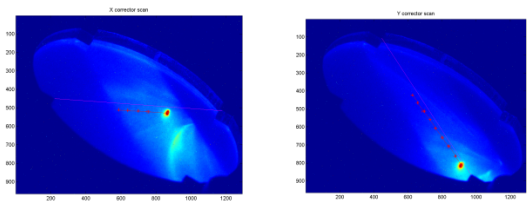

Figure 3: Beam centroid displacement as a function of (left) horizontal corrector and (right) vertical corrector settings.

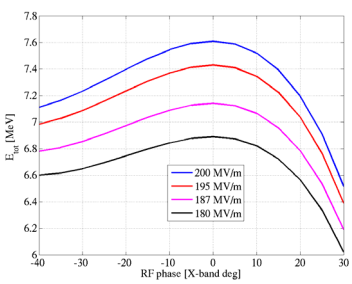

Figure 4: ASTRA-calculated energy at the gun exit for four cathode voltages:

Gun Tuning

To maximize the field in the gun, the reflected power was minimized by adjusting the gun temperature (the rf frequency is kept constant at 11.424 GHz). The gun operating temperature had been anticipated to be around 53 degC from design and cold test tuning. The minimization of reflected power indeed occurs at 53 degC as can be seen from the waveforms in Fig. 5. Systematic beam energy measurements as a function of temperature will be performed during the next run.

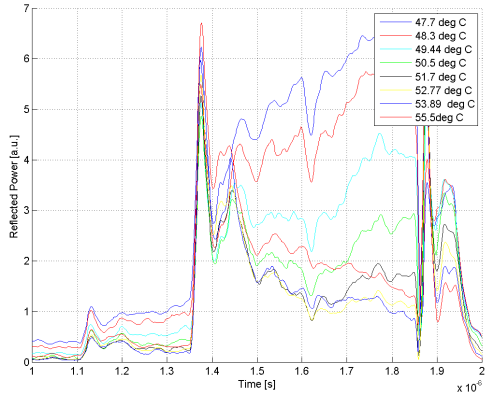

Figure 5: Reflected power waveforms from the gun for cathode temperatures between 47.7 degC and 55.5 degC.

Dark Current

The integrated dark current per pulse was measured as a function of the cathode temperature for 76 MW, 200 ns rf pulses from SLED II. The dark current was observed to increase as the temperature was lowered from the value that gives minimum reflected power (see Fig. 6). At the operating temperature of 53 degC, the dark current is about 150 pC, which should be manageable. The fluctuations in the dark current were of the order of 13%, and since the dark current increases as a high power (n > 10) of the peak voltage ($I \sim V^n$), the field stability appears to be at the 1% level or smaller.

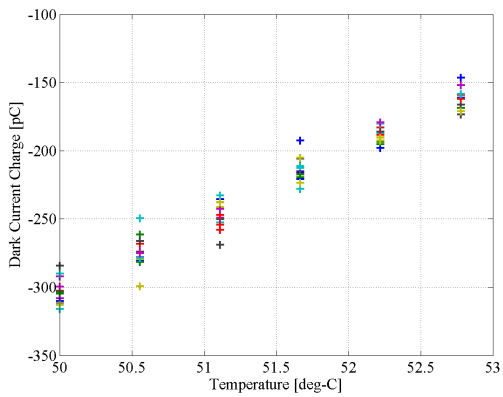

Figure 6: Gun dark current versus cathode temperature.

Beam Based Alignment

The laser should strike the cathode at the electromagnetic center of the rf gun and the electromagnetic axis of the gun should coincide with the magnetic axis of the solenoid. Preliminary measurements were made to establish a procedure to optimize the centering of the laser on the cathode. An rf phase scan was performed and the centroid of the photo-electron beam recorded on the first YAG screen. For the data shown in Fig. 7, the laser center is estimated to be offset from the gun center by 200 μm horizontally and 2.2 mm vertically.

Copyright © 2012 by the respective authors — cc Creative Commons Attribution 3.0 (CC BY 3.0)

Quantum Efficiency

Low energy (~7 μJ) laser pulses were used initally to avoid damage during laser alignment. This produced bunch charges of up to 15 pC. The quantum efficiency was thus around 10^{-5}.

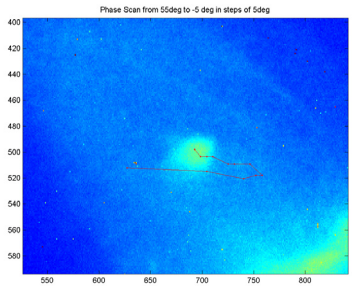

Figure 7: Electron beam centroid position on first YAG screen for various rf-to-beam phases.

HIGH ENERGY

Energy Measurement

The beam was accelerated in the linac and transported to the spectrometer at the end of the beamline. The gun-to-linac distance was not set precisely, and with the limited range of the phase shifters with full gun power operation, on-crest operation could not be achieved, although the phase offset was probably about 15 deg. The electron beam energy was measured to be 50 MeV. An appropriate positioning of the gun phase shifters should allow us to reach crest and 70 MeV. The T105 structure presently installed cannot be conditioned above about 65 MV/m due to pulse heating limits in the couplers. A new T105 structure with racetrack couplers will be installed next year and should allow up to100 MV/m acceleration.

Energy Jitter and Energy Spread

Large bunch energy jitter was measured at the spectrometer, about 2% at 50 MeV beam energy as shown in Fig. 8. This corresponds to excursions of +/- 3 deg X-band. Jitter levels of 3 deg could be traced back to the Low Level RF system. A new LLRF electronics system with higher initial power levels [5] will be installed and should lower this jitter. The additional jitter comes from the laser oscillator phase locking. The Tsunami oscillator is rated for 500 fs timing jitter, i.e., 2 deg X-band. However, we suspect that a larger oscillator phase jitter was present at the time of our experiment which would explain the +/- 3 deg total excursion. Acquiring a lower timing jitter (< 60 fs rms) oscillator is presently being considered.

Correlated energy spreads smaller than 50 keV were observed on the YAG screen of the spectrometer line. The YAG thickness and blurring effects hide the true beam size values. An OTR screen will be available for the next run.

Transverse Beam Characterization

The beam emittance was measured on a YAG screen as the OTR station was not equipped with appropriate lenses for capturing large cones of light. Small and intense spots were nevertheless observed on the OTR screen.

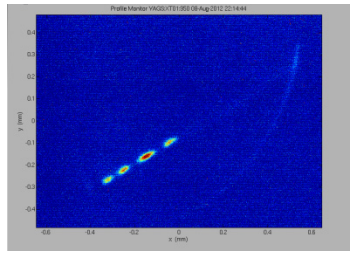

Figure 8: Five, 50 MeV pulses on the spectrometer YAG screen.

CONCLUSION

First photo-electron beam was successfully produced at the XTA facility after only 18 months of design, construction and installation. The rapid turn-on of this facility owes a lot to the expertise of various SLAC departments and the many years of X-band technology development. The results reported here cover only 11 days of commissioning and thus more work will be needed to fully optimize and understand the beam characteristics. However the early results look promising. In particular, the dark current levels and cathode QE are acceptable.

For the next run, an X-Band transverse deflector will be installed that will allow bunch length and slice emittance measurements. Many tools developed for optimizing the LCLS injector will be reused here. The OTR modules will be equipped with appropriate imaging systems for high resolution beam size determination. A peak brightness three to four times higher than that achieved at LCLS is expected with bunch lengths three times shorter than those obtained from S-Band guns.

ACKNOWLEDGMENT

We wish to thank E. Colby, R. Hettel and N. Holtkamp for their support and encouragement for this project and members of the many SLAC departments (alignment, magnetic measurement, mechanical engineering, laser, software and controls) for their valuable contributions

REFERENCES

[1] A.E. Vlieks, et al. “Recent measurements and plans for the SLAC Compton X-ray source”, SLAC-PUB-11689, 2006. 10pp. Published in AIP Conf.Proc.807:481-490, 2006.

[2] C. Limborg-Deprey, et al., “An X-band Gun Test Area at SLAC," MOP015, in Proceedings of the 2011 Particle Accelerator Conference, New York, NY (2011).

[3] Y.Sun “Low-charge, hard x-ray free electron laser driven with an X-band injector and accelerator,” Phys. Rev. ST Accel. Beams 15, 030703 (2012).

[4] F. V. Hartemann, et al., Phys. Rev. ST Accel. Beams 8, 100702 (2005).

[5] R.Akre “SLAC Linac RF Performance for LCLS,” SLAC-PUB-8574, Aug 2000.

Copyright © 2012 by the respective authors — cc Creative Commons Attribution 3.0 (CC BY 3.0)

PERFORMANCE OF THE FIRST C100 CRYOMODULES FOR THE CEBAF 12 GeV UPGRADE PROJECT*

M. Drury, A. Burrill, G. K. Davis, J. Hogan, L. King, F. Marhauser, H. Park, J. Preble, C. E. Reece, R. Rimmer, A. Reilly, H. Wang, and M. Wiseman,
Thomas Jefferson National Accelerator Facility, Newport News, VA 23606 USA

Abstract

The Thomas Jefferson National Accelerator Facility is currently engaged in the 12 GeV Upgrade Project. The goal of the 12 GeV Upgrade is a doubling of the available beam energy of CEBAF from 6 GeV to 12 GeV. This increase in beam energy will be due primarily to the construction and installation of ten "C100" cryomodules in the CEBAF linacs. The C100 cryomodules are designed to deliver an average 108 MV each from strings of eight seven-cell, electropolished, superconducting RF cavities operating at an average accelerating gradient of 19.2 MV/m. The new cryomodules fit in the same available linac space as the original CEBAF 20 MV cryomodules. Cryomodule production started in September 2010. Initial Acceptance Testing started in June 2011. Four C100 cryomodules were installed and tested from August 2011 through July 2012. The first two of these cryomodules were successfully operated during the last period of the CEBAF 6 GeV era, which ended in May 2012. This paper will present the results of Acceptance Testing and Commissioning of the C100 style cryomodules to date.

INTRODUCTION

Since July 2011, six C100 cryomodules have been delivered to the Cryomodule Test Facility (CMTF) for Acceptance Testing. Four of these cryomodules have been installed in the South Linac of CEBAF and commissioned. Two of these, C100-1 and C100-2, have been operated with beam during the final 6 GeV operations period for CEBAF which started in November 2011 and ended in May 2012.

Each cryomodule goes through two testing cycles, acceptance testing prior to installation in the linac and a final commissioning after installation.

Acceptance testing is generally a more comprehensive set of tests than the final commissioning and is meant to uncover any major problems before delivery to the linac. An example of such a problem would be the failure of an instrumentation feedthru during cooldown that leads to the loss of insulating vacuum. Such problems are more easily addressed while the cryomodule is in the CMTF.

During acceptance testing, each cavity is tested to insure proper operation of the mechanical and piezo tuners. Low power measurements using a network analyser are made to characterize the seven passbands of each cavity once the cavities have been tuned to 1497.000 MHz. The higher order modes of each cavity are also characterized at low power. Each cavity is then characterized in terms of maximum gradient, field emission, and unloaded Q (Q_0). Measurements of microphonics, pressure sensitivity, static Lorentz coefficients and static heat loads are also conducted.

Once the cryomodule has been installed in a linac, it is commissioned. Commissioning consists of a subset of the acceptance tests. The focus for commissioning is determining stable operating gradients, measuring field emitted x-ray production, Q_0 and microphonics.

MICROPHONICS

The measurement of cavity detuning due to external vibration sources is conducted in both the CMTF and in the tunnel. The results of these measurements, however, are location and time dependent. We now know that the CMTF has a large number of vibration sources that are not present in the tunnel environment. This paper will focus on measurements made on installed cryomodules.

A maximum peak detuning of 25 Hz was budgeted for the C100 cavities. Microphonics testing of the first unit (C100-1) met design goals, but results were higher than expected based on prototype testing. C100-1 as measured during operation in the CEBAF tunnel ranged as high as 21 Hz peak detuning during a 500 second sample time period [1]. While within the specification, the results were higher than predicted. These results led to a modification of the mechanical tuner system in order to gain margin. The tuner modification was first installed on the cavities in C100-4. Thicker plates at either end of the tuning structure led to an average reduction in peak detuning of 42% [1].

TUNING SENSITIVITY

Two other properties related to cavity detuning are measured during Acceptance testing. These are pressure sensitivity and the static Lorentz coefficient. As Tables 1 and 2 illustrate, these properties were also affected by the tuner modifications.

Table 1: Pressure Sensitivity (Hz / torr)

	C100-1	C100-2	C100-3	C100-4	C100-5
1	435	404	420	**250**	**254**
2	322	323	352	**226**	**234**
3	300	357	323	**215**	**203**
4	252	321	355	**200**	**188**
5	273	356	323	**205**	**183**
6	314	338	325	**230**	**203**
7		379	355	**213**	**214**
8		399	426	**243**	**243**

* Authored by Jefferson Science Associates, LLC under U.S. DOE Contract No. DE-AC05-06OR23177.

Copyright © 2012 by the respective authors — cc Creative Commons Attribution 3.0 (CC BY 3.0)

Table 2: Static Lorentz Hz/(MV/m)^2

	C100-1	C100-2	C100-3	C100-4	C100-5
1	-2.35	-2.23	-2.27	**-1.59**	**-1.60**
2			-2.18	**-1.58**	**-1.68**
3	-1.98	-2.08	-2.04	**-1.62**	**-1.43**
4	-1.95	-2.08	-2.14	**-1.63**	**-1.58**
5	-2.05	-2.11	-2.01	**-1.46**	**-1.55**
6		-2.19	-2.16	**-1.54**	
7	-1.94	-2.32	-2.18	**-1.61**	
8	-2.48	-2.36	-2.30	**-1.47**	

These two tables show that the tuner modification has led to a 37% reduction in pressure sensitivity and a 28% reduction in the static Lorentz detuning coefficient.

GRADIENT PERFORMANCE

The C100 cavities are required to have an average maximum usable gradient equal to or greater than 19.2 MV/m in order to meet the design goal of 108 MeV per cryomodule. The maximum gradient of each cavity is determined first in the CMTF and again after the cryomodules are installed in the linacs.

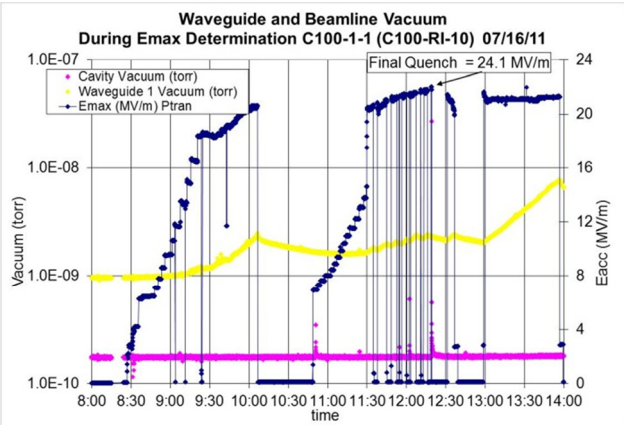

Figure 1: Maximum Gradient Determination

Figure 1 illustrates the process of raising a cavity to its maximum gradient (Emax) for the first time in a cryomodule along with the effects on both beam line and waveguide guard vacuums. This process can take as long as eight hours. Note that this cavity experienced multiple non-repeating quenches as the gradient was raised to its final maximum gradient at 24.1MV/m. This is typical behaviour for a cavity during this procedure.

In theory, there are a number of conditions that may limit the maximum gradient. These include, arcing in the waveguide vacuum space, vacuum degradation, rf window temperature, quenching, high dynamic (rf) heat load and an administrative limit of 25 MV/m. In practice, the cavities are limited by quenching, high rf heat load or the administrative limit. For single cavity operation, a dynamic heat load in the range of about 50–60 W would be considered to be too high for stable operation. Heat loads in this range will most likely cause "boiling" in the helium bath. This behavior manifests as large swings in the helium bath level and an increase in the helium bath pressure.

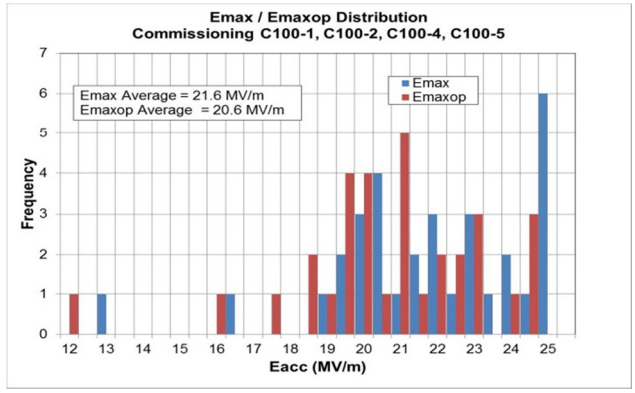

Figure 2: Emax / Emaxop Distribution.

Once the maximum gradient is known a determination must be made of the maximum stable operating gradient (Emaxop). This is done by lowering the gradient below Emax by an amount generally between 0.5 MV/m and 1.0 MV/m. The cavity is then operated at this new gradient for at least one hour. If no faults or cryogenic instabilities (such as boiling) occur, this gradient is designated as Emaxop for single cavity operation.

Figure 2 shows the distribution of maximum gradients for the first four installed C100 cryomodules. Note that there are three outliers in this distribution. The lowest gradient at 12.5 MV/m was the result of the beamline being vented to air during assembly, the next lowest suffered a quench induced field emitter during vertical test and was not reprocessed as would normally be done. The last of the three had a misadjusted stub tuner which led to waveguide vacuum problems. The stub tuner problem was later corrected after commissioning had been completed.

Field Emission

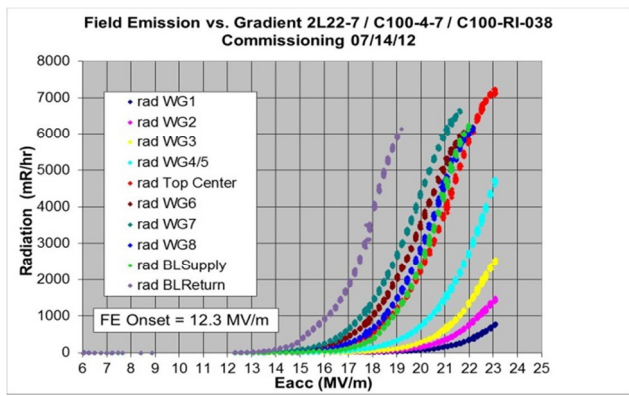

Figure 3: Typical Plot of X-Ray Production by Field Emission

After the Emaxop determination is completed, a measurement of x-rays produced by field emission as a function of gradient is made. A set of 10 Geiger –Mueller (GM) tubes are placed on the cryomodule at several locations including the beamline at either end of the cryomodule and at the Fundamental Power Couplers

Copyright © 2012 by the respective authors — cc Creative Commons Attribution 3.0 (CC BY 3.0)

(FPC's). Figure 3 shows the results for a typical cavity. Note that the GM tubes used saturate at approximately 7 R/hr. Figure 4 shows the distribution of field emission induced x-ray onset gradients for the four installed cryomodules.

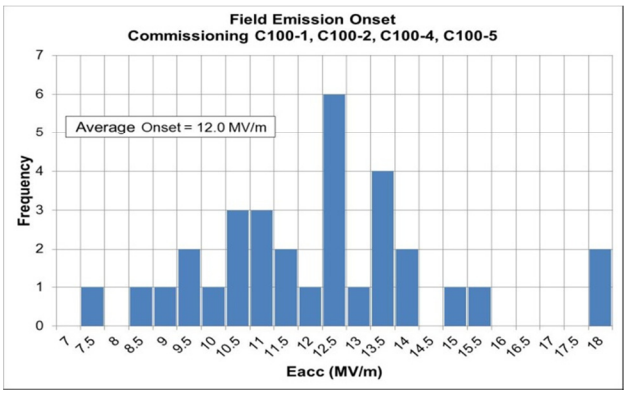

Figure 4: Field Emission Induced Onset of X-rays

Q_0 AND HEAT LOAD

After the operating gradients have been determined, Q_0 vs. E_{acc} is measured for each cavity. Q_0's are measured calorimetrically. The cryomodule is isolated by closing the JT and RT valves and the rate of rise of the helium bath pressure is used to determine the rf heat load [2]. Figure 5 shows a typical Q_0 vs. E_{acc} curve. Figure 6 shows the values of Q0 at Emaxop and at 2.07 K for the four installed cryomodules.

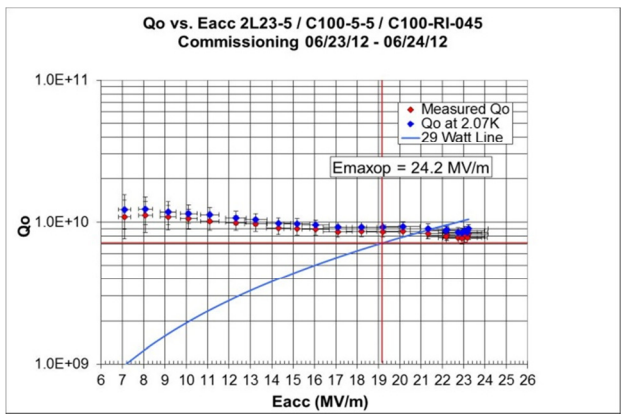

Figure 5: Typical Q_0 Plot

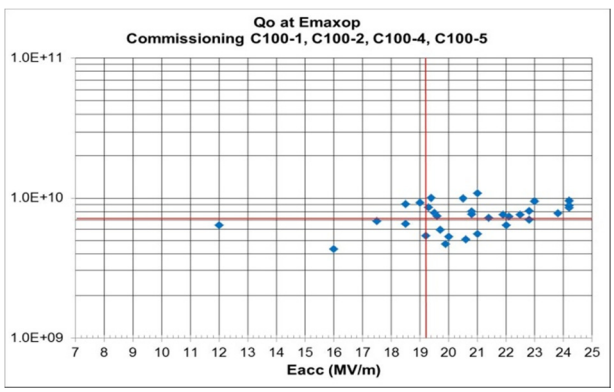

Figure 6: Q_0 at Emaxop

The Q_0 measurements are used to calculate a set of gradients at which the rf heat load equals 29 W but does not exceed Emaxop for a particular cavity. The 29 W value is based on a dynamic heat load budget for each cryomodule of 250 W that includes waveguide losses. If this budget is exceeded, boiling in the helium bath will begin and stable operations will not be possible. In cases where a cavity or cavities do not reach the 29 W heat load level due to other gradient restrictions, the gradients of other cavities in that cryomodule may be adjusted upwards. The final commissioning step is to attempt to operate all eight cavities simultaneously at these gradients for at least one hour. The average of these "ensemble" maximum operating gradients is 19.5 MV/m.

Table 3: Cryomodule Energy Gain (MeV)

	Acceptance	Commission	Ops
C100-1	111.7	104.3	94.5
C100-2	117.5	109.6	108
C100-3	118.7		
C100-4	115.1	105.8	106.2
C100-5	108.2	109.9	109.3

Table 3 lists energy gain for the first five cryomodules. It should be noted that the Acceptance test numbers are only predictions as the CMTF set up only allows for single cavity operation. Furthermore, only the first two cryomodules have been operated with beam. C100-1 has not yet been pushed to its maximum gradients with beam as efforts during the last physics run were focused on bringing C100-2 up to its maximum gradients with beam. On May 18, 2012, C100-2 was operated at 108 MV for over an hour at 465 µA, the design current for CEBAF [3].

SUMMARY

Five C100 cryomodules have been tested in the CMTF. Four of these have been installed in the CEBAF linacs, two of which have been operated with beam. In testing, all five have met or exceeded the specifications necessary for successful operation in the 12 GeV CEBAF accelerator. One of the five cryomodules has been shown to be operable at the design energy and beam loading.

REFERENCES

[1] K. Davis *et al.*, "Vibration Response Testing of the CEBAF 12GeV Upgrade Cryomodules," LINAC 2012, (2012).

[2] M. Drury *et al.*, "Commissioning of the CEBAF Cryomodules," PAC 1993, (1993).

[3] C. Hovater *et al.*, "Commissioning and Operation of the CEBAF 100 MV Cryomodules," IPAC 2012 (2012).

Copyright © 2012 by the respective authors — cc Creative Commons Attribution 3.0 (CC BY 3.0)

VIBRATION RESPONSE TESTING OF THE CEBAF 12 GeV UPGRADE CRYOMODULES*

K. Davis, J. Matalevich, T. Powers, and M. Wiseman
Thomas Jefferson National Accelerator Facility, Newport News, VA 23606, USA

Abstract

The CEBAF 12 GeV upgrade project includes 80 new 7-cell cavities to form 10 cryomodules. These cryomodules were tested during production to characterize their microphonic response *in situ*. For several early cryomodules, detailed (vibration) modal studies of the cryomodule string were performed during the assembly process to identify the structural contributors to the measured cryomodule microphonic response. Structural modifications were then modelled, implemented, and verified by subsequent modal testing and *in-situ* microphonic response testing. Interim and latest results from this multi-stage process will be reviewed.

VIBRATION TEST PROGRAM

A vibration test program was conducted during construction of the first C100 cryomodules, with the goal of improving the operational vibration response of the cryomodules. Beginning with C100-4, a simple modification was introduced that reduces the peak microphonic detuning to less than one-half of the original project design requirements.

The 12 GeV project "budgeted" for 25 Hz peak total detuning (4 Hz static plus 21 Hz dynamic) based on the available klystron power (13 kW), the design Q_{ext} (3.2×10^7) for the fundamental power couplers, and maximum beam load (465 μA) [1]. Tuner performance allowed the static detuning budget to be reduced, allowing the full 25 Hz for the peak dynamic detuning. Operational experience in CEBAF has established a 6× rule-of-thumb between standard deviation to peak detuning, giving us approximately 4.2 Hz rms detuning (one σ, assuming a Gaussian distribution).

Commissioning of the cryomodules in CEBAF includes measurement of the ambient microphonic response of each cavity in the cryomodule using established procedures and test equipment [2]. Microphonics testing of the first unit (C100-1) met design goals marginally, but results were higher than expected based on prototype testing. C100-1, as measured during operation in the CEBAF tunnel ranged as high as 21 Hz peak detuning over a 500 second time period. Early measurements taken in the cryomodule test facility were even higher, but were eventually attributed to anomalous local driving sources in that facility. The last full upgrade-style pre-production cryomodule ("Renascence") measured less than 15 Hz peak detuning for all cavities in the cryomodule test facility (historically, half this amplitude would be expected in the CEBAF tunnel due to the different vibration environment found there). The most relevant design changes between the two modules comprised removal of the stiffening rings from the cavity design and a completely different tuner design.

A typical spectrum from one of the noisier cavities in the first production cryomodule (C100-1) is shown in Figure 1. The spectrum is dominated by the peak at approximately 10.5 Hz. This peak shows up in the spectrum of all eight cavities, and is typically highest in amplitude in the middle of the string (cavities 4 and 5), becoming lower in amplitude as you move out to the ends of the string (cavities 1 and 8).

Vibration testing of the CEBAF 12 GeV upgrade cryomodules comprised FEA modelling, modal testing of cryomodule components, and operational RF testing of the completed, cold cryomodules. The end goal was to improve our understanding of the vibrational response of the cryomodule to the extent that it affects RF performance, and to improve that performance with minimal risk to the 12 GeV project.

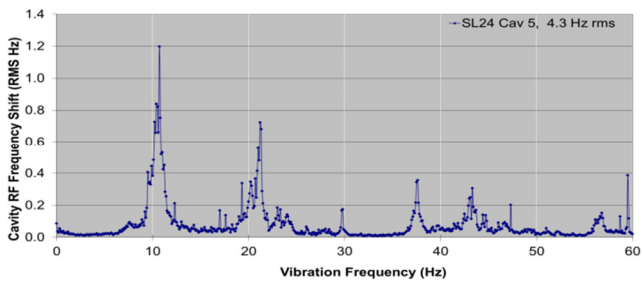

Figure 1: Spectra of Baseline (C100-1) Design

FEA Modelling

ANSYS™ finite element analysis software was used to create a 1-D simplified model of the string assembly. Once the model was validated against the modal test data, the model was used to vet various proposed design modifications including stiffening inside the cavity helium vessels, adding damping to the cavity string assembly, and changes to the cavity tuner. The conclusion of this analysis was that the tuner pivot plates were the least stiff component in the tuner assembly. Stiffening the pivot plate was judged to present low schedule, budget, and technical risk.

* Authored by Jefferson Science Associates, LLC under U.S. DOE Contract No. DE-AC05-06OR23177. The U.S. Government retains a non-exclusive, paid-up, irrevocable, world-wide license to publish or reproduce this manuscript for U.S. Government purposes.

Copyright © 2012 by the respective authors — cc Creative Commons Attribution 3.0 (CC BY 3.0)

Modal Testing

The second production cryomodule (C100-2) was instrumented with triaxial accelerometers during the assembly process [Figure 2]. Hammer impact testing was performed at various stages during the assembly process, beginning with the completed string of eight cavities suspended in its space frame, and ending with the finished cryomodule prior to cool-down. Because a complete cryomodule is such a complex mechanical assembly with limited internal access, waiting until the module is completed before testing makes it difficult or impossible to determine how individual components and subassemblies influence the vibration response of the completed cryomodule. Because of the extreme temperatures inside an operating cryomodule, cool-down marked the last opportunity to collect data from accelerometers on the cold-mass.

A parallel set of modal tests was performed using a single C100 cavity mounted to its tuner in a stand-alone test stand (the tuner test stand) [Figure 3]. The goal for this set of modal tests was to understand how these components contributed to the overall vibration response of the cryomodule, and to test various engineering solutions intended to improve the vibration response.

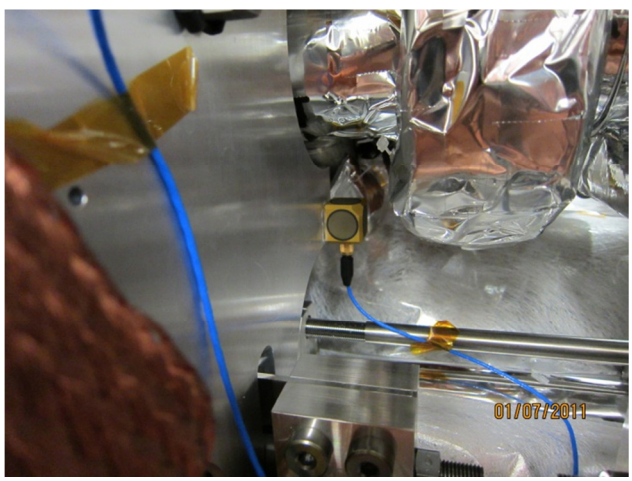

Figure 2: Accelerometer mounted to a tuner pivot plate during final assembly of the cryomodule.

TEST RESULTS

Results of String Modal Analysis

The following modes were identified as contributing to the operational microphonics:

1) First axial (10 Hz, beamline orientation) rigid body mode of the string: Center cavities have higher overall microphonics, most of which is accounted for by this mode. This effect is caused by the center axial nitronic rods, which impose a nearly fixed boundary at one end of cavity 4 and cavity 5. The warm tuner stacks actively participate in this mode, providing possible "hooks" to easily insert damping into the system.

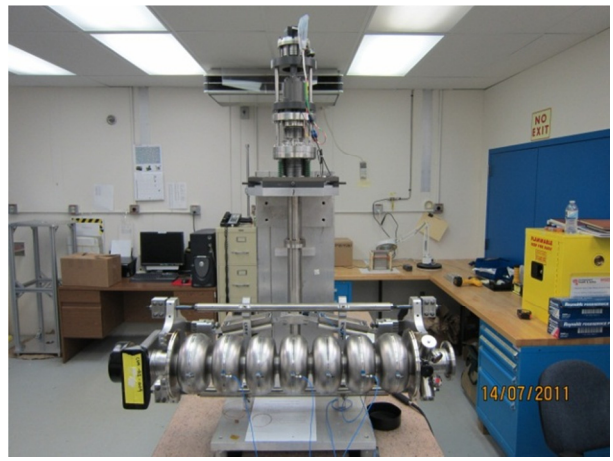

Figure 3: C100 Cavity in the Tuner Test Stand

2) Second axial modes of the string (20 to 25 Hz, varies with cryomodule): Each half-string (cav 1-4 or cav 5-8) has a mode where the four cavities move together, primarily in the axial (beamline) direction. The other half-string usually resonates at a slightly different frequency from cryomodule to cryomodule. The warm tuner stacks move very little in this vibration mode, any damping would involve changes to the cryomodule cold mass.
3) First bending mode of each individual cavity (40 to 45 Hz, varies cavity-to-cavity): The warm tuner stacks actively participate in this mode, providing possible damping "hooks" into the system.

Modified (stiffer) tuner plates were installed beginning with C100-4. The modal test of the cavity string was repeated during the assembly of C100-5. The results showed a decrease in the response at 10 Hz and between 40-45 Hz. The results also predicted a slight increase in response amplitude and frequency in the rage of 20-25 Hz.

Results of Tuner Test Stand Modal Analysis

In support of the investigation into microphonics on C100 cryomodules, a series of bench measurements were collected utilizing the tuner test stand [Figure 3]. The bench setup consisted of a bench-mounted C100 tuner, cavity, and in some test configurations, a helium vessel as well. The intent was to: perform a head-to-head comparison of several potential design modifications, experimentally define the vibrational modes of the system, and determine at what level measurements acquired on this fixture translated into actual performance of the tuner/cavity system in a fully assembled cryomodule. Because the boundary conditions on the bench are different than in the cryomodule, it was fully expected that the vibrational response would be different. But it was expected that at least portions of the system response would be similar enough that the results would prove useful to the overall study. The modifications that were studied include 1) a retrofit cell support device between the helium vessel and the cavity (both with and

Copyright © 2012 by the respective authors — cc Creative Commons Attribution 3.0 (CC BY 3.0)

without a cryogenic damping mesh material installed), and 2) stiffened tuner pivot plates.

The vibrational response of the cavity with and without the support devices was substantially the same with only modest reduction in amplitude with the support device. The results of the testing with and without the stiffened tuner pivot plates showed more promise. The overall modal response between the two configurations was similar as far as mode shapes and resonant frequencies. The configuration with the stiffened arms resulted in reduced vibrational amplitudes for several modes and a significant reduction in amplitude for a lateral bending mode of the cavity.

Operational Testing of the C100 Cryomodules

As of July, 2012, four C100 cryomodules have been installed and commissioned in CEBAF. Two of these cryomodules (C100-1 and-2, baseline tuner design) have been used to deliver beam to physics experiments during the final 6 GeV run. C100-2 demonstrated the ability to meet the 12 GeV design goals of 108 MeV per cryomodule with 465 μA of beam loading. Two more cryomodules (C100-4 and -5, modified tuner design) were installed at the beginning of the 12 GeV Long Shutdown. They have not been used to accelerate beam [3].

Since all of the cryomodules have not completed their construction, it was especially valuable to perform a validation test of the design modification: to compare the vibration response of a baseline cryomodule and a modified cryomodule. Because microphonic response is somewhat variable as a function of time and position in the linac, direct comparison of existing microphonics data (measured weeks or months apart) was not ideal. A baseline cryomodule and a modified cryomodule were operated in adjacent zones in the CEBAF tunnel with all sixteen cavities simultaneously at 10 MV/m, using the normal accelerating operating mode (constant frequency, fixed gradient regulation). The results are summarized in Table 1. Comparing the spectra of this data for C100-1 vs. C100-5, the dominant frequencies are similar; the relative contribution of the 10 Hz and 40-45 Hz components has been substantially reduced, at the expense of a moderate increase in the 20-25 Hz components. The overall ambient microphonic response of the cavities improved (decreased) by an average of 42%. This data is consistent with commissioning microphonics data measured independently on C100-1 through 5.

Table 1: Operational Microphonics in the CEBAF Tunnel, Baseline vs. Modified Design (peak detuning, Hz)

Cryomodule	C100-1 (baseline)	C100-5 (modified)	% Improved
Cavity 1	11.8	5.1	57%
Cavity 2	12.8	6.7	48%
Cavity 3	13.7	5.6	59%
Cavity 4	13.5	7.4	46%
Cavity 5	18.0	9.6	46%
Cavity 6	9.1	8.5	8%
Cavity 7	9.7	5.6	42%
Cavity 8	8.9	5.8	35%

Other Operational Issues

CEBAF accelerator operations group have had six months experience with first two C100 cryomodules. During this time, operations worked closely with the Low-Level RF group to define and improve the control system parameters and user interface [4]. One remaining issue that may be related to vibration response and/or controls: when operating at or near the limits of klystron power (high gradient and high beam loading), a single cavity trip can lead to a cascade that trips some, or all, of the other cavities in the zone. When a cavity trips, the associated loss of Lorentz force causes a step detuning of that cavity. Such trips contain substantial high frequency mechanical energy that travels through the string detuning other cavities (all eight cavities are rigidly coupled to each other). In some cases, all eight cavities trip within a few seconds. The root cause of these trips and how to control them are operational issues that are still being studied. Thus far, this has not proven to be a significant factor reducing beam availability. We are studying control system changes to reduce these trips, and to improve the associated recovery time once a trip happens.

SUMMARY

The first four C100 cryomodules have been commissioned; the first two were used to deliver beam to the CEBAF physics program over a six-month period. The microphonic response of the first two modules was within design requirements, but higher than expected. A vibration test program was performed. Various proposed changes were analysed, resulting in production changes to the cavity tuner. The first two cryomodules incorporating these modifications have been commissioned and tests show, on average, a 42% improvement in operational microphonic response (less than half of the original 12 GeV design envelope). This tuner modification will be included in the last seven C100 cryomodules, scheduled to be complete by the end of 2012.

REFERENCES

[1] C. Reece *et al.*, "Optimization of the SRF Cavity Design for the CEBAF 12GeV Upgrade," SRF2007.

[2] J. Delayen *et al.*, "Microphonics and Lorentz Transfer Function Measurements on the SNS Cryomodules," SRF2003.

[3] M. Drury *et al.*, "Performance of First C100 Cryomodules for the CEBAF 12 GeV Upgrade Project," these proceedings.

[4] C. Hovater, *et al.* in *Proc. Int. Part. Accel. Conf. 2012*. New Orleans, Louisiana: p. 2432-2434.

Copyright © 2012 by the respective authors — cc Creative Commons Attribution 3.0 (CC BY 3.0)

STABILIZATION OF THE BEAM INTENSITY IN THE LINAC AT THE CTF3 CLIC TEST FACILITY

A. Dubrovskiy, JINR, Dubna, Russia
F. Tecker, CERN, Geneva, Switzerland
B.N. Bathe, S. Srivastava, BARC, Mumbai, India

Abstract

A new electron beam stabilization system has been introduced in CTF3 in order to open new possibilities for CLIC beam studies in ultra-stable conditions and to provide a sustainable tool to keep the beam intensity and energy at its reference values for long term operations. The stabilization system is based on a pulse-to-pulse feedback control of the electron gun to compensate intensity deviations measured at the end of the injector and at the beginning of the linac. Thereby it introduces negligible beam distortions at the end of the linac and it significantly reduces energy deviations. A self-calibration mechanism has been developed to automatically configure the feedback controller for the optimum performance. The residual intensity jitter of 0.045% of the stabilized beam was measured whereas the CLIC requirement is 0.075%.

INTRODUCTION

CTF3 is a test facility, which is extensively used to uncover new frontiers of the Compact Linear Collider (CLIC) and to develop new technologies of normal conducting linear accelerators [1, 2]. In spite that the feasibility of most of the critical CLIC components has been demonstrated the demands on the beam with parameters closer to the CLIC ones are only rising [3]. The quality, the performance and the relevance to CLIC of each beam shot reduces with the beam deviation from the nominal parameters. In CLIC the beam stability and reproducibility are essential properties and they are required in order to keep the maximum luminosity up to 5.9×10^{34} $cm^{-2}s^{-1}$ at energies from 500 GeV to 3TeV during 20 years of high energy experiments [4]. The beam stability in CTF3 needs to be improved in order to meet CLIC requirements.

DRIVE BEAM GENERATION

In CTF3 an electron beam with the intensity of 4.5 A and the pulse length of 1.5 μs is created by a thermionic gun, bunched at 1.5 GHz or 3 GHz in the bunching system and then pre-accelerated up to 20 MeV (see Fig. 1). After the injector the beam passes through the cleaning chicane, where low energy particles are eliminated and the bunch length is reduced. The beam of 4.0 A with a low energy spread is injected into the linac. It is accelerated in the fully loaded mode at the average gradient of 7 MV/m up to 125 MeV. Then the beam goes through the stretching chicane, where the bunch length is increased. After that the beam goes around the delay loop and combiner ring, where the intensity is increased by the factor four or eight. The generated high-intensity, high-energy beam is delivered to the tests lines, where the beam is most required to be stable.

BEAM STABILITY OUTLINES

Beam current variations and drifts at the level of 10^{-4} in CTF3 cannot be associated with any one particular device as dominant source of influence. Apparently, it is a combination of imperfections of all components together: the electron gun, RF sources and the current control of magnets. On top of this each of components changes its properties due to fatigue processes, temperature variations and unknown sources. This study is limited to the consideration of the treatment of integrated deviations only in the linac.

The intensity and energy stabilities are the main properties of the beam, which are responsible for the stable pulse-to-pulse beam combination and delivery to the tests areas. In the fully loaded operation the beam energy deviation at the end of the linac can be approximated as follows:

$$\Delta E \propto -\frac{1}{2} I_L \Delta\varphi_L{}^2 - \Delta I_L + \frac{I_L}{E_L}\,\Delta E_I, \qquad (1)$$

where I_L and φ_L – the intensity and phase at the beginning of the linac and E_I is the energy at the end of the injector. The beam phase and intensity deviations propagate from the injector to the linac and they are coupled through the energy deviation in the cleaning chicane:

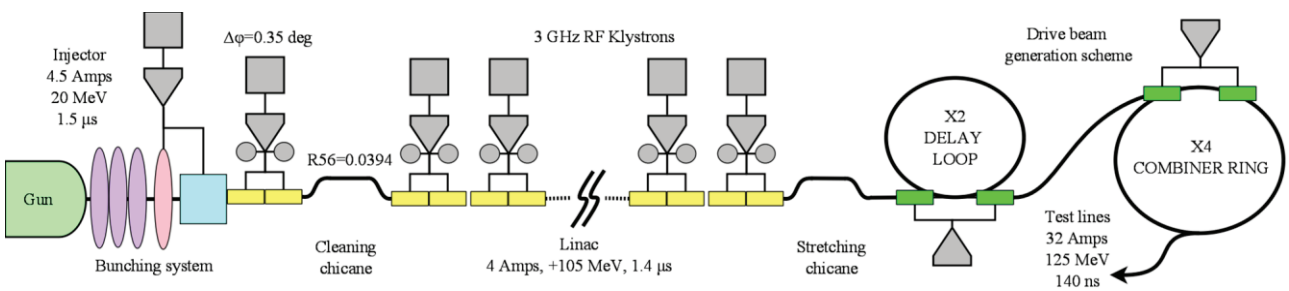

Figure 1: CTF3 layout.

Copyright © 2012 by the respective authors — cc Creative Commons Attribution 3.0 (CC BY 3.0)

$$\Delta I_L \approx \Delta I_I \frac{I_L}{I_I} - k\, I_L \frac{\Delta E_I}{E_I}, \quad (2)$$

$$\Delta\varphi_L \approx \Delta\varphi_I + R_{56} f_{RF}/c \frac{\Delta E_I}{E_I}, \quad (3)$$

where I_I and φ_I are the intensity and phase before the chicane, k is the cleaning sensitivity constant corresponding to a ratio of the relative current change through the chicane with a fixed R_{56} to the relative energy deviation, f_{RF} is the linac RF frequency and c is the speed of light. By eliminating the relative energy deviation in the injector $\frac{\Delta E_I}{E_I}$ and substituting Eq. 2 and 3 into Eq. 1 the beam energy deviation ΔE scales with a function of beam current deviations before and after the cleaning chicane.

One option to improve the stability is to keep the intensity stable in the injector ($\Delta I_I = 0$):

$$\Delta E \propto -\frac{\Delta I_L}{I_L}\left(I_L + \frac{E_I\, I_I}{E_L k}\right) - \frac{I_L}{2}\left(\Delta\varphi_I - \frac{R_{56} f_{RF}}{c\, k}\frac{\Delta I_L}{I_L}\right)^2. \quad (4)$$

This option is favourable when the beam energy and phase remain unchanged in the injector. Another alternative option is to keep the intensity stable right after the chicane ($\Delta I_L = 0$):

$$\Delta E \propto \frac{E_I\, I_I}{E_L k}\frac{\Delta I_I}{I_I} - \frac{I_L}{2}\left(\Delta\varphi_I + \frac{R_{56} f_{RF}}{c\, k}\frac{\Delta I_I}{I_I}\right)^2. \quad (5)$$

The second option copes with small energy and intensity variations and it keeps the intensity stable at the end of the linac. An option can be chosen that has the smallest absolute energy deviation. The preference shall be given to the second one if $|\Delta E|_{\Delta I_L=0}| < |\Delta E|_{\Delta I_I=0}|$ (Eq. 4 and 5), where the intensity deviations are linked through the Eq. 2. The condition can be resolved for negative deviations only when the phase deviation is small:

$$2|\Delta\varphi_I| < \left|\frac{c\, k}{R_{56} f_{RF}}\right|. \quad (6)$$

When the phase deviation is significantly smaller in the above equation and while keeping the linac intensity stable the total compensation must meet one of the following requirements:

$$-{\Delta\varphi_I}^2 \gtrsim \frac{\Delta I_L}{I_L} \gtrsim -\left(\frac{c\, k}{R_{56} f_{RF}}\right)^2 \quad \text{or} \quad \frac{\Delta I_L}{I_L} > 0. \quad (7)$$

The third option is to keep the total energy stable $\Delta E = 0$. An approximated solution from Eq. 4 and 5 is to compensate the sum of weighted deviations such that:

$$s\frac{\Delta I_L}{I_L} - (1-s)\frac{\Delta I_I}{I_I} = 0,$$
$$s \approx 1 - \frac{E_I I_I}{kE_L I_L + 2E_I I_I}. \quad (8)$$

Since $\frac{1}{2} < s < 1$ intensity deviations in the linac should also be significantly compensated.

CTF3 BEAM STABILITY

The CTF3 parameters used for the following estimations are shown in the Fig. 1. The cleaning sensitivity k can be estimated from the injector beam energy distribution function as a derivative at the cut-off energy level. It can also be measured as a ratio of the beam loss after the chicane to the injector energy change by the control of the RF field level in the last two accelerating structures. The cleaning sensitivity $k = 0.5$ was measured in a setup with a high energy acceptance, in the nominal setup the value is supposed to be higher.

The lower injector phase error is bound by the RF phase stability. All RF phases in accelerating and bunching cavities are locked by RF phase loops, which are stabilizing phases at the level of the minimum RF phase shifters step $\Delta\varphi_{RF}$ [5]. Thereby the injector phase error should be at least as $2\Delta\varphi_{RF} < \sup\Delta\varphi_I$. For the same reason the current reference can be established with an error given by the phase. Taking into account the above the criteria to compensate the intensity variations in the CTF linac can be derived from Eq. 7 as:

$$\left|\frac{\Delta I_L}{I_L}\right| \gtrsim 0.015\%. \quad (9)$$

The upper compensation limitation is restricted naturally by the performance of the thermionic gun and transient losses.

One of the current CTF3 goals is to establish a highly stable combined beam in terms of the energy and intensity at the same time: $\left|\frac{\Delta I_L}{I_L}\right| < 0.075\%$ and $\left|\frac{\Delta E}{E}\right| < 0.1\%$. For this type of operation an intermediate option should be chosen between the stable intensity (Eq. 5) and the stable energy with $s \approx 0.769$ (Eq. 8), where residual energy deviations should come only from beam phase deviations.

The proposed three options to keep the beam intensity stable give different energy deviations at the end of linac (see Fig. 2). Medium term observations of intensities showed very small deviations in the injector while the deviations in the linac were up to $\pm 0.4\%$. Thus the first option with the stable injector represents the current status with no compensation, where the energy deviation proportionally grows with the intensity deviation reaching levels over 0.6%. The second option with the stable linac should bring intensity deviations in the linac to zero and reduces energy deviations down to 0.2%, which is above the required value. The third option with the stable energy

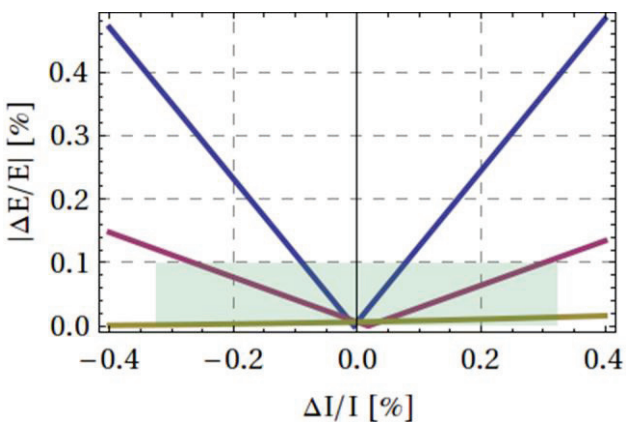

Figure 2: Total energy deviations at the end of the linac with corresponding intensity changes in the linac: blue line - stable injector, purple line – stable linac and yellow line – stable energy. The parts of the lines lying in the shaded area satisfy the stability goal.

Copyright © 2012 by the respective authors — cc Creative Commons Attribution 3.0 (CC BY 3.0)

at the end of the linac should bring deviations close to the requirements for both parameters.

DEVELOPED SOLUTION

In order to apply different intensity compensation options a beam feedback software system has been developed and integrated into the control system in CTF3. In all cases the actuator of the intensity compensation is the grid voltage control in the thermionic gun. The gun control allows modifying the beam intensity in the order of 10^{-5} Amps, which is sufficiently small. The beam intensity is measured by Beam Position Monitors (BPM) with a resolution of only 5.8 mA, which is more than 0.1%. The integration over the pulse length up to 1.4 μs and averaging over several consecutive BPMs improve the resolution and reduce the noise down to 0.3 mA, which is below 0.01%. For each mode of operation a set of BPMs and their weights are predefined, and they are used to calculate the weighted mean intensity. The calculated intensity is compared with the reference value specified by operators. Based on this information the controller estimates the needed gun voltage correction and applies it on the next pulse (see Fig. 3). In order to prevent strong or unnecessary influence on the beam energy the upper and lower deviation thresholds are respected (for example see Eq. 9). The best and sustainable feedback performance has been achieved by applying exponential moving average filter on the weighted mean intensity, which also prevents from undesirable additional high-frequency fluctuations.

CALIBRATION

A self-calibration process of the feedback controller has been implemented to automatically compute most of the controller parameters. It provides an accurate calibration for the optimum performance. Inaccurate settings may lead to oscillation around the reference value, a large correction time or overshoots of the beam current. In the calibration mode the gun voltage is applied in a predefined pattern and the beam current is logged to determine the beam response, the noise impact, control limitations, setup correctness and the best filter parameter. It can be carried out at any time after significant modifications in the injector setup or in the cleaning chicane or when the controller is losing its efficiency due to some slow processes.

CONCLUSIONS

The intensity stabilization system has been successfully developed in a way to minimize energy deviations by keeping the intensity stable. It was tested and used during the normal operation and during the night operation in CTF3. The implemented self-calibration process allows operatively adapting to new setups with the best performance. Using the developed system the beam intensity has been stabilized in the injector down to 0.045%, which improves the earlier result of 0.05%. The intensity stabilization in the linac successfully transfers

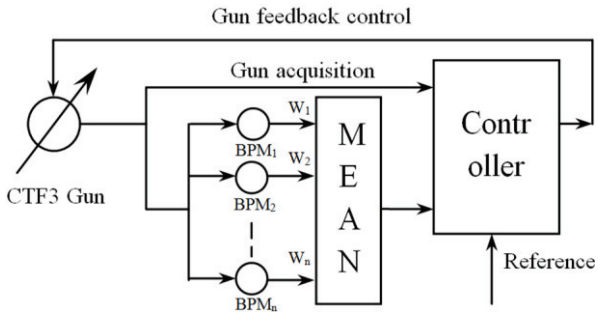

Figure 3: Intensity control layout.

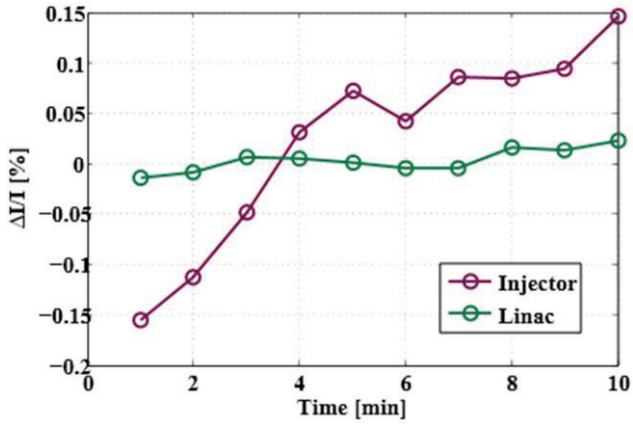

Figure 4: Illustration of the stabilization of the intensity in the linac by adjusting the intensity in the injector.

intensity variations over 0.15% from the linac into the injector within a small and preserved range of gun adjustments (see Fig. 4). Thereby it keeps the intensity stable at the end of the linac and it notably reduces energy deviations.

The effect of the stabilization system on possible changes of the emittance and bunch length must be additionally studied. Explicit energy correlation measurements will be performed soon.

The approach to cure integrated beam errors has been demonstrated to be a feasible and efficient technique at the cleaning chicane in CTF3 by transferring intensity variations from the linac into the injector.

ACKNOWLEDGMENT

The authors acknowledge Alexandra Andersson, Guido Sterbini and the whole CTF3 operation team.

REFERENCES

[1] G. Geschonke et al. *CTF3 Design Report. Technical Report*, CTF3 Note 2002-047, CERN, May 2002.

[2] A Multi-TeV linear collider based on CLIC technology: *CLIC Conceptual Design Report* edited by M. Aicheler et al. 2012.

[3] J.P. Delahaye, "*Towards CLIC Feasibility*",IPAC'10, Kyoto, 2010

[4] D. Schulte et al. Status of the CLIC Phase and Amplitude Stabilisation Concept, LINAC, 2010.

[5] A. Dubrovskiy, F. Tecker *RF pulse compression stabilization at the CTF3 CLIC Test Facility*, IPAC, 2010.

Copyright © 2012 by the respective authors — cc Creative Commons Attribution 3.0 (CC BY 3.0)

HIGH POWER COUPLER TEST FOR TRIUMF E-linac SC CAVITIES

A.K. Mitra, Z. Ang, S. Calic, P. Harmer, S. Koscielniak, R.E Laxdal, W.R. Rawnsley, R. Shanks
TRIUMF, 4004 Wesbrook Mall, Vancouver, BC, Canada, V6T 2A3

Abstract

TRIUMF has been funded to build an electron linac with a final energy of 50 MeV and 500 kW beam power using TESLA type 9-cell superconducting cavities operating at 1.3 GHz at 2 K [1]. The e-linac consists of an electron gun, buncher cavity, injector cryomodule (ICM), and two accelerator cryomodules (ACMs). The ICM has one 9-cell cavity whereas each of the ACMs contains two 9-cell cavities. One ICM and one ACM are scheduled to be installed by 2014. Six power couplers, each rated for 60 kW CW, have been procured for three cavities. The ICM will be fed by a 30 kW CW Inductive Output Tube (IOT) and each ACM will be powered by a 290 kW CW klystron. Before installing the power couplers with the cavities, they are to be assembled and conditioned with a high power RF source. A power coupler test station has been built and tests of two power couplers have begun. A 30 kW IOT has been commissioned to full output power and it will be used for the power coupler tests. In this paper, test results of the RF conditioning of the power couplers in pulse and CW mode will be described.

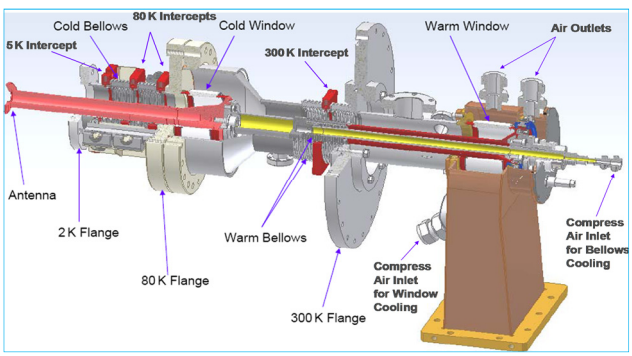

Figure 1: The CPI coupler is based on the Cornell 60 kW TTF-III coupler design.

INTRODUCTION

The power couplers that are being tested are manufactured by CPI, USA and have been adapted from the Cornell coupler shown in figure 1. The couplers, prior to installation with the accelerating cavities, are to be fully RF conditioned. A 30 kW IOT amplifier has been tested to full power and it will be used for RF conditioning of the couplers in both CW and pulse mode. Two couplers are mounted on to a waveguide box which has been designed such that RF power can be transmitted from the input coupler through the waveguide box and out through a second coupler to a 50 Ω waveguide load with minimum standing wave [2]. The coupler station is shown in figure 2. Each coupler has two ceramic windows, one cold and one warm. The cold window is the barrier for the ultra high vacuum pressure inside the SRF cavities which is on the order of 10^{-9} mbar and the warm window is a safeguard in the event of a failure of the cold window. Since the waveguide box and the couplers are at room temperature, the CW power applied to the couplers is kept to a level < 10 kW so as to limit the temperature of the inner conductor to 80 °C maximum. The couplers have Mega Industries WR650 coaxial to waveguide transitions which are at atmospheric pressure.

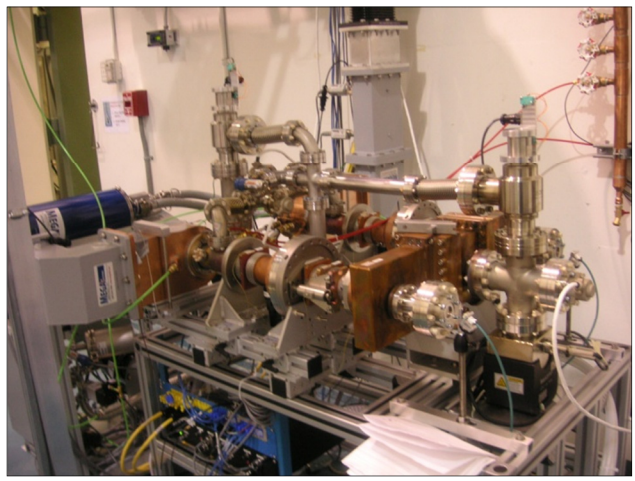

Figure 2: The power coupler test set up.

HIGH POWER TEST OF COUPLERS

The waveguide box was baked and found to be leak tight. The cold windows and the waveguide box were assembled in a clean room environment and leak checked. The warm window and waveguide to coaxial transition were assembled on the coupler test stand and all monitoring and instrumentation were attached.

Signal Level Measurement

The strength of the coupling to the waveguide box can be varied by moving the inner conductors of the couplers. Both couplers are adjusted for best matching (minimum VSWR). Measured values of S11 and S21 are 1.065:1 and 0.166 dB respectively. From the S21 measurement, the power loss in the two couplers and the waveguide box in total will be 39 W for an input power of 1 kW. Hence no cooling is required. However for 10 kW input power, the power loss increases to 390 W which requires cooling if run for a long time.

Interlocks and Monitoring

The vacuum system for the coupler test stand uses two systems; one vacuum common to the cold windows of the couplers and the waveguide box and the second system common to both of the warm windows of the couplers.

Copyright © 2012 by the respective authors — cc Creative Commons Attribution 3.0 (CC BY 3.0)

A hardware interlock system was built to protect the power couplers during RF conditioning, figure 3. A sample of the IOT output power is derived from a 60 dB directional coupler and a four way splitter. This signal is brought to the protection electronics ZX47-40LN-S+ logarithmic power detector module using Andrew Heliax cable. The log detector output and a reference level set by a potentiometer drive a comparator to generate a trip. When a trip occurs, the 1.3 GHz drive signal to the linear IOT RF power amplifier is cutoff by a Mini-Circuits ZASWA-2-50DR+GaAs switch with ~65 dB of isolation. This switch has no latching problems and it is designed in fail-safe mode. The response time of the system, a few μs, is fast compared to the RF pulse widths used for conditioning and thus trips on peak rather than on average power. It has been found to be very stable and not to cause false trips when operating just below the trip level.

The fast trip system includes vacuum cold cathode gauges and photomultiplier (PMT) arc detectors. A trip is generated if the pressure in the warm space exceeds $5{\cdot}10^{-6}$ Torr or the pressure in the cold space exceeds $5{\cdot}10^{-7}$ Torr [3]. One Hamamatsu H10722-01 PMT attached to each power coupler is sensitive to light generated by multipacting in the region between the warm and cold RF windows. Ten thermocouples are attached at various points to the exterior of the couplers and the waveguide box. PT100 temperature sensors are attached inside the inner conductor of the couplers near the warm window bellows. Two Raytek MI series IR sensors measure the temperature of the cold window ceramics through viewing windows in the waveguide box. The ion pump current for both cold and warm sections, air cooling of the coupler inner conductors and water cooling of the external parts of the waveguide to coaxial transitions are monitored.

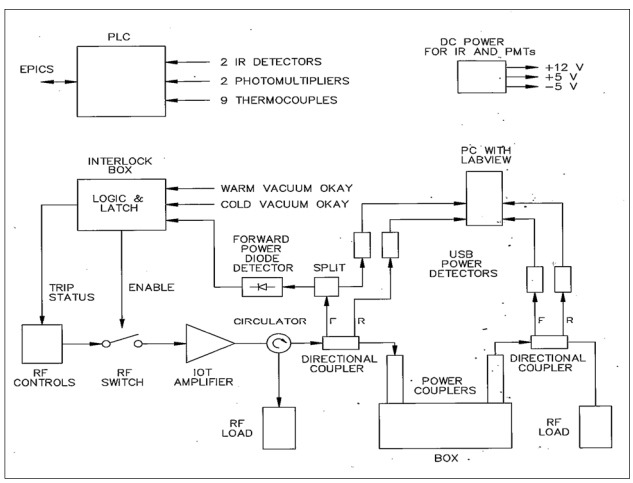

Figure 3: A block diagram of the RF set up.

RF Power Measurements

The couplers will be RF conditioned both in travelling wave mode and standing wave mode. The 30 kW IOT transmitter will be used for these tests. RF power will be initially pulsed with low duty cycle to allow high voltage conditioning of the coupler inner surfaces. Once no evidence of multipacting is observed and low pressure is established, < $1.0{\cdot}10^{-7}$ Torr, it will be driven in CW mode.

Travelling Wave Test

The RF drive power was pulse modulated, with a 200 ms period and pulse width varying from 100 μs to 10 ms. The duty ratio will eventually be changed to 10%, 20%, 50% and 100% and RF power reduced accordingly to stay within temperature and pressure limits.

Table 1: Travelling Wave Test in Pulse Mode

Width (ms)	Period (ms)	Duty Ratio (%)	Peak Power (kW)	Cold Vac (Torr)	Warm Vac (Torr)
0.1	200	0.05	7.50	1.19E-08	1.00E-07
0.2	200	0.10	10.00	1.70E-08	2.30E-07
1	200	0.50	9.00	2.30E-08	3.30E-07
2	200	1.00	7.60	2.50E-08	5.00E-08
10	200	5.00	7.20	1.48E-08	2.60E-08

Table 1 shows the vacuum pressure in the cold and warm sections for varying duty ratio and peak power ranging from 7 to 10 kW. There was no noticeable increase in temperature in the couplers or in the waveguide box. The results of a CW RF test are shown in figure 4 where the RF power was increased slowly from 0 to 9 kW over 2 hours. The pressure in the cold section remained unchanged whereas the pressure in the warm section deteriorated as the power was increased. The temperature increased from 22.6 to 29 °C for TCM-1 TC7 (the outer conductor of the coupler) and from 23.6 to 33.8 °C in TCM-2 TC3 (the inner conductor of the coupler). At 10 kW CW, the vacuum tripped and since then it has been difficult to condition at more than 1 kW CW. Both low level (<1 kW) pulse and CW RF conditioning were undertaken and severe multipacting was observed in the input coupler.

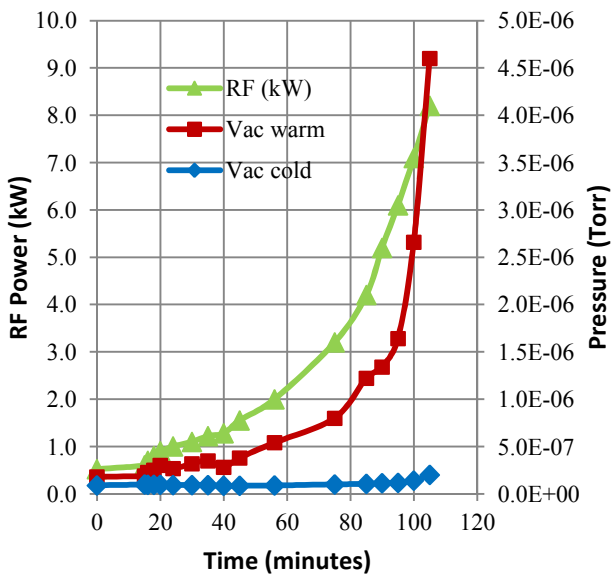

Figure 4: A travelling wave test in CW mode

Copyright © 2012 by the respective authors — cc Creative Commons Attribution 3.0 (CC BY 3.0)

Standing Wave Test

Standing wave mode will be used to establish higher peak power in the couplers using a movable waveguide short instead of the 50 Ω waveguide termination. The waveguide box is made in-house, figure 5. A variation of a half guide-wave length can be achieved by moving the shorting plunger by 180 mm. High standing wave was established near the vacuum side of the input coupler's warm window by observing the vacuum bursts as the shorting plunger was moved.

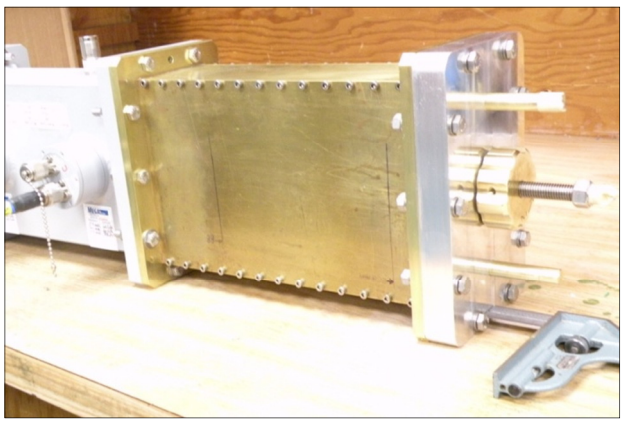

Figure 5: Movable WR650 waveguide short

A 500 W solid state amplifier was used in CW and pulse mode under standing wave conditions to locate the region of multipacting. Figure 6 shows the vacuum bursts as the waveguide shorting plate is adjusted to get high standing wave in the warm window region. The RF drive and the waveguide short were interchanged and the same cw and pulse tests were carried out. It was found out that coupler 2 vacuum settled to a steady, low value as shown in figure 7. It was concluded that the coupler 1 warm window shows signs of multipacting. Further investigation is to be carried out with higher power and higher duty ratio.

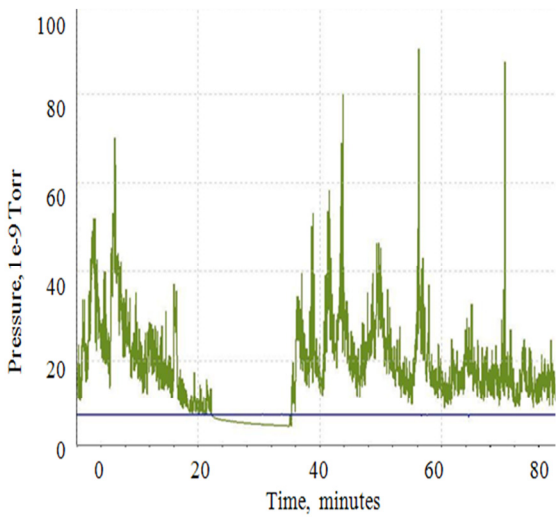

Figure 6: RF power applied to coupler 2 with the waveguide short at coupler 1.

CONCLUSION

The CW and pulse coupler tests were successful to a power level of 8 kW. However, after a vacuum trip at the warm window of the input coupler (coupler 1) at 8 kW, multipacting was observed at the 1 kW CW level. Afterwards, a solid state amplifier with 500 W output and a variable waveguide short were used to carry out coupler conditioning in standing wave mode in order to find the reason and location of the multipacting inside the coupler. The IOT transmitter will be used (it's going through some high voltage issues at present) again for conditioning after the low power test is concluded. It was observed that the warm window reacts to pulse conditioning much more than the cold window, hence another turbo pump and ion gauge will be installed so that the pressure at both of the warm windows can be observed simultaneously. The IR sensors which look at the cold windows are very helpful but their alignment is sensitive since their 20° field of view is partially obstructed and covers a small fraction of the ceramic. With improved cooling of the inner conductor of the coupler, possibly at liquid nitrogen temperature, it is envisaged to reach the final target of RF conditioned to 30 kW CW and 60 kW pulse. The RF conditioning of the coupler test is vital for the e-linac project since two such couplers are required to be installed with the ICM by mid 2013.

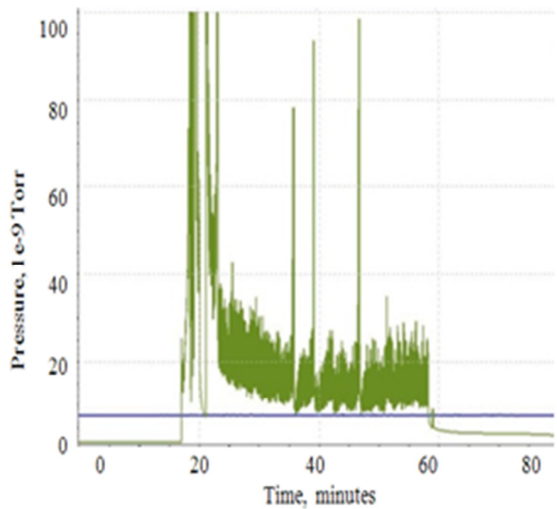

Figure 7: RF power applied to coupler 1 with the waveguide short at coupler 2.

REFERENCES

[1] S. Koscielniak et al, "Electron Linac Photo-fission Driver for the Rare Isotope Program at TRIUMF", IPAC10, Kyoto, Japan (2010)

[2] M. Stirbet et al, "RF Conditioning and Testing of Fundamental Power Couplers for the RIA Project", SRF03, Lübeck Travermünde, Germany (2003)

[3] V. Veshcherevich et al, "High Power Tests of Input Couplers for Cornell ERL Injector", SRF07, Peking University, China (2007)

Copyright © 2012 by the respective authors — cc Creative Commons Attribution 3.0 (CC BY 3.0)

NOVEL TECHNIQUE OF SUPPRESSING TBBU IN HIGH-ENERGY ERLS*

Vladimir N. Litvinenko #, Brookhaven National Laboratory, Upton, NY, USA
Department of Physics and Astronomy, Stony Brook University, Stony Brook, NY, USA

Abstract

Energy recovery linacs (ERLs) is an emerging generation of accelerators that promise to revolutionize the fields of high-energy physics and photon sciences. These accelerators combine the advantages of linear accelerators with that of storage rings, and augur the delivery of electron beams of unprecedented power and quality. However, one potential weakness of these devices is transverse beam break-up instability that could severely limit the available beam current. In this paper, I propose a novel method of suppressing these dangerous effects using the chromaticity of the transverse motion.

In this short paper I am able only to touch the surface of the method and a complete description of the method with all relevant derivations can be found in [1].

INTRODUCTION

Energy-recovery linacs (ERLs, see Fig.1) belong to a family of recirculating linacs (RLs) that accelerate a beam of charged particles multiple times in the same linear accelerator, accumulating the beam's energy on each pass.

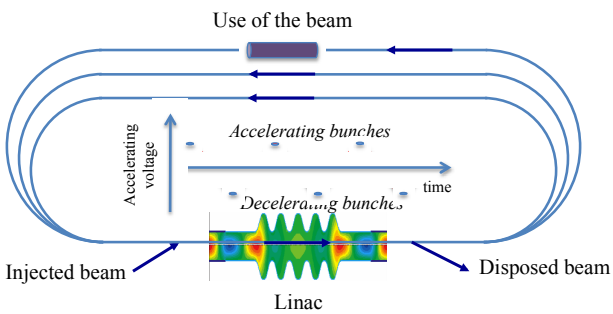

Figure 1: A sketch of a three-pass ERL.

One main challenge for these accelerators is the transverse beam break-up instability (TBBU) that especially is severe for SRF recirculating linacs. Early experiments with recirculating SRF accelerators at Stanford [2] and Illinois [3], where this instability occurred at a few microamperes of the average beam current, highlighted this problem. Dipole high-order modes (HOMs) of the SRF cavities were identified as the culprits driving this instability [4-5], and several remedies were developed for raising this threshold [6].

Detailed theoretical approaches and TBBU simulation programs were developed in the late 80s [7-9]. The renewed interest also stimulated refinements of the TBBU theory, simulation programs [10-12] and their experimental verification [13] all are driven by the need for high current ERLs, and also by the rewards of resolving this complex problem. Nevertheless, strong damping of HOMs in SRF linacs while maintaining high accelerating gradients remains one of the major unsolved issues. In the general ERL case, we can write a complete matrix of dispersion relations [7-12], but an analytical solution of the TBBU's instability threshold can be derived only for a single HOM mode, and a single-pass ERL, and as detailed in [5]:

$$I_{th} = \frac{2c^2}{e\,R_g \cdot Q \cdot \omega} \cdot \frac{1}{T_{12}\sin(\omega t_r)} \qquad (1)$$

where c is the speed of the light, e is the elementary charge, $R_g \cdot Q$ is the HOM's impedance (measured in Ω), ω is its frequency, and t_r is the beam's travel time through the returning loop. Since there are many HOM modes in the cavities encompassing a large range of the spectrum, there can be modes with $|\sin(\omega t_r)| \sim 1$; then, the only meaningful way of increasing the threshold is by reducing the values of Q and the $|T_{12}|$. As shown in [10], eq. (66), in an ERL with N passes through its linac, we can estimate the TBBU threshold by

$$I_{th} = \frac{2c^2}{e\,R_g \cdot Q \cdot \omega} \cdot \frac{1}{\sum_{J=1}^{2N}\sum_{I=J+1}^{2N} T^{IJ}\sin\omega(t_I - t_J)}, \qquad (2)$$

where $T^{IJ} \equiv T_{12}(s_J|s_I)$ is the element of transport matrix between the J^{th} and I^{th} pass through the linac. Analyzing eq. (3) the authors of ref. [10] offered their natural conjecture that the TBBU threshold scales as follows:

$$I_{th} \propto \left(R_g \cdot Q \cdot N^2 \left\langle \left|T^{IJ}\right| \right\rangle\right)^{-1}. \qquad (3)$$

The unfavorable scaling discussed above may have major implications on the cost of a high-energy ERL. Since an SRF linac usually more expensive than magnetic elements, cost-effective solutions [14-16] lead to three- to six-pass ERLs. If the current in such ERL designs suffer from severe beam current limitation, then the extent of their use and their energy reach will be restricted.

One way of resolving these confines lies in reducing the Q of all dangerous HOMs by developing complex HOM-damping schemes, and in addition, circumscribing the number of cells per linac module so to avoid trapping high-Q HOMs.

The other way of increasing the threshold current is by lowering $\left\langle \left|T^{IJ}\right| \right\rangle$. The latter is the topic of this paper.

*Work supported by Brookhaven Science Associates under Contract No. DE-AC02-98CH10886 with the U.S. DOE

#vl@bnl.gov

Copyright © 2012 by the respective authors — cc Creative Commons Attribution 3.0 (CC BY 3.0)

SUPPRESSION OF THE BEAM'S RESPONSE USING CHROMATICITY

Since the bunch is an ensemble of particles, its transverse response to the kick will be the average if the responses of the individual particles are

$$\langle x_r \rangle = \langle T_{12} \rangle \cdot x', \tag{4}$$

where $\langle a \rangle$ signifies the average value of a parameter, a. I suggest using the chromaticity of the returning loops and an energy spread in the beam (induced by an RF chirp, if needed) beam to reduce $\langle T_{12} \rangle \to 0$.

For a particle with a small energy-deviation $p = p_o(1+\delta);\ |\delta| << 1$, the envelope function $\beta_o \equiv \mathrm{w}_o^2$ and the phase advance can be extended as

$$\begin{aligned} \mathrm{w}(s,\delta) &\cong \mathrm{w}_\mathrm{o}(s)\left(1+\delta\cdot\upsilon(s)\right); \\ \psi(s,\delta) &\cong \psi_\mathrm{o}(s)+\delta\cdot\phi(s), \end{aligned} \tag{5}$$

where the subscript "o" indicates the values for particles with the designed energy. The straightforward perturbation theory (see [1]) yields the following expression:

$$\begin{aligned} \varphi(s) &= -\frac{1}{2}\int_0^s K(z)\mathrm{w}_\mathrm{o}^2(z)\left(1+\cos 2\left(\psi_o(z)+\phi_o\right)\right)dz; \\ \upsilon(s) &= -\frac{1}{2}\int_0^s K(z)\mathrm{w}_\mathrm{o}^2(z)\cdot\sin 2\left(\psi_o(z)+\phi_o\right)dz. \end{aligned} \tag{6}$$

One important (and well known) feature of this solution is that the phase deviation (i.e., the chromaticity of oscillations) is defined by a monotonic function with average rate of $-\langle K(z)\mathrm{w}^2{}_\mathrm{o}(z)\rangle_z/2$, while the envelope deviation is a fast oscillating function with double-betatron frequency. Hence, in a large accelerator system, chromaticity grows steadily, and can reach significant values $C(s) = \phi(s)/2\pi >> 1$, and, even for a modest deviation in relative energy, phase variation can be large, while the relative variation in the envelope function remains small $\delta\cdot\upsilon(s) << 1$.

Naturally, the level of suppression of the beam's response (transfer function, $\langle T_{12} \rangle$) depends on the energy-distribution function; Table 1 gives a few examples. Smooth bell-shape energy-distribution functions (Gaussian, Lorentzian, $\kappa - 2$) assure the strong suppression of $\langle T_{12} \rangle$ whose value falls fast with the increase of $|X| \equiv 2\pi|C|\sigma_\delta$; sharp-edged distribution functions (such as rectangular- or triangular-ones) cause the oscillating behavior of $\langle T_{12} \rangle$ which declines more slowly with the growth of $|X|$. In all cases, a highly chromatic lattice resulting in $|X| >> 1$ effectively suppresses the beam's response to transverse kicks.

In the TBBU theory [7-12], the low-energy passes through the linac are considered to be the ones most vulnerable to TBBU instability. Specifically, the conclusions are that the TBBU threshold is proportional to the lowest energy in the recirculating path, and also inversely proportional to number of the recirculating passes. The examples described in this paper as well in ref. [1] show that this rule is not applicable to an ERL wherein the accumulated chromatic phase spread is significantly larger than unity.

Examples

eRHIC's low-emittance ERL lattice has chromaticities $C_{x_t} \cong -175;\ C_{y_t} \cong -125$ per turn. The LHeC low emittance lattice has $C_{x_t} \cong -510;\ C_{y_t} \cong -460$ per turn. Hence, an induced correlated Gaussian energy spread of $\sigma_\delta = 5\cdot 10^{-3}$ will suppress $\langle T_{12}(s|s+C\rangle$ 3,000 –fold in vertical direction and by astronomic $3.7\cdot 10^6$ in horizontal direction. In LHeC ERL $\sigma_\delta \cong 1.3\cdot 10^{-3}$ will suffice for suppressing a single-turn response 1,000-fold.

Table 1. Suppression of the Beam's Response on a Transverse Kick by the Chromaticity: $X = \phi\sigma_\delta;\ Y = \upsilon\sigma_\delta$.

$f(\delta)$	Suppression factor $\langle T_{12} \rangle / \mathrm{w}_{\mathrm{io}}\mathrm{w}_\mathrm{o}$	Type
$\frac{1}{\sqrt{2\pi}\sigma_\delta}\exp\left(-\frac{\delta^2}{2\sigma_\delta^2}\right)$	$e^{-X^2/2}\cdot\left(\sin\psi + X\cdot Y\cos\psi\right)$	Gaussian
$\frac{1}{\pi\sigma_\delta}\left(1+\frac{\delta^2}{\sigma_\delta^2}\right)^{-1}$	$e^{-\lvert X\rvert}\cdot\left(\sin\psi + Y\cdot sign(X)\cos\psi\right)$	Lorentzian
$\frac{2}{\pi\sigma_\delta}\left(1+\frac{\delta^2}{\sigma_\delta^2}\right)^{-2}$	$e^{-\lvert X\rvert}\cdot\left((1+\lvert X\rvert)\sin\psi + X\cdot Y\cos\psi\right)$	$\kappa - 2$
$\frac{1}{2\sigma_\delta}\left(\theta(\delta-\sigma_\delta)-\theta(\delta+\sigma_\delta)\right)$	$\frac{\sin X}{X}\sin\psi + Y\frac{\sin X - X\cos X}{X^2}\cos\psi$	Rectangular

Copyright © 2012 by the respective authors — cc Creative Commons Attribution 3.0 (CC BY 3.0)

Numeric example

Some higher order effects can, in principle, reduce or at least, significantly modify the predictions given in Table 1. To address this concern, I tested the concept by directly calculating the response of the beam with a Gaussian energy-distribution propagating through a beam-line encompassing 1024 FODO cells. Each FODO cell comprises one focusing- and one defocusing-quadrupole. Hence, I use the exact analytical expression for the transport matrix of the FODO cell for an ultra-relativistic particle with arbitrary momentum $p = p_o(1+\delta)$: $T_{FODO}(\delta)$. The matrix is multiplied by the necessary number of times

$$T_{total}(\delta) = \left[T_{FODO}(\delta)\right]^{1024} \qquad (7)$$

to form the exact matrix of the beam-line. The beam's displacement at the end of the beam-line to an angular kick, θ, at its entrance entails a simple convolution:

$$\langle x \rangle = \langle T_{12\ total} \rangle \cdot \theta; \quad \langle T_{12\ total} \rangle = \int_{-\infty}^{\infty} T_{12\ total}(\delta) f(\delta) d\delta$$

where $T_{12\ total}(\delta)$ is an exact, analytical, nonlinear function of δ. For comparison, I define the suppression factor of the transverse response as

$$S = \max\left(\left|T_{12\ total}(\delta)\right|\right) / \left|\int_{-\infty}^{\infty} T_{12\ total}(\delta) f(\delta) d\delta\right|.$$

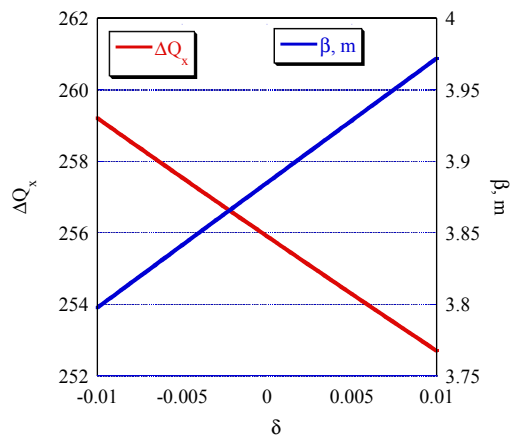

Figure 2. The FODO beam-line optics parameters as function of the particle momentum.

The exact matrix function was used to convolve it with Gaussian energy-distribution with $\sigma_\delta = 2 \cdot 10^{-3}$. I did not observe any significant deviations from the expected theoretical behavior either at a small values (as expected), or at large values of the of total beam-line's chromaticity. For example, the beam-line with tune advance of 0.22285 per cell has chromaticity of $C = -276.68$, and the calculated suppression factor of 428-fold that compares favorably with the theoretical estimation of 422-fold. Increasing the chromaticity further to $C = -328.51$ by increasing the tune advance per cell to 0.2499 increased the calculated suppression factor to $5.93 \cdot 10^3$. This also is reasonably close to the theoretical estimation of $5.02\ 10^3$.

CONCLUSIONS

I have shown in this paper that using the natural chromaticity of the arcs in ERLs affords an opportunity of suppressing the beam's transfer function (its response to transverse kicks), and either suppressing TBBU instability or significantly increasing allowable operating currents.

In an ERL comprising of a sequence of linacs and arcs, with the product of the chromaticity and the energy spread in the arcs $|\phi\sigma_\delta| >> 1$, the electron beam forgets the kick it received in the linacs while traveling through an arc. Then, the traditional ERL TBBU excitation scheme falls apart, and each linac effectively sees fresh electron beams.

ACKNOWLEDGMENT

The author would like to thank Ilan Ben-Zvi, Yue Hao, Dmitry Kayran (BNL) and Eduard Pozdeyev (FRIB) for fruitful, in-depth discussions of the methods, and Georg Hoffstaetter (Cornel University) and Frank Zimmermann (CERN) for their interest in the prospects of suppressing TBBU in high-energy ERLs.

REFERENCES

[1] V.N. Litvinenko, Physics Review Special Topics – Accelerators and Beams, Volume **15**, 074401 (2012)
[2] C M. Lyneis et al.,Trans. Nucl. Sci. **B**, 1979,
[3] P. Axel et al,., Trans. Nucl. Sci. **26**, 1979
[4] C.M. Lyneis et al., NIM 204 (1983) 269-28
[5] R.E. Rand, Recirculating electron accelerators, Harwood Acad. Publ., 1984
[6] R.E. Rand and T.I. Smith, Part Acc. **11,** p. 1 (1980)
[7] G.A. Krafft, J.J. Bisognano, S. Laubach, Tech-Note CEBAF-PR-90-39
[8] J.J. Bisognano, R.L. Gluckstern, Proc. PAC'87, Washington, DC, p. 1078.
[9] G.A. Krafft, J.J. Bisognano, Proc. PAC'87, Washington, DC, p. 1356.
[10] G.H. Hoffstaetter, I.V. Bazarov, PR ST-AB 7, 054401 (2004).
[11] E. Pozdeyev, PR ST-AB 8, 054401 (2005)
[12] G.H. Hoffstaetter, I.V. Bazarov and C. Song, PR ST-AB 10, (2007) 044401
[13] C.D. Tennant et al., PR ST-AB 8, 074403 (2005)
[14] C.W. Leemann, D.R. Douglas, G.A. Krafft, Ann. Rev. Nucl. Part. Sci. **51 (**2001) 413
[15] V.N. Litvinenko et al., (2011), 438 http://arxiv.org/pdf/1108.1713v1
[16] F. Zimmermann et al., Proc. EPAC08, Genoa, Italy (2008) 2847

Copyright © 2012 by the respective authors — cc Creative Commons Attribution 3.0 (CC BY 3.0)

THE LINEAR ACCELERATING STRUCTURE DEVELOPMENT FOR HLS UPGRADE *

K. Jin, S. C. Zhang, Y. L. Hong, G. R. Huang, D. C. Jia
National Synchrotron Radiation Laboratory, NSRL USTC,
P.O. Box 6022, Hefei Anhui 230029, China

Abstract

Hefei Light Source (HLS) is mainly composed of an 800 MeV electron storage ring and a 200 MeV constant-impedance Linac functioning as its injector. A new Linac is developed in view of the Full Energy Injection and the Top-up Injection scheme will be adopted in the HLS upgrade. In this paper, an 800MeV linear accelerating system construction, the constant-gradient structure design and the symmetry couplers consideration will be described in detail. The manufacture technology, the RF measurement, the high power test results and the accelerating system operation are presented.

INTRODUCTION

In order to ensure the low-emittance focusing parameters steady operation in the HLS Storage Ring, it's necessary to increase the injector energy to 800MeV. After realize Full Energy Injection, each system of Storage Ring can keep single operation state, the light source stability will be improved eminently. A new Linac is developed in view of the Full Energy Injection and the Top-up Injection scheme will be adopted in the HLS upgrade. An 800MeV Linac layout is shown in Fig.1.

The project is proceeding as planned at present. In this paper, an 800MeV linear accelerating system construction, the constant-gradient structure design and the symmetry couplers consideration will be described in detail. One section of accelerator structure has been fabricated successfully. The manufacture technology, the RF measurement, the high power test results and the project schedule are presented.

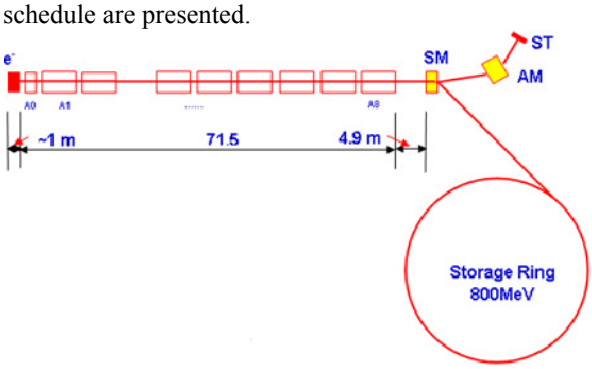

Figure 1: HLS 800MeV Linac layout

800MEV LINEAR ACCELERATING SYSTEM DESIGN

HLS accelerating system consists of a pre-buncher, a buncher and eight units of constant-gradient accelerating structures (6m accelerator unit). Total length is about 73meter. The electron beam energy can be achieved to 800MeV~1GeV. In general, seven such as units is in operation condition and another one is in standby state so that to assure storage-ring stability running (Fig.2).

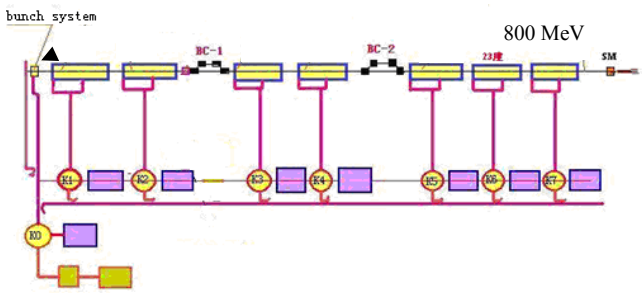

Figure 2: 800MeV electron Linac energy, phase and microwave System

Pre-buncher

Pre-buncher or velocity modulation cavity is a cylindrical reentrant resonator. Its resonance frequency is 2856 MHz, working at TM_{010} mode. Cavity dimensions and physical parameters are calculated with SUPERFISH. To reduce the errors of resonance frequency caused by temperature, beam loading etc., stainless steel is selected to make this cavity to reduce Q (~ 500), the cavity shunt impedance is Rs/Q = 220. So when 2kW power is feeding in, it will produce about 15kV microwave voltage in the cavity. According to beam dynamics calculation, bunching parameter is selected r = 1.92. The beam waist of electron beam from gun is focused at the center of pre-buncher. Through the preliminary bunching cavity and drift 35 cm, its phase width will be focused from 260°to 90°. The work was finished in a HLS phase I project. It is in good condition still. So it will continue to use after upgrading.

The fundamental mode buncher

The bunching system work frequency is 2856 MHZ, including pre-buncher and fundamental mode buncher. The beam from the gun is focused initially in the pre-buncher, then electron beam get into buncher to further complete beam phase bunching process, and further increase the beam energy. The fundamental mode buncher is constant gradient disk load accelerating structure. Solenoids are used to focus in the transverse direction. The length of fundamental mode buncher is 1.63 m, the accelerating gradient is about 8.2 MV/m, and beam energy is about 13.1 MeV after bunching section.

In order to optimize bunching effect, pre-buncher voltage is optimized to 15kV and the distance between buncher and pre-buncher is optimized to 35 cm. The

Copyright © 2012 by the respective authors — cc Creative Commons Attribution 3.0 (CC BY 3.0)

Table.1: parameters of buncher

No	a (1e-3m)	b (1e-3m)	D (1e-3m)	β	F (GHz)	betag	Q	Rs (Mohm/m)	alpha
1.	11.1550	41.6430	24.4929	0.70	2.855996	0.009970	10955	37.543	0.27400
2.	11.1550	41.6430	24.4929	0.70	2.855996	0.009970	10955	37.543	0.27400
3.	11.1550	41.3210	30.7910	0.88	2.856011	0.010174	12482	49.503	0.23568
4.	11.1550	41.2287	33.2403	0.95	2.856010	0.010202	12911	52.987	0.22722
5.	11.1550	41.1933	34.2900	0.98	2.856000	0.010216	13222	55.533	0.22156
6.	11.1550	41.1820	34.6399	0.99	2.856005	0.010226	13523	58.023	0.21642
7.	11.1550	41.1710	34.9894	1.0	2.855997	0.010230	13719	59.649	0.21325

buncher adopts traveling wave electron accelerating structure. It totally has 45 cavities; the first five cavity is vary phase velocity period structure. The phase velocities are 0.70, 0.88, 0.95, 0.98, 0.99, the others are relativistic accelerating section. The results are in the Table.1.

Accelerating Section

The constant-gradient structure can produce higher energies than an optimized constant-impedance structure when both are operating at the breakdown limit of electric field strength. Considering such structure reduces ration of maximum to average field strengths and increases some advantages [1], the constant-gradient structure was thus adopted for the HLS Linac upgrade.

The cavity type of constant-gradient disk-loaded structure was selected in HLS accelerating section. Operating frequency of 2856MHz, phase shit per cavity of 2π/3, i.e. cavity length of 34.989mm and disk thickness of 5.8mm is set. The optimum cell geometer and its EM performance, calculated with MAFIA-Code [2], are listed in Table 2. The curves of field strength and energy vs. axial distance z are shown in fig.3. Here the power range is 32.0 Mw to 10.1Mw in such accelerator section, the field strength E_z of 20.7Mv/m is acquired and the energy gain is about 62MeV.

In order to realize Full Energy Injection, one klystron of 80Mw provides power to a pre-buncher and a buncher as well as to a 6m accelerator unit which is constructed by two 3m standard sections. Another one of 80Mw and six klystrons of 50Mw with SLED technology will provide

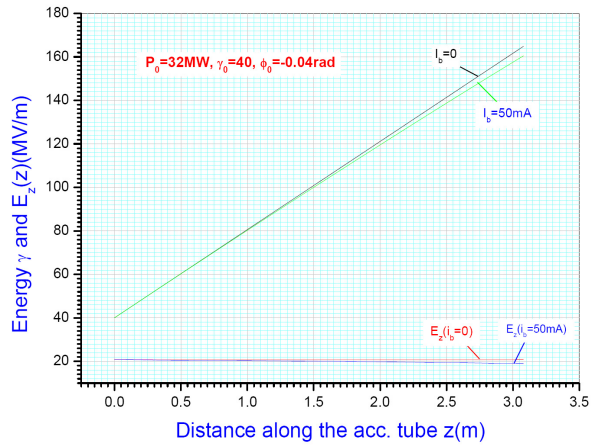

Figure 3: The field strength and energy gain in the 3m accelerating section.

power to each 6m accelerator unit individually.

The average accelerating gradient of 20Mv/m can be obtained in such away. The electron beam energy can be achieved to 800MeV~1GeV. In general seven 6m accelerator units are in operation condition and the other one is in standby state so that to assure storage-ring stability running. The electron beam energy gain in all accelerating structures is shown in Table 3.

Table 2:Final design and performance of the HLS accelerator structure

Parameters	**HLS Linac**
Operating frequency (f)	2856 MHz
Phase shit per cavity	2π/3
Iris diameter range of disk-loaded (2a)	25.386-19.260mm
Cavity diameter range of disk-loaded (2b)	83.118-81.718mm
Range of shunt impedance (R_s)	55-63 MΩ/m
Normalized group velocity range (Vg/c)	0.0177-0.0063
Attenuation parameters (τ)	0.585 Np
Filling time (t_F)	0.8995μsec
Operating state	42℃, vacuum
No. of standard 3m section	16
No. of cavities in each 3m section	86+2 coupler
Distance between inputs of two consecutive sections	31λ
No. of 6m accelerator unit	8

Copyright © 2012 by the respective authors — cc Creative Commons Attribution 3.0 (CC BY 3.0)

Table 3: The beam energy gain in HLS Linac Ⅱ

Equipments	Beam energy	Δφ
e-Gun	100keV	1ns
Pre-Buncher	140keV	500ps
Buncher	15.5MeV	10ps
1# 6m acc. unit	120.6MeV	10ps
2# 6m acc. unit	225.4MeV	10ps
3# 6m acc. unit	340.3MeV	10ps
4# 6m acc. unit	455.3MeV	10ps
5# 6m acc. unit	570.2MeV	10ps
6# 6m acc. unit	685.1MeV	10ps
7# 6m acc. unit	800.0MeV	10ps

HLS STANDARD 3M SECTION DEVELOMENT

According to the above-mentioned design, an 800MeV traveling wave linear accelerator is being developed. A standard 3m section of accelerator structure has been fabricated successfully. It consists of 86 disk-loaded accelerating cavities. The phase velocity of β_p=1, the operation mode of 2π/3 and the constant-gradient structure are considered.

The RF coupler is an important component for an accelerator structure. It consists of a tapered rectangular waveguide and a coupling cavity with a coupling aperture. It must be well matched to the feeding waveguide and has synchronous frequency for the proper phase advance in the structure so that ensure the input power is fed effectively and an excellent travelling wave is transmitted in the accelerating cavities train. Therefore the sizes of the coupling cavity and the coupling iris aperture should be designed exactly at operation frequency so that the optimum transmission parameter S21 and scattering parameter S11 are obtained. In order to compensate the amplitude asymmetry and the phase shift, offsetting the coupler cavity was adopted. The value of the offset was found by means of microwave perturbation measurement, for the input cavity, it is 1.8mm, and for the output cavity, 1.0mm. The amplitude asymmetry of the order of 1.58%, and the phase shift of the order of 1.0°was obtained over the beam aperture.

In our project, the numerical simulation design of RF coupler assembly was considered. In the wake of the computer program development, special the MAFIA-code [2], it made the three dimensions (3D) S-parameters calculation in time domain becoming possible and the change in dimensions can be easily implemented on the computer. Revising the sizes step by step in such a way, in conjunction with microwave measurement by Kyhl method [3], the optimal matching and tuning results is acquired finally.

The cavities were machined high-precisely in a constant temperature room. It was assembled with the input coupler and the output coupler. Also the external water pipes are used so that the structure can be cooled and keep constant operating temperature. Finally the module was brazed in a hydrogen furnace.

Then each cell of the accelerating structure was tuned to the phase shift φ=120°/cell. The RF parameters are measured with the Network Analyzer Agilent E5071C. The voltage standing wave ratio, VSWR=1.019, was achieved at the operation frequency and VSWR is less than 1.2 in a frequency-bandwidth of 4 MHz, which is shown in Fig.6 for the typical structure.

The high-power test of the 3m accelerator section was processed in May. 2012. The pulse length of 1uS, maximum input power to the section is approximately 50Mw peak; Steady operation of pulse length of 5uS, input power of 40MW peak for such section was obtained. The test results satisfied the design which input power to the section is 32Mw peak. It means that accelerating gradient of 20Mv/m can be achieved in HLS Linac. It is a basic guarantee of the 800MeV Linac upgrade project success.

CONCLUSION

At present a Buncher and all 16 standard 3m sections has been manufactured successfully in NSRL. Microwave measurement and cavities tuning will be finished end of Sep. The HLS Linac Ⅱ will be installed in Oct. and will be operated end of 2012.

ACKNOWLEDGMENT

We would like to thank all the members of the collaboration for their contributions. Special thanks are given to J. Wang, J. F. Gao, Y. Z. Liu, J. Y. Zhang, W. Wei, F. Hu, S. Y. Jiang, X. Y. He and Y. J. Pei, who were heavily involved in the HLS Linac Ⅱ fabrication.

REFERENCES

[1] R. B. Neal, et al., Theory and selection of characteristic parameters, The Stanford Two-mile Accelerator, Chapter 6-1.
[2] Mafia, the MAFIA Collaboration, December 1996.
[3] E. Westbrook, Microwave Impedance Matching of Feed Waveguide to the Disk-loaded Accelerator Structure Operating in the 2p/3 mode, SLAC-TN-63-103, December 1963.

Copyright © 2012 by the respective authors — cc Creative Commons Attribution 3.0 (CC BY 3.0)

FEASIBILITY STUDY OF SHORT PULSE MODE OPERATION FOR MULTI-TURN ERL LIGHT SOURCE*

T. Atkinson†, A. V. Bondarenko, A. N. Matveenko, Y. Petenev,
Helmholtz-Zentrum Berlin für Materialien und Energie GmbH (HZB), Germany.

Abstract

The optic and simulation group at HZB are designing a light source based on the emerging Energy Recovery Linac superconducting technology, the Femto-Science-Factory (FSF) will provide its users with ultra-bright photons of angstrom wavelength at 6 GeV. The FSF is intended to be a multi-user facility and offer a wide variety of operation modes. A low emittance $\sim 0.1\,\mu$m rad mode will operate in conjunction with a short-pulse ~10 fs mode.

INTRODUCTION

This paper continues on from a recent introductory study[1] and highlights the physical limitations when trying to offer interchangeable modes and preserve beam quality. The paper concentrates on the short bunch mode, introducing the multi stage compression schemes in a general manner and presents the first results of the start-to-end beam simulations.

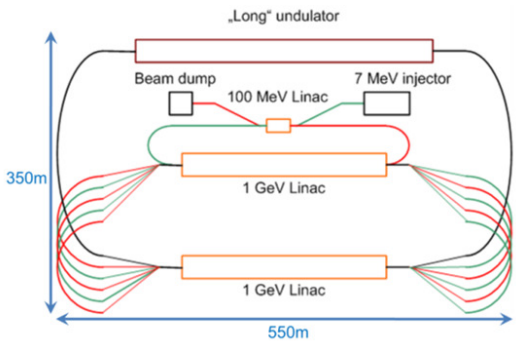

Figure 1: Schematic of the FSF Multi-Turn ERL.

The main design parameters of the FSF are listed in Table 1 and Fig. 1 shows the layout of the light source.

A SRF injector based on the design parameters of the BERLinPro[2] project delivers the 100 MeV electron beam into the main accelerator. Here two 1 GeV linacs are continually traversed until 6 GeV beam energy is reached. Each Arc contains straight sections for undulators and the final energy Arc permits a long straight section for 5000 period undulators.

The beam quality delivered to the long undulators and hence the photon brilliance attainable depends on the machine operating mode.

Table 1: Main design parameters of FSF

Parameter	High Brilliance Mode	Short Bunch Mode
Energy (GeV)	6	6
Charge (pC)	15	4
Bunch Length (fs)	>200	~10
<B> (ph/s/mm^2/mrad^2/0.1%)	10^{22}	10^{21}
B_{peak} (ph/s/mm^2/mrad^2/0.1%)	10^{26}	10^{26}

SHORT BUNCH MODE

Single pass machines do not suffer the same fate as storage rings as equilibrium is never reached. A design based on linear uncoupled optic, helps address a proof-of-principle for the short pulse mode, which is later then tested using a realistic input beam distribution from the BERLinPro injector project.

Compression in the Injector

Producing a femto-second pulse of low energy spread starts at the Gun, Table 2. Here the longitudinal electron beam properties are restricted by the photo-injector laser pulse and the superconducting RF acceleration. The primary subtle compression in the Merger between the Booster and linac minimizes transverse emittance growth.

Table 2: Injector ASTRA[3] simulations

Component	Bunch Length (mm)	Emittance (keV mm)	Energy (MeV)
Gun	0.7	0.3	1.8
Booster	1.0	2	6.6
Linac	0.45	2.2	50

The injector Arc is then used to prepare the beam for the main accelerator. The combination of a second linac to increase the beam energy to 100 MeV and the R_{56} in the Arc compress the beam to $\sigma_t \sim 660\,fs$ with a correlated energy spread of $\Delta E/E \sim 1.5 \cdot 10^{-4}$.

* Work supported by German Bundesministerium für Bildung und Forschung, Land Berlin, and grants of Helmholtz Association VH NG 636 and HRJRG-214.
† terry.atkinson@helmholtz-berlin.de

Copyright © 2012 by the respective authors — cc Creative Commons Attribution 3.0 (CC BY 3.0)

Telescopic Compression

The main acceleration stage uses a scheme based on telescopic compression. In this regime the combination of the linac chirps and the R_{56} in the Arcs are described as a simple focusing (F) and defocussing (f) lens, Eq. 1. The shortest pulse achievable from a multi-turn isochronous structure is with full compression in the final arc. This is however at the expense of a correlated energy spread, blue in Fig. 2.

$$\begin{pmatrix} z \\ \Delta E/E \end{pmatrix}_1 = \begin{pmatrix} f/F & F-f \\ 0 & F/f \end{pmatrix} \begin{pmatrix} z \\ \Delta E/E \end{pmatrix}_0 \quad (1)$$

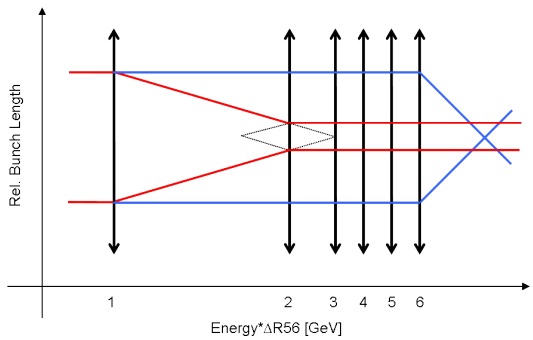

Figure 2: Telescopic bunch compression to preserve energy spread.

In order to remove the correlated energy spread and still produce a short pulse consider an alternative solution based on a telescopic lattice, red in Fig. 2. Implementing the first two arcs as achromats and accelerating either side of on-crest in each linac, the two "lenses" can share the same focal plane, just like in a telescope, to maximize the magnification and recover the energy correlation properties of the injector.

The minimal bunch length of the final beam into the long undulators is restricted by the requirement of an rms energy spread given by $\Delta E/E \sim 1/\text{UndulatorPeriods} \sim 10^{-4}$, to be $\sigma_t \sim 10\, fs$ when implementing purely linear optic.

Simulation Codes

Starting from previous calculations using ASTRA[4] up until the 50 MeV injector linac exit, the beam distribution was converted and tracked onwards through the FSF using Elegant[5].

Short Bunch Simulations

The first 50 m shown in Fig. 3 is the initial bunch compression in the injector Arc to prepare the beam for the first 1 GeV FSF linac of phase $\phi_1 = +8^\circ$ off crest . What follows this a step like bunch compression in the first Arc with $R_{56} = 20\, cm$ till the second 1 GeV linac at $\phi_2 = -20^\circ$ (placed at $s \sim 500\, m$). The second Arc of $R_{56} = 5\, cm$

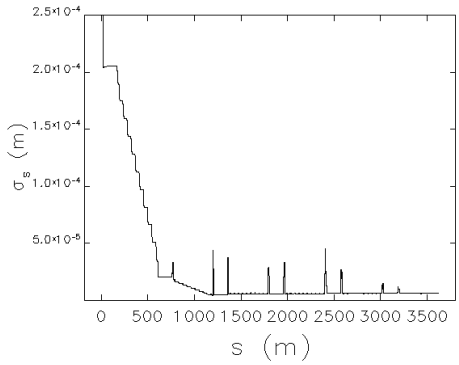

Figure 3: Bunch length variations in the FSF.

then completes the full bunch compression. These longitudinal bunch parameters are then preserved in the remaining isochronous Arcs, with some "spiking" shown due the vertical spreaders.

With the present optic a bunch length $\sigma_t \sim 20\, fs$ and energy spread $\Delta E/E \sim 1 \cdot 10^{-4}$ is achievable at the long undulator entrance Fig. 4.

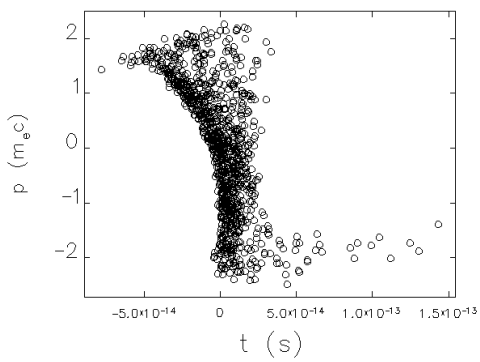

Figure 4: Phase space at long undulator entrance.

Large cumulative distortions due to radiation effects are not envisaged in this two stage process to achieve full compression as the energy after the first main linac is 1 GeV and the bunch charge is reduced for the short pulse mode.

LONGITUDINAL EMITTANCE

The longitudinal emittance can be described as an ellipse occupying a density of particles in $(c\Delta t, \delta)$ phase space. The non-linear properties of RF curvature acceleration can alter the phase distributions varying the normalized emittance.

2nd Order Aberrations

An emittance compensation scheme using higher order magnetic terms created in the Arcs is described here.

Copyright © 2012 by the respective authors — cc Creative Commons Attribution 3.0 (CC BY 3.0)

Using the linacs relative energy Eq. 2 and the Arcs bunch length Eq. 3 variations respectively one can calculate the emittance variation across the two stages as follows.

$$
\begin{aligned}
&LINAC \\
&\delta_1 = \delta_0 + R_{65} c\Delta t_0 + T_{655}(c\Delta t_0)^2 \quad (2) \\
&c\Delta t_1 = c\Delta t_0 \\
&+ARC \\
&\delta_2 = \delta_1 \\
&c\Delta t_2 = c\Delta t_1 + R_{56}\delta_1 + T_{566}\delta_1^2 \quad (3)
\end{aligned}
$$

Keeping only second order terms, assuming $\delta_0 = 0$ and substituting Eq. 2 and Eq. 3 the emittance can be approximated as Eq. 4

$$
\begin{aligned}
\epsilon^2 &= <(c\Delta t_2)^2><\delta_2^2> - <(c\Delta t_2 \delta_2>^2 \quad (4) \\
\epsilon^2 &\simeq <(c\Delta t_0)^4><(c\Delta t_0)^2> \left(T_{566}R_{65}^3 - T_{655}\right)^2
\end{aligned}
$$

Emittance Correction

One can interpret Eq. 4 as a useful tool to control the normalized emittance. The accelerating phase determines both the R_{65} and T_{655} terms and sextupoles in the Arc can adjust T_{566} to compensate for them.

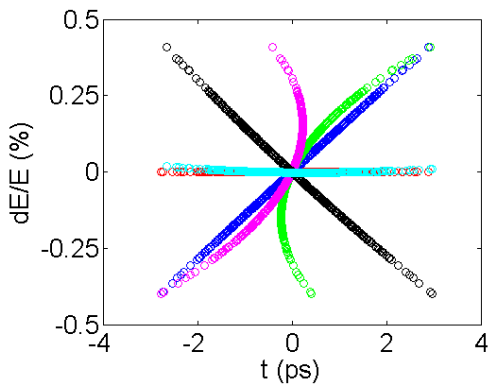

Figure 5: Correction of the 2nd order aberrations.

Fig. 5 demonstrates this concept, showing anticlockwise the variation of the beam phase space from an uncorrelated low emittance flat beam (red) through a non-linear RF chirp (blue). Then the introduction of first and second order magnetic correction, rotating and deforming the phase space (green - magenta - black) before finally a second linac is used to approximately recover the original distribution (cyan).

Emittance Correction Simulations

This scheme was adapted for the two stage telescopic bunch compression in the FSF machine simulations Fig. 6. The second order terms from the off-crest RF acceleration for the short bunch mode were optimized so that they would be fully compensated for by the T_{566} term created in the dipoles in the achromat Arcs.

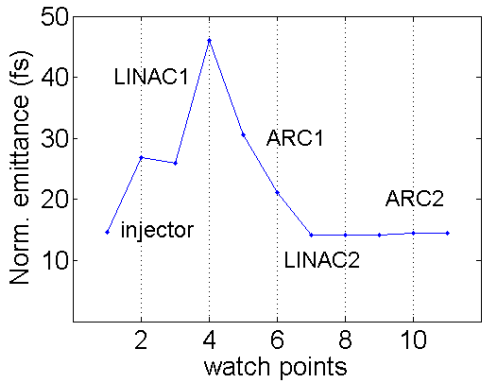

Figure 6: Recovering the injector properties.

Additional correction using sextupoles will be considered for future calculations as an essential tool for the recovery of the injectors longitudinal beam properties.

CONCLUSION

A two stage linear bunch compression scheme for the FSF light source has been presented and simulated using realistic beam parameters from the BERLinPro injector. A compensation scheme to recover the normalized emittance of the injector has been proposed.

REFERENCES

[1] Y. Petenev et al., "Feasibility Study of an ERL-Based GeV-scale Multi-turn Light Source", IPAC2012, New Orleans, USA.

[2] T. Kamps, et al., Journal of Physics: Conference Series 298 (2011) 012009.

[3] ASTRA code, A Space Charge Tracking Algorithm, http://tesla.desy.de/ meykopff/ 2012.

[4] J. Knobloch et al., Status of the BERLinPro Energy Recovery Linac Project, IPAC 2012, New Orleans, July 2012.

[5] M. Borland, "elegant: A Flexible SDDS-Compliant Code for Accelerator Simulation," Advanced Photon Source LS-287, September 2000.

Copyright © 2012 by the respective authors — cc Creative Commons Attribution 3.0 (CC BY 3.0)

LINAC OPTICS DESIGN FOR MULTI-TURN ERL LIGHT SOURCE*

Y. Petenev#, T. Atkinson, A.V. Bondarenko, A.N. Matveenko, HZB, Berlin, Germany.

Abstract

The optics simulation group at HZB is designing a multi-turn energy recovery linac-based light source. Using the superconducting Linac technology, the Femto-Science-Factory (FSF) will provide its users with ultra-bright photon beams of angstrom wavelength at 6 GeV. The FSF is intended to be a multi-user facility and offer a variety of operation modes. In this paper a design of transverse optic of the beam motion in the Linacs is presented. An important point in the optics design was minimization of the beta-functions in the linac at all beam passes to suppress beam break-up (BBU) instability.

INTRODUCTION

In this document we present a design of a Linac optics for a new 3 pass ERL-based LS with 6 GeV maximum energy of electron beam. This future facility is named Femto-Science Factory (FSF) [1].

The schematic layout of the facility is presented in Fig. 1. A beam is created in 1.3 GHz SRF gun with photo cathode. We consider an SRF injector with similar parameters to the B*ERL*inPro injector under development at HZB [2, 3]. Then it passes a 100 MeV Linac and is accelerated to 6 GeV after passing 3 times through each of two 1 GeV main Linac's. In the arcs between the acceleration stages it is assumed to have undulators with 1000 periods. In the long straight section (see Fig.1) a long undulator with 5000 periods is assumed. The main design parameters of FSF are presented in Table 1.

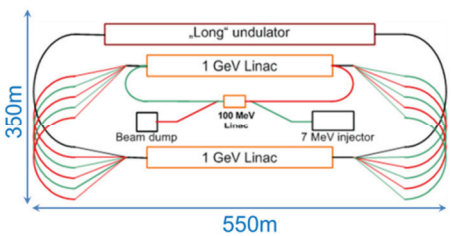

Figure 1: The scheme of FSF.

One potential weakness of the ERLs is transverse beam breakup instability, which may severely limit a beam current. If an electron bunch passes through an accelerating cavity it interacts with dipole modes (e.g. TM_{110}) in the cavity. First, it exchanges energy with the mode; second, it is deflected by the electro-magnetic field of the mode. After recirculation the deflected bunch interacts with the same mode in the cavity again which constitutes the feedback. If net energy transfer from the beam to the mode is larger than energy loss due to the mode damping the beam becomes unstable.

The actuality of this problem was recognized in early experiments with the recirculating SRF accelerators at Stanford [4] and Illinois [5], where threshold current of this instability was occurring at few microamperes of the average beam current. In the works of Rand and Smith in [6] dipole high order modes were identified as a driver of this instability. In late of the 80's the detailed theoretical model and simulation programs had been developed [7, 8]. Nowadays the interest to this problem was renewed. The requirements for more detailed theory and simulation programs [9-11] are given by the needs of high current (~100 mA) ERLs.

The threshold current for the transverse beam breakup may be estimated for the case of a single cavity and single mode for a multipass ERL in the form as [11]:

$$I_{th} \approx I_0 \frac{\lambda\!\!\!^{-2}}{Q_a L_{eff} \sqrt{\sum_{m=1}^{2N-1} \sum_{n=m+1}^{2N} \frac{\beta_m \beta_n}{\gamma_m \gamma_n}}}, \qquad (1)$$

where I_0- Alfven current, Q_a is the quality factor of HOM, $\lambda\!\!\!^{-} = \lambda/2\pi$, λ is the wavelength corresponding to the resonant frequency of the TM_{110} mode, γ_m is the relativistic factor at the m-th pass through the cavity, β_m – is the Twiss parameter, L_{eff} – is the effective length of the cavity, N is the number of passes during acceleration. It should be noted that (1) gives more realistic estimation of the BBU threshold current than a similar expression in [9] with a 1/N(2N-1) dependence on the number of passes. This is the result of an assumption in [9] of integer tunes in every turn of the ERL.

Table 1: Main Design Parameters of FSF

Parameter	High brilliance mode	Short bunch mode
E, GeV	6	6
<I>, mA	20	5
Q, pC	15	4
τ, fs	200-1000	~10
<B>, ph/s/mm2/mrad2/0.1%	$8 \cdot 10^{22}$	$\sim 4 \cdot 10^{21}$
B_{peak}, ph/s/mm2/mrad2/0.1%	10^{26}	$\sim 10^{26}$

Eq. 1 shows that it is preferable to have low β-functions at low energies. Therefore, the design was optimised to minimize beta functions of the beam in the Linac to increase the threshold current of BBU instability from one

* Work supported by German Bundesministerium für Bildung und Forschung, Land Berlin, and grants of Helmholtz Association VH-NG-636 and HRJRG-214.

#yuriy.petenev@helmholtz-berlin.de

Copyright © 2012 by the respective authors — cc Creative Commons Attribution 3.0 (CC BY 3.0)

point of view and to decrease the beats of the beta functions in the spreaders from another.

As it was shown in [1], for a scheme of FSF, presented in Fig. 1, BBU instability will develop in the 1st cavity of the 1st 1 GeV linac.

In this paper we analyze the influence of the energy gain in the preinjection linac (100 MeV) and two main linacs (1 GeV) on the BBU threshold and propose an optimized solution.

Preinjection Linac Pattern

In this part we would like to discuss BBU instability in the preinjection linac, which is coming after the merger section. In Fig. 1 it is suggested to have a 100 MeV linac. Therefore we have acceleration from 7 to 107 MeV, or deceleration for the same amount of energy. Therefore it is required to have one cryomodule with an acceleration gradient of the cavities of G = 15.5 MeV/m.

Now we would like to analyse model with a linac consisting of two cryomodules with acceleration up to 250 MeV and with a triplet of quadrupole magnets in between them, which role is to change the sign of the twiss parameter α of the beam. Let us find the initial injection twiss parameters to have the equal threshold currents for the entrance and for the middle of the linac. To find that we will use eq. 1 and a model of the linac with one dipole HOM, which we locate at different positions in the linac. In this case we assume that the 1st cryomodule is a long cavity with a transfer matrix M given by [12]:

$$\begin{pmatrix} \cos(\alpha)-\sqrt{2}\sin(\alpha) & \frac{\sqrt{8}\gamma_0 L\sin(\alpha)}{\Delta\gamma} \\ -\frac{3}{\sqrt{8}}\frac{\Delta\gamma\sin(\alpha)}{L\gamma_1} & \left(\cos(\alpha)+\sqrt{2}\sin(\alpha)\right)\frac{\gamma_0}{\gamma_1} \end{pmatrix}, \quad (2)$$

where $\alpha = \frac{1}{\sqrt{8}}\ln\left(\gamma_1/\gamma_0\right)$, $\gamma_{1(0)}$ is the final(initial) normalized energy of the particle, L – the length of the cavity (cryomodule). Also we assume that there is a symmetrical β-functions on acceleration and deceleration in the linac.

Therefore we can transfer the beta function through the 1st cryomodule as:

$$\beta_1 = \frac{\gamma_1}{\gamma_0}\left(\beta_0 m_{11}^2 - 2\alpha_0 m_{11}m_{12} + \frac{1+\alpha_0^2}{\beta_0}m_{12}^2\right) \quad (3)$$

.

The RF focusing in the second cryomodule is quite weak and we represent it with a cavity without RF focusing for simplicity. So the beta function at the end of the linac might be found as:

$$\beta_2 = \frac{\gamma_2}{\gamma_1}\left(\beta_1 - 2\alpha_1 L + \frac{1+\alpha_1^2}{\beta_1}L^2\right) \quad (4)$$

.

The minimum of the $\beta_2 = 2L^2/\beta_1$ is given, when

$$\alpha_1 = \frac{\beta_1}{L} \quad (5)$$

.

Now we can proceed with an equation for the thresholds:

$$\sqrt{\frac{\beta_0\beta_2}{\gamma_0\gamma_2}} = \frac{2\beta_1}{\gamma_2-\gamma_0} \quad (6)$$

.

To find the solution we will vary the initial twiss parameters and look for a maximum value of the thresholds. The numerical solution is presented in Fig. 2.

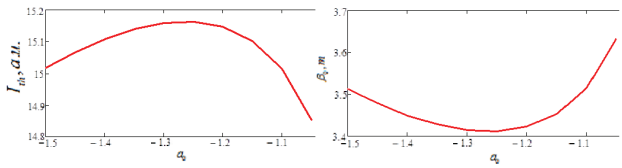

Figure 2: Threshold current, calculated using eq. 1 (without constants, which are the same for all cavities) and initial twiss parameters for preinjection Linac, consisting of two long cavities with a triplet in between.

One can see from Fig. 2 that the maximum threshold current is achieved at α_0 ~ -1.26 and β_0 ~ 3.41.

Different Acceleration Pattern

In this paragraph we would like to discuss an improvement of the present scheme of FSF, where we have 100 MeV preinjection and then two 1 GeV Linacs (Fig. 1), for the scheme, presented in Fig. 3.

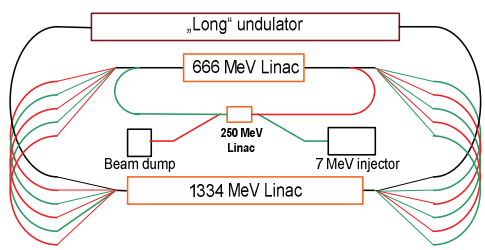

Figure 3: The improved acceleration scheme of FSF.

One of the motivations of this improvement was BBU instability. The new scheme gives roughly 1.7 times better threshold current for the 1-st cavity in the 1-st linac see Table 2, where the instability develops in the first scheme.

The easiest way to see the reason of rebalancing of the energies in the two main linacs is to analyse the eq. 1, specifically the square root in the denominator. We would

Copyright © 2012 by the respective authors — cc Creative Commons Attribution 3.0 (CC BY 3.0)

like to find a balance between the energy gains in two main linacs to have equal threshold currents for them. To do that, we will analyse a model with linacs, when a focusing from a triplets is neglected for the second and the third passes. In this model with the injection energy of about 250 MeV the transverse focusing inside the cavities can be neglected. So, we assume that the beta functions of a beam at the exit and at the entrance to the linac are about the length of the linac for the second and the third passes and for the end of the linacs at the first pass and it is about the length of the one cryomodule [1] at the entrance for the first pass.

Let's introduce G as a gradient of the cavities in MeV/m, $L= 2000$ [MeV] $/G$ is a length of the cavity structure, required to accelerate to the final energy of 2 GeV, x is the length of the first linac and, therefore, L-x is the length of the 2-nd. Now we can find energies $\gamma_{1(2),n}$ for each pass and as we said before $\beta_{1,1(6)} = \beta_{2,1(6)} \sim 12.57$ m and $\beta_{1,n} = x$ or $\beta_{2,n} = L$-x for the first and the second linac respectively and for n=2..5.

We can proceed with the following equation:

$$\sqrt{\sum_{m=1}^{2N-1}\sum_{n=m+1}^{2N}\frac{\beta_{1,n}\beta_{1,m}}{\gamma_{1m}(x)\gamma_{1n}(x)}} = \sqrt{\sum_{m=1}^{2N-1}\sum_{n=m+1}^{2N}\frac{\beta_{2,n}\beta_{2,m}}{\gamma_{2m}(x)\gamma_{2n}(x)}}, \quad (7)$$

when the threshold currents have the same values for the 1-st and last cavities in both linacs. This equation can be solved numerically and gives the result that x ~ L/3 with injection energy – $\gamma_{1,1} = 480$. This explains why we propose a new acceleration pattern in Fig. 3.

Now we proceed with a modeling of the linac optics in Elegant program [13]. Optics for all three passes through the first 666 MeV linac is presented in Fig. 4.

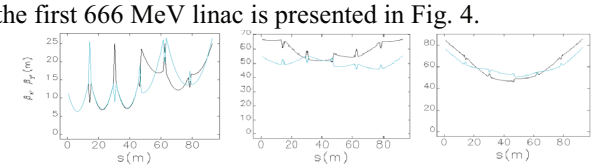

Figure 4: Optics design of the first 666 MeV linac. 3 passes with 250, 2.250 and 4.250 GeV beam injection energy from left to right correspondingly.

Also the optics was designed for the second 1334 MeV Linac and it is presented in Fig. 5.

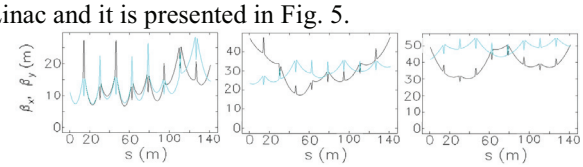

Figure 5: Optics design of the second 1334 MeV linac. 3 passes with 916, 2916 and 4916 MeV beam injection energy from left to right correspondingly.

The threshold currents for the schemes of FSF in Figs. 1 and 3 are presented in Table 2. For the estimations we used the following equation (which is a combination of eq. 1 and [9]):

$$I_{th} = \frac{2mc^3}{e\omega\left(\frac{R}{Q}\right)_d Q_d}\frac{1}{\sqrt{\sum_{m=1}^{5}\sum_{n=m+1}^{6}\frac{\beta_m\beta_n}{\gamma_m\gamma_n}}}, \quad (8)$$

and we took a mode with $(R/Q)_d \cdot Q_d = 6\cdot 10^5$ Ω, $\omega = 2\pi\cdot 2\cdot 10^9$ Hz.

Table 2: Threshold Currents for Different Schemes

Linac scheme	I_{th}, A		
	Preinjector	1st Linac	2nd Linac
0.100 + 1 + 1GeV	1.26	0.88	3.73
250 + 666 + 1334MeV	1.21	1.46	3.58

One can see from the Table 2 that the value of threshold current for the 1st main linac was improved. It was also slightly decreased for the 2nd linac and for the preinjection.

CONCLUSION

In the new proposed scheme BBU instability will develop in the preinjection Linac. In the future work we should find a way how to increase the thresholds in the preinjection linac and in the 1st by decreasing the threshold current value in the 2nd linac.

REFERENCES

[1] Y. Petenev et al., "Feasibility Study of an ERL-Based GeV scale Multi-turn Light Source", IPAC2012, New Orleans, USA.

[2] T. Kamps, et al., Journal of Physics: Conference Series 298 (2011) 012009.

[3] A.N. Matveenko, et al., "Status of the B*ERL*inPro optics design", Proc. of IPAC'11, pp.1500-1502;

[4] Claude M. Lyneis, Michael S. McAshan, Roy E. Rand, H. Alan Schwettman, Todd I. Smith and John P. Turneaure, The Stanford Superconducting Recyclotron, IEEE Transactions on Nuclear Science, Vol. NS-26, No. 3, June 1979.

[5] P.Axel, L.S.Cardman, H.D.Graef, A.O.Hanson, R.A.Hoffswell, D.Jamnik, D.C.Sutton, R.H.Taylor, and L.M.Young, Operating Experience with MUSL-2, IEEE Transactions on Nuclear Science, Vol. NS-26, No. 3, June 1979.

[6] R.E. Rand and T.I. Smith, Beam optical control of beam breakup in a recirculating electron accelerator, Particle accelerators, Vol. 11, pp. 1-13 (1980).

[7] J.J. Bisognano, R.L. Gluckstern, in Proceedings of the 1987 Particle Accelerator Conference, Washington, DC (IEEE Catalog No. 87CH2387-9), pp. 1078-1080.

[8] G.A. Krafft, J.J. Bisognano, in Proceedings of the 1987 Particle Accelerator Conference, Washington, DC (IEEE Catalog No. 87CH2387-9), pp. 1356-1358.

[9] G.H. Hoffstaetter, I.V. Bazarov, „Beam-breakup instability theory for the energy recovery linacs", Phys. Rev. ST AB 7, 054401 (2004).

[10] E. Pozdeyev, et al., "Multipass beam breakup in energy recovery linacs", NIM A 557 (2006) 176-188.

[11] N.A. Vinokurov et al., Proc. of SPIE Vol. 2988, p. 221 (1997).

[12] J. Rosenzweig, L. Serafini. "Transverse particle motion in radio-frequency linear accelerators". Phys. Rev., E49 (1994), p. 1601.

[13] M. Borland, "Elegant: A Flexible SDDS-Compliant Code for Accelerator Simulation," APS LS-287, 2000.

Copyright © 2012 by the respective authors — cc Creative Commons Attribution 3.0 (CC BY 3.0)

SINGLE SHOT BUNCH-BY-BUNCH BEAM EMITTANCE MEASUREMENT OF THE SPRING-8 LINAC

Yoshihiko Shoji# and Kouji Takeda, NewSUBARU/SPring-8, University of Hyogo, Japan

Abstract

The bunch-by-bunch emittance of a single shot beam from the SPring-8 electron linac was measured utilizing phase rotation in an electron storage ring. The linac beam was injected into the ring and the beam profiles of several revolutions were recorded using a dual sweep streak camera. The fast sweep separated the linac bunches in 1 ns macro pulse and the slow sweep separated the profiles at different turns. The bunch emittances were reconstructed from the profiles. The stability of the linac beam was evaluated from the recorded shot-to-shot fluctuation. We also identified differences in the orbit and the emittance of different bunches in a pulse.

INTRODUCTION

The SPring-8 linac has been operated as an injector to the electron storage ring, NewSUBARU. However, fine parameter tuning is required for stable top-up injection because of the small ring acceptance. In that process, single shot linac beam monitors were necessary to understand the shot-to-shot fluctuation of the injection. A single shot bunch-by-bunch emittance monitor would be a powerful tool to understand the shot-to-shot fluctuation of the injection efficiency.

We used the visible light profile monitor of the electron storage ring as a diagnostic for the linac beam. The dual sweep streak camera recorded multiple profiles of the injected beam in a single camera frame. The fast sweep separated linac bunches in a macro pulse and the slow sweep separated profiles of different turns. The betatron oscillation in the ring produced phase rotation allowing the reconstruction of the beam emittance. It was possible to fully optimize the ring parameters for our measurements since beam storage was not required.

A stability of the linac beam was evaluated from the shot-to-shot variation. We could also see differences in the bunch at the front of a macro pulse compared to the bunch at the rear.

PARAMETERS OF DAILY OPERATION

Averaged Beam Parameters

Figure 1 shows the layout of the SPring-8 linac, the booster synchrotron, and NewSUBARU storage ring. Table 1 shows the main parameters for the linac. The macro pulse width of the linac beam is normally 1 ns, which contains 3 linac bunches. The rf synchronization system between the linac and the ring [1] enables an injection to a single rf bucket of the ring with rf frequency of 500 MHz.

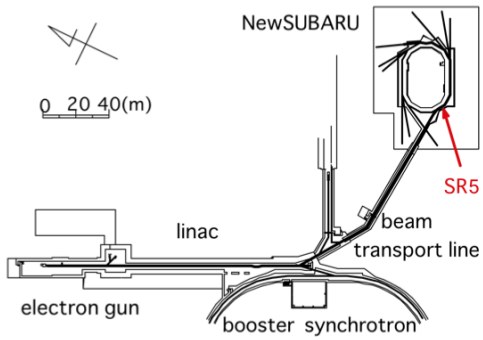

Figure 1: Layout of the 1 GeV SPring-8 linac, the booster synchrotron, and the NewSUBARU storage ring.

Table 1: Main Parameters of the Linac

Electron energy	1 GeV
Rf frequency	2856 MHz
Common pulse rate	1 Hz
Common pulse width	1 ns
FWHM bunch length; front/middle	10 ps / 14ps
Full energy spread; front / middle	0.4% / 0.6%
Transverse emittance (FWHM^2)	100 π nmrad.

The listed transverse emittance was calculated from the average over many shots, measured by Q-scanning at the beam transport line. The longitudinal parameters were obtained from the measurements of the synchrotron oscillation in the ring just after injection [2]. The listed bunch length and the energy spread were calculated from the average of 10 shots.

Bunch Structure and Injection Efficiency

The bunch structure was fluctuated by a jittering of the gate pulse of the electron gun. Figure 2 shows six typical dual sweep images of the streak camera with six typical bunch structures. The vertical axis in the images is the ring rf phase and the horizontal axis the revolution. The time structure at 1/4 of the synchrotron oscillation period (41 μs) gives the energy profile.

Figure 3 shows the injection efficiency with the ring parameters characteristic of daily operation. Shots with images A and B had comparatively worse efficiency. A separated data shows that the ring has a large enough longitudinal acceptance for the injected beam, suggesting that dependence on transverse parameters caused fluctuations in the injection efficiency.

shoji@lasti.u-hyogo.ac.jp

Copyright © 2012 by the respective authors — cc Creative Commons Attribution 3.0 (CC BY 3.0)

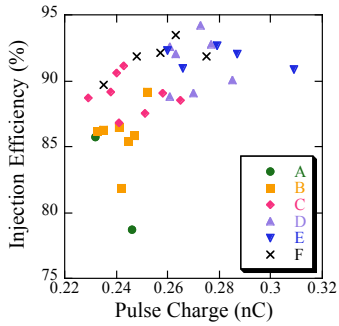

Figure 3: Injection efficiency for different bunch structure.

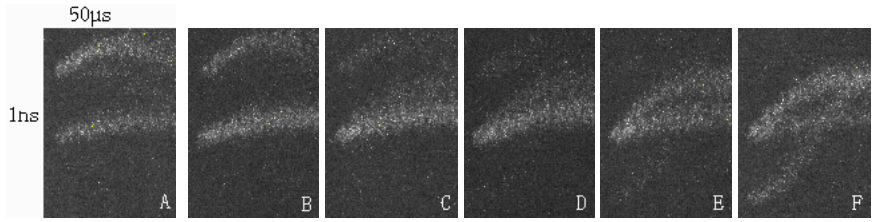

Figure 2: Typical dual sweep images.

SHOT-TO-SHOT MEASUREMENTS

Setup for the Measurement

Figure 4 shows the schematic layout near the injection point and the monitor line, named SR5. The dove prism on the line switches transverse measurement axis, in this case we selected the vertical with 90 degrees rotation.

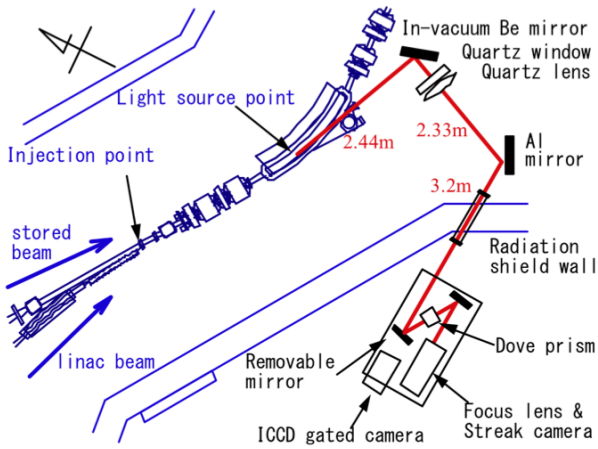

Figure 4: Layout of the visible light monitor line SR5.

The ring parameters were different from those of daily operation. The injection pulse bump was optimized so that the injected beam had a small dipole oscillation and maintained almost 100% injection efficiency. The vertical chromaticity was reduced to 0 in order to eliminate the betatron phase spread over multiple revolutions. The linear H/V coupling was reduced to less than 1%. The very small beam size of the stored beam was used to calibrate the vertical spatial resolution: 0.3 mm FWHM at the light source point with $\beta_y = 17$ m.

Data Analysis of a Typical Shot

Here we demonstrate our method of analysis using a representative shot (#12) as an example. Its total charge, measured by fast CT on the beam transport line, was 0.23 nC.

Figure 5 shows the dual sweep image of the streak camera frame and the projection to the fast sweep axis. The vertical axis is the horizontal position in space and the ring rf phase in time. The upper part of the figure corresponds to the head of the linac pulse with the tail in the lower part of the figure. The horizontal axis is the vertical position in space and the ring revolutions in time. The six spots correspnd to profiles from the 4th through 9th turns after the injection. Profiles at the initial 3 turns were out of the camera slit because of a large horizontal displacement. The horizontal profile in the figure of each spot corresponds to the vertical spatial profile in the experimental frame.

Figure 6 shows profiles of the 6 turns of the two respective bunches. They were fitted with Gaussian functions. We derived the peak position y and a divergence σ^2 as a function of the revolution number N.

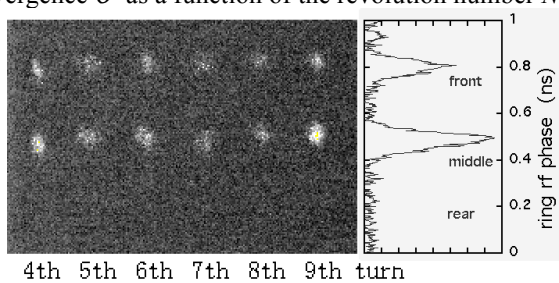

Figure 5: Dual Sweep image of the injected beam of the shot #12.

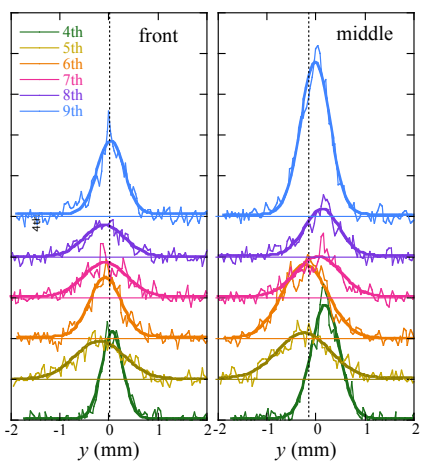

Figure 6: Vertical beam profiles from turns 4 through 9 of the front bunch and the middle bunch.

As shown in Figure 7, the data were fitted with the following sinusoidal functions

$$y = A_0 + A_S \sin(2\pi\Delta\nu_y N) + A_C \cos(2\pi\Delta\nu_y N) \quad (1)$$

$$\sigma^2 = B_0 + B_S \sin(4\pi\Delta\nu_y N) + B_C \cos(4\pi\Delta\nu_y N) \quad (2)$$

Here $\Delta\nu_y$ =0.224 is the sub-integer part of the vertical betatron tune. The dipole oscillations of two bunches were obviously different. The oscillations of the widths

Copyright © 2012 by the respective authors — cc Creative Commons Attribution 3.0 (CC BY 3.0)

were almost the same except for one data point, the 6th turn of the middle bunch.

The beam ellipse at the injection point is calculated using the phase advance to the light source point, 0.15 rad. Figure 8 shows the extrapolation of the fitted wave and the beam ellipses at the injection point.

The transverse emittance ε_y was obtained from

$$\varepsilon_y = \sqrt{(B_0 - \sigma_R{}^2)^2 - (B_S{}^2 + B_C{}^2)}/\beta_y. \quad (3)$$

Here $\sigma_R{}^2$=0.02 mm^2 is the spatial resolution.

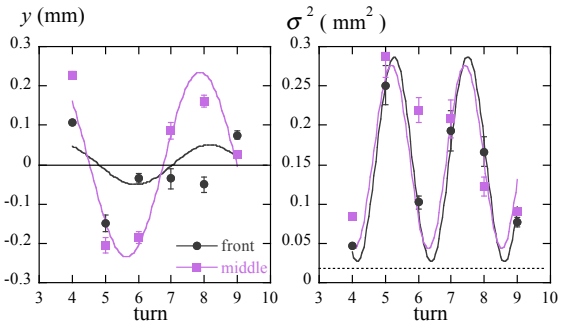

Figure 7: The dipole oscillation of the peak position (left) and the quadrupole oscillation of the divergence (right). The dotted line on the right indicates the spatial resolution.

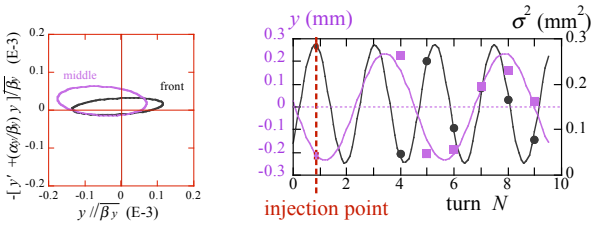

Figure 8: Extrapolation of the fitted waves and the calculated beam ellipses at the injection point.

Shot-to-Shot Fluctuation

We recorded the profiles of 20 shots in order to see the shot-to-shot fluctuation. Figure 9 shows the bunch charge for the 20 shots. They are grouped A-E, according to the charge of the front bunch.

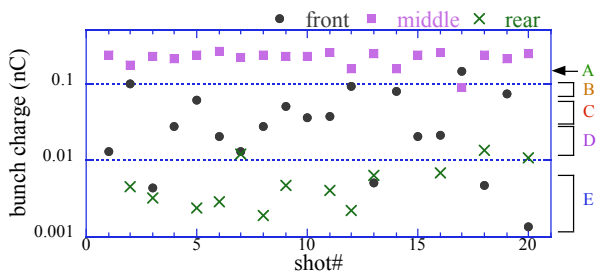

Figure 9: Bunch charge for the highlighted 20 shots.

The parameters quantifying the dipole oscillation, A_C and A_S, of the middle bunch are plotted in Figure 10. The fluctuation was correlated with the group and took place at the phase $\Delta A_S/\Delta A_C$ = 1.3. We added data points of the front bunch of groups A–C to the plot. The differences in the same pulse were roughly of the order of the fluctuation in phase.

The parameters for the quadrupole oscillation, B_C and B_S, of the middle bunch are plotted in Figure 11. No clear dependence on the group was observed. However, it seems to be no accident that the difference of two bunches satisfied $2\Delta B_S - \Delta B_C > 0$ for all 8 shots.

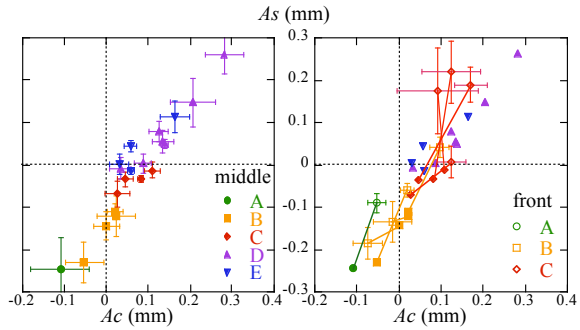

Figure 10: Shot-to-shot fluctuation of the dipole oscillation of the middle bunch (left) and those of the front bunch (right). The oscillations of different bunches in the same shot are connected with lines.

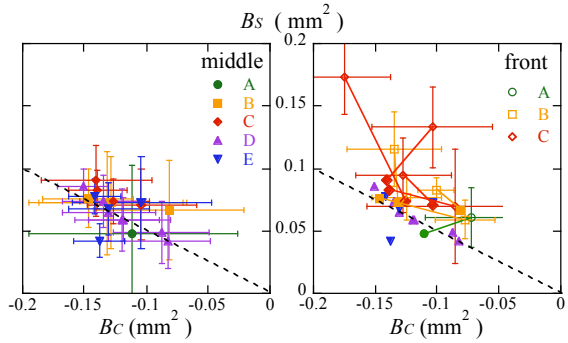

Figure 11: Shot-to-shot fluctuation of the quadrupole oscillation of the middle bunch (left) and those of the front bunch (right).

SUMMARY AND DISCUSSION

We succeeded in measuring the shot-to-shot, bunch-by-bunch fluctuations of the vertical emittance of the SPring-8 linac beam. A measurement of the horizontal parameter would be necessary to identify the mechanism that causes the correlation with the injection efficiency.

ACKNOWKEDGEMENT

We thank operators of NewSUBARU, Dr. Minagawa, Mr. Shinomoto, and Mr. Takemura for their help with the measurement. We thank members of the SPring-8 linac group for many helpful suggestions. We acknowledge technical and financial support by KEK on the construction of SR5 according to the "comprehensive support program for the promotion of accelerator science and technology".

REFERENCES

[1] Y. Kawashima, *et al.*, PR ST-AB 4, 082001 (2001).
[2] T. Matsubara, *et al.*, PR ST-AB 9, 042801 (2006).

Copyright © 2012 by the respective authors — cc Creative Commons Attribution 3.0 (CC BY 3.0)

ADVANCES IN BEAM TESTS OF DIELECTRIC BASED ACCELERATING STRUCTURES*

S. P. Antipov[1,2], C. Jing[1,2], A. Kanareykin[1,#], J.E. Butler[1], V.Yakimenko[3], W. Gai[2]
[1]Euclid Techlabs LLC, Solon, OH, USA,
[2]Argonne National Laboratory, Argonne, IL, USA
[3]Brookhaven National Laboratory, Upton, NY, USA

Abstract

Diamond is being evaluated as a dielectric material for dielectric loaded accelerating structures. It has a very low microwave loss tangent, high thermal conductivity, and supports high RF breakdown fields. We report on progress in our recent beam tests of the diamond based accelerating structures of the Ka-band and THz frequency ranges. Wakefield breakdown test of a diamond-loaded accelerating structure has been carried out at the ANL/AWA accelerator. The high charge beam from the AWA linac (~70 nC, σ_z ~ 2 mm) was passed through a rectangular diamond loaded resonator and induce an intense wakefield. A groove is cut on the diamond to enhance the field. Electric fields up to 300 MV/m has been generated on the diamond surface to attempt to initiate breakdown. Wakefield effects in a 250 GHz planar diamond accelerating structure has been observed at BNL/ATF accelerator as well. We have directly measured the mm-wave wake fields induced by subpicosecond, intense relativistic electron bunches in a diamond loaded accelerating structure via the dielectric wake-field acceleration mechanism. A surface analysis of the diamond has been performed before and after the beam test.

INTRODUCTION

Diamond has been proposed as a dielectric material for dielectric loaded accelerating (DLA) structures [1-3]. Dielectric Loaded Accelerator structures using ceramics or other materials and excited by a high current electron beam or an external high frequency high power RF source have been under extensive study for many years [4-7]. Low loss microwave ceramics, fused silica, and CVD polycrystalline and single crystal diamonds [11] have been considered as materials for dielectric based accelerating structures to study of the physical limitations encountered in developing field strengths > 100 MV/m at microwave [4-6] and > GV/m at THz frequencies in a dielectric based wakefield accelerator [6,7,11,12]. THz radiation has been generated recently by a short ~10 GV/m pulse within a 100 μm diameter quartz fiber [7]. A planar diamond-based DLA structure was proposed recently by Omega-P, Inc., where the dielectric loading of this structure was to be made of diamond slabs fabricated using CVD (chemical vapor deposition) technology [2].

Our choice of CVD (Chemical Vapor Deposition) diamond as a loading material will allow demonstration of high accelerating gradients; up to 0.5-1.0 GV/m as long as the diamond surface can sustain a 0.5-1.0 GV/m short pulse (~ 10 ns) rf field without breaking down. Diamond has the lowest coefficient of thermal expansion, highest thermal conductivity (2×10^3 Wm^{-1} K^{-1}) and extremely low loss tangent ($<10^{-4}$) at Ka-W frequency bands. Secondary emission from the CVD diamond surface can be dramatically suppressed by diamond surface dehydrogenation or oxygen termination [3,6,8-12]. The CVD process technology is rapidly developing, making the CVD diamond fabrication process fast and inexpensive. Given these remarkable properties, diamond should find numerous applications in advanced accelerator technology [3]. Planar diamonds are available commercially in various grades including single crystal diamonds. The goal of this research is to perform a wakefield acceleration experiment using a diamond loaded structure and to test diamond for breakdown.

Euclid Techlabs had performed two wakefield experiments with diamond loaded accelerating structures: a 25 GHz structure at the Argonne Wakefield Accelerator of ANL and a 250 GHz structure at the Accelerator Test facility of BNL [9].

BEAM EXPERIMENTS WITH THE DIAMOND BASED DLA STRUCTURES

Significant progress has been made in the development and testing of high gradient dielectric accelerating structures (DLA) [1]. As various engineering challenges (breakdown, dielectric losses, efficient RF coupling) have been overcome, the technology of high gradient RF or wakefield driven dielectric loaded structures appears increasingly attractive as a viable option for high energy accelerators. Typical DLA considered in experiments is a cylindrical, dielectric tube with an axial vacuum channel inserted into a conductive sleeve or a rectangular waveguide loaded with planar dielectric pieces. In this paper we will focus on the latter structure. The dielectric constant, thickness of dielectric and the size of a vacuum gap are chosen to adjust the phase velocity of the fundamental mode at certain frequency to the beam velocity ~ c. In the application to particle acceleration, the dominant TM_{01} mode is of main interest.

*Work supported by the Department of Energy SBIR program.
#alexkan@euclidtechlabs.com

Copyright © 2012 by the respective authors — cc Creative Commons Attribution 3.0 (CC BY 3.0)

We report here the results of a wakefield breakdown test of single crystal diamond-loaded rectangular accelerating structure [10]. The high charge beam from the AWA linac (~70 nC, σ_z = 2 - 2.5 mm) was transported through a rectangular diamond - loaded resonator and induced an intense wakefield [12]. A deep (200 μm) and narrow (20 μm) groove is cut on the diamond surface to enhance the field (by approximately a factor of ε). Electric fields at least of 300 MV/m were present on the diamond surface in the groove (decay time ~ 35 ns). A surface analysis of the diamond was performed before and after the beam test. No breakdown-type damage was observed on scanning electron microscopy images [10].

Structure design was presented earlier in [10], Fig.1. Parameters of the structure were determined via parametric simulations with constraint on the thickness of commercially available diamond plates, and the minimal gap size was determined by beam dynamics [11].

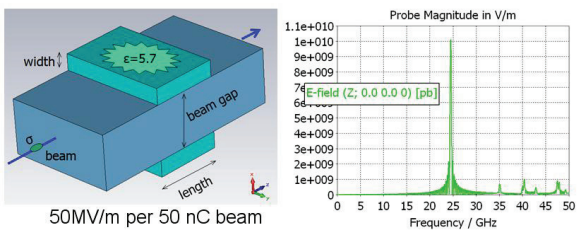

Figure 1: Left: geometry of the diamond resonator: length = 4mm, width = 1.2mm, beam gap = 4mm and overall width = 8mm. Right: spectrum of the wakefield (simulation).

To achieve stronger fields on the surface of the diamond two small 20 and 25 micron – wide, 220 micron deep grooves were laser cut on the diamond surface transverse to the beam propagation direction. There is a large field enhancement in these grooves: the field at the entrance to the groove is higher by a factor of ~ ε (5.7) than it would be in its absence [10] – a five time field enhancement because of the boundary conditions for the electric field at the surface of dielectric. For deep and narrow scratches (aspect ratio of 10 and higher) such enhancement is practically ε. As the groove becomes wider and shallower the field enhancement drops.

Diamond laser cutting is not a trivial procedure. Multistage cleaning was used to get rid of partial conductivity from carbon deposits. Special technology has been used that allowed removing practically all remaining carbon. SEM measurement confirmed that the laser cutting was successful as well as that target values of groove widths were achieved [11], Fig. 2.

In the experiment we manage to transport 72 nC charge through the structure, which corresponded to at least 300 MV/m on the surface of the groove. The bunch length measurement was not available, so for this estimate we used maximum value of 2.5mm. Shorter bunch length yields higher gradient.

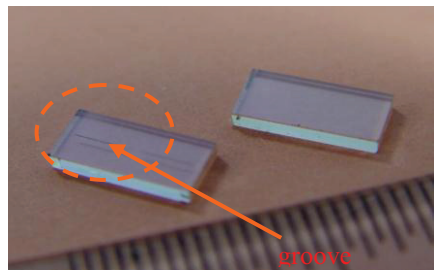

Figure 2: Field Enhancement groove machined in a planar diamond sample.

We used scanning electron microscopy to analyze the condition of the diamond surface before and after the experiment. Besides the presence of lint the surface did not undergo noticeable changes, Fig.3.

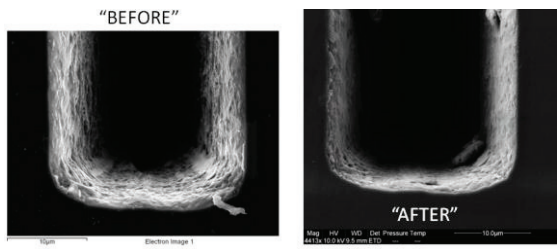

Figure 3: SEM measurement of the groove: right – before, left – after the test.

WAKEFIELD ACCELERATION IN A 250 GHZ DIAMOND STRUCTURE

Recently, we have directly measured THz wakefield acceleration/deceleration in a diamond loaded dielectric accelerating structure.

Proof of principle experiments at BNL/ATF [9] have studied wakefields in diamond structures in the 250 GHz regime. It should be noted especially that in this experiment diamond was for the first time used as a loading material for a wakefield dielectric based accelerating structure [9]. Fields produced by a leading (drive) beam were used to accelerate a trailing (witness) electron bunch, which followed the drive bunch at a variable distance. The energy gain of a witness bunch as a function of its separation from the drive bunch describes the time structure of the generated wakefield. By sweeping the separation between the drive beam and the witness beam and energy measurements of the witness beam a 0.25 THz frequency wakefield was directly sampled at the scale of about one wavelength [9,13].

The general experimental methodology is the following: a pair of beams is generated: - a high charge drive beam, followed by a smaller witness beam at a variable distance *d*. The drive beam generates a wake there and the witness beam is accelerated or decelerated depending on the delay between the two beams. We record the witness beam energy change, ΔE as a function of *d*.

Copyright © 2012 by the respective authors — cc Creative Commons Attribution 3.0 (CC BY 3.0)

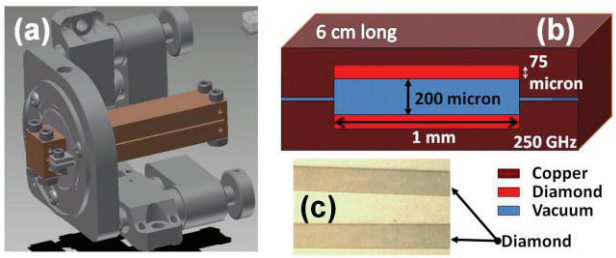

Figure 4: (a) 250 GHz structure mounted on a positioning holder; b) structure dimensions; c) photo of diamond after the experiment exhibiting no visible damage.

In the experiment we used 75 micron thick polycrystalline diamond plates loaded in a 6 cm long waveguide, Fig.4. The beam gap was 200 microns. This structure yields a wakefield dominated by a TM_{11} – like mode with 1200 micron wavelength (0.25 THz). The ATF drive beam is very short and also excites higher order modes, hence the wake is not a pure sine wave [9].

The subpicosecond drive and witness beams are produced by the technique described in [9]. A beam accelerated off-crest hence having a linear energy chirp (the head of the beam having lower energy than the tail) passes through a a dispersionless translating section. A mask is placed between the dogleg dipoles where the beam transverse size is dominated by the correlated energy spread. After the second dipole magnet the transverse pattern introduced by the mask becomes the longitudinal charge density distribution. In our case the mask was motorized and allowed creation of a drive beam followed by a witness beam at a variable delay [9].

Calibration is done via coherent transition radiation (CTR) interferometry. We fitted the recorded transverse profile by a gaussian distribution with σ_x = 50 μm, σ_y = 350 μm. The longitudinal wakefield produced by a beam with this current distribution was numerically calculated and compared with the experimental results.

The relative change in witness beam energy depending on the drive – witness separation is measured on the spectrometer. Compared to the beam energy, when it does not go through the structure, we observe energy gain and loss in the interval from -0.6 to +0.65 MeV for the witness beam following a drive beam through the DLA structure. This yields a 10.8 MV/m gradient for a 6 cm structure. The measurement accuracy was limited by the spectrometer resolution (σ = 0.028 MeV), estimated using the sharpest features obtained on the spectrometer by measuring the FWHM (full width half maximum) and dividing it by 2.355 to obtain the equivalent Gaussian width. Fig. 5 shows the measured energy change (diamonds) as a function of drive – witness separation with error bars. The shape of the experimentally mapped wake (diamonds) agrees well with the theoretical (scaled) prediction (circles) based on the wakefield (solid line) calculated for the drive beam current distribution (dashed line).

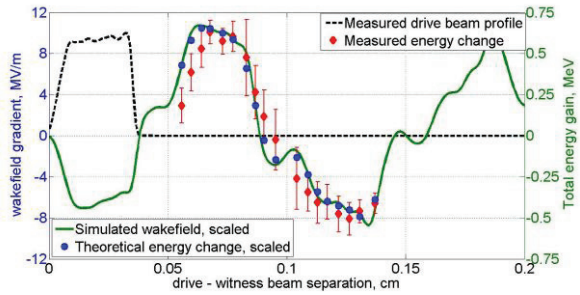

Figure 5: Energy gain of the witness beam as a function of separation from the drive beam.

SUMMARY

The emphasis of this paper is to present progress on development and fabrication of new types of diamond waveguides to be used for high gradient dielectric accelerating structures. We reported the results from development of a diamond DLA of GHz frequency range and wakefield tests of diamond-loaded rectangular accelerating structures at THz frequencies. We have directly measured THz wakefield acceleration and deceleration in a diamond loaded dielectric accelerating structure in an experiment where diamond was used for the first time in a wakefield dielectric based accelerating structure. In the 25 GHz frequency range, we achieved field levels on the order of 300 MV/m (35 ns pulse) in the structure using the 72 nC, 15 MeV beam at the Argonne Wakefield Accelerator Facility. Single crystal diamond plates produced by chemical vapor deposition (CVD) were used in the structure. A surface analysis of the diamond has been performed before and after the beam tests.

REFERENCES

[1] D. Whittum, SLAC-PUB-7910, July 1998.
[2] C. Wang, V.P. Yakovlev et al. PAC'05, 1282 (2005)
[3] A.Kanareykin et al. Proc. EPAC'06, 2460, (2006).
[4] W. Gai, AIP Conf. Proc.1086, 3, (2009).
[5] W. Gai et al. Phys. Rev. Lett. 61, 2756 (1988).
[6] A.Kanareykin. Journal of Physics, Conf. Ser., 236, p.012032, (2010).
[7] M. C. Thompson et al. AIP Conf. Proc. 877, 903 (2006).
[8] P Schoessow et al. AIP Conf. Proc. 1086, 398 (2009)
[9] S.Antipov et al. Appl. Phys. Lett. 100, 132910 (2012).
[10] S.Antipov et al. Proceedings IPAC'12, p. p.2813.
[11] A.Kanareykin. AIP Conference Proceedings, v. 1299, p. 286, 2010.
[12] S.Antipov et al. AIP Conference Proceedings, v. 1299, p. 359, 2010.
[13] S.Antipov et al. Phys. Rev. Lett. 108, 144801 (2012).

Copyright © 2012 by the respective authors — cc Creative Commons Attribution 3.0 (CC BY 3.0)

ON-LINE DISPERSION FREE STEERING FOR THE MAIN LINAC OF CLIC

J. Pfingstner*, D. Schulte, CERN, Geneva, Switzerland

Abstract

For future linear colliders as well as for light sources, ground motion effects are a severe problem for the accelerator performance. After a few minutes, orbit feedback systems are not sufficient to mitigate all ground motion effects and additional long term methods will have to be deployed. In this paper, the long term ground motion effects in the main linac of the Compact Linear Collider (CLIC) are analysed via simulation studies. The primary growth of the projected emittance is identified to originate from chromatic dilutions due to dispersive beam orbits. To counter this effect, an on-line identification algorithm is applied to measure the dispersion parasitically. This dispersion estimate is used to correct the beam orbit with an iterative dispersion free steering algorithm. The presented results are not only of interest for the CLIC project, but for all linacs in which the dispersive orbit has to be corrected over time.

INTRODUCTION

Linear colliders and light sources often require very small beam emittances and beam sizes to reach their goals. This fact makes these machines inherently sensitive to ground motion effects. For short time scales orbit feedbacks can be used to mitigate these effects by steering the beam with the help of beam positioning monitors (BPMs) (see [1] for the CLIC case). For longer time scales, this steering is not sufficient to preserve the beam quality as can be seen in Fig. 1. To be able to operate CLIC over longer time periods, it is essential to correct this remaining emittance growth. The development of such an algorithm is the topic of this paper.

The main reason for the remaining emittance growth is that the BPM positions itself will drift from their original position, which results in a dispersive beam orbit. The according chromatic dilutions decrease the beam quality over time. In the literature, a technique named dispersion free steering (DFS) can be found, which has been developed to correct similar chromatic dilutions (see [3] and [4]). In this paper we modify and extent this basic DFS method, such that it can be used to correct long term ground motion effects in an on-line mode. On-line means in this case that the DFS correction is applied during the normal accelerator operation in a parasitic way, without stopping the physics program. The methode will be explained an evaluated on the example of CLIC, but can be easily utilised for other accelerators.

* juergen.pfingstner@cern.ch

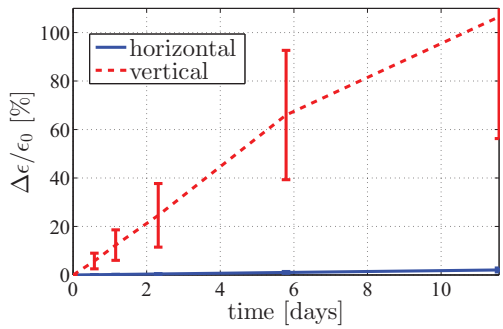

Figure 1: Simulations of the relative emittance growth over long time scales with orbit feedback in the main linac of CLIC. The used ground motion is generates according to the ATL law [2] with a constant A of $0.5\times10^{-6}\,\mu m^2/m/s$, which is the baseline for CLIC. The results have been averaged over 10 random samples of ground motion. For the initial horizontal and vertical emittance 600 nm and 10 nm have been used. The action of the orbit feedback was assumed to be perfect and therefore simulated by applying one-to-one steering without BPM noise, which is an optimistic approximation. It can be seen that already after 1 day the emittance has increased by about 10%.

ON-LINE DFS ALGORITHM

In this section, we will first introduce the basic DFS algorithm. After that the modifications necessary to apply this algorithm in an on-line mode will be discussed.

Basic DFS Algorithm

The DFS algorithm consists of two steps. In the first, the dispersion $\boldsymbol{\eta}$ at the BPMs is measured by varying the beam energy. This energy change can be created by changing the acceleration gradient, scaling the magnet strength and/or changing the initial beam energy. In the second step, corrector actuations $\boldsymbol{\theta}$ are calculated such that at the same time the measured dispersion $\boldsymbol{\eta}$ as well as the beam orbit $\boldsymbol{b}$ are corrected. Such actuations can be calculated by solving the following system of equations for $\boldsymbol{\theta}$ (see [5] for more details)

$$-\begin{bmatrix} \boldsymbol{b}-\boldsymbol{b}_0 \\ \omega(\boldsymbol{\eta}-\boldsymbol{\eta}_0) \\ \boldsymbol{0} \end{bmatrix} = \begin{bmatrix} \boldsymbol{R} \\ \omega\boldsymbol{D} \\ \beta\boldsymbol{I} \end{bmatrix}\boldsymbol{\theta}, \qquad (1)$$

where $\boldsymbol{b}_0$ and $\boldsymbol{\eta}_0$ are the reference beam orbit and target dispersion respectively. The third set of equations in Eq. (1) with the unity matrix $\boldsymbol{I}$ on the right side is used to damp too high corrector actuations. The weights ω and β can be

Copyright © 2012 by the respective authors — cc Creative Commons Attribution 3.0 (CC BY 3.0)

chosen to minimise the emittance, which is easiest done in simulation via a parameter scan. The matrices $\boldsymbol{R}$ and $\boldsymbol{D}$ are the orbit and dispersion response matrix.

To increase the robustness, this DFS algorithm is usually applied sequentially to overlapping sections of the accelerator. In the case of CLIC, the main linac is partitioned into 36 fully overlapping sections each consiting of about 28 FODO cells. Note that after the correction of one section, the dispersion of the sections downstream has changed as well. It is therefore necessary to re-measure the dispersion after each DFS correction of one section.

Problem of Low Energy Variations

The primary difference between the basic and the on-line DFS algorithm is that the dispersion cannot be measured straight forward. In the basic method, a large energy deviation will be used to create large dispersive offsets in the BPMs to increase the measurement accuracy. This is however not possible for an on-line algorithm, since only tiny energy variations can be tolerated due to the energy acceptance of the final focus system of CLIC. For the simulations in this paper an energy variation of only 0.5 per mill is used.

Two main problems arise from these small induced energy variations. First of all, the induced orbit variations will be small and the necessary accuracy of the dispersion measurement has to be recovered by combining many measured orbit samples in a stochastic way to filter the noise. This dispersion estimation will be discussed in the next section. The second problem due to the small energy variations comes from the fact that the used energy deviations are so small that they are in the order of the beam energy spread, which is strongly influenced by wakefields. Therefore, changes of wakefields due to the change of beam orbits or cavity positions start to influence the dispersion measurement. This problem can be resolved by an initial cavity alignment (see [6]) before the on-line DFS, which reduces the wakefield effects for the current beam orbit. It is also beneficial to perform a cavity alignment after each full DFS correction of the linac.

Dispersion Estimation

The dispersion is measured in this paper by changing the acceleration gradient, which can be accomplished for the main linac of CLIC by a modulation of the beam intensity of the drive beam. Additionally, the initial beam energy is varied with the help of a bunch compressor. Since the induced energy variations have to be small, the individual dispersion measurements will be disturbed strongly by the influence of BPM noise and the usual jitter of the initial beam energy and the accelerating gradients. Therefore, the dispersion is determined by using many measurements and combining them to a least squares (LS) estimate to ensure the necessary accuracy. Instead of determining the LS estimate via the usual calculation of the pseudo-inverse, a very efficient recursive version of the algorithm can be derived, if the induced energy variations are chosen to be the sequence $\{-\Delta E, +\Delta E, -\Delta E, +\Delta E, \dots\}$. In this case the LS estimate of the dispersion η_N at a BPM at time step $N \in 2\mathbb{N}$ can be written as

$$\eta_N = \left(\boldsymbol{E}^T\boldsymbol{E}\right)^{-1}\boldsymbol{E}^T\boldsymbol{b} = \frac{T_N}{N\Delta E} \quad \text{with} \qquad (2)$$

$$\boldsymbol{E} = \begin{bmatrix} -\Delta E \\ +\Delta E \\ \vdots \\ -\Delta E \\ +\Delta E \end{bmatrix} \quad \text{and} \quad T_N = \sum_{i=1}^{N} (-1)^i b_i,$$

where $\boldsymbol{b} \in \mathbb{R}^N$ is the vector of previous BPM measurements. The so obtained estimate η_N can subsequently be used to calculate corrections θ for the next accelerator section according to Eq. (1). The question how many samples N have to be used to create an accurate enough estimate will be answered in the results section of this paper.

Integration of On-Line DFS and Orbit Feedback

When using the on-line DFS algorithm in combination with the orbit feedback, the interaction of the two subsystems has to be considered. At the dispersion estimation the beam energy changes induced by the on-line DFS will create orbit offsets that will couple to the action of the orbit feedback. By choosing the excitation to be a constant value with alternating signs, the induced disturbances are of the highest resolvable frequency of the orbit controller. Due to its design, the orbit controller frequency response demagnifies this frequency component strongly and the orbit feedback will couple only very weakly to the induced orbit offsets.

Another modification to the basic DFS algorithm is necessary, since the orbit controller will react on the changed beam orbits due to the on-line DFS corrections. The orbit feedback would aim to steer the beam back on its previous orbit. Therefore, the BPM centres of the corrected section have to be shifted electronically to the new reference orbit after the DFS correction.

If a section would be DFS corrected without considering the beam orbit in the rest of the downstream linac, the beam would be steered far from its reference orbit. This would lead to an unacceptable emittance growth. Also the orbit feedback would react strongly on the large offsets, which would also decrease the accuracy of the next dispersion estimate. Therefore, the expected beam orbit change $\hat{\boldsymbol{b}}$ in the BPMs after the current section has to be corrected with the correctors after the current section. Simulation showed that it is sufficient to use only the correctors of the next section, which reduced the necessary calculation time of the performed all-to-all steering. The according corrector actuations $\hat{\theta}$ can be calculated by solving

$$-\begin{bmatrix} \hat{\boldsymbol{b}} \\ \boldsymbol{0} \end{bmatrix} = \begin{bmatrix} \hat{\boldsymbol{R}} \\ \beta_0 \boldsymbol{I} \end{bmatrix} \hat{\theta}, \qquad (3)$$

where β_0 is a damping factor for the corrector actuations.

Copyright © 2012 by the respective authors — cc Creative Commons Attribution 3.0 (CC BY 3.0)

RESULTS

To test the on-line DFS algorithm proposed, it was integrated in the simulation framework described in [1], which include the beam tracking in the main linac of CLIC, ground motion generation and the action of the orbit controller. The algorithm was tested on a beamline that was misaligned with about 11 days of ATL ground motion, followed by a one-to-one steering.

To determine how many samples are needed to estimate the dispersion sufficiently well, a simplified procedure was used. Instead of using full-scale simulations, the real dispersion was determined in simulations and corrupted with artificial BPM noise. The influence of the BPM resolution on the on-line DFS correction result is shown in Fig. 2. The effective BPM resolution in the estimate has to be about 5 nm to not worsen the average on-line DFS correction by more than 2%. Assuming a BPM resolution of 100 nm, the noise has to be reduced by a factor of 20. Since the averaging reduces the remaining noise by the factor $1/\sqrt{N}$, where N is the number of used samples, N has to be 400, which corresponds to 8 s of CLIC operation. Considering further that this procedure is repeated for 36 linac sections over two iterations, the full correction time needed is about 10 minutes not including the time needed for the cavity alignment. Additionally to the influence of noise, also the DFS algorithm itself cannot correct the chromatic dilutions fully. With perfectly known dispersion, the initial vertical emittance growth of 107.6% was reduced to 2.5% on average.

The long time periods necessary for the averaging cannot be simulated directly in reasonable time. We therefore only performed full-scale simulations with an N of 100, which corresponds to a real-time operation of about 2 minutes. Different imperfections were applied and on average the emittance growth could be reduced after two iterations to 2.8% with no imperfections, 3.7% with orbit feedback turned on and 10.4% with realistic BPM resolution.

The results for one particular ground motion sample are shown in Fig. 3. It can be observed that at the corrections of the final sections the emittance grows for a short time period. We believe that this behaviour is due to a worse steering and an improvement is subject to future work. Simulations were also performed including short-term ground motion (model B [1]) in combination with the orbit feedback for the dispersion estimation. The observed effect due to the ground motion was seen to be negligible. Another tested imperfection is the jitter of the acceleration gradients. Also here no significant degradation was observed for the maximal specification of 0.5%.

CONCLUSIONS

In this paper an on-line DFS algorithm was presented. Simulation results show that it is capable of correcting dispersive beam orbits due to long term ground motion misalignments efficiently. Two iterations of the algorithm have found to be enough to reduce the according beam emittance growth very efficiently, which takes for CLIC about 10 min. Since the time constant of the correction is much smaller than the emittance growth, there is no need to run the algorithm continuously. The mutual interaction of the algorithm with the orbit feedback was found to be small. Also the influence of ground motion and decelerator gradient jitter can be neglected. The presented algorithm is therefore an essential contribution for the successful operation of CLIC over longer time periods.

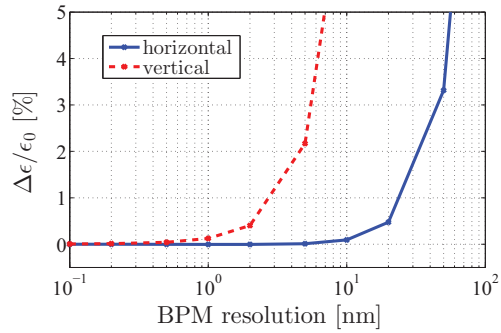

Figure 2: Relative emittance growth due to BPM resolution when using on-line DFS averaged over 20 random samples.

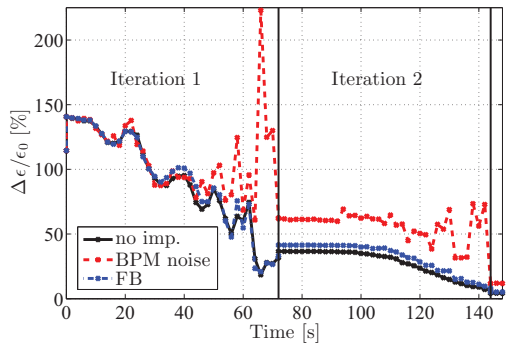

Figure 3: Relative vertical emittance during two iterations of the on-line DFS correction for one particular sample of ground motion. No imperfections are applied for the black curve (4% emittance growth). For the blue curve, the orbit feedback is turned on during the dispersion estimation. The mutual influence of the two subsystems is seen to be small (5% emittance growth). For the red curve a BPM resolution of 100 nm is used (12% emittance growth).

REFERENCES

[1] J. Snuverink et al., In Proc. of the IPAC11, TUPC023, 2011.

[2] V. Shiltsev, Phys. Rev. Spec. Top., 13:094801, 2010.

[3] T.O. Raubenheimer and R.D. Ruth, Nucl. Instrum. A 302(2), 191-208, 1991.

[4] D. Schulte, In Proc. of the PAC05, 1251-1253, 2005.

[5] A. Latina and P. Raimondi, In Proc. of the LINAC10, MOP026, 2010.

[6] N. Leros and D. Schulte, In Proc. of the EPAC02, 461-463, 2002.

Copyright © 2012 by the respective authors — cc Creative Commons Attribution 3.0 (CC BY 3.0)

DETAILED ANALYSIS OF THE LONG-RANGE WAKEFIELD IN THE BASELINE DESIGN OF CLIC MAIN LINAC

V.F. Khan and A. Grudiev
CERN, Geneva, Switzerland.

Abstract

The baseline design of the accelerating structure of the CLIC main linac relies on strong damping of transverse higher order modes (HOMs). Each accelerating cell is equipped with four damping waveguides that causes HOM energy to propagate to damping loads. Most of the HOMs decay exponentially with a Q-factor of about 10, however there are modes with higher Q-factors. Though the amplitude of the high Q modes is nearly two orders of magnitude smaller than the dominating lowest dipole mode, their cumulative effect over the entire bunch train may be significant and dilute the beam emittance to unacceptable level. In this paper we report on an accurate calculation of the long-range wakefield and its overall effect on beam dynamics. We also discuss possible measures to minimise its effect in a tapered structure.

INTRODUCTION

The CLIC baseline design of the main linac operates at 12 GHz [1]. Preserving the beam quality in linacs operating at high frequencies is primarily limited by the beam induced fields known as wakefields [2]. Inadequate suppression of wakefields may result in emittance dilution; hence it is essential to employ a damping mechanism. In the first section of this paper we present detailed calculation of the wakefields in the CDR [1] baseline design of the CLIC accelerating structure (CLIC AS) [3], which is based on strong waveguide damping of HOMs. We also investigate the presence of so called persistent wakefield [4] in this structure. In the CLIC scheme, the bunch train consists of 312 bunches [1]; in such multi-bunch acceleration, wakefield generated by a bunch often leads to kicking the following bunches. An analytical estimate of the effect of multi-bunch long range wakefields on the beam profile is presented in [5]. However, in [5], by considering the strong damping of the HOMs, it is assumed that only the first trailing bunch experiences a kick due to an off-axis driving bunch. Herein we calculate the very long range wakefields in CLIC AS which allows HOM kicks to be considered on all trailing bunches by applying the analytical model to estimate the long range multi-bunch wakefield effect. These results are discussed in the second section.

WAKEFIELDS IN CLIC AS

The CLIC AS is designed with tapered irises so as to keep the accelerating gradient (nearly) constant. The wakefield is strongly damped by means of four waveguides attached to each accelerating cell [1, 3]. The time domain code GdfidL [6] was utilised to calculate the long-range wakefields excited in the structure. The wakefield can also be reconstructed using the frequencies, kicks and Q factors of the dominating modes. The lowest dipole mode has the strongest impact on the off-axis beam as it contains the largest kick factor. The damping waveguides are carefully designed, in particular to damp this mode with a Q ~10 [3]. The envelopes of transverse wakefields of the sample cells, namely the first, middle and last are illustrated in the Fig. 1, and a disc of the CLIC AS is also shown inset. Beyond 1 m wake-length it is clear that only one mode dominates, which has low amplitude but high Q-factor. However, modes with high group velocity (v_g) and poor damping via these waveguides travel along the structure and are damped by means of evacuation from the structure volume through the input and output power couplers. Whereas the wakefield in the last cell does not seem to be affected by

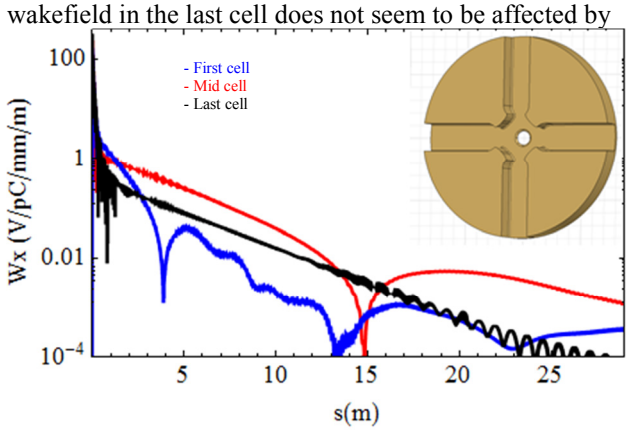

Figure 1: Envelope of transverse wakefield in single cells of CLIC AS.

the group velocity of the mode, the wakefields in the first and the middle cells are, resulting in reduction of the wakefield envelope at about 4 m and at about 15 m respectively. In this case, the wakefield is calculated including the group velocity term (β) as [1, 2]

$$W_{\perp}(s) = 2\sum_{p} K_p Exp\left[i\frac{\omega_p s}{c}\left(1+\frac{i}{2(1-\beta_p)Q_p}\right)\right]\left(1-\frac{\beta_p s}{L(1-\beta_p)}\right) \quad (1)$$

where K_p and ω_p are the frequency and kick factor of the mode p respectively, L is the structure length and $\beta=v_g/c$. The modes with non-negligible β_p travel rapidly through the structure which expedites wake suppression, hence it is necessary to include this term in the calculation. In order to understand the modal contribution in the wake beyond 1 m, we study the transverse impedance (Fourier transform of the wake) in these cells. The impedance of these cells is shown in Fig. 2. As can be seen, the first mode around 17 GHz has the largest impedance (i.e. kick factor) and better damping (width of the peak) compared to the other modes. The modes at 21 GHz, 26 GHz, 40

Copyright © 2012 by the respective authors — cc Creative Commons Attribution 3.0 (CC BY 3.0)

GHz and 55 GHz have non-negligible kicks. Among these, the mode at 21 GHz is poorly damped. Detailed Fourier analysis of the wakefield beyond 3 m indicates that only the 21 GHz mode contributes to the wakefield due to its poor damping. The impedance of the single cells beyond 3 m wake-length is shown in the inset of Fig. 2.

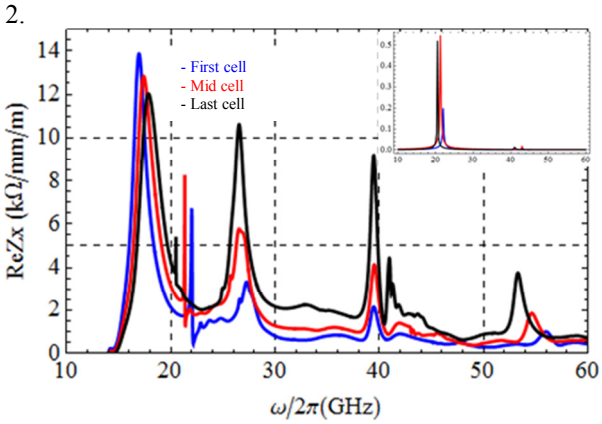

Figure 2: Transverse impedance in single cells of CLIC AS. Impedance for a window of 3m to 7m wake-length is shown inset.

The mode at 21 GHz has a detuning of ~1.5 GHz which assists in non-coherent addition of the wakefield. The wakefield excited in the CLIC AS is indicated in Fig. 3. The various modes contributing to the wakefield

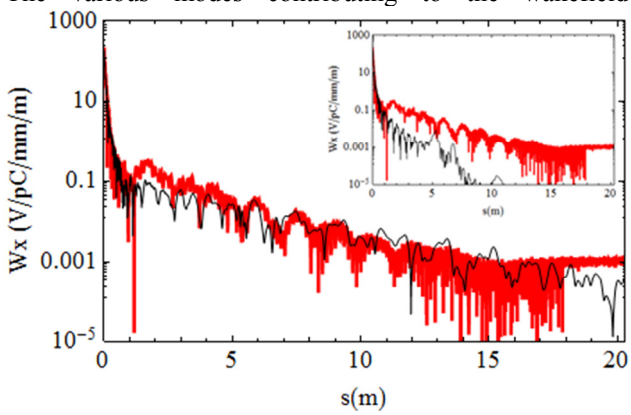

Figure 3: Comparison of the envelope of transverse wakefield in CLIC AS using GdfidL (red curve) and reconstruction using single cell modes (black curve). Inset compares the reconstruction excluding the 21 GHz mode.

are visualized in detail in Figs. 1 and 2. From these modes we reconstruct the wakefield (eq. 1) of the CLIC AS. We learned that the 21 GHz mode has a Q of few hundreds (it varies from cell-to-cell) and v_g ranging from 10% c in the first cell, 2.8% c in the middle cell and down to 0% c in the last cell. The reconstruction of the wake using single-cell modes is compared with the GdfidL simulation in Fig. 3. As the 21 GHz mode travels through the structure, it couples from cell to cell. We utilised single band of circuit model [7] to compute the coupled mode frequencies of this mode. Very good agreement has been found between the reconstructed and GdfidL wakefields. If we artificially remove this mode (using reconstruction), the wakefield does reduce for s > 1 m, which is indicated in the inset of Fig. 3.

If a mode is excited in a structure close to the cut-off frequency of the waveguide, then it does not travel through the waveguide, hence it cannot be damped. The wakefield pertaining to this mode is defined as persistent wakefield which does not decay exponentially [4]. Lingering of such a wakefield-tail is not acceptable from the beam dynamics point of view. We investigated the possibility of persistent wakefield in the CLIC AS. We observe that the modes contributing significantly to the wakefield decay exponentially. The reconstruction plot for a sample (mid) cell is presented in Fig. 4.

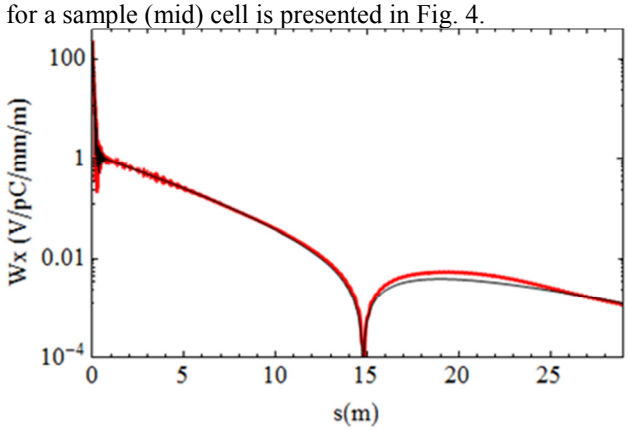

Figure 4: Reconstruction of wakefield in the middle cell using modal sum method. The black curve represents reconstruction, the coloured curve GdfidL simulation.

The only mode that does not decay rapidly is the 21 GHz mode. Detailed study of the e.m. fields in this mode using HFSS revealed that this is a TE-type dipole mode concentrated near the iris of the cell; the fields in this mode are far away from the damping waveguide aperture, hence this mode is poorly damped. The wakefield of this mode can be reconstructed using eq. 1. It is clearly visible that the wakefield decays exponentially with a Q of a few hundred. The reconstruction of this mode confirms the fact that there is no visible persistent wakefield in the CLIC AS. The multi-bunch wakefield effect causing beam amplification is discussed in the next section.

MULTIBUNCH WAKEFIELD EFFECT

In the CLIC scheme, the beam dynamics study defines an upper limit of 7 V/pC/mm/m wake on the first trailing bunch [1]. However, in multi-bunch acceleration, an off-axis driving bunch can cause serious deflections of the trailing bunches. In order to understand an overall effect of the wakefield on a multi-bunch beam profile, a matrix formulation was studied and is presented in [5]. This formulation involves two effects: an off-axis driving bunch deflecting a trailing bunch (direct effect), due to the deflection of this trailing bunch and, subsequent deflection of trailing bunches (indirect effect). In [5] it is assumed that every driving bunch exhibits wake only on the first trailing bunch. With this model a beam

Copyright © 2012 by the respective authors — cc Creative Commons Attribution 3.0 (CC BY 3.0)

amplification factor was calculated which is caused by coherent jitter (F_c ~1), r.m.s of jitter (F_{rms} ~4.9) and a worst case amplification factor (F_w ~20). Herein we extend this calculation to consider a more realistic case of very long range wake including the kicks on all trailing bunches even though the kicks have small amplitudes. For illustration a case of 3 bunches is assumed. The direct effect (a) and direct-indirect effect (A) matrix formulation in this case is [5]

$$a=\begin{pmatrix}0 & 0 & 0\\ ia_1 & 0 & 0\\ ia_2 & ia_1 & 0\end{pmatrix};\ A=Exp[a]=\begin{pmatrix}1 & 0 & 0\\ ia_1 & 1 & 0\\ \frac{i^2a_1^2}{2}+ia_2 & ia_1 & 1\end{pmatrix}. \quad (2)$$

In matrix a, a_1 and a_2 are the kicks experienced by the first and second trailing bunch respectively due to an off-axis leading bunch; which is nothing but a direct effect. Whereas $(ia_1)^2/2$ is the indirect effect on the second trailing bunch as is shown in matrix A. The aforementioned amplification factors are defined as [5]

$$F_c=\frac{1}{n}\sum_k\left|\sum_j A_{kj}\right|^2;\ F_{rms}=\frac{1}{n}\sum_{k=0}^{n-1}\sum_{j=1}^{k}A_{kj}A_{kj}^{*} \quad (3)$$

$$(u,\lambda,v)=\mathrm{SVD[A]};\qquad F_w=\lambda_1^2 \quad (4)$$

where SVD is the singular value decomposition of the matrix A. Using the matrix formulation, the amplification factors in CLIC AS are calculated and the results are presented in Fig. 4. Beyond 100 bunches (50 ns) the F_c does not change. This means a driving bunch kicks about 100 trailing bunches and beyond this its contribution is negligibly small. The consequence is that simulation over the time of an entire bunch train (47 m) is not needed. In Fig. 5 it can be observed that F_c does not change alarmingly compared to the previously calculated value [5] and the difference is about +5% which is within the beam dynamics limit [8]. The other two amplification factors are also within the acceptable limits [8]. In order to understand the sensitivity of the amplification factors we introduce +/-1% random errors in bunch spacing (r.m.s ~0.6%). Though this error changes the kicks on the bunches, the amplification factor F_c changes by only 1%. This is illustrated in Fig. 6.

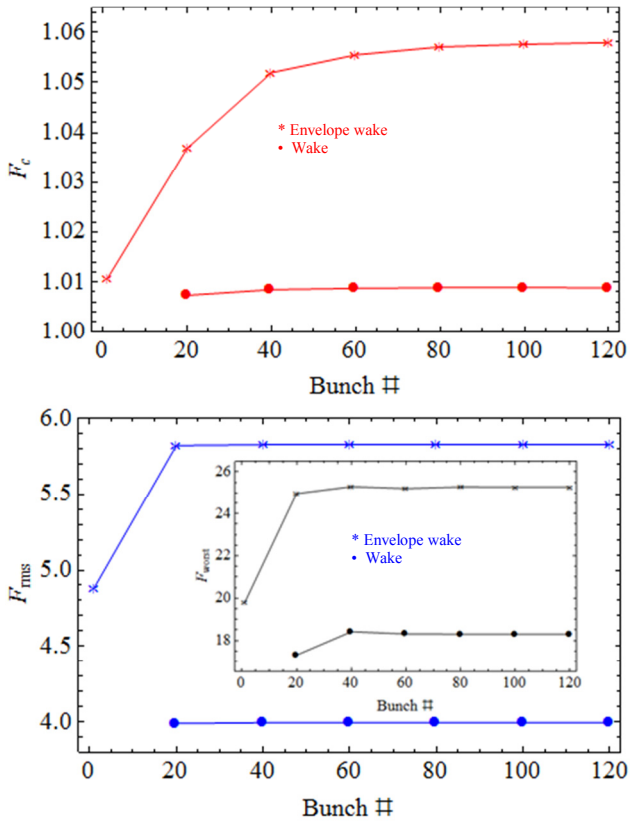

Figure 5: Amplification parameters of CLIC AS

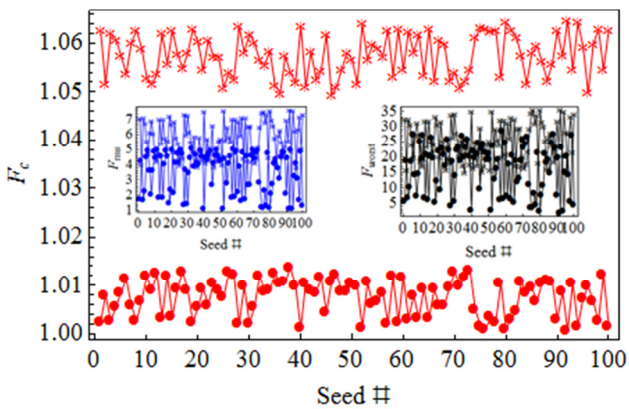

Figure 6: Amplification parameters of CLIC AS with random errors of +/- 1% in bunch spacing.

FINAL REMARKS

The baseline design of the CLIC AS for the CDR meets the beam dynamics criterion of damping HOMs. The maximum amplification of the beam due to coherent jitter considering the multi-bunch long range effect is about 6% which is within the acceptable limit.

ACKNOWLEDGEMENTS

The authors would like to thank D. Schulte and A. Latina for valuable discussions on beam dynamics constraints and multi-bunch matrix formulation as well as W. Wuensch for stimulating discussions and support for this work.

REFERENCES

[1] M. Aicheler, *et. al*, CLIC-CDR, SLAC-R-985, 2012.
[2] P. B. Wilson, SLAC-PUB 4547, 1989.
[3] A. Grudiev and W. Wuensch, LINAC10, MOP068, 2010.
[4] N. M. Kroll and X. Lin, SLAC-PUB-6144, 1993.
[5] D. Schulte, PAC09, FR5RFP055, 2009.
[6] www.gdfidl.de
[7] K. Bane and B. Gluckstern, SLAC-PUB-5783, 1992.
[8] D. Schulte, private communication.

Copyright © 2012 by the respective authors — cc Creative Commons Attribution 3.0 (CC BY 3.0)

SPECIFICATIONS OF THE DISTRIBUTED TIMING SYSTEM FOR THE CLIC MAIN LINAC

A. Gerbershagen, A. Andersson, D. Schulte, CERN, Geneva, Switzerland
P. N. Burrows, JAI, University of Oxford, Oxford, UK
F. Ömer Ilday, Bilkent University, Ankara, Turkey

Abstract

The longitudinal phase stability of the CLIC main and drive beams is a crucial element of the CLIC design. In order to measure and control the phase a distributed phase monitoring system has been proposed. The system measures the beam phase every 900 m. The relative phase between the measurement points is synchronized with an external reference system via a chain of reference lines. This paper presents the simulations of error propagation in the proposed distributed monitoring system and the impact on the drive and main beam phase errors and the luminosity. Based on the results the error tolerances for the proposed system are detailed.

INTRODUCTION

The Compact Linear Collider (CLIC) is a proposed 3 TeV center-of-mass energy e^+e^- collider. It is designed to extract the RF energy from high-current low-energy drive beams and use this energy for acceleration of the low-current high-energy main beams that are brought into collision.

Since the main beam acceleration is performed by the RF power extracted from the drive beam, the stability of the relative phasing of the drive and main beams is crucial for the preservation of CLIC's luminosity. A relative phase error of 0.2° @ 12 GHz between the drive and the main beam will cause a luminosity loss of 1% if the error is coherent between the 24 decelerator segments. The same luminosity loss can be caused by an incoherent error of 0.8°. [1]
Additionally to these requirements on the relative drive beam - main beam phase, the phase tolerance between the two main beams at the interaction point (IP) has been set to 0.6° @ 12 GHz [2]. Hence, in order to align the main beam phase a global phase reference over 50 km is needed.

The stated tolerance requirements have to be met on the timescale of ≈50 ns, since this is the beam loading time of the main beam accelerating structures and errors on the shorter time scale will be (at least partially) filtered out by the structures.

PROPOSED DISTRIBUTED TIMING SYSTEMS

The distributed timing system is required to establish the correct beam phase at each turn-around of the linac. This allows to measure and correct the main and drive beam phases along the main linac. There are two approaches for the design of such a system.

The first approach (A) is to use the outgoing main beams to transmit the phase information to a number of local oscillators (Fig. 1, top). These can maintain the phase accurately enough until the main beam returns on the way to the interaction point. This system requires accurate phasing between the outgoing main beams at the first booster linac near the interaction point (Fig. 2).
In the other approach (B) the master clock near the interaction point (IP) would define the nominal phase and distribute it as a signal cascade from one 900 m long decelerator segment to another (Fig. 1, bottom). This system would establish the relative phase of the local timing clocks by an optical connection independently of the beams.

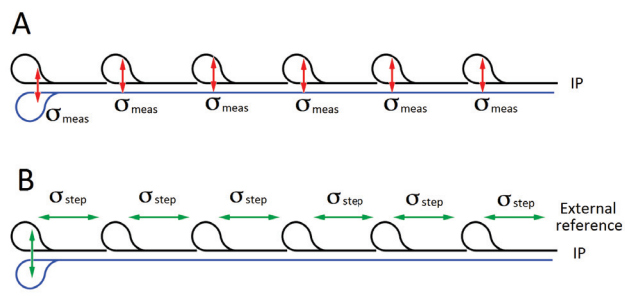

Figure 1: Phase signal propagation for the reference based on the main beam (A) and chained distribution of master clock signal (B).

Approach A has the advantage of having a relatively small error between the main and the drive beams, since the phase measurement at each drive beam decelerator is performed locally and hence no additional error is introduced during the distribution process (see Fig. 3, left). Approach B allows the correction of the main beam at its final turn-around, giving the possibility to reduce the jitter between the e^+ and e^- main beams (Fig. 3, right). However, if the drive beam correction signal is transported from the master clock via the distribution system, the noise introduced by this system would reduce the effectiveness of the phase correction. In the final CLIC design these approaches could be potentially combined.

The proposed timing distribution system is based on state of the art technology for signal distribution via optical fibers tested at XFEL (DESY, Hamburg) [3], [4]. This system is proven to provide <10 fs stability over the distance of several kilometers.
The following analysis determines the specifications of the

Copyright © 2012 by the respective authors — cc Creative Commons Attribution 3.0 (CC BY 3.0)

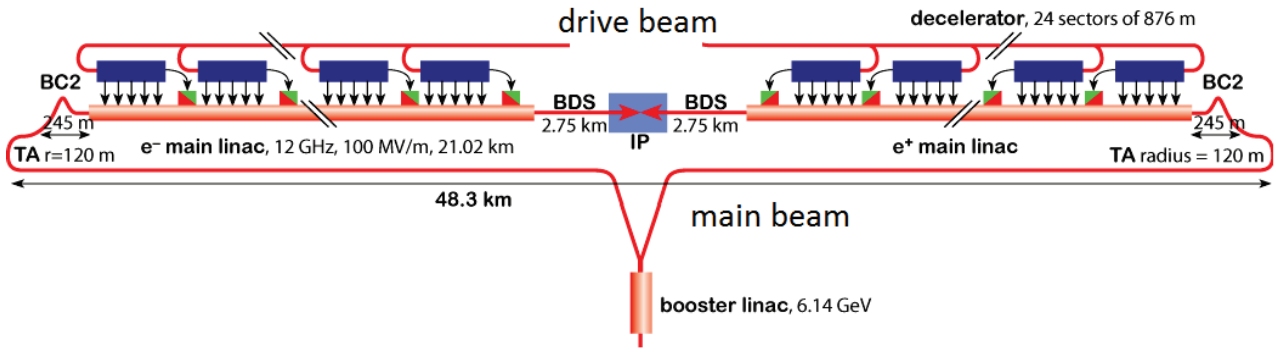

Figure 2: CLIC layout at 3 TeV.

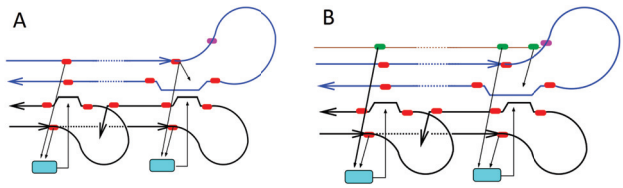

Figure 3: Phase correction system based on the main beam phase measurement (A) and on the external master clock (B) [2].

second approach (distributed timing system) and sets the requirements for the tolerances of this system.

ANALYSIS OF SPECIFICATIONS FOR THE DISTRIBUTED TIMING SYSTEM

Principle of time distribution and phase correction

As shown in Fig. 3 B, the signal from the master clock is used as the synchronization signal for the local oscillators. The master clock itself has a particular noise spectrum [5]. The impact of the noise on the local oscillators can be reduced by integrating the signal over the time intervals longer than the beam propagation time through the machine (≈ 0.2 ms).
The correction of the main beam is performed at the final turnaround with help of a kicker chicane, which can change the path length of the main beam bunches and hence their longitudinal position. The drive beam phase is also corrected via a chicane to the nominal value defined by the master clock at the turnarounds at each of the 24 decelerator modules.

The phase measurements on the main and drive beam after the chicanes ensure that the provided correction had the right value. If it is not the case, this could mean that the path length of the beams in the chicane is not as predicted, the chicane has the wrong R_{56} value or that the waveguide length has changed (e.g. due to temperature variation). To correct for these changes, a pulse-to-pulse feedback system can be introduced. Provided the changes are slow enough, the measured value of the correction error can be used to adjust the relative definitions of the monitors' nominal phase. The new definitions will ensure that the correction for the next pulse will set the drive beam bunches closer to their nominal position relatively to the main beam bunches. Hence, high stability of the local oscillator clocks must be ensured on a timescale of 20 ms, which is the pulse-to-pulse interval of CLIC.

In order to calculate the phase tolerance for signal transfer between the two subsequent decelerators, σ_{step}, (Fig. 1, B), one must calculate the impact of this error on the total phase error. We will assume a random walk of the phase error, which starts from the master clock at the IP and propagates along the machine step by step from one drive beam decelerator segment to another.

e^+ and e^- main beams phase tolerance

For the incoming main beams the relative phase tolerance at the IP is $0.6°$ @ 12 GHz $\hat{=}$ 42 μm $\hat{=}$ 140 fs [2] which corresponds to 1% of luminosity loss. Hence, one must assure that the total phase error introduced by the distributed timing system σ_{dts} is below $(140\text{ fs})/\sqrt{2}$ for each of the main beams.
Additionally to the 24 decelerator modules, each about 900 m long, we must consider that the beam delivery system of each main beam is about 2.75 km long [8]. To simplify the calculation it will be assumed that the distributed timing system for the main beam is 27, instead of 24, sectors long, hence about 2.7 km longer. One can consider the errors at each of the segments as linearly independent. Hence, the tolerance for the phase error introduced in each segment is given by

$$\sigma_{step,mm,1\%} = \frac{140\ fs}{\sqrt{27}\times\sqrt{2}} = 19.05\ fs \hat{=} 5.72\ \mu m. \quad (1)$$

The stated correction system error would cause a luminosity loss of 1%. However, in reality the largest part of the tolerance budget will be reserved for the beam itself and not for the reference jitter. Hence, the calculation only determines the upper limit for the distribution error but not

Copyright © 2012 by the respective authors — cc Creative Commons Attribution 3.0 (CC BY 3.0)

the effective system requirement, which will depend on the expected beam phase jitter. Defining the distribution system requirement to causing max. 0.1% luminosity loss, one obtains $\sigma_{step} = 5.72\ \mu m/\sqrt{10} = 1.81\ \mu m$
An advantage of the distributed timing system is that it allows to loosen the phase tolerances on the outgoing main beam by a factor of 7, since the phase correction at the final turnaround of the main beam can reduce the phase error [1], [7]. Also, the phase correction can compensate for the change in the main beam path length, given the path length change is slow enough ($\ll 20\ ms$ pulse interval).

Main beam - drive beam phase tolerance

The error σ_{step} causing 1% luminosity loss can be calculated from the main beam - drive beam relative phase error tolerance. The total error σ_{tot} introduced by the phase correction system at each decelerator must be below 0.8° @ 12 GHz for uncorrelated errors.

We assume a random walk of the distribution error segment by segment. The impact of each error is given by $\sum_{j=1}^{i} \sigma_{step}$ with i being the number of the segment counted from the IP. The total error introduced by the distributed timing system σ_{dts} is given by the sum of the errors in all segments. One should also consider that the main beam bunches are positioned at 30° of the RF wave in the four segments nearest to the IP and at 8° in other 20 segments. Hence σ_{dts} is given by

$$\sigma_{dts}^2 = \sum_{i=1}^{4}\left(\sum_{j=1}^{i}(\sigma_{step}\times\sin 30°)\right)^2 + \sum_{i=5}^{24}\left(\sum_{j=1}^{4}(\sigma_{step}\times\sin 30°)+\sum_{j=5}^{i}(\sigma_{step}\times\sin 8°)\right)^2$$

Normalising σ_{dts}^2 by the RMS value of the stated sine functions and calculating the sums, one obtains

$$\sigma_{step,md,1\%} = 0.059° \triangleq 4.12\ \mu m \qquad (2)$$

This value is of the same order of magnitude as the tolerance given by the main beam - main beam phase error consideration ($\sigma_{step,mm,1\%} = 5.72\ \mu m$) calculated in the previous sub-section. Defining as above the maximal 0.1% luminosity loss as a specification of the distribution system, the requirement for the reference stability will be $4.12\mu m/\sqrt{10} = 1.30\ \mu m$.

The 1% luminosity loss from the reference jitter has been calculated independently for main beam - main beam and main beam - drive beam phase error tolerances. In reality the same reference jitter σ_{step} would cause a luminosity loss via both channels,

$$\Delta\mathcal{L}_{total} = \Delta\mathcal{L}_{md} + \Delta\mathcal{L}_{mm} = 1\% \times \left(\left(\frac{\sigma_{step}}{\sigma_{step,md,1\%}}\right)^2 + \left(\frac{\sigma_{step}}{\sigma_{step,mm,1\%}}\right)^2\right)^2$$

Solving this equation for $\Delta\mathcal{L}_{total} = 1\%$ yields $\sigma_{step} = 3.34\ \mu m$. However, $\Delta\mathcal{L}_{total} = 0.1\%$ defines the specification of $\sigma_{step} = 1.06\ \mu m$ average error introduced by the distributed timing system at each decelerator segment.

CONCLUSIONS AND OUTLOOK

The phase jitter of the distributed timing system at each decelerator segment is calculated to be 3.34 μm for 1% luminosity loss from both the main to main and main to drive beam tolerances.This value is met by demonstrated performances [3], [4], which proves the feasibility of the distributed timing system. However, ideally the specification would be tighter - 0.1% luminosity loss, which requires a distribution system stability of 1.06 μm per segment. Hence, it has to be investigated whether the noise can be significantly reduced.

The demonstrated performance of the signal distribution includes the transformation of the optical signal into electrical and vice versa. One solution could be chaining the distribution by splitting the optical signal at each decelerator, using one part of the signal as a reference and amplifying the other part and sending it to the next decelerator. This would help to avoid transformation noise and might allow to reach the specified target. A dedicated approach would be needed to prove this concept experimentally.

It will be also necessary to demonstrate the reliability of the signal distribution technology to operate unattended in the tunnel.

REFERENCES

[1] D. Schulte et al., "Status of the CLIC Phase and Amplitude Stabilisation Concept", Proceedings of Linear Accelerator Conference LINAC2010, Tsukuba, Japan MOP024

[2] D. Schulte, First CLIC Phase Stability Meeting, November 24, 2011, http://indico.cern.ch/conferenceDisplay.py?confId=164428.

[3] F. Ömer Ilday, "Long-distance optical stabilization with femtosecond resolution", CLIC09 Workshop

[4] M. Felber, "Achievements and challenges during the first implementation phase of an engineered version in the accelerator", CLIC09 Workshop

[5] CLIC Conceptual Design Report, chapter 5.14, "Fine time generation and distribution"

[6] A. Andersson, "Phase reference system", CLIC collaboration meeting, May 10, 2012

[7] F. Stulle, "Beam phase and energy tolerances in the CLIC RTML", CLIC - Note - 874

[8] CLIC Parameter Table, http://clic-meeting.web.cern.ch/clic-meeting/clictable2010.html

Copyright © 2012 by the respective authors — cc Creative Commons Attribution 3.0 (CC BY 3.0)

A 10 MeV L-BAND LINAC FOR THE IRRADIATION APPLICATIONS IN CHINA

G.# Pei, Y. Chi, R. Shi, Z. Zhou, Q. Yuan, F. Zhao, D. He, X. Yang, C. Yu, M. Dai, J. Liu, Y. Feng, X. Li, X. He, X. Wang, Z. Zhu, E. Tang, H. Huang, J. Zhao, C. Ma,
Institute of High Energy Physics, IHEP, Beijing, P. O. Box 918, 100049, China
Z. Li, X. Zhang, Wuxi EL PONT Radiation Technology, Ltd, No 8 Weiye Road,
Qianqiaopeijianyuan District, Wuxi, 214151, Jiangsu, China

Abstract

The electron linear accelerator has wide applications, and the demands for the irradiation applications are keeping growing in China. A high beam power 10 MeV L-band Linac has been developed recently as a joint venture of Institute of High Energy Physics (IHEP) and Wuxi EL-PONT Company in China. The Thales TH2104U klystron, 2 A thermionic electron gun and 3 m long L-band disk-loaded constant impedance RF structure were adopted. A stable electron beam of 10 MeV / 40 kW has been obtained in the last April. In this paper the detailed design issues and beam commissioning results are reported.

INTRODUCTION

IHEP in China has very rich experience in the electron linac design and development. When requested to transfer the technology to industry, many S-band electron linacs have been developed for medical and irradiation applications. For the S-band irradiation linac, the beam power is limited to be ~20 kW because of the RF structure heating/cooling issues. Due to the scaling law of $P \sim f^{1}$ between the RF power consumption of the accelerating structure and the frequency, L-band structure [1][2] is usually adopted for the nature extending to much higher beam power up to ~100 kW level. For any high beam power machines the power efficiency is a concern. According to Eq. (1), the maximum conversion efficiency η_{max} of the RF power to the beam power dependents only on the attenuation factor τ [3], and smaller τ is preferred.

$$\eta_{\max} = \frac{1}{2}\left[\frac{\left(1-e^{-2\tau}\right)^2}{\left(1-e^{-2\tau}\right)-2\tau e^{-2\tau}}\right] \quad (1)$$

However, there is a compromise among power efficiency, power dissipation as well as heating, peak beam current and beam energy. It is known that τ is independent of frequency, and for SLAC type 3m long disk-loaded TW structure τ is ~0.57. Suppose a 3 m long L-band structure of 34 cavities is used, τ can be roughly estimated to be 0.57*34/86=0.225. With SUPERFISH simulation and cold test, τ is shown[4] to be 0.22, which is in good agreement with the simple scaling. By putting 0.22 into Eq. (1) one can get an efficiency η_{max} of 90%, which is very excellent. In this condition, the beam current is ~900 mA according to Eq. (2).

$$i_{\eta_{\max}} = \left(\frac{P_T}{rl}\right)^{1/2}\left[\frac{\left(1-e^{-2\tau}\right)^{3/2}}{\left(1-e^{-2\tau}\right)-2\tau e^{-2\tau}}\right] \quad (2)$$

Table 1 shows the design parameters for the 10 MeV / 40 kW L-band linac. The linac is a machine with very heavy beam loading; the beam energy range of 8 to 12 MeV can be easily controlled by simply adjusting the gun bias voltage (i.e. the gun emitting beam current), but above 10 MeV is not recommended for prevention of the neutron production.

Table 1: Design parameters for the 10MeV L-band linac

Beam energy (MeV)	10
Beam power (kW)	40
RF frequency (GHz)	1.3
Peak beam current (mA)	530
Duty cycle (%)	0.75
Klysron peak power (MW)	10

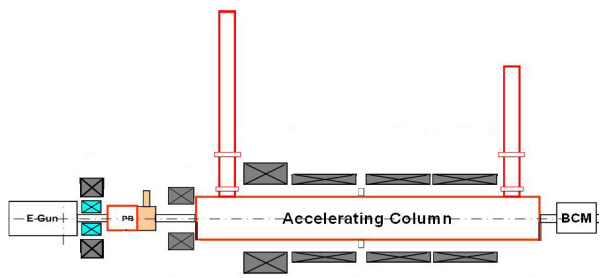

Figure 1: The schematic of the L-band linac.

DETAILED DESIGN AND SIMULATION

Figure 1 shows the schematic of the high power 10 MeV L-band linac, which mainly consists of an electron gun, an RF power source and an accelerating column. The electron gun is the 80 kV BEPC type [5] gun with 2 A Y646B cathode grid assembly. The gun system is separated from the other subsystems, which makes it easy for maintenance. The gun emitting current and the beam energy are adjustable. The RF power source is a 10 MW Thales TH2104U klystron with 130 kW average power, and the modulator was designed to make it work at 100 kW. Fig. 2 shows the Thales TH2104U klystron and its parameters.

*Work supported by the joint venture foundation of IHEP and the Wuxi EL-PONT Company in China.
#peigx@ihep.ac.cn

Copyright © 2012 by the respective authors — cc Creative Commons Attribution 3.0 (CC BY 3.0)

Frequency	1300	MHz
Output power	10	MW
Gain	> 47	%
Pulse width	> 55	μs
Duty cycle	> 1.1	%
Output average power	> 130	kW
Efficiency	45	%
Beam voltage	167	kV
Beam current	136	A

Figure 2: Thales TH2104U klystron and its parameters.

With 10 MW TH2104U klystron and a 3 m long L-band RF structure, a 10 MeV / 40 kW electron beam with a beam current of 530 mA as listed in Table 1 can be obtained. Except for the klystron, the RF structure is a key issue for the high power electron linac. The simple constant impedance structure with the cell dimension scaled from the 3 m long SLAC type disk-loaded TW structure was used, but the first 6 cells are β changed for the beam bunching requirement. Simulations with the EGUN and PARMELA codes have been conducted [6], and the simulation results were confirmed by measuring the beam performance in later commissioning. Even without the pre-buncher, a proper beam with more than 40% transmission efficiency was obtained, which is also confirmed with the machine commissioning. Fig. 3 shows the simulated beam energy spread and beam size, which are good enough for an irradiation machine.

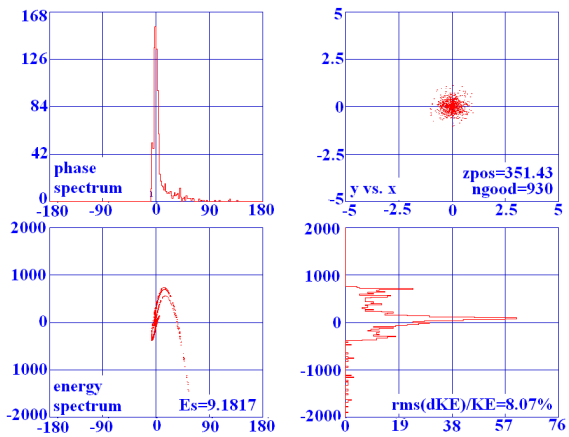

Figure 3: The simulated beam phase space.

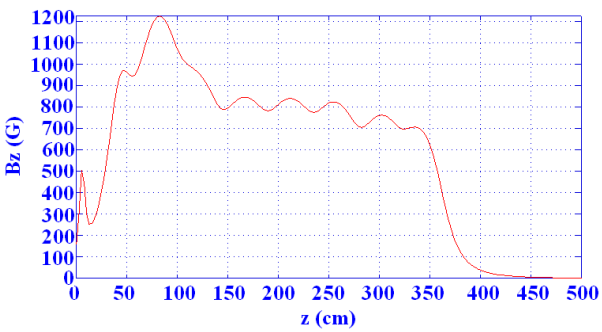

Figure 4: The solenoid magnetic field distribution along the 10 MeV / 40 kW linac.

Fig. 4 shows the designed solenoid magnetic field distribution along the whole linac. As the RF structure heating is a concern for the design of the high power electron linac, the structure iris temperature rise and its deformation were also simulated [7] and shown in Fig. 5, which indicates the maximum temperature of 62 °C under the design parameters and a tolerable deformation of ~17 μm. The cooling system is a simple water jacket around the accelerating column; A special cooling design is required if even higher beam power up to 100 kW is needed.

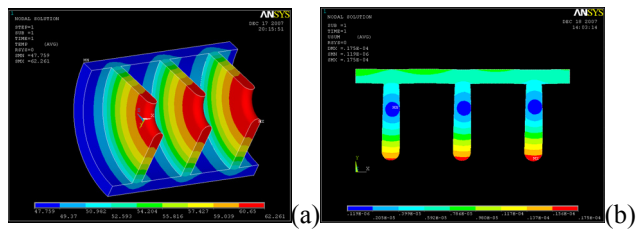

Figure 5: ANSYS results for the structure heating under the design parameters: (a) the iris temperature rise; (b) the structure deformation.

COMMISSIONING AND BEAM TEST

The machine was installed at EL PONT Company in 2009; the machine processing and commissioning were started right after the entire subsystems ready. The first beam was obtained on November 3rd, 2010. Fig. 6 is the picture of the whole linac, and Fig. 7 shows the modulator.

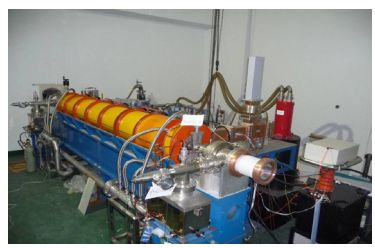

Figure 6: Picture of the L-band linac.

Figure 7: Pictures of the modulator.

Table 2 shows the milestones of the high power L-band electron linac development and commissioning progress. Almost two years were taken to get the first beam, and the main time consuming task is the klystron purchase, which takes one year and a half with almost 6 months delay. From the first beam @ 5Hz to the 40kW stable beam almost half year was taken to reach the design goal. During the high power processing process, many lessons have been learnt, such as beam instability, beam duct heating and degassing, beam loss and so on.

Copyright © 2012 by the respective authors — cc Creative Commons Attribution 3.0 (CC BY 3.0)

Fig. 8 is the beam testing results with the beam energy of 11.2MeV at 600mA beam current shown in (a) and the beam current profile measured with BCT shown in (b), which is better than the design prediction.

Table 2: Milestones of the L-band linac development

Date	Activity
October, 2007	Proposal and design
Auguest, 2008	Manufacture, purchase
September, 2009	Assembly at EL PONT
November 3rd, 2010	First beam
November 6th, 2010	Beam at 5 Hz
March 31st, 2011	30 kW
April 24th, 2011	40 kW

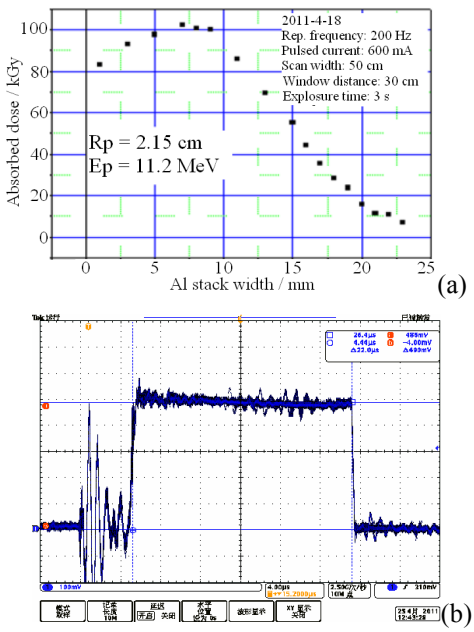

Figure 8: The beam testing results. Time-scale is 4 μs/division.

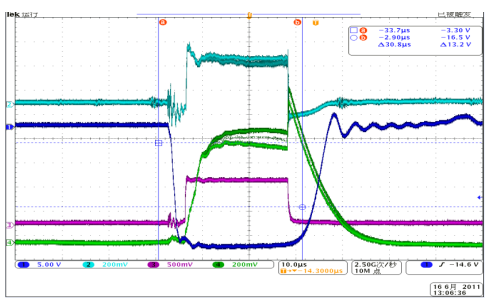

Figure 9: Machine status: blue line is the modulator high voltage waveform, turquoise the beam current from BCT, pink forward RF, and green reflected RF. Time-scale is 10 μs/division.

Many problems have been encountered during the beam testing and the machine commissioning; in particular the beam instability has very strong impact on the beam quality, the beam duct heating and the vacuum degradation, so systematic investigations were conducted for more than two months. Finally the RF driven source problem was found by monitoring the voltage standing-wave ratio (VSWR) as shown in Fig. 9, in which channel (1) in blue is the modulator high voltage waveform, channel (2) in turquoise the electron beam current from BCT, channel (3) in pink the forward RF, and channel (4) in green the reflected RF. It can be seen that the beam instability is correlated with the reflected RF (not the arcing but the VSWR change), which means the frequency is not correct even the indicator still shows 1300 MHz. After the problem was fixed, the beam instability was gone. In addition, the bunching effect of the pre-buncher was found not so strong, and taking out it would make the machine architecture much simpler.

SUMMARY

The high power 10MeV L-band electron linac is the first 40 kW irradiation linac developed and constructed in China. The first beam was obtained on November 3rd, 2010, which confirmed the design and the simulation predictions. After a few months machine processing, the designed beam parameters were achieved on April 24th, 2011. The formal beam testing was conducted by the National Institute of Metrology on December 26th, 2011, and the testing beam current is 720 mA with energy of 9.9 MeV. If the machine works at a duty cycle of 0.7% as already processed, the beam power can reach 50 kW. The conversion efficiency η from the RF power to the beam power is ~72%, a little bit lower than the theoretical prediction, which is partially because the RF power into the accelerating structure is lower than 10 MW, and/or the beam loss. Nonetheless, 72% is not bad. Now the machine has been put into operation at EL PONT Company.

ACKNOWLEGEMENT

The high beam power 10 kW / 40 MeV electron linac facility is a joint venture of IHEP and EL-PONT Company in China. Many works not mentioned here were accomplished by EL-PONT, such as infrastructure, power supply, cooling system, beam scan or deliver system and so on. Many thanks to all EL-PONT staffs for their contributions to the machine design, development, commissioning and operation.

REFERENCES

[1] J. Labrie et al., “AECL IMPELA Electron Beam Industrial Irradiations”, NIM in Physics Research, B40/41 (1989) 1153-1157.
[2] B. Park et al., “Intense L-band Electron Linac for Industrial Applications”, Proceedings of LINAC 2006, Knoxville, Tennessee, USA.
[3] The Stanford Two-Mile Accelerator, ed. by R.B. Neal, W.A. Benjamin, New York, 1968.
[4] Q. Yuan et al., private communication.
[5] 2.2/2.8GeV BEPC Injector Design (internal report, in Chinese), 1989.
[6] R. Shi, Y. Luo, private communication.
[7] H. Liu, private communication.

Copyright © 2012 by the respective authors — cc Creative Commons Attribution 3.0 (CC BY 3.0)

APPLICATIONS OF COMPACT DIELECTRIC BASED ACCELERATORS*

C. Jing#, S. Antipov, P. Schoessow, and A. Kanareykin, Euclid Techlabs LLC, Solon, OH, USA
J.G. Power, M. Conde, and W. Gai, ANL, IL, USA

Abstract

Important progress on the development of dielectric based accelerators has been made both experimentally and theoretically in the past few years. One advantage of dielectric accelerators over their metallic counterparts is their compact size, which make them attractive for industrial or medical applications. In this article, we discuss the design of dielectric based accelerators focusing on those technologies relevant toward these needs.

DIELECTRIC LOADED ACCELERATOR

The first studies of using RF driven dielectric-loaded circular waveguide for particle acceleration can be traced back to the early 1950's [1]. In recent years, because of its geometrical simplicity and availability of low loss dielectrics, theoretical and experimental investigations on dielectric based accelerators have been intensively revived. Among them, externally powered Dielectric-Loaded Accelerators (DLA), dielectric wakefield accelerators, and dielectric laser accelerators have attracted the most attention. In this paper, we concentrate on externally powered DLA technologies and possible application.

DLA structures can be made as simple as a dielectric tube surrounded by a conducting cylinder. Most of them use uniform, linear ceramic tubes so that they work as constant impedance accelerating structures. The TM_{01} mode (traveling wave accelerator) or TM_{01n} mode (standing wave) are the fundamental accelerating modes. Unlike conventional metallic accelerating structures, DLA structures do not require any structure periodicity to slow the phase velocity of the guided wave below the speed of light. For a given radius, the phase velocity of each guided wave mode in a DLA structure is governed by the dielectric constant of the material and its wall thickness. In general, for the same a/λ, where a is the radius of the beam opening and λ is the wavelength, the DLA structure can be made much smaller than a disk-loaded accelerating structure due to the high dielectric constant of the material used. This small size may be favored for applications with tight space requirements. It also facilitates the use of quadrupole lenses or a permanent solenoid around the structure to prevent the beam from breaking up in the case of high current beam acceleration. For example, for an X-band structure, given $a/\lambda=0.156$, the diameter of a cell of a 120-degree traveling wave disk-loaded accelerating structure is larger than 2 cm, but the outer diameter of the dielectric tube in a DLA structure is only 1 cm if the dielectric constant of the tube is 20.

However, the choice of dielectric constant should be considered as far more complicated than the requirement of a reduced transverse dimension. It is strongly linked with other accelerating parameters as well. A very good estimate of the group velocity of a traveling wave DLA structure is given by $V_g/c \approx 1/\varepsilon_r$ (where c is the speed of light and ε_r is the relative dielectric constant of the loaded material) when a/λ is less than 15%. The quality factor of a DLA structure can be roughly estimated as $Q \approx 5.22\times10^4/\{\sqrt{[f<GHz>\times(\varepsilon_r-1)]}+5.22\times10^4\times\tan\delta\}$, where f is the frequency of the TM01 mode in units of GHz and $\tan\delta$ is the loss tangent of the loaded material.

PARAMETER CHOICE

DLA structures are generally preferred for use in a short structure powered by short, high frequency RF pulses, which reduces the probability of RF breakdown but needs a short filling time to achieve a high RF-to-beam efficiency [2]. Consider the rough design of an X-band travelling wave DLA structure. From the group velocity estimate, we choose $\varepsilon_r=10$ for a structure with $V_g=10\%$ c. Then Q can be estimated to be 3400. Since the size of the beam opening (2a) is independent of Q but tightly related to the R/Q (figure of merit of an accelerating structure) and shunt impedance R (they both increase as the beam opening decreases), we can choose a as small as the beam emittance allows to obtain both a large R/Q and R. Meanwhile the filling time (defined as L/V_g, where L is the length of the structure) remains short since the group velocity is unrelated to the beam opening. It should be pointed out that a/λ of DLA structures cannot be chosen too small since it will increase the wakefield and thus the risk of beam break-up.

Transverse wakefield damping in DLA structures has been well studied [3]. Its implementation is rather simple: an axially slotted copper jacket filled with RF absorber or metallized strips on the outer surface of the dielectric tube surrounded with RF absorber. The low Q of the DLA structures also helps the damping of long range wakefields.

Figure 1 shows a few parameters of X-band (11.7GHz) travelling wave DLA structures. Three different dielectric constants are used in the plots, representing three commonly used low loss materials: Alumina ($\varepsilon_r=10$, $\tan\delta=1\times10^{-4}$), MgCaTiO ($\varepsilon_r=20$, $\tan\delta=1\times10^{-4}$) and Quartz ($\varepsilon_r=3.8$, $\tan\delta=6\times10^{-5}$). Figure 1(a) clearly shows that the group velocity is bounded by the reciprocal of the dielectric constant as the beam opening decreases. The quality factor of a DLA structure is the combined contribution of metal wall losses and dielectric losses, but

*Work supported by the Department of Energy SBIR program.
#jingchg@hep.anl.gov

Copyright © 2012 by the respective authors — cc Creative Commons Attribution 3.0 (CC BY 3.0)

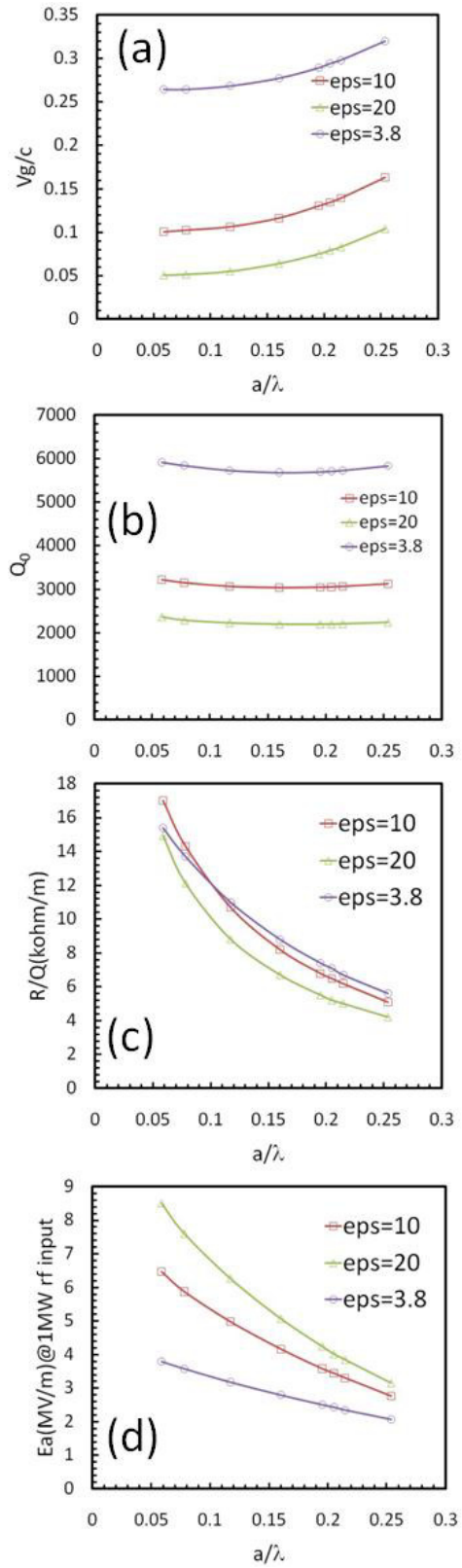

Figure 1: Dependence of parameters in DLA structures on the scaling parameter a/λ: (a) group velocity; (b) quality factor; (c) R/Q; (d) accelerating gradient.

it remains nearly constant across different size of beam channel (Fig. 1b).

From Fig. 1(c) and 1(d) we can see that the R/Q values for different dielectrics can approach or cross each other for small beam channels but the gradient in a higher ε_r DLA structure is always higher. This is because of the strong dependence of the gradient E_a on the group velocity, $E_a^2=[R/Q]\times 2\pi f\times P/V_g$, where P is the input RF power. Again, the low V_g leads to a long RF filling time which then requires a longer RF pulse to power the structure and accelerate the beam. The strong pulse length dependence of the RF breakdown rate will limit the accelerating gradient. However, in an application that does not need to operate with the gradient at a high risk level, a high dielectric constant material should be preferred since it will provide a higher gradient for a given RF power.

MULTIPACTOR

One principal effect that has limited further advances in DLA technology in the past is the problem of multipactor. The fraction of the power absorbed at saturation in the DLA structure was found to increase with the incident power, with as high as 30% of the incident power per unit length being absorbed if the dielectric material has a high Secondary Electron Yield (SEY). A thin film TiN coating, which reduces SEY, can reduce the multipactor loss below 10%. Using geometric factors, particularly the introduction of surface grooves to reduce the multipactor in DLA structures is also under investigation. However, lessons from other work show that one challenge to the success of this approach is the strong dependence upon a few critical dimensions of the groove design, which leads to a very tight machining tolerance and in turn increases the fabrication difficulties and costs.

In fact, the most effective approach to completely terminate multipactor is to use an external solenoid field. Analytical models, numerical simulations, and practical example in other applications have successfully demonstrated its effectiveness [4, 5]. In DLA structures, an external DC magnetic field in the longitudinal direction can continuously reduce the period for secondary electrons hopping on the dielectric surface (and thus spoil the resonance condition) when the ratio of the gyro-frequency to RF frequency is in the range of 0.7 to 1 (The gyro-frequency, Ω, is a plasma parameter; for electrons it is defined as $\Omega=eB/m_ec=1.76\times10^7B$ rad/s, where B is the magnetic field component perpendicular to the electron motion plane). It is equivalent to a solenoid field range from 2.8 kG to 4 kG for an X-band DLA structure. This approach is more attractive than other techniques since it can maintain all the advantages of regular DLA structures, and it is independent of the accelerator parameters other than the operating frequency.

TUNING

The need for frequency tuning (or phase velocity adjustment) of any accelerating structure arises from the fact that the phase velocity of the assembled accelerating

Copyright © 2012 by the respective authors — cc Creative Commons Attribution 3.0 (CC BY 3.0)

structure will, in general, differ from the design phase velocity due to various sources of error. In a DLA structure, these errors can be caused by machining tolerances of the dielectric dimensions, thermal expansion of the structure, dielectric constant heterogeneity, etc. The common way of tuning all-metal structures is using temperature variation or slight mechanical deformation of the accelerating structure walls. The DLA structure does not admit this possibility because the ceramic loading is usually made of a brittle microwave thermostabilized ceramic that does not allow any noticeable mechanical adjustment of its geometrical parameters. At the same time, the permittivity of BST ($Ba_xSr_{1-x}TiO_3$) ferroelectric has a strong temperature dependence. If a thin, low loss ferroelectric layer having relatively high dielectric constant (ε_r>100, tanδ<5×10^{-3}) is introduced, the DLA structure can be easily tuned by controlling its temperature. Introducing a relatively thin ferroelectric layer does not change the basic accelerating structure parameters significantly but it makes the overall average permittivity of the dielectric loaded resonator tunable in the range from tens of kHz to tens of MHz depending on the thickness of ferroelectric material [6].

RF COUPLING

Besides the dielectric loaded section, a DLA structure requires a RF coupler to feed in the high power RF signal. A well designed coupler should possess a high mode conversion efficiency (e.g. TE_{10} mode in rectangular waveguide to TM_{01} mode in DLA structure), and be less susceptible to high power breakdown. Figure 2 show three coupling schemes commonly used in DLA structures. In Fig. 2(a), the metallic RF coupler is separated from the DLA section. The tapered dielectric matching section is a part of the DLA structure that matches the impedance of the TM_{01} mode between the empty and dielectric-loaded waveguide. This coupling method can reach a very broad bandwidth at a cost of the extra length of the dielectric taper. It is worth pointing out the importance of fabricating the entire dielectric tube in a single piece. Any micro gap caused by a dielectric joint is subject to RF breakdown due to the strong field enhancement. Figure 2(b) shows a coaxial type coupling, where the impedance matching is accomplished in the coupler section so that the DLA section remains a simple straight tube. This design is very effective and compact, but the beam hole in the inner conductor of coaxial coupler may limit its usefulness in high gradient applications (i.e. where a/λ is small). Figure 3(b) shows a variation of the side coupling configuration, which is simple in fabrication but generally exhibits a smaller bandwidth than the axial coupling.

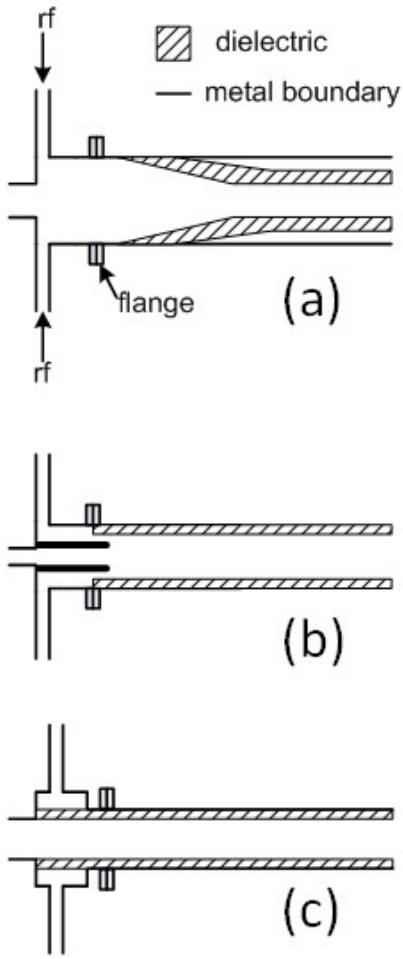

Figure 2: Three commonly used RF coupling schemes in DLA structures; (a) mode launcher; (b) coaxial coupler; (c) side coupling.

REMARKS

DLA technologies have seen significant progress for a decade. At present, it is possible to build and use a practical DLA structure. We expect that its compactness and low cost will eventually make it broadly useful in many applications.

REFERENCES

[1] G. Flesher and G. Cohn, AIEE Trans. 70 (1951): 887-893.
[2] C. Jing, et al, Proc. PAC11, NY, (2011): 2279-2281.
[3] W. Gai and C-H Ho, J. App. Phy. 70, (1991): 3955-3957.
[4] C. Chang, et al, J. Appl. Phys. 110, 063304 (2011).
[5] C-Y Yao, ANL, private communication.
[6] C. Jing, et al, Phy. Rev. Lett. 106, 164802 (2011),

Copyright © 2012 by the respective authors — cc Creative Commons Attribution 3.0 (CC BY 3.0)

LINEAR ACCELERATOR BASED ON PARALLEL COUPLED ACCELERATING STRUCTURE*

Yu. Chernousov, V. Ivannicov, I. Shebolaev, ICKC, Novosibirsk, RUSSIA
A. Levichev, V. Pavlov, A. Barnyakov, BINP, Novosibirsk, RUSSIA.

Abstract

Linear accelerator based on parallel coupled accelerating structure and RF-controlled electron gun is developed and produced. The structure consists of five accelerating cavities. The RF power feeding of accelerating cavities is provided by common exciting cavity which is performed from rectangular waveguide loaded by reactive pins. Operating frequency is 2450 MHz. RF-controlled Electron gun is made on the basis of RF triode. Linear accelerator was tested with different working regimes. The obtained results are following:

- energy is up to 4 MeV, accelerating current is up to 300 mA with pulse duration of 2.5 ns on the half of the width,
- energy is up to 2.5 MeV, accelerating current is up to 100 mA with pulse duration of 5 μs,
- energy is up to 2.5 MeV, accelerating current is up to 120 mA with pulse duration of 5 μs and beam capture of 100%.

The descriptions of the accelerator elements are given in the report. The features of the parallel coupled accelerating structure are discussed. The results of the measuring accelerator's parameters are presented.

INTRODUCTION

Compact linear electron accelerators have wide scientific and industrial applications. The more often linacs are used with energy up to 10 MeV, average beam power up to several kilowatts. In present there are two type of accelerating structures with travelling wave and standing wave. But all of these structures have sequential RF power feeding of the accelerating cells. This is cause of some problems. To supply the accelerating structure total RF power has to go from the first accelerating cell. As the power is attenuated along these structures the initial value of the power must be very high, therefore, there are breakdowns and thermal surface damage in the first accelerating cell. When the breakdown is happened in one of the accelerating cell the operating RF pulse is terminated because of all storage energy of the structure is dissipated in it. Developing of *accelerating structure with given distribution of the power along the cavities is very difficult task. Also there is problem of high order modes, vacuum pumping and etc.

The linear electron accelerator based on new type accelerating structure is developed and produced by Budker Institute of Nuclear Physics of SB RAS, Institute of Chemical Kinetics and Combustion of SB RAS and Institute of Catalysis of SB RAS [1]. The main elements of accelerator are parallel coupled accelerating structure, injector, waveguide track with vacuum RF window, focusing system and klystron KIU-111. The klystron's frequency is 2450 MHz, average power is 5 kW with pulse power of 5 MW [2]. The main goal of our efforts is to test new ideas and devices which are used in the accelerator. The mass of these elements are used in such accelerator for the first time and have some advantages.

PARALLEL COUPLED ACCELERTING STRUCTURE

The scheme of parallel coupled accelerating structure is shown in the Fig. 1 and Fig. 2. RF power from a klystron feeds the exciting cavity (1) through inductive coupling window (7). The exciting cavity supplies the accelerating cavities (2). The RF connection of the exciting cavity with the accelerating cavities is provided by magnetic field through coupling slots (5). The focusing alternative magnetic field is created along the beam axis by periodic permanent magnets (3) with radial magnetization inserted in the iron yoke (4). This kind of focusing provides large enough magnetic field while keeping the weight of the focusing system considerably small. The cupper pins (6) are used to tune the exciting cavity (1) at the resonance frequency.

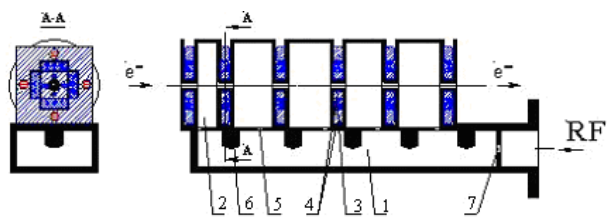

Figure 1: Scheme of the parallel coupled accelerating structure.

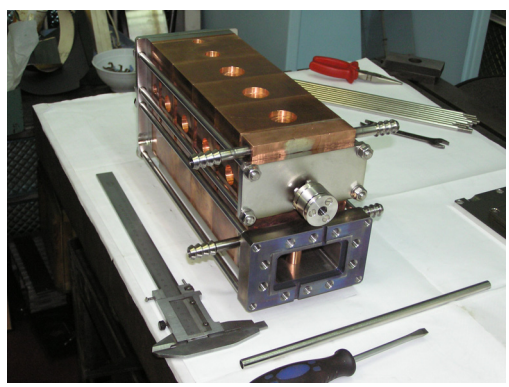

Figure 2: Parallel coupled accelerating structure.

* Work is supported by the Ministry of Education and Science of the Russian Federation, grants N 14.740.11.0836

Copyright © 2012 by the respective authors — cc Creative Commons Attribution 3.0 (CC BY 3.0)

Due to the scheme of RF power supplying this accelerating structure has some advantages versus structures with sequential power feeding. There is no need to have a high power in the first accelerating cavity. So the overvoltage and breakdown problems, thermal surface damage near the coupling slots are absent. The design of parallel coupled accelerating structure allows us to create compact periodic permanent magnet focusing system based on the permanent magnets with radial magnetization (see Fig. 1). The accelerating cavities are not connected with each other by electric field therefore aperture of the drift tubes between cavities is limited only by the beam focusing. By changing the coupling factor between exciting and accelerating cavities it is possible to make the free power distribution along the structure. If breakdown is happened in one of the accelerating cavities the storage energy only this cavity is dissipated, and only in this cavity. So the working RF pulse is not terminated but only amplitude of reflected signal is slightly changed, as it is presented on the Fig. 3.

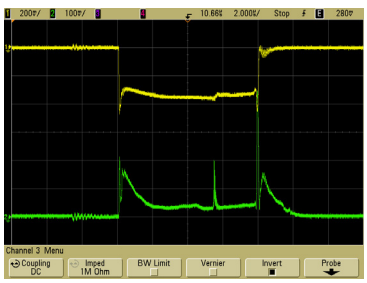

Figure 3: Breakdown in one of the accelerating cavities: 1 - signal from klystron; 2 - reflected signal from accelerating structure.

The accelerating structure can be used as for high average current with high average power as for short nano- and picoseconds duration current pulses with high amplitudes.

INJECTOR

Injector is the electron gun with DC voltage of 50 kV and pulse current up to 1 A. It is based on RF triode GS-34 and shown on the Fig. 4.

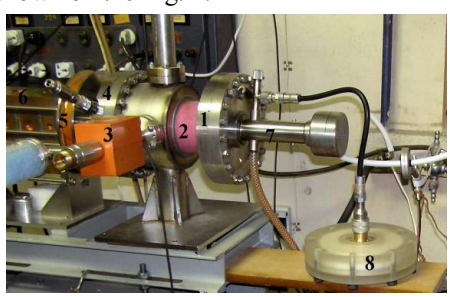

Figure 4: Injector: 1- cathode-grid unit, 2 – ceramics, 3 – vacuum pump, 4 – bunching cavity, 5 – matching solenoid, 6 - accelerating structure, 7 – coaxial cavity for RF beam control, 8 – antenna type RF lead.

Injector can work with following regimes: short pulses with duration of about nanoseconds, long pulses with duration of microseconds and long pulses with RF control for a beam π-chopper. Under using RF control the beam is modulated by coaxial cavity on bunches with length equaled to half wavelength of RF field. Due to this feature, the beam capture can be achieved up to 100%.

The cathode-grid unit 1 (see Fig. 4) is under potential of -50 kV. So, to feed the coaxial cavity 7 the antenna-type coaxial lead (8) was developed and produced. It is shown on the Fig. 5. The antenna-type lead consists of two symmetrical parts of coaxial half-wave resonator. The resonator is cut along perpendicular to the longitudinal axis plane of symmetry. The solid dielectric disk is located between the halves.

The Fig. 6 shows the measured bandpass characteristics. The reflection coefficient S_{11} at the operating frequency is 0.098 and the transmission coefficient S_{21} is 0.976. Bandwidth at the attenuation level of -3 dB is more than 1800 MHz (73%).

Figure 5: Antenna type RF lead.

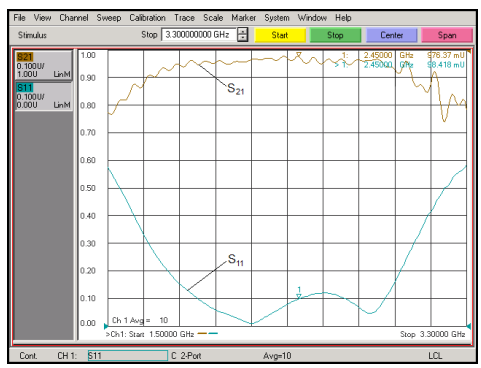

Figure 6: The transmission S_{21} and reflection S_{11} coefficients of the lead.

ACCELERATOR MEASUREMENTS

Accelerator was tested under three regimes.

The first regime is characterized by short beam pulse with duration of 2.5 ns on the half of width (see Fig. 7). The beam energy is about 4 MeV, beam current amplitude is about 300 mA. The Fig. 8 shows the cross section of the beam profile.

Copyright © 2012 by the respective authors — cc Creative Commons Attribution 3.0 (CC BY 3.0)

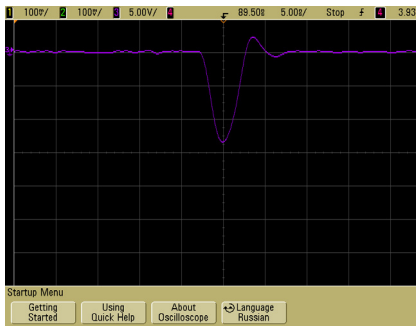

Figure 7: Oscilloscope of the accelerated beam current with duration of 2.5 ns (100 mA per cell).

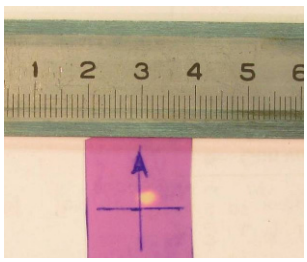

Figure 8: Cross section of the beam profile with pulse duration of 2.5 ns.

In the second regime the beam duration is 4 μs, energy is 2.5 MeV, beam capture is about 50%. Oscilloscope of the beam current and cross section of the beam profile are shown on the Fig. 10 and Fig. 11 correspondingly.

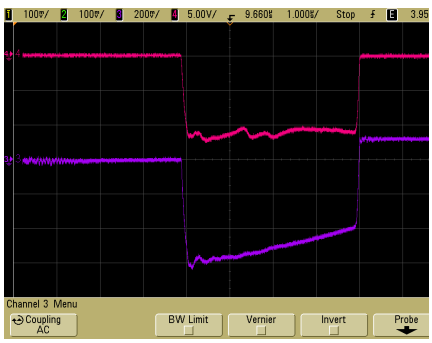

Figure 9: Oscilloscope of the accelerated beam current with duration of 4 μs: 3 – emission beam current (180 mA per cell), 4 – beam current in the end of accelerating structure (100 mA per cell).

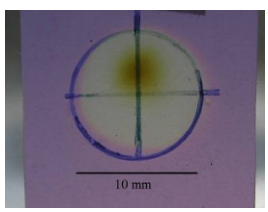

Figure 10: Cross section of the beam profile with pulse duration of 4 μs.

In the third regime the injector operated with RF control. The energy is equaled to 2.5 MeV. The feature of this regime is beam capture of 100%. Oscilloscope of the beam current and cross section of the beam profile are shown on the Fig. 12 and Fig. 13 correspondingly

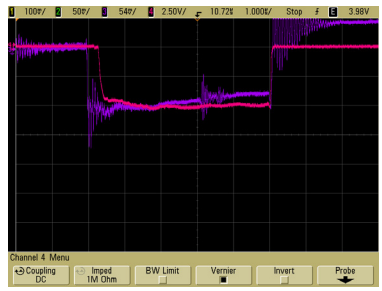

Figure 12: Oscilloscope of the accelerated beam current with RF control: 3 – emission beam current (50 mA per cell), 4 – beam current in the end of accelerating structure (50 mA per cell).

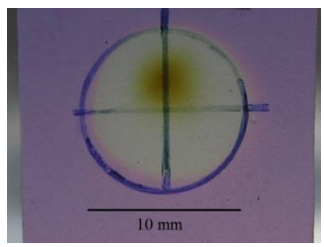

Figure 13: Cross section of the beam profile with RF control.

CONCLUSION

Linear electron accelerator based on parallel coupled accelerating structure and injector with RF control for a beam π-chopper is made, tested and measured. The beam energy is 2.5-4 MeV with total power of 2.4 MW, accelerated beam current is 100-300 mA. These values depend on the beam loading effect. The durations of the beam pulse were changed from 2.5 ns to 5 μs. With RF control the beam capture was achieved 100%. The diameter of cross section of the beam profile was about 3 mm. The beam loading effect is studying.

REFERENCES

[1] A.E. Levichev, V.M. Pavlov and et al., "Characteristics of the Parallel Coupled Accelerating Structure", IPAC'10, Kyoto, June 2010, THPEA040, p. 3765 (2010); http://www.JACoW.org.

[2] I.A. Frejdovich, P.V. Nevsky et al., JACoW, "Multy-beam klystrons with reverse permanent magnet focusing system as the universal RF power sources for the compact electron accelerators", RUPAC'06, Novosibirsk, September 2006, TUHO08, p. 100 (2006); http://www.JACoW.org.

Copyright © 2012 by the respective authors — cc Creative Commons Attribution 3.0 (CC BY 3.0)

DESIGN OF COMPACT C-BAND STANDING-WAVE ACCELERATOR FOR MEDICAL RADIOTHERAPY*

H. R. Yang#, M. H. Cho, and W. Namkung
Pohang University of Science and Technology, Pohang 790-784, Korea
S. H. Kim, Argonne National Laboratory, Argonne, Illinois 60439, USA
J. S. Oh, National Fusion Research Institute, Daejeon 305-333, Korea

Abstract

We design a C-band standing-wave accelerator for an X-ray and electron source of medical radiotherapy. The accelerator system is operated two modes, using the X-ray and electron beams. Since two modes require different energy, the accelerator is capable of producing 6-MeV, 100-mA pulsed electron beams with peak 2-MW RF power, and 7.5-MeV, 50 mA electron beams with peak 2.5-MW RF power. The beam is focused by less than 1 mm without external magnets. The accelerating structure is a bi-periodic and on-axis-coupled structure with a built-in bunching section, which consists of 3 bunching cells, 14 normal cells and a coupling cell. It is operated with the π/2-mode standing-wave. The bunching cells are designed to enhance the RF phase focusing. Each cavity is designed by the MWS code within 3.5% inter-cell coupling. In this paper, we present design details of RF cavities and the beam dynamics.

INTRODUCTION

The electron accelerator is widely used for industrial and medical applications: a contraband detection, material processing, a medical diagnosis and therapy, sterilizing food, and environmental processing [1, 2]. For the medical applications, the electron beam with 3 ~ 15 MeV, pulsed tens mA is required. These applications require the small beam spot size at the X-ray conversion target for reducing the penumbra [3]. In order to achieve such a small beam spot size, the RF focusing effect is maximized instead of the magnetic focusing with external magnets for a compact accelerator system.

We are developing a C-band standing-wave electron accelerator for an X-ray and electrons source of medical radiotherapy. This accelerator system is operated two modes, using the X-ray and electron beams. The X-ray beam is used to irradiate the viscera, and the electron beam is used to irradiate the inner and outer layers of skin. There is energy loss by two scattering foils which are between the accelerating column and the affected area in the electron mode, as shown in Fig. 1 [4]. The beam energy at the end of column has to be higher than irradiated energy in the affected area, 6 MeV which are widely used in the medical radiotherapy [5]. For such reasons, the accelerator is designed to produce 6-MeV, pulsed 100-mA electron beam with peak 2-MW power in the X-ray mode, and 7.5-MeV, pulsed 50-mA electron beam with peak 2.5-MW power in the electron mode. It is operated with a pulse length of 4 μs and with a pulse repetition rate of 250 Hz. The bunching cells are designed with beam dynamics simulation for enhancing the RF phase focusing. We design the RF cavities in the bi-periodic and on-axis-coupled accelerating structure with the MWS code. The beam dynamics simulations are conducted with PARMELA codes.

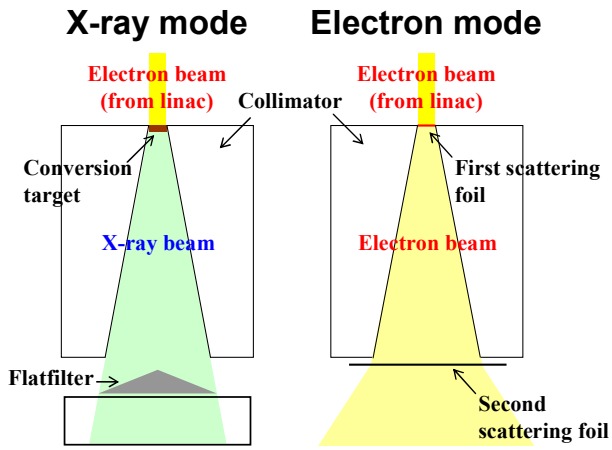

Figure 1: Schematic diagram of the X-ray and electron modes.

Table 1: The design parameters of the accelerator

Parameters	X-ray Mode	Electron mode
Operating Frequency	5712 GHz	
Input Pulsed RF Power	2.0 MW	2.5 MW
Pulse Length	4 μs	
Repetition Rate	250 Hz	
E-gun Voltage	19.0 kV	20 kV
Input Pulsed Beam Current	80 mA	180 mA
Output Beam Energy	6 MeV	7.5 MeV
Output Pulsed Beam Current	50 mA	100 mA
Type of Structure	Bi-periodic, On-axis coupled	
Operating Mode	SW π/2 mode	
Beam Aperture Diameter*	6 mm	
Average Accelerating Gradient	13.4 MV/m	16.7 MV/m
Number of Cells	18	
Inter-cell Coupling	3.5%	
Quality Factor*	9000	
Shunt Impedance*	113 MΩ/m	
Transit-time Factor*	0.84	

*Values for normal cells.

*Work supported by POSTECH Physics BK21 Program.
#highlong@postech.ac.kr

Copyright © 2012 by the respective authors — cc Creative Commons Attribution 3.0 (CC BY 3.0)

ACCELERATOR OVERVIEW

The accelerator uses a 5712-MHz magnetron as an RF source. It is capable of producing a max. 2.5 MW RF with a 4-μs pulse length and a 250-Hz repetition rate. It is supplied pulsed 2.0 MW RF in the X-ray mode, and pulsed 2.5 MW RF in the electron mode, as shown in Table 1. The RF power is transmitted to the accelerating column through the WR187 waveguide network, as shown in Fig. 2. Since there is a transient reflection during an RF filling time in the standing-wave accelerating structures, a circulator with the matched load is inserted in the waveguide network. The pulse modulator supplies a max. 65-kV and a 90-A pulsed power to the magnetron with a 4-μs pulse length. It also supplies a max. 20-kV pulsed voltage to an E-gun.

The E-gun is a diode-type thermionic DC gun with a dispenser cathode. Although the E-gun is capable of emitting electron beam of maximum 560 mA, the gun emits 80-mA electron beam with 20-kV pulse in the electron mode, and 180-mA e-beam with 19-kV pulse in the X-ray mode. The beam radius is 0.6 mm at the beam waist which is 15.2 mm from the anode. The direction of the beam is adjusted by the steering coils in the upstream and downstream of the accelerating column, as shown in Fig. 3.

The accelerating column is attached to the E-gun directly, as shown in Fig. 3. For a compact structure, it has a built-in bunching section without a pre-buncher, and any focusing magnet is not used, because the beam is focused enough by the enhanced RF phase focusing with the design of the bunching cells [6]. A bi-periodic and an on-axis coupled structure is adopted for the π/2-mode standing-wave structure [7]. The first three cells, in Fig. 3, are the bunching cells with phase velocities (βph) of 0.3, 0.5, and 0.85. The number of normal cells with βph = 1 is 14 units, and after these, the coupler cell is attached to the tapered C-band waveguide.

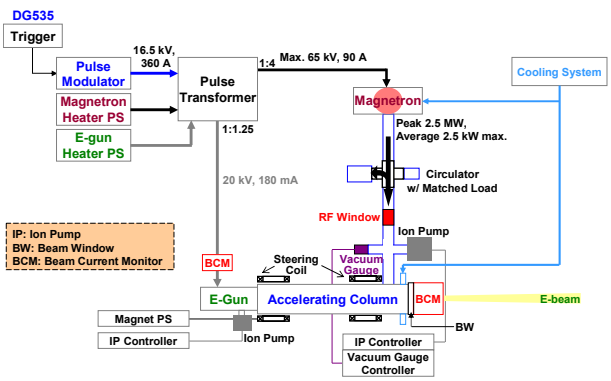

Figure 2: Schematic diagram of the accelerator system.

BEAM DYNAMICS

Beam dynamics simulations in the accelerating column are conducted by using the PARMELA code. The emittance of input beams is 20 mm-mrad and other parameters of input beams are described in the previous section. The phase velocities of bunching cells, and the asymmetric geometry of the first and second bunching cells are optimized to enhance the RF phase focusing, as shown in Fig. 3 [6]. In the electron mode, since the beam is scattered at two foils, the small beam spot is not required. Therefore, the efforts to enhance the RF phase focusing are optimized in the X-ray mode.

Fig. 4 is the phase trajectories of the X-ray and electron modes, and Fig. 5 is the beam envelopes of two modes. In the X-ray mode, the accelerating field is lower compared with that of the electron mode, because of the lower input RF power. Since the RF focusing is proportional to the square of the accelerating field, the beam is less focused in bunching cells, as shown in Fig. 5 [6]. However, since the beam is less accelerated in bunching cells, the average phase of the bunch is higher than that of the electron mode, as shown in Fig. 4. Then, the RF phase focusing is increased in normal cells [7]. Since these two effects cancel each other out, the beam spot size is almost the same in two modes. With effective RF focusing, the beam spot sizes of both are less than 1 mm at the end of column, as shown in Fig. 5.

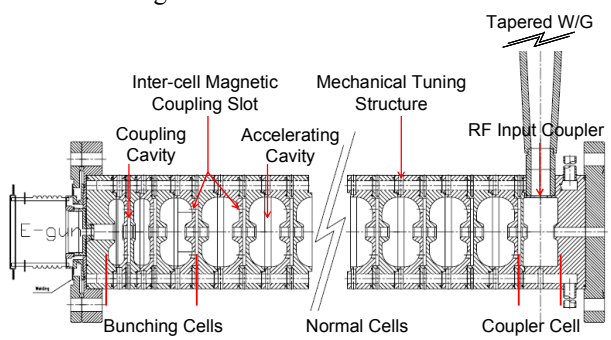

Figure 3: Cross-sectional view of the accelerator structure.

The output beam parameters of two modes are in Table 2. Since there is a lot of beam loss in the conversion target, collimator, and the flatfilter, as shown in Fig. 1, the beam current in the X-ray mode is higher than that of the electron mode, in order to obtain a lot of radiation. In the electron mode, the beam is accelerated near the crest, and more bunched, as shown in Fig. 4. Therefore, the beam energy spread is 10% less than that in the X-ray mode. It affects the increasing of the energy uniformity of beam in the electron mode.

RF CAVITY

Each cell in the accelerating column consists of the accelerating cavity and the coupling cavity, as shown in Fig. 3. Magnetic coupling slots are bored on the side wall between the accelerating cavity and the coupling cavity for the inter-cell coupling. The inter-cell coupling constant becomes 3.5%, restricted by the decrease of the shunt impedance. Due to these slots, the 3-D electro-magnetic simulation is conducted with the MWS code to obtain the resonant frequency for the π/2-mode of each cavity, as shown in Fig. 6. In the case of the coupling cavity, the transverse mid-plane can not be a symmetric boundary due to the magnetic coupling slots. To estimate an accurate resonant frequency for the coupling cavity,

Copyright © 2012 by the respective authors — cc Creative Commons Attribution 3.0 (CC BY 3.0)

the end cells are detuned for the frequency of the detuned cell to be lower than 3 GHz, as in Fig. 6(b) [8]. From the simulation result, the resonant frequencies of each cavity is obtained, 5711.5±0.5 MHz.

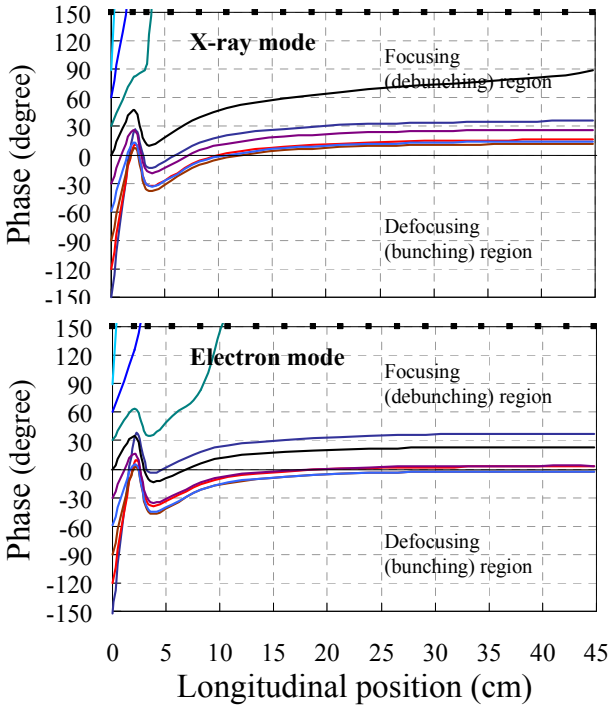

Figure 4: The phase trajectories of the X-ray and electron modes.

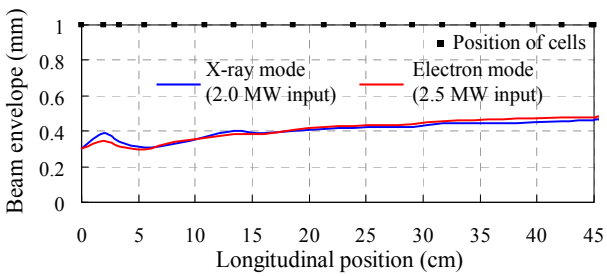

Figure 5: The beam envelopes of the X-ray and electron modes.

Table 2: The output beam parameters of the X-ray and electron modes

Beam parameters	X-ray Mode	Electron mode
Average Energy	6 MeV	7.5 MeV
Pulsed Beam Current	100 mA	50 mA
Energy spread	37%	27%
Beam spot size	~ 1 mm	~ 1 mm

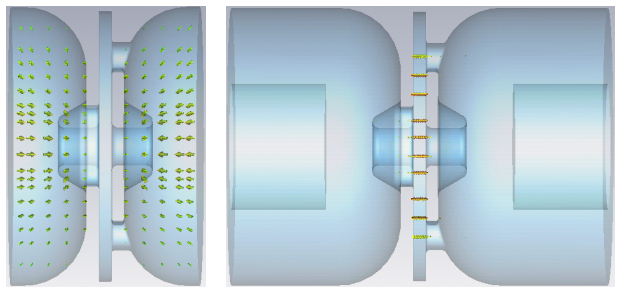

Figure 6: Simulation model to find the resonant frequency for (a): the accelerating cavity, (b): the coupling cavity.

SUMMARY

The C-band standing-wave accelerator is developed for the X-ray and electron source. This accelerator is capable of producing 6-MeV, 100-mA pulsed electron beams with an RF power of 2.0 MW for the X-ray source, and 7.5-MeV, 50-mA pulsed electron beams with an RF power of 2.5 MW for the electron source. In order to enhance the RF phase focusing, the phase velocities of bunching cells and the geometry of the first and second bunching cell are adjusted with beam dynamics simulations. Under these conditions, the beam is focused by less than 1 mm at the end of accelerating column in both of conditions. Since the beam is accelerated near the crest and more bunched in the electron mode, the beam energy spread 27% which is 10% less than that in the X-ray mode. The bi-periodic accelerating structure with on-axis coupling is designed. The cavity dimensions are determined for the π/2-mode frequency to be 5712 MHz with 3.5% inter-cell coupling by the MWS code simulation.

ACKNOWLEDGEMENT

This work is partly supported by MKE, Korea and POSTECH BK21 Program.

REFERENCES

[1] W. A. P. Calvo, et al., Rad. Phys. Chem. **81**, 1276 (2012).
[2] C. Tang, et al, "Present Status of the Accelerator Industry in Asia," in *Proc. of IPAC10* (Kyoto, Japan, May 23-28, 2010), p. 2447.
[3] L. W. Wang and K. Leszczynski, Med. Phys. **34**, No. 2, 485 (2007).
[4] G. X. Ding, et al., Med. Phys. **23**, No. 3, 361 (1996).
[5] G. A. Loew, SLAC-PUB-1830, 1 (1976).
[6] H. R. Yang, et al, "Self-focusing Effects in Compact C-band Standing-wave Accelerating Structure for X-ray Imaging Applications," in *Proc. of IPAC11* (San Sebastian, Spain, Sep. 4-9, 2011), p. 2046.
[7] H. Euteneuer, et al, "The 4.9 GHz Accelerating Structure for MAMI C," in *Proc. of EPAC 2000* (Vienna, Austria, June 26-30, 2006), p. 1954.
[8] S. H. Kim, et al, "Cold Test on C-band Standing-wave Accelerator," in *Proc. of PAC07* (Albuquerque, USA, June 25-29, 2007), p. 2823.

Copyright © 2012 by the respective authors — cc Creative Commons Attribution 3.0 (CC BY 3.0)

CHANGING ATTITUDE TO RADIATION HAZARDS AND CONSEQUENT OPPORTUNITIES FOR LINAC APPLICATIONS

Y. Socol, Falcon Analytics, POB 82 Netanya 42100, Israel

Abstract

High-energy LINACs unavoidably yield ionizing radiation. This fact makes them subject to strict regulations and considerably limits their possible applications. During the last two decades the attitude to ionizing radiation hazards seems to become more balanced, as opposed to "radiophobia" of the Cold-War era. Scientifically, the Linear No-Threshold (LNT) model of radiation damage is more frequently questioned. Moreover, the hypothesis of radiation hormesis – beneficial effect of low-dose radiation – is studied. While this scientific debate has not yet given fruit in terms of changes in radiation regulation policy, we may expect this to happen in the near to middle term. Namely, the ALARA (as low as reasonably achievable) demand is anticipated to be substituted by some tolerance level, which in turn is anticipated to be very high according to the present standards. The presentation will review the present status of the radiation-hazard debate, and outline anticipated opportunities for LINAC applications, like compact designs and wider industrial outreach.

TOLERANCE LEVEL VS. LINEAR NO-THRESHOLD

High-energy LINACs unavoidably yield ionizing radiation. Adverse effects of high doses of ionizing radiation were discovered nearly immediately after the discovery of X-rays and radioactivity back in the XIX century. However, it took about two decades before early medical practitioners began to control their exposures to ionizing radiation. For example, the British X-ray and Radium Protection Committee was formed in 1921. In 1924, at a meeting of the American Roentgen Ray Society, Arthur Mutscheller recommended "tolerance" (permissible) dose rate for radiation workers, a dose rate that could be tolerated indefinitely. This rate was 0.2 roentgen per day (R/day), based on applying a factor of 1/100 to the commonly accepted average erythema dose of 600 R (not accidentally – lethal dose in case of acute whole-body irradiation), spread over 30 days [1]. The International Commission on Radiological Protection (ICRP), established in 1928, accepted in 1931 this tolerance dose rate as a universal recommendation that was in effect for more than quarter of a century. This level corresponds to 70 R/year or about 700 mSv/year – 35 times higher than the present-day occupational (professional) exposure limit, and 700 times higher than the present-day public one. It was assumed that no harm will be caused by radiation below this tolerance level. To illustrate the extent of public confidence in the usefulness and safety of ionizing radiation we will remind that until after the Second World War X-ray machines were typical equipment of shoe shops (this fact was mentioned in passing in Rudolf Peierls' book from 1956 [2]).

It should be stressed that until now nobody succeeded to disprove the assumption of tolerance level (while it is clear that high dose is harmful: acute dose of 100 R leads to radiation sickness and 200 R may be already lethal). For example, a study of British radiological society members [3] reveals that while the pre-1921 radiologists (who had not controlled their exposure and therefore received high doses of ionizing radiation) had a 75% (4σ of the expected value) higher cancer mortality than other medical practitioners, the post-1920 radiologists had an insignificant 5% (0.4σ) excess. Furthermore, the studies of radium dial-painters, exposed to huge cumulative doses (mostly at low rates), revealed that no cancer excess was observed below the life-time dose of about 1000 rad [4]. For α-particles, emitted by radium, the radiation weighting factor w_R=20, i.e. 1000 rad = 10 Gray correspond to 200,000 mSv!

However, geneticists strongly believed the theory that the number of genetic mutations is linearly proportional to radiation dose just like the number of ionized atoms, that mutagenic damage was cumulative and therefore no tolerant (safe) dose for radiation could be set. According to this view, there is no absolute radiation safety, so that the safety level should only be weighed against the cost to achieve it [1].

After the bombing of Hiroshima and the start of the nuclear arms race, geneticists greatly amplified their concerns that exposure to radiation of atomic bomb fall-out would likely have devastating consequences on the gene pool of the human population. Hermann Muller was awarded the Nobel Prize in 1946 for his discovery of radiation-induced mutations. In his Nobel Prize Lecture, he argued that the dose-response for radiation-induced germ cell mutations was linear and that there was "no escape from the conclusion that there is no threshold" [5].

There was great controversy and extensive arguments during the following decade. Probably, both super-powers became interested in exaggerating the nuclear fall-out hazard. Ultimately all kinds of ionizing radiation became connected in public perception with nuclear apocalypse. As a result of (or at least in the wake of) this change in public perception, the ICRP and the national regulators changed their radiation protection policies in the mid-1950s. They rejected the tolerance dose concept and adopted the ALARA (as low as reasonably achievable) policy, i.e., to keep the radiation exposure ALARA. The accepted model for low-dose radiation-induced health damage became the so-called Linear No-Threshold (LNT) model. In LNT, the acute exposure, high-dose cancer

Copyright © 2012 by the respective authors — cc Creative Commons Attribution 3.0 (CC BY 3.0)

mortality data from the study on Hiroshima-Nagasaki survivors [6] was taken as the basis for extrapolation to low doses of radiation. (We should also mention in brackets, that the Life Span Study of the survivors, though dealing with vast amount of data, is performed by single organization that grants only a very limited access to its raw data for the scientific community). The ICRP has been progressively tightening its recommendations for occupational and public exposures, from 50 and 5 mSv/year in 1958 [7] to 20 and 1 mSv/year in 1990 [8], and national regulators usually followed. And probably even more importantly, these stringent norms were (and to a large extent are still being) considered unsafe by the general public.

NEW TRENDS

While the Linear No-Threshold (LNT) view is commonplace for the present regulation and for the public perception, it has never been a subject to scientific consensus. The absence of consensus has been always officially acknowledged – see e.g. the 1979 report of the US Congress Office of Technology Assessment [9]. Towards the end of the Cold War, the LNT model becomes more and more challenged.

In simple terms, the concept of a cumulative no-threshold damage to living organism by *any* possible factor contradicts most of the existing scientific evidence. E.g., for paracetamol – a widely used non-prescription medicine – the lethal dose LD_{50} is about 2 g/kg, i.e. below 200 g for a normal person (few weigh above 100 kg). Following the LNT logic, each caplet of paracetamol (0.5 g) has lethal probability of 50%×0.5/200=0.125% – i.e. a caplet should kill on average 1 out of 800 patients! Clearly, the LNT logic is completely inapplicable here, which is typical for biology. In more professional terms, an enormous amount of research has been underway on genetics and on the effects of radiation on DNA throughout the XX century. A very important review of this subject, as pointed by Jerry Cuttler [1], was published in 1990 by Daniel Billen in the Radiation Research Journal [10].

The above review points out that "DNA is not as structurally stable as once thought. On the contrary, there appears to be a natural background of chemical and physical lesions introduced into cellular DNA by thermal as well as oxidative insult. In addition, in the course of evolution, many cells have evolved biochemical mechanisms for repair or bypass of these lesions."

Billen points that spontaneous DNA damage occurs at a rate of about 10,000 natural events per cell per hour. Let us compare this with the damage caused by ionizing radiation. The number of DNA damaged sites per cell per roentgen (R) is estimated to be below 100 [10]. A radiation level of 0.2 R (or 2 mSv) per day (ICRP 1931 recommendation) would cause on average less than 20 events per cell per day, or below 1 event/cell per hour. This is 10,000 times lower (!) than the natural rate of DNA damage that occurs in every person. The above numbers have been known for more than 20 years, verified by numerous investigations and considered to be a solid scientific evidence.

Moreover, one can even suggest that low doses of X-rays and nuclear radiation are beneficial to human health ("hormesis" hypothesis) – just as the ultraviolet radiation (also a form of ionizing radiation) is clearly beneficial in low doses (sun tanning) while high doses are certainly harmful (sunburns and skin cancer). In that context it is worth mentioning that the healing properties of radon spas have been utilized for centuries before people heard the word "radiation", and that radon treatment is definitely not considered to be an "alternative therapy" by the mainstream medicine in Europe (as opposed to the US) [11]. Another fact worth mentioning is that in most of the nuclear industry workers studies, the rate of cancer mortality (as well as overall mortality) among the radiation workers is substantially lower than in the reference population [12]. These little-spoken facts and many others [11,13] comprise emerging (though not yet conclusive) scientific support for the hormesis hypothesis. The very idea of radiation hormesis and the term itself appeared back in 1920-s, but since 1950-s were missing in the scientific literature for decades till re-appearance in 1982. Since then, the scientific interest to hormesis steadily grows, as shown in Fig. 1.

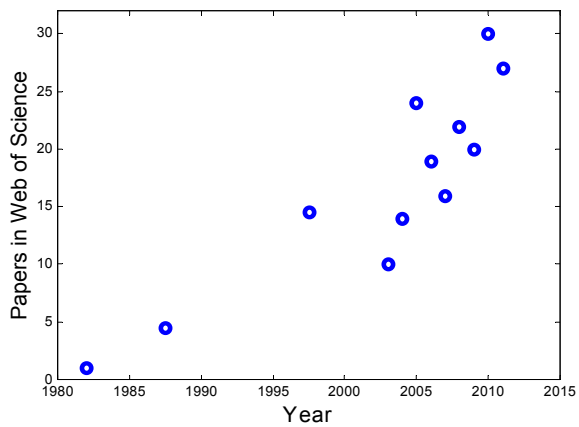

Figure 1: Growing number of scientific papers dealing with *radiation hormesis* (beneficial effects of low-dose ionizing radiation). The term "hormesis" appeared in 1920-s, but since 1950-s was missing in the scientific literature for decades till re-appearance in 1982. Source: Science Citation Index Expanded [14].

While this scientific debate has not yet given fruit in terms of changes in radiation regulation policy, we may expect this to happen in the near to middle term. For example, after the Fukushima accident it was publicly announced – probably for the first time after 1950-s – that no positive scientific evidence (besides extrapolation from high acute dose) supports carcinogenic or other harmful effect of radiation dose below 10 R (100 mSv). While the above understanding did not prevent the Japanese authorities from performing large-scale (and in our opinion unjustified) evacuation [1], it was still

Copyright © 2012 by the respective authors — cc Creative Commons Attribution 3.0 (CC BY 3.0)

essential in *ad hoc* setting higher radiation limits for the radiation workers, which led to ultimate solving of the damaged reactors' issues.

Instead of the ALARA (as low as reasonably achievable) demand, "as high as reasonably safe" AHARS approach was suggested [15]. Reasonably safe tolerance level is anticipated to be very high according to the present standards, probably orders of magnitude higher than the present limits, as discussed in the first part of this paper.

APPLICATIONS

Below we discuss how different applications of LINACs may benefit from the more realistic attitude to radiation hazards.

Food industry

Electron LINACs may be used for food sterilization, leading to the reduction in supply-chain losses and to extended shelf life. Since the irradiated food does not become radioactive, the main obstacle to the spread of this technology seems to be related to the public perception of radiation hazards. With more realistic attitude to radiation hazards, the market for LINAC-irradiated food is anticipated to considerably grow.

Manufacturing of plastics

Irradiation leads to intensification of important chemical processes, such as polymerization or curing in composites. In high-volume production, the radiation doses for the workers are relatively high. Since the plastics industry is generally regarded as low-tech with relatively cheap labour, upgrading the employees officially to a status of "radiation workers" does not seem to be a viable option in the present situation. However, the situation will change dramatically with easing of the radiation regulations and changing of the public perception of radiation hazards.

Other applications

All LINAC applications, especially compact Free-Electron Lasers still to be designed, will benefit from easing the radiation regulation and elimination of radiophobia. However, other applications seem to be less affected. For example, in medical applications (radiotherapy and end-point sterilization of equipment) there seems to be virtually no radiophobia whatsoever. It is as if these were different types of X-rays, electrons and isotopes being used for the different applications – harmless in medicine, yet extremely dangerous in all other fields of human endeavour. This topic by itself is worth of serious research, however more in relation to psychology and sociology than to physics.

CONCLUSIONS

During the last two decades the attitude to ionizing radiation hazards seems to become more balanced, as opposed to "radiophobia" of the Cold-War era. We may expect in the near or the middle term future a decline of radiophobia and easing of the radiation regulations. The ALARA (as low as reasonably achievable) demand is anticipated to be substituted by some tolerance level, which in turn is anticipated to be very high according to the present standards. The main anticipated opportunities for LINAC applications belong in our opinion to the food industry and plastic production technologies.

ACKNOWLEDGMENT

The author wishes to thank Dr. Jerry Cuttler (Cuttler & Associates Inc.) for drawing attention to his excellent recent publication [1], which provided a significant part of the historical background in the current publication.

REFERENCES

[1] J.M. Cuttler, "Commentary on the Appropriate Radiation Level for Evacuations," Dose-Response (Prepress), DOI: 10.2203/dose-response.12-013.Cuttler
[2] R.E. Peierls, *The Laws of Nature*, (New York: Charles Scribner's Sons, 1956), 90.
[3] P.G. Smith and R. Doll, "Mortality from Cancer and All Causes Among British Radiologists," British J. Radiology 54 (1981) 187-194.
[4] *Health Risks of Radon and Other Internally Deposited Alpha-Emitters: BEIR IV*. (Washington DC: The National Academies Press, 1988), 198.
[5] E.J. Calabrese, "Muller's Nobel lecture on dose–response for ionizing radiation: ideology or science?" Arch. Toxicol. 85 (2011) 1495-1498.
[6] Radiation Effects Research Foundation, www.rerf.jp
[7] ICRP, *Radiation protection; recommendations: Adopted September 9, 1958* (Oxford: Pergamon Press, 1959).
[8] *1990 Recommendations of the International Commission on Radiological Protection* (Oxford: Pergamon Press, 1991).
[9] *The Effects of Nuclear War*, Office of Technology Assessment, Congress of the United States 1979. (London: Croom Helm, 1980) 111.
[10] D. Billen, "Commentary: Spontaneous DNA Damage and Its Significance for the "Negligible Dose" Controversy in Radiation Protection." Radiation Research 124 (1990) 242-245.
[11] B.E. Erickson, "The Therapeutic use of Radon: a Biomedical Treatment in Europe; an "Alternative" Remedy in the United States," Dose Response. 5 (2007) 48–62. http://www.ncbi.nlm.nih.gov/pmc/articles/PMC2477705
[12] *Health Risks from Exposure to Low Levels of Ionizing Radiation: BEIR VII – Phase 2* (Washington DC: The National Academies Press, 2006) 194. http://www.nap.edu/catalog.php?record_id=11340 26
[13] J.M. Cuttler and M. Pollycove, "Nuclear Energy and Health: and the Benefits of Low-Dose Radiation Hormesis," Dose-Response 7 (2009) 52-89.
[14] Institute for Scientific Information www.isiknowledge.com
[15] W. Allison, *Radiation and Reason: Impact of Science on a Culture of Fear* (UK: York Publishing Services, 2009).
W. Allison, "Risk Perception and Energy Infrastructure," Evidence submitted to UK Parliament. Commons Select Committee. Science and Technology. December 22, 2011. http://www.publications.parliament.uk/pa/cm201012/cmselect/cmsctech/writev/risk/m04.htm

Copyright © 2012 by the respective authors — cc Creative Commons Attribution 3.0 (CC BY 3.0)

FERMILAB 1.3 GHz SUPERCONDUCTING RF CAVITY AND CRYOMODULE PROGRAM FOR FUTURE LINACS*

C.M. Ginsburg#, Fermilab, Batavia, IL 60510, USA

Abstract

The proposed Project X accelerator and the International Linear Collider are based on superconducting RF technology. As a critical part of this effort, Fermilab has developed an extensive program in 1.3 GHz SRF cavity and cryomodule development. This program includes cavity inspection, surface processing, clean assembly, low-power bare cavity tests and pulsed high-power dressed cavity tests. Well performing cavities have been assembled into cryomodules for pulsed high-power tests and will be tested with beam. In addition, peripheral hardware such as tuners and couplers are under development. The current status and accomplishments of the Fermilab 1.3 GHz activity will be described, as well as the R&D program to extend the existing SRF pulsed operational experience into the CW regime.

INTRODUCTION

Work by the International Linear Collider (ILC) [1,2] community, which includes Fermilab, has motivated substantial world-wide infrastructure development and cavity performance progress. At Fermilab, this has translated to a very large commitment of resources for infrastructure and personnel development. The developed capability has led to the possibility to use the 1.3 GHz infrastructure for development of Project X [3,4], although the performance requirements are somewhat different [5]. The Project X 3 GeV CW linac requires high Q_0 at gradients (E_{acc}) in the range $15<E_{acc}<20$ MV/m; 1.3 GHz cavities can be used to investigate high Q_0. In addition, the Project X 3-8 GeV pulsed section operates at 1.3 GHz and requires ILC-like cavities with E_{acc}~25 MV/m. The status of Fermilab 1.3 GHz infrastructure, accomplishments and plans are described.

INFRASTRUCTURE

The cavities are fundamentally of the Tesla design [6], made of high RRR niobium with an elliptical cell shape, for superconducting operation at 2K. Cavity qualification has been described in detail elsewhere [7] and includes cavity inspection, surface processing, clean assembly, and one or more cryogenic qualification tests which typically include performance diagnostics. Cavities which reach the performance requirement in vertical (bare) qualification test, typically $E_{acc}>35$ MV/m, are dressed and horizontally tested. Cavities which reach the performance specification in horizontal (dressed) qualification test, also typically $E_{acc}>35$ MV/m, are assembled into cryomodules.

The joint ANL/FNAL facility is the primary infrastructure [7] for surface processing of 1.3 GHz cavities, and includes electropolishing (EP). New infrastructure at Fermilab includes two high temperature furnaces for hydrogen degassing, see Fig.1. In addition, a centrifugal barrel polishing (CBP) machine for 1-cell and 9-cell 1.3 GHz cavities has been introduced for R&D and may be used for production cavity preparation in the future, see Fig.2. CBP may be used in place of the standard bulk electropolishing step, to reduce acid use. CBP has been demonstrated to be a useful repair technique [8], and may have other benefits as well, such as reducing cavity performance sensitivity to minor manufacturing or material defects; these studies are not yet complete. A new R&D surface processing facility [9] is now fully operational for the full suite of standard EP processing for 1-cell 1.3 GHz cavities. The R&D EP tool is shown in Fig.3.

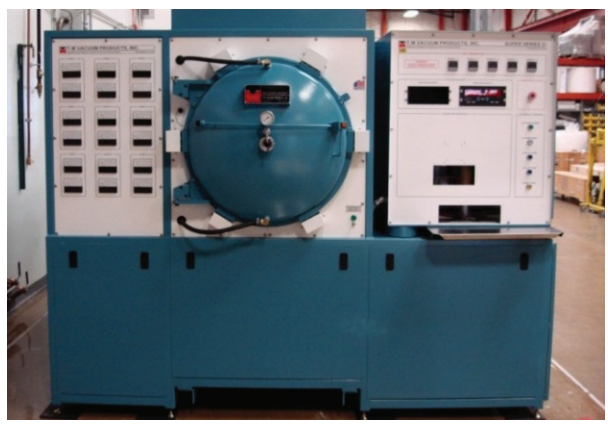

Figure 1: One of the two new vacuum furnaces.

Figure 2: Centrifugal barrel polishing machine.

*Operated by Fermi Research Alliance, LLC, under Contract DE-AC02-07CH11359 with the U.S. DOE
#ginsburg@fnal.gov

Copyright © 2012 by the respective authors — cc Creative Commons Attribution 3.0 (CC BY 3.0)

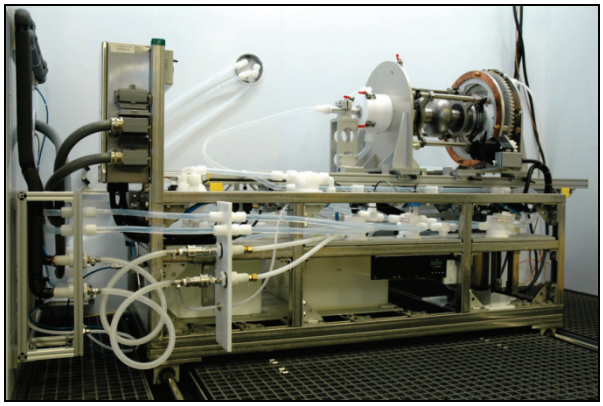

Figure 3: R&D EP tool.

ILC AND CONSIDERATIONS FOR CW

ILC R&D contributed substantially to cavity gradient performance. A worldwide effort by participating laboratories, including Fermilab, to optimize cavity processing and to develop new cavity vendors for high gradient cavities was implemented. As part of this work, a systematic analysis of cavity vertical test data was performed [10]. The data set is comprised of cavities fabricated by established vendors (ACCEL/RI, AES, MHI, Zanon), and processed by established laboratory surface processing (JLab, DESY, KEK), including electropolishing. If a cavity does not reach 35 MV/m after the initial EP processing stage, we assume it would be re-processed. Standard 2nd pass processes may include EP, HPR, or 120C bake, and are selected based on 1st pass performance at the discretion of the laboratory. There are 51 cavities in the 1st pass plot, and 35 in the 2nd pass plot. The difference in number of cavities reflects the fact that the 2nd pass may not have take place yet, or may have been done with a non-standard process. The gradient distribution of cavities which are not included in the 2nd pass yield is the same as those which are included. The ILC gradient yields, representing percentage of cavities reaching either 25 MV/m (blue points) or 35 MV/m (red points) are shown in Fig.4. ILC cavities reach 35 MV/m more than half the time after one or two EP processing cycles. For Project X, the gradient yield at 25 MV/m is of interest. In 1st pass, (69±6)% of all 51 cavities achieve >25 MV/m; and (86±13)% of 7 cavities achieve >25 MV/m considering only cavity tests taking place in 2012. In 2nd pass, (80±7)% of all 35 cavities achieve >25 MV/m; and (92±7)% of 13 cavities achieve >25 MV/m considering only cavity tests taking place in 2010-2012.

Ongoing efforts to improve cavity performance yields, either 1st pass or 2nd pass, include applying localized grinding (pioneered by KEK) to performance-limiting defects, and CBP. Many (~12) cavity repairs have been achieved through these two methods; however, at this time, cavity performance after these repairs has not been included in yield plots.

Two approaches for Q_0 optimization for Project X are being pursued at Fermilab now: venting cavities after hydrogen degassing in a nitrogen atmosphere [11], and using a hydrofluoric acid rinse as the final processing step [12]. Both approaches show promising results.

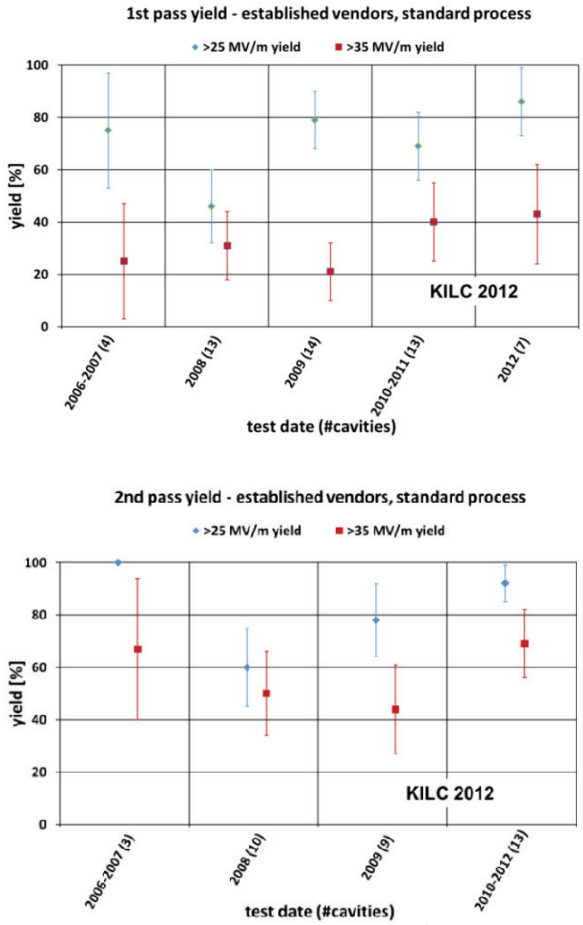

Figure 4: ILC cavity gradient yields: 1st pass (top) and 2nd pass (bottom), as a function of time. Blue points are >25 MV/m yield and red points are >35 MV/m yield.

ACCOMPLISHMENTS

Fermilab provides stewardship for 80 9-cell cavities for the ILC/Americas region. The status of these cavities is shown in Table 1. The bare cavities are processed and tested in strong collaboration with JLab, Cornell and ANL; see Fig.5 for vertical test performance.

Table 1: 9-cell Cavity Status August 31, 2012

ordered	80
received	69
processed	47
vertically tested	47
dressed	22
horizontally tested	19
CM2 installed	8

Copyright © 2012 by the respective authors — cc Creative Commons Attribution 3.0 (CC BY 3.0)

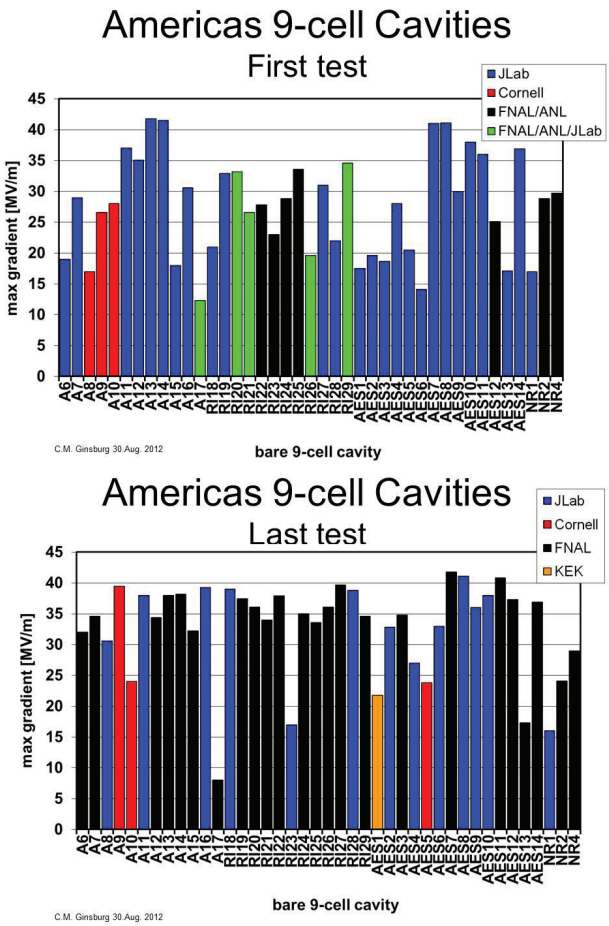

Figure 5: Gradient performance of all Americas cavities in first test (top) and last test (bottom). The test location is designated by the histogram bar color. An overall improvement is seen after additional process and test.

Two 1.3 GHz cryomodules have been assembled at Fermilab: CM1 and CM2. CM1 was built from a DESY "kit" containing parts from DESY and INFN, including surface processed, dressed, tested cavities. The magnet position is occupied by a "dummy" magnet. CM1 has been tested cold with excellent results [13]. CM2 is an 8-cavity string with a quadrupole package. CM2 is comprised of cavities which were surface processed and reached 35 MV/m in vertical test at JLab. These cavities were dressed and horizontally tested at Fermilab, then assembled into CM2. The summary of final cavity performance before CM2 assembly [14] is shown in Fig.6. CM2 will be tested at NML first without beam and then with beam within a year. All components are available for the assembly of CM3, which is expected to proceed within about a year.

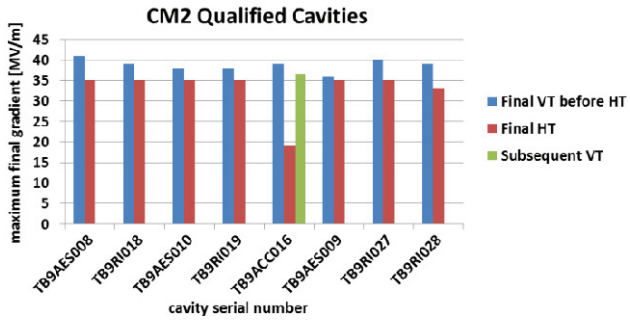

Figure 6: Gradient performance of CM2 cavities in vertical (blue) and horizontal tests (red). In one case, a subsequent dressed-cavity vertical test was performed after failed horizontal test.

ACKNOWLEDGMENTS

Material and information for this paper was provided by M. P. Kelly (ANL), R. Geng (JLab), A. Yamamoto (KEK), T. Arkan, M.S. Champion, L.D. Cooley, C. Cooper, E. Harms, A. Hocker, T. Khabiboulline, J.P. Ozelis, T. Peterson, A. Romanenko, A. Rowe, D. Sergatskov, A. Sukhanov, and V. Yakovlev (FNAL). I am grateful for their assistance. I thank my past and present colleagues in the ILC database group for providing their respective laboratories' data which were used in Figs.4-6: S. Aderhold (DESY), Z. Conway, F. Furuta (Cornell), R. Geng (JLab), Y. Yamamoto (KEK), and thank the DESY/ILC database group for their technical support. I thank the Fermilab technical staff for their hard work on cavities and cryomodules.

REFERENCES

[1] ILC Reference Design Report http://www.linearcollider.org/about/Publications/Reference-Design-Report
[2] A. Yamamoto, LINAC12, Tel-Aviv, TH3A01.
[3] Project X Reference Design Report, http://projectx-docdb.fnal.gov/cgi-bin/ShowDocument?docid=776
[4] S. Henderson, LINAC12, Tel-Aviv, TU1A01.
[5] V. Yakovlev and C.M. Ginsburg, LINAC12, Tel-Aviv, MO1A03.
[6] B. Aune et al., "The superconducting TESLA cavities," Phys. Rev. STAB **3**,092001 (2000).
[7] C.M. Ginsburg et al., LINAC10, Victoria, BC, Canada, 2010, THP026, and references therein.
[8] C. Cooper, SRF11, Chicago, WEIOA02, and references therein.
[9] C. Cooper et al., SRF2011, Chicago, TUPO025.
[10] C.M. Ginsburg et al., KILC12, Daegu, S. Korea, http://ilcagenda.linearcollider.org/contributionDisplay.py?contribId=85&sessionId=36&confId=5414
[11] A.Grassellino et al., LINAC12, Tel-Aviv, MOPB078.
[12] A. Romanenko, TTC Meeting, Beijing, 2011.
[13] E.R. Harms et al., LINAC12, Tel-Aviv, MOPB054.
[14] A. Hocker et al., IPAC12, New Orleans, WEPPC049.

Copyright © 2012 by the respective authors — cc Creative Commons Attribution 3.0 (CC BY 3.0)

NON-DESTRUCTIVE INSPECTIONS FOR SC CAVITIES

Y. Iwashita, Y. Fuwa, M. Hashida, K. Otani, S. Sakabe, S. Tokita, H. Tongu,
Kyoto University, Uji, Kyoto, JAPAN
H. Hayano, K. Watanabe, Y. Yamamoto, KEK, Ibaraki, JAPAN

Abstract

Starting from the high-resolution camera for inspection of the cavity inner surface – so-called Kyoto Camera, high resolution T-map, X-map and eddy current scanner have been developed. R&D for radiography techniques is also going on to detect small voids inside the Nb EBW seam, where the target resolution is 0.1 mm. Some radiography tests with X-rays induced from an ultra short pulse intense laser were carried out. The local treatment technique on the found defects is also realized by the Micro-Grinder.

INTRODUCTION

Non-destructive Inspections play important roles in improving yield on production of high performance SC Cavities. Starting from the high-resolution camera for inspection of the cavity inner surface [1], high-resolution T-map, X-map and eddy current scanner [2,3,4,5,6] have been developed. We are also investigating radiography to detect small voids inside the Nb EBW seam, where the target resolution is 0.1 mm. We are carrying out radiography tests with X-rays induced by irradiations of an ultra short pulse intense laser on a target metal sheet. Defects found by the inspection technique can be locally treated by the Micro-Grinder.

CAVITY CAMERA UPDATE

In order to inspect the SPL cavity at CERN, whose frequency is about a half of ILC cavity and the diameter is about twice larger, the illumination system has been enhanced to illuminate the wider surface area (see Fig. 1). Although the iris diameter is about twice larger than that of ILC's, the bore diameter at the flange position is limited (just below ø80mm). This limits the camera cylinder diameter is ø70mm. Fig. 2 shows the modification on the illumination system to illuminate the wider area with enough strength. While the former system used two LED's for each strip, the new system uses 14 LED chips on a line and two lines consist one strip. Thus 28 LED chips are used for a strip. Furthermore, the LED chip has three LED's in a package. This illumination system should provide enough light for the wider cavity surface area. Because of the larger cavity size, the working distance is longer than former model and a bigger lens system is adopted. Fig. 3 shows the overview of this system. The illumination plate on the cylinder is shown in Fig. 4. The camera cylinder can be rotated to see the annular area in a cavity without movement of the cavity, while the cavity table can rotate the cavity if it does not wear its He jacket around. The table has a function to move the cavity in its axial direction.

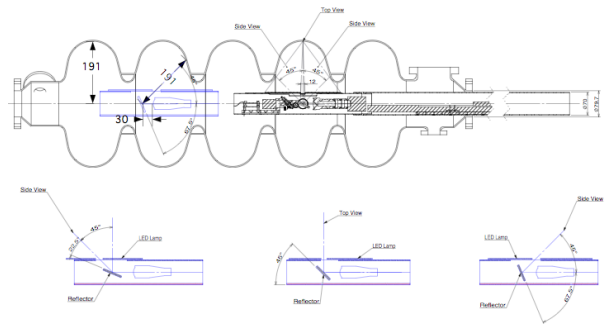

Figure 1: CavCam3 in SPL cavity.

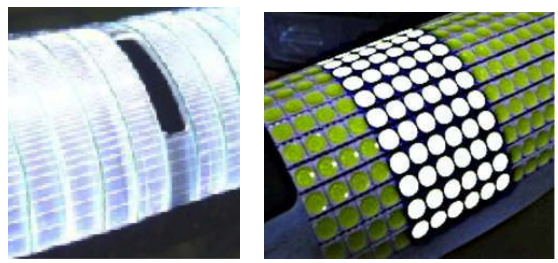

Figure 2: Enhanced illumination for wider surface area (Armadillo Illumination). 28 LED chips (right) instead of 2 LED's per strip (left) are installed.

Figure 3: Latest CavCam-3 for SPL cavity at CERN.

Figure 4: All the LED's are lighten. A diffusing panel will be install on the LED's to form the light strip. 14 chips/line x 2 lines/strip x 10 strips/side x 2 sides = 560 chips are used.

Copyright © 2012 by the respective authors — cc Creative Commons Attribution 3.0 (CC BY 3.0)

HIGH DENSITY T-MAP & X-MAP

The high density Temperature mapping system (T-map) and X-ray mapping system are under development. These systems utilize multiplexing technique to reduce the number of lines from the sensors to the measurement circuits. The temperature sensors are put on a Nb cavity surface during the vertical test to detect the temperature rise from the quench phenomena due to a defect on the inner surface, if any. Since one temperature sensor / cm^2 is assumed for the surface density, 1024 sensors will be installed on a cell and about nine thousands of sensors will be need to be connected to the measurement circuit. The number of lines needed for these connections is reduced by multiplexing the analog signals in the cryogenic area. The reduced lines include the three power supply lines (0V, ±5V), one clock line, one reset line, and two signal lines for each type of system (t-map and X-map) as shown in Fig. 5. T-sensors are installed on the inner side and X-sensors are located on the other side. T-sensors contact on the cavity surface (see Fig. 6). As shown in Fig. 7 the leaves can be instantly attached on a cell, which helps to reduce the installation time for a vertical test.

A dedicated X-map system for installation under the stiffener ring is also developed (see Fig. 8). Only X-sensors are installed on the PCB, which can slide into the space under the stiffener ring as shown in Fig. 9.

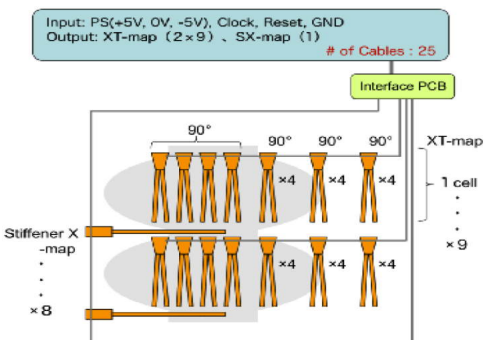

Figure 5: The inter-connection for the XT-map system.

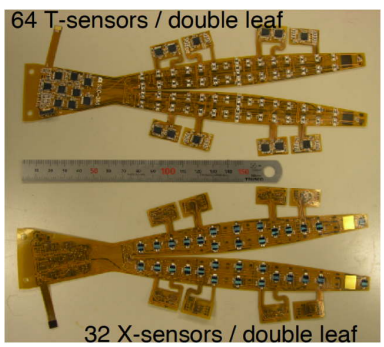

Figure 6: Leaf shaped flexible PCB.

HIGH RESOLUTION EDDY CURRENT SCAN

A Nb sheet before the press to form the cup will be inspected by a Eddy current scan [7]. Using a multi-frequency Eddy current probing system, a small void just under the surface, which may appear after surface treatments such as electropolishing (EP), would be detected. The depth information would be obtained from the three different frequency data simultaneously acquired during the measurement. The detected hole size is currently ø100µm x 50µm depth (see Fig. 10).

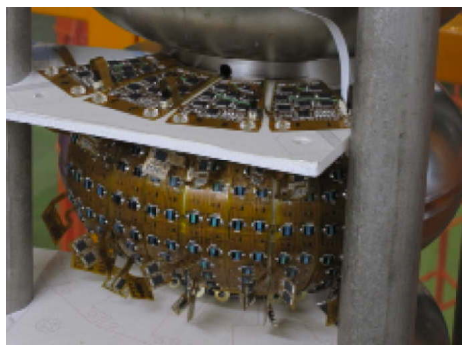

Figure 7: Installed XT-map leaves on a cell.

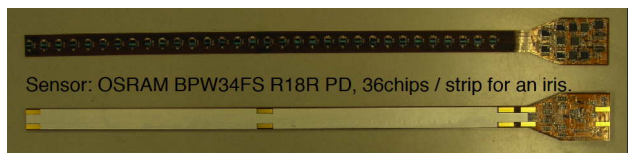

Figure 8: Stiffener X-map.

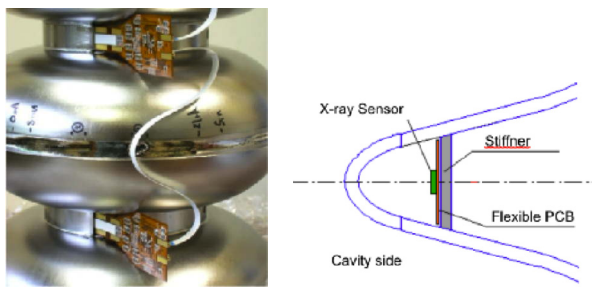

Figure 9: Installed stiffener X-map ribbons. The ribbons go under the stiffer ring.

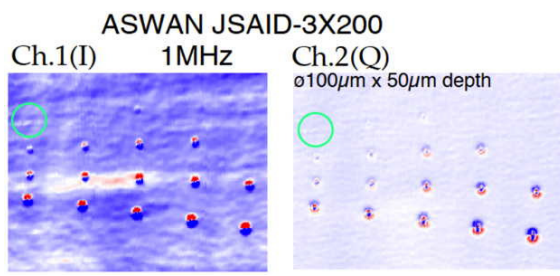

Figure 10: The high resolution eddy current scanner can detect the drilled holes on the Nb sheet down to ø100µm x 50 µm depth.

RADIOGRAPHY EFFORT

In order to inspect the EBW seam especially for possibly buried defects under the surface, various radiography techniques have been investigated such as

Copyright © 2012 by the respective authors — cc Creative Commons Attribution 3.0 (CC BY 3.0)

X-ray CT, and neutron CT. Since Nb has larger atomic number, high energy X-rays tend to be preferred for a better transmission. The contrast, however, becomes worse for high energy X-rays. Although the phase contrast techniques should have better contrast even in this case, it is not a handy way. After some trials, laser induced X-ray radiograph is under investigation (see Fig. 11). Fig. 12 shows the obtained radiography images for targets of Zr and Ag, where Zr is supposed to be better because of the X-ray energy just below the K absorption edge of the Nb. Further study is needed for better visibility and practical applications.

LOCAL REPAIR TECHNIQUE

Using the inspection devices, defects on the surfaces can be identified and analyzed. For those defects judged as harmful, the local repair technique should be applied. The micro-grinder can be inserted into the cavity, while the grinding head is retracted (see Fig. 13)[8]. After its positioning, some amount of water is applied to the area and the head with abrasives can start to grind. The grinding time can be limited by a timer up to 99 minutes. Additional EP and following processes are applied to the treated cavity to bring the cavity back to the line. Several cavities have been already repaired and show satisfactory results (see Fig. 14).

REFERENCES

[1] Y. Iwashita, Y. Tajima, H. Hayano, Development of High Resolution Camera for Observations of Superconducting Cavities, Phys. Rev. ST Accel. Beams, 11, [093501-1]-[093501-6], 2008

[2] A. Brinkmann, W.Singer, Nondestructive Testing of Niobium Sheets for Srf Cavities Using Eddy-Current and Squid Flaw Detection, Proc. LINAC08, Victoria, BC, Canada, pp.800-801

[3] L. Cooley, C. Antoine, G. Wu, D. Sergatskov, H. Jiang, R. Schuessler, O. Frianeza, Fermilab QA and QC activities, FNAL slides for TTC meeting Jan 2008

[4] Balle, Ch., Casas-Cubillos, J. et al, Influence of Thermal Cycling on Cryogenics Thermometers in Advances in Cryogenic Engineering 45B, Plenum, New York, 1999, pp. 1817.

[5] H. Tongu, et al., Multipoint T-maps for Vertical Test of the Superconducting Accelerator Tubes, Proc. of the 6th Annual Meeting of Particle Accelerator Society of Japan, (2009) 409-411.

[6] A. Canabal, et al., Development of a Temperature Mapping System for 1.3-Ghz 9-Cell Srf Cavities, Proc. PAC07 2406 - 2408 (2007).

[7] Updates on R&D of Non-destructive Inspection Systems for SRF Cavities, Y. Iwashita, H. Tongu, H. Hayano, T. Saeki, K. Watanabe, to be appeared as Proc. of SRF11, July 2011, Chicago.

[8] K. Watanabe, H. Hayano, E. Kako, S. Noguchi, T. Shishido, Y. Yamamoto, Y. Iwashita, Repair Techniques of Superconducting Cavity for Improvement Cavity Performance at KEK-STF, Proc. IPAC10, Kyoto, 2010

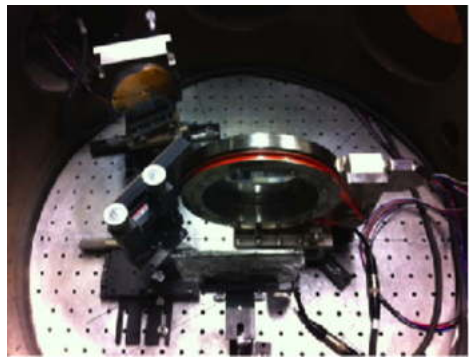

Figure 11: Layout for the laser induced X-ray radiography experiment. Various target materials can be irradiated by the laser to generate X-rays.

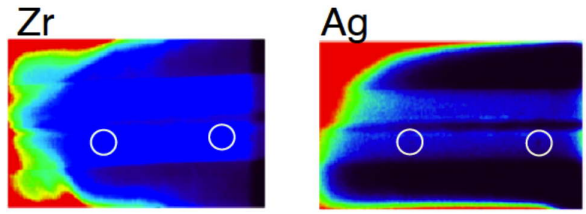

Figure 12: Obtained radiography images for targets of Zr and Ag. Both target materials give better visibility for the defects (sputter balls on the surface).

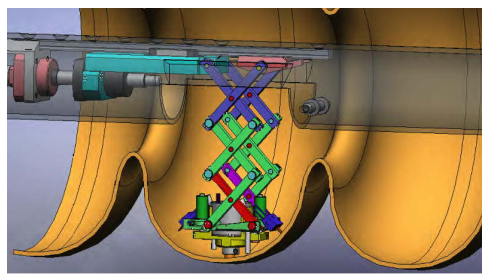

Figure 13: The grinding head assembly that has a tiny monitoring camera protrudes by a motor control towards the area to be treated.

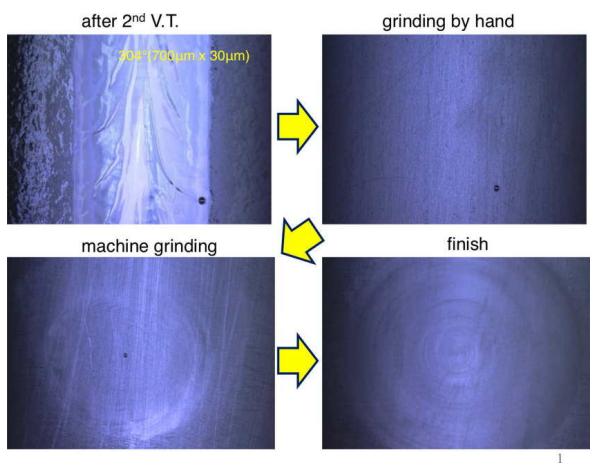

Figure 14: The progresses on the local grinding effect. The defect detected by the optical inspection was removed by the treatment.

Copyright © 2012 by the respective authors — cc Creative Commons Attribution 3.0 (CC BY 3.0)

TEST RESULTS OF TESLA-STYLE CRYOMODULES AT FERMILAB *

E. Harms#, K. Carlson, B. Chase, D. Crawford, E. Cullerton, D. Edstrom, A. Hocker, M. Kucera, J. Leibfritz, O. Nezhevenko, D. Nicklaus, Y. Pischalnikov, P. Prieto, J. Reid, W. Schappert, P. Varghese, Fermilab, Batavia, IL 60510 USA

Abstract

Commissioning and operation of the first Tesla-style Cryomodule (CM-1) at Fermilab was concluded in recent months. A second Tesla Type III+ module, RFCA002, will be replacing it. CM-1 is the first 8-cavity ILC style cryomodule to be built at Fermilab and also the first accelerating cryomodule of the Advanced Superconducting Test Accelerator (ASTA). We report on the operating results of both of these cryomodules.

INTRODUCTION

An electron Linac based on Superconducting RF technology has been proposed and is under construction at Fermilab. This Advanced Superconducting Test Accelerator (ASTA) has as its main components a Cs-Te 1-1/2 cell Photoinjector gun, two Capture cavities, and Tesla–style SRF cryomodules as well as low (40 MeV) and high energy user beam lines. This facility has been described previously [1]. It currently serves as the only test bed for multi-cavity cryomodules at Fermilab until a dedicated facility, the Cryomodule Test Facility (CMTF), now under construction is completed.

The setup for testing cryomodules at ASTA contains all of the necessary infrastructure including:

- 5MW 1.3 GHz klystron capable of pulsed operation at 10 Hz
- Cryogenics plant capable of providing 120 Watts of refrigeration at 2 Kelvin
- Interlock/protection systems
- Low Level RF (Feedforward & Feedback) system
- Vacuum system
- Controls integrated to Fermilab's Accelerator Controls system, ACNET.

CRYOMODULE 1

CM-1 was the first Tesla Type III Cryomodule to be placed into operation in the United States and the first multi-cavity cryomodule of any type to become operational at Fermilab. It was provided to Fermilab as a 'kit' from DESY in exchange for a 4-cavity 3.9 GHz module, ACC39, which was designed and assembled at Fermilab and is now in operation at DESY's FLASH facility. Table 1 highlights the major steps in bringing CM-1 into operation and completing the test program.

The test plan for CM-1 has been described previously as has been the performance characteristics of individual cavities [2]. Typical operating conditions were:

- 5 Hz repetition rate
- 700 μs fill time
- 500 μs flattop
- 2 Kelvin / 23.4 Torr temperature
- 3.9 MW peak Klystron power.

Table 1: CM-1 Commissioning Milestones

Milestone	Date
Cryomodule moved into final position and aligned	22 January 2010
5 MW RF/Klystron commissioning	June - July 2010
Warm coupler conditioning - one cavity at a time (4 - 14 days/cavity)	August – October 2010
Cool down from room temperature to 4 then 2 Kelvin	17 – 22 November 2010
Individual Cavity cold conditioning and evaluation	December 2010 – June 2011
Installation of Waveguide Distribution system and Water System upgrade	13 June - 5 July 2011
First powering of the entire module	6 July 2011
Long Pulse (9ms) tests	December 2011
Thermal cycling and lN_2 leak repair	January - February 2012
Cease operation/Removal	March 2012

Figure 2 provides a comparison of peak cavity gradients during qualification tests at DESY as well as during CM-1 full module operation while Table 2 summarizes individual cavity performance in CM-1. On average, the cavities' peak gradients in CM-1 are 85% of that measured previously.

Module Evaluation

The previous report [2] on CM-1 indicated some outstanding measurements to be performed including

- Demonstration of Lorentz Force Detuning Compensation on the entire module,
- Additional processing to attempt to improve the performance of deficient cavities,

*Operated by Fermi Research Alliance, LLC under Contract No. DE-AC02-07CH11359 with the United States Department of Energy.
#Harms@fnal.gov

Copyright © 2012 by the respective authors — cc Creative Commons Attribution 3.0 (CC BY 3.0)

- Possible thermal cycling to improve performance/uncover additional field emitters,
- Readjustment of VTO's to better match cavity pair outputs.

In large measure this was all carried out as was a Dynamic Heat Load measurement to determine the overall cryomodule Q_0 vs E.

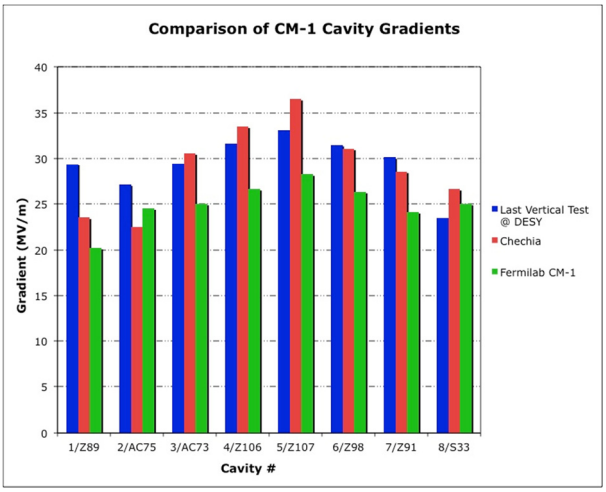

Figure 1: Comparison of cavity peak gradients – DESY single cavity vertical (blue), horizontal/Chechia (red), and the complete CM-1 at Fermilab (green).

Lorentz Force Detuning Compensation

Adaptive Lorentz Force Detuning Compensation (LFDC) measurements made on single cavities are documented elsewhere [3] prior to when all cavities were simultaneously powered and corrected. In this state gradients in the cavities ranged between approximately 8 and 27 MV/m. Without compensation, the highest gradient cavities would detune by up to 400 Hz during the flattop. With adaptive compensation on the detuning was negligible in all the cavities except for Cavity 1 which detuned by approximately 10 Hz during the RF pulse. Even for the cavities operating at the highest gradients, Lorentz force detuning could be compensated using relatively modest voltages to drive the piezoelectric tuners, approximately ±20V, and the waveforms did not exhibit fast transients that could potentially damage them.

Low Level RF

Development work on the Low Level RF system (LLRF) was a constant throughout the running period. By the end of the run it was possible to control the RF amplitude and phase over 50 pulses to a RMS magnitude error of $2.5X10^{-4}$% and RMS phase error of 0.005° as measured in-loop.

9 Millisecond Test

Once the cryomodule was well characterized a 'long pulse' study in support of an R&D program for Fermilab's proposed Project-X SRF Linac was performed. This proof-of-principle study entailed operating the two best-performing cavities (5 & 6) at a pulse length of up to 9 milliseconds and determining the LLRF and resonance control capabilities at various input powers and Q_L values. Operating parameters in this mode were:

- RF power limitations: 80 kW; 100 kW, 120 kW per two cavities,
- Use of the 'CC2' klystron capable of producing long pulses,
- External Q_L: 3 X 10^6; 6 X 10^6; 1 X 10^7,
- Gradient: 15MV/m; 20 MV/m; 25 MV/m,
- Pulse Width: up to 9 ms.

Table 2: Individual Cavity Performance Characteristics

Cavity	Peak E_{acc} (MV/m)	Estimated maximum Q_0 (E09)	Limitation/ Comments
1/Z89	20.2	11	'Soft' quench
2/AC75	22.5	12	Quench
3/AC73	23.2	0.43	'Soft' quench
4/Z106	24*	2.3	*RF-limited
5/Z107	28.2	39	Quench
6/Z98	24.5	5.1	Quench
7/Z91	22.3	4.7	'Soft' quench
8/S33	25	18	Tuner motor malfunction

This study proved to be a good first pass test. LFDC at the nominal parameters, Q_L= 1 X 10^7 and 25 MV/m, was demonstrated. LLRF feedback worked with phase stability good to ± 4°. The total range of detuning was found to be of order ±10 Hz peak-to-peak with comparable contributions from residual LFD and microphonics. The measured microphonics level was in range 2-4 Hz, similar to what was measured for short (1ms) pulses. Areas requiring further work were uncovered. Input power limitation for the low Q_L case (~3 X 10^6) limited the peak gradients to less than 20 MV/m. The system also proved to be less stable under dynamic conditions. Nearly constant attention was required under these conditions to maintain stable operation especially when adjusting the power.

Thermal Cycling

Additional processing of lower performing cavities did not noticeably alter their performance. The module was warmed up to room temperature and cooled also with no significant change in performance. During cooldown a

Copyright © 2012 by the respective authors — cc Creative Commons Attribution 3.0 (CC BY 3.0)

leak on the liquid nitrogen circuit appeared. In situ investigation revealed a failed feed-through on an in-line temperature sensor which was subsequently capped off and replaced with an externally mounted one. This experience proved to be valuable in both making diagnosis and repair without removing the cryomodule.

Summary of CM-1

Although issues with a tuner motor prevented all eight cavities from operating on resonance together and a subset of cavities exhibited sub-par performance, CM-1 did operate for an extended time stably and near the peak achievable gradients with both LLRF feedback enabled and LFDC. Valuable experience was gained and a larger cadre of staff was exposed to this type of operation.

As appropriate, components such as low performing cavities, tuner motors, and the like will be scrutinized and subjected to further testing once CM-1 is disassembled.

RFCA002

The second cryomodule planned for ASTA was delivered in March 2012 and installation work begun immediately. This device known as RFCA002 or CM-2 is also a Tesla Type III+ device. All cavities were fabricated by industry. Vertical testing was carried out at both Jefferson Lab and Fermilab and horizontal tests of the dressed cavities at Fermilab's Horizontal Test Stand. All facets of testing and assembly have been under the supervision of Fermilab staff. Since CM-2 is being installed in place of CM-1 the necessary infrastructure is already in place.

Expectations for the cryomodule are high as individual cavity testing results for these cavities met or exceeded the ILC design specification of 31.5 MV/m. These results are described previously [4]. Figure 3 summarizes the performance.

A final leak check of the 2-phase helium circuit gave indications of a leak, so the module has been returned to its assembly building, partially disassembled, and attempts to identify the source of the leak are in progress. The current expectation is for the cryomodule to be returned to ASTA late in 2012 with full warm and cold checkout completed in the first half of 2013.

LESSONS LEARNED

Operating experience with CM-1 in recent months is proving valuable in anticipation of bringing CM-2 and other cryomodules destined for this facility on-line in the near future as well as in preparation for possible future SRF facilities such as Project-X. Already the suite of instrumentation has been reviewed and modified for RFCA002 based on CM-1 experience. The sequence of commissioning steps has been reviewed and modified in light of the initial operating experience and will no doubt lead to faster and more efficient start-up of future modules.

Tuner motor issues with CM-1 led to a review of the motor controller circuitry, which led to modifications realizing a more robust and fail-safe system.

The Controls user interface system is also under regular updating as more experience is gained.

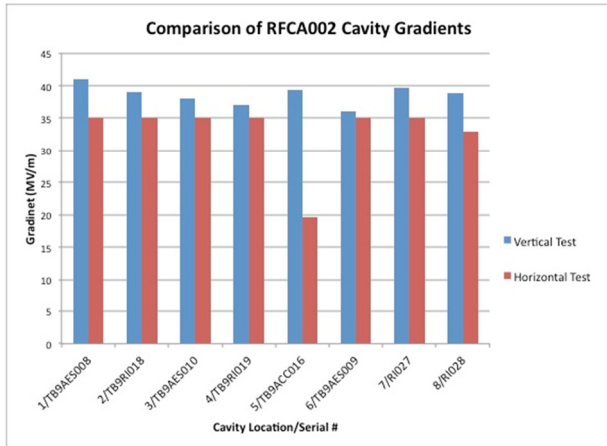

Figure 2: CM-2 peak cavity gradients as measured vertically (blue) and at Fermilab's HTS (red).

SUMMARY

Testing of the first Tesla-style SRF module at Fermilab has been successfully completed and preparation for installing and bringing a second module, capable of meeting ILC specifications, is well underway. With these achievements as well as operation of other SRF facilities, Fermilab is demonstrating its maturity in this field.

ACKNOWLEDGEMENTS

The achievements to date would not have been possible without the hard work and effort of many people in Fermilab's Technical and Accelerator Divisions. Shared expertise and contributions of hardware etc. from collaborators from many institutions around the world especially Argonne National Laboratory, DESY, INFN/LASA, Milano, Jefferson Lab, and SLAC, are noted and appreciated.

REFERENCES

[1] J. Leibfritz et al., 'Status and Plans for a Superconducting RF Accelerator Test Facility at Fermilab," IPAC2012, New Orleans, May 2012, MOOAC02.

[2] E.R. Harms et al., "RF Test Results from Cryomodule 1 at the Fermilab SRF Test Beam Facility," SRF'11, Chicago, July 2011, MOPO013.

[3] Y. Pischalnikov et al., "Lorentz Force Compensation for Long Pulses in SRF Cavities," IPAC2012, New Orleans, May 2012, THPPR012.

[4] A. Hocker et al., "Individual RF Test Results of the Cavities Used in the First US-built ILC-type Cryomodule," IPAC2012, New Orleans, WEPPC049.

Copyright © 2012 by the respective authors — cc Creative Commons Attribution 3.0 (CC BY 3.0)

DEVELOPMENT OF SUPERCONDUCTING RADIO-FREQUENCY DEFLECTING MODE CAVITIES AND ASSOCIATED WAVEGUIDE DAMPERS FOR THE APS UPGRADE SHORT PULSE X-RAY PROJECT*

J. Holzbauer†, A. Nassiri, G. Waldschmidt, G. Wu
Argonne National Laboratory, Argonne, IL 60439, U.S.A.

Abstract

The Advanced Photon Source Upgrade (APS-U) is a Department of Energy (DoE) funded project to increase the available x-ray beam brightness and add capability to enhance time-resolved experiments on few-ps-scale at APS. A centerpiece of the upgrade is the generation of short pulse x-rays (SPXs) for pump-probe time-resolved capability using SRF deflecting cavities [1]. The SPX project is designed to produce 1-2ps x-ray pulses for some users compared to the standard 100ps pulses currently produced. SPX calls for using superconducting rf (SRF) deflecting cavities to give the electrons a correlation between longitudinal position in the bunch and vertical momentum [2]. The light produced by this bunch can be passed through a slit to produce a pulse of light much shorter than the bunch length at reduced flux. The ongoing work of designing these cavities and associated technologies will be presented. This includes the design and prototyping of higher- (HOM) and lower-order mode (LOM) couplers and dampers as well as the fundamental power coupler (FPC). This work will be given in the context of SPX0, a demonstration cryomodule with two deflecting cavities to be installed in APS in early 2014.

INTRODUCTION

The SPX project calls for the use of an RF deflecting-mode cavity to chirp electron bunches, giving the electrons a correlation between their longitudinal position in the bunch and their vertical momentum. Synchrotron light produced from this bunch can then be passed through a physical slit to create a shorter light pulse at the proportional sacrifice of total flux. This scheme was first proposed by Zholents [1]; the scheme can be seen in Figure 1.

A significant amount of design work has gone into the RF cavities required for this project, details of which can be found in [2, 3, 4, 5, 6, 7]. This cavity application has many specific challenges including the need to heavily damp all non-operational modes to preserve beam quality for other APS users.

CAVITY DESIGN

The current design is a squashed elliptical dipole-mode cavity with a Y-shaped end group and an on-cell damping

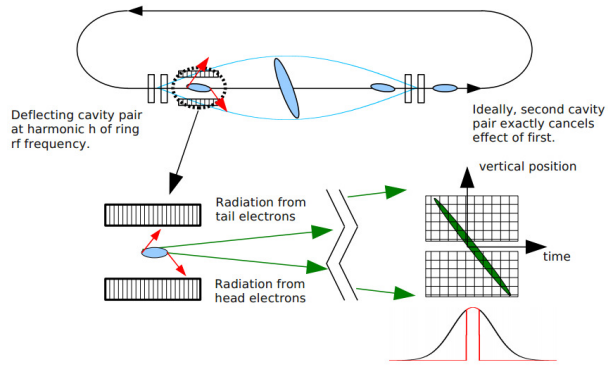

Figure 1: Schematic of Zholent's short pulse x-ray generation scheme. Image credit to [3].

port which can all be seen in Figure 2. Two of the waveguides from the Y end group will be used for damping of higher-order modes (HOMs) while the third will be primarily used as the forward power coupler. The on-cell damper is used primarily to damp the fundamental mode, called the lower-order mode (LOM). A list of the cavity parameters can be seen in Table 1.

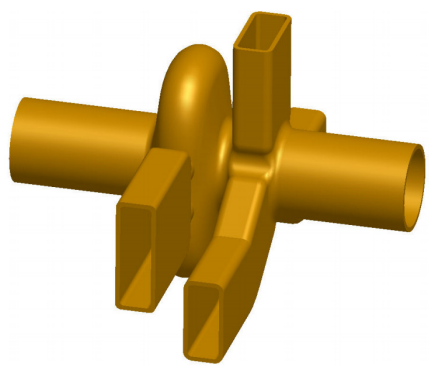

Figure 2: Schematic of a deflecting mode cavity for SPX. The LOM waveguide can be seen on-cell with the Y-end group (HOM dampers and FPC) to the right. Image credit to [3].

At this point, it is expected to use a BCP etching during cavity processing. Given the cavity parameters and this processing technique, 120 mT is the maximum expected reliable peak magnetic field. Given this and the requirement that each deflecting section have a total of 2 MV of

* Work supported by the U.S. Department of Energy, Office of Science, under Contract No. DE-AC02-06CH11357
† jholzbauer@aps.anl.gov

Copyright © 2012 by the respective authors — cc Creative Commons Attribution 3.0 (CC BY 3.0)

Table 1: Electromagnetic figures of merit

Parameter	Value
Frequency	2815 MHz
Q_0	10^9
Deflecting Voltage (V_t)	0.5 MV
Peak Surface Electric Field	41 MV/m
Peak Surface Magnetic Field	100 mT
Stored Energy	0.38 J
P_{loss} $Q_0 = 10^9$	7 W
(R/Q)'	18.6 Ω
Operational Temperature	2K

deflecting voltage to achieve 2-ps x-ray pulses [3], each cavity will be run at 0.5 MV deflecting voltage or 100 mT. In order to increase the operational margin, the possibility of electropolishing these cavities is being investigated.

HIGHER-ORDER MODE DAMPING

Because of the tight beam requirements, strong damping of non-operating modes was a focus of the overall cavity design. The squashed elliptical cavity geometry is meant to break the degeneracy of the dipole modes, increasing the frequency of the undesired dipole polarization as was done at KEK in the design of a similar deflecting mode cavity [8]. Significant work has been put into modeling of the cavities' broadband impedances [4], as well as the design of the HOM waveguides and dampers [7]. While the HOM waveguide design has been investigated in concept [9], their detailed design and packaging had not been considered until recently.

HOM Transitional Waveguide

Design of the SPX prototype cryomodule (SPX0) is well underway at JLab. Because of the broadband HOM damping requirements, it was decided to not use a window for the HOM dampers. This meant that all components of the HOM dampers would have to be assembled on the cold mass and had to fit inside the space frame for assembly. This is further complicated by the attachment of the tuner to the cavity very near to one of the HOM waveguide ports, making the HOM transitional waveguide (the waveguide running from the cavity to the damper itself) a very complex shape. This shape can be seen in Figures 3 and 4.

Despite these logistical requirements, the broadband transmission of this waveguide must not be compromised. The sizing of the HOM waveguide leading out of the cavity was chosen to have it's cutoff frequency between the operational frequency (2.815 GHz) and the first higher-order mode (estimated at 2.94 GHz). The waveguide must connect this custom sized waveguide to the HOM dampers which are based on WG340 waveguide. The placement and geometry of this taper was carefully considered to both give adequate attenuation of the operational mode and decent broadband transmission of HOM power.

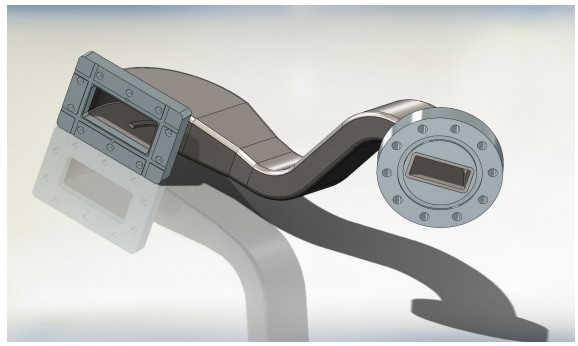

Figure 3: HOM Transitional Waveguide. Flange on the left connects to the cavity while the flange on the left connects to the damper assembly.

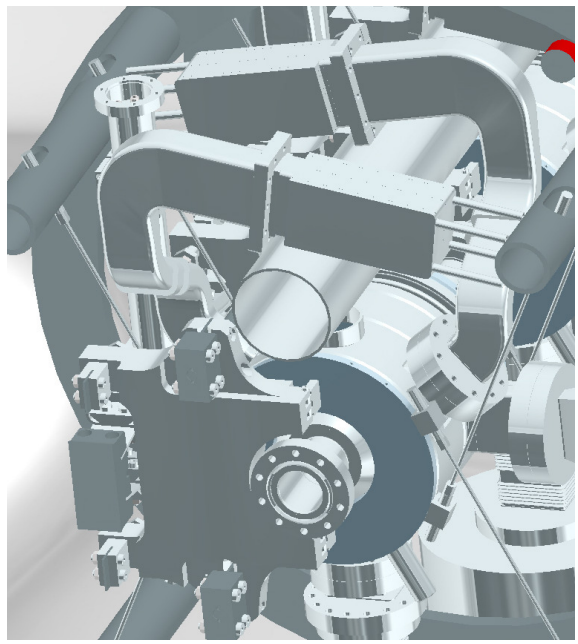

Figure 4: Section view of the SPX0 cryomodule space-frame mock-up. Cavity in helium vessel can be seen at the bottom of the image with tuner attached on the right side of the vessel. The HOM transitional waveguides and dampers can be seen crossing at the top of the image.

Given the space available, it was not possible to make the taper gradual enough to provide adequate broadband transmission because the first HOM (2.94 GHz) was still relatively close to cutoff. A ridge was added to this taper to improve transmission through the transition. The ridge was run through the taper on the wide wall and extended both toward the cavity into the S-Bend section and away from the cavity into the final, large radius bend. While this ridge improved transmission at 2.94 GHz, it also reduced transmission at some higher frequencies (3.0 GHz and 3.2 GHz) due to reflections off of the beginning of the ridge. The length of these ridge extensions was optimized to give the best broadband performance, the results of which can be see in Figure 5. The length of the ridge extension into

Copyright © 2012 by the respective authors — cc Creative Commons Attribution 3.0 (CC BY 3.0)

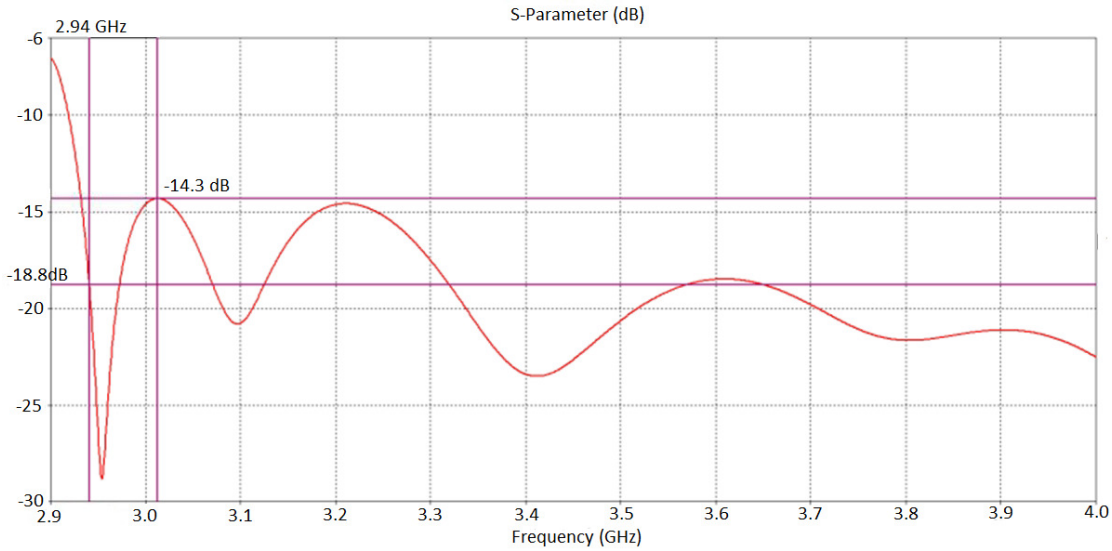

Figure 5: S11 parameter for the HOM Transitional Waveguide with optimized ridge. Reflection at the first HOM (2.94 GHz) is better than -18dB while the additional reflection cause by the ridge at 3.0 and 3.2 GHz is kept better than -14dB.

the S-Bend had the largest effect on performance. Longer ridges improved transmission at the first HOM frequency (2.94 GHz) but reduced performance at the higher frequencies. Without a ridge, S11 at 2.94 GHz was roughly -7dB, an unacceptably high reflection. Unfortunately, any reasonable ridge created the reflection at the higher frequencies which cannot be completely suppressed.

It is desired to keep the evanscant power from the operational mode reaching the HOM damper to below 10 W at full field to reduce total load on the damper. Simulations indicate that this traveling wave power should be 4.5 W, an acceptable number.

Waveguide Fabrication

When fabricated, the waveguide must be both mechancially robust and an adequate thermal barrier to keep the 2K heat load low. The HOM damper is water-cooled at room temperature outside the thermal shield and separated from the HOM transitional waveguide by a bellows, providing thermal resistance. The damper-end flange of this waveguide is expected to be strapped to the 80K cooling circuit. With a 1/8" wall of stainless steel and 10 microns of copper plating to improve RF performance, it is expected that this waveguide will contribute about 1.4 W (dynamic) to the 2 K heat load. Most of this comes from the evanescent fields in the beginning of the waveguide. Several fabrication methods are being considered for this complex geometry including fabrication from stainless steel sheet in parts, forming, and solid casting.

CONCLUSIONS

A credible design has been advanced for the HOM transitional waveguide. Prototyping is expected to begin in the coming months to validate the design and chosen fabrication process. SPX0 will provide an excellent test bed for this design and its interface with the cavity and HOM dampers. Results from this testing will be used to improved this design if necessary for the final SPX cryomodules.

REFERENCES

[1] A. Zholents et al., NIM A 425, 385 (1999).

[2] A. Nassiri et al., "Status of the Short-Pulse X-Ray Project at the Advanced Photon Source, IPAC 2012, New Orleans, LA, May 2012.

[3] Advanced Photon Source Upgrade Project - Conceptual Design Report, May 2011, http://www.aps.anl.gov/Upgrade/Documents/CDR/.

[4] H. Wang et. al., "Design, Prototype and Measurement of a Single-Cell Deflecting Cavity for the Advanced Photon Source", presented at the 2009 Particle Accelerator Conference, Vancouver, BC, Canada, May 2009, WE5PFP059.

[5] H. Wang et. al., "Crab Cavity and Cryomodule Prototype Development for the Advanced Photon Source", presented at the 2011 Particle Accelerator Conference, New York, NY, USA, March 2011, WEOCS7.

[6] G. Waldschmidt et. al., "Status of RF Deflecting Cavity Design for the Generation of Short X-Ray Pulses in the Advanced Photon Source Storage Ring", presented at the European Particle Accelerator Conference, Edinburgh, Scotland, June 2006, THPLS076.

[7] G. Waldschmidt et. al., "Superconducting Cavity Design for Short-Pulse X-Rays at the Advanced Photon Source", presented at the 2011 Particle Accelerator Conference, New York, NY, USA, March 2011, THP212.

[8] K. Hosoyama et. al., "Crab Cavity Development", presented at the 2005 Superconducting RF Workshop, Ithaca, NY, USA, June 2005, ThA09.

[9] L. Xiao et. al., "Higher Order Modes Damping Analysis for the SPX Deflecting Cavity Cryomodule", Proceedings of IPAC2012, New Orleans, Louisana, USA, pp 2414 - 2416.

Copyright © 2012 by the respective authors — cc Creative Commons Attribution 3.0 (CC BY 3.0)

MULTIPACTING ANALYSIS OF HIGH-VELOCITY SUPERCONDUCTING SPOKE RESONANTORS*

C. S. Hopper† and J. R. Delayen
Center for Accelerator Science, Department of Physics,
Old Dominion University, Norfolk, VA, 23529, USA and
Thomas Jefferson National Accelerator Facility, Newport News, VA 23606, USA

Abstract

Some of the advantages of superconducting spoke cavities are currently being investigated for the high-velocity regime. When determining a final, optimized geometry, one must consider the possible limiting effects multipacting could have on the cavity. We report on the results of analytical calculations and numerical simulations of multipacting electrons in superconducting spoke cavities and methods for reducing their impact.

INTRODUCTION

Superconducting multi-spoke cavities for frequencies of 325, 352, 500, and 700 MHz and velocities of β_0 = 0.82 and 1 have been designed and optimized [1, 2, 3] for a variety of possible applications. These applications include, but are not limited to, compact machines such as future light sources and high-energy proton or ion linacs. Here we focus on what regions of these resonators are most susceptible to multipacting events.

When the internal surface of a rf cavity is exposed to the high fields maintained in a superconducting cavity, electrons (known as primary electrons) can be emitted from the metal. The kinetic energy and trajectory of these electrons is determined by the electromagnetic fields, and in many cases, they will come in contact with another part of the surface with a certain amount of impact energy. If this energy falls within the secondary emission yield (SEY) range, then additional electrons, known as secondary electrons, will be ejected [4]. Figure 1 shows a generic SEY curve. The parameters E^I_{oc}, and E^{II}_{oc} are known as the crossover energies for which δ = 1. E_{om} marks the electron energy for which δ is maximum. These parameters can vary greatly between materials. Even for a given material, these parameters can vary widely based on both the bulk properties and surface condition.

For well prepared niobium cavities, the crossover energies are around 150 eV and 1050 eV, while E_{om} is around 375 eV [5]. We have presented preliminary results for crossover energies of 150 eV and 2000 eV previously [2]. When secondary electrons are in resonant trajectories, and each impact energy is in the range for which $\delta > 1$, then a cascade can occur generating excessive heat, thus leading to thermal breakdown. These regions are commonly called barriers, and they are classified as either "soft" or "hard." Soft barriers are those that can be conditioned through and thereby passed. It is believed conditioning occurs because multipacting electrons actually clean the surface to a point where the secondary emission yield is below unity [7]. Hard barriers are those which persist resulting in a limited achievable gradient and quenching.

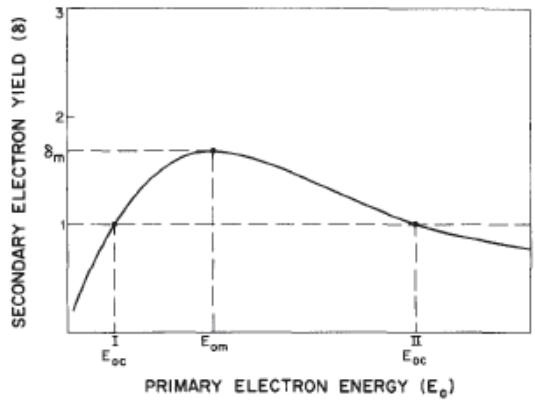

Figure 1: Definition of secondary-electron yield-curve parameters [6]

By improving the quality of the surface, the soft barriers on the gradient can be eliminated. On the other hand, hard barriers can only be overcome by changing the cavity geometry in such a way as to avoid resonant trajectories all together.

Multipacting is also characterized, most commonly, as either one-point or two-point. One-point multipacting occurs when the time of flight of the electron between two impacts is an integer number of rf cycles and that the electron's impact site is approximately the same as it's ejection site. This condition can be described in terms of the cyclotron and rf frequencies as [8],

$$\frac{f}{n} = \frac{eB}{2\pi m} \tag{1}$$

In the case of two-point multipacting, the time of flight is an odd number of half rf cycles and the impact site is not the same as the ejection site. The former condition can be described with the same parameters as (1) [9],

$$\frac{2f}{2n-1} = \frac{eB}{2\pi m} \tag{2}$$

* Work supported by U.S. DOE Award No. DE-SC0004094
† chopp002@odu.edu, chrsthop@jlbab.org

Copyright © 2012 by the respective authors — cc Creative Commons Attribution 3.0 (CC BY 3.0)

MULTIPACTING ANALYSIS

In order to analyze the multipacting conditions in our optimized multi-spoke cavities, the 3D parallel tracking code Track3P contained in the ACE3P code suite developed by SLAC was used [10]. The cavity was divided into three regions as seen in figure 2. The regions labeled 1 and 3 include the end caps, half of one spoke, and the outer conductor enclosing the end accelerating gaps. The region labeled 2 includes half of each spoke and the outer conductor enclosing the middle accelerating gap. Due to the symmetry, regions 1 and 3 give similar enough results that we will only discuss 1 and 2.

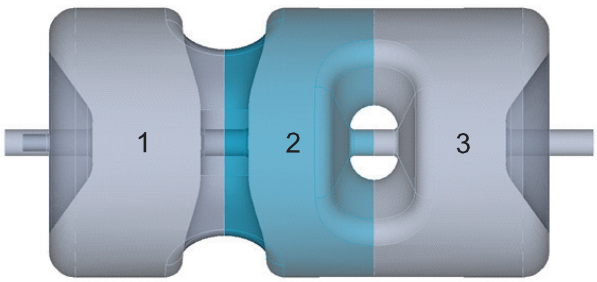

Figure 2: 325 MHz, β_0 = 0.82 cavity divided into three regions for multipacting analysis.

End cells

Figure 3 shows the resonant electrons surviving 50 rf cycles in region 1, along with their impact energies.

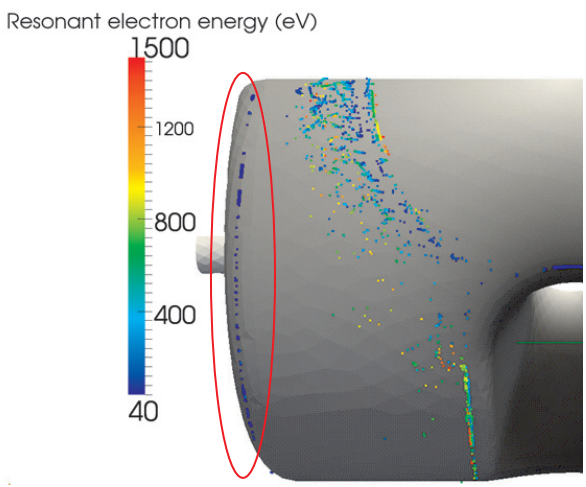

Figure 3: Resonant electrons and their impact energies surviving after 50 rf cycles as simulated by Track3P.

Figure 5 shows a plot of the resonant energies shown in figure 3. Upon inspection of figure 5, there are two observations to take note of. First, it appears that there are possible hard barriers between around 0.4 - 2 eV. Secondly, there are stable multipacting electrons at high field gradients. These electrons are found to be two-point, first order, and reside in the end cap area identified in figure 3. An example of these particle's trajectory is shown in figure 4.

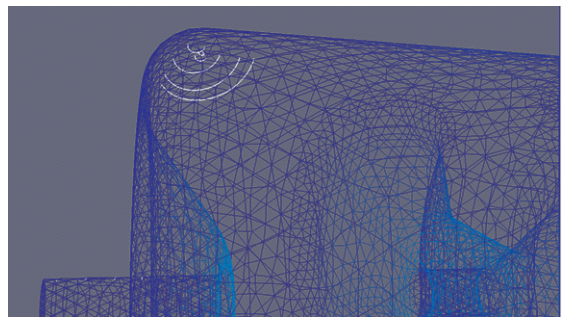

Figure 4: Two-point resonant electron trajectories in the end cap of the cavity.

The question of whether hard barriers exist has recently been tested on a similar cavity operating at 700 MHz, β_0 = 1. The cavity was designed and built in a collaboration between ODU and Niowave [3]. Multipacting analysis of that cavity showed a similar potential for hard barriers at low field gradients, but recent tests at 4.2 K have shown this not to be the case.

To address the question of soft barriers at high field gradient, the inset of figure 5 shows the multipacting electron energies present at 6 MV/m - 10 MV/m for this region of the end cap. The plots are for two different rounding radii at the outer edge, and the picture is of the end cap itself. A more subtle rounding (shown in black) has electrons with resonant impact energies of up to about 250 eV, although most fall below 150 eV. On the other hand, a larger rounding radius (shown in red), results in virtually all of the electron energies being below 100 eV.

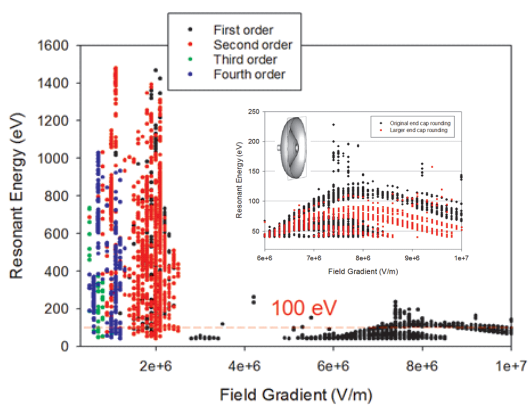

Figure 5: Resonant electron impact energy in region 1 for gradients up to 10 MV/m. The inset shows the impact energies for stable multipacting electrons for two different end cap outer rounding radii.

Copyright © 2012 by the respective authors — cc Creative Commons Attribution 3.0 (CC BY 3.0)

Center cell

The main regions of stable multipacting electron trajectories in the center accelerating gap are shown in figure 6. The low energy electrons (dark blue in color) are, as in the end caps, the ones that are still present even at high gradients. The energy of these electrons is shown in figure 7, and is similar, but slightly less than that of their counterparts at the end caps. These are also two-point, first order electrons which get trapped in the curvature where the spoke base meets the cylindrical outer conductor. As such, varying the curvature in this region can effect the electron's trajectory and impact energy. The inset of figure 7 is an example of this. For a smaller rounding radius (shown in black), there are a number of resonant electrons with energies between 100 and 120 eV for a field gradient of 7-9 MV/m. By increasing the rounding radius (shown in red), the maximum impact energy is now below 100 eV.

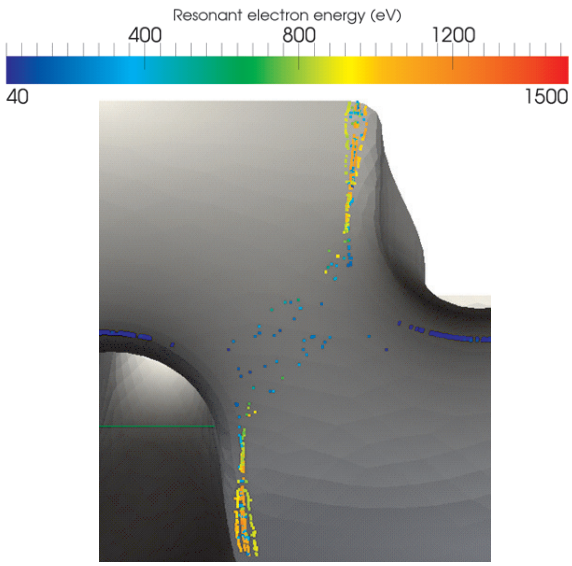

Figure 6: Resonant electrons and their impact energies surviving after 50 rf cycles as simulated by Track3P.

CONCLUSION

Multipacting simulations for multi-spoke cavities show that there is a potential for hard barriers at low field gradients and stable multipactors at high field gradients. However, recent prototype tests of an ODU designed, Niowave fabricated two-spoke cavity operating at 700 MHz has shown that these potential barriers should be able to be processed through.

Additionally, the soft barriers present at high gradients can be minimized by slightly altering the geometry in specific areas of the cavity. Both the end cap and spoke base rounding radius can be increased to a point where the stable, two-point, first order multipactors in these regions are likely to be conditioned away. Experiments at high gradients will have to be done in the future to verify this.

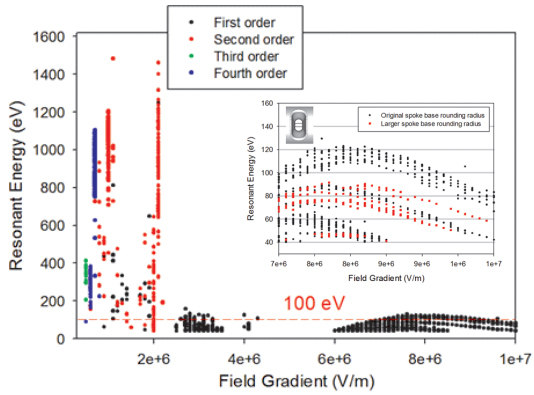

Figure 7: Resonant electron impact energy in region 2 for gradients up to 10 MV/m. The inset shows the impact energies for stable multipacting electrons for two different rounding radii where the spoke base meets the outer conductor.

ACKNOWLEDGMENT

We would like to thank Cho-Kuen Ng and Lixin Ge of SLAC for their helpful discussions on the Track3P code. We also thank Rocio Olave for her multipacting analysis of the 700 MHz cavity.

REFERENCES

[1] C. S. Hopper and J. R. Delayen, "Design of Superconducting Spoke Cavities for High-Velocity Applications," SRF2011, Chicago, July 2011.

[2] C.S. Hopper and J.R. Delayen, "Develpment of spoke cavities for high-velocity applications," Proc. of IPAC2012, New Orleans, LA, WEPPC103.

[3] D. Gorelov, C.H. Boulware, T. Grimm, J.R. Delayen, C.S. Hopper, R.G. Olave, S.U. De Silva, "Development of Superconducting 500 MHz Multi-spoke Cavity for Electron Linacs," Proc. IPAC2012, New Orleans, LA, WEPPC084.

[4] H. Padamsee and A. Joshi, J. Appl. Phys. 50 (1979) 1112.

[5] H. Padamsee, J. Knobloch and T. Hayes, "RF Superconductivity for Accelerators," John Wiley & Sons (1998).

[6] G. F. Dionne, "Origin of secondary-electron-emission yield-curve parameters," J. Appl. Phys. 46, 3347 (1975); doi: 10.1063/1.322061.

[7] F. L. Krawczyk, "Status of multipacting simulation capabilities for SCRF applications," Proc. 10th Workshop on RF Superconductivity, Tsukuba, Japan, 2001.

[8] P. Fernandes, R. Parodi and G. Bienvenu, "An Investigation on the Field Emitted Electrons in Travelling Wave Accelerating Structures," NIM A, 320 (1992) 1-8.

[9] P. Fabbricatore, G. Gemme, R. Musenich, R. Parodi and S. Pittaluga, "Experimental Evidence of MP Discharges in Spherical Cavities at 3 GHz," Proceeding of the 7^{th} Workshop on RF Superconductivity, Gif sur Yvette (1995).

[10] K. Ko et al, Advances in Parallel Electromagnetic Codes for Accelerator Science and Development, LINAC2010, Tsukuba, Japan.

Copyright © 2012 by the respective authors — cc Creative Commons Attribution 3.0 (CC BY 3.0)

MECHANICAL STUDY OF FIRST SUPERCONDUCTING HALF-WAVE RESONATOR FOR INJECTOR II OF CADS PROJECT*

Shoubo He#, Yuan He, Weiming Yue, Shenghu Zhang, Ruoxu Wang, Cong Zhang, Mengxin Xu, Fengfeng Wang, Shichun Huang, Yuzhang Yang, Shengxue Zhang, Hongwei Zhao
Institute of Modern Physics, Chinese Academy of Sciences, Lanzhou, Gansu 730000, China

Abstract

Within the framework of the China Accelerator Driven Sub-critical System (CADS) project, institute of modern physics (IMP) has proposed a 162.5MHz half-wave resonator (HWR) Superconducting cavity for low energy section (β=0.09) of high power proton linear accelerators. For the geometrical design of superconducting cavities structure mechanical simulations are essential to predict mechanical eigenmodes and the deformation of the cavity walls due to bath pressure effects and the cavity cool-down. Additionally, tuning analysis has been investigated to control the frequency against microphonics and Lorentz force detuning. Therefore, several RF, static structure, thermal and modal analyses with three-dimensional code Traditional ANSYS have been performed [1]. In this paper, we will present some results about mechanical analysis of the first superconducting HWR cavity in order to further optimization in the near future.

INTRODUCTION

The cavity geometry has been optimized to reach the design frequency 162.5MHz and β=0.09 and also we want to minimize value of peak electrical and magnetic field on the cavity surface relative to the accelerating electrical field on the cavity axes (Bpk/Eacc and Epk/Eacc) [2]. So the fabrication technology and resonator structural properties including cooling down, vacuum, etching and so on, also should be taken into account at the beginning of design. SC HWR cavities are highly sensitive to mechanical deformations due to the small loaded bandwidth of some SCRF applications. So accordingly for HWR the stability of the cavity structure against any external distortions is the primer design goal. In order to improve df/dP for a low Beta HWR cavity, the typical approach is to add some stiffening ribs on the cavity, but it will not be discussed in this paper. Here, we will investigate this type of structure and then we will improve it in the future. Primarily structural analysis was completed to determine the locations of the model that were beyond yield strength.

Since CADS accelerator will work in CW regime, the main goal of our cavity structural design is a minimization of the resonant frequency dependence on the external pressure fluctuations. The general basics of the cavity structural design are to avoid using the plane surfaces as illustrated in Figure 1. Besides, four access ports at each cavity (two at the bottom, two at the top) guarantee draining off of the chemical etching and easy access to the inner surfaces during the high pressure water rinsing (HPR).

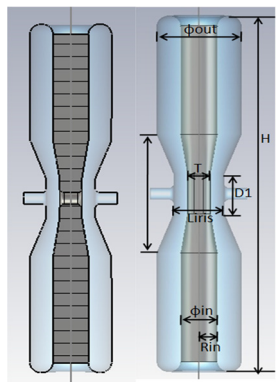

Figure 1: The cross section of HWR cavity with the main geometric parameters: Liris-iris to iris length, T-inner conductor thickness, D1-cavity diameter.

Table 1: Some Properties of HWR Cavity

Para.	Frequency	β	Diamater	Uacc	Epeak	Bpeak
Value	162.5	0.093	40	0.78	25	50
Unit	MHz	---	mm	MV	MV/m	mT

STRUCTURAL ANALYSIS

Injector II of CADS is composed by an ECR ion source, LEBT, RFQ and superconducting accelerating section. And in superconducting accelerating section, there are two cryomodules and each cryomodule is composed of 8 superconducting Half-Wave-resonator cavities and 9 superconducting solenoids. The proton beam will be accelerated from 2.1 MeV to 10MeV. Before structure analysis the geometry of HWR cavity was taken from a sat. model that was generated in software CST Microwave Studio and represented one cavity structure. The ANSYS RF results were compared to CST and to HFSS models of the same cavity for final verification. And the difference among these code result is only about 0.065%.

During mechanical analysis of HWR cavity, the variation of RF Eigen frequency was calculated, including pressure sensitivity, Lorentz force detuning, tuning sensitivity and resonant vibration and etc.. The

*This work is Supported by the National Natural Science Foundation of China (Grant Agreement 91026001)
#heshoubo@gmail.com

Copyright © 2012 by the respective authors — cc Creative Commons Attribution 3.0 (CC BY 3.0)

relationship between changes in RF frequency and mechanical deformations is given by the Slater Perturbation Theorem as the following equation 1, where E_0 and H_0 are the unperturbed electric and magnetic fields respectively, U_0 is the stored energy, f0 is the original cavity frequency, and Δf is the frequency shift:

$$\frac{\Delta f}{f_0} = \frac{\int_{\Delta v} (\mu_0 \left|\vec{H}_0(\vec{x})\right|^2 - \varepsilon_0 \left|\vec{E}_0(\vec{x})\right|^2) d^3x}{4 \cdot U_0} \quad (1)$$

PRESSURE SENSITIVITY

A sequential coupled field analysis RF-Structural-RF is used to predict the frequency shift due to cavity deformations under external pressure using codes ANSYS. As the cavity stiffening environment is hard to determine when cavity design, it is necessary to provide this research under two cavity beam port boundary conditions: fully fixed and completely free. The same meshed model was used for all types of simulations and that is very important as we can evaluate the frequency shift at the same scale.

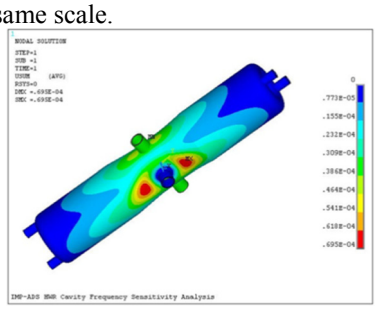

Figure 2: Structural analyses results of HWR with beam pipes fixed (cavity deformation).

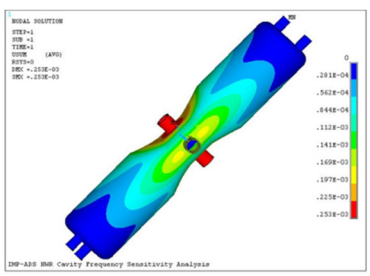

Figure 3: Structural analyses results of HWR with beam pipes free (cavity deformation).

Table 2: Pressure Sensitivity under 1 Atm

Boundary	Displacement	Stress	Δf	df/dp
fix	0.0695	5.786	17.892	23.54
free	0.252	19.066	110.773	145.6
Unit	mm	ksi	kHz	Hz/torr

From the above results we can see that the main frequency shift is caused by the beam port displacements. Although in this analysis the cavity has been simulated without helium vessel. While the helium vessel adds rigidity to the beam ports and in other words it is equivalent approximately to the fully constrained conditions. Whatever the different boundary condition, the cavity seems to be too soft so we need add some ribs on it for strength the cavity. And recently we just explore how to add these stiffening ribs.

Lorentz Force Detuning (LFD)

Since the superconducting HWR cavity will work in cw mode, so it will be static Lorentz force on the cavity walls. The pressure results in a deformation of the SC HWR cavity walls with changing the cavity volume by ΔV. And it creates the frequency shifts, which may be approximated as a perturbation using Slater's Theorem[3]. This shift is usually quantified by KL which is defined as

$$K_L = \frac{\Delta f}{(E_{acc})^2} \quad (2)$$

The numerical coupled analysis for LFD effect has been done and also an initial simulation of the cavity under beam pipes full constrain can be showed. From this formula, we can see that the frequency shift is proportional to the accelerating gradient. With the increase of accelerating gradient, the resonant frequency also decreases. Figure 4 shows the deformation of the cavity with LFD effect .

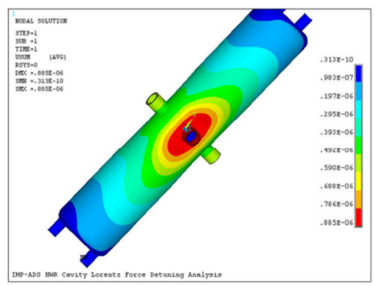

Figure 4: Deformation of the cavity wall (fix boundary condition)

From the above simulation the final fitting curve of the Δ f and E_{acc} is

$$\Delta f = -4.657 E_{acc}^2 - k \quad (3)$$

Finally according to the equation 2, the obtained Lorentz force detuning coefficient K_L is -4.657Hz/(MV/m)^2.

Modal Analysis

Generally speaking, it is difficult to eliminate vibrations in cavities because the situation around the cavity and the helium vessel is extremely complicated. In practice the structural modal analysis need to be provided with helium vessel fixed at the supports and tuner fixed by the tuner stem. While here the results is obtained from naked HWR cavity. And then we have the lowest frequency of modal analysis is 188Hz, which is far from the dangerous frequency obviously. Certainly it is need to

Copyright © 2012 by the respective authors — cc Creative Commons Attribution 3.0 (CC BY 3.0)

be further tested for all the accelerator with helium vessel, coupler, tuner and cryomudule etc. to verify the analysis.

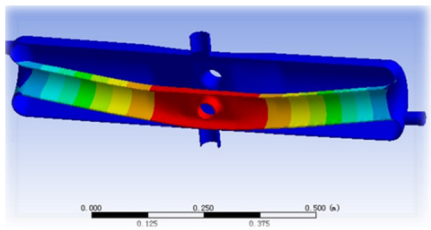

Figure 5: One of Model analyses results of HWR cavity with cleaning pipes free (cavity deformation).

Tuning Sensitivity

The role of the tuner is to ensure that the cavity resonance frequency will match the desired accelerator operating frequency. Tuners are generally made an active part of a complete RF control system which fulfills several functions. It stabilizes the frequency, amplitude, and phase variations induced by sources such as the RF drive, beam current variations, LFD, and microphonics. The usual tuning method for SC cavities is to change the length of the cells by mechanical adjustment of the overall length of the cavity. This method will not only bring in new HOM, but also not cause a big change for previous HOM[4].

The main factors that may be needed at the design of tuner are as follows:

- The tuning sensitivity of HWR cavity is 180KHz/mm;
- The spring constant of the HWR cavity is 2.2KN/mm;
- The limited space available (tuning range) is about 2mm.

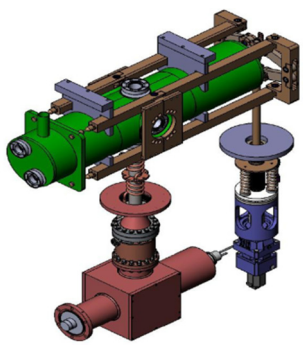

Figure 6: The IMP mechanical tuner: tuner(dark gray), helium vessel (green), and coupler (red).

Considering the fabrication tolerances for the cavity, the tuner may be able to retune the cavity over a range of 150 kHz cantered on the nominal operating frequency of 162.5 MHz.

Figure 7: Mechanical Tuner of HWR cavity test with copper HWR prototype .

CONCLUSION

We Mechanical analysis has been developed for 162.5 MHz SRF HWR cavities for the proposed CADS at IMP. The design of the tuner has been described and results of the static performance of the first copper HWR prototype have been got recently. In view of the mechanical results we find obviously that the SRF HWR cavity is much too sensitivity. So Some stiffening ribs must be added on the cavity wall. Besides, the coupled field analysis is in progress with more realistic boundary conditions ,including helium vessel.

ACKNOWLEDGMENT

We would like to thank Prof. Haipeng Wang and Dr. Gary Cheng of JLAB for the idea of simulations and helpful discussions.

REFERENCES

[1] ANSYS, Inc., Canonsburg, Pennsylvania, USA. www.ansys.com
[2] E. Zaplatin, IFMIF-EVEDA SC β=0.094 HALF-WAVE RESONATOR STUDY, SRF2009, THPPO015
[3] J.C. Slater, “Microwave Electronics,” D. Van Nostrand Co., Princeton, N.J., 1950, p8.
[4] H. Padamsee et al. RF Superconductivity for Accelerator, John Wiley & Sons, 1998.

Copyright © 2012 by the respective authors — cc Creative Commons Attribution 3.0 (CC BY 3.0)

THE SUPERCONDUCTING CH CAVITY DEVELOPING IN IMP*

M.X.XU#, Y.He, S,H.Zhang, Z.J.Wang, R.X.Wang, SH.B.He, W.M.Yue, C.Zhang, SH.CH.Huang, Y.ZH.Yang, SH.X.Zhang, T.C.Jiang, Y.L.Huang, H.W.Zhao, J.W.Xia, IMP, Lanzhou, Gansu 730000,China

Abstract

The Cross-Bar H-type (CH) cavity is a multi-gap drift tube structure operated in the H21 mode [1]. The Institute of Modern Physics (IMP) has been doing research and development on this type of superconducting CH cavity which can work at the C-ADS (accelerator driver sub-critical system of China). A new geometry CH cavity has been proposed which have smaller radius. It's suitable in fabrication, and it's can reduce cost too .Detailed numerical simulations with CST MicroWave Studio have been performed. An overall surface reduction of 30% against the old structure seems feasible. A copper model CH cavity is being fabrication for validating the simulations and the procedure of fabricating niobium cavity.

INTRODUCTION

C-ADS project with ambitious requirement regarding beam power and quality need new superconducting linac development. Superconducting Crossbar-H-Mode (CH)-cavities have two important features meet with the requirements of C-ADS. Superconducting CH cavity have high real estate gradients compared to conventional low-beta ion linacs, this feature will reduce the amount of cavity prominent. For the cross bar structure, CH cavities are more rigidly. This feature satisfy the harsh requirements of C-ADS about reliable. As this reasons, superconducting CH cavities have been choose as a backup cavity type for the C-ADS(see Fig.1). With respect to C-ADS actual application, one prototype of superconducting CH cavity (f=162.5MHz, beta=0.067, 6 cells) is presently being development in IMP.

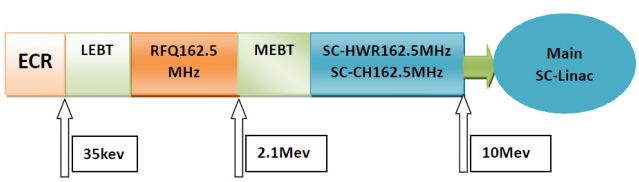

Figure 1: Layout of Injector-II for C-ADS.

NEW SHAPE SUPERCONDUCTING CH CAVITY

The superconducting CH cavity has electric and magnetic field structure similar with combine the 4-vane RFQ and DTL's. We can use a semi-analytical approach to estimate basic parameters like frequency. The parameter Rt and r1 are represent the radius of CH cavity and the tube radius of CH cavity respectively. Using this equivalent, we can get the resonance frequency with the radius Rt as following [1]:

$$\omega \approx c\left(\frac{0.73}{Rt^2\left(\frac{25}{144}+\frac{25}{72}Ln\left(\frac{Rt}{r1}\right)-0.2\right)}\right)^{1/2} \quad (1)$$

In case of the superconducting CH cavity of IMP, the frequency is 162.5MHz, r1 was 0.03m. Using the formula (1) can give radius Rt of the CH cavity is 0.29 meter. We have using the software CST to simulation. The radius of CH cavity is 0.32 meter [2].

The superconducting CH cavity is a complex cavity. With the radius of 0.32 meter, there are big surface. This means a large amount of high pure niobium needs and a more chance to come across defects. As in superconducting cavity, perfect surface is important for the cavity quality [3]. This size of CH cavity is not easy to protect from defects and contaminates or not suitable in the vacuum chamber of electric beam welding machine.

We try to cut a part of the girder called undercut [4] (see Fig.2).This undercut will increase inductance in the end of cavity, as this will increase the length of current flow. Increased inductance will lower the resonance frequency that we can get a smaller cavity structure in the same frequency (see Fig.3).

When we change the size of undercut in the girder of CH cavity, the radius will reduce with the width of girder liner. At most, we can reduce the radius of cavity by 20% (see Fig.4). As the radius reducing, the surfaces of the cavity reduce by 30% (see Fig.5).

*Work supported by 91026001 Nature Science Foundation of China
#xumx@impcas.ac.cn

Copyright © 2012 by the respective authors — cc Creative Commons Attribution 3.0 (CC BY 3.0)

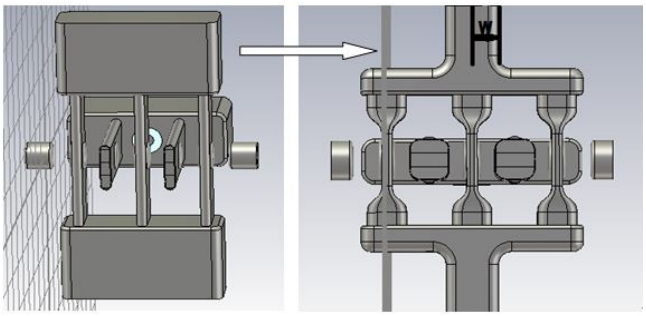

Figure 2: The copper CH cavity structure (left) and the CH cavity of use undercut in girder (right).

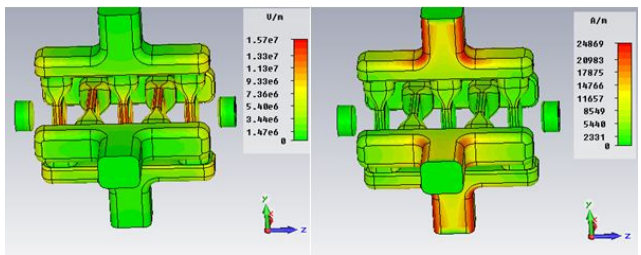

Figure 3: The electric field of use undercut CH cavity (left) and the magnet field of use undercut CH cavity.

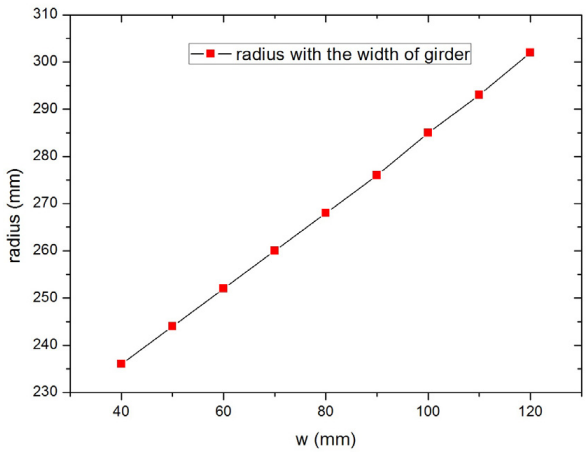

Figure 4: The radius of CH cavity with the width of girder.

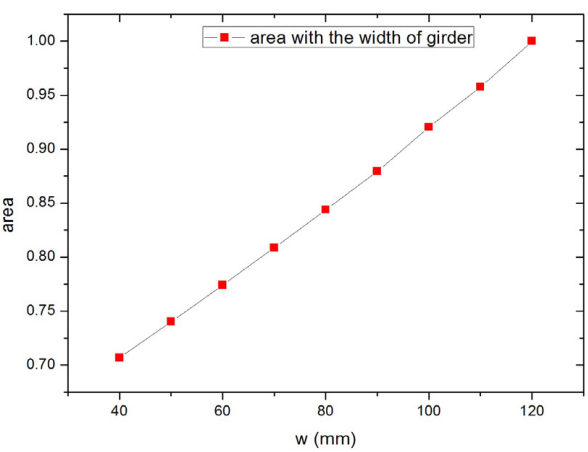

Figure 5: The surface of CH cavity with the width of girder.

This reduction has such advantages: as the cavity size became smaller, deep drawing dies became smaller too. It's easy to hand; the last electron beam welding joint have smaller length, less risk to burn a hole, easy to change position at the EBW; smaller use of high purity niobium, lower cost; less chance to come across defect in surface [4].

Field distribution variation with different undercut girder

The usage of undercut girder leads to a more homogeneous field distribution along the beam axis because the volume for the magnetic field is increased (see Fig.6).

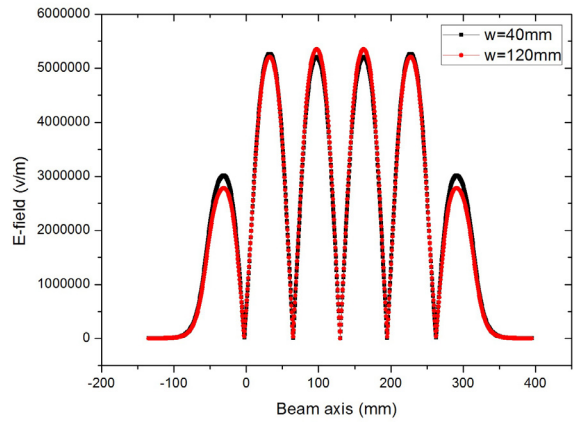

Figure 6: Field distribution of CH cavity with the different width of girder.

Frequency variation with different undercut girder

The frequency tuning is by compress and pulling the two side of cavity along beam axis. Different undercut girder influence the F/l (see Fig.7).

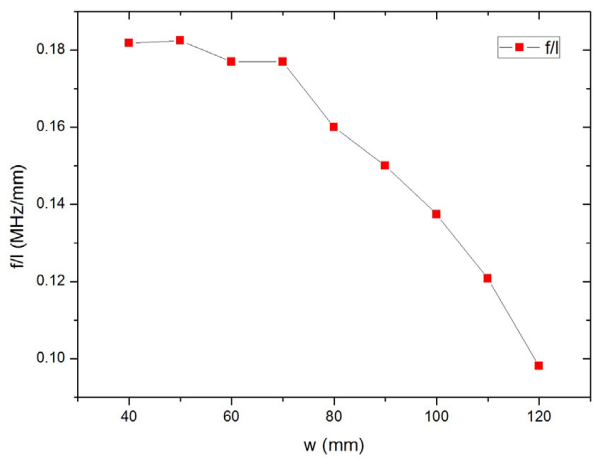

Figure 7: F/l of CH cavity with the different width of girder.

Copyright © 2012 by the respective authors — cc Creative Commons Attribution 3.0 (CC BY 3.0)

Copper prototype CH cavity fabrication

A copper prototype CH cavity has been built (see Fig.8) to validate the electromagnetic simulations, such as frequency (see Table1), field distribution along the beam axis, coupler size and position, tuning ability. And the CH cavity structure is complicate, need to check the design of dies and the path of electron beam weld in the fabrication.

Table 1: The EM parameters of the copper CH cavity

Parameter	Value	Unit
Frequency	162.5	MHz
Beta	0.067	
Ra/Q0	670	Ω
G	47	Ω
Epeak /Eacc	5.3	
Bpeak /Eacc	6.37	mT/ MV/m

OUTLOOK

We have design a superconducting CH cavity with smaller size. The future optimization will focus on lower the E_{peak} /E_{acc} and B_{peak} /E_{acc} , that it should be possible to reach higher effective voltages . The normal copper CH cavity will be finish at the end of 2012.

Figure 8: Parts of copper CH cavity.

REFERENCES

[1] H. Podlech, “New cavity shape developments for low beta applications”, Paper THOAAU06, Proc. of SRF2009, Berlin, Germany.
[1] http://www.cst-china.cn/
[3] Panamsee H, Knobloch J, Hays T. RF superconductivity for accelerators [M]. New York: John Wiley & Sons, 1998
[4] U. Ratzinger, H-type Linac structure, CERN Accelerator School,Lufthansa Training Center, Germany, 8 – 16 May 2000.

Copyright © 2012 by the respective authors — cc Creative Commons Attribution 3.0 (CC BY 3.0)

RF SURFACE IMPEDANCE CHARACTERIZATION OF POTENTIAL NEW MATERIALS FOR SRF-BASED ACCELERATORS*

B. P. Xiao[1,2#], G. V. Eremeev[1], M. J. Kelley[1,2], H. L. Phillips[1], C. E. Reece[1]
[1]Thomas Jefferson National Accelerator Facility, Newport News, VA 23606, USA
[2]College of William and Mary, Williamsburg, VA 23187, USA

Abstract

In the development of new superconducting materials for possible use in SRF-based accelerators, it is useful to work with small candidate samples rather than complete resonant cavities. The recently commissioned Jefferson Lab RF Surface Impedance Characterization (SIC) system [1] can presently characterize the central region of 50 mm diameter disk samples of various materials from 2 to 40 K exposed to RF magnetic fields up to 14 mT at 7.4 GHz. We report the recent measurement results of bulk Nb, thin film Nb on Cu and sapphire substrates, Nb_3Sn sample, and thin film MgB_2 on sapphire substrate provided by colleagues at JLab and Temple University.

INTRODUCTION

SRF accelerating cavities for particle accelerators made from bulk niobium materials are the state-of-art for particle accelerators. Other materials, like thin film Nb on Cu, Nb_3Sn, and MgB_2 are of interest because of their potential cost and performance benefits in SRF applications. In this paper, we report the measurement results from bulk Nb, thin film Nb on Cu substrates and thin film MgB_2 on sapphire provided by colleagues at JLab and Temple University.

DESCRIPTION OF APPARATUS

The sample has been put at the open end of a TE_{011} cylindrical Nb cavity with a sapphire rod inside, described in [1] . The system provides a resonant field at 7.4 GHz. The cavity body, from which the sample is thermally isolated, is surrounded by liquid helium during the test, which differs from the previous measurements [2-4] by making the RF effect on sample the only contribution to the induced heat and resonance frequency change. Heat can be conducted from the sample only via the calorimeter. The effective surface impedance of the sample is derived by directly substituting heater heat for RF heat under controlled RF field and temperature conditions. This system can detect as little as 1 μW dissipated on the sample, enabling the resolution of surface resistance as low as 1.2 nΩ at 5 mT peak magnetic field. A cross-section of the SIC system is shown in Figure 1.

The effective surface impedance can be calculated from:

$$Z_s = \frac{E_Z}{H_Y} = \frac{P_{rf}}{\frac{1}{2}\int H^2(S)dS} + i\omega\mu_0\lambda = \frac{P_{rf}}{kB_{pk}^{\ 2}} + i\omega\mu_0(\lambda_{ref} + \frac{f - f_{ref}}{M})$$

with: $k = \frac{1}{2}\int B^2(S)dS \Big/ (\mu_0 B_{pk})^2$

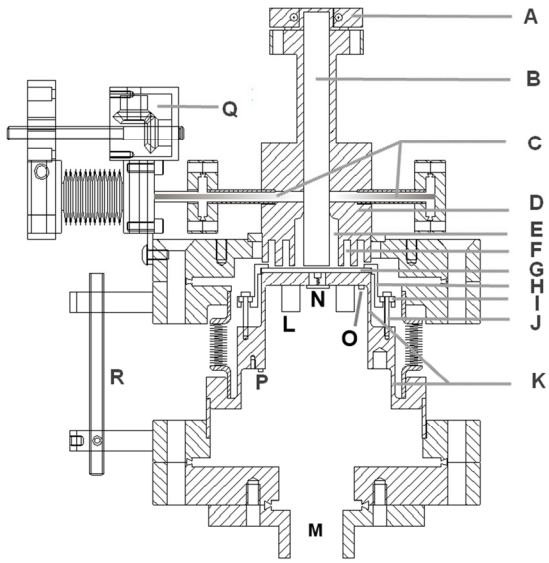

Figure 1: SIC system cross-section. A. Cap for sapphire rod, B. Sapphire rod, C. RF coupler, D. Nb cavity body, E. TE_{011} cavity, F. Double choke joints, G. Sample on top of copper sample holder, H. Stainless steel sample clamp, I. G-10 washer, J. Aluminium bolt, K. Upper and lower thermal insulators, L. Ring heater, M. Port for vacuum and wires. (Vacuum port of the cavity is not shown), N. Thermal sensor mounted on spring, O&P. Thermal sensor, Q. Coupler tuning mechanism, R. Gap tuning mechanism (1 of 3).

The real part is the effective surface resistance and imaginary part is the effective surface reactance. P_{rf} is the RF induced heat, $B(S)$ is the magnetic field distribution on the sample, M is the tuning sensitivity that represents the ratio between frequency change and penetration depth change. k and M are geometry dependent coefficients and ω is the resonant circular frequency. The RF induced heat is calculated from the difference between the power from the heater required to keep a constant sample temperature without RF fields in the cavity and the power from the heater required to keep the sample's equilibrium temperature unchanged when RF fields are present, so called power compensation technique. The change of effective surface reactance is proportional to the change of penetration depth. It may be discerned from the

* Authored by Jefferson Science Associates, LLC under U.S. DOE Contract No. DE-AC05-06OR23177. The U.S. Government retains a non-exclusive, paid-up, irrevocable, world-wide license to publish or reproduce this manuscript for U.S. Government purposes.

Copyright © 2012 by the respective authors — cc Creative Commons Attribution 3.0 (CC BY 3.0)

frequency dependence of the TE_{011} mode as a function of sample temperature.

EXPERIMENT

A set of commissioning measurements (Fig. 2) have been accomplished using bulk niobium, thin film niobium grown by energetic condensation (EC) on polycrystalline copper substrates, a Nb_3Sn film on niobium, and MgB_2 films on single crystal sapphire. The EC film samples were drawn from a batch produced by extracting niobium ions from an ECR plasma onto a biased and heated substrate [5].

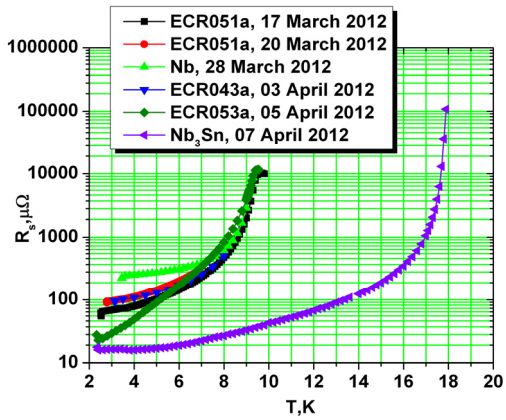

Figure 2: Measured surface resistance of several EC films, bulk Nb sample and Nb_3Sn sample.

Assuming 5% error in power measurement, 1% in current and voltage and 10% in loaded quality factor, the R_s measurement error is estimated to be ~ 20% (not shown). The measurements show high and inconsistent residual resistance at low temperature which is not yet understood.

Several EC samples were characterized with SIC the system. All samples show BCS resistance similar to that of bulk niobium. From the RF surface resistance at ~ 9.5 K in the normal conducting state, surface RRR of the films was estimated and is presented in Table 1 together with DC RRR measurements of co-deposited films. The difference between RF and DC measurement suggests variation in RRR values across the film.

Table 1: Transition temperatures, superconducting transition widths and surface RRRs of measured samples estimated from the data close to the transition temperature.

	RRR_{RF}	RRR_{DC}	T_c, K	ΔT, K
Bulk Nb	~ 60	>250	9.24	0.01
ECR051a	~ 40	54	9.30	0.30
ECR053a	~ 35	182	9.31	0.05
ECR043a	~ 50	289	9.29	0.20
Nb_3Sn			17.80	0.20

A Nb_3Sn sample that was produced at Jefferson Lab by a vapor deposition method was measured in the SIC system directly after the deposition. The R_s measurement shows the transition temperature of about 18 K, consistent with DC magnetization measurements. The film shows high RF surface resistance at the transition temperature suggesting a suboptimal film. This is consistent with the measurements done at Wuppertal University, which indicated that up to 0.5 μm needed to be oxypolished in order to achieve optimal RF performance. We plan to oxypolish the sample and measure the change in low temperature surface resistance as a function of removal.

MgB_2 on Sapphire

The principles of the HPCVD system used to produce the MgB_2 samples were described in references [6, 7]. Three 5 cm diameter samples were fabricated for SRF property characterization, two 200 nm thick (labelled MgB_2-200-I and MgB_2-200-II) and one 350 nm thick (labelled MgB_2-350). Small samples with 1×1 cm^2 size and 350 nm thickness have been fabricated for surface characterization.

The transition temperatures of MgB_2-200-I and MgB_2-200-II were both 39.3±0.2 K, while that of MgB_2-350 was 39.5±0.2 K.

The penetration depth λ_s may be derived from the effective penetration depth of thin films using the expression $\lambda_{eff} = coth(d/\lambda_s)$ [8] with d the film thickness. The results are plotted in Figure 3. The measurement errors of penetration depth and sample temperature are 5% and 0.01 K, respectively. Theoretical value based on BCS theory and Mattis-Bardeen's anomalous skin effect of a superconductor may be calculated using a code SRIMP, written by Halbritter [9]. Using the fitting routine developed by Ciovati [10], we find the suggested BCS model parameters for these MgB_2 samples $\Delta/kT_c = 1.08$, London penetration depth = 180 nm, coherence length = 6 nm, and mean free path = 38 nm.

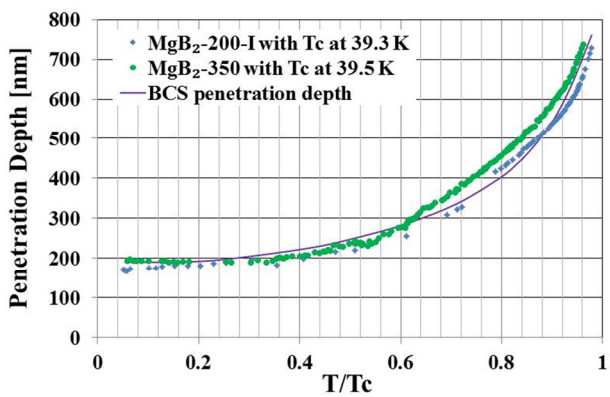

Figure 3: ◆MgB_2-200-I with T_c 39.3 K ● MgB_2-350 with T_c 39.5 K penetration depth versus sample temperature of MgB_2 on sapphire substrate – BCS penetration depth.

Figure 4 shows the effective surface resistance at 7.4 GHz of the MgB_2 samples, measured at temperatures between 2.1 K and 40 K, with peak fields between 0.6 mT

Copyright © 2012 by the respective authors — cc Creative Commons Attribution 3.0 (CC BY 3.0)

and 3.7 mT. The surface resistance of a large-grain Nb sample prepared by BCP etch, measured using the same apparatus, is plotted as a reference. At temperatures above 4 K, the MgB_2-350 sample has a lower surface resistance than Nb. At 2.2 K, the effective surface resistance decreased from 20 μΩ to 9 μΩ with the film thickness increase from 200 nm to 350 nm. The lowest effective surface resistance measured was 9±2 μΩ at 2.2 K, which is consistent with the previous best reported results [4, 11, 12] (using the f^2 rule for normalization) and with smaller systematic errors. We note that the 350 nm sample is less than two penetration depths thick at low temperatures and much less at higher temperatures. This must be taken into account when interpreting the effective surface resistance with respect to a BCS model. The microstructural defects or impurities revealed by XRD might explain why the samples' SRF performance <4K is not yet better than that of a near-perfect single crystal bulk Nb. These XRD measurements have been reported elsewhere [13] and suggest that the crystal quality of the epitaxial films may yet be improved. For the MgB_2-350 sample, the effective surface resistance versus magnetic field was measured with fields up to 10 mT at 3 K sample temperature. Results are shown in Figure 5. Effective surface resistance increased from 10 μΩ to 35 μΩ with increased fields from 0.5 mT to 10 mT.

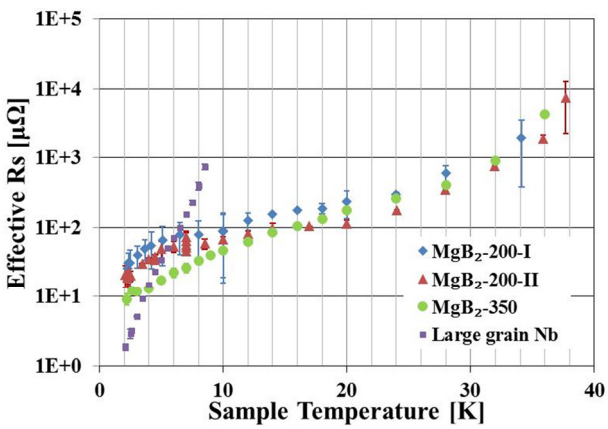

Figure 4: ◆MgB_2-200-I ▲MgB_2-200-II ●MgB_2-350 Effective surface resistance of MgB_2 on sapphire substrate ■Surface resistance of large grain Nb sample.

SUMMARY

The surface impedance characterization (SIC) system at Jefferson lab has been used to measure a variety of thin films on different substrates. In some circumstances the system appears to indicate anomalously high residual resistances that remain yet to be understood. From the data surface RRR values of the films were estimated. The first RF measurement of Nb_3Sn film produced at Jefferson Lab by the vapor diffusion method shows critical temperature of about 18 K consistent with DC magnetization measurements, but also suggests that the film performance may be improved by oxypolishing.

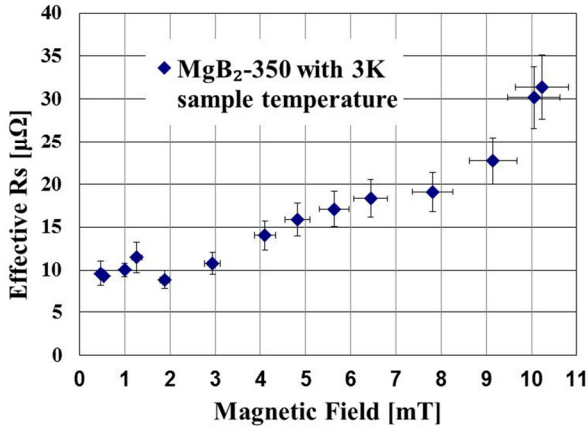

Figure 5: Effective surface resistance of MgB_2-350 versus magnetic field at 3 K.

Quality surface impedance characterization of MgB_2 films of two thickness has been accomplished. Extensive use of the SIC system for SRF material development is anticipated in the future.

REFERENCES

[1] B.P. Xiao, et al., Review of Scientific Instruments, 2011. **82**: p. 056104.
[2] A.G. Zaitsev, et al., 7th European Conference on Applied Superconductivity, 2006. **43**: p. 309.
[3] B.B. Jin, et al., Physical Review B: Condensed Matter and Materials Physics, 2001. **66**(10): p. 104521.
[4] N. Klein, et al., IEEE Transactions on Applied Superconductivity, 2003. **13**(2): p. 3253.
[5] A.-M. Valente-Feliciano, et al. in *Proc. Int. Part. Accel. Conf. 2012*. 2012. New Orleans, Louisiana: p. 2444-2446.
[6] X. ZENG, et al., Nature Materials, 2002. **1**: p. 35.
[7] C. Zhuang, et al., Superconductor Science and Technology, 2009. **22**: p. 025002.
[8] N. Klein, et al., Journal of Applied Physics, 1990. **67**(11): p. 6940.
[9] J.P. Turneaure, et al., Journal of Superconductivity, 1991. **4**(5): p. 341.
[10] G. Ciovati, *Investigation of the Superconducting Properties of Niobium Radiofrequency Cavities*, 2005, Old Dominion University: Norfolk VA. p. 218.
[11] A.V. Pogrebnyakov, et al., IEEE Transactions on Applied Superconductivity, 2007. **17**(2): p. 2854.
[12] D.E. Oates, et al., IEEE Transactions on Applied Superconductivity, 2007. **17**(2): p. 2871-2874.
[13] B.P. Xiao, et al., Supercond. Sci. Technol., 2012. **25**(9): p. 095006.

Copyright © 2012 by the respective authors — cc Creative Commons Attribution 3.0 (CC BY 3.0)

THE NEW 2ND-GENERATION SRF R&D FACILITY AT JEFFERSON LAB: TEDF*

C. E. Reece and A. Reilly
Thomas Jefferson National Accelerator Facility, Newport News, VA 23606, USA

Abstract

The US Department of Energy has funded a near-complete renovation of the SRF-based accelerator research and development facilities at Jefferson Lab. The project to accomplish this, the Technology and Engineering Development Facility (TEDF) Project has completed the first of two phases. An entirely new 3,100 m^2 purpose-built SRF technical work facility has been constructed and was occupied in summer of 2012. All SRF work processes with the exception of cryogenic testing have been relocated into the new building. All cavity fabrication, processing, thermal treatment, chemistry, cleaning, and assembly work is collected conveniently into a new LEED-certified building. An innovatively designed 800 m^2 cleanroom/chemroom suite provides long-term flexibility for support of multiple R&D and construction projects as well as continued process evolution. The detailed characteristics of this first 2nd-generation SRF facility are described.

JLAB SRF FACILITY HISTORY

In 1987 the construction of CEBAF began on a green-field site in Newport News, Virginia. Since CEBAF was to be the first major research institution fully dependent on superconducting RF (SRF) technology in the US, a self-contained set of facilities using then-current technology were setup to support construction of CEBAF. To assure project success and on-going support capability, investments were made in chemical, cleanroom, assembly, and testing facilities that have served multiple needs for the subsequent +20 years.

These facilities enabled the construction of the 42 cryomodules for CEBAF, two cryomodules for the JLab FEL, 24 cryomodules for SNS, rework with upgraded techniques of the ten weakest cryomodules from CEBAF as part of the "C50 program" to establish a 6 GeV program, several prototype cryomodules, and most recently ten "C100" cryomodules for the CEBAF 12 GeV Upgrade project. These projects plus additional R&D programs accumulated over 4200 cavity preparation and vertical cryogenic testing cycles.

Participation in the SNS construction project and the ILC R&D program provided opportunities to make some improvement to the cavity cleaning and testing capabilities. The evolution and aging of the infrastructure resulted in adequate, but constrained capabilities and significant on-going maintenance challenges.

* Authored by Jefferson Science Associates, LLC under U.S. DOE Contract No. DE-AC05-06OR23177. The U.S. Government retains a non-exclusive, paid-up, irrevocable, world-wide license to publish or reproduce this manuscript for U.S. Government purposes.

DOE SLI PROGRAM

The US Department of Energy has a program designed to upgrade existing substandard facility infrastructure within the Office of Science laboratory system. Jefferson Lab won a competitive award from this system, the Science Laboratory Infrastructure (SLI) program, to build the Technology and Engineering Development Facility Project (TEDF). The project allows elimination of substandard structures and provides improved:

- Energy efficiency
- Life-safety code compliance
- Work-flow efficiency
- Facility sustainability
- Human work environment
- Technical quality of facilities for future work

The completed TEDF project will provide new homes for members of several Jefferson Lab organizational units, including the SRF staff, most of the Engineering Division, and Physics Division instrumentation groups. The new building set will meet the "green building" standards of LEED Gold™.

TEDF CONCEPTUAL DESIGN

The architectural engineering firm EwingCole was retained to integrate user requirements into a coherent package. The firm took a blank-page approach to facility design, seeking to incorporate improved safety, energy efficiency, and work flow for SRF cavity development, fabrication, processing, assembly, testing, and provide increased build-out space for cryomodule assembly. Replacement of the cryomodule test facility and cavity vertical dewar test facility was briefly considered, but even simple duplication would have been much too expensive.

Lessons learned over the past +30 years of SRF cavity preparation were folded into facility requirements, as was equipment and support systems expertise from the semiconductor industry. This new facility was composed so as to strengthen our support of four parallel missions:

- Reliable on-going support for the CEBAF nuclear physics research program
- Research on performance-limiting aspects of SRF technology to push the net system costs down
- Development of new accelerating structures, improved SRF cavity processing methods, and prototype cryomodules for new applications
- Construction and delivery of SRF-based accelerator modules for Jefferson Lab and partner laboratories.

Anticipating the continued evolution of the designs, materials, and processes used in SRF cryomodules, the

Copyright © 2012 by the respective authors — cc Creative Commons Attribution 3.0 (CC BY 3.0)

new purpose-built facility was designed with flexibility of use in mind.

NEW FACILITY DESCRIPTION

The Technology and Engineering Development Facility Project has completed the first of two phases. A new 3,100 m^2 SRF technical work facility has been constructed and occupied in the summer of 2012. This new structure was appended to the south end of the existing Test Lab building, home to all previous SRF work at JLab. Each of the SRF work processes with the exception of cryogenic testing has been relocated into the new building.

The second phase of the TEDF project is now underway, fully renovating the existing Test Lab building. All internal structures and utilities are being demolished and removed with the single exception of the SRF cryogenic test areas, the vertical test area (VTA) and the cryomodule test facility (CMTF). A fully reconstructed office wing will reoccupy areas that were formerly technical work areas. A large concrete shielding wall originally constructed in the 1960s for the NASA synchrocyclotron has been removed from the center of the high bay to allow growth of the VTA staging and support areas. During this second phase construction period SRF staff are temporarily located in a new multi-use building that was also constructed during phase one. A schematic layout of the new facility is presented in Figure 1.

Chemroom/Cleanroom Suite

A unique feature of the new TEDF SRF facility is the ~800 m^2 chemroom/cleanroom suite. Two separate chemrooms are provided, one for larger components and more production-style cleaning and chemical processing activities, the other for developmental and research activities. Both of these rooms are outfitted with acid-compatible exhausted wet benches, ultrasonic cleaners, and robust safety systems. To minimize manual handling of acids, supply of standard BCP and EP electrolytes will be provided directly to use locations from a nearby external building. The existing JLab horizontal electropolish cabinet has been relocated into the production chemroom. The air supply to both chemrooms is 100% HEPA filtered. Both chemrooms also have cleaning stations and pass-throughs that connect to the 380 m^2 cleanroom. All material enters the cleanroom via one of these routes. The cleanroom is ISO Class 5 and meets International Standard 14644. It has 100% HEPA filter coverage with at-grade perforated floor return.

When complete, an appendage from the cleanroom will extend into the Test Lab and under the existing bridge crane. From this horizontal-flow cleanroom SRF cavity vertical dewar test inserts will be assembled and transferred via the crane to the VTA for cryogenic testing.

Adjoining both chemrooms and one wall of the cleanroom is the Process Support Area (PSA). The PSA contains all process piping for the chemrooms and the cavity processing equipment/tools that are accessed from inside the cleanroom.

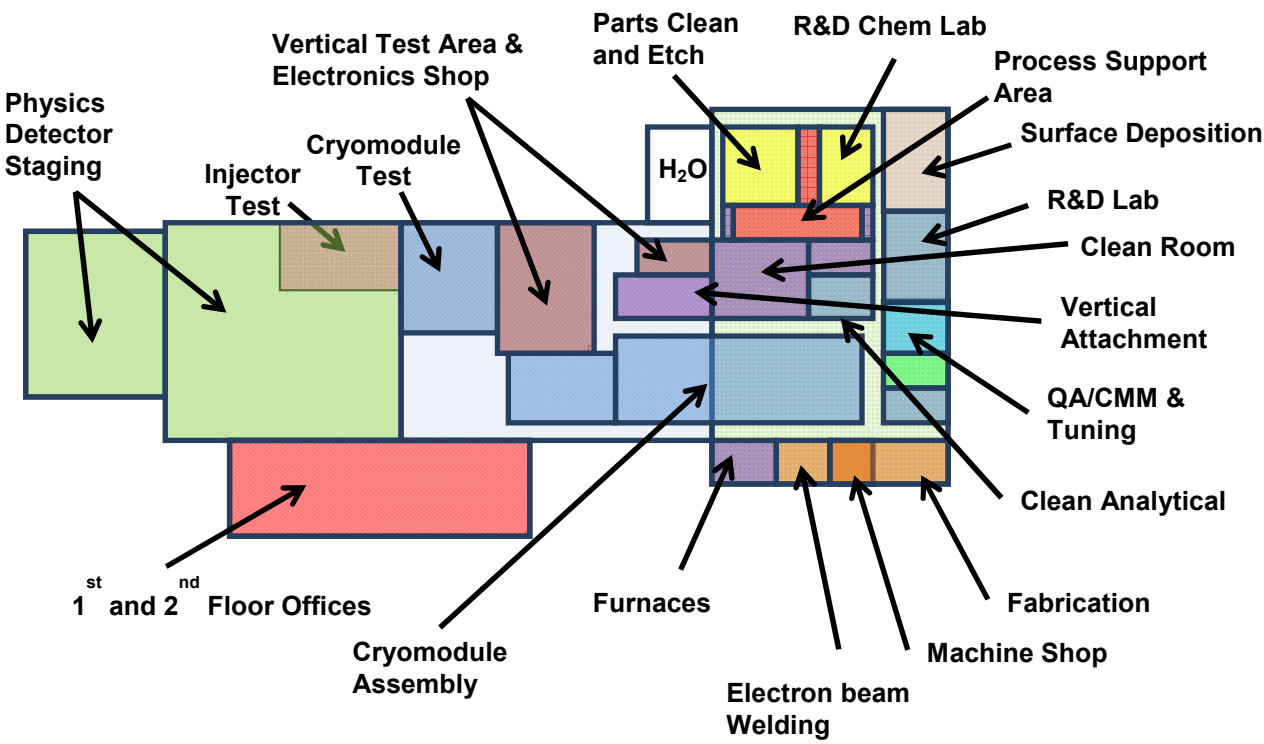

Figure 1: Overview schematic of new Test Lab/TEDF SRF facilities at Jefferson Lab, to be complete summer 2013.

Copyright © 2012 by the respective authors — cc Creative Commons Attribution 3.0 (CC BY 3.0)

The process tools are bulk-headed into the cleanroom from the PSA. Because of the actual and potential presence of hazardous acids, all effluent drains from the chemrooms and PSA, as well as any potential spills, gravity drain through the PSA to an external collection tank. A new acid neutralization system draws from this tank and increases the pH to an acceptable level before discharge to the sanitary system. The acid waste neutralization system has a capacity of 60 gpm.

The TEDF project provides new infrastructure, but not new equipment. The BCP acid etch cavity processing tool, high pressure cavity rinse tool, and vertical electropolish development tool have been relocated into the PSA, with front face open into the new cleanroom. (See Figure 2.) Hook-up and commissioning of the process tools are underway. The horizontal electropolish system, used for the 12 GeV Upgrade cavities and ILC cavity R&D, has been relocated into the production chemroom and is being recommissioned.

Figure 2: BCP and HPR tools bulk-headed into new cleanroom.

Water System

The new SRF ultrapure water (UPW) system has a makeup water capacity of 60 gallons per minute (gpm) and a polish water capacity of 120 gpm (90 gpm ambient loop and a 30 gpm hot UPW loop @ 60ºC). The UPW system is designed to produce microelectronics grade water with a resistivity of 18.2 Mohm-cm, total silica less than 3 ppb, total oxidizable carbon (TOC) below 2 ppb and an overall quality equivalent to type E-1.1 as specified in ASTM D5127-07, with the exception of dissolved gases and boron. This water is plumbed to all chemroom work locations and to each tool in the PSA.

Materials Research and Development

Within the large cleanroom an interior room is allocated to analytical equipment focused primarily on particulates that can generate field emission inside of accelerator cavities. The scanning electron microscope/scanning field emission microscope (equipped with EDS and EBSD) and field emission viewer systems have been relocated here.

The several JLab surface deposition systems have been collected into a common lab in the new facility. These include the general-purpose sputter coating system, the ECR plasma niobium energetic condensation research system, the UHV multi-technique deposition system, and a fledgling niobium HIPIMS deposition system. The infrastructure in this lab was also laid out to accommodate eventual addition of thin film coating systems for multi-cell cavities as those techniques mature.

Cavity Fabrication Facilities

The TEDF project has enabled JLab to retain and strengthen its SRF cavity development and prototyping capability. The sheet metal forming and machining equipment have been consolidated. The electron beam welder was relocated into a dedicated room in the new facility and its vacuum system was upgraded. The set of brazing and high temperature vacuum furnaces were collected into a common room. The cavity tuning and inspection stations were also collected together conveniently.

Cryomodule Assembly Facilities

As a result of the need to accommodate the concurrent assembly of 12 GeV cryomodules for CEBAF during the TEDF realization period and also address on-going maintenance and future construction projects, the cryomodule assembly facility is laid out as four parallel assembly lines. During the second phase of the TEDF project, when access to the Test Lab high bay is unavailable, only half of these four lines are available, and two are dedicated to completion of the remaining 12 GeV “C100” cryomodules. These extended assembly rail systems will create the opportunity to serve up to four independent activities/projects simultaneously in 2014 and beyond.

SUMMARY

Realization of a new state-of-the-art SRF facility is in progress at Jefferson Lab. Its purpose is to provide high-quality support to local, national, and international needs for SRF accelerator system development and construction.

Copyright © 2012 by the respective authors — cc Creative Commons Attribution 3.0 (CC BY 3.0)

A NEW INTERNAL OPTICAL PROFILOMETRY SYSTEM FOR CHARACTERIZATION OF RF CAVITY SURFACES – CYCLOPS*

C. E. Reece[1], A. D. Palczewski[1], H. Tian[1], J. Bearden[2], and L. Jacobs[2]
[1]Thomas Jefferson National Accelerator Facility, Newport News, VA 23606, USA
[2]MicroDynamics Inc., Woodstock, GA 30189, USA

Abstract

Jefferson Lab has received and is commissioning a new interferometric optical profilometer specifically designed to provide internal surface mapping of elliptical rf cavities. The CavitY CaLibrated Optical Profilometry System – CYCLOPS – provides better than 2 μm lateral resolution and 0.1 μm surface height resolution of programmatically selected locations on the interior surface of multi-cell cavities. The system is being used to provide detailed characterization of surface topographic evolution as a function of applied surface treatments and to investigate particular localized defects. We also intend to use the system for 3D mapping of actual interior rf surface geometry for feedback to structure design model and fabrication tooling. First uses will be illustrated. CYCLOPS was developed and fabricated by MicroDynamics Inc., Woodstock, GA, USA.

INTRODUCTION

The performance of superconducting resonant rf structures used for particle acceleration is quite often limited by localized surface defects. Developing an understanding of the nature of such defects and their origin is critical to confidently avoiding their occurrence. The surface of interest is the interior of a complex three-dimensional object, which presents a major impediment to the development of such an understanding.

External thermometry during cryogenic rf testing provides confident localization of anomalous heating to within ~1 cm. Use of such thermometric mapping has been followed up with visual inspection by careful non-contacting insertion of a camera and illumination system such as that developed at Kyoto University [1], and by use of long-range microscopes with mirror and lighting inserted into the cavity [2]. Such visual inspection provides valuable information about the morphology of the defect region, but is very difficult to interpret quantitatively. In addition to characterization of defects, quantitative topographical information is needed to refine the understanding of cavity surface topography evolution as a function of applied processing steps, whether mechanical or chemical, to optimize those processes for both effectiveness and economy.

One route to obtain quantitative topographic information from a location of interest is by forming a replica mold of the region which may then be examined with external profilometry tools. This has been successfully accomplished for a few defect spots in multi-cell cavities [3, 4], and even accomplished without affecting the performance of the cavity. Such technique, however, can hardly be envisioned for extensive use.

A more attractive solution would be provided by optical interferometric profilometry accomplished on the interior of the finished cavity. Though perhaps conceptually straightforward, the realization of such a system presents significant motion control challenges.

MicroDynamics Inc. [5] has developed such a system, called CavitY CaLibrated Optical Profilometry System (CYCLOPS) and delivered it to Jefferson Lab. Commissioning of the CYCLOPS is underway.

SYSTEM DESCRIPTION

This unique system provides optical inspection and quantitative profilometry of the interior surface of cylindrically symmetric structures that have axial clearance of at least 48 mm diameter. The system can accommodate structures up to 1.5 m in length and diameter up to 34 cm. See Figure 1.

Figure 1: CYCLOPS setup at Jefferson Lab.

The system is oriented vertically with the non-contacting optical probe traveling down the cylindrical axis. The probe consists of two concentric hollow cylinders, an outer probe which positions a lower mirror,

* Authored by Jefferson Science Associates, LLC under U.S. DOE Contract No. DE-AC05-06OR23177. The U.S. Government retains a non-exclusive, paid-up, irrevocable, world-wide license to publish or reproduce this manuscript for U.S. Government purposes.

Copyright © 2012 by the respective authors — cc Creative Commons Attribution 3.0 (CC BY 3.0)

and an inner probe which moves vertically with the balance of the optical system, including the reference leg of the interferometer. The displacement between the inner and outer probes establishes the distance of the focal plane away from the bottom mirror. The bottom mirror has a precision tilt control. The range of motion of the mirror provides a view 80º up to 30º down from horizontal.

Because the system is optimized for a very narrow depth of field for interferometric measurements, the cavity interior surface is best observed with the height of the bottom mirror and its tilt angle set to provide normal incidence on the surface of interest. A cavity to be inspected is mounted from below on a fixed-height rotary stage.

The four position control parameters of CYCLOPS are accessed via a computer interface and together establish a unique location in the 3D coordinate frame of the system to a precision of typically about 1 μm.

Reflections from the cavity surface return to a CCD camera. Surface profile data is derived by tracking the interference fringes from a blue LED through a series of acquired digital (1600 × 1200) optical images from an area approximately 2.6 × 2.0 mm. The focal plane is incremented through the surface during this series. Optical element position resolution is 78 nm, roughly $1/6^{th}$ of the optical wavelength. A non-interferometric, lower magnification mode provides a ~ 5 × 4 mm field of view for manual scanning operations.

OPERATION

A cavity to be examined may either be flange-mounted directly to the rotary headstock or aligned in a standard JLab cavity handling frame, which in turn is mounted to a spider fixture attached to the rotary table as in Figure 2.

Because best results are obtained when the surface is viewed with near-normal incidence, a CAD file of the cylindrically-symmetric design contour of the cavity is loaded as an input to CYCLOPS. Registration of the system's vertical coordinate, $z = 0$, to the design is accomplished by manual control and observation. Subsequently, the operator may specify the elevation of interest and request an auto setup of the system parameters so as to view that location in space with normal incidence to the design surface. Such setup is available except when the slope of the cavity wall is too steep to obtain normal incidence.

The operator then adjusts the position of the focal plane to the real surface and adjusts the field of view to the region of interest. The focus is then further refined to observe interference fringes. A series of digital images is acquired as the focal plane is scanned through the surface. Image processing then tracks the fringes between images and infers topographic information, finishing with a profilometry array for graphical display and further analysis, such as cross-section display, statistical characterization, etc.

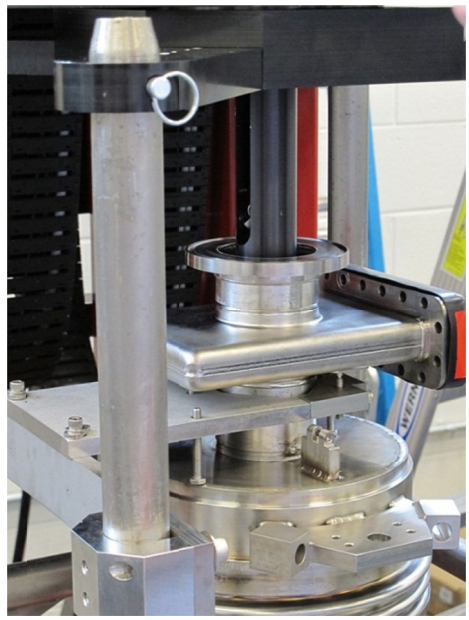

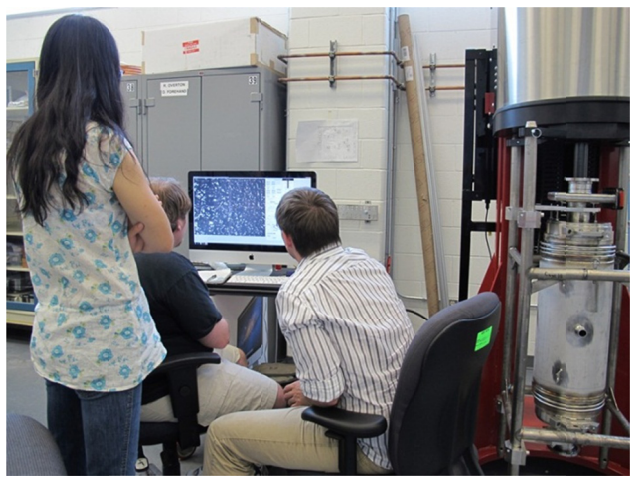

Figure 2: CEBAF upgrade cavity mounted on CYCLOPS for inspection.

Figure 3 shows the user interface while inspecting an intentionally drilled hole in a single cell test cavity. The right-most panel gives the operator graphical feedback on the location being viewed. The left panel is the live digital image. In between is the motion control panel for use by the operator.

Figure 4 is a rendering of the resulting profilometry scan for this defect. Due to the extreme depth of the hole, no interference fringes were observed there, so this region remains unresolved.

At present, operation is limited to user driven analysis of specific locations. Our intent is to continue to develop the user interface and to gradually increase the degree of automation in surface characterization and defect recognition.

Copyright © 2012 by the respective authors — cc Creative Commons Attribution 3.0 (CC BY 3.0)

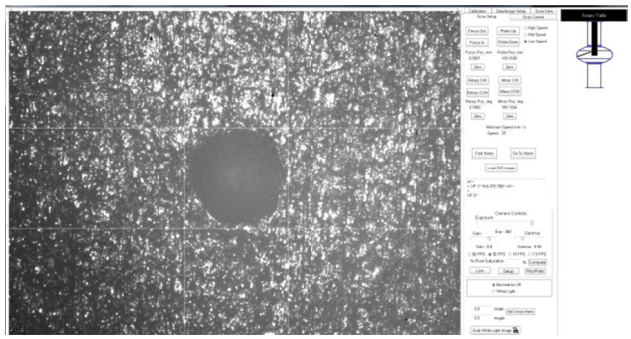

Figure 3: CYCLOPS user interface inspecting a 680 µm diameter drilled blind hole.

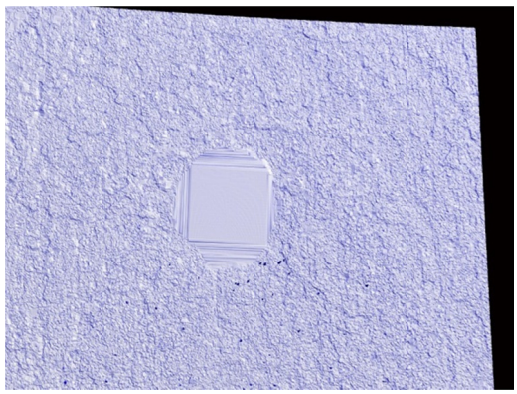

Figure 4. Interferometrically reconstructed surface profile from the surface imaged above.

Another intended use for CYCLOPS is as a tool for mapping the actual internal surface of multicell cavities for comparison with the theoretical design surface. Creating a 3D point cloud mapping of the actual surface will be valuable feedback to both the cavity sheet metal and welding fabrication processes. The feedback is also valuable for RF modelling, which is increasingly called upon to anticipate the field configurations of multiple higher-order modes as well as the fundamental accelerating mode. Subtle shape deviations from designs can have significant effects on the field configuration of such modes in multi-cell cavities. The CYCLOPS software to accomplish this mapping mission has not yet been commissioned.

SUMMARY

A new system for inspecting and characterizing the interior surface topography of cylindrically symmetric RF accelerating cavities has been developed. The system provides a helpful bridge between *ex situ* material studies and *in situ* visual inspections of "normal" and "defect" surfaces. Further automation of CYCLOPS is planned for the near future.

REFERENCES

[1] Y. Iwashita, *et al.*, Phys. Rev. ST Accel. Beams, 2008. **11**(9): p. 093501.

[2] R.L. Geng, *et al.* in *Proc. 15th Int. Conf. on RF Superconductivity*. 2011. Chicago, IL USA: p. 798-800.

[3] M. Ge, *et al.*, Supercond. Sci. Technol. , 2011. **24**(3): p. 035002 (8 pp).

[4] S. Berry, *et al.* in *Proc. 11th Int. Workshop on RF Superconductivity*. 2003. Travemunde, Germany: p. 591-595.

[5] MicroDynamics Inc., Woodstock, GA 30189, USA.

Copyright © 2012 by the respective authors — cc Creative Commons Attribution 3.0 (CC BY 3.0)

SUPERCONDUCTING RF LINAC FOR eRHIC*

S. Belomestnykh[1,2#], I. Ben-Zvi[1,2], J. C. Brutus[1], H. Hahn[1], D. Kayran[1], V. Litvinenko[1,2], G. Mahler[1], G. McIntyre[1], V. Ptitsyn[1], R. Than[1], J. Tuozzolo[1], Wencan Xu[1], A. Zaltsman[1]
[1)] Brookhaven National Laboratory, Upton, NY 11973-5000, U.S.A.
[2)] Stony Brook University, Stony Brook, NY 11794, U.S.A.

Abstract

eRHIC will collide high-intensity hadron beams from RHIC with a 50-mA electron beam from a six-pass 30-GeV Energy Recovery Linac (ERL), which will utilize 704 MHz superconducting RF accelerating structures. This paper describes the eRHIC SRF linac requirements, layout and parameters, five-cell SRF cavity with a new HOM damping scheme, project status, and plans.

INTRODUCTION

The proposed electron-ion collider eRHIC will collide ions from one of the rings of the existing heavy-ion collider RHIC with electrons from a new accelerator to be installed in the RHIC tunnel [1, 2]. eRHIC will utilize several superconducting RF accelerators. Layout of the SRF systems in the RHIC tunnel, their description, and main parameters were presented elsewhere [3]. The main electron accelerator, the subject of this paper, is a six-pass ERL with two 2.45-GeV SRF linac sections. After six re-circulations, the electron beam energy will be as high as 30 GeV.

SRF LINAC

Each SRF linac section will be 200-meters long. Due to rapid increase of the synchrotron radiation power at high energies, the beam current will be lowered at energies above 20 GeV to keep the total power loss below 10 MW. Thus, the highest luminosity will be achieved at 20 GeV. Parameters of the SRF linac are listed in Table 1.

Installing a shorter linac first and then gradually adding more SRF cryounits will stage the energy of the machine. The initial energy of the main ERL will be 10 GeV with three or four re-circulations. Only one linac section will be installed at this stage of the project.

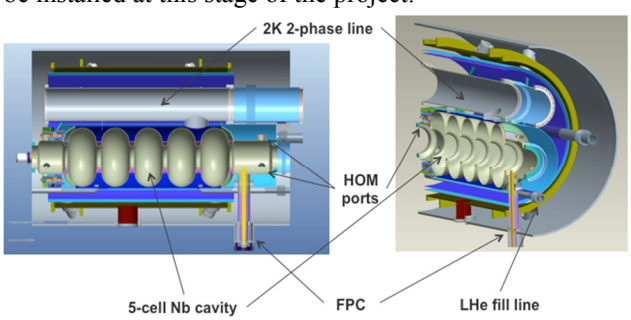

Figure 1: Preliminary layout of a cryounit for eRHIC.

Table 1: Parameters of the Main ERL Linacs

Energy gain per linac section at 30 GeV	2.45 GeV
Beam current per pass (E ≤ 20 GeV)	50 mA
Bunch frequency	14.1 MHz
Bunch length	2 mm rms
RF frequency	703.8 MHz
Linac length	2×200 m
No. of cavities per linac	2×120
Filling factor	0.64
Cavity type	Elliptical, 5-cell
E_{acc} at 30 (20) GeV	19.2 (12.7) MV/m
Peak detuning due to microphonics	6 Hz
Q_{ext} FPC	5.9×10^7
RF power per cavity	10 kW
Total heat load at 1.9 K	5,700 W
Total heat load at 50 K	12,000 W

The SRF linac utilizes five-cell, 704-MHz cavities, described in the next section. Each cavity will be housed in an individual cryounit (Figure 1). A series of such cryounits will form one long cryomodule per section of the linac, with one-meter long transitions to room temperature at each end. The linac's accelerating gradient will reach 19.2 MV/m when operating at the highest energy. At 6 Hz peak detuning due to microphonic noise, the RF power is under 10 kW per cavity. The cavities will be powered from individual solid-state RF amplifiers.

FIVE-CELL CAVITY AND OTHER COMPONENTS

Cavity and HOM Damping

A superconducting cavity for high-current applications [4-6] is shown in Figure 2. The cavity, named BNL3, has an optimized geometry that supports strong damping of higher order modes (HOMs) while maintaining good properties of the fundamental mode. The damping is accomplished via six antenna-type couplers attached to the large diameter beam pipes [7]. The simulations show that this HOM damping scheme provides sufficient suppression of the parasitic impedance to satisfy eRHIC requirements. The cavity parameters are listed in Table 2.

*Work is supported by Brookhaven Science Associates, LLC under contract No. DE-AC02-98CH10886 with the US DOE.
#sbelomestnykh@bnl.gov

Copyright © 2012 by the respective authors — cc Creative Commons Attribution 3.0 (CC BY 3.0)

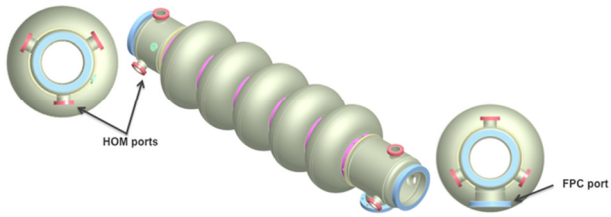

Figure 2: Five-cell 704-MHz SRF cavity for eRHIC.

Table 2: Parameters of the BNL3 Cavity

R/Q	506.3 Ohm
Geometry factor	283 Ohm
Cell-to-cell coupling factor	3.02%
Cavity loss factor (at σ_z = 2 mm)	3.96 V/pC
Cavity Q_0	4×10^{10}
E_{peak}/E_{acc}	2.46
B_{peak}/E_{acc}	4.27 mT/(MV/m)
Lorentz force detuning coefficient	0.45 Hz/(MV/m)^2
HOM power per cavity	7.3 kW
Operating temperature	1.9 K

Structural and thermal analysis, the cavity mechanical design, fabrication of a copper model and the first niobium cavity were done by AES, Inc. as part of collaboration with Stony Brook University and BNL. The full-scale copper model was designed and built with detachable end groups to provide more flexibility in studies of its HOM properties [6]. Because of a large cell-to-cell coupling, the initial field flatness was already very good at 90% right after manufacturing. It was improved to ±1.2% after tuning. The copper cavity is shown in Figure 3. A copper prototype of the HOM coupler is fabricated, and the HOM studies on this cavity are in progress [6].

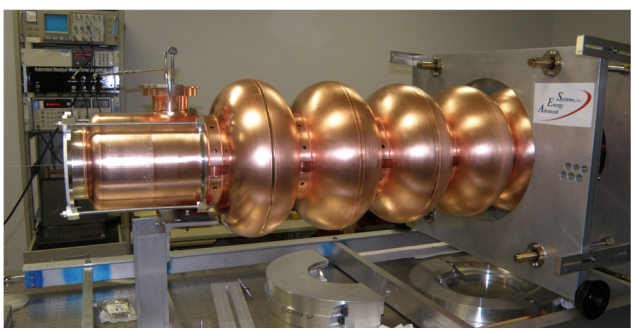

Figure 3: BNL3 cavity copper model undergoing frequency tuning at AES.

Fabrication of the first niobium cavity, BNL3-1, was completed recently at AES (Figure 4). It was made using 3-mm thick high-RRR material. All flanges are Conflat. RF measurements showed field flatness of ±3% and the resonant frequency within the specification so no cavity tuning was necessary after fabrication. The cavity is now being prepared for BCP, 600ºC vacuum bake and HPR. It will be tested at the BNL's vertical test facility in late 2012/early 2013.

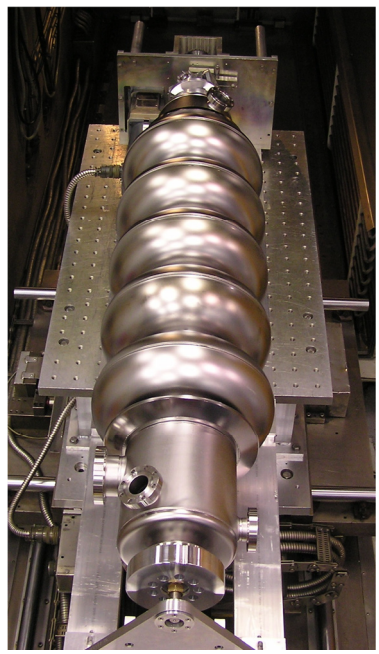

Figure 4: The first niobium BNL3 cavity (courtesy of AES).

Fundamental Power Coupler

As the RF power requirement for the eRHIC ERL cavities is relatively low (10 kW), the main emphasis of the fundamental power coupler (FPC) design is on minimizing its heat leak to 2 K system. Preliminary considerations [8] show that with a proper heat intercept the heat load at the cavity end is less than 0.4 W.

CRYOMODULE FOR COHERENT ELECTRON COOLING EXPERIMENT

The BNL3 cavity was chosen to provide an energy boost of 20 MeV to electrons in the Coherent electron Cooling Proof of Principle (CeC PoP) experiment in RHIC [9]. The new cavity (BNL3-2) and a single-cavity cryomodule are on order from Niowave, Inc. In addition to serving as the CeC PoP linac, it will provide valuable information for designing future eRHIC cryounits.

The BNL3-2 cavity will be fabricated from a 2.8-mm thick high-RRR niobium and will have a few design differences w.r.t. BNL3-1, while being interface-compatible with it. BNL3-2 will undergo processing similar to BNL3-1. The vertical testing at BNL is expected in mid-2013. Based on their vertical test

Copyright © 2012 by the respective authors — cc Creative Commons Attribution 3.0 (CC BY 3.0)

performance, one cavity will be chosen for incorporating in the cryomodule.

SUMMARY

A 30-GeV ERL is proposed for the future electron-hadron collider eRHIC. The main ERL linac is based on five-cell, 704 MHz elliptical SRF structures. The cavities will have to accommodate high average beam currents and will have to be strongly HOM-damped to satisfy requirements imposed by BBU. The optimized cavity shape has been developed and the design of the HOM coupling scheme is in progress at BNL. The first cavity, BNL3-1, has been fabricated by AES and is being prepared for vertical testing. The second cavity is on order from Niowave. One of these prototype cavities will be used for the CeC PoP experiment.

REFERENCES

[1] V. Ptitsyn et al., "High Luminosity Electron-Hadron Collider eRHIC," IPAC'2011, p. 3726.
[2] V.Ptitsyn, "Overview of Assymmetric Electron Hadron Colliders," IPAC'2012, p. 1025.
[3] S. Belomestnykh et al., "Superconducting RF Systems for eRHIC," IPAC'2012, p. 2474.
[4] Wencan Xu, et al., "High current cavity design at BNL," *Nucl. Instr. and Meth. A* **622** (2010) 17-20.
[5] Wencan Xu, et al., "High Current SRF Cavity Design for SPL and eRHIC," PAC'2011, pp. 2589.
[6] Wencan Xu et al., "Progress on the High-Current 704 MHz Superconducting RF Cavity at BNL," IPAC'2012, p. 2486.
[7] Wencan Xu et al., "New HOM Coupler Design for High Current SRF Cavity," PAC'2011, p. 925.
[8] P. Jain et al., "Development of Fundamental Power Coupler for High Current Superconducting RF Cavity," IPAC'2012, p. 2483.
[9] I. Pinayev et al., "Status of Proof-of-Principle Experiment for Coherent Electron Cooling," IPAC'2012, p. 400.

Copyright © 2012 by the respective authors — cc Creative Commons Attribution 3.0 (CC BY 3.0)

DEVELOPING OF SUPERCONDUCTING RF GUNS AT BNL*

S. Belomestnykh[1,2#], Z. Altinbas[1], I. Ben-Zvi[1,2], C.H. Boulware[3], J. C. Brutus[1], A. Burrill[4], R. Calaga[5], M. Cole[6], J. Dai[2], A. Favale[6], D. Gassner[1], T.L. Grimm[3], H. Hahn[1], L. Hammons[1,2], D. Holmes[6], J. Jamilkowski[1], D. Kayran[1], J. Kewisch[1], X. Liang[2], V. Litvinenko[1,2], G. Mahler[1], G. McIntyre[1], D. Pate[1], D. Phillips[1], T. Rao[1], J. Rathke[6], M. Ruiz-Osés[2], T. Schultheiss[6], S. Seberg[1], T. Seda[1], B. Sheehy[1], J. Skaritka[1], K. Smith[1], R. Than[1], A. Todd[6], J. Tuozzolo[1], E. Wang[1], Q. Wu[1], T. Xin[2], Wencan Xu[1], A. Zaltsman[1]

[1)] Brookhaven National Laboratory, Upton, NY 11973-5000, U.S.A.
[2)] Stony Brook University, Stony Brook, NY 11794, U.S.A.
[3)] Niowave, Inc., Lansing, MI 48906, U.S.A.
[4)] JLab, Newport News, VA 23606, U.S.A.
[5)] CERN, Geneva, Switzerland
[6)] Advanced Energy System, Inc., Medford, NY 11763, U.S.A.

Abstract

BNL is developing several superconducting RF guns for different applications. The first gun is based on a half-cell 1.3-GHz elliptical cavity. This gun is used to study generation of polarized electrons from GaAs photocathodes. The second gun, also of a half-cell elliptical cavity design, operates at 704 MHz and is designed to produce a high average current electron beam for the R&D ERL from multi-alkali photocathodes. The third gun is of a quarter-wave resonator type, operating at 112 MHz. This gun will be used for photocathode studies, including a diamond-amplified cathode, and to generate a high charge, low repetition rate beam for the coherent electron cooling experiment. In this paper we describe the gun designs, present recent test results, and discuss future plans.

INTRODUCTION

Developing superconducting RF (SRF) photoinjectors is a part of the SRF program that is important for several projects in progress or under consideration at the Collider-Accelerator Department of BNL. The SRF photocathode guns promise to generate high-bunch-charge, high-average-current, low-emittance electron beams. The three SRF guns described in this paper address different issues, from generating polarized electrons, to experimenting with different photocathodes, to producing high-intensity beams for energy recovery linacs and electron coolers.

1.3 GHz SRF PLUG GUN FOR GaAs PHOTOCATHODES

SRF guns, which combine excellent vacuum conditions of DC guns and high accelerating gradients of RF guns, potentially can generate very low emittance polarized electron beams from GaAs photocathodes with long lifetime. Our simulations show that a SRF gun can exceed the ILC's requirement for vertical beam emittance by a factor of two, if an ellipsoid charge distribution is used. There will be no need for a damping ring.

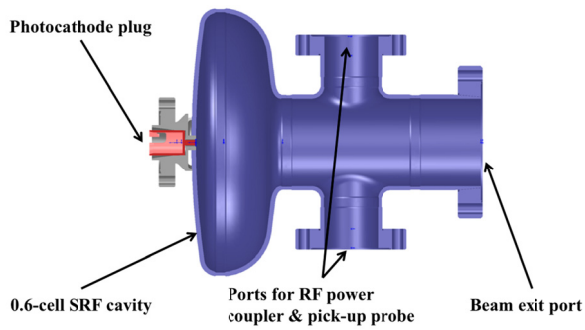

Figure 1: BNL 1.3-GHz plug SRF gun cavity.

Table 1: Parameters of the 1.3 GHz SRF gun

RF frequency	1300 MHz
Cavity active length	0.6 cell
Energy gain	0.6 MeV
Maximum field at the cathode	15 MV/m
e^- emission RF phase at 2.5 MV	20º
Cavity Q_0 at 2 K	7×10^9
Cavity operating temperature	2 K
Bunch repetition frequency	81.25 MHz
Bunch charge	0.12 pC
Bunch length	10 ps
Cathode spot size	2 mm dia.

We are using a 0.6-cell 1.3-GHz SRF plug gun to test the quantum efficiency (QE) and lifetime of a GaAs photocathode. It has got its name from a removable niobium plug holding a cathode and located at the back of the gun. The gun and cathode transfer system were

*Work is supported by Brookhaven Science Associates, LLC under contract No. DE-AC02-98CH10886 with the US DOE. The work at Niowave is supported by the US DOE under SBIR contract No. DE-FG02-07ER84861.
#sbelomestnykh@bnl.gov

Copyright © 2012 by the respective authors — cc Creative Commons Attribution 3.0 (CC BY 3.0)

designed and fabricated by AES, Inc. [1]. Figure 1 illustrates the cross section of the gun and Table 1 lists its main parameters. The Q_0 of 3×10^8 was obtained in a vertical test of the gun with a GaAs photocathode at JLab [2]. With our improved photocathode holder design, the Q_0 of the gun is estimated to be higher than 5×10^8.

A beam line for the beam test has been assembled and leak checked. A high temperature vacuum bake of the gun is necessary to achieve 10^{-11} Torr vacuum. Nb-Ti flanges began leaking during the bake. We plan to replace Nb-Ti flanges with two Conflat flanges, which can hold the high temperature easily. The refurbishment of the gun will be finished soon, and the final photoemission measurements are expected to take place in a few months.

The VTA test of the gun with the new holder and cathode is scheduled for mid-October of 2012. The goal of this is to test heat generating mechanism of the heavily doped GaAs in RF field. We successfully activated the bulk GaAs in a preparation chamber. The highest QE was 10% at 532 nm, which dropped to 0.8% after passing the photocathode through a transfer section to the gun [3].

704 MHz SRF GUN FOR R&D ERL

The R&D ERL at BNL is a facility dedicated to develop accelerator technologies for future energy recovery linac applications [4]. The project will be commissioned in several stages with an eventual goal to demonstrate operation with beam currents as high as 500 mA. A 704 MHz elliptical half-cell SRF gun was designed by BNL [5, 6] and fabricated by AES, Inc. Its main parameters are listed in Table 2.

Table 2: Parameters of the 704 MHz SRF gun

RF frequency	703.5 MHz
Cavity active length	8.5 cm (0.4 cell)
Maximum energy gain	2.5 MeV
Maximum field at the cathode	33.4 MV/m
E_{acc} at 2.5 MV	29.4 MV/m
e^- emission RF phase at 2.5 MV	33.4°
Energy gain at 500 mA	2.0 MeV
e^- emission RF phase at 2.0 MV	29.9°
Beam power at 500 mA	1 MW
R/Q	96.2 Ohm
Cavity geometry factor	112.7 Ohm
Cavity Q_0 at 2 K	3×10^{10}
Cavity operating temperature	2 K
Cavity RF losses (2 K) at 2.0 MV	1.4 W
Cathode operating temperature	80 K
Copper cathode RF losses (80 K) at 2.0 MV	226 W

The actual length of the nominally half-cell cavity is 0.4 cells. A copper cathode stalk is connected to the cavity via a specially designed quarter-wave choke joint. All surfaces of the choke joint are grooved to prevent multipacting [7]. The gun has two fundamental RF power couplers allowing delivery of 1 MW to a 500 mA electron beam. HOM damping is provided by a beamline ferrite load with a ceramic break [8]. A high temperature superconducting (HTS) solenoid is located inside the cryomodule near the beam exit.

The gun cryomodule was designed and fabricated by AES. Fundamental power couplers were manufactured by CPI/Beverly and were conditioned with maximum RF power of 250 kW pulsed and 125 kW CW in a full standing-wave mode [9]. The gun cavity was chemically etched, cleaned and vertically tested at Jefferson Lab. It reached accelerating gradient of 35 MV/m when tested without a cathode stalk.

The cryomodule was assembled at BNL, including its hermetic string (Figure 2) preparation in the clean room. It is installed in the ERL blockhouse for cold testing in Fall 2012 and subsequent beam operation. This gun will use a CsK_2Sb photocathode and is expected to operate with a gap voltage up to 2.5 MV and eventually generate a beam current of 500 mA at 2 MV.

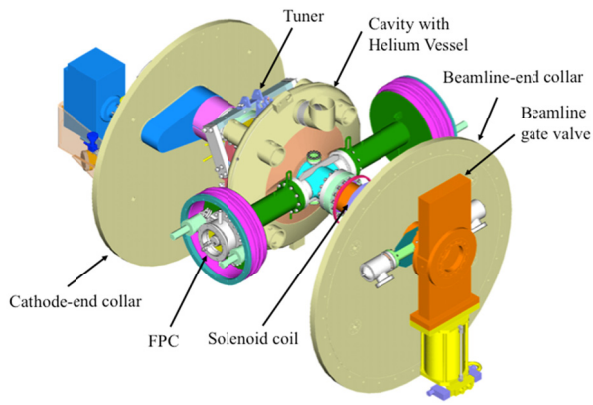

Figure 2: Hermetic string assembly of the 704-MHz SRF gun for R&D ERL.

112 MHz SRF GUN FOR COHERENT ELECTRON COOLING EXPERIMENT

A superconducting 112 MHz quarter-wave resonator (QWR) was developed for photocathode studies and electron gun experiments by collaborative efforts of BNL and Niowave, Inc. [10]. The low frequency was chosen to take full advantage of QWR benefits. The long wavelength allows generating long bunches and thus reducing space charge effects. A short, w.r.t. the wavelength, accelerating gap makes transit time factor close to unity and the gap field practically constant.

The gun will operate at 4.5 K with liquid helium provided from a quiet helium source via the cryomodule

Copyright © 2012 by the respective authors — cc Creative Commons Attribution 3.0 (CC BY 3.0)

cryogenic tower. Assuming a residual surface resistivity of 10 nOhm and a residual magnetic field of 60 mG, we expect to achieve the cavity quality factor of 1.8×10^9.

The QWR's center conductor geometry naturally accommodates a half-wavelength choke joint and allows mechanical decoupling of the cathode assembly from the niobium cavity [11]. A low RF loss photocathode stalk operates at room temperature. It is hollow, allowing inserting a small photocathode pack via a load lock system. Experiments are planned with multi-alkali and diamond-amplified photocathodes. The gun cryomodule is shown in Figure 3 and the gun parameters are listed in Table 3.

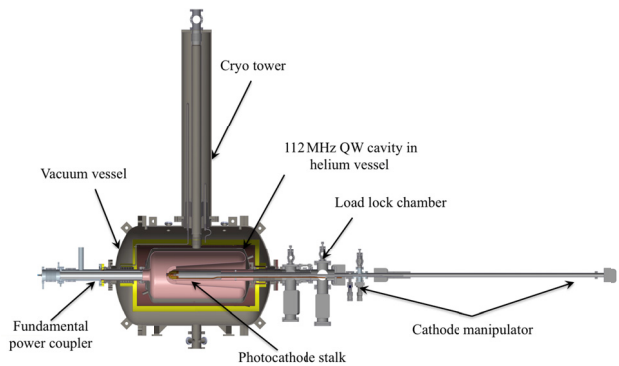

Figure 3: 112 MHz SRF gun cryomodule.

Table 3: Parameters of the 112 MHz QWR SRF gun

RF frequency	112 MHz
Maximum energy gain	2.0 MeV
Bunch charge	1 to 5 nC
Bunch repetition frequency	78 kHz
R/Q	127.3 Ohm
Geometry factor	38.5 Ohm
Cavity Q_0 at 4.5 K	1.8×10^9
Cavity RF losses at 2.0 MV	17 W
RF losses in the cathode stalk at 2.0 MV	38 W
Frequency tuning range	78 kHz
Frequency tuning with FPC	3 kHz
Q_{ext} of FPC, min.	1.25×10^7
Available RF power	2 kW

The 112 MHz gun will be equipped with a double-purpose fundamental RF power coupler/fine frequency tuning assembly [11]. The fine frequency tuning with a range of 3 kHz will be used for remote frequency adjustment. It will complement a larger range (78 kHz) tuner, which will be used only for an initial frequency set up. A focusing solenoid is placed on top of the FPC close to the cryomodule flange.

The cavity was chemically etched, high-pressure rinsed at Niowave, and first cold test of the gun was successfully performed there in December of 2010. The cavity Q of greater than 10^9 was measured and maintained up to ~0.5 MV accelerating voltage, and the pressure sensitivity of the fundamental mode was measured at 10 Hz/mbar [9]. At present, the gun cryomodule is undergoing modifications for compatibility with installation in RHIC tunnel, where it will become a part of the Coherent electron Cooling Proof-of-Principle (CeC PoP) experiment [12]. The first cool down of the modified gun at BNL is scheduled for 2013. The gun is expected to operate at an accelerating voltage up to 2 MV and generate electron beams with a charge per bunch from 1 to 5 nC.

SUMMARY

The superconducting RF photoemission sources of electron beams promise to provide high-quality electron beams for a variety of accelerator applications. At BNL, we are pursuing several design options. The 704 MHz gun for R&D ERL is assembled and its commissioning will begin soon. The other two guns are at different stages of modification with the goal to begin experiments in 2013.

REFERENCES

[1] D. Holmes et al., "Superconducting RF Photocathode Gun for Low Emittamce Polarized Electron Beams," SRF'2007, p. 434.
[2] Erdong Wang at al., *Chinese Physics C*, 2011, **35**(4): 387-391.
[3] Erdong Wang et al., "Testing a GaAs cathode in SRF gun," PAC' 2011, p. 388.
[4] D. Kayran et al., "Status of High Current R&D Energy Recovery Linac at Brookhaven national Laboratory," PAC'2011, p. 2148.
[5] R. Calaga et al., *Physica C* **441**, 159 (2006).
[6] A. Burrill et al., *Nucl. Instr. Meth. Phys. Res.* A **557**, 75 (2006).
[7] Wencan Xu et al., "Multipacting Simulation and Test Results of BNL 704 MHz SRF Gun," IPAC'2012, p. 2480.
[8] H. Hahn et al., *Phys. Rev. ST Accel. Beams* **13**, 121002 (2010).
[9] Wencan Xu et al., *Phys. Rev. ST Accel. Beams* **15**, 072001 (2012).
[10] S. Belomestnykh et al., "Superconducting 112 MHz QWR Electron Gun," SRF'2011, p. 223.
[11] T. Xin et al., "Design of the Fundamental Power Coupler and Photocathode Inserts for the 112 MHz Superconducting Electron Gun," SRF'2011, p. 83.
[12] I. Pinayev et al., "Status of Proof-of-Principle Experiment for Coherent Electron Cooling," IPAC'2012, p. 400.

Copyright © 2012 by the respective authors — cc Creative Commons Attribution 3.0 (CC BY 3.0)

IMPACT OF TRAPPED FLUX AND SYSTEMATIC FLUX EXPULSION IN SUPERCONDUCTING NIOBIUM

J. Vogt, O. Kugeler, J. Knobloch, Helmholtz-Zentrum für Materialien und Energie (HZB)

Abstract

The intrinsic quality factor Q_0 of superconducting cavities is known to depend on various factors like niobium material properties, treatment history and magnetic shielding. To study trapped flux in Niobium we constructed a test stand at Horizontal Bi-Cavity Test Facility (HoBiCaT) at HZB using niobium rods equipped with thermal, electrical and magnetic diagnostics. The focus in this study was on the behaviour of the trapped flux when the sample is slowly warmed up towards the critical temperature T_c. Besides the (incomplete) Meissner effect we observed additional flux expulsion starting at ≈0.1K below T_c. The reduced level of trapped flux is maintained when the sample is cooled down again and can even be improved by repeating the procedure. Possible explanations for the effect are discussed.

INTRODUCTION

We already reported on the impact of temperature gradients during the cool-down on the obtained Q_0 [1]. In the quest for minimization of RF losses in SRF cavities the impact of trapped vortices is one main topic. The vortices have a normal conducting core with a surface resistance about 6 orders above that of superconducting Niobium. This surface fraction is proportional to the trapped magnetic flux. The surface resistance was determined to be 2.2nΩ per μT for a 1.5GHz cavity [2]. A crucial step in avoiding trapped flux is an improved understanding of flux trapping behaviour of Niobium.

The energetically most favourable state of bulk Niobium at 1.8K (4.2K) is the Meissner phase, in which all magnetic field present in the normal conducting state is expelled. However, expulsion of flux can be incomplete, yielding a remaining magnetization of the material even after removing the external field source. The dynamics of this trapped flux is still not well understood. One approach was the investigation of flux that is permitted to penetrate a marginal type II superconductor in the mixed state. Here, the flux tubes form a lattice and several studies [3, 4] indicate a phase transition from localized (solid, fixed regular lattice) flux tubes towards moveable (liquid) flux tubes when the superconductor exceeds certain temperature / magnetic field combinations as indicated by the black dotted "melting line" in Figure 1.

The behavior of flux that is trapped in the Meissner state is uncertain. A continuation of the melting line in this phase is conceivable, so that flux lines in the check region (Figure 1) may be able to exit the Niobium below T_c. In our study, we examine the properties of the trapped magnetic flux in the Meissner phase when the rod is slowly warmed up.

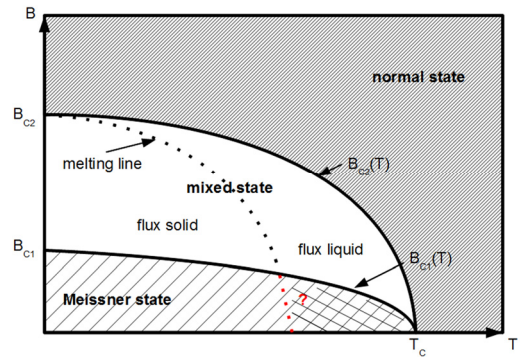

Figure 1: Magnetic phase diagram of marginal Type II superconductor [5]. The added red dotted line indicates a possible extension of the liquid/solid flux interface into the Meissner state. The size of the check region is exaggerated.

EXPERIMENTAL SETUP

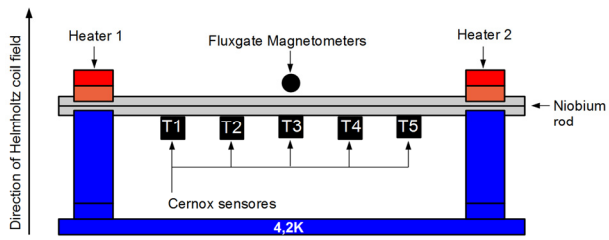

Figure 2: Experimental setup

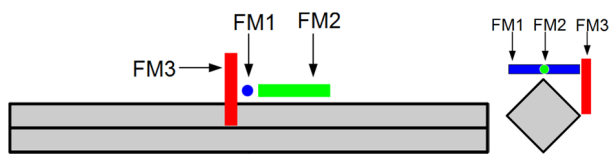

Figure 3: Positions of fluxgate magnetometers (FM): Longitudinal view (left) and cross section (right) of FM1 (black), FM2 (green) and FM3 (red)

For the experiments, a RRR=300 niobium rod (8.4x8.4x300mm) was positioned inside HoBiCaT [6]. It was conduction cooled through the posts to 4.2K. In order to reduce heat transfer into the Helium, heat conductivity was reduced by introducing a kapton foil between rod and support stands. Both ends of the rod were equipped with a resistive heater. They could be individually regulated to control the temperature of the rod with 10mK accuracy. Five Cernox temperature sensors with mK resolution and three fluxgate magnetometers with 1nT resolution (Bartington Mag-01H), one for each spatial direction,

Copyright © 2012 by the respective authors — cc Creative Commons Attribution 3.0 (CC BY 3.0)

were attached along the rod. A Helmholtz coil (HC) for the generation of a vertical magnetic field up to ±300μT enclosed the whole construction. The setup and the positions of the instruments are displayed in Figures 2 and 3.

MANIPULATION OF TRAPPED FLUX

In each of the performed experiments a magnetic field is applied using the HC while the Nb rod is cooled through T_c. Afterwards, the rod is smoothly warmed by manually adjusting the two heaters and the change in the magnetic field is observed by three fluxgate magnetometers (FM). Precise temperature control was exercised to ensure that at no time T exceeded T_c.

Manipulation without applied field

In the first set of experiments the HC is turned off after the rod has reached the minimum temperature. Hence, the signal registered subsequently by the FMs roughly corresponds to the frozen flux inside the rod. Referring to Figure 4, this is position (A).

When the rod is warmed up again, the magnetisation observed by the FMs stays constant until a temperature of T≈9.1K (<T_c) is reached. At this point the amount of trapped flux suddenly starts to drop (B) until a minimum level is reached (C). When the warming is stopped during the decrease and the rod is cooled, the level of trapped flux at the instance of stopping remains - even upon subsequent cooling.

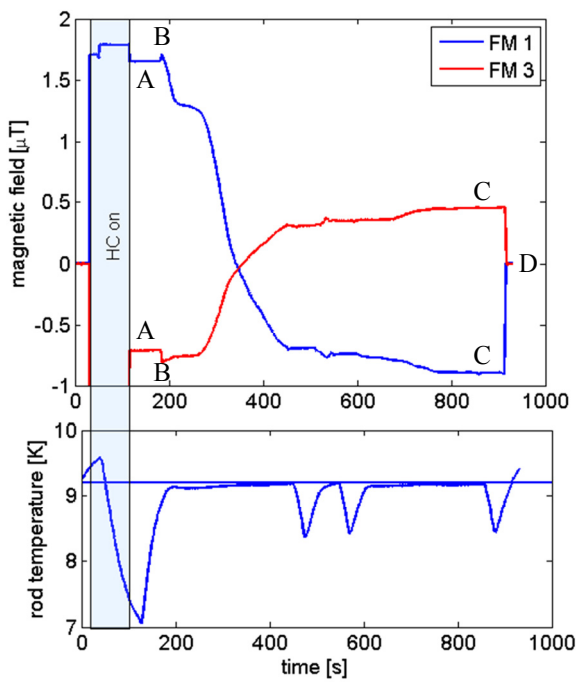

Figure 4: Behaviour of trapped flux and temperature when a HC field of 33μT is applied and trapped: Initially trapped flux (A), minimal trapped flux (C) and level of flux ambient in HoBiCaT ≈3μT (D). This value has been subtracted from all data points.

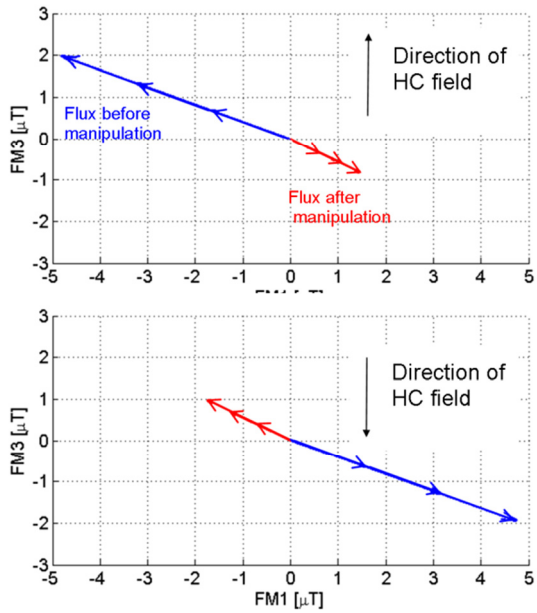

Figure 5: Trapping for HC fields: 33μT, 65μT, 97μT (above) and -32μT, -66μT, -98μT (below). The initially trapped field is blue and the field after additional expulsion is red.

The signals obtained by FM1 and FM3 are displayed in Figure 4. For better visualization their values can be combined to a vector indicating the spatial orientation of the trapped flux, see Figure 5. The signal of FM2 is more than one order of magnitude smaller than the signals of FM1 and FM3 due to the orientation of HC and rod and therefore is not displayed here.

The change in the trapped flux indicates that the warming enables the trapped flux lines to move. A possible explanation could be that the thermal energy exceeds the pinning potential and the pinning potential barrier does not hinder the movement of flux lines anymore ("liquid flux state"). Driving force for the movement could be the strive for approaching the energetically most favourable state – the complete Meissner state – given by a minimum of sc/nc interface area. Not all flux is expelled because different pinning centres have different pinning potentials [7] and not all of them can be exceeded by the thermal activation. Also the driving force reduces, the less flux remains in the sample. We observe:

(1) A redistribution of flux lines (here even change in sign due to geometry) and
(2) A reduction of the absolute amount of frozen flux

The latter is evident from the shortening of the vectors in Figure 5. Table 1 displays the values of the initially trapped field and the minimal trapped field in the end of the procedure for different HC fields. We achieved an expulsion of up to 75%.

Copyright © 2012 by the respective authors — cc Creative Commons Attribution 3.0 (CC BY 3.0)

Table 1: Magnetic field before and after expulsion

B_{HC} [µT]	$\lvert B_{trapped}\rvert$ [µT]	$\lvert B_{minimised}\rvert$ [µT]	Expulsion [%]
33	1.98	0.50	75
65	3.91	1.19	70
97	5.84	1.88	68
-32	1.87	0.88	53
-66	3.80	1.57	59
-98	5.73	2.26	61

Manipulation with applied field

These investigations raise the question how the flux tubes behave when an external field is not turned off during warm up as opposed to the above experiment, where an external field was trapped but only the ambient field remained during warm up.

Figure 6 displays a typically obtained signal of FM1. In the beginning the rod is normal conducting (A). It is cooled below T_c where flux is expelled by Meissner effect (B). The magnetic field probe measures an increase in the field density outside the rod. Afterwards the rod is slowly warmed using the heaters. Starting at a temperature of (9.08±0.01)K we observe a sudden decrease in expelled flux (C) which coincides with the onset of Paramagnetic Meissner Effect (PME) reported by Thompson [8]. The onset temperature does not depend on the applied field strength in the range of ±300µT tested here. The PME is a phenomenon observed in some high temperature superconductors and in Niobium. These materials exhibit a paramagnetic phase between the perfect diamagnetic behaviour in the Meissner state and the normal conducting state. Note the difference to classical frozen flux which is a topological coexistence of normal conducting and Meissner-like areas.

When the rod is warmed up further, a second effect occurs. When T_c is approached an additional expulsion of flux is evident (D) resulting in a lower level of residual frozen flux (i.e. a higher level of expelled flux). Subsequent repetition of cooling and heating leads to a minimized level of trapped flux (E) and each time we observe the PME. Further repetition leads only to the jumps in magnetisation due to PME but no further change in the level of trapped flux.

A possible explanation for this systematic flux expulsion could be an increased mobility of flux lines in a temperature regime close to T_c consistent with the data obtained in the first set of experiments.

In this set of experiments, HC fields of up to ±300µT were applied leading to expulsion pattern that were all similar to Figure 6. Hence, systematic flux expulsion works under these conditions.

CONCLUSION

The amount of trapped magnetic flux can be manipulated and systematically minimized while the material remains superconducting. The complete Meissner state is thus being approached.

If one could apply such a procedure to SRF cavities, this effect could lead to higher Q_0 values and operation close to the BCS-limit. In addition, the major impact of the cooling dynamics in the temperature range between 9.08K and T_c on the flux trapping behaviour could explain the impact of temperature gradients during the cool-down on the obtained Q_0 values as described in [1].

ACKNOWLEDGMENT

We would like to thank A. Frahm for the design of the testing apparatus and S. Klauke and M. Schuster for help with setting up the experiment.

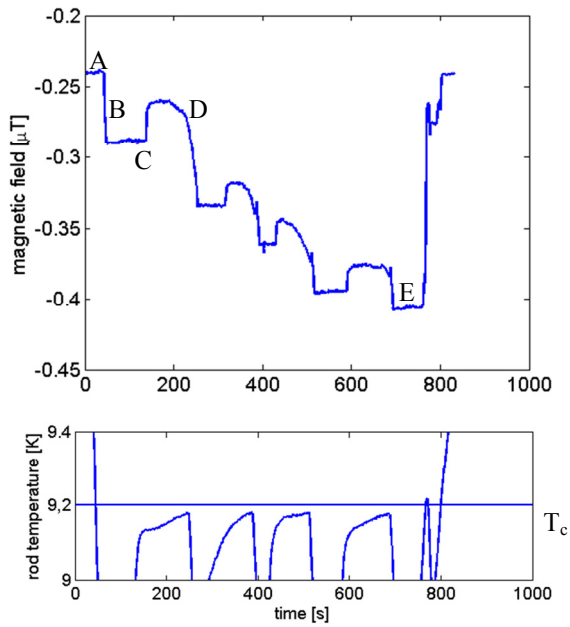

Figure 6: Behaviour of trapped flux (FM1) and temperature upon heating in ambient field (background field trapped and partially expelled)

REFERENCES

[1] O. Kugeler, J. Vogt, J. Knobloch, S. Aull, "Impact of Trapped Magnetic Flux and Thermal Gradients on the SRF Cavity Quality Factor", *Proc. 5th IPAC2012*, New Orleans (2012), p. 2203.
[2] P. Kneisel and B. Lewis, Tech. Rep. Tech. Note 94–028, Continuous Electron Beam Accelerator Facility, 1994
[3] J.W. Lynn, N. Rosov, T.E. Grigereit, H. Zhang, T.W. Clinton, Phys. Rev. Lett. 72, 1994
[4] J. Kierfeld, Phys. Rev. B 69, 2004
[5] C. Poole,"Handbook of Superconductivity", 2000
[6] O. Kugeler, A. Neumann, W. Anders, and J. Knobloch, Review of scientific instruments, vol. 81, Jul. 2010, p. 074701.
[7] W. Buckel, R. Kleiner, "Superconductivity", 2004
[8] D.J. Thompson, M.S.M. Minhaj, L.E.Wenger and J.T. Chen, Phys. Rev. Lett. 75, 1995

Copyright © 2012 by the respective authors — cc Creative Commons Attribution 3.0 (CC BY 3.0)

ALTERNATIVE APPROACHES FOR HOM-DAMPED CAVITIES*

Bernard Riemann†, TU Dortmund University, Dortmund, Germany
Axel Neumann, Helmholtz-Zentrum Berlin, Berlin, Germany
Thomas Weis, TU Dortmund University, Dortmund, Germany

Abstract

In this paper, we present two different ideas that may be useful for design and simulation of (superconducting) radio frequency cavities.

To obtain longitudinal and transverse voltages resp. shunt impedances in cavities without rotational symmetry, one or two integration paths are often used to get an approximate difference relation for the transverse voltage of higher order modes (HOMs). The presented approach uses a multipole decomposition that is valid in vicinity of the central axis to compute voltage multipole decomposition directly for paths of arbitrary number and position.

Elliptical cavities have been a standard in SRF linac technology for 30 years. We present another approach to base cell geometry based on Bezier splines that is much more flexible in terms of optimization, while reaching equal performance levels.

POLAR PATH INTEGRAL ANALYSIS

In the following section, the longitudinal and transverse voltages are expressed using a multipole decomposition. By pseudo-inversion of the resulting equation system (similar to polynomial interpolation), one can calculate the corresponding coefficients directly from an arbitrary number and position of integration paths.

This method also allows to check a) if the position and number of paths is appropriate to extract the desired coefficients, b) if there is any "noise" in the voltage paths that stem from computational errors or from a too large distance of the path from the central axis.

Signed Effective oltages

The effective longitudinal and transverse acceleration voltages can be written as complex Fourier integrals

$$\tilde{V}_{\parallel} = \int E_s(s) \exp\left(ik_\beta s\right)\, \mathrm{d}s \in \mathbb{C}, \tag{1}$$

$$\tilde{\vec{V}}_{\perp} = \frac{1}{q} \int \vec{F}_{\perp}(s) \exp\left(ik_\beta s\right)\, \mathrm{d}s \in \mathbb{C}^2, \tag{2}$$

where $\vec{F}_\perp$ is the total transverse Lorentz force, and E_s is the longitudinal electric field at the path position s. The complex angle $\Psi_0 = \arg(\tilde{V}_\parallel)$ corresponds to an optimal acceleration phase, and its magnitude to the acceleration voltage for this phase (see [6] for a special derivation of this relation with a fixed $\Psi_0 = 0$).

For each mode, the phases of $\tilde{V}_\parallel$ on all paths are equal up to an additional shift by π, corresponding to a sign change (deceleration). Using a fixed phase Ψ_0 that is one of the two possible optimal phases, we may define a real acceleration voltage for the optimal phase by

$$V_\parallel := \tilde{V}_\parallel \cdot e^{-\mathrm{i}\Psi_0} \in \mathbb{R}. \tag{3}$$

and, using the Panofsky-Wenzel theorem, a corresponding real transverse voltage may be defined by

$$\frac{\partial}{\partial t}\tilde{\vec{V}}_\perp = i\omega\tilde{\vec{V}}_\perp = -\vec{\nabla}_\perp \tilde{V}_\parallel \tag{4}$$

$$\vec{V}_\perp = \begin{pmatrix} V_x \\ V_y \end{pmatrix} = -i\tilde{\vec{V}}_\perp \cdot e^{-\mathrm{i}\Psi_0} \in \mathbb{R}^2. \tag{5}$$

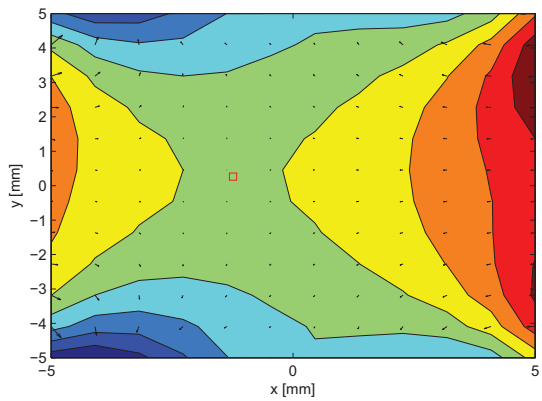

Figure 1: Reconstruction of the transverse (arrows) and longitudinal (isolines) voltages in the beam area with contributions from different multipole components. The corresponding coefficients were computed from voltages on circularly arranged integration paths at 5mm offset from beam axis for an eigenmode of the B*ERL*inPro main linac cavity. The red square marks the transverse forceless point z_0 which deviates from the axis by more than 1 mm.

Holomorphic Multipole Expansion

By using a complex analytic multipole decomposition

$$F(z) \approx \sum_p c_p\, z^p, \tag{6}$$

where $z = x+iy = re^{i\phi}$ is the transverse position of the integration path, and $c_p = a_p + ib_p$ are complex numbers that

* this work is supported by BMBF contract 05K10PEA
† bernard.riemann@tu-dortmund.de

Copyright © 2012 by the respective authors — cc Creative Commons Attribution 3.0 (CC BY 3.0)

describe the magnitude and orientation of different multipoles, the signed longitudinal and signed transverse voltages can be expressed as

$$V_{\parallel}(z) := \Im F(z) = \sum_p r^p [b_p \cos(p\phi) + a_p \sin(p\phi)] \quad (7)$$

$$\Rightarrow X(z) := \frac{\mathrm{d}}{\mathrm{d}z} F = -\omega(V_y + iV_x) = \sum_p p c_p \, z^{p-1} \quad (8)$$

Multiple Path Equation System

Assuming there are N numerical integration paths at transverse positions z_n set up for the computation, they can be combined into a vector thus summarizing the problem into two matrix equations.

$$\vec{V}_{\parallel} = \Im \left[\mathbf{M} \begin{pmatrix} c_0 \\ \vdots \\ c_{P-1} \end{pmatrix} \right] \quad , \quad \vec{X} = \mathbf{M} \begin{pmatrix} 1c_1 \\ \vdots \\ Pc_P \end{pmatrix} \quad (9)$$

where $\mathbf{M}$ denotes the $N \times P$ Vandermonde matrix defined by $M_{n,p} = z_n^{p-1}$.

The matrix equation for $\vec{V}_{\parallel}$ is sufficient to solve for the coefficients. On the other hand, the possible occurance of numerical errors in the path integral computation and the limited validity of the multipole decomposition, which only holds for small $|z|$, enforces cross-checking with the transverse data. To get the best results, information of all V should be used simultaneously. To do this, rectangular matrices $\mathbf{G}$ are defined by

$$\begin{pmatrix} c_0 \\ \vdots \\ c_{P-1} \end{pmatrix} = \mathbf{G}_1 \vec{c} \quad , \quad \begin{pmatrix} 1c_1 \\ \vdots \\ Pc_P \end{pmatrix} = \mathbf{G}_2 \vec{c}, \quad (10)$$

where $\vec{c}$ is a $P+1$-dimensional vector containing all c_p from 0 to P. The imaginary part of the bracketed term in (9) can be expressed in terms of the real and imaginary components $\vec{a}, \vec{b}$.One must now also separate $\vec{X}$ into its real and imaginary multipole components. Furthermore, the resulting matrix equation is still complex, since $\vec{X}$ is a complex vector, but $\vec{V}_{\parallel}$ must be real (which leads to inversion problems). To resolve this, the final equation system can be written as

$$\begin{pmatrix} \vec{V}_{\parallel} \\ \Re\vec{X} \\ \Im\vec{X} \end{pmatrix} = \begin{pmatrix} \Im\mathbf{M}\,\mathbf{G}_1 & \Re\mathbf{M}\,\mathbf{G}_1 \\ \Re\mathbf{M}\,\mathbf{G}_2 & -\Im\mathbf{M}\,\mathbf{G}_2 \\ \Im\mathbf{M}\,\mathbf{G}_2 & \Re\mathbf{M}\,\mathbf{G}_2 \end{pmatrix} \begin{pmatrix} \vec{a} \\ \vec{b} \end{pmatrix}. \quad (11)$$

To solve this equation system for $\vec{a}, \vec{b}$, singular value decomposition

$$\begin{pmatrix} \vec{V}_{\parallel} \\ \vec{X} \end{pmatrix} := \mathbf{u}\mathbf{\Sigma}\mathbf{v}^* \begin{pmatrix} \vec{a} \\ \vec{b} \end{pmatrix} \Rightarrow \begin{pmatrix} \vec{a} \\ \vec{b} \end{pmatrix} = \mathbf{v}\mathbf{\Sigma}^{-1}\mathbf{u}^* \begin{pmatrix} \vec{V}_{\parallel} \\ \vec{X} \end{pmatrix} \quad (12)$$

is used. For voltages of a number of eigenmodes Q to be processed, their column $2N$ vectors can be concatenated to form a $2N \times Q$ matrix.

Since multipole expansion of the longitudinal voltage is used, there must be at least one extremal point if components higher than dipolar are included. In fact, if the field is dominated by quadrupolar modes, one is interested in the exact position of this extremal point z_0, since the transverse voltages included in $X(z)$ cancel out for this path. The extremal point z_0 is given by

$$X(z_0) = \sum_p p c_p \, z_0^{p-1} \stackrel{!}{=} 0, \quad (13)$$

which can easily be solved numerically for z_0 by finding the roots of the given polynomial.

To check if the number and position of paths for the given multipole order is sufficient, one should check for the ratio σ_1/σ_P to be not too large. To check if the multipole decomposition method is valid for the integration path region, one should investigate if the components larger than P of the vector $\mathbf{u}^* \begin{pmatrix} \vec{V}_{\parallel} \\ \vec{X} \end{pmatrix}$ do vanish.

Preliminary Results and Outlook

Figure 1 shows a reconstructed area around the central axis path for the B*ERL*inPro main linac cavity for a mainly quadrupolar mode, and the forceless path position. The irregular isolines at the outer edge indicate a mixing with higher order multipole field components. For more results on the B*ERL*inPro main linac, see [1].

The obtained information is important in the consideration of coupler kicks that do not stem from the operational mode, but from quadrupolar or higher order modes (HOM coupler kicks). The question whether to include mainly quadrupolar modes into HOM damping considerations may be answered using such studies, especially the z_0 position distribution along all HOMs of the cavity. Such a study may also help to answer questions regarding alignment tolerances of cavities and cavity strings.

For including more distant points from the axis into the equation, one may consider to relax the multipole conditions and to include Bessel function terms into the modal decomposition basis, thus allowing for two or more different complex coefficients to describe each multipole. As an extreme case for all points of a cylindrical mesh, this would be equivalent to a waveguide mode-like decomposition of the generalized path voltages on an electric boundary plane with $V_{\parallel}, \mathrm{i}V_{\perp}$ instead of $\vec{E}_{\parallel}, \mathrm{i}\vec{H}_{\perp}$.

BEZIER SPLINE CAVITIES

In modern accelerator facilities, high acceleration gradients and duty cycles are achieved using SRF cavities. To protect these cavities from quenching and RF breakdown, sufficiently small peak surface electric fields in comparison to acceleration gradient $E_{\mathrm{surf}}/E_{\mathrm{acc}}$ are necessary. Therefore, the cavity shapes must be constructed from smooth profile curves.

Copyright © 2012 by the respective authors — cc Creative Commons Attribution 3.0 (CC BY 3.0)

From the disk-loaded cavity, design of such cavities has evolved from first rounding off the edges, and then substituting them by elliptical shapes, leading to modern SRF "re-entrant", "low-loss" and "TESLA-shape" [5] cavities which suppress resonant multipacting of secondary electrons. While elliptical shapes have shown superior performance, this parameterization is qualified by historical developments, as to the authors' knowledge, no other parameterizations of similar smoothness have been systematically researched for ultra-relativistic particles. The spline cavity geometry is such an alternative shape with additional desirable properties [2].

Figure of Rotation Parameters

A Bezier spline is a parameterized curve [3]

$$\vec{s}(t) = \vec{a}_0 + \vec{a}_1 t + \vec{a}_2 t^2 + ... = \sum_{n=0}^{N} \vec{s}_n b_{n,N}(t) \qquad (14)$$

with Bernstein polynomials $b_{n,N}$ and $t \in [0,1]$. The $N+1$ points $\vec{s}_n$ define the so-called control polygon and contain the free parameters of the spline. Let us consider the simplest possible case of a cubic ($N = 3$) Bezier spline as shown in Fig. 2. The geometry parameters are reduced by cell periodicity conditions and elementary RF constraints to a set of only three parameters [2], compared to five for an elliptical cavity. These parameters can be optimized according to the specific purpose of the cavity.

Implementation and Results

For the single cell computations with periodic boundary conditions, we used the well-known 2d code SUPERFISH [4]. Since the SUPERFISH mesher cannot use spline curves, a small wrapper for MATLAB was developed. The spline geometry was discretized by calculating a 200 point (halfcell) polygon from its parameters (Fig. 2), which was then used as input in SUPERFISH, also specifying a special localized mesh that matches the polygon discretization accuracy.

A parameter sweep for a given iris radius and an external equator tuning procedure were also implemented to tune all cavity sets to a π-mode frequency of 1.3 GHz [2]. The scan of the $(v_1, v_2)/L$ parameter space was processed in a spiral pattern to fully exploit the similarities between spline shapes with only slight parameter differences. A second scan with given radii for the 0-mode was performed, obtaining the corresponding frequency needed for the intercell coupling constant κ [6]. The procedure for a fixed iris radius took approx. 3.5 hours on a standard PC [2].

Figure 3 shows the results for a typial iris radius of 35 mm. It can be seen by comparison e.g. with [5] that the cubic spline shape geometry performance is in roughly the same range as the standard elliptical cavity geometries, although as stated, the cubic shape has two less free parameters. By inspecting the map, the trade-off between different figures of merit in the design process becomes visible (see e.g. red and black lines).

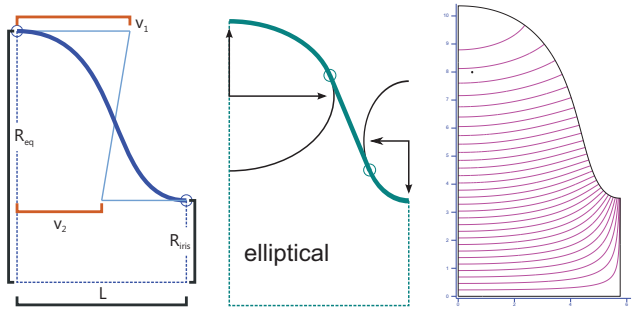

Figure 2: Parameterization for cubic Bezier shape (left), elliptical parameterization (center) and exemplary result for electric field lines ($v_1 = 0.9, v_2 = 0.65, R_{\mathrm{iris}} = 35\,\mathrm{mm}, R_{\mathrm{eq}} = 103.60\,\mathrm{mm}$, right)

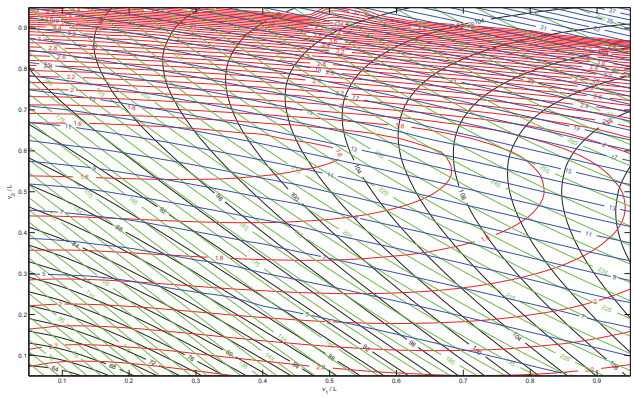

Figure 3: Cubic Bezier map for a 1.3 GHz cavity with iris radius 35 mm. The map shows the cubic interpolated isolines of $R/Q\,[\Omega]$ in black, $E_{\mathrm{surf}}/E_{\mathrm{acc}}$ in red, the Geometry factor $[\Omega]$ in green, and the intercell coupling constant $[10^{-3}]$ in blue.

REFERENCES

[1] A. Neumann et al., "Results and performance simulations of the main linac design for B*ERL*inPro", these proceedings.

[2] B. Riemann et al., "Design of SRF cavities with profiles based on Bezier splines", ICAP'12, Rostock, August 2012, WEP14.

[3] Paul De Casteljau. "Courbes à pôles", National Industrial Property Institute (France), 1959

[4] K. Halbach and R.F. Holsinger. "SUPERFISH - a computer program for evaluation of RF cavities with cylindrical symmetry", *Part. Acc.*, 7:213–222, 1976.

[5] Aune et al., "Superconducting TESLA cavities", *Phys. Rev. ST Accel. Beams* Vol. 3 pp. 092001 (2000)

[6] T. Wangler, *RF Linear Accelerators*, 2nd ed., Wiley-VCH, 2007

Copyright © 2012 by the respective authors — cc Creative Commons Attribution 3.0 (CC BY 3.0)

RESULTS AND PERFORMANCE SIMULATIONS OF THE MAIN LINAC DESIGN FOR B*ERL*inPro*

A. Neumann†, W. Anders, J. Knobloch, Helmholtz-Zentrum Berlin, Berlin, Germany
B. Riemann, T. Weis, TU Dortmund University, Dortmund, Germany
K. Brackebusch, T. Flisgen, T. Galek, K. Papke, U. van Rienen, Rostock University, Rostock, Germany

Abstract

The Berlin Energy Recovery Linac Project (B*ERL*inPro) is designed to develop and demonstrate CW LINAC technology for 100-mA-class ERLs. High-current operation requires an effective damping of higher order modes (HOMs) of the 1.3 GHz main linac cavities.

We have studied elliptical seven cell cavities damped by five waveguides at the adjacent beam tubes. Eigenmode calculations for geometrical figures of merit show that the present design should allow successful cw linac operation at the maximum beam current of 100 mA / 77pC bunch charge.

In this paper the progress in HOM calculations to avoid beam-breakup instabilities for the favored cavity structure is presented.

INTRODUCTION

B*ERL*inPro will be a CW driven ERL machine with a maximum current of 100 mA beam and a maximum energy of 50 MeV, while preserving a normalized emittance of better than 1 mm mrad at a pulse length of 2 ps [1]. The main linac cavity has strong HOM damping requirements since it is passed by two 100 mA beams that both resonantly interact with transverse deflecting (e.g. TM_{110}) cavity modes, leading to beam break up (BBU) [2].

An ERL cavity design must minimize the HOM's $R/Q_\perp$ and external quality factors Q_{ext} [8]. The mid-cell design influences the HOM spectrum, dispersion relation and operational mode acceleration performance (see [8] for op. mode parameters of the tuned structure). By proper end-cell tuning that preserves field flatness for the fundamental TM_{010}-π mode, mode localization (trapping) can be avoided and the Q_{ext} can be recuced to a sufficient extent.

In this paper updated HOM calculations of the main linac cavity using new methods are presented [8], and an outlook on ongoing activities to decompose the cavity structure into smaller parts is given [5] [9].

STRUCTURE EIGENMODE CALCULATIONS

The design under consideration is a seven cell structure using the Cornell ERL mid-cell design [6] and combining it with JLab 3-fold symmetric waveguide HOM couplers [7] (see Figure 1). Flexible input power coupling is enabled by replacing one waveguide with a TTF-III type coaxial fundamental power coupler (thus breaking the 3-fold symmetry). The design aims at combing the peak field properties of the Cornell design with the advantage of waveguide couplers having a natural cutoff above the fundamental, and further limiting the possibility of dust intruding from ferrite beam tube absorbers into the cavity.

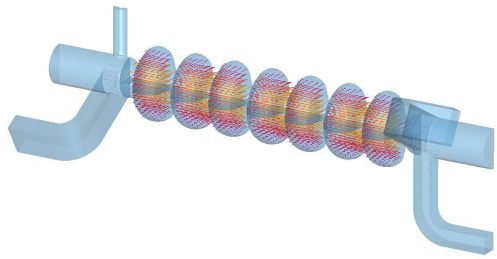

Figure 1: Rendering of the cavity design under consideration for B*ERL*inPro with a cut through the symmetry (FPC) plane and electric field magnitude of the operational mode.

	ERL shape Cornell U.	**Spline shape** TU Do, v4 / v5
$E_{\text{surf}}/E_{\text{acc}}$ (π mode)	2.07	2.08 / 2.07
$R_\parallel/Q$ (π mode)	111 Ω	113 Ω / 112 Ω
intercell coupling κ	2.1 %	1.7 % / 1,9 %
Geometry factor G	272.7 Ω	- / 269.5 Ω

Table 1: Cavity mid-cell figures of merit comparison.

Base cells

In parallel to periodic boundary mid-cell calculations, such calculations were also performed using Spline-based cells [4]. Table 1shows a preliminary comparison between 36 mm radius mid-cells for both designs. At the moment, development concentrates on the Cornell ERL mid-cell. Further development and degree elevation of the spline design may lead to a mid-cell shape with higher performance.

Transverse shunt impedance

The final goal will be to minimize the product $R/Q_\perp \cdot Q_{\text{ext}}$ for all HOMs. $|\vec{V}_\perp|^2 \propto R_\perp/Q$ can be computed di-

* Work supported by Federal Ministry for Research and Education BMBF under contract 05K10HRC and 05K10PEA
† Axel.Neumann@helmholtz-berlin.de

Copyright © 2012 by the respective authors — cc Creative Commons Attribution 3.0 (CC BY 3.0)

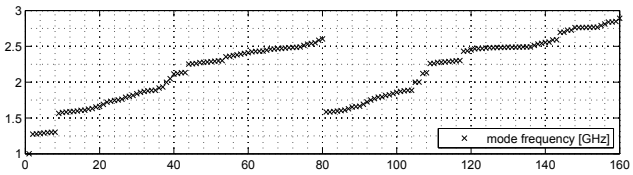

Figure 2: Frequency of all modes up to 2.85 GHz, about the lower range of the 4th dipole band. All modes were computed using the JDM eigenmode solver of CST MWS™.

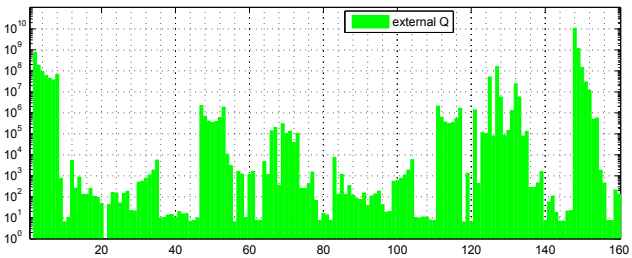

Figure 3: External Q of all TM/TE modes up to 2.85 GHz. While the dipole modes are sufficiently damped, some quadrupole modes exhibit large $Q_{\text{ext}} > 1 \cdot 10^6$.

rectly from the fields on the central axis by

$$\vec{V}_\perp = \frac{1}{q} \int \vec{F}_L(s) \exp\left(ik_\beta s\right)\, \mathrm{d}s \cdot \exp(-\mathrm{i}\Psi_0) \in \mathbb{R}^2 \quad (1)$$

simultaneously with its polarization and additional information about optimal phase relations in Ψ_0 [3]. The resulting $R/Q_\perp$ is shown in Figure 4. Again the dipole modes seem sufficiently damped while some quadrupole modes due to their high Q_{ext} and a small, but finite non-zero shunt impedance on axis show to be the most harming modes concerning BBU.

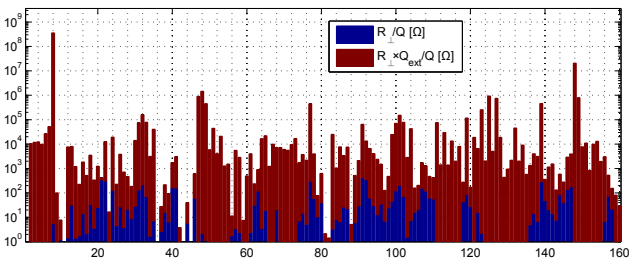

Figure 4: Transverse $R/Q_\perp$ and $R/Q_\perp \cdot Q_{\text{ext}}$ for all TM and TE modes up to 2.85 GHz (beginning of 4th dipole band). The arrow marks the coupler kick by the TTF-III power coupler at the fundamental mode.

Polar path analysis

The action of seemingly small voltages from mainly quadrupolar modes, giving rise to large instabilities, leads to the question if and to which extent quadrupole mode damping should be considered in realistic cavity designs, based on the influence of higher order mode coupler kicks and imperfections in beam path position and construction issues. Due to the broken rotational symmetry, any eigenmode may consist of different multipole components. A scheme named polar path analysis was developed [3] to extract the voltage components a_p, b_p of the longitudinal (and equivalently, transverse) voltage

$$V_\parallel(r,\phi) \approx \sum_p r^p [b_p \cos(p\phi) + a_p \sin(p\phi)] \quad (2)$$

from all available longitudinal and transverse voltages on an arbitrary number of integration paths N (the different paths are comprised into vectors of the respective voltages) by constructing and pseudo-inverting a rectangular matrix $\mathbf{A}$ in an equation system of the form [3]

$$\begin{pmatrix} \vec{V}_\parallel \\ \omega\vec{V}_x \\ \omega\vec{V}_y \end{pmatrix} = \mathbf{A} \begin{pmatrix} \vec{a} \\ \vec{b} \end{pmatrix}. \quad (3)$$

To investigate the possible shift of quadrupole modes a calculation of $R_\perp/Q$ along circular distributed integration paths at an arbitrary offset of 5mm was performed. Fig. 5 shows the results of the eigenmode computation for a mode with a dominating quadrupole component. Fig. 6 is a plot of the reconstructed transverse area with the result coefficients $|a_0 + \mathrm{i}b_0| = 3,5 \cdot 10^4$ V (monopole), $|a_1 + \mathrm{i}b_1| = 1.28 \cdot 10^5$ V/mm (dipole) $|a_3 + \mathrm{i}b_3| = 4.6 \cdot 10^4$ V/mm^2 (quadrupole) and $|a_4 + \mathrm{i}b_4| = 5.6 \cdot 10^2$ V/mm^3 (sextupole).

For quadrupolar modes, we are interested in the shift of the transverse forceless path. Fig. 6 also shows the marked forceless point given as a solution of the complex polynomial $X(z) \stackrel{!}{=} 0$ [3].

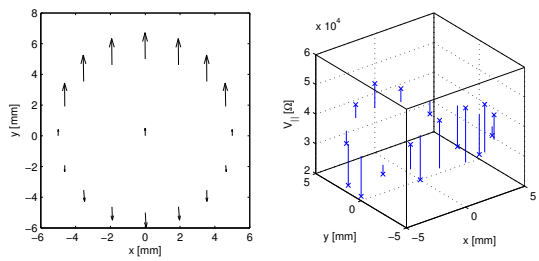

Figure 5: Polar plot of transverse (left, arrows) and longitudinal (right) voltages determined on circularly arranged integration paths at 5mm offset from beam axis for a mainly quadrupolar mode.

Most modes of these quadrupole bands are shifted more than the expected vertical beam size in the linac and thus mainly quadrupole modes may exhibit a non-neglectible dipole component. This effect needs to be investigated in more detail and it has to be understood how much the coupler's position influences this effective dipole component of the quadrupole modes.

Copyright © 2012 by the respective authors — cc Creative Commons Attribution 3.0 (CC BY 3.0)

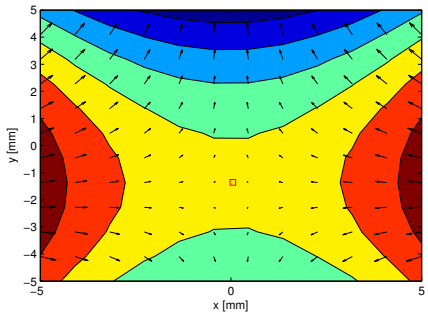

Figure 6: Reconstruction of the transverse (arrows) and longitudinal (isolines) voltages in the beam area from the data shown in Fig. 5. The red square marks the transverse forceless point.

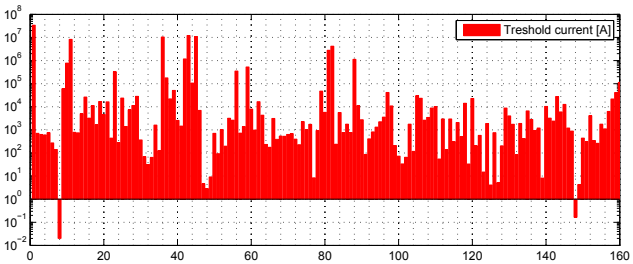

Figure 7: Approximate (orders of magnitude) calculations for the treshold current based on Eq. 4.

Treshold current

To evaluate and optimize the cavity, we use a simpflied equation for the treshold current

$$I_{\mathrm{th}} \approx \frac{2c}{e} \frac{E_0}{R_\perp/Q\, Q_{\mathrm{ext}} \omega} \qquad (4)$$

for one cavity HOM that still depends on the mode's transverse shunt impedance $R/Q_\perp$, its external quality factor Q_{ext} and frequency ω and the beam's energy E_0, but neglects the influence of recirculation time and the recirculation arc linear beam optics ("worst phase" assumption).

The results of our preliminary treshold current calculation for all modes are shown in Fig. 7. The seemingly smallest current value is not valid due to being equivalent to a coupler kick of the operational mode which is externally driven and cannot be described by the treshold current formula.

OUTLOOK

Full 3d structure eigenmode computations using several million mesh cells for hundreds of modes need too much computational resources to implement them as iteration steps into an optimizer routine for end-cell tuning (to lower the Q_{ext} for the dangerous HOMs). Thus, the next steps in B*ERL*inPro main linac cavity design will either consist of using Coupled S-parameter Calculations [11] of the segmented structure (see Fig. 8) with 2d eigenmode calculations of the rotationally symmetric cavity, or using a state-space equation system with a similarly separated structure [9] to find a set of end-cells with field-flat op. modes that are then optimized for maximum overall HOM damping ($R_\perp/Q \cdot Q_{\mathrm{ext}}$) [5]. The sufficient cavity sets will then be concatenated to the full three cavity string, as already the lowest order dipole modes propagate along the beam tube and couple to the neighboring rf structures.

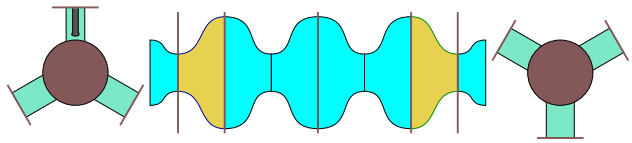

Figure 8: Cavity separation planned for CSC. The rotationally symmetric structure is decomposed along the equator radii, with an additional separation at the outer endcell iris. The resulting structure is concatenated with the 3d FPC/waveguide damping structure and the 2d (cartesian) 3-fold symmetric waveguide damping structure.

REFERENCES

[1] M. Abo-Bakr et al., "B*ERL*inPro - A Compact Demonstrator ERL for High Current and Low Emittance Beams", LINAC'10, Tsukuba, September 2010,.

[2] Y. Petenev et al., "Modeling of the Beam Break Up Instability for B*ERL*inPro ", IPAC'11, San-Sebstian, September 2011, MOPS051, p. 718, http://www.JACoW.org

[3] B. Riemann et al., "Alternative approaches for HOM-damped cavities," MOPB066, these proceedings

[4] B. Riemann et al., "Design of SRF cavities with profiles based on Bezier splines", ICAP'12, Rostock, August 2012, WEP14.

[5] T. Galek et al., "Traveling Poles Elimination Scheme and Calculations of External Quality Factors of HOMs in SC Cavities", ICAP'12, Rostock, August 2012, WEP07.

[6] N. Valles and M. Liepe, "Seven-cell Cavity Optimization for Cornell's Energy Recovery Linac", SRF'09, Berlin, September 2009, THPPO008, p. 538.

[7] F. Marhauser, "JLab High Current Cryomodule Development", ERL'09, Ithaca NY, September 2009, WG307.

[8] A. Neumann et al., "Status of the HOM calculations for the B*ERL*inPro main linac cavity", ICAP'12, Rostock, August 2012, FRAAC3.

[9] T. Flisgen et al., "Lumped equivalent models of complex RF structures", ICAP'12, Rostock, August 2012, THACI1.

[10] Computer Simulation Technology AG, Microwave Studio®, 64289 Darmstadt, Germany http://www.cst.com

[11] K. Rothemund, H.-W. Glock, U. van Rienen, "Eigenmode calculation of complex rf-structures using S-parameters", (2000) IEEE Transactions on Magnetics, 36 (4 I), pp. 1501-1503.

Copyright © 2012 by the respective authors — cc Creative Commons Attribution 3.0 (CC BY 3.0)

STUDY OF HPR CREATED OXIDE LAYER AT Nb SURFACES

P. V. Tyagi#, GUAS, Tsukuba, Japan
T. Saeki, M. Sawabe, H. Hayano, S. Kato, KEK, Tsukuba, Japan

Abstract

The performance of superconducting radio frequency (SRF) niobium (Nb) cavities mainly depends on final surface condition therefore the surface preparation of these SRF cavities becomes very important. The preparation of surface includes two steps; surface chemistry (in order to get a smooth surface) and cleaning/rinsing (in order to remove contaminants left after the surface chemistry). As high pressure rinsing (HPR) with ultra pure water (UPW) is most commonly used surface cleaning method after the surface chemistry, it's very interesting to characterize the Nb surfaces after HPR. The surface characterizations show the presence of a thicker oxide layer at Nb surface as an outcome of HPR. In this article, we report the production of oxide layer (FWHM thickness) based on different conditions such as high pressure and doses. The surface characterization was done by XPS (x-ray photoelectron spectroscopy) with depth profiling.

INTRODUCTION

Final surface preparations [1] of niobium (Nb) superconducting radio frequency (SRF) cavities play a critical role in order to achieve high performances. Final surface preparation includes mainly two steps 1) surface chemistry in order to make surface smoother and 2) post cleaning processes in order to remove chemical residues left after the surface chemistry. As a step two, the High Pressure Rinsing (HPR) with ultra pure water/deionized water (UPW/DI), is most commonly used surface cleaning procedure worldwide [2,3]. The HPR seems to be a most effective cleaning procedure and HPR treated cavities have shown high field gradient with a high Q value. For the last two decades, HPR has been successfully used on SRF cavity surfaces and became an integral part of the final surface preparation of Nb SRF cavities. In order to make HPR more effectively for removal of the contaminants from cavity surface, the HPR operating parameters such as high pressures and doses should be carefully determined.

In this paper, we report our efforts towards finding of the optimized pressure and doses for HPR. In this regard, three samples were initially buffer chemical polished (BCPed) and subjected to HPR with three different pressures and two doses. For the HPR experiments, a commercial high pressure washer machine was used which can reach to a maximum pressure of 15 MPa. After the experiments, sample surfaces were analyzed by XPS (x-ray photo-electron spectroscopy).

Email: puneet.tyagi@helmholtz-berlin.de
#Presently at Helmholtz Zentrum Berlin
Work was conducted in KEK, Tsukuba Japan.

EXPERIMENTAL DETAILS

Surface Analysis

After the experiments, all the samples surfaces were analysed by XPS and a depth profile can be obtained. Our surface analysis system contains one main chamber along with three loadloack mechanism. The main chamber is equipped with an electron energy analyzer, an ion mass spectrometer, a x-ray source, an electron gun, an ion gun for depth profiling, an extractor gauge, and a residual gas analyzer. The analysis system is capable of executing Auger electron spectroscopy (AES), secondary ion mass spectrometry (SIMS) with argon ion etching, and XPS with probing area of 2 mm. Fig. 1 is the overview of our surface analysis system. The main chamber is maintained at extremely high vacuum [4].

The three loadlock mechanism provides the facility to transfer the samples from vacuum environment to main chamber without exposing them in to air. A vacuum suitcase (maintained at UHV) can be attached to one of the loadloak chambers with it and sample can be transferred from the suitcase to the analysis chamber keeping in vacuum. A sample storage chamber, which maintains the base pressure of 10^{-8} Pa, is also connected to one of the loadlock chambers to keep remaining samples in the carousel in UHV. Also, samples can be mounted to one of the loadlock chambers directly from the atmosphere and can be transferred to main chamber after achieving UHV.

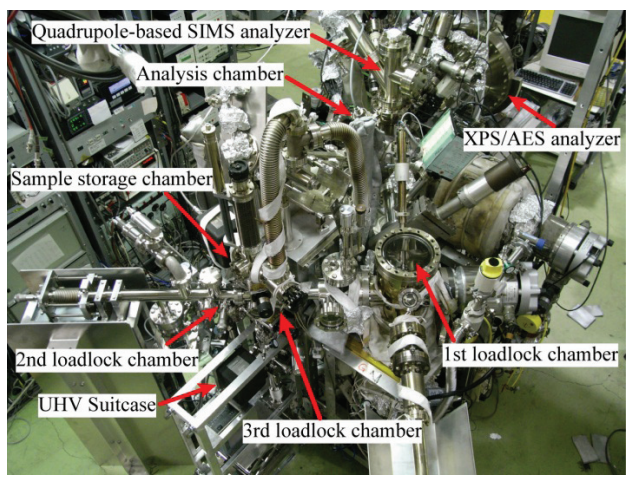

Figure 1: Overview of the surface analysis chamber.

HPR Experiments

We have conducted a series of HPR experiments on three Nb samples with three different pressures and two doses. The dose can be defined as the total injected

Copyright © 2012 by the respective authors — cc Creative Commons Attribution 3.0 (CC BY 3.0)

quantity of water/area. The aim of the experiment was to explore the effect of different parameters of HPR on contaminants removal after the surface chemistry.

A commercial Kranzle high pressure washer machine was used for the HPR experiments which can attain the pressure up to 15 MPa. The nozzle of the lance was made of ceramic with the diameter of 1 mm. For the experiments, three Nb samples (rectangular type: 20x14x2.8mm^3) were initially BCPed and a depth of 20 µm was removed. The sample (one by one) was mounted on a base plate which was fixed on a slide rail and can be slid during the HPR. We used one separator which separates the sample in two parts, to avoid the effect of rinsing of another position by side-streams of the water beam. Each sample was subjected to two doses at different places for each pressure. In order to keep the same dose as of other HPR facilities, we had calculated the total scanning time of the sample during the HPR was 1 second corresponding to a dose of 0.79l/cm^2. The other dose of 7.9l/cm^2 corresponding to a scanning time of 10 second was selected to compare the effect of different doses. During the HPR, each sample was manually scanned. Totally, six experiments were conducted with two doses for three different pressures. The distance between sample and nozzle was kept 50 mm to get highest pressure and to avoid the spreading of water beam. The experiment was conducted in class 1000 clean room. After the HPR experiment, all the samples were analyzed by XPS and a depth profile was obtained for each experiment.

EXPERIMENTAL RESULTS

XPS results of the BCPed sample followed by UPW rinsing only, showed that a huge amount of fluorine (up to 7 at. %) was found at top surface.

Table 1: The atomic composition present at top surface of the samples after HPR with different pressures as a function of dose

Elements	Atomic Composition Present at Samples Surface (Atomic %)						
	Dose=0.79l/ cm^2			Dose=7.9l/ cm^2			UPW rinsing
	8 MPa	10 MPa	15 MPa	8 MPa	10 MPa	15 MPa	
Nb	19	20	16	18	22	19	24
C	17	17	28	17	21	19	23
O	62	54	55	63	57	62	45
F	1.5	1.2	1	1.2	0.3	0.3	7

As it can also be encountered from the table 1 that the HPR was quite effective to mitigate the fluorine from the sample surfaces. The lowest fluorine was found on the surfaces treated with the higher dose. According to XPS results, it is evident that not only the higher pressure is effective in order to mitigate the chemical contaminants from the surface but higher dose is more advantageous over the high pressure.

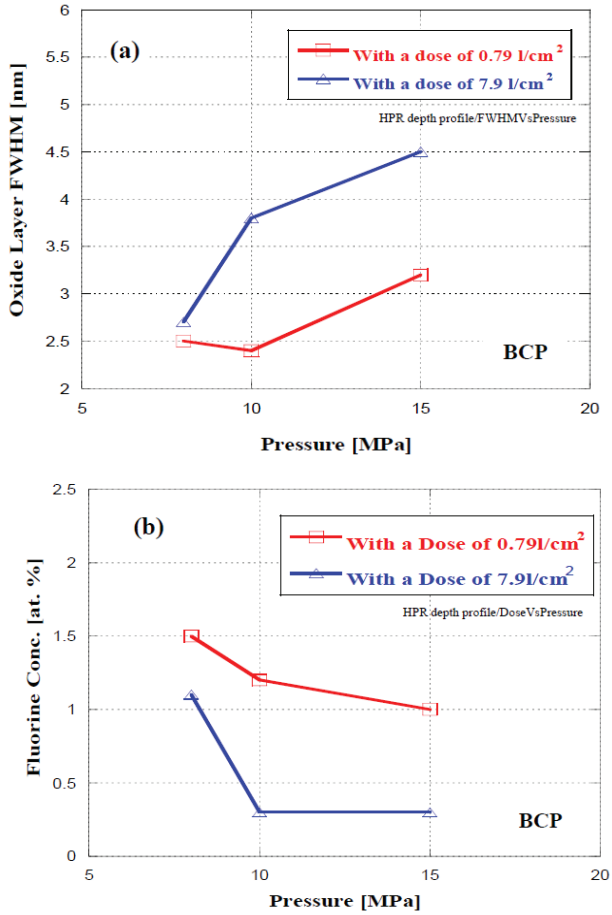

Figure 2: (a) Variation of oxide layer FWHM as a function of pressure and dose. (b) Reduction in fluorine concentration based on pressure and dose.

The depth profiles of all the samples showed a great increment in the thickness of oxide layer after the HPR. It can be seen from the fig. 2 (a) and (b) that the fluorine was reduced to same amount (up to 0.3 at.%) in case of the HPR with 10 MPa and 15 MPa with a high dose but a thicker oxide layer was produced by HPR with 15 MPa and a high dose. The FWHM oxide layer was found 0.7 nm thicker in case of 15 MPa than 10 MPa with a high dose (see table 2).

Copyright © 2012 by the respective authors — cc Creative Commons Attribution 3.0 (CC BY 3.0)

Table 2: The FWHM oxide layer thickness of after the HPR.

Pressure (MPa)	FWHM oxide layer thickness (nm)	
	Dose=0.79l/ cm^2	Dose=7.9l/ cm^2
8	2.5	2.7
10	2.4	3.8
15	3.2	4.5

It is also noticed that the amount of fluorine was increased at 1 nm depth and was similar in all the cases which shows that the HPR is effective to mitigate the contaminants from top layer of surface (<0.5 nm) only.

DISCUSSIONS

After the surface chemistry of Nb SRF cavities, the chemical residues such as fluorine and sulfur left after the process are expected to be the measure source of field emission during the operation of Nb SRF cavity. The HPR with optimum parameters will provide the better performance of SRF cavities ultimately a significant reduction in the production cost of Nb SRF cavities. Our surface analysis results of the HPR experiments showed that the HPR with high pressure and high dose was quite effective to remove contaminants after the surface chemistry. The depth profiles of the samples showed that the HPR with high pressure and dose produces a thicker oxide layer which might be a concern from SRF point of view. As it can be seen from our results, one side HPR with high pressure and dose seems to be very effective in order to mitigate the contaminants, another side it produces a thicker oxide layer. Therefore, in order to use HPR effectively, the balance in all the operating parameters should be carefully determined.

CONCLUSIONS

We have conducted a series of HPR experiments with three different pressures of 8, 10 15 MPa and two doses of 0.79l/cm^2 and 7.9l/cm^2. The experimental results showed that the fluorine was reduced to same amount after the HPR with high pressures of 10 and 15 MPa and a dose of 7.9l/cm^2 while a thicker oxide layer was created in case of the sample treated with 15 MPa and 7.9l/cm^2. Therefore it can be concluded from our experiments that the HPR with high pressures and doses is very effective to mitigate the contaminants after the surface chemistry but produces a thicker oxide layer.

ACKNOWLEDGMENT

The authors express their special thanks to Mr. T. Noguchi and Mr. V. Chouhan for their support in the experimental work.

REFERENCES

[1] TESLA Technology Collaboration, TTC Report No. 2008-05.
[2] D. Sertore et.al., "Study of the high pressure rinsing water jet interactions", Proceedings of EPAC08, MOPP154, June 2008, Genoa, Italy.
[3] E. Cavaliere et al., Physica C **441** (2006), 254-257.
[4] M. Nishiwaki et. al., "Surface study using niobium sample coupons for super conducting rf cavity" Proceedings of the PAC 09, TU5PFP070, May 2009, Vancouver, Canada.

Copyright © 2012 by the respective authors — cc Creative Commons Attribution 3.0 (CC BY 3.0)

QUALITY CONTROL OF CLEANROOM PROCESSING PROCEDURES OF SRF CAVITIES FOR MASS PRODUCTION*

R. Oweiss#, K. Elliott, A. Facco+, M. Hodek, I. Malloch, J. Popielarski, L. Popielarski, K. Saito
Facility for Rare Isotope Beams (FRIB), Michigan State University, East Lansing, MI 48824, USA
+INFN - Laboratori Nazionali di Legnaro, Padova, Italy

Abstract

Quality control is a key factor in the SRF cavity mass production. This paper summarizes ongoing research at the facility of Rare Isotope Beams (FRIB) to validate the quality assurance of SRF cavities while optimizing processing procedures for mass production. Experiments are conducted to correlate surface cleanliness for niobium surfaces with high pressure rinse time using β=0.085 quarter-wave resonators (QWR) cavities. Diagnostic devices, a liquid particle counter, a surface particle detector and a total organic carbon (TOC) analyzer are used to monitor key parameters for quality control. Rinse water samples are collected during high pressure rinsing to measure liquid particle counts. The SLS 1200 Sampler is used to detect the presence of liquid particles of 0.2µm and up to 1µm to set standards for acceptable cleaning thresholds and optimize high pressure rinse time. The QIII+ surface particle detector is used to scan the high electric field region of the β=0.085 QWR to ensure high pressure rinsing efficiency. The β=0.085 QWR RF testing data are analyzed and results are presented to investigate the correlation between attained acceleration gradients and surface cleanliness.

INTRODUCTION

A quality control (QC) system is in place for cleanroom processing of SRF cavities at FRIB. The FRIB QC system embeds diagnostic tools and stringent cavity processing procedures to control particle contamination, increase field emission onset level and attain high acceleration gradients. The e-traveler system is launched to document procedures and to provide a reporting tool for data mining and decision-making. This paper presents the findings of the commissioning and use of the liquid particle counter during the high pressure rinsing process. The paper also focuses on the QC steps for the clean assembly of β=0.085 QWR, and investigates the potential of predicting the cavity attained gradient (E_{acc}) at field emission onset based on its QC data collected during processing.

QUALITY CONTROL FOR CLEANROOM PROCEDURES

High Pressure Rinsing (HPR)

HPR is a key step that precedes the final SRF cavity assembly for RF vertical testing. HPR is proven the most effective tool as a final surface treatment to remove particles and to reduce field emission [1]. The FRIB HPR tool for production is still under development. The current HPR tool resides in an ISO5 cleanroom. Cavities are high pressure rinsed by rotating the cavity on a rotary aluminum cylinder flange as illustrated in Figure 1. A stainless steel spray nozzle wand with 8 jets moves in and out from below the rotating cavity. The HPR system utilizes a 3HP CAT pump and a final 0.1µm filter; both of which are located outside the cleanroom. The CAT pump pressurizes the ultra-pure water to ~ 8300 kPa.

Figure 1: β=0.085 QWR on high pressure rinse in ISO5 cleanroom

Ultra-pure Water (UPW) Quality Control

A reliable ultra-pure water system is essential to the successful operation and process quality of the HPR system. The current ultrapure water system is fed by a 7.6 l/m reverse osmosis system (RO). The resistivity of the ultrapure water system ranges between 17.2-17.6 MΩ-cm. The resistivity is monitored by an inline resistivity meter. The TOC is measured routinely for all points of use on the UPW distribution line using a TOC analyzer. The UPW TOC levels are consistently below 50 ppb. The microbiological quality of the system is analyzed every year to detect any bacterial buildup and assess the need for the system sterilization. Ultimately, a well-defined maintenance schedule is followed to replace critical system components. [2]

Another integral component for monitoring the UPW and the HPR process is the liquid particle counter. The Liquid particle counter (SLS-1200) is a device that pressurizes the water sample using a built in pump and a syringe. The device is capable of detecting 0.2µm size particles and up to 1µm. A ¼" stainless steel national pipe tapered thread (NPT) fitting was installed on HPR system tray to collect drain water samples during cavity HPR.

* Work supported by the U.S. Department of Energy Office of Science under Cooperative Agreement DE-SC0000661.
#oweiss@frib.msu.edu

Copyright © 2012 by the respective authors — cc Creative Commons Attribution 3.0 (CC BY 3.0)

Liquid Particle Counter Commissioning Experiments

An experiment was set up to HPR one β=0.085 QWR (SC246X) and commission the liquid particle counter. The cavity was high pressure rinsed for 140 minutes per standard operating procedure. Rinse water samples were collected off the NPT fitting with tygon tubing that fed directly into a glass beaker. Another set of samples was collected directly off the NPT fitting without the tygon tubing. Samples were analyzed for liquid particle counts to display a descending trend with time as the cavity gets cleaner (see Figure 2). Athough the tygon tubing was ultrasonic cleaned, the cumulative liquid particle counts in rinse water samples collected with the tubing attached were extremely higher than those collected without the tubing. It was concluded that liquid particle counts samples should be collected directly off the NPT fitting.

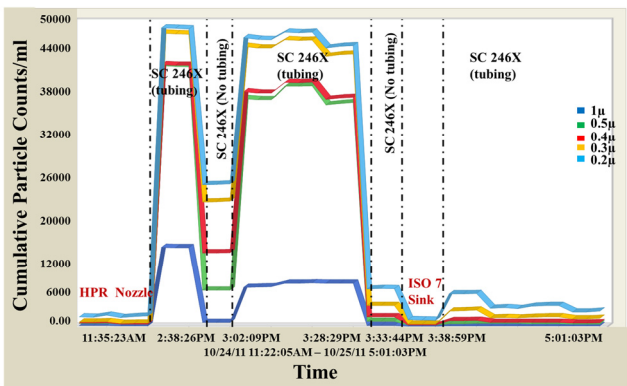

Figure 2: β=0.085 QWR (SC246X) HPR liquid particle counts time chart 10/24/2011

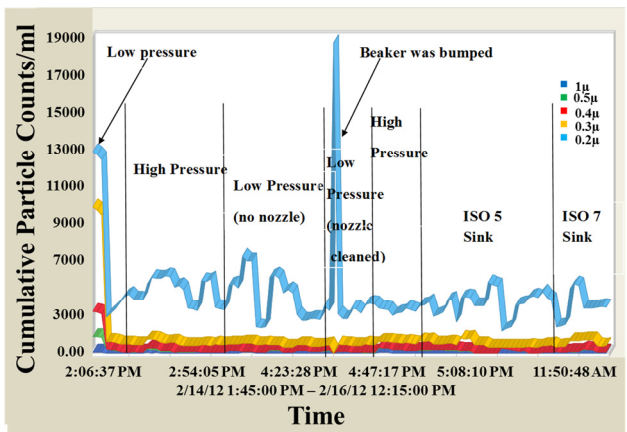

Figure 3: Liquid particle counts time chart for the UPW baseline experiment 02/14/12 - 02/15/12

Figure 3 displays the results for the baseline water quality experiment. This experiment was performed to investigate the water quality of the UPW system and to determine the HPR system baseline particle counts.

High and low pressure water samples were collected from the HPR wand with and without the spray nozzle. Samples were also collected from the ISO7 and ISO5 cleanroom sinks. Then the nozzle was disassembled from the wand, inspected, ultrasonic cleaned and re-installed to collect low and high pressure samples. UPW samples were also collected from ISO5 and ISO7 cleanroom sinks. Results were plotted for comparison (see Figure 3). TOC and resistivity were recorded for each sample with values of 58 ppb and 17.2 MΩ-cm respectively. It was concluded that UPW from HPR spray nozzle has the same quality as the cleanroom sinks. The 0.3µm cumulative liquid particle counts ranged between 400-500 particles/ml.

It was noted that on one of the samples the beaker was accidently bumped, creating a lot of bubbles. A sharp peak was recorded on the 0.2µm size counts (Figure 3), probably counting air bubbles as particles. Thus we will only report the 0.3µm cumulative liquid counts for all subsequent cavity processing and experimental work.

Components Preparation, Cleaning & Assembly QC Steps

Components used on cavity assembly undergo QC checks for residual magnetic field using a magnetometer. A demagnetizer is used to demagnetize components with residual field levels greater than 50 mG for ReA3 and greater than 15 mG for FRIB. The residual magnetic field is re-checked to ensure the acceptable threshold was attained. Components are prepared for the cleanroom using the following standard operating procedure: degrease with acetone, scrub using 1% solution of Micro-90®, rinse in deionized water, and wipe with ethanol. Components ultrasonic cleaning takes place in the ISO7 cleanroom for 30 minutes in a 1% solution of Micro-90® in UPW at 37.8°C, followed by a final ultrasonic rinse in UPW at 60°C for 40 minutes [3]. In the ISO5 cleanroom components are set to dry for assembly on the next day.

QC checks are performed on cleaned, dried components prior to their assembly to the cavity. The QIII+ surface particle counter is used to scan the seal surface on blanks, flanges, tuning plates, input and output couplers. The device is capable of detecting the presence of 0.3µm particles and up to 10µm. The surface particle detector uses a destructive sampling technique; as particles are removed from the surface, therefore the component gets cleaner. Surface particle counts are performed inside the cavity beam ports and RF ports. The inner surface of the outer conductor is also scanned for surface particle counts in the region below the beam and RF ports. These counts are illustrated as Q1, Q2, Q3 and Q4 in Figure 5. The surface particle count threshold for qualifying assembly components is set at 0.05 particles/cm^2 for the 0.3µm cumulative counts.

Air particle counts are performed at the cavity beam line before assembly to detect the 0.5µm particle size counts. The QC threshold of less than 1333 particles/m^3 must be attained for the clean assembly to take place.

CAVITY PROCESSING QC DATA & TEST RESULTS

Three β=0.085 QWR production cavities have passed the vertical Dewar testing at 4.3K and have been certified and assembled toReA3 coldmass string. During the tests, the amount of X-rays emitted from the cavity is measured

Copyright © 2012 by the respective authors — cc Creative Commons Attribution 3.0 (CC BY 3.0)

with an ion chamber approximately 1 meter from the cavity. Figure 4 shows that the acceleration gradient for SC251, 256 and 252 production QWRs had a large margin above the ReA3 goal of 3.4 MV/m. The figure also shows test results for two prototype cavities (SC246 & SC247).

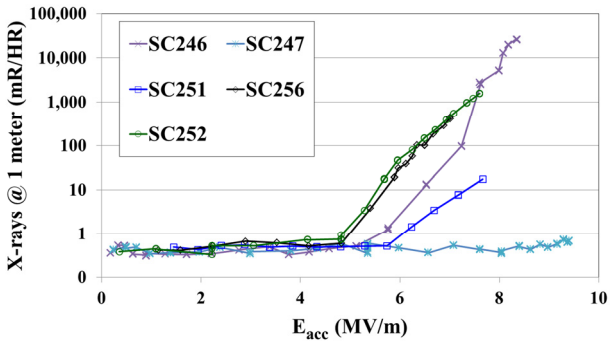

Figure 4: Field emission vs. E_{acc} for β=0.085 QWRs

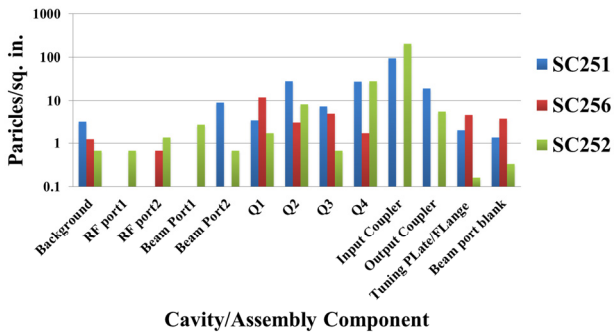

Figure 5: 0.3µm cumulative surface counts for β=0.085 QWR production cavities

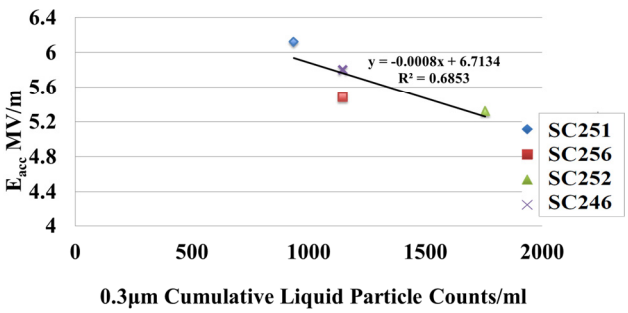

Figure 6: E_{acc} vs. 0.3µm cumulative final HPR liquid particle counts for β=0.085 QWR cavities

All cavities were processed per standard operating procedures; liquid particle counts were sampled every 20 minutes during HPR. QC checks and surface particle counts were performed on the cavities and assembly components to quantify cleanliness as in Figure 5.

Figure 6 is a plot for the 0.3µm cumulative liquid particle counts at the end of the β=0.085 QWR HPR vs. the cavity accelerating gradient at initial field emission onset. The figure illustrates a trend for an acceleration gradient at initial field emission onset of less than 5.9 MV/m if the cumulative liquid particle counts at the end of HPR is greater than 1000 particles/ml. We reported SC247 test results with no field emission and with the implementation of the QC system we recorded its final HPR cumulative liquid particle counts to be equal to the baseline particle counts of the UPW at HPR point of use.

CONCLUSION

FRIB cleanroom procedures have improved with the contribution of the QC system to ensure reproducibility of processing & clean assembly for mass production. The liquid and surface particle counters have been successfully commissioned and used. Acceptable cleaning thresholds have been identified. The overall surface cleanliness of cavities and assembly components has improved. The performance of β=0.085 QWR cavities that have been tested over the past year has improved; all production cavities were certified for ReA3. The processes are being optimized as this work paves the way for FRIB mass production through systematic procedures involving liquid, surface particle counts, field emission onset and acceleration gradient measurements. We reported findings on cavity liquid particle counts data during the HPR process that correlated to RF test results. Preliminary results show a trend for the acceleration gradient at FE onset that decreases as the 0.3µm cumulative liquid particle counts in cavity rinse water increases at the end of HPR. However many more cavity processes and tests are necessary to build a reliable statistical database and to define the right processing scheme for each cavity type.

AKNOWLEDGMENTS

The authors would like to thank all the members of the NSCL and FRIB for their significant contribution to this paper in particular Matthaeus Leitner, Steve Bricker, Chris Compton, Ken Witgen, Douglas Miller, David Norton, Andrew Wisniowiecki, Dan Victory and Nicholas Putman. We also would like to acknowledge and thank Bob Laxdal, John Mammosser and Peter Kneisel for their contributions and fruitful discussions.

REFERENCES

[1] N. Krupka et al., "Quality Control Update of the Cleanroom for Superconducting Multi Cell cavities at DESY", SRF 2005: Ithaca, New York, USA, 2005, CARE-Conf-05-032-SRF

[2] The ILC R&D Board Task Force on High Gradients, "Final Surface Preparation for Superconducting Cavities", TTC- Report 2008-05

[3] L. Popielarski et al., "Cleanroom Techniques to Improve Surface Cleanliness and Repeatability for SRF Mass Production", IPAC 2012: New Orleans, Louisiana, United States, 2012, WEPPC065

Copyright © 2012 by the respective authors — cc Creative Commons Attribution 3.0 (CC BY 3.0)

PROCESS DEVELOPMENTS FOR SUPERCONDUCTING RF LOW BETA RESONATORS FOR THE ReA3 LINAC AND FACILITY FOR RARE ISOTOPE BEAMS*

L. Popielarski#, C. Compton, L. Dubbs, K. Elliott, A. Facco(*), L. Harle, I. Malloch, R. Oweiss, J. Ozelis, J. Popielarski, K. Saito

Facility for Rare Isotope Beams (FRIB), Michigan State University (MSU), East Lansing, MI 48824, USA (*) INFN-Laboratori Nazionali di Legnaro, I-35020 Legnaro, Padova, Italy

Abstract

The Facility for Rare Isotope Beams (FRIB) will utilize over 330 superconducting radio frequency (SRF) low beta cavities for its heavy ion driver linac. The SRF department will process and test all cavities prior to string assembly in the cleanroom. The baseline processing procedures have been established. The methods are being optimized for production rate benchmarking. Additional processes are being developed to increase flexibility and reduce technical risks. This paper will describe developments and experimental results. Topics include high temperature heat treatment for hydrogen degassing, selective chemical etching for cavity frequency tuning, low-temperature bake out and process quality control.

INTRODUCTION

The ReAccelerator (ReA) and FRIB projects at MSU both utilize a 80.5 MHz β=0.085 quarter wave resonator (QWR) design [1]. For the ReA3 project eleven cavities have been fabricated and eight need to be certified, while for the FRIB project, 126 cavities need to be fabricated with 94 qualified for use in a cryomodule. The ReA project allows for the chance to gain valuable production experience. To meet the ReA3 cavity frequency specifications a differential etching technique with Buffered Chemical Polish (BCP) was developed for post fabrication tuning. The technical risks regarding cavity performance for ReA linac operation were reduced by establishing a low temperature bakeout method and a high temperature heat treatment - both of which improved cavity Q_0 values. The process steps for the ReA3 cavities are shown in Table 1. The process procedures will be optimized from lessons learned during the ReA cavity production.

Table 1: Summary of process steps for ReA3 cavities.

Step	Cavity Process Steps
1	Degrease, bulk BCP, dry, frequency measurements
2	Differential BCP, dry, frequency measurement
3	Degrease & hydrogen degas
4	Degrease, light BCP, High Pressure Rinse (HPR)
5	Clean assembly, evacuation, 120°C low temperature bake
6	*Test preparations and RF Dewar testing*
7	Clean removal from test stand and install to coldmass

*Work supported by the U.S. Department of Energy Office of Science under Cooperative Agreement DE-SC0000661.
#lpopiela@frib.msu.edu

In preparation for FRIB production, a comprehensive program is in place to improve process quality control and documentation. Innovative diagnostic tools allow for the quantification of process and assembly parameters for quality control [2]. The cavity fabrication, processing and vertical test parameters are recorded in a computer database (electronic traveler system), for cavity characterization and analysis. The database is accessible through a web-based interface, and will ease the analysis of 50 cavities before FRIB production.

HYDROGEN DEGASSING

The risk of Q-disease has been mitigated by implementing a hydrogen degassing step to the cavities after the bulk chemistry. The cavities are fired in a high temperature vacuum furnace for 10 hours at 600°C, while maintaining vacuum less than $5X10^{-6}$ Torr. The heat treatment removes much of the hydrogen from the bulk niobium material. Multiple QWRs and half wave resonators (HWRs) have been heat treated, using furnaces at Jefferson Lab and Fermilab, in an effort to quantify the benefits of the treatment both at 4.2 K and 2 K. The furnace design and heat treatment cycle have been optimized for production, considering both mechanical impacts to the cavity structure and overall schedule constraints. The current FRIB cavity furnace cycle is about 40 hours and includes pump down, temperature ramp up, steady state bake at 600 °C and cool down.

Figure 1: T-M Vacuum® high temperature vacuum furnace commissioned and being used to heat treat cavities at MSU.

Copyright © 2012 by the respective authors — cc Creative Commons Attribution 3.0 (CC BY 3.0)

The FRIB baseline calls for all SRF cavities to receive heat treatment. A high temperature vacuum furnace, shown in Figure 1, was procured from T-M Vacuum® in 2011 and installed and commissioned at MSU in 2012. The furnace fits two FRIB cavities per cycle.

DIFFERENTIAL REMOVAL AND TUNING

In an effort to compensate for frequency shifts during β=0.085 QWR fabrication, a program of frequency tuning by targeted material removal was undertaken. Removing material from the magnetic field region of the β=0.085 QWR will reduce the cavity frequency, while removing material from the electric field region (Fig. 2) will increase the cavity frequency. The process used to remove material from the RF surface must be reproducible, in order to accurately tune to the desired frequency goal after fabrication.

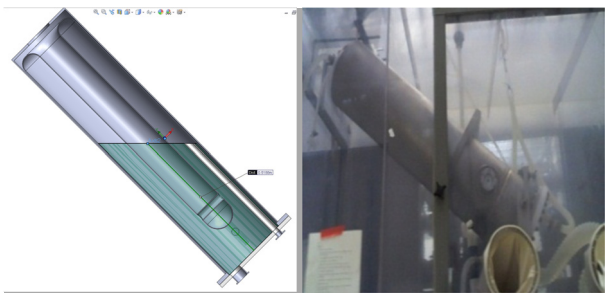

Figure 2: Differential etching setup for removal in high electric field region of the β=0.085 to increase frequency.

Etching with BCP was chosen to remove material because it was most likely to be uniform and repeatable. Simulations were performed to predict the expected amount of frequency shift per micron of niobium removed from the surface. The simulation predicted the cavity frequency would shift by 0.9 kHz/μm when etched in the high electric field region. A custom flange was fabricated to allow BCP circulation, while maintaining a specific fill height. After three trials an empirical tuning factor, kHz/μm, was calculated. The factor is recalculated after each custom etch for increased accuracy (Fig. 3).

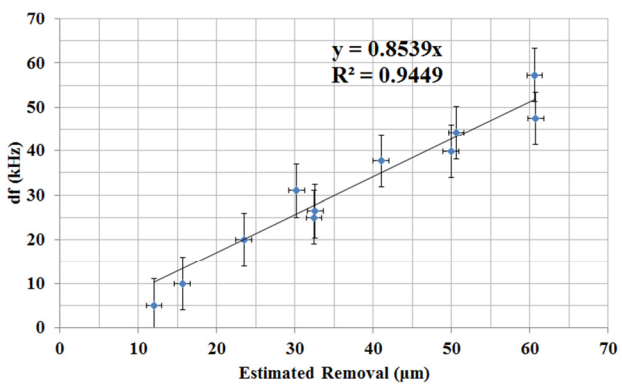

Figure 3: Measured frequency shift (kHz) versus the estimated material removal (microns).

Eight of the β=0.085 QWRs for ReA3 required a frequency increase and have been successfully tuned with this method. The current tuning factor is 0.8539 kHz/μm for removal in the electric field region. The average error is within 6 kHz of the desired frequency before the degassing procedure, which can cause unpredictable shifts up to 7 kHz. After degassing, the final frequency is set, to within 5 kHz (well within the operational fine tuning range) by attaching a custom length "puck" to the demountable niobium tuning plate with an e-beam weld which does not disturb the prepared cavity.

LOW TEMPERATURE BAKEOUT

Performing a 48-hour long 120ºC bakeout procedure, prior to cavity testing, has proven to be beneficial in improving the performance of the β=0.085 QWR at 4K (Fig. 4).

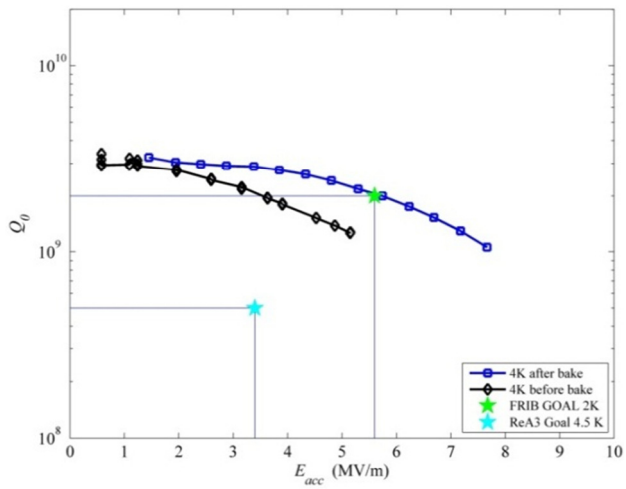

Figure 4: Q_0 versus E_a showing improvement in cavity performance after low temperature bakeout application.

After clean cavity assembly to the test stand and evacuation, the stand is removed from the cleanroom. The cavity is then wrapped in fiberglass heat tape and a gas heater is attached to the helium return flange on the vessel. Twelve thermocouples, five of which are connected to controllers, monitor the internal and external cavity temperatures to ensure that the temperature does not exceed 120ºC. Especially important to monitor is the bottom flange of the cavity, which cannot exceed 156ºC, the temperature at which the indium wire used in the vacuum seal will begin to melt. The cavity is wrapped in foil for insulation, and the temperature is slowly ramped up to 120ºC and then monitored for 48 hours. Residual gas analyzer scans are taken during the baking cycle to monitor the pressure in the cavity and to allow for the presence of any potential contaminants to be determined. The gradual stabilization of the pressure over time is indicative of the removal of water and other low-boiling contaminants in the vacuum space. The bakeout process has proven itself to be a low cost method by which to quickly improve the low field quality factor and somewhat recover the higher field Q-slope in an underperforming cavity. The bake application is being

Copyright © 2012 by the respective authors — cc Creative Commons Attribution 3.0 (CC BY 3.0)

considered as an optional process step for FRIB cavities exhibiting slightly low Q_0 during vertical test. A test stand bake oven is under development which will minimize the process time.

PROCESS QUALITY CONTROL & DOCUMENTATION

Overall cavity performance and certification rate in both the vertical Dewar and final cryomodule testing is improved by continuous documentation and aggressive quality control. Diagnostic tools are used to monitor and quantify the process data [2] and to discover problems quickly so they can be corrected. Documented process parameters include: water quality identifiers, niobium concentration in BCP, High Pressure Rinse (HPR) liquid particle counts, and surface particle counts of cavity RF surfaces and associated vacuum hardware. An inclusive process and maintenance management system, the electronic traveler (e-traveler), is used to record fabrication, process and test data for various devices (Fig. 5) and control process steps. The data can be searched, extracted, and analysed for correlations and post failure analyses (Fig. 6). Scheduled reports can be produced for various data fields or parameters and specified devices, being helpful to track trends and provide feedback.

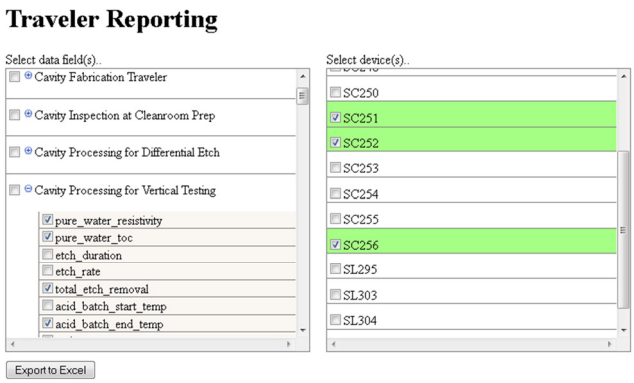

Figure 5: Screenshot of the reporting function which quickly exports any selected data field and device to an Excel® file.

Device SN	nb_concentration_solution	particle_count_end	spc_tuning_plate	initial_field_emission	low_field_q0	q0_120	xray_count_120
SC251	2.1	936	0	6.12	2.60E+09	1.50E+09	0.5
SC252	13	1775	0	5.32	2.80E+09	1.30E+09	0.8
SC256	13.3	1146	1.33	5.48	5.00E+09	3.25E+09	0.52

Figure 6: Sample of an e-traveler report for selected data fields and devices (in this case ReA3 cavities).

The initial release of the e-traveler system allows for its use during the ReA3 coldmass production. This has been beneficial to streamline the system and move toward production operations. The e-traveler reporting function reduces the time to identify the correlations between cavity process parameters and the cavity RF test results. These trends guide the optimization of the process procedures to ensure that they are effective, yet efficient.

Device routers, assembly work instruction and standard operating procedures are written and controlled as FRIB documents by the FRIB Manufacturing Engineering group and will eventually be embedded as links in each e-traveler form.

CONCLUSION

The recently developed procedures presented here have been applied to ReA3 cavities. Three of the cavities have been successfully RF tested, certified and installed to the coldmass string. The processing procedures and quality control techniques have proven to be effective at producing the required performance specifications for ReA3 cavities during vertical Dewar testing (Fig. 7).

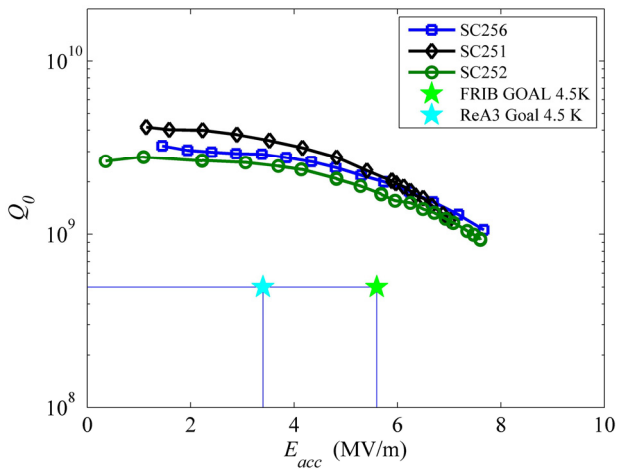

Figure 7: Q_0 vs. E_{acc} at 4K for ReA3 β=0.085 QWRs

ACKNOWLEDGEMENTS

The authors would like to thank the members of the NSCL & FRIB staff whose effort has made a significant contribution to this progress. In particular, Ed Bernard, Steve Bricker, Byambatsogt Enkhbat, Robert Gaul, Lee Harle, Matt Hodek, Doug Miller, Dave Norton, Sheng Peng, Nicholas Putman, Greg Velianoff, Michael Williams, Daniel Victory, Vasu Vuppala, Andy Wisniowiecki and Ken Witgen. We would like to acknowledge the impact of our weekly SRF teleconference on the overall success of our program with special thanks to Bob Laxdal and Peter Kneisel for their continued contributions. We thank our collaborators at JLab, Tony Reilly, and at Fermilab, Allan Rowe, for allowing us the use of their furnace while the MSU furnace was procured, installed and commissioned.

REFERENCES

[1] A. Facco et al., "Superconducting Resonators Development for the FRIB and ReA LINACS at MSU: Recent Achievements and Future Goals", Proc. in IPAC2012, New Orleans, USA, p.61

[2] R. Oweiss et al., "Quality Control of Cleanroom Processing Procedures of SRF Cavities for Mass Production", These proceedings, MOPB070.

Copyright © 2012 by the respective authors — cc Creative Commons Attribution 3.0 (CC BY 3.0)

MULTIPOLE EXPANSION OF THE FIELDS IN SUPERCONDUCTING HIGH-VELOCITY SPOKE CAVITIES *

R. G. Olave, J. R. Delayen, C. S. Hopper, Center for Accelerator Science, Old Dominion University
and Thomas Jefferson National Accelerator Facility, VA, USA †

Abstract

Multi-spokes superconducting cavities in the high-beta regime are being considered for a number of applications. In order to accurately model the dynamics of the particles in such cavities, knowledge of the fields off-axis are needed. We present a study of the multipoles expansion of the fields from an EM simulation field data for two-spokes cavities operating at 325 MHz, $\beta = 0.82$, and 500 MHz, $\beta = 1$.

INTRODUCTION

In recent years there has been considerable progress in the optimization and characterization of accelerating multi-spoke cavities in the high-velocity regime ($\beta_0 = v_0/c > 0.6$). Multi-spokes cavities have several advantages over the more traditional multi-cell elliptical cavities [1, 2], such as increased longitudinal acceptance, lower superconducting surface resistance and therefore lower heat load allowing for operation at 4K, and a cavity diameter on the order of half the rf wavelength, which allows for lower operating frequencies for a given size.

The lack of cylindrical symmetry of the multi-spokes cavities might result in the presence of non-negligible higher order multipole components of the operating mode. In order to study the impact of the cavity fields on the beam dynamics, it is necessary to characterize off-axis fields. To this end, we present a study of the multipoles expansion of the fields for the operating (fundamental) cavity mode for spokes operating at 325 MHz, $\beta = 0.82$, and 500 MHz, $\beta = 1$.

MULTIPOLAR RF KICKS AND FIELD EXPANSION

It has recently been demonstrated that surface fitting of field data around a virtual cylinder in the proximity of the beamline can be used to compute high-order transfer maps, interior fields, and non-linear beam dynamics including high-order multipole effects [3, 4].

From the interpolation of the electromagnetic fields on the surface of a virtual cylinder of radius R through the length of the cavity in a region with no charge, a general complete solution to the fields can be found. The accelerating electric field can then be expressed as:

$$E_{acc}(r,\phi,z) = E_z e^{i\omega t} = E^{(0)}_{acc-c} + \Big(\sum_{n=1}^{\infty} r^n \big(E^{(n)}_{acc-c} cos(n\phi) + E^{(n)}_{acc-s} sin(n\phi)\big)\Big) e^{i\omega t} \quad (1)$$

Where E_{acc} is the accelerating electric field along the beamline direction z and ω is the rf frequency. If the field $E_{acc}(R,\phi,z)$ is known, then the coefficients $E^{(0)}_{acc-c}$, $E^{(n)}_{acc-c}$ and $E^{(n)}_{acc-s}$ can be found via inverse Fourier integration of the surface fitted field.

Inserting this series into the Panofsky-Wenzel theorem we may then calculate the transverse change in momentum (kick) of the particles as a series of multipolar RF kicks:

$$\Delta p_{\perp} = \Big(\frac{e}{\omega}\Big) \int_{-\infty}^{+\infty} (-i)\nabla_{\perp} E_{acc}|_{t=z/v_z} dz \quad (2)$$

To get an idea of the impact of the nonlinear effects of the higher order field multipoles, it is useful to compare the strength of the multipolar RF-kicks with that of magnetic multipoles [7]. It is usual to express the magnetic potential and static magnetic kick to incoming particles as a Taylor series expansion [5, 6]. In magnets, the a_n and b_n terms are determined by the orientation of the magnet, such that a_1 corresponds to a vertical bend of the particle trajectory, b_1 to a horizontal bend, and in general a_n correspond to skew oriented magnets and b_n to normal oriented magnets. For simplicity we will continue to use this nomenclature. Obviously, the b_0 or monpole term is not dependent on the orientation of the cavity and corresponds to the accelerating voltage across the cavity. Following this idea, we find:

$$b_0 = \int_{-\infty}^{+\infty} E^{(0)}_{acc-c}(z)dz, \propto V_{acc}$$
$$b_n = \int_{-\infty}^{+\infty} \frac{ni}{\omega} E^{(n)}_{acc-c}(z)dz, (n = 1, 2, ...) \quad (3)$$
$$a_n = \int_{-\infty}^{+\infty} \frac{ni}{\omega} E^{(n)}_{acc-s}(z)dz, (n = 1, 2, ...)$$

Additionally, the rf multipole strength depends of the rf phase of particles traversing the cavity; so we can express them as complex numbers, where the real part corresponds to particles on crest, and the imaginary part corresponds to particles off-crest.

* Part of this work supported by U.S. DOE Award No. DE-SC0004094 Part of this work was done in collaboration with and supported by Niowave Inc. under the DOE STTR program.

† rolave@odu.edu

Copyright © 2012 by the respective authors — cc Creative Commons Attribution 3.0 (CC BY 3.0)

RF CAVITIES

We are in the process of design and characterization of a 325 MHz, $\beta = 0.82$ cavity; the optimization procedure, multipacting, and higher-order mode analyses have been presented elsewhere [8, 9, 10]. The 3D electromagnetic fields were obtained using CST Microwave Studio® 2012 (CST MWS). Table 1 lists the cavity's relevant RF parameters.

Table 1: RF Parameters of the 325 MHz cavity (At E_{acc} = 1 MV/m and reference length $\beta_0\lambda$)

Parameter		Units
Frequency	325	MHz
β_0	0.82	
R/Q	629	Ω
$(R/Q) * (QR_s)$	99200	Ω^2
E_p/E_{acc}	2.8	
B_p/E_{acc}	5.3	mT/(MV/m)
Bp/Ep	1.9	mT/(MV/m)
Energy Content	0.445	J

In order to get a better understanding of the beam dynamics, we present in Fig. 1 a plot of the transverse voltage (in the x and y directions) as a function of transverse offset from the design beamline. It is clear that focusing would occur in one direction while defocusing would occur in the other. This behavior is characteristic of quadrupole fields, so we may conclude that the dominant higher order multipole is a quadrupole. The transverse voltage due to higher-order multipoles is less than 1% with respect to the accelerating voltage. An open picture of the cavity with the electric surface fields is shown as well.

The results of the calculation of the multipole strength numbers are presented in table 2, up to the octupole terms. The numbers have been normalized to simulation field data such that V_{acc} = 1 V; notice that the deviation from this value gives us a measure of the error in our surface fitting calculation.

Table 2: RF Multipole components, normalized from simulation field data to $V_{acc} = 1V$, of the 325 MHz, $\beta = 0.82$ cavity.

Multipole component		Units
V_{acc}	0.89	V
V_x	0	V
V_y	0	V
b_2	-0.01 - 1.09 i	nT
a_2	0.003+0.22 i	nT
b_3	0	nT/m
a_3	0	nT/m
b_4	23.8 - 128.7 i	nT/m^2
a_4	-9.9 + 53.3 i	nT/m^2

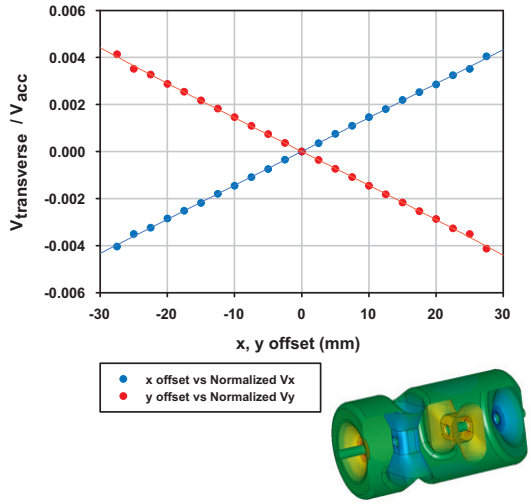

Figure 1: Normalized transverse voltage as a function of transverse offset, for the 325 MHz, $\beta = 0.82$ cavity. A CST MWS picture of the surface fields of the open cavity is shown for reference.

We have designed cavities operating at an rf frequency of 500 MHz, β = 1, optimized with racetrack-shaped spokes. It has recently been observed that there may be geometries in which the quadrupole effects can be minimized, specifically ring-shaped spokes, which exhibit more symmetry about the beamline [11]. Table 3 presents the relevant RF parameters for a cavity with racetrack shaped spokes, and for a cavity with ring spokes. This latter geometry has not been fully optimized yet for high shunt-impedance and/or low surface-fields, however it already exhibits promising rf characteristics.

Table 3: RF Parameters of the 500 MHz cavities (At E_{acc} = 1 MV/m and reference length $\beta_0\lambda$)

Parameter	Racetrack spokes	Ring spokes	Units
Frequency	500	500	MHz
β_0	1	1	
R/Q	725	737	Ω
$(R/Q) * (QR_s)$	124000	118000	Ω^2
E_p/E_{acc}	3.5	3.9	
B_p/E_{acc}	5.4	7.1	mT/(MV/m)
Bp/Ep	1.6	1.8	mT/(MV/m)
Energy Content	0.158	0.155	J

Picures of the cavities with racetrack-shaped spokes and ring-shaped spokes are presented in Figs. 2 and 3 respectively. Also presented are a plot of the transverse voltage field with respect to spatial offset from the design beamline. It is clear that there is a noticeable reduction in the

Copyright © 2012 by the respective authors — cc Creative Commons Attribution 3.0 (CC BY 3.0)

quadrupole strength, and an increase in effects from higher order multipoles, as evinced by the slightly oscillatory behavior. The same can be concluded from the multipole strength numbers presented in table 4, while we observe that the octupole term has indeed increased.

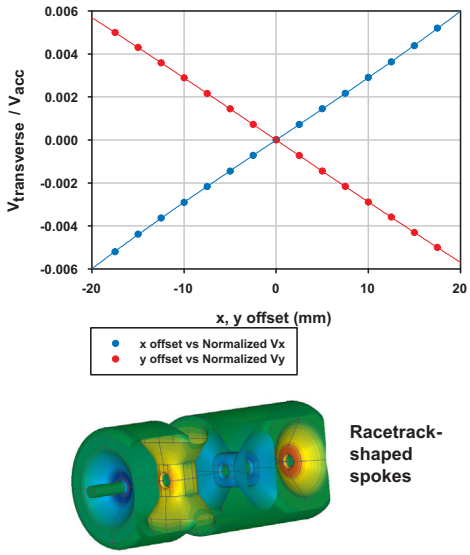

Figure 2: Normalized transverse voltage as a function of transverse offset, for the 500 MHz, $\beta = 1$ cavity with wide racetrack-shaped spokes. A CST MWS picture of the surface fields of the open cavity is shown for reference.

Table 4: RF Multipole components, normalized from field simulation data to $V_{acc} = 1V$, of the 500 MHz, $\beta = 1$ cavities.

Multipole component	Racetrack-shaped spokes	Ring-shaped spokes	Units
V_{acc}	1	1	V
V_x	0	0	V
V_y	0	0	V
b_2	-0.05 - 1.44 i	-0.002 - 0.66 i	nT
a_2	0.003+0.22 i	0 + 0.09 i	nT
b_3	0	0	nT/m
a_3	0	0	nT/m
b_4	304.5 +42.4 i	543.5 - 85.1 i	nT/m^2
a_4	-9.9 + 53.3 i	-146.6 + 22.8 i	nT/m^2

ACKNOWLEDGMENT

We would like to thank Subashini De Silva for her help with this work.

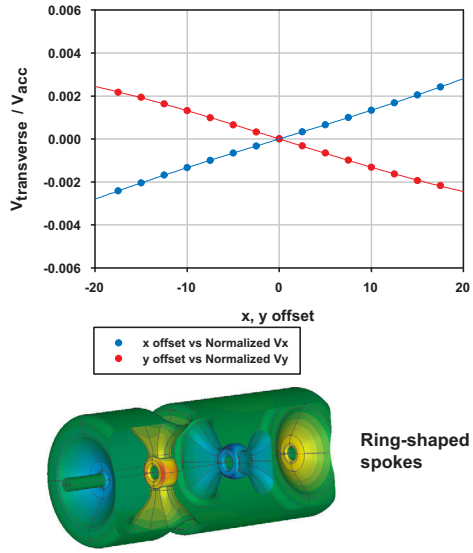

Figure 3: Normalized transverse voltage as a function of transverse offset, for the 500 MHz, $\beta = 1$ cavity with ring-shaped spokes. A CST MWS picture of the surface fields of the open cavity is shown for reference.

REFERENCES

[1] J. R. Delayen, "Superconducting spoke cavities for electron and high-velocity proton linacs," these proceedings.

[2] K. W. Shepard et al., "High-energy ion linacs based on superconducting spoke cavities," PRSTAB **6**, 080101 (2003).

[3] D. T. Abell, "Numerical computation of high-order transfer maps for rf cavities," PRSTAB **9**, 052001 (2006).

[4] C. E Mitchell and A. J. Dragt, "Accurate transfer maps for realistic beam-line elements: Straight elements," PRSTAB **13**, 064001 (2010).

[5] H. Wiedemann *Particle Accelerator Physics*, (Springer Berlind Heidelbergt New York, 2007), 63.

[6] D. H. Whittum, *Introduction to Microwave Linacs*, (SLAC-PUB 8026, Stanford CA, 1998).

[7] J. Barranco Garcia et al., "Study of Multipolar RF Kicks from the main deflecting mode in compact crab cavities for LHC," IPAC'12, New Orleans, USA, May 2012, TUPPR027.

[8] C. S. Hopper et al., "Development of Spoke Cavities for High-velocity application," IPAC'12, New Orleans USA, May 2012, WEPPC103.

[9] C. S. Hopper and J. R. Delayen, "Multipacting analysis of high-velocity superconducting spoke resonators," these proceedings.

[10] C. S. Hopper et al., "Higher Order Mode Properties of Superconducting two-spoke cavities," in preparation for submission to PRSTAB (2012).

[11] B. Mustapha et al., "A ring-shaped centered conductor geometry for a half-wave resonator," IPAC'12 New Orleans USA, May 2012, WEPPC037.

Copyright © 2012 by the respective authors — cc Creative Commons Attribution 3.0 (CC BY 3.0)

COLD TESTING OF SUPERCONDUCTING 72 MHz QUARTER-WAVE CAVITIES FOR ATLAS

M. P. Kelly, Z. A. Conway, S. M. Gerbick, M. Kedzie, T. C. Reid, R. C. Murphy,
P. N. Ostroumov, Argonne National Laboratory, Argonne, IL 60439, U.S.A.

Abstract

A set of seven 72 MHz β=0.077 superconducting quarter-wave cavities for a beam intensity upgrade of the ATLAS heavy-ion accelerator has been completed. Cavities have been fabricated using lessons learned from the worldwide effort to push the performance limits for niobium cavities close to the fundamental limits. Key developments include the use of electropolishing on the completed cavity. Polishing parameters, including temperature, are better controlled compared to the standard horizontal electropolishing systems for elliptical cavities. Wire EDM, used instead of traditional niobium machining, looks well suited for preparing weld joints that are, with respect to quench, defect free. Hydrogen degassing at 625 C has been performed after electropolishing, removing the need for fast cool down in with 2 K or 4 K operation. Tested cavities have useful accelerating voltages of >3 MV/cavity at 4 K, as for ATLAS, and 5 MV or more per cavity at 2 K with B_{PEAK}>130 mT in 3 of 4 cases.

INTRODUCTION

The essential components of the ATLAS Efficiency and Intensity Upgrade [1] are a new CW radio frequency quadrupole injector and one new cryomodule of 7 SC cavities for β=0.077, scheduled to replace three existing cryomodules of split-ring resonators in the middle portion of the ATLAS SC ion linac. This upgrade follows upon the 2009 β=0.15 ATLAS Energy Upgrade cryomodule, presently the world leading cryomodule for low velocity ions, providing 14.5 MV accelerating voltage over 4.5 meters.

The new cryomodule will nominally provide 17.5 MV of accelerating potential at a lower beta of 0.077 in a 5 meter cavity string (see Figure 1). ATLAS beam transport efficiency for both stable and radioactive ion beams will be improved dramatically by increasing overall acceptance and reducing emittance growth inherent in the split-ring designs.

Figure 1: Initial mock up of the 72 MHz cavity clean room assembly.

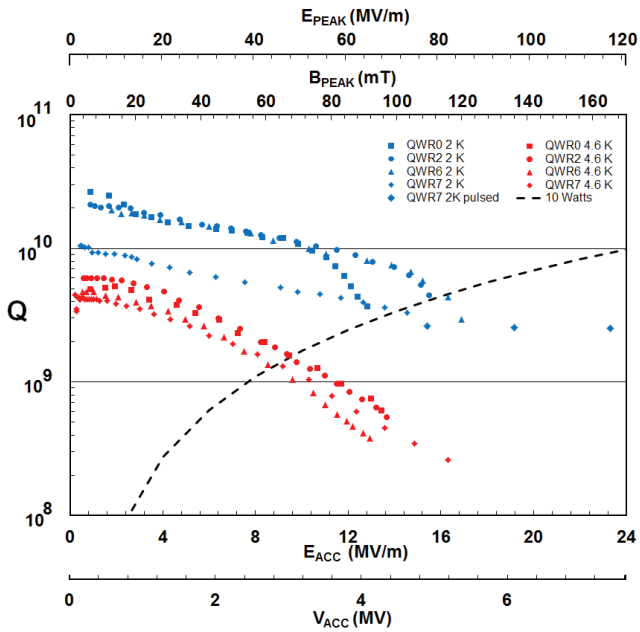

Figure 2: Quality factor versus accelerating gradient, voltage and surface fields at 2 and 4 K (l_{eff}=βλ=0.32m)

The planned cavity operating voltage of V_{ACC}=2.5 MV/cavity is roughly two times higher than for the present state-of-the-art at this beta, however, cavities and subsystems, including power couplers and cryogenics are all designed for operation with at least V_{ACC}~3 MV/cavity. Several improvements have been made since 2009 to achieve this performance, however, the two critical pieces are the improved rf design [2] and the unique capability to electropolish complete quarter-wave cavity/helium jacket assemblies [3].

CAVITY PERFORMANCE

Cold tests at 2 K and 4 K for four out of eight new 72 MHz cavities are complete and test results are shown in Figure 2. Seven of these cavities will be installed into ATLAS as part of the intensity upgrade and the eighth is for R&D and intended to advance the performance for this class of cavity [4]. Of the seven ATLAS cavities, four will be tested individually in the ANL test cryostat while the remaining three will be tested in the full cryomodule before installation into the ATLAS beamline. If a cavity requires a second round of cleaning, it can be removed

Copyright © 2012 by the respective authors — cc Creative Commons Attribution 3.0 (CC BY 3.0)

Table 1: Measured 72 MHz cavity performance characteristics

Quarter-wave number	0	2	6	7
Quench field (mT)	98	130	153	>165
R_{RES}* (nΩ)	1.0	1.2	1.2	2.5
Field emission onset# (MV/m)	37	74	74	77

*extracted from low field data at 2 K
#value of E_{PEAK}

from the cryomodule string using the previously developed up-to-air system [5].

Electropolishing

A key processing step for the cavities was the heavy, 150 μm, electropolishing on the complete cavity. Two separate rounds of polishing are performed. First, after fabrication, the cavities were electropolished on consecutive days, removing 65 μm of niobium each day. Total polishing time was about 12 hours. The cavities were then baked under vacuum at Fermilab for 14 hours at 625°C in order to degas hydrogen. Last, the cavities were returned to Argonne for a final light 20 μm electropolish.

Fundamentally, the ANL low-beta cavity electropolishing system and associated polishing parameters are similar to those for horizontal systems used with 1.3 GHz cavities for the global international linear collider effort. There is one major improvement, however. Since quarter-wave cavities do not require field flatness tuning or direct access to the niobium surface after polishing, final heavy electropolishing can be performed with the complete cavity with liquid helium jacket. The helium jacket is used to directly cool the niobium surface with chilled (22+/-0.5 °C) water in order to maintain a stable and uniform temperature over the entire cavity surface. As for elliptical cells, the cavities are rotated during the procedure at a speed of 1 rpm, however unlike with most e-cells, the maximum temperature on the niobium surface never rises above 32°C at any time during the rotation period.

4 Kelvin Performance

In ATLAS cavities are operated with 4.5 K helium from the ATLAS refrigerator. The nominal accelerating gradient is 7.9 MV/m ($l_{eff}=\beta\lambda=31.75$ cm) or 2.5 MV/cavity with a quality factor of $Q=1x10^9$ and a corresponding total surface resistance of 26 nΩ. At least 10 Watts of cryogenic cooling per cavity will be available.

In four cavities tested so far, achieved cw cavity accelerating gradients at 4.6 K range between E_{ACC}=12.4-16.2 MV/m, or double the requirement for ATLAS. Most cavities had approximately 3 hours of low-level (E_{ACC}=0-1.5 MeV) multipacting conditioning and one half to 1 hour of short pulse conditioning with 4 kW peak power in order to achieve the measured performance shown in Figure 2. Based on recent cavity results for Spiral-2 [6], an 'in-situ' bake at 110-120°C for 48 hours was performed for QWR0 by circulating warm helium gas through the cavity helium vessel. In this case, cold testing before and after showed no measureable difference from baking. This is not considered to be definitive since the temperature variations of 10°C both in time and over the cavity surface were larger than desirable.

2 Kelvin Performance

ANL is also pursuing the developments needed in order to demonstrate practical 2 K operation, the likely operating mode for future large SRF linacs. The high practical cavity field gradients possible at 2 K, combined with the compact lattice of the Argonne cryomodule design, can provide 'real-estate' gradients of 7 MV/m (at B_{PEAK}=120 mT), or about 2-3 times higher than for today's state-of-the-art at 4 K. This would make feasible the construction of a compact proton linac that would be extremely attractive for the next generation of high-power accelerators in areas of energy, national security, and medicine.

The four cavities tested to date support this goal. Cavities reach magnetic surface fields in the range B_{PEAK}=98-165 mT. In two of four cases, the thermal magnetic breakdown was extracted from pulsed 5% duty cycle measurements in order to limit x-ray radiation at very high fields. These points are not included on the Q curve for QWR's 2 and 6. The lowest quench at 98 mT for QWR0 is due to breakdown on the central conductor, based on second sound measurements. The location corresponds to that of a known welding defect, where contamination on the center conductor weld preparation is strongly suspected. At the other end, the QWR7 never quenched (B_{PEAK}=165 mT) and was administratively limited due to x-ray emission at the very high field of E_{PEAK}=115 MV/m, a regime that the present test cryostat shielding was not designed for. QWR7 was also fabricated from RRR 300 niobium, rather than RRR 250, and received particularly careful attention during fabrication [4]. Quench locations for the other two QWR's, numbers 2 and 6, were not measured.

Generally, each of the four tested cavities is much more efficient at 2 K, even considering the additional cost of refrigeration. The 2 K residual resistance, ranging from 1-2.5 nΩ comes directly from low field decay time measurements. Values of 5 nΩ for accelerating gradients up to 12 MV/m in three out of four cavities are, indeed, low for any cavity of any type. A goal for future cryomodules of B_{PEAK}=120 mT with R_s=5 nΩ and V_{ACC}=5 MV/cavity at T=2 Kelvin is within reach based on these results.

Other Performance Considerations

Improvements other than electropolishing have been made since the 2009 upgrade. Electromagnetic (EM) optimizations of the 72 MHz QWR accounts for about 20% of the performance increase relative to the previous 109 MHz ATLAS Energy Upgrade cavities. The design has been presented previously [2], however, the most substantial new feature is the conical-shaped outer

Copyright © 2012 by the respective authors — cc Creative Commons Attribution 3.0 (CC BY 3.0)

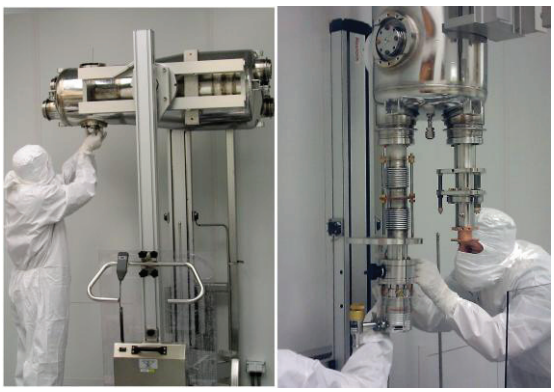

Figure 4: Clean room assembly for the 72 MHz QWR's.

housing which reduces B_{PEAK}/E_{ACC} by 20% compared to a straight cylindrical housing. No additional beam-axis space is needed since the expanded volume occupies the empty space already needed to join cavities together.

High values for E_{PEAK} in Table 1 are possible due to improved clean room fixturing. All of the assembly onto the six cavity ports is performed with the workers located well below the open cavity port (Fig. 4). Final rinsing of the cavities was performed for 1 hour through each of six ports in a class-100 clean room adjacent to the existing 1.3 GHz cavity rinsing area. The sequence for rinsing and assembly, as for e-cell cavities, includes mounting pickup probes, and blanks before the final rinse.

It is noted that wire electric discharge machining (EDM) was used to perform essentially all cutting on niobium subcomponents. The technique should, in principle, give similar results as for traditional mill machining, however, in practice it requires much less fixturing and technical skill with niobium and reduces the likelihood for embedding inclusions. Hydrogen contamination from EDM is not a major drawback since cavities require degassing anyway to achieve optimal performance at either 2 K or 4 K.

MICROPHONICS

Design and fabrication techniques for these quarter-wave cavities that nearly eliminate microphonic detuning include; (1) reduction of pressure sensitivity by EM design, (2) mechanical centering of the central conductor during fabrication, and (3) a passive mechanical damper to reduce the intrinsic mechanical Q of cavity vibrations. We show in Figures 5 and 6 early measurements of the effect of mechanical centering of the center conductor. Data is for QWR0 after all mechanical fabrication and electropolishing. Centering is done by inserting a long stainless bar into the center conductor through a 50 mm port in the top of the helium jacket and then inelastically bending the center conductor while monitoring the frequency on a network analyzer. The total bending was approximately 1 mm with a final accuracy of +/- 100 microns. The beneficial effect (Figure 5) is large, with a reduction in the peak-to-peak amplitude by a factor of 7, even before mechanical damper installation.

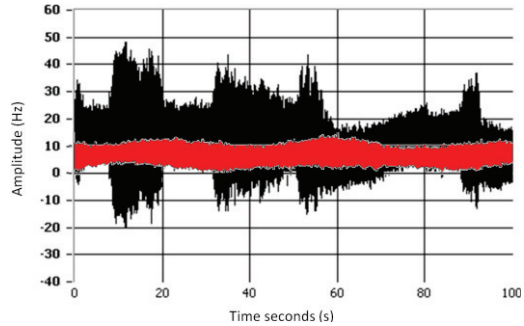

Figure 5: Microphonic amplitude reduction in a quarter-wave cavity due to centering the central conductor

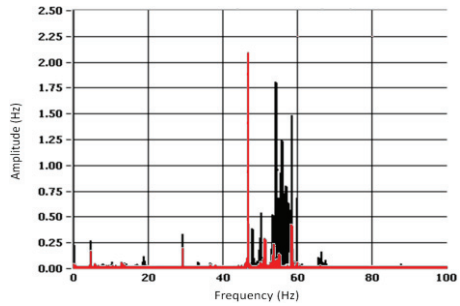

Figure 6: Fourier spectrum for data in previous Figure. Microphonics are lower (red) but the mechanical Q remains high when no mechanical damper is used.

CONCLUSION

The fabrication of eight quarter-wave cavities for β=0.077 and 72.75 MHz is complete and four of these have been tested. Horizontal electropolishing on the completed cavities was performed for the first time. Initial results at both 2 K and 4 K show remarkably good performance, easily exceeding the ATLAS requirements. Performance ranges from B_{PEAK}=98-165 mT, E_{PEAK}=70-120 MV/m, with practical acceleration at V_{ACC}>3 MV/cavity at 4 K and V_{ACC}>5 MV/cavity at 2 K.

ACKNOWLEGDEMENT

This work was supported by the U.S. Department of Energy, Office of Nuclear Physics, under Contract No. DE-AC02-06CH11357.

REFERENCES

[1] P.N. Ostroumov, et al., Proc. of LINAC 2012, TUPLB08
[2] B. Mustapha, et al., Proc. of LINAC-2010, Tsukuba, Japan, September 12-17, 2010.
[3] S.M. Gerbick et al., A New Electropolishing System for Low Beta Cavities, Proc. of SRF 2011.
[4] Z.A. Conway et al., Proc. of LINAC 2012, TUPLB07
[5] S.M. Gerbick et al., Proc. of SRF 2009, ThPPO029.
[6] R. Ferdinand et al., Status and Challenges of the Spiral2 Facility, Proc. of LINAC-2010, Tsukuba, Japan, September 12-17, 2010.

Copyright © 2012 by the respective authors — cc Creative Commons Attribution 3.0 (CC BY 3.0)

THERMO-MECHANICAL SIMULATIONS OF THE FREQUENCY TUNING PLUNGER FOR THE IFMIF HALF-WAVE RESONATOR

N. Bazin, P. Bosland, S. Chel, G. Devanz, N. Grouas, P. Hardy, J. Migne, F. Orsini, F. Peauger,
CEA, F-91191, Gif-sur-Yvette, France

Abstract

In the framework of the International Fusion Materials Irradiation Facility (IFMIF), which consists of two high power CW accelerator drivers, each delivering a 125 mA deuteron beam at 40 MeV [1], a Linear IFMIF Prototype Accelerator (LIPAc) is presently under design for the first phase of the project. A superconducting option has been chosen for the 5 MeV RF Linac, based on a cryomodule composed of 8 low-beta Half Wave Resonators (HWR), 8 Solenoid Packages and 8 RF couplers. The initial solution for the frequency tuning system of the HWR was an innovated system based on a capacitive plunger located in the electric field region, allowing a large tuning range of ±50 kHz, while keeping the cavity rigid enough to fulfill the Japanese regulations on pressurized vessel. Following the cold test results obtained on HWR equipped with the first design of plunger in 2011 [2], the project decided to change the tuning system by a more conservative solution based on the HWR wall deformation.

Nevertheless RF and thermal simulations were realized to understand the previous test results and the conceptual design of a new plunger in niobium was proposed to resolve the issue. The mechanical constraint is to sufficiently deform the plunger to tune the cavity while staying in the elastic range of the niobium material. For the thermal simulations, all the non-linear properties of the materials and the effects of the RF fields are taken into account: thermal conductivity and surface resistance are depending on the temperature, RF fields computed with dedicated software are leading to thermal dissipations in the materials and the vacuum seal.

FIRST DESIGN OF THE HWR PROTOTYPE TUNING SYSTEM

The low-β HWR prototype, whose RF and mechanical design has already been presented in [3] is made of niobium with a titanium helium vessel and niobium-titanium alloy flanges.

The tuning system is based on a capacitive plunger located in the electric field region of the HWR, perpendicular to the beam axis. This plunger, filled with liquid helium, is connected to a thin membrane – 1.7 mm thick – via a 5 mm stem where the tuning force is applied. In order to clean the cavity, the whole tuning system is dismountable from the cavity body and a Garlock Helicoflex joint is used for the vacuum tightness.

For mechanical reasons, the membrane was made of niobium-titanium alloy, whereas the stem and the plunger are made of pure niobium. The membrane can be deformed in the range of ±1 mm which is sufficient to achieve the required tuning sensitivity of ±50 kHz.

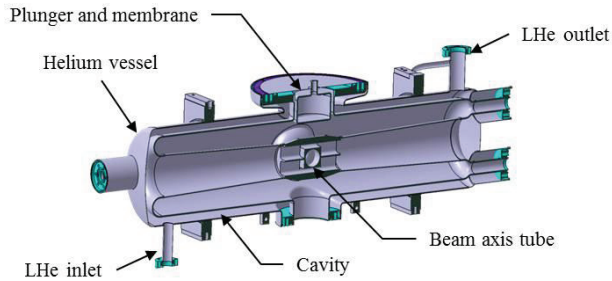

Figure 1: the IFMIF HWR prototype.

Vertical Test Results

After a proper preparation at IPN Orsay (BCP treatment, high pressure rinsing and assembly in an ISO 4 clean room), the prototype equipped with the tuning system was tested in a vertical cryostat at 4.2K.

Several multipactor barriers were observed starting at very low accelerating field (fist barrier at 12 kV/m) and up to 500 kV/m. To pass these barriers, the input power was increased on the incident antenna but the consequence was a quench of the NbTi membrane at the $E_{acc} \geq 1$ MV/m.

According to RF simulations, the magnetic field distribution over the membrane shows a maximum value of ~20% of peak field located on the centre of the membrane, which represents ~ 2.5 mT (Figure 2). This value may be sufficient to heat the membrane until its critical temperature.

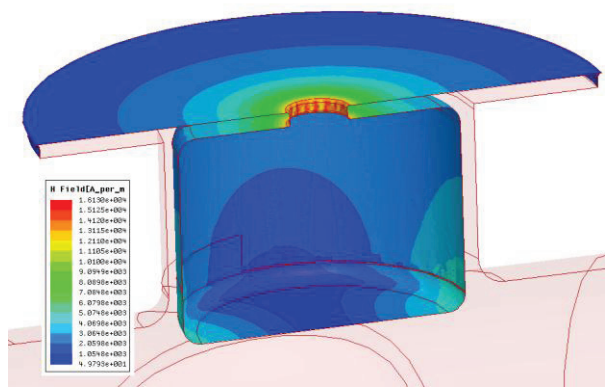

Figure 2: H-field in the plunger region.

Thermal Model of the Tuning System

In order to understand the behaviour of the tuning system, a thermal model has been developed taking into account all the non-linear properties of the materials and the effect of the RF field.

Copyright © 2012 by the respective authors — cc Creative Commons Attribution 3.0 (CC BY 3.0)

The thermal phenomena in the tuning system are:

- Convection with liquid helium inside the plunger and on the niobium-titanium flange
- Heat flux generated by the H-field on the RF surfaces of the membrane, the plunger and the flange, and
- RF dissipation in the seal (Figure 3).

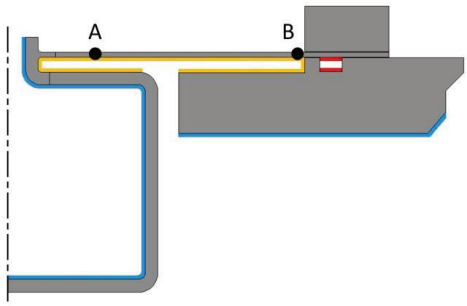

Figure 3: thermal loads on the 2D axis symmetrical model: in blue, the convection with the liquid helium, in orange, the RF losses, in red, the seal dissipation.

To determine the heat flux on each RF surface, the surface resistance of the niobium and the niobium – titanium alloy between the working temperature (4.2 K) and the critical temperature (9.2 K) at the cavity frequency must be introduced in the model. For both materials, the R_{BCS} was calculated using Halbritter's model [4], the parameters for the niobium can be found in [5] and the ones for the niobium-titanium alloy in [6].

As the thermal conductivity of the niobium is strongly dependent of its residual resistance ratio (RRR), the model developed in [7] was used to calculate this parameter between 4 K and 9.2 K. For the niobium-titanium alloy the temperature dependent thermal conductivity was given by the materials thermal properties database CryoComp.

In theory, the gasket placed in a groove on the niobium-titanium flange of the cavity does not produce RF dissipation. The plunger membrane is pinched between two flanges and so its contact with the rim of the cavity flange forbids the penetration of the field inside the gasket groove. In practical, the flatness of the contact surface of the two pieces is not perfect, and a gap may exist. The H-field value on the gasket is not calculated with the 3D software HFSS because of the scale difference between the gap flange (sub-millimeter scale) and the cavity (meter scale). Simulations on a simplified geometry made with 2D code Superfish show that whatever the size of the gap, 90% of the field on the rim penetrate on the gasket (Figure 4).

As the gasket is made of normal conducting material, its surface resistance is in the order of several milli-ohms at 175 MHz. In the worst case (i.e. half of the surface of the seal affected by the field) up to 25 W are dissipated at the nominal accelerating field.

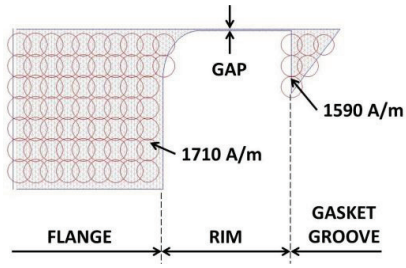

Figure 4: 2D simulation results of the influence of the gap between the membrane and the flange of the cavity on the gasket (H-field values are given for 4.5 M/m, the nominal accelerating field).

The thermal model was implemented in the finite element software Cast3M. The non-linear resolution procedure PASAPAS was modified and a new sub-procedure that redefines the RF heat load at each iteration has been introduced. For each boundary element, there is a surface resistance value attached at each element of the mesh. At each iteration this value is updated depending on the temperature of the element.

Simulation Results and Analysis

First, some simulations were done with no dissipation in the seal, heat load coming only from the RF field. For several values of the accelerating field, the peak temperature of the NbTi membrane (point A on Figure 3) is recorded. The result is presented in Figure 5: the higher the accelerating field, the warmer is the membrane. Above E_{acc} = 4.2 MV/m, the peak temperature is above the critical temperature of the niobium-titanium alloy.

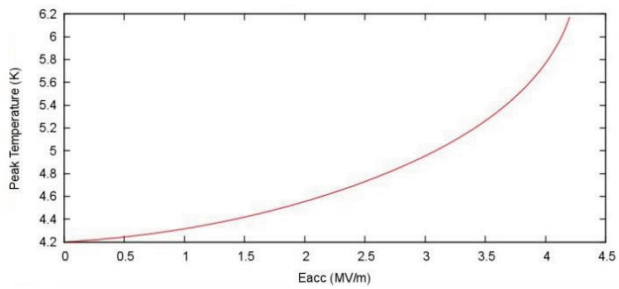

Figure 5: peak temperature of the membrane versus the accelerating field in the cavity (no dissipation in the seal).

The simulations show that even with the optimistic case of no dissipation in the seal, the RF losses lead to self-heating of the membrane due to the poor thermal conductivity of the niobium-titanium alloy.

Then the accelerating field was set at 1 MV/m, and simulations were done with several values for the power dissipated in the seal. Like before, the peak temperature of the membrane (point B on Figure 3) is recorded. Only 1.1 W is needed to reach the critical temperature of the material. The cause is the poor thermal conductivity of the niobium-titanium alloy which does not allow a good propagation of the heat in the material.

Copyright © 2012 by the respective authors — cc Creative Commons Attribution 3.0 (CC BY 3.0)

ALL-NIOBIUM PLUNGER TUNING SYSTEM

The previous thermal simulations have shown that the combination of the dissipated power in the seal, the poor thermal conductivity of the material and the high field due to the stem of the plunger can lead to a thermal quench of the membrane. These points were taken into account when designing a new all-niobium plunger tuning system.

Mechanical Design

The all-niobium tuning system was designed considering the following constraints:

- The overall dimensions are similar to the previous system in order to test it without modifying the cavity prototype.
- The displacement of the bottom surface of the plunger must be ±1 mm to achieve the frequency cavity tuning requirements.
- The system must sustain the atmospheric pressure with vacuum inside the cavity at room temperature.
- At room and helium temperatures, the stress must stay under the elastic limit of the niobium.

The resulting geometry is presented on Figure 6. There is no more liquid helium inside the plunger, the stem which was needed for manufacturing and was the cause of the field reinforcement has been suppressed. But as the length of the membrane is reduced and its flexibility is consequently limited, a flexible element similar to a wave was introduced.

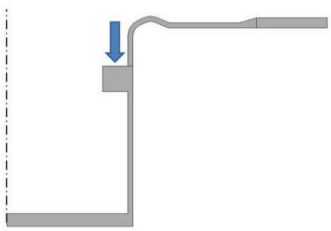

Figure 6: geometry of the niobium plunger. The arrow represents the force applied by the actuator.

The actuator force is no longer applied in the centre but on the side wall of the plunger. To achieve the ±1 mm displacement, a force of 4300 N is needed which can be easily delivered by the actuator designed for the first tuning system and slightly modified to be adapted to this system.

Thermal Design

The previously described thermal model was used to simulate the new plunger tuning system. First, RF simulations were done on the new geometry which showed that the field amplitude has marginally changed on the rim of the cavity flange. Indium seal is used instead of Helicoflex seal. The surface resistance is about the same (indium is superconducting under 3 K), but the surface of the indium seal affected by the RF field is much smaller. The dissipated power is estimated at 1.5 W at the nominal accelerating field.

A first simulation was carried out with no liquid helium cooling except the existing one on the bottom of the niobium-titanium flange of the cavity. At the nominal accelerating field, the plunger temperature is homogenous at 8.2 K, too close to the critical temperature to be acceptable.

We also observe that the dissipated power in the indium seal in the predominant heat source. It is necessary to prevent this heat to propagate along the niobium plunger. A second simulation was carried out with helium cooling on one side of the anchor piece of the actuator system. The plunger temperature is reduced to 5 K for the coolest part to 5.8 K for the warmest part (Figure 7).

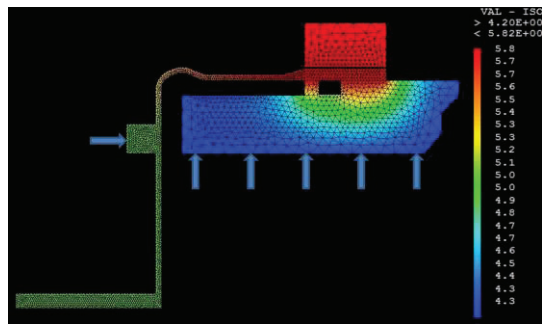

Figure 7: thermal simulation result. The blue arrows represent the liquid helium cooling.

CONCLUSION

The RF and thermal simulations made on the first tuning plunger allowed to understand the vertical test results and the limitations of the design.

In parallel of the design studies of the all-niobium plunger, the principle of tuning the cavity with a capacitive plunger was abandoned by the project and replaced by a more conservative solution of HWR deformed by beam noses compression. According to the project decision, a new tuner design is in progress.

REFERENCES

[1] "IFMIF Comprehensive Design Report", an Activity of the International Energy Agency (2004).
[2] F. Orsini et al., "Vertical tests preliminary results of the IFMIF cavity prototypes and cryomodule development", SRF 2011, Chigaco, USA, THIOB02, p.667 (2011)
[3] E. Zaplatin et al., "IFMIF-EVEDA SC β=0.094 Half Wave Resonator Study", SRF09, Berlin, Germany, THPPO015, p.569 (2009).
[4] J. Halbritter, "Comparison between measured and calculated RF losses in superconducting state", Z. Physik 238, 446-476 (1971)
[5] H. Padamsee, "RF Superconducting for Accelerators"
[6] M. Juillard et al., "Superconducting surface resistance measurements with a TE011 cavity", EPAC 1990, Nice, France, p.1106 (1990).
[7] F. Koechlin and B. Bonin, "Parameterization of the niobium thermal conductivity in the superconducting state", Supercond. Sci. Technol. 9 (1996), p. 453-460.

Copyright © 2012 by the respective authors — cc Creative Commons Attribution 3.0 (CC BY 3.0)

LORENTZ FORCE DETUNING COMPENSATION STUDIES FOR LONG PULSES IN ILC TYPE SRF CAVITIES

N.Solyak, G.Cancelo, B.Chase, D. Crawford, D. Edstrom, E. Harms, Y.Pischalnikov, W.Schappert,
Fermilab, Batavia, IL 60510, USA

Abstract

Project-X 3-8 GeV pulsed linac is based on ILC type 1.3 GHz elliptical cavities. The cavity will operate at 25 MV/m accelerating gradient, but in contrast with XFEL and ILC projects the required loaded Q is much higher (Q~10^7) and RF pulse is much longer (~8ms or even 26ms). For these parameters Lorence force detuning (LFD) and microphonics should be controlled at the level <30 Hz to minimize power overhead from the klystron. A new algorithm of LFD compensation, developed at Fermilab for ILC cavities was applied for Lorentz force compensation studies for 8ms pulses. In these studies two cavities inside TESLA-type cryomodule at Fermilab NML facility have been powered by one klystron. Studies done for different cavity gradients and different values of loaded Q demonstrated that required level of LFD frequency compensation is achievable. Detuning measurements and compensation results are presented.

INTRODUCTION

For the proposed second stage of Project X at Fermilab a 1mA H^- beam will be accelerated from 3 to 8 GeV in pulsed linac, based on XFEL/ILC technology. Each of 28 cryomodules with 8 cavities and one quadrupole will be powered by one RF power source. Efficient operation of the linac requires cavities operating at 25 MV/m with a higher loaded Q_L driven by longer pulses, (4ms fill and 4.3ms flattop) than has typically been used with Tesla style cavities until now. The period of the dominant mechanical modes of the cavities is typically several milliseconds and if left uncompensated, the Lorentz force at the planned gradient of 25MV/m can drive the cavities several bandwidths off resonance during the pulse. The RF power required to drive a detuned cavity for different values of Q_L is shown in Figure 1. Since detuned cavity requires extra power, it is critical to have LFD compensated to 30 Hz or better to keep RF power below 50 kW, enough to cover cavity detuning, RF distribution losses and provide overhead for LLRF control. The chosen value $Q_L=10^7$ is a compromise between cavity bandwidth and required power.

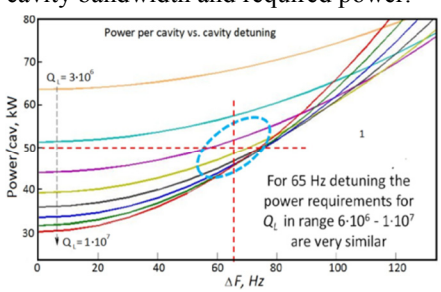

Figure1: Required power per cavity vs. cavity detuning

The feasibility of actively compensating Lorentz force during long pulses to the levels required for efficient operation of the linac under consideration for Project X was assessed during recent studies using two cavities from CM1 at the Fermilab SRF Test Facility.

EXPERIMENTAL SETUP

CM1 is a DESY Type II cryomodule containing eight 9-cell elliptical superconducting Tesla style cavities operating at a frequency of 1.3 GHz [1] , see Fig.2.

Figure 2: Cryomodule in NML at Fermilab

Following the successful commissioning of the cryomodule, the RF distribution system and modulator were reconfigured to drive only the two highest gradient cavities, C5 and C6, with 9 ms pulses from a 120 kW klystron at repetition rates of up to 1 Hz. These two cavities can operate at accelerating gradients, E_{acc}, of 25MV/m and 27MV/m respectively. The vector sum of the two cavities was controlled using an Esecon digital controller and the LFD compensation system developed for CM1 was adapted to handle the modified cavity configuration. The loaded Q_L of both cavities can be varied between 10^6 ($f_{1/2}$=650 Hz) and to 10^7 ($f_{1/2}$=65 Hz) by adjusting the ratios of the power couplers. Cavity baseband waveforms were recorded for the following matrix of operating conditions:

- Q_L: $3\cdot10^6$; $6\cdot10^6$; $1\cdot10^7$;
- E_{acc}: 15MV/m; 20 MV/m; 25 MV/m;
- RF power per cavity: 40 kW; 50 kW; 60 kW.

Current plans for the candidate Project X linac call for the cavities to operate with $Q_L=10^7$ at a gradient of 25 MV/m while driven by 50 kW of RF power required for RF distribution losses, control overhead and compensation of residual frequency detuning from LFD and microphonics.

Copyright © 2012 by the respective authors — cc Creative Commons Attribution 3.0 (CC BY 3.0)

ADAPTIVE COMPENSATION OF THE LORENTZ FORCE DETUNING

The CM1 LFD control system employs an adaptive feed-forward algorithm developed at FNAL to tailor the piezo drive waveform for each individual cavity [2]. This algorithm has been used successfully at FNAL [3] and KEK [4] to control LFD in a variety of SRF cavity designs and operating conditions.

In contrast to the approach commonly used, driving the piezo with a simple half-sine impulse with bias, width, amplitude, and timing adjusted to compensate detuning during the flattop of a short RF pulse, the FNAL algorithm measures the detuning response of the cavity to a series of piezo impulses timed to arrive between 10ms and 0ms in advance of the RF pulse. A least squares fit is then employed to determine the linear combination of impulses needed to cancel the detuning of the cavity by the Lorentz force. As the length of the RF pulse becomes comparable to the period of dominant mechanical mode of the cavities a more complex piezo waveform such as that produced by the FNAL algorithm is required to damp out mechanical oscillations.

An earlier test of adaptive algorithm for 8 ms pulse for dressed ILC-type cavity with blade-tuner in Horizontal Test Cryostat (HTS) at 22 MV/m the demonstrated LFD compensation at the level below 100 Hz peak-to peak [4]. This short test was performed at the end of routine testing of the cavity for short 1.3 ms pulses without optimizing of algorithm and cavity parameters. In current studies with two cavities at CM1, the main focus has been optimization of algorithm for long pulse operation.

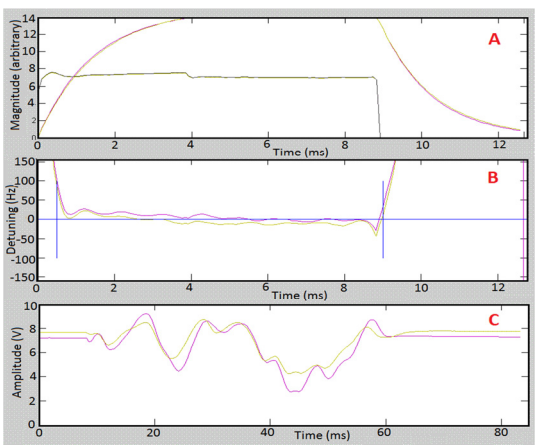

Figure 3: LFD compensation in C5 and C6 during a 9ms RF pulse at E_{acc}=25 MV/m. (A): Baseband envelopes of the forward and cavity field probe signals. (B): Residual detuning using following compensation by adaptive LFD algorithm. (C): Piezo drive waveforms.

Figure 3 shows a sample screenshot of the LFD controller online display. Compensation is applied over the window set by the two blue lines in Panel B. The piezo drive pulse begins 30msec prior to the arrival of the RF pulse and continues for the duration of the 9ms RF pulse. The LFD compensation algorithm was first tested and tuned for the modest set of cavity parameters Q_L~$3\cdot10^6$ (typical value for ILC cavity) and cavity gradient 18 MV/m. Large bandwidth provides robust operation in this regime.

RESULTS

The recorded baseband waveforms were analysed offline to determine the peak detuning during the flattop, pulse-to-pulse variation of detuning, and the phase and amplitude stability of both the vector sum and of the two individual cavities.

With an available RF power of 120 kW (~60 kW per cavity) the gradient was limited by 18 MV/m for Q_L=3.10^6. For higher values Q_L=6.10^6 and Q_L=10^7 the gradient ~25 MV/m was achieved.

Figure 4(left) shows the superposition of C6 detuning of 1800 pulses collected over a period of 30 minutes during operation at Q_L=10^7 and E_{acc} =24.5 MV/m. The red curve shows the detuning averaged over all the pulses while the white curve shows the std deviation of the sample at each point in time. The peak detuning during the flattop is 10Hz. Figure 4(right) shows a histogram of the average detuning for the same sample of pulses. The peak pulse-to-pulse variation during the flattop under these operating conditions is better than ±10 Hz peak-to-peak and 2.27Hz RMS. For all other operating conditions standard deviation of detuning was in range 2-4 Hz.

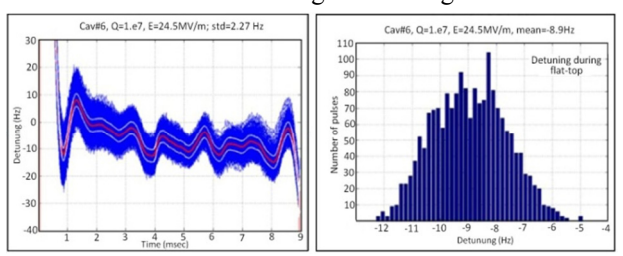

Figure 4: Residual detuning over 30 minutes during operation at Q_L=10^7 and E_{acc} =24.5 MV/m. (A) shows the detuning waveforms of 1800 pulses collected over (B) histogram of the average detuning for the same sample.

Figure 5 shows the closed loop amplitude and phase stability of the C5, C6 and of the vector sum of the two cavities during operation at 25 MV/m. While the individual cavities show pulse-to-pulse amplitude and phase variations of up to 0.2 MV/m and 4 degrees respectively, the variations of the two cavities is strongly anti-correlated (right plot) and the vector sum is stable to 0.01 MV/m (0.04%) in amplitude and 0.2° in phase.

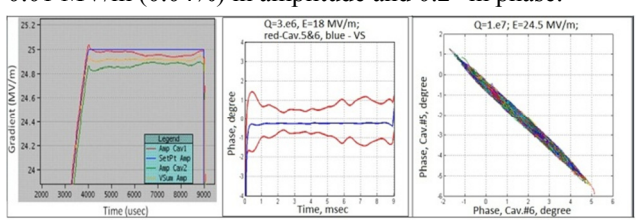

Figure 5: Ampitude (left) and phase (middle) waveforms of C5, C6 and VS. Cavity phase correlation plot (right).

The phase of the vector sum consistently shows a sinusoidal modulation at a frequency close to 1 kHz. This

Copyright © 2012 by the respective authors — cc Creative Commons Attribution 3.0 (CC BY 3.0)

modulation is not present when compensation is off. This modulation is almost certainly an artefact induced by the compensation algorithm but there was not sufficient time during these studies to adequately investigate it. Suppressing this component might allow compensation be further improved.

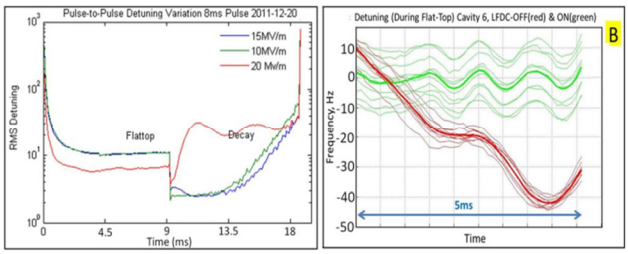

Figure 6: (A): RMS detuning for E_{acc}=10; 15; 20 MV/m. (B): Detuning (during 5ms flat-top) for the 10 RF pulses with LFDC system ON (green) and OFF (red). Thick line is average of 10 pulses.

An attempt was made to investigate the source of the pulse-to-pulse variations. Figure 6(A) shows the RMS detuning during and after of the RF pulse. During these measurements the adaptive portion of the compensation algorithm was turned off so that the compensation pulse did not change. The pulse to pulse variation drops dramatically when the RF feedback ends following the flattop. This may indicate that some of the pulse to pulse variation is due to pulse-to-pulse variations in the RF drive waveforms. Figure 6(B) compares the pulse-to-pulse detuning variation with compensation OFF and compensation ON while the RF controller was operating with feedback turned off. Although compensation is able to reduce the average detuning, the pulse-to-pulse variation becomes somewhat larger.

In these studies the settings for the shape of the cavity probe signal during filling time was optimized for Q_L=6.10^6. Some overhead in the forward power for Q_L=10^7 during the filling time can be seen in the Figure 7 (right).

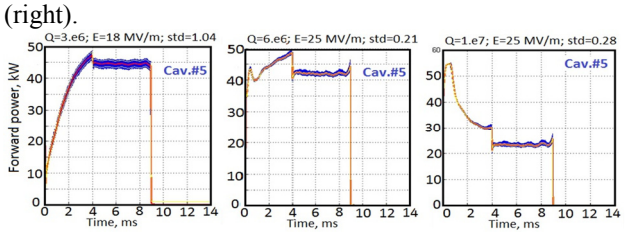

Figure 7: Forward power for Q_L=3.10^6 and E_{acc}=18 MV/m (left); Q_L=6.10^6 and E_{acc}=25 MV/m (centre); Q_L=10^7 and E_{acc}=24.5 MV/m (right)

DISCUSSIONS AND FUTURE PLANS

In these studies it was found that for a lower value of Q_L< 6.10^6 the tuning to operation regime was robust. The adaptive LFD compensation algorithm was able to react quickly enough during the period where gradient in cavity increases. Large bandwidth provides robust operation in this regime.

The tuning process for high Q_L=1.10^7 and E_{acc}=25 MV/m operation was more tricky in part of narrow bandwidth and because of operating gradient was close to the quench limit for C5. Also, in this regime klystron power was close to saturation (see Fig.7) complicating LLRF control. Additional difficulties for tuning of the cavity from low to high gradient arose from limitation in the drive signal applied for piezo-tuner. The later should be in range 0-200 Volts to ensure linear response. At high gradient the bias and voltage variation are increases and push required drive signal out of acceptable range. To put it back, it is required detune the cavity at intermediate gradient by using a mechanical frequency tuner, which complicates the tuning process due to hysteresis and non-linear response. As a result, after a quench it takes some time to tune cavity back to 25 MV/m again. This behavior depends on tuner design (Sacley-type tuner in these tests). The next long-pulse studies planned will involve on CM2 using two high gradient ILC cavities with blade-tuners. By that time we should have fixed known limitations of LFD compensation algorithm and LLRF system.

CONCLUSION

The results of the studies described here can be summarized as follows:

- Active compensation is able to limit LFD during long pulses in cavities operation with Q_L=10^7 and E_{acc}=25 MV/m to ±10 Hz peak-to-peak or better. This is comparable to the pulse-to-pulse detuning variations due to non-deterministic sources.
- The residual detuning is consistent from pulse-to-pulse and is dominated by a single deterministic sinusoidal component with a frequency near 1kHz. Compensation might be improved further if this component can be suppressed.
- Microphonics levels of 2-4 Hz were observed during long pulses. This is similar to the levels measured during 1 ms pulses.
- The detuning responses of the two cavities tested were different prior to compensation, but the levels of residual detuning following compensation were similar. The compensation algorithm is able to adapt the piezo waveform to the detuning response of each individual cavity.

While further improvements may be possible these studies clearly demonstrate that a pulsed linac employing active compensation of Lorentz force detuning could already meet the phase and amplitude stability requirements for Project X.

REFERENCES

[1] T. Arkan *et. al.*," Superconducting RF Cryomodule Production & Testing at Fermilab" Linac10, Japan.
[2] Y. Pischalnikov, W.Schappert, "Adaptive LFD Compensation" Fermilab Preprint-TM2476-TD
[3] W.Schappert *et. al.*," Resonance Control in SRF Cavities at FNAL", PAC2011, New York, USA.
[4] W.Schappert *et. al.*, "Adaptive Lorentz Force Detuning compensation in the ILC S1-G Cryomodule at KEK", SRF2011, Chicago, USA

Copyright © 2012 by the respective authors — cc Creative Commons Attribution 3.0 (CC BY 3.0)

NORMAL CONDUCTING DEFLECTING CAVITY DEVELOPMENT AT THE COCKCROFT INSTITUTE

G. Burt, P. K. Ambattu, A. C. Dexter, B. Woolley, C. Lingwood, Cockcroft Institute, Lancaster, UK
S. Buckley, P. Goudket, C. Hill, P. A. McIntosh, J. Mackenzie, A. Wheelhouse,
STFC, Daresbury, UK
V. Dolgashev SLAC, USA
A. Grudiev, CERN, Geneva, Switzerland
R M. Jones, UMAN, Manchester, UK

Two normal conducting deflecting structures are currently being developed at the Cockcroft Institute, one as a crab cavity for CERN linear collider CLIC and one for bunch slice diagnostics on low energy electron beams for Electron Beam Test Facility EBTF at Daresbury. Each has its own challenges that need overcome. For CLIC the phase and amplitude tolerances are very stringent and hence beamloading effects and wakefields must be minimised. Significant work has been undertook to understand the effect of the couplers on beamloading and the effect of the couplers on the wakefields. For EBTF the difficulty is avoiding the large beam offset caused by the cavities internal deflecting voltage at the low beam energy. Prototypes for both cavities have been manufactured and results will be presented.

INTRODUCTION

Transverse deflecting cavities are required for many applications on accelerators, including crab cavities, bunch separators, emittance exchange and for bunch length diagnostics. These cavities usually operate in a TM_{110}-like mode. The Cockcroft Institute in the UK is participating in the design of several deflectors for a range of applications including crab cavities for ILC [1], CLIC [2] and LHC [3] and a bunch length diagnostic for EBTF [4]. In this paper we concentrate on the normal conducting rf deflectors for CLIC and EBTF.

CLIC CRAB CAVITY

CLIC requires a crab cavity to rotate the bunches prior to the interaction point (IP) to achieve an effective head-on collision. As the bunch size at the IP is very small (~5 nm) the luminosity is very sensitive to the crab cavities RF phase and amplitude. This means that the beamloading must be minimised and correction applied. The beamloading is dependent on the longitudinal electric field experienced by the bunch. In crab cavities the longitudinal electric field is zero on axis but has a linear variation as the bunch goes off axis. This means the beamloading could be positive or negative depending on the beam offset. As the bunch train for CLIC is short (~200 ns), the beamloading cannot be compensated for in a single bunch train, the feedback would occur over several trains. Unless the jitter on the beam offset is much less than the bunch size the compensation will not be successful, hence the beamloading must be minimised instead [5]. In order to reduce the effect of beamloading the cavity is designed with a large power flow so that any power induced by beamloading is smaller in comparison. This is achieved by using a high group velocity travelling wave structure.

Another issue affecting beamloading is the perturbation of the input and output couplers. Couplers break the symmetry of the cavity and can give rise to monopole components to the deflecting field. A dual feed coupler keeps the symmetry of the structure and avoids monopole components but is more complex coupling arrangement requiring splitters. A single feed is the simpler coupling arrangement however this gives the end cells a large monopole component of the rf field. We have investigated methods of single feed coupling without inducing monopole component.

Single-feed Couplers

In order to minimise the monopole component of rf field in the end cells while using a single-feed coupler a number of options were investigated. Initially cancelling the monopole kick from the two end cells was studied. Consider particle moving at the speed of light. If the cell is rotated the monopole component has the sign of the real part of the voltage flipped. Hence if the input and output couplers are mounted on opposite side the real parts should cancel. If the lengths of the cells are adjusted so that the voltage is entirely real then the entire monopole component is cancelled. This however is not sufficient in travelling wave deflecting structures as the power put into the output cell will be extracted through the output coupler while the power in the input cell will travel down the structure. Hence it is necessary to cancel the beamloading in each cell individually.

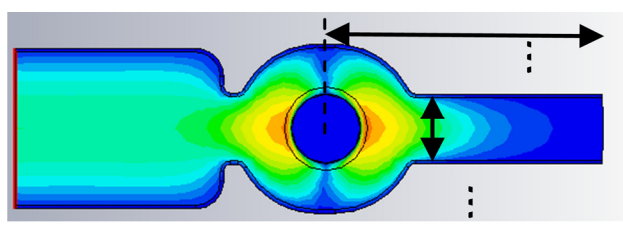

Figure 1: Dummy waveguide and input coupler on the CLIC crab cavity

In order to restore the symmetry of the cell a dummy waveguide opposite the coupler was studied. Using a

Copyright © 2012 by the respective authors — cc Creative Commons Attribution 3.0 (CC BY 3.0)

dummy waveguide was found to significantly reduce the monopole component but not reduce it to zero. The real part is reduced to zero, but the imaginary component is not and hence gives the minimum voltage. The reason for this is because there must be a power flow across the cell, from the coupler to the dummy waveguide. This means that there cannot be a full standing wave in the cavity and there must be a travelling wave component.

Another method of symmetrising the cell is to couple from the side with a TE_{02} mode coupler. This allows an equal power flow to each side hence avoiding a monopole component. However the cavity is now vertically asymmetric and hence there is a small vertical kick. However this symmetry can be recovered by adding a dummy waveguide. The TE02 mode splitter must carefully be designed to avoid excitation of a TE01 mode which gives rise to a monopole component to the fields.

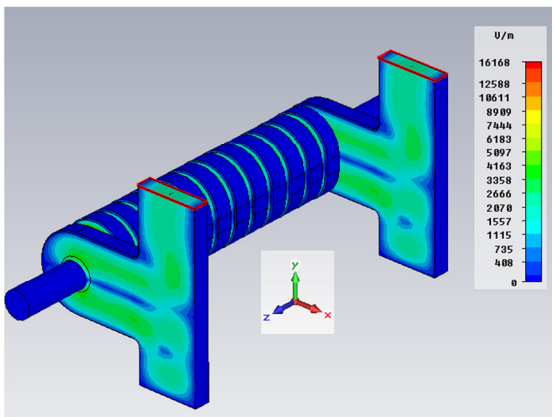

Figure 2: TE_{02} mode coupler

Wakefield Damping

As the cavity is close to the final focus magnets, where the beta function is large, it is very sensitive to transverse wakefields. It is necessary to damp any long-range wakefields within a few bunches to avoid large transverse offsets at the IP. The vertical wakefield is the most sensitive, due to the small vertical beam size, and is dominated by the opposite polarisation of the crabbing mode, known as the same order mode (SOM). As the wake is dominated by a single mode it is proposed to have this modes frequency at the zero-crossing, where the mode frequency is a half integer harmonic of the beam frequency. This means that each bunch induces a voltage 180 degrees out of phase with the previous bunch hence cancelling each other. For CLIC it is proposed that the cell has an elliptical cross-section such that the crabbing mode is at 11.99 GHz while the SOM is at 12.98 GHz. However the SOM still requires significant damping due to the very tight tolerances on vertical kicks. Choke damping and waveguide damping were both considered. Choke cavities are difficult for deflecting cavities as the choke must be polarised to damp one polarisation but not the other. Options are to use an elliptical cavity, an elliptical choke or a slotted choke [6]. The slotted choke achieved the best performance; however widening the slot to achieve better damping also reduces the Q of the crabbing mode which could be problematic due to enhanced heating. For this reason a waveguide damper was chosen for CLIC, as shown in Fig.3, as a waveguide coupler shows strong damping of the SOM without affecting the crabbing mode.

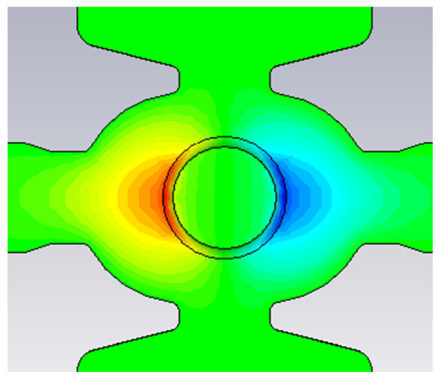

Figure 3: Damped elliptical cell of the CLIC crab cavity

Cavity Prototype

Two prototype cavities have been manufactured. One has been made by Shakespeare Engineering, a UK company, to be tested at SLAC and the other has been made at VDL, to be tested at CERN. The CERN cavity has had the parts machined and is due to be brazed soon. The SLAC cavity, shown in Fig. 4, has been fully manufactured and is currently undergoing tests at Cockcroft before shipping to SLAC.

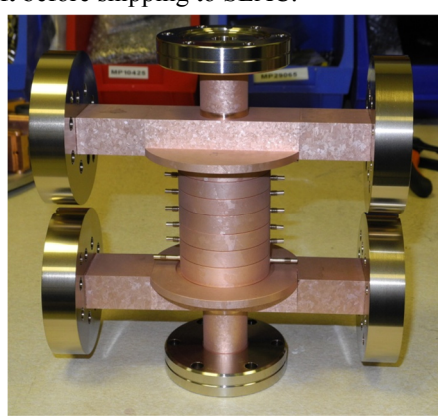

Figure 4: CLIC crab cavity prototype manufactured by Shakespeare Engineering.

EBTF TRANSVERSE DEFLECTING CAVITY

The Electron Beam Test Facility (EBTF) at Daresbury Laboratory will deliver low energy (5/6 MeV) short bunches (down to 40fs RMS) to a number of industrial experimental stations and for fundamental scientific research. In order to measure the longitudinal profile of the bunch an S-band transverse deflecting cavity will be inserted into the beamline. A transverse kick of around 5 MV is required, hence a 9 cell design has been chosen. The design of the transverse deflecting cavity has been influenced by the competing demands of high RF efficiency [7] and minimising the equal and opposite

Copyright © 2012 by the respective authors — cc Creative Commons Attribution 3.0 (CC BY 3.0)

unwanted transverse kick at the entrance and exit of the cavity which causes the low energy electrons to be displaced while traversing the cavity [8]. The coupler has a dummy waveguide to minimise the on-axis longitudinal electric field.

Minimising transverse offset

As a transverse deflecting cavity has a finite size the beam experiences a range of phases as it crosses the cavity. This means for a zero-crossing it experiences a finite force, initially in one direction and then in the other such that the net transverse momentum at the centre of the bunch is the same at the start and end of the cavity. However this does result in a transverse offset as the beam travels transversely inside the cavity. It was found that due to the beampipe the electrical centre of the end cell was not at the geometric centre. This resulted in an uneven kick producing a net transverse momentum when leaving this cell, which wasn't removed until experiencing the opposite force at the other end cell. This gave a much larger transverse offset in the cavity, of 4 mm, due to the low energy of the bunch. As the beam was offset the beamloading was much higher which significantly altered the beam energy. For ultra-relativistic beam this offset is small and typically ignored. For low energy beam of EBTF is could not be ignored and has to be minimized.

In order to counteract this effect the end cells were made much shorter such that transverse kick in the end cells for a zero-crossing particle was minimised. The final cavity is shown in Fig. 5. The particle tracking simulations in GPT [9] show the transverse offset inside the cavity is minimised, shown in Fig. 6.

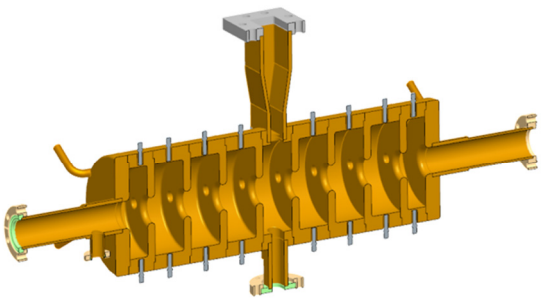

Figure 5: EBTF Transverse deflecting cavity with shortened endcells.

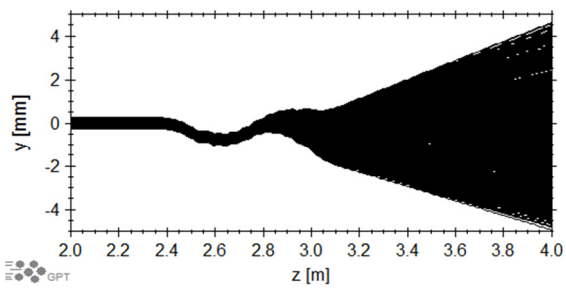

Figure 6: GPT tracking simulation of EBTF transverse motion.

Prototype Cavity

A 3-cell prototype has been produced by Research Instruments (shown in Fig. 7), to verify brazing procedure, and a contract has been placed with them for a full 9-cell structure.

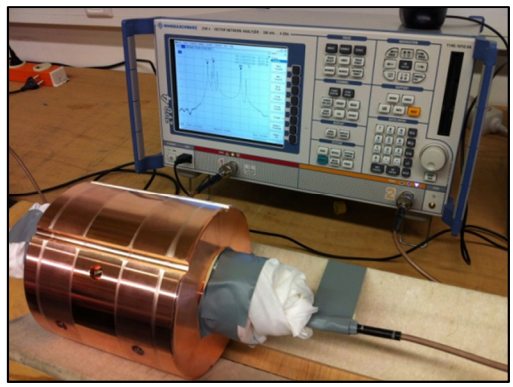

Figure 7: 3-cell prototype of the EBTF Transverse deflecting cavity.

SUMMARY

The Cockcroft Institute has a proven track record of designing deflecting cavities for numerous applications. High power testing is expected to be done on both cavities in the next few months.

ACKNOWLEDGEMENTS

This work has been supported by STFC via the Cockcroft Institute core grant and the EU through the EUCARD grant.

REFERENCES

[1] C. Adolphsen1 et. Al, Design of the ILC Crab Cavity System, EUROTeV-report-2007-010, 2007

[2] P.K. Ambattu, G. Burt, et al, An asymmetric crab cavity design for the CLIC, IPAC 2011

[3] R. Calaga, LHC Luminosity Upgrade Using Deflecting/Crabbing Cavities, ICFA DMC, Cockcroft Institute, September 2010

[4] P.A. McIntosh et al, A New Electron Beam Test Facility (EBTF) at Daresbury Laboratory for Industrial Accelerator System Development, IPAC 2012

[5] A. Dexter et.al, CLIC Crab Cavity Design Optimisation for Maximum Luminosity, Nucl. Instr. and Meth. A (2011)

[6] P.K. Ambattu et.al, Analysis and control of wakefields in X-band crab cavities for Compact Linear Collider, Nucl. Instr. and Meth. A (2011)

[7] G. Burt et al, A transverse deflecting cavity for the measurement of short low energy bunches at EBTF, IPAC 2012

[8] John Power , REPORT ON THE 2 CELL CAVITY SIMULATIONS WITH THE HALF – FULL – HALF GEOMETRY, ANL-AAI-TN-2007-003, 2007

[9] M.J. de Loos, S.B. van der Geer, General Particle Tracer,http://www.pulsar.nl/gpt

Copyright © 2012 by the respective authors — cc Creative Commons Attribution 3.0 (CC BY 3.0)

STATUS OF THE C-BAND RF SYSTEM FOR THE SPARC-LAB HIGH BRIGHTNESS PHOTOINJECTOR*

R. Boni, D. Alesini, M. Bellaveglia, G. Di Pirro, M. Ferrario, A. Gallo, B. Spataro,
INFN-LNF, Frascati, Italy
A. Mostacci, L. Palumbo, ULRS, Rome, Italy

Abstract

The high brightness photo-injector in operation at the SPARC-LAB facility of the INFN-LNF, Italy, consists of a 150 MeV S-band electron accelerator aiming to explore the physics of low emittance high peak current electron beams and the related technology. Velocity bunching techniques, SASE and Seeded FEL experiments have been carried out successfully. To increase the beam energy so improving the performances of the experiments, it was decided to replace one S-band travelling wave accelerating cavity, with two C-band cavities that allow to reach higher energy gain per meter. The new C-band system is in advanced development phase and will be in operation early in 2013. The main technical issues of the C-band system and the R&D activities carried out till now are illustrated in detail in this paper.

THE SPARC-LAB AT FRASCATI LNF

The SPARC-LAB is a research facility of the INFN Frascati Laboratory (LNF) whose purpose is to conduct advanced research in the field of high brightness, low emittance electron beams [1]. The facility, able to operate also in the velocity bunching configuration, feeds six 2m. long undulators and integrates the 150 MeV S-band photo-injector with a 220 Terawatt, Ti:Sa ultrashort laser system. FEL radiation in the SASE, Seeded and HHG modes have been performed from 500 nm down to 40 nm wavelength. The photo-injector SPARC, a single bunch electron accelerator, consists of a laser driven RF Gun followed by three traveling wave (TW), constant gradient, $2\pi/3$ accelerating cavities, with the first two immersed in a solenoidal field to keep down the beam emittance growth. A second beam line has been also installed and is now hosting a narrow band THz radiation source.

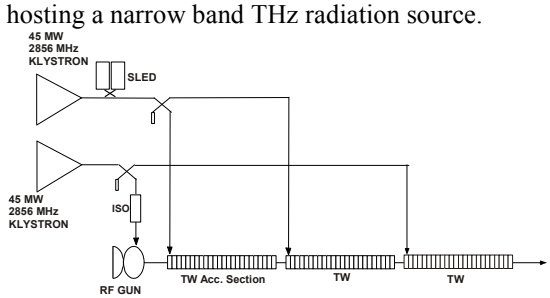

Figure 1: the SPARC photoinjector present layout.

To improve the performances of the experiments and recuperate the energy that is lost in the velocity bunching configuration. it was decided to increase the beam energy by replacing the third S-band section with two, 1.4 m. long, C-band TW accelerating structures that allow to operate at higher gradient. The choice of a higher frequency, e.g. the X-band, was also considered but then discarded because more expensive and technically more challenging.

THE C-BAND RF SYSTEM

The C-band technology is relatively new in linear accelerators compared to the standard and widely used S-band systems. Nevertheless it can be considered sufficiently mature since it is already employed in other accelerator laboratories like the Spring8 (JP) and the PSI FEL (CH) facilities.

R&D of the Accelerating Structure

The third S-band accelerating section, that is a 3 m. long SLAC-type unit, shown in Fig.1will be replaced with two, 1.4 m., C-band sections supplied with a 50 MW, 5712 MHz Toshiba klystron through a SKIP-type pulse-compressor [2]. In order to ease design and construction, the C-band sections are constant impedance (CI) structures with large (14 mm) iris diameter to minimize the surface electric field on the iris edges and improve the pumping speed. Also, the group velocity increases and this reduces the filling time. It must be remarked that the typical exponential decay of the input compressed pulse is partially compensated by the RF losses of the CI structure, resulting in a quasi-constant field amplitude along the section. Input and output waveguides are coupled to the beam-pipe instead of to the end-cells. A 50 cm long prototype was designed at LNF and built by a local firm. Brazing and vacuum test have been made at LNF [3].

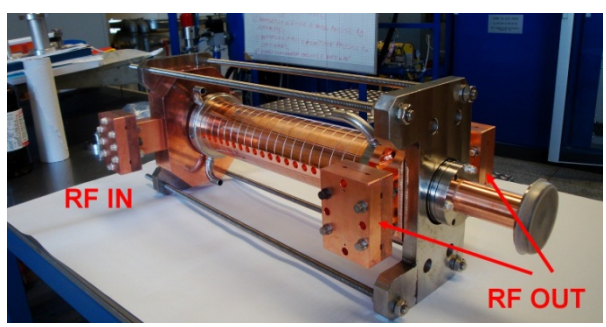

Figure 2: The C-band prototype tested at KEK.

* This research has received funding from the European Commission under the FP7-INFRASTRUCTURES-2010-1/INFRA-2010-2.2.11 project TIARA (CNI-PP). Grant agreement no 261905

Copyright © 2012 by the respective authors — cc Creative Commons Attribution 3.0 (CC BY 3.0)

The prototype, shown in figure 2, has been power tested at KEK, in the frame of a collaboration established ad hoc with the INFN.

The KEK RF station consists of a 50 MW - 2.5µsec Toshiba E37202 klystron, followed by a pulse compressor. The results of the power tests, reported in detail in the ref. [4], was very successful and well beyond our expectations. The C-band prototype was tested up to 110 MW peak - 200 nsec - 50 Hz to a maximum average gradient of 55 MV/m, with a breakdown rate of the order of 10^{-6} bpp/min after about 300 hours of RF conditioning. A picture of the prototype is shown in figure 2.

Following the positive results of the KEK power test, we started the construction of two 1.4 m accelerating sections. The next figure 3, shows the concept of the beam-pipe coupling. This type of coupling allows the first RF cell to be mechanically unperturbed, i.e. there are no slots on the cell outer wall that normally cause heating and degrade the performances.

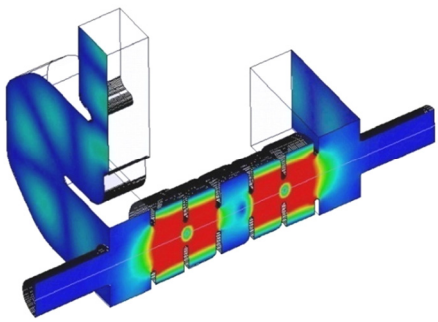

Figure 3: The waveguide beam-pipe coupling.

Further, the symmetric coupling guarantees low quadrupole components on the longitudinal axis [3]. The same concept of beam-pipe coupling is applied at the accelerating section output, with two opposite flanges without combiner. So we use 2 loads per section but the power dissipated by each load is halved.

The actual accelerating structures consist of 71 cells and are 1.4 m. long, to leave 20 cm for the insertion of a pumping unit in the 3 m. left available by the 3rd S-band section. The new C-band sections have been manufactured The cells and the waveguide couplers have been machined by a local firm; then, low power test and brazing of two halves have been made at LNF where a vacuum furnace of 80 cm of internal height is available. After joining mechanically the two halves, the first C-band section was tuned at LNF by adjusting the plungers on each cell wall. The last brazing will be made shortly by a local firm, where a 2 m. long vacuum furnace is available. The C-band actual section in shown in the next figure 4.

The figures 5 and 6 show the low power measurements made in laboratory with the bead perturbation technique. The following table 1 shows the main specifications of the C-band accelerating structures.

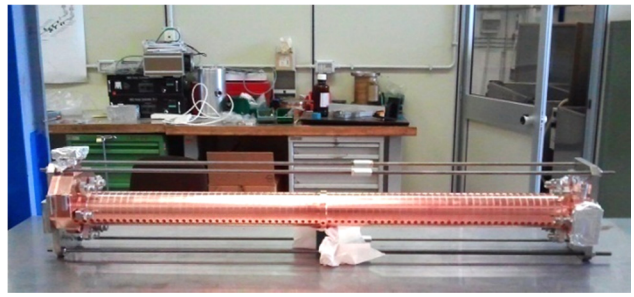

Figure 4: The two halves of one C-band section before the final brazing.

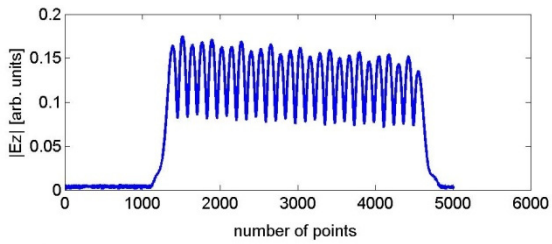

Figure 5: RF field profile of half C-band section.

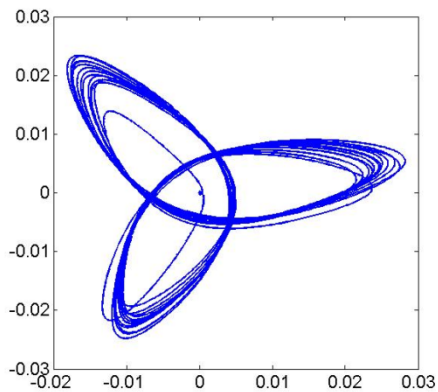

Figure 6: Phase advance per cell in the polar plane.

Table 1: C-band Structures Main Parameters

Frequency (MHz)	5712
type	TW, CI
structure	Disk loaded
Phase advance per cell	2π/3
n. of cells	71
Coupling type	beam-pipe
Iris radius (mm)	7.0
Group velocity/c	0.0283
Shunt impedance (MΩ/m)	82.9
Surf. peak E field/Acc. field	2.17
Filling time (nsec)	150
Total length with couplers (cm)	140

Copyright © 2012 by the respective authors — cc Creative Commons Attribution 3.0 (CC BY 3.0)

The RF power needed to produce the accelerating field is about 60% of input power. The residual 40% will be dissipated by two RF water-loads, supplied by CML-Engineering, connected to the output coupling ports of the accelerating sections.

The Power Transmission System

The layout of the complete C-band system is presented in figure 7. The RF power will be distributed to the accelerating structures by means of a network of rectangular WR187 waveguides (WG) made of OFHC copper. The total WG length from the klystron to the accelerating sections is about 10 m. and the RF losses are of the order of 10% since the attenuation is 0.035 dB/m.

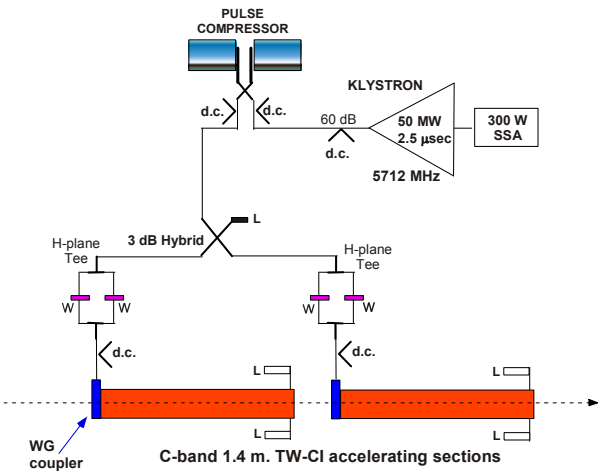

Figure 7: Layout of the SPARC C-band system

The C-band pulse compressor (PC) is under construction by the Division of Technology Development of the IHEP, Beijing, China. It is a double slot coupled cylindrical resonator system that follows the concept of the model "SKIP" developed by KEK. The PC output power is divided in two by a 3 dB hybrid junction and then delivered to the accelerating sections through two RF windows. The RF is split and recombined with two H-plane Tees. In this way the peak power through each RF window is halved as we are not sure of the actual capacity of them to handle power levels in excess of 100 MW peak.

The H-plane Tee s11 is -20 dB and the phase unbalance between outputs is about 1°. They have been designed and brazed at LNF. The machining was made by the local firm Comeb.

The RF Power Station

The RF power station consists of the Toshiba klystron E37202 driven by a solid state 400 W amplifier supplied by MitecTelecom. The pulsed klystron modulator is also a full solid state system made by Scandinova. The table 2 lists the main parameters of the RF power station. The klystron have been successfully RF tested on a dummy load up to 40 MW – 2 µsec – 10 Hz. The klystron RF conditioning is still ongoing.

Table 2: C-band Power Station Main Parameters

Frequency (MHz)	5712
Max klystron power (MW)	50
RF pulse width (µsec)	2.5
Klystron input RF power (W)	300
Klystron beam voltage (kV)	350
Max RF pulse rep. rate (Hz)	10

The Low Level RF System

The control of the C-band accelerating structures will be achieved by a digital low level RF (LLRF) system where all RF signals are down-converted to intermediate frequencies which are then digitized and processed with powerful digital processing platforms. The drive signal is finally up-converted to control the RF high power chain The schematic layout of the digital control system is shown in the figure 8..

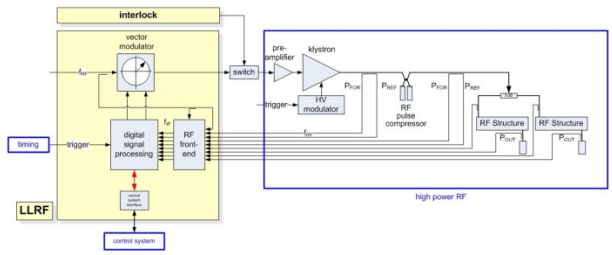

Figure 8: Schematic layout of the digital LLRF system.

A processing board based on VME64x is under development by the PSI laboratory (CH) in collaboration with INFN. It includes a multi-core PowerPC processor and a high performance field programmable gate array Xilinx Virtex-6 on the main board and provides a variety of I/O interfaces. The goal of the digital signal processing is to implement all static algorithms like the digital down-conversion from intermediate frequency to base-band, filtering, I/Q to amplitude/phase conversions and averaging calculations in firmware in the FPGA while using the PowerPC for more sophisticated high level applications like pulse-to-pulse feedback algorithms.

REFERENCES

[1] M. Ferrario et al., "Recent Results at the SPARC_LAB Facility", IPAC11, S. Sebastian, Spain.

[2] T. Sugimura et al., "SKIP, A Pulse Compressor for SuperKEKB", Proc. of Linac2004 Conference.

[3] D. Alesini et al., SPARC-RF-11-002, LNF Techn. Note.

[4] D. Alesini et al., " Design, Fabrication and Power Test of a C-band Acc. Structure", IPAC 11, S. Sebastian, Spain.

Copyright © 2012 by the respective authors — cc Creative Commons Attribution 3.0 (CC BY 3.0)

TRAVELING WAVE ACCELERATING STRUCTURES WITH A LARGE PHASE ADVANCE

V. Paramonov *, INR of the RAS, Moscow, 117312, Russia

Abstract

The Traveling Wave (TW) accelerating structures, operating with phase advance for the whole field more than 180^o per period (up to 1300^o) are considered in this report. To realize such phase advance, the structures should operate in higher branches of the Brillouine diagram for TM_{01} wave and have similar to TM_{01n} mode field distribution in the cell. RF parameters of the Disk Loaded Waveguide (DLW) cells are considered for such phase advance and some additions to improve RF efficiency are presented.

INTROSUCTION

There are a lot of papers, describing traveling wave structures with phase advance $\Theta \geq 180^o$ and particularities of particle acceleration. For example, see [1] and related references, higher current electron beams can be accelerated. If such structures operate in the first Brillouine zone for TM_{01} wave and field distribution in the cell corresponds to TM_{010} mode, it means acceleration with higher spatial harmonics. The subject of this paper is consideration of DLW structures, in which the main, dominating spatial harmonic has a phase advance $\Theta \geq 180^o$.

FIELD DISTRIBUTION

In Fig. 1 is shown well known formation of the DLW dispersion diagram from TM_{01} wave parabola in smooth waveguide, [2], and numbers of Brillouine zones are marked. For traveling wave the field distribution in the

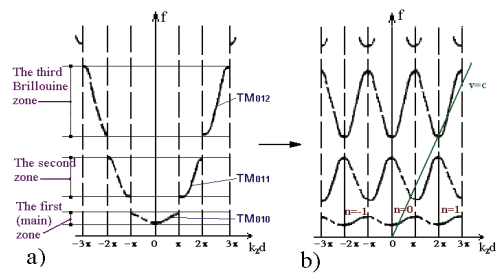

Figure 1: DLW dispersion diagram formation for TM_{01} wave.

aperture all time can be represented in complex form as:

$$E_j(r,z) = \Re E_j(r,z) - i\Im E_j(r,z) = \quad (1)$$
$$= e^{\frac{-i\Theta_0 z}{d}} \sum_{n\to-\infty}^{n\to+\infty} a_{jn}(r) e^{\frac{-i2n\pi z}{d}},$$

where d is the DLW period and $0 \leq \Theta_0 \leq 180^o$ is the phase advance. In the main zone, Fig. 1, the TM_{010} mode is implemented in DLW cell and expansion (1) starts with $n = 0$. For the second zone the field distribution is TM_{011}-like. For symmetrical DLW cell there is no $n = 0$ harmonic in the expansion (1), which starts now with $n = -1$, and field phase advance is in range $180^o \leq \Theta \leq 360^o$, including 180^o leap due to TM_{011} mode field structure.
So on, in higher zones with TM_{01N}-like field in the cell, we can provide field phase advance $N \cdot 180^o \leq \Theta \leq N \cdot 180^o + 180^o$.

DLW CELLS PARAMETERS

RF parameters of DLW cells in higher TM_{01} passbands investigated assuming operating frequency $3.0GHz$ in wide range of aperture radius a and Θ_0 similar to [3] with powerful 2D software. In each passband the cell length is defined from synchronism condition:

$$d_2 = \frac{\lambda(2\pi - \Theta_0)}{2\pi}, \quad d_3 = \frac{\lambda(2\pi + \Theta_0)}{2\pi}, \quad (2)$$

where d_2 and d_3 are the DLW cell length for the second and the third passband, respectively.
In Fig. 2 the surfaces of the group velocity β_g and effective shunt impedance Z_e are shown with parameters $\frac{a}{\lambda}$ and Θ_0 for the second and the third TM_{01} passbands.

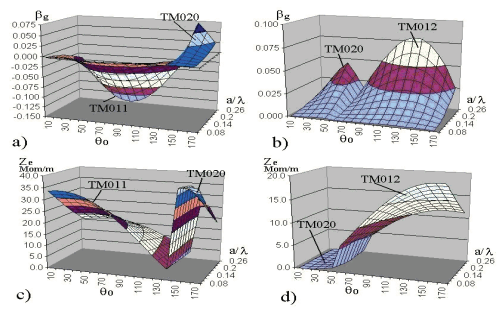

Figure 2: The surfaces $\beta_g(\frac{a}{\lambda}, \Theta_0)$, (a,b) and $Z_e(\frac{a}{\lambda}, \Theta_0)$, (c,d) for the second (a,c) and the third (b,d) passbands.

The regions of TM_{01} wave existence in each higher passbans are limited by interaction with TM_{02} wave, see Fig, 2. For the first and the second passbans possible Θ_0 values are in limits $0 < \Theta_0 < 140^o$ and $70^o < \Theta_0 < 180^o$, respectively. Outside these limits the cell radius R_c becomes large enough and TM_{02} wave comes in appropriate passband.
Without 2D investigations, these Θ_0 limitations were accepted and for appropriate higher passbands (the forth and so on).

* paramono@inr.ru

Copyright © 2012 by the respective authors — cc Creative Commons Attribution 3.0 (CC BY 3.0)

The examples of phase and amplitude distributions along

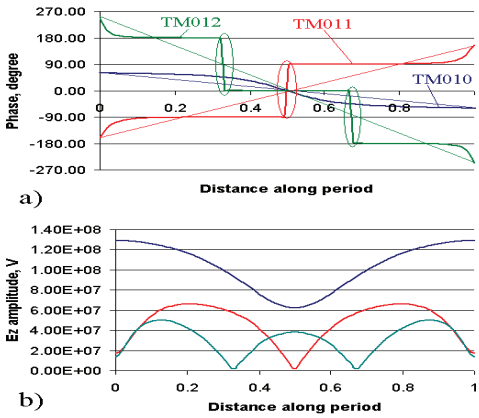

Figure 3: Phase (a) and amplitude distributions along DLW cell axis for the first ($\Theta = 120^o$), the second ($\Theta = 320^o$) and the third ($\Theta = 510^o$) passbands.

cell axis are plotted in Fig. 3 for several passbands, showing for the total field the phase advance per cell $\Theta > 180^o$ in higher passbands.

The relative dimensions of DLW cells for the first and the

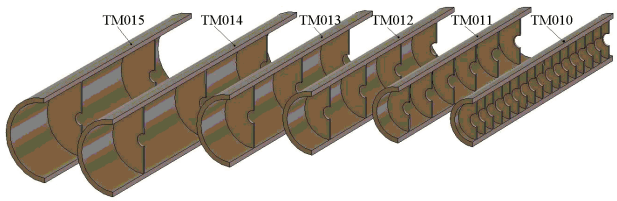

Figure 4: The relative DLW cells dimensions for operation in the first and in higher TM_{01} passbands.

higher TM_{01} wave passbands are compared in Fig. 4 and main RF parameters are listed in the Table 1.

As one can see from Fig. 4 and Table 1, the simple DLW

Table 1: The main RF parameters of DLW cells, $f_0 = 3GHz, a = 12mm$, for operation in the first and higher passbands.

Mode	Θ_0	R_c	$\beta_g \cdot 10^2$	$Q \cdot 10^{-3}$	Z_e
TM_{010}	120	39.49	2.19	14.1	60.86
TM_{011}	320	48.08	-1.36	18.7	24.93
TM_{012}	510	56.02	0.58	25.6	18.24
TM_{013}	680	65.51	-0.39	31.7	12.23
TM_{014}	840	70.73	0.22	36.4	9.48
TM_{015}	1040	79.55	-0.17	40.1	7.15
TM_{016}	1230	83.01	0.11	45.9	6.05

cells in higher passbands lose to classical DLW for the fist zone in transverse dimensions, group velocity and Z_e value.

EFFICIENCY IMPROVEMENT

Efficiency reduction of DLW cells in higher TM_{01} passbands is evident from the particularity in electric field distribution for TM_{01N} mode. In Fig. 5 electric field is shown in DLW cell for TM_{012} mode and one can see a strong E_r component along segments BE and CF.

Considering the balance

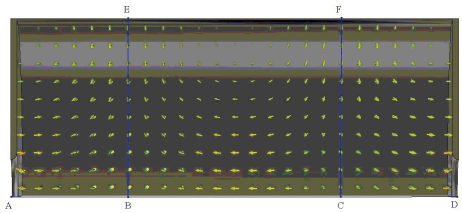

Figure 5: Electric field of TM_{012} mode in DLW cell.

$$\int_B^E E_r dr + \int_C^B E_z dz + \int_F^C E_r dr = \omega\mu\mu_0 \oint_S H_\varphi dS, \quad (3)$$

one can conclude - RF voltage along segments BE and CF spend magnetic flux, but doesn't takes a part in acceleration. It tells a way for RF efficiency improvement - we can substitute a part of segments BE and CF by conducting washers to reduce radial RF voltage part in (3). The maximum of E_r corresponds to minimum of H_φ and washers should not increase RF loss essentially.

Structures with washers in DLW cells are shown in Fig. 6 and main RF parameters are listed in the Table 2 for the same conditions as DLW cells in Fig. 3 and in the Table 1.

The washers lead to essential reduction in the cell radius

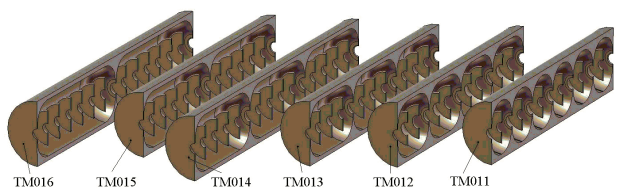

Figure 6: Structures with washers in DLW cells.

R_c, which is defined now mainly by washer diameter and for all structures in Fig. 6 $R_c \approx 65mm$. As one can see from the Table 2, the group velocity β_g and Z_e values are improved essentially due to stronger fields near axis. The DLW with washers is the structure with separated functions - β_g value for TW operations depends on the aperture radius in the disk. And Z_e value is defined by washers, which have similar to standing wave π mode field distribution - mostly effective with respect Z_e value. As one can see from the Table 2, Z_e value comes to saturation with increasing number of washers. The case $N = 3 \div 4$ (TM_{013}, TM_{014}) modes in the cell is a reasonable choice.

The accelerating structure with washers is known, [4], and further Z_e improvement is due to the drift tubes at washers. Such structure is shown in Fig. 7 and for the fifth passband,

Copyright © 2012 by the respective authors — cc Creative Commons Attribution 3.0 (CC BY 3.0)

Table 2: The RF parameters of DLW cells with washers.

Mode	$\beta_g \cdot 10^2$	$Q \cdot 10^{-3}$	Z_e
TM_{010}	2.19	14.1	60.86
TM_{011}	-0.91	24.4	50.32
TM_{012}	0.87	33.5	60.29
TM_{013}	-0.83	37.4	61.91
TM_{014}	0.77	40.2	64.01
TM_{015}	-0.76	42.4	65.85
TM_{016}	0.73	43.6	65.56

TM_{014} - like mode in the DLW cell has for bore hole diameter in drift tubes $2 \cdot a_b = 24mm$ calculated parameteres $Q = 34300, \beta_g = 0.822 \cdot 10^{-2}, Z_e = 75.5MOm/m$ and $Q = 35800, \beta_g = 0.812 \cdot 10^{-2}, Z_e = 99.1MOm/m$ for $2 \cdot a_b = 10mm$, showing essentially higher Z_e value, as compared to classical DLW.

The dimensions optimization for DLW cells with washers and drift tubes for further Z_e increasing was not performed and Z_e values, listed in the Table 2 and given for the structure in Fig. 7 may be not maximal.

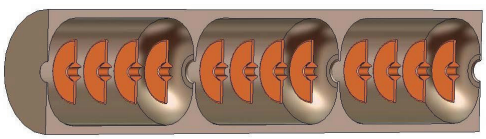

Figure 7: The structure with washers and drift tubes in DLW cell.

DISPERSION PROPERTIES

Due to the design idea, the operating branch of the dispersion diagram is not fundamental. Depending on the Θ value, below operating branch there are several lower branches of TM_{01j} modes and branches of modes with an azimuthal field variations. As an example, in Fig. 8 is shown the dispersion diagram for the structure with washers in the cell, operating with $\Theta = 510^o$ in the third TM_{01} passband with TM_{012}-like mode in the DLW cells. Instead of differences in details, there are common features for dispersion diagrams of all structures, considered in this report. All these structures are narrow band with strong dispersion and relatively small passband width for all branches.

The washers, or washers with drift tubes, do not change dispersion diagram significantly, as compared to diagrams for simple DLW cells, shown in Fig. 4. The lowest branch is all time for modes with one azimuthal field variation.

The line of synchronous interaction $v = c$ cross the lowest branch, and, therefore, upper branches, for $\Theta > 180^o$.

In the vicinity of operating point there are branches, with separation in frequency $(30 \div 100)MHz$, for modes with one and three azimuthal field variations. In this topic the situation with high order modes in the vicinity of operating point is the same as for the structure [4] and well known

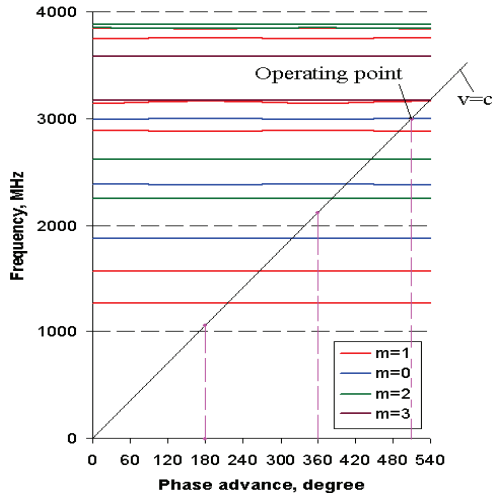

Figure 8: Dispersion diagram of DLW with washers, TM_{02}-like operating mode in the cell, $\Theta = 510^o$, m - number of azimuthal variations.

Disk And Washer (DAW) accelerating structure.

The density and placement of branches for high order modes in the vicinity of operating point is the limitation for washers number increasing in the cell.

SUMMARY

Traveling wave accelerating structures with the phase advance for the total field essentially larger than 180^o per period are possible using higher passbands of TM_{01} wave. It allows longer period length, but the simple DLW cell will lose to the classical case in RF efficiency. With washers and washers with drift tubes in DLW cells RF efficiency for higher passbands is improved in times, overlapping the classical case. The washer support, high order modes influence are the subjects for further consideration.

ACKNOWLEDGMENT

The author thanks Professor N.P. Sobenin for valuable discussion.

REFERENCES

[1] N.I. Aizatsky. DLW for acceleration high intensity short pulse electron beams. Proc. PAC1995 Conf., p. 3229, 1996

[2] O.A. Valdner, N.P. Sobenin et. al., Handbook for disk loaded waveguide. Moscow, Atomizdat, 1969 (in Russian)
G.A. Loew, R.B. Neal. Accelerating structures. In Linear Accelerators, ed. P. Lapostole, A. Septier. Amsterdam, North-Holl. Pub. Co, 1970, p. 39-107

[3] V. Paramonov. The data library for accelerating structures development. Proc. 1996 LINAC Conf., 1996, Geneva, CERN, v.2, p. 493

[4] V.G. Andreev, V.V. Pashkovskyj. Accelerating structure with washers and drift tubes for proton linear accelerators. Journ. of Techn. Physics, v. 40, n. 3, p. 523, 1970 (in Russian)

Copyright © 2012 by the respective authors — cc Creative Commons Attribution 3.0 (CC BY 3.0)

RF PARAMETERS OF A TE - TYPE DEFLECTING STRUCTURE FOR THE S-BAND FREQUENCY RANGE *

V. Paramonov †, L. Kravchuk, INR RAS, Moscow, Russia
K. Floettmann, DESY, Hamburg, Germany

Abstract

In [1]an effective compact deflecting structure has been proposed preferably for the L-band frequency range. RF parameters of this structure are now considered for S-band frequencies both for traveling and standing wave operation. Some methodical topics of the structure are discussed too.

INTRODUCTION

In [1] a deflecting structure was proposed with the original design idea to separate the functions of RF efficiency and RF coupling, which are coupled in the well known Disk Loaded Waveguide (DLW) by a single parameter - the aperture radius r_a. Two protrusions are introduces at the disk in order to concentrate the transverse electric field at the axis, Fig.1b. The magnetic field around the protrusions, Fig. 1d, provides the required flux for the transverse RF voltage. The structure has a small transverse diameter $2r_c \sim (0.6 \div 0.8)\lambda_0$, where λ_0 is the operating wavelength and looks promising at lower frequencies, including the L-band range. The structure dispersion is positive with a passband width $\Delta f \sim (0.10 \div 0.15) f_0$. It reaches a significant group velocity β_g for a Traveling Wave (TW) with a phase advance $0 < \theta < \pi$, which results in a significant power flow and thus suggest a Standing Wave (SW) operation, [2].

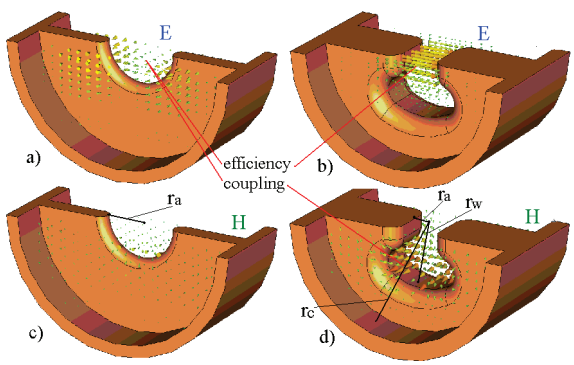

Figure 1: Electric (a, b) and magnetic (c, d) field distributions for the classical DLW structure (a, c) and the TE-deflector, (b, d).

The attractive features of the structure stimulate an additional study, including possible applications in the S - band frequency range.

* Work supported in part by RBFR N12-02-00654-a
† paramono@inr.ru

FIELD DISTRIBUTION

The classification of a structure with a complicated field distribution is always rather conditional. In the field distributions, Fig. 1b,d, one can see a strong transverse electric field, providing an argument for a structure classification in the RF sense as TE - type. But for the description of a deflecting field at $\beta = 1$ the generating hybrid waves HM_n and HE_n are used, see [3] for explanations, both with simultaneously non vanishing E_z and H_z components. For the deflecting force - the transverse component of the Lorenz force - in cylindrical or Cartesian coordinates we have:

$$\vec{F}^L_{r,x} = e(\vec{E} + [\vec{v}, \vec{B}]) = e(E_r - \beta Z_0 H_\varphi) = \\ = e(E_x - \beta Z_0 H_y), \quad Z_0 = \sqrt{\mu_0}\epsilon_0. \tag{1}$$

In contrast to a DLW, the structure under consideration has the same phasing for both transverse components E_r, H_φ or E_x, H_y and the deflecting effect of the electric field is partially compensated by an opposite deflection of the magnetic field. The phasing of transverse E, H components defines also the sign of the group velocity, which is positive in our case. For a deflection of particles this structure can be described as HE_1-dominating structure.
The effective transverse shunt impedance Z_e in the structure,

$$Z_e = \frac{|\frac{1}{k}\int_0^L \frac{\partial E_z}{\partial z} e^{ikz} dz|^2}{P_s L}, \quad \beta = 1, \tag{2}$$

where L is the structure length and P_s is the dissipated RF power, depends mainly on the distance between the ends of the protrusions, i.e. the effective aperture diameter $2r_a$, Fig. 1d, Fig. 2.
The structure has no rotational symmetry, which removes

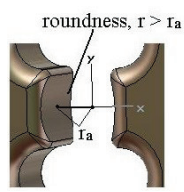

Figure 2: The structure shape near the axis for the reduction of multipole additions.

the problem of overlapping modes with perpendicular field orientation. But in the field distribution exist, together with the desirable dipole components $\sim cos(\varphi), sin(\varphi)$, multipole components $\sim cos(n\varphi), sin(n\varphi), n = 3, 5, 7, ..,$

Copyright © 2012 by the respective authors — cc Creative Commons Attribution 3.0 (CC BY 3.0)

which provide non linear additions $\sim r^{(n-1)}$ in the deflecting field. The relative amount of multipole additions can be effectively reduced by a special shape of the ends of the protrusions, Fig. 2. The roundness radius $r > r_a$, Fig. 2 should be optimized for the chosen value of r_a thus compromising the linearity of the field in the specified vicinity of the axis $r < r_0$ and the RF efficiency Z_e.

TW OPERATION

For a constant impedance structure the deflecting voltage V_d, the attenuation constant α and the normalized deflecting field $\frac{E_d^0\lambda}{\sqrt{P_t}}$ relate as:

$$V_d = \frac{E_d^0}{\alpha}(1-e^{-\alpha L}), \alpha = \frac{\pi}{\lambda|\beta_g|Q}, \frac{E_d^0\lambda}{\sqrt{P_t}} = \sqrt{\frac{2\pi\lambda Z_e}{|\beta_g|Q}}, \quad (3)$$

where P_t is the input RF power and Q is the quality factor of the structure .

In Fig. 3 the calculated surfaces $\beta_g(r_a,\theta_0)$ and $Z_e(r_a,\theta_0)$ for aperture radii $0.06 \le \frac{r_a}{\lambda} \le 0.15$ and phase advance $20^o \le \theta_0 \le 179^o$ are shown for a TW operation. As can be seen from Fig. 3b, high values of $Z_e \sim 70$MOm/m can be realized for $60^o \le \theta_0 \le 140^o$ and $\frac{r_a}{\lambda} \sim 0.07$. For $\frac{r_a}{\lambda} \sim 0.15$ both TE deflector and DLW reach comparable shunt impedances Z_e but, as compared to a DLW, the considered structure is not restricted in β_g, Fig.3a.

For each phase advance θ_0 the structure has an inversion

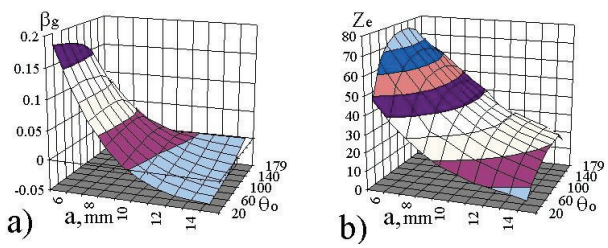

Figure 3: The surfaces of $\beta_g(r_a,\theta_0)$ (a) and $Z_e(r_a,\theta_0)$ for the TE-structure, $\lambda = 10cm$.

point at $r_a = r_{ai}$, where $\beta_g = 0$, as can be seen from Fig. 3a. The dependence $r_{ai}(\theta_0)$ is plotted in Fig. 4a as brown curve. The inversion point corresponds to the condition $H_y^0 = 0$, i.e. zero amplitude of the synchronous spatial harmonics in the transverse H_y component. In this report we consider the structure parameters for $r_a < r_{ai}$, assuming HE - domination. For $r_a > r_{ai}$ the components E_x and H_y have an opposite phasing. It is accompanied by a shunt impedance reduction, Fig. 3b.

For typical values of $\beta_g = 0.01, 0.02$ the dependencies of r_a, α and $\frac{E_d^0\lambda}{\sqrt{P_t}}$ on θ_0 are plotted in Fig. 4. Generally, the structure has a lower Q value, as compared to a DLW, especially for $\theta_0 < 60^o$ and the attenuation constant α for this region is rather high. But, in combination with the large value of $\frac{E_d^0\lambda}{\sqrt{P_t}}$ the structure reaches due to the higher Z_e a higher total deflecting voltage V_d. The deflecting field

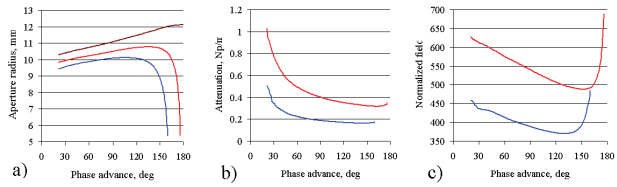

Figure 4: The dependencies of aperture radius r_a (a), attenuation α (b) and normalized field $\frac{E_d^0\lambda}{\sqrt{P_t}}$ (c)on θ_0 for $\beta_g = 0.01$ (red) and $\beta_g = 0.02$ (blue).

distributions for the TW mode are not considered in this report.

SW OPERATION

As can be seen from Fig. 3b, for SW operation, i.e. $\theta = 180^o$, the shunt impedance Z_e reaches not the maximal value. If an aperture radius r_a is specified, two parameters can be used to tune the operating frequency - the cell radius r_c and the window radius r_w, Fig.1. In Fig. 5 the dependence of Z_e on the aperture radius r_a is plotted for a fixed window radius r_w.

For small aperture radii the operating passband of the

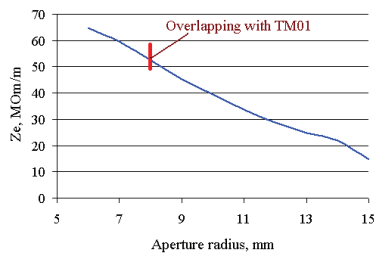

Figure 5: Z_e dependence on the aperture radius for $\theta_0 = 180^o, r_w = const$.

TE_{11}-like mode is the lowest band and the nearest TM_{01} passband is $\approx 500MHz$ higher. With increasing aperture the cell radius r_c increases too and the TM_{01} passband moves down. Due to the thick disk of approximately half a period length, modes of other types, except the operating mode, have a very weak coupling and a very narrow passband width of ($\sim 10MHz$). The vertical red line in Fig. 5 marks the range of r_a where the TM_{01} passband is closer to the operating frequency than $\pm 30MHz$.

Changing the window radius r_w both the operating frequency and the balance $\frac{Z_0 H_y^0}{E_x^0}$ in the deflecting field distribution are modified. A reduction of r_w simultaneously reduces both Z_e, and $\frac{Z_0 H_y^0}{E_x^0}$. The relative reduction of H_y^0 leads to a reduction of the operating passband width, which is just $\sim 16MHz$ for $H_y^0 = 0$. In Fig. 6 examples of deflecting field distribution are shown for different balance values $\frac{Z_0 H_y^0}{E_x^0}$, assuming the average deflecting field $10MV/m$. The plots of the amplitudes E_d are shown in

Copyright © 2012 by the respective authors — cc Creative Commons Attribution 3.0 (CC BY 3.0)

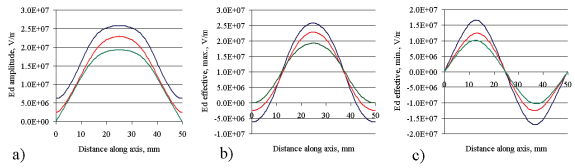

Figure 6: Distribution of the deflecting field amplitude (a), the effective field for bunch deflection (b) and bunch rotation (c) for harmonics balance $\frac{Z_0 H_y^0}{E_x^0} = 0.23$, (blue), 0.07 (red) and 0 (green) along the periodical axis.

Fig. 6a and $|E_d| \approx 0$ at the period ends for $\frac{Z_0 H_y^0}{E_x^0} = 0$. For bunch deflection the bunch center moves synchronously with the maximum of the total deflecting field, i.e. $\delta\psi = 0$. The effective deflecting field as seen by the particles is plotted in Fig. 6b. Sections with different sign of E_d can be seen, thus the deflected bunch will oscillate around the average deflected trajectory in this structure.

Today deflecting structures are widely used for another purpose, [4], related to bunch rotation. In this case the bunch center should move in a zero deflecting field, i.e. $\delta\psi = 90^o$, and the effective oscillating field becomes comparable to the amplitude of the average deflecting field, as shown in Fig. 6c. Thus together with the rotation, the bunch will oscillate as a whole along axis. Structure application for bunch rotation should hence be considered together with beam dynamics simulations. The high shunt impedance allows a higher deflecting voltage but large oscillations are not desirable from a beam dynamics point of view.

ADDITIONAL TOPICS

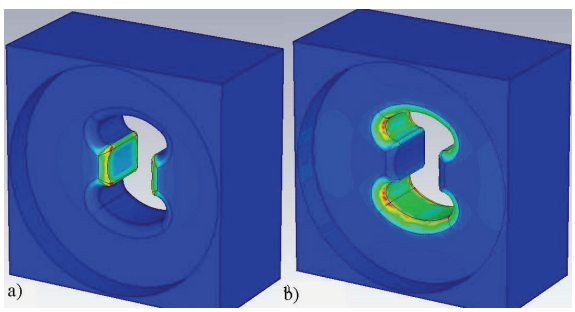

Figure 7: Electric (a) and magnetic (b) energy density distributions at the structure surface.

The somewhat more complicated structure shape, as compared to a DLW, presents no problem for modern numerically controlled tools. For the tuning after brazing the structure has an additional possibility: The distributions of the electric and magnetic energy densities at the structure surface are shown in Fig. 7 and a clear spatial separation can be seen. Four blind holes can be manufactured into the thick disk close to vicinity of the axis. After brazing of the structure small surface deformations in opposite holes, provide both positive and negative shift of the operating frequency.

With three independent parameters, $r_a < r_w < r_c$, the structure can be modified essentially. For $r_w \to r_a$ the structure transfers into the well studied DLW. Results for the opposite direction $r_w \to r_c$ are shown in Fig. 8.

The structure diameter becomes smaller, $2r_c \leq \lambda/2$ and

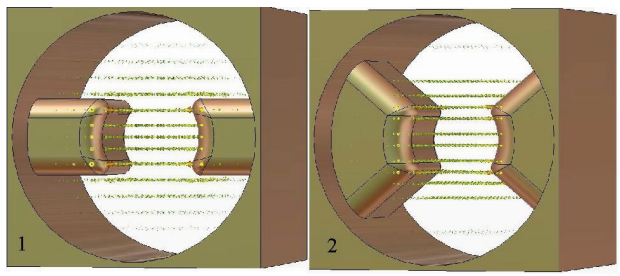

Figure 8: The structure modifications for $r_w = r_c$.

low frequency operation is possible. From an RF point of view the field distribution, can be considered either as for two transverse coaxial protrusions with opposite phasing or similar to a TM_{010} pillbox cavity with axis in x direction. For particle deflection along z-axis the structure remains HE_1 - dominated, with $\frac{Z_0 H_y^0}{E_x^0} \sim 0.4$, i.e. with stronger oscillations of the deflecting field, as shown in Fig. 6.

For manipulations of heavy ion beams, $\beta \ll 1$, [5], the magnetic component in the deflecting field (2) is negligible and the ions will see only the E_x component, similar to the case $\frac{z_0 H_y^0}{E_x^0} = 0$ in Fig. 6.

SUMMARY

RF parameters of a TE -type deflector are considered for the S - band frequency range. A higher shunt impedance, as compared to a classical DLW, can be obtained, leading to a higher deflecting voltage. Some methodical topics are considered too.

REFERENCES

[1] V. Paramonov, L. Kravchuk, S. Korepanov. Effective Standing Wave RF Structure for Particle Beam Deflector. Proc. 2006 LINAC Conf., p. 649

[2] V. Paramonov. Particularities of normal conducting L-band deflecting cavities. http://indico.cern.ch/conferenceDisplay.py?confId=83532

[3] H. Hahn, Deflecting Mode in Circular Iris-Loaded Waveguides, Rev. Sci. Inst., v. 34, n. 10, p. 1094, 1963

[4] R. Akre et. al., A Transverse RF Deflecting Structure for Bunch Length and Phase Space Diagnostic. Proc. 2001 PAC, p. 2353

[5] S. Minaev et.al., Electro-Dynamics Characteristics of RF Wobbler Cell for Heavy Ion Beam. Proc. 2010 LINAC Conf., p. 581

Copyright © 2012 by the respective authors — cc Creative Commons Attribution 3.0 (CC BY 3.0)

OPERATIONAL EXPERIENCE WITH THE FERMI@ELETTRA S-BAND RF SYSTEM*

A. Fabris#, P. Delgiusto, F. Gelmetti, M. Milloch, A. Milocco, F. Pribaz, C. Serpico, N. Sodomaco, R. Umer, L. Veljak, Sincrotrone Trieste, S.S. 14 – km. 163,5, in Area Science Park, 34149 Basovizza, Trieste, Italy

Abstract

FERMI@Elettra is a single-pass linac-based FEL user-facility covering the wavelength range from 100 nm (12 eV) to 4 nm (310 eV) and is located next to the third generation synchrotron radiation facility Elettra in Trieste, Italy. The machine is presently under commissioning and the first FEL line (FEL-1) will be opened to the users by the end of 2012. The 1.5 GeV linac is based on S-band technology. The S-band system is composed of fifteen 3 GHz 45 MW peak RF power plants powering the gun, eighteen accelerating structures and the RF deflectors. The S-band system has been set into operation in different phases starting from the second half of 2009. This paper provides an overview of the performance of the system, discussing the achieved results, the strategies adopted to assure them and possible upgrade paths to increase the operability of the system.

INTRODUCTION

The FERMI@Elettra FEL facility is based on a warm linac followed by a single pass seeded FEL [1]. Two FEL lines are foreseen: FEL-1 which produces fundamental output wavelength from 100 to 20 nm and FEL-2 which will extend the operation down to 4 nm applying High Gain Harmonic Generation schemes. The main parameters of the machine are reported in Table 1.

Table 1: Machine Parameters

Parameter	FEL-1	FEL-2	Unit
Wavelength	100-20	20-4	nm
Electron beam energy	1.2	1.5	GeV
Bunch charge	0.8	1	nC
Peak current	850	500	A
Bunch length (FWHM)	400	600	fs
Norm. emittance (slice)	0.8-1.2	1.0-2.0	mm mrad
Energy spread (slice)	150-250	100-200	keV
Repetition rate	10-50	50	Hz

The accelerator consists of an RF photocathode gun, an S-band linac, an X-band structure, a laser heater to control the uncorrelated energy spread and the beam transport system to the undulators. The machine is presently working at a repetition frequency of 10 Hz, which will be increased to 50 Hz in May 2013.

The commissioning of the facility is rapidly advancing and FEL-1 will be opened to external users at the end of the present year. Commissioning of FEL-2 will progress in the remaining time with the target of the first test experiment during 2013.

PRESENT STATUS OF THE S-BAND SYSTEM

Sixteen S-band accelerating structures are installed in the FERMI linac (Fig.1). The first nine structures are TW ones, while the last seven are BTW type and are equipped with SLED. Two more TW structures will be added in the future. They will replace the first two structures that will be finally relocated along the machine.

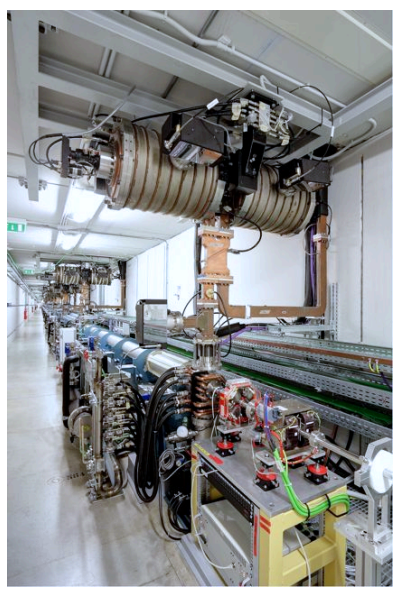

Figure 1: View of the linac from the high-energy end.

Fifteen 45 MW peak klystron (TH2132A) are installed, each one powered by pfn based modulators (Fig.2). Fourteen klystrons provide RF power to the accelerating structures, to the gun and to the low and high-energy RF deflectors. Two main power distribution schemes are used: one klystron feeding two TW structures or one klystron feeding one high gradient BTW structures. A spare power plant provides a backup solution to the first two, powering either the RF gun or the structures before the laser heater. The change of the operating mode is

*Work supported by the Italian Ministry of University and Research under grants FIRB-RBAP045JF2 and FIRB-RBAP06AWK3
#alessandro.fabris@elettra.trieste.it

Copyright © 2012 by the respective authors — cc Creative Commons Attribution 3.0 (CC BY 3.0)

performed by an array of remotely controlled waveguide switches.

Each RF plant is equipped with a low level RF (LLRF) system that maintains the stability of the RF below 0.1 % and 0.1° at 3 GHz. The system now in operation is an intermediate system, which implements a commercial processing board instead of the one specifically designed for FERMI and now in construction. All the needed loops are implemented such as amplitude, phase, cable calibration and phase locking. SLED phase reversal and phase modulation have been also implemented by means of the LLRF.

Figure 2: One of the fifteen modulators

The S-band RF system has been gradually set into operation starting with the first installation of the plant for the gun in the second half of 2009 [2]. All the fifteen RF plants and sixteen accelerating structures are now in operation. The machine routinely operates on a 24 hours basis for the commissioning of the accelerator and of the beamlines. The operating energy of the machine is 1.2 GeV and the repetition rate is 10 Hz.

ENERGY AND REPETITION FREQUENCY UPGRADE

Two major goals are foreseen for 2013: the upgrade of the repetition rate, following the installation of the new RF gun designed for 50 Hz, and the commissioning activities of FEL-2. Besides the proof of the double stage HGHG scheme, the latter also implies the upgrade of the machine energy to 1.5 GeV.

The transition to 50 Hz requires an upgrade of the modulators operation. This is particularly important for the first six built that, for time constrains, were installed re-using the components of the previous Elettra injector and therefore are limited by the hardware to 10 Hz. The upgrade of these modulators implies an almost complete rebuild, since many of the main components, such as pfn, pulse transformers, etc. have to be replaced. In addition, the upgrade activities must not affect the commissioning calendar and therefore they can be generally done only in the already planned shutdowns. The process is advancing according to the schedule and it will be completed in May 2013.

The energy upgrade to 1.5 GeV will be mainly realized by increasing the energy gain in the BTW high gradient accelerating structures, increasing the RF power and the RF pulse length. For the remaining structures there will be no major changes since an increase in the energy gain is basically limited either by the available RF power and the constraints due the energy requirements at various points along the machine, like the bunch compressors and the laser heater. The RF conditioning will be done using the automatic software already developed and available via the machine control system.

Table 2 shows the energy budget on crest for the two operating energies for FEL-1 and FEL-2. This should be decreased by the effects of:

- the deceleration of the X-band cavity (20 MeV typically);
- the longitudinal wakefields when operating at high bunch current (expected 30 MeV at 1.5 GeV);
- the loss in energy gain if running some structures off-crest for beam dynamic optimization.

Table 2: Energy gain per structure and total energy budget

Type	Quantity	1.2 GeV	1.5 GeV
Gun	1	5 MeV	5 MeV
TW-Elettra	2	47 MeV	47 MeV
TW-LIL	7	57 MeV	57 MeV
BTW	7	110 MeV	154 MeV
Total energy		**1268 MeV**	**1576 MeV**

In order to achieve the required energy gain in the BTW structures, overcoming the limitations encountered in their operation as injector for Elettra, the SLEDs will be phase modulated. This feature has been already implemented in all the plants with SLED since it has in any case a beneficial effect on the reliability. A preliminary test was done on one plant to investigate the energy gain limits [3]. After a first optimization of the parameters of a linear phase modulation, in this structure an energy gain of 165 MeV was reached, corresponding to an accelerating gradient of 27 MV/m. The klystron was operating at 38 MW peak power and 4 μsec pulse width. These results give confidence in the reaching of the target energy for FEL-2. Further studies will be done to evaluate the advantages of using a non-linear phase modulation to get a flatter RF pulse.

NEXT IMPLEMENTATIONS

New Accelerating Structures

The layout of the machine allows for the installation of two more accelerating structures powered by the existing plants. This gives the opportunity to move the first two structures along the machine and replace them with structures optimized for the beam dynamics needs at low

Copyright © 2012 by the respective authors — cc Creative Commons Attribution 3.0 (CC BY 3.0)

energy and high charge. The specification of the two structures calls for minimized phase and amplitude asymmetries in the coupler cells, to minimize the induced kick to the beam due to the multipole field components. The input and output coupling cells shall be of the dual-feed racetrack type with diametrically opposed sidewall-coupling aperture. Symmetrical feed coupling should allow to erase the dipole transverse momentum on the beam due to the total phase and amplitude symmetries in the coupling iris plane, while racetrack geometry permits to minimize quadrupole field components [4]. Each of the two structures will contribute with 50 MeV to the energy budget. This will extend the energy margin or allow operation at higher energy.

LLRF

The processing board presently used is a commercial board (LLRF4) and will be replaced by a new board under construction. This will allow to extend the capabilities of the system due to the higher computing power, adding new functionalities, such as intra-pulse feedback or real rime communications between LLRF units.

The present feedbacks are inter-pulse feedbacks and correct the RF drive to the klystron between pulses. This corrects mainly drifts in phase and amplitude, but does not correct jitter contribution which could be generally associated with modulator instabilities, for example due to the HV power supply or the pfn. In an intra-pulse feedback the information at beginning of the pulse is acquired and the correction applied inside the same pulse. This implementation requires higher performance capabilities on the processing hardware that should be achieved with the new board. The main issue to be taken into account for an intra-pulse feedback is the latency time, which is due to different contribution, such as the structure filling time, the digital acquisition time and the digital processing time.

The structure filling time varies from 0.8 to 1.5 μsec depending on the structure type and is the main contributor to the latency time. Since in the FERMI case the RF pulses are 4 μsec width, this makes not efficient to include the structure in the loop. Therefore a sample of the RF field at the output of the klystron will be acquired and used, allowing also the advantage of shorter cables.

Due to the high acquisition accuracy of the LLRF (0.017°, 0.029%), there is no need of averaging so we do not expect problems due to the digital acquisition time. The new board features low latency ADCs, high FPGA clock frequency and double data rate DACs, so also the digital processing time issue should be very much under control. Finally, the measurements taken on FERMI show that the phase and amplitude trend of the RF pulse can be considered constant between pulses. This leads to the conclusion that single amplitude and phase correction can be used within pulse.

RELIABILITY ANALYSIS AND RELATED ASPECTS

In the last years the effort has been mainly concentrated on installation aspects. The completion of these activities is shifting the attention on reliability and availability aspects. Some of these issues were already considered during the design phase, for example leading to the construction of a spare modulator. Some other aspects are being analyzed based on the operational results.

Current availability of the S-band system is 93 %, which is sufficient for the commissioning phase and the first users' periods. Klystron-modulator systems are the main source of short resettable faults affecting the uptime. A testing program has been launched to understand these events and figure out how to reduce them. Similar analysis will be applied to the other parts of the systems.

Other availability aspects are being considered, such as the ones related to reduction of the time needed for klystron or thyratron replacement. The possibility of having other spare plants cannot be pursued due to space limitations, so the spares should be ready to use for replacement. This is especially valid for the klystron in order to reduce activation and HV conditioning time once installed.

CONCLUSIONS

The commissioning of FERMI@Elettra is progressing and FEL-1 will be opened to external users at the end of 2012. The S-band RF system has been gradually set into operation during these years and it is being upgraded for 50 Hz operation. Fifteen RF power plants and sixteen accelerating structures are in operation, allowing the reaching of the required electron beam energy. Stability of the fields is well in specification as confirmed by the measurements on the beam parameters, such as the beam time jitter. Continuous efforts on reliability aspects are pursued since these are key points a users' facility.

REFERENCES

[1] M. Svandrlik et al., "Status of the FERMI@Elettra Project", IPAC'2012, New Orleans, May 2012, TUOBB03, p. 1092 (2012); http://www.JACoW.org

[2] A. Fabris et al., "FERMI@Elettra: Installation and Commissioning of the S-band RF System", LINAC'10, September 2010, TUP002, p. 395 (2010); http://www.JACoW.org

[3] C. Serpico et al., "Phase Modulation SLED Operation Mode at Elettra", IPAC'2011, San Sebastian, September 2011, MOPC010, p. 83 (2011); http://www.JACoW.org

[4] Z. Li et al., "Coupler Design for the LCLS Injector S-band Structures", PAC'2005, Knoxville, May 2005, TPPT031, p. 2176 (2005); http://www.JACoW.org

Copyright © 2012 by the respective authors — cc Creative Commons Attribution 3.0 (CC BY 3.0)

DESIGN OF A C-BAND DISK-LOADED TYPE ACCELERATING STRUCTURE FOR A HIGHER PULSE REPETITION RATE IN THE SACLA ACCELERATOR

Tatsuyuki Sakurai#, Takahiro Inagaki and Yuji Otake, RIKEN SPring-8 center, Hyogo, Japan
Hiroyasu Ego, JASRI/SPring-8, Hyogo, Japan

Abstract

It is expected that the high pulse-repetition rate of the SACLA accelerator provide a higher rate of X-ray laser pulses to expand ability of user experiments, such as simultaneously providing the laser to several beamlines and reducing a measuring time in the experiment. Therefore, we studied on a C-band accelerating structure for the higher pulse rate above 120 pps than the present rate of 60 pps. Since the higher repetition rate operation is inclined to increase vacuum electrical discharges, it is required to reduce the surface electric fields in the structure without decrease in accelerating voltage. We designed a cross sectional shape of ellipsoidal curvature, which reduces the maximum surface electric or rf field by 20%. The designed structure adopts a TM01-2π/3 mode disk-loaded type with a quasi-constant gradient. Since the high repetition rate also increases the heat load to the structure, in simulation, we optimized cooling channels. As a result of the design, an accelerating gradient of more than 40 MV/m will be expected, when an input RF power of 80 MW is fed into the structure.

INTRODUCTION

The SACLA (SPring-8 Angstrom Compact free electron LAser) facility succeeded to generate of the X-ray free electron laser (XFEL) with a wavelength of 0.12 nm in June, 2011[1]. Since March 2012, the X-ray laser is provided to the user experiments by mainly using one beamline.

To expend user experiment ability, SACLA has a space of five beamlines for the future expansion. The electron beam must be distributed to the beamlines by using a fast switching magnet in order to supply X-ray laser to many experiments users. However, the repetition rate of each beamline decreases inevitably. Therefore, we plan to operate SACLA with a repetition rate up to 120 pps for the upgrade of the beamlines.

Our present C-band (5712 MHz) accelerating structure to adopt multi-bunch operation has a choke-mode cavities [2] and an SiC absorbers outside of each cavity. The present structure generates an accelerator gradient of 37 MV/m to obtain a 8GeV electron beam and has a phase advance per cell of 3π/4 mode in order to machine the choke-mode cavity. Due to the heat dissipation, this complicated structure has distortions of the cavity, which leads large shifts of a resonant frequency and an RF phase. This distortion is a serious problem for 120 pps operation. Therefore, the newly designed accelerating structure does not have complicated choke structures and SiC absorbers. Furthermore, the simple structure gives reduction of the production costs and enable us high precise adjustment of the resonant frequency with the dimpling method after the brazed of the structure.

NEW STRUCTURE DESIGN

The designed disk-loaded structure has a phase advance per cell of 2π/3 for the accelerating TM01-mode and quasi-constant gradient. The highest shunt impedance for a travelling-wave structure occurs in the neighborhood of the phase advance. Therefore, an accelerating gradient of the new structure should be higher than the existing structure. Due to the compatibility of future replacement with the present choke-mode structure for future replacement, a structure length, a filling time and an attenuation parameter of new structure are designed to be the same as those of the choke-mode one.

We used the 3D electromagnetic field simulation codes, ANSYS-HFSS [3], in order to design the structure. By the simulation, the iris diameter (2a) of each cell is linearly changed over 100 cells and a quasi-constant gradient is obtained. The cell diameter (2b) was adjusted so that the resonance frequency for every cell is equal to the operation frequency of 5712 MHz. Table 1 shows the parameters of a new C-band disk-load type accelerating structure. Figure 1 shows variations of the 2a and the accelerating gradient at an input power of 80 MW. The averaged accelerating gradient is expected to be 43 MV/m, when an input RF power of 80 MW is fed into the structure.

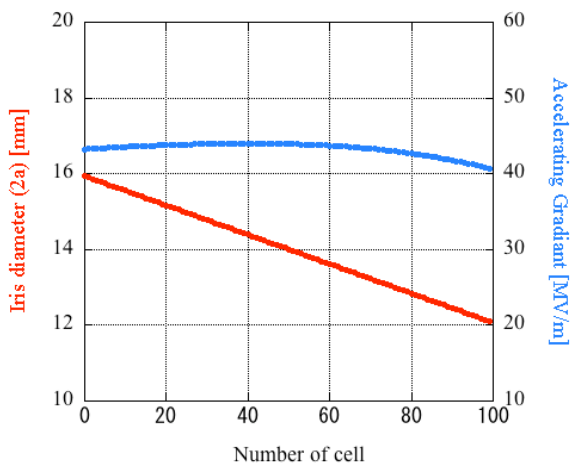

Figure 1: Variation of the iris diameters (red line/left axis) and an accelerating gradient at an input power of 80 MW (blue line/right axis).

#t-sakura@spring8.or.jp

Copyright © 2012 by the respective authors — cc Creative Commons Attribution 3.0 (CC BY 3.0)

The dipole HEM11 mode is the dominant source of beam wakefield instability [4] and hence the frequency and wakefield of the mode were also calculated. The variation of 2a was so determined that the wakefield of the HEM11 mode falls off in a few nsec and has drops within every bunch interval of 4.2 nsec in the which might be assumed as the minimum bunch-interval of multi-bunch operation in SACLA. Figure 2 shows the calculated envelope of the wakefield. It decreases sufficiently and drops at intervals of 4.2 nsec are less than 2% compare with peak value of the wakefield.

Table 1: Parameter of the new C-band accelerator

Operation frequency [MHz]	f_a	5712
Structure type		Quasi-Constant Gradient (quasi-CG) Disk-load type, Traveling wave structure
Resonant mode		TM01-2π/3
Total cavity length [m]	L	1.862
Unloaded Q factor	Q_0	8800
Group velocity	v_g/c	0.023
Filling time [nsec]	t_F	270
Attenuation parameter	τ	0.59
Average shunt impedance [MV/m]	r	66.0
Number of cell	N	100
Iris diameter [mm]	2a	15.941~12.109
Cell diameter [mm]	2b	43.761~42.451
Disk spacing [mm]	d	17.495
Disk thickness [mm]	t	4
Cross sectional shape of Iris		Ellipsoidal curvature

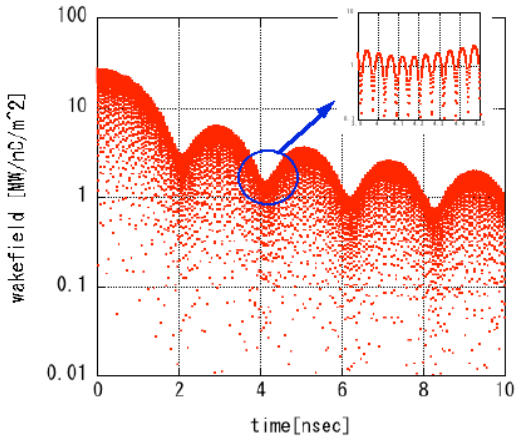

Figure 2: Wakefield envelope of HEM11 mode.

CROSS SECTIONAL SHAPE OF ELLIPSOIDAL CURVATURE

We designed a cross sectional shape of the iris as ellipsoidal curvature, which reduces the strength of surface electrical field. Figure 3 shows the cross sectional view of the ellipsoidal curved iris shape. We estimated the dependence of the maximum surface electrical field dependent on the axis ratio of major and minor axis of an ellipse iris (B/A), by using HFSS and decided the disk thickness (t) is 4.0 mm, as well as to maintain the compatibility to the existing choke-mode type accelerating structure. It is the same as the existing structure parameter in order to replace the choke-mode structure. Therefore, we fix A=2 mm and change the size of B. Figure 4 shows the ratio of the maximum surface electrical field to the on-axis electrical field (E_p /E_{acc}) depending on a ratio of B/A. E_p/E_{acc} becomes minimum at B/A = 2 and is 20% lower than that at B/A=1. Therefore, we adopted the cross sectional shape of the iris as ellipsoidal curvature of B/A = 2.

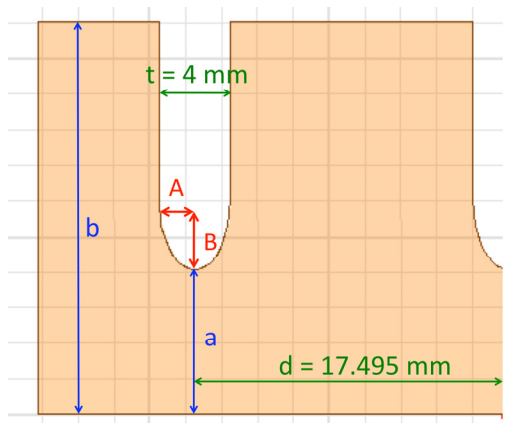

Figure 3: Cross sectional view of the ellipsoidal curved iris shape.

Copyright © 2012 by the respective authors — cc Creative Commons Attribution 3.0 (CC BY 3.0)

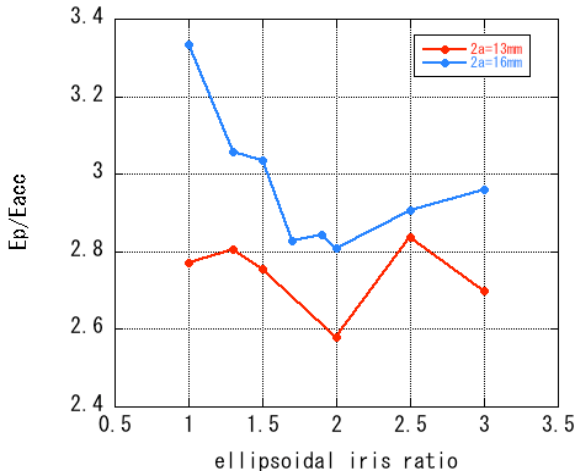

Figure 4: Ratio of maximum surface electrical field to the on-axis electric field (E_p /E_{acc}) depending on the ratio of B/A.

THERMAL EXPANSION EFFECT

The high repetition rate increases the heat load of the accelerating structure, which may causes the thermal expansion and the shift of the resonant frequency. Therefore we carefully optimized the cooling water channels of the accelerating structure. The heat load of the accelerating structure in 120 pps is educed to be 3.8 kW. The initial temperature of the cooling water from a cooling system is 26.5°C. We place eight water flow channels with an 8 mm in diameter as shown in Figure 5. A flow velocity of water is assumed to be 0.8 m/sec. A water flow rate per one channel and the total flow rate are assumed to be 2.5 L/min and 20 L/min, respectively. A counter-flow method is adopted the cooling of accelerating structure in order to make a temperature slope small. We employ a precise temperature-regulation system in order to stabilize the temperature of the accelerating structure by feedback control of the water heater [5]. A required temperature stability should be set at ±0.1°C.

To realize the above-mentioned conditions, we used the ANSYS thermal and structure analysis software to simulate the temperature distribution and expansion of the accelerating structure. Figure 5 shows the estimated temperature distribution of the accelerating structure operated at 120 pps. We designed the resonant frequency of the cavity is set at 5712 MHz with the cavity temperature at 33°C. When the cavity is heated with the heat load of 3.8 kW, 2b is expanded at about 2.8 μm from the original size, and the resonant frequency shifts at 430 kHz. The frequency shifts is compensated by lowering the water temperature by 4.4°C. The rise of the water temperature due to 3.8 kW is 2.7°C. Since we use the counter-flow method, the temperature of the input water temperature should be set at 33°C-4.4°C=28.6°C, which compensates the frequency shift. Since this input temperature is higher than 26.5°C of the initial temperature of the cooling water system, the precise temperature-regulation system can control the temperature by changing the heater power. On the other hand, when the repetition rate is low and the heat load is negligibly small, the temperature of cooling water can be controlled to be 33°C with a heater. Therefore, we can keep the resonant frequency at 5712 MHz for every operation rate by adjusting the heater power.

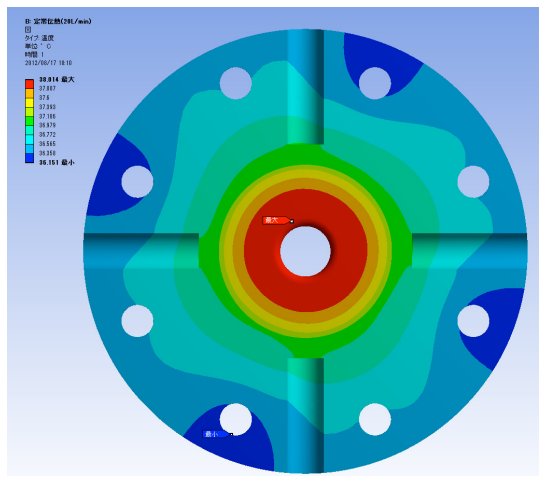

Figure 5: Temperature distribution of the accelerating structure in 120 pps operation

SUMMARY

We designed a new C-band accelerating structure adapted to a pulse repetition rate of 120 pps. The structure is a TM01-2π/3 mode disk-loaded type and has a quasi-constant accelerating gradient of 43 MV/m at an input RF power of 80 MW. Furthermore, the cross sectional shape of an iris having the ellipsoidal curvature decreases a surface electrical field by 20%. We confirmed that the new structure could be operated by 120 pps, by our thermal-expansion analysis. We will manufacture a prototype accelerating structure and perform a high power RF test in 2013.

REFERENCES

[1] H. Tanaka.et.al., “A compact X-ray free-electron laser emitting in the sub-Angstrom wavelength region”Nature photonics 6 (2012) 540-544.
[2] T. shintake et al., “The choke mode cavity.” J. J. Appl. Phys. 31 (1992) L1567.
[3] http://www.ansys.com
[4] K.A.Thompson.et.al.,”Design and simulation of accelerating structure for future linear collider.” SLAC-PUB-6032 (1993)
[5] T.Hasegawa. et. al., “Status of the precise temperature-regulation system for the C-band accelerator at XFEL/SPring-8.”IPAC10, Kyoto, May, 2010 TUPEA073.

Copyright © 2012 by the respective authors — cc Creative Commons Attribution 3.0 (CC BY 3.0)

THE NONRESONANT PERTURBATION THEORY BASED FIELD MEASUREMENT AND TUNING OF A LINAC ACCELERATING STRUCTURE *

W. C. Fang#, Q. Gu, Z. T. Zhao, SINAP, Shanghai, China
D. C. Tong, THU, Beijing, China

Abstract

Assisted by the bead pull technique, nonresonant perturbation theory is applied for measuring and tuning the field of the linac accelerating structure. The method is capable of making non-touching amplitude and phase measurements, real time mismatch feedback and field tuning. Some key considerations of the measurement system and of a C-band traveling-wave structure are discussed, and the bead pull measurement and the tuning of the C-band traveling-wave linac accelerating structure are presented at last.

INTRUDUCTION

The Shanghai soft X-ray Free Electron Laser test facility(SXFEL)is presently being planned and designed at the Shanghai Institute of Applied Physics, CAS [1]. This facility will be located close to the Shanghai Synchrotron Radiation Facility, which is the first 3rd generation light source in mainland China [2]and it requires a compact linac with a high gradient accelerating structure and high beam quality. As a key R&D item, a room temperature C-band (5712 MHz) accelerating structure has been developed [3, 4]. For fabricating the C-band structure with high performance, the bead pull measurement system based on nonresonant perturbation theory has been developed.

There are several methods for RF structure measurement or tuning, such as the resonant perturbation method [5] and the phase shift method, however several limitations appear when they are applied to a traveling-wave accelerating structure. The resonant perturbation method picks up the amplitude of the electromagnetic field, therefore it is limited in the measurement of the standing-wave accelerating structure and the phase shift method only shows the phase information in the RF structure. For the accurate and fast tuning of a traveling-wave linac RF structure, nonresonant perturbation theory is the preferable method, which can measure the electromagnetic field distribution with both amplitude and phase, and this method is capable of making non-touch measurement, which can maintain the clean inner surface of the accelerating structure and reduce its RF breakdown rate. Furthermore, this method is also very effective in performing an accurate and fast real-time tuning of the accelerating structure, which is economical for mass fabrication of accelerating structures.

In this paper we present a cold test application of nonresonant perturbation theory on a linac RF structure [6]. This method based on the bead pull technique can pick up the amplitude and phase distribution of a linac structure, particularly for a traveling-wave structure, and is a preferable and efficient method for accelerating structure cold testing and tuning. In the following we describe firstly the theory of nonresonant perturbation and the tuning procedure and then discuss the key considerations of our measurement system with the bead pull technique. At the end we give several experimental results of our newly developed C-band traveling-wave accelerating structure tuning, which verify the feasibility of this method.

*Work supported by SINAP project
#fangwencheng@sinap.ac.cn

NONRESONANT PERTURBATION THEORY AND TUNING PRINCIPLE

According to nonresonant perturbation theory, the variation of the reflection coefficient in the input port is measured with and without a perturbation bead, which is placed at different points along a line to pick up the amplitude and phase distribution of the electromagnetic field strength, a schematic drawing is shown in Figure 1. Based on the results and post-processing, RF tuning is processed with accurate and fast real-time feedback.

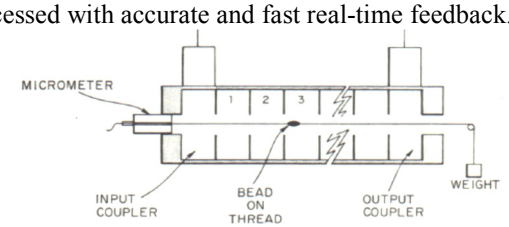

Figure 1: The field measurement based on nonresonant perturbation theory.

Nonresonant Perturbation Theory and Field Measurement

In nonresonant perturbation theory, the desired field strength is calculated as the following [6]:

$$2P_i(\Gamma_p - \Gamma_a) = -j\omega[k_e E_a^2 - k_m H_a^2] \quad (1)$$

For an accelerating structure, the TM mode is used for beam acceleration and the crucial longitudinal electrical field Ez is the unique field component on axis, thus the first equation of equation (1) is used for field measurement, and is renamed as equation(2) with reflected coefficient S11 of the Network Analyzer:

$$\Delta S11 = \Gamma_p - \Gamma_a = S11_P - S11_a = -\frac{j\omega k_e}{P_i} E_a^2 \quad (2)$$

whereS11p and S11a are acquired from the Network Analyzer, respectively corresponding to Γp and Γa in equation (1) above. In equation (2), Ea is complex data, its amplitude is the square root of the amplitude of ΔS11, and its phase is half of the phase ofΔS11. As the

Copyright © 2012 by the respective authors — cc Creative Commons Attribution 3.0 (CC BY 3.0)

bead goes through the RF structure, the distribution of Ez on axis can be measured step by step.

Tuning Principle

With the bead pull measurement, the amplitudes and phases of the field can be measured, and after post-processing the local reflected coefficient can be calculated for the later tuning procedure. For the accelerating structure, the field of the center of the ith cell can be expressed by $E_i e^{j\varphi_i}$, which is the superposition of forward and backward waves $a_n e^{j(-2\pi/3(i-n)+\psi_n)}$ and $b_n e^{j(2\pi/3(i-n)+\phi_n)}$, where the center cell is the nth cell of the three cells in Figure 2.

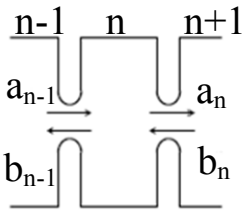

Figure 2: Forward and backward wave of nth cell.

It is supposed that the amplitudes in three adjacent cells are the same, according to [7],

$$a_n e^{j\psi_n} = E_{n-1} e^{j(\varphi_{n-1}-\pi/2)} + E_n e^{j(\varphi_{n-1}-\pi/6)}/\sqrt{3}$$
$$b_n e^{j\phi_n} = E_{n-1} e^{j(\varphi_{n-1}+\pi/2)} + E_n e^{j(\varphi_{n-1}+\pi/6)}/\sqrt{3} \quad (3)$$
$$b_{n+1} e^{j\phi_{n+1}} = E_n e^{j(\varphi_n+\pi/2)} + E_{n+1} e^{j(\varphi_{n+1}+\pi/6)}/\sqrt{3}$$

Based on equations (3), the local reflected coefficient of the nth cell is derived as equation (4)

$$\Gamma_{local,n} = \frac{b_n e^{j\phi_n} - b_{n+1} e^{j(\phi_{n+1}-2\pi/3)}}{a_n e^{j\psi_n}} = A + jB \quad (4)$$

where A and B represent the real and imaginary parts of the reflection respectively.

According to the conclusion in [8], the real part of the reflection coefficient in equation (4) is small and neglected relative to the imaginary part. The left imaginary part is dominated by the frequency detuning of each cell, which is shown in Equation (5).

$$\Gamma_{local} \approx -j\frac{2\beta Q_0 \Delta F}{(\beta+1)^2 + Q_0'^2(\Delta F)^2} \approx j\frac{Q_0' \Delta f_0}{f_0} \quad (5)$$

where f_0 is the eigenfrequency, $\Delta f_0 = f_0 - f$, and $Q_0' = c\varphi/vg$ is the eigen-parameter of each cell. In Equation (5), it is easy to find that the reflection coefficient Γ_{local} is more or less than zero respectively when f_0 is detuned above or below the operating frequency f. Based on this principle, every cell can be tuned independently according to the sign of Γ_{local}.

According to equation (5), in equation (4) A is neglected and B presents the frequency detuning. If B is more than zero, the frequency is more than the design value, and to the contrary, frequency is a little less. This is the rule for the automatic tuning process, and the process is not stopped until B reaches zero.

In equation (4), the left side represents the local reflection$\Gamma_{local,n}$of the nth cell, however in the automatic tuning process, only reflection coefficient Γ_{port} of the input port can be measured, which is the sum of the local reflection coefficients of all cells including coupling cells and periodic cells. Because of the attenuation and reflection of each cell, these reflections are added with different weight, and this is expressed as equation (6),

$$\Gamma_{port} = \sum_1^n C_n \Gamma_{local,n} \quad (6)$$

For a traveling-wave accelerating structure, the attenuated power for the nth cell is [9]

$$\left(\frac{dP}{dl}\right)_n = -2\alpha_n P \quad (7)$$

whereα_n is the attenuation factor of the nth cell and P is the power flow of the nth cell, and equation (7)can be solved as

$$P_n = P_0 e^{-2\sum_1^n \alpha_n} = P_0 e^{-2\tau_n} \quad (8)$$

so that the weight from attenuation can be expressed as

$$\Gamma_{port} = \sum_1^n e^{-2\tau_n} \Gamma_{local,n} \quad (9)$$

In equation (9), the global attenuation for all cells from the input waveguide should be added, and equation (9) is revised as

$$\Delta\Gamma_{port} = |S11| e^{-2\tau_n} \Delta\Gamma_{local,n} \quad (10)$$

where|S11|is the global attenuation factor from the input waveguide, which is equal to the reflection coefficient of the input port when detuning the input coupling cell.

Besides the effect of attenuation, the reflection of each cell also occupies some part of the weight C_n in equation (6),however the reflection of each cell is random. So the reflection of each cell cannot be derived analytically, however it can be calculated by the post-processing of the forward and backward waves in equation (3).

For a constant impedance traveling-wave accelerating structure, equation (10) is modified as

$$\Delta\Gamma_{port} = |S11| \left(\frac{a_n}{a_1}\right)^2 \Delta\Gamma_{local,n} \quad (11)$$

wherea_n is the same as that in equation (3), and $\left(\frac{a_n}{a_1}\right)^2$ includes both the attenuation factor in equation (10) and the reflection from each cell. The square represents the integrated effect of both forward and backward waves.

For a constant gradient traveling-wave accelerating structure, equation (10) is modified as

$$\Delta\Gamma_{port} = |S11| \left(\frac{a_n}{a_1}\right)^2 e^{-2\tau_n} \Delta\Gamma_{local,n} \quad (12)$$

where $\left(\frac{a_n}{a_1}\right)^2$ only represents the reflection factor, and $e^{-2\tau_n}$ is the attenuated factor, which can be calculated from design parameters.

TUNING EXPERIMENTS

Based on the design in [3], the 1.1m C-band traveling accelerating structure has successfully accomplished cold RF testing and tuning, which is shown in Figure 3. It is necessary to point out that a constant impedance structure is adopted for the 1.1m C-band structure at last, which is different from the preliminary one, for simplifying the fabrication process. The 1.1m C-band structure is tested vertically so that the pull-bead can be placed into the structure easily without touching the inner surface of the structure.

Copyright © 2012 by the respective authors — cc Creative Commons Attribution 3.0 (CC BY 3.0)

Figure 3: Vertical cold RF test for the 1.1m C-band traveling accelerating structure.

Before any tuning, the field distribution on axis is measured, which is shown in Figure 4 left. In Figure 4 left, the field distribution including amplitude and phase is very confused, and it predicts that there are complicated standing waves on axis in the accelerating structure. After the analysis by LABVIEW code in Figure4 right, apparently there are three peaks around the 15th, 22th and 50th cells and it is detuned severely. Similarly, the phase advance per cell has large fluctuation, which is expected to be about 120 degrees. Based on this severe detuning of the C-band accelerating structure, several tuning iterations are proceeded necessarily.

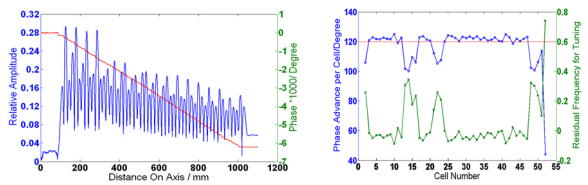

Figure 4: The field distribution and analysis before tuning

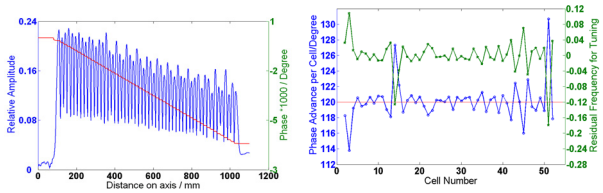

Figure: 5 The field distribution after 1st tuning.

After the first tuning phase, the field distribution and post-processing analysis are shown in Figure 5. In Figure 5 left the amplitude and phase on axis are distributed more smoothly with respect to that before tuning. In Figure 5 right, the phase advance mainly fluctuates between 118 and 122 degrees, and the amplitude of the residual frequency tuning per cell is mainly less than 0.05, which is within the permitted tolerance. However there is some slight detuning among cells, and after four water tubes are brazed, the last tuning phase eliminates the residual detuning finally.

After the final whole-structure tuning, the accelerating structure is almost matched, and the results are shown in Figure 6. According to the design target, the standing-wave ratio on axis is below 1.1 and the amplitude of phase advance fluctuation per cell is 2 degrees, corresponding to the baseline of 120 degrees per cell. In Figure 6 left, the field amplitudes in the center of cells are attenuated exponentially and the standing-wave ratio (SWR) on axis of the accelerating structure is below 1.1.In Figure 6 right, the phase advance per cell fluctuates between 118 and 122 degrees, and correspondingly the residual frequency detuning of all cells is from -0.04 to 0.04, which stays in the range of tolerance from -0.05 to 0.05. However on the both ends of accelerating structure in Figure 6 right, three cells on the each end are detuned out of the range above, which is used for the tuning of couplers.

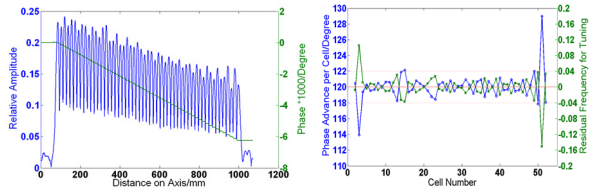

Figure 6: The field distribution after final tuning phase.

CONCLUSION

The nonresonant perturbation theory based on the bead pull measurement technique is an effective means for measuring and tuning a high gradient accelerating structure. The measurement system has been setup and successfully used in the R&D of a 1m long C-band traveling-wave accelerating structure for SXFEL. Now this prototype structure is ready for a high power RF test and since a 1.8 m long C-band constant gradient structure is under development, this measurement system becomes an indispensable tool in the accelerating structure developments.

ACKNOWLEDGEMENTS

We would like to thank Dr. Juwen Wang of SLAC for his helpful suggestion and useful discussion on the development of the measurement system, and appreciate our SINAP colleagues who join in the discussion on the nonresonant perturbation theory.

REFERENCES

[1] C. Feng et al., ChineseSci Bull, 2010, Vol.55 No.3: 221-227.
[2] M. H. Jiang et al., ChineseSci Bull, 2009, Vol54 No.22: 4171-4181.
[3] W. C. Fang et al., Chinese Sci Bull, 2011, Vol.56 No.1: 18–23.
[4] W. C. Fang et al., Chinese Sci Bull, 2011,56(32): 3420-3425.
[5] L. C. Maier et al., Journal of Applid Physics, 1952, 23(1) : 68-77.
[6] C. W. Steele, IEEE Trans.on microwave theory and techniques, 1966, MIT-14(2) : 70-74.
[7] T. Khabiboulline et al., PAC95, Dallas, TX , USA, 1995, Vol 3: 1666 – 1668.
[8] J. R. Shi et al., LINAC10, Japan, 2010, 97–99.
[9] C.G. Yao. Electron Linear Accelerator (in Chinese). Beijing: Science Press, Beijing, China, 1986,143-150.

Copyright © 2012 by the respective authors — cc Creative Commons Attribution 3.0 (CC BY 3.0)

S-BAND LOADS FOR SLAC LINAC*

A. Krasnykh, F.-J. Decker, SLAC National Accelerator Lab, Menlo Park, CA 94025, USA
R. LeClair, INTA Technologies, Santa Clara, CA 95051, USA

Abstract

The S-Band loads on the current SLAC linac RF system were designed, in some cases, 40+ years ago to terminate 2-3 MW peak power into a thin layer of coated Kanthal material as the high power absorber [1]. The technology of the load design was based on a flame-sprayed Kanthal wire method onto a base material. During SLAC linac upgrades, the 24 MW peak klystrons were replaced by 5045 klystrons with 65+ MW peak output power. Additionally, SLED cavities were introduced and as a result, the peak power in the current RF setup has increased up to 240 MW peak. The problem of reliable RF peak power termination and RF load lifetime required a careful study and adequate solution. Results of our studies and three designs of S-Band RF load for the present SLAC RF linac system is discussed. These designs are based on the use of low conductivity materials.

INTRODUCTION

The original RF system setup of the SLAC linac (see Fig. 1) was based on an array of 24 MW peak klystrons [1].

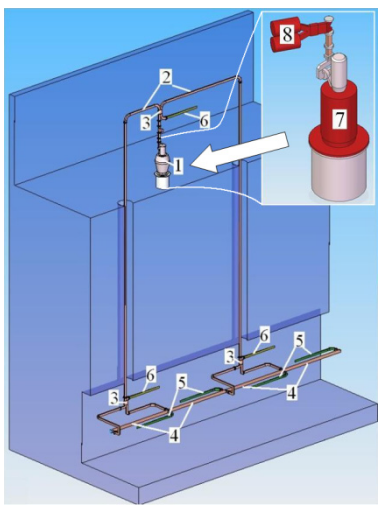

Figure 1: Original RF setup of the SLAC linac; 1 is XK-5 Klystron, 2 is WR284 Waveguide Branches, 3 is Power Dividers, 4 is Accelerating Sections, 5 is High Power RF Loads, 6 – Low Power RF Loads

Each RF station is equipped with a XK-5 klystron (1), feeding two branches of WR284 waveguide (2) and three 3dB power splitters (3) to supply four 10ft travelling accelerating sections (4). The residual klystron power after passing through the accelerator structure is absorbed by four high power loads (5).

* Work supported by the U.S. Department of Energy under contract number DE-AC02-76SF00515 and SBIR grant number DE-SC0007661

Three low power RF loads (6) absorb any mismatched (reflected) RF power. 240 such stations were in service of the original SLAC linac.

A high energy physics program (to reach 50 GeV output beam energy) was initiated and completed at the end of 1980 [2]. The original XK-5 klystrons were replaced by 5045 series klystrons with a 50 MW peak (subsequent production improvements the output power reached 65+ MW peak). SLED cavities were also introduced into the RF system thereby increasing the beam energy by a factor 1.7. The present typical RF setup is depicted in Fig. 1 where the new RF components (5045 klystron (7) and the SLED assembly (8)) are shown in right corner. A white arrow shows the location of the upgrade.

The residual power termination performance of the RF loads was not a concern during many years of service. For example, there were not any problems when the linac is used as the PEP-II injector. The RF absorption performance only became an item of concern after analyses of the LCLS RF phase stability issues [3].

It was found that the RF amplitude and phase of the reflected signals are unstable. It was shown also that these RF instabilities are associated with the processes inside of the load vacuum envelope. A detail of the RF structure layout that helps illustrate the high power load problem is shown in Fig.2.

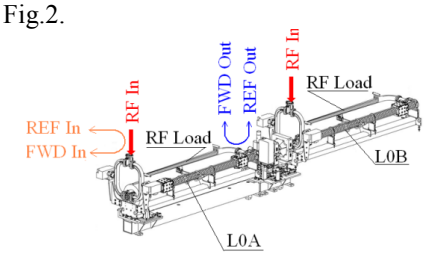

Figure 2: LCLS Injector layout

These two stations are working with detuned SLED cavities. The input and output couplers are employed for the monitoring of forward (FWD In and FWD Out) and reflection (REF In and REF Out) signals. The waveforms of these signals are shown in Fig. 3.

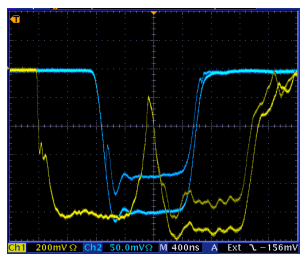

Figure 3: Waveforms of reflection signals

Ch1 (yellow trace) shows the reflection power from the input of the accelerating structure. Ch2 (blue trace) shows the reflection signal from the output of the accelerating

Copyright © 2012 by the respective authors — cc Creative Commons Attribution 3.0 (CC BY 3.0)

structure. One can see that the amplitude of the reflection signal from the input of the accelerating structure (the Ch1 trace) is stable in the beginning of the RF pulse, and after approximately 1600 nsec the amplitude is jumping between two stages. This is clear from the Ch2 trace, which corresponds to the signal from the output coupler on the end of the accelerating structure that has been terminated by the high power RF load.

The result of the activity inside of the RF load is also clearly seen in Fig. 4).

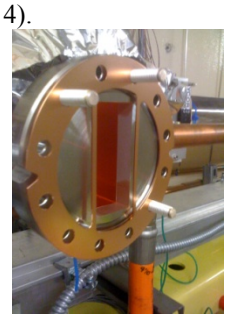

Figure 4: The grey area seen in copper waveguide

When the RF load was disassembled from the accelerating structure, a gray layer on a flange of the output coupler and waveguide wall could be seen. This gray area consisted of deposited particles that were created inside of the high power RF load and transported by a pumping gradient to the end of the accelerating structure. Due to coupler directivity limitation (approx. -25 dB) the RF instability can be seen on the FWD RF signal of many SLAC RF stations. We have no data on the lifetime of the original high power RF loads. Independently we tested dozen available (spare) original RF loads. The instability of the high power RF termination has been identified in all tested loads.

RESULTS OF STUDY

There was unsuccessful attempt to find (in national and world wide) vendors to purchase the needed vacuum load from industry. Two dry load designs were tested. One high power load was designed in BINP (Novosibirsk, Russia) and another S-Band dry load manufacturer was Nihon Koshuha Co. (NKC, Japan). The BINP load design does not meet the "*dry*" SLAC specification (i.e. with water leak proof) because the only brazing layer is the vacuum-water interface. It is not acceptable for 2 mile SLAC linac. The NKC loads cost and acceptance yield are not acceptable for SLAC (we tested five loads and only two were accepted).

SLAC's Designs and Results

The results above required find alternative solution for our linac within SLAC budget limitations. We are now working with a small business company that was granted a Phase I SBIRs to develop new S-Band RF loads for the SLAC linac. This work is being performed under a Cooperative Research and Development Agreement (CRADA) to design and build the RF load based on low conductive materials as a high power RF absorber. According to the CRADA, the high power load design will be performed by SLAC personnel. INTA will be a responsible for the technology and manufacting methodologies. Working together under the DoE SBIR support, the problem of high power RF load could be solved for the next 50 year linac service. A more detail decryption of SLAC RF load design will be published at SLAC.

The following RF load concepts are under consideration by INTA and SLAC:

- RF load design based on SiGraSiC group of composite materials
- RF load based on the bulk Kanthal APMT extruded tubing
- RF load based on the plasma deposition of ferritic FeCrAl alloy

Result of the RF Load Design Based on SiGraSiC Material. This is a rather new family of the carbon-carbon conductive materials and their composites. We contacted HITCO Carbon Composites, Inc. and realized that the manufacturing process allows us to tailor the conductivity based upon the constituents to some extent. Samples of this material was tested in a broadband power range (mW <P< 10 kW) range power. A design of the high power 3dB attenuator with SiGraSiC insertions was made and a prototype of the attenuator has been tested at 8 kW peak RF level. The 3dB prototype attenuator at test stand is shown in Fig. 5. Two black 12 inch insertions at H-planes of WR284 waveguide are made from SiGraSiC blocks.

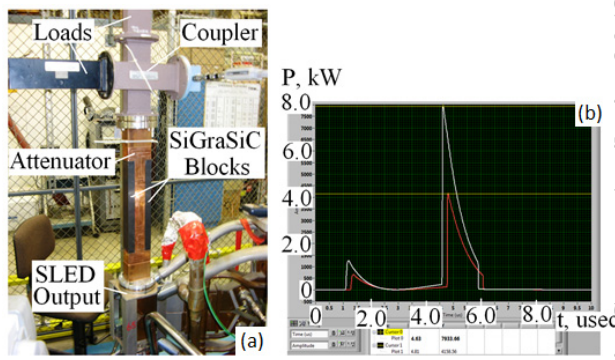

Figure 5: Experimental setup (a) and results (b)

shows input and output waveform of the RF power. White and red traces are the input and transmitted RF power though a device. We did not see any RF absorber degradations at kilowatt power levels. Attenuation rate with a special SiGraSiC shape is approx. 10 dB/m. A load (that possesses 10dB one-way-pass attenuation) will require two SiGraSiC blocks of a 40 inch length each. The technology of vacuum and heat transfer issues is under consideration.

Result of the RF Load Design Based on the Bulk APTM Kanthal Extruded Tubing. The Kanthal material is preferable because of its reasonable low electric conductivity, its stability under high temperature, and its good vacuum properties. Our discussion with experts from Kanthal indicated that a rectangular waveguide from the Kanthal material will require design of special

Copyright © 2012 by the respective authors — cc Creative Commons Attribution 3.0 (CC BY 3.0)

extruded tooling and a significant upgrade in technology. However extruded "cylindrical" tubing made from bulk Kanthal material is readily available. A proposed RF load concept is shown in Fig. 6.

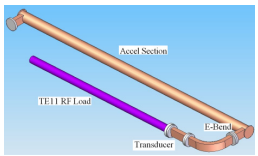

Figure 6: TE11 mode RF load concept

The RF load based on tubing will require a mode converter (transducer) because the RF mode from the output of the accelerating section is TE10 mode. For our experiments, we selected a tube with OD=75mm and wall thickness=4.5 mm because the wave length in this waveguide would be close to the critical wave length. In this case, we would expect a high attenuation of a propagated wave.

We evaluated two types of waveguide transducers. The first one is simply a rectangular-to-round waveguide with a conductive post (see HFSS half of model on Fig. 7a) and a smooth tapering transducer from rectangular-to-round waveguide is shown in Fig. 7 b).

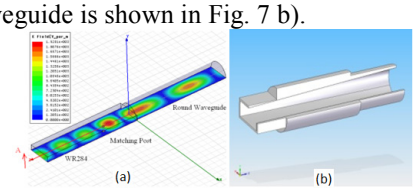

Figure 7: Mode converters with matching post (a) and rectangular-to-round transition (b)

A low level setup for a measurement of RF power attenuation of the APTM Kanthal extruded tube of 6 ft long is shown in Fig 8. We tested this load concept in a broadband power range too.

Figure 8: TE11 mode RF load under low power test

TE11 attenuation measurements of the bulk Kanthal APMT show approximately 2-2.5 dB/m attenuation rate. It is rather low compared to the attenuation rate of the original RF load [1] where a technology of "flame-spayed" Kanthal wire onto a stainless steel base was used. That fact confirms that both (1) a component matrix of absorber and (2) a technology of matrix deposition onto base material are important phases for the RF attenuation rates.

Result of the RF Load Design Based on the Plasma Deposition of Ferritic FeCrAl Alloy. A concept of the TE10 mode RF load can be seen from Fig. 9 where a cross section of modified WR284 waveguide is shown.

Figure 9: TE10 mode RF load concept

The modified WR284 waveguide is formed (extruded) from two identical parts made from aluminium alloy. Two halves are a base for the RF absorber layer. Both H-planes are with four thin vanes. A FeCrAl matrix is plasma sputtered onto the halves. Both coated halves are welded and a waveguide channel is formed. The RF load prototype was designed at SLAC and made by INTA Technologies. The RF load prototype had been conditioned and tested up to 30 MW peak power at SLAC high power test stand. Two power meter waveforms vs. time are shown in Fig. 10. Red and blue traces are forward and transmitted RF power.

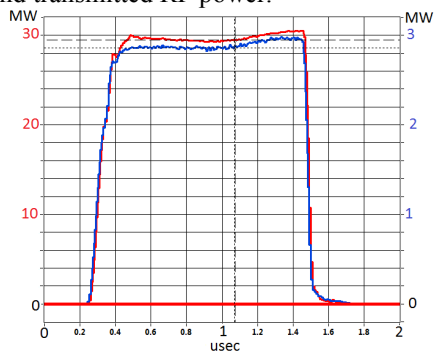

Figure 10: Input (red) and Output (blue) RF power wavforms

One can see that: (1) the RF load prototype runs at 30MW peak and 1 usec pulse width, and (2) one-way-pass attenuation is approx. 10 dB (~5.5 dB/m). No RF power instability was detected. More details of our studies and results will be published in SLAC-PUB-preprint.

CONCLUSION

There are indications that the present SLAC RF loads are near the end of their lifetime. SLAC and INTA Technology haves studied several alternatives for solving the RF load problem. The most promising results were obtained with the plasma deposition of ferritic FeCrAl alloy onto modified rectangular waveguide with vanes on H-planes. The technology achieved a 5.5 dB/m attenuation rate at 30 MW peak power and 1 usec pulse width with no evidence of breakdown activity in the vacuum envelope on the coated surfaces. We proposed a design and technology recommended for manufacture of a pilot series of the high power loads for the SLAC linac.

ACKNOWLEDGMENT

We thank Mr. R. Sviben and Mr. S. Schatz (Kanthal, SANDVIK) and Mrs. R. Hines (SiGraSiC, HITCO) for useful discussions.

REFERENCES

[1] "The Stanford Two-Mile Accelerator", p. 376-381, R. B Neal, General Editor, 1968, W. A. Benjamin, Inc., NY Amsterdam

[2] G. A. Loew, et. al., PAC 1985 Vancouver, Canada, 1985 (see also SLAC-PUB-3609)

[3] F.-J. Decker, et. al. "Indentifying Longitudinal Jitter Sources in the LCLS Linac", IPAC 2010, May 2010

Copyright © 2012 by the respective authors — cc Creative Commons Attribution 3.0 (CC BY 3.0)

FABRICATION TESTS FOR IMP 162.5 MHz RFQ*

Bin Zhang, Yuan He, Xiaofeng Jin, Jing Wang, Junhui Zhang, Aiming Shi, Xiaonan Du,
Zhouli Zhang, IMP, CAS, China
Derun Li, Matthew, D. Hoff, Steve Vireostek, Andrew Lambert, LBNL, USA

Abstract

The RFQ for one of front ends of C-ADS is designed. The frequency of the RFQ is 162.5 MHz and the energy is 2.1 MeV. The beam intensity is 15 mA and it works at CW mode. Because of low frequency, the four-wing structure is big size. It makes fabrication will take more risks. Therefore, four fabrication tests were planned and done to minimize the technic risks. The description about fabrication and testing results are presented .

STRUCTURE DESIGN

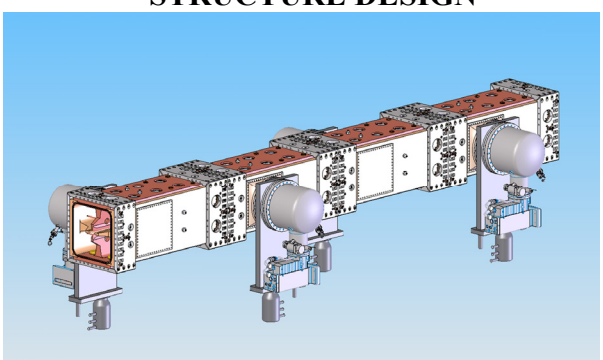

Figure 1: Structure of the ADS-Linac RFQ

Four 1.05 m long cavity modules were bolted together with a total length of 4.20 m, approximately 1000 kg for each complete module. All OFHC copper body were machined from solid billets, 4-vane cavity structure be choose with fly cut modulated vane tips. In this structure it includes 32 Pi-mode rods for mode stabilization, 20 fixed slug tuners/module 12 field sensing loops were designed per module. RF power feed through two loop couplers. 20 cooling channels per module will take the heat of RF power.

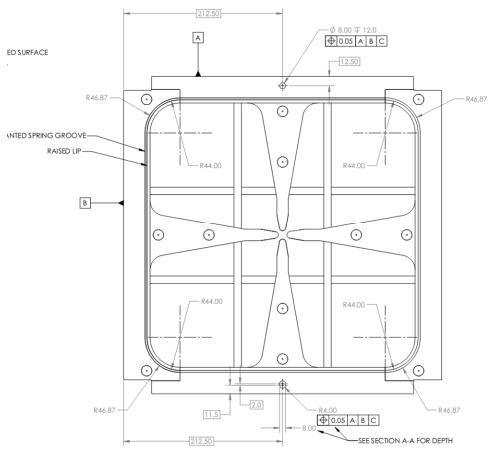

Figure 2: Section of RFQ

FABRICATION TESTS

Since the RFQ work in a low frequency, the four-wing structure is big size (425mm×425mm at section), four fabrication tests were planned and done to ensure fabricated process and minimize technic risks. It include fly cutting test, full length vane test, braze and clamp test and half-length test module. Two of them had finished the last one were rough machining now, as for hydrogen braze test, more tests were necessary before the last braze to take.

Flying cutting test

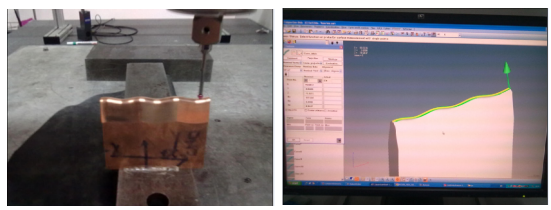

Figure 2: measurement vane

Flying cutting method were choice for RFQ modulation machined instead of ball drill. Two short pieces were cut and measurement with CMM. the result of measurement shows some point were out of tolerance ,some improvement with cutting tool will be take and the pieces will be measurement again in new CMM device.

Table 1: result of modulation measurement

	Max (mm)	Min(mm)
Profile tolerance	+0.0067	-0.0070
Section 1	+0.0056	-0.0097
Section 5	+0.0103	-0.0185
Section9	+0.0431	-0.0856
Radius of tip	8.5685	8.5315
Angle	19.9332	19.5164

Full length vane fabricated test

Full length of a single vane is about 1050mm, include all mechanic structure of RFQ, such as braze groove, cooling water deep hole, modulation of vane, vacuum seal groove etc. Main task were focused on the Gun-drill for deep hole, EBW for water plunger and the tolerance for vane pale. So far, it had been finished and all ports, holes and outside surface geometry tolerance will be checked by CMM this month.

Copyright © 2012 by the respective authors — cc Creative Commons Attribution 3.0 (CC BY 3.0)

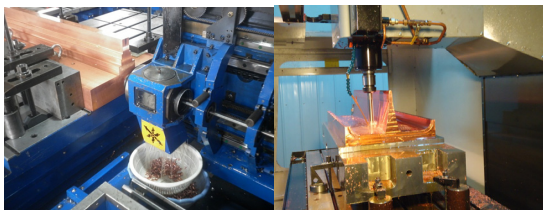

Figure 3: process of fabrication

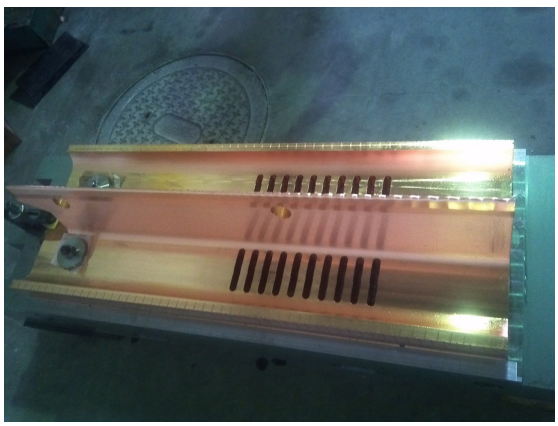

Figure 4: Single vane in full length

Braze and clamp test

Braze alloy is Ag-Cu28, and braze temperature is 790°C. Two braze test were carried out separately in hydrogen furnace and vacuum oven. The result shows braze in hydrogen has advantage attemperature uniformity. After checking with CMM the deformation of short braze pieces , nearly 0.8mm deformationwere be found. 3D ANSYS calculated were taken and it shows the same deformation trend. The reason is that OFC will get very soft at high temperature while braze clamp (SS) still keep intensity. Improved braze clamp had been redesign, and next test will be carry out later.

Figure 5: Short part were brazed in furnace

Half-length test module

The half-length module were rough machining now, however, fine machining will wait until braze test be finished.

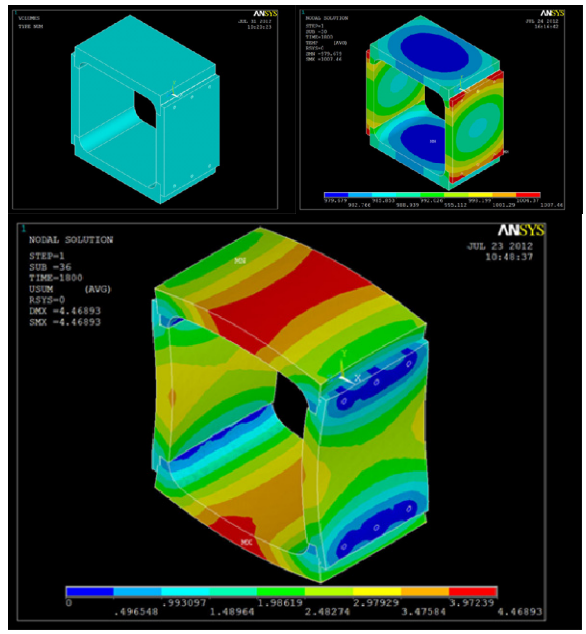

Figure 6 Deformation during brazing

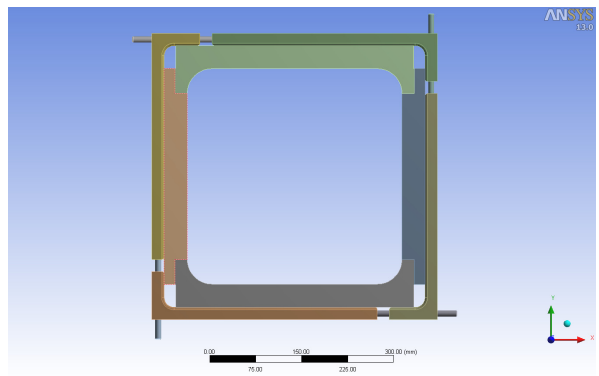

Figure 7 New structure of braze clamp

CONCLUSION

There are benefits in starting fabrication tests in parallel to the planned short module.

Gun drill (in addition to vane cutting test)

EB welding for the cooling channel

Inter-module assembly technique

Development of brazing for large copper components is critical.

Tooling and assembly procedures need to be discussed.

AKNOWLEDGEMENTS

We would like thank Xiaoqi Zhang and Guoping Sun (KTTJ)for their fruitful collaboration on the mechanic design and machining.

REFERENCES

[1] A. Pepato et al, “Mechanical Design of the IFMIF-EVEDA RFQ” PAC 2009 Vancouver.

[2] A.Pisent,et.al. “IFMIF-EVEDA RFQ DESIGN”EPAC2008, Genoa(Italy)

[3] S. Mathot “ RFQ Vacuum brazing at CERN” EPAC 2008, Genoa(Italy)

Copyright © 2012 by the respective authors — cc Creative Commons Attribution 3.0 (CC BY 3.0)

X-RAY LOCAL ENERGY SPECTRUM MEASUREMENT AT TSINGHUA THOMSON SCATTERING X-RAY SOURCE (TTX)*

Y.-C. Du#, Z. Zhang, L.-X. Yan , J.-F. Hua, H. Zha , W.-H. Huang , C.-X. Tang
Accelerator laboratory, department of engineering physics, Tsinghua University, Beijing, China
Key laboratory of Particle & Radiation Imaging (Tsinghua University), Ministry of Education, Beijing, 100084, China
Key laboratory of High Energy Radiation Imaging Fundamental Science for National Defense, Beijing, 100084, China

Abstract

Thomson scattering X-ray source, in which the TW laser pulse is scattered by the relativistic electron beam, can provide ultra short, monochromatic, high flux, tunable polarized hard X-ray pulse which is can widely used in physical, chemical and biological process research, ultra-fast phase contrast imaging, and so on. Since the pulse duration of X-ray is as short as picosecond and the flux in one pulse is high, it is difficult to measure the x-ray spectrum with traditional spectra measurement methods. In this paper, we introduce an iterative statistical algorithm (Expectation-Maximization) to reconstruct the spectra from the attenuation data, and the results of the X-ray spectrum measurement experiment on Tsinghua Thomson scattering is also presented.

INTRODUCTION

Thomson Scattering sources (also called Inverse Compton Scattering), which can be bright X-ray sources typically produce photons, have attracted a lot of interest as the technologies for producing low-emittance high-brightness relativistic electron sources and ultra-short high-power lasers have progressed. The X-rays that are generated by the interactions between laser and electron, exhibit high directivity, and have a polarized tunable quasi-monochromatic spectrum. The knowledge of the spectrum of an X-ray source is a key point for the development of any kind of application, for example in imaging both contrast and absorbed dose strongly depend on energy. However, direct methods performing a standard spectrometric measurement based on single photon energy measurement to detect the X-ray spectrum of Thomson Scattering sources have always been considered troublesome to implement because the beam is too intense to cause pulse pile up problems. Thomson Scattering source can produce up to 10^8 photons, bunched in 10ps long pulse [1]. An alternative way to measure the spectrum might request the measurement to be integral-type, which will not be affected by the high rate of incidence of photons. The analysis of attenuation data (transmission curves), which can provide some information about the spectral distribution of an X-ray source, as not affected by the rate of incidence of photons, is a good candidate to measure the X-ray spectrum of the Thomson Scattering X-ray source. Although there are several problems with this method, such as low accuracy, non-unique solution to ill-condition system and instability with different measurement error [2], this method can still give good estimation and reconstruction of spectra with some improvements based on the property of the measured spectra.

In this article, we introduce an iterative statistical algorithm (Expectation-Maximization) [3] to reconstruct the spectra from the attenuation data on simulated measurement. Results show that this method can give good approximations for the mean energy of the spectra, while it is not sensitive to the specific spectral distribution and the energy broadening. In order to reconstruct the shape of the spectra, especially the energy broadening, we present a new method based on the Expectation-Maximization algorithm. An preliminary experiment is also carried out on Tsinghua Thomson scattering X-ray source, the measured maximum X-ray energy is about 53keV, which is agreed well with the simulations.

OVERVIEW OF TTX

The scheme of TTX is shown in figure 1. This machine includes a 50MeV electron linac based on the photocathode RF gun and a Ti: Sapphire TW laser system. The laser system generates both the 266nm UV pulse for photocathode and the 800nm IR pulse for scattering interaction. The two pulses are derived from one 79.3MHz Ti:Sapphire oscillator in order to reduce the time jitter between the electron beam and the IR pulse. The linac system consists of a BNL/KEK/SHI type 1.6 cell S-band photocathode RF gun, a 3m S-band SLAC type travelling wave accelerating section, generates 40~50MeV ultra-short high brightness electron pulse for scattering interaction. The laser system is synchronized with the RF system through a timing circuit, with a timing jitter no greater than 0.5ps. The parameters of electron and laser were listed in the table 1.

In previous experiment, we succeed to generate and detect the X-ray signal with head-on colliding mode. The results from the MCP and X-ray CCD are shown in figure 2.

*Work supported by work is supported by NSFC under Grant Nos. 10735050, 10805031, 10975088 and 10875070 and by the 973 Program under Grant No. 2007CB815102.
dych@mail.tsinghua.edu.cn

Copyright © 2012 by the respective authors — cc Creative Commons Attribution 3.0 (CC BY 3.0)

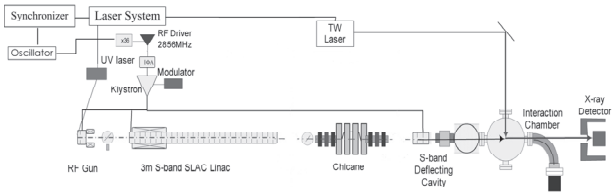

Figure 1: scheme of TTX.

Table 1: Parameters of Laser and Electron Beam

Electron		
Charge	200	pC
Energy	47	MeV
rms emittance	3	mm mrad
Bunch length	3	Ps
Beam size at interaction position	50	Um
Arriving time jitter	~500	Fs
Laser		
Wavelength	800	Nm
Pulse duration	60	Fs
Energy	<300	mJ
Beam size	~100	Um

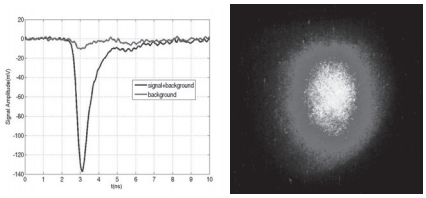

(a) (b)

Figure 2: typical X-ray signal and background from the MCP detector(a) and X-ray CCD.

LOCAL ENERGY SPECTRUM MEASUREMENT

X-Ray Spectrum Measurement from the Analysis of Attenuation Data

The relative transmission function $T(x)$ responding to an attenuator of thickness x is related with the spectrum of an X-ray beam in the following way[1]:

$$T(x)=\frac{S(x)}{S(0)}=\int_0^{E_{\max}} e^{-\mu(E)x}F(E)dE \qquad (1)$$

where $S(x)$ is the signal measured with an absorber of thickness x, and $S(0)$ is the signal measured without any absorber. $\mu(E)$ is the total attenuation coefficient of the attenuator in which are included both photoelectric and Compton effects for photons of energy E. $F(E)=\phi(E)\bullet C(E)$, where $\phi(E)$ represent the spectrum distribution of photons and $C(E)$ represent the energy response determined by the way to measure the signal $S(x)$. $E_{\max}$ is the maximum energy of the spectrum.

When we treat the problem from its numerical point of view by discretizing the integral, the Eq.(1) turns out a linear system of the form

$$T=A\bullet F \qquad (2)$$

where $T\in R^M$ represent the attenuation curve as a function of the attenuator and $F\in R^N$ is the discretized spectrum. Generally, the linear system described by Eq.(1) translates, after the disctretization, into an ill-conditioning linear system in Eq.(2). Here the Expectation-Maximization (EM) algorithm is used to obtain an approximation to the exact solution of the system Eq.(2)[2]. Expectation -Maximization algorithm is an iterative statistical algorithm with the form [3][4]:

$$F_n^{(k+1)}=F_n^{(k)}f_n,\quad f_n=\frac{\sum_m A_{nm}{}^t\dfrac{T_m}{\sum_{n'}A_{mn'}F_{n'}^{(k)}}}{\sum_m A_{nm}{}^t} \qquad (3)$$

Numerical Simulation

A Monte Carlo numerical simulation experiment is carried out to verify the method first. During the simulation process, Monte Carlo method is used to simulate the Thomson Scattering and calculate the attenuation curve through silicon with different thickness to justify the reliability and feasibility of this method. Figure 3 shows the results for the reconstruction of local spectra for different two points in the X-ray spot.

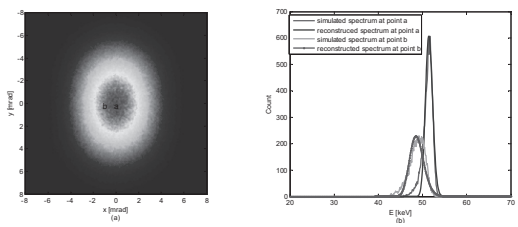

Figure 3: (a) X-ray profile simulated by CAIN and the two points selected to reconstruct local spectra. (b) Simulated and reconstructed spectra at two different points with 0.5 mrad collecting angles and 5% Gaussian random error.

It can be observed that the EM method performs well to reconstruct the local spectra of Thomson Scattering source. However, as the collecting angles increase, the X-ray spectra are not close to Gaussian distribution any more. To solve this problem, we propose an assumption that according to the spectral distribution features of Thomson Scattering, as the collecting angles increase, the right half of spectra remains almost unchanged. So we

Copyright © 2012 by the respective authors — cc Creative Commons Attribution 3.0 (CC BY 3.0)

can treat the right-half spectra of the small collecting angles given by EM algorithm as the right half for spectra of other angles within a certain range. Then we can reconstruct the spectra with the attenuation data more accurately as under this assumption, the mean energy will have direct and close relationship with the shape of spectra. Fig.4 shows the reconstruction result (top) and the simulation result (bottom) for Thomson Scattering spectra within the collecting angle range from 0.5mrad to 5mrad.

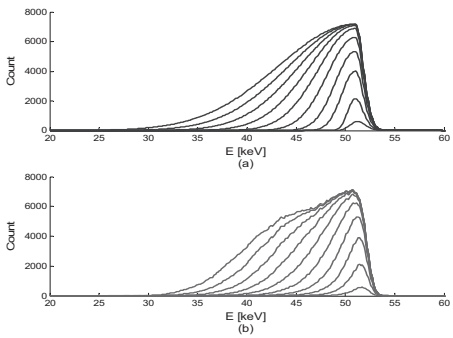

Figure 4: (a): Representative reconstruction results of spectra for collecting angles ranging from 0.5 mrad to 5 mrad with an equal interval of 0.5 mrad (b): The simulated spectra for the Thomson Scattering source with collecting angles of the same range with CAIN.

Experiment Results

A preliminary experiment is carried out on TTX to measure the X-ray spectrum. The scheme of the experiment is shown in figure 5. The silicon wafers with different thickness are used as attenuator, a CsI screen and CCD camera are used as the X-ray intensity monitor.

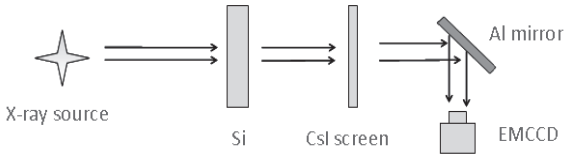

Figure 5: The scheme of the X-ray spectrum measurement.

The typical X-ray profile with attenuators is shown in figure 6. The sheltered part is used to obtain the attenuation curve and the unsheltered part is used to X-ray intensity normalization to cancel the jitter influence. The attenuation curves for point a, b, and c, the reconstructed X-ray spectrum from the attenuation curves are also shown in figure 6. The maximum X-ray energy at the center of profile is 53keV, which is agreed well with the theory expectation and simulations.

In Thomson scattering X-ray source, the X-ray energy is a function of scattered angle. In figure 7, the mean energy of the X-ray as a function of scattered angle is shown and compared with the theory and simulation expectations. The measured results are a little different to the theory curve but agreed well with the simulation results, since in theory curve the emittance effect of the electron beam is not included.

Reconstruction spectra results from measured attenuation for collecting angles ranging from 0.5mrad to 5mrad with an equal interval of 0.5mrad are shown in figure 8:The deposition efficiency of CsI screen is considered.

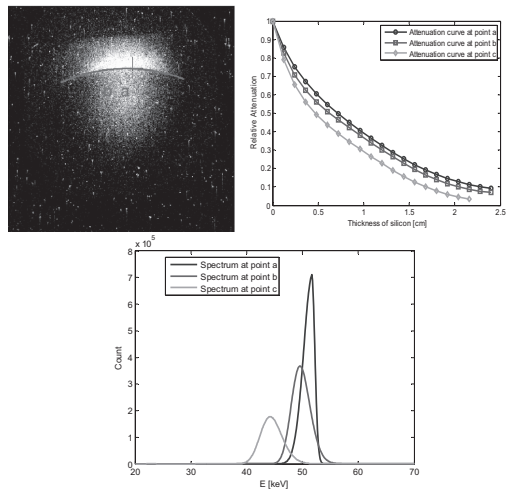

Figure 6: (top left)X-ray profile measured by EMCCD sheltered by 1.5cm silicon. (top right) Attenuation curves at points a, b, and c. (bottom) The reconstructed local X-ray spectrum from the attenuation curves.

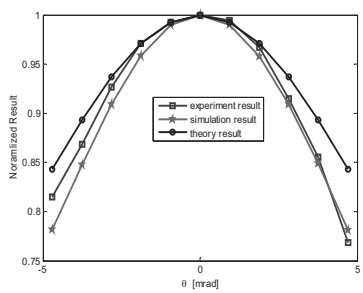

Figure 7: Mean energy along the line b-a-c in the profile, and compared with theory and simulation.

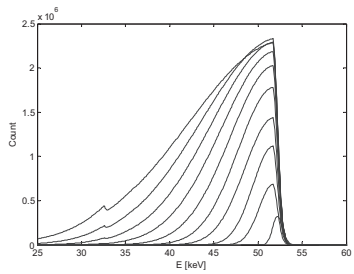

Figure 8: The x-ray spectrum with different collecting angle.

REFERENCE

[1] Emil Y. Sidky et al., "A robust method of x-ray source spectrum estimation from transmission measurement", Journal of Applied Physics 97, 124701(2005)
[2] Marian Manciu et al., Journal of X-ray Science and Technology 17 (2009) 85-99.
[3] Marco Endrizzi et al., , NIM A, 608(2009) S78-S82.
[4] Li Zhang et al., 2007 IEEE Nuclear Science Symposium Conference Record, 3089-3093, 2007.

Copyright © 2012 by the respective authors — cc Creative Commons Attribution 3.0 (CC BY 3.0)

FRIB TECHNOLOGY DEMONSTRATION CRYOMODULE TEST*

J. T. Popielarski*, E. C. Bernard, S. Bricker, C. Compton, S. Chouhan, A. Facco#, A. Fila, L. Harle, M. Hodek, L. Hodges, S. Jones, M. Klaus†, M. Leitner, D. Miller, S. Miller, D. Morris, J. P. Ozelis, R. Oweiss, L. Popielarski, K. Saito, N. Usher, J. Weisend, Yan Zhang, Z. Zheng, S. Zhao
FRIB, East Lansing, Michigan, USA
#INFN/LNL, Legnaro (PD), Italy, † Technische Universität Dresden, Dresden, Germany

Abstract

A Technology Demonstration Cryomodule (TDCM) has been developed for a systems test of technology being developed for FRIB. The TDCM consists of two half wave resonators (HWRs) which have been designed for an optimum velocity of beta=v/c=0.53 and a resonant frequency of 322 MHz. The resonators operate at 2 K. A superconducting 9T solenoid is placed in close proximity to one of the installed HWRs. The 9T solenoid operates at 4 K. A complete systems test of the cavities, magnets, and all ancillary components is presented in this paper.

INTRODUCTION

The SRF Department at Michigan State University had developed and tested four cryomodules prior to the first demonstration cryomodule for FRIB. Two of the cryomodules are working reliably in the ReA3 linac at MSU [1]. The TDCM, shown in figure 1, is the first cryomodule that demonstrates FRIB specific technology and encourages a transition to large scale engineering and quality assurance methods [2].

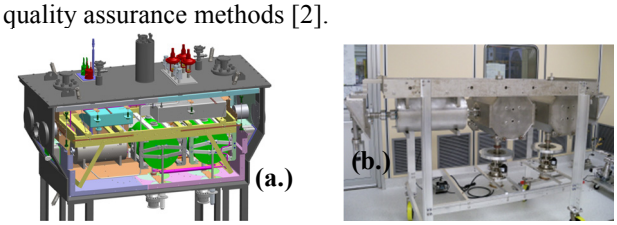

Figure 1: (a.) Rendering of TDCM in cryostat (b.) Cold mass assembly in cleanroom.

In developing the FRIB TDCM, a baseline cryomodule production method evolved for FRIB. The technical and schedule related setbacks encountered during the TDCM campaign eventually yielded reliable fabrication, processing, and certification techniques. SRF-related infrastructure and utility usage required for the TDCM assisted in finalizing planning for a new SRF high bay which will support FRIB cavity processing, vertical testing, cold mass assembly, and cryomodule bunker tests.

TDCM RELEVANCE TO FRIB

The TDCM is a developmental snapshot, and much of the technology improved as more detailed engineering analysis and sub component testing programs provided opportunities for design optimization [3- 5]. Some of the key differences are: a "bottom-up" style from the "top-down" TDCM style [4]; the rail system, support system, heat and magnetic shields assemblies were simplified; Improvements to alignment methods; an internal heat exchanger replaces the external heat exchanger; the 4K thermal intercepts will be parallel circuits as opposed the series connection in the TDCM.

With much of the cryogenic circuitry and alignment systems optimized in the baseline design before TDCM testing took place, alignment and continuous 2K operation aspects were not tested. The plumbing of the RF coupler 4K intercepts [6] required steady flow in the static state required continuous overfilling of the 4K header to ensure the couplers stayed cooled during RF conditioning.

TDCM DEVELOPMENT

Individual tests or more detailed engineering analyses conducted on the cavities, couplers, tuners, and cryogenic circuits used in the TDCM led to design optimizations and improved processing [7- 9].

Initial dunk tests showed low field emission onset values and thermal breakdown below the operating gradient; FRIB processing optimization for the HWR began during the TDCM campaign. The TDCM cavities were field emission-free [10] prior to the installation of the helium vessels.

Initial tests still showed signs of multipacting in the cavity. Repeated measurements on several cavities show a recurring barrier at 2 MV/m E_{acc}. This barrier self-conditioned as the RF power was raised, and in most tests only observed during initial 4K measurements.

During the initial dunk tests, it was discovered Q_0 was lower after a thermal cycle with no change otherwise. A closer investigation for Q-disease showed a strong reduction in the Q_0 after a 15 hour soak at 100K. The cavities were sent to JLAB for a furnace treatment to remove hydrogen from the bulk. Subsequent 'Q-soaks' and thermal cycles showed no signs of degradation. A 600°C furnace treatment was added to the baseline processing plan and a furnace has been installed at MSU [9].

After being jacketed with a helium vessel, the 1st cavity was certified using the vertical cryostat configuration [5], and no field emission was observed. This helium vessel design utilized a titanium bellows at the beamport to reduce the tuning force required for the scissor-jack tuner.

*This material is based upon work supported by the U.S. Department of Energy Office of Science under Cooperative Agreement DE-SC0000661.
#popielar@frib.msu.edu

Copyright © 2012 by the respective authors — cc Creative Commons Attribution 3.0 (CC BY 3.0)

After this cavity had been installed on the TDCM cold mass, the next jacketed cavity developed a large leak from the helium to insulating space found at the titanium bellows. The bellows were removed from the already certified cavity, requiring additional machining and welding.

TDCM TESTING

RF Amplitude and Phase Control

The resonators in the FRIB linac will operate with a very narrow BW for amplitude and phase control. For the HWR, the 30 Hz RF bandwidth available for control presents a technical challenge and increasing the RF BW has a very large impact on cost. The low level RF controller was developed at MSU and employs an ADRC algorithm [11] which is required to ensure a dynamic stability within 2% (peak-to-peak) amplitude and 2 degrees (peak-to-peak) phase. The resonators do not have fast tuning implemented to cancel microphonics. Measurements were done using a fast (1.6 kHz) data acquisition of the RF signals. The results are shown in figure 2, where the measured cavity and amplitude stability is within the limits of the measurement uncertainty. During the measurements, the cavity field was kept just below a multipacting barrier in the cavity and with the slow tuning feedback to the scissor-jack mechanical tuner turned off.

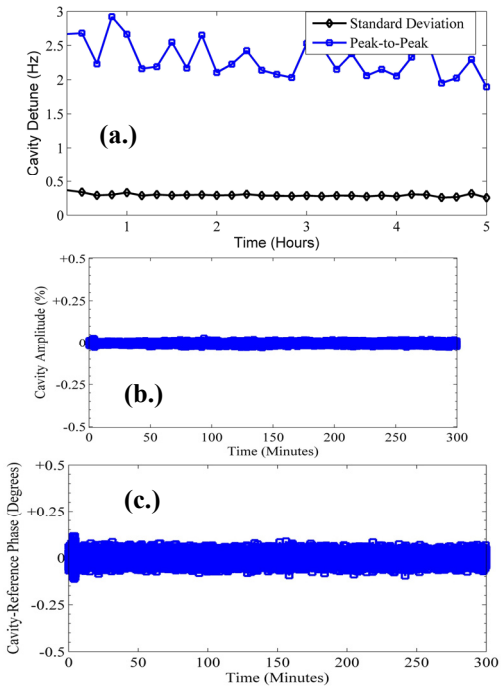

Figure 2: (a) Closed loop detuning, calculated from the forward phase changes while regulating with the cavity amplitude and phase (b, c) well within the design specification.

The 'cavity detune' (Δf) in Figure 2a is inferred from the changes in the forward phase ($\Delta\varphi_f$) and is calculated from $\Delta f = BW \times \Delta\varphi_f$. The closed loop detune inferred from the measurement agreed well with some shorter duration open loop measurements done a 2K. A slow drift of 8 Hz over five hours was measured, justifying the necessity of a slow tuner. During this measurement, the bath pressure was well regulated (less than 0.7 Torr peak-to-peak).

The next round of measurements was performed using the feedback to the slow tuner. The measured amplitude and phase stability was higher (1.4%, 0.6°, peak-to-peak), but still within the FRIB specification. It was noticed that the tuner drive was constantly moving, which created a mechanical oscillation at 110 Hz, causing a closed loop detune of 24 Hz peak-to-peak.

RF Couplers

The RF couplers had been conditioned for multipacting barriers prior to the installation into the cold mass [6]. The multipacting that was conditioned had returned after installation to and cooling of the TDCM, with similar onset levels. Coupler conditioning did not completely remove the multipacting from the coupler above 2 kW after 10 hours of RF pulses. The multipacting was suppressed by applying an external magnetic field through a coil winding around the coupler. Figure 3 shows a plot the current on the probe near the ceramic disk; 6.8 kW peak power was achieved with 4.5 kW average forward power while driving 1 MHz off-resonance. A detailed multipacting analysis [12] shows that the location of the two-point multipacting in the coaxial line depends strongly on the boundary condition at the cavity port. With the rf system 'detuned' from the cavity, the boundary condition at the coupler port is that of a short circuit, and a single two-point multipacting node exists at the voltage peak, which is approximately half way between the coupler port and the ceramic disk. However, when driving the cavity on resonance, two voltage peaks exist on the transmission line. The magnetic field suppression did not suppress the multipacting when locked to the cavity resonance.

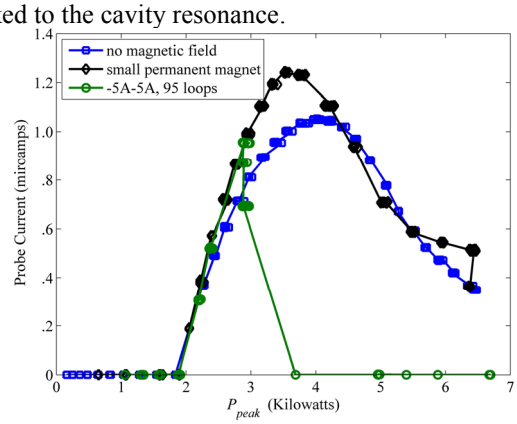

Figure 3: Multipacting suppression in the FPC while driving from the cavity off-resonance.

Tuners

The bellows used to reduce the force required to tune the cavity was replaced with a rigid connection to the helium vessel. A measurement of the tuning ratio of

Copyright © 2012 by the respective authors — cc Creative Commons Attribution 3.0 (CC BY 3.0)

360:1 greatly exceeds the expected 8:1 ratio showing that the scissor-jack mechanism was not performing as expected. This resulted in a reduced tuning sensitivity of the actuator controller (from 1.8 Hz/step to 0.03 Hz/step), which may explain the mechanical effects on the performance of the LLRF with the tuner engaged. Additional testing will be performed on an alternate tuning concept which utilizes a pneumatic drive.

Cryostat

Static load measurements on the TDCM cryostat were performed by recording liquid level as a function of time using the level sensor to infer the evaporation rate. This rate was calibrated by using a gas meter to measure the mass flow of the helium gas at room temperature. The mass flow measurement and nominal liquid volume boil-off from the header dimensions had roughly good agreement. Neither the level vs time nor the gas meter methods were calibrated with a known heat source. An evaporation rate of 2.85 W to the 2K header and 4.0 Watts to the 4K header was measured and repeated four times, with a spread of 0.22 W peak to peak.

Cavity Dynamic Load

The cavity dynamic loads, measured the same as the static load measurements described above, could not be accurately measured below the multipacting barriers (1.67 MV/m E_{acc}), since the resolution of this type of measurement is ~0.5 W. This resolution exceeds the heat load measured in the last Dewar test (0.10 Watts at 1.67 MV/m). With helium processing, a reasonable field level (4 MV/m) was reached. The dynamic load of 1.5W @ 4 MV/m yields a Q_0 of 1.2E10. This measurement was done in the last hours of the TDCM test. The load from the RF coupler at this field (850W forward power) was negligible considering a load measurement done with 4.5 kW forward power off resonance was less than the measurement resolution.

Magnets & Magnetic Field Interactions

The Earth's magnetic field is shielded from the cavities with a global mu-metal shield. Measurements on the shield showed an attenuation factor of at least 25 was achieved; however accurate measurements of the residual magnetic fields with the cold mass installed were not performed. Prior to energizing the magnets, the low field Q_0 (@1.67 MV/m) showed the possibility of high residual magnetic fields trapping fluxes up to 200 mG, but the Q drop at this field could also be explained as either measurement error or multipacting.

The 9T solenoid has a fringe field such that the flux at the nearest cavity surface is 250 Gauss. The revised FRIB specification for this fringe-field is 650 Gauss. The magnet was powered to full field; the cavities were warmed up to 30 K, and then re-cooled. The dynamic loads were measured again at 2K. The difference in the dynamic loads was less than the 0.5 W measurement resolution. A magnetic field cancellation procedure was performed by varying the power supply current, I, in a decreasing and alternating manner, e.g. a series, $\{(-0.9)^n I\}_{n=0}^{40}$ which took 5 hours to complete. The dynamic load measurement performed after this degaussing and further RF conditioning yielded a quality factor close to that measured in the vertical test.

TDCM Outlook and Future Tests

The TDCM test ended abruptly after taking only limited dynamic load data due to an unexpected cryoplant failure. A suspected helium leak in the transfer line that supplied the TDCM required mass flow rates of 3-5 g/s to maintain level in the liquid helium levels, though static load measurements indicate only 0.5 g/s is required. Therefore, running the TDCM test in parallel to NSCL experimental programs in impossible due to the unavailability of this LHe supply rate.

Though the TDCM completed a successful first round of testing in mid-2012, additional testing will be done by end of 2012. The next round of testing will focus primarily on the high power RF conditioning that commenced in the later stages of the TDCM measurements.

A new transfer line is being procured and installed to supply the TDCM from a refrigerator that is separate from the NSCL experimental program. While the transfer line is being built, the cryostat is being opened up to make some adjustments. Magnetic material found on the internal scissor jack tuning mechanisms is being removed. The RF couplers are undergoing an in-situ bake (~100-120C, 72 hours) in an effort to reduce the multipacting intensity. Additional measurement equipment will be installed to determine the dynamic load of the couplers to the intercepts and the remnant fields from the 9T solenoid before and after degaussing steps.

ACKNOWLEDGMENTS

The authors would like to thank Greg Velianoff, Jon Wlodarczak, Tom Russo, John Brandon, Mike Holcomb, and Jie Wei for their help in late night and evening shifts during RF conditioning; JLab for degassing the HWR's installed in the TDCM; Peter Kneisel, Curtis Crawford, and Bob Laxdal for their advice given regularly in weekly teleconference.

REFERENCES

[1] D. Leitner et al., Proc. of SRF 2011, pp. 674.
[2] M. Leitner et al., Proc. of SRF 2011, pp. 56.
[3] S. Miller, et al., Proc. of SRF 2011, pp. 213.
[4] M. Johnson et al., IPAC 2012, to be published.
[5] A. Facco, et al, IPAC 2012, to be published.
[6] J. Popielarski, et al, Proc. of SRF 2011, pp. 353.
[7] L. Popielarski, et al, Proc. of SRF 2011, pp. 526.
[8] R. Oweiss, these proceedings.
[9] L. Popielarski, these proceedings.
[10] J. Popielarski, IPAC 2012, to be published.
[11] J. Vincent, et al, Nuclear Instruments Methods in Physics Research A 643 (2011) pp. 11.
[12] Z. Zheng, et al, these proceedings.

Copyright © 2012 by the respective authors — cc Creative Commons Attribution 3.0 (CC BY 3.0)

THE INJECTOR CRYOMODULE FOR THE ARIEL E-LINAC AT TRIUMF

R.E. Laxdal, N. Muller, A. Koveshnikov, W.R. Rawnsley, G. Stanford, V. Zvyagintsev
TRIUMF, Vancouver, Canada
M. Ahammed, M. Mondrel, VECC, Kolkata, India

Abstract

The ARIEL project at TRIUMF includes a 50 MeV-10 mA electron linear accelerator (e-Linac) using 1.3 GHz superconducting technology. The accelerator is divided into three cryomodules including a single cavity injector cryomodule (ICM) and two accelerating cryomodules with two cavities each. The ICM is being built first. The ICM utilizes a unique top-loading box vacuum vessel. The shape readily allows the addition of a 4K/2K cryogenic unit that accepts near atmospheric LHe and converts to 2K liquid inside the cryomodule. The cryomodule design is complete and in fabrication. The 4K/2K cryogenic unit has been assembled with tests scheduled next month. The paper describes the design and status of the cryomodule.

INTRODUCTION

TRIUMF is now preparing a new high intensity superconducting electron linear accelerator[1], e-Linac, as a key element of the ARIEL project. The e-Linac is specified to produce 10mA of 50MeV electrons as a powerful 0.5MW photo-fission driver to add a complimentary second source of radioactive ion beams for the existing ISAC experimental infrastructure. The e-Linac consists of five 1.3GHz nine-cell niobium cavities each supplying 10MV acceleration with two 50kW power couplers supplying the required beam loaded rf power. The five cavities are housed in three cryomodules, with a single cavity in an injector cryomodule, EINJ, and two identical accelerating cryomodules EAC1 and EAC2 with two cavities in each module. The fully funded first phase of the e-Linac includes the first two cryomodules for a final energy and intensity of 30MeV and 5mA for 150kW driver capability by 2014. The EINJ is presently being fabricated and will serve as the working prototype for EAC1.

TRIUMF began developing EINJ in 2010 in collaboration with the VECC laboratory in Kolkata. VECC requires a photo-fission driver for the proposed ANURIB[2] facility. TRIUMF and VECC have an agreement to jointly design the EINJ cryomodule. Two EINJs are being fabricated and beam tested at TRIUMF with one EINJ being shipped to VECC and the second installed in the e-Linac. The initial EINJ is presently in fabrication. A beam test area is being installed in the ISAC-II building to utilize the existing cryogenics infrastructure with beam tests scheduled for early 2013.

CONCEPTUAL DESIGN

Cryomodules for 1.3GHz elliptical cavities utilize typically round vacuum chambers with end loaded cold mass assemblies. In applications such as X-FEL involving long linac structures the gas return pipe in the cryomodule acts as both the support strongback for the cold mass and the helium cold return distribution line for the overall cryogenic system. Operation is at 2K with the 2K produced either in a central 2K cold box or in a JT expansion valve close to the cryomodule that transforms a typical 3 bar stream from a 4K cold box to He-II. Heavy ion linacs such as the ISAC-II 40MV linac[3] operate at 4K due to typically lower rf frequencies and hence lower BCS resistance and are typically designed as box cryomodules with the cold mass loaded from above due to the large transverse size of the low frequency low beta cavities.

Although non-standard a top-loading box design (Fig. 1) has some advantages for the e-Linac over an end-loading round variant. Firstly the modular and staged testing/installation sequence of the e-Linac suggests that each cryomodule be self-reliant to convert 4K atmospheric LHe available from dewars or ISAC-II cryogenic system into 2K He-II. To this end the box

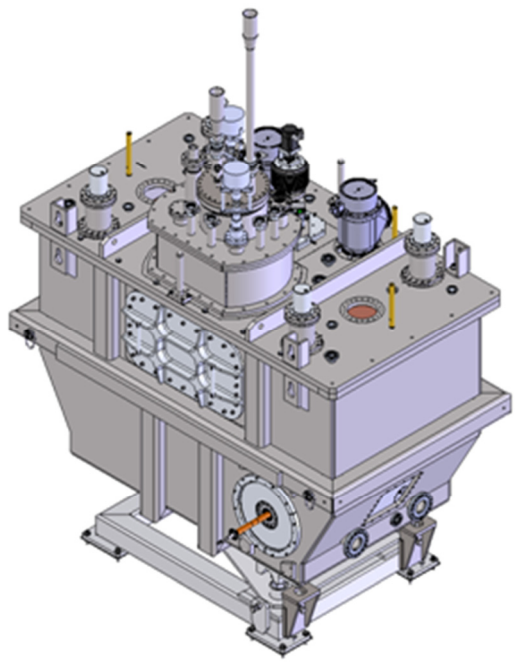

Figure 1: Model of the e-Linac Injector cryomodule.

Copyright © 2012 by the respective authors — cc Creative Commons Attribution 3.0 (CC BY 3.0)

cryomodule design has sufficient head room that makes possible the addition of a dedicated 4K/2K cryo-insert on each module. Secondly, incorporating features of the ISAC-II design reduces the engineering design effort within TRIUMF and takes best advantage of the existing infrastructure for assembly and test.

The basic concept of the e-Linac cryogenic system[4] replicates the ISAC-II system. A 4K cold box produces 4K liquid at 1.3Bar to a supply dewar that feeds LHe to a common delivery trunk with parallel 4K feed to each cryomodule. A 4K reservoir on board each cryomodule acts as phase separator and the 4K return vapor is sent back to the cold box. The 2K liquid is produced in each cryomodule by passing the 4K liquid through a heat exchanger in counterflow with the returning exhaust gas from the 2K phase separator and expanding the gas to 30 mbar through a JT expansion valve. The header pipe above the cavity string acts as a 2K phase separator and delivers cold gas back through the 4K/2K heat exchanger to the sub-atmospheric pumping system as a liquid load. A second on-board cryovalve delivers helium from the 4K phase separator to the bottom of the cavity string during cooldown. A siphon circuit from the 4K reservoir is used to cool the 4K temperature intercepts with vapour return back to the reservoir.

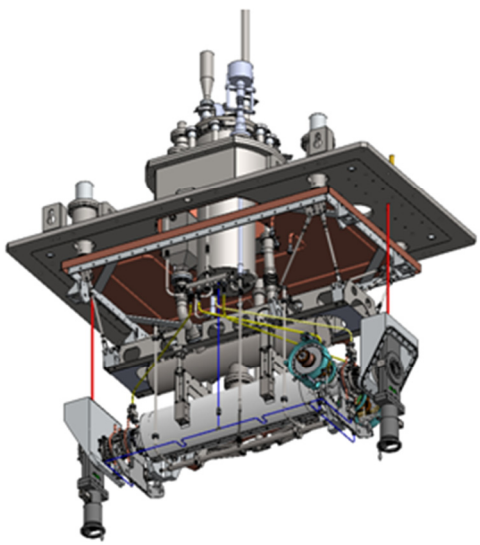

Figure 2: Top plate and cold mass assembly for EINJ.

DETAIL DESIGN

Vacuum Vessel

The vacuum vessel is a stainless steel vessel in a rectangular box shape with additional ribs welded on to strengthen against the vacuum load (Fig. 1). A warm layer of 1mm mu-metal sheet is placed in the vacuum space anchored to the vacuum vessel. The entrance and exit beam tube regions are angled to allow the installation of the cold mass as a hermetically sealed unit with warm isolation valves at either end.

The cold mass is supported from the top plate with the following minor exceptions. The beam pipe is connected at the warm isolation valve to the end flange. In addition each cavity is fed rf power through two couplers mounted horizontally and symmetrically opposed at the `coupler end' of the cavity. The cold part of the coupler is assembled with the cavity as part of the hermetically sealed unit. After the top assembly has been inserted into the cryomodule the warm end is assembled to the cold end through cutouts in the side of the cryomodule. Two Cornell/CPI 50 kW couplers will be used to feed rf power to each of the 9-cell cavities. The power couplers are on the downstream end to reduce coupler kicks. There are also flanges adjacent to the beam tubes for off-axis wire position monitors (WPM)[5] for alignment purposes. The top plate has a cut out opening to allow independent installation and removal of the cryo-insert (see below). In addition a side panel cut-out allows access to the cryo-insert connections to allow removal of the cryo-insert without pulling the cold mass.

Strongback and Cold Mass

The stainless steel strongback supports the cold-mass and forms a rigid assembly unit (Fig. 2). The cold-mass includes the cavity hermetic unit, cold mu-metal, tuner, 2K phase separator, lower cooldown supply pipe, and diagnostics. The strongback is supported from the top flange of the cryostat through struts. The support struts are equipped with spherical rod ends to avoid any mechanical stresses that may develop during thermal cycling. The hermetic unit consists of the niobium cavity and titanium helium jacket, the cold end of the power couplers, the warm-cold beam-pipe transition including HOM dampers, the cavity rf pick-up and isolation valves. The strongback and struts will thermally contract during cooldown though the reduced length of the module limits this to <4 mm. The vertical contraction does not affect the alignment since this can be compensated for during the initial set-up using the WPM and optical measurements and is repeatable.

4K / 2K Cryo-Insert

The 4K/2K cryo-insert is being built and tested as a separate package. The geometry of the cryogenic unit is chosen to be compatible with pre-testing in an existing cryostat. The insert, shown schematically in Fig. 3, includes a 4K phase separator, 4K/2K heat exchanger, JT expansion valve, 4K cooldown valve, LN2 cooled thermal shield, warm mu-metal layer plus siphon circuit for intercept cooling. The prototype heat exchanger is fabricated by DATE with an estimated capacity of 2.5 gm/sec. A dummy 2K phase separator and three dummy thermal intercept loads are added to the test unit. These are removed during installation to the cryomodules and replaced with the 2K phase separator and actual thermal intercept loads.

The 4K/2K test unit is assembled and tests are imminent. Tests will include (1) static load measurements (2) 2K production efficiency (3) thermal siphon circuit cooling capacity (4) cooldown procedure and (5) cryogenic diagnostics operation.

Copyright © 2012 by the respective authors — cc Creative Commons Attribution 3.0 (CC BY 3.0)

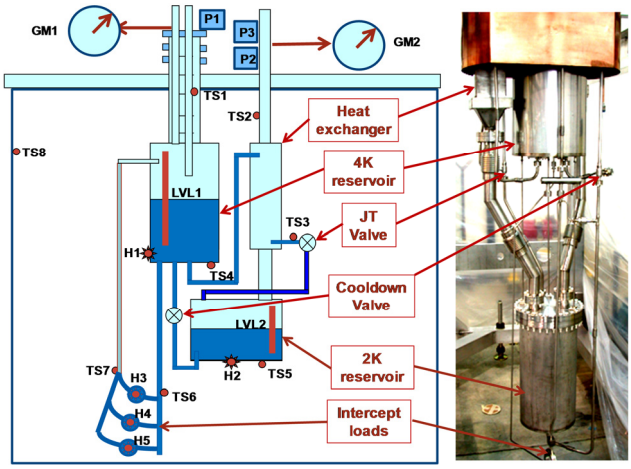

Figure 3: 4K/2K test unit with schematic and test diagnostics including temperature sensors (TS), variable heaters (H), gas meters (GM), pressure sensors (P) and level probes (LVL) and the actual unit as assembled prior to first cold test.

Alignment

A cavity alignment of ±0.5mm is specified. The alignment is done using a combination of Wire Position Monitor (WPM)[5] sensors and optical targets. Before final treatment of the cavity a WPM bracket is attached to the upstream and downstream cavity beam tube. The WPM holders on the bracket are indexed to the cavity center using beam tube reference targets. Each bracket is equipped with two WPM holders one right and one left of the beam center and two optical targets. The cavity is assembled in the clean room to form a hermetically sealed unit then assembled into the cold mass and supported from the lid resting on an assembly frame with for and aft features replicating the beam port and WPM and optical target positions. After the cold mass is inserted into the tank the support towers are adjusted using WPM and optical targets as reference to bring the cold mass on line. Later after cooldown and full thermalization the support towers are re-adjusted to final position.

Developments

Power coupler assembly mock-up: The alignment strategy requires that the cold mass be allowed to move during warm-up and cooldown without undo stress on components. Specifically the power couplers and warm-cold transition sections need sufficient flexibility. The coupler is flexibible through transition bellows and an internal universal coupling. An exoskeleton gymbal has been designed to allow the warm and cold end of the coupler to move while maintaining the concentricity of the inner to outer conductor and reduce stress build-up in the coupler windows. This gimbal was tested in a mock-up of the cavity and tank wall geometry. The mock-up is also useful to help establish the jigs and fixtures required to intall the warm- end of the coupler through the outer side wall.

Scissor tuner mock-up: A spare scissor tuner assembly has been loaned from J-Lab. A mock-up of the cavity tuning geometry is used to test the tuner using a mechanical spring with a force loading of 4500N/mm comparable to that of the cavity. The ISAC-II rotary servo motor with ball screw is being used to drive the tuner. The mock-up is useful in benchmarking the tuner motor under the typical loads and to test the rate, response and backlash in the mechanism (Fig. 4).

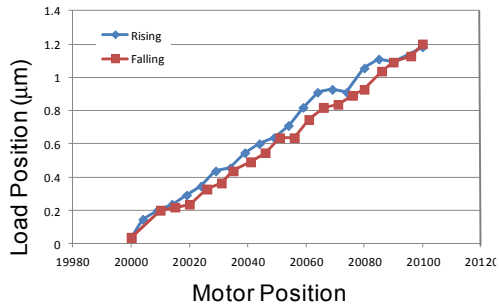

Figure 4: Correlation of mock cavity length with motor position for 1 micron cycling.

STATUS

The tank and lid are being manufactured by a local shop. The strongback and strut supports are being fabricated at TRIUMF. The cavity is being fabricated at PAVAC. A 7-cell replica cavity in copper has been fabricated and is being used for HOM studies. The first Nb cavity inner cells are nearing completion with coupler and tuner end groups to follow. Two 50kW couplers are being conditioned in a dedicated waveguide box station. The 4K/2K test stand will be tested first without MLI to check for cold leaks and function of diagnostics then wrapped in MLI for performance tests. The cold mu-metal has been designed and will be manufactured at Amuneal. The scissor tuner will be ordered from Incodema pending completion of performance tests at TRIUMF. The LN2 shield is in fabrication at TRIUMF. The warm-cold beam pipe transition section with HOM dampers is undergoing final studies to determine placement of HOM diagnostics.

REFERENCES

[1] S. Koscielniak, et al., `ARIEL Superconducting Electron Linac', these proceedings.
[2] R.K. Bhandari, et al, `Rare Ion Beam (RIB) Facility at VECC : Present and Future', IPAC11, San Sebastian, 2011.
[3] R.E. Laxdal, et al, `Operating Experience of the 20 MV Upgrade Linac', Linac10, Tsukuba, Sept. 2010.
[4] R.E. Laxdal, `Design Considerations for the e-Linac Cryogenic System', TRI-DN-11-04, internal TRIUMF document, 2011.
[5] W.R. Rawnsley, et al., `A Wire Position Monitor System for the ISAC-II Cryomodule Components Alignment', LINAC04, Lubeck, 2004.

Copyright © 2012 by the respective authors — cc Creative Commons Attribution 3.0 (CC BY 3.0)

THE UPGRADED ARGONNE WAKEFIELD ACCELERATOR FACILITY (AWA): A TEST-BED FOR THE DEVELOPMENT OF HIGH GRADIENT ACCELERATING STRUCTURES AND WAKEFIELD MEASUREMENTS*

M.E. Conde#, D.S. Doran, W. Gai, R. Konecny, W. Liu, J.G. Power, Z. Yusof,
ANL, Argonne, IL 60439, U.S.A.
S. Antipov, C. Jing, Euclid Techlabs LLC, Solon OH 44139, U.S.A.
E. Wisniewski, IIT, Chicago IL 60616, U.S.A.

Abstract

Electron beam driven wakefield acceleration is a bona fide path to reach high gradient acceleration of electrons and positrons. With the goal of demonstrating the feasibility of this concept with realistic parameters, well beyond a proof-of-principle scenario, the AWA Facility is currently undergoing a major upgrade that will enable it to achieve accelerating gradients of hundreds of MV/m and energy gains on the order of 100 MeV per structure. A key aspect of the studies and experiments carried out at the AWA facility is the use of relatively short RF pulses (15 – 25 ns), which is believed to mitigate the risk of breakdown and structure damage. The upgraded facility will utilize long trains of high charge electron bunches to drive wakefields in the microwave range of frequencies (8 to 26 GHz), generating RF pulses with GW power levels.

AWA FACILITY

The mission of the Argonne Wakefield Accelerator Facility (AWA) is to develop technology for future accelerator facilities. The AWA facility has been used to study and develop new types of accelerating structures based on electron beam driven wakefields. In order to carry out these studies, the facility employs a photocathode RF gun capable of generating electron beams with high bunch charges and short bunch lengths. This high intensity beam is used to excite wakefields in the structures under investigation.

The facility is also used to investigate the generation and propagation of high brightness electron beams, and to develop novel electron beam diagnostics.

The AWA high intensity electron beam is generated by a photocathode RF gun, operating at 1.3 GHz. This one-and-a-half cell gun typically runs with 12 MW of input power, which generates an 80 MV/m electric field on its Magnesium photocathode surface. A 1.3 GHz linac structure increases the electron beam energy, from the 8 MeV produced by the RF gun, to 15 MeV. The linac is an iris loaded standing-wave structure operating in the $\pi/2$ mode with an average accelerating gradient of 7 MV/m; it has large diameter irises to minimize the undesirable wakefields generated by the passage of high charge electron bunches.

The charge of the electron bunches can be easily varied from 1 to 100 nC, with bunch lengths of 2 – 2.5 mm rms, and normalized emittances of 3 to 100 π mm mrad.

The AWA laser system consists of a Spectra Physics Tsunami oscillator followed by a Spitfire regenerative amplifier and two Ti:Sapphire amplifiers (TSA 50). It produces 1.5 mJ pulses at 248 nm, with a pulse length of 2 to 8 ps FWHM and a repetition rate of up to 10 pps. A final KrF Excimer amplifier is optionally used to increase the energy per pulse to 15 mJ.

The generation of electron bunch trains (presently up to 16 bunches) requires each laser pulse to be divided by means of beam splitters into a laser pulse train. The charge in each electron bunch is determined by the energy in each laser pulse and the quantum efficiency of the photocathode material. Typically, single bunches of 100 nC can be produced (with a maximum of 150 nC occasionally reached).

WAKEFIELD ACCELERATION

The use of electron beam driven wakefields to achieve high gradient acceleration has received considerable attention. It offers the advantage of using a relativistic beam to transport the energy to the accelerating structures, decreasing the difficulties of generating and distributing RF power by conventional means; wakefields naturally constitute RF pulses that are of short duration and high peak intensity [1].

Research at the AWA facility has been exploring various types of wakefield structures, including photonic band gap structures, metallic iris loaded structures, and also more exotic schemes using metamaterials. The main focus of the facility, however, has clearly been the development of dielectric loaded structures. They offer the advantage of simple geometry and easy fabrication with accelerating properties that compare favourably with conventional iris loaded metallic structures: the axial electric field is uniform across the transverse cross section of cylindrical structures, and the uniform cross section of the structures presents no geometric features to cause field enhancement. The damping of the undesirable deflecting dipole modes seems to be more easily accomplished in dielectric loaded structures as well; planned experiments will explore the use of longitudinal slots on the metallic outer shell of dielectric structures, as a possible scheme to damp dipole modes. Dielectric structures also hold the promise of withstanding higher electric fields without material breakdown. A significant advantage offered by wakefield structures, in comparison

*Work supported by the U.S. Department of Energy under contract No. DE-AC02-06CH11357.
#conde@anl.gov

Copyright © 2012 by the respective authors — cc Creative Commons Attribution 3.0 (CC BY 3.0)

with other wakefield schemes, is the ability to accelerate positron bunches or electron bunches in basically identical fashion.

AWA FACILITY UPGRADES

The AWA Facility has several major upgrades presently underway, which will considerably enhance its capabilities.

A new one-and-a-half cell RF gun (Fig.1) has been commissioned, and it will replace the existing RF gun as the source of drive bunches. The new RF gun operates with a Cesium Telluride photocathode, and thus, due to the higher quantum efficiency of Cs_2Te, it will be able to generate longer bunch trains with high charge per bunch. We plan to generate trains with up to 32 electron bunches, each separated by one L-band RF period, and with up to 100 nC per bunch. (It should be noted that the two upper limits, i.e. 32 bunches and 100 nC per bunch, cannot be reached simultaneously, since this would load the accelerating fields in the RF gun to an unacceptable level.) These longer bunch trains will, of course, generate longer RF pulses when traversing the wakefield structures.

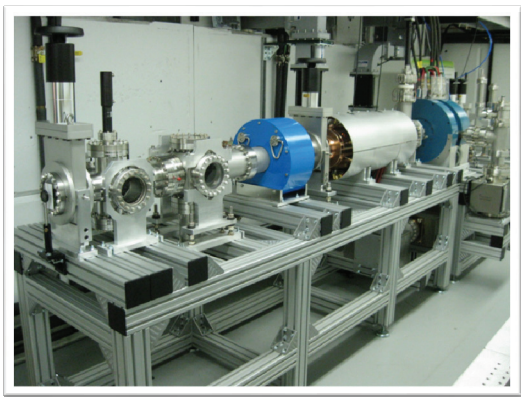

Figure 1: The new AWA RF gun (between the blue solenoids), followed by the first one of the six new linac tanks, another focusing solenoid, and two vacuum crosses for laser beam input and beam profile measurements (YAG screen). A combination of ICT and FCT (Integrating Current Transformer and Fast Current Transformer made by Bergoz) is installed in between the two crosses.

Three additional L-band RF power stations, consisting of one 30 MW Litton klystron and two 25 MW Thales klystrons, and their respective modulators, will power six new linac tanks in the drive beamline. These new klystrons have been commissioned to full power.

The new linacs [2] will be seven-cell standing-wave π mode structures, designed to operate with 10 MW of input power and 11.2 MeV energy gain. Thus, the operation of the six new linac tanks will increase the energy of the beam produced by the drive gun from 8 MeV to 75 MeV. This will, of course, allow significantly more energy to be extracted from the drive beam as it drives wakefields in the structures under test. The higher beam energy also implies a smaller physical transverse emittance of the bunches, facilitating their propagation through smaller aperture wakefield structures, and generating even higher wakefield amplitudes.

The fabrication of the first one of the six new linac tanks has been completed, and good field flatness across the cells has been achieved (Fig.2). It has been installed just downstream of the new RF gun (Fig.1). The fabrication of the remaining five linac tanks is under way, and their final brazing cycles are scheduled for October of 2012.

The commissioning of the new drive gun will free up the existing gun, which will then be used to generate a witness beam to probe the wakefields produced by the drive bunches.

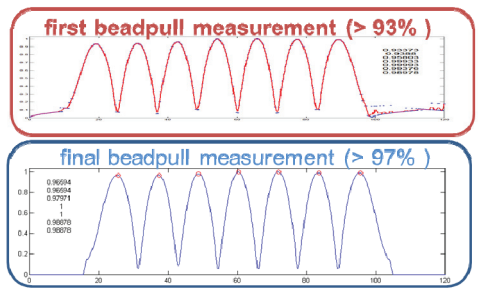

Figure 2: Bead-pulling RF measurement of first linac tank, showing good field balance across the cells.

A new beamline switchyard (Fig. 3) will be constructed to allow concomitant experiments: (a) collinear wakefield acceleration; (b) RF power generation and two beam acceleration; (c) phase space manipulation (emittance exchange, etc); (d) high brightness beam generation; (e) beam diagnostic development. This flexible beamline switchyard will allow a quicker and more efficient transition among several concurrent experimental setups.

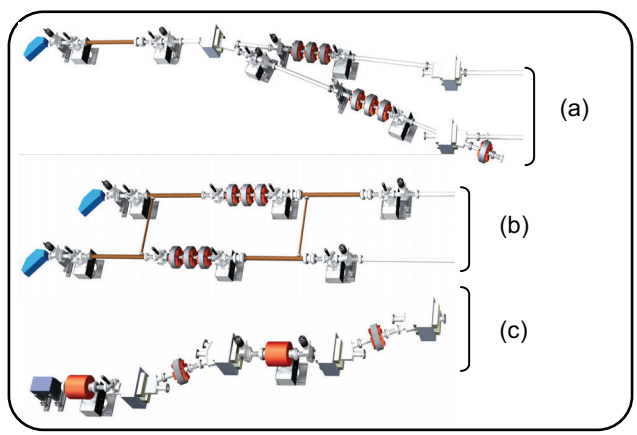

Figure 3: Different legs of the new AWA beamline switchyard will be dedicated to specific types of experiments: (a) collinear wakefield acceleration; (b) two-beam-acceleration and RF power generation; (c) phase space manipulation (emittance exchange) and beam diagnostic development.

Copyright © 2012 by the respective authors — cc Creative Commons Attribution 3.0 (CC BY 3.0)

In order to house the upgraded AWA Facility, the present bunker has been extended beyond the perimeter of the existing building, into a new annex. Figure 4 shows the interior and the roof of the expanded bunker.

(a)

(b)

Figure 4: The expanded AWA bunker: (a) plentiful interior space is now available for the installation of the new linac tanks and new beamline switchyard; (b) new RF power circulators and waveguides have been installed on the roof of the expanded bunker, ready to connect the new klystrons to the new linac tanks.

CONCLUDING REMARKS

In the past few years AWA has demonstrated high gradient fields (100 MV/m) in dielectric based wakefield structures [3]. Generation and extraction of RF power using beam driven dielectric structures has also been demonstrated [4 - 6]. Several experiments exploring new designs and new features of dielectric based wakefield structures will be conducted in the near future.

Concomitantly, AWA is undergoing upgrades that will enhance its capabilities. These upgrades will allow the generation of longer bunch trains with high charge per bunch. The higher beam energy will make it possible to excite high gradient wakefields in longer accelerating structures, thus generating hundreds of MV/m over meter scale structures. The second RF gun will provide "witness" bunches to probe the wakefields, demonstrating high gradient acceleration.

Once the upgrades are completed, the goal is to achieve accelerating gradients on the order of 0.5 GV/m in structures with approximately 3 mm apertures. The generation and extraction of RF pulses with power levels on the order of GW shall also be demonstrated. As an example, Table 1 shows the main parameters of a pair of structures that will be tested as soon as the upgraded AWA Facility becomes available. The actual hardware is seen in Fig. 5.

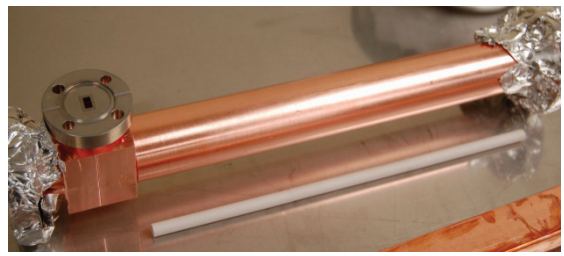

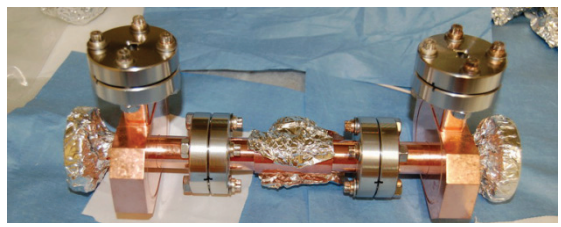

Figure 5: 26 GHz power extractor and accelerating structure.

Table 1: 26 GHz TBA Structures

Decelerating structure	**Accelerating structure**
ID / OD / length (mm) 7.0 / 9.068 / 300	ID / OD / length (mm) 3.0 / 5.025 / 300
Dielectric constant 6.64	Dielectric constant 9.70
Group velocity 0.254 c	Group velocity 0.111 c
R/Q 9.79 kΩ/m	R/Q 21.98 kΩ/m
RF Power (50 nC) 1.33 GW	R_{sh} 50.44 MΩ/m
Peak gradient 167 MV/m	E_0 (1.26 GW) 316 MV/m
Energy loss 20.5 MeV	E_{loaded} (1.26 GW) **267 MV/m**

REFERENCES

[1] W.Gai et al, "Short-pulse dielectric two-beam acceleration," J. Plasma Physics, p. 1, Feb. 2012.

[2] J.G. Power et al, "Upgrade of the Drive Linac for the AWA Facility Dielectric Two-Beam Accelerator," in proceedings of IPAC 2010, Kyoto, May 2010.

[3] M. Conde et al., "High Gradient Excitation and RF Power Generation using Dielectric Loaded Wakefield Structures," in proceedings of LINAC'08, Victoria, September 2008.

[4] F. Gao et al., "Design and Testing of a 7.8 GHz Power Extractor Using a Cylindrical Dielectric-loaded Waveguide," Physical Review ST Accel. Beams 11, 041301(2008).

[5] F. Gao et al., "Multi-Nanosecond High Power Pulse Generation at 7.8GHz with a Dielectric-loaded Power Extractor," IEEE Transactions on Nuclear Science **56** (3), p. 1492 – 1497, (2009).

[6] C. Jing et al., "The First Experiment of a 26 GHz Dielectric Based Wakefield Power Extractor," in proceedings of IPAC 2010, Kyoto, May 2010.

Copyright © 2012 by the respective authors — cc Creative Commons Attribution 3.0 (CC BY 3.0)

SIMULATION STUDY ON THE LONGITUDINAL BUNCH SHAPE MEASUREMENT BY RF CHOPPER AT J-PARC LINAC

T. Maruta*, J-PARC center, Japan Atomic Energy Agency, Tokai, Ibaraki, Japan
M. Ikegami, High Energy Accelerator Research Organization, Tsukuba, Ibaraki, Japan

Abstract

We propose to measure the longitudinal rms beam size by existing apparatuses in MEBT1 at J-PARC linac. The RF chopper cavity horizontally deflects beam particles at the frequency of 324 MHz, which is the same frequency as other accelerator cavities. By setting an adequate driving phase of the chopper, a horizontal deflection is proportional to relative phase difference from the centroid of a beam bunch. Then, the deflected beam distribution is measured by a wire scanner monitor. It is also possible to measure the longitudinal rms emittance by varying the amplitude of a buncher upstream. In this paper, we confirm the feasibility of the measurement scheme with particle simulation.

INTRODUCTION

The J-PARC linac is comprised from a 50 keV negative hydrogen (H^-) ion source (IS), a 3 MeV Radio Frequency Quadrupole (RFQ), a 50 MeV Drift Tube Linac (DTL), and a 181 MeV Separate-type DTL (SDTL). There is a medium energy beam transport section (MEBT1) between the RFQ and DTL. We place an RF chopper system in the middle of MEBT1 to shape a macro pulse configuration in accordance with RF frequency of following 3 GeV rapid cycling synchrotron (RCS).

In the J-PARC linac, a beam intensity upgrade project is currently underway. The project will replace the front end part (IS to RFQ) for the extension of the peak current to 50 mA in the next summer. A simulation study indicates that the longitudinal beam emittance in the 50 mA operation is 20 % larger than present one. The beam rejection power of the RF chopper system is inversely correlated to a beam width in phase direction, it motivated us to consider a reinforcement of the chopper. It is important to understand the current beam width for an inquest of the reinforcement. However, we have no monitors for the beam width measurement, and moreover, there is no space to install an additional monitors in MEBT1.

We devise a beam width measurement method only with an existing apparatus in MEBT1 to overcome the situation. Then we evaluate the feasibility with a three dimensional particle-in-cell code IMPACT [1].

MEBT1

MEBT1 is a 3 m long transport line between RFQ and DTL as shown in Fig. 1. There are two major issues. One is a matching of the beam to the DTL acceptance in both longitudinal and transverse phase space by eight quadrupole magnets and two buncher cavities while transferring the beam to DTL. To measure the beam qualitatively, we place beam current monitors (CT), beam position monitors (BPM) and wire scanner monitors (WSM) [2] throughout MEBT1. The other issue is a shaping of a macro pulse in accordance with the RF frequency of following RCS. The RF chopper system is involved in the shaping. It is comprised from an RF chopper cavity and a scraper which is located at 0.72 m downstream from the cavity. Unnecessary beam bunches are horizontally (x) deflected by the cavity and then they hit to the scraper.

RF Chopper Cavity

We employ an RF deflector (RFD) for beam chopping [3]. The RFD is operated in a TE_{11}-like mode with the frequency of 324 MHz, which is same as RFQ and DTL. The deflection angle of a RF gap is 6 mrad at the electric field of 1.6 MV/m of which an RF power is 22 kW. There are two RF gaps in the cavity at intervals of $3\beta\lambda$, where β is the velocity of beam normalized by the speed of light and λ is RF wave length. The two RF gaps are currently connected in series via a coaxial tube with length of 2λ to supply an RF from a single semiconductor amplifier. In this summer, we modify the configuration to individually supply an RF to each RF gap by introduction of an additional amplifier. It enable us to tune an asynchronous phase and an amplitude of each RF gap individually. The current amplifier stably supply an RF power up to 35 kW which corresponds a gap field of 2.0 MV/m. Moreover, we have a plan to upgrade the amplifier to 60 kW in the next summer.

MEASUREMENT METHOD

In the measurement, we use the RF chopper cavity, the upstream buncher and a WSM downstream of the chopper cavity. The measurement is comprised of two steps. In the first step, we measure the beam width in phase direction by the chopper cavity and the WSM. Then, the second step measures a longitudinal emittance and a Courant-Snyder parameter by adding the buncher to the beam width measurement. This measurement is similar to a transverse emittance measurement so-called "Q-scan" [4] in principle.

Beam Width in Phase Direction

In the nominal operation of J-PARC linac, the chopper is tuned to give a maximum deflection to a beam bunch. It is equivalent that we adjust the RF to be maximum when a beam bunch arrives at the middle of an RF gap as shown in Fig. 2(a). The integrated RF of a beam particle gradually attenuates in accordance with a phase difference from the

* tmaruta@post.j-parc.jp

Copyright © 2012 by the respective authors — cc Creative Commons Attribution 3.0 (CC BY 3.0)

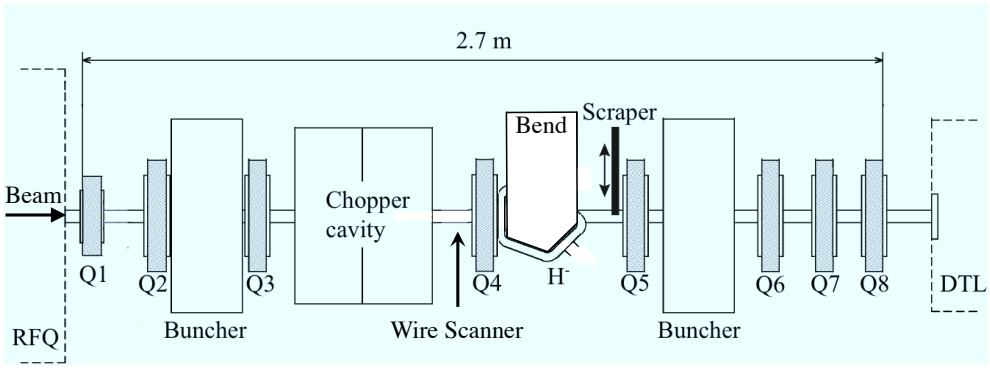

Figure 1: Layout of MEBT1. We use the chopper cavity, the upstream buncher cavity and the wire scanner between the chopper cavity and Q4 for the measurement.

centroid of a beam bunch. The earlier and later particles than the centroid are deflected in same amount if the phase deference is same. Consequently, it is hard to extract the beam width in phase direction from an x plane measurement.

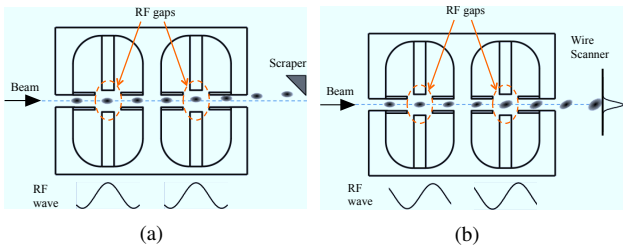

Figure 2: The RF setting and a beam bunch behavior — (a) In the nominal operation (b) In the measurement.

If we set the RF phase shifted by $\pi/2$ from the nominal operation, the centroid of a beam bunch is not deflected at an RF gap, because the centroid passes through a gap at zero-crossing. Whereas, particles away from the centroid are deflected in accordance with the relative phase difference from the centroid ($\Delta\phi$). Consequently, a beam bunch rotates on the $x' - \phi$ phase space as shown in Fig. 2(b). If the transverse emittance is negligibly small, the x position after the deflection is a function of $\Delta\phi$. We can obtain a beam distribution in phase direction by the measurement of the x distribution downstream of the chopper. Unfortunately, the beam is a finite transverse emittance. Instead we obtain a root-mean-square (rms) beam width (σ_ϕ).The deflected rms beam width on the x plane at the distance of D is

$$< (x + D\theta(\Delta\phi))^2 > = < x^2 > + D^2 < (\theta(\Delta\phi))^2 >, \quad (1)$$

where $< x^2 >$ is square of rms beam size without deflection and θ is deflection angle of each particle. This equation shows that we can obtain the σ_ϕ from the measurement of x distribution with and without the deflection.

Originally, this method is considered by Prof. Naito from KEK [5]. Although it is important to adjust the asynchronous phase of both RF gaps to a zero-crossing, the ambiguity of phase difference due to the series connection of RF gaps is an obstacle for an accurate measurement. The introduction of the additional amplifier in this summer resolves the ambiguity. Consequently, it is possible to conduct the measurement.

Emittance

The σ-matrix at the chopper (σ^C) is expressed from the σ-matrix at the upstream buncher (σ^B) and the transfer matrix between them (R) as $\sigma^C = R\sigma^B R^T$. The element σ_{55}, which is equivalent to the square of σ_ϕ, σ^C_{55}, is written as

$$\sigma^C_{55} = (\sigma^C_\phi)^2 = \varepsilon \left(\beta^B R^2_{55} - 2\alpha^B R_{55}R_{56} + \gamma^B R^2_{56}\right), \quad (2)$$

where ε is the emittance, and α^B, β^B and γ^B are Courant-Snyder parameters at the buncher, respectively. The lattice is RF gap + Quadrupole + Drift. The matrix elements without impulse from the space charge forces are $R_{55} = 1 + kL/\beta\gamma^3$ and $R_{56} = L/\gamma^2$, where k is an electric field of the buncher and L is the length of the lattice. Substituting them into Eq. 2 and deforming it with focusing on k, Eq. 2 is expressed as

$$(\sigma^C_\phi)^2 = \frac{\varepsilon\beta^B L^2}{\beta^2\gamma^6}\left(k + \frac{\beta\gamma^3}{L} - \frac{\alpha^B}{\beta^B}\beta\gamma\right)^2 + \varepsilon^2\frac{L}{\gamma^2}\frac{1}{\varepsilon\beta^B}. \quad (3)$$

Therefore, $(\sigma^C_\phi)^2$ is the second order polynominal function of k, and the minimum width is equivalent to the square of $\varepsilon^2 L/\gamma^2\varepsilon\beta^B$. Since $\varepsilon\beta^B$ can be calculated from the coefficient of k^2, it is possible to extract the ε from the correlation of the σ_ϕ and the k. The Courant-Snyder parameter also evaluate from Eq. 2. The R elements vary when we change k. Measurements at three k result three equations in three unknowns.

SIMULATION

We use a three dimensional particle-in-cell code, IMPACT, for an evaluation of the feasibility. In the simulation, the initial particles are launched at the entrance of MEBT1. Then, we track these particles to the WSM

Copyright © 2012 by the respective authors — cc Creative Commons Attribution 3.0 (CC BY 3.0)

which we use in the measurement. The output distribution from PARMTEQM [6] is taken as the initial distribution. The electro-magnetic field inside the chopper cavity is calculated with a finite element method (FEM) code, Micro Wave Studio (MWS) [7]. We treat the RFDs as two single cavity in MWS and obtain an electric field distribution at the frequency of 324 MHz.

We measure the deflection at the several electric fields to confirm the reproducibility of a simulation with the MWS field distribution. The horizontal beam distribution at the electric field of 0, 0.33, 0.50, 0.95 and 2.0 MV/m are measured by the WSM. Here we define the deflection as the displacement of the centroid of the distribution from the centroid without excitation. Figure 3 shows the comparison of the measured deflection with the simulation. The simulated deflection shows a linear correlation to the electric field. The measurements are well gathered around the simulation in the region less than 1 MV/m. Concerning to the 2.0 MV/m, we observe a decline of a beam current at the chopper downstream. It is supposed that a part of a beam bunch hits to an aperture inside the chopper and it becomes an obstacle for the calculation of the deflection properly.

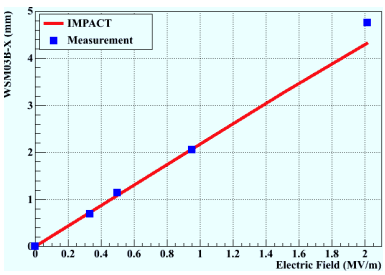

Figure 3: Correlation of the chopper electric field and the deflection at the WSM.

Figure 4(a) shows the σ_ϕ at each RF gap as a function of the buncher E_0TL. Red points are σ_ϕ at the upstream gap (#1) and blue points are that at the downstream (#2). Both distributions have a minimum σ_ϕ, and the E_0TL of minimum σ_ϕ at the gap #2 is lower than the gap #1. It is consistent that the k at minimum σ_ϕ is inversely proportional to L shown in Eq. 3. The σ_ϕ of the gap #2 is minimum at E_0TL of 0.19 MV. Since the maximum E_0TL is currently 0.17 MV, we may need to upgrade the semiconductor amplifier of the buncher to observe the minimum σ_ϕ.

Next, we calculate the boundary condition on the $\phi - E$ phase space at the buncher. From the measurement in Fig. 4(a), we extract the boundary of the ellipse at the buncher by using the R. We use a Trace3D [8] for the calculation of the R for each E_0TL. Figure 4(b) shows the boundaries and actual ellipse by IMPACT. Here we shows the boundaries at the buncher E_0TL of 0, 0.085 and 0.17 MV. Since an emittance growth is not taken into account to the Trace3D, the reproducibility of the boundaries becomes worse as the emittance growth being large. The calculated boundaries are close to the ellipse well. The effect of the emittance growth between the buncher to the chopper is supposed to be negligibly small. We consider to upgrade the semiconductor amplifier of the buncher currently. After the upgrade,It is expected to observe the minimum σ_ϕ in Fig.3 and to give more tight constraint for the ellipse in Fig. 4(a).

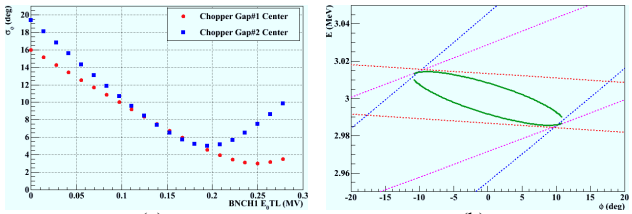

Figure 4: The simulation results — (a) σ_ϕ at both RF gaps of the chopper as a function of the buncher E_0TL (b) The ellipse and the boundaries obtained by σ_ϕ^C measurement. The dotted lines are the boundary at 0 (red), 0.085 (magenta) and 0.17 MV (blue), respectively.

SUMMARY AND FUTURE PROSPECTS

Because of the introduction of another semiconductor amplifier for the chopper, it is possible to measure the beam width in phase direction. Moreover, we also measure longitudinal beam emittance and Courant-Snyder parameters by adding the flexibility of the buncher amplitude to the beam width measurement. The data-taking is scheduled at the beginning of October. We confirm the feasibility of the measurement and evaluate the longitudinal beam profile.

REFERENCES

[1] J. Qiang, R.D. Ryne, S. Habib, V. Decyk, "An object-oriented parallel particle-in-cell code for beam dynamics simulation in linear accelerators", J. Comput. Phys. 163 (2000) 434-451.

[2] A. Miura, et al., "Operational Performance of Wire Scanner Monitor in J-PARC Linac", Proceedings of the 1st International Particle Accelerator Conference (IPAC10), Kyoto, Japan, May 23-28, 2010. pp. 1008-1010.

[3] S. Fu and T. Kato, "RF-chopper for the JHF proton linac", Nucl. Instr. and Meth. A 440 (2000) 296-306.

[4] A.W. Chao and M. Tigner ed., "Handbook of Accelerator Physics and Engineering".

[5] F. Naito, "Longitudinal Bunch Shape Monitor Using the Beam Chopper of the J-PARC", Proceedings of the 22nd International Linear Accelerator Conference (LINAC2004), Lübeck, Germany, August 16-20, 2004. pp.806-808

[6] K.R. Crandall et al., "RFQ design codes", LA-UR-96-1836 Revised December 7, 2005, Los Alamos National Laboratory (1996).

[7] Y. Kondo, et al., "Simulation Study of the RF Chopper", Proceedings of the 25th International Linear Accelerator Conference (LINAC10), Tsukuba, Japan, September 12-17, 2010. pp. 911-913.

[8] http://laacg1.lanl.gov/laacg/services/download_trace.phtml.

Copyright © 2012 by the respective authors — cc Creative Commons Attribution 3.0 (CC BY 3.0)

DESIGN OF MEBT FOR THE PROJECT X INJECTOR EXPERIMENT AT FERMILAB

A. Shemyakin#, C. Baffes, A. Chen, Y. Eidelman, B. Hanna, V. Lebedev, S. Nagaitsev, J.-F. Ostiguy, R. Pasquinelli, D. Peterson, L. Prost, G. Saewert, V. Scarpine, B. Shteynas, N. Solyak, D. Sun, M. Wendt, V. Yakovlev, Fermilab*, Batavia, IL 60510, USA
T. Tang, SLAC, Menlo Park, CA 94025

Abstract

The Project X Injector Experiment (PXIE) [1], a test bed for the Project X front end, will be completed at Fermilab at FY12-16. One of the challenging goals of PXIE is demonstration of the capability to form a 1 mA H- beam with an arbitrary selected bunch pattern from the initially 5 mA 162.5 MHz CW train. The bunch selection will be made in the Medium Energy Beam Transport (MEBT) at 2.1 MeV by diverting undesired bunches to an absorber. This paper presents the MEBT scheme and describes development of its elements, including the kickers and absorber.

REQUIREMENTS

The PXIE MEBT will be a ~10 m beam line between RFQ and the first Half-Wave Resonator cryomodule (HWR). It should form the required bunch pattern, match the optical functions between RFQ and SRF, include tools to measure properties of the beam coming out of RFQ and coming to SRF, and clean transverse halo particles while transporting the bunches selected for the following acceleration with a low emittance dilution and a low beam loss. The main MEBT requirements are listed in Table 1.

Table 1. The main MEBT functional requirements

Parameter	Value	Unit
Beam kinetic energy	2.1 +/-1%	**MeV**
Input frequency of bunches	162.5	MHz
Nominal input beam current	5	mA
Beam current operating range	1-10	mA
Nominal output beam current	1	mA
Relative residual charge of removed bunches	$< 10^{-4}$	
Beam loss of pass through bunches	< 5%	
Nominal transverse emittance	< 0.27	μm
Nominal longitudinal emittance	0.8	eV-μs
Relative emittances increase	<10%	

FOCUSING SCHEME

Transverse focusing in the MEBT is provided mainly by equidistantly placed quadrupole triplets (Fig.1); the only exception is two doublets at the MEBT upstream end. Below the regions between neighboring triplets or doublets are referred to as MEBT sections. These sections are represented in Fig. 2 by rectangles color-coded according to their main function. The regular period is 1140 mm, which leaves 650 mm (flange-to-flange) space for equipment (350 mm in the section #0).

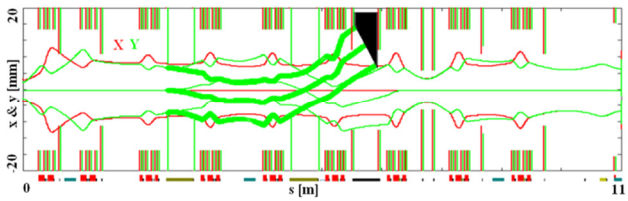

Figure 1: Scheme of MEBT optics [2] and the beam envelope. The thin lines are the central trajectory and 3σ envelope (ε_{rms_n}=0.25 mm mrad) of the passing beam, and the thick lines are the Y envelope of the chopped-out beam. Red- quadrupoles, blue- bunching cavities.

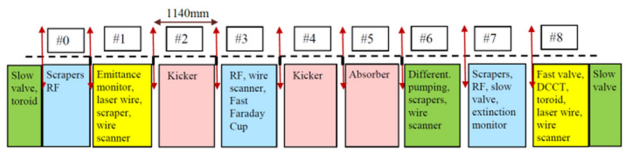

Figure 2: MEBT structure. Red - chopping system, blue- RF, yellow – diagnostics, green – vacuum.

Longitudinally the beam is focused (Fig.3) by three bunching cavities (Fig.4).

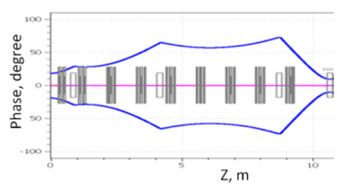

Figure 3: 3-σ bunch length through MEBT.

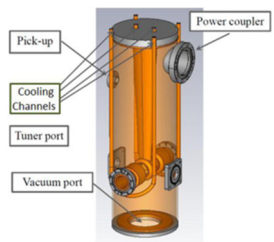

Figure 4: Conceptual design of the MEBT bunching cavity.

CHOPPING SYSTEM

The undesired beam bunches will be removed in the MEBT by a chopping system consisting of two identical kickers separated by 180° transverse phase advance and an absorber at 90° from the last kicker. In the broadband, travelling-wave kickers [3], the transverse electric field propagates through their structures with the phase velocity equal to the speed of H- ions, 20 mm/ns. Depending on polarity, bunches are either kicked toward the absorber surface or on a pass through path. In either

shemyakin@fnal.gov
* Operated by Fermi Research Alliance, LLC, under Contract No. DE-AC02-07CH11359 with the United States Department of Energy

Copyright © 2012 by the respective authors — cc Creative Commons Attribution 3.0 (CC BY 3.0)

case, the voltage on opposites plates is +/-250V with respect to ground. The gap between the kicker plates is 16 mm. Protection electrodes with 13 mm gap are installed on both sides of each kicker. To prevent extensive irradiation resulting from beam mismatch, an elevated electrode current will trigger a beam interruption. Because of critical importance of the kicker performance, presently two versions of the kicker are been developed.

In the first version having 50 Ohm characteristic impedance of the kicker structure, the beam is deflected by voltage applied to planar electrodes connected in vacuum by coaxial cables with the length providing necessary delays (Fig. 5). Each half of the ~0.5 m kicker has 25 copper plates with dimensions of 14.6 x 50 x 1 mm. The power loss induced by the electromagnetic wave (~100 W) and beam (~40W) is removed through the Teflon-insulated cables clamped to a water-cooled structure.

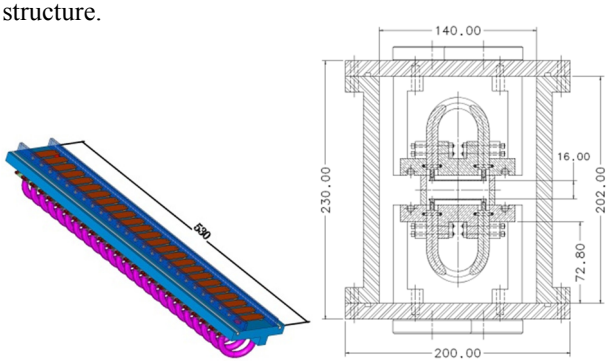

Figure 5: Mechanical schematic of the 50-Ohm kicker structure and the cross section of the kicker assembly.

The structure elements were simulated; a short mock-up was successfully measured; and presently a full-scale prototype is being designed.

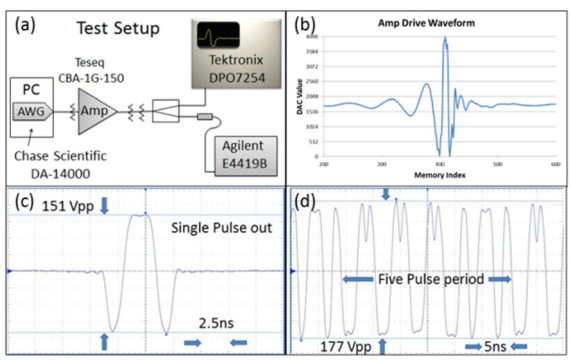

Figure 6: Test of the CBA 1G-150 amplifier with pre-distortion. (a) scheme of the test; (b) pre-distorted input signal and (c) corresponding output signal for a single pulse; (d) output for a CW pattern, corresponding to removal of four consecutive bunches followed by a one-bunch passage.

The kicker will be driven by a 1-kW linear amplifier. To decrease the lower frequency content of the output signal, the 6.15ns pulse affecting a single bunch is formed as shown in Fig.6c. Effects of a significant low frequency phase distortion in the commercially available amplifiers will be corrected by pre-distorting the driving signal generated according to an algorithm that has been successfully tested with a similar amplifier [4] of lower (150W) power (Fig.6).

The second version of the kicker has 200 Ohm impedance and consists of two helical structures (Fig. 7). Each helix is a flat wire wound with the 8.5mm helix pitch around a 28.6 mm OD copper grounded tube. The wire is suspended 4.8 mm above the tube surface by four ceramic spacers. The deflecting field is formed by flat copper 5.6x20x0.5 mm electrodes soldered to each turn of the helix.

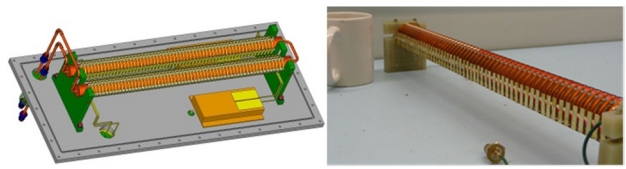

Figure 7: Mechanical drawing of 200 Ohm dual-helix kicker and photo of a single 200 Ohm helix prototype.

Simulations of the kicker structure agree well with prototype measurements (Fig. 8). Distortion during the propagation through the 200 Ohm helix is within specifications.

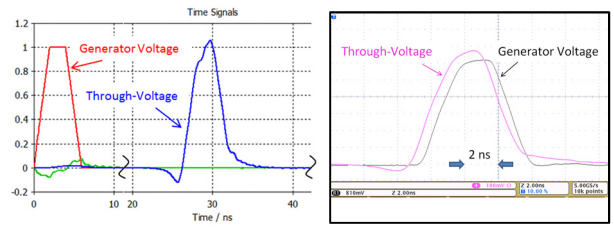

Figure 8: Simulation results of the helix kicker (left) and the prototype response (right). The traces at the right plot are time shifted.

The 200 Ohm kickers are intended to be driven by broadband, DC coupled switches in the push-pull configuration, which are under development [3].

The MEBT absorber should withstand irradiation by a 21 kW H- beam with the nominal rms beam radius of ~2mm. The design shown in Fig. 9 ([5]) addresses concerns about the heat load and resulting mechanical stresses as well as possible blistering issues.

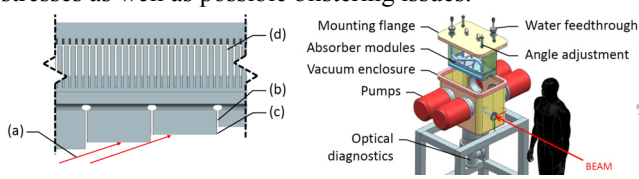

Figure 9: Conceptual design of the MEBT absorber. Left: side view of absorber showing (a) beam incident on surface, (b) axial stress relief slits, (c) shadowing step increment (magnitude exaggerated), (d) 300µm wide by 1mm pitch water cooling channels. Horizontal scale exaggerated. Right: exploded view.

To decrease the power density, the beam is directed to the 40-cm long absorber at a 29mrad grazing angle. The

Copyright © 2012 by the respective authors — cc Creative Commons Attribution 3.0 (CC BY 3.0)

absorber is made of the molybdenum alloy TZM and is cooled by water flowing through transverse micro-channels. The axial stress is relieved by transverse slits. Thermal and stress analysis showed feasibility of the design. A 10-cm long prototype is being manufactured, and its thermal properties will be tested with an electron beam.

OTHER SUBSYSTEMS

Several other subsystems are at different stages of development: quadrupoles, scrapers, vacuum system, and diagnostics.

The triplet assembly, which will consist of a central (larger) and two smaller quadrupoles, a pair of dipole correctors, and a button BPM mounted between the quadrupoles, is under technical design.

The scraping system concept assumes installation of 16 scrapers grouped in 4 sets with two X and two Y scarpers per set. Each scraper is an electrically isolated, ~100W-rated plate precisely movable across half of the aperture. The scrapers will be used for several purposes:

1. For beam halo measurements and removal
2. To protect the downstream equipment from beam losses. A high-loss signal from a scraper will trigger turning the beam turn-off.
3. As an axillary beam density distribution diagnostics (in a pulse mode)
4. To form a pencil H- beam for measurements downstream (in a pulse mode)

One pair of scraper sets is to be installed at the beginning of the MEBT to protect the MEBT elements (first of all, kickers), and the second pair is located after the absorber as a protection for cryomodules. The sets in each pair are separated by ~90º of the phase advance.

The vacuum system design is at a conceptual stage. The vacuum requirements are determined by the electron detachment in the H- beam and by the necessity to have a low gas flow into the HWR cryomodule. Obviously, the electron detachment results in a loss of H- beam intensity; an additional restrictive effect is a flux of created neutral hydrogen atoms that may reach the SRF cavities. For the design of the vacuum system, we adopted the requirement of keeping the integral of the pressure over the length of the MEBT to be below $1 \cdot 10^{-6}$ Torr·m, which corresponds to loosing $\sim 10^{-4}$ in the beam intensity and adding an additional ~0.1 W heat load to SRF by the neutrals.

The gas flow from the room-temperature MEBT to the 2K HWR cryomodule causes a gas deposition on the cryogenic surfaces. While there are no exhaustive experiments or a cohesive theory on the subject, there are indications in literature that such coverage at the surface of the cryogenic cavities degrades their performance. On the other hand, the closest analogue, a HWR in the Argonne National lab, successfully operates at the pressure of $5 \cdot 10^{-8}$ Torr immediately upstream of the cryomodule, though with the residual gas composed primarily by water [6]. To be on a safe side, we aim to keep the pressure upstream of PXIE's HWR at or below of $1 \cdot 10^{-9}$ Torr (H_2).

The main source of the vacuum load in the MEBT is expected to be a flow of hydrogen created from recombination of protons at the absorber. The worst scenario of 10 mA average absorber current corresponds to ~1 mTorr·l/s of the hydrogen load. To maintain a high vacuum near the SRF, first, the absorber is placed into a large box with effective pumping speed of 2500 l/s by turbo pumps and, second, the absorber is followed by a differential pumping section (#6 in Fig.2), where the vacuum chambers are separated by a 10mm ID, 200 mm long pipe. The calculated pressure profile is shown in Fig.10. Low particulate vacuum practices will be applied to the portion of the MEBT downstream of the section #6 to prevent degradation of the SRF cavities performance.

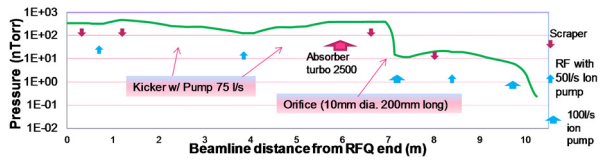

Figure 10: The pressure profile in the MEBT calculated for 10mA beam at the absorber.

The main purpose of two yellow-colored sections in Fig.2, #1 and #8, is to house beam diagnostics. A fully equipped MEBT diagnostics should allow characterizing the beam coming in and out of MEBT as well as its optics. The diagnostics are listed in Fig.2, and their detail description can be found in Ref. [7].

CONCLUSION AND PLANS

The proposed scheme of the MEBT contains all elements required for shaping and characterizing the beam coming to the Project X SRF linac. The extensive test of the MEBT operation is planned to be carried out in PXIE. The FY2013 schedule includes manufacturing and testing prototypes for the absorber, kicker, quadrupoles, and BPM.

ACKNOWLEDGMENT

The authors acknowledge multiple useful discussions of an alternative MEBT scheme with J. Staples.

REFERENCES

[1] S. Holmes et al., Proc. of IPAC'12, New Orleans, USA, May 20 - 25, 2012, THPPP090.
[2] V. Lebedev et al., ibid, THPPP057.
[3] V. Lebedev et al., ibid, WEPPD078.
[4] http://www.teseq.us/com/en/products_solutions/emc_radio_frequency/power_amplifiers/CBA_1G-150_e.pdf
[5] C. Baffes et al., Proc. of IPAC'12, New Orleans, USA, May 20 - 25, 2012, WEPPD035.
[6] P. Ostroumov, G. Zinkann, private communication, 2012.
[7] V. E. Scarpine et al., Proc. of IPAC'12, New Orleans, USA, May 20 - 25, 2012, MOPPR072.

Copyright © 2012 by the respective authors — cc Creative Commons Attribution 3.0 (CC BY 3.0)

BEAM LOSS MITIGATION IN J-PARC LINAC AFTER THE TOHOKU EARTHQUAKE

M. Ikegami, K. Futatsukawa, Z. Fang, T. Miyao, Y. Liu, KEK/J-PARC, Tokai, Japan
T. Maruta, A. Miura, H. Sako, J. Tamura, G. Wei, JAEA/J-PARC, Tokai, Japan

Abstract

In the course of the beam commissioning of J-PARC linac after nine-month shutdown due to an earthquake, we have experienced beam losses which were not seen before the earthquake. One of the main cause for the beam loss was the irregular RF setting for accelerating cavities to avoid multipactor at one of them, which started to pose difficulty in the nominal operation after the earthquake. In this paper, we discuss the beam loss mitigation effort putting the emphasis on the optimization of the RF setting for SDTL.

INTRODUCTION

We had a magnitude-9.0 earthquake in Tohoku region in Eastern Japan in March 2011. It caused severe damage to J-PARC facilities which forced us to shutdown for nearly nine months [1]. After significant restoration efforts, we started beam operation of J-PARC linac in December 2011 and user operation in January 2012. The linac beam power when we resumed the user operation was 7.2 kW. Then, it is increased to 13.3 kW in March 2012, which is the same as just before the earthquake. While the linac beam operation was restored in terms of the beam power, we have experienced higher beam losses than before the earthquake. Thus, we have been trying to mitigate the beam loss while supporting the user operation. The initial beam start-up in December 2011 and January 2012 was reported in another literature [2]. Therefore, we focus on the beam loss mitigation effort after restoring the user operation in this paper. It should be noted here that the history of residual radiation during the beam commissioning was summarized in the reference [3].

J-PARC linac consists of a 50-keV negative hydrogen ion source, 3-MeV RFQ (Radio Frequency Quadrupole linac), 50-MeV DTL (Drift Tube Linac), and 181-MeV SDTL (Separate-type DTL) [4]. For later reference, we should note here that the SDTL section consists of 30 SDTL tanks with $2\beta\lambda$ inter-tank spacing with β and λ being the particle velocity scaled by the speed of light and the RF wavelength, respectively. Then, each SDTL tank consists of five β-graded cells, and two neighboring SDTL tanks are driven by a klystron.

As reported in reference [2, 3], we experienced significant beam loss at the straight section after SDTL immediately after we resumed the beam operation. A main cause of the beam loss was identified to be insufficient alignment of some of the beam ducts. After conducting urgent realignment of the beam ducts [5], the beam loss was substantially reduced and become significantly less sensitive to the beam steering. However, multipactor of one of SDTL cavity has been gradually worsened and the irregular RF setting we adopted to avoid the multipactor started to cause beam losses.

In this paper, we mainly discuss the method we adopted to circumvent the SDTL multipactor while suppressing the beam losses.

MULTIPACTOR AT AN SDTL CAVITY

As mentioned above, a pair of SDTL tanks are driven by a klystron. The relative RF amplitude and phase of the tank pair are supposed to be kept balanced with the low-level RF control system. However, we noticed just before the resumption of beam operation in December 2011 that the fifth tank pair, or SDTL5, shows some unstable behavior. For this tank pair, one of the tanks tends to have arcing, or presumably multipactor, which makes the balance of RF amplitude and phase easily lost. This unstable behavior arises in a certain range of RF amplitude which contains its design amplitude. Although similar behavior has been noticed for SDTL1 to SDTL6 since before the earthquake, it caused no difficulty in operating with the design tank level [6]. Therefore, we suspect that the multipactor in SDTL5 become severer at the earthquake for some reason to cause practical difficulty in the nominal operation.

As we can avoid the multipactor by adopting higher or lower RF amplitude for SDTL5, we adopt 109 % of the design amplitude in starting the user operation in January 2012. The unstable band in the RF amplitude was widened during the beam operation and forced us to increase the operating amplitude to 116 % later. As of June 2012, we are operate SDTL5 with the same amplitude. However, the unstable region for SDTL5 is still widening gradually and reducing the operational margin.

We don't delve into the details on the multipactor itself in this paper. Instead, we discuss the irregular RF setting for SDTL we adopt to avoid the multipactor, its effect on the beam losses, and the countermeasure for the beam loss we adopted in the beam commissioning. Further detail of the multipactor will be found in the reference [7].

BEAM LOSS MITIGATION WITH IRREGULAR SDTL SETTING

Operation with 109 % Amplitude for SDTL5

In setting the RF amplitude and phase for SDTL tanks after the earthquake, it was required for us to perform the

Copyright © 2012 by the respective authors — cc Creative Commons Attribution 3.0 (CC BY 3.0)

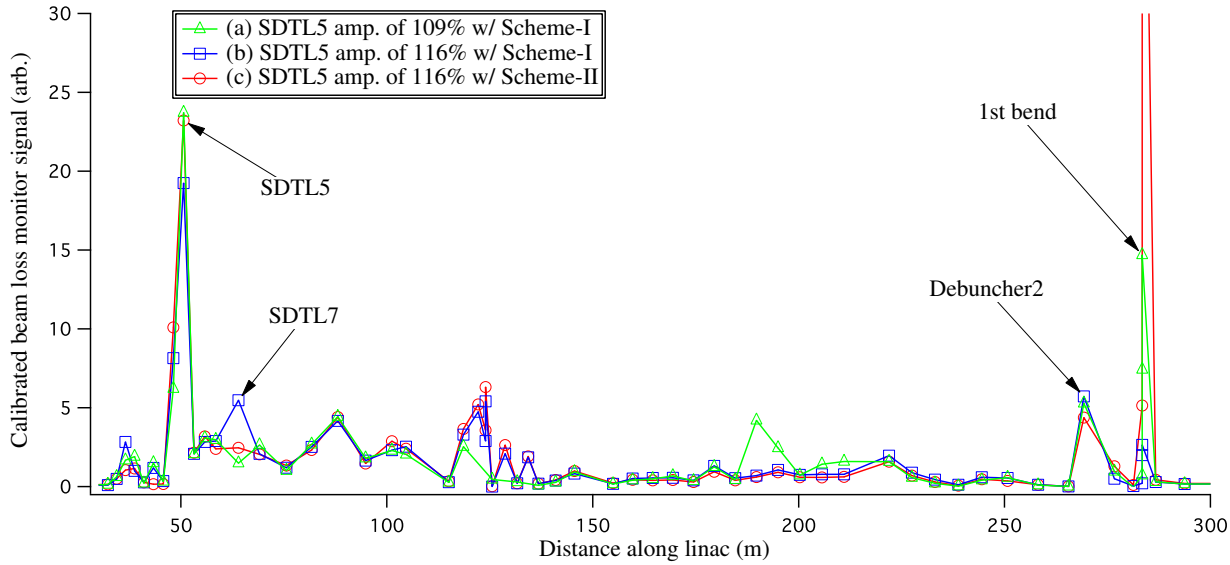

Figure 1: Calibrated beam loss monitor signal distribution along J-PARC linac and the following straight line of the beam transport line. Each marker shows the measured data with a beam loss monitor. The data are taken (a) with the SDTL amplitude of 109 % after Scheme-I tuning, (b) with the SDTL amplitude of 116 % after Scheme-I tuning, and (c) with the SDTL amplitude of 116 % after Scheme-II tuning.

phase and amplitude scan tuning [8]. At first, we adopted the RF amplitude of 109 % for SDTL5 to avoid the multipactor. In the phase and amplitude scan tuning, we needed an unusual treatment for SDTL5. Namely, we fixed the amplitude for SDTL5 and performed the phase scan only to find the phase setting to realize the design energy gain. After conducting the tuning for SDTL5, the tuning for SDTL6 and downer stream tanks were performed with the nominal procedure to set them to the design amplitude and synchronous phase.

After finishing the phase and amplitude scan tuning, we tried to operate with the determined RF setting. However, we experienced significant beam loss particularly at the straight section after the SDTL exit. We then tried to mitigate the beam loss by adjusting only the SDTL phases, because neighboring tanks also has unstable bands in their amplitude. In this tuning, we adopt the phase shift for SDTL5 and that for SDTL6 to SDTL15 as two tuning knobs. It should be noted that we assume the same phase shift for SDTL6 to SDTL15. This tuning was performed with the trial-and-error method to minimize the beam loss downstream with the phase-and-amplitude scan tuning result as the starting point. As a result, the phase for SDTL5 was shifted by +5 degree and those for SDTL6 to SDTL15 by -8 degree. Here, the positive phase shift is defined to increase the energy gain in the vicinity of the design phase. We call this tuning "Scheme-I" in this paper.

In the tuning, the beam loss is measured with BLM's (Beam Loss Monitors) of gas proportional counter type [9] distributed along the linac. As the output from BLM tends to saturate, we perform a calibration to linearize it [10]. The calibrated BLM signal after the Scheme-I tuning is shown in Fig. 1 as case (a). In the SDTL section with the horizontal axis of 30 to 115 m, the BLM is affected by X rays from SDTL cavity. A large peak is noticed at around 50 m, which is supposedly caused by X rays from SDTL5 operating with higher RF amplitude than usual. Another peak at around 280 m is the beam loss at the first bending magnet in the beam transport line. A large BLM signal there is often attributable to proton component generated in double stripping of negative hydrogen ions [10]. A peak at around 270 m is the beam loss at the second debuncher. As the aperture of the debuncher cavity is narrower than the neighboring beam transport lines, the beam loss naturally tends to concentrate on this location [11]. Aside from these peaks, a peak is also noticeable at around 190 m which is connected with significant residual radiation in the beam transport. This peak shows the beam loss caused by insufficient alignment of beam ducts which was avoided by realignment later. While a clear peak is not observed, we also had significant residual radiation at around 120 m. As the corresponding beam loss was not detected by the BLM's which then existed, we added BLM's in this area for later measurements (case (b) and (c) in Fig. 1).

Operation with 116 % Amplitude for SDTL5

While the beam loss was reasonably suppressed with a Scheme-I tuning for 109 % SDTL5 amplitude, gradual widening of the multipactor band of SDTL5 forced us to further increase its amplitude to 116 %.

With 116 % amplitude for SDTL5, we first tried Scheme-I tuning as in the previous subsection. However, we could not find a setting to fully suppress the beam loss this time. When we suppress the beam loss after the SDTL

Copyright © 2012 by the respective authors — cc Creative Commons Attribution 3.0 (CC BY 3.0)

exit, the beam loss in the middle of the SDTL section arises. Assuming the beam loss with lower energy would be preferable as the resultant residual radiation could be lower, we decided to adopt the setting to localize the beam loss at the upstream portion of the SDTL section. The resultant phase shift for SDTL5 was -6 degree and that for SDTL6 to SDTL15 was +8 degree. With this setting, the beam loss after the SDTL exit is comparable to before the earthquake, but we have visible beam loss at around SDTL7. It should be noted that the resultant phase shift is opposite to that in the previous subsection.

The beam loss distribution after the tuning is shown in Fig. 1 as case (b). In this figure, the peak at around 190 m was disappeared thanks to realignment. While the corresponding measurement with the same BLM configuration is not available for case (a), the peak at around 120 m was supposedly reduced judging from the reduction in the residual radiation [3]. Instead, a new peak arose at SDTL7 around 65 m as discussed above.

Operation with Design Longitudinal Focusing

After a certain period of user operation, we found that the beam loss at around SDTL7 caused significant residual radiation [3]. It motivated us to try an alternate scheme, namely, adoption of an optics with the design longitudinal focusing strength.

Keeping the design longitudinal focusing with increased RF amplitude, we naturally have higher energy gain. Consequently, we need to reduce the energy gain for neighboring cavities to compensate it. As mentioned above, we have multipactor for SDTL1 to SDTL6, which poses a constraint in choosing their RF amplitude. We conducted RF measurements to confirm that we can decrease the SDTL4 amplitude while avoiding the multipactor. Then, we tried an RF setting where we keep the longitudinal focusing for SDTL5 to the design strength with 116 % amplitude. Its excess energy gain is compensated by lowering SDTL4 amplitude. In this setting, the longitudinal focusing for SDTL4 is also kept to the design strength. We here call this tuning "Scheme-II". In calculating the longitudinal focusing force, we adopt the single gap approximation for SDTL4 and SDTL5 neglecting the phase slip. In the setting, the energy gain of SDTL5 is increased from the design value of 8.35 MeV to 10.00 MeV. Meanwhile, the energy gain of SDTL4 is decrease from its design 7.55 MeV to 5.90 MeV with the reduced amplitude of 83 %.

After adopting this setting, the beam loss was significantly reduced and become comparable to that before the earthquake. The beam loss at around SDTL7 disappeared by adopting this setting as shown as case (c) in Fig. 1. As seen in this figure, the beam loss at the first bending magnet around 280 m suddenly increased. While the reason for the sudden increase has not been fully understood, the beam loss was identified to be caused by protons and successfully mitigated by adjusting the chicane orbit we set up between RFQ and DTL [10].

SUMMARY

We had a large earthquake in March 2011 followed by a nine-month beam shutdown for restoration efforts. We resumed the beam operation of J-PARC linac in December 2011 and user operation in January 2012. Then, we recovered the beam power just before the earthquake in March 2012.

In the course of the beam commissioning, we have experienced beam losses which were not observed before the earthquake. Particularly, the multipactor in SDTL5 forced us to adopt irregular RF setting and it caused excess beam loss. In an effort to mitigate the beam loss, we have experimentally confirmed that we can suppress the beam loss by adopting an optics with the design longitudinal focusing. Although it may be an expected result, it would be a rare experimental demonstration because a high intensity β-graded linac is rarely operated with irregular RF setting for a long term. We have observed certain increase of the residual radiation at the second debuncher (not detected with BLM)[3] which might be attributable to the SDTL setting. Even with this reservation, this result provides valuable information in designing a counter-failure scenario for present and future high intensity linacs.

Thanks to the RF tuning and other efforts, we succeeded in reducing the beam loss in J-PARC linac to a comparable level to before the earthquake.

REFERENCES

[1] K. Hasegawa, "Recovery of the J-PARC Linac from the Earthquake", in these proceedings.

[2] M. Ikegami et.al., "Beam Start-up of J-PARC Linac after the Tohoku Earthquake", IPAC'12, New Orleans, May 2012, THPPC010, p. 3293 (2012).

[3] M. Ikegami et.al., "Beam Commissioning of J-PARC Linac after Tohoku Earthquake and Its Beam Loss Mitigation", to be published in Procs. of 9th Annual Meeting of Particle Accelerator Society of Japan.

[4] Y. Yamazaki ed., "Technical Design Report of J-PARC", KEK Report 2002-13 (2003).

[5] J. Tamura et.al., "Beam Loss Reduction by the Beam Duct Realignment in the J-PARC Linac Beam Transport Line", to be published in Procs. of 9th Annual Meeting of PASJ (Particle Accelerator Society of Japan) (in Japanese).

[6] T. Ito, K. Hirano, private communication.

[7] T. Ito, K. Hirano, K. Nammo, "Multipactor at SDTL Cavity in J-PARC Linac", to be published in Procs. of 9th Annual Meeting of PASJ (in Japanese).

[8] G. Shen, M. Ikegami, Nucl. Instrum. Meth. Phys. Res. A 598 (2009) 361.

[9] S. Lee, M. Tanaka, T. Toyama, J. Kishiro, "The Beam Loss Monitor System of the J-PARC Linac, 3 GeV RCS, and 50 GeV MR", EPAC'04, Lucerne, July 2004, THPLT074, p. 2667 (2004).

[10] H. Sako, M. Ikegami, IEEE Trans. Nucl. Sci., 57 (2010), 57.

[11] T. Maruta, "Beam Loss Study at J-PARC Linac by Using GEANT4 Simulation", IPAC'11, San Sebastián,September 2011, WEPS047, p 2595 (2011).

Copyright © 2012 by the respective authors — cc Creative Commons Attribution 3.0 (CC BY 3.0)

PLANNING FOR EXPERIMENTAL DEMONSTRATION OF TRANSVERSE EMITTANCE TRANSFER AT THE GSI UNILAC THROUGH EIGEN-EMITTANCE SHAPING

C. Xiao, O.K. Kester, Institute of Applied Physics, Goethe-University of Frankfurt a.M, Germany
L. Groening, GSI Helmholtzzentrum für Schwerionenforschung, Darmstadt, Germany

Abstract

The minimum transverse emittances achieved in a beam line are determined by the two transverse eigen-emittances of the beam. Without coupling, they are equal to the transverse rms-emittances. Eigen-emittances are constants of motion for all symplectic beam line elements. To allow for rms-emittance transfer, the eigen-emittances are changed by a non-symplectic action to the beam, preferably preserving the four-dimensional rms-emittance.

Unlike emittance swapping, the presented concept will allow the transformation of a beam of equal rms-emittances into a beam of different rms-emittances while preserving the four-dimensional rms-emittance. This contribution will introduce the concept for eigen-emittance shaping and rms-emittance transfer at an ion beam line. The actual work status towards the experimental demonstration of the concept at the GSI UNILAC is presented.

INTRODUCTION

For injection of beams into circular machines with different horizontal and vertical emittance acceptances, the injection efficiency can be increased if these beams are flat. However, beams provided from the linear accelerator are generally round, and the horizontal and vertical emittances are quite equal.

Round-to-flat transformation requires a change of the beam eigen-emittances by a non-symplectic transformation [1]. Such a transformation can be performed by placing a charge state stripper foil inside a longitudinal field region as proposed in [2]. Inside such a solenoidal stripper, the transverse inter-plane correlations are created non-symplectically. Afterwards they are removed symplectically with a coupling correction section. The new set-up providing round-to-flat transformation is shown in Fig. 1. Such a emittance transfer section is proposed to be integrated into the existing beam line between the UNILAC [3] and the SIS synchrotron.

EMITTANCE

The four-dimensional symmetric beam matrix C contains ten unique elements, four of which describe the coupling. The rms-emittances, ε_x and ε_y, are defined as the square roots of the determinants of the on-diagonal submatrices. If one or more of the elements of the off-diagonal

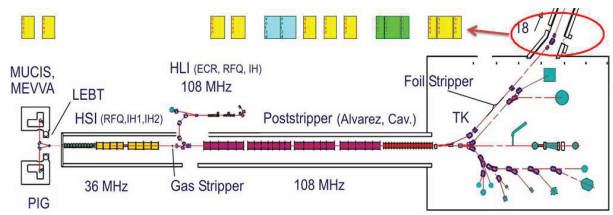

Figure 1: Conceptual layout of the transverse emittance transfer section in the GSI UNILAC.

submatrix is non-zero, the beam is x-y coupled. Diagonalization of the beam matrix yields the beam eigen-emittances, ε_1 and ε_2, and the values are calculated as:

$$\varepsilon_1 = \frac{1}{2}\sqrt{-tr(CJ)^2 - \sqrt{tr^2(CJ)^2 - 16|C|}} \quad (1)$$

$$\varepsilon_2 = \frac{1}{2}\sqrt{-tr(CJ)^2 + \sqrt{tr^2(CJ)^2 - 16|C|}} \quad (2)$$

The four-dimensional matrix J is the skew-symmetric matrix with non-zero entries on the block diagonal of form. Eigen-emittances are invariant under symplectic transformations, and the eigen-emittances are equal to rms-emittances when the inter-plane correlations are zero.

BEAM TO BE STRIPPED

Multi-particle beam dynamics simulations have been done using the TRACK code [4]. The uncoupled particle distribution at the entrance of this beam line is concluded from beam experiments and plotted in Fig. 2.

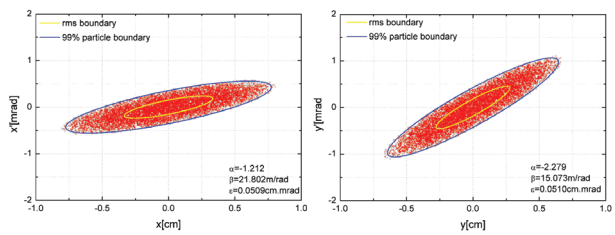

Figure 2: The particle distributions at the entrance of beam line.

The subroutines of the stripper in the TRACK code are based on the SRIM code [5]. The three-dimensional field

Copyright © 2012 by the respective authors — cc Creative Commons Attribution 3.0 (CC BY 3.0)

of the solenoid is calculated by the OPERA-3D code [6, 7], and the stripper foil is placed at the center. The oscillations of the rms-emittances and eigen-emittances along the longitudinal field with and without stripper are shown in Fig. 3.

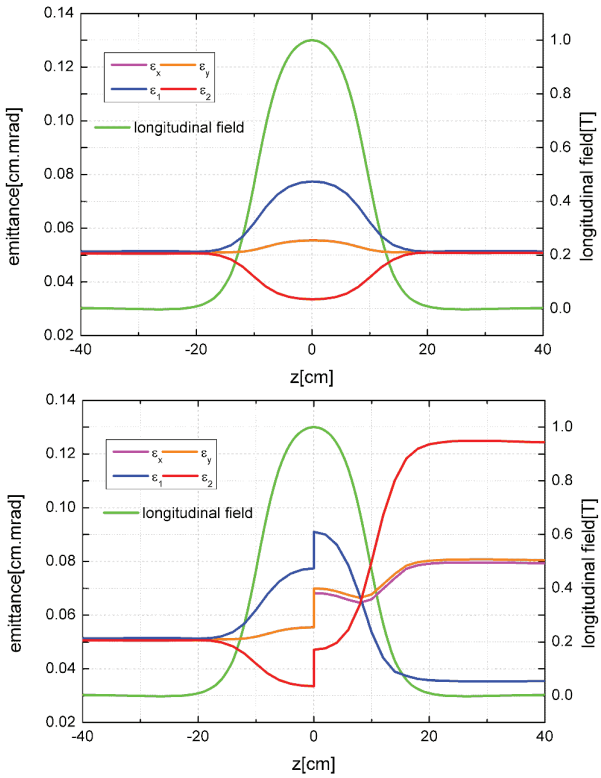

Figure 3: The rms-emittances and eigen-emittances along the longitudinal field without and with stripper foil.

Without the stripper, the eigen-emittance variation which is created by the entrance fringe field would be canceled by the exit fringe field and the beam experiences a symplectic transformation. The input and output rms-emittances are same. If the stripper is considered, the exit fringe is passed by the beam with reduced rigidity, thus overcompensating the eigen-emittances variation, and at the exit of longitudinal field region, a coupled output beam is achieved.

The foil stripper itself is modeled by increasing the spread of the angular distribution through scattering. Because of scattering the rms-emittances increase during the stripping process, and the output rms-emittances are larger than the input values. The particle distributions before and after the stripper are illustrated in Fig. 4.

COUPLING CORRECTION SECTION

The coupling correction section starts at the exit of the longitudinal field, which is then followed by a normal triplet and a skew triplet separated by appropriate drift space. A simple realization of such a system is sufficient to remove inter-plane correlations exhaustively. Along the subsequent elements after the solenoid, the gradients of

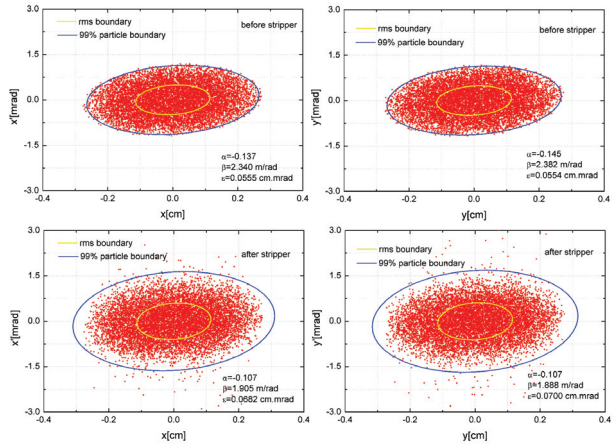

Figure 4: The particle distributions before and after foil.

normal and skew triplet are determined numerically to correct four ($\langle xy\rangle$, $\langle x'y'\rangle$, $\langle x'y\rangle$, and $\langle xy'\rangle$) beam correlations, respectively. This scheme allows total correction of any arbitrary linearly coupled beam with correction range limited only by the available quadrupole strength.

Our design process is to produce inter-plane correlations non-symplectically, thus changing the eigen-emittances in the longitudinal field, then remove them symplectically by the following quadrupole correction section. Fig. 5 shows the simulation of this process, the optics of the quadrupole correction section has been designed to bring the horizontal rms-emittance down to the lower eigen-emittance.

After the quadrupole correction section the output uncoupled beam is divergent, and since there is still a long drift space between the quadrupole correction section and the emittance measurement, another normal triplet is required. The particle distributions at the position of emittance measurement are shown in Fig. 6. The inter-plane correlations between the horizontal and vertical phase spaces are removed ($\varepsilon_x = \varepsilon_1$).

MACHINE-RELATED ERRORS

There are many sources of magnet imperfection, which are mainly generated by gradient fluctuations, rotational angle errors, and misalignment errors. The misalignment errors of the quadrupole cause the beam trajectory to deviate from and oscillate around the designed path in the beam line, but the values of rms-emitances and eigen-emittances are not affected. The gradient fluctuation errors and the rotational angle errors are the potential sources of inter-plane correlations not be removed exhaustively. We use a statistical method in which the error values of each magnet are randomly generated under given maximum values. The influences of these errors on the rms-emittances and eigen-emittances are shown in Fig. 7.

In the presence of the gradient errors, the fluctuations of the rms-emittances and eigen-emittances are not obvious, and the values of rms-emittances and eigen-emittances are almost the same and the cross-plane coupling beam after

Copyright © 2012 by the respective authors — cc Creative Commons Attribution 3.0 (CC BY 3.0)

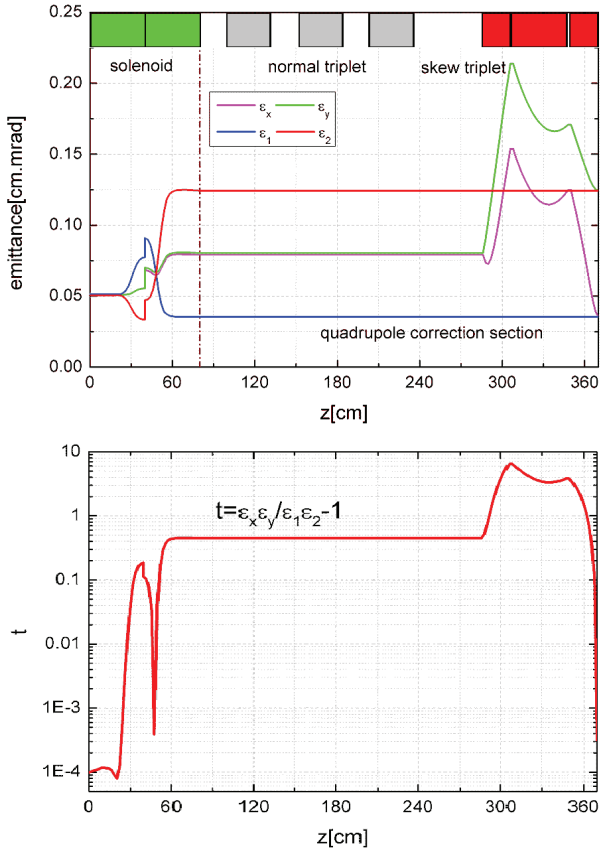

Figure 5: The emittances and the beam rms sizes along the longitudinal field and quadrupole correction section.

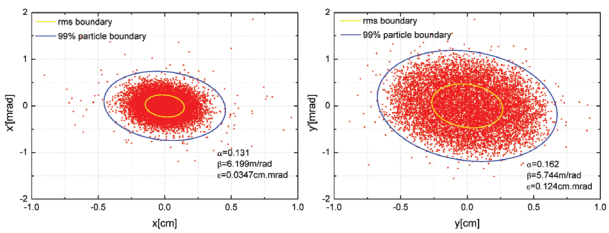

Figure 6: The particle distributions at the end of beam line.

stripper can be corrected to a large degree.

In the presence of the rotational angle errors, the values of lower eigen-emittances are almost constant but the values of horizontal rms-emittances are varied. This bias may lead to attempting to correct the implied coupling, which will actually introduce coupling rather than correct it.

Based on the manufacturing experiences of the UNILAC, the maximum values of gradient fluctuation, rotational angle and misalignment errors are 0.1% and 0.3 degree.

CONCLUSION AND OUTLOOK

The longitudinal field strength and beam sizes at the stripper foil are free parameters, the amount of emittance transfer scales with the field strength and beam rms sizes.

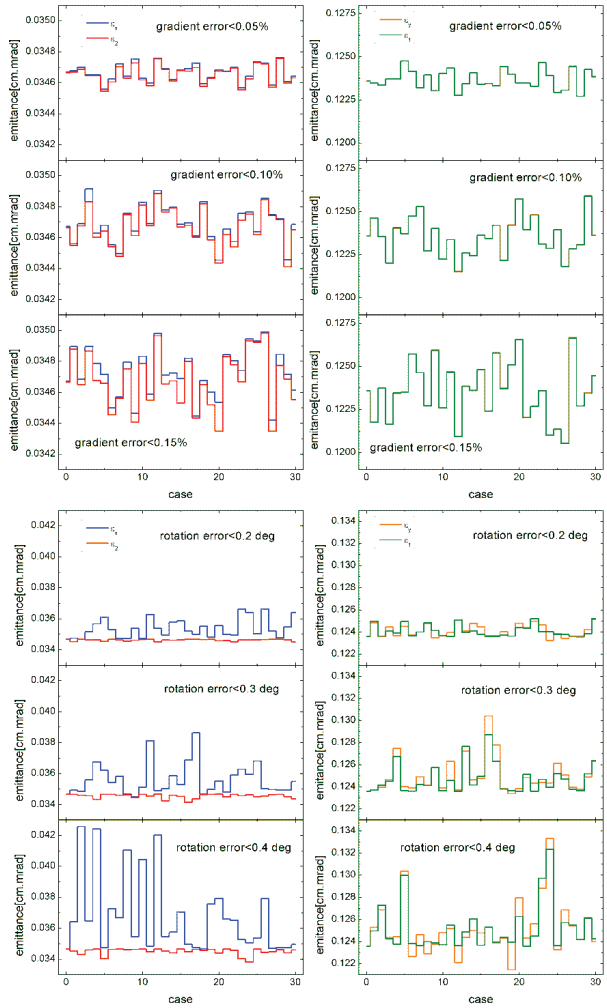

Figure 7: The influences of the gradient fluctuation and rotational angle errors.

This freedom makes the difference to a emittance swapping scheme. The simulations illustrate that the combination of a normal triplet and a skew triplet has ability to correct a coupled beam, and the beam line errors degrade the accuracy of correction.

GSI aims at experimental verification of emittance transfer by assembling the beam line presented in this paper, and the corresponding hardwire devices are under manufacturing. The beam experiment is planned for early 2014.

REFERENCES

[1] A.J. Dragt, PRA **45**, 4 (1992).

[2] L. Groening, PRST-AB **14**, 064201 (2011).

[3] W. Barth et al., Proc. XXIV Linac Conf., p. 175, (2008).

[4] http://www.phy.anl.gov/atlas/TRACK/.

[5] http://www.srim.org/

[6] http://www.cobham.com/.

[7] Goethe University Internal Report IAP-DYNA-190412

Copyright © 2012 by the respective authors — cc Creative Commons Attribution 3.0 (CC BY 3.0)

STATUS OF THE IFMIF-EVEDA 9 MeV 125 MA DEUTERON LINAC

A. Mosnier, Fusion for Energy, BFD Department, Garching, Germany

Abstract

The scope of IFMIF/EVEDA has been recently revised to set priority on the validation activities, especially on the Accelerator Prototype (LIPAc) extending the duration up to mid 2017 in order to better fit the development of the challenging components and the commissioning of the whole accelerator. The present status of LIPAc, currently under construction at Rokkasho in Japan, outlines of the engineering design and of the developments of the major components will be reported. In conclusion, the expected outcomes of the engineering work, associated with the experimental program will be presented.

INTRODUCTION

The International Fusion Materials Irradiation Facility (IFMIF) aiming at generating materials irradiation test data for DEMO and future fusion power plants is based on an accelerator-driven, D-Li neutron source to produce high energy neutrons at sufficient intensity and irradiation volume. IFMIF Engineering Validation and Engineering Design Activities (EVEDA) have been conducted since mid 2007 in the framework of the Broader Approach Agreement.

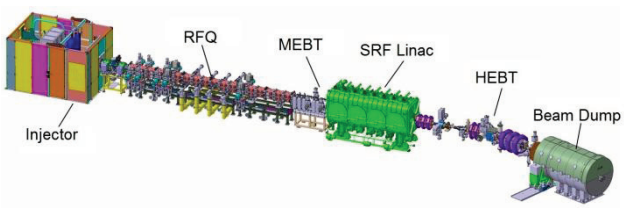

Figure 1: LIPAc layout

In order to demonstrate the feasibility and to develop the technology, a representative portion of one of the two IFMIF accelerators, up to the first section of the SRF Linac, is being designed and built. This high intensity linear accelerator prototype, called LIPAc (Fig. 1), will be assembled and commissioned at Rokkasho in Japan, with the objective to reach a stable 125 mA, 9 MeV continuous deuteron beam. These engineering validation activities are conducted since mid-2007 under the framework of the Broader Approach Agreement and are shared as follows:

- The accelerator components are designed, manufactured and tested by European institutions (CEA, CIEMAT, INFN, SCK-CEN): Injector, Radio Frequency Quadrupole (RFQ), Medium and High Energy Beam Transport lines, Superconducting RF Linac, Beam Dump, 175 MHz RF Systems, Local Control Systems, Beam Instrumentation;
- The conventional facilities (building and auxiliaries), the Central Control System, as well as the RFQ couplers, are provided by JAEA;
- The design integration and the interface management are coordinated by Fusion for Energy (F4E);
- The coordination and the integration on site are provided by the Project Team hosted in Rokkasho.

In 2010, the priority was set on the validation of the Accelerator Prototype [1] extending the duration up to mid 2017 in order to better fit the time required for the development of the challenging components and for the installation and sequential commissioning of the accelerator at Rokkasho.

ACCELERATOR COMPONENTS

Accelerator components [2] are designed, manufactured and individually tested in Europe, and then transported to Rokkasho for installation in the accelerator building.

Injector

The injector has to deliver a continuous low emittance deuteron beam (140 mA, 100 keV) with high reliability. The ion source is based on an electron cyclotron resonance cavity, excited by a 2.45 GHz magnetron [3]. The extracted beam is matched to the RFQ entrance by means of a dual solenoid focusing scheme in the LEBT. In order to meet emittance and matching requirements, the space charge must be highly compensated by injection of krypton gas and up to the RFQ entrance thanks to an electron repeller electrode. In addition, an electrostatic chopper will be implemented between the two solenoids to enable the operation of LIPAc with short pulses of very sharp rise/fall times.

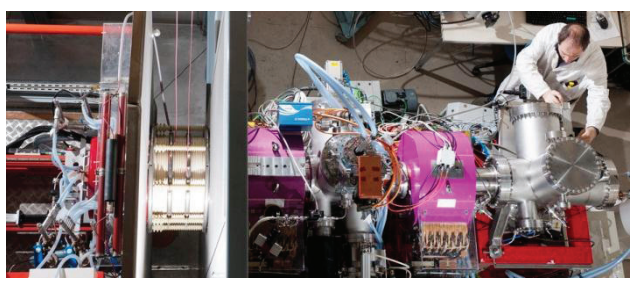

Figure 2: Top view of the Injector (P. Stroppa/cea credit).

The injector was assembled at CEA-Saclay in order to test the components in Europe before the shipment to Japan scheduled at the beginning of 2013 (Fig. 2). After the first H+ beam produced in May 2011, a test campaign was carried out in pulsed and continuous operation. Pulsed beams of 150 mA at 100 kV and continuous beams of 100 mA at 75 kV were routinely produced. The first D+ beam was extracted in April 2012, first in pulsed mode and then in continuous mode for a short period in order to limit the activation of the elements. However, as the continuous operation at 100 kV was limited by HV discharges in the extraction system, a new 5 electrode

Copyright © 2012 by the respective authors — cc Creative Commons Attribution 3.0 (CC BY 3.0)

system (instead of the former 4 electrode system) is being installed and injector tests will start gain at the end of September 2012 to complete the optimization (ion source plasma, krypton pressure, solenoid setting) and characterize the beam emittance which should be lower than 0.25 π mm mrad.

Radiofrequency Quadrupole

The 4-vane RFQ, under development by INFN, has to bunch the DC beam from the injector and to accelerate the beam from 0.1 to 5 MeV. The 10 m long cavity is composed of 18 x 0.54 m long modules flanged together (Fig. 3). The peak surface electric field is limited to a maximum value of 1.8 x Kilpatrick's criterion.

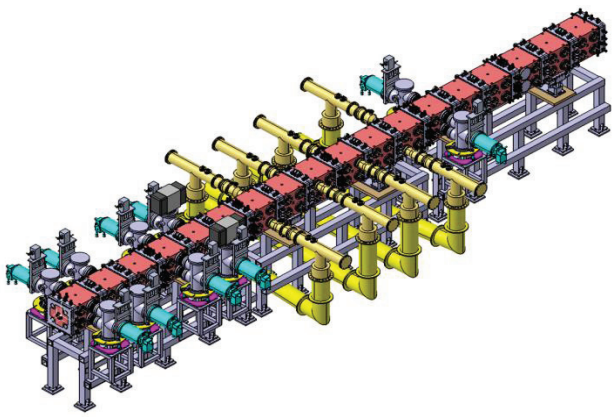

Figure 3: 3D mock-up of the RFQ equipped with RF couplers, cryo-pumps, slug tuners and cooling channels.

The RF power (about 1300 kW) is injected by 8 loop couplers, using 6 1/8" RF windows. High power tests have been performed with a high-Q load circuit at JAEA-Tokai. Final acceptance tests and RF conditioning in TW mode of two complete couplers (waveguide, window and tip modules) will be performed at INFN-Legnaro at the beginning of 2013 on a specific test bench [4] including a coupling cavity. The manufacturing of the other couplers will start just after approval of the acceptance tests.

The RF tuning of the RFQ is ensured by 22 slug tuners per quadrant. An aluminium full scale RFQ model has been built to validate the tuning procedures and the mode stabilization by means of bead-pull measurements. The tuning algorithm allowed reaching voltage errors of ±1% in 4 iterations only.

The cooling system is able to remove the dissipated power in the structure (more than 700 kW assuming 10% extra field) but also to regulate the resonance frequency and to keep the correct field profile, thanks to four independent circuits, enabling the temperature difference between the vane and the outer walls to be independently adjusted in the 3 super-modules.

A vacuum system, composed of dry primary and 10 cryogenic pumps, provides a high pumping speed to balance the gas load (dominated by beam losses), resulting in a pressure profile below 5 10^{-7} mbar all along the RFQ.

In order to test the production procedure, a full scale technological prototype (30% shorter) has been machined in INFN and brazed at CERN in two steps (1st horizontal, 2nd vertical). Leak tests and dimensional checks have been passed successfully (average vane displacement close to the target of 50 µm).

The module production [5] has been split into 3 super-modules (SM), composed of 6 modules each:

- high energy SM with homogenous aperture
- intermediate energy SM with z-dependent aperture
- low energy SM

One module of the high energy SM has been machined and brazed (Fig. 4). A maximum deformation of 100 µm has been measured, still acceptable but at the limit of the specification, and might be corrected for the next modules by using the appropriate annealing cycle and improved fixation tooling. Three modules (plus the RF plug) will be completed in November 2012 for high power tests, planned at the beginning of 2013 at INFN-Legnaro.

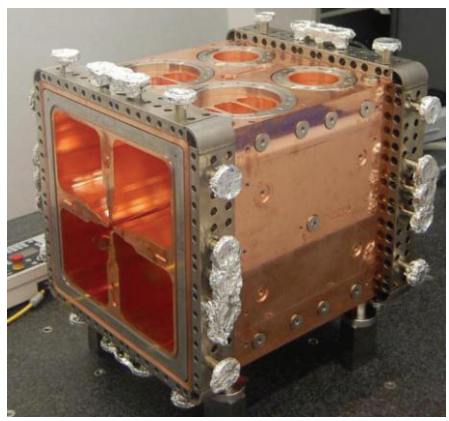

Figure 4: First RFQ module completed

SRF Linac

The high-energy section of LIPAc accelerates the beam to 9 MeV and consists of the first cryomodule (Fig. 5) of the IFMIF SRF Linac, housing eight superconducting half-wave resonators (HWR) and eight solenoid packages. The main cavity and magnet parameters are listed in Table 1.

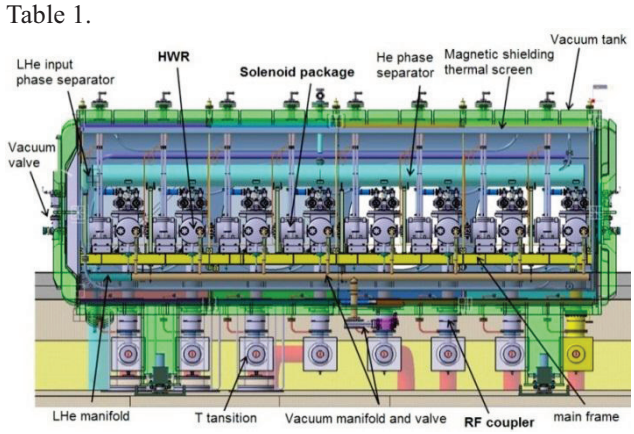

Figure 5: 3D mock-up of the LIPAc Cryomodule

Copyright © 2012 by the respective authors — cc Creative Commons Attribution 3.0 (CC BY 3.0)

RF optimisation of the HWR geometry lowered the electric and magnetic peak surface fields down to E_p/E_{acc}=4.4 and B_p/E_{acc}=10.1 mT/MV/m.

Table 1: Main Parameters of Cavity and Solenoid

Frequency	175	MHz
Cavity β	0.094	
Accelerating field Eacc	4.5	MV/m
Quality factor Qo	1.4 10^9	
Max. forward Power / coupler	200	kW
Max. Tuning range	± 50	kHz
Beam aperture cavity/solenoid	40 / 50	mm
Magnetic field Bz on axis	6	T
Field at cavity flange	≤ 20	mT

The original design of the tuner relied on a capacitive plunger with a large membrane to allow an elastic deformation of ±1 mm. Two prototype cavities have been fabricated (Fig. 6) and tested at cold temperature. Unfortunately, results showed a low Qo, as well as a quench at low field, pointing to a suspect plunger. In addition, potential problems occurring in the main cavity body cannot be also ruled out [6]. Following up the recommendations of a Review Panel, a new design based on a conventional compression tuner principle is under development [7]. Given the rigidity of the present resonator design, this solution implies a lengthening of the cryomodule lattice (about 10 cm) to ease the integration of the tuner between the HWR tank and the solenoid package.

Figure 6: HWR prototype.

The RF coupler [8] is composed of a water-cooled Cu antenna, a disk ceramic window, an external conductor made of helium cooled double wall tube and a tee transition between the input coaxial line and the coupler, including a duct for the cooling water. Pairs of couplers will be tested and conditioned at room temperature by means of a coupling box, especially developed to achieve large bandwidth and low losses. Two prototype couplers have been fabricated (Fig.7, left) and will be tested when the 200 kW RF source will be available, planned at the end of 2012.

The beam focussing and orbit corrections are performed by 8 sets of superconducting solenoids/steerers and beam position monitors, located before each HWR. The NbTi solenoid includes an active shielding made of a concentric outer solenoid in antiparallel configuration to lower the stray field below 20 mT at the cavity flanges. During the cold tests at 4.2K performed in a vertical cryostat (Fig. 7, right), the theoretical critical current of the magnet was reached (at about 260 A, well above the nominal current of 210 A) with a very short training [9].

The design of the cryomodule is now almost completed: cavity vacuum and cryostat insulation vacuum are separated in order to ensure a good vacuum quality. The 5-m long cryostat includes the magnetic shielding to protect the HWR from the earth magnetic field, two independent 4.5K helium circuits to cool down the cavities and the magnets, a helium phase separator and a thermal shield cooled at 60K by GHe.

Figure 7: coupler prototype (left) solenoid test (right).

MEBT, HEBT and Beam Dump

Five quadrupoles and two bunchers in the MEBT [10] fulfil the transverse and longitudinal matching conditions of the RFQ output beam to the SRF input (Fig. 8). A prototype magnet has been fabricated and validated in a magnetic test bench. A 5-gap IH buncher meets the voltage requirement (350 kV) with a minimum RF power dissipation. A prototype buncher is under fabrication and power tests are planned at mid-2013. The beam halo and out-of-energy particles coming from the RFQ are stopped in two movable scrapers, designed for a maximum 500 W

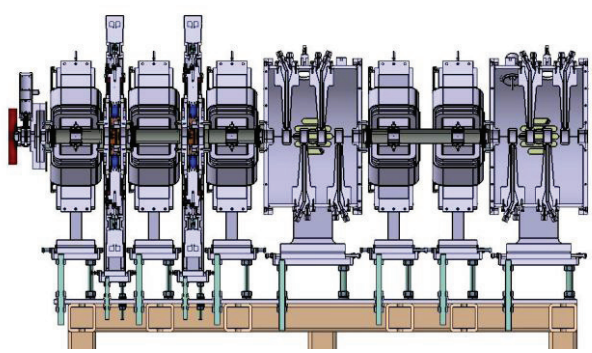

Figure 8: Medium Energy Beam Transport line.

Copyright © 2012 by the respective authors — cc Creative Commons Attribution 3.0 (CC BY 3.0)

The HEBT (Fig. 9) which transports the beam from the Linac to the beam dump includes the following elements:

- a Diagnostics Plate for the beam characterization
- a bending magnet to reduce the neutron radiation from beam dump towards upstream components
- a magnetic beam expander to limit the power density on the beam dump (< 200 kW/cm^2)
- a lead shutter, closed during beam shutdown to act as a gamma shield from the activated beam dump
- a beam scraper to protect the last portion of the vacuum pipe in front of the beam dump.

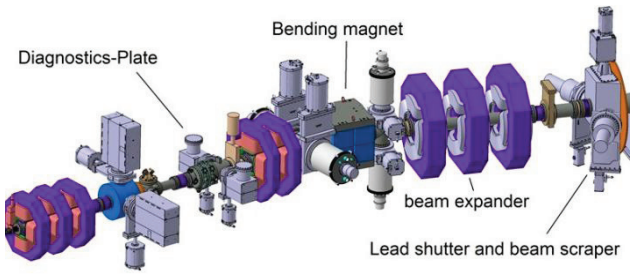

Figure 9: High Energy Beam Transport line.

A conical dump [11] made of copper has been designed to stop the 1.125 MW deuteron beam (Fig. 10). It is cooled by a high velocity water flow that circulates through an annular channel along the outer surface of the cone. Thermo-mechanical studies showed a high robustness to beam errors, CW and pulsed mode operation, buckling and high velocity coolant flow effects. A local shielding made of water tanks and polyethylene against neutrons and iron blocks against gamma rays associated with an extra frontal shielding made of a 70 cm thick concrete wall to fulfil the radiological protection requirements: low dose rates outside the accelerator vault during accelerator operation and manual maintenance inside the accelerator vault possible during beam-off phases. The HEBT and the beam dump are in the final stage of detailed design, and cartridge prototypes have been built. Hydraulic test of a full scale cartridge is on-going. Integration and test of the complete beam dump is planned at mid-2013.

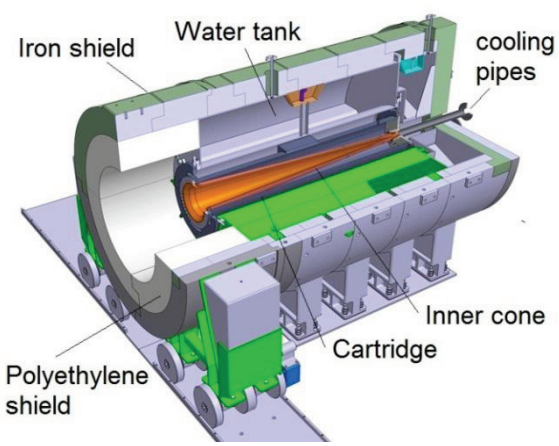

Figure 10: Beam Dump.

RF Power Systems

The RF Power System [12] is composed of 18 RF power generators to feed the 8 RFQ couplers (200 kW), the 8 superconducting half wave resonators of the SRF Linac (105 kW) and the 2 buncher cavities (16 kW). Except for the buncher cavities, which are fed by full solid-state amplifiers, the same topology has been chosen for all the power chains for standardization and scale economy reasons: they use the same main components (solid-state pre-driver and tetrodes for driver and final amplifier) which can be individually tuned to provide different RF output powers up to 200 kW (Fig. 11). The first prototype 200 kW RF source will be ready by the end of 2012 and will be used for the testing and conditioning of the HWR couplers while the first 2 x 100 kW RF module is expected at the beginning of 2013. The 16 kW solid-state amplifier should be ready for the high power tests of the buncher cavities at mid-2013.

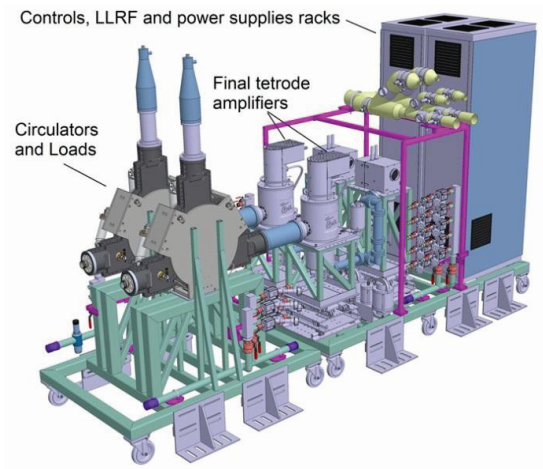

Figure 11: RF module with two 100 kW amplifiers.

Beam Diagnostics

A full set of non-interceptive diagnostics [13] to monitor and to characterize the beam all along the accelerator has been developed (Fig. 12): current monitors of various types (ACCT, DCCT, FCT), 20 beam position monitors (8 of them at cryogenic temperature), beam profile monitors (based on ionization and fluorescence of the residual gas), about 40 beam loss monitors (ion chamber LHC type), micro-loss monitors (based on CVD diamond operating at cryogenic temperature) and a bunch length monitor (residual gas). For short chopped beam pulses, SEM grids and slits will be used for emittance and energy spread measurement.

In addition, a Diagnostic plate (D-Plate) combines specific diagnostics to characterize the beam during commissioning with the beam, and will be located first at the exit of the RFQ and MEBT and second at the exit of the SRF Linac during LIPAc normal operation (Fig. 13).

The Control System (including Central Control System, Local Area Network, Personnel Protection System, Machine Protection System, Timing System, Local Control System) based on EPICS, is in progress [14].

Copyright © 2012 by the respective authors — cc Creative Commons Attribution 3.0 (CC BY 3.0)

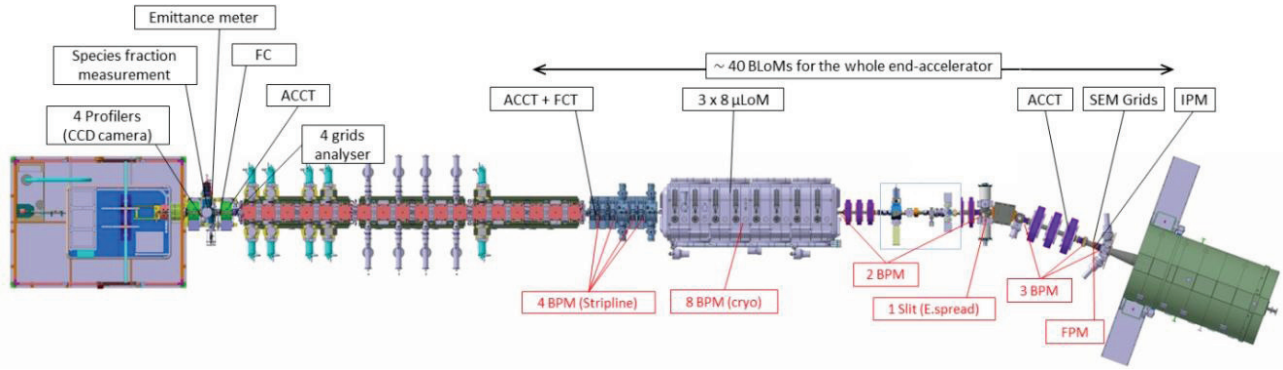

Figure 12: Beam instrumentation along the accelerator.

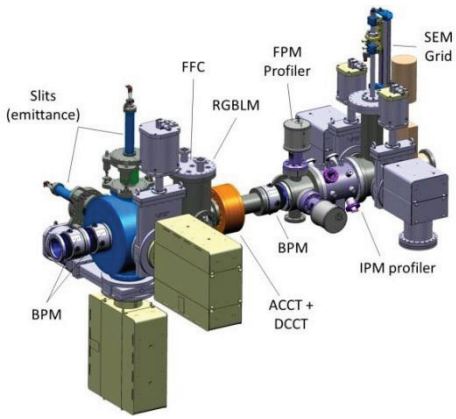

Figure 13: Diagnostics Plate.

ACCELERATOR BUILDING

The building (Fig. 14), completed in Rokkasho in March 2010, consists of an accelerator vault, a nuclear heating, ventilation and air conditioning (HVAC) area, a heat exchange and cooling water area for both radiation controlled and non-controlled areas, an access room, a control room, and a large hall for power racks, RF systems (HVPS and RF power chains) and the 4K refrigerator. The accelerator vault is surrounded by 1.5 m thick concrete walls and ceiling. The installation of the main auxiliaries has been completed and the first accelerator component, the injector, will be delivered and installed at the beginning of 2013.

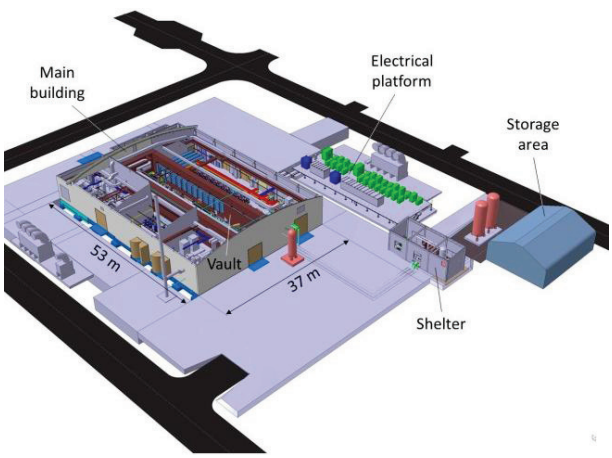

Figure 14: Building mock-up.

ACKNOWLEGMENT

This paper summarizes the collaborative work of many Institutions (F4E, CEA, CIEMAT, INFN, SCK-CEN in Europe and JAEA in Japan) for the LIPAc Project in the framework of the Broader Approach Agreement. Thus the author gratefully acknowledges the hard work and dedication of the entire staff involved in LIPAc which made possible the results presented herein.

REFERENCES

[1] P. Garin and M. Sugimoto, "IFMIF/EVEDA: Adjustment of Scope and Recent Technical Achievements", Fusion Science and Technology, Vol. 62, 219 (2012).
[2] A. Mosnier et al., "Present Status and Developments of the Linear IFMIF Prototype Accelerator (LIPAc)", IPAC2012, New Orleans, 20-25 May 2012.
[3] R. Gobin, "Light ion ECR sources state of the art for Linacs", these proceedings.
[4] S. Maebara, "Coupling cavity design of RF input coupler tests for the IFMIF/EVEDA RFQ", IPAC2012, New Orleans, 20-25 May 2012.
[5] A. Pisent et al, "Production and testing of the first modules of the IFMIF-EVEDA RFQ", IPAC2012, New Orleans, 20-25 May 2012.
[6] F. Orsini et al, "Preliminary results of the IFMIF cavity prototypes tests in vertical cryostat and cryomodule development", SRF2011 Workshop, Chicago, 2011.
[7] N. Bazin, "Thermo-Mechanical Simulations of the Frequency Tuning Plunger for the IFMIF Half-Wave Resonator", these proceedings.
[8] H. Jenhani, "Input power coupler for the IFMIF SRF Linac", IPAC2012, New Orleans, 20-25 May 2012.
[9] S. Sanz et al, "Fabrication and Testing of the First Magnet Package Prototype for the SRF Linac of LIPAc", IPAC2011, San Sebastián, Spain, 4-9 September 2011.
[10] I. Podadera et al, "The Medium Energy Beam Transport Line (MEBT) of IFMIF/EVEDA LIPAc", IPAC2011, San Sebastián, Spain, 4-9 September 2011.
[11] D. Iglesias et al, "The IFMIF-EVEDA Accelerator Beam Dump Design", Journal of Nuclear Materials, Vol. 417 (issues1-3), 1275 (2011).
[12] D. Regidor et al, "IFMIF-EVEDA RF Power System", IPAC2011, San Sebastián, Spain, 4-9 September 2011.
[13] J. Marroncle, "IFMIF-EVEDA LIPAc Diagnostics and its Challenges", to be submitted to IBIC2012, Tsukuba, Japan, Oct 1-4, 2012.
[14] H. Takahashi et al, "Development status of data acquisition system for LIPAc", IPAC2012, New Orleans, May 2012.

Copyright © 2012 by the respective authors — cc Creative Commons Attribution 3.0 (CC BY 3.0)

CHINESE ADS PROJECT AND PROTON ACCELERATOR DEVELOPMENT*

W.M. Pan#, Y.L. Chi, S.N. Fu, P. Sha, IHEP, Beijing, P.R.China
Q.Z. Xing, Tsinghua University, Beijing, P.R.China

Abstract

Significance of proton accelerator on the science and application has been widely recognized in the 21st century. The high-current proton accelerator can be utilized to drive the sub-critical nuclear reactor to build the clean nuclear power system. Moreover, it can serve in the field of high-energy physics, such as the neutrino factory and muon collider. For the spallation neutron source, the high-current proton accelerator provides the important platform for the multidisciplinary development of condensed matter physics, radiation physics, material science, aerospace science and life science. So proton accelerator is developing very fast in China nowadays. There're many proton accelerators under construction over China, which includes Accelerator Driven Sub-critical System (ADS), China Spallation Neutron Source (CSNS), Compact Pulsed Hadron Source (CPHS). These three projects will be introduced in this paper.

INTRODUCTION

ADS [1], CSNS [2] and CPHS have common ground, but are applied in different fields. They're all ongoing in China at present.

ADS ACCELERATOR

ADS project is a strategic plan to solve the nuclear waste problem and the resource problem for nuclear power plants in China [3]. It's supported financially by the central government and administrated by the Chinese Academy of sciences (CAS). With its long-term planning lasting until 2032, the project will be carried out in three major phases, see Figure 1.

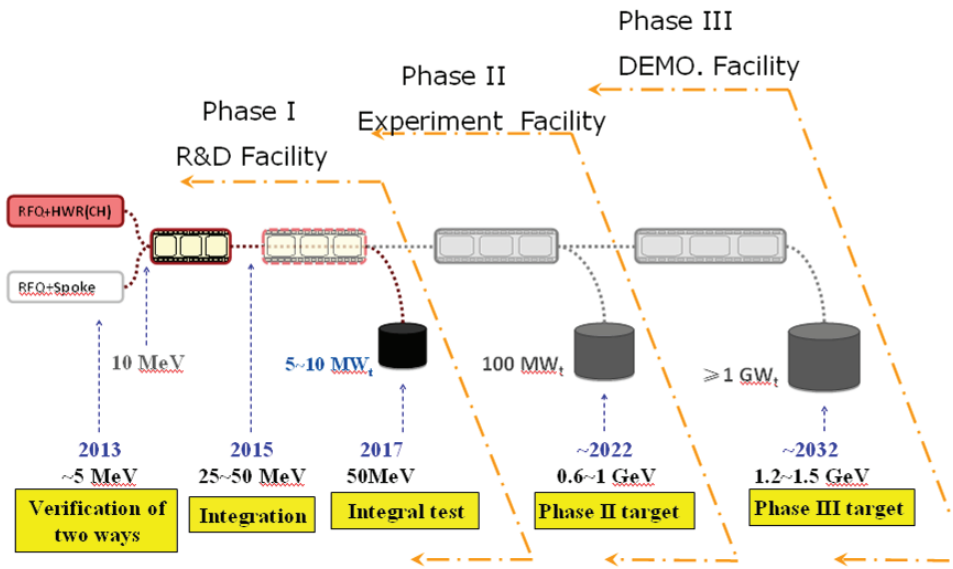

Figure 1: Road map of ADS

ADS accelerator will be built by two institutes of CAS: Institute of High Energy Physics (IHEP) and Institute of Modern Physics (IMP). It's a CW proton linac and uses superconducting acceleration structures except RFQ, the design specifications for the proton beam are shown in Table 1. For Phase I, the goal is to build a CW proton linac of 50 MeV and 10 mA by about 2015. Phase I will be executed progressively in several steps, with the 1st step to build two 5-MeV test stands of different front-end designs.

Table 1: ADS Proton Beam Specifications

Parameters	Value	Units
Energy	1.5	GeV
Current	10	mA
Beam power	15	MW
Frequency	162.5/325/650	MHz
Duty factor	100%	
Beam Loss	<1 (0.3)	W/m
Beam trips/year [4]	<25000 <2500 <25	1s<t<10s 10s<t<5m t>5m

*Work supported by CAS
#panwm@ihep.ac.cn

Copyright © 2012 by the respective authors — cc Creative Commons Attribution 3.0 (CC BY 3.0)

Design Philosophy

For the ADS accelerator, it has the characteristics of very high beam power and very high reliability which are not possessed by any of the existing proton linacs. However, several proposed CW proton/deuteron linac projects are good models for the physics and technical design, such Project-X, EFIT or MYRRHA, IFMIF and EURISOL. In addition, some pulsed high power proton linacs and some CW heavy ion linacs using superconducting cavities also serve as good examples. In general, there're several key points:

- It has been common understanding that superconducting proton linac is the best choice as an ADS driving accelerator, compared with other accelerator types which are still further away from the requirements as shown in Table 1. So hundreds of superconducting cavities (HWR, spoke, Elliptical) are widely used, as Figure 2 shows.
- High reliability is the most crucial for ADS. To achieve this goal, it's necessary to have enough redundancy for the entire accelerator. For the very low energy part, it's difficult to apply the local compensation as main linac, thus two parallel injectors are adopted. When one is on operation, the other is hot-spare and can be switched to the operation quickly. Figure 2 show that.
- Another key point of design is that beam losses should be kept as low as possible along the linac, with a usual acceptance of 1 W/m for all high-power proton accelerators. This is more difficult for the ADS, the beam power of which is 10 times higher. It also means a beam loss rate of 7e-8/m at the higher energy part, and requires very delicate error and beam loss studies.
- Beam emittance in the 3-D planes is very important. As the beam loss rate should be controlled at an extremely low level, all the measures should be considered to control the emittance growth along the linac, especially the halo emittance that is directly linked to the beam loss. Anyway, the total geometry emittance may increase during the acceleration due to all the errors and mismatches, so big physical aperture is adopted at higher energy section.

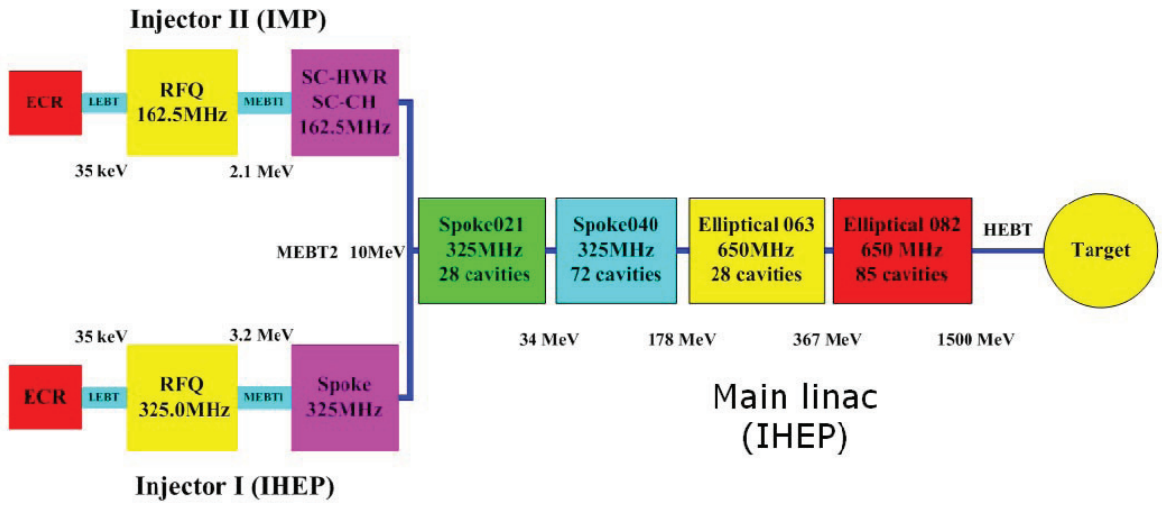

Figure 2: Layout of ADS accelerator

Injector I

Injector I will be built by IHEP, which Figure 2 demonstrates. The frequency of RFQ and Spoke cavity is 325 MHz, which is the same as Project-X. CW RFQ and low beta superconducting spoke cavity are the obstacles Injector I faces.

Currently, the design of RFQ has been determined, and the machining of prototype is ongoing now. Table 2 indicates main parameters of RFQ.

Table 2: Main RFQ Parameters

Parameters	Value	Units
Injection energy	35	keV
Output energy	3.2	MeV
Pulsed beam current	15	mA
Beam duty factor	100%	
Beam transmission	98.7%	
Total power	320.94	kW
Accelerator length	469.95	cm

Copyright © 2012 by the respective authors — cc Creative Commons Attribution 3.0 (CC BY 3.0)

Although very low-beta single spoke cavity are considered very difficult to develop and lack of experience, it's straightforward for IHEP to adopt such a spoke cavity for the superconducting acceleration structure in the Injector I since the main linac uses the same type of cavities but with higher beta, which will reduce the time and cost in the cavity development. Main parameters are listed in Table 3.

Table 3: Main Parameters of Spoke Cavity

Parameters	Value	Units
Diameter	468	mm
length	180	mm
Beam aperture	35	mm
Beta	0.12	
R/Q	142	Ω
G	61	Ω
Epeak/Eacc	4.54	
Bpeak/Eacc	6.37	mT/(MV/m)

Now the prototype of spoke cavity is under machining now (Figure 3), which may finish in Oct, 2012. Then the vertical test may be done at the end of 2012.

Figure 3: Spoke bars after welding.

Injector II

IMP is in charge of Injector II [5], the frequency of which is 162.5 MHz, half of the frequency of main linac. It can reduce the power density of RFQ, thus the difficulty of cooling. Therefore, 162.5-MHz half wave resonator (HWR) is adopted. Furthermore, superconducting CH cavity is also a potential choice.

The physics design of RFQ, which is developed by collaboration with LBNL, has been completed. Table 4 shows main parameters. And the prototype is being fabricated now. The fabrication of HWR cavity is together with spoke cavity. It may finish in October of 2012, too.

Table 4: Main Parameters of RFQ

Parameters	Value	Units
Injection energy	35	keV
Output energy	2.1	MeV
Pulsed beam current	15	mA
Beam duty factor	100%	
Beam transmission	99.5%	
Total length	420.8	cm

Figure 4: Outer tube of HWR.

CSNS LINAC

CSNS is the first large-scale, high-power accelerator project to be built in China. It locates at Dongguan, Guangdong province. Through years of preparation, it has began the construction in Sep, 2011. The goal is that it will provide 100 kW proton beam (1.6GeV) on a target in 2018. The total budget of CSNS is $260,000,000, which includes an 80-MeV H- linac, a 1.6-GeV cycling synchrotron, the spallation neutron target and 3 neutron spectrometers, as Figure 5 shows.

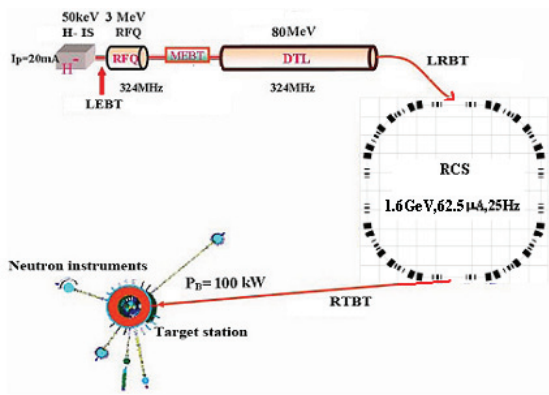

Figure 5: Schematics of CSNS.

Physics Design

CSNS accelerator [6] can produce proton beam of 1.6-GeV kinetic energy at 25 Hz repetition rate, striking a solid metal target to launch neutrons. Table 5 lists main parameters.

Copyright © 2012 by the respective authors — cc Creative Commons Attribution 3.0 (CC BY 3.0)

Table 5: CSNS Parameters

Project Phase	I	II
Beam Power on target [kW]	100	500
Proton energy t [GeV]	1.6	1.6
Average beam current [μA]	62.5	312.5
Linac energy [MeV]	80	250
Linac RF frequency [MHz]	324	324
Macropulse duty factor	1.0	1.7
RCS circumference [m]	228	228
RCS harmonic number	2	2
RCS Acceptance [πmm mrad]	540	540

The linac is made up of H- ion source, LEBT, RFQ, MEBT and DTL. But superconducting cavities (spoke or elliptical) will be applied in Phase II.

Present status

According to the plan, CSNS linac will start installation at the end of 2013 when the linac tunnel becomes available. Almost all the linac components have started fabrication or procurement at present.

CPHS PROJECT

CPHS in the Dept. Engineering Physics, Tsinghua University, is driven by one pulsed high-current proton linear accelerator. The accelerator consists of the Electron Cyclotron Resonance (ECR) ion source, Low Energy Beam Transport (LEBT) line, Radio Frequency Quadrupole (RFQ) accelerator, Drift Tube Linac (DTL) and High Energy Beam Transport (HEBT) line. The function of the whole accelerator system is to produce the proton beam, accelerate it to 13MeV, and deliver it to the target where one uniform round beam spot is obtained with the diameter of 5 cm. The whole performance of the CPHS facility relies critically on the accelerator system.

Four neutron beam lines are planned in the CPHS project at Tsinghua University, among which two lines are being constructed for the Small Angle Neutron Scattering (SANS) and neutron imaging. The neutron will be generated by the proton beam bombarding a Beryllium target.

Design

Main parameters of CPHS accelerator is listed in Table 6. Figure 6 is the layout of CPHS.

Table 6: Main Parameters

Parameters	Value	Units
Beam power	16	kW
Beam energy	13	MeV
Average current	1.25	mA
Pulse repetition rate	50	Hz
Protons per pulse	1.56×10^{14}	
Charges per pulse	2.5×10^{-5}	C
Pulse energy	0.325	kJ
Pulse length	500	μs
Peak current	50	mA
Beam duty factor	2.5	%
RF frequency	325	z MH
Output energy of the ion source	50	keV
Output energy of the RFQ	3	MeV
Output energy of the DTL	13	MeV

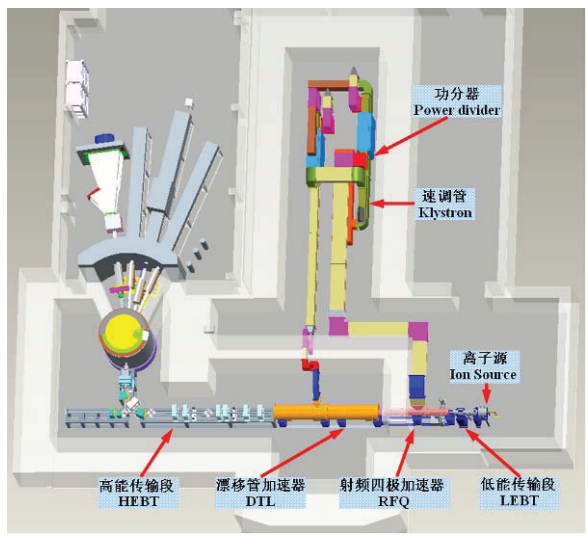

Figure 6: Layout of CPHS.

ECR Ion source and LEBT

The Electron Cyclotron Resonance (ECR) ion source is adopted to produce the proton beam. A three-electrode extraction system is to extract the 50keV proton beam from the plasma chamber. The LEBT matches the proton beam produced by the ion source to the RFQ accelerator. The 1.4m-long LEBT consists of two solenoid lens, two steering magnets, two diagnostic champers and one cone structure (the cone, ACCT and electronic trap).

The ECR proton source and LEBT are under conditioning now, and the maximum output proton beam has reached 60 mA, as Figure 7 shows.

Copyright © 2012 by the respective authors — cc Creative Commons Attribution 3.0 (CC BY 3.0)

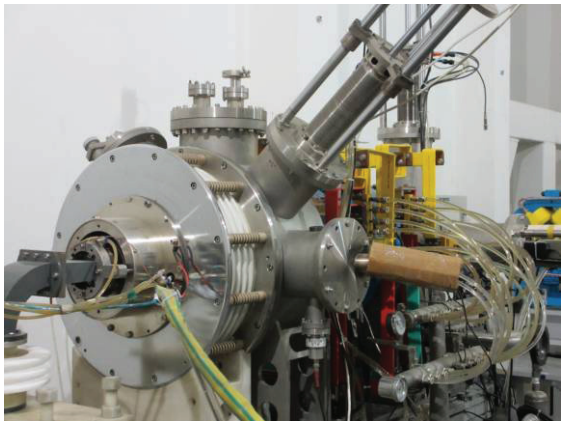

Figure 7: ECR and LEBT.

RFQ

Maintaining the good quality of the beam, Radio Frequency Quadrupole (RFQ) accelerator can bunch, focus and accelerate the low-energy CW proton beam from the ion source. The CPHS RFQ has a structure of four-vane and accelerates protons from 50keV to 3MeV. The inter-vane voltage increases with the beam energy. The total length of the RFQ is greatly shortened with a high transmission rate. The coupling plates are not necessary for the 3 m-long RFQ. The RFQ are designed to be matched to the DTL directly without MEBT.

Machining, brazing and assembly of the RFQ (3MeV/50mA) have been finished, and the result of the cold test at THU is satisfactory, which Figure 8 shows.

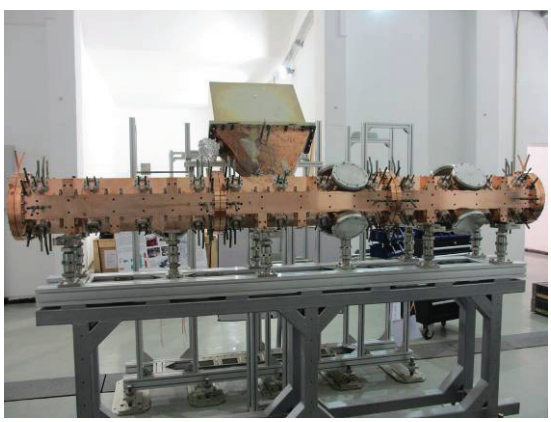

Figure 8: RFQ.

DTL

Samarium-cobalt permanent magnets are adopted as the transverse focusing quadrupoles for the CPHS DTL . The field gradient is designed to be almost constant (84.6 T/m). The lattice structure is FDFD, which ensures small envelop of the beam. The DTL is matched directly with the RFQ accelerator. The average accelerating field increases almost linearly from 2.2MV/m to 3.8MV/m.

The construction of the DTL will be completed in 2013.

HEBT and Target

The CPHS HEBT (Figure 9) is to deliver the 13MeV proton beam accelerated by the DTL to the target station, with minimum beam loss, and obtain one uniform round beam spot with the diameter of 5 cm on the target. To decrease the influence of the recoil neutrons on the DTL, the proton beam is deflected before it bombards the target.

To carry out the proton irradiation experiment with the 13MeV proton beam directly bombarding the target, one straight beam line is designed simultaneously. Two sweeping magnets are designed to obtain the uniform beam spot of 10cm×10cm on the target.

Figure 9: HEBT and target station.

While the HEBT beam line is ready, the 3 MeV proton beam will be used to produce the neutron at the end of 2012.

ACKNOWLEDGMENT

Colleagues of IHEP, IMP, Tsinghua University contribute to this paper. Thanks for them!

REFERENCES

[1] Z.H. Li, et al, “Physical design of the proton accelerator for China ADS,” Progress Report on China Nuclear Science & Technology (Vol.2), October 2011.

[2] H.C. Liu, et al, “Status of the China Spallation Neutron Source Project,” This proceedings.

[3] A. Stanculescu, “Accelerator Driven System (ADS) and Transmutation of Nuclear Waste,” Workshop on Nuclear Data and Nuclear Reactors: Physics, Design and Safety. Trieste, 13 March – 14 April 2000.

[4] R.L. Sheffield, “Utilization of accelerators for transmutation and energy production,” Proceedings of HB2010, Morschach, Switzerland.

[5] Y. He, et al, “Design and progress of Injector II for China ADS proton accelerator,” Progress Report on China Nuclear Science & Technology (Vol.2), October 2011.

[6] S.N. Fu, H.S. Chen, et al, “Status of the China Spallation Neutron Source Project,” PAC'09, Vancouver, May 2009, TH1GRI02, (2009).

Copyright © 2012 by the respective authors — cc Creative Commons Attribution 3.0 (CC BY 3.0)

FRIB ACCELERATOR STATUS AND CHALLENGES*

J. Wei#[1], D. Arenius[2], E. Bernard[1], N. Bultman[1], F. Casagrande[1], S. Chouhan[1], C. Compton[1], K. Davidson[1], A. Facco[1,4], V. Ganni[2], P. Gibson[1], T. Glasmacher[1], K. Holland[1], M. Johnson[1], S. Jones[1], D. Leitner[1], M. Leitner[1], G. Machicoane[1], F. Marti[1], D. Morris[1], J. Nolen[1,3], J. Ozelis[1], S. Peng[1], J. Popielarski[1], L. Popielarski[1], E. Pozdeyev[1], T. Russo[1], K. Saito[1], R. Webber[1], M. Williams[1], Y. Yamazaki[1], A. Zeller[1], Y. Zhang[1], Q. Zhao[1]

[1] Facility for Rare Isotope Beams, Michigan State University, East Lansing, MI 48824, USA
[2] Thomas Jefferson National Laboratory, Newport News, VA 23606, USA
[3] Physics Division, Argonne National Laboratory, Argonne, IL 60439, USA
[4] INFN - Laboratori Nazionali di Legnaro, Legnaro (Padova), Italy

Abstract

The Facility for Rare Isotope Beams (FRIB) at MSU includes a driver linac that can accelerate all stable isotopes to energies beyond 200 MeV/u at beam powers up to 400 kW. The linac consists of 330 superconducting quarter- and half-wave resonators operating at 2 K temperature. Physical challenges include acceleration of multiple charge states of beams to meet beam-on-target requirements, efficient production and acceleration of intense heavy-ion beams from low to intermediate energies, accommodation of multiple charge stripping scenarios (liquid lithium, helium gas, and carbon foil) and ion species, designs for both baseline in-flight fragmentation and ISOL upgrade options, and design considerations of machine availability, tunability, reliability, maintainability, and upgradability. We report on the FRIB accelerator design and developments with emphasis on technical challenges and progress.

INTRODUCTION

The Facility for Rare Isotope Beams (FRIB), baselined as a 7-year, US$680 million construction project, is to be built at the Michigan State University under a corporate agreement with the US DOE [1]. FRIB driver accelerator is designed to accelerate all stable ions to energies above 200 MeV/u with beam power on the target up to 400 kW (Table 1). As shown in Figure 1, the driver accelerator consists of Electron Cyclotron Resonance (ECR) ion sources, a low energy beam transport containing a pre-buncher and electrostatic deflectors for machine protection, a Radiofrequency Quadrupole (RFQ) linac, linac segment 1 (with Quarter-wave Resonators (QWR) of β=0.041 and 0.085) accelerating the beam up to 20 MeV/u where the beam is stripped to higher charge states, linac segments 2 and 3 (with Half-wave Resonators (HWR) of β=0.29 and 0.53) accelerating the beam above 200 MeV/u, folding segments to confine the footprint and facilitate beam collimation, and a beam delivery system to transport to the target a tightly focused beam. The reaccelerator (ReA) consists of similar β=0.041 and 0.085 accelerating structures [2].

*Work supported by the U.S. Department of Energy Office of Science under Cooperative Agreement DE-SC0000661
#wei@frib.msu.edu

Table 1: FRIB Driver Accelerator Primary Parameters

Parameter	Value	Unit
Primary beam ion species	H to ^{238}U	
Beam kinetic energy on target	> 200	MeV/u
Maximum beam power on target	400	kW
Macropulse duty factor	100	%
Beam current on target (^{238}U)	0.7	emA
Beam radius on target (90%)	0.5	mm
Driver linac beam-path length	517	m
Average uncontrolled beam loss	< 1	W/m

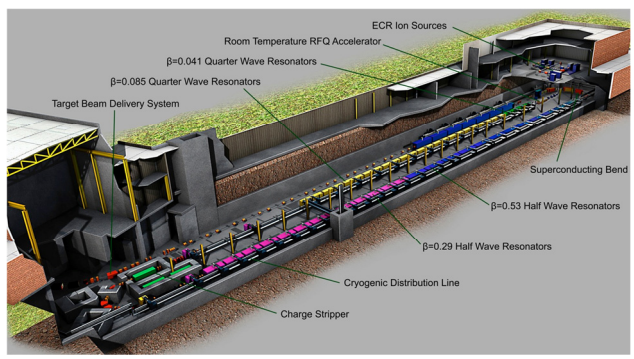

Figure 1: Layout of the FRIB driver accelerator.

DESIGN PHILOSOPHY

Full-energy linac technology is chosen to deliver primary beam that can meet the FRIB requirements of rare-isotope productivity and separation accuracy. Up to 400 kW of beams are focused to a diameter of 1 mm (90%), energy spread of 1% (95% peak-to-peak), and bunch length of < 3 ns (95%) on the target.

Superconducting (SC) technology is the energy-efficient choice for the CW linac. SC acceleration of heavy-ion beams is feasible from very low energy (500 keV/u) with practically sized cavity bores by housing both the cavities and solenoids in a cryomodule. A two-cell scheme is chosen throughout the entire linac providing both efficient acceleration and focusing. Developments of digital low-level RF control and solid-

Copyright © 2012 by the respective authors — cc Creative Commons Attribution 3.0 (CC BY 3.0)

state RF amplifier technologies have made individual cavity powering and control reliable and cost efficient.

Furthermore, high availability, maintainability, reliability, tunability, and upgradability are especially required for the FRIB accelerator to operate as a national scientific user facility.

- Availability: The accelerator is designed with high beam-on-target availability accommodating normal, alternative, and fault scenarios. In the normal scenario, a liquid lithium stripper is used to raise the average charge state of ^{238}U beam to 78+ for efficient acceleration. Alternatively, helium gas confined by plasma windows with differential pumping can be used to strip the ^{238}U beam to a lower average charge state of 71+. Fault scenarios include the situation when superconducting (SC) cavities underperform by up to 20% of the design gradients. Furthermore, key components and subsystems are implemented with spares and design redundancies.
- Maintainability: The average uncontrolled beam loss is limited to below 1 W/m level for all ion species from proton to uranium, to facilitate hands-on maintenance. For a proton beam at high energy, this level corresponds to an average activation of about 1 mSv/h measured at a distance of 30 cm from the beam chamber surface, 4 hours after operations shutdown. For heavy ions like uranium at low energies, activation and radiation shielding is of less concern; the 1 W/m limit addresses concerns in damage on superconducting cavity surfaces and in cryogenic heat load. To facilitate maintenance of individual cryomodules, warm interconnect sections are used between cryomodules, and U-tubes with bayonet connections are used for cryogenic distribution.
- Reliability: A Machine Protection System (MPS) minimizes component damage and operational interruption (e.g. magnet quench and cryogenic load increase) caused by both acute (fast) and chronic (slow) beam losses. Upon acute beam loss, the MPS response time is 35μs (including diagnostics, signal processing, and residual beam dumping). MPS responding to slow beam loss is complicated by low sensitivity of conventional ion chamber loss detection to low-energy heavy ions and beam-loss signal background from adjacent linac segments with which beam energies are significantly different. Beam-halo- scraping rings in the warm interconnect sections and possible thermal sensors at cold regions are planned for more sensitive loss detection [3].
- Tunability: The accelerator is designed to be easily tunable during both beam commissioning and operations. In linac segment 1, where beam transverse-phase advance is large, cold beam-position monitors (BPM) are implemented in the cryomodules. Efforts are made in establishing beam-tuning strategies based on virtual accelerators and on-line models under normal and fault conditions.
- Upgradeability: Space is reserved in linac segment 3 to house another 12 cryomodules to readily increase the energy of ^{238}U beam above 300 MeV/u. If cavities with 35% higher accelerating gradient are used in linac segments 2 and 3, the beam-on-target energy can be raised above 400 MeV/u for ^{238}U. The linac tunnel allows future expansion so that a dedicated light-ion injector can be added supporting rare isotope production using the isotope separation on-line (ISOL) method [1]. Using an RF deflector cavity and a Lambertson septum magnet, $^{3}He^{+}$ beam supplying protons to the ISOL target can share cycle with the ^{238}U beam feeding the fragmentation target; thus simultaneous users are supported. Furthermore, space is reserved to house instrumentations including non-destructive diagnostics and sub-harmonic buncher that are compatible with future user demands of experiments.

ACCELERATOR PHYSICS CHALLENGES

The FRIB accelerator design combines the complexity of heavy ion accelerators with the engineering challenges of high-power accelerators. Due to the low charge-to-mass ratio, heavy ion acceleration is often not efficient. Uncontrolled beam loss, which usually is not an issue for low-power heavy ion machines, is of primary concern for the FRIB accelerator. Comparing with high-power proton machines like the Spallation Neutron Source (SNS) linac where apertures of the elliptical SC cavities are large and beam amplitude reaches maxima in the warm locations of the focusing quadrupole magnets, the apertures of the FRIB QWR and HWR accelerating structures are small and beam amplitude reaches maxima in the cold solenoid locations inside cryomodules. Requirements on beam halo prevention, detection and mitigation are stringent.

To maximize beam intensity on the target, beams of multiple charge states are accelerated simultaneously (2 charge states of 33+ and 34+ before stripping, and 5 charge states of 76+ to 80+ after stripping for ^{238}U). Bends of second-order achromatic optics are used to fold the beams, and cavity phases are adjusted so that beams are longitudinally overlapping at the charge stripper.

Conventional charge strippers like solid carbon foils are not sustainable at the power of a ^{238}U beam at 17 MeV/u during normal operations [4]. FRIB accelerator lattice needs to accommodate beam acceleration of different charge states resulting from various stripping methods including liquid lithium and helium gas (average charge state from 63+ to 78+ for ^{238}U). Buncher cavities of fundamental (80.5 MHz and 322 MHz) and double (161 MHz) linac RF frequencies are strategically placed in the folding segments to preserve beam quality.

Due to the short stopping distance in surrounding materials, uncontrolled beam loss of the low-energy heavy ions can cause damage to the surface of accelerating structures much more easily than a proton beam. On the other hand, due to the low level of radio-activation, losses of low-energy heavy-ion beams are difficult to detect [3]. Beam-loss detection and machine

Copyright © 2012 by the respective authors — cc Creative Commons Attribution 3.0 (CC BY 3.0)

protection often rely on beam scraping. On the other hand, scraping of partially stripped ions may lead to higher ionization further complicating beam collimation and machine protection.

Due to requirements of frequent longitudinal and transverse focusing in the superconducting acceleration structure, focusing solenoids are placed inside cryomodules adjacent to cavities. Alignment tolerance of these solenoids is ±1 mm under cryogenic conditions. Horizontal and vertical steerers are needed to thread the beam and correct the beam orbit.

Stringent beam-on-target requirements demand tight optical control, error control, and advanced beam diagnostics. The primary beam of 400 kW needs to be focused into a diameter of 1 mm with below ±5 mrad transverse angular spread. The desired range of beam power variation on target is 8 orders of magnitude. Orbit stability needs to be controlled at 0.1 mm level.

TECHNOLOGY CHALLENGES

Charge Stripper

The FRIB baseline design of charge stripping [4] was based on the ANL work on a liquid-lithium high-power thick target where it was demonstrated power deposition of 20 kW (from an electron beam) with the liquid lithium operating well in an accelerator environment [5]. During the last couple of years the stability of a thin liquid film with the correct thickness for the FRIB stripper (~600 μg/cm^2) was achieved (Figure 2). The next step is to show that the power deposited by the primary beam on the moving film (~ 1 kW) will not destroy or perturb it.

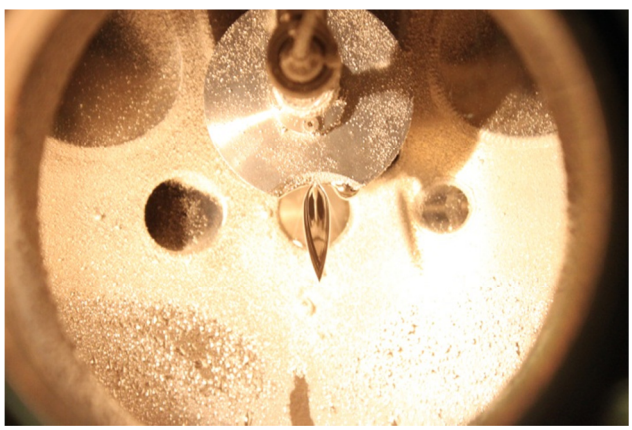

Figure 2: Liquid lithium film established at ANL.

A second option for the stripper consisting of a helium gas cell enclosed by plasma windows was considered. The RIKEN group has shown [6] that helium gas produces a higher average charge state than a nitrogen gas stripper. The purpose of the plasma windows is to limit the helium gas leaking out of the gas cell [4].

Superconducting RF

FRIB driver linac is the first full-size SC linac using a large quantity (340) of low-β cavities. Cavity design is optimized not only for optimum performance but also for low production cost. This requirement guided the choice of the cavity geometries, materials and mechanical solutions, avoiding complicated shapes, minimizing the amount of electron beam welds, eliminating bellows, optimizing construction and surface treatment procedures. FRIB cavities work with superfluid helium at 2 K. The increase in cavity Q more than compensates the energy required for the 2 K cryogenic system operation. This innovative choice in a low-β linac allows operation of cavities in stable pressure conditions with high safety margin on the maximum surface fields [7].

After a 10-year development, the 2nd generation QWR prototypes are used in the ReA3 linac (7 with β_0=0.041 in operation and 8 with β_0=0.085 under installation). This cavity type underwent modifications including the displacement of the RF coupler from the bottom plate to the resonator side and an increased distance between the tuning plate and the inner conductor tip, in order to remove a critical thermal problem in the design. The new tuning plate includes slots and undulations to increase its maximum elastic displacement and thus its tuning range, and a "puck" whose length can be adjusted for cavity tuning before final welding. Concerning the β_0=0.53 HWR prototype, which is similar in design to the β_0=0.29 cavity, 4 units of the 2nd generation have been built by 2 different vendors in addition to the one built in house. After positive test results, the β_0=0.085 QWR and the HWRs designs are further refined in a 3rd generation design with increased diameter that takes maximum advantage of the space available in FRIB cryomodules.

Test results and production cost considerations led to the choice of buffered chemical polishing (BCP) for FRIB cavity's surface treatment. The effort was concentrated in the development of a reliable procedure able to produce field-emission free, high gradient cavities. The treatment includes the following BCP steps: 1) bulk etch (~150μm removal), 2) differential etching in QWRs for final cavity tuning if required, 3) light etch (~30 μm removal). Thermal treatment in high vacuum at 600 °C is applied before step 3) for Hydrogen removal to prevent Q disease. High pressure water rinsing (HPR) is applied before cavity final installation. To assure surface cleanliness, dust particle count is performed on resonator surfaces during cavity assembly in the clean room and the water purity is continuously monitored during HPR. During BCP both the cavity and acid temperatures are stabilized to control the removal rate and to avoid excess of hydrogen absorption in Nb. The acid flow path in the β_0=0.53 HWR was studied by means of simulations and experiments to obtain homogeneous removal over the entire inner resonator surface. The implementation of the 120°C final thermal treatment showed negligible improvement of the Q-slope at 2 K but significant reduction at 4.2 K [8].

The 2nd generation prototypes of β_0=0.085 QWR and 0.53 HWR have been tested in vertical dewars at 2 K exceeding FRIB design specifications. The residual resistance measured in the prototype families was below 5 nΩ up to about 100 mT in QWRs, and about 80 mT in

Copyright © 2012 by the respective authors — cc Creative Commons Attribution 3.0 (CC BY 3.0)

HWRs. Considering that the FRIB specified limits are 11 nΩ and 70 mT, a large safety margin exists for upgrades.

The 3rd-generation cavity design optimization resulted in significant improvement of peak fields E_p/E_{acc}, B_p/E_{acc} and shunt impedance R_{sh}, with consequent reduction of the overall linac cost and operational risk. E_p and B_p in operation could be moved below the safe values of 35 MV/m and 70 mT in all cavities. The design gradients of the β_0=0.085 QWR and β_0=0.29 HWR are raised by 10% without increasing the total cryogenic load, allowing a reduction of two cryomodules. The apertures of all QWRs were enlarged from 30 to 34 mm, and their bottom rings were modified for efficient tuning-plate cooling using a low-cost design. The HWR designs were optimized to facilitate the mechanical construction and tuning procedure. In all cavities, the helium vessel is made of titanium to avoid brazed Nb-to-stainless-steel interface.

The Technology Demonstration Cryomodule (TDCM) consists of two β_0=0.53 HWRs operating at 2 K and a 9 T solenoid operating at 4.5 K arranged in a "top-down" configuration. The cryomodule was tested [9] at the design cryogenic temperatures demonstrating excellent cryogenic and LLRF control stabilities. Multipacting was found to impede the performance of the cavities and the coupler [9]. Future tests are planned on magnetic field and shielding studies, mechanical-type and pneumatic-type tuner evaluations, multipacting mitigation, and integrated tests with both β_0=0.29 and β_0=0.53 HWRs.

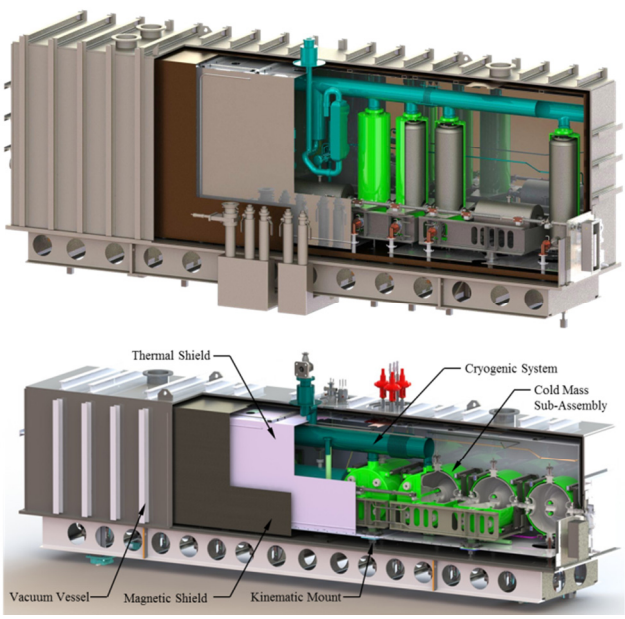

Figure 3: FRIB "bottom-up" cryomodule designs. The top cryomodule incorporates 8 β=0.085 QWRs, 3 solenoids, and 3 cold beam position monitors; the bottom cryomodule incorporates 8 β=0.53 HWRs and a solenoid.

The FRIB cryomodule design has evolved significantly from the "top-down" ReA3 style to a "bottom-up" design [10]. Key features including rail system, support system, heat and magnetic shields are simplified along with improvements in assembly and alignment. Figure 3 shows the current design incorporating a torque-resistant structural frame made of stainless steel. We incorporate machined fiberglass compression posts supporting the coldmass in the cryomodule vacuum vessel. Three posts on linear roller bearings oriented towards the center of thermal contraction serve as 6-degree-of-freedom kinematic supports. This design controls the alignment of the coldmass while allowing thermal contraction. Cavity and solenoid attachment points to the rails are all machined after welding to ensure assembly consistency.

DESIGN & ACQUISITION

A summary of the accelerator design status was given in Ref. [1] including the front end, linac segments, folding segments, beam-delivery system, and reaccelerator. Also discussed was subsystem status including the cryogenics, cryomodule, RF, ion source, RFQ, magnet and power supply, diagnostics, vacuum and alignment, controls, and utilities [1]. After the project baseline in April 2012, the FRIB project entered into its final design phase when detail-engineering designs are performed at MSU. While critical processing and assembly are to be performed in house, fabrication of a large quantity of repetitive components is planned through mass production and out-sourcing by industrial providers [11].

The FRIB project plans to place approximately 450 procurements valued at more than $50k each. The sum of all technical equipment procurements amounts to $217M excluding conventional facility construction. We have implemented a procurement strategy that strives to reduce vendor risks for the best value to the FRIB project:

- We work directly with the vendors understanding their individual risk concerns and proposing mitigations:
  - Perform certain tasks in-house if the vendor lacks capability;
  - Adjust engineering designs to allow vendor to implement familiar fabrication approaches;
  - Identify key-personnel bottlenecks at the vendor, and provide technical support where necessary;
  - Work closely with the vendor in mass-production planning and subsequent quality monitoring;
  - Accept components on mechanical (dimensional) properties instead of functional (e.g. electromagnetic, RF) performance;
  - FRIB to purchase high-cost materials that expose to market fluctuations (e.g., Nb).
- We evaluate how the project fits into the supplier's total capabilities and long-term business plans to gauge supplier management's commitment to solve production challenges and risks.
- We develop long-term supplier relationships for mass production. Phasing of procurements from prototypes to production sensitizes vendors to be able to successfully produce the unique components.

So far we have implemented this strategy to negotiated favorable prices for all the SRF material purchases and the production of 174 β=0.53 HRWs [9].

Copyright © 2012 by the respective authors — cc Creative Commons Attribution 3.0 (CC BY 3.0)

COLLABORATION & PARTNERSHIP

FRIB accelerator systems design has been assisted under work-for-others agreements by many national laboratories including ANL, BNL, FNAL, JLAB, LANL, LBNL, ORNL, and SLAC, and in collaboration with many institutes including BINP, KEK, IMP, INFN, INR, RIKEN, TRIUMF, and Tsinghua University.

The cryogenics system is designed in collaboration with the JLAB cryogenics team. The refrigeration process incorporates the cumulative experience from both JLab and SNS cryogenic systems. The recent experience gained from the JLab 12 GeV cryogenic system design is utilized for both the refrigerator cold box and the compression system designs. The Floating Pressure Process – Ganni Cycle [12] is to be implemented to provide efficient adaptation to the actual loads.

The charge stripping system is under development in collaboration with the ANL Physics Division. We borrowed the LEDA ion source and LEBT from LANL to modify the optics to obtain a 1 to 3 mm diameter beam spot on the liquid-lithium film at MSU. Once the new optics is checked on a new platform that is matched to the ANL lithium loop, the device will be moved to ANL for the integrated test.

The SRF development benefit greatly from the expertise of the low-β SRF community. Weekly teleconferences are held with participations from INFN, TRIUMF, JLAB, and ANL. FRIB is collaborating with ANL on the coupler and tuner developments, and assisted by JLAB on cavity processing.

FUTURE PERSPECTIVES

The FRIB accelerator design is advanced towards beginning construction in 2014. Early procurements before 2014 is strategically planned to establish the front end test stand to demonstrate critical components of the ECR ion source and the fully powered RFQ, to contract on long lead-time cryogenic refrigeration subcomponents, to acquire cryogenic distribution equipment that needs to be installed before accelerator tunnel completion, and to acquire SRF components to be assembled in the pre-production cryomodules. Upon fabrication, installation, and integrated tests, early beam commissioning is expected to be staged from 2017 to 2019. The facility is scheduled to meet key performance parameters supporting user operations before 2021. Full design capability is expected to be reached in 4 years after the beginning of operations. Science driven upgrade options may be pursued at any stage of the project.

ACKNOWLEDGMENTS

We thank the Accelerator Systems Advisory Committee chaired by S. Ozaki for their valuable advice and guidance, B. Laxdal, P. Kneisel, and A.C. Crawford for their participation in the FRIB weekly teleconference, colleagues who participated in FRIB accelerator peer reviews including A. Aleksandrov, G. Ambrosio, W. Barletta, G. Bauer, G. Biallas, J. Bisognano, S. Bousson, M. Champion, M. Crofford, R. Cutler, B. Dalesio, G. Decker, J. Delayen, H. Edwards, J. Error, J. Fuerst, K. Kurukawa, J. Galambos, J. Galayda, J. Gilpatrick, S. Gourlay, S. Henderson, L. Hoff, G. Hoffstaetter, J. Hogan, N. Holtkamp, H. Horiike, C. Hovater, H. Imao, R. Janssens, R. Keller, J. Kelley, P. Kelley, M. Kelly, J. Kerby, A. Klebaner, J. Knobloch, J. Mammosser, T. Mann, N. Mokhov, G. Murdoch, H. Okuno, P. Ostroumov, R. Pardo, S. Peggs, T. Peterson, C. Piller, J. Power, T. Powers, J. Preble, D. Raparia, T. Roser, R. Ruland, W.J. Schneider, D. Schrage, J. Sondericker, W. Soyars, C. Spencer, R. Stanek, M. Stettler, J. Stovall, V. Verzilov, P. Wanderer, M. Wiseman, L. Young, and A. Zaltsman, and colleagues who advised and collaborated with the FRIB team including A. Burrill, K. Davis, W. Hartung, D. Hseuh, A. Hutton, R. Kersevan, S.H. Kim, K. Macha, G. Maler, E.A. McEwen, W. Meng, T. Reilly, J. Sandberg, J. Tuozzolo, and J. Vincent. At Michigan State University, the FRIB accelerator design is executed by a dedicated team of the FRIB Accelerator Systems Division with close collaboration with the Experimental Systems Division headed by G. Bollen, the Conventional Facility Division headed by B. Bull, the Chief Engineer's team headed by D. Stout, and supported by the project controls, procurements, ES&H of the FRIB Project, by the NSCL, and by the MSU.

REFERENCES

[1] J. Wei et al, HIAT12, MOB01 (2012, in press)
[2] D. Leitner et al, SRF'2011, Chicago (2011, in press)
[3] Z. Liu, Y. Zhang et al, IPAC'12, New Orleans (2012)
[4] F. Marti, these proceedings
[5] Y. Momozaki et al, JINST 4 (2009) P04005
[6] H. Okuno et al, Phys. Rev. ST-AB 14 (2011) 033503
[7] A. Facco et al, IPAC'12 (2012, in press)
[8] L. Popielarski et al, these proceedings
[9] J. Popielarski et al; W. Zheng et al, these proceedings
[10] M. Johnson et al, IPAC'12, (2012, in press)
[11] M. Leitner et al, these proceedings
[12] V. Ganni, P. Knudsen, Adv. Cryo. Eng. 55, AIP, New York (2010) 1057.

Copyright © 2012 by the respective authors — cc Creative Commons Attribution 3.0 (CC BY 3.0)

STATUS AND COMMISSIONING PLAN OF PEFP 100-MEV LINEAR ACCELERATOR*

Hyeok-Jung Kwon#, Yong-Sub Cho, Ji-Ho Jang, Han-Sung Kim, Kyung-Tae Seol, Young-Gi Song, Dae-Il Kim, Bum-Sik Park, Sang-Pil Yun, Jin-Yeong Ryu,
PEFP/KAERI, Daejeon, Korea

Abstract

One of the goals of the Proton Engineering Frontier Project (PEFP) is to develop a 100-MeV proton linear accelerator, which consists of 50-keV proton injector, 3-MeV radio frequency quadrupole (RFQ), 20-MeV / 100-MeV drift tube linac (DTL) and 20-MeV / 100-MeV beam lines. The 100-MeV linear accelerator and beam line components have been installed in the tunnel and experimental hall. After the completion of the utility commissioning, the commissioning of the accelerator starts with a goal of the beam delivery to the 100-MeV target room located at the end of the beam line. The proton beams will be supplied to users from March 2013. In this paper, the status and commissioning plan of the PEFP 100-MeV linear accelerator are presented.

INTRODUCTION

The PEFP was launched by the Korean Government at 2002 as a 21st century Frontier R&D program. It has three main objectives; to develop a high power proton linac, to develop proton beam utilization and accelerator application technology, to industrialize developed technologies.

The specifications and schematics of the 100-MeV, 20mA proton accelerator developed by PEFP are shown in Table 1 and Figure 1 respectively. The PEFP proton accelerator has its own characteristics; to supply high duty & high average current beam to users, to supply proton beam with wide range in beam energy and current, to supply proton beam into 3 beam lines simultaneously, and to supply beam with large area up to 300mm in diameter. The main application fields of the accelerator are such that; industrial field with ion cut, semiconductor switch application, radio isotope production, medical field with proton therapy research, biological field with mutation of plants & micro-organism, space technology field with research on radiation effect on materials, and basic science field with neutron application.

The project host city is Gyeongju who supplies land and supporting buildings such as main office building, regional cooperation centre and dormitory and so on. The main buildings for accelerator and experimental hall, utility and substation are provided by the central government. The construction of the main buildings will be completed in October, 2012.

The development of 100-MeV DTL was completed in 2010. The main accelerator components such as RFQ and DTL were designed by PEFP, fabricated by the 17 Korean domestic industries, assembled and tested by PEFP. As a front end, a 20-MeV linac was developed, installed and operated since 2007 at KAERI Daejeon site waiting for the PEFP site preparation at Gyeongju. [1][2] The operation of 20-MeV linac at Daejeon was finished at November 2011. Since then, the machine was disassembled and delivered to Gyeongju site at February 2012 when the accelerator tunnel was prepared. The 100-MeV accelerator and two beam lines were installed inside the accelerator tunnel and the experimental hall, respectively. The commissioning of the accelerator will start at the end of 2012 after the klystron gallery, modulator room and utility are prepared.

Table 1: Specifications of the PEFP Proton Accelerator

Parameter	DTL-I	DTL-II
Output Energy (MeV)	20	100
Max. Peak Beam Current (mA)	20	20
Max. Beam Duty (%)	24	8
Average Beam Current (mA)	4.8	1.6
Max. Pulse Length (ms)	2	1.33
Max. Repetition Rate (Hz)	120	60
Max. Avg. Beam Power (kW)	96	160

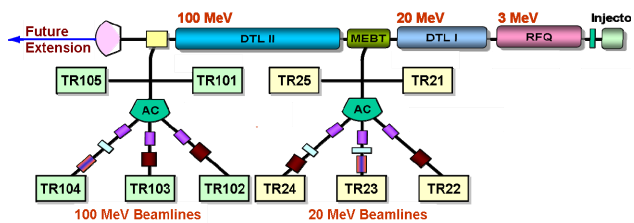

Figure 1: Schematic of the PEFP proton accelerator and beam lines

ACCELERATOR DEVELOPMENT

20-MeV Linac Operation

The 20-MeV linac was installed at Daejeon site temporarily in 2005 waiting for site preparation at Gyeongju. The 20-MeV linac got an operation license in 2007, since then the machine was used to study the machine itself and to test 100-MeV accelerator components in addition to supply proton beams to users. The key technologies developed during 20-MeV linac operation are as follows.

*Work supported by the MEST in Korean Government
#hjkwon@kaeri.re.kr

Copyright © 2012 by the respective authors — cc Creative Commons Attribution 3.0 (CC BY 3.0)

The digital LLRF system was developed from the analogue system in 2007 and upgraded in 2010. The digital LLRF system utilized a commercially available control board with FPGA. The control algorithm with PI was developed by PEFP. The board can produce synchronized NCO output signal equipped in the board, therefore it does not need an analogue IQ modulator. By installing mixers at input and output section symmetrically, the LLRF system became more stable against the external reference signal perturbation. The delay of the system was measured to be less than 1us. The OPI interface of the LLRF system is GUI mode with EPICS. Various waveforms, such as RF forward power, RF reflected power and cavity field level can be monitored as well as the resonant frequency error measurement function. [3][4] The high power test results showed that the amplitude and phase were maintained within 1% and 1degree respectively. By using the digital LLRF system, the beam current could be stabilized during operation. [5]

The klystron power supply was changed from DC high voltage power supply to the high voltage converter modulator (HVCM) in 2009. The design duty of the 20-MeV machine is 24%. A CW klystron and DC high voltage power supply were used in the initial operation period. At that time, the electron beam of the klystron was operated in DC mode and only the RF operation was in pulse mode. Therefore the operation efficiency was very low because the machine could not be operated at high duty due to the insufficient radiation shielding, whereas the power consumption was 4MW to drive two CW klystrons. To increase the efficiency, the high voltage converter modulator was developed as a klystron power supply for 100-MeV linac. When the modulator was delivered, it was installed in 20-MeV linac RF system with the purpose of testing the modulator itself and driving the 20-MeV linac. The system efficiency of the 20-MeV linac could be increased by driving the klystron electron beam in pulse mode. In addition, several problems of the first modulator were identified and fixed. The debugging of the first delivered modulator was reflected on the successive procurements of the modulator. [6]

The ion source was changed from duoplasmatron type to microwave type in 2011. The main purpose of this change was to meet the ion source requirement of more than 100 hours continuous operation without maintenance. The former duoplasmatron type ion source satisfied all the requirements such as beam current, beam emittance and so on except the life time. Due to the filament, its life time was limited to 40 hours. But the life time of the ion source should be more than 100 hours based on the operation scenario of the 100-MeV linac. Therefore microwave ion source was developed because one of its advantages was long life time. The developed microwave ion source was tested for 100 hours at the test bench and it showed no degradation of the performance. After the test at the test bench, it was installed at 20-MeV linac and used as a proton injector. The microwave ion source had been operated for 243 hours without maintenance until the November, 2011. [7][8]

For beam diagnostic devices, the beam position monitors (BPM) for 100-MeV linac and the beam transfer line were developed and tested at the 20-MeV beam line in 2011. The beam test results showed that the BPM produced the expected signal and was good enough for the beam phase measurement. [9]

In addition to the technology development of each accelerator components, the integrated test of the accelerator was carried out.

The long-time operation was tried to check the pulse loss statistics. The total number of pulses was 14,400 and the total pulse loss rate was 0.56%. Among them, 0.01% was due to the spark at the ion source and 0.55% was due to the spark at the RFQ. The spark at the RFQ was the main cause of the beam pulse loss. [10] For the long-pulse operation test, it was not difficult to increase the beam pulse width up to 500us. The 500us beam pulse is shown in Figure 2. The high repetition rate test was also carried out. The RF system was operated at 20Hz and the repetition rate of the beam from the ion source was increased from 1Hz to 15Hz. The beam pulse at 15Hz is shown in Figure 3. All the system including low level RF and data acquisition system was operated without any problems. The radiation dose was measured at the target room fence which is 1m apart from the radiation shielding block. The neutron dose rate was 500uSv/hr at 15Hz and gamma ray dose rate was 150uSv/hr. We did not increase the duty because of the insufficient radiation shielding at Daejeon site. [11]

The beam parameters such as beam energy, beam profile, beam emittance and beam phase were measured in parallel with the machine study. The beam energy was measured with the time-of-flight method by using two BPMs installed at the 20-MeV beam line. The result was 20.2MeV and this was compared with other two methods; dose measurement and range measurement with the aluminium foil, Gafchromic film and ion chamber. Both results showed a good agreement within 1% with each other. To measure the beam profile, we used the wire scanner. The beam profiles depending on various operating conditions of the quadrupole triplet installed at the 20-MeV beam line were measured and the beam radius was compared with the PARMILA results.

The beam emittance at the upstream of the RFQ was measured by using the electric sweep scanner. The measured emittance was 0.35 π mm mrad in normalized rms value which showed higher than the design value of 0.2 π mm mrad. It is necessary to optimize the operation parameters of the ion source and LEBT. The beam emittance at the downstream of the 20-MeV DTL was also measured by using quad scan method. The last magnet in the triplet was used to change the transfer matrix. The measured emittance was 0.22 π mm mrad, which was well agreed with the design value. [8]

The BPM signals were utilized for the beam phase measurement, which is important at the commissioning stage of the 100-MeV linac because a phase scan method

Copyright © 2012 by the respective authors — cc Creative Commons Attribution 3.0 (CC BY 3.0)

is considered as a tuning method of the RF amplitude and phase. The beam phase was measured at various amplitude and phase of the RFQ and DTL and the results were compared with the PARMILA results. Finally, we could establish the phase scan algorithm based on the measurement data. [12]

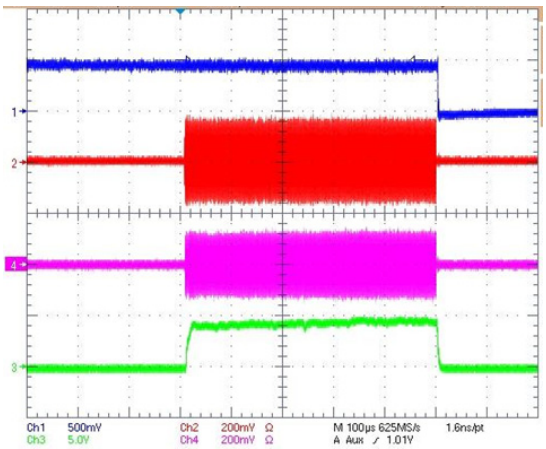

Figure 2: 500us beam operation (Time : 100us/div.)

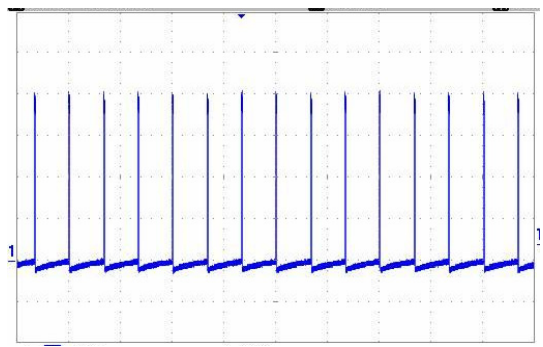

Figure 3: Beam pulse at 15Hz (Time span: 1s)

A 20-MeV beam was supplied to the users during the 20-MeV machine operation in Daejeon site. The users who want a beam service submit an application form through the Internet and the beam line operator contacts the users and discusses the irradiation conditions. After that, the beam line operator does the beam service by using the sample prepared by the users. During beam irradiation to the specimen, the beam line operator communicates with the linac operator through the control system which includes personal protection logics. The beam conditions were adjusted to the specific user demands however the typical operation conditions were 5mA peak current with 50us pulse width, 1Hz repetition rate during beam service. There were total 1603 samples irradiated by using 20-MeV linac for five years. The number of sample treatment increased from about 100 samples in 2007 to more than 680 in 2011 as shown in Figure 4. For five year beam service, most of the users (66%) come from the Research Institute, and the others come from the University (22%) and Industry (12%). The most frequent application field was Bio-Technology (60%) including the cancer cell irradiation and mutation study. The research and application field related to the Nano-Technology (17%) which included a nano-particle synthesis was next to Bio-Technology.

As mentioned above, the operation of 20-MeV linac at Daejeon site was finished at November 2011. Since then, the machine was disassembled and delivered to Gyeongju site at February 2012. The DTL tanks and klystrons were moved with the vibration free truck as shown in Figure 5. After the movement, the field profile of the DTL was measured and the difference was within 3% before and after the movement.

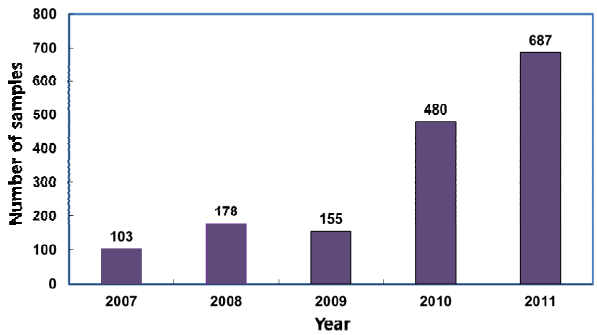

Figure 4: Number of samples depending on fiscal year

Figure 5: 20-MeV DTL tanks on the vibration free truck for the movement to Gyeongju site

100-MeV Linac Development

The fabrication of the 20-MeV ~ 100-MeV DTL tanks was completed at December 2010. It consists of seven tanks and total 163 ea. drift tubes. It has hollow type electromagnet for beam focusing whereas the 20-MeV DTL has a pool-type electromagnet. The length of each tank is 6.8m. The 100-MeV DTL tank has one klystron per one DTL tank and one Resonant Frequency Control Cooling System (RCCS) for each tank.

The fabrication of two Medium Beam Energy Transport (MEBT) tanks was also completed. MEBT tanks will be used as a longitudinal matching section between 20-MeV DTL and 100-MeV DTL because there is a long drift space between them for 20-MeV beam extraction. The MEBT tank is a kind of DTL tank with three gaps.

The 350MHz klystron is used as a RF amplifier for the PEFP linac. The specification of the klystron is 1.6MW peak power with 1.5ms pulse width, 60Hz repetition rate. It was modified from the TH2089F CW klystron to produce a higher peak power and reduced duty. There are

Copyright © 2012 by the respective authors — cc Creative Commons Attribution 3.0 (CC BY 3.0)

total 7 klystrons for 20-MeV ~ 100-MeV DTL, and all the klystrons were delivered to Gyeongju site and waiting for installation.

The high voltage converter modulator is used to drive the klystron. The specification of the modulator is 5.8MW peak power with 1.5ms pulse width, 60Hz repetition rate. There are two distinct features in the PEFP modulator. One is to keep the pulse voltage droop less than 1% by the adjustment of the switching frequency. The other is to limit the load arc energy less than 20J spontaneously by the internal resonant characteristics, which means that the crowbar is not necessary in the modulator. One modulator drives two or three sets of the klystrons simultaneously. Total 4 sets of modulator are necessary for whole accelerator including 3-MeV RFQ, 20-MeV DTL and 100-MeV DTL and all of them were delivered. One of the modulators was used to drive the 20-MeV linac at Daejeon site for 3 years. The normal operation conditions was 2.8MW peak power with 1ms pulse width, 4Hz repetition rate. It was tested up to 30kW in average power.

A RCCS is used to control the resonance frequency of each DTL tank by supplying the temperature–controlled water to drift tubes. The maximum heat load is 94kW. It should cover large range of heat load from lowest heat load from the magnet only to the highest heat load from the full duty RF power in addition to the magnet heat load. The operating temperature range of the RCCS was designed from 21°C to 33°C to reduce the DTL tuning requirement. Within the above temperature range, the RCCS can maintain the temperature accuracy within ±0.1°C by using two sets of three-way valves. Also the RCCSs were ready to installation.

One of the most important interfaces between machine and building was the waveguide connecting accelerator located in first floor with the klystron located second floor. The waveguide was specially designed, fabricated and tested with care and embedded inside the ceiling of the tunnel during the building construction.

Beam Line Development

The important components of the beam line are AC magnet which distribute the proton beams into three beam lines pulse by pulse successively and 300mm aperture beam window to extract large area beam into the air for irradiation, in addition to the main dipole and quadrupole magnets. All the dipole and quadrupole magnets were fabricated. The magnetic properties of the magnet were measured and the geometrical fiducialization was also finished. Two AC magnets, one for 20-MeV beam, the other for 100-MeV beam were also fabricated. The sweep frequencies of the AC magnets are 15Hz for 20-MeV beam line and 7.5Hz for 100-MeV beam line. The maximum bending angle of the AC magnet is 20 degree. The AC magnet will be driven by the power supply with fast switch technology. The material of beam window is a 0.5mm thickness AlBeMat with concave geometry. The energy loss through the beam window is 0.6MeV for 100-MeV beam. The window will be forced air-cooled by using the blower.

COMMISSIONING PLAN

Each of the high power devices such as modulator and klystron will be commissioned after the commissioning of the all utilities is completed. The first devices to be on-site commissioned are 4 sets of modulator. The modulator will be tested at low power level of 2kW in average power with non-inductive resistor. The beam and RF test of the klystron will be done after the modulator tests are completed. Initial test of the klystron will be done without connection to the DTL tank and reflecting all the RF power to the dummy load by using a shorting plate installed one arm of the circulator. The on-line RF conditioning of the DTL tank will be done after the high power test of the klystron-modulator system finishes.

The beam commissioning goal of the accelerator is to deliver a 100-MeV, 1kW beam to the beam dump located at the end of the accelerator. The commissioning goal of the beam line is to deliver a 100-MeV, 1kW beam to the beam dump located in the TR103 target room.

An important step of the beam commissioning process is to determine the RF amplitude and phase of each DTL tank. We adopt a phase scan method [12][13]. For this purpose, a strip line BPMs will be used at the downstream of each DTL tank to pick up the beam phase signal. Then the signal is delivered to the commercially available control board. The control board treats both the LLRF control signals as mentioned above and beam phase signal because both signal needs RF reference. In addition to the hardware, software to treat the phase scan data was implemented in Matlab. An experimental data of the beam phase as a function of RF phase with the fixed relative amplitude A/A_0 is compared with the implemented PARMILA simulation results to generate a χ-value for each case of A/A_0. The quadratic fitting of the χ-values can determine the RF amplitude and phase.

INSTALLATION AND SCHEDULE

The 100-MeV linac was installed inside the tunnel as shown in Figure 6 after the survey of the tunnel was performed and the supporting structures were prepared at March 2012. The total length from the ion source to the beam dump is 93m. The magnets of the 20-MeV / 100-MeV beam line were also installed at May 2012 as shown in Figure 7. [14]

Based on the construction schedule, the klystron gallery and modulator room will be prepared in September 2012, and the utility commissioning will be finished in October 2012. Form September, the modulator will be delivered to the modulator room in 3rd floor and installation starts. Also all the RF components including klystron, RCCS and waveguides will be installed in the klystron gallery of 2nd floor. The accelerator commissioning starts from the modulator commissioning step by step after the utility commissioning is completed. The DTL conditioning will start in January 2013 and the beam acceleration into the beam dump is planned in February 2013. The construction status of the accelerator building is shown in Figure 8.

Copyright © 2012 by the respective authors — cc Creative Commons Attribution 3.0 (CC BY 3.0)

Figure 6: The installed 100-MeV linac in the tunnel

Figure 7: The installed 20-MeV beam line magnets in the 20-MeV beam line hall

Figure 8: Construction of the accelerator building at Gyeongju project site

CONCLUSION

The PEFP launched by the Korean government in July 2002, is developing a 100-MeV proton linac and installing the facilities at Gyeongju project site. The 20-MeV part of the linac has been successfully developed, tested and operated for 5 years at Daejeon. After finishing operation at November 2011, it was moved to the project site at Gyeongju. The installation of the 100-MeV linac and beam line magnets were finished in March 2012. The modulators and klystrons will be installed from September 2012. The construction of the accelerator building including the commissioning of the conventional facility will be completed in October 2012. The commissioning of the accelerator starts from the modulator commissioning. The important milestones are to start the DTL tank conditioning in the tunnel in January 2013 and to deliver the 100-MeV proton beam into the beam dump in February 2013.

REFERENCES

[1] B. H. Choi, et al., "The Proton Engineering Frontier Project", Proceedings of IPAC10, Kyoto, p3616 (2010).
[2] Y. S. Cho, et al., "100-MeV High – Duty - Factor Proton Linac Development at KAERI", Proceedings of LINAC 2006, Knoxville, p501 (2006).
[3] Y. G. Song, et al., "Design and Implementation of Distributed Control System for PEFP 100-MeV Proton Accelerator", Proceedings of IPAC2011, San Sebastian, p2334 (2011).
[4] K. T. Seol, et al., "Improvement of the RF System for the PEFP 100-MEV Proton Linac", Proceedings of IPAC2011, San Sebastian, p139 (2011).
[5] H. S. Kim, et al., "Development of the PEFP Low Level RF Control System", Proceedings of PAC07, Albuquerque, p2167 (2007).
[6] D. I. Kim, et al., "Klystron and Modulator System for the PEFP 20-MeV Proton Linac", Proceedings of IPAC2011, San Sebastian, p3352 (2011).
[7] D. I. Kim, et al., "Beam Test of the Microwave Ion Source for the 20-MeV Proton Linac", Transactions of the Korean Nuclear Society Spring Meeting, Taebaek, May 2011.
[8] H. J. Kwon, et al., "Improvement of the 20-MeV Proton Accelerator at KAERI", Proceedings of IPAC2011, San Sebastian, p3466 (2011).
[9] J. Y. Ryu, et al., "Low Power Test of the PEFP Prototype Beam-line BPM and Linac BPM", Transactions of the Korean Nuclear Society Spring Meeting, Jeju, May, 2012.
[10] H. J. Kwon, et al., "100-MeV Proton Accelerator Component Tests by Using 20-MeV Linac", Proceedings of LINAC2010, Tsukuba, p443 (2010).
[11] S. P. Yun, et al., "Development of the Target Room for the 20-MeV PEFP Linac", Transactions of the Korean Nuclear Society Spring Meeting, Gyeongju, May 2008
[12] J. H. Jang, et al., "Beam Commissioning Plan of PEFP 100-MeV Linac", Proceedings of IPAC2011, San Sebastian, p2619 (2011).
[13] T. L. Owens, M. B. Popovic, E. S. Mccrory, C. W. Schmidt, and L. J. Allen, "Phase Scan Signature Matching for Linac Tuning", Particle Accelerators., 48 (1992) 169.
[14] B. S. Park, et al., "Positioning the 100-MeV Linac and Magnets with Two Laser Trackers", Proceedings of IPAC2012, New Orleans, p2912 (2012).

Copyright © 2012 by the respective authors — cc Creative Commons Attribution 3.0 (CC BY 3.0)

OVERVIEW OF SACLA MACHINE STATUS

Y. Otake#, on behalf of the members of XFEL division, XFEL Research and Development Division,
RIKEN SPring-8 Center, Harima Institute, RIKEN, 1-1-1,
Kouto, Sayo-cho, Sayo-gun, Hyogo JAPAN 679-5148
XFEL Division, JASRI, 1-1-1, Kouto, Sayo-cho, Sayo-gun, Hyogo JAPAN 679-5198

Abstract

SACLA, part of an X-ray free-electron laser, has been constructed, and was successfully lased at 0.06 nm in 2011. SACLA mainly comprises a low-emittance thermionic electron gun, an 8-GeV linear accelerator using C-band (5712 MHz) cavities and 18 in-vacuum undulators. A concept used to develop this machine involves compactness compared with the other machine, such as LCLS with a length of more than 1 km. Stable X-ray lasing of up to 0.06 nm to also be a concept demands extremely stable accelerator components, such as a 50 fs temporal stability of an rf phase at a cavity in an injector. We have now realized a 700 m compact machine by using low-emittance at an electron gun, an accelerating gradient of more than 35 MV/m by a C-band accelerator, and short-period undulators. Continuous lasing for more than several days is strongly supported by these stable components and small operator's trimming, and has also been established by reducing perturbation sources to laser instability. SACLA is regularly operated for user experiments, such as material imaging with an extreme amount of data.

INTRODUCTION

SACLA has been constructed in order to generate an X-ray laser of up to a wavelength of around 0.06 nm, and is now under operation for user experiments [1]. We can explore new science, such as revealing protein membrane structures, by this machine.

SACLA was designed in accordance with the following two concepts, called SCSS concepts [2]. One is a short machine length, like compactness, which is associated with low construction costs. Next, is an ultra stable machine, which guarantees stable laser intensity, contributing to reliable experiments. In order to realize this concept, we employ a method using a high-brightness, low-emittance thermionic electron gun operated at a 500 kV high-voltage pulse [3], a C-band accelerator with a high-gradient acceleration of more than 35 MeV/m [4] and an in-vacuum undulator with a short period and a narrow gap [5]. Their high-brightness electron beam and narrow gap as well as short period, λ_u, associated with a large undulator parameter, K, and a short radiation wavelength, λ, allow us to reduce the gain length of self-amplified spontaneous emission (SASE) along the undulator beam line. High-gradient acceleration is also effective to make a short accelerator. Hence, the machine length becomes shorter than other X-ray free electron laser (XFEL) machines of over 1 km, such as the linac coherent light source (LCLS) at SLAC [6] and Euro-XFEL at DESY [7]. This SCSS concept is the most prominent characteristic of our SACLA.

Ultimate stability of an X-ray laser, which is guided by ultra-stable accelerator components, is also a crucial part of SACLA. As examples to realize stable X-ray lasing conditions, it is necessary that the electron beams and related undulator radiation should spatially overlap within 4 μm in STD along the undulator line [8], if we allow for reduction of the SASE intensity up to half of the peak intensity (design value). The demanded rf phase (temporal) stability at cavities in an injector is around 100 fs in STD, if we also accept a peak electron-intensity fluctuation of 10% in STD, corresponding to a peak X-ray laser intensity fluctuation of 10% in STD [9], which is almost the intrinsic intensity jitter of statistical SASE generation. The amplitude of the Pierce gain parameter, ρ, for FEL amplification along an undulator section directly reflects the overlap factor, OF, between the electron beam and its radiation [10], and also the charge density of the electron beam [2]. For example, these component stabilities mean a stable low-emittance value and electron beam energy stability established by the emission stability of the electron beams form the thermionic electron gun, the rf phase and amplitude stabilities of acceleration cavities, the magnetic field stabilities of beam-transport magnets, undulator magnetic field stability, and components alignment in order to secure the interaction between the electron beams and the beam radiated field along the undulator line.

We must realize these required values to secure stable X-ray laser radiation, as well as the concept. This paper introduces accelerator components and their performances, X-ray lasing performance, and the present issues to deteriorate the lasing performance of SACLA.

SACLA'S MACHINE LAYOUT, ITS FUNCTION AND COMPONETS

Layout and Function

Figure 1 shows the machine configuration of SACLA, which mainly comprises a 500 kV thermionic electron gun, a 238, 476, 1428 MHz multi-sub harmonic bunching and accelerating system as an injector, 8 S-band detuned-accelerating structures, 128 C-band choke-mode accelerating structures, 18 in-vacuum undulators and an X-ray beam line. The individual components of SACL work as follows. At first, the electron gun emits electron beams with a low emittance of 0.6 πmm-mrad in rms, a pulse width of 3 μs in FWHM and a 1A peak current.

#otake@spring8.o.jp

Copyright © 2012 by the respective authors — cc Creative Commons Attribution 3.0 (CC BY 3.0)

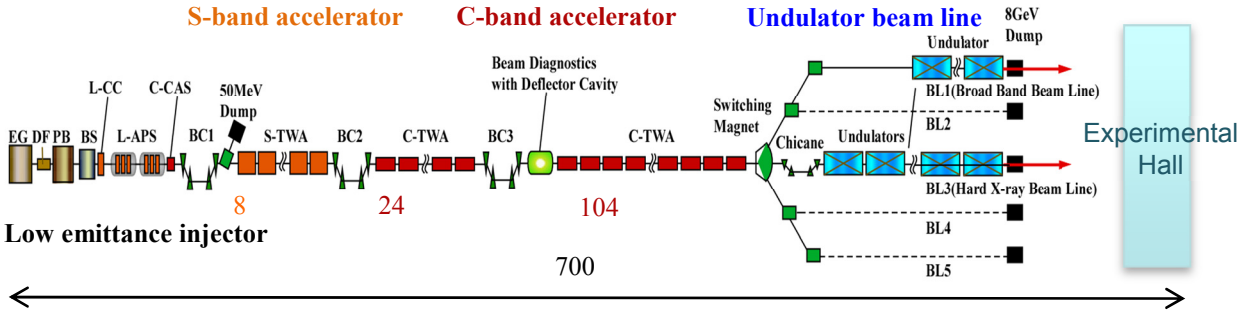

Figure 1: Machine layout of SACLA. SACLA comprises a low-emittance injector including a CeB6 500 kV thermionic electron gun (EG), a beam chopper (DF), a 238 MHz sub-harmonic buncher (SHB or PB), a 476 MHz booster cavity (BS), an L-band correction cavity (L-CC), L-band alternating periodic structures (L-APS) and a C-band correction accelerating structure (C-CAS)), a bunch compressor 1 (BC1), 8 S-band accelerating structures, a bunch compressor 2 (BC2), 24 C-band accelerating structures, a bunch compressor 3 (BC3), 104 C-band accelerating structures and undulator beam lines (BL1 and BL3) with 18 undulators.

Table 1: Present parameters of the X-ray and electron beam of SACLA

X-ray	
Wavelength (Å)	~ 0.6
Peak Power (GW)	10
Pulse Length (fs)	200 ~ 30
Photons per pulse	2 x 10^{11}
Pulse Energy (mJ)	0.1 ~ 0.5
Bandwidth	10^{-3}
Peak brilliance (ph/s/mm^2/mrad^2/0.1% BW)	1x 10^{33}
Coherence (transverse) (longitudinal)	2D coherent Multimode
Electron Beam	
Energy (GeV)	~ 8.5
Charge (nC)	0.2 ~ 0.3
Peak current (kA)	~ 3
Pulse width (fs)	10 ~ 70
Normalized Emittance (π mm mrad)	0.1 ~ 0.5
Repetition rate (Hz)	~ 60 (Max.)

Then, a high-voltage chopper forms a 1 ns beam width in FWHM from the 3 μs width to fit the rf phase space of a 238 MHz sub-harmonic buncher (SHB) in order to make velocity bunching. After this, the electron beam is accelerated up to 1 MeV by a 476 MHz booster cavity (booster), and the booster makes velocity bunching. Following the booster, L-band (1428 MHz) alternating-periodic structures (APS) develop further velocity bunching up to about a beam pulse width of 10 ps, produces energy chirp along an electron bunch for the following magnetic bunching process and accelerates up to a beam energy of around 30 MeV. Next, magnetic bunching using 4 bending magnets chicane as a bunch compressor 1 (BC1) compresses a bunch length up to about 3 ps. 8 S-band accelerating structures also cause energy chirp along the bunch for the bunch compression of BC2, and accelerate the electron beam up to 450 MeV. Following this, 24 C-band accelerating structures accelerate the beam up to 1.4 GeV, and provide energy chirp for bunch compression at BC3, which is the final bunch compression stage. These bunch compression processes correspond to an off-crest rf wave acceleration part, which is very sensitive to any outside perturbation, such as an environmental temperature change. A successive part of the bunch compressors, as mentioned above, is 104 C-band accelerating structures, which only accelerate the electron beam at the rf crest part up to an energy of ~ 8.5 GeV. The rf crest acceleration is relatively ten-times more insensitive to perturbations from the environment compared with off-crest acceleration. After obtaining full energy, such as 8.5 GeV, the electron beam passes through an undulator line with an effective length of 90 m in order to amplify an X-ray laser up to a wavelength of 0.063 nm by the SASE process, and to emit the laser to an experimental hall. Table 1 summarizes the characteristics of both the electron beam and the X-ray laser beam. In addition to the present configuration of SACLA, as mentioned above, we have a spare room for 4 other beam lines of BL1, 2 ,4, 5 to meet the requirements of multi-users. BL1 already and partly works for electron-beam tuning and emitting wide-band spontaneous light.

Low-emittance Thermionic Electron Gun

One of the key instruments of the SCSS concept is a thermionic electron gun [3], which is crucial to obtain a low-emittance electron beam. This electron gun uses cathode material of a CeB_6 single crystal heated up to about 1550 ºC; a high voltage pulse of around 500 kV with a pulse width of 3 μs in FWHM is added to the cathode. This single-crystal material is usually used for an electron microscope. This cathode with 3 mm in diameter and 5 mm long radiates an intense electron beam with

Copyright © 2012 by the respective authors — cc Creative Commons Attribution 3.0 (CC BY 3.0)

Figure 2: Outlook of the 500 kV, CeB_6 thermionic electron gun.

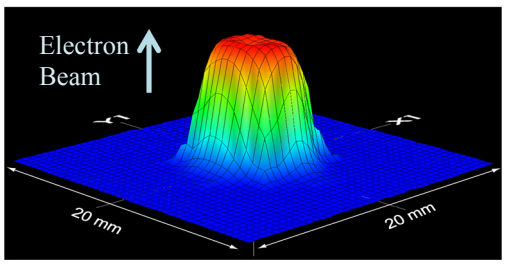

Figure 3: Spatial transverse profile of the beam emitted from the electron gun with a 0.6 πmm-mrad emittance.

a low emittance of 0.6 πmm-mrad from a very smooth surface within a flatness of several μm, when applying a high-voltage pulse. Figure 2 shows the outlook of the electron gun installed in to a SACLA accelerator tunnel. Figure 3 also shows the transverse profile of the radiated electron beam having 0.6 πmm-mrad emittance. The 500 kV high-voltage pulse is generated by almost the same high-voltage pulse modulator as in the klystron case, mentioned below. This modulator generates a 37.5 kV pulse. Then, this pulse is stepped up to 500 kV with a transformer. For impedance matching and interchangeability to a C-band high-power rf system, as also mentioned below, a 500 kV klystron like dummy tube without cavities is employed, because of the high-impedance of our cathode.

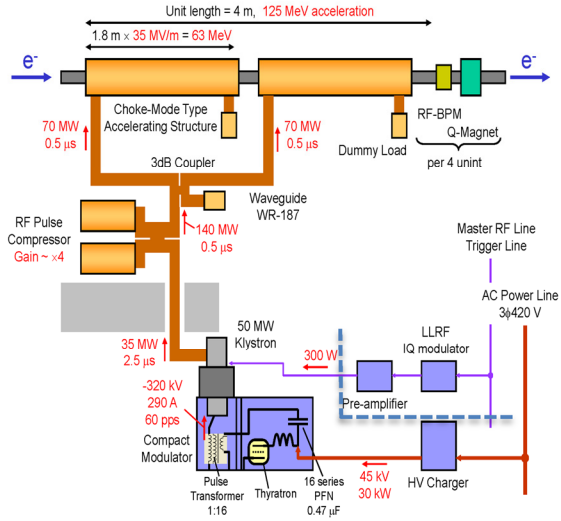

Figure 4: Schematic diagram of the C-band accelerator system. The system comprises 2 C-band accelerating structures, high-power waveguide components, a 50 MW klystron with a 2.5 μs rf output pulse width, a pulse modulator and a high-voltage inverter power supply.

C-band High-gradient Acceleration System

A C-band acceleration unit is depicted in Fig. 4 [4]. There are 64 units in a SACLA accelerator building. Each unit has two 1.8 m choke mode accelerating structures, a vacuum waveguide system including an rf pulse compressor, SLED, with an rf multiplication factor of 4, a 50 MW klystron generating a 2.5 μs width rf pulse, a 350 kV pulse modulator to drive the klystron, a 45 kV inverter power supply, and a low-level rf (LLRF) and timing system. When the klystron generates a 35 MW rf pulse, the SLED generates a 200 MW peak rf pulse fed into the 2 accelerating structures. Then, these structures provide a 35 MV/m acceleration gradient. Figure 5 shows the preset acceleration gradient produced by the C-band system. The 350 kV high-voltage pulse is formed with a pulse transformer placed under the klystron from a 45 kV pulse, which is generated by a pulse forming network (PFN). This PFN is charged with the 45 kV inverter power supply, and the 45 kV pulse is made by switching charge in capacitors constituting the PFN with a thyratron.

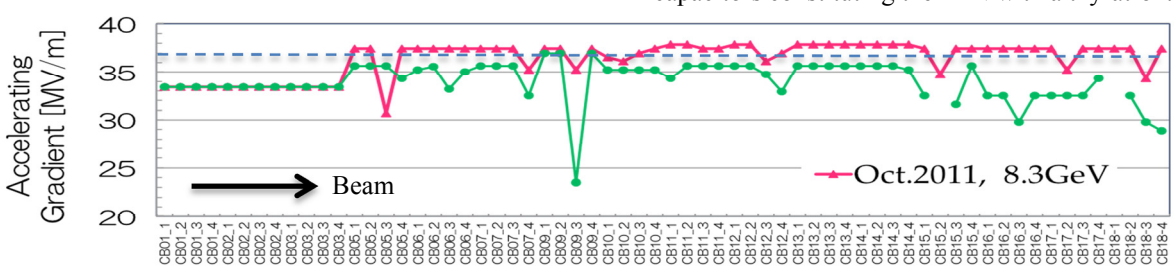

Figure 5: Acceleration electric-field gradients of all the C-band units along the SACLA accelerator. The electric-field gradients of almost all the C-band units after BC3 reach values of more than 37 MV/m. The red line with the solid triangle dots shows the case at a beam energy of 8.3 GeV; the green line with the solid round dots shows the case of 7 GeV. The blue dotted line is a reference value of 37 MV/m.

Copyright © 2012 by the respective authors — cc Creative Commons Attribution 3.0 (CC BY 3.0)

In-vacuum and Short Period Undulator

One of the effective methods to reduce a gain length of FEL amplification is an in-vacuum undulator [5], in which short period permanent magnets assemblies are installed into a vacuum chamber. Therefore, the gap distance between the magnets, which the electron beam passes through, is as narrower as possible compared with an out-vacuum undulator having a vacuum beam duct in the gap. This means we can obtain a large K value by a strong magnetic field conducting a large ρ value and a short gain length. Furthermore, since the gap is movable, the wavelength of the X-ray laser generated with the undulator is changeable. The present minimum gap is 3.5 mm. Figure 6 shows a view of SACLA's 18 undulators installed into a radiation shield room, and Table 2 summarizes the fundamental parameters of our in-vacuum undulator.

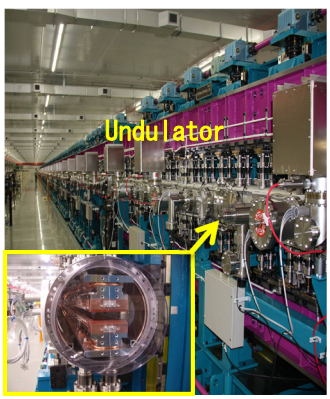

Figure 6: 18 undulators along the BL3 of SACLA.

Table 2: Fundamental parameters of the undulator of SACLA.

Magnet Structure	Hybrid Type
Permanent Magnet Material	NdFeB
Length (m)	5
Period Legth (mm)	18
Number of Periods	277
Number of Undularors for BL3	18
Minmum Gap of Magnet (mm)	3.5
Maximum K value	2.2
K at 0.12 nm, E = 7 GeV	1.8

Key Components to Support Stability

There are many crucial devices to secure SACLA's lasing stability. However, we do not have much space in this paper. Hence, the 2 key components of SACLA, as most important devises, are explained as follows. One is the inverter power supply for the klystron modulator, which decides the rf phase and amplitude stability of a klystron output. Because a change in the output voltage of the inverter power supply is associated with a klystron high-voltage change, it varies the electron beam velocity (energy) in the drift tube of the klystron. The demanded voltage stability of the power supply is less than 100 ppm (rms), which comes from a required rf temporal (phase) stability of 100 fs in the accelerating structures of the off-crest part, as mentioned in the introduction. Our developed inverter power supply employs hybrid coarse and fine voltage-control power supplies working in parallel. Figure 7 shows the voltage-control performance of the inverter power supply, which is sufficient for our demand.

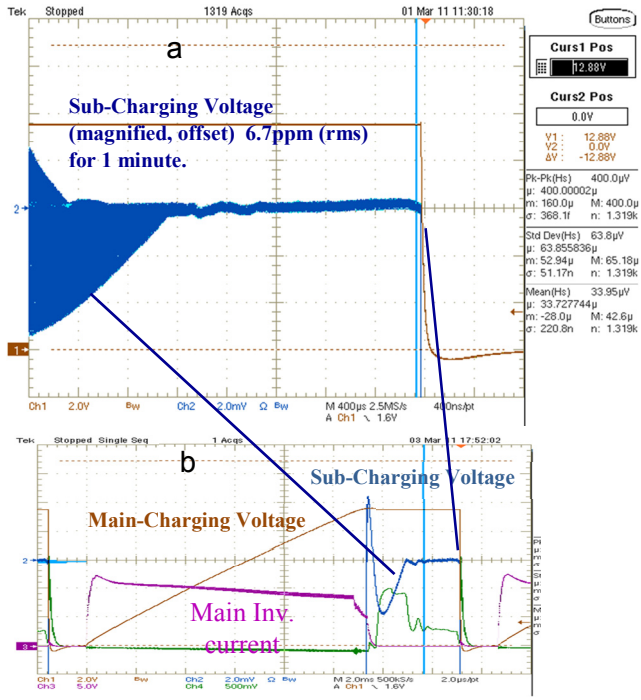

Figure 7: Voltage stability of the inverter power supply. The stability is 6.7 ppm in rms for 1 minute. The upper "a" drawing shows the magnified amplitude and time scales case. The lower "b" shows the reduced amplitude and time scales case.

Next, an indispensable part is the LLRF system [11], which mainly determines the beam temporal stability associated with lasing instability. This system comprises a master oscillator that generates 238, 476, 1428, 2856, 5712 MHz reference signals to drive the high-power rf source, like the klystron, through an in-phase quadrature modulator for pulse modulation and rf amplitude and phase control, and a 500 W solid-state pulse amplifier. These signals are transmitted by phase-stabilized optical fibers with a thermal optical length coefficient of 2ppm/K. The temperatures around these LLRF components, as well as the optical fibers, are controlled by cooling water within 0.1 K to reduce any rf phase and amplitude drifts. One of the performances of the LLRF system is shown in Fig. 8, which is the rf amplitude and phase stabilities at 238 MHz SHB driven with a 10 kW solid-state pulse amplifier. This amplifier is directly connected to the LLRF system. The rf phase and

Copyright © 2012 by the respective authors — cc Creative Commons Attribution 3.0 (CC BY 3.0)

amplitude stabilities are 0.0067 deg. and 1 x 10^{-4} in rms for 24 hours, respectively. These values are almost sufficient for our demand.

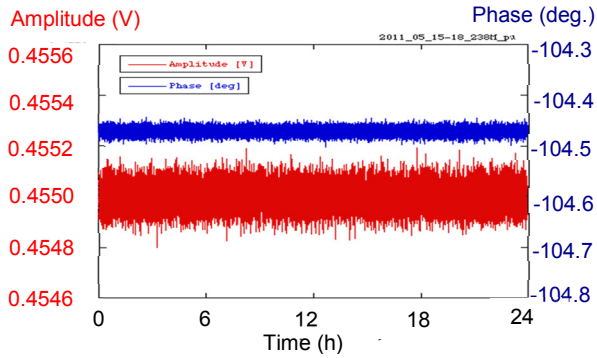

Figure 8: Phase and amplitude stabilities of the 238 MHz SHB. The phase stability is 0.0067 deg. in rms and the amplitude stability is 1 x 10^{-4} in rms for 24 hours.

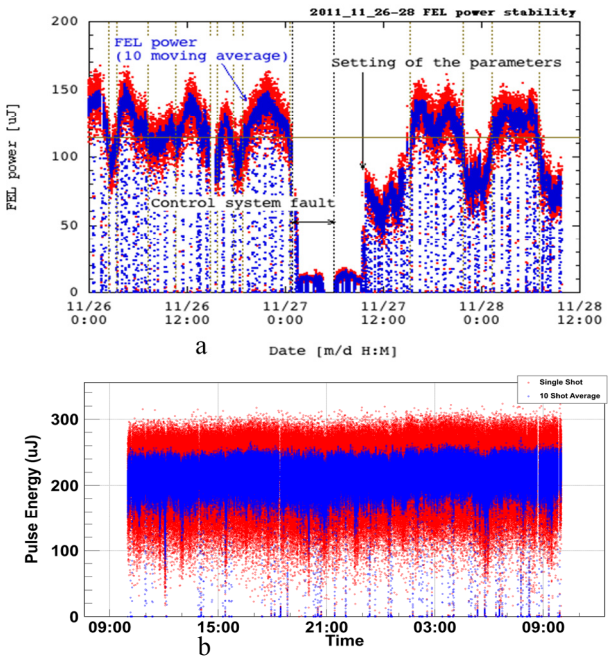

Figure 9: Lasing intensity stabilities. a, intensity variation for 3 days with the rf phase and amplitude control of all SACLA's cavities and the incident beam orbit control for BL3; b, lasing intensity stability with the operator's fine trimming for the rf phase and amplitude of the injector cavities.

LASING PERFORMANCE AND PROBLEM

SACLA lased at 0.1 nm in June, 2011, after beam commissioning by using the above-mentioned instruments. Then, the lasing intensity stability of SACLA, as shown in Fig. 9-a, was not sufficient. For 3 days, we could keep the X-ray lasing with only feedback control loops of the rf phases and amplitude of all the cavities and an incident beam orbit on the undulator of BL3. After this, improvements of the instrument stabilities, such as temperature regulation betterment in the injector cavities (e.g. SHB) from within 0.1 K to within 0.004 K, were performed [12]. Finally, we obtained further lasing intensity stability, as described in Fig. 9-b. However, this intensity stability was established by the operator's fine trimming of the rf phases and amplitude at the cavities around the injector. The frequency of the trimming is once or twice an hour.

SUMMARY

SACLA, 700 m long, which is shorter than the other XFEL machines, lased at up to 0.063 nm in 2011. This is the world shortest wavelength of a laser. The lasing intensity stability is an acceptable level for user experiments. This means the short-term instrument stabilities already reached at our demanded values, like a temporal electron beam stability of 100 fs. However there is still laser intensity drift caused by the characteristic drifts of accelerator instruments, such as insufficient temperature regulations of the rf cavities in an injector. Operator trimming of the rf phases and amplitude at the injector cavities cures the lasing intensity drift up to an acceptable level. We are now planning and executing improvements to obtain further laser-intensity stability without operator trimming.

ACKNOWLEDGMENT

The authors appreciate the members of the XFEL/SPring-8 construction group their support to our study and development.

REFERENCES

[1] T. Ishikawa et al., Nature Photonics **6**, 540-544, doi:10.1038/nphotonics (2012).
[2] T. Tanaka and T. Shintake, (Eds.): SCSS X-FEL Conceptual Design Report, (2005).
[3] K. Togawa, et al, *Phys. Rev. ST Accel. Beams* **10**, 020703 (2007).
[4] T. Inagaki et al, Proc. of IPAC11, 104-106 (2011).
[5] H. Kitamura, *J. Synchrotron Rad.* **7**, 121-130 (2000).
[6] J. Arthur, et al, Linac Coherent Light Source (LCLS) Conceptual Design Report, SLAC-R593 Stanford (2002).
[7] M. Altarelli, et al. (Eds), XFEL, The European X-Ray Free-Electron Laser, Technical Design Report. Preprint DESY 2006-097, (DESY Hamburg, 2006).
[8] T. Tanaka et al, *Nucl. Instrum. Meth.*, **A 528**, 172 (2004).
[9] H. Tanaka, Proc. of the 8th annual meeting of PASJ, 613-615 (2011), in Japanese.
[10] S. Hiramatsu, *Text of KEK OHO'98 high-energy accelrator seminer*, I-1 - I-55(1998), in Japanese.
[11] Y. Otake et al, proc. of ICALEPCS07, 706-710 (2007).
[12] T. Asaka et. al, Stability performance of the injector for SACLA/XFEL at SPring-8, in these proceedings.

Copyright © 2012 by the respective authors — cc Creative Commons Attribution 3.0 (CC BY 3.0)

LCLS OPERATIONAL EXPERIENCE AND LCLS-II DESIGN*

Tor O. Raubenheimer#, for the LCLS/LCLS-II Team, SLAC, Menlo Park, U.S.A.

Abstract

Five months after first lasing in April 2009, the Linac Coherent Light Source (LCLS) began its first round of x-ray experiments. The facility has rapidly attained and surpassed its design goals in terms of spectral tuning range, peak power, energy per pulse and pulse duration. There is an ongoing effort to further expand capabilities while supporting a heavily subscribed user program. The facility continues to work toward new capabilities such as fs-scale pulses, self-seeding, synchronized THz for pump-probe, and multiple-bunch operation. Future upgrades will include polarization control as well as hard and soft x-ray self-seeded operation. The facility is already starting to construct a major expansion, with two new undulator sources and space for four new experiment stations referred to as the LCLC-II.

LCLS FACILITY

The Linac Coherent Light Source Facility (LCLS) at SLAC National Accelerator Laboratory is based on the last third of the SLAC linac where a high brightness beam is generated in an off-axis injector and then accelerated to ~14 GeV [1,2]. The concept for the facility was laid out in 1992 at the Workshop on 4th Generation Light Sources at SLAC [3]. Now, the LCLS is well on its way to realizing all the scientific capabilities envisioned in *LCLS – the First Experiments* [4], which described six broad areas of opportunity for research with an x-ray laser.

The facility achieved its design goals during the first weeks of operation [5] and is developing new capabilities on an almost weekly basis. Essentially all the experiment techniques envisioned for LCLS are being tested and proven in operation and the full suite of three experimental stations in each of two experiment halls have been commissioned as indicated in Table 1.

Table 1: LCLS Experimental Stations

Experimental Station	Start of User Operations
Atomic, Molecular & Optical Science (AMO)	October, 2009
Soft X-ray Materials Science (SXR)	June, 2010
X-ray Pump-Probe (XPP)	October, 2010
Coherent X-ray Imaging (CXI)	February, 2011
X-ray Correlation Spectroscopy (XCS)	November, 2011
Matter in Extreme Conditions (MEC)	April, 2012

* Work supported in part by the DOE Contract DE-AC02-76SF00515.
# tor@slac.stanford.edu

The principal performance goals of LCLS-I were to produce:

- X-ray pulses of 230 femtoseconds duration or shorter
- Photon energies ranging from 800 eV to 8,000 eV
- 10^{12} photons per pulse at 8 keV

As noted, these goals were achieved or exceeded promptly at the outset of commissioning, in April- May 2009; a list of the present operating parameters can be found in Table 2. A rapid and productive research program commenced with a 1,300 hour operation run, October-December 2009, during which 152 experimenters participated in 11 experiments. Productivity has continued to increase; in FY2010, 359 experimenters participated in LCLS experiments. Demand for access to LCLS continues to grow as illustrated in Fig. 1 where the proposals for each the experimental stations is is plotted versus run number; each run is roughly 5 months in duration. However, as shown in Fig. 1, the LCLS productivity is already limited by capacity; only one in four proposals receive beam time.

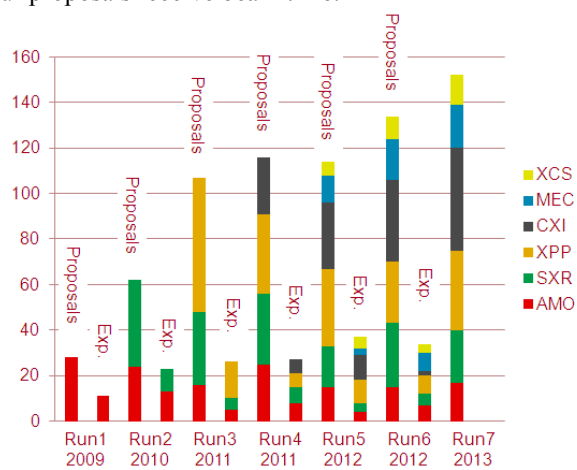

Figure 1: LCLS proposals and experiments receiving beam time by experimental station and run number.

OPERATIONAL EXPERIENCE EXTENDED LCLS CAPABILITIES

Rapid progress in accelerator research and accelerator commissioning has made it possible to expand LCLS capabilities well beyond the LCLS the goals listed in the previous section. The energy produced in a single x-ray pulse has reached 6 mJ. The operating range of photon energies, originally specified at 800-8,000 eV, has been expanded to 480-10,000 eV, limited by the electron beam energy and the fixed period and magnetic field in the undulator. The pulse duration can be varied between a few femtosecond (fs) and 500 fs with soft x-rays and a few fs to ~100 fs for hard x-rays.

Copyright © 2012 by the respective authors — cc Creative Commons Attribution 3.0 (CC BY 3.0)

Table 2: Typical LCLS X-ray Beam Characteristics

X-RayTuning Range	480 - 10,000	eV
Peak Power	up to 70	GW
Bandwidth, 8,000 eV	0.2 typical; <0.01 seeded	% FWHM
Bandwidth, 800 eV	0.5 typical	% FWHM
X-Ray pulse duration	~3-500	x 10^{-15} sec
Beam size at waist, 800 eV	20, typical	μm, RMS
Beam divergence, 800 eV	20, typical	μrad, FWHM
Beam size at waist, 8,000 eV	15, typical	μm, RMS
Beam divergence, 8,000 eV	3, typical	μrad FWHM
Energy/Pulse	> 2 typical, 6 max	mJ
Energy Jitter/Pulse	5 typical	%
Pulse Repetition Rate	120	Hz

Perhaps the most important measure by which LCLS has exceeded its design goals is in it's flexibility. The x-ray pulse length and pulse energy and the beam and photon energy can all be rapidly varied; typical x-ray parameters are listed in Table 2. For example, the LCLS routinely operates with 80 fs pulses, a duration at which it readily produces 2 mJ/pulse. But the pulse duration can be readily adjusted from a few fs to 500 fs in response to user needs. Such changes can be achieved in a matter of minutes in most cases. Generally, peak power remains constant or is increased somewhat as the pulse duration is reduced. This ability to change pulse length has proven to be extremely important and data collection at several pulse durations is now a routine part of most LCLS experiments.

Similarly, many experimenters will want to scan many x-ray photon energies during their shifts. With the fixed gap undulator in the LCLS, this requires adjusting the beam energy. The photon energy can be varied between 480 to 10,000 eV. Making small changes of a few % can be done in minutes while making larger changes can take as long as an hour.

This performance is due to an injector that significantly exceeds the design performance [6], a linac and bunch compression system that is extremely well understood [7], extensive feedback and control systems that allow varying across a broad range of parameters with minimal impact to the expected performance [8], and a long highly precise undulator and beam-based alignment system [9].

Finally, another critical performance metric is the x-ray availability for user experiments. The LCLS runs delivering x-rays over a 5-day block of time (typically two experiments) followed by two days for scheduled maintenance or machine development, The facility has been running extremely well, with better than 93% availability of x-rays for the users [10] as illustrated in Figure 2.

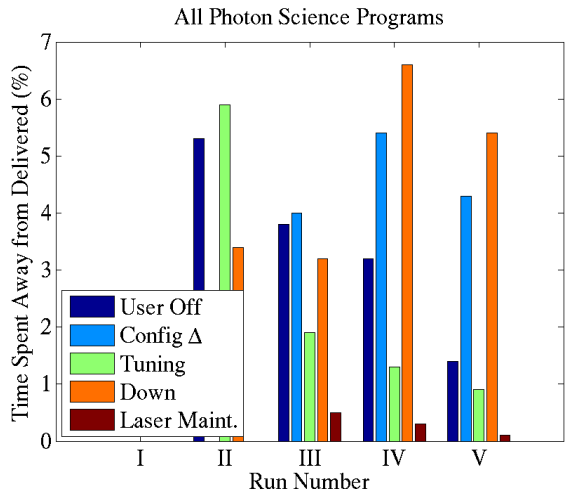

Figure 2: LCLS availability from May 2010 through May 2012; note that User Off and Configuration Δ are counted as available time to users while Tuning, Down and Maint. Are counted as unavailable time (Ref. [10]).

LCLS R&D PROGRAM [11]

The capabilities of LCLS continue to expand at a rapid pace. In the next few months and years, it will be possible to:

Produce pulses with duration approaching 1 fs: Two techniques for producing very short (~1 fs) x-ray pulses were proposed during the design of LCLS [12,13], and both have yielded very good results during accelerator studies and in x-ray experiments. Operation with low (20 picocoulomb) charge, it has been possible to produce electron bunches shorter than 10 fs with pulse energies of ~0.14 mJ. This configuration is used in routine operations at the request of x-ray experimenters. Using new techniques for measuring the electron bunch length [14,15], it may be possible to achieve 1 fs rms resolution. Direct measurement of the x-ray pulse length is perhaps even more important. A new X-band deflecting cavity is being installed after the undulator and it should provide fs-scale resolution of both the electron beam and the x-ray pulse [15]. Studies of the x-ray spectrum and development of accurate x-ray timing diagnostics will hopefully enable better understanding of the time structure of the x-ray pulse.

Produce short, hard x-ray pulses with full temporal coherence; A very attractive scheme for self-seeding short hard x-ray pulses [16,17] was proposed and has been demonstrated in the LCLS producing a bandwidth roughly 50 times smaller than SASE [18,19]. The scheme can be implemented without significant impact on other operating modes. Compatibility with normal operations has been established and seeded beams will be offered to users starting in the Fall of 2012 [20]. A soft x-ray self-seeding experiment is being design for the LCLS and will be tested in roughly two years.

Copyright © 2012 by the respective authors — cc Creative Commons Attribution 3.0 (CC BY 3.0)

Produce terawatt-level peak powers; When generating temporally coherent x-ray pulses, it is also possible to heavily taper the undulator to extract very high peak powers. Simulation studies appear to support the generation of terawatt-level peak powers with tapers on the order of 10% [21]. Studies are being performed on the LCLS to verify the physics of heavy tapering.

Provide polarization control: LCLS is presently developing options for polarization control. In specific, the DELTA undulator [22] is a novel compact design with a fixed gap that would fit with the LCLS undulator system. Both the polarization and the K are fully adjustable. SLAC is building a 3.2-m prototype to be installed and tested at the end of the LCLS undulator [23].

Provide a synchronized source of high-field pulsed THz radiation: Passing the electron beam through a thin conducting foil will generate Optical Transition Radiation (OTR). With a bunch length of 10-100 fs, one can expect OTR in the frequency range 10-100 THz; however it is more useful to think of the OTR as an electromagnetic pulse with time structure similar to the derivative of the beam current. SLAC researchers are presently investigating the feasibility of producing OTR pulse with electric fields in the range 0.1-1 volt per Ångstrom. If successful, these pulses might be transported to the Near Experiment Hall hutches for THz pump/x-ray probe investigations.

Provide two x-ray FEL pulses (using two electron bunches), separated by a few nanoseconds, has been demonstrated [24]. This is an enabling step toward novel techniques for pump/probe experiments with LCLS or simultaneous 120 Hz operation of multiple undulators using a single injector.

LCLS-II PROJECT [25]

The LCLS-II Project (LCLS-II) will provide a major enhancement of the LCLS. LCLS-II will enable operation and optimization of the electron beam for its two new undulator sources with complete independence from operation of the existing LCLS undulator x-ray source and experiment stations. LCLS-II will also construct the essential infrastructure necessary to enable LCLS to continue growth in both capacity (up to four x-ray sources and ten experiment stations) and capability (a range of photon energies from 250 eV to >20 keV, a 100x-1,000x increase in brightness and >10X increase in peak power). The design of LCLS-II draws heavily on experience from construction and operation of LCLS. In addition, key design features of LCLS-II have been chosen to support new capabilities presently under development at LCLS.

The LCLS-II will take advantage of existing SLAC infrastructure and accelerator facilities, most notably the second kilometer of the 3-km SLAC linac. The addition of this second electron source will greatly enhance LCLS operations flexibility. Experience has already shown a surprisingly high demand for changes in x-ray pulse duration. It is common practice to change pulse durations once or twice a day. With two completely independent sources of electrons, the new undulator sources for LCLS-II can be optimized without compromising the needs of experiments using the LCLS undulator. LCLS-II also re-uses the off-axis vault at Sector 10 to house the injector linac, and the beam transport facilities originally built to inject electrons into the PEP-II ring. This transport line passes through Sectors 20-30 of the SLAC linac, which provides electrons to LCLS. The operating range of the hard and soft x-ray undulators is illustrated in Figure 2 while Figure 3 is a schematic of the LCLS-II layout and associated electron beam diagnostics. Finally, Figure 4 shows the planned civil construction and the location of the new Undulator and Experimental Halls.

This expansion of the LCLS facility will build upon the proven performance characteristics of the LCLS, enabling groundbreaking research in a wide range of scientific disciplines. LCLS-II will create unbounded opportunity for research into atomic-level dynamics of processes that are fundamentally important to materials science, chemistry and the life sciences. The LCLS-II conceptual design provides greatly enhanced capacity and capability for the LCLS facility.

The Linac Coherent Light Source II (LCLS-II) Project conceptual design will provide the following facility enhancements:

- A hard x-ray undulator source (2-13 keV).
- A soft x-ray undulator source (250-2,000 eV).
- A dedicated, independent electron source for these new undulators, using sectors 10-20 of the SLAC linac.
- Modifications to existing SLAC facilities for the injector and a new shielded enclosure for the two new undulator sources, beam dumps and x-ray front ends.
- A new experiment hall capable of accommodating at least four experiment stations.

The undulator sources will produce spatially coherent plane-polarized x-rays by self-amplified spontaneous emission (SASE). They will be designed to be compatible with future upgrades to include full temporal coherence and polarization control.

Much of the new technical systems and facilities will be virtually identical to those constructed in the original LCLS Project (LCLS-I) and the LCLS Ultrafast Scientific Instruments equipment project (LUSI). The LCLS-II Project will build on experience and lessons learned during LCLS-I construction, commissioning and operation so as to reduce cost, schedule and technical risk.

There are, however, important differences between the LCLS-II design and LCLS:

- The LCLS-II undulators are variable-gap devices that are being produced at LBNL and are similar

Copyright © 2012 by the respective authors — cc Creative Commons Attribution 3.0 (CC BY 3.0)

in design to those planned for the European XFEL or in common use at many storage ring light sources

- The LCLS-II undulator hall is 302-m in length, 132-m longer than in LCLS. This will provide sufficient length to achieve SASE performance goals at 13 keV, and additional length for undulators and other hardware necessary to achieve 1 TW power levels at 13 keV.
- LCLS-II has one experiment hall, whereas LCLS-I constructed two halls
- The LCLS-II experiment hall is 80-m in length, an increase of 10-m compared to LCLS

The LCLS-II undulator hall will provide ample space for future upgrades such as self-seeding systems, polarization-control "afterburner" undulators and generation of multi-color x-ray pulses. The tunnel can also accommodate a large number of post-saturation tapering undulators to produce x-ray pulses with extreme peak powers (approaching one terawatt).

Much of the new technical systems and facilities will be virtually identical to those constructed in the original LCLS Project (LCLS-I). The LCLS-II Project will build on experience and lessons learned during LCLS-I construction, commissioning and operation so as to reduce cost, schedule and technical risk.

The LCLS-II Project will enable expansion of LCLS to keep pace with the explosive growth of research opportunities and user demand which will saturate the existing facility.

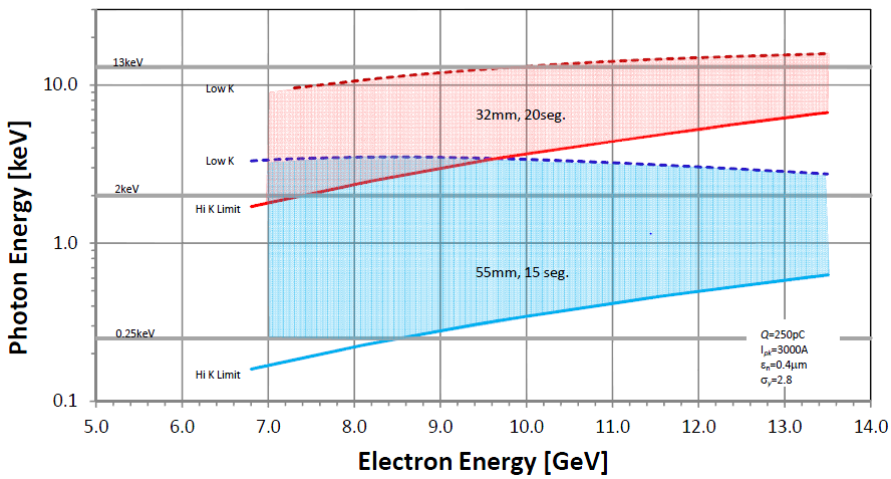

Figure 2: Photon energy versus electron beam energy at saturation for the two new undulator sources proposed in the LCLS-II Project. The blue field indicates the range of the soft x-ray (SXR) undulator source and the red field indicates the hard x-ray operating range range. The lower range on the curves is set by the largest *K* available for each undulator while the upper bounds on the curves is set by the installed length of undulator which is initially planned to be 66-meters in the SXR and 88-meters in the HXR; the upper bounds increase with the installation of additional undulator segments which can be accommodated in the long Undulator Hall which is roughly 300-meters in length.

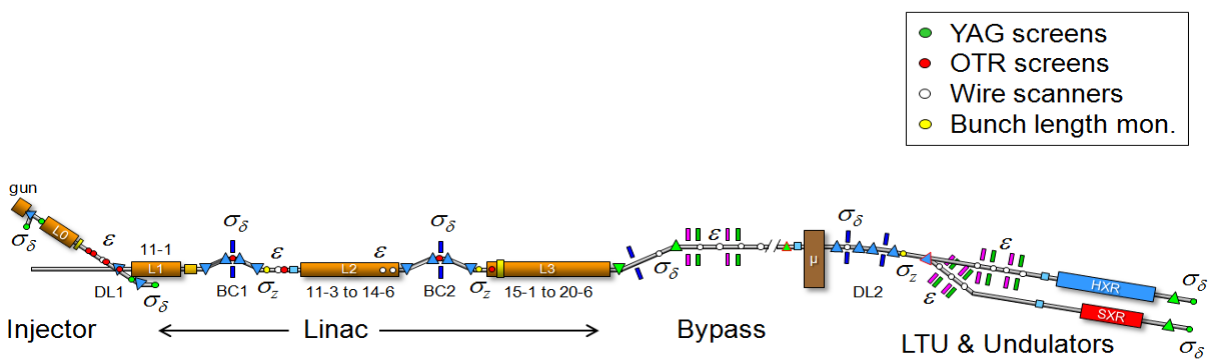

Figure 3: Schematic of the LCLS-II design illustrating the Injector, Linac and bunch compressors, the 1.2 km long bypass around LCLS-I and the Linac-to-Undulator (LTU) and undulators. The primary beam diagnostics are shown for each section.

Copyright © 2012 by the respective authors — cc Creative Commons Attribution 3.0 (CC BY 3.0)

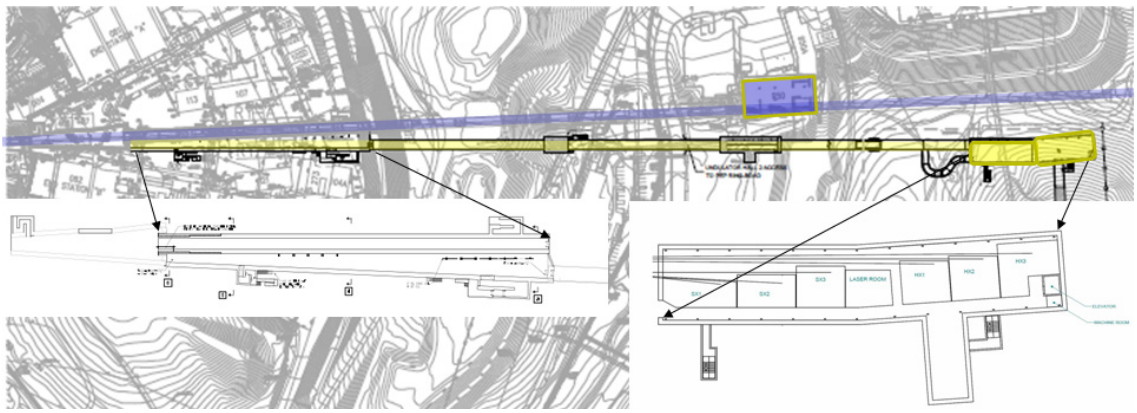

Figure 4: Layout of LCLS-I and LCLS-II. Items tinted blue are existing LCLS facilities. Items tinted yellow are new LCLS-II facilities. Blow-ups of the Beam Transport Hall extension and the new Experiment Hall are shown below the site layout. The LCLS-II Beam Transport Hall is attached to the existing facility at the "headhouse". The long Undulator Hall, roughly 300-meters in length, will be used to support a number of possible upgrades including self-seeding, multi-color generation, polarization control and the generation of terawatt-scale peak x-ray powers.

ACKNOWLEDGEMENTS

The author is grateful to John Galayda and Zhirong Huang for their careful reading of the paper and the LCLS and LCLS-II Teams for their assistance.

REFERENCES

[1] J. Arthur, *et al.*, *Linac Coherent Light Source (LCLS) conceptual design report*, SLAC-R-593, SLAC (2002).

[2] P. Emma, *et al.*, "*First lasing and operation of an ångstrom-wavelength free-electron laser,"* Nature Photon. **4**, 641 (2010).

[3] C. Pellegrini, "*A 4 to 0.1-nm FEL based on the SLAC Linac,"* Proc. of the Fourth generation light sources, Feb. 1992, Stanford, CA (1992).

[4] Shenoy, Stöhr, *ed.,* "LCLS: The first Experiments," SLAC-R-0611, Stanford, September 2000 (2003).

[5] P. Emma, "*First Lasing of the LCLS X-ray FEL AT 1.5 Å*," Proc. of PAC2009, May 2009, Vancouver, BC (2009).

[6] R. Akre *et al.*,"*Commissioning the Linac Coherent Light Source Injector*", Phys. Rev. STAB, **11**, 030703 (2008).

[7] F.J. Decker, *et al.*, "*Improving the beam stability in the LCLS Linac*," Proc. of PAC2009, May 2009, Vancouver, BC (2009).

[8] H. Loos, *et al.*, "*Operational Performance of LCLS Beam Instrumentation,"* 14th Beam Instrumentation Workshop (BIW10), Sept. 2010, Santa Fe, NM (2010).

[9] H.D. Nuhn, "*LCLS Undulator Commissioning, Alignment, and Performance,"* 31st Free Electron Laser Conf., Aug 2009. Liverpool, United Kingdom (2009).

[10] B. Allen, "*LCLS Availability*," Workshop on Accelerator Operations, Aug 2012, SLAC, California (2012).

[11] Z. Huang, "*Some R&D Towards Brighter X-ray FEL's*," Proc. of Future Light Sources, March 2012, Jefferson Lab., Virginia (2012).

[12] P. Emma, *et al.*, "*Femtosecond and Subfemtosecond X-Ray Pulses from a Self-Amplified-Spontaneous-Emission-Based-Free-Electron Laser"*, Phys. Rev. Lett. **92**, 074801(4) (2004).

[13] Y. Ding *et. al.* "*Measurements and Simulations of Ultra-low Emittance and Ultra-short Electron Beams in the Linac Coherent Light Source"*, Phys. Rev. Lett. **102**, 254801, (2009).

[14] Z. Huang, *et al.*, "*Ultrashort LCLS Bunch Length Measurement Using the SLAC A-line Spectrometer"*, Proc. PAC2011, March 2011, BNL, New York, p. 2459 (2011).

[15] Y. Ding, *et al.*, "*Femtosecond x-ray pulse temporal characterization in free-electron lasers using a transverse deflector,"* Phys. Rev. STAB, **14,** 120701 (2011).

[16] G. Geloni, *et al.*, "*Cost-effective way to enhance the capabilities of the LCLS baseline,*" DESY 10-133, August 2010, http://arxiv.org/abs/1008.3036v1.

[17] G. Geloni, V. Kocharyan, E. Saldin, "*A novel self-seeding scheme for hard X-ray FELs*," J. Mod. Opt. **58**, 1391 (2011).

[18] J. Amman, *et al.*, "*Demonstration of self-seeding in a hard-X-ray free-electron laser*;" Nature Photonics, DOI: 10.1038/NPHOTON.2012.180 (2012).

[19] R. Lindberg, *et. al.*, "Hard X-ray Self-Seeding at the LCLS," proceedings of FEL'12, Aug. 2012, Nara, Japan (2012).

[20] J. Welch, et al., "*Comparison of Hard X-Ray Self-Seeding with SASE after a Monochromator at LCLS*," Proc. of FEL'12, Aug. 2012, Nara, Japan (2012).

[21] W. Fawley, *et al.*, "*Toward TW-level LCLS Radiation Pulses*," proc. FEL'11, Aug. 2011, Shanghai, China (2011).

[22] A. Temnykh, "Delta undulator for Cornell energy recovery linac," Phys. Rev. STAB **11**, 120702 (2008).

[23] H.D. Nuhn, "*Delta Undulator R&D Project at SLAC*," Proc. of Future Light Sources, March 2012 Jefferson Lab., Virginia (2012).

[24] F.J. Decker, *et al.*, "*A demonstration of multi-bunch operation in the LCLS*," Proc. of FEL2010, Aug. 2010, Malmö, Sweden (2010).

[25] J. Galayda, *ed.,* LCLS-II Conceptual Design Report, https://slacportal.slac.stanford.edu/sites/lcls_public/lcls_ii/Published_Documents/CDR%20Index.pdf.

Copyright © 2012 by the respective authors — cc Creative Commons Attribution 3.0 (CC BY 3.0)

THE HIGH-CURRENT ERL AT BNL*

I. Ben-Zvi#, BNL, Upton NY, USA

Abstract

The electron hadron collider eRHIC will collide polarized or non-polarized electrons with a current of 50 mA and energy in the range of 5 GeV to 30 GeV with hadron beams, including heavy ions or polarized light ions of the RHIC storage ring. The electron beam will be generated in an Energy Recovery Linac (ERL) contained inside the RHIC tunnel, comprising six passes through two linac sections of about 2.5 GeV each. The electron ERL poses many challenges in term of a high-current high-polarization electron gun, HOM damping in the linac, crab cavities, harmonic cavities and beam stability. Three R&D projects are underway to provide experience with the eRHIC ERL components. A prototype high-current ERL is under commissioning to test performance at up to 300 mA of the ERL. A prototype polarized-electron gun based on funneling of 20 separate cathodes, providing 3.5 nC per bunch, is under construction and a Coherent electron Cooling (CeC) proof-of-principle experiment is under construction.

INTRODUCTION

RHIC, the Relativistic Heavy Ion Collider at Brookhaven Lab, found it first: a "perfect" liquid of strongly interacting quarks and gluons — a quark-gluon plasma (QGP) — produced by slamming heavy ions together at close to the speed of light. The fact that the QGP produced in these particle smashups was a liquid and not the expected gas, and that it flowed like a nearly frictionless fluid, took the physics world by surprise. Similarly, searches for the source of "missing" proton spin at RHIC have opened a deeper mystery: So far, it's nowhere to be found. To probe these and other puzzles, nuclear physicists would like to build a new machine: an electron-ion collider (EIC) designed to probe structures with extreme precision, at the scale of 10^{-15} meters, both protons and heavy ions to reveal their inner secrets.

The use of an Energy Recovery Linac (ERL) for the electron accelerator of eRHIC was suggested [1] as means to achieve high-luminosity, outstanding polarization and convenient upgradability features. Given a hadron machine design, a linac-ring configuration allows a 10- to 50-fold higher luminosity than an optimized ring-ring design. ERLs combine the advantages of linear accelerators, like beam quality, immunity to resonances, high degree of polarization and beam disruption with those of storage rings, such as high beam power and stability.

* Work supported by Brookhaven Science Associates, LLC under Contract No. DE-AC02-98CH10886 with the U.S. DOE
#benzvi@bnl.gov

A polarized electron beam with an energy up to 30 GeV would collide with a number of ion species accelerated in the existing RHIC accelerator complex, from polarized protons with a top energy of 250 GeV to fully-stripped uranium ions with energies up to 100 GeV/u covering a C.M. energy range from 45 to 175 GeV for polarized e-p, and from 32 to 110 GeV for electron heavy-ion-collisions. Using the present significant margin of the RHIC superconducting magnets the maximum beam energy could be increased by 10 or more percent.

The eRHIC design is based on using one of the two RHIC hadron rings and a multi-pass ERL. Using an ERL as the electron accelerator assures high luminosity in the range of 10^{33}~10^{34}cm^{2}s^{-1}. Locating the ERL inside the RHIC tunnel allows for significant cost savings and natural staging: the energy can be increased from the initial 5 - 10 GeV of the first stage to the final 30 GeV by incrementally adding additional accelerating cavities to the two main linacs. eRHIC will be able to provide electron-hadron collisions in up to three interaction regions. [2]

Polarized electrons will be generated in a high-current 20 photocathode funneling electron gun. The ion beams of the RHIC component will be cooled by a novel Coherent electron Cooling (CeC) system. The machine will heavily rely on SRF technology for production and acceleration of electrons, cooling of hadron beams and realizing crab crossing collision scheme.

In this paper we will describe the layout of the multi-pass eRHIC electron ERL, and describe R&D projects carried out in the Accelerator R&D Division of the BNL Collider-Accelerator Department (C-AD) towards the realization of eRHIC, including the polarized electron source, the SRF cavities (5-cell accelerating cavities, crab cavities), the R&D high-current ERL and the CeC Proof-of Principle (PoP) experiment.

LAYOUT OF THE ACCELERATOR

eRHIC General Layout

Figure 1 presents a layout of the collider with locations of various systems in the existing RHIC tunnel. The injection system consists of an electron gun, 10 MeV SRF injector linac (with no energy recovery) and 600-MeV single-pass SRF ERL. Two 2.45 GeV SRF linacs in combination with six passes make the main ERL. In addition to the main SRF linacs, eRHIC will have energy loss and energy spread compensation linacs (not shown in the figure). The CeC accelerator will consist of a low frequency SRF gun and buncher and a 136 MeV ERL. Finally, there will be SRF crab cavities for both hadrons and electrons (not shown in figure). The lattice provides separation of the electron orbits to individual arcs in the

Copyright © 2012 by the respective authors — cc Creative Commons Attribution 3.0 (CC BY 3.0)

arcs, similar combiners to bring the orbits on the axis of the linac sections and bypasses for the interaction points.

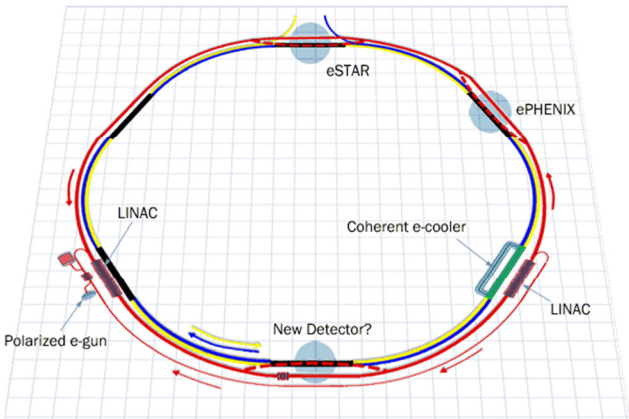

Figure 1: A schematic of the design for adding an electron ring (red), and possible future detector, to RHIC to create eRHIC, which would be the world's first electron-ion collider (EIC).

eRHIC Lattice

The lattice of recirculation passes is based on a low-emittance near-isochronous cell, which allows a flexible tuning R56 parameter and has a large dipole filling factor to minimize synchrotron radiation. The four splitters/mergers provide the transition between the beam line in the linacs and six vertically arranged recirculation passes in the arcs. The by-pass lines around the experimental detectors are provided for all recirculation passes except the top energy pass. The electron and proton bunch frequencies at different proton energies are matched by a combination of path length variation of the electrons and the electron RF harmonic. More details on the electron optics can be found in [3].

One potential weakness of the ERL is transverse beam break-up (BBU) instability that could severely limit the available beam current. Strong damping of HOMs has been the method of choice for suppressing BBU instabilities. A new method of suppressing BBU by many orders of magnitude has been recently proposed [4,5]. This method uses the chromaticity of the transverse motion, a naturally occurring effect, to dephase the transverse instability.

SRF Systems

The rather extensive SRF systems of eRHIC are described in detail by Belomestnykh [6,7]. These include ERL cavities at 704 MHz, low frequency injector cavities at 112 MHz, energy loss and energy spread compensation cavities at 1408 MHz, and crab cavities at a number of harmonics – 225 MHz, 450 MHz, 676 MHz and 1013 MHz. In this paper I will concentrate on the main linac cavities and the ERLs. The ERLs do not include any quadrupole magnets, still providing reasonably low beta-functions in the linacs. SRF linacs for the three ERLs (main ERL, 600-MeV pre-accelerator, and CeC) will utilize the same 704-MHz linac technology with minor modifications. Some parameters of these linacs are presented in Table 1. Two main ERL linacs will be located in the IP2 and IP10 straight sections, where their lengths are limited to 200 m for each linac. Parameters of the main linacs are listed in Table 1. The energy of the main ERL will be increased from 5 GeV in Phase I to 30 GeV in stages by adding cryomodules to the main linacs until they occupy all allotted space. Due to limitation on the beam loss power, the beam current will be lowered at energies above 20 GeV to keep the synchrotron radiation power loss below 10 MW.

Table 1: Parameters of the 704-MHz SRF Linacs [6,7]

Parameter	Main	Pre-acc.	CeC	injector
E gain [MeV]	2450	590	136	10
Current [mA]	50	50	70	50
Length [m]	200	60	19	5.2
No. of cavities	120	30	8	2
E_{acc} [MV/m]	19.2	18.5	15.1	4.7

eRHIC Main Accelerator Cavities at 704 MHz

A five-cell 703.8-MHz superconducting cavity for high-current applications (Figure 2) is under development at BNL and Stony Brook University [8,9,10]. This cavity has been designed as a universal high-current cavity with respect to damping yet with optimized shunt impedance and low surface electric fields, suitable for proton acceleration as well as electron ERL service.

The cavity has an optimized shape that supports strong damping of higher order modes (HOMs), which is accomplished via six antenna-type couplers attached to the large diameter beam pipes. The prototype copper cavity and niobium cavity were engineered and constructed by Advanced Energy Systems, Inc. (AES) and the niobium cavity is shown in Figure 3. Each cavity will be housed in an individual cryomodule. A series of such basic cryomodules will form one long cryomodule with 1-meter long transitions to room temperature at the ends.

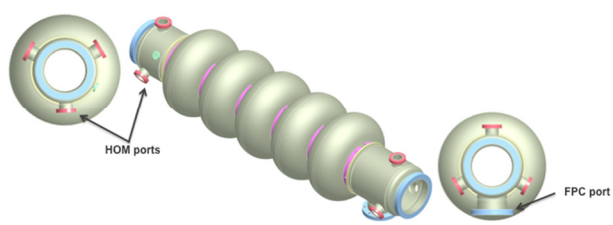

Figure 2: Schematic high-current 704 MHz SRF cavity.

Copyright © 2012 by the respective authors — cc Creative Commons Attribution 3.0 (CC BY 3.0)

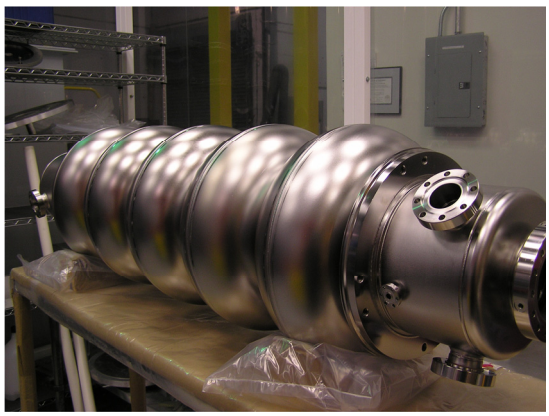

Figure 3: Niobium five-cell 704 MHz SRF cavity.

THE R&D HIGH-CURRENT ERL

The plan for the high-current eRHIC ERL calls for six acceleration passes (and six deceleration passes) of 50 mA in a SRF linac structure. This is a lot of current through each cavity – equivalent to 600 mA. Thus an important part of our R&D program is building a high-brightness 300 mA Energy Recovery Linac (ERL) [11] (see Figure 4).

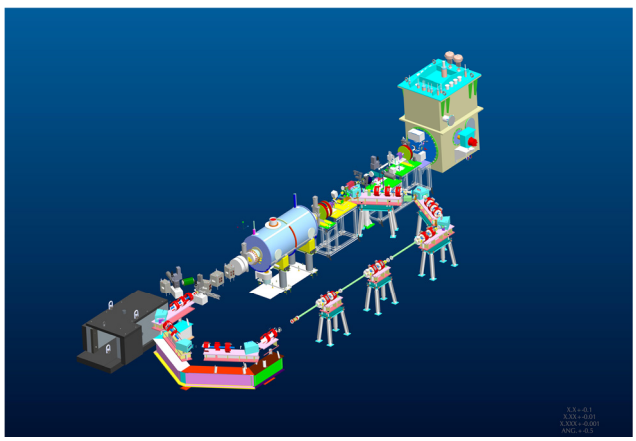

Figure 4: Schematic layout of the R&D Energy Recovery Linac at BNL. The electron gun is on the upper right side; the 5-cell accelerating cavity in the middle and the beam dump is on lower left.

The ERL is in final assembly stages, with commissioning of subsystems going on at present time. The objective of this ERL is to serve as a platform for R&D into high current ERL, in particular issues of halo generation and control, Higher-Order Mode (HOM) issues, coherent emissions for the beam and high-brightness, high-power beam generation and preservation.

BNL is developing several superconducting RF guns for different applications [12]. The first gun is based on a half-cell 1.3 GHz elliptical cavity, made by AES. This gun is used to study generation of polarized electrons from GaAs photocathodes. The second gun, made by Niowave Inc. is based on a quarter-wave resonator, operating at 112 MHz. This gun will be used for photocathode studies, including a diamond-amplified cathode, and to generate high charge, low repetition rate beam for the coherent electron cooling experiment. The third gun, shown in Figure 5, is a half-cell elliptical cavity operating at 704 MHz. It was engineered and constructed by AES and is designed to produce very high average current (up to 500 mA) electron beam at 2 MeV for the ERL prototype from a multi-alkali. This RF gun is equipped with a load-lock cathode delivery system. The accelerating unit of the ERL is a 704 MHz strongly HOM-damped 5-cell cavity built by AES. The AES built ERL ring has a highly flexible single-pass loop and a comprehensive system of beam instrumentation. At the time of writing of this manuscript, all elements of the ERL are in house and most are installed and surveyed to their exact positions. The first beam from the SRF gun is expected in December 2012, beam through the 5-cell cavity is anticipated in February 2012 and beam through the ERL loop in May 2013. We plan to study the performance of this unique machine: The high QE photocathodes and their load-lock delivery system, the SRF gun capable of 500 mA current at 2 MeV beam kinetic energy, the zig-zag beam merger, the highly damped 5-cell SRF accelerating cavity, and various advanced instrumentation elements.

Figure 5: The SRF Photocathode electron gun installed in the ERL vault, as seen from the cathode insertion side Notice the dual waveguide system of the fundamental power couplers.

Of particular interest are the high-current, low-emittance properties of the system, like coherent emissions, beam halo evolution and mitigation and emittance preservation. We plan to increase the current gradually from sub-mA to ampere-class in stages.

Copyright © 2012 by the respective authors — cc Creative Commons Attribution 3.0 (CC BY 3.0)

THE CEC POP EXPERIMENT

An effective cooling of ion and hadron beams at energy of collision is of critical importance for the productivity of present and future Nuclear Physics Colliders, such as RHIC, eRHIC and ELIC. Such cooling would allow to cool beam beyond their natural emittances and also to either overcome or to significantly mitigate limitations caused by the hour-glass effect and the intra-beam scattering. It also would provide for longer and more efficient stores, which would result in significantly higher integrated luminosity. To efficiently cool the transverse and longitudinal emittances of high-energy proton and ion beams by an order of magnitude, the novel technique of Coherent electron Cooling (CeC) is being considered [13].

The CeC principle of operation is as follows: Initially the hadron beam that is being cooled enters a drift space called "modulator", where it overlaps an electron beam of the exact same average velocity. In the modulator each hadron induces a density modulation in the electron beam. The electron beam is then sent to an undulator, which serves as a high-gain FEL. The density modulation is amplified by the FEL to a desired extent. Then both hadron beam and electron beam are brought to an overlap, following a precise temporal delay, in another drift space called the "kicker". There the hadrons interact with the self-induced electric field of the electron beam and receive energy kicks toward their central energy. The process reduces the hadron's energy spread, i.e. cools the hadron beam. The longitudinal cooling can be shared to cool transversally. Simulations show cooling times of tens of minutes can be achieved for the high-energy proton beam of RHIC, an achievement that cannot be done with traditional stochastic- or electron- cooling techniques.

The eRHIC CeC system will use a small ERL, with 136 MeV energy to produce the 70 mA electron beam for the cooler. A proof-of-principle experiment at RHIC for the CeC technique is under preparation [14]. The electron accelerator for this experiment will use a 20 MeV SRF linac at 704 MHz, based on the cavity described above, and injected by a 112 MHz SRF electron gun [12] equipped with 500 MHz copper buncher cavities.

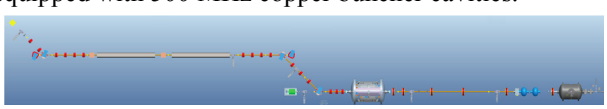

Figure 6: Layout of the Coherent electron Cooling POP experiment. See text for details.

Figure 6 shows the schematic layout of the Proof-of-Principle CeC experiment in RHIC. From right-to-left: 112 MHz SRF gun, normal conducting 500 MHz buncher cavities (blue), transport (solenoids in red), 704 MHz accelerating cavity, dog-leg, modulator section (focusing solenoid in red), FEL amplifier, kicker section (with focusing solenoids) then a bend to an electron beam dump.

THE POLARIZED GUN AND INJECTOR

Since the luminosity in a collider is proportional to the number of particles in each bunch, we want to increase the beam current, hence the bunch charge. When polarized electrons are required the gun performance is ultimately limited by the rapid aging of the cathodes caused by ion back-bombardment. The number of ions that are created in the gun and hit the cathode is proportional to the beam current and the vacuum pressure. A high beam current is therefore a direct cause of cathode aging. The approach we are taking at BNL is to multiplex a large number of cathodes in what is known technically as a funneling scheme. We call it the "Gatling gun" [15, 16], due to its similarity with a historical multiple barrels machine gun. The Gatling Gun R&D project aims to prove the concept of a DC gun with twenty separate cathodes. The beams from these cathodes are merged using a rotating magnetic field. We are carrying out R&D aimed at proving that the destruction caused by the back-scattered ions is reduced for each cathode by a factor of twenty. Each cathode will produce a pulse stream at a frequency of 700 kHz, controlled by a laser. The timing of firing the laser beams is such that each cathode is emitting with a delay relative to the previous one. The 20 cathodes combined thus produce a bunch stream at 14 MHz. As seen in Figure 7, the beams coming out of the cathodes pass through a hole in the anode, then a focusing solenoid, then a 30° fixed field bending-magnet. When the beams reach the central axis of the gun, they are bent onto the exit common path by a field, rotating at 700 kHz.

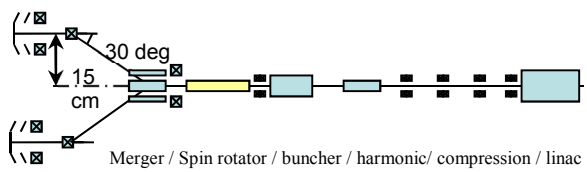

Figure 7: Schematic of the Gatling Gun injector.

The funneling device [17] generates combined dipole and quadrupole-magnetic fields; the symmetries of fields are well preserved, and they can bend and focus the 200 keV beam by 30° with little emittance growth. Our simulations demonstrate that the radius of the good field (0.1%) region is more than 6 cm; the power losses in the coils (including the eddy-current effect) are about 600 W, and the power losses (viz., eddy current, hysteresis, and residual) are about 650 W.

Low frequency SRF structures will be used at the initial stages of acceleration/bunching in the 10 MeV main ERL injector and in the CeC injector.

3.5-nC bunches of polarized electrons will be produced at each cathode for each pulse. The bunches will be relatively long to alleviate space charge effects and will

Copyright © 2012 by the respective authors — cc Creative Commons Attribution 3.0 (CC BY 3.0)

have to be shortened prior to injection into the 704 MHz SRF linac. This will be accomplished by velocity modulation in a 112 MHz quarter wave SRF buncher. A third harmonic single-cell elliptical SRF structure will be used for linearization. The buncher will operate at accelerating voltage of 1.3 MV and the third harmonica cavity – at 0.6 MV. The gun is in an advanced state of construction, as can be seen in Figure 8, showing the chamber accepting the fixed dipoles and the laser ports.

Figure 8: A component of the funneling polarized electron gun. Laser input ports are shown on top.

SUMMARY

The Accelerator R&D Division of the Collider-Accelerator Department at Brookhaven National Laboratory is carrying out R&D on eRHIC, a high-current, high-energy Energy Recovery Linac (ERL) designed for colliding 50 mA polarized electrons at an energy of 20 GeV with the beams of the Relativistic Heavy Ion Collider (RHIC). The R&D includes the design of the 6-pass ERL beam dynamics, accelerating cavities, crab cavities and other SRF devices. Three focused R&D efforts in this context include the construction, commissioning and testing of three major systems: A 20 MeV, 300 mA R&D ERL, a Proof-of-Principle (PoP) experiment in Coherent electron Cooling and a PoP experiment to demonstrate a funneling polarized electron gun, aimed at extending the current state-of-the-art 4 mA guns to as much as 20 times higher.

ACKNOWLEDGMENT

The various R&D projects described in this paper are the work of a very large number of colleagues at BNL in general, mostly in the Collider-Accelerator Department (C-AD) and in the Accelerator R&D Division of C-AD. The dedicated and expert work of these colleagues is gratefully acknowledged.

REFERENCES

[1] Ben-Zvi, I. Kewisch, J. Murphy and S. Peggs, "Accelerator Physics Issues in eRHIC", Nuclear Instruments and Methods in Physics Research **A463**, 94 (2001).
[2] V. Ptitsyn, et al., "High Luminosity Electron-Hadron Collider eRHIC," Proceedings of IPAC'2011, p. 3726.
[3] D. Trbojevic et al., "Recirculating Electron Linacs (REL) for LHeC and eRHIC", IPAC'2011, p. 1099
[4] V.N. Litvinenko, "Chromaticity of the lattice and beam stability in energy recovery linacs", Vladimir N. Litvinenko, Phys. Rev. ST Accel. Beams **15**, 074401
[5] V. N. Litvinenko, "Novel method of suppressing transverse beam-break-up instability in multi-turn energy recovery linacs", in the proceedings of this conference.
[6] S. Belomestnykh, et al., "Superconducting RF Systems for eRHIC", WEPPC109, Proceedings of IPAC'2012, page 2474.
[7] S. Belomestnykh, et al, Superconducting RF Linac for eRHIC", in the proceedings of this conference.
[8] Wencan Xu, et al., "High current cavity design at BNL," *Nucl. Instr. and Meth. A* **622** (2010) 17-20.
[9] Wencan Xu, et al., "High Current SRF Cavity Design for SPL and eRHIC," PAC'2011, pp. 2589.
[10] Wencan Xu, et al., "Progress on the High-Current 704 MHz Superconducting RF Cavity at BNL," WEPPC113, Proceedings of IPAC'2012, page 2486
[11] I. Ben-Zvi et al., "The Status of the BNL R&D ERL" ICFA Beam Dynamics News Letter # 58, 2012.
[12] S. Belomestnykh et al, "Developing of Superconducting RF Guns At BNL", in the proceedings of this conference.
[13] V. N. Litvinenko, Y. S. Derbenev, Physical Review Letters 102, 114801 (2009).
[14] V.N. Litvinenko et al., "Proof-of-Principle Experiment for FEL-Based Coherent Electron Cooling", Proceedings of PAC'2011, p. 2064
[15] V. N. Litvinenko, C-AD/AP/417 Note, (2011).
[16] X. Chang, et al., "A Multiple Cathode Gun Design for the eRHIC Polarized Electron Source," Proceedings of PAC'2011, p. 1969.
[17] I. Ben-Zvi, et al, "Generating high-frequency, rotating magnetic fields with low harmonic content", Physical Review ST-AB **14**, 092001 (2011).

Copyright © 2012 by the respective authors — cc Creative Commons Attribution 3.0 (CC BY 3.0)

THE SWISS FEL RF GUN: RF DESIGN AND THERMAL ANALYSIS

J.-Y. Raguin, M. Bopp, A. Citterio, A. Scherer
PSI, CH-5232 Villigen, Switzerland

Abstract

We report here on the design of a dual-feed S-band 2.5-cell RF gun, developed in the framework of SwissFEL, capable of operating at 100 Hz repetition rate. As in the LCLS RF gun, z-coupling, to reduce the pulsed surface heating, and a racetrack coupling cell shape, to minimize the quadrupolar component of the fields, have been adopted. The cell lengths and the iris thicknesses are as in the PHIN gun operating at CERN. However the iris aperture has been enlarged to obtain a frequency separation between the operating π mode and the $\pi/2$ mode higher than 15 MHz. An amplitude modulation scheme of the RF power, which allows one to obtain a flat plateau of 150 ns for multibunch operation and a reduced average power is presented as well. With an RF pulse duration of 1 μs it is shown that operation at 100 MV/m and 100 Hz repetition rate is feasible with very reasonable thermal stresses.

INTRODUCTION

Paul Scherrer Institut is completing the study of the accelerating systems of SwissFEL, a Free Electron Laser which targets a maximum electron beam energy of 5.8 GeV. SwissFEL is designed for two standard electron beam operation modes, one with a 200 pC charge per bunch and a core slice emittance of 0.43 mm·mrad and the second with a 10 pC charge per bunch and a core slice emittance of 0.18 mm·mrad. SwissFEL, the main linac frequency being the C-band American frequency 5712 MHz, operates with a repetition rate of 100 Hz and two electron bunches, with a spacing of 28 ns, are accelerated at each RF pulse.

The proposed 2.5-cell RF gun operates with a nominal body temperature of 40 °C in the π mode at the S-band frequency of 2998.8 MHz, such a frequency having a common sub-harmonic with the SwissFEL C-band main linac frequency. The beam energy at the exit of the RF gun is about 7 MeV. The two full cell lengths and the iris thicknesses of the RF gun are identical to the ones of the CTF3 PHIN RF gun [1]. The upstream cell, shorter than the two full cells, has a longitudinally adjustable backplane. The middle cell is coupled to two rectangular waveguides symmetrically arranged to cancel the dipolar component of the field. The racetrack interior shape of this coupling cell is optimized to minimize the quadrupolar field component, as in the LCLS RF gun [2]. Long lifetime and reliable operation with the targeted peak on-axis electric field of 100 MV/m requires the optimization of the two RF coupling port dimensions to reduce the dynamic thermal stress due to pulsed heating. With the high 100 Hz repetition rate, mechanical stresses caused by thermal loading have to be thoroughly addressed.

SWISSFEL RF GUN DESIGN

Design with 2D RF Simulations

Ignoring at this stage the middle cell coupling ports, RF simulations performed with the 2D electromagnetic code SUPERFISH [3] are used to determine the radius and the elliptical shape of the irises between the cells compatible with reduced surface electric fields and large frequency separation between the operating π mode ($TM_{010-\pi}$ mode) and the $\pi/2$ next lower mode ($TM_{010-\pi/2}$ mode). The radius of the upstream cell and of the two full cells are adjusted to reach a balanced on-axis field at the operating frequency. The 2D RF design was then guided by the requirements that the mode separation between the operating π mode and the $\pi/2$ mode be higher than 15 MHz and that the peak surface electric field is not higher than the electric field on the cathode. The large mode separation between the operating mode and the next lower mode reduces the impact of the lower mode on the electron bunch energy spread and projected emittance. It is also expected to make the field balance less sensitive to thermal expansion under operational conditions and to manufacturing dimension deviations that may occur during production [4].

Fig. 1 shows the electric field contour lines of the π mode. The cell radii are optimized to obtain field flatness at the operating frequency. The dimensions of some geometrical parameters, used also for the final 3D design, are specified in Table 1. The elliptical profile of the irises is characterized by an aspect ratio of 1.7:1 so that the maximum surface electric field is lower than the peak field on the cathode.

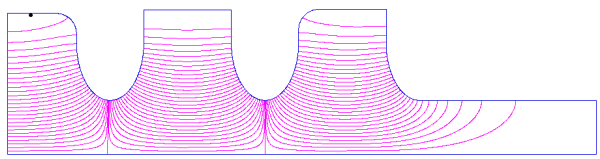

Figure 1: Electric field contour lines of the operating π mode

Table 1: Geometrical parameters of the SwissFEL RF gun

Parameter		Value	
Cell length	20.5 mm	26 mm	26 mm
Iris thickness		20 mm	
Iris radius		16 mm	
Drift radius		16 mm	

Final Design with 3D RF Simulations

The dimensions obtained with the 2D code SUPERFISH are used as input to complete the RF design of the gun with the 3D electromagnetic code HFSS [5], in particular the

Copyright © 2012 by the respective authors — cc Creative Commons Attribution 3.0 (CC BY 3.0)

design of the two RF coupling ports and of the racetrack shaped coupling cell [2, 6]. The coupling apertures, located in the middle cell, are optimized to minimize field distortion, to obtain a coupling coefficient β around 2 and to ensure that the temperature rise per pulse of the most exposed areas does not exceed 50^{o}C. To fulfill these three criteria, the two main features that have been adopted are coupling apertures running longitudinally all along the coupling cell, i.e. z-coupling scheme, and a large inner edge radius of the apertures. In addition, a balanced on-axis electric field is obtained with a minor change of the upstream and downstream cell radii. A cross-section of the RF gun is shown in Fig. 2.

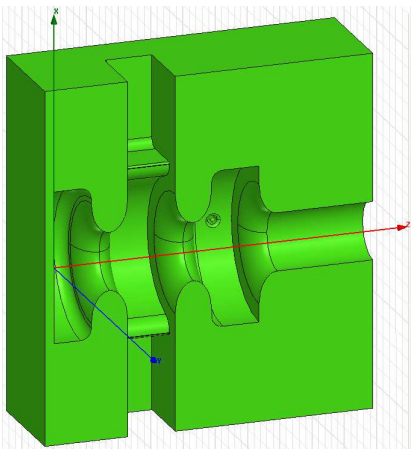

Figure 2: Cross-section of the SwissFEL RF gun.

Fig 3 shows the on-axis electric field along the RF gun in the final RF design. The ratios of the three maxima of the on-axis electric fields are higher than 98%.

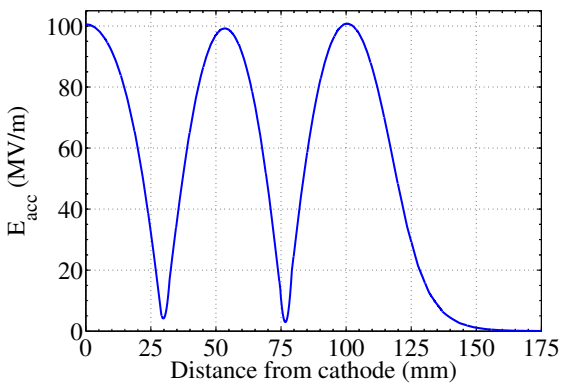

Figure 3: On-axis electric field of the SwisFEL RF gun.

The coupling apertures induce field distorsion in the vicinity of the gun axis that may deteriorate the electron bunch quality. The two symmetrically arranged apertures allow one to cancel the dipolar component of the fields. To reduce the quadrupolar fields, the coupling cell has a racetrack transverse profile. For a given inner edge radius of the apertures, there is some specific combination of aperture width and length of the racetrack straight section which minimizes the quadrupolar component. Fig 4 shows the amplitude of the longitudinal electric fields along both transverse directions of the coupling cell middle plane (see Fig 2 for the definition of the x- and y-axis). Such equal amplitudes are obtained for a width and an inner radius of the coupling apertures of 17.73 mm and 8.5 mm, respectively whereas the racetrack straight section is 7.1 mm long.

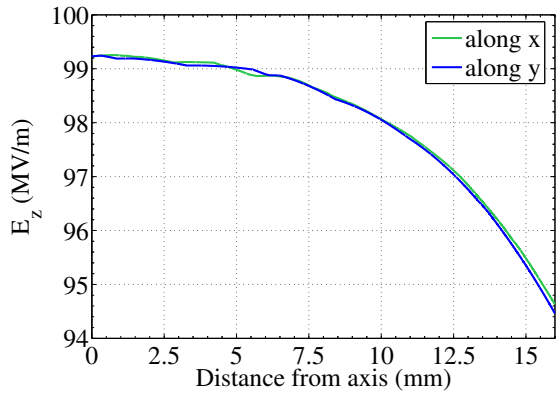

Figure 4: Amplitude of the longitudinal electric field along transverse directions of the SwisFEL RF gun.

The design coupling coefficient β has been chosen to be 2. Overcoupling the cavity at the operating frequency decreases the filling time of the RF gun. The nominal accelerating field can then be reached with a shorter RF pulse, a requirement for reducing the mechanical stresses on the gun body due to thermal loading. In the final design, the π-mode resonance frequency is within 100 kHz of the design frequency with a calculated coupling coefficient β of 1.98. The $\pi/2$ mode is about 16 MHz lower in frequency and the coupling coefficient β is 0.2.

An upper bound of the temperature rise per pulse on the inner surface of the RF gun can be analytically estimated by assuming a constant amplitude of the surface magnetic field over the whole pulse length. This limit $(\Delta T)_{max}$ is given by the formula: $(\Delta T)_{max} = (R_s/K)\sqrt{D/\pi}\sqrt{t_{pulse}}|H_s|^2$, where R_s, K and D are the surface resistance, the thermal conductivity and the specific heat of copper, respectively, at the operating frequency, whereas t_{pulse} and $|H_s|$ are the pulse length and the amplitude of the surface magnetic field, respectively. The distribution of the temperature rise for a 3 μs pulse on the surface of one of the coupling apertures is shown on Fig 5. The amplitude of the surface magnetic field corresponds to a peak on-axis electric field of 100 MV/m. The maximum temperature rise, located all along the aperture, is lower than 45 ^{o}C.

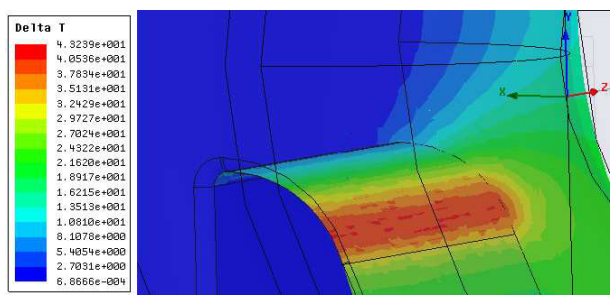

Figure 5: Coupling aperture temperature rise for a 3 μs RF pulse and a peak on-axis field of 100 MV/m.

Copyright © 2012 by the respective authors — cc Creative Commons Attribution 3.0 (CC BY 3.0)

TRANSIENTS AND THERMAL STRESSES

Since SwissFEL is planned for a two-bunch operation with a 28 ns spacing, an amplitude modulation scheme of the RF input power is proposed to maintain a constant amplitude of the peak accelerating field for a duration longer than the bunch spacing. Assuming zero rise and fall times, an RF power of about 14 MW is required to reach the 100 MV/m nominal peak accelerating field with a 3 μs rectangular RF pulse. In the amplitude modulation scheme, assuming a 1 μs total RF pulse and targeting the nominal peak accelerating field, an RF power of about 18 MW during the first 850 ns of the RF pulse feeds the cavity. The RF power is then quickly reduced to about 14 MW and is kept constant during the last 150 ns of the RF pulse. Such a scheme results in a flat-topped accelerating field of 100 MV/m (see Fig 6). The reflected power is maximum at the end of the RF pulse and is about 28 MW.

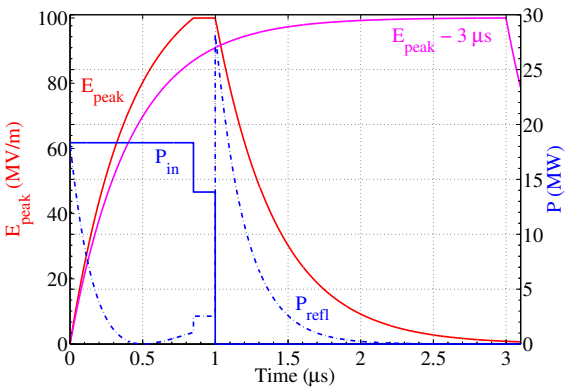

Figure 6: Transient-states of the peak accelerating field and of the RF input and reflected powers.

With this amplitude modulation scheme and with a repetition rate of 100 Hz, the average dissipated power is as low as 0.9 kW (see Fig 7). The temperature rise per pulse on the coupling apertures due to pulsed heating, estimated more rigorously by taking into account the transient behavior of the magnetic surface field during the whole pulse duration [7], is reduced to about 18 °C. With a 3 μs rectangular RF pulse, the average dissipated power is about three times higher and the temperature rise is about twice higher.

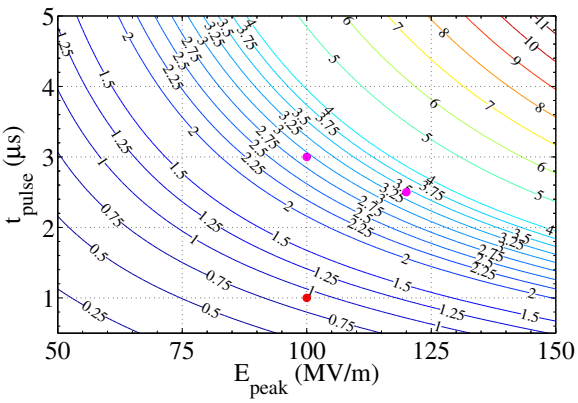

Figure 7: Average dissipated power (kW) vs. peak accelerating field and pulse length for a repetition rate of 100 Hz.

The number, size and location of the cooling channels in the RF gun body are determined with ANSYS [5] simulations for operation with an inlet water temperature of 40 °C and a maximum average dissipated power of 3.5 kW. The thermally induced stresses in the gun body are within an acceptable range with a 0.9 kW thermal load (see Fig 8).

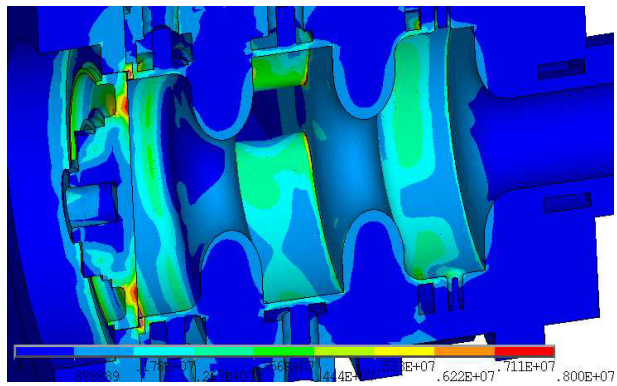

Figure 8: Thermal stress (N/m^2) for a 0.9 kW average load on the SwissFEL RF gun body.

CONCLUSIONS

A dual-feed S-band 2.5-cell RF gun operating in the π mode has been designed for SwissFEL which allows a two-bunch operation with an amplitude modulation scheme of the RF input power. A peak on-axis accelerating field of 100 MV/m can be maintained constant for 150 ns within a 1 μs total RF pulse length. For a pulse repetition frequency of 100 Hz, the total average power loss is then less than 1 kW and the temperature rise per pulse is well below the critical limit. Thermo-mechanical studies led to a design such that the RF gun can safely operate with a thermal load lower than 3.5 kW. The RF gun can then also operate safely at 120 MV/m in the single- and two-bunch regimes. However, the RF pulse length shall not exceed 2.5 μs when operating without amplitude modulation of the input power.

REFERENCES

[1] R. Roux, "Conception of Photoinjectors for the CTF3 Experiment", Int. J. Mod. Phys. A 22 (2007), pp. 3925-3941.
[2] L. Xiao et al., "Dual Feed RF Gun Design for the LCLS", Proc. PAC 2005, pp. 3432-3434, Knoxville, 2005, http://www.JACoW.org.
[3] J. H. Billen and L. M. Young, "Poisson / Superfish", Los Alamos National Laboratory, LA-UR-96-1834, 1996.
[4] D. H. Dowell et al., "The Development of the Linac Coherent Light Source RF Gun", ICFA Beam Dynamics Newsletter No. 46 (2008), pp. 162-192.
[5] http://www.ansys.com
[6] J. Haimson et al., "A Racetrack Geometry to Avoid Undesirable Azimuthal Variations of the Electric Field Gradient in High Power Coupling Cavities for TW Structures", Proc. 7th Workshop on Advanced Accelerator Concepts, Lake Tahoe, 1996, AIP Conf. Proc. 398, pp. 898-911.
[7] D. P. Pritzkau et al., "Experimental Study of RF Pulsed Heating on Oxygen Free Electronic Copper", Phys. Rev. ST Accel. Beams 5, 112002 (2002)].

Copyright © 2012 by the respective authors — cc Creative Commons Attribution 3.0 (CC BY 3.0)

DEFLECTING STRUCTURES WITH MINIMIZED LEVEL OF ABERRATIONS*

V. Paramonov †, INR of the RAS, Moscow, 117312, Russia

Abstract

Deflecting structures are now widely used for bunch phase space manipulations either in special bunch diagnostic or in emittance exchange experiments. As a tool for manipulation, the structure itself should provide the minimal phase space perturbations due to non linear additives in the field distribution. Criterion of the field quality estimation is developed and deflecting structures are considered for minimization of non linear additives.

INTRODUCTION

The Deflecting Structures (DS) - periodical structures with transverse components of the electromagnetic field - initially were introduced for charged particle deflection and separation. The bunch cross DS synchronously with the deflecting field Ed, corresponding the phase $\phi = 0$ in the structure and particles get the increment in the transverse momentum p_t. There are a lot of papers, see for example [1], describing DS design and application for such purpose. At present for short and bright electron bunches DS found another applications, either for bunch special diagnostic, [2], or emittance exchange experiments. Both directions are related to the transformation of particle distributions in the six dimensional phase space and DS operates in another mode - the bunch center cross DS at zero E_d value, $\phi = 90^o$. There are also a lot of papers, describing it in more details. Application for Particles Distributions Transformation (PDT) provide additional requirements - a tool for transformation should provide the minimal, as possible, own distortions to the original distributions.

FIELD DISTRIBUTION QUALITY

For deflecting field E_d description the widely used basis of $TM - TE$ waves can not be used due to degeneration into TEM at $\beta = 1$. A basis of hybrid waves $HE - HM$ was introduced, [3], [4] to avoid this methodical problem. The common representation for the field distribution in the DS aperture is

$$\vec{E} = C\vec{E}_{HE} + D\vec{E}_{HM}, \quad \vec{H} = C\vec{H}_{HE} + D\vec{H}_{HM}, \quad (1)$$

with the weighting coefficient C, D depending both on supporting structure and on operating mode. It is the method of description and results treatment. The physical object - the deflecting force - is the transverse component of the Lorenz force

$$\vec{F}^L = e(\vec{E} + [\vec{v}, \vec{B}]), F_x = eE_d = e(E_x - \beta Z_0 H_y), \quad (2)$$

where $Z_0 = \sqrt{\frac{\mu_0}{\epsilon_0}}$, expressed in (2) through the transverse E_x and H_y components in Cartesian coordinates.

In any periodical structure for Traveling Wave (TW) operating mode each field component $E_j(r, z)$ in the beam aperture can be represented in the complex form as the set over spatial harmonics:

$$E_j(r, z) = \widehat{E_j(r, z)} e^{i\psi_j(z)} = \quad (3)$$
$$= \sum_{n \to -\infty}^{n \to +\infty} a_{jn}(r) e^{\frac{-i(\Theta_0 + 2n\pi)z}{d}},$$

where $\widehat{E_j(r, z)}$ and $\psi_j(z)$ are the amplitude and the phase distributions, d is the structure period and $a_{jn}(r)$ is the transverse distribution for the n-th spatial harmonics. The period length is defined from synchronism with the main a_{j0} harmonic, $d = \frac{\Theta_0 \beta \lambda}{2\pi}$.

The bunch emittance deterioration during PDT take place due to non linear additions both in transverse and longitudinal distributions of the field. There is inevitable nonlinearity at $\beta < 1$ even in main harmonic distribution, vanishing for $\beta \to 1$, [3], [5]. But the main source of additions are higher spatial harmonics. For each harmonic the transverse and longitudinal distributions are rigidly coupled and are proportional to harmonic amplitude. To estimate field quality, we have to estimate the level of spatial harmonics, [5]. Spatial harmonics are essential at the aperture radius $r = a$ and higher harmonics attenuate to the axis as

$$a_{jn}(0) \sim a_{jn}(a) \cdot exp(-\frac{4\pi^2 n}{\beta\Theta_0} \cdot \frac{a}{\lambda}), \quad |n| \gg 1, \quad (4)$$

where λ is the operating wave length. At the axis $r = 0$ just lower harmonics $n = \pm 1, \pm 2, \pm 3$ are really presented. For harmonics estimations in details and 'in total', let us introduce parameters $\delta\psi_j(z)$ and Ψ_j at the axis $0 \le z \le d, r = 0$

$$\delta\psi_j(z) = \psi_j(z) + \frac{\Theta_0 z}{d}, \quad \Psi_j = max(|\delta\psi_j(z)|), \quad (5)$$

with the physical sense as the deviation and the maximal phase deviation of the real wave component from the synchronous harmonic. The qualitative estimation and correct value for $a_{jn}(0)$ one can get as

$$|a_{jn}(0)| < \frac{(\widehat{E_j(0, z)}_{max} + \widehat{E_j(0, z)}_{min})\Psi_j}{2n}, \quad (6)$$
$$a_{jn}(0) = \frac{\int_0^d \widehat{E_j(0, z)} sin(\delta\psi_j(z)) sin(\frac{2\pi n z}{d}) dz}{d}.$$

From linearity, we can apply $\delta\psi_j(z)$ and Ψ_j for quality

* Work supported in part by RBFR N12-02-00654-a
† paramono@inr.ru

Copyright © 2012 by the respective authors — cc Creative Commons Attribution 3.0 (CC BY 3.0)

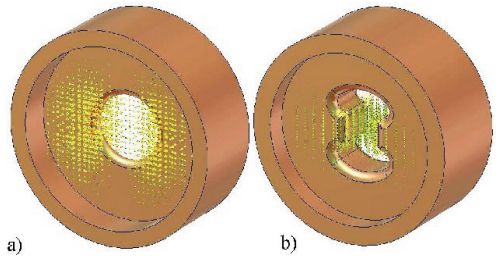

Figure 1: DLW (a) and TE - type (b) deflectors.

estimation both in longitudinal $E_z, \delta\psi_z(z), \Psi_z$ and transverse $E_d, \delta\psi_d(z), \Psi_d$ field components, also estimating PDT quality in these directions. To emphasize the differences in field distribution, the developed method is applied for analysis of DLW [6] and TE - type deflectors, Fig. 1.

OPERATING MODE

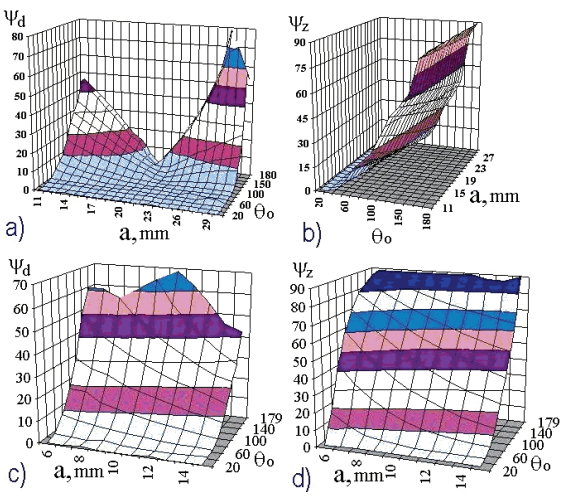

Figure 2: The surfaces $\Psi_d(a, \Theta_0)$ (a,c) and $\Psi_z(a, \Theta_0)$ (b,d) for the DLW (a,b) and TE - type (c,d) deflectors.

Assuming operating frequency $f_0 = 3GHz$, in Fig. 2 are shown the surfaces $\Psi_d(a, \Theta_0)$ and $\Psi_z(a, \Theta_0)$ for the DLW and TE - type deflectors both for TW $0 < \Theta_0 < 180^0$ and Standing Wave (SW, $\Theta_0 = 180^0$) operating mode,[5].

TW Operation

As can be seen from Fig. 2, small Ψ_d, Ψ_z values all time are at lower $\Theta_0 \leq 60^o$ values. For spatial harmonics the decrement of attenuation in (4) is inverse proportional to Θ_0 and $a_{zn}(0), a_{dn}(0)$ all time are small for low Θ_0. It is the common property of slow wave systems. Any periodical structure has reduced aberration level in TW operation with low Θ_0, both in E_z and in E_d distributions. For DLW harmonics attenuation is essentially stronger due to larger aperture radius.

Another effect is very important for E_d distribution and is in mutual phasing of transverse E and H components. For the opposite E_x and H_y phasing (DLW) electric and magnetic components work for deflection together (1), but E_x spatial harmonics compensate or even cancel $Z_0 H_y$ harmonics. It extends low Ψ_d region to higher Θ_0 values, Fig. 2a, and $\Psi_d < \Psi_z$. For the same E_x and H_y phasing (TE deflector) deflection form electric and magnetic components is partially compensated (1), but E_x and $Z_0 H_y$ harmonics add, $\Psi_d > \Psi_z$. The significant harmonics cancellation takes place at $|E_x^0| \sim |Z_0 H_y^0|$ - for comparable amplitudes of synchronous harmonics in E_x and H_y distributions. One can see clear canyon in $\Psi_d(a, \Theta_0)$ surface in Fig. 2a and for the bottom of this canyon $|E_x^0| \approx |Z_0 H_y^0|$. The structures with opposite phasing can provide very small aberrations level in E_d distribution.

In the Table 1 are listed the relative harmonics amplitudes for DLW TW operation. In comparison with DLW LOLA deflector, [6], or similar structures with $\Theta_0 = 120^o$, operation with $\Theta_0 = 60^o$ leads to aberrations reduction in times, especially for longitudinal force. Conditions for RF efficiency in TW case also are more flexible, as compared to SW case. The end cells with RF couplers are the points of special consideration, [5].

Table 1: The relative $a_{zn}(0) \cdot 10$ and $a_{dn}(0) \cdot 10$ values for DLW.

Operation $a =, mm$	Θ_0	E_z, $n=1$	E_z, $n=2$	E_d, $n=1$	E_d, $n=2$
TW,23.80	60	-0.048	-0.007	0.006	-0.009
TW,23.58	90	-0.581	-0.004	0.009	-0.001
TW,22.33	120	-1.950	-0.048	0.020	-0.015
SW,12.0	180	-6.103	-1.385	-3.818	-0.623
SW,19.4	180	-5.619	-0.691	-0.271	-0.148

SW Operation

In the case of short deflectors SW operation is more efficient in RF sense. But individual E, H components, including E_z at $\Theta_0 = 180^o$ have a single, either real or imaginary part in representation (1), resulting in $\Psi_j = 90^0$ for each component separately. For longitudinal force aberration reduction is possible just by aperture radius increasing -it is not so effective as for low Θ_0 TW case.

The deflecting field E_d is composed from two components, E_x, H_y and has in representation (1) both real and imaginary parts, similar to TW case. Relations (5),(6) work for E_d study even for Θ_0 SW case.

Because harmonics attenuation at $\Theta_0 = 180^o$ (assuming $\beta = 1$) is not effective, the single way for aberration reduction in E_d is harmonics cancellation for E_x and H_y distributions under opposite phasing. It can be realized in DLW by aperture radius choice for the preliminary specified disk thickness t_d, [8]. In the Table 1 are given results for optimized SW case ($a = 19.4mm, t_d = 5.4mm, \Psi_d \sim 1.5^o$, $\frac{Z_0 H_y^0}{E_x^0} = 0.98$). In SW DLW E_d aberration reduction is possible, but at the expense of moderate RF efficiency.

Copyright © 2012 by the respective authors — cc Creative Commons Attribution 3.0 (CC BY 3.0)

SUPPORTING STRUCTURE

The hybrid HE_n, HM_n waves exist in a supporting RF structure. But the classification of a supporting structure with a complicated field distribution is always rather conditional. In Fig. 3 the plots of $\frac{Z_0 H_y^0}{E_x^0}$ balance are shown,

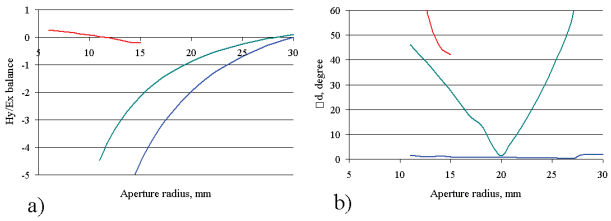

Figure 3: The field balance $\frac{Z_0 H_y^0}{E_x^0}$ (a) and $\Psi_d(a)$ plots (b) for DLW deflector $\Theta_0) = 60^o$ (blue), $\Theta_0) = 180^o$ (green) and TE - type deflector, $\Theta_0 = 180^o$ (red).

having even for well studied DLW in the first passband a large variety $-10 \le \frac{Z_0 H_y^0}{E_x^0} \le 0.5, 10mm \le a \le 30mm$ with different $\vec{E}, \vec{H}$ distributions, [5]. Similar field transformation we can provide in TE deflector, [7], Fig. 4.

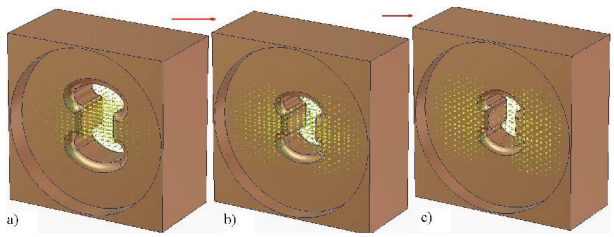

Figure 4: Field transformation for deflecting mode in the TE - type deflector.

At the structure axis we can define C, D in (1) from the already calculated E_d distribution and connect it with $\frac{Z_0 H_y^0}{E_x^0}$ balance. For E_d aberration minimization, especially for SW case, we need the opposite phasing of transverse $\vec{E}, \vec{H}$ components. Now it is the single sustainable sign for structure selection. Such phasing means the negative power flow near, but doesn't mean, in general, total negative flow, which define a negative dispersion in operating point. Even in simple DLW the inversion aperture radius a_i, corresponding to $\beta_g = 0$, essentially depends on Θ_0, [5].

For effective aberration reduction in E_d we need in the balance $|\frac{Z_0 H_y^0}{E_x^0}| \approx 1$. But the case of $|Z_0 H_y^0| = |E_x^0|$ is very close, probably coincides, to inversion point. It results in non monotonous (for TW case, [5]) or narrow (for SW case, [8]) dispersion curve. The method for DLW dispersion curve correction is described in [8]. Also the practice of Ψ_d minimization shows, that $(\Psi_d)_{min}$ is close, but not identical to $|Z_0 H_y^0| = |E_x^0|$ condition.

The DLW has just one parameter, effective for $\frac{Z_0 H_y^0}{E_x^0}$ balance control, aperture radius a, see Fig. 3a, which defines RF efficiency also. By splitting control over transverse $\vec{E}, \vec{H}$ components in TE - deflector, which is defined by r_a, r_w combination, see [7], we also can get opposite H_y and E_x phasing, Fig. 3a. Continuing the structure transformation, shown in Fig. 4, we come in the region $|Z_0 H_y^0| \approx |E_x^0|$ from the top in Fig. 3a. The field distribution becomes as in right picture in Fig. 3 and there are no evident reasons denote transformed option as TE-type. We lose in RF efficiency (Z_e value), as compared to original case, Fig. 1b, [7], but still remain essentially higher, as compared to simple DLW. The level of aberration is practically the same as for optimized in $(\Psi_d)_{min}$, see Table 1, case $a = 19.4mm$, classical DLW structure. The parameters of such SW deflectors in details, including end cells and RF coupler cell, are considered in [8].

SUMMARY

In any periodical DS aberrations, both in E_z and in E_d, are lowered in TW operation with $\Theta_0 \le 60^o$, especially for large aperture radius. Essential improvement in E_d distribution also takes place for opposite phasing of transverse $\vec{E}, \vec{H}$ components at the axis. Such TW DS provide the best results in PDT linearity. For TW operation with $\Theta_0 \ge 120^o$ and SW, $\Theta_0 = 180^o$, aberration reduction is possible in E_d only, by aberrations cancellation in oppositely phased and balanced transverse $\vec{E}, \vec{H}$ components. In a simple SW DLW it is realized for moderate RF efficiency. By splitting control over transverse $\vec{E}, \vec{H}$ components we get efficient SW DS with low E_d aberration level.

ACKNOWLEDGMENT

The author warmly thanks Dr. K. Floettmann, DESY, for support and collaboration with all beam dynamics conclusions.

REFERENCES

[1] T.H. Fieguth, R.A. Gearhart, RF Separators and Separated Beams at SLAC, Proc. 1975 PAC, p. 1533

[2] R. Akre et. al., RF Deflecting Structure for Bunch Length and Phase Space Diagnostic. Proc. 2001 PAC, p. 2353

[3] Y. Garault, CERN 64-43, CERN, 1964

[4] H. Hahn, Deflecting Mode in Circular Iris-Loaded Waveguides, Rev. Sci. Inst., v. 34, n. 10, p. 1094, 1963

[5] V. Paramonov, RF field distributions quality in deflecting structures. (in preparation).

[6] O.H. Altenmueller et. al., Investigations of Traveling-Wave Separators ..., Rev. of Sci. Instr., v. 35, n 4, 1964

[7] V. Paramonov, K. Floettmann, L. Kravchuk. RF Parameters of a TE-Type Deflecting Structure for the S-band frequency range. MOPB082, These proceedings.

[8] V. Paramonov et. al., Standing wave RF deflectors with reduced aberrations. WEPPD012, Proc. RuPAC 2012

Copyright © 2012 by the respective authors — cc Creative Commons Attribution 3.0 (CC BY 3.0)

RESULTS OF TESTING OF MULTI-BEAM KLYSTRONS FOR THE EUROPEAN XFEL

V. Vogel, L. Butkowski, A. Cherepenko, S. Choroba, I Harders and J. Hartung,
DESY, 22607 Hamburg, Germany

Abstract

For the European XFEL multi-beam klystrons, which can produce RF power of 10 MW at an RF frequency of 1.3 GHz, at 1.5ms pulse length and 10 Hz repetition rate, were chosen as RF power sources. Twenty-seven of horizontal multi-beam klystrons (MBK) together with connection modules (CM) will be installed in the XFEL underground tunnel. The CM will be installed on the MBK and connects the MBK to the pulse transformer with only one HV cable, because the CM has a filament transformer inside as well as all diagnostics for HV and cathode current measurements. MBK prototypes together with CM prototypes have been tested for long time at a test stand at DESY, about 4600 hours of operation for each of horizontal MBK with full RF output power, full pulse length and repetition rate of 10 Hz. Testing of first MBKs from series production has been started. In this paper we will give an overview of the test procedure, summarize the current test results and we will give a comparison of the most important parameters.

INTRODUCTION

For the XFEL project [1] as a source of RF power for 27 RF station were chosen the horizontal MBK made by two companies: MBK TH1802 from "Thales" [3] and MBK E3736H from "Toshiba" [4]. The main parameters of MBK are given in Table 1.

Table 1: Main parameters of L-band MBK for XFEL

Parameters	Design value	Test value
Output power (MW)	10	10.3
RF pulse length (ms)	1.5	1.5
Efficiency (%)	> 63	64
Repetition rate (Hz)	up to 30	10
Max average RF power (kW)	150	155
Max average power in collector (kW)	300	270
Max drive power (W)	<200	<150
Bandwidth (MHz)	3	>3

Both prototypes of MBK were tested on DESY MBK test stands [2], a total time of testing exceed of 4600 hours for both of tubes. The test was done with full RF power of 10 MW, full RF pulse length of 1.5 ms and with repetition rate of 10 Hz. Fig. 1 shows the top view of the test stands. Because the all of RF station will be located in the underground tunnel it is very important do not have the open oil during installation of MBK. It was proposed and tested the connection between MBK and HV pulse transformer through connection module (CM) [5, 6 and 7] and HV cable. Several types of HV cables and connectors as well as CM prototypes were tested. Big advances of using CM are that CM has inside a high voltage high frequency filament transformer and monitors for measurement of klystron voltage and cathode current. Fig. 2 shows the one of klystrons with CM and HV cable.

Figure 1: MBK test stands in DESY Hamburg

Figure 2: MBK with CM and HV cable "PFISTERER 3S"

RESULTS OF MBK PROTOTYPES TEST

Since February 2008 we started the test of the first of horizontal MBK prototype on DESY site. For the test of MBK it was specially developed two radiation protected

Copyright © 2012 by the respective authors — cc Creative Commons Attribution 3.0 (CC BY 3.0)

test chambers. Each of both klystron waveguides outputs was connected through WR650 directional coupler and RF power divider to the two of RF loads. Using four of RF loads for the one klystron allow us made the test of average output RF power up to level of 155 kW. The waveguide system was pressured by dry air up to 1.35 bars absolute. The pressured waveguide and air flow up to 10 litters per minute allow us work without breakdown on the level of pulse power of 5 MW in one of klystrons output arm with pulse length of 1.5 ms and repetition rate of 10 Hz. Fig. 3 shows the view of one of klystron output arms. During prototypes test all klystrons parameters were proofed and we have measured a bandwidth, the gain, the phase response and efficiency of the tubes [8, 9, 10 and 11]. Fig. 4 shows the tubes efficiency in depends of output power level and Fig. 5 shows the gain curve for the different value of klystron beam voltage. Fig. 6 shows the wave shape of beam voltage and cathode current.

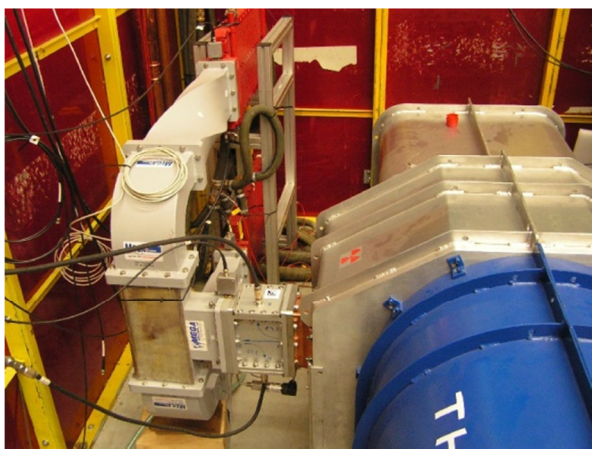

Figure 3: Connection between MBK and RF loads during test.

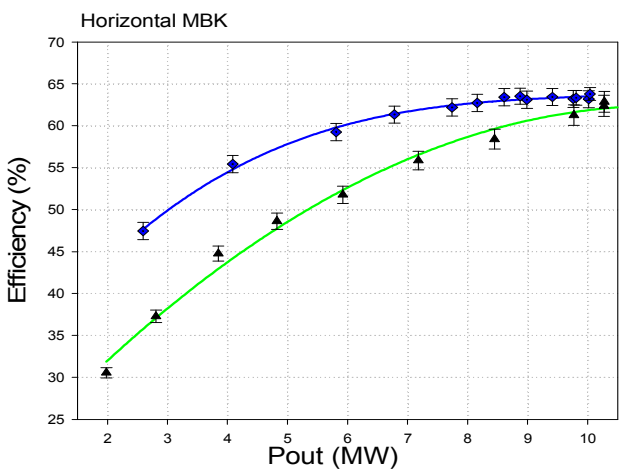

Figure 4: Efficiency for two types of MBK prototypes.

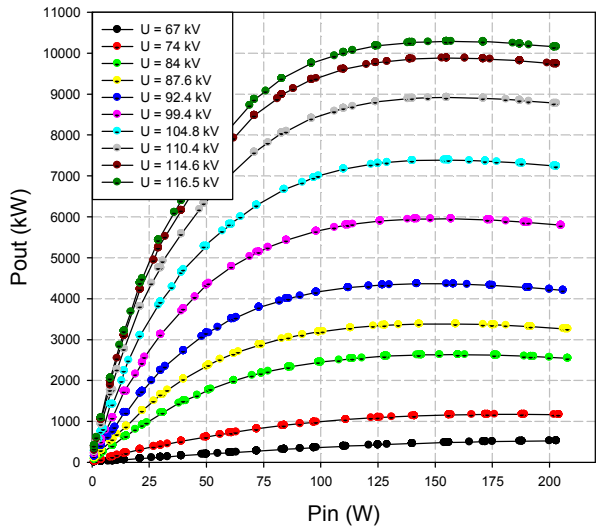

Figure 5: Gain curve for the different value of high voltage.

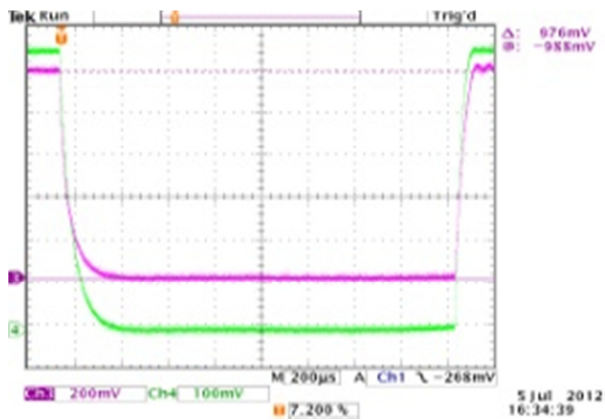

Figure 6: Wave shape of beam voltage and cathode current, the measurement from voltage and current monitors located inside CM.

PROTECTION SYSTEM

The horizontal MBK for XFEL will use the M type of dispenser cathode, for this type of cathode we can expect average tube lifetime of 145000 hours, but in the real operation the lifetime of tube can be thoroughly reducing by service conditions, several events can happen as: the gun arcing, RF breakdown, beam losses inside tube, operation of the tube in the bad vacuum and number of cathode switch cycles. To minimize the influence of service conditions to the klystrons lifetime the special fast protection system (KLM) [12] was developed and tested, the main task of KLM are: to detect as quickly as possible all events which can destroy the tube, then stop input power to the tube and send signal to stop HV pulse. The tube recovery procedure should depend on the kind of events has happened. To make decision which type of recovery procedure should be used, KLM accumulate the

Copyright © 2012 by the respective authors — cc Creative Commons Attribution 3.0 (CC BY 3.0)

signals from different type of sensors. At first, both outputs of klystron and klystron input should have a directional coupler (DC). DC is one of most important devices, the signal from that used for detection of reflected power from waveguide distribution system (WDS) and for analysing difference of expected output impulse shape and real impulse shape. At second, to detect a breakdown on the air side of output window of the klystron or breakdown in the waveguide section between window and DC it was used fast light sensors. To detect the gun arc in the klystron it was used HV breakdown sensor. The measurement of the level of vacuum inside tube, level of partial discharge in the HV system and information from sounds detectors help us to understand the reason of event and help use the right recovery procedure and make true estimation of time to recovery the RF station back to the normal operation.

Figure 7: The first serial MBK for XFEL on DESY site.

CONCLUSION

In February 2008 the first prototype of MBK for XFEL had been installed on the MBK test stand DESY. In March 2010 we have started the test of second MBK. Up to September 2012 the testing time for both of MBK prototypes reach about 4600 hours of operation at the level of 10 MW output power, RF pulse duration of 1.5 ms and repetition rate of 10 Hz. The value of pulse high voltage was about 117 kV, high voltage pulse duration 1.7 ms. The average time between two gun arcs for E3736H is about 230 hours and for TH1802 is about 460 hours. The klystrons were tested together with connection modules (CM) and different types of HV cables. During testing time we didn't observe any sign of degradation of klystrons parameters as well as CM parameters. The all of using testing equipment's work without any problem and DESY are ready to start the test of serial MBK and since August 2012 we have in DESY site the first serial MBK for XFEL. Fig. 7 shows our team and the first of serial MBK.

REFERENCES

[1] M. Atarelli et al. (Eds.), "XFEL: The European X-Ray "Free-Electron Laser: Technical Design report", DESY Report DESY 2006-097, July 2006.
[2] V. Vogel, S. Choroba, et al., "Testing of 10MW Multibeam Klystrons for the European X-Ray FEL at DESY", PAC07, Albuquerque, New Mexico, USA, 2007
[3] A. Beunas, G. Faillon, "10MW/1.5ms,L band multi beam klystron", Proc. Conf. Displays and Vacuum Electronics, Garmisch-Paterkirchen, Germany, April 29-30, 1998.
[4] A. Yano, S. Miyake, S. Kazakov, et al., "The Toshiba E3736 Multi-Beam-Klystron", LINAC'04, Lubeck, Germany.
[5] Ju. D. Valiaev, I.V. Kazarezov, V.I. Kuznetsov, V.P. Ostanin, "Small size high frequency isolation transformer for power supply of the devices located at high potential", BINP Preprint, Novosibirsk, 1989 (in Russian).
[6] V. Vogel, A. Cherepenko et al., "Connection Module for the European X-ray FEL 10MW Horizontal Multibeam Klystron," IPAC10, Kyoto, Japan, THPEB043, 2010
[7] P. Bak, V. Zabrodin, A. Korepanov and V. Vogel, "Klystron Cathode Heater Power Supply System Based on the High-Voltage Gap Transformer," PAC09, Vancouver, BC, Canada, TU6RFP016, 2009
[8] V. Vogel, S. Choroba et al., "Thales MBK test," http://www.xfel.eu/project/meetings/project_meetings/2010
[9] V. Vogel and S. Choroba, "Status of Horizontal MBK for XFEL" http://www.xfel.eu/project/meetings/project_meetings/2009
[10] V. Vogel and S. Choroba "Status of the Thoshiba MBK," http://www.xfel.eu/project/meetings/project_meetings/2006
[11] V. Vogel, S. Choroba, "Status of Multi-Beam Klystrons", Proc., 51th ILC DESY General Project Meeting. http://ilcagenda.cern.ch/categoryDisplay.py?categId=16
[12] V. Vogel "MBK protection" LLRF seminar, 2008 http://ttfinfo.desy.de/LLRFelog/index.jsp

Copyright © 2012 by the respective authors — cc Creative Commons Attribution 3.0 (CC BY 3.0)

COMPUTATIONAL MODEL ANALYSIS FOR EXPERIMENTAL OBSERVATION OF OPTICAL CURRENT NOISE SUPPRESSION BELOW THE SHOT-NOISE LIMIT

A. Nause, E. Gover, Tel Aviv University, Israel

Abstract

In this paper we present simulation analysis of experimental results which demonstrate noise suppression in the optical regime, for a relativistic e-beam, below the classical shot-noise limit. Shot-noise is a noise resulting from the granular nature of the space-charge in an e-beam. It is linear to the beam current due to its Poissonic distribution in the emission process. Plasma oscillations driven by collective Coulomb interaction during beam drift between the electrons of a cold intense beam are the source of the effect of current noise suppression. The effect was experimentally demonstrated [1] by measuring Optical Transition Radiation (OTR) power per unit e-beam pulse charge. The interpretation of these results is that the beam charge homogenizes due to the collective interaction (sub-Poissonian distribution) and therefore the spontaneous radiation emission from such a beam would also be suppressed (Dicke's subradiance [2]). Analysis of the experimental results using GPT simulations will demonstrate the suppression effect. For the simulation results we used a full 3D GPT model of the ATF section in which the experiment took place at.

INTRODUCTION

Shot-noise is a noise resulting from the granular nature of the space-charge in an e-beam. The discreteness of the particles and the randomness of electrons emission from the cathode causes time dependent fluctuations of the charge and current density at any cross section along the beam transport line. This noise was first reported in 1918 by Schottky who made experiments in vacuum tubes.

Noise is best characterized in terms of the Fourier transform of the time-varying fluctuations in electric current, namely, by its spectral density. Gover and Dyunin showed in a 1D model [3] that it is possible to observe and control optical frequency energy and current (shot noise) fluctuations in a dense relativistic charged particles beam. GPT simulations were used to demonstrate this effect for a real-like beam starting from Shot-noise [4]. Moreover, at certain conditions, when the dominant noise in the beam is current shot noise (density fluctuations), it is possible to reduce significantly the beam noise by virtue of a collective interaction process along an interaction length corresponding to a quarter period longitudinal plasma oscillation in the beam. This means that the charge distribution in the beam can be homogenized in this process.

First experimental observation of this phenomenon using OTR from a metallic foil was presented last year [1]. Noise suppression using a dispersive section (dog-leg bend) was demonstrated in SLAC [5]. TR is proportional to the current-noise amplitude [6], and therefore can be used in order to estimate the suppression in the current noise. In this paper we press analysis of the experimental results and demonstrate this effect using full 3D GPT simulations that were carried out for this purpose.

1D Model of Noise Dynamics in Charged Electron Beams

In electron-beam transport under appreciable space-charge conditions, the microdynamic noise evolution process may be viewed as the stochastic oscillations of Langmuir plasma waves [3]. In the linear regime, the evolution of longitudinal current and velocity modulations of a beam of average current I_b, velocity βc and energy $E = (\gamma - 1)mc^2$, can be described in the laboratory frame by [7]:

$$\frac{d}{d\phi_p}\breve{i}(z,\omega) = -\frac{i}{W(z)\breve{v}(z,\omega)} \quad (1)$$

$$\frac{d}{d\phi_p}\breve{v}(z,\omega) = -iW(z)\breve{i}(z,\omega) \quad (2)$$

where $\breve{i}(\omega) = \breve{I}(\omega)e^{i\omega z/\beta c}$, $\breve{v}(\omega) = \breve{V}(\omega)e^{i\omega z/\beta c}$. $\breve{I}(\omega)$, $\breve{V}(\omega)$ are the respective Fourier components of the beam current and kinetic-voltage modulations. The kinetic-voltage modulation is related to energy and longitudinal velocity modulations: $\breve{V}(\omega) = -(mc^2/e)\breve{\gamma} = -(mc^2/e)\gamma^3\beta\breve{\beta}$, $\phi_p(z) = \int_0^z \theta_{pr}(z')dz'$ is the accumulated plasma phase, $W(z) = r_p^2/(\omega A_e \theta_{pr}\epsilon_0)$ is the beam wave-impedance. A_e is the effective beam cross-section area, $\theta_{pr} = r_p\omega_{pl}/\beta c$ is the plasma wavenumber of the Langmuir mode, $r_p < 1$ is the plasma reduction factor, $\omega_{pl} = \omega_{po}/\gamma^{3/2}$ is the longitudinal plasma frequency in the laboratory frame. The single-frequency Langmuir plasma wave model expressions [3] can be solved straightforwardly in the case of uniform drift transport. After employing an averaging process, this results in a simple expression for the spectral parameters of stochastic current and velocity fluctuations (noise) in the beam assuming that they are initially uncorrelated[]:

$$\breve{i}(L,\omega) = \cos\phi_p(L)\breve{i}(0,\omega) + (\sin\phi_p(L)/W_d)\breve{v}(0,\omega) \quad (3)$$

where $\phi_p = \theta_{pr}z$, $\theta_{pr} = r_p\frac{\omega_p'}{v_0}$, $\omega_p' = (\frac{e^2 n_0}{m\epsilon_0\gamma^3})$, $W_d = \sqrt{\mu_0/\epsilon_0}/k\theta_{pr}A_e$.

The beam current noise evolution is affected by the initial axial velocity noise through the parameter

$$N^2 = \overline{|\breve{v}(0,\omega)|^2}/W^2\overline{|\breve{i}(0,\omega)|^2} = (\omega/c\beta k_D)^2 \quad (4)$$

Copyright © 2012 by the respective authors — cc Creative Commons Attribution 3.0 (CC BY 3.0)

where $k_D = \omega_{pl}/c\sigma_\beta$ is the Debye wavenumber and $c\sigma_\beta$ is the axial velocity spread. Equation (4) suggests that current noise suppression is possible if the beam is initially cold $N^2 < 1$, and if plasma phase accumulation of $\phi_p(L) \sim \pi/2$ is feasible.

NOISE SUPPRESSION EXPERIMENT

The noise suppression demonstration experiment was conducted on the 70 MeV RF-LINAC of ATF/BNL (figure 1). The OTR measurements were carried out at a fixed point (CTR-1) 6.5 m away from the LINAC exit. Keeping the beam spot sizes on viewer YAG4 wide in all experiments made it possible to measure similar OTR image patterns on the CCD screen in all experiments (see figure 3). The measured signal S_{OTR} was the integrated charge accumulated in all of the pixels of a CCD (charge-coupled device) camera exposed to the OTR emission on the incidence of single electron-beam pulse on the screen. The measured data of $S_{OTR} = Q_b$ in CTR-0 and CTR-1 are shown in figure 2 as a function of the varied bunch charge Q_b in the range 200 to 500 pC. The pulse duration in all experiments remained approximately the same (5 pS) corresponding to an average current of 40 to 100A (figure 4). In a shot-noise-dominated beam, in the absence of collective microdynamics, the current noise and consequently S_{OTR} are proportional to I_b. Our measured data of $S_{OTR} = Q_b$ in CTR-0 lie approximately on a horizontal line, confirming the absence of collective microbunching and current-velocity noise correlation or noise suppression before this point. On the other hand, the data measured on CTR-1 exhibit a systematic drop as a function of charge (200 to 500 pC) for all beam energies (50 to 70 MeV). As the measurement conditions at the two measurement positions and at different beam energies could not be made identical, the absolute suppression level between the two points could not be determined. However, the normalized data of all measurements of noise per unit charge depicted in figure 2 show the scaling with charge for all beam energies. This demonstrates attainment of 20 to 30% relative noise suppression, and confirms the predicted effect of collective microdynamic noise suppression process in the drift section.

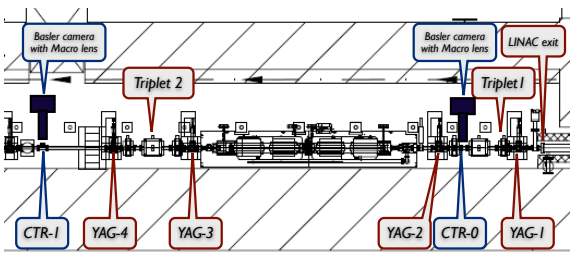

Figure 1: The ATF electron-beam transport set-up is shown from the injector RF-LINAC exit to the OTR viewer site (CTR-1).

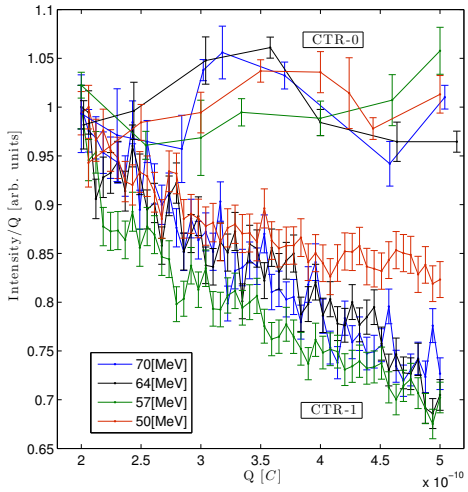

Figure 2: Integrated OTR intensity measurement signals divided by the electron pulse charge. The CTR-1 data correspond to OTR measurement from a screen, intercepting the electron beam 6.5m away from the LINAC exit. The curve's negative slope indicates relative current shot-noise suppression of 20-30% as the beam charge varies from 0.2 to 0.5 nC at different beam energies (50-70 MeV). The CTR-0 data correspond to OTR measurement right after the LINAC exit. Used for reference, its horizontal slope (linear scaling of S_{OTR} with beam charge) indicates that there was no charge suppression before the collective microdynamic process in the subsequent drift section. The error of the camera integrated signal measurement, 3%, was determined from the variance in the value of the signal due to pulse-to-pulse variation, measured repeatedly while keeping all beam control parameters fixed. The charge measurement error is 1%.

COMPUTATIONAL MODEL OF COLLECTIVE MICRODYNAMICS IN VARYING CROSS-SECTION BEAM TRANSPORT

At the exit of the Linac, the beam is current-noise dominated, and $N^2 \ll 1$. However, due to finite emittance, the axial velocity spread becomes significant as the beam is focused and consequently N^2 (Eq (4)) is no longer negligible. Furthermore, at tight focusing the uniform beam expression (Eq. (3)) cannot be used and in order to calculate the noise suppression, one should solve differential equations for variable beam parameters. In this section we show through a model case computational solution of equations (1) and (2), that the axially varying beam cross section and the excess axial velocity spread due to angular spread can account for a substantial moderation of the noise suppression effect that was realized in the experiment. This example also explains some parameter scaling features of the measurement data.

We turn the generic coupled current and ripple voltage

Copyright © 2012 by the respective authors — cc Creative Commons Attribution 3.0 (CC BY 3.0)

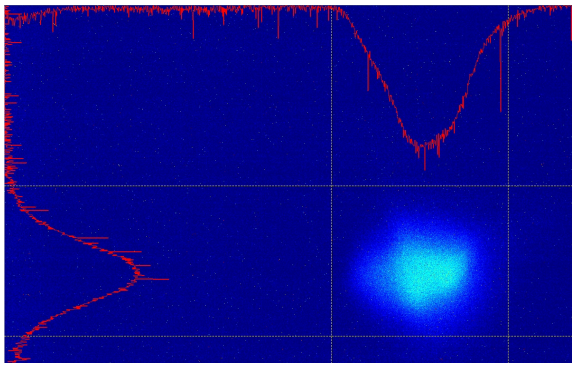

Figure 3: OTR image and axis intensity profiles. Photographed from CTR-1 with a macro lens of 1:1 magnification.

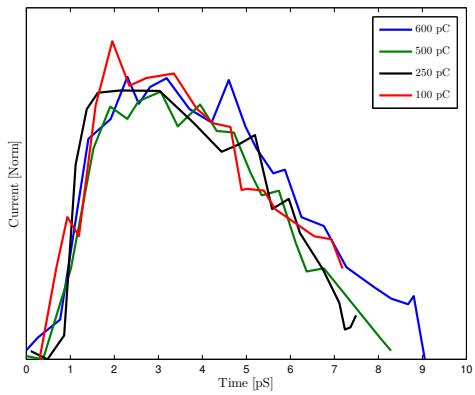

Figure 4: Temporal pulse profile of the e-beam bunch at different bunch charge levels. Pulse duration was approximately 5 pS for all experiments.

equations (1) and (2) into explicit equations in z by substituting $\frac{d}{d\phi_p} = \left(\frac{d\phi_p}{dz}\right)^{-1}\frac{d}{dz} = \frac{1}{\phi_{pr}(z)}\frac{d}{dz}$ and $W(z) = r_p^2/\omega\epsilon_0 A_e(z)\theta_p(z)$:

$$\frac{d}{dz}\breve{i}(z,\omega) = -i\omega\epsilon_0 A_e(z)\theta_p^2(z)\breve{v}(z,\omega) \tag{5}$$

$$\frac{d}{dz}\breve{v}(z,\omega) = -\frac{ir_p^2}{\omega\epsilon_0 A_e(z)}\breve{i}(z,\omega) \tag{6}$$

where $\theta_p^2(z) = eZ_0 I_0/mc^2 A_e(z)\gamma_0^3\beta_0^3$.

This set of equations can be solved explicitly numerically if $A_e(z) = 2\pi\sigma_x(z)\sigma_y(z)$ is given, and the initial conditions $\breve{i}(0,\omega), \breve{v}(0,\omega)$ are specified, and the solution at the end of the drift section L is a linear combination of the initial conditions: $\breve{i}(L,\omega) = A(L)\breve{i}(0,\omega) + B(L)\breve{v}(0,\omega)$. Assuming that the current modulation noise and the focusing enhanced velocity noise are uncorrelated at $z = 0$, we set

$$\overline{|\breve{i}(L,\omega)|^2} = |A(L)|^2\overline{|\breve{i}(0,\omega)|^2} + |B(L)|^2\overline{|\breve{v}(0,\omega)|^2} \tag{7}$$

$$\overline{|\breve{i}(0,\omega)|^2} = eI_b \tag{8}$$

$$\overline{|\breve{v}(L,\omega)|^2} = \left(\frac{mc^2}{e}\gamma_0\beta_0\right)^2\frac{e}{I_0}\sigma_{\beta z}^2 \tag{9}$$

To compute the noise evolution for the parameters of the reported experiment it is necessary to estimate the cross section dimensions $\sigma_x(z), \sigma_y(z)$ along the interaction length. This was done based on the measurements on screens YAG-1 to YAG-4, the recorded quad excitation parameters, and performing full 3-D simulation (with space-charge) using GPT.

The beam axial velocity spread due to energy spread ($\Delta E \simeq 3KeV$) is small, and its effect on the initial velocity noise is negligible. We assume that the initial velocity noise is determined by the standard deviation of the axial velocity spread (equation (9)), which was calculated for each quad setting from the angular spread standard deviations due to the focusing and emittance ($\epsilon_x, \epsilon_y \sim 2-5\mu m$):

$$\sigma_{\beta z} = \frac{1}{4}(\sigma_{\beta x}^2 + \sigma_{\beta y}^2) \tag{10}$$

The coefficients $A(z = L), B(z = L)$ were computed by

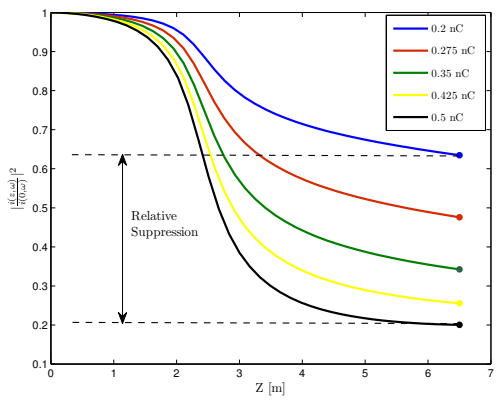

Figure 5: Noise suppression along the collective interaction region as calculated from solution of the coupled differential equations with $\sigma_x(z)$, $\sigma_y(z)$ of 70 MeV.

iterative integration of the coupled linear differential equations (5 and 6) with the initial conditions ((9)). In Figures 5 and 6 we display the results of the model computation of the variable parameters differential equations. The curves show the noise suppression as function of length and of the beam current for the two extreme energy cases E=50 MeV, 70 MeV. The relative suppression factor in the range Q_b=0.2-0.5nC at the drift section exit $L = 6.5m$ is displayed in Fig.() for the two beam-energy examples. Figure 7 can only be regarded as a model explanation for the reduced relative noise suppression effect observed in the experiment. As mentioned, there can be additional factors

Copyright © 2012 by the respective authors — cc Creative Commons Attribution 3.0 (CC BY 3.0)

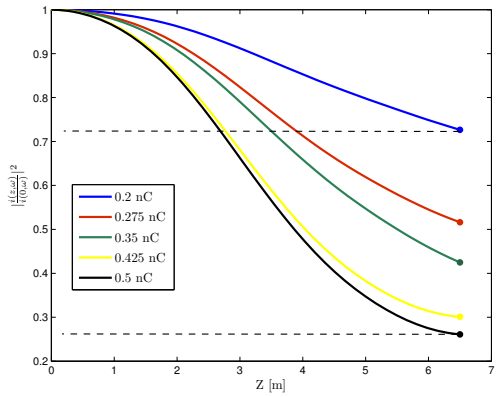

Figure 6: Noise suppression along the collective interaction region as calculated from solution of the coupled differential equations with $\sigma_x(z)$, $\sigma_y(z)$ of 50 MeV.

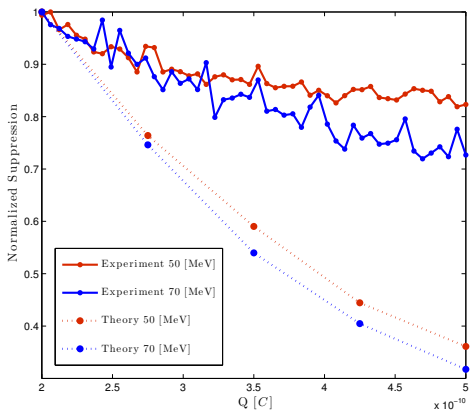

Figure 7: Relative noise suppression rate computed from Eq. 5 and 6 for E=50 MeV, 70 MeV compared to the experimental suppression results.

affecting the suppression rate. It is noted that the computed curves display significantly larger relative suppression in the range Q_b=0.2-0.5nC than the experimental curves, but in either case there is only little dependence on the acceleration energy. In the simple uniform beam model one would expect dependence of the noise suppression factor on the beam energy due to the $3/2$ power dependence of the plasma frequency on γ, which corresponds to smaller plasma phase accumulation at higher beam energy. However, the beam envelope had to be varied in the experiment in different beam energies, and one must keep in mind, that at the higher energy the beam focuses into a tighter waist due to the reduced space charge effect. This tends then to increase the plasma frequency at the waist, where most of the microdynamic process takes place.

This observation is consistent with the point of view that the beam envelope expansion and the beam charge homogenization process are in essence the same process of excess charge beam expansion when viewed in the beam rest frame (independent of the acceleration energy). This is consistent with the plasma phase accumulation theorem of constant plasma phase accumulation in a space charge dominated beam waist [3]. This provides qualitative physical explanation for the weak dependence of the relative noise suppression on the beam energy in the 50-70 MeV range, as depicted in both the experimental (figure 2) and model calculation (figure 7) curves.

REFERENCES

[1] A. Gover, A. Nause, E. Dyunin, Beating the shot-noise limit, Nature Physics, doi:10.1038/nphys2443.

[2] Dicke, R. H., "Coherence in Spontaneous Radiation Processes", Phys. Rev. 93 99–110 (1954).

[3] A. Gover, E. Dyunin, Collective-Interaction Control and Reduction of Optical Frequency Shot Noise in Charged-Particle Beams, Phys. Rev. Lett. 102, 15 (2009).

[4] A. Nause, E. Dyunin, "Optical frequency shot-noise suppression in electron beams: Three-dimensional analysis", Journal of App. Phys. 107, 103101 (2010).

[5] D. Ratner et el, "Observation of Shot Noise Suppression at Optical Wavelengths in a Relativistic Electron Beam", Phys. Rev Lett. 109, 3 (2012).

[6] Loos, H. and et al, "Observation of coherent optical transition radiation in the LCLS linac", Proceedings of the 2008 Free-Electron Laser Conference (Gyeongju, Korea).

[7] A. Gover, T. Duchovni, E. Dyunin, A.Nause, "Collective microdynamics and noise suppression in dispersive electron beam transport", Physics of Plasmas 18 123102, (2011).

Copyright © 2012 by the respective authors — cc Creative Commons Attribution 3.0 (CC BY 3.0)

STATUS OF THE RARE ISOTOPE SCIENCE PROJECT IN KOREA*

J. W. Kim for the RISP, Institute for Basic Science, Daejeon, Korea

Abstract

A heavy-ion accelerator facility has been designed in Korea for the production of rare isotope beams under the rare isotope science project (RISP). The project is funded and officially started in the end of 2011. The accelerator complex is composed of three main accelerators: a superconducting linac to use the in-flight fragmentation (IF) method to generate isotope beams, a 70 MeV proton cyclotron for the ISOL method, and a superconducting post accelerator for re-acceleration of rare isotope beams produced by ISOL to the energy range of 18 MeV/u. Minimum energy of a U beam requested for the IF driver is 200 MeV/u at the beam power of 400 kW. This facility will be unique in the aspect that the IF and ISOL systems can be combined to produce extreme exotic beams. In addition, standalone operation of each accelerator will accommodate diverse users in the beam application fields as well as in nuclear physics.

INTRODUCTION

A heavy ion accelerator facility is being designed in Korea to produce rare isotope beams by using both in-flight fragmentation (IF) and ISOL methods. The project is named as rare isotope science project (RISP), and was started from the end of 2011 after a period of conceptual design [1]. A conceptual layout of the facility is shown in Fig. 1.

The main accelerator is a superconducting linac, which can accelerate a ^{238}U beam to 200 MeV/u and protons to 600 MeV. It is divided into two sections, SCL1 before charge stripping at the energy of 18.5 MeV/u and SCL2 after the stripping. These parameters of the primary beam are similar to those of the FRIB project in the US [2]. A major difference from the planned FRIB facility is the use of an independent ISOL driver. A 70-MeV H- cyclotron will be employed to drive a 70-kW ISOL target system. The radioisotope beam extracted from the target will be further ionized in EBIS [3] or ECR ion sources to achieve a higher charge state before beam injection to the post accelerator (SLC3), which is also a superconducting linac to accelerate a beam up to the energy of around 18 MeV/u. Furthermore this isotope beam produced by ISOL can be accelerated using the SCL2 for the IF system to produce more exotic isotope beams.

*Work supported by the Rare Isotope Science Project of the MEST and National Research Foundation of Korea.

jwkim@ibs.re.kr

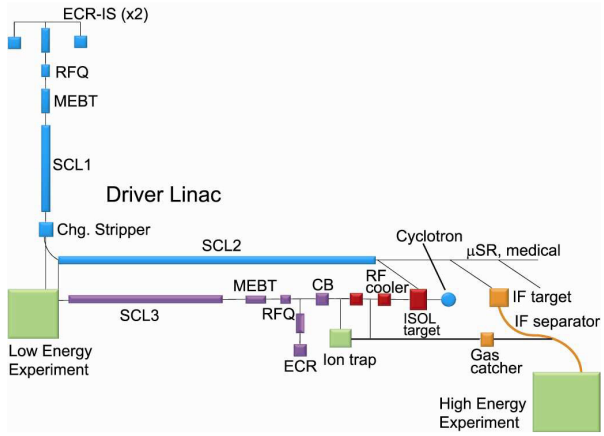

Figure 1: Conceptual layout of the heavy-ion accelerator complex of the RISP.

When the primary beam passes through a thin target, fast radioisotope beams are produced by the projectile fragmentation and fission mechanisms. Then the following isotope-beam selection system utilizes Bρ–energy loss–Bρ analysis to separate and identity an isotope beam of interest. This fast isotope beam can be stopped using a gas stopper, and the charge state of the beam extracted from the gas stopper can be boosted like in the ISOL method before being injected into the post accelerator. A main advantage of the IF method is that it is not subject to chemistry of the ions unlike in the ISOL. Hence rare isotope beams in a wider range can be produced.

The experimental areas are divided depending on the energy of the beam delivered as shown in Fig. 1. Different kinds of spectrometers are planned to be facilitated for nuclear reaction and structural studies [4]. In addition, the facility will accommodate beam users in various application fields including biomedical and material sciences using both stable and isotope beams. The stopping location of an isotope beam can be accurately traced by radiation measurement, which is a notable advantage of radioactive beam and is to be explored in some applications.

ACCELERATOR COMPLEX

To produce highly charged ion beams, a superconducting ECR ion source similar to the VENUS source of the LBL [5] is to be developed. To meet the goal of 400-kW beam power for U beam, envisioned scheme was to accelerate a beam in two charge states of 34+ and

Copyright © 2012 by the respective authors — cc Creative Commons Attribution 3.0 (CC BY 3.0)

35+ [6], but recent ECR test results showed that a single-charge-state U beam could be sufficient for the production of the full beam power.

The injection beam line is designed to accept a two-charge-state beam for very heavy ions such as U beam in case that higher beam power can be more easily achieved with a two-charge-state beam from the ECR. However, beam losses may be reduced for a singly charged beam especially in longitudinal phase space due to the mitigation of sensitivity to misalignment errors and so on.

To increase acceleration efficiency for a heavy ion beam, it is needed to strip electrons from the ions as the beam energy is increased. The charge stripping is set to be performed at the energy near 18 MeV/u to produce the charge state of around 78+ for the U beam. We plan to use a carbon foil for initial low-current beam testing, but not at the beam power over a kW because empirical results show that the lifetime of carbon foil is greatly shortened [7]. A liquid Li target is being studied as the stripper, which can handle the full power beam as has been developed by an ANL group [8]. A gas target is also a possibility. Higher pressure gas could be confined with plasma window to produce higher charge state beam. The equilibrium charge state by the gas stripper is significantly lower compared to that by a carbon foil, while liquid Li target is expected to produce higher charge states than by the gas.

The primary accelerator is a superconducting linac composed of two sections SCL1 and SCL2. Four different types of superconducting cavities are planned to be developed. In SCL1 quarter-wave resonators with the geometrical β of 0.047 operating at 81.25 MHz will accelerate a beam from the RFQ. Another type is a half-wave resonator operating at 162.5 MHz with β of 0.12. After the charge stripping, spoke-type cavities will be used in SCL2, which operate at 325 MHz. Two types of single-spoke cavity with β of 0.3 and 0.53 will be developed. Operating temperature of all the cavities is 2 K. Cryogenic system for the entire facility will have refrigeration capacity of around 15 kW at 4 K. The total number of cavities including the cavities in SCL3 is over 500, and the number of cryomodule is around 150.

Transverse focusing for the superconducting linac will be made by quadrupole magnet doublets in between the cryostat. A similar focusing lattice has been used for SPIRAL2 [9]. It is expected that alignment errors of the focusing elements can be corrected more easily when they are located in the room temperature. The steering coils will be incorporated together with the quadrupole magnets.

The post accelerator SLC3 shown in Fig. 1 will use the same kinds of sc-cavities and focusing elements of the driver linac SCL1. Main differences would stem from the lower beam current of rare isotope beam and the beam charge state depending on the performance of charge breeding in the EBIS or ECR source. The beam diagnostic elements in wide dynamic range will be placed to measure and transport very low-current isotope beams. A standard technology is to use a stable beam with similar q/A first to tune the beam line and then to transport rare isotope beam to the downstream target or detector.

An H- cyclotron of 70 MeV is to be used as a driver for the ISOL system. The maximum beam current is specified as 1 mA. We plan to purchase a commercial unit as similar energy cyclotrons have been developed for the production of medical isotopes and as an ISOL driver [10]. The beam current of 1 mA is higher than that of existent commercial cyclotrons, which is around 700 μA. However, the increase to 1 mA is foreseen to be not technically very challenging. In fact, there is a concern in the lifetime of carbon foil for electron stripping extraction of 1 mA beam. However, the use of carousel containing several units should allow the foil exchange period to be acceptable.

As the cyclotron can be procured and installed more readily compared to the planned superconducting linac, isotope beams produced by the cyclotron will be available earlier by the end of 2016 in the current project schedule, while the beam from the linac is expected by the end of 2017.

RARE ISOTOPE BEAM PRODUCTION

Both methods of in-flight fragment separation and ISOL will be used to produce rare isotope beams. In the present work plan, ISOL facility belongs to the experimental user group, while the IF separator is being designed by the accelerator group. Some details of the beam characteristics by the ISOL are described in Ref. [4].

The in-flight fragmentation method has been developed in major nuclear physics laboratories at the beam energy higher than tens of MeV per nucleon [11]. But the intensity of isotope beams was limited by the beam power available from the primary accelerator. The next generation IF facility requests the beam power of a few hundred kW to produce high intensity rare isotope beams. As a result of this high beam power, the high-power target and removal of the primary beam in the process of isotope beam separation using a beam dump have become technical challenges.

The in-flight isotope beam separation system can be largely divided into pre and main stages. In the pre-separator, the primary beam is separated by momentum dispersion, and a beam dump is used to remove the separated primary beam in the localized area. This pre-separator area has the high-level of radiation, and radiation heating on the magnetic elements is high [12]. A remote handling system based on servo-motor controlled crane is being considered. The design of beam dump is in fact complicated because the system needs to separate different kinds of rare isotope beam from the primary beam in different beam energies, also considering that the range of the primary heavy-ion beam is short. A rotating water drum, which can be displaced along the axis, is being considered.

Copyright © 2012 by the respective authors — cc Creative Commons Attribution 3.0 (CC BY 3.0)

The main separator is designed to identify the isotope beam of interest and to purify it by using the time of flight method and other nuclear physics techniques. The beam from the pre-separator is mixed with different kinds of isotope beams having similar q/A ratio. The use of a wedge-shaped degrader can remove some interfering isotope beams utilizing energy loss mechanism inside material at the cost of inducing additional nuclear reaction and beam energy straggling. The unwanted isotope beams identified by the time of flight method can be removed by an rf deflector located at the end of separator before the beam is delivered to the downstream experimental area. The rf deflector can be more effectively used to purify the isotope beam in the proton rich side.

SUMMARY

The rare isotope science project in Korea is in progress, which was started from the end of 2011. The high current heavy ion linear accelerator is a primary driver to produce rare isotope beams using the IF method. A 70-MeV cyclotron will be used to produce isotope beams using the ISOL method. A plan is that radio-isotope beam produced by ISOL can be further accelerated using the primary accelerator to a higher energy so as to utilize the IF method. This two-stage process is expected to produce more exotic isotope beams.

In the current schedule, the first proton beam from the cyclotron will be delivered to the target in the end of 2016, and the first IF beam by the end of 2017. This is very aggressive schedule to carry out, and the schedule is also subject to the construction of the building complex for the accelerators and experimental equipments. Achieving the permission to operate the high-level radiation facility from the Korea Institute of Nuclear Safety is also expected to be a tough task.

REFERENCES.

[1] J. Ahn et al., "Overview of the KoRIA facility for rare isotope beams", Few-Body Systems, Vienna, Springer (2012).

[2] X. Wu et al., "The overview of the accelerator system for the facility for rare isotope beams at Michigan State University", Proc. of LINAC2010, Tsukuba, Japan, Sep. 12-17, 2010, p.163 (2010).

[3] J. Alessi et al., "Construction of the BNL EBIS preinjector", Proc. of PAC09, Vancouver, Canada, May 4-8, 2009, p.407 (2009).

[4] M.S. Ryu et al., "Characteristics of rare isotope beams in the KoRIA facility", J. Korean Phys. Soc. 60, 19 (2012).

[5] D. Leitner et al., "Status of the Venus ECR ion source", Proc. of ECRIS2010, Grenoble, France, Aug. 23-26, 2010, p.11 (2010).

[6] E. Lessner, P. Ostroumov, "Multi-charge-state beam steering in high-intensity heavy-ion linacs", Proc. of EPAC 2004, Lucerne, Switzerland, July 5-9, 2004, p.1476 (2004).

[7] H. Kuboki et al., "Charge-state distribution of ^{238}U in nitrogen gas and carbon foil at 14 and 15 MeV/n", Phy. Rev. ST 14, 053502 (2011).

[8] J. Nolen et al., "Development of windowless liquid lithium targets for fragmentation and fission of 400-kW uranium beams", NIM B 204, 293 (2003).

[9] T. Junquera et al., "The high intensity superconducting linac for the SPIRAL 2 project at GANIL", Proc. of LINAC 2006, Knoxville, USA, Aug. 21-25, 2006, p.142 (2006).

[10] V. Sabaiduc et al., "New high intensity compact negative hydrogen cyclotrons", Proc. of CYCLOTRONS 2010, Lanzhou, China, Sep. 6-10, 2010, p.81 (2010).

[11] M. Bernas et al., "Projectile fission at relativistic velocities: a novel and powerful source of neutron-rich isotopes well suited for in-flight isotopic separation", Phys. Lett. B 331, 19 (1994).

[12] I. Baek et al., "Radiation simulations for a pre-separator area for rare isotope production via projectile fragmentation", Proc. of PAC07, Albuquerque, USA, June 25-29, 2007, p.1763 (2007).

Copyright © 2012 by the respective authors — cc Creative Commons Attribution 3.0 (CC BY 3.0)

REDUCED-BETA CAVITIES FOR HIGH-INTENSITY COMPACT ACCELERATORS*

Z.A. Conway#, S. Gerbick, M.J. Kedzie, M.P. Kelly, J. Morgan, R. Murphy, P.N. Ostroumov, and T. Reid, ANL, Argonne, IL 60439, USA

Abstract

This paper reports on the development and testing of a superconducting quarter-wave and a superconducting half-wave resonator. The quarter-wave resonator is designed for beta = 0.077 ions, operates at 72 MHz and can provide more than 7.4 MV of accelerating voltage at the design beta, with peak surface fields of 165 mT and 117 MV/m. Operation was limited to this level not by RF surface defects but by our administrative limits on x-ray production. A similar goal is being pursued in the development of a half-wave resonator designed for beta = 0.29 ions and operating at 325 MHz.

INTRODUCTION

The length and cost of the low-velocity portion ($\beta = v/c < 0.6$) of superconducting proton and heavy-ion linacs are dominated by the accelerator cavity performance. Accelerator cavities used in this velocity region, reduced-beta cavities, have not performed at the same peak-surface fields which are regularly achieved in elliptical-cell cavities optimized for velocity-of-light electrons [1], 160 mT and 80 MV/m peak surface fields. This performance disparity has been blamed on the greater complexity of the reduced-beta cavity fabrication and processing. Several advances at Argonne National Laboratory in cavity design [2]; fabrication and processing have disproved this hypothesis.

First, the results locating a defect which limited the performance of a prototype 72 MHz quarter-wave cavity (QWR) optimized for $\beta = 0.077$ ions for the ATLAS intensity upgrade will be presented. Second, the fabrication and processing of a subsequent geometrically identical quarter-wave cavity will be outlined. Finally, the impact of these results and future plans for a similarly constructed half-wave cavity will be discussed.

INITIAL PROTOTYPE PERFORMANCE

The QWR prototype fabrication and test results were presented in [3]. Since these papers were published we have refined our electromagnetic simulations of the cavity surface fields and the results used in this paper are given in table 1. This cavity was limited to peak surface fields of 96 mT and 70 MV/m by a surface defect which initiated a cavity quench. Figure 1, shows the cavity with the location of the defect highlighted in red along with a single channel record of the quench.

The defect was located by measuring the time-of-flight of second sound waves propagating from the cavity quenching defect to an array of oscillating superleak transducers [4]. The distance the second sound wave travelled was calculated with the wave velocity. This combined with the known location of the detectors allowed us to determine the defect location. Our detector array was 1-dimensional in nature and located the height of the defect in the quarter-wave cavity center conductor.

This defect was located at the same height as an electron beam weld blow-out which occurred during final welding of the center conductor. The center conductor is formed from two halves which are welded together. The center conductor halves were tack welded, but the final electron beam welds could not be finished within the desired 24-hour etch window between pre-weld etching and welding. The parts were etched again after tacking and the very small-gap joint between the two parts could not be properly cleaned. Some foreign debris was trapped in this joint which caused a blow-out during the final electron beam welding which was repaired.

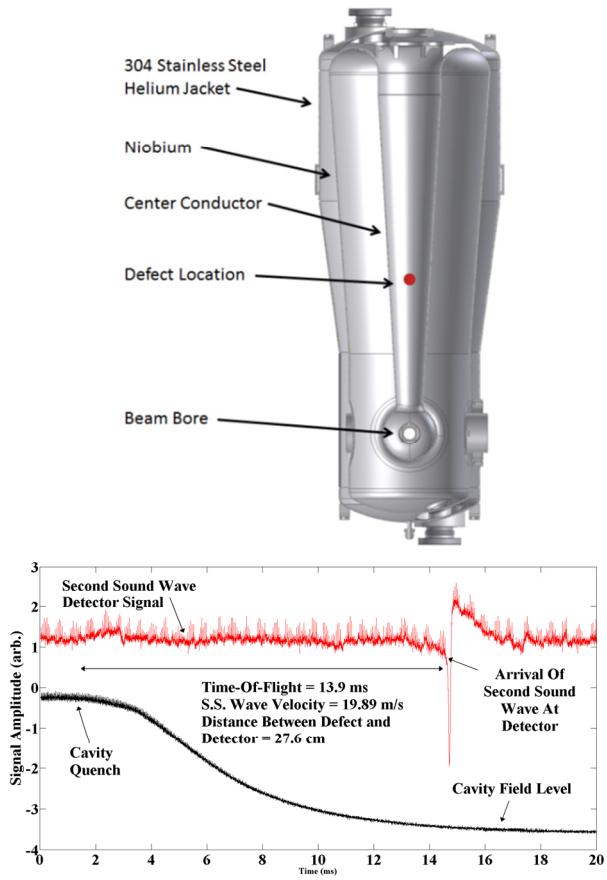

Figure 1: (Top) The cavity with a red dot placed at the height of the defect in the center conductor, the cavity is 53 inches from top to bottom . (Bottom) A single quench event with an oscillating superleak transducer signal and the cavity transmitted power.

* This work was supported by the U.S. Department of Energy, Office of Nuclear Physics, under Contract DE-AC02-06CH11357 and ANlLWFO 8R268 supported by DTRA.

zconway@anl.gov

Copyright © 2012 by the respective authors — cc Creative Commons Attribution 3.0 (CC BY 3.0)

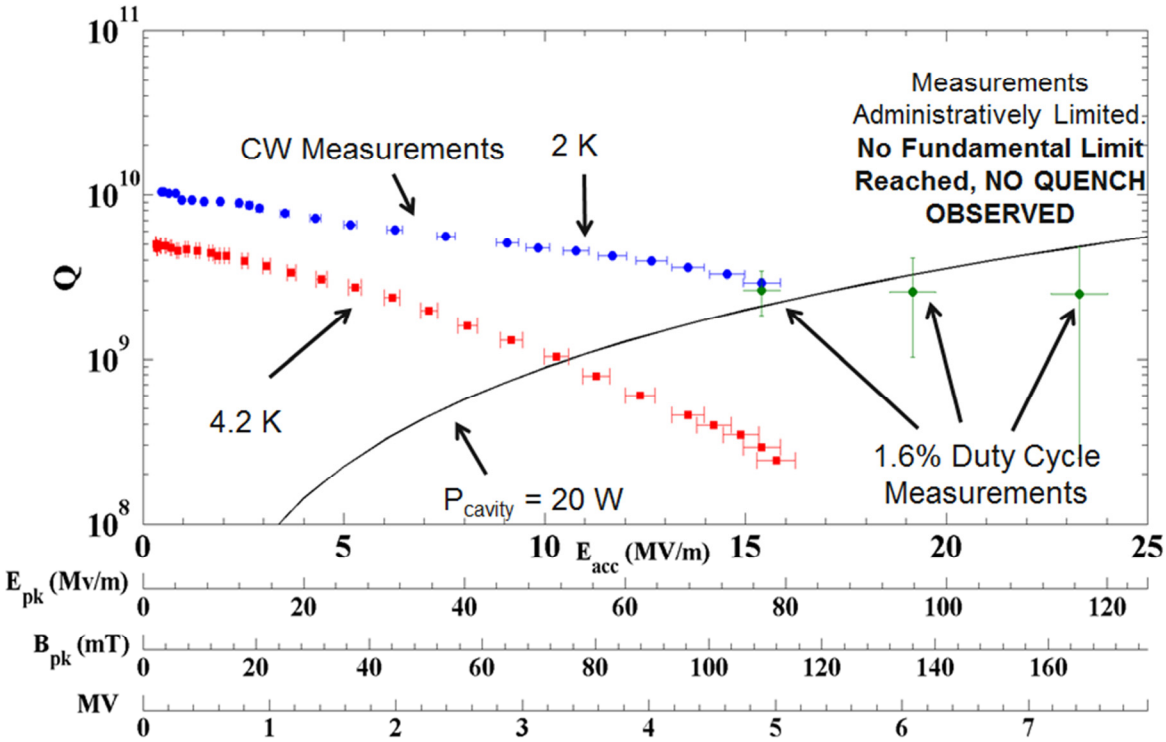

Figure 2: The measured performance of the QWR. There are 4 horizontal axes corresponding to the accelerating gradient, peak surface electric and magnetic fields, and the voltage gain of a synchronous β = 0.077 ion. The vertical axis corresponds to the cavity quality factor. The blue data points were measured at 2 K and the red data points were measured at 4.2 K in the cw mode, the green points were measured at 2 K with a 1.6% duty cycle, and the solid black line corresponds to 20 W of RF power dissipated in the cavity. No fundamental limit to the cavity performance was encountered and the cavity could have reached higher fields with appropriate radiation shielding

Table 1: Electromagnetic Properties of the QWR

Freq. (MHz)	72.75
β	0.077
l_{eff} (cm, βλ)	31.75
E_{pk}/E_{acc}	5.0
B_{pk}/E_{acc} (mT/(MV/m))	7.1
QR_s (Ω)	25.9
R_{sh}/Q (Ω)	568

FABRICATION AND PROCESSING

Here the fabrication details which differ from what was presented in [3] for the prototype QWR are listed:

1) Very careful attention was paid to the status of the weld joints and their preparation prior to electron beam welding. All components were soaked in DI water after every handling/machining step to look for inclusions.
2) Significantly more surface inspection and QA. The cavity RF surface was carefully hand-polished with 220 grit sandpaper to avoid fold-over and deep polishing marks. All pits, orange-peel, and scratches were polishing in this manner in the high field regions.
3) The temperature of the pre-weld etches were limited to $T < 16^0$C to limit hydrogen uptake. The bulk electropolish procedure (~120 μm removal) temperature was reduced to $25 < T < 30^0$C. The final light (~20 μm removal) electropolish temperature was $20 < T < 25^0$C.
4) The cavity was baked at 625^0C for 24 hours to degas the hydrogen dissolved in the bulk niobium. This prevents Q-disease and improves the 2 K performance of the cavity.

After fabrication was complete the electropolishing, baking, and cleaning proceeded. Recent tests of similar cavities have found that the Q may be improved by about a factor of 2 by reducing the 625^0C bake duration to 12 hours [5].

TEST RESULTS

The cavity vacuum was allowed to pump for 72 hours reaching a pressure < 1 e-7 torr prior to cooldown. The cavity was cooled to 4.2 K with care taken to limit the time spent between 50 and 165 K to about 45 minutes even with the hydrogen degassing. The cavity was conditioned using up to 10 watts of RF power to remove the low-level multipacting barriers over ~2 hours and then 5 minutes of pulsed power processing at 4.6 K with 4 kW

Copyright © 2012 by the respective authors — cc Creative Commons Attribution 3.0 (CC BY 3.0)

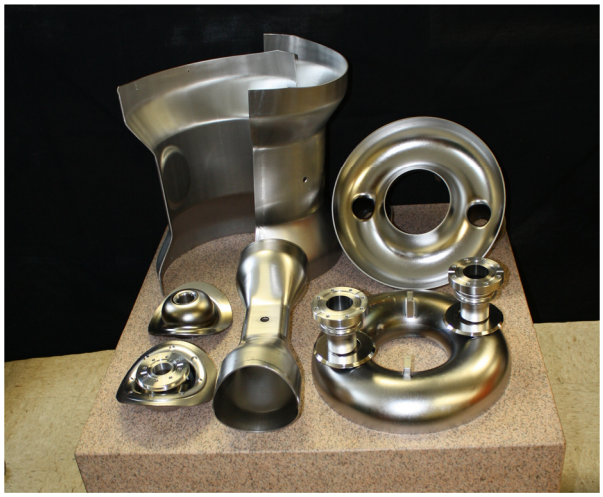

Figure 3: The niobium subassemblies which will be welded together to make the HWR. The parts clockwise from top left are outer-conductor halves, toroids, inner-conductor, and re-entrant noses.

of forward power. Following this conditioning the performance given in figure 2 was observed. Note that the residual resistance of the cavity at low-fields is less than 4.5 nΩ at 4.2 K and 2.5 nΩ at 2.0 K. The gradients presented in figure 2 were not limited by any fundamental phenomena, e.g., defect-initiated quench or field emission. The results were limited administratively to avoid exceeding the ANL limits on x-ray production. The cavity is only partially shielded behind a high-density concrete wall and is not in a complete cave-like enclosure. This allows considerable x-ray shine to reach experimenters. To reduce the average x-ray production the cavity was operated with a 1.6% duty cycle to safely comply with the ANL guidelines. The data points measured in this manner are highlighted in green and are the three highest gradient 2 K measured data points. Please note that the cavity dissipated power measurement accuracy decreased due to measuring these data points in the over-coupled limit but the relative accuracy of the field amplitude is unchanged. The highest data point measured was repeatable and corresponded to a voltage gain of 7.4 MV and peak surface fields of 165 mT and 117 MV/m. At no point was the QWR tested here quenched. The high field data points do not represent a fundamental limit on the cavity performance. With additional radiation shielding the maximum performance of this cavity can be determined.

The best 9-elliptical cell cavity built for the ILC program reached 175 mT and 84 MV/m. The quarter-wave cavity tested here reached comparable peak surface magnetic fields relative to the best 9-cell cavity and exceeds the peak surface electric field by 40% [1]. The previous best reduced beta cavity was a spoke cavity tested at FNAL which reached 127 mT and 85 MV/m after extensive conditioning [6].

IMPACT AND FUTURE WORK

The test results presented here characterize the world's highest peak-field performance in a reduced-beta cavity designed for heavy-ion particle accelerators. The results approach the theoretical maximum of performance of any niobium resonator and allow for the proposal of future accelerators with higher base line gradients, shortening and reducing the cost of these installations.

We are now in the final stages of fabricating a half-wave resonator (HWR) designed to operate at 325 MHz and optimized for $\beta = 0.29$ ions [7]. This cavity builds upon the success of the conical geometries developed at ANL for quarter-wave cavities which optimize the cavity field distributions maximizing accelerator performance. The HWR is being fabricated in a manner identical to the record setting QWR. Figure 3 shows the subassemblies which will be combined to make the niobium cavity in the next several weeks. We expect to finish fabrication of this cavity in October 2012 with cold testing sometime in late November or early December. Results will be published once available.

ACKNOWLEDGMENTS

We would like to thank Joel Fuerst and Josh Kaluzny of the ANL APS for the sub-atmospheric testing of the cavity and Allan Rowe and Mayling Wong-Squires of FNAL for help with the 625^{0}C bake of the cavity. We would also like to acknowledge Glenn Cherry and Rick Fischer, of the ANL Nuclear Engineering Engineering-Support-Group, for numerous contributions to the hardware development required for testing.

REFERENCES

[1] R.L. Geng, "Overview of ILC High Gradient Cavity R&D at Jefferson Lab," In the Proceedings of SRF11, Chicago, Illinois, USA, Pg. 74 (2011).

[2] P.N. Ostroumov et al, "A New ATLAS Efficiency and Intensity Upgrade Project," In the Proceedings of SRF09, Berlin, Germany, Pg. 218 (2009).

[3] M.P. Kelly et al, "SRF Advances for ATLAS and Other beta<1 Applications," In the Proceedings of SRF11, Chicago, Illinois, USA, Pg. 680 (2011).

[4] Z.A. Conway et al, "Defect Location in Superconducting Cavities Cooled with He-II Using Oscillating Superleak Transducers," In the Proceedings of PAC09, Vancouver, British Columbia, Canada, Pg. 921 (2009).

[5] M.P. Kelly et al, "Cold Testing of Superconducting 72 MHz Quarter-Wave Cavities for ATLAS," MOPB073, these proceedings.

[6] L. Ristori et al, "Development of 325 MHz Single Spoke Resonator For HINS at Fermilab: Recent Results," In the Proceedings of PAC09, Vancouver, British Columbia, Canada, Pg. 963 (2009).

[7] P.N. Ostroumov et al, "Beta = 0.285 half-Wave Resonator for FRIB," In the Proceedings of SRF11, Chicago, Illinois, USA, Pg. 132 (2011).

Copyright © 2012 by the respective authors — cc Creative Commons Attribution 3.0 (CC BY 3.0)

R&D TOWARDS CW ION LINACS AT ANL*

P.N. Ostroumov#, A. Barcikowski, Z. Conway, S. Gerbick, M. Kedzie, M.P. Kelly, S. Kutsaev, J. Morgan, R. Murphy, B. Mustapha, D. Paskvan, T. Reid, D. Schrage, S. Sharamentov, K. Shepard, G. Zinkann,
Argonne, IL 60439, U.S.A ANL, Argonne, IL 60439, U.S.A.

Abstract

The accelerator development group in ANL's Physics Division has engaged in substantial R&D related to CW proton and ion accelerators. Particularly, a 4-meter long 60.625-MHz CW RFQ has been developed, built and commissioned with beam. Development and fabrication of a cryomodule with seven 72.75-MHz quarter-wave resonators (QWR) is complete and it is being assembled. Off-line testing of several QWRs has demonstrated outstanding performance in terms of both accelerating voltage and surface resistance. Both the RFQ and cryomodule were developed and built to upgrade ATLAS to higher efficiency and beam intensities. Another cryomodule with eight 162.5-MHz SC HWRs and eight superconducting SC solenoids is being developed and built for Project X at FNAL. We are also developing both an RFQ and cryomodules (housing 176-MHz HWRs) for proton & deuteron acceleration at SNRC (Soreq, Israel). In this paper we discuss ANL-developed technologies for normal-conducting and SC accelerating structures for medium- and high-power CW accelerators, including the projects mentioned above and other developments for applications such as transmutation of spent reactor fuel.

INTRODUCTION

Technologies for CW RFQ and SC RF successfully developed for ATLAS upgrade for higher efficiency and beam intensities [1,2] can be applied in future high-power CW accelerators. Particularly, we are developing a CW RFQ and two cryomodules with different β_{OPT} for the SARAF accelerator facility at SNRC [3]. Similar SC RF technology is being used for the development and construction of the HWR cryomodule for Project X [4]. Below we discuss beam commissioning of the RFQ and results of QWRs testing and cryomodule assembly for the ATLAS upgrade project. Status of the SARAF and PXIE cryomodule development is presented.

CW RFQ

This summer we commissioned a CW RFQ designed and built for the ATLAS Facility [5]. Several innovative ideas were implemented in this CW RFQ. By selecting a multi-segment split-coaxial structure we have achieved moderate transverse dimensions for a 60.625 MHz resonator. For the design of the RFQ resonator and vane tip modulations we have developed a full 3D approach which includes MW-Studio and TRACK simulations of the entire structure. A novel trapezoidal vane tip modulation is used in the acceleration section of the RFQ which resulted in increased shunt impedance. To form an axially symmetric beam exiting the RFQ, a very short output radial matcher, only $0.75\beta\lambda$ long, was developed.

An advanced fabrication technology was applied for the construction of the RFQ which includes precise machining and two-step high temperature brazing. Thanks to the high accuracy of the overall fabrication, the assembly of the 5-segment RFQ was straightforward and resulted in excellent alignment. The resonance frequency control system based on water temperature regulation showed excellent performance. The RF measurements show excellent RF properties for the resonator, with a measured intrinsic Q equal to 94% of the simulated value for OFE copper. The multi-segment split-coaxial structure creates strong coupling between the quadrants and individual RFQ segments which reduces the effect of local frequency deviations on electromagnetic field distortions. Therefore, no bead-pull measurements were required for tuning of the accelerating field. Figure 1 shows the complete RFQ assembly after installation of

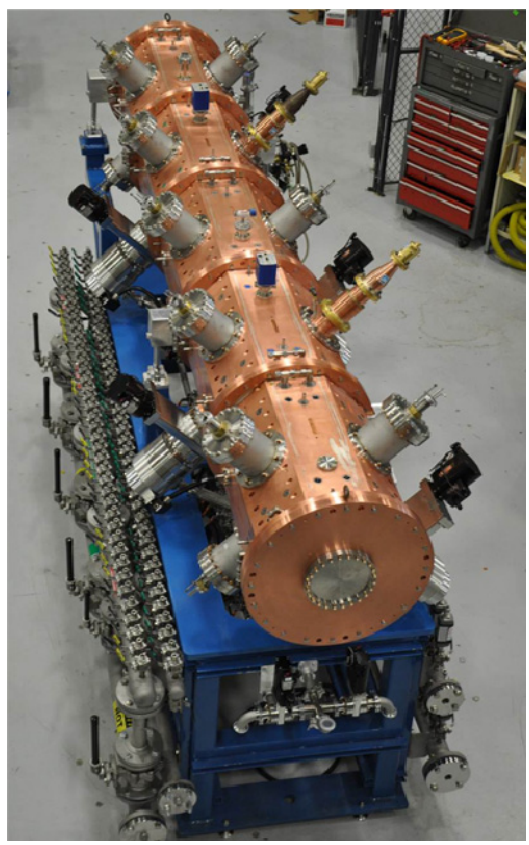

Figure 1: Completed RFQ assembly.

* This work was supported by the U.S. Department of Energy, Office of High Energy Physics and Nuclear Physics, under Contract DE-AC02-76CH03000, DE-AC02-06CH11357 and ANL WFO 85Y47
#ostroumov@anl.gov

Copyright © 2012 by the respective authors — cc Creative Commons Attribution 3.0 (CC BY 3.0)

the tuners, vacuum pumps, vacuum gauges, RF couplers, and pick-up loops.

An O^{5+} ion beam extracted from an Electron Cyclotron Resonance (ECR) ion source was used for the RFQ commissioning. In off-line beam testing, we found excellent agreement of the measured beam parameters with the results of beam dynamics simulations. For example, the beam energy spread was determined by scanning the magnetic field level in the 70° bending magnet located downstream of the RFQ. The results of these measurements are shown in Fig. 2.

The great success of this advanced design and fabrication technology is reflected in the measured beam parameters after the RFQ which are nearly identical to the simulated data. Currently we are developing the design for a 4-vane RFQ operating at 176 MHz for acceleration of protons or deuterons up to 1.5 MeV/u. This design takes full advantage of the ATLAS RFQ experience.

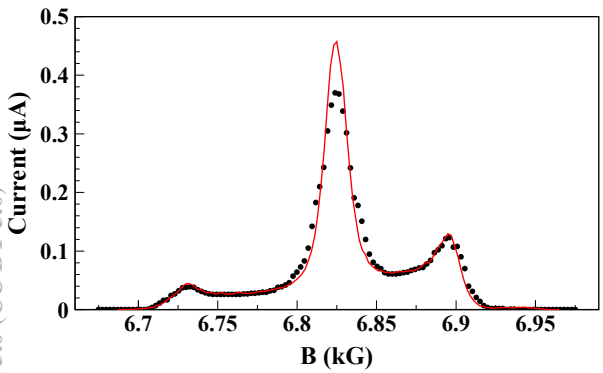

Figure 2: Measured (dots) and simulated (red curve) beam intensity as a function of the magnetic field.

QWR CRYOMODULE

While split-ring resonators are successfully operated at ATLAS with low-intensity ion beams, they exhibit a fundamental limit in the acceleration of high-intensity beams due to RF steering. Therefore we are replacing all ATLAS split-ring resonators with QWRs. Three years ago we commissioned a new cryomodule containing seven 109 MHz β_{OPT}=0.15 QWRs to provide an additional 15 MV voltage. Now, we have developed and built a new cryomodule which consists of seven β_G=0.077 QWRs at 72.75 MHz SC cavities and four 9-Tesla SC solenoids. The new high-performance cryomodule will replace three existing ATLAS cryomodules with split-ring cavities to increase the intensities of accelerated ion beams.

Compared to the previous generation of quarter-wave resonators, several innovations were implemented into the cavity design, fabrication and RF surface treatment. The cavity geometry is highly optimized to reduce both electric and magnetic peak fields: both outer and inner conductors are conical as shown in Fig. 3. During the fabrication of the niobium components, a wire EDM technique instead of machining was used to maintain clean surfaces prior to electron-beam welding. Electropolishing of the cavities was performed for a completed cavity with the integral helium vessel installed. The cavity is equipped with a double-window 4-kW adjustable RF coupler with a nitrogen cooled cold window. The new QWRs will create accelerating gradients a factor of three higher, on average, than in the existing split-ring cavities, and are designed to provide an accelerating voltage of 2.5 MV per cavity. Four 72.75 MHz QWRs were cold tested in the test cryostat and all of them provided more than 4 MV voltage, E_{PEAK}>70 MV/m and B_{PEAK}>105 mT [6,7]. The fabrication of the cryomodule, all the 72.75-MHz QWRs and SC solenoids is complete. Figure 4 shows the assembled cavities being loaded into the box cryostat during a trial fitting. The new cryomodule was designed to produce 17.5 MV total voltage but will provide up to 21 MV which will be limited only by the available cryogenic capacity.

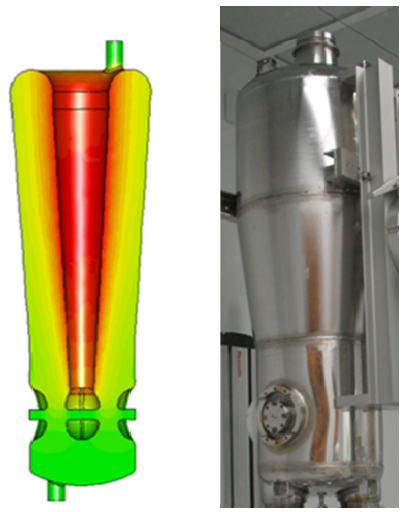

Figure 3: Cavity MWS model showing magnetic field distribution (left) and completed cavity assembly in the HPR apparatus (right).

Figure 4: Cavity string is being lowered into the box vacuum vessel during mock assembly.

Copyright © 2012 by the respective authors — cc Creative Commons Attribution 3.0 (CC BY 3.0)

HWR CRYOMODULES

In high-intensity light ion accelerators, to reduce space charge effects, the fundamental frequency should be high as compared to heavy-ion linacs. SC HWRs are superior to QWRs at operational frequencies above ~150 MHz and optimal beta $\beta_{OPT} \geq 0.1$. The fundamental frequency of Project-X is 162.5 MHz which is defined by the RFQ. Therefore we are developing a cryomodule with 8 HWRs for the acceleration of H-minus ions from 2.1 MeV to 11 MeV [8]. Similar HWRs operating at 176 MHz are designed for the SARAF Phase II 5-mA proton and deuteron linac. To increase the available accelerating voltage, the HWR shape is highly optimized reducing both B_{PEAK}/E_{ACC} and E_{PEAK}/E_{ACC} [9]. Optimization of the cavity shape was performed taking into account die-forming fabrication technology available from industry [10,11]. The final cavity shape has tapered central and outer conductors as shown in Fig. 5. The confidence in the proposed HWR design and predicted performance is based on the very successful design, construction and testing of a conical QWRs for the ATLAS upgrade. The results of the EM optimization are summarized in Table 1.

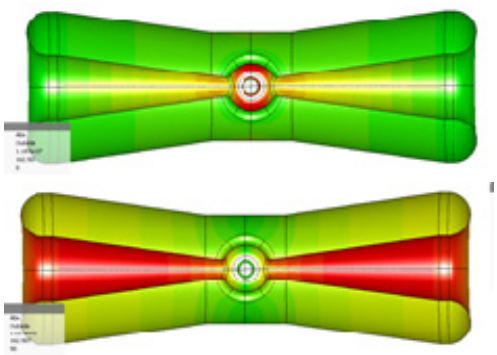

Figure 5: A half-wave resonator model in MWS. The electric (top) and magnetic field (bottom) distributions on the surface are shown.

Table 1: HWR main parameters

Parameter	PXIE	SARAF	
Frequency, MHz	162.5	176	
Operating temperature, K	2	4	
Optimal beta, β_{OPT}	0.11	0.089	0.16
$L_{EEF} = \beta_{OPT}\lambda$, cm	20.7	15.2	27.3
Aperture, mm	33	33	36
Accelerating voltage, MV	1.7	1.0	2.1
E_{PEAK}/E_{ACC}	4.7	5.3	4.7
B_{PEAK}/E_{ACC}, mT/(MV/m)	5.0	5.6	5.6
$G = Q_0R_S$, Ω	48	40	60
R/Q_0, Ω	272	231	296

Both PXIE and SARAF HWR cryomodule designs are an evolution of the top-loaded box cryomodule design used successfully for the ATLAS Upgrade. The PXIE and the first HWR SARAF cryomodules layout were determined with careful beam-dynamics simulations and estimates of recent cavity performance. As a result of these studies, a focusing period contains a solenoid-BPM-HWR sequence. Each solenoid is equipped with dipole coils for beam steering in both planes. The cryomodule design is developed around these requirements. The cryomodule beam-line assembly along with the strong-back, vacuum and helium manifolds, and cavity subsystems is shown in Figure 6.

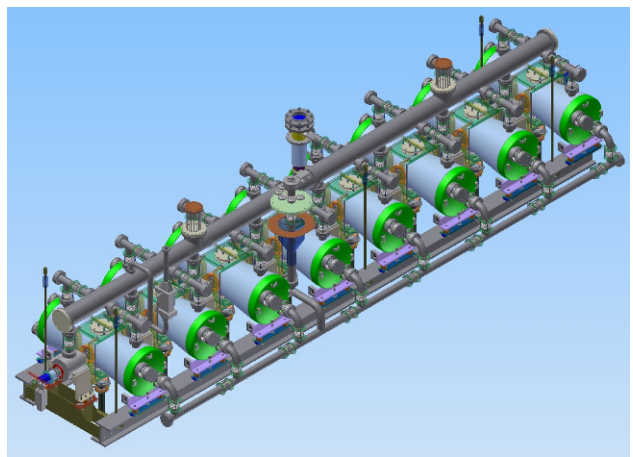

Figure 6: PXIE HWR cryomodule design

REFERENCES

[1] P.N. Ostroumov, et al, LINAC-10, September 12-17, Tsukuba, Japan, p. 157.
[2] P.N. Ostroumov, et al, PAC-11, March 28- April 1, New York, p. 2110.
[3] D. Berkovits et al, Paper MO1A01 in these proceedings.
[4] S. Nagaitsev, PAC'11, New York, March-April 2011, p. 2566.
[5] P.N. Ostroumov, et al, Development and Beam Test of a CW Radio Frequency Quadrupole Accelerator, submitted to PRST-AB.
[6] M. Kelly, et al, Paper MOPB073 in these proceedings.
[7] Z. Conway, et al, Paper TUPLB66 in these proceedings.
[8] Z. Conway, et al, Paper TUPB068 in these proceedings.
[9] B. Mustapha, et al, Proceedings of the IPAC-12, p. 2289.
[10] P.N. Ostroumov, et al, Proceedings of the IPAC-12, p. 2295.
[11] Z. Conway, et al, Paper TUPB067 in these proceedings.

Copyright © 2012 by the respective authors — cc Creative Commons Attribution 3.0 (CC BY 3.0)

DESIGN AND BEAM TEST OF SIX-ELECTRODE BPMS FOR SECOND-ORDER MOMENT MEASUREMENT

K. Yanagida*, S. Suzuki, and H. Hanaki, JASRI/SPring-8, Sayo Hyogo, Japan

Abstract

To enhance a beam observation system during top-up operation, we developed in the SPring-8 linear accelerator non-destructive beam position monitors (BPMs) that can detect second-order moments of electron beams. BPMs have six stripline-type electrodes with circular or quasi-elliptical cross-sections. We tested a BPM with a circular cross-section using electron beams, and our results showed that its normalized moments were determined accurately by electrostatic field calculation. We studied a precise calibration method to determine the relative attenuation factors between the electrode channels based on the principle that the relative moments must not vary with a change of the beam position using a steering magnet in drift space.

INTRODUCTION

The SPring-8 linear accelerator provides electron beams toward a storage ring about every twenty seconds because of the top-up operation of the storage ring. To enhance the beam observation system during the top-up operation, a non-destructive BPM system is being upgraded to a six-electrode BPM system that can detect the second-order moments of electron beams because the second-order moments are physical quantities related to beam sizes, which can be deduced by measuring second-order moments at more than six locations in FODO magnetic lattices [1].

Therefore, we developed the major components of a six-electrode BPM system: BPMs, a signal processor, and a digital input board. We installed our developed six-electrode BPMs with a circular cross-section in the beam transport line and tested them using electron beams. This paper describes the BPM designs as the parts of the six-electrode BPM system, the principle of multipole moment measurement, and the beam test results.

SIX-ELECTRODE BPMS

This section describes the designs of six-electrode BPMs and the principle of absolute moment measurement.

BPM designs

We developed two kinds of six-electrode BPMs for second-order moment measurement. One is a BPM with a circular cross-section for the non-dispersive section, and the other is a BPM with a quasi-elliptical cross-section for the dispersive section (Fig. 1). In the figure the numbers represent electrode number d. Both BPMs have stripline-type electrodes as signal pick-ups. The stripline length is 27 mm, which corresponds to $\lambda/4$ of the acceleration radio frequency. The characteristic impedance is designed as 50 Ω. One electrode of both BPMs shares 30 ° with respect to the duct center. The aperture radius of a BPM with a circular cross-section is 16 mm, and the long and short radii of a BPM with a quasi-elliptical cross-section are 14 mm and 28 mm. These BPMs were or will be installed instead of the existing four-electrode BPMs with circular and quasi-elliptical cross-sections [2][3].

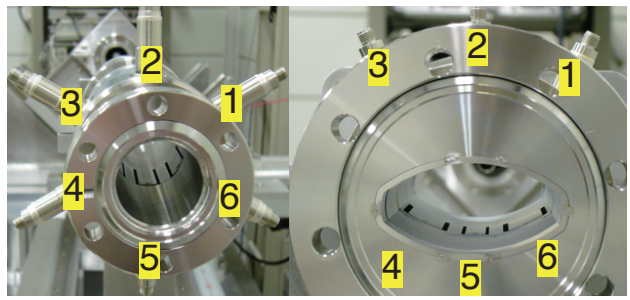

Figure 1: Six-electrode BPMs with circular and quasi-elliptical cross-sections. Numbers represent electrode number d.

Absolute Moment Measurement

A BPM with symmetrical arranged electrodes can detect multipole moments with respect to the duct center. These are called absolute moments P_n and Q_n, where n is the order of the multipole moment. For example, first-order absolute moments represent the transverse positions of beam centroid P_1 (horizontal position) and Q_1 (vertical position). The two-dimensional position (P_1, Q_1) is generally called the beam position.

Our developed six-electrode BPMs have two electrodes in the vertical direction, but none horizontally. This configuration enables us to measure three higher-order ($n \geqq 2$) absolute moments: P_2, Q_2, and Q_3.

Because the signal voltage of each electrode V_d is proportional to the integral of the electric field strength on the electrode, we can obtain the absolute moments with normalized moments $R^n_{Pn}/2$, $R^n_{Qn}/2$ and geometrical factors k, K, as described in Eq. (1). In the equation, R_{Pn} or R_{Qn} is called an effective aperture radius. The effective aperture radii and the geometrical factors are calculated analytically, especially for a BPM with circular cross-section, or numerically [4].

The calculation result is summarized in Table 1. A smaller effective aperture radius is preferable for accurate

* ken@spring8.or.jp

Copyright © 2012 by the respective authors — cc Creative Commons Attribution 3.0 (CC BY 3.0)

measurement, but R_{Q1} is rather large:

$$
\begin{aligned}
P_1 &= \frac{R_{P1}}{2}\frac{V_1 - V_3 - V_4 + V_6}{V_1 + V_3 + V_4 + V_6},\\
Q_1 &= \frac{R_{Q1}}{2}\frac{V_1 + V_3 - V_4 - V_6}{V_1 + V_3 + V_4 + V_6},\\
P_2 &= \frac{R_{P2}^2}{2}\frac{kV_1 - 2V_2 + kV_3 + kV_4 - 2V_5 + kV_6}{kV_1 + 2V_2 + kV_3 + kV_4 + 2V_5 + kV_6},\\
Q_2 &= \frac{R_{Q2}^2}{2}\frac{V_1 - V_3 + V_4 - V_6}{V_1 + V_3 + V_4 + V_6},\\
Q_3 &= \frac{R_{Q3}^3}{2}\frac{KV_1 - V_2 + KV_3 - KV_4 + V_5 - KV_6}{KV_1 + V_2 + KV_3 + KV_4 + V_5 + KV_6}.
\end{aligned}
\tag{1}
$$

Table 1: Effective aperture radii and geometrical factors

	circular (analytical)	quasi-elliptical (numerical)
R_{P1} [mm]	18.69	18.03
R_{Q1} [mm]	32.38	54.84
R_{P2} [mm]	18.91	18.42
R_{Q2} [mm]	17.59	22.48
R_{Q3} [mm]	16.57	18.55
k	1.000	1.918
K	1.000	3.056

RELATIVE MOMENTS

As described above, the absolute moments of six-electrode BPMs can be obtained using Eq. (1). However, they are rather complicated because they involve not only the moments of a beam intensity distribution called relative moments P_{gn} and Q_{gn} but also the moments of the beam centroid. For easier comparison of the multipole moments, we define the relative moments and extract them from the absolute moments.

Relative moments are defined as the moments with respect to the beam centroid. It is considered that the origin is transferred from the duct center (0, 0) to the beam position (P_1, Q_1) to cancel the first-order relative moments, i.e., P_{g1}=0 and Q_{g1}=0. Consequently, we can obtain the relative moments from the absolute moments using the following relations [4]:

$$
\begin{aligned}
&P_1 = b_G\cos\beta_G,\ Q_1 = b_G\sin\beta_G,\\
&P_{g2} = a_{g2}^2\cos 2\alpha_{g2} = P_2 - b_G^2\cos 2\beta_G,\\
&Q_{g2} = a_{g2}^2\sin 2\alpha_{g2} = Q_2 - b_G^2\sin 2\beta_G,\\
&Q_{g3} = Q_3 - b_G^3\sin 3\beta_G - 3b_G a_{g2}^2\sin(\beta_G + 2\alpha_{g2}).
\end{aligned}
\tag{2}
$$

SCREEN MONITOR FOR RELATIVE MOMENT MEASUREMENT

At the beam test, the relative moments were also measured by a screen monitor that records the two-dimensional beam intensity distribution on the screen (DESMARQUEST AF995R) into the intensity distribution on a charge-coupled device (CCD) using an optical focusing lens when the electron beams hit the screen.

We define the intensity distribution on the screen as $I(x_i, y_j)$, where x_i and y_j indicate the position of the data cell. The origin is defined as the screen center, i.e., the duct center, but not the CCD center. To calculate the absolute moments from $I(x_i, y_j)$, we define nth-order absolute intensity moments $m_{h(n-h)}$ in the Cartesian coordinates, as described in Eq. (3), and consequently obtain the absolute moments using Eq. (4) [4]:

$$
\begin{aligned}
&m_{00} = \sum_i\sum_j I(x_i,y_j),\ m_{10} = \sum_i\sum_j x_i I(x_i,y_j),\\
&m_{01} = \sum_i\sum_j y_j I(x_i,y_j),\ m_{20} = \sum_i\sum_j x_i^2 I(x_i,y_j),\\
&m_{11} = \sum_i\sum_j x_i y_j I(x_i,y_j),\ m_{02} = \sum_i\sum_j y_j^2 I(x_i,y_j),\\
&m_{21} = \sum_i\sum_j x_i^2 y_j I(x_i,y_j),\ m_{03} = \sum_i\sum_j y_j^3 I(x_i,y_j).
\end{aligned}
\tag{3}
$$

$$
\begin{aligned}
&m_{00}P_1 = m_{10},\ m_{00}Q_1 = m_{01},\\
&m_{00}P_2 = m_{20} - m_{02},\ m_{00}Q_2 = 2m_{11},\\
&m_{00}Q_3 = 3m_{21} - m_{03}.
\end{aligned}
\tag{4}
$$

Figure 2 shows the example data of the beam intensity distribution (contour plot) on the screen. Using Eqs. (3) and (4), the multipole moments of this distribution were obtained as P_1=2.334 mm, Q_1=−0.989 mm, P_{g2}=−0.391 mm^2, Q_{g2}=1.366 mm^2, and Q_{g3}=0.161 mm^3.

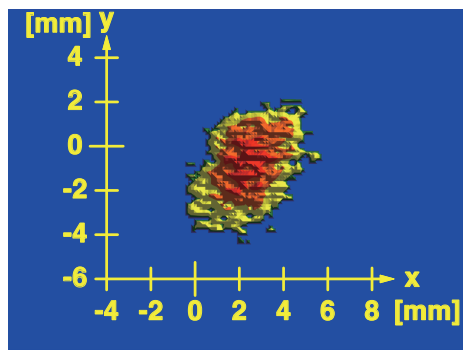

Figure 2: Two-dimensional beam intensity distribution (contour plot) on screen

BEAM TEST

We performed a beam test of a six-electrode BPM with a circular cross-section to verify whether the normalized moments measured by the beam test agree with those calculated analytically.

Entire Calibration

Even though each element of the system is calibrated precisely, entire calibration is very difficult and is not eas-

Copyright © 2012 by the respective authors — cc Creative Commons Attribution 3.0 (CC BY 3.0)

ily achieved. To resolve this problem we studied a method for entire calibration using electron beams.

The principle is very simple. We assume that the electron beams are stable during the beam test and that the steering magnets change the beam position without changing the beam intensity distribution with respect to the beam centroid. If we change the beam position at the BPM location using upstream steering magnets, observed relative moments P_{g2}, Q_{g2} and Q_{g3} must be constant. Conversely speaking, we can easily determine the relative attenuation factors between the electrode channels so that all the obtained relative moments are constant.

After we determined the relative attenuation factors, we applied them to all the data including the entire calibration data. Figure 3 shows example data of the multipole moments of the entire calibration. The beam position (P_1, Q_1) and second-order absolute moments P_2 vary by means of steering magnets, but second-order relative moments P_{g2} do not.

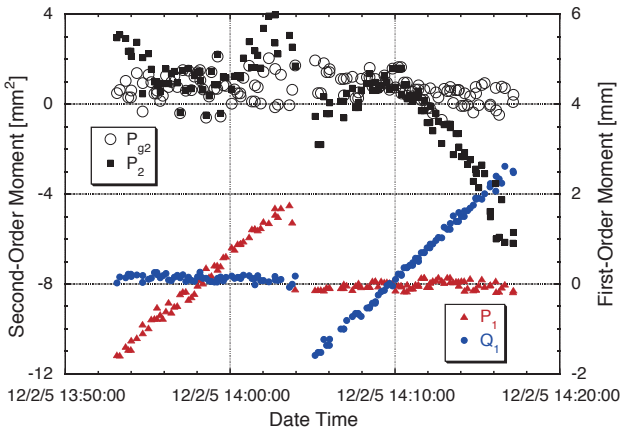

Figure 3: Multipole moments of entire calibration. Relative attenuation factors are applied.

Correlation Measurement

Finally, we compared the second-order relative moments taken by the screen monitor to those by the BPM when we changed the beam intensity distribution by changing the magnetic field of the upstream quadrupole magnet. Because the screen monitor was located upstream of the BPM in the drift space, we did not take both bits of data at the same beam shot. The distance between the screen monitor and the BPM is ∼2 m.

Figure 4 is the correlation plot between the second-order relative moments taken by the screen monitor (abscissa) and the BPM (ordinate). In the plot the spread data points were caused by the shot by shot fluctuation of the beam intensity distribution. However, the correlation plot apparently indicates a direct proportionality relation with a proportionality coefficient of 1.

This result provides the following important consequences. One, for such BPMs with stripline-type electrodes, normalized moments can be obtained accurately by

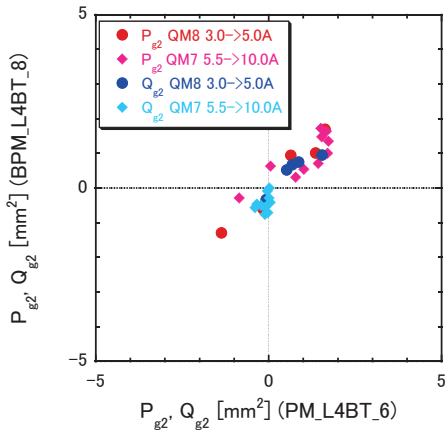

Figure 4: Correlation plot between second-order relative moments taken by screen monitor (abscissa) and BPM (ordinate)

analytical or maybe numerical electrostatic field calculation, i.e., the correlation plot with a proportionality coefficient of 1. The other is that an entire calibration is useful as is a self-consistent method for precise calibration to determine the relative attenuation factors between electrode channels, i.e., the correlation plot passing through the origin.

SUMMARY

We developed six-electrode beam position monitors with circular and quasi-elliptical cross-sections for second-order moment measurement. From the beam test results normalized moments of BPM with circular cross-section were accurately determined by analytical electrostatic field calculation. The entire calibration is useful and a self-consistent method for precise calibration to determine the relative attenuation factors between electrode channels.

REFERENCES

[1] R. H. Miller, et al., "Nonintercepting Emittance Monitor," Proc. 12th Int. Conf. High-Energy Accel. (HEAC'83), Fermilab USA, 1983, pp. 603-605.

[2] K. Yanagida, et al.,"A BPM System for The SPring-8 Linac", Proc. of the 20th Int. Linac Conf., Monterey USA, Aug. 2000, pp. 190-192.

[3] K. Yanagida, et al., "Beam Instrumentation Using BPM System of The SPring-8 Linac," Proc. of the 22th Int. Linac Conf., Lubeck Germany, Aug. 2004, pp. 438-440.

[4] K. Yanagida, et al., Phys. Rev. ST Accel. Beams **15**, 012801 (2012).

Copyright © 2012 by the respective authors — cc Creative Commons Attribution 3.0 (CC BY 3.0)

NON-DESTRUCTIVE REAL-TIME MONITOR TO MEASURE 3D-BUNCH CHARGE DISTRIBUTION WITH ARRIVAL TIMING TO MAXIMIZE 3D OVERLAPPING FOR HHG-SEEDED EUV-FEL

H. Tomizawa, K. Ogawa, T. Sato, and M. Yabashi
RIKEN Hariama Institute, 1-1-1 Kouto, Sayo-cho, Sayo-gun, Hyogo, Japan
Y. Okayasu, S. Matsubara, and T. Togashi
JASRI/SPring-8, 1-1-1 Kouto, Sayo-cho, Sayo-gun, Hyogo, Japan
E. J. Takahashi
RIKEN Advanced Science Institute, Hirosawa 2-1, Wako, Saitama 351-0198, Japan
M. Aoyama
Kansai Photon Science Institute, Japan Atomic Energy Agency,
8-1-7 Umemidai, Kizukawa-shi, Kyoto 619-0215, Japan
A. Iwasaki and S. Owada
Department of Chemistry, The School of Science, The University of Tokyo,
7-3-1 Hongo, Bunkyo-ku, Tokyo 113-0033, Japan
H. Minamide and T. Matsukawa
RIKEN 519-1399, Aramaki-aza, Aoba, Aoba-ku, Sendai, Miyagi, 980-0845, Japan

Abstract

We have developed a three-dimensional bunch charge distribution (3D-BCD) monitor with arrival timing for an FEL seeded with a high-order harmonic (HH) pulse. A 3D-BCD monitor is based on an Electro-Optic sampling (EOS) technique with multiple EO crystal detectors in spectral decoding. Utilizing this EO-multiplexing technique, we obtained the relative positioning in the transverse and the timing in the longitudinal of the electron bunch with respect to arriving timing of a seeding HH pulse at the undulator in real-time with non-destructive measurements. In our EUV-FEL accelerator, we prepared a seeded FEL with an EOS-based feedback system for user experiments. For obtaining a higher seeding hit rate, 3D overlapping between the electron bunch and the seeding pulse must be maximized at the optimal point. Keeping the peak wavelength of EO signals at the same wavelength with our feedback system, we provided seeded FEL pulses (intensity >4σ of SASE) with a 20-30% hit rate during pilot user experiments. For achieving the upper limit of temporal resolution, we are planning to combine high-temporal-response EO-detector crystals and an octave broadband probe laser pulse with a linear chirp rate of 1 fs/nm. We are developing an EO-probe laser pulse with ~10 μJ pulse energy and bandwidth over 300 nm (FWHM). In 2011, we successfully demonstrated the first bunch measurement with an organic EO crystal in the FEL accelerator at SPring-8.

INTRODUCTION

Since 2010 at SPring-8, we have been demonstrating a seeded free-electron laser (FEL) in the extreme ultra violet (EUV) region by high-order harmonics (HH) generation from an external laser source in a prototype test accelerator (EUV-FEL) [1]. In FEL seeding as a full-coherent high-intensive light source for EUV user experiments, a high hit rate of successfully seeded FEL pulses is required. Precise measurements of the electron bunch charge distribution (BCD) and its arrival timing are crucial keys to maximize and keep 3D (spatial and temporal) overlapping between the high-order harmonics (HH) laser pulse and the electron bunch. We constructed a timing drift monitor based on Electro-Optic (EO) sampling, which simultaneously measures the timing differences between the seeding laser pulse and the electron bunch using a common external pulsed laser source (Ti: Sapphire) of both the HH driving and EO-probing pulses (Fig. 1). The EO-sampling system can use timing feedback for continuous (without interruption) operation of HH-seeded FELs.

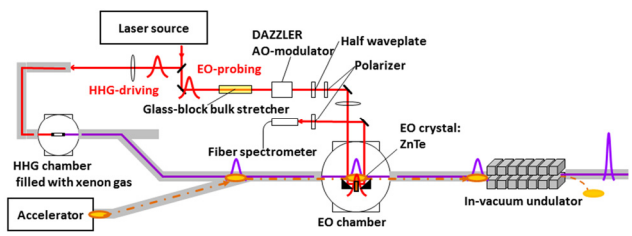

Figure 1: Experimental setup of seeded FEL with EO-sampling feedback at EUV-FEL accelerator: relative positioning in transverse and timing in longitudinal of electron bunch with respect to arriving timing of a seeding HH pulse are monitored at entrance of the first in-vacuum undulator to keep in a best seeding condition.

The R&D of a non-destructive 3D-BCD monitor (proposed in 2006 [2]) with bunch-by-bunch detection and real-time reconstructions has been extensively investigated at SPring-8. This ambitious monitor is based on an EO-multiplexing technique that resembles real-time spectral decoding and enables simultaneous non-destructive measurements of longitudinal and transverse BCDs. This part of the monitor was simultaneously materialized for probing eight EO crystals that surround

Copyright © 2012 by the respective authors — cc Creative Commons Attribution 3.0 (CC BY 3.0)

the electron beam axis with a radial polarized, hollow EO-probe laser pulse. In 2009, we verified the concept of a 3D-BCD monitor through electron bunch measurements in the photoinjector test facility at SPring-8 [3].

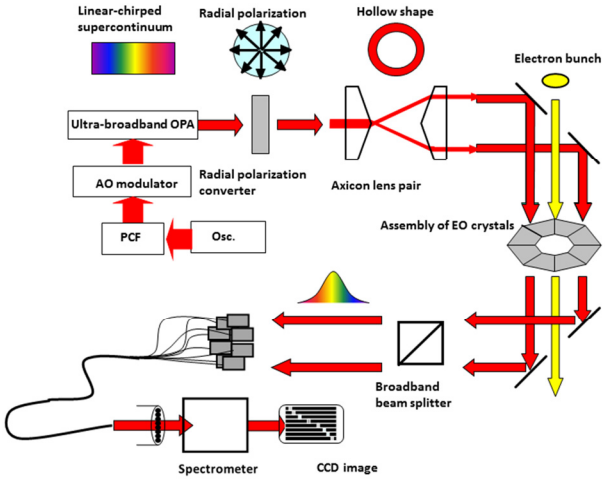

Figure 2: Schematic drawing of 3D-BCD monitor based on EO-multiplexing technique, utilizing simultaneous detection in imaging spectrographs with multi-track (eight tracks) of area array CCD of an image intensified (I.I.) camera.

As part of the Self-Amplified Spontaneous Emission (SASE) XFEL project at SPring-8, an additional target of temporal resolution is ~30 fs (FWHM), which utilizes an organic EO crystal (DAST) instead of conventional inorganic EO crystals (ZnTe, GaP, etc.). EO sampling with DAST crystals is expected to measure a bunch length that is less than 30 fs (FWHM). In 2011, we demonstrated the first EOS bunch measurements with DAST crystal in the EUV-FEL accelerator.

In this paper, we describe the development status and application of 3D-BCD as a 3D-overlapping monitor for FEL seeding.

3D-BCD AND OVERLAPPING MONITOR

EO-sampling measures a probe-pulse's retardation by changing the refraction index of a non-linear optical crystal by the radial Coulomb field of relativistic electron bunch slices. The EO-probe laser pulse is injected into the EO crystal at the same time as the electron bunch arrives at the EO crystal. The BCDs are bunch-by-bunch encoded as polarization modulations on the spectra of the EO-probe pulses. In spectral decoding to detect with a multi-channel spectrometer in real-time, the polarization modulations are converted into spectral intensity modulations by a polarized beam splitter.

A 3D-BCD monitor evolved from simple encoding of EOS into a multiplexing technique with a single probe laser pulse for multiple EO crystal detectors in a manner of spectral decoding (demultiplexing). A schematic drawing of a 3D-BCD monitor with eight EO crystals that surround the electron beam axis is shown in Fig. 2. It is applied for a multiplexing technique to simultaneously probe eight EO crystals with a radial polarized, hollow (ring beam) laser pulse. We realized demultiplexing as an imaging spectrograph with eight-track simultaneous detection in the area array CCD of a high-speed gated I.I. camera. Transverse detections of bunch slices are done by analyzing the multipole moments of the bunch slice charge density distributions (Ref. [3]).

For obtaining a higher hit rate of FEL seeding, 3D overlapping between the electron bunch and the seeding laser pulse is necessary to maintain a constant seeded FEL pulse. Utilizing this multiplexing EOS technique, relative positioning in the transverse and the timing in the longitudinal of the electron bunch with respect to arriving timing of the seeding HH pulse is obtained at the entrance of the first in-vacuum undulator in real-time with a non-destructive measurement.

In a 3D-overlapping monitor for FEL seeding, the probe pulse is split from the HH-driving Ti: Sapphire laser pulse (Fig. 1). For higher temporal resolution, the probe pulse is broadened by a photonic crystal fiber (PCF) up to over 300 nm. For real-time reconstructions of the 3D information, the octave broadband pulse is squarely shaped and linearly chirped by an Acousto-Optic (AO) modulator. Then the probe pulse passes through the radial polarization converter and an axicon lens pair to obtain a ring beam shape with radial polarization. This ring beam is simultaneously injected into eight EO crystals. As the spectral decoding of conventional EOS, the demultiplexing of the probe pulse is measured through eight-bunched bundle fibers that are matched to the f-number of the grating optics of a spectrometer (imaging spectrograph). In addition, for a high S/N ratio of EO signals, over 1000 counts of signal intensity per channel are necessary.

FEASIBILITY TESTS WITH THE EUV-FEL ACCELERATOR

Pilot user experiments with seeded FEL were demonstrated with a high hit rate with the EUV-FEL accelerator, at SPring-8 in July 2012. The EOS system shown in Fig. 1 was used for feedback to the timing delay unit of a common laser source as a real-time monitor for the relative difference of arrival timing between an electron bunch and a seeding HH pulse. We realized a sophisticated feedback system of timing drift with real-time data processing of EO-signal spectra that encoded the arrival timing as the central wavelengths of the peak signals of spectra and the BCD of the electron bunches. Maintaining the peak wavelength of EO signals at the same wavelength is the most optimal timing for HH seeding. Our feedback system realized a half-day seeded FEL operation with a hit rate of 20-30% (Seeded FEL pulse intensity >4σ of SASE). Compared with a hit rate of seeded FEL operation without EOS feedback [1], the hit rates became 100 times higher. This result shows that only keeping a temporal-overlapping constant at the optimal condition is effective to seed a single-pass SASE FEL pulse shot-to-shot with a HH pulse.

Copyright © 2012 by the respective authors — cc Creative Commons Attribution 3.0 (CC BY 3.0)

The other feasibility tests were done by bunch measurements with an organic EO crystal (DAST) in the EUV-FEL accelerator. DAST-EOS allows a few tens of femtosecond temporal resolution in the 3D-BCD measurements. In 2011, we successfully demonstrated BCD measurements with a bunch charge of 0.28 nC by a 230-μm thick, organic DAST crystal EO-sampling method. The edges of the EO crystals were set 2.0 mm from the electron beam axis. In a comparable EOS condition, double EO-signal intensity was observed by DAST over a conventional, 1-mm thick inorganic ZnTe crystal. The comparison of EO signals is shown in Fig. 3.

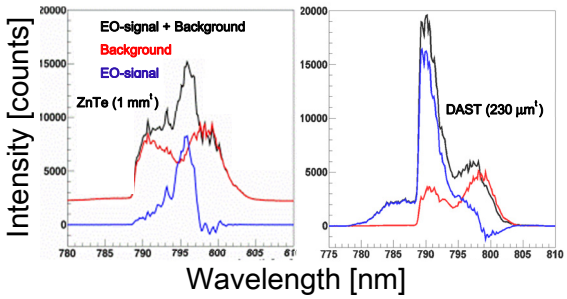

Figure 3: First BCD measurements with 230-μm thick organic DAST crystal compared with EO signals with a 1-mm inorganic ZnTe crystal. The both of the crystals were set 2.0 mm from the electron beam axis.

OCTAVE BROADBAND LASER PROBE PULSE GENERATION TAWARD ULTIMATE TEMPORAL RESOLUTION

For obtaining higher resolution feasible with DAST EO crystal, we developed an octave broadband probe pulse with a linear chirp rate of 1 fs/nm using a high pulse energy oscillator (FEMTOSOURCE scientific XL 500 (550 nJ/pulse; Femtolasers GmbH) and a PCF to generate a 5-MHz supercontinuum pulse train.

In spectral decoding (demultiplexing), temporal resolution T_{Res} depends on the bandwidth of the probe pulse, as in the following relationship $T_{Res} \sim (\tau_0 \tau_c)^{1/2}$, where τ_0 is the pulse width of a Fourier transform limited pulse and τ_c is the chirped probe pulse duration. If we utilize a laser pulse with 300 nm of square spectrum bandwidth (FWHM) at a center wavelength of 800 nm and 300-fs pulse duration as an EO-probe pulse, we can obtain temporal resolution of 30 fs.

We are developing an EO-probe laser pulse with a few tens of micro-Joules and bandwidth over 300 nm (FWHM). For obtaining such bandwidth and pulse energy, this EO-probe pulse is a supercontinuum amplified with optical parametric amplification (OPA). Especially for amplification that maintains bandwidth >350 nm, a non-collinear OPA (NOPA) using BBO crystal and a pump source with a 460-nm wavelength must be prepared (Fig. 4, upper diagram).

The EO-probe pulse energy of 10 μJ provides a high S/N ratio per decoding (demultiplexing) detector. In addition, the probe laser spectrum is shaped adaptively as a square spectrum by a broadband AO-modulator, DAZZLER (UWB-650-1100, FASTLITE) at the detectors.

The octave-broadband supercontinuum pulse is temporally stretched with nonlinear chirping due to the Group Velocity Dispersion (GVD) and even higher dispersion of the material of transparent optics, including the DAZZLER crystal. Hence, since dispersion controls are applied to roughly compress laser pulses by a Grism pair and linearly chirped by DAZZLER, we can finely adjust the pulse duration of the broadband probe laser with a linear chirp rate of 1 fs/nm for probing EO crystals. Owing to the characterization of the nonlinear chirp of the laser pulse with chirp scanning measurement, DAZZLER works as adaptive optics with two functions that provide control of spectral amplitude and phase up to 7th order dispersions: an intensity spectrum shaper and a linear chirp keeper.

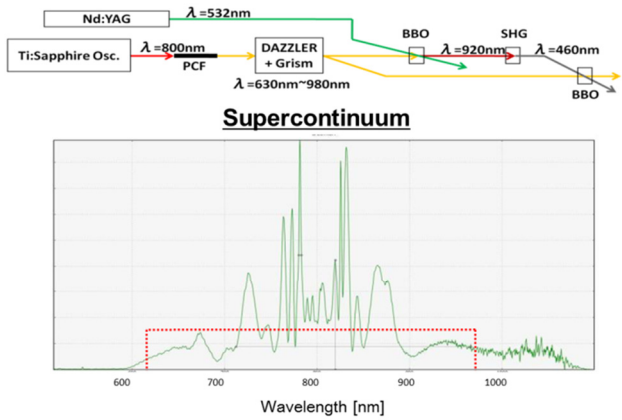

Figure 4: Schematic drawing of generation of broadband linear-chirped laser pulse with square-shaped spectrum (shaping region is shown as red dashed lines on supercontinuum spectrum). Pump source with 460 nm is not available commercially. It is generated from Nd: YAG laser (SHG: 532 nm) pump pulse and the super-continuum signal pulse with additional NOPA stage.

CONCLUSIONS

In several experiments, we successfully demonstrated and proved that the principle experiment of the 3D-BCD monitor as an application for an HH-seeded EUV-FEL is completely feasible. In addition, we successfully demonstrated BCD measurements with single organic DAST crystal (230-μm thick) by the EO-sampling method. We made the world's first electron bunch measurements by organic EO crystals. This crystal makes a few tens of femtosecond temporal resolution in 3D-BCD measurements possible with our octave broadband EO-probe pulse with a linear chirp rate of 1 fs/nm. The complete version of a 3D-overlapping monitor with a feedback system will be installed in our EUV-FEL.

REFERENCES

[1] T. Togashi et al., Optics Express, Vol. 19, Issue 1 (2011)
[2] H. Tomizawa et al., *Proc. of FEL07*, Novosibirsk, Russia, 317 (2007) 472.
[3] H. Tomizawa et al, *Proc. of FEL10*, Malmo, Sweden, (2010) 445.

Copyright © 2012 by the respective authors — cc Creative Commons Attribution 3.0 (CC BY 3.0)

DEVELOPMENT OF PERMANENT MAGNET FOCUSING SYSTEM FOR KLYSTRONS

Y. Fuwa, Y. Iwashita, H. Tongu, Institute for Chemical Research, Kyoto University, Kyoto, Japan
S. Fukuda, S. Michizono, High Energy Accelerator Research Organization, Ibaraki, Japan

Abstract

A permanent magnet focusing system for klystrons is under development to improve reliability of RF supply system and reduce power consumption. To save production cost, anisotropic ferrite magnets are used in this system. A test model has been fabricated and the power test of a 750 kW klystron with this focusing magnet is carried out. 60 % of the nominal output power has been achieved at a preliminary power test so far.

INTRODUCTION

Distributed Klystron Scheme (DKS) is proposed as one of the RF supply scheme for International Linear Collider (ILC) to reduce the cost and the down time by raising the reliability [1]. Because thousands of relatively small modulating anode (MA) klystrons ware required in DRFS scheme, the failure rate of each component must be reduced. Especially thousands units of electromagnet for klystron beam focusing would cause maintenance problems. Replacing the electromagnets by permanent magnets can eliminate their power supplies and cooling system. Hence the failure rate of the RF supply system can be reduced and cut down the operation cost. A klystron beam focusing system with ferrite magnets is under development is described.

FABRICATION OF FOCUSING MAGNET

Magnetic Materials

There have been precedents for electron beam focusing in klystrons with permanent magnets such as ALNICO, the rare earth (RE) [2,3,4]. Figure 1 shows the B-H curves for these magnet materials and anisotropic ferrite magnets. ALNICO magnets, which have high remanence, shows less coercivity and easily demagnetize. Although RE magnets such as NdFeB has high remanence and coercivity, they are rather expensive and have the resource problem. The anisotropic ferrite magnets have less remanence but higher coercivity than ALNICO. The required magnetic field for beam focusing in klystrons is less than 1 kGauss, therefore the remanence of the anisotropic ferrite magnets is enough high. And the material costs are not expensive, because anisotropic ferrite magnets are composed of iron oxide.

Magnet Field Distributions

Periodic Permanent Magnet (PPM) focusing scheme has relatively well-known magnetic field distribution. In a focusing system with permanent magnet, the alternating magnetic field can be easily generated because an integrated value of magnetic field vector along closed

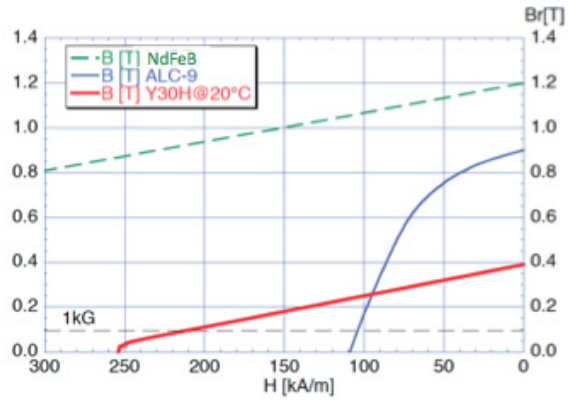

Figure 1: B-H curves of rare earth, ALNICO and ferrite magnets.

curve or infinitely-long axis is zero by the Ampere's law. However, periodicity cause stop bands. For pulse operations, the operating point always crosses such region during pulse rising time and the beam loss causes wall heating and prevents stable operation.

For safe operation, unidirectional magnetic field distribution is applied. Because the required magnet field is not high, anisotropic ferrite magnets can be used. RADIA 4.29[5,6] is used for the magnetic field design. Applied design is shown in Figure 2. Magnets shown in Figure 2 are categorized into two groups. The one group consists of magnets surrounding the klystron body

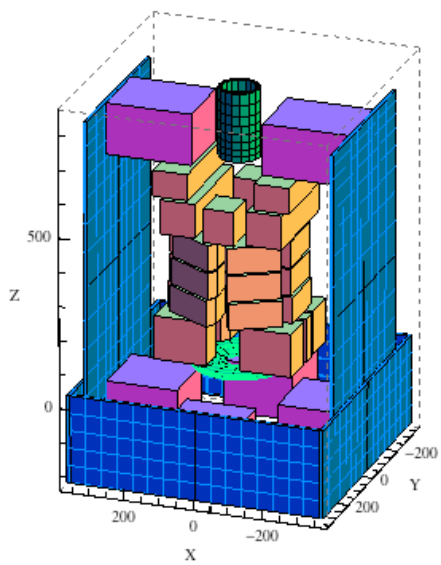

Figure 2: Layout of magnet and iron yoke.

Copyright © 2012 by the respective authors — cc Creative Commons Attribution 3.0 (CC BY 3.0)

(yellowish ones in Fig. 2), whose easy axes are parallel to the klystron beam axis. The other group consists of the bottom and the top large magnet bricks (purplish ones in Fig. 2) to form the magnetic field around the cathode and the collector area. Their easy axis is perpendicular to the klystron axis. All magnets are retractable for the insertion of the klystron. Klystrons are usually inserted from the top of the focusing magnets and thus the minimum aperture of the magnets must be larger than most fat part of the klystron such as ceramic insulator. The retractable magnets can open their aperture at the klystron installation time and close at the operation. (see Figure 3). This retracting mechanism can also be used for the field adjustment.

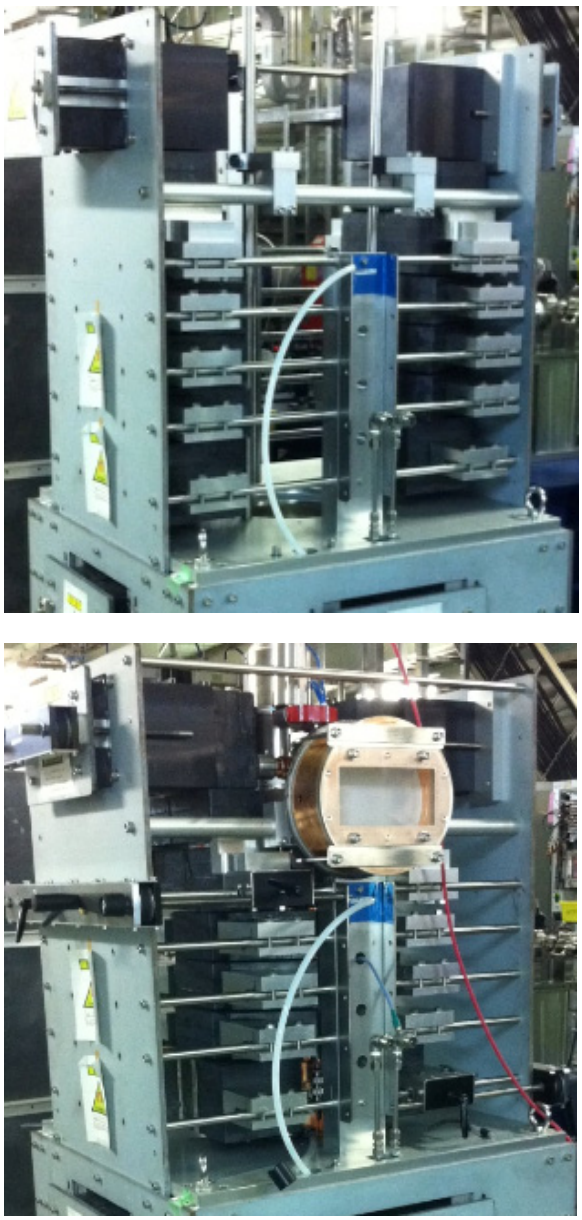

Figure 3: The magnets have larger aperture than the klystron body before the klystron installation (upper). After the klystron installation, the magnets are brought close to the klystron (lower).

KLYSTRON POWER TEST

To evaluate performance of the fabricated focusing magnet, a power test with real klystron (Toshiba E37501) is carried out. Figure 4 shows the E 37501 and Table 1 shows its nominal specification. The magnet field distribution, which is measured, adjusted is applied for power test. Figure 5 shows the longitudinal magnetic field. The blue line shows measured magnetic field generated by permanent magnets and the red line shows that by the electromagnet. The beam transport simulation has been performed by DGUN[7] using measured longitudinal magnetic field. The result of the simulation shows that the beam can pass through the klystron body without loss in the DC state (see Figure 6). Figure 7 shows transverse magnetic field components. The transverse magnetic field components are adjusted less than 10 Gauss by moving magnet's position. In the power test, the klystron was operated with 1 Hz repetition rate and the RF pulse duration was 1 ms so as not to damage the klystron body by unexpected beam loss. The result of the preliminary power test where the klystron cathode voltage is from 45 kV to 65 kV is shown in Figure 8. In Figure 8, red plots are the output maximum output power with our permanent magnets and blue plots are the max output power with an electromagnet measured by Toshiba. About sixty percent of the nominal output power at Toshiba is attained by the permanent

Figure 4: The klystron using in power test (Toshiba E37501).

Table 1: Specification of E37501

frequency	1.3 GHz
Max Output Power	750 kW
Max Efficiency	55 %
Max Gain	43 dB
Max Pulse Length	1.5 msec
Max Repetition Rate	5 Hz
Max Beam Voltage	66 kV
Max Beam Current	50 A

Copyright © 2012 by the respective authors — cc Creative Commons Attribution 3.0 (CC BY 3.0)

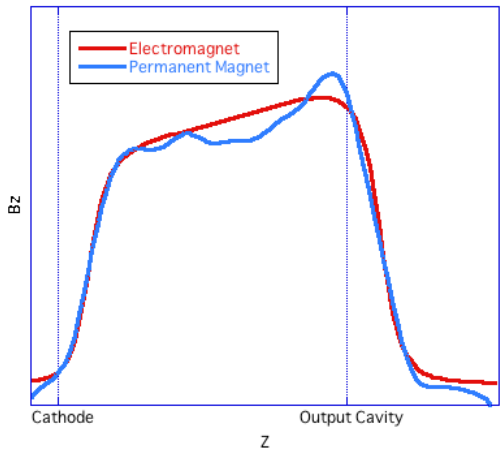

Figure 5: The longitudinal magnetic fields.

Figure 6: The result of DGUN simulation with the measured longitudinal magnetic field.

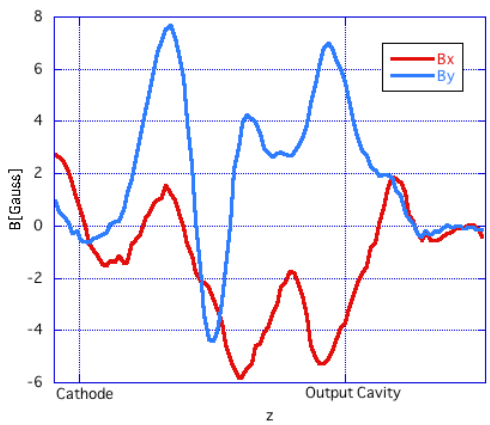

Figure 7: The measured transverse magnetic fields.

magnets in this early stage experiment. And the energy efficiency is about 33 % for our permanent magnets. This low output power and efficiency are supposed to be caused by the not optimized magnetic field in the cathode area. Figure 9 shows the calculated magnetic field in the cathode area. Although the magnetic field near the axis looks good, that on the outskirts may not be optimum, which results in beam mismatch.

Electric discharges occurred frequently in the operation and prevent stable operation. The electric discharges seem to be caused by the shape of the oil tank; the oil tank has a smaller diameter than that for the electromagnet focusing in order to reduce the distance from the magnets to the axis. This problem will be fixed by a remodeling of the tank. Further study will be continued for a better performance through magnetic field adjustment and so on.

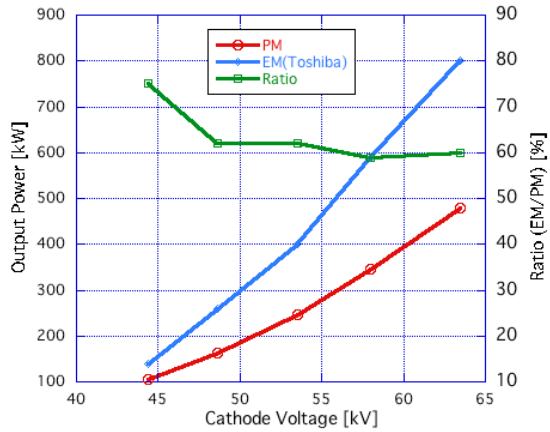

Figure 8: The preliminary result of the klystron power test.

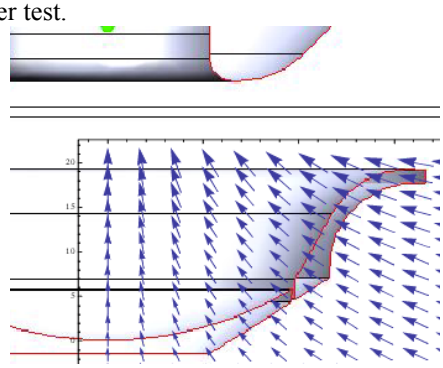

Figure 9: The calculated magnetic field in the cathode area

REFERENCES

[1] S. Fukuda, Distributed RF Scheme (DRFS) – Newly Proposed HLRF Scheme for ILC, LINAC2010, Tsukuba, pp.112-114, 2010.

[2] Jane V. Lebacqz, Status Report on Klystron Improvements, IEEE, Trans., NS-22, 3 pp.1324-1327, June1975.

[3] Fukuda, S., Shidara, T., Saito. Y., Hanaki, H., Nakao, K., Homma. H., Anami, S., Tanaka, J., PERFORMANCE OF HIGH POWER S BAND KLYSTRONS FOCUSED WITH PERMANENT MAGNET, 198624009 KEK-86-9, Feb. 1987.

[4] S. Masumoto, et al., STUDY OF PPM-FOCUSED X-BAND PLUSE KLYSTRON, Proc. of LINAC 2006, Knoxville, pp.628-630.

[5] P. Elleaume, O. Chubar, J. Chavanne, Computing 3D Magnetic Field from Inserted Devices, proc. of the PAC97, May 1997, p.3509-3511.

[6] O. Chubar , P. Elleaume, J. Chavanne, A 3D Magnetostatics Computer Code For Insertion Devices, SRI97 Conf. Aug. 1997, J. Synchrotron Rad. (1998). 5, 481-484.

[7] A. Larionov, K. Ouglekov, "DGUN-code for simulation of intensive axial-symmetric eletron beams", 6th ICAP, TU Darmstadt, Germany, 2000, p. 17.

Copyright © 2012 by the respective authors — cc Creative Commons Attribution 3.0 (CC BY 3.0)

THE FINE STRUCTURE FOR THE ZONE OF PARTICLE INTERACTION WITH A FINITE LENGTH PERIODIC STRUCTURE

V. Paramonov*, INR of the RAS, 117312, Moscow, Russia

Abstract

Interaction of the charged particle with finite length periodic structure is considered to estimate the long range wakefield effects in the constant impedance periodic deflecting structure for the special bunch diagnostic. In each structure passband there is a narrow zone with three modes, effectively interacting with the particles. To separate these modes, both frequency domain and time domain simulations are considered and compared.

INTRODUCTION

To describe long range wakefield effects for the $m-$th mode of the cavity, both longitudinal and transversal, loss factor k_m^l and kick factor k_m^t are used.

$$k_m^l = \frac{|\int_0^L E_{zm}(r=0,z)e^{\frac{i\omega_m \cdot z}{c}}dz|^2}{4U_m}, \qquad (1)$$
$$k_m^t = \frac{|\int_0^L E_{zm}(r=r_e,z)e^{\frac{i\omega_m \cdot z}{c}}dz|^2}{4r_e^2 U_m}$$

where $E_{zm}(r,z)$, ω_m and U_m are the distribution of z component, the frequency and the stored field energy of the m-th mode. For more details and explanations one can see [1], for example.

To estimate effects in a wide frequency range, one should either simulate frequencies and fields distributions in the structure, or directly simulate wakefields of the short bunch in the long structure. Below we consider some particularities of the long range wakefields in the periodic structure with finite number of periods.

PARTICLE INTERACTION WITH FINITE LENGTH PERIODIC STRUCTURE

For the traveling wave in the infinite periodic structure each field component can be represented in complex for and expanded in a series of spatial harmonics:

$$E_{fj}(r,z) = \Re E_j(r,z) - i\Im E_j(r,z) = \qquad (2)$$
$$= \sum_{p\to-\infty}^{p\to+\infty} a_{jp}(r)e^{\frac{-i(\Theta_0+2p\pi)z}{d}}, \quad 0 \le \Theta_0 \le \pi.$$

where d is the structure period, Θ_0 is the phase advance per period. Suppose the structure has a finite number of periods N and appropriate (half cells) terminations. For the standing wave a discrete set of possible phase advance $\Theta_m = \frac{mpi}{N}, m = 0, 1, ..., N$ is possible and the field distribution can be described, [2], as:

$$E_{sjm}(r,z) = \sum_{p\to-\infty}^{p\to+\infty} 2a_{jp}(r)cos(\frac{(\Theta_m + 2p\pi)z}{d}) \qquad (3)$$

with the same coefficients $a_{jp}(r)$ as in appropriate traveling wave representation (2). For such field representation of the standing wave let us consider the weighting function $S(\Theta_{mp})$, $\Theta_{mp} = \Theta_m + 2p\pi$, which describes interaction of relativistic $\beta = 1$ particle with p-th spatial harmonics in the field expansion (3):

$$S(\Theta_{mp}) = \int_0^L cos(\frac{\Theta_{mp}z}{d})e^{\frac{i\omega_m z}{c}}dz = \qquad (4)$$
$$= \frac{1}{2}\{\frac{e^{iL(\frac{\omega_m}{c}+\frac{\Theta_{mp}}{d})}-1}{i(\frac{\omega_m}{c}+\frac{\Theta_{mp}}{d})} + \frac{e^{iL(\frac{\omega_m}{c}-\frac{\Theta_{mp}}{d})}-1}{i(\frac{\omega_m}{c}-\frac{\Theta_{mp}}{d})}\}.$$

The functions $\Re S(\Theta)$, $\Im S(\Theta)$ and $|S(\Theta)|$ are plotted in

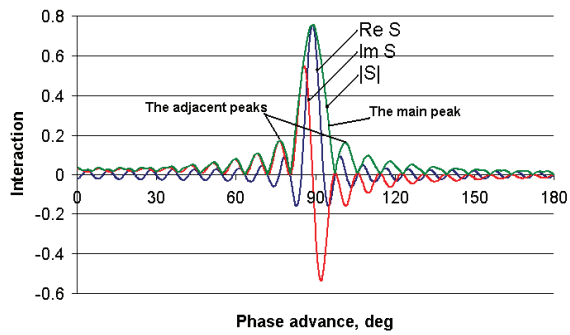

Figure 1: The functions $\Re S(\Theta)$, $\Im S(\Theta)$ and $|S(\Theta)|$ for the first monopole passband of the LOLA IV deflecting structure, $N = 46$

Fig. 1 for the first monopole passband of the LOLA IV [3] deflecting structure.

The maximal value $\Re S(\Theta_s)_{max} = |S(\Theta_s)|_{max} = \frac{L}{2} = \frac{Nd}{2}$ corresponds to the synchronous interaction $\frac{\omega_m}{c} = \frac{\Theta_s}{d}$ and linearly increases with the increasing number of cells in the structure. The width of the main peak $|S(\Theta)|$ (the distance in Θ between points $|S(\Theta)| = 0$ is $d\Theta = \frac{4\pi}{N}$ and for longer structure the main peak is narrowed. Because the separation between standing wave modes at Θ axis is of $\frac{\pi}{N}$, all time three or four modes belong to the main peak. The adjacent peaks in $|S(\Theta)|$, see Fig. 1, are placed at the distance $\delta\Theta = \pm\frac{3\pi}{N}$ with respect to the main peak $\Theta = \Theta_s$. The width of adjacent peaks is $\frac{2\pi}{N}$ - twice less, as compared to the width of the main peak. The maximal values of the

* paramono@inr.ru

Copyright © 2012 by the respective authors — cc Creative Commons Attribution 3.0 (CC BY 3.0)

adjacent peaks are $|S(\Theta_s \pm \delta\Theta)| = \frac{Nd}{3\pi}$ and also linearly rise with the increasing number of cells in the structure. But, with respect to the main peak, the adjacent peaks are lower in $1.5\pi \approx 4.7$ times. In the expression for k_m^l, k_m^t the values (1) the weighting function $S(\Theta)$ is in the second power and all modes, which do not belong to the $\pm\frac{2\pi}{N}$ vicinity of the synchronous point, will have at least one order lower k_m^l, k_m^t values.

In the interaction of the particle with the field in the periodical structure the synchronism has the effect of a band pass filter - only three modes with the phase advance $\Theta_m = \Theta_s \pm \frac{2\pi}{N}$ in the vicinity of the synchronous point can have a significant k_m^l, k_m^t values.

One can directly check with (4), that total loss or kick factor of modes owned by the main peak, is approximately twice as for synchronous interaction, regardless to the precise modes position with respect Θ_s, $\sum k_m^{l,t} \approx 2k_s^{l,t}$.

FREQUENCY DOMAIN APPROACH

The method, essentially based on the properties of the structure periodicity, was developed to estimate in the wide frequency range k_m^l and k_m^t values of the Transverse Deflecting Structure (TDS) for special beam diagnostic in the European XFEL. XFEL TDS has sections of the constant impedance deflecting structure with $N = 16$ and $N = 46$. The TDS prototype for $N = 14$ is considered in [4].

At first, considering only one period of the structure, we simulate with traveling wave regime in wide frequency range frequencies ω_n and complex fields distributions E_{zn} of all modes for the reference set of the phase advance $\Theta_n = \frac{n\pi}{N_1}, n = 0, 1, ..., N_1$. To simplify simulations, symmetry properties of the structure should be used actively. Defining for the m-th mode three intermediate functions,

$$I_m^{ee,eo,oo}(\Theta_n) = \int_0^{d/2} \begin{matrix} \Re E_{zm} cos \\ \Re E_{zm} sin \\ \Im E_{zm} sin \end{matrix} (\frac{\omega_m z}{c}) dz, \quad (5)$$

and taking into account (3), we can express the integral in (1) as:

$$\frac{k_m^l}{U_M} = (\frac{I_m^{ee}(\Theta_m)\{1 + (-1)^m cos(N\phi_m) + 2S_m^{cc}\}}{U_m} + \quad (6)$$
$$+\frac{I_m^{eo}(\Theta_m)(-1)^m sin(N\phi_m) - 2I_m^{oo}(\Theta_m)S_m^{ss}}{U_m})^2 +$$
$$+(\frac{I_m^{ee}(\Theta_m)\{(-1)^m sin(N\phi_m) + 2S_m^{cs}\}}{U_m} +$$
$$+\frac{I_m^{eo}(\Theta_m)\{1 - (-1)^m cos(N\phi_m)\} + 2I_m^{oo}(\Theta_m)S_m^{sc}}{U_m})^2$$

where the coefficients

$$S_m^{cc,cs,sc,ss} = \sum_{n=1}^{N-1} \begin{matrix} cos \\ cos \\ sin \\ sin \end{matrix} (n\Theta_m) \begin{matrix} cos \\ sin \\ cos \\ sin \end{matrix} (n\phi_m) \quad (7)$$

are discrete analogs of the weighting function $S(\Theta_{mp})$ in (4) with the same filtering properties. The intermediate functions in (5) are slow functions of the phase advance Θ_n and for intermediate Θ_m values one can apply smooth interpolation. Similar expression can be obtained for kick factor values k_m^t, (1).

The relation (6) describes the general case of interaction. In the case of synchronism this formula is more simple:

$$k_{m_{max}}^l = \frac{N^2(I^{ee}(\Theta_s) + (-1)^{n_b} I^{oo}(\Theta_s))^2}{U_m}, \quad (8)$$

where $n_b = \frac{\omega_s \pi}{\omega_0 \Theta_0}$ is the number of Brillouine zone for synchronous particle - wave interaction. The relation (8) provides also the upper estimation for k_m^l, k_m^t values in each passband of the structure.

The results of this method were compared with k_m^l, k_m^t values, obtained from the direct frequencies and fields distribution for the lowest monopole and dipole passbands in TDS sections with $N = 16$ and $N = 46$ and one can see comparison in Fig. 2.

The method has been applied to estimate k_m^l, k_m^t values

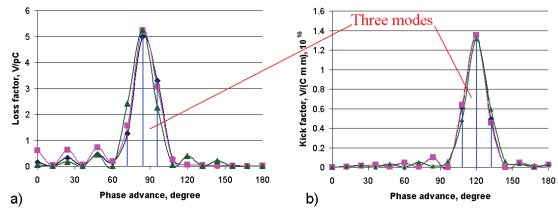

Figure 2: The loss factor k_m^l values calculated from direct field distributions simulations (blue) and from field reconstruction (magenta) for the TDS with $N = 16$ cells (a) and $N = 46$ (b). The green triangles are for the full end cell terminations.

in the XFEL TDS sections and results to be published in details in another papers. For example, in Fig.3 the TDS dispersion diagram for monopole modes in wide frequency range.

The frequency resolution of our method doesn't depend

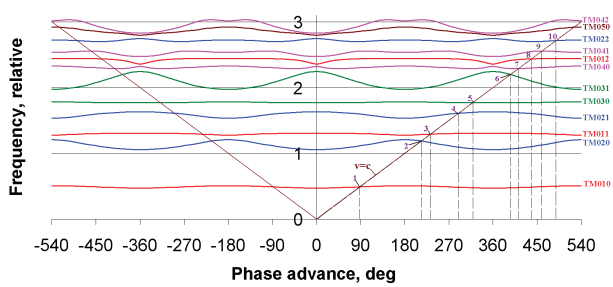

Figure 3: The diagram of interaction for the particle $v = c$ with monopole modes in the TDS XFEL structure.

both on the structure type and number of cells in the structure. All time for each passband three or four modes are allocated with maximal k_m^l, k_m^t values for this passband.

Copyright © 2012 by the respective authors — cc Creative Commons Attribution 3.0 (CC BY 3.0)

TIME DOMAIN SIMULATIONS

For more confidence, the special set of simulations with our method has been performed for LOLA IV structure and results for $N = 104$ were compared with results of time domain simulations [5].

In Fig. 4 the longitudinal wake potential, calculates with PS CST [6] for Gaussian bunch with $\sigma = 6mm$ is shown at the distance $s = 500m$ for the LOLA IV structure with $N = 16$. One can clearly see the beating with the length $\lambda_b \approx 25m$, corresponding to the frequency of $\frac{c}{\lambda_b} \approx 12MHz$. It is exactly the frequency difference between neighbor modes at the first monopole passband in LOLA IV for $N = 16$ in the vicinity of synchronous point $\Theta_s \approx 96^o$. In general case the modes separation in frequency for vicinity of synchronous point is $\delta\omega = \frac{\omega_s \beta_g \pi}{N\Theta_s}$, where β_g is the group velocity.

To extract the wake impedance from wake potential with the Fourier transform, highlighting the contributing modes, transform resolutions should be much better than $\delta\omega$.

To extract contributing modes reliably, the wake potential should be calculated at the distance $s > \frac{2\pi c}{\delta\omega} \sim \frac{cN\Theta_s}{\pi f_s \beta_g}$. Another case the information in wake potential is not sufficient for reliable modes separation. In Fig.5 the plots are shown for wake impedance, extracted with sufficient Fourier transform resolution from longitudinal wake potential, calculated at the distances 5m, 25m and 50m.

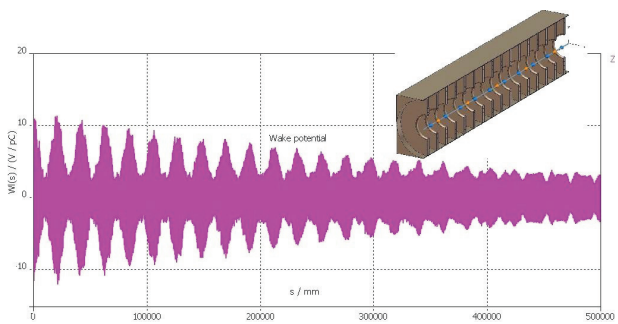

Figure 4: The longitudinal wake potential in LOLA IV structure ($N = 16$) at the distance of 500 m.

With simulations at short distance with time domain approach one get the total value of the wake impedance for the total passband, without separation to contributing modes.

SUMMARY

In the interaction of particle with finite length periodical structure at the phase advance scale in each structure passband there is the zone of effective interaction in the vicinity of synchronous interaction. The width of this zone decreases with increasing number of periods in the structure, but all time four or three modes at each passband belong to such zones. The total value of loss or kick factors for modes owned by each such zone is approximately twice as for synchronous interaction, regardless to precise modes placements inside zone.

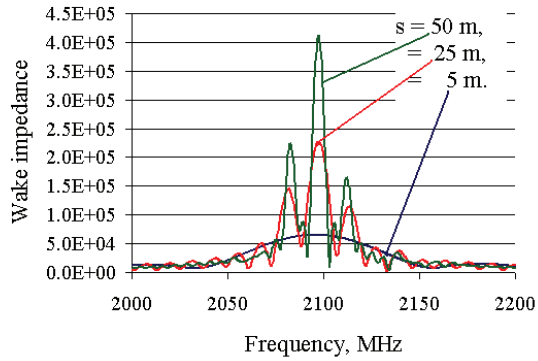

Figure 5: The calculated wake impedance of monopole modes in LOLA IV structure for simulations $s = 5m, 25m$ and $50m$, $N = 16$

Frequency domain approach, essentially use periodicity properties of the structure, developed to estimate long range wakefields of the structure. The method resolution doesn't depends on the structure type and number of periods in the section, all time showing the fine structure for the zones of effective interaction at each passband.

With time domain simulation the modes separation is also possible, but for long structures with small group velocity requires wake potential calculation at long distance and results treatment with high Fourier transform resolution.

ACKNOWLEDGMENT

The author thanks Dr. I. Zagorodnov and Dr. M. Dohlus (DESY) for very useful discussion.

REFERENCES

[1] K. L. F. Bane, P. B. Wilson, T. Weiland, Wake Fields and Wake Field Acceleration, SLAC-PUB-3528, SLAC, 1984

[2] G. Loew, R. Neal, Accelerating Structures, G. Dome, Review and Survey of Accelerating Structures, in Linear Accelerators, ed. P. Lapostolle, E. Septier, North-Holland Pub. Co., Amsterdam, 1970

[3] O.H. Altenmueller, R.R. Larsen, G.A. Loew, Investigations of Traveling-Wave Separators for the Stanford Two-Mile Linear Accelerator, The Rev. of Sci. Instr., v. 35, n 4, 1964

[4] L. Kravchuk et. al., Layout of the PITZ Transverse Deflecting System for Longitudinal Phase Space and Slice Emittance Measurements. Proc. Linac2010, p. 416, 2011

[5] I. Zagorodnov, T. Weiland, Wake Fields Generated by the LOLA-IV Structure and the 3rd Harmonic Section in TTF-II, TESLA Report 2004-01, DESY, 2004

[6] `http://www.cst.com`.

Copyright © 2012 by the respective authors — cc Creative Commons Attribution 3.0 (CC BY 3.0)

DEFLECTING STRUCTURES WITH MINIMIZED LEVEL OF ABERRATIONS*

V. Paramonov †, INR of the RAS, Moscow, 117312, Russia

Abstract

Deflecting structures are now widely used for bunch phase space manipulations either in special bunch diagnostic or in emittance exchange experiments. As a tool for manipulation, the structure itself should provide the minimal phase space perturbations due to non linear additives in the field distribution. Criterion of the field quality estimation is developed and deflecting structures are considered for minimization of non linear additives.

INTRODUCTION

The Deflecting Structures (DS) - periodical structures with transverse components of the electromagnetic field - initially were introduced for charged particle deflection and separation. The bunch cross DS synchronously with the deflecting field Ed, corresponding the phase $\phi = 0$ in the structure and particles get the increment in the transverse momentum p_t. There are a lot of papers, see for example [1], describing DS design and application for such purpose. At present for short and bright electron bunches DS found another applications, either for bunch special diagnostic, [2], or emittance exchange experiments. Both directions are related to the transformation of particle distributions in the six dimensional phase space and DS operates in another mode - the bunch center cross DS at zero E_d value, $\phi = 90^o$. There are also a lot of papers, describing it in more details. Application for Particles Distributions Transformation (PDT) provide additional requirements - a tool for transformation should provide the minimal, as possible, own distortions to the original distributions.

FIELD DISTRIBUTION QUALITY

For deflecting field E_d description the widely used basis of $TM - TE$ waves can not be used due to degeneration into TEM at $\beta = 1$. A basis of hybrid waves $HE - HM$ was introduced, [3], [4] to avoid this methodical problem. The common representation for the field distribution in the DS aperture is

$$\vec{E} = C\vec{E}_{HE} + D\vec{E}_{HM}, \quad \vec{H} = C\vec{H}_{HE} + D\vec{H}_{HM}, \quad (1)$$

with the weighting coefficient C, D depending both on supporting structure and on operating mode. It is the method of description and results treatment. The physical object - the deflecting force - is the transverse component of the Lorenz force

$$\vec{F}^L = e(\vec{E} + [\vec{v}, \vec{B}]), F_x = eE_d = e(E_x - \beta Z_0 H_y), \quad (2)$$

where $Z_0 = \sqrt{\frac{\mu_0}{\epsilon_0}}$, expressed in (2) through the transverse E_x and H_y components in Cartesian coordinates.

In any periodical structure for Traveling Wave (TW) operating mode each field component $E_j(r, z)$ in the beam aperture can be represented in the complex form as the set over spatial harmonics:

$$E_j(r, z) = \widehat{E_j(r, z)} e^{i\psi_j(z)} = \\ = \sum_{n\to-\infty}^{n\to+\infty} a_{jn}(r) e^{\frac{-i(\Theta_0 + 2n\pi)z}{d}}, \quad (3)$$

where $\widehat{E_j(r, z)}$ and $\psi_j(z)$ are the amplitude and the phase distributions, d is the structure period and $a_{jn}(r)$ is the transverse distribution for the n-th spatial harmonics. The period length is defined from synchronism with the main a_{j0} harmonic, $d = \frac{\Theta_0 \beta \lambda}{2\pi}$.

The bunch emittance deterioration during PDT take place due to non linear additions both in transverse and longitudinal distributions of the field. There is inevitable nonlinearity at $\beta < 1$ even in main harmonic distribution, vanishing for $\beta \to 1$, [3], [5]. But the main source of additions are higher spatial harmonics. For each harmonic the transverse and longitudinal distributions are rigidly coupled and are proportional to harmonic amplitude. To estimate field quality, we have to estimate the level of spatial harmonics, [5]. Spatial harmonics are essential at the aperture radius $r = a$ and higher harmonics attenuate to the axis as

$$a_{jn}(0) \sim a_{jn}(a) \cdot exp(-\frac{4\pi^2 n}{\beta\Theta_0} \cdot \frac{a}{\lambda}), \quad |n| \gg 1, \quad (4)$$

where λ is the operating wave length. At the axis $r = 0$ just lower harmonics $n = \pm 1, \pm 2, \pm 3$ are really presented. For harmonics estimations in details and 'in total', let us introduce parameters $\delta\psi_j(z)$ and Ψ_j at the axis $0 \le z \le d, r = 0$

$$\delta\psi_j(z) = \psi_j(z) + \frac{\Theta_0 z}{d}, \quad \Psi_j = max(|\delta\psi_j(z)|), \quad (5)$$

with the physical sense as the deviation and the maximal phase deviation of the real wave component from the synchronous harmonic. The qualitative estimation and correct value for $a_{jn}(0)$ one can get as

$$|a_{jn}(0)| < \frac{(\widehat{E_j(0, z)}_{max} + \widehat{E_j(0, z)}_{min})\Psi_j}{2n}, \quad (6)$$

$$a_{jn}(0) = \frac{\int_0^d \widehat{E_j(0, z)} sin(\delta\psi_j(z)) sin(\frac{2\pi n z}{d}) dz}{d}.$$

From linearity, we can apply $\delta\psi_j(z)$ and Ψ_j for quality

* Work supported in part by RBFR N12-02-00654-a

† paramono@inr.ru

Copyright © 2012 by the respective authors — cc Creative Commons Attribution 3.0 (CC BY 3.0)

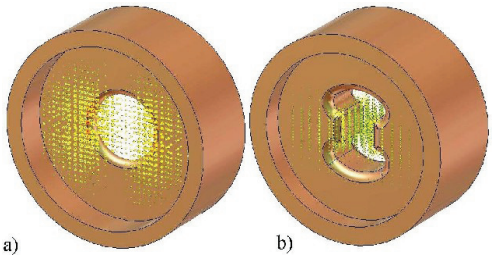

Figure 1: DLW (a) and TE - type (b) deflectors.

estimation both in longitudinal $E_z, \delta\psi_z(z), \Psi_z$ and transverse $E_d, \delta\psi_d(z), \Psi_d$ field components, also estimating PDT quality in these directions. To emphasize the differences in field distribution, the developed method is applied for analysis of DLW [6] and TE - type deflectors, Fig. 1.

OPERATING MODE

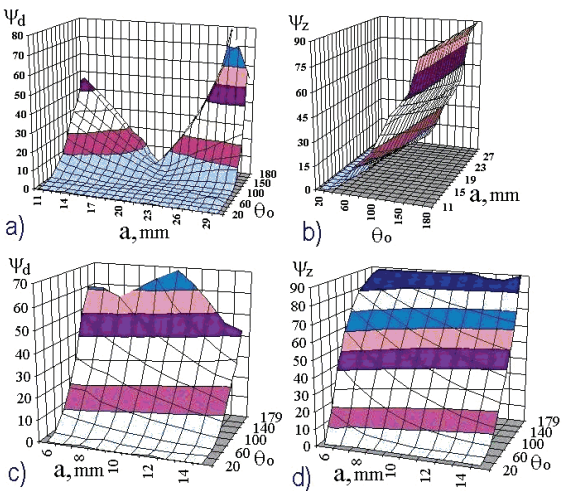

Figure 2: The surfaces $\Psi_d(a, \Theta_0)$ (a,c) and $\Psi_z(a, \Theta_0)$ (b,d) for the DLW (a,b) and TE - type (c,d) deflectors.

Assuming operating frequency $f_0 = 3GHz$, in Fig. 2 are shown the surfaces $\Psi_d(a, \Theta_0)$ and $\Psi_z(a, \Theta_0)$ for the DLW and TE - type deflectors both for TW $0 < \Theta_0 < 180^0$ and Standing Wave (SW, $\Theta_0 = 180^0$) operating mode,[5].

TW Operation

As can be seen from Fig. 2, small Ψ_d, Ψ_z values all time are at lower $\Theta_0 \leq 60^o$ values. For spatial harmonics the decrement of attenuation in (4) is inverse proportional to Θ_0 and $a_{zn}(0), a_{dn}(0)$ all time are small for low Θ_0. It is the common property of slow wave systems. Any periodical structure has reduced aberration level in TW operation with low Θ_0, both in E_z and in E_d distributions. For DLW harmonics attenuation is essentially stronger due to larger aperture radius.

Another effect is very important for E_d distribution and is in mutual phasing of transverse E and H components. For the opposite E_x and H_y phasing (DLW) electric and magnetic components work for deflection together (1), but E_x spatial harmonics compensate or even cancel $Z_0 H_y$ harmonics. It extends low Ψ_d region to higher Θ_0 values, Fig. 2a, and $\Psi_d < \Psi_z$. For the same E_x and H_y phasing (TE deflector) deflection form electric and magnetic components is partially compensated (1), but E_x and $Z_0 H_y$ harmonics add, $\Psi_d > \Psi_z$. The significant harmonics cancellation takes place at $|E_x^0| \sim |Z_0 H_y^0|$ - for comparable amplitudes of synchronous harmonics in E_x and H_y distributions. One can see clear canyon in $\Psi_d(a, \Theta_0)$ surface in Fig. 2a and for the bottom of this canyon $|E_x^0| \approx |Z_0 H_y^0|$. The structures with opposite phasing can provide very small aberrations level in E_d distribution.

In the Table 1 are listed the relative harmonics amplitudes for DLW TW operation. In comparison with DLW LOLA deflector, [6], or similar structures with $\Theta_0 = 120^o$, operation with $\Theta_0 = 60^o$ leads to aberrations reduction in times, especially for longitudinal force. Conditions for RF efficiency in TW case also are more flexible, as compared to SW case. The end cells with RF couplers are the points of special consideration, [5].

Table 1: The relative $a_{zn}(0) \cdot 10$ and $a_{dn}(0) \cdot 10$ values for DLW.

Operation $a =, mm$	Θ_0	E_z, $n=1$	E_z, $n=2$	E_d, $n=1$	E_d, $n=2$
TW,23.80	60	-0.048	-0.007	0.006	-0.009
TW,23.58	90	-0.581	-0.004	0.009	-0.001
TW,22.33	120	-1.950	-0.048	0.020	-0.015
SW,12.0	180	-6.103	-1.385	-3.818	-0.623
SW,19.4	180	-5.619	-0.691	-0.271	-0.148

SW Operation

In the case of short deflectors SW operation is more efficient in RF sense. But individual E, H components, including E_z at $\Theta_0 = 180^o$ have a single, either real or imaginary part in representation (1), resulting in $\Psi_j = 90^0$ for each component separately. For longitudinal force aberration reduction is possible just by aperture radius increasing -it is not so effective as for low Θ_0 TW case.

The deflecting field E_d is composed from two components, E_x, H_y and has in representation (1) both real and imaginary parts, similar to TW case. Relations (5),(6) work for E_d study even for Θ_0 SW case.

Because harmonics attenuation at $\Theta_0 = 180^o$ (assuming $\beta = 1$) is not effective, the single way for aberration reduction in E_d is harmonics cancellation for E_x and H_y distributions under opposite phasing. It can be realized in DLW by aperture radius choice for the preliminary specified disk thickness t_d, [8]. In the Table 1 are given results for optimized SW case ($a = 19.4mm, t_d = 5.4mm, \Psi_d \sim 1.5^o, \frac{Z_0 H_y^0}{E_x^0} = 0.98$). In SW DLW E_d aberration reduction is possible, but at the expense of moderate RF efficiency.

Copyright © 2012 by the respective authors — cc Creative Commons Attribution 3.0 (CC BY 3.0)

SUPPORTING STRUCTURE

The hybrid HE_n, HM_n waves exist in a supporting RF structure. But the classification of a supporting structure with a complicated field distribution is always rather conditional. In Fig. 3 the plots of $\frac{Z_0 H_y^0}{E_x^0}$ balance are shown,

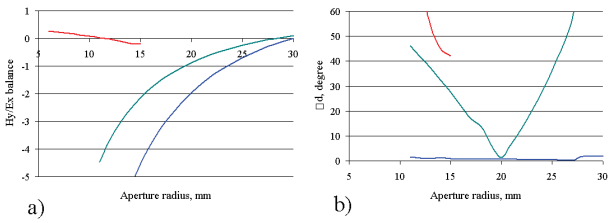

Figure 3: The field balance $\frac{Z_0 H_y^0}{E_x^0}$ (a) and $\Psi_d(a)$ plots (b) for DLW deflector $\Theta_0) = 60^o$ (blue), $\Theta_0) = 180^o$ (green) and TE - type deflector, $\Theta_0 = 180^o$ (red).

having even for well studied DLW in the first passband a large variety $-10 \le \frac{Z_0 H_y^0}{E_x^0} \le 0.5, 10mm \le a \le 30mm$ with different $\vec{E}, \vec{H}$ distributions, [5]. Similar field transformation we can provide in TE deflector, [7], Fig. 4.

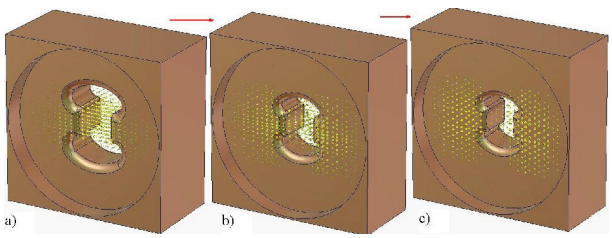

Figure 4: Field transformation for deflecting mode in the TE - type deflector.

At the structure axis we can define C, D in (1) from the already calculated E_d distribution and connect it with $\frac{Z_0 H_y^0}{E_x^0}$ balance. For E_d aberration minimization, especially for SW case, we need the opposite phasing of transverse $\vec{E}, \vec{H}$ components. Now it is the single sustainable sign for structure selection. Such phasing means the negative power flow near, but doesn't mean, in general, total negative flow, which define a negative dispersion in operating point. Even in simple DLW the inversion aperture radius a_i, corresponding to $\beta_g = 0$, essentially depends on Θ_0, [5].

For effective aberration reduction in E_d we need in the balance $|\frac{Z_0 H_y^0}{E_x^0}| \approx 1$. But the case of $|Z_0 H_y^0| = |E_x^0|$ is very close, probably coincides, to inversion point. It results in non monotonous (for TW case, [5]) or narrow (for SW case, [8]) dispersion curve. The method for DLW dispersion curve correction is described in [8]. Also the practice of Ψ_d minimization shows, that $(\Psi_d)_{min}$ is close, but not identical to $|Z_0 H_y^0| = |E_x^0|$ condition.

The DLW has just one parameter, effective for $\frac{Z_0 H_y^0}{E_x^0}$ balance control, aperture radius a, see Fig. 3a, which defines RF efficiency also. By splitting control over transverse $\vec{E}, \vec{H}$ components in TE - deflector, which is defined by r_a, r_w combination, see [7], we also can get opposite H_y and E_x phasing, Fig. 3a. Continuing the structure transformation, shown in Fig. 4, we come in the region $|Z_0 H_y^0| \approx |E_x^0|$ from the top in Fig. 3a. The field distribution becomes as in right picture in Fig. 3 and there are no evident reasons denote transformed option as TE-type. We lose in RF efficiency (Z_e value), as compared to original case, Fig. 1b, [7], but still remain essentially higher, as compared to simple DLW. The level of aberration is practically the same as for optimized in $(\Psi_d)_{min}$, see Table 1, case $a = 19.4mm$, classical DLW structure. The parameters of such SW deflectors in details, including end cells and RF coupler cell, are considered in [8].

SUMMARY

In any periodical DS aberrations, both in E_z and in E_d, are lowered in TW operation with $\Theta_0 \le 60^o$, especially for large aperture radius. Essential improvement in E_d distribution also takes place for opposite phasing of transverse $\vec{E}, \vec{H}$ components at the axis. Such TW DS provide the best results in PDT linearity. For TW operation with $\Theta_0 \ge 120^o$ and SW, $\Theta_0 = 180^o$, aberration reduction is possible in E_d only, by aberrations cancellation in oppositely phased and balanced transverse $\vec{E}, \vec{H}$ components. In a simple SW DLW it is realized for moderate RF efficiency. By splitting control over transverse $\vec{E}, \vec{H}$ components we get efficient SW DS with low E_d aberration level.

ACKNOWLEDGMENT

The author warmly thanks Dr. K. Floettmann, DESY, for support and collaboration with all beam dynamics conclusions.

REFERENCES

[1] T.H. Fieguth, R.A. Gearhart, RF Separators and Separated Beams at SLAC, Proc. 1975 PAC, p. 1533

[2] R. Akre et. al., RF Deflecting Structure for Bunch Length and Phase Space Diagnostic. Proc. 2001 PAC, p. 2353

[3] Y. Garault, CERN 64-43, CERN, 1964

[4] H. Hahn, Deflecting Mode in Circular Iris-Loaded Waveguides, Rev. Sci. Inst., v. 34, n. 10, p. 1094, 1963

[5] V. Paramonov, RF field distributions quality in deflecting structures. (in preparation).

[6] O.H. Altenmueller et. al., Investigations of Traveling-Wave Separators ..., Rev. of Sci. Instr., v. 35, n 4, 1964

[7] V. Paramonov, K. Floettmann, L. Kravchuk. RF Parameters of a TE-Type Deflecting Structure for the S-band frequency range. MOPB082, These proceedings.

[8] V. Paramonov et. al., Standing wave RF deflectors with reduced aberrations. WEPPD012, Proc. RuPAC 2012

Copyright © 2012 by the respective authors — cc Creative Commons Attribution 3.0 (CC BY 3.0)

RESULTS OF TESTING OF MULTI-BEAM KLYSTRONS FOR THE EUROPEAN XFEL

V. Vogel, L. Butkowski, A. Cherepenko, S. Choroba, I Harders and J. Hartung,
DESY, 22607 Hamburg, Germany

Abstract

For the European XFEL multi-beam klystrons, which can produce RF power of 10 MW at an RF frequency of 1.3 GHz, at 1.5ms pulse length and 10 Hz repetition rate, were chosen as RF power sources. Twenty-seven of horizontal multi-beam klystrons (MBK) together with connection modules (CM) will be installed in the XFEL underground tunnel. The CM will be installed on the MBK and connects the MBK to the pulse transformer with only one HV cable, because the CM has a filament transformer inside as well as all diagnostics for HV and cathode current measurements. MBK prototypes together with CM prototypes have been tested for long time at a test stand at DESY, about 4600 hours of operation for each of horizontal MBK with full RF output power, full pulse length and repetition rate of 10 Hz. Testing of first MBKs from series production has been started. In this paper we will give an overview of the test procedure, summarize the current test results and we will give a comparison of the most important parameters.

INTRODUCTION

For the XFEL project [1] as a source of RF power for 27 RF station were chosen the horizontal MBK made by two companies: MBK TH1802 from "Thales" [3] and MBK E3736H from "Toshiba" [4]. The main parameters of MBK are given in Table 1.

Table 1: Main parameters of L-band MBK for XFEL

Parameters	Design value	Test value
Output power (MW)	10	10.3
RF pulse length (ms)	1.5	1.5
Efficiency (%)	> 63	64
Repetition rate (Hz)	up to 30	10
Max average RF power (kW)	150	155
Max average power in collector (kW)	300	270
Max drive power (W)	<200	<150
Bandwidth (MHz)	3	>3

Both prototypes of MBK were tested on DESY MBK test stands [2], a total time of testing exceed of 4600 hours for both of tubes. The test was done with full RF power of 10 MW, full RF pulse length of 1.5 ms and with repetition rate of 10 Hz. Fig. 1 shows the top view of the test stands. Because the all of RF station will be located in the underground tunnel it is very important do not have the open oil during installation of MBK. It was proposed and tested the connection between MBK and HV pulse transformer through connection module (CM) [5, 6 and 7] and HV cable. Several types of HV cables and connectors as well as CM prototypes were tested. Big advances of using CM are that CM has inside a high voltage high frequency filament transformer and monitors for measurement of klystron voltage and cathode current. Fig. 2 shows the one of klystrons with CM and HV cable.

Figure 1: MBK test stands in DESY Hamburg

Figure 2: MBK with CM and HV cable "PFISTERER 3S"

RESULTS OF MBK PROTOTYPES TEST

Since February 2008 we started the test of the first of horizontal MBK prototype on DESY site. For the test of MBK it was specially developed two radiation protected

Copyright © 2012 by the respective authors — cc Creative Commons Attribution 3.0 (CC BY 3.0)

test chambers. Each of both klystron waveguides outputs was connected through WR650 directional coupler and RF power divider to the two of RF loads. Using four of RF loads for the one klystron allow us made the test of average output RF power up to level of 155 kW. The waveguide system was pressured by dry air up to 1.35 bars absolute. The pressured waveguide and air flow up to 10 litters per minute allow us work without breakdown on the level of pulse power of 5 MW in one of klystrons output arm with pulse length of 1.5 ms and repetition rate of 10 Hz. Fig. 3 shows the view of one of klystron output arms. During prototypes test all klystrons parameters were proofed and we have measured a bandwidth, the gain, the phase response and efficiency of the tubes [8, 9, 10 and 11]. Fig. 4 shows the tubes efficiency in depends of output power level and Fig. 5 shows the gain curve for the different value of klystron beam voltage. Fig. 6 shows the wave shape of beam voltage and cathode current.

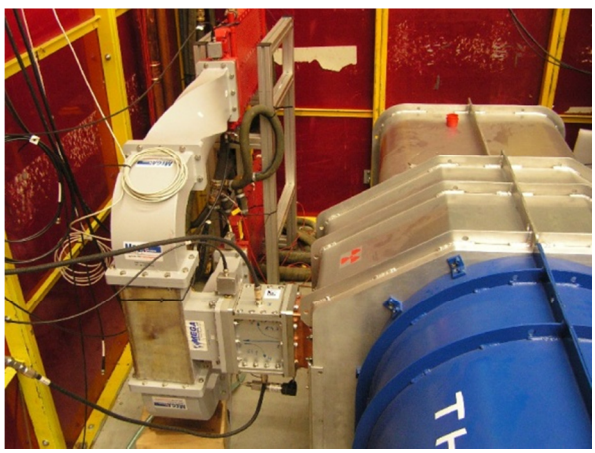

Figure 3: Connection between MBK and RF loads during test.

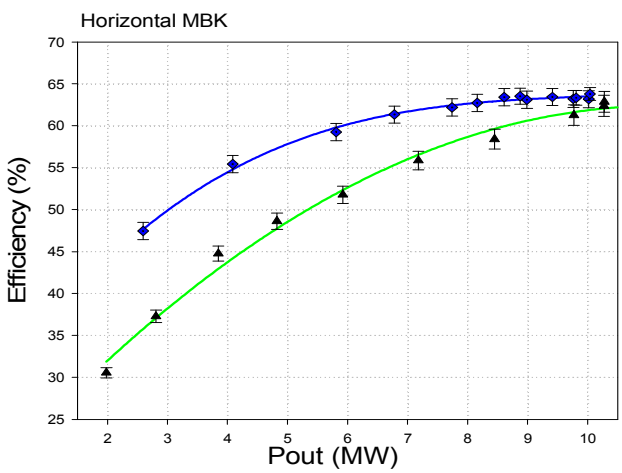

Figure 4: Efficiency for two types of MBK prototypes.

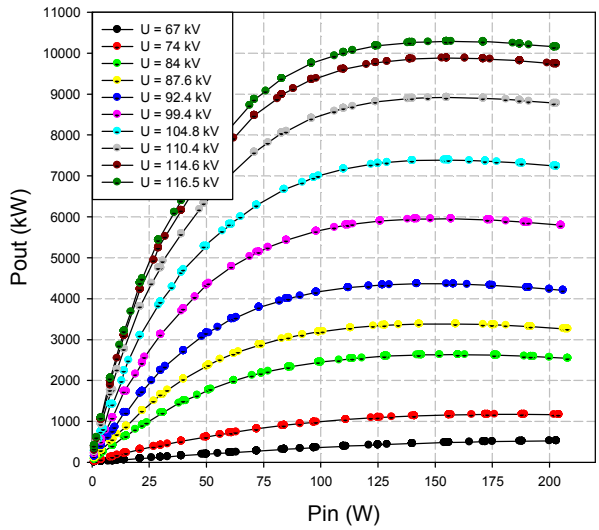

Figure 5: Gain curve for the different value of high voltage.

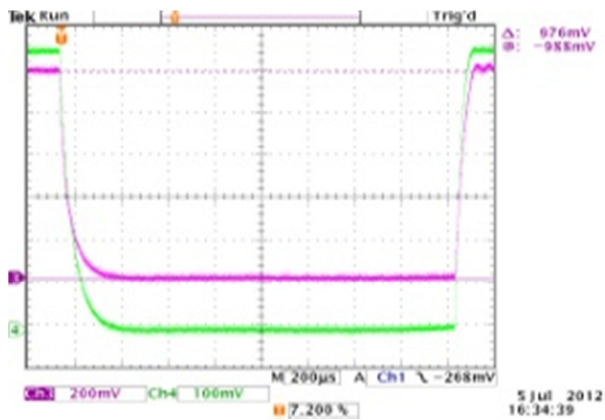

Figure 6: Wave shape of beam voltage and cathode current, the measurement from voltage and current monitors located inside CM.

PROTECTION SYSTEM

The horizontal MBK for XFEL will use the M type of dispenser cathode, for this type of cathode we can expect average tube lifetime of 145000 hours, but in the real operation the lifetime of tube can be thoroughly reducing by service conditions, several events can happen as: the gun arcing, RF breakdown, beam losses inside tube, operation of the tube in the bad vacuum and number of cathode switch cycles. To minimize the influence of service conditions to the klystrons lifetime the special fast protection system (KLM) [12] was developed and tested, the main task of KLM are: to detect as quickly as possible all events which can destroy the tube, then stop input power to the tube and send signal to stop HV pulse. The tube recovery procedure should depend on the kind of events has happened. To make decision which type of recovery procedure should be used, KLM accumulate the

Copyright © 2012 by the respective authors — cc Creative Commons Attribution 3.0 (CC BY 3.0)

signals from different type of sensors. At first, both outputs of klystron and klystron input should have a directional coupler (DC). DC is one of most important devices, the signal from that used for detection of reflected power from waveguide distribution system (WDS) and for analysing difference of expected output impulse shape and real impulse shape. At second, to detect a breakdown on the air side of output window of the klystron or breakdown in the waveguide section between window and DC it was used fast light sensors. To detect the gun arc in the klystron it was used HV breakdown sensor. The measurement of the level of vacuum inside tube, level of partial discharge in the HV system and information from sounds detectors help us to understand the reason of event and help use the right recovery procedure and make true estimation of time to recovery the RF station back to the normal operation.

Figure 7: The first serial MBK for XFEL on DESY site.

CONCLUSION

In February 2008 the first prototype of MBK for XFEL had been installed on the MBK test stand DESY. In March 2010 we have started the test of second MBK. Up to September 2012 the testing time for both of MBK prototypes reach about 4600 hours of operation at the level of 10 MW output power, RF pulse duration of 1.5 ms and repetition rate of 10 Hz. The value of pulse high voltage was about 117 kV, high voltage pulse duration 1.7 ms. The average time between two gun arcs for E3736H is about 230 hours and for TH1802 is about 460 hours. The klystrons were tested together with connection modules (CM) and different types of HV cables. During testing time we didn't observe any sign of degradation of klystrons parameters as well as CM parameters. The all of using testing equipment's work without any problem and DESY are ready to start the test of serial MBK and since August 2012 we have in DESY site the first serial MBK for XFEL. Fig. 7 shows our team and the first of serial MBK.

REFERENCES

[1] M. Atarelli et al. (Eds.), "XFEL: The European X-Ray "Free-Electron Laser: Technical Design report", DESY Report DESY 2006-097, July 2006.

[2] V. Vogel, S. Choroba, et al., "Testing of 10MW Multibeam Klystrons for the European X-Ray FEL at DESY", PAC07, Albuquerque, New Mexico, USA, 2007

[3] A. Beunas, G. Faillon, "10MW/1.5ms,L band multi beam klystron", Proc. Conf. Displays and Vacuum Electronics, Garmisch-Paterkirchen, Germany, April 29-30, 1998.

[4] A. Yano, S. Miyake, S. Kazakov, et al., "The Toshiba E3736 Multi-Beam-Klystron", LINAC'04, Lubeck, Germany.

[5] Ju. D. Valiaev, I.V. Kazarezov, V.I. Kuznetsov, V.P. Ostanin, "Small size high frequency isolation transformer for power supply of the devices located at high potential", BINP Preprint, Novosibirsk, 1989 (in Russian).

[6] V. Vogel, A. Cherepenko et al., "Connection Module for the European X-ray FEL 10MW Horizontal Multibeam Klystron," IPAC10, Kyoto, Japan, THPEB043, 2010

[7] P. Bak, V. Zabrodin, A. Korepanov and V. Vogel, "Klystron Cathode Heater Power Supply System Based on the High-Voltage Gap Transformer," PAC09, Vancouver, BC, Canada, TU6RFP016, 2009

[8] V. Vogel, S. Choroba et al., "Thales MBK test," http://www.xfel.eu/project/meetings/project_meetings/2010

[9] V. Vogel and S. Choroba, "Status of Horizontal MBK for XFEL" http://www.xfel.eu/project/meetings/project_meetings/2009

[10] V. Vogel and S. Choroba "Status of the Thoshiba MBK," http://www.xfel.eu/project/meetings/project_meetings/2006

[11] V. Vogel, S. Choroba, "Status of Multi-Beam Klystrons", Proc., 51th ILC DESY General Project Meeting. http://ilcagenda.cern.ch/categoryDisplay.py?categId=16

[12] V. Vogel "MBK protection" LLRF seminar, 2008 http://ttfinfo.desy.de/LLRFelog/index.jsp

Copyright © 2012 by the respective authors — cc Creative Commons Attribution 3.0 (CC BY 3.0)

COMPUTATIONAL MODEL ANALYSIS FOR EXPERIMENTAL OBSERVATION OF OPTICAL CURRENT NOISE SUPPRESSION BELOW THE SHOT-NOISE LIMIT

A. Nause, E. Gover, Tel Aviv University, Israel

Abstract

In this paper we present simulation analysis of experimental results which demonstrate noise suppression in the optical regime, for a relativistic e-beam, below the classical shot-noise limit. Shot-noise is a noise resulting from the granular nature of the space-charge in an e-beam. It is linear to the beam current due to its Poissonic distribution in the emission process. Plasma oscillations driven by collective Coulomb interaction during beam drift between the electrons of a cold intense beam are the source of the effect of current noise suppression. The effect was experimentally demonstrated [1] by measuring Optical Transition Radiation (OTR) power per unit e-beam pulse charge. The interpretation of these results is that the beam charge homogenizes due to the collective interaction (sub-Poissonian distribution) and therefore the spontaneous radiation emission from such a beam would also be suppressed (Dicke's subradiance [2]). Analysis of the experimental results using GPT simulations will demonstrate the suppression effect. For the simulation results we used a full 3D GPT model of the ATF section in which the experiment took place at.

INTRODUCTION

Shot-noise is a noise resulting from the granular nature of the space-charge in an e-beam. The discreteness of the particles and the randomness of electrons emission from the cathode causes time dependent fluctuations of the charge and current density at any cross section along the beam transport line. This noise was first reported in 1918 by Schottky who made experiments in vacuum tubes.

Noise is best characterized in terms of the Fourier transform of the time-varying fluctuations in electric current, namely, by its spectral density. Gover and Dyunin showed in a 1D model [3] that it is possible to observe and control optical frequency energy and current (shot noise) fluctuations in a dense relativistic charged particles beam. GPT simulations were used to demonstrate this effect for a real-like beam starting from Shot-noise [4]. Moreover, at certain conditions, when the dominant noise in the beam is current shot noise (density fluctuations), it is possible to reduce significantly the beam noise by virtue of a collective interaction process along an interaction length corresponding to a quarter period longitudinal plasma oscillation in the beam. This means that the charge distribution in the beam can be homogenized in this process.

First experimental observation of this phenomenon using OTR from a metallic foil was presented last year [1]. Noise suppression using a dispersive section (dog-leg bend) was demonstrated in SLAC [5]. TR is proportional to the current-noise amplitude [6], and therefore can be used in order to estimate the suppression in the current noise. In this paper we press analysis of the experimental results and demonstrate this effect using full 3D GPT simulations that were carried out for this purpose.

1D Model of Noise Dynamics in Charged Electron Beams

In electron-beam transport under appreciable space-charge conditions, the microdynamic noise evolution process may be viewed as the stochastic oscillations of Langmuir plasma waves [3]. In the linear regime, the evolution of longitudinal current and velocity modulations of a beam of average current I_b, velocity βc and energy $E = (\gamma - 1)mc^2$, can be described in the laboratory frame by [7]:

$$\frac{d}{d\phi_p}\breve{i}(z,\omega) = -\frac{i}{W(z)\breve{v}(z,\omega)} \quad (1)$$

$$\frac{d}{d\phi_p}\breve{v}(z,\omega) = -iW(z)\breve{i}(z,\omega) \quad (2)$$

where $\breve{i}(\omega) = \breve{I}(\omega)e^{i\omega z/\beta c}$, $\breve{v}(\omega) = \breve{V}(\omega)e^{i\omega z/\beta c}$. $\breve{I}(\omega)$, $\breve{V}(\omega)$ are the respective Fourier components of the beam current and kinetic-voltage modulations. The kinetic-voltage modulation is related to energy and longitudinal velocity modulations: $\breve{V}(\omega) = -(mc^2/e)\breve{\gamma} = -(mc^2/e)\gamma^3\beta\breve{\beta}$, $\phi_p(z) = \int_0^z \theta_{pr}(z')dz'$ is the accumulated plasma phase, $W(z) = r_p^2/(\omega A_e \theta_{pr}\epsilon_0)$ is the beam wave-impedance. A_e is the effective beam cross-section area, $\theta_{pr} = r_p\omega_{pl}/\beta c$ is the plasma wavenumber of the Langmuir mode, $r_p < 1$ is the plasma reduction factor, $\omega_{pl} = \omega_{po}/\gamma^{3/2}$ is the longitudinal plasma frequency in the laboratory frame. The single-frequency Langmuir plasma wave model expressions [3] can be solved straightforwardly in the case of uniform drift transport. After employing an averaging process, this results in a simple expression for the spectral parameters of stochastic current and velocity fluctuations (noise) in the beam assuming that they are initially uncorrelated[]:

$$\breve{i}(L,\omega) = \cos\phi_p(L)\breve{i}(0,\omega) + (\sin\phi_p(L)/W_d)\breve{v}(0,\omega) \quad (3)$$

where $\phi_p = \theta_{pr}z$, $\theta_{pr} = r_p\frac{\omega_p'}{v_0}$, $\omega_p' = (\frac{e^2 n_0}{m\epsilon_0\gamma^3})$, $W_d = \sqrt{\mu_0/\epsilon_0}/k\theta_{pr}A_e$.

The beam current noise evolution is affected by the initial axial velocity noise through the parameter

$$N^2 = \overline{|\breve{v}(0,\omega)|^2}/W^2\overline{|\breve{i}(0,\omega)|^2} = (\omega/c\beta k_D)^2 \quad (4)$$

Copyright © 2012 by the respective authors — cc Creative Commons Attribution 3.0 (CC BY 3.0)

where $k_D = \omega_{pl}/c\sigma_\beta$ is the Debye wavenumber and $c\sigma_\beta$ is the axial velocity spread. Equation (4) suggests that current noise suppression is possible if the beam is initially cold $N^2 < 1$, and if plasma phase accumulation of $\phi_p(L) \sim \pi/2$ is feasible.

NOISE SUPPRESSION EXPERIMENT

The noise suppression demonstration experiment was conducted on the 70 MeV RF-LINAC of ATF/BNL (figure 1). The OTR measurements were carried out at a fixed point (CTR-1) 6.5 m away from the LINAC exit. Keeping the beam spot sizes on viewer YAG4 wide in all experiments made it possible to measure similar OTR image patterns on the CCD screen in all experiments (see figure 3). The measured signal S_{OTR} was the integrated charge accumulated in all of the pixels of a CCD (charge-coupled device) camera exposed to the OTR emission on the incidence of single electron-beam pulse on the screen. The measured data of $S_{OTR} = Q_b$ in CTR-0 and CTR-1 are shown in figure 2 as a function of the varied bunch charge Q_b in the range 200 to 500 pC. The pulse duration in all ex-

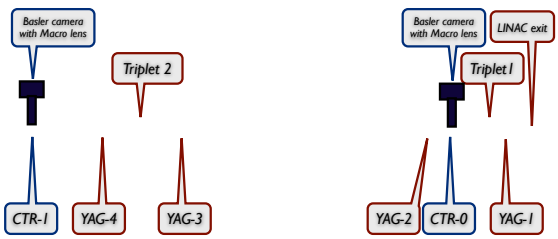

Figure 1: The ATF electron-beam transport set-up is shown from the injector RF-LINAC exit to the OTR viewer site (CTR-1).

periments remained approximately the same (5 pS) corresponding to an average current of 40 to 100A (figure 4). In a shot-noise-dominated beam, in the absence of collective microdynamics, the current noise and consequently S_{OTR} are proportional to I_b. Our measured data of $S_{OTR} = Q_b$ in CTR-0 lie approximately on a horizontal line, confirming the absence of collective microbunching and current-velocity noise correlation or noise suppression before this point. On the other hand, the data measured on CTR-1 exhibit a systematic drop as a function of charge (200 to 500 pC) for all beam energies (50 to 70 MeV). As the measurement conditions at the two measurement positions and at different beam energies could not be made identical, the absolute suppression level between the two points could not be determined. However, the normalized data of all measurements of noise per unit charge depicted in figure 2 show the scaling with charge for all beam energies. This demonstrates attainment of 20 to 30% relative noise suppression, and confirms the predicted effect of collective microdynamic noise suppression process in the drift section.

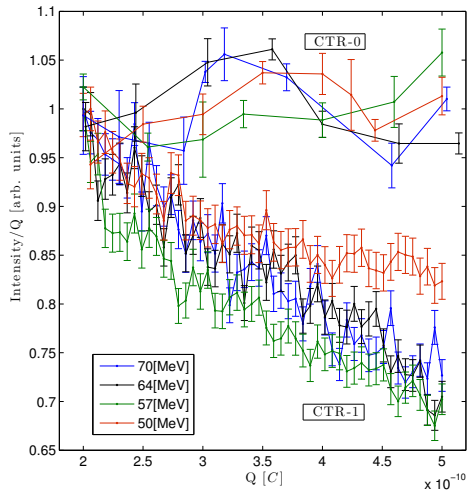

Figure 2: Integrated OTR intensity measurement signals divided by the electron pulse charge. The CTR-1 data correspond to OTR measurement from a screen, intercepting the electron beam 6.5m away from the LINAC exit. The curve's negative slope indicates relative current shot-noise suppression of 20-30% as the beam charge varies from 0.2 to 0.5 nC at different beam energies (50-70 MeV). The CTR-0 data correspond to OTR measurement right after the LINAC exit. Used for reference, its horizontal slope (linear scaling of S_{OTR} with beam charge) indicates that there was no charge suppression before the collective microdynamic process in the subsequent drift section. The error of the camera integrated signal measurement, 3%, was determined from the variance in the value of the signal due to pulse-to-pulse variation, measured repeatedly while keeping all beam control parameters fixed. The charge measurement error is 1%.

COMPUTATIONAL MODEL OF COLLECTIVE MICRODYNAMICS IN VARYING CROSS-SECTION BEAM TRANSPORT

At the exit of the Linac, the beam is current-noise dominated, and $N^2 \ll 1$. However, due to finite emittance, the axial velocity spread becomes significant as the beam is focused and consequently N^2 (Eq (4)) is no longer negligible. Furthermore, at tight focusing the uniform beam expression (Eq. (3)) cannot be used and in order to calculate the noise suppression, one should solve differential equations for variable beam parameters. In this section we show through a model case computational solution of equations (1) and (2), that the axially varying beam cross section and the excess axial velocity spread due to angular spread can account for a substantial moderation of the noise suppression effect that was realized in the experiment. This example also explains some parameter scaling features of the measurement data.

We turn the generic coupled current and kinetic voltage

Copyright © 2012 by the respective authors — cc Creative Commons Attribution 3.0 (CC BY 3.0)

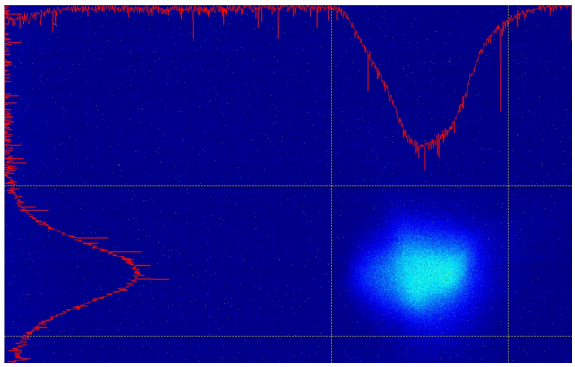

Figure 3: OTR image and axis intensity profiles. Photographed from CTR-1 with a macro lens of 1:1 magnification.

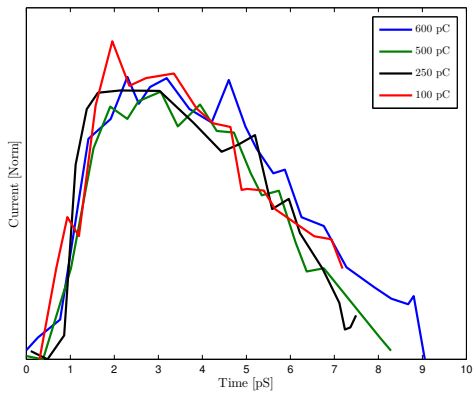

Figure 4: Temporal pulse profile of the e-beam bunch at different bunch charge levels. Pulse duration was approximately 5 pS for all experiments.

equations (1) and (2) into explicit equations in z by substituting $\frac{d}{d\phi_p} = \left(\frac{d\phi_p}{dz}\right)^{-1}\frac{d}{dz} = \frac{1}{\phi_{pr}(z)}\frac{d}{dz}$ and $W(z) = r_p^2/\omega\epsilon_0 A_e(z)\theta_p(z)$:

$$\frac{d}{dz}\breve{i}(z,\omega) = -i\omega\epsilon_0 A_e(z)\theta_p^2(z)\breve{v}(z,\omega) \tag{5}$$

$$\frac{d}{dz}\breve{v}(z,\omega) = -\frac{ir_p^2}{\omega\epsilon_0 A_e(z)}\breve{i}(z,\omega) \tag{6}$$

where $\theta_p^2(z) = eZ_0 I_0/mc^2 A_e(z)\gamma_0^3\beta_0^3$.

This set of equations can be solved explicitly numerically if $A_e(z) = 2\pi\sigma_x(z)\sigma_y(z)$ is given, and the initial conditions $\breve{i}(0,\omega), \breve{v}(0,\omega)$ are specified, and the solution at the end of the drift section L is a linear combination of the initial conditions: $\breve{i}(L,\omega) = A(L)\breve{i}(0,\omega) + B(L)\breve{v}(0,\omega)$ Assuming that the current modulation noise and the focusing enhanced velocity noise are uncorrelated at $z = 0$, we set

$$\overline{|\breve{i}(L,\omega)|^2} = |A(L)|^2\overline{|\breve{i}(0,\omega)|^2} + |B(L)|^2\overline{|\breve{v}(0,\omega)|^2} \tag{7}$$

$$\overline{|\breve{i}(0,\omega)|^2} = eI_b \tag{8}$$

$$\overline{|\breve{v}(L,\omega)|^2} = \left(\frac{mc^2}{e}\gamma_0\beta_0\right)^2\frac{e}{I_0}\sigma_{\beta z}^2 \tag{9}$$

To compute the noise evolution for the parameters of the reported experiment it is necessary to estimate the cross section dimensions $\sigma_x(z), \sigma_y(z)$ along the interaction length. This was done based on the measurements on screens YAG-1 to YAG-4, the recorded quad excitation parameters, and performing full 3-D simulation (with space-charge) using GPT.

The beam axial velocity spread due to energy spread ($\Delta E \simeq 3KeV$) is small, and its effect on the initial velocity noise is negligible. We assume that the initial velocity noise is determined by the standard deviation of the axial velocity spread (equation (9)), which was calculated for each quad setting from the angular spread standard deviations due to the focusing and emittance ($\epsilon_x, \epsilon_y \sim 2-5\mu m$):

$$\sigma_{\beta z} = \frac{1}{4}(\sigma_{\beta x}^2 + \sigma_{\beta y}^2) \tag{10}$$

The coefficients $A(z = L), B(z = L)$ were computed by

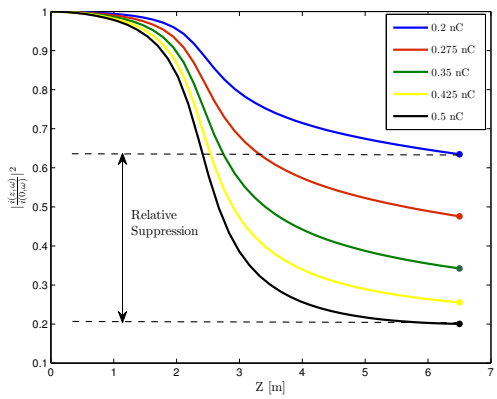

Figure 5: Noise suppression along the collective interaction region as calculated from solution of the coupled differential equations with $\sigma_x(z)$, $\sigma_y(z)$ of 70 MeV.

iterative integration of the coupled linear differential equations (5 and 6) with the initial conditions ((9)). In Figures 5 and 6 we display the results of the model computation of the variable parameters differential equations. The curves show the noise suppression as function of length and of the beam current for the two extreme energy cases E=50 MeV, 70 MeV. The relative suppression factor in the range Q_b=0.2-0.5nC at the drift section exit $L = 6.5m$ is displayed in Fig.() for the two beam-energy examples. Figure 7 can only be regarded as a model explanation for the reduced relative noise suppression effect observed in the experiment. As mentioned, there can be additional factors

Copyright © 2012 by the respective authors — cc Creative Commons Attribution 3.0 (CC BY 3.0)

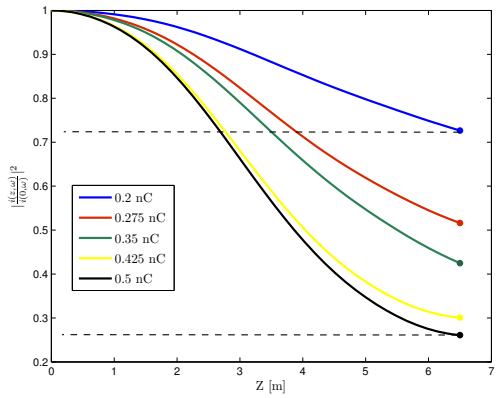

Figure 6: Noise suppression along the collective interaction region as calculated from solution of the coupled differential equations with $\sigma_x(z)$, $\sigma_y(z)$ of 50 MeV.

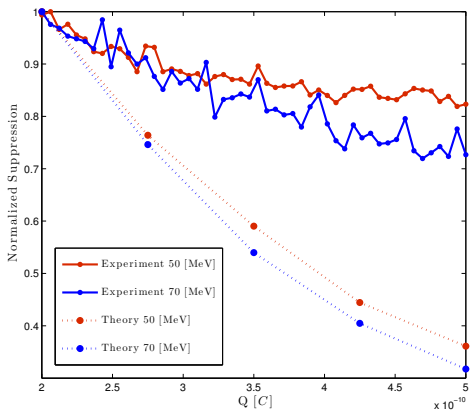

Figure 7: Relative noise suppression rate computed from Eq. 5 and 6 for E=50 MeV, 70 MeV compared to the experimental suppression results.

affecting the suppression rate. It is noted that the computed curves display significantly larger relative suppression in the range Q_b=0.2-0.5nC than the experimental curves, but in either case there is only little dependence on the acceleration energy. In the simple uniform beam model one would expect dependence of the noise suppression factor on the beam energy due to the $3/2$ power dependence of the plasma frequency on γ, which corresponds to smaller plasma phase accumulation at higher beam energy. However, the beam envelope had to be varied in the experiment in different beam energies, and one must keep in mind, that at the higher energy the beam focuses into a tighter waist due to the reduced space charge effect. This tends then to increase the plasma frequency at the waist, where most of the microdynamic process takes place.

This observation is consistent with the point of view that the beam envelope expansion and the beam charge homogenization process are in essence the same process of excess charge beam expansion when viewed in the beam rest frame (independent of the acceleration energy). This is consistent with the plasma phase accumulation theorem of constant plasma phase accumulation in a space charge dominated beam waist [3]. This provides qualitative physical explanation for the weak dependence of the relative noise suppression on the beam energy in the 50-70 MeV range, as depicted in both the experimental (figure 2) and model calculation (figure 7) curves.

REFERENCES

[1] A. Gover, A. Nause, E. Dyunin, Beating the shot-noise limit, Nature Physics, doi:10.1038/nphys2443.

[2] Dicke, R. H., "Coherence in Spontaneous Radiation Processes", Phys. Rev. 93 99–110 (1954).

[3] A. Gover, E. Dyunin, Collective-Interaction Control and Reduction of Optical Frequency Shot Noise in Charged-Particle Beams, Phys. Rev. Lett. 102, 15 (2009).

[4] A. Nause, E. Dyunin, "Optical frequency shot-noise suppression in electron beams: Three-dimensional analysis", Journal of App. Phys. 107, 103101 (2010).

[5] D. Ratner et el, "Observation of Shot Noise Suppression at Optical Wavelengths in a Relativistic Electron Beam", Phys. Rev Lett. 109, 3 (2012).

[6] Loos, H. and et al, "Observation of coherent optical transition radiation in the LCLS linac", Proceedings of the 2008 Free-Electron Laser Conference (Gyeongju, Korea).

[7] A. Gover, T. Duchovni, E. Dyunin, A.Nause, "Collective microdynamics and noise suppression in dispersive electron beam transport", Physics of Plasmas 18 123102, (2011).

Copyright © 2012 by the respective authors — cc Creative Commons Attribution 3.0 (CC BY 3.0)

STABILITY PERFORMANCE OF THE INJECTOR FOR SACLA/XFEL AT SPRING-8

T. Asaka#, T. Hasegawa, T. Inagaki, H. Maesaka, T. Ohshima, S. Takahashi, K. Togawa, Y. Otake,
RIKEN SPring-8 Center, Hyogo 679-5148, Japan

Abstract

To realize stable lasing of an X-ray free electron laser, it is required to obtain more stability of more than one or two figures compared with a conventional accelerator technology. At SACLA, stabilities of 100 ppm and 50 fs in the amplitude and timing of the accelerating RF field, respectively, have been attained, resulting in an achievement of a beam energy stability of 0.02% (std.) or less at 8-GeV. However, two variations with different cycle periods were found in the laser power. One was a long-term variation over several hours, which was in agreement with the phase drift of a 238 MHz/SHB. The other was caused by a variation of the beam position in a 30-MeV injector section. A periodically changed beam position of 30 μm (std.) was found out at a cycle of 0.5 Hz by a fast Fourier transform method using BPM data. The temperatures of all the injector RF cavities are kept within 28±0.04˚C by controlling the cooling water temperature. The AC power supply of the controller to heat the cooling water is operated at 0.5 Hz by a pulse width modulation control with alternatively turning on and off. A strong correlation between the laser intensity fluctuation and the modulation frequency of the AC power supply was found out. We are planning to improve the RF cavity temperature variation to an order of less than 0.01 K by establishing a new temperature regulation system using a continuous level control with a DC power supply. This plan will reduce the XFEL power fluctuation.

INTRODUCTION

User experiment at SACLA started in March of this year after beam commissioning for one year [1]. Toward increasing laser intensity, an accurate beam adjustment of a linear accelerator was carried out during the beam commissioning. At the same time, we have conducted some research and analysis aiming at high-level laser stability.

In order to realize a stable X-ray Free Electron Laser (XFEL) at SACLA, the peak current of an electron beam, passing through a 90-m long undulator section, should reach 3 kA with a normalized emittance of 1π mm mrad or less. In addition, it is important to maintain this beam performance with a high-level stability. Because even a slight beam orbit variation of without 4μm (rms) in the accelerator end causes unstable laser oscillation, which measures decreasing half of the peak laser intensity, in the undulator, RF equipment has to be very carefully designed so as to minimize its variation in the RF amplitude and phase [2]. We took thorough stabilization countermeasures against all of the RF equipment, such as controlling a cooling water temperature for each RF cavity by using a precise temperature regulation system, employing a low-noise power supply and the suppressing of a mechanical vibration. As a results, stability performances of the RF cavities were improved to almost satisfy the target values, that is the RF amplitude and time jitter were <100 ppm and <50 fs, respectively. Accordingly, the beam energy stability of 0.02% (std.) or less has been achieved at the end of the 8-GeV accelerator because of the highly stabilized RF system.

However, it was observed that the laser power with an optimized lasing parameter decreased in a few hours. We were forced to spend about one hour in readjustment of the lasing parameter for recovering the laser power. To make the user experiment more efficient, it was urgent to investigate the cause of the laser power variation and fix it. The possible causes are as follows: (1) a variation of the beam arrival time with the velocity bunching process in the injector section, (2) RF phase drift due to a low level RF system of the injector section, which depends on the environment temperature, and (3) RF phase fluctuation of the cavities, which depends on the cooling water temperature. To clarify the causes, the correlations between each apparatus and surrounding factors were investigated. Consequently, the dominant factors were clarified, and a readjustment procedure for recovery of the laser power was established. The laser power is kept stable during user experiment at present, as shown in Fig. 1. This report presents details of the analysis of beam fluctuation and improvement of laser performance.

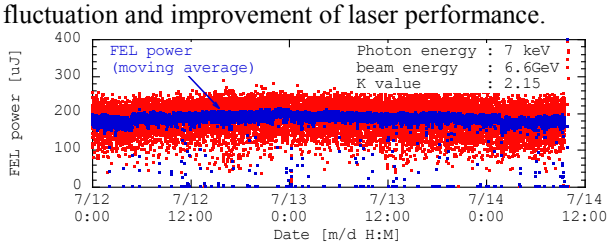

Figure 1: Stability of laser power in user experiment measured using photo detectors.

LONG-TERM VARIATION

Measurement of Laser Power Stability, Beam Arrival Time and Beam Energy

Accelerator operation was performed during three days to reveal which part of the accelerator caused beam variation. First, the condition of the lasing parameter was optimized for 10-keV photon energy at 7-GeV. The laser power immediately after the optimization reached 0.13 mJ.

#asaka@spring8.or.jp

Copyright © 2012 by the respective authors — cc Creative Commons Attribution 3.0 (CC BY 3.0)

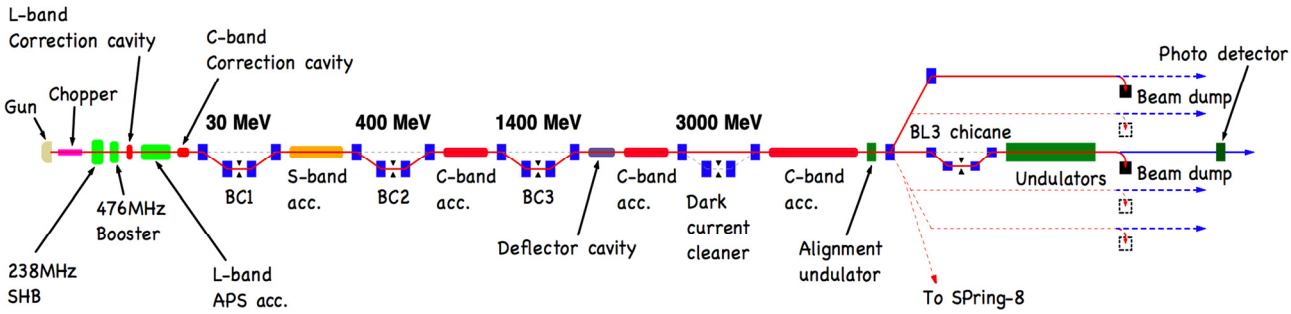

Figure 2: Schematic view of the linear accelerator and undulator section in SACLA.

The laser power was measured by using photo detectors located at the downstream of the undulators, as illustrated in Fig. 2. Figure 3 shows a trend of the laser power over three days. The operation setting points to control accelerator components, such as the RF phase of 238 MHz/SHB, were not changed, although the laser power decreased rapidly dozens of times because of occurring self-fire or firing miss on klystron modulator. Moreover, regardless of a control system failure in November 27th, all parameters were maintained under the same conditions before and after the failure.

To ascertain the cause of the laser power variation shown in Fig. 3, the beam position and the beam arrival time were also measured by using beam position monitors (BPMs), which were installed at intervals in the accelerator. In addition, the variation of the beam energy was measured by using a BPM with a multi stripline installed in each bunch compressor (BC1, BC2, BC3). Figure 4 (a) and (b) show trends of the beam arrival time after BC1 and the beam energy in BC2, respectively. Since a beam is fixed at off crest RF phase in BC, the beam energy is affected significantly by the slight variation of the beam arrival time. We find out that the laser power level decreases to less than 70% of the peak of 0.13 mJ (green line in Fig. 3) when the variation of beam phase shift at the BPM after BC1 exceeds a tolerance of 0.6 degree specified in Fig. 4 (a).

The RF phase drift of the cavity for velocity bunching process in the injector section was considered to be a primary cause for the variation in the beam arrival time. Figure 5 shows trends of the beam arrival time obtained from the phase information on beam-induced voltage in 238 MHz/SHB, 476 MHz/Booster and L-band correction cavity. As shown in Fig. 5, because the drifts of the beam phase after 476 MHz/Booster had similar tendency, the RF phase drift of 238 MHz/SHB was estimated to be a dominant factor of the long-term variation in the laser power.

Although low-level RF instruments for 238 MHz/SHB are stabilized by a thermally controlled 19" enclosure, the beam in the SHB is affected by a temperature variation of less than 0.1˚C [2]. It turned out that a band-pass filter of a reference signal of 238 MHz/SHB has a temperature dependence of -10.6 ps/K. Thus, we are planning to replace it with another band-pass filter with 2 ps/K and to improve the temperature stability of the 19" enclosure with a precision temperature control of ±0.002 K.

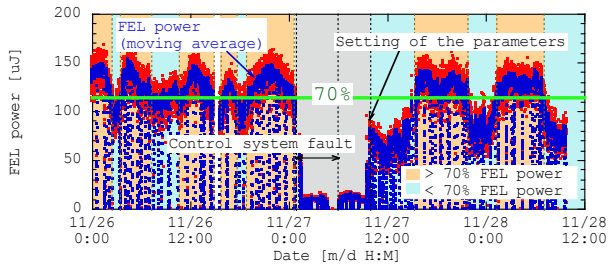

Figure 3: Measurement result for the laser power.

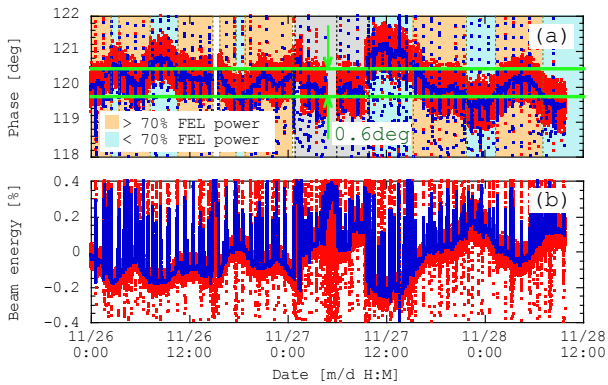

Figure 4: (a) Beam arrival time after BC1. The beam phase is equivalent to 0.58 ps/1 degree. (b) Beam energy in BC2, where the energy dispersion is η = -345mm.

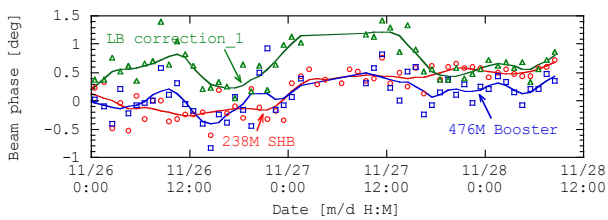

Figure 5: Beam arrival time obtained by an induced voltage from the beam in each RF cavity of the injector.

BEAM POSITION FLUCTUATION

To clarify a cause of the shot-by-shot laser power fluctuation, a correlation analysis and a frequency analysis of the fluctuation were carried out for the data measured simultaneously by using the BPMs. The beam parameters were optimized for 10-keV photon energy at a repetition rate and a beam energy of 10 Hz and 7-GeV, respectively. The beam orbit at the undulator section and the beam energy were corrected by using a slow feedback control (time constant of more the one second) during measurements.

Copyright © 2012 by the respective authors — cc Creative Commons Attribution 3.0 (CC BY 3.0)

Correlation Plots

The laser power and the position fluctuated significantly during beam commissioning. To trace an origin of the short-term fluctuation, the correlations between the beam position in each place of the accelerator and the laser power were investigated by using BPM data of 3000 shots for 5 minutes. The beam position fluctuation at the entrance of the undulator section was 10 μm (std.). A significant correlation between the beam position at the entrance of the undulator section and the laser power was recognized, as shown in Fig. 6 (a). Judging from Fig. 6 (b), the correlation between the beam positions after BC1 and at the entrance of the undulator section, the laser power fluctuation was obviously generated from a beam position jitter of 30 μm in the injector section.

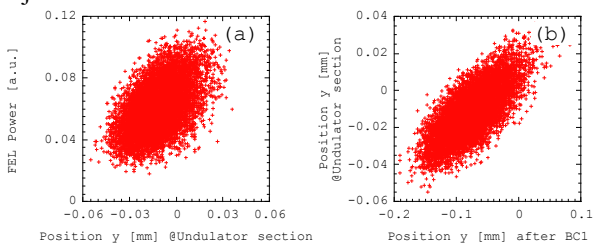

Figure 6: (a) Correlations between the beam position at the entrance of the undulator section and the laser power. (b) Correlations between the beam position after BC1 and at the entrance of the undulator section.

Fourier Transform Analysis

In order to analyze the frequency components of the beam position jitters in the injector section, a fast Fourier transform analysis was performed, as shown in Fig. 7. The highest peak was observed at a periodic cycle of 0.5 Hz, which coincided with an operating cycle of the temperature controller equipped with the precise temperature regulation system for RF cavities. In addition, it shifted to 2 Hz when the operating cycle of the temperature controller was changed from 0.5 Hz to 2 Hz, as shown in Fig. 7. It means that the beam position was affected by the operating cycle of temperature controller in RF cavities, although each temperature of RF cavity was regulated within 28±0.04˚C [3].

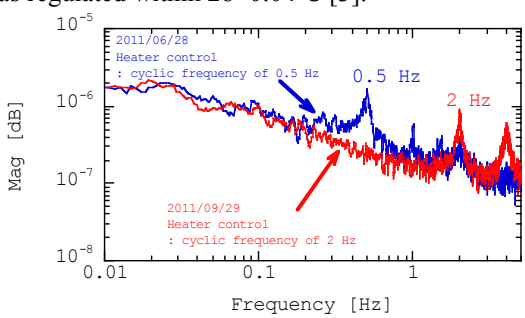

Figure 7: Results of a period analysis using the beam position jitters data after BC1. Blue and red lines are the spectra when the temperature controller of RF cavities was operated at a cycle of 0.5Hz and 2Hz for the heating regulation, respectively.

Moreover, different beam position jitters were observed to be synchronized with the operating cycle of the temperature controller for each RF cavity, as shown in Fig. 8. For example, the maximum magnitude at 1.1 Hz corresponds to the operating cycle of L-band APS accelerating structure. The slight variation in each RF cavity contributed to the beam position jitters in the injector section.

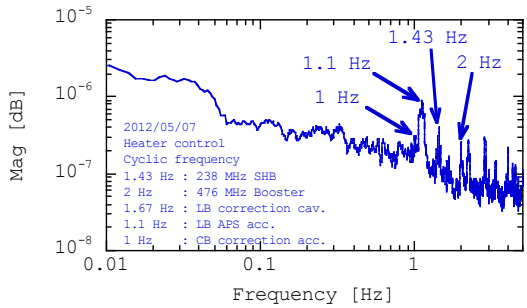

Figure 8: Spectrum of the beam position jitters after BC1 under different conditions of the operating cycle of the cooling water temperature controller in the RF cavity.

CONCLUSION

The 8-GeV accelerator of SACLA is required to continuously supply a stable beam with extreme high quality. Thus, we started to research the cause of instabilities in the accelerator during beam commissioning. It was clarified that the RF phase drift of 238 MHz/SHB might be dominant factor of the long-term variation in the laser power, judging from the phase information on beam-induced voltage. In the user experiment, the laser power can be recovered easily and promptly by tuning the RF phase of 238 MHz/SHB at the moment.

One possible factor for the laser power fluctuation was the influence of the switching frequency of temperature controller equipped with a precise temperature regulation system in the injector section. In order to reduce the laser power fluctuation, a new precise temperature regulation system by using a continuous level control with a DC power supply is installed in the injector section in August. In addition, a temperature measurement and control module with extremely high temperature resolution of 0.001 K has been adopted in place of a conventional less-accurate PLC temperature measurement module. The laser power can be expected to be more stable.

REFERENCES

[1] H. Tanaka, “The SPring-8 Angstrom Compact Free Electron Laser (SACLA)”, in proceedings the IPAC’12, New Orleans, p2106.

[2] Y. Otake, “Construction Status of XFEL/SPring-8 (Its Stability Issure)”, in proceedings the FEL08, Gyeongju, p222.

[3] T. Hasegawa et al., “Upgrade of a Precise Temperature Regulation system for the Injector at SACLA”, in proceedings FEL2012, Nara.

Copyright © 2012 by the respective authors — cc Creative Commons Attribution 3.0 (CC BY 3.0)

MAJOR TRENDS IN LINAC DESIGN FOR X-RAY FELS*

A.A. Zholents#, ANL, Argonne, IL 60439, USA

Abstract

Major trends in the contemporary linac designs for x-ray free-electron lasers (XFELs) are outlined starting with identification of the key performance parameters, continuing with considerations of the design options for the electron gun and linac, and finishing with electron beam manipulation in the phase space.

KEY PERFORMANCE PARAMETERS

Pursuit of the XFEL demands improvements in accelerator technology for producing and accelerating high-brightness electron beams. The brightness of the electron beam $B_n = N_e (\lambda_c)^3/\varepsilon_x\varepsilon_y\varepsilon_z$, where N_e is the number of electrons in the electron bunch; $\varepsilon_x\varepsilon_y\varepsilon_z$ are the normalized horizontal, vertical, and longitudinal emittances; and $\lambda_c \approx 3.86\cdot10^{-11}$ cm is the Compton wavelength, plays the most important role in the FEL process. It was shown in [1, 2] that in the best possible scenario when electron beam and FEL parameters are optimized to yield the fastest growth rate of the microbunching, the inverse gain length in the FEL scales linearly with brightness and quadratically with the electron beam energy (a typo in [1] shows linear dependence), i.e.,

$$\frac{\lambda_u}{L_g} \propto \frac{K^2}{2+K^2}\left(\frac{E_b}{\hbar\omega_s}\right)^2 B_n, \qquad (1)$$

where L_g is the gain length, $\hbar\omega_s$ is the x-ray photon energy, E_b is the electron beam energy, λ_u is the undulator period, and K is the undulator parameter.

The electron beam energy is the next most important parameter (after brightness) that strongly affects FEL performance. Besides Eq. (1), E_b appears in the optimization of FEL performance in a few other places. The first is a constraint on the geometrical emittance $\varepsilon_{x,y}/\gamma \le \lambda_s/4\pi$, providing that the electron beam size matches the light beam and electrons do not de-phase over the FEL gain length due to betatron oscillations. Here the relativistic factor γ was used instead of E_b. The second is a constraint on the relative energy spread σ_E/E_b, which is basically driven by the same de-phasing concern. The third is the FEL resonance condition $\lambda_s = \lambda_u/2\gamma^2\times(1+K^2/2)$. Finally, the electron beam energy almost solely defines the cost of the electron beam delivery system. According to these listed constraints, the next-generation FELs should rely on the increased brightness of the electron beam and undulators with short periods in order to lower E_b and, thus, the cost of the FEL. Although, clearly, the undulator technology is extremely important, it is out of the scope of this review and, thus, we refer the reader to a recent publication [3].

*Work supported by the U.S. Department of Energy, Office of Science, under Contract No. DE-AC02-06CH11357.

#azholents@aps.anl.gov

ELECTRON GUN

Production and acceleration of high-brightness electron beams are the two most challenging tasks for the electron gun and linac. The brightness is largely defined by the ability of the electron gun to produce a small emittance, and at present, the rf photocathode guns yield the brightest electron beams. Any advances in this area will allow for lowering the linac energy, thus saving on the construction cost of the facility, and also on the operation cost, as a smaller linac can be used. The ultimate brightness is defined by a so-called "intrinsic emittance" (IE), which is solely dependent on the cathode material work function φ_0 and an electron extraction mechanism. For example, measurements of the IE in the case of the photoemission from a Cu cathode shown in Figure 1 [4] demonstrate that it depends on the difference between photon energy $\hbar\omega$ and the effective work function $\varphi_{eff} = \varphi_0 - (e^3E_c)^{1/2}$ (in CGS units), where e is the electron charge, and E_c is the applied electric field on the cathode

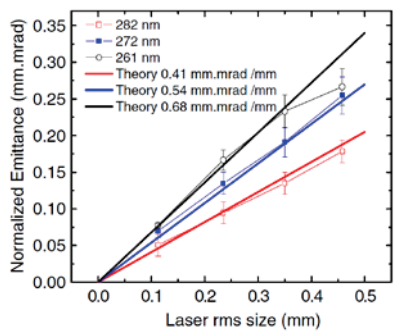

Figure 1: Normalized projected emittance versus laser spot size for three different laser wave lengths as shown in Ref [4]. Measurements were carried out for a copper cathode using a low charge less than 1 pC and E_c=25 MV/m. Theoretical fit assumes φ_0 = 4.3 eV. Thermal effects are not included.

surface responsible for reduction of the potential barrier due to the work function φ_0. Here one can see that the smaller the excess energy $\hbar\omega - \varphi_{eff}$, the smaller the IE [5]:

$$\varepsilon_{\text{intrinsic}} = \sigma_r\sqrt{\frac{\hbar\omega-\varphi_{eff}}{3mc^2}}, \qquad (2)$$

where σ_r is the rms size of the laser beam on the cathode, and m is the electron mass. This trend was also observed with Mo, Nb, Al, and bronze cathodes [4] and is expected in semiconductor cathodes such as Cs_2Te and SbK_2Cs [6]. Thus, matching the work function of the cathode material to laser photon energy is expected to yield better IE. Some ideas aimed at production of the photocathode materials with desirable work function were proposed recently [6, 7]. For example, it was found that ternary alkali metal transition metal acetylides (Cs_2TeC_2) [8]

Copyright © 2012 by the respective authors — cc Creative Commons Attribution 3.0 (CC BY 3.0)

exhibit substantial reduction of work function down to 1.7-2.4 eV from ~ 3 eV for a Cs_2Te photocathode.

In theory, the quantum efficiency (QE) of the cathode, i.e., the number of extracted electrons per incident photon, is directly connected to excess energy. A drop in QE is expected when one approaches the limit where the photon energy barely exceeds the effective work function. However, for small charge bunches, the drop in QE can be compensated with a more powerful laser, and for future x-ray FELs this could be a viable approach to an ultimately small emittance and, thus, ultimately bright beams.

Other effects such as surface roughness, electron-electron scattering near the cathode surface, and non-uniformity of electron emissivity over the cathode surface could also affect IE. Cathode contamination and lifetime are also important issues for a light source operating nonstop for long periods of time. Besides aiming for more robust cathodes, the current approach for overcoming adverse effects consists of improving the vacuum inside the rf gun. A promising concept has been proposed [9, 10], where a very-high-frequency (VHF) rf gun is projected to achieve low 10^{-11} Torr vacuum while holding a relatively high E_c = 20 MV/m in cw operation (see Figure 2). Assisting in achieving high vacuum are numerous high-conductance vacuum ports seen on the periphery of the central part of the cavity coupled to a pumping plenum containing non-evaporative getter (NEG) modules.

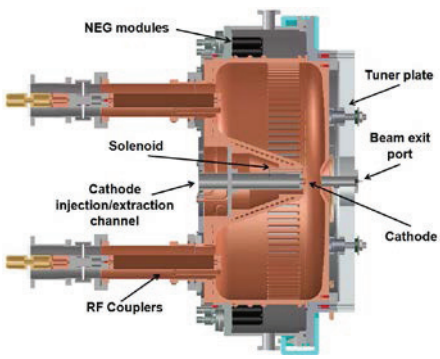

Figure 2: The VHF electron gun cavity showing main components and NEG pumping modules [10].

LINAC

According to Liouville's theorem, in an ideal case, the normalized brightness of an electron bunch is invariant along the electron beamline, but in reality, its conservation can only occur with carefully considered design of the electron beam delivery system. A good example of this practice is the LCLS linac equipped with a laser heater [11], two bunch compressors [12, 13], and a beam transport line where the normalized slice emittance remains practically unchanged over the entire process of the electron bunch acceleration and compression, resulting in an increase of the electron peak current from a few tens of amperes in the injector to up to a few kiloamperes at the end of the linac. Similar attention to all details of the beam delivery system, including field quality of magnetic elements, precision alignment of all magnetic elements and linac modules, transverse and longitudinal wakefields, coherent synchrotron radiation, intrabeam scattering, transverse and longitudinal space charge effects, microbunching instability, and diagnostics and feedback systems should be expected in the next generation of x-ray FELs. Obviously, the impact of all collective effects can be greatly reduced by using lower-charge bunches. Additionally, the uncorrelated energy spread that is artificially increased in the LCLS by the laser heater to suppress the microbunching instability in intense bunches can be reduced for low-charge bunches, resulting in brighter beams.

Evidently, a lower-charge bunch gives fewer photons. Increasing the bunch repetition rate will help to compensate this loss and boost the total number of photons integrated over the same period of time. However, normal-conducting linacs are quite limited in repetition rate under realistic operating conditions, and pragmatically, only superconducting rf (SRF) linacs can support high bunch repetition rate. Currently, an accelerating gradient over 20 MV/m can be reliably achieved in SRF in cw operation, but a lower gradient may be preferred when full construction and operating costs are considered. Aiming for future applications in the x-ray FELs, current R&D is focused on increasing the Q-factor of cavities at a 25 MV/m gradient. Promising results have been obtained using atomic layer deposition (ALD), where it seems possible to control the surface composition of niobium SRF cavities, control multipactoring, improve the Q-factor, and synthesize superconducting structures with a significantly improved critical field [14, 15]. It is then assumed that multiple FEL lines will be simultaneously supported by a single SRF linac [16-18], providing uniformly spaced electron bunches at a few-MHz repetition rate. The same high-repetition-rate performance is expected from the electron gun, and various scenarios are currently being considered including a DC gun [19], a superconducting gun [20], and a normal-conducting VHF gun, briefly described above.

The linear accelerator is usually the main cost driver for a FEL facility and substantial efforts are being devoted worldwide to the development of new acceleration technologies [21]. It is conceivable that future accelerators will be compact and inexpensive. One promising concept is to use hollow, cylindrical, dielectric tubes powered by a high-charge electron "drive" bunch whose main purpose is to produce Čerenkov radiation and excite strong electromagnetic waves in the structure. Trailing behind, a second low-charge "main" bunch navigates these waves and enjoys a speedy acceleration [22]. Preliminary studies [23] show that not only does a dielectric wakefield accelerator (DWFA) reduce the accelerator footprint afforded by speedy acceleration, but the DWFA is also capable of supporting high bunch repetition rates with uniform bunch spacing up to one million cycles per second.

Copyright © 2012 by the respective authors — cc Creative Commons Attribution 3.0 (CC BY 3.0)

PHASE SPACE BEAM MANIPULATION

Precise control over the electron partitioning in a 6D phase space and manipulation of the phase space occupancy offer enormous opportunities for optimization of XFEL performance. Currently, only manipulation in the 2D longitudinal phase space is widely used. It involves inducing the energy chirp with the RF system and compressing the electron bunch using one or more magnetic chicanes. Typically when the bunch leaves the last chicane it is not fully compressed and has some remaining chirp that is removed by off-crest acceleration in the downstream linac (which is an inefficient and costly option) or by using the wakefield created by the beam itself. However, often the wakefield produced in the linac is too weak and, thus, the task of removing the energy chirp can be better accomplished by a dedicated wakefield inducing element, like, for example, the dielectric channel tested in [24, 25] or corrugated pipe considered in [26].

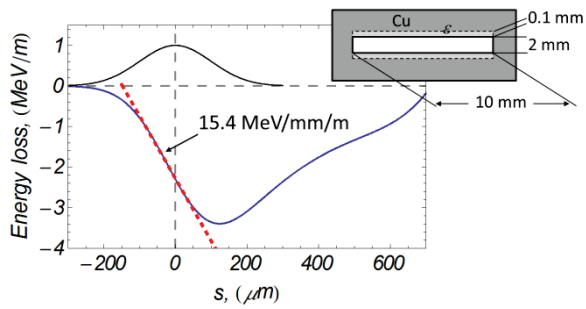

Figure 4: The energy loss distribution along the electron bunch (blue curve) in the 1-m long rectangular copper channel coated inside with 100 μm thick dielectric layer with the dielectric constant $\varepsilon = 4.4$ (insert). The bunch charge is 300 pC with density distribution shown by the black curve (courtesy of A. Kanareikin).

The emittance exchange technique proposed in [27] goes further and considers reduction of the transverse emittance at the expense of increasing the uncorrelated energy spread, thus, doing two useful things at the same time while preserving the 6D phase-space volume produced in the electron gun, i.e., obtaining small emittance and eradicating a need in the laser heater. This technique is particularly effective when it is combined with a round-to-flat emittance adapter [28]. Other approaches include non-symplectic applications for emittance partitioning [29]. Currently, all these techniques are undergoing intense theoretical and experimental studies [30-33]. Moreover, a double emittance exchange [34] was recently proposed as a convenient tool for beam manipulation in the longitudinal phase space including preparation of microbunching for seeded FELs.

Another direction of promising new research is centered on suppression of the shot noise of electrons and, thus, mitigation of the microbunching instability (i.e., see Ref. [35] and references therein).

REFERENCES

[1] M. Zolotorev, Nucl. Instrum. Methods in Phys. Res. A 483 (2002) 445.
[2] M. Gullans, G. Penn, J.S. Wurtele, M. Zolotorev, Phys. Rev. ST Accel. Beams 11 (2008) 1.
[3] J. Bahrdt, Yu. Ivanyushenkov, to be published in Proc. of SRI Conf. (2012).
[4] C. P. Hauri et al., Phys. Rev. Lett. 104 (2010) 2234802.
[5] D. Dowell, J. Schmerge, Phys. Rev. ST Accel. Beams 12 (2009) 074201.
[6] D. Dowell et al., Nucl. Instrum. Methods in Phys. Res. A 622(3), (2010) 685.
[7] K. Németh et al., Phys. Rev. Lett. 104 (2010) 046801.
[8] J.Z. Terdik et al., Phys. Rev. B (2012), in press.
[9] K. Baptiste et al., Nucl. Inst. Methods in Phys. Res. A 599 (2009) 9.
[10] F. Sannibale et al., Proc. of IPAC'12, New Orleans, USA, WEEPPB004, p. 2173 (2012); http://www.JACoW.org.
[11] Z. Huang et al., Phys. Rev. ST Accel. Beams 13 (2010) 020703.
[12] R. Akre et al., Proc. of FEL'08, Gyeongju, Korea, FRAAU04, p. 548 (2008); http://www.JACoW.org.
[13] P. Emma, SLAC-TN-05-004, November 14, 2001.
[14] A. Gurevich, SRF Material Workshop, FNAL, Batavia, IL, May 23-24, 2007.
[15] M.J. Pellin, J.W. Elam, J. Moore, ECS Trans. 11(7), (2007) 23-28.
[16] A. Zholents et al., Proc. of Linac'08, Victoria, Canada, TUP046, p. 502 (2008); http://www.JACoW.org.
[17] R. Bartolini et al., Proc. of FEL'09, Liverpool, UK, WEOB02, p. 480 (2009); http://www.JACoW.org.
[18] K. Jacobs et al., Proc. of IPAC'12, New Orleans, USA, paper, TUPPD079, (2012); http://www.JACoW.org.
[19] F. Löhl et al., Proc. of IPAC'10, Kyoto, Japan, MOZRA01, p. 45 (2010); http://www.JACoW.org.
[20] R. Xiang et al., Proc. of FEL'09, Liverpool, UK, WEOB04, p. 408 (2009); http://www.JACoW.org.
[21] See, for example, W. Leemans, E. Esarey, Physics Today, 62 (2009) 44.
[22] W. Gai et al., Phys. Rev. Lett. 61 (1988) 2756.
[23] C. Jing, J. Power, and A. Zholents, APS Light Source Note ANL/APS/LS-326 (2011).
[24] S. Antipov et al., Phys. Rev. Lett. 108 (2012) 144801.
[25] S. Antipov et al., Conf. Proc., IPAC'12, New Orleans, MOPPP013, (2012) 598.
[26] K. Bane and G. Stupakov, Nucl. Instrum. Methods in Phys. Res. A 690, (2012) 106.
[27] M. Cornacchia, P. Emma, Phys. Rev. ST Accel. Beams 5 (2002) 084001.
[28] R. Brinkmann, Y. Derbenev, and K. Flöttmann, Phys. Rev. ST Accel. Beams 4 (2001) 053501.
[29] B. Carlsten et al., Microbunching Workshop (2012), http://www.umer.umd.edu/events_folder/uBi12/
[30] P. Emma, Z. Huang, K.-J. Kim, and P. Piot, Phys. Rev. ST Accel. Beams 9 (2006) 100702.
[31] J. Ruan et al., Phys. Rev. Lett. 106 (2011) 244801.
[32] D. Xiang and A. Chao, Phys. Rev. ST Accel. Beams 14 (2011) 114001.
[33] B. Carlsten et al., Phys. Rev. ST Accel. Beams 14 (2011) 050706.
[34] A. Zholents and M. Zolotorev, APS Light Source Note ANL/APS/LS-327; presented at PAC 2011, NY, (2011).
[35] D. Ratner and G. Stupakov, Phys. Rev. Lett. 109 (2012) 034801.

Copyright © 2012 by the respective authors — cc Creative Commons Attribution 3.0 (CC BY 3.0)

C-BAND ACCELERATOR STRUCTURE DEVELOPMENT AND TESTS FOR THE SWISSFEL

R. Zennaro, J. Alex, H. Blumer, M. Bopp, A. Citterio, T. Kleeb, L. Paly, J.-Y. Raguin
Paul Scherrer Institute, Villigen

Abstract

The SwissFEL requires a 5.8 GeV beam provided by a C-band linac consisting of 104 two-meter accelerating structures [1]. Each structure is of the constant-gradient type and is composed of 113 cups [2]. The cup shape is double-rounded to increase the quality factor. No tuning feature is implemented. For this reason ultra-precise turning is exploited. A strong R&D program has been launched on structure fabrication, which will be followed by a future technology transfer to a commercial company. The program includes the production and test of short structures that can be brazed in the existing PSI vacuum oven and will be completed with the production of the full two-meter prototype once the new full scale brazing oven, presently under construction, is operational. The status of the R&D program, including the production and power test results of the first two test structures, is reported here.

INTRODUCTION

The baseline of the R&D program includes the production and test of four short constant-impedance structures. The first and the second test structures are composed of eleven regular cells and two matching cells. Each cell geometry and volume are defined by two joined half cups. The dimensions of the regular cells are close to the one of the first regular cell of the two-meter structure prototype [2] whereas the regular cells of the third structure have a geometry close to the one of the last regular cell. The connection to the input waveguides and output loads is provided by removable mode launchers which are mechanically connected to the structure via two flanges and two RF chokes [3]; see Figure 1.

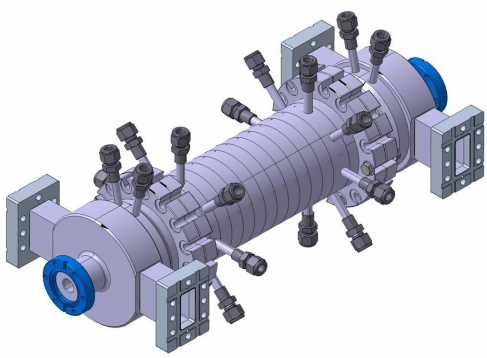

Figure 1: Short test structure.

The fourth test structure is under construction and will be equipped with an RF J-type coupler, the same type than the ones of the two-meter structure [2].

The main parameters of the test structures are summarized in Table 1.

Table 1: Main parameters of the test structures

Test Structure	Structure 1,2	Structure 3, 4
Type	Constant impedance	Constant impedance
Number of regular cells	11	11
Frequency	5.712 GHz	5.712 GHz
Phase advance/cell	2π/3	2π/3
Iris aperture radius /thickness	7.267/2.5 mm	5.478/2.5 mm
Group velocity	3.1 % c	1.4 % c
Q	10400	10350
R/Q	7214 Ohm/m	8522 Ohm/m
Nominal gradient (MV/m)	28 MV/m at 28 MW	28 MV/m at 10.84 MW

CUP PRODUCTION AND CONTROL

Extremely high accuracy in structure production is required to avoid tuning. The specified tolerance for the cup diameter is ±4 μm. In order to verify the cup size all the cups had metrology control. The histogram in Figure 2 shows the metrology results for the inner diameters of the cups produced for structure 3 and 4: the cups have a systematic error of -0.9 μm, the error distribution has a standard deviation of 0.4 μm and a peak to peak difference of 2.0 μm.

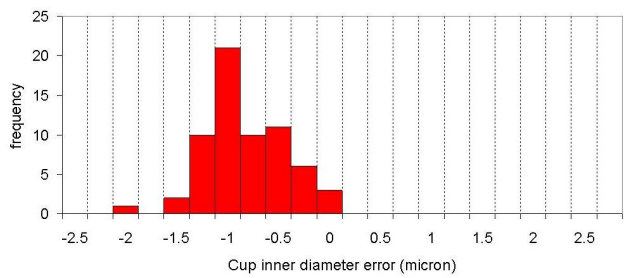

Figure 2: Histogram of the errors on the inner cup diameter for cups produced for structure 3 and 4.

To have a cheap and quick system to verify the cup dimensions we developed a single cup resonant frequency measurement tool. A resonating volume is defined by closing a half cup with a copper plate by applying a pressure of 14 MPa and by detuning the opposite half cup. The repeatability of the measurements in constant temperature conditions is excellent, with a standard deviation of the frequency of less than 5 kHz.

Copyright © 2012 by the respective authors — cc Creative Commons Attribution 3.0 (CC BY 3.0)

The cups used for structure 2 were individually controlled via metrology and RF frequency measurements. Each single cup is composed of two half cells that are individually measured.
Keeping the metrology results as reference, the frequency measurements have a systematic error of roughly 80 kHz i.e. one micron between the two halves and a random error of one micron or less.

COLD RF MEASUREMENTS

All the RF cold measurements were made in stable operating conditions obtained by cooling the structure using temperature stabilized water and by filling it with dry nitrogen.
Figure 4 shows the reflection coefficients for structure 1 (see also reference 3), 2 and 3. At the nominal frequency the reflection is respectively -31 dB for structure 1, -23 dB for structure 2 and -20 dB for structure 3.

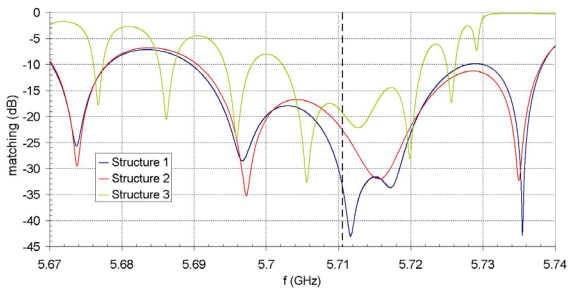

Figure 3: Reflection coefficient (S_{11}) of the three structures.

Field distributions, as shown in Figure 4, have been obtained by bead-pull measurements. Each structure was measured in two configurations, by swapping alternately the input with the output.

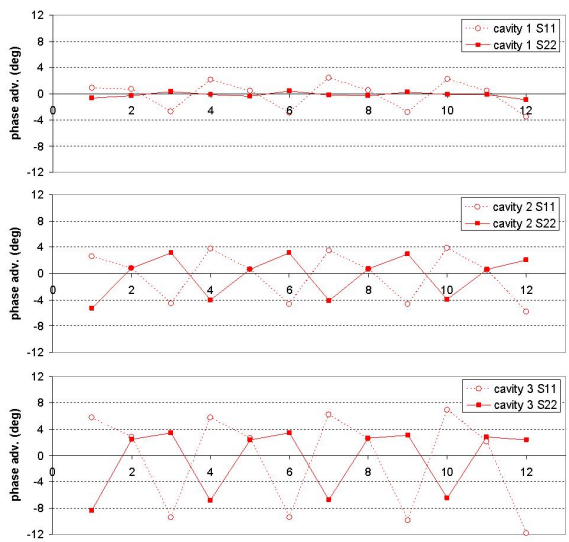

Figure 4: Error in the phase advance vs. cell number.

A standing-wave component in the field pattern is evident in the three cavity tests. This component is negligible for S_{22} in structure 1 and is very large in cavities 2 and 3 for both S_{11} and S_{22} (N.B. since the structures are fully symmetric port1 and port2 are arbitrarily defined). The three-cell periodicity in the standing-wave component is a clear indication that the mismatch is located in a single cell, either the output matching cell or the previous one.

A post-mortem inspection of structure 2 showed a brazing problem in the two matching cells; however all the regular cells were fine. Some brazing alloy penetrated into the matching cells, modifying the geometry as illustrated in Figure 5.

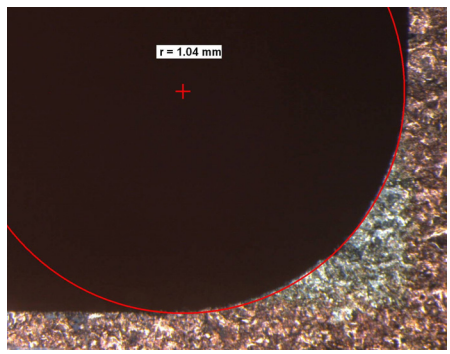

Figure 5: Fillet radius of 1 mm generated at the base of the matching iris due to brazing alloy penetration.

Unlike the regular cells where the braze joint is placed in the middle of each cell, in the matching cells, it is at the base of the matching iris. At this location, a fillet, azimuthally uniform and with a radius of roughly 1 mm, has been measured in both matching cells. As final verification the electromagnetic field distribution from the modified geometry, including the brazing error, was simulated with HFSS and the resulting error in the phase advance per cell is in good agreement with the measurements illustrated in Figure 6.

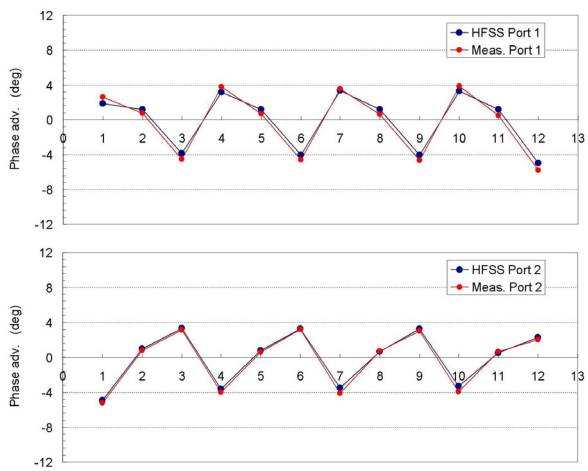

Figure 6: Error in the phase advance vs. cell number in structure 2, measure (red line) and computed (blue line) taking into account the brazing error.

Copyright © 2012 by the respective authors — cc Creative Commons Attribution 3.0 (CC BY 3.0)

CONDITIONING AND BREAKDOWN ANALYSIS

The power tests were made in TRFCB (Test RF for C-Band) which is the PSI test stand for C-band components. It is presently equipped with a SCANDINOVA K2-2S solid-state modulator and a newly developed Toshiba E37210 100-Hz 50-MW klystron which is directly connected to the structure without a pulse compressor, which is under construction.

In case of structure 1 the conditioning and power test was made at only 10 Hz. A gradient of 33.5 MV/m at the nominal pulse length (350 ns) was reached with a low breakdown rate (BDR) BDR=$8 \cdot 10^{-7}$ after 490 hours of conditioning [3]. Due to limited repetition rate it was not possible to get enough statistics to provide the dependence of the breakdown rate (BDR) on the gradient and on the pulse length.

Instead, in case of structure 2 and 3 we operated at 100 Hz; the conditioning was faster even without bake-out and after only 120 (334) hours of operation of structure 2 (structure 3) we could already acquire data for the BDR analysis.

Even operating at 100 Hz breakdowns were very rare at the nominal gradient in both structures, for this reason the pulse length dependence was studied operating almost at full klystron power; see Figure 7.

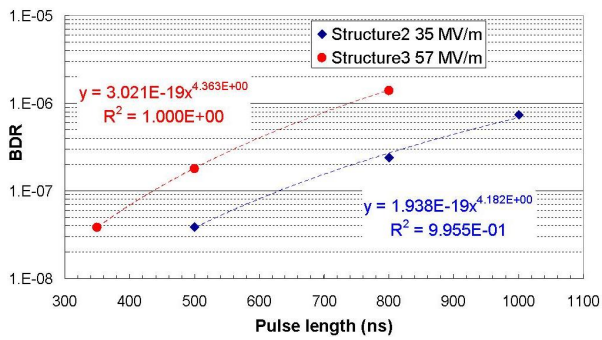

Figure 7: Pulse length dependence of BDR for structure 2 at 35 MV/m and structure 3 at 57 MV/m.

Due to the rarity of events in structures 2 and 3 and in order to have significant statistics, the BDR dependence on the gradient was measured for a pulse length of 1 μs, much longer then the nominal one (350 ns); see Figure 8.

The x-rays produced during the RF pulse were measured by a scintillator placed transversally to the structure. The integrated signal generated by the scintillator (I_s) has been acquired for different gradients. The surface field enhancement factor (β) was estimated by extrapolation from the Fowler Nordheim formula [4] by assuming I_s proportional to the emitted electrons.

A β of 68 was measured for both structures 1 and 2, by contrast structure 3 has a β of only 48.

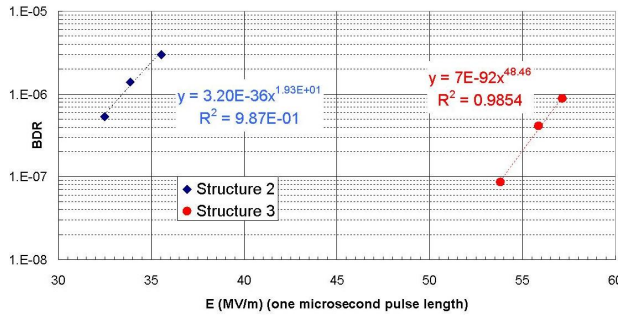

Figure 8: Gradient dependence of BDR for structure 2 and 3 for 1 μs pulse.

CONCLUSIONS AND OUTLOOK

Three of the four short test structures have been produced and power tested. The fourth structure is presently under construction; it will provide information concerning the robustness of the J-coupler design.

The machining precision required to avoid tuning has been reached and the cups are well inside the tolerances. The stacking and brazing techniques are proven for the regular cups. Some brazing problems have been encountered in the matching cells which however are not part of the nominal two-meter structure. The presence of brazing alloy in the matching cells seems to be the reason for the large phase advance error in structure 2 and for the poor matching; this problem is still under investigation. An equivalent post mortem analysis is planned for structure 3.

High accelerating gradients have been reached without difficulties and the breakdown rate is largely lower than required for operation. Breakdown localization by means of acoustic sensors is under test and will be fully operational with the two-meter prototype structure.

REFERENCES

[1] R. Ganter et al., SwissFEL CDR, PSI Bericht Nr. 10-04, April 2012.

[2] J.-Y. Raguin and M. Bopp, "The Swiss FEL C-band Accelerating Structure: RF Design and Thermal Analysis", this conference, TUPB012.

[3] R. Zennaro et al., "Design, production and power conditioning of the first C-band test accelerating structure for the SwissFEL", IPAC 2012, New Orleans, USA.

[4] R.H. Fowler and L. Nordheim, Proc. R. Soc. (London) A119, 173 (1928).

Copyright © 2012 by the respective authors — cc Creative Commons Attribution 3.0 (CC BY 3.0)

THE SWISS FEL RF GUN: RF DESIGN AND THERMAL ANALYSIS

J.-Y. Raguin, M. Bopp, A. Citterio, A. Scherer
PSI, CH-5232 Villigen, Switzerland

Abstract

We report here on the design of a dual-feed S-band 2.5-cell RF gun, developed in the framework of SwissFEL, capable of operating at 100 Hz repetition rate. As in the LCLS RF gun, z-coupling, to reduce the pulsed surface heating, and a racetrack coupling cell shape, to minimize the quadrupolar component of the fields, have been adopted. The cell lengths and the iris thicknesses are as in the PHIN gun operating at CERN. However the iris aperture has been enlarged to obtain a frequency separation between the operating π mode and the $\pi/2$ mode higher than 15 MHz. An amplitude modulation scheme of the RF power, which allows one to obtain a flat plateau of 150 ns for multibunch operation and a reduced average power is presented as well. With an RF pulse duration of 1 μs it is shown that operation at 100 MV/m and 100 Hz repetition rate is feasible with very reasonable thermal stresses.

INTRODUCTION

Paul Scherrer Institut is completing the study of the accelerating systems of SwissFEL, a Free Electron Laser which targets a maximum electron beam energy of 5.8 GeV. SwissFEL is designed for two standard electron beam operation modes, one with a 200 pC charge per bunch and a core slice emittance of 0.43 mm·mrad and the second with a 10 pC charge per bunch and a core slice emittance of 0.18 mm·mrad. SwissFEL, the main linac frequency being the C-band American frequency 5712 MHz, operates with a repetition rate of 100 Hz and two electron bunches, with a spacing of 28 ns, are accelerated at each RF pulse.

The proposed 2.5-cell RF gun operates with a nominal body temperature of 40 °C in the π mode at the S-band frequency of 2998.8 MHz, such a frequency having a common sub-harmonic with the SwissFEL C-band main linac frequency. The beam energy at the exit of the RF gun is about 7 MeV. The two full cell lengths and the iris thicknesses of the RF gun are identical to the ones of the CTF3 PHIN RF gun [1]. The upstream cell, shorter than the two full cells, has a longitudinally adjustable backplane. The middle cell is coupled to two rectangular waveguides symmetrically arranged to cancel the dipolar component of the field. The racetrack interior shape of this coupling cell is optimized to minimize the quadrupolar field component, as in the LCLS RF gun [2]. Long lifetime and reliable operation with the targeted peak on-axis electric field of 100 MV/m requires the optimization of the two RF coupling port dimensions to reduce the dynamic thermal stress due to pulsed heating. With the high 100 Hz repetition rate, mechanical stresses caused by thermal loading have to be thoroughly addressed.

SWISSFEL RF GUN DESIGN

Design with 2D RF Simulations

Ignoring at this stage the middle cell coupling ports, RF simulations performed with the 2D electromagnetic code SUPERFISH [3] are used to determine the radius and the elliptical shape of the irises between the cells compatible with reduced surface electric fields and large frequency separation between the operating π mode ($TM_{010-\pi}$ mode) and the $\pi/2$ next lower mode ($TM_{010-\pi/2}$ mode). The radius of the upstream cell and of the two full cells are adjusted to reach a balanced on-axis field at the operating frequency. The 2D RF design was then guided by the requirements that the mode separation between the operating π mode and the $\pi/2$ mode be higher than 15 MHz and that the peak surface electric field is not higher than the electric field on the cathode. The large mode separation between the operating mode and the next lower mode reduces the impact of the lower mode on the electron bunch energy spread and projected emittance. It is also expected to make the field balance less sensitive to thermal expansion under operational conditions and to manufacturing dimension deviations that may occur during production [4].

Fig. 1 shows the electric field contour lines of the π mode. The cell radii are optimized to obtain field flatness at the operating frequency. The dimensions of some geometrical parameters, used also for the final 3D design, are specified in Table 1. The elliptical profile of the irises is characterized by an aspect ratio of 1.7:1 so that the maximum surface electric field is lower than the peak field on the cathode.

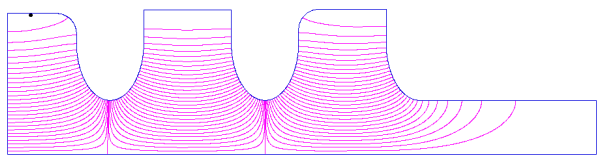

Figure 1: Electric field contour lines of the operating π mode

Table 1: Geometrical parameters of the SwissFEL RF gun

Parameter		Value	
Cell length	20.5 mm	26 mm	26 mm
Iris thickness		20 mm	
Iris radius		16 mm	
Drift radius		16 mm	

Final Design with 3D RF Simulations

The dimensions obtained with the 2D code SUPERFISH are used as input to complete the RF design of the gun with the 3D electromagnetic code HFSS [5], in particular the

Copyright © 2012 by the respective authors — cc Creative Commons Attribution 3.0 (CC BY 3.0)

design of the two RF coupling ports and of the racetrack shaped coupling cell [2, 6]. The coupling apertures, located in the middle cell, are optimized to minimize field distortion, to obtain a coupling coefficient β around 2 and to ensure that the temperature rise per pulse of the most exposed areas does not exceed 50^{o}C. To fulfill these three criteria, the two main features that have been adopted are coupling apertures running longitudinally all along the coupling cell, i.e. z-coupling scheme, and a large inner edge radius of the apertures. In addition, a balanced on-axis electric field is obtained with a minor change of the upstream and downstream cell radii. A cross-section of the RF gun is shown in Fig. 2.

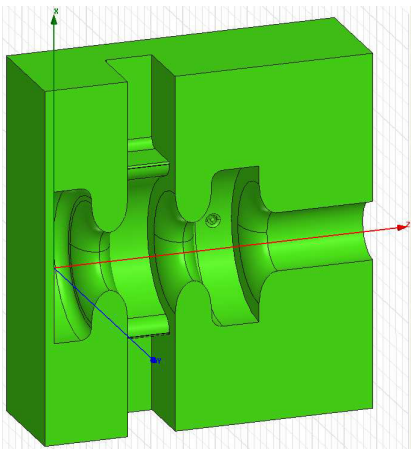

Figure 2: Cross-section of the SwissFEL RF gun.

Fig 3 shows the on-axis electric field along the RF gun in the final RF design. The ratios of the three maxima of the on-axis electric fields are higher than 98%.

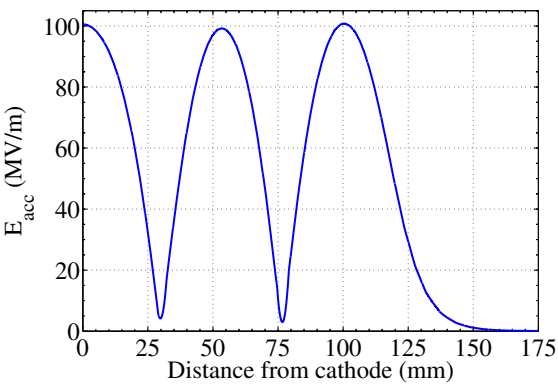

Figure 3: On-axis electric field of the SwissFEL RF gun.

The coupling apertures induce field distorsion in the vicinity of the gun axis that may deteriorate the electron bunch quality. The two symmetrically arranged apertures allow one to cancel the dipolar component of the fields. To reduce the quadrupolar fields, the coupling cell has a racetrack transverse profile. For a given inner edge radius of the apertures, there is some specific combination of aperture width and length of the racetrack straight section which minimizes the quadrupolar component. Fig 4 shows the amplitude of the longitudinal electric fields along both transverse directions of the coupling cell middle plane (see Fig 2 for the definition of the x- and y-axis). Such equal amplitudes are obtained for a width and an inner radius of the coupling apertures of 17.73 mm and 8.5 mm, respectively whereas the racetrack straight section is 7.1 mm long.

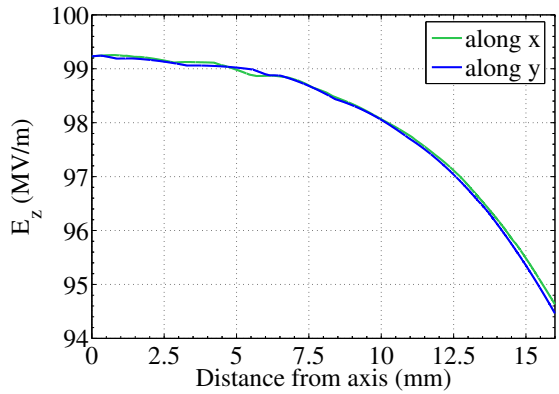

Figure 4: Amplitude of the longitudinal electric field along transverse directions of the SwisFEL RF gun.

The design coupling coefficient β has been chosen to be 2. Overcoupling the cavity at the operating frequency decreases the filling time of the RF gun. The nominal accelerating field can then be reached with a shorter RF pulse, a requirement for reducing the mechanical stresses on the gun body due to thermal loading. In the final design, the π-mode resonance frequency is within 100 kHz of the design frequency with a calculated coupling coefficient β of 1.98. The $\pi/2$ mode is about 16 MHz lower in frequency and the coupling coefficient β is 0.2.

An upper bound of the temperature rise per pulse on the inner surface of the RF gun can be analytically estimated by assuming a constant amplitude of the surface magnetic field over the whole pulse length. This limit $(\Delta T)_{max}$ is given by the formula: $(\Delta T)_{max} = (R_s/K)\sqrt{D/\pi}\sqrt{t_{pulse}}|H_s|^2$, where R_s, K and D are the surface resistance, the thermal conductivity and the specific heat of copper, respectively, at the operating frequency, whereas t_{pulse} and $|H_s|$ are the pulse length and the amplitude of the surface magnetic field, respectively. The distribution of the temperature rise for a 3 μs pulse on the surface of one of the coupling apertures is shown on Fig 5. The amplitude of the surface magnetic field corresponds to a peak on-axis electric field of 100 MV/m. The maximum temperature rise, located all along the aperture, is lower than 45 ^{o}C.

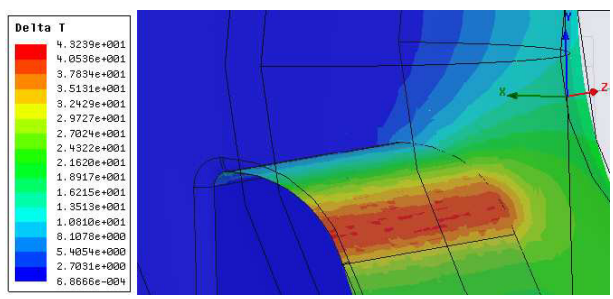

Figure 5: Coupling aperture temperature rise for a 3 μs RF pulse and a peak on-axis field of 100 MV/m.

Copyright © 2012 by the respective authors — cc Creative Commons Attribution 3.0 (CC BY 3.0)

TRANSIENTS AND THERMAL STRESSES

Since SwissFEL is planned for a two-bunch operation with a 28 ns spacing, an amplitude modulation scheme of the RF input power is proposed to maintain a constant amplitude of the peak accelerating field for a duration longer than the bunch spacing. Assuming zero rise and fall times, an RF power of about 14 MW is required to reach the 100 MV/m nominal peak accelerating field with a 3 μs rectangular RF pulse. In the amplitude modulation scheme, assuming a 1 μs total RF pulse and targeting the nominal peak accelerating field, an RF power of about 18 MW during the first 850 ns of the RF pulse feeds the cavity. The RF power is then quickly reduced to about 14 MW and is kept constant during the last 150 ns of the RF pulse. Such a scheme results in a flat-topped accelerating field of 100 MV/m (see Fig 6). The reflected power is maximum at the end of the RF pulse and is about 28 MW.

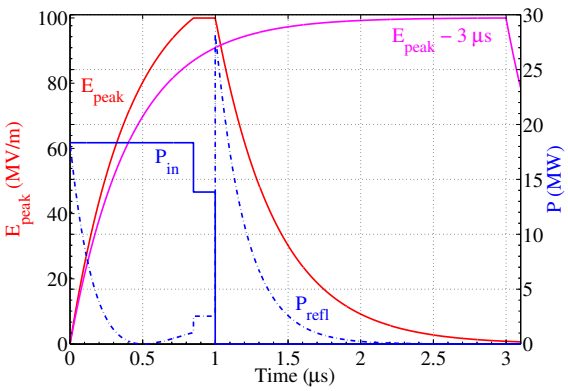

Figure 6: Transient-states of the peak accelerating field and of the RF input and reflected powers.

With this amplitude modulation scheme and with a repetition rate of 100 Hz, the average dissipated power is as low as 0.9 kW (see Fig 7). The temperature rise per pulse on the coupling apertures due to pulsed heating, estimated more rigorously by taking into account the transient behavior of the magnetic surface field during the whole pulse duration [7], is reduced to about 18 °C. With a 3 μs rectangular RF pulse, the average dissipated power is about three times higher and the temperature rise is about twice higher.

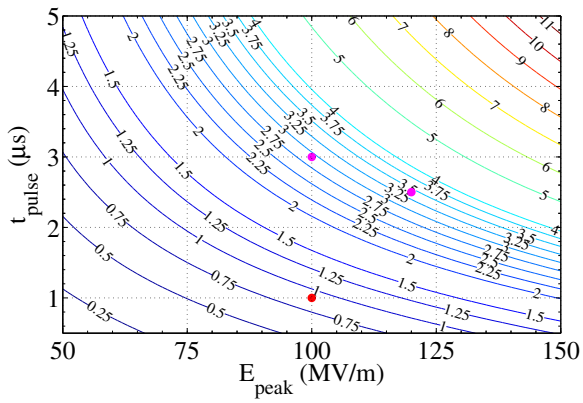

Figure 7: Average dissipated power (kW) vs. peak accelerating field and pulse length for a repetition rate of 100 Hz.

The number, size and location of the cooling channels in the RF gun body are determined with ANSYS [5] simulations for operation with an inlet water temperature of 40 °C and a maximum average dissipated power of 3.5 kW. The thermally induced stresses in the gun body are within an acceptable range with a 0.9 kW thermal load (see Fig 8).

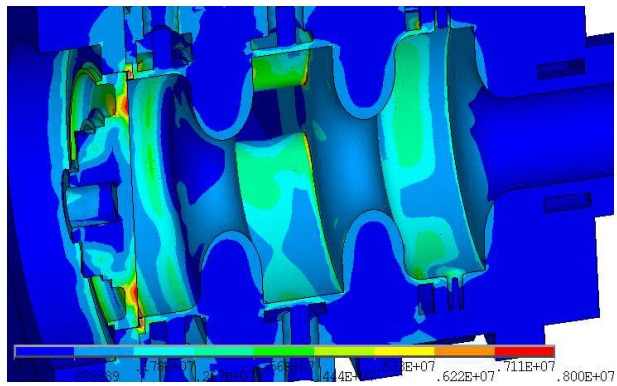

Figure 8: Thermal stress (N/m^2) for a 0.9 kW average load on the SwissFEL RF gun body.

CONCLUSIONS

A dual-feed S-band 2.5-cell RF gun operating in the π mode has been designed for SwissFEL which allows a two-bunch operation with an amplitude modulation scheme of the RF input power. A peak on-axis accelerating field of 100 MV/m can be maintained constant for 150 ns within a 1 μs total RF pulse length. For a pulse repetition frequency of 100 Hz, the total average power loss is then less than 1 kW and the temperature rise per pulse is well below the critical limit. Thermo-mechanical studies led to a design such that the RF gun can safely operate with a thermal load lower than 3.5 kW. The RF gun can then also operate safely at 120 MV/m in the single- and two-bunch regimes. However, the RF pulse length shall not exceed 2.5 μs when operating without amplitude modulation of the input power.

REFERENCES

[1] R. Roux, "Conception of Photoinjectors for the CTF3 Experiment", Int. J. Mod. Phys. A 22 (2007), pp. 3925-3941.
[2] L. Xiao et al., "Dual Feed RF Gun Design for the LCLS", Proc. PAC 2005, pp. 3432-3434, Knoxville, 2005, http://www.JACoW.org.
[3] J. H. Billen and L. M. Young, "Poisson / Superfish", Los Alamos National Laboratory, LA-UR-96-1834, 1996.
[4] D. H. Dowell et al., "The Development of the Linac Coherent Light Source RF Gun", ICFA Beam Dynamics Newsletter No. 46 (2008), pp. 162-192.
[5] http://www.ansys.com
[6] J. Haimson et al., "A Racetrack Geometry to Avoid Undesirable Azimuthal Variations of the Electric Field Gradient in High Power Coupling Cavities for TW Structures", Proc. 7th Workshop on Advanced Accelerator Concepts, Lake Tahoe, 1996, AIP Conf. Proc. 398, pp. 898-911.
[7] D. P. Pritzkau et al., "Experimental Study of RF Pulsed Heating on Oxygen Free Electronic Copper", Phys. Rev. ST Accel. Beams 5, 112002 (2002)].

Copyright © 2012 by the respective authors — cc Creative Commons Attribution 3.0 (CC BY 3.0)

THE SWISS FEL S-BAND ACCELERATING STRUCTURE: RF DESIGN

J.-Y. Raguin, PSI, CH-5232 Villigen, Switzerland

Abstract

The Swiss FEL accelerator concept consists of a 330 MeV S-band injector linac at 2998.8 GHz followed by the main linac at the C-band frequency aiming at a final energy of 5.8 GeV. The injector has six four-meter long S-band accelerating structures that shall operate with gradients up to 20 MV/m and with a 100 Hz repetition rate. Each structure has 122 cells, including the two coupler cells and operates with a $2\pi/3$ phase advance. The design presented is such that the average dissipated RF power is constant over the whole length of the structure. The cells consist of cups and the cell irises have an elliptical profile to minimize the peak surface electric field. The coupler cells are of the double-feed type with a racetrack cross-section to cancel the dipolar components of the fields and to minimize its quadrupolar components.

INTRODUCTION

The injector linac foreseen for SwissFEL at the Paul Scherrer Institut (PSI) [1] consists of two boosters, one with two S-band accelerating structures located between the PSI-designed RF gun [2] and the laser heater, the second with four S-band structures positioned between the laser heater and the two X-band structures used to complete the linearization of the longitudinal phase space. These accelerating structures are designed to operate at 40 °C with a pulse repetition frequency of 100 Hz and at 2998.8 MHz, an S-band frequency identical to the design frequency of the RF gun and which has a common sub-harmonic with the C-band main linac.

The presented S-band structure is of the travelling-wave type and operates with a $2\pi/3$ phase advance per cell. With a flange-to-flange length of 4.15 m, it consists of 122 cells - 120 regular cells and two coupler cells. Two cells, located upstream and downstream of the structure, are equipped with an RF pickup for monitoring and controlling the amplitude of the RF fields during operation. Since the energy of the electron bunches accelerated in the RF gun is about 7 MeV, any RF field distortion in the vicinity of the longitudinal axis of the structure may severely deteriorate the bunch emittance. In conventional travelling-wave structures, these field distortions are caused by the breaking of the azimuthal symmetry of the structure due to the topology of RF input and outport ports. The remedies against these field distortions are to equip the coupler cells with symmetrically arranged double feeds and to adopt a racetrack shape of these cells [3]. These two geometrical features are selected for designing the coupler cells.

The peculiarity of the presented S-band structure is the optimized cell-to-cell iris and cell radii to obtain an RF dissipated power per cell *constant* all along the structure. In addition, the cell-to-cell irises have an elliptical cross-section. Such a profile allows to reduce the ratio of the peak surface electric field to the accelerating gradient E_{peak}/E_{acc} and is expected to inhibit the generation of dark current. The accelerating gradient of the structure is 20 MV/m. Table 1 summarizes some main parameters of the designed S-band structure.

Table 1: Main parameters of the SwissFEL S-band structure

Parameter	Value
Operating frequency	2998.8 MHz
Phase advance per cell	$2\pi/3$
Total number of cells	122
Accelerating gradient	20 MV/m
Maximum pulse repetition frequency	100 Hz
Operating temperature	40 °C

DESIGN OF THE REGULAR CELLS

The regular cells of the designed structure have a cup-like shape with a curvature radius of 10 mm at the manufacturing temperature (see Fig. 1). The cell-to-cell iris thickness is 5 mm and is constant all along the structure. These irises have all the same elliptical cross-section with an aspect ratio of 1.5:1. Due the difficulty to tune and to match coupler cells with low group velocity, the radius of the last iris of the structure has been chosen to be 9.31 mm. The length of each cell is 33.324 mm at 40 °C to operate the structure in the TM_{010}-like mode with a $2\pi/3$ phase advance per cell,

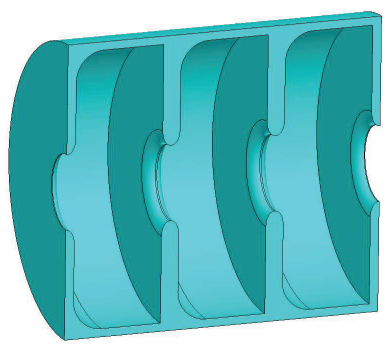

Figure 1: 3D model of the S-band structure cells.

The RF design of the regular cells is performed with the 2D electromagnetic code SUPERFISH [4]. By modelling three identical cells and by applying the appropriate boundary conditions, one obtains the standing-wave field map and the eigenfrequency from which the travelling-wave fundamental RF mode parameters characterizing the

Copyright © 2012 by the respective authors — cc Creative Commons Attribution 3.0 (CC BY 3.0)

cell and corresponding to the required $2\pi/3$ phase advance can be calculated: the group velocity v_g, the *effective* shunt impedance per unit length r and the quality factor Q. The 3D electromagnetic code HFSS [5] is used for cross-checking the cell design. HFSS can solve for the complex eigenfrequencies of a 3D domain with periodic boundary conditions i.e. with a prescribed phase shift per periodic length. The group velocity and the *effective* shunt impedance per unit length are then computed by post-processing the modal electromagnetic fields.

To design a tapered travelling-wave structure with a prescribed phase advance requires the modelling of a set of single cells with different iris radii. The radius of these cells is optimized for the desired phase advance at the design frequency. The cell irises are identical. With the RF mode parameters of these sample cells and with fitting and interpolating procedures, a travelling-wave structure with specific electrodynamic properties can be synthesized. This methodology is used here to design a structure for the RF dissipated power per cell to be *constant*.

Let us consider the RF power P_{n-1} flowing *in* the nth cell and the RF power P_{n-1} flowing *out*. Both quantities are related by the equation:

$$P_n = P_{n-1} e^{-2\alpha_n L_{cell}},$$

where L_{cell} is the cell length and α_n is the attenuation *per unit length* of this cell defined by:

$$\alpha_n = \frac{\omega_0}{2 v_{g,n} Q_n}.$$

$v_{g,n}$ and Q_n are the group velocity and the quality factor of the nth cell, respectively. The RF power dissipated in the nth cell $P_{diss,n}$ is defined by the difference between the power flowing in and the power flowing out of the cell. It is then trivial to obtain the condition for which the power $P_{diss,n}$ dissipated in the nth cell is equal to the power $P_{diss,n-1}$ dissipated in the preceding cell. This condition is:

$$e^{2\alpha_{n-1} L_{cell}} = 2 - e^{2\alpha_n L_{cell}}.$$

or:

$$v_{g,n-1} Q_{n-1} = \frac{\omega_0 L_{cell}}{\ln\left(2 - e^{-2\alpha_n L_{cell}}\right)}.$$

A MATLAB-based optimization tool has been written to calculate the cell and iris radii of the 120 regular cells with the above recurrence formula. The highest ratios of the peak surface electric field to the accelerating gradient E_{peak}/E_{acc} are on the structure's first irises. The 1.5:1 aspect ratio of the iris elliptical cross-section minimizes E_{peak}/E_{acc} on the first regular cell irises. In this design, it decreases monotonically from 2.15 for the structure's second iris to 1.81 for the penultimate iris. The filling time of the structure is 840 ns.

Fig 2 shows the accelerating gradient and the *average* power dissipated per cell along the optimized structure for a 3 μs pulse and for a 100 Hz repetition rate. The required RF input power to obtain an overall average gradient of 20 MV/m is 44 MW. The *average* dissipated power per cell is about 80 W.

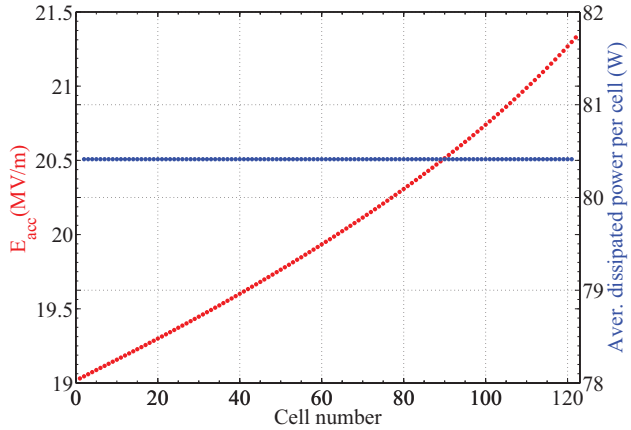

Figure 2: Variation of the accelerating gradient and the average dissipated power per cell.

The variation of the cell and iris radii along the optimized structure at 20 °C are shown in Fig 3. Fig 4 shows the variation of v_g/c and r/Q. Fig 5 shows the variation of the quality factor Q at 40 °C. These Qs are corrected to 85 % of the values computed with SUPERFISH.

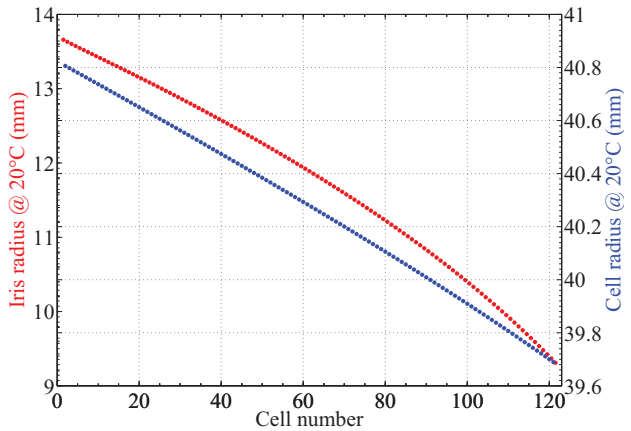

Figure 3: Variation of the iris and cell radii.

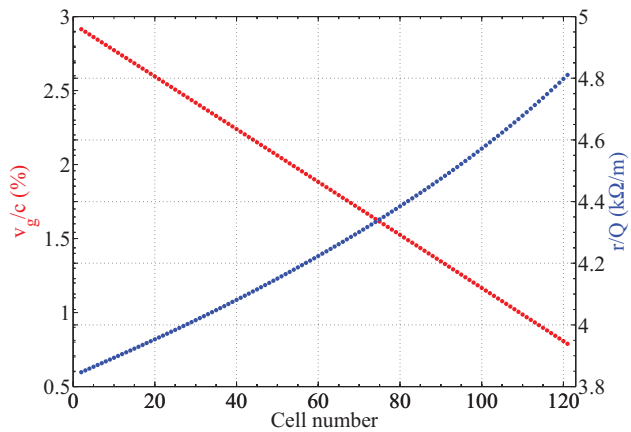

Figure 4: Variation of the group velocity and r/Q.

The dimensions of the first, middle and last regular cells at 20 °C are given in Table 2. The RF mode parameters -

Copyright © 2012 by the respective authors — cc Creative Commons Attribution 3.0 (CC BY 3.0)

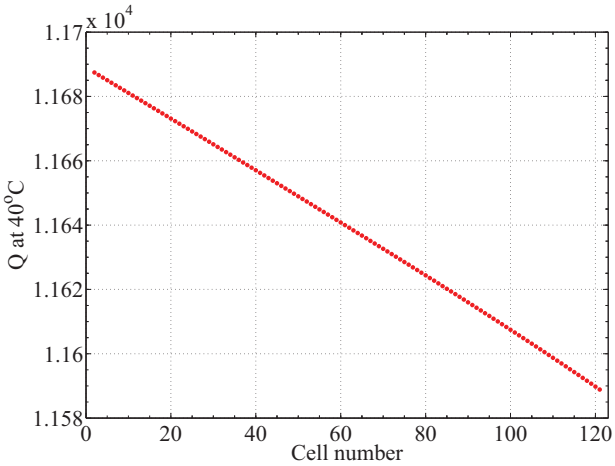

Figure 5: Variation of the quality factor.

v_g/c, r/Q and quality factor Q - are presented in Table 3. The Qs are given at 40 °C and are corrected.

Table 2: Dimensions for the first, middle and last cells.

	Iris radius (mm)	Cell radius (mm)
First cell	13.659 upstream	40.806
Middle cell	11.906 average	40.284
Last cell	9.310 downstream	39.689

Table 3: RF mode parameters for the first, middle and last cell - Q at 40 °C and corrected.

	v_g/c (%)	r/Q (kΩ/m)	Q
First cell	2.91	3.85	11688
Middle cell	1.87	4.23	11640
Last cell	0.79	4.81	11589

DESIGN STUDIES OF THE COUPLER CELLS

The conventional double-feed type coupler, in which two waveguide-to-cell irises are symmetrically arranged [6], is selected as RF input and output ports of the structure. The beneficial impact of the racetrack shaped coupler cells on the RF field amplitudes in the transverse planes is illustrated in Fig 6. For nearly optimized waveguide-to-cell iris width and cell radius of the output coupler, the amplitudes of the longitudinal electric field along the transverse directions of the cell's middle plane are nearly equal over a 2 mm distance from the structure's axis. The length of racetrack straight section, not yet optimized, is 16 mm.

Pulsed surface heating [7] studies on the on-going design of the couplers is performed. For the output coupler, the maximum temperature rise per pulse is below 6 °C with a radius of inner edge of the waveguide-to-cell irises of 3 mm, a 3 μs RF pulse and an overall average accelerating gradient in the structure of 20 MV/m.

CONCLUSIONS

The regular cells of a four-meter S-band travelling-wave accelerating structure for the injector linac of SwissFEL,

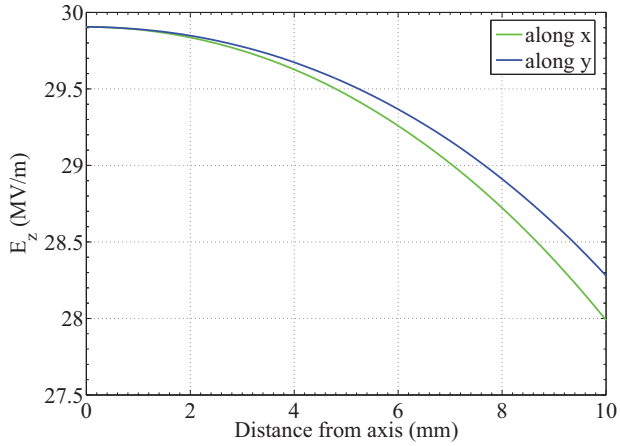

Figure 6: Amplitude of the longitudinal electric field along transverse directions in the middle plane of the output coupler cell.

operating at 40 °C with a $2\pi/3$ phase advance per cell, have been designed at the S-band frequency 2998.8 MHz. The structures are expected to run at, or below, an accelerating gradient of 20 MV/m with a pulse repetition frequency of 100 Hz. The RF pulse length shall be long enough to efficiently control the gradient with a dedicated feed-back control system. Since the combination of the high repetition rate and long RF pulse significantly increases the thermal load, the cell and iris radii of the structure are optimized for an RF dissipated power to be constant in each of the 120 regular cells and for a last iris radius of the structure to be 9.31 mm. The two dual-feed input and output coupler cells with a racetrack shape are under study. A model of the transient-state for determining the minimum RF pulse length after which the accelerating gradient has reached a steady-state is also elaborated.

REFERENCES

[1] SwissFEL Conceptual Design Report, PSI Bericht Nr. 10-04, April 2012.

[2] J.-Y. Raguin et al., "The Swiss FEL RF Gun: RF Design and Thermal Analysis", these proceedings, TUPB010, http://www.JACoW.org.

[3] J. Haimson et al., "A Racetrack Geometry to Avoid Undesirable Azimuthal Variations of the Electric Field Gradient in High Power Coupling Cavities for TW Structures", Proc. 7th Workshop on Advanced Accelerator Concepts, Lake Tahoe, 1996, AIP Conf. Proc. 398, pp. 898-911.

[4] J. H. Billen and L. M. Young, "Poisson / Superfish", Los Alamos National Laboratory, LA-UR-96-1834, 1996.

[5] http://www.ansys.com

[6] H. Deruyter et al., "Symmetrical Double Input Coupler Development", Proc. LINAC 1992, pp. 407-409, Ottawa, 1992.

[7] D. P. Pritzkau et al., "Experimental Study of RF Pulsed Heating on Oxygen Free Electronic Copper", Phys. Rev. ST Accel. Beams 5, 112002 (2002)].

Copyright © 2012 by the respective authors — cc Creative Commons Attribution 3.0 (CC BY 3.0)

THE SWISS FEL C-BAND ACCELERATING STRUCTURE: RF DESIGN AND THERMAL ANALYSIS

J.-Y. Raguin, M. Bopp, PSI, CH-5232 Villigen, Switzerland

Abstract

The Swiss FEL accelerator concept consists of a 330 MeV S-band injector linac followed by the main linac in C-band aiming at a final energy of 5.8 GeV. The two-meter long C-band accelerating structures have 113 cells, including the two coupler cells, and operate with a $2\pi/3$ phase advance. The structure is of the constant-gradient type with rounded wall cells and has an average iris radius of 6.44 mm, a radius compatible with the impact of the short-range wakefields on the whole linac beam dynamics. The cell irises have an elliptical profile to minimize the peak surface electric fields and the coupler cells are of the J-type. We report here on the RF design of the structure, as well as on its thermal analysis, to target operational conditions with an accelerating gradient of about 28 MV/m and a repetition rate of 100 Hz.

INTRODUCTION

The main linac of SwissFEL at the Paul Scherrer Institut (PSI) is designed to consist of 28 RF modules operating at the C-band American frequency 5712 MHz with a pulse repetition frequency of 100 Hz. Each module is composed of one solid-state modulator, one 50-MW klystron, one PSI-designed C-band pulse compressor - a barrel-open cavity (BOC) - and four accelerating structures. Since SwissFEL aims for two-bunch operation with a 28 ns spacing, it is crucial that the acceleration through the structures is identical for *both* bunches. Such a feature can be achieved by performing phase modulation on the klystron drive signal. With a 3 μs, 40 MW klystron RF pulse, and taking into account the RF losses along the waveguide network of the module, the RF pulse, compressed by the BOC to 350 ns, is tailored so that *both* bunches gain an energy per accelerating structure as high as 56 MeV.

A 56 MeV energy gain per structure is achievable with a constant-gradient travelling-wave structure having in total 113 cells - 111 regular cells and two coupler cells. The length of each regular cell is fixed by the imposed $2\pi/3$ phase advance per cell. It can indeed be shown that the resulting energy gain is nearly optimal with such a choice of phase advance and the adopted pulse compression scheme. The accelerating gradient is then about 28 MV/m, a smaller - and safer - gradient than the 35 MV/m gradient corresponding to the state of the art [1].

One peculiarity of the designed C-band structure is the optimized cell-to-cell iris and cell radii theoretically resulting in *identical* accelerating gradient for each regular cell of the structure. In addition, J-type coupler cells [2] are selected since this type is mechanically the least complex to manufacture. Table 1 summarizes some main parameters of the designed C-band structure.

Table 1: Main parameters of the SwissFEL C-band structure

Parameter	Value
Operating frequency	5712.0 MHz
Phase advance per cell	$2\pi/3$
Total number of cells	113
Accelerating gradient	28 MV/m
Maximum pulse repetition frequency	100 Hz
Operating temperature	40 °C

DESIGN OF THE REGULAR CELLS

The regular cells of the designed structure have rounded outer walls to reduce the RF losses. For a defined cell-to-cell iris geometry, the quality factor of such cells is typically 10 % higher than the cells of a disk-loaded structure. At the manufacturing temperature of 20 °C, the length of each cell is 17.489 mm so as to operate the structure at 40 °C on the TM_{010}-like mode with a $2\pi/3$ phase advance per cell. The cell-to-cell iris thickness is 2.5 mm at 20 °C, a compromise between the desired high *effective* shunt impedance and the high mechanical rigidity, and is constant all along the structure. These irises have an elliptical cross-section with an aspect ratio of 1.375:1. Due the impact of the longitudinal short-range wakefields on the whole linac beam dynamics, the average iris radius of the structure is required to be about 6.44 mm.

Since the regular cells that composed the accelerating structure are axisymmetric, their RF design can be performed with the 2D electromagnetic code SUPERFISH [3]. SUPERFISH provides modal standing-wave eigenfrequencies and field maps from which the travelling-wave fundamental RF mode parameters of a cell under design can be calculated: the group velocity v_g, the effective shunt impedance per unit length r and the quality factor Q. The 3D electromagnetic code HFSS [4] is used for cross-checking the cell design.

The design of a tapered structure, such as a constant-gradient type, can be performed by modelling at first a set of single cells with different iris radius, the cell radii being optimized to have the required phase advance at the design frequency. The upstream and downstream iris radii of each of these individual cells are equal. With the mode parameters of these sample cells and with fitting procedures, a *pure* constant-gradient travelling-wave structure can be synthesized with an average iris radius of 6.436 mm at 40 °C.

Let us consider the gradient $E_{acc,n}$ in the nth cell and

Copyright © 2012 by the respective authors — cc Creative Commons Attribution 3.0 (CC BY 3.0)

the power P_{n-1} flowing in this cell. These quantities are related:

$$E_{acc,n} = \sqrt{\alpha_n r_n P_{n-1}},$$

where r_n and α_n are the *effective* shunt impedance and the attenuation *per unit length* of this cell, respectively. The attenuation α_n is defined by: $\alpha_n = \omega_0/(2v_{g,n}Q_n)$, where $v_{g,n}$ and Q_n are the group velocity and the quality factor of the cell, respectively. The power P_n flowing out the cell is related to the power P_{n-1} flowing in:

$$P_n = P_{n-1}e^{-2\alpha_n L_{cell}},$$

where L_{cell} is the cell length. From these relations, it is straightforward to obtain the recurrence formula for which the accelerating gradient is identical in two consecutive cells, the $(n-1)$th cell and the nth cell:

$$\frac{v_{g,n}}{(r/Q)_n} = \frac{v_{g,n-1}}{(r/Q)_{n-1}} e^{-2\alpha_{n-1}L_{cell}}.$$

A small MATLAB-based optimization tool that makes use of these relations has been written to provide the final cell and iris radii of the 111 regular cells. The aspect ratio of 1.375:1, which characterizes the elliptical cross-section of all the cell-to-cell irises, corresponds to the optimal profile which ensures the lowest ratio of the peak surface electric field to the accelerating gradient E_{peak}/E_{acc} on the structure's *first* iris. The ratio E_{peak}/E_{acc} decreases monotonically from 2.16 for the first iris to 1.89 for the last iris. The filling time of the structure is 330 ns.

Fig 1 shows the accelerating gradient and the power flow along the designed constant-gradient structure. The input power required to obtain a 28 MV/m constant gradient is about 28 MW for a rectangular RF pulse .

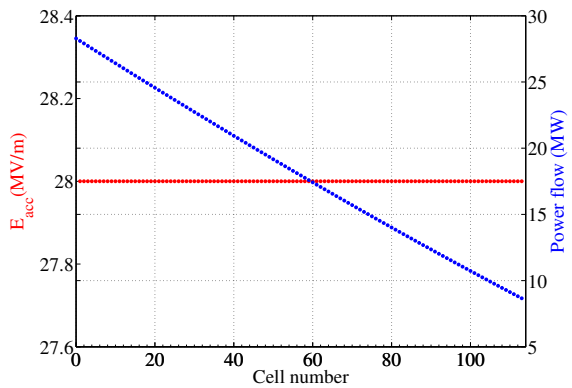

Figure 1: Accelerating gradient and variation of the power flow.

The dimensions of the first, middle and last regular cells at 20 °C are given in Table 2.

Table 2: Dimensions for the first, middle and last cells.

	Av. iris radius (mm)	Cell radius (mm)
First cell	7.244	22.431
Middle cell	6.481	22.194
Last cell	5.436	21.929

Table 3: RF mode parameters for the first, middle and last cell - Q at 40 °C and corrected.

	v_g/c (%)	r/Q (kΩ/m)	Q
First cell	3.10	7.23	10036
Middle cell	2.17	7.84	9995
Last cell	1.19	8.70	9951

The RF mode parameters - group velocity normalized to the speed of light v_g/c, r/Q and quality factor Q - are presented in Table 3. The Qs, given at 40 °C, are 94 % of the values computed with SUPERFISH.

The variation of the cell and iris radii along the structure at 20 °C are shown in Fig 2. The variation of v_g/c and r/Q are shown in Fig 3. Fig 4 shows the corrected Qs at 40 °C.

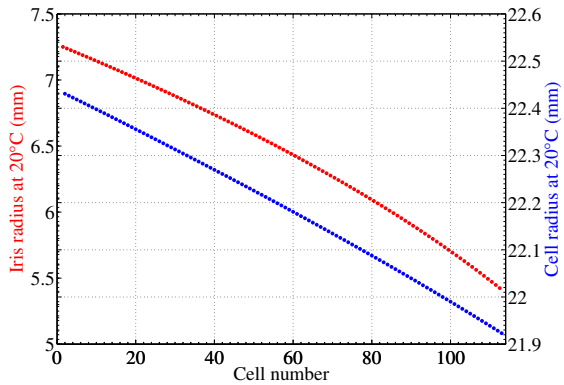

Figure 2: Variation of the iris and cell radii.

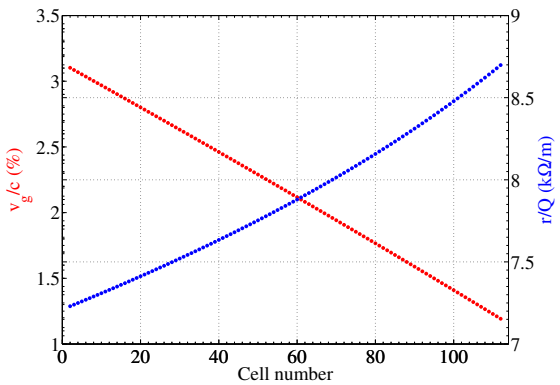

Figure 3: Variation of the group velocity and r/Q.

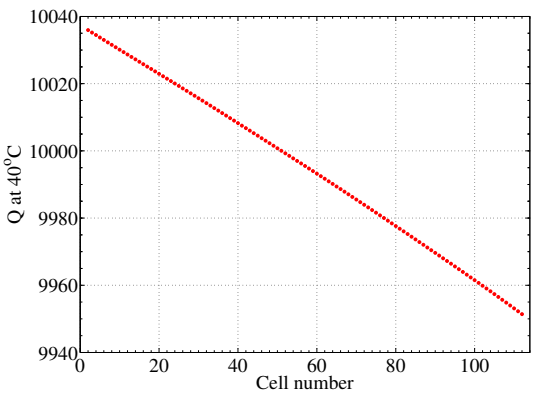

Figure 4: Variation of the quality factor.

Copyright © 2012 by the respective authors — cc Creative Commons Attribution 3.0 (CC BY 3.0)

DESIGN OF THE COUPLER CELLS

Comparative studies of several types of coupler cell revealed that the J-type, its topology and design methodology having been described in [2], provides satisfying RF characteristics to feed the C-band structure. The width of the two symmetrically arranged waveguide-to-cell irises is moderately small to avoid detrimental field distortions in the vicinity of the structure longitudinal axis when the coupler is properly matched and tuned. In addition, its intrinsic mechanical simplicity makes it suitable for reliable mass production. Such a coupler is then selected for the RF input and output ports of the structure. The length of both coupler cells is 14.8 mm at 20 °C. Fig 5 shows a 3D computer model of the input coupler.

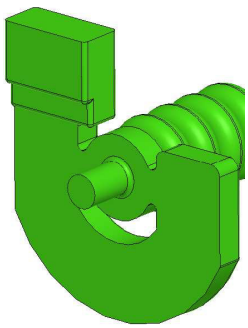

Figure 5: 3D computer model of the J-type coupler.

The determination of the optimal waveguide-to-cell iris widths and cell radii for both couplers is performed with the module Optimetrics of the 3D code HFSS [4]. For the input coupler, the optimal cell radius and the width of the irises are 20.342 mm and 16.170 mm, respectively, with inner and outer edge radii of the irises of 2.5 mm. For the output coupler, the optimal cell radius is 20.372 mm and the width of the irises is 13.289 mm with edge radii of 2.0 mm.

An estimation of the dynamic stress induced by pulsed surface heating is provided by calculating the maximum temperature rise per pulse on the critical areas [5]. The highest amplitudes of the magnetic field on the structure inner surface are located at the inner edge of the waveguide-to-cell irises of the coupler cells. Assuming a 350 ns *rectangular* RF pulse and an accelerating gradient of 28 MV/m, the maximum temperature rise per pulse, about 4 °C, is negligibly small, a consequence of the chosen fairly large inner edge radii of the irises.

THERMAL ANALYSIS

The temperature stabilization of a C-band accelerating structure is achieved by water flowing through eight azimuthally distributed channels integrated in each disk of the structure and running all along it. The design pressure of these 8 mm-diameter channels is 6 bar and the foreseen water speed is around 1 m/s. The nominal inlet temperature of the water is 40 °C for each of the four accelerating structure of an RF module and shall be stabilized within ±0.01 °C. With a 3 μs long klystron RF pulse and a 100 Hz repetition rate, the average thermal load per disk is expected to be around 13 W. Fig 6 shows a typical temperature distribution in one of the copper disks that composed the structure with such thermal load.

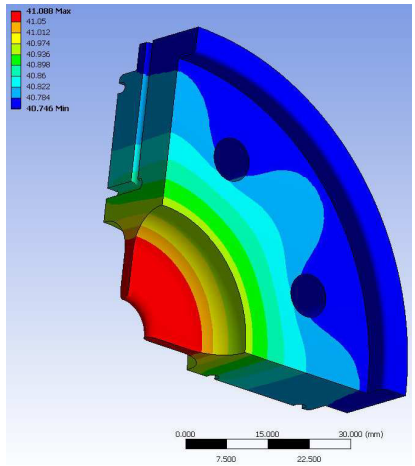

Figure 6: Temperature distribution in a disk of the C-band structure for a 40 °C inlet water temperature.

A global tuning of the four accelerating structures of an RF module can be performed by varying the inlet temperature of the water within ±5 °C of the nominal temperature.

CONCLUSIONS

A two-meter long C-band travelling-wave accelerating structure operating at 40 °C with a $2\pi/3$ phase advance per cell has been designed at the C-band frequency 5712 MHz for the main linac of SwissFEL. The structures are expected to run at a peak accelerating gradient of 28 MV/m with a compressed RF pulse of 350 ns. The cell and iris radii are optimized for a constant gradient in each of the 111 regular cells and for the averaged iris radius of the structure to be about 6.44 mm during operation. The two coupler cells are of the J-type. The eight integrated water cooling channels running along the structure allow one to maintain the structure at the nominal temperature with a pulse repetition frequency of 100 Hz. The manufacturing at PSI of some prototype short C-band structures and their successful high-power tests are presented in [6].

REFERENCES

[1] T. Sakurai et al., "High-Power RF Test on the Mass-Producted C-Band RF Components for XFEL/SPRING-8", Proc. IPAC 2010, pp. 3694-3696, Kyoto, 2010, http://www.JACoW.org.

[2] C. Suzuki et al., "Input Coupler Design for C-Band Accelerating Structure", Proc. PAC 1997, pp. 536-538, Vancouver, 1997, http://www.JACoW.org.

[3] J. H. Billen and L. M. Young, "Poisson / Superfish", Los Alamos National Laboratory, LA-UR-96-1834, 1996.

[4] http://www.ansys.com

[5] D. P. Pritzkau et al., "Experimental Study of RF Pulsed Heating on Oxygen Free Electronic Copper", Phys. Rev. ST Accel. Beams 5, 112002 (2002)].

[6] R. Zennaro et al., "C-Band Accelerator Structure Development and Tests for the SwissFEL", these proceedings, TUPB009, http://www.JACoW.org.

Copyright © 2012 by the respective authors — cc Creative Commons Attribution 3.0 (CC BY 3.0)

UPDATE ON THE COMMISSIONING EFFORT AT THE SwissFEL INJECTOR TEST FACILITY

T. Schietinger for the SwissFEL team,
Paul Scherrer Institut, CH-5232 Villigen PSI, Switzerland

Abstract

The SwissFEL Injector Test Facility at the Paul Scherrer Institute is the principal test bed and demonstration plant for the SwissFEL project, which aims at realizing a hard-X-ray Free Electron Laser by 2017. Since the spring of 2012 the photoinjector facility has been running with all RF cavities in full operation, allowing beam characterization at energies around 230 MeV with bunch charges between 10 and 200 pC. We give an overview of recent commissioning efforts with particular emphasis on efforts to optimize the emittance of the uncompressed beam.

INTRODUCTION AND MOTIVATION

The Paul Scherrer Institute (PSI) is planning an X-ray Free Electron Laser (FEL) user facility, which is to deliver ultrashort coherent photon pulses with wavelengths ranging between 0.1 and 0.7 nm by the year 2017 [1]. For cost and space reasons the driving linac is foreseen to feature a relatively modest end energy, thus calling for very low emittance to still achieve lasing at the target wavelengths. In preparation of SwissFEL, PSI is commissioning a 250 MeV photo-injector, which allows gaining experience with high-brightness electron beams and serves as a realistic test bed for crucial components in development for SwissFEL.

The SwissFEL Injector Test Facility [2] has been in operation in various configurations since 2010 [3]. Only recently the RF system was completed and the design energy of 250 MeV could be reached. At the same time, a flexible magnetic chicane, designed to compress the electron bunch longitudinally, was put into operation. The results of the first beam characterization around this energy as well as the first experience with the bunch compressor were reported in an earlier note [4]. In this paper we report on the ensuing work on emittance optimization with uncompressed beam, performed in a high-charge (about 200 pC) and low-charge (about 10 pC) mode.

MACHINE SETUP

Electrons are extracted from a copper cathode by a TW class drive laser, which is based on a frequency tripled Ti:sapphire chirped-pulse amplifier [5]. A pulse-stacking method, where the laser beam is sent through several birefringent BBO-crystals, is applied to approximate a flat-top longitudinal intensity profile. In the high-charge mode (typically 200 pC), the FWHM pulse length is 10.3 ps, in the low-charge mode (10 pC) it is 3.6 ps. Figure 1 shows a comparison of the two pulse shapes, as measured with a cross-correlation method. Transverse pulse shaping is performed with an aperture mask. The laser spot diameter on the cathode is about 0.84 mm for the high-charge mode and about 0.38 mm for the low-charge mode. A smaller back up laser system based on a Nd:YLF amplifier is used for simple tasks not requiring high beam quality.

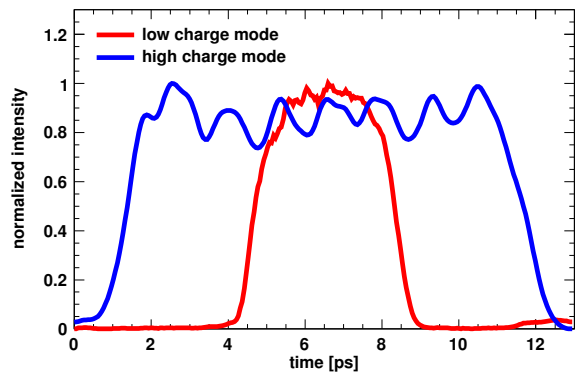

Figure 1: Laser longitudinal profile measurement for the two charge modes.

The first acceleration of the electrons to 7.1 MeV/c momentum is provided by the CTF3 Gun Nr. 5, an S-band RF gun originally built for the CLIC test facility at CERN [6].

A movable gun solenoid is used for initial focusing and optimization of the projected emittance. Energy and energy spread of the electrons emitted by the gun can be measured with a small dispersive beamline upstream of the booster.

The booster consists of four S-band travelling-wave structures, each surrounded by four solenoids for additional focusing. A fifth accelerating structure, operating at a harmonic frequency (X-band), was recently installed. Its purpose will be the approximate linearization of the longitudinal electron phase space for optimal bunch compression in the magnetic chicane following the booster. The bunch compressor was not in use (left in the straight position) during the measurements presented here, i.e., all results shown were obtained with uncompressed bunches.

An extensive diagnostic section equipped with a series of quadrupoles allows various kinds of optics-based emittance measurements. A transverse-deflecting RF cavity (S-band, five cells) is used for bunch length and slice-resolved measurements (resolution 20 fs). Transverse beam profiles are obtained by imaging the beam with either, for overview images, scintillating crystal screens (YAG or LuAG) or, for precision measurements, OTR screens (thin metal foils

Copyright © 2012 by the respective authors — cc Creative Commons Attribution 3.0 (CC BY 3.0)

emitting optical transition radiation). The beam orbit is tracked by a series of resonant strip-line beam-position monitors. The absolute bunch charge is measured by means of a wall current monitor with an uncertainty of 10–15%.

The measurements presented here were performed at a beam energy of 230 MeV, with the phases of all travelling-wave structures set to their on-crest values.

EMITTANCE OPTIMIZATION

Given the moderate size of the SwissFEL main linac, low emittance is a key requirement for the SwissFEL electron beam to achieve lasing in the X-ray domain. In particular a small core slice emittance is crucial for the FEL process in the undulator section. For the matching of the beam optics, however, it is vital to keep the projected emittance under control as well.

The primary method used to measure emittance is a single-quadrupole scan, where the beam optics are set up in a way that allows the generation of phase advance simultaneously in the horizontal and the vertical plane. The precondition for this to work is that the beam optics are equal in both planes at the location of the scanning quadrupole, i.e., $\beta_x = \beta_y = \beta_0$ and $\alpha_x = \alpha_y = \alpha_0$, with $\beta_0 = \alpha_0 L$ where L marks the distance to the observing screen. Under these conditions, the beam waist occurs in both planes for zero quadrupole gradient and is equal to $\beta_{\min} = L^2/\beta_0$ in a thin-lens approximation. The method has the advantage that an operator can easily verify how well the beam is matched to the desired optics. The beam size is then measured as a function of phase advance from Gauss fits to background-subtracted beam profiles using the OTR screens. Figure 2 shows an example of an emittance scan at 10 pC charge. The plots show normalized phase space with beam size measurements under different phase advance as tangential lines (top), measured beam sizes in comparison to the model expectation (middle), and the corresponding statistical pulls defined as the difference between measurement and model normalized by the measurement error (bottom).

The emittance of a photo-injector at a given bunch charge is mainly determined by the laser spot size, the strength of the initial focusing at the gun solenoid, and the gradient of the first booster cavity. In our optimization procedure we set the laser spot size and the gradient of the first cavity to design values and scan the gun solenoid field strength for the lowest projected emittance. We then minimize the transverse couplings of the beam by adjusting two small corrector quadrupoles integrated in the coil of the gun solenoid. Further reduction of couplings is achieved by tuning the solenoids surrounding the first S-band cavity.

A sizable dependence of the emittance on the orbit through the S-band structures was observed after this first optimization. The next step was therefore a beam-based alignment of the orbit in the S-band section.

In this procedure an orbit feedback loop is closed to fix the beam orbit through the S-band section during a measurement. The optimal orbit is found empirically by measuring the emittance as a function of the reference BPM offsets used by the feedback.

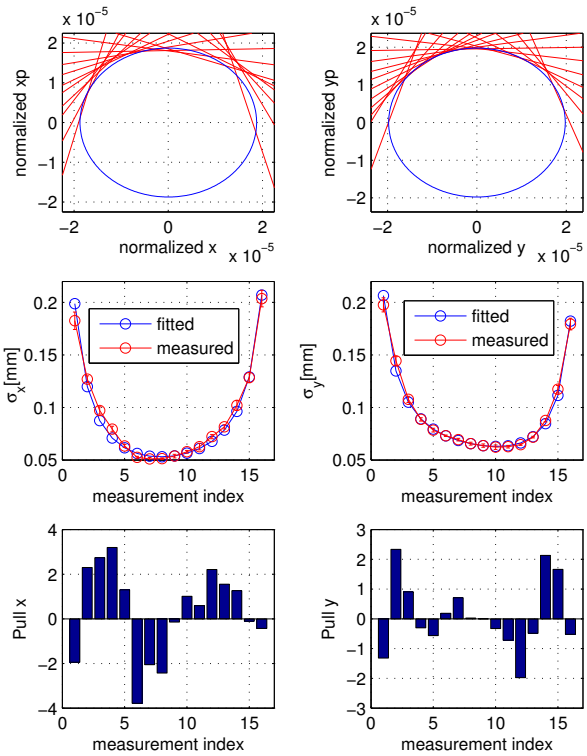

Figure 2: Example of a single-quadrupole emittance measurement performed at 10 pC charge. See text for details.

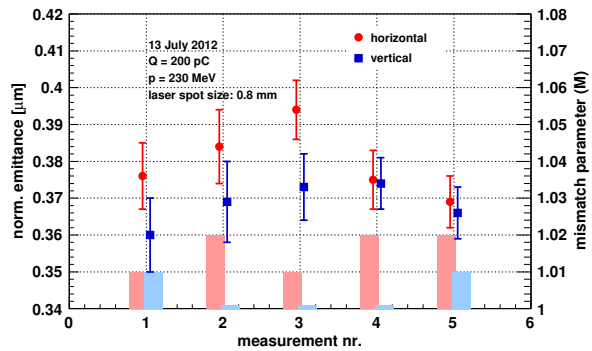

Figure 3: Stability of emittance measurement: the same single-quadrupole scan was repeated five times with 2 minutes between measurements. The measured emittance is shown in µm (left-hand scale), error bars are determined from the evaluation of 10 images per set point.. Also shown (bars, right-hand scale) is the mismatch parameter determined by the fit to the optics as a measure for the matching quality (optimum value is 1).

After adjusting the orbit some asymmetry between the horizontal and the vertical emittance remains (see also [4]). The asymmetry could be traced to dispersion effects dis-

Copyright © 2012 by the respective authors — cc Creative Commons Attribution 3.0 (CC BY 3.0)

torting the beam at the observation point. A correction of the dispersion then results in symmetric emittance values as expected. Figure 3 shows the stability of the emittance measurement over a series of five measurements taken at intervals of two minutes.

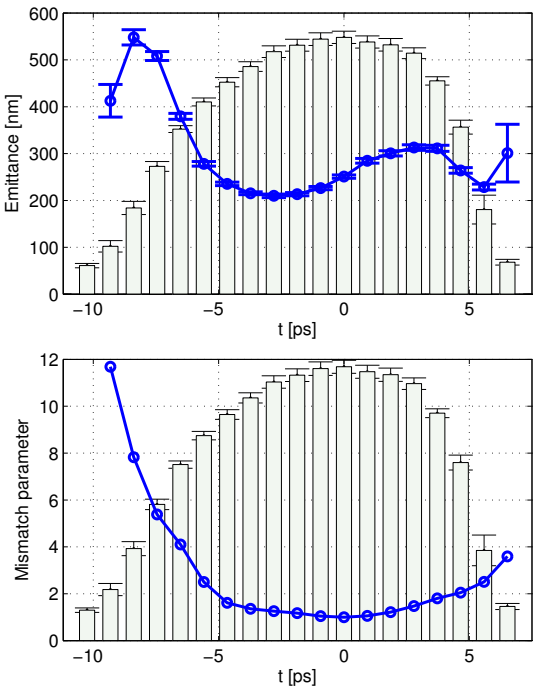

Figure 4: Slice emittance measurement at 200 pC: charge profile (bars) in comparison to slice emittance (top) and relative mismatch parameter (bottom) as a function of position along the bunch.

Once the projected emittance is optimized, we measure the horizontal emittance of individual longitudinal beam slices along the bunch by streaking the beam vertically with the RF deflector. Figure 4 shows an example measurement. For the low-charge mode, the slice emittance measurement is compromised by a weak signal-to-noise ratio on the observing screen. Improved diagnostics is currently being installed.

Table 1 summarizes the emittance values measured so far and compares them to design values. The reported errors are statistical; they are obtained by repeating the measurement a few times at a given setting.

OTHER MEASUREMENTS

Further commissioning work in the past few months mainly concerned the understanding and setup of the movable bunch compressor chicane. The activities include measurements of R_{56} and R_{16} as a function of the dipole current to obtain a complete characterization of the compressor. A setup procedure was worked out which ensures the correction of both the residual dispersion downstream of the bunch compressor and the effect of geomagnetism in the drift lengths of the chicane. First studies on mitigating the effect of coherent synchrotron radiation using the small quadrupoles inside the chicane have also been carried out, with encouraging results. The detailed findings of these studies will the subject of future reports.

Table 1: Measured normalized projected and core slice emittances in comparison to simulated values for the two different charge modes. Errors are statistical.

type	σ_{laser} [mm]	$\varepsilon_{n,x}$ [µm]	$\varepsilon_{n,y}$ [µm]	$\varepsilon_{n,\mathrm{sim}}$ [µm]
high-charge mode (≈200 pC):				
proj.	0.21	0.379 ± 0.004	0.369 ± 0.004	0.350
slice	0.21	0.251 ± 0.004	–	0.330
low-charge mode (≈10 pC):				
proj.	0.10	0.161 ± 0.001	0.181 ± 0.002	0.096
slice	0.10	≤ 0.15	–	0.080

CONCLUSION AND OUTLOOK

The commissioning of the SwissFEL Injector Test Facility is progressing steadily towards the final characterization of the high-brightness beam required to drive SwissFEL. The last months were dedicated to emittance optimization with uncompressed bunches, yielding promising results.

During a recent shutdown, the last main component of the injector test facility was installed, a harmonic X-band (12 GHz) cavity in front of the bunch compressor, which will finally allow beam characterization after linear bunch compression, the crucial next step towards the demonstration of the validity of the SwissFEL design concept.

ACKNOWLEDGMENT

We thank the numerous expert groups at PSI who contributed to the success of the SwissFEL Injector Test Facility.

REFERENCES

[1] R. Ganter (ed.), PSI Report 10-06 (2010).

[2] M. Pedrozzi et al., in Proceedings of the 31st International Free Electron Laser Conference (FEL), Liverpool, UK, 2009; M. Pedrozzi (ed.), PSI Report 10-05 (2010).

[3] T. Schietinger et al., in Proceedings of the 25th Linear Accelerator Conference (LINAC), Tsukuba, Japan, 2010; T. Schietinger et al., in Proceedings of the 2nd International Particle Accelerator Conference (IPAC), San Sebastian, Spain, 2011.

[4] T. Schietinger et al., in Proceedings of the 3rd International Particle Accelerator Conference (IPAC), New Orleans, USA, 2012.

[5] A. Trisorio et al., Optics Express 19 (2011) 20128.

[6] R. Bossart, M. Dehler, in Proceedings of the 5th European Particle Accelerator Conference (EPAC), Sitges (Barcelona), Spain, 1996.

Copyright © 2012 by the respective authors — cc Creative Commons Attribution 3.0 (CC BY 3.0)

COMPARATIVE DESIGN OF SINGLE PASS, PHOTO-CATHODE RF-LINAC FEL FOR THE THz FREQUENCY RANGE: SELF AMPLIFICATION vs. ENHANCED SUPER-RADIANCE

Yu. Lurie*, Y. Pinhasi, Ariel University Center of Samaria, Ariel, Israel

Abstract

Self amplified spontaneous emission and enhanced super-radiance are discussed and compared as possible configurations in the construction of a single-pass, photo-cathode RF-LINAC FEL source for THz radiation, being developed in Ariel University Center of Samaria. Numerical simulations carried out using 3D, space-frequency approach demonstrate the charge squared dependence of the radiation power in both cases, the characteristic typical to super-radiant emission. The comparison reveals a high efficiency of an enhanced super-radiance FEL, which however can only be achieved with ultra-short (the radiation wavelength long or shorter) drive electron beam bunches at a proper energy chirping.

INTRODUCTION

Tera-Hertz radiation is of interest for a basic science, medical and biological applications, spectrometry, remote detection, and etc. Free-electron lasers (FELs), which often can fit on or scale to the size of a table-top, are able to provide intense coherent electromagnetic radiation over a wide range of THz frequencies. In the present work, we consider a *single pass* FEL (without any oscillator resonant cavity) for production of such radiation. The FEL is designed to be driven by trains of short electron pulses, produced by a photo-injector RF-LINAC. The Israeli RF-LINAC FEL project under development is considered here as an example of such a radiation source [1]. Basic operational parameters of the FEL are given in table 1. Two possible configurations of the FEL are considered and compared in the work: a self amplified spontaneous emission (SASE) FEL, and an enhanced super-radiance (ESR) FEL [2]. The following discussion is concentrated just on the processes taking place in the FEL radiator section (wiggler), leaving aside any consideration of other FEL components.

SASE is a well-known FEL configuration, which is widely used at the far ultra-violet and X-ray wavelengths but also at the infra-red and THz frequencies. An initial spontaneous emission of electron beam is self amplified in SASE FELs, giving rise to a non-linear beam-radiation interaction which results in an exponential growth of the emission up to a saturation. ESR FEL [2] is supposed to utilize a constructive energy-phase correlation [3], what enhances the undulator super-radiant emission of short (a radiation wavelength long or shorter) electron pulses. Energy chirping is a well-known technique used in accelerator physics for density compression of electron pulses. In an ESR FEL, it is suggested to cause a longitudinal density compression of short electron pulses just inside the FEL interaction region, i.e. inside the wiggler.

Table 1: Operational parameters of the THz FEL.

Accelerator	
Type:	Photo-injector RF-LINAC
Electron beam energy:	E_k=3÷6 MeV
Pulse duration:	$T_b \gtrsim 0.1$ pS
Bunch charge:	Q_b=30-500 pC
Wiggler	
Magnetic induction:	B_w=2 kGauss
Period:	λ_w=25 mm
Waveguide	
Rectangular waveguide:	15×10 mm^2

THE MODEL

To simulate and compare between both FEL configurations, 3D space-frequency approach [4] was applied. The method is based on an expansion of the high-frequency electromagnetic field in terms of transverse eigen modes of the medium (free-space or a waveguide) in which the field is excited and propagates. The interaction between the electromagnetic field and the gain medium is fully described by a set of coupled equations, expressing the evolution of mode amplitudes along the interaction region. The model was realized in a numerical code WB3D and has been successfully applied to the analysis of various effects in FEL devices [5]-[11].

A drive electron beam pulse is considered in the model as a consisting of charged electron "macro-clusters" distributed over the beam. An initial distribution of the clusters in the beam is of great importance in simulations of radiation emission processes. Random Gauss longitudinal distribution of a fixed number (N_q=300) of equal charges was considered in the present work. Unfortunately this approach produces an artificial level of spontaneous emission, what prevents from a correct description of radiation build-up process. However this model seems to be adequate enough in description of a coherent emission of ultra-short (much shorter than the radiation wavelength) or highly-bunched electron beam pulses. To improve the description of spontaneous emission and of transition effects, the unified model of electron beam short noise from Ref. [12] was also applied to simulate the initial electron beam short noise in a wide frequency range.

* ylurie@ariel.ac.il

Copyright © 2012 by the respective authors — cc Creative Commons Attribution 3.0 (CC BY 3.0)

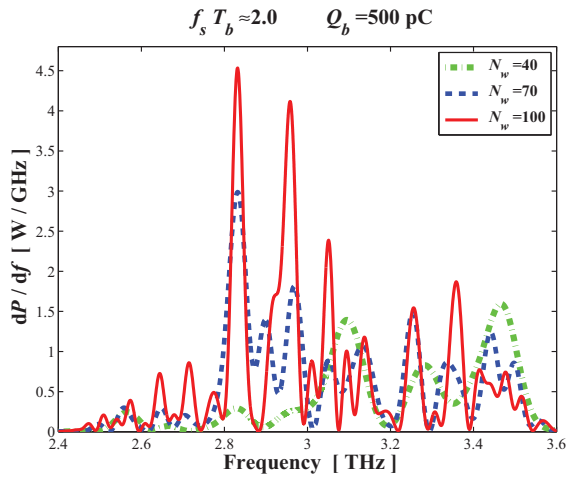

Figure 1: Example of SASE radiation spectrum.

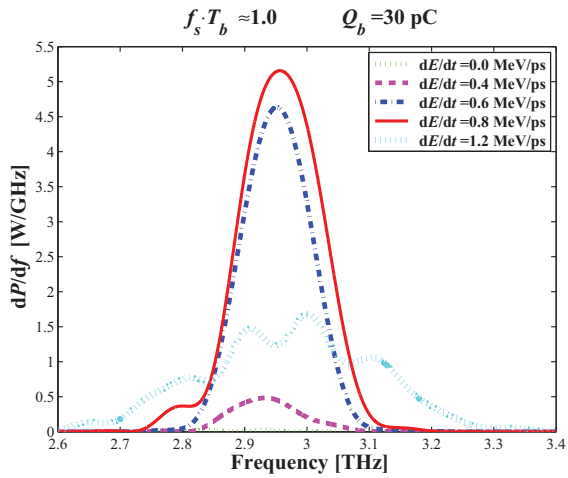

Figure 3: Radiation spectrum of ESR FEL.

THE RESULTS

The simulations were carried out supposing the beam energy of E_k=5.5 MeV, what corresponds to the FEL synchronism frequency of $f_s \approx 2.96$ THz ($\lambda_s \approx 100\ \mu m$).

Typical spectrum of SASE emission is given in figure 1. The example corresponds to the Q_b=0.5 nC electron beam pulse of relative duration $f_s\, T_b \approx 2$. The unified model of electron beam short noise was applied to simulate an initial distribution of $N_q = 3501$ clusters. Total power of the emitted radiation is demonstrated in figure 2 as function of the wiggler length (in the units of the wiggler's period). The results presented were received in the unified model of electron beam short noise for electron beam pulses of the charges of Q_b=0.1 nC, 0.5 nC, and 1.0 nC. Convergency of the results with the number of macro-clusters considered in the simulations are also shown.

Enhanced super-radiance can be achieved in FELs driven by a train of short electron pulses which are subjected to a controlled energy chirp. Coherent emission of an electron bunch is strongly depressed if the bunch is about the radiation wavelength long or longer. Energy chirp gives rise to a longitudinal density compression of the bunch just while it propagates along the wiggler, enhancing super-radiance [2]. We consider such FEL configuration as a competitor to SASE in construction of compact FELs for the Tera-Hertz frequency spectral range. Simulations of ESR FEL were carried out supposing the L_w=1 m long wiggler (N_w=40 periods); a shorter wiggler can actually be taken, depending on the initial beam pulse duration, and on the energy chirp rate. Figure 3 demonstrates the radiation spectrum of ESR FEL, obtained in the example of the beam charge of Q_b=30 pC, and of the initial relative beam pulse duration $f_s\, T_b \approx 1$. A proper choice of the energy chirp rate ($\frac{dE}{dt} \gtrsim 0.6$ MeV/ps in the example given) provides a remarkable increase in the total radiation power (about two orders of magnitude) as one can see in the picture. This energy chirp rate level means the total energy variance during the beam pulse of $\frac{\Delta E}{E_b} = \frac{1}{E_b}\frac{dE}{dt}\, T_b \approx 3.6\%$. Such energy chirping can be achieved in RF-LINAC FEL scheme by means of some phase de-synchronization of the accelerated electron pulses relative to the accelerating electromagnetic wave in the RF-LINAC cavities, similar to the application of the "phase-matching" section within the FEL beam line [3]. Figure 4 shows dependence of the radiation power on the energy chirp rate used.

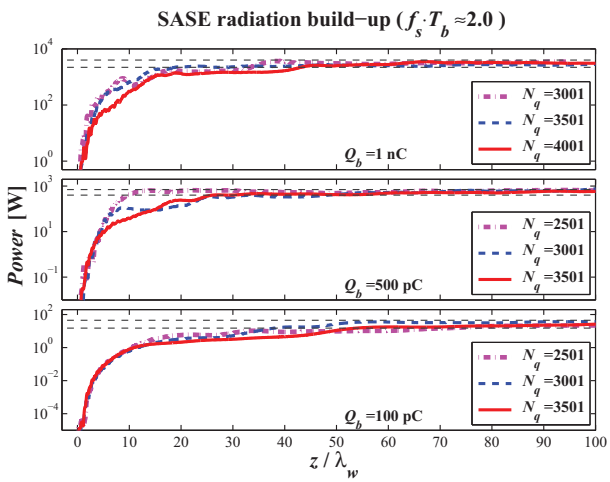

Figure 2: SASE FEL power build-up.

Radiation power obtained in the both FEL configurations considered is presented in figure 5 as a function of the beam charge. Up to considerably high beam charges where space-charge effects reduce a coherent emission, the power in both FEL configurations seems to grow linearly with the beam charge squared what is characteristic to super-radiant emission process.

CONCLUSIONS

Simulations of SASE FEL with initial random Gauss distribution of macro-charges seem to overestimate the saturation power and the saturation length. The unified model of

Copyright © 2012 by the respective authors — cc Creative Commons Attribution 3.0 (CC BY 3.0)

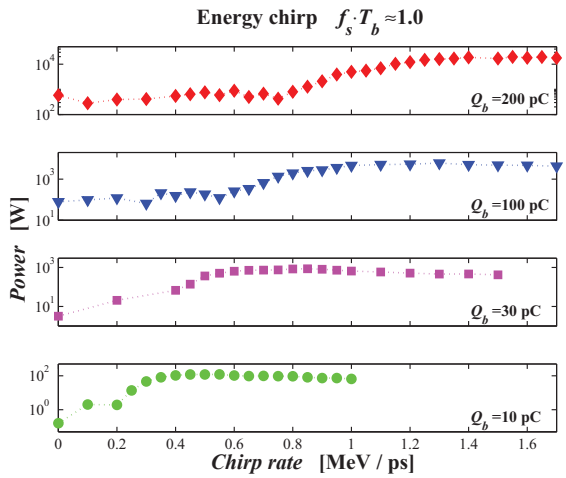

Figure 4: ESR FEL power dependence on the chirp rate.

electron beam short noise [12] is applied instead to a more realistic description of an initial spontaneous emission of noisy drive beam (short noise) and of the transition radiation build-up process. In contrast, nearly the same results were received in simulations of ESR FEL in both models. This difference can be explained by a much stronger bunching taking place in ESR FEL (bunching factor of about 5-6% in comparison with more than 90% at SASE and at ESR FELs, respectively). In ESR FEL, most of the radiation is emitted coherently at the moment of a maximum density compression of the beam pulse; spontaneous emission has a negligible effect at this moment.

A considerably long (about 100 periods) wiggler is required for a SASE FEL in order to enable saturation. The beam bunching is found to be rather weak, and the power of the emitted radiation is much lower than that of ESR FEL driven by electron bunches with similar charges. Spectrum of SASE emission includes a number of narrow peaks,

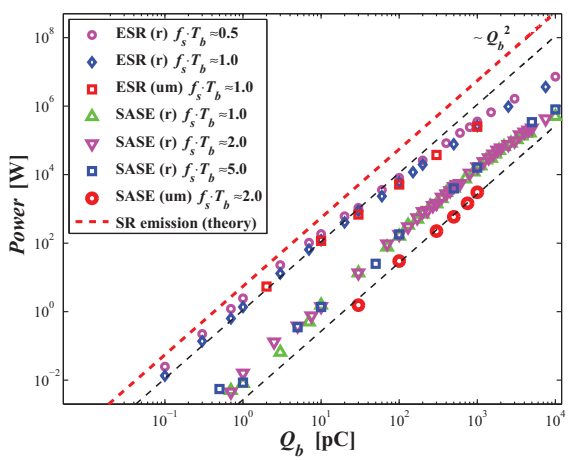

Figure 5: Radiation power of ESR and SASE FELs as a function of the beam charge.

competing each other at saturation. At the range of the beam charges considered, the power of saturated SASE emission is found to demonstrate a super-radiant proportionality to the beam charge squared.

An ESR FEL utilizes short (the radiation wavelength or shorter) electron bunches with a controlled energy chirping. Train of such bunches can be obtained by means of a photo-injector RF-LINAC enabling some phase desynchronization of the accelerated electron pulses relative to the accelerating wave. At a proper chirping, ESR FEL is found to provide a high beam bunching, promising a high efficiency of such radiation source. Unfortunately, destructive space-charge forces emerge to reduce ESR FEL efficiency if overcharged bunches are applied. To overcome this limitation, low-charged bunches at a higher bunch repetition rate can be used. Concluding, ESR FEL seems to be a perspective concept for construction of a photo-injector, THz spectral range RF-LINAC FEL being under development in AUC in cooperation with UCLA.

REFERENCES

[1] E. Dyunin, Yu. Lurie, Y. Pinhasi, A. Gover, H. Marks, IEEE 25-th convention of electrical and electronics engineers in Israel, December 3-5, 2008, Eilat, Israel, p. 825. DOI: 10.1109/EEEI.2008.4736655

[2] Yu. Lurie, Y. Pinhasi, Phys. Rev. ST Accel. Beams **10**, 080703 (2007).

[3] A. Doria et al., Phys. Rev. Lett. **80**, 2841 (1998); Nucl. Instr. Meth. A, **475** (2001), p. 296; Phys. Rev. Lett. **93**, 264801 (2004).

[4] Y. Pinhasi, Yu. Lurie, A. Yahalom, Phys. Rev. E **71** (2005), 036503.

[5] Y. Pinhasi, Yu. Lurie and A. Yahalom, Nucl. Instr. and Meth. in Phys. Res. A **475**, no. 1-3 (2001), 147.

[6] Y. Pinhasi, and Yu. Lurie, Phys. Rev. E **65** (2002) 026501.

[7] Y. Pinhasi, Yu. Lurie, A. Yahalom, and A. Abramovich, Nucl. Instr. Meth. Phys. Res. A **483** (2002), 510.

[8] Y. Pinhasi, Y. Lurie, A. Yahalom, Nucl. Instr. Meth. Phys. Res. A **528** (2004), 62.

[9] A. Gover, E. Dyunin, Y.Lurie, Y. Pinhasi, M.V. Krongauz, Phys. Rev. ST Accel. Beams. **8** (2005), 030702.

[10] Yu. Lurie and Y. Pinhasi, Phys. Rev. ST Accel. Beams **13**, 050701 (2010).

[11] V. Zhaunerchyka, R.T. Jongma, Yu. Lurie, Y. Pinhasi, W.J. van der Zande, Appl. Phys. Lett. **97**, 231109 (2010).

[12] B.W.J. McNeil, M.W. Poole and G.R.M. Robb, Phys. Rev. ST Accel. Beams **6**, 070701 (2003).

Copyright © 2012 by the respective authors — cc Creative Commons Attribution 3.0 (CC BY 3.0)

WARM BEAMLINES AND INFRASTRUCTURE IN THE EUROPEAN XFEL

M. Hüning, DESY, Hamburg, Germany

Abstract

The European XFEL is driven by a superconducting linear accelerator. In the main accelerator tunnel the accelerator modules will be suspended from the tunnel ceiling. The warm sections like bunch compressors will be installed on girders supported from the floor. The accelerator infrastructure like klystrons and electronic racks will be installed in the accelerator tunnel in close proximity to the electron beam line.

INTRODUCTION

The layout of the European XFEL [1] is depicted in figure 1. There are two injector linacs, each consisting of a normalconducting RF gun, one accelerating module with 8 superconducting cavities, one 3rd harmonic module with 8 superconducting cavities as well, and a warm beam line with laser heater and extensive beam diagnostics.

Two dogleg chicanes guide the beam onto the axis of the main linac. To transport the beam with relatively large energy spread, the chicanes consist of a large number of narrowly spaced dipoles, quadrupoles and sextupoles. At the entrance of the main linac tunnel follows the first bunch compressor chicane (B0). The chicane is C-shaped and deflects vertically. Subsequently the beam is matched into a string of four accelerator modules (L1) which is followed by the second bunch compressor (B1) and a diagnostic section for transverse and longitudinal beam diagnostics. This scheme is repeated once (L2, B2) before the beam is boosted to the final energy in the main linac. There is space reserved for an extension of the main linac. Still in the main linac tunnel the collimation section is located to limit the energy deviation and the maximum transverse excursions the beam might develop coming out of the main linac. Afterwards the beam is distributed to the undulator beam lines necessary for the SASE process.

COLD LINAC SECTIONS

The superconducting RF cryo modules in the main linac are suspended from the ceiling of the tunnel. This provides the shortest connection between the cavity axes and the fixture on the tunnel wall. The specifications for the tunnel straightness were comparatively relaxed, so that the ceiling frames have to allow for ±50 mm adjustment both horizontally and vertically. This is achieved by making them out of two parts which are cut to length and shifted against each other before they are welded together in situ. The whole setup is welded to steel bands which were cast in the tubbings of the tunnel wall at the time of manufacture. Including the suspension frames and the modules inner structure the beam axis is located 2.2 m from the tunnel ceiling.

Under the modules there is room for klystrons, high voltage pulse transformers, pumps, electronic racks, and other equipment. To protect the electronics from radiation caused by beam loss or dark current in the cavities the racks are shielded by concrete blocks. Two blocks are located in front of and behind the racks along the direction of the beam. A layer of blocks is put on top of the racks. The maximum top load on the racks needed to be increased to support the weight of the concrete. There is no shielding to the sides where the electronics are accessed. An assessment of the expected dose rate was done and a sideways shielding appeared unnecessary. The radiation dose in the racks however is monitored and should additional shielding be required additional shielding plates can be attached.

Short distance cable connections within one RF section comprised of 4 cryo modules are made on a cable tray on top of the shielding. Long distance connections are reduced to the absolute minimum and consist of fibre cables wherever possible. These connections are traced in a compartment below the tunnel floor.

The room under the tunnel floor is used for water supply lines, high voltage pulse cables for the klystrons, main lines of the electric supplies, and fibre cables.

BUNCH COMPRESSOR SECTIONS

The bunch compressor sections comprise of the actual bunch compressor chicane and a diagnostic sections for

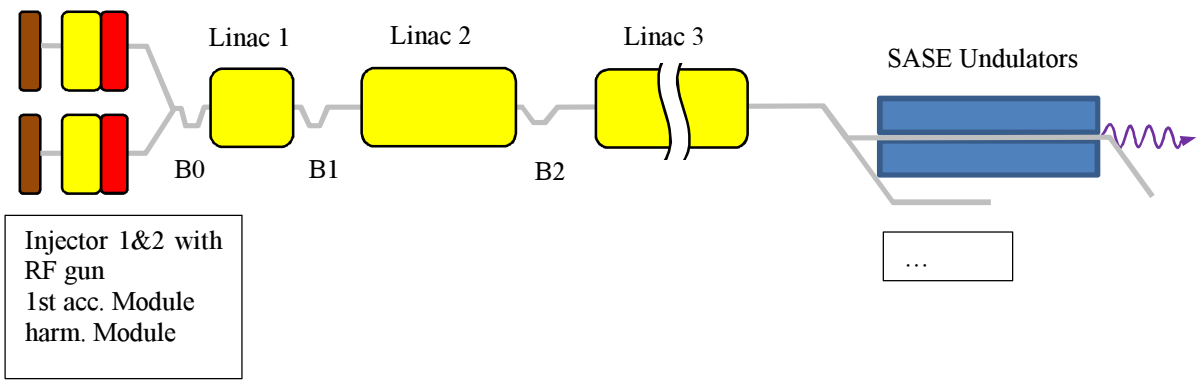

Figure 1: Layout of the European XFEL.

Copyright © 2012 by the respective authors — cc Creative Commons Attribution 3.0 (CC BY 3.0)

transverse and longitudinal beam diagnostics. In contrast to the cold sections in the warm sections beam line elements are supported from the floor. Due to the short distance of the beam axis to the ceiling, the distance from the floor is comparatively large, namely 2.2 m from the floor and even 3.5 m from the lower tunnel walls.

The larger parts of the bunch compressor sections are erected on girders. This reduces the number of installation and alignment steps at the inconvenient height and the number of bellows is dramatically reduced. The girders come in lengths of 3.2 m and 4.6 m. They are made as a sandwich-structure of steel and concrete. Aluminium plates are fixed to the upper side and machined for precise flatness and provided with grooves for easy and precise mounting of the elements (see figure 4). The girders are supported by two concrete pillars fixed to the tunnel floor. Studies were made to minimize the susceptibility of the whole setup to vibrations given the unfavourable conditions [4]. It was possible to increase the lowest resonance of the setup above 35 Hz. A test setup is in preparation in the main tunnel to verify these assessments.

Between the concrete pillars electronic racks are placed. The pillars and the girder provide a limited amount of radiation shielding. Additional shielding is provided by concrete blocks on top of the racks in analogy to the setup in the cold linac sections. To reduce the detrimental influence of the shielding on the vibrational behaviour of the setup, the shielding blocks on top of the racks are decoupled from the pillars. Like in the cold section this results in increased specs for the maximum load on the roof of the racks. Figure 2 depicts the 3D model of the setup.

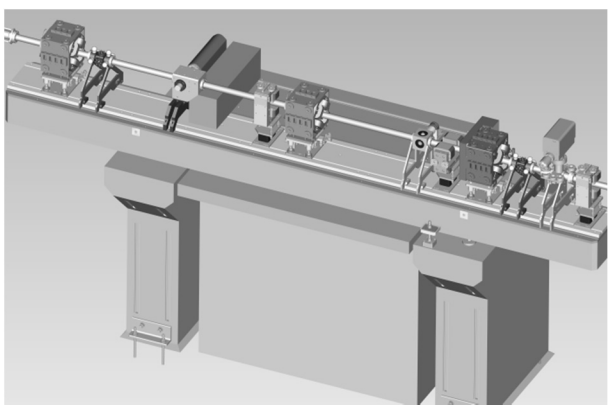

Figure 2: Bunch compressor girder setup with support columns, racks, and rack shielding.

DOGLEG SECTION

There are two injectors foreseen for the European XFEL. They are located in two storeys of the underground injector building. The floors are symmetrically shifted upwards respectively downwards against the main tunnel floor. The injected beam has to pass a dogleg chicane to enter the main tunnel. The dogleg crosses the main cavern of the main entrance shaft. The distance to bridge is 18 m, the height difference 2.5 m. The largest distances are 4.8 m from the cavern floor, 7.9 m from the ceiling, 5.5 m from the side walls.

The bunch compression scheme is such that the first compression chicane is located right at the entrance of the main tunnel. The beam is accelerated with an off-crest

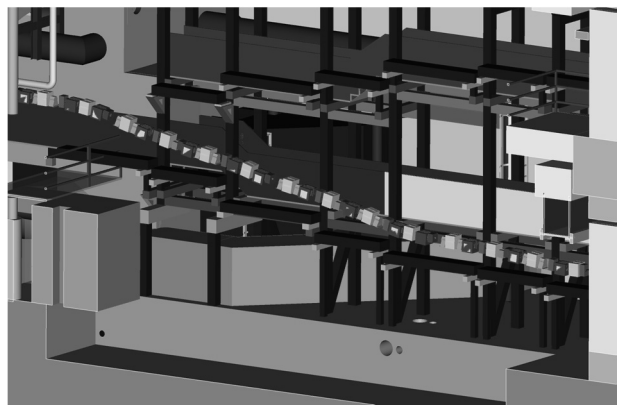

Figure 3: Dogleg support structure.

phase in the injector to provide the energy chirp for the bunch compression. Third harmonic modules are placed in the injectors to linearize the energy modulation. Extreme care has to be taken to transport the beam with large energy spread to avoid emittance degradation [2]. This is achieved by splitting the deflection into many undulating kicks along this section.

This means that the section is filled with 16 dipoles, 17 quadrupoles, and 16 sextupoles. Between the magnets diagnostic elements and vacuum equipment need to be supported. This is accomplished by putting the beam line on girders which in turn are supported by a large steel frame. The frame consists of two rows of columns made from I-beams. The girders are attached to protruding beams welded to two one column of each row. Diagonal struts help stiffening the structure [3]. By this the lowest resonance frequency of this structure was raised to 14 Hz. Figure 3 shows a 3D model of this structure.

Since the beam is inclined for the larger part of this section, most of the components have to be installed with a slope against the girder underneath. Moreover the

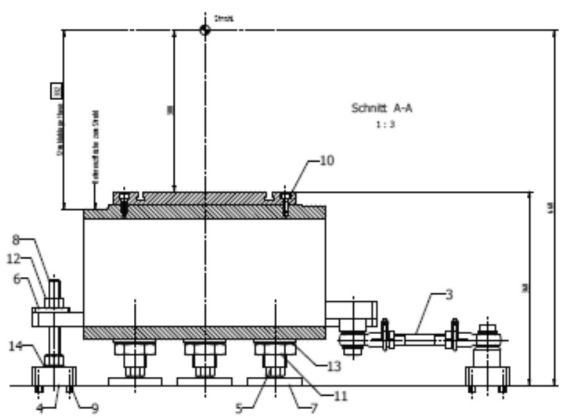

Figure 4: Cross-section of the bunch compressor girder.

Copyright © 2012 by the respective authors — cc Creative Commons Attribution 3.0 (CC BY 3.0)

slope changes many times. To accommodate this, the fixtures for the beam line elements allow for easy inclination.

INJECTOR SECTION

The injectors are each located in a separate enclosure so that they can be operated independently from each other and from the main accelerator. Here all beam line elements are supported from the floor, the beam axis is 1.4 m from the floor. Originally it was intended to locate all electronics outside the tunnel in a higher floor. Meanwhile the demands on beam diagnostics and RF control tightened and essential parts of the electronics had to be put near the beam line. Eleven racks are placed under the first accelerator module. Because of the restricted space the racks only have half height. In the close vicinity of the RF gun a high level of radiation from dark current is expected, therefore the racks are shielded all around. The shielding is made from a sandwich of aluminium, lead, boron and polyethylene. This is expected to be more powerful than a shielding made out of concrete.

The warm beam line is tightly packed with elements and therefore put on girders. The girders are of the same kind as in the bunch compressors. The room below the girders however is too small to place racks there. The electronics that does not fit under the modules is placed into shielded racks besides the beam line. The detailing is on-going with respect to accessibility of the machine elements behind the racks.

ACKNOWLEDGMENT

The author would like to thank G. Weichert, C. Schulz, T. Möhring, R. Platzer, N. Meyners, H. Hügelmann, A. Wagner, N. Mildner, M. Postigo, M. Körfer, and M. Hoffmann for their contributions to this work and providing material for this paper.

REFERENCES

[1] "The European X-Ray Free-Electron laser; Technical Design Report", DESY 2006-097 (2007). http://xfel.eu/en/document

[2] V. Balandin, W. Decking, N. Golubeva, "Large Energy Acceptance Dogleg for XFEL Injector", Proc. of IPAC2011, WEPC007, San Sebastian, Spain (2011).

[3] R. Platzer, "Studie Schwingung Stahlgerüst", Technical Note, DESY, Hamburg, Germany (2012).

[4] R. Platzer, "Studie Schwingung Girder", Technical Note, DESY, Hamburg, Germany (2012).

Copyright © 2012 by the respective authors — cc Creative Commons Attribution 3.0 (CC BY 3.0)

STUDY OF BEAM-BASED ALIGNMENT FOR SHANGHAI SOFT X-RAY FEL FACILITY

Duan Gu#, D.Z.Huang, Meng Zhang, Qiang Gu, M.H.Zhao
Shanghai Institute of Applied Physics, Shanghai 201800, China

Abstract

In linear accelerators, dispersion and transverse wake-field from alignment errors will lead to a significant emittance growth. The performance of the Free Electron Laser (FEL) process imposes stringent demands on the transverse trajectory, dispersion and emittance of the electron beam. So finding an effective Beam-Based Alignment(BBA) procedure is crucial for the success of Shanghai X-Ray FEL facility. This paper presents the preliminary study of different BBA method performances in SXFEL Linac. In addition, a MATLAB based simulation including quadrupole misalignment, dipole field errors and beam position monitor errors have been used to predict the orbit and emittance growth along the beamline and the required corrector current. Comparison with other codes is also presented.

INTRUDUCTION

As a critical development step towards constructing a hard X-ray FEL in China, a soft X-ray FEL facility (SXFEL) was proposed and will be constructed to verify the cascaded HGHG scheme and carry out the research on key technologies for X-Ray FEL. The SXFEL facility will be working at 9 nm soft X-ray band which consists of a 130MeV photo cathode injector, a main linac accelerating the beam to an energy of 840MeV, an undulator section with two stages of HGHG scheme and a diagnostic beamline. The local energy spread is 0.1%-0.15%, the peak current is about 600A and the normalized emittance is 2 mm·mrad[1].

In FEL facilities, misalignments between Quadrupoles and Beam Position Monitors(BPM) cause an increase of the transverse beam size and emittance which turns into an increase of normalized emittance. To keep the normalized emittance due to misalignment below 2 mm·rad, the average Quad-BPM misalignment in the linac must be smaller than 100um.

The traditional optical alignment can no longer meet such strict requirements, but a lot of analytical and numerical studies have been done and proved that Beam-Based Alignment technology can simultaneously eliminate the misalignment and dispersion in linac and undulator section, which obviously will leads to a much smaller emittance growth and transverse beam size. With the method above, a software based on MATLAB has been designed and simulation results have been compared with other software.

guduan@sinap.ac.cn

BBA TECHNOLOGY OVERVIEW

Over past decade, a number of different realizations have been developed to measure the offset of magnetic center of quadrupole magnet[2][4]. Most techniques are based on a common approach, which is to change the quadrupole strength and measure the resulting deflection.

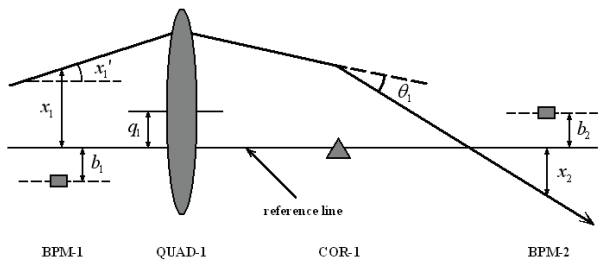

Figure 1: Common approach of BBA.

With respect to the reference line, m_i is the BPM reading at BPM-i. According to Linear optics theory (regardless wakefield effect and Quad-tilt), the transverse misalignment of upstream Quadrupole can be calculated using orbit response matrices, corrector values and inject parameters:

$$m_i = x_i - b_i = (x_i)_1 - b_i$$

$$x_i = R^{(B_1:i)}x_1 + \sum_j^{N_{Ci}} R^{(C_j:i)}c_j + \sum_j^{N_{Qi}} R^{(Q_j:i)}(I - R^{(Q_j)})q_j \quad (1)$$

Where b_i is BPM reading error due to off-axis between electronic center and geometric center. R is the 2×2 transport matrix form BPM-1 or corrector c_j or Q_j to BPM-i.

x_1 is initial incoming parameters, the unknown c_j the corrector strength and Q_j is Quadrupole misalignments, which are defined as:

$$x_1 = \begin{bmatrix} x_1 \\ x_1' \end{bmatrix};\ c_j = \begin{bmatrix} 0 \\ \theta_j \end{bmatrix};\ q_j = \begin{bmatrix} q_j \\ 0 \end{bmatrix} \quad (2)$$

Further more, we can simultaneously correct both orbit and dispersion using so called "Dispersion Free Steering" method. The optimal settings are calculated using the orbit and dispersion response matrices, which are defined as the shift of the orbit or dispersion due to corrector strength change:

$$R_{i,j} = \frac{\Delta x_i}{\Delta \theta_j}\ ;\quad D_{i,j} = \frac{\Delta d_i}{\Delta \theta_j} \quad (3)$$

Copyright © 2012 by the respective authors — cc Creative Commons Attribution 3.0 (CC BY 3.0)

Where Δx_i and Δd_i is the change of the orbit and dispersion in the BPM-i, and $\Delta\theta_j$ is the change of the strength of corrector-j. The basic aim is to find a setting of $\Delta\theta_j$ which induces orbit and dispersion that minizes in a least squares sense the final orbit and dispersion:

$$(1-w^2)\| x_{meaus}+O\Delta\theta\|^2+w^2\| d_{meaus}+D\Delta\theta\|^2=\min \quad (4)$$

More details about the algorithm procedure and successful correction results can be found at [3].

SIMULATION ON SXFEL LINAC

Soruces of the emittance growth and misalignment in the LINAC of FEL facilities has already been well-studied[2][6]. Usually it consists of field errors and stray magnet fields in the beam line as well as dispersion created upstream of the BPM, for instance, misalignment of Quadrupole, Dipole, Accelerator modules and even BPMs themselves. The Errors and launch parameters used in simulation are shown in Table 1.

Table 1: SXFEL linac Simulation Parameters

Parameter	Δx, Δy/μm (+/-)	Δθ/μrad (+/-)
DIPOLE	150	10
QUAD	150	10
ACC.MODULE	100	--
BPM	150	--
Launching error	100	150

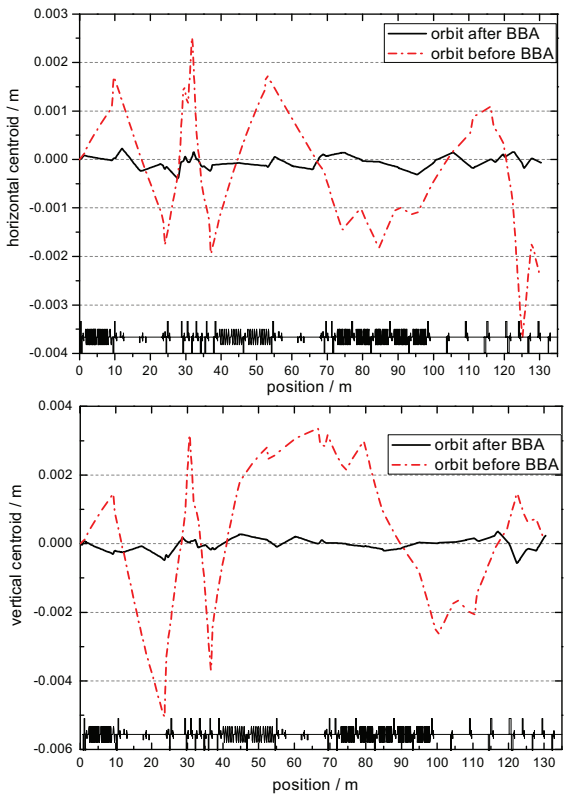

Figure 2: Comparison of orbit before and after correction.

SXFEL linac BBA simulations have been done using Elegant [7] as shown in Figure 2. After applying magnet errors and launch parameters in Table 1, we can get the correct result with Global correction method. As one can see in Figure 2, the deviation can be very large. When the electron beam travels across chicanes, the deviation will be notable increase due to the magnet effects, so these errors must be controlled in a reasonable region during BBA procedure.

In simulation results one can see that after 1st correction, the transverse orbit deviation is decline from 10^{-3}m to 10^{-4}m. Meanwhile the Smoothness of orbit and RMS orbit deviation can meet design requirement for SXFEL linac. Naturally, the impact of these errors on orbit kick and dispersion generation depend on the actual operating conditions of the accelerator, so the orbit must be measured and controlled frequently.

Further more, transverse wakefield effects caused by structure misalignment in accelerate modules is also an important factor which should be considered, as it can lead to a significant emittance growth[8]. By doing simulations, the emittance growth before and after correction are shown in Figure 3. As one can see, after BBA the final emittance growth can be controlled within 5%, and in vertical plane the correct result is much better.

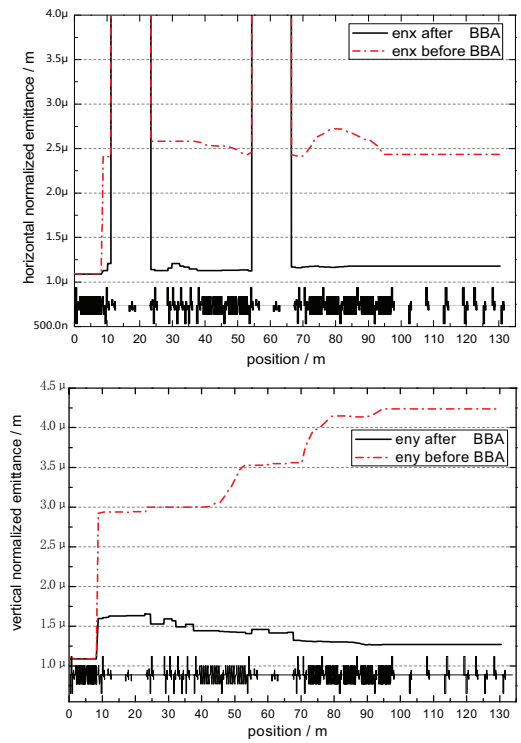

Figure 3: Comparison of emittance growth before and after correction.

CONTROL SOFTWARE DESIGN AND DEVELOPMENT

To assist the design and measurement, an automated control software based on MATLAB has been designed

Copyright © 2012 by the respective authors — cc Creative Commons Attribution 3.0 (CC BY 3.0)

with interfaces to EPICS. This software aims to connecting BBA methods and bottom devices, so we can seem it as a middle level application.

After setting launch parameters and using the BBA method above, the final offset could be determined. The flow diagram of the simulation code is shown in Figure 4.

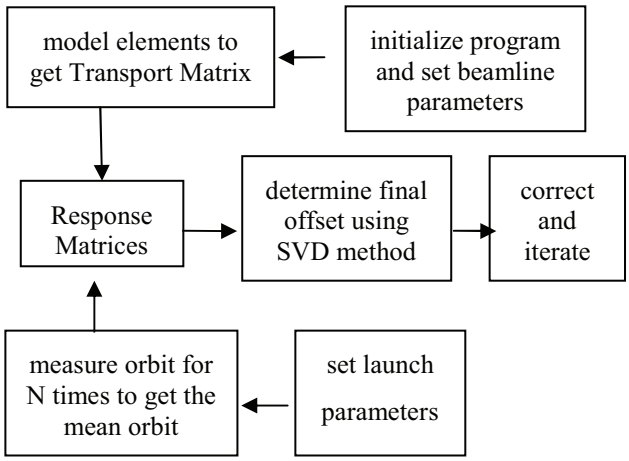

Figure 4: Flow diagram of the control program.

The response matrices are calculated from the quadrupole currents and the estimated energy along the machine. In this case, energy uncertainties such as magnets field errors and calibration errors are not take into account in this preliminary study.

After applying magnet errors and launch parameters in Table 1, we can get the correct result with Global correction method within the Matlab application. The correction results are shown in Figure 5.

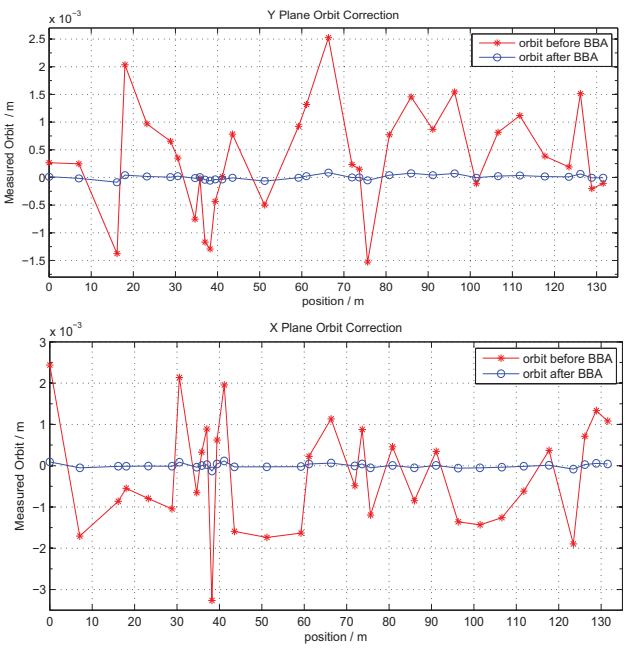

Figure 5: Simulation results from MATLAB BBA codes.

CONCLUSIONS

Preliminary design and simulations of the SXFEL Beam-based Alignment procedure have been presented in this paper, including brief introductions to main linac alignment method, beam dynamics simulations with nominal parameters, and orbit sensitivity studies. Simulations show SXFEL linac beam qualities are well within the capabilities of Beam-based Alignment technology. Further study is on the way to optimize and properly implement this technology into the SXFEL facility.

REFERENCES

[1] W.H. Huang et al, Design and Beam Dynamics Simulation for the Photoinjector of Shanghai Soft X−ray Free Electron laser Test Facility. Proceedings of FEL2011, Shanghai, China.

[2] Tor Raubenheimer, Peter Tenenbaum. Brief Review of Linear Collider Beam-Based Alignment for Linacs. LCC-0129 SLAC-TN-03-071,2004.

[3] E. Prat et al, “Measurement and Correction of Dispersion in the VUV-FEL”, EPAC’06, Edinburgh, June 2006, p. 1951..

[4] SUN Bao-gen, HE Duo-hui, LU Ping. Development of beam-based alignment system using a switchable shunt resistor for HLS. High Power Laser and Particle Beams, 2001, V13(06): 0-0).

[5] Tenenbaum P，Hendrickson L，Raubenheimer T O. Developments in beam-based alignment and steering of the Next Linear Collider main Linac. Proceedings of the 2001 Particle Accelerator Conference 2001:3837,2001.

[6] Emma P. Beam based alignment of sector-1 of the SLC Linac.EPAC-1625-1627,1992.

[7] Borland M. Elegant: A Flexible SDDS-Compliant Code for Accelerator Simulation. Advanced Photon Source LS-287,2000.

[8] John Irwin, Chun-xi Wang, Karl Bane. Transverse wakefield effect measurement via Model-independent Analysis.SLAC-PUB-7917,1979.

Copyright © 2012 by the respective authors — cc Creative Commons Attribution 3.0 (CC BY 3.0)

SECOND CW AND LP OPERATION TEST OF XFEL PROTOTYPE CRYOMODULE

J. Sekutowicz, V. Ayvazyan, J. Branlard, M. Ebert, J. Eschke, A. Gössel, D. Kostin, F. Mittag, W. Merz, R. Onken, DESY, 22607 Hamburg, Germany
W. Cichalewski, W. Jałmużna, A. Piotrowski, K. Przygoda, TUL, 90-924 Łódź, Poland
K. Czuba, Ł. Zembala, WUT, 00-665 Warsaw, Poland
I. Kudla, J. Szewiński, NCNR, 05-400 Świerk-Otwock, Poland

Abstract

In summer 2011, we performed the first test of continuous wave and long pulse operation of the XFEL prototype cryomodule [1], which originally has been designed for a short pulse operation. In April and June 2012, the second test took place, with the next prototype. For that test, cooling in the cryomodule was improved and new LLRF system has been implemented. In this contribution we discuss results of the second test of these new types of operation, which can in the future extend flexibility in the time structure of the electron and photon beams of the European XFEL facility.

INTRODUCTION

The XFEL cryomodules are based on TESLA collider cryomodules [2] and as such, they still have many features of that original design from early 90's. The TESLA cryomodules have been compromised to keep the cost possibly low. In these 8-cavity containers, unlike for example, in 2-cavity HERA cryomodules, only cells of cavities are immersed in the superfluid liquid helium (LHe). The energy dissipated in their superconducting surface is transferred to the LHe bath thru ~3 mm thick high purity Nb wall. The situation is very different for so-called end-groups, the end-beam tubes with attached input couplers and/or HOM couplers, located outside the LHe vessels. Energy dissipated in the end-groups is transported to the helium bath via much longer distance and much higher thermal resistance, which depends on the heat conductivity of niobium the end-groups are made of. The losses are often enhanced on the HOM antennae, which are made of niobium and should stay superconducting for an operation. The TESLA cavity and cryomodule designs prove to operate very successfully in the XFEL nominal short pulse mode, when the duty factor (DF) does not exceed 1.3 %, RF-pulses are ca. 1.3 ms long and their rep-rate is 10 Hz. This operation is demonstrated since many years at FLASH, which linac comprises 56 TESLA cavities.

A continuous improvement in the performance of superconducting 9-cell TESLA cavities, especially the remarkable increase of the intrinsic quality factor, and minor cooling improvements for the end-groups, should make possible operation of the XFEL cryomodules in continuous wave (cw) mode at gradients up to ~7.5 MV/m and in the long pulse (lp) mode up to the XFEL nominal gradient E_{acc}= 23.4 MV/m. These estimated gradients result from splitting of the XFEL linac in to 12-cryomodule long cryogenic strings, which leads to the maximum allowed total 2K (1.8 K) heat load (HL) per cryomodule of 20 W. For the nominal operation, the estimated maximum 2 K heat load is ca. 11 W. The maximum gradient of 23.4 MV/m in the lp-mode seems to be achievable for up to 100 ms long RF-pulses.

The new operation modes will allow for more flexibility it the time structure of both the electron and photon beam. In the nominal operation, the intra RF-pulse bunch-to-bunch spacing is 220 ns. The new operation modes will offer significantly larger bunch spacing, of the order of few microseconds, keeping the average XFEL brilliance superior to other facilities. The enlarged spacing is advantageous. For example, it allows for less expensive detectors. Further, in the new operation modes, the photon burst rep-rate can be in the kHz range. This will make optical lasers for pump-and-probe experiments less technically challenging, still providing ca. 1000 photon-bursts in the cw operation and ca. 100 at the maximum electron beam energy in the lp runs. For the nominal short pulse operation, one will have only 10 bursts /s.

PREPARATION OF THE SECOND TEST

Thermal improvements in cryomodule

Two thermal improvements were done in cryomodule PXFEL3_1, which was foreseen for the tests in 2012. Each made cooling of the HOM antennae more effective. At first, five cavities could be equipped with prototypes of the high conduction HOM feedthrough, in which low conduction standard alumina window was replaced with the sapphire window and the niobium antenna was brazed to the inner-conductor pin. Secondly, all sixteen HOM feedthroughs were thermally connected, with copper strips, directly to the 2 K tube.

Cavity performance and Q_{ext} of input couplers

Prior to the cw/lp studies, the cryomodule was tested in the nominal mode. For that test, Q_{ext} of all input couplers had been set to $3 \cdot 10^6$. The test showed malfunctioning of two cavities. Cavity No 7 had strongly detuned HOM coupler and could be operated cw up to 4 MV/m. At this gradient, the out-coupled power was already 24 W, from which 20 % was dissipated in the cable, contributing significantly to the total HL at 2 K. Cavity No 8 showed strong electron emission, leading in the cw operation to enhanced HL and to quenching already at 9.3 MV/m.

For the cw/lp tests Q_{ext} of all cavities was set to $1.5 \cdot 10^7$, which corresponds to the 3 dB resonance width of 87 Hz.

Copyright © 2012 by the respective authors — cc Creative Commons Attribution 3.0 (CC BY 3.0)

RF distribution system and IOT amplifier

The RF-power distribution system was re-arranged in 2012 to make switching between a 10 MW klystron (used for nominal test) and the IOT amplifier for the cw/lp operation less time consuming. The new waveguide arrangement was not sufficiently balanced and reflected ca. 5% (1%) RF-power in the lp (cw) mode. A better balancing requires very careful RF-characteristics for all components and thus it is lengthy procedure, which could not be done during the test period. The IOT amplifier is protected with technical interlock, which stops operation when the reflected power at the output exceeds 0.9 kW. In addition during the IOT performance test in February this year, prior the amplifier was attached to the cryomodule, we observed a mismatch of the IOT input circuit, which was not technically understood and thus could not be fixed in-house. The tube will be sent to CPI in November 2012, after the second 120 kW IOT prototype will be delivered to DESY. The waveguide reflection and mismatch of the input circuit limited the IOT output power to ca. 18 kW. Even though, the power was low, with high Q_{ext} of input couplers we could expected to reach gradients up to 11 MV/m.

Low Level RF: VME and µTCA

New LLRF based on the µTCA architecture was used in the studies for the monitoring and for stabilization of phase and amplitude of the accelerating gradient, both in the cw and lp mode. The VME standard, LLRF system used in 2011, was in 2012 employed only once for verification of the stability we achieved with µTCA. The new LLRF system shall operate two feedback loops, for the RF and for piezo-tuners. The later one is meant as an additional compensation of microphonics and it was implemented in April 2012 for the first time. The piezo-bias with DC-voltage only was successfully used in 2011 and 2012 for fine frequency adjustment of all cavities.

Cryogenic plant and vacuum system

The cryogenic plant at DESY supplies with liquid helium (LHe) both the FLASH facility and the cryomodule test hall. The LHe pressure at 2 K can be stabilized for several hours within the range of ±30 µBar, when the total HL does not vary rapidly (no quench). The accelerating mode frequency modulation caused by this pressure variability is ±1.1 Hz. The pressure at 1.8 K is not as stabile. In 2012 we did not attempted to test the cryomodule at 1.8 K. This test is scheduled for the end of this year. In 2011 we observed that dominant modulation of the field amplitude was at frequencies 47-50 Hz. Further investigation, after the first cw/lp studies had been finished, showed that the modulation was caused by vacuum pumps located close to the middle of the cryomodule. The pumps, which are needed only for cool-down, were switched off during the test in 2012.

CW OPERATION

Several dynamic HL tests for cw/lp operations were conducted in April and June 2012. The dynamic HL is calculated as difference between actual heat dissipation in cryomodule and heat capacity of the superfluid helium flowing through a cryomodule. It takes always a while to balance that difference, which oscillates vs. time around its final value. Prior to the dynamic HL tests in 2011 and 2012 we measured the static HL for the investigated cryomodules. For PXFEL3_1, the static HL at 2K was 4.5W. It was lower by 3W than static HL of the cryomodule tested in 2011. Here we present the result for one of the 2012 cw tests at 5.6 MV/m. Table 1 shows conditions for the test. The result is shown in Figure 1.

Table 1: Conditions for the dynamic HL test at 2K

Condition /Parameter	Value/Status
Number of cavities in operation	7
$< E_{acc} >$	5.6 MV/m
Q_{ext}	$1.5 \cdot 10^7$
RF-power / Input coupler	550 W
RF-feedback	off
Piezo-feedback	on

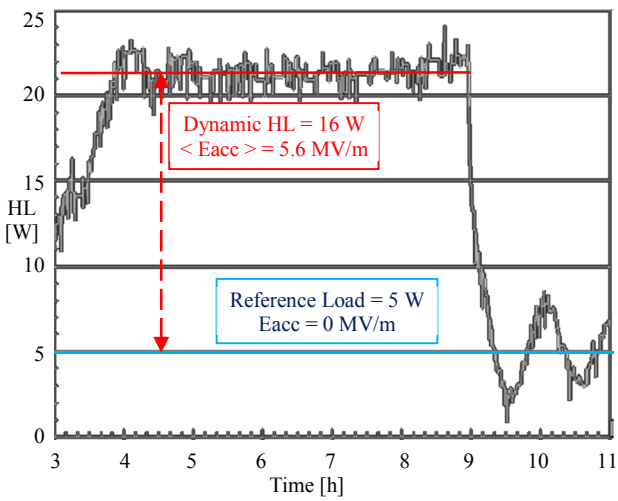

Figure 1: (Colour) Dynamic HL measured at 5.6 MV/m.

The measured 2 K dynamic HL at $<E_{acc}>$ = 5.6 MV/m was 16 W. The operation was very stable over more than 5 hours. Knowing intrinsic quality factors of cavities assembled in PXFEL3_1 from the vertical tests, we could estimate dynamic HL, which shall be 13.7 W. The 2.3 W difference between the measured and estimated HL can be attributed to enhanced dissipation in the 14 end-groups of 7 active cavities.

Projecting this result on 8 cavities operating at 1.8 K and assuming the same static loss of 4.5 W, one might expect that XFEL cryomodules can operate cw at ~7 MV/m, staying within 20 W budget for the total HL per cryomodule.

LP OPERATION

We performed also several lp tests in 2012. For some of these tests we could operate only 6 cavities and two cavities No 7 and 8 were detuned off resonance. In other lp tests cavity 8 operated at slightly lower gradient.

Copyright © 2012 by the respective authors — cc Creative Commons Attribution 3.0 (CC BY 3.0)

Dynamic Heat Load vs. DF

In one of the lp experiments, we measured dynamic HL vs. duty factor at 8.1 MV/m. The tested DF range was from 15-47 %. In that experiment we set the rise time of RF-pulse to 100 ms to avoid overvoltage in the high voltage supply. 1/3 of the rise time was added to the RF-pulse flattop duration to calculate an effective DF. Conditions for the experiment are shown in Table 2. Figure 2 summarizes the result. For DF between 15-30% the measured dynamic HL is slightly lower than the estimated value. For DF higher than 30%, the measured dynamic HL is higher than the estimated one and the difference increases with DF. For DF=47% the difference is 3.4 W, which is 280mW/end-group. Again, projecting the result on 8 cavities at 1.8 K, it seems possible to operate XFEL cryomodules at 20 MV/m with DF=14% and the pulse rep-rate of 1 Hz, keeping the 20 W budget for total HL.

Table 2: Conditions for the dynamic HL test vs. DF

Condition /Parameter	Value/Status
Number of cavities in operation	6
$< E_{acc} >$	8.1 MV/m
Q_{ext}	$1.5 \cdot 10^7$
RF-pulse repetition rate	0.7 Hz
RF-power / Input coupler	1200 W
RF-feedback	off
Piezo-feedback and bias	on

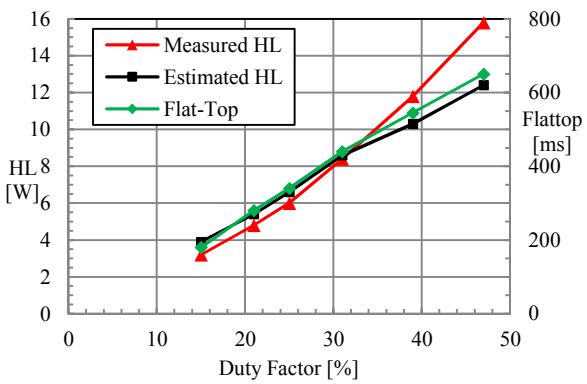

Figure 2: (colour) Measured and estimated dynamic HL, and flattop vs. effective duty factor at $<E_{acc}>$ = 8.1 MV/m.

Maximum gradient vs. DF

We set 6 good performing cavities at 10.5 MV/m and cavity No 8 at 8.1 MV/m. The RF-power was 18 kW, close to the IOT limit. The cryomodule operated for more than two hours very stable. The DF was 17%, flattop 200 ms and rep-rat 0.7Hz. The measured dynamic HL was 5.3W and it was higher than the estimated value by 0.8W, which is 64 mW/end-group. The test proved that XFEL cryomodules should run at 21 MV/m with 140 ms flattop and DF=17%, keeping total HL below 20W.

LLRF

As mentioned already, we used mainly µTCA LLRF electronics, which performed very reliable, both in the cw and lp mode. Amplitude and phase of the vector sum (VS) for 8 cavities operating cw at 3.5 MV/m could be stabilized by the RF-feedback (piezo feedback was off) to $6.5 \cdot 10^{-5}$ and 0.0098° rms respectively (see Figure 3). When the RF-feedback was switched off, standard deviation for the VS amplitude and phase was $1.5 \cdot 10^{-3}$ and 0.5° respectively.

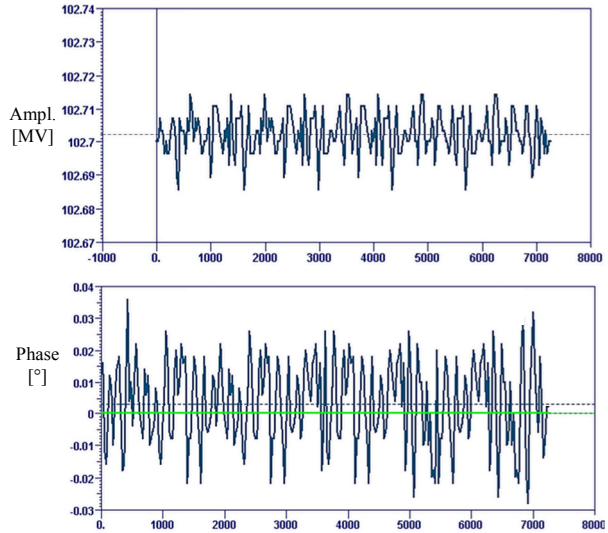

Figure 3: Amplitude (upper) and phase (lower) for cw mode when the RF-feedback was on. The whole range of horizontal axes is 1 s and the displayed units are arbitrary.

Similar stability was achieved for the lp operation. We also observed that the piezo-feedback suppressed microphonics by at least factor of 2, however we were not able to integrate operation of the piezo- and RF-feedback simultaneously.

FINAL REMARKS

The cw and lp operation test result are encouraging. These operations seem to be possible, even though the total HL/cryomodule is rather limited for the XFEL linac. We still do not have the final proof, and following has to be demonstrated or measured in the near future:

1. Lp operation at gradients ~20 MV/m.
2. HL for operation at 1.8 K at higher gradients.
3. Integration of the piezo- and RF-feedback.

We are planning to conduct these experiments in fall 2012 and in 2013.

ACKNOWLEDGMENT

We want to express our gratitude to A. Bruesewitz, R. Gabler, V. Katalev, S. Knoop, T. Prien, I. Sandvoss, T. Wölflick for their technical support.

REFERENCES

[1] J. Sekutowicz et al., "Cw and lp operation test of XFEL-like cryomodule", IPAC12, New Orleans, USA, 21-25 May, 2012.

[2] R. Brinkmann et al. (editors), TESLA TDR, DESY-Report-2001-23, 2001.

Copyright © 2012 by the respective authors — cc Creative Commons Attribution 3.0 (CC BY 3.0)

STATUS OF THE EUROPEAN XFEL 3.9 GHZ SYSTEM

P. Pierini#, A. Bosotti, P. Michelato, L. Monaco, C. Pagani, R. Paparella, D. Sertore,
INFN Milano/LASA, Italy
E. Vogel, DESY, Germany
E. Harms, FNAL, USA

Abstract

The third harmonic system at 3.9 GHz of the European XFEL injector section will linearize the bunch RF curvature, induced by first accelerating module, before the first compression stage. This paper presents qualification tests on cavity prototypes and the on-going activities towards the realization of the third harmonic section of the European XFEL in view of its commissioning in 2014.

INTRODUCTION

The European XFEL injector foresees a third harmonic section after the RF photocathode gun and the first 1.3 GHz accelerating module [1-3], just before the first bunch compression stage. The 3rd harmonic system is similar to the ACC39 module built by FNAL [4-7] and nowadays operated at FLASH in DESY Hamburg.

The XFEL 8-cavity module will provide a maximum voltage of 40 MV, with gradients well within the cavity performances already achieved by the FLASH experience.

This paper reports on the status of the main on-going activities related to different components of the 3.9 GHz section, namely testing of prototype cavities, procurement of components and finalization of the 3rd harmonic system design.

CAVITY PROTOTYPES

The baseline fabrication process for the 3.9 GHz resonators is based on the experience earned by the production of the 1.3 GHz TTF cavities. Moreover, since the maximum gradient required for these kinds of resonators is 20 MV/m, we chose a standard chemical processing (BCP) as bulk treatment. Minor adaptations were performed to the FLASH FNAL cavity design, mainly in order to conform to the different module design or to adapt them to standard XFEL components (e.g. flanged HOM/PU feedthroughs). In preparation for the realization of the final system, three full dressed prototype cavities (3HZ01-3) have been tendered for fabrication and processing at E. Zanon SpA, one of the qualified vendors for the XFEL main linac resonators [2].

To finalize the production phase, Cu and Nb mockups were used. After the mechanical fabrication, a bulk BCP etched 150 um from the inner surface and an 800 °C UHV oven treatment (at DESY) was performed to remove the hydrogen content. The cavities were tuned to a final Field Flatness to > 95 %, with a length spread of ±0.4 mm from the nominal dimensions, well within the structure length specifications. Each cavity has then undergone the final light BCP chemistry (10-30 um), HPRs and final preparation for cold vertical test.

After fabrication and processing, vertical testing of the cavities has been performed at INFN Milano - LASA, where the cavity preparation area and vertical RF test station was refurbished, adapted for the 1.3/3.9 GHz XFEL workprogram and qualified through test of 1.3 GHz single cells of proven performances provided by DESY.

TEST RESULTS

3HZ01

This was the first 3.9 GHz cavity tested at LASA with the upgraded infrastructure. Besides few glitches due the infrastructure commissioning, an error in the variable coupler setup prevented a consistent RF characterization of the cavity. We had indications of high losses, possibly located in the antenna region, but the absence of a complete temperature mapping of the cavity prevent its confirmation.

Moreover, due to the new changes in the cryogenic system and as a measure to limit LHe consumption, we performed LN_2 precooling, resulting in a long permanence of the cavity between 77 K and 150 K, possibly driving "Q-disease" effects that were concurrent, in our interpretation, with antenna losses.

To rule this effect out in preparation for a new test, the cavity has been newly heat-treated after warmup and it is now waiting the final chemistry and further testing.

Although the first test was not fully successful, it was a very important step for the final commissioning of the 3.9 GHz test infrastructure and highlighted the need for improved diagnostics. During the cryogenic operation, the overall static losses of the test stand were measured at values lower than 1 W. The lesson learned in this first cooldown and low He consumption required for operation allowed avoiding LN_2 precooling in the successive tests.

3HZ02

After the commissioning of the facility with the 3HZ01 test, the RF power feed was changed to a fix coupling scheme through the cavity main coupler port. Cavity 3HZ02 was therefore sent to measurement after a light final BCP chemistry of 10 um. For this test temperature sensors were installed on the cavity.

After the subcooling from 4.2 K to 2.0 K the surface resistance reached a final value of about 320 nΩ. The cavity reached a maximum field of 15 MV/m with a Q_0 of

#paolo.pierini@mi.infn.it

Copyright © 2012 by the respective authors — cc Creative Commons Attribution 3.0 (CC BY 3.0)

8 10^8 (see Fig. 1), without any detectable X-Ray or field emission. Analysis of the fundamental pass-band modes power rises indicate that the limiting cells are #2 or #8 (numbering starts from the coupler side), but do not allow discrimination between the two.

Given the high residual resistance with respect to the foreseen value and to the FNAL experience [5], we proceeded by removing further 20 um from the cavity surface with a further BCP etch. The subsequent RF vertical test was comparable to the previous one, reaching a maximum accelerating field around 15 MV/m with a Q_0 of 6 10^8, without indications of X-Ray or field emission. This time OST (Oscillating Superleak Transducers) (provided by FNAL and Cornell) were installed around the cavity [8] to detect second sound signals produced during cavity quenches. For this task we developed the signal processing electronics, the data acquisition system and the quench region reconstruction software.

Even if the spatial resolution of the OST reconstructed signal is still not precise enough to allow identify precisely the position of the quench origin, the analysis of the OST signals correlated with the result from the mode analysis shows that all the cell except #2 and #8 could reach approximately 20 MV/m and cell #2 is most likely the limiting one because its maximum field is similar to the overall cavity maximum field. Moreover, the OST signal shows cell #2 as quench origin and not cell #8 confirming the results of the mode analysis [9].

A cross-check of the quench locations with the optical inspection survey of the cavities does not allow identifying any geometrical features on the inner surface as quench origins. Further analysis will be also performed in order to assess the presence of contaminations during welding or geometrical features that may be responsible for the quenches at these moderate field levels.

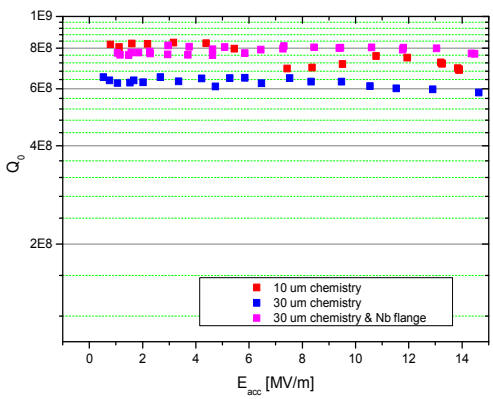

Figure 1: Q_0 versus E_{acc} at 2.0 K for cavity 3HZ02 in three tests following different treatments: 10 um BCP, 10+20 um BCP and after installation of a Nb-sputtered flange. In all cases, the maximum field at 15 MV/m was limited by a hard quench, without X-Ray and field emission activity.

As a final test we installed a Nb-coated flange on the upper beam pipe port to exclude the possible influence of fringe fields reaching the beam pipe flange on the overall dissipation. We installed also a temperature sensor on the flange to detect possible temperature increase. This third test confirmed the previous results, ruling out contribution of additional dissipation effects at the beam pipe flanges. We observed temperature rise on HOM cans.

3HZ03

The last cavity prototype, 3HZ03, underwent 30 um of surface removal by final BCP and was tested with the fixed coupling antenna.

After subcooling, the surface resistance dropped to the final value of ~90 nΩ, comparable to FNAL experience at 2.0 K [5]. The maximum accelerating field at 2.0 K is 19 MV/m with a Q_0 of 9 10^8, limited by quench. The Q_0 increases to 1 10^9 at 1.8 K, where we reached a maximum accelerating field of 21 MV/m, followed by a quench. RF test results of the fundamental power rises at 2.0 and 1.8 K are presented in Figure 2. As for the previous cavities, we did not observe any X-ray or field emission activity.

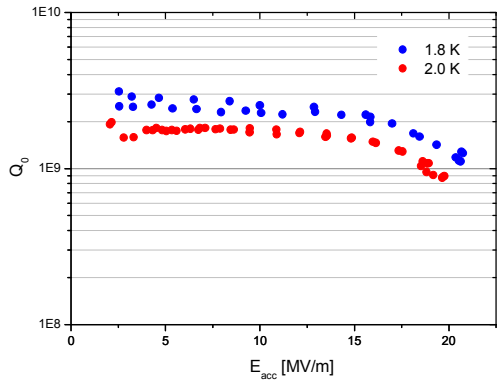

Figure 2: Q_0 versus E_{acc} for cavity 3HZ03 at 2.0 K and 1.8 K. The cavity is quench limited without X-ray or field emission.

Figure 3 shows the power rise of all cavity modes of the fundamental pass-band. As for the case of cavity 3HZ02, the cavity performance on the π mode is limited by cells #2 or #8.

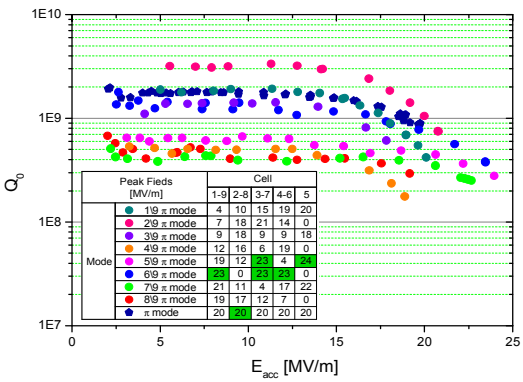

Figure 3: Q_0 vs E_{acc} for all fundamental pass-band modes of cavity 3HZ03. The mode analysis shows that cells #2 and #8 are limiting the cavity performance in the π mode, while the other individual cells reach 23 MV/m and above (values highlighted in green).

Copyright © 2012 by the respective authors — cc Creative Commons Attribution 3.0 (CC BY 3.0)

Besides these cells, all other cells have been excited to fields above 23 MV/m during the power rises. The table inset in Figure 3 summarizes the maximum accelerating field reached in each cell, and the maximum fields are highlighted in color.

Future Activities

The vertical testing program is now focused on the qualification of 3HZ01 and later on a second round of tests for qualification of the three cavities with HOM antennas installed. The HOM tuning procedure has been tested on the Nb mockup cavity and the cavity HOM antennas fabrication will start soon.

After this second round of tests, the three prototypes will be integrated with the helium tanks (nearly ready) prior to horizontal test qualification with power couplers.

"QUENCH SIMULATOR" FOR OST

In order to check the OSTs response and to validate and calibrate the reconstruction routines, we have developed a "quench simulator", based on pulsed resistors placed at known locations around the cavity in the LHe bath. At present, we have installed two SMD two ceramic supported resistors.

Fig.4 shows the experimental setup (photograph on the left) and an example of reconstruction of the position of the second "quench simulator" (yellow sphere), as determined by the reconstruction routines (model on the right). The estimated position of the origin of the signal detected by the OSTs is currently within +/- 5 mm from its physical location, larger than the uncertainty associated to the absolute position of the sensors in the setup and still not adequate for the quench origin determination in these small structures (the cavity iris-to-iris nominal distance is only 38 mm). Improvements in the quench reconstructions algorithms, to account for sensor finite dimensions and proper handling of signal propagation in the correct geometry, are on-going to increase this resolution.

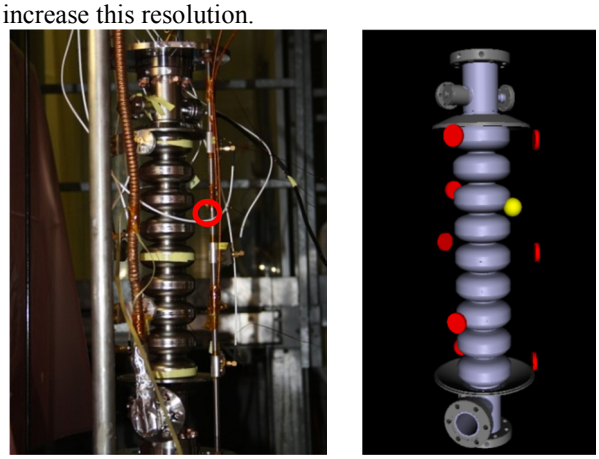

Figure 4: OSTs around the cavity (left photograph of the cavity in the insert) and reconstruction of the quench origin (model on the right). The source is highlighted by the red circle on the left and represented by the yellow sphere on the right, where OSTs are shown in red.

THE XFEL 3.9 GHZ SYSTEM

The 3.9 GHz complete system is provided to the European XFEL Project as an In-Kind contribution by INFN and DESY, and builds on the successful FNAL experience demonstrated by FLASH ACC39 system. The general layout of the 3.9 GHz system at the XFEL injector has been presented in Ref. [3]. Since the European XFEL injector commissioning is foreseen to start in mid 2014, the procurement of the third harmonic section components is entering its final stages. Call for tenders for cavity fabrication is going to be placed late this summer.

The 8-cavity cryomodule design, which includes a quadrupole magnet placed at the beginning of the cavity string, is nearly completed. Fig. 5 shows its view with installed cavities. The call for tender is ready to be launched fall this year.

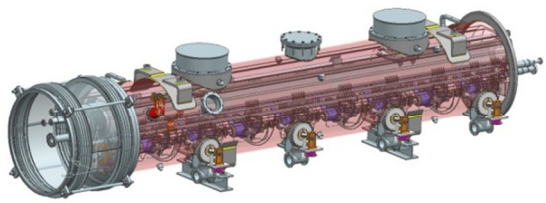

Figure 5: View of the XFEL 3.9 GHz cryomodule full equipped with cavities. Power couplers are alternated to reduce kicks to the beam.

REFERENCES

[1] E. Vogel et al. "Status Of The 3rd Harmonic Systems For FLASH And XFEL In Summer 2008," LINAC08, Victoria, BC, Canada, 2008, TUP034, p. 821.

[2] P. Pierini et al. "Third harmonic Superconducting Cavity Prototypes for the XFEL," LINAC08, Victoria, BC, Canada, 2008, THP019, p. 821.

[3] P. Pierini et al., "Status of the XFEL 3.9 GHz Injector Section", IPAC11, San Sebastian, Spain, 2011, MOPC091, p. 289.

[4] E. Vogel et al. "Test And Commissioning Of The Third Harmonic RF System For FLASH," IPAC10, Kyoto, Japan, 2010, THPD003, p. 4281.

[5] E. Harms et al, "Third Harmonic System at FERMILAB/FLASH", SRF09, Berlin, Germany, 2009, MOOBAU01, p. 11.

[6] H. Edwards et al, "3.9 GHz Cavity Module For Linear Bunch Compression At FLASH," LINAC10, Tsukuba, Japan, 2010, MO304, p. 41.

[7] E. Harms et al, "Commissioning And Early Operating Experience Of The FLASH Third Harmonic RF System," LINAC10, Tsukuba, Japan, 2010, TUP013, p. 422.

[8] Z. A. Conway et al., "Oscillating Superleak Transducers For Quench Detection In Superconducting ILC Cavities Cooled With He-II", LINAC08, Victoria, BC, Canada, 2008, THP036, p. 863.

[9] P. Pierini et al., "Status of the European XFEL 3.9 GHz system", IPAC12, New Orleans, USA, 2012, WEPPC009, p. 2224.

Copyright © 2012 by the respective authors — cc Creative Commons Attribution 3.0 (CC BY 3.0)

STUDY OF PLASMA EFFECT IN LONGITUDINAL SPACE CHARGE INDUCED MICROBUNCHING INSTABILITY*

Dazhang Huang†, Qiang Gu, SINAP, Shanghai, 201800, China, P. R.
King-Yuen Ng‡, Fermilab, Batavia, IL 60616, USA

Abstract

Microbunching instability (μBI) usually exists in the LINAC of a free electron laser facility. If it is not well-controlled, the beam quality will be seriously damaged and the machine will not operate properly. In many cases, the longitudinal space charge (LSC) is a dominant factor that generates the instability; therefore its contribution must be studied in details. The current model of the LSC impedance [1] derived from the fundamental electromagnetic theory [2] has been widely used to explain the physics of the LSC-induced μBI. [3] However, in the case of highly bright electron beams, the plasma effect may also play a role. In this article, the basic model of the LSC impedance including the plasma effect is constructed by solving Vlasov and Poisson equations in the 6-D phase space, and preliminary investigation is carried out to study the modification to the instability gain. The solution indicates that the μBI gain depends not only on the spatial information of the beam, but also on the velocity (momentum) and time information. The comparison of the gains of the μBI in the LINAC of Shanghai soft X-ray Free Electron Laser Facility (SXFEL) computed by various methods is given and the discrepancy is illustrated.

INTRODUCTION

The possibility of oscillation in a plasma due to local separation of charges and the consequent restoring forces was discussed by J. D. Jackson long time ago. [4] The theory is based on a neutral plasma, which has both the positively (ion) and negatively (electron) charged components. For a charged particle beam in an accelerator, although it is not neutral in terms of charges, there is still density fluctuation due to the graininess of the individual particles — in our case, the individual electrons. Such graininess is usually smoothed out in the fluid model and ignored in most computations. In a highly intensive beam, however, it may introduce the "plasma-like" oscillation (for convenience, "plasma oscillation" is used hereafter), and must be investigated in details in order to reveal its magnitude and to discover its physics. Similar discussions in the 2-D phase space for this effects on the free electron laser have been addressed by Kim, et. al. [5]

In this article, we start our discussions in the 6-D phase space by employing Vlasov and Poisson (Gauss) equations, which describe the evolution of the distribution function of the electron bunch and the electric field induced by the charge distribution. We then use a method similar to Jackson's [4] to linearize the Vlasov equation and obtain the solution of the initial-value problem. The solution includes the contributions from both the perturbed and unperturbed parts of the initial distribution. As the result, the contribution from the velocity distribution is also included. From the solution, we see that the plasma oscillation introduces a "relative dielectric factor (permittivity)" ϵ_r, and also an extra factor coming from the initial velocity distribution.

* Work supported by National Science Foundation of China (NSFC), Project No. 11275253, and US DOE, contract DE-FG02-92ER40747.
† huangdazhang@sinap.ac.cn
‡ ng@final.gov

SOLUTION OF INITIAL-VALUE PROBLEM

We carry out the investigations with the equations describing the evolution of beam distribution under the influence of the electromagnetic force. The discussion is in laboratory frame hereafter. In cylindrical coordinates system, the linearized Vlasov-Poisson equation and the Poisson (Gauss) equation can be written:

$$\frac{\partial f_1}{\partial t}+v_z\frac{\partial f_1}{\partial z}+v_\perp\frac{\partial f_1}{\partial r}-\frac{eE_z}{\gamma m}\frac{\partial f_0}{\partial v_z}+\frac{F_\perp}{\gamma m}\frac{\partial f_0}{\partial v_\perp}=0, \quad (1)$$

$$\frac{\partial E_z}{\partial z}+\frac{1}{r}\frac{\partial}{\partial r}(rE_r)=-\frac{e}{\epsilon_0}\int f_1 dv_z, \quad (2)$$

where $-e$ is charge of an electron, $f(t,\vec{r},\vec{v})=f_0(t,\vec{r},\vec{v})+f_1(t,\vec{r},\vec{v})$, with f_0 being the unperturbed background of the beam and f_1 the density perturbation due to plasma oscillation. We assume that f_0, f_1 and $\vec{E}$ have no azimuthal dependence, which is reasonable. The Gauss's law or Poisson equation, Eq. (2), will be solved in the particles' rest frame and then Lorentz transformed to the lab frame in the next section.

Since the transverse velocity $v_\perp$ is small, we can assume $v_z\approx v$ and $F_\perp \ll F_z$. Then Eq. (1) simplifies to

$$\frac{\partial f_1}{\partial t}+v\frac{\partial f_1}{\partial z}-\frac{eE_z}{\gamma m}\frac{\partial f_0}{\partial v}=0. \quad (3)$$

Let us focus on Eqs. (3) and (2). Following Jackson, [4] we perform Fourier transform in t and Laplace transform in z on Eq. (3), and integrate by parts to obtain

$$\int dz\left[e^{-ikz+i\omega t}f_1(v,z,t)\right]_{t=0}^{t=\infty}+\int_{-\infty}^{\infty}dz\int_0^\infty e^{-ikz+i\omega t}dt \times\left[(-i\omega+ikv)f_1-\frac{e}{\gamma m}\frac{\partial f_0}{\partial v}E\right]=0. \quad (4)$$

Copyright © 2012 by the respective authors — cc Creative Commons Attribution 3.0 (CC BY 3.0)

For ω in the upper half plane, the upper limit of the first term on the right hand side of Eq. (4) vanishes as $t \to \infty$. We have then the solution in (v, ω, k) space,

$$f_1(v,\omega,k) = \frac{1}{i(kv-\omega)}\left[\Phi(v,k) + \frac{e}{m}\frac{\partial f_0}{\partial v}E(\omega,k)\right], \tag{5}$$

where

$$\Phi(v,k) = \int_{-\infty}^{\infty} dz e^{-ikz} f_1(v,z,t=0). \tag{6}$$

Both Eq. (5) and Eq. (6) form the solution depending on the initial-value of the density perturbation. If we perform inverse Fourier transform on ω, we will obtain the density perturbation $f_1(v,t,k)$ at later time, which represents the time revolution of the density fluctuation. In the regular LSC theory, the density fluctuation is neglected. However, it will be taken into account under certain conditions in the following discussions.

ELECTRIC FIELD INDUCED BY LSC

Based on the classical electromagnetic theory, the solution of Eq. (2) can be written as

$$E_z(\vec{x}) = \frac{e\lambda}{4\pi\epsilon_0}\int G(\vec{x},\vec{x'})\rho(\vec{x'})d^3\vec{x'}, \tag{7}$$

with the Green function

$$G(\vec{x},\vec{x'}) = \frac{(z-z')\gamma}{[(x-x')^2+(y-y')^2+(z-z')^2\gamma^2]^{3/2}}. \tag{8}$$

Here the same notations of Venturini's [1] have been used, with beam density $\lambda\rho(x,y,z)$, uniform linear density λ, $\rho(x,y,z) = \rho_\perp(x,y)\rho_z(z)$, and normalization $\int \rho_\perp(x,y)dxdy = 1$.

In cylindrical coordinates, the Green function can be expanded as [2]

$$G(\vec{x},\vec{x'}) = -\frac{i}{\pi\gamma^2}\sum_{m=-\infty}^{\infty} e^{im(\phi-\phi')}\int_{-\infty}^{\infty} kdk e^{ik(z-z')} \times I_m\left(\frac{kr_<}{\gamma}\right)K_m\left(\frac{kr_>}{\gamma}\right), \tag{9}$$

where $r_<$ and $r_>$ denotes the smaller and larger between r and r', respectively, and I_m and K_m are the modified Bessel function of the first and second kind. Thus the longitudinal electric field E_z in the k-space becomes

$$E_z(k) = i\frac{e}{4\pi\epsilon}\frac{\lambda}{\pi\gamma^2}\sum_{m=-\infty}^{\infty}\int dV'\rho(r',\phi',z')e^{im(\phi-\phi')} \times ke^{-ikz'}I_m^< K_m^>. \tag{10}$$

In our study, the unperturbed density distribution serves as the smooth background, therefore it does not contribute to the longitudinal electric field at all. For this reason, only the perturbed one (Eq. (5)) plays a role. Assuming that the beam is of radius r_b and has a uniform transverse distribution $f_\perp = 1/\pi r_b^2$ when $r \le r_b$, we write the beam distribution as $\rho(r,\phi,z) = f_\perp f_1(v,z,t=0)$. For an observation point located on axis (only $m=0$ term contributes), [1] finally we obtain

$$E(\omega,k) = \frac{e\lambda}{2\pi\epsilon_0\epsilon_r\pi r_b^2}\int_W dv \times \int_{-\infty}^{\infty} dz \frac{e^{-ikz}f_1(v,z,t=0)}{kv-\omega}\Big[1-\xi K_1(\xi)\Big], \tag{11}$$

where $\xi = kr_b/\gamma$, and

$$\epsilon_r = k - \frac{e^2\lambda}{2\pi\epsilon_0\gamma m}\int_W \frac{\partial f_0}{\partial v}\frac{dv}{kv-\omega} \tag{12}$$

is the relative dielectric factor (permittivity). The path of integration W is from $v=-\infty$ to ∞ passing below the pole $v=\omega/k$. This path comes from the analytic continuity from the upper ω-half-plane to the whole ω-plane. Introducing the frequency of plasma oscillation in lab frame, $\omega_p = \sqrt{e^2\lambda/2\pi\epsilon_0\gamma m}$, Eq. (12) can be written as

$$\epsilon_r = k - \omega_p^2\int_W \frac{\partial f_0}{\partial v}\frac{dv}{kv-\omega}. \tag{13}$$

Equation (13) is also called the dispersion relation, it is a function of the wavenumber k of the density fluctuation. Equation (11) is the expression of the longitudinal electric field induced by the LSC under the influence of density fluctuation (plasma oscillation). Apparently, it includes the contribution due to the velocity distribution of the beam.

In most of the cases, where the momentum and location of the electron are decoupled, the perturbation can also be written as $f_1(v,z,t=0) = f_{v1}(v,t=0)f_{z1}(z,t=0)$. Equation (11) becomes

$$E(\omega,k) = \frac{e\lambda\big[1-\xi K_1(\xi)\big]}{\epsilon_0\epsilon_r\pi r_b^2}\int_W dv\frac{f_{v1}(v,t=0)}{kv-\omega} \times \frac{1}{2\pi}\int_{-\infty}^{\infty} e^{-ikz}f_{z1}(z,t=0)dz. \tag{14}$$

Equation (14) decouples the contributions from the beam density distribution and velocity/momentum distribution.

INFLUENCE ON μBI

In this section, we start our preliminary discussions on the effects of the modified LSC impedance in microbunching instability. As already known, the gain of μBI due to the LSC impedance (linear in beam current) reads [6]

$$G = Ck|R_{56}|\frac{I_0}{\gamma_0 I_A}\frac{|Z(k)|}{Z_0}\exp\left(-\frac{C^2k^2R_{56}^2\sigma_\gamma^2}{2\gamma_0^2}\right), \tag{15}$$

where C is the compression factor of a bunch compressor (chicane), R_{56} is the transport matrix element of the whole bunch compressor, and σ_r is the uncorrelated energy spread. In Eq. (15), one can see that the gain is proportional to the absolute value of LSC impedance per unit length $Z(k)$.

Copyright © 2012 by the respective authors — cc Creative Commons Attribution 3.0 (CC BY 3.0)

The impedance per unit length of the longitudinal space charge is defined as

$$Z(k) = -E_z(k)/I(k), \quad (16)$$

where $I(k)$ is the Fourier transform of the beam current, i.e., $I(k) = ec\lambda\rho_z(k)$. Note that in our discussion $\rho_z(k) = (2\pi)^{-1}\int e^{-ikz} f_1(z, t = 0)dz$. Based on Eq. (14), we can derive the LSC impedance in the existence of density fluctuation:

$$Z(\omega, k) = -\frac{Z_0}{\pi\gamma\epsilon_r r_b}\frac{1-\xi K_1(\xi)}{\xi}\int_W \frac{f_1(v, t=0)dv}{kv-\omega}. \quad (17)$$

Comparing with the regular expression of the LSC impedance without density fluctuation, [1, 3] we can see that the difference comes from the relative dielectric factor ϵ_r and the initial velocity perturbation $f_1(v, t = 0)$. Moreover, it is also a function of the oscillation frequency ω.

At this point, we believe that more investigations are needed to obtain the exact picture of the development of the μBI induced by the longitudinal space charge field. For an example, assuming the Gaussian distribution of electron velocity, and performing inverse Fourier transform on ω, we will find the explicit time and wavelength dependence of the microbunching instability.

In the proposed Shanghai X-ray Free Electron Laser Facility (SXFEL), [7] at the exit of the LINAC injector, the momentum distribution is Gaussian-like (Fig. 1) and the current profile is Gaussian with a number of small spikes, i.e., initial modulation (Fig. 2). Although the numerical simulation and analytic solution of the μBI gain at the exit of LINAC are both not-so-significant, we can still see the discrepancy between them (Fig. 3).

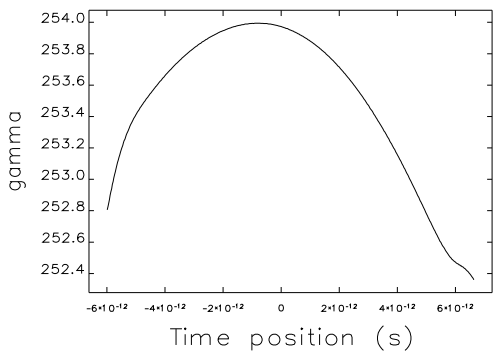

Figure 1: Beam momentum distribution at the exit of SXFEL injector.

CONCLUSIONS

The electric field introduced by the longitudinal space charge (LSC) with density fluctuation (plasma oscillation) is studied in detail by solving the Vlasov and Poisson equations. Its influence on the LSC-induced microbunching instability (μBI) is carried out. The preliminary investigation implicates that the gain curve of μBI does not depend only on the spatial information of the beam, but also on the beam's momentum/velocity information as well. Further study is ongoing to reveal the details of the development of the LSC-induced μBI.

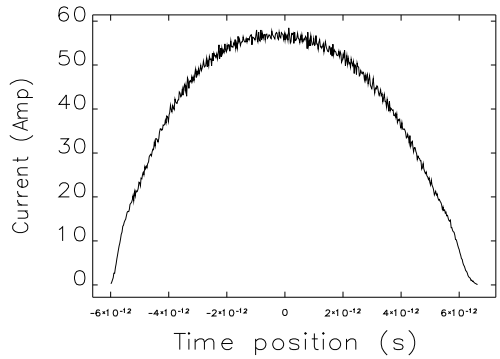

Figure 2: Current profile at the exit of SXFEL injector.

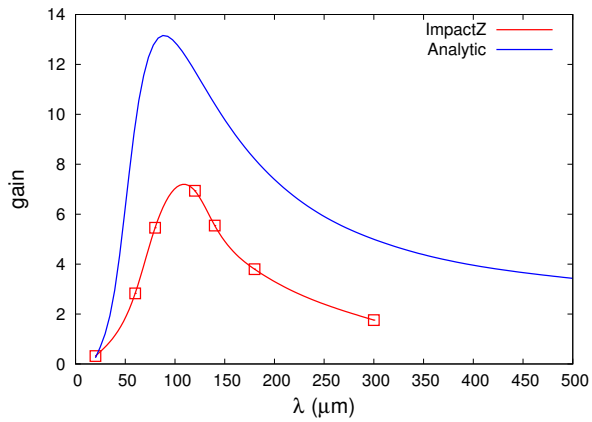

Figure 3: (color) μBI gain at the exit of SXFEL LINAC computed by different methods: ImpactZ simulation (red), and analytic solution (blue).

REFERENCES

[1] Marco Venturini, Phys. Rev. ST Accel. Beams 11, 034401 (2008)

[2] J. D. Jackson, Classical Electrodynamics (Wiley, 1999)

[3] Z. Huang, et. al., Phys, Rev. ST Accel. Beams 7, 074401 (2004)

[4] J. D. Jackson, J. Nucl. Energy, Part C: Plasma Physics, 1960, Vol 1, 171-189

[5] K.-J. Kim and R. R. Lindberg, FEL11-proceedings, Aug. 2011, Shanghai, China

[6] E.L. Saldin, et. al., NIMA 483 (2002) 516-520

[7] The feasibility study report of the Shanghai X-ray Free Electron Laser Facility, Nov. 28, 2011

Copyright © 2012 by the respective authors — cc Creative Commons Attribution 3.0 (CC BY 3.0)

A PASSIVE LINEARIZER FOR BUNCH COMPRESSION

Q. Gu#, M. Zhang, M. H. Zhao, SINAP, Shanghai, China

Abstract

In high gain free electron laser (FEL) facility design and operation, a high bunch current is required to get lasing with a reasonable gain length. Because of the current limitation of the electron source due to the space charge effect, a compression system is used to compress the electron beam to the exact current needed. Before the bunch compression, the nonlinear energy spread due to the finite bunch length should be compensated; otherwise the longitudinal profile of bunch will be badly distorted. Usually an X band accelerating structure is used to compensate the nonlinear energy spread while decelerating the beam. But for UV FEL facility, the X band system is too expensive comparing to other system. In this paper, we present a corrugated structure as a passive linearizer, and the preliminary study of the beam dynamics is also shown.

INTRODUCTION

In a high gain free electron laser facility, the electron beam will be accelerated and compressed before lasing. Because of the finite length of the electron beam and the sinusoidal accelerating voltage of the RF field, a nonlinear energy chirp has been induced. With this energy chirp, a ramped or a spiky [1] [2] current profile will be generated after the compressor, which will cause the partial lasing to the whole bunch and prevent getting higher peak current. To correct the nonlinear energy chirp, a higher harmonic RF linearizer was proposed and successfully used [2] [3] [4].

The corrugated structure is a metallic, cylindrical tube with periodic, shallow corrugations (see Figure 1). This structure was used for a model of roughness wake, a source of the THz radiation [5] and a dechirper for the high gain FELs [6]. By choosing the parameters of the structure, one can change both the wake length and the amplitude of the wake. With these two wake function parameters, one can easily match the duration (bunch length) and the amplitude of the nonlinear energy chirp.

In this paper, we will report the principle to setup a passive linearizer and the application to the Dalian UV FEL facility.

THE CORRUGATED STRUCTURE AS AN ENERGY CHIRP LINEARIZER

The structure of the corrugated cylindrical pipe is shown in Figure 1. The pipe radius is a, the corrugation periodis p, the corrugation gap is g, and the corrugation depth isδ, while p,δ « a, and δ≥ p. The earlier work on corrugated structure [7] [8] [9] has shown that when a short, ultra-relativistic charged beam passes through the structure, a strong fundamental mode with a frequency above the cut-off frequency of the cylindrical pipe will be excited. The longitudinal point charge wakefield of this mode is approximatelywritten as,

$$W(s) = 2 \cdot \chi \cdot H(s) \cdot cos\,(k \cdot s). \qquad (1)$$

The χ is the loss fact by

$$\chi = \frac{Z_0 \cdot c}{2 \cdot \pi \cdot a}, \qquad (2)$$

the H(s) is a unit step function by,

$$H(s) = \begin{cases} 1, s \geq 0 \\ 0, s < 0 \end{cases}, \qquad (3)$$

and the k is the wave number of the fundamental mode by

$$k = \sqrt{\frac{2 \cdot p}{a \cdot \delta \cdot g}}. \qquad (4)$$

The wake potential is given by the convolution

$$W_\lambda(s) = \int W(s') \cdot \lambda(s - s') ds', \qquad (5)$$

the λ (s) is the line charge density of the charged beam. And the energy loss along the beam can be easily calculated as

$$E_{loss}(s) = W(s) \cdot \lambda(s). \qquad (6)$$

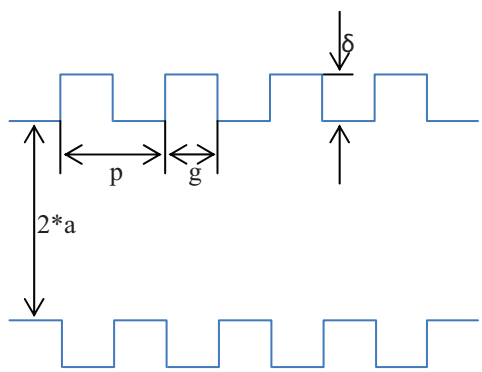

Figure 1: The drawing of the corrugated structure

Considering a beam with infinitesimal rising time and falling time, and with a length of l without any current fluctuation, we choose the wave length of the point charge wake potential twice as the bunch length. We simplify the calculation by only considering the field within the beam. The result is written as

$$E_{loss}(s) = -2 \cdot \chi \cdot \lambda \cdot \frac{l}{\pi} \cdot sin\,(\frac{\pi}{l} \cdot s). \qquad (7)$$

#guqiang@sinap.ac.cn

Copyright © 2012 by the respective authors — cc Creative Commons Attribution 3.0 (CC BY 3.0)

And some results are shown in Figure 2.

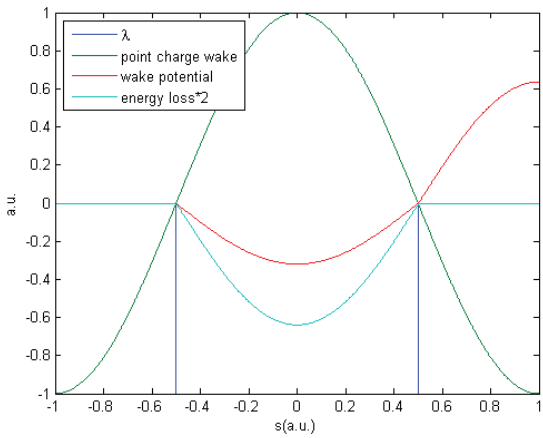

Figure 2: The energy loss along the beam. The energy loss (cyan) is multiplied by a factor of 2; otherwise it overlaps with the wake potential. The amplitude of the line charge density of the beam and the loss factor of the point charge wake function are normalized

In this case, the corrugated structure induced energy loss along the bunch is with a sinusoidal waveform and with a wavelength of two times as the bunch length, which could be used as a linearizer for the temporary phase space manipulation. This structure will work as the harmonic cavity but with short wavelength and lower correcting voltage.

To optimize the parameters of the corrugated structure for linearizing the energy chirp, one should find out the proper wavelength κ and the loss factor χ. With a given quadratic energy chirp and the beam current, we can get the loss factor through equation 7 and by equation 2 one can determine the radius of the corrugated structure. Then by properly choosing the parameters p, δ and g using the equation 4, we should get the right wavelength of the point charge wake potential which is twice as the bunch length. During this calculation, we must keep the condition of p, δ « a, and δ≳ p.

APPLICATION TO DALIAN COHERENCE LIGHT SOURCE

Dalian Coherence Light source (DCL) is a free electron laser (FEL) facility withhigh gain harmonic generation (HGHG) scheme [10]. By using the OPA technique in the seed laser system, the FEL output wavelength can be continuously tuned from 50 to 150 nm. The DCL consists of a linear accelerator, a radiator, and the beamlines (see Figure. 3). The radiatorconsists of undulators system and seeding laser system. The beamlines consist of the transport lines and experimental stations.

The linac consists of a photo-cathode RF gun, 7 SLAC-type accelerating tubes (2.856 GHz), and a magnetic bunch compressor. The linaccan deliver a high brightness electron beam to the radiator (see Table 1).

Table 1: Main parameters of the DCL linac

Parameters	Values	Units
Energy	~300	MeV
Energy spread(global)	<0.2	%
Peak Current	~300	A
Charge	~500	pC
Normalized emittance (slice)	~4	mm·mrad

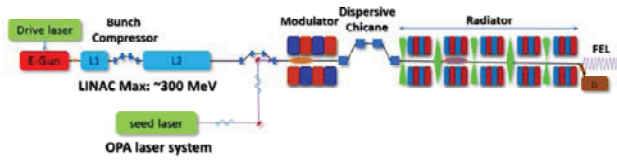

Figure 3: Schematic layout of the DCL.

In the original design, there is no X-band linearizer due to the budget limit. Because of the quadratic term of the energy chirp before the bunch compressor, we could not get the higher current, and suffer from the large peak with a long tail (see Figure 5). This turns out to be that the lasing will only take place at a small part of the whole bunch, which will limit the laser pulse energy and cause the bandwidth degradation in the long pulse mode for the energy resolved experiments.

Table 2: Main parameters of corrugated structure

Parameters	Values	Units
a	3.3	mm
p	1.25	mm
δ	0.5	mm
g	0.9	mm
L (total length)	0.45	m

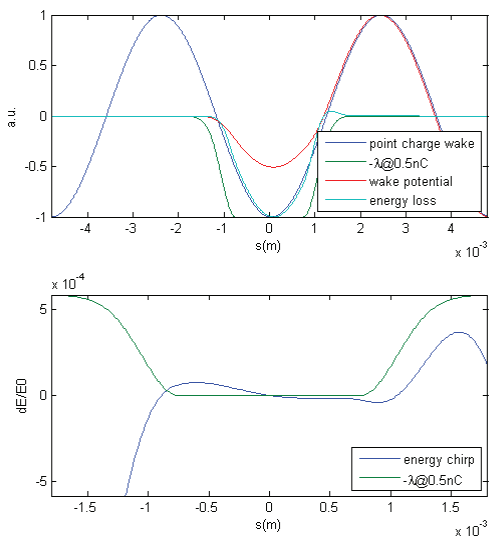

Figure 4: Linearizing of the energy chirp. The energy loss along the bunch (up) and the final result (bottom).

Copyright © 2012 by the respective authors — cc Creative Commons Attribution 3.0 (CC BY 3.0)

To use the corrugated structure as a linearizer for the DCL, we must choose the proper corrugated parameters by the method mentioned above. Through some calculations and tests due to the imperfect beam profile, the parameters are shown in Table 2, and the estimated result of energy chirp linearizing is shown in Figure 4. It shows the quadratic chirp has been compensated in the middle, but remains in the head and tail.

To ensure this structure will work in a real linac, the code LiTrack [11] is used for simulation study on the longitudinal tracking (see Figure 5). The results shows that by optimizing the parameters of the corrugated structure, we can make current profile of the compressed beam even more flat that the X-band case. But there still has a sharp edge due to the finite rising time of the bunch. The sensitivity of the jitter is also studied by the code for the three cases. With a set of given hardware jitters, the jitter of the beam parameters is not significantly from one to another (see Table 3).

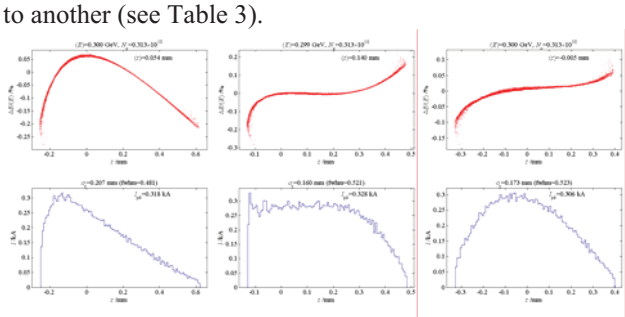

Figure 5: The longitudinal phase space at the exit of the linac. Without linearizing (left), with corrugated structure (middle), with X-band (right)

Table 3: Jitter budget comparison

Parameters	without linearizing	corrugated structure	X-band
R56,opt.(mm)	-50	-75	-75
Beam energy (0.1%)	1.0	0.87	0.96
Peak current (%)	5.3	3.4	6.2
Arriving time (fs)	132	173	186

The code Elegant [12] is used for the 3D beam dynamics study taking account of the strong transverse wake of the structure [9] with the structure wake field, coherence synchrotron radiation (CSR) and longitudinal space charge (LSC) effect(see Figure 6). The result shows there is a minimum emittance around the 50um displacement of the corrugated structure. This means that the transverse wake of the structure gives a kick along the bunch in advance which is opposite to the kick due to the CSR, and compensates the emittance mismatching by the CSR, at some point.

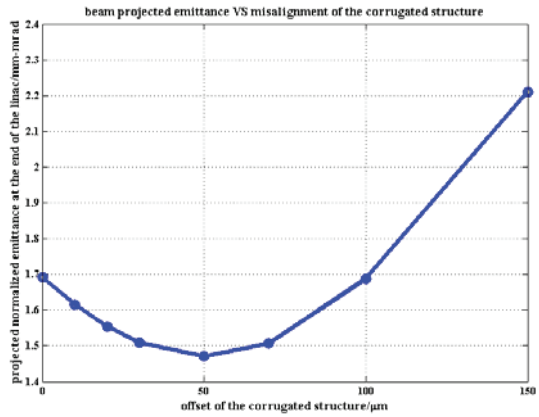

Figure 6: The emittance growth due to the displacement of the corrugated structure.

CONCLUSION

The corrugated structure could be used as a linearizer for the linac. In practise, the structure could be divided into several sections to be more flexible to fit to the beam parameters changing.

ACKNOWLEDGMENT

The authors would like to thank Dr. B. C. Jiang for useful discussions.

REFERENCES

[1] G. De Ninno, et. al., FEL COMMISSIONING OF THE FIRST STAGE OF FERMI@ELETTRA, WEPC55, Proceedings of FEL2009.
[2] H. Edwards, et. al., 3.9 GHz CAVITY MODULE FOR LINEAR BUNCH COMPRESSION AT FLASH, MO304, Proceedings of Linear Accelerator Conference LINAC2010.
[3] Linac Coherent Light Source (LCLS) Conceptual Design Report, 2002
[4] SCSS X-FEL Conceptual Design Report, 2005
[5] K. Bane and G. Stupakov, Nucl. Inst. Meth.A 677 (2012) 67~73.
[6] K. Bane and G. Stupakov, Corrugated Pipe as a Beam Dechirper, SLAC-PUB-14925, 2012
[7] S. Kheifets, Longitudinal Impedance of Simple Cylindrically Symmetric Structures, SLAC-PUB-4133, 1986
[8] K.L.F. Bane, G. Stupakov,Impedance of a Beam Tube with Small Corrugations, XX International Linac Conference
[9] Karl L.F. Bane, The Resonator Impedance Model of SurfaceRoughness Applied to the LCLS Parameters, SLAC-AP-117, 1999
[10] Conceptual design report of Dalian Coherence Light source, 2011
[11] K.L.F. Bane, P. Emma, Litrack: A Fast Longitudinal Phase Space Tracking Code with Graphical User Interface, SLAC-PUB-11035
[12] M. Borland, elegent: A Flexible SDDS-Compliant Code for Accelerator Simulation, Advanced Photon Source LS-287, September 2000.

Copyright © 2012 by the respective authors — cc Creative Commons Attribution 3.0 (CC BY 3.0)

THE OPTIMIZATION OF RF DEFLECTOR INPUT POWER COUPLER

A. Smirnov, O. Adonev, P. Binyukov, N. Sobenin,
NRNU MEPhI, Moscow, 115409, Kashirskoe sh., 31, Russia

Abstract

This paper concerns the investigation of different types of input power cell for S-band RF electron deflector. This device serving for slice emittance diagnostics is a disc-loaded waveguide which operates with TE_{11}-like wave in travelling wave regime with 120 deg phase shift per cell. Since this deflector meets the restriction on its length and has to provide high enough deflecting potential to a particle during its flight time it is significant to increase the transversal field strength in coupling cell or to shorten it so that the deflecting potential remains constant. The total structure consists of 14 regular cells and two couplers. As it is now all cells have the same length equal to D=33.34 mm and the field in couplers is lower than that of regular cells. In this paper different lengths are considered and numerically simulated in order to choose the best one.

INTRODUCTION

A deflecting voltage seen by a particle travelling along the axis of a disc-loaded waveguide driven with dipole TE_{11} (Fig. 1) mode can be calculated using transversal values of on-axis electric and magnetic fields or using longitudinal value of the electric field at some offset from the axis (Panofsky-Wenzel theorem) [1].

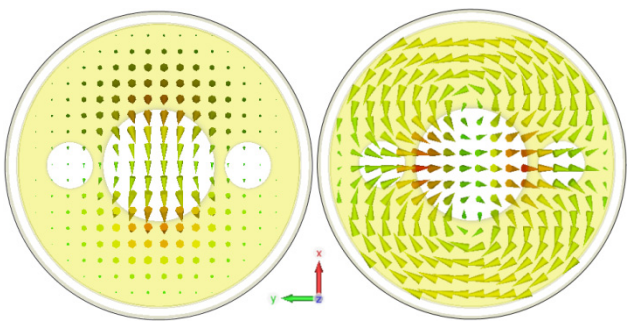

Figure 1: Electric (left) and magnetic (right) fields of TE11 mode.

In the first method, we can use x-component (vertical) of E-field and y-component (horizontal) of H-field distributions along the axis z, since the particle experiences actions from both fields. Electric and magnetic fields are orthogonal to each other. The equivalent transversal deflecting field can be derived from the expression of Lorentz force $F_L=eE_d=e(E_x\pm vB_y)$:

$$\dot{E}_d(z)=\dot{E}_x(z)\pm\mu_0\beta c\dot{H}_y(z)\,, \qquad (1)$$

where (and further on) the sign '±' refers to the interplay of the particle and the wave propagation directions. According to time dependence of field components as $\exp(i[\omega t+\theta])$, this gives the equation for the transversal potential that is gathered by electron on a path from $z=0$ to $z=L$ (structure length):

$$V_d(\theta)=\int_0^L \Re\left(\dot{E}_d(z)\right)dz=$$

$$=\int_0^L \left|\dot{E}_d(z)\right|\cos\left(\varphi_{E_d}(z)\pm\frac{2\pi}{\lambda}z+\theta\right)dz\,, \qquad (2)$$

where $\lambda=c/f$ is the wavelength and θ is the initial phase of the deflecting voltage with respect to particle. Now by varying θ through the range from 0 to 2π one can find the maximal value of the deflecting voltage V_{dmax}.

An approach through Panofsky-Wenzel theorem requires longitudinal component of the electric field only, which is taken at some small enough vertical offset from the structure axis a – $E_z(z, x=a)$. The transverse deflecting field in this case is

$$\dot{E}^{PW}(\theta)=\frac{\lambda}{2\pi}\frac{\partial\dot{E}_z(z)}{\partial x}\bigg|_{x=0}\approx\frac{\lambda\dot{E}_z(z,x=a)}{2\pi a} \qquad (3)$$

due to the fact that longitudinal on-axis field $E_z(x=0)$ is nil for hybrid waves. And the corresponding potential V_{dmax} can be found from the following expression by varying θ from 0 to 2π:

$$V_d(\theta)=\frac{\lambda}{2\pi a}\times$$

$$\times\int_0^L\left|\dot{E}_z(z,x=a)\right|\cos\left(\varphi_{E_z}(z,x=a)\pm\frac{2\pi}{\lambda}z+\theta\right)dz. \qquad (4)$$

Both dependencies (2) and (4) are sin-shaped and shifted with 90^0, which is result of Maxwell equations.

TRANSVERSE DEFLECTING STRUCTURE

The structure layout [2] is presented in Fig.2. Cell irises have two additional holes used both for coupling between the cells and for stabilization of the mode polarization plane. The deflector consists of 14 regular cells with length of D=33.34mm (required for a phase shift of 120^0 per cell) and two power couplers, therefore total length is $16D$=533.44mm. It operates at frequency of 3 GHz. The input power is 2.5 MW, which provides total deflecting

Copyright © 2012 by the respective authors — cc Creative Commons Attribution 3.0 (CC BY 3.0)

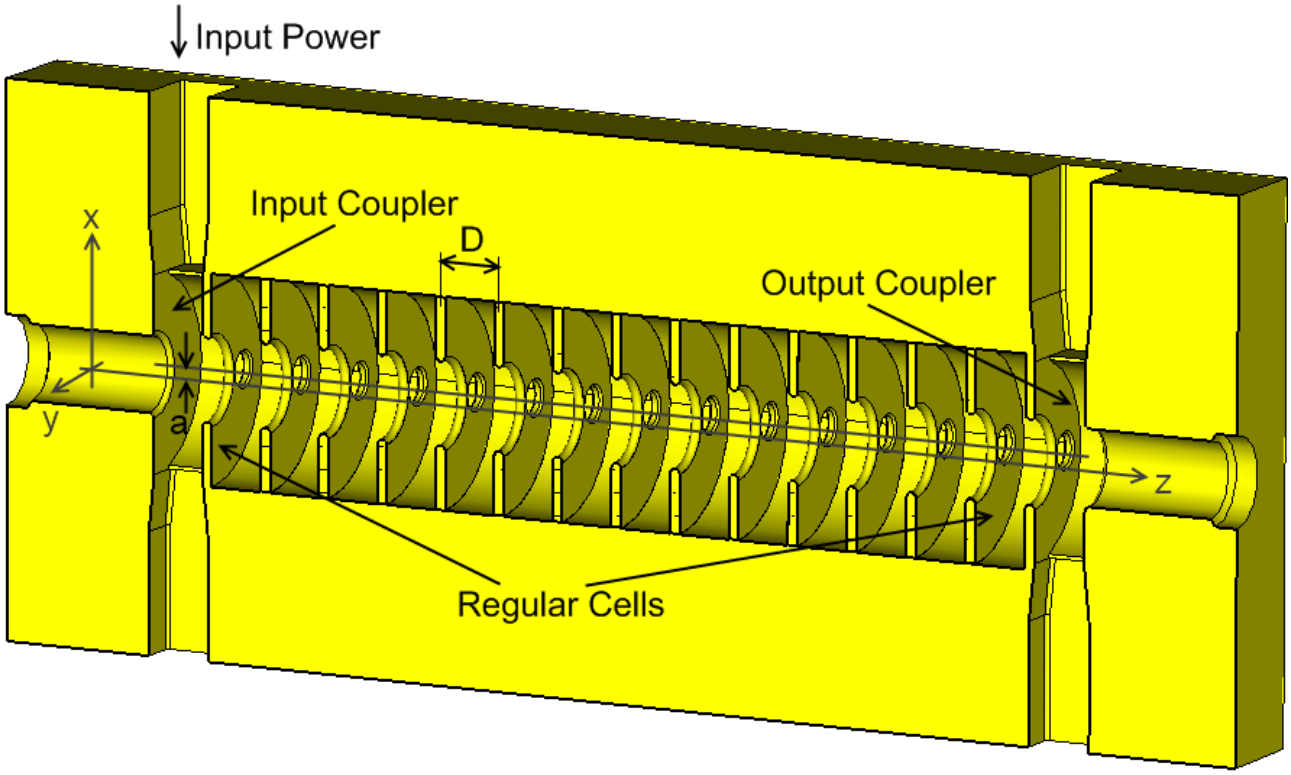

Figure 2: Transverse deflecting structure (longitudinal section).

voltage of 1.8 MV. Both couplers are equal and are tuned to provide matching with feeding rectangular waveguides at the operating frequency, which results in travelling wave regime inside the structure.

COUPLERS COMPARISON

In this section we will describe the investigation of three couplers with different lengths – D, $3D/4$ and $D/2$, (the latter one is shown on Fig. 3) in terms of deflecting efficiency.

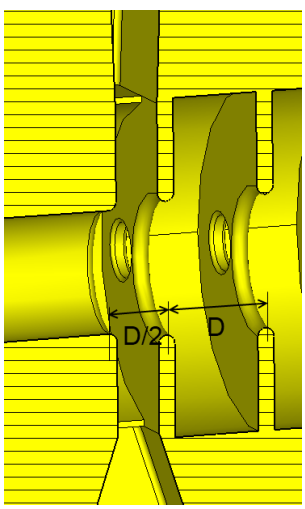

Figure 3: Coupler with length of $D/2$.

In order to calculate the transversal voltage we first tune all couplers by adjusting its radius and the width of coupling window to have good matching at 2997.2 MHz (as shown on Fig.4) and travelling wave with phase shift of $120^0 \pm 1^0$ per cell.

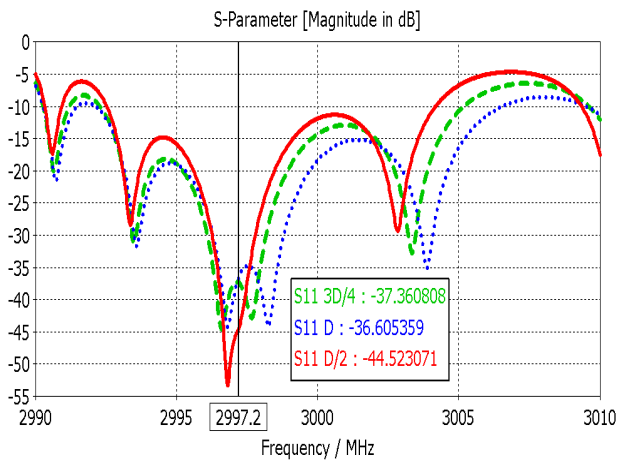

Figure 4: S11 vs. frequency for different coupler lengths: D (blue, dotted), $3D/4$(green, dashed), $D/2$ (red, solid).

Second, we extract required field distributions along the specified lines from numerical simulations and then we renormalize these values for input power of 2.5 MW in order to calculate deflecting fields with (1) and (3). The corresponding curves are plotted on Fig.5 and Fig.6 respectively.

Copyright © 2012 by the respective authors — cc Creative Commons Attribution 3.0 (CC BY 3.0)

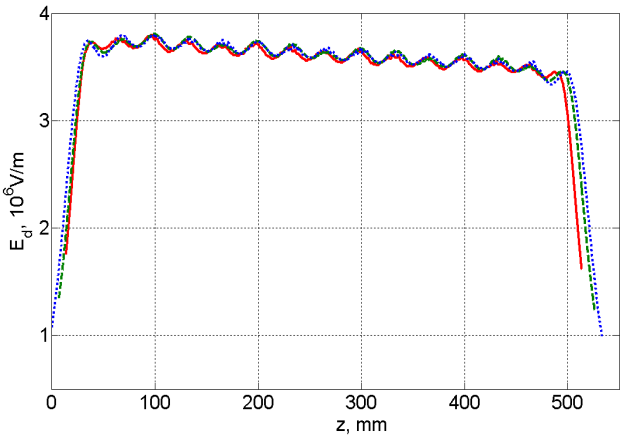

Figure 5: E_d (z) for different coupler lengths: D (blue, dotted), 3D/4(green, dashed), D/2 (red, solid).

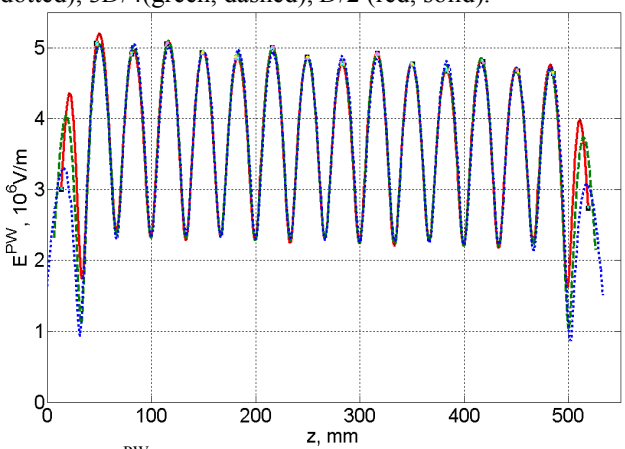

Figure 6: E^{PW} (z,x=a=4mm) for different coupler lengths: D (blue, dotted), 3D/4(green, dashed), D/2 (red, solid).

The plots on Fig.5 and Fig.6 are snapped over the range from D to 15D (33.34..500.10 mm) to indicate that the deflecting fields corresponding to the regular cells are equal and do not depend on the coupler geometry. The only difference appears in couplers. The slope along z-axis is due to the RF power dissipation in copper walls.

Third, using (2) and (4) we calculate the deflecting voltages inside two regions: the full structure including all cells and in regular cells only. The field penetration inside the beampipes is not considered. The difference between potentials of these two regions is sum of both couplers potentials. The results of the calculations are listed in Table 1.

Table 1: Deflecting Voltages with Different Couplers

Coupler Length	Method	V_{dmax}, MV		
		Full Structure	Regular Cells	Couplers
D	On-axis	1.8356	1.6858	0.1498
	P-W	1.8138	1.6782	0.1356
3D/4	On-axis	1.8164	1.6864	0.130
	P-W	1.8012	1.6791	0.1221
D/2	On-axis	1.7982	1.6924	0.1058
	P-W	1.7863	1.6832	0.1031

It is shown that the two methods coincide well. The average value of potential contribution from each regular cell is 0.1202 MV. The renormalization of the deflecting potentials to the same coupler length gives the following relation between the coupler efficiencies with respect to a regular cell:

D : 3D/4 : D/2
62.5% : 72.1% : 83.2%

CONCLUSIONS

In this work the three types of power coupler for RF deflector were considered. The total deflecting voltage seen by a particle was calculated with direct approach using on-axis fields and with Panofsky-Wenzel theorem. It was shown that twice as shorter coupler provides 1.33 times better deflecting efficiency. This fact can be used when it is preferable to increase the total deflecting potential of the deflector but also to keep its length the same by adding one regular cell.

REFERENCES

[1] W.K.H. Panofsky, W.A. Wenzel, Rev. Sci. Instr. 27, 967, 1956.

[2] L.V. Kravchuk et al., "Layout of the PITZ Transverse Deflecting System for Longitudinal Phase Space and Slice Emittance Measurements", Proc. of LINAC10, Tsukuba, Japan, 2010.

Copyright © 2012 by the respective authors — cc Creative Commons Attribution 3.0 (CC BY 3.0)

MEASUREMENTS OF A REDUCED ENERGY SPREAD OF A RECIRCULATING LINAC BY NON-ISOCHRONOUS BEAM DYNAMICS*

F. Hug#, C. Burandt, M. Konrad, N. Pietralla, TU Darmstadt, Darmstadt, Germany
R. Eichhorn, Cornell University, Ithaca, NY, USA

Abstract

The Superconducting Linear Accelerator S-DALINAC at the University of Darmstadt (Germany) is a recirculating linac with two recirculations providing beams for measurements in nuclear physics at small momentum transfers. For these experiments an energy spread of better than 10^{-4} (rms) is needed. Currently acceleration in the linac section is done on crest of the accelerating field. The recirculation path is operated achromatic and isochronous. In this recirculation scheme the energy spread of the resulting beam in the ideal case is determined by the electron bunch length. Taking into account the stability of the RF system the energy spread increases drastically to more than 10^{-3} (rms**).**

We will present a new non-isochronous recirculation scheme which helps cancelling out these errors coming from the RF-jitters. This scheme uses longitudinal dispersion in the recirculation paths and an acceleration off-crest on a certain phase with respect to the maximum. We will present results of the commissioning of the new system including measurements of the longitudinal dispersion in the recirculation arcs as well as measurements of the resulting energy spread using an electron spectrometer.

INTRODUCTION

Operating since 1987 the Superconducting DArmstadt LINear Accelerator (S-DALINAC) is used as a source for nuclear- and astrophysical experiments at the university of Darmstadt [1]. It can accelerate beams of either unpolarized or polarized electrons [2] to beam energies of 1 up to 130 MeV with beam currents from several pA up to 60 µA. The layout of the S-DALINAC is shown in Fig. 1.

Acceleration in the injector and main linac is done by superconducting elliptical cavities with a quality factor of $Q_0 \approx 10^9$. These cavities are operating at a frequency of 3 GHz with a maximum accelerating gradient of 5 MV/m.

The main linac consists of 8 standard 20-cell cavities and can provide an energy gain of 40 MeV. By recirculating the beam two times the maximum energy of 130 MeV can be achieved. In the adjacent experimental hall this beam can be used for different experiments such as electron scattering in two electron spectrometers or experiments with tagged photons. For these experiments an energy spread of $\pm 1 \cdot 10^{-4}$ is required.

* Work supported by DFG through SFB 634
# hug@ikp.tu-darmstadt.de

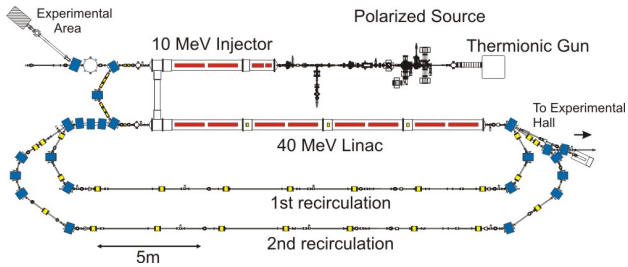

Figure 1: Floor plan of the S-DALINAC.

LONGITUDINAL BEAM DYNAMICS

The S-DALINAC is designed to use an isochronous recirculation scheme originally. On a isochronous working point the electrons are accelerated in the maximum of the accelerating field (on crest) in every turn and the bunch length is kept constantly small ($\pm$ 1°) using achromatic and isochronous recirculation paths. Isochronicity is a property of beam optics and can be described as $dl/dE = 0$ meaning that the length of the flight path of all electrons is independent from their energy. Acceleration on crest of the RF-field is the common mode for linear accelerators. Usually amplitude and phase jitters of the cavities are not correlated and the resulting energy spread is mainly determined by the short bunch length. In a recirculating linac the errors can add up coherently throughout the linac passages in a way that every electron sees the same errors in all passes through the linac due to the large time constant of field variations in the superconducting cavities compared to the short time of flight of the ultra relativistic electrons through the linac.

A way to overcome these correlated errors is changing the longitudinal working point to a non-isochronous one. This is the common operation mode for synchrotrons or microtrons In a non-isochronous recirculation scheme the recirculation paths provide a longitudinal dispersion $dl/dE = D_L \neq 0$ while the accelerating field is operated at a certain synchrotron phase $\Phi_S \neq 0$ (on edge). The electrons then perform synchrotron oscillations in the longitudinal phase space. Compared to synchrotrons a quite large phase advance per turn is needed to cancel out the RF jitters. In fact a half or full integer number of synchrotron oscillations leads to the best energy resolution of the extracted beam in a way that the resulting energy spread at extraction is only determined by the energy spread at injection while the errors caused by the RF jitters of the main linac are cancelled out. [3,4]

The usability of such a non-isochronous recirculation scheme at the S-DALINAC has been verified already by numerical simulations (see Fig. 2). The new longitudinal

Copyright © 2012 by the respective authors — cc Creative Commons Attribution 3.0 (CC BY 3.0)

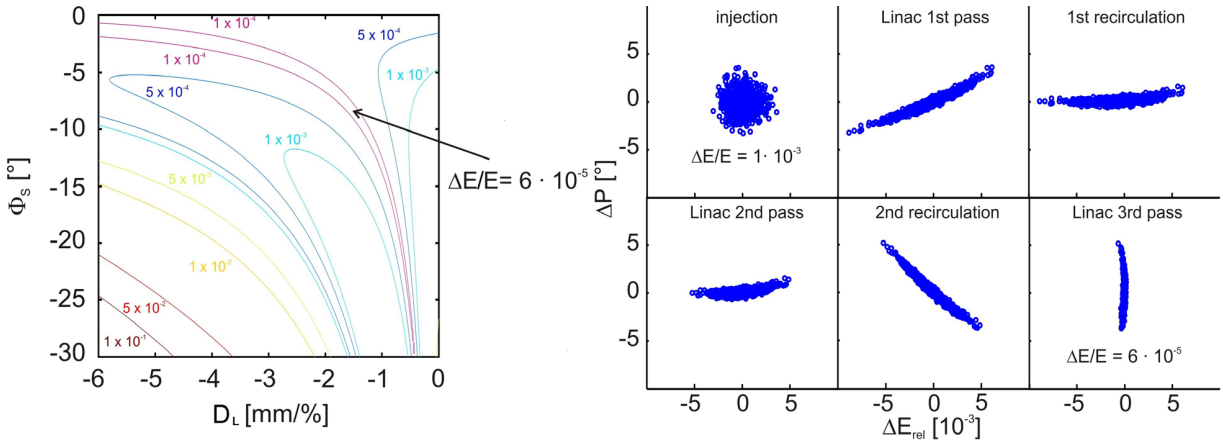

Figure 2: Hillplot of the resulting energy spread at extraction for different sets of longitudinal dispersion and synchrotron phase (left). Beside the isochronous point exist areas of reduced energy spread. The minimum has been determined to D_L = -1.5 mm/% and Φ_S = -9.5° On the right side a bunch of 5000 particle has been tracked through the linac using the optimized parameters. The particles perform a half oscillation in longitudinal phase space ending up on a reduced energy spread.

working point has been determined to D_L = -1.5 mm/% and Φ_S = -9.5° and would lead to a reduction of the energy spread to $\Delta E/E = 6.03 \cdot 10^{-5}$ which satisfies the requirements mentioned above very well. (for more details see [5,6,7])

LATTICE OPTIMIZATION

In order to tune the S-DALINAC to different non-isochronous working points in future optimizations at the recirculation paths had to be carried out. In particular the quadrupole lattice of the recirculation arcs needed to be reviewed to change the value of D_L easily while the transverse dispersion D and the transverse angular dispersion D' both equal zero at the end of every recirculation arc. The result of these optimizations are lattices for both arcs in which D_L can be manipulated easily by changing only the quadrupole gradients in the arcs. Keeping these gradients on a fixed ratio in addition D and D' remain at zero at the end of every arc like required. (for more details on this topic see [7,8])

MEASUREMENT OF LONGITUDINAL DISPERSION

The idea of adapting the concept of non-isochronous recirculation for the S-DALINAC was presented many years before [5], while the realisation, especially tuning the machine to the new longitudinal working point, needed some time. One reason was a lack of beam diagnostics developed meanwhile and described in the section below.

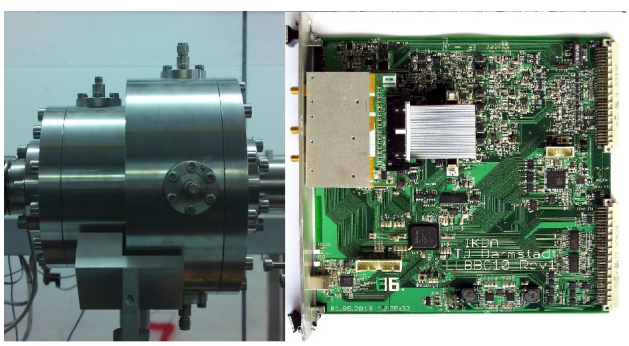

Figure 3: Measurement setup consisting of rf monitor (left) and rf board with FPGA board (right).

For the measurement of the longitudinal dispersion of the recirculation arcs RF monitors located at the beginning of the straight sections behind the last dipoles has been used. Usually, these intensity monitors, which are pillbox cavities at a 3 GHz resonant frequency (see Fig. 3 left), are used for non-destructive measurement of the beam current during operation. The passing cw beam excites an oscillation and the RF signals can be coupled out. Matter of interest is the detection of the phase of the 3 GHz oscillation excited by the beam. This can be done by mixing the RF signal of the monitor with the local oscillator frequency of the RF control system. This down conversion to the base band [9] is done on a RF board (see Fig. 3 right) leading to I/Q values describing the relative oscillation phase of the RF monitor. The I/Q values are converted into real phase values on a FPGA board then. This board is also used for setting amplifications and offsets of the measurement. The hardware is mainly part of the new developed digital LLRF system of the S-DALINAC with minor modifications due to the weak signals coming out of the RF monitors [8,9,10].

To determine D_L out of the phase values the time of flight method is used. For every quadrupole setting, corresponding to a certain dispersion D_L the energy of the beam is changed and the phase on the RF monitor is measured. If $D_L \neq 0$ the time of flight in the arc changes with respect to the beam energy and so does the phase. The results of the measurements on both recirculations is shown in Fig. 4.It can be seen that the measurement fits very well with the simulation results and that D_L can be changed over a large interval including the envisaged value of D_L = -1.5 mm/%.

Copyright © 2012 by the respective authors — cc Creative Commons Attribution 3.0 (CC BY 3.0)

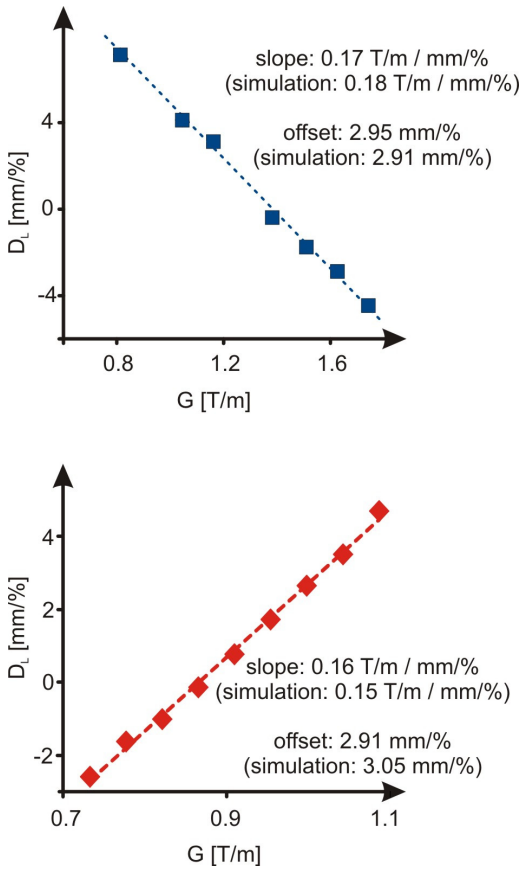

Figure 4: Measured values of D_L in the first recirculation (top) and second recirculation (bottom) for different quadrupole gradients in the arc.

MEASUREMENT OF THE ENERGY SPREAD

Having set up a detection system for D_L and characterized the recirculation arcs allowed to tune the accelerator to its new non-isochronous working point. In order to check the energy resolution of the beam an electron scattering experiment on a thin gold target has been performed. The obtained data is shown in Fig. 5. The energy spread could be reduced from ΔE = 120 keV in the isochronous mode to ΔE = 30 keV in the non-isochronous mode. Both spectra have been measured for about 30 min, which is a typical time between two saves of experimental runs for nuclear physics experiments. After this first proof of principle the following beam time has been successfully performed in the non-isochronous mode.

SUMMARY AND OUTLOOK

Using a new non-isochronous recirculation scheme for the S-DALINAC the energy spread of the electron beam could be reduced significantly. Nevertheless additional experiments are planned to check the effect of different longitudinal working points on the energy spread and compare the data with simulations shown in Fig. 2.

In addition the concept of using a non-isochronous working point to reduce the energy spread of multi-pass linacs might be interesting to overcome beam break-up limits in high current linacs or ERLs as the bunchlength during acceleration is naturally longer which generally leads to weaker excitations of HOMs [11].

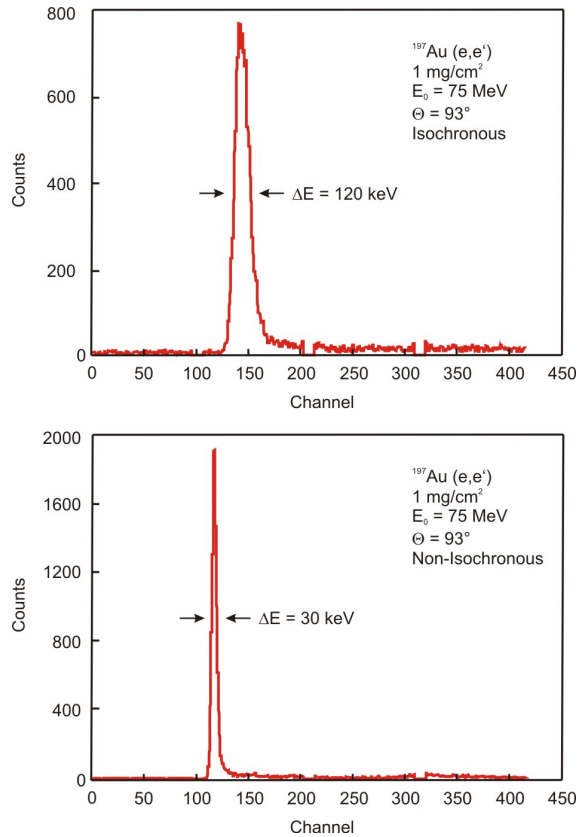

Figure 5: Energy spread of the beam obtained by elastic scattering on a thin gold target. Top: isochronous acceleration. Bottom: Non-isochronous recirculation.

REFERENCES

[1] A. Richter., EPAC '96, Sitges (1996) 110.
[2] C. Eckardt et al., IPAC '10, Kyoto (2010) 4083.
[3] H. Herminghaus, NIM A305 (1991) 1.
[4] H. Herminghaus, NIM A314 (1992) 209.
[5] R. Eichhorn et al., LINAC '06, Knoxville, Tennessee (2006) 73.
[6] F. Hug et al., IPAC '10, Kyoto (2010) 4470.
[7] R. Eichhorn et al., LINAC '10, Tsukuba, Japan (2010) 64.
[8] F. Hug et al., DITANET Conference, Seville, Spain (2011) in press.
[9] A. Araz et al., Phys. Rev. ST Accel. Beams 13, 082801 (2010).
[10] Konrad et al., Phys. Rev. ST Accel. Beams 15, 052802 (2012).
[11] J-L. Biarrotte, PAC '01, Chicago, Illinois (2001) 1098.

Copyright © 2012 by the respective authors — cc Creative Commons Attribution 3.0 (CC BY 3.0)

STATUS OF THE RARE ISOTOPE SCIENCE PROJECT IN KOREA*

J. W. Kim for the RISP, Institute for Basic Science, Daejeon, Korea

Abstract

A heavy-ion accelerator facility has been designed in Korea for the production of rare isotope beams under the rare isotope science project (RISP). The project is funded and officially started in the end of 2011. The accelerator complex is composed of three main accelerators: a superconducting linac to use the in-flight fragmentation (IF) method to generate isotope beams, a 70 MeV proton cyclotron for the ISOL method, and a superconducting post accelerator for re-acceleration of rare isotope beams produced by ISOL to the energy range of 18 MeV/u. Minimum energy of a U beam requested for the IF driver is 200 MeV/u at the beam power of 400 kW. This facility will be unique in the aspect that the IF and ISOL systems can be combined to produce extreme exotic beams. In addition, standalone operation of each accelerator will accommodate diverse users in the beam application fields as well as in nuclear physics.

INTRODUCTION

A heavy ion accelerator facility is being designed in Korea to produce rare isotope beams by using both in-flight fragmentation (IF) and ISOL methods. The project is named as rare isotope science project (RISP), and was started from the end of 2011 after a period of conceptual design [1]. A conceptual layout of the facility is shown in Fig. 1.

The main accelerator is a superconducting linac, which can accelerate a ^{238}U beam to 200 MeV/u and protons to 600 MeV. It is divided into two sections, SCL1 before charge stripping at the energy of 18.5 MeV/u and SCL2 after the stripping. These parameters of the primary beam are similar to those of the FRIB project in the US [2]. A major difference from the planned FRIB facility is the use of an independent ISOL driver. A 70-MeV H- cyclotron will be employed to drive a 70-kW ISOL target system. The radioisotope beam extracted from the target will be further ionized in EBIS [3] or ECR ion sources to achieve a higher charge state before beam injection to the post accelerator (SLC3), which is also a superconducting linac to accelerate a beam up to the energy of around 18 MeV/u. Furthermore this isotope beam produced by ISOL can be accelerated using the SCL2 for the IF system to produce more exotic isotope beams.

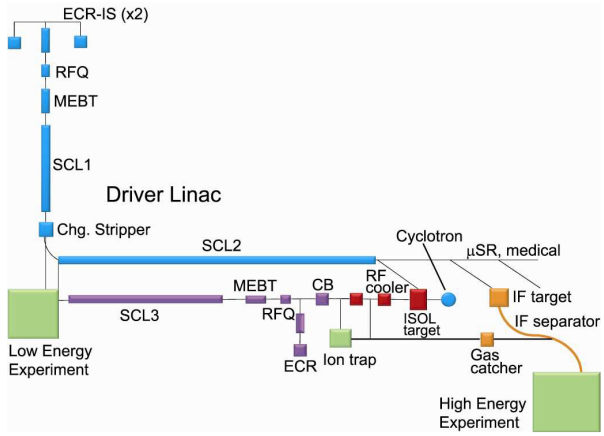

Figure 1: Conceptual layout of the heavy-ion accelerator complex of the RISP.

When the primary beam passes through a thin target, fast radioisotope beams are produced by the projectile fragmentation and fission mechanisms. Then the following isotope-beam selection system utilizes Bρ–energy loss–Bρ analysis to separate and identity an isotope beam of interest. This fast isotope beam can be stopped using a gas stopper, and the charge state of the beam extracted from the gas stopper can be boosted like in the ISOL method before being injected into the post accelerator. A main advantage of the IF method is that it is not subject to chemistry of the ions unlike in the ISOL. Hence rare isotope beams in a wider range can be produced.

The experimental areas are divided depending on the energy of the beam delivered as shown in Fig. 1. Different kinds of spectrometers are planned to be facilitated for nuclear reaction and structural studies [4]. In addition, the facility will accommodate beam users in various application fields including biomedical and material sciences using both stable and isotope beams. The stopping location of an isotope beam can be accurately traced by radiation measurement, which is a notable advantage of radioactive beam and is to be explored in some applications.

ACCELERATOR COMPLEX

To produce highly charged ion beams, a superconducting ECR ion source similar to the VENUS source of the LBL [5] is to be developed. To meet the goal of 400-kW beam power for U beam, envisioned scheme was to accelerate a beam in two charge states of 34+ and

*Work supported by the Rare Isotope Science Project of the MEST and National Research Foundation of Korea.
jwkim@ibs.re.kr

Copyright © 2012 by the respective authors — cc Creative Commons Attribution 3.0 (CC BY 3.0)

35+ [6], but recent ECR test results showed that a single-charge-state U beam could be sufficient for the production of the full beam power.

The injection beam line is designed to accept a two-charge-state beam for very heavy ions such as U beam in case that higher beam power can be more easily achieved with a two-charge-state beam from the ECR. However, beam losses may be reduced for a singly charged beam especially in longitudinal phase space due to the mitigation of sensitivity to misalignment errors and so on.

To increase acceleration efficiency for a heavy ion beam, it is needed to strip electrons from the ions as the beam energy is increased. The charge stripping is set to be performed at the energy near 18 MeV/u to produce the charge state of around 78+ for the U beam. We plan to use a carbon foil for initial low-current beam testing, but not at the beam power over a kW because empirical results show that the lifetime of carbon foil is greatly shortened [7]. A liquid Li target is being studied as the stripper, which can handle the full power beam as has been developed by an ANL group [8]. A gas target is also a possibility. Higher pressure gas could be confined with plasma window to produce higher charge state beam. The equilibrium charge state by the gas stripper is significantly lower compared to that by a carbon foil, while liquid Li target is expected to produce higher charge states than by the gas.

The primary accelerator is a superconducting linac composed of two sections SCL1 and SCL2. Four different types of superconducting cavities are planned to be developed. In SCL1 quarter-wave resonators with the geometrical β of 0.047 operating at 81.25 MHz will accelerate a beam from the RFQ. Another type is a half-wave resonator operating at 162.5 MHz with β of 0.12. After the charge stripping, spoke-type cavities will be used in SCL2, which operate at 325 MHz. Two types of single-spoke cavity with β of 0.3 and 0.53 will be developed. Operating temperature of all the cavities is 2 K. Cryogenic system for the entire facility will have refrigeration capacity of around 15 kW at 4 K. The total number of cavities including the cavities in SCL3 is over 500, and the number of cryomodule is around 150.

Transverse focusing for the superconducting linac will be made by quadrupole magnet doublets in between the cryostat. A similar focusing lattice has been used for SPIRAL2 [9]. It is expected that alignment errors of the focusing elements can be corrected more easily when they are located in the room temperature. The steering coils will be incorporated together with the quadrupole magnets.

The post accelerator SLC3 shown in Fig. 1 will use the same kinds of sc-cavities and focusing elements of the driver linac SCL1. Main differences would stem from the lower beam current of rare isotope beam and the beam charge state depending on the performance of charge breeding in the EBIS or ECR source. The beam diagnostic elements in wide dynamic range will be placed to measure and transport very low-current isotope beams. A standard technology is to use a stable beam with similar q/A first to tune the beam line and then to transport rare isotope beam to the downstream target or detector.

An H- cyclotron of 70 MeV is to be used as a driver for the ISOL system. The maximum beam current is specified as 1 mA. We plan to purchase a commercial unit as similar energy cyclotrons have been developed for the production of medical isotopes and as an ISOL driver [10]. The beam current of 1 mA is higher than that of existent commercial cyclotrons, which is around 700 μA. However, the increase to 1 mA is foreseen to be not technically very challenging. In fact, there is a concern in the lifetime of carbon foil for electron stripping extraction of 1 mA beam. However, the use of carousel containing several units should allow the foil exchange period to be acceptable.

As the cyclotron can be procured and installed more readily compared to the planned superconducting linac, isotope beams produced by the cyclotron will be available earlier by the end of 2016 in the current project schedule, while the beam from the linac is expected by the end of 2017.

RARE ISOTOPE BEAM PRODUCTION

Both methods of in-flight fragment separation and ISOL will be used to produce rare isotope beams. In the present work plan, ISOL facility belongs to the experimental user group, while the IF separator is being designed by the accelerator group. Some details of the beam characteristics by the ISOL are described in Ref. [4].

The in-flight fragmentation method has been developed in major nuclear physics laboratories at the beam energy higher than tens of MeV per nucleon [11]. But the intensity of isotope beams was limited by the beam power available from the primary accelerator. The next generation IF facility requests the beam power of a few hundred kW to produce high intensity rare isotope beams. As a result of this high beam power, the high-power target and removal of the primary beam in the process of isotope beam separation using a beam dump have become technical challenges.

The in-flight isotope beam separation system can be largely divided into pre and main stages. In the pre-separator, the primary beam is separated by momentum dispersion, and a beam dump is used to remove the separated primary beam in the localized area. This pre-separator area has the high-level of radiation, and radiation heating on the magnetic elements is high [12]. A remote handling system based on servo-motor controlled crane is being considered. The design of beam dump is in fact complicated because the system needs to separate different kinds of rare isotope beam from the primary beam in different beam energies, also considering that the range of the primary heavy-ion beam is short. A rotating water drum, which can be displaced along the axis, is being considered.

Copyright © 2012 by the respective authors — cc Creative Commons Attribution 3.0 (CC BY 3.0)

The main separator is designed to identify the isotope beam of interest and to purify it by using the time of flight method and other nuclear physics techniques. The beam from the pre-separator is mixed with different kinds of isotope beams having similar q/A ratio. The use of a wedge-shaped degrader can remove some interfering isotope beams utilizing energy loss mechanism inside material at the cost of inducing additional nuclear reaction and beam energy straggling. The unwanted isotope beams identified by the time of flight method can be removed by an rf deflector located at the end of separator before the beam is delivered to the downstream experimental area. The rf deflector can be more effectively used to purify the isotope beam in the proton rich side.

SUMMARY

The rare isotope science project in Korea is in progress, which was started from the end of 2011. The high current heavy ion linear accelerator is a primary driver to produce rare isotope beams using the IF method. A 70-MeV cyclotron will be used to produce isotope beams using the ISOL method. A plan is that radio-isotope beam produced by ISOL can be further accelerated using the primary accelerator to a higher energy so as to utilize the IF method. This two-stage process is expected to produce more exotic isotope beams.

In the current schedule, the first proton beam from the cyclotron will be delivered to the target in the end of 2016, and the first IF beam by the end of 2017. This is very aggressive schedule to carry out, and the schedule is also subject to the construction of the building complex for the accelerators and experimental equipments. Achieving the permission to operate the high-level radiation facility from the Korea Institute of Nuclear Safety is also expected to be a tough task.

REFERENCES.

[1] J. Ahn et al., “Overview of the KoRIA facility for rare isotope beams”, Few-Body Systems, Vienna, Springer (2012).

[2] X. Wu et al., “The overview of the accelerator system for the facility for rare isotope beams at Michigan State University”, Proc. of LINAC2010, Tsukuba, Japan, Sep. 12-17, 2010, p.163 (2010).

[3] J. Alessi et al., “Construction of the BNL EBIS preinjector”, Proc. of PAC09, Vancouver, Canada, May 4-8, 2009, p.407 (2009).

[4] M.S. Ryu et al., “Characteristics of rare isotope beams in the KoRIA facility”, J. Korean Phys. Soc. 60, 19 (2012).

[5] D. Leitner et al., “Status of the Venus ECR ion source”, Proc. of ECRIS2010, Grenoble, France, Aug. 23-26, 2010, p.11 (2010).

[6] E. Lessner, P. Ostroumov, “Multi-charge-state beam steering in high-intensity heavy-ion linacs”, Proc. of EPAC 2004, Lucerne, Switzerland, July 5-9, 2004, p.1476 (2004).

[7] H. Kuboki et al., “Charge-state distribution of ^{238}U in nitrogen gas and carbon foil at 14 and 15 MeV/n”, Phy. Rev. ST 14, 053502 (2011).

[8] J. Nolen et al., “Development of windowless liquid lithium targets for fragmentation and fission of 400-kW uranium beams”, NIM B 204, 293 (2003).

[9] T. Junquera et al., “The high intensity superconducting linac for the SPIRAL 2 project at GANIL”, Proc. of LINAC 2006, Knoxville, USA, Aug. 21-25, 2006, p.142 (2006).

[10] V. Sabaiduc et al., “New high intensity compact negative hydrogen cyclotrons”, Proc. of CYCLOTRONS 2010, Lanzhou, China, Sep. 6-10, 2010, p.81 (2010).

[11] M. Bernas et al., “Projectile fission at relativistic velocities: a novel and powerful source of neutron-rich isotopes well suited for in-flight isotopic separation”, Phys. Lett. B 331, 19 (1994).

[12] I. Baek et al., “Radiation simulations for a pre-separator area for rare isotope production via projectile fragmentation”, Proc. of PAC07, Albuquerque, USA, June 25-29, 2007, p.1763 (2007).

Copyright © 2012 by the respective authors — cc Creative Commons Attribution 3.0 (CC BY 3.0)

BEAM INTENSITY AND ENERGY CONTROL FOR THE SPIRAL2 FACILITY

C. Jamet, T. Andre, B. Ducoudret, C. Doutressoulles, W. Le Coz, G. Ledu, S. Leloir, S. Loret,
GANIL, Caen, France

Abstract

The first part of the SPIRAL2 facility, which entered last year in the construction phase at GANIL in France, consists of an ion source, a deuteron and a proton source, a RFQ and a superconducting linear accelerator delivering high intensities, up to 5 mA and 40 MeV for the deuteron beams.

Diagnostic developments have been done to control both beam intensity and energy by non-interceptive methods at the linac exit. The beam current is measured by using couples of ACCT-DCCT installed along the lines and the beam energy by using a time of flight device.

This paper gives explanations about the technical solutions, the results and resolutions for measuring and controlling the beam.

ACCELERATOR CHARACTERISTICS

The SPIRAL2 accelerator, an extension of the GANIL laboratory is under construction at CAEN in France [1].

The beams accelerated by the Linac will range in intensity from a few 10 µA to 1mA for ions, up to 5 mA for deuterons, and in energy from 0.75 up to 14.5 MeV/A for ions, 20 MeV/A for deuterons and 33 MeV for protons.

BEAM CONTROLS

In order to control these beam characteristics, measuring chains and controlling devices are under development by the Electronic Machine Group at GANIL.

Controls of the beam intensity, efficiency, energy and beam power, will be necessary for the kick-off authorization issue by the French Nuclear Safety Authority (ASN).

These surveillances are part of the Machine Protection System (MPS) [2] and have to bring:

- A thermal protection, against direct beam damages, requiring a fast response time (few 10 µs)
- An enlarged protection which controls the operation domain from the safety point of view.

Characteristics of the Beam Intensity

Intensity range:

- Few 10µA to 5mA

Duty cycle of the slow chopper:

- From 1/10000 to 1/1 (frequency of 1Hz from 1/10000 to 1/2000 and a frequency of 5Hz from 1/2000 to 1/1)

Duty cycle of the fast chopper:

- From 1/1000 to 1/100 (repetition frequency from 8,88 kHz to 880 kHz)

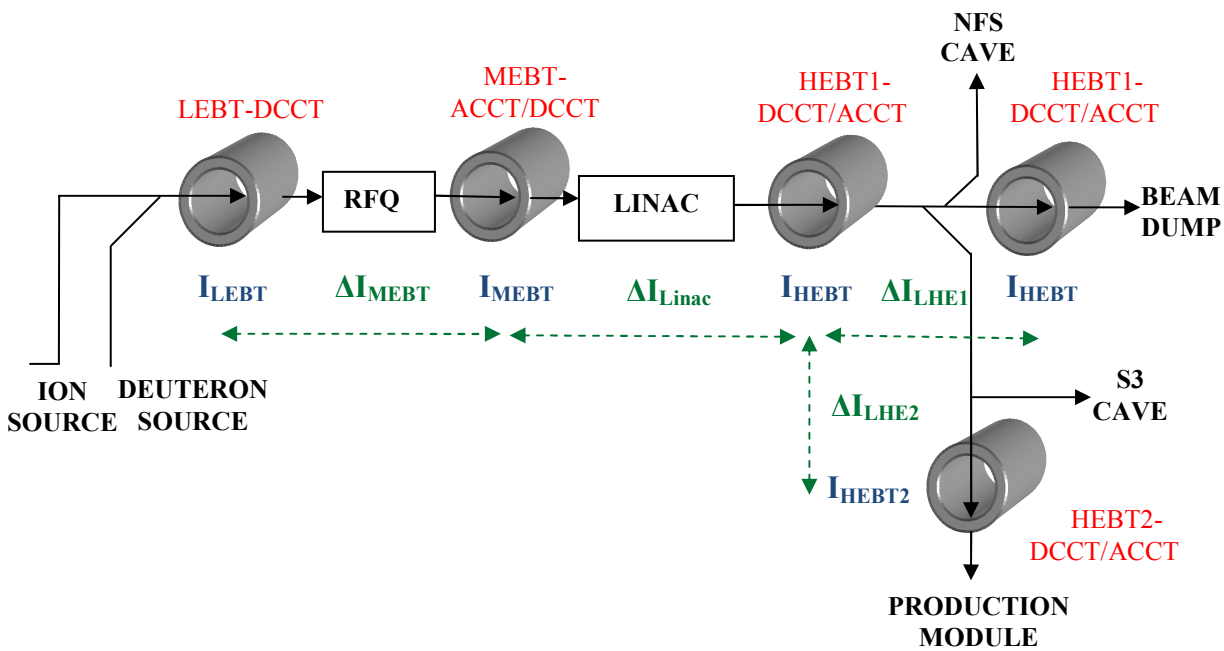

Figure 1: Scheme of the beam intensity and the beam efficiency control.

Copyright © 2012 by the respective authors — cc Creative Commons Attribution 3.0 (CC BY 3.0)

BEAM INTENSITY DIAGNOSTICS

Two kinds of transformers are used to measure the beam intensity by a non-interceptive method, DCCT (NPCT) and ACCT. A Bergoz NPCT and a homemade ACCT inside a magnetic shield, compose an ACCT-DCCT couple.

In a first time, three ACCT-DCCT blocks are built and under qualification.

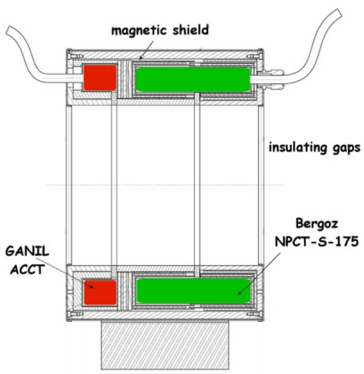

Figure 2: Design of an ACCT-DCCT couple.

Transformer Descriptions

DCCT: NPCT-175-C030-HR
ACCT:
Torus: Nanocristalin
Turn ratio: 300:1
Internal diameter: 184 mm
External diameter: 220 mm

ACCT and DCCT diagnostics are complementary. The DCCT, a commercial device, measures the intensity of continuous and chopped beams (response time around 50 µs for a bandwidth of 10 kHz), the minimum intensity is around a few dozens of µA without offset compensation. The ACCT chain is faster with a response time less than 1 µS (bandwidth more than 300 kHz) and an intensity accuracy better than 10 µA but it needs a chopped beam.

Uncertainty Evaluation

Controls are done by comparison between the beam characteristics and thresholds. Each applied threshold value has to take account of the chain accuracy, to ensure that the beam characteristic is under the intended threshold.

The ACCT-DCCT measurement chains are limited by the following parameters:

- The offset
- The thermal noise
- The electromagnetic disturbances
- The linearity and accuracy of the gain
- The temporal shift between two chains for the efficiency measurement
- The low drop for the ACCT

Each uncertainty has been evaluated and added.

For the DCCT, the main influences, which limit the accuracy, are the thermal noise and the offset due to the temperature and the magnetic field level. In order to decrease the effect of the offset, a beam periodic interruption is planned to deduct the signal without beam (offset). Few measures per hour are foreseen. The noise is limited by reducing the electronic bandwidth.

For the ACCT, the main parameters are also the electronic offset (estimation of 10 µA) and the thermal noise (1µA with a bandwidth of 100 kHz). Currently, an optimization of the electronic is to decrease the offset value.

Electronic Monitoring

In order to control quickly the beam intensity, with an important duty cycle and a slow frequency of the chopper, the electronic monitoring consists in integrating the beam intensity on a given period (fig. 3). The control is based on a beam charge threshold rather than a beam intensity threshold.

The required performances [2] are the following:

- For a 200 kW 20 MeV/A beam loss (5 mA), response time is 35 µs
- For a 50 W 20 MeV/A beam loss (1.25 µA), response time is 140ms

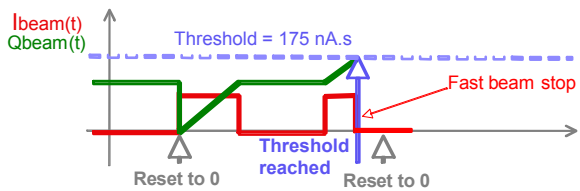

Figure3: Principle of beam intensity integration.

BEAM ENERGY MEASUREMENTS

Three electrodes installed along the HEBT will measure the beam energy at the exit of the LINAC by a time of flight method (TOF). The required performances are the following:

- Intensity range: from 50 µA to 5 mA
- Energy range: from 2 MeV/A to 33 MeV/A
- Response time: 1 s
- Required accuracy:
  +/-1 per mille for the beam tuning
  +/-1 per cent for the beam control

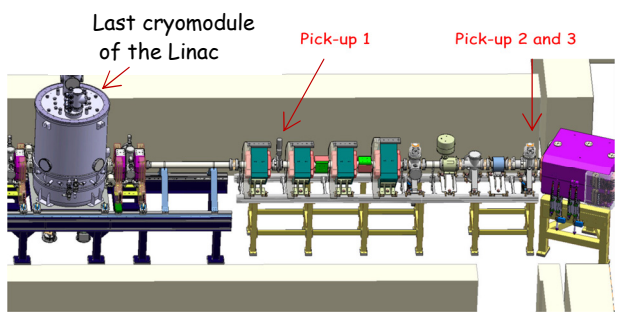

Figure 4: Electrodes along the HEBT line.

Copyright © 2012 by the respective authors — cc Creative Commons Attribution 3.0 (CC BY 3.0)

The first unit includes the Pick-up1 and the second unit is composed by the Pick-up2 and 3. The pick-up3 is designed to determine the bunch number between the two first pick-ups [3], the length between the second and the third pick-up is calculated to be smaller than the distance between two bunches.

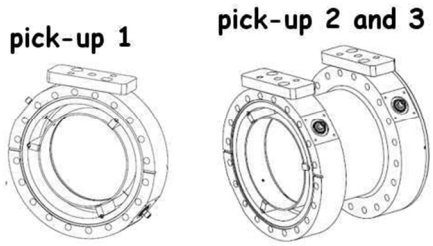

Figure 5: Design of the pick-up electrodes

Time of Flight Values

Table1: Lengths, Bunch Number at Min and Max Energy

	Linac	
Energy	2Mev/A	33MeV/A
β	0.066	0.2607
L_{12} (mm)	3878.8	
L_{23} (mm)	130	
L_{acc} (mm)	224.4	886.4
N	17	4

L_{12} : Length between the pick-up 1 and 2
L_{23} : Length between the pick-up 2 and 3
L_{acc} : Length between 2 bunches
N: Bunch number between the pick-up 1 and 2
v: Beam velocity
φ12: Pick-up1 phase - Pick-up2 phase

$$v = \frac{L_{12}}{T_{12}} = \frac{L_{12}}{T_{acc}(N + \frac{\varphi_{12}}{360})} = 360.\frac{L_{12}}{360.N + \varphi_{12}}.F_{acc}$$

The energy accuracy (ΔE) is function of the length accuracy (ΔL) and the phase accuracy (Δφ).

$$\left|\frac{\Delta E}{E}\right| \approx 2.\left|\frac{\Delta L_{12}}{L_{12}}\right| + 2.\left|\frac{2\Delta\varphi}{360.N + (\varphi_{12})}\right|$$

Electronic Developments

A new electronic device has been developed at GANIL to measure the phase and amplitude of pick-up signals and calculate the beam energy. The principle consists in directly digitizing the pick-up pulses by under-sampling. The phase and amplitude of different harmonics are then calculated with a FPGA by an I/Q method before the beam energy calculation [4].

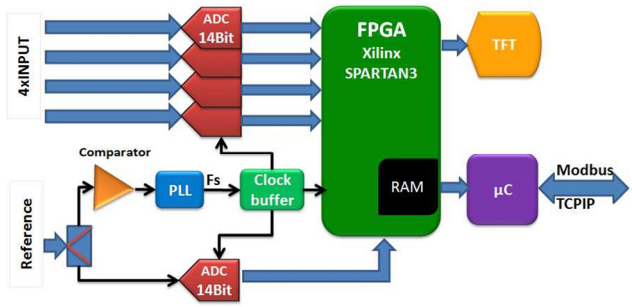

Figure 6: Synoptic of the acquisition electronic.

Beam Tests at the GANIL's Accelerator

Beam Tests have been done at GANIL to compare the beam energy measurements by the TOF method and the spectrometer method. The goal is to compare the values between these two methods and evaluate the TOF accuracy. The gap of the measured values is included between -1 ‰ and -3 ‰ in energy corresponding to -0.5° to -1.5° in phase (with a beam intensity from 1µA to 5 µA).

By projection of these results and by taking account of the length accuracy, calculations give an energy accuracy included between 1 to 3 per thousand in the HEBT.

CONCLUSIONS

Currently the ACCT-DCCT blocks are made, the ACCT electronic is under development, and an optimization to decrease the electronic offset is in progress. The next step consists in studying and in carrying out the intensity and efficiency control device. The required performances in response time and in sensitivity are very restrictive.

For the TOF device, the chain uncertainties are under evaluation in order to characterize this device. The electronics will be ready at the end of this year to measure the beam energy at the exit of the RFQ. For the HEBT, an evolution of this electronic is scheduled to make the device safer and to fulfil the safety requirements.

REFERENCES

[1] P. Bertrand et al., "SPIRAL2 accelerator construction progress", this conference.
[2] M. Moscatello et al., Machine Protection System for the SPIRAL2 Facility, IPAC2012, New Orleans, Louisiana, USA.
[3] C. Jamet et al., Spiral2 Beam Energy Measurement, DIPAC11, Hamburg, Germany.
[4] C. Jamet et al., Phase and amplitude measurement for the SPIRAL2 Accelerator, DIPAC09, Basel, Switzerland.

Copyright © 2012 by the respective authors — cc Creative Commons Attribution 3.0 (CC BY 3.0)

OVERVIEW OF THE RISP SUPERCONDUCTING LINAC

D. Jeon#, H.J. Kim, H.C. Jung, S.K. Kim, Y.Y. Lee, S. Matlabjon, H.J. Kim, C.J. Choi, J. Joo, J.H. Lee, Y. Kim, G.T. Park, J. Song, RISP, Institute for Basic Science, Daejeon, Republic of Korea

Abstract

The Rare Isotope Science Project (RISP) is launched in Korea to build the IF and ISOL facilities to support researches in various science fields. Superconducting linac with 200 MeV/u, 400 kW is the driver for the IF (In-flight Fragmentation) facility and the 70 MeV, 70 kW cyclotron is the driver for the ISOL (Isotope Separation On-Line) facility. These facilities are to produce high intensity RI beans with high purity near the neutron-rich drip line. Design aspects of the driver SCL is presented.

INTRODUCTION

The International Science and Business Belt (ISBB) was initiated by the Republic of Korea government to promote the research in the forefront basic science and to seamlessly couple science and business. As the core institute of the International Science and Business Belt plan, the Institute for Basic Science was founded in November 2011 and under the IBS the Rare Isotope Science Project (RISP) was launched. The RISP is to construct a world-class multi-purpose facility to support a wide range of cutting edge science programs in but not limited to nuclear science, material science, bio & medical science, astrophysics, and atomic physics as well as interdisciplinary science programs. To meet the diverse demands, the RISP design is optimized to provide various high intensity stable ion beams and radioactive isotope (RI) beams from proton to uranium for domestic and international users. The RISP facility includes the In-Flight Fragmentation (IFF) facility and the Isotope Separator On-Line (ISOL) facility. The driver accelerator for the IFF facility is a superconducting linac that can accelerate to 200 MeV/u in case of uranium beam and that for the ISOL facility is a 70-MeV cyclotron. The IFF superconducting linac can deliver 400 kW beam power to the IFF target and the 70-MeV cyclotron can deliver 70 kW beam power to the ISOL target.

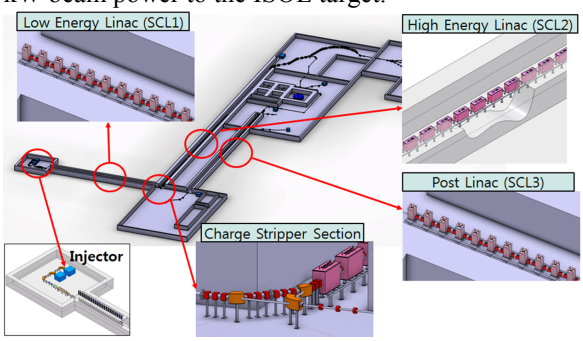

Figure 1: Schematic plot of the RISP facility layout phase.

#jeond@ibs.re.kr

The assessment of conceptual design is done and design changes are introduced [1].

THE DRIVER SCL DESIGN

Superconducting Cavities

The driver SCL for the IF facility is designed to accelerate high intensity heavy ion beams and to meet the needs of various users. Large cavity apertures (4 and 5 cm) are chosen to reduce uncontrolled beam loss on the superconducting cavities because beam loss is a serious issue for heavy ion beams. Cavity types are chosen and optimization of the geometric betas of SC cavities is done and an optimum set of β_g = [0.047, 0.12, 0.30, 0.53] is obtained. Its results are shown in Fig. 2. The Half Wave Resonator (HWR) is chosen to minimize the asymmetric field effects and to improve the quality. And for each type of SC cavities, optimization of the cavity geometry was conducted with respect to R/Q, QR_s, E_{peak}/E_{acc} and B_{peak}/E_{acc} etc. Table 1 lists the cavity parameters. Figs. 3 and 4 show the electromagnetic fields of the optimized SC cavities.

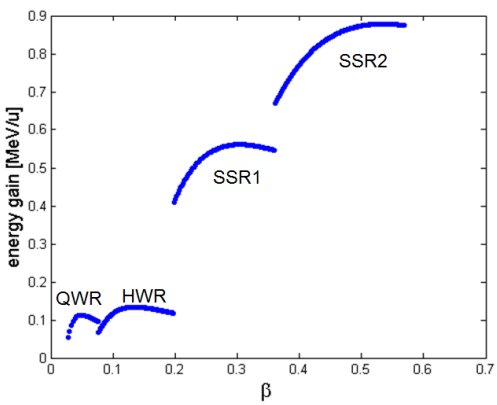

Figure 2: Plots of the optimized geometric betas of the superconducting cavities employed by the RISP.

Table I: Cavity Parameters

Parameters	Unit	QWR	HWR	SSR1	SSR2
β_g	-	0.047	0.12	0.30	0.53
Resonant frequency	MHz	81.25	162.5	325	325
No of cavities	-	24	138	88	136
Aperture diameter	mm	40	40	50	50
QR_s	Ohm	17.5	41.2	86.1	104.7
R/Q	Ohm	472.3	264.8	237.0	298.0
V_{acc}	MV	1.02	1.07	2.04	3.53
E_{peak}	MV/m	30	30	30	30
B_{peak}	mT	54.1	40.8	52.2	62.3
Operating temp	K	2	2	2	2
P_0	W	2.7	2.0	4.8	8.4
Beam current (U)	pmA	9.5	9.5	8	8

Copyright © 2012 by the respective authors — cc Creative Commons Attribution 3.0 (CC BY 3.0)

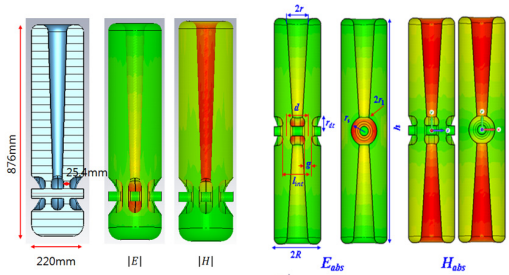

Figure 3: Plots of optimized QWR and HWR showing their electromagnetic fields.

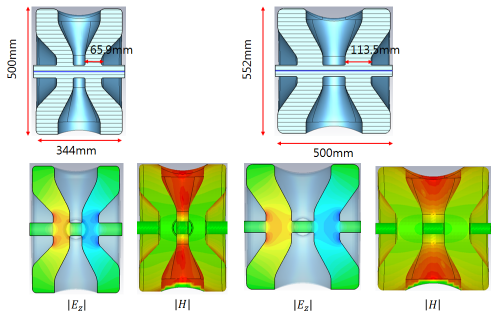

Figure 4: Plots of optimized SSR1 and SSR2 showing their electromagnetic fields.

SCL Layout

It is known that the position of each component in a cryomodule changes by no less than a millimeter in a random fashion during the cool-down of a cryomodule and it is not trivial to predict accurately enough alignment of superconducting solenoids in a cryomodule after the cool-down. Accurate alignment of focusing elements such as superconducting (SC) solenoids is very crucial for maintaining the beam quality of high intensity beams which is envisioned for the heavy ion accelerator. For high intensity operations, the foreseen uncertainty of no less than a millimeter displacement can induce intolerable level of beam loss, leading to activation of accelerator components and potential quench of superconductors inside cryomodules.

The previous SCL design with SC solenoids presents the following challenges and issues:

- Alignment of SC solenoids is not trivial to control. It is known that components in a cryomodule can move no less than a millimeter during cool-down.
- Small misalignment of SC solenoids by ±0.5 mm generates significant emittance growth (simulations indicate factor 2.5 emittance growth by the end of the short beta=0.047 SCL11).
- Heat deposit by the beam loss in the SC solenoids can be an issue such as quench.
- Operation of the SCL is not trivial for example due to the magnetization of surrounding elements in the cryomodule.
- The SCL employing long cryomodules that contain multiple cavities and solenoids can impose significant restriction on the beam diagnostics access. This leads to difficulties in the accelerator tuning for a high intensity operation.

These points raised concerns and studies have been initiated to come up with a better SCL lattice design that can enable high intensity beam operations by improving the beam quality and straightening complexities. These are crucial design considerations in designing the SCL, for the intensity heavy ion beams has increased steadily. The SPIRAL2 project also adopted quadrupole doublet focusing lattice for the high intensity ion beam acceleration (for instance 1 mA of heavy ion beams and 5 mA deuteron beam) [2].

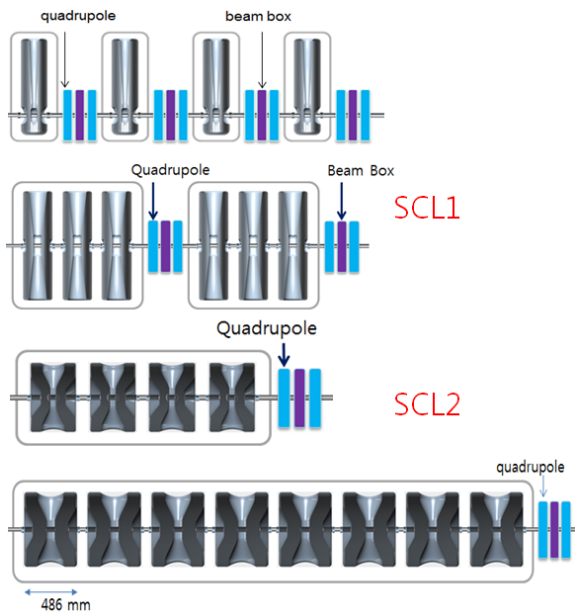

Figure 5: Plots of the SCL layout for each SC cavity type..

Cryomodule, Coupler and Tuner

The project can profit from the existing knowledge base, accelerating the learning process and minimizing the R&D workload and the project can concentrate on developing core design and technologies. Existing designs and products of cryomodules, couplers and tuners will be utilized as much as possible for the SCL design. It is planned to carry out R&D for couplers.
For the couplers and tuners, there are a few existing prototypes and products such as the SPIRAL2 project, the Project-X, and the FRIB etc. These are natural candidates for the frequencies are quite close or identical to the frequency of the RISP cavities.

Charge Stripper Section

One of the critical components of the driver SCL is the charge stripper because of high power deposited in the stripping material in a small area. Charge stripper strips

Copyright © 2012 by the respective authors — cc Creative Commons Attribution 3.0 (CC BY 3.0)

electrons from heavy ion beams to enhance the acceleration efficiency in the following SCL2. Recent studies done by FRIB indicate that carbon foils show fast decay of performance, which makes this type of stripper is very unlikely to satisfy the requirements [4]. The FRIB looks at other options of the charge stripper which include liquid lithium stripper developed at the ANL, gas stripper, gas stripper with plasma windows, and plasma stripper [5]. These options are being considered for the project as well. Even though carbon foils may have defects in full beam power, it is still useful for low beam power operation especially during the testing, commissioning, and possibly early low power operation stages.

Beam Diagnostics and Collimation

The beam boxes located at every doublet are reserved for various diagnostics devices such as beam profile monitors, beam current monitors (BCM), Faraday cups, emittance scanners, bunch shape monitors (BSM), etc. Beam position monitors (BPM) will be installed with quadrupoles, providing beam position and phase data. This feature is a very strong merit in light of beam diagnostics for beam operation and commissioning. There are beam boxes periodically placed for necessary beam diagnostics and this is critical for operation and accurate machine tuning. For instance four profile monitors installed in series can easily establish matching [3]. Because the beam box is in the warm section, maintenance and alignment are straightforward.
Figure 6 shows a preliminary beam diagnostics configuration of the driver SCL. For the charge stripping station, required beam diagnostics are BPMs, beam profile monitors, beam current monitors, and beam loss monitors, etc.

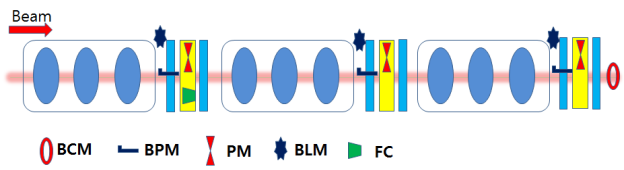

Figure 6: Schematic plot of the SCL beam diagnostics configuration.

Another advantage is that collimators can be installed at the beam boxes to improve beam quality as shown in Fig. 7. These collimators can minimize the uncontrolled beam loss to the superconducting cavities.

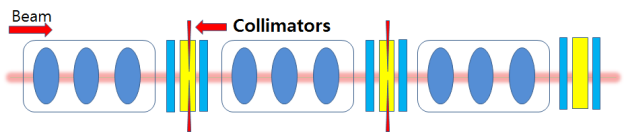

Figure 7: Schematic plot of the SCL beam collimation configuration.

Cost Estimation

Cost estimation is conducted including the cost for cavity, tuner, coupler, internal cryogenics, vacuum system, cryomodule and processing & cryomodule assembly cost. Cost comparison between the two driver SCL options shows that the cost difference between the two options is in the error range of cost estimation, which is less than 1 % of the driver SCL cost. And cost estimation is made for both the driver SCL and the ISOL SCL assuming that we keep the same lattice choice for the ISOL SCL as well. The cost estimation shows that the overall combined cost difference is less than 2 % of the total cost when switching to the SCL lattice with NC quadrupoles. This difference is in the error range of cost estimation and it is concluded that cost is not an issue in adopting the proposed SCL lattice.

CONCLUSION

The design of the RISP driver SCL is conducted, optimized for the acceleration of high intensity heavy ion beams. Types and parameters of SC cavities are chosen to facilitate the goal. Geometric beta and cavity geometry are optimized for better performance.The driver SCL consists of QWR and HWR, SSR1 and SSR2 with relatively large beam apertures of 4 cm and 5 cm to minimize the heavy ion beam loss. The SCL adopts the lattice with normal conducting quadrupoles rather than superconducting solenoids. There are regularly placed beam boxes for the beam diagnostics and collimation.

ACKNOWLEDGEMENT

This work is made possible by the support of the Ministry of Education, Science (MEST) and Technology and the National Research Foundation (NRF) of the Republic of Korea.

REFERENCES

[1] Baseline Design Summary, The Rare Isotope Science Project, Institute for Basic Science, Korea
[2] R. Ferdinand et al., Proc. of LINAC Conference 2010, p. 16, Tsukuba, Japan.
[3] D. Jeon, C.M. Chu, J. Stovall, S. Assadi, *Practical Transverse Matching of the High Intensity SNS Linac*, Nucl. Instr. and Meth. A **607** (2009) 517..
[4] F. Marti et al., Proc. of LINAC Conference 2010, p. 659, Tsukuba, Japan.
[5] F. Marti et al., Proc. of LINAC Conference 2010, p. 662, Tsukuba, Japan.

Copyright © 2012 by the respective authors — cc Creative Commons Attribution 3.0 (CC BY 3.0)

BEAM ENVELOPE ANALYSIS AND SIMULATION

V.S. Dyubkov*, A.S. Plastun, NRNU MEPhI, Moscow, Russian Federation

Abstract

Forming the charge particle beams with small cross-sections and low energies is an actual problem for linac design. That beams are used actively for isotope therapy, ion implantation, etc. Beam emittance is its quality factor, and it should be matched with a facility channel acceptance. The method for beam dynamics analysis at linac is developed in terms of non-coherent particle oscillation study. Nonlinear beam dynamics is investigated by using this method. It is shown that this technique allows one to realize effective beam handling and emittance control. Analytical results obtained are verified by means of numerical simulation.

INTRODUCTION

One of the most interesting problems of accelerator engineering to date are the design and development of high-performance high-current compact systems for an injection and acceleration of low-velocity heavy-ion beams. This problem as well as others cannot be solved without taking into account problem solution on beam emittance matching with an acceptance of an accelerator channel. Effective acceptance evaluation for the resonance accelerator channel depends on a mathematical model used for describing a beam dynamics. Effective acceptance evaluation of the resonance accelerator channel was performed previously on basis of charged particle beam oscillation as a whole [1] – [4], that is under the assumption of coherent oscillations of individual particles. It is of particular interest to consider a model, which is taking into account non-coherent particle oscillations in the beam, and analyse results based on it.

BEAM DYNAMICS

It is difficult to analyse a beam dynamics in a high frequency polyharmonic field. Therefore, we will use one of methods of an averaging over a rapid oscillations period, following the formalism presented in [1] – [4]. One first expresses RF field in an axisymmetric periodic resonant structure as Fouriers representation by spatial harmonics of a standing wave assuming that the structure period is a slowly varying function of a longitudinal coordinate z

$$E_z = \sum_{n=0}^{\infty} E_n I_0\left(k_n r\right) \cos\left(\int k_n\, dz\right) \cos\omega t,$$

$$E_r = \sum_{n=0}^{\infty} E_n I_1\left(k_n r\right) \sin\left(\int k_n\, dz\right) \cos\omega t,$$

where E_n is the nth harmonic amplitude of RF field on the axis; $k_n = (1+2n)\pi/D$ is the propagation wave number for the nth RF field spatial harmonic; D is the resonant structure geometric period; ω is the RF frequency; I_0, I_1 are modified Bessel functions of the first kind.

As it was stated above, we will take into account non-coherent particle oscillations in the beam being accelerated. To this end, one introduces a notion of a reference particle, i.e. a particle moving on the channel axis. A magnetic force can be neglected for low-energy ions. We will assume that $dr/dz \ll 1$. Then, one passes into the reference particle rest frame. There is a differentiation over longitudinal coordinate in the beam motion equation. Thus, the motion equation together with an equation of particle phase variation can be presented in a view of a system of the first order differential equations as follows

$$\begin{cases} \dfrac{d\Gamma}{d\xi} = e_z(\xi, 0, \tau^*) - e_z(\xi, \rho, \tau), \\ \dfrac{d\beta_r}{d\xi} = \beta_z^{-1} e_r(\xi, \rho, \tau). \end{cases} \quad (1)$$

Here we introduced the following dimensionless variables: $\Gamma = \gamma^* - \gamma$; γ^* and γ are the Lorentz factors for the reference and given particles respectively; $\xi = 2\pi z/\lambda$ is dimensionless longitudinal coordinate; $e_{z,r} = eE_{z,r}Z\lambda/2\pi m_0 c^2$; e is the elementary charge; Z is a charge state of an ion; λ is a wave length of RF field; m_0 is an ion rest mass; c is the light velocity in free space; $\beta_{z,r}$ is normalized velocity component.

Let us introduce a new dynamical variable $\psi = \tau - \tau^*$ ($\tau = \omega t$, τ^* is a normalized motion time of the reference particle at the laboratory coordinate system). Note, that

$$\frac{d\psi}{d\xi} = \beta_s^{-3}\Gamma, \quad (2)$$

β_s is normalized synchronous particle velocity, s is the field harmonic number.

Suppose that $|\beta_z - \beta_s| \ll 1$ one can obtain

$$\frac{d^2\psi}{d\xi^2} + 3\varkappa\frac{d\psi}{d\xi} = \frac{1}{\beta_s^3}\frac{d\Gamma}{d\xi} \quad (3)$$

upon differentiation of Eq. 2. The second equation of Eq. 1 can be rewritten as

$$\frac{d^2\delta}{d\xi^2} + \varkappa\frac{d\delta}{d\xi} = \frac{e_r}{\beta_s^3}, \quad (4)$$

where $\delta = \rho/\beta_s$, $\rho = 2\pi r/\lambda$, $\varkappa = \ln'_\xi \beta_s$.

* vsdyubkov@mephi.ru

Copyright © 2012 by the respective authors — cc Creative Commons Attribution 3.0 (CC BY 3.0)

On averaging Eq. 3 and Eq. 4 over rapid oscillation period one can present the motion equation in the smooth approximation with the restrictions mentioned above in the following matrix form

$$\ddot{\Upsilon} + \Lambda\dot{\Upsilon} = -L\Phi_{\text{ef}}, \qquad (5)$$

where the dot above stands for differentiation with respect to the independent longitudinal coordinate and

$$\Upsilon = \begin{pmatrix}\psi\\ \delta\end{pmatrix}, \qquad \Lambda = \begin{pmatrix}3\varkappa & 0\\ 0 & \varkappa\end{pmatrix}, \qquad L = \begin{pmatrix}\frac{\partial}{\partial\psi}\\ \frac{\partial}{\partial\delta}\end{pmatrix}.$$

Now, ψ and δ mean its averaged values. Φ_{ef} plays role of an effective potential function (EPF) describing a beam interaction with the polyharmonical field of the system subject to the incoherent particle oscillations.

For example, we consider there are two spatial harmonics at the linac. One of it is the synchronous harmonic with $s = 0$, and another one is the nonsynchronous (focusing) with $n = 1$. In this case we have

$$\begin{aligned}\Phi_{\text{ef}} = {} & \frac{e_0}{2\beta_s}\left[I_0(\delta)\sin(\psi+\varphi^*) - \psi\cos\varphi^* - \sin\varphi^*\right]\\ & + \frac{e_0^2}{64}\left[I_0^2(\delta) + I_1^2(\delta) - 1\right]\\ & + \frac{5e_1^2}{256}\left[I_0^2(3\delta) + I_1^2(3\delta) - 1\right]\\ & - \frac{e_0^2}{32}\left[I_0(\delta)\cos\psi - 1\right] - \frac{5e_1^2}{128}\left[I_0(3\delta)\cos\psi - 1\right]\\ & - \frac{e_0e_1}{32}\left\{[I_0(\delta) + I_0(3\delta)]\cos(\psi+2\varphi^*) - 2\cos 2\varphi^*\right\}\\ & + \frac{e_0e_1}{32}\left\{[I_0(\delta)I_0(3\delta) + I_1(\delta)I_1(3\delta)]\cos 2(\psi+\varphi^*)\right.\\ & \left. - \cos 2\varphi^*\right\},\end{aligned}$$

where $e_n = eE_nZ\lambda/2\pi\beta_s^2m_0c^2$.

To define eigenfrequencies of small system vibrations, EPF is expanded in Maclaurins series

$$\Phi_{\text{ef}} = \frac{1}{2}\Omega_{0\psi}^2\psi^2 + \frac{1}{2}\Omega_{0\delta}^2\delta^2 + o(\Upsilon^{\text{T}}\Upsilon),$$

and the coefficients in which are given by

$$\Omega_{0\psi}^2 = -\frac{e_0}{2\beta_s}\sin\varphi^* - \frac{e_0e_1}{16}\cos 2\varphi^* + \frac{e_0^2}{32} + \frac{5e_1^2}{128},$$

$$\Omega_{0\delta}^2 = \frac{e_0}{4\beta_s}\sin\varphi^* + \frac{3e_0e_1}{64}\cos 2\varphi^* + \frac{e_0^2}{128} + \frac{45e_1^2}{512}.$$

NUMERICAL SIMULATION

The analytical results obtained above were used to investigate the beam matching possibility at the linac output. The beam was the unbunched 2.5 keV/u lead ions Pb^{25+} with charge-to-mass ratio is equal to 0.12. Self-consistent beam dynamics simulations were conducted by means of a modified version of the specialized computer code BEAMDULAC-ARF3 based on CIC technique to calculate beam self-space-charge field. Computer simulation was carried out for the linac structure under the following parameters: $\lambda = 8.88$ m, system length is equal to 2.5 m, channel aperture is equal to 5 mm; input and output values of the equilibrium particle phase are equal to $-\pi/2$ and $-\pi/6$ respectively, synchronous harmonic maximal value at the axis is equal to 16 kV/cm, $e_1/e_0 = 9$. The equilibrium particle phase linearly increases at the bunching length (1.75 m) and plateaus further. Note that the variation of the synchronous harmonic amplitude against longitudinal coordinate (at 1.75 m) was calculated by using the technique described in [1]. Initial beam radius and current were 1 mm and 5 μA respectively. This parameters guarantee a positivity of the eigenfrequency of the small transverse tunes and, therefore, provide beam matching at the linac output. The output beam energy and current transmission coefficient were 100 keV/u and 85% respectively.

4D beam phase volume projection onto $(\psi, \dot{\psi})$ phase plane together with phase paths calculated in keeping with Eq. 5 at linac output is shown in Fig. 1. There are channel longitudinal acceptance in conservative approximation (curve 1) as well as channel dynamical acceptance in Fig. 1 too.

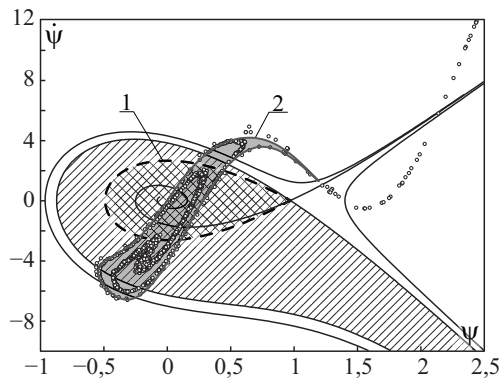

Figure 1: 4D beam phase volume projection and phase paths.

The size of beam envelope and transmission are shown in Fig. 2 and Fig. 3 respectively. The output beam radius is nearly 1.5 times greater than the input one because of this fact. This result is acceptable. It is clear that main linac

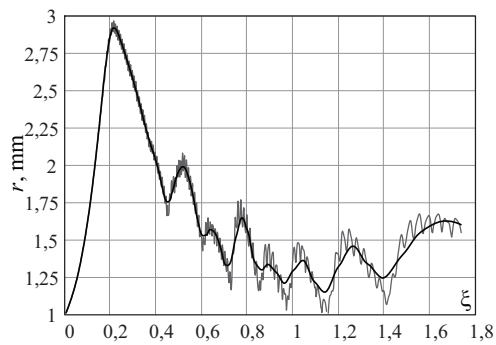

Figure 2: Beam envelope.

Copyright © 2012 by the respective authors — cc Creative Commons Attribution 3.0 (CC BY 3.0)

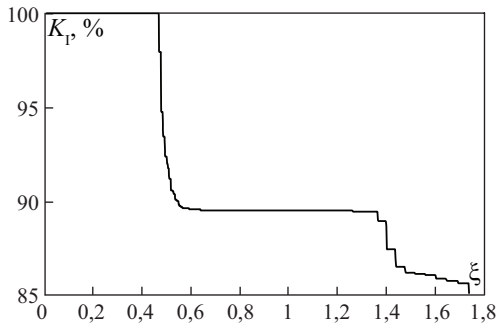

Figure 3: Current transmission.

parameters choice based on proposed technique is rather efficient to realize beam envelope (emittance) control.

SUMMARY

Beam dynamics model with regard for particles non-coherent oscillations was made. Effective acceptance evaluation in terms of this model was evaluated. The necessary restrictions on the linac parameters were imposed to make beam matching at the output. The numerical simulations of the self-consistent low-velocity heavy-ion beam dynamics confirmed the analytical results obtained.

REFERENCES

[1] V.S. Dyubkov and E.S. Masunov, International Journal of Modern Physics A, 24 (2009) 843.

[2] E.S. Masunov and N.E. Vinogradov, Zhurnal Tekhnicheskoi Fiziki, 71 (2001) 79.

[3] E.S. Masunov and S.M. Polozov, Zhurnal Tekhnicheskoi Fiziki, 75 (2005) 112.

[4] E.S. Masunov and V.S. Dyubkov, Problems of Atomic Science and Technology, 3 (2008) 166.

Copyright © 2012 by the respective authors — cc Creative Commons Attribution 3.0 (CC BY 3.0)

BEAM DYNAMICS OF THE LINAC ALPI-PIAVE IN VIEW OF POSSIBLE UPGRADES SCENARIO FOR THE SPES PROJECT

M. Comunian, C. Roncolato, INFN/LNL, Legnaro,
B. Chalykh, ITEP, Moscow

Abstract

At the Legnaro National Laboratories it is operating a Super Conducting linac for nuclear studies named ALPI. The ALPI linac is injected either by a XTU tandem, up to 14 MV, or by the s-c PIAVE injector, made with 2 SC-RFQ. In this article will be report the beam dynamics simulations for some possible scenario upgrade of the linac operate by a new injector, made with a new RFQ.

INTRODUCTION

The SPES strategy is to develop a facility for Nuclear Physics research together with a facility for applied Physics based on the same technology and infrastructure.

SPES [1] is designed to provide neutron-rich radioactive nuclear beams (RIB) of final energies in the order of 10 MeV/A for nuclei in the A= 9-160 mass region. The radioactive ions will be produced with the ISOL technique using the proton induced fission on a Direct Target of UCx [2] and subsequently reaccelerated using the PIAVE-ALPI accelerator complex. A Uranium fission rate of 10^13 fission/s is foreseen.

Fig. 1 shows schematically the SPES main elements located at underground level, a second floor at ground level hosting laboratories and services is not shown.

The driver is the proton cyclotron delivering beam on different targets. Two production ISOL targets are planned to be installed. The production target and the first mass selection element will be housed in a high radiation bunker. Before the High Resolution Mass Spectrometer (HRMS) a cryopanel will be installed to prevent the beam line to be contaminated by radioactive gasses and a RFQ cooler to reduce the input emittance of the HRMS. After passing through the HRMS, the selected isotopes will be stopped inside the Charge Breeder and extracted with increased charge (n+). A final mass selector will be installed before reaching the PIAVE-ALPI accelerator, to clean the beam from the contaminations introduced by the Charge Breeder itself.

THE NEW RFQ INJECTOR

The injection to the ALPI Linac is based on the use of a new Radio Frequency Quadrupole, with the adiabatic bunching inside. In this way a high voltage platform can be avoided, and a higher overall transmission could be achieved.

The new RFQ will operate in a CW mode (100% duty factor) at a resonant frequency of 80MHz. This frequency is the same as that of the lowest energy ALPI superconducting structures. The injection energy of ions was set to 5.7 keV/u. This choice is a compromise between the desire to reduce the ion energy to simplify the LEBT and RFQ bunching section design and the need to increase the injection energy to reduce space charge effects. The extraction energy was set to 727 keV/u, higher than the output of PIAVE RFQ, to optimize the beam dynamics of the SRF linac. Table 1 summarizes main new RFQ parameters [3].

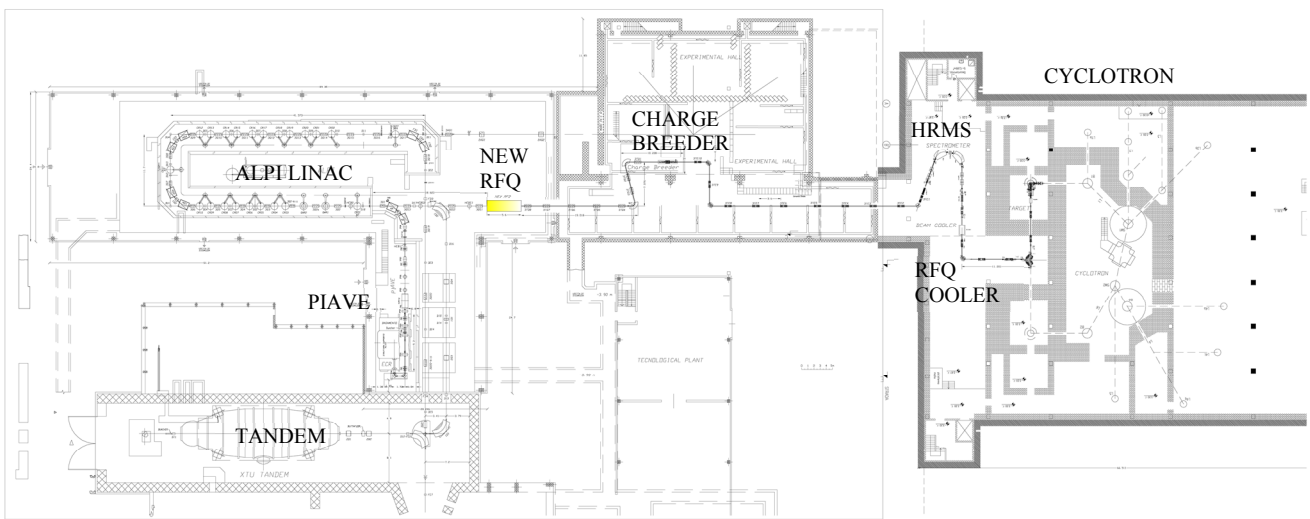

Figure 1: Layout of the SPES and ALPI facility; the dark black part on right is the new Cyclotron area. In yellow the new RFQ as ALPI injector.

Copyright © 2012 by the respective authors — cc Creative Commons Attribution 3.0 (CC BY 3.0)

Table 1: Principal RFQ parameters

Operational mode	CW
Frequency (MHz)	80.
Injection Energy (keV/u)	5.7 (β=0.0035)
Extraction Energy (keV/u)	727 (β=0.0395)
Accelerated beam current (μA)	100
Ratio Charge over Mass (Q/A)	7 – 3
Internal bunching section	Yes

The design goals were to minimize the longitudinal and transverse emittances and to optimize the RF losses and transmission of the RFQ structure.

A comparison with the PIAVE injector, show the advantage of the new RFQ: it has better transmission with a lower total longitudinal emittance, see table 2. The PIAVE SRFQ is with a lower RMS longitudinal emittance due to the external 3 Harmonic buncher.

Table 2: Comparison PIAVE-new RFQ

Parameter [units]	PIAVE SRFQ	NEW RFQ
A/q	8.5	7.0
Input Tr. Norm. RMS emittance [mmmrad]	0.071	0.1
Output Energy [keV/u]	587 (β=0.0355)	727 (β=0.0395)
Output RMS Long. emittance [degkeV/u]	2.2	4.3
Output 90% Long. emittance [degkeV/u]	62	16
Transmission [%]	72	95
QWR 0.047 TTF	0.85	0.95
QWR 0047 DY' [mrad]	-0.48	-0.32

THE ALPI LINAC UPGRADE

The present configuration of the Legnaro super-conducting accelerator complex (PIAVE injector and ALPI main accelerator) fits the requirements for SPES post acceleration too. Nevertheless an upgrade of its performances both in overall transmission and final energy is needed and a solution which minimizes the impact on the present structures [4].

The super-conducting linac ALPI is injected either by a XTU tandem or by the s-c PIAVE injector, see Fig. 2. The linac (at the present 64 cavities and a total voltage of 48 MV) is build up in two branches connected by an achromatic and isochronous U-bend. ALPI period consists in one triplet and 2 cryostats (4 cavities in each cryostat), and a diagnostic box (profile monitor and Faraday cup) in between.

The PIAVE-ALPI complex is able to accelerate beams up to A/q = 7. Higher A/q ions suffer from too low injection energy to the medium-β cryostats, where the RF defocusing is too strong and the beam gets easily lost onto the cavity beam ports. In the last years the average cavity accelerating field has been enhanced by more than a factor of two with respect to the original design value. The strength of the focusing lenses on the other hand, has remained the same, 20 T/m, therefore, even for 6 < A/q < 7 it is hard to design a proper longitudinal beam dynamics such that it will not cause problems on the transverse plane. To fully exploit the available acceleration gradient, some improvements are required in the layout of ALPI.

In this framework, it has been proposed to promote the presently "bunching" cryostats CRB2 and CRB4 (at the beginning and end of ALPI) to the role of "accelerating" cryostats CR21 and CR22, equipping them with 8 additional Nb-sputtered QWRs.

The role of the 160 MHz buncher CRB2 can be taken by the already existing 80 MHz NC buncher HEB2 for relatively light beams injected by the Tandem directly into the 160 MHz medium β_{opt} section, with negligible beam loss.

For SPES, the Radioactive Ion Beam at 727 keV/A will be injected into ALPI by means of the QWRs actual present into PIAVE, that will be moved in at the begin of ALPI, with a different period: QWR1, triplet, QWR2, triplet, to reduce the longitudinal phase advance, see figure 2 and figure 3 and the envelopes in figure 4, the other parts of ALPI remain unchanged.

In this scenario the ALPI configuration is with qwr1-2 at 4 MV/m, CR03-CR18 at 4.5 MV/m and CR19-CR22 at 6.5 MV/m.

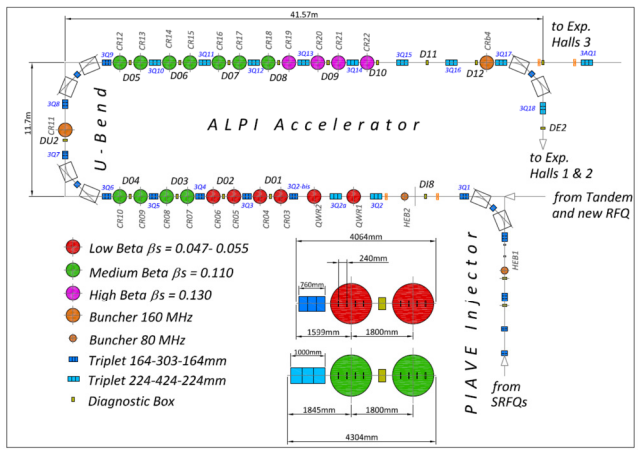

Figure 2: New ALPI Layout: the low Beta, red circles, begins with a shorted period.

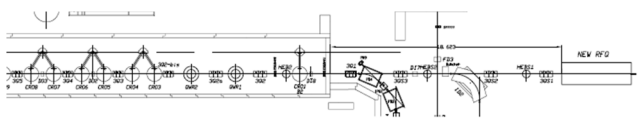

Figure 3: Layout of ALPI with the new RFQ as Injector.

THE ALPI BEAM DYNAMICS

By using this new ALPI layout and with the help of the new RFQ the losses in the ALPI linac are reduced at about 6%: 3% in the first branch of the linac and the other 3% in the high energy branch of the ALPI linac see figure 5. The input distribution is assumed gaussian at 3σ, with a longitudinal cut on +/-50° on phase. The transverse emittance is below in the case of PIAVE, because it has been measured, in the case of the new injector it has been assumed a larger margin on the emittance, probably by a factor 2.

Copyright © 2012 by the respective authors — cc Creative Commons Attribution 3.0 (CC BY 3.0)

The beam is focused between the cryostat with a spot size of about 0.3 mm RMS. In the first half of ALPI the synchronous phase is set +/- 20° as needed to focalize/steerer the beam and to reduce the longitudinal phase advance. After the U bend of ALPI, the cavities phase is set to -20°.

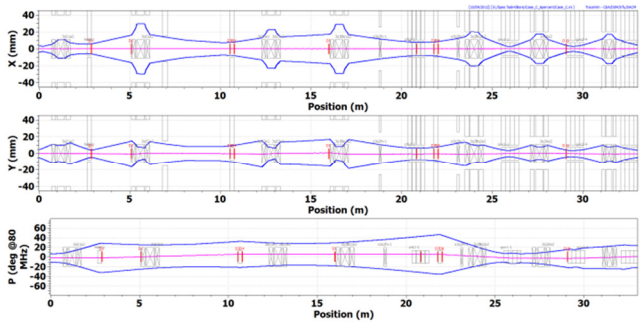

Figure 4: Multiparticles beam envelopes from the new RFQ to CR03, from left to right.

CONCLUSIONS

In table 3 is reported the comparison on performance between the PIAVE and the new RFQ as injectors of ALPI, the main advantage of the new RFQ is in term of global transmission, i.e. taking into account the performance of the internal bunching section of the new RFQ. The low longitudinal emittance, produce by the new RFQ, play an important role to permit a good transport through ALPI, but at linac end this high transmission can induce a larger beam emittance on the longitudinal plane. An upgrade of the triplets of ALPI are not been take into account due to the high cost, in this scenario this is the principal limit, i.e. the maximum gradient force of 20 T/m do not permit to reduce the losses at zero on any injectors. The actual limit on energy is also connected to the dipoles maximum rigidity and with the problems/costs connected with the installation of new cryostats.

Table 3: PIAVE-ALPI versus new RFQ-ALPI

Parameter [units]	PIAVE-ALPI	new RFQ-ALPI
A/q	7.0	7.0
Output Energy [MeV/u]	10.1	10.3
Output RMS Long. emittance [degkeV/u]	18	32
Alpi Transmission [%]	88	94
Total Transmission [%]	62	90

REFERENCES

[1] G. Prete et al., "The SPES project: a second generation ISOL facility", Physics Procedia 26 (2012) 274 – 283.
[2] A. Andrighetto et al., "Production of high-intensity RIB at SPES", Nuclear Physics A 834 (2010) 754c–757c.
[3] M. Comunian et al., "The RFQ injector for the Radioactive ion beam of SPES Project", these proceedings.
[4] G. Bisoffi et al., "A Cost-Effective Energy Upgrade of the Alpi Linac at Infn-Legnaro", Proceeding of HIAT 2012.

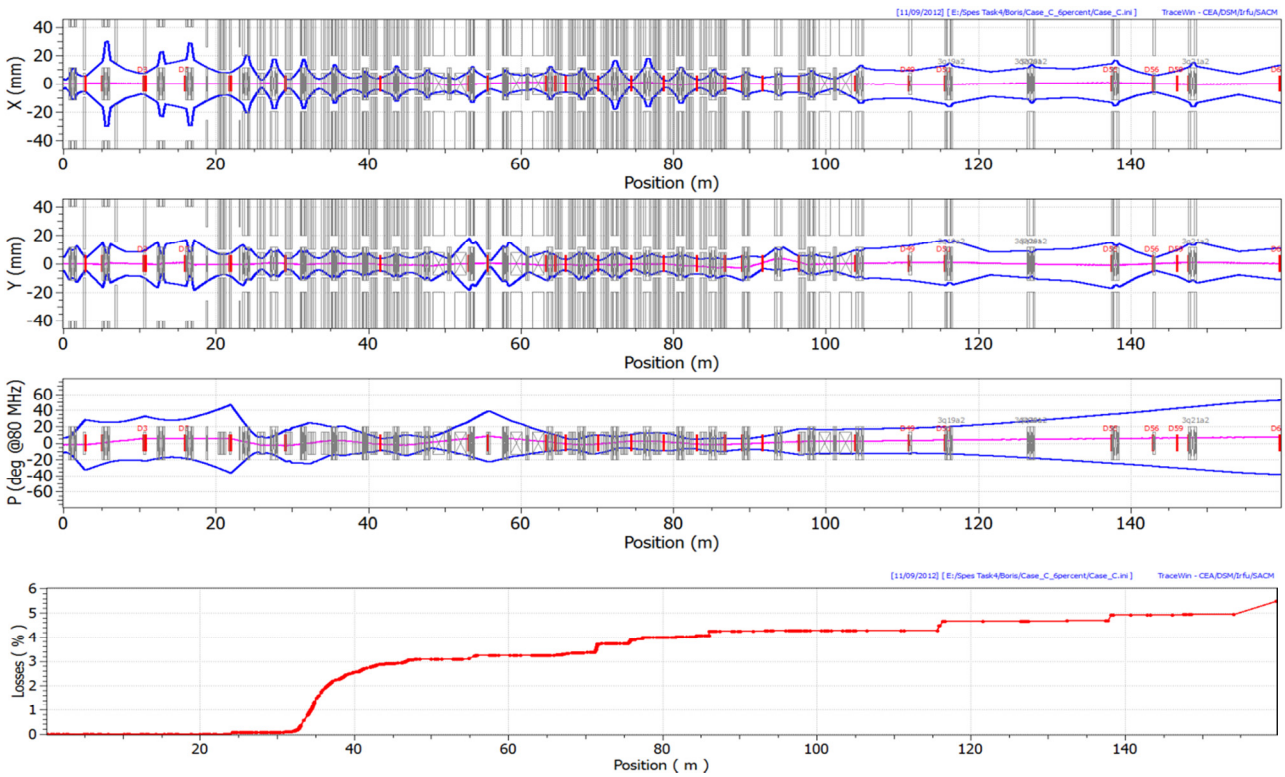

Figure 5: Multiparticles beam envelopes of the ALPI and losses, with the beam coming out from the new RFQ, from left to right.

Copyright © 2012 by the respective authors — cc Creative Commons Attribution 3.0 (CC BY 3.0)

PIEZOELECTRIC ACTUATOR BASED PHASE LOCKING SYSTEM FOR IUAC LINAC

B.K.Sahu, R. Ahuja, Rajesh Kumar, S.K. Suman, A.Rai, P.Patra, A.Pandey , J Karamkar, G.K.Chowdhury, Mukesh Kumar, R.N. Dutt, D.S.Mathuria, S. Ghosh, D.Kanjilal and A.Roy, Inter University Accelerator Centre (IUAC), Aruna Asaf Ali Marg, New Delhi – 110067, India

Abstract

The linac of IUAC consists of five cryostats having a superbuncher(SB), three accelerating modules, having eight quarter wave resonators (QWR) each, and a rebuncher(RB). At present SB, two accelerating modules and RB are operational and testing of the last linac module is being carried out. In the operational linac modules the phase locking is achieved by a combination of fast I-Q based electronic tuner and helium gas flow based mechanical tuner. Microphonics measurement on the resonators confirms the presence of low frequency vibrations along with main mechanical mode of the resonator. The existing gas flow based mechanical tuner working in the time scale of seconds can't arrest these vibrations, In a parallel development we have tested a piezoelectric actuator based fast tuner operating in the time scale of milli seconds. The test results showed that the piezoelectric based tuner can arrest all low frequency vibrations and reduce a substantial load from the electronic tuner to improve the dynamics of the phase locking scheme. The implementation of this scheme along with test result is presented in this paper.

INTRODUCTION

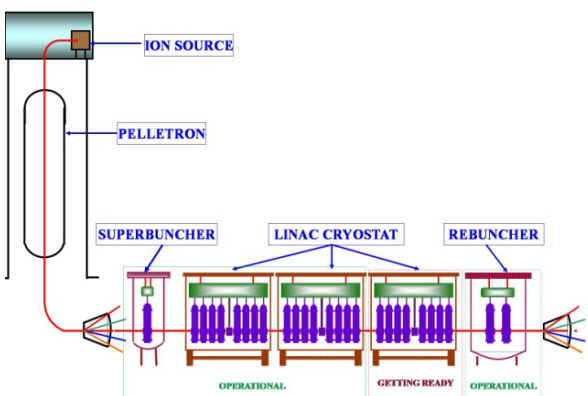

Figure 1: The schematic of IUAC linac.

At Present, the first two accelerating modules of IUAC superconducting (SC) linear accelerator (linac) are operational with superbuncher and rebuncher to provide accelerated heavy ion beams to conduct experiments in nuclear physics and materials science [1]. The third linac module is almost ready for beam acceleration. Each module has eight SC niobium Quarter Wave Resonators (QWR) operating at a resonance frequency of 97MHz and are independently phase locked with the master oscillator. The phase locking of the SC QWR consists of fast I-Q based dynamic phase control along with the helium gas flow based mechanical tuner [2]. The vibration related fluctuations around master frequency (microphonics) are mainly controlled by the fast I-Q based electronic tuner and the slow drifts of the central frequency are arrested by closed loop helium gas flow based mechanical tuner, to reduce the load on the electronic tuner. The gas flow based tuner operates in the time scale of seconds. Thus it can control frequency drifts less than a Hz. All the faster component of frequency jitter put an extra load on the electronic tuning mechanism of the resonator. An alternate piezoelectric actuator based tuner along with stepper motor based coarse tuner is successfully developed and tested with one of the QWRs in the test cryostat [3].

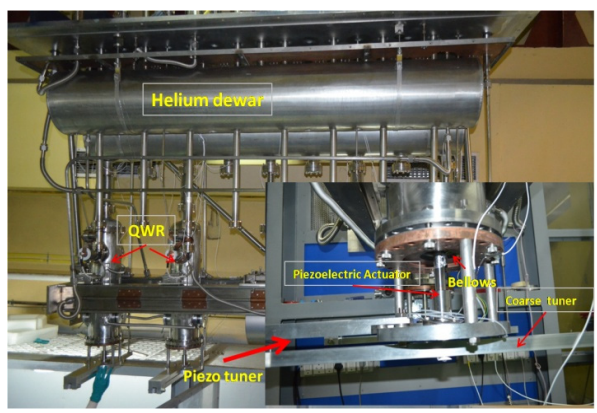

Figure 2: The piezoelectric actuator based mechanical tuner in third linac cryo module along with close view.

The stepper motor based coarse tuner brings frequency close to the master frequency and then the control is given to the piezoelectric actuator based tuner. The piezoelectric tuner operates in the time scale of tens of milli seconds and thus takes considerable load away from the fast tuner to reduce the average power during operation. After the successful operation of piezoelectric based tuner in test cryostat it is decided to optimise the tuner performance for linac operation and the new piezoelectric actuator based mechanical tuners are installed in two of the resonators in third linac module. The control scheme is tested with conditions similar to actual operation.

Copyright © 2012 by the respective authors — cc Creative Commons Attribution 3.0 (CC BY 3.0)

MEASUREMENT OF MICROPHONICS OF QWRS DURING LINAC OPERATION

External vibrations caused by vacuum pumps and pressure changes of the helium bath are coupled to the resonator and they may excite any natural resonance frequency associated with this resonator. This phenomenon produces to a jitter in the resonance frequency of a resonator and known as microphonics. The amount and nature of microphonics will determine the achievable field stability and also the required amount of control to be shared between electronic tuner and piezoelectric based mechanical tuner. To reduce this frequency jitter by damping the main mechanical mode an unique vibration damper using ordinary SS balls have been used in our resonators with great success[4]. Microphonics measurements have been performed on the resonators of first and second linac module cooled at liquid helium temperature in the closed loop cryogenic operational mode. Existing resonator control electronics used to lock the cavity field to an external master oscillator with the help of self-excited loop (SEL) and separate feedback loops to lock both the phase and amplitude of the resonator. The control electronics have been used to stabilize the phase and amplitude of the accelerating field of a superconducting resonator using RF power from the 400 Watt RF amplifier.

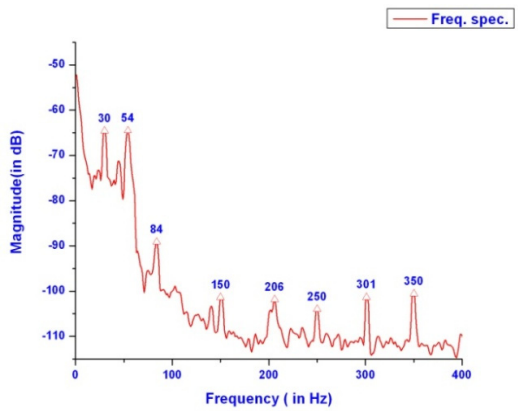

Figure 3: All the resonant modes of the resonator in linac cryostat.

The probability for cavity eigen frequency shift due to microphonics is measured using Agilent signal analyser model 35670A. The total frequency spectrum of the vibrations a resonator is shown in figure 3. It is observed from figure 3 that most of the microphonics is caused by internal mechanical resonances in the frequency range of 1Hz to 100Hz where as higher order modes up to 400 Hz are also present with much reduced amplitude. The main mechanical mode of the resonator is 54 Hz in this resonator and around 60 Hz in most of the resonators. During measurement of microphonics some low frequency vibration less than 30 Hz is also observed in some of the resonators.

CHARACTERISATION OF PIEZOELECTRIC ACTUATOR BASED MECHANICAL TUNER FOR OPERATION

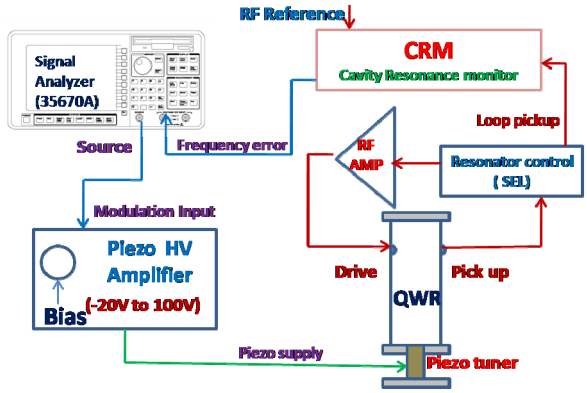

Figure 4: Set up for measurement of frequency response or piezoelectric based mechanical tuner.

The dynamics of the piezoelectric actuator based tuner is optimised to implement on the resonators of the linac cryostat after proper characterisation of the overall system with the piezoelectric mechanical tuner. The dynamic characteristics of the final piezoelectric actuator with attached bellows for the resonator are studied extensively at cold temperature using SEL to understand the different resonant modes of the system. Figure.4 shows the set-up for the measurement of the transfer function between the piezoelectric amplifier input and the frequency range of the resonator around the mean centre frequency. To measure the frequency response of the piezoelectric actuator based mechanical system a periodic chirp signal from the source of the signal analyser in the frequency range of 1 to 400 Hz.

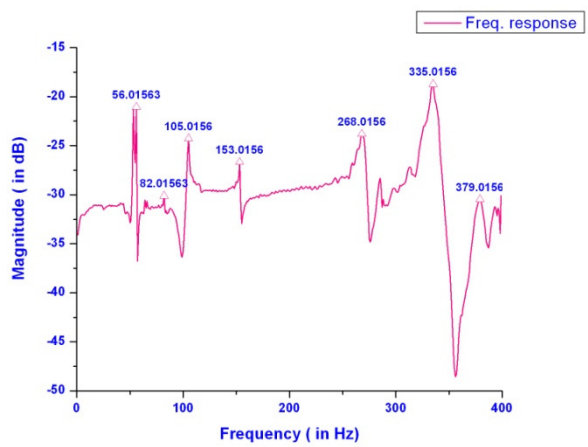

Figure 5: Frequency response of the piezoelectric tuner.

Since the periodic chirp provides an equal amount of energy at all the frequencies within the span, the measurement covers all the resonant modes of the system. The same resonant modes are also verified by using swept sine analysis of the analyser. The various resonant modes

Copyright © 2012 by the respective authors — cc Creative Commons Attribution 3.0 (CC BY 3.0)

are shown in Figure. 5. The DC bias of the piezoelectric amplifier is varied to obtain the transfer function. The first resonant mode is found to be the main mechanical mode of the resonator. The response time of the system is also studied by applying a step function of 10 msec. Based on the results we have concluded that the closed loop system can be safely operated around 10 msec.

CLOSED LOOP OPERATION OF PIEZOELECTRIC ACTUATOR TO PHASE LOCK LINAC RESONATOR

The superconducting resonator frequency is first brought close to the master oscillator by operating the coarse tuner. The piezoelectric bias voltage is kept at a mid voltage range to have maximum closed loop dynamic range in both the direction. The Resonator is first phase locked using the dynamic phase control loop. The phase error of the resonator controller is processed in a dedicated PI based control to compensate the frequency drift around the central frequency of the resonator and to eliminate the hysteresis effects. The block diagram for the closed loop control of the piezoelectric actuator with existing dynamic phase control based resonator controller is shown in figure 6.

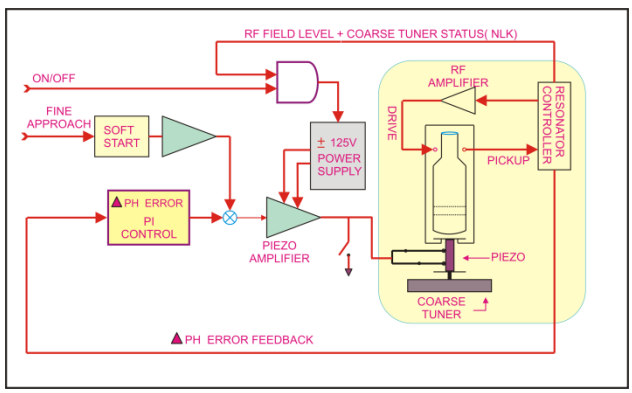

Figure 6: Block diagram of Piezoelectric close loop control scheme.

The electronics for the closed loop control is designed in house. The control consists of a high voltage amplifier along with P-I based closed loop control and necessary safety interlocks. In the existing resonator control electronics, the phase error calibration is set for ~ 5mV for 1 Hz change in frequency whereas the high voltage amplifier for the piezoelectric actuator need to supply ~125mv to correct 1Hz frequency drift from the master. Hence the DC gain of the loop was decided and 3 dB bandwidth of the control loop was optimised at 16 Hz with unity gain at 32 Hz. The total phase margin for control was 80 degree. During the test, the overall locking performance was found to be satisfactory. The proportional gain and integration time constant was optimised to have a correction of +/- 80 Hz variation in the central frequency within 12 milli second time scale. The stability of the lock was found to be good and the average power for locking was reduced drastically with piezoelectric actuator taking away a substantial load from the fast tuner. It was observed that for both, large and small variation of resonance frequency from its central value, the piezoelectric voltage was kept on varying at the same rate to correct the variation. When a large mechanical vibration was coupled intentionally with the resonator the resonator's frequency started fluctuating widely (~160 Hz), but the controller was able to hold the lock with increase in forward power momentarily. The total range of the piezoelectric actuator based tuner is found to be 990 Hz along with coarse tuner range of 42 kHz for this particular set of resonator and mechanical tuner. The stability of the lock was observed for a few hours at an accelerating field of 3.8 MV/m. The amplitude and phase lock stabilities were measured to be 0.1% and ±0.2 degree respectively at this field level.

CONCLUSION

Piezoelectric actuator based control scheme is successfully implemented in a resonator in third linac cryostat. It is found to improve the phase locking performance. The mechanical coarse tuning mechanism with the piezoelectric actuator also performed well and we are in the process of replacing the ferrofluid based coarse movement with linear motion feed through for ease of coarse operation. We are planning to use piezoelectric based tuners in four of the resonators installed in linac-3 along with existing gas flow based tuners in the other four to have detailed operational statistics. Piezoelectric tuners will be installed on all the other linac resonators in place of gas operated mechanical tuners.

ACKNOWLEDGEMENT

Authors would like to acknowledge the help and cooperation received from the cryogenic group and resonator fabrication group of IUAC. The authors acknowledge the technical help and suggestion received from Mr. Gopal Joshi and S. Khole of Electronics Division, BARC during testing.

REFERENCES

[1] S. Ghosh et al, Proc of Heavy Ion Accelerator Techonology (HIAT) Accelerator Conference held during 18-21 June 2012 in Chicago,IL, USA.
[2] G. Joshi et al. Pramana, J. of Physics, Vol. 59, No.6, Dec 2002, page – 1035.
[3] B.K.Sahu et al. Proc. of International Particle Accelerator Conference (IPAC'10) Kyoto, Japan.
[4] S.Ghosh, et al Physical Review Special Topic – Accelerator and Beams, 10, 042002 (2007).

Copyright © 2012 by the respective authors — cc Creative Commons Attribution 3.0 (CC BY 3.0)

A HELIUM INJECTOR FOR COUPLED RFQ AND SFRFQ CAVITY PROJECT AT PEKING UNIVERSITY

Haitao Ren, Shixiang Peng*, Pengnan Lu, Jia Chen, Jie Zhao, Yuan XU, Shuli Gao, Zhi Wang, Zhiyu Guo and Jia'er Chen
INST, KLNPT & IHIP, School of Physics, Peking University, Beijing 100871, China

Abstract

A new acceleration structure named as coupled radio frequency quadrupole and separated function radio frequency quadrupole cavity (Coupled RFQ & SFRFQ) is under design at Peking University (PKU). A pulsed or CW He^+ beam injector will be needed to transport 30 keV 20 mA He^+ beam and normalized rms emittance less than 0.15 pi.mm.mrad for this composited type cavity. For pulsed mode, the factor is 1/6, the pulse width is 1 ms. Based on the experimental results obtained on the PKU LEBT test bench, an injector with a 2.45GHz permanent magnet ECR ion source and a 1.16 m long two-solenoid type low energy beam transport (LEBT) line was developed. In this paper we will address the 30 keV He^+ ion beam transportation experimental results on the test bench as well as the specific design on the helium injector.

INTRODUCTION

The development of advanced materials is a key to the achievement of nuclear fusion as a safe, environmentally attractive and economically competitive energy source [1]. Therefore, the study of material irradiation damage effects is increasingly important for advanced nuclear energy systems. An accelerator-based material irradiation facility with beam energy of MeV is a good choice to address the challenges presented by fusion wall materials andto study the form of the resulting waste. A coupled RFQ-SFRFQ accelerator for materials irradiation has been developed at Peking University [2]. It is a new acceleration structure that couples RFQ and SFRFQ electrodes in a single cavity. This material irradiation project is designed to accelerate the helium beam to 0.8 MeV with the peak current of 5 mA. In this paper we will address the general description of the He+ injector design in part 2. In part 3, we will present the bench experimental results on He^+ ion beam production and transmission efficiency on the space charge compensation with Ar gas. In part 4, we will give out the concept and specific design of the helium injector. A summary will follow at the end of this paper.

GENERAL DESCRIPTION

A helium injector is used to generate plasma, to create an expected ion beam and to transport it into an accelerator. It consists of an ion source and a low energy beam transport part (LEBT).

* Corresponding author Email: sxpeng@pku.edu.cn

Among sorts of ion source we choose a permanent magnet 2.45 GHz Electron Cyclotron Resonance Ion Source (PKU PMECRIS) for this coupled RFQ and SFRFQ accelerator at PKU. One reason is that this type of ion source has very unique features, such as high ion beam density, high reliability, ability to operate both in CW mode and in pulsed mode, good reproducibility and low maintenance and long lifetime. And those outstanding characteristic make 2.45 GHz ECRIS popular as a High Current Ion Source in the world [3-7]. Another reason of out chosen is that researchers at PKU are skilful on this kind of ECRIS [5,7]. By replacing the solenoid with permanent magnet, the ECR ion source body is more compact.

LEBT is used to transport and to match the beam created and extracted from the ion source to accelerator. Beam focus can be done with electrostatic or magnetic elements[8] within LEBT. Compared with electrostatic type LEBT, the advantage of magnetic LEBT is obvious on the neutralization of space charge, on the emittance growth suppressing and on the improvement of beam transmission efficiency within the injector [8]. When the injector dimension is not the limitation, magnetic type LEBT is a good choice for a high intensity low energy ion beam. Based on the above understanding and our experience on D+ injector design for PKUNIFTY[5], a magnetic low energy beam transport (LEBT) line with two solenoids is chosen to transport the He^+ beam into the coupled RFQ-SFRFQ. This injector must produce and transport at least 20 mA (peak current) of helium beam with energy of 30 keV to the entrance of RFQ, and the normalized rms emittance of the beam should be less than 0.15 πmm.mrad. Parameters of the injector are listed in table 1.

Table 1: Parameters of the Helium Injector

He+ beam current	mA	20
Energy	keV	30
Duty cycle	Hz	166
Pulse length	ms	1
Emittance(norm rms)	πmm.mrad	0.15

BENCH EXPERIMENTS

Nonlinear space charge force for low energy intense beam is a main reason of beam divergence and emittance growth, which leads to low transmission efficiency [4]. In LEBT line, the space charge effect is more obvious,

Copyright © 2012 by the respective authors — cc Creative Commons Attribution 3.0 (CC BY 3.0)

especially for the beams with lower beam energy part. Compared with proton beam, the He^+ has lager mass and then the beam extraction and transport is more difficult. As the beam diverges a lot, electrode temperatures increase and the spark rate becomes important. Moreover, in these conditions, even after source extraction tuning, the LEBT transmission improvement is a big challenge [9].

In order to obtain the beam characteristics required at the entrance of the RFQ-SFRFQ cavity, beam transmission efficiency of He^+ has been carefully studied on the LEBT test bench (Fig. 1) [6]. The distances from the emission aperture of the ion source to FC1, FC2 and FC3 are 50 mm, 1195 mm and 1995mm.

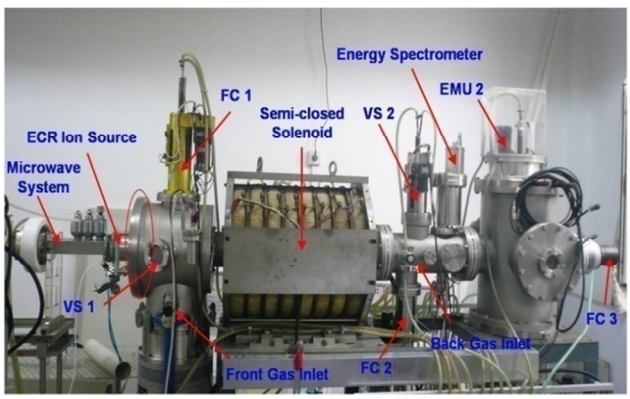

Figure 1: PKU LEBT test bench.

On the test bench we adopt a 2.45GHz permanent magnetic ECR (PMECR) ion source which has a compact structure, similar to the one reported before [5, 7]. Equipped with a tri-electrode extraction system, this ion source has ability to produce high-current ion beams of various gaseous elements, such as H^+, D^+, He^+, N^+, O^+, Ar^+ [7]. With pulsed mode about 65 mA peak current of He^+ beam can be extracted, and the normalized rms emittance is less than 0.2 π mm.mrad. There are two gas inlets on our test bench, named as the front gas inlet and the rear gas inlet. The front one can mainly contribute to the space charge compensation of ion beams around the region of extraction system, and the rear one mainly works behind the semi-closed solenoid. Fig. 2 shows the experimental results of He^+ ion beam compensated by Ar gas through the front or rear gas inlets. As shown in Fig.2, He^+ beam transmission efficiency (IFC3/IFC1) can be increased from 39% to 48% when injected Ar flow from 0 to 1.5 sccm at the rear injection location(rear case). Once when the injection location changes to the front that near the extraction system, He^+ transmission efficiency increases from 39% to 55%, 8% higher than the rear injection case when the gas flow increase up to 0.4 sccm. In the meantime, the current needed by the solenoid for front case is 3A less than that for the rear case. From beam dynamics point of view, less focusing force means higher beam quality[10]. This is understandable for the beam density within extraction region is the highest along the injector and the space charge force is proportionality to the beam intensity. And this phenomenon is co-accordant with the theoretical analysis in [8].

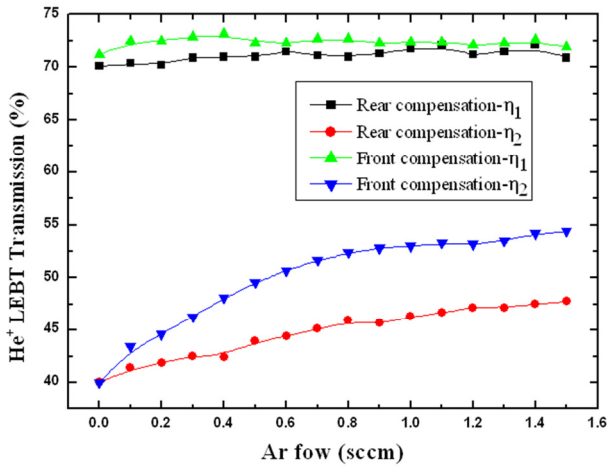

Figure 2: LEBT transmission of 30keV/65mA He^+ beam with front compensation and rear compensation.

HELIUM IN JECTOR

Based on the above experimental results, a He^+ injector with a permanent magnet 2.45 GHz ECR ion source and a two-solenoid LEBT with a front and a rear extra gas injection points was designed for Coupled RFQ & SFRFQ accelerator. Fig.3 is the schematic view of this injector. The entire LEBT length is about 1160 mm. It consists of five sections, drift 1: 280 mm, solenoid 1: 200 mm, drift 2: 200 mm, solenoid 2: 200 mm, drift 3: 280 mm. Two solenoids are more flexible than one solenoid for the beam match at the entrance of RFQ accelerator when beam extraction from the ion source is not in ideal condition.

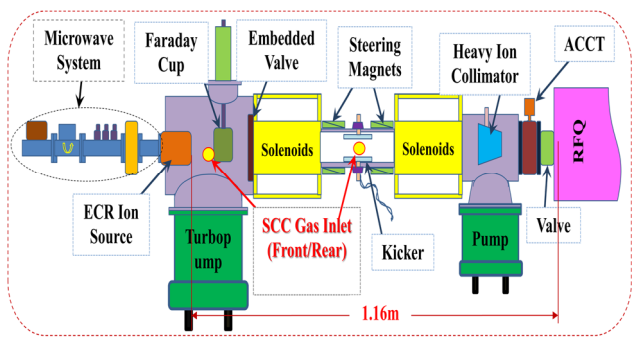

Figure 3: Schematic view of the helium injector.

Details of this injector are a 2.45GHz PMECR ion source with a tri-electrode extraction system for He+ beam producing, a Faraday cup for measuring the total current output, an embedded valve to break-up the vacuum between the ion source and the LEBT, two semi-closed solenoids for beam focusing, two steering magnets for beam trajectory adjusting, a kicker for pulse molding, a heavy ion collimator, an ACCT and a small valve at the entrance of RFQ to make the injector and RFQ cavity vacuum independent. Compensation gas can be injected

Copyright © 2012 by the respective authors — cc Creative Commons Attribution 3.0 (CC BY 3.0)

from the extraction region and between two solenoids. The kicker will installed between two steering magnets and the kick-off beams will be absorbed at the water-cooling collimator just behind the solenoid 2.

SUMMARY

To satisfy the requirement of Coupled FRQ and SFRFQ accelerator, a 30keV/20mA He+ injector based on the PKU 2.45 GHz PMECRIS and two-solenoid LEBT is being developed at PKU. The experimental results obtained on PKU LEBT test bench give a strong support for this design. Fabrication is on the way and commissioning will start at the beginning of year 2013.

ACKNOWLEDGMENTS

This work is supported by National Science Foundation of China No. 91126004, No.11075008 & No.11175009.

REFERENCES

[1] Kohyama, Y. Katoh, M. Ando, K. Jimbo, A new Multiple Beams–Material Interaction ResearchFacility for radiation damage studies in fusion materials, Fusion Engineering and Design 51–52 (2000) 789–795.

[2] Z. Wang, J. E. Chen, M. L. Kang, Y. R. Lu, W. L. Xia, S. L. Gao, Z.Y. Guo, G. Liu, S. X. Peng, H. T. Ren, X. Q. Yan, J. Zhaoand K. Zhu, Design of coupled cavity with energy modulated electron cyclotron resonance ion source formaterials irradiation research, PHYSICAL REVIEW SPECIAL TOPICS - ACCELERATORS AND BEAMS **15,** 050101 (2012).

[3] L. Celona, G. Ciavola, S. Gammino, et. al., **Rev. Sci. Instrum**. **75**, 1423 (2004).

[4] R. Gobin, P.-Y. Beauvais, O. Delferrière, et. al., *Rev. Sci. Instrum*. **79**, 02B303 (2008).

[5] H. T. Ren, S. X. Peng, P. N. Lu, Q. F. Zhou, Z. X. Yuan, J. Zhao, M. Zhang,Z. Z. Song, J. X. Yu, Z. Y. Guo and J. E. Chen, Deuteron injector for Peking University Neutron Imaging Facility project. *Review Science Instrument.* **83**, 02B711 (2012) .

[6] Gobin, R., Blideanu, V., Bogard, D., et. Al., Rev. Sci. Instrum. 81, 02B301_2010.

[7] H. T. Ren, S. X. Peng, P. N. Lu, S. Yan, Q. F. Zhou, J. Zhao, Z. X. Yuan, Z. Y. Guo, and J. E. Chen, Intense beams from gases generated by a permanent magnet ECR ion source at PKU, *Rev. Sci. Instrum* **83**, 02B905 (2012).

[8] N. Chauvin, O. Delferrière, R. Duperrier, R. Gobin, P. A. P. Nghiem, and D. Uriot, Transport of intense ion beams and space charge compensation issues in low energy beam lines (invited). *Rev. Sci. Instrum.***83**, 02B320 (2012).

[9] Shixiang PENG, Pengnan LU, Haitao REN, Jie ZHAO, Jia CHEN, Yuan XU, Zhiyu GUO and Jia'er Chen, Principal Elements of Space Charge Compensation on a Low Energy High Intensity Beam Injector. *Rev. Sci. Instrum.* **Sumitted**, 2012/8

[10] P. N. Lu, S. X. Peng, H. T. Ren, M. Zhang, Z. X. Yuan, Z. Z. Song, J. Zhao,J. X. Yu, Y. J. Ma, R. Xu and Z. Y. Guo, Preliminary studies on space charge compensation by analyzing residual Argon gas ion signals. *Rev. Sci. Instrum.* **81**, 02B711 (2010).

Copyright © 2012 by the respective authors — cc Creative Commons Attribution 3.0 (CC BY 3.0)

A NEW DESIGN OF THE RFQ CHANNEL FOR GSI HITRAP FACILITY

S. Yaramyshev#, W. Barth, G. Clemente, L. Dahl, V. Gettmann, F. Herfurth, M. Kaiser, M. Maier, D. Neidherr, A. Orzhekhovskaya, H. Vormann, G. Vorobjev, GSI, Darmstadt, Germany
R. Repnow, MPI-K, Heidelberg, Germany

Abstract

The HITRAP linac at GSI is designed to decelerate ions with mass to charge ratio of A/Z<3 from 4 MeV/u to 6 keV/u for experiments with ion traps. The particles are decelerated to 500 keV/u with an IH-DTL structure and finally to 6 keV/u with a 4-rod RFQ. During commissioning stage the deceleration to approx. 500 keV/u was successfully demonstrated, while no particles behind the RFQ with an energy of 6 keV/u were observed. Dedicated simulations with DYNAMION code, based on 3D-fotometrie of the fabricated RFQ electrodes were successfully performed comprehending the commissioning results. In a second step the simulations have been experimentally confirmed at a test-stand (MPI-K, Heidelberg). An input energy, accepted by the RFQ is significantly higher than design value. For this reason the longitudinal beam emittance after deceleration with IH structure does not fit to the longitudinal RFQ acceptance. To solve this problem a new design of the RFQ channel with a correct input energy has been started. New RFQ parameters and the results of the beam dynamics simulations are presented in this paper.

INTRODUCTION

The **H**eavy **I**on **Trap** (HITRAP) facility of the GSI Helmholtzcenter for Heavy Ion Research at Darmstadt has been built to decelerate highly charged heavy ions to an energy of 6 keV/u. Then ions can be captured in a Penning trap, cooled further to cryogenic temperatures, extracted and transported to the experiments for atomic, nuclear and solid state physics [1-2].

The HITRAP linac (Fig. 1) is foreseen to decelerate heavy ions with an energy of 4 MeV/u down to 500 keV/u by IH-DTL section and to 6 keV/u by a 108 MHz RFQ [3], designed by Prof. A. Schempp (IAP Frankfurt, Germany) and fabricated by NTG Company (Gelnhausen, Germany). A deceleration of the beam to 500 keV/u at HITRAP facility was successfully demonstrated, while until now all efforts providing for complete deceleration to 6 keV/u failed. Therefore a beam dynamics study for the RFQ by means of the advanced multiparticle code DYNAMION [4] has been carried out. As a basis for precise and reliable simulations the RFQ electrodes have been disassembled from the tank and measured by Sigma3D Company (Aachen, Germany). The photometric data has been used to build a 3D surface of the electrodes "as fabricated" (Fig. 2). Detailed distribution of the electrical potential inside an RFQ channel was calculated by means of a relaxation scheme. Obtained 3D electrical field mapping was used as an input data.

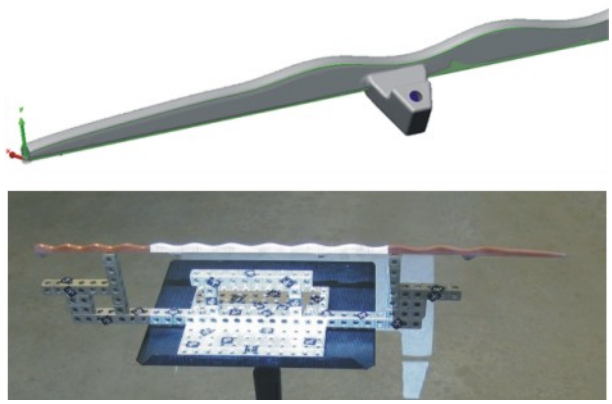

Figure 2: 3D surface of the rods (top) used for the simulations and created from the measurements (bottom)

The results of DYNAMION simulations for the HITRAP-RFQ demonstrated significantly higher (approx. 525 keV/u) beam energy than the design value of 500 keV/u. This fact can be the most probable explanation of the not reached deceleration of the beam to the design energy of 6 keV/u at HITRAP facility.

HITRAP-RFQ EXTERNAL TESTS

In 2011 the HITRAP-RFQ was transported to MPI-K (Heidelberg, Germany), installed at Pelletron accelerator and tested with H_2^+ beam (Fig. 3).

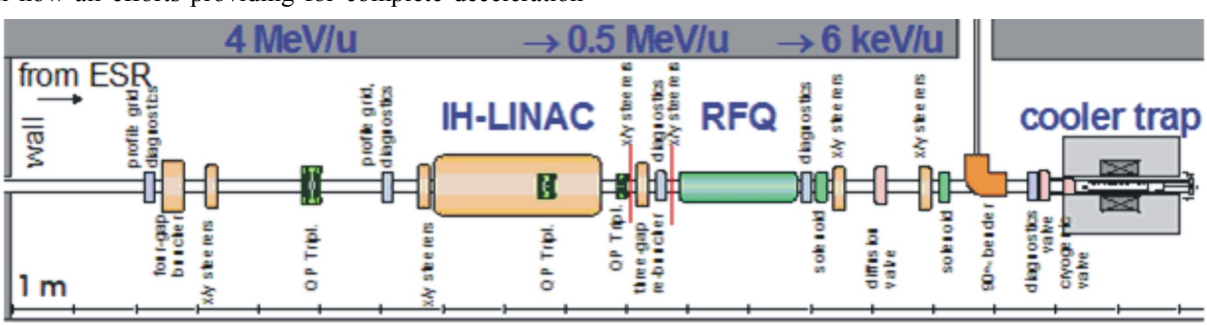

Figure 1.Schematic layout of the HITRAP facility

#S.Yaramyshev@gsi.de

Copyright © 2012 by the respective authors — cc Creative Commons Attribution 3.0 (CC BY 3.0)

Figure 3: Test stand at MPI-K.

The results of DYNAMION simulations were confirmed: the HITRAP-RFQ decelerates ions only with an energy of approximately 517±10 keV/u. Slight discrepancy between measurements and DYNAMION simulations could be explained by a significant misalignments of the rods, especially not fixed ends at the RFQ high energy entrance.

DESIGN OF THE NEW RFQ CHANNEL

On the base of the numerical study and experimental confirmation a decision to design new RFQ electrodes was done. The main goals were to provide for the correct input energy of 495 keV/u, as well as for an increased longitudinal acceptances. An additional complication for a design makes the requirement to the exact input- and output -energies, simultaneously with already fixed length of the electrodes (1981.0±0.5 mm).

New RFQ accelerating-focusing channel was designed with the interactive code DESRFQ [5], written at ITEP (Moscow, Russia). A typical screenshot, which illustrates a final stage of a design process, is shown on Fig. 4

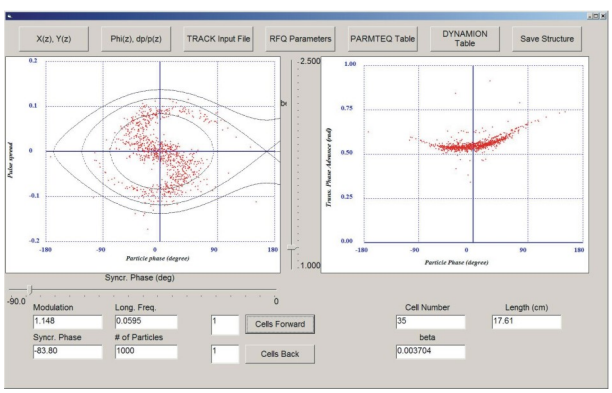

Figure 4: Typical screenshot from the code DESRFQ: beam portrait on longitudinal phase space (left) and stability diagram (right).

Main parameters for old and new design are presented in Tab. 1. New electrodes are designed with the constant average radius (average aperture). It allows for easier fabrication of the rods, as well as for machine tuning.

Table 1: Main RFQ parameters

	Old	**New**
Input energy (keV/u)	525	495
Voltage (kV)	77.5	89.5
Average radius (cm)	1.0-0.58-0.68	0.65
Rods rounding and width	variable	constant
Max. field strength (kV/cm) *Kilpatrick crit. 125 kV/cm*	~ 220	~ 175
Max. modulation	3.0	2.35
Min. aperture (cm)	0.34	0.39
Transverse normalized acceptance (cm mrad)	0.145	0.223
Long. acceptance (arb.u.)	~35	~70
Length (cm)	198.1	198.1

New laws for modulation and synchronous phase (Fig. 5) provides for the almost constant electrical field strength on the electrode surface, significantly lower than existing one, even in spite of higher voltage between adjacent electrodes.

An increased RFQ voltage allows to the lower modulation, what enlarges an aperture and subsequently a transverse acceptance of the RFQ.

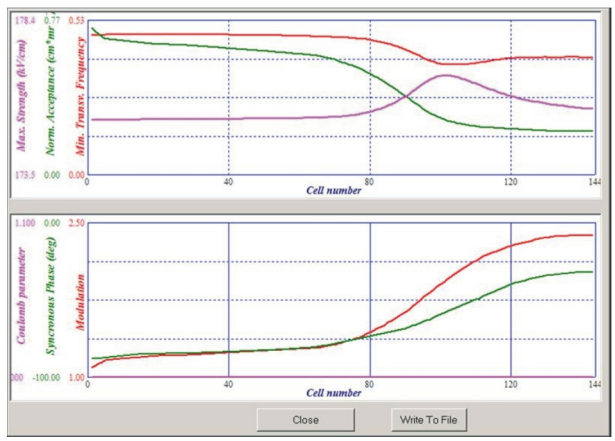

Figure 5: Main parameters of the new RFQ design along the structure: max. field strength, transverse acceptance, min. phase advance (top); modulation and synchronous phase (bottom).

The IH-**DTL structure** decelerate ions from 4 Mev/u to 500 keV/u. Beam dynamics simulations, as well as experiments demonstrate wide energy spread with a significant part of the high energy particles behind the DTL. It strongly hampers measurements of the beam parameters at the RFQ entrance. Therefore the beam parameters at the RFQ entrance were estimated from the results of beam dynamics simulation for the IH-DTL.

To keep the installation as flexible, as possible the design of the new RFQ channel was directed to provide for significantly higher longitudinal acceptance.

Calculations of the channel acceptance were performed with the input particle distribution, widely distributed in 6D phase space. For a comparison of both design the only particles with an energy below 7 keV/u behind RFQ are treated as accepted. These particles, filling the acceptance at the RFQ entrance, are shown on Fig. 6. The

Copyright © 2012 by the respective authors — cc Creative Commons Attribution 3.0 (CC BY 3.0)

longitudinal acceptance for the new channel is increased on about factor of two. The transverse acceptances are some percent lower due to the strong coupling between transverse and longitudinal properties of the RFQ. Nevertheless the total 6D acceptance for the new design is significantly higher.

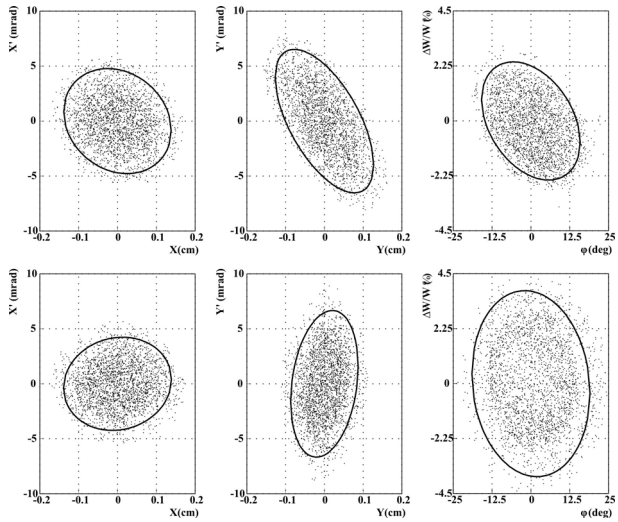

Figure 6: Particle distribution representing the transverse and longitudinal acceptances for old (top) and new (bottom) designs. The ellipses describe 90% of the particles.

The total transverse output beam emittances for the new design are significantly higher than for the old one due to the increased 6D RFQ acceptance. However the difference between output transverse rms beam emittances and brilliance is much smaller (Fig. 7).

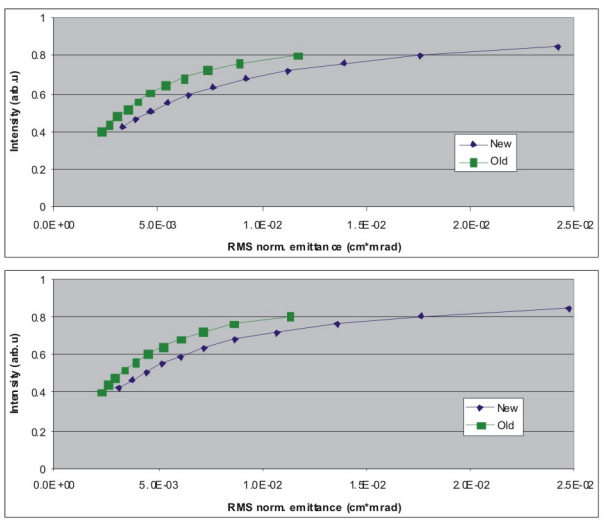

Figure 7: Beam intensity inside given horizontal (top) and vertical (bottom) normalized rms emittance behind RFQ.

The simulated energy distribution behind new and old RFQs is presented on Fig. 8. Longitudinal particle distribution on phase (space) is almost DC with some variation of the particle density.

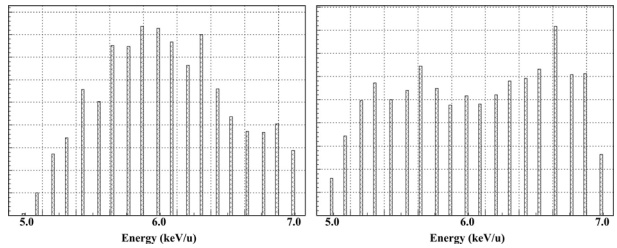

Figure 8: Low energy particle distribution behind RFQ for old (left) and new (right) design.

CONCLUSION AND OUTLOOK

An improved design of the HITRAP-RFQ channel was proposed. Main goals of the design are the correct input energy and twice increased longitudinal acceptance. This should provide for easier beam matching to the RFQ and successful deceleration of the ions to the design energy of 6 keV/u at GSI HITRAP facility.

The fabrication of the new rods and stems is ongoing. Commissioning and the test experiments with the upgraded RFQ are planned in November 2012 at MPI-K (Heidelberg). Afterwards the RFQ will be installed into the HITRAP beam line at GSI.

A completely new RFQ design, including new tank with improved rf properties, as well as mechanical and thermal stability is strongly recommended. In parallel a new design of the RFQ channel, based on the refined experimental and numerical information about beam parameters behind IH-DTL, should be elaborated.

Further improvement of the RFQ beam dynamics might be reached with a special law of synchronous phase along channel, as well as with use of the trapezoidal modulation [6] for the RFQ high energy part.

REFERENCES

[1] O. Kester et al., "DECELERATION OF HIGHLY CHARGED IONS FOR THE HITRAP PROJECT AT GSI", LINAC 2006, Knoxville, Tennessee USA, MOP063 (2006).

[2] F. Herfurth et al., "HITRAP Decelerator and According Beam Instrumentation", HIAT 2012, Chicago, Illinois USA, THB05 (2012).

[3] B. Hofmann et al., "A RFQ-DECELERATOR FOR HITRAP", PAC07, Albuquerque, New Mexico, USA, TUPAN020 (2007).

[4] S. Yaramyshev et al., "Development of the versatile multi-particle code DYNAMION" NIM A, Vol 558/1, pp 90-94, (2005).

[5] S. Yaramyshev et al., "Advanced beam dynamics simulations with the DYNAMION code for the upgrade and optimization of the GSI-UNILAC", HB2010, Morschach, Switzerland, THO1A04 (2010).

[6] O. Belyaev et al., "IHEP EXPERIENCE ON CREATION AND OPERATION OF RFQS", LINAC-2000, Monterey, California, USA, MOD21 (2000).

Copyright © 2012 by the respective authors — cc Creative Commons Attribution 3.0 (CC BY 3.0)

DESIGN OF RE-BUNCHER CAVITY FOR HEAVY-ION LINAC IN IMP

L. Sun#, Y. He, A. Shi, X. Du, Z. Zhang, C. Zhang
Institute of Modern Physics, Chinese Academy of Sciences, Lanzhou 730000, China

Abstract

A re-buncher with spiral arms for a heavy ion linear accelerator named as SSC-LNAC at HIRFL (the heavy ion research facility of Lanzhou) has been constructed. The re-buncher, which is used for beam longitudinal modulation and match between the RFQ and DTL, is designed to be operated in continuous wave (CW) mode at the Medium-Energy Beam-Transport (MEBT) line to maintain the beam intensity and quality.

Because of the longitudinal space limitation, the re-buncher has to be very compact and will be built with four gaps. We determined the key parameters of the re-buncher cavity from the simulations using Microwave Studio software, such as the resonant frequency, the quality factor Q and the shunt impedance. The detailed design of a 53.667 MHz spiral cavity and measurement results of its prototype will be presented.

INTRODUCTION

The spiral cavity shown in Fig.1 is a kind of characteristic RF structure other than QWR (Quarter Wave Resonator) cavity, whose remarkable properties are attributed to a high efficiency, compact design and a big variety of possible fields. In comparison to other available designs, the advantage of this structure lies in its small size. Furthermore it can easily be tuned to expected frequency point by varying the length of the spiral. Of course, due to the small size the required budget can also be kept low. This re-buncher resonator, having four gaps in it, operates at a fixed frequency of 53.667MHz to provide the longitudinal focusing of 7.12MeV heavy ion beam. To reduce the risk of sparking, the voltage of gaps is well optimized at 30kV. The bunching voltage, which is defined as the sum of the four gap voltages, has reached 120kV at a power consumption of 0.95kW.

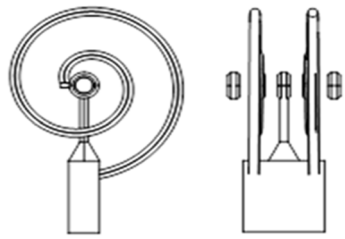

Figure 1: Schematic drawing

DYNAMICS DESIGN

According to the design for LINAC [1] which are presented in Fig.2, the re-buncher is located between the RFQ and the IH-DTL cavities, and it can be used to provide adjustable longitudinal focusing force to guarantee that most particles do not exceed the longitudinal acceptance of the DTL. The longitudinal emittance of the main bunch and the longitudinal acceptance of the DTL at its entrance are illustrated in Fig.3. The void region is the longitudinal acceptance of the whole DTL. The area occupied by black dots is the matched longitudinal particle distribution at the entrance of the DTL. Obviously, without bunching function, the majority of particles will lost, only 23.2% particles can be accelerated by the DTL. When the re-buncher is turned on, a satisfying result can be acquired by optimizing the re-buncher structure and its bunching voltages

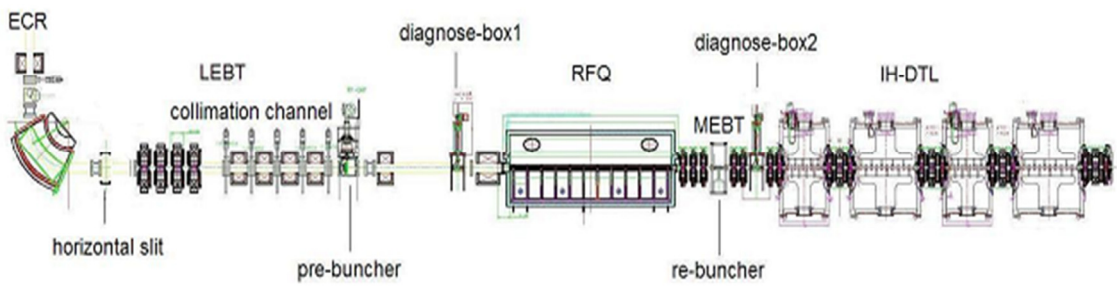

Figure 2: The layout of the SSC-LINAC

sunlp@impcas.ac.cn

Copyright © 2012 by the respective authors — cc Creative Commons Attribution 3.0 (CC BY 3.0)

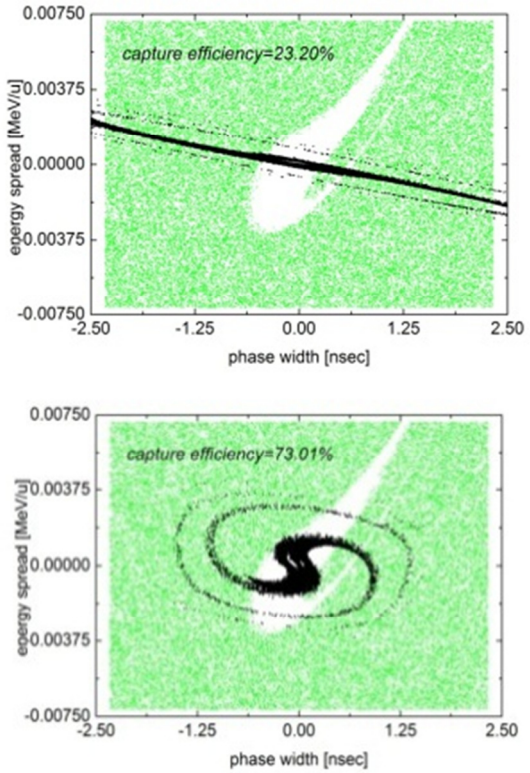

Figure 3: The particle longitudinal distribution when the re-buncher turned on (bottom) and off (top) respectively.

MAIN PARAMETERS

According to the specification of re-buncher shown in Fig.4 and Tab.1, the sizes of all parts need to be confirmed to meet the requirement of the accelerators' conditioning. The dimension of the resonator is coming from the process of EM optimization and mechanical consideration. With the repeated parameters' sweep, the size of every part has already obtained.

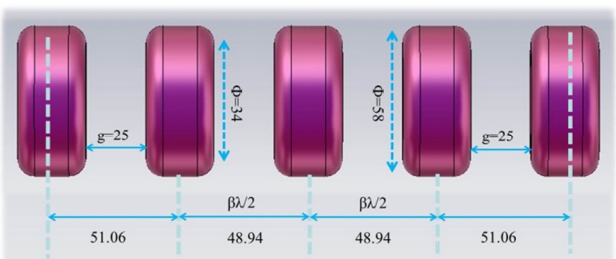

Figure 4: The dimension of drift tubes.

Table 1: The parameters of dynamics design

specification	value	unit
resonant frequency, f	53.667	MHz
velocity, β	0.0175	
charge to mass ratio	1/7	
operating energy	0.143	MeV/u
accelerating voltage, V	30	kV/gap
length of cavity, βλ	22.9	cm
tank diameter	60	cm
diameter of aperture	3.4	cm
voltage stability	±1%	
phase stability	±0.3%	
vibration amplitude	±0.1	mm
operating mode	CW	

SIMULATION RESULTS

The main results of the dynamics simulation for the complicated multi-gap resonator using RF design software named Microwave Studio are presented in Tab.2.

Table 2: The simulated results

characteristic parameters	results	unit
resonant frequency	53.7676	MHz
total energy	1	joule
total power loss	83.04	kW
shunt impedance	2248	kΩ
gap voltage	227.38	kV
R/Q	153.044	Ω
Q-factor	4068.2	

The main consideration for cooling is to analyze the surface current distribution [2] which is indispensable to the structural and thermal designs. Another concern is the voltage distribution along z-axis.

POWER SIMULATION

The power consumption of the cavity can be estimated easily from the above calculated results. First of all, the shunt impedance of four gaps R (about 2248 kΩ) is a key factor. According to the simulated results and the design voltage of each accelerating gap, the magnitude of total power consumption of the cavity can be estimated roughly by using formula as follow:

$$P = (16V_{gap}^2/2R) = 0.95 \text{ kW}$$

We can also estimate the cavity power loss which usually accounts for the power margin, thus a 2 kW amplifier is needed.

COUPLING LOOP [4]

The RF power will be fed into this cavity by a coupling loop which is located near the root of the spiral. The loop area of 100 cm^2 will provide impedance matching of 50

Copyright © 2012 by the respective authors — cc Creative Commons Attribution 3.0 (CC BY 3.0)

ohms. Now this coupler has been designed and simulated at IMP.

PROTOTYPE CAVITY

By May 2011 the prototype cavity has already been manufactured at IMP. The structures are shown in Fig.4.

Considering the cavity cost, we decided to choose the carburizing steel for the outer housing and the aluminum for the inner conductor. The measurement results are shown in Tab.3 and Fig.5:

Table 3: Measurement results

characteristic parameters	measured results	unit
resonant frequency	53.678	MHz
scattering parameter(S_{11})	-24	dB
tuning range	±152	kHz
R/Q	142.5	Ω
Q-factor	702	
flatness of Electric field	≤2.65%	

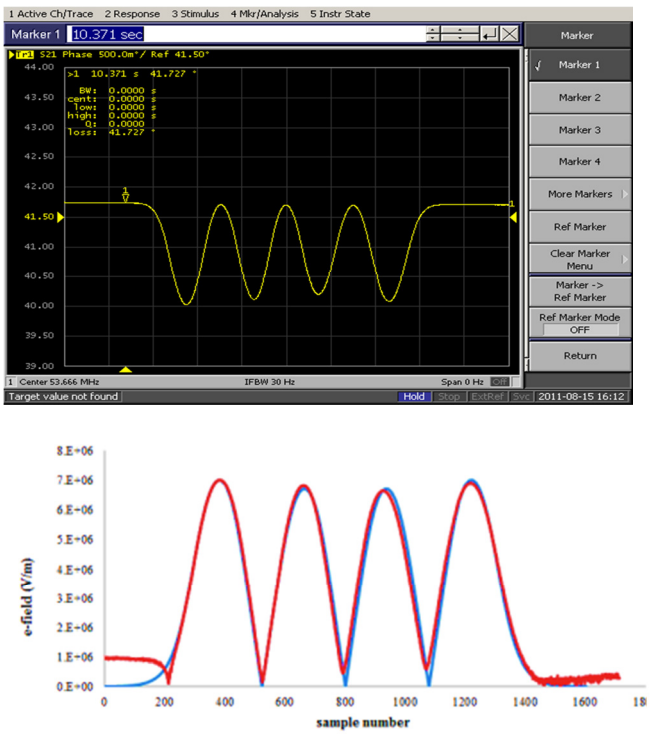

Figure 5: Measurements and analysis of the electric field flatness, the top figure shows the measured results of the phase shift and the bottom figure is the comparison between the simulated results (blue line) and the measured results (red line).

SUMMARY

From the measured Q value as above, we found that the material conductivity could be the primary problem. Through the analyzing the power loss in the lossy resonator presented in Fig.6, the spiral arms and wall are realized to consume the majority of the RF power. And the materials of the prototype are the carburizing steel and duralumin with low conductivity. Using these materials, the simulated Q-factor is no more than 1200. According to the simulations and measurements, we think that a copper spiral cavity will improve its performance greatly, especially for the Q value and shunt impedance. Of course, a good contact and careful assembly are not to be neglected.

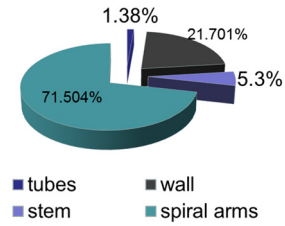

Figure 6: the power distribution

The re-buncher at the MEBT is very important for the longitudinal matching between the DTL and the RFQ cavity. The RF performance of the cavity with two spiral arms has been simulated. Now a full-scale prototype has already been manufactured. The primary measurement shows that the re-buncher design can meet the requirements of the linear accelerator. Although the Q factor is only 702, a little far away from the original design, this value agrees well with the calculated value of the lossy metallic material. In addition, the trajectory tracking results based on the electromagnetic simulation have been finished to help understand the dynamics process.

Now further study of various properties for this cavity is in progress, including all the basic tests using vector network analyzer and the bead-pull measurement [5].Then, a lot of work still need to be done, including fabricating a solid-state amplifier and developing a real copper cavity.

REFERENCES

[1] Xiao Chen, He Yuan, Yuan Youjin, et al. Particle-in-cell mode beam dynamics simulation of the low energy beam transport for the SSC-linac injector, Chinese Physics C, 2011,35(5):500-504.

[2] Schuh M, Kuhnel K U, Welsch C P, Optimization of spiral-load cavities using the 3D code opera/soprano[C]. Proceedings of LINAC, 2008.

[3] Mitra A K, Poirier R L, A 35MHz spiral re-buncher cavity for the TRIUMF ISAC facility[C]. Proceedings of 1999 particle conference, 1999.

[4] Welsch C P, Kunel K U, Schempp A, Development of rebunching cavities at IAP[C]. Proceeding of LINAC2000, 2000.

[5] Mitra A K, Poirier R L, High power test of the 35 MHz spiral re-buncher cavity for the TRIUMF ISAC Facility[C],1999.

Copyright © 2012 by the respective authors — cc Creative Commons Attribution 3.0 (CC BY 3.0)

CONCEPTUAL DESIGN OF SUPERCONDUCTING HEAVY ION LINEAR INJECTOR FOR HIAF*

Z.J. Wang, Y. He, H. Jia, S.H. Liu, C. Li, X.B. Xu, B. Zhang,
W. Wu, H.W. Zhao IMP, Lanzhou,730000,China

Abstract

A heavy ion accelerator facility, High Intensity Heavy Ion Accelerator Facility (HIAF), has been promoted by Institute of Modern Physics IMPof Chinese Academy of Sciences (CAS). The injector of the accelerator facility is a superconducting linac(HIAF-linac). It is a high intensity heavy ion linac and works on pulse mode. The final energy is 100 MeV/u. The accelerated species are from Prton to Uranium. The linac works with both laser and ECR ion source. The designed current is 1.0 emA. The general concept of HIAF and the preliminary design of linear injector are presented in the paper.

INTRODUCTION

High Intensity Heavy Ion Accelerator Facility (HIAF) will be a national user facility. The proposed HIAF facility is based on a heavy-ion linac with a minimum energy of 100 MeV/u for all ions at a beam current 1.0emA. This advanced facility will provide high intensive ion beam for high energy nuclear science to understand the fundamental forces and particles of nature as manifested in nuclear matter. The HIAF project will include three parts, ion linac injector, the rings and experiments facility. The concept HIAF-linac design will be introduced as following.

The proposed linac design is based on the goal of constructing a reliable, low-maintenance, state-of-the-art accelerator with proven technology and robust operating stability that will minimize downtime and ensure production of intense beams for world-class experiments. The design of the driver linac is largely determined by the requirement of a 100 MeV/u, 1.0 mA uranium beam, and the need to accelerate a wide range of ions while limiting the uncontrolled beam loss below 1 W/m, high power SC machine to facilitate hands-on maintenance. The accelerator lattice design must provide adequate transverse and longitudinal acceptance.

Fig. 1. shows a concept schematic layout of the linac facility.

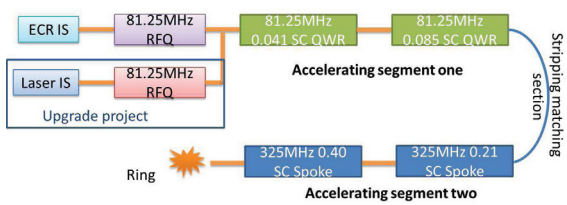

Figure 1: The concept layout of HIAF-linac.

* Supported by the National Natural Science Foundation of China (Grant No.11079001)

As shown in the Fig.1, HIAF-linac will be consisted of front end, superconducting(SC) accelerating segment one, stripping and matching section and superconducting accelerating segment two.

In this paper, concept design of each section are presented.

FRONT END DESIGN

Front end section includes ECR, LEBT and RFQ. The ECR will provide high charge ions beam at both CW and pulse mode. LEBT has two functions, one is to select the charge state from hybrid charge beam, the other is to match the beam to RFQ entrance. The RFQ will accelerator ion beam from 0.02MeV/u to 0.4MeV/u. The layout of the front is shown in Fig. 2 shows the schematic layout of front end. As shown in the figure, one prebuncher is located in

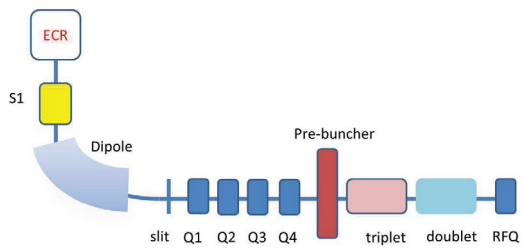

Figure 2: The schematic layout of front end.

the LEBT to decrease the longitudinal emittance to meet the requirement of the acceptance in superconducting section.

The design goals were to minimize the longitudinal emittance and transverse emittance, the RF power, and the structure length. After several optimizations, the parameters of RFQ were found to minimize output longitudinal emittance and maximum transmission. The RFQ was designed using DESRFQ[1] code. The final design structure parameters will be simulated by Track code[2]. RFQ cell profile at different section are shown in the Fig. 3

SUPERCONDUCTING ACCELERATING SEGMENT ONE

Beam from the front end will be injected into the SC linac. Two types of accelerating structures in fourteen cryomodules are used to achieve energy of 15MeV/u for uranium in segment one. Segment one will be approximately 80.2m long and will accelerate the uranium beam from 0.4 to 15 MeV/u when the beam current is 1mA. Segment one includes two periodic structures. Three cryomodules, each containing six β_{opt}=0.041 λ/4 cavities op-

Copyright © 2012 by the respective authors — cc Creative Commons Attribution 3.0 (CC BY 3.0)

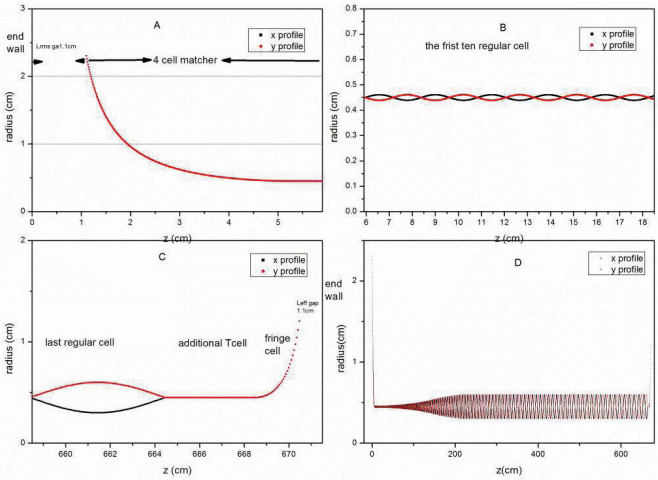

Figure 3: RFQ cell profile at different section: (A) input matcher,(B) regular cell(C) output T cell and fringe cell (D) all cells along the RFQ.

erating at 81.25MHz and three superconducting solenoidal magnets will accelerate the beam from 0.4 to 1.54MeV/u as the first period structure. For the β_{opt}=0.041 λ/4 section, the full periodic structure will be adopted instead of compact periodic structure which need matching between cryomodules[3]. The full periodic structure can avoid the formation of beam halo caused by mismatch. The disarrange is the period phase advance for long periodic structure is lager than 90°, while for the low beam current, this is not an issue.

The other kind of periodic structure consists of four β_{opt}=0.085 λ/4 cavities and one superconducting solenoidal magnets. Eleven cryomodules, each containing eight β_{opt}=0.085 λ/4 cavities operating at 81.25MHz and two superconducting solenoidal magnets will accelerate the uranium beam to 15MeV/u. Fig. 4shows the schematic layout of the cryomodules for each type in segment one. Fig. 5shows the transverse and longitudinal phase advance

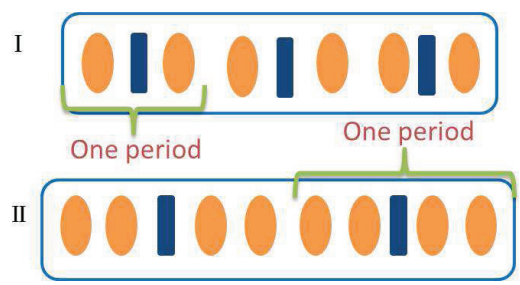

Figure 4: The schematic layout of the cryomodules for each type in segment one.

for the uranium beam. As shown in the Fig.5, the phase advance changes smoothly in the regular section. While there are some jumps at the cavity type transition section where

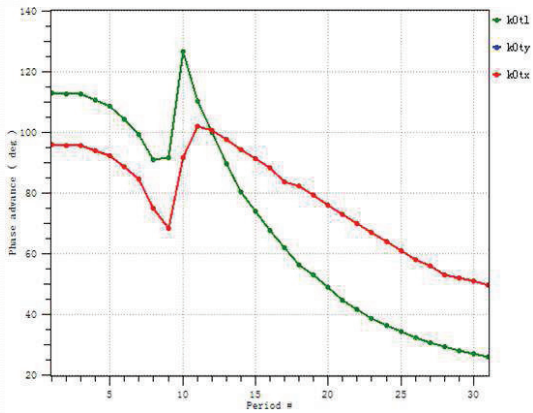

Figure 5: The transverse and longitudinal phase advance for the uranium beam .

several period are used to do match. The beam parameters on entering and exiting the segment one are summarized in Table. 2. The simulation results substantiate that the design will meet performance requirements.

Table 1: Beam parameters in superconducting acceleration segment one

parameter	Qty or Type	Unit
Segment one length	80.18	m
Charge states	34+	
Input energy	0.4	MeV/u
Output energy	15	MeV/u
Cavity Cryomodule Configuration		
λ/4 β_{opt} 0.041		
Number of cryomodules	3	
Number of cavities/cryomodule	6	
Number of solenoids/cryomodule	3	
Number of cavities	18	
Number of solenoids	9	
Rf frequency	81.25	MHz
Epk 31.25	MV/m	
Cryomodule length	5.46	m
Cavity Cryomodule Configuration		
λ/4, β_{opt} 0.085		
Number of cryomodules 11		
Number of cavities/cryomodule 8		
Number of solenoids/cryomodule 2		
Number of cavities 88		
Number of solenoids 22		
Rf frequency	81.25	MHz
Epk	31.25	MV/m
Cryomodule length	5.8	m

STRIPPING AND MATCHING SECTION

The stripping and matching section will be an 180° arch structure to save the longitudinal space. Stripping section

Copyright © 2012 by the respective authors — cc Creative Commons Attribution 3.0 (CC BY 3.0)

will strip the U^{34+} beam to U^{76+} at 15 MeV, the energy is choose referring the stripping experiment in RIKEN[4]. The type of stripping film is under study. Also the longitudinal matching function will be realized with a serial of bucher cavities are used to match the beam from 81.25MHz to 325MHz. A set of quadrupoles are used to match the beam to stripping film and the entrance of superconducting accelerating segment two.

SUPERCONDUCTING ACCELERATING SEGMENT TWO

In the baseline driver linac, two kind of uranium beam, which are U^{76+}(stripped beam) and U^{34+}(un-stripped beam), will be accelerated in superconducting accelerating segment two. The section will be approximately 96 m long consisting of a total of twenty four accelerating cryomodules. The first fifteen cryomodules, each containing six spoke 021cavities operating at 325 MHz, will be used to accelerate the uranium beam from 15 MeV/u to 34 MeV/u. There is one superconducting solenoidal magnet in each cryomodule of Segment two for transverse focusing. Each period in the Spoke021 section consists of six spoke cavities (β_{opt}=0.21) and one superconducting solenoid. The period length is 3.76 m. The subsequent nine cryomodules, each containing six spoke cavities operating at 325MHz, will be used to accelerate the beam from 34 MeV/u to 50MeV/u.Each period in the Spoke040 section consists of six spoke cavities (β_{opt}=0.40) and one superconducting solenoid.

The section two will accelerate U^{34+} beam from 15MeV/u to 50MeV/u and U^{76+} beam from 15MeV/u to 100MeV/u. The superducting spoke cavity, whose β is 0.21 and 0.40, will be adopted for the mature technology in the ADS project. The transit time factor of superconducting spoke cavity for U^{76+} and U^{34+} is shown in Fig. 6 As shown in Fig. 6, the transit time factor of superconducting spoke cavity are larger than 0.5 for the two charge state beam. The beam parameters on entering and exiting the segment one are summarized in Table. 2. The simulation results substantiate that the design will meet performance requirements.

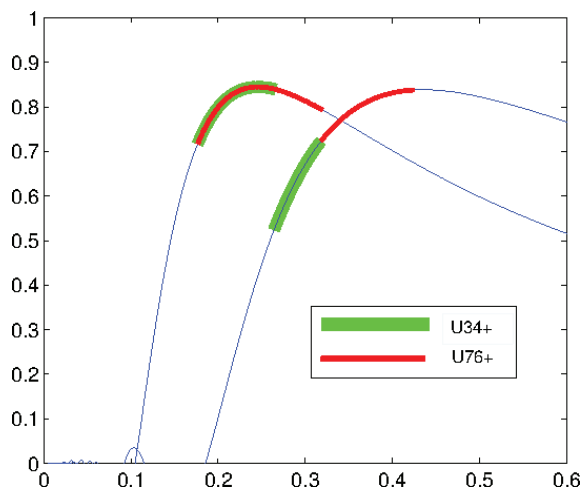

Figure 6: The transit time factor of superconducting spoke cavity for two kinds of beam.

Table 2: Beam parameters in superconducting acceleration segment one

parameter	Qty or Type	Unit
Segment two length	80.18	m
Charge states	76+	
Input energy	15	MeV/u
Output energy	100	MeV/u
Cavity Cryomodule Configuration		
Spoke β_{opt} 0.21		
Number of cryomodules	15	
Number of cavities/cryomodule	6	
Number of solenoids/cryomodule	1	
Number of cavities	90	
Number of solenoids	15	
Rf frequency	325	MHz
Epk 35	MV/m	
Cryomodule length	3.76	m
Cavity Cryomodule Configuration		
Spoke, β_{opt} 0.40		
Number of cryomodules 9		
Number of cavities/cryomodule 6		
Number of solenoids/cryomodule 1		
Number of cavities 72		
Number of solenoids 9		
Rf frequency	325	MHz
Epk	35	MV/m
Cryomodule length	4.36	m

SUMMARY

The general concept of HIAF and the preliminary design of linear injector are presented in the paper. The preliminary design of each section is finished. While more optimization work need to be done in the further.

REFERENCES

[1] Kolomiets.A.A, DESRFQ - a code for generation of Radio Frequency Quadrupole

[2] P.N. Ostroumov, V.N. Aseev, B. Mustapha, TRACK - a Code for Beam Dynamics Simulation in Accelerators and Transport Lines with 3D Electric and Magnetic Fields,2007.http://www.phy.anl.gov/atlas/TRACK/Trackv37/Manuals/tv37_man_index.html

[3] R. C. York, X. Wu, Q. Zhao et al., BEAM DYNAMICS IN THE FRIB LINAC,Proceedings of HB2010, Morschach, Switzerland. http://accelconf.web.cern.ch/accelconf/HB2010/papers/tuo1b05.pdf

[4] H. Kuboki, H. Okuno, H. Hasebe, et al., Charge-state distribution of 238U in nitrogen gas and carbon foil at 14 and 15 MeV/nucleon, Physical Review Special Topics - Accelerators and Beams 14, 053502 (2011).

Copyright © 2012 by the respective authors — cc Creative Commons Attribution 3.0 (CC BY 3.0)

STATUS OF THE LINAC SRF ACQUISITION FOR FRIB*

M. Leitner#, E. Bernard, J. Binkowski, B. Bird, S. Bricker, S. Chouhan, C. Compton, K. Elliot, B. Enkhabat, A. Fox, L. Harle, M. Hodek, M. Johnson, I. Malloch, D. Miller, S. Miller, T. Nellis, D. Norton, R. Oweiss, J. Ozelis, J. Popielarski, L. Popielarski, K. Saito, M. Shuptar, G. Velianoff, J. Wei, M. Williams, K. Witgen, Y. Xu, Y. Yamazaki, Y. Zhang
FRIB, Michigan State University, East Lansing, MI 48824, U.S.A.
A. Facco, INFN-Laboratori Nazionali di Legnaro, I-35020 Legnaro, Padova, Italy

Abstract

The Facility for Rare Isotope Beams (FRIB) will utilize a high-intensity, superconducting heavy-ion driver linac to provide stable ion beams from protons to uranium up to energies of >200 MeV/u and at a beam power of up to 400 kW. The ions are accelerated to about 0.5 MeV/u using a room-temperature 80.5 MHz RFQ and injected into a superconducting cw linac consisting of 330 individual low-beta cavities in 49 cryomodules operating at 2 K. This paper discusses the current status of the linac SRF acquisition strategy as the project phases into construction mode.

INTRODUCTION

Due to the heavy mass and correspondingly low velocity of the accelerated ions the FRIB driver linac [1] utilizes four different low-beta SRF resonator designs as shown in figure 1 and figure 2. The status of SRF system designs and overall acquisition strategies have been summarized in [2]. For high-beta applications superconducting RF has become an established technology with a history of industrial optimization efforts. However, for low-beta structures, FRIB will most likely be the first facility requiring industrially produced components on a larger scale.

FRIB is a US$ 680 million construction project with an 8-year timetable: According to the current FRIB baseline schedule fabrication and procurement of linac components will start mid-2014. Actual linac installation will begin end of 2016 after completion of conventional facilities and cryoplant construction. Accelerator commissioning is scheduled to initially proceed in parallel with installation and to conclude at the earliest by end of 2019 (beginning of 2021 if schedule contingency is included). 2015 to 2018 will be the peak period for industrial SRF cavity and cryomodule production.

The FRIB project plans to place approximately 450 procurements above US$ 50,000 each. The sum of all technical equipment procurements (excluding conventional facility construction) issued to industry amounts to US$ 217 million. Roughly 30% of that procurement value will be spent on cryomodule components not including RF amplifier equipment.

* This material is based upon work supported by the U.S. Department of Energy Office of Science under Cooperative Agreement DE-SC0000661.

LeitnerM@frib.msu.edu

SRF PROCUREMENT SPECIFICS

A major challenge for the FRIB project is the need to develop, qualify, and industrialize four independent cryomodule and cavity types before start of construction. Optimization of the linac resulted in a design with 49 cryomodules incorporating 106 quarter-wave (QWR) and 224 half-wave (HWR) resonators (330 total) with four different optimum velocities as shown in figure 2. A detailed cavity count table can be found in [2].

Unlike prior superconducting low-β linacs, the large size of FRIB has required optimization of the resonator designs for both maximum performance and for low cost in the view of a large production. This requirement guided the choice of the resonator geometries, materials and mechanical solutions avoiding complicated shapes, minimizing the amount of electron beam welds, eliminating bellows, as well as optimizing construction and surface treatment procedures. The history of the resonator development and detailed FRIB cavity specifications are summarized in [3].

Cavity Procurement Status

Including development, pre-production, spare, and 10% excess cavities FRIB will procure more than 400 cavities within the next six years. FRIB can select from a highly qualified cavity supplier base due to world-wide strong, industrial interest in SRF cavity fabrication. Six vendors have consistently bid for FRIB cavity production: AES, Niowave, Roark, and Pavac on the American continent; Research Instruments and Zanon on the European continent. So far AES, Niowave, and Roark have produced physical cavity prototypes for FRIB.

β=0.53 Cavities:

The first and largest (several M$) FRIB cavity production contract (for a total of 160 undressed β=0.53 cavities: 2 development, 10 pre-production, 148 linac cavities) has been awarded to Roark, Inc. as a firm price contract. For FRIB procurement quantities the cost reduction between development cavities and mass-produced cavities falls around 3. The β=0.53 cavities are the largest and most expensive cavities used in the driver linac.

β=0.29 Cavities:

Due to federal funding delays FRIB has slowed down the procurement of the other cavity types. At present two

Copyright © 2012 by the respective authors — cc Creative Commons Attribution 3.0 (CC BY 3.0)

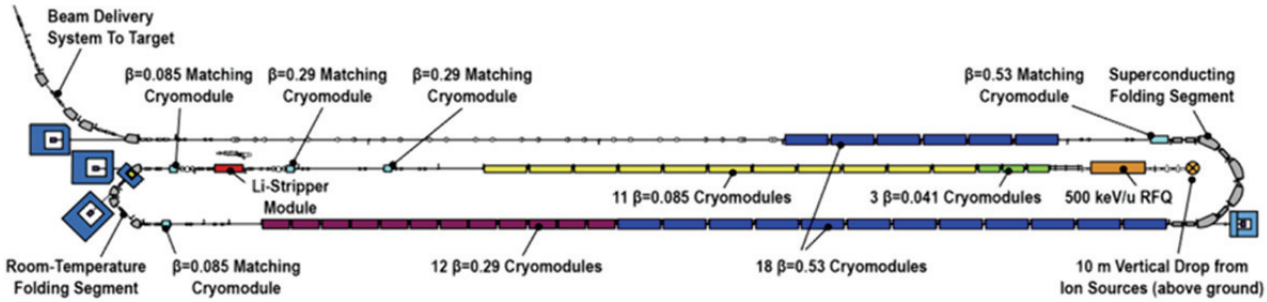

Figure 1: A schematic layout of the FRIB driver linac.

development β=0.29 cavities are being fabricated by Roark, Inc. with delivery expected in the beginning of 2013. Requests for proposals to deliver 10 pre-production cavities, 76 FRIB linac cavities, and 2 spare cavities will be issued in 2013.

β=0.085 Cavities:

For the quarter-wave resonators, ten early β=0.085 cavity designs have been fabricated by Niowave, Inc. in 2010. They are utilized in the MSU Re-Accelerator project RεA [4]. FRIB is currently building two β=0.085 FRIB cavity prototypes in-house. An additional two development cavities have been purchased from Pavac Industries Inc. The request for proposal for 10 pre-production cavities, 94 FRIB linac cavities, and 11 spare cavities will be issued in 2013.

β=0.041 Cavities:

The initial section of the FRIB linac requires a small amount of β=0.041 cavities. Since these cavities are similar to cavities operational in the first two cryomodules of the existing RεA linac [4] 12 FRIB linac cavities plus 4 spare cavities will be purchased in 2014 without a development program.

Helium Vessels

All FRIB cavities are dressed in titanium helium vessels which are directly connected to the cavities through Nb-Ti transition pieces. No bellows are required in the designs. The helium vessels are designed according to the ASME pressure vessel code, but will not be code-stamped.

FRIB has successfully adopted the Jefferson Lab titanium-inert-gas (TIG) welding technique for titanium which utilizes oversize (~2 inch diam.) argon shielding gas nozzles made of quartz glass. That way the welding operator can work in direct contact with the equipment without requiring inert-gas chambers. As a result, welding times have been dramatically reduced. FRIB will work with vendors to transfer that knowledge.

Cavity Surface Preparation

Bulk cavity etching (~150 μm removal) will be performed by industry. Test results and cost considerations for a large production led FRIB to the choice of BCP (buffered chemical polishing) as surface treatment for the resonators. Once cavities are received and inspected at FRIB, 600°C heat treatment, final light etch, and high pressure rinse will be performed at MSU.

Niobium Procurement Status

The FRIB niobium procurement amounts to US$ 13 million and includes RRR>250 niobium sheets, plates, tubes, and rods, as well as Nb-Ti alloy material. The contract for thin niobium sheets used for deep drawing has been awarded to Tokyo Denkai Co. Ltd.; Ningxia Orient Superconductor Technology Co. will produce all niobium tubes, rods, and thick sheets; ATI Wah Chang is responsible for delivering all Nb-Ti material. Based on vendor capacity the delivery is phased according to the following schedule: 5% of material volume in Feb. 2013, 23% in Aug. 2013, 5% in Oct. 2013, 29% in Jan 2014, 38% in Oct. 2014.

Niobium will be accepted based on dimensional checks at MSU, confirmation of mechanical properties (tensile strength, hardness), profilometry, as well as thermal conductivity and chemical composition confirmation.

Cryomodule Status

After the conceptual design, the FRIB cryomodule design has evolved significantly from a "top-down"

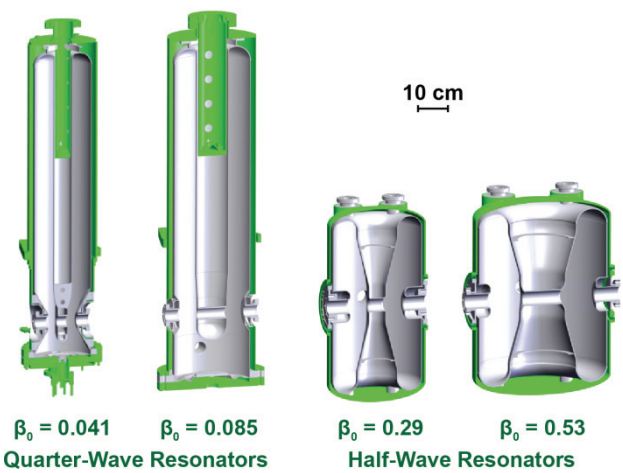

Figure 2: The FRIB driver linac requires four different low-beta cavity types as shown. Due to the large quantity of cavities in the driver linac the current development effort focuses strongly on minimization of fabrication costs [2].

Copyright © 2012 by the respective authors — cc Creative Commons Attribution 3.0 (CC BY 3.0)

cryomodule style, widely used in the low-beta community, to a "bottom-up" design which has advantages for mass-produced applications. Figure 3 shows the current design incorporating a torque-resistant structural frame made of stainless steel. The design incorporates machined fiberglass compression posts supporting the coldmass in the cryomodule vacuum vessel. Three posts on linear roller bearings oriented towards the center of thermal contraction serve as 6-degree-of-freedom kinematic supports. This novel design maintains the alignment of the coldmass while allowing thermal contraction. Cavity and solenoid attachment points to the rails are all machined after welding and full annealing at 1100 °C to ensure assembly consistency.

The FRIB cryomodules contain separate cryogenic circuits at 4 K for the solenoids and at 2 K for the cavities with the 2 K heat exchanger residing inside.

The project schedule calls for a production rate of 1.5 cryomodules per month. Cavity processing, vertical tests and coldmass assembly are planned to be performed at MSU. The cryomodule thermal shield, magnetic shield, cryogenic plumbing, and vacuum vessel will be procured from industry as complete "plug-in" units ready for assembly in the cryomodules. Based on initial experience with vendors significant cost savings could be gained by ordering fully assembled subcomponents which are fit to tolerance at a single vendor instead of procuring individual parts from independent vendors requiring tight tolerances for overall assembly fits.

FRIB INDUSTRIAL ACQUISITION STRATEGY

Cost discipline has been strongly ingrained into the FRIB engineering culture since the overall project cost is capped. Designs are optimized towards low-cost manufacturability while still utilizing high-quality suppliers. In addition, MSU procurement overhead and labor rates are low compared to other national laboratories leading to 30% reduced cryomodule costs compared to similar projects.

Nevertheless, the most significant cost containment is achieved by a well-managed industrial acquisition strategy. Based on initial procurement experiences we can identify three main contributing factors to cost reduction:

(1) Actively reduce risks to the vendors. In dedicated engineering meetings designs are adjusted to allow suppliers to implement familiar or more cost-effective fabrication approaches. Components including cavities are accepted built-to-print instead of built-to-specification (e.g. electromagnetic or RF). Manufactures are given the option that high-risk manufacturing steps are performed at MSU. High-cost materials that are exposed to market fluctuations (e.g. niobium) are purchased by FRIB.

(2) Through FRIB-management vendor visits, a good rapport is developed with suppliers by ensuring that the project fits into the supplier's total capabilities and long-term business plans. For FRIB procurement volumes (50 to 200 production units) this favours suppliers with a strong "fabricator" background, contrary to smaller vendors with a R&D focused, more collaborative business model. Successful manufacturing companies with a long-standing manufacturing history are skilled in effective work-flow management (hence cost-reduction) and committed to solve manufacturing challenges and risks on the production floor together with their clients.

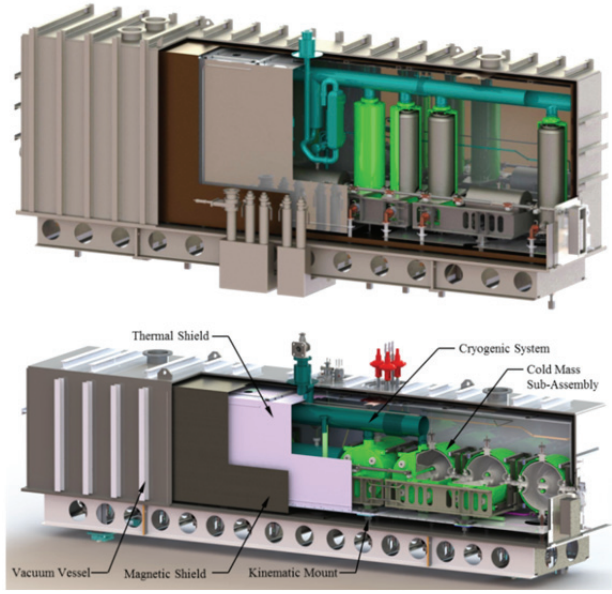

Figure 3: FRIB "bottom-up" cryomodule designs. The top cryomodule incorporates eight β=0.085 QWRs, three solenoids, and three cold beam position monitors; the bottom cryomodule incorporates eight β=0.53 HWRs and a single solenoid.

(3) Actively develop the vendor base with a goal of six to ten companies bidding after request for proposals. Vendor interest is assured by tailoring the request for proposal to long-term business plans of the vendor base. It is important to attractively size procurement packages and volumes. Phasing of procurements from prototypes to production prepares vendors to be able to successfully produce and attractively price the unique components required for FRIB.

REFERENCES

[1] J. Wei et al., The FRIB Project - Accelerator Challenges and Progress, Proc. of HIAT 2012, to be published

[2] M. Leitner et al., Design Status of the SRF Linac Systems for the Facility for Rare Isotope Beams, Proc. of SRF 2011, pp. 56–64

[3] A. Facco et al., Superconducting Resonator Development for the FRIB and ReA Linacs at MSU: Recent Achievements and Future Goals, Proc. of IPAC 2012, to be published

[4] D. Leitner et al., Status of the ReAccelerator Facility RεA for Rare Isotopes Beam Research, Proc. of SRF 2011, pp. 674-679

Copyright © 2012 by the respective authors — cc Creative Commons Attribution 3.0 (CC BY 3.0)

SCATTERING OF H⁻ STRIPPED ELECTRONS FROM SEM GRIDS AND WIRE SCANNERS AT THE CERN LINAC4

B.Cheymol*, E. Chevallay, M. Duraffourg, G.J. Focker, C. Hessler, U. Raich, F. Roncarolo†, C. Vuitton, F. Zocca, CERN, Geneva, Switzerland

Abstract

At the CERN LINAC4, wire grids and scanners will be used to characterize the H^- beam transverse profiles from 45 keV to 160 MeV. The wire signal will be determined by the balance between secondary emission and number of charges stopped in the wire, which will depend on the wire material and diameter, the wire polarization and the beam energy. The outermost electrons of H^- ions impinging on a wire are stripped in the first nanometers of material. A portion of such electrons are scattered away from the wire and can reach the neighboring wires. In addition, scattered electrons hitting the surrounding beam pipe generate secondary electrons that can also perturb the measurement. Monte Carlo simulations, analytical calculations and a laboratory experiment allowed quantifying the amount of scattering and the scattered particles distributions. The experiment was based on 70 keV electrons, well reproducing the case of 128 MeV H^- ions. For all the LINAC4 simulated cases the predicted effect on the beam size reconstruction results in a relative error of less than 5%.

INTRODUCTION

When H^- ions interact with matter the outer electron is stripped almost immediately. These electrons can be considered free with an energy of: $E_e = E/1836$ where E is the energy of the H^- beam. For LINAC4 the stripped electrons energy ranges from about 25 eV at the source exit to about 87 keV. Some data about electron scattering can be found in literature [1, 2, 3] for the energy range and materials considered for LINAC4. For electron energies below the MeV range, the proportion of backscattered electrons is around 10 % for low Z materials and up to 50 % in case of materials with higher density.

TWO WIRE SIMULATIONS

The Monte Carlo code FLUKA [4] code was used to simulate an electron beam hitting two parallel wires of the same material and diameter separated of 500 μm. This was done for H^- energies above 50 MeV. Below such energy, the corresponding electron energy is not properly simulated by FLUKA. A beam composed of 10^6 electrons, with a rectangular shape of width equal to the wire diameter was sent to one wire in order to investigate the amount of scattered particles reaching the second wire. The simulation was repeated for 27 keV and 87 keV electrons (corresponding to 50 MeV and 160 MeV H^- energy respectively) and 33 μm Carbon wires or 40 μm Tungsten wires. Fig 1 shows the angular distribution of the particles emerging from the first wire for the four simulated settings. At the position of the second wire (i.e. 90^o or symmetrically 270^o), the ratio of particles varies from 2×10^{-4} to 3×10^{-3}. It drops for angles between 90^o and 270^o and reaches its minimum for an angle equal to 180^o. For Tungsten the angular distribution is independent of the beam energy and at 180^o the flux is less than 10^{-5} for both energies. For Carbon, at the lowest energy, the flux is around 10^{-5} at 180^o. At 87 keV some electrons have enough energy to cross the wire and 44 % of the particles exiting the wire have angles between 150^o and 210^o. Table 1 shows the percentage of scattered electrons emerging from the first wire and how many of them reach the second wire. At both energies, about 55 % of incident electrons are scattered on a Tungsten wire and in the worst case less than 0.7 % reach the side wire. For a Carbon wire and 27 keV electrons, about 17 % of the impinging particles are scattered, while at 87 keV the amount of scattered electrons is hardly distinguishable from the ones traversing the wire. At both energies, it can be estimated that the percentage of scattered electrons reaching the second wire is below 0.3 %. Even if these results (wire cross talk below 1 %) arise from a simplified case not considering Secondary Emission (SE) electrons, the scattering coefficients determined with the FLUKA simulations agree very well with the data found in literature [3]. Both the scattering coefficients and the scattering angles are also in agreement with similar studies performed at INR with GEANT4 [5].

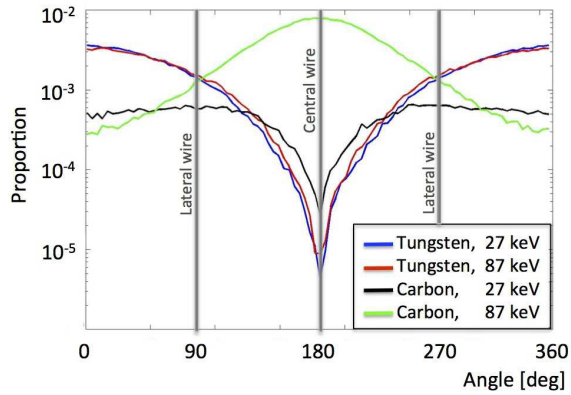

Figure 1: Angular distribution of particles emerging the wire, normalized to the number of primary electrons.

* Now at ESS, Lund, Sweden
† federico.roncarolo@cern.ch

Copyright © 2012 by the respective authors — cc Creative Commons Attribution 3.0 (CC BY 3.0)

	Carbon (33 μm)		Tungsten (40 μm)	
Energy [keV]	27	87	27	87
$\frac{N_1}{N_{tot}}$	17 %	N.A.	55 %	55 %
$\frac{N_2}{N_{tot}}$	0.24 %	0.05 %	0.6 %	0.66 %

N_{tot} = electrons hitting the first wire, N_1 = scattered electrons emerging form the first wire, N_2 = scattered electrons emerging from the first wire and reaching the second.

Table 1: Percentage of scattered particles that emerging from the first wire reach the second.

ELECTRON GUN MEASUREMENTS AND SIMULATIONS

An experimental measurement of electron scattering was performed by means of a 70 keV electron beam (4.3 ns pulse length and about 5 nC pulse charge) reproducing the case of 128 MeV H^- ions. A set of three 40 μm tungsten wires was mounted on a fork support with 0.5 mm pitch. The electron beam was collimated on the central wire through a 0.4 mm slit, so that the lateral wires could be reached only by the electrons scattered by the central wire. Each wire was connected to an electronic acquisition channel, composed of an integrating amplifier and an ADC (Analog to Digital Converter). The typical signals of the central and lateral wires, at the integrator output, as the beam is passing through the collimator, are shown in Fig. 2. The negative peak represents the integral of the negative and positive peak induced by the beam charge when approaching and drifting away from the conductive wires. The integral is non zero due to wake-field ringing, as discussed below. The integral of the wire signals as sampled by the ADC are shown in Fig 3. Since the sampling time was 6 μs, the negative peak provided by the integrator cannot be seen, with only the tail sampled. The decay time constant generated by the integrator itself is now visible, as the ADC signal is shown on a much larger time scale. The lateral wire signals are actually the cross-talk signals we are interested in, due to the electrons scattered by the central wire. I this case, we defined the *cross-talk* among wires as the ratio between the lateral and the central wire, averaged over the first 3 ADC samples. Using the raw data shown in Fig 3, the cross talk observed is about 7 %, whereas if it is accounting for the offset subtraction of individual ADC channels, this value decreases to about 4 %.

The wakefield effect on the wire signal shape could be demonstrated through a wakefield simulation performed with the CST Particle Studio software [6] in the case of a lateral wire, modeled with the tank and fork geometries. The lateral wire signals as sampled by a scope and calculated by the simulations are shown in Fig 4. The simulations reproduce with an acceptable accuracy the measurements, considering that the simulations consisted of a simplified geometry and perfectly conducting materials. The fact that in the simulations only the two ideal peaks (negative and positive as the beam passes close to the wire) sur-

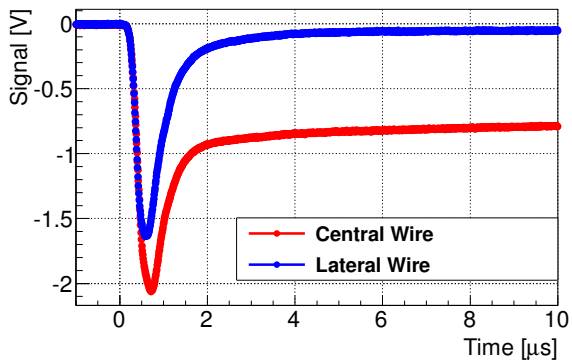

Figure 2: Signals of the central and one lateral Tungsten wires as recorded by a scope at the integrating amplifier output.

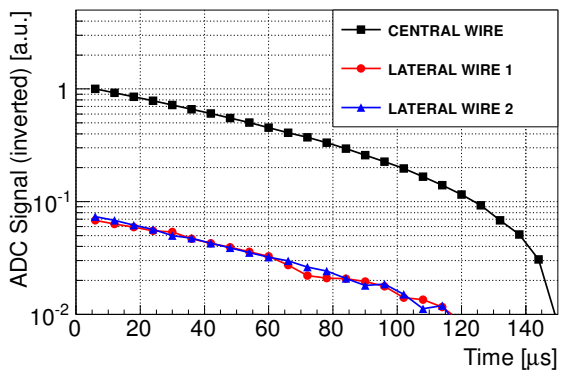

Figure 3: Central and lateral wire signals as sampled by the ADC.

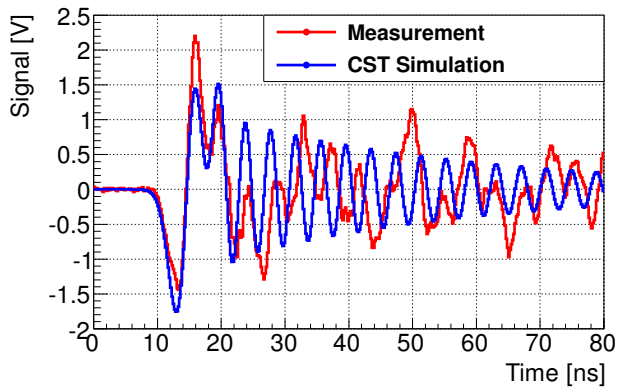

Figure 4: Lateral wire signal before integration, as sampled by a scope and simulated with CST Particle Studio

Copyright © 2012 by the respective authors — cc Creative Commons Attribution 3.0 (CC BY 3.0)

Wire Pol.	Cross-Talk		Central wire signal*	
	Meas.	Simul.	Meas.	Simul.
0 V	4 %	1.4%		
20 V	13.5 %	7 %	+ 27 %	+ 12 %
50 V	15.4 %	14.4 %	+ 36.5 %	+ 35.5 %
100 V	N.A.	13.0 %	N.A.	+ 39.0 %

* w.r.t. 0 V polatization

Table 2: Cross-talk and signal intensity measured for different polarization voltages of the tungsten wires.

vive when deleting the wire fork structure, confirms that the signal ringing is due to wakefield effects.

The scattered electron energy is too high to foresee any polarization to suppress them. However, a polarization can be applied to any wire in order to suppress SE electrons and enhance the wire signal. The effect of such polarization on the wire cross-talk was studied in the electron gun experiment and benchmarked with a very detailed model including: i) FLUKA simulations to estimate the location of SE sources (wires, collimator in front of the wire), ii) analytical models predicting the SE yield and iii) CST particle studio simulations to account for EM fields and track the electrons. The results are summarized in Table 2. Both measurements and simulations agree that the cross-talk between wires increases with polarization voltages. Even though SE is more and more suppressed (see the central wire signal in the table), the field lines created by the biased wires result in more secondary electrons trapped by the lateral wires. With no polarization and with 20 V the measured cross-talk is larger than that predicted by the simulations. This could well be related to effects other than scattered electrons, such as coupling in the electronics channels. With 50 V wire polarization, the agreement between measurement and simulations is remarkably good, within 1 %. In the laboratory setup, it was not possible to exceed 50 V due to the HV power supply module used.

Using the cross-talk results presented above, we calculated the effect of the cross talk among wires due to scattered and SE electrons on the accuracy of a wire grid profile measurement. This was done assuming a Gaussian beam. The results are shown in Fig. 5 for different beam sizes and for a wire grid pitch of 0.5 mm. With a cross-talk of 5 %, which is a realistic estimation with no wire polarization, the error is less than 4 % even for a σ=0.5 mm beam, smaller than what expected at LINAC4.

CONCLUSIONS AND OUTLOOK

Simulations of electron scattering between two wires reproduced the scattering coefficient data found in literature for Carbon and Tungsten. For both materials the number of electrons scattered from one wire and reaching the neighboring one is below 1 % of those incident on the first wire. A laboratory experiment supported by analytical calculations, EM simulations and particle tracking provided results for Tungsten wires when considering also SE electrons and wire polarizations to suppress them. The overall result yields an acceptable uncertainty (below 4%) on the beam profile determination with wire grids due to Tungsten wires cross-talk. This also applies to the Carbon wire grids and the wire scanners (Carbon and Tungsten) foreseen for LINAC4, as will be discussed in a more complete note [7], that will also study wire cross-talk in case of a multi bunch beam. A source of uncertainty could arise from the fact that the electron beam was considered as representative of the H^- beams interacting with the wires with the consequent scattering of stripped electrons. For the moment, however, we could not find any phenomena (e.g. space charge from H^-) that would invalidate this assumption.

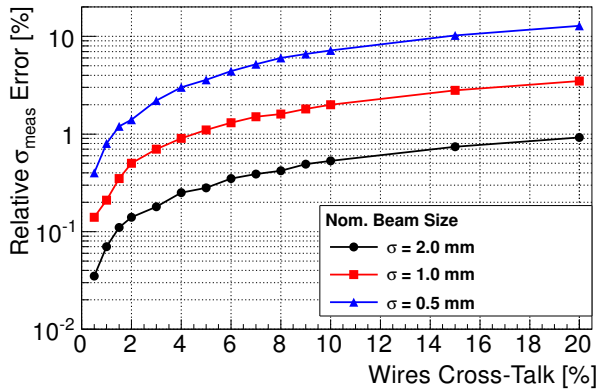

Figure 5: Estimated beam size error as a function of the cross-talk, for three typical beam sizes.

ACKNOWLEDGMENT

The authors would like to thank E. Bravin, V. Fedosseev, J.J. Gras and R. Jones for the support, fruitful discussions and comments.

REFERENCES

[1] J.G. Trump and R. J. V. , de Graaff, *Phys. Rev.,* Vol 75, p. 44, 1949 .

[2] P.Verdier and F.Arnal, *Compt. Rend.*, Vol. 267, p. 1443, 1968.

[3] T. Tabata and R. I. S. Okabe, *Nucl. Instrum. and Meth.*, no 94, p. 509-553, 1971

[4] A. Fasso, A. Ferrari, J. Ranft, and P. Sala, Fluka: a multi-particle transport code, CERN-2005-10 (2005)

[5] A. Feshenko, *Private communication*

[6] CST- Computer Simulation Technology AG - www.cst.com

[7] F.Zocca et al., "Effect of H^- stripped electrons on the LINAC4 profile measurements", CERN-ATS-NOTE, to be published

Copyright © 2012 by the respective authors — cc Creative Commons Attribution 3.0 (CC BY 3.0)

PROGRESS ON RFQIII FABRICATION IN J-PARC LINAC

T. Morishita, Y. Kondo, K. Hasegawa, JAEA, Tokai, Japan
H. Kawamata, T. Sugimura, F. Naito, KEK, Tsukuba, Japan

Abstract

For the beam current upgrade in J-PARC linac, the fabrication of a new RFQ, which is designed for 50mA beam acceleration, has been started. The engineering design and the fabrication technologies were carefully chosen to reduce the discharge risk during the operation. For good vacuum pumping, vanes and ports are brazed for the direct pumping through slits at the tuners. Also, we tried a chemical polishing to improve the smoothness of the vane surface.

INTRODUCTION

The J-PARC accelerator comprises an injector linac, a 3-GeV Rapid-Cycling Synchrotron and a 50-GeV Main Ring. The J-PARC linear accelerator consists of an ion source, an RFQ, DTLs, separated DTLs (SDTL), and the beam transport line to the RCS synchrotron [1].

The J-PARC linac has been operating for users with the beam energy of 181 MeV. The currently operating RFQ is a four-vane type cavity used to accelerate a negative hydrogen beam from 50 keV to 3 MeV with peak current of 30mA. The RF duty factor is 3% (600 μs at50 Hz). For the quick replacement in case of the RFQ trouble, we fabricated a spare RFQ (RFQII) as a backup machine. [2, 3, 4]

The energy (to 400MeV) and current (to 50mA) upgrade of the linac is scheduled for 1MW operation at RCS. The beam dynamics of an RFQ is newly designed for beam current upgrade to 50 mA operation. [4, 5] Then, we started a fabrication of RFQIII last year.

In this paper, we present the fabrication progress of an RFQIII for J-PARC linac.

ENGENEERING DESIGN

Table 1 shows the RFQ III parameters. For the beam current upgrade, the vane length is longer than RFQII about 0.5 m. The RFQ cavity is divided into three unit tanks. Each tank (about 1.2 m long) will be integrated together on a platform after the brazing of the major and the minor vanes.

Engineering design topics are listed in Table 2. The high-power test of the RFQII has been done successfully at April 2012. Basically the mechanical design and the fabrication procedure are the same as RFQII. Followings are the points which are changed from RFQII

Drilled Hole Plugging

The drilled hole plugging technique was changed from electron beam welding to the brazing. In the fabrication of RFQII, there was a vacuum leak at the welding spot after the brazing (one of seventy-two welding points). Then we changed it to brazing along with the vane brazing in the RFQIII fabrication.

Table 1: Main Parameters of RFQIII

parameter	RFQ III
Beam current [mA]	50
Frequency [MHz]	324
Acceleration energy [MeV]	0.05 to 3
Vane length [m]	3.6
Inter-vane voltage[kV]	81
Maximum surface field [MV/m]	30.7 (1.72 Kilpatrick)
Average bore radius [mm]	3.5
Vane-tip curvature [mm]	0.75r0(2.617)

Table 2: Mechanical Design Features

Material	High-purity oxygen-free copper with HIP(Hot Isostatic Pressing)
Drilled hole plugging	RFQII : Electron beam welding RFQIII : Brazing
Annealing	600 degree C in vacuum furnace
Vane machining	Numerical-controlled machining with ball-end mill RFQIII: Introduced non-contact measurement [6]
Surface treatment	Chemical polishing (3-5μm)
Integration method	Vanes and ports are jointed in one step brazing
Unit cavities connection	RFQII : Welding for vacuum sealing, bolting for mechanical alignment RFQIII : bolting for mechanical alignment and vacuum sealing

Dry Cutting for the Fitting of End Flanges

Figure 1 shows a schematic drawing of the unit cavity components to be assembled for brazing. After the final cutting of vanes, those are assembled and machined for a flange fitting at each ends. In the RFQII, vanes were disassembled for the surface treatment to remove cutting oil, then, reassembled for brazing. In the RFQIII, to reduce costs and production period, dry-machining for a flange fitting is adopted after the surface treatment. Then we can reduce the disassemble-reassemble process.

#takatoshi.morishita@j-parc.jp

Copyright © 2012 by the respective authors — cc Creative Commons Attribution 3.0 (CC BY 3.0)

Additionally, the displacements by the reassembling could be removed.

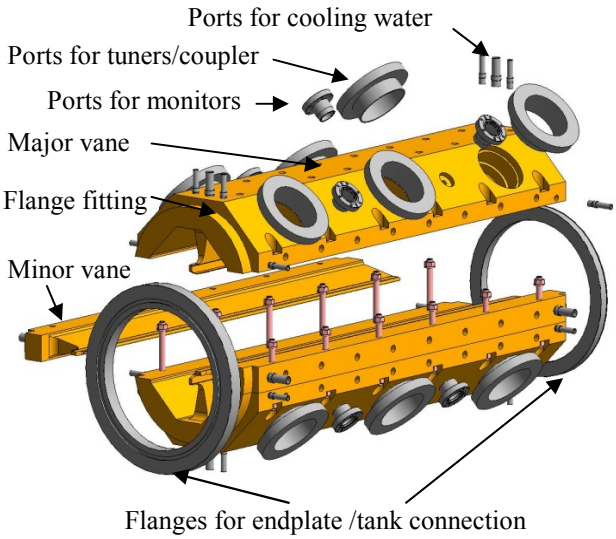

Figure 1: Assembling of vanes and other components of the unit tank for brazing.

Unit Cavities Connection

Unit cavities are bolted together with a vacuum seal and an RF conductor. This configuration is simple and decomposable easily. However, the angle error between flanges at the connection will cause the alignment errors for the straightness between unit tanks. In the experience from RFQII fabrication, the angle error of the brazed flange was less than 0.07mm/(flange diameter). Then we put the 0.1 mm gap between flanges for a margin to correct the angle error. By adjusting the gap locally within the squashing tolerance of a vacuum seal and an RF contactor, t he angle error will be compensated.

Dividing Point of the Unit Cavity

The longitudinal dividing point (i.e. the edges of the second unit cavity) of the RFQII cavity is taken at the top/bottom of the modulation. In the RFQIII, dividing point is taken at the position where the longitudinal effect for the beam bunch is small. The gaps between unit cavities are 0.3 mm.

SURFACE TREATMENTS

To reduce the discharge risk in the high electric field, the inner surface of the cavity was chemically polished after the machining. The surface treatment procedure is summarized in Table 3. Figure 2 shows a chemical-polishing major vane in the bath.

Four kinds of solutions were tested before the fabrication of RFQII. Figure 3 shows the surface conditions for solutions and polishing depths.

- Solution #3 cannot produce a smooth surface.
- A smooth surface can be obtained by the solution #4, however, outshoots are found occasionally.
- Grain-boundary appears for over-polished (more than 10 μm) with the solutions #1,2, and 3.
- Lightly-polished (less than 10 μm) surface seems well with the solutions #1 and 4.

Table 3: Surface Treatment Procedure

Process	Tools/Solutions	procedure
Cleaning	Water, methyl alcohol, MEK	wiping
Masking	Taping, caulking	Screw holes, brazing surface
Degreasing	Alkaline solution	Submerging
Acid wash	Sulfuric acid aqueous solution	Submerging
Chemical polishing	Nitric acid + Phosphoric acid + Surfactant	Polishing depth is controlled by temperature and submerging time
Acid wash	Sulfuric acid aqueous solution	Submerging
Anticorrosion	Chromate solution	Submerging
Cleaning /drying-out	Ultrapure water / drie	Running water Air blow

Figure 2: Major vane is submerging in solution #1.

Figure 4 shows the surface roughness for the cases of before polishing, 3μm polished, and 10μm polished by the solution #4.

Copyright © 2012 by the respective authors — cc Creative Commons Attribution 3.0 (CC BY 3.0)

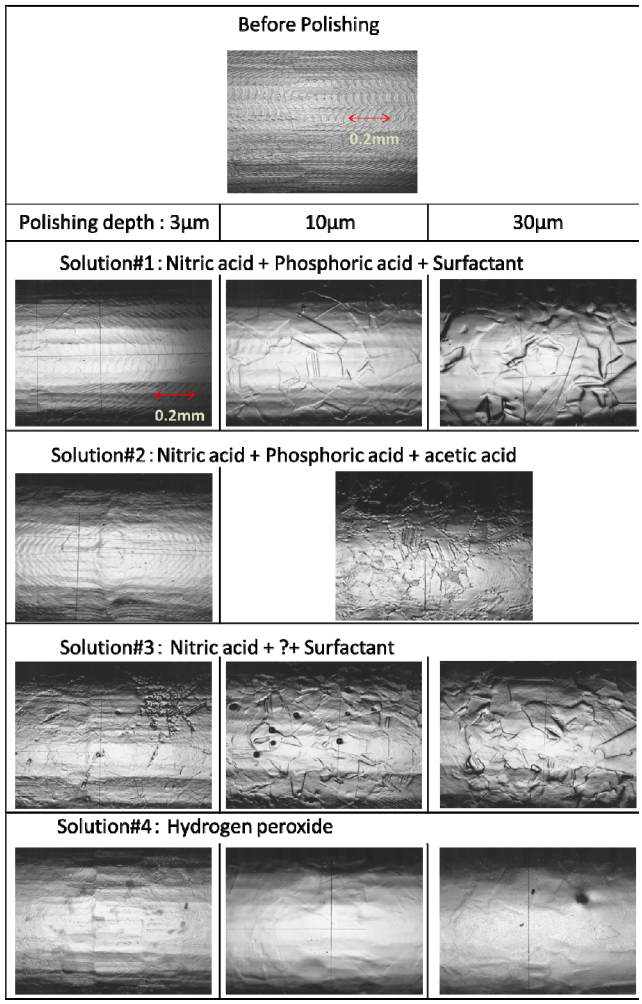

Figure 3: Close-up view of polished surface. Test pieces are machined with the same condition of the vane.

- Calculated average roughness (Ra) improved by the light polishing. The difference between 3μm and 10μm is small.
- Maximum height (Ry) decreased from 1.8μm to 1.2μm by 3μm polishing. Another 7μm polishing, the effect is 0.28μm.

Based on these examinations, we chose the solution #1 and 5μm polishing for the surface treatment.

PROGRESS OF RFQIII FABRICATION

Final machining and surface treatment for first and second units have been finished. The brazing of the first unit is in process. The machining of vanes for third unit is in the finishing step.

SCHEDULE

The third unit will be brazed this November. After the assembling, the RF tuning will be done at end of this year. The high-power test is scheduled next spring. The RFQIII will be installed in the accelerator tunnel at the shutdown period in 2013 after the off-line beam test with ion source and diagnostic beam line on the ground.

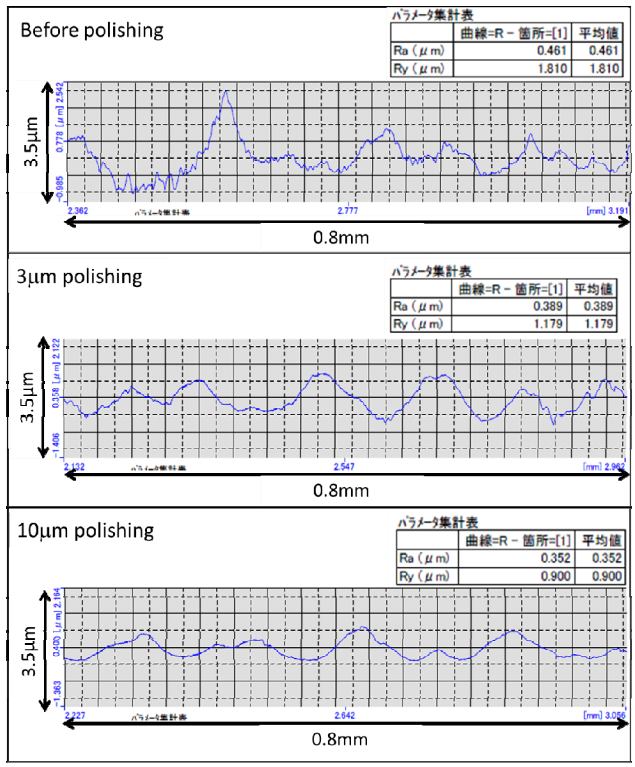

Figure 4: Surface roughness before/after the polishing. Test pieces are machined with the same condition with the vane tip.

ACKNOWLEDGMENT

The authors would like to thank Mr. Y. Iino and Mr. H. Hatanaka of TOYAMA Co., Ltd. for the mechanical design and fabrication of RFQs II and III. It should also be acknowledged that Mr. T. Yoshida of Asahi Kinzoku Kogyo Inc., Y. Hori and Y. Saito of KEK to establish a method of the surface treatment process.

REFERENCES

[1] Y. Yamazaki (eds), "Accelerator Technical Design Report for J-PARC"JAERI-Tech 2003-044; KEK-Report 2002-13.
[2] T. Morishita et al., "Fabrication of the New RFQ for the J-PARC Linac", Proc. of 2010 International Particle Accelerator Conference, Kyoto, Japan, p. 783 (2010).
[3] T. Morishita et al., Procs. of LINAC2010, Tsukuba, Japan, p. 518 and p.521 (2010).
[4] Y. Kondo et al., THPB052, this conference.
[5] Y. Kondo et al., Phys. review STAB, to be published.
[6] Y. Kondo et al., NIMA, **667,** p. 5(2011).

Copyright © 2012 by the respective authors — cc Creative Commons Attribution 3.0 (CC BY 3.0)

ONE DESIGN OF HEAVY ION LINAC INJECTOR FOR CSRm

X.H. Zhang, Y.J. Yuan, J.W. Xia
Institute of Modern Physics, Chinese Academy of Sciences, CHINA

Abstract

The design of heavy ion linac as one new injector of the main Cooling Storage Ring (CSRm) has been discussed. The linac design is based on interdigital H mode drift tube with KONUS (Kombinierte Null Grad Struktur). A high acceleration rate with zero degree synchronous particle phase acceleration reduces the length of IH-KONUS linac and the cost in comparison with conventional linac based on Alvarez structure. To reduce the effect of emittance growth, he RFQ structure is used in front of the IH-KONUS linac. In this linac, the design particle $^{238}U^{28+}$ will be accelerated to 7 AMeV, and the transmission of Uranium beam can reach up to 80%. In this report, the initial physics design of the main linac is presented.

INTRODUCTION

HIRFL-CSR (Heavy Ion research Facility in Lanzhou-Cooling storage Ring) has been built and supplied 7000 hours operation time. As the user number increasing and the experimental requirement improved, the injection linac is proposed, which will make the operation time to improve by 2000 hours. The whole HIRFL-CSR Layout with CSR-LINAC injector is shown in figure.1.

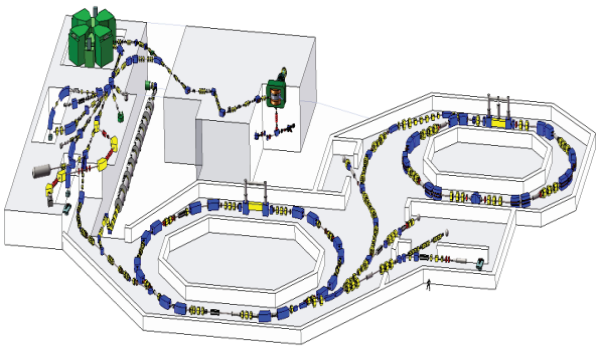

Figure 1: The whole HIRFL-CSR Layout with CSR-LINAC injector.

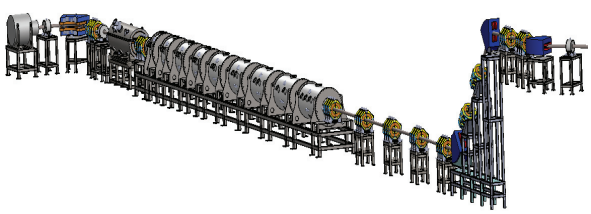

Figure 2: The 3-Dimensional Map of the heavy ion linac for CSRm.

The new linac injector will accelerate $^{238}U^{28+}$ to 7AMeV and the operation frequency is chosen to 108.48 MHz [1] [2]. The main parameters are summarized in table.1. The heavy ion linac consists of electron cyclotron resonance ion source, low energy beam transport, radio frequency quadrupole linac, medium energy beam transport and drift tube linac. The 3-Dimensional Map of the heavy ion linac injector for CSRm is shown in figure.2.

Table 1: Heavy Ion Injection Linac Main Parameters

Ion source	parameter
Particles	C, Ar, Xe, Pb, U
Superconducting ECRIS	$^{208}Pb^{35+}$, $^{238}U^{28+}$
Beam current (emA)	0.05-0.15 (pulsed)
Emittance (pi.mm.mrad)	0.4 (normalized, 90%)
Voltage（KV）	25-40
RFQ	parameter
Input energy (AkeV)	4
Exact energy (AkeV)	300
q/A	1/8.5
Frequency (MHz)	108.48
maximum power (kW)	250
Duration (ms)	10
Repetition (Hz)	10
Duty factor	2%
Transmission (design)	>90%
emittance (pi.mm.mrad)	<0.8 (normalized, 90%)
IH-DTL	Parameter
Input energy (AkeV)	300
Exact energy (AMeV)	7
q/A	1/8.5
Frequency (MHz)	108.48/216.96
Duration (ms)	10
Repetition (Hz)	10
Duty factor	2%
emittance (pi.mm.mrad)	0.8 (normalized, 90%)
Output momentum spread	< ±0.15%
Transmission (design)	> 90%

zhangxiaohu@impcas.ac.cn

Copyright © 2012 by the respective authors — cc Creative Commons Attribution 3.0 (CC BY 3.0)

RFQ BEAM DYNAMICS DESIGN

Because of the transverse focusing and longitudinal bunching simultaneously, Radio Frequency Quadrupole is greatly important in linear accelerator. In this scheme, 4-rod structure is adopted in order to high impedance and good electric field stability at 108.48MHz. The energy acceleration range is from 4AkeV to 300AkeV and the pole length is 202 cm [3]. the 0 mA and 3 mA simulation is done and the comparison is shown table.2.

Table 2: 0mA and 3mA RFQ Main Parameter Comparison

Beam	$^{238}U^{28+}$	$^{238}U^{28+}$	
structure	4rod	4rod	
Frequency	108.48	108.48	MHz
Duty cycle	2	2	%
Beam current	0	3	mA
Input energy	4	4	AkeV
Output energy	300	300	AkeV
Vane Length	202	202	Cm
Voltage	80	80	KV
Transmission	98	94	%
Power losses	100	100	KW
Impedance	130	130	KΩ/m
RF power	100	108	KW
Cell number	157	157	
Modulation	2.5	2.5	
Min. aperture	2.7	2.7	Mm
Ein_total	200	200	Pi.mm.mrad
Ein_norm	0.1	0.1	Pi.mm.mrad
Eout_norm	0.1	0.1	Pi.mm.mrad
TiwssP_in	-0.47 0.03 40.7	-0.47 0.03 40.7	— mm/mrad mrad/mm
TiwssP_out,x	-1.39 0.22 13.3	-1.56 0.25 13.89	— mm/mrad mrad/mm
TiwssP_out,y	1.67 0.285 12.1	1.77 0.3 13.8	— mm/mrad mrad/mm
TiwssP_out,z	0 0.087 11.4	- 0.1450. 125 8.17	— ns/AkeV AkeV/ns

DTL DESIGN

The IH-KONUS structure is used in the main acceleration section. The frequency is 108.48MHz until the particle energy reaches 1.4AMeV and in the post acceleration section 217.96MHz is applied until the particle energy reach 7AMeV. The total length is 19.96 m, including 10 cavities. The main parameter is shown in table.3.

LORASR code is applied for the IH-KONUS drift tube linac design, which is dedicated for KONUS structure. In case of the minimum emittance growth, the initial physics design is finished [4]. Figure.3 shows the x and y transverse envelope along the linac. Figure.4 shows the energy and phase spread along the linac. Figure.5 exhibits the phase space distribution at the entrance and exit of the DTL section. Figure.6 exhibits the relative emittance along the linac.

Table 3: The Main Acceleration Section Parameters

Particle	$^{238}U^{28+}$	
Current	0	mA
A/q	8.5	
Frequency	108.48/216.96	MHz
No. of Tank	10	
No. of Gaps	217	
Energy range	0.3-7	AMeV
Total length	1996.1	Cm
Transmission	100	%
Pulse cycle	2	%
TwissP_out,x	1.8588 3.0821 1.4454	— mm/mrad mrad/mm
TwissP_out,y	1.3666 2.8722 0.9984	— mm/mrad mrad/mm
TwissP_out,z	0.8435 0.0061 281.314	— ns/AkeV AkeV/ns
Emittance_x (Norm, 90%)	0.15718	Pi.mm.mrad
Emittance_y (Norm, 90%)	0.14135	Pi.mm.mrad
Emittance_z (Norm, 90%)	0.62009	AkeV*ns

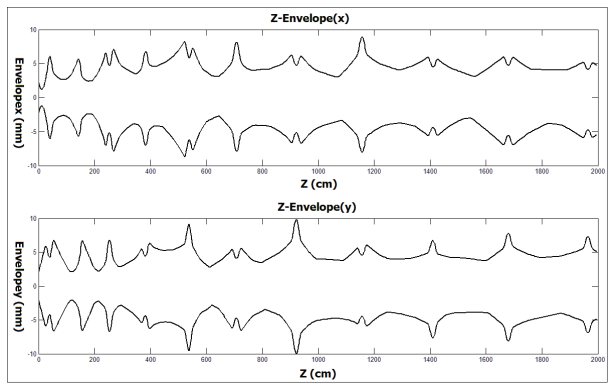

Figure 3: The x and y transverse envelope along the linac.

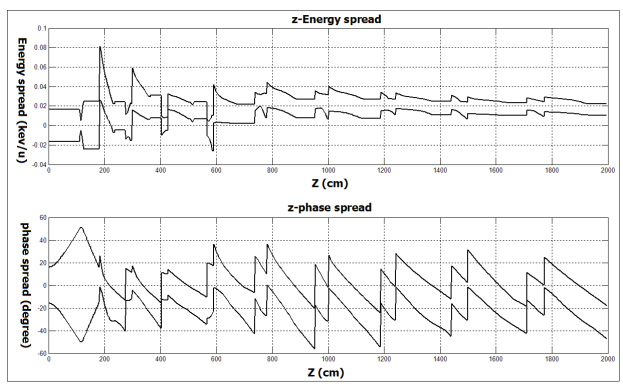

Figure 4: The energy and phase spread along the linac

Copyright © 2012 by the respective authors — cc Creative Commons Attribution 3.0 (CC BY 3.0)

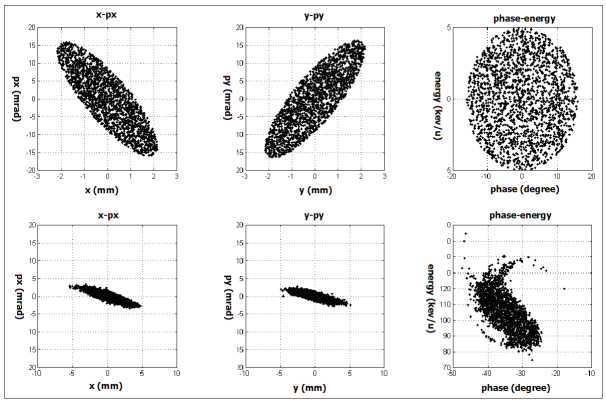

Figure 5: The phase space distribution at the entrance and exit of the DTL section.

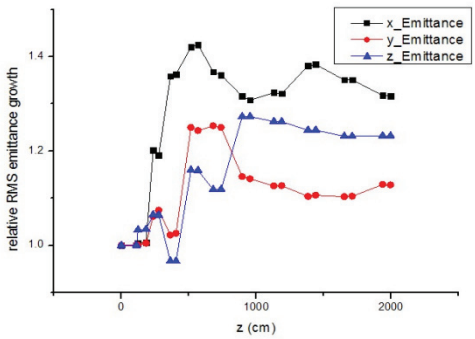

Figure 6: The relative emittance growth along the linac.

CONCLUSIONS

The heavy ion linac injector is very important for staring more comprehensive physical experiments and improving operation efficiency. Compared with the cyclotron injector, the linear accelerator can supply higher current and smaller emittance beam. Moreover, the Linac has larger beam acceptance and higher transmission [5].

LORASR and Beampath code will be applied for the whole physical design and optimization process. Beampath code will be well used for the end-to-end simulation and optimization, besides error analysis.

However, much more work will be done in the future.

REFERENCES

[1] P.-Y. Beauvais, Recent Evolutions in the Design of the French High Intensity Proton Injector (IPHI) Proc. of the EPAC 2004, Lucerne, Switzerland, 1273-1275.

[2] U. Ratzinger, the Upgraded Munich Linear Heavy Ion Post AcceleratorProc. of the PAC 1987, 367-368.

[3] www.gsi.de

[4] H. Podlech, U. Ratzinger, A. Schempp, Institute of Applied Physics IAP,J.W. Goethe University Frankfurt/Main, Germany Design Study of A 3.7 AMeV Linac for A/Q Up To 8.5, 2009.

[5] S. Yamada et al. Injector System of HIMAC Proc. of the LINAC 1990, Albuquerque, USA, LA-12004-C, p. 593.

Copyright © 2012 by the respective authors — cc Creative Commons Attribution 3.0 (CC BY 3.0)

CRYOGENIC SYSTEM FOR THE ADS INJECTOR II IN IMP, CAS*

X. H. Guo[1] , T. Jin[1], H. L. Su[1], X. F. Niu[1], Y. N. Han[1],J.H.Zhang[1]
N. Peng[2], L. Y. Xiong[2], L. Q. Liu[2]
[1]Institute of Modern Physics, Chinese Academy of Sciences, Lanzhou, 730000, China
[2]Key Laboratory of Cryogenics, Technical Institute of Physics and Chemistry
Chinese Academy of Sciences, Beijing, 100190, China

Abstract

In order to meet the requirements of ADS Injector II project which is now designing and building in IMP, CAS, a liquid helium cryogenic system with 4.5K&850W cooling power is building. This paper presents the primary design and the status of this cryogenic system with deferent operation models according to the need of superconducting tests.

INTRODUCTION

In order to produce energy and transmute radioactive wastes in a possibly, cleaner and safer way, the Accelerator Driven Sub-critical (ADS) program has been officially started under the coordination of Chinese Academy of Sciences (CAS). The final aim of this program is to build a 1000 MW demo facility in 2032. The road map of this program is shown in Figure 1. There are two beam lines will be built before 2015, which respectively called ADS injector I and II with deferent design idea. The upper line is ADS injector II (RFQ + HWR) [1], will build by Institute of Modern Physics (IMP), Chinese Academy of Sciences (CAS). It has three cryomodules, two of them are on-line operation and the other one is off-line test module. Each of them includes 8 superconducting HWR cavities and 9 superconducting solenoids [2]. The superconducting solenoids are bath-cooled with saturated liquid helium near the atmospheric pressure and the superconducting cavities are bath-cooled with 2 K saturated liquid helium. For the steady operation, the pressure fluctuation of the liquid helium in the cryomodules of cavities should be less than ±0.3 mbar, while the liquid level should be kept in a small band of ±1%.

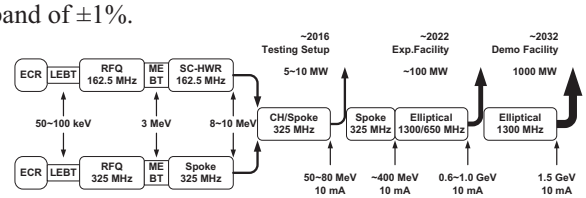

Figure 1: Road map of ADS program.

CRYOGENIC SYSTEM

The flow diagram of the cryogenic system is shown as Figure 2. It consists of a helium refrigerator, a 2000 L helium storage dewar, a purification system, three identical valve boxes, three cryomodules, four 100 m3 pure helium gas buffer tanks and several cryogenic lines. The helium refrigerator system, a standard helium refrigerator LR280 developed by LINDE, is based on 2-turbine-in-series and 1 additional JT turbine Claude cycle. It consists of a compressor module, an oil removal system, gas management panel, a cold box. An oil lubricated screw compressor (FSD 571 made by KAESER Ltd.) is used to compress 95 g/s helium gas from 105 kPa to 1.4 MPa. The oil remove system comprises a bulk oil separator, two coalescing filters mounted in series and a final activated charcoal absorber. The gas management system consists of two by-pass recycle valves (for roughly and finely adjusting, respectively) to automatically recycle excess flow from compressor discharge to suction line and two control valves to automatically adjust the helium inventory in the refrigeration system. The cold box is a vertical cylinder consisting of 5 stages of brazed aluminium plate-fin heat exchangers, two gas-bearing turbo-expanders arranged in series, one additional JT turbine, valves, one 80 K absorber and one 20 K absorber furnished to remove contaminants from the helium stream. The three valve boxes are used to distribute and control the helium flow and nitrogen flow in different operation models such as cool-down, warm-up, 4.3 K bath-cooled mode, 2 K bath-cooled mode and to protect the cryomodules against any possible damages. The cryogenic transfer lines used for delivering LHe, GHe and LN2 include a coaxial transfer line, a multi-channel transfer line and several single channel transfer lines.

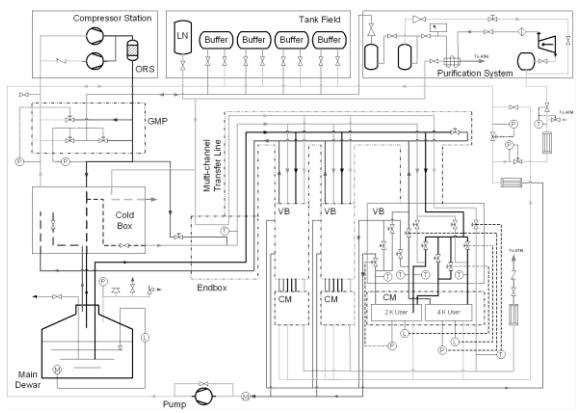

Figure 2: Flow diagram of the ADS Injector II cryogenic system.

*Work supported by Accelerator Driven Sub-critical (ADS) program of CAS, China. guoxh@impcas.ac.cn

Copyright © 2012 by the respective authors — cc Creative Commons Attribution 3.0 (CC BY 3.0)

HELIUM GAS RECOVERY SYSTEM

In order to reduce the cost of superconducting test, a helium gas recovery system is build. This system consist of a helium gas collecting sub-system and a high pressure purifier sub-system. These sub-system include gas balloon, multi component detector, diaphragm compressor, pure high pressure tank, impure high pressure tank and LN2 tank. Figure 3 is the diagram of helium gas recovery system. The impure helium is first collected in a 50m3 gas balloon. There are two position sensors are used to protect the gasbag from over filled and to control the compressor too. As soon as the gas bag is filled with impure helium gas enough, the higher position sensor is triggered, the diaphragm compressor will run automatically to pressurize the impure helium gas go through the purifier to a 5000m3@15MPa impure helium gas tank. The multi component detector can monitor the purity of the helium gas, if the purity of helium gas reach 99.999%, the relevant valve open, pure helium gas goes into the 3000m3@15MPa pure high pressure tank, otherwise, purify cycle again.

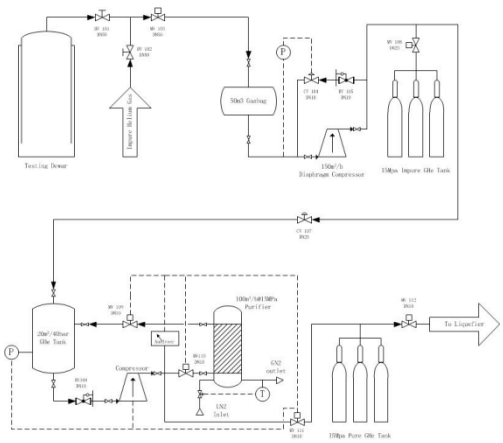

Figure 3: The diagram of helium gas recovery system.

OPERATION MODELS

According to the cooling requirements of superconducting test, this cryogenic system can supply mainly four operation models, such as 300 K ~ 80 K cool-down mode, 80 K ~ 5 K cool-down mode, warm-up mode and nominal cooling operation. For 300 K ~ 80 K cool-down mode, to control the cool-down speed, the cooling temperature is mixed from 300 K gas and 80 K gas. The mass flow rates of the cryogen are adjusted in the valve boxes. As the temperature of the return gas in this model is high, the return gas will go to the compressor suction via the by-pass valve and a heater. For 80 K ~ 5 K cool-down mode, the cool-down temperature and mass flow rate also can be controlled. The return gas will go to the cold box to recover the cooling capacity. Warm-up mode is the reverse procedure of cool-down, the suitable temperature and mass flow rate of the warm gas will be used. Under the nominal cooling operation, the superconducting solenoids are 4.3 K bath-cooled and the superconducting cavities are 2 K bath-cooled. The levels in the 4.3 K and 2 K cryomodules are adjusted by the supply valves, respectively. The pressure in the 4.3 K and 2 K cryomodules are adjusted by the return valves. Almost of the 4.3 K vapour helium will return to the cold box; other helium from current leader and coupler will return to compressor suction directly. All of the 2 K vapour helium will return to the compressor suction via an electrical heater and a pump station

ESTIMATED HEAT LOAD

The estimated heat load @ 4.5 K of the system is listed in Table 1. The total load for operating will be 335 W + 120 L/hr. allowing for margin, the equivalent load for nominal operating mode will be 850 W @ 4.5 K

Table 1: Estimated 4.5 K Heat Load

Items	**Equivalent Heat load @ 4.5 K**
Cryomodules	50 W×3 = 150 W 1.4 g/s×3 = 4.2 g/s ~ 120 L/h
Valve boxes and End box	30 W×3+10 W = 100 W
multi-channel transfer line	10 W
single channel transfer lines	45 W
2000L dewar	30 W
Total	335 W + 120 L/h ~ 700 W
With margin	**850 W**

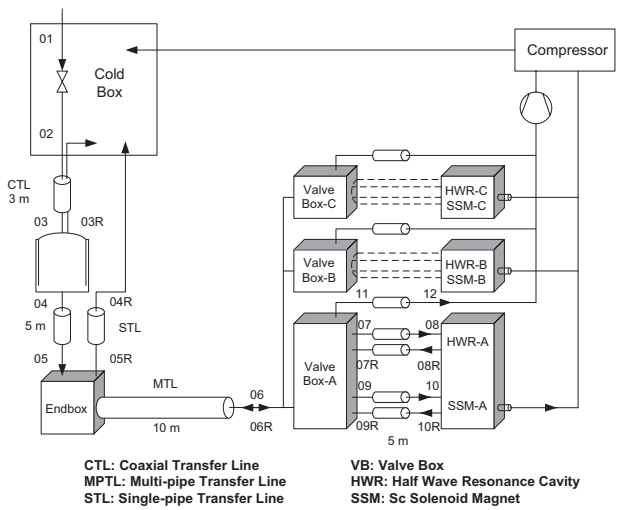

Figure 4: Simplified flow scheme of the ADS Injector II cryogenic system.

PROCESS SIMULATION

The thermodynamic analysis of the system was carried out based on the simplified flow scheme (see Figure 4) and the estimated heat loads. The simulation boundary conditions are based on the Ts-Diagram for specific mixed mode of refrigerator. The pressure, temperature, mass flow rate and cryogen quality have been calculated. The results of the static processing simulation for

Copyright © 2012 by the respective authors — cc Creative Commons Attribution 3.0 (CC BY 3.0)

superconducting solenoids and superconducting cavities are presented by T-s diagrams in Figure 5 and Figure 6.

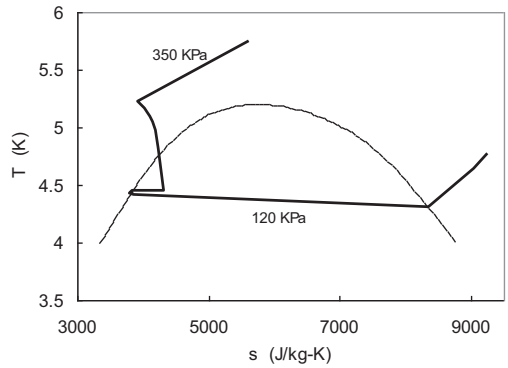

Figure 5: T-s diagram for the cooling of superconducting solenoids.

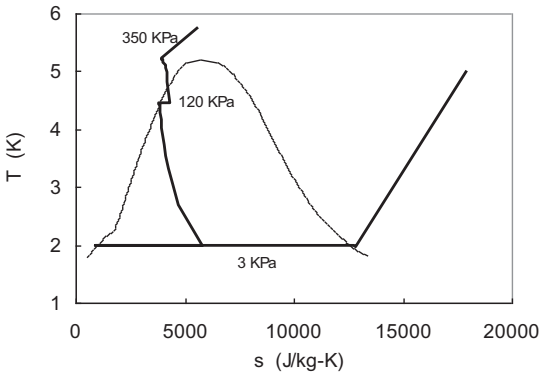

Figure 6: T-s diagram for the cooling of superconducting cavities.

SUMMARY

Basically, the cryogenic system for cooling ADS injector II System was designed by considering a various requirements of operation modes. The static and dynamic heat load of the cryomodules was estimated. The thermodynamic analysis of the cryogenic system was carried out based on the simplified flow scheme. The procurement of the components of the cryogenic system, such as refrigerator, dewar, buffer tanks have been ordered and are under fabrication in factories. The helium gas recovery and purification system are also built. All the cryogenic system will be completed in 2013.

REFERENCES

[1] Z.J. Wang, et al., The comparison of ADS injector II with HWR cavity and CH cavity, Proceedings of IPAC2011 (2011), 26162618

[2] Y. He, et al., The conceptual design of injector II of ADS in China, Proceedings of IPAC2011 (2011), 2613-2615

[3] Peng N., Guo X. H., Jin T., Su H. L., Niu X. F., Han Y. N., Xiong L. Y., Liu L. Q.. Conceptual Design of the Cryogenic System for the ADS System Injector II. ICEC 24: International Cryogenic Engineering Conference. 17P-P06-02.

Copyright © 2012 by the respective authors — cc Creative Commons Attribution 3.0 (CC BY 3.0)

R&D TOWARDS CW ION LINACS AT ANL*

P.N. Ostroumov#, A. Barcikowski, Z. Conway, S. Gerbick, M. Kedzie, M.P. Kelly, S. Kutsaev, J. Morgan, R. Murphy, B. Mustapha, D. Paskvan, T. Reid, D. Schrage, S. Sharamentov, K. Shepard, G. Zinkann,
Argonne, IL 60439, U.S.A ANL, Argonne, IL 60439, U.S.A.

Abstract

The accelerator development group in ANL's Physics Division has engaged in substantial R&D related to CW proton and ion accelerators. Particularly, a 4-meter long 60.625-MHz CW RFQ has been developed, built and commissioned with beam. Development and fabrication of a cryomodule with seven 72.75-MHz quarter-wave resonators (QWR) is complete and it is being assembled. Off-line testing of several QWRs has demonstrated outstanding performance in terms of both accelerating voltage and surface resistance. Both the RFQ and cryomodule were developed and built to upgrade ATLAS to higher efficiency and beam intensities. Another cryomodule with eight 162.5-MHz SC HWRs and eight superconducting SC solenoids is being developed and built for Project X at FNAL. We are also developing both an RFQ and cryomodules (housing 176-MHz HWRs) for proton & deuteron acceleration at SNRC (Soreq, Israel). In this paper we discuss ANL-developed technologies for normal-conducting and SC accelerating structures for medium- and high-power CW accelerators, including the projects mentioned above and other developments for applications such as transmutation of spent reactor fuel.

INTRODUCTION

Technologies for CW RFQ and SC RF successfully developed for ATLAS upgrade for higher efficiency and beam intensities [1,2] can be applied in future high-power CW accelerators. Particularly, we are developing a CW RFQ and two cryomodules with different β_{OPT} for the SARAF accelerator facility at SNRC [3]. Similar SC RF technology is being used for the development and construction of the HWR cryomodule for Project X [4]. Below we discuss beam commissioning of the RFQ and results of QWRs testing and cryomodule assembly for the ATLAS upgrade project. Status of the SARAF and PXIE cryomodule development is presented.

CW RFQ

This summer we commissioned a CW RFQ designed and built for the ATLAS Facility [5]. Several innovative ideas were implemented in this CW RFQ. By selecting a multi-segment split-coaxial structure we have achieved moderate transverse dimensions for a 60.625 MHz resonator. For the design of the RFQ resonator and vane tip modulations we have developed a full 3D approach which includes MW-Studio and TRACK simulations of the entire structure. A novel trapezoidal vane tip modulation is used in the acceleration section of the RFQ which resulted in increased shunt impedance. To form an axially symmetric beam exiting the RFQ, a very short output radial matcher, only $0.75\beta\lambda$ long, was developed.

An advanced fabrication technology was applied for the construction of the RFQ which includes precise machining and two-step high temperature brazing. Thanks to the high accuracy of the overall fabrication, the assembly of the 5-segment RFQ was straightforward and resulted in excellent alignment. The resonance frequency control system based on water temperature regulation showed excellent performance. The RF measurements show excellent RF properties for the resonator, with a measured intrinsic Q equal to 94% of the simulated value for OFE copper. The multi-segment split-coaxial structure creates strong coupling between the quadrants and individual RFQ segments which reduces the effect of local frequency deviations on electromagnetic field distortions. Therefore, no bead-pull measurements were required for tuning of the accelerating field. Figure 1 shows the complete RFQ assembly after installation of

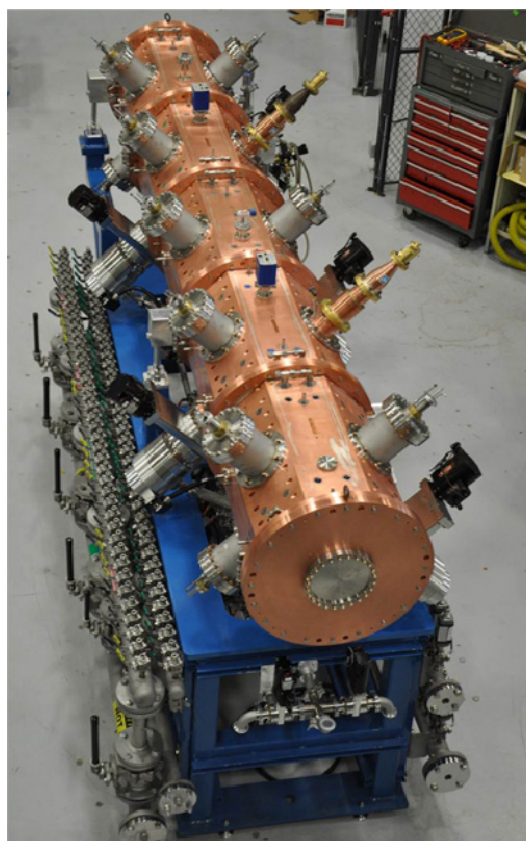

Figure 1: Completed RFQ assembly.

* This work was supported by the U.S. Department of Energy, Office of High Energy Physics and Nuclear Physics, under Contract DE-AC02-76CH03000, DE-AC02-06CH11357 and ANL WFO 85Y47
#ostroumov@anl.gov

Copyright © 2012 by the respective authors — cc Creative Commons Attribution 3.0 (CC BY 3.0)

the tuners, vacuum pumps, vacuum gauges, RF couplers, and pick-up loops.

An O^{5+} ion beam extracted from an Electron Cyclotron Resonance (ECR) ion source was used for the RFQ commissioning. In off-line beam testing, we found excellent agreement of the measured beam parameters with the results of beam dynamics simulations. For example, the beam energy spread was determined by scanning the magnetic field level in the 70° bending magnet located downstream of the RFQ. The results of these measurements are shown in Fig. 2.

The great success of this advanced design and fabrication technology is reflected in the measured beam parameters after the RFQ which are nearly identical to the simulated data. Currently we are developing the design for a 4-vane RFQ operating at 176 MHz for acceleration of protons or deuterons up to 1.5 MeV/u. This design takes full advantage of the ATLAS RFQ experience.

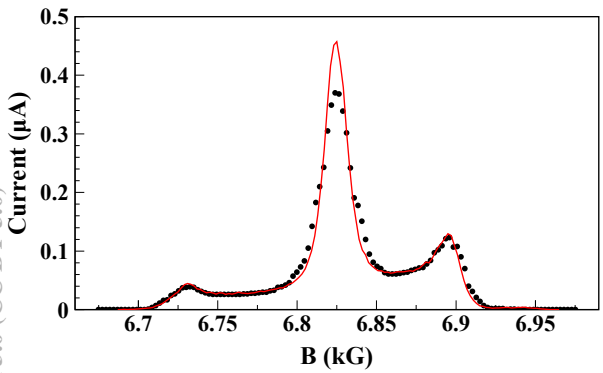

Figure 2: Measured (dots) and simulated (red curve) beam intensity as a function of the magnetic field.

QWR CRYOMODULE

While split-ring resonators are successfully operated at ATLAS with low-intensity ion beams, they exhibit a fundamental limit in the acceleration of high-intensity beams due to RF steering. Therefore we are replacing all ATLAS split-ring resonators with QWRs. Three years ago we commissioned a new cryomodule containing seven 109 MHz β_{OPT}=0.15 QWRs to provide an additional 15 MV voltage. Now, we have developed and built a new cryomodule which consists of seven β_G=0.077 QWRs at 72.75 MHz SC cavities and four 9-Tesla SC solenoids. The new high-performance cryomodule will replace three existing ATLAS cryomodules with split-ring cavities to increase the intensities of accelerated ion beams.

Compared to the previous generation of quarter-wave resonators, several innovations were implemented into the cavity design, fabrication and RF surface treatment. The cavity geometry is highly optimized to reduce both electric and magnetic peak fields: both outer and inner conductors are conical as shown in Fig. 3. During the fabrication of the niobium components, a wire EDM technique instead of machining was used to maintain clean surfaces prior to electron-beam welding. Electropolishing of the cavities was performed for a completed cavity with the integral helium vessel installed. The cavity is equipped with a double-window 4-kW adjustable RF coupler with a nitrogen cooled cold window. The new QWRs will create accelerating gradients a factor of three higher, on average, than in the existing split-ring cavities, and are designed to provide an accelerating voltage of 2.5 MV per cavity. Four 72.75 MHz QWRs were cold tested in the test cryostat and all of them provided more than 4 MV voltage, E_{PEAK}>70 MV/m and B_{PEAK}>105 mT [6,7]. The fabrication of the cryomodule, all the 72.75-MHz QWRs and SC solenoids is complete. Figure 4 shows the assembled cavities being loaded into the box cryostat during a trial fitting. The new cryomodule was designed to produce 17.5 MV total voltage but will provide up to 21 MV which will be limited only by the available cryogenic capacity.

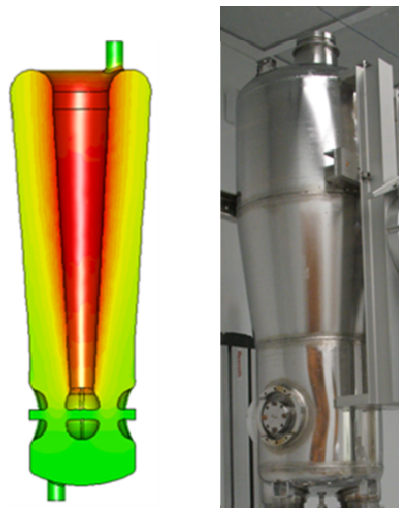

Figure 3: Cavity MWS model showing magnetic field distribution (left) and completed cavity assembly in the HPR apparatus (right).

Figure 4: Cavity string is being lowered into the box vacuum vessel during mock assembly.

Copyright © 2012 by the respective authors — cc Creative Commons Attribution 3.0 (CC BY 3.0)

HWR CRYOMODULES

In high-intensity light ion accelerators, to reduce space charge effects, the fundamental frequency should be high as compared to heavy-ion linacs. SC HWRs are superior to QWRs at operational frequencies above ~150 MHz and optimal beta $\beta_{OPT} \geq 0.1$. The fundamental frequency of Project-X is 162.5 MHz which is defined by the RFQ. Therefore we are developing a cryomodule with 8 HWRs for the acceleration of H-minus ions from 2.1 MeV to 11 MeV [8]. Similar HWRs operating at 176 MHz are designed for the SARAF Phase II 5-mA proton and deuteron linac. To increase the available accelerating voltage, the HWR shape is highly optimized reducing both B_{PEAK}/E_{ACC} and E_{PEAK}/E_{ACC} [9]. Optimization of the cavity shape was performed taking into account die-forming fabrication technology available from industry [10,11]. The final cavity shape has tapered central and outer conductors as shown in Fig. 5. The confidence in the proposed HWR design and predicted performance is based on the very successful design, construction and testing of a conical QWRs for the ATLAS upgrade. The results of the EM optimization are summarized in Table 1.

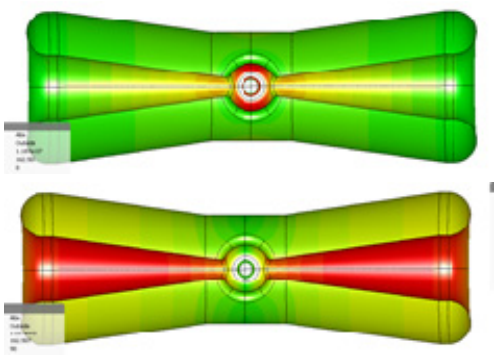

Figure 5: A half-wave resonator model in MWS. The electric (top) and magnetic field (bottom) distributions on the surface are shown.

Table 1: HWR main parameters

Parameter	PXIE	SARAF	
Frequency, MHz	162.5	176	
Operating temperature, K	2	4	
Optimal beta, β_{OPT}	0.11	0.089	0.16
$L_{EEF} = \beta_{OPT}\lambda$, cm	20.7	15.2	27.3
Aperture, mm	33	33	36
Accelerating voltage, MV	1.7	1.0	2.1
E_{PEAK}/E_{ACC}	4.7	5.3	4.7
B_{PEAK}/E_{ACC}, mT/(MV/m)	5.0	5.6	5.6
$G = Q_0R_S$, Ω	48	40	60
R/Q_0, Ω	272	231	296

Both PXIE and SARAF HWR cryomodule designs are an evolution of the top-loaded box cryomodule design used successfully for the ATLAS Upgrade. The PXIE and the first HWR SARAF cryomodules layout were determined with careful beam-dynamics simulations and estimates of recent cavity performance. As a result of these studies, a focusing period contains a solenoid-BPM-HWR sequence. Each solenoid is equipped with dipole coils for beam steering in both planes. The cryomodule design is developed around these requirements. The cryomodule beam-line assembly along with the strong-back, vacuum and helium manifolds, and cavity subsystems is shown in Figure 6.

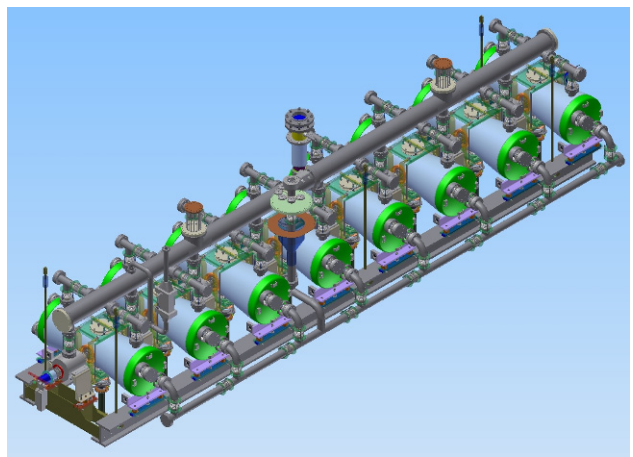

Figure 6: PXIE HWR cryomodule design

REFERENCES

[1] P.N. Ostroumov, et al, LINAC-10, September 12-17, Tsukuba, Japan, p. 157.
[2] P.N. Ostroumov, et al, PAC-11, March 28- April 1, New York, p. 2110.
[3] D. Berkovits et al, Paper MO1A01 in these proceedings.
[4] S. Nagaitsev, PAC'11, New York, March-April 2011, p. 2566.
[5] P.N. Ostroumov, et al, Development and Beam Test of a CW Radio Frequency Quadrupole Accelerator, submitted to PRST-AB.
[6] M. Kelly, et al, Paper MOPB073 in these proceedings.
[7] Z. Conway, et al, Paper TUPLB66 in these proceedings.
[8] Z. Conway, et al, Paper TUPB068 in these proceedings.
[9] B. Mustapha, et al, Proceedings of the IPAC-12, p. 2289.
[10] P.N. Ostroumov, et al, Proceedings of the IPAC-12, p. 2295.
[11] Z. Conway, et al, Paper TUPB067 in these proceedings.

Copyright © 2012 by the respective authors — cc Creative Commons Attribution 3.0 (CC BY 3.0)

STATUS OF THE SUPERCONDUCTING RF ACTIVITIES FOR THE HIE-ISOLDE PROJECT

W. Venturini Delsolaro, L. Alberty Vieira, S. Calatroni, O. Capatina, B. Delaup, A. D`Elia*, I. Mondino, E. Montesinos, M.A. Fraser, P. Maesen, Y. Kadi, N. Jecklin, M. Therasse, D. Valuch.
CERN, Geneva, Switzerland; *Manchester University and Cockroft Institute

Abstract

The planned upgrade of the REX ISOLDE facility at CERN will boost the energy of the machine from 3 MeV/u up to 10 MeV/u with beams of mass-to-charge ratio $2.5 < A/q < 4$. For this purpose, a new superconducting post accelerator based on independently phased 101.28 MHz Quarter Wave Resonators (QWR) will replace part of the normal conducting Linac. The QWRs make use of the Niobium sputtering on Copper technology which was successfully applied to LEP2, LHC and to the energy upgrade of the ALPI Linac at INFN-LNL. The status of advancement of the project will be detailed, limited to the SRF activities.

INTRODUCTION

The upgrade of the REX ISOLDE facility [1] relies on a new superconducting Linac to bring the energy of the radioactive beams from 3 MeV/u up to 10 MeV/u with beams of mass-to-charge ratio $2.5 < A/q < 4$.

The project is staged in three phases in order to optimize the beam delivery to the physicists and to take advantage of the scheduled shut down periods of the CERN accelerator complex. The first phase will consist in the installation of two cryomodules, each housing 5 high beta Quarter Wave Resonators (QWR) and a superconducting solenoid for beam focusing.

The core element of the HIE ISOLDE Linac is the QWR, which will make use of the sputtered Nb/Cu technology pioneered at CERN for LEP2 [2], and subsequently developed for the complex QWR shape in INFN-LNL for the energy upgrade of ALPI [3], [4]. The elliptical cavities in use at CERN were coated by magnetron sputtering at relatively low temperatures, whereas the QWR for ALPI were realized by bias diode sputtering at higher temperatures.

The design of the high beta cavity is reported in [5], the main parameters are listed in Table 1.

Work to set up a production chain for sputtered QWR started in CERN in 2008 and the early reached milestones are reported in [6], [7]. The most recent project schedule requires series production of the cavities to start at CERN in early 2013.

Besides the cavity itself, ancillaries like the power coupler and tuning system are being developed. This paper reports on the latest developments in the SRF frame, while a recent and detailed update on the whole HIE ISOLDE project is given in [8]

Table 1: Parameters of the high β HIE ISOLDE QWR

Frequency (MHz)	101.28
β (%)	10.3
Active length (m)	0.3
$\Gamma = Rs\ Q$ [Ω]	30.34
E_{acc} (MV/m)	6
Q_0 @ E_{acc}=6 MV/m	$5\ 10^8$
E_{apk}/E_{acc}	5.4
B_{apk}/E_{acc}(Gauss/MV/m)	96

STUDY OF CAVITY MECHANICAL TOLERANCES

The high substrate temperatures reached during the sputtering process called for a reconsideration of the mechanical tolerances for the manufacture of the cavity. Indeed, it was not clear to what extent the induced mechanical deformations would affect the beam quality. A study was launched in early 2012 to understand the effect of the misalignment of the internal conductor of the quarter-wave resonator on the beam. In previous error studies only misalignments of the ideal cavity were considered, see [9]. In the new study, the outer conductor of the cavity was assumed as ideal but the internal conductor was misaligned in each independent mode: Δx, Δy, Δz and $\Delta\theta_y$, where the magnitude of each error was parameterized at the beam ports. The misalignments were implemented by pivoting the internal conductor about its point of attachment at the top of the cavity. In fact, the field perturbation seen by the beam is dominated by the fringing electric fields in the vicinity of the beam ports. Moving the position of the drift-tube on the inner conductor could attain analogous results. Systematic RF simulations were performed with CST-MWS: many cavities were generated with regular increments in each independent type of misalignment; the field profiles on the axis were extracted and kick factors calculated. An example of these results is shown in Fig. 1.

Copyright © 2012 by the respective authors — cc Creative Commons Attribution 3.0 (CC BY 3.0)

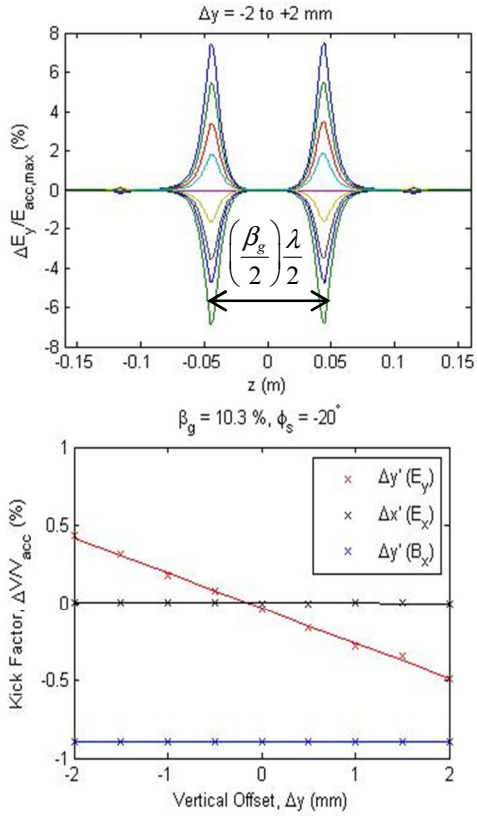

Figure 1: The perturbation to the vertical electric field seen on axis for Δy = -2 to +2 mm in steps of 0.5 mm (top) and the resulting kick factors (bottom), calculated at the geometric velocity of the cavity and at the nominal synchronous phase.

Table 2: Kick factors from misalignment of the inner conductor compared to the kick generated from the misaligned cavity.

Misalignment Type	$\Delta V/V_{acc}$ **(%/mm)** (β = 0.103, φ_s = -20 °)
Δx ($\approx 579.5\Delta\theta_z$)	0.20
Δy	0.21
Δz ($\approx 579.5\Delta\theta_x$)	0.25
Δx ($\approx 45\Delta\theta_y$)	1.10
Ideal cavity misaligned: Δx, Δy	0.41

The intrinsic magnetic field present in the nominal case is largely unperturbed with vertical misalignment and is compensated by systematically offsetting the beam axis in the aperture [9], [10].

As expected, the kick factors for misalignment of the inner conductor are of the same order of magnitude as the kick factors from the misalignment of the ideal cavity, at the level of a few tenths of 1%.

The kick factors per mm of misalignment are collected in Table 2, calculated at the geometric velocity and nominal synchronous phase. The most significant error is the rotation of the inner conductor about its axis. However, this is not likely to occur during the coating process.

In order to avoid any perturbation to the beam, the inner conductor should be aligned to within σ_{rms} = ±0.3 mm. The results allowed relaxing the previous conservatively set tolerances by a factor 5. First metrology results after sputtering indicate that this should be sufficient.

CAVITY PROTOTYPE TESTS

The workflow to produce and characterize a test Nb coated cavity is rather complex and labour intensive. The copper cavity substrate must first be stripped of its previous film; then the surface is chemically prepared, and rinsed with ultra-high purity water in a clean environment. The cavity is then mounted onto the coating system in a class 100 clean room. After pump down and baking the cavity is coated and left to cool down in the sputtering system. It is then removed from the vacuum chamber, rinsed again, dried, and transported to the cold test area where it is mounted into a test cryostat, equipped for the RF measurement at liquid helium temperature.

A total of 6 coating tests have been accomplished since the end of 2011, all with the bias diode method. Different sets of sputtering parameters were adopted as the coating system was being refurbished to allow for higher baking temperatures and higher sputtering power.

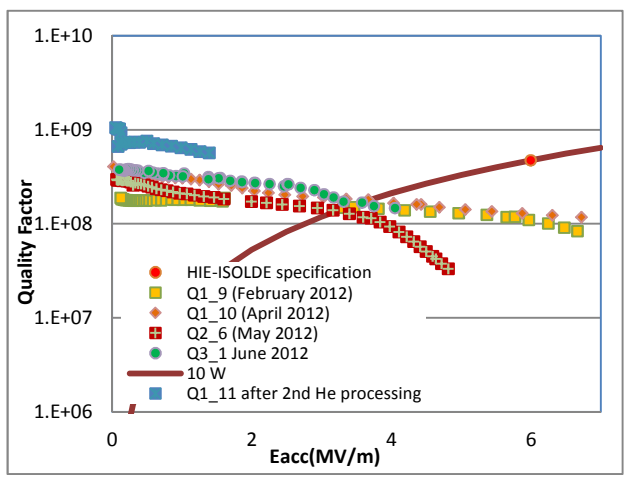

Figure 2: Performance of the test cavities in 2012. The red dot indicates the HIE-ISOLDE specification.

The cavity performances are displayed in Fig 2. Initially the effect of increasing the coating temperature was explored. Following [3] the process temperature was increased from previous 150 ºC to more than 600 ºC, with very encouraging results. The design accelerating field

Copyright © 2012 by the respective authors — cc Creative Commons Attribution 3.0 (CC BY 3.0)

could be reached for the first time, although Q values were still a factor 3-4 below the specification.

The latest test was done at higher sputtering power and resulted in a further improvement of Q_0 without any degradation of the initial slope. The limit in accelerating field which appeared on this last cavity could be shifted up by applying He conditioning. It is believed to be due to a localized area and is still under investigation.

ANCILLARIES

The fundamental power coupler and tuning systems were designed and prototypes are available [11], [12]. However, a continuing effort is being put in reviewing and improving the existing designs, both on economic and on technical grounds.

The first model of fundamental power coupler showed some mechanical problems after several thermal cycles between warm and operational temperatures. At the end of 2011 a redesign of this element was launched and the first prototype was successfully tested in March 2012.

The new design is based on a stainless steel external body to minimize the thermal load on the cavity, an all in one machined copper antenna including N connector inner contact, a movable copper outer line sliding inside the external body, a Vespel© ring to ensure concentricity between the antenna and the outer line, a ceramic ring with an EB weld between outer line and outer N connector, sliding RF contacts, and a displacement system and guidance rails made of stainless steel and brass to ensure positioning of the antenna in the cryogenic environment. A schematic view of the new power coupler is shown in Figure 3.

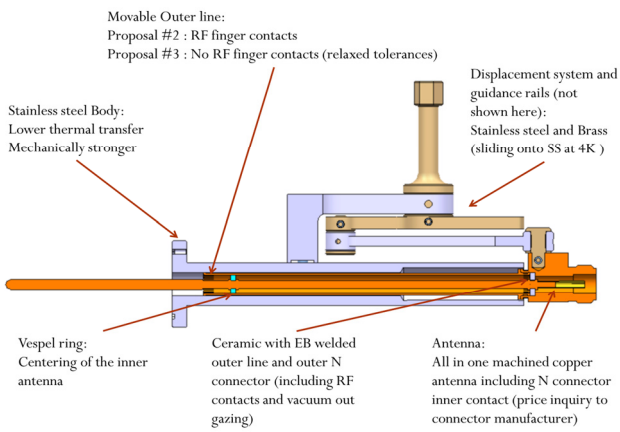

Figure 3: Prototype fundamental power coupler

The available tuning system will have to be tested in the next future with the final – stiffer – cavity design prototype, to assess the level of microphonics which is a necessary input to continue the development of a suitable low level RF system.

CONCLUSION

The SRF program for the HIE-ISOLDE project, focused on the development of Nb sputtered QWR generating 6 MV/m accelerating field at 10 W power dissipation was vigorously pursued in 2012 with encouraging results.

The effect of internal cavity misalignments was quantified and new tolerances were issued. This provided confidence that the high sputtering temperatures will not cause significant beam degradation through cavity deformations. Recent results marked a further step towards the achievement of the cavity specifications.

In parallel, work continues on cavity ancillaries, aiming to be ready for the first cryomodule in summer 2013.

ACKNOWLEDGMENT

We wish to thank all the technical staff at CERN who daily make possible the progress of this work.

The precious support of G. Bisoffi, E. Palmieri, A. Porcellato and S. Stark from INFN-LNL is warmly acknowledged.

We acknowledge funding from the Swedish Knut and Alice Wallenberg Foundation (KAW 2005-0121) and from the Belgian Big Science program of the FWO (Research Foundation Flanders) and the Research Council K.U. Leuven.

We would like to acknowledge as well the receipt of fellowships from the CATHI Marie Curie Initial Training Network: EU-FP7-PEOPLE-2010-ITN Project number 264330.

REFERENCES

[1] M. Pasini et al, `A SC upgrade of the REX ISOLDE accelerator at CERN` Proceedings of LINAC08 – MOP028, p. 124

[2] S. Calatroni, "Niobium coating techniques" Journal of Physics: Conference Series **114** (2008) 012006

[3] S. Stark et al., "Niobium sputter-coated QWRs", Particle Accelerators, Vol.61 (1998) p. 383

[4] A.M. Porcellato et al., "Performance of ALPI new Medium Beta Resonators" to be published in the Proceedings of HIAT12, and references therein

[5] S. Calatroni et al, "The HIE-ISOLDE Superconducting Cavities: Mechanical Design and Fabrication" Proceedings of SRF09 - THPPO010, p. 546

[6] G. Lanza et al.,"The HIE-ISOLDE Superconducting Cavities: Surface Treatment and Niobium Thin Film Coating", Proceedings of SRF09 - THPPO075, p. 801

[7] M. Therasse et al., "HIE-ISOLDE SRF development activities at CERN", Proceedings of IPAC11, MOPC104.

[8] Y. Kadi et al., "Status and future perspectives of the HIE-ISOLDE project at CERN", Proceedings of IPAC12, MOOBA02.

[9] M.A. Fraser, "Beam Dynamics Studies of the ISOLDE Post-accelerator for the HIE-ISOLDE Upgrade", PhD Thesis, University of Manchester, 2011.

[10] M.A. Fraser, R.M. Jones, M. Pasini, Phys. Rev. ST Accel. Beams **14** 020102, 2011.

[11] A. D'Elia, "Design and characterisation of the power coupler line for the HIE-ISOLDE high-beta cavity", HIE-ISOLDE-Project-Note-011, CERN, August 2011.

[12] A. D'Elia et al, "HIE-ISOLDE high-beta cavity study and measurements", Proceedings of SRF09 – THPPO027, p. 609

Copyright © 2012 by the respective authors — cc Creative Commons Attribution 3.0 (CC BY 3.0)

DISCUSSION OF THE OPTIMISATION OF A LINAC LATTICE TO MINIMISE DISRUPTION BY A CLASS OF PARASITIC MODES

S. Molloy*, ESS, Lund, Sweden
R. Ainsworth, Royal Holloway, University of London, Egham,UK

Abstract

It is well known that each resonant mode in the RF spectrum of multi-cell accelerating cavities will split into a passband containing a number of modes, and that the coupling of these modes to the beam is dependent on the velocity of the accelerated particles. If these modes are found to degrade the quality of the beam, it is possible to take various measures to damp them, and thus keep their effect below some critical threshold. In the case of the parasitic modes within the same passband as the fundamental accelerating mode, their frequency is typically too close to that of the fundamental to allow their power to be safely extracted, and so cavity designers must rely on the natural damping of the cavity itself. This note contains a theoretical discussion of the coupling of the beam to these passband modes for a large class of accelerating cavities, and provides a mathematical model for use during the design and optimisation of linacs.

INTRODUCTION

In general, π-mode accelerating cavities act as several coupled cells, each of which resonates at almost the same frequency. The cell-cell coupling splits each of the resonances into a passband containing the same number of modes as there are coupled cells. Each of these will have the same character (i.e. TM_{mnp}, TE_{mnp}, etc.) as the single cell resonance, but may be differentiated by their frequency and cell-cell phase difference.

Modes lying within the same passband as the accelerating mode will be referred to as Same Order Modes (SOMs), while others will be called Higher Order Modes (HOMs).

Various schemes are used to damp the power in these parasitic modes so that their amplitude has fallen below some threshold value by the time a subsequent beam pulse arrives at the cavity, however the SOMs remain problematic since the similarity of their frequency and structure with the desired fundamental mode mean that it is normally not possible to damp their power sufficiently.

In storage rings or CW linacs, the pulses last long enough that modes whose frequency, f_m, does not lie within a very small region around an integer multiple of the bunch repetition frequency, $n{\cdot}f_b \pm \Delta f$, will be "washed out", and will not obtain an amplitude large enough to cause problems. In other words, these modes will be excited at all phases, thus resulting in almost complete cancellation.

In the case of pulsed machines, the shortness of the pulse will increase the window, Δf, in which damaging parasitic modes might exist. Equivalently, decreasing the pulse length will increase the proportion of the bunch train that will experience high field amplitudes for the parastic modes before their phase slip with respect to the bunch frequency begins to damp them. Therefore, studies of these modes are important for pulsed machines such as the European Spallation Source (ESS).

Velocity range

In machines that accelerate "heavy" particles such as protons or ions, the accelerating cavities must be designed so as to handle the changing velocity of the beam. Often, linacs are divided into various families of cavities, each of which is optimised for a particular beam velocity. These cavities will have a velocity range over which the efficiency of the acceleration is considered to be acceptable, and so optimisation of the linac design proceeds while taking these boundaries into account.

Just as the efficiency of the accelerating mode (i.e. the coupling of the mode to the beam) is a function of the beam velocity, so is the coupling to the SOMs, and there may be a velocity range where the coupling to a SOM exceeds that of the accelerating mode. In this case, it is likely that this mode will cause significant deterioration of the quality of the beam pulse.

Therefore, the function of the beam's coupling to the SOMs may provide a tighter limit on the acceptable velocity range of the cavity than would otherwise be expected.

CAVITY MODEL

The cavity model used here follows the derivation used in [1], although note that there are several typos in that paper that make the quantitative conclusions unreliable. Much of the calculation may also be extrapolated from [2].

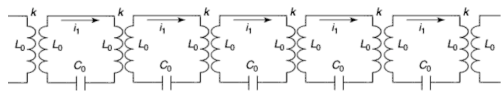

Figure 1: Lumped circuit model of a a five-cell cavity connected at both ends to a beam-pipe.

Figure 1 shows the lumped circuit used to model a five-cell cavity coupled to a beam-pipe.

The coupling, k, between each cell, and between the end cells and the beam pipe, is modeled as a transformer, and the cells are modelled as resonant circuits. The values of k, L_0, & C_0, may be derived from the desired response of the circuit (i.e. resonant frequency, etc.).

* stephen.molloy@esss.se

Copyright © 2012 by the respective authors — cc Creative Commons Attribution 3.0 (CC BY 3.0)

Note that the model shown in figure 1 is appropriate for a cavity composed of identical cells. The standard presentation of this circuit removes the transformers from either end cell, each of which are terminated with a short. The halving of the cell's inductance is compensated by doubling the value of the capacitance in each of these end cells. This results in a string of cells with the correct amplitude variation, however, as noted in [1], the phase relationship between the cells is no longer modelled correctly.

A more correct approach would be to start with the model shown in figure 1, but add an error, δf, to the resonant frequency of the final cells. This error will alter the frequency & phase characteristics of each of the modes in the passband, and can be set so as to achieve the desired field characteristics for the accelerating mode.

BEAM-CAVITY COUPLING

The purpose of this note is to determine the functional relationship between the beam's velocity, $v = \beta c$, and its coupling to the fundamental mode & the nearest SOM. The permissible velocity range of the cavity is then arbitrarily defined as the points on either side of this maximum where the couplings to the two modes has become equal.

Cell amplitudes

In the model presented here, each cell has the same frequency, $\omega_0 = 2\pi f_0 = 1/\sqrt{2L_0C_0}$; i.e. the frequency error usually introduced to tune the field is not present.

For each cell, an equation can be written by summing the currents around each circuit.

$$X_1\left[1-\frac{\omega_0^2}{\omega_q^2}\right]+X_2\frac{k}{2}=0 \quad n=1 \tag{1}$$

$$X_n\left[1-\frac{\omega_0^2}{\omega_q^2}\right]+\left(X_{n-1}+X_{n+1}\right)\frac{k}{2}=0 \quad 2\geq n\geq N-1 \tag{2}$$

$$X_N\left[1-\frac{\omega_0^2}{\omega_q^2}\right]+X_{N-1}\frac{k}{2}=0 \quad n=N \tag{3}$$

These equations describe the current, $X_n \equiv i_k\sqrt{2L_n}$, in the k-th cell of the cavity, oscillating in the q-th mode with an angular frequency, ω_q. They may be rearranged as a matrix equation as follows.

$$LX = AX \tag{4}$$

$$L \equiv \omega_0^{-2}\begin{bmatrix} 1 & \frac{k}{2} & & \dots & 0 \\ \frac{k}{2} & 1 & \frac{k}{2} & & \\ & \ddots & \ddots & \ddots & \vdots \\ \vdots & & \frac{k}{2} & 1 & \frac{k}{2} \\ 0 & \dots & & \frac{k}{2} & 1 \end{bmatrix} \quad (N\times N) \tag{5}$$

$$X \equiv \begin{bmatrix} X_1 \\ \vdots \\ X_N \end{bmatrix} \quad (N\times 1) \tag{6}$$

$$A \equiv \omega_q^{-2} \tag{7}$$

Note that equation 4 has the same form as an eigenvalue equation, and so the vector, X, is an eigenvector of the matrix, L, while the scalar, A, is an eigenvalue.

Therefore, the frequencies & distribution of the cell amplitudes can be found for each of the N modes by finding the eigenvalues/vectors of the $N\times N$ matrix, L.

For a general mode, q, it can be shown that the j-th component of the eigenvector, $X_{q,j}$, is as follows.

$$X_{q,n} = K_q\cdot\sin\left(\pi n\left(1-\frac{q}{N+1}\right)\right) \quad q,n=1,\dots,N \tag{8}$$

Here K_q is an arbitrary scaling constant that may be used to normalize the eigenvector to be of unit length.

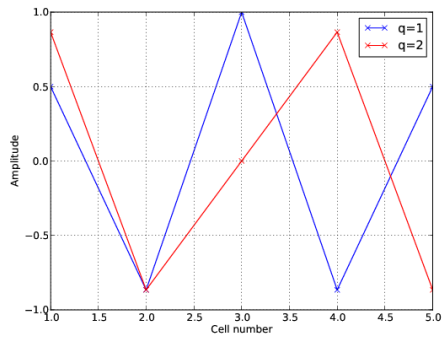

Figure 2: Amplitude of the accelerating mode, $q=1$, & the nearest SOM, $q=2$, in each cell of a five-cell cavity. Note that the scaling constants have been set, $K_1 = K_2 = 1$.

Figure 2 shows the expected eigenvector amplitudes for the accelerating mode, $q=1$, & the nearest SOM, $q=2$, of a five-cell cavity. Note that the accelerating mode is significantly different from the usual flat field-profile due to the fact that each of the cells in this calculation are modelled as having the same resonant frequency. This is due to the fact that the usual shift in frequency of the end-cells has not been taken into account.

In the remainder of this note, it will be assumed that this tuning has occurred, and that the amplitudes of the accelerating mode in each cell are identical. This assumption will not be used for the remaining modes, thereby introducing a small error into the results.

The symmetry of the nearest SOM around the central cell of the cavity can be seen quite clearly, as well as the fact that this mode has an odd distribution; i.e. a negative parity under reflection about the centre cell.

Field profile

In order to simplify subsequent calculations, the field profile of the beam is modelled as a concatenation of a series of half-cycles of sine-waves (one for each cell) whose amplitude is determined by equation 4. Figure 3 shows the

Copyright © 2012 by the respective authors — cc Creative Commons Attribution 3.0 (CC BY 3.0)

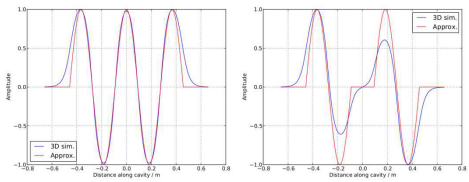

Figure 3: Approx. profile of the accelerating mode in a 5 cell cavity compared with a 3D simulation.

results of this in comparison to data extracted from a 3D simulation of a similar cavity.

These figures show that this approximation is sufficient for the accelerating mode – although remember that these amplitudes are set to be constant, and not gathered from equation 4. The approximation for the SOM is not so good, however it can be argued that the locations where the approximation over-estimates the field are cancelled by those where it is under-estimated.

Integration with beam velocity

This approximation to the field profile can then be integrated with a term that provides the necessary phase variation of the RF oscillating with frequency, $\omega = 2\pi f$.

The following determines the voltage, $V_{q,n}$, experienced by a particle moving with velocity, $v = \beta c$, along the z axis of cell, n. Note that the limits of the integral are defined as the beginning & end of a cell designed for a particle moving with speed, $v_0 = \beta_0 c$.

$$V_{q,n} = X_{q,n} \int_{z_n}^{z_{n+1}} \sin\left(\frac{\omega_q}{\beta_0 c}(z - z_n)\right) \sin\left(\frac{\omega_q}{\beta c} z\right) dz \quad (9)$$

$$z_n \equiv (2n - N)\frac{\beta_0 \lambda}{2} \quad (10)$$

This integral may be solved by integrating by parts twice in order to obtain the following.

$$V_{q,n} = X_{q,n} \frac{\beta^2}{\beta_0^2 - \beta^2} \frac{\beta_0 c}{\omega_q} \cdot \left[\sin\left((2n-N)\frac{\beta_0}{\beta}\frac{\pi}{2}\right) + \sin\left((2n-N-2)\frac{\beta_0}{\beta}\frac{\pi}{2}\right)\right] \quad (11)$$

Note that equation 11 is completely general in that no assumptions have been made about the eigenvector, $X_{q,n}$, or about the number of cells, N.

To obtain the voltage for the entire cavity, this result is then summed over the number of resonant cells.

$$V_q = \sum_{n=1}^{N} V_{q,n} \quad (12)$$

It can be seen that symmetric structure within $X_{q,n}$, in combination with the parity property of the sin function, will lead to cancellations in equation 11, and a substantial reduction in the number of terms within the summation.

RESULTS

The consequences of equations 11 & 12 are examined for the case of a 5-cell cavity (i.e. $N = 5$).

$$V^{(4)} = \frac{\beta^2}{\beta_0^2 - \beta^2} \frac{\beta_0 c}{\omega} \left[\sin\left(\frac{\beta_0}{\beta}\frac{5\pi}{2}\right) - \sin\left(\frac{\beta_0}{\beta}\frac{\pi}{2}\right)\right] \quad (13)$$

$$V^{(5)} = -\frac{2}{\sqrt{5}} \frac{\beta^2}{\beta_0^2 - \beta^2} \frac{\beta_0 c}{\omega} \cos\left(\frac{\beta_0}{\beta}\frac{5\pi}{2}\right) \quad (14)$$

Here the voltages, $V^{(4)}$ & $V^{(5)}$, correspond to the voltages obtained for the nearest SOM ($4\pi/5$ mode, $q = 2$), and the accelerating mode ($5\pi/5$, $q = 1$) respectively.

Note that the integral performed to obtain the result in equation 14 used a cosine variation of the field due to the even parity of the eigenvector for that mode (i.e. the second $\sin()$ in equation 9 was exchanged for a $\cos()$).

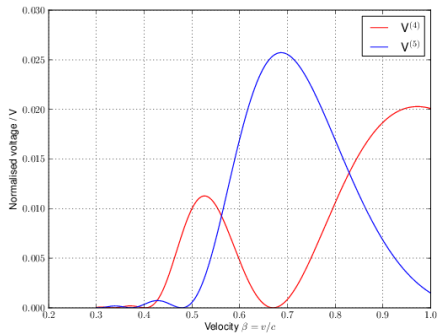

Figure 4: $V^{(4)}$ & $V^{(5)}$ vs β for a 5-cell, $\beta_0 = 0.67$, cavity.

Figure 4 shows the variation of $V^{(4)}$ and $V^{(5)}$ for a 5-cell cavity designed for $\beta_0 = 0.67$.

Note that an estimation of the acceptable velocity range based purely on the coupling to the accelerating mode might conclude with $0.54 \geq \beta \geq 0.92$, which could lead to subsequent problems due to the excessive excitation of the SOM at either end of the range.

DISCUSSION

Many computer codes used to optimise high power linacs neglect to take account of these additional modes, and so it is possible that the optimisation will lead to solutions whereby a SOM is sufficiently excited to disrupt the phase space of the beam [3].

While a general solution to the problem, $V^{(N-1)}(\beta) = V^{(N)}(\beta)$, may be difficult to write down explicitly, it would be possible to add such limits to a computer code.

REFERENCES

[1] Z. Qian, "The effects of tuning and terminating on the operating mode of multi-cell coupled cavity", Proceedings of the Particle Accelerator Conference, 1995

[2] T. Wangler, "RF Linear Accelerators", Wiley-VCH, 2008

[3] R. Ainsworth, "Studies of Parasitic Cavity Modes for Proposed ESS Linac Lattices", TUPB052, this conference

Copyright © 2012 by the respective authors — cc Creative Commons Attribution 3.0 (CC BY 3.0)

SUPERCONDUCTING LOW BETA NIOBIUM RESONATOR FOR HEAVY IONS

Prakash N. Potukuchi, Amit Roy, K.K. Mistri, J. Sacharias and S.S.K. Sonti
Inter-University Accelerator Centre, Aruna Asaf Ali Marg, New Delhi - 110067, India

Abstract

A High Current Injector, as an alternate injector for the superconducting linac, is currently under development at Inter-University Accelerator Centre. To provide some cushion for velocity matching of the beams from HCI, a superconducting low beta module is also being planned for which a new niobium resonator optimized for β=0.05 operating at 97 MHz, has been designed. This resonator has the highest frequency in its class among the superconducting structures designed for such low velocity particles. The resonator has been carefully modeled to optimize its parameters. Even though the frequency of the resonator is high, its physical dimensions are large enough to allow processing of the superconducting surface effectively. The first niobium prototype has been built and bead pull measurements have been done. It will be tested at 4.2 K shortly. This paper briefly presents the resonator design and fabrication; results from bead pull measurement and expected beam energy from the system.

INTRODUCTION

Presently the 15 UD Pelletron accelerator injects heavy ion beams into the superconducting booster linac at Inter-University Accelerator Centre (IUAC) [1]. In order to provide larger beam currents at high charge states than are currently available from the Pelletron accelerator, a high current injector (HCI) is being developed. In figure 1, a block diagram of the HCI system is shown. The high temperature superconducting electron cyclotron resonance (HTS-ECR) ion source [2] will inject heavy ion beams of mass to charge ratio (A/q) =6 at an energy of ~8 keV/u into a room temperature radio frequency quadrupole (RFQ) [3] which will accelerate it to ~180 keV/u. The beam would be further accelerated through a drift tube linac (DTL) section [4] which will have half a dozen tanks, the maximum number that can be accommodated in the new HCI-hall. The expected maximum energy at the end of the DTL section is around 1.8 MeV/u. However, long term stable operation may require restricting its operation to ~1.5 MeV/u only. This corresponds to a velocity β (=v/c)=0.056, which is very close to the lower velocity cut off of the quarter wave resonators employed in the linac [5]. In order to provide some cushion for velocity matching of the beams from HCI into the linac, a superconducting low beta module (LBM) is being planned after the DTL section. The low beta module, however, will be positioned in such a way that it can accelerate beams from HCI as well as the Pelletron accelerator. A new superconducting niobium quarter wave resonator optimized for β_0=0.05 operating at 97 MHz has been designed for this module.

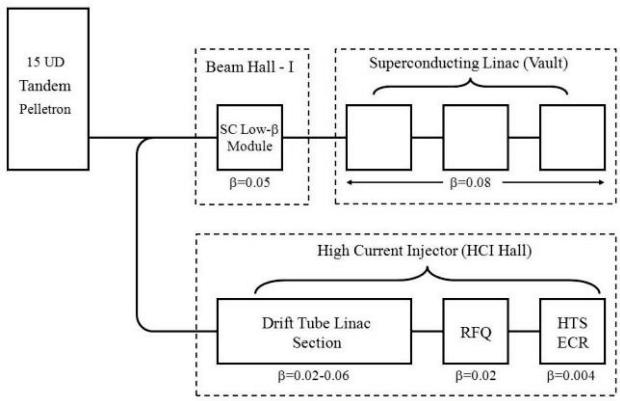

Figure 1: Block diagram of the HCI system. The dashed boxes indicate the location of the various components.

LOW β RESONATOR

Design

TEM class superconducting niobium resonators are used in linacs for accelerating heavy ions. Several variants of this class of structure have been designed and developed around the world [6]. Among them, the two gap quarter wave co-axial line resonator (QWR) is characterized by its excellent mechanical stability and broad velocity acceptance. In addition, QWRs are simpler to fabricate compared to other structures, although more number of resonators are required to reach the final beam energy. Over the past two decades many techniques have been developed to effectively address the extrinsic effects that limit the achievable accelerating gradient in niobium resonators and these have helped in pushing the gradients up [7]. Besides, it is well known that quarter wave resonators achieve higher gradients as compared to, say half wave structures [8]. Overall the QWR structure therefore offered a very good choice for the low beta resonator design.

The LBM will be located in beam hall-I (figure 1) where the ceiling height is slightly less than that in the linac vault. The overall height of the resonator was therefore an important design parameter. In order to restrict it we decided to keep the frequency high and chose 97 MHz, which is also the frequency of the quarter wave resonators used in the linac. The electromagnetic parameters of the low beta resonator were carefully optimized using Microwave Studio code [9]. The main goal in the optimization was to reduce the peak magnetic and electric fields in the resonator while maintaining high values for the shunt impedance and geometric factor, and a small value of stored energy. To achieve these, the drift tube length and accelerating gaps were chosen to obtain

Copyright © 2012 by the respective authors — cc Creative Commons Attribution 3.0 (CC BY 3.0)

maximum energy gain. The central coaxial line was tapered and the tapering was gradually increased until the magnetic field reduced to a low value. Tapering the central conductor has the additional advantage of providing better mechanical stability while reducing resonance electron multipacting. In the second step of the optimization the diameter of the outer housing was gradually increased to further reduce the peak magnetic field while increasing the shunt impedance and geometric factor. However, beyond a certain diameter of the outer housing, the real estate gradient begins to suffer.

For frequency tuning of the resonator the existing slow tuner bellows design, which has been well tested and suitably modified for reliable performance [1], will be used. In table 1, the various parameters of the low beta resonator are shown. The resonator is jacketed with an outer stainless steel (SS) vessel which will hold the liquid helium needed for cooling it. This design was originally developed for the resonators employed in the IUAC-linac [5]. Details of the low beta resonator design can be found in reference 10. In figure 2, a cut away 3-D view of the resonator is shown.

Table 1: Design Parameters of the Low Beta Resonator

Resonance frequency f_0	97 MHz
Synchronous velocity β_0	0.051
Effective length L_{eff}	10.4 cm
Stored energy U_0 @ 1 MV/m	26 mJ
E_{Peak} @ 1 MV/m gradient	3.4 MV/m
B_{Peak} @ 1 MV/m gradient	64.2 G
Geometric Shunt impedance R_{sh}/Q	650 Ω
Geometry factor QR_s	16.1 Ω
Frequency tunability Δf_{ST}	100 kHz

Figure 2: Cut away 3D view of the low beta quarter wave resonator. The overall height is about 85 cm.

Niobium Prototype

After validating the electromagnetic parameters of the low beta resonator design on a room temperature copper model, the niobium prototype resonator was built. Except for the beam ports and the niobium flange that joins the tapered co-axial line to the outer housing; all other components are rolled or die-formed from sheet material. The central tapered co-axial tube was die-formed in a single length but in two halves and electron beam welded along the seam. The outer SS vessel was fabricated and then cut into two halves and brought around the resonator like a clamshell assembly. Where the niobium joined SS, flanges made of explosively bonded niobium-SS were used to provide the transition. In figure 3, the prototype niobium resonator is shown.

Bead pull measurements were performed on the niobium prototype to measure the various parameters of the resonator. The frequency tunability was measured using a mock slow tuner. In figure 4, the frequency perturbation data and transit time factor are shown. In table 2, the various parameters have been summarized.

(a) (b)

Figure 3: (a) Niobium outer housing (left) and central co-axial conductor (right), (b) low beta resonator complete with the outer SS vessel.

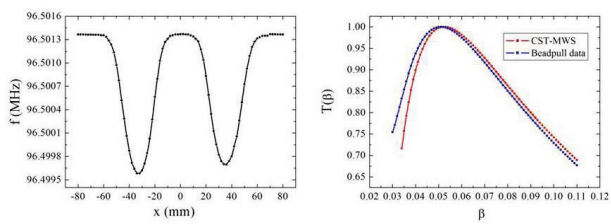

Figure 4: Bead pull measurement (left) and transit time factor (right) of the niobium prototype. The blue curve is from the bead pull measurement and the red curve is from Microwave Studio calculations.

Table 2: Parameters of the Prototype Resonator Obtained from Bead Pull Measurement.

Parameter	Measured value
f_0	96.5 MHz
β_0	0.051
U_0	26.4 mJ
R_{sh}/Q	620 Ω
Δf_{ST}	90 kHz

Copyright © 2012 by the respective authors — cc Creative Commons Attribution 3.0 (CC BY 3.0)

LOW BETA MODULE

Numbers of Resonators

In figure 5, the final ion velocity β_f as a function of the initial velocity β_i for different number of low beta resonators in the cryomodule, all operating at the modest gradient of 5 MV/m, is shown. For finalizing the number of low beta resonators needed, we have assumed the initial velocity corresponding to an energy of ~1 MeV/u (β_i=0.046) keeping both the DTL section as well as the Pelletron accelerator in mind. At β_i=0.046 the final velocity with six resonators is ~0.056 which is very close to the lower velocity cut off of the QWRs in the linac. With eight resonators, however, the final velocity is ~0.059, which is better. At 6 MV/m gradient (not shown), this value is ~0.062. Keeping these in mind it has been decided to have eight resonators in the low beta module.

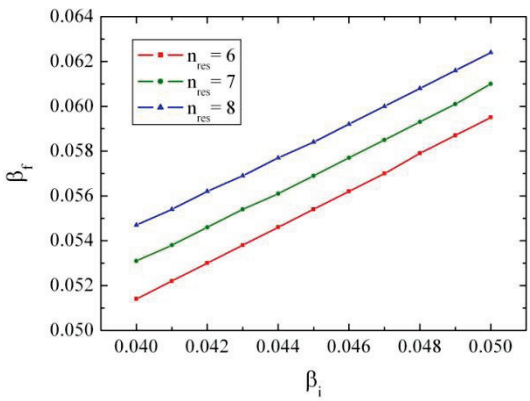

Figure 5: Final velocity β_f as a function of initial velocity β_i for different number of low beta resonators all operating at 5 MV/m accelerating gradient.

Energy Gain

Energy gain for beams from the two combinations, namely (i) HCI and superconducting linac, and (ii) Pelletron accelerator and linac, have been done. In figure 6, the energy gain for the HCI-Linac combination with and without the LBM, is shown.

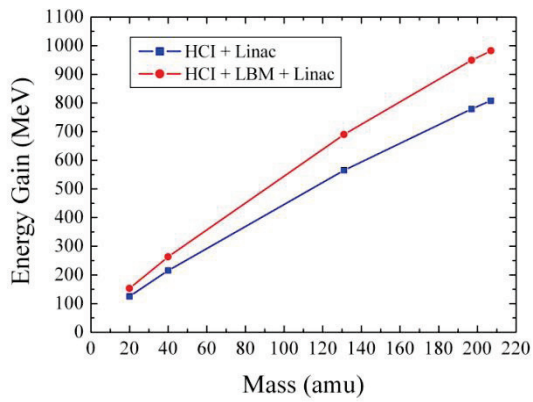

Figure 6: Energy gain as a function of ion mass for the HCI-Linac combination with and without the LBM.

For the HCI-LBM-Linac combination the beam energy out of the DTL section is taken to be 1.5 MeV/u. A foil stripper has been assumed after the DTL section for increasing the charge state of the ions. All resonators in the LBM were assumed to operate at 5 MV/m. Based on the operational experience with the superconducting linac, the QWRs in the linac were assumed to operate at 3.5 MV/m accelerating gradient.

In figure 7, the energy gain from the Pelletron accelerator-Linac combination with and without the LBM, is shown. Gas stripper in the terminal and foil stripper in the high energy dead section in the Pelletron (operating at 12.5 MV terminal potential) have been assumed. The resonator gradients in the LBM and linac are assumed to be 5 MV/m and 3.5 MV/m respectively.

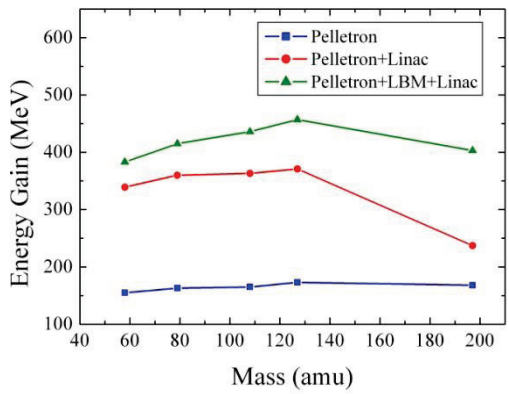

Figure 7: Energy gain as a function of ion mass for the Pelletron-Linac combination with and without LBM.

CONCLUSION

A new superconducting niobium quarter wave resonator for the low beta module has been designed and the prototype has been built. It will be tested at 4.2 K shortly.

REFERENCES

[1] S. Ghosh et al., Phys. Rev. ST AB **12**, 040101 (2009).
[2] D. Kanjilal et al., Rev. Sci. Intr., **77** (2006) 03A317.
[3] Sugam Kumar et al., Proc. of Indian Particle Accel. Conf., InPAC2011, Feb. 15-18, 2011, IUAC, New Delhi, India, www.iuac.res.in/InPAC2011/
[4] B.P. Ajith Kumar et al., Proc. of Indian Particle Accel. Conf., InPAC2009, Feb. 10-13, 2009, RRCAT, Indore, India, www.inpac.rrcat.gov.in
[5] P.N. Prakash et al., Proc. of 1997 SRF Workshop, Oct. 6-10, 1997, Abano Terme (Padova), Italy, p633
[6] M.P. Kelly, Proc. of 2006 Linac Conf., LINAC06, August 20-25, 2006, Knoxville, TN, USA, p2.3
[7] Hasan Padamsee, Jens Knobloch and Tom Hays, RF Superconductivity for Accelerators, Wiley-VCH Verlag GmbH & Co. KGaA, Weinheim, 2nd Ed. 2008.
[8] A. Facco, TTC Meeting, April 2010, Fermi Lab, USA, http://conferences.fnal.gov/ttc10/
[9] Computer Simulation Technology: www.cst.com
[10] Prakash N. Potukuchi and Amit Roy, PRAMANA - Journal of Physics, Vol. 78, No. 4, April 2012, p565.

Copyright © 2012 by the respective authors — cc Creative Commons Attribution 3.0 (CC BY 3.0)

STUDIES OF PARASITIC CAVITY MODES FOR PROPOSED ESS LINAC LATTICES

R. Ainsworth*, Royal Holloway University of London, UK
S. Molloy, European Spallation Source AB, Lund, Sweden

Abstract

The European Spallation Source (ESS) planned for construction in Lund, Sweden, will be the worlds most intense source of pulsed neutrons. The neutrons will be generated by the collision of a 2.5 GeV proton beam with a heavy-metal target. The superconducting section of the proton linac is split into three different types of cavities, and a question for the lattice designers is at which points in the beamline these splits should occur. This note studies various proposed designs for the ESS lattice from the point of view of the effect on the beam dynamics of the parasitic cavity modes lying close in frequency to the fundamental accelerating mode. Each linac design is characterised by the initial kinetic energy of the beam, as well as by the velocity of the beam at each of the points at which the cavity style changes. The scale of the phase-space disruption of the proton pulse is discussed, and some general conclusions for lattice designers are stated.

INTRODUCTION

The European Spallation Source is a facilty, currently in its design phase [1], for the generation of intense pulses of neutrons for studies in applied science. The neutrons are generated through the spallation process when a 5 MW (average) proton pulse is made to impact a heavy metal target.

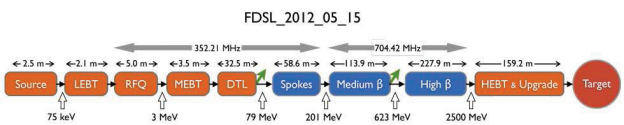

Figure 1: Block diagram of the ESS linac.

	Value	Unit
Final kinetic energy	2.5	GeV
Macropulse current	50	mA
Macropulse repetition rate	14	Hz
Bunch frequency	352.21	MHz

Table 1: Main ESS linac parameters.

A cartoon of the ESS linac is shown in Figure 1, and the main parameters of the proton beam are given in Table 1.

This note concerns the beam dynamics within the superconducting sections of the machine:

Spokes: Two–spoke cavities operating at 352.21 MHz. This section accelerates the beam from the exit of the DTL at 79 MeV to 201 MeV.

Medium β: Five–cell elliptical cavities operating at 704.42 MHz. The geometrical beta of this section is still under discussion, but is likely to be set at a value close to, $\beta_g = 0.65$. In this section, the beam is accelerated from 201 MeV to 623 MeV.

High β: Five–cell elliptical cavities operating at 704.42 MHz. As with the previous section, the geometrical beta is still under discussion, but the likely value is close to, $\beta_g = 0.92$. This section accelerates the beam to its final energy of 2.5 GeV

Given the high intensity of the beam, one major concern is that strong resonances will be excited in the superconducting cavities that will then act to disrupt subsequent bunches. In particular parasitic modes that lie close in frequency to that of the accelerating mode. They are of concern due to there small frequency spread and high R/Q relative to the accelerating mode. If they are found to be a problem, the geometric beta of the cavity may need to be altered or the velocity partitioning between the cavity families may need to be shifted.

LINACS

For the studies into Same Order Modes (SOMs), that is, modes that are part of the same passband as the fundamental accelerating mode, four linacs are investigated as shown in Table 2 where cavities per family denotes the number of cavities in the spoke, medium β and high β sections.

Linacs	Cavities per family	Energy In [MeV]
HS_2011_11_23	36-64-12	50
FD_SL_2012_04_13	32-60-120	79
FD_SSCL_2012_04_16	32-52-128	80
FD_SL_2012_05_15	28- 60-120	79

Table 2: Linacs investigated for SOM simulations.

* rob.ainsworth.2009@live.rhul.ac.uk

Copyright © 2012 by the respective authors — cc Creative Commons Attribution 3.0 (CC BY 3.0)

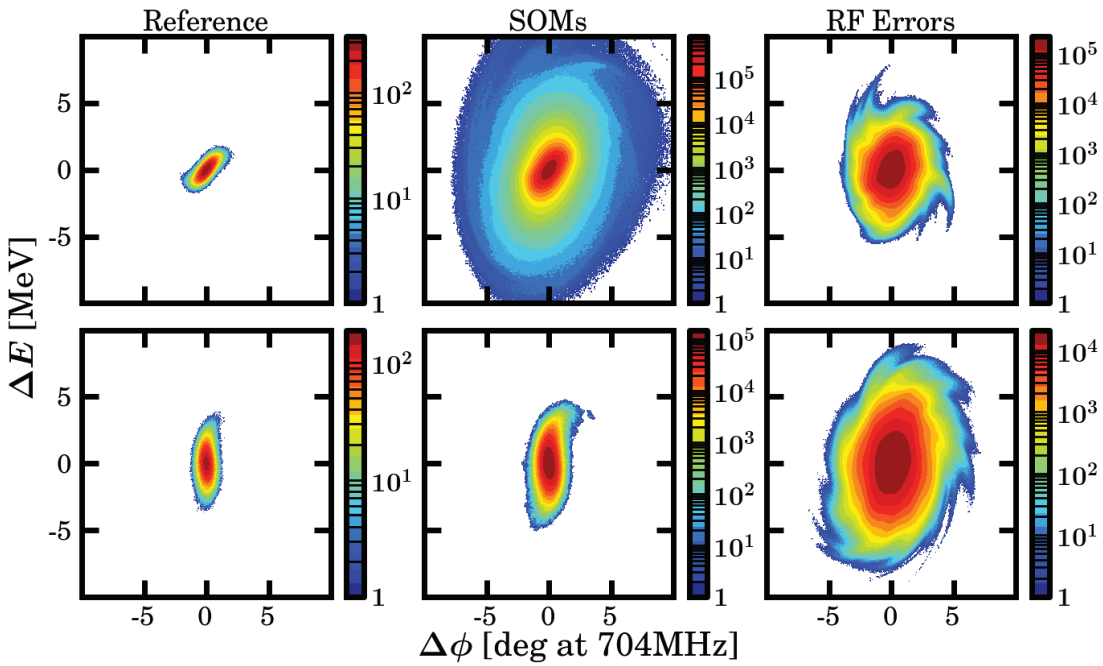

Figure 3: The Pulse phase space distribution at the end of the linac due to different effects.

SIMULATIONS

To explore the effect of these modes, a pulse train of one million point-like bunches was tracked through the superconducting section of the linac. Each bunch adds to the induced fields, these act on subsequent bunches through a kick-drift-kick model [2], and the resulting bunch energy and time errors are calculated.

For each cavity family, the SOM with the highest R/Q is used for simulations. For the spokes, the second mode is used and for the ellipticals, the $4\pi/5$ mode is used. The R/Q that will be seen in each cavity for the whole HS_2011-11-23 linac is shown in Figure 2. Of particular concern are the regions at the beginning of the spoke and medium beta sections where the R/Q of the SOMs are larger than that of the accelerating mode.

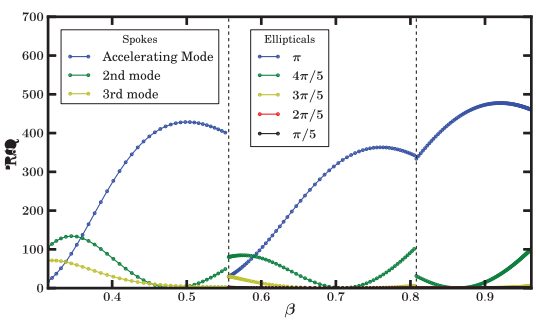

Figure 2: The R/Q for each cavity as a function of particles velocity.

The simulation is performed 1000 times using a different seed for the random number generator to set the frequencies of the SOMs. All other parameters are left constant. In addition, a charge scatter of 1% was also used [3].

Jitter from the RF system will also lead to energy and phase errors. Uniformly distributed errors of $1\%, 1^\circ$ are used in each linac with the exception of the HS_2011_11_23 linac which uses errors of $0.5\%, 0.5^\circ$. Each linac is simulated 1000 times with a different set of uniformly distributed random errors each time. The growth due to RF errors will be used as the acceptable limit in order to gauge the effect of the SOMs.

FREQUENCY SPREAD

The frequency spread of the SOMs will have a large effect on their influence. A smaller frequency spread will result in a larger coherence resulting in a larger influence on the beam. Therefore, it is important to use an reasonable value. In the late 1980's, Ron Sundelin performed a series of studies measuring the distribution of resonant frequencies of SCRF cavities [4]. The frequency spread based on empirical results is given by

$$\sigma = 1.09 \times 10^{-3} \cdot |f_n - f_0|. \quad (1)$$

This means that for the elliptical cavities where the $4\pi/5$ mode is only ~ 1 MHz away from the accelerating mode, the frequency spread will be ~ 1 kHz.

Copyright © 2012 by the respective authors — cc Creative Commons Attribution 3.0 (CC BY 3.0)

GROWTH

To quantify the growth, the area, ϵ, of the phase space created all the bunches are compared where the area is given by

$$\epsilon = \pi\sqrt{\langle\Delta E^2\rangle\langle\Delta\phi^2\rangle - \langle\Delta E\Delta\phi\rangle^2}, \qquad (2)$$

where ΔE and $\Delta\phi$ are the energy and phase error of the bunch with respect to the synchronous bunch. The growth ϵ_{RF}/ϵ is used to determine the effects of the RF and set the tolerable growth due to SOMs.

RESULTS

Figure 3 shows the effect of these modes on the pulse phase space of two linacs with different velocity partitioning over the three cavity families. The first column shows the phase space distribution with no external effects such as SOMs or RF errors acting providing a reference distribution to compare to. The middle column shows the case where a SOM is present in each cavity. The last column shows the case when RF errors are applied to the linac in form of amplitude and phase errors. The growth due RF errors is used as an acceptable limit It can be seen that the linac of the top row, which represents an earlier ESS layout, is susceptible to these modes. The bottom row, corresponding to the May 2012 linac layout, shows significantly better performance.

Table 3 shows the growth in due to SOMs and RF errors for each of the linacs simulated. It can be seen that all linacs due except the HS_2011_11_23 linac show negligible growth due to SOMs. It is thought that increasing the Energy input to the spoke section from 50 MeV to 79 MeV was the main reason the effect of SOMs was less in the other linacs. This is because at 79 MeV, the R/Q of the SOMs no longer crossed the accelerating mode in the spoke section.

SOMs	Average Growth	Max Growth
HS_2011_11_23	3.1	56.6
FD_SL_2012_04_13	1.02	1.2
FD_SSCL_2012_04_16	1.01	1.5
FD_SL_2012_05_15	1.02	1.47
RF Errors	Average Growth	Growth
HS_2011_11_23	3.3	13
FD_SL_2012_04_13	4.24	16.2
FD_SSCL_2012_04_16	3.9	14.5
FD_SL_2012_05_15	3.7	16.6

Table 3: Growth in each linac due to SOMs and RF errors.

CURRENT AND DAMPING SCAN

The final investigation was to vary the current, Ib and Q_{ex} for the simulations involving the May Baseline linac FD_SL_2012_05_15. The current was varied from the nominal current of 50 mA to a relatively high current of 150 mA in order to determine a threshold if there is one and how close the nominal current is to the threshold. The Q_{ex} is also varied from 10^4 to 10^9, previous simulations used a relatively high value of 10^8 as the actual value will not be known however it is expected to be similar to that of the fundamental mode which has a $Q_{ex} \sim 10^6$. The results are shown in Figure 4 where the dashed line represents the growth due to RF errors. At the nominal current, negligible growth is observed and it is not until 90 mA where the growth starts to exceed that of RF errors. Losses are also seen at this current for $Q_{ex} > 10^7$.

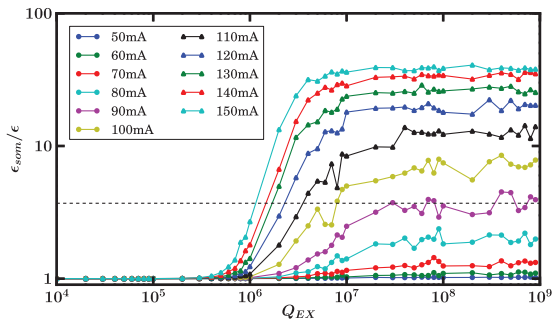

Figure 4: The average longitudinal phase space increase for 100 linacs at varying currents and Qex of the SOMs.

SUMMARY

The influence of parasitic modes in the ESS linac have been investigated with emphasis on modes that lie in the same passband as the fundamental mode. It has been shown that although it is possible to design a linac susceptible to modes in the fundamental passband, the current baseline is not affected at the nominal current and should operate up to currents on 100 mA if upgrades are desired in the future. Therefore, no change is needed to the velocity partitioning of the linac nor the geometric beta of the cavities.

ACKNOWLEDGEMENTS

The authors would like to thank Marcel Schuh for his help in benchmarking the code used in the above simulations.

REFERENCES

[1] H. Danared, " Design of the ESS Accelerator", THPPP071, IPAC12.

[2] M. Schuh et al., Phys. Rev. ST Accel. Beams 14 (2011) 051001.

[3] J. Tuckmantel et al., Phys. Rev. ST Accel. Beams 13 (2011) 021001.

[4] S. Molloy, Note, ESS Doc 92-V2.

Copyright © 2012 by the respective authors — cc Creative Commons Attribution 3.0 (CC BY 3.0)

MAIN COUPLER DESIGN FOR PROJECT X*

S. Kazakov, O. Pronitchev, S. Cheban, M. Kramp, V. Poloubotko,
V. P. Yakovlev, T. N. Khabiboulline, Y. Orlov, FNAL, Batavia, IL 60510, USA
M. S. Champion, ORNL, Oak Ridge, Tennessee, USA

Abstract

325MHz and 650MHz multi-kilowatt CW main couplers for superconducting linac of Project X and their design parameters are presented. Experimentally measured effectiveness of antenna air cooling is introduced.

INTRODUCTION

A multi-megawatt proton/H^- source, Projec X, is under development at Fermi National Accelerator Laboratory [1]. Main element of it is 3 GeV superconducting proton linac which includes 5 families of superconducting cavities of three frequencies: 162.5, 325 and 650 MHz. 162.5 MHz cavities and main couplers are under developing in Argonne National Laboratory. Scope of this paper is development of power couplers for 325 and 650 MHz at FNAL. Superconducting linac of Poject X is supposed to accelerate 1 mA average proton beam and it is considered a possibility to increase beam current up to 5mA in the future. This upgraded version of accelerator will require two types of couplers, which reliably can operate at CW power level ~ 25kW at 325MHz and ~100 kW at 650MHz respectevly. In this paper we are describing current design of these couplers.

COUPLERS DESIGN AND PARAMETERS

Recent Changes in the Design

There were several earlier publication on subject of Project X couplers [2,3]. Since the last publication, several changes were made in the design, which resulted in a change of some coupler parameters.

In the previous design there was a large bellows, which is housed outside the cryomodule. The purpose of the bellows was compensation an accelerating cavity shift and thermal shrink/expansion of coupler parts during cool down/warming up. Due to the bellows location outside of cryomodule, a sufficiently large force (~ 200kg) due to the atmospheric pressure was applied to the accelerating cavity. It had to be compensated by special springs. In this design a coupler had to be rigidly fixed to cryomodule body after completion of the cooling dawn/warming up and had to be unfixed during these procedures. It was deemed inconvenient and potential reason of accidents.

A large bellows was replaced by four bellows. Two of them are located on the outer conductor of coaxial coupler, two - in the internal conductor. Bellows are located inside the cryomodule and coupler does not require to be fixing/unfixing during cooling down and warming up. The atmospheric pressure difference driven force is reduced to 40 kg. The bellows are still located on the non-vacuum side of the coupler and requirements are not as high as if they were located in vacuum close to an accelerating cavity. Current set of bellows can accommodate ±3mm displacement in any direction.

The second important change: a copper plating was removed from coaxial outer conductor of vacuum side of 350 MHz coupler. It decreases static and increases dynamic cryo-loadings, but improves the reliability of the coupler. Previous experience shows that the copper coating often is a source of many problems. Dynamic cryo-loading still is in an acceptable range.

The third change: the temperatures of thermal interceptors were increased. Now temperature of interseptor nearest to 2 K cavity flange is considered as 15 K instead of 5 K and temperature of second interceptor is considered to be 125 K instead of 80 K. We think these values are more realistic, though perhaps are too conservative. It increases calculated static cryo-loading of the coupler.

The fourth change: in order to decrease a static cryo-loading, the thickness of stainless outer conductor of vacuum part of couplers was changed from 0.8mm to 0.4mm

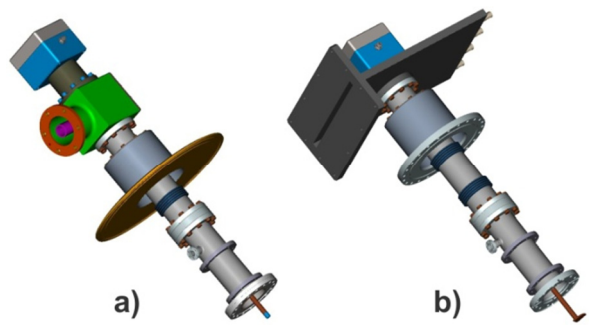

Figure 1: General view of a) 325MHz and b) 650 MHz couplers

Current Design and Electrical Parameters

General views of 325 MHz and 650 MHz couplers are presented in Figure1. Couplers have similar structures and have many common parts and technologies. Cut view of 325 MHz coupler with details is shown in Figure 2. 650 MHz coupler has the same internal structure but waveguide input port instead of coaxial one. We would like to remind the design approach: to keep a geometry of vacuum part of couplers, which connected to superconducting cavity, as simple as possible. We think it should increase reliability. All complicated elements like a bellows and matching elements are moved to the air part of devices. Main features of the design: single RF

*Work supported by DOE

Copyright © 2012 by the respective authors — cc Creative Commons Attribution 3.0 (CC BY 3.0)

window at room temperature, air cooled antenna, ability to apply HV bias to suppress multipactor, fixed coupling. Table 1 shows some electrical parameters of couplers.

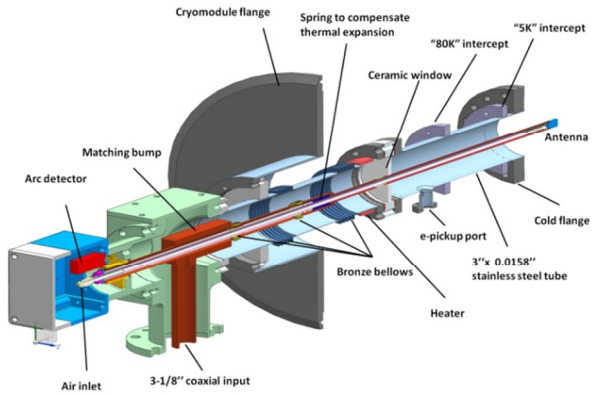

Figure 2: Cut view of 325 MHz coupler.

Table 1: Design Parameters of Couplers

Parameter	325MHz coupler	650MHz coupler
CW power	30 kW	120 kW
Maximum pulse power	0.4 MW	3 MW
Multipactor threshold	25 kW, TW	1 MW, TW
Passband	50 MHz	30 MHz
Input	3-1/8" coaxial	11.5" x 0.524" WG
Output	3" x 0.5" coaxial	3" x 0.5" coaxial
Output impedance	105 Ohm	105 Ohm

Thermal Parameters

Figure 3 shows a 2D model for calculation of thermal properties. Scheme is the same for both 325 and 650 MHz couplers.

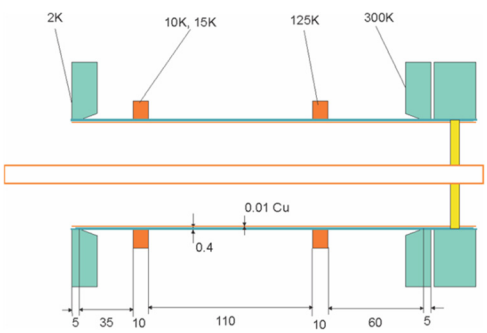

Figure 3: Scheme of vacuum part of coupler which was used for calculation of thermal properties.

For 325 MHz coupler two cases were considered: with 10 μm copper coating and without. 650 MHz coupler has to be used with copper coating only because of high dynamic cryo-loading at 120 kW power level. Results of thermal parameters calculations are presented in the tables 2 and 3.

Table 2: Thermal Properties of 325 MHz Coupler, Columns 2, 3 - no Copper, Columns 4, 5 – 10 μm Copper

Cryo-loading	P = 0 kW	P = 30 kW	P = 0 kW	P = 30 kW
2 K	0.06 W	0.50 W	0.24 W	0.28 W
5 K	0.58 W	2.82 W	1.76 W	1.91W
80 K	2.02 W	5.36 W	4.40 W	4.63 W

Table 3: Thermal Properties of 650 MHz coupler

Cryo-loading	P = 0 kW	P = 120 kW
2 K	0.24 W	0.45 W
5 K	1.76 W	2.65 W
80 K	4.40 W	6.03 W

AIR COOLING OF ANTENNA

High average RF power coming through coupler requires forced cooling of antenna. Air was chosen as cooling media because of simplicity, easy availability and higher reliability. 325 MHz coupler is supposed to be used at 30 kW CW maximum power level and 650 MHz coupler at 120 kW CW level. Power losses in the copper antenna is 10W and 60W respectively. It is obvious that antenna will be heated to high temperature in vacuum without forced cooling. It will cause high thermal radiation from antenna tip into superconducting cavity. Therefore forced cooling is necessary.

Recently we made an experiment to measure a performance of air cooling of the antenna. Scheme of experiment is presented in Figure 4.

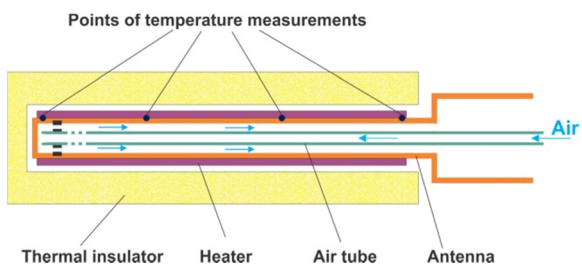

Figure 4: Scheme of measurements of antenna air cooling effectiveness.

Measured parameters were a power of heater, temperatures at four points along the antenna, air flow

Copyright © 2012 by the respective authors — cc Creative Commons Attribution 3.0 (CC BY 3.0)

rate and pressure at the entrance of the air pipe. Knowing of the temperature distribution along the antenna without air cooling we could calculate a power flow through the antenna end (right at the drawing). This allow us to estimate an efficiency of thermal insulator and to find a power flow coming through it insulator as function of average antenna temperature.

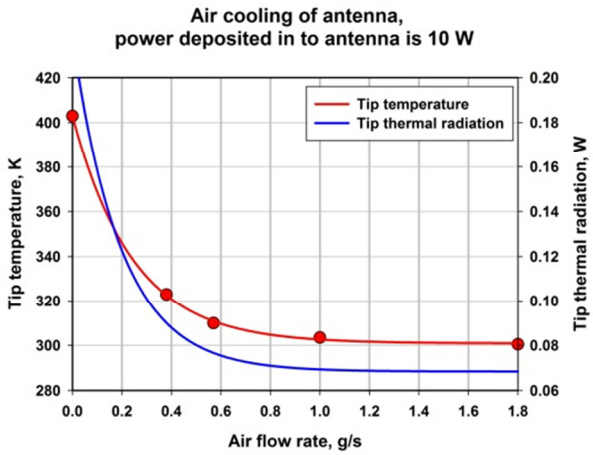

Figure 5: Antenna air cooling, case of 10 W deposition into antenna (325MHz, 30kW, TW). ~0.3 g/s flow rate provides acceptable temperature of antenna tip. Thermal radiation at this point ~0.1W

Graph at Figure 5 shows dependences of antenna temperature and thermal radiation of the antenna tip on the air flow rate for 10 W power deposition to the antenna. Pressure of this range of flow rate was so small that we could not measure it with our pressure gauge. We can see that flow rate 0.3g/s is enough to cool the antenna if we accept 0.1 W of thermal radiation as a criterion. It corresponds to 330 K temperature of the antenna tip. Coefficient of emissivity was taken as 0.05 (polished copper).

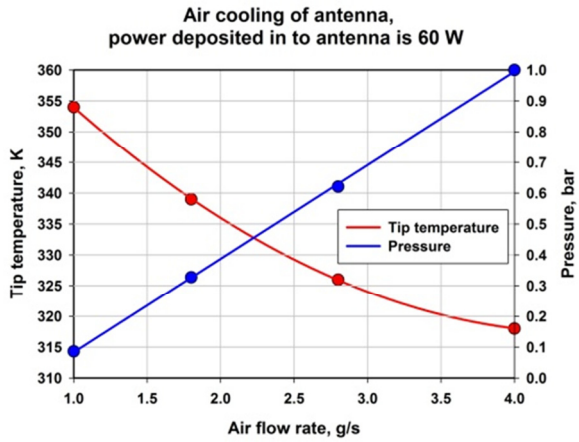

Figure 6: Antenna air cooling, case of 60 W deposition into antenna (650MHz, 120kW, TW). ~2.5g/s flow rate and ~0.5 bar pressure provide acceptable temperature of antenna tip. Thermal radiation at this point ~0.1W

Graph at Figure 6 presents results of measurements for 60 W of deposited power. From this figure we can see that 2.5 g/s flow rate and 0.5 bar pressure is enough for 120 kW, 650MHz operation.

REFERENCES

[1] S. Holmes, “Project X: News, Strategy, Meeting Goals”, Project X Document 1026-v2, April 2012.

[2] S. Kazakov et al., “High Power Couplers for Project X”, PAC' 11, New York, March 2011, TUP072, p. 952

[3] S. Kazakov et al., “High Power Couplers for Project X Linac”, SRF’11, Chicago, March 2011, TUPO006.

Copyright © 2012 by the respective authors — cc Creative Commons Attribution 3.0 (CC BY 3.0)

COHERENT EFFECTS OF HIGH CURRENT BEAM IN PROJECT-X LINAC

A. Sukhanov*, A. Lunin, V. Yakovlev, I. Gonin, T. Khabiboulline, A. Saini, N. Solyak, and A. Vostrikov, Fermilab†, Batavia, IL 60510, USA

Abstract

Resonance excitation of longitudinal high order modes in superconducting RF structures of Project-X continuous wave linac is studied. We analyze regimes of operation of the linac with high beam current, which can be used to provide an intense muon source for the future Neutrino Factory or Muon Collider, and also important for the Accelerator-Driven Subcritical systems. We calculate power loss and associated heat load to the cryogenic system. Longitudinal emittance growth is estimated. We consider an alternative design of the elliptical cavity for the high energy part of the linac, which is more suitable for high current operation.

INTRODUCTION

A multi-megawatt proton source, Project-X (PX) is now under development at Fermilab [1]. PX will provide high quality muon, kaon and neutrino beam, unavailable at existing facilities, and support physics program at the intensity frontier. Eventually, PX may become a driver for a future Neutrino Factory and/or Muon Collider at Fermilab.

Technology, which is being developed for Project-X, may be directly applied to Accelerator-Driven Subcritical systems (ADS) for energy generation and transmutation of nuclear waste [2]. ADS applications require continuous wave (CW) multi-MW proton beam with high average current and high availability. Thus, exploration of the capability of PX technology to deliver beam of $\geq$ 10 mA is important.

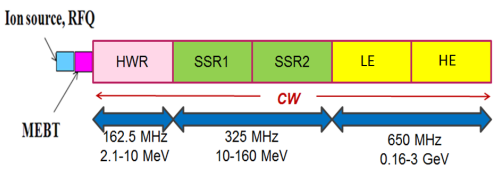

Figure 1: Project-X linac layout.

A key component of Project-X is the CW superconducting RF linear accelerator. It accelerates bunches of H^- ions from 2.1 MeV to 3 GeV. Layout of the linac is shown in Fig. 1. The high energy (HE) section of the linac uses 650 MHz 5-cell elliptical cavities. Coherent excitation of monopole high order modes (HOMs) in these cavities may affect stable operation of the linac due to rise of cryogenic losses and deterioration of beam quality. Our study [3] shows, that it is not a problem for the present PX parameters, CW regime, and 1 mA average beam current. However, HE cavities have a potential problem, when monopole HOMs of the 5^{th} passband may become trapped in the internal cells of a cavity [4]. This, together with the fact that cryogenic losses increase as square of an average beam current, $P_{loss} \sim I^2_{beam}$, may lead to losses up to hundred Watt for 10 mA beam.

In this paper we calculate cryogenic heat load and estimate growth of the longitudinal beam emittance due to coherent excitation of monopole HOMs during operation of PX CW linac with an average beam current up to 10 mA. We compare results of these calculations for the present and alternative [4] designs of the HE elliptical cavities.

COHERENT HOM EXCITATION

A bunched continuous beam passing through a superconducting cavity may coherently excite one of the cavity HOM with a high quality factor, Q. The bunch sequence frequency in PX linac is 162.5 MHz. A broad-band chopper provides the beam structure needed for experiments. A typical bunch timing structure required for muon, kaon and nuclear experiments running in parallel at 3 GeV is shown in Fig. 2. Average beam current in this mode is 1 mA. Fig. 3 shows the spectrum for the idealized 3 GeV beam structure, assuming very short bunches of equal charge and in the absence of timing jitter.

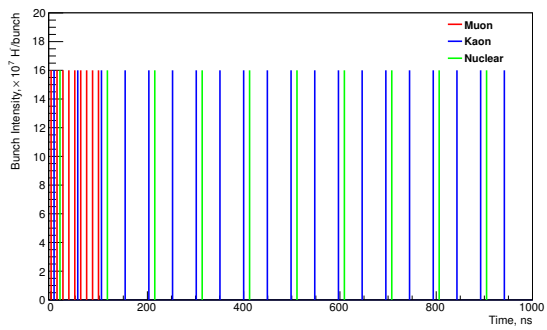

Figure 2: Beam structure for 3 GeV program.

Spectrum and (R/Q) values of PX HE structure are shown in Fig. 4. Amplitude of an excited monopole HOM depends on the amplitude of the nearest beam spectrum line, $\tilde{I}$, and detuning δf, the distance between the HOM frequency f and the beam spectrum line frequency, and

* ais@fnal.gov

† Operated by Fermi Research Alliance, LLC under Contract No. DE-AC02-07CH11359 with the United States Department of Energy.

Copyright © 2012 by the respective authors — cc Creative Commons Attribution 3.0 (CC BY 3.0)

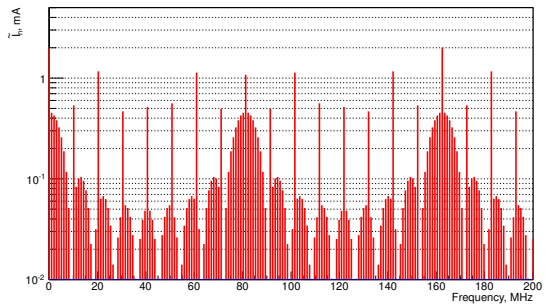

Figure 3: Beam spectrum of 3 GeV program.

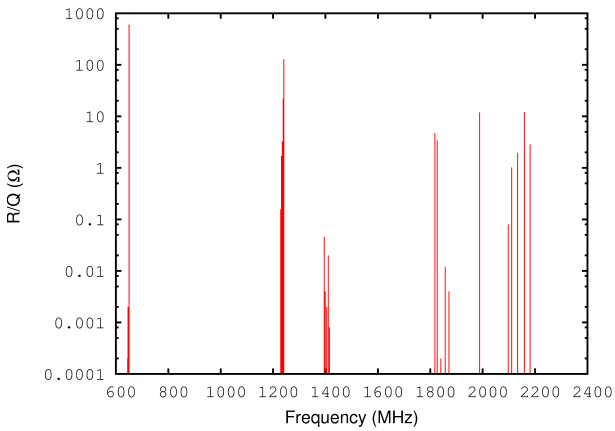

Figure 4: (R/Q) of the monopole HOMs in PX HE section.

for a high Q resonance[1] can be estimated as $U_{HOM} \approx \frac{\tilde{I}(R/Q)}{4\sqrt{2}\delta f/f}$. If the HOM mode is exactly at the resonance, $U_{HOM} = \frac{1}{2}\tilde{I}(R/Q)Q_L$, where Q_L the loaded quality factor of the mode.[2] The cryogenic losses depend on square of HOM amplitude: $P_{loss} \approx \frac{U^2_{HOM}}{(R/Q)Q_0}$. Requiring that P_{loss} is much smaller than the sum of the static heat load and the cryogenic losses due to accelerating mode (∼20 W), and assuming that the intrinsic quality factor is $Q_0 = 5 \times 10^9$, we estimate that the maximum allowable value of the monopole HOM loaded quality factor is $Q_L \ll 6 \times 10^7$.

Similarly, requiring, that excitation of a monopole mode does not increase longitudinal emittance, $\varepsilon_z \gg U_{HOM}\sigma_z/c$, where σ_z is a bunch length, and c is speed of light, we obtain estimation of safe frequency detuning: $\delta f \gg f\frac{\tilde{I}(R/Q)\sigma_z}{4\sqrt{2}\varepsilon_z c}$. We have the worst case at the start of the HE section, where the bunch length is at the maximum ($\sigma_z/c = 7.7 \times 10^{-3}$ ns), the second pass-band monopole HOM (1241 MHz and highest $R/Q = 130\ \Omega$), the nearest large amplitude beam spectrum line ($\tilde{I}$ = 1 mA). Using value of emittance $\varepsilon_z = 1.5$ keV·ns (see [5] for more details), we find $\delta f \gg 140$ Hz.

For a more accurate estimation of the probability of coherent HOM excitation in PX linac we perform statistical analysis based on spread of the data for the HOM parameters (frequency, impedance and quality factor). Since experimental data on HOM parameters are not available, we obtain this information from simulation of cavity HOMs taking into account manufacturing mechanical tolerances. While running the simulation, we allow random variations of the cavity profile within ±0.2 mm of the ideal shape. We tune the individual cell frequency by changing its length but preserving the field flatness along the cavity. Finally, we calculate HOM spectrum, (R/Q), and Q_{ext} of the derived 5-cell structure. Fig. 5 shows results of simulation of Q_{ext} of the 5^{th} passband. One can see from this plot, that variations of the cavity geometry within the manufacturing tolerances may result in very high values for Q_{ext}, which violate condition for Q_L, established above, and may possibly lead to high cryogenic losses.

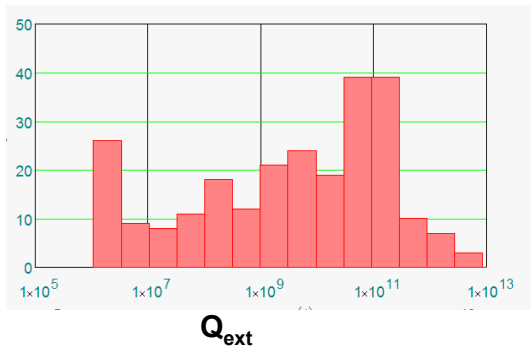

Figure 5: Variation of Q_{ext} for the monopole HOMs in the 5^{th} passband of HE cavity.

An alternative design of HE cavity with larger aperture and $\beta_G = 0.92$ is suggested (see [4], and [6, 7] for more details). The new cavity shape suppresses high Q_L of the monopole HOM completely and mitigates the problem of large cryogenic losses.

RESULTS

In order to estimate probability of cryogenic losses per cryomodule, and relative change of longitudinal emittance, we generate ∼ 10^5 random linacs using predicted deviations of frequency, Q_L, and (R/Q) value of monopole HOMs.

Cryogenic losses

The results of computation of losses for both present and alternative PX HE cavities are presented in Fig. 6 for 1 mA (top) and 5 mA (bottom) average beam current. We can see from these plots, that for the present HE cavity the probability to have losses above 0.1 W per cryomodule increases from 10^{-4} to 10^{-3}, when the average beam current changes from 1 mA to 5 mA. For the alternative HE cavity probability of the same losses is less than 10^{-5}, even for 5 mA PX operation.

[1] Here we assume that $\delta f/f \ll 1/Q$.

[2] $1/Q_L = 1/Q_0 + 1/Q_{ext}$, where Q_0 is intrinsic quality factor, and Q_{ext} is external quality factor of HOM.

Copyright © 2012 by the respective authors — cc Creative Commons Attribution 3.0 (CC BY 3.0)

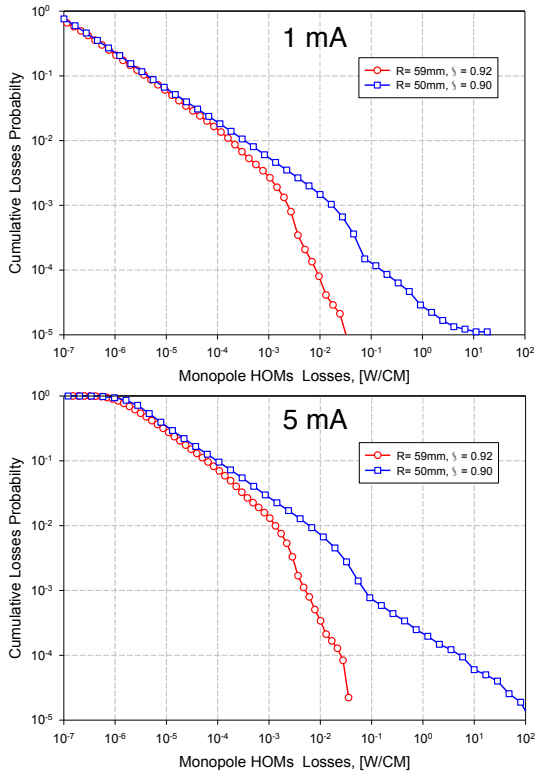

Figure 6: Probability of power loss per cryomodule for the monopole HOMs for the present (blue) and alternative (red) HE cavities.

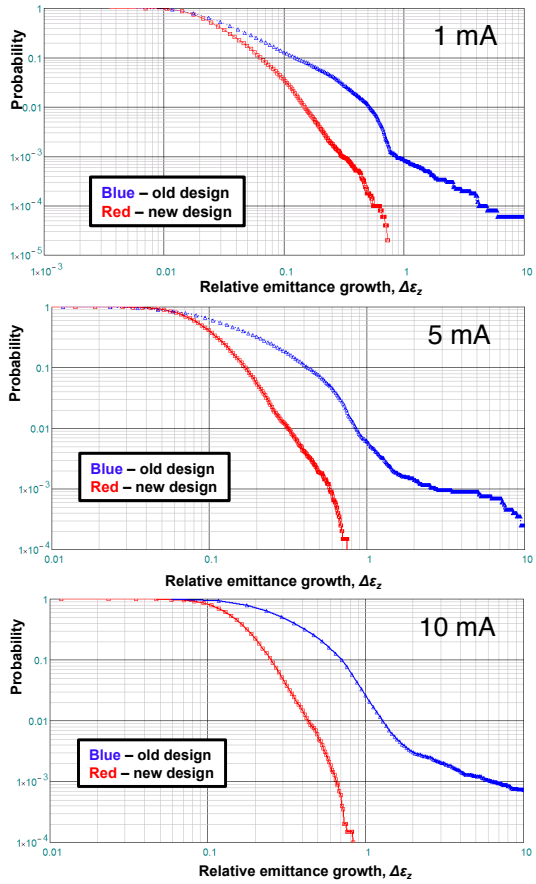

Figure 7: Probability of longitudinal emittance growth in the HE section of PX linac for 1 mA (top), 5 mA (middle), and 10 mA (bottom) average beam current. Data for the present design of the cavity are shown in blue, data for the alternative design are in red.

Longitudinal emittance growth

Beam structure of PX consists of three sub-components (1 MHz, 10 Mhz and 20 MHz, see Fig. 2). The phase of the voltage of an HOM excited by the resonance with one of the beam components is random with respect to two other components of the beam. In case of a high-Q resonance, such an HOM may introduce a significant energy variation and longitudinal emittance growth along the beam train.

The results of statistical analysis are summarized in Fig. 7. For the present PX HE cavity the probability of the emittance to increase by 100% is changing from 10^{-3} to $\sim 2 \times 10^{-2}$, when average beam current increases from 1 mA to 10 mA. The high probability of emittance growth is explained by presence of high Q resonances in the 2^{nd} and the 5^{th} passbands of HE cavity. As expected, for the alternative cavity the probability of the same change in the emittance is much smaller and is below 10^{-4} for 10 mA PX linac operation.

CONCLUSION

We analyze regimes of high beam current operation of PX CW linac. We calculate cryogenic power loss and growth of longitudinal emittance. We find that PX linac of the present design can be safely operated with an average beam current up to 5 mA. High Q monopole HOM resonances in PX HE cavities may create problems for operation with a higher beam current. An alternative design of HE cavity mitigates these issues and allows to run PX linac with an average beam current of 10 mA and higher.

REFERENCES

[1] http://projectx.fnal.gov/

[2] P. Singh, "SRF accelerator for Indian ADS Program: Present & future prospects", SRF 2011, Chicago, Illinois, USA, July 25–29 2011.

[3] V. Yakovlev *et al.*, "High Order Modes in Project-X Linac", HOMSC 2012, Daresbury, UK, June 25-27, 2012.

[4] A. Lunin, *et al.*, "Alternative Cavity for the HE Part of the Project X Linac", IPAC 2012, New Orleans, Louisiana, USA, May 20–25, 2012.

[5] N. Solyak, *et al.*, "Design of the Project X CW Linac", LINAC 2010, Tsukuba, Japan, September 12–17, 2010.

[6] A. Lunin, "Design of alternative $\beta = 0.92$ cavity for Project-X" http://ProjectX-docdb.fnal.gov/cgi-bin/ShowDocument?docid=926

[7] A. Lunin, "Design of alternative $\beta = 0.92$ cavity for Project-X (part II)" http://ProjectX-docdb.fnal.gov/cgi-bin/ShowDocument?docid=1087

Copyright © 2012 by the respective authors — cc Creative Commons Attribution 3.0 (CC BY 3.0)

R&D OF IMP SUPERCONDUCTING HWR FOR CHINA ADS

Weiming Yue, Yuan He, Shenghu Zhang, Bin Zhang, Shoubo He, Cong Zhang, Mengxin Xu,
Pingran Xiong, Shengxue Zhang, Ruoxu Wang, Xueliang Guo, Hongwei Zhao,
Institute of Modern Physics, Chinese Academy of Sciences Lanzhou 730000, China

Abstract

The R&D program of IMP superconducting HWR is based on the China ADS, The aim is to build and test a HWR prototype on December 2012. We have designed a 162.5 MHz β=0.09 half-wave resonator (HWR), and a copper HWR has been fabricated in January 2012. The fabrication of a Nb HWR will be completed by September 2012, and the fabrication of a slow tuner and a high power coupler for this HWR will be completed then. In this poster, we present the HWR electromagnetic design, mechanical design, fabrication arts, copper HWR RF test result, the design of the slow tuner and the power coupler.

INTRODUCTION

At present, many energy researchers agree that nuclear energy is the best way to solve the issue of an energy shortage. In order to apply nuclear energy in a safe and clear way, the accelerator and nuclear scientists obtained a reasonable way to apply nuclear energy and dispose the nuclear wastes, this is an accelerator-driven system (ADS). IMP and IHEP are developing a high-intensity CW H- ion linac for China ADS (Accelerator Driven Sub-critical System), The main design parameters of linac are listed in Table1 [1]. Two injectors are being constructed by IMP and IHEP to demonstrate the most critical R&D issue related to the front-end of a CW high-power and proton linac. Injector Ⅰ chose Superconducting spoke cavity to accelerate H- from 3.2MeV to10MeV，which is being constructed by IHEP. Inject Ⅱ chose Superconducting Half-wave Resonator to accelerate H- from 2.1MeV to10MeV, which is being constructed by IMP. HWR is a well built superconducting cavity international, there are many labs in the word have designed and constructed HWR cavities.

Table 1: China ADS Linac Main Design Parameters

Parameters	Value	Unit
Particle	Proton	
Frequency	162.5/325/650	MHz
Energy	1.5	GeV
Current	10	mA
Beam power	15	MW
Duty factor	100	%

ELECTROMAGNETIC DESIGN

The design of the HWR consists in reaching a reasonable compromise between optimal electromagnetic performances, acceptable mechanical characteristics, and ease of fabricating and preparation [2]. The first step in this HWR design is to optimize the RF properties of the HWR.

The goal of the RF properties is to get a lower heat load and a higher accelerating gradient, which are determined by a higher R/Q0 (R is the shunt impedance and Q0 is the quality factor) and lower peak surface fields (Bpk/Eacc and Epk/Eacc). There are four electron beams welding in the cavity high magnetic region when welding our HWR, and we can't grinding this region, so the performance limitation in the HWR is the thermal-magnetic quench, which leads us to put more care to minimize Bpk/Eacc.

RF Optimization

The most important design parameters to optimize were: Bpk/Eacc, Epk/Eacc, R/Q0 and G [3]. A selected number of cavity geometry parameters were used during this optimization. They are shown on Fig. 1.

In order to optimize the HWR geometry parameters, CST-MWS is used to conduct the RF simulation. Starting from a initial HWR model showed in Fig. 1 and varying the geometry parameters one at a time we were able to establish the general dependence of the important design parameters on the geometry parameters, Fig. 2 shows the quantitative dependence in %.

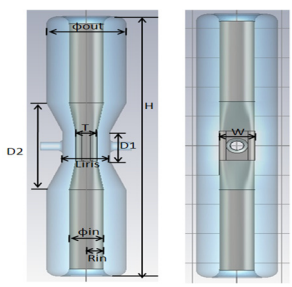

Figure 1: Parameters of the cavity geometry used in the RF optimization.

We notice that the design parameters to optimize are more sensitive to the parameters, namely, Rout, Rin, T, Liris, W and Rblend2. Increasing the HWR outer conductor radius (Rout), a significant improvement in all parameters of interest. Beyond 92 mm we begin to sacrifice real-estate gradient. We choose Rout as 92 mm. By decreasing the inner conductor radius (Rin) while

Copyright © 2012 by the respective authors — cc Creative Commons Attribution 3.0 (CC BY 3.0)

keeping the same outer conductor at 92 mm, R/Q0 goes up, but Emax/Eacc also goes up when Rin is smaller than 40 mm. We choose Rin as 40 mm. By Varying the W and Rblend2, Emax/Eacc is smallest when W is 90 mm and Rblend2 is 17 mm, while other RF parameters change a little. We choose W as 90 and Rblend2 as 15.

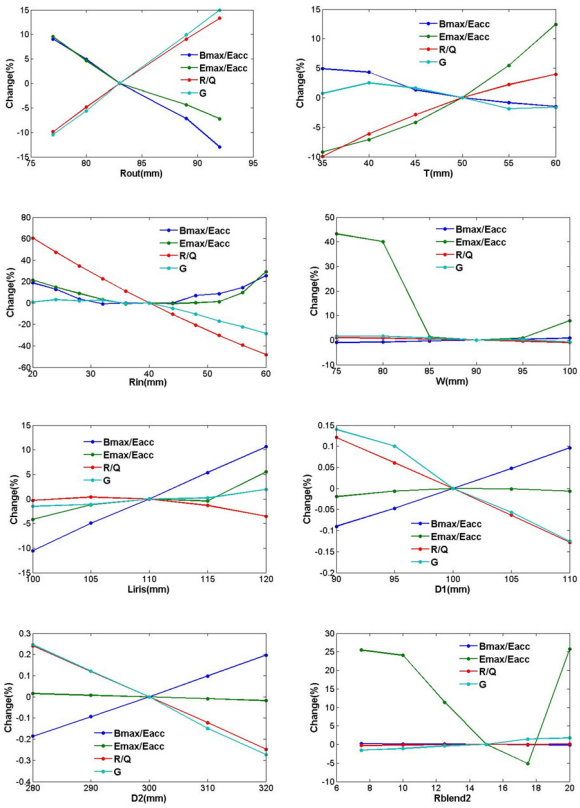

Figure 2: Quantitative dependence of the design parameters in % as function of the geometry parameters.

Optimized Geometry Parameters and RF Parameters

Table 2: Final design parameters of the IMP HWR

Parameters	Value	Unit
Frequency	162.5	MHz
β opt	0.095	
Uacc	0.78	MV
Epeak	25	MV/m
Bpeak	50	mT
R/Q0	148	Ω
G=Rs*Q0	28.5	Ω
Q0(4.4)	6.7E8	

TUNER AND COUPLER

The working of IMP HWR tuner bases on the principle of a slight elastic deformation by applying a pushing and pulling force at the beam tubes. This causes a change in the gap width and the accompanying variation of capacity finally results in a frequency shift. The Diagram of the HWR tuner is shown in Fig. 3. The rf-response of the cavity was simulated with ANSYS and CST-MWS. The tuning sensitivity of the HWR is 179.9 kHz/mm. The spring constant of the HWR is 2.178kN/mm.

The HWR assembled with coupler and tuner is shown in Fig 3. The HWR coupler is a 50-ohm coaxial line with Single ceramic window. This coupler was designed to run at 15 kW power. The parameters of the coupler antenna are in table 3. These parameters are simulated by CST-MWS.

Table 3: Parameters of the Coupler Antenna

Port diameter	Antenna diameter	Antenna length	Qext
40mm	17.4mm	43mm	6.88E5

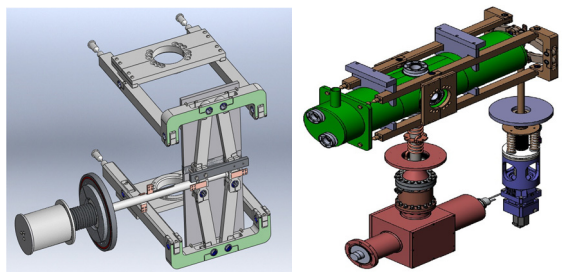

Figure 3: Tuner and HWR assembled with coupler and tuner.

HWR COPPER MODEL

A HWR copper model was built at IMP to test the HWR fabrication procedure and to study the low-level RF behavior of the resonator. Fig. 4 is the HWR copper model. We got the biggest input RF power is 563 W during the RF measurement. The biggest voltage between two gaps is about 60 kV. The RF measurement and CST-MWS simulation result are shown in table 4. The frequency simulation result is a little smaller than the measurement result. The Q0 simulation result is about 20% higher than the RF measurement result.

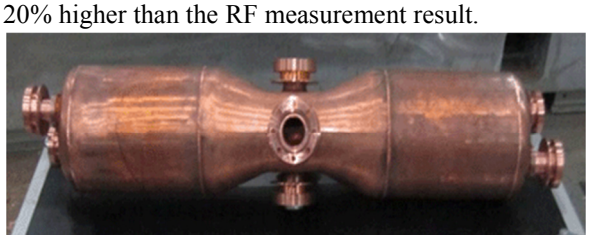

Figure 4: HWR copper model.

Copyright © 2012 by the respective authors — cc Creative Commons Attribution 3.0 (CC BY 3.0)

Table 4: Copper Model RF Measurement and CST-MWS Simulation Result

Parameters	Measurement	Simulation
Frequency	162.6MHz	162.18MHz
Q0	7040	8561

NIOBIUM HWR FABRICATION

The IMP HWR mainly consists of three parts, inner conductor, outer conductor and top/bottom covers. The inner conductor and outer conductor were fabricated from niobium sheets by deep drawing and electron-beam welding. The top/bottom covers were fabricated from niobium sheets by deep drawing. The beam pipes, coupler pipes and process ports pipes were fabricated form niobium rods by machining.

Figure 5: The main parts of IMP HWR.

The residual resistance ratio (RRR) of niobium sheets and rods is 250. The main parts of IMP HWR are shown in Fig 5. Particularly critical are the four electron- beam welds between inner conductor, outer conductor and top/bottom covers, which are made from the outside, and a reliable method for obtaining a smooth weld seam at the inner cavity surface was required. We assembled the three parts for HWR frequency measurement before final welding, as shown in Fig 6.

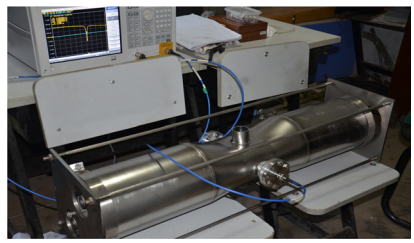

Figure 6: Frequency measurement before final welding.

SUMMARY

The HWR introduced in this paper can be used to accelerate proton from 2.1 MeV to 10 MeV. The fabrication of the HWR will be completed by September 2012. We expect to vertical test this HWR on December 2012.

REFERENCES

[1] Shinian Fu, “Chinese Plan for ADS and CSNS”, SRF’11, Chicago, July 2011, FRIOB03.

[2] J-L.Biarrotte, S.Blivet, S.Bousson et al. T.Junquera, Design study of a 176MHz SRF wave resonator for the Spiral-2 project, Proceedings of the 11th Workshop on RF Superconductivity , Lübeck/Travemünder, 2003.

[3] B.Mustapha, P.N.Ostroumov, Electro-magnetic optimization of a quarter-wave resonator, Linac2010, Tsukuba, Japan, MOPO49.

Copyright © 2012 by the respective authors — cc Creative Commons Attribution 3.0 (CC BY 3.0)

THE MULTIPACTING SIMULATION FOR THE NEW-SHAPED QWR USING TRACK3P*

C. Zhang#, S. He, Y. He, S. Huang, Y. Huang, T. Jiang, R. Wang, M. Xu, Y. Yang, W. Yue, S.H. Zhang, S. Zhang, H. Zhao
Institute of Modern Physics, Lanzhou, Gansu 730000, China

Abstract

In order to improve the electro-magnetic performance of the quarter wave resonator, a new-shaped cavity with an elliptical cylinder outer conductor has been proposed [1]. This novel cavity design can provide much lower peak surface magnetic field and much higher R_a/Q_0 and G. The multipacting simulation has been done for this new QWR cavity using ACE3P/TRACK3P code, in this paper the simulation results will be presented and analyzed.

INTRODUCTION

In the Heavy Ion Accelerating Facility (HIAF) of IMP, superconducting quarter wave resonators (QWRs) with frequency of 81.25 MHz and β of 0.041, 0.085 will be applied to accelerate the ion beams from 0.3 MeV/u to 17 MeV/u. Because of the extremely high design voltage for the β =0.085 QWR cavity, an elliptical cylinder outer conductor shape has been proposed for it (see Fig. 1).

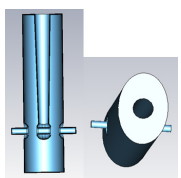

Figure 1: The elliptical cylinder outer conductor QWR model for multipacting simulation.

MULTIPACTING SIMULATION

Parallel codes Omega3P and Track3P which are developed at SLAC have been used, to obtain the field maps and then to analyse the multipacting barriers [2, 3]. When doing the multipacting simulation, one half of the QWR cavity was used taking advantage of the symmetry. Seed particles were initiated on all the RF surfaces. The accelerating gradient was scanned up to 6 MV/m firstly to locate the multipacting band, and then much finer scan interval was used in order to study the multipacting band in detail. 2 eV was used as the initial energy for primary and secondary emissions to study its effect on multipacting and typical niobium secondary electron yield *(SEY) was applied to estimate the multipacting strength* (see Fig. 2). At each field level, 50 RF cycles were used as total running time to obtain resonant trajectories.

* Work supported by 91026001 Nature Science Foundation
# claire335@gmail.com

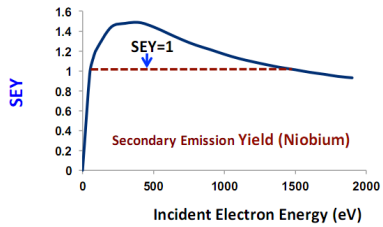

Figure 2: Secondary electron yield (SEY) for Niobium on the dependence of impact energy. The impact energy range relevant to the peak SEY is 150~700 eV. Resonant electrons with impact energies in this range are most dangerous to lead to hard multipacting.

MULTIPACTING SIMULATION RESULTS

Multipacting Band at Low Field Level

The distribution of resonant particles identified by Track3P presented the multipacting bands occurred at low field levels, Figure 3, 4 show the expanded plot around this multipacting band and impact positions.

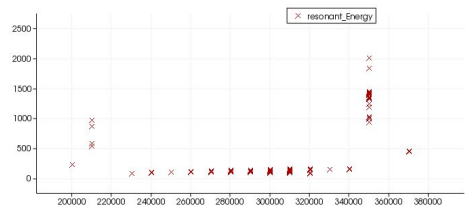

Figure 3: Impact energy vs. accelerating gradient at low field level.

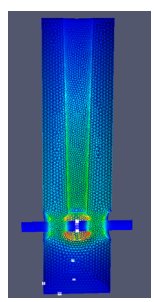

Figure 4: Impact positions at all field levels.

There are two multipacting bands, one at field levels of 0.2 ~0.34 MV/m with impact energies 80~160 eV in the beampipe region (see Fig. 5, 6); the other at around the accelerating gradient of 0.35 MV/m with impact energies 700~2000 eV in the bottom part of the cavity. In consideration of the peak SEY energy for Nb (see Fig. 2), such two bands are expected to be a soft barrier.

Copyright © 2012 by the respective authors — cc Creative Commons Attribution 3.0 (CC BY 3.0)

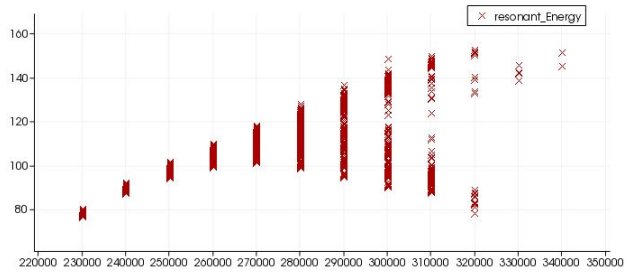

Figure 5: Impact energy vs. accelerating gradient of 0.2~0.34 MV/m.

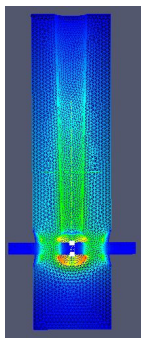

Figure 6: The beampipe impact positions for the accelerating gradient of 0.2~0.34 MV/m.

Rounding Effects on Multipacting

Since it is a common method of reducing the B_{peak} near the short plate location by rounding the joints between the short plate and the inner and outer conductors, here let's see what this procedure will bring to the multipacting activities in the cavity. In order to check how the rounding will affect the multipacting status, the simulation will be done for the three situations-(a) rounding only the inner conductor joint, (b) rounding only the outer conductor joint (see Fig. 7) and (c) rounding both joints, separately.

As for the first two cases, the multipacting occurrences are very similar to that of the flat short plate QWR, both in the impact energy span (see Fig. 8, 9) and in the impact positions (see Fig. 10, 11).

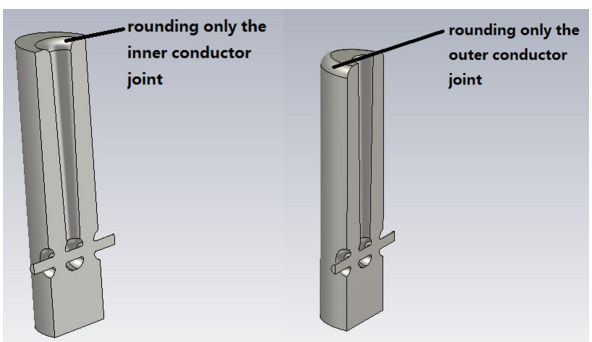

Figure 7: Rounding only one joint between the short plate and the inner or the outer conductor.

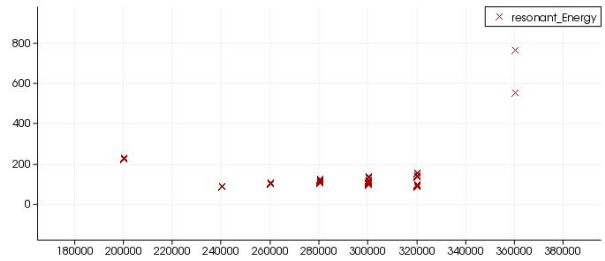

Figure 8: Resonant particle distribution for the case of just rounding the inner conductor joint.

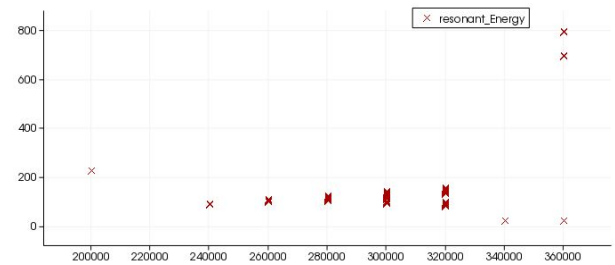

Figure 9: Resonant particle distribution for the case of just rounding the outer conductor joint.

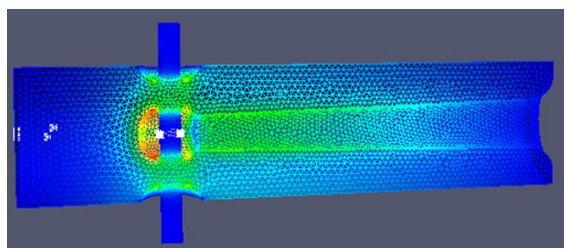

Figure 10: Impact positions for the case of just rounding the inner conductor joint.

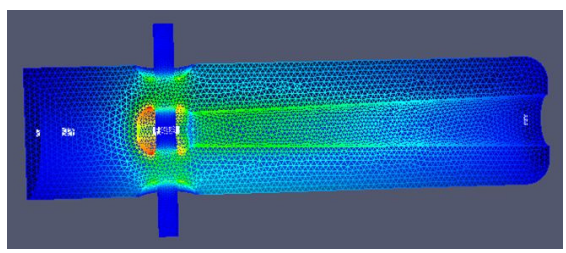

Figure 11: Impact positions for the case of just rounding the outer conductor joint.

However, the multipacting resonances are very critical for the third situation (see Fig. 12). Firstly, the resonant trajectories are expanded to the short plate region and the middle outer conductor (see Fig. 13); and secondly, the impact energies have spread around the peak of the SEY curve (see Fig. 14, 2). As a result, the attempting to lower the Bpeak by rounding both the joints can incur a very serious multipacting in the cavity. The final electro-magnetic design choose not to round the either of the joints speciously since the elliptical cylinder outer conductor cavity shape can offer low enough B_{peak}.

Copyright © 2012 by the respective authors — cc Creative Commons Attribution 3.0 (CC BY 3.0)

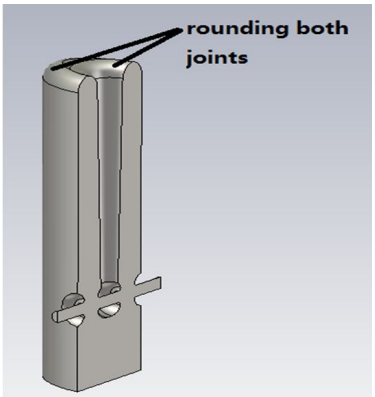

Figure 12: Rounding both joints between the short plate and the inner and the outer conductor.

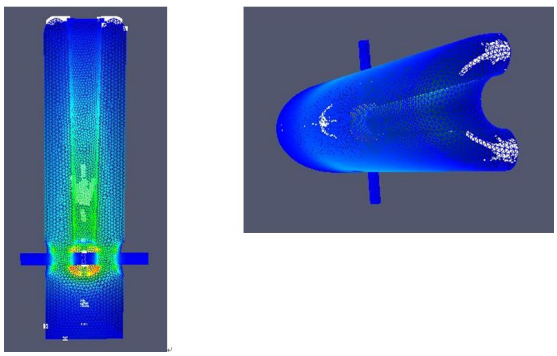

Figure 13: Impact positions for the case of rounding both joints.

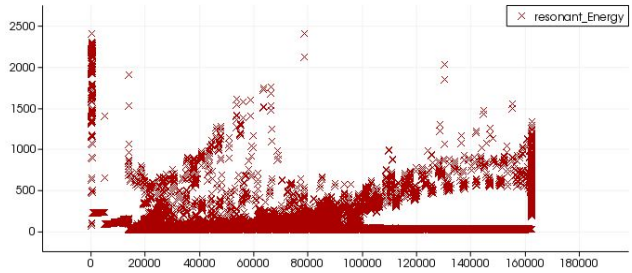

Figure 14: Resonant particle distribution for the case of rounding two joints.

SUMMARY

Track3P was used to analyze the multipacting bands in the elliptical cylinder outer conductor shaped QWR cavity. Only multipacting bands at low field levels were found and the impact energy distributions showed that no hard multipacting bands exist in the cavity. However, rounding the joints between the short plate and both the inner and outer conductors will cause more multipacting bands. The fabrication and test of the prototype cavity is in need in order to see if the experimental data will be in agreement with the simulation results.

REFERENCES

[1] C. Zhang et al, "Electro-magnetic optimization of a quarter-wave resonator.", Proc. SRF 2011, Chicago, USA, 2011.

[2] K. Ko, et al, "Advances in Parallel Computing Codes for Accelerator Science and Development", Proc. LINAC2010, Tsukuba, Japan, 2010.

[3] Lixin Ge et al, "Multipacting simulation and analysis for the FRIB Half Wave resonator using Track3P", Proc. LINAC2010, Tsukuba, Japan, 2010.

Copyright © 2012 by the respective authors — cc Creative Commons Attribution 3.0 (CC BY 3.0)

STRUCTURAL ANALYSIS OF THE NEW-SHAPED QWR FOR HIAF IN IMP*

C. Zhang#, S. He, R. Wang, M. Xu, W. Yue, S. Zhang, S. Huang, Y. Yang, Y. Huang
T. Jiang, S. Zhang, Y. He, H. Zhao
Institute of Modern Physics, Lanzhou, Gansu 730000, China

Abstract

Since the QWR cavity is very successful for the operation with frequency of 48 to 160 MHz and beta value of 0.001 to 0.2, a new-shaped QWR is being designed for the low energy superconducting section of HIAF in the Institute of Modern Physics [1]. The cavity will work at 81.25 MHz and beta of 0.085，with an elliptical cylinder outer conductor to better its electro-magnetic performance and keep limited accelerating space. Structural design is an important aspect of the overall cavity implementation, and in order to minimize the frequency shift of the cavity due to the helium bath pressure fluctuations, the Lorentz force and microphonics excitation, stiffening elements have to be applied. In this paper, structural analyses of the new-shaped QWR are presented and stiffening methods are explored.

INTRODUCTION

A stable resonant frequency for the superconducting cavity is desired, because excessive frequency fluctuations require extra power to control the RF amplitude and phase. The reasons that lead to frequency fluctuations include the fluctuations in the liquid helium pressure, Lorentz force detuning, mechanical vibration modes and the etching effect from the cavity surface treatment. Since the operating temperature for the QWR cavities is 4.5 K, the helium pressure stability will be determined by the extent to which the cryogenic plant can be controlled. The stiffening measures were intended primarily to reduce the pressure sensitivity.

MECHANICAL SIMULATION

When the EM design has been completed, the mechanical performance of the cavity should be evaluated. We tried to figure out the cavity's helium pressure sensitivity, severity of Lorentz Force Detuning plus the vibration frequency of mechanical modes, and further, to minimize the instabilities using different stiffening measures. Simulations and optimizations have been done by the 3D Multiphysics solver ANSYS-APDL [2]. In the simulation, niobium sheet of 3 mm thickness was firstly used, with the mechanical properties of Young modulus of 105000 N/mm2, Poisson ratio of 0.38 （see Fig. 1）.

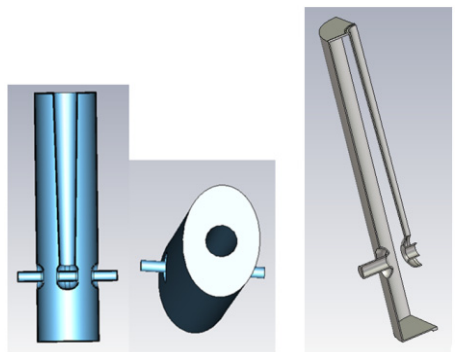

Figure 1: Mechanical model of the elliptical cylinder outer conductor QWR for the structural analysis.

Etching Effects

Surface processing is very important in order to achieve good performance of the superconducting cavity. Either the BCP or the EP is to etch proper thickness of the inner surface, which will change the frequency. According to Slater's perturbation theory, a small deformation in the cavity boundary will lead to a frequency shift.

Using the ANSYS-APDL code, the change in the frequency because of the etching can be calculated. Firstly, you have to get the electro-magnetic field distribution, and then the frequency change caused by the cavity wall's deformation can be obtained. The simulation results show that 1 μm etching thickness will lead to 27Hz increase in the frequency.

Lorentz Force Detuning

The Lorentz force on the cavity surface results from the interaction of the surface electromagnetic fields with the induced surface currents, which will exert pressure to the cavity wall, and the resulting cavity shape deformation ΔV will cause the change in the resonant frequency. The frequency shift caused by Lorentz force is often quantified by K_L which is defined as: $K_L=\Delta f/(E_{acc})^2$.

If the cavity works at the continuous wave mode, then the frequency change will be invariant, it is the static Lorentz force detuning; otherwise, when the cavity works at the pulsed wave mode, the dynamic Lorentz force detuning will be caused. In this paper, only the static situation was considered and 2.5 MV accelerating voltage was to be scaled for the naked cavity whose

*Work supported by 91026001 Nature Science Foundation
#claire335@gmail.com

Copyright © 2012 by the respective authors — cc Creative Commons Attribution 3.0 (CC BY 3.0)

beam port is fixed. The simulation result gives the K_L with the value of -0.34 Hz/(MV/m)2 (see Fig. 2).

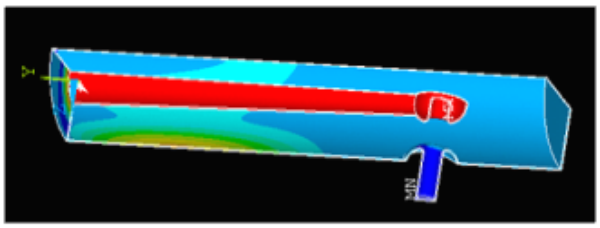

Figure 2: Deformation of the elliptical cylinder outer conductor QWR caused by Lorentz force.

Mechanical Vibration Modes

Mechanical wave in the environment can be transmitted to the cavity by various mediums, and the cavity can resonate mechanically at certain frequencies. Firstly, the naked cavity was simulated for its three lowest modes and results are shown as following, with the vibration frequency of 11 Hz, 13 Hz and 20 Hz, respectively (see Fig. 3).

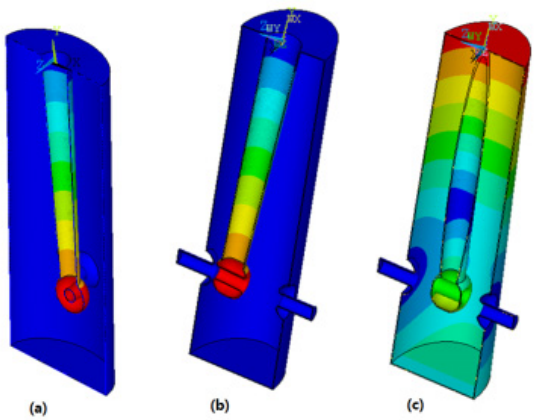

Figure 3: The lowest three vibration modes for the new-shaped naked QWR cavity.

Secondly, stiffening elements were added. A stiffening ring was added on the shorting plate and fixed in the simulation, and in order to reflect more accurately the influence of the tuner, the tuner button was fixed too (see Fig. 4-up). Different radius rings were tested to find out the strengthening effect (see Fig. 4-down). Obviously, the smallest radius ring with 60 mm can increase the mechanical frequency the highest. The vibration mode for the 60 mm stiffened-ring QWR is illustrated in Fig. 5.

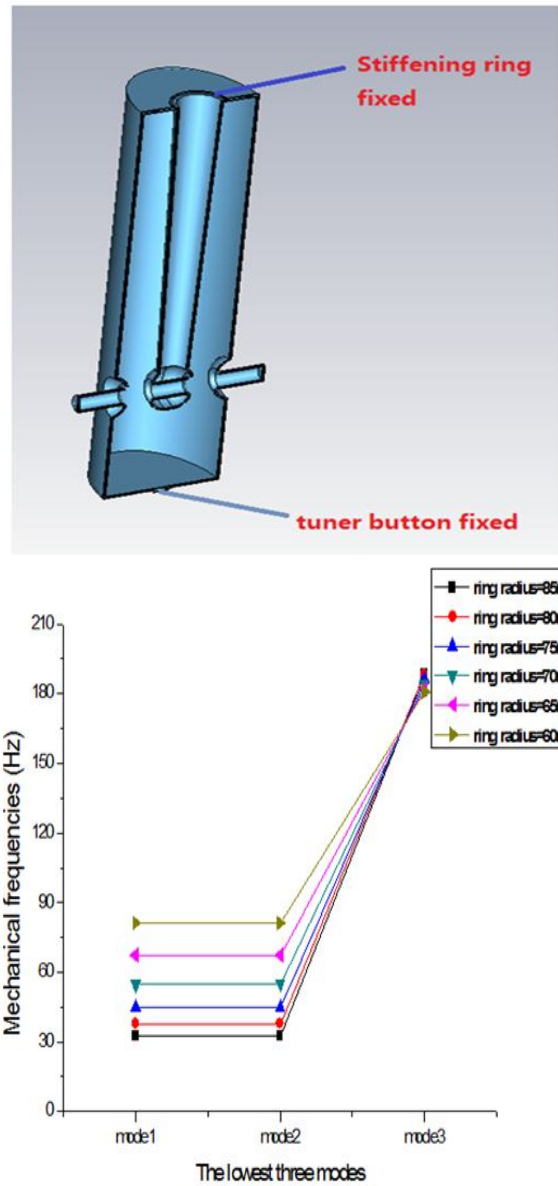

Figure 4: Stiffening ring on the short plate (up); the lowest three vibration modes frequency on the dependence of the radius of stiffening ring (down).

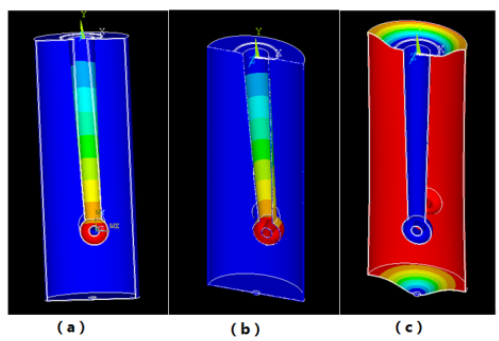

Figure 5: The lowest three vibration modes for stiffened-ring with radius 60mm QWR cavity.

Copyright © 2012 by the respective authors — cc Creative Commons Attribution 3.0 (CC BY 3.0)

Helium Pressure Detuning

In operation, the superconducting quarter wave resonator cavity with frequency of 81.25 MHz works at 4.3K, at which temperature the liquid helium's pressure fluctuates momently. The optimization goal of the mechanical design should be to minimize the cavity's pressure sensitivity. Mechanical simulations were done to quantify the displacements and the resulting frequency vibration from a constant pressure outside the cavity wall [3].

Firstly, the model we used is the one which have the stiffening ring with radius of 60mm and found that the max displacement appeared on the outer conductor corresponding to longer axis of the elliptical cylinder (see Fig. 6).; then we added two supporting rods on the shorting plate attempting to decrease the deformation caused by squeezing on the cavity wall, but the efficacy is not so good (see Fig. 7); later, thicker material (4mm) was used for the cavity wall and the simulation results showed the max displacement was reduced more than in a factor of 2 (see Fig. 8).

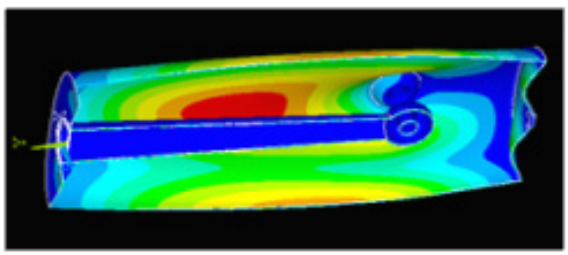

Figure 6: Deformation of ring-stiffened QWR caused by the external pressure, the frequency shift Δf due to the change in ambient pressure ΔP: df/dP~-37 Hz/mbar.

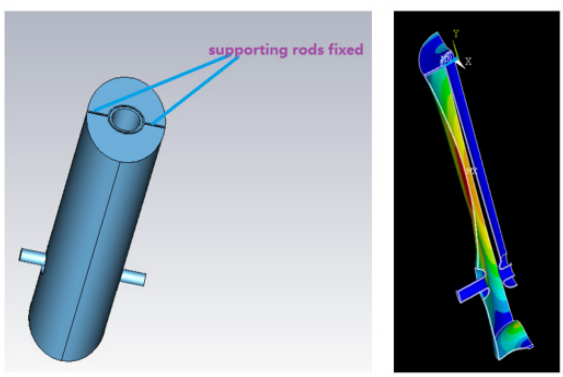

Figure7: Supporting rods on the short plate (left); deformation of ring-and-supporting-rods-stiffened QWR by external pressure: df/dP~-29 Hz/mbar.

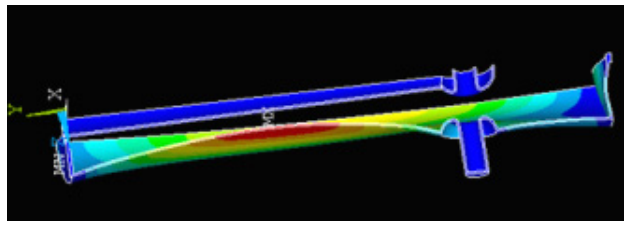

Figure 8: Deformation of ring-and-supporting-rods –stiffened-and-thickened QWR by external pressure: df/dP~-11 Hz/mbar.

CONCLUSIONS

Numerical models have been used to predict the stability of the elliptical cylinder outer conductor quarter wave resonator and relevant stiffening elements have been explored. Major flaws have been encountered in the mechanical models due to the outer conductor's elliptical cylinder shape. Better stiffening measures should be kept searching. In the next stage, the cavity with helium vessel need to be simulated and the fabrication of prototype should be carried out to verify experimentally the mechanical performance.

REFERENCES

[1] C. Zhang et al, "Electro-magnetic optimization of a quarter-wave resonator.", Proc. SRF 2011, Chicago, USA, 2011.

[2] ANSYS, Inc., Canonsburg, Pennsylvania, USA. www.ansys.com.

[3] Zaplatin E., et. al., "Structural Analyses of MSU Quarter-Wave Resonators", in Proceedings SRF 2009: 14th International Conference on RF Superconductivity: Berlin, Germany, Helmholz-Zentrum Berlin, Berlin, Germany, 2009, p.560-563.

Copyright © 2012 by the respective authors — cc Creative Commons Attribution 3.0 (CC BY 3.0)

AN ANALYTICAL CAVITY MODEL FOR FAST LINAC-BEAM TUNING*

Zhengqi He#, Zhihong Zheng (FRIB, East Lansing, Michigan; TUB, Beijing),
Zhengzheng Liu, Yan Zhang, Jie Wei, (FRIB, East Lansing, Michigan)

Abstract

Non-axisymmetric RF cavities can produce axially asymmetric acceleration fields. Conventional method using numerical 3-D field tracking to address this feature is time-consuming and thus not appropriate for on-line beam tuning applications. In this paper, we develop analytical treatment of non-axisymmetric RF cavities. Multipole models of cavities are derived using realistic 3-D field in both longitudinal and transverse dimensions. Then, beam dynamics formulism is established. Finally, special case of FRIB quarter-wave resonators are calculated by the model and benchmarked against 3-D field tracking to ensure the efficiency and accuracy of the model.

INTRODUCTION

Non-axisymmetric RF cavities, such as quarter-wave resonators (QWR), half-wave resonators (HWR) and spoke cavity, can produce dipole and quadrupole terms in transverse direction, and can cause beam steering and deformation. Up to now, no model can handle this problem except for multi-particle tracking. So, we aim at building longitudinal and transverse model for non-axisymmetric RF cavities to solve this problem. The model will be implemented into on-line beam tuning application[1], therefore the basic requirement is accuracy and efficiency.

LONGITUDINAL DYNAMICS

For linac acceleration, keeping track of kinetic energy and phase evolution would be important. Particle tracking by iteration is the traditional way, while revealing lack of efficiency when applying to online beam tuning. To solve the problem, the thin lens model is implemented, describing the energy gain and phase advance after a RF cavity, which can be considered as a drift-kick-drift model as below[2][3]:

$$\begin{cases} W_f = W_i + qV_0T(k)\cos\phi_i - qV_0S(k)\sin\phi_i \\ \phi_f = \phi_i + \dfrac{qV_0}{2W_i}k\left[T'(k)\sin\phi_i + S'(k)\cos\phi_i\right] \end{cases} \quad (1)$$

where W_i and W_f stands for initial and final kinetic energy and φ_i and φ_f are initial and final particle phase. V_0 are the static electric voltage. T, T', S and S' are the transit-time factors calculated from numerical electric field data. In order to analyse the error introduced by constant beta assumption during drift section, two kinds of thin lens model is developed comparatively for multi-gap cavities. 1) One gap kick model treats the whole cavity as one thin accelerating gap. 2) Multi-gap kick model treats each accelerating gap separately.

Comparison with Simulation

Facility of Rare Isotope Beams (FRIB)[4] linac segment is implemented for comparison between model and numerical calculation. FRIB linac segment one, which consists of three β=0.041 QWR cryomodules and eleven β=0.085 QWR cryomodules, accelerates ions from 0.5MeV/u to 16.6MeV/u. By adding cavity driven phase onto absolute particle phase, we obtain the initial phase of the certain particle, which can be described as: $\varphi_i = \varphi_{abs} + \varphi_{drive}$; The driven phase is set so that the synchrotron phase is -30 deg. After setting the driven phase, linac segment acceleration simulation is performed via 4 different methods, namely, IMPACT[5] tracking (used as reference), particle tracking, 2-gap kick model, 1-gap kick model. For 2-gap kick model, we can achieve the phase precision of 0.31% when divided by 2π, and kinetic energy gain prediction precision of 0.042% of the 16.1MeV/u kinetic energy gain (figure 1). The numerical electric field data comes from CST[6] simulation.

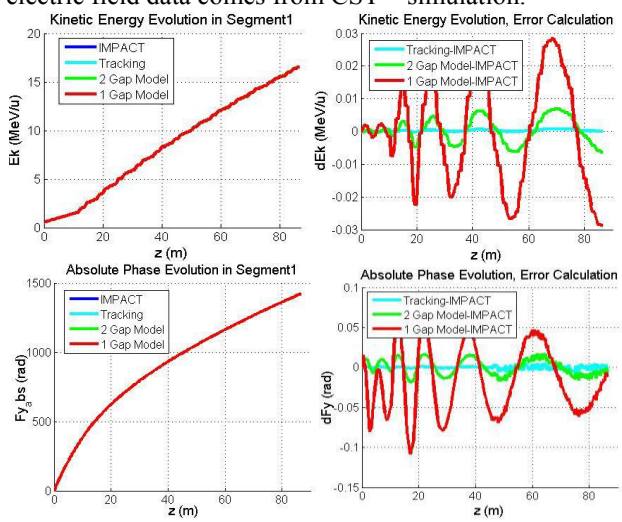

Figure 1, Kinetic energy and Absolute phase evolution and error calculation; a) Kinetic Energy evolution; b) Difference between different models and IMPACT simulation in Kinetic energy prediction; c) Absolute phase evolution; d) Difference between different models and IMPACT simulation in absolute phase prediction.

TRANSVERSE DYNAMICS

Traditional treatment of transverse RF cavity field usually only consists of focusing electric field terms. However, early studies already show that field dipole terms and quadrupole terms exist in non-axisymmetric RF

* Work supported by the U.S. Department of Energy Office of Science under Cooperative Agreement DE-SC0000661

Copyright © 2012 by the respective authors — cc Creative Commons Attribution 3.0 (CC BY 3.0)

cavities[7][8]. Therefore, we are developing a transverse model including multipole terms derived directly from numerical data.

Field Multipole Expansion

In 3-D cylindrical coordinate system the zeroth order of φ represents focusing term, the first order represents dipole or steering term and the second order represents quadrupole term. The 2-D Taylor-Fourier series expansion is conducted for each x-y plane field. In a 2-D polar coordinate, we first transfer 2-D vector field into two 2-D scalar field by projection. Then, we expand the ρ direction into Taylor series and ϕ direction into Fourier series. The coefficient is proportional to the relative strength of a certain field mode. The process can be expressed as:

$$F_{\rho,nm}(\rho,\theta)=F_{max}\cdot\begin{bmatrix}1\\ \rho\\ \rho^2\\ \rho^3\\ \vdots\\ \rho^n\end{bmatrix}^T\cdot\begin{bmatrix}a_{00}-ib_{00} & a_{01}-ib_{01} & a_{02}-ib_{02} & \cdots & a_{0m}-ib_{0m}\\ a_{10}-ib_{10} & a_{11}-ib_{11} & a_{12}-ib_{12} & \cdots & a_{1m}-ib_{1m}\\ a_{20}-ib_{20} & a_{21}-ib_{21} & a_{22}-ib_{22} & \cdots & a_{2m}-ib_{2m}\\ \vdots & \vdots & \vdots & \ddots & \vdots\\ a_{n0}-ib_{n0} & a_{n1}-ib_{n1} & a_{n2}-ib_{n2} & \cdots & a_{nm}-ib_{nm}\end{bmatrix}\cdot\begin{bmatrix}1\\ e^{i\theta}\\ e^{i2\theta}\\ e^{i3\theta}\\ \vdots\\ e^{im\theta}\end{bmatrix} \quad (2)$$

$$=F_{max}\cdot\sum_{n,m=0}^{\infty}P_nA_{hm}\Theta_m$$

In a specific case, if the geometry of the cavity is symmetric, we can apply this condition to simplify the Taylor-Fourier series expansion. Theoretically, we should expand the field to infinite order while in practice we have to truncate it to satisfy certain precision.

For the case of FRIB β=0.085 QWR, we transfer CST numerical electric field data, which is in Cartesian coordinate system, to Polar coordinate system by bilinear interpolation. Multipole expansion results show that in coefficient matrix of E_r, the linear term is A_{21} (focusing term), A_{12} (dipole term) and A_{23} (quadrupole term). In coefficient matrix of H_r, the linear term is A_{21}(monopole term), A_{12} (dipole term) and A_{23} (quadrupole term). Then longitudinal direction is scanned and multipole term coefficient is calculated for all the x-y planes of field data (figure 2).

Inversely, we can rebuild the field by using the coefficient. Only high order and random noise still exist and the precision would be at the order of 0.1% if we truncate the expansion to 4th order.

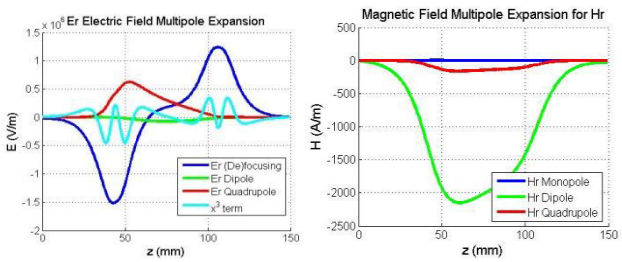

Figure 2, Result of multipole term strength $C_{max,i,j}$ curve for E_r and H_r; a) E_r multipole term strength, defined as E_{max} times multipole term coefficient, vs. longitudinal coordinate z; b) H_r multipole term strength, defined as H_{max} times multipole term coefficient, vs. longitudinal coordinate z;

Multipole Beam Kick Model

The multipole beam kick model is utilized to calculate beam kick caused by multipole terms. We start from the Lorentz force equation:

$$\Delta y'=\frac{qe\mu_0}{\gamma m_0}\int_{t_s}^{t_e}H_x(x,y,z,t)\,dt+\frac{qe}{\gamma m_0\beta c}\int_{t_s}^{t_e}E_y(x,y,z,t)\,dt$$
$$=\Delta y'_{H,y}+\Delta y'_{E,y} \quad (3)$$

Beam kick can be caused by electric field and magnetic field. Take electric field as example. Assume the field is a sinusoidal function with time and get replaced by z as an independent variable. The expansion is done under cylindrical coordinate system, substitute the result:

$$\begin{cases}E_y(x,y,z)=E_\rho(\rho,\phi,z)\cdot\sin\phi+E_\phi(\rho,\phi,z)\cdot\cos\phi\\ E_\rho=E_{\rho,max}\sum_{j,k=0}^{n}(a_{\rho,jk}-ib_{\rho,jk})e^{ik\theta}\rho^j\\ E_\phi=E_{\phi,max}\sum_{j,k=0}^{n}(a_{\phi,jk}-ib_{\phi,jk})e^{ik\theta}\rho^j\end{cases} \quad (4)$$

where x=ρ·cosφ, y=ρ·sinφ. After simplification and axis transformation, we can write E_y into the following form:

$$E_y(x,y,z)=\sum_{i,j=0}^{n}E_{max}(z)\cdot c_{ij}(z)\cdot t_{ij}(x,y) \quad (5)$$

Make use of the concept of time transit factors, we can finally get the expression of vertical beam kick by electric multipole components:

$$\Delta y'_{E,y}=\frac{qe}{\gamma\beta^2m_0c^2}\int_{z_s}^{z_e}\sum_{i,j=0}^{n}E_{max}(z)\cdot c_{ij}(z)\cdot t_{ij}(x,y)\cdot\cos(kz+\phi_0)\,dz$$
$$=\frac{qe}{\gamma\beta^2m_0c^2}\cdot\sum_{i,j=0}^{n}t_{ij}(x,y)\int_{z_s}^{z_e}C_{max,ij}(z)\cdot\cos(kz+\phi_0)\,dz \quad (6)$$
$$=\frac{qe}{\gamma\beta^2m_0c^2}\cdot\sum_{i,j=0}^{n}t_{ij}(x,y)\cdot V_{ij}\cdot(T_{ij}\cos\phi_0-S_{ij}\sin\phi_0)$$

Similarly, we can also get the expression of vertical beam kick by magnetic multipole components:

$$\Delta y'_{H,y}=\frac{qe\mu_0}{\gamma\beta m_0c}\cdot\sum_{i,j=0}^{n}t_{ij}(x,y)\cdot U_{ij}\cdot(T_{ij}\cos\phi_0-S_{ij}\sin\phi_0) \quad (7)$$

For general case, $c_{i,j}(z)$ and $t_{i,j}(z)$ would be quite complicate except for some special linear case.

Focusing: The term with i=1, j=0, stands for beam focusing term. When at this case, for y electric field, $E_{max}(z) = E_{max,\rho}(z)$, $c_{10}(z) = a_{\rho,10}(z)$ and $t_{ij} = y/\rho_{max}$; for magnetic field, $H_{max}(z) = H_{max,\varphi}(z)$, $c_{01}(z) = a_{\varphi,01}(z)$ and $t_{ij} = - y/\rho_{max}$. Using the model we can evaluate the focusing effect of the cavity.

Beam Steering: The term with i=0, j=1, stands for beam steering term, or dipole term. When at this case, for y electric field, $E_{max}(z) = E_{max,\rho}(z)$, $c_{01}(z) = b_{\rho,01}(z) = a_{\varphi,01}(z)$ and $t_{ij} = 1$; for magnetic field, $H_{max}(z) = H_{max,\rho}(z)$, $c_{01}(z) = a_{\rho,01}(z) = -b_{\varphi,01}(z)$ and $t_{ij} = 1$. Using the model we can derive the dipole kick and predict beam steering for FRIB β=0.085 QWR. The result is then benchmarked with particle tracking (figure 3a).

Quadrupole Terms: The term with i=1, j=2, stands for quadrupole term. When at this case, for y electric field, $E_{max}(z) = E_{max,\rho}(z)$, $c_{12}(z) = -a_{\rho,12}(z) = b_{\varphi,12}(z)$ and $t_{ij} =$

Copyright © 2012 by the respective authors — cc Creative Commons Attribution 3.0 (CC BY 3.0)

y/ρ_{max}; for magnetic field, $H_{max}(z) = H_{max,\rho}(z)$, $c_{12}(z) = b_{\rho,12}(z) = a_{\varphi,12}(z)$ and $t_{ij} = y/\rho_{max}$. Using the model we can derive the quadrupole kick for FRIB β=0.085 QWR and then benchmarked against particle tracking (figure 3b).

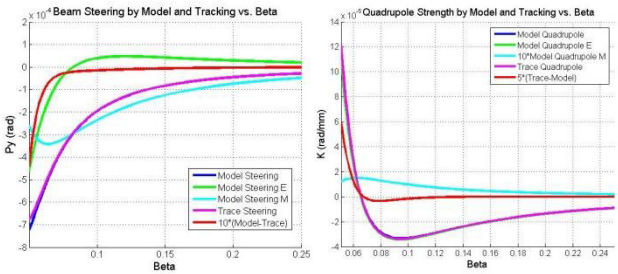

Figure 3, Prediction of beam steering and quadrupole strength by Model and Tracking vs. beta, φ_0=-π/6; a) Blue: beam steering by model, green: electric field steering, cyan: magnetic field, magenta: particle tracking, red: 10 times of error between model and tracking. b) Blue: quadrupole strength by model, cyan: electric field quadrupole, magenta: 10 times magnetic field quadrupole, green: particle tracking, red: 10 times of error between tracking and model.

Comparison with Simulation

After multipole expansion of FRIB β=0.085 QWR FRIB cavity, we derived all the linear terms including focusing term, dipole term, quadrupole term in transverse electric and magnetic fields. Then, we develop the transverse drift-kick-drift thin lens model and compare the result with particle tracking simulation. The thin lens model includes a series of multipole kicks located at their own components' electric (magnetic) centre separated by a series of drift spaces.

We implement the method to the second gap of FRIB β=0.085 QWR cavity, and the multipole thin lens components can be seen in table 1. Units: mm for position, V for V_0 and A for U_0. In order to check the correctness of this thin lens model, the result is benchmarked against particle tracking simulation (figure 4). The blue circles represent initial phase space and red triangle represent final phase space calculated by real field tracking after one β=0.085 QWR cavity. Green squares shows thin lens model with focusing components only, which tilt both x and y phase space eclipse. Blue stars represent the phase space after adding steering term into the thin lens model. There is no steering effect in x direction, while in y direction the steering effect is around -0.245 mrad. The RMS error of blue stars for x, x', y, y' is 1.3%, 23%, 1.2%, 8.4%. Red crosses represent the phase space after adding quadrupole term into the thin lens model. Then the x and y phase space tilt to an opposite direction and get closer to particle tracking. The RMS error of red crosses for x, x', y, y' becomes 0.034%, 3.7%, 0.29%, 3.6%. The model shows good agreement with particle tracking while the calculation speed is about 200 times faster.

Table 1, Optics line of transverse thin lens model

Type	Position	T	S	V0(U0)
E Defocusing	41.4319	0.9806	0	0.1203
E Quad. Pole	61.7142	-0.9530	0	0.0739
H Dipole	72.0426	0.8921	0	4.84e-4
E Dipole	77.4354	0.9530	0	0.0103
E Focusing	104.1544	-0.9650	0	0.1200

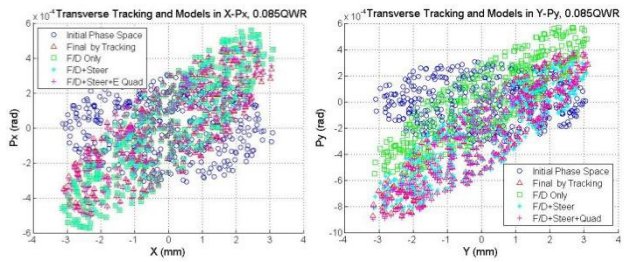

Figure 4, X-Px phase space and Y-Py phase space of a KV distribution beam using tracking and models; a) X-Px phase space when including different field terms and benchmark against particle tracking; b) Y-Py phase space when including different field terms and benchmark against particle tracking.

CONCLUSION

A longitudinal and transverse model designed for on-line beam tuning application which needs both precision and speed has been established for non-axisymmetric RF cavities and has been checked with the case of FRIB QWR. The procedure of building both longitudinal and transverse model is universal and can be easily extended to other cavities such as half-wave resonators, crab cavities and spoke cavities. The model can achieve better precision in transverse direction than traditional model where beam steering and quadrupole terms are usually omitted. An enhancement of 200 times in calculation speed has been seen when using model in transverse direction and a faster speed can be expected if database such as TTF factors are made beforehand.

REFERENCES

[1] Y. Zhang, proceedings for IPAC12
[2] T. P. Wangler, in Principles of RF Linear Accelerators, Wiley-Interscience Publication, p. 181~p.183
[3] K. R. Crandall, D. P. Rusthoi, Trace 3-D Documentation
[4] J. Wei et al, proceedings for HIAT12
[5] IMPACT, by J. Qiang, LBNL, (2002)
[6] Computer Simulation Technology, http://www.cst.com
[7] A. Facco, et al, in PRS-TAB, Vol. 14, 070101 (2011)
[8] M. Cavenago, in Nuclear Instruments and methods in Physics Research A311 (1992) 19-29

Copyright © 2012 by the respective authors — cc Creative Commons Attribution 3.0 (CC BY 3.0)

MULTIPACTING SUPPRESSION MODELING FOR HALF WAVE RESONATOR AND RF COUPLER *

Z. Zheng[1,2], A. Facco[1,3], Z. Liu[1], J. Popielarski[1], K. Saito[1], J. Wei[1], Y. Xu[1], Y. Zhang[1]
[1] FRIB, East Lansing 48824, Michigan, USA
[2] TUB, Beijing, China
[3] INFN - Laboratori Nazionali di Legnaro, Padova, Italy

Abstract

In prototype cryomodule test of Facility of Rare Isotope Beam (FRIB) β=0.53 half-wave-resonators (HWRs) severe multipacting barriers, prevented RF measurement at the full field specified. The multipacting could not be removed by several hours of RF conditioning. To better understand and to eliminate multipacting, physics models and CST simulations have been developed for both cavity and RF coupler. The simulations have good agreement with the multipacting discovered in coupler and cavity testing. Proposed cavity and coupler geometric optimizations are discussed in this paper.

INTRODUCTION

While the multipacting can be categorized by different physics features, the 1st order multipacting with electrons bouncing between two points is significantly stronger than other kinds of multipacting. First order two point multipacting is related primarily to the geometric structures. During the prototype cryomodule test with the final cavity coupler, multipacting barriers which did not show up or that could be easily conditioned in the vertical test prevented us from reaching full gradient. RF conditioning had very little effect. Since the only significant change from the successful vertical test was the coupler, we attributed these new barriers to the change of geometry in the coupler region. The fact that MP could be suppressed by magnetic field around the coupler confirmed our hypothesis. We developed physics models to help simplify the coupler geometry optimization to eliminate MP. Simulations done with CST [1] reassured the physics models. In this paper, Section 1 gives the physics model and CST simulation results of FRIB β=0.53 HWR 1st generation prototype; Section 2 discusses the physics model and optimization scheme for the RF coupler.

MULTIPACTING IN HWR

Multipacting Conditions in the HWR

From CST simulation, multipacting in the HWR cavity mainly locates at the short plate as shown in Figure 1 (green semi-circle). The two-point, 1st order multipacting can thus be described with a cyclotron model, as shown in Figure 2.

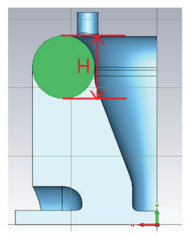

Figure 1: 1/8 structure of FRIB β=0.53 cavity, the short plate is marked as green semi-circle, which is the conjunction between cavity inner and outer conductor.

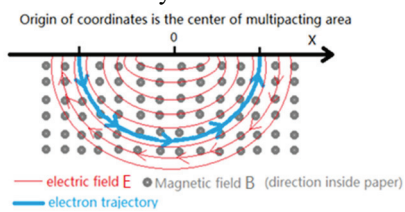

Figure 2: Physics picture of two point 1st order multipacting at a short plate. The flat is the infinitesimal approximation of the semi-circle short plate.

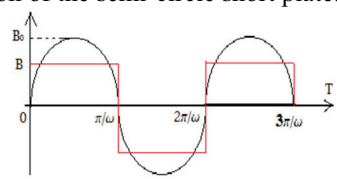

Figure 3: Assumption of B field (red line) as an approximation of the real field B_0.

The magnitude of B is assumed to be $1/\sqrt{2}$ of B_0 to simplify the analytical model, as the red step function shown in Figure 3. Electric field has the same assumption.

According to this cyclotron model, conditions of two-point 1st order multipacting are:

$$E_0(-x) = -E_0(x) \quad (1)$$

$$T = T_{rf} = \frac{2\pi}{\omega} \quad (2)$$

$$W_1 < K_{impact} < W_2 \quad (3)$$

B_0 and E_0 are the magnetic and electric field amplitudes on the plate surface, ω is the cavity's circular frequency, T is the cyclotron period of electron and T_{rf} is the RF period, $[W_1, W_2]$ is the region of impact energy corresponding to SEY>1.

To further interpret Eq. (3) of K_{impact} in terms of electric and magnetic field, we obtain:

$$r \approx \frac{\sqrt{K_{impact} m}}{B_0 e} \quad (4)$$

*Work supported by the U.S. Department of Energy Office of Science under Cooperative Agreement DE-SC0000661

Copyright © 2012 by the respective authors — cc Creative Commons Attribution 3.0 (CC BY 3.0)

$$K_{impact} = \frac{mE_0^2\pi^2}{B_0^2} \quad (5)$$

Therefore, Equation (3) for the two point 1st order multipacting condition becomes:

$$\frac{1}{\pi}\sqrt{\frac{W_1}{m}} < \frac{E_0}{B_0} < \frac{1}{\pi}\sqrt{\frac{W_2}{m}} \quad (6)$$

The conditions for two-point multipacting at half wave cavity must satisfy Eq. (1) and Eq. (6), while an additional condition can be deduced from:

$$B_0 = \sqrt{2}A\frac{m\omega}{e} \quad (7)$$

where m and e are electron mass and charge, A is the correction coefficient for the real field. The surface magnetic field is a fixed value of ~23 mT from CST simulation.

All the conditions described above have been verified by CST simulation, which is also an evidence of the domination of two-point 1st order multipacting.

Confirmation with TDCM Test

In the prototype cryomodule test of β=0.53 HWRs, multipacting is found when E_{acc} > 2.4 MV/m. As we process the cavity to suppress it, we can only ramp the peak electric field up to 15MV/m which corresponds to E_{acc} = 3.6MV/m as shown in Figure 4.

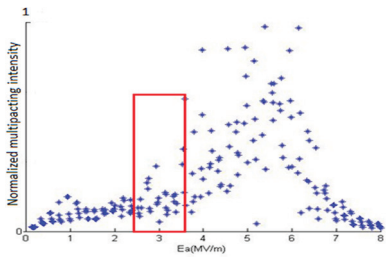

Figure 4: CST simulation of the cavity's multipacting in the cryomodule test. The red box marks the region of multipacting in the cryomodule test.

From CST simulation, the multipacting intensity grows significantly at about 3.6 MV/m, the same barrier as we observed in the cryomodule test. In the sense, CST model is reliable to predict experimental results.

The multipacting barrier was also observed in vertical testing of the HWR's. In the vertical tests, the multipacting barriers were easily conditioned. Most likely, the hard multipacting barriers in the coupler prevented efficient RF conditioning of the cavities and acted as a source of free electrons, eventually captured by MP in the cavity vacuum. Experimental results of the cavities and couplers installed in the test cryomodule are discussed in [4].

Optimization for FRIB HWR

Geometric modification on short plate is naturally the first choice. To keep cavity performance, we consider changing the height H of the circle as shown in Figure 1 for optimization.

Figure 5 gives the effect of H on multipacting intensity. As the current design is 52mm, we change H from 5mm to 82mm in the simulation. The CST simulation shows that two-point 1st order multipacting disappears at H = 5mm with only one-point 1st order multipacting left.

In the CST simulation, we also found that the two-point 1st order multipacting moves to the outer conductor while decreasing H. This phenomenon can be explained by the physics model of multipacting condition, where the area that satisfied Eq. (1) and Eq. (6) has been moved to outer conductor as H decreases. At the same time, the area is reduced. Finally, two-point 1st order multipacting disappears at H=5mm.

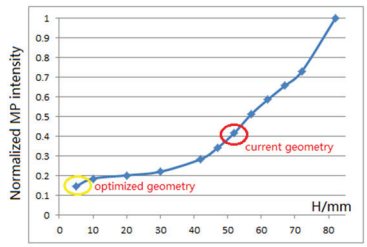

Figure 5: MP intensity versus H from CST simulations.

According to our analysis, the two-point 1st order multipacting can be suppressed by a flat short plate design (H=5mm). However, a flat plate is more sensitive to helium pressure fluctuation. If we make the plate thick, although the effect of helium pressure fluctuation becomes less, the cost increases a lot and thermal stability of the cavity is reduced. Moreover, this multipacting barrier is easily conditioned in the same cavities with the vertical test coupler. Due to such a trade-off and improvable test result, we currently prefer to condition the HWR to overcome multipacting. The solution is to remove MP from the coupler which is triggering the one in the cavity.

MULTIPACTING IN RF COUPLER

Physics Model for RF Coupler

Multipacting in RF coupler is caused by its coaxial structure, demonstrated by CST simulations. The coupler's multipacting locates at peak electric field region where magnetic force is very little. Assuming constant radial electric field, motion of electrons is

$$E_r = \frac{E_0 r_1}{r_2 - r_1}\ell n\frac{r_2}{r_1} \quad (8)$$

$$s(t) = \frac{eE_r}{\omega^2 m}(\omega t - \sin\omega t) \quad (9)$$

r_1 , r_2 is the inner and outer conductor radius, E_0 is electric field at inner conductor, e is electron charge, m is electron mass, ω is RF circular frequency, and $s(t)$ is the distance an electron travels.

Conditions for two-point multipacting thus become:

$$s(t=\frac{(2n-1)\pi}{\omega}) = r_2 - r_1 \Rightarrow E_0 r_1 = \frac{\omega^2(r_2-r_1)^2 m}{(2n-1)\pi e}(\ell n\frac{r_2}{r_1})^{-1} \quad (10)$$

$$W_1 \le \frac{2m\omega^2(r_2-r_1)^2}{(2n-1)^2\pi^2} \le W_2 \quad (11)$$

The RF power at which coupler has multipacting is

Copyright © 2012 by the respective authors — cc Creative Commons Attribution 3.0 (CC BY 3.0)

$$P_n = \frac{A\omega^4 (r_2 - r_1)^4 m^2}{(2n-1)^2 \pi \eta e^2} (\ell n(\frac{r_2}{r_1}))^{-1} \quad (12)$$

where n is the order of two-point multipacting, η is the wave impedance in vacuum (377Ω), A is 1 for traveling wave and 0.25 for standing wave (full reflection) from superposition theorem.

Figure 6 is the comparison between the widely known scaling law from E. Somersalo's paper [2] and Eq. (12).

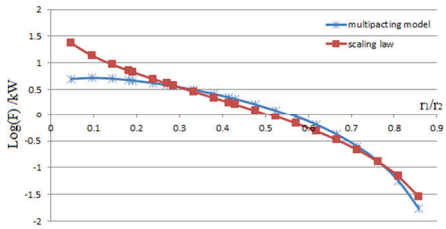

Figure 6: Comparison of the Eq. (12) results (blue line) and E. Somersalo's scaling law (red line) for two-point 1st order multipacting in the FRIB coupler, as we change the inner radius. Outer radius is 21mm.

In spite of our rough assumption for constant radial electric field, which should only valid with short gap between inner and outer conductor, the two lines have a rather good agreement and start having a larger discrepancy when r_1 is less than 4.

Confirmation with TDCM Test

Figure 7 shows the geometry of the FRIB HWR coupler, which is scaled from the SNS RF coupler. While the SNS coupler works at peak pulsed power 550 kW with little multipacting issue, the FRIB coupler must work at the power of 5kW CW, just at the multipacting barrier as shown in Figure 8. We define total secondary electrons in 8 RF cycles as multipacting strength. Density of primary electrons is identical for both couplers. As a result of CST simulation, the maximum multipacting of the SNS coupler is only 5% of FRIB's one. We compared CST simulation with TDCM test for the FRIB coupler, and they agree well as indicated in Figure 8.

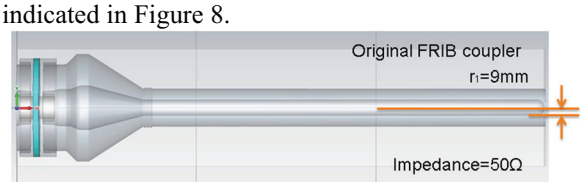

Figure 7: Geometry of FRIB coupler

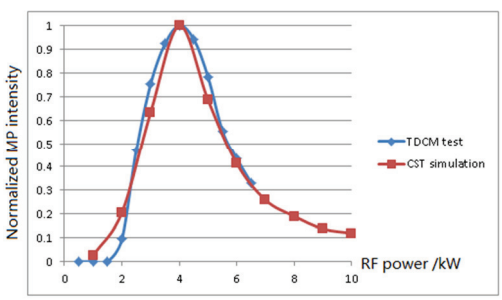

Figure 8: FRIB RF coupler's multipacting in cryomodule test and CST simulation. The peak electron intensity is normalized to 1.

Geometric Optimization of RF Coupler

Suggested by our analysis, there are two methods to suppress multipacting with geometric modification and two optimizations are proposed:

1) Reduce inner radius from 9mm to 6mm. The impedance will be changed from 50Ω to 75Ω though. Cavity design and CF flanges will be kept the same. RF power condition for two-point multipacting will shift to a higher point by 1.5 kW according to our model.

2) Enlarge outer radius to 31.4mm. Coupler impedance is also 75Ω. This change requires modification of the cavity at the port and a larger CF flanges. However, the RF power condition has been moved much higher - to about 18.2 kW.

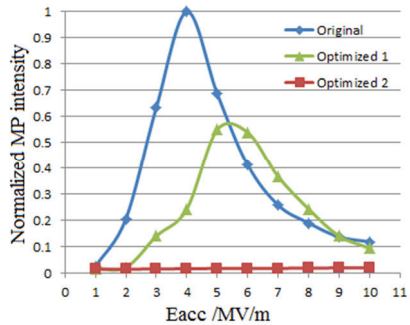

Figure 9: CST comparison of multipacting with the original coupler and two optimized designs. Green line corresponds to a smaller inner radius (6mm), while red line corresponds to a larger outer radius (31.4mm).

Figure 9 shows the comparison of multipacting intensity before and after the optimizations. Although we would prefer not to modify the cavity port, enlarging outer radius gives a much better mitigation of multipacting, and we are currently inclined to implement this modification.

CONCLUSION

In this paper, we verified CST simulations of multipacting with cryomodule test results for both HWR and RF coupler at FRIB. As the two-point 1st order multipacting dominates, we developed model and explained its physics for both HWR and RF coupler. Geometric optimizations have been proposed to mitigate multipacting, which are considered to be important changes and are under discussion and review.

REFERENCES

[1] http://www.cst.com/
[2] E. Somersalo, P. Yla-Oijala, D. Proch, "Analysis of multipacting in coaxial lines," 1996 IEEE.
[3] Hasan Padamsee, Jens Knobloch, Tom Hays, "RF Superconductivity for Accelerators", pp. 190-191.
[4] J. Popielarski, et al, "FRIB Technology Demonstration Cryomodule Test," MOPLB10.

Copyright © 2012 by the respective authors — cc Creative Commons Attribution 3.0 (CC BY 3.0)

ADRC CONTROL FOR BEAM LOADING AND MICROPHONICS *

Z. Zheng# (FRIB, East Lansing, Michigan; TUB, Beijing)
Z. Liu, J. Wei, S. Zhao, Y. Zhang (FRIB, East Lansing 48824, Michigan, USA)

Abstract

Superconducting RF (SRF) cavities are subject to many disturbances such as beam loading and microphonics. Although we implemented Proportional Integral (PI) control and Active Disturbance Rejection Control (ADRC) in the Low Level RF (LLRF) system at FRIB to stabilize the RF field, the control loop gains are inadequate in the presence of beam loading and microphonics. An improved scheme is proposed and simulated with much higher gains are achieved. The feasibility to include piezo tuner in ADRC and PI circuit is also presented in this paper.

INTRODUCTION

For a SRF cavity, there exist many disturbances, either external or self-induced, in which beam loading and microphonics are two most important ones. While beam loading disturbs the cavity voltage and RF phase with beam induced voltage, microphonics detunes cavity by mechanical perturbations. To reject the disturbances, PI control strategy and ADRC method have been considered. PI handles disturbances in a passive way, reacting to tracking errors caused by the disturbances, while ADRC rejects the disturbances actively by estimating the disturbances directly.

In the original LLRF system of FRIB cavities, both PI and ADRC solutions are implemented to control the amplitude and phase separately, because it was assumed that independent amplitude and phase control will benefit more to operation. Simulation shows that such a scheme presents potential difficulties in phase control, with both ADRC and PI, where the loop gain can be inadequate to reject microphonics. Figure 1 shows the phase fluctuation of ADRC exceeds the cavity phase stability limit of 0.5 degree. PI control performs worse than ADRC with much larger phase and amplitude fluctuations with separated phase and amplitude controllers.

According to SNS LLRF control experience [1], we proposed a new scheme to process and control the cavity voltage as a vector instead of separating amplitude and phase. Section 1 explains the new model of ADRC control. Section 2 shows the comparison of ADRC and PI with the new scheme, from which one can see the stable loop gain increased significantly and rejected beam loading and microphonics effectively. Section 3 discusses the feasibility to reject microphonics by a piezo-tuner.

*Work supported by the U.S. Department of Energy Office of Science under Cooperative Agreement DE-SC0000661
#zhzheng@msu.edu

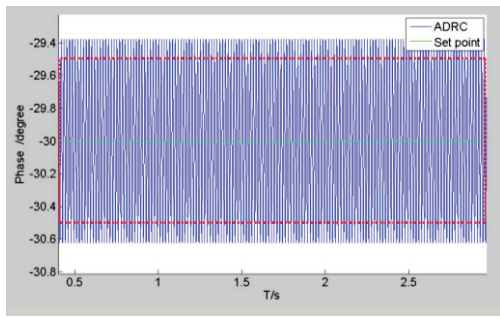

Figure 1: Phase fluctuation to reject microphonics by the original ADRC scheme. The red line marks the fluctuation limit due to stability concern of cavity phase. Microphonics amplitude is assumed to be 20Hz in this calculation.

MODEL OF ADRC CONTROL

The cavity dynamics is represented by a parallel RLC circuit as shown in Figure 2. According to Kirchhoff's law, we have:

$$\frac{d^2\hat{V}_c}{dt^2}+\frac{\omega_0}{Q}\frac{d\hat{V}_c}{dt}+\omega_0^2\hat{V}_c=\frac{R\omega_0}{Q}\frac{d\hat{I}_c}{dt} \quad (1)$$

$$\hat{I}_c=\frac{(\hat{I}_g+\hat{I}_b)Z_{ext}}{Z_{ext}+Z_{cav}} \quad , \quad Z_{ext}=\frac{R}{\beta} \quad (2)$$

$$\hat{V}_c(t)=\vec{V}(t)e^{jw_gt}=V_c(t)e^{j\varphi_v(t)}e^{jw_gt} \quad (3)$$

$$\hat{I}_c(t)=\vec{I}_c(t)e^{jw_gt}=I_c(t)e^{j\theta(t)}e^{jw_gt} \quad (4)$$

Since $\dot{\vec{V}}_c << \omega_g\vec{V}_c$ and $\dot{\vec{I}}_c << \omega_g\vec{I}_c$, Eq. (1) can be simplified to first-order differential equation as:

$$\dot{\vec{V}}_c+\omega_{1/2}(\vec{V}_c-\frac{\hat{I}_bZ_{ext}}{Z_{ext}+Z_{cav}}R)+\frac{\Delta\omega}{j}\vec{V}_c=\omega_{1/2}\frac{\hat{I}_gZ_{ext}}{Z_{ext}+Z_{cav}}R \quad (5)$$

where ω_0 is cavity resonant frequency and Q is quality factor, β is coupling factor, $\tilde{I}_g$ is generated current, $\tilde{I}_b$ is beam induced current due to beam loading effect, $\tilde{I}_c$ is total current of cavity, $\tilde{V}_c$ is cavity voltage, ω_g is generator circular frequency, $\Delta\omega=\omega_0-\omega_g$ is the total cavity detuning by microphonics and tuner, $\omega_{1/2}=\omega_0/2Q$ is cavity half bandwidth, Z_{cav} and Z_{ext} is cavity and external impedance.

According to the model, we can define the output of cavity system as $y=\alpha\vec{V}_c$, cavity input as $u=I_g/A$. Eq. (5) can be simplified as $\dot{y}=f+bu$, where

$$f=-\alpha\omega_{1/2}(\vec{V}_c-\frac{\hat{I}_bZ_{ext}}{Z_{ext}+Z_{cav}}R)-\alpha\frac{\Delta\omega}{j}\vec{V} \quad (6)$$

Copyright © 2012 by the respective authors — cc Creative Commons Attribution 3.0 (CC BY 3.0)

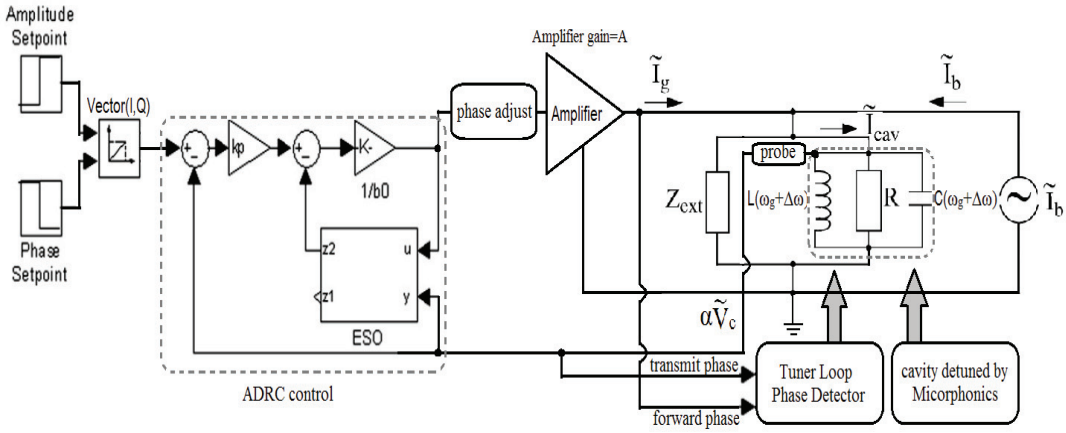

Figure 2: Model of ADRC control with new vector-control scheme

$$b = \alpha\omega_{1/2} AR \frac{Z_{ext}}{Z_{ext} + Z_{cav}} \quad (7)$$

f is considered as the total disturbance, b is design parameter of cavity system. This conventional ADRC model [2] is simulated as shown in Section 3.

COMPARISON OF PI AND ADRC

We took an example of FRIB β=0.085 quarter-wave resonators (QWR085), which has a bandwidth of 40 Hz. Data sampling rate is set to be 25 kHz. For ADRC, the controller and observer bandwidths are set to 10000 and 20000 rad/s respectively. PI controller is tuned with a proportional gain of 600 and an integral gain of 2500. Those parameters were picked to achieve best stable response and far exceeded the limit of old scheme.

Compensation of Beam Loading

The average beam current for QWR085 cavity is 352 μA [3]. A bunch beam (2~2.5s) is assumed. Figure 3 and Figure 4 show the comparison of PI and ADRC control for amplitude and phase control. Both PI and ADRC can reject the beam loading effectively, with small amplitude fluctuation of ±0.08% and phase fluctuation of ±0.03°. PI takes much longer to get back to set point than ADRC.

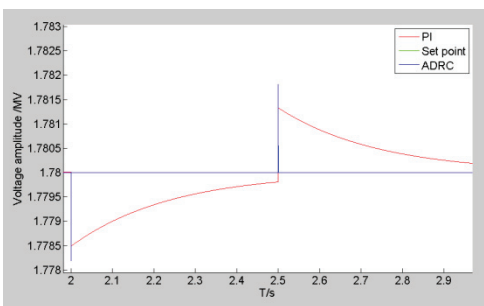

Figure 3: Cavity voltage amplitude fluctuation to reject beam loading. Amplitude's set point (1.78MV) is overlap with blue line.

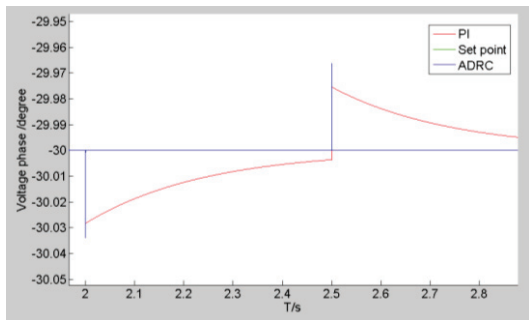

Figure 4: Cavity voltage phase fluctuation to reject beam loading. Phase set point (-30°) is overlap with blue line.

Microphonics

The frequency of microphonics is 60Hz and amplitude is set to be 20Hz, same as the maximum cavity detuning tolerance. Figure 5 and Figure 6 compare PI and ADRC to reject microphonics. The amplitude fluctuation is ±0.001% for PI and vanishing small for ADRC. Phase fluctuation is ±0.31° for PI and ±0.03° for ADRC. Obviously, ADRC performs better than PI in rejecting microphonics.

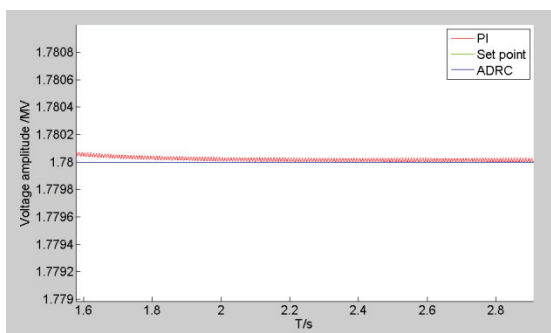

Figure 5: Cavity voltage amplitude fluctuation for microphonics. Amplitude's set point (1.78MV) is overlap with blue line.

Copyright © 2012 by the respective authors — cc Creative Commons Attribution 3.0 (CC BY 3.0)

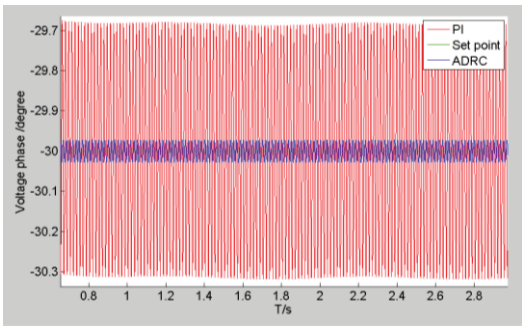

Figure 6: Cavity voltage phase fluctuation for microphonics. Green is set point=-30°.

PIEZO TUNER FOR MICROPHONICS

Piezo-tuner is driven by piezo actuators for fast and fine adjustments of cavity's frequency. Since piezo tuner is commonly used to compensate Lorenze Force Detuning (LFD) and microphonics for pulsed power accelerators, we also studied its feasibility to be included in PI and ADRC control systems.

In the simulation as shown in Figure 7, piezo tuner is assumed to be linear with a sampling rate of 25 kHz. Its tuning range is ±40 Hz without mechanical backlash.

Simulation shows that the response time of piezo tuner in ADRC should be smaller than 0.03 ms for stable response. Considering most piezo tuner response time is 0.1~1 ms, it is not the right choice for the current ADRC control. In PI control, the required piezo tuner response time should be less than 0.6 ms and it could be achievable. Figure 7 shows phase fluctuation reduced by a 0.5 ms piezo tuner. Figure 8 shows RF power used by ADRC for successful rejection without assistance from piezo tuner. Figure 9 shows RF power used by PI for successful rejection with help of piezo tuner.

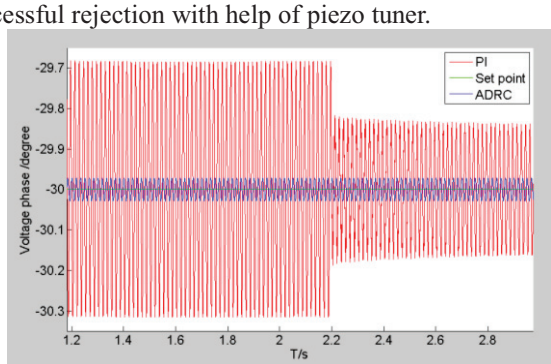

Figure 7: Phase fluctuation reduced by piezo-tuner. Piezo-tuner response time is set to 0.5 ms. Blue is ADRC without piezo-tuner, red is PI with a piezo-tuner turned on at 2.2 s.

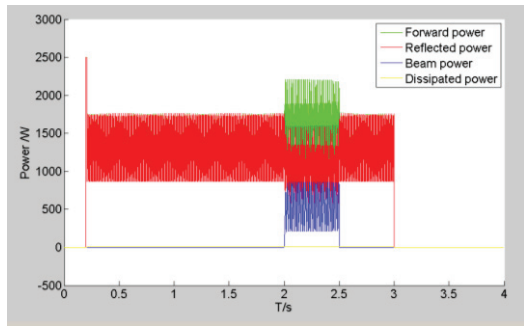

Figure 8: Power needed in ADRC without piezo-tuner. RF power is turned on at t=0.2s and off at t=3s. PI without piezo-tuner consumes similar RF power.

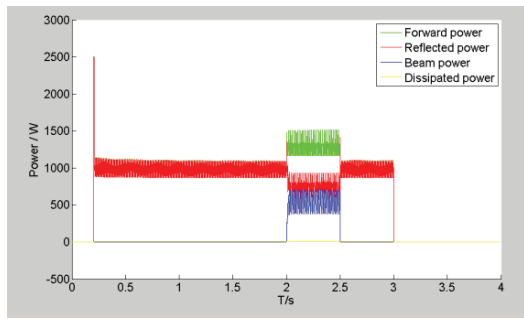

Figure 9: Power needed in PI with piezo-tuner. RF power is turned on at t=0.2s and off at t=3s.

Although piezo tuner can help save RF power by ~650W in PI control (compare with RF power by PI without piezo tuner), we still prefer a smaller phase fluctuation without piezo tuner with ADRC. Since FRIB cavity is operated at CW without Lorentz Froce Detuning (LFD), the RF power consumed to compensate microphonics without piezo tuner is still tolerable. In this sense, we prefer ADRC without piezo tuner to reject microphonics.

CONCLUSION

In this paper, we developed new control model with improved vector-control scheme to reject disturbances. ADRC and PI method have been studied respectively to compensate beam loading and microphonics. As ADRC reacts more quickly and fluctuates much less, we are inclined to use ADRC for FRIB LLRF system to reject beam loading and microphonics.

REFERENCES

[1] Hengjie Ma, private conversation.
[2] J. Vincent, et al, "On active disturbance rejection based control design for superconducting RF cavities". Nuclear Instruments and Methods in Physics Research A 643 (2011) 11–16.
[3] Y. Zhang, et al, "Simulation study and initial test of the SNS ring RF system", PAC'07 (2007) 2520.

Copyright © 2012 by the respective authors — cc Creative Commons Attribution 3.0 (CC BY 3.0)

LONGITUDINAL DYNAMIC ANALYSIS FOR THE PROJECT X 3-8 GeV PULSED LINAC

G. Cancelo, B. Chase, Nikolay Solyak, Yury Eidelman, Sergei Nagaitsev
Fermi National Accelerator Laboratory, Batavia, IL 60510, U.S.A.

Abstract

The Pulsed Linac requires over 200 9-cell, 1300 MHz cavities packed in 26 ILC type cryomodules to accelerate 1 mA average beam current from 3GeV to 8 GeV. The architecture of the RF must optimize RF power, beam emittance, and energy gain amid a large number of requirement and constraints. The pulse length is a critical issue. Ideally, a 26 ms pulse would allow direct injection into the Fermilab's Main Injector, bypassing the need of the Fermilab's Recicler. High loaded quality factors (QL) are also desirable to minimize RF power. These requirements demand an accurate control of the cavity resonant frequency disturbed by Lorentz Force Detuning and microphonics. Also the LLRF control system must regulate the RF amplitude and phase within tight bounds amid a long list of dynamic disturbances.

INTRODUCTION

The H^- 3-8 GeV LINAC for Project X [1] is optimized for accelerating the synchronous particle at a small negative phase close to the RF peak voltage. At 3 GeV beam β's and transit time factors (TTF) along the 200+ cavity LINAC are near 1and monotonically increasing along z. Although TTF and β_b impact in the longitudinal dynamics most longitudinal problems arise from the fact that, to cut costs, modern accelerators are being designed powering a string of cavities from one klystron. As multiple cavities are connected to a single klystron the setting and control of RF system parameters becomes more complex. A low level RF (LLRF) control loop controls the amplitude and the phase of the klystron's RF power. However, the loop cannot dynamically control individual cavity amplitude and phases. This is further complicated due to Lorentz forces (LFD) and microphonics that severely detune superconducting cavities. One more problem arises from the fact that to achieve the maximum possible acceleration cavities are operated at their maximum operating gradient, close to their quenching limit. Since some disturbances are pulse to pulse repetitive we can use some feedforward compensation. For instance LFD can be minimized at the single cavity level using piezoelectric tuners. The setting of RF cavity parameters such as synchronous phases (Φs), predetuning (Δω) and RF power P_{for_i} and fill time t_0 are very important.

LONGITUDINAL DYNAMICS SIMULATIONS

For small phase-energy oscillations the stability of the longitudinal dynamics can be studied using a Hamiltonian equation (1) relating the phase and energy stability [2] (Figure 1).

$$H_\phi = \frac{A w^2}{2} + B(\sin\phi - \phi\cos\phi_s), \qquad (1)$$

where the first term represents the kinetic energy of the particle and the second term the potential energy. A and B are constants:

$$A = \frac{2\pi}{\beta_s^3 \gamma_s^3 \lambda} \quad , \quad B = \frac{qE_0T}{mc^2}$$

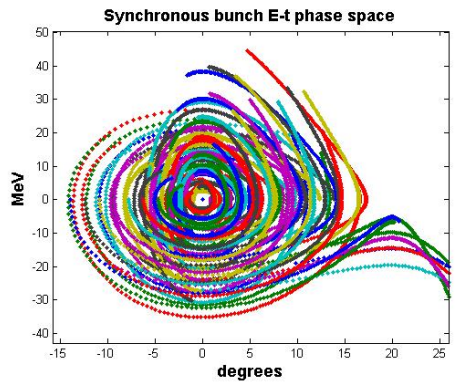

Figure 1: Synchronous bunch E-T phase space.

As shown in Figure 2, at 3 GeV the small amplitude oscillation frequency is 1.24 MHz (i.e. 0.8μs period). The oscillation frequency slows down as energy increases.

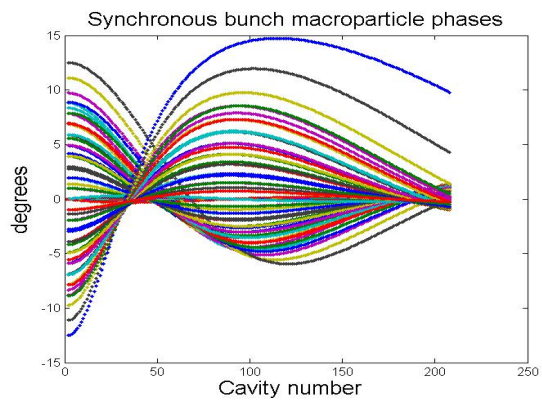

Figure 2: Synchronous bunch macroparticle phases.

$$\omega_{osc} = \sqrt{\frac{\omega_0 E_0 TTF \sin(\phi_s) c}{mc^2 \beta_s \gamma_s^3}}$$

$\phi_s = -10°$	*sync_phase*
$TTF = 0.97$	*TransitTimeFactor*
$E_0 = 3GeV$	*InitEnage*
$\beta_s = 0.95$	*syncbeta*
$\omega_0 = 2\pi 1.3GHz$	*RFfreq*

These simulations are performed using a bunched beam represented by 73 macroparticles and a Gaussian profile in E and t. The total number of particles is 6.24 10^{12} per mA of current.

The simulated conditions are:

*Work supported by Fermi Research Alliance, LLC. under Contract No. DE-AC02-07CH11359 with the United States Department of Energy.
cancelo@fnal.gov

Copyright © 2012 by the respective authors — cc Creative Commons Attribution 3.0 (CC BY 3.0)

- Average gradient amplitude 25 MV/m.
- 13 RF Stations: 2 cryomodules with 8 cavities/cryomodule and a total of 16 cavities/RF Station.
- Total Energy gain ~5 GeV.
- Beam current: 1 mA (try also 2 mA).
- Beam phase: -10 degrees.
- RF pulse: 4.3 to 30 ms flattop.
- Fill Time: 4.243 ms.
- Qload: up to a maximum of 10^7.
- R/Q=1036 Ohm/cav.

At 25MV, I_b=1mA and (R/Qo)=1036Ω the Q_L for power matching is 2.5e7, implying a $BW_{1/2}$ of 26Hz. In order to better deal with LFD and u-phonic disturbances a Q_L=1x10^7 has been set.

Major concerns studied are:

- Energy spread inside the RF station. Despite a well regulated VS there may be emmitance grow and beam loss due to tilts in amplitudes and phases of individual cavities under the same close loop.
- LFD: peak to peak detuning, in particular for long pulses (4, 8 and 30ms flattops)
- Impact of fill time in LFD.
- Active compensation.
- Maximum RF accelerating energy: cavity gradients close to quenching limits.
- Influence of cavity gradient spread in the RF station.
- Optimum cavity loaded quality factors (QL) as a function of cavity gradients.

CAVITY ELECTRICAL AND MECHANICAL MODELS

The electrical model is represented by a 1st order differential equation modeled with 2 state-variables, the I and Q components of the cavity voltage.

$$\begin{bmatrix} \dot{V}_r \\ \dot{V}_i \end{bmatrix} = \begin{bmatrix} -\omega_{1/2} & -\Delta\omega \\ \Delta\omega & -\omega_{1/2} \end{bmatrix} \cdot \begin{bmatrix} V_r \\ V_i \end{bmatrix} + \begin{bmatrix} \omega_{1/2} R_L \\ \omega_{1/2} R_L \end{bmatrix} \cdot \begin{bmatrix} I_r \\ I_i \end{bmatrix} \quad (2)$$

The model is time-varying because the detuning (Δω) varies along the pulse. Δω is coupled through the mechanical model. The mechanical model is represented by 2nd order differential equation of the cavity detuning as a function of the square of the gradient for each mechanical resonant mode.

$$\frac{d^2(\Delta\omega_m)}{dt^2} + \frac{\omega_m}{Q_m}\frac{d(\Delta\omega_m)}{dt} + (\omega_m)^2 \Delta\omega_m = (\omega_m)^2 2\pi K_m V^2(t)$$

$$\Delta\omega_m = \sum_{m=1}^{3} \Delta\omega_m \qquad m = 1,2,3$$

ILC type 9-cell niobium cavities detune about 600Hz at 25MV by effect of LFD. This number is prohibitive in terms of RF power required. We assume that LFD can be controlled to 60Hz or better. We also assume a microphonic detuning of ±5Hz RMS (Figure 3).

The LFD is a function of V^2. Longer flattops do not imply worse LFD after the first minimum which occurs at 4ms. Predetuning the cavities increases the LFD oscillations although shortens the time of the first minimum to 2ms (Figure 3).

A possible way for reducing the LFD using the RF is to make a smoother Off to On power transition. For instance if instead of applying a power step we ramp the power during part or all the fill time, the detuning becomes,

$$\Delta\omega = \frac{V_0^2}{t_{fill}^2}\left[t^2 - at + \frac{e^{-t/\tau}}{\sqrt{4Q_m^2 - 1}}\left(1 - \sin\left(\sqrt{4Q_m^2 - 1}\,\omega_m t + \phi_0\right)\right)\right]$$

For $0<t<t_{fill}$. And where a is the slope of the ramping power. For small t we can achieve a substantial LFD reduction at the expense of a longer fill time. However single digit peak to peak LFD numbers can, so far, only be achieved using piezotuners.

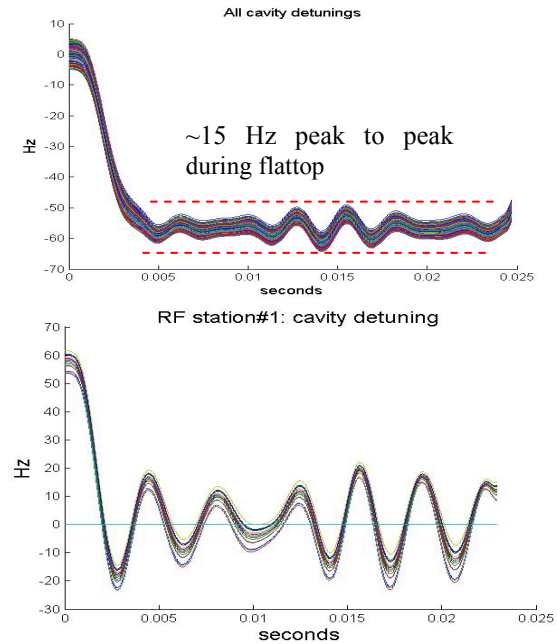

Figure 3: All cavity detunings (upper trace) and with pre-detuning (lower trace).

RF PARAMETER SETTING

A key problem is the control of a string of cavities operating at different gradients, synchronous phases and beam loading. A real life example we simulated using the gradients of the two highest accelerating cryomodules at DESY-FLASH (ACC6 and ACC7), which average 24.8 and 27.5 MV/cav and a total of ~420MeV. The RF station gradient spread can be about 20% of the mean gradient.

A simplistic option is to operate all cavities at the same gradient and loaded Q's (Q_L), below the gradient of the cavity with the lowest quenching limit. This option avoids individual cavity tilts at all beam loading conditions. The advantage is simplicity. We can use a fix RF distribution and, in principle, fix couplers, but we give up 20% of the gradient.

A fixed proportional power distribution allows individual gradients to approach higher limits. However, this approach must be accompanied with adjustable couplers to be able to flatten individual cavities for each beam loading.

Cavity tilts arise due to mismatch between RF, beam and cavity parameters including magnitude, phase and detuning.

Copyright © 2012 by the respective authors — cc Creative Commons Attribution 3.0 (CC BY 3.0)

Cavity tilts force us to lower gradients to avoid quenches. Cavity tilts and cryomodule misalignment generate transverse kick and large emitance growth. And tilts are proportional to the flattop length.

The most common approach for finding optimum longitudinal parameters is to consider zero reflected power at beam injection [3]. During the fill time of the RF pulse the cavity gradient increases exponentially from 0 to V_{cav0} and, if at beam injection, the RF forward power equals the beam power then the system suddenly enters the steady state and a flat pulse is achieved. Unfortunately this is seldom the case when the RF station operates cavities at different gradients, synchronous phases and beam loadings. The steady state approach finds:

$$\beta_{opt} = 1 + \frac{2RI_{b0}}{V_{cav}}\cos\phi_s \quad , \quad \varphi_{opt} = -\phi_s, \quad P_{ref_cav}=0. \quad (3)$$

A simulation with parameters calculated by (3) and LFD show gross cavity amplitude and phase deviations during the pulse which translates into up to 5MeV energy spread between the head and the tail of the bunch train (Figure 4). Even when the RF Vector Sum is well control by the feedback loop.

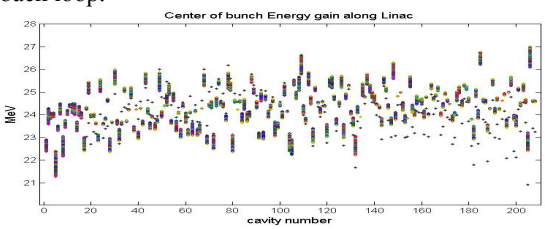

Figure 4: Simulation of bunch energy.

As a consequence the zero reflected power premise is not met either. An alternative approach is using the transient response of the cavity equations and setting $V_{cav_i}=0$ for $t>T_{fill}$, without constraining the reflected power [4].

The RF system voltages and currents are modelled by equations (2).

For fix or null LFD the system is linear, the cavity voltage is the superposition of the cavity response to the generator and beam currents (power) $I_g e^{j\theta}$ and $I_b e^{j\pi}$.

The solution to equation (2) is given by:

$$\begin{pmatrix} V_r \\ V_i \end{pmatrix} = \frac{\omega_{12}R_L}{\omega_{12}^2+\Delta\omega^2}\left\{ e^{-\omega_{12}t}I_g\begin{pmatrix} -\omega_{12}\cos(\Delta\omega t+\theta)+\Delta\omega\sin(\Delta\omega t+\theta) \\ -\Delta\omega\cos(\Delta\omega t+\theta)-\omega_{12}\sin(\Delta\omega t+\theta)\end{pmatrix}u(t) + I_g\begin{pmatrix} \omega_{12}\cos\theta-\Delta\omega\sin \\ \Delta\omega\cos\theta+\omega_{12}\sin \end{pmatrix} \right.$$
$$\left. e^{-\omega_{12}(t-t_o)}I_b\begin{pmatrix} -\omega_{12}\cos\Delta\omega(t-t_o)+\Delta\omega\sin\Delta\omega(t-t_o) \\ -\Delta\omega\cos\Delta\omega(t-t_o)-\omega_{12}\sin\Delta\omega(t-t_o)\end{pmatrix}u(t-t_0) - I_b\begin{pmatrix}\omega_{12}\\ \Delta\omega\end{pmatrix}u(t-t \right. \quad (4)$$

Where u(t) is the Heaviside function (i.e. u(t)=1 t≥0 and 0 otherwise).

To obtain a flattop at the injection time $t=t_0$ we must eliminate the time dependency in equation (4). That is achieved by making

$$I_g = e^{\omega_{12}t_o} I_b \quad (5a) \quad \text{and} \quad \Delta\omega = -\theta/t_0 \quad (5b)$$

Equations (5a,b) guarantee a flattop for $t\geq t_0$. The appropriate value for the flattop amplitude and phase can be obtained from equation (4) at $t=t_0$- given by

$$\begin{pmatrix} V_r \\ V_i \end{pmatrix}_{t=t_o} = \frac{\omega_{12}R_L}{\omega_{12}^2+\Delta\omega^2}\left\{ e^{-\omega_{12}t_o}I_g\begin{pmatrix} -\omega_{12} \\ -\Delta\omega\end{pmatrix} + I_g\begin{pmatrix} \omega_{12}\cos\theta-\Delta\omega\sin\theta \\ \Delta\omega\cos\theta+\omega_{12}\sin\theta\end{pmatrix}\right\}$$

Using the tuning angle equation $\tan\psi = \frac{\Delta\omega}{\omega_{12}}$, the cavity voltage amplitude and phase are given by:

$$|V_c| = \frac{R_L I_b}{1+\tan^2\psi}\sqrt{\left(-1+e^{\omega_{12}t_o}(\cos\theta-\tan\psi\sin\theta)\right)^2+\ldots} \quad (6)$$
$$\ldots+\left(-\tan\psi+e^{\omega_{12}t_o}(\tan\psi\cos\theta+\sin\theta)\right)^2}$$

$$\phi_s = \tan^{-1}\left(\frac{\tan\psi\cos\theta+\sin\theta-\tan\psi e^{-\omega_{12}t_o}}{\cos\theta-\tan\psi\sin\theta-e^{-\omega_{12}t_o}}\right) \quad (7)$$

Equations (6) and (7) have 3 unknowns: the RF cavity phase θ (i.e. ψ), β (i.e. Q_L) and t_0. Both R_L and the half bandwidth ω_{12} are a function of β. (6) and (7) with constrains (4) and (5) are solved for for θ and β for a fix t_0. Also t_0 can be used to optimize the reflected power. Figure 5 shows how amplitudes and phases are maintained fairly flat even in high LFD and RF closed loop.

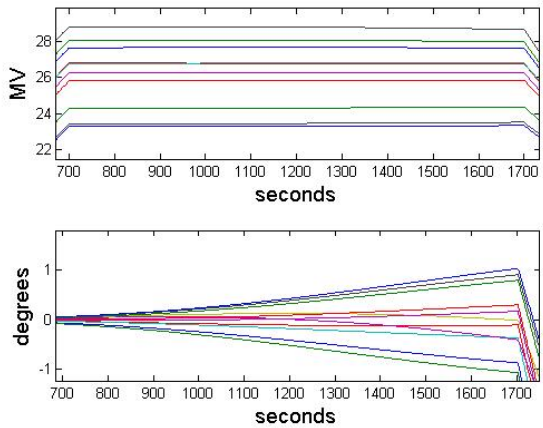

Figure 5: Stabilized amplitude and phases.

As part of the ILC 9mA experiment at DESY-FLASH we have reduced tilts even further using an iterative procedure that fine tunes the Q_L's. Tilts better 0.2% RMS over 800us have been obtained in an RF station with 16 cavities [5].

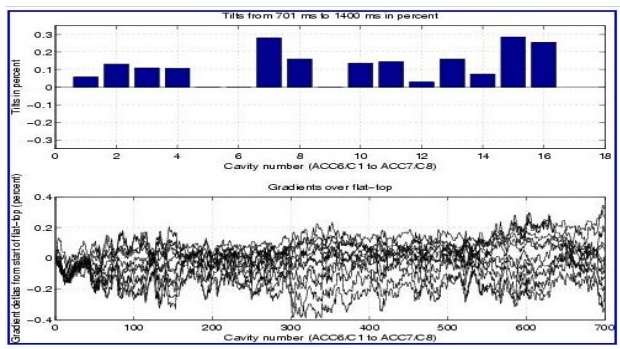

Figure 6: Cavity tilts in FLASH ACC 6 and 7.

REFERENCES

[1] Holmes, S.. "Project X reference Design Report", http://projectx-docdb.fnal.gov., Nov. 2010.

[2] T.P. Wangler. *Principles of RF Linear Accelerators*, John Wiley&Sons, Inc., NY, 1998.

[3] Schilcher, T. "Vector Sum Control of Pulsed Accelerating Fields in Lorentz Force Detuned Superconducting Cavities", Ph.D thesis, DESY, Hamburg, August 1998.

[4] Cancelo et al. "Optimizing cavity gradients in pulsed (6) Linacs using the cavity transient response",LINAC08, Canada, Sep. 1998.

[5] Carwardine et al. "The ILC 9mA experiment at DESY-FLASH", in preparation.

Copyright © 2012 by the respective authors — cc Creative Commons Attribution 3.0 (CC BY 3.0)

REDUCED-BETA CAVITIES FOR HIGH-INTENSITY COMPACT ACCELERATORS*

Z.A. Conway#, S. Gerbick, M.J. Kedzie, M.P. Kelly, J. Morgan, R. Murphy, P.N. Ostroumov, and T. Reid, ANL, Argonne, IL 60439, USA

Abstract

This paper reports on the development and testing of a superconducting quarter-wave and a superconducting half-wave resonator. The quarter-wave resonator is designed for beta = 0.077 ions, operates at 72 MHz and can provide more than 7.4 MV of accelerating voltage at the design beta, with peak surface fields of 165 mT and 117 MV/m. Operation was limited to this level not by RF surface defects but by our administrative limits on x-ray production. A similar goal is being pursued in the development of a half-wave resonator designed for beta = 0.29 ions and operating at 325 MHz.

INTRODUCTION

The length and cost of the low-velocity portion ($\beta = v/c < 0.6$) of superconducting proton and heavy-ion linacs are dominated by the accelerator cavity performance. Accelerator cavities used in this velocity region, reduced-beta cavities, have not performed at the same peak-surface fields which are regularly achieved in elliptical-cell cavities optimized for velocity-of-light electrons [1], 160 mT and 80 MV/m peak surface fields. This performance disparity has been blamed on the greater complexity of the reduced-beta cavity fabrication and processing. Several advances at Argonne National Laboratory in cavity design [2]; fabrication and processing have disproved this hypothesis.

First, the results locating a defect which limited the performance of a prototype 72 MHz quarter-wave cavity (QWR) optimized for $\beta = 0.077$ ions for the ATLAS intensity upgrade will be presented. Second, the fabrication and processing of a subsequent geometrically identical quarter-wave cavity will be outlined. Finally, the impact of these results and future plans for a similarly constructed half-wave cavity will be discussed.

INITIAL PROTOTYPE PERFORMANCE

The QWR prototype fabrication and test results were presented in [3]. Since these papers were published we have refined our electromagnetic simulations of the cavity surface fields and the results used in this paper are given in table 1. This cavity was limited to peak surface fields of 96 mT and 70 MV/m by a surface defect which initiated a cavity quench. Figure 1, shows the cavity with the location of the defect highlighted in red along with a single channel record of the quench.

The defect was located by measuring the time-of-flight of second sound waves propagating from the cavity quenching defect to an array of oscillating superleak transducers [4]. The distance the second sound wave travelled was calculated with the wave velocity. This combined with the known location of the detectors allowed us to determine the defect location. Our detector array was 1-dimensional in nature and located the height of the defect in the quarter-wave cavity center conductor.

This defect was located at the same height as an electron beam weld blow-out which occurred during final welding of the center conductor. The center conductor is formed from two halves which are welded together. The center conductor halves were tack welded, but the final electron beam welds could not be finished within the desired 24-hour etch window between pre-weld etching and welding. The parts were etched again after tacking and the very small-gap joint between the two parts could not be properly cleaned. Some foreign debris was trapped in this joint which caused a blow-out during the final electron beam welding which was repaired.

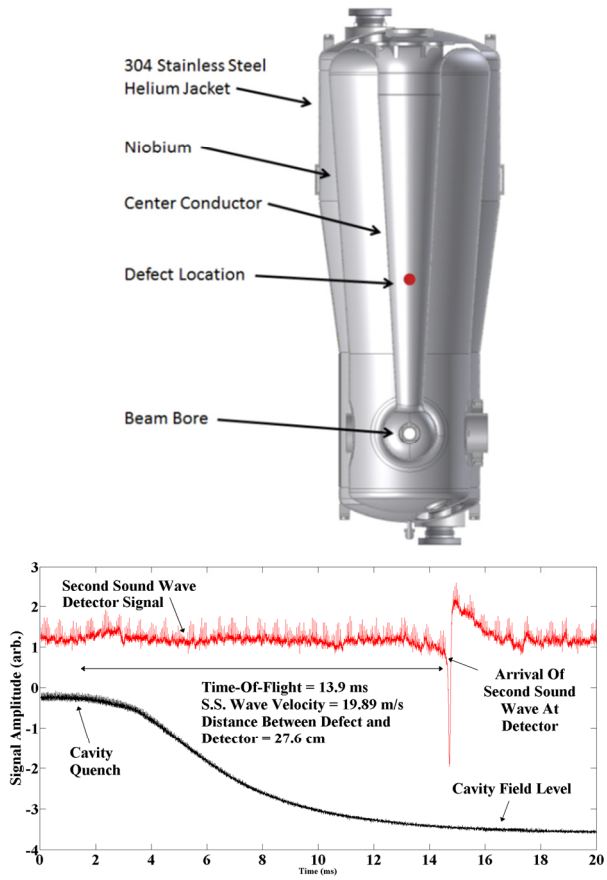

Figure 1: (Top) The cavity with a red dot placed at the height of the defect in the center conductor, the cavity is 53 inches from top to bottom . (Bottom) A single quench event with an oscillating superleak transducer signal and the cavity transmitted power.

* This work was supported by the U.S. Department of Energy, Office of Nuclear Physics, under Contract DE-AC02-06CH11357 and ANlLWFO 8R268 supported by DTRA.
# zconway@anl.gov

Copyright © 2012 by the respective authors — cc Creative Commons Attribution 3.0 (CC BY 3.0)

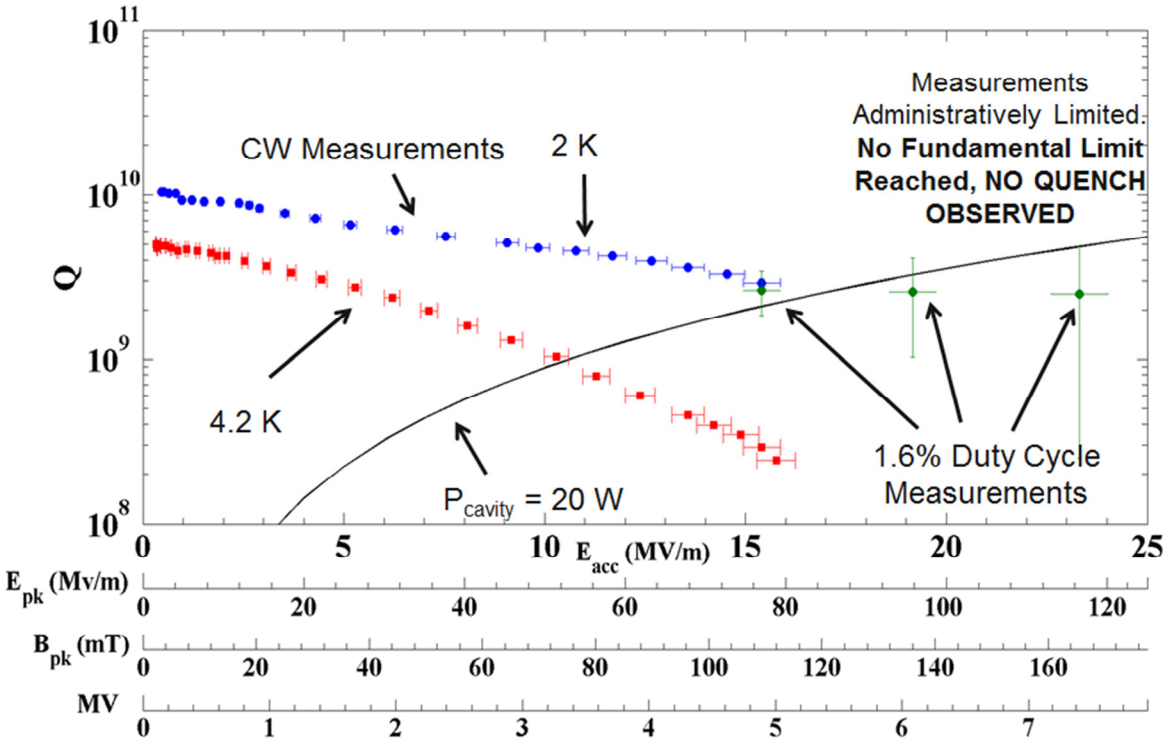

Figure 2: The measured performance of the QWR. There are 4 horizontal axes corresponding to the accelerating gradient, peak surface electric and magnetic fields, and the voltage gain of a synchronous β = 0.077 ion. The vertical axis corresponds to the cavity quality factor. The blue data points were measured at 2 K and the red data points were measured at 4.2 K in the cw mode, the green points were measured at 2 K with a 1.6% duty cycle, and the solid black line corresponds to 20 W of RF power dissipated in the cavity. No fundamental limit to the cavity performance was encountered and the cavity could have reached higher fields with appropriate radiation shielding

Table 1: Electromagnetic Properties of the QWR

Freq. (MHz)	72.75
β	0.077
l_{eff} (cm, βλ)	31.75
E_{pk}/E_{acc}	5.0
B_{pk}/E_{acc} (mT/(MV/m))	7.1
QR_s (Ω)	25.9
R_{sh}/Q (Ω)	568

FABRICATION AND PROCESSING

Here the fabrication details which differ from what was presented in [3] for the prototype QWR are listed:

1) Very careful attention was paid to the status of the weld joints and their preparation prior to electron beam welding. All components were soaked in DI water after every handling/machining step to look for inclusions.
2) Significantly more surface inspection and QA. The cavity RF surface was carefully hand-polished with 220 grit sandpaper to avoid fold-over and deep polishing marks. All pits, orange-peel, and scratches were polishing in this manner in the high field regions.
3) The temperature of the pre-weld etches were limited to T < 16^{0}C to limit hydrogen uptake. The bulk electropolish procedure (~120 μm removal) temperature was reduced to 25 < T < 30^{0}C. The final light (~20 μm removal) electropolish temperature was 20 < T < 25^{0}C.
4) The cavity was baked at 625^{0}C for 24 hours to degas the hydrogen dissolved in the bulk niobium. This prevents Q-disease and improves the 2 K performance of the cavity.

After fabrication was complete the electropolishing, baking, and cleaning proceeded. Recent tests of similar cavities have found that the Q may be improved by about a factor of 2 by reducing the 625^{0}C bake duration to 12 hours [5].

TEST RESULTS

The cavity vacuum was allowed to pump for 72 hours reaching a pressure < 1 e-7 torr prior to cooldown. The cavity was cooled to 4.2 K with care taken to limit the time spent between 50 and 165 K to about 45 minutes even with the hydrogen degassing. The cavity was conditioned using up to 10 watts of RF power to remove the low-level multipacting barriers over ~2 hours and then 5 minutes of pulsed power processing at 4.6 K with 4 kW

Copyright © 2012 by the respective authors — cc Creative Commons Attribution 3.0 (CC BY 3.0)

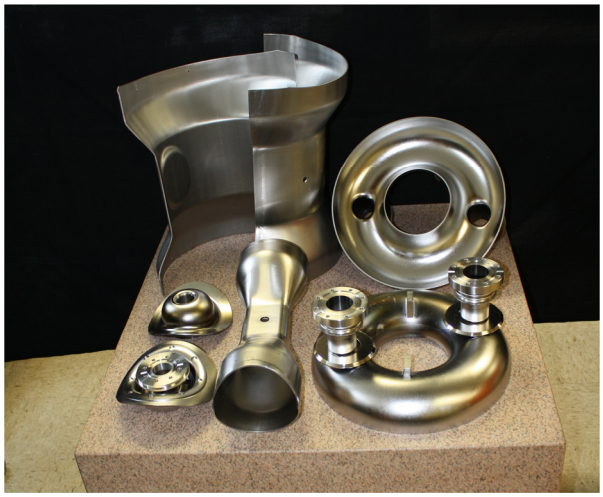

Figure 3: The niobium subassemblies which will be welded together to make the HWR. The parts clockwise from top left are outer-conductor halves, toroids, inner-conductor, and re-entrant noses.

of forward power. Following this conditioning the performance given in figure 2 was observed. Note that the residual resistance of the cavity at low-fields is less than 4.5 nΩ at 4.2 K and 2.5 nΩ at 2.0 K. The gradients presented in figure 2 were not limited by any fundamental phenomena, e.g., defect-initiated quench or field emission. The results were limited administratively to avoid exceeding the ANL limits on x-ray production. The cavity is only partially shielded behind a high-density concrete wall and is not in a complete cave-like enclosure. This allows considerable x-ray shine to reach experimenters. To reduce the average x-ray production the cavity was operated with a 1.6% duty cycle to safely comply with the ANL guidelines. The data points measured in this manner are highlighted in green and are the three highest gradient 2 K measured data points. Please note that the cavity dissipated power measurement accuracy decreased due to measuring these data points in the over-coupled limit but the relative accuracy of the field amplitude is unchanged. The highest data point measured was repeatable and corresponded to a voltage gain of 7.4 MV and peak surface fields of 165 mT and 117 MV/m. At no point was the QWR tested here quenched. The high field data points do not represent a fundamental limit on the cavity performance. With additional radiation shielding the maximum performance of this cavity can be determined.

The best 9-elliptical cell cavity built for the ILC program reached 175 mT and 84 MV/m. The quarter-wave cavity tested here reached comparable peak surface magnetic fields relative to the best 9-cell cavity and exceeds the peak surface electric field by 40% [1]. The previous best reduced beta cavity was a spoke cavity tested at FNAL which reached 127 mT and 85 MV/m after extensive conditioning [6].

IMPACT AND FUTURE WORK

The test results presented here characterize the world's highest peak-field performance in a reduced-beta cavity designed for heavy-ion particle accelerators. The results approach the theoretical maximum of performance of any niobium resonator and allow for the proposal of future accelerators with higher base line gradients, shortening and reducing the cost of these installations.

We are now in the final stages of fabricating a half-wave resonator (HWR) designed to operate at 325 MHz and optimized for $\beta = 0.29$ ions [7]. This cavity builds upon the success of the conical geometries developed at ANL for quarter-wave cavities which optimize the cavity field distributions maximizing accelerator performance. The HWR is being fabricated in a manner identical to the record setting QWR. Figure 3 shows the subassemblies which will be combined to make the niobium cavity in the next several weeks. We expect to finish fabrication of this cavity in October 2012 with cold testing sometime in late November or early December. Results will be published once available.

ACKNOWLEDGMENTS

We would like to thank Joel Fuerst and Josh Kaluzny of the ANL APS for the sub-atmospheric testing of the cavity and Allan Rowe and Mayling Wong-Squires of FNAL for help with the 625^{0}C bake of the cavity. We would also like to acknowledge Glenn Cherry and Rick Fischer, of the ANL Nuclear Engineering Engineering-Support-Group, for numerous contributions to the hardware development required for testing.

REFERENCES

[1] R.L. Geng, "Overview of ILC High Gradient Cavity R&D at Jefferson Lab," In the Proceedings of SRF11, Chicago, Illinois, USA, Pg. 74 (2011).

[2] P.N. Ostroumov et al, "A New ATLAS Efficiency and Intensity Upgrade Project," In the Proceedings of SRF09, Berlin, Germany, Pg. 218 (2009).

[3] M.P. Kelly et al, "SRF Advances for ATLAS and Other beta<1 Applications," In the Proceedings of SRF11, Chicago, Illinois, USA, Pg. 680 (2011).

[4] Z.A. Conway et al, "Defect Location in Superconducting Cavities Cooled with He-II Using Oscillating Superleak Transducers," In the Proceedings of PAC09, Vancouver, British Columbia, Canada, Pg. 921 (2009).

[5] M.P. Kelly et al, "Cold Testing of Superconducting 72 MHz Quarter-Wave Cavities for ATLAS," MOPB073, these proceedings.

[6] L. Ristori et al, "Development of 325 MHz Single Spoke Resonator For HINS at Fermilab: Recent Results," In the Proceedings of PAC09, Vancouver, British Columbia, Canada, Pg. 963 (2009).

[7] P.N. Ostroumov et al, "Beta = 0.285 half-Wave Resonator for FRIB," In the Proceedings of SRF11, Chicago, Illinois, USA, Pg. 132 (2011).

Copyright © 2012 by the respective authors — cc Creative Commons Attribution 3.0 (CC BY 3.0)

DEVELOPMENT OF A SUPERCONDUCTING HALF-WAVE RESONATOR FOR PXIE *

Z.A. Conway#, R.L. Fischer, S.M. Gerbick, M.J. Kedzie, M.P. Kelly, S.V. Kutsaev, B. Mustapha, P.N. Ostroumov and K.W. Shepard, ANL, Argonne, IL 60439, USA
I.G. Gonin, A. Lunin and V.P. Yakovlev, FNAL, Batavia, IL 60510, USA

Abstract

An ambitious upgrade to the FNAL accelerator complex is progressing in the Project-X Injector Experiment (PXIE). The PXIE accelerator requires 8 superconducting half-wave resonators optimized for the acceleration of 1 mA $\beta = 0.11$ H^- ion beams. Here we present the status of the half-wave resonator development, focusing particularly on cavity design, with a brief update on prototype fabrication.

INTRODUCTION

Project-X is based upon a 1-5 mA H^- linear accelerator to be constructed at FNAL to support advanced intensity frontier physics over the next several decades in the US [1]. The Project-X Injector Experiment (PXIE), is being designed, built and commissioned as a demonstration of the most critical R&D issues related to the front-end of the driver linac [2].

The PXIE project will include the beam source, LEBT, RFQ, MEBT, and two superconducting cavity cryomodules. The first superconducting cavity cryomodule will house 8 half-wave resonators, 8 magnets which integrate the focusing solenoids with x-y steering coils [3], and all of the necessary peripherals for operation, e.g., power couplers, slow tuners, etc. This half-wave cryomodule is being designed and built at Argonne National Laboratory.

The initial half-wave resonator design was presented in [4, 5], which contains the main cavity RF performance parameters. In this paper we update the status of the half-wave resonator design. We address methods of minimizing cavity frequency dependence on changes in external pressure (df/dP), simulations of the slow-tuner performance and the pressure safety analysis of the cavity.

MINIMIZING df/dP

The half-wave resonators in PXIE will be operated at 2 K. While this greatly reduces the external fluctuations in helium pressure relative to a 4 K cryogenic system, variations of 1-2 mbar are expected. To accommodate this, the cavities were designed to have a df/dP = 6 Hz/mbar. This enables operation with RF amplifiers of ~4 kW, requiring no mechanical fast tuner, at the desired accelerating gradient of 8.2 MV/m for a 1 mA beam current.

* This work was supported by the U.S. Department of Energy, Office of High Energy Physics and Nuclear Physics, under contract DE-AC02-76CH03000 and DE-AC02-06CH11357
# zconway@anl.gov

df/dP ~ 6 Hz/mbar is a good compromise minimizing the fabrication cost and complexity simultaneously with the df/dP, which results in a more stable and reliable accelerator system and smaller RF amplifiers. A 0.125 inch helium jacket with a df/dP = 6 Hz/mbar satisfies our design requirements, but we spent a little additional time to determine how we may zero df/dP if it proves necessary after prototyping or in future projects.

The cavity Nb design is the results of detailed electromagnetic studies and was taken as the starting point for our design [4, 5]. The cavity is formed from 0.125 inch thick Nb sheet. We have recent experience with using 0.125" and 0.187" thick stainless steel helium jackets on superconducting cavities. We prefer to use 0.125 inch thick stainless steel but were unsure of its effect on df/dP. The cavity is shown in figure 1. Table 1 gives the results of varying the stainless steel material thickness of this model.

A novel technique to reduce df/dP is to add a flat or a dish to the side of the cavity in the high-electric field region. This increases the negative frequency shift due to deformations resulting from increases in the external pressure. Figure 2 shows a dish geometry in a half-symmetry cavity model and its displacement, please note that the helium jacket is not shown in this picture. Table 2 gives the results of varying the dish depth, where the depth is measured inward from the cavity surface. The peak surface electric field was not increased by more than 2% in these simulations.

Notice that df/dP may be controlled in finished cavities by choosing a dish which yields df/dP < 0. The dish may then be stiffened with a small gusset which may be subsequently weakened via machining to tune df/dP to zero. A similar gusset weakening procedure was employed in [6].

SLOW-TUNER PERFORMANCE

Our half-wave resonator design is highly re-entrant at the beam ports. This breaks the cylindrical symmetry in the high-electric field region which, in the past, has limited the slow-tuning range of half-wave cavities squeezed at the beam ports. We will employ the pneumatic ANL slow-tuner design discussed in [4]. Our simulations found that the tuning sensitivity for an applied force will be 84 kHz/kN for the 0.187 inch thick and 93 kHz/kN for the 0.125 inch thick helium jackets. The later sensitivity will be verified with the prototype cavity which is under construction.

Copyright © 2012 by the respective authors — cc Creative Commons Attribution 3.0 (CC BY 3.0)

Figure 1: The half-wave cavity. (Top) the helium jacket. (Bottom) the niobium parts of the cavity.

Table 1: df/dP Dependence on Helium Jacket Thickness

Wall Thickness (inches)	0.125	0.187	0.250	0.312”
df/dP (Hz/mbar)	6.0	6.8	7.1	7.2

PRESSURE SAFETY

A critical design constraint is proving that the cavity design satisfies the FNAL pressure safety guidelines. The pressure safety analysis follows the American Society of Mechanical Engineers (ASME) Boiler and Pressure Vessel Code (BPVC) [7]. To satisfy these requirements we successfully demonstrated:

- That the cavity assembly is structurally stable under loading
- That the cavity structure will not buckle.
- That the cavity will not fail due to localized stresses.
- That the cavity will not fail due to thermal or pressure cycling and the fatigue associated with it.

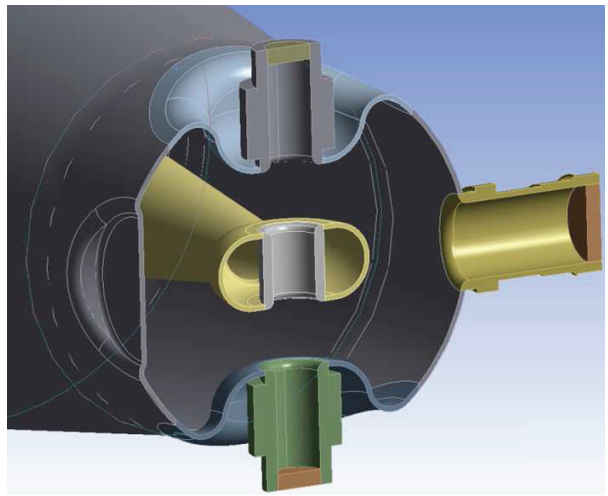

Figure 2: Dish in half-symmetry model of cavity.

Table 2: df/dP Dependence on Dish Depth

Depth (cm)	None	0.5	1	3
df/dP (Hz/mbar)	6.0	5.9	5	2.5

The room temperature and 2 K material properties we used for the simulations are given in [8]. For the design, the maximum allowable working pressures are given, by FNAL for this project, to be 2 bar at 293 K and 4 bar at 2 K.

The limit-load method specified in the BPVC, which uses an elastic-perfectly plastic material model (Figure 3), was used to check for plastic collapse. Plastic collapse is indicated if the ANSYS program fails to converge on a stable solution. The assumption of perfectly plastic response and the use of load factors to account for modelling uncertainty produce a fairly conservative result. Under all loading conditions, the analysis converged on a structurally stable solution, demonstrating protection against plastic collapse. This is largely due to the fact that high stresses were localized, and loads were easily transferred to the rest of the structure after plastic action at these locations.

Figure 4 shows the niobium stress when applying the maximum allowable working pressure at room temperature with a few almost negligible loads (e.g., the weight of the slow tuner and helium gas). Notice that the regions of maximum stress occur around the doughnut shaped center conductor. This is due to the inner conductor pushing in on the doughnut. The toroids on either end of the cavity roll inward upon pressurizing the helium space, a mode which may result in the buckling of the center conductor. The results at 2 K and for the helium jacket are not shown since they resulted in much higher levels of safety.

A linear-elastic pre-stressed eigenvalue buckling analysis was used to check for buckling. The BPVC specifies a baseline minimum buckling load factor, with additional capacity reduction factors applied to account for manufacturing uncertainty in cylindrical and spherical

Copyright © 2012 by the respective authors — cc Creative Commons Attribution 3.0 (CC BY 3.0)

sections. The load factor calculated by ANSYS for the first mode was 4.57, with buckling occurring in a cylindrical shell. After applying the appropriate capacity reduction factor, the required load factor was 2.5, for a safety factor with respect to buckling of 1.83. In the torispherical heads, a load factor less than this value (0ver 60) were extracted and none were found to show buckling in this area. Figure 5 shows two of the buckling modes found. These figures show normalized mode shapes, so they are snap-shots of the cavity during buckling and are not equilibrium solutions.

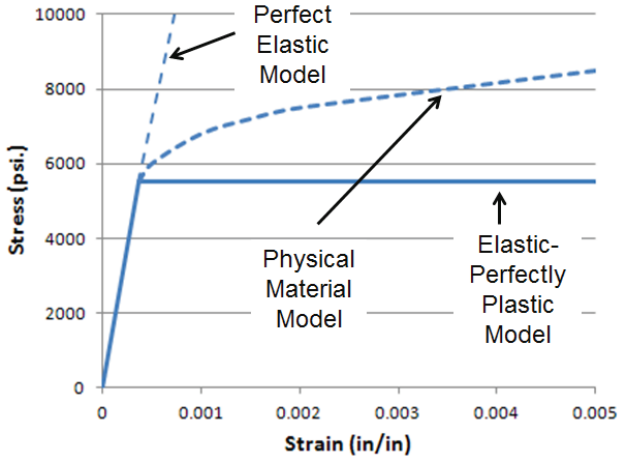

Figure 3: Material stress strain curves for Nb. For our plastic collapse simulations we used the elastic perfectly plastic material model.

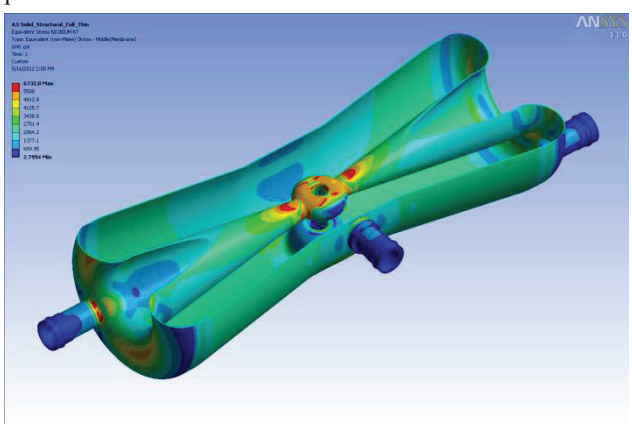

Figure 4: Niobium stresses at room temperature due to a static pressure gradient of 1.5 times the maximum allowable working pressure. The maximum stress (red) is 6700 psi, the minimum (dark blue) is 3 psi.

FUTURE WORK

The cavity structural design is well understood in simulations. We are currently building two prototype cavities to develop our fabrication procedures and to benchmark our simulation results against experimental measurements. We expect to finish the first prototype late summer 2013. Experimental results will be presented as they are collected.

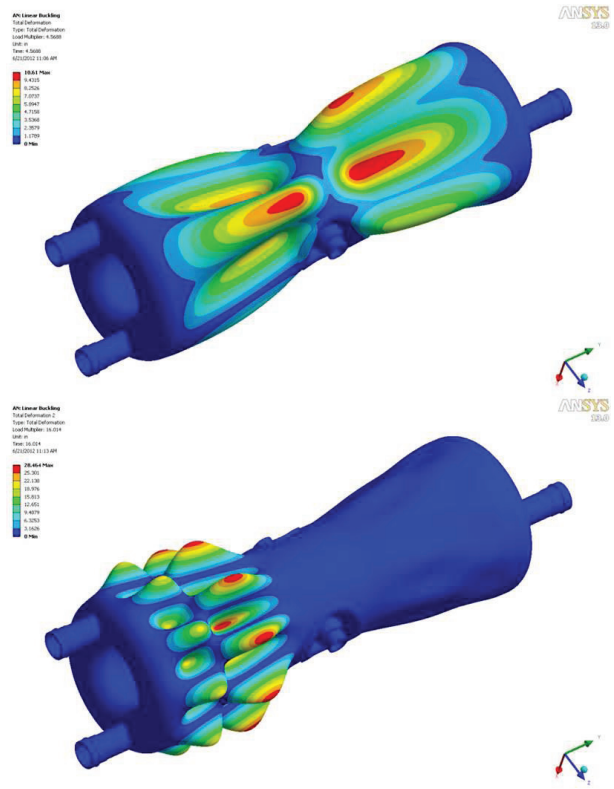

Figure 5: Two examples of buckling modes of the cavity. (Top) The mode with the lowest factor of safety; 1.8. (Bottom) factor of safety of 6.4 times the code requirement.

ACKNOWLEDGMENTS

We would like to thank Joel Fuerst of the ANL APS and Leonardo Ristori and Tom Nichols of FNAL for many helpful and interesting discussions.

REFERENCES

[1] S. Nagaitsev, “Project X - New Multi Megawatt Proton Source at Fermilab”, PAC’11, New York, March-April 2011, p. 2566
[2] S. Nagaitsev et al, “PXIE: Project X Injector Experiment,” IPAC’12, New Orleans, May 2012, p. 3874
[3] P.N. Ostroumov et al, “A New Generation of Superconducting Solenoids for Heavy-Ion Linac Applications,” LINAC’02, Gyeongju, Korea, August 2002, p. 332
[4] P.N. Ostroumov et al, “Development of a Half-Wave Resonator for Project-X,” IPAC’12, New Orleans, May 2012, p. 2295
[5] B. Mustapha et al, “A Ring-shaped Center Conductor Geometry for a Half-wave Resonator,” IPAC’12, New Orleans, May 2012, p. 2289
[6] Z.A. Conway et al, “Mechanical Properties of Spoke Resonators,” SRF’2005, July 2005, Ithaca, p. 185
[7] ASME International, 2010 ASME B&PV Code, Section VIII, Division 2.
[8] FNAL Technical Division Technical Note TD-09-005, “Guidelines for the Design, Fabrication, Testing and Installation of SRF Nb Cavities,” 2010.

Copyright © 2012 by the respective authors — cc Creative Commons Attribution 3.0 (CC BY 3.0)

CRYOMODULE DESIGNS FOR SUPERCONDUCTING HALF-WAVE RESONATORS*

Z.A. Conway#, G.L. Cherry, R.L. Fischer, S.M. Gerbick, M.J. Kedzie, M.P. Kelly, S.H. Kim, J.W. Morgan, P.N. Ostroumov and K.W. Shepard, ANL, Argonne, IL 60439, USA

Abstract

In this paper we present advanced techniques for the construction of half-wave resonator cryomodules. Recent advances in superconducting low-beta cavity design and processing have yielded dramatically improved cavity performance which reduces accelerator cost and improves operational reliability. This improvement has led to the proposal and construction of half-wave resonators by ANL for the acceleration of $0.1 < \beta < 0.5$ ions, e.g., the SARAF Phase-II project at SNRC (SOREQ, Israel) and Project-X at Fermilab. These cryomodules build and improve upon designs and techniques recently implemented in upgrades to ATLAS at ANL. Design issues include the ease of assembly/maintenance, resonator cleanliness, operating at 2 or 4 Kelvin, and ancillary system interfacing.

INTRODUCTION

We are developing three separate cryomodules for two distinct projects: one for Project-X at FNAL [1] and two for SARAF Phase-II at SOREQ [2]. The cryomodules for these projects will house superconducting half-wave resonators [3, 4] which require similar layouts but differ in operation modes and dimensions. To reduce risk and optimize the cost of the cryomodule fabrication we are developing the three designs together. All designs are modifications and improvements on box-cryomodules fabricated at ANL in the past 5 years [5, 6].

In this paper several aspects of the designs and their differences will be presented. First, the cryomodule requirements will be discussed. This is followed by a discussion of a few select aspects of the cryomodule designs, differences and plans for addressing these differences. Finally, this paper concludes with a short statement of our future plans.

CRYOMODULE REQUIREMENTS

Project-X is a high intensity, 1 mA, H^- linear accelerator facility being developed at FNAL. A single half-wave resonator cryomodule will house 8 $\beta = 0.11$ 162.5 MHz superconducting cavities, 8 superconducting magnets and will operate at 2 K.

The SARAF Phase-II project is an upgrade of the current SARAF accelerator to accelerate >5 mA, 40 MeV/u, proton/deuteron beams. Four cryomodules are required of two types, all of which will operate at 4 K. The first type, the low-beta cryomodule, contains 7 $\beta = 0.09$ 176 MHz superconducting cavities and 7 superconducting magnets. The second type, two high-beta cryomodules, each housing 7 $\beta = 0.16$ 176 MHz superconducting cavities and 4 superconducting magnets [7].

While the accelerator lattice and operating temperature differ between the cryomodules enough similarities exist such that we see significant cost savings in designing a cryomodule which may be adapted to each case, with minor modifications.

CRYOMODULE DESIGN

Vacuum Vessel

The cryomodule designs all build upon past ANL experience with box-cryomodules (see for example [5]). Here the cryomodules are much wider due to the half-wave cavities being mounted on their sides. To keep the half-cylinder bottom would make the vacuum vessels unacceptably tall. We have arrived at making the vacuum vessel a box which appears to be a good compromise between fabrication cost, structural integrity and minimizing cryostat height. The radii of the rounded corners were chosen to fit the contents of the box minimizing overall height including the depth of the required gussets.

Figure 1 shows the results from ANSYS calculations of the structural deformations due to vacuum being pulled on the inside. Notice that the structure pulls in about 0.25" on average due to evacuation, the maxima are between 0.5" and 0.67". We are currently evaluating whether or not to stay with this or reinforce the box further. Motion of the vacuum vessel wall moves the internal magnetic shielding and stresses the baton points which may degrade performance. Reducing the maximum displacement to less than 0.25" will avoid this but it adds the cost of additional gusseting. Future tests are planned here to evaluate the magnetic shielding.

With the rounded corners the vacuum vessel dimensions may be scaled between the three different sizes required by varying the length of the straight sections. Other designs we considered included straight sides (too mechanically compliant), angled corners (more expensive to fabricate), and a half-cylinder bottom (makes the cryomodule too tall). All of these designs were discarded for the mentioned reasons.

Beam-Line Component Support and Alignment

While the required accelerator lattice varies between the cryomodules the same support scheme may be used. All of the cryomodules require the solenoids to be aligned to better than ± 1.0 mm_{peak} transversely with $\pm 0.1^0$ for all of the rotation angles with similar constraints on the cavities. The beam-line string length varies from 4 to 6

* This work was supported by the U.S. Department of Energy, Office of High Energy Physics under contract DE-AC02-76CH03000 and by Soreq-NRC under work for others agreement 85Y47.

zconway@anl.gov

Copyright © 2012 by the respective authors — cc Creative Commons Attribution 3.0 (CC BY 3.0)

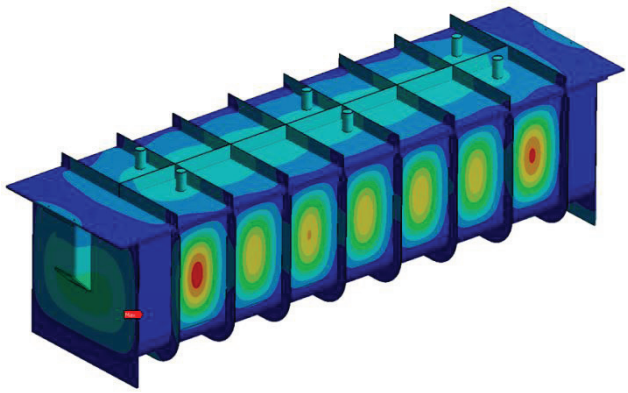

Figure 1: ANSYS results of the vacuum vessel deformation due to a 14.7 psi static pressure gradient across the walls. The red color corresponds to displacements greater than 0.6 inches with the maximum being 0.67 inches.

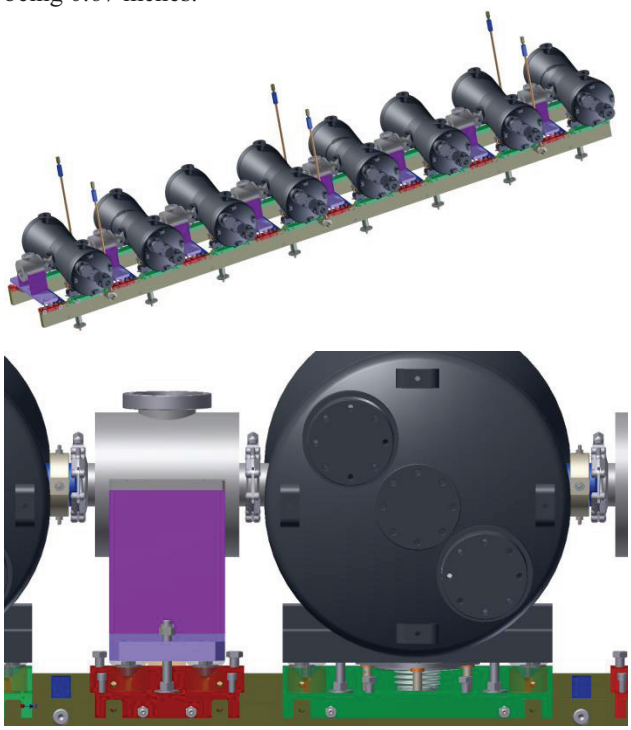

Figure 2: (Top) A cavity/solenoid string mounted on a strong-back. (Bottom) A close up of the alignment hardware for a solenoid and a cavity. The runners move transversely by adjusting two screws which push and two screws which pull (screws not shown but threaded holes they mate with are). One of each adjustment type is on each corner. The runners can be moved up and down by adjusting two vertical screws and placing shims between it and the strong-back.

meters and will be supported and aligned on a cryomodule spanning titanium rail system, called the strong-back. The strong-back is composed of 2 inch x 8 inch grade 2 titanium plates formed into a box and supported by titanium hangers. Each component is mounted on top of the strong back with its own independent kinematic-alignment hardware. Figure 2 shows the strong-back assembly for a cryomodule string. Notice the green and red (colors chosen for contrast) runners each of the cavities and solenoids sit on. These runners are adjustable on the strong-back for final fine-alignment. Recent experience with a 7 cavity and 4 solenoid cryomodule demonstrated that using this technique all of the components over a 4.5 meter length can be aligned to better than ±0.25 mm_{peak} transversely with $\pm 0.15^0$ for all of the rotation angles, exceeding our current transvers requirements by a factor of 4. The angular alignment was only limited by the travel in our alignment system and our future hardware will have an additional 0.125 inches of motion.

Our favourable result at room temperature will be verified at 4 K in the next several months. To address this in our developing designs we have studies the behaviour of the strong-back due to loading and cool-down. Figure 3 shows the loading of the strong-back. We have optimized the position of the hangers to minimize distortion due to the weight of the components and their ancillary equipment. The hanger positions may be very closely calculated by hand. One must only balance the torque about each support to get a hanger distribution which varies from the ANSYS optimum by 1 cm over the 6 meter length of the model shown. Figure 4 shows the change in the strong-back shape due to thermal contraction. The loading elements are part of this simulation; they are suppressed in this figure to show more of the strong-back. The side-views are shown in figures 3 and 4 since there is negligible twisting of the strong-back.

In all of the simulations no component is perturbed by more than 0.1 mm_{peak} and 0.0005^0 well within our alignment tolerances. If tests with current hardware confirm similar simulations we will be able to align the entire beam-line assembly at room temperature without having to adjust for differential displacements of components due to cool-down.

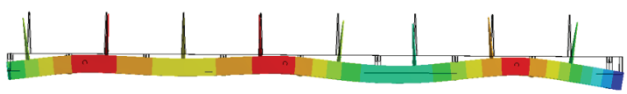

Figure 3: Side view of the strong-back showing the displacement due to the weight of the beam-line components. The maximum displacement is 0.13 mm, dark blue. The outlined shape is the undeformed model.

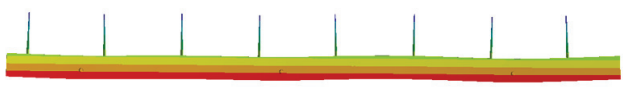

Figure 4: Side view of the strong-back showing the displacement due to thermal contraction and component loading. The maximum displacement is 0.05 mm. The outlined shape is the undeformed model. Notice the displacements decrease as the titanium elasticity decreases due to cool-down.

These results demonstrate that the beam-line components can all be aligned on a single long (> 4 m) strong-back. Short independently alignable cryomodules housing one or two components are not required. This

Copyright © 2012 by the respective authors — cc Creative Commons Attribution 3.0 (CC BY 3.0)

saves significant cost in fabricating one large vacuum vessel instead of several shorter ones.

Cryomodule Cryogenics

A major difference between all of the cryomodules we are currently developing is the operating temperature. To accommodate this we are designing almost identical 2-4 K helium distribution systems. The 2 K option has a sub-cooled heat exchanger and a J-T valve. These components are removed from the design and replaced with direct bayonet connections to the helium distribution system for the 4 K option.

Several smaller differences of operating at 4 instead of 2 K:

- Shorter beam-line gate valves, remove one of the thermal transition sections. Figure 5 shows a cross-section of the 2 K beam-line gate valve model.
- Eliminates the need for conduction cooled superconducting magnet leads.
- Eases the leak checking of the cryomodule since superleaks are no longer an issue.
- All of the 5 K intercepts are either eliminated or not connected.
- Radiative warming of the 4 K helium system by the slow tuners is neglected, resulting in an increase in the thermal load of 0.5 W. This load is reduced in the 2 K design using multi-layer insulation and larger washer stacks to thermally isolate the slow tuners.

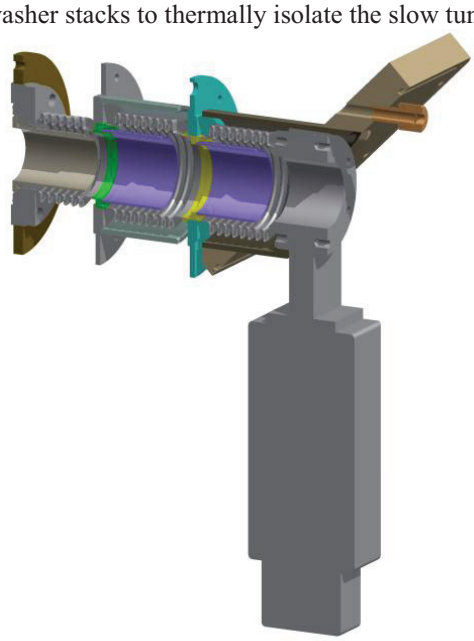

Figure 5: Cross section view of the beam-line gate valve. The total heat leak to 2 K in this design is < 0.05 W. For the 4 K cryomodules the final bellows segment on the left will be removed.

FUTURE PLANS

Our plans are two fold; (1) continue the modelling and (2) benchmark the modelling with physical measurements. The future modelling will be focused on reducing the number of vacuum vessel gussets (to minimize fabrication cost at $5k apiece), evaluating the structural integrity of the final design to ensure compliance with all US and DOE safety requirements, and to refine our understanding of the beam-line string alignment. In the next 6 months we will be able to measure and quantify the motion of a 4.5 meter long titanium strong-back which will provide useful insight into the simulations. We hope to begin fabrication of the first of these three cryomodules in the next two years.

ACKNOWLEDGMENTS

We would like to thank Joel Fuerst of the ANL APS and Tom Nichols of FNAL for many helpful and interesting discussions.

REFERENCES

[1] S. Nagaitsev, “Project X - New Multi Megawatt Proton Source at Fermilab”, PAC’11, New York, March-April 2011, p. 2566.

[2] D. Berkovits et al, “Operational Experience and Future Goals of the SARAF Linac at SOREQ,” MO1A01, these proceedings.

[3] P.N. Ostroumov et al, “Development of a Half-Wave Resonator for Project-X,” IPAC’12, New Orleans, May 2012, p. 2295.

[4] Z.A. Conway et al, “Half-Wave Resonators for SARAF Phase II Upgrade,” TUP067, these proceedings.

[5] J. Fuerst et al, “The ATLAS Energy upgrade Cryomodule” SRF’09, Berlin, Germany, September 2009, p. 52.

[6] M. Kedzie et al, “Design and Development of a New SRF Cavity Cryomodule for the ATLAS Intensity Upgrade,” Advances in Cryogenic Engineering: Cryogenic Engineering Conference –CEC, Spokane, WA, 2011, p. 937.

[7] P.N. Ostroumov et al, “SARAF Phase 2 Linac Physical Design Study,” FR1A05, these proceedings.

Copyright © 2012 by the respective authors — cc Creative Commons Attribution 3.0 (CC BY 3.0)

BEAMDULAC-SCL CODE FOR COMPLEX APPROACH OF BEAM DYNAMIC INVESTIGATION IN SC LINAC

A.V. Samoshin
National Research Nuclear University "MEPhI", Moscow, Russian Federation

Abstract

Periodic sequences of independently phased accelerating cavities and focusing solenoids are used in MeV and GeV energy range linacs. The beam dynamic investigation is difficult for such superconducting linear accelerator. The matrix calculation was preferably used for primary choused of accelerating structure parameters. This method does not allows properly investigate the longitudinal motion. The smooth approximation can be used to investigate the nonlinear ion beam dynamics in such accelerating structure and to calculate longitudinal and transverse acceptances. The advantages and disadvantages of each method will describe, the results of investigation will compare. The user friendly software BEAMDULAC-SCL for ion beam dynamic analysis was created. A numerical simulation of beam dynamics in the real field are carried out for the different variants of the accelerator structure based on previously analytically obtained results.

INTRODUCTION

High-current accelerators have great perspectives for problems of thermonuclear fusion, safe nuclear reactors, transmutation of radioactive wastes and free electron lasers. A large number of low energy particle accelerators are applied in micro- and nanoelectronics, material science, including the study of new construction materials for nuclear industry, in medical physics, in particular for cancer treatment by using of the accelerators of protons and light ions, in radiation technology. It is proposed to use one universal accelerator, consisting of independently phased cavities and solenoids sequence to solve these problems.

An ion superconducting linac is usually based on the superconducting (SC) independently phased cavities. This linac consists of the niobium cavities which can provide typically 1 MV or more of accelerating potential per cavity. Such structures can be used for ion acceleration with different charge-to-mass ratio in the low energy region [1] and for proton linac in the high-energy region (SNS, JHF, ESS project). It is desirable to have a constant geometry of the accelerating cavity in order to simplify manufacturing and to decrease the linac cost. Such geometry leads to a non-synchronism but a stable longitudinal particle motion can be provided by proper RF cavities phasing. The beam can be both longitudinally stable and accelerated in the whole system by control of the accelerating structure driven phase and the distance between the cavities. In this paper two methods of the beam dynamics investigation are compared for low ion velocities and for the charge-to-mass ratio $Z/A = 1/66$. This comparison can be demonstrated as an example of a post-accelerator of radioactive ion beams (FRIB) linac, where beam velocity increases from $\beta = 0.01$ to $\beta = 0.06$ [1].

The beam transverse focusing can be provided with the help of SC solenoid lenses, following each cavity and with the help of special RF fields. As it was shown early the beam focusing can be realized for the solenoid field near $B \sim 20$ T. The value of magnetic field B can be reduced by using of addition alternating phase focusing (APF). The smooth approximation has been applied to study the APF in RIB linac. By adjusting the drive phase (φ_1 and φ_2) of the two cavities, we can achieve the acceleration and the focusing by less magnitude of the magnetic field B [2]. Adding a solenoid into focusing period will also allow the separate control of the transverse and longitudinal beam dynamics. A schematic plot of one period of the accelerator structure is shown in Figure 1. The low-charge-state low velocity beams require stronger transverse focusing than one is used in existing SC ion linac. Early investigation of beam dynamics shows that with the initial normalized transverse emittance $\varepsilon_T = 0.1\pi$·mm·mrad and the longitudinal emittance $\varepsilon_V = 0.3\pi$·keV/u·nsec the connection between the longitudinal and transverse motion can be neglected if maximum beam envelop $X_m < 3$-4 mm and inner radius of drift tubes $a = 15$ mm.

Beam dynamics in such systems cannot be studied by means of analytical methods only. The initial setup of the system consisting of different types superconducting resonators and focusing solenoids or quadrupoles, can be performed using the transfer matrix calculation and the method of smooth approximation, and then refined the beam dynamics simulation in polyharmonic field.

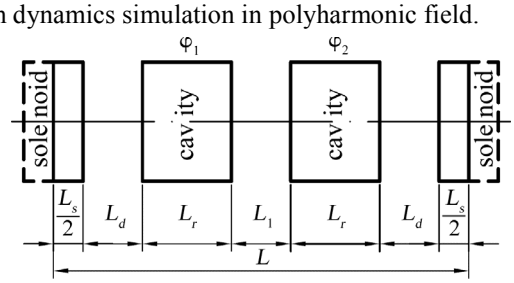

Figure 1: Layout of structure period.

The BEAMDULAC-SCL code is developed in the laboratory DINUS and allows to do the comprehensive research of ion beam dynamics in a different structures that satisfy the acceleration of many methods. To evaluate the accelerator parameters implemented transfer matrix calculation method. Using a smooth averaging technique we can to determine the stability region and to calculate

Copyright © 2012 by the respective authors — cc Creative Commons Attribution 3.0 (CC BY 3.0)

the dynamics of a single particle and beam. For completion, to verify selections, we perform the calculation of beam dynamics in polyharmonic field.

MATRIX CALCULATIONS

Conditions of longitudinal and transverse beam stabilities for the structure consisting from the periodic sequence of the cavities and solenoids were studied early using transfer matrix calculation [2]. The code window shows dependencies of dimensionless parameter $\alpha = \pi eZUL/2A\lambda mc^2\beta_g^3\gamma_g^3$ (for stable motion it must be less than 2), here U is accelerating potential per cavity, L is period length, phase advances per period (Floke parameters), magnetic field which is need for beam stable motion with envelope value X_m = 3 mm is shown in Figure 2.

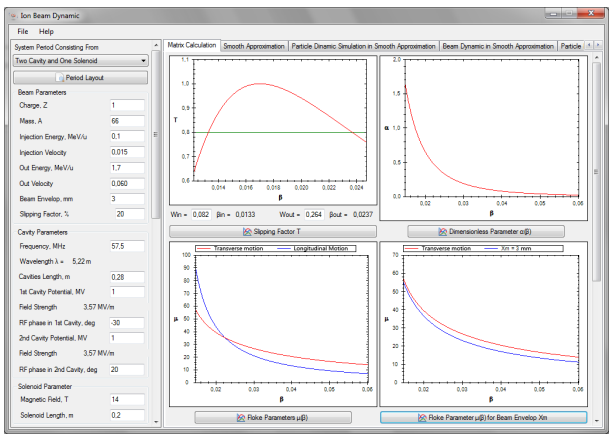

Figure 2: Beam dynamic transfer matrix calculation.

BEAM DYNAMICS IN SMOOTH APPROXIMATION

In SC linac design, it is very important to know the bucket size since it relates to the longitudinal RF focusing. But the linac longitudinal acceptance cannot be obtained by matrix method because of the assumption that the particles have small longitudinal oscillation amplitude. In order to investigate the nonlinear ion beam dynamics in such accelerated structure and to calculate the longitudinal and transverse acceptances it can be used smooth approximation [3, 4].

We realize two smooth approximation methods in this program. In the first case take into account the coherent oscillations of bunches and the effective potential function describe slowly oscillations in the reference particle frame (Fig. 3a). In the second case the effective potential function was found in the frame where averaged velocity of the reference particle $\overline{\beta}_c = 0$ (Fig. 3b) [5].

The analysis of the effective potential function makes it possible to study the condition of the beam phase and radial stability and to calculate the longitudinal acceptance.

The code window contain plots of longitudinal and transverse oscillations frequencies, the cross section of the potential function and change the size of the separatrix is shown in Figure 3.

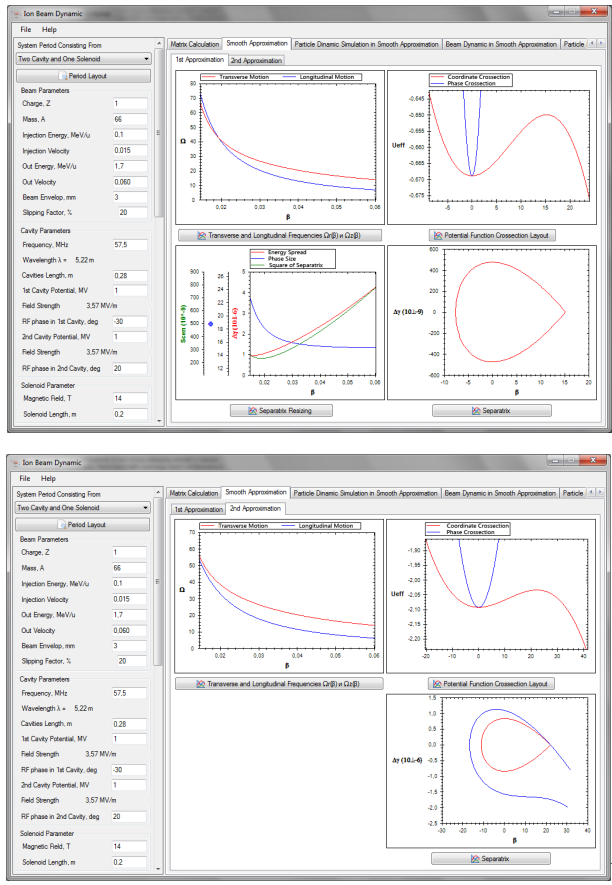

a

b

Figure 3: The frequencies of longitudinal and transverse oscillations, potential function cross-section and separatrixes for different approximation cases.

NUMERICAL SIMULATION OF ION BEAM DYNAMICS

Single Particle Motion

The particle dynamic was studied in averaged on fast oscillations field for the analyses of longitudinal and transverse motions. Field's components can be obtained from the effective potential function in smooth approximation. The solution can be obtained only by numerical simulation because the field components are nonlinear functions. The greatest interest has the modeling of the dynamics of the full field. The results of ion beam numerical simulations in polyharmonic field with Z/A = 1/66 are shown in Figure 4.

Beam Dynamics

As Initial parameters of numerical simulation for this system (see on figures) are similar to the previous one. The initial particle phase in the cavity are $\varphi_1 = -30°$ and $\varphi_2 = 20°$, and magnetic field of solenoid is B = 14 T. The beam moves through 8 periods in this case. The numerical simulation in polyharmonic field was performed to verify of the result obtained bellow. The геометrical velocity β_G

Copyright © 2012 by the respective authors — cc Creative Commons Attribution 3.0 (CC BY 3.0)

varies in each cavity. Results of ion beam numerical simulations in a polyharmonic field are close to results received in smooth approximation. The beam longitudinal size increase is negligible and transverse emittance slowly vying. The results are shown in Figure 5 agree with previously analyze.

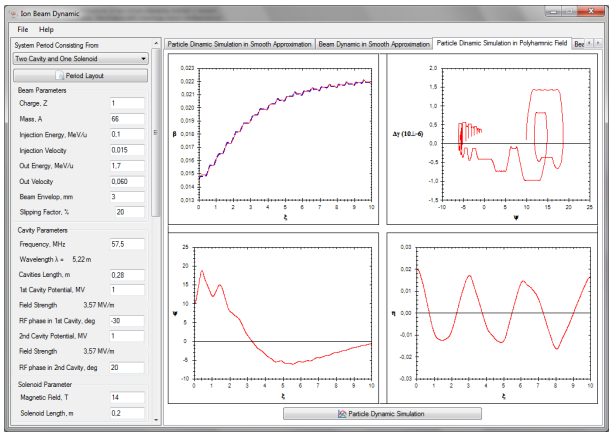

Figure 4: Particle trajectories during acceleration.

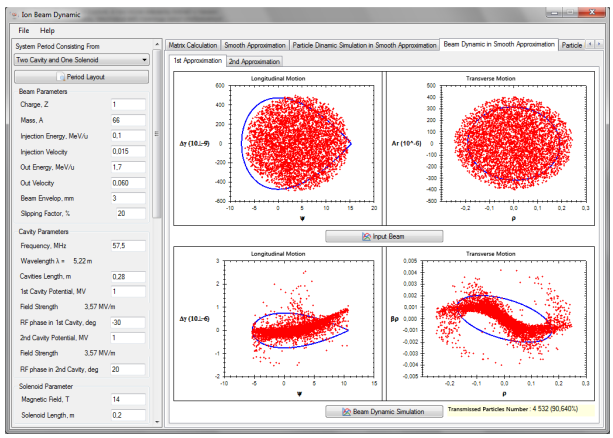

a

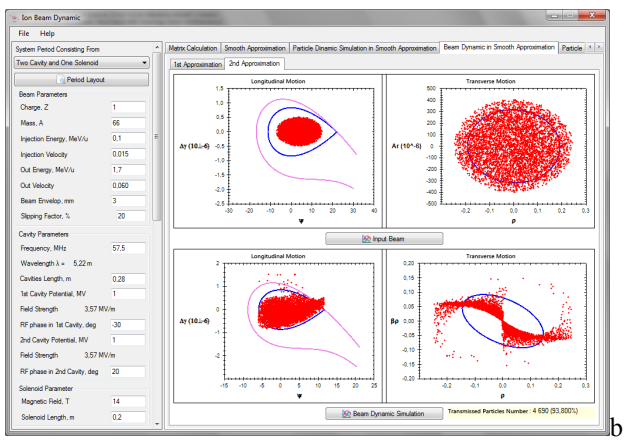

b

Figure 5: Beam dynamics simulation for 1st smooth approximation.

NUMERICAL SIMULATION OF ION BEAM DYNAMICS

The numerical simulation in polyharmonic field was performed to verify of the result obtained bellow. The simulation was spent for the same focusing periods and the same initial parameters. Geometrical velocity β_G varies in each cavity too. The results of ion beam numerical simulations in a polyharmonic field are close to results received in smooth approximation. The beam longitudinal volume increase negligible and transverse emittance slowly vying.

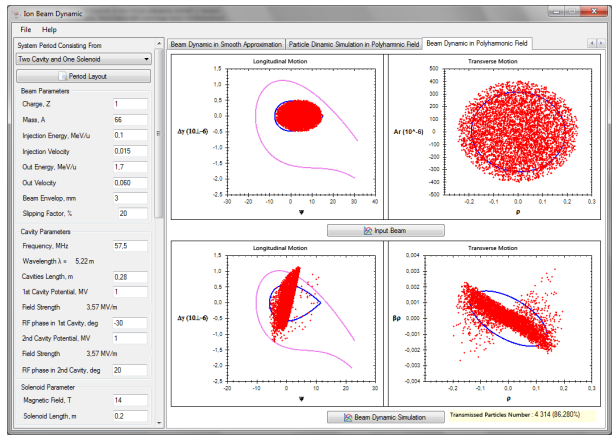

Figure 6: Beam dynamics in the polyharmonic field.

CONCLUSION

New BEAMDULAC-SCL code, developed for the beam dynamics analysis and accelerator parameters optimization (for linacs as SNS, FRIB etc) was described. The program window contains several tabs with different beam dynamics calculating methods: the matrix calculation, which is used to advance parameters choice of the accelerating structure, and nonlinear particle dynamics analysis in a smooth approximation, the calculation of the beam dynamics in the real field with slipping coefficient account to verify and refine the choosen accelerator parameters.

REFERENCES

[1] P.N. Ostroumov and et al. / Proc. of PAC'2001, 2001, p. 4080.
[2] E.S. Masunov, D.A. Efimov, P.N. Ostroumov / Proc. of EPAC'2004, p. 1405-1407.
[3] E.S. Masunov, N.E. Vinogradov // Phys. Rev. ST-AB 4, 2001, 070101.
[4] Ji Qiang, R.W. Garnett // Nucl. Instr. and Meth. A 496, 2003, p. 33.
[5] E.S. Masunov, A.V. Samoshin / Proc. of PAC'2007, p.1568-1570.
[6] E.S. Masunov, A.V. Samoshin / Proc. of RuPAC'2006, p. 162-164.

Copyright © 2012 by the respective authors — cc Creative Commons Attribution 3.0 (CC BY 3.0)

DEVELOPMENT OF PROTON THERAPY AT THE SC LINAC WITH BEAMDULAC-SCL CODE

S.M. Polozov, A.V. Samoshin
National Research Nuclear University "MEPhI", Moscow, Russian Federation

Abstract

Proton cancer therapy complexes are conventionally developing based on synchrotrons and cyclotrons. High electrical power consumption and especial devices necessary to energy variation (as slow extraction systems and degraders) are the main problems of such complexes. At once SC linacs based on short independently phased cavities have a serious progress at present. Linear accelerator consumes less power comparably with cyclic and the energy variation can be easily realized by means of RF field amplitude and phase variation in a number of cavities. The accelerator's modular configuration which is now widely used in FRIB's or SNS's can be applied for therapy linac also. It is possible to choose the SC linac parameters and to do the proton and ion beams stability study with help of the BEAMDULAC-SCL code. This software also allows providing of the structure optimization and the beam dynamics control.

INTRODUCTION

Development of a simple in operation and cost-effective cancer treatment proton accelerator is very important now. Normal conducting cyclotrons and synchrotrons are conventionally uses for treatment. A number of comparatively compact SC synchrocyclotrons are under development. But contemporary progress in SC linacs development, construction and operation experience let to propose their using for medical application. Such linacs have a very high rate of energy gain and can by compact thus, need low RF power feeding and large scale and power-intensive magnets are not necessary for it. But the possibility of easily beam energy variation by means of a number of the resonator turn-off (deeply variation) or RF field phase in last resonators (slow variation) can be the main advantage of SC linac.

A number of cancer therapy linacs projects as TOP [1], LIBO [2], TOP-IMPLART [3] are under R&D at present. The novel CYCLINAC concept combines compact low energy cyclotron and short linac is also discussed [4].

Contemporary SC linac technologies are used for development of spoliation neutron sources (SNS) and facilities for radioactive ion beams (FRIB). High-gradient quarter- and half-wave, elliptical and side-coupled cavities are used for beam acceleration and SC solenoids of quadrupoles for transverse focusing. The average rate of energy gain in SNS linac is about 4 MeV/m for example. It can be proposed that 200 MeV low intensity linac can be compact that 50 m.

The optimization of linac structure will done in this paper using BEAMDULAC-SCL code with was developed for heavy ion beam dynamics simulation in FRIB's. The possibility of permanent magnet using for transverse beam focusing will discussed, the limit gradient for different energy ranges will defined. The beam quality (beam envelope control in main) preservation is one of the main goals.

PERIOD LAYOUT

Let's we consider the linear accelerator, consisting of independently phased cavities and solenoids sequence first (fig. 1).

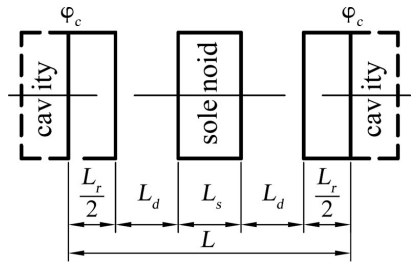

Figure 1: Layout of structure period.

For low-velocity ion beams the quarter- and half-wave resonators with few amounts of gaps are commonly used as accelerating structures. If SC resonators are used they should be the same, otherwise the cost of facility rapidly increase. This means that the phase velocity of the wave should be constant in each cavity. With a large number of resonators is economically advantageous to divide them into several groups, consists of identical resonators. Obviously, in this acceleration system will always violate the principle of synchronicity, when the synchronous particle velocity equal to the phase velocity of the accelerating wave at any time. I.e. in this case, appear a slipping of the particles relative to the accelerating wave. The slipping value must not exceed acceptable value, if not acceleration rate and rapidly reduced and beam longitudinal and transverse stability worse, and the transmission coefficient decreases. Therefore the number of identical resonators should be limited, and the number of groups consisting of identical geometry should be minimal.

Ions are accelerated and slipping relative to the RF field in dependence of the ratio between the particle velocity β and the phase velocity of the wave in cavity β_G.

The beam motion can be both longitudinally stable and accelerated in the whole system by control the driven phase of the accelerating structure and the distance between the cavities [5]. The beam focusing can be provided by solenoids or permanent magnet lenses (PML) which follow each of the cavity [6].

The conditions of longitudinal and transverse beam stability for the structure consisting from the periodic

Copyright © 2012 by the respective authors — cc Creative Commons Attribution 3.0 (CC BY 3.0)

sequence of cavities and solenoids were studied early using transfer matrix calculation [7]. It is very important to know the bucket size since it relates to the longitudinal RF focusing in SC linac design. The smooth approximation can be used in order to investigate the nonlinear ion beam dynamics in such accelerating structures and to calculate the longitudinal and transverse acceptances [7].

The results of self-consistent beam dynamics investigation in accelerating structures by means of BEAMDULAC-SCL code are discussed in this paper. The BEAMDULAC code is developing in MEPhI since 1999 for high current beam dynamics simulation in linear accelerators and transport channels.

SOLENOID FOCUSING

If we require that the slipping factor value does not exceed 20%, the accelerator should be divided into three parts with βg = 0.18, 0.3 and 0.5 respectively (see fig. 2).

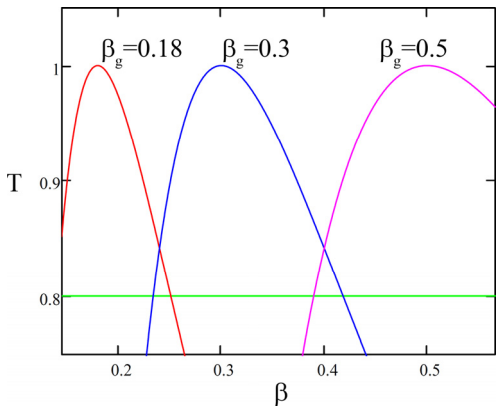

Figure 2: Slipping factor value.

Parameters of each part are given in Table 1. To reduce the paper size we present beam dynamics analysis results only for the last part having the beam energy range from 82 MeV to 200 MeV. The field strengthfor each cavity is equal 4 MV/m, the cavity length 2 m, the particle phase into RF field -20º, frequency f = 150 MHz. Figure 3 shows that with the chosen accelerator parameters the phase advance of the longitudinal and transverse oscillations are not close to each other, which will not lead to a coupling resonance, so beam motion will be stable. Note that the chosen value of the magnetic field makes it possible to keep the beam envelope lower than 3 mm.

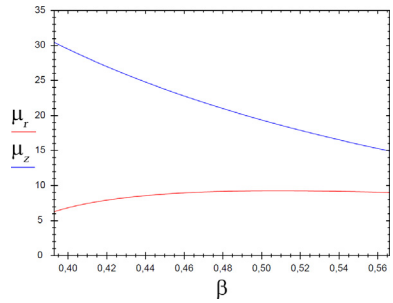

Figure 3: Longitudinal and transverse Floke parameters.

Figure 4 shows the separatrix size (maximum energy spread, red curve), the phase size (blue curve) and the separatrix area (green curve). We can see that the acceptance increases with the chosen parameters of the accelerator.

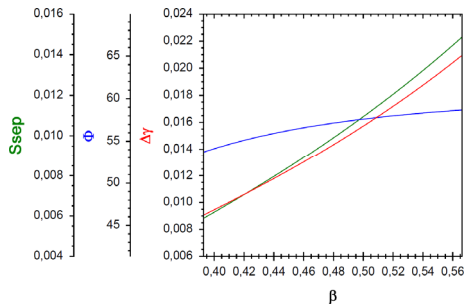

Figure 4: Separatrix dimension during acceleration.

Beam dynamics in the real field were carried out basing on the chosen parameters. The simulation results are shown in the Figure 5. The transmission efficiency is equal 92%.

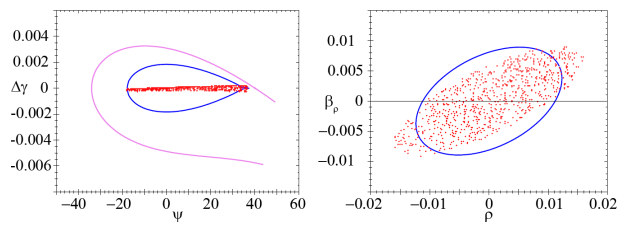

Figure 5: Longitudinal and transverse phase space.

With help of BEAMDULAC-SCL code, the number of periods of the accelerating structure can be defined, and therefore the total length of the accelerator. The total length of the accelerator, which consists of three sections, will be equal 46.72 m (see Table 1).

Table 1: The Accelerator Parameters with Solenoid Focusing

	W_{in}, MeV	W_{out}, MeV	β_g	L_{res}, m	E, MV/m	L_{sol}, m	B, T	N_{per}
1 range	10	28	0.18	0.72	4	0.2	1.5	6
2 range	28	82	0.3	1.2	4	0.2	1.5	10
3 range	82	200	0.5	2	4	0.2	1.5	10

Copyright © 2012 by the respective authors — cc Creative Commons Attribution 3.0 (CC BY 3.0)

APF AND SOLENOID FOCUSING

By using of an additional alternating phase focusing (APF) we can reduce the value of the magnetic field necessary for transverse focusing. In this case the period will consist of two cavities and one solenoid. If the entry phase of cavities are differs by the sign but are equal by value, the longitudinal stability region is small, therefore we choose $\varphi_1 = -25$ ° and $\varphi_2 = 20$ ° (in Figure 6 this value is represent as x). Note that the absolute value of negative phase must be greater than positive, otherwise the beam stability worse.

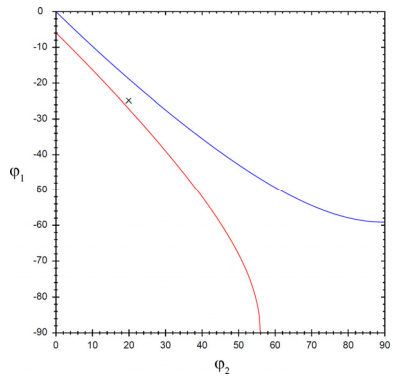

Figure 6: Stability diagram in terms of (φ_1,φ_2).

Chosen parameters of the accelerator are shown in Table 2. Other linac parameters are the same as in the previous case. Figure 7 shows that with the chosen parameters stability is keeping.

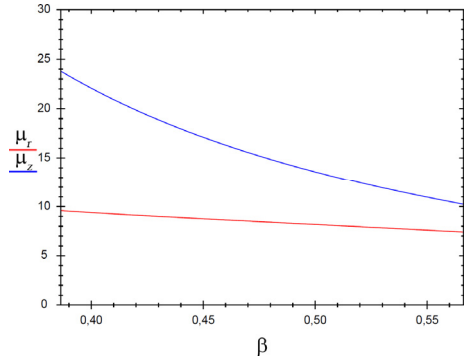

Figure 7: Longitudinal and transverse Floke parameters.

As in the previous case we consider the variation of separatrix size. In this case, the acceptance is much smaller than in the previous case (see Fig. 5 and Fig. 8), but also growing. Separatrix size can be increased by tuning the entry phase into neighboring cavities, but in this case we shift to higher phases area, which reduces the acceleration rate.

Table 2: The Accelerator Parameters with Solenoid Focusing

	W_{in}, MeV	W_{out}, MeV	β_g	L_{res}, m	E, MV/m	L_{sol}, m	B, T	N_{per}
1 range	10	27	0.18	0.72	4	0.2	0.6	3
2 range	27	79	0.3	1.2	4	0.2	0.7	5
3 range	79	200	0.5	2	4	0.2	0.8	5

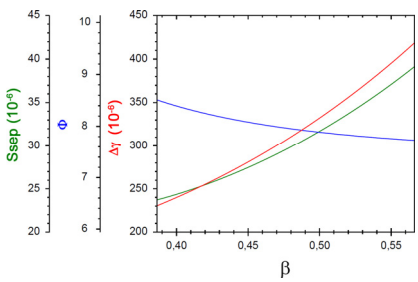

Figure 8: Separatrix size during acceleration.

The beam dynamics numerical simulation results in the real field are shown in Figure 9. The total length of the accelerator in this case is equal 42.82 m which is smaller than in previous case.

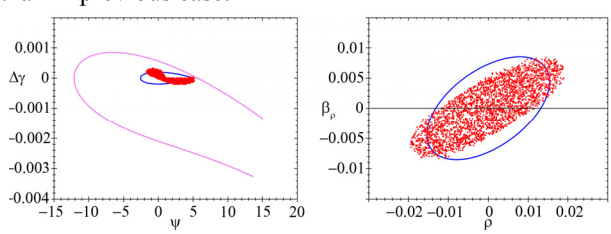

Figure 9: Longitudinal and transverse phase space.

CONCLUSION

A complex analysis of the proton beam dynamics stability was done with the help of especially designed BEAMDULAC-SCL code. The analysis shows that it is possible to develop a proton treatment linear accelerator with length less than 50 m and necessary for transverse focusing magnetic field will less than 1 T. Beam envelope control is possible this case. Optimal choosing linac parameters are shown in Tables 1 and 2.

REFERENCES

[1] L. Picardi et al., Proc. of EPAC'02, p. 248.
[2] V. G. Vaccaro et al., Proc. of PAC'05, p. 2494.
[3] C.Ronsivalle et al., Proc. of IPAC 2011, p. 3580.
[4] U.Amaldi, Proc. of CYCLO'07, p. 166.
[5] P.N. Ostroumov and et.al., Proc. of the PAC'2001, Chicago, IL, June 2001, p.4080.
[6] E.S. Masunov, et.al., Proc. of the EPAC'2004, Lucerne, Switzerland, p. 1405 – 1407.
[7] E.S. Masunov and A.V. Samoshin, Proc. of the PAC'07, Albuquerque, June 2007, p. 1568.

Copyright © 2012 by the respective authors — cc Creative Commons Attribution 3.0 (CC BY 3.0)

FIRST MEASUREMENTS ON THE 325 MHz SUPERCONDUCTING CH CAVITY*

M. Busch†,[1], F. Dziuba[1], H. Podlech[1], U. Ratzinger[1], W. Barth[2,3], S. Mickat[2,3], M. Amberg[3], M. Pekeler[4]
[1]IAP Frankfurt University, 60438 Frankfurt am Main, Germany
[2]GSI Helmholtzzentrum, 64291 Darmstadt, Germany
[3]Helmholtz-Institut Mainz (HIM), 55099 Mainz, Germany
[4]RI Research Instruments, Bergisch Gladbach, Germany

Abstract

At the Institute for Applied Physics (IAP), Frankfurt University, a superconducting 325 MHz CH-Cavity has been designed and built. This 7-cell cavity has a geometrical β of 0.16 corresponding to a beam energy of 11.4 AMeV. The design gradient is 5 MV/m. Novel features of this resonator are a compact design, low peak fields, easy surface processing and power coupling. Furthermore a new tuning system based on bellow tuners inside the resonator will control the frequency during operation. After successful rf tests in Frankfurt the cavity will be tested with a 10 mA, 11.4 AMeV beam delivered by the GSI UNILAC. In this paper first measurements and corresponding simulations will be presented.

CAVITY LAYOUT

Worldwide there is a growing interest in applications demanding high beam power and quality (e.g. MYRRHA (**M**ulti Purpose H**Y**brid **R**esearch **R**eactor for **H**igh-Tech **A**pplications) [1]). The superconducting CH-cavity is an appropiate structure for these specifications being characterized by a small number of drift spaces between adjacent cavities compared to conventional low-β ion linacs [2]. Applying KONUS beam dynamics, which decreases the transverse rf defocusing and allows the development of long lens free sections, this results in high real estate gradients with moderate electric and magnetic peak fields. In the past a 19-cell, superconducting 360 MHz CH-prototype has been developed and successfully tested [3]. For future operations a new design proposal for high power applications has been investigated. Presently a new cavity operating at 325.224 MHz, consisting of 7 cells, β = 0.16 and an effective length of 505 mm (see table 1) is undergoing first measurements. Referring to the previous structure this cavity utilizes some novel features (see fig. 1):

- inclined end stems
- additional flanges at the end caps for cleaning procedures
- two bellow tuners inside the cavity
- two ports for large power couplers through the girders

* Work supported by GSI, BMBF Contr. No. 06FY7102, 06FY9089I
† busch@iap.uni-frankfurt.de

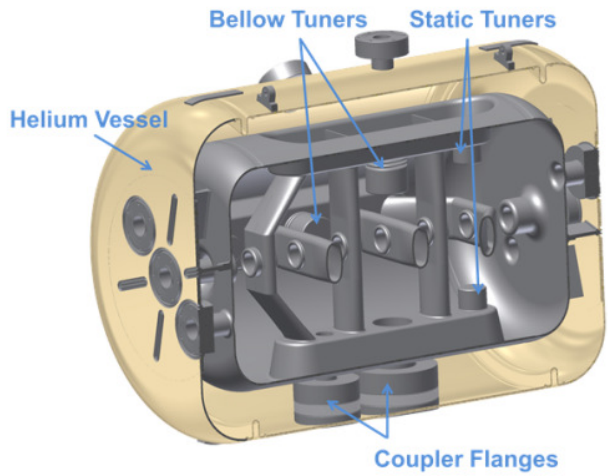

Figure 1: Layout of the superconducting 7-cell CH-Cavity (325.224 MHz, β = 0.16)[4].

Table 1: Specifications of the 325 MHz CH-Cavity.

β	0.16
frequency [MHz]	325.224
no. of cells	7
length ($\beta\lambda$-def.) [mm]	505
diameter [mm]	352
E_a [MV/m]	5
E_p/E_a	5
B_p/E_a [mT/(MV/m)]	13
G [Ω]	64
R_a/Q_0	1248
R_aR_s [$k\Omega^2$]	80

SCOPE FOR THE DYNAMIC BELLOW TUNERS

Rf, mechanical properties as well as Multipacting studies of the novel bellow tuner system can be reviewed in [5],[6], [7].

Copyright © 2012 by the respective authors — cc Creative Commons Attribution 3.0 (CC BY 3.0)

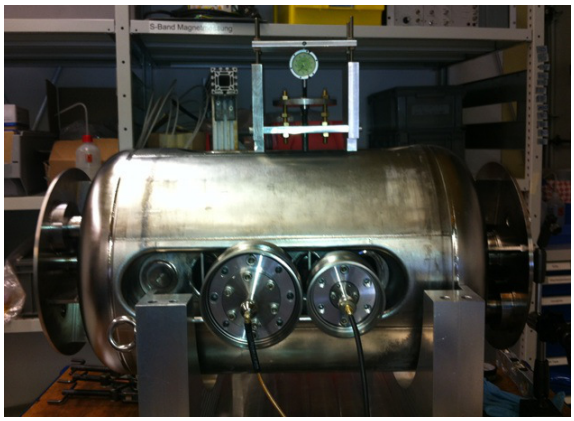

Figure 2: Setup for the test of the dynamic bellow tuners.

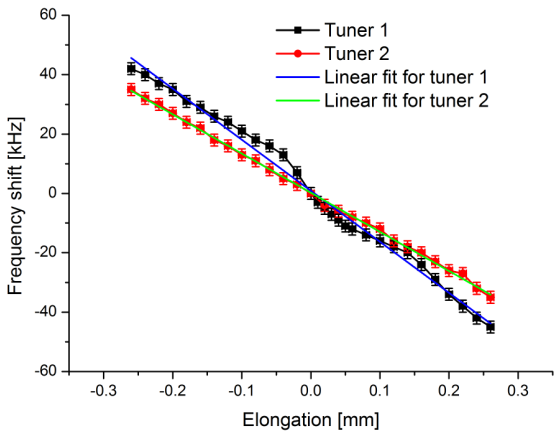

Figure 3: Frequency shift caused by elongation of tuner 1 and tuner 2.

First mechanical and rf tests regarding the scope of the dynamic bellow tuners have been performed at RI (Research Instruments GmbH [8]). The measuring configuration consisted of a framework housing a probe indicator and three spindles applying force via a metal plate on the rod of the tuners in each case (see fig. 2). Proceeding at room temperature the mechanical range of the bellow tuners was limited to $\Delta x = -0.3\ mm..0.3\ mm$ preventively. The measured frequency shift averaged $\Delta f = -172\ kHz/mm$ for tuner 1 and $\Delta f = -132\ kHz/mm$ for tuner 2. The simulated shift for the tuners is ($\Delta f = -150\ kHz/mm$) (see fig. 3).

PRELIMINARY COLD TEST

Prior to the final assembly of the cavity a preliminary cold test was arranged cooling down the cavity to LN_2 temperature. For this purpose the structure has been evacuated and inserted into an insulated metal box (see fig. 4). Three thermal sensors were attached to the top, alongside and bottom of the end caps. The cavity was leak-proof and the last remaining tuner hole was sealed with a Viton plug. This setup allowed a measurement down to an average temperature of roughly -120 °C (see fig. 5). Showing good agreement to the expected shrinkage the frequency shift at LHe should total up to 450 kHz corresponding to a shrinkage of 0.14 %.

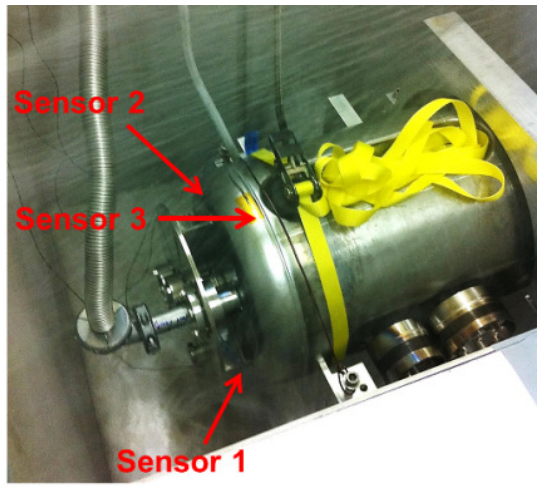

Figure 4: Setup for the preliminary cold test. Thermal sensors on top, alongside and bottom of the end cap.

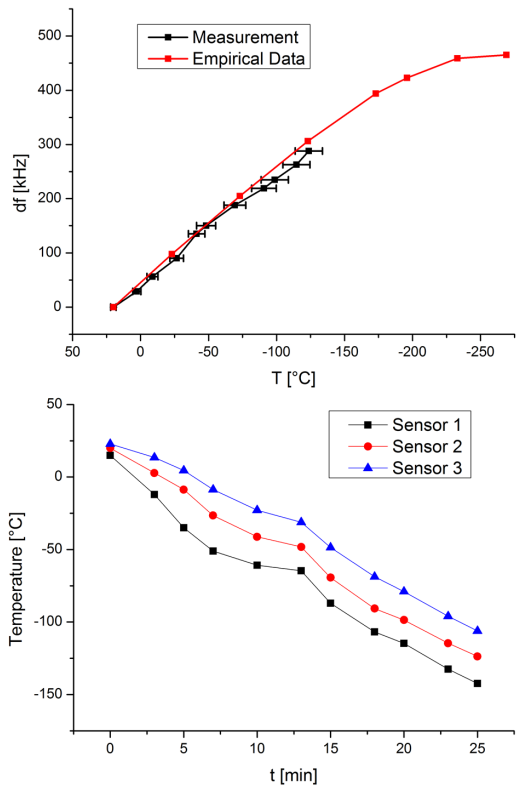

Figure 5: Top: Measured and expected frequency shift due to thermal shrinkage (Empirical data taken from: A.F. Clark, Materials at Low Temperatures). Bottom: Temperature behaviour for all three sensors.

Copyright © 2012 by the respective authors — cc Creative Commons Attribution 3.0 (CC BY 3.0)

PRESSURE SENSITIVITY

Furthermore pressure sensitivity measurements have been performed. Therefore three probe indicators were positioned on both end caps and on one cavity quarter shell (see fig. 6) to measure the deformation at the according spots. Then the cavity has been evacuated with a rotary vane pump down to 100 mbar and 1 mbar in another measurement, respectively. The frequency shift according to the measurements added up to ≈190 kHz and ≈180 kHz, respectively. According to simulations the shift is 205 kHz. The deformation on the cavity quarter shell was 0.22 mm at 100 mbar residual pressure while the simulated reference value amounts to 0.19 mm (see fig. 7).

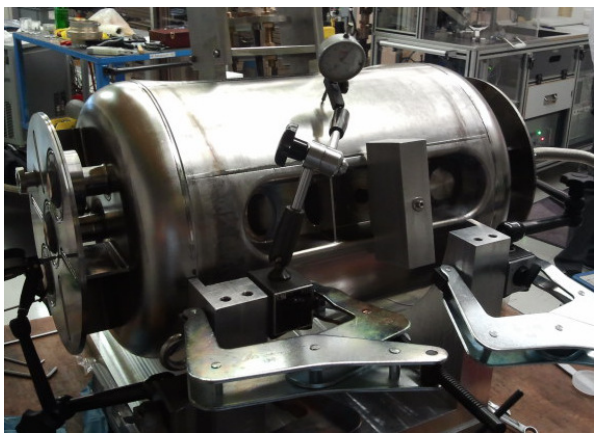

Figure 6: Setup for pressure sensitivity measurement.

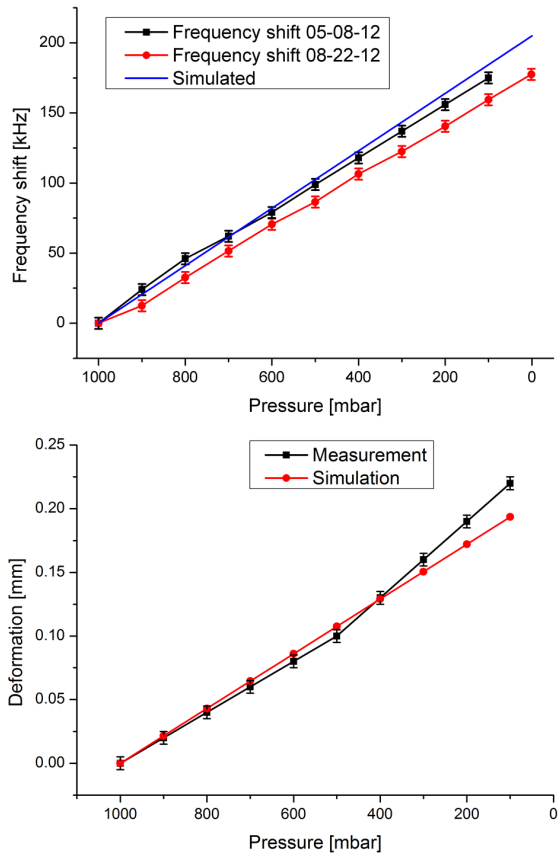

Figure 7: Top: Frequency shift due to evacuation. Bottom: Deformation of the cavity quarter shell versus residual pressure.

ACKNOWLEDGEMENT

This work has been supported by Gesellschaft für Schwerionenforschung (GSI), BMBF contr. No. 06F134I and EU contr. No 516520-FI6W. We acknowledge also the support of the European Community-Research Infrastructure Activity under the FP6 Structuring the European Research Area program (CARE, contract number RII3-CT- 2003-506395). This work was (financially) supported by BMBF 06FY161I, 06FY7102 and by the Helmholtz-InternationalCenter for FAIR within the framework of the LOEWE program (Landesoffensive zur Entwicklung Wissenschaftlich-Ökonomischer Exzellenz) launched by the State of Hesse. We'd like to thank our contact persons and the staff at RI for the close collaboration and the kind assistance for the measurements during this project.

REFERENCES

[1] H. Podlech, M. Amberg, H. Klein, D. Mder, U. Ratzinger, A. Schempp, R. Tiede, M. Vossberg, C. Zhang "General Layout of the 17 MeV Injector for MYRRHA", Proceedings of IPAC 2011, San Sebastian, Spain, p. 2574-2576 .

[2] H. Podlech, A. Bechtold, H. Liebermann, M. Busch, G. Clemente, H. Klein, U. Ratzinger, R. Tiede, C. Zhang Development of Room Temperature and Superconducting CH-Structures for High Power Applications, Proc. of the HPPA5 workshop, Mol, Belgium, 2007, p. 115-124.

[3] H. Podlech, U. Ratzinger, H. Klein, C. Commenda, H. Liebermann, A. Sauer, "Superconducting CH-Structure", Phys. Rev. STAB 10, 080101, 2007.

[4] CST Microwave Studio, http://www.cst.com.

[5] M. Busch, H. Podlech, M. Amberg, F. Dziuba, U. Ratzinger, "Superconducting CH-Cavity development", Proceedings of IPAC 2010, Kyoto, Japan, p. 753-755.

[6] M. Amberg, W. Barth, S. Mickat, M. Busch, F. Dziuba, H. Podlech, U. Ratzinger, K. Aulenbacher, "Structural Mechanical Analysis of Superconducting CH-Cavities", Proceedings of SRF 2011, Chicago, USA, p. 162-164.

[7] M. Busch, F. Dziuba, H. Podlech, U. Ratzinger, W. Barth, S. Mickat, M. Amberg, K. Aulenbacher, "Status of the 325 MHz sc CH-Cavity at IAP Frankfurt", Proceedings of IPAC 2011, San Sebastian, Spain, p. 265-267.

[8] RI, Research Instruments GmbH, Bergisch Gladbach, Germany, http://www.research-instruments.de

Copyright © 2012 by the respective authors — cc Creative Commons Attribution 3.0 (CC BY 3.0)

STATUS OF THE SUPERCONDUCTING CW DEMONSTRATOR FOR GSI*

F. Dziuba†,[1], M. Amberg[1,3], K. Aulenbacher[3,4], W. Barth[2,3], M. Busch[1], H. Podlech[1], U. Ratzinger[1], S. Mickat[2,3]

[1]IAP University of Frankfurt, 60438 Frankfurt am Main, Germany
[2]GSI Helmholtzzentrum, 64291 Darmstadt, Germany
[3]Helmholtz Institut Mainz (HIM), 55099 Mainz, Germany
[4]KPH Mainz University, 55128 Mainz, Germany

Abstract

Since the existing UNILAC at GSI will be used as an injector for the FAIR facility a new superconducting (sc) continuous wave (cw) LINAC is highly requested by a broad community of future users to fulfill the requirements of nuclear chemistry, especially in the research field of Super Heavy Elements (SHE). This LINAC is under design in collaboration with the Institute for Applied Physics (IAP) of Frankfurt University, GSI and the Helmholtz Institut Mainz (HIM). It will consist of 9 sc Crossbar-H-mode (CH) [1] cavities operated at 217 MHz which provide an energy up to 7.3 AMeV. Currently, a prototype of the cw LINAC is under development. This demonstrator comprises the first sc CH cavity of the LINAC embedded between two sc solenoids mounted in a horizontal cryomodule. One important milestone of the project will be a full performance test of the demonstrator by injecting and accelerating a beam from the GSI High Charge State Injector (HLI) in 2014. The status of the demonstrator is presented.

THE SUPERCONDUCTING CW LINAC DEMONSTRATOR

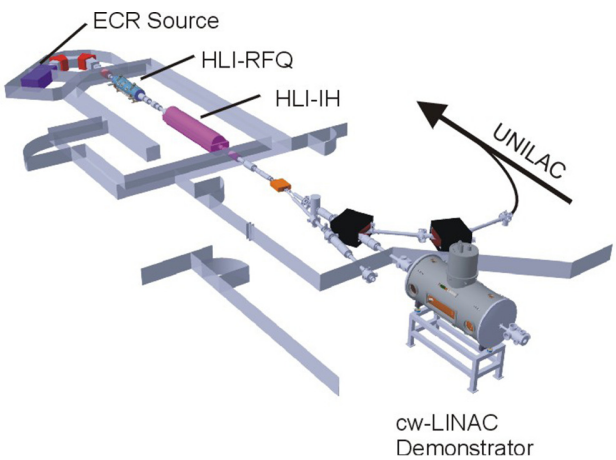

Figure 1: Demonstrator setup with the High Charge Injector at GSI.

The demonstrator will be the first section of the new sc cw LINAC at GSI. It will be operated at 217 MHz which is the second harmonic of the existing 1.4 AMeV GSI HLI. A test of the sc 217 MHz CH cavity, which is the key component of the project, under real operational conditions is the main aim of the demonstrator [2, 3]. It is planned to run a full performance test by injecting and accelerating a beam from the HLI in 2014. Figure 1 shows the cw demonstrator setup and the HLI.

STATUS OF THE SC 217 MHZ CH CAVITY

The sc 217 MHz CH cavity for the cw LINAC demonstrator (see fig. 2) will consist of 15 accelerating cells at a total length of 690 mm while the maximum gradient is 5.1 MV/m. Furthermore, the cavity is designed with the special EQUUS (EQUidistant mUlti-gap Structure) beam dynamics [4].

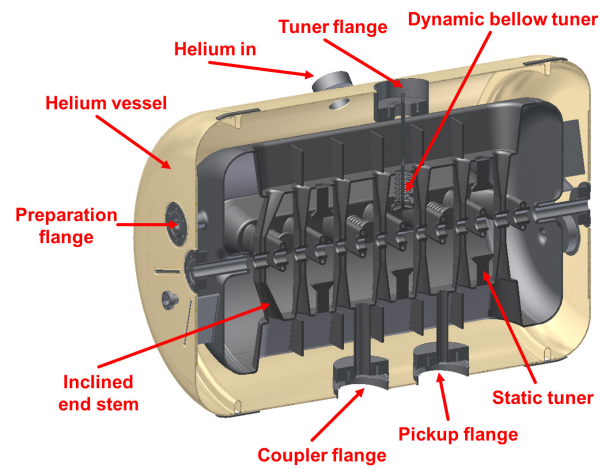

Figure 2: Side view of the sc 217 MHz CH cavity for the cw demonstrator at GSI.

The rf design of the cavity is finished. All main parameters of the cavity are shown in table 1. In June 2012 the production of the cavity has started at Research Instruments (RI) GmbH, Bergisch Gladbach, Germany. It is scheduled to be delivered to the IAP in 2013.

The cavity will be equipped with all necessary auxiliaries like a 10 kW cw power coupler, a titanium helium

* Work supported by HIM, GSI, BMBF Contr. No. 06FY7102
† dziuba@iap.uni-frankfurt.de

Copyright © 2012 by the respective authors — cc Creative Commons Attribution 3.0 (CC BY 3.0)

Table 1: Main parameters of the 217 MHz CH-cavity

β		0.059
Frequency	MHz	216.816
Accelerating cells		15
Total length	mm	690
Cavity diameter	mm	410
Cell length	mm	40.8
Accelerating gradient	MV/m	5.1
U_a ($\beta\lambda$ definition)	MV	3.12
E_p/E_a		6.4
B_p/E_a	mT/(MV/m)	5.4
R_a/Q_0	Ω	3320

vessel, several preparation flanges and a frequency tuning system. Since matching the design frequency during the fabrication and the operation process of a sc CH cavity is a serious challenge, the tuning will be done by capacitive static and dynamic tuners positioned between the stems.

Nine static tuners will be adapted accordingly during the fabrication to hit the design frequency. At a maximum height of 65 mm the frequency shift range of the static tuners is 3.6 MHz. Additionally, three slow bellow tuners (see fig. 3), driven by stepping motors control the frequency of the cavity during operation. They will readjust frequency changes and pressure effects at 4.2 K. Furthermore, two of these bellow tuners are connected to fast reacting piezo elements to compensate limitations like microphonics and Lorentz-Force-Detuning (one in operation, one in spare). The expected frequency shift range for one fast tuner during operation is ± 50 Hz/μm.

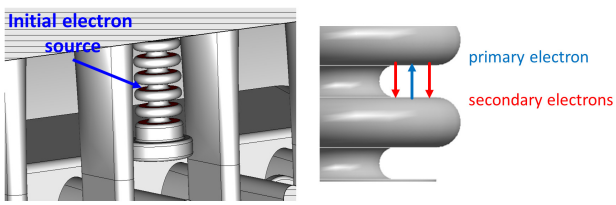

Figure 3: Final design of the 6-cell bellow tuner with the initial electron sources for the multipacting analyses.

To determine the geometry of the bellow tuners several mechanical, rf and multipacting simulations have been performed with ANSYS Workbench, CST MICROWAVE STUDIO and CST PARTICLE STUDIO. The gaps of the bellows are critical spots for multipacting. Figure 3 shows the final geometry of the 6-cell bellow tuner with a gap width of 3.5 mm and the initial electron sources for the multipacting analyses. For the simulations 12000 initial particles were chosen while the energy of the initial electrons has been varied from 2 to 5 eV with an kinetic spread of 50%. The simulated secondary emission yield (SEY)

$$\langle \mathrm{SEY} \rangle = \frac{\text{Total number of secondaries}}{\text{Total number of hits}}$$

for different accelerating gradients is shown in figure 4 as an example for an initial electron energy of 3 eV. As all simulations show, the effect of multipacting does not appear in the tuner gaps.

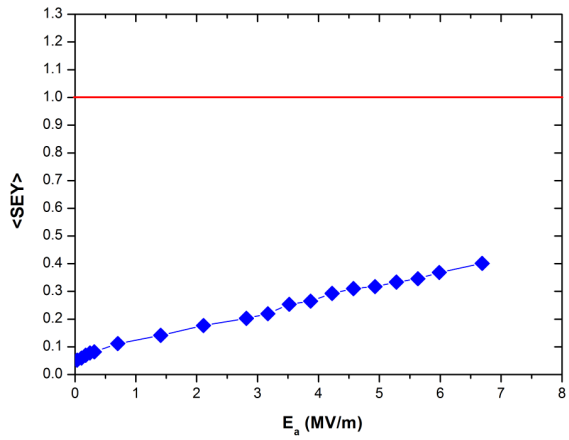

Figure 4: Simulated secondary emission yield for different accelerating gradients at an initial electron energy of 3 eV.

THE HORIZONTAL CRYOSTAT

For the planned beam tests at the GSI HLI a new horizontal cryostat is needed which houses the two sc solenoids and the sc CH cavity (see fig. 5). The final design phase of the cryostat is in progress at the moment. It is going to be built by Cryogenic Limited, London, United Kingdom and scheduled to be delivered in 2014. In comparison to a first concept study [5] the material of the vacuum vessel was changed from stainless steel to aluminum due to cost-efficient production.

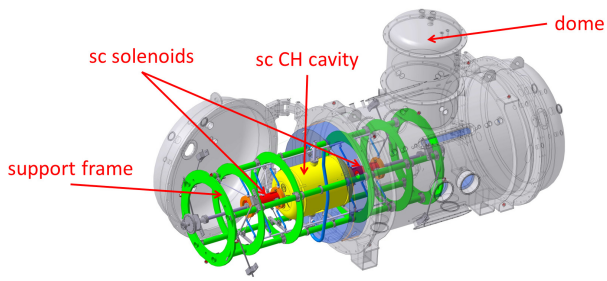

Figure 5: Layout of the horizontal cryostat close to the final design. In the center of the support frame the cavity (yellow) is embedded by two sc solenoids (red).

The main design criteria for the new cryostat are:

- modular design, universally usable - tests of various types of solenoids and CH cavities with different lengths and diameters
- various flanges for assembling options
- a dome for electrical supplies with a reservoir for cryogenic liquids
- a measuring system to control the positions of the cold masses on the beam axis

Copyright © 2012 by the respective authors — cc Creative Commons Attribution 3.0 (CC BY 3.0)

Furthermore, the LHe reservoir will have a flow rate of 100 l/h while the estimated losses of the cryostat are roughly 2 l/h.

Table 2: Design parameters of the cryostat

Inner length	mm	2200
Inner diameter	mm	1120
Material tank		Aluminum
Insulating vacuum	mbar	$< 1 \cdot 10^{-5}$
Max. system pressure	bar	< 0.5
Operating temperature	K	4.2
Temperature thermal shield	K	77
Max. static losses (stand by)	W	< 10

To investigate the behavior of the cryostat's support frame under a cryogenic environment, first thermal and mechanical simulations have been performed with CST MPHYSICS STUDIO. Therefore, three different temperature sources were added to a simple model of the cryostat and the cavity to run the stationary solver (see fig. 6). Figure 6 shows the 3D temperature distribution of the support frame with the suspension rods. Heat transfer caused by radiation was not considered in the simulations as well as insulating materials. The outer suspension rods of the support frame were fixed during the simulations. As the contour plots of figure 7 show, the total displacement in x and y direction is roughly 3 mm while in z direction a displacement of 10 mm appears.

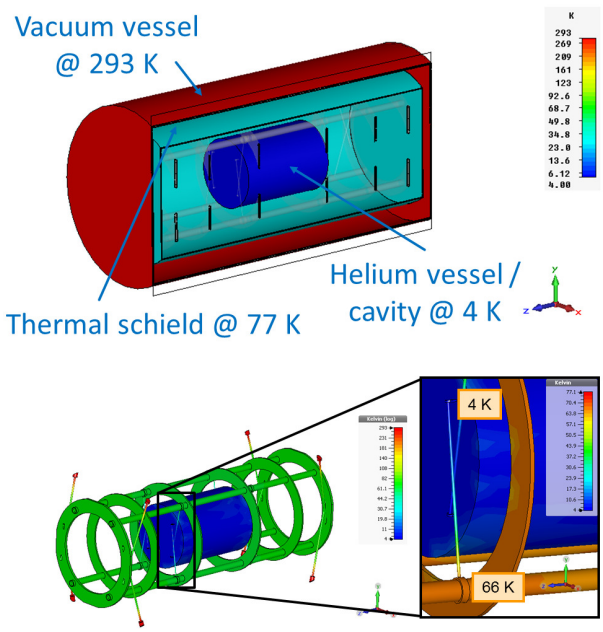

Figure 6: Temperature sources for the thermal stationary solver (top) and 3D temperature distribution of the support frame (bottom).

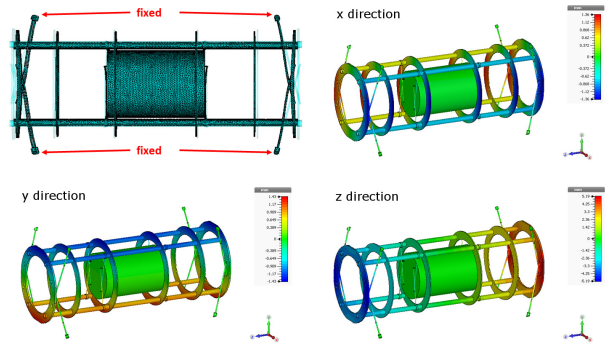

Figure 7: Deformed mesh of the support frame (scaling factor 10) and total displacement in x,y,z direction.

SUMMARY & OUTLOOK

First preparations were done to set up the cw LINAC demonstrator at the GSI HLI. A 3000 l LHe-tank as well as a helium recovery system have been delivered to GSI.

The rf design of the sc 217 MHz CH cavity is completed and its fabrication has started in June 2012 at RI. At present, the final design phase of the horizontal cryostat is in progress. The cryostat as well as the sc solenoids have been ordered from Cryogenic Limited.

The delivery of all main components is expected in 2013/14. After the assembling under clean room conditions and first rf test at the IAP, a full performance test with beam at the HLI is foreseen in 2014. Successful tests of the demonstrator are a fundamental step on the way to the proposed sc cw LINAC.

ACKNOWLEDGMENT

This work has been supported by Helmholtz-Institut Mainz (HIM) and Gesellschaft für Schwerionenforschung (GSI). This work was (financially) supported by BMBF Contr. No. 06FY7102 and by the HelmholtzInternational-Center for FAIR within the framework of the LOEWE program (Landesoffensive zur Entwicklung Wissenschaftlich-Ökonomischer Exzellenz) launched by the State of Hesse.

REFERENCES

[1] H. Podlech et al., Superconducting CH structure, Phys. Rev. STAB 10, 080101 (2007).

[2] S. Mickat et al., The sc cw-LINAC-Demonstrator - SRF Technology finds the way to GSI, in Proc. of SRF2011 (to be published), Chicago, USA (2011).

[3] F. Dziuba et al., Development of superconducting crossbar-H-mode cavities for proton and ion accelerators, Phys. Rev. STAB 13, 041302 (2010).

[4] S. Minaev et al., A Superconducting Energy Variable Heavy Ion Linac with Constant Beta, Multi-Cell Cavities of CH-Type, Phys. Rev. STAB 12, 120101 (2009).

[5] V. Gettmann et al., The sc cw-LINAC Demonstrator - an R&D project for SRF technology, in Proc. of SRF2011, Chicago, USA (2011).

Copyright © 2012 by the respective authors — cc Creative Commons Attribution 3.0 (CC BY 3.0)

DESIGN AND SIMULATION OF A TEST MODEL FOR A TRI-SPOKE CAVITY AT RIKEN *

L. LU, N. Sakamoto, K. Suda, K. Yamada, O. Kamigaito,
RIKEN Nishina Center for Accelerator-Based Science,
RIKEN, 2-1, Hirosawa, Wako, Saitama 351-0198, JAPAN

Abstract

A design for a tri-spoke-type superconducting cavity for uranium beams with β = 0.303 and a 219 MHz operational frequency is presented. And a test model designed and assembled by two end-wall flanges and one triparted part of the designed tri-spoke cavity, was expected to be built using the same fabrication technology that is supposed for Nb cavity manufacture. The designs and simulations of the tri-spoke cavity and the test model will be reported in this paper.

INTRODUCTION

Very heavy ions such as uranium can be accelerated to very high energy using an accelerator chain, which consists of a new linear injector named RILAC2 with a powerful superconducting ECR ion source and four booster cyclotrons in the RIKEN RI-beam factory (RIBF) [1-4]. However, two charge-stripping sections cause an increase in the phase width of the beam in subsequent cyclotrons. Thus, we aim to design a tri-spoke type superconducting cavity as a rebuncher in order to focus the beam in the longitudinal direction. This tri-spoke cavity would be placed between fRC and IRC. The frequency of the tri-spoke cavity was chosen to be 219 MHz, which is the 12th harmonic of the fundamental frequency of 18.25 MHz. This frequency yields a cell length of $\beta\lambda/2 = 207$ mm at β = 0.303 [5]. The total voltage is estimated to be a few megavolts at this frequency.

We have not experiences and facilities of fabrication of superconducting cavity. Thus, the novelty of SC rf technology, the complexity of mechanical construction, and use of electron beam welding, a substantial effort should first be invested and researched in fabricating a test model from oxygen-free copper. The test model is assembled from two end-wall flanges and a triparted tri-spoke cavity, as shown in Fig. 1 [6]. The parameters of the tri-spoke cavity and the fabrication model are listed in Table 1.

Table 1: Parameters of tri-spoke cavity model and fabrication model

Parameter	Tri-spoke	Test model
Frequency (MHz)	219	228
Length (mm)	828.8	346.4
Cavity Dia. (mm)	580	580
Beam Bore (mm)	15	15
R/Q (Ω)	241.21	155.6
E_{pk}/E_{acc}	2.75	2.04
H_{pk}/E_{acc} (Oe/MV/m)	58.21	
G (Ω)	81.17	79.4
R_{res} @ 4.2K (nΩ)	25	25
Q @ 4.2K (Ω)	3.25E+09	3.17E+09
Power@ 4.2K (W)	0.42	0.45

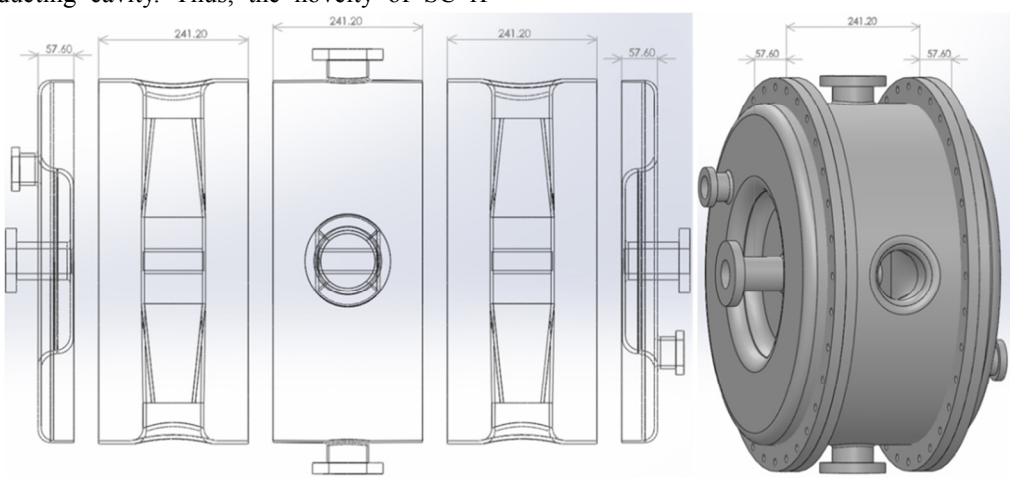

Figure 1: Images of wall flanges and triparted cavity parts (left) and the assembled image of the test model (right).

*luliang@riken.jp
*Work supported by Foreign Postdoctoral Researcher

Copyright © 2012 by the respective authors — cc Creative Commons Attribution 3.0 (CC BY 3.0)

DESIGN

Designs and Simulations

In order to train technicians and for practice in welding technique, a test model will be built from copper sheets using the same fabrication technology that is expected to be used in Nb cavity manufacture. Feedback from this model will be helpful for Nb model design and eventual Nb model fabrication through low temperature tests. The test model is designed to be assembled from two end-wall-flanges and one triparted cavity, as shown in the right part of Fig. 1.

Tri-spoke cavity and test model designs have been optimized using Microwave Studio (MWS) software [7]. Fig. 2 and Fig. 3 show the main geometrical designs of the tri-spoke cavity and the test model used for optimization. The position of the coupler was designed to be at the center of the cavity, oriented in the vertical direction of the 2nd stem. The vacuum port can be installed on either side. This symmetrical position of this design is attractive as the magnetic field is zero in this region [8-9]. Two maintenance ports for cavity cleaning were designed in the side wall because the magnetic field is not concentrated in these positions.

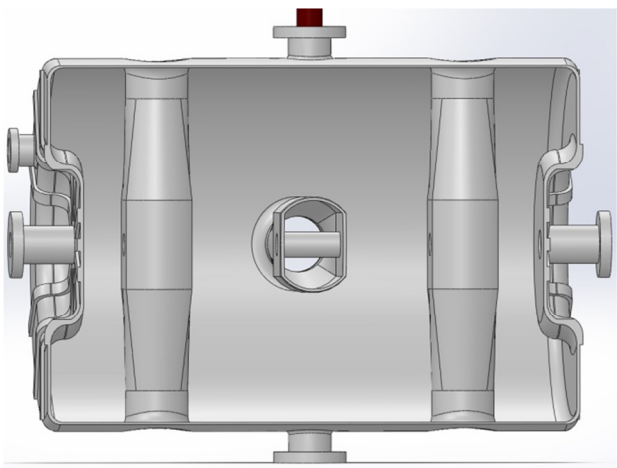

Figure 2: Cross section of the tri-spoke cavity with stiffening ribs.

Electron beam welding and normal braze techniques, which will be adopted in the manufacture of this test model, will be studied in this training process. The test results of the model will also be studied for feedback on RF cavity and cavity mechanical design. A full scale Nb test model, identical to the copper test model, will also be manufactured and assembled after low temperature testing of the copper model is complete.

The RF cavity is designed to minimize the peak surface electric and magnetic field ratios: E_{peak} / E_{acc} and B_{peak} / E_{acc}, respectively. Surface electric and magnetic fields in an optimized cavity are shown in Fig 4. The main RF parameters of this cavity are summarized in Table 1.

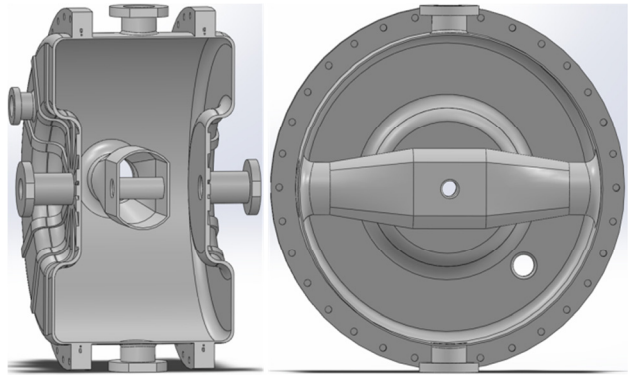

Figure 3: Cross section of the test model with ribs.

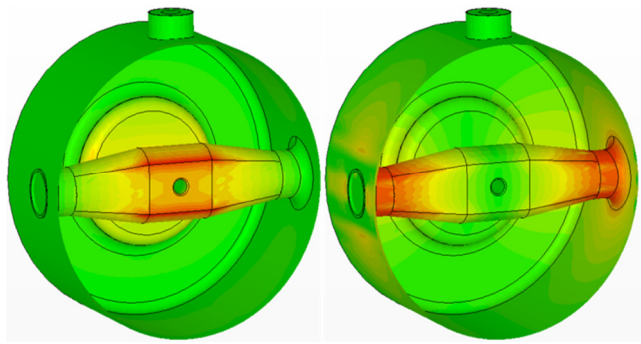

Figure 4: Surface electric (left) and magnetic (right) fields in the test model. The field strength increases as the color changes from green to yellow to red.

The walls and spokes will be formed from 3 mm thick copper sheets. End wall flanges will be made from a 5 mm thick sheet. The initial cavity fabrication design will specify that the spokes will be formed in halves and seam welded together. Cavity walls will also be manufactured from two 3 mm thickness halves and longitudinally welded. Two press-formed end wall flanges will be assembled from cavity walls by two connection ring ribs in test model manufacturing. A conductor and a metal O-ring will be adopted in the connection ring rib. All cavity welds will be formed using outsourced electron beam technology. The outer cavity stiffening structure will be brazed to the cavity body.

However, there are other opinions about the manufacturing method which is use numerical control machine (NC) tools to shape the spokes from Nb ingots or bulk copper. The assembly method should then include two flanges with stiff ribs. However, the design and fabrication of a stiff cavity with an inflexible structure are attractive for our research because a buncher cavity with an inflexible frequency shift is not required for a high power system.

The manufacturing method of shaping spokes using NC machine tools has been discussed. Further, the simulation of the maximum displacement using a model with ribs has been discussed along with the relationship between the

Copyright © 2012 by the respective authors — cc Creative Commons Attribution 3.0 (CC BY 3.0)

displacement and the tuning effects. The design of stiff ribs was discussed for several structure types. The final rib design and the simulated results for the maximum deformation of a rib model are shown in Fig. 5 using Microwave Studio. The total pressure acting on the surface of the cavity is set to 0.121325 MPa. The observed 0.39 mm deformation is tolerable and easy to tune. The calculated pressure sensitivity (df/dP) is -172 Hz/mBar.

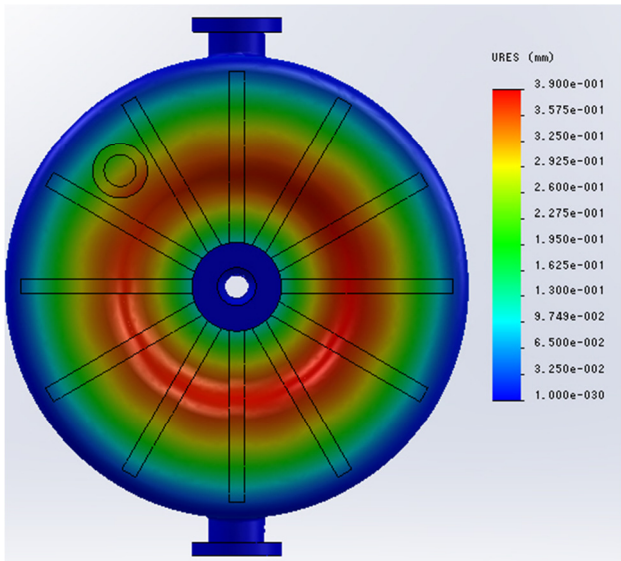

Figure 5: The image of the maximum displacement of the test model with ribs.

This cavity tuning method will be adopted for the end-wall tuners. Inward deformation of the end-walls (the region of high electric field shown in the left side of Fig. 4) increases the capacitance and hence reduces the frequency. Both the tuning effects of the tri-spoke cavity and the test model are shown in Fig. 6. As shown in Fig. 6, both the frequency changes of the tri-spoke cavity and the test model decrease linearly with tuning length.

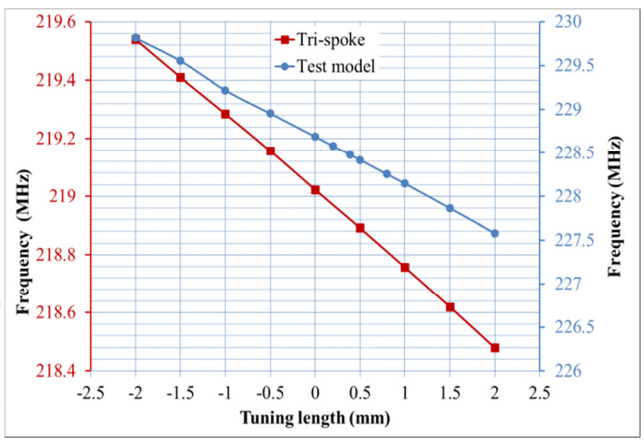

Figure 6: Shifts in resonator frequency of the tri-spoke cavity (red line) and the test model (blue line).

The details of coupler design are not finalized, but calculations of the external Q (Qext) are being simulated. The simulated results obtained using MWS are presented in Fig. 7.

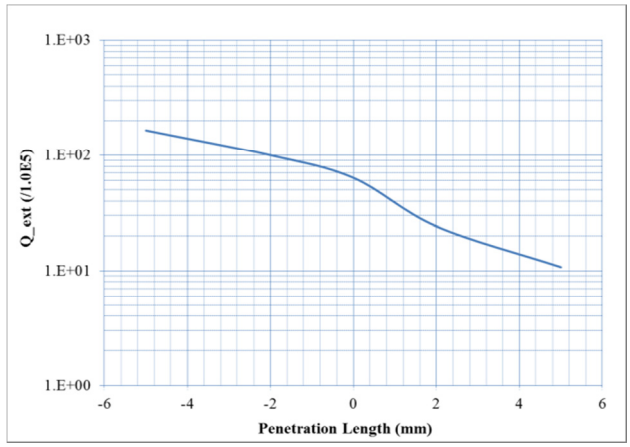

Figure 7: The Qext dependence on the penetration length of the coupler.

FUTURE WORK

There are three important works to be considered in the future: post processing, design of the power coupler, and the design of the helium and vacuum vessels. For post processing of the cavity, such as surface polishing, cleaning, and baking, we have begun to study the basis of these techniques and prepare the equipment for initial research. The power coupler will be designed as a coaxial structure with inner and outer conductors and is required to contain both warm and cold insulating windows, which enable the whole coupler to be divided into warm and cold sections. The design of the helium vessel and the vacuum vessel will be considered after the measurements of the fabrication model are complete.

REFERENCES

[1] Y. Yano, Nucl. Instr. and Meth. B261 (2007) 1009.
[2] Y. Higurashi, *et al.*, in Proceedings of IPAC10, Kyoto, Japan, THPEC060, (2010).
[3] K. Yamada, *et al.*, Proceedings of the IPAC10, Kyoto, Japan, MOPD046, (2010).
[4] K. Suda, *et al.*, Proceedings of the IPAC10, Kyoto, Japan, THPEA023, (2010).
[5] L. Lu, N. Sakamoto, et al., Proceedings of the SRF2011, Chicago, USA, MOPO028, (2011).
[6] L. Lu, N. Sakamoto, et al., Proceedings of IPAC2012, New Orleans, USA, WEPPC018, (2012).
[7] "CST Microwave Studio ™", Version 2011
[8] E. Zaplatin, W. Braeutigam, et al., Proceedings of the EPAC2004, Lucerne, Switzerland (2004).
[9] G. P. Zinkann, S. Sharamentov, et al., Proceedings of PAC2005, Knoxville, Tennessee, USA, WPAT082, (2005).

Copyright © 2012 by the respective authors — cc Creative Commons Attribution 3.0 (CC BY 3.0)

SUPERCONDUCTING CW HEAVY ION LINAC AT GSI

Winfried Barth, Peter Gerhard, Viktor Gettmann, Sascha Mickat
HIM, Mainz
Gesellschaft für Schwerionenforschung, D-64291 Darmstadt, Germany

Abstract

An upgrade program has to be realized in the next years, such that enhanced primary beam intensities at the experiment target are available. For this a new sc 28 GHz full performance ECR ion source is under development. Via a new low energy beam line an already installed new RFQ and an IH-DTL will provide for cw-heavy ion beams with high average beam intensity. It is planned to build a new cw-heavy ion-linac behind this high charge state injector. In preparation an R&D program is still ongoing: The first linac section comprising a sc CH-cavity embedded by two sc solenoids (financed by HIM and partly by HGF-ARD-initiative) as a demonstrator will be tested with beam at the GSI High Charge Injector (HLI). The new linac should feed the GSI flagship experiments SHIP and TASCA, as well as material research, biophysics and plasma physics experiments in the MeV/u-area. The linac will be integrated in the GSI-UNILAC-environment; it is housed by the existing constructions. Different layout scenarios of a multipurpose high intensity heavy ion facility will be presented as well as the schedule for preparation and integration of the new cw-linac.

INTRODUCTION

Table 1: Design Parameters of the cw-LINAC

Mass/Charge		6
Frequency	MHz	217
Max. beam current	mA	1
Injection Energy	MeV/u	1.4
Output energy	MeV/u	3.5 – 7.5
Output energy spread	keV/u	+- 3
Length of acceleration	m	12.7
Sc CH-cavities		9
Sc solenoids		7

The HLI in combination with the Universal Linear Accelerator (UNILAC) is a powerful high duty factor (25%) accelerator to provide heavy ion beams for the ambitious SHE-research program at GSI. In future the UNILAC is designated as an injector for FAIR (Facility for Antiproton and Ion Research). Beam time availability for SHE-research will be decreased due to the limitation of the UNILAC in providing a proper beam for SHE and in fulfilling the requirements for FAIR simultaneously. To keep the SHE program at GSI competitive on a high level, an upgrade program of the HLI was initialized comprising a new 28 GHz ECR source and a new cw capable RFQ [1,2]. As a result of a long term cost-benefit analysis a standalone sc cw-LINAC in combination with the upgraded HLI is assumed to fit the requirements of SHE best. Significant higher beam intensities will be provided and lead to an increase of the SHE production rate.

The technical design and the realisation of such a sc cw-LINAC in parallel to the existing UNILAC at GSI is assigned to a collaboration of GSI, the IAP, and the Helmholtz-Institute Mainz (HIM), which was founded in 2009. A conceptual layout [3] of a sc cw-LINAC was worked out, which allows the acceleration of highly charged ions with a mass to charge ratio of 6 at 1.4 MeV/u from the upgraded HLI. Nine superconducting CH-cavities [4] operated at 217 MHz accelerate the ions to energies between 3.5 MeV/u and 7.3 MeV/u, while the energy spread should be kept smaller than ±3keV/u. As beam focusing elements seven superconducting solenoids are applied. The general parameters are listed in table 1. The commissioning of the cw-LINAC is scheduled in 2019 at earliest.

CW-LINAC-DEMONSTRATOR

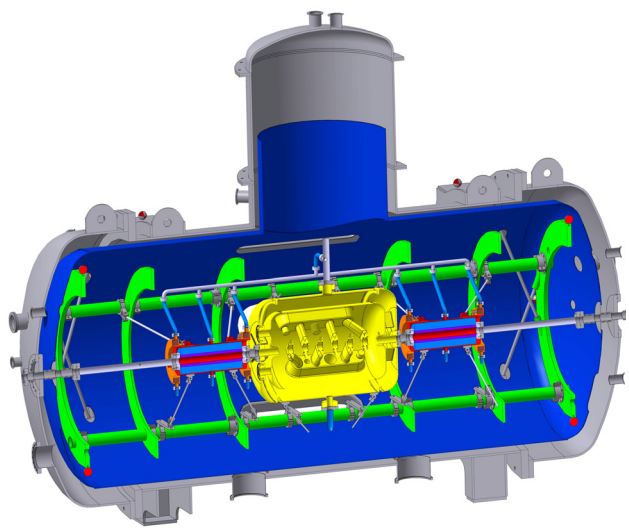

Figure 1: Scheme of the cw-LINAC Demonstrator; CH-cavity (yellow) in its centre embedded by two sc solenoids (red-orange).

The first section of the cw-LINAC comprising a sc CH-cavity embedded by two sc solenoids (financed by HIM and ARD) as a demonstrator (see fig. 1) will be tested with beam at the HLI (see fig. 2).

Copyright © 2012 by the respective authors — cc Creative Commons Attribution 3.0 (CC BY 3.0)

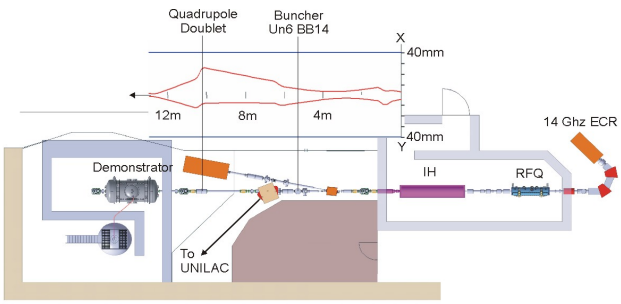

Figure 2: Existing HLI serves as an injector for the cw-LINAC demonstrator. A re-buncher as well as a quadrupole doublet provide for matching to the demonstrator.

A study has been worked out which provides a concept to assemble the cryostat [5] with the solenoids and the cavity as well as to align the three components to the beam axis. An sc CH-structure was chosen as key component for the whole linac. In a prototype test of a 360 MHz sc CH-cavity (β=0.16, 19 gaps) at the IAP maximum gradients of up to 7 MV/m at Q_0-values between 10^8 and 10^9 were achieved in a vertical cryostat. The rf-cavities have an operating frequency of 217 MHz and provide gradients of 5.1 MV/m at a total length of minimum 0.6 m [6]. The CH-prototype cavity [7, 8] is surrounded by two sc-solenoids with maximum design fields of 9.3 T at an effective length of 290 mm and a free beam aperture of 30 mm. The fringe fields are reduced from the maximum field to 50 mT at the inner NbTi-surface of the neighbouring cavity, based on the 9T solenoid design for the ISAC-II cryomodule [9].

The favoured location to set up the Demonstrator is in straightforward direction of the GSI-HLI (fig. 2 and 3). Two existing experiments at the HLI have to move since the space is needed for the demonstrator test environment including a new radiation protection cave. The liquid helium (LHe) supply is covered by a 3000 ltr tank. The consumed helium is collected in a 25 m^3 recovery balloon and bottled by a compressor. In operation a consumption of 20 ltr LHe per hour is predicted. For longitudinal matching of the beam from the HLI to the demonstrator an existing re-buncher can be used, while for transverse focusing an additional quadrupole doublet is foreseen. Additional beam diagnostic elements (profile grids, emittance meter) have to be integrated in the beam line in front of and behind the cryostat. Beam energy measurements by time of flight method (TOF) have to be performed with phase probes.

In 2012 the new test area was cleared completely. After this the radiation shielding bunker was built; assembly of the matching line is now completed and an emittance meter is in place of the demonstrator. First beam measurements were successfully accomplished to check the capabilities of the matching beam line. In autumn a dedicated beam test with a full performance argon beam is scheduled to verify the assumed beam parameters at the entrance of the demonstrator.

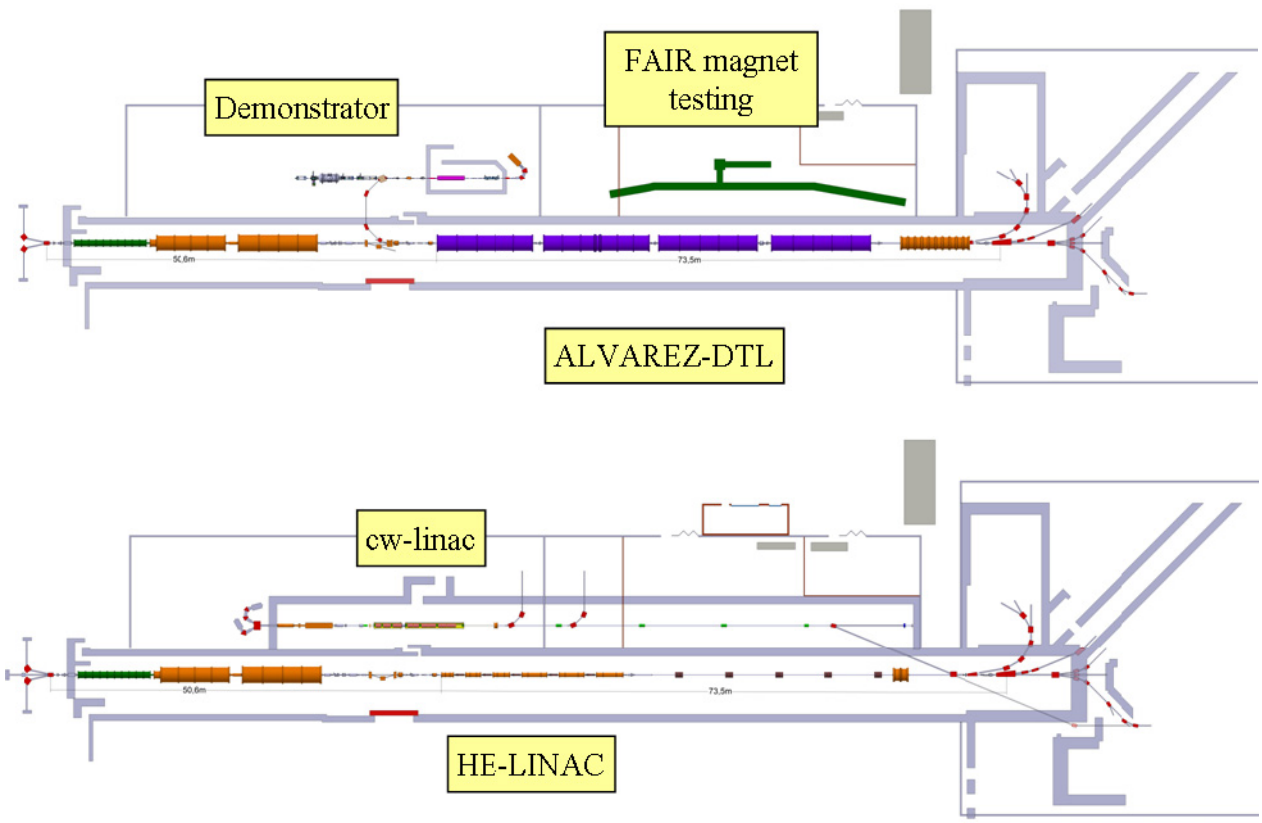

Figure 3: Complete GSI-injector environment; with demonstrator in place as scheduled for 2014 (top), after completion with HE-linac and cw-LINAC in place (bottom).

Copyright © 2012 by the respective authors — cc Creative Commons Attribution 3.0 (CC BY 3.0)

MULTIPURPOSE HIGH INTENSITY HEAVY ION LINAC

Successful R&D at the cw-CH-linac demonstrator is a milestone for the realization of the sc-cw-linac-project [10, 11]. This new injector linac could be an integrated part of a revised multipurpose heavy ion linac at GSI. A proposal for this advanced GSI-injector environment including all beam transfer lines was elaborated in 2011 [12]. Beam could be delivered by the cw-linear accelerator for highly charged ions and by the synchrotron injector (HE-linac) on a pulse to pulse basis (fig. 3). Additional beam lines would be required in order to avoid restrictions on beam operation during construction times of the different linac systems. Then the warm cw-linac (HLI) in combination with the HE-linac could also serve as a synchrotron injector for rare isotopes delivered by the ECR-ion sources. Optionally heavy ions, mainly uranium ions, from the HSI would be transferable to the cw-linac (cold), where a high duty factor ion beam could be accelerated for UNILAC experiments (e.g. for the material research cave). Additionally a high intensity proton beam from the new FAIR-p-linac will serve the synchrotron only. A maintenance program dedicated to the complete UNILAC will be performed in the next years. During this time the High Current Injector will be upgraded as a high intensity heavy ion FAIR-injector. The FAIR p-linac should be mounted until 2017. After completion of the technical design in the next three years, the HE-linac is gradually built up until the end of this decade.

STATUS & OUTLOOK

Table 2: Time Schedule

	cw-LINAC – Demonstrator-Project
2005	HLI-upgrade program comprising sc ECR-source, LEBT, and cw-capable RFQ defined
2009	Proposal of a sc cw LINAC Foundation of HIM
2010	sc cw-LINAC-project evaluated Successful commissioning of the cw capable RFQ Tendering of demonstrator components
2011	Delivery of LHe-supply and rf-amplifier Ordering of cavity, solenoids, cryostat Assembly of test area@GSI started
2013	Delivery of cavity, solenoid, cryostat 1st tests (warm + cold) at IAP
2013/14	Full performance test at GSI HLI
>2019	*Commissioning "sc cw-LINAC"*

The mechanical assembly of the demonstrator at GSI-HLI is still in preparation. Components like the 3000 ltr LHe-tank, the 25 m^3 recovery balloon and the compressor are in house. The order of the CH-cavity is placed to Research Instruments (RI) at Bergisch Gladbach, Germany, the 5 kW rf-amplifier was delivered in may 2010. The cryostat, the two sc-solenoids and the support system were ordered at Cryogenic (London, U.K.). Cryogenic will also provide for the integration, alignment in cryogenic environment of the cryostat.

REFERENCES

[1] W. Barth et al., Unilac-upgrade programme for the heavy element research at gsi-ship, Proceedings of EPAC 2006, Edinburgh, Scotland, TUPLS034, 04 Hadron Accelerators, A08 Linear Accelerators, p.1565, (2006)

[2] P. Gerhard et al., Commissioningof a new cw RFQ at GSI, Proceedings of IPAC10, Kyoto, Japan, p.741-743, (2010)

[3] S. Minaev et al., Superconducting, energy variable heavy ion linac with constant β, multicell cavities of CH-Type, Phys. Rev. ST Accel. Beams 12, 120101 (2009)

[4] H. Podlech et al., Superconducting CH structure, Phys. Rev. ST Accel. Beams 10, 080101 (2007)

[5] V. Gettmann et al., The sc cw -LINAC Demonstrator – an R&D project for SRF technology, SRF2011, Chicago, USA (2011)

[6] F. Dziuba et al., Development of superconducting crossbar-H-mode cavities for proton and ion accelerators. Phys. Rev. ST Accel. Beams 13, 041302 (2010)

[7] M. Amberg et al., Structural Mechanical Analysis of Superconducting CH-Cavities, SRF2011, Chicago, USA (2011)

[8] F. Dziuba et al., Development of Superconducting CH-Cavities, SRF2011, Chicago, USA (2011)

[9] R.E. Laxdal et al., Magnetic field studies in the ISAC-II cryomodule, Physica C 441, p.225–228 (2006)

[10] S. Mickat et al., The sc cw-LINAC-demonstrator – srf technology finds the way to GSI, SRF2011, Chicago, USA (2011)

[11] S. Mickat, et. al., The sc cw LINAC Demonstrator – 1st test of an sc CH-cavity with heavy ions, 12th HIAT Conference, Chicago, U.S.A. (2012)

[12] W. Barth, et. al., Future Heavy Ion Linacs at GSI, IPAC2011, San Sebastian, Spain (2011)

Copyright © 2012 by the respective authors — cc Creative Commons Attribution 3.0 (CC BY 3.0)

BEAM DYNAMICS DESIGN OF CHINA ADS PROTON LINAC*

Z.H. Li, F. Yan, P. Cheng, H.P. Geng, Z. Guo, C. Meng, B. Sun, J.Y. Tang, IHEP, Beijing, China

Abstract

It is widely accepted that the Accelerator Driven System (ADS) is one of the most promising technical approach to solve the problem of the nuclear wastes, a potential threaten to the sustainable development of the nuclear fission energy. An ADS study program was approved by Chinese Academy of Sciences at 2011, which aims to design and built an ADS demonstration facility with the capacity of more than 1000 MW thermal power within the following 20 years. The 15 MW driver accelerator will be designed and constructed by the Institute of High Energy Physics (IHEP) and Institute of Modern Physics (IMP) of China Academy of Sciences. This linac is characterized by the 1.5 GeV energy, 10mA current and CW operation. It is composed by two parallel 10 MeV injectors and a main linac integrated with fault tolerance design. The superconducting acceleration structures are employed except the RFQ. In this paper the general considerations and the beam dynamics design of the driver accelerator will be presented.

INTRODUCTION

The C-ADS project is a strategic plan to solve the nuclear waste and resource problems for nuclear power plants in China. It is supported financially by the central government and administrated by the Chinese Academy of Sciences. With its long-term planning lasting until 2032 aiming at construction of an ADS demonstration facility with 1000MW thermal power, the project will be conducted in three major phases.

As part of the whole project, the C-ADS driver accelerator is a CW proton linac and uses superconducting acceleration structures except the RFQs. The design specifications for the proton beams are shown in Table 1. For the first phase, the project goal is to build a CW proton linac of 50 MeV and 10 mA by about 2015. The first phase itself will be executed progressively in several steps, with the first step to build two 5-MeV test stands of different designs.

Table 1: Specifications for C-ADS Accelerator

Energy	1.5 GeV	
Current	10 mA	
Beam Power	15 MW	
Frequency	(162.5)325/650MHz	
Duty factor	100%	
Beam loss	<1 W/m	
Beam Trips/Year[1]	<25000	1s<t<10s
	<2500	10s<t<5min
	<25	t>5min

GENERAL

The C-ADS accelerator is a CW proton linac characterised by the properties of very high beam power and stringent requirements for reliability and availability that are not possessed by any of the existing proton linac. Therefore, the linac design had to integrate the stringent requirements from the very beginning [2]. The C-ADS linac is composed by two parallel 10 MeV injectors, main linac and a section of beam line (MEBT2) used to transfer and match beams from injectors to the main linac. The total length of the linac is about 450 m and the layout of the C-ADS driver linac is show in Figure 1.

Injectors

Two parallel 10MeV Injectors are designed working at "hot spare" mode to satisfy the stringent requirements on reliability and availability. This is the most difficult part of the whole linac. At present different technical

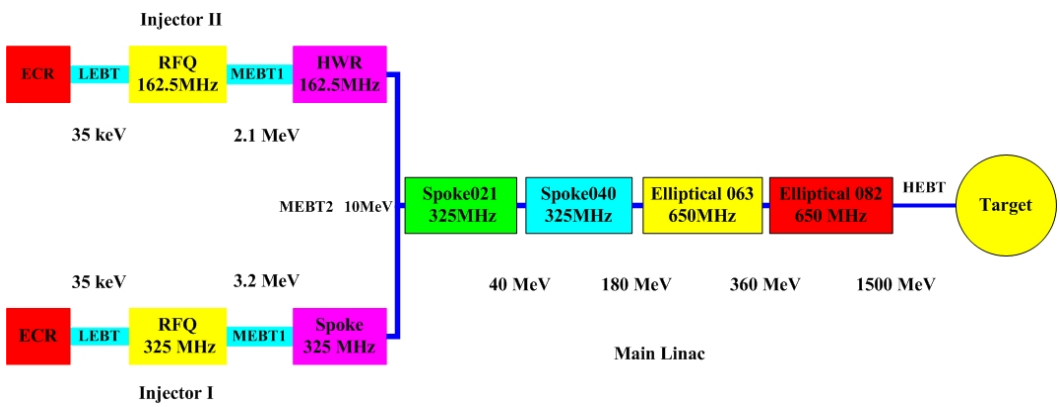

Figure 1: Layout of China ADS linac.

*Work supported by NSFC (10875099, 91126003), the China ADS Project (XDA03020000), IHEP special funding (Y0515550U1)
#lizhihui@ihep.ac.cn

Copyright © 2012 by the respective authors — cc Creative Commons Attribution 3.0 (CC BY 3.0)

approaches are applied for the two injectors reliability and availability. This is the most difficult part of the whole linac. At present different technical approaches are applied for the two injectors.

The Injector I, which is designed and built by the Institute of High Energy Physics (IHEP), is composed by a 15 mA ECR ion source with 35 keV output energy, then followed by a LEBT integrated with charge neutralization, which is used to transfer and match the beam to a 325MHz 3.2MeV 4-Vane RFQ. As the only normal conducting acceleration structure, the thermal management is believed to be one of the most difficult tasks for a CW machine, and several measures have been taken to decrease the surface energy density, such as 55 kV inter-vane voltages, much smaller than the popular design. This RFQ is also characterised by low input energy, which helps to get a relatively smaller output longitudinal emittance (0.16 mm.mrad), about 0.8 times the transverse one, which makes the following part more efficiency. Then a 2.06 m long MEBT (MEBT1) [3] is followed. It is composed by two bunchers, 6 quadrupoles and beam instruments devices, it is employed to match and transfer the beam to the superconducting section of Injector I.

The superconducting section of Injector I has one 9 m long cryogenic module with 12 single spoke cavities [4] and 11 solenoids inside, it will accelerate the beam to 10MeV. The geometry beta of the cavity is only 0.12 and is the smallest of the same type cavity, the Multipacting may be one of threatens for its steady operation. The physical and mechanical designs of the cavity have finished and the main parameters of the cavity are shown in table 2. Now the cavity is under construction, and the vertical test is foreseen at the October this year. The compact lattice with short solenoid (150 mm) and larger absolute synchronous phase (-46~-30 deg) is applied to improve the longitudinal beam dynamics.

Table 2: Main parameters of the Spoke012 cavity

β_g	Freq. MHz	V. Max MV	Emax MV/m	Bmax mT	R/Q Ω
0.12	325	0.82	32.5	47.5	148.7

The main difference between Injector I and Injector II is the working frequency. The half frequency of the spoke sections of main linac, 162.5 MHz, is applied for Injector II and the main motivation is to decrease the surface energy density of the RFQ. The details of the Injector II design can be found in reference [5].

At first step, two 5 MeV test stand based on the two different technical solutions will be built at the end of 2013 and the final solution of the two identical injectors will be chosen based on the behaviour of the two test stands.

MEBT2

Paragraphs The main function of the MEBT2 is to transfer and merge beams from two injectors and match it to the following main accelerator. As the only bending section of the linac, it is our only chance to collimate the tail particles coming from upstream here.

The bending angle is 15 degree and the distance from the injector axis to the main linac axis is 1.2 m. For each of the mainstream lines of the MEBT2, eight quadrupoles, two bending magnets and four bunchers are used. The design scheme satisfies the requirements of more-or-less uniform transverse focusing, achromatic bending and good control in the beam phase width. In the common part, three quadrupoles, two Spoke021 cavities and two solenoids are used for the matching in the phase spaces. Besides the main line, there is also an auxiliary line for each injectors and is used to transfer beams to the dump when the injector is working in offline mode. Another scheme without bunchers in bending section is under study too.

Main linac

The main linac is composed by two single spoke cavity sections working at 325MHz with geometry beta of 0.21 and 0.4 respectively, and then two 5-cell 650MHz elliptical cavity sections with geometry beta of 0.63 and 0.82 are applied to boost the beam to the final energy. The main parameters of the cavities are listed in table 3.

Table 3: Main parameters of the cavities in the main linac

Cavity type	βg	Freq. MHz	Vmax MV	Emax MV/m	Bmax mT
Single Spoke	0.21	325	1.64	31.14	65
Single Spoke	0.40	325	2.86	32.06	65
5-cell elliptical	0.63	650	10.26	37.72	65
5-cell elliptical	0.82	650	15.63	35.80	65

As a high power machine, beam loss control becomes more and more important as the energy increase. In order to satisfy the specifications listed in the table 1, we have followed the following considerations in the main linac design:

- Redundancy and fault tolerance design: for the nominal operation, the cavities only work at about 2/3 of maximum value listed in table 3, the maximum value is used when the cavity is involved in the local compensation, by which means the fault tolerance design is achieved [6].
- The mismatch is one of the sources of halo formation, which may cause particle loss. In order to keep the possibility of mismatch as small as possibility, periodic lattice structures are adopted. This is achieved by adding two long drifts at each side of the unit cell.
- Large transverse and longitudinal acceptance: this is very important for beam loss control. The aperture is

Copyright © 2012 by the respective authors — cc Creative Commons Attribution 3.0 (CC BY 3.0)

set as more than 10 times transverse RMS beam size and the absolute value of the synchronous phases are kept larger than 10 time RMS beam width throughout the whole main linac. The RMS beam size and synchronous phase are shown in figure 2.

- The tune depression along the main linac is about 0.7, which indicates significant space charge effect. We follow the high current proton linac design recipes proposed by Gerick. The zero current phase advances per period are kept below 90 degree for three phase planes. The ratio between transverse one and longitudinal one is set to 0.75 according to the values of emittance in both directions, so that the working points can be located in the resonance free region in Hofmann Chart to avoid the emittance exchange.
- Keep the zero current phase advance per meter smooth at the transition of different sections.
- The normal conducting triplet is used in the 650 MHz sections, which makes the local compensation not so difficult when one of the quadrupole is failed in working compared with the case of doublet.

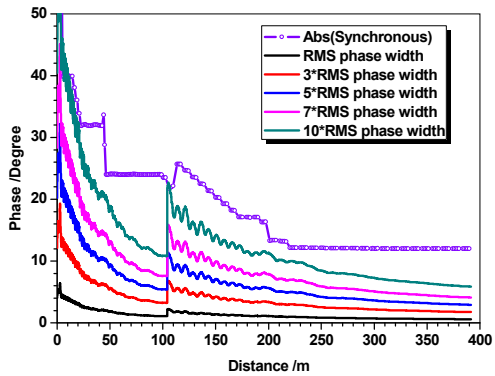

Figure 2: Synchronous and RMS phase width along main linac

END TO END SIMULATION AND ERROR ANALYSIS

The end to end multi-particle simulations are performed with TraceWin and Track. The initial particle distribution is obtained from RFQ simulation with ParmteqM and the total number of particles is 100000. The RMS envelop is very smooth even at the transitions between sections. Figure 3 shows the normalized RMS emittance evolution along the linac. We can see the transverse emittance growth is controlled about 10%, but significant longitudinal emittance growth can be observed at the junction between MEBT2 and main linac, the reason for emittance growth partly comes from the fact that the beam width is relatively large at the exit of RFQ, and partly comes from the imperfect matching between MEBT2 and the main linac. The optimization of MEBT2 is still on going.

The error analysis with proper correction scheme is performed with TraceWin code, 1000 linacs are produced with 10000 particles for each linac. The error settings are listed in table 4. The results show that particle loss is within the specification given in table 1 and prove the robustness of the design. Further error analysis with more particles will be performed with Track later.

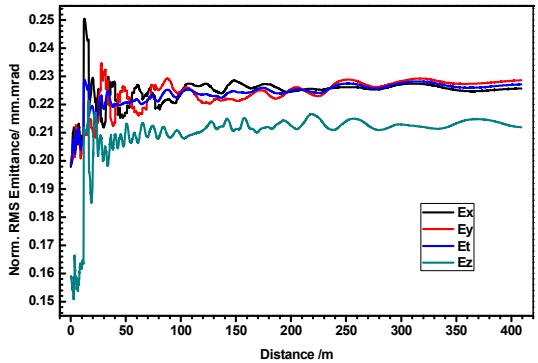

Figure 3: Norm. RMS emittance along linac

Table 4: Error settings for error analysis

Errors	Solenoid S/D	S.C. Cav. S/D	N.C. Quad. S/D
Align. Errors Translation x/y/z (mm)	±1/±0.01 ±1/±0.01 ±1/±0.01	±1/±0.01 ±1/±0.01 ±1/±0.01	±0.2/±0.002 ±0.2/±0.002 ±0.5/±0.002
Align Errors Rotation x/y/z (mrad)	±2/±0.02 ±2/±0.02 --/--	±2/±0.02 ±2/±0.02 --/--	±2/±0.02 ±2/±0.02 ±2/±0.02
RF Amp. Errors (%)	--/--	±1/±0.5	±1/±0.5
RF Phase errors (deg.)	--/--	±1/±0.5	±1/±0.5

Note: S stands for static and D stands for dynamic;

REFERENCES

[1] R.L. Sheffield, "Utilization of accelerator for transmutation and energy production", HB2010, Morschach, Switzerland, p.1.
[2] J-L.Biarrotte, Preliminary design studies of an experimental Accelerator-Driven System, XADS-DEL04-063, 2004.
[3] H.Geng et al., "The MEBT Design for the China Accelerator Driven System", IPAC'11, San Sebastian, Spain, p.2604.
[4] LI Han et al., Chinese Physics C, V.36, 2012, p.761.
[5] Y.He et al., "The Conceptual Design of Injector II of ADS in China", IPAC'11, San Sebastian, Spain, p.2613.
[6] J-L.Biarrotte, "Beam dynamics studies for the fault tolerance assessment of the PDS-XADS Linac design", EPAC 2004, Lucerne, Switzerland, 2004, p.1282.

Copyright © 2012 by the respective authors — cc Creative Commons Attribution 3.0 (CC BY 3.0)

THORIUM ENERGY

S. Peggs, BNL, USA and ESS, Sweden
R. Seviour, ESS, Sweden and Huddersfield U., UK and Lund U., Sweden
R. Cywinski, Huddersfield U., UK

SAFETY, PROLIFERATION, AND WASTE

Uranium-based nuclear fission technologies are an important energy source for many industrialised nations, although use has been limited by: high cost; perceived adverse safety; the potential for proliferation; and the management of nuclear waste. A thorium fuel cycle, combined with alternative technologies, presents numerous potential advantages [1]. Thorium fuel cycles are intrinsically more proliferation-resistant, reduce plutonium production, and can consume legacy plutonium and waste actinides. The different characteristics of the thorium cycle options arise not only from the different system designs, but also from the physical properties of the fuels themselves [2, 3].

Safety: Molten salt reactor (MSR) and high-temperature gas-cooled reactor (HTGR) thorium reactors have safety advantages over conventional light water reactors (LWR) [2, 3, 4]. The liquid fuel in an MSR may provide improved reactivity feedback and can be removed from the reactor core [4]. HTGRs can withstand very high temperatures in excess of 2000 K without fuel failure [5]. As demonstrated at the German AVR, these designs may survive a complete loss of power event [2]. The use of thorium in LWR fuel can have advantages over solely U-Pu systems because of its better thermal, physical, and irradiation performance [5].

Proliferation: Thorium occurs in nature as a single fertile isotope. In itself, it cannot be enriched to produce weapons grade material. Consequently it has been argued that thorium is "proliferation resistant" [6, 7]. Additionally, production of Pu-239 is extremely small in most proposed thorium cycles, due to the different actinide distribution, thereby posing a significantly lower proliferation risk. However, thorium cycles do generate U-233 as the fissile isotope, rather than the Pu-239 bred from U-238 in the U-Pu cycle. U-233 is in principle useable in nuclear weapons, but the inherent co-generation of U-232 provides significant protection due to the steady growth of hard-gamma emitting Tl-208 in its decay chain. This makes non-state weapons manufacture difficult, and easily detectable.

Waste: Thorium systems have the ability to burn actinides, and provide several routes to plutonium stockpile disposal [6]. Waste forms for thorium-bearing fuels have been studied and shown to have advantages based on their physical and chemical properties [3, 5, 8, 9].

SOLID FUEL REACTORS

Thorium can in principle be used as a solid fuel component in all the main reactor types that have operated to date: boiling and pressurised light water reactors (BWRs and PWRs), heavy water reactors (HWRs), HTGRs, and sodium-cooled fast reactors. Thoria based fuels offer higher operational safety margins and accident tolerance due to various favourable, robust, properties: a very high melting point; non-oxidizability; general chemical inertness; reasonable thermal conductivity; and a strong ability to retain fission products within its crystal lattice.

Reactors without accelerators: Thorium cycles have been investigated in a variety of reactors, including Gas-Cooled Reactors (GCRs), BWRs, and PWRs [10, 11, 12]. These studies demonstrated good performance of thorium in oxide form in LWRs and in carbide form in GCRs [13]. The Light Water Breeder Reactor programme in a PWR [14] demonstrated the feasibility of a closed Th-U-233 fuel cycle, confirming that U-233 breeding is achievable using a heterogeneous epi-thermal spectrum U-Th core. Near-complete transuranic waste incineration has been suggested in a thorium-fuelled PWR [15]. India has operated thorium-fuelled research reactors for many years: first the Purnima-II reactor (1984-6) and, since 1997, in the 30 kW Kamini research reactor [16], which uses U-233 bred from thorium in another reactor.

Accelerator-driven subcritical cores: The accelerator provides a controlled external source of fast neutrons in the reactor core, to breed fissile material at the same rate or faster than it is consumed. Some neutrons maintain a chain reaction while others breed Th-232 to U-233. Eventually the U-233 becomes the fissile fuel, with fertile thorium being added to the mix as necessary.

Proton-driven spallation is the usual choice (especially for GW-scale reactors), although other particles including electrons have also been proposed. Heavier nuclei bring little advantage at considerable cost. The required beam current I is given by

$$I = e\,\frac{(1-k)P}{nfE_f} \qquad (1)$$

where $k < 1$ is the "criticality" factor of the reactor, P is the thermal power, n is the number of neutrons produced per incident proton, of which a fraction f induce fission, and E_f is the mean energy release per fission. A typical 1 GWe reactor requires average currents of about 10 mA and a beam power of about 10 MW, beyond today's most powerful accelerators.

In 1996 the Indian Atomic Energy Commission initiated design studies for a 200 MWe PHWR ADS system fuelled by uranium and thorium [17]. Jacobs Engineering Group Inc. (Jacobs) have produced a conceptual design of an Accelerator-Driven Thorium Reactor (ADTR™) 600 MWe power station, based on the lead-cooled fast reactor illustrated in Figure 1 [18, 19]. The ADTR™ challenges previously established criticality margins, with a proposed k value of 0.995 [20].

Copyright © 2012 by the respective authors — cc Creative Commons Attribution 3.0 (CC BY 3.0)

MOLTEN SALT REACTORS

The Molten-Salt Reactor Experiment (MSRE) operated from 1965 until 1969 using a fuel/moderator mixture of lithium, beryllium, thorium and uranium fluorides [21]. It built on the success of the 1954 Aircraft Reactor Experiment [22], and on other early liquid-fuel schemes; the basic feasibility of such designs is well demonstrated. The graphite moderator ensures the correct neutron spectrum while the fuel salt circulates in a closed loop. Increased power (in a fluctuation) expands the liquid fuel, in turn reducing the power output. This safety feature was tested during MSRE operation, performing as expected. MSRs have further safety advantages and some disadvantages in comparison to solid-fuel reactors [23]. More modern Lithium Fluoride Thorium Reactor designs are being proposed as an alternative fuel cycle solution by several advocacy groups [24, 25].

Most MSR advantages are maintained in an ADS implementation. The target in the salt bath produces additional neutrons, making it easier to optimise performance. One promising target design, from BARC, uses an inert gas injected into a long vertical column to create a mass imbalance that circulates the lead-bismuth eutectic (LBE) and also removes gaseous poisons [26].

It is sometimes said that the accelerator trip requirements for an ADS MSR are considerably relaxed compared with a solid-fuel ADS reactor, because the timescales for stresses are longer since there is no Hastelloy cladding on the fuel rods. The comparison depends on the power rating of the fuel pins in the solid-fuel reactor. Recent studies have shown that in some cases the fuel cladding is the limiting factor [27] while in others it is the inner barrel [28]; an ADS MSR has no need for fuel cladding but does require an inner barrel.

ACCELERATOR IMPLICATIONS

Optimising spallation output in terms of proton energy cost per neutron gives a broad plateau beginning at about 1 GeV, a value chosen by the Spallation Neutron Source (SNS) [29]. A lower value of 600 MeV reduces the capital costs of the MYRRHA proposal, but provides enough neutrons for a power of 57 MWth [30]. The European Spallation Source [31] energy of 2.5 GeV is rather higher.

At least 20 neutrons are produced for each incident 1 GeV proton in a typical spallation target – 1 neutron per 50 MeV of beam energy. About 150 MeV of wall-plug energy is therefore required for each neutron, assuming a typical accelerator efficiency of 30%. Maximising this efficiency is an important accelerator design goal.

Beam losses must be kept to a low level to allow hands-on maintenance: a proton loss rate of 1 W/m is considered a maximum. This is also a major design challenge.

Reliability and availability: Extremely high accelerator reliability is required in a full-scale ADS power station. Repeated short trips lead to thermal stresses in reactor components, and long trips lead to economically very damaging losses of generating power [32]. Recent analyses of maximum allowable beam trip durations considering thermal stress and damage to reactor components suggest that the required accelerator reliability is much less severe than originally thought (but is still very challenging) [28]. Several uncertainties remain, especially concerning irradiated materials properties, erosion and corrosion related aspects in an LBE environment, and reactor restart sequences.

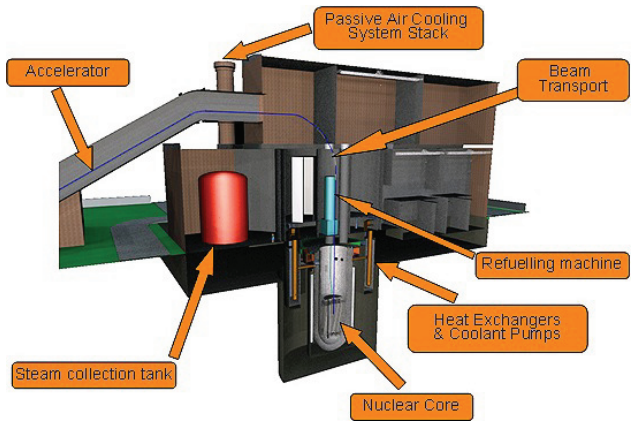

Figure 1: The ADTR^{TM} power station reactor building.

Erroneous initial optimistic predictions of the number of allowed emergency reactor stops due to beam trips could lead to premature replacements of components, reduction of reactor lifetime, and to a dramatic decrease of availability. Thus, the MYRRHA project requirements conservatively allow fewer than 5 beam trips (longer than 3 seconds) per 3-month operating period, following PHENIX reactor experience [33, 34]. In any case, major improvements in accelerator reliability are most certainly required for the ADS mission.

Industrial experience shows that reliability is achievable – at a cost – through redundancy, under-rating, graceful failure, and planned maintenance, using a holistic analysis of the complete system. It may be advantageous to use several independent accelerators, so that when one is off-line the current in the others can be increased.

Accelerator technologies

Linear accelerators (linacs) can provide the necessary energy and current, and appear to offer sufficient reliability, availability, and rapid fault recovery. However, they are expensive relative to cyclotrons or synchrotrons. A 1.4 MW linac like the SNS would be ∼300 m long, at a cost of ∼0.7 B$, so that it would nonetheless not dominate the total project cost, assuming that a thorium reactor costs about the same as a uranium reactor, ∼5 B$.

Cyclotrons are restricted to non-relativistic energies, and are limited by space-charge effects and by the need for orbit separation, but achieve MW-class beam powers at PSI and TRIUMF. A recent proposal for a 5 MW, 800 MeV, strong-focusing cyclotron would overcome both of these limitations [35]. There are also other proposals for ADS

Copyright © 2012 by the respective authors — cc Creative Commons Attribution 3.0 (CC BY 3.0)

cyclotrons [36].

Rapid Cycling Synchrotrons (RCS) like ISIS operate at frequencies as fast as 50 Hz with beam powers well above 100 kW. Much faster repetition rates are attractive, but face the need to develop rapid frequency swing Radio Frequency (RF) systems, and also face technical issues with magnet and vacuum chamber eddy currents.

Fixed-Field Alternating Gradient (FFAG) accelerators currently exist only as low power prototypes, both proton [37] and electron [38]. An isochronous FFAG could be run with continuous beam like a cyclotron to achieve large currents. Non-isochronous designs face the same frequency swing challenges as RCS RF systems.

NECESSARY RESEARCH

A recent study assessed the technological readiness of accelerator and target technology for ADS systems, and outlined the necessary R&D activities [39]: it concluded that accelerator and target technology had advanced significantly in the last two decades, and was now ready for a full scale demonstration of the coupling of a MW-class accelerator to a subcritical core. Recent experimental accelerator/reactor coupling demonstrations have been made at low power at GUINEVERE [40] and KURRI [37]. The key performance requirements are very high proton beam power ($\simeq$ 10 MW), very low beam loss ($<$ 1 W/m) and very high reliability. Key research areas include:

1. development of highly reliable and fault tolerant accelerator systems and accelerator components;
2. advancing the state-of-the-art in accelerator systems, including linacs, FFAGs and RF systems;
3. improved understanding of beam loss mechanisms, emittance and halo growth.

Required spallation target R&D includes: 1) LBE handling, oxygen control and cleanup; 2) development of windowless target technologies; 3) materials irradiation studies; 4) full scale mock-up of cooling systems; 5) engineering the accelerator-to-target sub-critical blanket interfaces.

ACKNOWLEDGEMENTS

Active and profound contributions were made by V. Ashley, R. Ashworth, R. Barlow, J.-L. Biarrotte, S. Henderson, W. Horak, A. Hutton, J. Kelly, M. Lindroos, P. McIntyre, A. Norlin, H. Owen, G. Parks, and T. Roser.

REFERENCES

[1] "Towards an Alternative Nuclear Future", Thorium Energy Association, ThorEA, (2010).

[2] M. Lung & O. Gremm, V.180, 2, p.133-146, (1998).

[3] P. Rodriguez & C.V. Sundaram, J. of Nucl. Mats., V.100, p.227-249, (1981).

[4] K. Furukawa et al., Energy Conversion and Management, V.49, 7, p.1832-1848, ISSN 0196-8904, (2008).

[5] A. Talamo, Prog. in Nucl. Energy, V.51, p.274-280, ISSN 0149-1970, (2009).

[6] A. Galperin at al., Sci. & Global Sec. V.6, 3, (1997).

[7] R. Sollychin, IAEA Bulletin 51-1, p.43-44, (2009).

[8] P. Demkowicz et al., Nucl. Tech., V.147, p.157, (2004).

[9] D. Barrier et al., J. of Nucl. Matls., 352, p.357, (2006)

[10] IAEA, IAEA-TECDOC-1450, (2005).

[11] M. Todosow et al., Nucl. Tech., 151, 168-176, (2005).

[12] T.K. Kim & T. Downar, Nucl. Tech., 138, 17-29, (2002).

[13] J. Belle & R.M. Berman, Eds., US DOE/NE-0060, (1984).

[14] R. Atherton, Ed., WAPD-TM-1600, (1987).

[15] B.A. Lindley & G.T. Parks, Annals of Nucl. En., 40, 106-115 (2012).

[16] "(Indian) Nuclear Power Programme – Thorium", http://www.dae.gov.in/publ/ar0203/chap3.pdf

[17] S. Banerjee, "Towards a Sustainable Nuclear Energy Future", WNA Symposium (2010).

[18] C. Rubbia et al., CERN-AT-95-44(ET), (1995).

[19] V. Ashley & R. Ashworth, "The Technically Viable ADTR™ Power Station", Nuclear Future V.7 3, (2011).

[20] C. Rubbia, PCT Patent, PCT/EP2010/054132, (2010).

[21] R.C. Briant et al., Nucl. Sci. Eng., 2, 797 (1957).

[22] P. N. Haubenreich & J.R. Engel, Nucl. Appl. Tech., 8, 118 (1970).

[23] C.W. Forsberg, Trans. Am. Nucl. Soc. Ann. Meeting, (2004).

[24] Thorium Energy Alliance, http://thoriumenergyalliance.com

[25] The Weinberg Foundation, http://www.the-weinberg-foundation.org

[26] P. Satyamurthy, L. M. Gantayet & A. K. Ray, PRAMANA 68, No 2, 343 (2007).

[27] A. Ahmad, S.L. Sheehy & G.T. Parks, Annals of Nuclear Energy, 46, 97-105 (2012).

[28] H. Takei et al., Journal of Nuclear Science & Technology, 49:4, p.384-397, (2012).

[29] "Spallation Neutron Source Project Completion Report", SNS 100000000-BL0005-R00 (2006).

[30] D. De Bruyn et al., Technology & Components of ADS, Karlsruhe, OECD - NEA, p. 47-52, (2011).

[31] S. Peggs, Ed., "ESS Conceptual Design Report", ESS report ESS-2012-1, (2012).

[32] S.J. Steer et al., Elec. Pwr. Sys. Res., 81, 1662-1671 (2011).

[33] J-L. Biarrotte et al., LINAC 2010, (2010).

[34] G. Rimpault et al., submitted to ANS Nucl. Tech., (2013).

[35] P. McIntyre, IPAC 2012, (2012).

[36] L. Calabretta, Cyclotrons-10, (2010).

[37] M. Tanigaki et al., APAC 2004, (2004).

[38] S. Machida et al., Nature Physics **8**, p 243 (2011).

[39] H. Ait Abderrahim et al., http://science.energy.gov/~media/hep/pdf/files/pdfs/ADS_White_Paper_final.pdf, (2011).

[40] A. Degtyarev et al., Proc. of GLOBAL 2011, (2011).

Copyright © 2012 by the respective authors — cc Creative Commons Attribution 3.0 (CC BY 3.0)

DESIGN AND BEAM TEST OF SIX-ELECTRODE BPMS FOR SECOND-ORDER MOMENT MEASUREMENT

K. Yanagida*, S. Suzuki, and H. Hanaki, JASRI/SPring-8, Sayo Hyogo, Japan

Abstract

To enhance a beam observation system during top-up operation, we developed in the SPring-8 linear accelerator non-destructive beam position monitors (BPMs) that can detect second-order moments of electron beams. BPMs have six stripline-type electrodes with circular or quasi-elliptical cross-sections. We tested a BPM with a circular cross-section using electron beams, and our results showed that its normalized moments were determined accurately by electrostatic field calculation. We studied a precise calibration method to determine the relative attenuation factors between the electrode channels based on the principle that the relative moments must not vary with a change of the beam position using a steering magnet in drift space.

INTRODUCTION

The SPring-8 linear accelerator provides electron beams toward a storage ring about every twenty seconds because of the top-up operation of the storage ring. To enhance the beam observation system during the top-up operation, a non-destructive BPM system is being upgraded to a six-electrode BPM system that can detect the second-order moments of electron beams because the second-order moments are physical quantities related to beam sizes, which can be deduced by measuring second-order moments at more than six locations in FODO magnetic lattices [1].

Therefore, we developed the major components of a six-electrode BPM system: BPMs, a signal processor, and a digital input board. We installed our developed six-electrode BPMs with a circular cross-section in the beam transport line and tested them using electron beams. This paper describes the BPM designs as the parts of the six-electrode BPM system, the principle of multipole moment measurement, and the beam test results.

SIX-ELECTRODE BPMS

This section describes the designs of six-electrode BPMs and the principle of absolute moment measurement.

BPM designs

We developed two kinds of six-electrode BPMs for second-order moment measurement. One is a BPM with a circular cross-section for the non-dispersive section, and the other is a BPM with a quasi-elliptical cross-section for the dispersive section (Fig. 1). In the figure the numbers represent electrode number d. Both BPMs have stripline-type electrodes as signal pick-ups. The stripline length is 27 mm, which corresponds to $\lambda/4$ of the acceleration radio frequency. The characteristic impedance is designed as 50 Ω. One electrode of both BPMs shares 30 ° with respect to the duct center. The aperture radius of a BPM with a circular cross-section is 16 mm, and the long and short radii of a BPM with a quasi-elliptical cross-section are 14 mm and 28 mm. These BPMs were or will be installed instead of the existing four-electrode BPMs with circular and quasi-elliptical cross-sections [2][3].

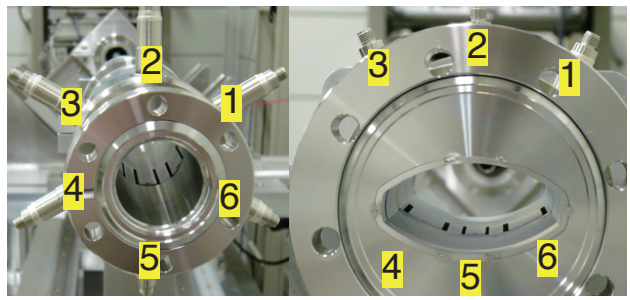

Figure 1: Six-electrode BPMs with circular and quasi-elliptical cross-sections. Numbers represent electrode number d.

Absolute Moment Measurement

A BPM with symmetrical arranged electrodes can detect multipole moments with respect to the duct center. These are called absolute moments P_n and Q_n, where n is the order of the multipole moment. For example, first-order absolute moments represent the transverse positions of beam centroid P_1 (horizontal position) and Q_1 (vertical position). The two-dimensional position (P_1, Q_1) is generally called the beam position.

Our developed six-electrode BPMs have two electrodes in the vertical direction, but none horizontally. This configuration enables us to measure three higher-order ($n \geqq 2$) absolute moments: P_2, Q_2, and Q_3.

Because the signal voltage of each electrode V_d is proportional to the integral of the electric field strength on the electrode, we can obtain the absolute moments with normalized moments $R^n_{Pn}/2$, $R^n_{Qn}/2$ and geometrical factors k, K, as described in Eq. (1). In the equation, R_{Pn} or R_{Qn} is called an effective aperture radius. The effective aperture radii and the geometrical factors are calculated analytically, especially for a BPM with circular cross-section, or numerically [4].

The calculation result is summarized in Table 1. A smaller effective aperture radius is preferable for accurate

* ken@spring8.or.jp

Copyright © 2012 by the respective authors — cc Creative Commons Attribution 3.0 (CC BY 3.0)

measurement, but R_{Q1} is rather large:

$$
\begin{aligned}
P_1 &= \frac{R_{P1}}{2}\frac{V_1 - V_3 - V_4 + V_6}{V_1 + V_3 + V_4 + V_6},\\
Q_1 &= \frac{R_{Q1}}{2}\frac{V_1 + V_3 - V_4 - V_6}{V_1 + V_3 + V_4 + V_6},\\
P_2 &= \frac{R_{P2}^2}{2}\frac{kV_1 - 2V_2 + kV_3 + kV_4 - 2V_5 + kV_6}{kV_1 + 2V_2 + kV_3 + kV_4 + 2V_5 + kV_6},\\
Q_2 &= \frac{R_{Q2}^2}{2}\frac{V_1 - V_3 + V_4 - V_6}{V_1 + V_3 + V_4 + V_6},\\
Q_3 &= \frac{R_{Q3}^3}{2}\frac{KV_1 - V_2 + KV_3 - KV_4 + V_5 - KV_6}{KV_1 + V_2 + KV_3 + KV_4 + V_5 + KV_6}.
\end{aligned}
\tag{1}
$$

Table 1: Effective aperture radii and geometrical factors

	circular (analytical)	quasi-elliptical (numerical)
R_{P1} [mm]	18.69	18.03
R_{Q1} [mm]	32.38	54.84
R_{P2} [mm]	18.91	18.42
R_{Q2} [mm]	17.59	22.48
R_{Q3} [mm]	16.57	18.55
k	1.000	1.918
K	1.000	3.056

RELATIVE MOMENTS

As described above, the absolute moments of six-electrode BPMs can be obtained using Eq. (1). However, they are rather complicated because they involve not only the moments of a beam intensity distribution called relative moments P_{gn} and Q_{gn} but also the moments of the beam centroid. For easier comparison of the multipole moments, we define the relative moments and extract them from the absolute moments.

Relative moments are defined as the moments with respect to the beam centroid. It is considered that the origin is transferred from the duct center (0, 0) to the beam position (P_1, Q_1) to cancel the first-order relative moments, i.e., P_{g1}=0 and Q_{g1}=0. Consequently, we can obtain the relative moments from the absolute moments using the following relations [4]:

$$
\begin{aligned}
&P_1 = b_G\cos\beta_G,\ Q_1 = b_G\sin\beta_G,\\
&P_{g2} = a_{g2}^2\cos 2\alpha_{g2} = P_2 - b_G^2\cos 2\beta_G,\\
&Q_{g2} = a_{g2}^2\sin 2\alpha_{g2} = Q_2 - b_G^2\sin 2\beta_G,\\
&Q_{g3} = Q_3 - b_G^3\sin 3\beta_G - 3b_G a_{g2}^2\sin(\beta_G + 2\alpha_{g2}).
\end{aligned}
\tag{2}
$$

SCREEN MONITOR FOR RELATIVE MOMENT MEASUREMENT

At the beam test, the relative moments were also measured by a screen monitor that records the two-dimensional beam intensity distribution on the screen (DESMARQUEST AF995R) into the intensity distribution on a charge-coupled device (CCD) using an optical focusing lens when the electron beams hit the screen.

We define the intensity distribution on the screen as $I(x_i, y_j)$, where x_i and y_j indicate the position of the data cell. The origin is defined as the screen center, i.e., the duct center, but not the CCD center. To calculate the absolute moments from $I(x_i, y_j)$, we define nth-order absolute intensity moments $m_{h(n-h)}$ in the Cartesian coordinates, as described in Eq. (3), and consequently obtain the absolute moments using Eq. (4) [4]:

$$
\begin{aligned}
&m_{00} = \sum_i\sum_j I(x_i,y_j),\ m_{10} = \sum_i\sum_j x_i I(x_i,y_j),\\
&m_{01} = \sum_i\sum_j y_j I(x_i,y_j),\ m_{20} = \sum_i\sum_j x_i^2 I(x_i,y_j),\\
&m_{11} = \sum_i\sum_j x_i y_j I(x_i,y_j),\ m_{02} = \sum_i\sum_j y_j^2 I(x_i,y_j),\\
&m_{21} = \sum_i\sum_j x_i^2 y_j I(x_i,y_j),\ m_{03} = \sum_i\sum_j y_j^3 I(x_i,y_j).
\end{aligned}
\tag{3}
$$

$$
\begin{aligned}
&m_{00}P_1 = m_{10},\ m_{00}Q_1 = m_{01},\\
&m_{00}P_2 = m_{20} - m_{02},\ m_{00}Q_2 = 2m_{11},\\
&m_{00}Q_3 = 3m_{21} - m_{03}.
\end{aligned}
\tag{4}
$$

Figure 2 shows the example data of the beam intensity distribution (contour plot) on the screen. Using Eqs. (3) and (4), the multipole moments of this distribution were obtained as P_1=2.334 mm, Q_1=−0.989 mm, P_{g2}=−0.391 mm^2, Q_{g2}=1.366 mm^2, and Q_{g3}=0.161 mm^3.

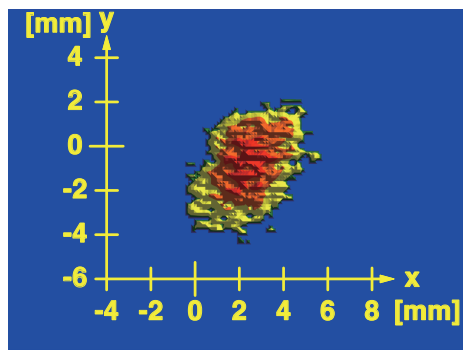

Figure 2: Two-dimensional beam intensity distribution (contour plot) on screen

BEAM TEST

We performed a beam test of a six-electrode BPM with a circular cross-section to verify whether the normalized moments measured by the beam test agree with those calculated analytically.

Entire Calibration

Even though each element of the system is calibrated precisely, entire calibration is very difficult and is not eas-

Copyright © 2012 by the respective authors — cc Creative Commons Attribution 3.0 (CC BY 3.0)

ily achieved. To resolve this problem we studied a method for entire calibration using electron beams.

The principle is very simple. We assume that the electron beams are stable during the beam test and that the steering magnets change the beam position without changing the beam intensity distribution with respect to the beam centroid. If we change the beam position at the BPM location using upstream steering magnets, observed relative moments P_{g2}, Q_{g2} and Q_{g3} must be constant. Conversely speaking, we can easily determine the relative attenuation factors between the electrode channels so that all the obtained relative moments are constant.

After we determined the relative attenuation factors, we applied them to all the data including the entire calibration data. Figure 3 shows example data of the multipole moments of the entire calibration. The beam position (P_1, Q_1) and second-order absolute moments P_2 vary by means of steering magnets, but second-order relative moments P_{g2} do not.

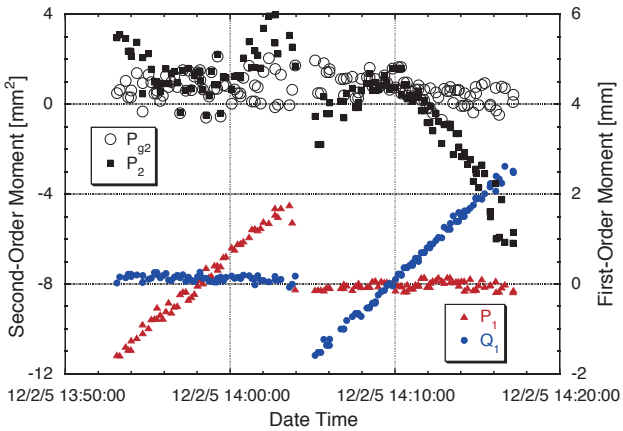

Figure 3: Multipole moments of entire calibration. Relative attenuation factors are applied.

Correlation Measurement

Finally, we compared the second-order relative moments taken by the screen monitor to those by the BPM when we changed the beam intensity distribution by changing the magnetic field of the upstream quadrupole magnet. Because the screen monitor was located upstream of the BPM in the drift space, we did not take both bits of data at the same beam shot. The distance between the screen monitor and the BPM is ∼2 m.

Figure 4 is the correlation plot between the second-order relative moments taken by the screen monitor (abscissa) and the BPM (ordinate). In the plot the spread data points were caused by the shot by shot fluctuation of the beam intensity distribution. However, the correlation plot apparently indicates a direct proportionality relation with a proportionality coefficient of 1.

This result provides the following important consequences. One, for such BPMs with stripline-type electrodes, normalized moments can be obtained accurately by

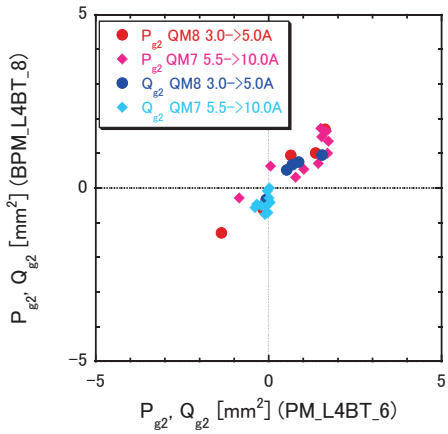

Figure 4: Correlation plot between second-order relative moments taken by screen monitor (abscissa) and BPM (ordinate)

analytical or maybe numerical electrostatic field calculation, i.e., the correlation plot with a proportionality coefficient of 1. The other is that an entire calibration is useful as is a self-consistent method for precise calibration to determine the relative attenuation factors between electrode channels, i.e., the correlation plot passing through the origin.

SUMMARY

We developed six-electrode beam position monitors with circular and quasi-elliptical cross-sections for second-order moment measurement. From the beam test results normalized moments of BPM with circular cross-section were accurately determined by analytical electrostatic field calculation. The entire calibration is useful and a self-consistent method for precise calibration to determine the relative attenuation factors between electrode channels.

REFERENCES

[1] R. H. Miller, et al., "Nonintercepting Emittance Monitor," Proc. 12th Int. Conf. High-Energy Accel. (HEAC'83), Fermilab USA, 1983, pp. 603-605.

[2] K. Yanagida, et al.,"A BPM System for The SPring-8 Linac", Proc. of the 20th Int. Linac Conf., Monterey USA, Aug. 2000, pp. 190-192.

[3] K. Yanagida, et al., "Beam Instrumentation Using BPM System of The SPring-8 Linac," Proc. of the 22th Int. Linac Conf., Lubeck Germany, Aug. 2004, pp. 438-440.

[4] K. Yanagida, et al., Phys. Rev. ST Accel. Beams **15**, 012801 (2012).

Copyright © 2012 by the respective authors — cc Creative Commons Attribution 3.0 (CC BY 3.0)

NON-DESTRUCTIVE REAL-TIME MONITOR TO MEASURE 3D-BUNCH CHARGE DISTRIBUTION WITH ARRIVAL TIMING TO MAXIMIZE 3D OVERLAPPING FOR HHG-SEEDED EUV-FEL

H. Tomizawa, K. Ogawa, T. Sato, and M. Yabashi
RIKEN Hariama Institute, 1-1-1 Kouto, Sayo-cho, Sayo-gun, Hyogo, Japan
Y. Okayasu, S. Matsubara, and T. Togashi
JASRI/SPring-8, 1-1-1 Kouto, Sayo-cho, Sayo-gun, Hyogo, Japan
E. J. Takahashi
RIKEN Advanced Science Institute, Hirosawa 2-1, Wako, Saitama 351-0198, Japan
M. Aoyama
Kansai Photon Science Institute, Japan Atomic Energy Agency,
8-1-7 Umemidai, Kizukawa-shi, Kyoto 619-0215, Japan
A. Iwasaki and S. Owada
Department of Chemistry, The School of Science, The University of Tokyo,
7-3-1 Hongo, Bunkyo-ku, Tokyo 113-0033, Japan
H. Minamide and T. Matsukawa
RIKEN 519-1399, Aramaki-aza, Aoba, Aoba-ku, Sendai, Miyagi, 980-0845, Japan

Abstract

We have developed a three-dimensional bunch charge distribution (3D-BCD) monitor with arrival timing for an FEL seeded with a high-order harmonic (HH) pulse. A 3D-BCD monitor is based on an Electro-Optic sampling (EOS) technique with multiple EO crystal detectors in spectral decoding. Utilizing this EO-multiplexing technique, we obtained the relative positioning in the transverse and the timing in the longitudinal of the electron bunch with respect to arriving timing of a seeding HH pulse at the undulator in real-time with non-destructive measurements. In our EUV-FEL accelerator, we prepared a seeded FEL with an EOS-based feedback system for user experiments. For obtaining a higher seeding hit rate, 3D overlapping between the electron bunch and the seeding pulse must be maximized at the optimal point. Keeping the peak wavelength of EO signals at the same wavelength with our feedback system, we provided seeded FEL pulses (intensity >4σ of SASE) with a 20-30% hit rate during pilot user experiments. For achieving the upper limit of temporal resolution, we are planning to combine high-temporal-response EO-detector crystals and an octave broadband probe laser pulse with a linear chirp rate of 1 fs/nm. We are developing an EO-probe laser pulse with ~10 μJ pulse energy and bandwidth over 300 nm (FWHM). In 2011, we successfully demonstrated the first bunch measurement with an organic EO crystal in the FEL accelerator at SPring-8.

INTRODUCTION

Since 2010 at SPring-8, we have been demonstrating a seeded free-electron laser (FEL) in the extreme ultra violet (EUV) region by high-order harmonics (HH) generation from an external laser source in a prototype test accelerator (EUV-FEL) [1]. In FEL seeding as a full-coherent high-intensive light source for EUV user experiments, a high hit rate of successfully seeded FEL pulses is required. Precise measurements of the electron bunch charge distribution (BCD) and its arrival timing are crucial keys to maximize and keep 3D (spatial and temporal) overlapping between the high-order harmonics (HH) laser pulse and the electron bunch. We constructed a timing drift monitor based on Electro-Optic (EO) sampling, which simultaneously measures the timing differences between the seeding laser pulse and the electron bunch using a common external pulsed laser source (Ti: Sapphire) of both the HH driving and EO-probing pulses (Fig. 1). The EO-sampling system can use timing feedback for continuous (without interruption) operation of HH-seeded FELs.

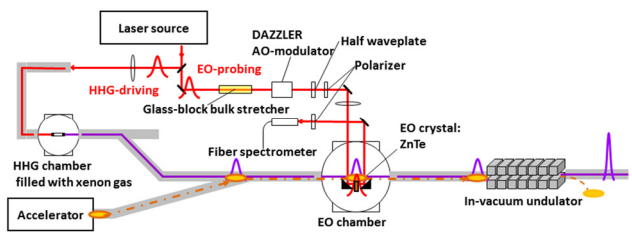

Figure 1: Experimental setup of seeded FEL with EO-sampling feedback at EUV-FEL accelerator: relative positioning in transverse and timing in longitudinal of electron bunch with respect to arriving timing of a seeding HH pulse are monitored at entrance of the first in-vacuum undulator to keep in a best seeding condition.

The R&D of a non-destructive 3D-BCD monitor (proposed in 2006 [2]) with bunch-by-bunch detection and real-time reconstructions has been extensively investigated at SPring-8. This ambitious monitor is based on an EO-multiplexing technique that resembles real-time spectral decoding and enables simultaneous non-destructive measurements of longitudinal and transverse BCDs. This part of the monitor was simultaneously materialized for probing eight EO crystals that surround

Copyright © 2012 by the respective authors — cc Creative Commons Attribution 3.0 (CC BY 3.0)

the electron beam axis with a radial polarized, hollow EO-probe laser pulse. In 2009, we verified the concept of a 3D-BCD monitor through electron bunch measurements in the photoinjector test facility at SPring-8 [3].

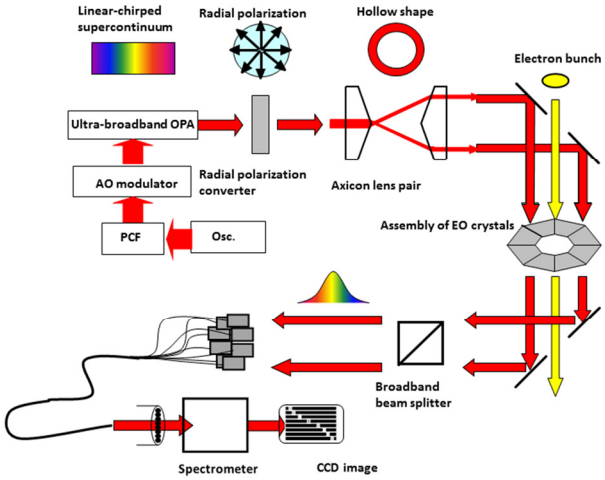

Figure 2: Schematic drawing of 3D-BCD monitor based on EO-multiplexing technique, utilizing simultaneous detection in imaging spectrographs with multi-track (eight tracks) of area array CCD of an image intensified (I.I.) camera.

As part of the Self-Amplified Spontaneous Emission (SASE) XFEL project at SPring-8, an additional target of temporal resolution is ~30 fs (FWHM), which utilizes an organic EO crystal (DAST) instead of conventional inorganic EO crystals (ZnTe, GaP, etc.). EO sampling with DAST crystals is expected to measure a bunch length that is less than 30 fs (FWHM). In 2011, we demonstrated the first EOS bunch measurements with DAST crystal in the EUV-FEL accelerator.

In this paper, we describe the development status and application of 3D-BCD as a 3D-overlapping monitor for FEL seeding.

3D-BCD AND OVERLAPPING MONITOR

EO-sampling measures a probe-pulse's retardation by changing the refraction index of a non-linear optical crystal by the radial Coulomb field of relativistic electron bunch slices. The EO-probe laser pulse is injected into the EO crystal at the same time as the electron bunch arrives at the EO crystal. The BCDs are bunch-by-bunch encoded as polarization modulations on the spectra of the EO-probe pulses. In spectral decoding to detect with a multi-channel spectrometer in real-time, the polarization modulations are converted into spectral intensity modulations by a polarized beam splitter.

A 3D-BCD monitor evolved from simple encoding of EOS into a multiplexing technique with a single probe laser pulse for multiple EO crystal detectors in a manner of spectral decoding (demultiplexing). A schematic drawing of a 3D-BCD monitor with eight EO crystals that surround the electron beam axis is shown in Fig. 2. It is applied for a multiplexing technique to simultaneously probe eight EO crystals with a radial polarized, hollow (ring beam) laser pulse. We realized demultiplexing as an imaging spectrograph with eight-track simultaneous detection in the area array CCD of a high-speed gated I.I. camera. Transverse detections of bunch slices are done by analyzing the multipole moments of the bunch slice charge density distributions (Ref. [3]).

For obtaining a higher hit rate of FEL seeding, 3D overlapping between the electron bunch and the seeding laser pulse is necessary to maintain a constant seeded FEL pulse. Utilizing this multiplexing EOS technique, relative positioning in the transverse and the timing in the longitudinal of the electron bunch with respect to arriving timing of the seeding HH pulse is obtained at the entrance of the first in-vacuum undulator in real-time with a non-destructive measurement.

In a 3D-overlapping monitor for FEL seeding, the probe pulse is split from the HH-driving Ti: Sapphire laser pulse (Fig. 1). For higher temporal resolution, the probe pulse is broadened by a photonic crystal fiber (PCF) up to over 300 nm. For real-time reconstructions of the 3D information, the octave broadband pulse is squarely shaped and linearly chirped by an Acousto-Optic (AO) modulator. Then the probe pulse passes through the radial polarization converter and an axicon lens pair to obtain a ring beam shape with radial polarization. This ring beam is simultaneously injected into eight EO crystals. As the spectral decoding of conventional EOS, the demultiplexing of the probe pulse is measured through eight-bunched bundle fibers that are matched to the f-number of the grating optics of a spectrometer (imaging spectrograph). In addition, for a high S/N ratio of EO signals, over 1000 counts of signal intensity per channel are necessary.

FEASIBILITY TESTS WITH THE EUV-FEL ACCELERATOR

Pilot user experiments with seeded FEL were demonstrated with a high hit rate with the EUV-FEL accelerator, at SPring-8 in July 2012. The EOS system shown in Fig. 1 was used for feedback to the timing delay unit of a common laser source as a real-time monitor for the relative difference of arrival timing between an electron bunch and a seeding HH pulse. We realized a sophisticated feedback system of timing drift with real-time data processing of EO-signal spectra that encoded the arrival timing as the central wavelengths of the peak signals of spectra and the BCD of the electron bunches. Maintaining the peak wavelength of EO signals at the same wavelength is the most optimal timing for HH seeding. Our feedback system realized a half-day seeded FEL operation with a hit rate of 20-30% (Seeded FEL pulse intensity >4σ of SASE). Compared with a hit rate of seeded FEL operation without EOS feedback [1], the hit rates became 100 times higher. This result shows that only keeping a temporal-overlapping constant at the optimal condition is effective to seed a single-pass SASE FEL pulse shot-to-shot with a HH pulse.

Copyright © 2012 by the respective authors — cc Creative Commons Attribution 3.0 (CC BY 3.0)

The other feasibility tests were done by bunch measurements with an organic EO crystal (DAST) in the EUV-FEL accelerator. DAST-EOS allows a few tens of femtosecond temporal resolution in the 3D-BCD measurements. In 2011, we successfully demonstrated BCD measurements with a bunch charge of 0.28 nC by a 230-μm thick, organic DAST crystal EO-sampling method. The edges of the EO crystals were set 2.0 mm from the electron beam axis. In a comparable EOS condition, double EO-signal intensity was observed by DAST over a conventional, 1-mm thick inorganic ZnTe crystal. The comparison of EO signals is shown in Fig. 3.

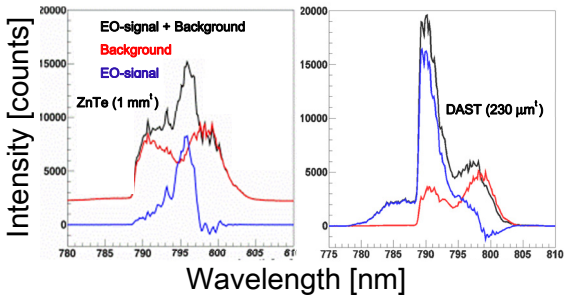

Figure 3: First BCD measurements with 230-μm thick organic DAST crystal compared with EO signals with a 1-mm inorganic ZnTe crystal. The both of the crystals were set 2.0 mm from the electron beam axis.

OCTAVE BROADBAND LASER PROBE PULSE GENERATION TAWARD ULTIMATE TEMPORAL RESOLUTION

For obtaining higher resolution feasible with DAST EO crystal, we developed an octave broadband probe pulse with a linear chirp rate of 1 fs/nm using a high pulse energy oscillator (FEMTOSOURCE scientific XL 500 (550 nJ/pulse; Femtolasers GmbH) and a PCF to generate a 5-MHz supercontinuum pulse train.

In spectral decoding (demultiplexing), temporal resolution T_{Res} depends on the bandwidth of the probe pulse, as in the following relationship $T_{Res} \sim (\tau_0 \tau_c)^{1/2}$, where τ_0 is the pulse width of a Fourier transform limited pulse and τ_c is the chirped probe pulse duration. If we utilize a laser pulse with 300 nm of square spectrum bandwidth (FWHM) at a center wavelength of 800 nm and 300-fs pulse duration as an EO-probe pulse, we can obtain temporal resolution of 30 fs.

We are developing an EO-probe laser pulse with a few tens of micro-Joules and bandwidth over 300 nm (FWHM). For obtaining such bandwidth and pulse energy, this EO-probe pulse is a supercontinuum amplified with optical parametric amplification (OPA). Especially for amplification that maintains bandwidth >350 nm, a non-collinear OPA (NOPA) using BBO crystal and a pump source with a 460-nm wavelength must be prepared (Fig. 4, upper diagram).

The EO-probe pulse energy of 10 μJ provides a high S/N ratio per decoding (demultiplexing) detector. In addition, the probe laser spectrum is shaped adaptively as a square spectrum by a broadband AO-modulator, DAZZLER (UWB-650-1100, FASTLITE) at the detectors.

The octave-broadband supercontinuum pulse is temporally stretched with nonlinear chirping due to the Group Velocity Dispersion (GVD) and even higher dispersion of the material of transparent optics, including the DAZZLER crystal. Hence, since dispersion controls are applied to roughly compress laser pulses by a Grism pair and linearly chirped by DAZZLER, we can finely adjust the pulse duration of the broadband probe laser with a linear chirp rate of 1 fs/nm for probing EO crystals. Owing to the characterization of the nonlinear chirp of the laser pulse with chirp scanning measurement, DAZZLER works as adaptive optics with two functions that provide control of spectral amplitude and phase up to 7th order dispersions: an intensity spectrum shaper and a linear chirp keeper.

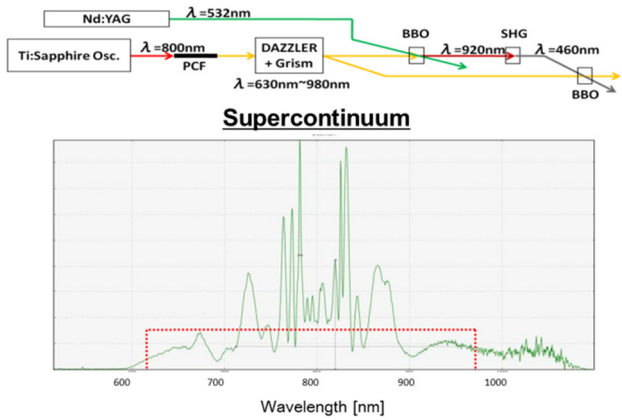

Figure 4: Schematic drawing of generation of broadband linear-chirped laser pulse with square-shaped spectrum (shaping region is shown as red dashed lines on supercontinuum spectrum). Pump source with 460 nm is not available commercially. It is generated from Nd: YAG laser (SHG: 532 nm) pump pulse and the super-continuum signal pulse with additional NOPA stage.

CONCLUSIONS

In several experiments, we successfully demonstrated and proved that the principle experiment of the 3D-BCD monitor as an application for an HH-seeded EUV-FEL is completely feasible. In addition, we successfully demonstrated BCD measurements with single organic DAST crystal (230-μm thick) by the EO-sampling method. We made the world's first electron bunch measurements by organic EO crystals. This crystal makes a few tens of femtosecond temporal resolution in 3D-BCD measurements possible with our octave broadband EO-probe pulse with a linear chirp rate of 1 fs/nm. The complete version of a 3D-overlapping monitor with a feedback system will be installed in our EUV-FEL.

REFERENCES

[1] T. Togashi et al., Optics Express, Vol. 19, Issue 1 (2011)
[2] H. Tomizawa et al., *Proc. of FEL07*, Novosibirsk, Russia, 317 (2007) 472.
[3] H. Tomizawa et al, *Proc. of FEL10*, Malmo, Sweden, (2010) 445.

Copyright © 2012 by the respective authors — cc Creative Commons Attribution 3.0 (CC BY 3.0)

BEAM DIAGNOSTICS DEVELOPMENT FOR TRIUMF E-LINAC*

V.A. Verzilov#, P. Birney, D.P. Cameron, J. Van Holek, S.Y. Kajioka, S. Kellogg, M. Lenckowski, B. Minato, W.R. Rawnsley, TRIUMF, Vancouver, Canada
J.M. Abernathy, D. Karlen, D.W. Storey, Victoria University, Victoria, Canada

Abstract

TRIUMF is currently in a phase of the construction of a superconducting 50 MeV 10 mA CW electron linear accelerator (e-linac) to support the photo-fission based rare radioactive isotope beam production program. The project imposes certain technical challenges to various accelerator systems including beam diagnostics. In the first place these are a high beam power and widely varying beam operating modes: from very short beam pulses to the CW regime. A number of development projects have been started with the aim to construct the diagnostic instrumentation required for commissioning and operation of the facility. The paper reports the present status of the projects.

INTRODUCTION

As a part of the effort to expand the Rare Radioactive Isotope Beam (RIB) program, TRIUMF has started the construction of a 50 MeV 10mA CW superconducting electron linac as a driver for production of neutron-rich isotopes via photo-fission reactions [1]. The facility will comprise a gridded 300 keV thermionic electron gun operated at 650 MHz, a 1.3 MHz superconducting linac, a 70 m long transfer line and the Target Stations for RIB production. Future expansion foresees a recirculation ring to bust the beam energy up to 75 MeV. While civil construction works are carried on, chosen design and operation strategies can be proved at the injector test facility that produced the first beam in November of 2011.

Design challenges are largely associated with a substantial (half a Megawatt) beam power in the CW mode. Clearly, commissioning and tune-up modes are necessary to safely deliver the beam all the way to the targets or dedicated beam dumps. It is presently seen that the beam tuning may require beam pulses of a few microseconds short. A number of development projects were launched about two years ago in order to design the diagnostics capable of supporting all the variety of beam modes. As for today all these projects are either close to completion and moving into production phase or at least reached the maturity state.

DIAGNOSTICS SYSTEMS

Not all the e-linac diagnostics devices are presented and discussed below. Some were reported elsewhere [2]. The beam loss monitoring and machine protection, which are both critical for the operation of the facility are subjects for a dedicated paper.

*Funding is received from National Research Council of Canada
#verzilov@triumf.ca

Beam Position Monitors (BPM)

The general absolute accuracy of beam position measurements is expected to be better than 500 μm. The required relative position resolution of 50 μm is not very high and should be easily achievable. Both button and stripline BPM monitors have been designed for the project. The stripline BPM provides a higher signal strength and better absolute accuracy. The button BPM, which is substantially smaller in dimensions, was demanded for locations with tight space constraints.

Each button electrode, that is 12 mm in diameter, is mounted at the pin tip of a SMA vacuum feedthrough welded to a NW16 flange (see Fig. 1). A special alignment groove is machined to improve the position accuracy. The required absolute accuracy is expected to be achieved by a torque adjustment in situ of the fastening bolts to balance the calibration signal strength delivered by individual pickups composing a BPM. The button pickups are manufactured by Kyocera Corporation according to TRIUMF drawings. Three complete BPM were installed at the injector test facility. First beam data are available.

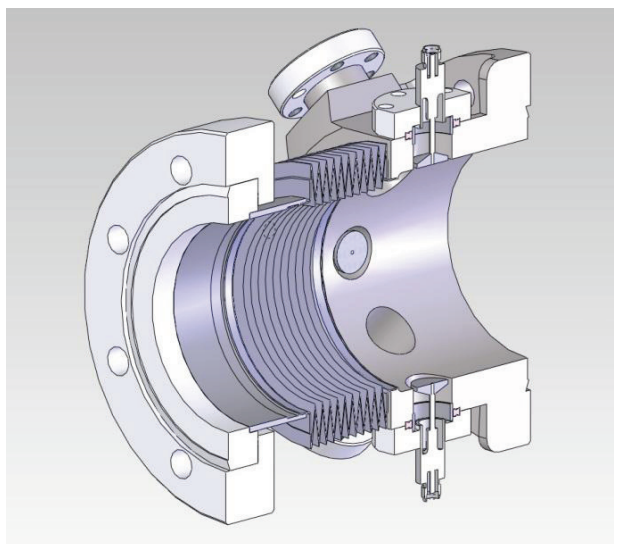

Figure 1: A cross-section view of the button BPM.

The stripline BPM (see Fig. 2) was developed based on work done at Cornell. The Cornell design was adjusted to comply with the 650 MHz bunch repetition frequency and a smaller diameter (50 mm) of the beam pipe. The prototype unit is currently being assembled. Position sensitivity of both button and stripline BPMs is 1.4 dB/mm. The estimated signal strength of the button BPM is about −30 dBm (confirmed by measurements) at the

Copyright © 2012 by the respective authors — cc Creative Commons Attribution 3.0 (CC BY 3.0)

nominal beam current of 10mA. The stripline BPM signal is expected to be stronger by 13 dB.

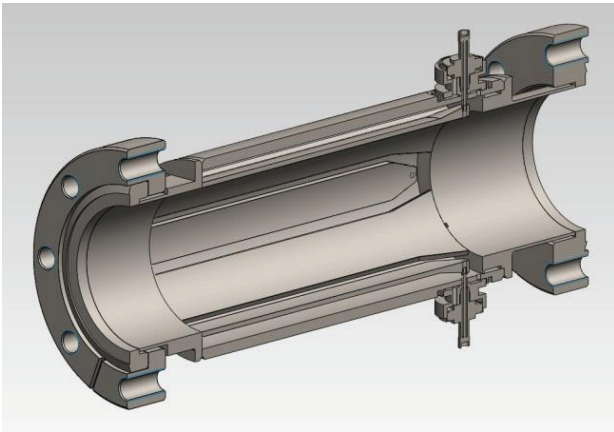

Figure 2: A cross-section view of the stripline BPM.

The BPM signal processing electronics was challenged to operate in both the pulsed beam tune-up mode with the pulse width as short as 1us and the CW operation mode. The electronics development has required a substantial amount of efforts and presently the prototype module is fully ready for beam tests. Electronics comprises a front-end unit, a digitizer and a digital signal processing (DSP) module. The front-end is a commercial BERGOZ Instrumentation AFE board customized for the frequency of 650MHz. This four channel plug-in module down converts the input signals to the IF frequency of 26MHz and performs subsequent amplification. The IF signals are digitized by an in-house developed module based on a 14-bit ADS6445 ADC from Texas Instrument The IF signal sampling is performed at rates of up to 125 MHz. Data are then transferred to Xilinx Spartan-6 FPGA. The FPGA performs the ADC data deserialization, signal demodulation and filtering. Fresh data are available approximately each microsecond. The same FPGA runs the Xilinx MicroBlaze soft processor that accesses the FPGA registers and outputs data via Ethernet and RS232 ports. The electronics is assembled inside a 1U rack enclosure.

Current Monitors

The beam current will be measured using Faraday Cups (FC) at energies of 100-300 keV and DC current transformers at higher energies. Even at low energies the beam power reaches substantial values making the Faraday Cup design quite challenging. Two FC designs have been developed. A 300W version was designed to operate in combination with a 1mm slit scanner, thus, allowing measuring the beam transverse profile at beam currents substantially higher than it is possible with view screens. Four FC monitors are currently in use at the test facility. The devices were proved to have a bandwidth of about 1 MHz on a 50 Ohm load.

Design of a higher power version was recently completed. The high power Faraday Cup can dissipate up to 3kW of the beam power provided the beam size is not too small (typically larger than 1mm rms). The design was verified by thermal and stress analysis using COMSOL Multiphysics. A special feature of the TRIUMF design is the modularity achieved by employing a high vacuum compatible VCR fitting which significantly simplifies device serviceability.

The beam current in the CW regime and with long beam pulses will be measured with DC current transformers. Presently, one unit, model NPCT-115-HR, has been purchased from Bergoz Instrumentation. The associated development is reduced to the design of the transformer enclosure which has to provide the required attenuation of the external magnetic field, in particular, the residual field of the TRIUMF cyclotron. The transformer protection during bake-outs and temperature control with an accuracy of better than 0.2 C are incorporated into design.

View Screen

Sixteen view screen monitors will be installed at the beginning and this number is likely to increase in the future. Each monitor includes two or three targets, optics and a camera (Fig. 3). Possible target options are a 0.5 mm thick piece of gold-plated Yttrium Aluminium Garnet (YAG) scintillator, an Optical Transition Radiation (OTR) screen and a calibration target. To sustain higher beam currents we presently plan to use a 10-30 μm thick Pyrolytic Graphite foil as the OTR screen. The targets are positioned into the beam with a stepper motor driven actuator. All targets are rotated by 45° with respect to the beam direction.

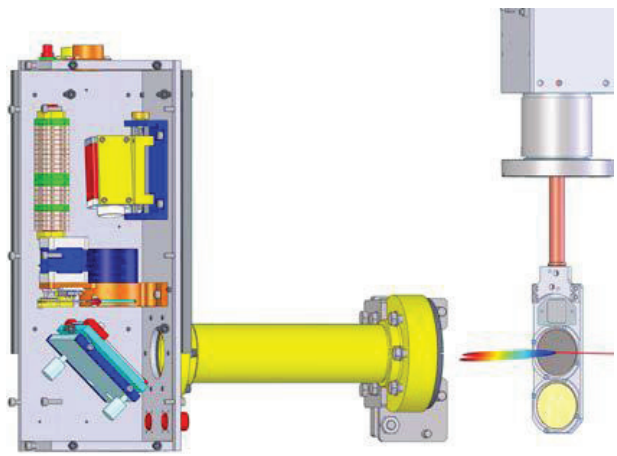

Figure 3: The view screen monitor.

Light produced by the beam on targets is extracted through a fused silica window, reflected by a flat mirror by 90° and collected by a lens on a 12bit GigE CCD camera. The camera is tilted by 7° with respect to the optical axis to correct for the target tilt. A motorized iris adjusts the light intensity on the camera. The whole optical pathway is encompassed into the light tight enclosure. The camera is protected by a lead shield. The monitor control, image acquisition and processing are entirely implemented within the EPICS environment.

Copyright © 2012 by the respective authors — cc Creative Commons Attribution 3.0 (CC BY 3.0)

Wire Scanner

In addition to view screens, wire scanner monitors are being developed to extend capabilities of beam profile measurements. Wire scanners typically possess a much higher dynamic range that makes possible measuring the beam halo. Another attractive possibility is to design the device sufficiently fast so it can operate at the full beam current. Calculations show that a carbon wire needs to travel through the beam at speeds of about 3m/s to survive the 10 mA and 50 MeV electron beam with the size of about 0.5 mm rms.

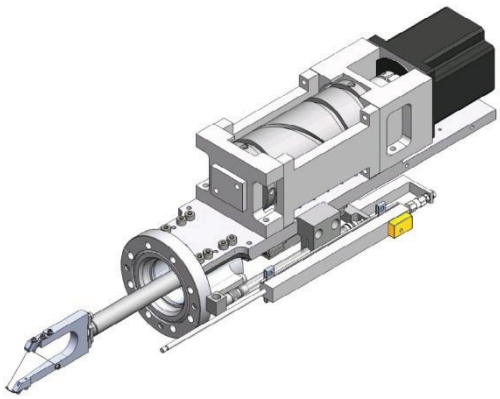

Figure 4: The preliminary design of the fast wire scanner.

To achieve such high speeds we closely followed earlier DESY-Zeuthen design [3] but replaced their slot winding cylinder with a drum having a variable pitch helical slot. The pitch is 144 mm per revolution in the constant speed zone. Close to the park position, the pitch is small to facilitate acceleration and deceleration of the drive mechanism. Two orthogonal wires will move through the beam at 45°. There will be slow and fast modes of operation. With low duty cycle beam pulses, wire motion may be paused for each measurement. For high power CW beams the wires will fly through the beam at a high speed. The preliminary design of the mechanics has been completed (see Fig.4) and the prototype unit is being manufactured.

The motor control electronics based on commercially available components have been purchased and is presently in the evaluation phase.

Beam Phase and Bunch Length Monitors

The thermionic gun produces electron bunches with the duration of about 100 ps and longer. Two broadband devices were designed with a purpose to evaluate the bunch length on this time scale. The first one is a beam intercepting pickup resembling a piece of a tapered coaxial line attached to a high frequency vacuum SMA feedthrough. The pickup is built in to a standard conflate flange (see Fig. 5) and was simulated and later measured to have a bandwidth of 8-10 GHz. A bunch length of 200 ps (fwhm) was measured with this device that was consistent with the beam dynamic expectations.

In contrast, the second broadband monitor is a non-intercepting capacitive pickup. By construction it can be thought of as a 50 Ohm transmission line bent to form a nearly closed circle (see Fig.5). Signals are available from both ends of the line and can be either combined or used independently. Due to a high pass frequency response of the monitor the direct data interpretation is complex. It was used to measure the beam phase. To reduce the beam position dependence of phase measurements both outputs need to be combined.

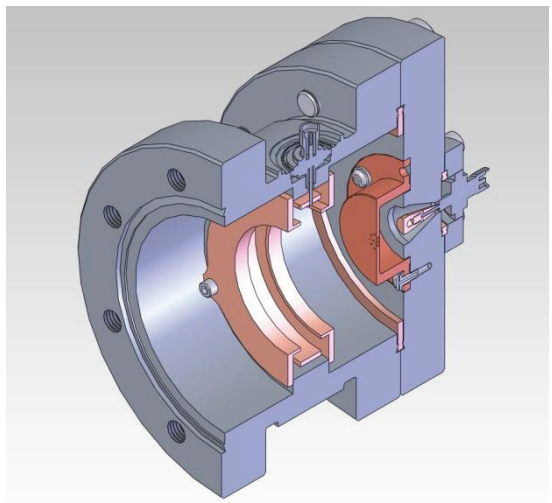

Figure 5: A cross-section of the capacitive and coaxial pickups assembly.

After bunches are compressed by the buncher cavity to sub 10 ps durations they are outside of the reach by the described monitors. A RF deflecting structure was designed for this purpose and is currently being commissioned.

ACKNOWLEDGMENT

The authors would like to thank C. Sinclair for valuable recommendations and assistance with the design of various diagnostics systems, M. Sachwitz for sharing details of the DESY-Zeuthen wire scanner design and M. Rivers for the development of the areaDetector EPICS module.

REFERENCES

[1] L. Merminga et al., "ARIEL: TRIUMF's Advanced Rare Isotope Laboratory," IPAC'11, San Sebastian, Spain, September 2011, WEOBA01, p. 1917 (2011);

[2] A. Laxdal *et al*: "High Power Allison Scanner for Electrons" BIW 2012, Newport News, USA, TUCP04; http://www.JACoW.org.

[3] U. Hahn, N.V. Bargen, P. Castro, O. Hensler, S. Karstensen, M. Sachwitz, H. Thom, "Wire scanner system for FLASH at DESY," DESY, Hamburg, NIM A 592 (2008) 189-196.

Copyright © 2012 by the respective authors — cc Creative Commons Attribution 3.0 (CC BY 3.0)

BEAM LOSS TRACK MEASUREMENTS BY A FAST TRIGGER SCHEME IN J-PARC LINAC*

H. Sako#, T. Maruta, and A. Miura, Japan Atomic Energy Agency, Tokai, Japan

Abstract

In J-PARC Linac, highest beam loss has been observed at the ACS (Annular-Coupled Structure linac) section. The primary source of the beam loss is considered to be H^0 produced by an interaction of H^- beams with remnant gas. The H^0 hits the beam duct, converted to H^+, and escapes from the beam duct.

To detect the H^+'s and estimate the absolute magnitude of the beam loss, we constructed a detector system, which consists of 6 planes of hodoscopes made of 16 scintillation fibers with 64 x 64 mm^2 area. The scintillation light is measured by multi-anode photomultipliers. In the ACS section, two planes to measure horizontal positions are installed, and at about 1 m downstream positions, two planes for horizontal measurements and two for vertical measurements are placed. We will reconstruct charged particles passing through all the 6 planes, and measure the velocity by time-of-flight and energy loss to identify particle species.

We present new measurements since the recovery of the J-PARC after the earthquake started in April 2012 by a new fast trigger scheme using dynode signals of photomultipliers in order to improve signal-to-noise ratios.

INTRODUCTION

The H^0 ion produced by a beam H^- interacted with a remnant gas atom is considered to be the main source of the beam loss in the J-PARC ACS section. The primary goal of this work is to measure H^+'s converted from the H^0's through the beam duct. For this measurement, we constructed 6 planes of scintillating fiber detectors. Each plane consists of 16 4 x 4 x 64 mm^3 plastic scintillating fibers. There are 2 upstream horizontal-measuring planes (H0, H1), 2 downstream horizontal-measuring planes (H2, H3) 1130 mm apart from H0/H1, and 2 downstream vertical-measuring planes (V0, V1) 58 mm apart from H2/H3. 32 fibers in each pair of planes are connected to a multi-anode photo-multipliers (PMT's) Hamamatsu H8500C. This pairing is to reduce inefficiency when a charged particle passes through a boundary between adjacent fibers in a plane and also to suppress accidental background.

Charged particle tracks are reconstructed by combining hits at the fiber planes. Energy of each track is measured with the time-of-flight, and energy loss in each plane is measured by the amplitude of the signal. The energy and the amplitude are used to identify protons and reject other particle species such as electrons, X ray, gamma ray, and neutrons.

The second goal of this work is to measure beam loss source positions along the beam duct and identify hot spots, by projecting each track to the beam axis.

Since 2010, we have measured beam loss with these detectors in ACS section, where we already observed charged particle tracks by beam loss. Detailed description of the scintillating fiber counters and data acquisition system, see [1,2].

FAST TRIGGER SCHEME

In 2012 measurements, the trigger scheme was improved significantly. Until 2011, we used a scheduled timing of the beginning of the macro pulse as the start signal for TDC (Time-to-Digital Converter) CAEN V785 and the gate signal for QDC (charge (Q)-to-Digital Converter) CAEN V792. There were two serious problems with this scheme. First, since the TDC cannot record multiple hits, in case there is another hit before the interesting signal, a wrong timing was recorded, and therefore signal-to-background (S/N) ratio was significantly deteriorated. To solve this problem, we utilized final-stage dynode signals (DY) which are available for PMT H8500C. The polarity of DY signals is opposite to the negative anode signals. Since the PMT has multiple anodes, the DY signal serves as analog sum signal over all the anode channels. We discriminate the DY signals of the three PMT's (DY1 for H0/H1, DY2 for H2/H3, and DY3 for V0/V1), and form coincidence signal from discriminated signals of DY1 and DY3 for the start timing of TDC's and the timing gate of QDC's. The DY1 and DY3 coincidence signal (DY1&DY3) is used as a trigger of a charged particle track penetrating from H0 to V1. Timing and charge of individual anode signal can be measured with low accidental background by narrowing the duration from the start timing to the anode signals for TDC's, and the gate width for QDC's. We also formed a time gate (TG) from the scheduled beam start timing to define the timing within the macro pulse. The coincidence DY1&DY3&TG is used for the data taking. The timing offset and time interval per TDC channel for each fiber was calibrated by injecting a pulse generator signal split to all the detector signal cables end and measuring the timing with the data acquisition system.

RESULTS

The analysis shown here is based on the data taken from Apr. to Jun. 2012. The fiber geometry for H0, H1, H2, and H3 is shown in Fig. 1. By moving H2 and H3, we cover three different track angles, 3.6°-5.0°, 6.0°-7.0°, and 9.0°-11.0°.

*Work supported by JSPS KAKENHI Grant Numbers 23656063, 24510134.

#hiroyuki.sako@j-parc.jp

Copyright © 2012 by the respective authors — cc Creative Commons Attribution 3.0 (CC BY 3.0)

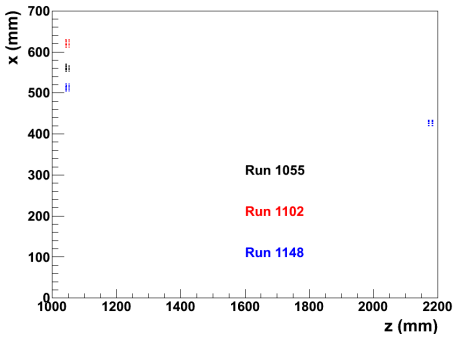

Figure 1: Fiber geometry is shown as a function of the z-position (mm) along the beam axis and the horizontal x-position (mm). The upstream fiber positions at z around 2170 mm are common, while there are three different downstream fiber positions at z around 1050 mm.

With TDC hits, we reconstruct a 3-dimensional track with the horizontal fiber position x^{hit}_i, the timing t^{hit}_i, and the z-position z_i at Plane Hi (i=0, 1, 2, 3). The positive direction of z is upstream. We require TDC hits in all the 4 Planes H0-H3, and search for straight line tracks and fit with the following formulae in the z-x and the z-t planes simultaneously;

$$x^{track} = X_0 + X_1 z^{track}$$
$$t^{track} = T_0 + T_1 z^{track} \quad ,$$

where X_0, X_1, T_0, T_1 are fit parameters. Fig. 2 shows residuals of the horizontal position x^{hit}_p- x^{track}_p and the time t^{hit}_p- t^{track}_p, where t^{track}_p is t^{track} at z=z_p (Plane Hp, p=1,2). A sharp signal peak (colored small spot in the center) for charged tracks with very low background is seen. The width of the time residual of the Gaussian fit is 0.40 nsec in r.m.s.

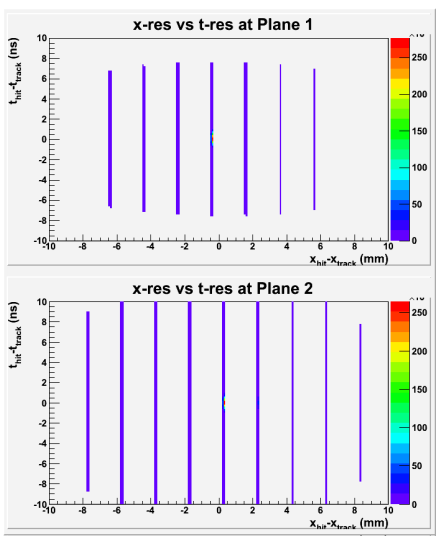

Figure 2: Residuals of hit timing (nsec) in the horizontal axis and horizontal hit positions (mm) in the vertical axis is plotted for H1 (top) and H2 (bottom) with respect to the projected timing from the track.

Fig. 3 shows TDC distributions at each fiber at Plane H2. The peaks at each fiber show protons. Before the calibration, the timing variations of ~100 TDC channel corresponding to ~3.2 nsec were observed. We calibrated the timing at each fiber by injecting pulse generator signals at the PMT signal outputs in the linac tunnel, and measured the timings with the DAQ system. We also changed used several known delay settings for generator signals. We corrected at each fiber both for timing offset and time per TDC channel. The resulting proton timing was adjusted within 1 TDC channel, namely 32 psec.

Fig. 4 shows two-dimensional distributions of time-of-flight and the track angle at different geometries. The signal peak is the highest at the lowest angle configuration. The energies at the peaks are 72.49 MeV at 3.6°-5.0°, 114.7 MeV at 6.0°-7.0°, and 79.05 MeV at 9.0°-11.0°, which are within the simulated H^+ energy ranges of 40-110 MeV. The observed energies have decreasing tendency at a higher angle, which may be due to higher energy loss with larger effective thickness of the beam duct.

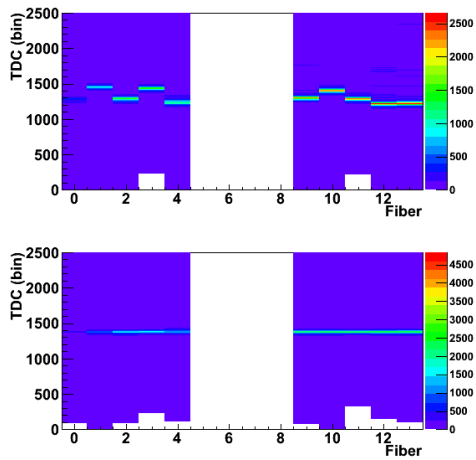

Figure 3: TDC distributions before (top) and after (bottom) the timing calibrations at Plane H2.

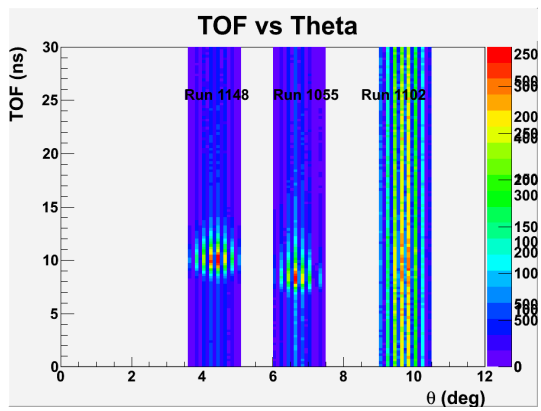

Figure 4: Time-of-flight (nsec) between H0 and H2 as a function of the track angle (degrees) at the three geometry configurations. Note that the z-scales of each geometry configurations are different.

Copyright © 2012 by the respective authors — cc Creative Commons Attribution 3.0 (CC BY 3.0)

Fig. 5 shows the projected z-position of each track to x=0, namely to the beam axis. The raw data (solid line) shows decreasing numbers of tracks toward upstream (larger z) positions.We estimated H^+ numbers from time-of-flight distributions at each geometry as shown with dashed lines in Fig. 5. After the correction, the H^+ peak heights are similar at 6.0^o-7.0^o and 3.6^o-5.0^o, and corresponding z-ranges of 5400-6300 mm and 6900-9000 mm, while lower by the factor of 6 at 9.0^o-11.0^o and 4400-5000 mm.

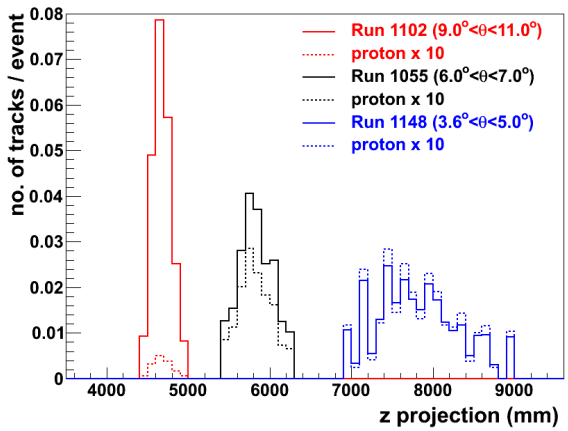

Figure 5: Projected z-positions of x-z tracks at three geometry configurations. Solid lines show raw numbers of tracks including accidental tracks, whereas the dashed lines are after the time-of-flight cuts and corrected to obtain proton numbers.

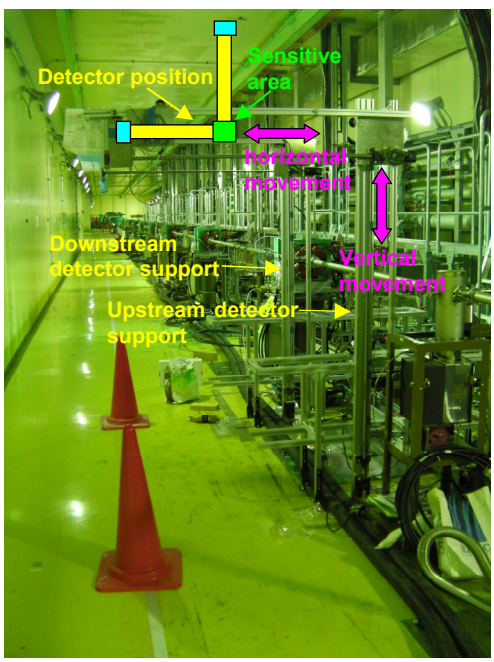

Figure 6: Remotely controlled detector moving system. The base plate for the detector moves in horizontal and vertical directions.

CONCLUSIONS

A clear time-of-flight signal consistent with H^+ has been observed with the fast trigger scheme with PMT dynode signals. Assuming H^+, the energy is 72.5-114.7 MeV, which is cosistent with simulation. In the measured angle ranges, the H^+ rate is highest at the lowest angle ranges of 3.6^o-5.0^o. The beam loss distributions along the beam axis are demonstrated.

In the summer shutdown period in 2012, we have been upgrading the detectors for the next beam operation starting from Oct. 2012. We are currently constructing two fiber planes for vertical position measurements at the upstream position, which enables both horizontal and vertical track reconstruction. Also, the new detector is expected to have better position resolutions by weighted mean positions of fibers in two planes with their amplitudes, since we adopt scintillating fibers with a 4 mm diameter circular cross section, instead of existing fibers with a 4 mm x 4 mm square cross section. We are installing a remotely-controlled detector moving supports in x- and y-positions as shown in Fig. 6. With these upgrades, we expect to increase acceptance of beam loss tracks significantly. We are also preparing detailed detector simulation in order to estimate detector acceptance for absolute beam loss rate estimation.

ACKNOWLEDGEMENT

We thank J-PARC linac monitor group for helping us detector installation and tests. This work was supported by JSPS KAKENHI Grant Numbers 23656063 and 24510134.

REFERENCES

[1] H. Sako, *et al.*, "Beam Loss Particle Tracking in J-PARC Linac," 8th Annual Meeting of Particle Accelerator Society in Japan, Tsukuba, Japan, p. 501 (2011).

[2] H. Sako, *et al.*, "Measurement of Beam Loss Tracks by Scintillating Fibers at J-PARC Linac," IPAC11, San Sebastian, Spain, 2011, p. 1251 (2011).

Copyright © 2012 by the respective authors — cc Creative Commons Attribution 3.0 (CC BY 3.0)

HIGH DYNAMIC-RANGE HIGH SPEED LINAC CURRENT MEASUREMENTS *

C. Deibele, D. Curry, R. Dickson, ORNL, Oak Ridge, TN 37831 USA

Abstract

It is desired to measure the linac current of a charged particle beam with a consistent accuracy over a dynamic range of over 120 dB. Conventional current transformers suffer from droop, can be susceptible to electromagnetic interference (EMI), and can be bandwidth limited. A novel detector and electronics were designed to maximize dynamic range of about 120 dB and measure rise-times on the order of 10 nanoseconds.

BACKGROUND/GENERAL THEORY

An ideal beam of current in a linac can be expressed as a series of Gaussian pulses of current separated by a unit of time, t_o, as described $I(t) = \sum_{n=-\infty}^{\infty} I_m(t - nt_o)$, where $I_m(t) = \frac{1}{\sigma\sqrt{2\pi}} e^{\frac{-t^2}{2\sigma^2}}$. Since the current, I(t), is periodic, the current can be realized as a Fourier series $I(t) = \sum_{n=0}^{\infty} a_n \cos(n\omega_o t), \omega_o = \frac{2\pi}{t_o}$. Many linac beam measurement systems make use of this spectral analysis technique and rely on a measurement of a particular harmonic. For example, beam position and phase measurement systems measure the first and/or second harmonic component, and draw various conclusions about the beam position within the beampipe or beam phase relative to some rf source.

Measurements of a beam harmonic have an inherent advantage that baseband noise, interference, or EMI can be easily filtered and therefore not contaminate the intended spectral measurement. For example, switched power supplies can easily inject parasitic baseband signals into the intended measurement signal and therefore reduce the signal-to-noise ratio. It is desired, therefore, that thermal noise be the limiting factor in many of the linac beam measurements.

To measure the beam current, a measurement of a signal that can be calibrated to an individual harmonic of the beam and is directly proportional to beam harmonic is desired. Many BPM (Beam Position Monitoring) systems rely on this technique, and a signal that is proportional to beam current is reported. Unfortunately, output signals from BPM electrodes by its design are strongly dependent on beam position, and therefore the design of the BPM electrodes can produce a nonlinear calibration of the reported current. Also, many linac BPM systems use an IQ under-sampled/down converted signal processing technique which may not adequately measure the sharp rise/fall times of linac beam, which is essential in any chopped linac current.

* Work performed at (or work supported by) Oak Ridge National Laboratory, which is managed by UT-Battelle, LLC, under contract DE-AC05-00OR22725 for the U.S. Department of Energy.

A detector is sought that:

- can successfully measure a signal that is proportional to a beam harmonic,
- does not intercept the beam and can support high intensity operation,
- has an output signal that is independent of beam position as beam traverses through it,
- has a low quality factor (or "Q"), so that accurate rise-times and fall-times can be measured,
- is optimized for measuring high dynamic range.

SYSTEM DESIGN

A description of the overall beam current measurement system is described. Particular and practical design issues are discussed.

Detector Design

The detector design was inspired by a stripline BPM, as it possesses most of the design criteria in the preceding section. A stripline can be optimized for beam response for a particular harmonic, and thereby is optimal for high dynamic range. The output of most BPM designs, however, is dependent on beam position. This effect can be reduced by placing the BPM striplines outside of the beampipe diameter. A schematic of the envisioned detector is depicted in Fig. 1.

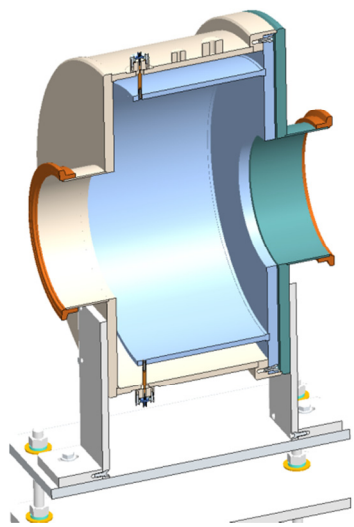

Figure 1: Schematic of the beamline detector.

A circumferentially continuous electrode that is λ/4 in length is short circuited to the wall of the vacuum vessel. Two of the four feed-thrus are shown.

Copyright © 2012 by the respective authors — cc Creative Commons Attribution 3.0 (CC BY 3.0)

To optimize the output signal, a single electrode was envisioned to encircle the beampipe, and it was designed to be λ/4 in length. The inside diameter of the electrode and number of feed-thrus were simulated and optimized to have an output signal that is minimally dependent on beam position inside of the detector. Initially, only one feed-thru was simulated for the design. The single feed-thru permitted, however, a strong output signal dependence which was proportional to beam position inside of the electrode. Additional feed-thrus were added to the design until the output sum signal had less than 1% variation on beam position in the beampipe, and the inside diameter of the electrode was close to a factor of two of the diameter of the beampipe. The number of feed-thrus necessary for any particular beampipe is determined by the pipe diameter and frequency of harmonic which is measured. An additional schematic of the detector is shown in Fig. 2.

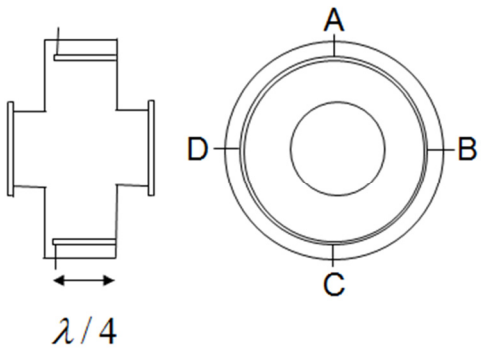

Figure 2: Schematic of detector. Output signal is the sum of the four feed-thrus, A+B+C+D. The frequency and beampipe dimensions required 4 feed-thrus for a 1% variation in output signal for beam signal.

A photo of the installed detector in the injection dump beamline at the Spallation Neutron Source (SNS) is shown in Fig. 3. A combiner is located inside of a green radiation shielded enclosure. Also inside the enclosure is a small circulator tuned to the SNS first beam harmonic, 402.5 MHz, and small single stub tuner.

Analog Electronics and System Design

The analog electronics and overall system design are shown in Figure 4. The signals from the electrode are sent to a summing hybrid. The reflection from the detector itself is 0 dB, and therefore a circulator and single stub tuner is introduced to reduce the reflection from the detector to about -60 dB. The output from the tuner is sent to the long haul cable that goes from the beam enclosure in the tunnel to the service building where the analog and digital electronics are housed in a rack.

From the long haul cable, the signal enters into an rf enclosure chassis. Spurious signals were observed using conventional simple enclosures due to overlap from the first harmonic of the beam signal and cellular devices carried by personnel. The signal then passes through two diplexers. The diplexers are used to properly terminate any out-of-band signals (i.e. baseband and higher order harmonics) and then be properly terminated into a load resistor and not spoil the intended signal measurement.

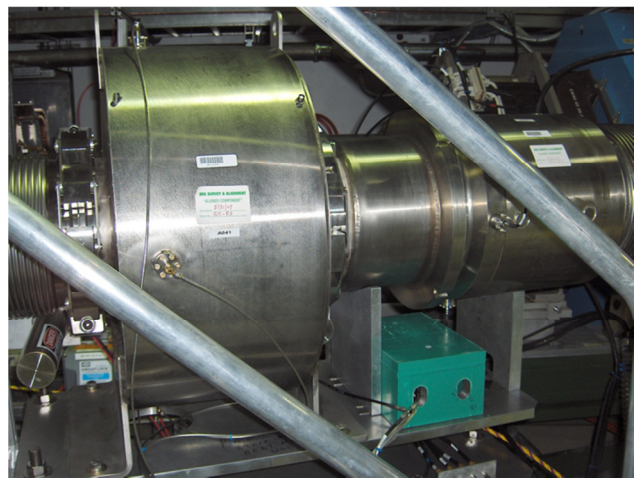

Figure 3: Installed detector and shielded box (in green) with analog combining hybrid, circulator, and single stub tuner.

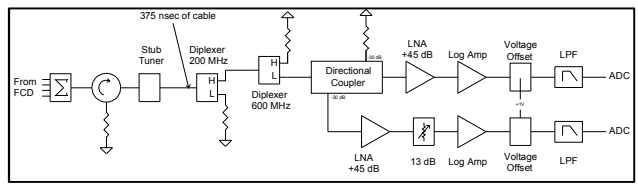

Figure 4: Schematic of cabling and analog electronics.

The next part of the analog signal processing involves taking advantage of the properties of logarithmic amplifiers. As with all conventional amplifiers, logarithmic or otherwise, there exists an operational region where the device was intended to be used. The logarithmic amplifiers that were chosen [1] for this system have a fairly fast rise/fall time of 10 nsec, but also, has an operational region of input power from -70 dBm to 0 dBm. The directional coupler therefore was used to create two data channels from the detector, and then use digital signal processing to recombine the two data channels into a single data channel.

It was desired, therefore to keep the thermal noise floor as low as possible by using low noise amplifiers (LNA). The LNAs are Miteq AMF-2F-00250050-06-10P, which has a noise figure of 0.5 dB and gain of 45 dB. As shown, the logarithmic amplifier follow the LNA. One of the features of the logarithmic amplifier is that its output ranges from about 2.4 volts to 0.5 volts. Since most ADCs (Analog to Digital Convertors) are bipolar, an advantage exists to add a DC offset to the output of the logarithmic amplifier. This permits the full range of the ADC to be utilized. The final component in the analog chassis is an antialiasing low pass filter.

Copyright © 2012 by the respective authors — cc Creative Commons Attribution 3.0 (CC BY 3.0)

Digital Electronics

A commercially available platform was chosen to implement the digital front end electronics. It was assembled using a BenNUEY VME Field Programmable Gate Array (FPGA) carrier card from Nallatech [2] with a single BenADDA-V4 DC coupled 14-bit dual channel Analog to Digital Converter (ADC) module operating at a 105 MHz sampling rate. The ADC channels are connected to the analog electronics and are driven by the high and low gain outputs respectively.

The key advantage of designing with commercially available hardware was in the deployment of rapid prototype designs. The initial basic implementation was completed in two weeks. This provided a simple and effective method for verifying the performance of the entire system early in the design cycle. It also let users work with the interface and enabled the collection of feedback immediately.

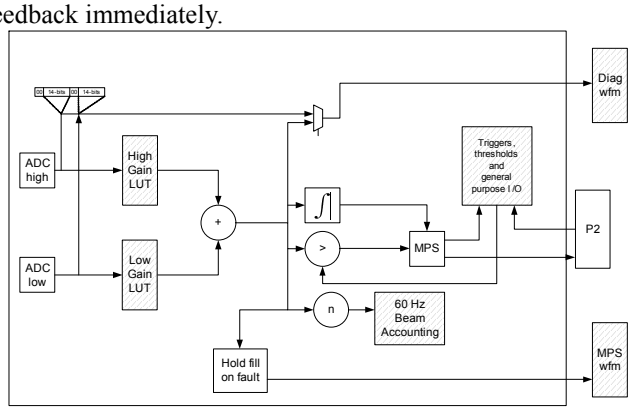

Figure 5: Simplified block diagram of the final digital design implementation.

A pipeline architecture was used to implement the final design. An overview of the digital design is shown in Fig. 5. Each of the 14-bit ADC's possible values are converted to a beam current value by referencing a local look-up table contained within the FPGA. The high and low gain channels are then combined into a single 32-bit value. The contribution from each channel is dependent on the operating range of its associated analog amplifier. The look-up tables are aligned to ensure each channel's impact on the final value is contained within its usable dynamic range. The look-up tables can be bypassed to preserve the raw ADC values if desired. This allows a simple method for calibrating the ADCs and troubleshooting without requiring special firmware builds to be loaded into the FPGA. The technique to calibrate the analog and digital electronics is described in [3] [4] [5].

To prevent incurring loss of critical data due to bandwidth limitations of the VMEbus, the waveforms and beam accounting information is stored in the large banks of local dynamic memory that are connected to the FPGA. It can take several cycles for the VME processor to retrieve these waveforms depending on the system load. Utilizing this memory relaxes the processor's requirement to respond immediately upon receiving an interrupt from the hardware that the waveforms are available.

An additional advantage of utilizing a real-time parallel processing-based design was the integration of a 60Hz shot-to-shot beam accounting scheme and a Beam Dump protection component without compromising the functionality of the original system requirements. The machine protection portion of the design incorporated four independent power measurements that utilized a sliding window technique to calculate the integrated power on the dump for monitoring high losses over a few micro-seconds to low losses that occur over several seconds. The necessary hardware required to interface the machine protection system was included on the rear transition card.

A sample beam measurement of current is shown in Fig. 6.

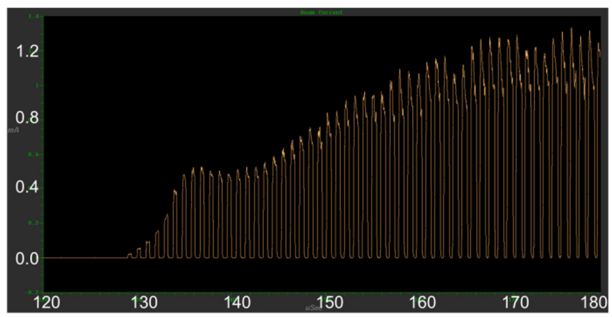

Figure 6: Sample measurement of beam current in the injection dump. Vertical units are in milliamps, horizontal in microseconds. Individual minipulse are clearly visible and the noise floor is a microamp.

ACKNOWLEDGMENTS

We wish to thank J. Bryan, A. Webster, S. Murray III, R. Taylor, J. Diamond, R. Hardin, G. Link, T. Davidson, D. Bartkoski, Z. Xie, S. McTeer, M. Holding, S. Assadi, and K. Gawne for their technical contribution and discussion.

REFERENCES

[1] www.eltac.co.uk
[2] www.nallatech.com
[3] D. Thompson et. al, "HIGH DYNAMIC RANGE CURRENT MEASUREMENTS WITH MACHINE PROTECTION," ICALEPS 2007, Knoxville, TN, WPPB24.
[4] D. A. Bartkoski et. al, "HIGH-DYNAMIC-RANGE CURRENT MEASUREMENTS IN THE MEDIUM-ENERGY BETA TRANSPORT LINE AT THE SPALLATION NEUTRON SOURCE," Linac 2006, Knoxville, TN, TUP002.
[5] D. A. Bartkoski et. al, "Log Amp Calibration and Setup," SNS-NOTE-DIAG-177, http://neutrons-staff/sites/Notes/Shared%20Documents/sns0177.pdf

Copyright © 2012 by the respective authors — cc Creative Commons Attribution 3.0 (CC BY 3.0)

DEVELOPMENT OF PERMANENT MAGNET FOCUSING SYSTEM FOR KLYSTRONS

Y. Fuwa, Y. Iwashita, H. Tongu, Institute for Chemical Research, Kyoto University, Kyoto, Japan
S. Fukuda, S. Michizono, High Energy Accelerator Research Organization, Ibaraki, Japan

Abstract

A permanent magnet focusing system for klystrons is under development to improve reliability of RF supply system and reduce power consumption. To save production cost, anisotropic ferrite magnets are used in this system. A test model has been fabricated and the power test of a 750 kW klystron with this focusing magnet is carried out. 60 % of the nominal output power has been achieved at a preliminary power test so far.

INTRODUCTION

Distributed Klystron Scheme (DKS) is proposed as one of the RF supply scheme for International Linear Collider (ILC) to reduce the cost and the down time by raising the reliability [1]. Because thousands of relatively small modulating anode (MA) klystrons ware required in DRFS scheme, the failure rate of each component must be reduced. Especially thousands units of electromagnet for klystron beam focusing would cause maintenance problems. Replacing the electromagnets by permanent magnets can eliminate their power supplies and cooling system. Hence the failure rate of the RF supply system can be reduced and cut down the operation cost. A klystron beam focusing system with ferrite magnets is under development is described.

FABRICATION OF FOCUSING MAGNET

Magnetic Materials

There have been precedents for electron beam focusing in klystrons with permanent magnets such as ALNICO, the rare earth (RE) [2,3,4]. Figure 1 shows the B-H curves for these magnet materials and anisotropic ferrite magnets. ALNICO magnets, which have high remanence, shows less coercivity and easily demagnetize. Although RE magnets such as NdFeB has high remanence and coercivity, they are rather expensive and have the resource problem. The anisotropic ferrite magnets have less remanence but higher coercivity than ALNICO. The required magnetic field for beam focusing in klystrons is less than 1 kGauss, therefore the remanence of the anisotropic ferrite magnets is enough high. And the material costs are not expensive, because anisotropic ferrite magnets are composed of iron oxide.

Magnet Field Distributions

Periodic Permanent Magnet (PPM) focusing scheme has relatively well-known magnetic field distribution. In a focusing system with permanent magnet, the alternating magnetic field can be easily generated because an integrated value of magnetic field vector along closed

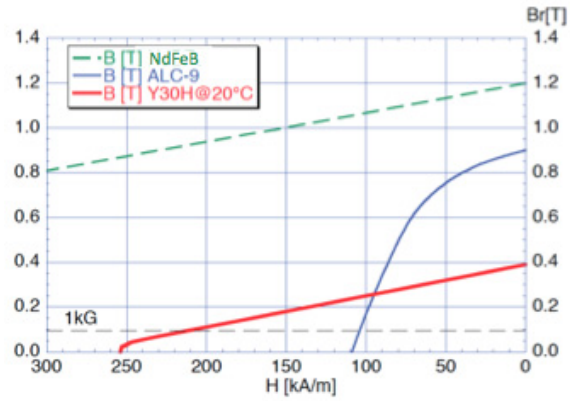

Figure 1: B-H curves of rare earth, ALNICO and ferrite magnets.

curve or infinitely-long axis is zero by the Ampere's law. However, periodicity cause stop bands. For pulse operations, the operating point always crosses such region during pulse rising time and the beam loss causes wall heating and prevents stable operation.

For safe operation, unidirectional magnetic field distribution is applied. Because the required magnet field is not high, anisotropic ferrite magnets can be used. RADIA 4.29[5,6] is used for the magnetic field design. Applied design is shown in Figure 2. Magnets shown in Figure 2 are categorized into two groups. The one group consists of magnets surrounding the klystron body

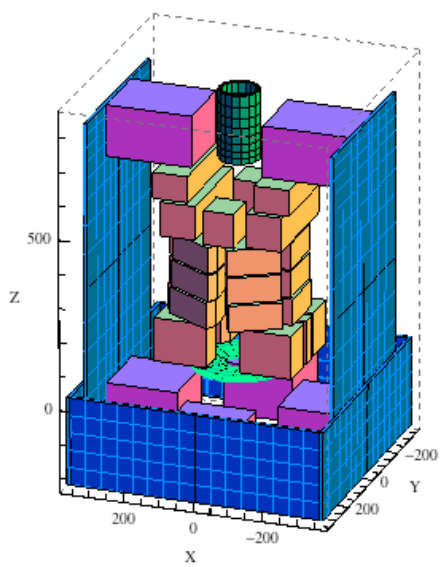

Figure 2: Layout of magnet and iron yoke.

Copyright © 2012 by the respective authors — cc Creative Commons Attribution 3.0 (CC BY 3.0)

(yellowish ones in Fig. 2), whose easy axes are parallel to the klystron beam axis. The other group consists of the bottom and the top large magnet bricks (purplish ones in Fig. 2) to form the magnetic field around the cathode and the collector area. Their easy axis is perpendicular to the klystron axis. All magnets are retractable for the insertion of the klystron. Klystrons are usually inserted from the top of the focusing magnets and thus the minimum aperture of the magnets must be larger than most fat part of the klystron such as ceramic insulator. The retractable magnets can open their aperture at the klystron installation time and close at the operation. (see Figure 3). This retracting mechanism can also be used for the field adjustment.

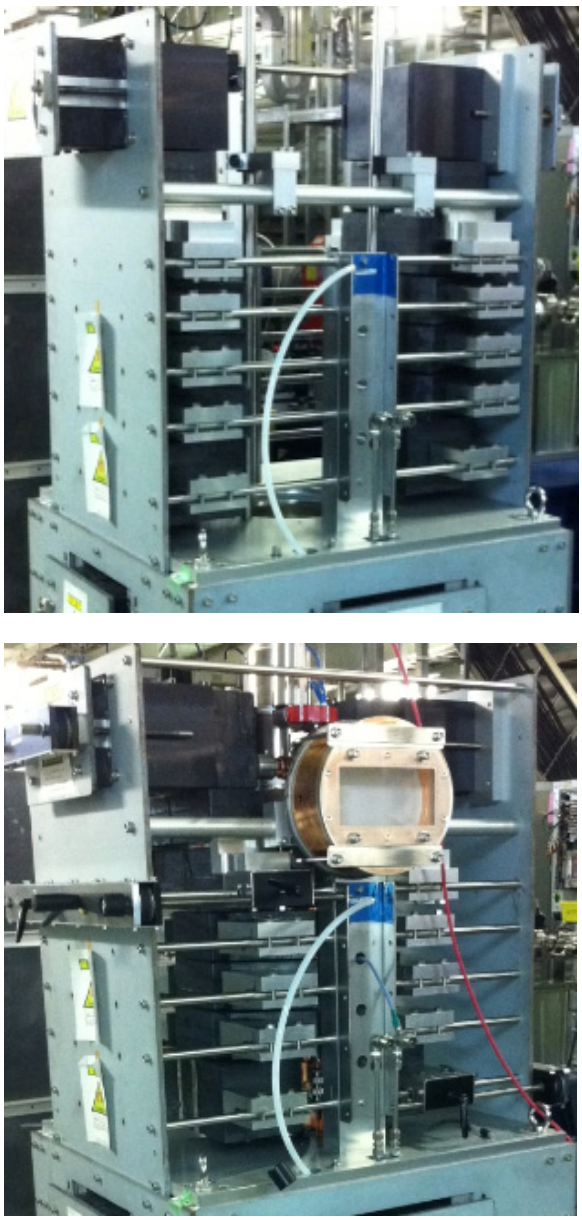

Figure 3: The magnets have larger aperture than the klystron body before the klystron installation (upper). After the klystron installation, the magnets are brought close to the klystron (lower).

KLYSTRON POWER TEST

To evaluate performance of the fabricated focusing magnet, a power test with real klystron (Toshiba E37501) is carried out. Figure 4 shows the E 37501 and Table 1 shows its nominal specification. The magnet field distribution, which is measured, adjusted is applied for power test. Figure 5 shows the longitudinal magnetic field. The blue line shows measured magnetic field generated by permanent magnets and the red line shows that by the electromagnet. The beam transport simulation has been performed by DGUN[7] using measured longitudinal magnetic field. The result of the simulation shows that the beam can pass through the klystron body without loss in the DC state (see Figure 6). Figure 7 shows transverse magnetic field components. The transverse magnetic field components are adjusted less than 10 Gauss by moving magnet's position. In the power test, the klystron was operated with 1 Hz repetition rate and the RF pulse duration was 1 ms so as not to damage the klystron body by unexpected beam loss. The result of the preliminary power test where the klystron cathode voltage is from 45 kV to 65 kV is shown in Figure 8. In Figure 8, red plots are the output maximum output power with our permanent magnets and blue plots are the max output power with an electromagnet measured by Toshiba. About sixty percent of the nominal output power at Toshiba is attained by the permanent

Figure 4: The klystron using in power test (Toshiba E37501).

Table 1: Specification of E37501

frequency	1.3 GHz
Max Output Power	750 kW
Max Efficiency	55 %
Max Gain	43 dB
Max Pulse Length	1.5 msec
Max Repetition Rate	5 Hz
Max Beam Voltage	66 kV
Max Beam Current	50 A

Copyright © 2012 by the respective authors — cc Creative Commons Attribution 3.0 (CC BY 3.0)

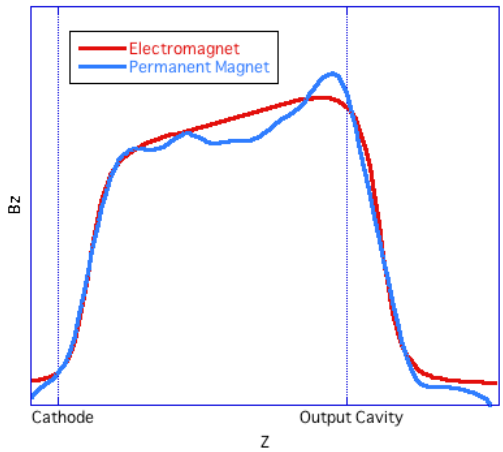

Figure 5: The longitudinal magnetic fields.

Figure 6: The result of DGUN simulation with the measured longitudinal magnetic field.

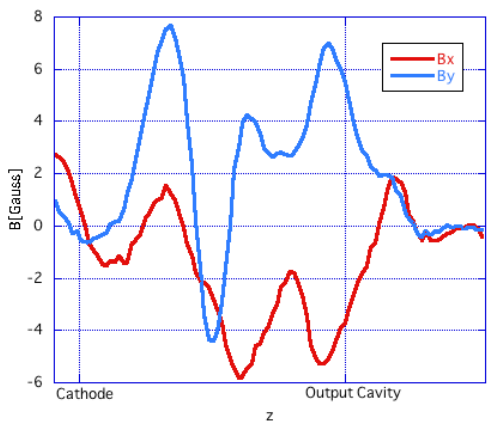

Figure 7: The measured transverse magnetic fields.

magnets in this early stage experiment. And the energy efficiency is about 33 % for our permanent magnets. This low output power and efficiency are supposed to be caused by the not optimized magnetic field in the cathode area. Figure 9 shows the calculated magnetic field in the cathode area. Although the magnetic field near the axis looks good, that on the outskirts may not be optimum, which results in beam mismatch.

Electric discharges occurred frequently in the operation and prevent stable operation. The electric discharges seem to be caused by the shape of the oil tank; the oil tank has a smaller diameter than that for the electromagnet focusing in order to reduce the distance from the magnets to the axis. This problem will be fixed by a remodeling of the tank. Further study will be continued for a better performance through magnetic field adjustment and so on.

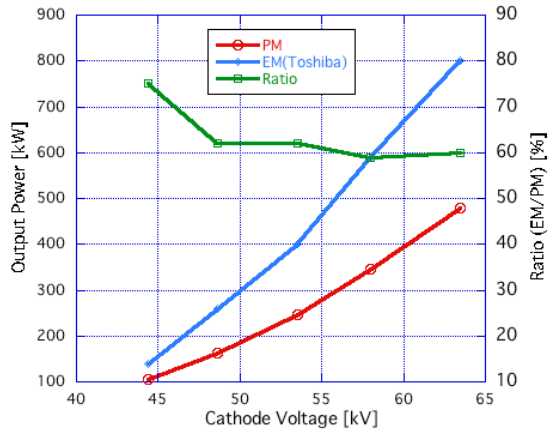

Figure 8: The preliminary result of the klystron power test.

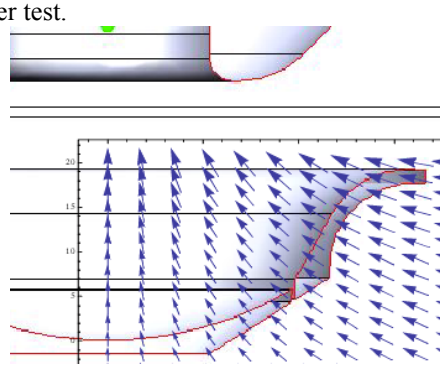

Figure 9: The calculated magnetic field in the cathode area

REFERENCES

[1] S. Fukuda, Distributed RF Scheme (DRFS) – Newly Proposed HLRF Scheme for ILC, LINAC2010, Tsukuba, pp.112-114, 2010.

[2] Jane V. Lebacqz, Status Report on Klystron Improvements, IEEE, Trans., NS-22, 3 pp.1324-1327, June1975.

[3] Fukuda, S., Shidara, T., Saito. Y., Hanaki, H., Nakao, K., Homma. H., Anami, S., Tanaka, J., PERFORMANCE OF HIGH POWER S BAND KLYSTRONS FOCUSED WITH PERMANENT MAGNET, 198624009 KEK-86-9, Feb. 1987.

[4] S. Masumoto, et al., STUDY OF PPM-FOCUSED X-BAND PLUSE KLYSTRON, Proc. of LINAC 2006, Knoxville, pp.628-630.

[5] P. Elleaume, O. Chubar, J. Chavanne, Computing 3D Magnetic Field from Inserted Devices, proc. of the PAC97, May 1997, p.3509-3511.

[6] O. Chubar , P. Elleaume, J. Chavanne, A 3D Magnetostatics Computer Code For Insertion Devices, SRI97 Conf. Aug. 1997, J. Synchrotron Rad. (1998). 5, 481-484.

[7] A. Larionov, K. Ouglekov, "DGUN-code for simulation of intensive axial-symmetric eletron beams", 6th ICAP, TU Darmstadt, Germany, 2000, p. 17.

Copyright © 2012 by the respective authors — cc Creative Commons Attribution 3.0 (CC BY 3.0)

176 MHz SOLID STATE MICROWAVE GENERATOR DESIGN

A. Smirnov, A. Krasnov, K. Nikolskiy, N. Tikhomirova, E. Ivanov,
Siemens Research Center, Moscow, Russia
O. Heid, T.Hughes, Siemens AG, Erlangen, Germany

Abstract

This paper concerns the R&D work upon design of a compact RF amplifier to be used for linear accelerators. The machine under development will operate at 176 MHz with output power of 25 kW in continuous wave regime. It consists of 50 push-pull PCB modules (approx. 500W output power each), connected in parallel to several radial filter rings, which both allow class-F operation and combine the power from the modules, delivering it to a single 50 Ohm coax cable. The CST simulations and the design of 324 MHz test prototype are presented.

INTRODUCTION

High power RF sources are important elements for most of linear accelerators that have found growing number of applications in physics and medicine.

The main benefits of the generator under development will be its smaller size, perspective of lower cost, better reliability and higher efficiency, achieved with class-F operation, compared to conventional RF power sources like klystrons. The solid-state microwave power modules based on SiC vJFET transistors arranged in parallel push-pull circuits, will be designed on PCB boards.

All modules will be connected to a power combiner with common output 50 Ohm coaxial cable.

This generator is planned to be a predecessor to the 'big' 324 MHz machine with pulsed RF output power of 3 MW.

RF POWER MODULES

We have designed and manufactured compact RF power modules with one pair of SiC transistors arranged in circlotron topology [1] as shown on Fig.1.

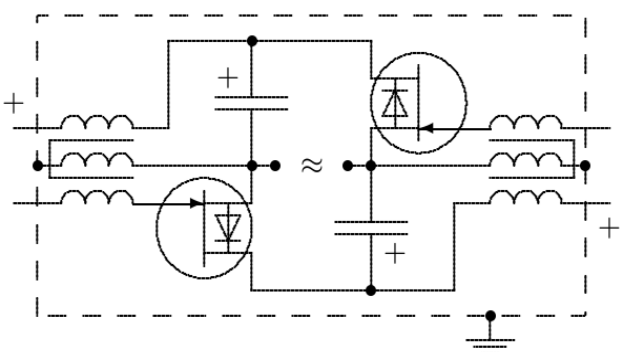

Figure 1: Parallel push-pull circuit.

The manufactured module layout is presented on Fig.2. We used Rogers 4003C with ε=3.55 as a substrate material. The transistors are fed with 180^0 phaseshift, provided with external balun. The module provides maximum available gain of 18.9 dB at output power of 2.0 kW and with supply voltage of 150 V.

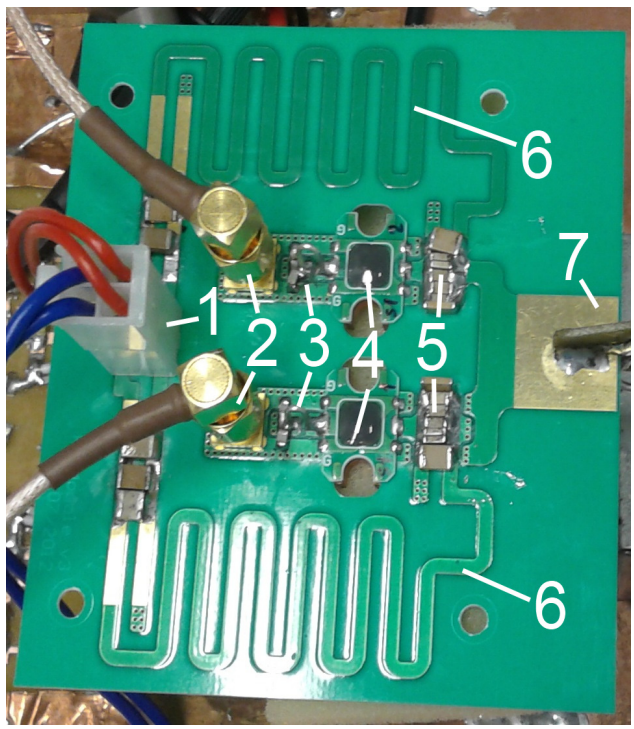

Figure 2: RF power module (heat sink is not shown): 1 – DC supply voltage; 2 – RF inputs; 3 – input matching circuit; 4 – SiC transistors; 5 – DC-blocking capacitors; 6 – quarter-wavelength lines; 7 – symmetric output stripline.

Each transistor will be mounted on a water-cooled heat-sink with a sinter paste, as shown on Fig. 3, which can dissipate up to 300 W average thermal power.

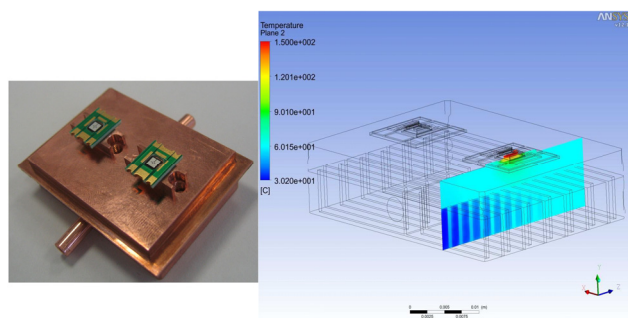

Figure 3: Transistor package mounted on a water-cooling module with temperature distribution.

Copyright © 2012 by the respective authors — cc Creative Commons Attribution 3.0 (CC BY 3.0)

POWER COMBINER

In [2], a possibility of parallel power combining with use of a resonant cavity was shown. In this work, we present a non-resonant power combiner concept based on a stepped coaxial line, shown on Fig 4. It benefits in avoidance of energy storage and thus in lower power dissipation.

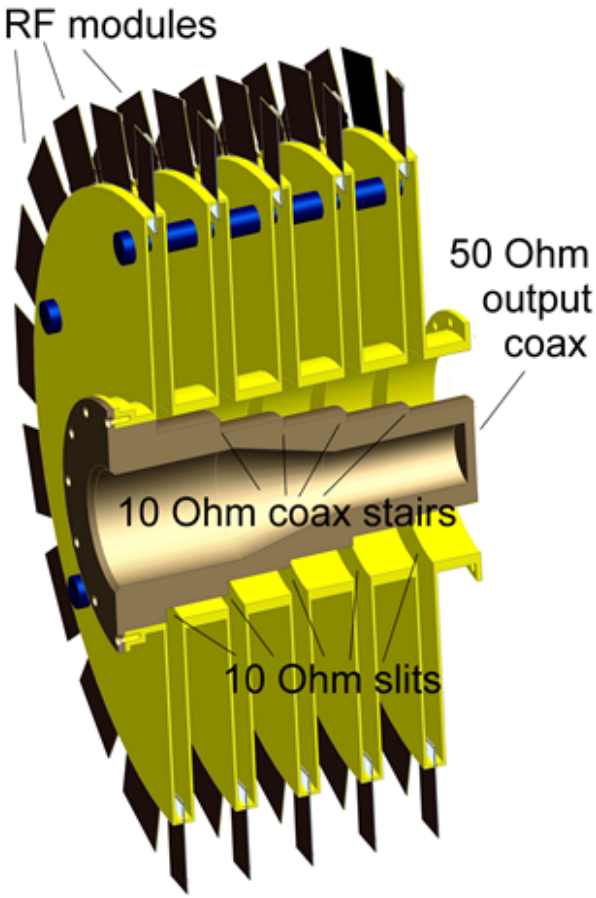

Figure 4: Stepped-line power combiner.

The inner conductor represents sequence of coaxial segments with impedances from 10 to 50 Ohm with 10 Ohm steps. The whole number of modules can be distributed among 5 rings that are mounted on the outer conductor of the coaxial cable and feed it through 5 circumferential slits, each ring having output impedance of 10 Ohm.

Due to the offsets between the rings the drive amplifier must provide the phase shift between the groups of RF modules hooked up to each ring. Meanwhile, the distance between the first and the last slits must not exceed quarter-wavelength to avoid the resonance in the coaxial cable.

Each ring has to be surrounded with metal housing that introduces high shunt inductance which will serve to reduce the power leakage.

RADIAL FILTER

In combination with a suitable resonant load, the RF module can operate in class-F mode at very high efficiencies (over 85%). In an ideal class-F operation, current and voltage are shifted in phase by 180^0, the output voltage waveform having square shape and the drain current being sine-like. A filter at the drain of the transistor with the proper values of input impedances at fundamental frequency and at odd harmonics is required to shape the waveforms [3]. The shaping minimizes the overlap of the voltage and current waveform which reduces power dissipation in the transistor and increases the efficiency.

Henceforth, we consider the third harmonic filter only. Even harmonics are shorted inside each RF module.

The input impedance constraints for the filter are as follows:

let

$$Z_{module}{}^{1}=R^{1}+jX^{1}$$
$$\text{and } Z_{module}{}^{3}=R^{3}+jX^{3}$$

be the output series impedances of a single RF power module at fundamental frequency and at the third harmonic respectively. Since we need to extract the power at fundamental with high efficiency and to reflect the third harmonic back in-phase, the input impedance Z_{filter} has to

- compensate the imaginary part at both frequencies;
- provide power dissipation in the load higher than in the transistors by a factor of 10 (~90% efficiency);
- behave as an open-circuit at odd harmonic

or

$$Z_{filter}{}^{1}=10R^{1}-jX^{1}$$
$$\text{and } Z_{filter}{}^{3}=500R^{3}-jX^{3}$$

at the fundamental frequency and the third harmonic respectively.

We design the filter which fulfills these two complex constraints using four λ/16 transmission lines (four segments) with different line impedances. We calculate the line impedance of each filter segment using scattering matrix approach, taking into account that the filter eventually acts like an impedance transformer of the load R_{load}; see Fig. 5.

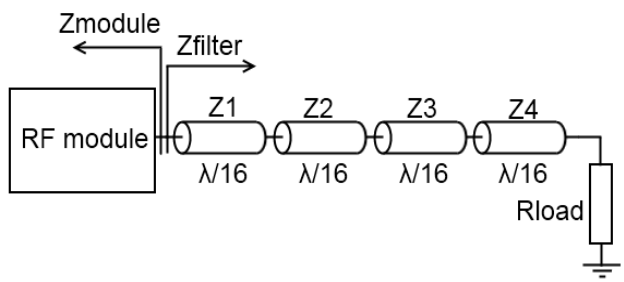

Figure 5: Filter schematics .

The preferable concept of the filter design is to use segments formed from radial transmission lines, driven with non-dispersive TEM-like wave. This leads to a filter

Copyright © 2012 by the respective authors — cc Creative Commons Attribution 3.0 (CC BY 3.0)

that serves to a plurality of the RF modules connected in parallel through horn antennae as shown on Fig.6.

We use CST Microwave Studio to optimize the filter interior shape in order to get desired input impedance values at the antennae tips, to which the modules are connected.

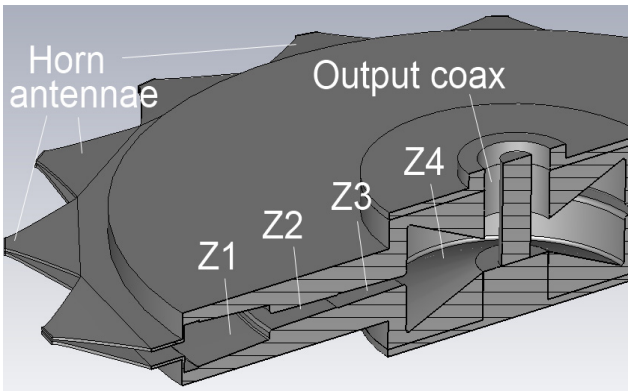

Figure 6: Radial filter CST model

The numerical simulations showed that the radial filter made of copper will dissipate 4.5 times less power than in case of using stripline-based filters connected to the output of each RF module individually. This filter geometry can be easily embedded inside every ring of the power combiner.

Test Prototype

In order to verify the CST predictions we have designed one filter ring with 16 horn antennae (see Fig. 7), which is currently under manufacture.

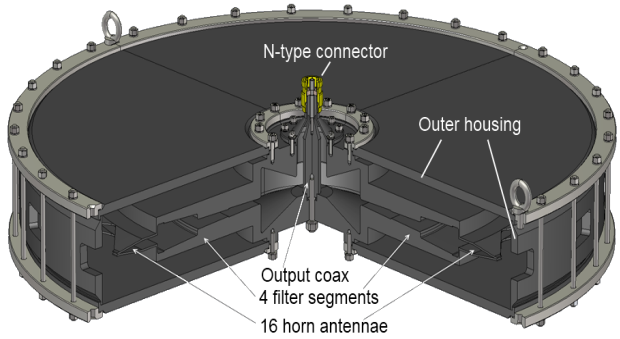

Figure 7: Test prototype CST model

SUMMARY

We have described our preliminary design of the basic RF generator components. The next steps will improve the RF modules' performance in terms of output power and gain; reduce the size of the power combiner by shortening each filter segment and by tuning each horn antenna shape to make it work as the first filter segment itself.

REFERENCES

[1] R. Irsigler, M. Back, O. Heid, Th. Kluge, J. Sirtl, "Compact Solid State RF-modules for Direct Drive RF-Linacs", IPAC2011, San Sebastian, Spai.n

[2] O. Heid, T. Hughes, "Compact Solid State Direct Drive RF Linac Experimental Program", HB2010, Morschach, Switzerland.

[3] F. H. Raab, "An introduction to class-F power amplifiers", RF Design, vol 19, no. 5m pp. 79-84, May 1996.

Copyright © 2012 by the respective authors — cc Creative Commons Attribution 3.0 (CC BY 3.0)

HIGH POWER AMPLIFIER SYSTEMS FOR SARAF PHASE II

I. Fishman, I. Gertz, B. Kaizer, D. Har-Even, Soreq NRC, Yavne, Israel

Abstract

Soreq NRC initiated the establishment of SARAF- Soreq Applied Research Accelerator Facility. SARAF is based on continuous wave (CW), proton/deuteron RF superconducting linear accelerator with variable energy (5-40 MeV) and current (0.04-5 mA). RF power to each cavity is driven by a High Power Solid State Amplifier. The paper outlines the design concept of 10 and 15 kW at 176 MHz power amplifiers. 10 kW amplifier was successfully tested at the beginning of 2012. 15 kW system is now under final design stage. The amplifiers are combined from basic 5.5 kW compact 19" 7U water cooled drawers.

INTRODUCTION

The paper describes the basic 5.5 kW amplifier drawer and method of building and construction of High Power amplifier systems. The need of High Power Amplifiers appears when the 6 exiting 2 kW 176 MHz amplifier built by "Accel" for Prototype Cryogenic cavities limits to rise the current of the accelerator. The 4 kW amplifiers were designed and built to exchange the 2 kW.

The 5.5 kW is designed and built for future design of high energy cavities for the Phase II project.

BASIC 5.5 kW RF POWER AMPLIFIER

The 5.5 kW High Power Amplifier (HPA) consists of following sub modules and components:

- 4 double 800 W water cooled RF modules.
- 8 ways 100 W RF Power Splitter.
- 8 ways 5.5 kW RF Power Combiner.

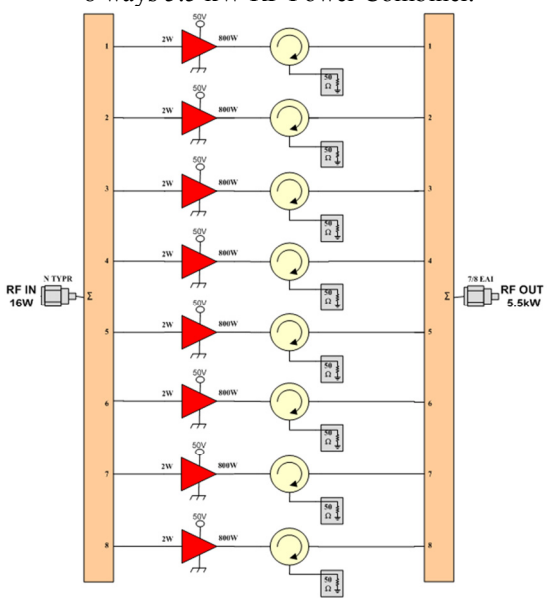

Figure 1: 5.5 kW block diagram.

800 W RF Power Module

The power amplifiers are attached to opposite sides of a joint heat sink to reduce separate water cooling and optimize the design. This permits to enter in very small volume 100x200x350 mm. Each amplifier delivers 800 Watt P1dB CW RF power. The amplifiers are protected by two circulators and two 800 Watt RF resistors. This permits safe operation with full reflected RF power.

The following control signals are available from each amplifier:

- C max, normally high, low in case overheat.
- Temperature measurements, 10 mV / deg C.
- REF Power Detector Pout@800W 40ºC-1.5v.
- FWR Power DetectorPout@800W40ºC-1.5v.

This signals permits to monitor the status of each amplifier in the drawer.

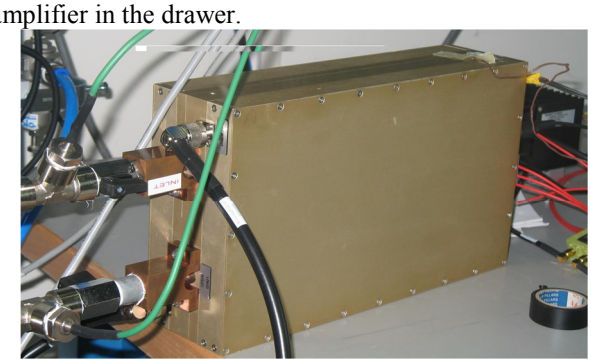

Figure 2: The double 800 W amplifier module view.

8 way 100 W RF Power Splitter

The splitter divides the driver's RF power into 8 equal signals to drive each of eight Power Amplifier modules up to 800 Watt. The splitter is designed by micro strip line technology and is mounted in aluminium milled case. The splitter was computer simulated and has very low loss and good matching. The RFin connector is N-type and 8 output connectors are SMA type.

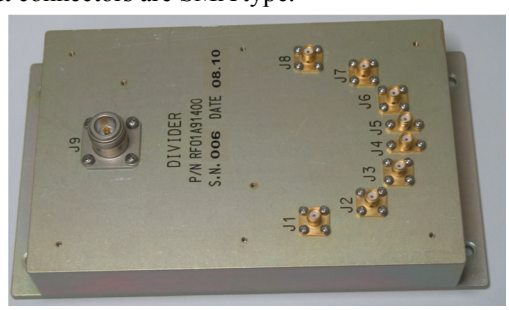

Figure 3: 8 way 100 W splitter (divider) view.

Copyright © 2012 by the respective authors — cc Creative Commons Attribution 3.0 (CC BY 3.0)

8 way 5.5 kW RF Power Combiner

The RF Power Combiner is summing the RF power of 800 Watt from 8 modules and applies the 5.5 kW into the output connector of the Combiner. The Combiner is built as a quarter wave air dielectric coaxial line technology. The combiner model was simulated using RFSim99 and has extremely low insertion loss (0.15 dB) and very good matching on the operating frequency 176 MHz . The 8 input connectors are special N-type – low loss and high power. The 7/8" EIA output connector is the part of the air dialectic coaxial line. Input to output port ratio is measured 9.03 dB; and returned loss is 66 dB at 176 MHz.

Figure 4: 5.5 kW 8 way Combiner view.

5.5 kW HPA RF conceptual diagram

The RF conceptual electrical diagram is shown on Fig. 1. RF input from driver is connected to the RFin on the rear panel. The RF cable delivers the 16 W driving signal to the N-type input of the 8 way RF Power Splitter. The Splitter divides 16 W into 8 equal 2 W signals. The equal length (phased) RG223/U cables connect the output SMA connectors of the RF Power Splitter to the RF input SMA connector of the eight RF Power Modules. The equal length (phased) H2000 cables connects the output N-type connectors of the RF Power Modules to the N-type input connectors of the RF Power Combiner. The 5.5 kW RF output connector 7/8" EIA is built in into RF Power Combiner. The Combiner is mounted on rear panel of the drawer, so that the connector is the Output Connector of the Drawer.

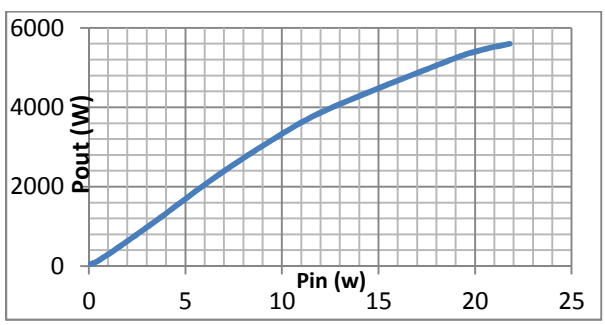

Figure 5: 5.5 kW drawer power test data graph.

5.5 kW HPA Drawer Assemblies

The 4 double RF power modules, RF Splitter , RF Power Combiner and some another components are assembled in 19" 7 U 550 mm long drawer. The drawer is purchased as a Kit. The front panel, rear panel and the mounting chassis were reconstructed. The Front panel includes: DC ON green Led, Fault red Led, water coolant quick pipe connectors and drawer handles. The Rear panel includes: 8 x 30 Ampere Breakers for current protection of 8 amplifier modules, N-type "RF in" connector, 7/8" EIA RF connector "RF output", DC Input bolts +/-50VDC, 200 Ampere with protection cover and control D-type connector. Four RF Double Power modules are mounted on chassis one aside one. Two six mm aluminium plates are placed on each two modules. One plate is the base of the splitter. Another is a base for two fans for air cooling of the combiner. The combiner is mounted on the rear panel and has two supports on each plate. The 12 mm plastic tubes connect the RF modules inlet and outlet with the water dividers 1:4, mounted on the front panel. Equal (phased) input RF cables RG223/U connects the input SMA connectors of the modules to the outputs of the splitter. The RF outputs of the modules are connected with equal (phased) H2000 cable to the combiner's N-type inputs.

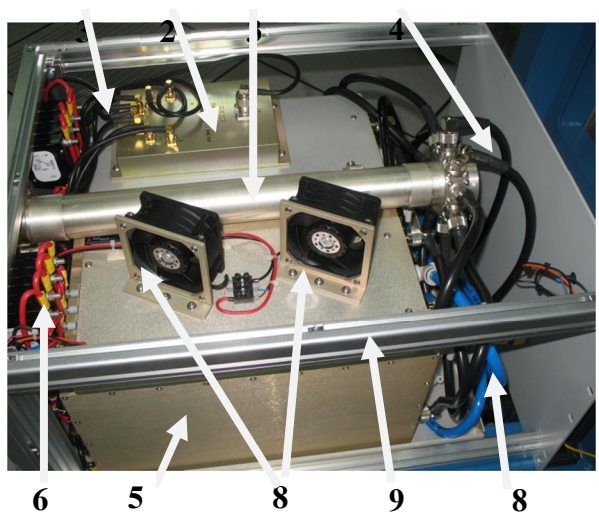

1. RF power splitter
2. RF power combiner
3. RF input RG232/U phased cables (equal length)
4. RF output H2000 phased cables (equal length)
5. Double 800 Watts module
6. 30 A DC breakers
7. Fans
8. Water coolant distributing pipes
9. Drawer aluminium frame

Figure 6: Inside view of the 5.5 kW drawer.

10 kW RF AMPLIFIER SYSTEM

The 10 kW system is built by combining the RF power from two 5.5 kW drawers using 3 dB 90º High Power Quad Hybrid Coupler (HPQHC). The HPQHC requires 90º shifted signals so the same kind coupler, but 100 W, is used as a splitter between the driver and the inputs of

Copyright © 2012 by the respective authors — cc Creative Commons Attribution 3.0 (CC BY 3.0)

the 5.5 kW amplifiers. The conceptual electrical diagram is presented in Fig. 7.

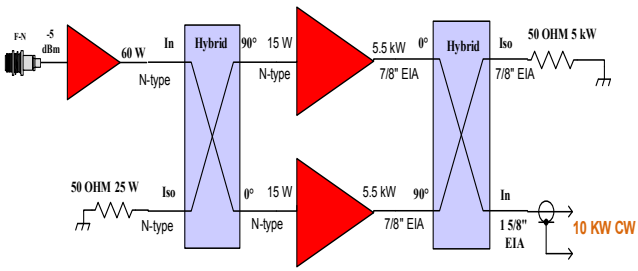

Figure 7: 10 kW HPA conceptual diagram.

The two amplifier system required a single 60 Watt driver. The driver is built from 100 Watt pallet with 2.5 Watt hybrid amplifier as the first stage. The total gain is 48 dB, so 0 dBm is enough to get the required 10 kW. The driver has a circulator in the output for better matching.

Figure 8: 60 W Driver inside view.

The driver case is mounted on cooper water cooled plate and has a thermal switch disconnecting voltage of the pallet and the hybrid if the temperature riches 50º C. The system is mounted in 25" 48 U Rack. Two 5.5 kW drawers, two 12 kW power supplies and Driver occupied 1/2 of 19" inner cage. The combiner and splitter are mounted on the sides of the 19" cage, as well as the cooling PVC pipes and valves. Two 10 kW systems will be installed in total 48" rack. The mains distributing board is mutual for two systems. First 10 kW system is recently tested and shows good linear results. See test data graph Fig.9.

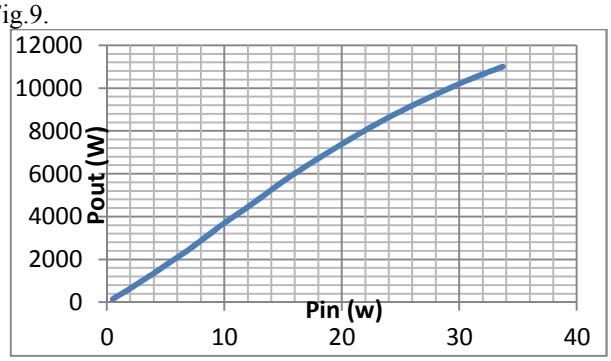

Figure 9: The 10 kW system test data graph.

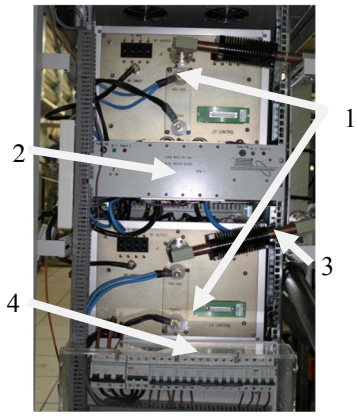

1 – 5.5 kW amplifier drawers
2 – 60 W driver
3 – 3 dB 90º hybrid combiner
4 – Mains electric board

Figure 10: 10 kW Amplifier system view.

15 kW RF AMPLIFIER SYSTEM

The 15 kW system is built by combining the RF power from three 5.5 kW drawers using 3:1 RF Power combiner.

The combiner is in phase type and has very low loss 0.3 dB and good isolation 22 dB. The electrical diagram is presented in Fig 11.

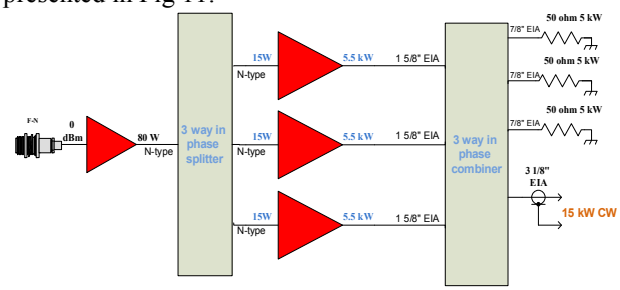

Figure 11: 15 kW HPA conceptual diagram.

The three amplifier system requires a single 80 Watt driver. The same driver as in 10 kW systems is used. The in phase type 1:3 splitter is installed in the driver 19" 2 U drawer.

The 15 kW system is installed in 25" 48 U Rack. Three 5.5 kW drawers, three 12 kW power supplies, Combiner and Driver occupied the total height of the 19" inner cage of the Rack. The inlet and outlet cooling pipes are on the sides of the cage. Equal length 1 5/8" rigid coaxial lines are connecting the Combiner with the RF output connector of the 5.5 kW drawers. Three 5 kW water cooled resistors mounted direct on the 7/8" EIA connectors in the rear of the combiner. The 3 1/8" EIA output connector is in the front of the Combiner and serves as the output connector of the 15 kW system.

SUMMARY

The 10 kW system is tested and shows good results.
The 15 kW system is now under advanced design.
The project is very low risk design and production.

Copyright © 2012 by the respective authors — cc Creative Commons Attribution 3.0 (CC BY 3.0)

COMPACT 4 kW VARIABLE RF POWER COUPLER FOR FRIB QUARTER-WAVE CAVITIES *

M.P. Kelly#, S.V. Kutsaev, Z.A. Conway, M. Kedzie,
ANL, Argonne, IL 60439, U.S.A.
J.L. Crisp, L.L. Harle, FRIB, East Lansing, Michigan, USA

Abstract

A new compact 4 kW power coupler has been designed and prototyped at Argonne National Laboratory in collaboration with Michigan State University. The coupler is intended for use on the β=0.085 80.5 MHz superconducting quarter-wave cavities for the FRIB driver linac and also for the ReA6 cryomodule using the same quarter wave cavity design. The coupler has a cold RF window and a 3 cm variable bellows section. The short 16 cm length of the RF window plus bellows facilitates a simple and compact clean room installation onto the cavity coupling port. A prototype has been fabricated in collaboration with U.S. industry and cold tested at 3 kW forward power under realistic operating conditions at Argonne. Simulation and test results are presented.

INTRODUCTION

The front-end of the superconducting linac for the Facility for Rare Isotope Beams (FRIB) at Michigan State University includes two different types of 80.5 MHz quarter-wave resonators (QWR's) operating with β=0.041 and β=0.085. [1] The rf power coupler will be the primary means of locking the cavity rf phase to a master oscillator in the presence of microphonics and, at the same time, will provide the required beam power. The proposed full β=0.085 cavity rf bandwidth is 40 Hz, with a corresponding total rf power of 2.5 kW. In order to provide reasonable margin, coupler specifications call for reliable coupler operation at 4 kW CW power under all conditions of reflection angle.

DESIGN APPROACH

As always, a coupler should reliably deliver rf power to the beam at the nominal Qext and also be suitable for other modes of operation such as cavity rf (pulse) conditioning. The coupler should not adversely impact cleanliness of the high-gradient SC cavities either in assembly or long-term operation. Considerations for the previously tested ANL 4 kW, 72 MHz coupler are similar [2], and the early 4 kW design served as the starting point for the new coupler. RF parameters are given in Table 1.

The modular design has four separate components. These include a variable bellows, a 'cold' rf window, a 55-to-300 K transition and a room temperature rf window. Both window assemblies are built around a donut-shaped alumina disc with a hole for the center conductor. The discs have been fabricated from alumina ceramic and brazed between the copper inner and outer conductors at MPF Products Inc.. The ceramic material was chosen for its good combination reliable brazing characteristics and good rf performance.

Adjustability of the center conductor by 3 cm into or out of the cavity coupling port is performed by compressing a cold bellows, formed from thin-walled stainless steel with 20 μm of copper deposited on the inner (rf) surface. The cold window is anchored to 55 K by circulating cold He

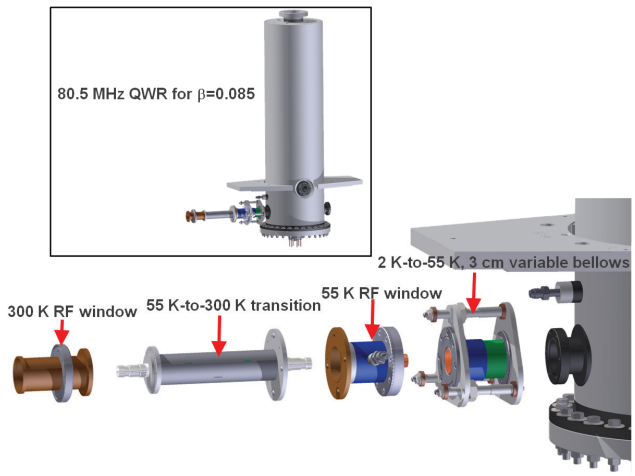

Figure 1: Prototype 4 kW coupler for FRIB quarter-wave cavity.

Table 1: Coupler Design Parameters

Parameter	Value
Nominal design power (kW)	4
Type	Coaxial capacitive
Outer diameter (cm)	4.1
Length (cm)	37
Impedance, nominal (Ω)	50
S11 @ 80.5 MHz (dB)	-31
Static load to 2K (W)	0.36
Static load to 55K (W)	4.1
Dynamic load to 2K (W)	0.15
Dynamic load to 55K (W)	8.4

* This work was supported by the U.S. Department of Energy, Office of High Energy Physics and Nuclear Physics, under Contract DE-AC02-76CH03000 and DE-AC02-06CH11357.
#mkelly@anl.gov

Copyright © 2012 by the respective authors — cc Creative Commons Attribution 3.0 (CC BY 3.0)

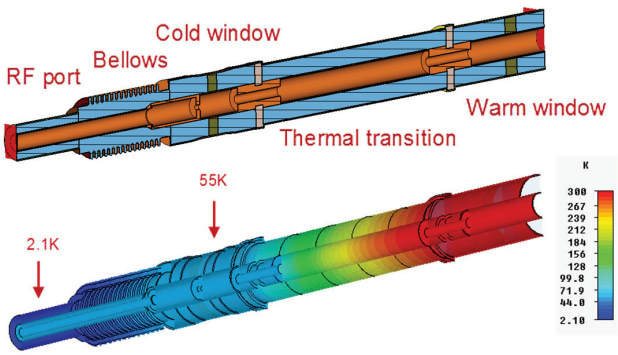

Figure 2: Coupler electromagnetic/thermal model in CST Studio for 4 kW forward power.

gas through the cold window assembly (see Figure 1). The ceramic window also separates cavity and cryomodule vacuum spaces. The center conductor is conductively cooled through the ceramic disc (λ~50 W/m-K at 55 K), so that the center conductor operates just above the intercept temperature of 55 K for all planned FRIB operating modes. The cold bellows and rf window are easily cleanable to the standards required for a clean SC cavity. The warm window, located near the wall of the cryomodule, separates the cryomodule vacuum from atmosphere.

FABRICATION

A pair of prototype couplers have been built and then tested at ANL on a 72.5 MHz QWR cavity. The cavity will be installed as part of an upgrade of ATLAS and is sufficiently close in terms of frequency to the FRIB QWR that rf performance should differ little. Fabrication for the MSU coupler also borrows heavily from techniques used for the ANL 72 MHz 4 kW coupler reported on previously [2].

Both warm and cold window assemblies are built around a 4 cm diameter, 6.4 mm thick alumina disc with a hole for the center conductor. The discs were in turn fabricated from 97.6% pure WESGO Al 300 alumina and brazed using a copper-gold alloy between the copper inner and outer conductors by MPF Products Inc. The ceramic material was chosen for its combination reliable brazing characteristics and good rf performance. For the cold window, a vacuum tight stainless vessel surrounds the outer conductor and is used to directly cool the outer conductor and the ceramic using circulating helium or liquid nitrogen.

The cold bellows assembly is made by TIG welding a thin- wall (150 μm thick) formed 321 stainless steel bellows directly into a pair of CF flanges (see Figure 1). A three post and bushing guide mechanism, both from 304 stainless steel, is located just outside the bellows/flange assembly. The posts and bushings are Dicronite coated to maintain clean, low friction sliding under vacuum and at cryogenic temperatures. Critically, the 20 μm of copper plating is deposited as the last fabrication step by Saporito

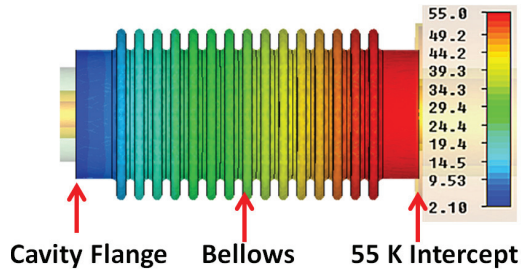

Figure 3: Temperature map for a copper-plated stainless steel bellows for P_{for}=4 kW in full reflection

Finishing. The necessity of the copper plating is discussed below.

ELECTROMAGNETIC AND THERMAL MODELS

To provide a large operating margin at the highest power levels of 4 kW, the electromagnetic and thermal analyses have been performed in CST studio. The intent is to design so that no part of the coupler approaches a condition where thermal runaway might occur. CST simulations have been checked analytically, where reasonable, to establish confidence in the results. Multipacting is not predicted to be a problem at 80.5 MHz in the range 0-4 kW. Even so, it can be suppressed by the straightforward application of a bias voltage to the center conductor [3].

Temperature dependent physical properties of the materials (copper, stainless steel, ceramic), including thermal conductivities, resistivities, and heat capacities have been modelled by breaking the CST 2011 model into discrete pieces. Results in Figure 2 and 3 (note that temperature scales are different) show no localized heating for the case of 4 kW forward power in full reflection and overcoupled. Generally, the coupler is far from overheating.

The low-conductivity thin-wall thermal transitions are the most susceptible to overheating since the thin wall 'thermal break' also reduces the capabilty to dissipate rf losses. Figure 3 shows a detailed view of the CST model for the cold bellows, which includes an accurate model for the 20 μm copper plating onto 150 μm of stainless steel. The copper cryogenic properties were taken to be those for OFHC copper. Higher accuracy could be gained with detailed knowledge of the composition of the copper plating. OFHC represents a middle ground in terms of thermal and electrical conductivity in the range of 2 K to 55 K.

For the case of 4 kW forward power in the overcoupled condition, the total calculated rf loss in the bellows was 260 mW, concentrated near the 55 K intercept due to the higher electrical resistivity at that temperature. Even so, the temperature gradient is smooth and monotonically changing and no significant heating is predicted. Since rf losses increase as the square root of the electrical resistance, an unplated stainless bellows would have losses roughly 15 times higher losses or about 4 W at 4

Copyright © 2012 by the respective authors — cc Creative Commons Attribution 3.0 (CC BY 3.0)

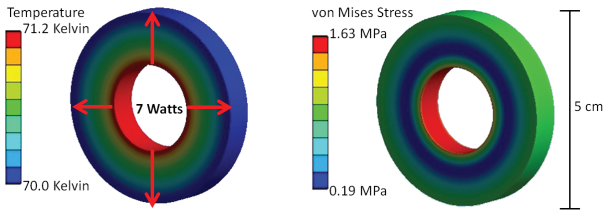

Figure 4: Internal stress in a ceramic window due to a temperature gradient.

kW forward power. More than half of the losses would go into 2 K helium and for this reason alone an unplated bellows at this diameter was not considered.

As discussed, both the warm and cold windows are fabricated from the 97.6% WESGO Al 300 alumina. To verify that the ceramic will operate far away from its physical and mechanical limits, ANSYS model simulations were performed to estimate the induced stresses in the ceramic due to (cyclic) temperature gradients. ANSYS permits the direct incorporation of temperature dependent thermal conductivity, Young's modulus and Poisson's ratio. Here, values were taken from the Ref [4]. The model in Figure 4. is a slightly more demanding case than anticipated for the FRIB coupler, with a 5 cm diameter ceramic and a higher radial heat flow (7 W versus 2 Watts). For this case the temperature gradient is 1.2 K and the maximum von Mises stress of 1.6 MPa is located at the inner diameter of the ceramic. This value is about 100 times lower that the values (120-220 MPa) where cyclic fatigue loading has been shown to be important. It does indicate that cooling the ceramic very rapidly, by immersing in liquid nitrogen, should be avoided.

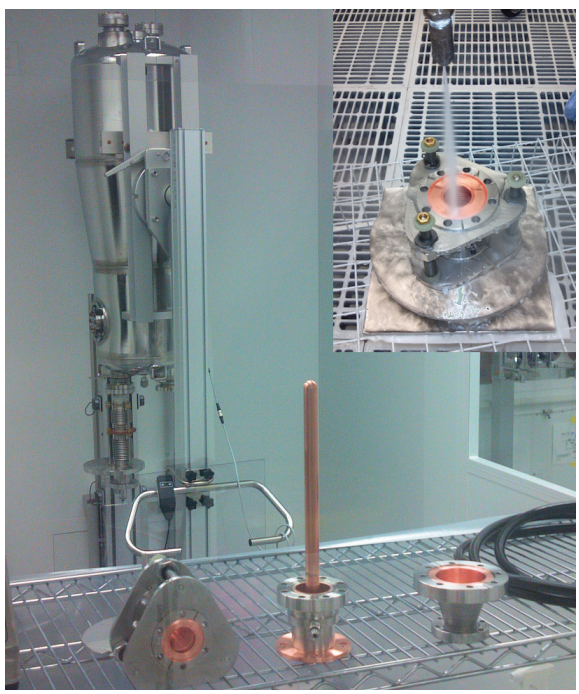

Figure 5: Prototype bellows assembly (inset) and cold window in the clean room

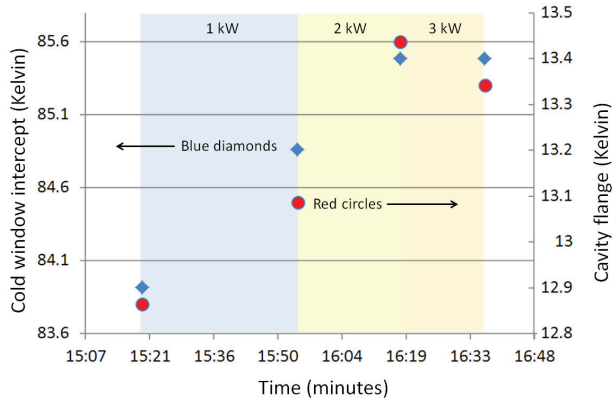

Figure 6: Thermometry for cold rf testing.

CLEAN ASSEMBLY AND TESTING

The copper plated bellows assembly and the cold window were manually high-pressure rinsed and assembled in the clean room as shown in Figure 5. Particulate measurements performed using a Climet model 750i particle counter placed below the parts with air flow from above indicate components are cleanable consistent with ISO class 5 standards.

The coupler assembly was tested cold with forward power levels of 1-3 kW. For these tests the cavity temperature was 4 K and the intercept was at 80 K. Results of temperature measurements are shown in Figure 6. The temperature rise at the 80 K intercept of 2 degrees corresponds to a heat load of 2.5 W, as determined using a reference heater. Similarly, at the cavity coupler flange the heat load was 120 mW. Both values are about 30% lower than the CST predictions, a difference not unexpected due to uncertainty in the copper cryogenic properties which are very sensitive to purity.

CONCLUSION

A pair of prototype power couplers intended for the MSU/FRIB β=0.085 QWR's have been designed, simulated, built and tested at ANL. RF performance on a cavity with up to 3 kW forward power is in good agreement with simulations. The coupler should provide ample performance margin for planned operating conditions at FRIB.

REFERENCES

[1] A. Facco et al, "Superconducting Resontators Development for the FRIB and ReA LINACS at MSU: Recent Achievements and Future Goals", Proc. of the IPAC'12, New Orleans, Lousianna, May 2012

[2] M.P. Kelly et al, "A New Fast Tuning System for the ATLAS Intensity Upgrade Cryomodule", Proc. of PAC'11, New York, NY, March 2011

[3] S.V. Kutsaev et al, "Electromagnetic Design for a 15 kW CW RF Input Coupler, "Proc. of the IPAC'12, New Orleans, Lousianna, May 2012

[4] P. Auerkari, "Mechanical and physical properties of engineering alumina ceramics" , Espoo 1996

Copyright © 2012 by the respective authors — cc Creative Commons Attribution 3.0 (CC BY 3.0)

HIGH POWER TESTS OF TRASCO RFQ COUPLERS

E. Fagotti, F. Grespan, L. Antoniazzi, A. Palmieri, F. Scarpa, INFN/LNL, Legnaro, Italy
M. Desmons, CEA, Saclay, France
O. Brunasso Cattarello, R. Panero, INFN, Torino, Italy

Abstract

The TRASCO RFQ is powered by eight coaxial power couplers, magnetically coupled to the cavity by a loop-antenna. Couplers were designed to support up to 140 kW in cw operation. After a test-stand validation with a 10 kW power amplifier in Legnaro, the system was tested up to full power at CEA-Saclay. This paper covers the main steps of the coupler validation and conditioning results.

INTRODUCTION AND LOW POWER TESTS AT LNL

Two RF couplers were constructed based on the design developed in [1]. The RF coupler consists of the drive loop, the coaxial transmission line (inner diameter 19.4 mm, outer diameter 38 mm) and its associated cooling channels, and the coaxial alumina window (Figure 1).

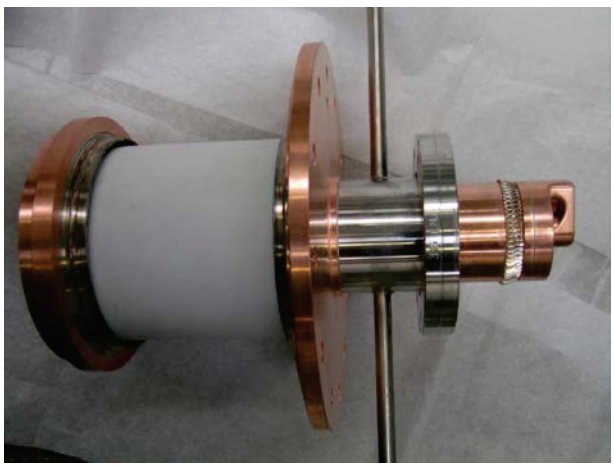

Figure 1: RF coupler system with loop, coaxial transmission line and coaxial alumina window.

In order to match the impedance of the coaxial line with the WR2300 waveguide used for the RF distribution, a "half doorknob" matching device is employed. The relatively small dimension of the coupler is determined by the 57 mm diameter of the RFQ port, in turn due to the small cross-sectional construction of the RFQ structure. The inner conductor of the loop is cooled via a coaxial SS tube and the outer conductor with a cooling SS sleeve. In particular, the CU OFE (inner coaxial, outer coaxial and drive loop) and the LN316 (flange and cooling sleeves) sub-assemblies were constructed and cleaned separately and then brazed together in a single brazing step. Prior to the brazing, the dimensions of the loop were determined after a set of measurements performed on the first two modules of the RFQ with on-purpose built aluminium dummy couplers. Finally, the cylindrical RF alumina windows were TIG welded on the coupler body. Such windows are the same used for the NC LEP couplers and can withstand up to 140 kW CW RF power.

In order to allow the RF processing of the couplers a bridge waveguide cavity was employed. Such cavity is made with aluminium and is water cooled through the cooling sleeves on its walls. An aluminium strip acts both as RF joint and vacuum seal. The cavity has two ports in order to allow the conditioning of two couplers, one connected to the RF source and the other connected to the load, with minimum reflection (RL=-15 dB). HFSS simulations showed that about 30% of the input power is dissipated on the cavity walls. Figure 2 shows the couplers connected with the bridge cavity.

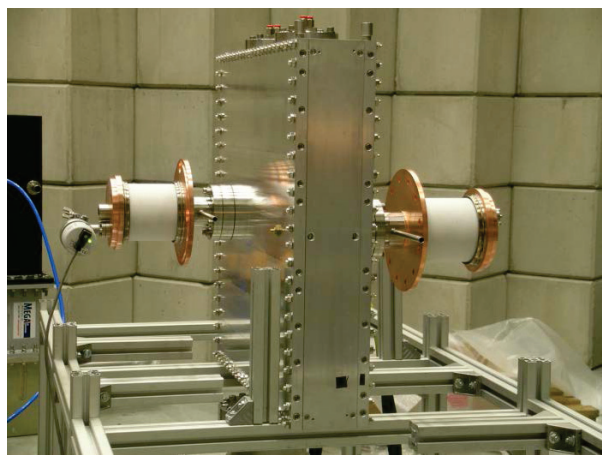

Figure 2: View of the two couplers connected with the bridge cavity. It is possible to notice the cooling channels and the RF windows.

A dedicated low power test-stand was installed at LNL for system validation, in which the RF source was provided by a 10 kW solid state amplifier. Before the final assembly, the coupler components were cleaned; the two couplers were inserted in the bridge cavity and baked out under vacuum with a maximum temperature of 150°C. During this baking process, one of the O-rings used to close the interface SS flange on the bridge cavity experienced problems at high temperature and started melting. The problem was not discovered during this test, because no vacuum analysis was available at the time and the O-ring melting had no impact on the vacuum level (later, it came out that the O-ring was not made of Viton®, as requested, but of NBR). However, after baking, a vacuum level of 1.9×10^{-8} mbar at the ceramic window location was measured.

The test in pulsed mode with 20 μs pulse length and a 500 ms repetition period started in March 2011. The power was increased from 100 W up to 9.5 kW playing

Copyright © 2012 by the respective authors — cc Creative Commons Attribution 3.0 (CC BY 3.0)

with pulse length and repetition rate in order to speed up conditioning time. Two power levels required some hours conditioning time in pulsed mode: 400 W and 2 kW. Once these two levels were conditioned, CW operation was reached at 1 kW in few minutes and then power was increased up to 2 kW CW. At this point, power was raised with a 1.1 ms pulse length and 50 ms period length, thus reaching 9.5 kW in a short time. After conditioning in pulsed mode, CW operation at 8 kW was reached without any problem in a few minutes. The two observed multipacting levels were foreseen with Multipacting Calculator code with a 10% error.

HIGH POWER TESTS AT CEA SACLAY

After low power tests at Legnaro, the coupler test stand was disassembled and reassembled at CEA/Saclay (France). This installation differs from the previous one for the power amplifier, the RF distribution up to the coupler waveguide and for the power load. In particular, a 1 MW power klystron was used. The RF distribution consisted of a long WR2300 waveguide path connected to the coupler test system through a taper and a half height bellow. The power exiting from the bridge cavity via the output coupler was collected by a 100 kW coaxial water load (Figure 3).

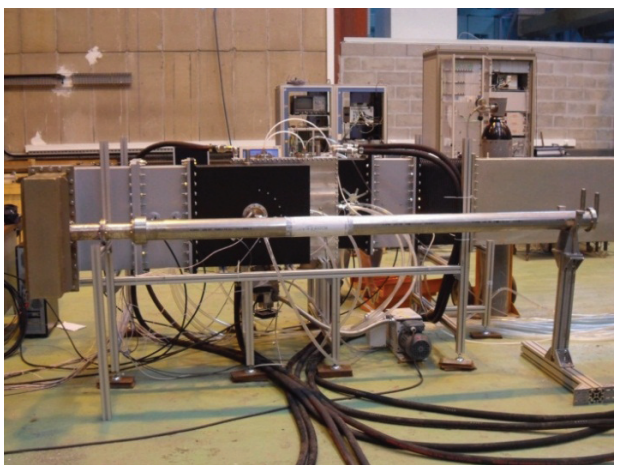

Figure 3: The RF couplers test stand assembled at CEA Saclay

The diagnostics equipment of the test stand included: forward and reflected power detection for both couplers, vacuum level on the two couplers in correspondence of the vacuum gauges placed on the top of the coaxial line, temperatures on the critical parts of the bridge cavity, of the couplers and of the water load, arc detectors placed in correspondence of the two RF windows on the air side and arc detectors placed on bridge cavity in front of couplers loops. Due to the fact that the power on the coupler connected to the load was less than the power on the drive coupler, the conditioning proceeded in two steps. In the first step, one of the couplers was conditioned up to 140 kW and the second one at 100 kW. In the second step the couplers configuration was reversed and the second couplers was conditioned up to 140 kW.

The Local Control System (LCS) manages data acquisition and storage, as well as diagnostics and interlock managements. Data acquisition and storage was performed by Siemens® S7-300 PLC connected via ethernet to a PC equipped with the HMI. The HMI, which includes archive functions, was developed with the software *WinCC*. In pulsed mode RF power levels had to be acquired in time correspondence with the power pulses. In order to do that, a particular PLC synchronization procedure was developed. In this way, it was possible to take measurements with an update frequency up to 50 Hz, for power pulses with width greater than 1.07 ms. For shorter pulse length the readings were taken manually, by looking at the vacuum controllers and the oscilloscope. As for interlocks is concerned, the LCS permits to set thresholds for vacuum, forward and reflected powers and temperatures, which, once they are overcome, the slow interlock (100 ms) is fired and RF power is cut, while the threshold value is overcome. As for arc detection, once an arc is detected, the fast interlock (few μs) directly connected with the klystron input cuts the RF drive signal, and permits the recovery of the RF power in 100 ms.

As a general rule, the conditioning rate was paced by the vacuum level or multipacting. As the duty cycle was increased, the presence of vacuum instabilities (typically above 10^{-6} mbar) drove the maintenance of the pulse length and rep rate up to re-establishment of the baseline vacuum level (from 10^{-7} mbar to 10^{-6} mbar depending on the average RF power). In case the vacuum instability was persistent, typically the pulse length was decreased in order to limit the outgassing activity before proceeding with higher power levels. In any case, during the absence of the operator overnight, the system was always left in a stable condition (no vacuum instabilities). As for multipacting is concerned, in addition to the level already conditioned at LNL, another level associated with the bridge cavity (also predicted by calculations) appeared at about 90 kW. The usage of short pulses in the order of 20 μs with 1 to 10 Hz rep rate allowed the conditioning of these levels, too.

Conditioning started on June 27th and, during the first part of the process, power was fed at very low duty cycle (0.05% at maximum) in full reflection conditions. This was caused by the lack of water in the load. After fixing the problem, full transmission was obtained with a reflected power at the first coupler of about 5%. This value was in perfect agreement with HFSS simulations. In this condition, the entire power range up to 155 kW peak power was explored with up to 2% duty cycle on June 30th. On the following day, the duty cycle was set to CW and the power was raised from 5 kW up to 116 kW. In this condition, the vacuum level did not exceed $4*10^{-6}$ mbar for most of the time.

The conditioning resumed at the end of July, but due to some issues involving the PLC cards of the LCS, it was only possible to act manually. In this session, the

Copyright © 2012 by the respective authors — cc Creative Commons Attribution 3.0 (CC BY 3.0)

conditioning proceeded up to 75 kW average power. Above 130 kW peak power, outgassing phenomena up to 10^{-4} mbar and discharge events increased strongly. An enhancement of the radiation emitted by the cavity also appeared and this forced the improvement of lead shielding configuration. At power stop, the problem of the melted O-ring appeared. The system recovered in two hours, but it was decided to stop the conditioning and to start again after summer.

After the summer break and a period of scheduled maintenance of the CEA test stand cooling system, operations resumed on October 21st with 100 ms rep rate and with pulse length up to 0.5 ms up to the nominal power. Then RF pulse duration was increased on October 25th up to CW and 140 kW. At this point, in the afternoon of the same day, a series of severe arcs occurred and consequently the vacuum level deteriorated up to $5*10^{-5}$ mbar. This phenomenon forced the conditioning to restart by drastically reducing the pulse duration to 0.15 ms up to 7 ms and by ramping again the RF power from 30 kW to 140 kW on the following three days.

In the following week, RF average power was gradually increased, both by increasing pulse length and peak power. In Figure 4 it is possible to see the conditioning results between Nov 7th and Nov 10th.

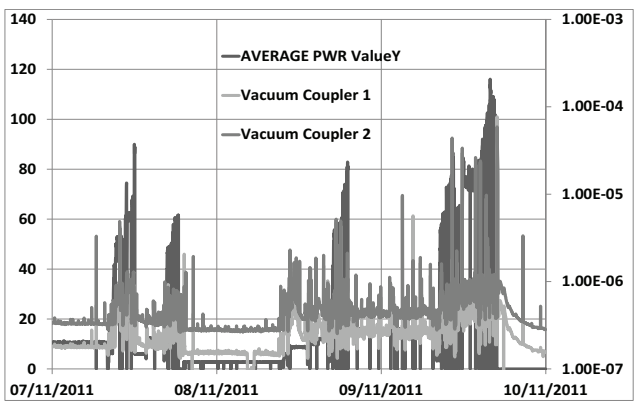

Figure 4: The average power and the vacuum level in the two couplers vs time.

On the following week, it was finally possible to get the nominal value of 140 kW for a run of some hours.

At this point, the system was disassembled to reverse coupler configuration. While the coupler close to the water load did not present any particular problem, the coupler conditioned at high power showed a strong aluminum sputtering on external surface. The problem can be explained in the following way: the melted O-ring was responsible for the vacuum tightness very near to the zone where the problem appears. In the same point the RF seal is present. As the SS flange and the aluminum cavity experience a thermal cycling due to average power variation, the bad vacuum seal due to the melted NBR O-ring causes some gas to penetrate in the zone of the RF seal. During conditioning, electric field penetrated in a region with poor vacuum, caused by the damaged O-ring, in which free electrons generated by aluminum oxide as well as brazing material in the brazing groove were present. This fact generated sparks at high values of electric field and aluminum sputtering on the copper surface (Figure 5), as already observed in July 2011. Moreover, since HFSS simulations showed that H field on the RF seal zone was equal to about 7000 A/m at 150 kW input power, during a discharge the current on a louver is likely to overcome the maximum design current of 1500 A. This caused a deterioration of the contact resistance of the seal itself and therefore a non-zero voltage across the gap between the coupler and the bridge cavity port that could enhance electron emission and sputtering on the copper.

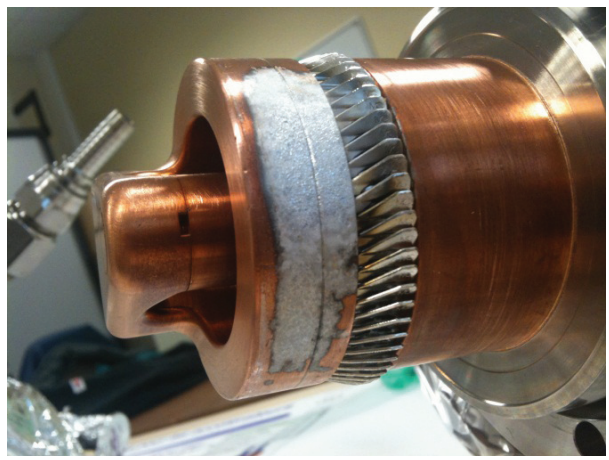

Figure 5: Particular of the coupler after the tests: the aluminum sputtering on the copper surface and the damaged spring contact are visible.

In order to mitigate the problem during conditioning of the reversed configuration, the vacuum threshold on the coupler was decreased and the recovery time after vacuum interlock was extended. With this new procedure, the conditioning of the second coupler was fast and with fewer sparks and the nominal power was reached as well.

CONCLUSIONS

Both the couplers were successfully tested up to nominal power and then they were used for the high power tests on the RFQ [2]. It should be noted that the issues met during conditioning were mainly due to a component, the O-ring, not pertaining to the coupler itself. Anyway, in order to improve reliability of the coupler itself, it will be necessary to improve the RF joint and, more generally, the interface volume between the coaxial and the RFQ body in terms of vacuum and field strength.

REFERENCES

[1] A. Palmieri et al, "Study and design for TRASCO RFQ high power coupler", LINAC'02, Gyeongju, August 2002, TH453, p.722 (2002), http://www.jacow.org.

[2] E. Fagotti et al., "High Power RF Conditioning of the TRASCO RFQ", THPB040, these proceedings.

Copyright © 2012 by the respective authors — cc Creative Commons Attribution 3.0 (CC BY 3.0)

DESIGN OF COUPLER FOR DIRECT COUPLED AMPLIFIER TO DRIFT TUBE LINAC CAVITIES OF THE INJECTOR RILAC2 FOR RIKEN RI BEAM FACTORY

K. Suda*, S. Arai, Y. Chiba, O. Kamigaito, M. Kase, H. Okuno, N. Sakamoto, Y. Watanabe, K. Yamada
RIKEN Nishina Center for Accelerator-Based Science, Wako-shi, Saitama, Japan

Abstract

Drift Tube Linac cavities for the new injector RILAC2 for RIKEN RI-Beam Factory were designed and constructed. To reduce an installation area and cost, we adopted a direct coupling method for a power amplifier to the cavity without using a long transmission line. A change of resonant frequency of the cavity caused by the coupler and amplifier must be accurately taken into account. The lumped element circuit model was not sufficient to estimate such a change. A complicated design procedure for the coupler and cavity was performed using a three-dimensional electromagnetic calculation software. The required input impedance seen from the amplifier was successfully achieved.

INTRODUCTION

The new heavy-ion linac RILAC2 was successfully constructed and commissioned at RIKEN RI Beam Factory [1, 2]. The main part of the accelerating cavity consists of three drift tube linac (DTL) cavities, operate in continuous wave mode at a fixed frequency of 36.5 MHz. Their structure is a quarter wavelength resonator because the size of the resonator is the smallest available in this frequency range. In order to reduce an installation area further, and to save a construction cost, we adopted a direct coupling method for a power amplifier to each DTL cavity without using a long transmission line. However, the direct coupling of the power amplifier changes the resonant frequency of the coupled system considerably from that of the cavity itself. Thus, the cavity design is dependent on that for the amplifier. Therefore, a detailed cavity and coupler design was carried out by using the three-dimensional electromagnetic calculation software, CST Microwave Studio (MWS).

REQUIRED PERFORMANCES FOR DTL CAVITIES

The design parameters of DTL cavities as determined by beam dynamics calculations [3] are listed in Table 1. The required gap voltages were 110, 210, and 260 kV for DTL1, DTL2, and DTL3, respectively. The height and diameter of the cavity to be used were required to be less than 3 m and 1.3 m, respectively, due to space restrictions in the AVF cyclotron hall. Each cavity consists of an outer and inner conductor, drift tubes, a capacitive coupler, and a capacitive tuner. The amplifiers for the three DTLs were based on the tetrode 4CW50,000E (Eimac). Their maximum output powers were 25, 40, and 40 kW for the respective DTLs. The required gap voltages were obtained when the parallel shunt impedances of each cavity are higher than 1.1 M Ω. The first two cavities (DTL1 and DTL2) were newly constructed, while the DTL3 cavity was modified from the decelerating cavity of the Charge State Multiplier (CSM) [4]. The design of the cavity without a coupler and amplifier was performed by MWS [5].

Table 1: Design Parameters for DTL Cavities

Cavity	DTL1	DTL2	DTL3
Frequency (MHz)	36.5	36.5	36.5
Duty (%)	100	100	100
Mass-to-charge ratio	7	7	7
Input energy (keV/u)	100	220	450
Output energy (keV/u)	220	450	670
Diameter (m)	0.8	1.1	1.3
Height (m)	1.32	1.429	1.890
Gap number	10	10	8
Gap length (mm)	20	50	65
Gap Voltage (kV)	110	210	260
Drift tube aperture radius (mm)	17.5	17.5	17.5
Peak surface field (MV/m)	8.9	12.3	13.7
Synchronous phase (°)	−25	−25	−25
Power amp. (Maximum: kW)	25	40	40

AMPLIFIER DIRECT COUPLING

Figure 1 shows images of the amplifiers and coupler, coupled to the DTL3 cavity. The RF coupler consists of

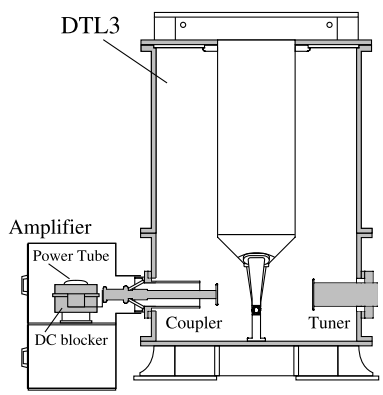

Figure 1: Schematic of the amplifiers coupled to cavity of DTL3. The output from the amplifier is directly connected to the coupler through a capacitor (DC blocker).

* ksuda@ribf.riken.jp

Copyright © 2012 by the respective authors — cc Creative Commons Attribution 3.0 (CC BY 3.0)

a non-50 Ω coaxial cylinder and a coupler disk attached to the tip of the inner cylinder. A position of the inner cylinder is manually adjustable within ± 20 mm to tune input impedance.

The standard method is that an output impedance of the amplifier is matched to 50 Ω using a stub and an output capacitor. As compared with that, the direct coupling method of the power amplifier to the cavity reduces the number of the parts used in the amplifier. Thus its cost and size are reduced. However, it is required to match the input impedance to the cavity taking into account the capacity of the tetrode as well as the characteristic impedance and length of the coaxial part. The resonant frequency changes considerably by a value more than that for the case of the standard method. In particular, the assumed tunable frequency range of the capacitive tuner for DTL3 was ±0.6% (±220 kHz). To tune the resonant frequency of the whole system within the range, the frequency of the cavity alone should be within a third of it (±73 kHz). It means that, in the design of the cavity, the calculation of the resonant frequency of the cavity must be performed with an accuracy of ±0.2 %.

DESIGN OF RF COUPLER

We first tried to calculate frequency changes due to a direct coupling scheme by using a lumped element circuit. The circuit model for the direct coupled system is shown in Fig. 2. Here, $Z_{cav}, C_{cpl}, Z_w, l, C_p$, and L_{choke}

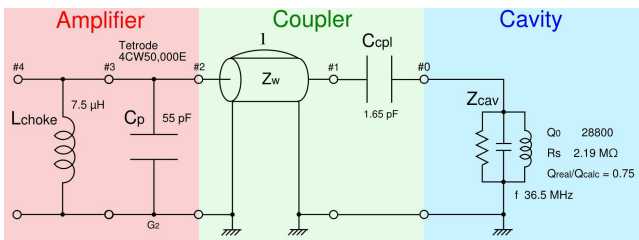

Figure 2: Lumped circuit element diagram of the coupled system of the amplifier, coupler, and cavity of DTL3.

denote the impedance of the cavity, coupling capacitance, impedance and length of the coaxial line, parallel capacitance of the tetrode, and parallel inductance of the choke coil, respectively. The optimum input impedance seen from #4 is 700–1100 Ω, which corresponds to the optimum output impedance of the tetrode. The frequency of the cavity alone was temporarily set to be 36.5 MHz, the actual value of Q_0 was assumed to be 75% of the calculated value, and C_p was 55 pF as obtained from the specification sheet of the tetrode. The input impedance was matched when C_{cpl} was 1.65 pF, where the frequency change was −458 kHz. The lumped element circuit calculation overestimated the frequency change (c.f. actual change is ∼ −300 kHz).

The lumped element circuit model calculation was also performed with a 50-Ω coupler system. The impedance seen from #2 in Fig. 2 was calculated assuming $Z_w = 50\Omega$, $l = 1700$ mm, and the resonant frequency of the cavity alone was 36.975 MHz. The input impedance was matched to 50 Ω when C_{cpl} was 0.5 pF. The calculated input impedances are shown in Fig. 3 as well as the measured data. The frequency change by the coupling was −162 kHz for the lumped element circuit calculation, whereas −30 kHz for the measured data. The lumped element circuit calculation overestimated again the actual value by a factor of more than five. The result of the MWS frequency domain solver shows a poor agreement of the frequency change (+78 kHz), however, the distribution of the impedance was well reproduced. The frequency change was more precisely calculated by using the MWS eigenmode solver. The frequency change by the eigenmode solver was −21 kHz, which was close to the measured value. Therefore, by combining the frequency domain and eigenmode solver of the MWS, the coupled system of the coupler and cavity can be designed. The tetrode, which was difficult to be treated in MWS, was taken into account by a method of the lumped circuit element.

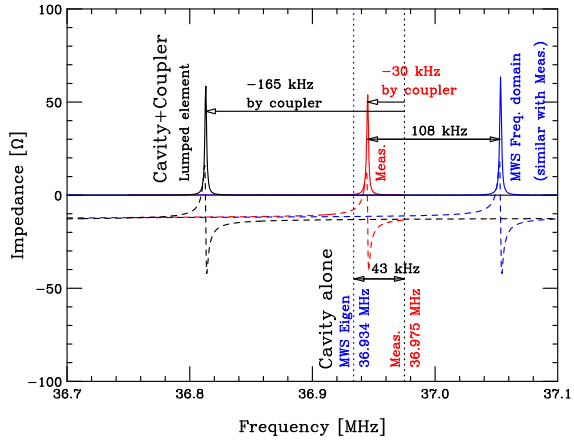

Figure 3: Input impedance for 50 Ω-coupler calculated by lumped circuit element. The real and imaginary parts of the input impedance are shown by solid and broken lines, respectively. The measured values are shown by red lines.

DETERMINATION OF COUPLING STRENGTH AND CAVITY HEIGHT

Input impedances were calculated by using the frequency domain solver of MWS. The calculations with MWS were performed without accounting for the tetrode, and subsequently, the tetrode was taken into account as a parallel capacitor by the method of lumped element circuits. In order to simulate the ratio of the Q_0 factor (78% of the ideal value), the electric conductivity was set to be 61 % of the conductivity of copper ($5.8 \times 10^7 \times 0.78^2 = 3.53 \times 10^7$ [S/m]). The tuner position measured from the center of the cavity was set at 362.8 mm, at which distance the frequency attained the center of its variable range. To determine the coupling strength, calculations were performed by varying the diameter of the coupling disk from 110 to 170 mm. The impedances without the tetrode are plotted

Copyright © 2012 by the respective authors — cc Creative Commons Attribution 3.0 (CC BY 3.0)

on a Smith chart in Fig. 4. Without the tetrode, the desired impedance Z' is written as $1/Z' = 1/700 - j\omega C_p$. The plot of impedances against frequency is shown in

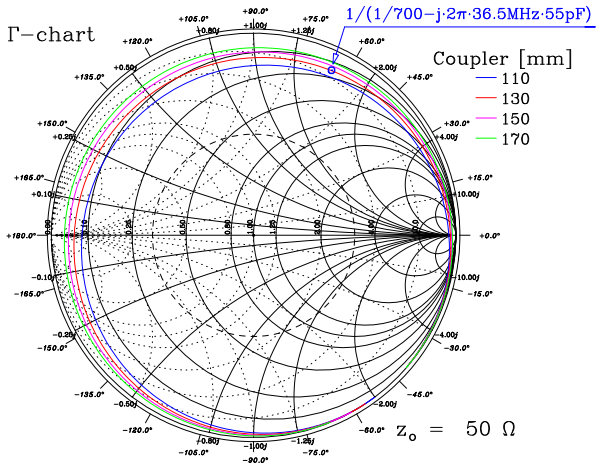

Figure 4: Calculated input impedance without the tetrode shown in a Smith chart. Desired impedance Z' is shown by a blue circle.

Fig. 5. The impedance with the tetrode was calculated with $1/Z = 1/Z' + j\omega C_p$. The calculations showed the frequency change by the coupler was −290 kHz, and the change by the tetrode was −19 kHz (−309 kHz in total). The input impedance was calculated to be 750 Ω, which was close to the desired value of 700 Ω. The size

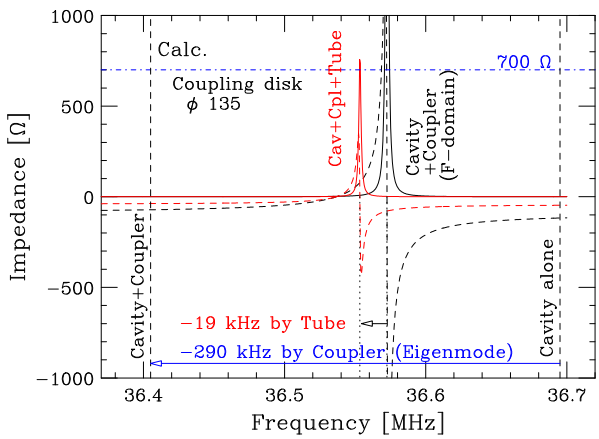

Figure 5: Calculated input impedances for DTL3 with the coupling disk of ϕ 135 mm. Black solid and broken lines indicate the real and imaginary impedances, respectively, for the case without the tetrode. Red solid and broken lines denote the real and imaginary impedances, respectively, when the tetrode was attached in parallel as a lumped element.

of the coupling disk was finely tuned by measuring the impedance with the actual cavity. Figure 6 shows the measured impedance with a coupling disk of ϕ130 mm. The input impedance was 690 Ω at 36.5 MHz. The frequency changes by the coupling of the coupler and tetrode agreed well with the calculation.

Based on these results, the cavity height was determined as follows. The frequency of the cavity alone was set to

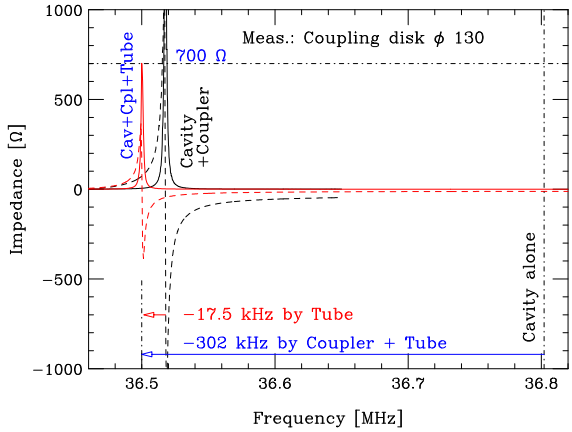

Figure 6: Measured coupling impedances for DTL3 with the coupling disk of ϕ130 mm. The notation is the same as that in Fig. 5.

be 36.725 MHz (0.225 MHz higher than the required frequency of 36.5 MHz). When the CSM cavity was modified to DTL3, a movable shorting plate was removed, and a flange was attached between the inner conductor and the top plate. The frequency was estimated to be increased by 0.125 MHz using the eigenmode solver. Based on the relation between the cavity height and frequency measured before the modification, the cavity height of DTL3 was determined to be 1890 mm (Fig. 7).

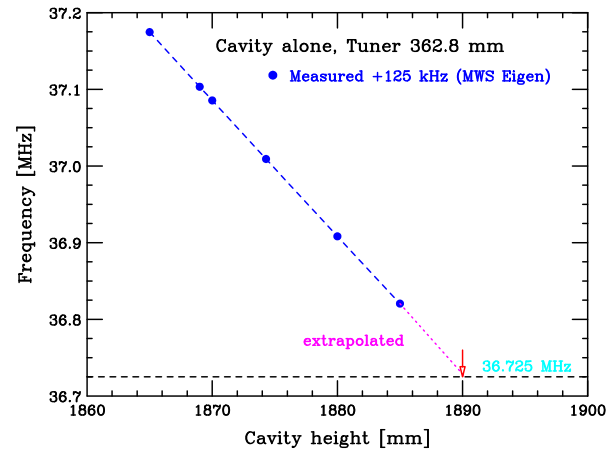

Figure 7: Measured resonant frequency of DTL3 with a movable shorting plate. The frequency shift caused by a removal of the shorting plate (0.125 MHz) is taken into account.

REFERENCES

[1] K. Yamada et al., Proc. IPAC'12, TUOBA02, 1071 (2012).

[2] N. Sakamoto et al., Proc LINAC12, MO3A02 (2012).

[3] O. Kamigaito et al., Proc. PASJ6, WOOPD02, 38 (2009).

[4] O. Kamigaito et al., Rev. Sci. Instrum. **76**, 013306 (2005).

[5] K. Suda et al., Proc. IPAC'10, THPEA023, 3726 (2010).

Copyright © 2012 by the respective authors — cc Creative Commons Attribution 3.0 (CC BY 3.0)

THE C-BAND RF PULSE COMPRESSION FOR SOFT XFEL AT SINAP

W.C. Wang, Z.T. Zhao, Q. Gu, SINAP, Shanghai, China

Abstract

A compact soft X-ray free electron laser facility is presently being constructed at Shanghai Institute of Applied Physics Chinese Academy of Science (SINAP) in 2012 and will be accomplished in 2014. This facility will be located to the shanghai synchrotron radiation facility (SSRF) which is a third generation light source in china. It requires a compact linac with a high-gradient accelerating structure for a limited overall length less than 230m.The c-band technology which is already used in KEK/Spring-8 linear accelerator is a good compromise for this compact facility and a c-and traveling-wave accelerating structure was already fabricated and tested at SINAP[1], and a c-band pulse compression will be required. There are some reasons, why RF pulse compression devices are quite useful to be applied in RF power supply of the soft XFEL. For it can enhance the peak RF power by expense of RF pulse length, so it will not increase the average power and at the same time reduce the total number of the klystron, it also increases the gradient of the accelerating structure, so we need the c-band pulse compressor. AND a SLED type RF pulse compression scheme is proposed for the C-band RF system of the soft XFEL and this scheme uses TE0.1.15 mode energy storage cavity for high Q-energy storage.

The C-band pulse compression under development at SINAP has a high power gain about 3.1 and it is designed to compress the pulse width from 2.5μs to 0.5μs and multiply the input RF power of 50MW to generate 160MW peak RF power, and the coupling coefficient will be 8.5. It has three components: 3-dB coupler, mode convertors and the resonant cavities. In this paper C-band pulse compression and some components for the c-band pulse compression will be described.

INTRODUCTION

The future c-band accelerator structure of SXFEL is supposed to operate at high acceleration gradient about 40MeV per meter, this requires very high peak RF power about 160MW at frequencies 5712MHz. So as to reduce the total number of the klystron and enhance the peak RF power, the RF pulse compression is needed.

RF pulse compression is one of the methods to compress the RF pulse length and at the same time increase the peak RF power that klystron deliver. RF pulse compression is based on the principle that the RF pulse is stored in a resonance cavity or a delay line and emitted within a short time to create the short RF pulse with high peak power and then deliver it into accelerating section. At present, several RF pulse compressions systems have been already utilized successfully in the s-band or c-band linear accelerator, such RF pulse compression, the SLAC Energy Double (SLED) was the first, it was successfully applied in SLC operation, and now SLED-I，SLED-II，SLED-III（coupled cavities），BPC，DLDS and VPM（BOC）were already developed.

BPC，SLED-II and DLDS use the delay line as the energy storage cavity, have the flat output, high power gain and high efficiency, but the delay line is long and not economical. SLED-III（coupled cavities）use coupled cavities as the energy storage cavity, reduce the length of the delay line, but the output power irregular. It is applied a complex amplitude modulation on the input RF power, it is hard to control the accuracy and the stable. SLED-I has the simple structure and work stable, but it has the low power gain and less efficiency and a decaying exponential output pulse shape, so the technology AM-PM is applied for the flat output pulse shape.

In the soft XFEL, the design goal of the pulse compression is to compress the pulse width from 2.5μs to 0.5μs and to multiply the input RF power of 50MW to generate 160MW peak RF power. To satisfy this requirement for the soft XFEL, we adopted a SLED type pulse compression as the c-band pulse compressor. This scheme use TE0.1.15 mode for the storage cavity to compress an RF pulse into a short square high peak-power pulse for the course of R＆D study of the soft XFEL. Figure 1 shows the schematic diagram. This scheme consists of one 3-db coupler, two mode convertors, and a pair of high-Q resonant cavities.

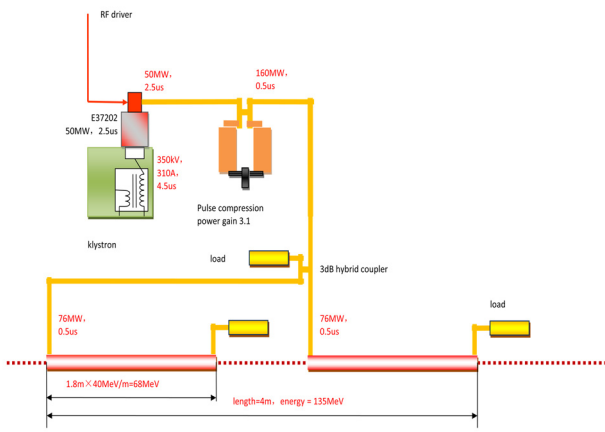

Figure1: C-band 50WM RF Scheme.

C-BAND PULSE COMPRESSOR

C-band Pulse Compressor

For the SLED type RF pulse compression, the expression of the power for the resonant cavity is[2]

$$T_C \frac{dE_e}{dt} + E_e = -\alpha E_K \quad (1)$$

Copyright © 2012 by the respective authors — cc Creative Commons Attribution 3.0 (CC BY 3.0)

where $\alpha = 2\beta/(1+\beta)$, $T_c = \frac{2Q_L}{\omega}$, Ee: emitted wave from the coupling aperture, EK: reverse wave that is equal in magnitude to the incident wave Ei from the klystron.

The expression of the energy multiplication factor Vmax is

$$V_{max} = \gamma * e^{-\frac{T_a}{T_c}}[1-(1+g)^{1+v}] * [g*(1+v)]^{-1}\text{-}(\alpha-1) \quad (2)$$

where $\gamma = \alpha(2-e^{-T_1})$, $T_a = (L/gv_{g0})\ln[1/(1-g)]$ is the filling time for the structure.

g is the gradient of group velocity along accelerating structure, v=Ta/TC[ln(1-g)]-1.

Q value of the TE_{0115}mode[3]

TE_{0115}mode was chosen as the resonant cavity mode and the Q factor can be expressed as:

$$Q_0 = \frac{\lambda*[\upsilon_{mn}^2+(p\pi R/l)^2]^{\frac{3}{2}}}{2\pi\delta\left[2p^2\pi^2\frac{R^3}{l^3}+\upsilon_{mn}^2\right]} \quad (3)$$

Optimize the cavity diameter：

The relation among resonant frequency, mode and geometry dimensions can be expressed as:

$$\left(\frac{f_0 D}{c}\right)^2 = \left(\frac{\nu_{mn}}{\pi}\right)^2 + \left(\frac{pD}{2l}\right)^2 \quad (p \neq 0) \quad (4)$$

Considering the resonant frequency, the cost, unloaded Q value, it is suitable to choose the resonant cavity length is 429.18mm and the diameter is 152.6mm. And a tuner also is designed at the end of the each resonant cavities, it used to tune the frequency.

Table 1: Parameters of the pulse compression cavity

Operation frequency	5712MHz
mode	TE0.1.15
Cavity diameter	152.6mm
Cavity length	429.18mm
Iris diameter	48mm
Cavity length	15mm
Quality factor	181710
Power gain	3.1
Coupling coefficient	8.5

The results of simulation by CST are shown in Fig. 2.

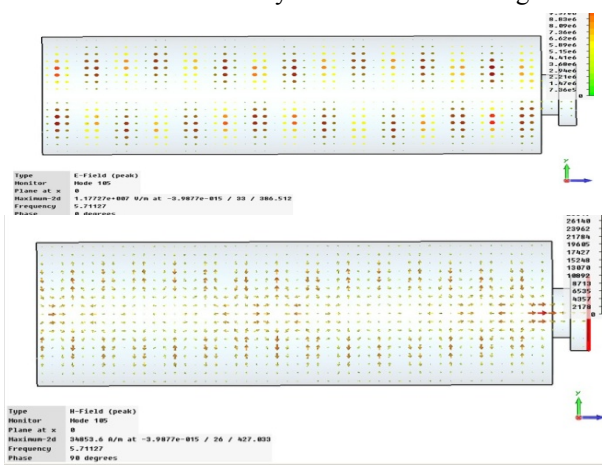

Figure 2: The cavity mode simulated by CST.

COMPONENTS FOR THE C-BAND PULSE COMPRESSION

3-dB Coupler Hybrid

3-dB coupler hybrid is an essential element to direct the flow of RF power for the RF pulse compression system. In the cavity type compressor, through this coupler an output RF power of the klystron is guided to two over coupled cavities, and waves from the each cavity are combined so as to add and transmitted to the accelerating structure. The value of the coupling depends on the width and the length of the coupling region. For 3-dB coupling, they were designed 76mm and 60mm, respectively.

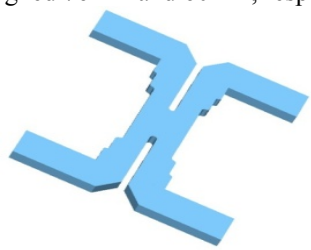

Figure 3: The 3-db hybrid coupling.

The distance of the coupling section L is a function of the width 2a as followings,

$$L = \frac{1}{4\left(\frac{1}{\lambda_{g10}}-\frac{1}{\lambda_{g20}}\right)} \quad (5)$$

Where $\lambda_{g10} = \frac{\lambda}{\sqrt{1-(\frac{\lambda}{4a})^2}}$; $\lambda_{g20} = \frac{\lambda}{\sqrt{1-(\frac{\lambda}{2a})^2}}$

Here we used a ladder type hybrid which has excellent divided ratio, phase condition, broad frequency response characteristics and the coupling is 3dB.

Table 2: Parameters of the 3-db coupler

Coupling region width	76mm
Coupling region length	60mm
First ladder length	176mm
First ladder depth	6.2mm
Second ladder length	124mm
Second ladder depth	13mm
Simulation coupling	S_{21},S_{31}=-3dB; S_{11},S_{41}<-30dB

The results of simulation by CST are shown in Fig. 4.

Mode Converter

Many modes are concentrated around the target TE0.1.nmode in the high-Q cavity of the RF Pulse Compressor. The high purity of the cylindrical TE_{01}mode must be needed to produce the designed Q-value and efficiency. Thus the many unnecessary modes can reduce the high Q-value and the efficiency if we directly connect the rectangular waveguide to the TE_{01}nmode cavity, so that a mode converter is applied between the 3-db coupler and the cavity to reduce unnecessary modes. The mode converter is shown in Fig. 5.

Copyright © 2012 by the respective authors — cc Creative Commons Attribution 3.0 (CC BY 3.0)

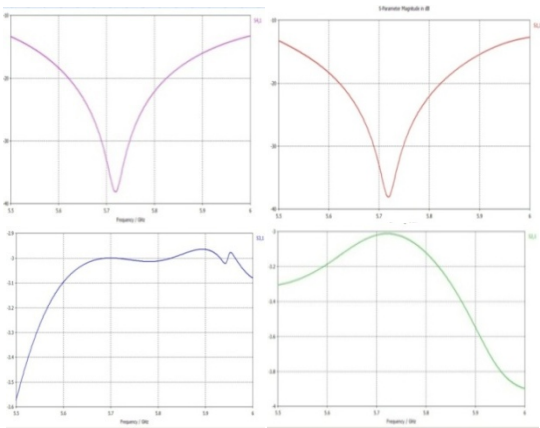

Figure 4: The simulation of the 3-db hybrid coupling.

The simulated S-parameters of the mode converter shows that the transmission coefficients of the other inconvenient modes become lower that 0.1 as S_{11}.

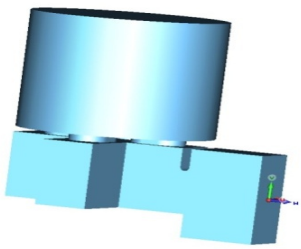

Figure 5: Mode convertor

Table 3: Parameters of the Mode Convertor

Rectangular:	BJ48, l=31.25mm
Cross rectangular:	l=80mm h=35mm
Cylindrical:	R=40mm,l=65mm
Coupling hole: Coupling height	h=4mm,a=22.18mm,b=16mm
Simulation	S_{11}<-30dB; S_{21}=0dB

The results of simulation by CST are shown in Fig. 6.

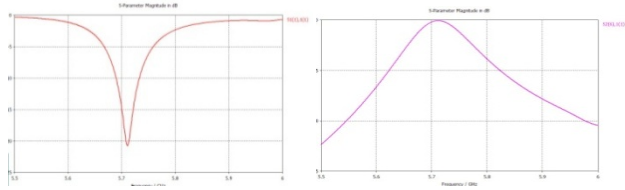

Figure 6: The simulation of the mode convertor.

CONCLUSION

In this paper we designed c-band pulse compression use TE_{0115} mode for the soft the SINAP SXFEL, and it will be fabricated in the future. And also some components for the c-band pulse compression are also designed. The low mode RF pulse comression cavity is fabricated in the SINAP.

REFERENCES

[1] Fang W C, Gu Q, Tong D C et al., Design optimization of a c-band traveling-wave accelerating structure for a compact X-ray free electron laser facility, Chinese Sci. Bull, 2011,56(32):3420-3425

[2] Z.D. Farkas, H.A. Hogg, G.A. Loew and P.B.Wilson, SLED:A METHOD OF DOUBLING SLAC's ENERGY, SLAC-pub-1453, June 1974

[3] XIAO Ou-Zheng, ZHAO Feng-Li, HE Xiang, Design and simulation of a c-band pulse compressor, CPC,2012,36(4):360-363

[4] Mitsuhiro Yoshida, Ph.D Thesis, The Research and Development of High Power C-band RF Pulse Compression System using Thermally Stable High-Q Cavity

Copyright © 2012 by the respective authors — cc Creative Commons Attribution 3.0 (CC BY 3.0)

INPUT COUPLER OF THE J-PARC DTL

Fujio Naito*, Hirokazu Tanaka, Kesao Nanmo, KEK, Japan
Takashi Ito, Koichiro Hirano, JAEA, Japan

Abstract

DTL of the J-PARC has two input couplers in one tank. The coupler has a movable coupling loop with an capacitive element which increase the coupling with the tank. The loop position is the outside of the tank, where is in the atmosphere. The tank vacuum is kept by the ceramic window on the wall in the coupler port. The rf properties and the mechanical structure of the coupler were designed to achieve the larger coupling constant. Features of the coupler design for J-PARC DTL is described.

INTRODUCTION

Japan Proton Accelerator Research Complex (J-PARC) is a high-intensity proton accelerator facility constructed in the Tokai campus of Japan Atomic Energy Agency (JAEA) under the collaboration between KEK and JAEA. The accelerator consists of a 181-MeV linac, a 3-GeV rapid cycle synchrotron and a 30-GeV synchrotron main ring. The 181-MeV injection linac comprised of the an H^- ion source, RFQ linac, DTLs, and separated type DTLs (SDTLs). The resonant frequency of whole rf cavities in operation is 324MHz. The beam energy of linac will be increased to 400MeV by adding the annular-ring coupled structure (ACS) linac at the end of 2013[1].

The DTL section is composed of three long tanks. The length of each tank is approximately 9m. Each drift tube in the tank accommodates the compact electric quadrupole magnet. The beam is accelerated to approximately 50-MeV by the three DTL tanks.

The SDTL is a short DTL which has 5 gaps in a tank. Drift tubes in the SDTL do not accommodate the quadrupole magnet but the quadrupole doublet is set between the tanks. J-PARC has 30 SDTL tanks for the beam acceleration and two SDTL tanks as a debuncher.

The input coupler of the DTL has a different design from that of the SDTL. In the following sections the different points are mainly described.

REQUIREMENT ON THE COUPLER

The high-power rf is provided to each DTL tank independently. Each DTL tank has two input couplers so that the rf power which one coupler should transfer is reduced by half compared to the case that one tank has one coupler. However it is not simple to tune the coupling constant for both couplers adequately. In order to simplify the tuning procedure, the coupling constant of the coupler must be changed easily keeping the vacuum in the tank.

* fujio.naito@kek.jp

Rf coupling method we usually use is a loop coupling for DTL because it is much easier to adjust the coupling constant than an iris coupling. The coupling constant of the loop coupler is tuned by changing the tilt of the loop to the tank or changing the distance from the cavity.

The input coupler has a ceramic window to keep the vacuum in the tank. If the coupling loop of the coupler is in the vacuum side, the vacuum is usually broken when the loop tilt or the loop position is changed. Of course it is possible in principle to make a certain mechanical structure to move the loop in vacuum. However it is not reliable because the structure is probably too complicated.

For the DTL of J-PARC the coupling loop is set outside of the tank, where is in the atmosphere. The tank vacuum is kept by the ceramic window on the wall in the coupler port. The schematic view of the coupler design is shown in figure 1. The distance between the loop and the window is changeable by sliding the inside cylinder of the coaxial waveguide on which the loop is brazed. The loop is not fixed on the outer cylinder of the coaxial waveguide but the loop is contacted to the outer by the finger type rf contact.

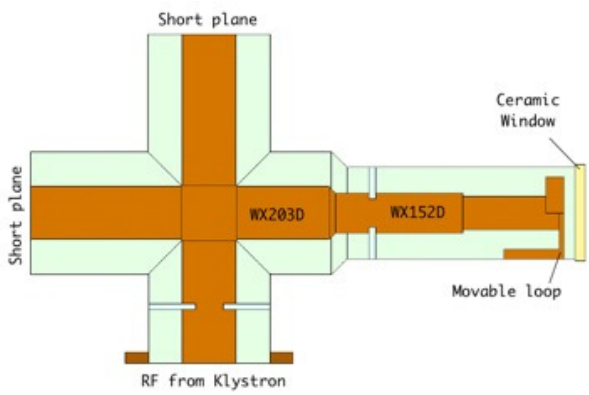

Figure 1: Coupler design.

As the loop is located outside of the tank, it is hard to have the large coupling constant with the tank. As the result, the coupling strength achieved by the loop is not enough for the DTL in spite of the fact that one DTL tank has two couplers as mentioned before.

Consequently the movable loop of the coupler has been put an capacitive element as shown in figure 2, which increase the coupling with the tank. In the figure 2 the rectangle plate on the right of the coaxial waveguide is the coupling loop. The half circle on the left is the capacitive element. Figure 3 shows the loop of the coupler for the SDTL. It is the simple loop. It is described that how we fixed the radius and thickness of the element in the next section.

Copyright © 2012 by the respective authors — cc Creative Commons Attribution 3.0 (CC BY 3.0)

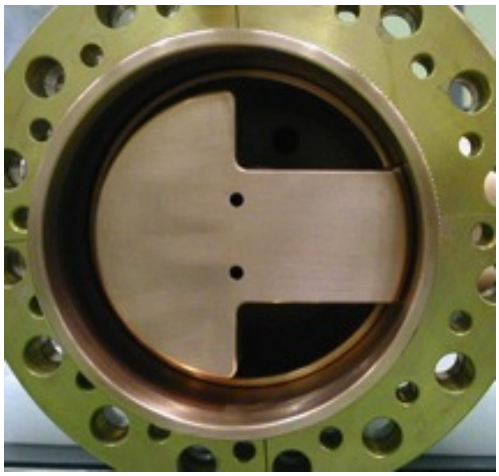

Figure 2: Rf coupling loop of DTL
The left semicircle is the capacitive element.

Figure 3: Rf coupling loop of SDTL
The white ceramic window is placed in the coupler.

Design of the coupling loop

The rf simulator HFSS was used for the design of the coupling structure. The example of the input shape of the loop for the simulater is shown in figure 4. It includes the magnetic coupling loop and the capacitive element. The parameters are the radius and thickness of the capacitive element. The loop is connected the cylindrical cavity in the simulator. The resonant frequency is tuned around 324-MHz.

In the simulation, there is no wall loss in the cavity. Thus $\S_{11}$ is always one. To determine the coupling strength of the loop to cavity, the phase shift of $\S_{11}$ was used. Here we defined the width as the measure of the coupling strength by the frequency span in which the phase is changed from -45 degree to +45 degree. The $\frac{1}{Q_{ext}}$ is proportional to the width. The results are shown in figure 5 and figure 6, respectively. The vertical line of both figures shows the width as mentioned just before. The simulation results has fixed the radius and the thickness of the capacitive element at 60mm and 30mm, respectively.

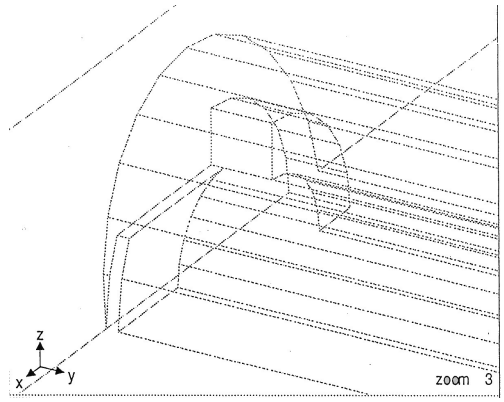

Figure 4: Loop for simulation

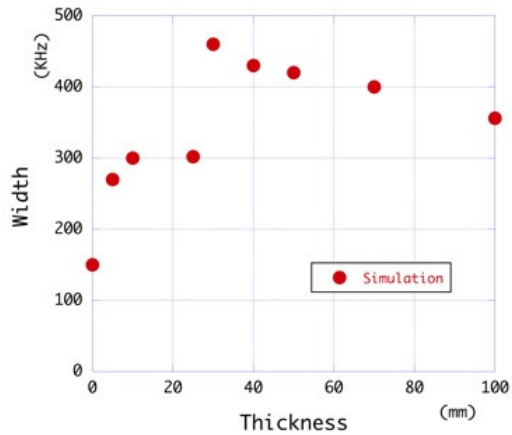

Figure 5: Frequency width vs the thickness of C
Simulation result. The Radius is constant (55mm).

Design of the ceramic window

The ceramic window is made of aluminum oxide of 99.7% purity. The shape of the window is a disk of which the thickness and the diameter are 17mm and 160mm, respectively. The oxide TiN is coated on the surface of the vacuum side in order to reduce the secondary electron emission coefficient.

The vacuum seal for the window is a metal seal. To put the window inside the tank as many as possible, we designed the step shape cross section shown in the upper of figure 7 at first. However the window was broken during the high-power test by the sparking problem happened at the step. Thus we modified the shape as shown in the lower of figure 7. It has no step. It has a simple shape but the window position is more outside compare to the first design.

MEASURED COUPLING CONTSANT FOR DTL-1

The coupling constant was measured by using DTL-1 of J-PARC. Figure 8 shows the measured relation between the loop position and the observed coupling constants (β_1 and

Copyright © 2012 by the respective authors — cc Creative Commons Attribution 3.0 (CC BY 3.0)

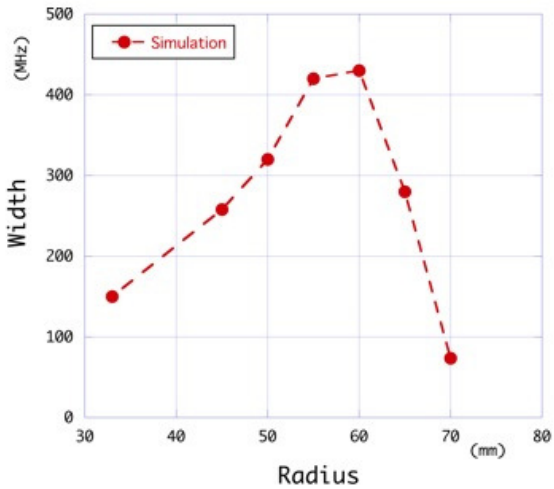

Figure 6: Frequency width vs the radius of C
Simulation result. The thickness is constant (50mm).

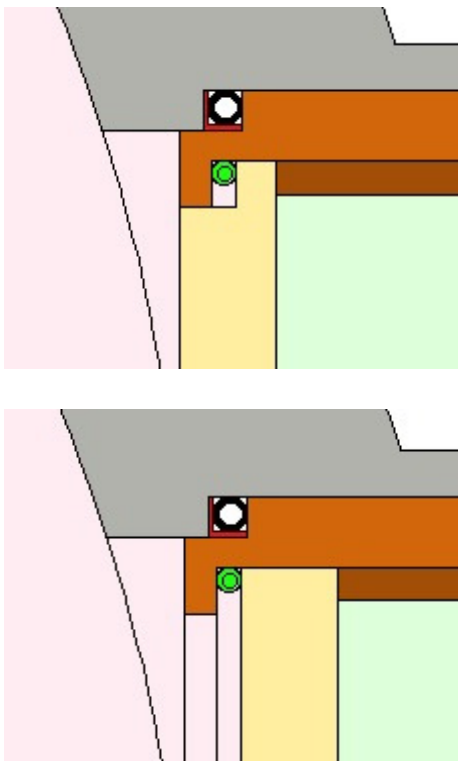

Figure 7: Cross sectional view of the cerarmic window
Yellow:window, Brown:outside cylinder of the waveguide
Green:vacuum seal, Red:rf contact, Gray:cavity wall

β_2) for two couplers. It also shows the measured unloaded-Q (Q_0) values. Since the unloaded-Q (Q_0) does not depend on the coupling constant, it shows that the moving coupler works well.

The maximum coupling constant we can have by two coupler is approximately 2. It is large enough for us, because the required total coupling is usually less than 1.5. Thus the distance of the loop from the window is around 10mm.

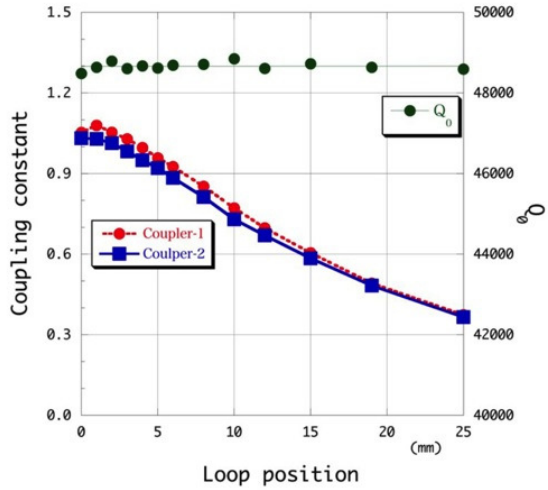

Figure 8: Measured coupling constant for DTL1 [2].

In the two port cavity, the measured coupling constant β_1^* and β_2^* by using a network analyzer do not mean the true coupling constant β_1^* and β_2^*. This we use the following relations to estimate the true values.

$$\beta_1 = \frac{\beta_1^*(1+\beta_2^*)}{1-\beta_1^*\beta_2^*}, \quad \beta_2 = \frac{\beta_2^*(1+\beta_1^*)}{1-\beta_1^*\beta_2^*}$$

CONCLUSION

The high-power rf coupler with a movable coupling loop has been developed for the DTL of J-PARC. The coupling loop has the capacitive element which increases the coupling constant. Its design was fixed by using the rf simulator. The shape of the ceramic window was checked by the high-power test. Finally the performance of the coupler has been confirmed by real DTL cavity. The couplers are working well after the earthquake also.

ACKNOWLEDGMENT

The authors would like to acknowledge Professor emeritus Kato and Professor emeritus Takasaki for their essential suggestions and the continuous encouragement.

REFERENCES

[1] K. Hasegawa, “STATUS OF THE J-PARCT LINAC”, Proc. of LAC 2010, Tsukuba, JAPAN, 449 (2010)

[2] F. Naito, et. al, “RESULTS OF THE HIGH-POWER CONDITIONING AND THE FIRST BEAM ACCELERATION OF THE DTL-1 FOR J-PARC” Proc. of LAC 2004, Lubeck, GERMANY, 300 (2004)

Copyright © 2012 by the respective authors — cc Creative Commons Attribution 3.0 (CC BY 3.0)

RECOVERY AND STATUS REPORT OF DTL/SDTL FOR THE J-PARC AFTER EARTHQUAKE

T. Ito#, K. Hirano, Japan Atomic Energy Agency, Tokai, Japan
K. Nanmo, F. Naito KEK, Tsukuba, Japan

Abstract

The Japan Proton Accelerator Research Complex (J-PARC) facilities had big damages because of an earthquake on March 11, 2011. A DTL and an SDTL that were installed at the linac area had also damages. The alignment of the cavity was deformed more than 40mm and there had been observed about 0.2mm misalignment of the DT position in the DTL, and so on. However the result of the recovery work over eight months, we restarted proton beam acceleration at the linac section. As is the case with before earthquake, the DTL and the SDTL are operating with a few trips per day, as of April 2012. In this paper, we will present the recovery works from the earthquake and the operating status of the DTL and the SDTL.

DAMAGES OF THE DTL AND THE SDTL

By the earthquake, the Drift Tube Linac (DTL), Separated type DTL (SDTL) and various equipment of the cavity had damages [1] [2]. The situation damage is described below.

Drift Tube Alignment

Fortunately there were no damages, like a dent and a crack, on the outside of cavity and focusing magnets between SDTL tanks by the visual inspection. A movable Tuner and an RF coupler attached on the cavity was also no damage. However, it was observed that the alignment of the all tanks of DTL and SDTL was broken by the deformation of the floor of the tunnel. Furthermore a few misaligned drift tubes in the DTL were also observed.

First, we check the DT position by using a digital camera and the alignment telescope. Figure 1 shows the pictures of the DT bore of the DTL and the SDTL.

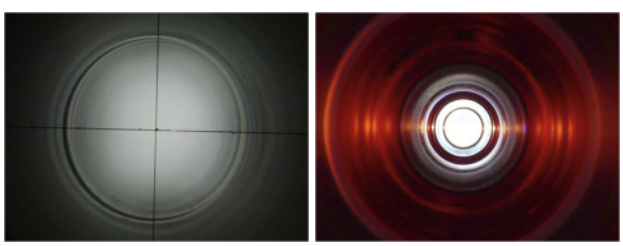

Figure 1: Pictures of the DT bore. Left:DTL, Right:SDTL

For the DTL bore picture (left picture), the black circular arc of the left side is broader than right side. This means that the DT bore center or DT position is decidedly sifted in a horizontal direction. On the other hand, the circles in the SDTL picture (right picture) were nearly arranged in a concentric pattern. Therefore we judged that there was no clear displacement of the alignment of the DT position for the SDTL.

Next we measured the center position of the DT bore of the DTL by using alignment telescope. Figure 2 is a schematic view of the measurement system and the measured center position of the DT bore for a D1-1 (unit tank #1 of the DTL1).

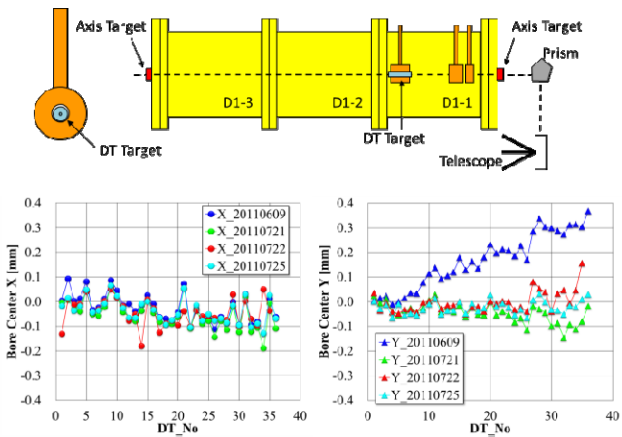

Figure 2: Schematic view of the measurement system and the measured center position of the DT bore.

The telescope axis was set on a line defined by the two axis targets and the DT target center position from the telescope axis was measured.

The graph shows the measured displacement of the DT bore center for the unit tank D1-1. The abscissa is DT number and the ordinate is the displacement of the bore center from the telescope axis.

There is about 0.2mm misalignment of bore center for X direction. The displacement for Y direction is less than X displacement except for the large DT number with large reading error. The reason is that the DT is swung like pendulum by horizontal vibration of earthquake because the DT is fixed at the top of the cavity.

There is a line with large tilt for Y measurement. This means that the unit tank D1-1 is inclined with respect to the telescope axis. This tilt line was measured before re-alignment of the DTL unit tank. Namely, the accelerator tunnel was deformed by the earthquake and the DTL was deformed along a floor of the tunnel. After re-alignment of the unit tank, the deformation of the DTL for Y direction is resolved (i.e. other three lines).

We did not measure the DT bore center of other cavities, because we could not prepare the target for DTL2 and the DTL3 soon. However, a drift of a resonant frequency of the cavity and an abnormal Q value were not observed. Therefor we concluded that there was no serious displacement of the DT.

#itou.takashi@jaea.go.jp

Copyright © 2012 by the respective authors — cc Creative Commons Attribution 3.0 (CC BY 3.0)

Cavity and Magnet Alignment

As mentioned before, Each DTL was deformed along the floor level [3]. The deformation was occurred at the joint part of the unit tanks (i.e. connection of cavity flanges). Maximum displacement was about 0.8mm for X direction and 1.5mm for Y direction.

SDTLs and the focusing magnets that are set on the same supporting frame of the SDTL tank were displaced very much. It had been measured that there are about 25mm misalignment of the horizontal position and 45mm of vertical position. The vertical displacement was due to the deformation of the floor level same as the DTL. The cause of the horizontal displacement was deformation of the floor. The SDTL cavity and the focusing magnet moved horizontally beyond the movable range of a cavity stage.

Furthermore, the tilt of the tank around the beam axis has been observed. The angle of it is 3-mrad. This tilt was also happened by the deformation of the tunnel.

Vacuum Pump

The linac tunnel was broken. As the result the floor and the wall of the tunnel are cracked in several places.

Groundwater was leaked and the accelerator tunnel was flooded up to 10cm. Therefore a lot of the mechanical vacuum pumps put on the floor were sunk. All soaked pumps were tested and broken pump was replaced with the new one.

Ion pumps and turbo molecular pumps were no damage because these pumps were attached to the cavity directly and the height of the ion pump is a few dozen centimeters above the floor.

Monitor

Monitors installed between the cavities had big damage. Many Beam Position Monitors (BPM), Current Monitors (CT) and bellows jointed to these monitors were broken. Therefore, the vacuum cannot be kept and the inner surface of the DTL and the SDTL were exposed to the air. Figure 3 shows the broken current monitor and bellows. The CT was broken at the brazing point between the ceramic cylinder and the metal pipe.

As it was impossible to repair the damaged monitors and the bellows, new equipment was made immediately.

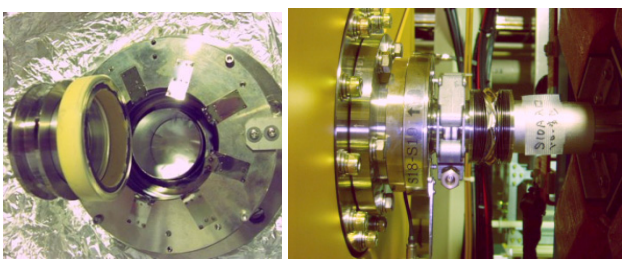

Figure 3: Broken CT (left) and bellows (rigtht)

Magnet Power Supply

Just after the earthquake, there was no damage for the outside of all magnet power supplies. At that time, the electric power was not available to turn on the power supply. However the power supply had been exposed to high humidity and high temperature atmosphere during several months because the air conditioning system of linac building was broken by the earthquake. Consequently, a lot of the power supply does not work well by the failure of the electric control boards in the power supply. We still continue to repair the broken power supply.

RE-ALIGNMENT

Drift Tube Alignment

Each DT in the DTL contains an electric quadrupole magnet (DTQ). Therefore the misalignment of the DT should be corrected in order to accelerate the beam with good quality. However it is necessary for the realignment of the DT to remove all electric cable for the DTQ and to separate the long DTL into the short unit tanks. It is really hard work to re-align the DTs. Since the beam simulation with the observed misalignment of DTs shows that the effect of the misalignment of DT is allowable level for the beam loss, we decided not to re-align the displaced DTs. [4] [5].

Cavity and Magnet Alignment

It is necessary to align the cavity and the focusing magnet. As mentioned previous section, there had been observed about 45mm and 25mm displacement for vertical and horizontal position respectively at the SDTL section in the accelerator tunnel. If we want to align the all tanks and magnets on the ideal one straight beam line, the adjustment length of the cavity is beyond the bounds of adjustable range of the cavity stage. So we decided to re-align the cavity at the DTL section and the SDTL section to the different axes respectively.

For DTL section, we determined the beam axis as the adjustment length of the unit tank was the minimum (~ a few mm). The unit tank was also aligned with docking condition and without removing the feeder cable to reduce the recovery work time.

Two targets of a laser tracker are mounted on each unit tank. The measured unit tank position of the DTL after the installation, the earthquake and the re-alignment by using a laser tracker is shown in Figure 4. The abscissa is the Z position of the DTL and the ordinate is the displacement from an axis defined by the two targets (see figure 4).

After the earthquake, the unit tank had large displacement for both directions X and Y. As the result of the re-alignment of the unit tank, the position was nearly equal to the position the after the installation measured in 2005.

For the SDTL section, the beam axis is different from the axis of DTL section. The axis is bent after the DTL section. The acceleration beam is bent by using first steering magnet installed between the S01A and the S01B. Because of this, it is possible to adjust the position of the cavities and the magnets within the limits of the adjustable range of the cavity stage.

Copyright © 2012 by the respective authors — cc Creative Commons Attribution 3.0 (CC BY 3.0)

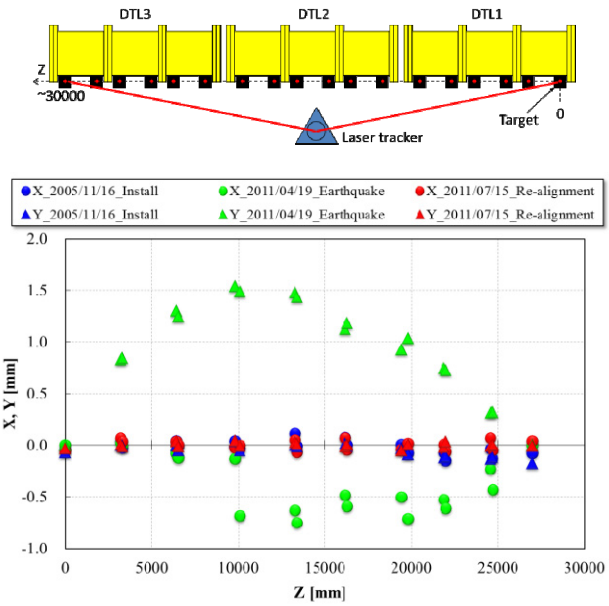

Figure 4: Displacement of the unit tank position.

Figure 5 shows measured position of the SDL and the focusing magnets after re-alignment. The SDTL and the magnets were measurement by using the laser tracker same as the DTL. The horizontal axis is the displacement of the Z (longitudinal). The vertical axis is the displacement of the X and Y (transverse) from the new beam axis. X and Y=0 is on axis.

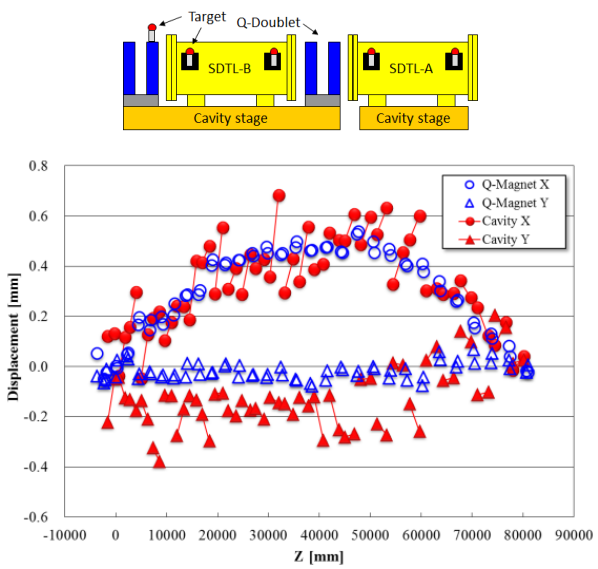

Figure 5: Displacement of the SDTL and the magnet.

Every focusing magnet has a target, and Each SDTL cavity has two targets as with the unit tank of the DTL. A cavity-A (S01A - A15A) is aligned individually. A cavity-B (S01B - S15B) and two doublets (four magnets) are aligned together on the cavity stage. The SDTL and the magnet are aligned smoothly within about 0.6mm from the new beam axis. The measured displacement of the X direction is larger than Y. This reason is an alignment error by the measurement limit of the laser tracker. The circumferential angle was corrected at the same time as the re-alignment of the X and Y direction.

After the vacuum pumps, the beam monitors and so on were attached, the final alignment of the cavity and the magnet was done. Figure 6 shows the result of the final alignment. It may be seen from figure 6 that the DTL and the SDTL is aligned to the different beam axis.

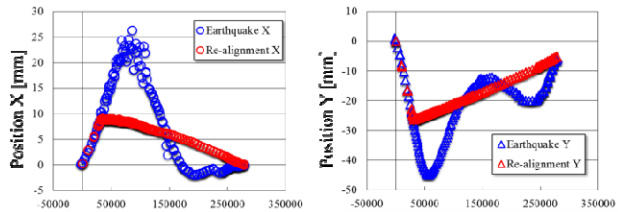

Figure 6: Result of the final alignment.

OPERATION STATUS

On November 2011, a conditioning of the DTL and the SDTL was started. The beam acceleration was re-started on December and we successfully accelerated the beam (the beam current is15mA, the pulse length is 500 micro seconds) at the linac section. It was almost the same as before the earthquake. Then, the user operation of the Materials and Life Science Experimental Facility (MLF) and the Neutrino Experimental Facility (NU) was started in January.

However, the several issues have been revealed. The beam loss is higher than it before the earthquake in several locations of the linac tunnel. For the S05B cavity, it was impossible to input an rf power from 300kW to 400kW. The operating power of the S05B was included in this range. Therefore the operating power was increased to 510kW that is about 1.4 times of those before the earthquake. After the investigation, a possibilities of a multipactor on the inner surface of the cavity emerged. We have continued our efforts to solve these problems.

ACKNOWLEDGMENT

We would like to thank members of J-PARC, JAEA and Mitsubishi SC for helping the recovery work of the DTL and the SDTL.

REFERENCES

[1] T. Ito et al., Proc. of 8th Annual Meeting of Particle Accelerator Society of Japan, August 1-3, 2011, p1316. (in Japanese)
[2] K. Hasegawa, et. al., Recovery of the J-PARC Linac from the Earthquake, FR2A01, in these proceedings
[3] T. Morishita, et. al., Floor Deformation of J-PARC Linac after the Tohoku Earthquake in Japan, Proc. of IPAC10, San Sebastian, Spain (2011), p2601, WEPS049
[4] M. Ikegami, Proc. of the 8th Annual Meeting of Particle Accelerator Society of Japan, August 1-3, 2011, p1131. (in Japanese)
[5] M. Ikegami, et. al., Study on the Realignment Plan for J-PARC Linac after the Tohoku Earthquake in Japan, , p44, MOOCB01

Copyright © 2012 by the respective authors — cc Creative Commons Attribution 3.0 (CC BY 3.0)

BEAM LOSS OCCURRED AT DTL CAVITY IN J-PARC LINAC*

A. Miura#, T. Ito, K. Hirano, T. Maruta
J-PARC Linac, Japan Atomic Energy Agency, Tokai, Ibaraki, Japan
T. Miyao, K. Nanmo, M. Ikegami, F. Naito
J-PARC Linac, High Energy Acceleartor Organization, Oho, Tsukuba, Japan

Abstract

We measured the residual radiation along the beam line during short operation intervals. Because the dependence on the operational condition of higher residual radiation was recognized at the surface of drift tube linac (DTL) cavity by radiation survey, we installed scintillation beam loss monitors at some points with particularly high radiation to investigate the cause of the radiation. Although the DTL section is low energy part of the linac, fine structure of the beam loss was observed by the scintillation BLM. We also measured the beam loss occurred at the DTL varying the beam orbit. In this paper, the result of the radiation measurement and beam loss signals obtained by the scintillation BLM's are presented.

INTRODUCTION

There was big damage in J-PARC caused by the Tohoku earthquake in March 2011[1-3]. And the beam operation of J-PARC linac was suspended. We resumed the beam operation and delivered to the laboratory from December. After resuming the operation, we measured the residual radiation along the beam line during short intervals. Because the dependence on the operation condition and history of higher residual radiation was recognized at the surface of drift tube linac (DTL) cavity by radiation survey, we installed scintillation beam loss monitors (BLM's) at some points with particularly high radiation to investigate the cause of the radiation. We also measured the beam loss occurred at the DTL varying the beam orbit.

RESIDUAL RADIATION IN DTL SECTION

DTL (Drift Tube Linac) in Linac

J-PARC linac consists of the IS (ion source), RFQ (Radiofrequency Quadrupole), DTL (Drift Tube Linac), SDTL (Separated type DTL) and the beam transport to downstream RCS (Rapid Cycling Synchrotron) as fig. 1. Negative hydrogen ion beam is accelerated up to 50 keV in the ion source chamber. After the beam is accelerated up to 3 MeV by RFQ and had matching by the quadrupole magnets in MEBT (middle energy beam transport) section, it is injected to DTL through SDTL to be accelerated.

J-PARC linac has three DTL cavities, and each cavity consists of connected 3 unit tanks. Length of a unit tank reaches 3 m, then a DTL cavity reaches about 9 m. The first DTL cavity consists of 75 drift tubes (DTs) and quadrupoles. All DTs are aligned within 50 μm to the center of the magnetic fields [4].

#miura.akihiko@jaea.go.jp

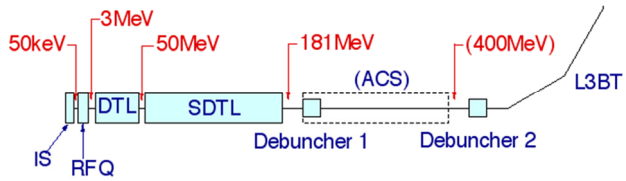

Figure 1: Configuration of J-PARC Linac. DTL section is located to the downstream of RFQ, the beam energy is accelerated from 3 to 50 MeV. (IS: Ion source, RFQ: Radio Frequency Quadrupole, DTL: Drift Tube Linac, SDTL: Sparated-type DTL)

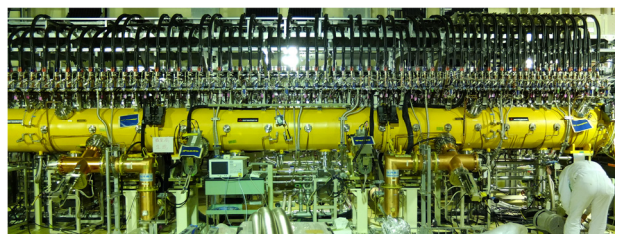

Figure 2: Overview of DTL Cavity. One DTL cavity consists of 3 unit tanks.

Residual Radiation in DTL Section

Intervals of the first operation after resuming the operation, residual radiation at the surface of DTL cavities was measured using Geiger-Muller counter. Most of all points are measured under 1.0 μSv/h, but higher residual radiation was recognized at DT25 (the 25th DT) and DT55 (the 55th DT) of 1st DTL cavity. Measured points are described in fig. 3 and measured values are listed in table 1.

Based on these results, we measured the residual radiation every interval of beam operation. As described in fig. 4, dependences on the operational conditions and

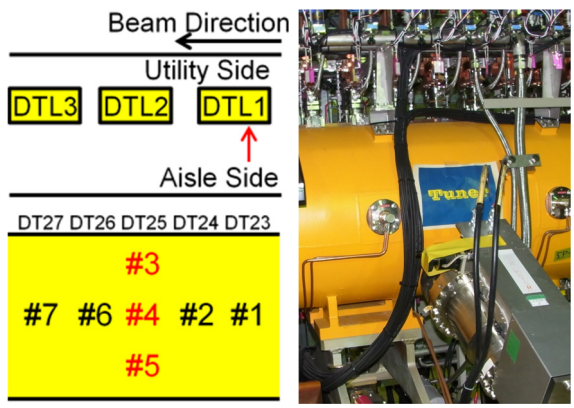

Figure 3. Measurement Points of 1st DTL1 Cavity. Axis is defined to the x-y-z coordination, +y as a top of vertical, +z as a beam direction, +x as a inevitably defined for aisle direction.

Copyright © 2012 by the respective authors — cc Creative Commons Attribution 3.0 (CC BY 3.0)

the operation history are recognized. Because the beam energy is not enough high to detect the gas-proportional BLM (beam loss monitor) and the installed position of them is not close to the surface of cavities, there was no difference of beam loss signals from gas-proportional BLM during the operation. Based on the less sensitivity of gas-proportional BLM, we employed scintillation BLMs to observe the beam loss carefully through an operation at the points where the higher residual radiation was detected.

Table 1: Residual Radiation around DT25 and DT55 of 1st DTL Cavity

Aisle Side(+x direction)		Utility Side(-x direction)	
Position	Dose value [μSv/h]	Position	Dose value [μSv/h]
# 1	4.2	# 1	5.30
# 2	4.58	# 2	8.87
# 3	8.7	# 3	9.04
# 4	6.59	# 4	6.98
# 5	6.7	# 5	8.78
# 6	5.50	# 6	5.17
# 7	2.49	# 7	2.51

BEAM LOSS DETECTION BY SCINTILLATION BLM

Plastic Scintillation Beam Loss Monitor

Plastic scintillation monitors with less X-ray sensitivity are employed and installed to measure the beam loss. We used photo-multipliers of Hamamatsu H3164-10 with the gain of 1.1 x 10^6, the peak wavelength of 420 nm, and the rise time of 0.8 nsec (Figure 4). The plastic scintillator is Saint-Gobain BC-408 with the peak emission wavelength of 425 nm and rise time of 0.9 nsec, which matches the photomultiplier [5].

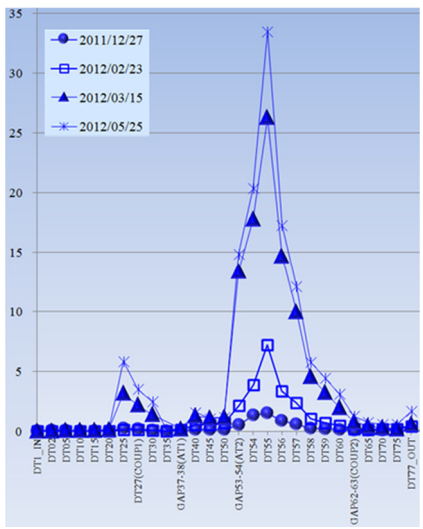

Figure 4: Residual Radiation at DTL1. Radiation depends on the operation history and beam outputs. Unit of longitudinal axis is in μSv/h and horizontal axis describes the position.

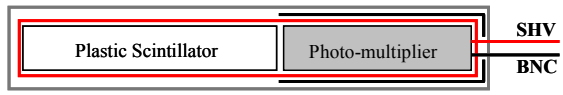

Figure 5: Configuration of Plastic Scintillation Beam Loss Monitor.

Beam Loss Measurement

In the first DTL section, beam energy is at least 10 to 20 MeV. Peak sensitivity of plastic scintillator (BC-408) is slightly sifted to higher energy, but it would have low sensitivity even the low beam energy. We employed the four scintillation BLMs to install +x side (aisle side) and –x side (utility side) at both DT25 and DT55 (fig. 6). In order to confirm the beam orbit dependence of beam loss at DT25 and DT55, we use the steering magnet installed at upstream part (MEBT1) to shift a beam orbit. In addition, high voltage supplied for the photo multiplier is suppressed under -800V to prevent from a saturation of signal responce. Waveform of the signal is obtained to observe the beam loss events using high speed sampling oscilloscope.

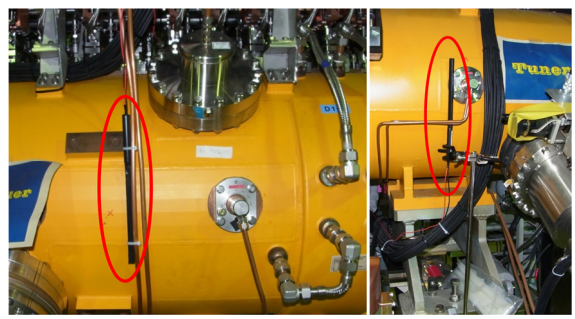

Figure 6: Scintillation BMLs Installed at the Surface of DTL Cavity. Installation situation of DT25 is on left side and it of DT55 is on right side.

Discussions of Beam Loss Measurement

Because beam loss signals are successfully obtained even in low beam energy and fine waveforms are obtained using scintillation BMLs, discussions can be useful.

Waveforms obtained at DT25 are shown in fig. 7 and fig.8. Figure 7 shows the waveform obtained after the beam orbit correction. The beam orbit is corrected with observing beam losses occurring from DTL to downstream section.

Figure 8 shows the waveform obtained after the slightly shift of beam orbit. In this case, beam loss events are recognized more at the corrected orbit than those at the shifted orbit.

Copyright © 2012 by the respective authors — cc Creative Commons Attribution 3.0 (CC BY 3.0)

In case of DT55, characteristic beam loss events are shown in fig. 9 and 10. In fig. 9, the less beam loss occurs at the corrected orbit. If the beam orbit is misaligned, many beam loss events are observed in figure 10. In this case, a beam orbit dependence of beam loss events is recognized, but these patterns show a different contribution.

SUMMARY

Beam orbit dependence of beam loss at two point of DTL cavity is obtained by the measurement using scintillation BLMs, after the beam orbit is corrected. Result obtained at the upstream point suggests that the misalignment which would be caused by the earthquake is still left in the DTL cavity. The result at the downstream points has a tendency of beam orbit dependence, but the misalignment is not remarkably suggested. Alignment of DTs should be confirmed more in detail.

Beam loss which is detected at the surface of DTL cavity is successfully measured by the scintillation BLM even the low beam energy. Beam loss occurs at DTL1 depends on the beam orbit which pass through the cavity inside. This is a predictable result by the specification of scintillation. Because the serious beam loss had not been seen in this section, we had not focused it. But these residual radiation and beam orbit dependence of beam loss show the important lessons for beam commissioning. Also, the scintillation BLM would become an essential beam commissioning tool, based on the development of electrical circuits which has the functions of high speed beam loss detection system, qualification of the beam loss events and high accuracy. In future, the beam loss detection system using scintillation will be developed.

ACKNOWLEDGMENT

We would like to express thanks to the engineers of Mitsubishi Electric System & Service Co., Ltd. for their efforts and help.

REFERENCES

[1] K. Hasegawa et al., "Status of J-PARC Accelerator Facilities after the Great East Japan Earthquake", Proc. of IPAC2011, WEPS095, San Sebastian, Spain.
[2] T. Morishita et al., "Floor Deformation of J-PARC Linac after the Tohoku Earthquake in Japan", Proc. of IPAC2011, WEPS049, San Sebastian, Spain.
[3] A. Miura, et. Al., “Beam Monitor Deformation by Tohoku Earthquake and its Recovery Project”, Proc. of IPAC2011, WEPC144, San Sebastian, Spain.
[4] Y. Yamazaki, eds. *Accelerator Technical Design Report for J-PARC*, KEK Report 2002-13.
[5] A. Miura, et. Al., “Beam Loss Detected by Scintillation Beam Loss Monitor”, Proc. of DIPAC2011, MOPD43, Hamburg, Germany.

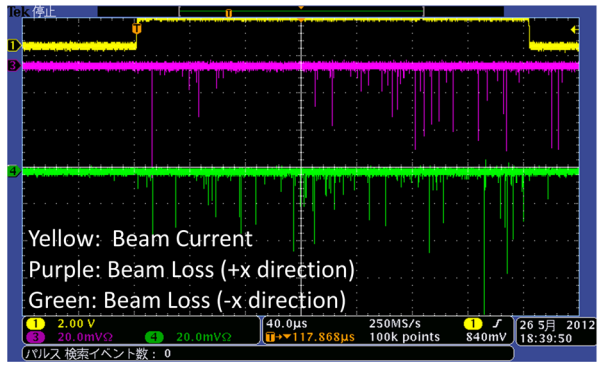

Figure 7: Beam Loss Events Occurred at DT25. Beam orbit is corrected with observing beam losses occurring from DTL to downstream section.

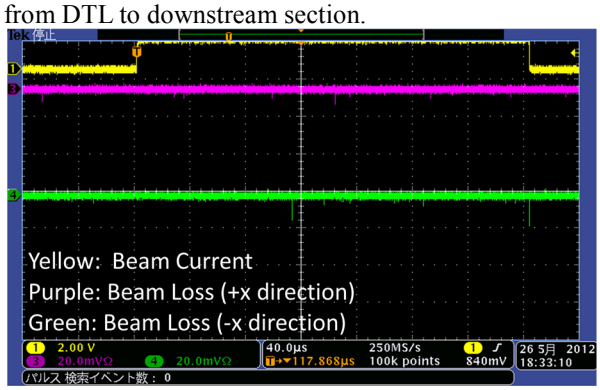

Figure 8: Beam Loss Events Occurred at DT25. Many beam loss events are disappeared, after the beam orbit is slightly shifted.

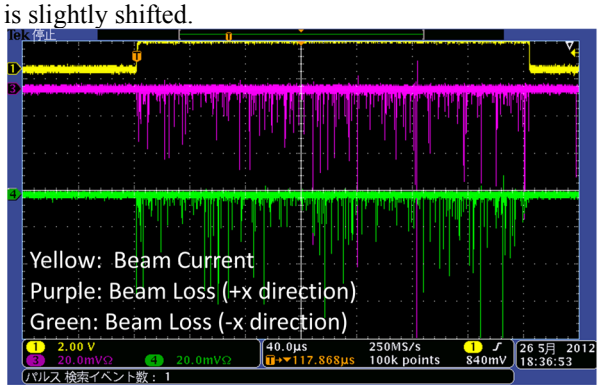

Figure 9: Beam Loss Events Occurred at DT55. Beam orbit is corrected with observing beam losses occurring from DTL to downstream section.

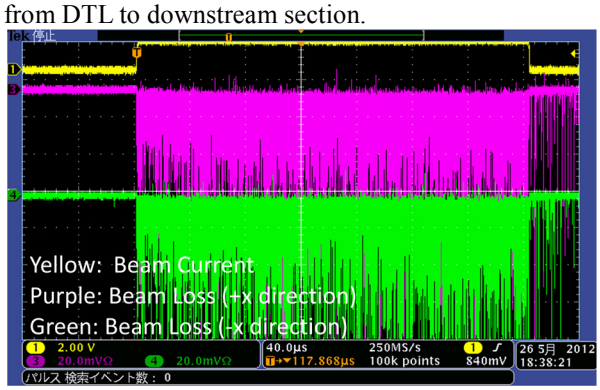

Figure 10: Beam Loss Events Occurred at DT25. Many beam loss events are observed, after the beam orbit is slightly shifted.

Copyright © 2012 by the respective authors — cc Creative Commons Attribution 3.0 (CC BY 3.0)

DESIGN AND PERFORMANCES OF PHASE MONITOR IN J-PARC LINAC

A. Miura*,
J-PARC Linac, Japan Atomic Energy Agency, Tokai, Ibaraki, 319-1195, Japan
T. Miyao, Z. Igarashi,
J-PARC Linac, High Energy Acceleartor Organization, Oho, Tsukuba, 305-0801, Japan

Abstract

J-PARC linac employs a fast current transformer (FCT) as a beam phase monitor to calculate the beam energy by time-of-flight method, and the 4-stripline beam position monitors (BPMs) for the beam position measurement. We designed, fabricated and have been used them to the beam operation. Performances of fabricated monitors and their calibration data have been measured. Here, we will discuss the structure and frequency performance of the FCT monitor. At the great earthquake occurred off the Pacific coast of Tohoku, some CT monitors, such as a phase monitor and beam current monitor had damage and the vacuum leakage was observed. But no damage of BPMs was found. It has been considered that the signals from striplines of BPM would be useful for a phase measurement. A phase measurement using a BPM has been successfully conducted. Above the lessons learnt from the damage by the quake, we consider to employ the BPM for the FCT backups after evaluation of the performances of BPM as the phase measurement device. Finally, these performances of BPM are compared with those of FCT. Based on the results of the evaluations, we will discuss the performance to measure the beam phase both FCT and BPM.

INTORODUCTION

Energy upgrade project is now progressed in J-PARC linac. Currently, J-PARC linac accelerates the negative hydrogen beam up to 181 MeV, but 400 MeV accelerated beam can be obtained with 21 ACS cavities[1]. We designed and fabricated the beam monitors, such as BPM (beam position monitor), SCT (slow current transfer) as the beam current monitor, FCT (fast current transfer) as the beam phase monitor, WSM (wire scanner monitor) as the beam profile monitor) for this project[2]. After fabricated BPM and CT monitors, the performance of each monitor had been obtained to confirm the design parameters and for calibration[3].

There was big damage in J-PARC caused by the Tohoku earthquake in March 2011[4-5]. As for the beam monitors in J-PARC Linac, there was no damage of BPMs and WSMs, but deformation of CT monitors (SCT and FCT) was found and vacuum leak occurred. Damage was mainly observed at the part where the ceramics and metal parts were brazed. BPM has a strong structure for shaking by quakes, on the other hand, FCT monitor has a such structural weak point for shaking. Because the BPM also can measure the beam phase using an electrical circuit for phase detection, it has been considered to use the BPM for the backup of FCT.

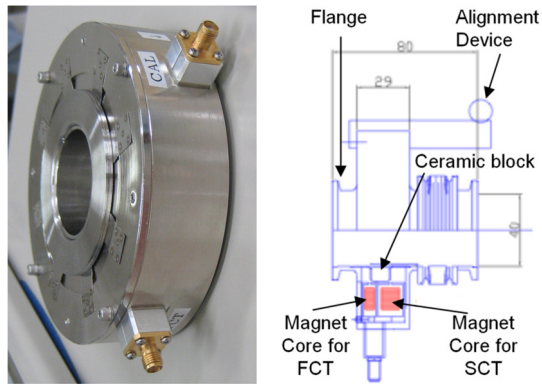

Figure 1: Overview and drawing of FCT and SCT monitor. In the drawing figure, cross-section is described in the bottom half.

FCT is well calibrated to detect the beam phase for 324 MHz acceleration frequency. If the BPM is employed for phase measurement, it is though that it also needs to calibrate to 324 MHz. Then, we obtained the performance of BPM as the phase monitor. And the data are compared with the data obtained from FCT monitor.

In this paper, we describe the design parameters and performances of FCT and compared results obtained from BPM.

DESIGN OF FCT MONITOR

The beam phase monitor is the other kind of beam current monitor, which is specially designed for high frequency response. The beam phase measurement related to the RF signal provides key information in order to tune the acceleration RF phase. So that the most important information should be extracted from the fundamental RF component, 324MHz. The beam phase monitor has to have an efficient response to this RF fundamental component.

The conventional current transformer is difficult to extend its high frequency cut-off, $1/CR=\omega_H$, because of the stray-capacitance. Using crystallized magnetic alloy makes the beam phase monitor transformer, and a single winding is taken to reduce the stray-capacitance. The frequency response of the Fast-Current-Transformer (FCT) has been sufficiently extended up to GHz region.

Finemet^{TM} core (Hitachi Metals, Ltd.) with high magnetic permeability is employed for the FCT, a single tern coil is combined with the Finemet core with 5 mm thickness is for a coil (fig. 1). Except for MEBT and DTL subsection, each current transformer has its inductive core

*miura.akihiko@jaea.go.jp

Copyright © 2012 by the respective authors — cc Creative Commons Attribution 3.0 (CC BY 3.0)

outside of the vacuum chamber in order to avoid any outgas from the monitor parts. Therefore a small ceramic block is employed for RF signal to be transmitted through (toward the inductive core) while a vacuum enclosure is tightly kept (fig. 1).

A signal can be picked up with the reference frequency as ω, and the output is described below.

$$V = \frac{j\omega L/Z}{1+j\omega L/Z} \cdot \frac{RI}{N} \quad (1)$$

Here, I shows a beam current, Z shows the characteristic impedance, N shows the number of coil and L shows self-inductance.

DESIGN OF BPM

J-PARC Linac employs the strip-line type beam position monitor to avoid the space problem (fig. 2). The diameter and the length depend on the aperture size and the accelerated energy.

Accuracy of the position is stably maintained at 0.1 mm using a test bench. Because new BPMs are also required the same accuracy, we designed the pickups and the body. Basic design is taken over from the present BPMs and in order to define the design of the pickup, two-dimensional electro-magnetic simulation is conducted. After obtained the simulation results, we fabricate the prototype one for the measurement. A variety of the width of pickup are tried to match the corresponding impedance (50 ohm) and finally decide the pickup and body design. Calibration of the BPMs has already completed.

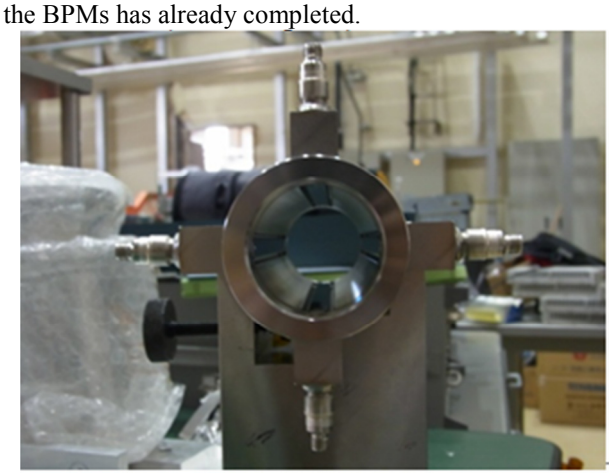

Figure 2: Beam Position Monitor (BPM).

BPM signal which is induced from the electrical charge of beam pulse on the strip-line is obtained. When we consider the equivalent circuit of BPM based on the induction principal, inducted output signal is described below.

$$V = \frac{I\theta/2\pi}{1/R+1/Z} \quad (2)$$

Here, Z is the characteristic impedance and it is adjusted to 50 ohms. θ is a composed angle from the beam centre to each strip-line. This is proportional to the width of a strip-line.

BENCH TEST OF FCT AND BPM

Setups at Test Bench

Figure 3 shows the overview of the test bench to measure the characteristic features of phase measurement devices. In the case of figure 3 on the left side, FCT is set on the bench. Waveguides are connected with both flanges and the one side (top) is terminated. From the other side (bottom), RF conductor with ϕ17 mm diameter is inserted to supply the RF signal using network analyzer. Reflected signal and output signal from FCT terminal are measured (fig. 4).

About the characteristic measurement of BPM (fig. 3 right side), BPM is set as same as the FCT. But in this

Figure 3: Overview of the test bench. An FCT is set on left side and a BPM is set on right side.

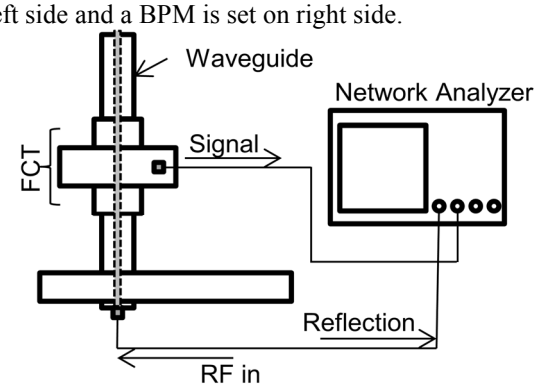

Figure 4: Signal network of characteristic measurement of FCT.

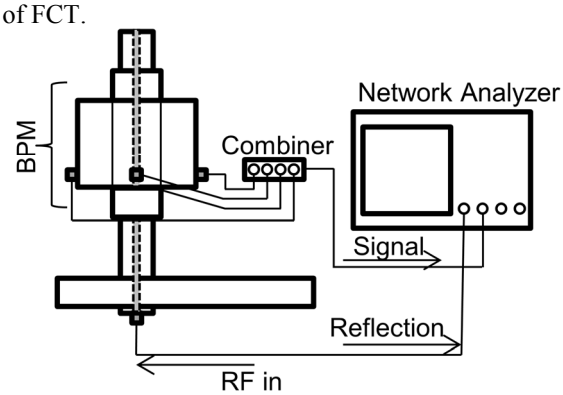

Figure 5: Signal network of characteristic measurement of BPM. Because four strip-lines feel the beam pulse, a combiner is employed for taking the sum of output signal.

Copyright © 2012 by the respective authors — cc Creative Commons Attribution 3.0 (CC BY 3.0)

case, because four strip-lines feel the beam pulse, a combiner is employed for taking the sum of output signal from all strip-lines. And there are two pick-ups as upstream and downstream for each strip-line. One is used in this measurement to obtain the signal, the other side is terminated. When the BPM is installed in the beam line, because the impedance of each cable is matched 50 ohms, one is used for beam position measurement and the other one can be used for the phase measurement.

Performances of FCT and BPM for Phase Measurement

Measured performance data of FCT and BPM using network analyser are shown in figure 6 and 7. Measured signal level at 324 MHz are -15.742 dB for FCT and -25.967 dB for BPM. If the signal loss is calculated using following formula, we can discuss the signal level.

$$\text{Signal Loss(dB)} = -20\log(\text{V_out/V_in}) \quad (3)$$

Input signal level from network analyser is corresponding to 0.5 V, and estimated signal from FCT is

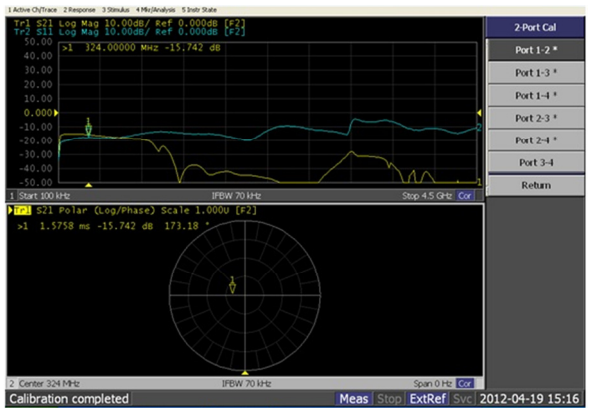

Figure 6: Measured performance of FCT using network analyzer.

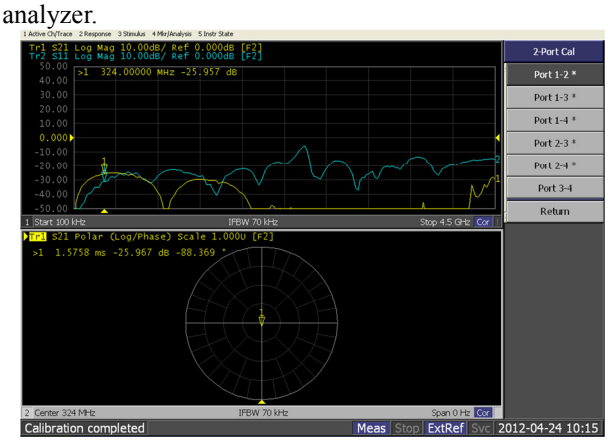

Figure 7: Measured performance of BPM. For the figure 6 and 7, in the upper box, yellow line shows the reflection of the input RF. And water color shows the characteristic response from FCT and BPM respectively. Arrow sign shows the 324 MHz which is the acceleration frequency in J-PARC accelerator cavities. In the lower box, shifted phase is measured through the FCT/BPM head, flanges, cables connectors.

82 mV and that from BPM is 25 mV. By this estimation, the signal from FCT is three times higher than that from BPM.

Three times higher frequency (972MHz) is used for the ACS accelerator cavity. Because the characteristic response of FCT is kept for the higher frequency and cut-off frequency is very high, FCT will be employed up to GHz region. But the characteristic response of BPM is periodical for the higher frequency, BPM will have a good performance at 324 MHz. If we employ the BPM for phase measurement at higher frequency, we need to consider the obtained data.

SUMMARY

We have measured the performances of FCT which is designed for energy upgraded linac. Signal level of FCT is so high to be transferred to a phase detection circuit that it achieved good performance at the acceleration frequency. And it would be used for the higher frequency, because the output level is stable up to 3.0 GHz. Signal revel of BPM designed for the energy upgraded linac is also acceptable to be used for the phase measurement. But, when these monitors are compared in the phase measurement, FCT has a superiority at the acceleration frequency.

Because the width and length of strip-line is depending on the beam energy, signal level is also depending on the beam energy. Then, this consideration is not general, it can be only referred for both FCT and BPM designed for energy upgraded linac. But FCT is confirmed to be sufficiently used for the higher frequency region.

When the ACS cavities are installed for energy upgrade, both FCTs and BPMs are installed at the same time. We will confirm above performance and compare them.

ACKNOWLEDGMENT

We would like to express thanks to the engineers of Mitsubishi Electric System & Service Co., Ltd. for their efforts and help.

REFERENCES

[1] H. Ao, et. al., “Status of J-PARC Energy Upgrade”, Proc. of LINAC10, TU201, Tsukuba, Japan.
[2] A. Miura, et. al., “Beam Diagnostics in the J-PARC Linac for ACS Upgrade”, Proc. of DIPAC2011, MOPD08, Hamburg, Germany.
[3] T. Miyao, et. al., “Beam Position Monitors for ACS Section of the J-PARC Linac”, Proc. of DIPAC2011, TUPD018, Hamburg, Germany.
[4] K. Hasegawa et. al., “Status of J-PARC Acceleration Facilities after the Great East Earthquake in Japan”, Proc. of IPAC2011, WEPS095, San Sebastian, Spain.
[5] A. Miura, et. al., “Beam Monitor Deformation by Tohoku Earthquake and its Recovery Project”, Proc. of IPAC2011, WEPC144, San Sebastian, Spain.

Copyright © 2012 by the respective authors — cc Creative Commons Attribution 3.0 (CC BY 3.0)

CSNS DTL PROTOTYPING AND RF TUNING

H.C. Liu, X.J. Yin, J. Peng, A.H. Li, K.Y Gong, Y.C. Xiao, Q. Chen, S.N. Fu
Institute of High Energy Physics, Beijing, China

Abstract

The 324MHz Alvarez-type Drift Tube Linac (DTL) for the China spallation neutron source will be used to accelerate the H^- ion beam of up to 15mA peak current from 3 to 80MeV. It consists of four independent tanks, of which the average length is about 8.6 m. Each tank is divided into three short unit tanks about 2.8 m in length for easy manufacture. A full-scale prototype of the first unit tank with 28 drift tubes containing electromagnetic quadrupoles has been constructed to validate the design and to demonstrate the technology. The overall features of the prototype in both key technology and RF tuning are presented. In particular, the influence of the post couplers was studied in the ramped field DTL.

INTRODUCTION

The China Spallation Neutron Source (CSNS) Linac mainly consists of an H^- ion source, a LEBT, a 3 MeV RFQ, a MEBT and an Alvarez-type Drift Tube Linac (DTL) as shown in Figure 1[1]. The DTL will accelerate H^- ion beam of up to 15mA peak current from 3 to 80 MeV in 4 accelerating cavities over a length of 35m. These four RF cavities operating at 324MHz and at 1.05 duty cycles are 560mm in diameter. Several new features have been incorporated in the basic design, leading to many technical difficulties, especially in the low energy section. A 2.8m long full-scale prototype thus has been built to validate the design principles. RF low-power measurements were performed to verify the electro-magnetic properties of the cavity and to define the most appropriate tuning strategy.

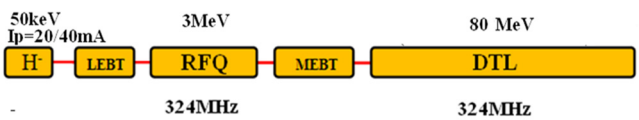

Figure 1: CSNS Linac layout

RF STRUCTURE

The Prototype RF structure includes a single tank, 28 drift tubes accommodated with electromagnetic quadrupoles, end walls, slug tuners, and post couplers. See Figure 2 for a general layout of the prototype Model.

Tank Fabrication

The tank is a vacuum vessel that provides a RF envelope and a mechanically stable platform for the array of drift-tube assemblies, post couplers, and slug tuners. It is made of a carbon steel tube with copper plated in the inner surface to increase its electrical conductivity. It contains 9 large ports for tuners, vacuum, and approximately 60 small ports for drift-tubes, post couplers and pickups. Tank inner surface and all ports were coated with Oxygen-Free Copper (OFC) applying successfully the Periodic Reverse (PR) copper electroforming technology.

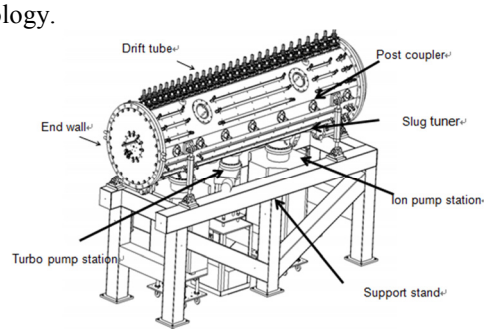

Figure 2: CSNS prototype DTL

Figure 3 shows the tank prototype module after electro-forming. The inner copper surface has been polished and the ports have been finish machined for high accuracy and high flatness. The measured inner surface roughness is between 0.26 and 0.29μm. The average copper thickness is 0.2 mm (design 0.15 mm).

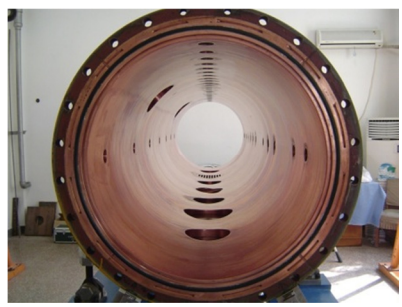

Figure 3: Internal view of DTL prototype

Drift tube

Each drift tube assembly is comprised of a body and stem, see Figure 4. One of the main features of the CSNS DTL is the use of OFC in all parts of DTs. Long-term deformation test has been done which convinced us of the material selection and design.

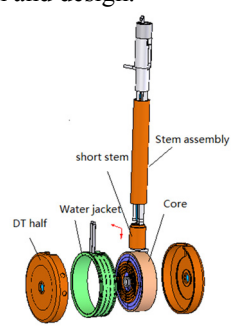

Figure 4: View of a typical Drift tube

liuhc@mail.ihep.ac.cn

Copyright © 2012 by the respective authors — cc Creative Commons Attribution 3.0 (CC BY 3.0)

The fabrication process is complex and time consuming accompanied with many kind of tests. All parts of the DT and the stem (34 mm in diameter) are fabricated by the electron beam welding (EBW) after the installation of the EMQ into the DT. The space around the magnet in the DT is filled with the epoxy resin by a vacuum impregnation method.

The magnetic field is measured several times by a rotating coil measurement system during the DT fabrication process [3]. Modifications have been introduced to make the rotating coil system more accuracy. Figure 5 shows the records which compare the deviations of the mechanical centre from the magnetic field centre before and after the measurement system upgrade. It can be found that most of the deviations (round one) fall into the tolerable area ±30 μm after the measurement system upgrade compared with those (squares) before the upgrade. The average deviation decreases from 28.6 to 14.5μm, approximately 51%. Correspondingly the ratio of the dipole component and the quadrupole component becomes less than 0.05% at the magnetic centre compared with 0.3% before the upgrade. Higher-order multi-pole components are also sufficiently small at the field centre.

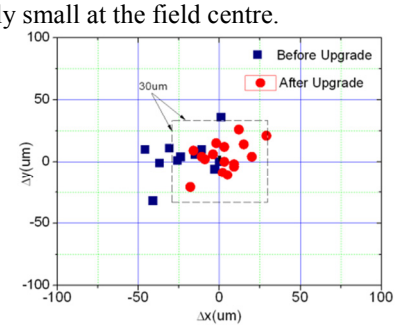

Figure 5: Deviation of the mechanical centre from magnetic field centre before and after upgrade.

Other Components

Some aluminium cold models needed in the low power tuning of prototype DTL cavity include post couplers and slug tuners, have been developed. The vacuum grill and tank end wall containing a half DTL also have been fabricated for test.

Figure 6: Aluminium cold models: post coupler (a), slug tuner (b), vacuum grill (c) and end wall (d).

ACCELERATING FIELD

The tuning of the DTL tank basically includes three items, namely resonant frequency tuning, field profile tuning and stability tuning against perturbations. A bead perturbation method was chosen for field distribution measurement. Normally, it's required an aluminium bead, monofilament fishing line, a motor to step the bead through the cavity, and a network analyser to measure the phase changes due to bead. The space resolution was about 1mm per data point.

The general technique to tune the cavity is as follows [3]:

- Using the slug tuners, with the post couplers removed. Tune the cavity fields so that the fields follow the design field.
- After the fields are to within a few percent of the design field, insert the post couplers to establish the stabilization.
- Orient the post couplers to tune the fields and adjust the length of post couplers to maintain required tile sensitivity.

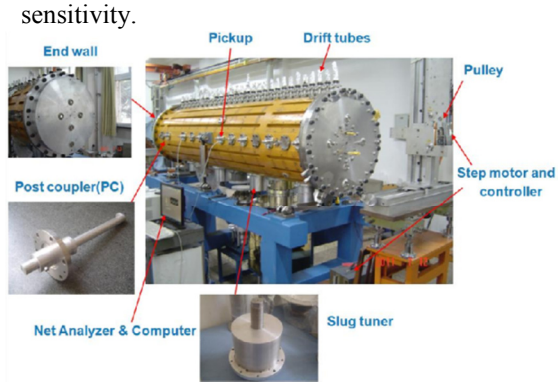

Figure 7: Tuning setup for DTL tank

Adjustment of the Tuners

The prototype DTL tank has 4 slug tuners for resonant frequency and field tuning. Firstly, the field with all the slug tuners penetrating into the cavity to an identical penetration depth has been measured, about 20% maximum deviations from the design value. The frequency sensitivity for each slug tuner has been obtained in advance. After adjustment of the slug tuners, the electric field distribution along the beam axis is within ±2% as shown in Figure 8.

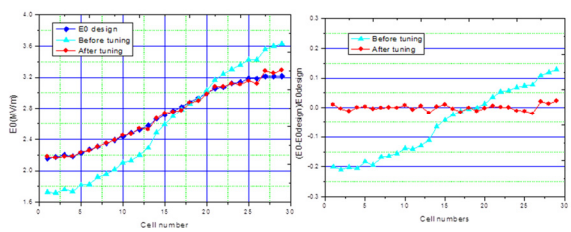

Figure 8: Slug tuner adjustment.

Adjustment of the Post-couplers

The post-couplers are used in DTL cavities to create a secondary coupled resonator system, which is then coupled with the main resonator system, formed by the accelerating cells resonating in the TM_{01} mode. The purpose of the PC is to stabilize the accelerating field in

Copyright © 2012 by the respective authors — cc Creative Commons Attribution 3.0 (CC BY 3.0)

case of local frequency errors. This can be done by tuning the dispersion curve of PC band and TM_{01} band such that the stop band between these two curves to be very small. The PCs are expected to have a negligible effect on the nominal accelerating field, and we start with all PCs inserted into the cavity as far as possible to get a lower enough frequency for PC mode. For the field stabilization of the TM_{010}, the mode with the highest resonant frequency in the PC band (PC1) should locate in the symmetric position in the frequency spectrum to the TM_{011} mode in most cases. However, in the prototype DTL design, the average accelerating field linear ramp from 2.2 to 3.1MV/m and then keeps constant. When the post-couplers inserted into the cavity, the field distribution and the resonant frequency change by quite a bit according to the measurement. The Q value of the accelerating mode as a function of the post-coupler insertion depth also has been investigated, see Figure 9. While the stop band between the dispersion curve of the PC mode and that of the TM-band was adjusted to be zero by means of gradually pull out all PCs, the Q value of the TM_{010} decreased by a factor of two at a PC-DT length of about 3cm. It has confirmed us that the conventional tuning method for flat field will not work in the ramping field structure. Unlike the flat field structure, the PC influence on the single cell differs significantly from the others in the ramping field cavity, especially in the low energy section, results in unsymmetrical locations between PC1 and TM_{011}. On the other hand, the loss in the aluminium material is bigger compared with that of copper, leading to a negative impact on Q value. Therefore, we modified the post-couplers shape and material in order to increase the cavity Q value and better understand the PC stabilization mechanism in the ramping field cavity.

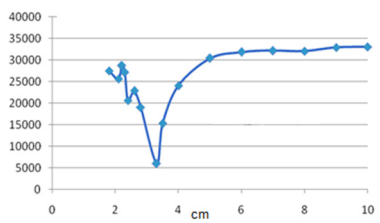

Figure 9: Unloaded Q value of TM010 versus PC-DT gap length

After adjusting the PC-DT gap to define the region where the Q value appeared to be insensitive to the PC penetration length, we get the tilt sensitivity directly by making two repetitive bead-pull measurements. The initial adjustment of the post-couplers has been done by keeping up the PC-DT length constant within the limited region. The axial field profile has been measured before and after frequency perturbation of the two end tuners. A considerable number of tests with finely adjusting the PC-DT gap have been undertaken to make the tilt sensitivity less than ±100%/MHz, some individual PC adjustment results in a smooth TS curve. At this stage, the orientation angles of all the post-couplers keep constant. It is noticed that small TS fully compatible with the design value do not guarantee that the fields are at the design value. Achieving the fields to be at the design value requires that the post couplers be rotated. Rotating the post coupler in a particular direction will reduce the fields in that particular direction. Since the fields are generally only locally perturbed by rotating the post coupler, the field tuning can be done step by step. Once the fields are flat from rotating the post couplers, the fields should be checked for tilt sensitivity. This tuning procedure is basically iteration process. Figure 10 shows the field profile after stabilization. The overall RF properties of the prototype DTL are listed in Table 1.

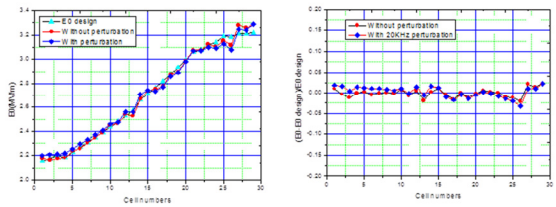

Figure 10: Field profile after post-couplers adjustment.

Table 1: RF properties of prototype tank

	Design	measurement
Resonant frequency	323.9@20°C	323.923@26°C
Unloaded Q	>80% calculation	81.9% calculation
Field flatness	⩽2%	-2%~1%
Tilt sensitivity	⩽100%/MHz	99%~-68%/MHz

CONCLUSION

The prototypes of the tank and the DT containing 28 EMQs for 324 MHz DTL have been developed in IHEP for the CSNS project. The RF properties have been measured for this prototype DTL. The tuning scheme and the procedures for ramping field DTL tank are established and the prototype was successfully tuned to meet the tuning requirement. The CSNS DTL will be constructed based on the experienced gained in the manufacture, assemblies and test of this prototype cavity.

REFERENCES

[1] Yin X J, Gong K Y, Peng J, et al. Development of a 324 MHz drift tube Linac for CSNS, TUP062, Proceedings of LINAC2010.

[2] Takasaki E, Naito F, Tanaka H, et al. Results of the magnetic field, measurements of the DTL quadrupole magnets for the J-PARC, Proceedings of LINAC.2004.

[3] C. Deibele, DTL Cavity Tuning at SNS, SNS-NOTE-ENGR-74.

Copyright © 2012 by the respective authors — cc Creative Commons Attribution 3.0 (CC BY 3.0)

STUDY ON THE BEAM DYNAMICS IN THE RISP DRIVER LINAC

H. J. Kim, J.-G. Hwang, and D. Jeon, RISP, Deajeon, Korea

Abstract

Rare Isotope Science Project (RISP) has been proposed as a multi-purpose accelerator facility for providing beams of exotic rare isotopes of various energies. The RISP driver linac which is used to accelerate the beam, for an example, Uranium ions from 0.3 MeV/u to 200 MeV/u consists of superconducting RF cavities and warm quadrupole magnets for focusing heavy ion beams. Requirement of the linac design is especially high for acceleration of multiple charge beams. In this paper, we present the RISP linac design and the requirements of dynamic errors to minimize the beam centroid oscillation and preserve beam losses under control.

INTRODUCTION

The RISP (Rare Isotope Science Project) accelerator has been planned to study heavy ion of nuclear, material and medical science at the Institute for Basic Science (IBS). It can deliver ions from proton to Uranium with a final beam energy, for an example, 200 MeV/u for Uranium and 600 MeV for proton, and with a beam current range from 8.3 pμA (Uranium) to 660 pμA (proton) [1, 2]. The facility consists of three superconducting linacs of which superconducting cavities are independently phased and operating at three different frequencies, namely 81.25, 162.5 and 325 MHz.

The layout of the RISP accelerator is shown in Fig. 1. The Uranium ions produced in an electron cyclotron resonance ion source are preaccelerated to an energy of 300 keV/u by a radio frequency quadrupole and transported to the superconducting cavities by a medium energy beam transport. The driver linac is divided into three different sections: low energy superconducting linac (SCL1), charge stripper section and high energy superconducting linac (SCL2). Figure 2 shows a conceptual structure of SCL1 and SCL2. The SCL1 uses the two different families of superconducting resonators, i.e., quarter wave resonator (QWR) and half wave resonator (HWR). The SCL11 consists of 24 QWR's whose geometrical β is 0.047 and 24 doublets. The resonance frequency of QWR is 81.25 MHz. The cryomodule of the SCL11 hosts one superconducting cavity. The SCL12 consists of 138 HWR's whose geometrical β is 0.12 and 36 doublets. The resonance frequency of HWR is 162.5 MHz. This segment has the two families of cryomodules: one type of cryomodule hosts three superconducting cavities and the other hosts six superconducting cavities.

The SCL2 consists of the SCL21 and the SCL22, each consisting of geometric β 0.30, resonance frequency 325 MHz Single Spoke Resonators (SSR) and geometric β 0.53, resonance frequency 325 MHz SSR. Single Spoke Resonator type is chosen mainly because it can have a larger bore radius compared with the Half Wave Resonator type, which is very essential to reduce the uncontrolled beam loss in the high energy linac section. The number of cavities in the SCL21 and SCL22 is 88 and 138 respectively. The cryomodule of the SCL21 and SCL22 hosts 4 and 8 cavities respectively. Table 1 summarizes the parameter of four different superconducting cavities. The charge stripper section is located between SCL1 and SCL2. The charge stripper strips electrons from heavy ion

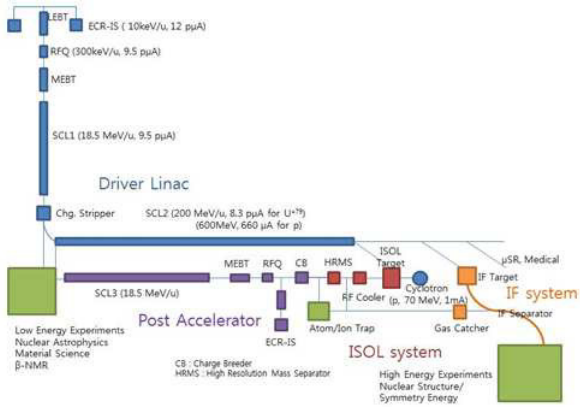

Figure 1: Layout of the RISP accelerator.

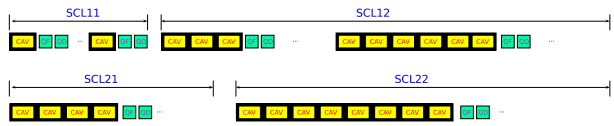

Figure 2: Layout of the SCL: SCL1 (top) and SCL2 (bottom).

Table 1: Superconducting cavity parameters.

Parameter	unit	QWR	HWR	SSR 1	SSR 2
β_g		0.047	0.12	0.30	0.53
Frequency	MHz	81.25	162.5	325	325
Aperture	mm	40	40	50	50
V_{acc}	MV	1.02	1.07	2.04	3.53
E_{peak}/E_{acc}		5.08	6.2	4.06	4.15
B_{peak}/E_{acc}	mT/(MV/m)	9.16	8.4	7.07	8.6
QR_s	Ohm	37	47	86	108
R/Q	Ohm	480	319	242	304
Temperature	K	2	2	2	2
Q_0	10^9	3.6	4.6	8.1	10

Copyright © 2012 by the respective authors — cc Creative Commons Attribution 3.0 (CC BY 3.0)

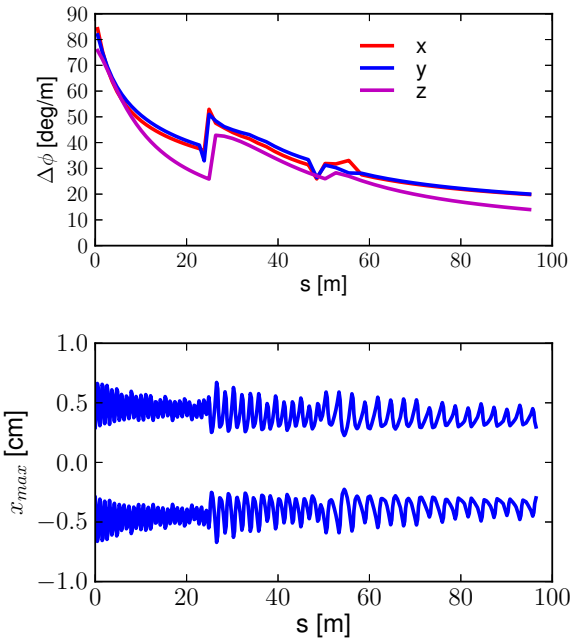

Figure 3: Phase advance per unit length (bottom) and maximum horizontal beam size envelope along the length of SCL1 (top) without machine imperfections.

Table 2: Machine imperfection of RISP lattice using quadrupole as a focusing element. Displacement and rotation errors are uniformly generated. Phase and amplitude errors are 3 σ Gaussian.

Parameters	SC Cavity	Quadrupole
Displacement (mm)	$\pm$1	$\pm$0.15
Phase (deg)	$\pm$1	-
Amplitude (%)	$\pm$1	-
Rotation (mrad)	-	$\pm$5

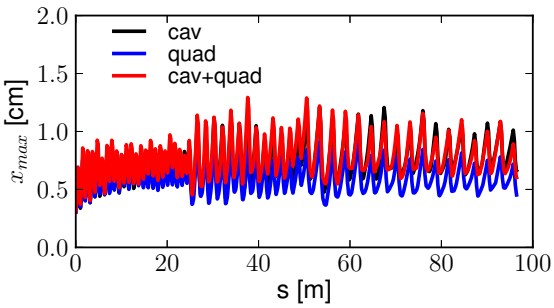

Figure 4: Plot of maximum horizontal envelope for SCL1 due to machine imperfections.

beams to enhance the acceleration efficiency in the high energy linac section. The charge stripping section consists of four normal conducting quadrupole triplets and two room-temperature 45 degree bending magnets. The quadrupole magnets provide adequate transverse focusing and beam matching to the SCL2 and bending magnet provides the momentum dispersion for the charge selection.

The post accelerator (SCL3) is designed to accelerate the rare isotopes produced in the ISOL (Isotope Separation On-Line) system up to 18.5 MeV/u. The SCL3 is, in principle, a duplicate of the driver linac up to low energy linear accelerator. The accelerated rare isotope beams are reaccelerated in the SCL2. Hence, the RISP accelerator provides a large number of rare isotopes with high intensity and with various beam energies.

BEAM DYNAMICS SIMULATIONS

The RISP linac is a flexible structure to deliver heavy ions from proton to Uranium. The linac lattice is optimized by minimizing emittance growth and potential for beam loss by keeping a beam envelope smooth and regular. A transverse phase advance per period is kept under 90 degrees to prevent envelope instabilites. The ratio of transverse to longitudinal phase advance is kept in the range of 1.2 to 1.6 to avoid a resonance due to parametric coupling between longitudinal and transverse planes. Figure 3 shows phase advance per unit length along the length of SCL1. The maximum beam envelopes shown in Fig. 3 are kept less than 7 mm along the linac.

For the actual SCL, machine imperfections cannot be avoided. The error comes from the misalignment of the linac elements and the limitation of manufacturing accuracy and various control errors. For instance, steering magnets are used to correct beam orbit displacements. In the baseline design of the RISP linac, steering magnets are placed where normal conducting quadrupoles are. The misalignment analysis includes all superconducting cavities and focusing elements assuming a uniform distribution. Table 2 summarizes tolerances for the lattice consisting of superconducting cavity and normal conducting quadrupole. It has been well known that the normal conducting quadrupole can be aligned in an accuracy of $\pm$150 μm [4]. The rotation angle about the z-axis is set to 5 mrad. The rotation angle is important due to the skew quadrupole term while it is independent of the solenoid due to symmetry of solenoid field. In the misalignment and RF error analysis, charge states of 33+ and 34+ of Uranium beams are used. Effect of machine imperfection on beam envelope is shown in Fig. 4. The maximum envelope is kept well below the transverse aperture 20 mm of SCL1.

In order to examine the quality of the present quadrupole-based driver linac lattice, effects of machine imperfections on the beam parameters are investigated, compared with the previous linac design based on superconducting solenoids. To summarize the layout of the previous SCL design of briefly, the SCL11 consists of three cryomodules where each cryomodule hosts eight superconducting cavities and eight superconducting solenoids. The solenoid is used to focus the beam. The SCL12 consists of twelve cryomodules where each cryomodule hosts eight cavities and three solenoids. Diagnostic devices and steer-

Copyright © 2012 by the respective authors — cc Creative Commons Attribution 3.0 (CC BY 3.0)

Table 3: Machine imperfection of superconducting solenoid-based lattice. Displacement and rotation errors are uniformly generated. Phase and amplitude errors are 3 σ Gaussian.

Parameters	Quadrupole	Solenoid
Displacement (mm)	$\pm$0.15	$\pm$0.5
Phase (deg)	-	-
Amplitude (%)	-	-
Rotation (mrad)	$\pm$5	$\pm$5

Table 4: Variation of beam parameters due to machine imperfections.

Parameters	Initial	Doublet	Solenoid
x_{max} (cm)	0.3	0.7	1.7
y_{max} (cm)	0.6	1.0	1.5
ϕ_{max} (deg)	26.8	10.2	75.6
ϵ_x (cm-mrad)	0.013	0.016	0.026
ϵ_y (cm-mrad)	0.013	0.016	0.024
ϵ_z (keV/u-ns)	1.3	2.74	1.33
$x_{centroid}$ (cm)	0.0	0.32	1.20
$y_{centroid}$ (cm)	0.0	0.50	0.97
$\phi_{centroid}$ (deg)	0.3	3.25	5.60

ing magnets can be placed in the drift spaces between cavity and quadrupole or between quadrupoles in the doublet lattice while they should be placed between cryomodules in the solenoid lattice. The length of quadrupole-based linac is commensurate with solenoid-based linac. The particle tracking with machine errors is performed with the TRACK code which has been developed in ANL [3]. Table 3 summarizes tolerances for the lattice consisting of superconducting solenoids. The maximum transverse displacement of solenoid is set to 0.5 mm. This displacement is half of the offset of superconducting cavities, but the effect of solenoid displacement is expected to be detrimental to beam dynamics in the linac. Only the SCL11 is used for comparison of beam performance. For multi-charge state beam acceleration, a strong focusing is required. The misalignment of superconducting solenoids is, from the error simulations, found to affect the beam properties more than that of normal conducting quadrupole. As shown in Fig. 5, the misalignment of superconducting solenoid increases the maximum beam envelope by 3.5 times while the normal conducting quadrupole error increases the envelope only by 0.8 times. The aperture radius of quadrupole and solenoid is 20 mm. The envelope due to solenoid misplacement goes high up to 1.7 cm just after the SCL11The maximum increase of rms emittance is 10% for doublet lattice, while it is 140% for solenoid lattice. The effects of cavity misalignment and RF error on longitudinal emittance are less sensitive than focusing elements. The dynamics simulation results are summarized in Table 4.

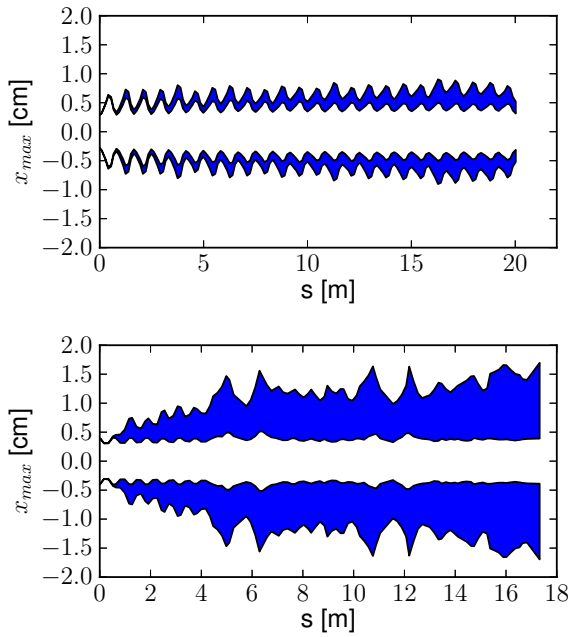

Figure 5: Plot of maximum horizontal beam envelope: doublet lattice (top) and solenoid lattice (bottom). The shade region represents the bounds of envelope variation.

SUMMARY

Beam dynamics design of the RISP low and high energy linac has been presented. In the design, the focusing in the superconducting linacs is provided by normal conducting quadrupole doublets. Four different cavities, such as QWR, HWR, SSR 1 and SSR 2, are used to accelerate the beam in the linac. The number of cavities per cryomodule at each section is optimized to minimize the total number of cavities required for the efficient acceleration. We emphasize the stability of operation, flexibility of maintenance, and the minimization of beam loss. The linac design with normal conducting quadrupole gives a good beam quality.

ACKNOWLEDGMENTS

We thank B. Mustapha for help with the TRACK code. This work was supported by the Rare Isotope Science Project which is funded by the Ministry of Education, Science and Technology (MEST) and National Research Foundation (NRF) of KOREA.

REFERENCES

[1] S.K. Kim et al, "Rare Isotope Science Project: Baseline Design Summary", http://www.risp.re.kr/.

[2] D. Jeon et al, "Overview of the Superconducting Linacs of the Rare Isotope Science Project", this conference.

[3] V.N. Aseev et al, Proceedings of 2005 Particle Accelerator Conference, Knoxville, Tennessee, p. 2053.

[4] S. Nath et al., ASAC Review presentation, October 2001, SNS/ORNL, Tennessee., USA

Copyright © 2012 by the respective authors — cc Creative Commons Attribution 3.0 (CC BY 3.0)

AMPLITUDE AND PHASE CONTROL OF THE ACCELERATING FIELD IN THE ESS SPOKE CAVITY

V.A. Goryashko *, V. Ziemann, R. Yogi, R. Ruber, Uppsala University

Abstract

We report about numerical simulations of the accelerating field dynamics in the ESS spoke cavity in the presence of the beam loading and Lorentz detuning. A slow feedforward is used to cure the Lorentz detuning whereas a fast feedback through a signal oscillator and cavity pre-detuning technique are applied to eliminate the beam loading effect. An analysis performed with a Simulink model shows that a combination of feedforward, feedback and cavity pre-detuning result in a substantially shorter stabilization time of the field voltage and phase on a required level as compared to a control method using only the feedforward and feedback. The latter allows one to obtain smaller magnitude but longer duration deviations of the instantaneous voltage and phase from the required nominal values. As a result, a series of cavities only with feedforward and feedback needs an extra control technique to mitigate a cumulative systematic error rising in each cavity. In addition, a technique of adiabatic turning off of the RF power in order to prevent a high reflected power in the case of a sudden beam loss is studied.

INTRODUCTION

To obtain the beam of a high quality in terms of the energy spread and emittance the cavity voltage magnitude and phase should be controlled very accurately. According to the ESS design [1], the voltage magnitude deviation must be below 0.1% of the total value and its phase deviation must not exceed 0.5 degrees. This can be achieved by means of an appropriate control. The most widely used control technique is the negative feedback based on a PID controller. The idea is to control a system's output by comparing it to a desired setpoint and feeding the error back to the input dynamically. At the same time, when a perturbation can be foreseen like the Lorentz detuning, it is useful to use a feed-forward technique to prevent such a perturbation. Combined feedback and feed-forward control can significantly improve performance over simple feedback architectures when there is a major disturbance to the system that can be measured beforehand [2]. In the present paper we apply aforementioned techniques of the control to stabilize the spoke cavity voltage magnitude and phase.

THE BEAM-CAVITY INTERACTION: FEEDBACK AND FEED-FORWARD

To study the evolution of the accelerating field in a spoke cavity we will adopt the traditional model [3], in which the cavity is presented by the lumped RLC circuit, the coupler

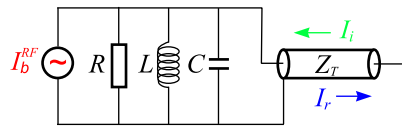

Figure 1: The lumped model: cavity modeled by an RLC circuit, the coupler by a connected transmission line of impedance Z_T and the beam by a current source.

by the transmission line with impedance Z_T on which we have the incident (generator) wave current I_i and the reflected wave current I_r. The latter is assumed to disappear without re-reflection. The beam is modeled as a current source I_b^{RF}, where I_b^{RF} is the RF beam current that is twice of the DC beam current, $I_b^{RF} = 2I_b^{DC}$. The cavity characterized by the resonant frequency ω_0 is excited to voltage V_c under these conditions.

We will assume that variations of the generator and beam currents as well as external perturbations are slow as compared to the RF period such that a dynamic quantity may be represented as a product of a slow varying envelope multiplied by $\exp(i\omega t)$ (in general case ω is not identical to ω_0), e.g. $V_c(t) = \mathrm{Re}\{A(t)\exp(i\omega t)\}$ and $\omega^{-1}\mathrm{d}\ln A/\mathrm{d}t \ll 1$. Impedances of the loaded cavity and transmission line can be expresses in terms of the shunt cavity resistance R, and three quality factors: Q_0 is the quality factor of the bare cavity, Q_{ext} is the quality factor of the cavity with the coupler, $Q_L = (Q_0^{-1}+Q_{ext}^{-1})^{-1}$ is the total quality factor. For a superconducting cavity the loaded quality factor is mainly determined by the external Q-factor, $Q_L \approx Q_{ext}$. Then, using the slow varying approximation we arrive at a first order differential equation for the complex cavity voltage amplitude [3]

$$t_F\frac{\mathrm{d}A}{\mathrm{d}t}+A(1-2i\delta Q_L) = 2Q_L\frac{R}{Q}\left[I_i(t)-I_b^{DC}(t)F_b\mathrm{e}^{-i\phi_e}\right], \quad (1)$$

where $\delta = (\omega_0-\omega)/\omega$ is the normalized detuning, ϕ_e is the synchronous phase defined according to the electron linac convention (the energy transfer from the field to the beam is maximal when $\phi_e = 0$), F_b is the beam form-factor, t and $t_F = 2Q_L/\omega$ are the observation and filling time, respectively.

The current reflected by the cavity reads

$$I_r(t) = \frac{1}{2Q_L(R/Q)}\left[A(1+2i\delta Q_L) - t_F\frac{\mathrm{d}A}{\mathrm{d}t}\right] - I_b^{DC}(t)F_b\mathrm{e}^{-i\phi_e}. \quad (2)$$

and the power coming to the cavity from the coupler (incident power) and the power reflected by the cavity to the

* vitaliy.goryashko@physics.uu.se

Copyright © 2012 by the respective authors — cc Creative Commons Attribution 3.0 (CC BY 3.0)

coupler are

$$P_{i,r} = \frac{R/Q}{2} Q_{ext} |I_{i,r}|^2. \quad (3)$$

The energy conservation low reads

$$\frac{1}{t_F} \frac{\mathrm{d}U_{st}}{\mathrm{d}\tau} = P_g - P_r - P_b, \quad (4)$$

where $U_{st} = |A|^2/2\omega Q_L$ is the energy stored in the cavity and

$$P_b = \mathrm{Re}\{A I^*_{b,DC}\, \mathrm{e}^{i\phi_e}\} \quad (5)$$

is the power transferred to the beam.

Within the steady-state limit ($A(t) = \mathrm{const}$) one can minimize the reflected power by tuning the cavity, the so-called 'reactive beam loding compensation',

$$\frac{\Delta\omega^{opt}}{\omega} = \frac{(R/Q) I_b^{DC} F_b \cos\phi}{V_c} \quad (6)$$

and the reflected power completely disappears if the coupler is also adapted such that

$$Q_{ext}^{opt} = \frac{V_c}{2(R/Q) I_b^{DC} F_b \sin\phi}. \quad (7)$$

For a high Q resonator such as superconducting cavities, the narrow electromagnetic bandwidth makes the coupling between the cavity and the RF feeding source sensitive to rather small amount of detuning. As a result, small mechanical deformations due to, for example, the surronding vibration noise (microphonics) or Lorentz forces (due to the radiation pressure), are a source of concern. Whereas microphonics are usually critical for CW operation, the dynamic detuning associated to Lorentz forces is the main issue for pulsed operation as in the SNS [4]. Then, one can also expect the Lorentz detuning to be especially relevant to the ESS spoke cavity. In the case of the static field pressure the frequency deviation is proportional to the negative square of the accelerating field $\Delta f = -|K_L| E_{acc}^2$, where $K_L < 0$ is referred to as the Lorentz detuning factor in Hz/(MV/m)^2. If we now take into account only the main mechanical mode, then the frequency deviation may be approximately described by a 1st order differential equation

$$\tau_m \frac{d\Delta\omega}{dt} = -[\Delta\omega(t) - \Delta\omega_T(t)] + 2\pi K_L E_{acc}^2, \quad (8)$$

where $E_{acc}^2 = |A|^2/L_{acc}^2$ and $L_{acc} = (n+1)\beta\lambda/2$ are the accelerating electric field and length, respectively, β is the velocity factor, n is the number of spoke bars, λ is the wavelength of the accelerating field, τ_m is the mechanical damping time constant and $\Delta\omega_T(t)$ is a frequency shit due to an external mechanical excitation (such as a piezoelectric tuner).

Analysis of the cavity voltage evolution in the presence of the beam loading and Lorentz detuning with applied feed-forward and feedback controls was performed with a model developed in the Simulink MatLab in a way similar to that realized in [2]. A typical diagram of the control system is shown in Fig. 2.

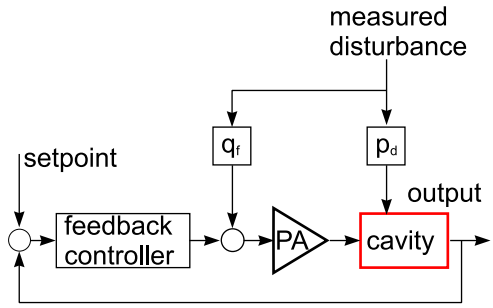

Figure 2: Feedback and feed-forward control of the accelerating voltage of a cavity fed by a power amplifier (PA).

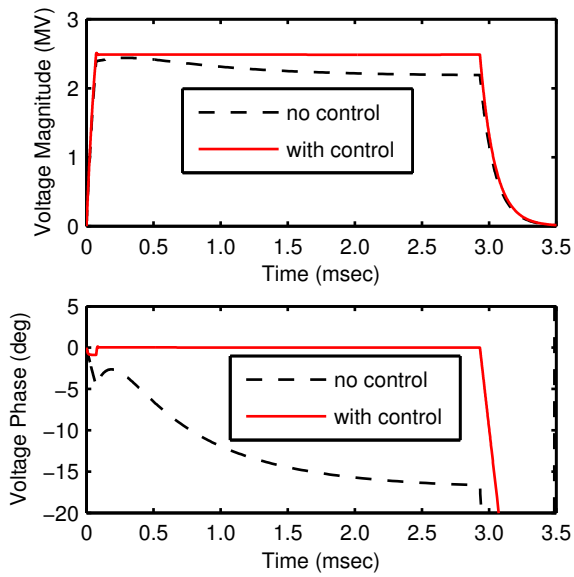

Figure 3: The cavity voltage magnitude and phase vs. time. The solid red curves stand for the spoke cavity with the implemented feedback and feed-forward control whereas the dashed black curves stand for the case with no control.

SIMULATION RESULTS

We performed simulations of the spoke cavity using Eqs. (1)-(8) for the following set of parameters: $I_b^{DC} = 50$ mA, the nominal power ought to be transferred to the beam P_{b0} is 240 kW, $F_b = 1$, $\phi_e = 15.2^o$, $Q_0 = 1.2 \cdot 10^{10}$, $R/Q = 426\Omega$, frequency $f = 351.8$ MHz, optimal initial detuning $\Delta f^{opt} = -395$ Hz, $V_c = 4.974$ MV, $Q_{ext}^{opt} = 1.21 \cdot 10^5$, $t_F = 72\mu$s.

The beam during its passage through the cavity induces the voltage that adds to the voltage induced by the incident (from coupler) current so that the magnitude and phase of the total induced voltage changes during the interaction of the beam with the cavity, see dashed black curves in Fig. 3 representing the cavity voltage magnitude and phase as a function of time. Filling of the cavity with the electromagnetic field is also accompanied by the Lorentz detuning

Copyright © 2012 by the respective authors — cc Creative Commons Attribution 3.0 (CC BY 3.0)

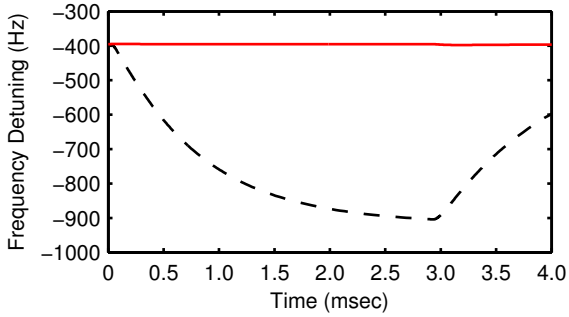

Figure 4: Dynamic detuning of the frequency caused by the electromagnetic pressure vs. time. The red solid curve and the black dashed curve stand for the cavity with and without control, respectively.

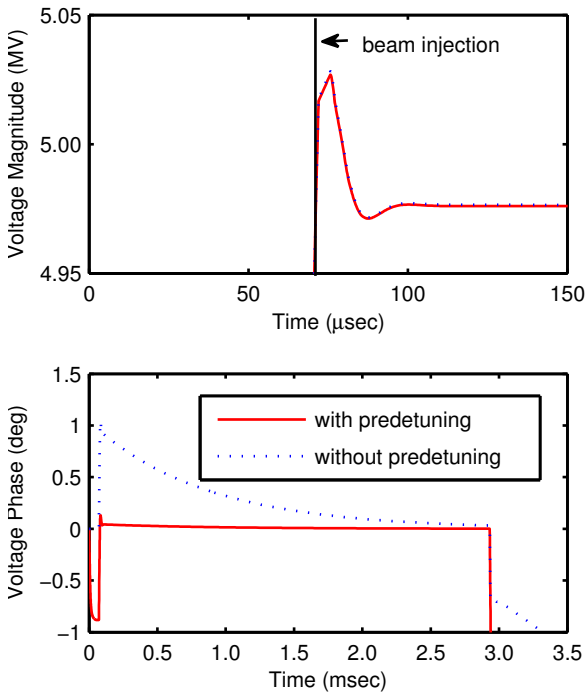

Figure 5: The voltage magnitude and phase of the controlled cavity with (red solid curve) and without (blue dotted curve) the cavity predetuning vs. time. Note that the time scales are different.

shown by the dashed black curve in Fig. 4. One can see that the cavity voltage and phase deviate substantially from the required nominal values. As we mentioned the cavity voltage can be controlled by means of a fast feedback to cure the beam loading and by a slow feed-forward to cure the Lorentz detuning. The results for the controlled cavity are shown at the same Figs. 3, 4 by solid red curves. In addition, in Fig. 5 the voltage magnitude and phase are shown

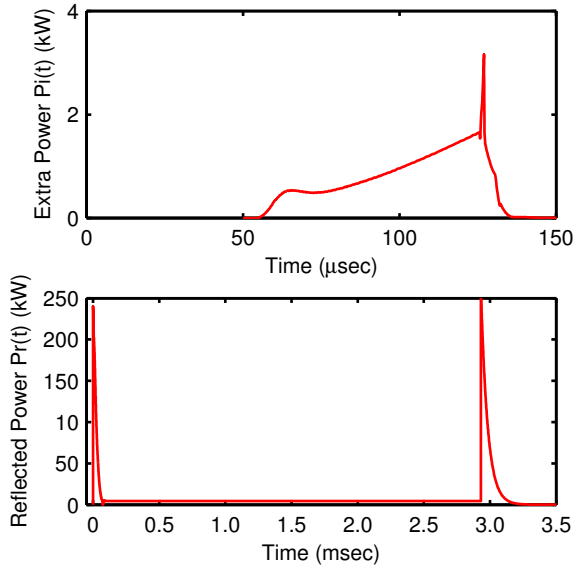

Figure 6: The extra incident power $P_i(t)$ required to compensate the beam loading and the reflected power $P_r(t)$ vs. time. Note that the time scales are different.

in detail. It turns out that using the cavity predetining defined by Eq. (6) one can stabilize the voltage magnitude and phase on the nominal level within 10 μs whereas without the cavity predetuning the phase stabilization can not be achieved. An additional required incident power from the coupler and the reflected power are shown in Fig. 6.

CONCLUSION

We found that that a combination of feedforward, feedback and cavity pre-detuning allows one to stabilize the ESS spoke cavity voltage and phase within 10 μs on the nominal level such that the voltage magnitude error and phase error are 0.5% do not exceed 0.2^o, respectively. The maximal required additional power is around 4.2%.

ACKNOWLEDGMENT

One of the authors (V.A.) is thankful to Dr. Joachim Tückmantel for explaining some elements of the theory of the beam-wave interaction in a cavity.

REFERENCES

[1] S. Pegg, "Conceptual Design Report," ESS-2012-001, 2012.

[2] M. Hermandez, W. Höfle, sLHC Project Report 0054, CERN, April 2001.

[3] J. Tuckmantel, Internal Note, CERN-ATS-NOTE-2011-002 TECH.

[4] M. Doleans, "Studies in reduced-beta elliptical superconducting cavities," PhD, 2003.

Copyright © 2012 by the respective authors — cc Creative Commons Attribution 3.0 (CC BY 3.0)

UPPSALA HIGH POWER TEST STAND FOR ESS SPOKE CAVITIES

R.A. Yogi, A. Rydberg, D. Dancila, K. Gajewski, L. Hermansson, M. Noor, R. Wedberg,
R. Santiago-Kern, T. Ekelöf, T. Lofnes, V. Ziemann, V. Goryashko, R. Ruber,
Uppsala University, Uppsala, Sweden

Abstract

The European Spallation Source (ESS) is one of the world's most powerful neutron source. The ESS linac will accelerate 50mA pulse current of protons to 2.5GeV in 2.86 ms long pulses at a repetition rate of 14 Hz. It produces a beam with 5MW average power and 125MW peak power. ESS Spoke Linac consist of 28 superconducting spoke cavities, which will be developed by IPN Orsay, France. These Spoke Cavities will be tested at low power at IPN Orsay and high power testing will be performed in a high power test stand at Uppsala University.

The test stand consists of tetrode based RF amplifier chain (352MHz, 350 kW) power and related RF distribution. Outputs of two tetrodes shall be combined with the hybrid coupler to produce 350 kW power. Preamplifier for a tetrode shall be solid state amplifier. As the spoke cavities are superconducting, the test stand also includes horizontal cryostat, Helium liquefier, test bunker etc. The paper describes features of the test stand in details.

INTRODUCTION

The European Spallation Source (ESS) is the world's most powerful neutron source. The ESS linac will accelerate 50mA pulse current of protons to 2.5GeV in 2.86ms long pulses at a repetition rate of 14 Hz [1].

ESS Linac has twenty eight superconducting Spoke cavities. The power coupled to the beam ranges from 162 kW to 239 kW per coupler for beam current of 50mA. The RF amplifier for Spoke will power the spoke cavities via RF distribution system. Considering 5% loss overhead in RF distribution system and 25% power overhead for LLRF, the power for RF amplifier will range from 225 kW upto 350 kW.

ESS Specifications for Spoke Linac amplifier:

Frequency = 352.21 MHz
Power = 350 kW
3 dB Band-width = 200 kHz.
Pulse width = 3.5 ms
Pulse repetition rate = 14 Hz

RF amplifier at ESS specifications doesn't exist. Hence there is a need for prototyping it.

Also the superconducting spoke cavity for ESS Spoke Linac is being developed at IPN Orsay. It needs to be tested for high power.

Hence there is a need for High Power Test Stand. The ESS spoke cryomodule consists of two spoke cavities. Hence the test stand shall consist of two high power RF chains. A facility called FREIA is being built at Uppsala University to serve these purposes.

FREIA FACILITIES RELATED TO ESS

FREIA (Facility for Research and Instrumentation for Accelerators) is a facility being developed at Uppsala. First project of FREIA is High Power Test Stand for ESS superconducting Spoke Cavities (fig.1).

High Power Amplifier:

The various technologies of RF sources like tetrodes, solid state, IOTs and klystrons are compared [2] and Tetrode is finalized as the first high power amplifier for the first chain at FREIA.

Three Thales tetrodes TH781, TH391 and TH595 can serve the purpose.

Table 1: Comparison of Tetrodes

Specification	TH781	TH391	TH595
Maximum power at 352MHz	350kW	200kW	200kW
Efficiency	50 – 55%	> 65 %	> 65 %
Gain	11 dB	15 dB	15 dB
Cavity	Doesn't exist	Exist	Exist
Cooling	Water	Air	Water

The calculations show that TH781 can produce 350 kW at 352 MHz but at reduced gain and efficiency. Though TH391 offers improved gain and efficiency, it is air cooled, which allows anode dissipation of only 12 kW. Type of cooling will also affect the size of the system. Air cooling my lead to system with bigger size. TH595 is water cooled and hence it has higher anode dissipation of 40 kW, in addition the system will also be compact.

So 350kW power will be generated by combining outputs from the two tetrodes (TH595) which produce 175 kW each. Power combining will be achieved with help with the 3dB Hybrid coupler.

The specifications for Tetrode amplifier are:

Frequency = 352.21 MHz
Power = 175 kW
3 dB Band-width = 200 kHz.
Pulse width = 3.5 ms
Pulse repetition rate = 14 Hz
Gain > 15 dB
Efficiency > 65%

It is well known that gain of the tetrode reduces with aging. While calculating power needed from the pre-driver, this fact was taken into consideration, so gain of 13 dB is assumed and output power of predriver is 10 kW.

Copyright © 2012 by the respective authors — cc Creative Commons Attribution 3.0 (CC BY 3.0)

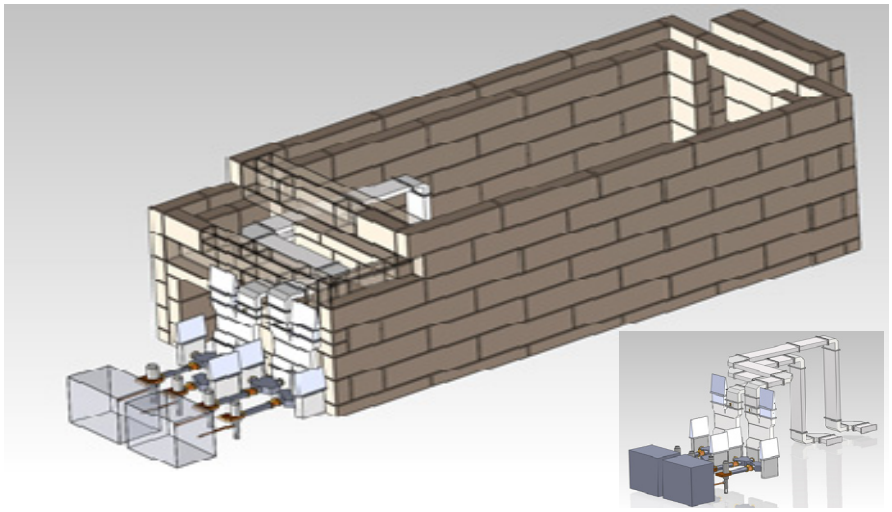

Figure 1: Model of bunker and high power RF chain for ESS spoke cryomodule with inset containing high power RF amplifier and RF distribution at FREIA.

TH595 characteristics [3] show that anode current more than 45 A is not permissible. Hence the tetrode can't be operated in deep class C mode. Hence the design suggests to operate it in class B, thus achieving low harmonic distortion than class C as well as more efficiency than class A.

The calculations show that there will be quicent current of 2 A flowing through the tetrode, which will lead to dissipation and hence decreased efficiency. To avoid this, control grid power supply will be modulated ie. it should be made more negative before and after the RF pulse to get nearly zero quicent current.

Power Supplies for Tetrode Amplifier

The Tetrode amplifier will need four power-supplies. Anode power supply (18kV, 18 A, average output power = 31 kW), screen-grid power-supply (1.3 kV, 0.7 A), control-grid power-supply (400 V, 0.7 A), filament power supply (8.8 V, 190 A rms). As there are two tetrodes in the first chain, it will need two sets of power-supplies.

Instead of using two anode power-supplies, a single anode power-supply powering both the tetrodes will be used, thus achieving lower cost and size [4]. Instead of crow-bar, series switch will be used for protection, thus increasing reliability of the system.

Pre-Amplifier

Solid state topology is chosen for the preamplifier. The amplifier will be modular. Each module provides more than 700W power. Each module has its own circulator. To avoid non-linearity, each module will be driven in class AB. To avoid power dissipation and hence to have high efficiency, a blanking signal is applied to the amplifier during absence of RF pulse. Power input to the preamplifier is given by signal generator.

Thus specifications of pre-driver are:

Frequency = 352.21 MHz
Power = 10 kW
3 dB Band-width = 200 kHz.
Pulse width = 3.5 ms
Pulse repetition rate = 14 Hz
Gain > 73 dB
Efficiency ≥ 50-55 %

RF Distribution

Basic layout of RF distribution is as shown in fig. 2.

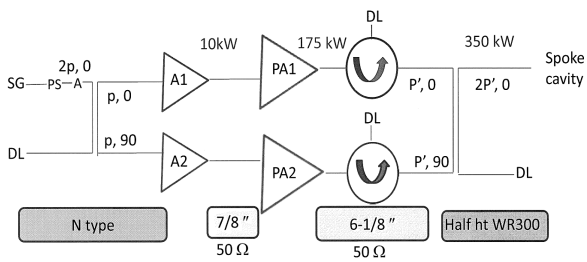

Figure 2: Schematic for high power RF layout for FREIA. SG: Signal generator, PS: Phase shifter, A:Attenuator DL: Dummy load, A1, A2: Preamplifier (352 MHz, 10 kW), PA1, PA2: High Power Amplifier (352 MHz, 175 kW)

Various types of RF distributions are studied. The RF distribution shown in (fig.2) is finalized considering space requirements, ease of handling and cost. Mainly three types of RF distribution are needed depending upon power level (fig. 1, fig. 2).

Peak power = 350 kW: Half height WR2300
Peak power = 175 kW: 6-1/8 inch, 50 Ω coaxial line
Peak power = 10 kW: 7/8 inch, 50 Ω coaxial line

He Liquifier and Cryostat

As the ESS spoke cavities are superconducting, it needs to be cooled down to 2 K . To achieve this, FREIA will have He liquefier with capacity of 100 lit./hour. It will also have horizontal cryostat for holding the Spoke cavities.

Copyright © 2012 by the respective authors — cc Creative Commons Attribution 3.0 (CC BY 3.0)

FREIA Bunker

Particles will not be injected in the spoke cavities during testing in the test stand. But cavities will be operated at high electric gradients, capable of generating X-rays. Thus there is requirement for the bunker. The bunker will be made up of Concrete blocks with iron. Simulations have been done to optimise thickness of the concrete block. Fig. 1 shows layout of the bunker.

FREIA hall will also have other facilities described in the next section.

FEATURES OF FREIA HALL

Following are the features of FREIA hall.

- 1000m^2 hall
- Electrical input power = 1.2 MW
- Cooling capacity = 800 kW power
- Helium liquefier (> 70 l/h) with LN_2 precooling
- Distribution box to users
- Impure gas recovery from users
- RF amplifiers (two chains): 352 MHz, 350 kW
- RF distribution system
- Test cryostat vertical and horizontal
- Test bunkers.

SUMMARY

FREIA facility is being developed at Uppsala. The first project of FREIA is High Power Test Stand for ESS superconducting Spoke Cavities. It will serve two purposes i.e. prototyping of RF amplifier at ESS specifications and high power testing of superconducting spoke cavities of ESS. As cryomodule consists of two spoke cavities, the test stand will have two chains of RF amplifier (352 MHz, 350kW peak) and RF distribution. As the cavities are superconducting, He liquefier is needed.

Construction of FREIA hall will be completed by Q2 of 2013. The target is to complete installation of first amplifier chain, related RF distribution and liquefier by Q4 of 2013

REFERENCES

[1] S. Pegg, “Conceptual Design Report,” ESS-2012-001, 2012.

[2] R.Yogi et al, “Selection of RF power source and distribution scheme at 352 MHz for spoke cavities for ESS and at FREIA,” FREIA Report 2012/1, May 2012.

[3] Thales data sheet for TH595

[4] R.Wedberg et al., ‘Technical design report on power supplies for spoke cavities at FREIA’, FREIA Report 2012/2, May 2012.

Copyright © 2012 by the respective authors — cc Creative Commons Attribution 3.0 (CC BY 3.0)

ERL-BASED LIGHT SOURCE CHALLENGES

Yukinori Kobayashi#, KEK, Oho 1-1 Tsukuba, Ibaraki 305-0801, Japan

Abstract

The challenges of the design and technology for the future Energy Recovery Linac (ERL) based light source are reviewed. The developments of a high-brightness electron source, including the drive laser, and the CW high gradient superconducting cavities for both injector and main linac as key components of the accelerator are described. In addition, the status of the compact ERL (cERL) for R&D which is going to be constructed at KEK is presented.

INTRODUCTION

The Energy Recovery Linac (ERL) is a future X-ray light source based on state-of-the-art superconducting linear accelerator technology, which will offer far higher performance than the existing storage ring. The high repetition rate, short pulse, high spatial coherence and high brightness will enable the filming of ultrafast atomic-scale movies and determination of the structure of heterogeneous systems on the nano-scale. These unique capabilities of ERL will lead to a distinct paradigm shift in X-ray science from static and homogeneous systems to dynamic and heterogeneous systems, in other words, from time- and space-averaged analysis to time- and space-resolved analysis. In short, ERL will be an unprecedented tool that will bridge the critical gaps in our understanding of material science and technology [1].

In addition, continuous improvements in linear accelerator technology may result in dramatic progress in X-ray science in the future, such as the realization of a fully coherent X-ray free-electron laser. Although self-amplified spontaneous emission X-ray free-electron lasers (SASE-XFELs) are in use around the world, the X-ray beam from SASE-XFEL is essentially not fully coherent in the temporal domain. By configuring a Bragg diamond cavity for lasing in the X-ray region, it may be possible to create an X-ray free-electron laser oscillator (XFEL-O) by taking full advantage of the unprecedented electron beam quality of ERL [2-4]. Construction of the XFEL-O is planned in the second stage of the ERL project.

KEK established the ERL Project Office in April 2006. Because a GeV-class ERL machine has not been constructed anywhere in the world, it is first necessary to construct a compact ERL (cERL) with an energy of 35 MeV that can be used for developing several key accelerator components such as a high-brilliance DC photocathode electron gun and superconducting cavities for the injector and main linac. During 2011, such main accelerator components were successfully developed and operation of the beam will start at the end of March 2013.

#yukinori.kobayashi@kek.jp

In this conference, the development of high-brightness electron sources and superconducting cavities, which are key accelerator components for the ERL, and construction of the compact ERL for R&D at KEK, will be mainly presented.

DESIGN CONCEPT OF THE 3-GEV ERL AT KEK

For the future project of the KEK Photon Factory, we propose constructing a 3-GeV ERL that can be upgraded to become the XFEL-O [5-7]. A conceptual layout of the 3-GeV ERL is shown in Fig. 1. In the first stage of the project, a 3-GeV ERL which comprises an injector linac, a superconducting main linac, and a return loop will be constructed. In the return loop, 20–30 insertion devices which are used to emit synchrotron radiation will be installed. Using state-of-the-art undulator technology, a broad spectrum of synchrotron radiation from vacuum ultra-violet (VUV) to hard X-rays will be covered.

In the second stage of the project, an XFEL-O system which comprises a long undulator and an X-ray resonator will be built. To deliver high-energy beams for the XFEL-O system, the path length in the return loop by a half rf wavelength of 115.3 mm will be adjusted. Under this configuration, the beams are firstly accelerated to 3 GeV through the main linac and pass through the return loop. The beams are then accelerated again (without energy recovery) through the main linac up to 6 GeV. Finally, the beams are used to drive the XFEL-O, and dumped without energy recovery.

Target parameters of the 3-GeV ERL are given in Table 1. Since the ERL is a very flexible light source, this table shows some typical operational modes. For the major users requiring highly brilliant SR, we provide high-coherence or high-flux modes of operation. Among these modes, the high-flux mode imposes a greater challenge for the lifetime of the photocathodes. The “ultimate” mode requires both very-low emittance and high currents; this imposes much greater challenges for the accelerator physics and engineering, and thus is a long-term goal. In the ultra-short-pulse mode, we compress the electron bunches down to a hundred femto-seconds or shorter. In this mode, the beam emittances are largely influenced by the coherent synchrotron-radiation in the return loop. Then, bunch charges in this mode will be chosen by balancing the SR intensity and the beam emittance.

Copyright © 2012 by the respective authors — cc Creative Commons Attribution 3.0 (CC BY 3.0)

Table 1: Target Parameters of the 3-GeV ERL Integrated with the X-Ray Free-Electron-Laser Oscillator (XFEL-O)

Operation modes	High-coherence mode	High-flux mode	Ultimate mode	Ultra short-pulse mode	XFEL-O mode
Beam energy (E)	3 GeV	3 GeV	3 GeV	3 GeV	7 (6) † GeV
Average beam current (I_0)	10 mA	100 mA	100 mA	Typically, 77 mA (flexible)	20 mA
Charge/bunch (q_b)	7.7 pC	77 pC	77 pC	Typically, 77 pC (flexible)	20 pC
Repetition rate of bunches (f_{rep})	1.3 GHz	1.3 GHz	1.3 GHz	Typically, 1 MHz (flexible)	1 MHz
Normalized beam emittances (ε_{nx}, ε_{ny})	0.1 mm·mrad	1 mm·mrad	0.1 mm·mrad	To be investigated (typically, 1-10 mm·mrad)	0.2 mm·mrad
Beam emittances at full beam energy (ε_x, ε_y)	17 pm·rad	170 pm·rad	17 pm·rad	To be investigated (typically, 1 - 10 nm·rad)	7 pm·rad
Energy spread of beams; in rms (σ_E/E)	2×10^{-4}	2×10^{-4}	2×10^{-4}	To be investigated	5×10^{-5}
Bunch length; in rms (σ_t)	2 ps	2 ps	2 ps	100 fs	1 ps

† Parameters for the XFEL-O at a beam energy of 7 GeV [2-4] are shown. Parameters at a lower beam energy of 6 GeV are under investigation.

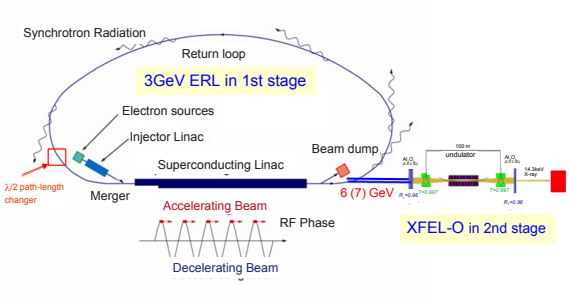

Figure 1: Conceptual layout of 3-GeV ERL plan integrated with an X-ray free electron-laser oscillator (XFEL-O).

DEVELOPMENT OF KEY COMPONENTS FOR ERL

High-Brightness DC Photocathode Gun and Gun Test Beamline

Two high-brightness photocathode DC electron guns are under development at the Japan Atomic Energy Agency (JAEA) and KEK site to meet the requirements for the Energy Recovery Linac (ERL) of a normalized emittance of less than 1 mm·mrad and a sufficiently long cathode lifetime. To suppress the increase in emittance induced by the space-charge effect, the gun voltage must be 500 kV or higher. An extreme high vacuum of the gun chamber is required to preserve the negative electron affinity (NEA) surface of the cathode. All of the vacuum components in the gun system (a titanium chamber, ceramic insulators, guard rings, etc.) should have a low outgassing rate, and the pumps should function under the extreme high vacuum.

The first gun developed at JAEA has successfully extracted an electron beam of 10 mA with a voltage of 180 kV and has applied a high voltage of up to 500 kV with a cathode electrode and NEG pumps in place. The pressure of the gun chamber reached 6×10^{-10} Pa (N_2 equivalent) with 18000 l/s NEG pumps after baking at 180ºC for 50 h. The 1/e static lifetime of the NEA GaAs cathode is 1000 h in a cathode preparation chamber.

The second gun developed at KEK has been constructed with a gun chamber and a pair of ceramic insulators with guard ring electrodes fixed inside as shown in Fig. 2. In order to understand the actual performance of the vacuum system, we have precisely measured the outgassing rate by the rate-of-rise method. The gun system was baked at 150–200ºC for 100 hours. After the baking process, a total outgassing rate of 1.0×10^{-10} Pa m^3/s (H_2 equivalent) was measured.

To study the properties of the cathode, the initial beam emittance and temporal response have been measured by using a 200-kV gun and a beam diagnosis system. The 200-kV gun was originally developed at Nagoya University and the beam diagnosis system, which has a RF deflector, a double slit system, solenoids and screen monitors, was constructed at KEK. Typical results for the temporal response of photocathodes with different thickness of active layer are shown in Fig. 3. The measured photoemission response depends on the thickness of the active layer [8].

Drive Lasers

A drive laser system that has a repetition rate of 1.3 GHz, pulse duration of 20 ps, and average power of 15 W is required for 10 mA beam operation in cERL. The wavelength was originally specified to be ~800 nm to minimize the emittance, however, our studies on the emittance and time response of photocathodes have

Copyright © 2012 by the respective authors — cc Creative Commons Attribution 3.0 (CC BY 3.0)

shown that ~500 nm is a better choice. A stable oscillator that can be synchronized to the accelerator timing system, a high-power amplifier, and a wavelength conversion system are the main components of the laser system. Various other issues related to beam operation include spatial and temporal shaping, various operational modes of pulse structure, delivery to the gun, position and intensity control, and fast interlock system.

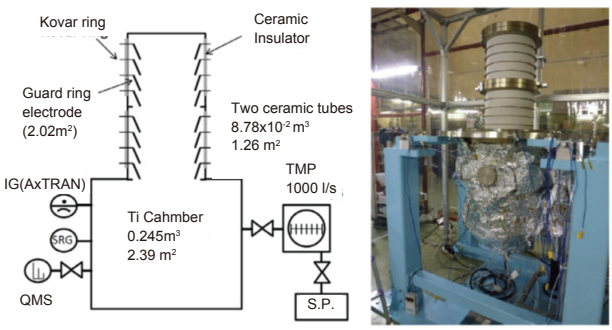

Figure 2: Layout of the vacuum system for the 2nd gun at KEK (left), and a photograph of the system (right).

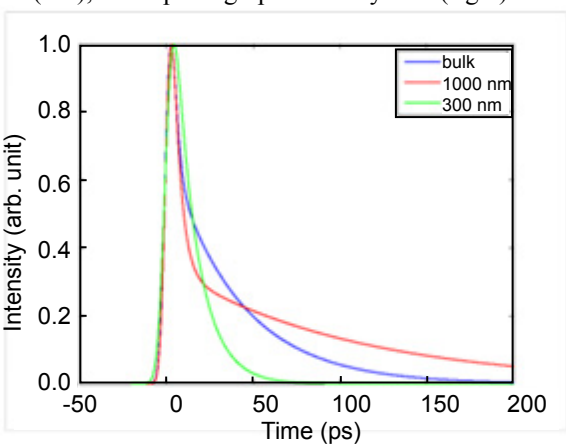

Figure 3: Temporal response of NEA GaAs photocathode by irradiation of short laser pulses (~ ps, λ = 785 nm) to a thickness of 300 nm, 1000 nm and bulk sample.

Work on developing the drive laser system has been under way since 2007. Various schemes for the 1.3 GHz oscillator have been tried and a 10 W-class fiber amplifier has been demonstrated, but the results were not sufficient to achieve the above target values.

We have therefore introduced a commercially available 1.3-GHz laser oscillator and a fiber amplifier in a gun test stand, and have studied the performance of the oscillator. Although the long-term stability is still questionable, we confirmed that it could operate in a mode-lock state synchronized to the given RF reference. In order to improve the wavelength conversion efficiency, a new scheme utilizing an enhancement cavity has been proposed and tested as shown in Fig. 4.

SC Cavities for the Injector

The injector for the cERL is required to accelerate CW electron beams of 10 mA from the beam energy of 500 keV to 5 MeV. An injector cryomodule, which contains three 2-cell cavities equipped with two input couplers and five HOM couplers, was designed as shown in Fig. 5. Three 2-cell cavities and six input couplers for installing into the cryomodule were fabricated in 2011. Vertical tests to confirm the cavity performance were carried out

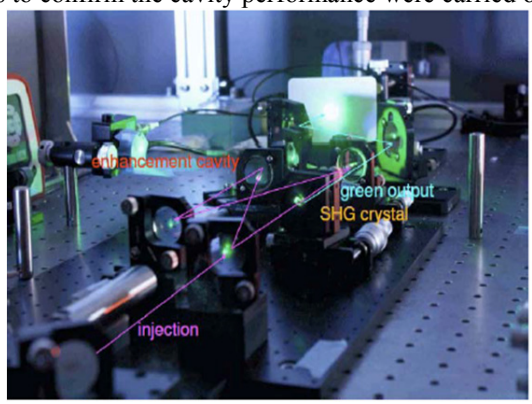

Figure 4: Laser system with cavity wavelength conversion.

at KEK-STF (Superconducting RF Test Facility), and RF conditioning of the input couplers with a CW high-power RF source were performed at KEK-ETF (ERL Test Facility).

The vertical tests investigated not only the high gradient performance of the cavities but also the thermal properties of several types of RF feedthrough for the HOM couplers. The final vertical test results of three 2-cell cavities are shown in Fig. 6. After confirming the cavity performance, the 2-cell cavities were sent back to the manufacturer in order to weld with a He jacket made of titanium. As shown in Figure 5, a high-pressure gas examination of the 2-cell cavities covered with the He jacket and two He panels made of stainless steel was carried out in compliance with the Japanese law concerning the safety of high-pressure vessels. The main components of the injector cryomodule were delivered to KEK in March of this year and assembly work was started in April. The injector cryomodule was completed in June, and has already been connected with the cold-box for cool-down. The first cool-down test of the injector cryomodule will be started by this September.

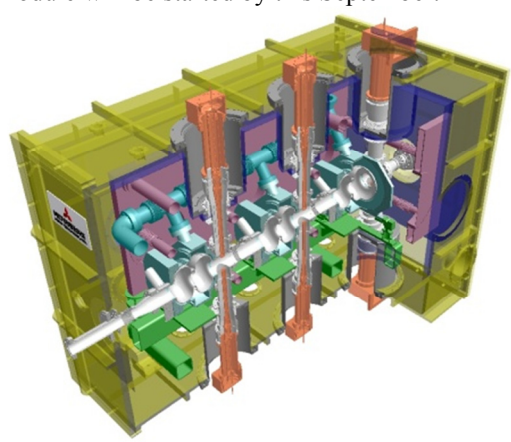

Figure 5: Schematic drawing of the injector cryomodule containing three 2-cell cavities and six input couplers.

Copyright © 2012 by the respective authors — cc Creative Commons Attribution 3.0 (CC BY 3.0)

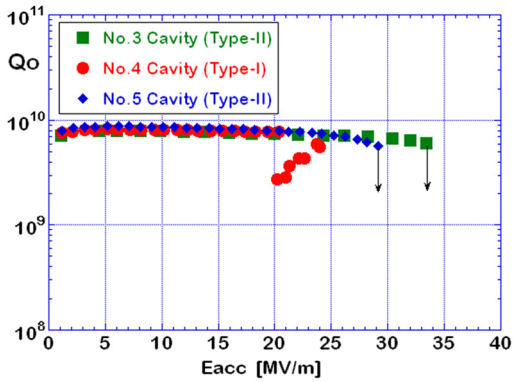

Figure 6: Final vertical test results of three 2-cell cavities with five RF feedthroughs (Type-I or Type-II) for five HOM couplers.

SC Cavities for the Main Linac

Development of the basic technologies of the main components has finished and the components for the prototype module of the main linac are now being manufactured. Cold tests of two 9-cell cavities were carried in a vertical cryostat and a maximum accelerating gradient of 25 MV/m was achieved, as shown in Fig. 7. Field emission at 15 MV/m was sufficiently low and a Q value of $>1\times10^{10}$ was obtained.

As main components, a pair of input couplers was completed and assembled in a clean room to the power test station. Power conditioning up to 20 kW will be performed before installing the couplers in the cavity. Fabrication of the two types of HOM dampers is now under way. A ferrite cylinder of IB004 is bonded on the copper pipe by the hot-isostatic-pressing method. Movement of the frequency tuner was tested on a prototype tuner, which is based on the slide-jack structure developed for the ILC cavities. Movement of several micro-meters was smoothly obtained by a piezo tuner to compensate the cavity frequency response of 300 kHz/mm.

The main linac module as shown in Fig. 8 is going to be assembled, which will be followed by a cool test in autumn.

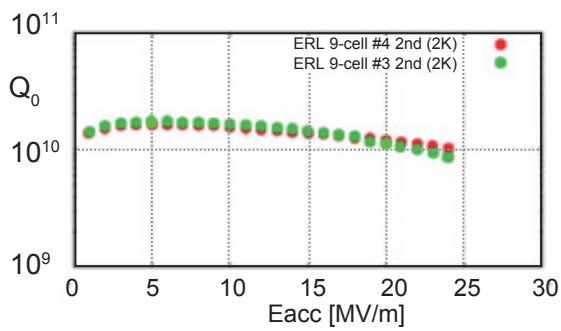

Figure 7: Q-E plot of the 9-cell cavities for the cERL main linac module.

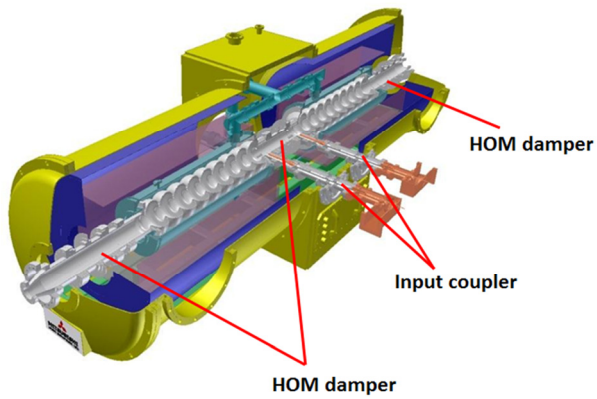

Figure 8: Schematic drawing of the prototype module of the cERL main linac. A pair of 9-cell cavities is connected with LN_2-cooled HOM dampers.

COMPACT ERL PROJECT

Overview of cERL

Figure 9 shows the current plan of the cERL for the first stage of commissioning [9]. It will comprise a 5-MeV injector including a 500-kV DC photocathode gun and three 2-cell superconducting (SC) cavities, a main SC linac having a single cryomodule, a single return loop of 35 MeV, and supporting facilities. The principal parameters of the cERL are shown in Table 2.

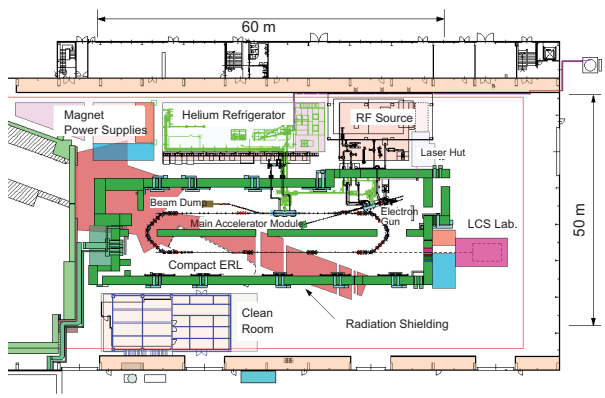

Figure 9: Current plan of the Compact ERL for commissioning.

Construction of the Radiation Shield for the cERL

The KEK-ETF was selected as the construction site for the cERL. This hall was fully renovated in 2009, at which time we removed large amounts of concrete blocks and radioactive components from the old proton beamlines. In 2010, remaining radioactive matter, such as radioactive iron plates attached to the floor and a lot of polyethylene shielding stuffed in the floor pit, was removed. In parallel with cleaning the hall, we started designing the radiation shielding for the cERL. After checking the maximum safety load of the floor, the structure of the radiation shielding was designed. The shielding will be made of

Copyright © 2012 by the respective authors — cc Creative Commons Attribution 3.0 (CC BY 3.0)

reinforced concrete, and the thickness of the surrounding walls and ceiling blocks are 1.5 m and 1.0 m, respectively. The ceiling blocks can be removed when large instruments are installed in the shield. Calculations for the structure, assuming both horizontal and vertical loads (acceleration) of 0.25 G, were carried out, and it was confirmed that the structure was sufficiently strong. Soon after finishing the radiation shielding design, the Great East Japan Earthquake struck on 11 March 2011. Fortunately no one was working in the building, there were no injuries, and there was no serious damage to the building. However, the specifications of the shielding needed to be changed: the limit of horizontal and vertical excitation force was raised from 0.25 G to 0.5 G for resisting a similar large earthquake.

Construction and installation of the radiation shield in ETF started in February and will be completed by the end of this September.

Table 2: Principal Parameters of the Compact ERL

Parameter	Initial goal	Final goal
Beam energy at recirculation	35 MeV (single loop)	125 MeV (single loop)
		245 MeV (double loops)
Injection energy	5 MeV	5 MeV
Average beam current	10 mA	100 mA
RF frequency	1.3 GHz	1.3 GHz
Accelerating gradient of main SC cavities	15 MV/m	15 MV/m
Bunch repetition frequency	1.3 GHz	1.3 GHz
Normalized emittance	1 mm·mrad	1 mm·mrad (77 pC/bunch) 0.1 mm·mrad (7.7pC/bunch)

Construction and Commissioning Schedule

The schedule for constructing the cERL is shown in Fig. 10. Fabrication of the accelerator components such as the injector part, superconducting cavities, RF sources and He cryogenic systems will be completed by the end of next March. Then, beam commissioning for the injector part will be started and will continue until mid-July 2013. Then, the recirculation loop will be installed in the summer of 2013 and commissioning will be started in October 2013. To avoid radiation problems from the cERL, the beam current will be carefully increased and the beam quality of the cERL, including unwanted beam loss, will be examined during 2014. The beam current of 10 mA with the normalized emittance of 1 mm·mrad will be achieved as the first stage, and then the emittance will be gradually reduced to 0.3 mm·mrad with 7.7 pc/bunch. In addition, the emittance of 1 mm·mrad with a higher bunch charge of 77 pc is also expected.

Commissioning of the beam at cERL will yield much important information on whether the components need to be improved as well as information on the drawbacks of the design of the 3-GeV class ERL.

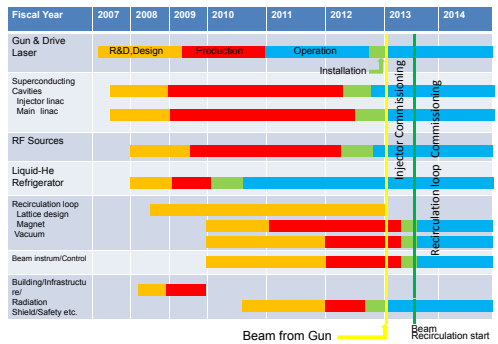

Figure 10: Construction and commissioning schedule of cERL.

ACKNOWLEDGMENT

The author thanks the Japanese ERL collaboration team who provided materials for this paper.

REFERENCES

[1] See, for example, D. Bilderback, J.D. Brock, D.S. Dale, K.D. Finkelstein, M.A. Pfeifer, Sol M. Gruner, New J. Phys. **12** (2010) 035011.

[2] K. -J. Kim, Y. Shvyd'ko, S. Reiche, Phys. Rev. Lett. **100** (2008) 244802.

[3] R.R. Lindberg and K.-J. Kim, Proceedings of the 23rd Particle Accelerator Conference (PAC09), 4-8 May, 2009, Vancouver, Canada, pp. 1198-1200.

[4] K. -J. Kim and Y. Shvyd'ko, Phys. Rev. ST Accel. Beams. **12** (2009) 030703.

[5] S. Sakanaka et al., Proceedings of the first International Particle Accelerator Conference (IPAC'10), May 23-28, 2010, Kyoto, Japan, pp. 2338-2340.

[6] S. Sakanaka, H. Kawata, Y. Kobayashi, N. Nakamura, R. Hajima, Proceedings of the XXV Linear Accelerator Conference (LINAC10), September 12-17, 2010, Tsukuba, Japan, pp. 398-400

[7] N. Nakamura, Proceedings of the third International Particle Accelerator Conference (IPAC'12), May 20 - 25, 2012, New Orleans, USA, pp. 1040-1044.

[8] S. Matsuba, Y. Honda, X. Jin, T. Miyajima, M. Yamamoto, T. Uchiyama, M. Kuwahara, and Y. Takeda, Jpn. J. Appl. Phys. **51** (2012) 046402.

[9] R. Hajima, N. Nakamura, S. Sakanaka, Y. Kobayashi (ed.), "Design Study of the Compact ERL", KEK Report 2007-7/JAEA-Research 2008-032, February, 2008 [in Japanese].

Copyright © 2012 by the respective authors — cc Creative Commons Attribution 3.0 (CC BY 3.0)

STATUS AND FUTURE OF THE CLIC STUDY

R. Corsini*, CERN, Geneva, Switzerland

Abstract

The Compact Linear Collider (CLIC) International Collaboration is carrying out an extensive R&D program towards a multi-TeV electron-positron collider.

The CLIC concept is based on the use of high-gradient normal-conducting accelerating structures in conjunction with a novel two-beam acceleration scheme, where the RF power needed to accelerate the colliding beams is extracted from a high-current drive beam running parallel to the main linac. In order to establish the feasibility of such concept a number of key issues were addressed, both experimentally and theoretically, and the results of the study were documented in the recently completed CLIC Conceptual Design Report (CDR). The conclusions reached in the CDR constitute also an important contribution to the European strategy group. A short summary of the present status will be given, together with an outlook on the program for the next period, aimed at the preparation of an implementation plan.

INTRODUCTION

CLIC is a high-energy linear e^+e^- collider with the potential to operate at centre-of-mass energies ranging from a few hundred GeV up to 3 TeV and with luminosities of a few 10^{34} $cm^{-2}s^{-1}$.

In CLIC the colliding beams are produced in conventional electron and positron sources and accelerated to about 2.8 GeV. The beam emittances are reduced in a pre-damping ring followed by a damping ring. In the ring-to-main-linac transport system (RTML) the beams are compressed longitudinally and accelerated to 9 GeV. The main linac uses 100 MV/m, 12 GHz, normal conducting accelerating structures to achieve the final beam energy. In the beam delivery system (BDS) the beams are cleaned by collimation and compressed to their final sizes at the collision point. The main challenges for the CLIC main beam are the accelerating gradient needed to get to the high centre-of-mass energy and the good beam quality (i.e., the ultra low beam emittances and sizes) needed to reach high luminosity.

The RF power used to accelerate the electron and positron beams is extracted from a high-current, low-energy drive beam running in parallel to them. The drive beam is generated in a dedicated accelerator complex located in the central area. The other challenges for CLIC are related to the two-beam concept: the efficient generation of the drive beam, the power production in special RF structures called PETS (power extraction and transfer structures) and the stable drive beam deceleration. The fundamental CLIC parameters and its conceptual layout can be found in Table 1 and in Fig. 1. More details about the CLIC machine are given in the recently completed Conceptual Design Report.

*On behalf of the CLIC Collaboration

Table 1: Fundamental CLIC parameters at 3 TeV centre-of-mass. The luminosity quoted is within 1% of the nominal energy.

Centre-of-mass energy	3	TeV
Luminosity	2×10^{34}	$cm^{-2}s^{-1}$
Particles per bunch	3.72×10^9	
Horizontal beam size at IP	≈ 40	nm
Vertical beam size at IP	≈ 1	nm
Bunches per pulse	312	
Bunch separation	0.5	ns
Repetition rate	50	s^{-1}

The CLIC accelerator complex and the CLIC physics and detector studies are described in separate documents. The CLIC accelerator CDR [1] provides detailed descriptions of the accelerator layout, its components and the expected performance of CLIC. In particular, it describes technical solutions to the key feasibility issues, thus proving the validity of the CLIC concept. In this framework, prototypes of many of the technical subsystems have been successfully tested at the CLIC test facility CTF3 at CERN and at other facilities around the world. The test results are reported in detail in the CDR.

This paper gives a status update on the most important design challenges of CLIC, namely:

- The main linac gradient and issues related to the accelerating structures.
- The experimental verification of the two beam concept, which is essential to provide the main linac RF power.
- The ultra low beam emittances and sizes to reach high luminosity. In particular alignment and stabilization of the main linac and BDS components.

In order to have energy flexibility a possible staged implementation of the machine is being studied. The future program of the studies is focused on an implementation plan by 2016, at the same time as results from LHC running at full energy are expected to provide results guiding the way for a possible implementation. The main elements of the future program are also briefly discussed at the end of the paper.

ACCELERATING STRUCTURES

Each main linac contains about 70000 23 cm long accelerating structures. The total ratio of active length to total linac length reaches almost 80%, resulting in an extremely high "real estate" gradient. The structure design has been carefully optimized using empirical constraints to achieve a gradient of 100 MV/m, as described in [1].

Copyright © 2012 by the respective authors — cc Creative Commons Attribution 3.0 (CC BY 3.0)

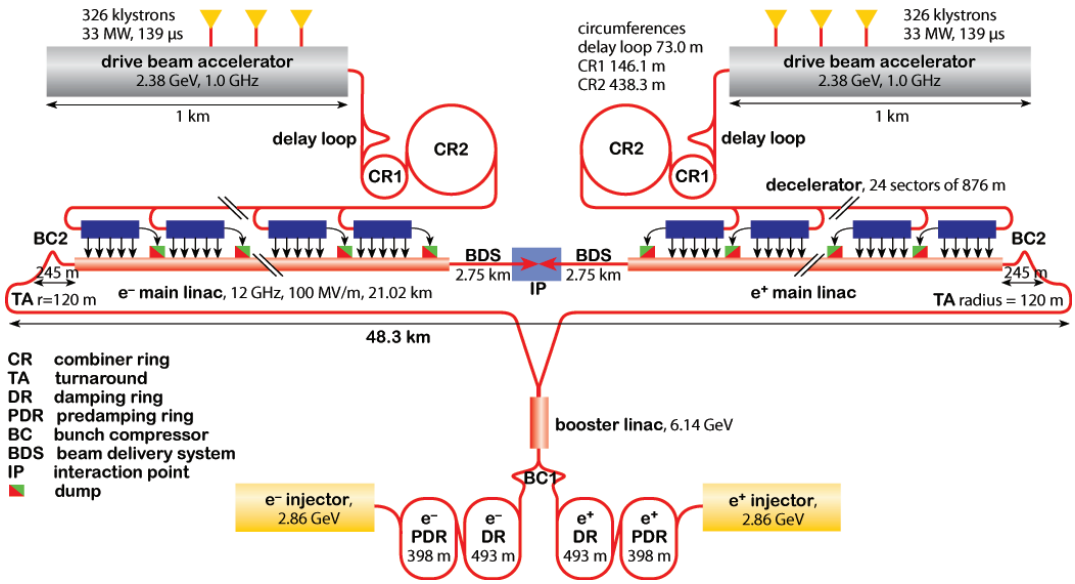

Figure 1: Conceptual CLIC layout.

The main limitation arises from RF breakdowns, i.e. electrical arching that may occur in the structure during the RF pulse. Breakdowns may damage the structure, reducing its performance, and can give transverse kicks to the beam. Typically the breakdown probability p increases with the gradient G and pulse length τ as $p \propto G^{30} \tau^5$ [2]. We conservatively assume that a single breakdown in a main linac structure completely spoils the beam pulse for luminosity. This must happen only in 1% of the beam pulses at the target gradient of 100 MV/m, which results in a required breakdown rate of $\leq 3 \times 10^{-7}$ m^{-1} pulse^{-1}. Four accelerator structure designs have recently been tested: T18, TD18, T24 and TD24 (see Fig.2). TD24 is the present CLIC baseline structure; T24 is a simplified version without damping waveguides. T18 and TD18 correspond to an earlier, less efficient design. Again "D" indicates the presence of damping waveguides. At SLAC and KEK [3] klystrons operating at 11.424 GHz are being used for testing such structure types, scaled in all dimensions to the klystron frequency.

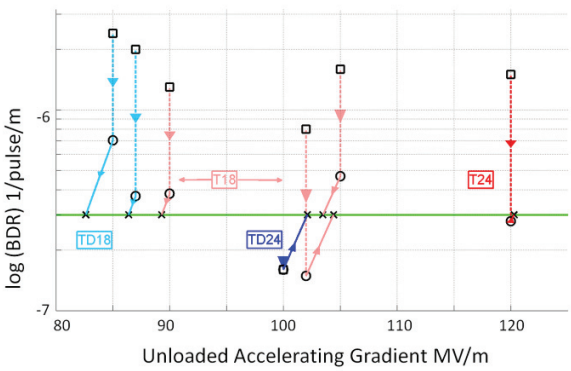

Figure 2: Gradient and breakdown rate achieved with different CLIC structures. Squares mark actual measurements, circles the expected breakdown rate at the nominal pulse length and crosses the expected gradient at the nominal breakdown rate.

At CERN 12 GHz power can be produced in the CTF3 two-beam test stand (TBTS), in which however the low repetition rate does not allow to fully condition the structures under test, and a 12 GHz klystron-based test stand has been recently put in operation.

The tests have been performed with pulse lengths and breakdown rates close to the CLIC ones. The measurement data is shown in Fig. 2 together with the expected CLIC gradients, obtained by scaling the pulse length and breakdown rate to the CLIC values using the scaling formula above. The TD24 structure has achieved an unloaded gradient of 103 MV/m. A dedicated experiment is planned in CTF3 to investigate the effect of beam loading, expected to be in the range of 0 to -16% due to the changed power flow in the presence of beam.

TWO-BEAM ISSUES

The RF frequency of the CLIC drive beam accelerator (DBA) is 1 GHz. The injector produces a 140 μs long electron beam pulse composed by 240 ns long sub-pulses in which only odd or even RF buckets are alternatively filled. The DBA accelerates the beam to about 2.4 GeV with a nominal RF to beam efficiency of 97%. A 500 MHz RF deflector separates the sub-pulses and sends every other into a delay loop, so that its bunches can be interleaved with those of the next sub-pulse. This produces a sequence of 240 ns sub-pulses spaced by 240 ns long gaps. These are then merged (first with a three-fold, then a four-fold combination) in two rings using a time-dependent closed bump generated by transverse deflectors. Thus each of the 24 final sub-pulses has 24 times the initial current and only 2.5 cm bunch spacing. Each will feed one drive beam decelerator in the main linac. To demonstrate the two-beam scheme, the CLIC Test facility CTF3 has been build and commissioned at CERN by an international collaboration [4]. Its layout is shown in Fig. 3.

Copyright © 2012 by the respective authors — cc Creative Commons Attribution 3.0 (CC BY 3.0)

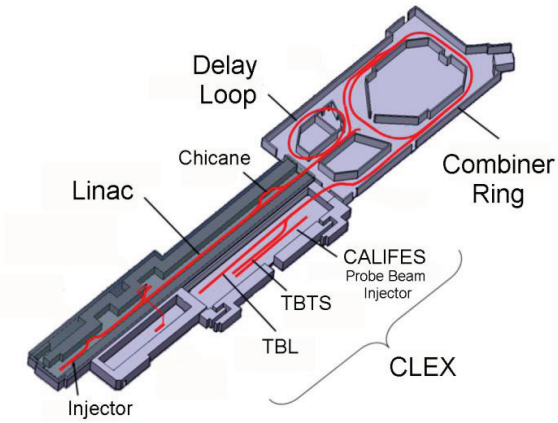

Figure 3: CTF3 Overall Layout.

CTF3 consists of a 120 MeV electron linac followed by a 42 m long delay loop and a 84 m combiner ring. The beam current is first doubled in the delay loop and then multiplied again by a factor four in the ring, for a total increase of the initial beam current by a factor eight. The drive beam can then be sent to the CTF3 experimental area (CLEX) to be used for two-beam experiments. In the CLEX area the Test Beam Line (TBL) is used to test drive beam deceleration in a string of PETS. The drive beam can alternatively be sent to a second beam line (Two-Beam Test Stand, TBTS), where a PETS powers one or more CLIC accelerating structures. A 200 MeV injector (CALIFES) provides the probe beam used in the TBTS to verify two-beam acceleration.

Drive Beam Generation

The CTF3 linac accelerates routinely a current of about 4 A. It is operated in full beam-loading, and a 95% RF-to-beam energy transfer efficiency was measured [5]. HOM damping is used to prevent any transverse instability. Isochronous operation of the loop, ring and transfer lines is needed in order to avoid bunch lengthening. Tuning of the momentum compaction below the required value ($\alpha_p < 10^{-4}$) was demonstrated already in the CTF3 preliminary phase, and is now part of standard operation [6]. In order to be able to separate and recombine sub-pulses in the delay loop, leaving a hole for ring extraction, the sub-harmonic bunching system RF phase is periodically switched by 180° to phase-code the bunches. A switching time of 6 ns was measured, well below the required value [7]. The residual charge in satellite bunches is ~ 7 %, acceptable for CTF3 and close to the CLIC needs. CTF3 target emittance for the drive beam is 150 π μm in both planes after combination; 50 π μm is routinely obtained in the linac, while measurements on the fully recombined beam typically give values 2 to 4 times the target. The main source of emittance growth was identified as orbit mismatch between delay loop and combiner ring, and non-perfect orbit closure in the ring itself. Several correcting measures were put in place, and we expect to reach the target before the end of 2012. The required CLIC drive beam current stability is extremely tight (7.5 10^{-4} for pulse-to-pulse rms charge variations). After reduction of slow drifts by a feedback, the rms pulse-to-pulse variation measured in the linac was ~ 5 10^{-3}, well below the CLIC specs [8]. The charge jitter is about 8 10^{-4} for the combination 4 beam. The same orbit errors causing emittance growth still push the jitter of the fully combined beam, to the percent level. One of the goals of this year run is reduce it to a few 10^{-3}. CLIC has also tight requirements for RF phase and amplitude stability in the linac (0.05° rms phase jitter for a coherent error along the drive beam train and 0.2% for the RF amplitude). In CTF3 an RF phase jitter of 0.035° has been measured with respect to the external reference; the amplitude stability was 0.21%.

RF Power Production, Deceleration and Two-Beam Acceleration

Each of the 48 CLIC drive beam decelerators contains about 1500 21.3 cm long PETS. All PETS have an aperture of 23 mm and produce about 130 MW RF power each, split by half in an RF waveguide network to be fed into two main linac accelerating structures [9].

In TBTS, in order to get high power at a limited drive beam current, a 1 m long PETS is used. Furthermore, part of the output power can be injected back at the PETS entrance, amplifying RF production. Thus, RF power levels above 200 MW, well beyond the 130 MW nominal values, were reached inside the PETS at the 240 ns nominal pulse length. In CLIC it is mandatory to rapidly switch off RF power production from individual PETS in case of repetitive breakdowns. A mechanism based on a variable external reflector, yielding full control of the RF power sent to the accelerating structure and a reduction of the power level inside the PETS by a factor of 4, has been developed and successfully tested [1]. A PETS was also tested at SLAC using klystrons. After some conditioning, the PETS ran for 80 hours with no breakdown, for an estimated breakdown rate of less than 2.4×10^{-7} m^{-1} per pulse [1] (CLIC target 1×10^{-7} m^{-1}). More than 100 MW of peak RF power was delivered to the first accelerating structure tested (CLIC nominal 65 MW). Gradients up to 150 MV/m have been achieved (see Fig. 4) [4].

The measured drive beam deceleration, the RF power produced and the probe beam acceleration are consistent

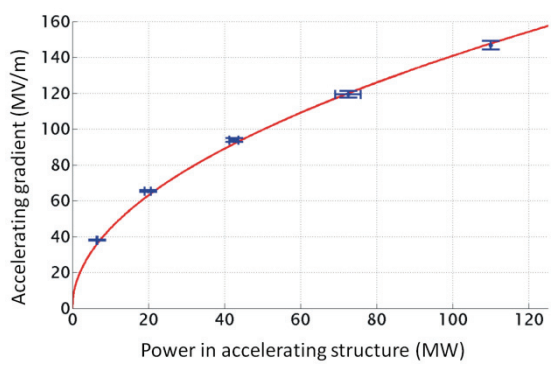

Figure 4: Measured accelerating gradient as function of the accelerating structure RF input power.

Copyright © 2012 by the respective authors — cc Creative Commons Attribution 3.0 (CC BY 3.0)

between them and with the theoretical predictions. The TBTS is used to study in detail the physics of RF breakdowns. In this context, measurements on breakdown transverse kicks were recently performed [10].

The CLIC decelerator will decelerate the beam from 2.4 GeV to 0.24 GeV. It is mandatory to achieve small losses and avoid any instability. Simulations of the impact of static and dynamic imperfections on drive beam stability in the decelerator were performed. They show that the beam remains stable with a good margin on the achievable wake-field damping and with alignment tolerances less stringent than for the main linac [11].

In CTF3 a test beam line (TBL) is being constructed to test the deceleration. It contains 13 PETS and has space available for 16. The initial TBL beam energy (120 MeV) is much smaller than even the final CLIC decelerator energy (240 MeV). The resulting larger beam size will limit the maximum deceleration. The TBL has been operated last year with a total of 9 PETS and a beam current of 21 A. Under these conditions a beam deceleration of 26% was measured in the spectrometers. The energy loss was correlated with predictions from beam current and the PETS RF power [12].

LUMINOSITY AND OPERATION

CLIC has very small target normalized transverse emittances. A conceptual design of the CLIC damping ring exists that meets the CLIC specifications, according to extensive simulation studies including intra-beam scattering, electron cloud build-up and fast beam-ion instability. Existing third generation light sources and damping ring test facilities have normalized emittances that are not too far from the CLIC damping ring goal. In particular, the Swiss Light Source (SLS) has achieved a normalized vertical emittance slightly better than the CLIC target [13]. The Accelerator Test Facility (ATF) at KEK reached values 7 times larger in the horizontal plane and a 2.5 times larger in the vertical one than the CLIC nominal values. Such emittances would be sufficient to obtain in CLIC 40% of the nominal luminosity.

Emittance budgets have been defined for the RTML and the main linac to account for static and dynamic imperfections. In the BDS the beam develops tails, hence the performance budget has been defined in terms of the luminosity: with no imperfections in the BDS the luminosity would be 20% larger than nominal.

Survey, Beam-Based Alignment, Stabilization

Transverse misalignments of the main linac and BDS components are the main source of static emittance dilution. The survey reference system consists of overlapping wires that run along the machine. The beam line elements are mounted on girders that can be moved with motors while sensors measure the offset of the girders to the wires. The beam position can be measured with high resolution beam position monitors (BPMs) at each quadrupole and with wake-field monitor in each accelerating structure [1]. The main linac performance target is a vertical emittance growth of less than 5 nm with a probability of 90%. Simulations were performed using a detailed model of the mechanical pre-alignment following methods verified in test-setups [1]. Dispersion free steering (DFS) is used to correct the dispersion by moving BPMs and quadrupoles. Girders holding structures are aligned to the beam by minimizing the signal in the wake-field monitors. The performance target has been clearly met [1]. The target for the BDS is to achieve 110% of the nominal luminosity with 90% probability, in presence of static imperfections. An rms misalignment of 10 μm is assumed for all components, which is close to the main linac accuracy. Beam-based alignment is used followed by optimization of tuning knobs that change the beam properties at the IP. Currently, 70% of the simulated machines reach the target of 110% luminosity and 90% reach at least 90% [1].

The main beam is very sensitive to magnet motions in the main linac and BDS, due to site dependent ground motion or technical noise. As a conservative benchmark, we use a ground motion model based on measurements of the CMS experimental hall floor [14], which includes some technical noise. The main linac and BDS magnets are equipped with active stabilization systems, using motion sensors and piezo-electric actuators controlled by a local feedback/feed-forward system [1]. A prototype system has been developed and the transfer of the ground motion to the magnet was measured and compared to simulations. The final quadrupoles are mounted on a large concrete block supported by air-springs [15]. The different transfer functions are implemented in the simulation code. The luminosity budget for dynamic imperfections is about 20%. Simulations show that 13% of this budget is used assuming the calculated curve of the prototype stabilization and beam-based feedback. An improved stabilization system, under development, should lose only 3%.

A basic machine protection system concept has been developed to cope with a wide variety of failures [1]. Based on the LHC experience, a strategy was established: slow errors and drifts that grow over several pulses will be detected by a post-pulse analysis while faster failures that can develop between pulses are addressed by an interlock system detecting the equipment failure directly. Failures that occur immediately before the beam pulse and cannot be caught by the interlock system are avoided by “safe-by-design” components, with large enough inertia to slow down the process enough to catch it on the next pulse. Against even faster failures the machine is protected by masks and other passive protection. A first start-up procedure for the drive and main beam has also been defined based on the CTF3 experience.

IMPLEMENTATION STUDIES AND OUTLOOK

In order to satisfy the physics demands to provide luminosity at very different energies the construction of CLIC in stages is being studied. The stage choice will

Copyright © 2012 by the respective authors — cc Creative Commons Attribution 3.0 (CC BY 3.0)

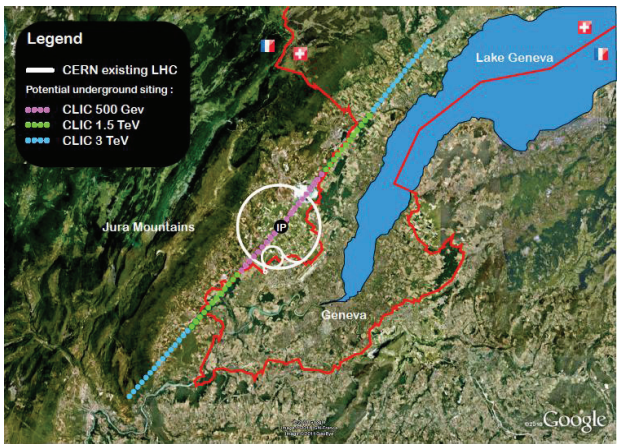

Figure 5: Linear Collider footprints near CERN, showing various implementation possibilities, as studied for example for the CLIC CDR.

depend on the results of the LHC, however with the current status one can draw the preliminary conclusion that a linear collider should be able to run from the 230 GeV up to the highest possible energy. For a given construction stage, unless other measures are taken, the luminosity at CLIC drops proportionally to the energy as this is decreased. Beam stability imposes further limitations and the bunch charge must be reduced with decreasing energy. This can be partly compensated by several measures, allowing for an energy flexibility of a factor 3 to 4, within which the luminosity will scale more favorably with the centre-of-mass energy [16]. As a result, a few stages may cover all the needed range up to Multi TeV, each stage having the possibility to lower the energy by a factor 3 or so without excessive luminosity losses. The possibility of constructing the machine in stages has advantages and imposes constraints, most of which have not yet been studied in detail. Topics include fast and resource-optimized access to the initial physics goals; i.e. scope (energy, luminosity) and schedule for each stage, based on the best knowledge of the physics potential of the machine; approval and construction planning for civil engineering and key technology components risk reduction, flexibility and use of operational experiences, potential reuse of parts going from one stage to another; power and energy consumption as function of energy and luminosity taking into account optimized yearly and daily operation scenarios. While several of these are discussed in the CDR they are also a main focus for the next phase.

The overall objective for the next phase of the project is to develop an implementation plan for the project by 2016, and a detailed work-plan has been prepared. Key studies will address stability and alignment, timing and phasing, stray fields and dynamic vacuum including collective effects. Other studies will address failure modes and operation issues. The collaboration will continue to identify and carry out system tests, where priorities are the measurements in CTF3, ATF and CLIC drive beam injector system tests. Further X-band structure development and tests are high priorities as well as the construction of integrated modules where a number of key elements are included and need to be optimized.

Initial site studies have already been carried out and preliminary footprints have been identified for an initial 500 GeV machine as well as an ultimate 3 TeV layout, as shown in Figure 5, and these studies will continue. The 44 CLIC institutes are all participating in the planning and execution of these activities.

CONCLUSIONS

The focus of the CLIC R&D over the last years has been a set of key feasibility issues that are essential to prove the fundamental validity of the CLIC concept. The feasibility studies have successfully addressed the key technical challenges of such a machine and were described and summarized in a recently completed CDR [1]. Several large systems tests were performed to validate the two-beam scheme, and of particular importance are the results from the CLIC test facility, CTF3 [4]. Both the machine and detector/physics studies for CLIC have primarily focused on the 3 TeV implementation of CLIC as a benchmark for the CLIC feasibility. Performance issues linked to operation over a wide energy range, and considerations of a staged construction program are included in the final part of the CDR.

ACKNOWLEDGMENT

For this paper material I am indebted to the CLIC Collaboration, and in particular to the authors of the various chapters and sections of the CDR. The paper is based on what was previously presented at IPAC 2012 by S. Stapnes and at IPAC 2011 by D. Schulte.

REFERENCES

[1] "The CLIC accelerator CDR: A multi-TeV linear collider based on CLIC technology." http://project-clic-cdr.web.cern.ch/project-CLIC-CDR/
[2] A. Grudiev et al., PRST-AB 12, 102001 (2009).
[3] T. Higo et al., Proc. IPAC 2010.
[4] R. Corsini et al., Proc. IPAC 2012.
[5] P. Urschütz et al., Proc. LINAC'06 and CLIC note 697.
[6] R. Corsini et al., PRST-AB 7, (2004).
[7] P. Urschütz et al., Proc. EPAC'06 and CLIC note 683.
[8] G. Sterbini, LCWS 2010 and T. Persson, P. Skowronski, Proc. IPAC 2012.
[9] I. Syratchev et al., Proc. PAC 2007.
[10] A. Palaia et al., Proc. IPAC 2012.
[11] E. Adli, CERN-THESIS-2010-024.
[12] R. Lillestol, Proc. IPAC 2012.
[13] M.Aiba, M.Boge and A.Streun, "Ultra low vertical emittance at SLS through systematic and random walk optimization", (2012), Subm. to Nucl. Instr. Meth. A.
[14] A. Kuzmin et al., CERN EDMS 1027459 (2009).
[15] A. Gaddi et al., LCD-2010-011.
[16] D. Schulte et al., Proc. IPAC 2010.

Copyright © 2012 by the respective authors — cc Creative Commons Attribution 3.0 (CC BY 3.0)

APPLICATION OF X-BAND LINACS

G. D'Auria
Sincrotrone Trieste, Trieste, Italy

Abstract

Since the late 80's the development of Normal Conducting (NC) X-band technology for particle accelerators has made significant progress and has witnessed tremendous growth. The driving force behind this technological development, has been, and is, the interest of the scientific community in the construction of a Multi-TeV e^+e^- Linear Collider at a reasonable size and cost. The use of the X-band frequency allows for a much higher accelerating gradient per meter, when compared to the S and C bands. SLAC, with a major contribution from KEK, has been pioneering this development since the late 80's in the framework of the NLC/JLC projects. Later, in 2007, the same technology was chosen by CERN for CLIC, the 12 GHz Linear Collider based on the Two-Beam Acceleration (TBA) concept. In addition to these applications, X-band technology is also rapidly expanding in the field of X-ray FELs and other photon sources where it shows great potential. Here, a selection of X-band projects as well as the main applications of this technology at different international laboratories, is reported. The paper also includes a brief report on X-band medical and industrial applications.

INTRODUCTION

In radar engineering the X-band is specified as frequencies in the range of 8-12 GHz. Already by the mid 60's, the SLAC "Blue Book" reported a clear interest for X-band technology in the process of selecting the best frequency for the SLAC Linac [1]. From the late 80's up to 2004, groups from SLAC, KEK, and later Fermilab, began a dedicated development of accelerating structures and components at 11.4 GHz (four times the frequency of the SLAC Linac), for a TeV-scale e^+e^- Linear Collider. A slowdown of these activities occurred in 2004, after the decision of the International Technology Review Panel (ITRP) to select L-band superconducting technology for the International Linear Collider (ILC). However, in 2007 CERN decided to lower the frequency of the Compact Linear Collider (CLIC) to 12 GHz (previously at 30 GHz), resulting in a renewed, and more vigorous, interest in X-band. Significant progress has been made in the last decade to raise the achievable accelerating gradients from the 65-70 MV/m declared at the end of the NLC/JLC program [2], up to the 100 MV/m reached on CLIC test structures [3], values far beyond those reached with the present S and C band technology. Today X-band developments are rapidly expanding due to their demonstrated potential in different segments of accelerator technology. X-band structures are currently used for very accurate beam diagnostics and e-bunch manipulations at many X-ray FEL facilities worldwide [4,5,6]. Very ambitious projects using X-band Linacs, and based on Inverse Compton Scattering (ICS) for "extreme light" sources, are under construction or have been proposed [7,8]. Moreover, with the low bunch charge option currently considered for future X-ray FELs, X-band technology offers a low cost, compact solution for generating multi-GeV low emittance bunches. With the accelerating gradients mentioned above, an entire 1 GeV Linac can be easily housed in less than 20 m, representing a very cost effective solution for application with limited space [9].

HIGH ENERGY COLLIDER

CERN's decision to lower the CLIC frequency to 12 GHz, has been a key factor in the revival of X-band work. The intense activity carried out in the framework of the CLIC international collaboration has led to important developments. At present the CLIC CDR has been completed [10] and the project is moving into the technical design of the main components. Concerning the high gradient X-band structures, two different modules, called T24 and TD24 (Dumped), have been successfully tested, with the CLIC RF pulse shape, to the CDR specifications of 100 MV/m (unloaded average gradient), $\tau_{RF} > 170$ ns flat-top and a BDR/m $< 3 \times 10^{-7}$. Moreover, the measured RF breakdown rate (BDR) has shown good agreement with theory [11]. The baseline design of the CLIC structure, named TD26, has been completed and is very similar to TD24 [12]. The structure is designed for a $2/3\pi$, quasi-constant gradient, operating mode, with an average iris radius of 2.75 mm ($r_{av}/\lambda_{rf}=0.11$). Four damping waveguides, with SiC absorbers, are integrated in each cell to provide for adequate HOM damping. Each structure is composed of 26 cells plus two couplers.

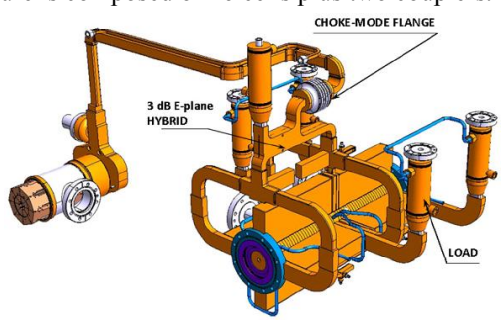

Figure 1: CLIC RF module

Two TD26, assembled together, make up what is called a "Superstructure" (SAS). Wakefield monitors, used for beam-based alignment, and accurate trajectory correction, are integrated into the first cell of every second structure of a SAS. To achieve the CLIC luminosity, the accelerating structures must be aligned to an accuracy of 5 μm with respect to the beam. Figure 1 shows one CLIC

Copyright © 2012 by the respective authors — cc Creative Commons Attribution 3.0 (CC BY 3.0)

RF module, including its Power Extraction Transfer Structure (PETS), which extracts the RF power from the primary beam and transfers it to the main beam. The first TD26 structure is currently being fabricated and is expected to be ready for tests, in an RF module, early 2013. Other important tests planned for 2013 concern the effect of the beam loading on the RF breakdown rate, and a new wake field test to be performed at SLAC.

X-RAY FELS AND PHOTON SOURCES APPLICATIONS

Low charge X-ray FELs

Forth generation light sources are based on FELs, driven by normal conducting (NC) or superconducting (SC) linacs. Soft and hard X-ray NC FEL facilities are presently operational (LCLS, SACLA, FERMI), in the construction phase (SwissFEL, PAL-XFEL, etc.), or are newly proposed in many international laboratories. While some use pre-existing S-band linacs, operating at 3 GHz (LCLS, FERMI), others (SACLA, PSI, PAL-FEL) use newer designs, based on the C-band technology, operating at 6 GHz. This choice increases the linac operating gradients, with an overall reduction of the machine length and cost. However, these advantages could be further enhanced using X-band linacs that can operate with gradients twice as high than the C-band linacs. The choice of the X-band is particularly advantageous for FEL operation using extremely short e-pulses (< 50 μm) in the so called low charge regime (10-20 pC). These parameters guarantee very low wake field effects as well as reduced non-linear energy correlation along the bunch (no harmonic linearization needed). For example, a layout of a very compact hard X-ray FEL, with the same performance achieved by LCLS in low charge mode, driven by a 6 GeV X-band linac, has recently been studied at SLAC [13].

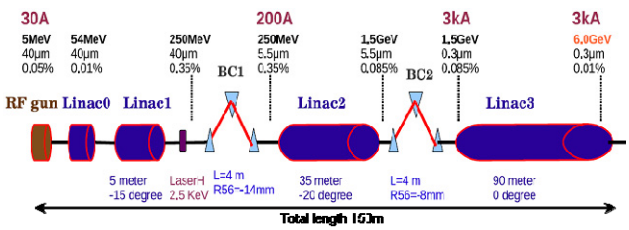

Figure 2: Layout of a 6 GeV X-band linac for a compact hard X-ray FEL

Beam simulations made with ASTRA and ELEGANT show that with two bunch compressors and a peak gradient of 80 MV/m (corresponding to an average gradient ≤ 60 MV/m), it is possible to produce 6 GeV e-pulses, with a length of 2-6 fs, 10 pC charge, and peak currents up to 3-4 kA. The slice energy spread and the normalized transverse emittance are less than 0.02% and 0.2 mm mrad respectively. No emittance dilution is observed for a 20 μm rms, random offsets of the x-y structure axes. Figure 2 shows the proposed layout with a total linac length of 150 m. The study also considers an overall undulator chain of 30 m (λ_w=1.5cm) to reach a saturated power level above 10 GW. This performance is equivalent to the low charge mode of LCLS and is obtained in 180 m, as opposed to the 1230 meters of LCLS. Another study of a an X-band linac for a soft ray X-FEL operating at a 1 KHz rep-rate, is discussed in [14].

Extreme light sources based on ICS

Extremely bright, narrow bandwidth gamma ray sources, based on the Inverse Compton Scattering process (ICS) are attracting a growing interest among scientists for applications in what is called "Nuclear Photonics", the study of nuclei with light. Gamma rays are the most energetic part of the EM spectrum and can penetrate through lead and other thick containers to detect the presence of nuclear weapons, radioactive waste, etc. Following the T-REX project at LLNL, that successfully demonstrated the feasibility of a Mono-Energetic Gamma-ray (MEGa-ray) source, ranging from 75 keV to 0.9 MeV, using a 120 MeV S-band linac [15], LLNL is currently assembling a new very compact source, VELOCIRAPTOR, to extend the production of radiation up to 2.5 MeV [16]. This new source is based entirely on a 250 MeV X-band linac. Figure 3 shows the layout of the machine under development at LLNL in collaboration with SLAC.

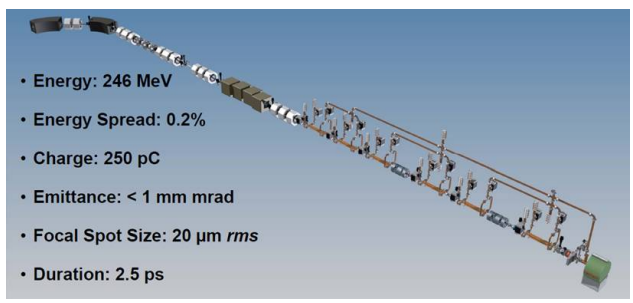

Figure 3: LLNL γ-ray source with expected performance

The electron source is a revised version of a the first X-band photo-injector developed and tested at SLAC in 2003, Mark-0 [17]. The original design, tested up to 200 MV/m, has been improved with wider mode separations (>25 MHz), a longer initial half cell, elliptical irises, and racetrack coupler, Mark-1. The main accelerator is composed of six SLAC T53 accelerating structures, developed and tested at SLAC at the beginning of 2000, in the framework of the NLC program. Although these structures have been operated up to 90 MV/m, with an acceptable BDR, for the LLNL project they will be operated at 70 MV/m, to keep an adequate margin. Two XL4 klystrons with an RF pulse compressor systems (SLED II) will provide the RF power. for the entire machine. Operation is foreseen at 120 Hz, with 250 pC per pulse. LLNL is also assembling a X-band test station with a photo-injector, a single accelerating section, and beam diagnostics, to investigate accelerator optimization and future upgrades of the MEGa-ray technology. A very important (and challenging) issue for these sources is increasing the gamma-ray flux and the pulse repetition rate of the machine. Work is underway to investigate the photo-injector performance, with different cathode

Copyright © 2012 by the respective authors — cc Creative Commons Attribution 3.0 (CC BY 3.0)

materials (Cu and Mg) in multi-bunch mode, lowering the bunch charge to 25 pC and filling up to 1000 micro-pulses, at 11.4 GHz, in a macro-pulses train. The process must produce a significant increase in the average beam power while maintaining the beam brightness.

X-band photo-injectors

As part of a joint effort with LLNL, SLAC has recently started a dedicated R&D effort on X-band photo-injectors, with the assembly of the X-Band Test Area (XTA) in the NLCTA tunnel [18]. SLAC began their activity on X-band photo-injectors in the first years of 2000. The first photo-injector, installed at XTA has been Mark-0, that will provide operational experience before testing an improved version Mark-1, which is currently being fabricated at SLAC for XTA and LLNL, in the framework of the MEGa-ray program [19]. For the high gradients where they can operate (i.e. 200 MV/m), these photo-injectors produce very high brightness beams compared with the present S-band ones (i.e. a factor 3-4 over the LCLS injector). Figure 4 shows the Mark-0 gun and a plot of the energy gain of a 1.6 cell S-band gun operated at 115 MV/m, compared with a 5.5 cell X-band one operated at 200 MV/m. A $\beta_{Lorentz}$ factor of 0.5 is reached after 3 mm at S-band and only at 1.2 mm at X-band.

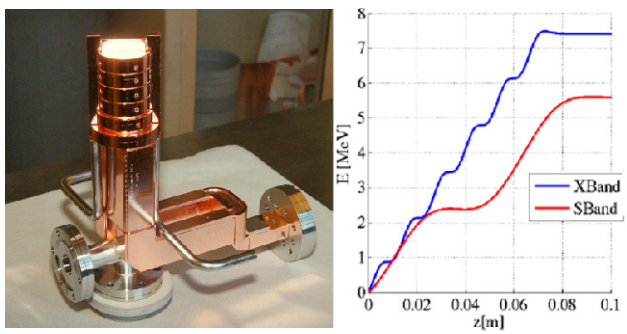

Figure 4: SLAC Mark-0 photo-injector and S-X band energy gain comparison.

Table 1 shows a comparison between the simulation results obtained running the XTA injector at 200 MV/m, with 250 and 20 pC, and results obtained with the same charge at LCLS at 115 MV/m.

Table 1: XTA and LCLS performance comparison

X-band			
Q (pC)	$\varepsilon_{x,95\%}$ (mm mrad)	σ_l (mm)	B_p (Q/σ_l/ε/1E3)
250	0.28	0.184	4.85
20	0.075	0.109	2.44
LCLS			
Q (pC)	$\varepsilon_{x,95\%}$ (mm mrad)	σ_l (mm)	B_p (Q/σ_l/ε/1E3)
250	0.40	0.620	1.01
20	0.15	0.220	0.61

Concerning the XTA activities and achievements, RF power tests started last March and the first photo-electrons were collected at the YAG screen, at the gun exit, in the end of July. At the beginning of August the beam was accelerated to 50 MeV with a 1 m (T105) accelerating structure.

R&D programs on X-band photo-injectors are also ongoing at UCLA, Particle Beam Physics Lab. (PBPL), in collaboration with INFN-LNF and "La Sapienza" University, in Rome. Two research lines are now in progress: the development of an hybrid photo-injector, a single accelerating unit made up of a Standing Wave (SW) gun and a Travelling Wave (TW) structure [20], and an asymmetric emittance photo-injector, for flat beams production [21]. Figure 5 shows the conceptual schematic of the hybrid photo-injector and the electric field on the axis.

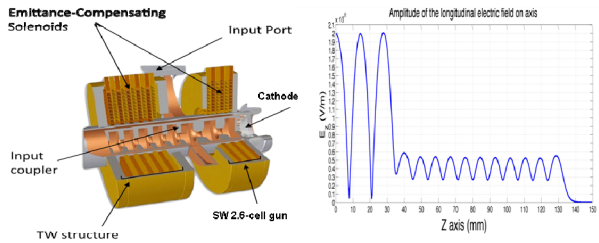

Figure 5: Hybrid photo-injector schematic with

The latest UCLA design for the hybrid photo-injector foresees a 2.6-cell SW gun followed by a 11-cell TW section (9 regular cells + input-output RF couplers). This structure strongly focuses the electrons in the longitudinal plane, acting as a velocity buncher. Two emittance compensating solenoids, with a peak field up to 6 kGauss on the SW gun and 2.5 kGauss on the TW structure, are foreseen. This novel design, more compact than a standard split system, exhibits a good RF matching and no circulator is need on the main RF line. Table 2 summarizes the input and output parameters, obtained with numerical simulations, operating the gun at 200 MV/m. The extremely short pulse and low emittance obtained prove that these sources can reach a brightness higher than 10^{16} (A/mrad^2).

Table 2: Input/Output beam parameters

Input beam		Output beam @30 cm	
Charge	6.75 pC	Energy	4 MeV
Radius	67.5 μm	Transv. size	58 μm
Length	416 fs	Length	80 fs
$\varepsilon_{Ter.}$	0.03 mm mrad	$\varepsilon_{n,x,y}$	0.065 mm mrad
		$\Delta E/E$	0.60 %

The concept behind the asymmetric emittance photo-injector is based on a magnetized photo-cathode, which produces a beam already impressed with an angular momentum. The beam is then passed through a skew-quad triplet that splits the emittances. The project under development at UCLA employs a 9.3 GHz, 2.5-cell SW structure, operated at 200 MV/m, with 5.5 MW. Beam dynamics simulations show that with 1pC bunch charge, 1ps pulse length, and 25 μm transverse beam size at the cathode, it is possible to have a 4.9 MeV beam, with a normalized transverse emittance of 1.3 x 10^{-7} mm mrad (circularly-magnetized) at the photo-injector exit. After the skew-quad array, (k_1, k_2, k_3 = -9.4, 6.0, 5.9, T/m), the emittances are splitted in ε_{nx}= 2.6 x 10^{-7} mm mrad and ε_{ny}= 2.9 x 10^{-9} mrad. The axial magnetic field at cathode is 6500 Gauss.

Copyright © 2012 by the respective authors — cc Creative Commons Attribution 3.0 (CC BY 3.0)

Diagnostics and beam manipulation

The Transverse Deflecting Cavity (TDC) is a diagnostic tool widely used at FEL linacs to measure the temporal profile and the slice properties of very short e-bunches [22]. The idea is to streak the e-bunches, using a RF structure operating in a properly polarized TM_{11} mode, and measure the beam profile on a screen downstream of the cavity. The diagnostics is further enhanced if the deflected beam is observed after an energy dispersion dipole, perpendicular to the RF deflection. The dispersion properties of the dipole allow each bunch slice to be measured, thus reconstructing the beam longitudinal phase space. Figure 6 shows the principle of operation of a TDC. With the beam energy and optics fixed, the measurement resolution depends on the TDC frequency and the gradient seen by the beam. The combined effect of these two parameters is that a X-band TDC can provide much higher resolutions (by a factor of 10) than a S-band one.

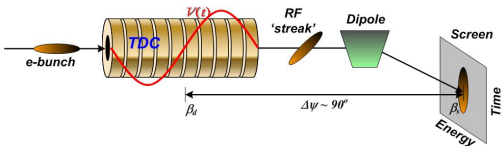

Figure 6: Operating principle of a TDC

A new application of this technique is now being implemented at LCLS for measuring the femtosecond temporal profile of the FEL photon beam [23]. An X-band deflecting system, made of 2 adjacent X-band sections, is being installed downstream the LCLS undulator for the continuous monitoring of all e-bunches. The two TDCs are positioned just before the beam dump and can be operated without interfering with the FEL users. The current design, at 13.6 GeV, is expect to achieve resolutions down to 2 fs, rms. The shot-to-shot slice analysis of each e-bunch, with FEL On and FEL Off, will indicate the parts of the beam that have radiated (loosing energy), allowing a reconstruction of the current/photons time profiles. Figure 7 shows these reconstructed profiles [24].

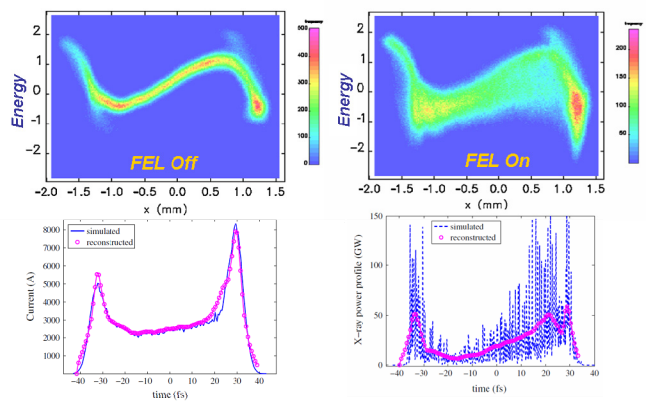

Figure 7: Reconstructed current profile and photon intensityy with FEL Off (left) and FEL On (right).

Short X-band structures are also used for longitudinal phase space linearization at FEL linacs. They optimize the compression process, compensating for the second-order RF time-curvature and the second-order momentum compaction term, T_{566} at magnetic chicane. The first system, operating at 11.4 GHz, was installed and successfully commissioned at LCLS [25]. A second system recently came into operation at FERMI@Elettra FEL [26] and a third one is being installed at SwissFEL. The latter two are based on the same multipurpose 12 GHz accelerating structure developed in the framework of a collaboration between CERN, PSI and Sincrotrone Trieste [27]. The RF design, featuring 72 cells, 75 cm (active length), 5/6π constant gradient, integrates two alignment monitors for accurate beam steering and trajectory correction. Moreover it is also possible to move the entire structure in the x-y plane by ± 500 µm, with fine remote adjustments. The low energy part of FERMI linac is shown in Figure 8, with the X-band structure installed at roughly 180 MeV and the first bunch compressor (BC1) at 320 MeV.

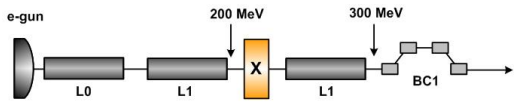

Figure 8: FERMI layout up to the first bunch compressor

The RF system is based on a 50 MW klystron (XL5), a 12 GHz scaled version of the SLAC XL4. The entire system has been installed in the last quarter of 2011 and commissioned up to June 2012. At present, for the nominal integrated gradient on the structure of 20 MV, it is operated at 50% of its nominal power. The measured RF phase and amplitude stabilities of 0.2 deg X-band and 0.05% rms are well in the specs. Tests have been carried out on the idle structure to verify the transverse wakes effects and the beam emittance degradation. Data, collected steering 350 pC, 6.5 ps (FWHM) beam ± 1.0 mm off-axes (x-y), did not show any particular emittance degradation if the beam stays aligned on the axes within one hundred microns.

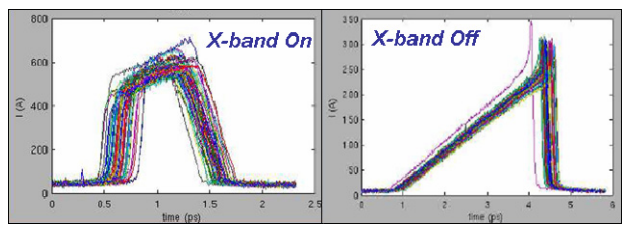

Figure 9: Current temporal profiles at BC1

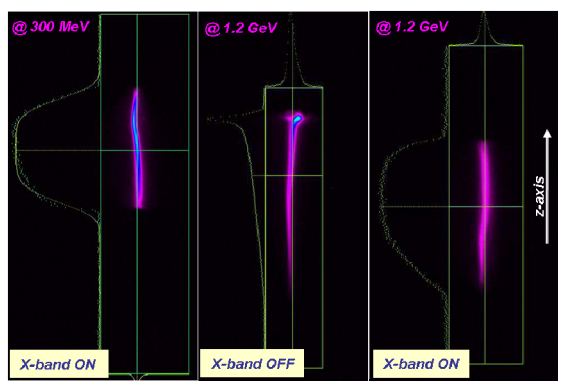

Figure 10: Bunch charge distribution at linac exit

Copyright © 2012 by the respective authors — cc Creative Commons Attribution 3.0 (CC BY 3.0)

Beam tests, performed at different cavity set-ups (17-20 MV) and compression factors (5-10) provided very good results. Figures 9-10 show the current temporal profile downstream BC1, and the bunch charge distributions at linac exit, with X-band On/Off, taken with two TDCs at 300 MeV and 1.2 GeV, on 150 e-pulses (15 sec).
For the tests, the machine was operated with only one bunch compressor. The flat-toping effect induced by the X-band in the two distributions is evident, with a net increase of the peak current (up to 600 A), and a very positive impact of the on the FEL performance.

INDUSTRIAL AND MEDICAL APPLICATIONS

In the last decade, the industrial and medical applications of X-band linacs have experienced significant growth. The advantages in using higher frequencies with respect to the most widely used S-band technology, came from its compactness, reduced weight and ease in handling and control. At X-band, the higher structure shunt impedance allows for higher efficiency in RF power conversion at a given beam energy. Moreover the breakdown voltages are much higher and filling time shorter. Most of the industrial and medical X-band linacs, cover the 1-10 MeV energy range and are operated at 9.2-9.4 GHz, using 1-2 MW pulsed magnetrons, at up to 0.1% duty cycle. A high power pulsed klystron (5 MW-20 kW) is also available at 9.3 GHz, but the offer at higher frequency is very limited. Portability makes X-band widely used for on-site inspections, i.e. bridges, chemical plants, pipe lines [28] and non-destructive analysis, i.e. cargo screening, food processing, etc. Novel compact inexpensive linacs, 1-2 MeV/10-100 μA average current, are also being developed for replacement of radionuclides sources, used for industrial radiography, Ir-192, Cs-137, Co-60 [29]. Medical applications greatly benefit from X-band for the reduced size of the beams and the possibility to easily have "self-shielded machines", minimizing stray radiation and leakages in treatment rooms. The most common applications that use X-band linacs are the Intra-Operative Radiation Therapy (IORT), where the electron beam radiation is directly delivered during surgery, and Stereotactic Radiosurgery, that uses an image-guided system to precisely deliver intensity modulated radiation to the focal lesion. For their compactness, X-band linacs are also being considered for Hadrontherapy, where it would be desirable to have "single room facilities" in which a proton linac rotates around the patient [30].

CONCLUSION

Applications of X-band technology in linacs is rapidly expanding due to its great potential already shown in different areas of particle accelerators. Recent results, concerning the accelerating gradients obtained at CLIC, demonstrate the feasibility of 100 MV/m operation with NC accelerating structures at 12 GHz. This will also benefit the interest for very compact linacs for X-ray FELs. The developments of very high brightness X-band photo-injectors are very promising and the use of X-band structures for diagnostics and beam manipulation at FEL linacs is continuously evolving. Very challenging R&D programs with X-band linacs have been undertaken in laboratories pursuing high intensity gamma sources, to increase the average power of the machines with multibunch operations.

Moreover, the great attention shown in the last two years by the scientific community for the use of X-band technology has also stimulated the interest in industry for the production of high power RF components. Two 50 MW, 12 GHz klystrons are currently at an advanced stage of manufacturing at industry.

ACKNOWLEDGEMENTS

The author is very grateful to U. Amaldi, S. Döbert, A. Degiovanni, J. Kovermann, G. McMonagle, I. Syratchev, W. Wuensch (CERN); C. Adolphsen, C. Limborg, P. Krejcik, T. Raubenheimer, S. Tantawi, A. Vlieks (SLAC); C. Barty, R. Marsh (LLNL); J. Rosenzweig, A. Valloni (UCLA); B. Spataro (INFN-LNF); M. Uesaka (University of Tokyo); E. Tanabe (AET Inc.); A. Tafo (Accuray); F. Manelli (Elekta) for providing informations about their activities and R&D programs on the X-band. Furthermore, the colleagues of the Linac group and FERMI commissioning team are acknowledged.

REFERENCES

[1] R.B. Neal "The SLAC Two Mile Accelerator", W.A. Benjamin, 1968.
[2] C. Adolphsen, SLAC-Pub 11224 (2005).
[3] W. Wuensch, HG2012 Workshop, 18-20 April 2012, KEK, Tsukuba, Japan.
[4] P. Emma, LCLS-TN-01-1, (2001).
[5] G. D'Auria et al., IPAC'10, Kyoto, Japan, TUPE015.
[6] J.W. Wang et al., SLAC-Pub 13444 (2008).
[7] F.V. Hartemann, LINAC'10, Tsukuba, Japan MOP005.
[8] ELI-NP, Magurele, Romania, http://www.eli-np.ro/
[9] G. D'Auria, NIM A 657 (2011).
[10] http://clic-study.org/accelerator/CLIC-ConceptDesignRep.php
[11] A. Grudiev et al., PRST 12, 102001 (2009).
[12] A. Grudiev et al., LINAC'10, Tsukuba, Japan, MOP068.
[13] Y. Sun et al., PRST 15, 030703 (2012).
[14] R. Walker et al., FEL'11, Shanghai, Cina, TUPB18.
[15] D. Gibson et al., PRST 13, 070703 (2010).
[16] S. Anderson et al., NIM A 657 (2011).
[17] A. Vlieks et al., AIP Conf. Proc. 691, June 2003.
[18] C. Limborg et al., PAC'11, New York, USA, MOP015.
[19] A. Vlieks et al., IPAC'12, New Orleans, LA, USA, WEEPPB007.
[20] J. Rosenzweig et al., NIM A 657 (2011).
[21] A. Valloni et al., AAC'12, Austin, Texas, USA.
[22] P. Emma et al., LCLS-TN-00-12, (2000).
[23] P. Krejcik et al., BIW'12, Newport News, VA, USA.
[24] Y. Ding et al., PRST 14, 120701 (2011).
[25] P. McIntosh et al., SLAC-Pub 11270.
[26] G. D'Auria et al., IPAC'12, New Orleans, LA, USA, TUPPP054.
[27] M.Dehler et al., IPAC'12, New Orleans, USA, MOOBC03.
[28] M. Uesaka et al., NIM A 657 (2011).
[29] S. Boucher et al., IPAC'12, New Orleans, LA, USA, THPPR069.
[30] U. Amaldi et al., RAST Vol. 2 (2009) 111–131.

Copyright © 2012 by the respective authors — cc Creative Commons Attribution 3.0 (CC BY 3.0)

ARIEL SUPERCONDUCTING ELECTRON LINAC

S. Koscielniak, F. Ames, R. Baartman, I. Bylinskii, Y. Chao, D. Dale, R. Dawson, E. Guetre, N. Khan, A. Koveshnikov, A. Laxdal, R. Laxdal, F. Mammarella, M. Marchetto, L. Merminga, A. Mitra, T. Planche, A. Sitnikov, Y.N. Rao, V. Verzilov, D. Yosifov, V. Zvyagintsev, TRIUMF*, 4004 Wesbrook Mall, Vancouver, B.C. Canada;
D. Karlen, R. Langstaff, University of Victoria, Victoria, B.C. Canada

Abstract

The TRIUMF Advanced Rare Isotope Laboratory (ARIEL) is funded since 2010 June by federal and BC Provincial governments. In collaboration with the University of Victoria, TRIUMF is proceeding with construction of a new target building, connecting tunnel, rehabilitation of an existing vault to contain the electron linear accelerator, and a cryogenic compressor building. TRIUMF starts construction of a 300 keV thermionic gun, and 10 MeV Injector cryomodule (EINJ) in 2012; the designs being complete. The 25 MeV Accelerator Cryomodule (EACA) follows in autumn 2013. TRIUMF is embarking on major equipment purchases and has signed contracts for 4K cryogenic plant and four sub-atmospheric pumps, a 290 kW c.w. klystron and high-voltage power supply, 80 quadrupole magnets, EINJ tank and lid, and four 1.3 GHz niobium 9-cell cavities from a local Canadian supplier. The low energy beam transport and beam diagnotics are being installed at the ISAC-II/VECC test facility. Procurement is anticipated October 2012 for the liquid He distribution system.

CONVENTIONAL INFRASTRUCTURE

The ARIEL project is described in Refs. [1,4]. The conventional infrastructure consists of four contracts: the main ARIEL construction, demolition and excavation, and the Stores and Badge buildings replacements. The latter are necessitated by site congestion. The new Compressor Building (CB), for gaseous helium management, forms part of the ARIEL package. In addition there are major renovations that will transform the former Proton Hall to the Electron Hall (e-hall).

Chernoff-Thompson Architects led a successful bid for the overall architecture and engineering contract, awarded October 2010. The Stores and Badge building construction is complete and occupancy was taken Sept 2011 and Dec 2011, respectively.

The demolition and excavation work started October 2011, and completed April 2012. The ARIEL main construction package was awarded Feb 2012. There is substantial completion of the tunnel and B2 level of the actinide target preparation labs, target hall and Rare Isotope Beams annexe. The annexe will contain mass separators and front-end accelerators. The CB is well advanced: roofing and envelope cladding, mechanical and electrical rough-in, are all proceeding on-track for occupancy in December 2012.

*TRIUMF is funded under a contribution agreement with the National Research Council of Canada.

The e-hall was emptied of legacy proton spectrometers in March 2012. The e-hall shielding, south wall upgrade and new north wall (that will protect e-hall from the future BL4N proton beam), is complete. The 10T full-coverage crane, and egress stairway are installed. Sealing of the concrete roof beams is pending final shield block moves. E-hall occupancy is anticipated October 2012.

Figure 1: ARIEL construction site, view north.

To accommodate the power requirements of e-linac systems a new 12.5 kV, 5 MW switchgear will be installed atop the e-hall roof. The gear will be close to the klystron power supplies and other local loads including a 0.5 MW emergency power bus. Further, the gear will feed north to the ARIEL building (2 MW) and south to the He CB (1 MW) housing the compressors and SA pumps.

The contract was awarded to Siemens Electric Canada April 2012. Fabrication is complete, and factory tests satisfactory. Delivery and installation will occur Sept-December, followed by connection to the TRIUMF grid, commissioning and energization.

ELECTRON GUN

The thermionic gun provides 300 keV kinetic energy electron bunches with charge up to 16 pC at a repetition frequency of 650 MHz. Aspects of the gun design were reported [2] previously. The main components are a gridded gun in a 2 bar SF6 filled vessel, and in-air HV power supply. Unique features of the gun are its inverted cathode/anode geometry to reduce dark current, and transmission of RF modulation via a dielectric (ceramic) waveguide and chokes through the SF6. The latter obviates the need for an HV platform inside the vessel to carry the RF transmitter, and results in a significantly smaller/simpler vessel. The modulation is applied to a CPI Y-845 gridded dispenser cathode via a stepped

Copyright © 2012 by the respective authors — cc Creative Commons Attribution 3.0 (CC BY 3.0)

coaxial line impedance matching section from the RF-collecting choke. The gun bias and heater power are applied through an isolation transformer.

The grid biasing and modulation is tested on a 100 kV prototype source; a conductance angle ±16° at 650 MHz is inferred from the transconductance. The same source confirmed the beam intensity can be varied by applying a macro pulse structure (over the RF) with a variable duty factor from 99.9% down to 0.1%; the lowest value is essential for intercepting profile monitors. The RF waveguide was subject to bench testing on scale models and extensive simulation and optimization with HFSS, and has been ordered from Kyocera. The gun electrodes, the vessel internal corona domes and shroud, were subject to extensive 3D electrostatic modelling and optimization. The electrodes are fabricated, ready for polishing. The gun ceramic, anode-tube internal steering coil, gun solenoid, isolation transformer, conditioning resistors and 350kV Glassman HV power supply are all delivered. Detailing of the gun support struts, HV shroud SF6 vessel is complete; and will be fabricated in autumn 2012, and components assembly and integration follow thereafter.

INJECTOR TEST FACILITY

The VLBT test facility at ISAC-II, under collaboration between TRIUMF and VECC of Kolkata, India, provides an ideal proving ground for e-linac design and operation strategies. It prototypes the injector up to the exit of the cryomodule with enhanced diagnostic capability for benchmarking the performance of the gun, various diagnostic devices and procedures, and demonstrating sustained operation at the design parameters. Refs. [8,9] detail recent beam dynamics simulations and beam tests.

The extant part of the ELBT, Fig. 2, comprises the sequence: box DB1A after 1st solenoid, DB1B after buncher cavity, DB3 after 3rd solenoid, all in the mainline; and MB0 dipole, RF deflector cavity, DB0 in the analyzer stub. Button BPMs are installed between the first and second solenoids. View screens VS1A, VS1B, VS3 are installed and tested at each of the diagnostic boxes (DB). An Allison type emittance scanner [3], a wideband capacitive pickup (a.k.a non-intercepting monitor, NIM) and fast Faraday cup are moveable.

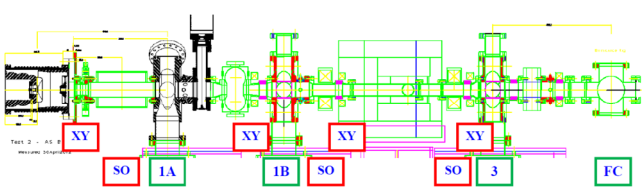

Figure 2: ELBT mainline major components.

Do date there have been two rounds of beam tests: phase (i) to DB1B; and phase (ii) transport to DB3 and DB0 is underway. In the intervening period, a crane was installed for shielding block lifts and moves; and shielding (for an eventual 25 kW beam test) is configured.

The outcome of the phase-one test: (i) The solenoid and correctors successfully controlled beam trajectory and shape as designed. (ii) Low level control of buncher cavity, and phase lock to the gun grid, was demonstrated. (iii) The beam horizontal emittance was measured directly with the Allison scanner, and indirectly with scintillator screen and solenoid scan. Both methods confirmed the Gaussian distribution from the gun. (iv) BPM, Faraday cups, slit scanner, chromox and YAG scintillator screens, capacitive pickup, PMT based loss monitor, were tested [5] and areas for improvement identified. The time structure of the electron source was measured with the NIM. The measured bunch length of 200 ps agrees with beam dynamics simulations.

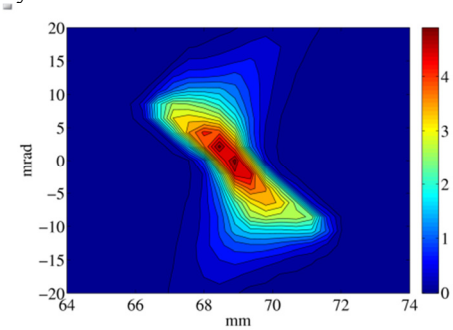

Figure 3: Phase space as mapped by the Allison emittance scanner, for a 60 keV, 10 mA peak electron beam. The normalized r.m.s. emittance is 4.6 microns.

For the phase-two test under way, two solenoids and diagnostic boxes were added; and the Allison rig and FC reinstalled after DB3. The analyzer magnet MB0 and deflecting cavity are now installed for measurement of longitudinal parameters. The 1.3 GHz deflector LLRF is synchronized with the gun modulation; and electron beam deflections are recently demonstrated in a RF phase scan.

BEAM DIAGNOSTICS

Status of diagnostic devices is reported in Refs. [5,10]. Initial beam threading will be with view screens, followed by orbit correction with 4-button type BPMs each measuring in two planes H &V. Sixty button electrodes were delivered by Kyocera Corp; all were inspected and verified to be within tolerance of 0.05 mm. The position sensitivity is 1.4dB/mm between opposite pickups. The signal power of -27dBm was measured at VLBT with the beam current of 10 mA (peak), and agrees well with the expected value of -30dBm. About 140 more buttons are still to be procured and tested. The prototype of the stripline BPM is being manufactured for test at VLBT.

The BPM electronics design is complete; a prototype unit has been successfully tested in the laboratory. This consists of a commercially available, *Bergoz*, analog front-end (AFE) customized for 650 MHz and a TRIUMF developed intermediate frequency (IF) processing unit based on a 125 MHz 14-bit ADC and Spartan-6 FPGA. The output bandwidth is around 1 MHz.

Preliminary design of the fast wire scanner, speed goal of 3 m/s, was completed. The prototype unit is presently being fabricated at TRIUMF for test at VLBT.

A *Bergoz* DC current transformer is housed in a magnetic and vibration shielded and temperature

Copyright © 2012 by the respective authors — cc Creative Commons Attribution 3.0 (CC BY 3.0)

stabilized enclosure. Initial bench tests reveal a drift of ~ 40 uA over 48 hours; the cause is being investigated.

BEAM LINES

The beam line sections are: ELBT, the 300 keV transport; EMBT 5-10 MeV transfer between EINJ and EACA; EABT 25 MeV transfer to future EACB; EHAT 25-50 MeV transport downstream of the cryomodules to a switching magnet; EHDT leading to a 100 kW beam dump; and EHBT 25-75 MeV transport to the photo-fission targets. The EMBT layout anticipates a "Merger" section in a future scenario that will merge the injector beam with a recirculating beam to provide RLA and/or ERL functionality. The EHBT, in the tunnel, consists mainly of a periodic section consisting of six 90° FODO cells, each 4m in length. The EMBT contains a 36° bend section, the EHDT, a 90-degree section formed of four bends, and the EHBT two doglegs and bend sections to the west and east targets. All insertions are achromatic.

Quadrupoles

From the Injector linac onward, the most convenient focusing device is the magnetic quadrupole. However, at lowest envisioned beam energy of 5 MeV, the focal power required is rather small. This forces us to shortest possible quadrupoles, else the fields are too low compared with expected remanent field of low-carbon steel. A theoretical study was made to derive the optimal pole shape for short quadrupoles whose length is comparable to or smaller than the aperture. Conventional 2-D treatment and fabrication practice, assuming sufficiently large pole length, break down in such cases. We have derived [6] analytically a new 3D shape, and demonstrated that it yields smaller aberrations. For short quads it is well approximated by a simple spherical pole provided the sphere radius is 1.65 times the quadrupole aperture radius.

The beamlines in the e-hall adopt weak and medium quadrupoles, with integrated strengths up to 0.2 T and 0.7 T respectively. This is easily achieved with the short quadrupoles of aspect ratio 1 and cylindrical poles with spherical faces. The weak quads are also used for the periodic section in the tunnel. At highest envisioned energy of 75 MeV, the shortest required focal length is 0.24 m in the EHBT dogleg sections. The required integrated gradient is 1.05 T; this will be achieved with a more conventional strong quadrupole design with rectangular cross-section poles and hyperbolic faces. The strong quads will be water-cooled, the weaker ones air-cooled, and the medium ones indirectly cooled. All have aperture diameter equal to 52.0 mm. In total, there are 80 quadrupoles; the contract for their manufacture was awarded to Buckley Systems Ltd., New Zealand, August 2012 with delivery scheduled January to March 2013.

Dipoles

The different beam lines contain a total of fifteen dipoles, which have been divided into four groups, depending on their required integrated field and field quality. for the purpose of design and procurement. Longitudinal space constraints in the beamline layout, particularly in “Merger” and doglegs, lead us to design the magnets as small as possible. Thus, many of these dipoles are short compared with their aperture leading to low strength because the field does not “plateau” inside the magnet. Proximity of other magnets implies also the use of field clamps to contain the field fall-off. These features combine to make essential their modeling with a 3D finite element code such as OPERA. Moreover, one must ensure that the second order aberrations (sextapole) will causes negligible emittance growth (<0.01% per dipole). To study the non-linear optical properties of our models, we used the differential algebra and particle tracking code COSY INFINITY with field maps imported from OPERA. Satisfactory pole, field clamp and yoke geometries were obtained (0.1% fringe field at 10cm from magnet edge) and are being used as the basis for tender. The first dipole, the EMBT momentum analyzer, contract was awarded to Alpha Magnetic Inc. August 2012.

Vacuum

ARIEL e-linac has 13 vacuum volumes with requirements ranging from 10^{-10} Torr in the gun, 10^{-9} in ELBT, 10^{-8} in EMBT and EABT, to 10^{-7} in EHAT, EHDT and EHBT when the beam is present. The limits arising from residual gas (Rutherford) scattering and ion neutralization are an order of magnitude relaxed compared with these values. The pipes inside the cryomodules will naturally cryopump to 10^{-11}Torr, and the issue there is of cleanliness and particulates free. The insulating and coupler vacuums are 10^{-6} Torr. The beam line volumes are separated by RF screened all metal electro-pneumatic gate valves. The vacuum volumes are evacuated from atmospheric pressure to high vacuum level with turbo-molecular pumps, which are also used during the in-situ bake out. After the bake out is completed, the turbo-pumps are isolated via gate valves and the pressure is further lowered by ion pumps. The ion gauges are used only during the initial evacuation and bake out. Once the ion pumps are turned on, the ion gauges are turned off. The pressure is observed on the cryo-pumps controllers.

CRYOMODULES

Due to heavy beam loading, five 9-cell cavities at 100kW/cavity are required to reach the 0.5 MW beam power. The injector cryomodule (EINJ) contains a single 9-cell cavity, and is designed [11] and constructed in collaboration with VECC. The accelerator cryomodules (EACA,B) each house two 9-cell cavities.

The cryomodule design utilizes a box vessel with a top-loading cold mass. A 4 K phase separator, 4K/2K heat exchanger and Joule-Thomson valve are installed within each module to produce 2 K liquid. The cold mass is suspended from the lid with mounting posts, struts and strong back; and is surrounded by a LN2-cooled copper box for thermal isolation. A 1 mm warm mu-metal shield is fastened to the inside of the vacuum vessel. The cold mass consists of the cavity hermetic unit, a cold mu metal

Copyright © 2012 by the respective authors — cc Creative Commons Attribution 3.0 (CC BY 3.0)

layer and the tuner. The tuner cold part is the Jefferson-lab style scissor type; and is followed by a long actuator and warm ISAC-II style rotary servo motor mounted on the lid. The hermetic unit includes the cavity(s), power couplers, RF pick-up(s), the warm-cold transitions with HOM damping material and warm isolation valves. A carbon fibre reinforced silicon carbide material CESIC is chosen for the damping material with measured conductance at 1.3 GHz and 80 K of 2200 Si/m.

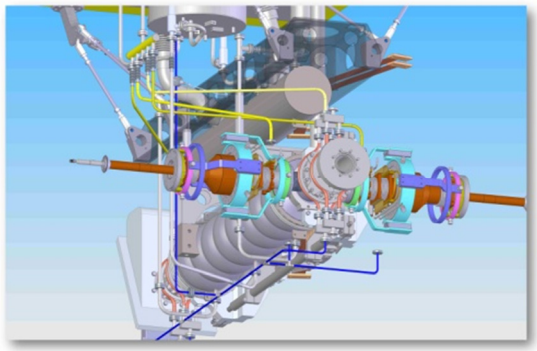

Figure 4: Injector cryomodule internal assembly.

The e-linac cryogenic distribution is based on a parallel feed of atmospheric LHe from a main trunk to each cryomodule. The LHe is drawn from a main dewar supplied from the 4 K cold box. A LHe reservoir in each cryomodule acts as a phase separator. Cold gas returns in parallel back to a common return trunk and is delivered back to the cold box where it represents a refrigerator load. 2 K liquid is produced in each cryomodule by passing the 4 K liquid through a heat exchanger in counter flow with the returning exhaust gas from the 2 K phase separator and expanding the gas to 31 mbar through a JT expansion valve. The header pipe above the cavity string acts as a 2 K phase separator. The cold helium gas passes through 4K/2K heat exchanger; and then, after warming up to ambient temperature, reaches the warm sub-atmospheric pumping system. This fraction constitutes a liquefaction load to the He cryoplant. A siphon circuit from the 4 K reservoir is used to cool the 4 K intercepts, with vapour return back to the reservoir. Initial cool down is done by delivering 4 K liquid from the 4 K phase separator to the bottom of the cold mass through a dedicated cool down valve.

The 4K/2K cryo-insert is being built and tested as a separate package. The insert includes a 4 K phase separator, 4K/2K heat exchanger, JT expansion valve, 4 K cool down valve plus siphon circuit for intercept cooling. The prototype heat exchanger is from DATE, France, with an estimated capacity of 2.5 gm/sec. All components plus fabricated parts are now being assembled for cold test in October 2012. The lid, tank, support posts, strong back and cavity support detailing is complete. LN2 shield detailing is in progress. Manufacture of the tank and lid was awarded August 2012.

SRF Cavities

The nine-cell 1.3 GHz elliptical cavity borrows the TESLA/ILC type inner cell geometry but uses modified end groups to accommodate the large power couplers and to mitigate HOMs. A multi-pass beam break up (BBU) criterion establishes a limit of R_d/Q^*Q_L < 1e7 Ohm. End group beam tubes of inner radius 48 mm and 39 are used for the power coupler and RF pick-up end, respectively.

The first of four niobium cavities is presently being fabricated at PAVAC Industries of Richmond Canada. A 7-cell cavity in copper was completed Feb 2012 to test all fabrication procedures and manufacturing jigs; lessons learnt are now applied to the Nb cavity production to improve quality assurance.

Processes have been developed at PAVAC that will expedite the fabrication of future cells and cavities – in terms of reproducibility, true to shape and frequency. A main study was on forming. The original dies produced cells too short at the equator - causing material stress and some multipacting. PAVAC developed a forming tool with male die against a plastic that becomes almost fluid at high pressure and “hydroforms” - all cells formed since then are exceptionally reproducible. Next the fixturing during welding of half cells became an issue. Our equator weld set-up initially was a butt weld of two identical ½ cells. During forming and machining, and due to grain structure, the niobium ½ cells can go slightly out of a true circle. The question became how to hold them nicely true to a circle while not touching the newly etched weld zone. A self-fixturing solution is adopted: an interleaving feature is machined into the equator of unique male and female half-cells so they fit together and ‘self-fixture’ during welding. Two Nb cells have been prepared in this way, and frequency is very repeatable. Success at equator suggested we prepare the iris in the same way to better control weld and reduce centroid drift over multi-cell length. All cell parts are coming out very true and the self fixturing is better suited for production. The near term milestone is to have a complete Nb 9-cell cavity in November 2012.

CRYOGENIC EQUIPMENT

Since the project start, June 2010, the e-linac cryogenic system 13], Fig. 5, has moved from conceptual design phase to the engineering design and procurement stages. Conceptual design of e-linac cryomodules and cryogenic system went through external reviews Sept 2010 and March 2011, respectively. In parallel with SRF cavity and injector cryomodule engineering design, the helium refrigerator-liquefier specification was produced and tendered June 2011. The contract for supplying He cryoplant consisting of HELIAL 2000 cold-box, main and recovery compressors with oil removal and gas management systems (OR/GMS), and multi-component purity analyzer was awarded to Air Liquide Advanced Technologies (France). This is class 700 W cooling power at 4.6 K machine with maximum liquefaction rate of 288 l/h. The final design was approved June 2012, and the cryoplant has moved to the production phase; concluding in delivery the second quarter of 2013. The contract for helium gas storage was awarded May 2012 with delivery scheduled January 2013.

Copyright © 2012 by the respective authors — cc Creative Commons Attribution 3.0 (CC BY 3.0)

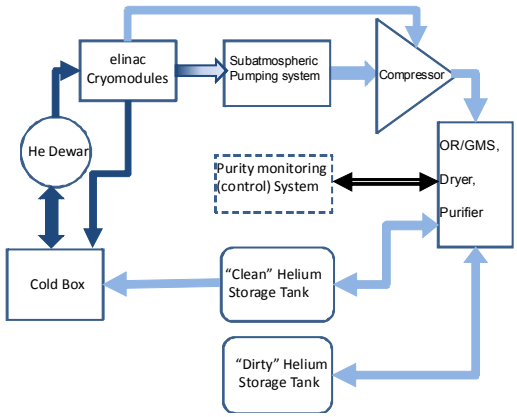

Figure 5: e-linac cryogenic system overview.

The cold-box with 1000 litre liquid helium storage dewar are positioned in the immediate vicinity of the e-linac cryomodules in order to minimize losses associated with LHe transfer. The warm part of installation, including two Kaeser He compressors, OR/GMS, and sub-atmospheric helium pumps, will be located outside the e-hall in the separate compressor building.

Recent activity has focused on design and tender of the liquid helium distribution system, and procurement of SA pump units. Further development is related to SA helium and LN2 system design and manufacturing, installation of services and auxiliaries, instrumentation.

The sub-atmospheric units will pump continuously on He gas to maintain a suction pressure within 24-28 mbar measured at the pumps inlet. The exhausting clean He gas is sent to a helium compressor at 1.05–1.1 Bara. A modular design is adopted with 4 units for EINJ and EACA having a combined through-put totalling 5.6 gm/sec, and 6 units totalling 9.3 gm/sec after the addition of EACB. The contract for supply of four sub-atmospheric helium pumps, type DS3010-B, was awarded to Busch Vacuum Technics Inc. in August 2012; and delivery is scheduled first quarter 2013.

RADIO-FREQUENCY EQUIPMENT

The e-linac 1.3 GHz high power RF system will be installed in stages: in the first, to be completed in 2014, the injector cryomodule (EINJ) is fed by a 30 kW c.w. Inductive Output Tube (IOT); and the first accelerator cryomodule (EACA), will be powered by a high power c.w. klystron and power divider. At a later stage, EINJ is upgraded to 100 kW, and a second accelerator cryomodule (EACB) is added along with another klystron and power supply. EINJ and EACA contain one, and two, SRF cavities respectively. Each cavity is equipped with two 50 kW c.w. input couplers – manufactured by CPI following the Cornell (ERL injector prototype) design. Ref. [12] details the coupler conditioning station.

The IOT with solenoid and trolley is purchased from CPI, USA, and its HV power supply and drive amplifier from Bruker BioSpin, France. The system is installed and tested to the maximum rated output power of 30 kW on a water cooled load, and can now be run routinely.

The c.w. klystron is specified with a saturated power of 290 kW and usable linear range (incremental gain of 0.5 dB/dB) up to 270 kW, leaving plenty of margin for transmission loss to the 200 kW nominal rated EACA. After a tender process, coordinated as a joint venture with Helmholtz Zentrum Berlin, orders were placed with CPI, USA: one for TRIUMF and 3 units for HZB. The klystron is a factory-tuned multi-cavity, high efficiency, high gain, broadband, water cooled tube. The final design was complete August 2012. The klystron is to be factory tested January 2013 prior to shipment to TRIUMF.

The contract for the klystron high voltage power supply, rated at 65 kV 8.65 A, and focus, filament and vacuum ion pump power supplies, and trunk RF distribution system including all control, interlocks and protection and integration of the klystron was awarded to Thomson Broadcast June 2012. The power supply is based on a voltage controlled power module type *PM-14-10-VR-1* derived from the modulator PSM12-2400 for DESY. A description of this technology and its advantages is provided in Ref. [7]. The 300 kW c.w. circulator and loads are subcontracted to AFT Microwave.

CONCLUSION

The ARIEL e-linac project has witnessed outstanding progress across all areas. The building's construction is on schedule for completion 2013 April. Beamlines, cryogenic and high-power RF equipment design and procurements are on schedule. The facility two key milestones, the Injector Cryomodule beam test in 2013 March and Accelerator Cryomodule initial beam test in 2014 June, are on track.

REFERENCES

[1] L. Merminga *et al*: "ARIEL: TRIUMF's Rare IsotopE Laboratory", WEOBA001, proc IPAC 2011, San Sebastian, Spain.
[2] C. Beard *et al*: Conceptual design of ARIEL 300 keV electron gun", proc PAC 2011, NY. City NY.
[3] A. Laxdal *et al*: "High Power Allison Scanner for Electrons", TUCP04, proc. BIW 2012, Jefferson Laboratory, Newport News VA.
[4] S. Koscielniak *et al*: MOOBC01, proc. IPAC12, New Orleans LA.
[5] D. Karlen *et al*: "Beam Diagnostic Systems for the TRIUMF e-linac", MOPPR003, *ibid.*
[6] R. Baartman, "Quadrupole Shapes", Phys. Rev. ST Accel. Beams 15, 074002 (2012).
[7] M. Bader, M. Frei, J. Troxler: "Low Ripple Vacuum Tube Power Supply Based on Enhanced PSM Technology", Thomson Broadcast AG, 2012.
[8] A. Chakrabati *et al*: MOPB024, these proceedings.
[9] R.E. Laxdal *et al*: MOPB026, these proceedings.
[10] V.A. Verzilov *et al*: TUPB081, these proceedings.
[11] R.E. Laxdal *et al*: MOPB091, these proceedings.
[12] A.K. Mitra *et al*: MOPB033, these proceedings.
[13] Y. Bylinskii *et al*: "ARIEL e-linac cryogenic system development at TRIUMF", proc. International Cryogenics Conference, May 2012, Tsukuba, Japan.

Copyright © 2012 by the respective authors — cc Creative Commons Attribution 3.0 (CC BY 3.0)

LINAC-BASED LASER COMPTON SCATTERING X-RAY AND GAMMA-RAY SOURCES

R. Hajima*, JAEA, Ibaraki 3191195, Japan

Abstract

Laser Compton scattering (LCS) light sources can provide high-energy photons from keV to MeV range. Many research and development projects of linac-based LCS sources are carried on. For the photon energies of tens keV, linac-based LCS sources realize laboratory-size X-ray sources, of which performance is potentially comparable to 2nd generation synchrotron light sources. Linac-based LCS also realizes unparalleled γ-ray sources of high-brightness and narrow bandwidth. In the present paper, status and perspectives of linac-based LCS X-ray and γ-ray sources are reviewed.

LASER COMPTON SCATTERED PHOTON SOURCES

The combination of a high-energy electron accelerator and a laser realizes high-energy photon sources based on laser Compton scattering (LCS) [1].

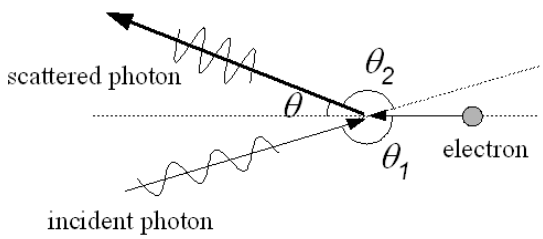

Figure 1: Laser Compton scattering.

Figure 1 shows a schematic representation of laser Compton scattering, where a high-energy photon (X-ray or γ-ray) is generated via the Compton back-scattering of an incident laser photon with a relativistic electron. The energy of the scattered photon, E_x, is a function of the incident photon energy, $E_L = hc/\lambda$, electron energy $E_e = \gamma mc^2$, and scattering geometry, and approximated for a head-on collision:

$$E_x \approx \frac{4\gamma^2 E_L}{1+(\gamma\theta)^2+4\gamma E_L/(mc^2)} \qquad (1)$$

The above equation shows that the LCS photon energy is tunable by changing electron beam energy, laser wavelength or collision angle. The LCS photon energy also has a correlation to the scattered angle. Therefore, monochromatic photon beam can be obtained by putting a collimator to restrict the LCS beam divergence at the downstream. We can produce linear- and circular-polarized high-energy photons by using polarized lasers. The electron energy necessary for generation of hard X-ray (20 keV, for example) is only 30 MeV, which is much smaller than the electron energy to produce hard X-ray via synchrotron radiation.

Owing to the above features of LCS photon source, energy tunability, monochromatic and polarized photon generation, compactness, LCS sources have been developed by using various types of accelerators such as storage rings, linacs and microtron [2-6]. In the present review, we focus on linac-based LCS photon sources in X-ray and γ-ray energies.

A photon flux from laser Compton scattering at an ideal head-on geometry integrated over the entire scattering angle is given by

$$F_{total} = \frac{16}{3} N_e N_L f \frac{r_0^2}{w_0^2} \qquad (2)$$

where N_e and N_L are the number of electrons and laser photons at the collision, respectively, f is the collision frequency, r_0 is the electron classical radius and w_0 is the collision spot size.

Spectral brightness of laser Compton scattered photon sources can be calculated as

$$B \approx F_{total} \frac{\gamma^2}{\varepsilon_n^2} \times 0.1\% \qquad (3)$$

where ε_n is normalized emittance and the factor 0.1% is for the conventional unit of spectral brightness, (photons/sec/mm^2/mrad^2/0.1%BW).

In order to obtain a high-flux and high-brightness photon beam from laser Compton scattering, it is necessary to increase the density of both electrons and photons at the collision point and to reduce normalized emittance. An electron beam of small emittance and high-average current is, thus, essential to high-flux and high-brightness photon generation via laser Compton scattering.

LINAC-BASED LCS X-RAY SOURCES

Linac-based LCS X-ray source enable us to produce energy-tunable X-ray beams with a laboratory-size apparatus, of which flux and brilliance is potentially comparable to synchrotron radiation from a bending magnet of GeV-class storage rings. There are many R&D programs carried out for realizing LCS X-ray sources. Here, we see research activities on-going in Japan.

A LCS X-ray source has been developed at AIST (National Institute of Advanced Industrial Science and Technology) [7]. They employed a 42-MeV S-band linac equipped with a photocathode RF gun. For the laser Compton scattering, they use a Ti:Sapphire laser. Two

*hajima.ryoichi@jaea.go.jp

Copyright © 2012 by the respective authors — cc Creative Commons Attribution 3.0 (CC BY 3.0)

collision angles, 90-degree and 165-degree, are possible to generate LCS X-rays. Ultrashort X-ray pulses, 150 fs (rms), are obtained at the 90-degree collision and a high-flux X-ray, 10^7 photons/s, is available at the 165-degree collision. The LCS X-ray source has been used mainly for imaging applications such as phase contrast imaging of rat's lumber vertebra [8] and K-shell absorption angiography of rabbit [9]. In order to improve X-ray flux, they are developing a multi-collision system, in which a train of electron bunch generated from the photocathode gun collides with a train of laser pulse to produce LCS X-rays with a flux of $3.3\text{x}10^9$ photons/s [10].

There are two LCS X-ray source under development at High Energy Accelerator Research Organization (KEK). One is based on an S-band normal conducting linac and the other is based on an L-band superconducting linac. Both the LCS sources are utilizing multi-collision configuration. The S-band LCS source named LUCX (Laser Undulator Compact X-ray) has already demonstrated X-ray generation and imaging application [11]. They obtained an X-ray beam at 30 keV with a flux of $2.1\text{x}10^5$ photons/s.

The superconducting LCS X-ray source at KEK is based on an L-band superconducting linac originally developed for ILC (International Linear Collider). They have constructed an electron beam transport line for the LCS X-ray generation at the downstream of an ILC cryomodule [12]. A 4-mirror type laser enhancement cavity is employed for the multi-collision LCS X-ray generation. Generation of electron bunch, 162500 bunches in a train of 1-ms duration, has been successfully demonstrated [13]. The first X-ray generation is scheduled by the end of 2012 using a 40-MeV electron beam. Expected performance of LCS X-ray is energy of 30 keV and flux of $1.4\text{x}10^{11}$photons/s/10%BW.

Table 1 is a summary of the LCS X-ray sources in Japan, where the average spectral brightness is evaluated by Eqn.(3) with assuming normalized emittance of 1 mm-mrad, a typical value obtained from a photocathode electron gun.

Table 1: Linac-based Laser Compton X-ray sources

Facility	X-ray Energy	X-ray Flux #1	X-ray Brightness #2
AIST (demonstrated)	40 keV	10^7	$\sim10^8$
AIST (upgrade)	38 keV	$3.3\text{x}10^9$	$\sim10^{10}$
LUCX (demonstrated)	30 keV	$2.1\text{x}10^5$	$\sim10^6$
STF (design)	30 keV	$1.4\text{x}10^{12}$	$\sim10^{13}$

#1 photons/sec/100%BW

#2 photons/sec/mm^2/mrad^2/0.1%BW, evaluation by Eq. (3) with assuming a normalized emittance of 1 mm-mrad

From Table 1, we can see that linac-based LCS X-ray sources are surpassing the brightness of X-ray tubes and approaching to the brightness of bending magnet radiation from a 2nd generation synchrotron light source.

LINAC-BASED LCS GAMMA-RAY SOURCES

Since synchrotron radiation light sources cannot cover photon energies above ~1MeV, LCS is the only photon source to produce energy-tunable photon beams in MeV energy region. So far, LCS γ-ray sources have been developed utilizing storage rings [2,3].

Storage-ring based LCS γ-ray sources, however, have a limitation of spectral brightness due to quantum excitation. An electron beam in a LCS photon source suffers from quantum excitation from collision with laser photons. This quantum excitation causes growth of emittance and energy spread of the electron beam. Degradation of electron beam quality, growth of emittance and energy spread, is summarized in ref [14]. In the limit of high-density collision, energy spread of an electron beam in a storage ring LCS source reaches to an equilibrium, where the quantum excitation balances with the radiation dumping:

$$\left(\frac{\sigma_E}{E}\right)_{eq} = \sqrt{\frac{7}{5}\frac{\lambda_c}{\lambda_L}\gamma} \qquad (4)$$

where $\lambda_c = h/mc = 2.43\text{x}10^{-12}$ m is the Compton wavelength of the electron, λ_L is the laser wavelength. For example, in a 350-MeV storage ring operated with a 1 μm laser to produce 2-MeV γ-rays, the electron energy spread at the equilibrium is calculated to be 4.6% (rms). This growth of energy spread becomes a serious limitation of spectrum brightness of storage ring-based LCS γ-ray sources.

According to Eq. (3), the spectral brightness of LCS photon source is proportional to γ^2 as far as the normalized emittance is preserved. In order to receive the full benefit of γ^2 scaling, linac is the best platform for LCS γ-ray source. An electron beam preserves its normalized emittance during acceleration in a linac and the electron beam after the LCS interaction goes to a beam dump, thus, we can keep the collision of fresh electrons with laser photons to produce high-flux and high-brightness γ-rays in linac-based LCS sources.

In Lawrence Livermore National Laboratory (LLNL), they have developed a linac-based LCS γ-ray source, T-REX, for a homeland security application, which is detection of special nuclear material hidden in a cargo container [15]. The detection is based on nuclear resonance fluorescence (NRF), isotope specific photonuclear reaction [16]. The γ-ray source, T-REX, utilized a 120-MeV S-band normal conducting linac equipped with a photocathode RF gun. They generated γ-rays, 200-500 keV, from T-REX and demonstrated the detection of concealed material of a specific isotope, Li-7 beyond a shield, by using 478 keV γ-ray from T-REX [17].

Copyright © 2012 by the respective authors — cc Creative Commons Attribution 3.0 (CC BY 3.0)

Following the successful demonstration of LCS γ-ray generation at T-REX, a new LCS γ-ray source, VELOCIRAPTOR, is under development at LLNL [18]. For the γ-ray source, VELOSILAPTOR, they employed an X-band linac developed by SLAC for making the γ-ray source compact. Since the fissile isotopes, U-235 and Pu-239, have resonant energy around 2 MeV, they chosen machine parameters to produce 2 MeV γ-rays. An electron beam from the X-band linac has energy of 250 MeV to produce 0.5-2.5 MeV γ-ray by collision with frequency-doubled Nd:YAG laser.

In the detection of nuclear material using NRF, narrow-band γ-rays are essential for the better signal-to-noise ratio in the measurement, because the resonant width of NRF is less than 1 eV and incident γ-rays out of this resonant width become background noise. In LLNL, they optimized electron beam parameters to obtain narrow-band γ-rays [19].

In Japan, another application of LCS γ-ray has been proposed, which is non-destructive measurement of fissile material in melted nuclear fuel at Fukushima Daiichi Nuclear Power Plant [20]. The Great East Japan Earthquake on March 11, 2011 brought a severe accident in Fukushima Daiichi Nuclear Power Plant. Most of nuclear fuels in the plant has been melted due to loss of coolant. It is currently being thought that the complete decommissioning of the plant will take 30-40 years. During this long-term decommissioning process, the removal of melted fuels will most probably start from 2021 or later and will continue for 10-15 years. In this removal process, it is considered that debris of melted fuel are contained in a water-filled canister. Under the nuclear safeguards agreement, we need to measure the amount of fissile material in each canister to declare no fissile material is diverted into a weapon. Taking into consideration the available time prior to the removal of the melted fuel from the reactors, we have time to develop some techniques for the measurements of fissile material in the melted fuels.

A research group of JAEA proposed a non-destructive measurement system for plutonium in spent nuclear fuel by nuclear resonance fluorescence triggered by LCS γ-ray source based on an energy-recovery linac (ERL) [21,22]. It is considered that the ERL γ-ray source is also applicable to the measurements of fissile material in the melted fuel.

In order to demonstrate the performance of ERL LCS γ-ray source for the application of nuclear material measurement, JAEA has launched a 3-year R&D program (2011-2013) supported by Ministry of Education, Culture, Sports, Science and Technology (MEXT) in Japan [20]. The program aims at generation of a high-flux and narrow-bandwidth LCS photon beam at the Compact ERL in collaboration with KEK. Figure 2 shows a schematic view of the proposed experiment at the Compact ERL. Since the initial commissioning of the Compact ERL is conducted at electron beam of 35 MeV and 10 mA, generated LCS photon energy will be 22 keV and the flux is expected to be ~10^{11} photons/sec.

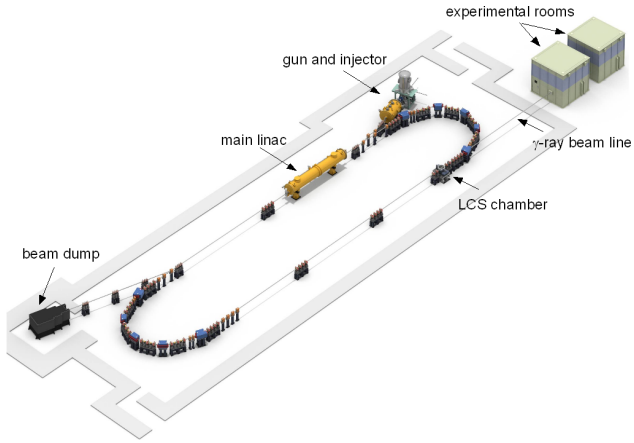

Figure 2: A schematic view of the LCS γ-ray experiment at the Compact ERL

For the measurement of fissile material, 2-MeV γ-rays are required to cover NRF energies of uranium and plutonium isotopes. For this purpose, a 350 MeV ERL to produce 2-MeV γ-ray at a flux of 10^{13} photons/sec was designed [23]. For the more compact and efficient LCS γ-ray source, utilization of a multi-turn ERL with spoke cavities operated at 4K is also under consideration.

LCS γ-ray source will be an innovative tool for scientific applications as well. A research facility of LCS γ-ray is to be built at Bucharest, Romania. The facility is ELI-NP (ELI Nuclear Physics), which is one of the four pillars of Extreme Light Initiative (ELI), pan-European laser facility aiming to host the most intense lasers world-wide [24].

The ELI-NP is a complex facility of petawatt lasers and LCS γ-rays, where two 10-petawatt class lasers and a 600-MeV linac for LCS γ-rays are constructed in the same facility. In the Whitebook of ELI-NP, many experimental proposals are described [25], for example, probing the pair creation from the vacuum in the focus of strong electrical fields with a high energy γ-ray beam, which is a validation of QED. Production of medical isotope using narrow-band γ-ray beam is also proposed at ELI-NP [26].

SUMMARY

The performance of linac-based LCS X-ray and γ-ray sources shows continuous improvement following advancement of laser and accelerator technologies. LCS X-ray source is able to provide energy-tunable, polarized and quasi-monochromatic hard X-rays with a laboratory-size apparatus. Spectral brightness of recently developed LCS X-ray source exceeds the brightness of X-ray tubes. The flux and brightness can be further increased by multi-collision configuration. Expected performance of curently-developing LCS X-ray source is comparable to bending magnet radiation from 2nd generation synchrotron sources.

Copyright © 2012 by the respective authors — cc Creative Commons Attribution 3.0 (CC BY 3.0)

LCS also provides energy-tunable narrow-bandwidth γ-rays in photon energies above 1 MeV, where synchrotron radiation source is not available. Since a linac is free from electron beam degradation due to accumulation of the quantum excitation, linac-based γ-ray source is unparalleled in terms of its narrow bandwidth and spectral brightness. Development of LCS γ-ray sources are carried out in the world towards homeland security, nuclear industrial applications and innovative science.

ACKNOWLEDGMENT

The author thank to Drs. J. Urakawa, R. Kuroda and K. Sakaue for providing materials to complete the review. The author also thank to MEXT Quantum Beam Technology Program for the support of LCS source development in Japan.

REFERENCES

[1] G.A. Krafft and G. Priebe, Review of Accelerator Science and Technoogy 3 (2010) 147.
[2] H.R. Weller et al., Progress in Particle and Nuclear Physics 62 (2009) 257.
[3] H. Ohgaki et al., Nucl. Instr. Meth. A455 (2000) 54.
[4] M. Bech et al., J. Synchrotron Radiation, 16, 43-47 (2009).
[5] R.W. Schoenlein et al., Science 274 (1996) 236.
[6] I. Daito et al., Proc. IPAC-2012 (2012) 4124.
[7] R. Kuroda et al., Nucl. Instr. Meth. A637 (2011) S183.
[8] H. Ikeura-Sekiguchi et al., Appl. Phys. Lett. 92 (2008) 131107.
[9] K. Yamada et al., Nucl. Instr. Meth. A608 (2009) S7.
[10] R. Kuroda et al., Proc. IPAC-2012 (2012) 4139.
[11] K. Sakaue et al., Proc. IPAC-2012 (2012) 2146.
[12] H. Shimizu et al., Proc. IPAC-2011 (2011) 1470.
[13] M. Kuriki et al., Proc. IPAC-2012 (2012) 1479.
[14] Z. Huang and R.D. Ruth, Phys. Rev. Lett. 80 (1998) 976.
[15] F. Albert et al., Phys. Rev. ST-AB 13 (2010) 070704.
[16] J. Pruet et al., J. Appl. Phys. 99 (2006) 123102.
[17] F. Albert et al., Opt. Lett. 35 (2010) 354.
[18] S.G. Anderson et al., Nucl. Instr. Meth. A657 (2011) 140.
[19] F. Albert et al., Proc. IPAC-2011 (2011) 1488.
[20] R. Hajima et al., Proc. 52nd INMM Annual Meeting (2011).
[21] R. Hajima et al., J. Nucl. Sci. and Tech. 45 (2008) 441.
[22] T. Hayakawa et al., Nucl. Instr. Meth. A621 (2010) 695.
[23] R. Hajima et al., Nucl. Instr. Meth. A608 (2009) S57.
[24] http://www.eli-np.ro
[25] The Whitebook of ELI Nuclear Physics (2010).
[26] D. Habs and U. Köster, Appl. Phys. B103 (2011) 501.

Copyright © 2012 by the respective authors — cc Creative Commons Attribution 3.0 (CC BY 3.0)

RF POWER PRODUCTION AT THE TWO BEAM TEST STAND AT CERN

I. Syratchev, CERN, Geneva, Switzerland.

Abstract

The generation of short (250 ns) high peak power (135 MW) RF pulses by decelerating a high current (100 A) bunched (12 GHz) drive beam is one of the key components in the CLIC two beam acceleration scheme. Recent tests with drive beam deceleration at CERN's CTF3, using specially developed 1 m long CLIC Power Extraction and Transfer Structure (PETS) operated in a re-circulation regime have successfully demonstrated this concept. The results of these tests are presented.

INTRODUCTION

The CLIC PETS is a low impedance, high group velocity iris loaded 0.213 m long structure with a relatively large ($2\ a/\lambda = 0.92$) beam aperture. Each PETS is comprised of eight octants separated by damping slots. Each slot is equipped with damping loads in order to provide the strong damping of the transverse higher order modes [1]. In operation, the high peak power RF pulses (135 MW × 240 ns) are generated in the PETS via interaction with a high current (100 A) bunched (12 GHz) drive beam. These pulses are extracted at the downstream end of the PETS using a special high power coupler and are distributed to the two CLIC accelerating structures using an RF waveguide network. The snapshot of such a process simulated with computer code T3P [2] is shown in Fig. 1.

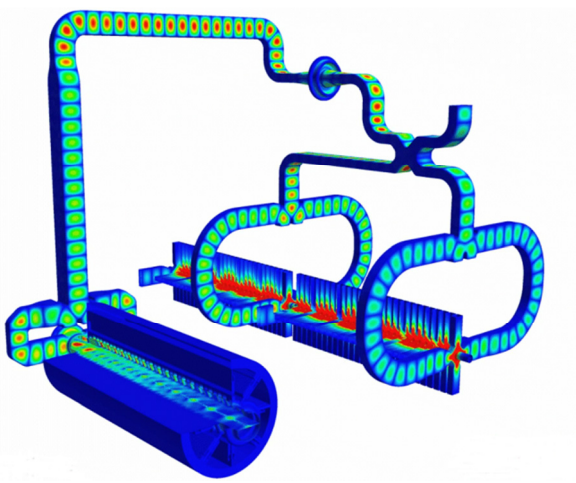

Figure 1: Electric filed plot in the CLIC two-beam accelerator unit. Here the PETS (shown left) is driven by the steady state drive beam current (courtesy SLAC).

During the period of 2008-2012, a thorough high RF power testing program was conducted at CERN in order to demonstrate experimentally the feasibility of all the issues associated with high RF power generation using the drive beam. In parallel, complimentary tests using X-band high power klystrons as a RF power source were done at ASTA (SLAC). Operated at a repetition rate of 60 Hz, such experiments provided high enough statistics to quantify the RF breakdown trip rate. To do these tests, an 11.424 GHz scaled version of the 12 GHz PETS was designed and fabricated, see Fig. 2. The feasibility of the PETS operation at a peak RF power level ~7% higher and with RF pulses ~10% longer compared to CLIC requirements was successfully demonstrated in these experiments [3]. The tests at a fixed power level (see Fig. 3) were ended when the measured breakdown trip rate was close enough to the CLIC specification of 1.0E-7/pulse/m. In the ASTA test, it occurred after 80 hours of operation without breakdown (BDR <2.4E-7/pulse/m).

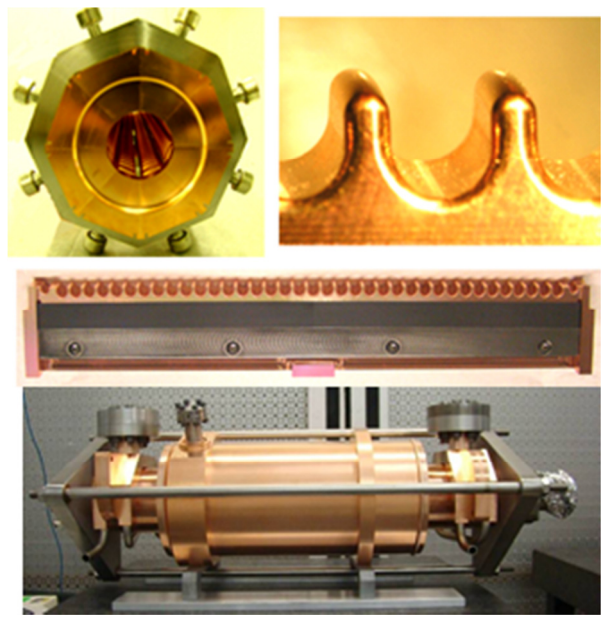

Figure 2: The front view of the assembled PETS body (top left), zoom of the PETS single bar period (top right), the single bar equipped with damping loads (centre) and fully assembled structure (bottom).

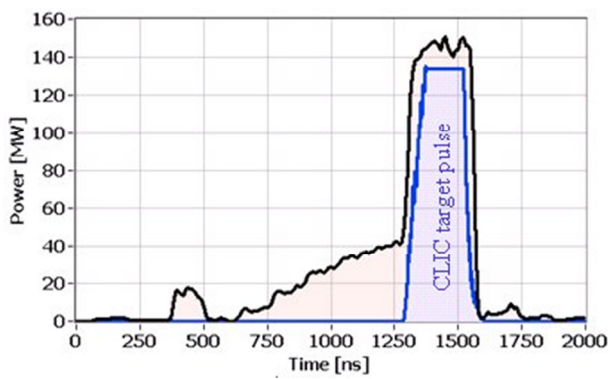

Figure 3: Typical RF pulse shape in ASTA. Here, for convenience, we also have plotted the shape of the CLIC target pulse.

Copyright © 2012 by the respective authors — cc Creative Commons Attribution 3.0 (CC BY 3.0)

PETS TESTING PROGRAM IN CTF3

PETS Operation at Two Beam Test Stand

The generation in the PETS of 12 GHz RF power from the drive beam was demonstrated in the CLIC experimental area (CLEX), which is a part of the CLIC Test Facility (CTF3) [4]. The CLEX is equipped with a number of experiments. One of them is the Two Beam Test Stand (TBTS). The TBTS is a unique and versatile facility where the two-beam acceleration experiments are conducted. It comprises two beam lines equipped with various types of beam diagnostics. One line is for the drive beam, which is generated in the CTF3 complex and then delivered to the TBTS via a beam transfer line, the other is dedicated to the probe beam, which is prepared in the CALIFES accelerator complex. As it is shown in Fig. 4, CTF3 will allow for different scenarios of the drive beam generation in terms of the beam current and pulse length.

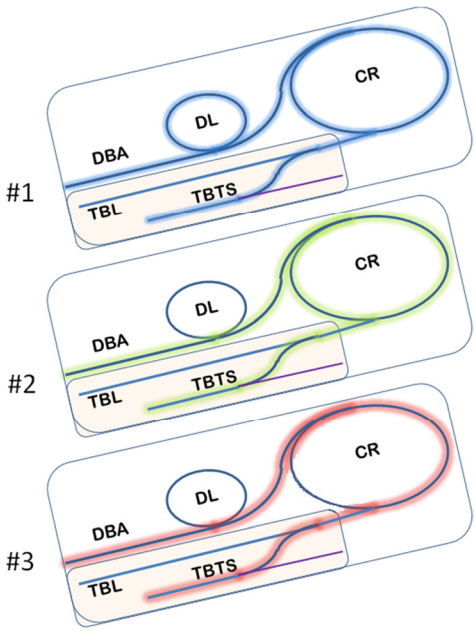

Figure 4: The drive beam generation modes in CTF3: 1– with full recombination (×8), 2 – with partial recombination (×4), and 3 – without recombination.

Because the drive beam current available in CTF3, even with full recombination, will be about four times lower than the CLIC design, the TBTS PETS design was modified to be able to generate the nominal CLIC RF power. To recover the lack of current, the active PETS length was significantly increased from original 0.213 m to 1m. The fully assembled, 1 meter TBTS PETS equipped with water cooling channels and power couplers on its girder and ready for the installation into the vacuum tank is shown in Fig. 5. The TBTS PETS power production capability for the different CTF3 modes of operation (assuming the single bunch form factor =1) is summarized in a Table 1. Mode 1 of the PETS operation provides power levels well above CLIC nominal values; unfortunately, the pulse length of 140 ns is rather short compared to the CLIC nominal pulse of 240 ns. To improve this, it was decided to implement a different configuration – PETS with external re-circulation [5]. In this case, the PETS operates in an amplification mode, similar to that in the classical resonant rings. The only difference is that now we have a beam as an internal source of RF power.

Table 1: The TBTS PETS Power Production Modes

Operation mode	#1	#2	#3
Current, A	<30	14	4
Pulse length, ns	140	<280	<1200
Bunch Frequency, GHz	12	12	3
PETS power (12 GHz), MW	<280	61	5

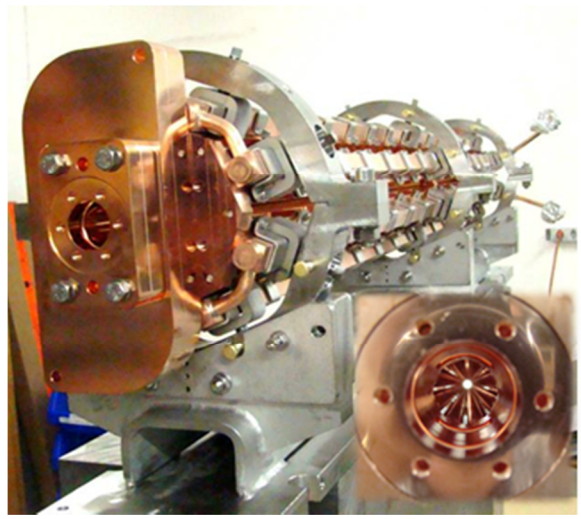

Figure 5: The TBTS PETS general view.

The implementation of re-circulation required development of several special RF components. High RF power variable splitter and variable (2π) RF phase shifter were ordered and received from industry (GYCOM, Russia) [6]. In 2008, a PETS tank equipped with all the RF components was installed into the drive beam line in the TBTS experimental area, as is shown in Fig. 6. With re-circulation, the power gain of the system in a steady can be written as:

$$P_G = \frac{1}{1 - 2g\cos(\phi) + g^2}$$
$$g = \sqrt{S\eta_{loop}} \qquad (1)$$

where S is fractional power delivered back to the PETS input, ϕ is RF phase advance in the loop and η_{loop} is total round trip efficiency. Following (1), in a phased loop (ϕ=0) with 50% re-circulation (S=0.5) and 75% measured ohmic efficiency (η_{loop}=0.75), the steady state power gain is about 6.5. Thus, driven with only 8.6 A drive beam current, the PETS generates the required CLIC RF peak

Copyright © 2012 by the respective authors — cc Creative Commons Attribution 3.0 (CC BY 3.0)

power. At the same time, the RF power extracted from the re-circulating loop (50%) and received by the single accelerating structure would also be as high as required. Providing enough margin in drive beam current and pulse length, the PETS operation mode 2, together with ~50% re-circulation was chosen as a working point for the PETS power production and two-beam acceleration program. In this configuration, the TBTS PETS was operated until September 2011. After start up and initial conditioning, it was reliably generating RF peak power well in excess of the CLIC nominal value. In Fig. 7 the example of a typical pulse generated at the PETS output is shown. One can see clearly the expected stair-case nature of the RF power build-up, where the duration of each step corresponds to the round-trip delay in the re-cycling loop.

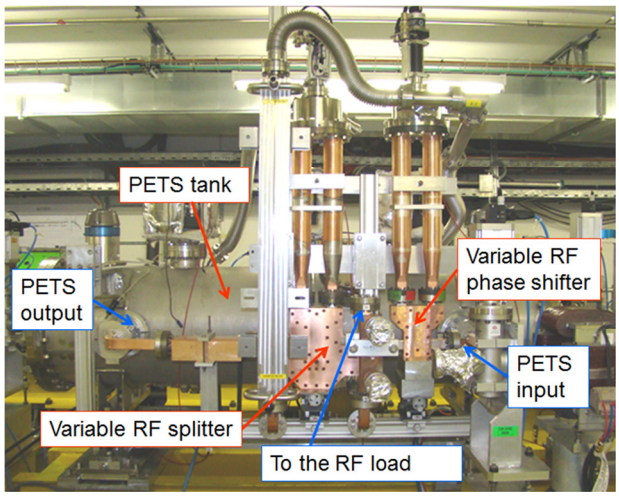

Figure 6: The PETS tank installed in the TBTS test area.

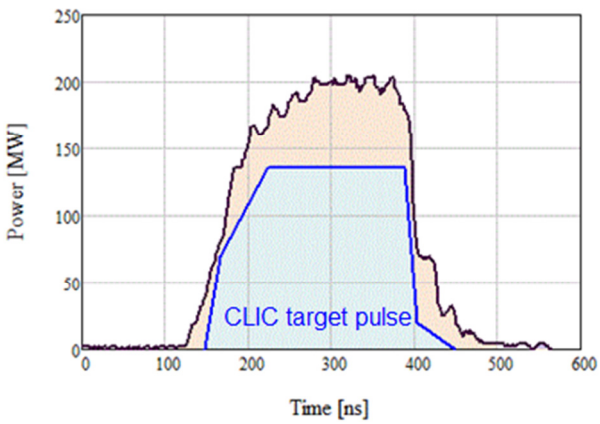

Figure 7: Typical RF pulse shape measured at the PETS output. Here, for convenience, we also plotted the shape of the CLIC target pulse.

We have developed a number of computer models of varying complexity which accurately reconstruct and predict the processes in the system with re-circulation [7-9]. In order to illustrate this, in Fig. 8 and Fig. 9, the simulated results are compared to measurements. In this example, we used a rather simple model [9] based on the known settings of re-circulation (ϕ and g) and measured profile of the drive beam current. One can see good agreement between the simulations and experiments.

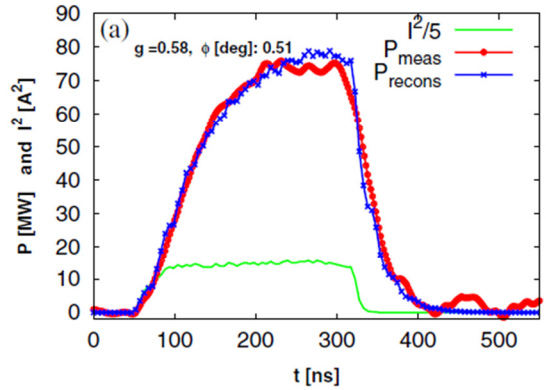

Figure 8: Measured RF pulse (red line) and reconstructed signal (blue line) are shown together with the current pulse used as an input for reconstruction (green line).

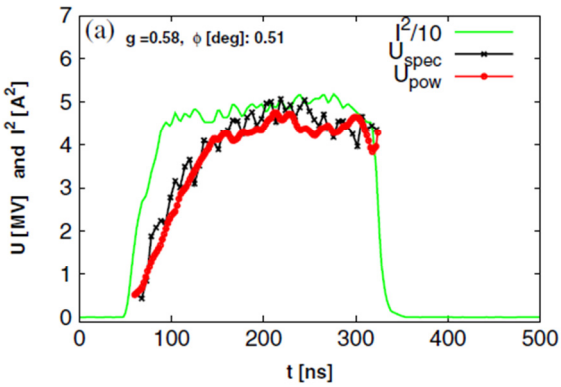

Figure 9: Measured with the spectrometer the drive beam deceleration (black line) and the one calculated from power measurements (red line) are shown together with the pulse current (green line). It shows the same pulse as in Fig. 8.

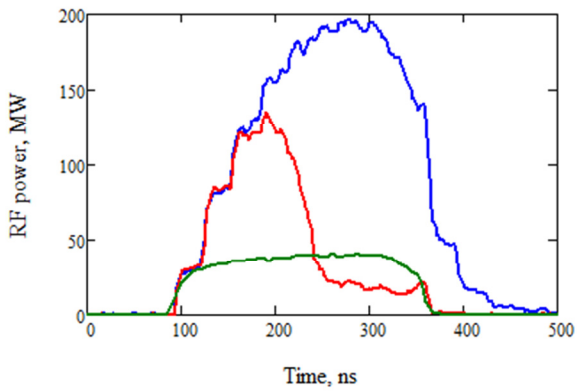

Figure 10: The normal RF pulse (blue line) followed by the RF pulse with breakdown (red line). Here the expected direct (without re-circulation) RF power production (green line) is shown for the reference.

Here we cannot give a firm conclusion about the breakdown trip rate in our experiments in the TBTS, because of insufficient statistics (CTF3 operates at 1 Hz repetition rate) and some difficulties with providing stable

Copyright © 2012 by the respective authors — cc Creative Commons Attribution 3.0 (CC BY 3.0)

drive beam generation during long enough periods. Nevertheless, an important observation concerning the pulse shape modifications due to the RF breakdown was made: power production is normally quenched just after the RF breakdown happens. This may be explained by the fact that the RF breakdown products modify the gain and phase advance in the loop. In most of the cases (>90%), the PETS continued to generate RF power at a much lower level, which is close to the direct power production level, see Fig. 10. This indicates that most probably, the breakdown happened in the re-cycling waveguide loop and not the PETS itself. Relying on this "self-protecting" effect, a quite aggressive operational procedure was implemented, where the control system followed up the integrated level of residual gas pressure in the PETS tank, rather than reacting on each individual breakdown event.

Demonstration of the PETS ON/OFF Operation

One of the feasibility issues of the CLIC two-beam scheme, is the possibility of rapidly switching off the RF power production in an individual PETS in case of breakdowns, which can occur either in the PETS or one of the main beam accelerating structures. The proposed solution is to use a variable external reflector connected to the PETS. When activated, this scheme allows us to continuously manipulate the RF power transfer to the accelerating structure and to reduce the RF power production in the PETS itself by a factor of 4 [10].

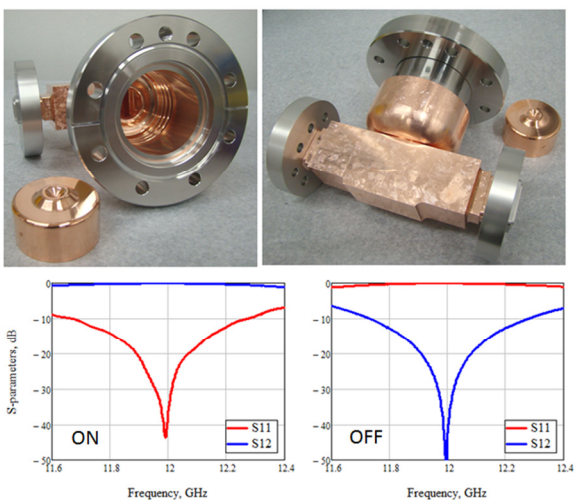

Figure 11: The general view of the variable reflector body and movable piston (up). S-parameters measured at two extreme positions of the piston.

An external high power variable RF reflector is the key component of the system [11]. Providing the whole range of reflections from 0 to 1, it can fully or partially terminate the RF power transfer from the PETS to the accelerating structure. In general, the reflected RF power will be returned back to the PETS. In order to mitigate this effect, a fixed RF reflector is placed at the upstream end of the PETS, in order to establish re-circulation of the RF power inside the PETS. If, at the operating frequency, the electric length of such an RF circuit is tuned to $L=\lambda_0(n+1/4)$, then a destructive interference with the RF power generated by the drive beam is achieved. A prototype of the new high RF power variable reflector was fabricated and low RF power measurements were in good agreement with HFSS [13] simulations, see Fig. 11. We also built a separate variable RF short circuit to enable the tuning of RF phase advance in the system. In 2011, these new components replaced the external re-circulation circuit on the TBTS PETS tank as shown in Fig. 12.

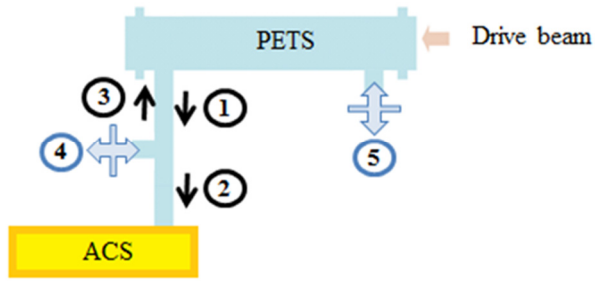

Figure 12: Layout of the PETS ON/OF setup in TBTS. The black arrows show RF power flows in the system: 1) RF power extracted from the PETS; 2) RF power transmitted to the accelerating structure; 3) RF power reflected back into the PETS. The new components are: 4) variable RF reflector; 5) variable RF short circuit.

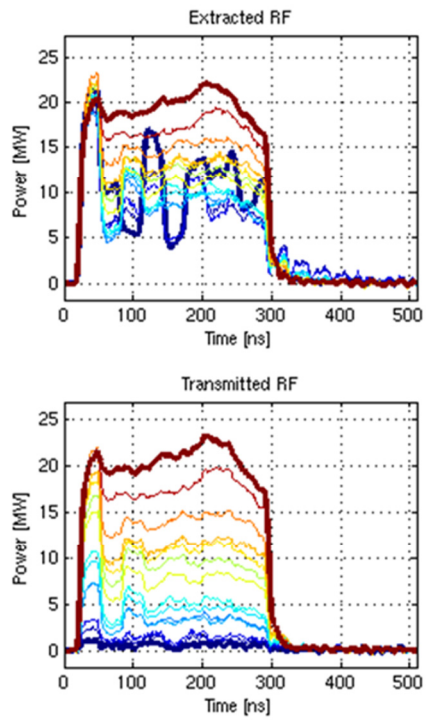

Figure 13: TBTS PETS ON/OFF demonstration with the beam. Here the line colors correspond to different settings of variable reflection. The colors are gradually changed from red (ON) to blue (OFF).

During experiments with the beam, the variable reflector settings were changed gradually from full reflection to full transmission. The RF powers produced by PETS and delivered to accelerating structure were measured at different intermediate piston positions. The

Copyright © 2012 by the respective authors — cc Creative Commons Attribution 3.0 (CC BY 3.0)

results of one of the tests are shown in Fig. 13. These results were in a good agreement with the system computer modeling, where measured S-parameters of all components were used as an input [12].

At the time of the experiment, the available drive beam current in CTF3 made it impossible for us to run the system at the nominal CLIC RF power level in direct RF power production mode. To demonstrate the power capability of the new RF components used in the ON/OFF RF circuit, we set the recirculation loop parameters to their amplification mode, similar to the setup that was routinely used in the TBTS PETS with external recirculation. The processing of the PETS with ON/OFF circuit went rather fast. In about 100 hours ($2x10^5$ pulses) the system was conditioned up to 150 MW × 200 ns. The PETS processing and operation history is summarized in Fig. 14 and Fig. 15.

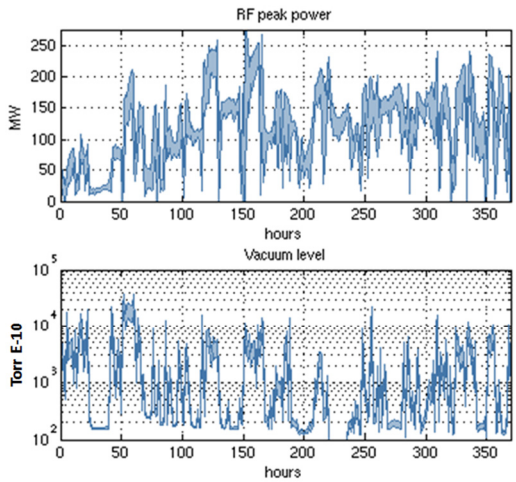

Figure 14: The PETS ON/OFF operation history: peak RF power (top) and vacuum level (bottom).

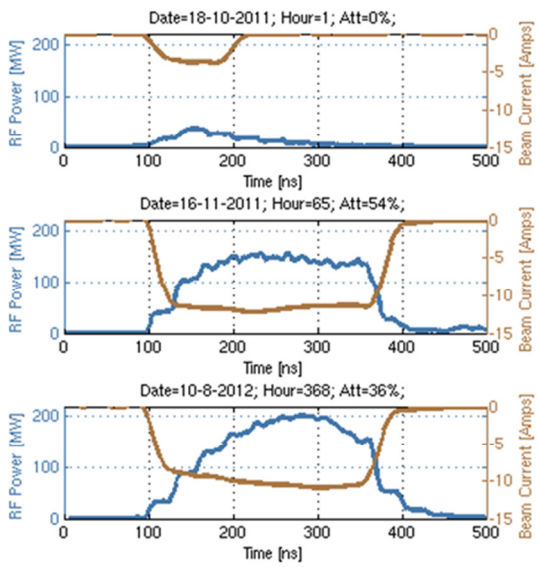

Figure 15: Typical drive beam current (brown lines) and RF power (blue lines) pulses at the different stages of operation.

SUMMARY

The feasibility of all the issues associated with high RF power generation using the drive beam was successfully demonstrated in the dedicated testing program that was conducted at CERN during the period of 2008-2012.

The scaled, 1 m long, PETS was installed and operated in beam driven mode with external RF re-circulation in order to compensate for the lack of drive beam current and pulse length. The PETS routinely produced RF power with peak levels well in excess of the CLIC specifications.

The new high RF power variable RF reflector and variable RF short circuit were designed and fabricated. These devices have replaced the external recirculation in the special, 1 m long PETS installed in CTF3. The PETS ON/OFF operational principle and high peak RF power capability were successfully demonstrated in experiments with the CTF3 drive beam.

REFERENCES

[1] I. Syratchev *et al.,* 'High RF Power Production for CLIC', Proceedings of PAC 2007, Albuquerque, New Mexico, USA.

[2] A. Candel *et al.,* "Numerical verification of the power transport and Wakefield coupling in the CLIC Two-Beam accelerator", SLAC-PUB-14439.

[3] A. Cappelletti *et al.,* "Demonstration of the high RF power production feasibility in the CLIC power extraction and transfer structure [PETS]", NIMA, Vol. 667, Issue 1, pp. 78-81, 2011.

[4] P. Skowronski *et al.*, "The CLIC feasibility demonstration in CTF3", CERN-ATS-2011-117.

[5] I. Syratchev *et al.,* 'CLIC RF High Power Production Testing Program', Proceedings of EPAC 2008, Genoa, Italy.

[6] S. Kuzikov *et al.*, "A 12 GHz Pulse Compressor and Components for CLIC Test Stand", Proceedings of RuPAC-2010, Protvino, Russia.

[7] R. Ruber and V. Ziemann, CERN CTF3 Note Report No. 092, 2009.

[8] E. Adli, CERN CTF3 Note Report No. 096, 2009.

[9] E. Adli *et al.*, "*X*-band RF power production and deceleration in the two-beam test stand of the Compact Linear Collider test facility", PRST Accelerators and Beams, 14, 081001, 2011.

[10] I. Syratchev, 'On-Off option and operation', 2nd CLIC Workshop 2008, Geneva, CERN.

[11] I. Syratchev *et al.*, "High Power Operation with Beam of a CLIC PETS Equipped with ON/OFF Mechanism", Proceedings of IPAC-2012, New Orleans, USA.

[12] I. Syratchev, "The high power demonstration of the PETS ON/OFF operation", 5th High Gradient Workshop, KEK, Tsukuba, Japan, 2012.

[13] Ansoft Corporation – HFSS: http://www.ansoft.com

Copyright © 2012 by the respective authors — cc Creative Commons Attribution 3.0 (CC BY 3.0)

SOLID STATE MARX MODULATORS FOR EMERGING APPLICATIONS*

M.A. Kemp#, SLAC National Accelerator Laboratory, Menlo Park, CA, USA

Abstract

Emerging linear accelerator applications increasingly push the boundaries of RF system performance and economics. The power modulator is an integral part of RF systems whose characteristics play a key role in the determining parameters such as efficiency, footprint, cost, stability, and availability. Particularly within the past decade, solid-state switch based modulators have become the standard in high-performance, high power modulators. One topology, the Marx modulator, has characteristics which make it particularly attractive for several emerging applications. This paper is an overview of the Marx topology, some recent developments, and a case study of how this architecture can be applied to a few proposed linear accelerators.

THE MARX TOPOLOGY

It is a futile task to completely capture all the implementations of Marx which have been developed. However, presented in this section is one way in which to describe a Marx and highlights several particular implementations which embody many of the strengths of the topology.

The Ideal Modulator

In the context of RF sources, the modulator is typically defined as the power converter interfacing the AC mains with the RF tube. In CW systems, it is common to refer to this interface simply as the power supply. Hence, the modulator is usually a pulsed supply.

The desired characteristics of a modulator are most effectively optimized in view of a specific implementation. However, some general positive attributes are common. First, the pulse quality of a modulator must be appropriate for the RF system. Output voltage, output current, pulse width, and pulse repetition frequency broadly classify the modulator. However, especially in linacs for light sources, secondary parameters such as timing jitter, pulsed amplitude stability, and flat-top droop are increasingly important.

The power input to the modulator is most commonly the AC mains. While it is possible to further sub-divide some modulators into a power supply and a pulse shaping unit, the view is typically most straightforward considering these to be one system. A consideration for the modulator is to draw a constant power with near-unity power factor from the mains. Some facilities are bound by regulatory requirements which dictate harmonic content at the point of common coupling with the utility, such as IEEE 519. An ideal modulator is lossless. Short of this, waste heat is most typically rejected to the facility water cooling system or the ambient atmosphere.

The availability, A, of a system is typically defined in terms of the mean time to repair (MTTR) and the mean time between failures (MTBR),

$$A = \frac{MTBF}{MTBF + MTTR} \tag{1}$$

To enable very high availability numbers, redundant architectures can be used. This allows a component to fail without bringing down the system.

The cost of a modulator might be divided into three categories: the procurement costs, the maintenance costs, and the operation costs. The maintenance costs might include the manpower and replacement parts to repair and refurbish the system. Operation costs include utility needs and system configuration adjustments.

Secondary characteristics of interest include the ability of a modulator to operating into different impedance loads. During commissioning or operation of an accelerator at different configurations, the modulator may most efficiently interface with the RF source at a lower or higher output voltage. In the case, for example, of the klystron, this would necessitate modulator operation into a different effective impedance. The pulse shape characteristics must be appropriately preserved at these varying load conditions.

In addition, it is critical that the system is appropriately protected in the case of a load short. Both the modulator should remain undamaged and the modulator must prevent excess energy transfer to the load arc. This is one of the more challenging parameters for a modulator to produce.

General Marx Description

The Marx bank has been used as a high voltage generator since the patent from Erwin Marx in 1923. While there have been demonstrations utilizing inductive elements and opening switches, the most common embodiment uses capacitors and closing switches to construct the output pulse. Specifically: *A Marx modulator is a topology in which capacitors are charged in parallel during the recharge period and discharged in series during the output pulse.* A generic Marx circuit is shown in Fig. 1. In the case of modulators for linac applications, the pulse is repetitive, has a flat or shaped output, and can be terminated in the event of a detected fault. Therefore, turn-on and turn-off switching is necessary, and hence so is solid-state switching.

*Work supported by Department of Energy contract DE-AC02-76SF00515.
#mkemp@slac.stanford.edu

Copyright © 2012 by the respective authors — cc Creative Commons Attribution 3.0 (CC BY 3.0)

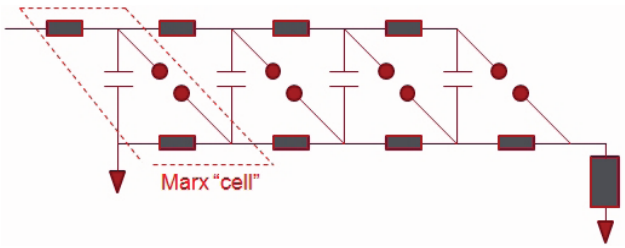

Fig. 1. Simple schematic of a capacitor-based Marx generator.

Turn-on Marx banks primarily using gas switches have been the work-horse of high voltage generators for many decades. At low powers, Marx-like topologies have been proposed with solid-state switching since the 1980's [1,2]. Only recently has the technology of solid state devices advanced to the point to enable solid modulators with peak powers capable of driving high-power vacuum tubes [3].

The simplest pulse characteristic that a Marx generator can produce is the RC-decay. The capacitance of the erected Marx discharges into a resistive load. The advantage of using the Marx topology rather than a single large capacitor and switch is that the maximum voltage across components in a Marx cell is the charge voltage. Therefore, relatively low voltage components can be used.

Further taking advantage of this characteristics, more complex circuits can be used in the Marx cell. For example, the output of the cell during a pulse might be a "chopped" waveform. In other words, a periodic square-wave can be generated during the pulse. Or, the cell itself can produce a square pulse. This can be enabled by placing a power electronics converter within the Marx cell. Finally, the cell can potentially produce an arbitrary shape on the output by using a pulse width modulated switching scheme in tandem with a low-pass filter.

In general, there are three characteristics of the Marx topology which are advantageous for emerging applications: modularity, low-voltage sub-units, and electrostatic adding. Recalling the ideal attributes of a modulator mentioned above, four attributes are desired: low cost, maintainability, availability, and pulse quality. A mapping of the Marx characteristics on the desired attributes of a modulator is given in table 1.

Table 1: Characteristics of the Marx topology compared with desired attributes for an ideal modulator.

	Modularity	**Low-Voltage Sub-Units**	**Electrostatic Adding**
Low Cost	All things being equal, many smaller units are more cost-effective to manufacture in bulk than fewer, larger units.	Components, in particular switches are commoditized and low-voltage. Synergy with other fields, such as the high-volume traction control market, can be used to develop modulators with off-the-shelf components.	Magnetics are not needed to support the whole pulse width. Therefore, large transformers are not necessary.
Maintainability	Several voltage or power levels of modulators within the same facility can utilize the same Marx sub-unit. This simplifies maintenance and lowers spares counts.	Pristine and carefully maintained surfaces are not critical at lower voltages. The most-maintained components are within the lower-voltage cells.	-
Availability	Redundancy can be built into the modulator. One or more modules can fail and not disable the RF station.	At lower voltage, precision diagnostics are more easily implemented. Therefore, for example, monitoring end of life indicators at the volt level is straightforward, while it would not be possible using a high-voltage diagnostic.	Each cell has a similar role in producing the output pulse; location within the array is not critical. Therefore, reconfiguration in the case of module failure is straightforward.
Pulse Quality	-	The macro pulse generated from the modulator is a combination of the individual modules. As such, fine details can be produced at the low-voltage level and preserved at the high voltage level.	Without using high-voltage magnetics, it is more-straightforward to produce a fast rise and fall-time pulse.

Copyright © 2012 by the respective authors — cc Creative Commons Attribution 3.0 (CC BY 3.0)

SELECTED IMPLEMENTATIONS

There are several recent embodiments of the Marx modulator topology which highlight some of the advantageous characteristics listed above. These are highlighted below.

Prompt turn-on

For the Electra krypton fluoride laser program, the Naval Research laboratory developed a solid-state short-pulse Marx modulator [4]. Using thyristors, the modulator produces the characteristics given in table 2. Magnetic assist is used in series with the switches to enable high di/dt (54 kA/μs) switching. The modulator has been operated for over 10 million shots and the switches have been separately tested for over 300 million shots without failure. This Marx represents a prompt turn-on scenario where all cells are triggered simultaneously. In addition, low-inductances techniques are used with magnetic switching to enable a very fast pulse.

Table 2. Characteristics of the NRL Marx modulator.

Voltage Output	-200 kV
Current Output	-5 kA
Repetition Rate	10 Hz
Pulse Width	~300 ns

Staggered turn-on

For the International Linear Collider (ILC) klystron modulator, several developments took place to provide an alternative to the previous baseline, the bouncer modulator. The characteristics of the modulator are shown in Table 3. Two particular modulators that were produced based upon the staggered turn-on mode of Marx modulator operation. The modulator from DTI [5] is shown in Fig. 2 while the SLAC P1 Marx [6] is shown in Fig. 3.

While these Marx banks have different implementations of the technology, they do a common characteristic with how they produce the flat output pulse. Because it is a long-pulse modulator, there must be an active correction scheme to ensure the output pulse remains flat. To achieve this, some cells do not turn on at the beginning of the pulse. They have delayed turn-on such that when the overall output droops to a certain level, the delayed cell turn-on raises the overall voltage to within the appropriate tolerance. The saw-tooth waveform on the top of the pulse remains within the +/-0.5% level.

Table 3. Characteristics of the ILC Marx Modulators.

Voltage Output	-120 kV
Current Output	140 A
Repetition Rate	10 Hz
Pulse Width	1.6 ms
Flat-top	+/- 0.5%

Figure 2. Photograph of the DTI ILC Marx Modulator.

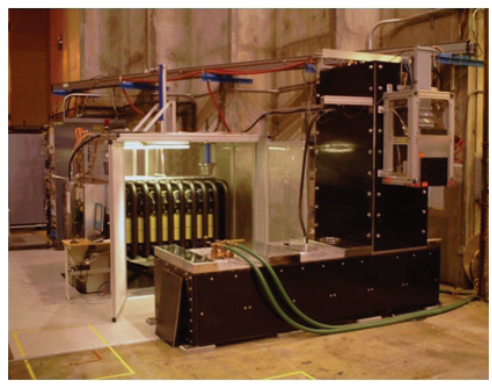

Figure 3. Photograph of the SLAC P1 Marx.

Filtered PWM output

For the European XFEL project, Thompson Scientific produced a "pulse step" Marx modulator [7]. The characteristics of this Marx are shown in Table 4. In this modulator, the cell output is a chopped pulse width modulated signal. By interleaving the outputs of the Marx cells, the ripple adds deconstructivly. A low pass filter on the output smooths the modulator output into a square pulse. This modulator pulses into output cables which feed a step-up transformer. The output is closed loop, enabling operation into many different impedance loads [8].

Table 4. Characteristics of the XFEL Modulator

Voltage Output	12kV
Current Output	2 kA
Repetition Rate	30 Hz
Pulse Width	1.7 ms

Flat-pulse output

The second-generation modulator developed at SLAC for the ILC application is the SLAC P2 Marx [9]. The characteristics of this Marx are given in Table 3. Among many structural and electrical evolutions from the P1 Marx, the P2 Marx uses a fundamentally different correction scheme. Each cell produces a square output

Copyright © 2012 by the respective authors — cc Creative Commons Attribution 3.0 (CC BY 3.0)

pulse. A buck converter is placed in series with the main cell capacitance. This converter produces a "ramp-up" which exactly compensates the "ramp-down" of the main capacitor droop. The sum of the two signals is constant over the length of the pulse. A photograph of the finished modulator is shown in Figure 4.

Because large step-up transformers are not necessary, the rise-time of the Marx can be reduced compared to the baseline. For the P2 Marx, the rise and fall are <10μs. This is important such that wasteful energy is not deposited in the klystron collector prior to and after the RF pulse. In addition, as shown in Figure 5, a very flat output pulse is possible. Each cell has a deterministic ripple at a constant carrier frequency. Therefore, the cells can be interleaved, similar to the Thompson modulator, to cancel the ripple on the output of the modulator. Measured ripples of less than 0.05% have been demonstrated.

Figure 4. Photograph of the SLAC P2 Marx.

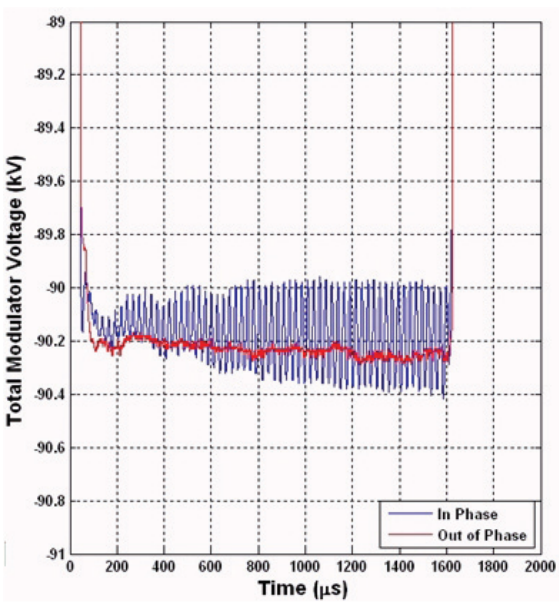

Figure 5. Measured output voltage for the SLAC P2 Marx. Shown is the output with the cells in phase and out of phase.

In addition, the SLAC P2 Marx uses the characteristic of the cells having relatively low voltage by having abundant diagnostic access. Each cell contains twelve, 12-bit, 1 MS/s ADCs to monitor parameters of interest within the cell.

EMERGING APPLICATIONS

One attribute of the Marx modulator is that it is a repeated structure of a modular cell. Fundamentally, the research and development can focus on this cell unit, such that it can be applied to many different applications. For example, several cells can be placed in series to produce a higher voltage. Alternatively, several can be placed in parallel to increase the output current. This is illustrated in Figure 6. The application of the SLAC P2 Marx cell for several emerging accelerator applications is presented in this section.

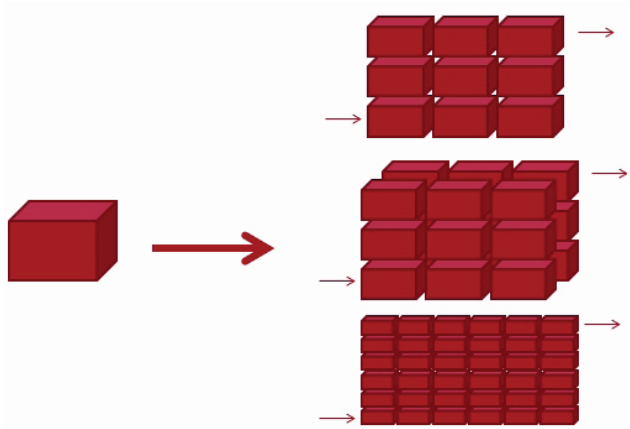

Figure 6. Scaling of a single Marx building block to several configurations.

ESS

The European Spallation Source is a next generation proton accelerator that is proposed to be implemented in Sweden [10]. While the characteristics of the RF system have not been finalized as of this publication, some preliminary values are given in Table 5. Using the same SLAC P2 Marx cell, a Marx modulator can be developed for the ESS application. While the average power requirements are higher, the cell dissipation is within the limits of the Marx cell. Assuming two different klystron operating voltages, two different Marx banks can be constructed. These are shown in Table 6.

Table 5. Preliminary characteristics of an ESS RF station.

Klystron Peak Power	4.8 MW
RF Pulse Width	14 Hz
Repetition Rate	3.4 ms

Copyright © 2012 by the respective authors — cc Creative Commons Attribution 3.0 (CC BY 3.0)

Table 6. Characteristics of an ESS Marx based upon the SLAC P2 Marx cell topology.

	# of cells	Max single cell loss	DC to pulse efficiency
SLAC P2 Marx	32	410 W	95%
80 kV ESS Marx	23	780 W	95.8%
113 kV ESS Marx	31	610 W	95.5%

CLIC

The Compact Linear Collider (CLIC) is a proposed high energy physics machine at CERN. [11] While the parameters of the drive beam klystron modulator are not finalized, some preliminary figures are shown in Table 7 [12]. The two particularly challenging parameters are the AC-pulse efficiency and the pulse amplitude reproducibility.

In the case of the pulse amplitude reproducibility, the characteristic of the P2 Marx of having precision diagnostics within the cell can be taken advantage of. If, for example, the modulator were to regulate on the output pulse of the modulator using a waveform digitized with a 12-bit ADC, the best possible resolution would be $1/2^{12}$, or 244 ppm. However, if the same 12-bit ADC we used on each of the *n* cells, the best possible resolution becomes $1/2^{12}/n^{0.5}$, or 38 ppm for a 40-cell Marx.

Table 7. Preliminary modulator characteristics for the CLIC drive beam klystron modulator.

Pulse Voltage	150 kV
Pulse Current	160 A
Pulse Width	140 µs
Reproducibility	10-50 ppm
AC-pulse Efficiency	90%
Pulse Repetition Frequency	5 Hz

Fermi 201 MHz Linac Upgrade

Fermi National Accelerator Laboratory desires to upgrade its 201MHz linac RF systems. One proposed method to improve the reliability of the system would be to replace the existing series-pass regulator based triode modulator with a Marx modulator. This application is particularly challenging because of the shaped output pulse. On a pulse to pulse basis, the output waveform of the modulator must change. For example, when the proton beam arrives in the cavity, the cavity voltage must be quickly increased to compensate for the loading. As such, the modulator output must rise. The timing of this is not consistent and also the magnitude must be dynamically changed.

This application is suited for the Marx modulator because of the ability of the modulator to both have staggered turn-on and off, and also because of the ability of the modules to produce ramping outputs. For example, if during the beam arrival time the voltage out of the modulator must increase gradually, the individual cells could produce a rising output. In a simple sense, the modulator can perform as an arbitrary waveform generator.

REFERENCES

[1] H.I. Swanson, "Amplifier Employing Digital Modulator Circuit," US patent 4403197.
[2] R.B. Frey, "Pulse Step Modulator and Transformer," US patent 5710520.
[3] A. Krasnykh, *et al.,* "A sold state Marx type modulator for driving a TWT," Power Modulator Symposium, 2000.
[4] F. Hegeler, *et al.*, "A Durable Gigawatt Class Solid State Pulsed Power System," Trans. Plasma Sci., 2011.
[5] J. Casey, *et al.*, "Long Pulse Marx Bank Modulator for the ILC," PAC'09, TU6RFP074, 2009.
[6] C. Burkhart *et al.,* "P1-Marx Modulator for the ILC," IEEE Power Modulator and High Voltage Conference, 2010.
[7] W. Decking, "Status of the European XFEL- Constructing the 17.5 GeV Superconducting Linear Accelerator," LINAC'12, MO1A02, 2012.
[8] H. Leich, *et al*., "Towards a Modulator for the XFEL RF Stations," LINAC'10, THP061, 2010.
[9] M.A. Kemp, *et al*., "The SLAC P2 Marx," IEEE Power Modulator and High Voltage Conference, 2012.
[10] M. Lindroos, *et al.*, "Parameter Choice for the ESS Linac Design," LINAC'12, TH2A01, 2012.
[11] R. Corsini, "Status and Future of the CLIC Study," LINAC'12, WE1A02, 2012.
[12] D. Aguglia, *et al.*, "Klystron Modulator Technology Challenges for the Compact Linear Collider," Pulsed Power Conference, 2011.

Copyright © 2012 by the respective authors — cc Creative Commons Attribution 3.0 (CC BY 3.0)

RESULTS ACHIEVED BY THE S1-GLOBAL COLLABORATION FOR ILC

H. Hayano, M. Akemoto, S. Fukuda, K. Hara, N. Higashi, E. Kako, H. Katagiri, Y. Kojima, Y. Kondo, T. Matsumoto, S. Michizono, T. Miura, H. Nakai, H. Nakajima, K. Nakanishi, S. Noguchi, N. Ohuchi, T. Saeki, M. Satoh, T. Shidara, T. Shishido, T. Takenaka, A. Terashima, N. Toge, K. Tsuchiya, K. Watanabe, S. Yamaguchi, A. Yamamoto, Y. Yamamoto, K. Yokoya,
KEK, Tsukuba, Japan
K. Jensch, D. Kostin, L. Lilje, A. Matheisen, W. -D. Moeller, M. Schmoekel, P. Schilling, N. Walker, H. Weise, DESY, Hamburg, Germany
T. Arkan, S. Barbanotti*, M. Battistoni, H. Carter, M. Champion, A. Hocker, R. Kephart, J. Kerby, D. Mitchell, Y. Pischalnikov, M. Ross, T. J. Peterson, W. Schappert, B. Smith,
FNAL, Chicago, USA
A. Bosotti, C. Pagani, R. Paparella, P. Pierini, INFN, Milano, Italy
C. Adolphsen, C. Nantista, SLAC, Menlo Park, USA

Abstract

The S1-Global cryomodule experiment [1] by ILC-GDE (International Linear Collider, Global Design Effort) was planned to achieve "S1" goal, which is to operate at least one of cryomodule with 31.5MV/m ILC average gradient. The design, fabrication, assembly, experiment, and disassembly were done by the international collaboration based on ILC-GDE. The experiment hosted by KEK STF (Superconducting RF Test Facility at KEK) was performed from June 2010 to February 2011. The achieved gradient performance of the contributed cavities was average 30.0MV/m before installation, 27.7MV/m for single cavity operation after installation, and 26.0MV/m for 7 cavities simultaneous operation [2, 3].

The other goal of the S1-Global is to perform plug-compatibility concept by building one set of cryomodule from brought-in cavities and couplers of each laboratories. The half-size cryomodule-C was its demonstration built from INFN cryostat, two set of DESY cavities and couplers, and two set of FNAL cavities and couplers. The connection of cryomodule-C and KEK cryomodule-A was also another aspect of plug-compatibility.

The S1-Global program was the truly international cryomodule experiment by the effort of GDE members and GDE participation laboratories. The program has demonstrated to realize the international cryomodule and their performance close to ILC specification. The issues of the current cryomodule technologies and what we need to solve in the next were identified.

INTRODUCTION

The S1 is one of the identified tasks by the GDE R&D board, where an RF operation of a cryomodule with an average accelerating gradient of 31.5MV/m is to be demonstrated. The S1-global experiment was the world's first program of building a segment of a superconducting linac system and testing a string of superconducting RF cavities by a global collaboration in the Technical Design phase of the ILC project. The proposal was to bring eight 9-cell superconducting cavities and associate hardware components from institutions in the world, install them in common cryomodules, and demonstrate their operation by a global collaboration. The participating institutions contributed their hardware and human resources on an equal footing. The picture of the cryomodules is shown in Fig.1. While the S1-Global program lacked beam operation, it involved all the essential steps that are required prior to beam acceleration. The program successfully addressed numerous critical issues such as the plug-compatibility (i.e. compatible but not identical) of hardware components, as well as single- and multiple-cavity operation with pulsed microwave power and associated LLRF controls. While the tests were all completed by the end of February 2011, disassembly of the S1-Global cryomodules was started on May 2011 toward the end of the year 2011, practically all of the contributed cavity components were brought back to their home institutions for post-mortem diagnosis studies.

CAVITIY PACKAGE

A new half-length cryomodule (Cryomodule-C) was designed and prepared by INFN, while the other half cryomodule (Cryomodule-A) was built by modifying an existing 6-m STF cryomodule at KEK.

The upstream module, Cryomodule-C, has 2 FNAL cavities, TB9AES004 for slot C1 and TB9ACC0112 for slot C2, and two DESY cavities; Z108 for slot C3 and Z109 for slot C4. Four cavities are equipped with TTF3 type main input couplers. In Fig.2, the illustrations of their cavity packages are shown. TB9AES004 was last tested in the horizontal test stand at FNAL before shipment, while TB9ACC011 was last tested in the vertical test stand. They are processed and tested at JLAB, ANL and FNAL. DESY cavities were processed with the DESY EP treatment and had been previously installed in the module 8 and tested on the CMTB at DESY. Before shipment to KEK, Z108 and Z109 underwent 6 HPR cycles and were tested in the DESY vertical cryostat.

*Current affiliation: DESY

Copyright © 2012 by the respective authors — cc Creative Commons Attribution 3.0 (CC BY 3.0)

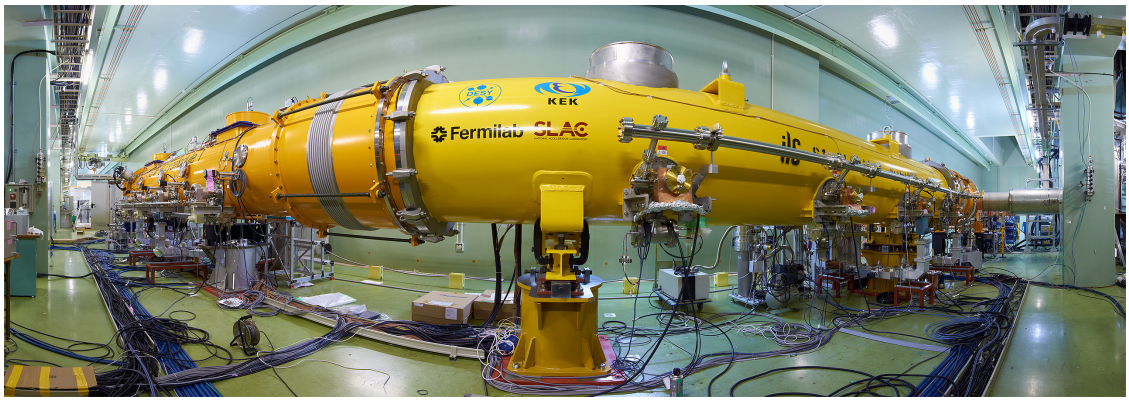

Figure 1: The S1-Global cryomodule from the view of the input coupler side. Right cryomodule is from INFN.

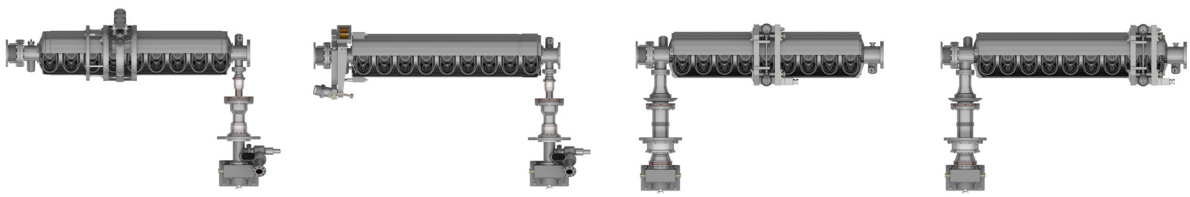

(a) FNAL cavity (b) DESY cavity (c) KEK cavity (d) KEK cavity

Figure 2: Cavity package contribution from each laboratory. There are two cavities in each type. (a) FNAL cavity with blade tuner and TTF3 coupler, (b) DESY cavity with Saclay/DESY tuner and TTF3 coupler, (c) KEK cavity with slide-jack tuner in centre and STF2 coupler, (d) KEK cavity with slide-jack tuner in the end and STF2 coupler.

These cavities were sent to KEK with input coupler cold section mounted in a vertically upward position, and the cavity under vacuum.

The downstream module, Cryomodule-A, has four KEK supplied cavities, in slots A1 – A4. The cavities were TESLA-like cavities, named MHI05, MHI06, MHI07, and MHI09. Each cavity was processed and tested at KEK. There are two types of tuners utilized, central slide-jack tuner on MHI05 and MHI06, and lateral slide-jack tuner on MHI07 and MHI09. STF2 Couplers for each cavity were produced by Toshiba, and pre-conditioned at KEK up to 1.0MW in pulsed operation, with a 1.5 msec pulse width at 5 Hz.

CRYOMODULES

The design of the Cryomodule-C cross section is almost the same as the TTF-type III cryomodule. The cryomodule mainly consists of the cavity-packages, input couplers, the gas return pipe (GRP), magnetic shields, two sets of thermal shields, cooling pipes and the vacuum vessel. The distance of 1383.6 mm between the input couplers, same as the TTF-type III and XFEL design, was used for four cavities although the cavity-packages of FNAL and DESY have different lengths, 1247.4 mm and 1283.4 mm, respectively. This mismatch was resolved with the bellow pipes between the cavities. The designs of these two cavity jackets are different because of the different type of frequency tuner, the blade tuner and the Saclay-type tuner, as shown in Fig. 2. However, the cavity support lugs have the same distance of 750 mm between two lugs along their axis, and the fixed distance 197.5 mm from the input coupler axis, independent of the type of cavity package design and as a result, the cavity package supports to the GRP, are identical, i.e. 'plug compatible'. The frequency tuners of these cavities were driven by the cold motor and the Piezo element. The cold motors were installed inside the 5 K shied. The DESY and FNAL cavities were designed to be enclosed with the magnetic shields.

The Cryomodule-A was used in STF phase-1. The thermal and mechanical designs of Cryomodule-A were based on the TTF-type III cryomodule. However the components in the Cryomodule-A have different dimensions from those in the Cryomodule-C. The KEK cavities for Cryomodule-A have two designs with different locations of the frequency tuner as shown in Fig. 2. Upstream two cavity-packages have the tuner located at the centre of the helium jacket. The distance between the support lugs along the cavity axis is designed to be 750mm, i.e. the same distance as the FNAL and DESY cavities. The downstream two cavity packages have the tuner placed at the opposite end of the jacket with respect to the input coupler. The distance of the support lugs is changed to 650 mm and the tuning action does not require sliding of cavity at the support pads in this case. Since the KEK tuners have the driving motor outside the vacuum vessel, they were driven by the warm motor, while the Piezo element is in the cold side.

Copyright © 2012 by the respective authors — cc Creative Commons Attribution 3.0 (CC BY 3.0)

(a) (b)

Figure 3: (a) Cold mass assembly of Module-C in clean-room by DESY-FNAL-KEK team (b) Cavity package assembly of Module-C by INFN-FNAL-KEK team.

Assembly of both Cryomodule-C and Cryomodule-A is mainly divided into two processes: the cavity string assembly in the class-10 clean room (CR), and the cold mass assembly outside of the CR. Fig. 3 pictures shows the STF assembly work done by international cooperation. For the cavity assembly in the clean room, two weeks were scheduled for each module. For the cold mass assembly, two months for Cryomodule-C and one month for Cryomodule-A were scheduled. The Cryomodule-C assembly was scheduled first to ease final assembly of the two modules in the STF tunnel. After moving the cavity-string out of the clean room, the cold mass was assembled from January 25 to March 19, 2010. Transportation of the two cryomodules down to the STF tunnel was completed on April 28th.

The operation of the cryogenic system was done a day-by-day basis. The operation started in the mornings and stopped in the evenings. No operation on Saturdays and Sundays. It took almost 2 weeks (10 workdays) to complete cooling-down of the 8 cavities from room temperature to 2 K. During the experiment weeks, the study was possible to start at noon from Tuesday to Friday.

HLRF AND LLRF

Two HLRF systems were used for the S1-global. They are the No. 1 station and the No.2 station. TH2104C was for the No.1 station and the other was newly procured TH2104A for the No.2 station. Both were capable to output 5-MW power at the frequency of 1.3 GHz with the pulse width of 1.5ms and repetition rate of 5Hz. In power distribution system (PDS) in RDR, there are two types of PDS proposed, that is, the linear PDS and the tree type PDS using 3dB power dividers. Both systems were evaluated in the S1-global test [3], as shown in Fig. 4. A tree type power-dividing scheme (3-dB Hybrid PDS) using variable 3-dB hybrids was employed to cryomodule-C. In this system variable power divider of the variable tap-off (VTO) supplied by SLAC was introduced. The linear distribution system (TESLA type PDS) was used in cryomodule-A. The variable QL system using a reflector and a phase shifter was introduced in each coupler port.

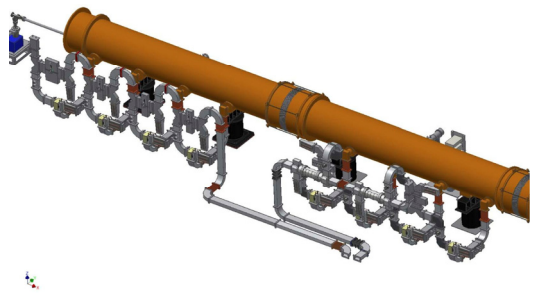

Figure 4: Power distribution system used in S1-global test. Linear PDS in the left, and tree-type PDS in the right. SLAC VTO are installed in the right PDS.

To examine each cavity performance efficiently, two RF power sources were used. A conventional digital low-level RF (LLRF) system was adopted in this evaluation. An FPGA board on a commercial digital signal processing (DSP) board (Barcelona) was used to control the RF output from each klystron. The FPGA board has 10 of 16-bit ADCs and 2 of 14-bit DACs with an FPGA and installed to cPCI [7]. In the vector-sum performance evaluation, to maximize each cavity's gradient, the ratios of the RF input powers to the cavities are optimized using tuneable hybrids and variable tap-offs. One cPCI became the FB controller and operated a vector-sum control.

SINGLE CAVITY PERFORMANCE TEST

The cryomodules were cooled down three times during the test. The first cool-down test was carried out from June to July 2010 for measurement of the thermal and mechanical performance of the cryomodules, together with RF tests of all cavities with low power. The second test was done from September to December 2010 for check-up of the cavity performance, the LFD measurement, its compensation by piezo tuners, a long-term operation, and the dynamic loss measurement by high RF power. The DRFS power system [8,9] was tested in the third cold test from January to February 2011 by using two 800 kW klystrons that were placed in the tunnel.

In the low power RF tests [4] done by INFN/FNAL/KEK team, it was found that tuners attached in TB9ACC011 and MHI-09 were not controllable, and it was not possible to set the frequency of these cavities to 1300.000 MHz. Therefore, simultaneous operation of multiple cavities was limited to 7 cavities rather than 8. Results of low power tuner tests are shown in Fig. 5.

Copyright © 2012 by the respective authors — cc Creative Commons Attribution 3.0 (CC BY 3.0)

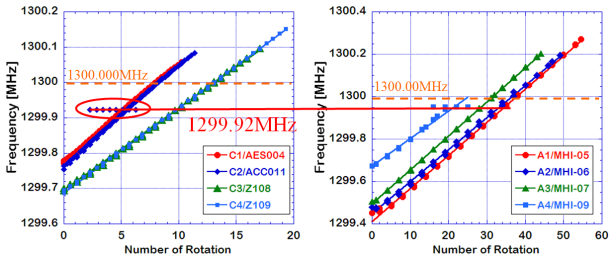

Figure 5: The result of the drive test for the motor tuner at low power. The tuner of TB9ACC011 did not work at 2K, and MHI-09 could not be set to 1300.000 MHz.

The slow tuner of TB9ACC011 failed after only a single tuning cycle (Fig. 5). In addition, one of the two-piezo actuators installed on the same cavity discharged at approximately half the nominal maximum operating voltage of 200V and the fast tuning range was smaller than expected. After disassembly, the reason of this slow tuner fail was found that the two M3 set screws in the shaft connecting the motor and the harmonic drive had worked loose presumably due to vibration during operation. One of the two screws had worked completely loose. The second was unable to transmit the full torque of the motor and was allowing the shaft to slip.

A visual inspection of the TB9ACC011 piezo actuators during disassembly showed that the two brass end caps holding the actuator stack were not well aligned. Misalignment of the caps can result in the transmission of excessive shear forces to the actuator stack. Further inspection revealed the actuator installed on the coupler side of the cavity had fractured on one edge. The physical damage to the stack can account for the both the discharges observed during operation and for the reduced tuning range.

The slow tuner of MHI-09 failed during the first excursion test (Fig. 5). The rotation of the motor became slow and finally stopped in the point of 1299.95MHz. After the several trial of the motor rotation, the frequency finally did not change even the motor was rotating. After the disassembly, the tuner was carefully checked. When the fixed bolts of the slide-jack were loosen from the thick flange, the tuner mechanism became smooth and no stuck. In that case there were 0.55mm to 0.6mm gap space between flange and the slide-jack. This was caused by the flange bending deformation, which came from the welding heat.

After the second cool-down, the conditioning of each cavity with high power was carried out. The achieved gradient values in vertical and cryomodule tests are summarized in Fig. 6. The maximum average gradient was 30.0 MV/m at vertical test, however, went down to 27.7 MV/m for single cavity operation and 26.0 MV/m for simultaneous operation of seven cavities at the cryomodule test. In this conditioning, the performance of MHI-06 was drastically improved from 28MV/m in vertical test to 38MV/m. On the other hand, the gradient of the two cavities (TB9ACC011 and Z108) were significantly reduced by 27% and 38% each. Issues during the assembly processes or transportation to KEK are suspected. This problem should be certainly addressed by the post-mortem diagnosis studies. MHI-05 performance (actually, performance of the input coupler) also degraded to 16MV/m during the adjustment for the feedback control due to the abnormally excess of the input power.

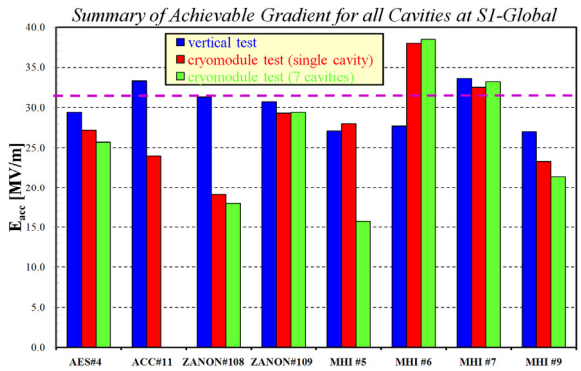

Figure 6: The achieved gradient values for eight cavities in vertical and cryomodule tests. The purple dotted line shows 31.5 MV/m of the ILC average operation gradient.

The LFD measurement for each cavity was carried out by using 'pulse shortening' method. The detuning frequency for three periods -- rise-up, flattop, and full-pulse -- was evaluated for the comparison of the stiffness of all the cavities. The slopes of linear fitting between the detuning frequency for the three periods and the square of the gradient shows the cavity stiffness, as shown in Fig. 7. The MHI cavities are found to be stiffer than others. The effect is remarkable in the flattop period, while the difference is smaller in the rise-up period.

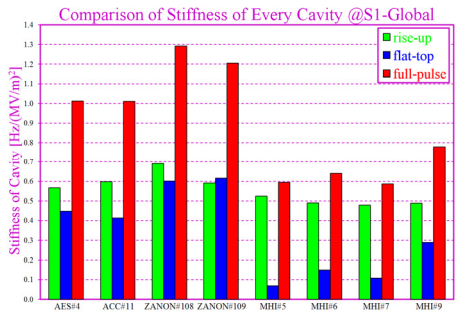

Figure 7: Comparison of the slopes from rise-up, flattop and full-pulse

Two kind of the LFD compensation were tried. The 'single pulse compensation' by a half sine waveform, which was used at STF Phase-1 [4] and the 'adaptive compensation', a new method presented in [5], were tried. Both methods turned out to be successful. As the compensation of LFD, a pulse corresponding to half period of a sine waveform is applied to piezo before the

Copyright © 2012 by the respective authors — cc Creative Commons Attribution 3.0 (CC BY 3.0)

start of the RF pulse. Four adjustable parameters for the piezo drive exist, that is, drive frequency, delay time, pulse height, and pulse offset. The excursion peak-to-peak of the detuning frequency at the flattop of the pulse was introduced as a measure of the compensation. After the compensation, MHI cavity still has a smaller peak-to-peak of the detuning frequency at the flattop period. In addition to the standard method of LFD compensation, an adaptive feed-forward method developed at FNAL for CM1 was employed to compensate detuning in six of the eight S1G cavities. This compensation method also successfully suppressed LFD in each of the S1-G cavities tested to the point where residual detuning should have no significant impact on the design, the cost, or operation of a machine such as the ILC.

The static heat loads of the cryomodules at 2 K, 5 K, and 80 K were measured by calorimetric methods [6]. The total heat load at 2 K for eight cavities was evaluated to 7.2W. The 5K heat load was evaluated to 7.3W for module-A and 5.3W for module-C. The 80K heat load was also evaluated to 48.7W for module-A and 34.4W for module-C. They are good agreement with calculated values. The dynamic losses of several cavities were evaluated by the cavity-tuned operation and the cavity-detuned operation for cavity loss and coupler loss. Q_0 value by this calorimetric method shows 4 to 9 x 10^9. For the heat loss estimation of the input couplers, four cavities in each module were detuned and operated at a power level of 32 MV/m. The four couplers losses of Module-C and A were 0.5 W and 4.6 W, respectively. The loss of the TTF-III coupler is consistent with this estimation. The loss of the STF-2 couplers was found to be one order bigger than the TTF-III. The temperature rises were found at the connection flanges between the STF-2 couplers and the cavity beam pipes. This temperature rise is considered to be due to heat generation at the 3 μm Cu layer on the inner surface of the outer conductor.

OPERATION OF SEVEN CAVITIES WITH VECTOR-SUM FEEDBACK CONTROL

In the final stage of the experiment, one 5-MW klystron feeds its power to all eight cavities. The performance of operation with vector-sum feedback control was evaluated [7]. During this operation, one cavity (C-2) could not be used for the vector-sum control because its mechanical tuner failure. The input powers to the cavities were adjusted by the tuneable hybrids and the variable tap-offs to yield the maximum gradient for each cavity. The detuning of each cavity during the RF pulse flat-top (1 ms) was set near 0 Hz by using the Piezo tuners. The result of vector-sum feedback control operation for seven cavities is shown in Fig. 8. The average gradient of seven cavities after input power optimization for each cavity was 26 MV/m. Since the average of each cavity's quench limit was 26.7 MV/m, the operation near quench limit of each cavity was achieved. The amplitude and phase stabilities were 0.005%rms and 0.015°rms, respectively, which satisfy the ILC requirements of 0.07%rms in amplitude and 0.24°rms in phase.

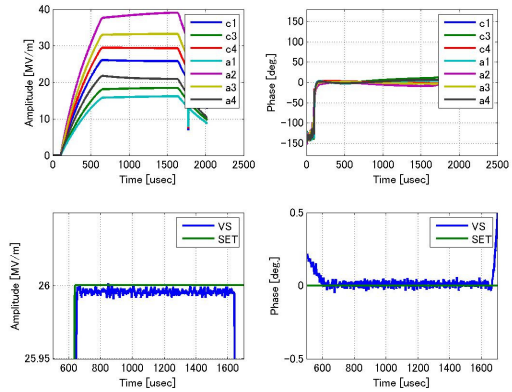

Figure 8: Vector-sum operation. Left: each cavity's gradient and vector-sum gradient, right: each cavity's phase and vector-sum phase.

ACKNOWLEDGMENT

The authors gratefully acknowledge the participating laboratory directors and collaborating personnel for their understanding and cooperation throughout this program. The continuous encouragement, appropriate advice, and strong support of the GDE director, Barry Balish, and the executive boards, including the project manager, are also acknowledged and greatly appreciated.

REFERENCES

[1] S1-Global team, "S1-Global Report," to be published in GDE web site, (2012).
[2] Y. Yamamoto, et al., "Test Results of the International S1-Global Cryomodule," SRF2011, Chicago, (2011).
[3] E. Kako, et al., "S1-Global module tests at STF/KEK," IPAC2011 San Sebastian, (2011).
[4] R. Paparella, et al., "Tuner Performance in the S1-Global Cryomodule," IPAC20111, San Sebastian, (2011).
[5] W. Schappert, et al., "Adaptive Lorentz Force Detuning Compensation in the ILC S1-Global Cryomodule at KEK," SRF2011, Chicago, (2011).
[6] N. Ohuchi, et al., "Thermal Performance of the S1-Global Cryomodule for ILC," IPAC20111, San Sebastian, (2011).
[7] S. Michizono, et al., "Performance of LLRF System at S1-Global in KEK," IPAC2011, San Sebastián, (2011).
[8] T. Miura, et al., "Performance of the μTCA Digital Feedback Board for DRFS Test at KEK-STF," IPAC2011, San Sebastián, (2011).
[9] T. Matsumoto, et al., "Operation Test of Distributed RF System with Circulator-less Waveguide Distribution in S1-Global Project at STF/KEK," IPAC2011, San Sebastián, (2011).

Copyright © 2012 by the respective authors — cc Creative Commons Attribution 3.0 (CC BY 3.0)

COMPACT SUPERCONDUCTING CRABBING AND DEFLECTING CAVITIES*

S. U. De Silva[1,2#]
[1]Center for Accelerator Science, Old Dominion University, Norfolk, VA 23529, USA.
[2]Thomas Jefferson National Accelerator Facility, Newport News, VA 23606, USA.

Abstract

Recently, new geometries for superconducting crabbing and deflecting cavities have been developed that have significantly improved properties over those of the standard TM_{110} cavities. They are smaller, have low surface fields, high shunt impedance and, more importantly for some of them, no lower-order-mode with a well-separated fundamental mode. This talk will present the status of the development of these cavities.

INTRODUCTION

Primarily the crabbing and deflecting structures are used to restore luminosity in particle colliders or in separating a single beam into multiple beams. The crabbing concept was initially proposed by R.B. Palmer for collider rings [1] and was later proven for linear colliders [2] as well. The applications of crabbing and deflecting cavities are not limited to the above-mentioned applications but also can be used in many applications for beam diagnostics, emittance exchange, in generating compressed x-ray beams etc. Some of the potential applications at present are the deflecting cavity needed for the Jefferson Lab 12 GeV upgrade [3] to separate the maximum energy beam into the three experimental halls and the deflecting cavity system required for the multi experimental project under Project-X [4]. One of the crabbing applications is the LHC luminosity upgrade that requires a crabbing system for vertical and horizontal crossing at the integrations regions of IP_1 and IP_5 [5].

The stringent dimensional constraints set by these current applications especially operating at low frequencies demands the design and development of compact crabbing and deflecting cavities. Compared to the crabbing and deflecting cavities operating in TM_{110} these compact designs that has been developed have improved properties with low surface fields, high shunt impedance. Most of the designs have no lower order modes (LOMs) with a widely separated higher order mode (HOM) spectrum.

The First Superconducting Deflecting Cavity

The early research in superconducting crabbing and deflecting structures was done in 1970s where the first superconducting rf deflecting cavity as shown in Fig. 1

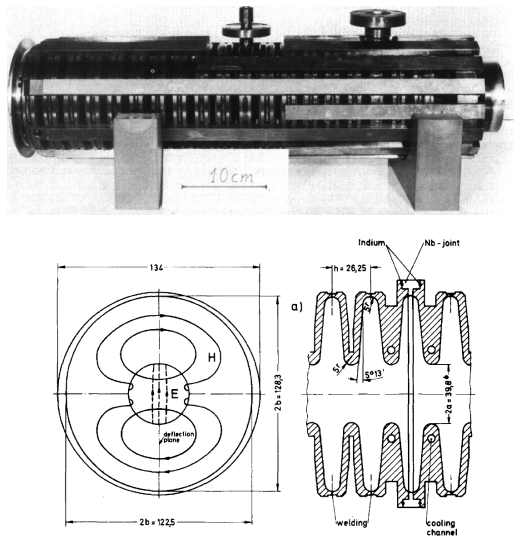

Figure 1: 19-cell end section of the 2.865 GHz rf separator cavity (top) and bi-periodic TM_{110} operating mode (bottom).

was designed and developed in KfK, Karlsruhe in collaboration with CERN [6]. The 2.865 GHz, 104-cell cylindrical-shaped standing wave rf particle separator shown in Fig. 1 installed at CERN in 1977 was capable of delivering a deflection in the vertical plane. The rf separator driven at 1.8 K, in a bi-periodic TM_{110}-type mode (Fig. 1) was in operation until 1981.

The First Superconducting Crabbing Cavity

The first crabbing cavity system was developed and installed in 2007 at KEK [7] for the KEKB electron-positron collider. The crabbing cavity shown in Fig. 2, operating in TM_{110} mode at 508.9 MHz was the only crabbing cavity system that has been in operation in a particle collider until 2010 after the installation in 2007.

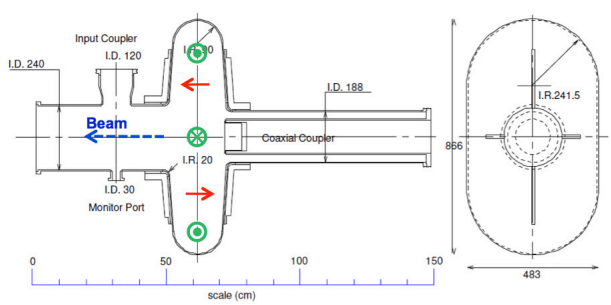

Figure 2: Superconducting 508.9 MHz KEK crabbing cavity.

*Authored by Jefferson Science Associates, LLC under U.S. DOE Contract No. DE-AC05-06OR23177. The U.S. Government retains a non-exclusive, paid-up, irrevocable, world-wide license to publish or reproduce this manuscript for U.S. Government purposes.
Part of this work was done in collaboration with and supported by Niowave Inc. under the DOE STTR program.
#sdesilva@jlab.org

Copyright © 2012 by the respective authors — cc Creative Commons Attribution 3.0 (CC BY 3.0)

The KEK crabbing cavity has a squashed elliptical geometry in order to separate the two polarizations of the TM_{110} mode. Since the TM_{110} mode is not the lowest mode in the cavity the crabbing cavity system has larger dimensions to that of a TM_{010} mode of the same frequency and was also required to have a complex higher order mode (HOM) damping scheme in order to damp the lower order mode (LOM) and near by HOMs that were close to the operating crabbing mode. The properties of the KEK crabbing cavity are listed in Table 1. The squashed elliptical geometry at 508.9 MHz operating frequency has higher surface magnetic fields with low shunt impedance.

COMPACT CAVITY DESIGNS

The standard crabbing and deflecting cavities with elliptical geometries operate in TM_{110} mode, which is not the lowest mode in these geometries. Also the squashed elliptical have very large structures at low frequencies. The current compact designs operate in TE or TEM like modes, where the deflection is given by either the electric field or by both the electric and magnetic fields. Some of those compact superconducting crabbing and deflecting cavity designs are

- 4-Rod Cavity by University of Lancaster and Jefferson Lab
- Quarter-Wave Cavity by Brookhaven National Laboratory
- Parallel-Bar Cavity/RF-Dipole Cavity by Old Dominion University and SLAC Accelerator National Laboratory

4-Rod Cavity - U. of Lancaster/Jefferson Lab

The 400 MHz superconducting 4-rod crabbing cavity [8] is an adaptation of the 499 MHz normal conducting rf separator designed by C. Leemann and C.G. Yao at Jefferson Lab for separating the 6 GeV beam into the three experimental halls in the beam switchyard area [8]. The rf separator is a two cell design as shown in Fig. 3, with each cell of ~λ/2 length and diameter.

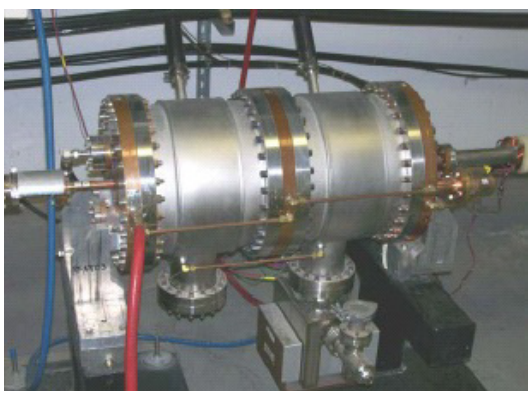

Figure 3: Normal conducting 499 MHz 4-rod rf separator cavity at Jefferson Lab.

The normal conducting 4-rod cavity has a rod configuration that gives 4 fundamental modes, with the electric field configuration shown in Fig. 4. The top left field configuration corresponds to the accelerating mode, which is the lowest mode in the design. The next mode is the deflecting/crabbing mode with the field configuration shown in bottom left of Fig. 4 with the magnetic field circulating around the rods near the end plates. In this geometry both electric and magnetic fields contribute to the net deflection.

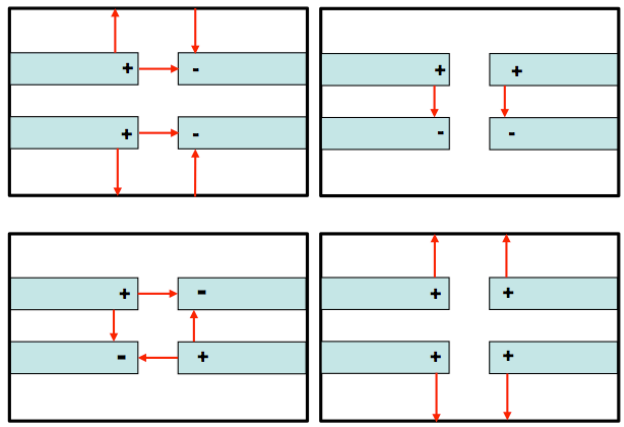

Figure 4: Electric field configuration of the 4 fundamental modes in the 4-rod geometry.

The superconducting 4-rod cavity design (Fig. 5) [9] adapted from the normal conducting design has improved bar geometry and outer conductor that gives a compact design with low surface electric and magnetic fields. The rods are further curved to suppress the higher order multipole components in the cavity.

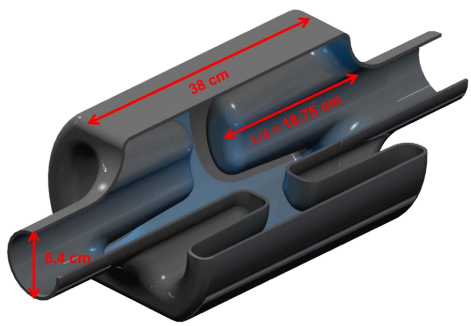

Figure 5: Superconducting 400 MHz 4-rod cavity design from University of Lancaster/Jefferson Lab.

The properties of the superconducting 4-rod cavity are shown in Table 1. This design has very high transverse [R/Q] therefore high shunt impedance compared to other compact crabbing and deflecting cavities. However the LOM at 375 MHz present close to the fundamental operating mode and the low separation between the operating mode and the next HOM as shown in the HOM spectrum in Fig. 6 require a complex damping scheme in order to damp these modes. The compact crabbing and deflecting structures have a HOM configuration with modes giving a net deflection in horizontal direction or in vertical direction and accelerating modes as shown in Fig. 6. Additionally in the 4-rod cavity there are no hybrid modes present in the geometry.

Copyright © 2012 by the respective authors — cc Creative Commons Attribution 3.0 (CC BY 3.0)

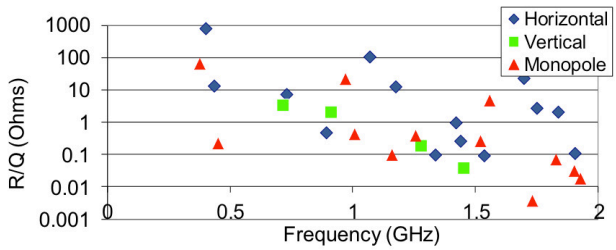

Figure 6: HOM spectrum of the 4-rod crabbing cavity.

Quarter-Wave Cavity - BNL

The standard quarter-wave cavity is modified into a crabbing and deflecting cavity utilizing the strong reentrant shape that gives a TEM field configuration near the outer conductor [10]. However the quarter-wave cavities have a strong on axis longitudinal electric field component that gives rise to an accelerating mode, present within the fundamental deflecting/crabbing mode. The quarter-wave design is modified with a pedestal at the bottom of the cavity to suppress the accelerating field component as shown in Fig. 7 [11]. The length of the longer pedestal at the top of cavity controls the frequency of the design. As shown in Fig. 7 the quarter-wave geometry at 400 MHz is optimized to reduce the surface fields and minimize the longitudinal accelerating component present in the cavity.

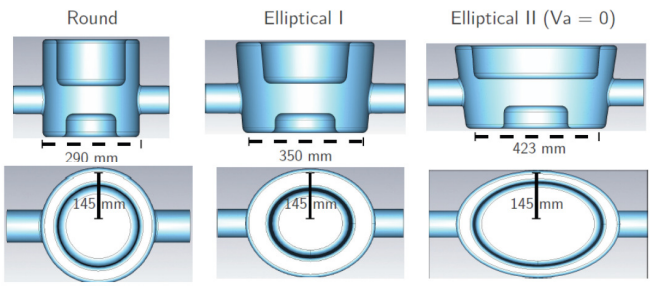

Figure 7: Superconducting 400 MHz quarter-wave deflecting/crabbing cavity by BNL.

The electric and magnetic field content of the quarter-wave crabbing cavity is shown in Fig. 8.

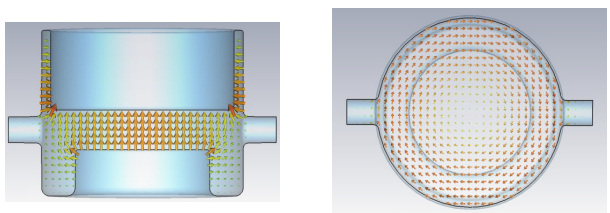

Figure 8: Electric field (left) and magnetic field (right) content of the 181 MHz quarter-wave crabbing cavity designed for eRHIC [11].

The quarter-wave cavity has two design options with the initial asymmetric geometry and a symmetric geometry to completely eliminate the longitudinal accelerating component as shown in Fig. 9. Compared to the asymmetric cavity the symmetric cavity doesn't have a longitudinal electric field component, however has a reduced mode separation between the fundamental deflecting/crabbing mode and the next HOM. The properties of the asymmetric and symmetric quarter-wave cavities are shown in Table 1. The symmetric design has improved surface fields and transverse [R/Q] however has smaller shunt impedance due to the decreased geometrical factor.

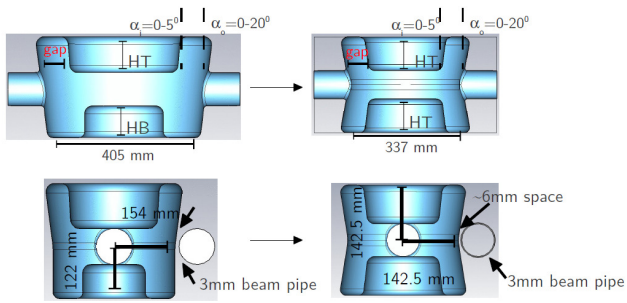

Figure 9: Asymmetric and symmetric 400 MHz quarter-wave crabbing cavities.

The HOM spectrum [8] of the asymmetric quarter-wave cavity is shown in Fig. 10, with a similar mode configuration described in the 4-rod cavity. However the asymmetric cavity also has hybrid modes present in the geometry. One of the attractive features in this design is the absence of any lower order modes.

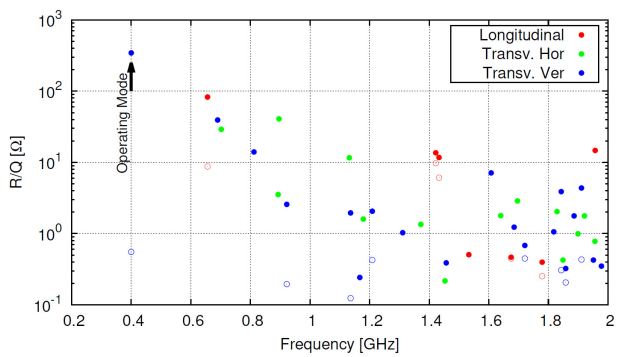

Figure 10: HOM spectrum of the asymmetric quarter-wave crabbing cavity [12].

Parallel-Bar and RF-Dipole Cavity - ODU/SLAC

The parallel-bar cavity [13] with a rectangular outer conductor with cylindrical-shaped bars operating in a TEM-like mode is being evolved into a cylindrical-shaped design with trapezoidal-shaped bar geometry [14] (Fig. 11). The latter design named rf-dipole cavity operates in a TE_{11}-like mode, where the main contribution to the net deflection is given by the transverse electric field.

A similar design was proposed by Zenghai Li at SLAC named the ridged waveguide cavity as shown in Fig. 12 [11] operates in TE_{11}-like mode. Currently ODU and SLAC are collaborating on designing a 400 MHz compact crabbing cavity. Currently the rf-dipole cavity is considered as the 499 MHz rf separator for the Jefferson Lab 12 GeV upgrade, as one of the crabbing cavity

Copyright © 2012 by the respective authors — cc Creative Commons Attribution 3.0 (CC BY 3.0)

Table 1: Properties of superconducting crabbing and deflecting cavities.

Parameter	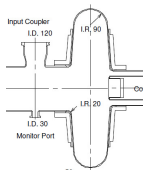 KEK Cavity	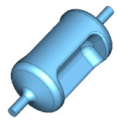 RF-Dipole Cavity	RF-Dipole Cavity	4-Rod Cavity	Asymmetric ¼-Wave Cavity	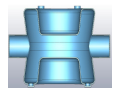 Symmetric ¼-Wave Cavity	Units
Frequency	508.9	499.0	400.0	400.0	400.0	400.0	MHz
Aperture diameter (d)	100.0	40.0	84.0	84.0	84.0	84.0	mm
d/(λ/2)	0.34	0.13	0.22	0.22	0.22	0.22	
LOM	410.0	None	None	375.2	None	None	MHz
Nearest HOM	630.0	777.0	589.5	436.6	657.0	577.8	MHz
Peak electric field (E_P^*)	4.24	2.86	3.9	4.0	5.38	4.04	MV/m
Peak magnetic field (B_P^*)	12.23	4.38	7.13	7.56	7.6	7.2	mT
B_P^* / E_P^*	2.88	1.53	1.83	1.89	1.42	1.77	mT/(MV/m)
$[R/Q]_T$	48.9	982.5	287.2	915.0	344.0	401.1	Ω
Geometrical factor	227.0	105.9	138.7	62.8	131.0	82.4	Ω
$R_T R_S$	1.1×10^4	1.0×10^5	4.0×10^4	5.7×10^4	4.5×10^4	3.3×10^4	Ω^2

At E_T^* = 1 MV/m

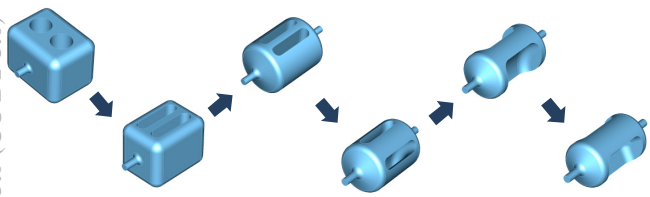

Figure 11: Design evolution of the parallel-bar cavity into the rf-dipole cavity.

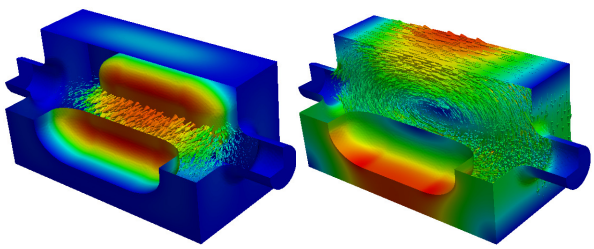

Figure 12: Ridged waveguide cavity by SLAC.

options for the LHC luminosity upgrade operating at 400 MHz, and as the 750 MHz crabbing cavity for the medium energy electron ion collider (MEIC). The field profile of the rf-dipole cavity is shown in Fig. 13.

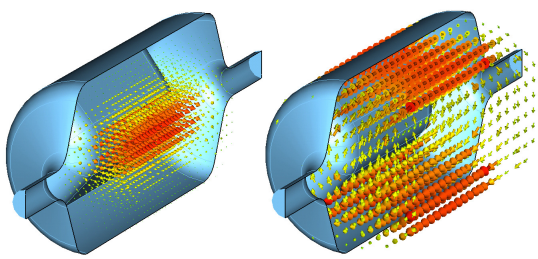

Figure 13: Electric field (left) and magnetic field (right) content in the 499 MHz rf-dipole cavity.

The properties of the 499 MHz and 400 MHz rf-dipole cavities are given in Table 1. The inner bar height and the angle of the trapezoidal shaped bars connecting to the outer conductor allows the rf-dipole design to have both reduced surface electric and magnetic fields. Therefore an rf-dipole cavity can be designed at a given design frequency and beam aperture, with a balanced ratio of peak surface magnetic field to the peak surface electric field as required by the application.

The HOM spectrum of the rf-dipole cavity is shown in Fig. 14. The rf-dipole cavity has no low order modes and the HOMs are well separated.

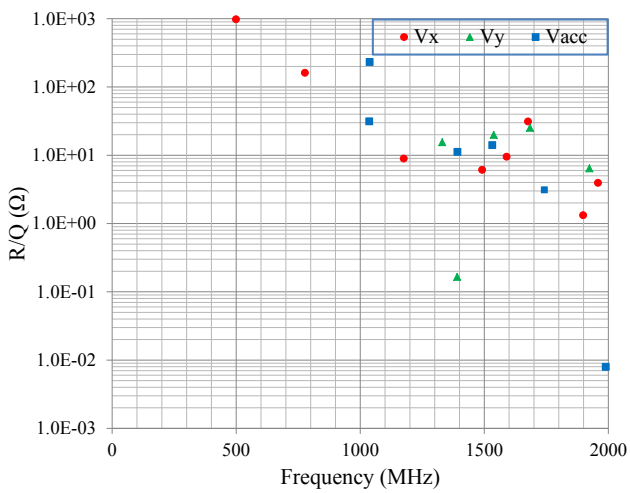

Figure 14: HOM spectrum of the 499 MHz rf-dipole cavity.

The rf-dipole design can be reduced into a more compact design with fixed transverse dimensions with a square-shaped outer conductor as shown in Fig. 15 where

Copyright © 2012 by the respective authors — cc Creative Commons Attribution 3.0 (CC BY 3.0)

the frequency of the design is controlled by the curvature of the edges of the cavity. The rf-dipole design is further modified with curved trapezoidal-shaped bar geometry to suppress the higher order multipole components.

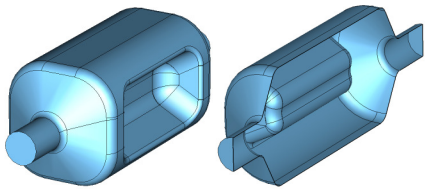

Figure 15: Square-shaped rf-dipole cavity with flat trapezoidal-shaped bar geometry (left) and with curved bar geometry (right).

CAVITY FABRICATION

First prototypes of some of the compact deflecting and crabbing cavities have already being fabricated. Fig. 16 shows the fabricated cavity designs. The prototypes of the 400 MHz 4-rod cavity, the 400MHz and 750 MHz rf-dipole cavities are fabricated at Niowave Inc. and the 499 MHz rf-dipole cavity is currently being fabricated at Jefferson Lab.

Figure 16: Prototype of the 400 MHz 4-rod cavity (top left), 400 MHz (top right), 400 MHz (bottom left) and 750 MHz (bottom right) rf-dipole cavities.

CONCLUSIONS

The development of compact deflecting/crabbing cavities was in response to the strict dimensional requirements in some current applications. All these compact designs have attractive properties in meeting the requirements. The low and balanced surface fields and high shunt impedance in these compact superconducting crabbing and deflecting cavities make them very attractive designs compared to the standard cavities operating in TM_{110} mode. The absence of lower order modes and wide separation in the higher order modes in most of the designs reduces the lower and higher mode damping complexity.

The 4-rod cavity design uses coaxial type couplers in damping the LOM and HOMs. The quarter-wave cavity design uses magnetic loop type couplers placed at the bottom of the cavity to damp the HOMs. The rf-dipole cavity is considering both the options of using the waveguide or a coaxial high-pass filter type coupling in damping the HOMs. Further studies are done on these compact cavities on addressing the important rf-related issues such as multipacting, mechanical analysis, field non-uniformity etc. The fabricated prototypes are in preparation for rf testing.

REFERENCES

[1] R. B. Palmer, "Energy Scaling, Crab Crossing and the Pair Problem", Tech. Rep. SLAC-PUB-4707 (SLAC, 1988).

[2] K. Oide and K. Yokoya, Phys. Rev. A 40, 315 (1989).

[3] J.R. Delayen et al., "Options for an 11 GeV RF Beam Separator foe the Jefferson Lab CEBAF Upgrade", Proc. of the Particle Accelerator Conference, Vancouver, BC, Canada, p. 1644, (2009).

[4] V. Yakovlev and M. Champion, "A Beam Splitter for the Project-X", LHC- CC11, (2011).

[5] R. Calaga, in Proceedings of the 2011 Conference on RF Superconductivity, Chicago, Illinois, (2011) p. 988.

[6] A. Citron et al., NIM 164, 31-55, (1979).

[7] K. Hosoyama et al, "Crab Cavity for KEKB", Proc. of the 7th Workshop on RF Superconductivity, p.547 (1998).

[8] C. Leemann and C.G. Yao, "A Highly Effective Deflecting Structure", Proc. of the 1990 Linear Accelerator Conference, p.232-234, (1991).

[9] B. Hall, "LHC-4R Crab Cavity", EUCARD SRF Annual Review, March 2012.

[10] E. Haebel, "Superconducting Cavities and Minimum RF Power Schemes for LHC", CERN/EF/RF 84-4.

[11] Q. Wu et al., "Novel Deflecting Cavity Design for eRHIC", Proc. of the15th International Conference on RF Superconductivity, p.707, (2011).

[12] R. Calaga et al., "HOM Damping and Multipacting Analysis of the Quarter-Wave Crab Cavity", Proc. of the 3rd International Particle Accelerator Conference, p. 2260, (2012).

[13] J. R. Delayen and H. Wang, Phys. Rev. ST Accel. Beams 12, 062002 (2009).

[14] J. R. Delayen, S.U. De Silva, "Designs of Superconducting Parallel-Bar Deflecting Cavities for Deflecting/Crabbing Applications", Proc. of the15th International Conference on RF Superconductivity, p.219, (2011).

[15] Z. Li and L. Ge, "Compact Crab Cavity Design and Modeling Using Parallel Code ACE3P", LHC-CC11, (2012).

Copyright © 2012 by the respective authors — cc Creative Commons Attribution 3.0 (CC BY 3.0)

SUPERCONDUCTING SPOKE CAVITIES FOR ELECTRONS AND HIGH-VELOCITY PROTON LINACS*

J. R Delayen#
Center for Accelerator Science, Old Dominion University, Norfolk, VA 23529, U.S.A
Thomas Jefferson National Accelerator Facility, Newport News, VA 23606, USA

Abstract

Over the last two decades, spoke resonators have been developed for the medium-velocity range of many proton and ion machines. These structures are now being considered and developed for electron linacs and high velocity proton linacs. The status of these developments and the properties of high-velocities spoke cavities are presented.

FEATURES OF THE SPOKE CAVITY

Thc spokc cavity, shown in Fig. 1, is a variant of thc coaxial half-wave geometry. In its fundamental mode of operation, the spoke sustains a TEM mode where the length of the spoke is approximately half the wavelength. The current (and magnetic field) is large where the spoke meets the outer conductor, and the voltage (and electric field) is large in the middle of the spoke.

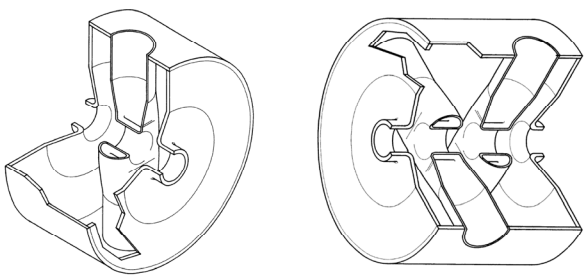

Figure 1: Single-spoke and double-spoke cavity [1].

In multi-spoke cavities, shown in Fig. 2, each spoke operates 180^0 out of phase with the nearest ones and is usually perpendicularly oriented with respect to them.

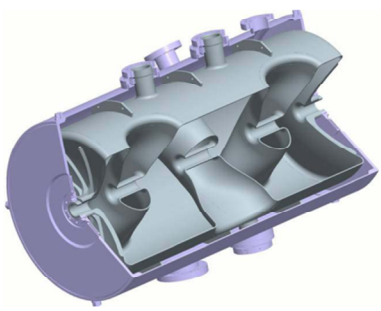

Figure 2: triple-spoke cavity [2].

* Work supported by U.S. DOE Award No. DE-SC0004094
# jdelayen@odu.edu

The spoke cavity was initially developed for the mid-velocity range because of a number of attractive features [3, 4].

Size

For the same frequency and in the medium-velocity region, spoke cavities are smaller than TM-class cavities. The transverse size of a spoke cavity is in the range 0.5-0.55 λ while that of a TM cavity is about 0.95λ. As a result accelerators can be designed for low frequency where 4.2K operation is practical, while maintaining cavities of a reasonable size. At half the frequency of a TM cavity of the same β, a multi-spoke cavity of the same length would have half the number of cells. Therefore its velocity acceptance is broader and the cavity is useful over a wider range of velocities. Lower frequency would also result in a higher longitudinal acceptance, which might be beneficial in high current applications.

As will be shown later, thc size difference is not as dramatic with spoke cavity designs that maximize the shunt impedance and minimize the surface fields. These optimizations lead to geometries of the spoke themselves which deviate substantially from cylinders; as a consequence, in order to maintain the frequency, the spokes have to be longer and the diameter of the cavity larger.

Cell-to-cell Coupling

Unlike TM cavities where the cell-to-cell coupling occurs through the iris opening, a multi-spoke cavity is much more open and magnetic field lines couple all the cells. The cell-to-cell coupling is much higher in multi-spoke cavities than in multi-cell TM cavities and they are much more robust with respect to manufacturing inaccuracies. Tuning to achieve field profile balance is probably unnecessary while it is an important and necessary step for TM cavities.

The strong cell-to-cell coupling, together with the fact that multi-spokc cavitics havc only a rclativcly small number of spokes, implies that the accelerating mode will be well separated from the nearest mode. In addition, unlike multi-cell TM cavities, the fundamental accelerating mode in multi-spoke cavities is the lowest frequency mode, and there are no lower-order modes. This was known to be true in the medium-velocity regime and it has been confirmed in all the high-velocity spoke cavities designed to-date.

Copyright © 2012 by the respective authors — cc Creative Commons Attribution 3.0 (CC BY 3.0)

Surface Fields and Energy Content

In a spoke cavity, the electromagnetic fields are concentrated around the spoke and decay rapidly moving away from it. In contrast, in a TM cavity, a much larger volume is uniformly filled with electromagnetic energy. Thus, spoke cavities tend to have a small energy content and high shunt impedance.

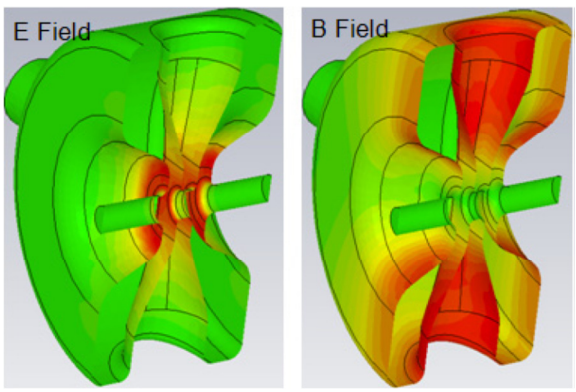

Figure 3: Distribution of surface electric and magnetic field in a single-spoke cavity [5].

This also means that the power couplers (both fundamental and for higher-order mode extraction if needed) can be located on the outer conductor instead of on the beamline as shown in Figs. 2, and 3. The impact of this aspect on the use of the beam line is illustrated in Fig. 4. [6]

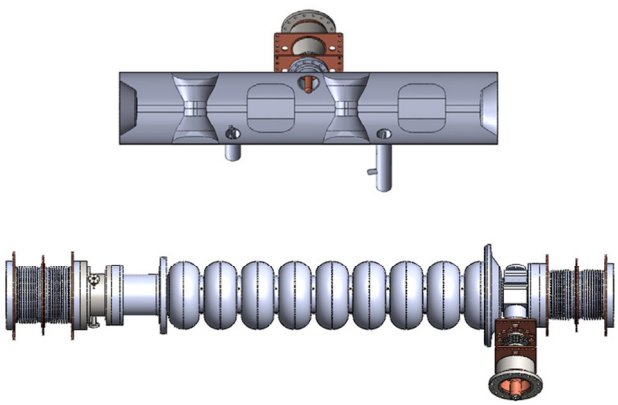

Figure 4: Relative location of couplers in spoke and TM-type cavities [6]

Electromechanical Properties

Unlike multi-cell TM cavities, spoke cavities have only a few mechanical modes that couple to the electromagnetic field, and they are at relatively high frequency. Spoke cavities can also be designed with very sensitivity to helium pressure fluctuations (~0.5 Hz/torr) by compensating the electric and magnetic effects instead of stiffening and have shown very low levels of microphonics (<1 Hz rms) [7-9].

POTENTIAL APPLICATIONS OF HIGH-VELOCITY SPOKE CAVITIES

One type of accelerator where high-velocity spoke cavities may find an application is in small, low-energy (a few 10's of MeV) electron accelerators where 2K refrigeration is not available or affordable. One example is the type of x-ray source based on Inverse Compton Scattering first proposed by MIT [10] and shown in Fig. 5. This concept for the accelerator is now being developed at Jefferson Lab. Minimization of 4K cryogenic losses implies low frequency, modest gradients, and high shunt impedance which are the characteristics of spoke cavities.

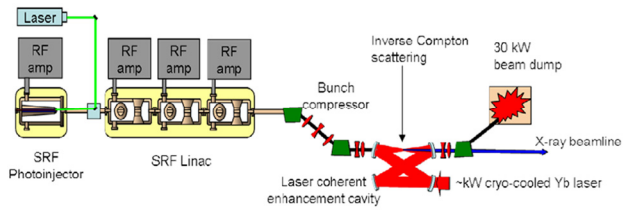

Figure 5: Concept layout for an Inverse Compton Source

In Japan there is a proposal for a non-destructive assay system of nuclear materials (uranium, plutonium, and minor actinides) in spent fuel using nuclear resonance fluorescence [6, 11]. An energy-recovering linac would be combined with a laser to produce high-brightness, monochromatic x/γ-rays via inverse Compton scattering. To be practical the ERL needs to be compact but still be able to deal with the high current and the instabilities due to the high-order modes. The rationale for considering spoke cavities in this application is that, since the fundamental and high-order mode couplers can be located radially instead of on the beamline, the cavities can be located closer to each other, increasing the "real estate" gradient. A schematic view of this ERL is shown in Fig. 6.

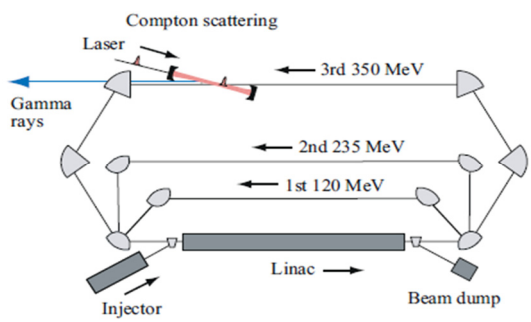

Figure 6: Schematic view of ERL for non-destructive assay of nuclear materials [6, 11]

Another potential application is in GeV-scale proton accelerators such as spallation sources. The use of spoke cavities would result in an accelerator with constant frequency from a few MeV to a few GeV, avoiding

Copyright © 2012 by the respective authors — cc Creative Commons Attribution 3.0 (CC BY 3.0)

frequency transitions which can be the source of beam loss, and standardizing in equipment, in particular rf sources [12].

Finally, spoke cavities could also be considered in GeV-scale cw electron accelerators with low repetition bunch frequency, such as light sources. In this case, cryogenic losses would be an important consideration and, because of the low bunch frequency, there is no need to use high rf frequency. Spoke cavities could offer a low-frequency alternative while maintaining a reasonable size.

DESIGN OPTIMIZATION AND PROPERTIES OF HIGH-VELOCITY SPOKE CAVITIES

Spoke cavities have many more "degrees of freedom" that TM-type cavities and the parameter space to be explored is much larger [3]. This can lead to different strategies in their design.

KEK employed a multi-objective optimization procedure with a genetic algorithm for the design of 650 MHz, β=1 multi-spoke cavities for an ERL-based linac for non-destructive assay of nuclear materials [6]. The three objective were: the minimization of E_p/E_{acc}, B_p/E_{acc}, and $1/(R/Q)$. The results are shown in Fig. 7. This technique is quite powerful, rapid, and, if the objective, carefully chosen, can lead to excellent results. Its limitation is that the trade-offs are not always apparent.

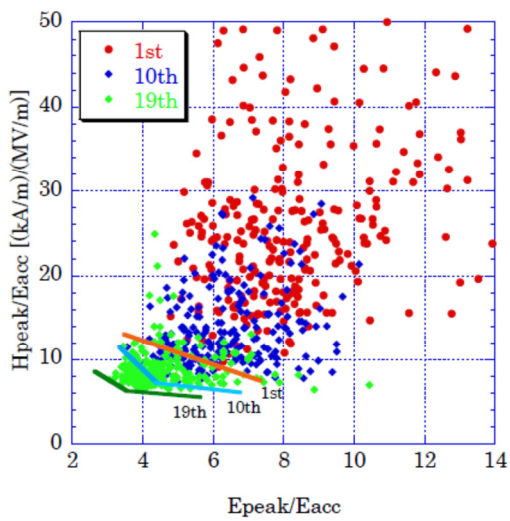

Figure 7: Distribution and Pareto front lines of E_p/E_{acc} and B_p/E_{acc} at successive generations [6].

ODU opted for a more systematic approach where each parameter was modified independently (keeping the frequency and beta constant) in order to assess its impact on the cavity properties [13-16]. This approach was probably slower but led to a good understanding of the importance of each design parameter and how it affects the final design, as well as providing a good basis for the design choices and the trade-offs involved. A number of single- double-, and triple-spoke cavities have been designed this way for a number of applications: GeV-scale proton linacs, small compact electron accelerators for inverse-Compton Scattering light sources, and larger electron accelerators for FELs or light sources. The design frequencies were 325 MHz, 352 MHz, 500 MHz, and 700 MHz; and the βs were 0.82 and 1.

Jefferson Lab has focused on 352 MHz, β=1, double-spoke cavities for a small light source [17].

In the end, as could be expected, all designs look fairly similar. The differences can be attributed to the different application and goals. Some designs had the goal of minimizing the peak surface fields (which in itself means deciding whether to minimize E_p/E_{acc} or B_p/E_{acc}), maximizing the shunt impedance, or a combination of both.

Spoke Shape

Since the highest surface electric and magnetic fields are located on the spoke –close to the beam line for the electric field and close to the outer cylinder for the magnetic field, (see Fig. 3) – the properties of the cavity will depend strongly on the geometry of the spoke and significant design effort is directed toward the shape of the spoke.

The simplest shape is that of a straight cylinder with a possible flattening in the beam line region (see Fig. 1). For multi-spoke cavities, the peak surface magnetic field can be significantly reduced by a non-circular cross-section near the outer conductor. The first attempt in that direction was by elongating the spoke parallel to the beam line, which resulted in a lower peak surface magnetic field [18]. It turns out, however, that even lower surface fields could be obtained by elongating the spoke cross-section perpendicularly to the beam line; the circular cross-section being the one with the highest surface magnetic field. This is illustrated in Fig. 8. The maximum peak surface magnetic field is for a near-circular cross-section at the spoke base. As the spoke is elongated longitudinally, the peak surface magnetic field first decreases and goes through a minimum. If instead the spoke is elongated transversally, the peak surface magnetic field decreases even further [13, 14, 16]. Transversally elongated spokes also lead to higher shunt impedance.

The peak surface magnetic field can be reduced even further by increasing the cross-section near the outer cylinder, further deviating from a straight cylinder. This can also be used to control the ratio of the peak surface magnetic field and peak surface electric field. For cavities designed to operate at 4.2 K, a ratio of B_p/E_p ~1.8

Copyright © 2012 by the respective authors — cc Creative Commons Attribution 3.0 (CC BY 3.0)

mT/(MV/m) would be a realistic goal given the state of the SRF technology; for cavities operating at 2 K, a ratio of ~2.2 mT/(MV/m) would be more appropriate. These numbers are of course very dependent on the state of the art and could evolve, and have evolved, in time. The resulting shape, shown in Fig. 9, yields low surface fields and a high shunt impedance; it has however the disadvantage of increasing the outer diameter of the cavity in order to maintain a constant frequency, thus reducing somewhat one of the main attraction of the spoke geometry. Nevertheless, even with these extreme spoke shapes, the spoke cavity is about 75% the transverse size of a TM cavity of the same frequency.

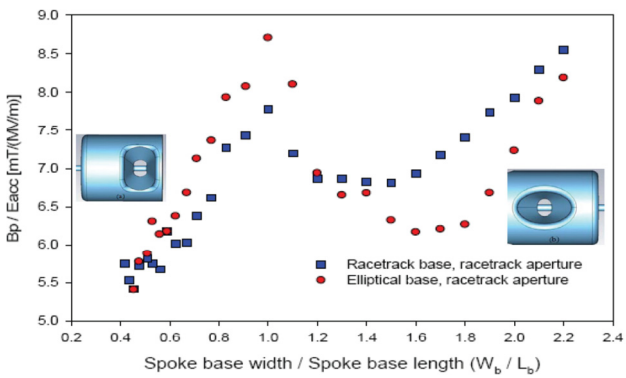

Figure 8: Peak surface magnetic field as a function of the shape of the base of the spoke. The field is maximum for a near-cylindrical spoke.

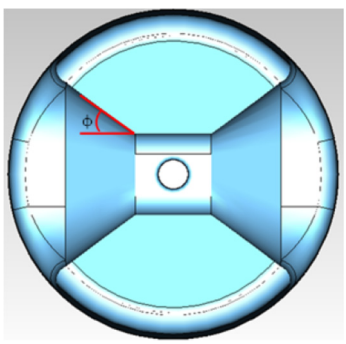

Figure 9: Typical spoke shape for low surface fields and high shunt impedance.

Similarly, the shape of the spoke near the beam line affects the peak surface magnetic field, with cross-sections elongated transversally reducing the peak surface magnetic field.

Higher-order modes

It was known that, in the low and medium-β regime, spoke cavities did not have any lower-order mode and that the first higher-order mode was will separated from the fundamental. That was cited as one of the attractive features of spoke cavities. Extensive simulations have confirmed that it is also the case for β~1 spoke cavities [19]. This is illustrated in Fig. 10 which shows the *R/Q* for a 325 MHz, β=0.82 double-spoke cavity.

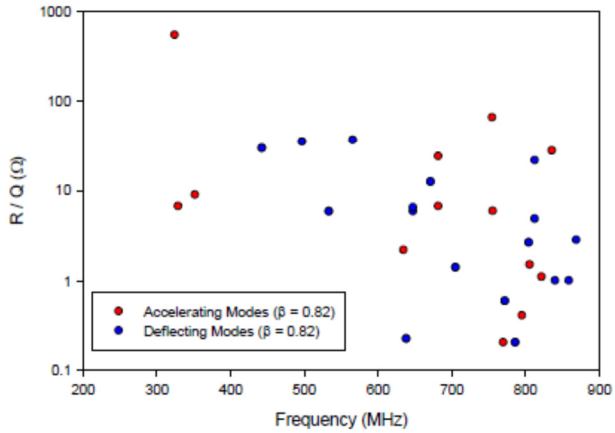

Figure 10: *R/Q* for particles of optimal velocity in a 325 MHz, β=0.82, double-spoke cavity.

Multipoles

Spoke cavities lack the circular cylindrical symmetry and therefore the electromagnetic fields of the fundamental accelerating field will have multipole components besides the accelerating monopole [20]. In some applications, the multipole components will need to be reduced and limited. One strategy would be to have a ring-shaped geometry near the beamline as was recently suggested for the half-wave geometry [21]. In such geometry, shown in Fig. 11, the quadrupole component was reduced by more than a factor of [20].

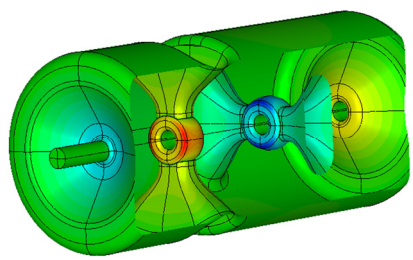

Figure 11: Double-spoke cavity with ring-shaped spoke near the beam line in order to reduce the multipole components.

Multipacting

As is always the case for new geometries for superconducting cavities, the presence of multipacting is a concern. As more and more complex and powerful simulation tools are developed extensive simulations can be made, but no definitive answer can be found until a cryogenic test on a real cavity. Such extensive simulations have been done both at Jefferson Lab [17] and ODU [22, 23] with similar results. Multipacting resonances occur at low field with high impact energy. The resonances that are found at expected operating fields have low impact energy.

The only data point that exists at present is a preliminary test of a 700 MHz, β=1, double-spoke cavity.

Copyright © 2012 by the respective authors — cc Creative Commons Attribution 3.0 (CC BY 3.0)

Multipacting levels were found at low field but were processed away [24].

Hardware

The only high-velocity spoke cavities in existence to-date are a 500 MHz and a 700 MHz, both double-spoke and β=1 [25]. They were designed by ODU and manufactured by Niowave Inc. Testing of the 700 MHz cavity is under way.

ACKNOLEDGMENTS

I would like to thank S. U. de Silva, C. S. Hopper, R. G. Olave (ODU); F. He, HyeKyoung Park (Jefferson Lab); Peter Ostroumov (ANL); Frank Krawczyk (Los Alamos); M. Sawamura (JAEA, Tokai); and C. Boulware, D. Gorelov, T. Grimm (Niowave Inc.) for their contributions and providing material for this talk.

REFERENCES

[1] J. R. Delayen, "Superconducting Accelerating Structures for High-Current Ion Beams," Proc. LINAC'88, Newport News, October 1988, p. 199.
J. R. Delayen and C. L. Bohn, "Prototype Resonators for High-Current Ion Beams," Proc. 4th Workshop on RF Superconductivity, Tsukuba, August 1989, p. 427.

[2] K. W. Shepard, M.P. Kelly, J.D. Fuerst, M. Kedzie, and Z.A. Conway, "Superconducting Triple-spoke Cavity for β=0.5 Ions", Proc. PAC 2005, paper TPPY100.

[3] J. R. Delayen, "Medium-β Superconducting Accelerating Structures", Proc. SRF 2001, paper FA007.

[4] J. R. Delayen, "Applications of Spoke Cavities", Proc. LINAC 2010, paper TU302.

[5] I. Gronin, M. Champion, T. Khabibouline, A. Lunin, N. Perunov, N. Solyak, and V. Yakovlev, "Single-spoke cavities for Low-energy Part of CW Linac of Project X", proc. IPAC 2010, paper WEPEC 057.

[6] M. Sawamura, R. Hajima, R. Nagai, N. Nishimori, "Design Optimization of Spoke Cavity of Energy-recovering Linac for Non-destructive Assay Research", Proc. SRF 2011, paper MOPO036.

[7] Z. A. Conway, J. D. Fuerst, K. W. Shepard, G. K. Davis, J. R. Delayen, "Electromechanical Properties of Spoke-loaded Superconducting Cavities", proc. SRF 2007, paper WE205.

[8] Z.A. Conway, M.P. Kelly, S.I. Sharamentov, K.W. Shepard, G.K. Davis, J.R. Delayen, .proc. SRF 2007, paper WEP 67.

[9] Z. A, Conway, "Electromechanical Interactions in Spoke-loaded Superconducting Cavities", PhD thesis, University of Illinois Urbana-Champaign (2007).

[10] W. S. Graves, W. Brown, F. X. Kaertner, D. E. Moncton, "MIT Inverse Compton Source", NIM A 608, Issue 1, Supplement 1 (2009) p. S103.

[11] T. Hayakawa, N. Kikuzawa, R. Hajima, T. Shizuma, N. Nishimori, M. Fujiwara, M. Seya, "Nondestructive Assay of Plutonium and Minor Actinide in Spent Fuel Using Nuclear Resonance Fluorescence with Laser Compton Scattering γ-rays", NIM A 621 (2010) p. 695.

[12] P. Ostroumov, "The Whole SC Linac", Presentation at the 4th Meeting of the ESSS Linac Reference Group.

[13] J. R. Delayen, S. U. de Silva, C. S. Hopper, "Design of Superconducting Spoke Cavities for High-velocity Applications", proc. PAC 2011, paper TUP100.

[14] C. S. Hopper, J. R. Delayen, ""Design of Superconducting Spoke Cavities for High-velocity Applications", proc. SRF 2011, paper MOP033.

[15] J. R. Delayen, C. S. Hopper, R. G. Olave", "Design of Low-velocity Superconducting Spoke Cavities for High-velocity Applications", proc. IPAC 2011, paper MOPC121.

[16] C. S. Hopper, J. R. Delayen, "Superconducting Spoke Cavities for High-velocity Applications" to be submitted to PRSTAB.

[17] Feise He, private communication.

[18] G. Apollinari, I. Gonin. T. Khabibouline, G. Lanfranco, F. McConologue, G. Romanov, "Design of 325 MHz Single and Triple Spoke Resonators at FNAL", Proc. LINAC 2006, paper THP056.

[19] C. S. Hopper, J. R. Delayen, R. G. Olave, "Higher Order Mode Properties of Superconducting Two-spoke Cavities", Proc. SRF 2011, paper MOPO022.

[20] R. G. Olave, J. R. Delayen, C. S. Hopper, "Multipole Expansion of the Fields in Superconducting High-velocity Spoke Cavities", these proceedings, paper MOPB072.

[21] B. Mustapha, P. N. Ostroumov, Z. A. Conway, "a Ring-shaped Center Conductor Geometry for Half-wave Resonator", proc. IPAC 2012, paper WEPPC037.

[22] C. S. Hopper, R. G. Olave, J. R. Delayen, "Development of Spoke Cavities for High-velocity Applications", proc. IPAC 2012, paper WEPPC103.

[23] C. S. Hopper, J. R. Delayen, "Multipacting analysis of High-velocity Superconducting Spoke Resonators', these proceedings,

[24] C. Boulware, private communication.

[25] D. Gorelov, C. Boulware, T. Grimm, J. R. Delayen, C. S. Hopper, R. G. Olave, S. U. de Silva, " Development of a Supercondeucting 500 MHz Multi-spoke Cavity for Electron Linacs", proc. IPAC 2012, paper WEPPC084.

Copyright © 2012 by the respective authors — cc Creative Commons Attribution 3.0 (CC BY 3.0)

SUPERCONDUCTING LINAC AND ASSOCIATED DEVELOPMENTS AT IUAC DELHI

A. Roy, Inter-University Accelerator Centre, Aruna Asaf Ali Marg, New Delhi – 110067, India

Abstract

A superconducting linear accelerator system has been developed as a booster of heavy ion beams available from the existing 15UD Pelletron accelerator. Two linac modules having eight niobium quarter wave resonators (QWRs) each have been installed and are fully operational for regular scheduled experiments. The third module is being added to the system. A new high current injector has been planned to couple to the superconducting linac. For this a high temperature superconducting electron cyclotron resonance ion source (HTS-ECRIS) was designed, fabricated and installed successfully. A radio frequency quadrupole (RFQ) accelerator is being developed for accelerating accelerate ions from the ECR (A/Q ~ 6) to an energy to of about 180 keV/A. The beams will then be accelerated further by drift tube linacs (DTL) to the required velocity to inject them to the existing superconducting linac booster. Prototypes of both these have been tested for power and thermal studies. Details of these developments and associated systems are presented in this paper.

INTRODUCTION

A superconducting linac boosters for increasing the energy of heavy ions from the Pelletron accelerator at Inter-University Accelerator Centre (IUAC), New Delhi is in operation for the past four years [1,2,3]. Heavy ions from the 15 UD Pelletron Accelerator have been accelerated through two modules, each with eight Nb quarter wave cavity resonators and used for many experiments in Nuclear Physics and Materials Science. The third module is in the process of installation and testing. The layout of the accelerator is shown in figure 1.

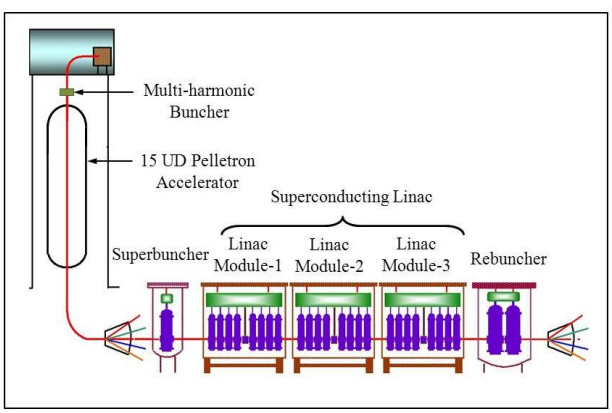

Figure 1: Sketch of the Pelletron – Linac accelerator system at IUAC, New Delhi.

Improvements were made in cooling the drive couplers of the resonators and an alternate frequency tuning mechanism based on piezo tuners has been developed. The novel method of reducing the microphonic noise in the cavity using steel balls to reduce the power required to amplitude and phase lock the cavities has been improved further. Automation of the phase tuning of the resonators was successfully tested out.

The High Current Injector planned to increase the ion flux has been designed and prototype of a suitable low beta Nb resonator with $\beta = 0.05$ has been fabricated. Prototypes of room temperature radio frequency quadrupole and drift tube linac have been built and tested for design validation.

IUAC is fabricating two $\beta = 0.22$, 325 MHz Single Spoke Resonators for the Project X of Fermi National Accelerator Lab (FNAL), USA. Several single cell 1.3 GHz TESLA type cavities and a 5-Cell cavity have been built in collaboration with RRCAT, Indore.

SUPERCONDUCTING LINAC

The complete linear accelerator (Linac) of Inter University Accelerator Centre (IUAC) will consist of five cryostats, the first one acting as superbuncher (SB) consists of a single quarter wave resonator (QWR), the next three linac cryomodules house eight QWRs each, and the last one has two QWRs used as rebuncher (RB).

In recent past, with the help of superbuncher, the first linac accelerating module and the rebuncher, Pelletron ion beams from ^{12}C to ^{107}Ag were further accelerated and delivered to conduct experiments in Nuclear Physics and Material Science. In 2011 another eight niobium resonators were installed in the linac cryostat-2 and a couple of off-line cold tests were conducted followed by beam acceleration through linac without the last accelerating module. During the beam acceleration, all sixteen resonators of cryostat 1 and 2 took part along with the single resonator operated each in superbuncher and rebuncher cryostat. During this entire period of beam acceleration extending for more than a month, three different beam species: ^{19}F, ^{28}Si and ^{31}P were accelerated and beam was delivered in the beam line of HYRA (Hybrid Recoil mass Analyzer) and NAND (National Array of Neutron Detectors). The results of the beam acceleration, in brief, are given in Table 1.

Copyright © 2012 by the respective authors — cc Creative Commons Attribution 3.0 (CC BY 3.0)

Table 1: The Beam Species and Their Total Energies Delivered for Experiments

Beam	Pell. energy (MeV)	Linac energy gain (MeV)	Total energy (MeV)
$^{19}F^{+7}$	100	37	137
$^{28}Si^{+11}$	130	60	190
$^{31}P^{+11}$	130	56	186

To increase the performance of the accelerating fields and hence the energy gain of the ion beam from the linac, several steps are adopted and they are listed in the following:

A warm water ultrasonic rinsing facility was installed for the final rinsing of the resonator before installation in the linac cryostat. It is observed that warm water ultrasonic rinsing reduces the field emission and helps to improve the accelerating fields of the niobium resonators.

A separate cooling arrangement for the power coupler of the resonator is designed and fabricated for the drive couplers of the resonators being installed in the linac cryostat-3. A Cu cold finger cooled to LN2 temperature is connected to the drive coupler as shown in figure 2. The coupler could then handle up to 400 watts without overheating and the temperature on the coupler remained below 268 K. This will allow operation of the resonator at higher rf power and increase the accelerating field,

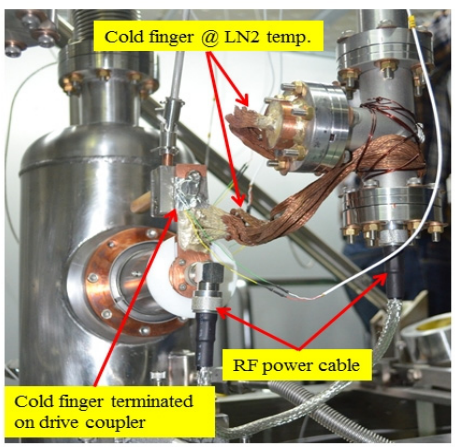

Figure 2: The additional cooling arrangement of the drive coupler at LN2 temperature.

To make the Linac operation smooth and trouble free, automatic locking of the resonators (when they go out of phase lock occasionally) without any human intervention has been taken up and some substantial progress is also achieved. In the next beam acceleration cycle, the auto tuning mechanism on linac resonators will be implemented.

In order to bring flexibility in the phase tuning of the resonators, a computer code has been developed to calculate the optimum phase at which the ion bunch would be injected in to each resonator in the linac. The programme varies the phase for each resonator at random to achieve the optimum time bunch at the target position. The results have been validated with beam during operation of the linac.

At present, the installation work of the remaining eight resonators in the last accelerating module (number-3 in figure 1) of linac is going on. After that, a couple of offline cold tests are planned to validate the performances of the resonators installed in linac-3. After the successful off-line testing of linac, the operation of the complete linac and the delivery of the ion beam for scheduled experiments are expected to start within a few months.

Reduction of Microphonics

During early on-line beam tests of linac, high RF power of about 300 watts was required to lock the resonators in over-coupled mode due to presence of microphonics. The requirement of RF power was successfully reduced by a novel technique of damping the mechanical mode of the resonator by inserting stainless steel balls of suitable diameter inside the central conductor of the QWR[4]. Further improvements were made in the reduction of the frequency jitters by experiments with combination of different diameters of the steel balls.

Piezo Tuner

The frequency fluctuations of the resonators are controlled by a feedback control for the fast components and the slow components by a mechanical tuner operated using helium gas. It was observed that often the forward rf power required by the feedback control system was rather high. To reduce the average power and to improve the dynamics of control mechanism, an alternate fast tuning mechanism has been tried out successfully and presently being implemented on all the resonators of the last accelerating module of linac. In this scheme, the tuner plate is deflected initially by a mechanical course tuner operated by a stepper motor driven shaft from outside and once the mean frequency is achieved, the control is handed over to the Piezo tuner controller (figure 3).

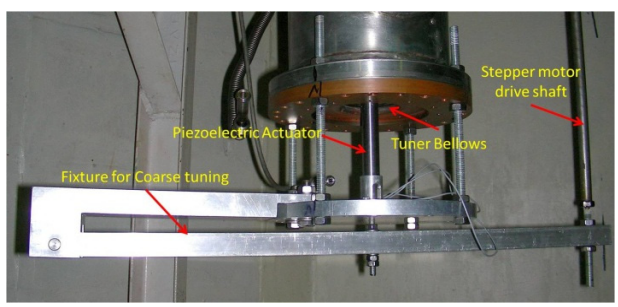

Figure 3: Detail of the piezo-actuator and its accessories connected at the bottom end of a resonator.

The piezoelectric actuator works in closed loop along with existing resonator control scheme to phase lock the

Copyright © 2012 by the respective authors — cc Creative Commons Attribution 3.0 (CC BY 3.0)

resonator. The response time for the Piezo to correct the frequency deviation is of the order of tens of milli second. During this short time, the deviation in frequency is very small and the extra power supplied by the amplifier is of negligible amount. Consequently the average power required by the resonator is negligible so the overall power requirement gets reduced substantially. During a recent test, a resonator could be phase locked at 3.6 MV/m field level with forward power of 100 W using the piezo tuner [5].

CRYOGENIC SYSTEM

The liquid helium cooling needs of RF accelerator cavities were being met by an existing piston based LHe plant. This plant was commissioned in 1996 and has been running since then to take care of the cooling needs of the stand alone resonator testing or actual beam delivery through the resonators to the users. Over last couple of years the plants performance has deteriorated because of non availability of proper spares and other wear and tear issues. At present the maximum tested heat load capacity of this machine is ~280W. So keeping in mind the running of existing facility and also the future expansion in cryogenic activities a new LHe plant of higher capacity (LINDE Cryotechnique,750W) has been commissioned recently. The machine has been tested for a maximum load of 950W @ 4.4K (with LN_2), 500W @4.4K (without LN_2) and maximum liquefaction capacity is 225 l/h (with LN_2). This plant has some more features built in so that cool down and continuous operation of LINAC becomes easier. These are (i) availability of 10K gas @ 3 g/s for initial cryostat cool down, (ii) return cold gas from distribution system can be routed to the low pressure stream of the cold box at 3 different positions depending on the temperature of the stream and (iii) automation features for non-stop operation.

Figure 4 : New Liquid Helium Plant with the central dewar in beam hall.

The new LHe plant has recently been connected to the existing distribution system at Valve Box-4 near rebuncher cryostat with the addition of a new LHe distribution line. Also to automate the distribution side all the inlet and outlet valves to the 5 cryostats has been automated. The inlet valve flow coefficient C_v has also been changed to incorporate the new flow scenario.

HIGH CURRENT INJECTOR

The High Current Injector (HCI) would consist of an Electron Cyclotron Resonance (ECR) ion source followed by a Radio Frequency Quadrupole (RFQ), six sections of Drift Tube Linac (DTL) and one low beta module with eight superconducting QWRs.

ECR Source

The 18 GHz High Temperature Superconducting ECR Ion Source, PKDELIS [6] will be used for delivering multiply charged ions (A/q ~ 6) covering a wide mass range (up to ^{238}U) with beam intensities much higher than those available from the Pelletron. The beams extracted from the ion source will be further accelerated using a high voltage platform and subsequent acceleration will done using room temperature RFQ and DTL. The emittance of different ion beams extracted from the ECR source were measured and the measurements showed clearly a mass and charge state dependence with highest emittance for the lightest ions. The energy spread of various ions was determined by measuring the plasma potentials of the source for different ion species as a function of different source parameters. The plasma potential was found to play a significant role in determining the longitudinal focussing and transport of the beam through the HCI.

Beam Transport

The Beam Transport System (BTS) for High Current Injector (HCI) from ECR source in BH-III to LINAC in BH-II has been thoroughly exercised using CODES Trace 3D, GICOSY, TRANSPORT and TRACK. Both transverse and longitudinal optics were considered so that good beam matching was maintained btween different HCI components and also with the superconducting linac. The layout based on the calculated optics has been finalised. The technical specifications of the magnets are being determined for placing the order for magnet fabrication. The high voltage deck for the ECR has been designed and order has been placed with a local vendor for fabrication.

Copyright © 2012 by the respective authors — cc Creative Commons Attribution 3.0 (CC BY 3.0)

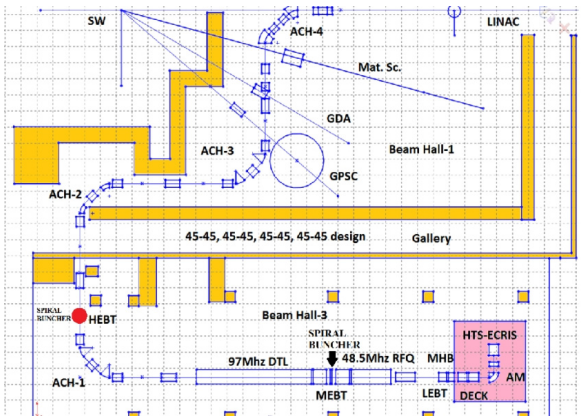

Figure 5: Plan of the layout of the high current injector for the linac.

Radio Frequency Quadrupole

A prototype of four-rod RFQ with operating frequency of 48.5MHz is designed and constructed as an accelerator section of High Current Injector (HCI) system to accelerate ions with A/q of 6 from 8keV/A to 180keV/A. Last year the high power tests for the prototype RFQ were completed. Various problems seen in the original model were corrected and satisfactorily solved. Based on the lessons learned, the final RFQ design was finalised, drawings made and is now under actual fabrication.

One of the major issues was the overheating of the base plate. The original model had a stainless steel base plate which was copper plated. The base plate was found to be hot at several places near the walls. A new base plate of copper was again manufactured and it was found that this solved the problem of localised heating. It was also found that the input and output flanges were also getting warm, but were within tolerable limits.

Some problems with the high power RF amplifier was also observed, especially unexpected tripping of the amplifier, even when there was no reflected power from the RFQ cavity. This was traced to high reflections from the high power section to the driver amplifier due to shifts in the frequency response at higher powers. A tuning of the high power section at high output power solved this issue.

Figure 6: Test set up for the prototype radio frequency quadrupole.

The final RFQ cavity mechanical design and drawings were completed, keeping in mind the lessons learnt from the prototype. Additional cooling options on the side and end flanges have been provided. The chamber has been fabricated at Bangalore, leak tested at IUAC and has been copper plated at RRCAT. The welding and surface finishes have been maintained at a higher standard compared to the prototype as they were found to be the limiting factor earlier in the surface treatment and plating.

The vanes, base plate and vane holders have been finalised, and is under fabrication at vendor's site in Ahmedabad.

Drift Tube Linac

The specification of the drift tube linac, which will operate at 97 MHz, is given in the Table 2.

Table 2: Specification of Six Tanks of the Drift Tune Linac

Tank #	Cells	Length (cm)	E_{out} (MeV/u)
1	11	38.5	0.32
2	13	73.4	0.55
3	13	94.4	0.85
4	11	86.5	1.15
5	11	99.2	1.46
6	9	81.6	1.80

Complete design validation has been done on a full scale prototype DTL resonator. Low level RF tests using bead pull technique were carried out. These tests validated the design frequency and electric field profile along the beam axis.

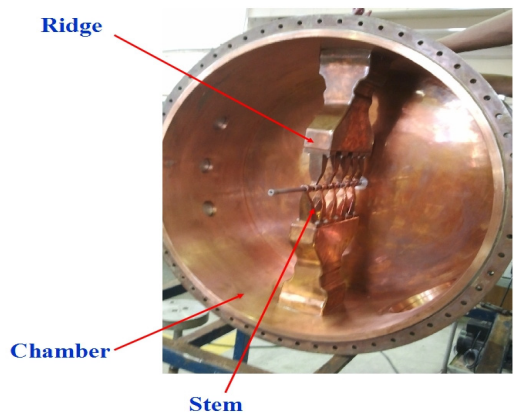

Figure 7: Prototype Drift Tube Linac with 11 gap sections.

Prototype resonator has been tested up to 6 kW input power. Total duration of high power test was ~ 100 hrs. Frequency and temperature variation has been measured. These tests have validated the complete resonator design parameters, power coupler and efficiency of water

Copyright © 2012 by the respective authors — cc Creative Commons Attribution 3.0 (CC BY 3.0)

cooling. Design modification is on to further improve the cooling efficiency near ridge base.

Low Beta Resonator

In order to provide flexibility in the beam injection from the HCI to the Linac, a superconducting module containing eight quarter wave resonators with $\beta = 0.05$ at 97 MHz has been designed. A prototype QWR has been fabricated and validated with bead-pull tests and is shown in figure 8 .

(a) (b)

Figure 8: (a) Niobium outer housing (left) and central co-axial conductor (right), (b) low beta resonator complete with the outer SS vessel.

This module with low beta resonators will also be able to match the velocities of an wider range of heavy ions from the Pelletron to the superconducting linac [7].

OTHER RESONATORS

In addition to in-house projects, two niobium single spoke resonators (β=0.22, f=325 MHz) for Project-X at Fermi National Lab, USA are in the final stage of fabrication. Four 1.3 GHz Tesla-type single cell niobium cavity have been fabricated in collaboration with RRCAT, Indore and tested at Fermilab. Two of the single cell cavities reached 35 MV/m and 40 MV/m in cold tests at 2 K. A multi-cell Tesla type cavity is also being fabricated in collaboration with RRCAT, Indore.

ACKNOWLEDGEMENT

The work from IUAC reported here is on behalf of all the members of the Linac, Resonator Fabrication, Cryogenics and High Current Injector groups of Inter-University Accelerator Centre.

REFERENCE

[1] S.Ghosh, et al Physical Review Special Topic – Accelerator and Beams, 12, 040101 (2009).
[2] A.Rai et al. Proc. of 14th International Conference on RF Superconductivity (SRF2009), p – 244.
[3] S.Ghosh et al, Proc. of 12th International conference on Heavy Ion Accelerator Technology (HIAT2012).
[4] S.Ghosh, P.N.Patra, B.K.Sahu, A.Rai, G.K.Chaudhuri, A.Pandey, D.Kanjilal and A.Roy, Physical Review STAB 10 (2007) 042002.
[5] B.K.Sahu et al. In this proceedings, contribution TUPB033.
[6] D.Kanjilal, G.Rodrigues, P.Kumar, A.Mandal, A. Roy, C.Bieth, S.Kantas and P.Sortais, Rev. Sci. Instr. Vol 77, (2006) 03A317.
[7] Prakash N. Potukuchi et al , In this proceedings, contribution TUPB049.

Copyright © 2012 by the respective authors — cc Creative Commons Attribution 3.0 (CC BY 3.0)

THE ESS LINAC DESIGN

M. Lindroos*, S. Molloy, D. McGinnis, C. Darve, H. Danared, ESS AB, Lund, Sweden
and the ESS Accelerator Collaboration

Abstract

The European Spallation Source (ESS) is a 5 MW, 2.5 MeV long pulse proton machine. It represents a big jump in power compare to the existing spallation facilities. The design phase is well under way, with the delivery of a Conceptual Design Report published in the beginning of 2012, and a Technical Design Report in December 2012. Why and how the 5 MW goal influences the parameter choices will be described.

INTRODUCTION

Spallation is a nuclear process in which neutrons of different energies are emitted in several stages following the bombardment of heavy nuclei with highly energetic particles. The spallation process is the most practical and feasible way of producing neutrons for a reasonable effort (or cost) of the neutron source cooling system. Spallation sources come in at least three types: short pulse sources (a few μs), long pulse sources (a few ms) and continuous sources. The future European Spallation Source (ESS) will be a long pulse source and the first spallation source with a time average neutron flux as high as that of the most intense research reactors.

The highest power spallation source currently in operation – the Spallation Neutron Source (SNS) in Oak Ridge – combines a full energy SC linear accelerator with an accumulator ring to provide very high intensity short pulses of neutrons to the instruments. The European Spallation (ESS) source will provide even higher intensities, but is developing instruments able to use longer linac pulses directly for spallation, avoiding the need for a costly and performance-limiting accumulator ring [1].

The obvious advantage of a linac is that beam passes only once through the accelerating structures, enabling it to accelerate a high current beam with a minimum of constraints. The current limit is mainly set by space charge effects at low energy, as well as the power that can be delivered to the beam in each accelerating cavity at medium and high energies, and by beam losses.

The spallation cross section for protons on heavy nuclei increases as a function of proton energy up to several tens of GeV [2]. Nonetheless it is generally agreed that a kinetic proton energy between 1-3 GeV is optimal for practical target and moderator designs, and in order to keep the shielding requirements reasonable.

The ESS has the ambitious goal of becoming a sustainable research facility with zero release of carbon dioxide. This will be achieved through a combination of actions, but with the linac being the most energy hungry part of ESS, the energy efficient design of the RF power sources and the cryogenics systems and high-Q cavities are important issues.

THE ESS BASELINE

The ESS accelerator high level requirements are to provide a 2.86 ms long proton pulse at 2.5 GeV at repetiton rate of 14 Hz, with 5 MW of average beam power on target. The configuration of the current, May 2012 Baseline linac is shown schematically in Fig. 1, and selected linac parameters are listed in Tab. 1 [3]. The warm linac has contributions from INFN Catania, CEA Saclay, ESS-Bilbao and INFN Legnaro, the superconducting cavities and their cryomodules are designed at IPN Orsay and CEA Saclay, and the HEBT will come from ISA in Aarhus. The 50-mA proton beam is produced in a pulsed microwave-discharge source on a platform at 75 kV. A low-energy beam transport, LEBT, with two solenoid magnets as focusing elements brings the beam to the entrance of the RFQ. The LEBT has a chopper that cuts away the beam while the proton pulses from the ion source stabilize, preventing a beam with off-nominal parameters from being accelerated in the RFQ and lost at high energy. The 4-vane RFQ accelerates the beam to 3 MeV with small losses and a minimal emittance growth. It is designed specifically for ESS but it is based on the IPHI RFQ at Saclay. The RF frequency of the RFQ and the warm linac is 352.21 MHz. After the RFQ there is a medium-energy beam transport, MEBT, with three buncher cavities and 10 quadrupole magnets. The MEBT has several different functions: it has optics to match and steer the beam from the RFQ into the drift-tube linac, it has a comprehensive set of beam-instrumentation devices, it has a chopper which acts faster than the LEBT chopper since space-charge neutralization is not an issue in the MEBT, and it allows collimation of the transverse particle distribution. A drift-tube linac, DTL, with four tanks takes the beam from 3 MeV to 79 MeV. It has a FODO structure with permanent-magnet quadrupoles. Every second drift tube is empty or used for steering magnets and beam-position monitors. The superconducting linac has three types of cavities: double-spoke resonators, five-cell medium-beta elliptical cavities and five-cell high-beta elliptical cavities. The May 2012 linac has 14 spoke cryomodules with two double-spoke resonators in each, and between the cryomodules there are warm quadrupole doublets. The spoke resonators operate at 352.21 MHz like the warm linac, but then there is a frequency doubling to the 704.42 MHz of the elliptical cavities. There are 15 medium-beta cryomodules with four cavities in each and

* E-mail: mats.lindroos@esss.se

Copyright © 2012 by the respective authors — cc Creative Commons Attribution 3.0 (CC BY 3.0)

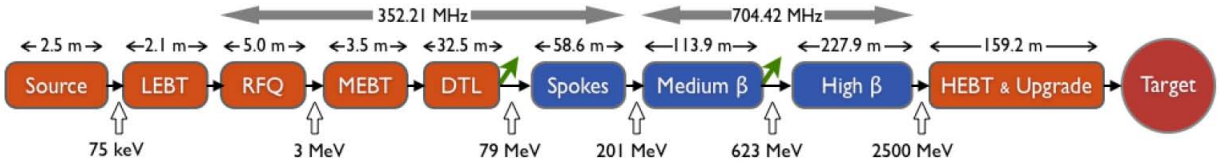

Figure 1: A block diagram of the ESS linac design. The Radio Frequency Quadrupole (RFQ) and Drift Tube Linac (DTL) are normal conducting while the spoke resonator and low beta and high beta elliptical cavities are superconducting

Table 1: The ESS RF parameters

	Length m	**Input energy** MeV	**Frequency** MHz	**Geometric** β	**No of sections**	**Temp** K
LEBT	2.1					
RFQ	5.0	75 $\times 10^{-3}$	352.2		1	RT
MEBT	3.5					
DTL	32.5	3	352.2		3	RT
Spoke	58.6	79	352.2	0.50 (optimal)	14 (2c)	≈ 2
Medium β	113.9	201	704.4	0.67	15 (4c)	≈ 2
High β	227.9	623	704.4	0.92	30 (4c)	≈ 2
HEBT	100	2500				

quadrupole doublets between, and there are 30 high-beta cryomodules with four cavities in each and quadrupole doublets between every second cryomodule. All accelerating structures will be powered by klystrons, except the spoke resonators where tetrodes will be used. With one klystron per elliptical cavity plus a few for the warm linac, there will be close to 200 large klystrons and almost 100 modulators since one modulator will drive two klystrons. The density of components in the klystron building would become too high if these were to be positioned linearly. Instead they will be located in groups of eight klystrons and four modulators across the klystron building. After the last cryomodule there is 100 m of tunnel where additional cryomodules can be installed for an energy upgrade. Then the beam is brought from the tunnel to the spallation target at the surface through two vertical bends and an expansion section. Quadrupole and octupole magnets are used to blow the beam up onto the desired profile of the proton-beam window and the target window.

SUPERCONDUCTING LINAC

The superconducting part of the linac consists of three families of SC cavities. The beam dynamics has been discussed in the previous section. We will here give some insight to the specific issues relating the superconducting technology for a high power linac like ESS.

Cryomodules

The cryomodules are installed in a $\approx$ 400 m long ESS cold linac section. There are three families of cryomodules: the spoke resonator cryomodules, the medium- and the high-beta elliptical cavity cryomodules. The cryomodules are composed of the cavity packages, the supporting system, the alignment system, the thermal and magnetic shieldings, the internal cryogenic piping and the diagnostic instrumentation. Each elliptical cryomodule contains four superconducting cavity packages, which include cavities (or resonator), fundamental power coupler, cold tuning system, its helium tank and the RF pick-up coil. Each spoke cryomodule contains two spoke resonator packages. The main functions of the cryomodules are to provide the positioning and alignment of the cavity package w.r.t. the beam axis, and to reduce the thermal losses to the 2 K helium tank. The cryomodules have the capacity 1) to transfer energy from RF system to the beam, 2) to confine the protons longitudinally and 3) to steer the protons longitudinally. To lower the construction and operating risk, the ESS cold linac take advantage of the de-velopment done on the cryomodules design and the procedures developed at the Spallation Neutron Source (SNS), Desy (X-FEL) and CEA for module integration. In an effort to standardize the solution and to lower the technical unknown/risk, the ESS has contracted the same institute (IPNO) to design the cryomodule of both the spoke and the elliptical cavities. The design of the cryomodules and its jumper connection are in compliance with the European Pressure Equipment Directive 97/23/EC and is driven by the ALARA principle.

Tab. 2 gives the length of the individual cryomodule types and the length of different SC sections. Warm quadrupole doublets and beam instrumentation systems are installed in between the cryomodules to correct and to monitor the beam profile. Fig. 2 shows the conceptual de-

Copyright © 2012 by the respective authors — cc Creative Commons Attribution 3.0 (CC BY 3.0)

Table 2: The ESS Cryomodule parameters

Section	Cryomodule length [m]	Cavities count per section
Spoke	≈ 2.9	28
Medium-beta	≈ 6.7	60
High-beta	≈ 6.7	120

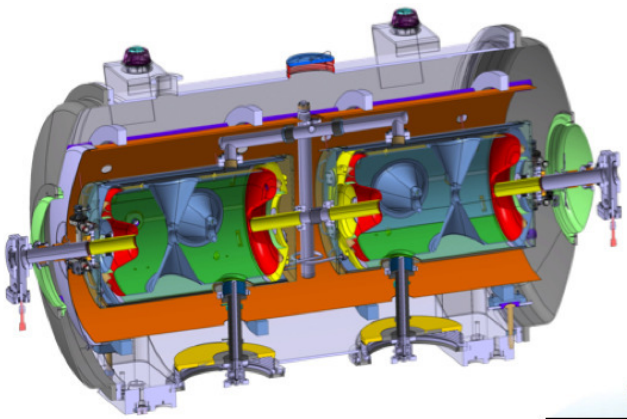

Figure 2: Spoke cavity cryomdoule for ESS

sign of the spoke resonator cryomodule and Fig. 3 shows the conceptual design of the RF elliptical cavities cryomodule. A space-frame is used to position and align the elliptical cryomodules.

Cavities

The three families of SC cavities intended for use in the ESS linac are:

1. Double spoke cavities operating at 352.21 MHz
2. Medium-β elliptical cavities operating at 704.42 MHz
3. High-β elliptical cavities operating at 704.42 MHz

Double spoke cavities The proton beam will be accelerated from 79 MeV to 201 MeV by 28 spoke cavities. These will be installed in 14 cryomodules (i.e. 2 cavities per cryomodule), operating at 2 K.

It should be noted that ESS will be the world's first accelerator to make use of spoke cavities.

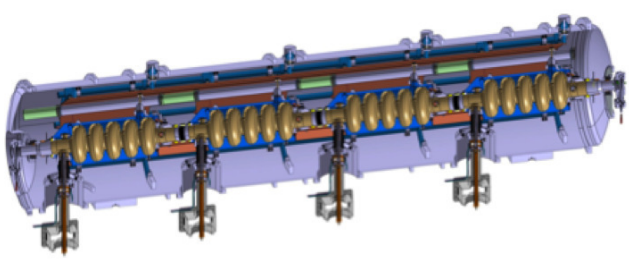

Figure 3: Elliptical cavity cryomdoule for ESS

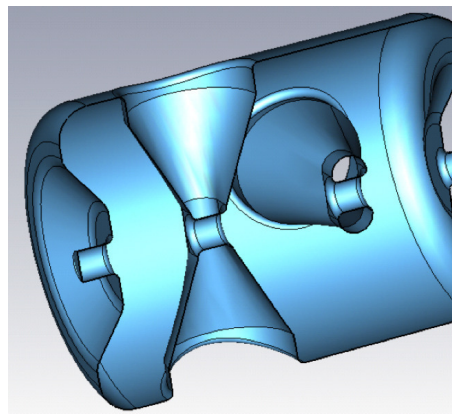

Figure 4: A cross-section through a spoke cavity design for ESS.

Figure 4 shows a cross-sectional view through a spoke cavity designed for use in ESS.

These cavities are designed to have an optimal beam velocity, $\beta_{opt} = 0.50$, and a peak accelerating gradient, $E_{acc} = 8$ MV/m.

The design of these cavities is driven by some quite conservative limits on the maximum surface fields – $B_{peak} \leq 70$ mT, $E_{peak} \leq 35$ MV/m – in order to minimise the risk associated with this new technology.

The expected quality factor, $Q_0 \geq 2 \times 10^9$, at the nominal gradient.

Medium-β cavities Following the spokes, the proton beam is then accelerated from 201 MeV to 623 MeV by 60 SC elliptical cavities. This is the first section to use the higher accelerator frequency of 704.42 MHz

These cavities contain five resonant cells operating in the π-mode, and they are designed with a geometric beta, $\beta_G = 0.67$.

At the nominal gradient, $E_{acc} = 15$ MV/m, the cavity surface will be treated such that a quality factor, $Q_0 \geq 5 \times 10^9$, is achieved.

High-β cavities The final section of the ESS linac consists of 120 high-β cavities that are used to accelerate the protons from the 623 MeV with which they exit the medium-β section, to the final energy of 2.5 GeV.

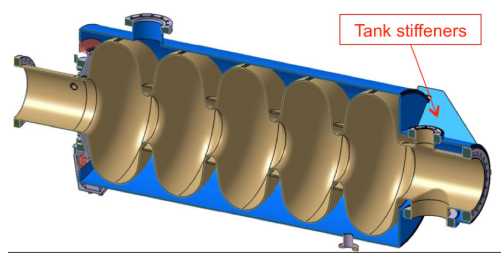

Figure 5: A cross-section through a high-β elliptical cavity installed within its cryo-vessel.

Copyright © 2012 by the respective authors — cc Creative Commons Attribution 3.0 (CC BY 3.0)

As with the medium-β section, these are also π-mode cavities with five resonant cells, however their geometric beta, $\beta_G = 0.92$ in the current baseline.

At the nominal gradient, $E_{acc} = 18$ MV/m, the cavity surface will be treated such that a quality factor, $Q_0 \geq 6 \times 10^9$, is achieved.

RF SOURCES

Because the vast majority of accelerating structures in the ESS linac are superconducting, the dominant feature of the ESS RF system is the number of RF stations. To handle variations in cavity coupling, Lorentz detuning, there is one RF power amplifier per superconducting resonator; totaling over 208 individual RF stations. The core of each RF station is an RF power amplifier which is typically a klystron. For the high beta section of the linac consisting of 120 stations, the peak power required for the cavities is 900 kW. Even though the loaded Q of the cavities is quite low (7×10^5) to compensate for heavy beam loading, the Lorentz detuning for ESS can be quite severe. Without any Lorentz-detuning compensation, the resonant frequency of the cavities could shift up to 50 degrees of RF phase during the beam pulse. In addition, the beam pulse for the ESS linac is very long (2.86 ms) which is about a factor of three longer than the mechanical response time of the cavity to the Lorentz detuning. To save on RF power overhead, all superconducting cavities will be equipped with fast piezoelectric tuners to negate the Lorentz detuning of the cavities. The klystrons are operated with 30 % below the maximum saturated power so that variations in the RF system such as modulator droop, cavity coupling, residual Lorentz detuning, and power loss in the waveguide distribution system can be compensated. Also part of the overhead is used for stable regulation of the feedback loop. The target efficiency of the klystrons at maximum saturated power is 60 % which will give an operational efficiency of about 45 %. The required maximum saturated power for the klystrons is 1.2 MW. The klystron is energized with a modulator. For stability, reliability and economic reasons, the klystrons will be powered in the pulsed cathode configuration. The modulators must supply a 3.5 ms long pulse at a rate of 14 Hz. The cathode voltage is for each klystron is about 100kV with a peak current of about 20 Amperes. For a modulator efficiency of 90 % and a power factor of 0.9, 120 kVA will be required for each klystron. For economical and space reasons, it has been decide to power two klystrons per modulator which limits the required power per modulator to 240 kVA. To handle the long pulse length of 3.5 ms, the modulators will implement solid-state switches at relatively moderate voltages and the output voltage pulse will be stepped up by a pulse transformer or equivalent technology. The modulator topology will not be imposed by ESS but functional specifications will be given to vendors. The regulation of each RF system will be done independently with the low level RF system. Using modern digital technology, most of the regulation will be done with adaptive feed-foward algorithms. Feedback regulation will play a secondary role to the adaptive feed-forward so the required power overhead can be minimized. With the large number of RF systems, it will be un-economical for the high power waveguide of each RF system to have its own penetration to the tunnel. ESS will use a stub concept for distributing 16 RF systems into the tunnel as shown in Figure 6. The stubs will provide access to additional conventional services such as water and power as well. In addition, the radiation shielding issues are best handled with the stub concept. ESS is also considering the use of Inductive Output Tubes (IOTs) in place of klystrons for the high beta section of the linac. IOT shows the promise of high efficiency and much lower capital cost. IOTs can be thought of as a cross between klystrons and tetrodes. As in tetrodes, IOTs employ a grid to control electron flow from cathode to collector. These grids are very robust with the advent of pyrolithic carbon technology. Since IOTs are gridded tubes, no pulsed modulation system is needed to energize the cathode. This eliminates costly high voltages switches in the power supply for the IOT. Also a gridded tube can be run in deep class C that can produce very high efficiencies (less than 70 %). Also IOTs do not exhibit the severe saturation effect of klystrons. This permits the operation of IOTs at the maximum rated power in feedback loops which increases the efficiency of the RF system significantly. It is estimated that 3-4 MW of power consumption can be saved if klystrons are replaced by IOTs. Like klystrons, IOTs use a resonant output cavity to efficiently couple power from the electron beam at high frequencies. However the gain of an IOT is much lower than a klystron because an IOT uses a single output cavity while a klystron may employ 4-5 stages of cavities. With the advent of low cost solid stage RF amplifiers as pre-drivers, the high gain provided by multi-cavity klystrons is not required. Because of this low gain, IOTs require cathode voltages on the order of 35kV as compared to 100 kV for high gain klystrons. The lower cathode voltage also reduces the cost of the power supply that energizes the IOT. Current estimates for a power supply for an IOT is 60 % the cost of a klystron modulator of comparable power. Currently there are no commercially available IOTs for the ESS power range. However there has been very good progress made in higher order mode multi-beam IOTs in which power levels of 1 MW have been achieved [4]

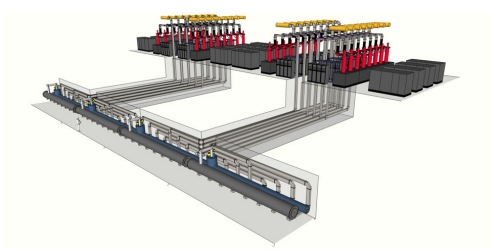

Figure 6: The ESS RF sources in stub lay-out

Copyright © 2012 by the respective authors — cc Creative Commons Attribution 3.0 (CC BY 3.0)

DISCUSSION

The ESS accelerator design update is approaching completion. Work is being done in all areas from ion-source, thorough accelerating structures to the target. We have here reported on the work on RF, cavities and cryomodules but major progress has also been made for the normal conducting magnets, the Low, Medium and High energy beam transsport, controls and instrumentation. The design update work for the accelerator and for all other areas of the project will enable ESS to enter construction in early 2013 provided the negotiations between ESS member states can complete in time.

ACKNOWLEDGMENT

We wish to thank all our colleagues at ESS Acceleraror division and in the ESS accelerator collaboration.

REFERENCES

[1] F. Mezei,"Comparison of neutron efficiency of reactor and pulsed source instruments", Proc. of ICANS-XII (Abingdon 1993) (RAL Report No. 94-025), I-137 and F. Mezei,"The raison dłtre of long pulse spallation source", J. Neutron Research 6 (1997) 3-32.

[2] K. van der Meer et al., Nucl. Instr. and Meth. in Phys. Res. B 217 (2004) 202220

[3] H. Danared, Proc. IPAC 2012, p. 2073.

[4] Progress in CPI Microwave Tube Development, Wright, Edward L.; Bohlen, Heinz, AIP Conference Proceedings;2006, Vol. 807 Issue 1, p145

Copyright © 2012 by the respective authors — cc Creative Commons Attribution 3.0 (CC BY 3.0)

SPIRAL2 ACCELERATOR CONSTRUCTION PROGRESS

P. Bertrand, R. Ferdinand, GANIL, Caen France,
on behalf of the SPIRAL2 team and partners.

Abstract

The installation of the SPIRAL2 superconducting accelerator at GANIL is almost started. All the major components have been tested in the various partner laboratories, and the building construction is now well engaged. The management of the interfaces between the process and the buildings is a strategic point in an underground accelerator, with strong space constraints. This paper describes the performances of the various components.

INTRODUCTION

Officially approved in May 2005, the SPIRAL2 radioactive ion beam facility at GANIL (Caen-Normandy) has been launched in July 2005, with the participation of many French laboratories (CEA, CNRS) and international partners. Figure 1 describes the project layout. In 2008, an important decision has been taken to build the SPIRAL2 complex in two phases:

- *Phase one* includes the complete accelerator and two new experimental halls, the Super Separator Spectrometer (S3) and the Neutron-based research area (NFS), all to be installed in a new dedicated building.
- *Phase two* includes the RIB production process and building, the low energy RIB experimental hall (DESIR) and the transfer line connection to the present GANIL facility for RIBs post-acceleration by means of the existing SPIRAL1 cyclotron called CIME.

The planning objective of the first phase is to have installed and tested the whole accelerator in order to start the experiments with NFS and S3 in 2014-2015. A complete presentation of the SPIRAL2 scientific case can be found in the White Book of SPIRAL2, and through the large number of Letters of Intent for physics [1] [2] [3].

Recalled in table 1, the SPIRAL2 accelerated beams will include protons, deuterons, $A/q<3$ ions, and optionally $A/q<6$ ions in the future. As indicated, a maximum beam power of 200kW is expected for deuterons in CW mode.

Table 1: Beam Specifications

beam	P+	D+	ions	ions
Q/A	1	1/2	1/3	1/6
Max. I (mA)	5	5	1	1
Min. output E (MeV/A)	2	2	2	2
Max output E (MeV/A)	33	20	14.5	8
Max. beam power (kW)	165	200	44	48

During the last years, our strategy for the accelerator itself was the following:

We decided a few years ago to install the low energy heavy ion transfer line and ECR source at LPSC laboratory (Grenoble), and the Deuteron/proton ones at IFRFU/Saclay, in order to operate a maximum of technical and beam tests, to check the validity of our design, and to improve with all partner laboratories our knowledge and collaboration. This will also gain time for the definitive installation and tests at GANIL.

Thanks to our partnership with existing accelerators (SARAF, INFIN-HH, GANIL…), we were also able to test various components like diagnostics in presence of existing beams, and to have some irradiation tests on samples to check their resistance to radiations and to validate the activation codes.

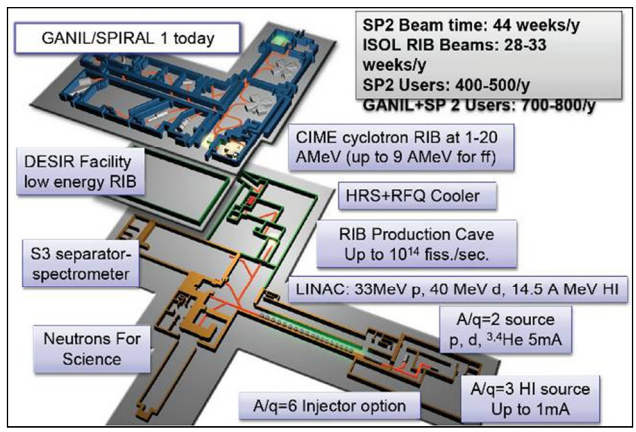

Figure 1: SPIRAL2 project layout, with experimental areas and connexion to the existing GANIL.

In the next paragraphs, we will focus essentially on the first phase of the project, providing the status of the main parts of the accelerator, the progress of construction of its building, and some scheduling.

SPIRAL2 INJECTOR STATUS

The Spiral2 injector, dedicated to protons, deuterons and heavy ions of $q/A>1/3$, is mainly composed of two ECR ion sources with their associated LEBT lines, a warm RFQ and the MEBT line connected to the LINAC.

Heavy ECR ion source, and LBET1

The 18GHz ECR heavy ion source, called Phoenix-V2, and its analysis beam line LEBT1 have been installed at the LPSC/Grenoble for a few years (Figure 2). The ECR source was updated these last years, in particular to host metallic ovens developed at GANIL.

Here are summarised the main results obtained: (see also [4] and [5] for more details) :

- Using automated optimization algorithms developed

Copyright © 2012 by the respective authors — cc Creative Commons Attribution 3.0 (CC BY 3.0)

from the TraceWin code, we obtained in a first step 30% more than 1mA of $^{16}O^{6+}$ (goal for SPIRAL2), and 70µA of $^{40}Ar^{12+}$,with a good transmission (95%). Around 2mA of $^{4}He^{2+}$ were also obtained, which is of interest to mimic the deuteron beam and learn how to tune the Linac.

- As expected, we measured transverse emittances of around 0.25 π.mm.mrad.norm.rms., with an efficient action of the hexapole corrector associated to the analysis bending magnet. Very similar transverse beam profiles in both pulsed and CW source mode were also obtained.
- The separation power of the LEBT1 line is found better than specified. (<1/100), which is a good sign for future Linac acceleration.
- Recent improvements allowed us to reach our 60 KV voltage goal in routine operation, mandatory for RFQ injection of A/Q=3 beams.
- We also obtained more than 20 µA of $^{58}Ni^{19+}$, which is very promising (Figure 3).

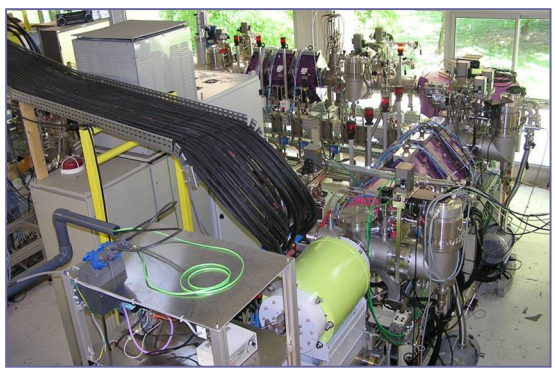

Figure 2: View of ECR source (green) and Spiral2 LEBT1 installed at LPSC (Grenoble) for beam tests.

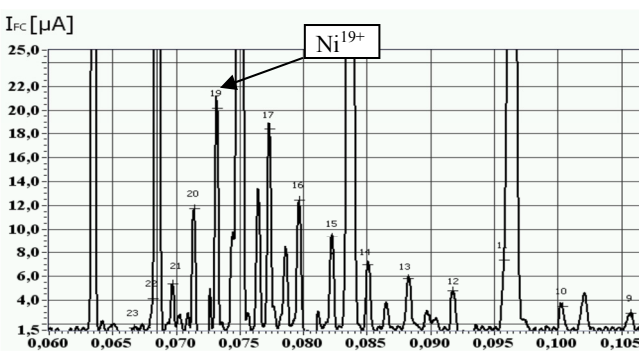

Figure 3: Spectrum optimized for Ni^{19+} (~20 µA), using the Large Capacity High Temperature Oven from GANIL (please zoom for details).

Several actions are now conducted: a development is underway to increase the volume of the plasma chamber, and a study is conducted by LPSC, GANIL and IPN/Lyon to develop a new fully superconductive 18/28 GHz ECR source.

Moreover, LEBT1 having been dismounted last June to be moved to the SPIRAL2/GANIL site, Phoenix-V2 will be reconnected to another LPSC test bench in order to continue metallic beam development with $^{40}Ca^{14+}$ and $^{40}Ca^{16+}$ up to the last moment.

Deuteron ECR ion source, LEBT2 and LEBC

Important results were also obtained in 2010-2012 at IRFU/Saclay, where the deuteron/proton ECR source, the transfer lines LEBT2 (achromatic analysis section) and LEBC (merging transport and matching line to the RFQ) have been installed in several successive steps (Figure 4).

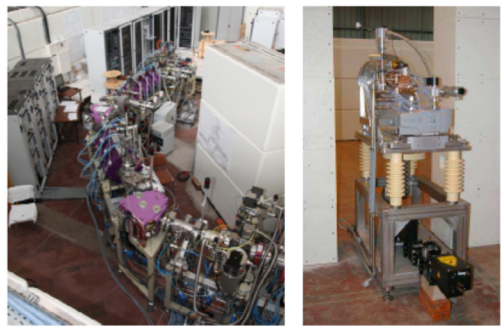

Figure 4: View of ECR source, and LEBT2+LEBTC installed at IRFU (Saclay) for beam tests

Here are the main results obtained during the last months:

- First of all, the 2.45GHz permanent magnet ECR source [6], confirms its capability to produce a very stable and reproducible 6.7 mA 40 kV deuteron CW or pulsed beam (and also down to 50 µA in CW), with an emittance between 0.1 and 0.22 π.mm.mrad.norm.rms, depending upon the tuning of the slits and the vacuum level.
- Beam alignment and automatic optical procedures showed very efficient behaviors, with transverse emittance portraits and perfect RFQ matching parameters achievements: By installing the emittance-meter at the *exact* RFQ injection point, we could measure the emittance (distorted) figures and by generating a set of 10^6 particle reproducing them, we could check with the Tracewin code that the real beam should be correctly bunched and accelerated through our RFQ (Figure 5).

- We also verified that the set of movable LEBT slits were efficient to clean optimally the generated halo, and that we could chose the vacuum level in order to optimize the space charge compensation parameter.
- The slow chopper, developed by INFN Catania, could be tested on line and gave excellent results [7]: Transition times below 30 ns were confirmed as well as the duty cycle range from 0.1‰ to 99.99%. The device can operate up to 10 kV, up to 1 kHz. The chopper will be used to manage the beam duty cycle. It is also a Machine Protection System device which stops the beam when an unwanted event occurs (lost beam, internal failure, etc…)
- Finally, we had also the opportunity to discover some technical weak points like the response delay of the magnet power supplies, and test successfully on line the corrections proposed by the constructors.

The entire installation will be dismounted this month, to be moved to the SPIRAL2/GANIL site.

Copyright © 2012 by the respective authors — cc Creative Commons Attribution 3.0 (CC BY 3.0)

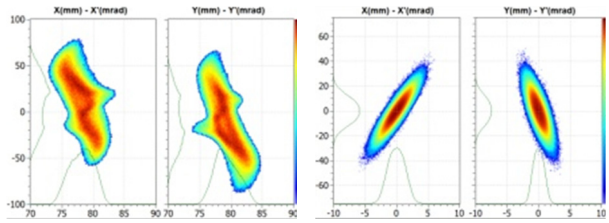

Figure 5: D^+ measured emittances as input for Toutatis RQF transport, and output emittances obtained.

Status of the 88 MHz room temperature RFQ

Developed by IRFU/Saclay, the RFQ is a 4-vane, 88MHz, 5-meter copper cavity ensuring bunching and acceleration of the continuous beam up to 0.75Mev/u [8].

The first RFQ segment was constructed, 3D-measured and accepted in May 2010, while the 4 other segments are in progress: The 4 last tubes are manufactured and assembled with their respective vanes in pre-machined state (≈500 µm) and measured with success (Figure 6). Final vane machining and geometrical checks should be achieved by end 2012.

The main issue is a vacuum leak observed last year for the first segment: this point, under strong investigation, is perhaps due to a too soft copper, to non conformities on surface roughness, and to previous non conformities of vacuum seals.

In parallel the integration system of the RFQ segments is ready, and the cooling system call for tender launched.

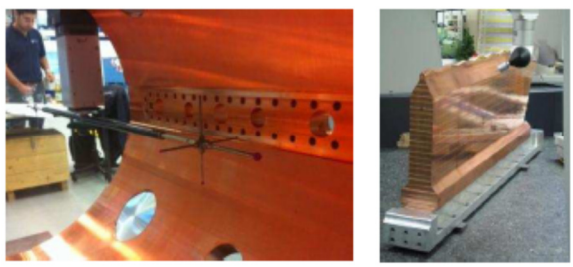

Figure 6: 3D measurement of RFQ tubes and vanes

Medium energy beam transfer line

The intermediate 8-meter MEBT line ensures several essential functions: the matching of the 0.75 MeV/A bunched beam from the RFQ exit to the SC Linac, the connection of a future *q/A*=1/6 heavy ion injector, a very fast selection by clean chopping of the beam bunches for NFS experiments, and the suppression of the beam halo before injection into the Linac.

The first (among three) *rebuncher* (Figure 7) [9] was intensely tested last year at full power, results leading to an increased cooling of the trimmer plates. The other two cavities are now being built. Recently, the 1st rebuncher was also used for tests of the whole RF system, including the amplifier, the LLRF, the PLC for the controlled trimmer motor and EPICS/Xal related applications.

The fast chopper (figure 7), or "single bunch selector" must reduce by 100 to 10000 the bunch rate for NFS experiments. It is based on the superposition of a steerer magnet and 2 high impedance meander electrodes driven with high voltage pulses of opposite sign. A vacuum chamber prototype equipped with 100Ω meanders and feed-through have been constructed in collaboration with INFN-LNS and successfully tested in Catania [10].

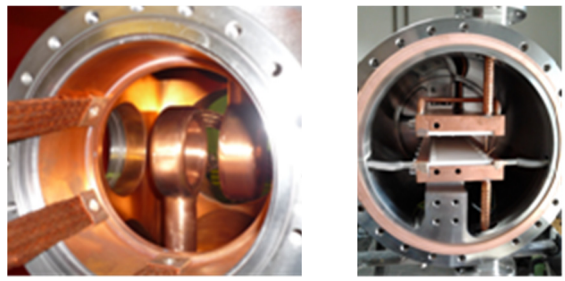

Figure 7: MEBT 3-gap rebuncher and single bunch selector.

For the beam commissioning, a diagnostic plate will be installed after the 1st MEBT rebuncher, allowing precise measurement of the RFQ output beam parameters.

SPIRAL2 LINAC AND HEBT STATUS

The LINAC accelerator [11][12][13][14] is a super-conducting linac composed of two types of QWR cavities, beta=0.07 and 0.12 operating at 88.05 MHz, with intermediate warm sections, housing quadrupole doublets, diagnostics and vacuum pumps.

The 12 low-β cavities were all qualified in vertical cryostat, the last one in July 2012 at IRFU/Saclay (in charge of the development of the A-type cryomodules). The 14 high-β ones were already successfully tested in 2010 at IPNO/Orsay (in charge of the B-type cryomodules). LPSC/Grenoble is in charge of the development, production and ongoing commissioning of the 12kW power couplers. For each family, a "qualification" cryomodule has been tested with some success before the production of the series cryomodules (although not with completely nominal performances).

RF power tests campaigns were performed on the qualification and pre-series cryomodules. The results showed several major difficulties, mainly related to high RF dissipations in the cavities on both cryomodule types. The main source of dissipation in the cavity, even at low accelerating field (i.e. < 6.5 MV/m), was the electron field emission. The pollution sources are now understood, coming from unexpected dirty parts from vendors, partly inadequate cryomodule assembly procedures, inappropriate venting procedure, and probably also from power coupler surface cleanliness. Qualification of the cryomodules subcomponents and the power coupler preparations were entirely reviewed.

We are still facing a long commissioning time. The low Q_{ext} coupler values ($5.5\ 10^5$ for CMA and $1\ 10^6$ for CMB) are obtained by a deep penetration of the antennas inside the cavity. Thus, the field at the antenna tip is of the same order of magnitude than the accelerating field of the cavity. As a consequence the RF processing of the power coupler mounted on the cavity had to be also improved.

Copyright © 2012 by the respective authors — cc Creative Commons Attribution 3.0 (CC BY 3.0)

All these efforts lead recently to the acceptance of the first A-type cryomodule for installation on the machine.

In parallel, all the vacuum boxes of the *warm section*s are achieved, with mechanics assembly in a clean room.

The *cryogenic system* is almost finished [15]: the valve boxes and 1.1kW Helium liquefier are constructed, with the cold box tested with success in the company last June. [15]

The *HEBT lines* are completely defined, with all dipoles constructed and being measured, while qpoles and steerers are under construction, and the call for tender of the main beam dump imminent [16].

DIAGNOSTICS

A set of 50 semi-interceptive multi-wire profile monitors and 5 non interceptive monitors (residual gaz ionization) are developed at GANIL, using the same specific modular electronic and acquisition software. We will be able to measure all types of beams from 10pA to 5mA (pulsed mode), and from 1nA to 5mA (CW mode) [17][18]. The complete series is underway. The new electronics has been validated.

LEBT and MEBT Emittance-meters developed by IPHC/Strasbourg are now fully operational.

BPM capacitive probes have been developed (IPN/Orsay and BARC/India) [19]. They are buried into the LINAC qpoles, allowing position, ToF measurement, and transverse beam tuning (±0.15mm resolution). One prototype was tested with success using the SARAF facility beam. Beam Extension Monitors (BEM) are under development for longitudinal tuning (IPNO and GANIL).

The survey of the beam intensity and the energy, is ensured by several ACCT/DCCT devices, and a ToF system installed at the exit of the Linac ([20][21]).

Several Faraday cups, developed by GANIL are already operational, the remaining ones being launched.

The BLM scintillator detectors associated with photo-multipliers are developed by IFIN-HH/Bucarest, and will be disposed along the Linac (1.5 m) and HEBT in order to deliver a “beam stop” signal in case of excessive beam losses. The BLM detector is now developed and tested with beam, and the final associated fast acquisition system ready (10µs) to be reviewed before fabrication.

AMPLIFIERS

Figure 8: First cabinets of solid state amplifiers being tested at GANIL on the variable VSWR test bench.

Recent RF system progress concerns the solid state amplifiers. First 2.5 kW, 5 kW, 10 kW and 19 kW units are being commissioned and fit the project requirement: 4% of reflected power, at any phase and at nominal output power (figure 8). The amplifiers are class AB, use in-phase combiners and show good operating symmetry and phase shift. They are equipped with BLF 578 transistors, each of them providing up to 700W continuous power.

The architecture is based on 5 kW water cooled racks (<25Kg), installed in a 750A-48V cabinet. It includes the combiners installed behind the racks and the drivers with fast protection digital controllers. A single main cabinet contains the control, fuses and a PLC for supervision.

COMMAND/CONTROL

The Spiral2 control system [22][23][24] is based on the Epics environment, and graphic user interfaces using CSS/BOY or home-programmed Java applications within a specific SPIRAL2 framework derived from OPEN-Xal. PLCs have in charge specific devices (ion source, RF, vacuum, cryogenic distribution…), and handle safety processes (beam interlocks, run permit system…).

During the Grenoble and Saclay beam tests, many C/C components and high level applications were successfully used, with the opportunity to validate most of the interfaces (power supplies, profilers, Faraday cups, emittance-meters…).We could also perform the beam alignment and optimization, and halo suppression.

Other developments are also in progress, like equipment description tools, relational database, archiving system, e-logbook, and specific interfaces with beam loss diagnostics and the Machine Protection System [25].

PHASE-1 BUILDING

Figure 9: View of the construction site (May 2012)

Figure 1 in the introduction indicates the positioning of phase-1 and phase-2 buildings with respect to the existing GANIL facility. The sufficient advancement of the phase-2 process and its building concept made it possible to define and start the construction of the accelerator-S3-NFS building as a first step of the entire project (Figure 9). The phase-1 building is positioned in such a way to allow a future Linac extension. The main steps and dates of the phase-1 construction are recorded below:

- Acceptation of the construction permit (October 2010)
- Beginning of excavation (January 2011)

Copyright © 2012 by the respective authors — cc Creative Commons Attribution 3.0 (CC BY 3.0)

- Geotechnical and geologic studies (May 2011)
- First concrete (September 2011)
- Installation of geodesic surface network (January 2012)
- Infrastructure equipments (tanks, insert) (March 2012)
- First paintings and resins of the low energy building block (July 2012).

INSTALLATION SCHEDULE

The schedule of the construction site is organised in such a way, that it is possible to install progressively the process inside the building, starting with the low energy beam lines (underground) and the corresponding power supply and utilities (superior floors), in parallel with other part of the building construction (HEBT for example).

On site, the process installation already started with the geodesic inserts. Using the outside geodesic network installed in 2011 and linked to the topometric network of the existing GANIL, land surveyors are now transferring the information underground (-9.5m) to prepare SPIRAL2 accelerator, NFS and S3 installations [26].

The installation of the accelerator parts will start during the last 2012 trimester with the various LEBTs. Then, the integration will continue as fast as the building construction, accelerator part deliveries and human resources permits. A great care is obviously taken to coactivity between the process and building teams. The injector beam commissioning, including the RFQ beam on the D-plate, should be made possible before the building final reception. Otherwise, the first deuteron Linac acceleration is linked to the safety authorisations and cannot happen before the first months of 2014. A strong work from the whole GANIL team is ongoing in order to provide beam to physics as soon as possible.

CONCLUSION

All the SPIRAL2 accelerator components are in a phase of technical tests and/or final construction. The progress of the accelerator building allows us to begin now the installation of the process, thanks to the work and motivation of all our partners.

AKNOWLEDGEMENT

The two authors thank all the colleagues who helped them to collect the information presented in this document.

REFERENCES

[1] The scientific objectives of the SPIRAL2 project. http://pro.ganil-spiral2.eu/spiral2/what-is-spiral2/physics-case/at_download/file

[2] R. Ferdinand and P. Bertrand, “Status and challenges of the SPIRAL2 facility”, LINAC2010, Tsukuba, Japan, September 2010.

[3] E. Petit, “progress of the SPIRAL2 project”, IPAC2011, San Sebastian, Spain, September 2011.

[4] C. Peaucelle et al., “First A/Q=3 Beams of Phoenix V2 on the heavy low energy beam transport line of SPIRAL2”, Ecris2010, Grenoble, France

[5] J.L. Biarrotte et al., “First beams produced by the SPIRAL2 injectors”, Linac 2010, Tsukuba, Japan.

[6] R. Gobin et al, “Development of a permanent magnet ECR source to produce a 5mA deuteron beam at CEA Saclay”, LINAC 2004, Lübeck, Germany.

[7] A. Caruso et al., “The LEBT chopper for the SPIRAL2 project”, IPAC2011, San Sebastian, Spain, September 2011.

[8] R. Ferdinand et al, “Spiral2 RFQ design”, EPAC 2004, Luzern, Switzerland, July 2004.

[9] M. Di Giacomo et al., “Design of the MEBT rebunchers for the SPIRAL2 driver”, LINAC08, Victoria, Canada, September 2008

[10] M. Di Giacomo, A. Caruso et al., “Measurement of the first prototype of the SPIRAL2 SBS selector”. IPAC2012, New Orleans, Mai 2012.

[11] P. Bosland et al. “Status of the low beta 0.07 cryomodules for SPIRAL2”, IPAC 2011, San Sebastian, Spain, September 2011.

[12] P.E. Bernaudin et al., “Status of the SPIRAL2 superconductiong linac”, IPAC 2010, Kyoto, Japan.

[13] G. Olry et al “SPIRAL2 Cryomodules: Status and First Tests Results”, SRF2009.

[14] Y. Gomez-Martinez et al., “Power Couplers for SPIRAL2”, SRF2011.

[15] S. Crispel et al., “Cryogenic system design for SPIRAL2 project at GANIL”, IPAC2010, Tokyo.

[16] L. Perrot et al., “HEBT lines for SPIRAL2 facility: What to do with the accelerated beams”, HB2010, Morschbach, Switzerland, October 2010.

[17] L.L. Vignet et al., “the beam profile monitors for SPIRAL2”, DIPAC2009, Basel, Switzerland.

[18] P. Ausset et al. “SPIRAL2 injector diagnostics”, DIPAC2009, Basel, Switzerland”.

[19] M. Abdillah et al. “Development of the beam position monitors for the SPIRAL2 Linac”, IBIC 2012, to be published.

[20] W. Lecoz et al., “SPIRAL2 Beam energy measurement”, DIPAC2011, Hamburg, Germany.

[21] Ch. Jamet et al. “Beam intensity and energy control on the SPIRAL2 facility”, this conference.

[22] E. Lecorché et al., “Overview of the SPIRAL2 control system progress”, ICALEPS1011, Grenoble, France, October 2011.

[23] P. Gillette et al., “SPIRAL2 control command: first high-level JAVA applications based on the IPEN-XAL library”, ICALEPS1011, Grenoble, France, October 2011.

[24] D. Touchard et al., “The SPIRAL2 radiofrequency command control”, ICALEPS1011, Grenoble, France, October 2011.

[25] M-H. Moscatello, “Machine protection system for the SPIRAL2 facility”, IPAC2012, New Orleans, USA, May 2012.

[26] R. Beunard et al. “Overview on the Preliminary Geodetic Network for SPIRAL2 Process Installation at GANIL”, IWAA2012, Batavia, USA, Sept. 2012.

Copyright © 2012 by the respective authors — cc Creative Commons Attribution 3.0 (CC BY 3.0)

DESIGN AND CONSTRUCTION OF THE LINAC4 ACCELERATING STRUCTURES

F. Gerigk, Y. Cuvet, A. Dallocchio, G. Favre, L. Gentini, J.M. Geisser, J.M. Giguet, S. Mathot
M. Polini, S. Ramberger, B. Riffaud, C. Rossi, P. Ugena Tirado, R. Wegner, M. Vretenar,
CERN, Geneva, Switzerland M. Naumenko, VNIITF, Snezhinsk, Russia
E. Kendjebulatov, Ya. Kryuchkov, A. Tribendis, BINP, Novosibirsk, Russia

Abstract

The Linac4 project at CERN is at an advanced state of construction. Prototypes and/or operational modules of the different types of accelerating structures (RFQ, buncher, DTL, CCDTL, and PIMS) have been built and are presently tested. This paper gives the status of the cavity production and reviews the RF and mechanical design of the various structure types. Furthermore the production experience and the first test results shall be presented.

INTRODUCTION

Linac4 [1] consists of four sections, which accelerate the beam up to its final energy of 160 MeV. The recently completed Radio Frequency Quadrupole (RFQ) [2] creates the 352.2 MHz bunch structure and raises the beam energy from 45 keV to 3 MeV. It is further accelerated by three Drift Tube Linac (DTL) tanks up to 50 MeV, followed by seven Cell-Coupled Drift Tube Linac (CCDTL) modules up to 103 MeV and 12 Pi-Mode Structures (PIMS) up to 160 MeV. Figure 1 shows a block diagram of Linac4 and the general parameters of each structure are summarized in Table 1.

Table 1: General Structure Parameters

Parameter	DTL	CCDTL	PIMS
f [MHz]	352.2	352.2	352.2
$E_{in/out}$ [MeV]	3-50.3	50.3-102.9	102.9-160
E_0T [MV/m]	2.65 - 2.95	3.6 - 2.7	3.74
ϕ_s [deg]	-35 → -24	-20	-20
ZT^2 [MΩ] †	44-52	40-33	24.6-26.2
av. Q_0 ‡	41000	42500	21600
P_{peak} [MW]	1.0/2.0/2.0	0.95-1.0	0.92-1.0
cav. length [m]	3.9/7.3/7.3	0.7-1.04	1.3-1.54
$N_{cavities}$	3	21	12
$N_{cav./module}$	n.a.	3	n.a.
$N_{gaps/cavity}$	39/42/30	3	7

† linac definition, operational value ‡ operational value

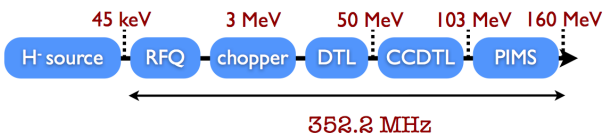

Figure 1: Linac4 block diagram.

The Linac4 accelerating structures are designed, constructed and tested under the supervision of the CERN RF group, supported by the CERN purchasing office, the vacuum group, the mechanical design office and by the CERN workshops for prototyping and qualification of construction procedures at the contractors. In general the prototyping and mechanical development was done at CERN and then exported for external construction. However, for certain critical construction processes – as outlined in the following – it was decided to "in-source" them.

All accelerating structures are designed for a maximum duty cycle of 10%, having in mind a future intensity upgrade of Linac4 as an injector to a high (average) power proton linac [3]. Linac4 itself will operate at a duty cycle of 0.04%, limited by the 1 Hz repetition rate of the PS Booster (PSB) into which the Linac4 beam is injected.

Due to LHC operational constraints the connection of Linac4 to the PSB is now foreseen to take place during the 2nd long LHC shutdown, which is expected for 2017/18 [1]. Commissioning with beam will take place in 2014/15 to leave sufficient time for improving reliability prior to operation in the LHC injection chain. The planning for the construction and commissioning of the accelerating structures has been adapted to this target date and is shown in Table 2.

Table 2: Key Dates for Linac4 RF Structures

date	status
10/12 - 11/13	RFQ, DTL, CCDTL assembly, tuning and testing
10/12 - 10/14	PIMS assembly, tuning and testing
09/13 - 04/14	DTL installation and commissioning
09/14	ready for 50 MeV protons
05/14 - 12/14	CCDTL commissioning
01/15 - 06/15	PIMS commissioning
07/15 - 12/15	160 MeV beam tests
01/16 - 11/16	reliability run
11/16	ready for 160 MeV H- operation
2017 - 2018	foreseen connection to PSB

RFQ

The RFQ is the only Linac4 accelerating structure which was completely constructed at CERN. Its design was elaborated in collaboration with CEA Saclay making use of experience with the IPHI RFQ [4]. In August 2012 the

Copyright © 2012 by the respective authors — cc Creative Commons Attribution 3.0 (CC BY 3.0)

Figure 2: Completed Linac4 RFQ in the 3 MeV test stand.

completed structure was delivered by the CERN workshops to the 3 MeV test stand, where presently the water stabilisation (precision $\pm 0.1^\circ$ C) is commissioned (see Fig. 2). Vacuum tightness was confirmed with a leak rate of 3×10^{-10} mbar l/s and the final RF tuning will be done in September/October. High-power tests will follow and the RFQ will see first beam before the end of the year. The RFQ construction history is given in Table 3 and more details can be found in [2].

Table 3: Timeline of RFQ: 5 Years from Concept to Construction

year	status
2007	1st conceptual design of the Linac4 RFQ
2008	beam dynamics, RF, and mechanical design ready
2008	order of 3D forged Cu
2009-12	construction at CERN
today	RFQ installed in Linac4 3 MeV test stand
end 2012	first beam in 3 MeV test stand

DTL

The Linac4 DTL consists of 3 tanks with permanent magnet quadrupoles (PMQ) and receives $\approx$ 5 MW of RF power from 3 klystrons. Preliminary design work started in 2004 and continued from 2006/7 at CERN with the development of a new drift tube alignment concept [5] tested on a proof-of-principle prototype. The mounting mechanism has since been filed as patent (see Table 4). Whereas in most DTLs the fine adjustment of the drift tubes is made after their installation, CERN chose a principle, which relies solely on the machining precision of tanks, girders and drift tubes. As a result no bellows are needed between stems and tanks, and vacuum leak tightness is achieved with a small metal gasket per stem. The principle was confirmed with a prototype built in collaboration with INFN Legnaro in 2008 [6]. The prototype allowed to confirm the drift tube alignment concept, to test post-coupler tuning procedures using an equivalent circuit model [7], and to make high power tests without and with PMQs in the first cell [8].

The series manufacturing takes place mostly in Spanish companies and was launched with the support of ESS-Bilbao. Heat treatment of the tanks to avoid deformations during final machining is done at CERN, as well as i) the Cu plating of the tanks, ii) the assembly of drift tubes by e-beam welding (EBW), and iii) the final assembly and tuning of the tanks. At present the drift tubes of the first tank segment are being installed after having successfully tested the segment for vacuum leaks (see Fig. 3).

Figure 3: First segment of the first DTL tank.

DTL: Lessons Learned

Materials: The use of stainless steel for the tanks proved very beneficial, since it is relatively easy to strip the Cu-plating and to repeat the plating process. This became necessary when the first plating attempt revealed some insufficiently covered areas in the tuner ports. Stripping the copper from mild steel surfaces attacks these surfaces to a degree that requires complete re-machining of all inner surfaces, as happened with a Linac4 DTL prototype that was made of mild steel. Thermal conductivity of stainless steel proved sufficient for the 10% design duty cycle, and the material could be procured at acceptable cost.

Tolerances: Relying on machining tolerances for the alignment of the drift tubes allows for the use of highly reliable metal gaskets at the drift tubes, eases the assembly, and makes it basically impossible to accidentally misalign drift tubes after their installation. However, this principle requires tight tolerances (20 μm range) on 2 m long pieces (girders and tanks). During the market survey and tendering exercise a lot of companies had to be disqualified because they either did not have milling machines for the required tolerances or the temperature controlled working conditions or the necessary experience to circumvent some of the shortcomings of their equipment. This led to many company visits and some prototyping effort in industry, which could probably have been reduced if the companies had clearly understood the required tolerances before making a bid. The advice is to prescribe the minimum machining equipment in the technical specification based on a survey of a number of capable companies.

Spring loaded metal gaskets: This kind of gasket is used in all Linac4 accelerating structures to seal the vac-

Copyright © 2012 by the respective authors — cc Creative Commons Attribution 3.0 (CC BY 3.0)

uum and to provide a good RF contact. Once they are installed correctly the experience so far is very good, but when using these gaskets one should consider a certain learning period until it is understood how to prepare the contact surfaces and until appropriate installation procedures have been established.

Table 4: Timeline of DTL: 9 Years for Development &Construction of Series (7 years for actual design)

year	status
2000	1st conceptual DTL design for new proton linac at CERN
2004	start of a collaboration with VNIIEF and ITEP in Russia for the design and construction of a Linac4 DTL tank
2005	2nd conceptual DTL design, decision to use PMQs
2006-7	start of mechanical design at CERN
2008	construction of DTL prototype in collaboration with INFN Legnaro
2009	successful high-power testing of the CERN/INFN prototype
2010	filing of patent on the "mounting mechanism" to position drift tubes
2008-11	purchase of 30 tons of raw material ($\approx$ 3000 pieces of stainless steel cylinders, Cu drift tubes/stems, Al girders, flanges, etc
2011	start of construction of tanks and drift tube parts in industry
2012	start of girder construction in industry
today	assembly of first tank segment at CERN
start 2013	first tank assembled
2013	assembly and tuning of tank 2,3, low-power testing of tank 1,2,3
2013-14	installation in Linac4 tunnel and high-power testing

CCDTL

Following the successful high-power tests [9] of a prototype built at CERN and a 2nd prototype built by the All-Russian Institute of Technical Physics (VNIITF) and the Budker Institute for Nuclear Physics (BINP) in Russia, it was decided to use a CCDTL for Linac4 for the intermediate energy range of 50 - 103 MeV. In 2009 a collaboration was launched with VNIITF (Snezhinsk) and BINP (Novosibirsk) for the design and construction of 7 CCDTL modules with 3 accelerating cavities and 2 coupling cells per module. The collaboration takes place within two contracts through the International Science and Technology Center (ISTC), which are jointly financed by CERN and the EU (via ISTC).

CERN provided a structure layout calculated with Superfish and BINP and VNIITF finalized the 3D electromagnetic and mechanical design of this section. In the beginning of 2010 46 tons of raw material were delivered to both institutes for the start of construction (see timeline in Table 5). The stainless steel for the tanks came in the form of pre-shaped half cells made by forging, which were then machined and Cu-plated at VNIITF. The needed technologies for i) cutting and welding of cooling channels, ii) surface finishing, iii) Cu plating were developed at VNIITF and then qualified via samples at CERN. BINP developed the technologies for i) brazing of drift tubes, ii) EBW of stems and drift tubes, and iii) alignment of drift tubes inside of the tank, which were also qualified by CERN experts during various technical visits. Finally in November 2011 a first completely assembled CCDTL module was successfully vacuum tested at BINP (see Fig. 4). In June 2012 another module was successfully aligned on its support, which is also constructed at BINP. The alignment goal was to have all beam pipe openings and drift tubes of a mounted module ($>$ 3 m long) within an envelope of $\pm$0.3 mm, which was achieved at the first attempt. The first two modules are presently on their way to CERN where they will be assembled by a BINP team and then high-power tested at the end of summer/beginning of autumn 2012.

Figure 4: CCDTL module during vacuum test at BINP, Novosibirsk.

CCDTL: Lessons Learned

Project set-up: The complete design and construction process was very efficiently managed by BINP. Having a single partner who takes care of a complete cavity construction removes a lot of problems, which arise when different industries or collaboration partners are involved. In case of the Linac4 DTL for instance CERN has to guarantee that all the interfaces between the different contributions from industry (e.g. tanks, giders, drift tubes) are correctly executed and actually fit together. This involves a very time-consuming quality control at all the different industrial partners, whereas in the case of the CCDTL all interface questions are automatically handled by the single partner. Here, CERN only intervened to make sure that all construction processes (Cu-plating, welding, brazing)

Copyright © 2012 by the respective authors — cc Creative Commons Attribution 3.0 (CC BY 3.0)

Table 5: Timeline of CCDTL: 12 years for Development & Construction of Series

year	status
1994	first CCDTL concept at LANL [10]
2000	Conceptual CCDTL design for new proton linac at CERN [11]
2001	13-cell cold model in aluminum
2004-5	design/construction of CERN prototype: 2 full size half tanks + coupling cell
2006	successful high-power testing of CERN prototype
2006	construction of prototype with 2 complete tanks + coupling cell in Russia (BINP/VNIITF)
2007	successful high-power testing of ISTC prototype at CERN
2009	start of ISTC contracts # 3888, # 3889 to construct 7 CCDTL modules for Linac4
1/2010	shipping of 46 tons of raw material (in ≈ 1500 pieces) to Russia
11/2011	successful vacuum and low-power tests of first complete module at BINP
today	delivery of first 2 modules to CERN
10/2012	assembly and high-power tests of first 2 modules
3/2013	delivery of last modules to CERN

are qualified according to CERN standards and the Russian partners solved autonomously all interface problems.

Raw materials: All raw materials were bought and delivered by CERN, which automatically ensured that they conform to CERN specifications. Special care was taken to have 3D forged stainless steel to reduce the risk of having inclusions or interior volumes, which might give problems during Cu-plating or on surfaces, where spring-loaded metal gasket are used. Nevertheless, in one instance we found a small void on a surface, which carries a gasket. Fortunately it is not located directly under the gasket and does not result in a leak.

Spring loaded metal gaskets: same comment as for DTL above.

Shipping: So far shipping and customs procedures between CERN and Russia went very smoothly due to the combined efforts of ISTC, BINP, and CERN logistics.

PIMS

The decision to use a 7-cell Pi-Mode Structure (PIMS) instead of a Side-Coupled Linac (SCL) was taken only in 2007 (see Table 6). The main arguments were that firstly a PIMS can be used at 352.2 MHz – the same frequency as the other RF structures – whereas a SCL would have required a 2nd RF system with 704.4 MHz for only a very short section of Linac4. Secondly the structure design is simpler and relatively easy to tune, reducing the overall manpower effort for the Linac4 accelerating structures and making the design more robust. The PIMS is constructed within a collaboration involving the National Centre for Nuclear Research (NCBJ) in Swierk/Poland, Forschungszentrum Jülich (FZJ) in Jülich/Germany and CERN. NCBJ is responsible for machining of all parts and the brazing of i) circular flanges to the tuner ports/RF pick-up ports and of ii) a rectangular flange to the central ring to connect the RF waveguide coupler. The ports for tuners and RF pick-ups are electron-beam welded to the cavity rings by FZJ and finally the discs and cylinders are transported to CERN. There the structure will be clamped and tuned via machining of the tuning islands (1st tuning step). In the last assembly step the rings and discs are electron-beam welded at CERN and then the fixed tuners (one per cell) are cut to their final length in the 2nd tuning step.

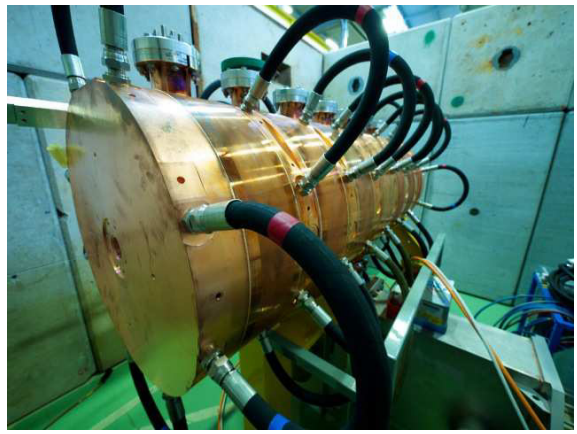

Figure 5: PIMS prototype in test bunker.

The mechanical design was made at CERN and tested with a prototype, which was built in the CERN workshops (see Fig. 5). After successful high-power tests [12] the design was exported to the collaboration partners to start the series construction. At present most production processes (machining, welding, brazing) have been qualified by CERN and roughly half of the discs and rings are in a rough-machined state. We expect to receive and assemble the parts for the first cavity shortly and the final pieces are foreseen to be delivered to CERN in spring 2014.

PIMS: Lessons Learned

Prototyping: An experience that was not only made with the PIMS but also with the other Linac4 structures is that one needs to plan for two prototypes: a first proof-of-principle "in-house" prototype plus a second one (or pre-series) with the contractor for the series. Having constructed a successful prototype does not necessarily mean that a contractor can use exactly the same processes, which have been developed for the "in-house" construction. They have to be adapted to the manufacturers equipment and capabilities and furthermore the machine operators have to be trained for the specific requirements of the project. The only way out is to develop from the beginning a prototype

Copyright © 2012 by the respective authors — cc Creative Commons Attribution 3.0 (CC BY 3.0)

Table 6: Timeline of PIMS: 7 Years from Concept to Final Delivery

year	status
1977	5-cell pi-mode structure used in PEP storage ring (el.) at SLAC (353.2 MHz)
1989	5-cell PIMS used in LEP (el.) at CERN (352.2 MHz)
2007	Decision to use PIMS (352.2 MHz) instead of Side-coupled linac (704.4 MHz) between 100 and 160 MeV in Linac4 for proton acceleration
2007	tendering for 3D forged OFE copper
2007-8	construction and measurements on scaled aluminum cold model
2008	order of 26 tons of 3D forged OFE copper (last piece delivered: 11/2011)
2009-10	design and construction of full size 7-cell PIMS prototype at CERN
2010	successful high-power testing at CERN and decision to use prototype as PIMS-1 in Linac4
11/2010	collaboration start with NCBJ (National Centre for Nucl. Research, Poland) and FZJ (Forschungszentrum Jülich, Germany) for the construction of 12 PIMS cavities
1/2011	1st shipment of altogether 31 tons of raw material (in ≈1500 pieces)
today	most machining and welding procedures are qualified, half of the discs and rings are rough-machined
10/2012	delivery of first series cavity to CERN, assembly (EBW) and tuning at CERN
2013	start of high-power testing of PIMS cavities
3/2014	delivery of last PIMS cavity pieces to CERN

together with the contractor for the series, which is forbidden by the CERN tendering rules.

Tolerances: After having developed a mechanical design (for the PIMS it took rougly one year), one should plan for sufficient time to work on relaxing the tolerances and simplifying the assembly procedures. In the case of the PIMS we immediately went into prototyping when the design was ready. Spending some extra months of design effort in reducing the tolerances before going into prototyping can drastically reduce the technological development and qualification period and also has the potential to reduce the manufacturing cost.

Raw material: For the construction of the PIMS we used 3D forged OFE copper, which is i) difficult to find on the market in the required size and quantity, ii) expensive, iii) and which requires long delivery times (3.5 years from ordering until receiving the last pieces at CERN). The advantages are: i) significantly improved results (less cavity formation in the welds, less deformation) for EBW [13, 14], which conform to ISO 13919-2 level B, ii) less deformation during machining, which is especially important for large pieces, iii) guaranteed yield strength of $R_p > 200$ MPa, which in case of the PIMS is needed to avoid plastic deformation through heating during high duty cycle operation. For Linac4 the material was ordered in time but the price did exceed the originally allocated budget. In general one should carefully assess the risk, which is taken with cheaper material, the requirements for the specific cavities (e.g. in terms of yield strength), and the cost and delivery delay for 3D forging.

OUTLOOK

After long years of design work, material procurement, setting up of contracts and collaborations, qualification of construction processes we are now receiving the first cavities and parts of the series. It is a pleasure to see the equipment coming in and everyone is looking forward to the assembly and testing period.

REFERENCES

[1] M. Vretenar et al., "Progress in the construction of Linac4 at CERN", LINAC12, Tel Aviv.

[2] C. Rossi et al., "Assembly and RF tuning of the Linac4 RFQ at CERN", LINAC12, Tel Aviv.

[3] F. Gerigk et al.,"Layout and machine optimisation for the SPL at CERN"

[4] P-Y. Beauvais, "Recent evolutions in the design of the French High Intensity Proton Injector (IPHI)", EPAC04, Lucerne.

[5] S. Ramberger, et al., "Drift tube linac design and prototyping for the CERN Linac4", LINAC08, Victoria.

[6] S. Ramberger, et al., "Production design of the drift tube linac for the CERN Linac4", LINAC10, Tsukuba.

[7] F. Grespan, G. De Michele, S. Ramberger, M. Vretenar, "An equivalent circuit for post coupler stabilization in a drift tube linac", LINAC10, Tsukuba.

[8] G. De Michele, S. Ramberger, J.M. Giguet, J. Marques-Balula, "The Linac4 DTL Prototype: Low and High Power Measurements", CERN-ATS-Note-2012-003 TECH.

[9] M. Pasini, M. Vretenar, R. Wegner, "CCDTL prototypes: test results", CARE-Report-2007-036-HIPPI.

[10] J.H. Billen, F.L. Krawczyk, R.L. Wood, L.M. Young, "A new RF structure for Intermediate Velocity Particles", LINAC94, Tsukuba.

[11] F. Gerigk, M. Vretenar, "Design of the 120 MeV Drift Tube Linac for the SPL", CERN-Nufact-Note 37.

[12] F. Gerigk, J.M. Giguet, P. Ugena Tirado, R. Wegner, "High power test for the first PIMS cavity for Linac4", IPAC11, San Sebastian.

[13] G. Favre et al., "Manufacturing the LINAC4 PI-Mode Structure at CERN", IPAC11, San Sebastian.

[14] F. Gerigk et al., "The hot prototype of the PI-Mode Structure for Linac4", LINAC10, Tsukuba.

Copyright © 2012 by the respective authors — cc Creative Commons Attribution 3.0 (CC BY 3.0)

COMPUTATIONAL MODEL ANALYSIS FOR EXPERIMENTAL OBSERVATION OF OPTICAL CURRENT NOISE SUPPRESSION BELOW THE SHOT-NOISE LIMIT

A. Nause, E. Gover, Tel Aviv University, Israel

Abstract

In this paper we present simulation analysis of experimental results which demonstrate noise suppression in the optical regime, for a relativistic e-beam, below the classical shot-noise limit. Shot-noise is a noise resulting from the granular nature of the space-charge in an e-beam. It is linear to the beam current due to its Poissonic distribution in the emission process. Plasma oscillations driven by collective Coulomb interaction during beam drift between the electrons of a cold intense beam are the source of the effect of current noise suppression. The effect was experimentally demonstrated [1] by measuring Optical Transition Radiation (OTR) power per unit e-beam pulse charge. The interpretation of these results is that the beam charge homogenizes due to the collective interaction (sub-Poissonian distribution) and therefore the spontaneous radiation emission from such a beam would also be suppressed (Dicke's subradiance [2]). Analysis of the experimental results using GPT simulations will demonstrate the suppression effect. For the simulation results we used a full 3D GPT model of the ATF section in which the experiment took place at.

INTRODUCTION

Shot-noise is a noise resulting from the granular nature of the space-charge in an e-beam. The discreteness of the particles and the randomness of electrons emission from the cathode causes time dependent fluctuations of the charge and current density at any cross section along the beam transport line. This noise was first reported in 1918 by Schottky who made experiments in vacuum tubes.

Noise is best characterized in terms of the Fourier transform of the time-varying fluctuations in electric current, namely, by its spectral density. Gover and Dyunin showed in a 1D model [3] that it is possible to observe and control optical frequency energy and current (shot noise) fluctuations in a dense relativistic charged particles beam. GPT simulations were used to demonstrate this effect for a real-like beam starting from Shot-noise [4]. Moreover, at certain conditions, when the dominant noise in the beam is current shot noise (density fluctuations), it is possible to reduce significantly the beam noise by virtue of a collective interaction process along an interaction length corresponding to a quarter period longitudinal plasma oscillation in the beam. This means that the charge distribution in the beam can be homogenized in this process.

First experimental observation of this phenomenon using OTR from a metallic foil was presented last year [1]. Noise suppression using a dispersive section (dog-leg bend) was demonstrated in SLAC [5]. TR is proportional to the current-noise amplitude [6], and therefore can be used in order to estimate the suppression in the current noise. In this paper we press analysis of the experimental results and demonstrate this effect using full 3D GPT simulations that were carried out for this purpose.

1D Model of Noise Dynamics in Charged Electron Beams

In electron-beam transport under appreciable space-charge conditions, the microdynamic noise evolution process may be viewed as the stochastic oscillations of Langmuir plasma waves [3]. In the linear regime, the evolution of longitudinal current and velocity modulations of a beam of average current I_b, velocity βc and energy $E = (\gamma - 1)mc^2$, can be described in the laboratory frame by [7]:

$$\frac{d}{d\phi_p}\breve{i}(z,\omega) = -\frac{i}{W(z)\breve{v}(z,\omega)} \quad (1)$$

$$\frac{d}{d\phi_p}\breve{v}(z,\omega) = -iW(z)\breve{i}(z,\omega) \quad (2)$$

where $\breve{i}(\omega) = \breve{I}(\omega)e^{i\omega z/\beta c}$, $\breve{v}(\omega) = \breve{V}(\omega)e^{i\omega z/\beta c}$. $\breve{I}(\omega)$, $\breve{V}(\omega)$ are the respective Fourier components of the beam current and kinetic-voltage modulations. The kinetic-voltage modulation is related to energy and longitudinal velocity modulations: $\breve{V}(\omega) = -(mc^2/e)\breve{\gamma} = -(mc^2/e)\gamma^3\beta\breve{\beta}$, $\phi_p(z) = \int_0^z \theta_{pr}(z')dz'$ is the accumulated plasma phase, $W(z) = r_p^2/(\omega A_e \theta_{pr}\epsilon_0)$ is the beam wave-impedance. A_e is the effective beam cross-section area, $\theta_{pr} = r_p\omega_{pl}/\beta c$ is the plasma wavenumber of the Langmuir mode, $r_p < 1$ is the plasma reduction factor, $\omega_{pl} = \omega_{po}/\gamma^{3/2}$ is the longitudinal plasma frequency in the laboratory frame. The single-frequency Langmuir plasma wave model expressions [3] can be solved straightforwardly in the case of uniform drift transport. After employing an averaging process, this results in a simple expression for the spectral parameters of stochastic current and velocity fluctuations (noise) in the beam assuming that they are initially uncorrelated[]:

$$\breve{i}(L,\omega) = \cos\phi_p(L)\breve{i}(0,\omega) + (\sin\phi_p(L)/W_d)\breve{v}(0,\omega) \quad (3)$$

where $\phi_p = \theta_{pr}z$, $\theta_{pr} = r_p\frac{\omega_p'}{v_0}$, $\omega_p' = (\frac{e^2 n_0}{m\epsilon_0\gamma^3})$, $W_d = \sqrt{\mu_0/\epsilon_0}/k\theta_{pr}A_e$.

The beam current noise evolution is affected by the initial axial velocity noise through the parameter

$$N^2 = \overline{|\breve{v}(0,\omega)|^2}/W^2\overline{|\breve{i}(0,\omega)|^2} = (\omega/c\beta k_D)^2 \quad (4)$$

Copyright © 2012 by the respective authors — cc Creative Commons Attribution 3.0 (CC BY 3.0)

where $k_D = \omega_{pl}/c\sigma_\beta$ is the Debye wavenumber and $c\sigma_\beta$ is the axial velocity spread. Equation (4) suggests that current noise suppression is possible if the beam is initially cold $N^2 < 1$, and if plasma phase accumulation of $\phi_p(L) \sim \pi/2$ is feasible.

NOISE SUPPRESSION EXPERIMENT

The noise suppression demonstration experiment was conducted on the 70 MeV RF-LINAC of ATF/BNL (figure 1). The OTR measurements were carried out at a fixed point (CTR-1) 6.5 m away from the LINAC exit. Keeping the beam spot sizes on viewer YAG4 wide in all experiments made it possible to measure similar OTR image patterns on the CCD screen in all experiments (see figure 3). The measured signal S_{OTR} was the integrated charge accumulated in all of the pixels of a CCD (charge-coupled device) camera exposed to the OTR emission on the incidence of single electron-beam pulse on the screen. The measured data of $S_{OTR} = Q_b$ in CTR-0 and CTR-1 are shown in figure 2 as a function of the varied bunch charge Q_b in the range 200 to 500 pC. The pulse duration in all experiments remained approximately the same (5 pS) corresponding to an average current of 40 to 100A (figure 4). In a shot-noise-dominated beam, in the absence of collective microdynamics, the current noise and consequently S_{OTR} are proportional to I_b. Our measured data of $S_{OTR} = Q_b$ in CTR-0 lie approximately on a horizontal line, confirming the absence of collective microbunching and current-velocity noise correlation or noise suppression before this point. On the other hand, the data measured on CTR-1 exhibit a systematic drop as a function of charge (200 to 500 pC) for all beam energies (50 to 70 MeV). As the measurement conditions at the two measurement positions and at different beam energies could not be made identical, the absolute suppression level between the two points could not be determined. However, the normalized data of all measurements of noise per unit charge depicted in figure 2 show the scaling with charge for all beam energies. This demonstrates attainment of 20 to 30% relative noise suppression, and confirms the predicted effect of collective microdynamic noise suppression process in the drift section.

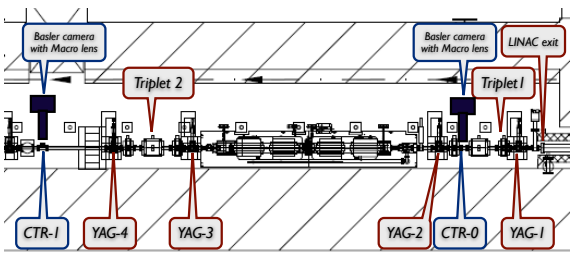

Figure 1: The ATF electron-beam transport set-up is shown from the injector RF-LINAC exit to the OTR viewer site (CTR-1).

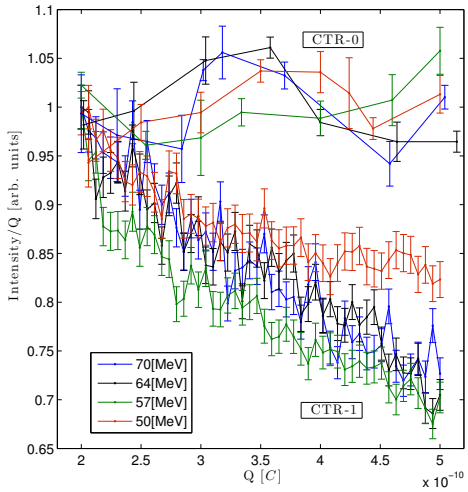

Figure 2: Integrated OTR intensity measurement signals divided by the electron pulse charge. The CTR-1 data correspond to OTR measurement from a screen, intercepting the electron beam 6.5m away from the LINAC exit. The curve's negative slope indicates relative current shot-noise suppression of 20-30% as the beam charge varies from 0.2 to 0.5 nC at different beam energies (50-70 MeV). The CTR-0 data correspond to OTR measurement right after the LINAC exit. Used for reference, its horizontal slope (linear scaling of S_{OTR} with beam charge) indicates that there was no charge suppression before the collective microdynamic process in the subsequent drift section. The error of the camera integrated signal measurement, 3%, was determined from the variance in the value of the signal due to pulse-to-pulse variation, measured repeatedly while keeping all beam control parameters fixed. The charge measurement error is 1%.

COMPUTATIONAL MODEL OF COLLECTIVE MICRODYNAMICS IN VARYING CROSS-SECTION BEAM TRANSPORT

At the exit of the Linac, the beam is current-noise dominated, and $N^2 \ll 1$. However, due to finite emittance, the axial velocity spread becomes significant as the beam is focused and consequently N^2 (Eq (4)) is no longer negligible. Furthermore, at tight focusing the uniform beam expression (Eq. (3)) cannot be used and in order to calculate the noise suppression, one should solve differential equations for variable beam parameters. In this section we show through a model case computational solution of equations (1) and (2), that the axially varying beam cross section and the excess axial velocity spread due to angular spread can account for a substantial moderation of the noise suppression effect that was realized in the experiment. This example also explains some parameter scaling features of the measurement data.

We turn the generic coupled current and ripple voltage

Copyright © 2012 by the respective authors — cc Creative Commons Attribution 3.0 (CC BY 3.0)

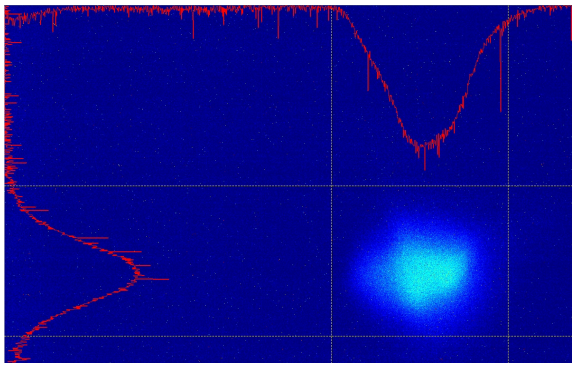

Figure 3: OTR image and axis intensity profiles. Photographed from CTR-1 with a macro lens of 1:1 magnification.

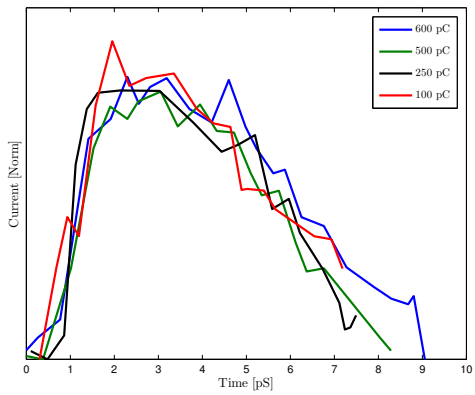

Figure 4: Temporal pulse profile of the e-beam bunch at different bunch charge levels. Pulse duration was approximately 5 pS for all experiments.

equations (1) and (2) into explicit equations in z by substituting $\frac{d}{d\phi_p} = \left(\frac{d\phi_p}{dz}\right)^{-1}\frac{d}{dz} = \frac{1}{\phi_{pr}(z)}\frac{d}{dz}$ and $W(z) = r_p^2/\omega\epsilon_0 A_e(z)\theta_p(z)$:

$$\frac{d}{dz}\breve{i}(z,\omega) = -i\omega\epsilon_0 A_e(z)\theta_p^2(z)\breve{v}(z,\omega) \tag{5}$$

$$\frac{d}{dz}\breve{v}(z,\omega) = -\frac{ir_p^2}{\omega\epsilon_0 A_e(z)}\breve{i}(z,\omega) \tag{6}$$

where $\theta_p^2(z) = eZ_0 I_0/mc^2 A_e(z)\gamma_0^3\beta_0^3$.

This set of equations can be solved explicitly numerically if $A_e(z) = 2\pi\sigma_x(z)\sigma_y(z)$ is given, and the initial conditions $\breve{i}(0,\omega), \breve{v}(0,\omega)$ are specified, and the solution at the end of the drift section L is a linear combination of the initial conditions: $\breve{i}(L,\omega) = A(L)\breve{i}(0,\omega) + B(L)\breve{v}(0,\omega)$. Assuming that the current modulation noise and the focusing enhanced velocity noise are uncorrelated at $z = 0$, we set

$$\overline{|\breve{i}(L,\omega)|^2} = |A(L)|^2\overline{|\breve{i}(0,\omega)|^2} + |B(L)|^2\overline{|\breve{v}(0,\omega)|^2} \tag{7}$$

$$\overline{|\breve{i}(0,\omega)|^2} = eI_b \tag{8}$$

$$\overline{|\breve{v}(L,\omega)|^2} = \left(\frac{mc^2}{e}\gamma_0\beta_0\right)^2\frac{e}{I_0}\sigma_{\beta z}^2 \tag{9}$$

To compute the noise evolution for the parameters of the reported experiment it is necessary to estimate the cross section dimensions $\sigma_x(z), \sigma_y(z)$ along the interaction length. This was done based on the measurements on screens YAG-1 to YAG-4, the recorded quad excitation parameters, and performing full 3-D simulation (with space-charge) using GPT.

The beam axial velocity spread due to energy spread ($\Delta E \simeq 3KeV$) is small, and its effect on the initial velocity noise is negligible. We assume that the initial velocity noise is determined by the standard deviation of the axial velocity spread (equation (9)), which was calculated for each quad setting from the angular spread standard deviations due to the focusing and emittance ($\epsilon_x, \epsilon_y \sim 2-5\mu m$):

$$\sigma_{\beta z} = \frac{1}{4}(\sigma_{\beta x}^2 + \sigma_{\beta y}^2) \tag{10}$$

The coefficients $A(z = L), B(z = L)$ were computed by

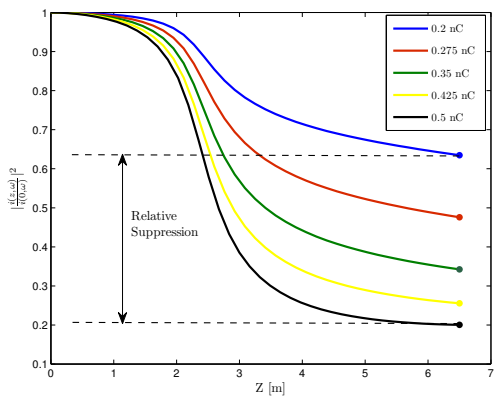

Figure 5: Noise suppression along the collective interaction region as calculated from solution of the coupled differential equations with $\sigma_x(z)$, $\sigma_y(z)$ of 70 MeV.

iterative integration of the coupled linear differential equations (5 and 6) with the initial conditions ((9)). In Figures 5 and 6 we display the results of the model computation of the variable parameters differential equations. The curves show the noise suppression as function of length and of the beam current for the two extreme energy cases E=50 MeV, 70 MeV. The relative suppression factor in the range Q_b=0.2-0.5nC at the drift section exit $L = 6.5m$ is displayed in Fig.() for the two beam-energy examples. Figure 7 can only be regarded as a model explanation for the reduced relative noise suppression effect observed in the experiment. As mentioned, there can be additional factors

Copyright © 2012 by the respective authors — cc Creative Commons Attribution 3.0 (CC BY 3.0)

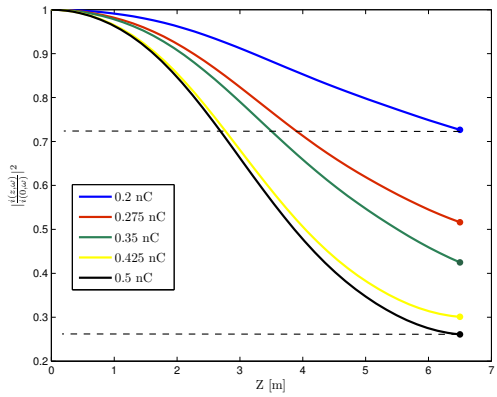

Figure 6: Noise suppression along the collective interaction region as calculated from solution of the coupled differential equations with $\sigma_x(z)$, $\sigma_y(z)$ of 50 MeV.

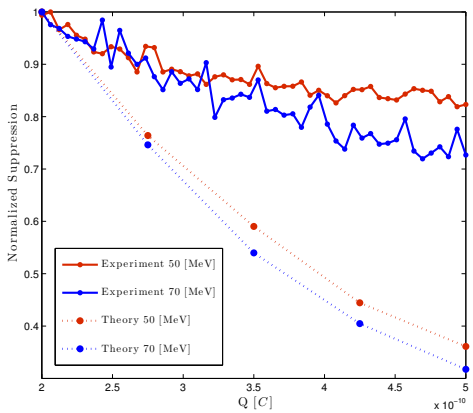

Figure 7: Relative noise suppression rate computed from Eq. 5 and 6 for E=50 MeV, 70 MeV compared to the experimental suppression results.

affecting the suppression rate. It is noted that the computed curves display significantly larger relative suppression in the range Q_b=0.2-0.5nC than the experimental curves, but in either case there is only little dependence on the acceleration energy. In the simple uniform beam model one would expect dependence of the noise suppression factor on the beam energy due to the $3/2$ power dependence of the plasma frequency on γ, which corresponds to smaller plasma phase accumulation at higher beam energy. However, the beam envelope had to be varied in the experiment in different beam energies, and one must keep in mind, that at the higher energy the beam focuses into a tighter waist due to the reduced space charge effect. This tends then to increase the plasma frequency at the waist, where most of the microdynamic process takes place.

This observation is consistent with the point of view that the beam envelope expansion and the beam charge homogenization process are in essence the same process of excess charge beam expansion when viewed in the beam rest frame (independent of the acceleration energy). This is consistent with the plasma phase accumulation theorem of constant plasma phase accumulation in a space charge dominated beam waist [3]. This provides qualitative physical explanation for the weak dependence of the relative noise suppression on the beam energy in the 50-70 MeV range, as depicted in both the experimental (figure 2) and model calculation (figure 7) curves.

REFERENCES

[1] A. Gover, A. Nause, E. Dyunin, Beating the shot-noise limit, Nature Physics, doi:10.1038/nphys2443.

[2] Dicke, R. H., "Coherence in Spontaneous Radiation Processes", Phys. Rev. 93 99–110 (1954).

[3] A. Gover, E. Dyunin, Collective-Interaction Control and Reduction of Optical Frequency Shot Noise in Charged-Particle Beams, Phys. Rev. Lett. 102, 15 (2009).

[4] A. Nause, E. Dyunin, "Optical frequency shot-noise suppression in electron beams: Three-dimensional analysis", Journal of App. Phys. 107, 103101 (2010).

[5] D. Ratner et el, "Observation of Shot Noise Suppression at Optical Wavelengths in a Relativistic Electron Beam", Phys. Rev Lett. 109, 3 (2012).

[6] Loos, H. and et al, "Observation of coherent optical transition radiation in the LCLS linac", Proceedings of the 2008 Free-Electron Laser Conference (Gyeongju, Korea).

[7] A. Gover, T. Duchovni, E. Dyunin, A.Nause, "Collective microdynamics and noise suppression in dispersive electron beam transport", Physics of Plasmas 18 123102, (2011).

Copyright © 2012 by the respective authors — cc Creative Commons Attribution 3.0 (CC BY 3.0)

STATUS OF ILC

A. Yamamoto*, High Energy Accelerator Research Organization (KEK), Tsukuba, Japan,
M. Ross*, SLAC National Accelerator Laboratory, Menlo Park, CA, USA
N. Walker*, DESY, Hamburg, Germany
* Project Managers of ILC Global Design Effort

Abstract

The International Linear Collider (ILC) is anticipated to be the next energy-frontier electron-positron accelerator based on superconducting radio-frequency (SCRF) technology, and to accelerate electron and positron beams up to 250 GeV each with having extend-ability up to 500 GeV each. This paper describes the progress of the technical design and R&D efforts progressed in the ILC Technical Design phase since 2007 and includes further effort after the completion of Technical Design Report (TDR) in 2012.

INTRODUCTION

The International Linear Collider (ILC) is proposed as the next energy-frontier electron-positron accelerator to be built with a global effort [1 - 3]. The ILC accelerator is based on SCRF accelerator technology, as recommended by the International Technology Recommendation Panel [4] and endorsed by the International Committee for Future Accelerators. The ILC Global Design Effort (ILC-GDE) was launched to advance the accelerator design and R&D efforts. It published the Reference Design Report (RDR) in 2007 [2]. The ILC design assumes an averaged cavity field gradient of 31.5 MV/m to achieve a center-of-mass energy of 500 (=2 x 250) GeV with two 11-km long main linacs. The technical design work and R&D efforts have significantly progressed during the Technical Design (TD) phase started in 2007 and are completed with the Technical Design Report (TDR) in 2012.

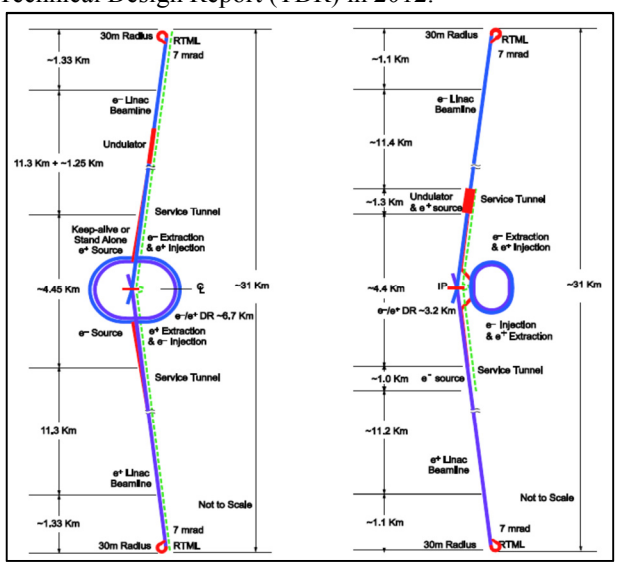

Figure 1: Layouts of ILC in RDR (left) and TDR (right).

A major update of the accelerator design has been made for TDR, seeking for the best cost-effective design with a 'cost-containment' guideline [5]. Figure 1 shows the TDR accelerator layout with the RDR accelerator layout, and Table 1 summarizes the main parameters.

Table 1: ILC accelerator and SCRF requirement.

Parameter	RDR	TDR
Energy (cms: GeV)	500	500
L ($cm^{-2}s^{-1}$)	2 x 10^{34}	1.5 x 10^{34}
Beam current (mA)	9	5.8
Beam Rep. (Hz)	5	5
Bunch spacing (ns)	369	554
Bunch train length (μs)	1.000	0.727
Numbers of bunches	2625	1312
Cav. Grad. (MV/m)	31.5	31.5
# 1.3-GHz, 9-cell cavity	15,941	16,024
# 1.3-GHz, Cryomodule	1,824	1,855
# 10-MW Klystron	646	413+α / 378+β (KCS/DKS)

GENERAL DESIGN UPDATES

The ILC accelerator design has been updated in the middle of the Technical Design Phase [5]. It has been motivated by i) overall cost containment and balancing among sub-system, ii) improved understanding of system functionality, iii) more complete and robust design, and iv) re-optimized R&D plans. The major design update includes:

- A Main Linac length consistent with an *average* accelerating gradient of 31.5 MV/m with a spread within +/-20%, and maximum operational beam energy of 250 GeV,
- A single-tunnel solution for the Main Linac and RTML, with two possible variants for the High-Level RF (HLRF) configuration:
  - Klystron cluster scheme (KCS):
  - Distributed Klystron scheme (DKS).
- Undulator-based positron source located at the end of the electron Main Linac (250 GeV),
- A lower beam-power parameter set with the number of bunches per pulse reduced by a factor of two,
- Reduced circumference Damping Rings (~3.2 km) at 5 GeV with a 6 mm bunch length,

Copyright © 2012 by the respective authors — cc Creative Commons Attribution 3.0 (CC BY 3.0)

- Integration of the positron and electron sources into a common "central region beam tunnel", together with the Beam Delivery System, resulting in an overall simplification of civil construction in the central region.

R&D PLAN AND PROGRESS

In the Technical Design phase, four critical main linac R&D topics were identified and have been pursued as follows [3,5, 6]:

- **S0:** SCRF cavities to exceed a gradient of 35 MV/m in individual performance test in vertical position,
- **S1:** Cavity-string in cryomodule to perform at 31.5 MV/m on average.
- **S2:** Cryomodule-string to perform with beam acceleration, including associated systems such as HLRF, LLRF, cryogenics, and beam diagnostics.
- **Industrialization:** Study and preparation for cost-effective production of SCRF accelerator components.

The notation of *S0, S1, and S2* refers to the shorthand for the individual goals introduced in the RDR period. Figure 2 shows the general SCRF R&D plan in the TD phase together with the foreseen development.

Year	07	2008	2009	2010	2011	2012
Phase	TDP-1			TDP-2		
Cavity Gradient in test to reach 35 MV/m	→ Yield 50%			→ Yield 90%		
Cavity-string to reach 31.5 MV/m, with one-cryomodule		Global effort for string assembly and test (DESY, FNAL, INFN, KEK)				
System Test with beam acceleration			FLASH (DESY) , NML/ASTA (FNAL) QB, STF2 (KEK)			
Preparation for Industrialization				Production Technology R&D		
Communication with industry:	1st Visit Vendors (2009), Organize Workshop (2010) 2nd visit and communication, Organize 2nd workshop (2011) 3rd communication and study contracted with selected vendors (2011-2012)					

Figure 2 : The main goals and timeline for SCRF R&D established at the beginning of the TD phase.

The highlighted results from the SCRF R&D are summarized as follows:

- Successful construction and functioning of SCRF facilities at FLASH at DESY [7], FNAL-ANL [8-10, JLab [11], and KEK [12].
- Identification of the preferred process for consistent production of 35 MV/m cavities (worldwide), and ultimately a successful demonstration of the TDP goal of a *production yield* of 90% [13].
- Encouragement of new cavity vendor participation, in cooperation with laboratories, for qualification in the Americas and Asia, to complement those already existing in Europe, so as to scope global mass production for the ILC.
- International collaboration on the construction of a cryomodule (S1-Global) hosted at KEK, enabling exploration of plug-compatible design philosophies and comparisons of technologies [14]. Construction and testing of cryomodules with beam acceleration, such as FLASH at DESY, ASTA/NML at Fermilab, and STF at KEK.
- Study of SCRF mass-production, including R&D for cost-effective industrialization.
- Associated system R&D such as HLRF/LLRF, cryomodule including quadrupoles and beam position monitor, and cryogenics.

Worldwide activities addressing these goals may be recognized with the progress of cavity and cryomodule developments and the facilities extended at DESY, FNAL and KEK as shown in Fig. 3: (a) TTF-FLASH at DESY, (b) STF/S1-Global at KEK, and (c) NML/ASTA at Fermilab. The cryomodule activity at KEK stands out in its truly global nature of cryomodule assembly.

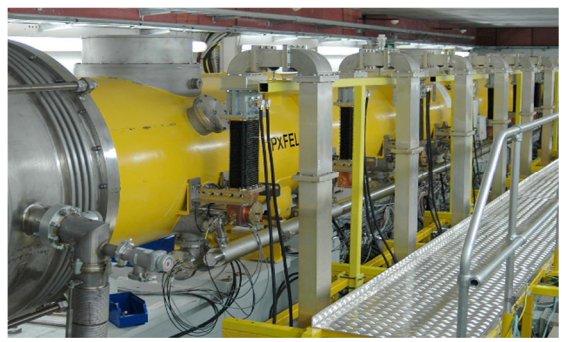

(a)

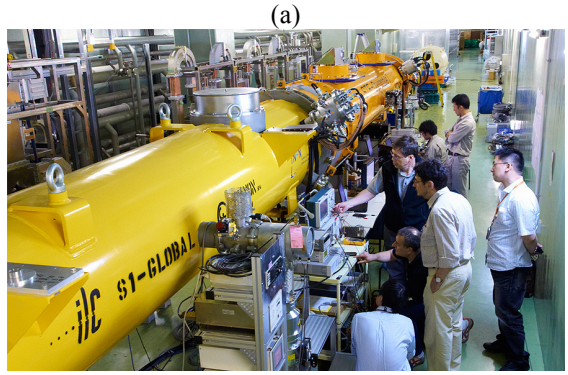

(b)

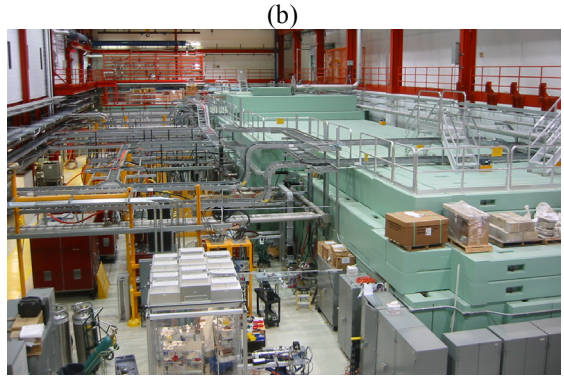

(c)

Figure 3: Photos of SCRF and accelerator beam test facilities progressed at (a) FLASH at DESY, (b) STF/S1-Global at KEK, and (c) NML/ASTA at Fermilab.

Copyright © 2012 by the respective authors — cc Creative Commons Attribution 3.0 (CC BY 3.0)

PROGRESS IN SUBSYSTEM

The progress in each subject is summarized as follows.

Cavity (S0)

- Establishment of the baseline sequence of cavity fabrication and surface preparation, based on the TESLA cavity design, and development a production yield evaluation scheme.
- Understanding of the field limitation and overcoming quench and field- emissions as major reasons for gradient limitation.
- Achievement of a production yield of ~70% at 35 MV/m, as described above, and ~80% with allowing gradient spread of 35 MV/m +/-20% (from 28 MV/m ~42 MV).

Figure 4 shows the progress of the ILC-SCRF 1.3 GHz cavity gradient R&D systematically monitored by the ILC SCRF global data base team led by C. Ginsburg: (a) integrated production yield in the 2nd pass of the surface process with the data available since 2006, and (b) differential production yield in each 1 ~ 2 years [9]. The production yield evaluation has been updated, six times during a period of 2009 through 2012, with the most recent updated time in April. 2012. In the 2nd pass, (69±13)% of cavities achieve >35 MV/m; and (92±7)% of cavities achieve >25 MV/m considering only cavity tests taking place in 2010-2012 [9]. It should be noted that the production yield reaches ~80 % with an interpolation and as the most practical evaluation, if the gradient spread of 35 MV/m +/-20 % would be applied.

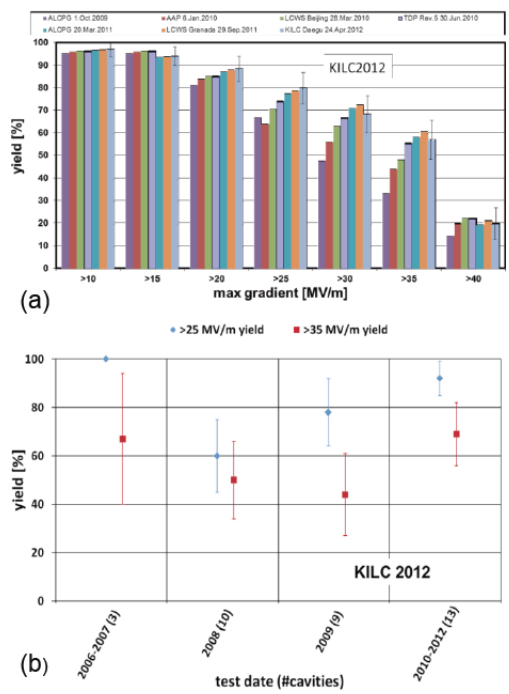

Figure 4: Progress of the ILC-SCRF 1.3 GHz cavity gradient R&D (a) integrated production yield in the 2nd pass process, with the data available since 2006, and (b) differential production yield. [9]. The blue points are for >25 MV/m yield and red points are for >35 MV/m yield.

Ongoing efforts to improve cavity production yields include applying mechanical tumbling [15] or localized grinding [16] for removal of known performance-limiting defects and centrifugal barrel polishing to the baseline cavity processing recipe. Many (~12) cavity repairs have been achieved through these two methods; however, at this time, cavity performance after these repairs is still to be discussed how we include these repaired cavities in yield plots, hopefully in near future [17].

Several manufacturers have engaged in the production of cavities [6]. While originally only two companies provided cavities qualifying for the ILC demands we now see companies in all three regions successfully manufacturing high-gradient cavities as updated in Table 2. The number of successfully tested cavities achieving the ILC specification has now reached several dozen.

Table 2: Progress in SCRF cavity vendors/laboratories and their successes in achieving the 35 MV/m gradient goal in fabrication.

Year / # cavity	Cavity manufactures	Laboratories
2006 / 10	Accel, Zanon	DESY
2011 / 41	RI, Zanon, AES, MHI	DESY, JLab, Fermilab, KEK
2012 / 45	RI, Zanon, AES, MHI, Hitachi	DESY, JLab, Fermilab, KEK, Cornell-U

Cavity String in Cryomodule (S1)

- A prototype cryomodule for the European XFEL program achieved an averaged field gradient of 32 MV/m [7].
- A cryomodule was assembled and tested in an international effort (S1-Global hosted at KEK) with contributions of FNAL, SLAC, DESY, INFN and KEK. S1-Gobal succeeded in realizing 26 MV/m on average in a 7- cavity string operation. The plug-compatible assembly of various cavities and the respective interfaces has been verified successfully [14, 18, 19].
- The cavity string assembly in the cryomodule, CM1, achieved 24 MV/m at Fermilab [10].

Figure 5 shows recent progress in the cryomodule performance test at (a) DESY/FLASH, (b) KEK/S1-global, and (c) Fermilab/NML-ASTA. The figure shows the cavity field gradient performance per each cell, measured in the vertical test and in the horizontal test (in case of Fermilab) and in the cyromodule test [7, 14, 10]. As an important message, the gradient degradation has been observed after installation into the cryomodules, and it will be an important subject to be settled as a major subject beyond TDR.

Copyright © 2012 by the respective authors — cc Creative Commons Attribution 3.0 (CC BY 3.0)

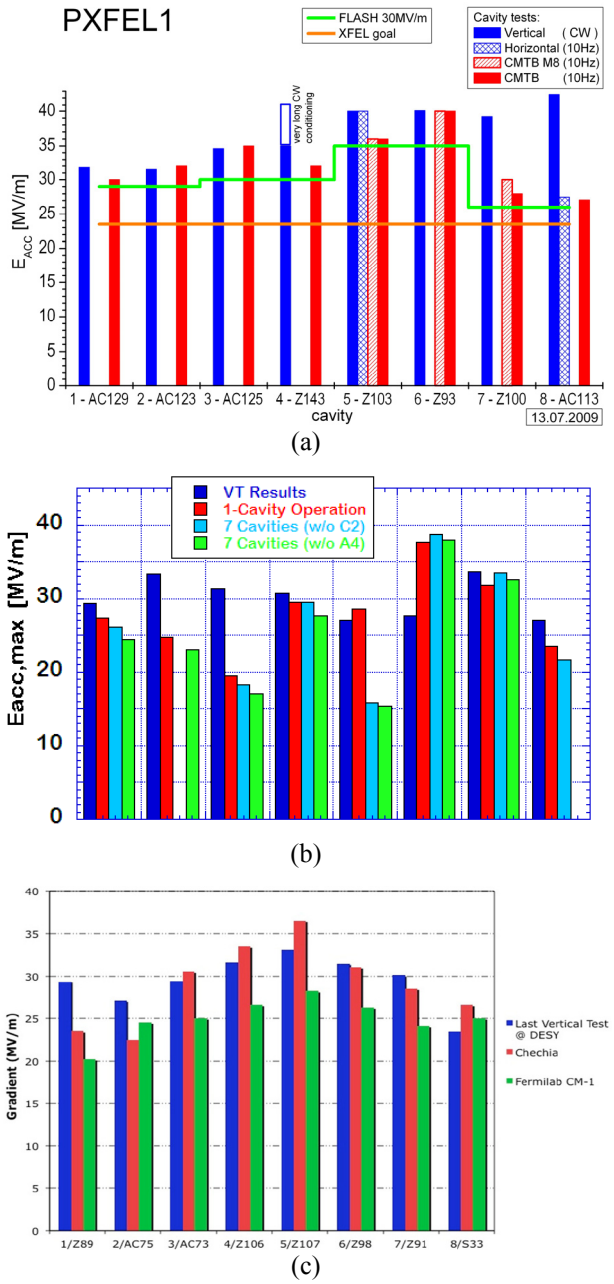

Figure 5: Field gradient achieved in cryomodules developed at (a) DESY/FLASH-PXFEL1 [7], (b) KEK/S1-Global [14], and (c) Fermilab/NML/ASTA-CM1 [10].

Cryomodule and HLRF Design

- The ILC cryomodule system design has been fixed with two design variants: a longer design consisting of an 8-cavity string plus 1 quadrupole at the centre, and a shorter design consisting of an 8-cavity string.
- The removal of the bottom 5 K shield has been explored; the shield is retained for TDR [20, 21].
- The R&D for superconducting magnet using condition cooling has been successfully made [22, 23]. It will help to assemble the magnet separately from the cavity string assembly that require specially arranged clean rooms.
- The Klystron Cluster System (KCS) for flat-land topography has been proposed; the R&D continues [24].
- The distributed RF with 800-kW klystron has been proposed for a mountainous topology, has been demonstrated during the S1-Gloabal program at KEK [25]. Finally, the Distributed Klystron scheme (DKS) with 10 MW klystrons has been chosen as the baseline for the mountainous topography.
- Marx modulator development has been successfu3 at SLAC as the baseline power source [26].
- The LLRF control study succeeded in adapting various cavity tuner designs [27,28], and demonstrated successful handling of cavity string performance variation and proved the general feedback operation with a RF power overhead margin below 10% [29, 30].

The KCS and DKS HLRF power system concepts are shown in Fig. 6, and Fig. 7, respectively.

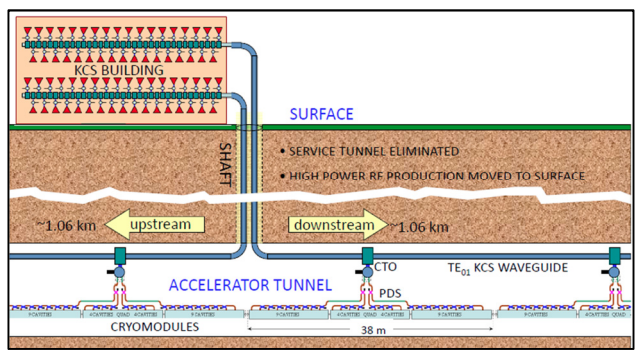

Figure 6: The KCS concept for the main linac HLRF power distribution system considered in flat-land site topography.

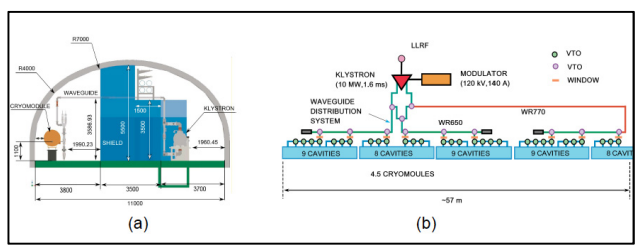

Figure 7: The DKS concept for the main linac HLRF power distribution system considered in mountainous site topography finalized in TDR.

PROGRESS IN BEAM-TEST FACILITIES

The beam acceleration tests by using SCRF beam test facilities have progressed at DESY/FLASH and KEK/STF, will be realized soon at Fermilab/NML-ASTA. Major progresses are summarized in Table 3 [29, 30].

Copyright © 2012 by the respective authors — cc Creative Commons Attribution 3.0 (CC BY 3.0)

Table 3: Progress in Beam Test Facilities to Demonstrate the ILC Beam Parameters

Subject	R&D goal	Achievement	Facility
- High beam power and long bunch trains (Feb. 2009)			
Pulse current	9 mA	9 mA	FLASH
Bunches per pulse	2400 x 3 nC	1800 x 3 nC 2400 x 2nC	FLASH
Cavity gradient	31.5 MV/m +/-20 %	> 30 MV/m with 4 cavities	FLASH
- Gradient operating margins (Feb. 2012):			
Gradient flatness	2%ΔV/V (0.8ms, 5.8mA)	<0.3% ΔV/V (0.8ms, 4.5mA)	FLASH
Gradient margin	3 % to quench limit	5% to limit (0.8ms, 4.5mA)	FLASH
Energy stability	0.1% rms	<0.15%(0.4ms) <0.02% (5 Hz)	FLASH
- Beam duration (April 2012) :			
Pulse width	1 ms	1ms	STFQB

EFFORTS BEYOND TDR

Technical R&D has progressed as described above, and the TDR as the progress report is to be completed by in 2012, as the time chart shown in Fig. 8.

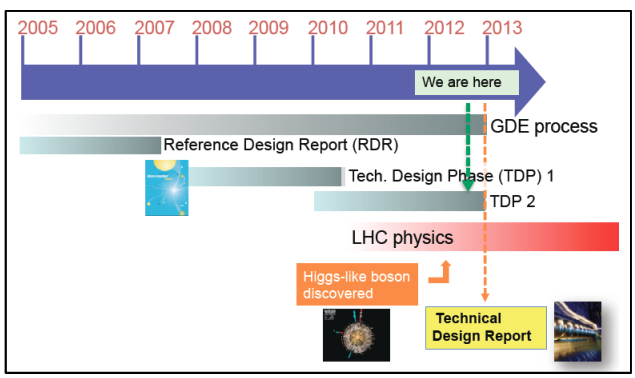

Figure 8: The ILC time line for Technical Design Report.

Further R&D efforts beyond TDR completion are discussed as follows:

- Higher gradient with an R&D target of 45 MV/m, motivated with further cost-effective cavity production including the energy upgrade phase,
- Mitigation of the field gradient degradation the cavity after installation into the cryomodule.
- Preparation for industrialization in optimization of mass-production models in close communication with industry.

SUMMARY

The ILC TD phase has been successfully carried out, and the TDR will be completed in 2012. ILC can be realized, based on the TDR technology.

We may consider multiple scenario of the ILC construction including staging the energy starting with lower energy depending on the physics output from LHC experiments, discovering Higgs-like boson in an energy range of 126 GeV.

Beyond the TDR completion, further R&D shall be extended, focusing on preparation of industrialization of major components with international industrial cooperation keeping plug-compatible mass-production with the best cost-effective approach.

ACKNOWLEDGMENT

We would thank all of worldwide ILC-GDE Collaborators for their cooperation to proceed the Technical Design and R&D effort carried out in the Technical Design Phase.

REFERENCES

[1] International Linear Collider; http://www.linearcollider.org.
[2] ILC Reference Design Report (RDR). http://www.linearcollider.org/about/Publications/Reference-Design-Report
[3] A. Yamamoto, EPAC08, Genova, MOYBGM01.
[4] ITRP Recommendation, (2004); http://www.fnal.gov/directorate/icfa/ITRP_Report_Final:pdf
[5] The International Linear Collider: A Technical Progress Report (Interim report). http://www.linearcollider.org/about/Publications/interim-report
[6] A. Yamamoto et al., SRF11, Chicago, MOIOA02
[7] D. Reschke et al., SRF11, Chicago, MOIOA01.
[8] V. Yakovlev, C. Ginsburg, LINAC12, Tel-Aviv, MO1A03.
[9] C.M. Ginsburg, LINAC12, Tel-Aviv, MOPB052.
[10] E.R. Harms et al., LINAC12, Tel-Aviv, MOPB054.
[11] C. Reece et al., SRF11, Chicago, MOTIOA04.
[12] H. Hayano et al., to be published in ILC-TDR.
[13] R. Geng et al., SRF11, Chicago, TUPO015.
[14] H. Hayano et al., LINAC12, Tel-Aviv, TH1A01.
[15] C. Cooper et al., SRF11, Chicago, TUPO025.
[16] Y. Iwashita et al., LINAC12, Tel-Aviv, MOPB053.
[17] Y. Yamamoto, published in IPAC12, New Orleans.
[18] Y. Yamamoto et al., SRF11, TH0101.
[19] E. Kako et al., IPAC11, San Sebastian, MOODA02.
[20] N. Ohuchi et al., IPAC11, San Sebastian, WEP035.
[21] P. Pierini, T. Peterson, to be published in ILC-TDR.
[22] V. Kashikhin et al., IEEE Trans. ASC, 22 (2012) 4002904.
[23] M. Tartaglia et al., to be reported in ASC12, Portland.
[24] C. Adolphsen, C. Nantista, LINAC12, MOPB044.
[25] S. Fukuda et al., LINAC10, Tsukuba, MOPO021.
[26] M. Kemp et al., LINAC12, Tel-Aviv, WE2A02.
[27] S. Michizono et al., IPAC11, San Sebastian, MOODA02.
[28] W. Schappert et al., SRF11, Chicago, FRIOA01.
[29] N. Walker et al., PAC09, Vancouver, WE6F109.
[30] J. Carwardine et al., to be reported in ILC-TDR.

Copyright © 2012 by the respective authors — cc Creative Commons Attribution 3.0 (CC BY 3.0)

THE 12 GeV ENERGY UPGRADE AT JEFFERSON LABORATORY

F. Pilat
Thomas Jefferson National Accelerator Facility, Newport News, VA 23606, USA

Abstract

Jefferson Laboratory has undertaken a major upgrade of its flagship facility, the CW re-circulating CEBAF linac, with the goal of doubling the linac energy to 12 GeV. I will discuss here the main scope and timeline of the upgrade and report on recent accomplishments and the present status. I will then discuss in more detail the core of the upgrade, the new additional C100 cryomodules, their production, tests and recent successful performance. I will then conclude by looking at the future plans of Jefferson Laboratory, from the commissioning and operations of the 12 GeV CEBAF to the design of the MEIC electron ion collider.

INDRODUCTION AND OVERVIEW

The CEBAF (Continuous Electron Beam Accelerator Facility) started operations in 1995 as the first CW re-circulating linac and first large accelerator based on superconducting RF technology. Designed for a maximum energy of 6 GeV, CEBAF has operated continuously serving a large nuclear physics community of more than 1400 users for 17 years, its last run at 6 GeV successfully completed in the spring 2012. With 5 recirculation passes and an injector able to tailor different beam characteristics (energy, intensity and polarization) independently for 3 experimental Halls capable to run concurrently, the linac has been a flexible and reliable source that has sustained a rich and successful nuclear physics program.

In the late 1990's the concept for an energy doubling to 12 GeV was defined, and the plan was approved and funded starting in 2004.

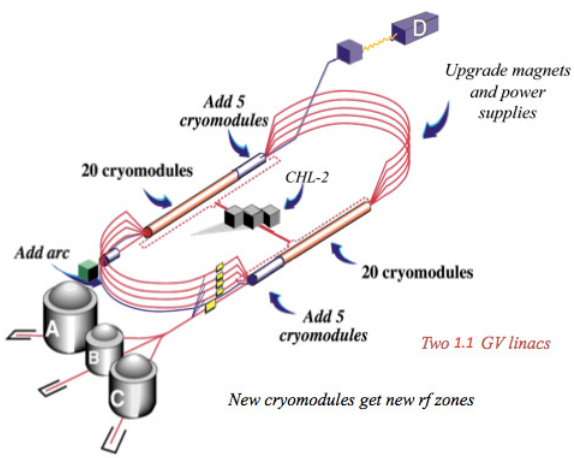

Figure 1: The main components of the CEBAF upgrade to 12 GeV.

The energy doubling is achieved by adding 10 new C100 to the existing 40 CEBAF cryomodules in free space at the end of each linac and by upgrading the magnets in the original 9 arcs to higher fields. The higher cryogenic load necessitates the doubling of the cryogenics capability with the addition of a second cryogenics plant, CHL-2 to the existing CHL-1. In addition, a new arc (Arc 10) provides an additional pass to deliver 12 GeV beam to the new Hall D. Beam for the existing Halls A, B and C is extracted at 11 GeV. The design is for a maximum of 3 Halls operating at the same time. The new Hall D adds the capability of a photon beam dedicated to the new Glue-X experiment. Included in the scope of the upgrade are new experimental detectors for the Halls B and C and infrastructure upgrades for Hall A. The injection line also needs to double the energy to match the linac.

A comparison of the high-level machine parameters between the 6 and 12 GeV CEBAF is given in Table 1.

Table 1: High-level parameters for the 6 and 12 GeV CEBAF.

Parameter	Unit	6 GeV	12 GeV
Max Energy to Halls	GeV	6	12
Passes for Hall ABC/D		5	5/5.5
Max current Hall A,C/B	μA	200 / 5	85/5
Emittance at max E H/V	nm-rad	1 / 1	10 / 2
Energy spread at max E	10^{-5}	2.5	50 at 11 GeV 500 at 12 GeV
Bunch length (rms)	ps	0.2	~1
Polarization	%	80	80

TIMELINE AND STATUS

The 12 GeV Upgrade is being managed as the 12 GeV Project, with project management structure and practices in place. The total Project cost is 310 M$ (excluding the injector upgrade, the path-length adjustors, the 5-pass RF separators and necessary machine maintenance, that are funded and managed off Project) and the Project is at the time of writing 68% complete and 79% obligated. The overall Project timeline is shown in Figure 2.

While procurement and subsystem work as well as civil construction have been in progress since FY04, the bulk of the construction and installation work has been planned during 2 operations shut-downs, the 6 month shutdown, May-November 2011 and the ongoing 16 month long shut-down, May 2012 to September 2013.

The present timeline has machine commissioning at 12 GeV starting in the fall of 2013, beam to Hall A in February 2014, followed by Hall D commissioning in October 2014, and Hall B and C in April 2015. Project completion, assuming the planned funding, is foreseen in June 2015.

The rationale of distributing the installation for the upgrade over 2 separate shutdowns in lieu of one was mainly motivated by two objectives: concluding the 6

Copyright © 2012 by the respective authors — cc Creative Commons Attribution 3.0 (CC BY 3.0)

GeV physics program in a timely fashion and capitalizing on the opportunity of testing with beam critical components of the upgrade, primarily the refurbished magnets and the new C100 cryo-modules during the final 6 GeV run from November 2011 to May 2012.

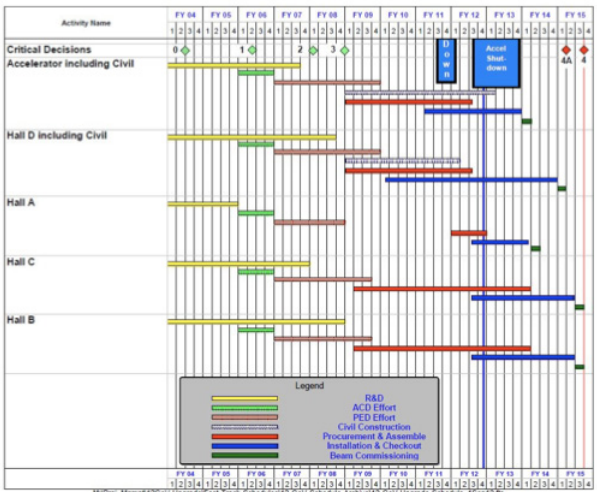

Figure 2: Timeline of the 12 GeV CEBAF Upgrade.

With 12 GeV upgrade activities being planned together with other programs going on concurrently at Jefferson Lab (operations of the JLAB FEL, preparation for CEBAF operations, construction of the TEDF, Technology and Engineering Development Facility, comprising 2 new buildings for a total project cost of 30 M$, a centralized engineering building and a doubling of the present infrastructures for SRF at JLAB, Ref [1]), the shutdowns are being managed by a laboratory-wide coordination structure that uses project management practices and integrated scheduling to minimize interferences of concurrent activities and insure overall proper activity prioritization.

The 6-month shutdown was successfully executed, all the scope of work was completed within the planned resources and budget, and in the area of magnet rework the goals were exceeded with the completion of 8 arcs instead of the baseline plan for 5. Operations started as planned in the middle of November 2011 and the ensuing run saw the completion of the 6 GeV physics program as well as operation of the machine with 2 new C100 cryo-modules. The 16 months long shutdown is in progress now and on schedule as of end of August 2012.

THE C100 CRYOMODULES

The main and more technically challenging components of the 12 GeV upgrade are the 10 new C100 cryomodules, each consisting of 8 seven cell SC cavities. The production and testing of the 80 cavities is completed and as of September 2012, 5 out of 10 cryomodules are in the tunnel and the entire production and installation will be completed by the spring of 2013.

Cavity Preparation and Testing

The 80 seven-cell 1497 MHz SC cavities for the C100s have been supplied by Research Instruments (RI) and, together with 8 pre-production cavities, have been processed, tested and assembled at JLAB. The C100 cavity production and qualification process consists of 19 steps, all documented with Pansophy travellers. [2] The electro-polishing (EP) process in particular was derived from the experience with the EP for the 9-cell JLAB high gradient cavities for the ILC, an excellent example of synergy between different R&D efforts.

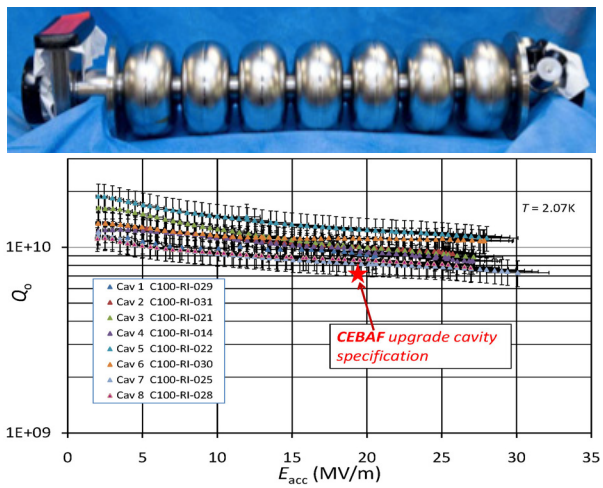

Figure 3: Vertical acceptance test results of the 8 cavities for the C100-3 cryomodule.

The cavity tests are performed at the Vertical Test Area (VTA), a facility specifically designed for measurement of cavities in super-fluid helium. A typical result of unloaded Q as a function of accelerating gradient for cavities in a C100 string is shown in Figure 3. The cavity specification is 19.2 MV/m average, with 29 W of average heat per cavity. The operational limit at 12 GeV is 25 MV/m, limited by the klystron RF power.

C100 Cryomodules: Design and Production

The design of the C100, started in 2001 and finalized by 2009, is an evolution from the original C20 CEBAF cryomodule and has capitalized on the experience of the C50 program. The goal of the latter was to reduce field emission and raise the gradient from 5.5 MV/m to 12.5 MV/m for 10 of the weakest C20 cryomodules. The latter were disassembled, baked, tuned, surface-processed and reassembled resulting in excellent gradient improvements.

The fact that 10 C100 cryo-module can output the same accelerating voltage of 40 original CEBAF modules is a testimony to the impressive progress in CW SRF in the past 20 years.

To meet the energy upgrade specifications, the C100 need to provide a minimum of 98 MeV but the C100 are designed for 108 MeV output in order to allow for sufficient margin. The production model had the primary components procured from industry and the modules assembled and qualified at JLAB. [3] The cryomodule

Copyright © 2012 by the respective authors — cc Creative Commons Attribution 3.0 (CC BY 3.0)

cost is evenly split between procurements and labor, and the most resource-consuming aspects are the assembly and QA processes.

Figure 4: C100 leaving the assembly building.

C100: Tests and Performance

Once assembled, each cryomodule goes through 2 testing cycles, acceptance testing in the Cryomodule Test Facility (CMTF) prior to installation and a final commissioning in the tunnel after installation. [4] During the acceptance procedure, every cavity is tested and tuned to 1497 MHz, HOM are characterized and maximum gradient, field emission and Q_o measured together with microphonics and static heat loads. Commissioning in the tunnel after installation consists of a subset of the acceptance tests.

The measurement of cavity detuning from external vibration sources has been particularly extensive given the potential operational consequences. [5] The peak detuning budget for the C100 cavities is 35 Hz. While within the specifications the initial measurements were higher than predicted, one possible cause being the lack of stiffening rings in the cavity design. The will to retain operational margin for the cavity powering led to a modification of the mechanical tuner system for the successive C100 cryomodules that in turn led to an average reduction in peak detuning of 42%.

In a modification of the original plan, the first 2 production C100 cryomodules were installed in the South Linac during the 6-month shutdown in the Summer 2011. The change in the plan provided a means to validating the main components of the upgrade by testing the modules in the tunnel, performing dedicated studies of HOM modes with beam at the end of the down, and by commissioning and operating the units with beam during the ensuing physics run.

Previous detection of BBU at 40 μA in CEBAF in 2007 with an earlier high gradient prototype motivated the effort to improve the C100 HOM damping and to undertake dedicated studies to measure HOM and compare them with predictions. [6] The predicted BBU threshold for the 12 GeV CEBAF beam is 26 mA, much higher than the nominal 465 μA maximum beam loading. Despite a dedicated beam test at low energy, 282 MeV/linac, and a special optics aimed at lowering the BBU threshold, we were unable to directly observe BBU, which is reassuring. The C100 HOMs were carefully surveyed, in particular the most important TE111, TM110 and TM111 for all cavities in C100-1 and C100-2 by beam transfer function measurements. These measurements and the comparison with prediction allowed us to conclude that BBU is not a likely concern for 12 GeV CEBAF (see Figure 5).

Figure 5: Measured dipole HOM impedances for the first 2 production C100 cryomodules.

C100: Commissioning and Operations

C100-1 and C100-2 were first commissioned and then used in operation with beam continuously from January to May 2012. [7]

The RF system is completely new for these cryomodules: each cavity is powered by one klystron, output power of 12 kW linear and 13 kW saturated, and controlled by the LLRF system. After a test of the RF controls and power systems, the cryomodule is attached to the waveguides, commissioned and handed over to operations.

During operations the cryomodule voltage ranged from 50 to over 100 MV. The fact that the C100 cavities have narrower bandwidth and much higher gradients than the original CEBAF cavities translated into the necessity to progressively learn to operate the C100 efficiently. In particular, turn-on and trip recovery applications proved critical to minimize downtime in operations. A critical aspect was to learn to minimize mechanical coupling between adjacent cavities, of the order of 10% if left uncorrected.

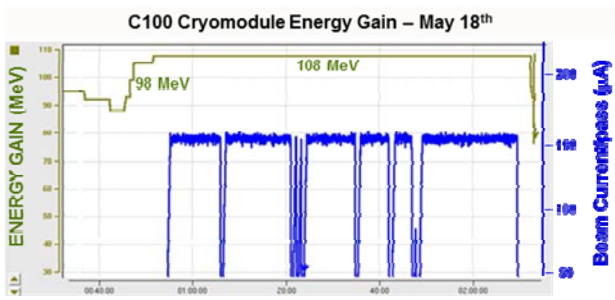

Figure 6: C100 reached the design gradient with the nominal 460 μA of total beam loading.

The goal of demonstrating that the new cryomodules could achieve an energy gain of 108 MeV at the 12 GeV design current of 465 μA for over 1 h of continuous

Copyright © 2012 by the respective authors — cc Creative Commons Attribution 3.0 (CC BY 3.0)

operations was achieved on May 18, 2012 (Figure 6). The operational experience of the first 2 C100 will be invaluable during the machine commissioning in the fall of 2013.

MAGNET UPGRADE

The magnet field needed to be increased to accommodate the higher energy. Adding H-steel to the original C- dipoles in order to reduce saturation solved the problem for most of the arc dipoles in the arc. New magnets were needed for the new Arc 10, the spreaders and recombiners and some transfer lines.

Figure 7: Re-worked and new magnets in the West Arc.

Most of the arc dipoles have been successful re-worked and measured during the 6-month shutdown. All magnets have met their design goals with no post construction modifications needed and performed well in operations. The upgrade of spreaders, recombiners and the remaining beam transport elements is in presently in progress.

CRYOGENICS

The upgrade to 12 GeV for the CEBAF linacs requires the doubling of the JLAB cryogenics capability so a new Central Helium Liquefier (CHL-2) is being added to the existing CHL-1. In addition a new cryo plant for Hall D (HDR – Hall D Refrigerator) is being installed to serve the SC solenoid for the Glue-X experiment. CHL-2 compressors are installed and the lower and upper cold-boxes are being commissioned as well.

As part of the upgrade, the CHL-1 refrigerator has been warmed up in a controlled way together with the linacs for the first time in the CEBAF history. The warm-up started on August 1st 2012 and was successfully completed in less than 2 weeks. An unplanned warm-up in 2005 was caused by Hurricane Isabelle, which resulted in loss of gradient for the CEBAF cryomodules as a consequence of uncontrolled thermo-cycling. Lessons learned from that experience were included in the planning of the controlled warm-up this summer.

Figure 8: CHL-2 compressors are installed and are being commissioned.

The controlled warm-up so far did not appear to present unforeseen challenges, and we are seizing the opportunity for needed cryogenics and cryomodule maintenance activities, including a global realignment of the cryogenics transfer lines and the linac cryomodules. In addition, new cooling towers for CHL-1 are being built that will add reliability and flexibility during the planned cool-down of the linacs in December 2012. The linacs need to be cooled down to commission the remaining C100 cryomodules and to run the JLAB FEL as planned starting in January 2013.

INJECTOR

The CEBAF elements responsible for the generation of polarized electrons, spin manipulation, acceleration up to the injection energy and merging into the North Linac is called the CEBAF Injector. For 12 GeV CEBAF operations the Injector will be upgraded in several phases to achieve an increase in the final injection energy and improvements geared toward improving the helicity correlated beam parameters. The increase in the final injector energy from 67 MeV to 123MeV is accomplished by replacing an original CEBAF cryomodule in the final acceleration portion of the injector with a new 100MeV C100 cryomodule. This upgrade is required to maintain the same injection to first pass energy ratio as in the original 4GeV CEBAF design.

Parity violated experiments have been one of the highlights of the 6 GeV CEBAF program and several parity violated experiments have been approved for the 12GeV physics program. In order to improve beam helicity correlated beam parameters required for these demanding experiments and reduce the amount of beam tuning to maintain the required beam quality the front-end of the Injector will be upgraded during the initial years of 12GeV operation. This upgrade includes raising the DC gun from 130keV to 200keV to reduce space charge effects and a new ¼-cryomodule. The ¼- cryomodule will eliminate the X-Y coupling of the old asymmetric module.

Copyright © 2012 by the respective authors — cc Creative Commons Attribution 3.0 (CC BY 3.0)

JEFFERSON LAB OUTLOOK

I will conclude by giving an overview of JLAB future plans in the 12 GeV era and beyond.

12 GeV Commissioning and Operations

Commissioning of the 12 GeV CEBAF will start in the fall of 2013. A draft-commissioning plan exists already and it will get finalized during the long shutdown. The most relevant difference from operations at 6 GeV is synchrotron radiation at 12 GeV. Hall commissioning will start with A, followed by D, C and B respectively. The projections for the out-years are for 30-34 weeks of machine operations per year. The Physics Advisory Committee has already approved more than 50 experiments for the 12 GeV era and we project at least 15 years of productive physics running.

The Electron-Ion Collider

The nuclear physics community is developing a strong physics case for an electron-ion collider as the next needed step in the development of the field. Jefferson Laboratory has just completed the conceptual design for a Medium Energy Ion Collider [8] that would fit strategically in the laboratory future plans as well as physically in within the laboratory footprints.

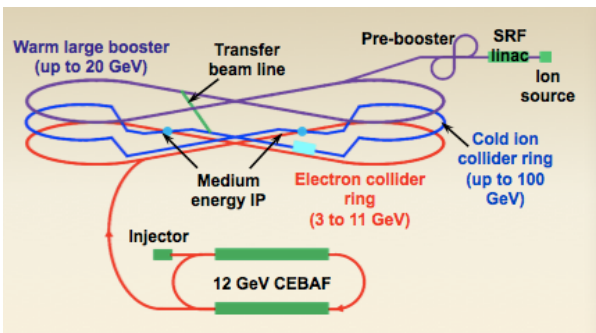

Figure 9: The MEIC collider complex at JLAB.

The design is for a ring-ring collider, with an energy range of 3-11 GeV for the electrons and 20-100 GeV for protons and ions, a luminosity of a few 10^{34} e-nucleons cm^{-2} s^{-1} and longitudinal and transverse polarization. CEBAF is the e- injector while the ion complex is new. Unique characteristics of this design are the figure-8 rings to insure preservation of polarization. Figure 10 outlines a possible timeline for the project that is compatible with 12 GeV CEBAF running and the long-term plans for DoE Office of Nuclear Physics.

CONCLUSIONS

The 12 GeV Upgrade for CEBAF at JLAB is progressing well and the start of commissioning is planned for the fall of 2013. A robust program of nuclear physics will follow. JLAB will complete a doubling of its SRF infrastructure in summer 2013 greatly enhancing its SRF R&D and production capabilities. An electron-ion collider is the long-term strategic goal of the laboratory.

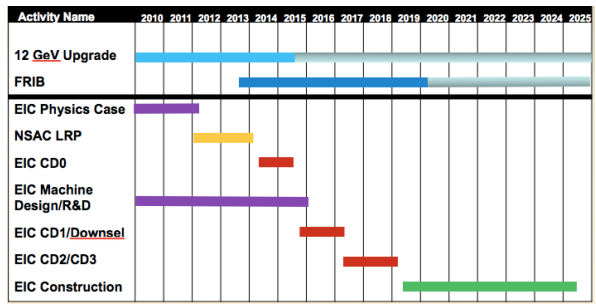

Figure 10: A possible timeline for the EIC realization consistent with DoE Nuclear Physics and JLAB plans.

ACKNOWLEDGEMENTS

I would like to thank M.Bevins, M. Drury, A. Freyberger, J. Hogan, C. Hovater, C. Reece, T. Satogata and Y. Zhang for technical input as well as A. Hutton, L. Harwood and C. Rode for reviewing the paper.

REFERENCES

[1] C. Reece, A. Reilly, "The New 2nd Generation SRF R&D facility at Jefferson Lab: TEDF", LINAC 2012.
[2] A. Reilly et al., "Preparation and Testing of the SRF Cavities for the CEBAF 12 GeV Upgrade", SRF2011
[3] J. Hogan et al., "12 GeV Upgrade Project – Cryomodule Production", IPAC 2012.
[4] M. Drury et al., "Performance of the First C100 Cryomodules for the CEBAF 12 GeV Upgrade project", IPAC 2012.
[5] K. Davis et al., "Vibration Response Testing of the CEBAF 12 GeV Upgrade Cryomodules", LINAC 2012.
[6] T. Satogata et al., "Re-circulating Beam Breakup Study for the 12 GeV Upgrade at Jefferson Lab" IPAC 2012.
[7] C. Hovater et al., "Commissioning and Operation of the CEBAF 100 MV Cryomodules", IPAC 2012.
[8] Y. Zhang, J. Bisognano (editors) et al., "Science Requirements and Conceptual Design for a Polarized Medium-Energy Electron-Ion Collider at Jefferson Lab", August 2012.

Copyright © 2012 by the respective authors — cc Creative Commons Attribution 3.0 (CC BY 3.0)

ERL-BASED LEPTON-HADRON COLLIDERS: eRHIC AND LHeC

F. Zimmermann, CERN, Geneva, Switzerland

Abstract

Two hadron-ERL colliders are being proposed. The Large Hadron electron Collider (LHeC) plans to collide the high-energy protons and heavy ions in the Large Hadron Collider (LHC) at CERN with 60-GeV polarized electrons or positrons. The baseline scheme for this facility adds to the LHC a separate recirculating superconducting (SC) lepton linac with energy recovery, delivering a lepton current of 6.4 mA. The electron-hadron collider project eRHIC aims to collide polarized (and unpolarized) electrons with a current of 50 (220) mA and energies in the range 5–30 GeV with a variety of hadron beams — heavy ions as well as polarized light ions — stored in the existing Relativistic Heavy Ion Collider (RHIC) at BNL. The eRHIC electron beam will be generated in an energy recovery linac (ERL) installed inside the RHIC tunnel.

INTRODUCTION

The LHeC and eRHIC projects would involve one of the proton or ion beams of the LHC and RHIC, respectively. They, therefore, represent interesting possibilities for further efficient exploitation of the LHC and RHIC infrastructure investments. These and other (non-linac) lepton-hadron colliders, e.g. MEIC at TJNAF, are reviewed in [1].

For the LHeC [2], with 60-GeV lepton beam energy and using the 7 TeV proton (and few TeV / nucleon ion) beam, centre-of-mass collision (CM) energies in the TeV range are attained, significantly exceeding the CM energy of HERA, the first (ring-ring) ep collider built. The LHeC ep target luminosity is 10^{33} cm^{-2}s^{-1}. Extensions to 10^{34} cm^{-2}s^{-1} are being considered. In order to keep the power consumption of the LHeC facility at a realistic level, the total electrical power for the LHeC lepton branch has been limited to 100 MW. A Conceptual Design Report (CDR) has been published [3]. The LHeC physics program comprises precision QCD, electroweak physics, high parton densities, and new physics at high energy.

The LHeC CDR considered both ERL-ring and ring-ring options for the LHeC. Recently [4] the ERL-ring design was chosen as the baseline scheme for several reasons: (1) the installation of the ring-ring machine would interrupt the ongoing and planned LHC program as well as imply extended tunnel work and interference with the existing LHC, and (2) the development of a CW SC recirculating energy-recovery linac for LHeC would prepare for many possible future projects, e.g., for an International Linear Collider, for a neutrino factory, for a proton-driven plasma wake field accelerator, or for a muon collider. With some additional arcs, using 4 instead of 3 passes through the linacs, a machine like the LHeC ERL (without energy recovery) could also operate as Higgs factory $\gamma\gamma$ collider [5].

The eRHIC [6] will collide 5–30 GeV polarized electron beams with 250–325 GeV polarized protons or 100–130 GeV / nucleon heavy-ion beams. The ultimate eRHIC luminosity per nucleon, achieved with lower hadron-beam emittances and with larger electron-beam currents than for the LHeC, is a factor 100–400 higher. In particular, eRHIC will employ a novel system of Coherent Electron Cooling (CEC) [7] to reduce the transverse and longitudinal emittances of the RHIC hadron beams, so that the normalized transverse emittances are about a factor 10 lower than those of the LHC. The enhanced space-charge tune shift requires a dedicated compensation by another electron beam [8]. For eRHIC, the total beam power loss, mainly due to synchrotron radiation, has been limited to about 10 MW. The ERL design offers a natural staging of the eRHIC facility where the beam energy is planned to be raised in steps as progressively additional SC cavities are installed and powered in the linac straights. The eRHIC physics program includes unraveling the origin of the proton spin, quantum phase space tomograpy of the nucleon, and the physics of strong color fields [9].

The luminosity of an ERL-ring collider can be written as

$$L = \frac{1}{4\pi e}\frac{N_{b,h}}{\varepsilon_h}\frac{1}{\beta_h^*} I_e H_{hg} H_D \ , \qquad (1)$$

where e denotes the elementary charge, H_D the disruption enhancement factor ($H_D \approx 1.3$ for $e^- p/A$ and $H_D \approx 0.3$ for $e^+ p/A$ collisions), and matched round colliding beams are considered. To obtain the maximum luminosity one aims for a large hadron bunch population $N_{b,h}$, a small geometric hadron-beam emittance ε (or large hadron-beam brightness $N_{b,h}/\varepsilon_h$), a small hadron beam interaction-point (IP) beta function β_h^*, a high geometric overlap factor H_{hg} (head-on collision, and small lepton beam emittance), and, provided by the ERL, a large lepton beam current I_e.

Table 1 compares parameters for the two projects. In case of the LHC the geometric emittances for proton and ion beams are the same, and correspond to the values available in present operation. The projected eRHIC hadron beam emittances are determined from the expected performance of the CEC system and from imposing consistent requirements for the space-charge compensation system. As a result, in the case of eRHIC it is the normalized, not the geometric emittances, which is the same for heavy-ion and proton beams.

LINACS, ARCS AND BEAM DYNAMICS

Both LHeC and eRHIC ERLs comprise two linacs. Their parameters are compared in Table 2. The LHeC linac is about 5 times longer and provides 4 times the energy gain, at comparable cavity voltage. The lower cavity filling factor for LHeC is partly due to the presence of about

Copyright © 2012 by the respective authors — cc Creative Commons Attribution 3.0 (CC BY 3.0)

Table 1: Collider parameters for eRHIC (ultimate) and LHeC (ultimate)

parameter [unit]	eRHIC		LHeC	
species	e^-	p, $^{197}Au^{97+}$	$e^\pm$	p, $^{208}Pb^{82+}$
beam energy (/nucleon) [GeV]	15 (30)	325, 130	60	7000, 2760
bunch spacing [ns]	18	18	25, 100	25, 100
bunch intensity (nucleon) [10^{10}]	2.4	40, 60	0.1, 0.4	17, 2.5
beam current [mA]	220 (12.6)	3330, 2000	6.4	582, 6
rms bunch length [mm]	2	49	0.6	75.5
polarization [%]	80	70, none	90 (e^+ none)	none, none
normalized rms emittance [μm]	5.8–57	0.2, 0.2	50	3.75, 1.5
geometric rms emittance [nm]	0.8	0.6, 1.4	0.43	0.50
IP beta function $\beta^*_{x,y}$ [m]	0.05	0.05	0.12	0.1
IP spot size [μm]	6	6, 8	7	7
synchrotron tune Q_s	—	4.6×10^{-4}	—	1.9×10^{-3}
hadron beam-beam parameter	0.015		0.0001	
lepton disruption parameter D	52, 22		6	
crossing angle	0 effectively (crab crossing)		0 (detector-integrated dipole)	
hourglass reduction factor H_{hg}	0.85		0.91	
pinch enhancement factor H_D	1.2–1.3		1.35 (0.3 for e^+)	
CM energy [TeV]	140 (197), 88 (125)		1300, 810	
luminosity / nucleon [10^{34} cm^{-2}s^{-1}]	14 (4), 8.4 (2.1)		0.1, 0.02	

100 quadrupoles along the LHeC linac, whereas the eRHIC linac, of shorter length, does not include any focusing elements. No focusing in the linac implies larger linac beta functions and, thereby, a greater potential susceptibility to multi-pass beam break-up instabilities. For realizing the LHeC linac quadrupoles several options are being considered: electromagnets powered individually, electromagnets in clusters of 4 together with trims, and permament magnets. The eRHIC will not use any cryomodules, but each eRHIC cavity will be an individual "cryounit" [10], designed for easy addition or removal. Estimated electrical power budgets for eRHIC and LHeC SC are dominated by the RF and cryo power required for the two SC linacs, as is illustrated in Table 3. The cryo power required and, therefore, also the size of the cryoplants are directly linked to the unloaded quality factor of the cavities, Q_0, since the cavity cryogenic RF loss at 1.8 K, $U_{\rm loss}$, follows from $U_{\rm loss} = V_{\rm cav}^2/((R/Q)Q_0)$. The RF parameters, in addition to power needed for the control of microphonics (with 10 kW available per cavity in eRHIC [10]), must take into account the beam energy loss due to synchrotron radiation. For the LHeC, with an arc-dipole bending radius of 764 m, an electron loses about 2 GeV over all arc passes (including the deceleration) to be compared with a maximum beam energy of 60 GeV. LHeC and eRHIC plan to install dedicated RF systems to compensate for this energy loss. For LHeC the highest compensating RF voltage required is 750 MeV for the energy loss at 60 GeV, for which a fundamental 721 MHz system is to be used. At lower energies higher-harmonic RF systems operating at 1.44 GHz can simultaneously compensate for energy losses experienced on the accelerating and decelerating arc passes at the same beam energy. For eRHIC at 30 GeV peak lepton energy, with a dipole bending radius of 234 m, the total energy loss per electron due to synchrotron radiation is about 770 MeV over all arc passes; at 20 GeV it is only 150 MeV. A single double harmonic compensator at (almost) the highest energy delivering 389 MeV per passage compensates for the energy loss from synchrotron radiation and other, smaller effects like resistive wall and linac-cavity HOMs [11].

Table 2: Parameters for eRHIC and LHeC SC linacs

parameter [unit]	eRHIC	LHeC
number of linacs	2	2
length / linac [km]	0.2	1.0
injection energy [GeV]	0.6	0.5
energy gain / linac [GeV]	2.45	10.0
number of acceleration passes	6	3
max. final energy [GeV]	30	60
real-estate gradient [MV/m]	12.45	10.0
energy gain / cavity [MeV]	20.4	20.8
cells / cavity	5	5
cavities / cryomodule (/cryounit)	1	8
cryomodules (cryounits) / linac	120	60
cryomodule length [m]	(100)	15.6
cavities / linac	120	480
RF frequency [MHz]	703.8	721
cavity length [m]	1.065	1.04
R/Q [linac Ω]	506	570
Q_0 [10^{10}]	4.0	2.5
power loss / cavity [W/cavity]	23.7	32
"W per W" (1.8 K to R.T.)	700	700
filling factor	0.64	0.50
length / GeV [m]	82	97
cryopower / linac [MW]	2	10

In hadron storage rings, the proton and ion revolution and RF frequencies vary as a function of beam energy and species. For the LHC at top energy, it is possible to operate

Copyright © 2012 by the respective authors — cc Creative Commons Attribution 3.0 (CC BY 3.0)

Table 3: Electrical power budget for eRHIC and LHeC

parameter [unit]	electrical power [MW]	
	eRHIC	LHeC
total main-linac cryopower	4	21
RF microphonics control	5	24
extra-RF power for SR losses	20	23
extra-RF cryopower	0.3	2
electron injector	2.6	6
arc magnets	11	3
total	∼43	78

the ion beams with the same RF frequency and harmonic number as the protons — a feature which will already be exploited for the first LHC *p-Pb* collision run in early 2013. This means that the LHeC electron linac frequency can be held constant. In any case small electron path length changes are easily accomplished in the LHeC ERL with the help of dogleg-pairs downstream of each spreader [3]. For eRHIC the hadron-beam frequency variation is more important, due to the lower energy and smaller circumference, and due to a wide range of hadron-beam energies. Changing the eRHIC proton beam energy from 250 GeV to 50 GeV would imply an electron circumference change of 66 cm, which exceeds the maximum range (15 cm) of the planned path-length insertion. The path length changes required are brought into the tolerable range by switching the electron "harmonic number," with a change by one unit (out of 9024) being equivalent to a path length change by one ERL RF wavelength, or 42.6 cm.

The lattice of the 6-passes for the eRHIC ERL arcs is based on low-emittance near-isochronous arc modules [12], supporting perfect isochronicity of complete paths. The standard building block is 35 m long, and contains 7 dipoles and 9 quadrupoles. The lattices for the 3 passes of the LHeC ERL arcs are based on a flexible-momnentum compaction (FMC) optics design [13]. The standard building block is 52 m long, and contains 4 quadrupoles and 2 (split into 10) dipoles. The values of the curly-H function $< H >$ and M_{56} are taylored as required by emittance dilution and isochronicity or beam-size conditions, respectively, for arcs of different energies, transiting from a quasi-isochronous optics yielding a small beam size for the two lowest energy arcs, to a TME-optics for the two arcs at highest energy [13]. At the ends of each linac the beams are directed into the appropriate energy-dependent arcs for recirculation. For this purpose at both eRHIC and LHeC the beams are separated vertically and the arc dipoles for successive passes are stacked on top of each other. The LHeC arc dipoles have a 25 mm gap and a maximum field of 0.264 T, at 60 GeV [3, 14]. The eRHIC arc dipoles have a much smaller gap of 5 mm and, at 30 GeV, a maximum field of 0.43 T. In view of the small gap and high beam current, resistive-wall wake fields and surface-roughness effects are under careful investigation for eRHIC.

Concerning multi-pass beam-break up (BBU) [15] in the recirculating linac, simulations demonstrate that for LHeC beam stability requires both damping ($Q \approx 10^5$) and detuning ($\Delta f / f_{\rm rms} \approx 0.1\%$) of the higher-order modes (HOMs) in the 721-MHz linac cavities [16]. For eRHIC assuming the HOMs of the "BNL3 cavity" design and an HOM rms frequency spread of 0.1–0.2% the simulated BBU threshold is higher than the 50-mA design current [17]. If needed, for both eRHIC and LHeC the threshold of the transverse ERL-type beam-break up is substantially increased thanks to the natural chromaticity of the return arcs with a moderate (correlated) relative energy spread of order 10^{-3} [18].

Collision of the leptons with the residual gas in the linac and arc beam pipes leads to the production of positive ions. With a CW beam, almost of these ions are trapped. Their presence adds additional focusing, modifying the optics, and can give rise to ion-driven transverse beam break up. The LHeC ERL circumference is chosen as 1/3 of the LHC circumference, so that ion clearing gaps can be introduced in the bunch train whose arrival times for successive passes coincide in the linacs and which, in addition, always correspond to the same partner hadron bunches in the LHC (so that the LHC would comprise hadron bunches which collide on every turn and some others which never collide). In these clearing gaps the ions drift away from the beam orbit. A good vacuum quality is also needed to further slow down the build up of a significant ion density during the bunch-train passages between successive clearing gaps. For the LHeC cold linacs partial gas pressures of 10^{-11} hPa at 1.8 K are required at the position of the beam to render the residual fast beam-ion instability harmless. Pressures of, or below, this magnitude were achieved in the cold parts of LEP, HERA and LHC [3]. In the warm arcs of the LHeC a partial pressure below 10^{-9} hPa should be sufficient [16]. Similar tolerances apply to eRHIC.

INJECTORS

The LHeC electron injector is composed of a DC gun, where a photocathode is illuminated by a laser beam, generating a 7-mA polarized electron beam, and of a downstream linac bringing this electron beam to the 500-MeV injection energy of the ERL. After the linac, a bunch compressor system allows shortening the bunches to 1 ps. The transport efficiency to the IP as assumed to be 90%. A possible concern is the shape of the electron beam [19] and its effect on the hadron beam. The larger polarized-beam current of 50 mA required for eRHIC is provided either by means of a single large-size GaAs photocathode [20] or with a Gatling gun [21] combining beams from a large array of GaAs cathodes. An unpolarized SRF electron gun [22] could generate significantly higher beam current up to 220–250 mA CW. Table 4 summarises the electron beam parameters at the exit of the DC gun.

The 60-m long 600-MeV eRHIC injector linac is operated in energy recovery mode with the spent and fresh beams propagating in the same direction on a single passage. After deceleration the spent 50-mA beam is dumped with about 10 MeV energy (500 kW power). For the LHeC dumping the 6.4-mA spent beam at the ERL injection energy of 500 MeV amounts to 3 MW of power loss, which could be absorbed by a 3 m^3 water dump (0.5 m in diame-

Copyright © 2012 by the respective authors — cc Creative Commons Attribution 3.0 (CC BY 3.0)

Table 4: Source e^- beam parameters for eRHIC and LHeC.

parameter	eRHIC	LHeC
electrons / bunch [10^9]	5.6, 24	1.1
charge / bunch [nC]	0.9, 3.8	0.18
rms bunch length [mm]	2	3–30
bunch spacing [ns]	18	25
average current [mA]	50, 220	7
bunch peak current [A]	50, 200	7–70
polarization	85–90%, none	$> 90\%$

ter and 8 m long) with a 3 m × 3 m × 10 m long shielding. If the LHeC injector is configured for energy recovery as in the case of eRHIC, decelerating the spent beam to 10 MeV, the beam power at the dump decreases to 64 kW.

LHeC also assumes positron-hadron collisions. Obtaining the desired e^+ rate is challenging. The source requirements may be relaxed by positron recycling, re-colliding, and cooling. A compact tri-ring scheme has been proposed for recooling the spent and recycled e^+ [3, 23]. If, through these measures, the required positron intensity needed from the source is reduced by an order of magnitude, several concepts could provide the e^+ intensity and the beam quality required, for example a Compton ring, a separate Compton ERL, or coherent pair production [3, 23].

IR AND BEAM-BEAM EFFECTS

The eRHIC interaction-region (IR) design avoids high-energy X-rays from synchrotron radiation through a large crossing angle, complemented by crab cavities (for the hadron beam with about 23 MV crab RF voltage at a fundamental RF frequency around 200 MHz, plus two higher harmonic crab RF systems, and for the electron beam with a 1-MV crab voltage at 700 MHz [24]), and through arranging for zero or extremely low magnetic fields on the electon beam trajectory, over the last 130 m before the IP. Only 1.9 W of soft radiation propagates through the detector (from a 2.4-mT field). At the other extreme, the LHeC IR design achieves head-on collisions by means of two detector integrated dipoles surrounding the IP, each with a field of about 0.3 T and a length of about 9 m, leading to the emission of 48 kW of X-rays (1.78×10^{18} γ/s) with a critical energy of 718 keV. About 73% of this power will be absorbed by dedicated SR absorbers located in front of the final SC hadron-beam quadrupole at 10 m from the IP.

The final quadrupole for eRHIC, 5.475 m from the IP, is a combined function magnet with a dipole field of 2.23 T and 88 T/m gradient, The final quadrupole for LHeC is a "half quadrupole" with a low-field exit hole for the electron beam and for the second (non-colliding hadron) beam, while the colliding proton beam should experience a gradient of 187 T/m [14, 25]. Both eRHIC and LHeC final quadrupoles could be realized using Nb_3Sn SC magnet technology, presently under development in the frame of the LHC luminosity upgrade program.

For LHeC the hadron-beam beam-beam tune shift of $\Delta Q \approx 10^{-4}$ is tiny — less than 1% of the LHC total p-p tune shift and of opposite sign — and, with 36σ separation at the first encounter provided by the near-IP dipole magnets, the effect of long-range collisions can be neglected. For eRHIC parasitic collisions are also unimportant, thanks to the 10-mrad crossing angle. Considering three collision points the maximum total beam-beam tune shift at eRHIC would be about 0.045, which is large, but consistent with experience at other colliders. A bigger concern is the hadron-beam emittance growth due to lepton-beam position jitter at the collision point. Extrapolating from Ref.[26] for LHeC the random orbit jitter from turn to turn should be less than 0.08σ at the IP. For both LHeC and eRHIC the lepton beam is heavily disrupted during the collision, as is indicated by the large disruption parameters $D \equiv N_{b,h} r_e \sigma_{z,h} / (\gamma_e \epsilon_h \beta_h)$ in Table 1. For LHeC the lepton beam emittance increases by about 15% with a proper matching of the extraction optics or by 180% if the exit optics does not take into account the optical effect of colliding with the proton beam. Similarly, the eRHIC lepton beam emittance grows by about a factor of 2 during the collision. The energy recovery path of the respective ERLs must accommodate these larger-emittance beams. For eRHIC the beam-beam kink instability is suppressed with a broad-band feedback system on the hadron beam [27]. At LHeC, with lower disruption parameter, much smaller hadron beam tune shift, and larger synchroton tune the kink instability is not expected to occur [27].

POLARIZATION

RHIC is the only polarized proton collider. In collisions at a beam energy of 250 GeV polarization at the level of 55% has been demonstrated and there are plans and means to push this polarization up to 70%. Proton polarization in the RHIC IPs is controlled by spin rotators. The heavy ions in RHIC, and all hadron beams in the LHC are unpolarized.

Polarized electron guns provide polarization at the 80-90% level. The direction of the electron spin can be flipped from one bunch to the next by changing the helicity of the gun laser photons. For eRHIC an economical way is chosen to maintain much of the source polarization and to orient it at the IP in the longitudinal direction. Namely there are no spin rotators and the spin is kept in the horizontal plane, rotating around the electron direction as a function of net bend angle and electron energy. In the proposed eRHIC layout the required orientation is obtained at RHIC Point 6 for collisions at discrete electron energies $E_e = n0.07216$ GeV, with n denoting an integer. Due to the finite energy spread the spin precession differs for different electrons in the beam. The effective polarization loss is given by the cosine of the spin vector spread angle; e.g. for an angle of 30^{deg}, the effective polarization is about 86% of the initial beam polarization. For eRHIC, an rms energy spread of 2×10^{-4} (6 MeV) leads to a loss in polarization by about 5% for the 30-GeV electron beam. Applying the same approach as for eRHIC to the 60-GeV electron beam in the LHeC a relative rms energy spread of 3×10^{-4} (18 MeV) would cause about 10% polarization loss due to the spread of the spin vectors. Since this

Copyright © 2012 by the respective authors — cc Creative Commons Attribution 3.0 (CC BY 3.0)

does not satisfy the polarization requirement imposed by the physics program, for LHeC a different approach has been chosen. Namely, the LHeC lepton polarization is preserved by rotating it into the vertical direction before the beam gets accelerated to high energy. Since the spin vector is then aligned with the main bending magnetic field direction, this prevents the spread of the spin vector due to the momentum spread. RHIC type spin rotators [32, 33] are considered for the LHeC leptons. Besides being compact, they offer independent control of the spin vector orientation, as well as nearly energy independent spin rotation for the same magnetic field. The four helical dipoles are arranged in a similar fashion as for the RHIC spin rotator [3]. Each helical dipole is 15 m long and the helicity alternates between right hand to left hand. To align the spin vector of the polarized electrons in the longitudinal direction at the IP, the magnetic fields of the inner and outer pairs need to be 0.46 T and 0.37 T, respectively. About 0.31 MW of synchrotron radiation power is then emitted by the 60-GeV electron beam passing through these magnets [34]. An alternative HERA type spin rotator, consisting of a series of 8 dipoles, has also been studied. For the same total length of the system the required dipole fields are 0.46 T (H) and 0.56 T (V) with a total SR power of 0.39 MW [34].

PLANS, OUTLOOK, AND THANKS

For the LHeC, in 2012 the R&D activities are focusing on preparation and on the exploration of possible collaborations with other research laboratories. This includes the choice of the preferred ERL RF frequency (721 MHz or 1.3 GHz). In 2013 the LHeC aims at the construction of a first SC IR model of the final quadrupole magnet with measurements on a short SC half-quadrupole magnet in 2014. A prototype of the IR beam pipes is also targeted for 2014. A final prototype RF cryostat including cavity and coupler is expected by 2015 [28]. The LHeC project will pursue the construction of a dedicated LHeC ERL test facility (Fig. 1), the design of which will be prepared over the next two years, with the goal of finalizing beam measurements by 2017. This test facilty could later be converted into the LHeC injector, including energy recovery. In parallel, a proto-collaboration is scrutinizing the detector design [28]. The above steps would allow a project decision on the LHeC by the time when results from the 7-TeV beam energy operation of the LHC are expected to be available.

For eRHIC the list of needed accelerator R&D [29] includes the 50-mA CW polarized source, CEC, and testing multiple aspects of the SRF ERL technology in BNL's already existing R&D ERL [30]. A final prototype RF cryostat is envisioned for 2014. By 2015 a CEC proof-of-principle demonstration is expected at a RHIC-based experiment set up in collaboration with JLAB, Daresbury, BINP and Tech-X [31]. Other important eRHIC R&D focuses on prototyping small-gap magnets and vacuum chambers for the eRHIC arcs, with final prototype magnets expected by 2013. Also the space-charge compensation by an electron beam is part of the eRHIC R&D plan. Other

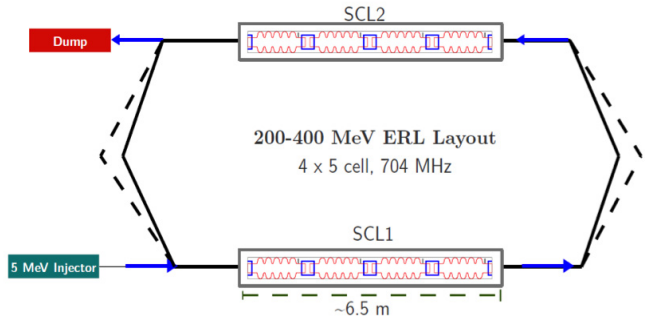

Figure 1: Schematic LHeC ERL test facility with two passes "up" and two passes "down", using two SC RF prototype cryo modules (R. Calaga).

eRHIC R&D relates to studies with hadron beams in RHIC for the various eRHIC operation modes. Speculatively, the eRHIC operation could start around 2020, with collisions of 250 GeV protons and 5–10 GeV electrons, followed by 10-GeV steps in electron energy every 2–3 years.

I thank S. Belomestnykh, I. Ben-Zvi, V. Litvinenko and V. Ptitsyn for updated information about eRHIC, and M. Bai, A. Bogacz, O. Brüning, R. Calaga, E. Jensen, J. Jowett, M. Klein, L. Rinolfi, S. Russenschuck, D. Schulte, D. Tommasini, R. Tomas, and J. Tückmantel for many helpful discussions on the LHeC.

REFERENCES

[1] ICFA Beam Dynamics Newsletter No. 58, August 2012
[2] LHeC web site: *http://cern.ch/lhec*
[3] J.Phys.G: Nucl.Part.Phys. 39, 075001 (2012)
[4] CERN-ECFA-NuPECC LHeC Workshop 14–15 June 2012
[5] S.A. Bogacz et al., arXiv:1208.2827 (2012)
[6] eRHIC web site: *http://www.bnl.gov/cad/eRhic*
[7] V.N. Litvinenko, Y.S. Derbenev, PRL. 102, 114801 (2009)
[8] V. Shiltsev et al., FERMILAB-CONF-9-152-APC
[9] E. Aschenauer, eRHIC Review 2011
[10] S. Belomestnykh et al., Proc. IPAC2012 Orleans, p. 2474
[11] V. Ptitsyn, eRHIC Review 2011
[12] D. Trbojevic et al., AIP CP 530 (2000) p. 333
[13] A. Bogacz, et al, Proc. IPAC2011 San Sebastian, p. 1120
[14] S. Russenschuck et al., IPAC2012 New Orleans, p. 1996
[15] E. Pozdeyev, PRST-AB 8, 054401 (2005)
[16] D. Schulte, private communication; and [3]
[17] D. Kayran, eRHIC Review 2011
[18] V. Litvinenko, PRST-AB 15, 074401 (2012)
[19] Y. Saveliev, CERN ATS Seminar 5 Sept. 2012
[20] E. Tsentalovich, 18th Int. Spin Physics Symp. (2008)
[21] V. Litvinenko, CA/AP/417; X. Chang et al., PAC11, p. 1969
[22] R. Calaga et al., Physica C 441 (2006), p. 159
[23] F. Zimmermann et al., IPAC2012 New Orleans, p. 3108
[24] V.N. Litvinenko, "Crab Crossing," eRHIC Review 2011
[25] R. Tomas et al., Proc. IPAC2011 San Sebastian, p. 2796
[26] K. Ohmi et al, Proc. PAC07 Albuquerque, p. 1496
[27] Y. Hao et al., Proc. IPAC12 New Orleans, p. 2017
[28] O.S. Brüning et al., Proc. IPAC2012 New Orleans, p. 1999
[29] V.N. Litvinenko et al., in Ref.[1], p. 52
[30] I. Ben-Zvi et al., in Ref.[1], p. 151
[31] V.N. Litvinenko et al., Proc. PAC2011, p. 2064
[32] I. Alekseev et al., Nucl.Inst.Meth. A499, 392 (2003)
[33] V. Ptitsyn, AGS/RHIC/SN No. 5 (1996)
[34] M. Bai, "Spin Rotator" at [4]

Copyright © 2012 by the respective authors — cc Creative Commons Attribution 3.0 (CC BY 3.0)

PLASMAS, DIELECTRICS AND THE ULTRAFAST: FIRST SCIENCE AND OPERATIONAL EXPERIENCE AT FACET*

C.I. Clarke†, E. Adli, S. Corde, F.J. Decker, R.J. England, R. Erickson, A. Fisher, S. Gessner, C. Hast, M.J. Hogan, S.Z. Li, N. Lipkowitz, M. Litos, Y. Nosochkov, J. Seeman, J.C. Sheppard, I. Tudosa, G. White, U. Wienands, M. Woodley, Z. Wu, G. Yocky, SLAC, Menlo Park, CA 94025, USA
C. Clayton, C. Joshi, W. Lu, K.A. Marsh, N. Vafaei, University of California, Los Angeles, USA

Abstract

FACET (Facility for Advanced Accelerator and Experimental Tests) is an accelerator R&D test facility that has been recently constructed at SLAC National Accelerator Laboratory. The facility provides 20 GeV, 3 nC electron beams, short (20 μm) bunches and small (20 μm wide) spot sizes, producing uniquely high power beams. FACET supports studies from many fields but in particular those of Plasma Wakefield Acceleration and Dielectric Wakefield Acceleration. FACET is also a source of THz radiation for material studies. We present the FACET design, initial operating experience and first science from the facility.

INTRODUCTION

Accelerators are our primary tool for discovering the fundamental laws to the universe. Each new frontier we probe requires a new, more powerful machine. Accelerators using conventional technologies are therefore increasing in size and cost. The future of this field will require new accelerating techniques that can reach the high energies required over shorter distances. New concepts for high gradient acceleration include utilizing the wakes in plasma and dielectric and metallic structures. FACET was built to provide a test bed for novel accelerating concepts with its high charge, highly compressed beams. As a test facility unlike any other, it has also attracted groups interested in beam diagnostic techniques and studies using terahertz radiation. In addition, the SLAC linac continues to offer opportunities to study conventional acceleration structures and accelerator physics.

FACET construction was completed in May 2011 and it became a United States Department of Energy User Facility for High Energy Physics in January 2012. FACET was commissioned and the first User Run took place over 12 weeks in 2012.

FACET has a five year program, operating four to five months every year through to 2016. Proposals are solicited every year and peer reviewed with the highest ranked experiments gaining beam time.

THE FACILITY

FACET delivers electron bunches to experiments with tightly focused transverse beam sizes and ultra-short bunch lengths. Positron bunches will be commissioned in 2013 for delivery to FACET experiments in 2014.

Multiple experiments share the same beam line and the waist of the beam is shifted according to the location of the experiment. The design parameters are given in Table 1 along with the best beam parameters that have been the achieved during the 2012 user run and typical parameters that were delivered regularly.

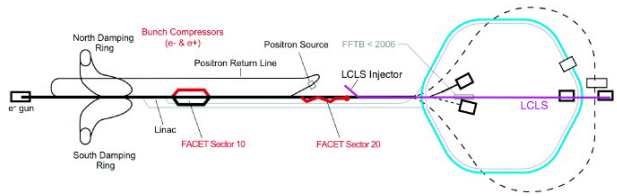

Figure 1: The SLAC linear accelerator and associated facilities. Two kilometers of s-band accelerating structures lead into FACET's final focus section. FACET's dump separates the first 20 sectors of the linac from the final 10 which are used by LCLS.

Linear Accelerator

FACET uses the first two-thirds of the SLAC linac to accelerate electrons up to 20 GeV (Fig. 1). An extraction kicker after the accelerating structures can direct the electrons to either the FACET experimental area and dump or into a positron target. Positrons are generated at the target and boosted to 200 MeV. They are then transported to the start of the linac and accelerated such that they enter the positron damping ring at 1.2 GeV. The positrons are then accelerated to an energy above 20 GeV using the same beamline as the electrons.

Bunch Compression

Three stages of bunch compression deliver the ultrashort bunches (with a design value of σ_z of 17 μm or 57 fs) to FACET experiments.

The first stage of compression occurs on injection from the damping ring to the linac. The bunches are compressed from 5.5 mm in the damping ring to 1.5 mm in the linac.

The next stage was built in 2002 for the Sub-Picosecond Pulse Source (SPPS) to compress electron bunches further to ~50 μm. This is a magnetic chicane in Sector 10 of the linac. The positron arm of the chicane was built in March 2012 and is exactly symmetric to the electron chicane.

* Work supported by the U.S. Department of Energy under contract number DE-AC02-76SF00515.
† cclarke@slac.stanford.edu

Copyright © 2012 by the respective authors — cc Creative Commons Attribution 3.0 (CC BY 3.0)

Table 1: FACET beam design parameters compared to the best beam parameters and the typical beam parameters achieved during the FACET User run 2012 without significant beam tuning.

Parameter	Design Goal	2012 Best	2012 Typical
Energy [GeV]	23	20.35	20.35
RMS Energy Spread [%]	1.5	1.5	1.5
Charge [nC]	3	3.2	2.9
Bunch Length σ_z	<30	20	20
Beam size $\sigma_x \times \sigma_y$	<15×15	20×23	35×35
Repetition Rate [Hz]	30 Hz	1-10 Hz	1-10 Hz

The third and final compression occurs in another magnetic chicane 20 m upstream of the experimental area. This brings the length of the bunch to a σ_z of ∼17 μm. This chicane can be set to compress either electrons or positrons.

Final Focus

The optics in FACET are designed to deliver a small, round beam at the "Interaction Point" (IP). The longitudinal position of the IP can be changed using upstream quadrupoles. Therefore, a series of experiments that require small spot sizes at different locations along the beam line can be supported by changing the optics.

Notch Collimator and Jaw Collimator

The notch collimator was installed in March 2012 to selectively collimate the incoming electron or positron bunches, effectively producing two bunches [2]. In wakefield acceleration studies, these bunches are termed the drive and witness bunch. The two bunches are separated by ∼160 μm (from simulation), which is ideal for wakefield studies.

The notch collimator is a tantalum blade that can be inserted into the beam path in the middle of the last chicane. At this location, energy is strongly correlated with position in x so by removing a portion of the beam in x, two bunches separated in time are formed after the chicane. The separation can be changed as well as the amount of charge in each of the drive and witness bunch.

A significant change of the optics is necessary in the final chicane which nominally has a R_{56} setting of 5 mm but needs to be changed to 10 mm to over-compress the bunch. In 2012, we saw the successful production of two bunches separated in time. More work will follow in 2013 to characterize this chicane setting and the notch collimator.

A jaw collimator immediately downstream is able to shape the bunch, producing ramped-charge drive bunches.

Transverse Deflecting Cavity

An x-band transverse deflecting cavity (xTCAV) allows single-shot measurement of the longitudinal profile of the bunch. Located upstream of the experiments but downstream of the notch collimator, it deflects the bunches transversely according to the longitudinal position in the bunch. The deflected bunch is then intercepted by a downstream profile monitor screen providing an image of the temporal distribution of the bunch. The resolution is designed to be 10 μm.

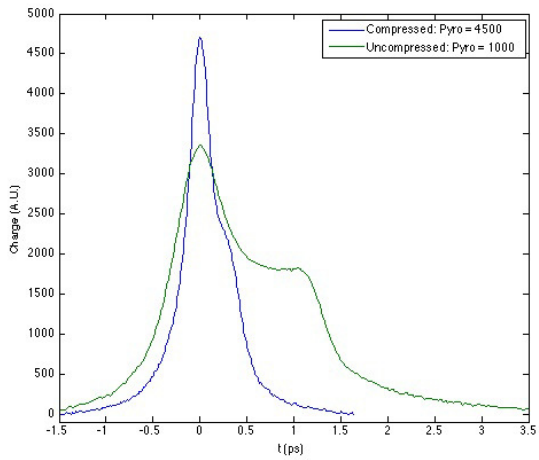

Figure 2: Preliminary results for longitudinal bunch profiles as measured by the xTCAV. Shown are two bunch profiles for the maximally compressed bunch (blue) and an uncompressed bunch (green).

Data were taken with the xTCAV in 2012. Studies are ongoing to understand the effects of the beamline optics and how to correct for intrinsic tilt. A variety of longitudinal profiles were observed from near-Gaussian bunches at maximum compression to two-peaked structures off-compression (Fig. 2).

Experimental Area

The main area for experiments at FACET is the "IP Area" (Fig. 3) immediately after the final focus system. The optics are designed to focus the beam in this area. 8 meters of optical breadboard support experiments and diagnostics.

Upstream of the IP Area, there is a 2.5 m optical table currently used for studies of the THz coherent transition radiation from the beam being intercepted by thin titanium foils.

The experiments are supported by diagnostics [3]. There are beam position monitors and toroids through the linac. Optical transition radiation (OTR) beam profile monitors

Copyright © 2012 by the respective authors — cc Creative Commons Attribution 3.0 (CC BY 3.0)

and a wirescanner provide beam spot size information in the IP Area. Pyroelectric detectors measure coherent transition radiation (CTR) providing a monitor of the bunch length. Synchrotron x-rays from a wiggler magnet in the third-stage bunch compressor chicane are intercepted and imaged to measure the energy spread. As part of the support for acceleration studies, there is an energy spectrometer at the dump table that uses Cerenkov light emitted in a defined air gap.

INITIAL OPERATING EXPERIENCE

The SLAC linac was turned off in April 2008 after the final PEP-II run. The last third continued to be used for LCLS however, the first two-thirds of the linac were unused, aside from a short check, until June 2011. Bringing the linac back for FACET after this period of dormancy came accompanied by challenges with the expected hardware failures which were systematically dealt with; for the 2012 User run, accelerator hardware uptime was over 90%. There were also significant operational challenges related to the new operation of the linac for highly compressed beams, the strong chromatic correction to the FACET lattice and the demands of the experimental program.

Commissioning the electron beam for FACET

The electron beams at FACET were commissioned during two periods [1]. The first period comprised 12 weeks in the summer of 2011. There followed a downtime period to complete the upgrade of the sector 10 chicane to allow compression of positrons as well as electrons. This downtime period of nearly 6 months also permitted several upgrades and improvements to the beamline and diagnostics including bunch length monitors in sectors 2 and 18 and movers on two sextupoles in the sector 20 chicane plus realignment of portions of the linac. The second commissioning period was in spring 2012 and comprised 5 weeks. The downtime work was of considerable benefit to achieving the goal of "20x20x20" bunches in 2012.

Operating the linac as a User Facility

The experiments were scheduled for 12 weeks immediately following the 2012 commissioning period. The beam time in these 12 weeks was divided between the experiments, access days and machine development days.

FACET tunnel access days were scheduled and planned in advance due to the large amount of support required by SLAC staff to both do the scheduled work during the access and recover from the access. Recoveries from shutting down the linac for at least half a day often took an equivalent amount of time before beam could be delivered with close-to-ideal parameters in FACET.

The day after the access was scheduled for machine development and beam set-up for experiments. Continuous machine development was necessary to study the beam and study new optics or lattices. As a result of weekly study, beam parameters, stability and reliability at FACET steadily improved.

Experiments ran 24 hours a day and efforts were taken to schedule each experiment in long blocks of time to minimize the time spent changing the configuration of the optics from one experiment to another. This was challenging as it put a strain on personnel on both the experimenter and machine side. Configuration changes and beam tuning took considerable amounts of time making this a large burden on the accelerator physicists and operators but systematic procedures and experience led to improvements. Accesses by experimenters outside of the access days were detrimental to the beam quality and the target beam parameters were difficult to achieve following an access without considerable beam tuning.

An operational difficulty at FACET in 2012 involved the frequent failure of the OTR screens. This affected the ability to tune the beam's transverse size quickly as the only diagnostic capable of measuring it at the focus was the wirescanner which took minutes per measurement. The 1 μm thick titanium foils were destroyed by the high power electron beams at high bunch compression and small transverse spot-size. A 500 μm titanium disk was successfully used for beam spot-size tuning towards the end of the run and these thicker disks will be used throughout the IP Area in 2013.

There were also electronic hardware failures in the experimental areas from radiation damage. We estimate that the experimental area sees between 2 and 4 kilorad of dose each week depending on location, a tenth of the dose being from neutrons. Most electronics in FACET suffered from the radiation, in particular the cameras used for the diagnostics.

FIRST SCIENCE FROM EXPERIMENTAL PROGRAM

Two rounds of proposals for FACET have been peer-reviewed and awarded beam time. A third round of proposal review is scheduled for October 2012. In the first FACET user run, which lasted 12 weeks in 2012, six experiments had beam time and two test-beam studies.

Plasma Wakefield Acceleration

SLAC has a history of plasma wakefield acceleration (PWFA) with studies at the Final Focus Test Beam (FFTB) culminating in the acceleration of electrons from 42 GeV to 85 GeV in 85 cm [4]. The 2012 studies at FACET used field-ionized lithium and rubidium plasma. Plasma density was $10^{14} - 10^{17} \mathrm{e}^{-}/\mathrm{cm}^3$ and the length of the plasma column was 20-30 cm. The plasma was contained within cooled buffer-gas, helium in the case of lithium and argon in the case of rubidium.

Field-ionized plasma wakefield acceleration using lithium resulted in signs of a small amount of beam-plasma interaction and acceleration of 3-4 GeV. Changing to rubidium, which has a lower first ionization energy, led to significantly more beam-plasma interaction and more consistent results, less dependent on the quality of the beam

Copyright © 2012 by the respective authors — cc Creative Commons Attribution 3.0 (CC BY 3.0)

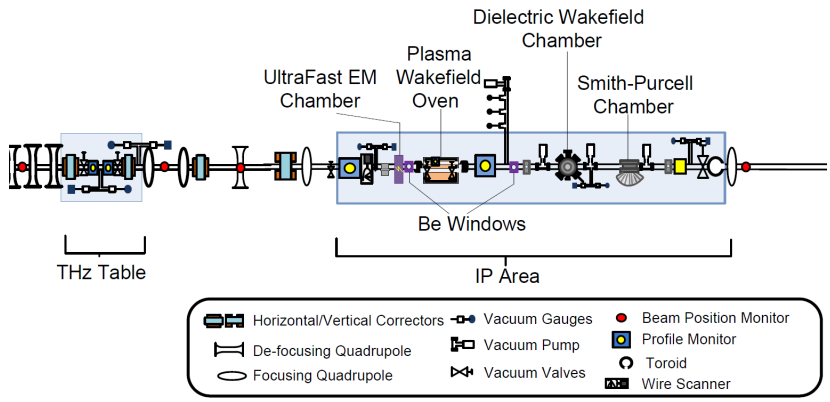

Figure 3: The IP Area includes two chambers that can be used to insert samples into or near the beam (UltraFast EM Chamber and Dielectric Wakefield Chamber). There is also an oven used in plasma acceleration studies plus experimental diagnostic devices such as the Smith-Purcell Chamber.

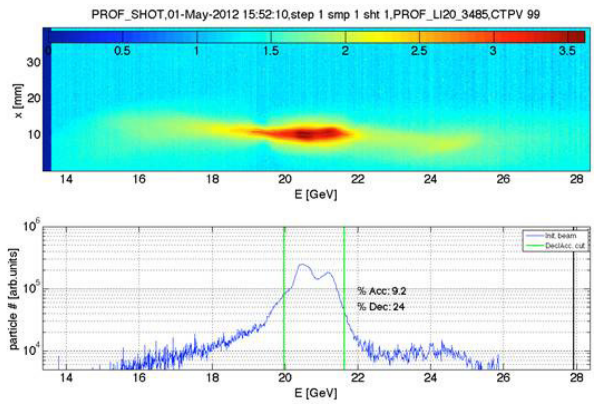

Figure 4: Image from cherenkov spectrometer from beam after passing through lithium vapor. Approximately a quarter of the bunch has interacted with the plasma and lost energy and just under 10% has gained energy.

(Fig. 4). It was estimated that between 10-20 GV/m acceleration gradients were seen. Dark current was produced from double-ionizing the rubidium and the also ionizing the argon buffer gas.

The next step is to put two bunches produced by the notch collimator through the rubidium vapor. A 10 TW laser will be installed for the next run as to get 20 GV/m gradients with the inevitable loss in charge density that comes from dividing the bunch into two, the vapor needs to be pre-ionized.

Head Erosion Study Head erosion is one of the limiting factors in PWFA. The head of the drive bunch becomes de-focused as the bunch traverses the plasma, lowering the charge density until it no longer ionizes the plasma therefore moving the ionization front further down the drive bunch with length of plasma traversed. Studies purposefully spoiling the emittance of the electron bunch at FACET using 50 μm gold foils demonstrated that the beam-plasma interaction could be slowly diminished and stopped altogether by increasing the emittance of the incoming bunch [5].

Betatron Radiation Diagnostic Hard X-rays and gamma rays are produced by the betatron oscillation of electrons in a beam-driven plasma wake. This betatron radiation was used as a diagnostic for beam matching into the plasma in 2012. Beam matching is critical for maximizing the energy extraction efficiency of a plasma accelerator stage. The detector was built immediately in front of the FACET dump. It comprised a 30 cm x35 cm phosphorescent screen which observed the transverse extent of the radiation and a sampling electromagnetic calorimeter with photodiodes for measuring the on-axis spectrum. To estimate the spectrum, the observed intensity patterns across the calorimeter are fit with a Gaussian-integrated synchrotron spectrum and compared to simulations [6].

Wakefield Acceleration in dielectric and metallic structures

Other concepts for accelerating structures involve wakefields in dielectric or metallic structures. These structures are also of considerable interest as THz sources.

Wakefield measurements in structures are common to facilities around the world but FACET offers high bunch charge and short bunch length which can drive multi-GV/m fields. This is where the longitudinal breakdown thresholds are for dielectric structures [7] so studies at FACET push the limits of the technology.

Dielectric structure studies at FACET in 2012 placed cylindrical structures of silica, diamond, alumina and sapphire and looked at the narrow-band, high-power coherent cherenkov radiation (CCR) produced to identify the modes being excited. Future plans include using slab-symmetric structures of diamond and silica and a Bragg-mirror structure.

Copyright © 2012 by the respective authors — cc Creative Commons Attribution 3.0 (CC BY 3.0)

Bunch length and profile measurement

Measuring bunch profiles of a few fs in a non-invasive and cost-effective manner is a challenge for future light-sources and accelerators. FACET provides a test-bed for bunch profile measurements in this regime.

In one experiment, coherent Smith-Purcell radiation is detected and used to reconstruct the temporal profile of the electron bunch [8]. Another experiment reconstructs temporal profiles from the power spectrum of the coherent transition radiation (CTR) from 1 μm titanium foils using a Michelson interferometer [9]. The results from these techniques are being bench marked against each other and also the measurement of the longitudinal bunch profile seen by the xTCAV.

THz studies

The short bunch length and high bunch charge at FACET makes it an excellent broadband THz source with high-peak field. When the beam passes through thin metal foils, transition radiation is produced with little degradation to the main electron beam so THz extraction is essentially parasitic to the other FACET experiments.

Calculations indicate that the CTR electric fields created are 0.6 V/Å or more when the beam's transverse size and length are optimized (20 μm) and the pulse contains 13 mJ making FACET potentially the brightest THz light source in the world [9]. Preliminary measurements with a large and flat beam (σ_x = 317 μm, σ_y = 36 μm) at 3 nC charge show 0.46 mJ of THz energy per pulse [10] as measured by a pyroelectric joulemeter. A knife-edge scan of the THz radiation at its focus measured σ_x = 1.36 mm and σ_y = 1.08 mm. The Michelson interferometer scan measured the length of the THz pulse as σ_z = 39 μm. The peak electric field of this THz pulse is 0.057 V/Å.

The THz radiation can be extracted, focused and delivered to experiments. A THz transport line has been designed to bring the THz radiation out of the accelerator tunnel to a local laser room to study materials in these intense fields and perform biological and chemical imaging.

Ultrafast processes in materials

Currently an experiment is taking advantage of the intense electromagnetic fields associated with the electron beam to probe domain switching in magnetic solids on the femtosecond timescale. This "Ultrafast Electromagnetic Switching" experiment inserts thin magnetic foils into the beam to be exposed to a single electron bunch. The exposed foils are removed from the beamline and analyzed with a spin-sensitive scanning electron microscope which can image the pattern of the magnetic domains. The resulting figure-eight pattern (Fig. 5) is from precessional switching [11]. The full characteristics of the pattern cannot be explained by the magnetic field alone; there is an effect where the electric field provides a torque, linear with the electric field strength.

The materials have expanded from simple magnetic solids to magnetic films such are as used in spintronics applications for MRAM memory and also ferroelectrics and multiferroics. Signs of femtosecond scale switching of electric polarization were seen in samples of PZT in 2012.

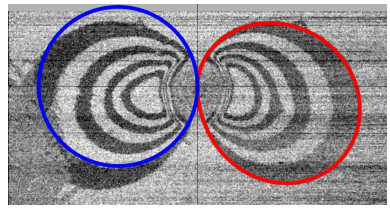

Figure 5: Image from a spin-sensitive SEM of a thin film of iron grown on a tungsten crystal after exposure from a single electron bunch. The full size of the image is ~900 μm. The blue circle shows the hypothetical switching boundary when only the magnetic field effect is included. The red circle takes into account the torque on the magnetization induced by the electric field. The distorted lines near the center are due to reduced magnetization as the film is heated near Curie temperature by the electron bunch.

FUTURE FOR FACET

FACET will operate for four to five months each year for the next four years. There will be periods of dedicated beam tuning prior to each user run to ensure good beam delivery to the users. In 2013, positron beams will be commissioned for delivery to FACET's experiments in 2014. A large upgrade to the facility next year will be the installation of a 10 TW laser for pre-ionisation of the plasma. This expands the plasma program at FACET beyond multi-GeV PWFA to Trojan Horse Plasma Wakefield Acceleration which can produce exceptionally low emittance electron beams and the study of the Self-Modulation of Long Lepton Bunches which paves the way towards PWFA with protons.

New proposals for experiments, whether a part of the wakefield acceleration program or a general beam physics or material science program, can be submitted throughout the year.

REFERENCES

[1] J. Yocky et al., IPAC'12, New Orleans, May 2012

[2] R.J. England et al., AIP Conf. Proc., 1299, pp. 478-482 (2010)

[3] S.Z. Li and M.J. Hogan, PAC'11, New York, March 2011.

[4] I. Blumenfeld et al., Nature 445, 741-744 (2007).

[5] S.Z. Li, SLAC Publication SLAC-PUB-15212

[6] M. Litos and S. Corde, SLAC Publication SLAC-PUB-15215

[7] M.C. Thompson et al., Phys.Rev.Lett., 100, 214801 (2008).

[8] R. Bartolini, IPAC'11, San Sebastian, Sept. 2011.

[9] Z. Wu et al., PAC'11, New York, March 2011.

[10] Z. Wu et al., IPAC'12, New Orleans, May 2012

[11] I. Tudosa et al., Nature 428, 831-833 (22 April 2004).

Copyright © 2012 by the respective authors — cc Creative Commons Attribution 3.0 (CC BY 3.0)

LINAC CONSTRUCTION FOR CHINA SPALLATION NEUTRON SOURCE

Shinian Fu, Jian Li, Huachang Liu, Huafu Ouyang, Xuejun Yin, IHEP, Beijing 100049, China

Abstract

Construction of China Spallation Neutron Source (CSNS) has been launched in September 2011. CSNS accelerator will provide 100kW proton beam on a target at beam energy of 1.6GeV. It consists of an 80MeV H^- linac and 1.6GeV rapid cycling synchrotron. Based on the prototyping experience, CSNS linac, including the front end and four DTL tanks, has finalized the design and started procurement. In this paper, we will first present an outline of the CSNS accelerator in its design and construction plan. Then the some prototyping results of the linac will be presented. Finally the linac construction progress in recent will be updated.

INTRODUCTION

China Spallation Neutron Source(CSNS) project was approved by the Chinese central government in 2008[1-2]. It has been launched in September 2011. Figure 1 shows the linac tunnel construction status up to now. It is planed to provide neutrons to the users in the first half of 2018. CSNS has a total budget of $260 M for construction of the accelerator, the spallation neutron target and 3 neutron spectrometers. Its site is at Dongguan, south part of China. The local government will support free land, additional budget of $57M, infrastructure, dedicated high-way and power transformer station.

Figure 1: Civil construction status of the linac tunnel.

CSNS accelerator is the first large-scale, high-power accelerator project to be constructed in China. The CSNS is designed to accelerate proton beam pulses to 1.6 GeV kinetic energy at 25 Hz repetition rate, striking a solid metal target to produce spallation neutrons The accelerator provides a beam power of 100 kW on the target in the first phase and then 500 kW in the second phase by increasing the average beam intensity 5 times while raising the linac output energy to 250 MeV. A schematic layout of CSNS phase-I complex is shown in Figure 2. The major design parameters of the CSNS accelerator complex for the two phases are listed in Table 1. In the phase-I, an H^- ion source produces a peak current of 25 mA H^- beam. RFQ linac bunches and accelerates it to 3 MeV. DTL linac raises the beam energy to 80 MeV. After H^- beam is converted to proton beam via a stripping foil, the RCS accumulates and accelerates the proton beam to 1.6 GeV before extracting it to the target.

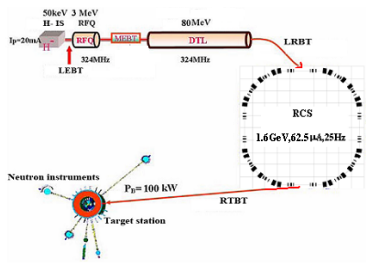

Figure 2: Schematics of the CSNS complex

Table 1: CSNS Design Parameters

Project Phase	**I**	**II**
Beam power on target [kW]	100	500
Proton energy [GeV]	1.6	1.6
Average beam current [μA]	62.5	312.5
Pulse repetition rate [Hz]	25	25
Linac energy [MeV]	80	250
Linac type	DTL	+SC Spoke
Linac RF frequency [MHz]	324	324
Macropulse. ave current [mA]	15	40
Macropulse duty factor	1.0	1.7
RCS circumference [m]	228	228
RCS harmonic number	2	2
RCS acceptance [πmm-mrad]	540	540

LINAC DESIGN AND DEVELOPMENT[3]

Penning H^- ion source is adopted for CSNS linac. The source provides 25 mA peak current, 0.5 ms long, 0.2πμm normalized emittance (rms) pulses at 50 kV and 25 Hz repetition rate for Phase-I.

The LEBT is for matching and transporting the H^- beam from ion source to RFQ accelerator, and pre-chopping the beam according to the requested time structure by the RCS with a chopping rate of 50%. Three-solenoid focusing structure is adopted for space charge neutralization, as shown in Figure 3. An electrostatic deflector is chosen as pre-chopper, positioned at the end of the LEBT. A prototype pre-chopper was installed at the entrance of the 352MHz proton RFQ, and it reached a fast rise time of 15 ns in the beam measurement at the exit of the RFQ[4].

Copyright © 2012 by the respective authors — cc Creative Commons Attribution 3.0 (CC BY 3.0)

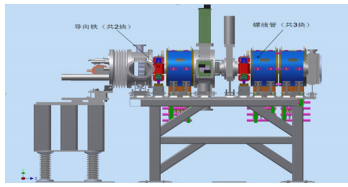

Figure 3: Front end of CSNS linac.

The CSNS RFQ construction is based on our experience of ADS RFQ design and manufacture[5]. A four-vane type RFQ is adopted with RF frequency of 324MHz. It accelerates H- beam from 50 keV to 3 MeV, with duty factor of 1.05%. The inter-vane voltage is 80 kV with Kilpatrick factor of 1.78. It has a total length is 3.62 m and is separated in two segments(Figure4). They are resonantly coupled with the coupling cell in the middle. Each segment technically consists of two modules and each module is composed with two major vanes and two minor vanes, and they are brazed together to form a vacuum cavity. Three sets of 1000 l/s ion pumps and 500 l/s turbo-molecular pumps are designed for an order of 10^{-7} torr dynamic vacuum pressure. Along the RFQ cavity there are 12 tuners in each quadrant for tuning field flatness and minimal dipole component. 20 cooling-water channels are distributed in the cross-section of the cavity for thermal stabilization and frequency tuning during operation. Four RF power couplers feed a pulse power of 510 kW into the cavity.

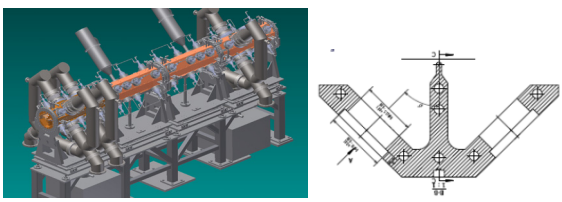

Figure 4: RFQ cavity (right), major vane with cooling-water channels (left).

The total length of MEBT is about 3 m, majorly including 10 qaudrupoles, two bunchers in the first phase. Two J-PARC type RF choppers will be added for the second phase. Beam instruments for beam current, beam position and beam loss are also installed in the MEBT. Figure 5 shows a scheme of the MEBT elements installation. Multi-particle simulation indicates the linac emittance growth majorly occurs in the MEBT. The RMS emittance growths in the x, y, z directions are respectively about 20%, 19% and 16% for 15mA beam in the first phase.

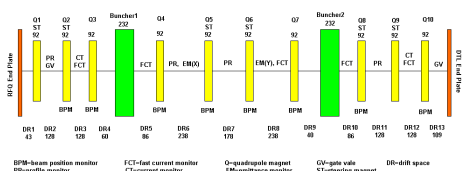

Figure 5: CSNS MEBT elements arrangement.

The DTL accelerates the 3 MeV beam from the RFQ to 80 MeV. The maximum surface field is below 1.3 times the Kilpatrick limit. In the old vision of the DTL design, we used FD lattice with a small drift tube bore radius[4]. It was found the particle losses was more than the limit of 1W/m when all errors were taken into account in the end-to-end multiparticle simulations. So FFDD focusing lattice is used in the new vision of DTL design with a lager bore radius for the drift tubes and lower quadrupole gradient. In this new design, the accelerating field keeps constant in each tank. The major parameters of the DTL tanks are listed in Table 2.

Table 2: The Major Parameters of the DTL Tanks

Tank number	1	2	3	4	total
Output energy (MeV)	21.67	41.41	61.07	80.1	80.1
Length (m)	8.51	8.56	8.78	8.8	
Number of cell	64	37	30	26	157
Cavity power (MW)	1.35	1.32	1.32	1.34	5.33
Total RF power (MW)	1.91	1.92	1.92	1.93	7.68
Accelerating field (MV/m)	2.86	2.96	2.96	3.0	
Synchronous phase (degree)	-35 to -25	-25	-25	-25	

A tank consists of three unit tanks with a length about 2.8 m for fabrication. Drift tubes are mounted on the tank through holes on the top of the tank. DC power supply is used for the focusing quadrupole in the drift tube. Each tank has 12 plug tuners and 2 dynamic tuners. A power coupler with ridged waveguide feed 2 MW RF power to a tank from a klystron. Vacuum of 1×10^{-6} Pa is guaranteed with 6 ion pumps and 3 molecular turbo pumps in each tank. The first tank of the DTL is plotted in Figure 6.

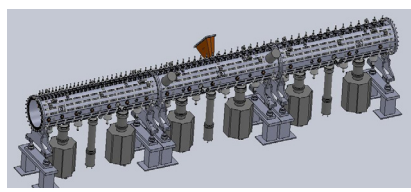

Figure 6: First tank of the CSNS DTL.

A prototype DTL has been fabricated for the technology development and cold measurement[6]. Figure 7 shows the prototype tank and measured alignment result of the drift tubes with error less than 0.03 mm.

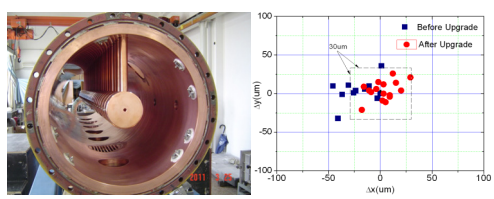

Figure 7: Prototype DTL and the measured center of the drift tubes.

Copyright © 2012 by the respective authors — cc Creative Commons Attribution 3.0 (CC BY 3.0)

LINAC CONSTRUCTION

CSNS linac is planed to start installation at the end of 2013 when the linac tunnel becomes available. Now most of the linac components have started fabrication or procurement.

The ion source has been ready for assembly. Figure 8 shows the major components of the source body. As we have set up a prototype H^- ion source at IHEP with a satisfactory beam current, we can take the advantage of this experience to start beam extraction test and beam transmission tuning in the LEBT in the early of the next year at IHEP before the laboratory at CSNS site becomes available.

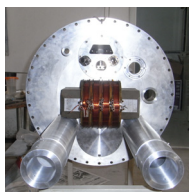

Figure 8: H^- ion source body during assembly.

RFQ cavity is now under fabrication. The 16 major vanes have been drilled the cooling water channels and will start semi-fine machining, while the 16 minor vanes are under fine machining. It is planed to complete the cavity fabrication in the middle of the next year. The RFQ will be powered by two 4616V4 tetrode amplifiers at 324 MHz with an output pulsed power of 350 kW for each. We replaced klystron in the old design with this tetrode just for less cost. Now one of the tetrode power sources has been set up at IHEP, and the test result shows it reached the output power 400 kW with a pulse length of 700㎳ at 25 Hz. Based on this successful experience, another set of the power source will soon start construction. Figure 9 shows the RFQ vanes under fabrication and tetrode power source.

Figure 9: RFQ vanes under fabrication (right) and tetrode power source (left).

For the MEBT, we will not fabricate any magnet and its power supply, as we are going to make use of the existing magnets of the beam line for ADS experiment. Two bunchers will start fabrication in recent and their solid state power sources of 25 kW have been ordered.

The DTL manufacture started in the end of the last year at the workshop of IHEP, at which a prototype DTL has been made. We will basically follow the manufacture technology of the prototype. The tank is made of carbon steel and the inner surface is copper-plated, with a thickness of 0.15mm after polishing. The drift tube is made of full copper and so does the stem. The quadrupole coil is SAKAE type, the same as J-PARC DTL. As the coincident of the mechanical center of the drift tube with the magnetic center of the quadrupole is rather essential requirement beam loss control and the work is very time costing during the manufacture of the drift tube, we built a new rotating-coil measurement system so as to reach a high accuracy of 6㎜ and high efficiency in the measurement of the magnetic center, as well as high-order modes, of the quadrupole. The system is now under test, as shown in Figure 10.

Figure 10: Rotating-coil magnetic measurement system.

Now the first tank is under fabrication, as shown in Figure 11. It is expected the first tank can be installed in the linac tunnel in the January 2014 after the beam commissioning of the RFQ. Then the following three tanks will be installed after the beam commissioning of the MEBT and the first DTL tank in August of 2014.

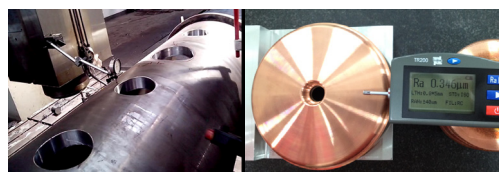

Figure 11: The DTL tank and drift tube under machining.

ACKNOWLEGEMENT

The authors are very grateful to the CSNS linac team members for their great efforts in the design and construction of the linac.

REFERENCES

[1] J. Wei, S.Fu, et al. China Spallation Neutron Source - an overview of application prospects, Chinese Physics C 2009, 33(11): 1033-1042.

[2] Shinian Fu, Hesheng Chen, et al, “Status and Challenges of the Chinese Spallation Neutron Source”, IPAC2011, San Sebastian, Spain, Sept. 2011, TUXA01.

[3] S.N.Fu, H.F.Ouyang, et al., “Status of a High Current Linaer Accelerator at CSNS”, LINAC2008. Victoria, Canada, Sept. 2008, MO202.

[4] H.F.Ouyang, S.N.Fu, J. Li, T. G. Xu, X. J. Yin, “The High Intensity Linac for CSNS”, LINAC2010, Tsukuba, Japan, Sept. 2010, TU202.

[5] S.N.Fu, S.X.Fang, et al., “Construction of a High Current RFQ for ADS Study”, LINAC2006. Knoxville, Tennessee USA, August 2006, MOP053.

[6] H.C. Liu, X.J.Yin, et al, “CSNS DTL Prototyping and RF Tuning”, this proceedings.

Copyright © 2012 by the respective authors — cc Creative Commons Attribution 3.0 (CC BY 3.0)

PERFORMANCE OF FERRITE VECTOR MODULATORS IN THE LLRF SYSTEM OF THE FERMILAB HINS 6-CAVITY TEST*

P. Varghese†, B. Chase, E. Cullerton, C. Tan, B. Barnes
Fermi National Accelerator Laboratory (FNAL), Batavia, IL 60510, USA

Abstract

The High Intensity Neutrino Source (HINS) 6-cavity test is a part of the Fermilab HINS Linac R&D program for a low energy, high intensity proton/H- linear accelerator. One of the objectives of the 6-cavity test is to demonstrate the use of high power RF Ferrite Vector Modulators(FVM) for independent control of multiple cavities driven by a single klystron. The beamline includes an RFQ and six cavities. The LLRF system provides a primary feedback loop around the RFQ and the distribution of the regulated klystron output is controlled by secondary learning feed-forward loops on the FVMs for each of the six cavities. The feed-forward loops provide pulse to pulse correction to the current waveform profiles of the FVM power supplies to compensate for beam-loading and other disturbances. The learning feed-forward loops are shown to successfully control the amplitude and phase settings for the cavities well within the 1% and 1° requirements specified for the system.

INTRODUCTION

The use of FVMs to regulate the phase and amplitude of individual cavities in a multi-cavity system driven by a single klystron helps to reduce the cost of the RF system for linear accelerators[1]. High power waveguide FVMs have been developed and the dynamic range of their phase shifting and amplitude attenuating capabilities have been studied[2]. Modeling and simulation of RF control systems with FVMs have shown their potential for field control of individual cavities in a multi-cavity system[3]. A learning feed-forward[LFF] control for the HINS six cavity test accelerator was integrated into the LLRF system. All RF components are driven by a single 325 MHz, 2.5MW pulsed klystron. The LFF algorithm is described and the results of its performance with beam are presented .

LLRF SYSTEM

The RF control block diagram for the 6-cavity test is shown in Fig.1. The LLRF control system regulates the phase and amplitude of the RF field vectors of the RFQ and the six room temperature copper cavities. There is a traditional wide-band proportional and integral feedback control loop around the klystron and the RFQ. Because the RFQ is a low Q device, it behaves much like a resistive load. Therefore, by regulating the RFQ field, the klystron output to the six cavities is effectively regulated as well. This RFQ control loop greatly reduces errors from klystron modulator voltage variations and from changing beam current. There are several disturbances to the six cavities that must be corrected by the FVM controllers. These are static amplitude and phase errors, drifts in cavity resonance frequency, differences in cavity Qs, and variations in cavity beam loading. Field errors in the cavities are corrected by an adaptive feed-forward system.

The primary feed-back loop is implemented as a PI controller in a FPGA with a sampling frequency of 56 MHz. The 325Mhz RF is downconverted to a 13 MHz IF which is sampled and downconverted to baseband. A 2.1 MSPS DAQ system acquires baseband I,Q signals for pulses upto 4ms wide. The data from all channels is uploaded to the slot0 controller between pulses and is available for processing in the CPU or for transmittal through an ethernet port to both the Fermilab ACNET control system and Labview user interfaces, for waveform display and parameter control.

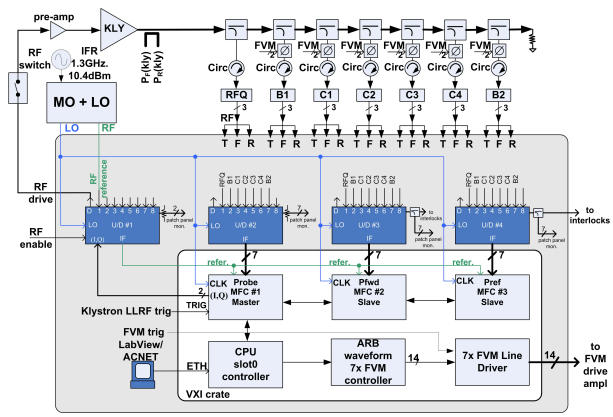

Figure 1: LLRF system configuration

LEARNING ALGORITHM

The learning feed-forward algorithm implementation for one cavity is shown in Fig.2. The wideband RFQ/klystron primary control loop is processed at the full 56 MHz sample rate of A/D converters, while the FVM control loops decimate the data to a 100 kHz rate, where it is processed and the feed-forward controller output is written to a VXI 16 channel arbitrary waveform generator module. Regulation waveforms are recalculated at the machine repetition rate of 0.5 Hz. Decimating the DAQ data by 21 brings the sample rate close to the 100 kHz sampling rate of the output DACs to the FVM. With 1024 points in the FVM waveform, the maximum width of the FVM profile is 10ms

* Work supported by Fermi Research Alliance LLC. Under DE-AC02-07CH11359 with U.S. DOE.
† varghese@fnal.gov

Copyright © 2012 by the respective authors — cc Creative Commons Attribution 3.0 (CC BY 3.0)

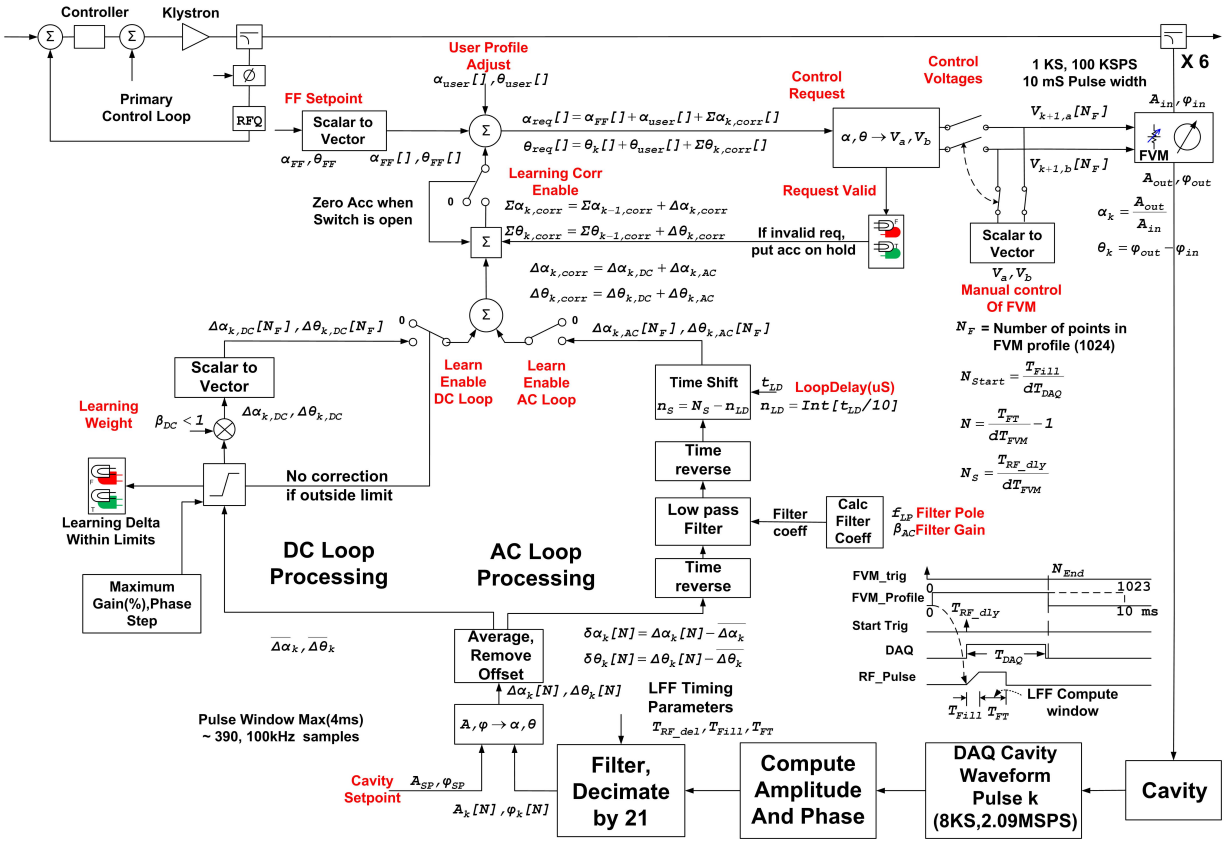

Figure 2: Learning Feedforward Algorithm

which allows for the 4ms RF pulse to be completely included within the FVM pulse. The FVM trigger starts the play-out of the waveform which is 2.5 ms before the start of the RF pulse. This allows the FVM to settle well before the arrival of the RF pulse and beam. The error in the cavity field amplitude and phase is transformed into a correction in the attenuation and phase shift parameter inputs to the FVM. The corrections are computed, based on zeroing the error in the next pulse. They can be computed exactly with an amplitude and phase computation of the cavity field read-back from the DAQ.

$$\Delta\alpha_k = \alpha_k \times (\frac{A_{SP}}{A_k} - 1) \quad (1)$$

$$\Delta\theta_k = \phi_{SP} - \phi_k \quad (2)$$

They can also be approximated with formulas based on the I,Q values by a linearization around the operating point as follows. With $I_e = I_{SP} - I_{cav}, Q_e = Q_{SP} - Q_{cav}$. the correction formulas are given by

$$\Delta\alpha_k = \alpha_k \times \frac{I_{cav}I_e + Q_{cav}Q_e}{I_{cav}^2 + Q_{cav}^2} \quad (3)$$

$$\Delta\theta_k = \frac{Q_e I_{cav} - I_e Q_{cav}}{I_{cav}^2 + Q_{cav}^2} \quad (4)$$

The approach taken in this design is to split the error into a DC component and an AC component with separate control loops. The DC loop is intended to correct offsets due to drift and parameter variations and the AC loop corrects for errors only in the flattop portion of the RF pulse to compensate for beam loading and other disturbances associated with the beam. The correction from the DC loop is an offset that is combined with the AC loop correction to add to the FVM output for the next pulse. A fault detection scheme detects large fluctuations in correction and places the learning on hold till the field recovers.

The transformation of the control request to the voltages to the FVM current coil power supplies is done using a lookup table and interpolation. Due to the highly nonlinear and restricted mapping from the α and θ domain to the Va , Vb domain, the operating point of the FVM needs to be chosen carefully to provide maximum headroom for the closed loop operation[2],[3]. There are large regions where there are no valid solutions which must be kept clear of. Motorized trombones allowed the tuning of the phase and waveguide distribution taps were adjusted to obtain the desired attenuation, to bring the FVM operating point to regions with the required dynamic range.

Treating the AC error as a disturbance input as shown in Fig.3 helps to understand the correction scheme. Since the FVM input profile for pulse k+1 is calculated based on the complete cavity field waveform acquired during pulse k, anti-causal time-reversal filters can be used for disturbance detection[4]. If the transfer function of the combined FVM

Copyright © 2012 by the respective authors — cc Creative Commons Attribution 3.0 (CC BY 3.0)

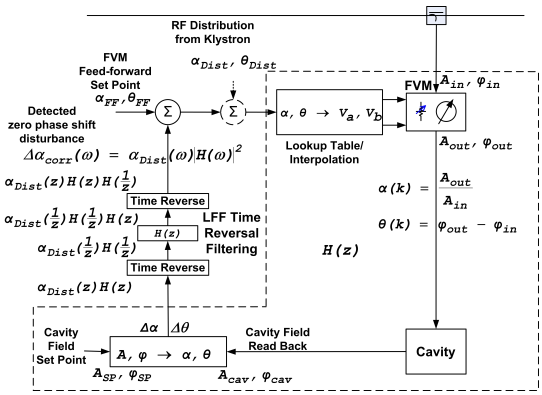

Figure 3: Time reversal filtering for FVM error detection

and the cavity system is represented by H(z), then passing the error through the anti-causal filtering shown in Fig.3, produces a zero phase shift, detected disturbance to which the appropriate gain and time advance (to account for the loop delay) can be added to cancel out the disturbance. The transfer function H(z) is modeled as a first order IIR filter whose pole and the loop delay parameter become the key tuning parameters to correct the disturbance input.

RESULTS

The learning feed-forward algorithm was tested under beam loading conditions. Fig.4 and Fig.5 show magnitude and phase plots for the cavity field with a 300 μS beam pulse with and without the LFF control. The convergence of the DC loop is determined mainly by the gain parameter. The AC loop needs to be tuned primarily with the filter pole and the loop delay parameter.

The regulation during beam was $< 0.2\%$ for amplitude and $< 0.21^\circ$ for phase. Cavity 1 shows only a partial suppression of the disturbance because its FVM request parameters overshot the valid region and the FVM inputs are held at the last valid value.

CONCLUSION

The application of a learning feed-forward loop for FVMs showed that they are capable of regulating cavity field and phase within specifications in applications with one klystron driving multiple cavities. Tuning the AC loop was critical to the stability of the system. It was shown that with a DC loop alone, it is not possible to accurately compensate for the beam-loading disturbances. The six cavity test was specified with a longer pulse width of 1ms. Due to technical issues with the RFQ, the RF pulse widths were limited to < 500 μS.

The feasibility of using FVMs in a single klystron multiple cavity application was demonstrated in the Hins 6-cavity test. The learning feed-forward loops around the FVMs provided independent control for cavities with differing characteristics and set-points.

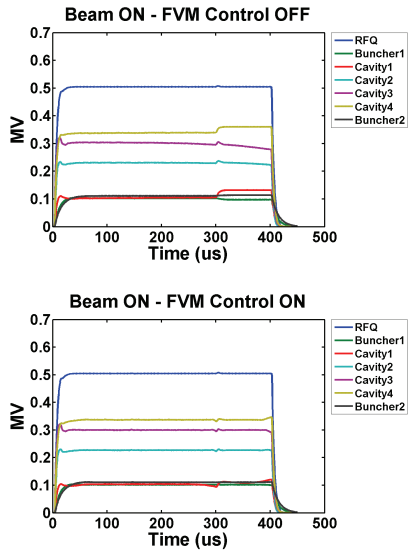

Figure 4: Cavity Magnitude with FVM LFF loops OFF/ON

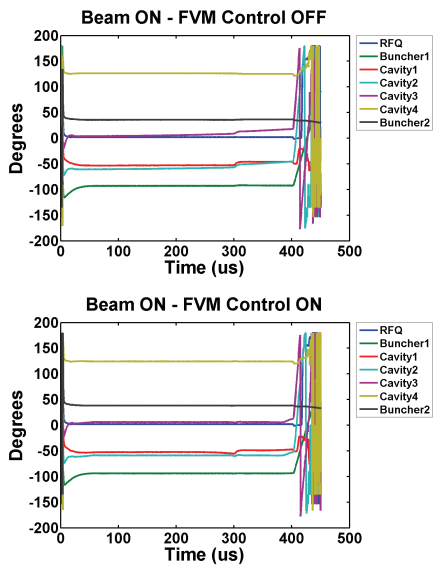

Figure 5: Cavity Phase with FVM LFF loops OFF/ON

REFERENCES

[1] J. Steimel et al.,"The Six-Cavity Test - Demonstrated Acceleration of Beam with Multiple RF Cavities and a single Klystron", IPAC'12, New Orleans, USA, June 2012, THPPP062.

[2] R.L.Madrak and D.Wildman, "High Power 325 MHz Vector Modulators for the Fermilab High Intensity Neutrino Source (HINS)", Linac'08, Victoria, B.C., Canada, September 2008, THP088.

[3] J.Branlard and B.Chase, "Modelling the LLRF control of a Multi-Cavity RF Station for Project-X", PAC'09, Albuquerque, NM, June 2009, WE3RAC05.

[4] A.Brandt,"Development of a Finite State Machine for the Automated Operation of the LLRF Control at FLASH", Doctoral Dissertation, University of Hamburg,2007.

Copyright © 2012 by the respective authors — cc Creative Commons Attribution 3.0 (CC BY 3.0)

FRONT-END LINAC DESIGN AND BEAM DYNAMICS SIMULATIONS FOR MYRRHA *

C. Zhang#, H. Klein, D. Mäder, H. Podlech, U. Ratzinger, A. Schempp, R. Tiede, M. Vossberg
Institut für Angewandte Physik, Goethe-Universität, D-60438 Frankfurt a. M., Germany

Abstract

A 17MeV, 176MHz, and CW (Continuous Wave) proton linac is being developed as the front end of the driver accelerator for the MYRRHA facility in Mol, Belgium. Based on the promising preliminary design, further simulation and optimization studies have been performed with respect to code benchmarking, RFQ simulation using realistic LEBT output distributions, and an updated CH-DTL design with more detailed inter-tank configurations. This paper summarizes the new results.

PRELIMINARY DESIGN

Following the EUROTRANS project [1], MAX [2] (MYRRHA Accelerator eXperiment research and development programme) is the ongoing European ADS (Accelerator-Driven System) project. For the front end of the driver linac, the EUROTRANS-style injector [3] that consists of one RFQ (Radio-Frequency Quadrupole), two RT (room-temperature) and four SC (superconducting) CH (Cross-bar H-mode)-DTL (Drift-Tube Linac) cavities will be still adopted, but with many new concepts [4].

The most important idea is to halve the RF frequency from 352MHz to 176MHz, which improves the RFQ shunt impedance significantly (see Fig. 1), enlarges the minimum gap between electrodes, and allows replacing the 4-vane RFQ structure by the simple 4-rod one. Consequently, for keeping the RFQ length at ~4m and the warm part still compact, the RFQ-DTL and RT-SC transition energies are reduced from 3MeV and 5MeV to 1.5MeV and 3.5MeV, respectively, which indeed brings more difficulties to the beam dynamics design but helps improving the RT-CH shunt impedance.

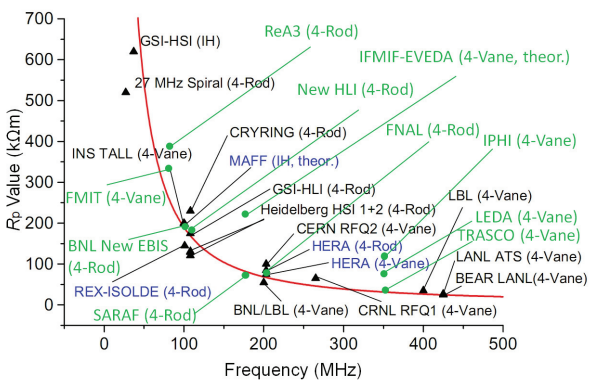

Figure 1: A survey of R_p values for RFQs [5].

From EUROTRANS to MAX, the injector design has lowered the RF power consumption per unit length and the Kilpatrick factor to ≤30kW/m and 1, respectively, for all warm cavities, even shortened the whole layout from 11.4m to 10.6m, and kept the beam dynamics performance satisfying. Being very conservative for CW operation and more cost-saving, this design has been taken as the baseline for further studies [5].

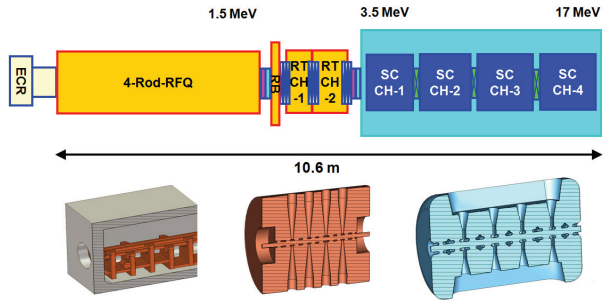

Figure 2: Preliminary layout for the MAX injector.

CODE BENCHMARKING

For the preliminary design of the MAX injector, the ParmteqM [6] and Lorasr [7] codes were used to simulate the beam transport in the RFQ and CH-DTL parts, respectively. Recently, the Toutatis [8] and TraceWin [8] codes have been introduced for benchmarking.

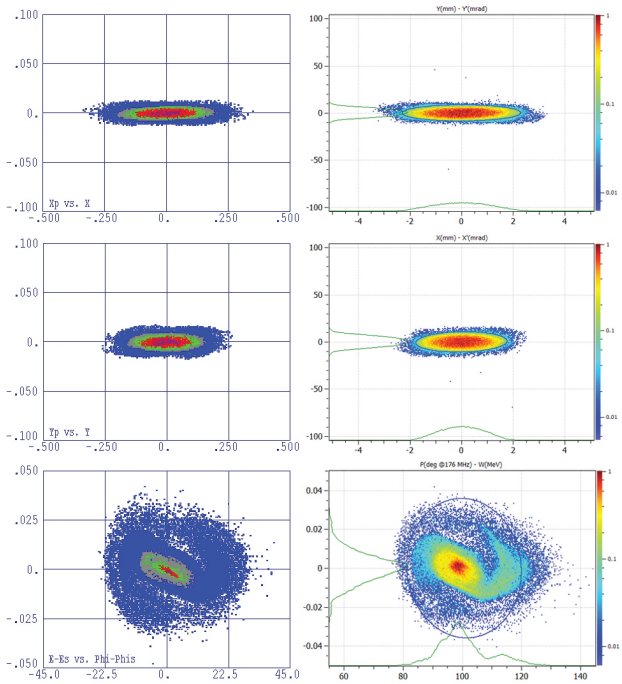

Figure 3: RFQ output particle distributions given by the ParmteqM (L) and Toutatis (R) codes.

Fig. 3 shows the RFQ output beams simulated by the ParmteqM and Toutatis codes. It's clear that the shape,

* Funded by the European Atomic Energy Community's (Euratom) 7th Framework Programme under Grant Agreement n°269565.
# Chuan Zhang: zhang@iap.uni-frankfurt.de

Copyright © 2012 by the respective authors — cc Creative Commons Attribution 3.0 (CC BY 3.0)

orientation, and size of the particle distributions are all quite similar on the three planes (the *x* and *y* planes are exchanged in Toutatis), respectively. Fig. 4 compares the emittance evolutions along the RFQ. Obviously, all transverse-emittance curves are almost identical, while the longitudinal-emittance ones have a small difference (which might be caused by a few halo particles) after *z*=0.5m, but they have nearly same evolution shape.

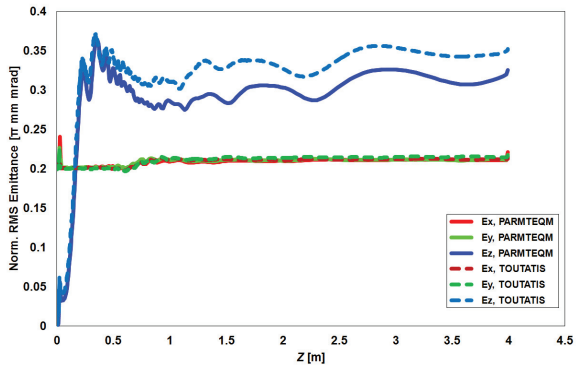

Figure 4: Emittance evolutions along the RFQ.

For the CH-DTL benchmarking, the first CH cavity with the integrated two triplets (see Fig. 5) has been used.

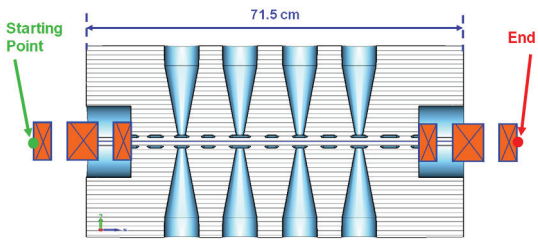

Figure 5: Benchmarking sample from the CH-DTL.

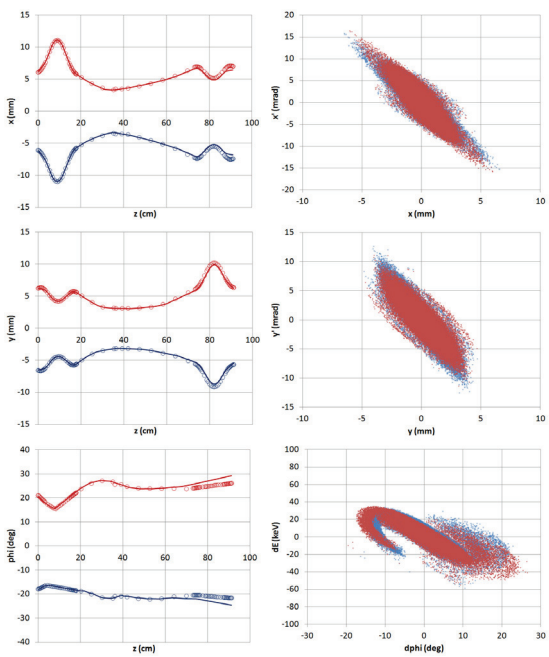

Figure 6: Beam envelopes (L) with circles by Lorasr and curves by TraceWin and output particle distributions (R) with blue dots by Lorasr and red dots by TraceWin.

In Fig. 6, the plots of the CH-DTL beam envelopes and output particle distributions show a good agreement between the Lorasr and TraceWin codes.

RFQ SIMULATION WITH LEBT OUTPUT

The MAX RFQ was designed using the New Four-Section Procedure [9] with a 4D-Waterbag input distribution. Table 1 summarizes the new simulation results based on the output particle distributions from the LEBT (Low Energy Beam Transport) designs [10]. It is seen that no matter the short or long version of LEBT will lead to similar results in the nominal (CW beam) and transient (with chopper) cases. All performance is still satisfying, except the longitudinal emittances have some relatively bigger but still acceptable growths due to the wing-form halo particles (see Fig. 7) from the LEBTs. However, the RFQ output distributions are always clean.

Table 1: LEBT-Based RFQ Simulation Results.

Parameter	Waterbag	Short LEBT transient	Short LEBT nominal	Long LEBT transient	Long LEBT nominal
$\varepsilon_{in}^{t.,\,n.,\,rms}$ [π mm-mrad]	0.20	0.18	0.16	0.14	0.14
$\varepsilon_{out}^{x.,\,n.,\,rms}$ [π mm-mrad]	0.22	0.20	0.17	0.17	0.15
$\varepsilon_{out}^{y.,\,n.,\,rms}$ [π mm-mrad]	0.22	0.20	0.16	0.17	0.15
$\varepsilon_{out}^{l.,\,rms}$ [π keV-deg]	64.6	92.4	92.7	108	80.0
T [%]	100	99	98.5	98.2	98.6

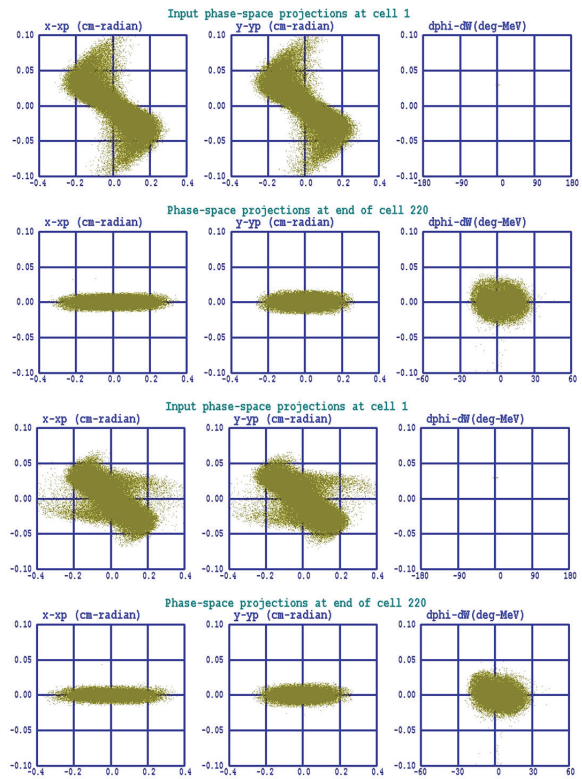

Figure 7: RFQ phase spaces with the short (T) and long LEBTs (B) in the transient case.

Copyright © 2012 by the respective authors — cc Creative Commons Attribution 3.0 (CC BY 3.0)

NEW MAX INJECTOR DESIGN

In the previous beam dynamics studies, the space needed for the inter-tank components was reserved by estimation. The inter-tank sections have been newly redesigned including all the details, e.g. the bellows for connecting cavities, the magnetic-field shielding for the solenoids, and the real dimensions of the cryomodule. The drift spaces between the cavities become longer, especially at the RFQ-DTL and RT-SC transitions, which increases the difficulty for the beam dynamics design.

The most critical area is the RT-SC transition where the drift space was extended by ~50cm. To overcome the negative consequences in both longitudinal and transverse planes, a new rebunching cavity (so-called RB-2) working at the -90° synchronous phase and a new solenoid have been added in front of the first SC-CH.

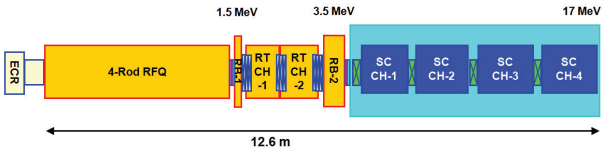

Figure 8: New layout for the MAX injector.

The beam dynamics of the new CH-DTL shown in Fig. 8 was re-optimized by tuning the focusing strength of all lenses and the gap voltages of the rebunching cavities while the design of the CH-cavities was kept almost unchanged.

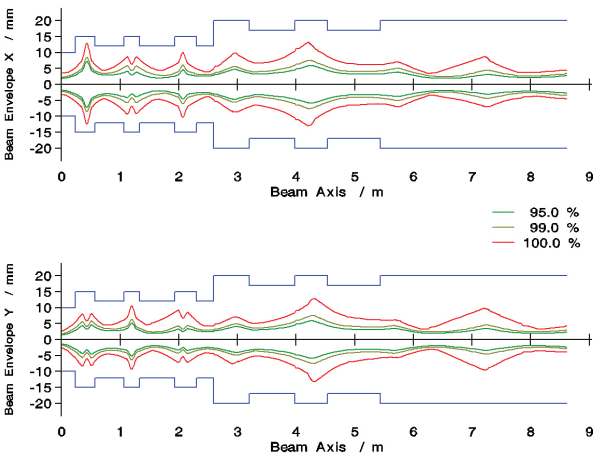

Figure 9: Transverse beam envelopes along the CH-DTL.

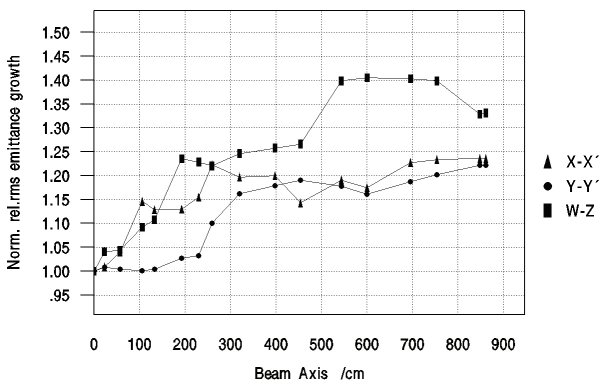

Figure 10: Emittance evolutions along the CH-DTL.

Fig. 9 plots the transverse beam envelopes along the new CH-DTL. In the first triplet, a few beam losses might happen when errors are included, but at 1.5MeV this beam energy they don't play any role. Therefore, a large safety margin is available for the beam throughout the CH-DTL. In addition, the emittance growths are still modest, as shown in Fig. 10.

CONCLUSIONS AND OUTLOOK

The correctness of the simulation results of the MAX injector design was successfully crosschecked by different codes. It was also proven that realistic LEBT output beams accelerated by the MAX RFQ will be transported into the CH-DTL with excellent beam quality. In addition, the simulation of the new CH-DTL updated with detailed inter-tank configurations has shown good performance. To sum up, an advanced new design is now available for the MAX injector. In the next step, systematic error studies will be performed.

ACKNOWLEDGEMENTS

Special thanks go to J.-L. Biarrotte and D. Uriot for their valuable contributions to the benchmarking using the Toutatis and TraceWin codes.

REFERENCES

[1] http://nuklear-server.ka.fzk.de/eurotrans/.
[2] http://ipnweb.in2p3.fr/MAX/.
[3] C. Zhang, M. Busch, H. Klein, H. Podlech, U. Ratzinger, J.-L. Biarrotte, "Reliability and Current-Adaptability Studies of a 352MHz, 17MeV, Continuous-Wave Injector for an Accelerator-Driven System", Phys. Rev. ST - AB 13, 080101 (2011).
[4] C. Zhang, H. Klein, D. Mäder, H. Podlech, U. Ratzinger, A. Schempp, R. Tiede, "From EUROTRANS to MAX: New Strategies and Approaches for the Injector Development", Proceedings of the 2nd IPAC in San Sebastian, Spain, September 4-9, 2011.
[5] C. Zhang, H. Klein, D. Mäder, H. Podlech, U. Ratzinger, A. Schempp, R. Tiede, M. Vossberg, MAX Deliverable 2.1: "352 MHz vs. 176 MHz Injector Comparison & Choice", January 31, 2012.
[6] K.R. Crandall, LANL Internal Report, Nr. LA-UR-96-1836, Revised December 7, 2005.
[7] R. Tiede, G. Clemente, H. Podlech, U. Ratzinger, A. Sauer, S. Minaev, "LORASR Code Development", Proceedings of the 10th EPAC in Edinburgh, Scotland, United Kingdom, June 26-30, 2006, pp. 2194-2196.
[8] http://irfu.cea.fr/Sacm/logiciels/.
[9] C. Zhang, A. Schempp, "Beam Dynamics Studies on a 200mA Proton Radio Frequency Quadrupole Accelerator", Nucl. Instrum. Methods Phys. Res., Sect., A, Volume 586, Issue 2, pp.153-159 (2008).
[10] J.-L. Biarrotte, "MYRRHA LEBT Preliminary Design Report", July 18, 2011.

Copyright © 2012 by the respective authors — cc Creative Commons Attribution 3.0 (CC BY 3.0)

PRELIMINARY STUDY OF PROTON BEAM TRANSPORT IN A 10 MeV DIELECTRIC WALL ACCELERATOR*

J. Zhu#, L.S. Xia, Y. Shen, W. Wang, H. Zhang, Y. Liu, S.F. Chen, W.D. Wang, J.S. Shi, L.W. Zhang, J.J. Deng
Institute of Fluid Physics, CAEP, Mianyang, Sichuan, 621900, China

Abstract

A novel proton accelerator based on Dielectric Wall Accelerator (DWA) technology is being developed at Institute of Fluid Physics (IFP). The accelerating gradient will be 25 MV/m or even higher based on current high gradient insulator (HIG) performance. Theoretical study and numerical simulation of accelerating the proton beam to 10 MeV by virtual travelling wave method are presented in this paper. The beam injection at the DWA entrance is also discussed.

INTRODUCTION

The proton dielectric wall accelerator is being developed at Institute of Fluid Physics. The DWA system is a block structure which is similar to the linear induction accelerator. Each block of cell is consist of a ring-shape high gradient insulator, parallel-plate Blumlein pulse forming lines and photon conductive switches. To obtain the highest accelerating gradient, the DWA will be operated in the "virtual" travelling wave mode with the accelerating pulse as short as no more than 2 nanoseconds in the majority of the HGI tube [1]. These technologies are now being tested individually and will soon be tested integrally. The proton bunch will first be accelerated to 1 MeV with the accelerating gradient of about 20 MV/m and then upgraded to higher energy by adding more DWA cells. The accelerating gradient is also expected to be 25 MV/m or even higher, which is mainly determined by the performance of the HGI tube.

The major advantageous of a DWA system used for cancer treatment is that the total length of the system will be less than 3 meters so that it can be equipped in a single treatment room and the large and costly gantry can be neglected. Moreover, the energy, spot size of the proton bunch can be changed from shot-to-shot by adjusting the pulsed power system.

ION SOURCE AND LEBT

The layout of a 10-MeV DWA system is shown in Fig.1. It will start with a proton beam generated in an ECR ion source and extracted at about 40 keV. The main purpose of the LEBT is to transport the beam to the entrance of the DWA and match the injection requirements. Since a DWA system should be short and light enough to be rotated for intensity modulated proton therapy (IMPT), a two Einzel lens structure was chosen as the LEBT system. The pulse width of the proton bunch generated by the ion source is expected to be much longer than the DWA requirement. A fast kicker system will be mounted at the exit of the LEBT. Most of the protons will be deflected and hit on the metal wall at the DWA entrance, and only a small part of protons is allowed to enter the DWA. Design and fabrication of the ion source and LEBT is performed by Institute of Heavy Ion Physics, Peking University.

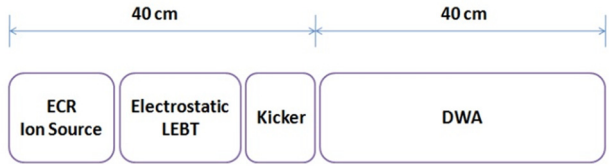

Figure 1: Layout of a 10 MeV DWA.

BEAM INJECTION

Generally, there is no any external focusing element or grid in the DWA system. The proton bunch is supposed to be focused to the downstream of the DWA by the radial electric field produced by the field gradient at the entrance [2]. The focusing effect is generally determined by the beam parameters, the accelerating gradient, the electric field and the time sequence. Chen [3] has demonstrated transporting a 2-MeV (injection energy) proton bunch in a 120-MeV DWA system at the accelerating gradient of 60 MV/m. For a 40-keV proton bunch, the radial electric field can easily cause the bunch pinching at the front of the DWA first and then defocusing. To demonstrate the focusing effect of the radial electric field at the entrance, the envelop equation

$$R'' = -\frac{\gamma'}{\gamma\beta^2}R' - \frac{\gamma''}{2\gamma\beta^2}R + \frac{K}{R} + \frac{\varepsilon_n^{\,2}}{\beta^2\gamma^2R^3} \quad (1)$$

for a 40-keV, 20-mA, 1-mm-mrad proton bunch at its waist is solved, where R, β, γ, ε_n and K is the beam's radius, velocity relative to the speed of light, Lorentz factor, normalized edge emittance and generalized perveance, respectively. We consider the case that the length of the DWA is 40 cm and the proton bunch rides on the flattop of the electric field (25 MV/m) except that there is a constant field gradient at the beginning 5 cm of the DWA. The proton bunch envelop as a function of the proton energy is plotted in Fig.2 (a). It is obvious that the focal spot of the beam will move upstream as the proton energy decreases. The focal spot of proton bunch with 2-MeV injection energy just locates at the end of the drift

*Work supported by National Natural Science Foundation of China (11035004) and Nuclear Energy Development Project of State Administration of Science, Technology and Industry for National Defence
#zhujun98@tsinghua.org.cn

Copyright © 2012 by the respective authors — cc Creative Commons Attribution 3.0 (CC BY 3.0)

tube, while the proton bunch with 40-keV injection energy will pinch at the front of the DWA and then diverge. If we adjust the injection timing to make only the last 1 cm of field gradient is seen by the bunch, the 40-keV proton bunch will also be tightly focused throughout the simulation region, as shown in Fig.2 (b).

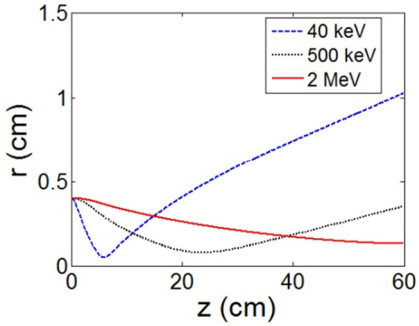

(a)

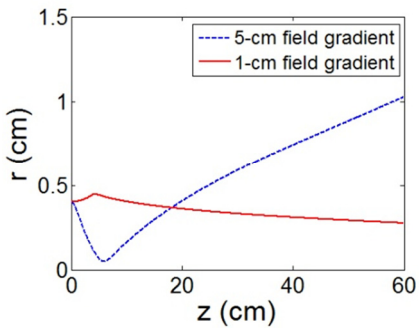

(b)

Figure 2: Beam envelop for (a) different injection energies, (b) two different lengths of field gradient at the DWA entrance for a 40-keV proton beam.

TRANSPORT SIMULATION

We have simulated the proton beam transported through a 40-cm DWA by using a self-consistent, 2.5-dimensional particle-in-cell code. The inner radius of the HGI tube is 1.5 cm and the average accelerating gradient is about 25 MV/m. Blumleins are grouped to form a 2-cm block which was triggered together. The accelerating voltage pulse was given a rise/fall time of 1 ns each. The simulation transports a 40-keV, 1-ns proton beam from 3 cm upstream of the DWA entrance to 20 cm downstream of the DWA exits. The flattop of each electric pulse and the triggering sequence were carefully chosen to ensure that the DWA worked in the "virtual" travelling wave mode and the proton bunch just rode on the flattop throughout the DWA except at the entrance and exits. To make sure that the proton bunch was not over-focused, the first two groups of HGI were triggered together when the proton bunch entered the HGI tube. An entrance metal screen was employed to further increase the accelerating field at the entrance and reduce the electric field gradient seen by the proton bunch. The simulation results with and without entrance screen are shown in Fig.3.

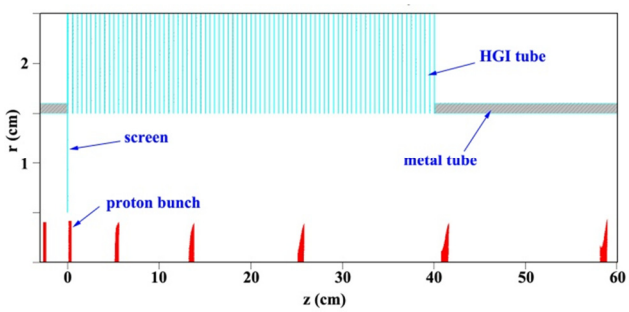

(a)

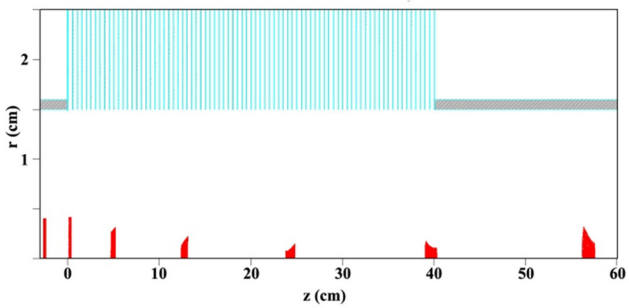

(b)

Figure 3: Beam transports in a 10-MeV DWA, (a) entrance screen can further reduce the focusing force at the entrance, (b) the proton bunch was over-focused when there was no entrance screen.

The bunch was first accelerated by the leading side of waveform, and a radial focusing force is applied on the bunch at the same time. The longitudinal and radial electric field profiles at the DWA entrance are shown in Fig. 4. When the entrance screen was employed, the accelerating field is higher at the entrance comparing to the case when there is no entrance screen. So the protons can be accelerated to higher energy in a shorter distance to avoid over-focusing. And the radial focusing force is also smaller. After that, the virtual travelling wave with a flattop was formed and the proton bunch rode on the flattop of the accelerating waveform, as shown in Fig.5. At this stage, the radial electric field vanished. The shape of the accelerating field nearly kept constant as the proton bunch travelling through the accelerator. However, the electric pulse flattop applied on the HGI reduced from about 4 ns at the entrance to 1.5 ns at the end, as shown in Fig.6. The pulse duration at the second group of Blumleins is longer than the first one since they are triggered together to increase the accelerating field and reduce the length of the waveform leading side at the entrance. At the exits of the DWA, a de-focusing force will be applied on the bunch because of the opposite field gradient to that of the entrance. So the last HGI should be turned off as quickly as possible. For the 10-MeV DWA, the transport systems with or without the entrance screen are both acceptable though the bunch was slightly over-focused when there was no entrance screen. However, the radial focusing force at the DWA entrance is proportional to the accelerating gradient, and the entrance screen could be an alternative method to avoid over-focusing for a longer DWA with higher accelerating gradient,

Copyright © 2012 by the respective authors — cc Creative Commons Attribution 3.0 (CC BY 3.0)

The proton energy and current profile at the exits of the DWA is shown in Fig.7. Because the bunch rode on the falling side of the acceleration waveform at the DWA entrance, the bunch underwent longitudinally compressing and the average peak current increased to about 100 mA at the DWA exits. This longitudinally compressing effect is useful in a DWA system for IMPT. It is desirable for such a system to have an accelerating gradient of 100 MeV/m with 1-ns accelerating pulse width. To ensure that the proton bunch rides on the flattop of the accelerating waveform, the bunch length should be sub-nanosecond. And how to extract such a proton bunch is still a challenge. However, by adjusting the charging sequence of the HGI, the proton bunch can be placed at the falling side of the accelerating waveform and the bunch will be compressed longitudinally in the front of the accelerator. Moreover, the proton bunch should be about 200 mA and 0.2 ns for a 50-Hz DWA system for IMPT. It is obvious that the current exceeds the maximum capability of the ion source. And the beam radius at the DWA entrance can't be kept small if the current extracted from the ion source is large enough. Therefore, the proton bunch should be extracted at lower current and then be compressed to higher current and shorter pulse length.

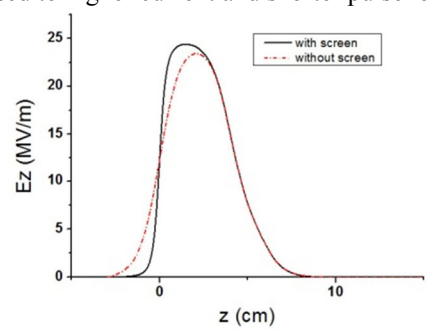

(a)

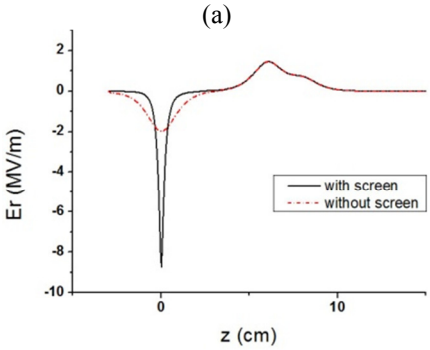

(b)

Figure 4: Longitudinal (a) and radial (b) electric field profiles at the DWA entrance with and without entrance screen.

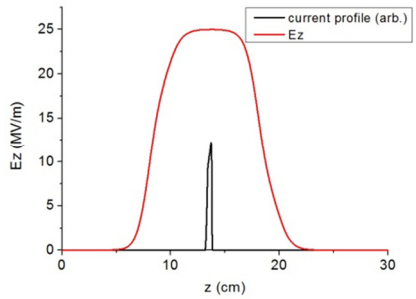

Figure 5: Longitudinal electric field and proton current profile in the middle of the DWA.

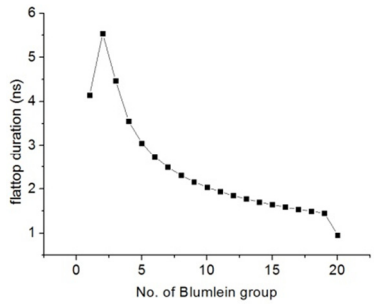

Figure 6: Electric pulse flattop duration as a function of the No. of HGI group.

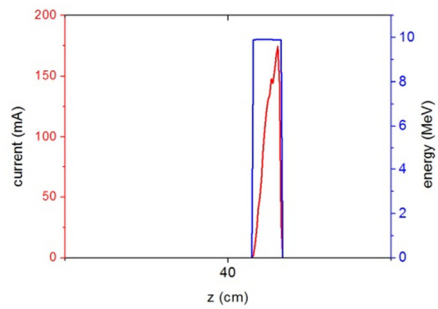

Figure 7: Proton energy and current profile at the exits of the DWA (with screen).

SUMMARY

The design of the ion source and LEBT for a 10-MeV DWA is introduced in this paper. We have discussed the beam injection by using the focusing force produced by the field gradient at the DWA entrance. We also have demonstrated that a 40-keV proton bunch can be transport through a 40-cm-long DWA with an accelerating gradient of 25 MV/m.

REFERENCES

[1] G.J. Caporaso, et al., "A Compact Linac for Intense Modulated Proton Therapy Based on a Dielectric Wall Accelerator", Physica Medica, 24, p. 98 (2008).

[2] Y-J Chen, et. al., "Beam Transport in a Compact Dielectric Wall Accelerator for Proton Therapy", Proceedings of Linear Accelerator Conference, Tsukuba, Japan, 2010.

[3] Y.J. Chen, et al., "Beam Transport in a Dielectric Wall Accelerator for Intense Modulated Proton Therapy", Proceedings of IPAC2011, Sebastian, Spain, 2011.

Copyright © 2012 by the respective authors — cc Creative Commons Attribution 3.0 (CC BY 3.0)

R&D ACTIVITIES ON HIGH INTENSITY SUPERCONDUCTING PROTON LINAC AT RRCAT

S.C. Joshi, S.B. Roy, P.R. Hannurkar, P. Kush, A. Puntambekar, P. Shrivastava, G. Mundra, J. Dwivedi, P. Khare, P.D. Gupta, Raja Ramanna Centre for Advanced Technology, Indore, India

Abstract

Raja Ramanna Centre for Advanced Technology (RRCAT), Indore has taken up a program on R&D activities of 1 GeV, high intensity superconducting proton linac for Spallation Neutron Source. This will require several multi-cell superconducting cavities operating at different RF frequencies. To start with, a number of single-cell prototype cavities at 1.3 GHz have been developed in high RRR bulk niobium. These single-cell cavities have exhibited high quality factor and accelerating gradients. Superconducting properties of niobium are being studied for varying composition of impurities and different processing conditions. Physics design of linac configuration and various accelerating structures have been initiated. Development activities on cryomodules, cavity test facilities and solid state RF amplifiers to power the SRF cavities at various RF frequencies are being pursued. Infrastructure setup required for SRF cavity fabrication, processing and testing is under progress at RRCAT.

INTRODUCTION

A programme is envisaged to develop a pulsed, MW range Spallation Neutron Source based on 1 GeV, 1 MW superconducting RF H- Ion linac, a full-energy injector for a 1GeV Accumulator Ring. The pulsed Spallation Neutron Source will be used for applications in the field of condensed mater physics, material sciences, chemistry, biology and engineering. In addition to setting up of SNS facility, it will enhance capacity building in the area of high intensity proton accelerators in India.

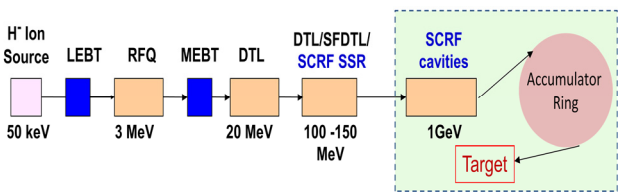

Figure 1. Schematic of Pulsed Proton Linac for Indian Spallation Neutron Source.

R&D ACTIVITIES

R&D activities for a SRF linac and accumulator ring for SNS would include prototype development of various sub-systems and setting up of infrastructure in the following areas:

- Ion source and front end component
- Materials R&D, cavity & cryomodule development
- Niobium cavity fabrication and processing facility
- Test facility for large number of SRF cavities and cryomodules
- Cryogenics setup for large size LHe Plant & supply network
- RF power sources and control electronics
- Sub-systems for 1 GeV accumulator ring including magnets, power supplies, RF cavity, UHV system and controls
- Manpower development and training

Ion Source and Front End

Development of a 3 MeV H- ion linac front end has been initiated for 1 GeV proton accelerators for a pulsed Spallation Neutron Source [1]. The front-end system will comprise of a filament driven multi-cusp H- ion source, Low Energy Beam Transport (LEBT) system, Radio Frequency Quadrupole (RFQ), RF power sources, Controls, Beam dump and Beam diagnostics.

H- Ion Source: In order to meet the requirement of H- ion front end linac system, a multicusp filament based 50 keV, 30 mA, low emittance H- ion-source operating in pulsed mode with a repetition rate of 25 Hz has been initiated. Physics design of the multicusp source was carried out analytically and also using computer simulations based on finite element method. This system has recently been tested for extraction of hydrogen ion current of 1.0 mA at 15 kV accelerating field. Figure 2, shows the multi-cusp H- ion source system.

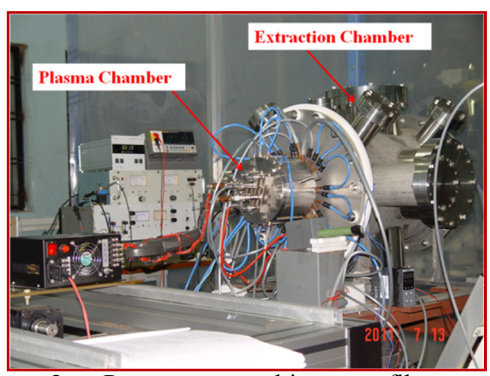

Figure 2. Prototype multi-cusp filament based source pulsed H^- ion source.

LEBT and RFQ: For prototype studies, design has been carried out for a suitable LEBT for beam transport from Ion Source to RFQ and a 3 MeV, 352 MHz RFQ. A Low Energy Beam Transport (LEBT) line, consisting of solenoid magnets of maximum strength 3.5 kG and steering coils having a maximum field of 100 G has been

Copyright © 2012 by the respective authors — cc Creative Commons Attribution 3.0 (CC BY 3.0)

designed for transporting the beam from Ion Source to RFQ with the matched beam parameters at RFQ entrance, and with minimum emittance growth.

For prototype RFQ, physics and engineering design has been carried out for a 352.2 MHz, 3.47 m long, four vane type RFQ to accelerate 50 keV, 30 mA pulsed H- ion beam with 1.25% duty factor to 3 MeV. The inter-vane voltage has been chosen to be 80 kV, the optimized value of the minimum aperture radius is 2.31 mm and modulation parameter has been varied in the range 1 – 1.95. The synchronous phase is initially kept at -90 degree to maximize the capture efficiency, which is ramped to -30 degree.

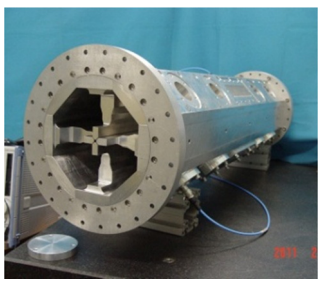

Figure 3. Prototype fabrication of 1st segment of RFQ structure.

Materials R&D for SRF Cavities

Since the major part of proton linac will be build using SRF cavities, intensive materials R&D activities have been taken up at RRCAT. The SRF cavity materials studies include superconducting properties of fine grain (50 micron average grain size), large grain (1 mm average grain size) and single crystal samples of Niobium materials. It was observed that a buffered chemical polishing of these Niobium materials caused a distinct reduction in the superconducting parameters like transition temperature (T_C), lower critical field (H_{C1}) and upper critical field (H_{C2}) [2.3]. These results indicate that BCP treatment possibly introduces Oxygen and Hydrogen in quantities large enough to degrade the superconducting properties of the Niobium materials, which, in turn, adversely affects the performance of the Niobium-SRF cavities.

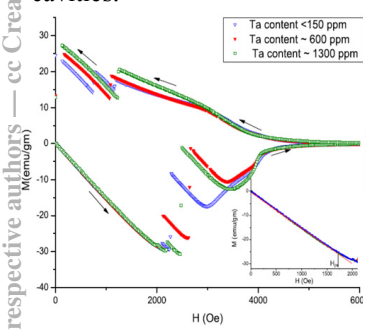

Figure 4. Magnetization v/s magnetic field plot of pristine fine grain Niobium with different Tantalum-contents at T=2 K [3].

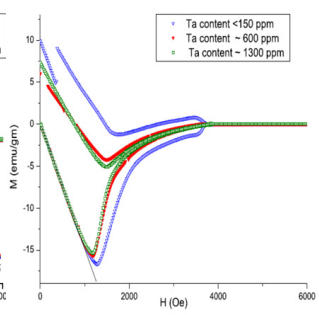

Figure 5. Magnetization v/s magnetic field plot of fine grain Niobium with different Tantalum-contents, subjected to BCP & annealing at 600^{O}C[3].

It was also seen that tantalum impurity content even up to several hundred to ~1300 ppm does not significantly affect the superconducting properties of Niobium materials [3]. These observations suggest that a less refined Niobium material may be deployable for cavity applications, provided the inclusions of the impurity elements do not influence the surface conductivity of Niobium materials significantly.

SRF Cavity Development

As an initial effort, four prototype 1.3 GHz single cell bulk niobium cavities have been developed under Indian Institutes Fermi Lab Collaboration (IIFC).

Figure 6. Prototype 1.3 GHz Single Cell cavities fabricated, processed and tested under IIFC Program.

Development of forming tools, forming of half-cells, machining of components, development of welding fixtures along with RF & vacuum qualification were carried out at RRCAT. The electron beam welding was carried out at IUAC. The fabricated prototype cavities were tested for RF and vacuum leak tightness up to 77 K at RRCAT before shipment to Fermi Lab. Processing, consisting of Centrifugal Barrel Polishing (CBP), Electro Polishing (EP), heat treatment and high pressure rinsing (HPR) was carried out jointly by Fermi Lab and Argonne National Laboratory in USA [4].

The cavity TE1CAT004 was successfully tested in the first test itself to achieve Eacc of 37.5 MV/m with a Q > 8.4 x E09 as shown in Figure 7.

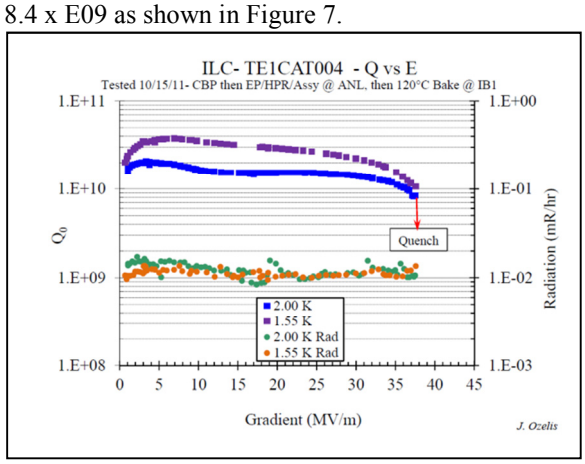

Figure 7. 2 K Performance test curve of 1.3 GHz single cell SRF cavity TE1CAT004 at VTS Facility, Fermi lab.

Prototype development of SRF cavities for medium energy is also under progress. Forming tools for 650 MHz cavities are undergoing forming trials for the first prototype single cell cavity.

Copyright © 2012 by the respective authors — cc Creative Commons Attribution 3.0 (CC BY 3.0)

Design and Development of Cryomodule

Design studies for a medium beta cryomodule for eight SRF cavities (Frequency 600-700MHz) are under progress. This work is in parallel to the cryomodule studies for Project-X under IIFC. The cavity support system will be a modified support system. The cavities will be supported from a helium gas return pipe with the help of a laser welded C-T shaped joint. This improvisation will reduce the machining time and cost for cavity support. Prototype Laser welded joints have been made and tested. The system has been designed and a scaled down prototype has been fabricated (Fig8).

The system will be tested under cryogenic conditions in the cryomodule component test rig.

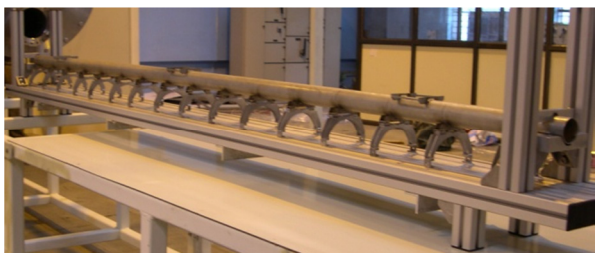

Figure 8. Laser welded prototype cavity support system

SRF Cavity Test Facility

A Vertical Test Stand Facility is under commissioning at RRCAT for testing SRF cavities at 2K. The 2K cryostat was designed by RRCAT along with Fermi Lab. To test the cavities, 1.3 GHz, 500W CW/600 W peak power solid state RF amplifier system has been designed and tested.

The building for VTS is also ready for commissioning.

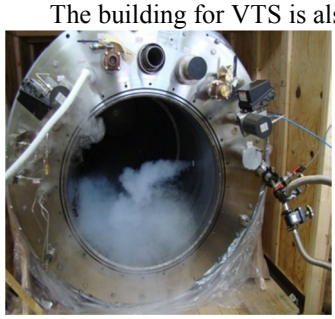

Figure 9. VTS Cryostat under cold shock testing

Figure 10. 500 W Solid State RF system for VTS

A Horizontal Test Stand for testing SRF cavities at high power RF, is being designed under collaboration with Fermi lab. The horizontal test stand cryostat is a continuous flow type cryostat and capable of testing two dressed SRF cavities/SC magnets in a single test cycle.

Development of RF Power Sources

Design and development of 30 kW, 650 MHz high powers solid state RF source for CW as well as pulse power, has been initiated at RRCAT[5]. The indigenous development efforts will be useful for the proposed high power proton accelerators for SNS applications. In this 650 MHz amplifier scheme, 30 kW CW RF power will be generated using modular combination of 8 kW amplifier units. Each 8 kW amplifier unit will be housed in a standard cabinet employing 32 numbers of 300W RF amplifier modules , 2 power dividers, 2 power combiners and high power directional coupler. The RF power unit will have provision for safety interlocks, data acquisition system and water cooling circuit. developed indigenously.

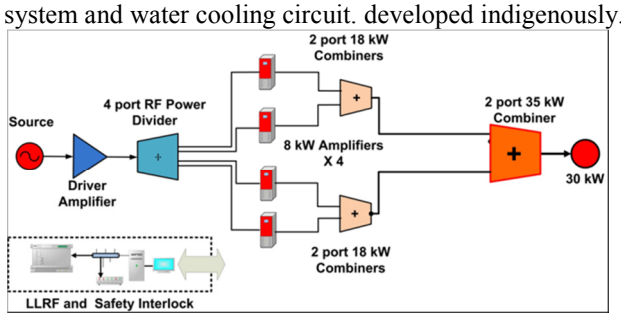

Figure 11. Solid State High Power RFM Amplifier Scheme.

Infrastructure Facility Development

A dedicated building for SRF infrastructure facilities has been completed. Cavity forming facility which includes a 120 Ton Hydraulic Press, suitable tooling have been established for SRF cavity parts. A 15 kW electron beam welding machine and a high vacuum annealing furnace are being procured. Cavity processing facilities including Barrel Polishing Machine for 1.3 GHz single cell cavity, prototype Electro polishing setup, high pressure rinsing facility, clean room facility, for low power RF characterization facility etc. have been set up. A Secondary Ion Mass Spectrometer (SIMS) has been set up for surface characterization of Niobium samples. A Confocal Microscope for defects identification and surface roughness measurement and a high accuracy 3D Co-ordinate measuring machine for mechanical measurement of a cavity profile have been installed [6].

ACKNOWLEDGEMENT

We acknowledge contributions of the team members from PLSCD,IMAS, PHPMS,ACDFS, RFSD, RRCAT. We acknowledge contribution of IUAC, N Delhi & Fermilab, USA for cavity & VTS development under IIFC.

REFERENCES

[1] S. C. Joshi et al., “Status Report of Development of High Current Front End H- Injector Linac for SNS”, Workshop on ADSS, BARC, Mumbai, Dec, 2011.
[2] S. B. Roy et al., Supercond. Sci. Tech. **22** 101514 (2009).
[3] S. B. Roy et al.,AIP. Conf. Proc. **1352** 56 (2011).
[4] A.M. Puntambekar et.al., “Development of 1.3 GHz Single Cell SRF Cavity under IIFC" PAC,New York USA, 2011
[5] A. Jain et at., “Development of 650 MHz Solid State RF Amplifier for Proton Accelerator", Workshop on ADS, BARC Mumbai, Dec, 2011.
[6] S.C. Joshi et at., “Status of Infrastructure Facilities for SRF Cavity” ADS, BARC Mumbai, Dec, 201. 1

Copyright © 2012 by the respective authors — cc Creative Commons Attribution 3.0 (CC BY 3.0)

THE NEW OPTION OF FRONT END OF ION LINAC

A. Kovalenko, JINR, Dubna, Russia
A. Kolomiets, ITEP, Moscow, Russia

Abstract

The standard set of elements consisting of RFQ, two tanks of accelerating IH-structures, external matching and focusing sections is modified to achieve better performances. Special insertions corresponding to buncher and quadrupole triplet are combined within the RFQ tank, whereas superconducting focusing elements are install between the DTL - structure tanks. Simulation of the system parameters was performed to provide the output beam energy of 5 MeV/u for the ions with charge – to - mass ratio of $0.33 \leq Z/A \leq 1$. Possible application of the considered scheme for the NICA facility at JINR (Dubna, Russia) is discussed.

INTRODUCTION

The work was motivated by our desire to find optimal way of the constructing linear accelerator chain aimed at injection of light ions and protons for the NICA complex at JINR [1] and also for other applications, in particular for the future carbon/proton superconducting (SC) medical synchrotrons [2].

The physics research program at NICA [3] requests the beams of heavy and light ions, protons, polarized deuterons and protons as well. The facility is based on the existing SC synchrotron - Nuclotron that is in operation since 1993 [4] and that was upgraded in 2008-2010[5]. The accelerator complex will include also two separate injection chains, 25 T·m SC booster synchrotron, the collider SC rings, beam transfer channels. The collider will provide heavy ion collisions of average luminosity of 10^{27}cm^{-2}s^{-1} at the energies of $\sqrt{s_{NN}} \sim (4 - 11)$ GeV. The collider detector MPD is scheduled for starting data taken in 2017. The fixed target experiment Baryonic Matter at Nuclotron (BM@N) is planned to start data taking in 2015 in the beam of gold ions extracted from the Nuclotron. The NICA will provide polarized proton and deuteron collisions up to $\sqrt{s}$ = 26 GeV and 12.5 GeV/u, respectively, with the average luminosity of 10^{31} cm^{-2} s^{-1}.

The two injection chains aimed at heavy ions and protons/light ions (including polarized ones) injection contain respectively the following: high charge state heavy ion source → the new heavy ion linac → SC booster → Nuclotron → collider and the sources of protons, deuterons (including polarized) and light ions → upgraded existing linac LU-20 → Nuclotron → Collider.

The Alvarez type proton linac LU-20 was commissioned in 1974. At the present time LU-20 provides proton beam with energy 20 MeV and light ions ($Z/A \geq 1/3$) up to 5 MeV/u. The LU-20 planned upgrade includes, at the first stage, replacement of old high voltage preinjector by the new one having much lower voltage of the ion source platform (U = 100 kV) and the use of RFQ to provide the ion energy required for injection to LU-20.

It is clear, however, that use of LU-20 for acceleration of ions heavier than protons is not very efficient. Moreover it would be very risky to expect reliable operation of the old linac in the coming decades even in the case of complete and very expensive replacement of the drift tubes containing quadrupoles inside.

The main goal of the work is design of compact and efficient linac that can be considered as an option of light ion injector for NICA project.

LIGHT ION INJECTOR

General Layout

Particles that will be accelerated in this device are protons, deuterons (including polarized) and other ions with charge - to - mass ratio of $1/3 \leq Z/A \leq 1/2$, in particular $^{12}C^{6+}$ and $^{12}C^{4+}$ as well. The specified values of the beam currents and the expected transverse emittance define the choice of the injector layout and basic parameters of its accelerating structures. After analysis of different possibilities, the scheme shown in Figure 1 is proposed.

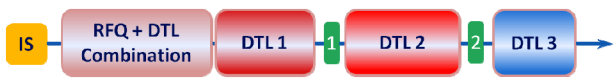

Figure1: Structural scheme of the NICA injector of light and polarized ions. (IS – ion sources)/

Initial part is a combination of RFQ and the DTL that was designed following the idea proposed in [6]. This combination allows to form at output of initial part beam parameters required for injection to DTL 1 and to exclude MEBT with focusing and rf elements for beam matching between RFQ and DTL 1.

DTL 1 and DTL 2 are designed for acceleration of ions with Z/A = 0.33 up to final energy 5 MeV/u. DTL 3 is aimed only for proton acceleration and has to be switched off in the other cases.

Superconducting solenoids are used for beam focusing between DTL sections. It allows reducing drift space between cavities and improving longitudinal beam dynamics. Application of superconducting elements in the proposed new injector is logically follows from the NICA basic technology concept and the advanced level of cryogenics in the Laboratory of High Energy Physics.

RFQ

The RFQ is based on a resonant structure with coupling windows developed in ITEP for TWAC facility injector [7]. The main attention at the design stage was devoted to

Copyright © 2012 by the respective authors — cc Creative Commons Attribution 3.0 (CC BY 3.0)

minimization of the beam longitudinal emittance formed by the RFQ in the case of rather high (> 90%) transmission coefficient. Following to the results obtained in [8], the sinusoidal modulation of the RFQ vanes is used only at the gentle buncher part whereas the trapezoidal one is applied at the main acceleration part with constant modulation coefficient. The trapezoidal modulation provides 15 – 20% higher RFQ accelerating efficiency at the same modulation.

The main feature of the RFQ is the new approach to the beam formation at the RFQ output that provides converging beam in both transverse planes as well as in longitudinal one. It is achieved by adding after regular RFQ vanes several drift tubes connected with opposite vanes with increased distance from axis. Potential difference between tubes is the same as applied to regular vanes.

Drift tube part accelerates ions with higher accelerating efficiency compare with modulated vanes. Due to absence of transverse focusing in this part of structure transverse envelopes amplitude increases approximately by a factor of two. Drift tubes aperture is chosen to exclude the particle losses. Two additional pieces of vanes with quadrupole symmetry βλ long each are installed after the last gap. The distance between the vane sets is βλ also. The model of the front end output is shown in Figure. 2.

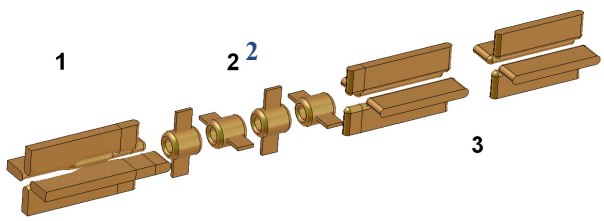

Figure 2: 3D model of the RFQ output part: 1 – the end of regular RFQ vanes, 2 - drift tubes, 3 - rf quadrupoles.

Basic parameters of RFQ + Hybrid combination are given in Table 1.

Table 1: The RFQ Main Design Parameters.

Parameter	Value
Accelerating frequency, MHz	109.0
Voltage between the vanes and tubes, kV	132.0
Average radius, mm	7.50
Thickness of the electrodes, mm	5.25
Maximum modulation coefficient	2.0
Betatron phase advance at the focusing period (minimum), deg.	36
Transverse acceptance (normalized), cm·mrad	0.42
Regular RFQ length, m	3.0
Total combination length, m	3.55
Output beam energy, MeV/u	0.82
Injection energy, MeV/u	0.03
Beam transmission @ I = 10 mA	95%
Maximum electric field at the electrodes surface, kV/cm	227

Hybrid structure consisting of a number of drift tubes without any transverse focusing whereas the focusing is provided by rf quadrupoles placed between the drift tube sections is described in [9]. It is possible to say that described design is a combination of conventional RFQ with a short length hybrid structure. The rf quadrupoles geometry is chosen to provide the bunch enter and exit at the field level closed to zero, i.e. at the accelerating field phase of ±90°. The influence of the output quadrupoles is equivalent to the four static quadrupole lenses forming the FDODF period, i.e. triplet. The distances between the opposite vanes in output quadrupoles are chosen to provide transformation of the beam with quadrupole symmetry at regular RFQ output into converging axially symmetric beam.

Drift Tube Structures

The DTL section is introduced by a crossbar type structure based on the same resonant structure with the coupling windows that has been used for the RFQ. The advantages of such option in compare with the commonly used IH structure are the following: 1) it is possible to equalize gap field level along the section including the first and the last gaps and to exclude dipole component of the field at the system axis and moreover 2) unification of the resonant structures for all cavities leads to lower production and operation cost of the injector. The main design parameters of the DTL sections are presented in Table 2.

Table 2: Design Parameters of DTL Cavities

Parameter	DTL 1	DTL 2	DTL 3
Frequency, MHz	109	109	218
Aperture, mm	10.0	10.0	10.0
Number of acceleration gaps	10	13	11
Electric field at the drift tube surface, kV/cm	230	230	230
Gap length, mm	30.0	50.0	50.0
Gap voltage, kV	600.0	700.0	700.0
Cavity length, mm	830	1605	1200
Output energy, MeV/u	2.58	5.06	10.72

BEAM DYNAMICS SIMULATION

Computer code PreRFQ, ALFIL and TRANSIT, created by the ITEP, were used for the beam dynamics simulation. The first code is aimed for calculations of field distribution in RFQ cell with different types of the vane modulation. ALFIL was used for field calculations in accelerating gap. TRANSIT is the program for multi-particle beam dynamic simulation. The 3D representations of the field are used in TRANSIT for all RFQ cells, accelerating gaps and solenoid. PIC solver is used for calculating particle interactions.

Copyright © 2012 by the respective authors — cc Creative Commons Attribution 3.0 (CC BY 3.0)

The transverse envelopes of the beam of $_{12}C^{4+}$ ions at beam current I = 10 mA calculated by the TRANSIT code are shown in Figure 3.

Twiss parameters of transverse emittances at RFQ output are given in Table 4. It shows that the parameters have very small dependence on beam current. It confirms that the proposed modification of RFQ output provides converged beam with axial symmetry that can be directly injected into DTL 1 cavity for wide range of beam current.

Calculated beam transmission in injector is showed in Figure 4. It shows that in design range of beam current 0 < I < 10 mA it is fully defined by RFQ transmission. Additional particle losses in DTL cavities for higher beam current are explained by increasing phase width of bunch at RFQ output due to space charge.

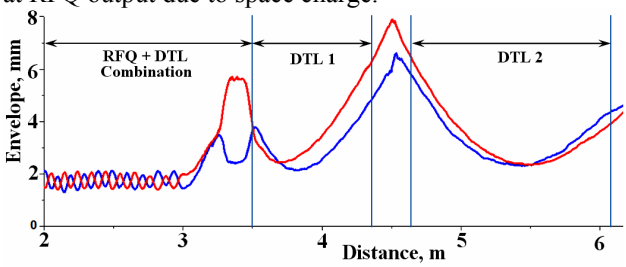

Figure 3: Calculated envelopes of $_{12}C^{4+}$ – ions at 10 мА for x (blue curve) and y (red curve) planes.

Table 3: Twiss Parameters of the Beam at RFQ Output

Beam current, mA	α_x	α_y	β_x m/rad	β_y m/rad
0	-1.82	-1.95	0.468	0.656
5	-2.04	-2.40	0.494	0.767
10	-2.00	-2.63	0.484	0.833
15	-1.96	-2.04	0.477	0.650

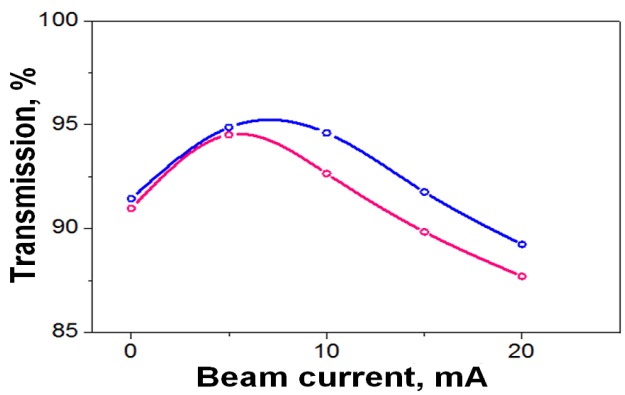

Figure 4: The dependence of $_{12}C^{4+}$ transmission on the beam current. Blue curve represent transmission at RFQ output, red one – at DTL 2 output.

CONCLUSION

Results of development and computer study of light ion injector for NICA project show that proposed combination of RFQ and Hybrid structure provides beam with parameters required for direct injection into following DTL cavity. Beam parameters have only slight dependence on beam current. This approach allows designing injector front end without use of MEBT with additional focusing and rf elements. It can be useful option for design heavy ion linac.

Computer simulations showed that RFQ and DTL cavities can be built using the same type of resonant structure – four vane with coupling windows that reduces manufacture and operation cost of injector.

Injector with total length L_{tot} = 6 m accelerates ions with Z/A = 0.33 up to energy W = 5 MeV/u. Accelerating structures are designed for conservative surface field $E_s \leq 230$ kV/cm to guarantee reliable operation. Injector has only two additional short DTL cavities comparing with structure required for upgrade of LU-20. Nevertheless injector provides higher beam parameters and more efficient and reliable operation. With adding short DTL cavities designed for acceleration of proton injector can completely replace old LU-20 linac for NICA project.

The proposed and considered design is adequate also to carbon ion and proton injector of the future medical synchrotrons.

REFERENCES

[1] Nuclotron-based ion collider facility NICA at JINR, http://nica.jinr.ru/.

[2] A.Kovalenko, N.Agapov et al. “Superconducting Magnet Technologies as basis for Design of Medical Carbon and Proton Synchrotron at Dubna”, Workshop “Physics for Health in Europe”, CERN, February 2-4, 2010. http://cern.ch/physics-for-health

[3] V.Kekelidze et al. Physics Program at NICA@JINR. 35th Int. Conf. on High Energy Physics (ICHEP2010), Paris, France, July 22-28, 2010.

[4] A.D.Kovalenko, “Status of the Nuclotron”, EPAC94, London, June 1994, Proc.v.1, pp.161-164, (1995).

[5] A.Eliseev, N.Agapov et al. “Results of the Nuclotron Upgrade Program”. Proc. IPAC’2011, September 4-11, 2011, San Sebastian, Spain, paper WEPS013.

[6] A. Bechtold, U.Bartz, M. Heilmann, P. Kolb, H. Liebermann, D. Mader, O. Meusel, H. Podlech, U. Ratzinger A. Schempp, C. Zhang, G. Clemente, “A Coupled RFQ – Drift Tube Combination for FRANZ, LINAC 2008, Victoria, 2008, MOP001, p. 46, (2002); http://www.JACoW.org

[7] V.A. Andreev at al., Injector of High Current Multi-charge Heavy Ion Beam for the TWAC Project, EPAC 2000, THP4B06, http://www.JACoW.org

[8] O.K. Belyaev et al., “IHEP Experience on Creation and Opereation of RFQs”,MOD21, LINAC 2000, Monterey, California, http://www.JACoW.org

[9] P.N. Ostroumov and A.A. Kolomiets, “New Concept for Acceleration of Slow, Low-Charge State Heavy Ion Beams”, Proceedings of the 2001 Particle Accelerator Conference, Chicago, p.4077.

Copyright © 2012 by the respective authors — cc Creative Commons Attribution 3.0 (CC BY 3.0)

EXPERIENCE WITH A 4-ROD CW RADIO FREQUENCY QUADRUPOLE

P. Gerhard*, W. Barth, L. Dahl, W. Hartmann, G. Schreiber, W. Vinzenz, H. Vormann
GSI Helmholtzzentrum f. Schwerionenforschung mbH (GSI), 64291 Darmstadt, Germany

Abstract

The High Charge State Injector (HLI) provides heavy ion beams for the linear accelerator UNILAC at GSI [1]. After 20 years of successful operation its four–rod Radio Frequency Quadrupole (RFQ) was replaced in 2010 [2]. Besides higher beam transmission, the principal intention of this upgrade was to raise the duty factor up to 100%. Commissioning and operational experience from the first years revealed that this goal could not be reached easily. After serious problems with melting of rf contacts were overcome, operation is still restricted. There is strong, modulated rf power reflection, most likely due to mechanical instabilities of the structure. In this paper we present the RFQ design, commissioning results, operational experience and future activities.

INTRODUCTION

The HLI is equipped with an ECR ion source and an RFQ-IH linac which accelerates highly charged ion beams with high duty factor of up to 30% to 1.4 MeV/u for further acceleration in the Alvarez DTL of the UNILAC. Since 1991 main user of these beams is the Super Heavy Element (SHE) research, one of the outstanding projects at GSI [3]. Experiments like TASCA and SHIP strongly benefit from the high average beam intensities. A dedicated cw linac for SHE research at GSI is seriously proposed, with the HLI as its injector. The existing HLI is not designed for cw operation. The replacement of the RFQ in 2010 was the first step towards a cw capable injector.

DESIGN & COMMISSIONING

Due to the high average rf power caused by the cw operation, all parts of the new 4-rod RFQ (electrodes, stems, tuning plates, plungers and coupling loop) had to be directly water cooled. This results in 72 connections and vacuum feedthroughs for cooling water, equipped with prevacuum sealing, making the mechanical engineering rather complex. More design properties are given in Tab. 1.

Table 1: Design properties of the new HLI RFQ.

Injection / extraction energy [keV/u]	2.5 / 300
RF frequency [MHz]	108.408
A/q (cw / max.)	6.0 / 8.5
Power (max. avg. / max. pulse) [kW]	60 / 120
Intervane voltage (cw / max.) [kV]	55 / 78
RMS emittance in / out [π mm mrad]	0.1 / 0.1009
Electrode length [m]	2.0

* p.gerhard@gsi.de

The new RFQ was delivered to GSI in autumn 2009. RF and beam commissioning was finished in spring 2010. Achievement of the design beam parameters (transmission, energy, emittance) could be demonstrated (Fig. 1 and [4]). Extensive beam measurements at different locations of the HLI beam line were performed.

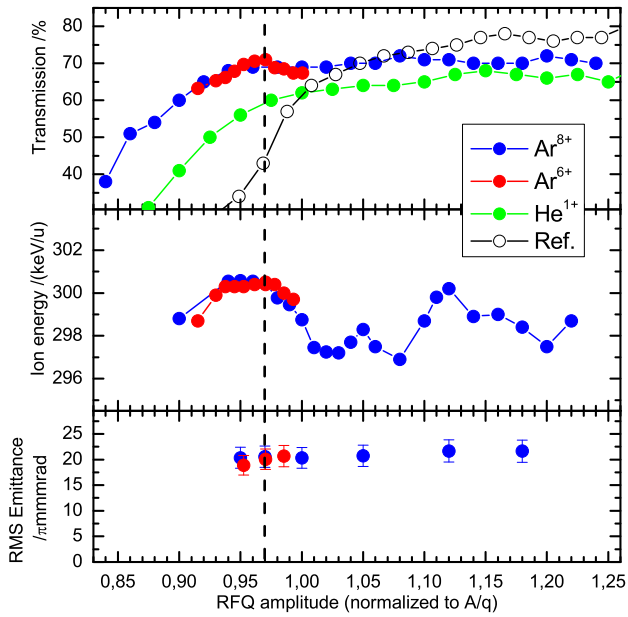

Figure 1: Beam commissioning results (top to bottom): Transmission, ion energy and beam emittance for different ions as a function of the rf amplitude, normalized to the mass-to-charge ratio. Reference data: Old RFQ; dashed line: Derived working point.

THERMAL ASPECTS

During rf commissioning two issues were discovered:

- Insufficient rf contact springs and
- the thermal instability of the 4-rod structure.

Rf contact springs

Several breakdowns of contact springs between the tuning plates and the stems occurred at rf power levels far below the design (s. Fig. 2). The first burning occurred at 16 kW avg. power, possibly due to incorrect mounting of the springs. After two breakdowns, complete renewal with more robust contacts and careful mounting was employed. Nevertheless, damages were found after operation at 24 and 30 kW. Obviously this type of contacts could not handle enough power safely in routine operation. Therefore it was decided to introduce a different contact mechanism using

Copyright © 2012 by the respective authors — cc Creative Commons Attribution 3.0 (CC BY 3.0)

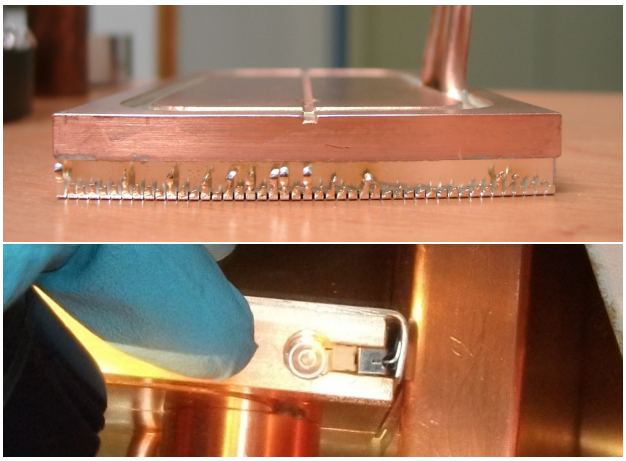

Figure 2: Tuning plate with burnt contact springs (top) and new contacts (bottom). The thick silver foil is pressed against the stem by spring steel foil and steel wedges.

solid silver foils (Fig. 2) [5]. After the new contacts were mounted in November 2010, 30 kW avg. and 110 kW pulse power were reached. Due to other limitations, the avg. design power could not be demonstrated so far.

Thermal instability

Although all relevant parts of the structure are directly water cooled, the structure reacts rapidly to changes of the thermal load. The frequency changes by approx. 200 kHz from rf off to 50% design power; elaborate estimates as well as tests with warm water indicate a temperature change of 10-20 K. Even small changes of the thermal load ($\ll 1\%$) have a significant and almost immediate effect, posing a challenge for the frequency or plunger controller. In normal operation, the average power can only be changed in small steps to allow the controller to follow. After rf breakdowns (sparking), the RFQ immediately cools down and is off resonance. It has to be restarted manually after the plungers have moved to the 'cold' position.

MECHANICAL ASPECTS

Observations

It was known from similar 4-rod RFQs, that the rf power reflected by the cavity can show a modulation [6]. In this case, the magnitude of the modulation turned out to be a major problem (Fig. 3). While the amplitude controller is still able to provide a perfect flattop (at its reference probe), the plunger controller is severely affected, since it relies on the phase difference between forward and reflected rf, which is also modulated. At higher power, it also leads to a significant fraction of the power being reflected. Besides heating up the transmitter, this limits the rf amplitude.

Most probably this modulation originates from mechanical vibrations of the electrode rods or the coupling loop. These vibrations may affect the rf resonance and rf matching. Rf power is then reflected due to the mismatch. The

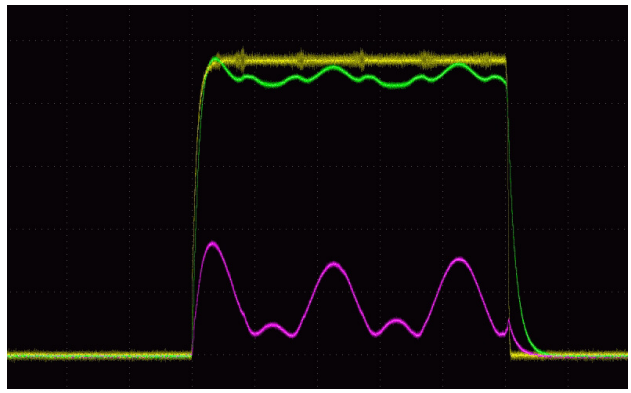

Figure 3: Modulation of the rf tank signals. Magenta: Reflected power; green: Forward power; yellow: Tank amplitude (read out).

modulation has a frequency of about 520 Hz, which is confirmed by simulations considering mechanical vibrations of the rods. A more detailed analysis of the rf signals revealed that the modulation is damped with a time constant between 6 and 10 ms. In order to identify the origin, we tried to increase the damping by putting Vespel clamps on every cell of the RFQ (Fig. 4). Operating the RFQ up to

Figure 4: RFQ structure with mounted Vespel clamps. A plunger is moved in from the top right corner.

moderate rf levels, we found the damping of the modulation to be slightly faster (5–6 ms), but also the modulation frequency slightly higher.

The RFQ is typically operated at 50 Hz pulse repetition rate and pulse lengths of up to 6 ms. During commissioning it turned out, that the RFQ can only be operated at certain pulse lengths, which have to be adjusted carefully in order to minimize the amplitude of the modulation (s. Fig. 5, left, curve 1, 5 and 9 from top). At other values, phase error exceeds the dynamic range of the control loop, rf behavior becomes unstable, reflected power increases and sparking occurs. The behavior changes when the RFQ is operated at 1 Hz. Now every pulse duration is possible and gives the same signal shape. Fig. 5 shows a comparison between the 50 Hz and the 1 Hz operation.

Copyright © 2012 by the respective authors — cc Creative Commons Attribution 3.0 (CC BY 3.0)

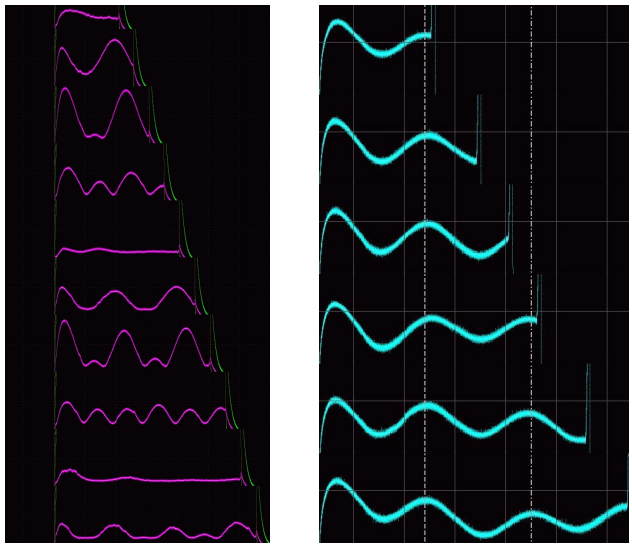

Figure 5: Rf signal modulation at 50 Hz (reflected power, left) and 1 Hz (phase difference forward/reflected, right) pulse repetition rate for pulse lengths of appr. 2-6 ms.

Discussion

The comparison shows, that 15-20 ms after the rf pulse a feedback between successive pulses is observed, while the damping has eliminated the modulation after 1 s. At 50 Hz, the remaining mechanical oscillations interfere with the excitation by the next pulse, leading to different appearances of the modulation for different pulse sequences. This fits nicely to the damping time of 5-10 ms found above. The unexpected rise of the modulation frequency with the Vespel clamps attached can be explained by a raised stiffness of the oscillator, i. e. the electrode rods, when they are pressed by the clamps. The changes induced by the clamps are indicating towards mechanical vibrations of the rods as the origin of the modulation, but they are not significant enough to prove this.

The rf field oscillates 5 orders of magnitude faster than the modulation observed, making it impossible to excite the vibrations. This is supported by the fact, that during the flattop the oscillation is damped. However, the envelope of the rf pulse is of almost rectangular shape. Therefore the rising and falling edges contain a broad frequency spectrum, which could be the origin of excitation. Tests with a trapezoid pulse shape showed a reduction of the modulation, on the cost of rf power used up outside of the flattop.

PULSED & CW OPERATION

After the serious breakdowns in the beginning, beam times with up to 30% duty cycle were conducted successfully in the past years. Handling of the RFQ is complicated due to the fast thermal reactions and the high, modulated power reflection. This also limits the applicable rf amplitude, depending on the duty cycle. A high risk of damage to the rf (pre-)amplifier is obvious. Interruptions like sparking cause long breakdowns, because the rf has to be raised slowly by hand from low levels. Pulsed operation requires absolutely stable repetition of identical pulses (length of pulse and pause, amplitude) at certain pulse lengths, which have to be fine adjusted to the thermal conditions.

So far no cw operation could be established. This is partly due to the low level rf, which is tailored to pulsed operation at 50 Hz rep. rate and 50% duty cycle at most. During a test period, the LLRF was reconfigured to enable cw operation. It turned out that no steady state could be reached. One would have expected that the perturbing modulation was damped out, but this was not the case.

In cw mode the thermal load is much higher than in pulsed mode at the same rf amplitude, hence rf power changes lead to larger thermal and consequently resonance frequency changes. The resonance changes much faster than the reaction time of the frequency controller. This leads to severe fluctuations of the power reflected and, despite the rapid compensation by the amplitude controller, of the power coupled into the cavity, too. The (slow) movement of the plungers also affects the amplitude controller. Finally, the rf amplitude is constantly changing, the system never reaches a steady state and the modulation is excited all the time, in spite of the cw operation.

CONCLUSION AND OUTLOOK

The new RFQ was intended to enable cw operation and enhance operational stability. Both aims could not be reached so far. Pulsed operation is possible with restrictions and special handling instructions. Cw operation has to be established in the framework of the upcoming cw linac.

In order to improve the situation, more tests and simulations are planned concerning the mechanical stability of the rods and the coupling loop. New electrodes with enhanced vibrational resistivity and cooling will be developed and implemented. Tests concerning the thermal stability have to be conducted in order to decide whether the stems and tuning plates have to be redesigned, too.

REFERENCES

[1] N. Angert et al., "Commissioning and First Operation Experience of the New Heavy Ion Injector of the UNILAC", EPAC'92, Berlin, Germany, March 1992, p. 167

[2] L. Dahl et al., "UNILAC Upgrades for Coulomb Barrier Energy Experiments", LINAC'10, Tsukuba, Japan, September 2010, MOP042, p. 148, and references therein

[3] S. Hofmann and G. Münzenberg, The discovery of the heaviest elements, Rev. Mod. Phys. 72, 733 (2000)

[4] P. Gerhard et al., "Commissioning of a new CW Radio Frequency Quadrupole at GSI", IPAC'10, Kyoto, Japan, May 2010, MOPD028, p. 741

[5] This type of contact is similar to and based on contacts implemented at SARAF.

[6] W. Vinzenz, "Resonanzfrequenzanalyse HLI RFQ", GSI internal report, 1997

Copyright © 2012 by the respective authors — cc Creative Commons Attribution 3.0 (CC BY 3.0)

HIGH-POWER RF CONDITIONING OF THE TRASCO RFQ

E. Fagotti, L. Antoniazzi, A. Palmieri, F. Grespan, , INFN-LNL, Legnaro, ITALY
M. Desmons, CEA, Saclay, FRANCE

Abstract

The TRASCO RFQ is designed to accelerate a 40 mA proton beam up to 5 MeV. It is a CW machine which has to show stable operation and provide the requested availability. It is composed of three electromagnetic segment coupled via two coupling cells. Each segment is divided into two 1.2 m long OFE copper modules. The RFQ is fed through eight loop-based power couplers to deliver RF to the cavity from a 352.2 MHZ, 1.3 MW klystron. After couplers conditioning, the first electromagnetic segment was successfully tested at full power. RFQ cavity reached the nominal 68 kV inter-vane voltage (1.8 Kilp.) in CW operation. Moreover, during conditioning in pulsed operation, it was possible to reach 83 kV inter-vane voltage (2.2 Kilp.) with a 0.1% duty cycle. The description of the experimental setup and procedure, as well as the main results of the conditioning procedure will be reported in this paper.

EXPERIMENTAL SETUP

The test was performed at CEA Saclay in January, February and March 2012.

The systems involved in the test are:

- RFQ cavity
- RFQ power system
- Vacuum system
- Cooling system
- Control system

The cavity under test is the first electromagnetic segment of the TRASCO RFQ [1], composed by two 1.2 m long OFE copper modules. The first module accommodates 12 gridded vacuum ports, the second one the 2 coupler ports. The RFQ end plates are equipped with dipole stabilizers [2, 3]. RFQ power level and field flatness are monitored by 16 pick-up loops, located inside the tuners along the 4 quadrants. The preservation of field flatness was verified looking at the pick-up signals, after transportation and positioning inside the CEA tunnel (Figure 1).

The core of the RF power system is the CEA 1.3 MW klystron, protected from the reverse power by a 1 MW circulator. The RF power is led into the RFQ tunnel through full-height WR2300 waveguide and then it is tapered to half-height WR2300 for the final distribution to the RFQ. Just upstream the RFQ, the RF power is split by a magic-TEE: two waveguide arms are coupled into the RFQ through 2 coupling loops, the 4th arm goes to a 100 kW water load. Forward and reverse powers are measured by directional couplers in the two waveguide arms before power couplers.

The vacuum system is composed by a dry primary pump, a turbo pump and two cryogenic pumps. The system was designed to maintain a pressure level $P \leq 1.3 \times 10^{-6}$ mbar under proton gas load. In particular, cryogenic pumps are unnecessary in absence of proton beam and they have not been used for this test. Vacuum gauges are located above couplers and on the vacuum manifold. Gate valves and nitrogen filling channel allow keeping the cavity in inert atmosphere during transports.

Cooling system is designed to remove 300 kW of power and to finely tune the resonant frequency by temperature regulation. For this purpose, it is necessary to have two independent water loops with two regulating temperatures. In the cooling skid, the temperature of each water circuit can be regulated by mixing the cold inlet water with part of the warm water coming from the cavity. Furthermore, the global temperature of the system can be adjusted by regulating the amount of warm water circulating in the heat exchanger. Water flow inside RFQ cooling channel is finely set by flow regulating valves located on each cooling channel. These valves maintain the required flow within ±2% when input pressure varies in the range 1-10 bar. Water flows and input/output temperatures of both water loops are monitored.

Control system [4] is connected to the other subsystems in order to monitor their characteristic parameters (temperature, powers, water flows, pressures), to command their actuators (valves, pumps) and set-up variables (interlock thresholds, water temperatures). In particular, interlocks on temperature, pressure, water flow, forward power are processed by PLC (response time =10 ms), while arc detectors and reflected power are directly sent to klystron to interrupt power in a few μs.

Figure 1: A view of TRASCO RFQ test in the IFMIF tunnel at CEA.

Copyright © 2012 by the respective authors — cc Creative Commons Attribution 3.0 (CC BY 3.0)

RFQ CONDITIONING

The unloaded quality factor Q_0=8460 was measured in the RFQ equipped with two aluminum couplers. Once the copper couplers were installed, the sum of the coupling coefficients ($\beta1+\beta2$) = 1.036 were obtained from the measurement of the cavity filling time τ=3.75 µs, at resonant frequency = 352.329 MHz. The two coupling coefficients are slightly mismatched, then we expect different values of reflected power in the 2 arms of the magic TEE, with less than 1% total reflected power in steady state operation. With that value of Q_0, the nominal voltage of 68 kV corresponds to cavity power P_{cav} = 192 kW (80 kW/m).

The RFQ resonant frequency control loop was not implemented for this conditioning test. The cavity was let free to be detuned, while the master frequency generator followed the RFQ resonant frequency. At low power level, a by-hand frequency control was sufficient. At high power operation (P_{cav} > 100 kW) an automatic frequency feedback control was required.

Three main phases of the RFQ conditioning are distinguishable, as highlighted in Figure 2 and 3.

From 24/01 to 30/01, RFQ was conditioned at very low duty cycle (<0.1%), to reproduce and never exceed Linac4 operating conditions (pulse length = 400 µs, rep.rate = 1.1 Hz, 82 kV), in order to allow the characterization of the X-ray emission at this regime. This phase was completed in 1 week, without any problem from the cavity point of view. In particular no discharges at 2.2 Kilp, no temperature changes or anomalous detuning were observed. Passing through all field levels, an important multipacting zone between 40 kV and 60 kV was noticed, to be treated with longer pulses. The presence of electron loading can be noticed in Figure 2, where the red squares are above the nominal curve, meaning that a large fraction of the power is not converted in accelerating voltage.

The period from 31/01 to 22/02 was dedicated to condition multipacting levels between 40 kV and 60 kV with pulses longer and longer. We adopted the following conditioning strategy:

- Fix a field level, with short pulse and long period;
- Lengthen the pulse length up to the complete conditioning of the level;
- Move on the next working point.

Because of 10 days of stop, the integrated time of this phase was 12 days.

Up to that time, the cavity frequency detuning caused by RF power was followed by changing the frequency of the signal generator by hand. Once the average power passed the 100 kW thresholds, the detuning at the power start was so fast that an electronic circuit was implemented, to give the frequency feedback to the signal generator. From 06/03 the CEA LLRF control was used.

From 23/02 to 14/03 the RFQ voltage was kept above 60 kV, except for the restart after large outgassing activity. In this phase of operations at high power level we noticed the first important discharge phenomena in the couplers, with consequent high vacuum levels (P > 10^{-4} mbar). To avoid long periods of vacuum recovery, interlock threshold of the reflected power was reduced and compensated with a longer blanking time, in order to skip the cavity filling time when the power is fully reflected.

The nominal voltage (68kV – 192 kW) in CW regime was reached in 07/03, and for 6 days the cavity was conditioned at this field with different duty cycles, always higher than 20 %.

Test was considered successfully closed in March 14th, after a continuous running at nominal voltage for 2 h. Temperature monitors did not show anomalous heating in high power steady state operation.

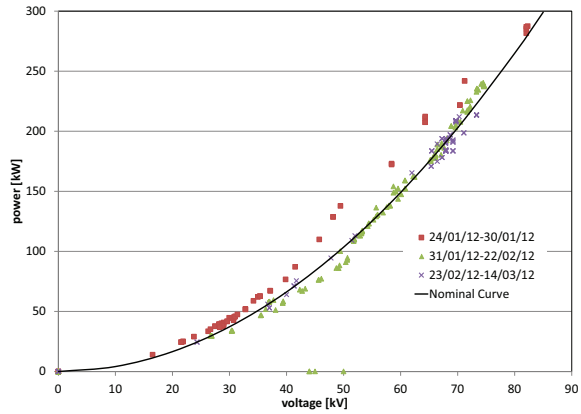

Figure 2: Peak cavity power, obtained as $P_{cav} = P_{forward} - P_{reverse}$, as function of the cavity voltage.

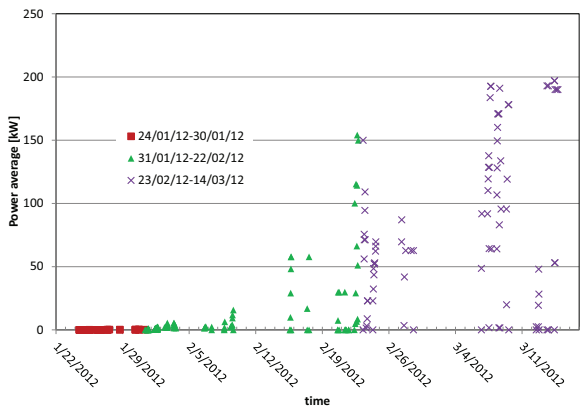

Figure 3: Cavity average power throughout the test.

RESULT ANALYSIS

Once the nominal steady state operation was reached, we observed an anomalous frequency detuning at 192 kW: Δf_{meas}= -238 kHz, to be compared with 2D simulation result Δf_{2D}= -132 kHz. Looking at the pick-up loops, we noticed that this frequency detuning was accompanied by an effect on the field flatness (Figure 4). A detailed simulation of the RFQ end-cells was performed with COMSOL [5], showing an important bending of the vane nose. The frequency perturbation profile obtained from simulation was imported in the

Copyright © 2012 by the respective authors — cc Creative Commons Attribution 3.0 (CC BY 3.0)

transmission line model of the RFQ, to evaluate the induced field and frequency detuning. Figure 5 shows field shape reproduced. The simulated detuning is -245 kHz. The asymmetric field shape, as observed in measurements, is caused by the differences on the end cell geometries. It is important to notice that this is a steady effect, not degenerative.

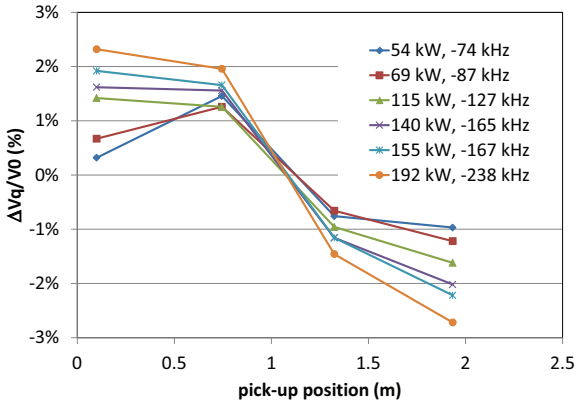

Figure 4: Field perturbation and frequency detuning measured at different power level.

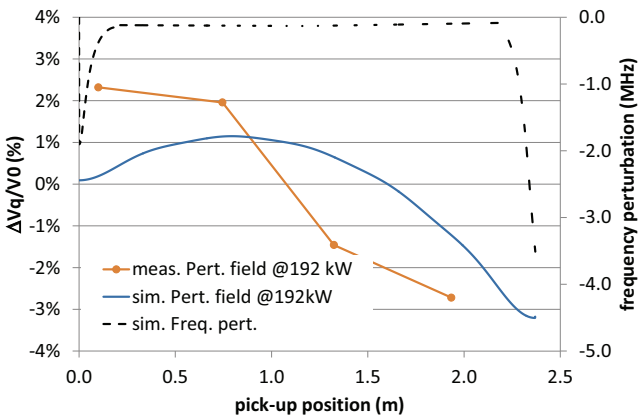

Figure 5: The measured voltage tilt at high power operation is reproduced by a transmission line analysis of the geometry deformation.

At the cavity open after the test, the power couplers showed evident copper sputtering. The RF coupler contacts were damaged and tainted by aluminium during the RF coupler test [6]. The contact degradation and aluminium oxide increase the resistance between hole and coupler wall. This could have generated a voltage difference with consequent discharges and copper sputtering, triggered off by cavity outgassing at high power operation. Sputtering phenomena was also found on the electrodes tip region, near the high energy termination plate. In this zone, R_0 changes and the electric field is a 6 % lower than the maximum value.

Finally, the chemical analysis of the cooling water revealed a copper concentration of 6.65 mg/l, due to the absence of a demineralization station in the cooling skid. In this condition, water conductivity was measured 35.8 μS/cm and PH of the water was measured 6.0.Before the test beginning, the cooling skid was filled with deionized water with 0.4 μS/cm resistivity and neutral PH.

Before removing termination plates (Figure 6), the unloaded quality factor Q_0 and coupling coefficients β_1 and β_2 were measured resulting in agreement with measurements before high power test. The quality of RF joint [7] was tested removing termination plates and then reinstalling them to look for a degradation of the unloaded quality factor. No Q_0 degradation was measured.

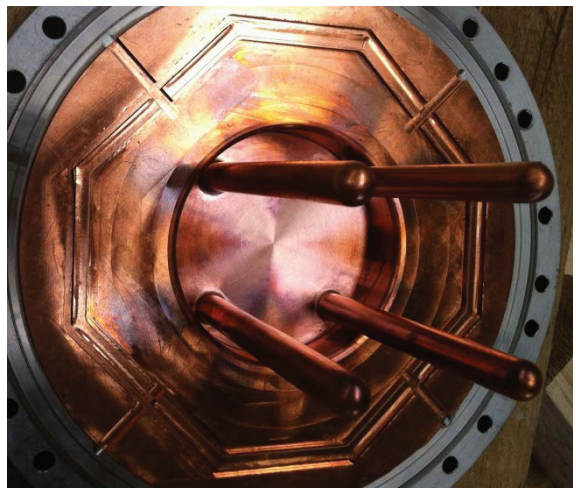

Figure 6: High energy termination plate inspection after high power test. V-shaped violet shadows caused by discharge phenomena are visible around dipole stabilizing rods.

ACKNOWLEDGMENT

We are very grateful to O. Brunasso and R. Panero for their technical support on the test assembly and disassembly. We acknowledge all the CEA team for the availability of people and facilities during the long test period.

REFERENCES

[1] A. Pisent et al., "The TRASCO-SPES RFQ", LINAC'04, Lübeck, August 2004, MOP16, p.69 (2004); http://www.jacow.org.

[2] F. Grespan et al., "Dipole stabilizing rods system for a four-vane RFQ: Modeling and measurement on the TRASCO RFQ aluminium model at LNL", EPAC'06, Edinburgh, June 2006, TUPCH123, p.1301 (2010); http://www.jacow.org.

[3] F. Grespan et al., "RF measurements for TRASCO RFQ characterization", LNL Annual Report, 2010, p. 262; http://www.lnl.infn.it.

[4] L. Antoniazzi et al., "Control System Implementation for TRASCO RFQ High Power Test", LNL Annual Report, 2012, p. 264; http://www.jacow.org.

[5] http://www.comsol.com/.

[6] E. Fagotti et al., "High Power Tests Bench for the TRASCO RFQ Coupler", TUPB094, these proceedings.

[7] E.Fagotti et al., "Completion of the fabrication of TRASCO RFQ", LINAC'10, Tsukuba, September 2012, TUP057, p.536 (2010); http://www.jacow.org.

Copyright © 2012 by the respective authors — cc Creative Commons Attribution 3.0 (CC BY 3.0)

STATUS OF E-XFEL STRING AND CRYOMODULE ASSEMBLY AT CEA-SACLAY

C. Madec, S. Berry, P. Charon, J.-P. Charrier, C. Cloué, A. Daël, M. Fontaine, O. Napoly, N. Sacépé, C. Simon, B. Visentin, A. Brasseur, Y. Gasser, S. Langlois, R. Legros, G. Monnereau, J.-L. Perrin, D. Roudier, Y. Sauce, T. Vacher, CEA/Irfu, Gif-sur-Yvette, France

Abstract

As In-Kind contributor to the E-XFEL project, CEA is committed to the integration on the Saclay site of the 100 cryomodules (CM) of the superconducting linac as well as to the procurement of the magnetic shieldings, superinsulation blankets and 31 cold beam position monitors (BPM) of the re-entrant type. The assembly infrastructure has been renovated from the previous Saturne Synchrotron Laboratory facility: it includes a 200 m^2 clean room complex with 112 m^2 under ISO4, 1325 m^2 of assembly platforms and 400 m^2 of storage area. In parallel, CEA has conducted industrial studies and three cryomodule assembly prototyping both aiming at preparing the industrial file, the quality management system and the commissioning of the assembly plant, tooling and control equipment. In 2012, the contract of the integration has been awarded to ALSYOM. The paper will summarize the outputs of the preparation and prototyping phases and the status of the up-coming industrial phase.

INTRODUCTION

The 17.5 GeV superconducting RF linac of the E-XFEL project [1] will comprise 100 cryomodules (cf fig.1), after the injector module. These twelve-meter long cryomodules, deriving from the FLASH technology, include a string of eight 1.3 GHz RF cavities with an average gradient of 24 MV/m, followed by a BPM and a superconducting quadrupole.

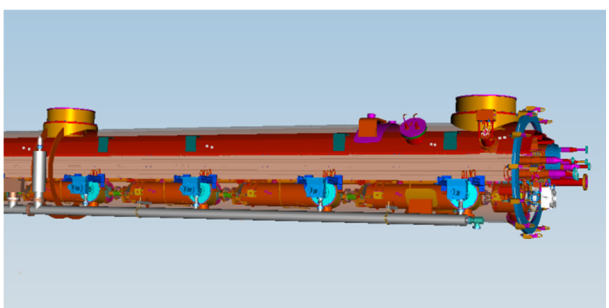

Figure 1: XFEL Cryomodule 3D-model

This string is closed by two gate valves at both ends. Within the Accelerator Consortium (AC), CEA is committed to the assembly of the 103 cryomodules over 2013 to mid-2015 with the goal to deliver one cryomodule per week to DESY for RF acceptance. Strategic decisions, shared by the AC, were taken in 2008 first to host the assembly plant on CEA premises at Saclay, using the former Saturne Synchrotron Laboratory accelerator and experimental halls, second to subcontract the 103 modules, assembly work, including 3 pre-series modules, to an industrial company for. The layout of the assembly plant (see Fig. 2), was optimized by breaking down the assembly work in seven successive blocks of one-week procedures, leading to one clean room complex for coupler and string assembly, and five cryostating workstations for the remaining cryostating work, including alignment and control operations. To allow for a fluid circulation of the cryomodules along the assembly chain even when a repair is needed at one workstation, each workstation, but the vacuum vessel cantilever (see Fig. 3), has been doubled to offer module parking possibilities.

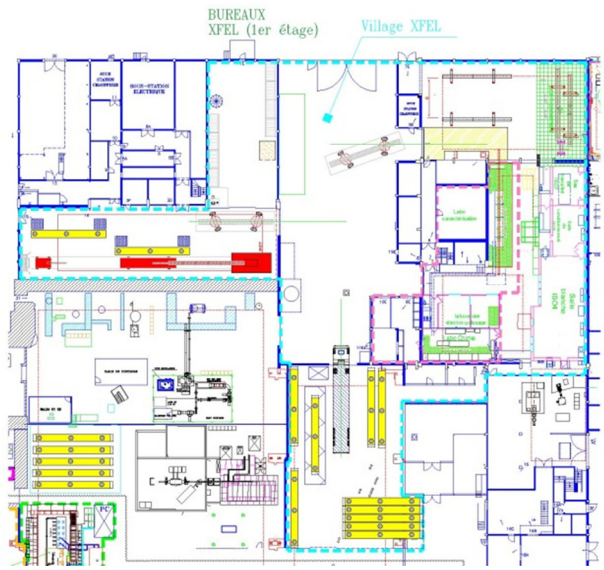

Figure 2: Layout of the XFEL infrastructure

Figure 3: Vacuum vessel and cold mass on the cantilever

OUTPUTS FROM THE PREPARATION PHASE

To ensure the integration of 103 CM at the rate of one cryomodule per week, CEA has set up a program to form

Copyright © 2012 by the respective authors — cc Creative Commons Attribution 3.0 (CC BY 3.0)

an expert team and to commission the facility. This program includes a training phase, a prototyping phase and the industrial phase.

Training phase:

In 2007, CEA and DESY have started the transfer of the knowledge by a period of observation by CEA personnel at DESY (M3 CM for FLASH) followed by a "hands-on" assembly period where CEA personnel participated in the assembly of the FLASH M8-PXFEL1 CM with the DESY team.

Pre-industrial studies:

Meanwhile, CEA has conducted industrialisation studies aiming at defining industrial equipment and methods for the cryomodule assembly. The first study has determined the workflow from the storage to the shipment, with cavity reception, clean room assembly, roll-out, alignment, vessel roll-over and coupler assembly (see Figs.2-7). The areas have been dimensioned accordingly and matched to the infrastructure which was renovated from the previous Saturne Synchrotron Laboratory facility: the 200m2 clean room complex with 112 m2 under ISO4 allows us to assemble the couplers to the cavity and two cavity strings in parallel; the *cryostating* will be held on the 1325 m2 of assembly platforms and 400 m2 are dedicated to storage.

Figure 4: PXFEL2_2 in the ISO4 clean room facility

The first fabrication file included assembly procedures with task description, duration and manpower skills definition. It included also the big tools drawing updates, tasks schedules and risk analysis. The cost estimate of the 103CM integration has been estimated. The outputs of this first study lead CEA to launch the big tool fabrication, speed-up the infrastructure set-up, establish the quality insurance plan and start the prototyping phase where CEA team is training in house on assembling 3 CM using its infrastructure and tools.

The second more detailed study finalized the tools such as the clean room tools specific to CEA infrastructure, the detailed assembly procedures with tools in use, duration of the task, incoming and outcoming parts; the parts flow has been consolidated, the stock needs have been evaluated. This study has defined the product breakdown structure, updated the risk analysis and detailed the schedule in tasks. The outputs of this study were used to place the call for tender for the 103 CM integration.

Prototyping phase:

The prototyping phase consisted of the assembly of 3 CM (namely PXFEL2_1, PXFEL3_1 and PXFEL2_2) at CEA by both CEA and DESY staff allowing qualifying the team, the tools and the infrastructure.

The infrastructure was equipped with the services and fluids for the CM assembly. Big tools such as girders and pillars (cf Fig 5) have been manufactured ahead of time and commissioned along the prototyping phase.

Figure 5: PXFEL2_2 cold mass and string hooked to the girder in the Roll-Out area

Small tools, especially those dedicated to clean room assembly (cf Fig. 6), were manufactured and commissioned during the prototype phase. Ionized gun and particle counters for clean room assembly were ordered and used to insure the required low level of particles on the part to be assembled (less than 10 particles over 1 minutes of 0.3 mm on the part to be assembled).

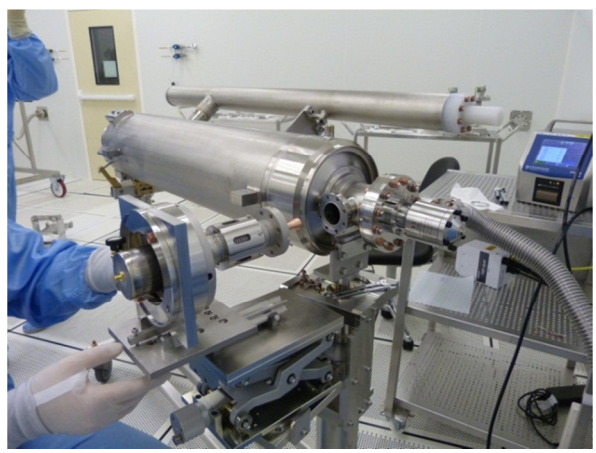

Figure 6 : coupler to cavity assembly in the clean room with tools (elevator table and coupler holding) and particle counter

Vacuum groups, equipped with RGA and slow pumping-venting system, have been installed on the clean room wall and in the coupler hall. Those groups, provided

Copyright © 2012 by the respective authors — cc Creative Commons Attribution 3.0 (CC BY 3.0)

by DESY, are designed to reduce the particles migration when pumping or venting a cavity or a coupler.

CEA has designed specific vacuum groups with a turbo pump and gauge attached to the cavity in the clean room and the primary pumps outside the clean room. Those groups are dedicated to the leak detection and venting of the cavity during the assembly. They have been ordered for the XFEL CM assembly.

The tests and controls have been detailed (RF, mechanical, vacuum, electrical), implemented and validated. The automated RF and tuner test bench have been developed for systematic measurements and recordings as well as the alignment and particle counter software. They have been tested on the prototypes.

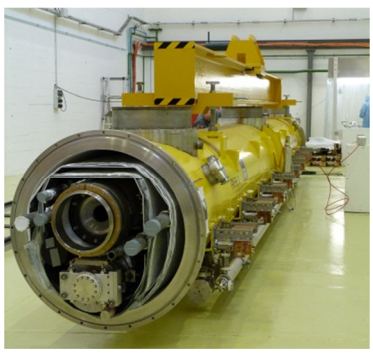

Figure 7 : CM after warm coupler assembly

The assembly procedures have been tested during a first assembly, then modified according to CEA's infrastructure and tools and rechecked on a last assembly for repetitive tasks. The part workflow from the reception to the assembly halls has been validated. Improvements on a few workstations are under evaluation, aiming at saving assembly time.

During the prototype phase, CEA and DESY established the Manufacturing Bill Of Material (MBOM [2]) which is collecting, recording, and archiving the complete mandatory fabrication information. It is focused on the parts that are needed to manufacture a CM at CEA. The MBOM also includes information about how the parts relate to each other, the inspection to be performed, the tests to be recorded, the assembly procedures, the documentation etc... The XFEL cryomodule MBOM contains roughly 500 lines i.e. 500 elements are assembled on a CM at CEA.

PROCUREMENTS

CEA is in charge of the procurement of the 800 cavity magnetic shields. The awarded company proposed some closing improvements as well as a new Cryophy™ material which was qualified on the CM prototypes.

Precut and assembled multilayer blankets for the 2K and 70K superinsulation have been ordered: they facilitate the assembly and reduce its duration. Cryogenic loss measurements on the prototype modules qualified them for the series.

CEA is also in charge of 31 cold re-entrant BPM (cf. figure 8). These BPM have been studied and prototyped at CEA [3], and tested on FLASH. The integration with the cold quadrupole is done at DESY. The electronics developed by CEA in collaboration with PSI will be implemented in the modular BPM unit [4].

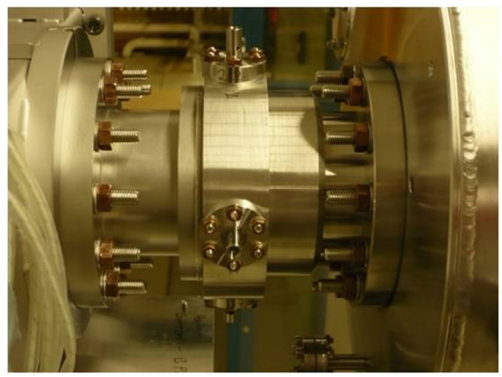

Figure 8 : BPM installed on PXFEL3_1

INDUSTRIAL PHASE

The contract for 103 CM integration has been awarded to ALSYOM in July 2012. The first phase (until Dec 2012), consists of the observation by ALSYOM of the assembly by CEA of the first pre-series cryomodule (XM-3) and the deployment of their industrial method based on the outputs of the prototyping. It also includes the set-up of the storage area, the ERP (entreprise resource planning) parameterization and the consumable parts ordering. The second phase is the training of the company team attended by the CEA team on the assembly of the second and third pre-series modules XM-2 and XM-1. From XM1 on, ALSYOM will be in charge of the series module assembly. A ramp-up period of six months is foreseen to reach the production rate of 1 CM per week. Based on quality assurance and quality control, the Acceptance Data Package (ADP) will support the first step of CM acceptance by CEA. It includes the certificate of conformity, the "as-built" configuration, the traveler, and the test and non-conformities reports. PXFEL2_2 CM ADP was built following our experience and needs, and it was delivered to DESY with the CM on Sept 4th, 2012 for approval. The second CM acceptance stage will be based on the RF test at DESY.

CONCLUSIONS

The CM factory is ready to start the assembly of the XM-3 pre-series XFEL cryomodule on September 17th, 2012.

REFERENCES

[1] E. Vogel et al. , 'Integration of the European XFEL accelerating modules', MOPB017 (this conference)
[2] L. Hagge, et al., "Parts management during fabrication at the European XFEL", IPAC2012, WEPPC005
[3] C. Simon, et al., Physical Review, 11, 082802 (2008)
[4] C. Simon, et al., the European XFEL BPM system, IPAC2010, MOP064

Copyright © 2012 by the respective authors — cc Creative Commons Attribution 3.0 (CC BY 3.0)

EXPERIMENTAL AND SIMULATION STUDY OF THE LONG-PATH-LENGTH DYNAMICS OF A SPACE-CHARGE-DOMINATED BUNCH*

I. Haber, B. L. Beaudoin, S. Bernal, R. A. Kishek, T. W. Koeth, Y. C. Mo
University of Maryland, College Park, MD 20742, USA

Abstract

The University of Maryland Electron Ring (UMER) is a low-energy (10 KeV) electron facility built to study, on a scaled machine, the long-propagation-length evolution of a space-charge-dominated beam. Though constructed in a ring geometry to achieve a long path length at modest cost, UMER has observed important space-charge physics directly relevant to linear machines. Examples are presented that emphasize studies of the longitudinal dynamics and comparisons to axisymmetric simulations. The detailed agreement obtained between axisymmetric simulation and experiment is presented as evidence that the longitudinal physics observed is not strongly influenced by the ring geometry. Novel phenomena such as soliton formation, unimpeded bunch-end interpenetration, and an instability that occurs after this interpenetration, are discussed.

BACKGROUND

The University of Maryland has had a long-standing program, inspired and nurtured by the late Prof. Martin Reiser, of using electron beams to conduct research, on a scaled basis, into the fundamental physics of intense charged particle beams when the beam evolution is dominated by the influence of space charge. An important and continuing element of this research has been its emphasis on comparison of theory and simulation to experiment. The early successes achieved are a strong motivation for the current research.

During the early years, the primary experimental facility was a 240 mA, 5 KeV electron beam injected into a transport system that consisted of 38 discrete iron core solenoid magnets, placed 13.6 cm apart [1]. Particle-in-cell (PIC) simulations [2] that carefully modelled the iron core solenoids [3] were successful in reproducing, in detail, experimentally observed behavior. The influence of space charge on beam characteristics such as emittance growth in the presence of misalignments and small errors in the initial match [4] were quantitatively reproduced and explained.

A significant milestone in simulation/experiment benchmarking [5] was achieved in an experiment where a mask was placed immediately downstream of the electron gun to produce a five beamlet pattern. This experiment was performed to test the theory that a nonuniform transverse current profile will relax to the lowest-potential-energy uniform profile. The excess energy would be converted to kinetic energy, causing the beam emittance to grow [6]. Agreement was obtained on the emittance growth between experiment and simulation and theory.

An unexpected downstream re-emergence of the initial five-beamlet pattern was observed on a series of downstream phosphor screen images. Furthermore, the image evolution was reproduced in striking detail in simulation. The simulations assumed uniform emission from the gun with the intrinsic emittance calculated from the cathode temperature and employed no adjustable free parameters. In addition, evolution of the current cross-section was sufficiently sensitive to the initial emittance that only a few percent variation in the initial emittance assumed in the simulation resulted in a noticeable deviation from the experimentally observed patterns. Comparison between simulation and experiment could therefore be used to deduce beam emittance.

To study conversion of the space charge potential energy in a mismatch to kinetic energy, an additional series of experiments was performed where the beam was purposely mismatched. Theoretical predictions of the energy exchange were verified. However, unlike the matched beamlet case where a final distribution with a uniform cross section was observed, the extra kinetic energy was transferred mostly to a beam halo [7].

Additional experiments were also conducted to test longitudinal beam dynamics. Generally good agreement between theory and experiment was also obtained [8]. In investigating both transverse and longitudinal dynamics, many experiments were conducted that validated both theoretical predictions of the physics of the evolution of space-charge dominated beams, as well as, the ability of simulations to predict the observed behavior. However, because of the limited length of the linear transport line, it was not possible to address many significant questions about the physics of space-charge-dominated beams. For example, what are the characteristic of the equilibrium distribution that is reached after long time relaxation of a space-charge-dominated beam? In addition, many questions concerning the longitudinal dynamics, which have a much slower evolution time than the transverse dynamics are inaccessible in a short linear transport system.

UNIVERSITY OF MARYLAND ELECTRON RING (UMER)

Ring Description

In order to address the long pathlength physics of a space charge dominated beam, while remaining within the available space and budgetary limits, the University of Maryland Electron Ring (UMER) was constructed. A

*Work supported by the United States Department of Energy and the Office of Naval Research.

Copyright © 2012 by the respective authors — cc Creative Commons Attribution 3.0 (CC BY 3.0)

substantial number of simulation studies was first conducted. From these studies it was determined that emittance growth of the propagating bunch would remain within acceptable limits with achievable construction tolerances [9].

UMER is a 11.52m circumference electron ring with 36 alternating-gradient (A-G) quadrupole periods and an approximate 60° phase advance per period. Immediately downstream of the 10KeV electron gun is an aperture wheel that can selectively insert different apertures without breaking vacuum. The apertures allow injected beam currents to be varied from 0.6mA to 100mA. Normalized beam emittances for the range of injected currents range between ~0.3μm and ~3μm. As a result, the beam space charge phase advance can range from moderately to substantially depressed. Under usual operating conditions, a 100ns constant current bunch is injected covering approximately half of the ring. The injection dipole is then switched to recirculate the bunch. Details of the UMER ring as well as performance measured during conditioning are beyond this discussion, but are documented in detail elsewhere [10-12].

Longitudinal Dynamics in UMER

A consequence of employing a ring is the added complexity of the transverse dynamics compared with a linear machine. For example, there are potential distortions of the transverse equilibrium as the beam is bent and the possibility of resonances that are not present in a linear geometry. This is a complex area of space-charge physics currently under study and is beyond the scope of the current discussion. However, because of the separation of time scales between the transverse and longitudinal evolution, the conventional wisdom expects that the longitudinal evolution will be averaged over the more rapid transverse dynamics and the two will be decoupled. Evidence is presented that this is what actually happens.

Bunch-End Expansion and Interpenetration

Because the injected UMER bunch does not fill the entire ring, unless the bunch ends are contained by an applied bunching force, the space charge forces in the bunch will cause the ends to expand [13]. The front of the bunch will eventually overtake the rear end of the previous turn. Because the bunch length is much greater than the pipe radius, the longitudinal electric field is largely shorted-circuited by the conducting pipe. This results in a longitudinal self-electric field that is proportional to the derivative of the line density. Consequently, at the minimum in current that occurs between overtaking bunch ends, the self-electric field vanishes and the ends freely interpenetrate.

This behavior and the consequent evolution of the longitudinal bunch toward uniformly filling the ring, is illustrated in Fig. 1, which is a plot of the time evolution of the beam current passing a resistive wall current monitor about half way around ring circumference downstream of the injection. Also plotted on the same axes is a simulation using a straightened-pipe axisymmetric numerical PIC model with a uniform constant applied solenoid focusing force. The simulated curve is corrected for the measured transverse beam loss and also for the characteristics of the measurement circuit, primarily the inductance that is in parallel with the resistance of the current monitor [14].

Multi-Stream Instability

As the bunch ends overtake and interpenetrate more than once, there are eventually several interpenetrating streams with different longitudinal velocities at any location along the bunch. Owing to the multiple streams, development of space-charge-driven instability is predicted by simulation, and is observed experimentally. There are small differences in details of the instability onset time and the details of the current modulation. However, this can be expected, since instability onset is generally sensitive to fine details of the initial distribution. This instability, which occurs at a wavelength several times larger than the pipe diameter, differs from the usual plasma two-stream instability. The usual two-stream instability is observed in simulations but occurs at a much shorter wavelength and saturates at too low a level to be observed experimentally.

Solitons

Another series of experiments where excellent agreement has been obtained between experiment and simulation, is the propagation of a short large-amplitude perturbation in the initial beam current created by laser excitation of the cathode [15]. In this case also, axisymmetric simulations reproduce, in detail, the measured current evolution, including the breakup of the large-amplitude initial pulse into a soliton train. Several parametric tests have been conducted to verify that the observed behavior reproduces what is expected from soliton propagation.

SUMMARY

Several experiments have been described where the beam evolution is reproduced in detail by “straightened” axisymmetric simulations. These simulations replace the flutter in the alternating-gradient focusing with a constant axisymmetric focusing force. In addition to neglecting the A-G flutter, these simulations also neglect the consequences of beam bending. The major effect that must be included to obtain agreement between simulation and experiment is to account for transverse current loss. This was done by assuming that such loss occurs uniformly along the bunch.

The degree to which agreement is obtained notwithstanding these assumptions argues strongly for the assumption that the transverse and longitudinal dynamics are decoupled. The UMER ring is therefore an excellent vehicle for the general exploration of space-charge-dominated longitudinal beam dynamics, and the results obtained should be directly applicable to linear machines.

Copyright © 2012 by the respective authors — cc Creative Commons Attribution 3.0 (CC BY 3.0)

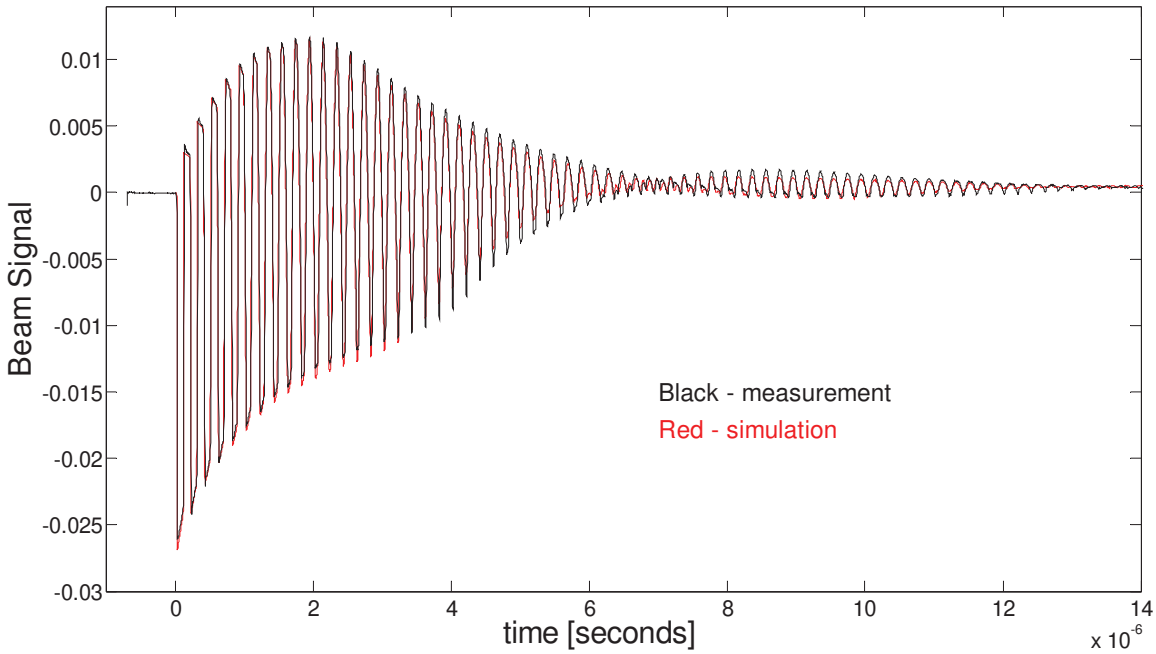

Figure 1: Excellent simulation/experiment agreement is seen in a comparison of the 6 mA wall-current monitor signal with simulated current profile adjusted to include beam loss and the equivalent circuit model of the detector.

REFERENCES

[1] D. Kehne, K. Low, M. Reiser, T. Shea, C.R. Chang, Y. Chen "Experimental studies of electron beam transport in the Maryland periodic solenoid channel," Nucl. Instrum. Methods A **278,** 194 (1989).

[2] David P. Grote, Alex Friedman, Jean-Luc Vay, and Irving Haber, "WARP – A Parallel Framework Combining Features of Plasma (Particle in Cell) and Accelerator Codes," AIP Conf. Proc 749(1) 2005.

[3] P. Loschialpo, W. Namkung, M. Reiser, J. D. Lawson, "Effects of space charge and lens aberrations in the focusing of an electron beam by a solenoid lens," J. Appl. Phys. **57** 10 (1985).

[4] H. Rudd, C. R. Chang, D. Kehne, K. Low, M. Reiser, T. Shea, and I. Haber, "Comparison of Simulation Theory & Measurement for the Maryland Transport Experiment," Nucl. Instr. & Methods in Physics Res. A278, 198 (1989).

[5] I. Haber, D. Kehne, M. Reiser, and H. Rudd "Experimental, Theoretical and Numerical Investigation of the Homogenization of Density Nonuniformities in the Periodic Transport of a Space-Charge Dominated Beam," Phys. Rev. A15, 44, 5194 (Oct. 15, 1991).

[6] T. P. Wangler, K.R. Crandall. R.S. Mills. and M. Reiser, "Relation Between Field Energy and RMS Emittance in Intense Particle Beams," IEEE Trans. Nucl. Sci. NS-32. 2196, 1985.

[7] D. Kehne, M. Reiser, H. Rudd, "Experimental Studies of Emittance Growth Due to Initial Mismatch of a Space Charge Dominated Beam in a Solenoidal Focusing Channel," Proc. of the 1991 Particle Accelerator Conf. http://www.JACoW.org

[8] D. X. Wang, J. G. Wang, D. Kehne, M. Reiser, I. Haber, "Experimental Studies of Longitudinal Beam Dynamics of Space-Charge Dominated Beams,". Proc. of the 1993 Particle Accel. Conf. http://www.JACoW.org

[9] R.A. Kishek, S. Bernal, M. Reiser, M. Venturini, J.G. Wang, I. Haber, and T. Godlove "Beam Dynamics Simulations of the University of Maryland Electron-Ring Project" Nuclear Instruments and Methods **A415**, 417-421 (1998).

[10] I. Haber, S. Bernal, B. Beaudoin, M. Cornacchia, D. Feldman, R.B. Feldman, R. Fiorito, K. Fiuza, T.F. Godlove, R.A. Kishek, P.G. O'Shea, B. Quinn, C. Papadopoulos, M. Reiser, D. Stratakis, D. Sutter, J.C.T. Thangaraj, K. Tian, M. Walter, and C. Wu, "Scaled electron studies at the University of Maryland," Nuclear Instruments and Methods A **606**, 64-68 (2009).

[11] R.A. Kishek, B.L. Beaudoin, S. Bernal, M. Cornacchia, K. Fiuza, I. Haber, T. Koeth, P.G. O'Shea, D.F. Sutter, and H. Zhang, "Advances in Modeling the University of Maryland Electron Ring," PAC 2011, New York, (2011). http://www.JACoW.org

[12] http://www.umer.umd.edu

[13] A. Faltens, E.P. Lee, S.S. Rosenblum, "Beam end erosion," J. of Appl. Phys., Vol. **61**, 12, p.5219, (1987).

[14] T. Koeth, B. Beaudoin, S. Bernal, I. Haber, R.A. Kishek, and P.G. O'Shea, "Longitudinal Relaxation of a Space-Charge Dominated Bunch," Proceedings of the 2011 IEEE Particle Accelerator Conference.http://www.JACoW.org

[15] Y. Mo, B.L. Beaudoin, D. Feldman, I. Haber, R.A. Kishek, P.G. O'Shea, and J.C.T. Thangaraj, "Experimental Observations of Large-amplitude Solitary Waves in Electron Beams," Paper ID TUPPC094, IPAC 2012, New Orleans (2012).

Copyright © 2012 by the respective authors — cc Creative Commons Attribution 3.0 (CC BY 3.0)

PHOTOINJECTOR SRF CAVITY DEVELOPMENT FOR B*ERL*inPro *

A. Neumann†, W. Anders, T. Kamps,
J. Knobloch - Helmholtz-Zentrum Berlin, Berlin, Germany
E. Zaplatin - FZJ Jülich, Jülich, Germany

Abstract

In 2010 HZB has received approval to build B*ERL*inPro , an ERL project to demonstrate energy recovery at 100 mA beam current by pertaining a high quality beam. These goals place stringent requirements on the SRF cavity for the photoinjector which has to deliver a small emittance 100 mA beam with at least 1.8 MeV kinetic energy while limited by fundamental power coupler performance to about 230 kW forward power. In oder to achieve these goals the injector cavity is being developed in a three stage approach. The current design studies focus on implementing a normal conducting cathode insert into a newly developed superconducting photoinjector cavity. In this paper the fundamental RF design calculations concerning cell shape for optimized beam dynamics as well as SRF performance will be presented. Further studies concentrate on HOM properties, the field-flatness and tuning mechanism for that design.

REQUIREMENTS TO THE CAVITY DESIGN

The B*ERL*inPro ERL will be a prototype facility demonstrating energy recovery with a 100 mA beam at 50 MeV beam energy while preserving a normalized emittance of better than 1 mm mrad at a pulse length of 2 ps or less [1]. This machine will make fully use of superconducting RF technology operated in continuous wave (CW). The injector has to deliver a high brightness beam at a high repetition rate, filling every RF bucket, a low emittance allowing for emittance compensation and a compression of the longitudinal phase space in the ps regime. At this high average current also higher order mode excitation and damping have to be considered as well as coupling strongly to the fundamental. The high beam brightness will be achieved by inserting a high quantum efficiency normal conducting semi-conductor cathode within the SC environment of the cavity. This cathode insert will mainly rely on the design by HZDR used in the ELBE SC 3.5 cell injector cavity [2]. As these are demanding goals, the injector and cavity are developed in a three stage approach. First results of an all superconducting gun cavity with a SC lead cathode were published in [5][6].

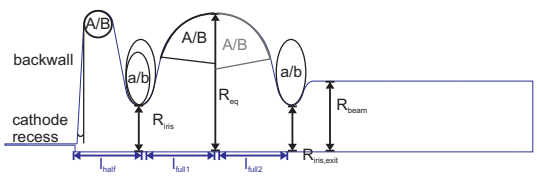

Figure 1: Geometry design parameters used for the cavity optimization scheme.

RF DESIGN STUDIES

The gun cavity has to fulfill several objectives while limited by some fundamental boundary conditions. The available total power will be limited to about 230 kW by using two KEK-style [3] fundamental power couplers (FPC), whereas the maximum electric peak field E_{peak} was recently demonstrated to reach 45 MV/m [4]. To name a few, regarding SRF and beam based properties the injector cavity has to be designed regarding the following aspects:

- Minimize E_{peak}/E_0 with $E_{\text{cathode}} < E_0$: This maximizes the field during beam extraction $E_{\text{launch}} = E_{\text{cathode}} \cdot \sin\Phi$ compared to the field anywhere on the surface E_{peak}, while it might be helpful to have the maximum on-axis field E_0 away from the cathode to reduce the probability of dark current.
- Minimize $H_{\text{peak}}/E_{\text{peak}}$ and maximize R/Q to minimize losses. Consider the cutoff of the beam tube and iris diameter for a compromise between R/Q and HOM propagation and cell-to-cell coupling.
- The resonators length determines the launch phase Φ and field level during emission and thus energy gain and emittance. Thereby it also defines the field level for the field emitted dark current at about $\Phi = 90 \pm 20$ degrees.
- Transverse beam properties are influenced by the field during emission (>10 MV/m [7]) as by the transverse focussing due to e.g. retraction of the cathode, backwall inclination and the transverse field component when the bunch leaves the RF structure.

Figure 1 shows the geometric parameters used in this work to run different optimization steps to converge to a suitable design. The design iteration was done by implementing different optimization schemes, like golden section search and Nead-Melder Simplex algorithms within a MATLAB™ wrapper to run the 2-D RF field solver Superfish [8]. The obtained fields were used in the same loop to perform a first field-phase scan of the longitudinal phase space using a simple self written tracking code. Following, a set of candidates were included in ASTRA-based [9] beam dynamics simulations including the solenoid or the whole injector

* Work supported by Bundesministerium für Bildung und Forschung and Land Berlin
† Axel.Neumann@helmholtz-berlin.de

Copyright © 2012 by the respective authors — cc Creative Commons Attribution 3.0 (CC BY 3.0)

chain of B*ERL*inPro . The outcome of these calculations delivered the feedback for further changes to the cavity's geometry.

Half-cell optimization

In a first iteration the half-cell was optimized to maximize the launch phase via a scan of the half cell's length taking transit time effects into account. Figure 2 shows the launch phase for maximum energy gain for half-cells varying from 0.4-0.6 $\lambda/2$. The 0.4 cell design shows the best performance with respect to launch phase, as all of them after fine tuning achieved comparable RF properties. Going to even shorter half-cells was omitted due to mechanical stability and peak field considerations. As can be seen in Table 1 the resultant E_{launch} of a pure 0.4 design is still rather low. Hence another full cell, starting from a TESLA shape, was added to the design. As can be seen in the energy-field-phase scan presented in Figure 3, a 1.4 cell design features a quite high launch field making full use of the offered 230 kW at $E_0 = 30$ MV/m. The corresponding field distribution is shown in Figure 4. A 1.X cell design has the further advantage, that the dark current emitted at field maximum on the cathode still can propagate out of the cavity which limits the danger of back bombardment.

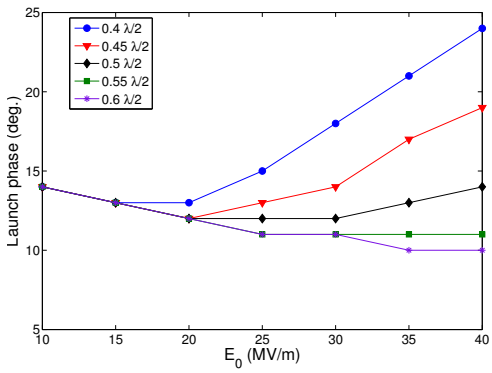

Figure 2: Energy-phase-field scan vs. half-cell length showing the phase with the highest energy gain in the half-cell.

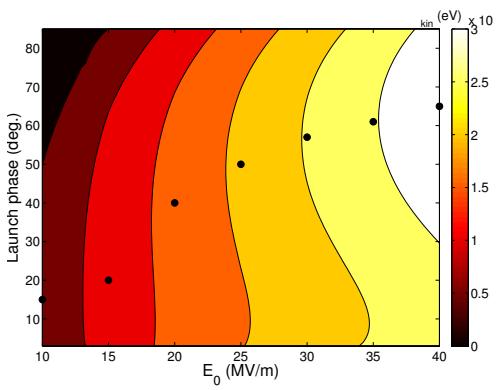

Figure 3: Energy-phase-field scan of a 1.4 cell cavity. The black dots denote the phase with the maximum energy gain at the given maximum on-axis field E_0.

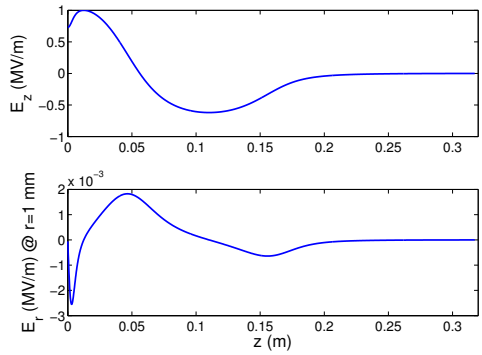

Figure 4: Field distribution (E_z, E_r) of a 1.4 cell gun cavity design with 35 mm exit iris and 53 mm beam tube radius.

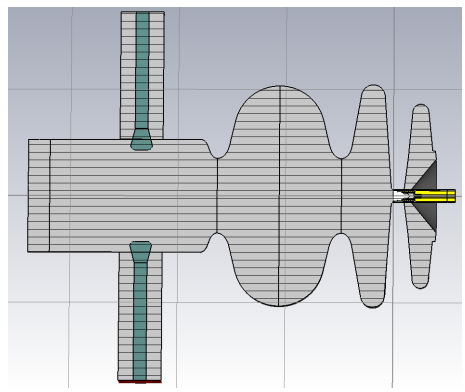

Figure 5: Possible design of the next 1.4 cell gun cavity featuring the HZDR-style choke cell, a modified cathode stock, two TTF-III type FPC having a 35 mm exit iris.

Figure 5 shows the current design for the next gun cavity which should demonstrate a beam of some mA using two modified TTF-III FPCs [10]. This cavity will mainly be used to study the cathode insert mechanism within the SC environment, beam dynamics and the HOM properties.

CELL TUNING

Preliminary investigations of the cell mechanical properties (the structure without helium vessel and any stiffening rings) showed that by simultaneous tuning of both cells E_z along the beam path varies within 2%. At the same time because of the cell deformations under external LHe pressure the field profile in the 0.4-cell changes up to 10%. With an installation of stiffening rings there are possibilities to find ring positions that the total effect of external pressure applied on the whole cavity and liquid helium vessel walls results in nearly complete compensation of the frequency shifts caused by cavity and vessel wall deformations (df/dp is close to zero, Figure 6). For df/dp=0 the field profile change is within 5%, being near the accuracy limit of that calculation.

Copyright © 2012 by the respective authors — cc Creative Commons Attribution 3.0 (CC BY 3.0)

Table 1: Cavity figures of merit for the TM_{010}-π mode of three gun cavity options at E_0= 30 MV/m and cathode retracted by 1.5mm. Note, that Q_{ext} relates to the limit in total forward power of 230 kW. All values are for β =1 as calculated by Superfish.

Parameter	0.4 cell	1.4 cell 35 mm exit iris	1.4 cell 40 mm exit iris
$R/Q(\Omega)$	93	151	146
E_{peak}/E_0	1.5	1.5	1.57
$E_{cathode}/E_0$	0.75	0.75	0.75
H_{peak}/E_{peak} (mT/(MV/m))	1.9	2.2	2.1
$\Phi_{launch}(E_{kin,max})$ (deg.)	18	52	50
E_{launch} (MV/m)	6.9	17.7	17.3
E_{kin} (MeV)	1.2	2.67	2.6
k_{cc} (%)	-	1.6	1.5
Q_{ext} at 100 mA	$1.44 \cdot 10^5$	$1.52 \cdot 10^5$	$1.58 \cdot 10^5$

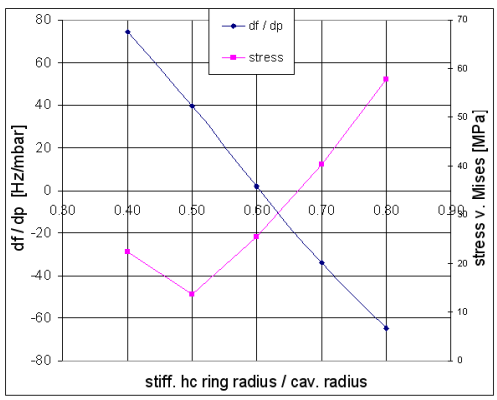

Figure 6: Detuning vs. LHe pressure coefficient and v. Mises stress versus position of a stiffening ring for the 1.4 cell design.

OUTLOOK

The current design work focusses on studying 3-D aspects using CST MWS [11] of the gun cavity design including optimizing the FPC's position and beam tube size for a minimized coupler kick by the fundamental to the beam while preserving the HOM damping capabilities. Further studies aim for calculation of the HOM losses and damping, especially taking the $\beta(z,t)$ dependent loss factor into account as depicted in Table 2. Beam dynamics based tolerance studies have to show how susceptible the beam properties are with respect to field flatness variations with respect to cavity tuning to decide whether two independent tuners for each cell are needed.

ACKNOWLEDGEMENTS

The authors acknowledge the fruitful discussions with J. Sekutowicz (DESY), J. Teichert and A. Arnold (both HZDR).

Table 2: Launch field dependent $R/Q(\Omega)$ of the TM monopole modes

f (MHz)	$R/Q_{\parallel}$ ($\beta = 1$)	$R/Q_{\parallel}$ E_0=16MV/m	$R/Q_{\parallel}$ E_0=30MV/m
1270	59	4.9	0.51
1300	150	125	147
2403	16.1	3.0	14.8
2510	49	24.9	20.8
2663	36.8	3.5	0.9
2750	28.6	3.5	0.04

REFERENCES

[1] J. Knobloch et al., ICFA Beam Dynamics Newsletters, No.58, p. 118, August 2012, http://www-bd.fnal.gov/icfabd/Newsletter58.pdf.

[2] A. Arnold et al., Nuclear Instruments and Methods in Physics Research Section A, Volume 593, Issues 12, 1 August 2008, Pages 57-62, DOI 10.1016/j.nima.2008.04.035.

[3] S. Noguchi et al., IPAC'10, Kyoto, 2010, WEPEC024, p. 2944, http://www.JACoW.org.

[4] P. Kneisel et al., PAC'10, New York, 2010, TUP109, p. 1047, http://www.JACoW.org.

[5] A. Neumann et al., IPAC'11, San-Sebstian, September 2011, MOODA03, p. 41, http://www.JACoW.org

[6] T. Kamps et al., IPAC'11, San-Sebstian, September 2011, THPC109, p. 3143, http://www.JACoW.org

[7] T. Kamps et al., LINAC'12, Tel Aviv, September 2012, THPB069, these proceedings.

[8] K. Halbach and R.F. Holsinger, SUPERFISH - a computer program for evaluation of RF cavities with cylindrical symmetry, Part. Acc., 7:213222, 1976

[9] K. Flöttmann, A Space Charge Tracking Algorithm (ASTRA), http://www.desy.de/~mpyflo/.

[10] O. Kugeler et al., SRF'09, Berlin, Germany, September 2009, THPPO046, p. 683, http://www.JACoW.org

[11] Computer Simulation Technology AG, Microwave Studio®, 64289 Darmstadt, Germany http://www.cst.com

Copyright © 2012 by the respective authors — cc Creative Commons Attribution 3.0 (CC BY 3.0)

PRELIMINARY STUDY OF PROTON BEAM TRANSPORT IN A 10 MeV DIELECTRIC WALL ACCELERATOR*

J. Zhu#, L.S. Xia, Y. Shen, W. Wang, H. Zhang, Y. Liu, S.F. Chen, W.D. Wang, J.S. Shi, L.W. Zhang, J.J. Deng
Institute of Fluid Physics, CAEP, Mianyang, Sichuan, 621900, China

Abstract

A novel proton accelerator based on Dielectric Wall Accelerator (DWA) technology is being developed at Institute of Fluid Physics (IFP). The accelerating gradient will be 25 MV/m or even higher based on current high gradient insulator (HIG) performance. Theoretical study and numerical simulation of accelerating the proton beam to 10 MeV by virtual travelling wave method are presented in this paper. The beam injection at the DWA entrance is also discussed.

INTRODUCTION

The proton dielectric wall accelerator is being developed at Institute of Fluid Physics. The DWA system is a block structure which is similar to the linear induction accelerator. Each block of cell is consist of a ring-shape high gradient insulator, parallel-plate Blumlein pulse forming lines and photon conductive switches. To obtain the highest accelerating gradient, the DWA will be operated in the "virtual" travelling wave mode with the accelerating pulse as short as no more than 2 nanoseconds in the majority of the HGI tube [1]. These technologies are now being tested individually and will soon be tested integrally. The proton bunch will first be accelerated to 1 MeV with the accelerating gradient of about 20 MV/m and then upgraded to higher energy by adding more DWA cells. The accelerating gradient is also expected to be 25 MV/m or even higher, which is mainly determined by the performance of the HGI tube.

The major advantageous of a DWA system used for cancer treatment is that the total length of the system will be less than 3 meters so that it can be equipped in a single treatment room and the large and costly gantry can be neglected. Moreover, the energy, spot size of the proton bunch can be changed from shot-to-shot by adjusting the pulsed power system.

ION SOURCE AND LEBT

The layout of a 10-MeV DWA system is shown in Fig.1. It will start with a proton beam generated in an ECR ion source and extracted at about 40 keV. The main purpose of the LEBT is to transport the beam to the entrance of the DWA and match the injection requirements. Since a DWA system should be short and light enough to be rotated for intensity modulated proton therapy (IMPT), a two Einzel lens structure was chosen as the LEBT system. The pulse width of the proton bunch generated by the ion source is expected to be much longer than the DWA requirement. A fast kicker system will be mounted at the exit of the LEBT. Most of the protons will be deflected and hit on the metal wall at the DWA entrance, and only a small part of protons is allowed to enter the DWA. Design and fabrication of the ion source and LEBT is performed by Institute of Heavy Ion Physics, Peking University.

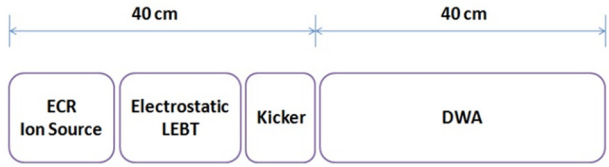

Figure 1: Layout of a 10 MeV DWA.

BEAM INJECTION

Generally, there is no any external focusing element or grid in the DWA system. The proton bunch is supposed to be focused to the downstream of the DWA by the radial electric field produced by the field gradient at the entrance [2]. The focusing effect is generally determined by the beam parameters, the accelerating gradient, the electric field and the time sequence. Chen [3] has demonstrated transporting a 2-MeV (injection energy) proton bunch in a 120-MeV DWA system at the accelerating gradient of 60 MV/m. For a 40-keV proton bunch, the radial electric field can easily cause the bunch pinching at the front of the DWA first and then defocusing. To demonstrate the focusing effect of the radial electric field at the entrance, the envelop equation

$$R'' = -\frac{\gamma'}{\gamma\beta^2}R' - \frac{\gamma''}{2\gamma\beta^2}R + \frac{K}{R} + \frac{\varepsilon_n^{\,2}}{\beta^2\gamma^2R^3} \quad (1)$$

for a 40-keV, 20-mA, 1-mm-mrad proton bunch at its waist is solved, where R, β, γ, ε_n and K is the beam's radius, velocity relative to the speed of light, Lorentz factor, normalized edge emittance and generalized perveance, respectively. We consider the case that the length of the DWA is 40 cm and the proton bunch rides on the flattop of the electric field (25 MV/m) except that there is a constant field gradient at the beginning 5 cm of the DWA. The proton bunch envelop as a function of the proton energy is plotted in Fig.2 (a). It is obvious that the focal spot of the beam will move upstream as the proton energy decreases. The focal spot of proton bunch with 2-MeV injection energy just locates at the end of the drift

*Work supported by National Natural Science Foundation of China (11035004) and Nuclear Energy Development Project of State Administration of Science, Technology and Industry for National Defence
#zhujun98@tsinghua.org.cn

Copyright © 2012 by the respective authors — cc Creative Commons Attribution 3.0 (CC BY 3.0)

tube, while the proton bunch with 40-keV injection energy will pinch at the front of the DWA and then diverge. If we adjust the injection timing to make only the last 1 cm of field gradient is seen by the bunch, the 40-keV proton bunch will also be tightly focused throughout the simulation region, as shown in Fig.2 (b).

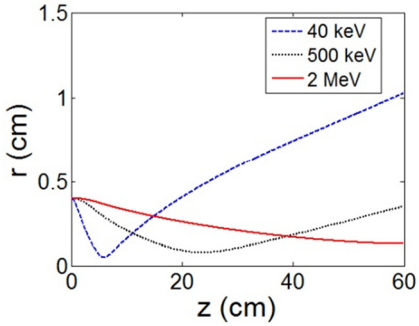

(a)

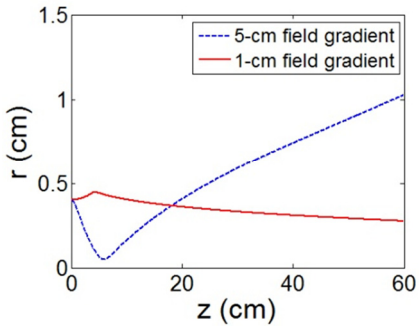

(b)

Figure 2: Beam envelop for (a) different injection energies, (b) two different lengths of field gradient at the DWA entrance for a 40-keV proton beam.

TRANSPORT SIMULATION

We have simulated the proton beam transported through a 40-cm DWA by using a self-consistent, 2.5-dimensional particle-in-cell code. The inner radius of the HGI tube is 1.5 cm and the average accelerating gradient is about 25 MV/m. Blumleins are grouped to form a 2-cm block which was triggered together. The accelerating voltage pulse was given a rise/fall time of 1 ns each. The simulation transports a 40-keV, 1-ns proton beam from 3 cm upstream of the DWA entrance to 20 cm downstream of the DWA exits. The flattop of each electric pulse and the triggering sequence were carefully chosen to ensure that the DWA worked in the "virtual" travelling wave mode and the proton bunch just rode on the flattop throughout the DWA except at the entrance and exits. To make sure that the proton bunch was not over-focused, the first two groups of HGI were triggered together when the proton bunch entered the HGI tube. An entrance metal screen was employed to further increase the accelerating field at the entrance and reduce the electric field gradient seen by the proton bunch. The simulation results with and without entrance screen are shown in Fig.3.

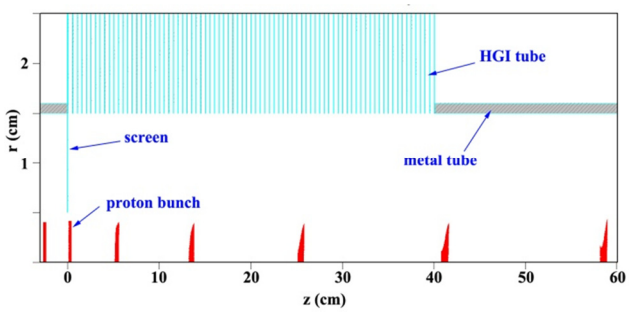

(a)

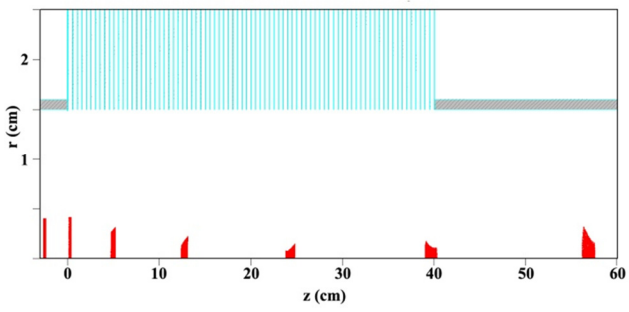

(b)

Figure 3: Beam transports in a 10-MeV DWA, (a) entrance screen can further reduce the focusing force at the entrance, (b) the proton bunch was over-focused when there was no entrance screen.

The bunch was first accelerated by the leading side of waveform, and a radial focusing force is applied on the bunch at the same time. The longitudinal and radial electric field profiles at the DWA entrance are shown in Fig. 4. When the entrance screen was employed, the accelerating field is higher at the entrance comparing to the case when there is no entrance screen. So the protons can be accelerated to higher energy in a shorter distance to avoid over-focusing. And the radial focusing force is also smaller. After that, the virtual travelling wave with a flattop was formed and the proton bunch rode on the flattop of the accelerating waveform, as shown in Fig.5. At this stage, the radial electric field vanished. The shape of the accelerating field nearly kept constant as the proton bunch travelling through the accelerator. However, the electric pulse flattop applied on the HGI reduced from about 4 ns at the entrance to 1.5 ns at the end, as shown in Fig.6. The pulse duration at the second group of Blumleins is longer than the first one since they are triggered together to increase the accelerating field and reduce the length of the waveform leading side at the entrance. At the exits of the DWA, a de-focusing force will be applied on the bunch because of the opposite field gradient to that of the entrance. So the last HGI should be turned off as quickly as possible. For the 10-MeV DWA, the transport systems with or without the entrance screen are both acceptable though the bunch was slightly over-focused when there was no entrance screen. However, the radial focusing force at the DWA entrance is proportional to the accelerating gradient, and the entrance screen could be an alternative method to avoid over-focusing for a longer DWA with higher accelerating gradient,

Copyright © 2012 by the respective authors — cc Creative Commons Attribution 3.0 (CC BY 3.0)

The proton energy and current profile at the exits of the DWA is shown in Fig.7. Because the bunch rode on the falling side of the acceleration waveform at the DWA entrance, the bunch underwent longitudinally compressing and the average peak current increased to about 100 mA at the DWA exits. This longitudinally compressing effect is useful in a DWA system for IMPT. It is desirable for such a system to have an accelerating gradient of 100 MeV/m with 1-ns accelerating pulse width. To ensure that the proton bunch rides on the flattop of the accelerating waveform, the bunch length should be sub-nanosecond. And how to extract such a proton bunch is still a challenge. However, by adjusting the charging sequence of the HGI, the proton bunch can be placed at the falling side of the accelerating waveform and the bunch will be compressed longitudinally in the front of the accelerator. Moreover, the proton bunch should be about 200 mA and 0.2 ns for a 50-Hz DWA system for IMPT. It is obvious that the current exceeds the maximum capability of the ion source. And the beam radius at the DWA entrance can't be kept small if the current extracted from the ion source is large enough. Therefore, the proton bunch should be extracted at lower current and then be compressed to higher current and shorter pulse length.

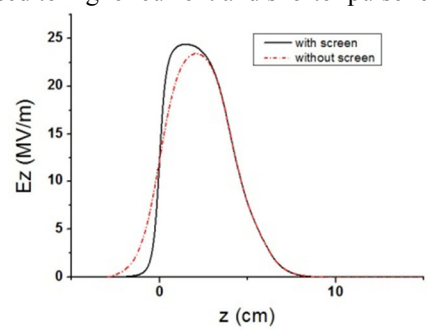

(a)

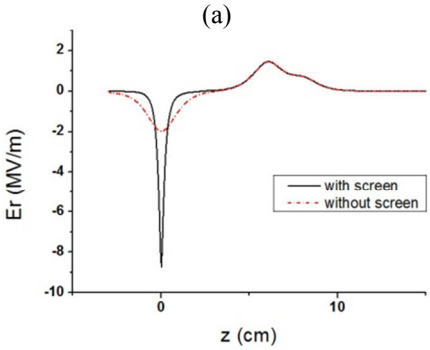

(b)

Figure 4: Longitudinal (a) and radial (b) electric field profiles at the DWA entrance with and without entrance screen.

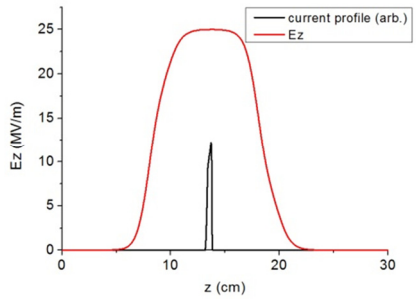

Figure 5: Longitudinal electric field and proton current profile in the middle of the DWA.

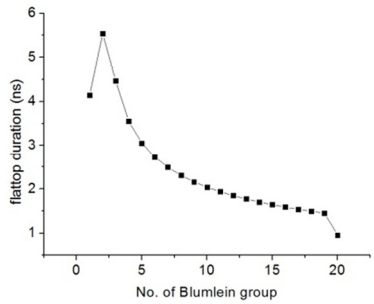

Figure 6: Electric pulse flattop duration as a function of the No. of HGI group.

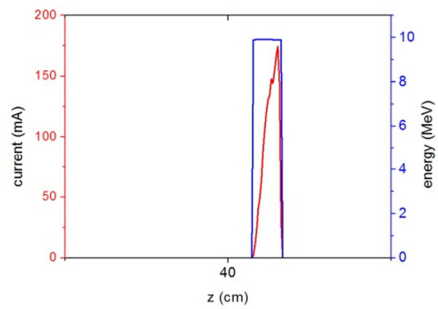

Figure 7: Proton energy and current profile at the exits of the DWA (with screen).

SUMMARY

The design of the ion source and LEBT for a 10-MeV DWA is introduced in this paper. We have discussed the beam injection by using the focusing force produced by the field gradient at the DWA entrance. We also have demonstrated that a 40-keV proton bunch can be transport through a 40-cm-long DWA with an accelerating gradient of 25 MV/m.

REFERENCES

[1] G.J. Caporaso, et al., "A Compact Linac for Intense Modulated Proton Therapy Based on a Dielectric Wall Accelerator", Physica Medica, 24, p. 98 (2008).

[2] Y-J Chen, et. al., "Beam Transport in a Compact Dielectric Wall Accelerator for Proton Therapy", Proceedings of Linear Accelerator Conference, Tsukuba, Japan, 2010.

[3] Y.J. Chen, et al., "Beam Transport in a Dielectric Wall Accelerator for Intense Modulated Proton Therapy", Proceedings of IPAC2011, Sebastian, Spain, 2011.

Copyright © 2012 by the respective authors — cc Creative Commons Attribution 3.0 (CC BY 3.0)

R&D ACTIVITIES ON HIGH INTENSITY SUPERCONDUCTING PROTON LINAC AT RRCAT

S.C. Joshi, S.B. Roy, P.R. Hannurkar, P. Kush, A. Puntambekar, P. Shrivastava, G. Mundra, J. Dwivedi, P. Khare, P.D. Gupta, Raja Ramanna Centre for Advanced Technology, Indore, INDIA

Abstract

Raja Ramanna Centre for Advanced Technology (RRCAT), Indore has taken up a program on R&D activities of 1 GeV, high intensity superconducting proton linac for Spallation Neutron Source. This will require several multi-cell superconducting cavities operating at different RF frequencies. To start with, a number of single-cell prototype cavities at 1.3 GHz have been developed in high RRR bulk niobium. These single-cell cavities have exhibited high quality factor and accelerating gradients. Superconducting properties of niobium are being studied for varying composition of impurities and different processing conditions. Physics design of linac configuration and various accelerating structures have been initiated. Development activities on cryomodules, cavity test facilities and solid state RF amplifiers to power the SRF cavities at various RF frequencies are being pursued. Infrastructure setup required for SRF cavity fabrication, processing and testing is under progress at RRCAT.

INTRODUCTION

A programme is envisaged to develop a pulsed, MW range Spallation Neutron Source based on 1 GeV, 1 MW superconducting RF H- Ion linac, a full-energy injector for a 1GeV Accumulator Ring. The pulsed Spallation Neutron Source will be used for applications in the field of condensed mater physics, material sciences, chemistry, biology and engineering. In addition to setting up of SNS facility, it will enhance capacity building in the area of high intensity proton accelerators in India.

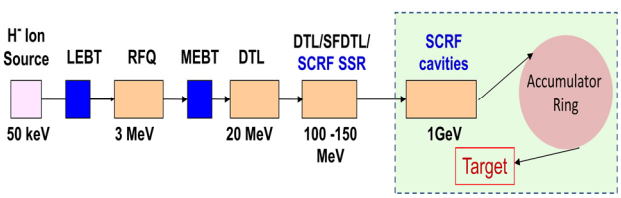

Figure 1. Schematic of Pulsed Proton Linac for Indian Spallation Neutron Source.

R&D ACTIVITIES

R&D activities for a SRF linac and accumulator ring for SNS would include prototype development of various sub-systems and setting up of infrastructure in the following areas:

- Ion source and front end component
- Materials R&D, cavity & cryomodule development
- Niobium cavity fabrication and processing facility
- Test facility for large number of SRF cavities and cryomodules
- Cryogenics setup for large size LHe Plant & supply network
- RF power sources and control electronics
- Sub-systems for 1 GeV accumulator ring including magnets, power supplies, RF cavity, UHV system and controls
- Manpower development and training

Ion Source and Front End

Development of a 3 MeV H- ion linac front end has been initiated for 1 GeV proton accelerators for a pulsed Spallation Neutron Source [1]. The front-end system will comprise of a filament driven multi-cusp H- ion source, Low Energy Beam Transport (LEBT) system, Radio Frequency Quadrupole (RFQ), RF power sources, Controls, Beam dump and Beam diagnostics.

H- Ion Source: In order to meet the requirement of H- ion front end linac system, a multicusp filament based 50 keV, 30 mA, low emittance H- ion-source operating in pulsed mode with a repetition rate of 25 Hz has been initiated. Physics design of the multicusp source was carried out analytically and also using computer simulations based on finite element method. This system has recently been tested for extraction of hydrogen ion current of 1.0 mA at 15 kV accelerating field. Figure 2, shows the multi-cusp H- ion source system.

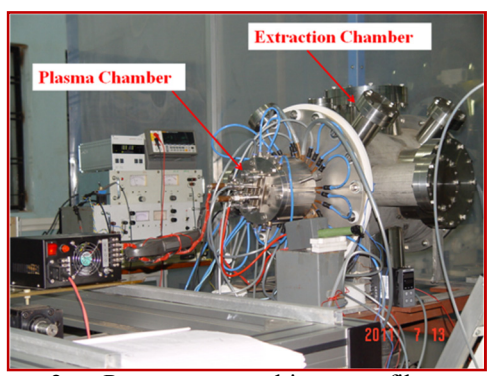

Figure 2. Prototype multi-cusp filament based source pulsed H^- ion source.

LEBT and RFQ: For prototype studies, design has been carried out for a suitable LEBT for beam transport from Ion Source to RFQ and a 3 MeV, 352 MHz RFQ. A Low Energy Beam Transport (LEBT) line, consisting of solenoid magnets of maximum strength 3.5 kG and steering coils having a maximum field of 100 G has been

Copyright © 2012 by the respective authors — cc Creative Commons Attribution 3.0 (CC BY 3.0)

designed for transporting the beam from Ion Source to RFQ with the matched beam parameters at RFQ entrance, and with minimum emittance growth.

For prototype RFQ, physics and engineering design has been carried out for a 352.2 MHz, 3.47 m long, four vane type RFQ to accelerate 50 keV, 30 mA pulsed H- ion beam with 1.25% duty factor to 3 MeV. The inter-vane voltage has been chosen to be 80 kV, the optimized value of the minimum aperture radius is 2.31 mm and modulation parameter has been varied in the range 1 – 1.95. The synchronous phase is initially kept at -90 degree to maximize the capture efficiency, which is ramped to -30 degree.

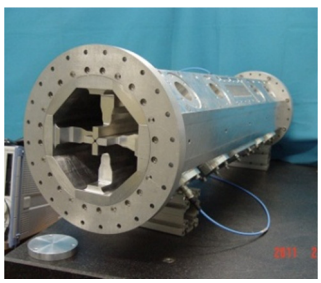

Figure 3. Prototype fabrication of 1st segment of RFQ structure.

Materials R&D for SRF Cavities

Since the major part of proton linac will be build using SRF cavities, intensive materials R&D activities have been taken up at RRCAT. The SRF cavity materials studies include superconducting properties of fine grain (50 micron average grain size), large grain (1 mm average grain size) and single crystal samples of Niobium materials. It was observed that a buffered chemical polishing of these Niobium materials caused a distinct reduction in the superconducting parameters like transition temperature (T_C), lower critical field (H_{C1}) and upper critical field (H_{C2}) [2.3]. These results indicate that BCP treatment possibly introduces Oxygen and Hydrogen in quantities large enough to degrade the superconducting properties of the Niobium materials, which, in turn, adversely affects the performance of the Niobium-SRF cavities.

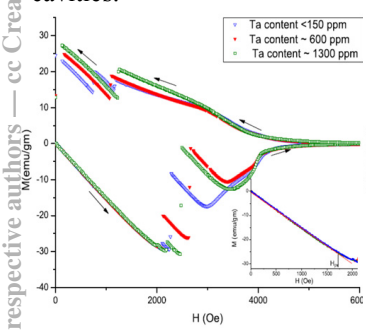

Figure 4. Magnetization v/s magnetic field plot of pristine fine grain Niobium with different Tantalum-contents at T=2 K [3].

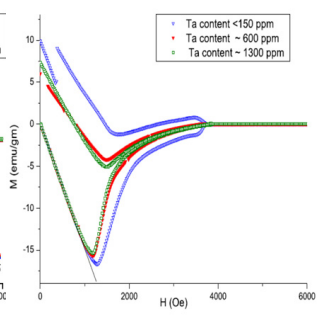

Figure 5. Magnetization v/s magnetic field plot of fine grain Niobium with different Tantalum-contents, subjected to BCP & annealing at 600^{O}C[3].

It was also seen that tantalum impurity content even up to several hundred to ~1300 ppm does not significantly affect the superconducting properties of Niobium materials [3]. These observations suggest that a less refined Niobium material may be deployable for cavity applications, provided the inclusions of the impurity elements do not influence the surface conductivity of Niobium materials significantly.

SRF Cavity Development

As an initial effort, four prototype 1.3 GHz single cell bulk niobium cavities have been developed under Indian Institutes Fermi Lab Collaboration (IIFC).

Figure 6. Prototype 1.3 GHz Single Cell cavities fabricated, processed and tested under IIFC Program.

Development of forming tools, forming of half-cells, machining of components, development of welding fixtures along with RF & vacuum qualification were carried out at RRCAT. The electron beam welding was carried out at IUAC. The fabricated prototype cavities were tested for RF and vacuum leak tightness up to 77 K at RRCAT before shipment to Fermi Lab. Processing, consisting of Centrifugal Barrel Polishing (CBP), Electro Polishing (EP), heat treatment and high pressure rinsing (HPR) was carried out jointly by Fermi Lab and Argonne National Laboratory in USA [4].

The cavity TE1CAT004 was successfully tested in the first test itself to achieve Eacc of 37.5 MV/m with a Q > 8.4 x E09 as shown in Figure 7.

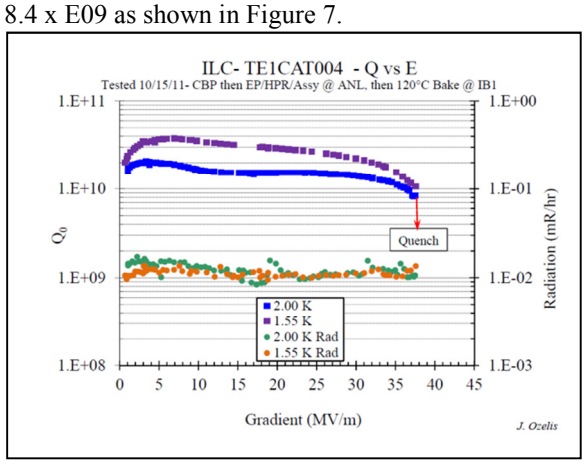

Figure 7. 2 K Performance test curve of 1.3 GHz single cell SRF cavity TE1CAT004 at VTS Facility, Fermi lab.

Prototype development of SRF cavities for medium energy is also under progress. Forming tools for 650 MHz cavities are undergoing forming trials for the first prototype single cell cavity.

Copyright © 2012 by the respective authors — cc Creative Commons Attribution 3.0 (CC BY 3.0)

Design and Development of Cryomodule

Design studies for a medium beta cryomodule for eight SRF cavities (Frequency 600-700MHz) are under progress. This work is in parallel to the cryomodule studies for Project-X under IIFC. The cavity support system will be a modified support system. The cavities will be supported from a helium gas return pipe with the help of a laser welded C-T shaped joint. This improvisation will reduce the machining time and cost for cavity support. Prototype Laser welded joints have been made and tested. The system has been designed and a scaled down prototype has been fabricated (Fig8).

The system will be tested under cryogenic conditions in the cryomodule component test rig.

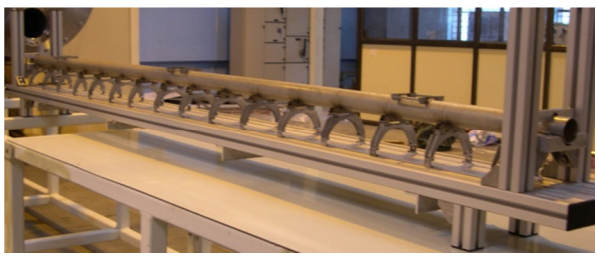

Figure 8. Laser welded prototype cavity support system

SRF Cavity Test Facility

A Vertical Test Stand Facility is under commissioning at RRCAT for testing SRF cavities at 2K. The 2K cryostat was designed by RRCAT along with Fermi Lab. To test the cavities, 1.3 GHz, 500W CW/600 W peak power solid state RF amplifier system has been designed and tested.

The building for VTS is also ready for commissioning.

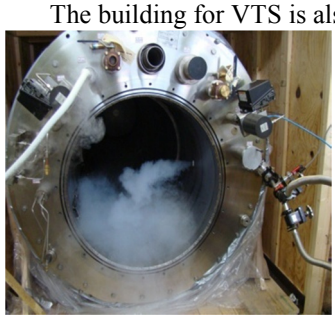

Figure 9. VTS Cryostat under cold shock testing

Figure 10. 500 W Solid State RF system for VTS

A Horizontal Test Stand for testing SRF cavities at high power RF, is being designed under collaboration with Fermi lab. The horizontal test stand cryostat is a continuous flow type cryostat and capable of testing two dressed SRF cavities/SC magnets in a single test cycle.

Development of RF Power Sources

Design and development of 30 kW, 650 MHz high powers solid state RF source for CW as well as pulse power, has been initiated at RRCAT[5]. The indigenous development efforts will be useful for the proposed high power proton accelerators for SNS applications. In this 650 MHz amplifier scheme, 30 kW CW RF power will be generated using modular combination of 8 kW amplifier units. Each 8 kW amplifier unit will be housed in a standard cabinet employing 32 numbers of 300W RF amplifier modules , 2 power dividers, 2 power combiners and high power directional coupler. The RF power unit will have provision for safety interlocks, data acquisition system and water cooling circuit. developed indigenously.

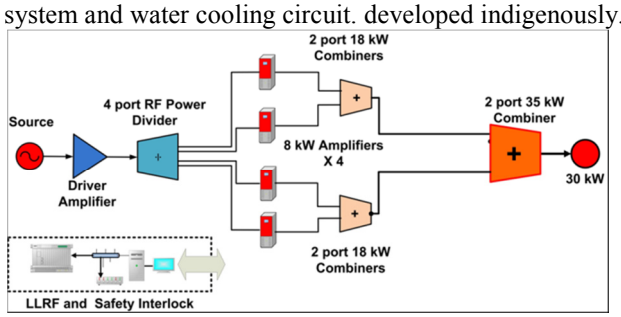

Figure 11. Solid State High Power RFM Amplifier Scheme.

Infrastructure Facility Development

A dedicated building for SRF infrastructure facilities has been completed. Cavity forming facility which includes a 120 Ton Hydraulic Press, suitable tooling have been established for SRF cavity parts. A 15 kW electron beam welding machine and a high vacuum annealing furnace are being procured. Cavity processing facilities including Barrel Polishing Machine for 1.3 GHz single cell cavity, prototype Electro polishing setup, high pressure rinsing facility, clean room facility, for low power RF characterization facility etc. have been set up. A Secondary Ion Mass Spectrometer (SIMS) has been set up for surface characterization of Niobium samples. A Confocal Microscope for defects identification and surface roughness measurement and a high accuracy 3D Co-ordinate measuring machine for mechanical measurement of a cavity profile have been installed [6].

ACKNOWLEDGEMENT

We acknowledge contributions of the team members from PLSCD,IMAS, PHPMS,ACDFS, RFSD, RRCAT. We acknowledge contribution of IUAC, N Delhi & Fermilab, USA for cavity & VTS development under IIFC.

REFERENCES

[1] S. C. Joshi et al., “Status Report of Development of High Current Front End H- Injector Linac for SNS”, Workshop on ADSS, BARC, Mumbai, Dec, 2011.
[2] S. B. Roy et al., Supercond. Sci. Tech. **22** 101514 (2009).
[3] S. B. Roy et al.,AIP. Conf. Proc. **1352** 56 (2011).
[4] A.M. Puntambekar et.al., “Development of 1.3 GHz Single Cell SRF Cavity under IIFC" PAC,New York USA, 2011
[5] A. Jain et at., “Development of 650 MHz Solid State RF Amplifier for Proton Accelerator", Workshop on ADS, BARC Mumbai, Dec, 2011.
[6] S.C. Joshi et at., “Status of Infrastructure Facilities for SRF Cavity” ADS, BARC Mumbai, Dec, 201. 1

Copyright © 2012 by the respective authors — cc Creative Commons Attribution 3.0 (CC BY 3.0)

CURRENT STATUS OF THE RAL FRONT END TEST STAND (FETS) PROJECT

A. Letchford, M. Clarke-Gayther, D. Faircloth, S. Lawrie, STFC/ISIS, Rutherford Appleton Laboratory, Harwell, UK

S. Alsari, M. Aslaninejad, A. Kurup, J. Pozimski, P. Savage, Imperial College of Science and Technology, London, UK

C. Gabor, C. Plostinar, STFC/ASTeC, Rutherford Appleton Laboratory, Harwell, UK

G. Boorman, A. Bosco, Royal Holloway University of London, London, UK

S. Jolly, University College London, London, UK

J. Back, University of Warwick, Coventry, UK

A. Garbayo, AVS, Eibar, Gipuzkoa, Spain

Abstract

The UK proton accelerator strategy aims to develop a viable high power proton driver with applications including spallation neutrons, the neutrino factory and ADSR. An essential first ingredient, identified as one of the main UK R&D accelerator projects, is the Front End Test Stand (FETS) at the Rutherford Appleton Laboratory (RAL), aimed at producing a high quality, high current, cleanly chopped H^- beam. Through its component parts, FETS has triggered development of a high brightness, 60 mA H^- ion source, a three-solenoid Low Energy Beam Transport line (LEBT), a 3 MeV four-vane Radio-Frequency Quadrupole (RFQ) and a Medium Energy Beam Transport line (MEBT) with a high speed chopper. The project is well advanced and when operational should be sufficiently versatile to explore a range of operating conditions. In this paper we present the current status of the construction, and plans for operation, experiments and future development.

THE FRONT END TEST STAND

The Front End Test Stand was first proposed nearly a decade ago [1], as a demonstrator for fast, high quality beam chopping. Since then, FETS has become the main proton R&D project in the UK, being a collaborative effort between Rutherford Appleton Laboratory where it is being built, and several universities as well as international partners [2]. FETS is of high relevance for the next generation of high power proton accelerators that are aiming to deliver beam powers in the megawatt range, in particular, the ISIS upgrade plans [3] and the UK neutrino factory design efforts [4].

A schematic FETS layout can be seen in Figure 1. It consists of five main components: an H^- ion source, a LEBT based on three solenoids, a 3 MeV RFQ, a MEBT with a fast chopping system and a wide-ranging set of diagnostics. When completed it will deliver a 60 mA, 2 ms, 50 Hz chopped beam at 3 MeV [5]. With the commissioning efforts in full swing, in this paper we will briefly present the current status of each section, highlighting recent progress as well as future plans.

ION SOURCE

A Penning surface plasma H^- ion source is used in FETS. The source is a modified version of the existing ISIS ion source that has successfully been used in routine operation for nearly 30 years. To meet the FETS requirements, a systematic development programme was started several years ago. This has led to a number of modifications including: geometry changes, transport optimisations, cooling improvements, power supply upgrades and operating parameter investigations.

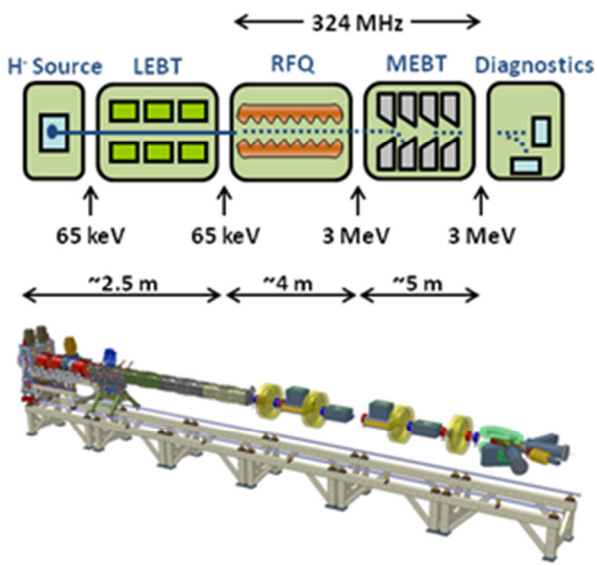

Figure 1: Schematic FETS layout.

Copyright © 2012 by the respective authors — cc Creative Commons Attribution 3.0 (CC BY 3.0)

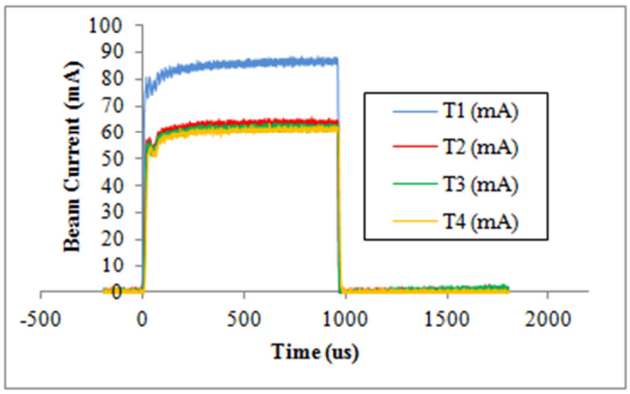

Figure 2: 1 ms beam current profiles at 50 Hz, at different positions: ion source (T1), inside the LEBT (T2, T3) and LEBT output (T4).

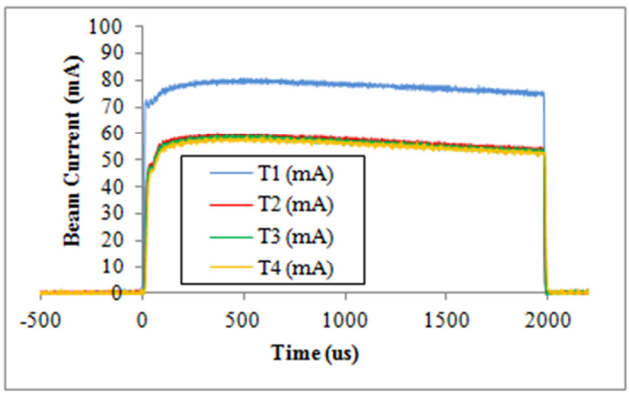

Figure 3: 2 ms beam current profiles at 25 Hz.

As a result, the ion source is now very close to delivering the FETS specifications [6].

However, not all the operating parameters have been met simultaneously. While the source can routinely produce 80 mA beams (see Figure 2), a significant droop in the H^- beam current can be seen for pulse lengths above 1 ms, at 50 Hz. By retuning the ion source and reducing the repetition rate to 25 Hz, 2 ms pulse lengths have been achieved (see Figure 3) [7].

To overcome this limitation, a new set of developments is under way, aimed at gaining a deeper understanding of the processes involved in the plasma formation. These include optical spectroscopy studies [8], plasma modelling simulations as well as geometry modifications with the intention of having a larger discharge volume by scaling the source [9].

LEBT

The LEBT design is based on the existing ISIS LEBT. It consists of three solenoids separated by drift sections of various lengths as it can be seen in Figure 4 [10]. Detailed and extensive parametric studies have been performed in order to understand the optimal operating parameters and the effects of the ion source. At present, a beam loss of ~20% is observed between the ion source and the first pumping vessel. However, the LEBT is capable of

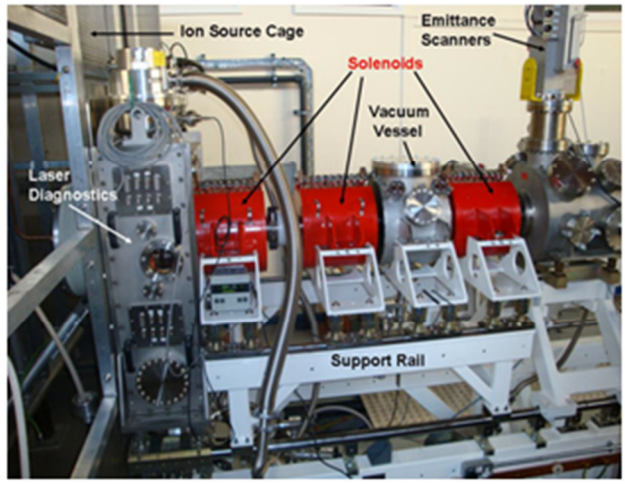

Figure 4: LEBT setup overview.

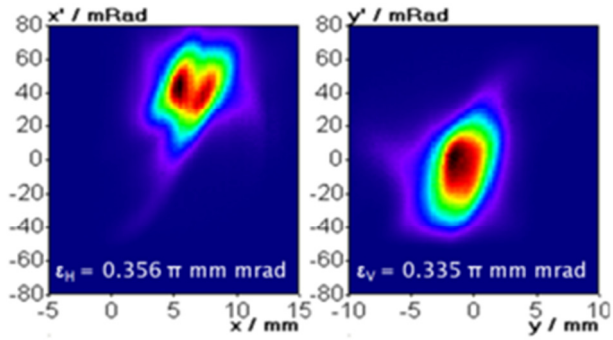

Figure 5: Measured LEBT output beam.

transporting the remaining beam with nearly 100% transmission, such that matched 60 mA beams can be effectively delivered at the input of the RFQ. Figure 5 shows the measured phase space distribution of the beam at the end of the LEBT. The normalised RMS emittance is larger than the FETS requirements and work is in progress to reduce it further [11], [12].

The LEBT is also being used for generic studies on the space charge compensation process. Preliminary results have already given an indication of the degree of variation of the Twiss parameters with time throughout the pulse, a process that can lead to beam mismatch. In addition, the recently installed residual gas ion spectrometer is expected to allow a direct measurement of the beam potential and a much more detailed analysis of the beam transport conditions [13].

RFQ

The RFQ has been designed and optimised using an innovative method which integrates the CAD design with the 3D electromagnetic modelling and the beam dynamics simulations within a single simulation framework [14]. The result is a 4 m long, 4-vane RFQ, operating at 324 MHz with a final energy of 3 MeV. Simulation efforts have concentrated on benchmarking the new method against results obtained with RFQSIM [15]: a good agreement has been observed in both transmission

Copyright © 2012 by the respective authors — cc Creative Commons Attribution 3.0 (CC BY 3.0)

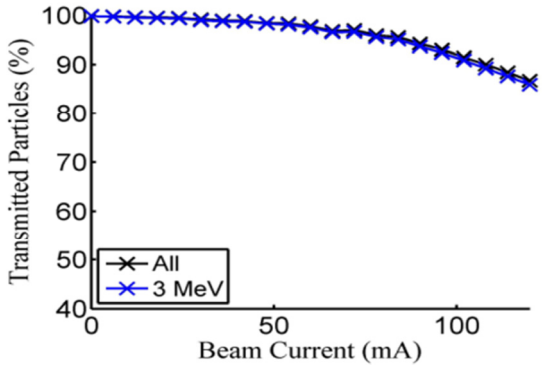

Figure 6: RFQ beam transmission.

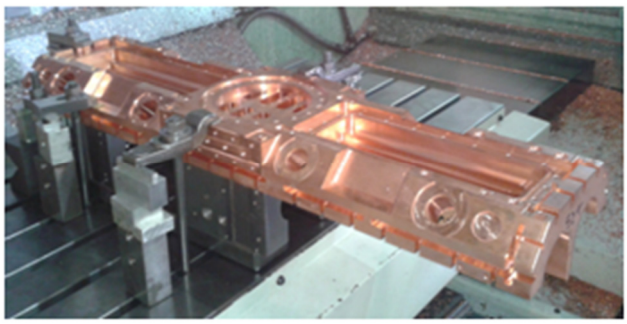

Figure 7: RFQ vane being manufactured.

and acceptance. For nominal RFQ input parameters, beam transmission is above 97% (Figure 6), while the RMS emittance growth is relatively small (< 20%) and largely independent of the beam current. In preparation for manufacturing, detailed studies have also been performed in order to estimate the machining and alignment tolerances.

With the design completed, the RFQ is currently being manufactured as four, 1 m long, separate sections. All the copper segments have been rough machined to +2 mm in order to discover the optimum finishing cut parameters, while the first section has already been finished to the final geometry and will be assembled, aligned and installed in the near future (Figure 7). This will allow us to gain a deeper understanding of the commissioning process before proceeding to install the remaining sections. The manufacturing of the RFQ ancillary equipment is well advanced [16], [17].

MEBT, CHOPPER AND DIAGNOSTICS

The MEBT baseline design consists of a series of quadrupoles, re-bunching cavities and the beam chopping system with its dedicated beam dumps. The lattice design is particularly challenging as it has to address two conflicting requirements: provide strong uniform focussing to maintain the beam quality under the influence of strong, non-linear space charge forces, while making available sufficiently long drifts for the chopping elements. Simulations indicate that beam loss can kept to ~1.5% with a nearly 100% chopping efficiency [18], [19].

More recently, a new lattice has been proposed that has the advantage of having fewer elements and therefore a reduced construction cost while offering more space for diagnostics (Figure 8). Optimisation work on improving the beam transmission is ongoing while efforts are being put into designing a suitable chopper beam dump.

The chopping system uses an innovative “fast-slow” deflection scheme. It is a tandem combination of fast transition time, short duration and slow transition time, long duration choppers. The “fast-chopper” removes 3 adjacent bunches at the beginning and at the end of the chopping interval, creating 2 gaps in the bunch train that will be used by the “slow-chopper” as a transition interval, thus preventing bunches being partially chopped. Work has been progressing well on electrode design, modelling and prototyping as well as on testing the master timing system [20].

On the diagnostics side, in addition to the standard MEBT diagnostics, progress has been made on designing an emittance measurement instrument to be located at the end of the MEBT. Non-destructive methods are under consideration, in particular laser photo-detachment. Tomographic reconstruction techniques from measured profiles are also being investigated [21].

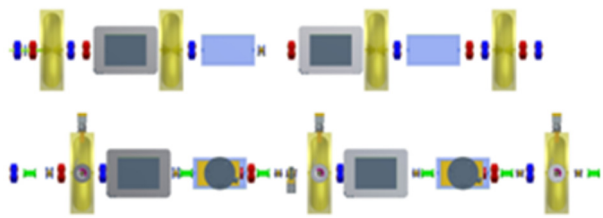

Figure 8: Schematic MEBT baseline layout (top) and a proposed alternative design (bottom).

REFERENCES

[1] D. Findlay et al., Proc. of NuFact’04, p. 323.
[2] A. Letchford et al., Proc. of IPAC’12, THPPP051.
[3] J. Thomason et al., Proc. of HB’08, WGE15.
[4] S. Choubey et al., RAL-TR-2011-018.
[5] A. Letchford et al., Proc. of IPAC’10, MOPEC075.
[6] D. Faircloth et al., Rev. Sci. Instrum. 81, 02A721.
[7] D. Faircloth et al., Rev. Sci. Instrum. 83, 02A701.
[8] S. Lawrie et al., Rev. Sci. Instrum. 83, 02A704.
[9] D. Faircloth et al., Proc. of NIBS’2012, O-3 08.
[10] J. Back et al., Proc. of IPAC’10, MOPEC078.
[11] C. Gabor et al., Rev. Sci. Instrum. 83, 02B719.
[12] C. Gabor et al., Proc. of IPAC’12, MOPPR056.
[13] J. Pozimski et al., Proc. of IPAC’12, MOPPD037.
[14] S. Jolly et al., Proc. of IPAC’10, MOPEC076.
[15] J. Maus et al., Proc. of EPAC’08, TUPP099.
[16] P. Savage et al., Proc of IPAC’10, MOPD056.
[17] P. Savage et al., Proc of IPAC’12, THPPP053.
[18] C. Plostinar, Proc. of IPAC’10, MOPD059.
[19] C. Plostinar et al., Proc of IPAC’11, WEPC039.
[20] M. Clarke-Gayther, Proc. of IPAC’10, WEPD095.
[21] C. Gabor et al., Proc. of DIPAC’09, TUPB022.

Copyright © 2012 by the respective authors — cc Creative Commons Attribution 3.0 (CC BY 3.0)

FRONT-END LINAC DESIGN AND BEAM DYNAMICS SIMULATIONS FOR MYRRHA *

C. Zhang#, H. Klein, D. Mäder, H. Podlech, U. Ratzinger, A. Schempp, R. Tiede, M. Vossberg
Institut für Angewandte Physik, Goethe-Universität, D-60438 Frankfurt a. M., Germany

Abstract

A 17MeV, 176MHz, and CW (Continuous Wave) proton linac is being developed as the front end of the driver accelerator for the MYRRHA facility in Mol, Belgium. Based on the promising preliminary design, further simulation and optimization studies have been performed with respect to code benchmarking, RFQ simulation using realistic LEBT output distributions, and an updated CH-DTL design with more detailed inter-tank configurations. This paper summarizes the new results.

PRELIMINARY DESIGN

Following the EUROTRANS project [1], MAX [2] (MYRRHA Accelerator eXperiment research and development programme) is the ongoing European ADS (Accelerator-Driven System) project. For the front end of the driver linac, the EUROTRANS-style injector [3] that consists of one RFQ (Radio-Frequency Quadrupole), two RT (room-temperature) and four SC (superconducting) CH (Cross-bar H-mode)-DTL (Drift-Tube Linac) cavities will be still adopted, but with many new concepts [4].

The most important idea is to halve the RF frequency from 352MHz to 176MHz, which improves the RFQ shunt impedance significantly (see Fig. 1), enlarges the minimum gap between electrodes, and allows replacing the 4-vane RFQ structure by the simple 4-rod one. Consequently, for keeping the RFQ length at ~4m and the warm part still compact, the RFQ-DTL and RT-SC transition energies are reduced from 3MeV and 5MeV to 1.5MeV and 3.5MeV, respectively, which indeed brings more difficulties to the beam dynamics design but helps improving the RT-CH shunt impedance.

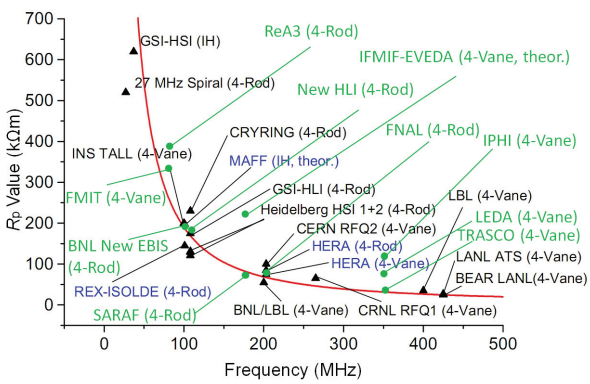

Figure 1: A survey of R_p values for RFQs [5].

From EUROTRANS to MAX, the injector design has lowered the RF power consumption per unit length and the Kilpatrick factor to ≤30kW/m and 1, respectively, for all warm cavities, even shortened the whole layout from 11.4m to 10.6m, and kept the beam dynamics performance satisfying. Being very conservative for CW operation and more cost-saving, this design has been taken as the baseline for further studies [5].

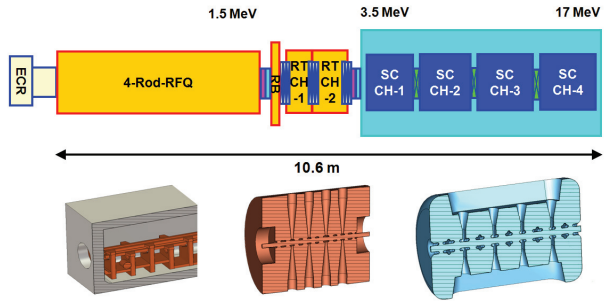

Figure 2: Preliminary layout for the MAX injector.

CODE BENCHMARKING

For the preliminary design of the MAX injector, the ParmteqM [6] and Lorasr [7] codes were used to simulate the beam transport in the RFQ and CH-DTL parts, respectively. Recently, the Toutatis [8] and TraceWin [8] codes have been introduced for benchmarking.

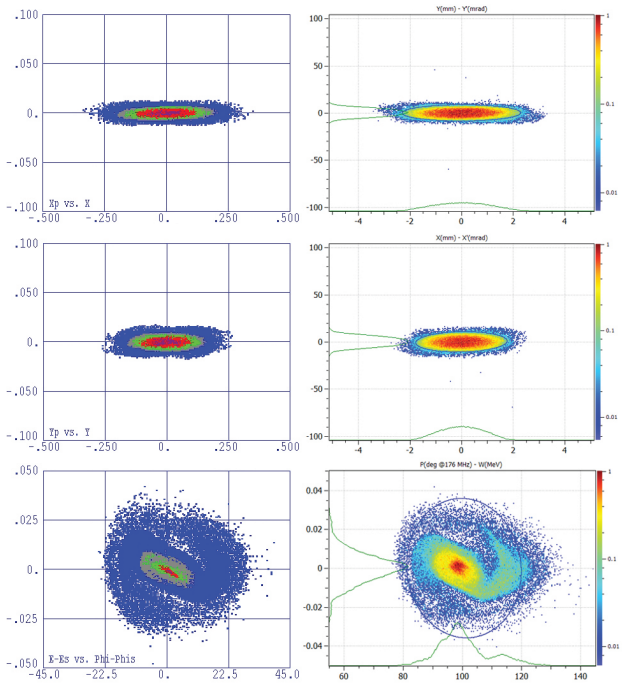

Figure 3: RFQ output particle distributions given by the ParmteqM (L) and Toutatis (R) codes.

Fig. 3 shows the RFQ output beams simulated by the ParmteqM and Toutatis codes. It's clear that the shape,

* Funded by the European Atomic Energy Community's (Euratom) 7th Framework Programme under Grant Agreement n°269565.
# Chuan Zhang: zhang@iap.uni-frankfurt.de

Copyright © 2012 by the respective authors — cc Creative Commons Attribution 3.0 (CC BY 3.0)

orientation, and size of the particle distributions are all quite similar on the three planes (the *x* and *y* planes are exchanged in Toutatis), respectively. Fig. 4 compares the emittance evolutions along the RFQ. Obviously, all transverse-emittance curves are almost identical, while the longitudinal-emittance ones have a small difference (which might be caused by a few halo particles) after *z*=0.5m, but they have nearly same evolution shape.

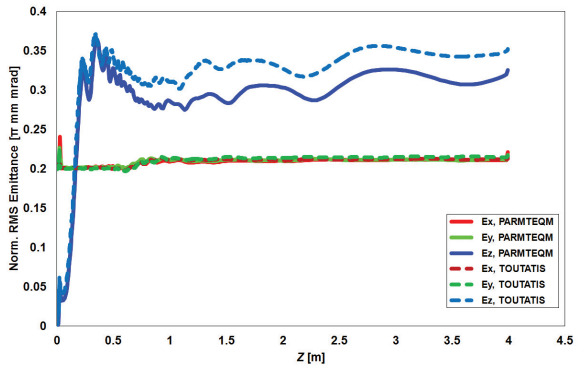

Figure 4: Emittance evolutions along the RFQ.

For the CH-DTL benchmarking, the first CH cavity with the integrated two triplets (see Fig. 5) has been used.

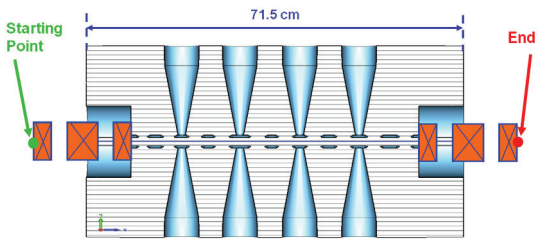

Figure 5: Benchmarking sample from the CH-DTL.

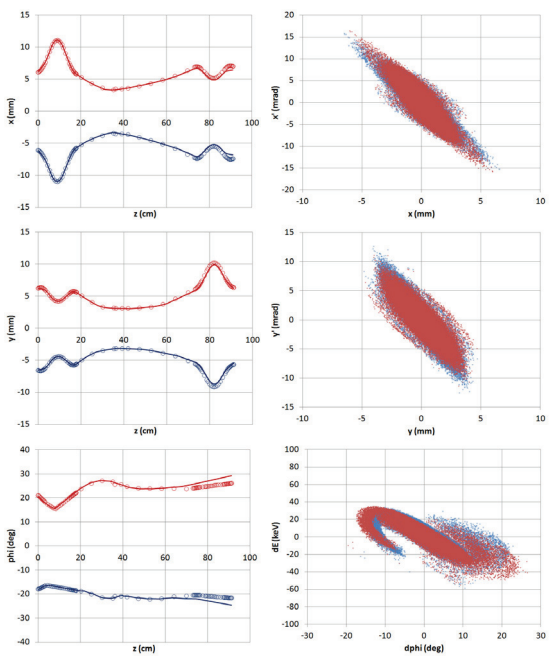

Figure 6: Beam envelopes (L) with circles by Lorasr and curves by TraceWin and output particle distributions (R) with blue dots by Lorasr and red dots by TraceWin.

In Fig. 6, the plots of the CH-DTL beam envelopes and output particle distributions show a good agreement between the Lorasr and TraceWin codes.

RFQ SIMULATION WITH LEBT OUTPUT

The MAX RFQ was designed using the New Four-Section Procedure [9] with a 4D-Waterbag input distribution. Table 1 summarizes the new simulation results based on the output particle distributions from the LEBT (Low Energy Beam Transport) designs [10]. It is seen that no matter the short or long version of LEBT will lead to similar results in the nominal (CW beam) and transient (with chopper) cases. All performance is still satisfying, except the longitudinal emittances have some relatively bigger but still acceptable growths due to the wing-form halo particles (see Fig. 7) from the LEBTs. However, the RFQ output distributions are always clean.

Table 1: LEBT-Based RFQ Simulation Results.

Parameter	Waterbag	Short LEBT transient	Short LEBT nominal	Long LEBT transient	Long LEBT nominal
$\varepsilon_{in}^{t.,\,n.,\,rms}$ [π mm-mrad]	0.20	0.18	0.16	0.14	0.14
$\varepsilon_{out}^{x.,\,n.,\,rms}$ [π mm-mrad]	0.22	0.20	0.17	0.17	0.15
$\varepsilon_{out}^{y.,\,n.,\,rms}$ [π mm-mrad]	0.22	0.20	0.16	0.17	0.15
$\varepsilon_{out}^{l.,\,rms}$ [π keV-deg]	64.6	92.4	92.7	108	80.0
T [%]	100	99	98.5	98.2	98.6

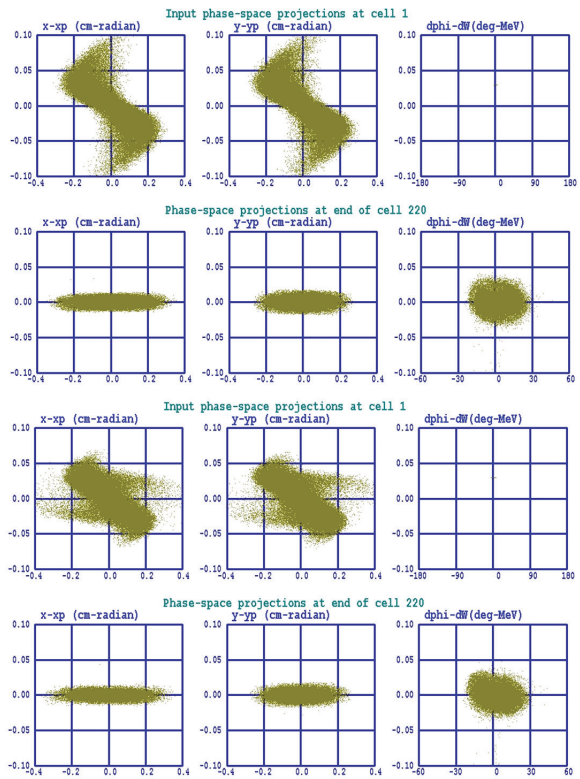

Figure 7: RFQ phase spaces with the short (T) and long LEBTs (B) in the transient case.

Copyright © 2012 by the respective authors — cc Creative Commons Attribution 3.0 (CC BY 3.0)

NEW MAX INJECTOR DESIGN

In the previous beam dynamics studies, the space needed for the inter-tank components was reserved by estimation. The inter-tank sections have been newly redesigned including all the details, e.g. the bellows for connecting cavities, the magnetic-field shielding for the solenoids, and the real dimensions of the cryomodule. The drift spaces between the cavities become longer, especially at the RFQ-DTL and RT-SC transitions, which increases the difficulty for the beam dynamics design.

The most critical area is the RT-SC transition where the drift space was extended by ~50cm. To overcome the negative consequences in both longitudinal and transverse planes, a new rebunching cavity (so-called RB-2) working at the -90° synchronous phase and a new solenoid have been added in front of the first SC-CH.

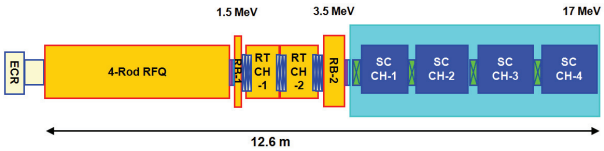

Figure 8: New layout for the MAX injector.

The beam dynamics of the new CH-DTL shown in Fig. 8 was re-optimized by tuning the focusing strength of all lenses and the gap voltages of the rebunching cavities while the design of the CH-cavities was kept almost unchanged.

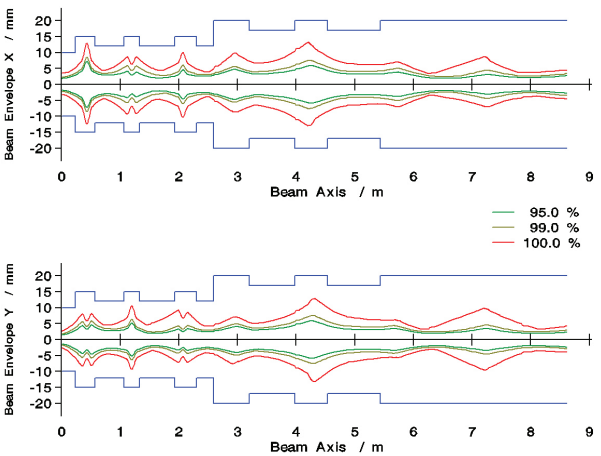

Figure 9: Transverse beam envelopes along the CH-DTL.

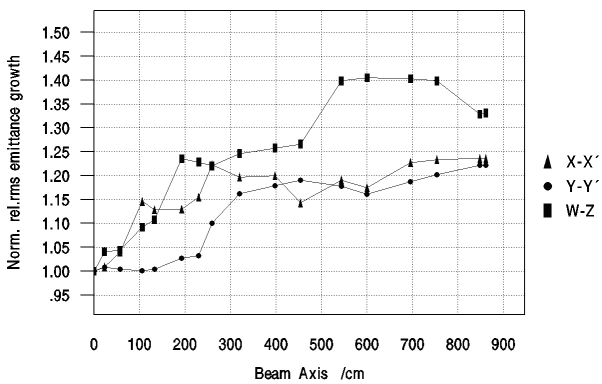

Figure 10: Emittance evolutions along the CH-DTL.

Fig. 9 plots the transverse beam envelopes along the new CH-DTL. In the first triplet, a few beam losses might happen when errors are included, but at 1.5MeV this beam energy they don't play any role. Therefore, a large safety margin is available for the beam throughout the CH-DTL. In addition, the emittance growths are still modest, as shown in Fig. 10.

CONCLUSIONS AND OUTLOOK

The correctness of the simulation results of the MAX injector design was successfully crosschecked by different codes. It was also proven that realistic LEBT output beams accelerated by the MAX RFQ will be transported into the CH-DTL with excellent beam quality. In addition, the simulation of the new CH-DTL updated with detailed inter-tank configurations has shown good performance. To sum up, an advanced new design is now available for the MAX injector. In the next step, systematic error studies will be performed.

ACKNOWLEDGEMENTS

Special thanks go to J.-L. Biarrotte and D. Uriot for their valuable contributions to the benchmarking using the Toutatis and TraceWin codes.

REFERENCES

[1] http://nuklear-server.ka.fzk.de/eurotrans/.
[2] http://ipnweb.in2p3.fr/MAX/.
[3] C. Zhang, M. Busch, H. Klein, H. Podlech, U. Ratzinger, J.-L. Biarrotte, "Reliability and Current-Adaptability Studies of a 352MHz, 17MeV, Continuous-Wave Injector for an Accelerator-Driven System", Phys. Rev. ST - AB 13, 080101 (2011).
[4] C. Zhang, H. Klein, D. Mäder, H. Podlech, U. Ratzinger, A. Schempp, R. Tiede, "From EUROTRANS to MAX: New Strategies and Approaches for the Injector Development", Proceedings of the 2nd IPAC in San Sebastian, Spain, September 4-9, 2011.
[5] C. Zhang, H. Klein, D. Mäder, H. Podlech, U. Ratzinger, A. Schempp, R. Tiede, M. Vossberg, MAX Deliverable 2.1: "352 MHz vs. 176 MHz Injector Comparison & Choice", January 31, 2012.
[6] K.R. Crandall, LANL Internal Report, Nr. LA-UR-96-1836, Revised December 7, 2005.
[7] R. Tiede, G. Clemente, H. Podlech, U. Ratzinger, A. Sauer, S. Minaev, "LORASR Code Development", Proceedings of the 10th EPAC in Edinburgh, Scotland, United Kingdom, June 26-30, 2006, pp. 2194-2196.
[8] http://irfu.cea.fr/Sacm/logiciels/.
[9] C. Zhang, A. Schempp, "Beam Dynamics Studies on a 200mA Proton Radio Frequency Quadrupole Accelerator", Nucl. Instrum. Methods Phys. Res., Sect., A, Volume 586, Issue 2, pp.153-159 (2008).
[10] J.-L. Biarrotte, "MYRRHA LEBT Preliminary Design Report", July 18, 2011.

Copyright © 2012 by the respective authors — cc Creative Commons Attribution 3.0 (CC BY 3.0)

POST ACCELERATION OF LASER GENERATED PROTON BUNCHES BY A CH-DTL*

Ali Almomani, Martin Droba, Ulrich Ratzinger, Ingo Hofmann, IAP-Frankfurt University, Germany

Abstract

Laser driven proton beam sources applying the TNSA process show interesting features in terms of energy and proton number per bunch. This makes them attractive as injectors into RF linacs at energies as high as 10 MeV or beyond. The combination shows attractive features like a very high particle number in a single bunch from the source and the flexibility and reliability of an RF linac by one pulsed magnetic solenoid lens only. A Crossbar H-type CH – structure is suggested because of its high acceleration gradient and efficiency at these beam energies. It is intended to realize the first cavity of the proposed linac and to demonstrate the acceleration of a laser generated proton bunch within the LIGHT collaboration at GSI Darmstadt. Detailed beam and field simulations will be presented.

INTRODUCTION

With advanced lasers like PHELIX (Petawatt High Energy Laser for Heavy Ion eXperiments), one can achieve focused intensities approaching 10^{20} W/cm^2. Under these conditions, intense protons with energies of ten to several tens on MeV are accelerated normally from the rear surface of the target by quasistatic electric fields of the order TV/m [1-2]. This process is called Target Normal Sheath Acceleration (TNSA) [2].

An interesting application for these proton beams is the matching into the acceptance of a succeeding RF accelerator for further post acceleration.

The LIGHT (Laser Ion Generation, Handling and Transport) collaboration aims to inject the laser accelerated protons into a conventional accelerator structure [3-4]. Due to the available energies, drift tube linacs are the most adequate choice. A CH – DTL is suggested as the linac structure [5-6].

This work is intended to realize the first cavity of the proposed CH-DTL and to demonstrate the acceleration of a laser generated proton bunch within the LIGHT project.

HYBRID RF ACCELERATOR OF THE LASER GENERATED PROTON PULSE

In PHELIX experiments protons with energies up to 30 MeV and with a total yield of 10^{13} protons per bunch were observed [7]. For the reference energy of 10 MeV, the yield within ± 0.5 MeV was exceeding 10^{10} protons. To compare this number with the conventional currents, the equivalent current of these bunches might add up to 500 mA beam current if every bucket would be filled with that proton number at 325 MHz.

The matching of laser – accelerated protons into a conventional RF linac is difficult due to the high particle number at large energy spread and large beam divergence. The coupling will be done by a pulsed magnetic solenoid. Figure 1 shows a schematic view for the hybrid accelerator.

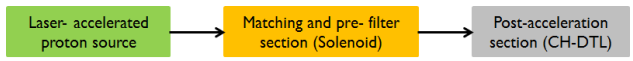

Figure 1: Scheme of the hybrid configuration.

Magnetic Solenoid

In order to collimate the laser – accelerated protons, a pulsed magnetic solenoid was chosen [5]. The 10 MeV p bunch in this lens layout (Figure 2) affords a magnetic field level of about 18 T in order to focus directly into a CH-DTL at a distance of about 210 mm from the target.

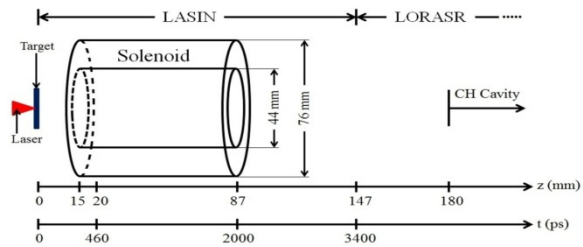

Figure 2: Schematic view on the laser target, the focusing solenoid and the drift to the rf linac. The longitudinal axis is marked in mm and in ps time of flight for a 10 MeV proton beam.

The output distributions, 60 mm behind the solenoid, are shown in Figure 3. The beam dynamics studies including the effect of co-moving electrons is described in Ref. 5.

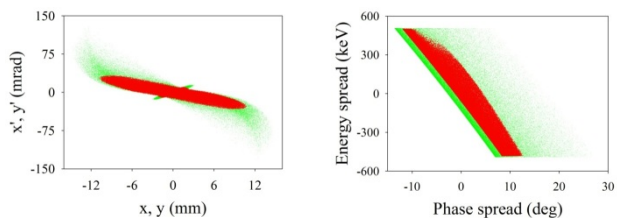

Figure 3: Particle distribution in transversal (left) and longitudinal (right) planes at the DTL – entrance within the energy range 10 MeV ± 0.5 MeV (green). The red 72% subsets of the particle distribution fall within the CH – DTL acceptance area and are used for DTL beam dynamics simulations.

Dedicated 40 MeV CH - DTL

The layout of the CH-DTL [5] was performed in two main steps. At first a 500 mA equivalent beam current design was developed by using a waterbag - type input distribution. In a second step, this linac layout was used to simulate the acceleration of the laser – accelerated bunch,

* This work is supported by HIC for FAIR and by BMBF: Contract number. 06FY7104I.

Copyright © 2012 by the respective authors — cc Creative Commons Attribution 3.0 (CC BY 3.0)

resulting from the complex transport simulations along the matching section (Figure 3).

The linac design consists of four CH cavities operating at 325 MHz, to accelerate the bunch from 10 to 40 MeV. The accelerating field gradient per cavity varies from 9 to 12 MV/m.

Due to the shape of protons in phase space behind the solenoid, it was not possible to match the whole distribution into the CH-DTL. Consequently, 70% of the total number of the protons is effectively fitted into the acceptance of the CH-DTL (see Figure 3).

All particles were effectively accelerated through the whole structure to the exit. Figure 4 shows the transverse 90, 99 and 100% beam envelopes. The quadruploes between the cavities were adapted allowing a loss free transport along the structure.

The longitudinal and transversal output distributions are shown in Figure 5 for 25000 macroparticles.

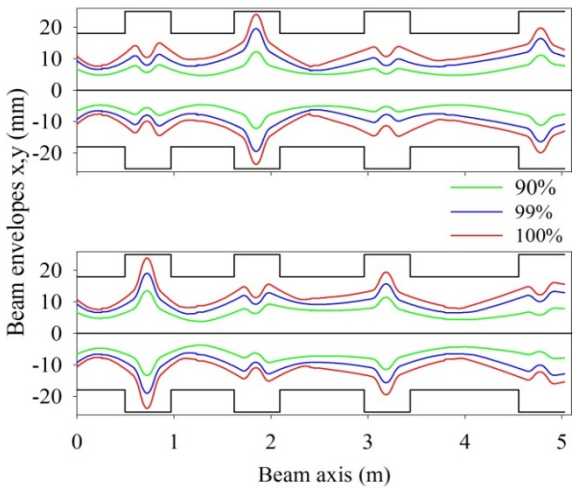

Figure 4: Transverse 90, 99 and 100% beam envelopes.

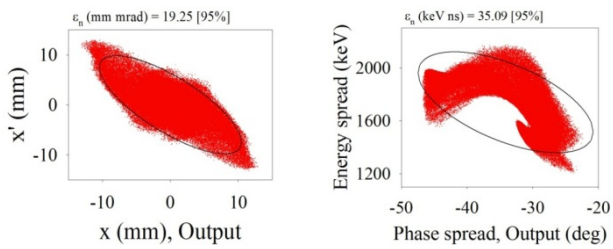

Figure 5: Transverse (left) and longitudinal (right) particle distributions at the CH – DTL exit.

THE FIRST CAVITY OF THE PROPOSED CH – DTL

The first cavity in the proposed linac has a length of about 668 mm and an outer diameter of about 386 mm (Figure 6). In this cavity, the proton bunch will be accelerated from 10 – 16.1 MeV.

In the CH – structure, the current flows from the outer cylinder to the drift tubes along the stems in order to generate the axial electric field which is needed for particle acceleration.

The stems are supporting the mechanical stability in the CH – structure, and they show the highest surface current density (Figure 7).

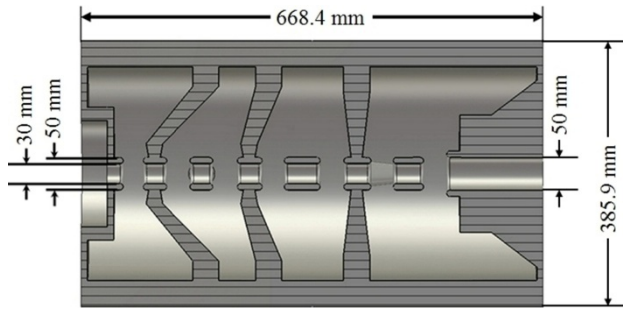

Figure 6: Schematic view for the first CH – cavity of the proposed linac.

The stem array allows for an efficient water cooling. Close to the beam axis the stems have to be kept slim to reduce the capacitance between neighbored stems and drift tubes.

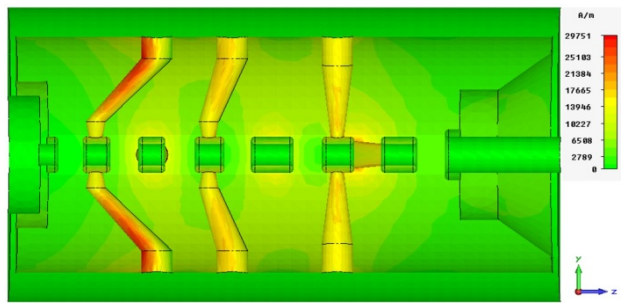

Figure 7: A MWS plot of the surface current density flowing along the stems. The inclined stems are carrying the highest density because the magnetic field flux is turning transversally into the neighbored quadrants at the cavity ends.

The on axis electric field distribution as calculated with MWS [8] is shown in Figure 8. The corresponding voltage value for this electric field distribution in each gap is calculated accordingly, and the results are compared with the reference values as given by the LORASR code (see Figure 9).

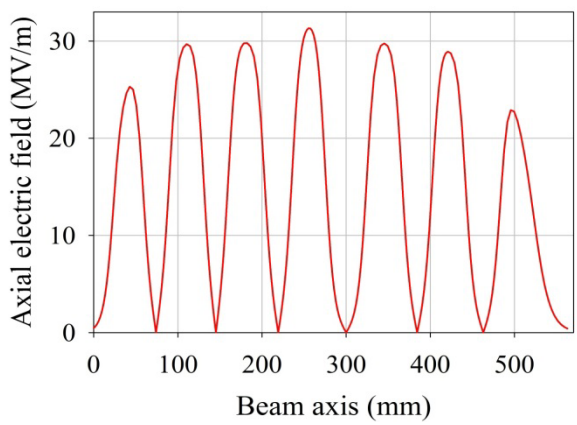

Figure 8: The axial electric field distribution as calculated by MWS along the beam axis.

Copyright © 2012 by the respective authors — cc Creative Commons Attribution 3.0 (CC BY 3.0)

The electric field is roughly uniform along the central 5 gaps and is reduced in the end gaps. This gives the optimum effective shunt impedance values.

In order to increase the magnetic flux in the end cells, the concept based on an inclined stem geometry for the end cells was applied. This choice helps to increase the voltage values in the end gaps.

The main characteristic parameters of this cavity are given in Table 1.

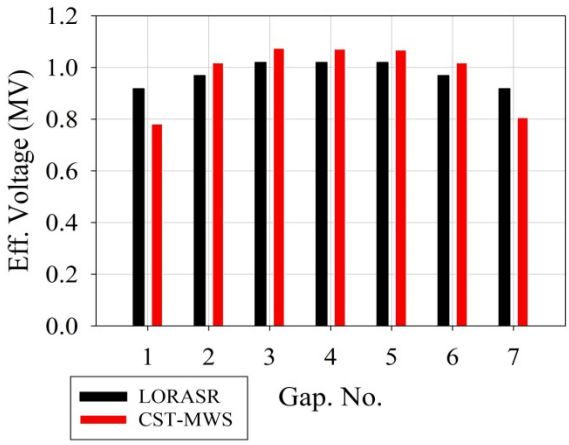

Figure 9: A comparison between the corresponding voltage distribution as calculated from the electric field which is given in Figure 8 with the reference design values as given from the LORASR code.

Table 1: The Main Parameters of the First CH – Cavity of the Dedicated Linac for Laser Accelerated Protons

Number of Gaps	7
Frequency (MHz)	325.2
Energy Range (MeV)	10.05 – 16.09
Power Loss (MW)	1.92
Q_0 – value	13289
Effective Shunt impedance (MΩ/m)	45.7
Accelerating Field Gradient (MV/m)	12.6
Beam Aperture (mm)	30
Outer Drift Tube Diameter (mm)	50
Total Length (mm)	668.4

Because of no internal focusing elements in this CH – DTL, the adaption of slim drift tubes is possible. This drift tube geometry results in attractive features like a very high sparking limit when compared to other structures like an Alvarez DTL.

The maximum effective accelerating gradient for this cavity layout would reach 12.6 MV/m. This corresponds to a 94 MV/m surface electric field spot at the third drift tube. The reason to have the maximum surface field on this position is mainly due to the inclined stems. As a consequence, these stems will be redesigned to reduce this effect.

In order to get a good estimation for the real peak field values, the drift tube edges have to be modelled carefully in the input files.

CONCLSION AND OUTLOOK

Laser driven proton beam sources have attractive features as rf linac injectors at energies above 10 MeV. They might become superior to the ion source, RFQ, and the first DTL stage of conventional linacs for special applications.

A CH linac with high space charge limit and large transverse and longitudinal acceptance was designed to accept a maximum fraction of the laser generated proton bursts.

Attractive applications for single bunch operation as delivered naturally by laser driven systems might occur, involving time of flight techniques or the study of secondary reactions at low noise level, for instance.

The study of the surface electric field for this cavity shows, that maximum local surface fields of about 94 MV/m are occurring on one drift tube. This value is about 5.2 times greater than the Kilpatrick limit. However, it appears very locally only - at the drift tube ends.

Further optimization and development is needed in order to optimize the proposed CH - cavities by using the CST – MicroWave Studio (MWS), and by improving cavity surface preparation techniques. This concept might lead towards intense single proton bunch acceleration with bunch particle numbers far above levels reached at present.

Within a funded project, cavity 1 of the proposed linac will be further developed towards a high gradient cavity. The availability of the GSI 3 MW klystron test stand will be very important for these investigations. The results will influence the rebuilt of the Unilac - Alvarez section, where the existing 1m thick concrete linac cave with fixed length should house a powerful pulsed heavy ion linac, optimized for achieving finally the beam intensities specified for the GSI-FAIR project. The 1.4 to 11.4 AMeV Alvarez section is in operation at duty factors up to 25 % since 4 decades now and was not optimized for pulsed high current operation.

REFERENCES

[1] S.C. Wilks st al., Phys. Plasmas **8**, 542 (2001).
[2] H. Schwoerer at al., Nature (London) **439**, 445 (2006).
[3] hppt://www.gsi.de/documents/DOC-2010-Nov-36-1.pdf.
[4] S. Yarameshiv et al., Proc. IPAC11, San Sebastián, Spain, MOODB03 (2011).
[5] A. Almomani et al., Phys.Rev. Special Topics – Accelerator and Beams **15**, 051302 (2012).
[6] A. Almomani et al., Proc. IPAC11, San Sebastián, Spain, WEPS033 (2011).
[7] V. Bagnoud et al., Appl. Phys. **B 100**, 137 (2009).
[8] CST Studio Suite, http://www.cst.com.

Copyright © 2012 by the respective authors — cc Creative Commons Attribution 3.0 (CC BY 3.0)

A PULSED LINAC FRONT-END FOR ADS APPLICATIONS

U. Ratzinger, H. Podlech, A. Schempp, K. Volk, IAP, Goethe Universität Frankfurt am Main, Germany
O. Heid, T. Hughes, U. Hagen, SIEMENS AG
H. Höltermann, BEVATECH, Frankfurt*

Abstract

Quite a number of projects worldwide develop proton driver linacs for neutron sources and for other Accelerator Driven Systems. One trend is to use a high duty factor and superconducting cavities as much as possible. Alternatively, one can aim on short duty factor and count on a continuing rapid development of pulsed rf amplifiers based on power transistor technology. A 500 mA, 5% duty factor layout of a proton injector is presented, consisting of a filament driven volume ion source, of a 150 keV transport section and of a 4.5 m long 162.5 MHz RFQ up to 2 MeV beam energy. Results of beam dynamics and technical designs will be presented.

INTRODUCTION

Worldwide there is an increasing interest in high power ADS (Accelerator Driven System) applications in the multi-MW range. Most of the planned facilities are using low to moderate beam currents (2-50 mA) with cw operation like MYRRHA [1] or the Chinese ADS [2]. The concept described in this paper is based on a pulsed linac with a duty factor of about 5% with very high beam currents of up to 500 mA of protons. The average beam current on the target should be larger than 20 mA. The advantage of lower duty factors is the economic use of room temperature RF structures alternatively to superconducting cavities.

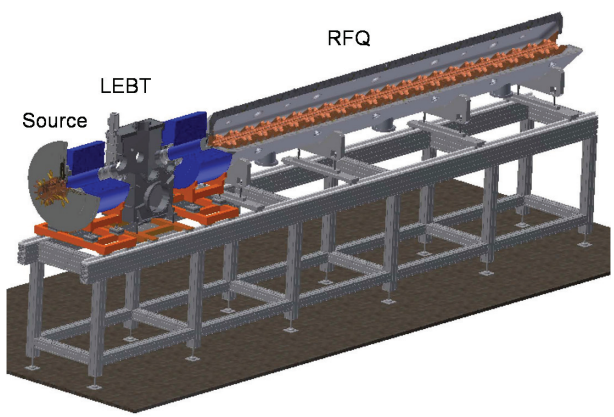

Figure 1: Schematic view of the high current 2 MeV front-end.

Of course, the required RF peak power is significantly larger because of the high beam load. But ongoing developments in pulsed solid state amplifiers will lead to a further reduction of the costs for RF power sources. Alternatively it may be possible to use Solid State Direct Drive^{TM} technology [3] in the future.

The 500 mA front-end consists of a high current proton volume source, a short LEBT-section and a 2 MeV 162.5 MHz 4-Rod-RFQ. Figure 1 shows schematically the layout and table 1 summarizes the main parameters.

Table 1: Main parameters of the 500 mA front-end

Parameter	Value	Unit
Particles	protons	NA
Current	500	mA
Platform voltage	150	kV
Source	volume type	NA
LEBT	magnetic	NA
RFQ	4-Rod	NA
Frequency	162.5	MHz
Energy	2	MeV
Duty factor	5	%

PROTON SOURCE

The proton source is a filament driven volume source which is based on the 220 mA proton source for the FRANZ project [4]. The extraction voltage has been set to 150 kV to keep emittance growth due to space charge small and to limit the technical effort as much as possible. A single hole extraction will be used to minimize the emittance. Numerical simulations have been performed to optimize the triode-extraction system. The other two beam species H_2^+ or H_3^+ can be reduced by source tuning and the proton content will be around 90% of the total beam current. Figure 2 shows schematically the 500 mA proton source.

LEBT

To optimize the beam parameters for injection into the RFQ a very compact LEBT-section consisting of two solenoids and a diagnostic chamber has been chosen. This enables the space charge compensated beam transport of high proton currents with only modest emittance growth. The space charge compensation in the simulations was 90%. Beam transport simulations have been performed with a simplified solenoid model. The solenoid aberrations can be kept small by designing for low aperture filling factor below 0.5. The transmission for the different ion species along the LEBT has been simulated to 100% for protons, 40% for H_2^+ and 24% for H_3^+. Figure 3 shows the loss profile for the two last mentioned species. The unwanted

* bevatech.com

Copyright © 2012 by the respective authors — cc Creative Commons Attribution 3.0 (CC BY 3.0)

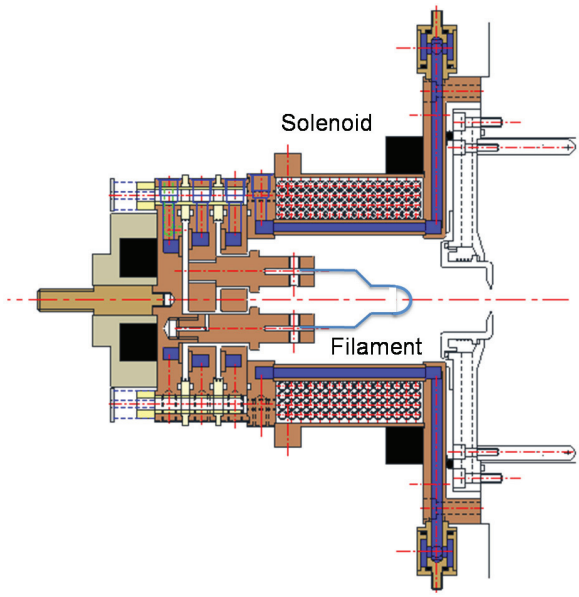

Figure 2: Schematic view of the 500 mA proton source (without extraction system).

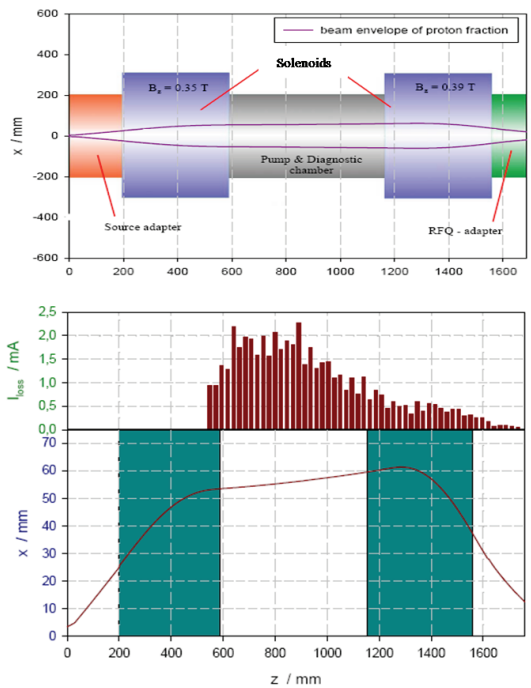

Figure 3: LEBT layout and proton beam envelopes as well as loss profile for other beam species.

species are not matched into the acceptance of the RFQ. Most of these particles will be lost in the RFQ.

RFQ

A 4-Rod RFQ has been chosen as first RF structure. This cavity type is the most common RFQ-structure for proton and ion beams below 200 MHz. The 4-Rod RFQ has several advantages:

- Excellent possibilities for tuning (field, frequency)
- Easy handling and access
- Reliability
- Cost efficient when compared to other structures

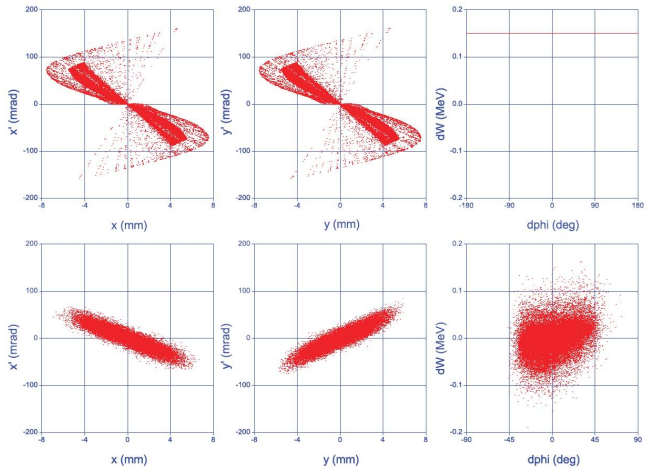

Figure 4: Input and output particle distribution of the RFQ with realistic input distribution.

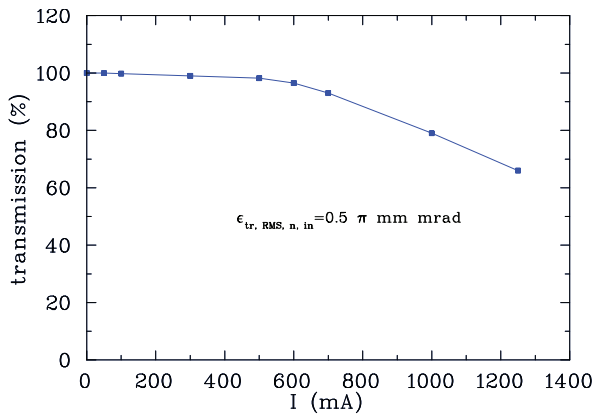

Figure 5: Simulated transmission as function of the input current.

As RF frequency 162.5 MHz has been chosen which gives the possibility to switch to the commercially available frequency of 325 MHz at higher energies. Beam dynamics simulations have been performed to optimize the transmission through the RFQ. Figure 4 shows the input and output phase space. As input the realistic particle distribution given by LEBT simulations has been used. The normalized transverse input RMS emittance is 0.6 π mm·mrad. A high electrode voltage of 150 kV is required to guarantee enough focusing strength for the high current proton beam.

Copyright © 2012 by the respective authors — cc Creative Commons Attribution 3.0 (CC BY 3.0)

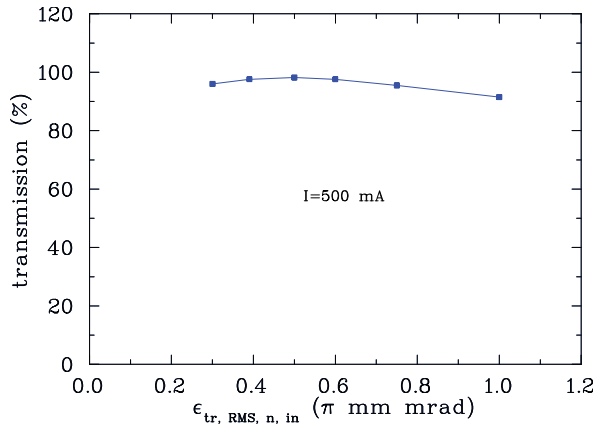

Figure 6: Transmission as function of the transverse input emittance.

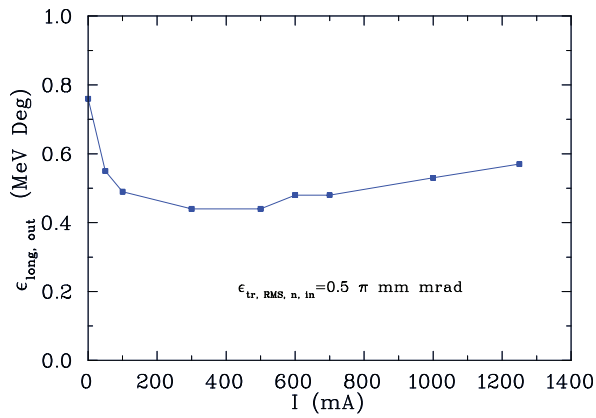

Figure 7: Longitudinal output emittance as function of the beam current.

The length of the RFQ is about 4.5 m, the calculated transmission is > 90 %.

Several simulations have been performed to study the influence of different input parameters like current or emittance on the transmission and output beam quality. Figure 5 shows the transmission as function of the beam current. The transmission stays constant for beam currents of up to about 600 mA, while for higher values there is a significant decrease of the transmission. Figure 6 shows that the transmission is relatively insensitive for the transverse input emittance between 0.3 and 1.0 π mm·mrad. For the simulations in figures 5-8 an ideal input phase space distribution has been used.

The longitudinal output emittance is influenced by the beam current with a minimum close to the design current (Fig. 7). The transverse output emittance increases linearly with the transverse input emittance (Fig. 8).

RF simulations have been performed to estimate the required RF power. Figure 9 shows the RF structure, the surface current density and the magnetic field distribution. The expected shunt impedance is 75 kΩm. This leads to a specific peak power of 300 kW/m without beam loading. The thermal load is expected to be 15 kW/m.

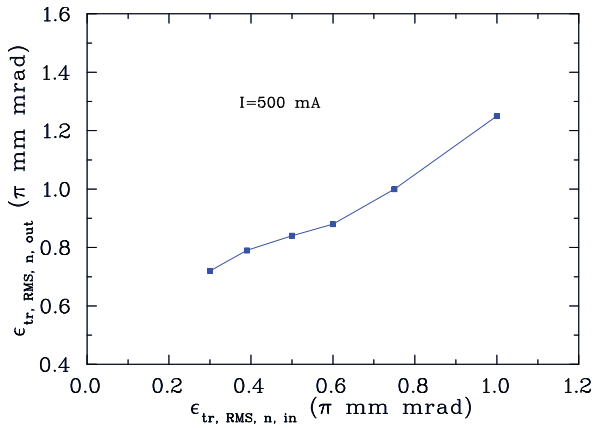

Figure 8: Transverse output emittance as function of the transverse input emittance (bottom).

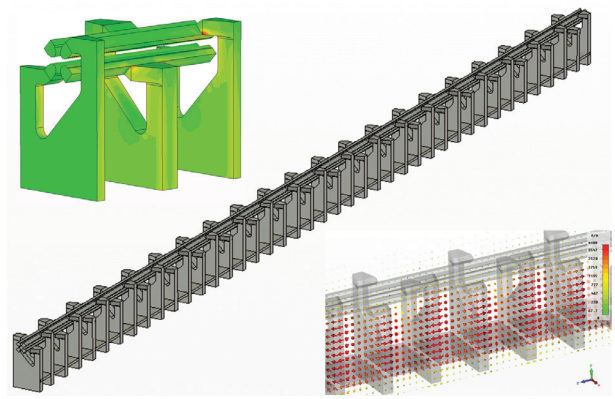

Figure 9: RF simulations of the 4-Rod RFQ.

CONCLUSION

A 500 mA proton front-end consisting of a high current volume source, a compact LEBT and and a 4-Rod RFQ has been investigated. Despite of the challenges due to the high beam current it seems to be feasible to build and to operate such a machine.

REFERENCES

[1] D. Vandeplassche et al., "The MYRRHA Linear Accelerator", IPAC'11, San Sebastian, September 2011, WEPS090, p. 2718 (2011)

[2] S. Fu et al., "Proton Linac for ADS Application in China", LINAC'10, Tsukuba, September 2010, TUPO019, p. 437 (2010)

[3] O. Heid, T. Hughes, "Solid State RF Power: The Route to 1 W per EURO-Cent", PAC'11, New York, April 2011, THOas2, p. 2047 (2011)

[4] U. Ratzinger et al., "The Driver Linac of the Neutron Source FRANZ", IPAC'11, San Sebastian, September 2011, WEPS040, p. 2577 (2011)

Copyright © 2012 by the respective authors — cc Creative Commons Attribution 3.0 (CC BY 3.0)

A COUPLED RFQ-IH CAVITY FOR THE NEUTRON SOURCE FRANZ*

M. Heilmann, D. Mäder, O. Meusel, U. Ratzinger†, A. Schempp, M. Schwarz
IAP, Frankfurt University, 60438 Frankfurt am Main, Germany

Abstract

The Frankfurt neutron source FRANZ [1] will deliver neutrons in the energy range up to 500 keV with high pulsed intensities. A 2 MeV proton beam will produce protons via the $^7Li(p,n)^7Be$ reaction. The 175 MHz accelerator cavity (Table 1) consists of a 4-rod-RFQ [2] coupled with an 8 gap interdigital H-type drift tube [3] section, the total cavity length being 2.3 m. The combined cavity will be powered by one RF amplifier to reduce investments and operation costs. The inductive power coupler will be at the RFQ part. The coupling into the IH-section is provided through a large aperture - mainly inductively. By CST-MWS-simulations [4] as well as by an RF model (Fig. 1) the voltage tuning along the cavity was investigated, and with special care the balance between both cavity sections. A first set of RFQ electrodes should allow to reach beam currents up to 50 mA in cw operation. The beam is pulsed with 100 ns, 250 kHz, while the cavity has to be operated cw due to the high repetition rate. The layout of the cavity cooling is adequate for a maximum heat load of 200 kW.

Figure 1: Coupled 1:2 RFD-DTL model for investigation of the coupling between two different accelerator structures. The RF-dipole (RFD)-model shows s capacity load per meter which is equivalent to the RFQ structure.

INTRODUCTION

The coupling of RF components is beneficial in many cases to reduce the RF amplifier costs and to profit from short drifts between accelerator sections - usually an advantage in high current beam dynamics. A IH-RFQ IH-DTL combination was suggested in ref. [5]. Such a combination was realized for the first time recently [6]. One difficulty in this case is the large diameter difference between RFQ and IH-section, due to the high capacitive load of an RFQ. The coupled structure for FRANZ consists of a 4-rod-RFQ and an IH-DTL. The resonance frequency is the same in both structures and can be driven in 0 and π-mode. It's possible to switch between these two modes after adapting the drift between both sections. The FRANZ-combination is investigated for the 0-mode [7, 8, 9]. The coupling between RFD and IH-DTL is mainly inductive.

Table 1: Parameters of FRANZ-RFQ-IH combination at 140 mA beam current. Parameters in brackets are valid for the 50 mA electrode design.

Parameter	Unit	
Particle		Proton
Frequency	MHz	175
Current	mA	(50) 140
RFQ Input-Energy	keV	120
IH-DTL Input-Energy	keV	700
IH-DTL Output-Energy	MeV	2.03
RFQ Thermal Losses	kW	139
IH Thermal Losses	kW	75
RFQ $\epsilon_{in}^{trans.,norm.,rms}$	mm mrad	0.4
IH $\epsilon_{X,out}^{trans.,norm.,rms}$	mm mrad	0.9
IH $\epsilon_{Y,out}^{trans.,norm.,rms}$	mm mrad	1.09
IH $\epsilon_{Z,out}^{trans.,norm.,rms}$	keV ns	5.2
RFQ - # of Cells		(97) 95
IH - # of Cells		8
RFQ - # of Stems		18
IH - # of Stems		6
RFQ - Aperture	mm	4
IH - Aperture	mm	22-24
RFQ - Dimension	mm	300x340x1825
IH - Dimension	mm	412x642x560
Electrode voltage	kV	(61) 75
Coupling constant		0.03
Q - Factor		8000
Shunt impedance	MΩ/m	69

* Work supported by HIC for FAIR and DFG
† u.ratzinger@iap.uni-frankfurt.de

Copyright © 2012 by the respective authors — cc Creative Commons Attribution 3.0 (CC BY 3.0)

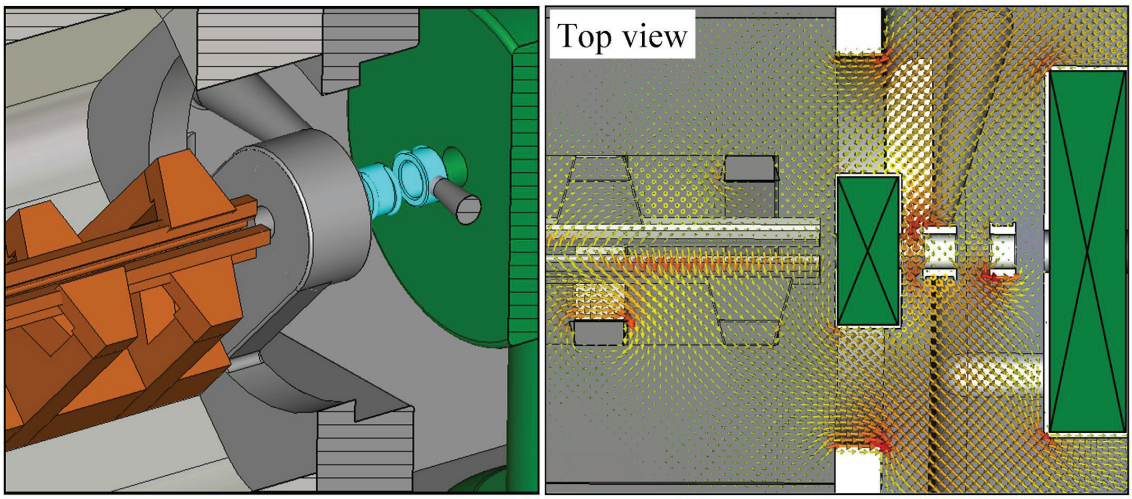

Figure 2: Side and top view of the coupling area. The RFQ is on the left side and the IH-DTL on the right. The arrows represent the magnetic field in the coupling area. The inductive coupling occurs through a large aperture from the RFQ to the IH-section.

COUPLED RFD-IH COMBINATION

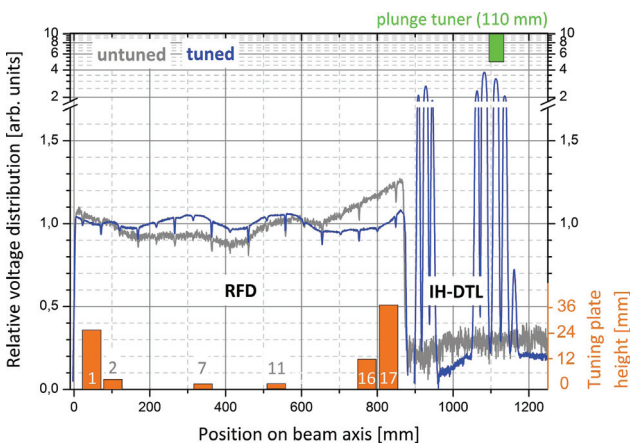

Figure 3: The relative voltage distribution along the coupled 1:2 RFD-DTL model (blue for optimized tuner positions). In green the IH-plunger position and in orange the heights of tuning plates in the RFD are shown. The voltage profile directly after coupling the untuned cavities is shown in grey.

The results from simulations by CST-MWS and from measurements can be summarized as follows:

- While the IH simulation results are well reflected by measurements, the voltage distribution along the RFD as well as the absolute resonance frequency of the ground mode are showing significant error bars. The coupled cavity simulation (Fig. 2) results can be used only as a first orientation. Therefore the construction of a 1:2 scaled rf model was well justified in this case.

- The shift of the resonance frequency of both cavities before and after coupling are within the 0.2 % range. This means that it makes sense to tune both structures individually first, while the coupling hole has to be kept open in both cases.

- The 4-rod-RFQ provides powerful tuning capabilities along the whole structure by the tuner plates at the bottom of each RF cell between two neighboured stems. The tuner configuration as shown in Fig. 3 is valid for the matched coupled case (orange bars). It had to be slightly modified against the separated RFQ-tuning to get a reasonable voltage distribution along the RFQ in the coupled case (resonance frequencies of cells close to the IH-cavity had to be increased to reduce the voltage amplitude in the coupling zone).

- From tuning experience it was decided to provide an RF tuning range of 0 to +1 % in resonance frequency for the IH cavity by capacitively acting plunges.

HEAT DISTRIBUTION

The heat distribution is shown in Fig. 4 for the IH-DTL and in detail for the IH-tube no. 6. The thermal losses in the IH-DTL are 75 kW. All components of this structure are water cooled to dissipate the losses. Half of the thermal losses are dissipated in tank, girder and steerer at an averaged temperature increase of 7 K. A temperature increase between 20 and 40 K is seen along the stems and tubes (Table 2). For reasons of mechanical stability the stems and drift-tubes are made from stainless steel with a wall thickness of 1.5 mm. IH-tube no. 6 is the component with the highest surface currents and a heat load of 3.2 kW. The highest surface currents are on the stem surfaces pointing towards the cavity end wall: Here the cavity magnetic field of the H_{110}-mode is pointing perpendicular to the beam axis, closing the field lines from the upper and lower half of the cavity. The direct water cooling of each

Copyright © 2012 by the respective authors — cc Creative Commons Attribution 3.0 (CC BY 3.0)

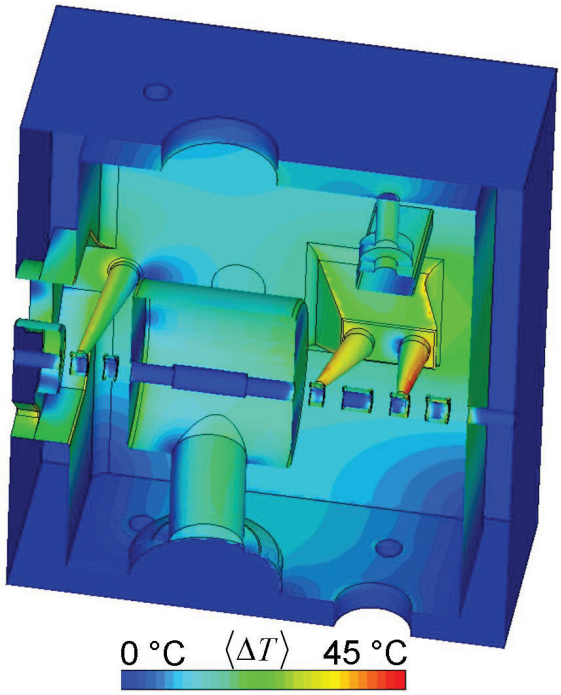

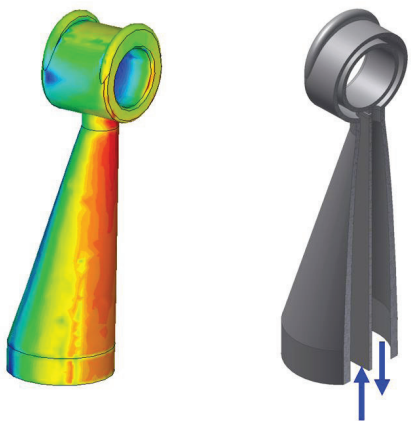

Figure 4: The heat distribution is shown for the IH-DTL (top). All surfaces of the IH-DTL are directly water cooled to remove the heat load efficiently. The heat distribution in detail for the IH-tube no. 6 and the cooling concept are shown below. The water flows along the stem around the tube and back.

stem and drift tube is needed in this case to allow cw operation at gap voltages amplitudes of up to 300 kV.

CONCLUSIONS

Combinations of RFQ-sections and DTL-sections into a coupled cavity are investigated at several laboratories currently. Main problems are the very different capacitive load per meter in these sections leading to nontrivial rf coupling szenarios. The Frankfurt coupled cavity shows promising features in simulations and RF model investigations. The power cavity is under construction and will be tested with intense pulsed beams from the FRANZ 120 keV high voltage platform. Due to the very demanding beam current request of up to 140 mA for experiments it was decided to stage the project: In a first step, RFQ electrodes for a design current of 50 mA will be realized, which already allows an attractive nuclear astrophysics program at FRANZ for several years.

Table 2: Parameters of power losses and heat distribution

Parameter	P_{norm} **[kW]**	$\langle\Delta T\rangle$**[K]**
Tube + Stem 1	2.9	23.6
Tube + Stem 2	4.6	31.3
Tube + Stem 3	3.2	30.8
Tube + Stem 4	3.8	33.0
Tube + Stem 5	3.3	38.6
Tube + Stem 6	3.2	44.7
Lens	5.8	4.8
Tuner	1.4	4.7
Tank, Steerer, Girder	35.9	7.0

REFERENCES

[1] U. Ratzinger, B. Basten, L.P. Chau, H. Dinter, M. Droba, M. Heilmann, L. Lotz, D. Mäder, O. Meusel, I. Müller, Y.C. Nie, D. Noll, H. Podlech, A. Schempp, W. Schweizer, K. Volk, C. Wiesner and C. Zhang, The Driver Linac of the Neutron Source FRANZ, Proceedings of IPAC12 Conference, WEPS040.

[2] A. Bechtold, A. Schempp, M. Vossberg, Recent High Power RFQ Development, Proceedings of International Topical Meeting on Nuclear Research Applications and Utilization of Accelerators, 4-8 may, 2009, Vienna, Austria.

[3] U. Ratzinger, Effiziente Hochfrequenz-Linearbeschleuniger fr leichte und schwere Ionen, Habilitationsschrift, Goethe Universität Frankfurt, 1998.

[4] CST MicroWave Studio, `www.cst.de`.

[5] U. Ratzinger, High Current IH Structures, Proc. of the 1994 EPAC Conf., London, Vol. 1, p. 264

[6] L. Lu, T. Hattori, N. Hayashizaki, Design and Simulation of C^{6+} hybrid single cavity linac for cancer therapy with direct plasma injection scheme, NIMA 688(2012)11-21.

[7] A. Bechtold, U. Bartz, G. Clemente, M. Heilmann, P. Kolb, H. Liebermann, D. Mäder, O. Meusel, H. Podlech, U. Ratzinger, A. Schempp, C. Zhang, A coupled RFQ-drift tube combination for FRANZ, Proceedings of LINAC08, Victoria, Canada, MOP001, p.46.

[8] D. Mäder, Kopplung der Beschleunigerkavitäten RFQ und IH-DTL am FRANZ-Projekt, Master Thesis, Uni. Frankfurt, 2011.

[9] M. Schwarz, Hochfrequenzabstimmung und Feldoptimierung des gekoppleten 1:2 RFD-IH-Modells fr FRANZ, Bachelor Thesis, Uni. Frankfurt, 2012.

Copyright © 2012 by the respective authors — cc Creative Commons Attribution 3.0 (CC BY 3.0)

STATUS OF CH CAVITY AND SOLENOID DESIGN OF THE 17 MeV INJECTOR FOR MYRRHA*

D. Mäder†, H. Klein, H. Podlech, U. Ratzinger,
C. Zhang, IAP, Goethe-Universität, Frankfurt am Main, Germany

Abstract

The multifunctional subcritical reactor MYRRHA (**M**ulti-purpose h**y**brid **r**esearch **r**eactor for **h**igh-tech **a**pplications) will be an accelerator driven system (ADS) located in Mol (Belgium). The first accelerating section up to 17 MeV is operated at 176 MHz and consists of a 4-rod-RFQ followed by two room temperature CH cavities with intertank quadrupole triplet focusing and four superconducting CH structures with intertank solenoids. Each room temperature CH cavity provides about 1 MV effective voltage gain using less than 30 kW of RF power. The superconducting resonators have been optimized for electric peak fields below 30 MV/m and magnetic peak fields below 30 mT. For save operation of the superconducting resonators the magnetic field of the intertank solenoids has to be shielded towards the CH cavity walls. Different coil geometries have been compared to find the ideal solenoid layout.

INTRODUCTION

Transmutation of long-lived radioactive waste and advanced technologies for future power generation will be investigated with the MYRRHA ADS [1]. The IAP of Frankfurt University is responsible for the development of the 17 MeV injector, a 13 meter long front end of the 600 MeV MYRRHA linac. To achieve the extremely high reliability of the beam supply for the reactor, two injectors will be driven at the same time. With this parallel redundancy the beam can be provided even during a failure of one injector. Because of thermal stress in the reactor not more than 11 beam trips of $t > 3s$ per year are allowed. The following accelerating structures up to 60 MeV are using the concept of serial redundancy [2].

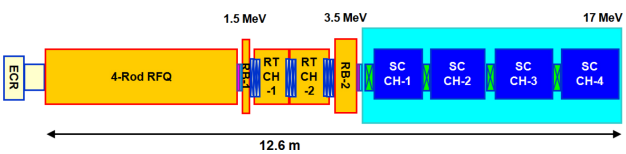

Figure 1: Overview of the MYRRHA injector.

A 4-rod-RFQ will bunch and accelerate the proton beam up to 1.5 MeV [3]. After a five gap CH rebuncher the proton bunches will be accelerated to 3.5 MeV with room temperature CH structures. Quadrupol triplets for focusing and phase probes for diagnostics are placed between the structures. 3 MV/m will be provided by the superconducing accelerators. Four bulk niobium CH cavities are assembled together with four 4.5 Tesla solenoids with coils made of NbTi in one cryomodule [Figure 1].

CH CAVITY DESIGN

Crossbar H-mode (CH) cavities are excellent candidates for acceleration of ions in the low and medium energy range. These resonators driven in the TE_{211}-Mode will be used for all accelerating and rebunching cavities after the 4-rod-RFQ from 1.5 to 17 MeV.

Room temperature CH cavities

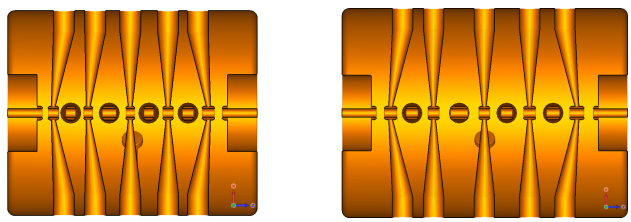

Figure 2: Scheme of the two room temperature CH structures.

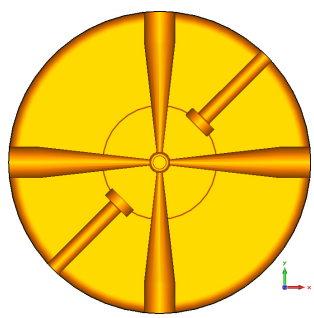

Figure 3: The diagonal tuners act mainly capacatively and provide a total frequency shift of 1 MHz.

CH-1 consists of three and CH-2 of two inclined stems [Figure 2]. Together with the extra volume around the vaults the inclination of the stems increases the induction on the outer stems. This flattens the gap voltage distribution and consequently the thermal load on the stems. The vaults at the resonator ends create additional space outside the cavity and are used for the quadrupole triplet lenses.

Each CH structure is tuned by two mainly capacitively acting tuners that provide a total frequency shift of 1 MHz.

* Work supported by the EU, FP7 MAX contract number 269565
† d.maeder@iap.uni-frankfurt.de

Copyright © 2012 by the respective authors — cc Creative Commons Attribution 3.0 (CC BY 3.0)

The tuners are mounted on the cavity wall under 45 degree to the horizontal plane [Figure 3].

Table 1: Parameter list of the room temperature CH-1 and CH-2 of MAX.

Parameter	RT CH-1	RT CH-2
Frequency [MHz]	176	176
Q-Factor (85% MWS)	14539	14964
P_{sim} [kW]	16.5	18.5
P_{real} (85% MWS) [kW]	19.4	21.8
$Z_a(\beta\lambda - def.)$ [MΩ/m]	113.5	100.6
U_0 [MV]	1.26	1.37
U_a [MV]	1.03	1.14
β_{avg}	0.066	0.077
No. of Gaps	10	10
Energy Range [MeV]	1.5 – 2.5	2.5 – 3.5
$E_a(\beta\lambda - def.)$ [MV/m]	1.8	1.6
L [mm]	715.2	833.6
$L(\beta\lambda - def.)$ [mm]	568.7	699.3
Diameter [mm]	584	608
Aperture [mm]	25	25

Superconducting CH cavities

One cryo-module will contain all cold parts of the injector. For manufacturing and transportation reasons the superconducting CH structures are not longer than 1.2 m. For this reason the number of gaps decreases with higher β_{avg} from 10 to 7.

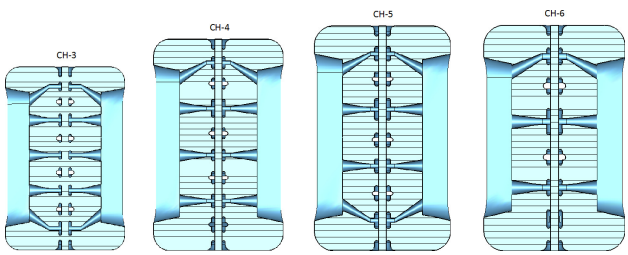

Figure 4: The four superconducting CH cavities in scale relatively to each other.

All superconducting cavities will be made of bulk Niobium and are optimised for an acceleration gradient between 3.5 and 3.9 MV/m and for a flat electric peak field distribution along the gaps. Low electric peak surface fields below 30 MV/m minimise the risk of quenching and ensure a safe operation [Table 2].

SC SOLENOID DESIGN

Superconducting solenoids driven at a maximum magnetic field of 4.5 T are used in the cold part of the injector for transversal focusing. The current densitiy of 300 A/mm^2 in the main coil is ten times smaller than the critical current density, where the solenoid is quenching [4].

Four superconducting solenoids of the same type will be placed between the accelerating cavities. The main coil

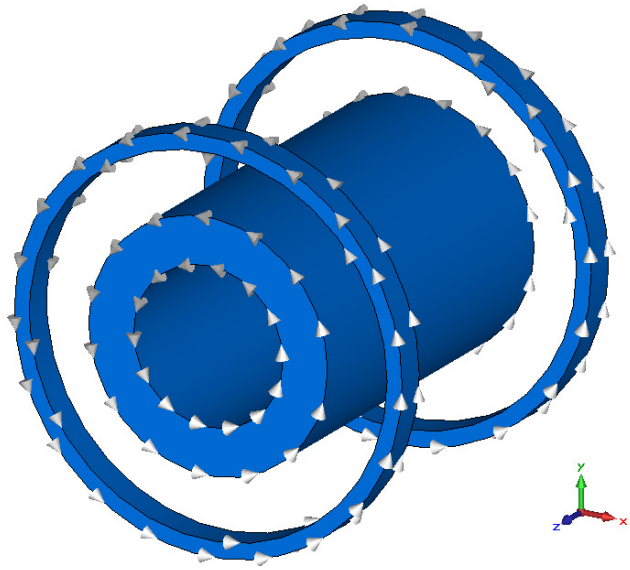

Figure 5: Main and bucking coils of the superconducting solenoid.

of the solenoid is 120 mm long and has 4300 windings of Niobium-Titanium in a copper matrix. To avoid quenching of the neighbouring accelerators the magnetic field of the solenoid has to be reduced. Two bucking coils with 420 windings at the ends of the main coil [Figure 5] minimise the fringe field [Figure 6 and 7]. All multi-filamentary superconducting wires in the solenoid can carry a total current of 120 A.

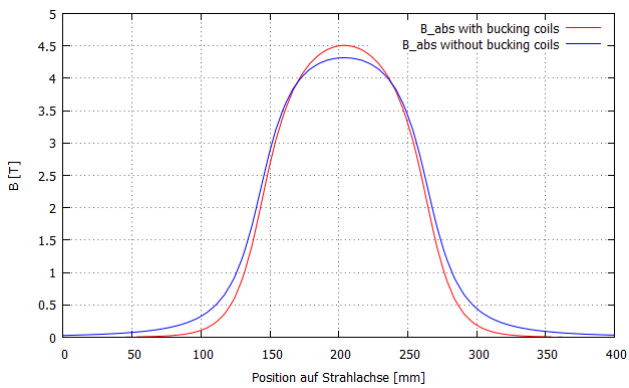

Figure 6: A solenoid with bucking coils has a lower fringe field in comparison with a simple solenoid. Both solenoids are normalized to the same focusing strength.

OUTLOOK

The new tuning concept of superconducting CH structures with static and dynamic tuners on the girders between the stems will be applied for the four sc injector cavities for MAX after a successful demonstration of this concept with a 325 MHz cavity at IAP [5].

The effects of the solenoids fringe field on the CH cavity are under investigation. Further simulations to shield the magnetic flux are necessary.

Copyright © 2012 by the respective authors — cc Creative Commons Attribution 3.0 (CC BY 3.0)

Table 2: Parameter list of the superconducting CH-3 to CH-6 of MAX.

Parameter	SC CH-3	SC CH-4	SC CH-5	SC CH-6
Frequency [MHz]	176	176	176	176
U_0 [MV]	4.25	4.72	4.93	4.78
U_a [MV]	3.50	3.98	4.18	4.09
β_{avg}	0.102	0.131	0.157	0.178
No. of Gaps	10	9	8	7
Energy Range [MeV]	3.5 – 6.7	6.7 – 10.4	10.4 – 14.2	14.2 – 17
$E_a(\beta\lambda - def.)$ [MV/m]	3.9	3.7	3.6	3.5
Geometry Factor [Ω]	62.6	67.6	70.2	73.2
$R_0/Q_0[\Omega]$	2216	2165	1817	1577
$R_0R_S[\Omega^2]$	138849	146345	127558	115473
E_{max} [MV/m]	29.27	28.06	30.59	28.92
$B_{max}[mT]$	27.8	29.7	35.27	31.35
E_{max}/E_a	7.5	7.6	8.5	8.3
L [mm]	915.9	1075.3	1129.0	1126.9
L $\beta\lambda - def.$ [mm]	901.1	1071.1	1162.1	1178.8
Diameter [mm]	600	650	684	708
Aperture [mm]	30	30	40	40

Additional measurements with a test solenoid close to a CH structure at 4.2K will be performed together with GSI in the demonstrator experiment [6]. A main focus in this layout is to put on high safety margins to reach the specified reliability.

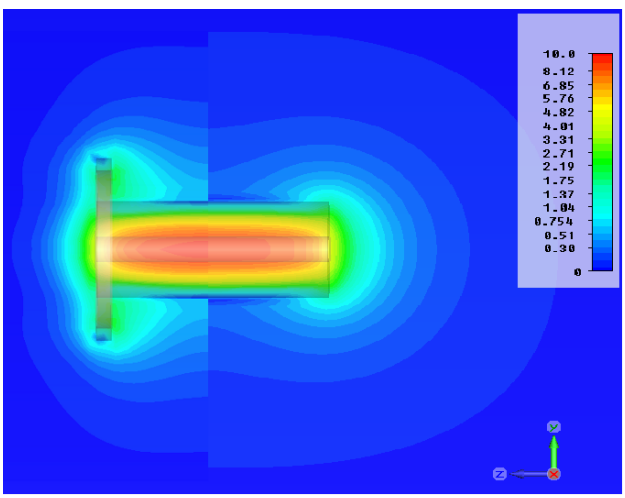

Figure 7: In this graphic two pictures with the magentic flux of a solenoid are merged. On the left side the solenoid with bucking coils is shown. The simple solenoid without bucking coils on the right side creates more spacious magnetic flux. The coloured scale is normalized to the highest field level of the left solenoid (4.5T). Both solenoids would have the same focusing strength, so the simple solenoid would have a less peak field (compare with figure 5).

ACKNOWLEDGEMENTS

This work has been supported by the EU (FP7 MAX contract number 269565).

REFERENCES

[1] J.-L. Biarrotte, A.C. Mueller, H. Klein, P. Pierini, D. Vandeplassche, "Accelerator reference design for the MYRRHA European ADS demonstrator", LINAC2010, Tsukuba, Japan, September 2010, p. 440-442

[2] D. Vandeplassche, J.-L. Biarrotte, H. Klein, H. Podlech, "The MYRRHA Linear Accelerator", IPAC2011, San Sebastian, Spain, September 2011, p. 2718-2720

[3] M. Vossberg, H. Klein, H. Podlech, A. Schempp, A. Bechtold, "4-rod-RFQ for MYRRHA", this proceedings, Paper ID:THPB047.

[4] A. Chao, "Handbook of Accelerator Physics and Engineering", World Scientific Publishing Co Pte Ltd, 1999

[5] M. Busch, F. Dziuba, H. Podlech, U. Ratzinger, W. Barth, S. Mickat, M.Amberg , M. Pekeler , "First Measurements on the 325 MHz Superconducting CH-Cavity", this proceedings, Paper ID: TUPB071

[6] F. Dziuba, M. Amberg, K. Aulenbacher, W. Barth, M. Busch, H. Podlech, U. Ratzinger, S. Mickat, "Status of the Superconducting cw Demonstrator for GSI", this proceedings, Paper ID: TUPB072

Copyright © 2012 by the respective authors — cc Creative Commons Attribution 3.0 (CC BY 3.0)

PROGRESS IN THE CONSTRUCTION OF LINAC4 AT CERN

M. Vretenar, L. Arnaudon, P. Baudrenghien, C. Bertone, Y. Body, J. Broere, O. Brunner, G. Bellodi, M. Buzio, C. Carli, J.P. Corso, J. Coupard, A. Dallocchio, N. Dos Santos, J.F. Fuchs, A. Funken, R. Garoby, F. Gerigk, L. Hammouti, K. Hanke, J. Hansen, I. Kozsar, J. Lettry, J.B. Lallement, A. Lombardi, L.A. Lopez-Hernandez, C. Maglioni, S. Mathot, B. Mikulec, D. Nisbet, M. Paoluzzi, B. Puccio, U. Raich, S. Ramberger, F. Roncarolo, C. Rossi, N. Schwerg, R. Scrivens, G. Vandoni, J. Vollaire, R. Wegner, S. Weisz, T. Zickler, CERN, CH1211 Geneva, Switzerland

Abstract

As first step of the LHC luminosity upgrade program CERN is building a new 160 MeV H^- linear accelerator, Linac4, to replace the ageing 50 MeV Linac2 as injector to the PS Booster (PSB). Linac4 is an 86-m long normal-conducting linac made of a 3 MeV injector followed by 22 accelerating cavities of three different types.

The general service infrastructure has been installed in the new tunnel and surface building and its commissioning is progressing; high power RF equipment is being installed in the hall and installations in the tunnel will start soon. Construction of the accelerator parts is in full swing involving industry, the CERN workshops and a network of international collaborations. The injector section including a newly designed and built H^- source, a 3-m long RFQ and a chopping line is being commissioned in a dedicated test stand. Beam commissioning of the linac will take place in steps of increasing energy between 2013 and 2015. From end of 2014 Linac4 could deliver 50 MeV protons in case of Linac2 failure, while 160 MeV H^- could be injected into the PSB from 2016; connection to the PSB will take place during a long LHC shut-down foreseen to begin end of 2017.

MOTIVATIONS AND PARAMETERS

The peak luminosity of the LHC has been constantly increased during its first years of operation and the nominal value of 10^{34} $cm^{-2}s^{-1}$ is now expected to be reached after the 2013-14 shut-down in parallel with the increase in energy. In this way, the LHC could provide to its experiments about 40 fb^{-1}/year, a value sufficient for Higgs physics but most likely too low for new physics discoveries. Extending the physics reach of the LHC during the next decade is therefore a priority for CERN: specific projects have been launched to overcome the present luminosity limitations, related both to the LHC interaction regions and to its injector chain, with the goal of achieving a levelled luminosity of 5×10^{34} $cm^{-2}s^{-1}$ with integrated luminosities of 250 fb^{-1}/year.

In particular, the LHC Injectors Upgrade (LIU) project aims at increasing the beam brightness from the injectors, limited now by several factors of which the most severe are related to space charge tune shift at the injection into the low-energy synchrotrons in the chain, the PS Booster (PSB) and the Proton Synchrotron (PS) [1]. Increasing their injection energies is thus required to reduce tune shift permitting higher beam brightness; to reach the LIU goals, injection energy from the linac into the PSB has hence to go up from 50 to 160 MeV and from the PSB into the PS from 1.4 to 2 GeV. For the PSB injection, an energy upgrade of the present 50 MeV Linac2 was ruled out because of the lack of space and of its obsolete technology; instead, the construction of the new 160 MeV Linac4 (the 4th hadron linac built at CERN) was approved by the CERN Council in 2007. The new linac will bring other advantages related to injecting into the PSB H^- instead of protons, to a modern construction technology exempt from the reliability concerns of Linac2, and to the possibility of increased beam intensity for non-LHC users [2]. Linac4 is being built in a location parallel to the present Linac2 (Fig. 1); a new surface building houses the RF and all other infrastructure and equipment.

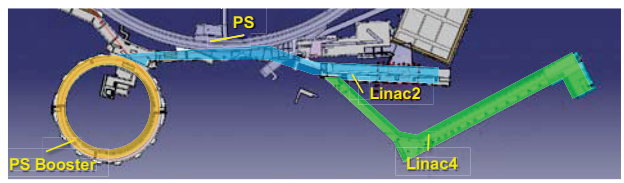

Figure 1: Linac4 and the other low-energy accelerators.

The new linac is dimensioned to double the maximum intensity from the PSB with the same transverse emittances, providing up to 10^{14} protons per pulse; this charge will be supplied by 400 μs long pulses at 40 mA current. The pulse repetition frequency is limited to a maximum of about 1 Hz by the PSB magnetic cycle. In case Linac4 would be used in a future high-intensity facility for neutrino physics, the accelerating structures have been designed for a maximum duty cycle of 10%; nevertheless, infrastructure and power supplies are dimensioned only for the duty cycle corresponding to PSB injection. Chopping of about 35% of the beam at 3 MeV is foreseen to allow low-loss injection in the PSB, bringing the required current out of the ion source to 80 mA. The accelerator (Fig. 2) is composed by a 3 MeV Front end (source, LEBT, RFQ and chopper line) followed by three normal-conducting accelerating structures all at 352 MHz, for a total length of 76 m. Adopting three different accelerating sections allows maximising the RF efficiency reducing at the same time the construction costs; using the same RF frequency as in the old LEP machine allowed to recover an important stock of klystrons, circulators and waveguides. A 70-m long transfer line connects to the existing Linac2 line.

Copyright © 2012 by the respective authors — cc Creative Commons Attribution 3.0 (CC BY 3.0)

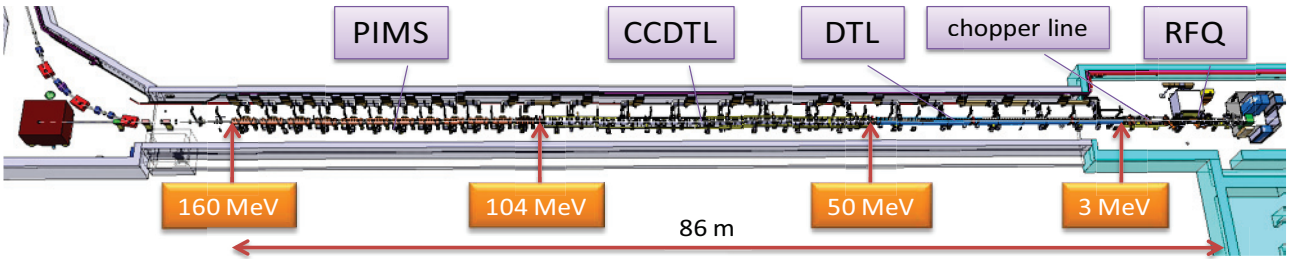

Figure 2: Linac4 layout.

THE 3 MeV FRONT END

The section up to 3 MeV is being installed and commissioned in a dedicated test stand, and will be transferred in 2013 to its location in the Linac4 tunnel. After an initial unsuccessful operation of the original RF volume source at 45 kV extraction voltage due to the high power of the co-extracted electron beam, tests have continued with protons and in parallel the design and construction of two new H^- sources has started [3]. The first source, based again on volume production but with improved beam extraction and electron dumping and a pulsed extraction voltage, is presently being tested and will feed the RFQ on the test stand. The second source foresees the addition of Caesium to enhance H^- current via surface production; it will be completed and installed in 2014 for the linac commissioning. A magnetron source is also being investigated for a possible future upgrade.

The 3-m long RFQ of the brazed-copper 4-vane type has been entirely built in the CERN Workshop [4]. A sequence of machining steps and thermal treatments allowed keeping vane position errors after brazing within the 30 μm tolerance, resulting in field errors within ±1% after adjustment of the slug tuners. Figure 3 shows the RFQ recently installed in the test stand. Vacuum and cooling tests have been completed; RF conditioning followed by beam tests will take place in the next months.

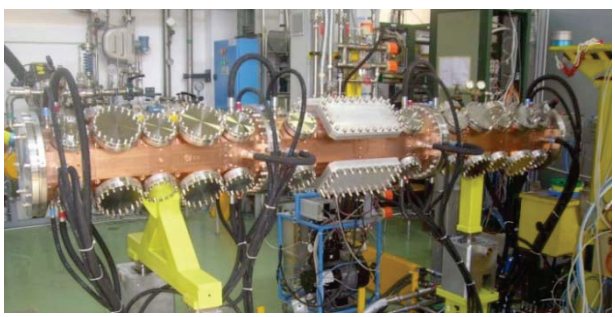

Figure 3: The Linac4 RFQ in the 3 MeV test stand.

The 3.6 m long chopper line connecting the RFQ to the DTL is completed and ready for beam tests. It contains a fast chopper made of two 40-cm long meander-line electrostatic deflectors, together with rebunching cavities, quadrupoles, diagnostics and the chopper dump.

ACCELERATING SECTION

The 50 MeV Drift Tube Linac (DTL) is divided in three tanks, with focusing provided by 113 Permanent Magnet Quadrupoles (PMQ) placed in vacuum inside the drift tubes and end walls. The innovative design which allows precise positioning of the drift tubes inside the tank, without the need for flexible connections, has been tested on a 1.2 m long prototype conditioned up to full RF power; construction of the three tanks is progressing at CERN with contributions from ESS-Bilbao (Spain). Figure 4 shows the assembly of the first DTL tank.

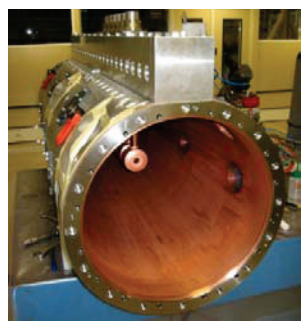

Figure 4: Assembly of DTL Tank1.

The 102 MeV Cell-Coupled DTL (CCDTL) is composed of 7 modules; a module contains 3 tanks with two drift tubes each, connected by coupling cells. Focusing is external to the drift tube structure, provided by a combination of PMQs (between tanks) and electromagnetic quadrupoles (between modules). After the successful high-power test of a prototype, the modules are being built by a collaboration of Russian laboratories (VNIITF Snezinsk and BINP Novosibirsk); delivery of the completed modules (Fig. 5) to CERN just started.

Figure 5: CCDTL module 2 during tests at Novosibirsk.

Copyright © 2012 by the respective authors — cc Creative Commons Attribution 3.0 (CC BY 3.0)

The PIMS (Pi-Mode Structure) section is composed of 12 EB-welded 7-cell copper cavities operating in pi-mode. The first cavity has been built at CERN and tested to full RF power; construction of the others has started at NCBJ Swierk (Poland), with part of the assembly being done at CERN and at FZ Jülich (Germany).

CONSTRUCTION PROGRESS

Installation of the machine infrastructure has been progressing since delivery of the Linac4 building and tunnel by the civil engineering company at end 2010; this includes electrical network, safety and communication equipment, cooling and ventilation, installation of racks and laying of all the cables. All equipment has been preliminarily integrated into an extensive 3-D computer model which allowed an early solution of interference problems. The infrastructure installation will be completed in September 2012, to leave place to the installation of machine components.

The complex RF network (Fig. 6) has been installed in the hall and tunnel as well as in the 15 shafts connecting the two levels. Its peculiarity comes from the fact that Linac4 will initially use a combination of thirteen 1.3-MW-klystrons from the old LEP feeding one cavity each and six new 2.8-MW-klystrons feeding two cavities (or two couplers) each. In a following phase, as the stock of LEP klystrons runs out, pairs of LEP klystrons will be replaced by new klystrons equipped with a power splitter, leaving the waveguide network unchanged and progressively extending the number of RF stations feeding two cavities. Prototypes of the newly developed 2.8-MW klystrons have been successfully tested at the factory, while testing and refurbishing of the LEP klystrons is progressing.

Figure 6: RF Network installed in the Linac4 Hall.

The 110 kV long-pulse klystron modulators developed at CERN are now being produced in the frame of a collaboration with the LAL Laboratory (France). A digital Low-Level RF derived from the LHC system and equipped with feed-forward capability is being completed to be used in Linac4. Construction of diagnostics equipment is progressing and most of the devices will be tested in the 3 MeV test stand.

Figure 7 shows the tunnel ready for the installation of the linac components.

Figure 7: Linac4 tunnel (August 2012).

COMMISSIONING PLANS

After completion of the infrastructure installation, the Linac4 tunnel will be used for ion source testing until the transfer of the 3 MeV line (RFQ and chopper line) foreseen for mid-2013. Additional time in 2013 for beam commissioning of the low-energy part has been recently foreseen to reduce use of critical resources (mainly survey and vacuum) during the long LHC shut-down that will take place in 2013/14. From 2014 it is foreseen to restart commissioning at the normal pace, in progressive steps of energy and sending for every step the beam into a dedicated temporary measurement bench. The different commissioning steps are DTL tank1 (January 2014), full DTL (spring 2014), CCDTL (end 2014), PIMS (mid-2015, on the final measurement section). The beam commissioning will be followed by an extensive series of beam measurement to prepare for the injection in the PSB and by a long reliability run in 2016, to assess and improve Linac4 reliability in preparation for the moment when it will become a critical element in the LHC injection chain. The connection of Linac4 to the PSB requires a long shut-down because of the upgrade to H^- of the PSB injection; it will take place at the next long LHC shut-down, indicatively in 2017/18.

Temporary operation with 50 MeV protons of Linac4 is being considered as a back-up solution in case of problems with Linac2 in the period between the two long shut-downs.

REFERENCES

[1] R. Garoby et al., "Upgrade Plans for the LHC Injector Complex", IPAC 2012, New Orleans.
[2] F. Gerigk, M. Vretenar (eds.), "Linac4 Technical Design Report", CERN-AB-2006-084 ABP/RF.
[3] J. Lettry et al., "H^- ion sources for CERN's Linac4", NIBS Symposium, Jyväskylä, Finland, 2012.
[4] C. Rossi, A. Dallocchio, J. Hansen, J.B. Lallement, A.M. Lombardi, S. Mathot, D. Pugnat, M. Timmins, G. Vandoni, M. Vretenar, M. Desmons, A. France, Y. Le Noa, J. Novo, O. Piquet "Assembly and RF Tuning of the Linac4 RFQ at CERN", this Conf.

Copyright © 2012 by the respective authors — cc Creative Commons Attribution 3.0 (CC BY 3.0)

LINAC4 45 keV PROTON BEAM MEASUREMENTS

G. Bellodi, V. A. Dimov, L. M. Hein, J-B. Lallement, A. M. Lombardi, O. Midttun, R. Scrivens,
CERN, Geneva, Switzerland
P. A. Posocco, Imperial College of Science and Technology, London, UK

Abstract

Linac4 is a 160 MeV normal-conducting H^- linear accelerator, which will replace the 50 MeV proton Linac2 as injector for the CERN proton complex.

Commissioning of the low energy part - comprising the H^- source, a 45 keV Low Energy Beam Transport line (LEBT), a 3 MeV Radiofrequency Quadrupole (RFQ) and a Medium Energy Beam Transport (MEBT) - will start in fall 2012 on a dedicated test stand installation.

In preparation to this, preliminary measurements were taken using a 45 keV proton source and a temporary LEBT setup, with the aim of characterising the output beam by comparison with the predictions of simulations. At the same time this allowed a first verification of the functionalities of diagnostics instrumentation and acquisition software tools.

Measurements of beam profile, emittance and intensity were taken in three different setups: right after the source, after the first and after the second LEBT solenoids respectively. Particle distributions were reconstructed from emittance scans and used as input to simulation studies of the beam transport through the line (forward and backward tracking). Comparison of the results with the measurements at different locations allowed an experimental validation of the LEBT (in terms of misalignments and calibration points) and qualification of the beam at the source output.

INTRODUCTION

The Linac4 [1] 3 MeV frontend is presently in the process of being assembled for the start of commissioning on a dedicated test stand in autumn 2012. While waiting for completion of the RFQ construction and final developments on the H- ion source, a preliminary campaign of measurements was carried out in 2011 to characterise the performance of a prototype Low Energy Beam Transport (LEBT) section of Linac4 and provide first validation of the beam simulation models used in the design of Linac4 as well as of the beam diagnostics and software acquisition tools functionality.

The LEBT is a critical part of the machine in the control of beam emittance and parameters for optimised matching into the RFQ acceptance of the beam extracted from the source. It consists of two solenoids, two steerers, a beam current transformer (BCT) and a diagnostics box containing a Faraday cup, a profile monitor, a moveable iris device for the production of lower intensity beams [2] and a pre-chopper (not operational at the time of the measurements). The layout has been kept as compact as possible in its 1.8 m length, to minimise space charge effects, predominant at these low energies. Beam dynamics simulations studies carried out with the PATH code [3] show that in the case of nominal beam parameters (45 keV, 80 mA, 90% space charge compensation, ε=0.25 mm mrad), and using a uniform input particle distribution, we can achieve almost lossless transmission through the LEBT and good matching to the RFQ. The LEBT acceptance is largely determined by the distance between the source output plane and the first solenoid, together with the first solenoid aperture.

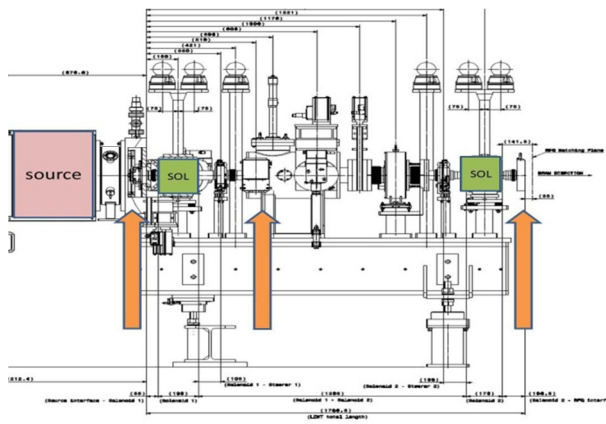

Figure 1: LEBT prototype setup (orange arrows indicate measurement positions).

MEASUREMENTS

A prototype version of the H- ion source was used for the measurements, in proton operation mode. Different neutralisation effects have to be expected, but beam dynamics in the LEBT is overall charge state insensitive, making the results of this pre-commissioning still meaningful for the final setup of the machine. Goal of the campaign was to calibrate the response of solenoids and steerers in the LEBT layout, and study the dependence of beam transport conditions and final parameters on the source settings (extraction voltage, RF power and gas pressure). The output beam was characterised via beam current and emittance measurements taken with the aid of a Faraday cup and a slit-and-grid device respectively at three distinct locations along the LEBT: at the source exit, between the two solenoids and downstream of the RFQ matching plane (see Figure 1).

Source Exit

Figure 2 shows the measured total beam current at the exit of the source when varying the RF power at a constant pulsed hydrogen gas flux. The beam consists of protons (about 70% of the total), as well as H2+ and H3+ ions (15% each), overlapped at this point, and which will

Copyright © 2012 by the respective authors — cc Creative Commons Attribution 3.0 (CC BY 3.0)

only later become separated in the transverse phase space. A representative beam distribution in the x-x' plane is shown in Figure 3, for the case of 40 kW applied RF power to the source: emittance was reconstructed by applying a 0.1% threshold of the maximum signal on the profile monitor. Near symmetry exists between the x and y plane (not shown here). The beam turned out to be considerably more divergent than expected on the basis of some extrapolations, with direct consequence on the transmission through the LEBT.

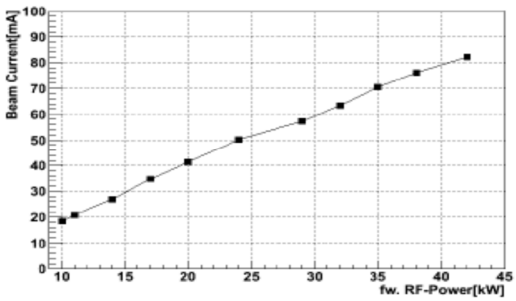

Figure 2: Measured beam current vs source RF power

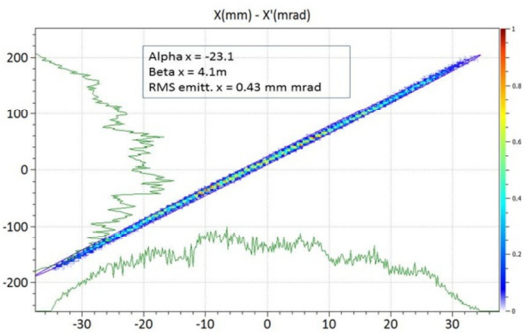

Figure 3: Beam emittance after the source at 40kW RF power.

LEBT

Several measurements at the source output were superimposed to produce a representative beam input distribution to be used in tracking simulation studies. Phase space measurements were used to calibrate the solenoid field maps generated with the code SUPERFISH/POISSON [4] and the response of the steerers. The LEBT transmission is mostly determined by the settings of the first solenoid: Figure 4 (left) shows measurements (red dots) taken at the exit of the LEBT while scanning the current fed to the first solenoid. Agreement with simulated values (superimposed) is very good. Maximum transmission of 60% is achieved for a 600 A setting. Figure 5 shows beam dynamics envelopes resulting from simulations with the reconstructed beam as measured at the source exit (red and blue lines) compared to the case of lossless transport for a uniform particle distribution input (green line). The aperture of the first solenoid is the main bottleneck for transmission, with 40% of the beam lost.

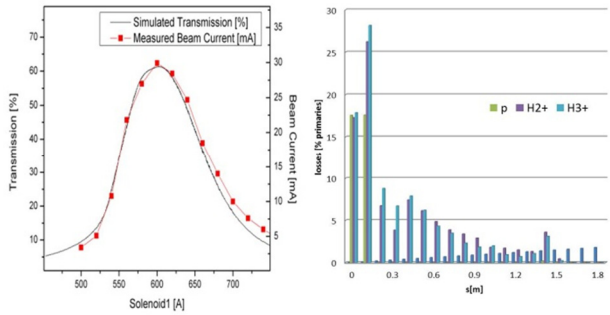

Figure 4: Beam transmission through the LEBT.

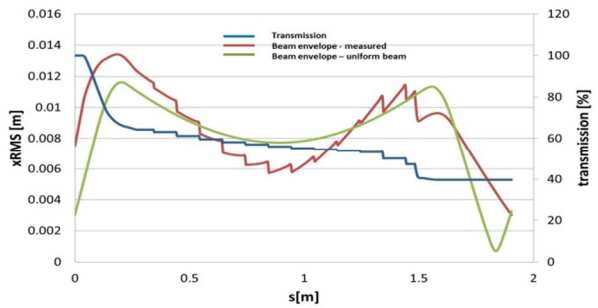

Figure 5: Beam envelopes and transmission for 685A-350A solenoid currents.

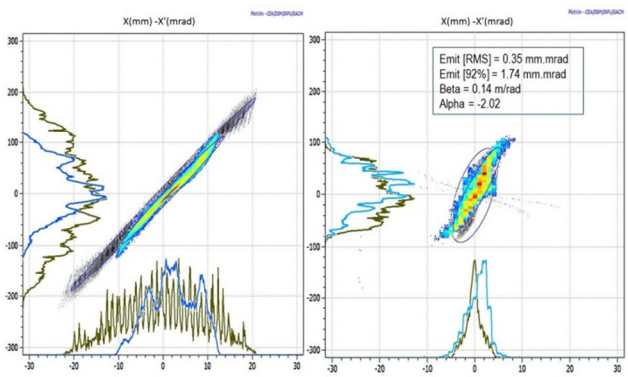

Figure 6: LEBT acceptance and output (600A-330A solenoid currents).

Figure 4 (right) shows a histogram of losses for the three distinct particle species: H2+ and H3+ losses are more evenly spread out along the LEBT structure, whereas all proton losses are concentrated at the first solenoid. Figure 6 (left) shows a comparison between the beam phase space measured after the source (in the background in grey) and the LEBT acceptance for the maximum transmission solenoid settings of 600 A and 330 A (as results from backtracking the LEBT output beam to the source measurement plane, in the foreground in colour). Only particles with a divergence within 100 mrad are transmitted through the structure. The right hand side shows the beam measured at the LEBT output for these configuration settings, in the foreground in colour, overlapped with the output beam distribution (in grey in the background) resulting from tracking the beam

Copyright © 2012 by the respective authors — cc Creative Commons Attribution 3.0 (CC BY 3.0)

measured at the source exit through the LEBT structure with the PATH code. Again, a very good agreement between measurements and simulations is obtained.

RFQ Matching Plane and Acceptance

The second solenoid allows flexibility in finding best matching conditions to the RFQ.

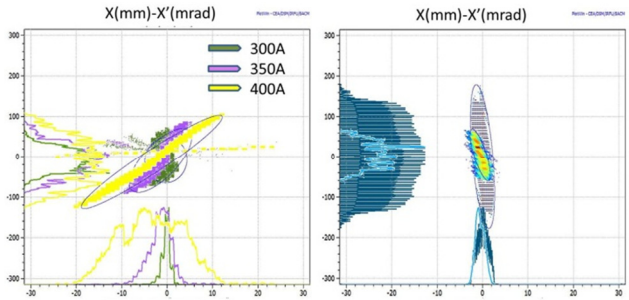

Figure :7 Phase space plots of the LEBT output beams (left) and RFQ acceptance (right).

Figure 7 on the left shows the measured beam phase space distributions at the LEBT output when varying the current settings on the second solenoid (300 A, 350 A and 400 A respectively) while keeping the first solenoid current fixed at 665 A. Figure 7 on the right illustrates a good matching case to the RFQ. Shown in grey in the background is the zero current acceptance of the RFQ in the x-x' plane, as obtained from Parmteqm [5] simulations; overlapped in colour is a beam distribution measured at the profile monitor at the LEBT output and backtracked by 83 mm to the point corresponding to the RFQ input plane. The settings used in this configuration are 685 A and 350 A for the first and second solenoid respectively. Assuming that measured offsets can be re-absorbed through some steering, the beam can be tracked to the end of the RFQ with >95% transmission (see Figure 8).

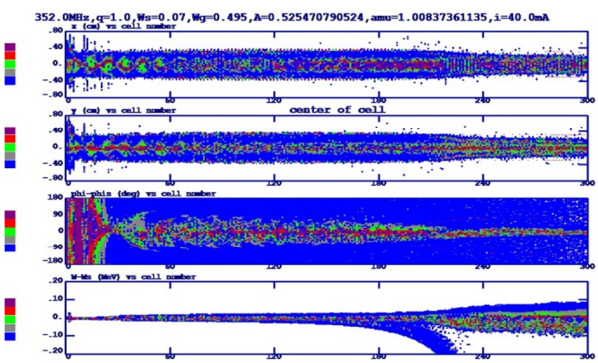

Figure 8 Transport through the RFQ: beam profiles in x, y, $\phi - \phi_s$, and $W - W_s$ vs cell number.

For different settings (non-optimised matching), RFQ transmission can drop to 60-70%, as indicated in Table 1, where simulation results for different LEBT configurations are shown. That matching to the RFQ is a critical point of the beam dynamics in Linac4 is otherwise illustrated in Figure 9, which shows the results of zero space charge acceptance studies, whereby a very large input beam distribution is tracked through each single structure at one time in a nominal machine setup. The plot shows that the RFQ and MEBT chopper line present the most stringent limitations in both transverse planes.

Table 1: Transmission Results for Different Solenoid Settings

Solenoid settings		Beam current [mA]		Transm.
Sol1	Sol2	LEBT	RFQ	RFQ
600	330	31	22.3	72%
600	350	31	19.2	62%
620	340	30	18.5	62%
640	350	26	22.1	85%
665	350	17	15.2	89%
685	350	14	13.3	95%

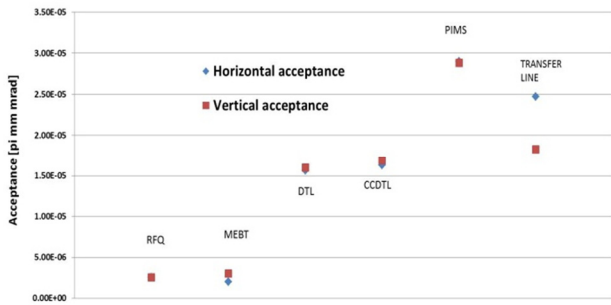

Figure 9 : Linac4 structures zero space charge acceptance (π mm mrad).

CONCLUSIONS

The 2011 pre-commissioning campaign at the Linac4 test stand has provided a means of detailed investigation of the LEBT optics using proton beam transport through prototype versions of the source and LEBT. Characterisation of the beam at the source output was made to cross-check measurements against simulation, as well as test beam diagnostics performance and software acquisition tools. Results were overall very satisfactory and a maximum proton beam current of 30 mA was successfully transported to the RFQ matching plane.

REFERENCES

[1] L. Arnaudon, et al. Linac4 technical design report. Technical Report CERN-AB-2006-084, CERN (2006).
[2] J B Lallement, A. M Lombardi, CERN-sLHC-Project-Note-0017 (2010.)
[3] A.Perrin,J.F.Amand,Travelv4.06user manual, CERN(2003)
[4] J Billen and L. Young, "SUPERFISH/POISSON Manual", LA-UR-96-1834.
[5] J Billen, "RFQ design codes", LA-UR-96-1836.

Copyright © 2012 by the respective authors — cc Creative Commons Attribution 3.0 (CC BY 3.0)

HIGH RESOLUTION EMITTANCE MEASUREMENTS AT SNS FRONT END

A. Zhukov, A. Aleksandrov, ORNL, Oak Ridge, TN 37831, USA

Abstract

The Spallation Neutron Source (SNS) linac accelerates an H- beam from 2.5MeV up to 1GeV. Recently the emittance scanner in the MEBT (2.5 MeV) was upgraded. In addition to the slit - harp measurement, we now can use a slit installed on the same actuator as the harp. In combination with a faraday cup located downstream in DTL part of the linac, it represents a classical slit-slit emittance measurement device. While a slit – slit scan takes much longer, it is immune to harp related problems such as wire cross talk, and thus looks promising for accurate halo measurements. Time resolution of the new device seems to be sufficient to estimate the amount of beam in the chopper gap (the scanner is downstream of the chopper), and probably to measure its emittance. This paper describes the initial measurements with the new device and some model validation data.

BEAM TIME STRUCTURE

The SNS runs a pulsed H- beam at 60Hz. The pulse can be up to 1 mS long. It consists of a train of mini-pulses having a 945 nS period. The LEBT chopper creates such a train by periodically kicking the beam into a target to create gaps between the mini-pulses. In addition, the MEBT chopper cleans up the gap further downstream. The LEBT chopper cyclically kicks the beam in four different directions, effectively creating periodicity with a period of 4 mini-pulses. This can cause variation of emittance along the beam pulse due to mini-pulse on/off transients, improper MEBT chopper and other causes.

EMITTANCE SCANNER

The emittance scanner is a classical slit-harp device [1]. It was recently upgraded to have additional capabilities of a slit-slit scan. The harp actuator also holds a plate with a slit in it. A faraday cup located in the DTL part of accelerator is used as a collector for slit-slit scans. Table 1 shows the most important properties of the beam and emittance device.

Table 1: Scanner and Beam Parameters

Parameter	Value
Ion Energy (H^-)	2.5 MeV
$\beta = v/c$	0.073
Slit – harp distance	353 mm
Signal wires	16
Distance between wires	1 mm
HV Bias	+300 V
Macro pulse length	~ 40 uS when using scanner
Beam current	~ 30 mA
Slit	0.1 mm carbon
Wire	0.1 mm tungsten
Second slit	0.15 mm
Harp Faraday Cup distance	24.45 m

Raw Signals

In order to measure signals from harp wires we use a custom-made transimpedance amplifier with 16 independent channels. A raw signal, digitized by a GE ICS-645 (5MS/s 16 bits) ADC, is shown on figure one.

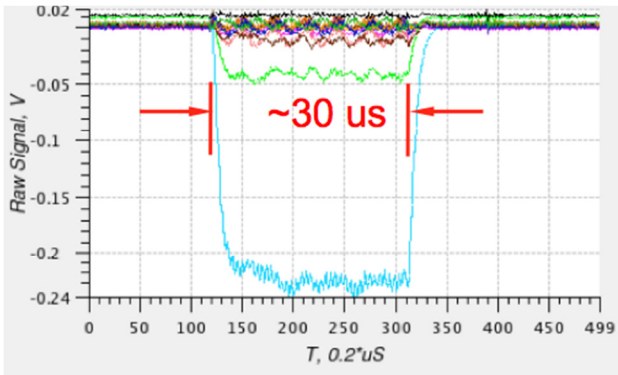

Figure 1: Raw signal from harp wires.

The time resolution of the harp signals is ~1us, and is a fundamentally limited by the current harp's design that introduces different coupling mechanisms [1].

The signal from a faraday cup is amplified by the commercially available SR445 wide-bandwidth amplifier and sampled with a 200MS/s 12 bit NI-5124 digitizer.

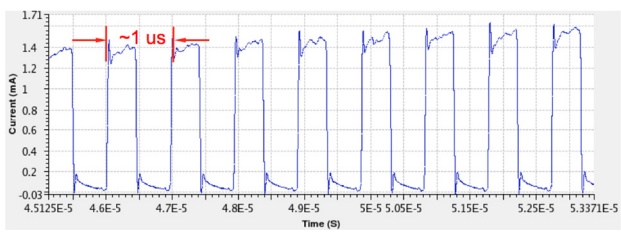

Figure 2: Raw signal from Faraday Cup.

The time resolution of the FC signal is at least 10 times better than from the harp. It clearly resolves the mini-pulse structure of SNS beam.

HIGH TIME RESOLUTION

In order to investigate the emittance variations along the beam pulse, we performed a slit-slit emittance scan and calculated emittance at different locations along the

Copyright © 2012 by the respective authors — cc Creative Commons Attribution 3.0 (CC BY 3.0)

pulse. The dependence of emittance on mini-pulse number is shown in Fig.3 [2]. Blue bars represent emittance calculated around the mini-pulse's rising edge (chopper switching) and the red ones show emittance calculated in the middle, "flat", part of a mini-pulse.

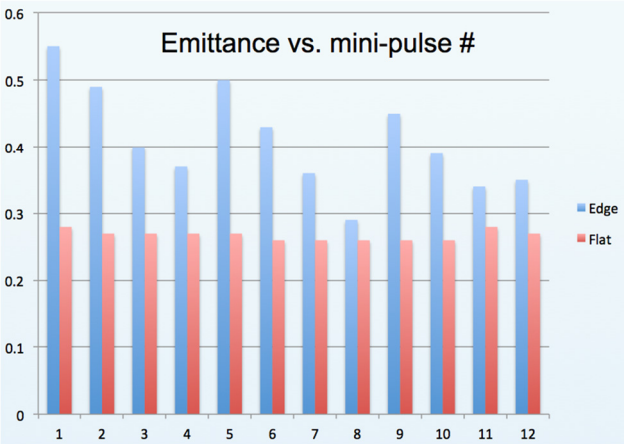

Figure 3: Emittance variation along beam pulse

It is clear that emittance calculated at the rising edge has the 4 mini-pulse periodicity.

BACKGROUND NOISE AND ARTIFACTS

Any emittance measurement contains some noise artifacts caused by electronic noise, wire coupling (in the case of harp measurements), electron coupling [1] and slit scattering. A common technique to mitigate this is the introduction of a threshold value with which signals that are lower than it are neglected. The emittance value depends on the threshold. Practically, it can be hard to select such a threshold value on a per measurement basis and consistently compare different measurements.

Figures 4-5 show a typical slit-slit scan and emittance dependence on the threshold value.

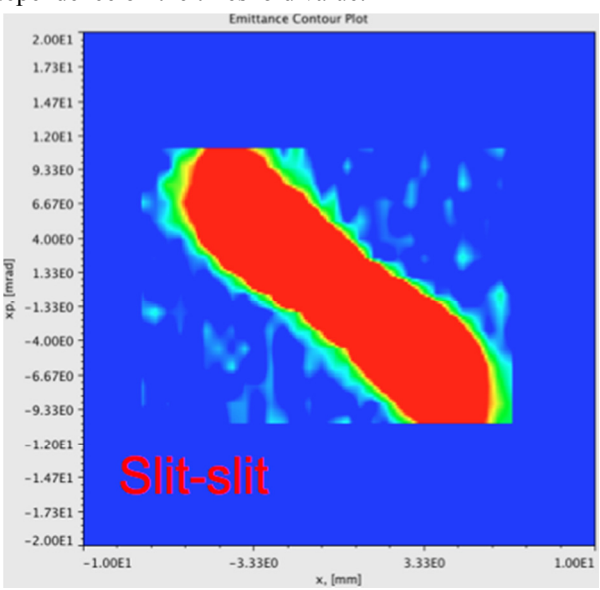

Figure 4: Horizontal emittance obtained with slit-slit scan.

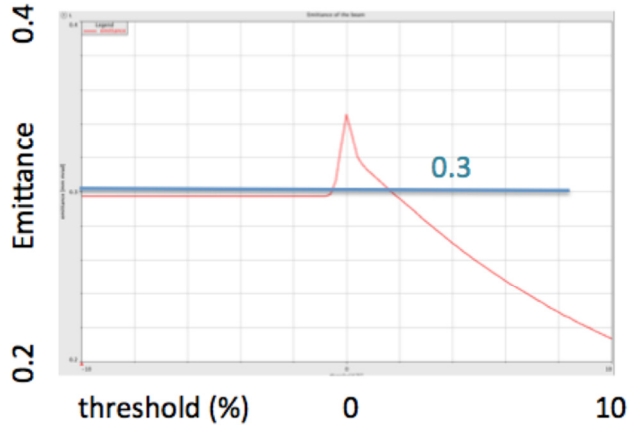

Figure 5: Emittance dependence on threshold value for slit-slit scan at Fig. 4.

The same beam was measured with slit-harp and corresponding plots are shown in Fig. 6-7. The shape of the emittance vs. threshold curve significantly differs for different types of measurements. In the case of a slit-harp measurement, there is a definite turning point where the slope of the curve changes. This change corresponds to the threshold value below which all artifacts (like the vertical stripe in Fig. 6) are neglected and only real beam is integrated. In contrast, the slit-slit scan doesn't show any artifacts, and the curve smoothly decreases while the threshold is increased.

Thus, in case of slit-slit scan, one can set the threshold to a small negative number (to account for negative noise signal being averaged with the positive noise signal). In the case of a slit-harp measurement, more analysis is needed, and it's hard to automate the process of comparing emittance values for different beam conditions.

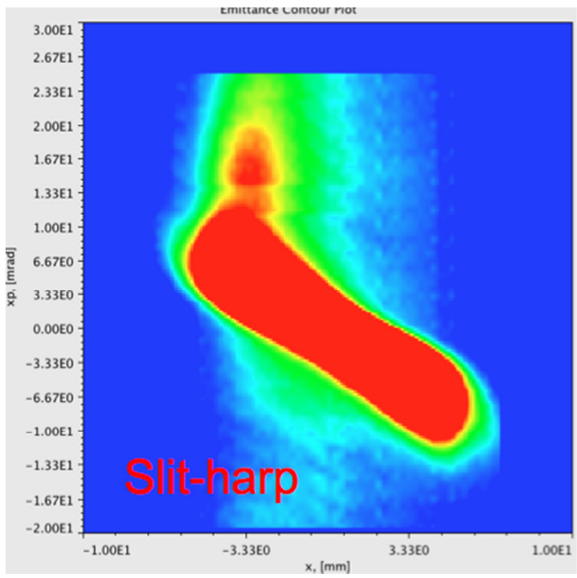

Figure 6: Horizontal emittance obtained with harp-slit scan.

Copyright © 2012 by the respective authors — cc Creative Commons Attribution 3.0 (CC BY 3.0)

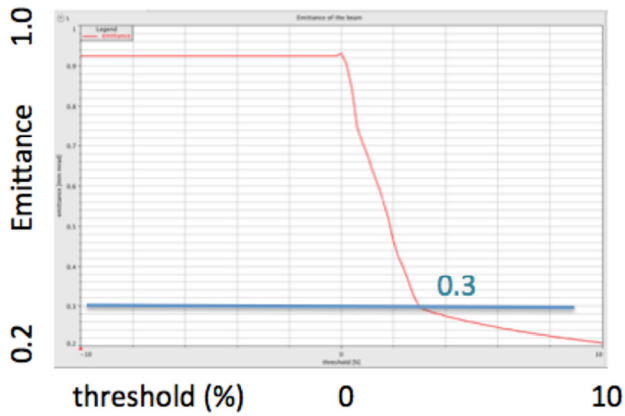

Figure 7: Emittance dependence on threshold value for slit-harp scan at Fig. 6.

WIRE IMPRINT IN PHASE SPACE

To perform a sanity check of the emittance device we inserted an upstream wire scanner into the beam. The particles intercepted by the wire form a vertical straight line in XX' space at wire scanner location. If we neglect non-linear effects, the beam line optics should transform it into a line at a different angle in the emittance slit location.

Figures 8 and 9 clearly present the wire shadow for two different wire positions.

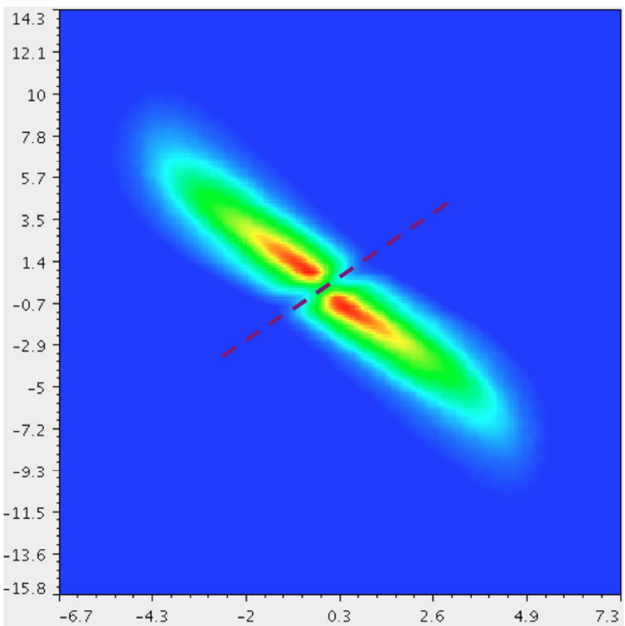

Figure 8: Emittance showing an upstream wire parked in the center of the beam.

SLIT VS. HARP COMPARISON

The MEBT emittance scanner now has two modes of operations: slit-slit and slit-harp. The slit-slit method provide fine time resolution (20nS) and has much better signal to noise ratio

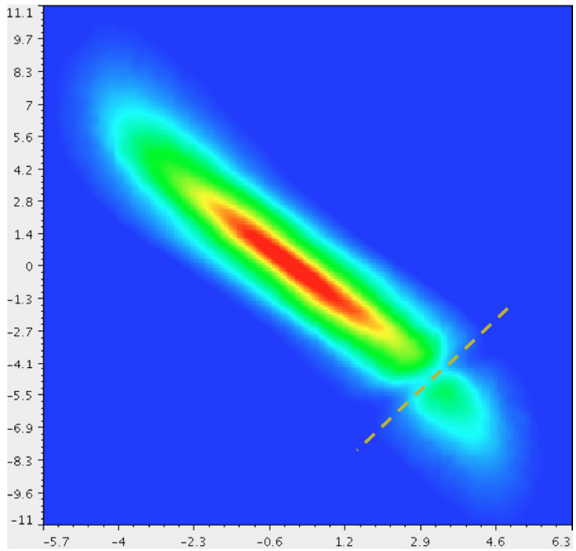

Figure 9: Emittance showing an upstream wire parked in the outer part of the beam.

The harp-harp scans can be used for fast scans when the core parameters are of main interest.

Table 2: Slit vs. Harp

Slit-Slit	Slit Harp
Time resolution ~20nS	Time resolution ~1uS
Dynamic range at least 10^4	Dynamic range ~ 10^3
One channel	16 channels (hard to calibrate)
No HV needed	Absolute values depend on HV
Cleaner scans	Artifacts and cross talk
Possibility to set threshold as a global absolute value	Threshold adjustment needed (hard to automate)
FC or loss monitor can be used as signal source	Only direct wire signal
Scan speed 30 minutes	Scan speed 4 minutes

ACKNOWLEDGMENT

ORNL/SNS is managed by UT-Battelle, LLC, for the U.S. Department of Energy under contract DE-AC05-00OR22725.

REFERENCES

[1] A. Zhukov et al, "Transverse Emittance Measurements in MEBT at SNS", proceedings of LINAC2010, TUP089

[2] A. Aleksandrov et al, "Diagnostic Tools for Beam Halo Investigation at SNS Linac", THPB013, these proceedings.

Copyright © 2012 by the respective authors — cc Creative Commons Attribution 3.0 (CC BY 3.0)

DIAGNOSTIC TOOLS FOR BEAM HALO INVESTIGATION IN SNS LINAC

A. Aleksandrov, W. Blokland, Y. Liu, C. Long, A. Zhukov.
Oak Ridge National Laboratory, Oak Ridge, TN 37830 USA

Abstract

Uncontrolled beam loss is a major concern in the operation of a high intensity hadron linac. A low density cloud of particles with large oscillation amplitudes, so called halo, can form around the dense regular beam core. This halo can be a direct or indirect cause of beam loss. There is experimental evidence of halo growing in the SNS linac and limiting the further reduction of beam loss. A set of tools is being developed for detecting of the halo and investigating its origin and dynamics. The set includes high resolution emittance measurements in the injector, laser based emittance measurements at 1 GeV, and high resolution profile measurements along the linac. We will present our experience with useful measurement techniques and data analysis algorithms.

INTRODUCTION

The SNS linac is operating routinely at beam power of about 1 MW with typical levels of uncontrolled beam loss within the design limit of 1W/m. This small level of beam loss, while considered to be acceptable, still creates significant activation of the beam line equipment, which affects the lifetime and complicates maintenance. Moreover, the SNS power upgrade plan requires a 50% increase in beam intensity while keeping uncontrolled beam loss at the present level. The major area of beam loss reduction efforts at SNS is the Super Conducting Linac (SCL). The SCL has large transverse aperture, therefore it was expected to be essentially lossless. Nonetheless, a significant beam loss was observed during commissioning and initial operation. It was discovered later that an intra-beam stripping is the main mechanism of the observed losses [1].

Intra-beam stripping losses are proportional to charge density in the bunch and, therefore, are inversely proportional to the bunch size. Increasing the bunch size is the easiest way to reduce the losses caused by the intra-beam stripping. On the other hand, the direct losses on the vacuum pipe aperture increase proportionally to the bunch size. There is an optimal beam size that can be easily calculated for a Gaussian bunch distribution. Unfortunately, as our measurements show, the bunch distribution in the SCL is not Gaussian. It consists of a dense Gaussian-like core and a less dense cloud surrounding the core. We call this cloud a "halo" without giving it a formal definition. Our goal is to reduce the number of particles in the halo or extension of the halo to allow further increase of the bunch core size.

The halo can be created at several places along the SNS linac: In the process of forming the bunches in the injector, at the transitions between the linac sections due to mismatch, and in the linac due to non-linear RF and space charge forces. Therefore, ideally, we need several measurement points to study the halo creation and propagation: at the exit of the injector, at the exit of the linac, and at as many points inside the linac as practical.

If, at this point of our study we do not understand the halo well and we do not define it quantitatively, then how do we measure it? We will use the "I know it when I see it" approach until we have sufficient understanding for developing a more sophisticated quantitative measure. In our experience, a 2-d emittance plot is a good halo visualization tool. An example of a comparison between measured emittance at 2.5MeV and at 1 GeV is shown in Fig.1. An ellipse drawn on the upper plot encloses 99% of the beam; an ellipse on the bottom plot has the same normalized area (area divided by $\beta\cdot\gamma$). If the normalized emittance was conserved than the ellipse on the bottom plot would enclose 99% of the beam as well. One can clearly see that in this case there is a significant amount of beam outside of the ellipse, which looks like a low density cloud. In other words, there is a halo at 1GeV, which was not present at 2.5MeV.

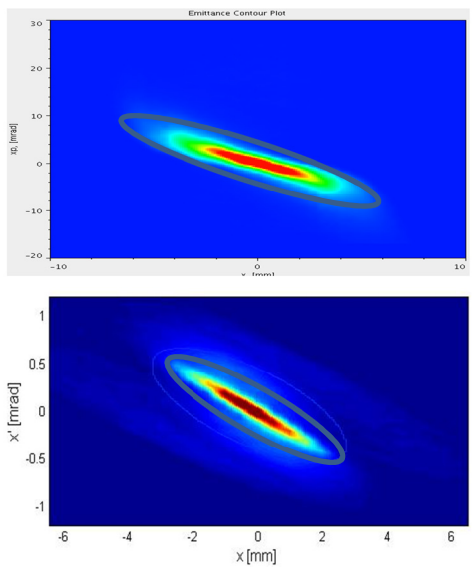

Figure 1: A comparison of two emittance measurements: one is measured at 2.5MeV (top) and the other at 1GeV (bottom). The ellipses superimposed on the images have same area in normalized coordinates.

In the next sections we will describe the tools we have or are developing to obtain the 2-d emittance plots along the SNS linac.

Copyright © 2012 by the respective authors — cc Creative Commons Attribution 3.0 (CC BY 3.0)

HALO MEASUREMENT TOOLS

The Requirements

Dynamic range and time resolution are the two major requirements for halo measurements. We do not define the halo in terms of charge density but the ultimate goal is to be able to reveal details on the level of 10^{-6}, corresponding to 1 W/m losses at 1 GeV. In the near term we set a more realistic goal of 10^4 dynamic range, which should be sufficient for studying the halo origin and behavior.

Beam in the SNS linac has a complicated time structure imposed by a fast chopper in the injector. Measurements with better than ~100ns resolution are required to study the halo variation with time. An example of the measured emittance difference between two parts of the mini-pulse, steady state and transient, is shown in Fig. 2.

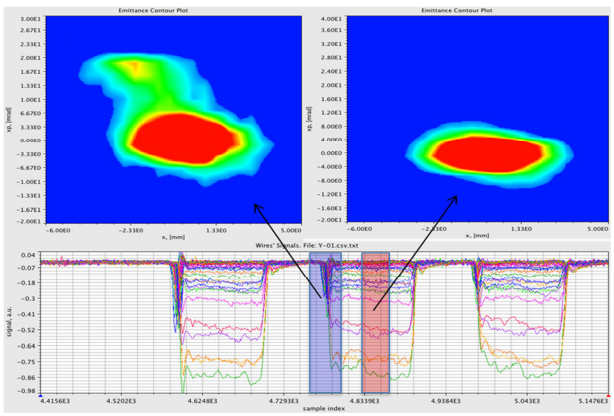

Figure 2: Emittance distortion during the chopper transient (left) revealed by a measurement with high time resolution.

Emittance Measurements in 2.5 MeV MEBT

The SNS MEBT has always had an in-line emittance measurement device of the slit-harp type [2]. Significant efforts have been applied to maximize the dynamic range and the resolution of the device. We believe that the best achieved parameters of ~1μs time resolution and ~ 10^3 dynamic ranges represent the fundamental limits of the design and cannot be further improved. Therefore a new system of the slit-slit type was developed. This device has demonstrated significantly improved time resolution of ~100ns and better than 10^3 dynamic range [2]. We believe with further improvements the time resolution can reach ~20ns the dynamic range can be higher than 10,000. These parameters allow a detailed characterization of the beam emittance in the injector, including halo.

Emittance Measurements in 1 GeV HEBT

Measuring the emittance of a hadron beam with energy in the GeV range is difficult. Fortunately, laser based diagnostics can be used in the case of H^- beam. We have developed a laser based system for direct measurement of 2-d emittance in the SNS HEBT at 1GeV [3]. An example of the measurement is shown on the bottom image of Fig.1. This system has an excellent 10ns time resolution. The dynamic range of ~100 requires improvement which is the focus of our current efforts.

Reconstruction of 2-D Emittance from 1-D Profiles

There are no tools for a direct measurement of the 2-d emittance in the SNS linac between the 2.5 MeV MEBT and the 1 GeV HEBT but there is a large number of 1-d transverse profile diagnostics: Conventional wire scanners in the normal conducting linac and laser wire scanners in the super conducting linac. We are developing tomographic reconstruction techniques for re-creating 2d emittances from multiple 1-d profile measurements. The MENT algorithm works well in the HEBT, where we have a sufficient number of diagnostics in the FODO transport line as shown in Fig. 3.

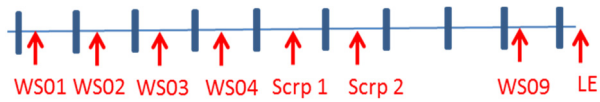

Figure 3: A layout of the HEBT lattice with diagnostics locations shown by arrows.

An example of a 2-d charge density distribution in phase space at the HEBT entrance created by the MENT algorithm is shown in Fig. 5. There is an excellent agreement between the transverse beam profiles measured by the four HEBT wire scanners (solid lines) and reconstructed by the MENT algorithm (dots) as illustrated in Fig. 4.

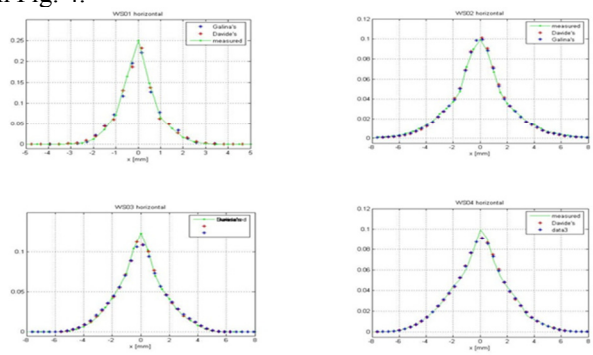

Figure 4: A comparison of transverse beam profiles measured by four HEBT wire scanners (solid lines) and reconstructed by the MENT algorithm (dots).

A comparison of a reconstructed emittance with a one measured with the laser emittance system reveals a significant difference in the distribution function shape, as illustrated by images in Fig. 6. It is interesting to note that RMS parameters of both distributions, given in the table below, are very close.

	Emittance [mm*mrad]	α	β [m]
Laser emittance	.42	2.49	15.9
MENT reconstruction	.41	2.47	13.4

Copyright © 2012 by the respective authors — cc Creative Commons Attribution 3.0 (CC BY 3.0)

Understanding of this difference is the subject of the current study.

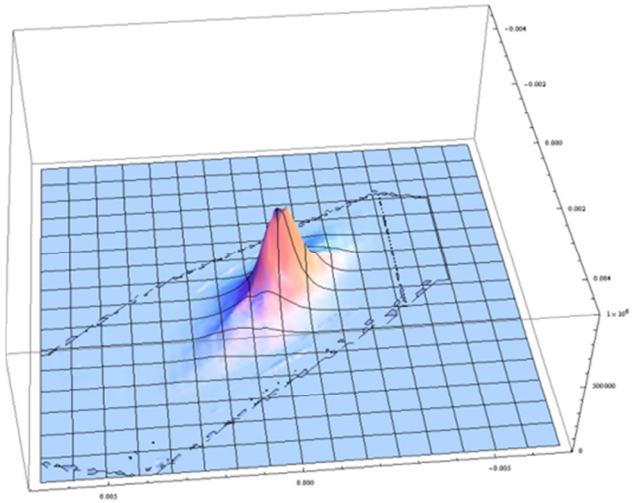

Figure 5: An example of 2-d charge distribution function reconstructed from four 1-d profiles using the MENT algorithm.

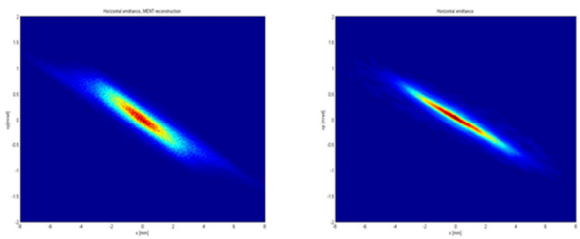

Figure 6: A comparison of charge distribution functions for the same beam: MENT reconstruction (left) and laser emittance measurement (right).

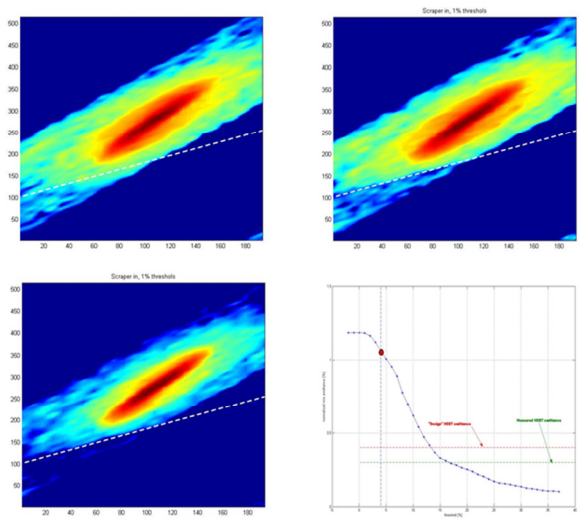

Figure 7: An example of the threshold determination for background subtraction in noisy emittance data using the upstream HEBT scraper (as explained in the text).

Use of Scrapers for Halo Study

We have several sets of scarpers in several locations along the SNS accelerator. The primary goal of the scrapers is to reduce the uncontrolled losses by intercepting stray particles (i.e. eliminating the halo). We found the scrapers to be useful for our halo study as well.

One example is finding the threshold for background subtraction in noisy emittance measurements. This is particularly important for the laser emittance measurements, which currently have a relatively large level of noise. The procedure is illustrated in Fig. 7, where top left image shows the emittance measured with an upstream scraper retracted, and the top right image shows the emittance measured with the scraper inserted. There is a shadow of the scraper clearly seen on the image. Also there is a background noise visible in the shadowed area. The threshold is increased until that background disappears as shown on the bottom left image. The bottom right plot in Fig. 7 shows a dependence of the emittance vs. the threshold, which is often used to find the proper threshold level. There are no distinct features on the curve near the correct threshold, and therefore this method is not reliable for identifying the proper threshold setting.

Another useful application is scraping the beam in the injector and observing propagation of the shadow along the linac. An example of such measurement using the wire scanners and the MENT reconstruction is shown in Fig. 8. The beam is scraped from one side in the MEBT as seen on the bottom left image. The measured distribution in the HEBT is shown on the right image. There is no a visible asymmetry or shadow. The distribution is completely homogenized during the process of acceleration.

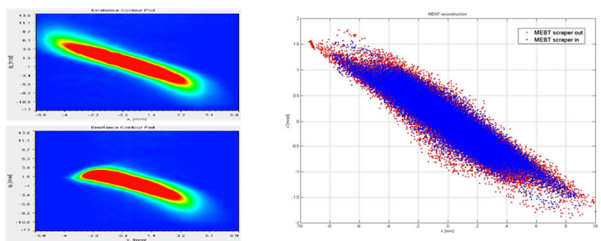

Figure 8: An example of measuring scraper shadow propagation along the linac. Explanation is in the text.

ACKNOWLEDGEMENTS

Authors are grateful to T. Gorlov for providing the MENT algorithm software and to A. Shishlo for help with the beam simulation and useful discussions.

ORNL/SNS is managed by UT-Battelle, LLC, for the U.S. Department of Energy under contract DE-AC05-00OR22725.

REFERENCES

[1] G. Galambos, et al, these proceedings.
[2] A. Zhukov, et.al, these proceedings.
[3] Y. Liu, et al., NIM A 675 (2012) 97–102.

Copyright © 2012 by the respective authors — cc Creative Commons Attribution 3.0 (CC BY 3.0)

LATTICE DESIGN AND BEAM DYNAMICS STUDIES FOR PROJECT-X*

J.-F. Ostiguy†, A. Saini, N. Solyak, J.-P. Carneiro, V. Lebedev
Fermilab, Batavia IL 60510, USA

Abstract

Project-X is a proposed proton accelerator complex at Fermilab to support a diversified experimental program at the intensity frontier. As currently envisioned, the complex would employ a CW superconducting linac to accelerate a 1 mA average, 5 mA peak H^- beam from 2.1 MeV to 3 GeV. A second superconducting linac –operating in pulsed mode– would ultimately accelerate a small fraction of this beam up to 8 GeV. The CW linac is based on five families of resonators operating at three frequencies: half-wave (1 family at 162.5 MHz), spoke (2 families at 325 MHz) and elliptical (2 families at 650 MHz). We discuss the latest iteration (v 6.0) of the CW linac baseline lattice.

INTRODUCTION

From 2.1 MeV up to 3 GeV, Project X employs SC linac technology operating in CW mode. The front-end MEBT incorporates a high bandwidth chopper with the ability to reject individual bunches. In conjunction with CW operation, this arrangement enables a variable and flexible bunch structure that can simultaneously accommodate a variety of experiments. The (multiplexed) beam structure can be quite complex; however, the average current over a time interval $T \sim \frac{Q_L}{2\omega_0}$ must remain 1 mA. While the overall concept is by now relatively mature, details are still evolving.

Some recent developments are worthy of mention. The first one is the decision to rely on 162.5 MHz half-wave resonator technology from Argonne National Laboratory to handle acceleration from 2.1 to 11 MeV. The considerations that led to this decision were many and include improved acceleration efficiency and longitudinal acceptance. It also allows the project to leverage ANL's expertise and infrastructure for fabrication. The second is the decision to build a test facility[1], dubbed PXIE (Project X Injector Experiment), to validate the concept of wide bandwidth chopping in the MEBT and to mitigate technical risks. PXIE comprises the ion source, LEBT and MEBT followed by one 162.5 MHz cryomodule (HWR) and one 325 MHz (SSR1) cryomodule. The intent is to maximally re-use the PXIE infrastructure for Project-X. In the interest of allowing PXIE to physically fit into existing available space and to minimize its cost – and eventually that of the Project-X CW linac itself – our recent lattice iterations strive to make maximum use of available cavity gradient even at the expense of some deviation from traditional design rules. Finally, it is becoming clear that in the current budgetary context the 3 GeV CW linac should be planned and build in stages. The existence of a compelling nuclear physics experimental program at 1 GeV makes this energy a logical choice for a first stage. Our most recent lattice iterations therefore assume 1 GeV as output energy. The default option for acceleration from 1 to 3 GeV would be to continue with cryomodules based on $\beta_g = 0.9$, 650 MHz cavities, as described in [3]. Recently, a number of other projects including NGLS at LBNL and X-FEL at DESY have been seriously looking into CW operation with 1.3 GHz ILC-style cavities. Given the larger size and overall cost of 650 MHz cavities, standardized CW 1.3 GHz technology and power sources from 1 to 3 GeV might prove a better and more cost-effective choice. We intend to study this option at a later time.

* Work performed under US DOE contract DE-AC02-76CH03000.
† ostiguy@fnal.gov, solyak@fnal.gov

LINAC LAYOUT

A high level block diagram of the latest linac layout (dubbed "v6.0"), starting for completeness, at the ion source, is shown in Fig. 1. Relevant details for each regular sections are summarized in Table 1. Overall transverse and longitudinal rms beam envelopes are shown in Fig. 2.

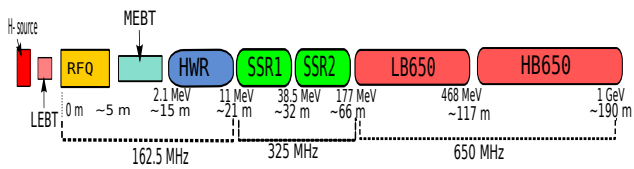

Figure 1: High Level Block Diagram for the (stage 1) 1 GeV CW Linac.

Table 1: Details of Linac Sections. Key: CM: cryomodule; D:doublet, S:solenoid, R:resonator, R^n: n-resonator sequence.

Section	f[MHz]	Cav/mag/CM	Period [m]	Cell
HWR	162.5	8/8/1	0.686	S-R
SSR1	325	16/8/2	1.250	R-S-R
SSR2	325	36/20/4	1.720	$S\text{-}R^2$
LB650	650	30/20/5	5.1	$D\text{-}R^3$
HB650	650	40/10/5	14.3	$D\text{-}R^8$

Ion source, LEBT, RFQ and MEBT

The ion source –which has been obtained from industry and tested– nominally supplies 5 mA of H^- at 30 keV continuously. It is followed by a LEBT section whose primary function is to match the beam into a RFQ operating at 162.5 MHz. Beam chopping is provided in the LEBT primarily to reduce beam power during machine commisioning and tuning. The 4.4 m RFQ, which is designed and ready for

Copyright © 2012 by the respective authors — cc Creative Commons Attribution 3.0 (CC BY 3.0)

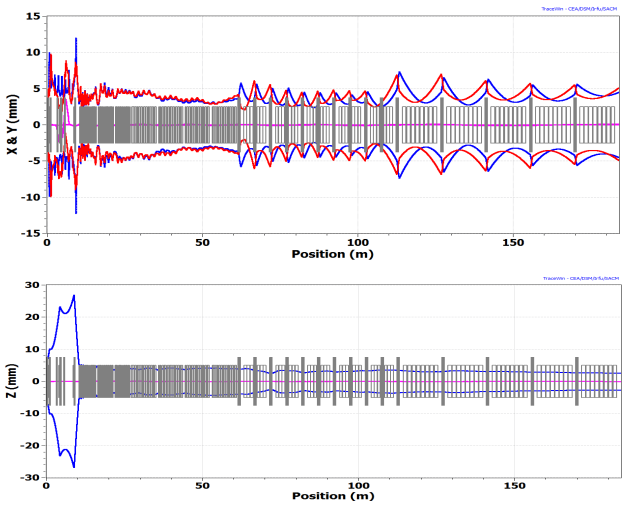

Figure 2: Beam Envelopes.

fabrication, accelerates the beam from 30 keV to 2.1 MeV in CW mode. Both the LEBT and RFQ are designed and constructed by LBNL, which is also responsible for the integration of the source. The output energy was selected to lie below the neutron production cross-section threshold in Cu. The beam transverse and longitudinal emittances at the RFQ output are expected to be 0.15 and 0.21 mm-mrad respectively, under nominal operating conditions. These values were obtained from simulations by tracking a distribution matching the *measured* beam parameters downstream of the ion source all the way to the RFQ output.

Details of the MEBT concept and operation have been presented elsewhere [2]. We only mention here two significant changes. The first is a decision to shorten and simplify the MEBT by using a two, rather than four, kicker configuration; with this configuration both the rejected and the transmitted beam are kicked. The second is to use 162.5 MHz rather than 325 MHz quarter wave bunchers. This results in a longitudinal acceptance better matched to that of the downstream 162.5 MHz HWR section; furthermore, although 162.5 MHz cavities are physically larger, they consume about half the power (< 2 vs 5 kW) of the 325 MHz versions.

HWR, SSR1 and SSR2 Sections

The HWR section comprises a single 6 m cryomodule and uses eight half-wave resonators to accelerate the beam from 2.1 to 11 MeV. The SSR1 sections comprises two cryomodules, each spanning four periods. The SSR2 sections consists of four cryomodules spanning four and a half periods each. Both sections are based on 325 MHz single-spoke cavities developed at Fermilab and employ solenoids for transverse focusing. The transitions upstream of SSR1 and downstream of SSR2 both involve two-fold frequency jumps; from a matching standpoint, the transition between SSR2 and LE650 is delicate since it also involves a change from solenoidal to quadrupole doublet focusing.

LB650 and HB650 Sections

Both the ("low beta") LB650 and the ("high beta") HB650 sections are based on 5-cell elliptical cavities operating at 650 MHz. The LB650 section uses $\beta_g = 0.6$ cavities to accelerate the beam from 177 to 468 MeV. An LB650 cryomodule spans two periods. While the first doublet is external and warm, the second is superconducting. In the HB650 section –based on $\beta_g = 0.9$ cavities – the beam ultimately reaches a final energy of 1 GeV; each HB650 cryomodule spans almost a single period (contains only cavities). Transverse focusing is handled by warm quadrupole doublets which provide natural locations for collimation and instrumentation. Matching from the upstream SSR2 into LE650 section is accomplished using independently powered magnets in the first doublet of the LE650 section. A notable change in this current v6.0 iteration with respect to the v5.3 iteration [3] is that the last two cryomodules of the LB650 sections ($\beta_g = 0.6$) have been replaced with a single ($\beta_g = 0.9$) HB650 cryomodule, resulting in a reduction by four in cavity count and by one in cryomodules. While the transit time factor is now a bit less favorable in the first HB650 cryomodule, the loss in acceleration was easily compensated by slightly raising the field in the downstream cavities.

BEAM DYNAMICS

Theoretically, in the presence of space charge, envelope oscillations are unconditionally stable only when the structural phase advances $\sigma_{\ell 0}, \sigma_{t0} < 90°$. In addition, to inhibit single particle synchro-betatron parametric resonances, one usually chooses $\sigma_\ell < \sigma_t$. Since longitudinal focusing is proportional to field amplitude, a limit on structural phase advance effectively sets a limit on achievable acceleration. In high peak current machines, $\sigma_{\ell 0}$ is generally conservatively kept below 90° even though the permissible advance is actually higher at low tune depression. Our modest peak current of 5 mA ($\frac{\sigma}{\sigma_0} \simeq 0.75$) provides some headroom to increase $\sigma_{\ell 0}$ beyond 90°/period in the HWR and SSR1 sections. Accordingly, the longitudinal structural phase advance per period starts around 100°. To get stable transverse envelopes and to avoid exceeding a practical field limit for the solenoids ($\sim$ 6 T), the corresponding transverse structural advances cannot initially be higher than the longitudinal. While having $\sigma_t < \sigma_\ell$ may excite 2nd order synchro-betatron resonances, the later are weak.

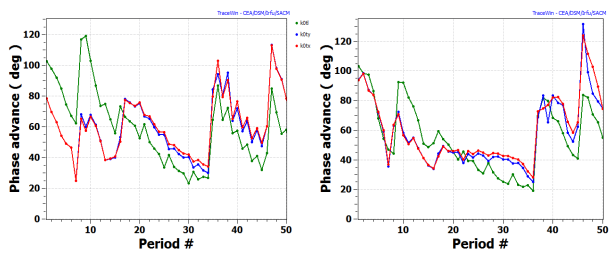

Figure 3: Structural phase advances along the CW linac.

Copyright © 2012 by the respective authors — cc Creative Commons Attribution 3.0 (CC BY 3.0)

Plots of the structural phase advances per period, for both the v5.3 (left-hand side) and current v6.0 (right hand side) lattice iterations are shown in Fig. 3. Using the cavity synchronous phase settings as an estimate of bucket half-width (i.e. longitudinal "aperture"), the latter is greater than $8\sigma_\phi$ in v6.0. This is an improvement over v5.3. where this ratio was somewhat smaller. Both lattices exhibit a "cross-over" point where the transverse phase advance becomes greater than its longitudinal counterpart. For the v5.3 lattice, the cross-over occurs at period no 16 (the entrance of the SSR2 section); in v6.0 it occurs later at period no 20, translating into a reduction in longitudinal phase advance in both the SSR1 and SSR2 sections. One of the objectives in v6.0 was to eliminate the emittance exchange observed in v5.3 and apparent in Fig. 4 which compares rms emittance growth in both lattices with v5.3 on the left-hand side. Fig. 5 compares Hofmann diagrams for v5.3 (left-hand side) and the current v6.0 (right-hand side) lattices. Note that while the v5.3 lattice had a few periods in high exchange rate regions, v6.0 has none. Furthermore, as seen on the right hand side of Fig. 4, emittance exchange has disappeared in v6.0. While emittance exchange is not always problematic, it does result in an increase in transverse beam size; avoiding it is preferable.

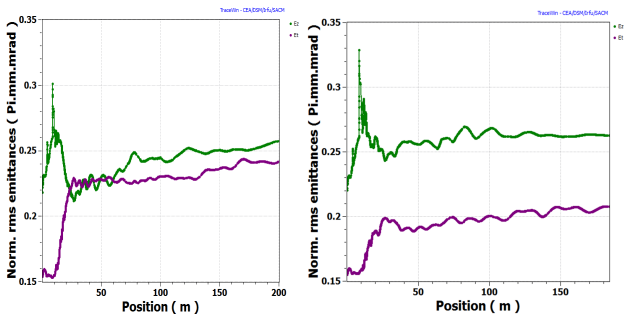

Figure 4: RMS emittances along the CW linac.

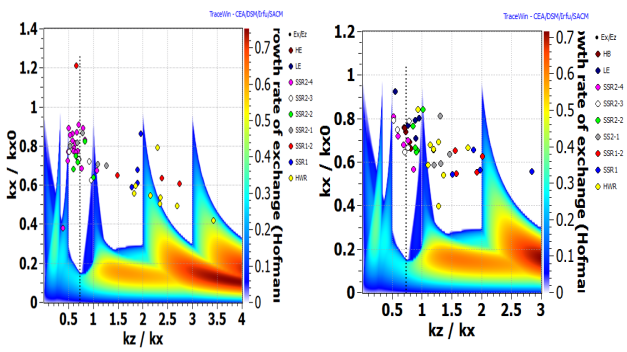

Figure 5: Hofmann Diagrams.

STATISTICAL ERROR ANALYSIS

Using the code TRACK from ANL, statistical errors studies were performed on the the FermiGrid computers. For each type of error(s) –individually and in combination– statistics from a total of 400 linacs were compiled, except for longitudinal errors where the number of linacs considered reached 5000. With a low energy beam directly injected into high gradient superconducting cavities, tolerances on dynamic rf phase and amplitude errors are expected to be an issue. No loss is observed at 0.5 deg, 0.5%; however at 1 deg, 1% 20 out of 5000 seeds cause beam losses in excess of a few W/m; in a few of those instances a significant fraction of the beam is lost. While dynamic phase and amplitude control is expected to be significantly better than 1 deg, 1%, these results suggests a possible resonant excitation. One issue is that the ratio of the longitudinal and transverse phase advance per period in the HWR section is probably too close to 1. Additional tuning will be performed in future iterations based on analysis of the problematic seeds. Preliminary runs performed to study focusing errors indicate that losses begin to appear when errors reach the 1 % level. Quadrupole misalignments have not been studied but the tolerances are expected to be similar to those of the solenoids.

Table 2: Losses due to Errors. Average over 400 Linacs

Element	Err. Type	Value	Avg. Loss (%)
Sol	δ_{xy}	$100\,\mu m$	0
Sol	δ_{xy}	$200\,\mu m$	0
Sol	δ_{xy}	$300\,\mu m$	3×10^{-3}
Sol	δ_{xy}	$400\,\mu m$	1.6×10^{-1}
Sol	δ_{xy}	$500\,\mu m$	5.7×10^{-1}
Cav	$\delta_\phi + \delta_E$	$0.5^\circ + 0.5\%$	0
Cav	$\delta_\phi + \delta_E$	$0.5^\circ + 1.0\%$	1.8×10^{-2}
Cav	$\delta_\phi + \delta_E$	$0.5^\circ + 1.5\%$	1.15
Cav	$\delta_\phi + \delta_E$	$0.5^\circ + 2.0\%$	6.25
Cav	$\delta_\phi + \delta_E$	$2.5^\circ + 2.5\%$	15.5

CONCLUSION

The Project-X CW linac lattice has been re-optimized to avoid emittance exchange, improve longitudinal aperture and reduce longitudinal phase advance. The latest lattice assumes a final energy of 1 GeV. The cryomodule count has been reduced by one by replacing the last two LB650 cryomodules with a single HB650 cryomodule. For a second phase, (1-3 GeV), the default plan is to use HB650 cryomodules and cavities; however, recent developments indicate that CW technology at 1.3 GHz might be worth pursuing. This will be the subject of future studies.

REFERENCES

[1] V. Lebedev et al. , "PIXIE Optics and Layout", IPAC12, New Orleans, May 2012

[2] A. Shemyakin, "Design of MEBT for the Project X Injector Experiment at Fermilab".

[3] J.F. Ostiguy et al.,"Status of the Project-X CW Linac Lattice", New Orleans, May 2012

Copyright © 2012 by the respective authors — cc Creative Commons Attribution 3.0 (CC BY 3.0)

PERFORMANCE OF FERRITE VECTOR MODULATORS IN THE LLRF SYSTEM OF THE FERMILAB HINS 6-CAVITY TEST*

P. Varghese†, B. Chase, E. Cullerton, C. Tan, B. Barnes
Fermi National Accelerator Laboratory (FNAL), Batavia, IL 60510, USA

Abstract

The High Intensity Neutrino Source (HINS) 6-cavity test is a part of the Fermilab HINS Linac R&D program for a low energy, high intensity proton/H- linear accelerator. One of the objectives of the 6-cavity test is to demonstrate the use of high power RF Ferrite Vector Modulators(FVM) for independent control of multiple cavities driven by a single klystron. The beamline includes an RFQ and six cavities. The LLRF system provides a primary feedback loop around the RFQ and the distribution of the regulated klystron output is controlled by secondary learning feed-forward loops on the FVMs for each of the six cavities. The feed-forward loops provide pulse to pulse correction to the current waveform profiles of the FVM power supplies to compensate for beam-loading and other disturbances. The learning feed-forward loops are shown to successfully control the amplitude and phase settings for the cavities well within the 1% and 1° requirements specified for the system.

INTRODUCTION

The use of FVMs to regulate the phase and amplitude of individual cavities in a multi-cavity system driven by a single klystron helps to reduce the cost of the RF system for linear accelerators[1]. High power waveguide FVMs have been developed and the dynamic range of their phase shifting and amplitude attenuating capabilities have been studied[2]. Modeling and simulation of RF control systems with FVMs have shown their potential for field control of individual cavities in a multi-cavity system[3]. A learning feed-forward[LFF] control for the HINS six cavity test accelerator was integrated into the LLRF system. All RF components are driven by a single 325 MHz, 2.5MW pulsed klystron. The LFF algorithm is described and the results of its performance with beam are presented .

LLRF SYSTEM

The RF control block diagram for the 6-cavity test is shown in Fig.1. The LLRF control system regulates the phase and amplitude of the RF field vectors of the RFQ and the six room temperature copper cavities. There is a traditional wide-band proportional and integral feedback control loop around the klystron and the RFQ. Because the RFQ is a low Q device, it behaves much like a resistive load. Therefore, by regulating the RFQ field, the klystron output to the six cavities is effectively regulated as well. This RFQ control loop greatly reduces errors from klystron modulator voltage variations and from changing beam current. There are several disturbances to the six cavities that must be corrected by the FVM controllers. These are static amplitude and phase errors, drifts in cavity resonance frequency, differences in cavity Qs, and variations in cavity beam loading. Field errors in the cavities are corrected by an adaptive feed-forward system.

The primary feed-back loop is implemented as a PI controller in a FPGA with a sampling frequency of 56 MHz. The 325Mhz RF is downconverted to a 13 MHz IF which is sampled and downconverted to baseband. A 2.1 MSPS DAQ system acquires baseband I,Q signals for pulses upto 4ms wide. The data from all channels is uploaded to the slot0 controller between pulses and is available for processing in the CPU or for transmittal through an ethernet port to both the Fermilab ACNET control system and Labview user interfaces, for waveform display and parameter control.

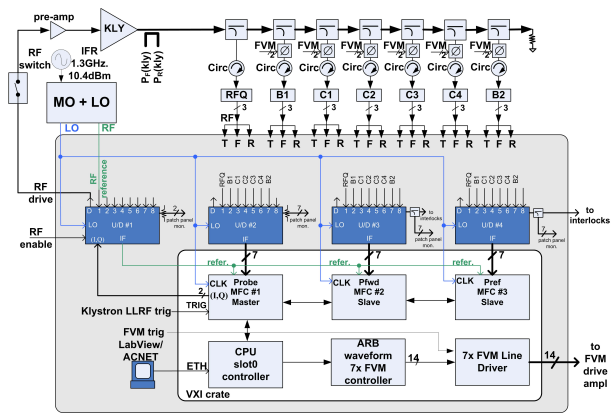

Figure 1: LLRF system configuration

LEARNING ALGORITHM

The learning feed-forward algorithm implementation for one cavity is shown in Fig.2. The wideband RFQ/klystron primary control loop is processed at the full 56 MHz sample rate of A/D converters, while the FVM control loops decimate the data to a 100 kHz rate, where it is processed and the feed-forward controller output is written to a VXI 16 channel arbitrary waveform generator module. Regulation waveforms are recalculated at the machine repetition rate of 0.5 Hz. Decimating the DAQ data by 21 brings the sample rate close to the 100 kHz sampling rate of the output DACs to the FVM. With 1024 points in the FVM waveform, the maximum width of the FVM profile is 10ms

* Work supported by Fermi Research Alliance LLC. Under DE-AC02-07CH11359 with U.S. DOE.
† varghese@fnal.gov

Copyright © 2012 by the respective authors — cc Creative Commons Attribution 3.0 (CC BY 3.0)

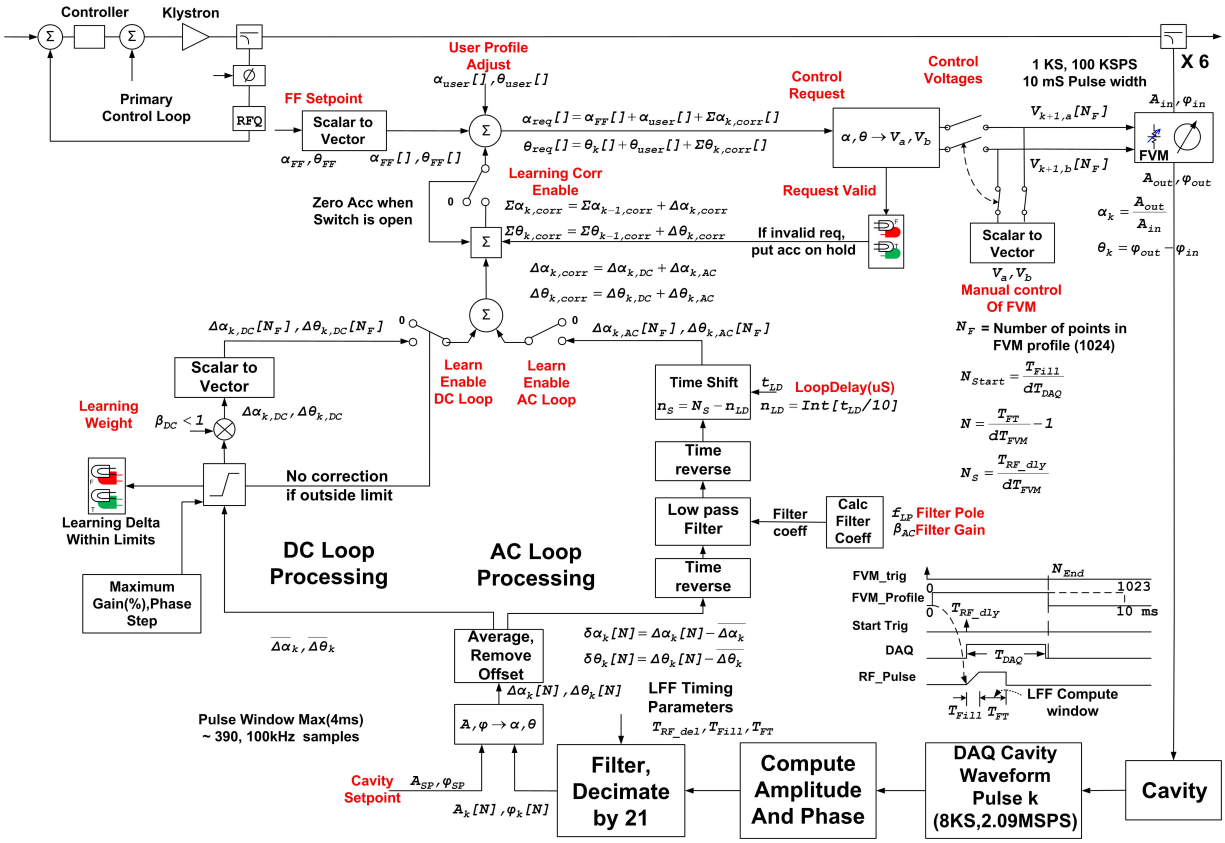

Figure 2: Learning Feedforward Algorithm

which allows for the 4ms RF pulse to be completely included within the FVM pulse. The FVM trigger starts the play-out of the waveform which is 2.5 ms before the start of the RF pulse. This allows the FVM to settle well before the arrival of the RF pulse and beam. The error in the cavity field amplitude and phase is transformed into a correction in the attenuation and phase shift parameter inputs to the FVM. The corrections are computed, based on zeroing the error in the next pulse. They can be computed exactly with an amplitude and phase computation of the cavity field read-back from the DAQ.

$$\Delta\alpha_k = \alpha_k \times (\frac{A_{SP}}{A_k} - 1) \quad (1)$$

$$\Delta\theta_k = \phi_{SP} - \phi_k \quad (2)$$

They can also be approximated with formulas based on the I,Q values by a linearization around the operating point as follows. With $I_e = I_{SP} - I_{cav}, Q_e = Q_{SP} - Q_{cav}$. the correction formulas are given by

$$\Delta\alpha_k = \alpha_k \times \frac{I_{cav}I_e + Q_{cav}Q_e}{I_{cav}^2 + Q_{cav}^2} \quad (3)$$

$$\Delta\theta_k = \frac{Q_eI_{cav} - I_eQ_{cav}}{I_{cav}^2 + Q_{cav}^2} \quad (4)$$

The approach taken in this design is to split the error into a DC component and an AC component with separate control loops. The DC loop is intended to correct offsets due to drift and parameter variations and the AC loop corrects for errors only in the flattop portion of the RF pulse to compensate for beam loading and other disturbances associated with the beam. The correction from the DC loop is an offset that is combined with the AC loop correction to add to the FVM output for the next pulse. A fault detection scheme detects large fluctuations in correction and places the learning on hold till the field recovers.

The transformation of the control request to the voltages to the FVM current coil power supplies is done using a lookup table and interpolation. Due to the highly nonlinear and restricted mapping from the α and θ domain to the Va , Vb domain, the operating point of the FVM needs to be chosen carefully to provide maximum headroom for the closed loop operation[2],[3]. There are large regions where there are no valid solutions which must be kept clear of. Motorized trombones allowed the tuning of the phase and waveguide distribution taps were adjusted to obtain the desired attenuation, to bring the FVM operating point to regions with the required dynamic range.

Treating the AC error as a disturbance input as shown in Fig.3 helps to understand the correction scheme. Since the FVM input profile for pulse k+1 is calculated based on the complete cavity field waveform acquired during pulse k, anti-causal time-reversal filters can be used for disturbance detection[4]. If the transfer function of the combined FVM

Copyright © 2012 by the respective authors — cc Creative Commons Attribution 3.0 (CC BY 3.0)

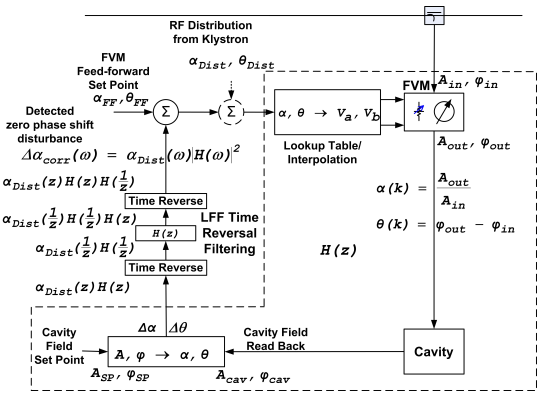

Figure 3: Time reversal filtering for FVM error detection

and the cavity system is represented by H(z), then passing the error through the anti-causal filtering shown in Fig.3, produces a zero phase shift, detected disturbance to which the appropriate gain and time advance (to account for the loop delay) can be added to cancel out the disturbance. The transfer function H(z) is modeled as a first order IIR filter whose pole and the loop delay parameter become the key tuning parameters to correct the disturbance input.

RESULTS

The learning feed-forward algorithm was tested under beam loading conditions. Fig.4 and Fig.5 show magnitude and phase plots for the cavity field with a 300 μS beam pulse with and without the LFF control. The convergence of the DC loop is determined mainly by the gain parameter. The AC loop needs to be tuned primarily with the filter pole and the loop delay parameter.

The regulation during beam was $< 0.2\%$ for amplitude and $< 0.21^\circ$ for phase. Cavity 1 shows only a partial suppression of the disturbance because its FVM request parameters overshot the valid region and the FVM inputs are held at the last valid value.

CONCLUSION

The application of a learning feed-forward loop for FVMs showed that they are capable of regulating cavity field and phase within specifications in applications with one klystron driving multiple cavities. Tuning the AC loop was critical to the stability of the system. It was shown that with a DC loop alone, it is not possible to accurately compensate for the beam-loading disturbances. The six cavity test was specified with a longer pulse width of 1ms. Due to technical issues with the RFQ, the RF pulse widths were limited to < 500 μS.

The feasibility of using FVMs in a single klystron multiple cavity application was demonstrated in the Hins 6-cavity test. The learning feed-forward loops around the FVMs provided independent control for cavities with differing characteristics and set-points.

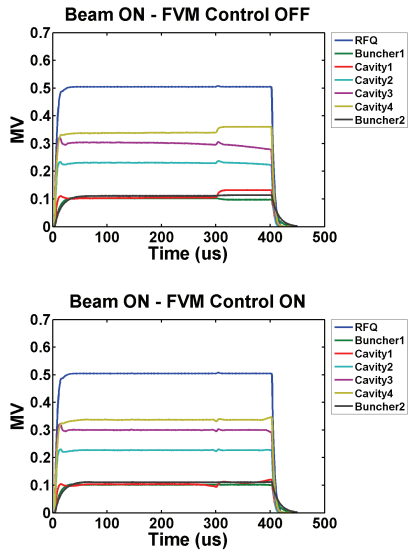

Figure 4: Cavity Magnitude with FVM LFF loops OFF/ON

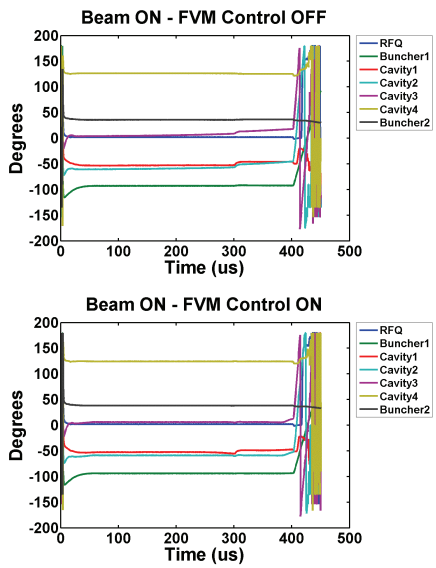

Figure 5: Cavity Phase with FVM LFF loops OFF/ON

REFERENCES

[1] J. Steimel et al.,"The Six-Cavity Test - Demonstrated Acceleration of Beam with Multiple RF Cavities and a single Klystron", IPAC'12, New Orleans, USA, June 2012, THPPP062.

[2] R.L.Madrak and D.Wildman, "High Power 325 MHz Vector Modulators for the Fermilab High Intensity Neutrino Source (HINS)", Linac'08, Victoria, B.C., Canada, September 2008, THP088.

[3] J.Branlard and B.Chase, "Modelling the LLRF control of a Multi-Cavity RF Station for Project-X", PAC'09, Albuquerque, NM, June 2009, WE3RAC05.

[4] A.Brandt,"Development of a Finite State Machine for the Automated Operation of the LLRF Control at FLASH", Doctoral Dissertation, University of Hamburg,2007.

Copyright © 2012 by the respective authors — cc Creative Commons Attribution 3.0 (CC BY 3.0)

CONCEPT: LOW ENERGY, LOW INTENSITY NF FROM PROJECT X*

Milorad Popovic#, FERMILAB, Batavia, IL 60510, USA

Abstract

This paper describes the concept of a Low Luminosity Low Energy Neutrino Factory (L^3ENF) using a Project X pulsed, or CW, Linac at 8GeV. By collecting π and μ with energy ~ 1 GeV, and accelerating them to 10 GeV, it is possible to store ~10^{20} μ per year. Most of the concepts suggested here can be tested using the Booster beam, Recycler, Antiproton Target Station, the Main Injector and the Tevatron. Once the VLENF Muon Storage Ring is built, components needed for L^3ENF could be used in experiments before Project X completion.

INTRODUCTION

The beam from the Project-X Linac [1] has a 162.5 MHz structure, and the accumulation ring is a multiple of this frequency so that the beam is transferred bunch to bucket in the ring. There will be a gap of ~10 buckets, 61ns long, in the linac beam train to create a beam gap in the ring for extraction. Accumulation of protons is carried continuously for 100 ms for CW linac, or for 16 ms for a pulsed linac, and then beam is sent onto a Be target using a single turn extraction and accumulation is continued.

The Li lens is used to collect as many 1 GeV pions as possible, and that bunched pion beam is injected into the linac structure used as a 200 meter long decay/buncher channel. Finally, the 1 GeV muon beam with a bunch structure of 162 MHz is accelerated to 10 GeV using 325 MHz superconducting beta=1 cavities.

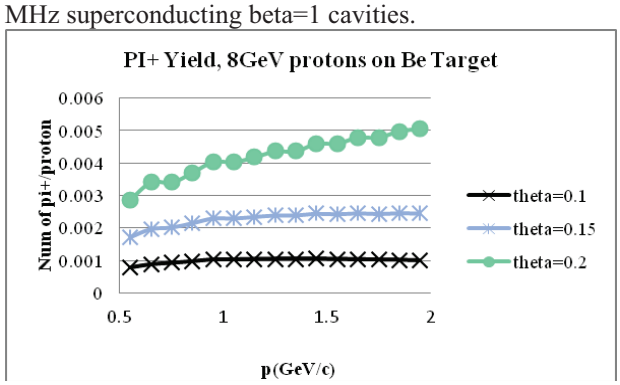

Figure 1: The pion yield curves above are produced using Striganov calculations.

Figure 1 shows number of positive pions produced with 8 GeV protons on a Be target with energy bins of +/- 0.1 GeV for three different values of forward acceptance angle theta. Table 1 lists conponents and main parameters of each stage of L^3ENF. Figure 2 shows a sketch of the whole complex.

*Work supported by Fermi Research Alliance, LLC, under contract No. DE-AC02-07CH11359 with the U.S. Department of Energy.

#popovic@fnal.gov

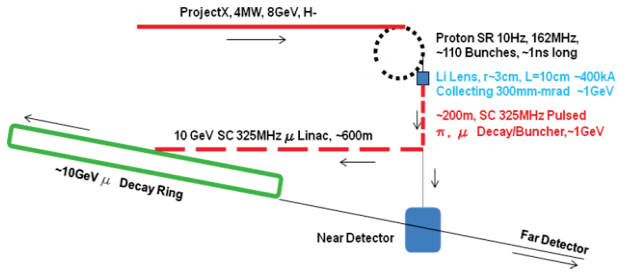

Figure 2: Protons are accelerated with ProjectX linac, then accumulated and targeted.

Table 1: Basic Beam Parameters

Protons	Parameters
Linac, H- Beam, 650MHz SC RF	BeamPower=4MW, CW I=0.5mA ~600ns on, ~60ns off, or 10Hz, 16ms Ekin=8GeV, Bunch Structure=162MHz
Proton Accumulation Ring	RingLength~200m, h=110, of 162MHz, 0.4MW stored per pulse, 100 bunches, ~$4*10^{12}$ protons per bunch, bunch length ~ 1ns, emittance 50mm-mrad, SC tune shift ~0.005 LongLimit ~ 0.1MW per bunch
Pions/Muons	**Parameters**
Target & Collection & Matching, at 1 GeV, energy spread of +/- 0.15GeV. Collecting E_un95%=300mm-mrad, L=3.5m, Yield~$5x10^{-3}$ pi+/proton	Target: Be or Hg, Li Lens, 15cm long, 3 cm radius, 10 Hz, Peak Current ~ 600kA, Focal length ~ 20cm. Quad doublet, Q1 g=4.1T/m, l_q1=0.35m, Q2 g=9T/m l_q2=0.7m
Linac/Pi Decay Chanel from 1.0 to 1.2 GeV, SC, pulsed, 325MHz	~20 FODO cells, ~8m, two 3-cell cavities beta=1, ~17MV/m, Cavity bore radius 0.2m L_quad=0.35m, g ~3T/m, Synch Phase~0 degree, Bunching mode
Linac/Mu from 1.2 to 10 GeV, SC, pulsed, 325MHz	~100 FODO cells, ~8m, two 3-cell cavities beta=1 , ~17MV/m, Cavity bore radius 0.2m L_quad=0.35m, g from 3T/m, rumped

In the rest of this note detailed descriptions of each stage and its building blocks are given. The assumption is that the Project X Linac accelerates H^- beam to 8 GeV with a bunch structure of 162.5 MHz and a programmable pulse width.

ACCUMULATION RING

The ring size is dictated by the space needed for RF, injection and extraction devices. The ring should be based on iron dominated magnets and be able to store an 8 GeV beam. The length of the ring should be a multiple of λ_{rf}=1.845m.

Copyright © 2012 by the respective authors — cc Creative Commons Attribution 3.0 (CC BY 3.0)

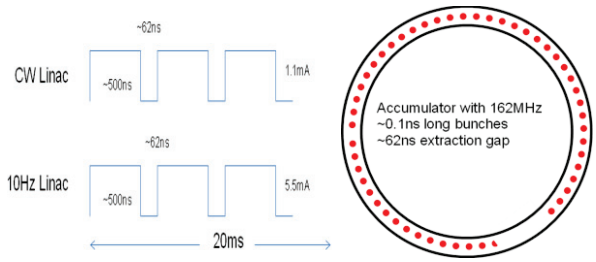

Figure 3: Beam accumulation.

The beam from the CW linac has a 95% normalized transverse emittance of ~1 mm-mrad and a total energy spread of ~5 MeV. It is assumed that during injection this beam is painted into a beam with transverse emittances of ~50 mm-mrad with the 162.5MHz beam structure from the Linac preserved.

The main limitations on beam parameters arise from longitudinal instabilities at injection. The maximum allowable beam power per bunch is:

$$P_{MAXperBuch} \leq f_{rep}\, m_o c^2 (\gamma - 1) \frac{\beta^2 \gamma^3 (\frac{\sigma_p}{p_0})^2 L_b \eta_{lattice}}{p_r \ln(\frac{a_{pipe}}{1.5\sigma_{beam}})}$$

For our choice of parameters, the longitudinal limits require less than ~100 kW per bunch.

Another limit related to the accumulation and bunching of a very large number of protons is set by the space charge tune shift. To produce very short proton bunches we need to have an accumulation ring of small circumference in conjunction with large transverse beam emittances.

$$B_{fact} = \frac{\sigma_s}{2\pi R_{aver}} \quad , \quad \Delta\nu_{sc} = -N_{ppB} \frac{p_r}{4\pi B_{fact} \beta\gamma^2 \varepsilon_{Nrms}}$$

With the parameters listed in Table 2, we conclude that direct space charge tune shift is ~ 0.02 and is therefore not an issue.

The accumulation ring is made with a bending field limited to ~1.8 T. Dipole magnets are combined function magnets. The distance between magnets is minimized to ~0.2 m. There are 32 magnets grouped in eight cells with six 8-meter straights and two 21-meter straights for injection and extraction.

Table 2: Lattice parameters (obtained from a MAD run)

total length = 191.0m	Qx = 2.59	Qy = 2.26
delta(s) = 0.0 mm	Qx' = -3.90	Qy' = 0.34
alfa = 0.1304	betax(max) = 24.77	betay(max) = 69.40
gamma(tr) = 2.76840	Dx(max) = 5.11	Dy(max) = 0.0
Dx(r.m.s.) = 4.310250	Dy(r.m.s.) = 0.0	

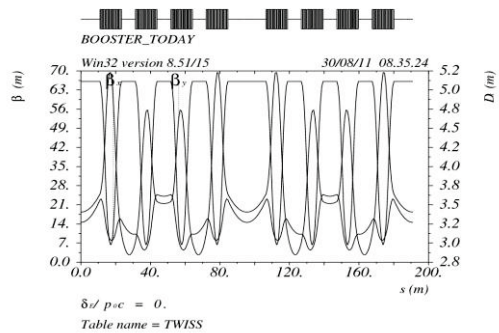

Figure 4: MAD output, for half of the ring.

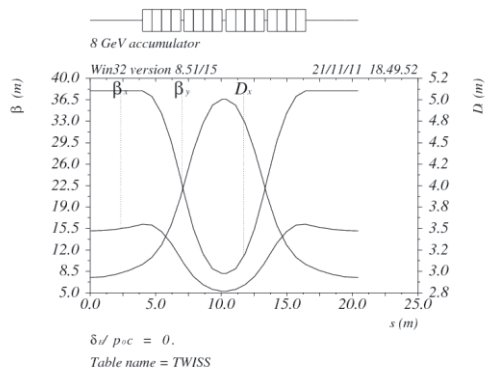

Figure 5: MAD output, the basic magnet group and lattice functions.

The lattice can be improved in the event that the long injection and extraction straight sections and the six 8-meter long straights can be shortened. If the injection and extraction will need less space, the lattice can be improved by shortening the straight sections.

TARGET AND PION COLLECTION

The proton beam is extracted every 100 ms and targeted on a Mercury jet target or Be target. The beam power of each pulse is 0.4 MW and the beam train is ~600 ns long with a bunch structure of 162 MHz and bunch length of ~1 ns. Right after the target there will be a lithium lens and set of collection quadrupoles. In this note we assume that we collect pions and muons from a 1 mm spot with kinetic energy of 1 GeV and within 0.3 radians in forward direction. The Litium lens is 15 cm long, with a radius of 3 cm, a peak current of 600 kA and a focal length of ~0.2 m.

PION DECAY CHANNEL

This section is identical to the Acceleration Linac. It is about 200 meters long with the RF phase close to zero so that the Linac is effectively a long decay channel with bunching cavities. The particles from the target are captured in the RF buckets, preserving the bunching structure and reducing the momentum spread off the target. The beam collected off the target is 1 GeV, with unnormalized 95% transverse emittances of 300mm-mrad

Copyright © 2012 by the respective authors — cc Creative Commons Attribution 3.0 (CC BY 3.0)

and energy spread of +/- 200 MeV. The bunch is 30 degrees (of 325MHz) long. Figure 6 shows PARMILA simulation of X, Y and Z planes.

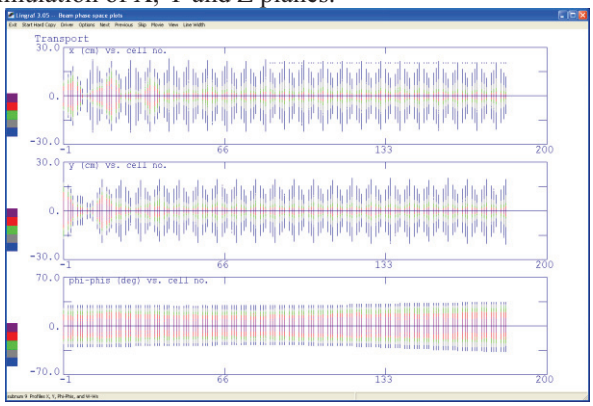

Figure 6: PARMILA run with 10000 particles and synchronous phase of ~2 degrees. FODO cell is around 8 meters long, G=3.1T/m

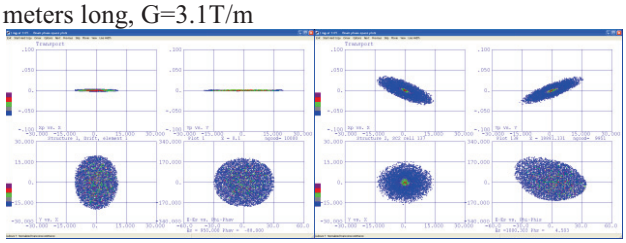

Figure 7: The pion beam phase space at the start and the end of the channel.

There are 28 FODO cells in the channel; G4beamline simulations start at the target and end at a virtual detector after the FODO channel.

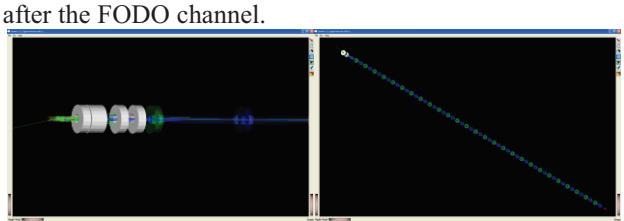

Figure 8: Target, Li lens, matching quads, G4Beamline model of the decay channel.

Starting with 10^5 protons on the target, G4beamline shows ~300 muons with energy spread and longitudinal spread as shown on graphs in Figure 9.

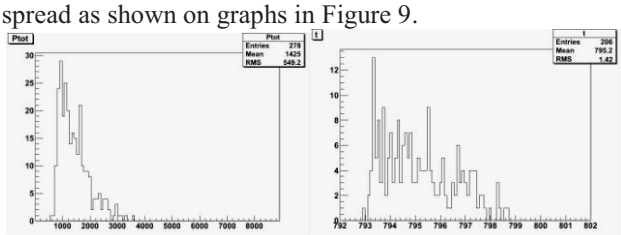

Figure 9: These graphs are with cuts; μ^+ only, with P_{tot}=[900:2000]MeV/c.

Figure 9 shows distributions of μ on the detector at the end of the channel. The whole channel consists of the target, Li lens, matching quads and 28 FODO Cells. In the simulation the space is provided for RF but RF is off.

MUON ACCELERATION

Pion/muon acceleration starts right after the Bunching Linac. The linac is based on 325MHz SC 3-cell cavities with FODO focusing, Figure 10. Figure 11 shows results of SuperFish calculation and dimensions of basic FODO cell.

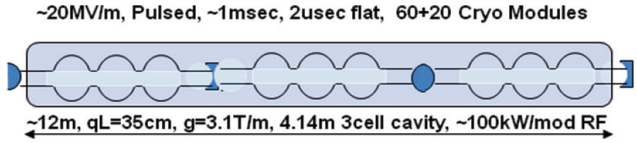

Figure 10: Cryostat has three cavities and two quads to reduce the number of warm-cold transitions.

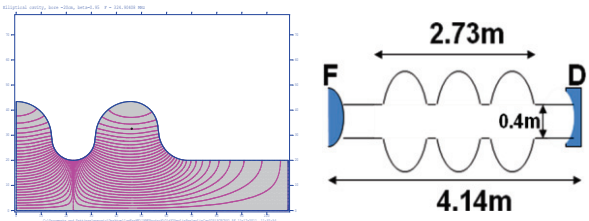

Figure 11: SuperFish result of 3-cell cavity

To design the Linac, the PARMILA code was used, Figure 12. The FODO lattice starts with 3.1T/m quad gradients and ramps to 6T/m. The distance between quads is 4.14 m, and it is constant along whole Linac. Acceleration is done using SC 3cell Beta=1 cavity with resonant frequency of 325MHz. The design requires constant energy gain per cavity to be 42MeV. The linac has a -20 degree synchronous phase which is ramped to -5 degrees in the first 3GeV. Injected beam has unnormalized 95% transvers emittances of 300 mm-mrad and an energy spread of +/-150MeV. The particles in the bunch are spread +/-15 degree (of 162.5MHz) around the synchronous particle.

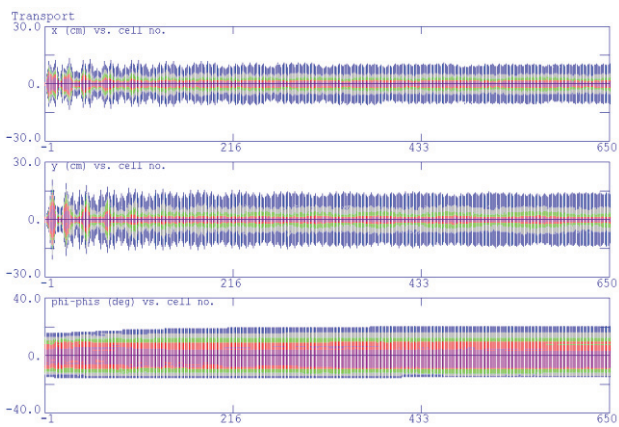

Figure 12: PARMILA outputs.

The entire Linac is ~900 meters long. A muon beam at 10 GeV has more than +/-150MeV spread. If needed the energy spread can be made smaller using coupled RF cavities with a higher synchronous phase.

The linac is pulsed with 10 Hz repetition rate and pulse length of few microseconds plus needed fill time.

REFERENCES

[1] S. Holmes et al., "Project X Reference Design Report," Project X Document 776-v1 (2010), http://projectx-docdb.fnal.gov

Copyright © 2012 by the respective authors — cc Creative Commons Attribution 3.0 (CC BY 3.0)

A CONCEPT: 8 GeV CW LINAC, STAGED APPROACH*

Milorad Popovic#, J-F. Ostiguy, FERMILAB, Batavia, IL 60510, USA

Abstract

This paper describes a concept for a CW Proton Linac on the Fermilab site. Except for the RFQ, the linac is based on superconducting technology. The linac has three segments that accelerate to 1 GeV, 3 GeV, and 8 GeV, respectively. It is located near the existing Fermilab Proton Source so that each section of the linac can be used as soon as it is commissioned. The whole design is based on the designs suggested for the Proton Driver and Project X. The suggested site and linac segmentation allow for the construction to start as soon as approval is granted. Additional benefits come from the fact that the present linac (the oldest machine in the Fermilab complex) is replaced, and the functionality of the existing Proton Source is preserved for the future.

INTRODUCTION

In order to create more opportunities for beam-based experiments using existing Fermilab infrastructure and in light of the expressed interest in a proton source capable of delivering multi-megawatt beam, a linac similar in design to Project X[1], but located near the existing linac, is proposed. The proposed linac, when completed, would be used to feed the existing 8 GeV program with increased intensity. Additionally, the proposed staged scenario would allow make use of some of the existing infrastructure.

The energy profile of the beam as suggested for Project X is shown in Figure 1.

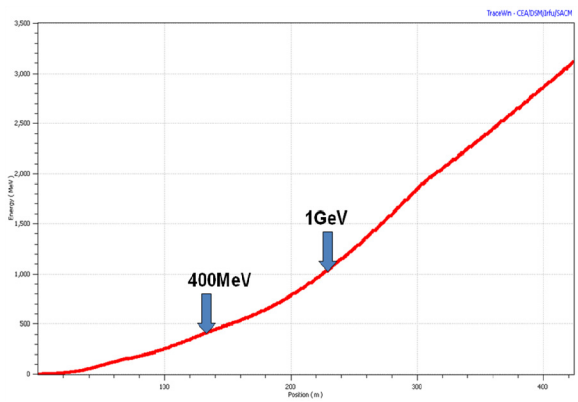

Figure 1: The arrows show the energies of the beam at the indicated distances from the ion source.

The proposed location of the new linac is indicated in Figure 2. The present 400-MeV linac (indicated by the blue line in Figure 2) is ~150 meters long and will be replaced with the new linac starting ~90 meters further upstream (as indicated by the red line in Figure 2). This will allow use of the existing tunnels for the linac and the beam transport line to inject 1-GeV beam into the Booster.

The injection can be bunch to bucket, as shown later. As in the case of the 400-MeV linac upgrade, the increase in injection energy will decrease the space charge tune shift in the Booster. For example, for typical present-day beam intensity and normalized transverse emittances, the space charge tune shift will decrease from 0.33 to 0.18. That in turn will allow more intense Booster beam at 8 GeV. This will also reduce the needed frequency swing of the RF cavities, allowing an increase of the total RF voltage per turn. The second blue line in Figure 2 indicates a CW linac from 1 to 3 GeV, and the long yellow line directed toward MI30 (the left side of Figure 2) shows the position of the 3 to 8 GeV linac.

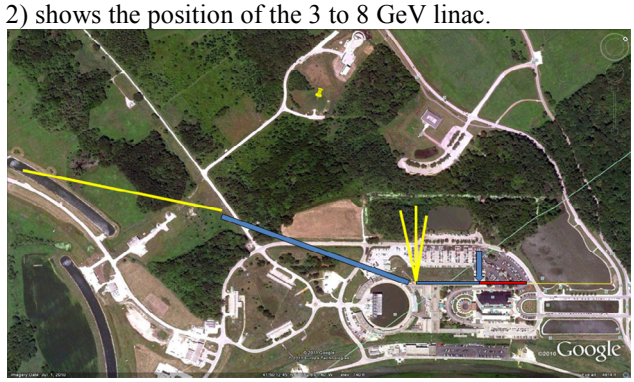

Figure 2: Proposed layout of the new linac on the Fermilab site.

In the rest of this note, a plan for staging of the new linac and the resultant effect on operation of the complex at each stage are described.

LOW ENERGY LINAC-CONCEPT

The low energy portion of the linac complex consists of ion source(s), LEBT, RFQ, MEBT, and linac up to some energy. For a high power CW machine with multiple users, redundancy in the form of multiple ion sources is needed. Also needed to provide the various required beam time structures is a wideband low energy beam chopping system. All these elements are indicated in Figure 3 and will be described in the following sections

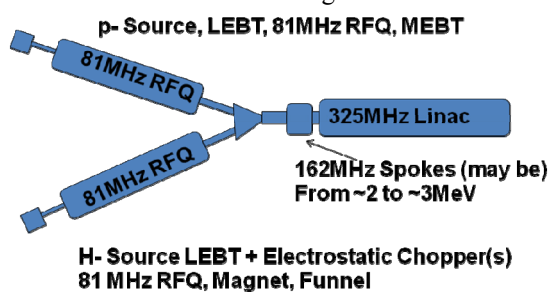

Figure 3: Low energy section of proposed linac. Details of components are described below.

*Work supported by Fermi Research Alliance, LLC, under contract No. DE-AC02-07CH11359 with the U.S. Department of Energy.
#popovic@fnal.gov

Copyright © 2012 by the respective authors — cc Creative Commons Attribution 3.0 (CC BY 3.0)

RFQ

One of the requirements of Project X is the ability to feed several experiments in parallel with flexible bunch structures. The highest beam repetition rate is expected to be ~ 20-30 MHz for kaons with a maximum bunch intensity up to 1.9E+8 protons. Following these requirements and the desire to have bunch separation long enough to make bunch by bunch kickers possible, we consider 81MHz RFQ. For input energy to the RFQ we chose 30 keV, beam energy from the existing D-Pace ion source and for the output energy, to stay below neutron production, we chose 2 MeV. Figure 4 shows graphical outputs from the Parteq simulation code

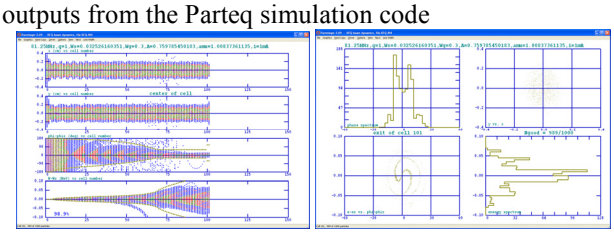

Figure 4: Horizontal, Vertical, Phase and Energy envelopes. The beam profiles at 2MeV.

The lists below show basic design parameters of RFQ.

Using the following parameters to create Parmteq input file

Particle symbol	= H-
Frequency	= 81.25 MHz
Beam current	= 1 mA
Normalized RMS emittance	= 0.2 pi mm mrad
Input energy	= 0.02752616 MeV
Shaper energy	= 0.03252616 MeV
Shaper phase	= -81.2368007 deg
Gentle-buncher energy	= 0.3 MeV
Gentle-buncher phase	= -30 deg
Final energy	= 2 MeV
Final synchronous phase	= -30 deg
Vane voltage	= 0.106381129 MV
Accelerating efficiency	= 0.759778545
Focusing parameter	= 13.4765212
Number of radial matching cells	= 4
Transition cell with no m=1 section	

Section lengths	
Radial matching section	= 5.64955674 cm
Shaper	= 41.5701789 cm
Gentle buncher	= 83.9719811 cm
Accelerating section	= 265.101211 cm
Transition region	= 10.3606282 cm
Total	= 406.653556 cm

Power estimates	
Copper power	= 78.4952518 kW
Beam power	= 1.97247384 kW
Total power	= 78.4678412 kW
Capture	98.6%

z	B	phi	m	V	W	A	a	psi
-5.650	0.674	-90.000	1.000	0.106	0.020	0.000	4.784	360.000
0.000	13.477	-90.000	1.000	0.106	0.020	0.000	1.870	360.000
10.393	13.477	-87.809	1.032	0.106	0.020	0.010	1.853	319.624
83.560	13.477	-59.552	1.166	0.106	0.071	0.104	0.982	187.142
91.766	13.477	-53.441	1.235	0.106	0.099	0.142	0.959	166.956
97.823	13.477	-48.860	1.293	0.106	0.119	0.163	0.935	150.795
102.621	13.477	-45.276	1.360	0.106	0.128	0.228	0.907	139.891
106.880	13.477	-42.375	1.427	0.106	0.147	0.276	0.877	129.710
109.994	13.477	-39.966	1.525	0.106	0.166	0.326	0.844	122.866
112.957	13.477	-37.924	1.628	0.106	0.195	0.382	0.808	115.595
120.090	13.477	-33.276	2.070	0.106	0.243	0.500	0.679	101.035
122.953	13.477	-32.068	2.292	0.106	0.262	0.624	0.627	97.279
125.963	13.477	-30.982	2.536	0.106	0.281	0.691	0.568	93.912
125.542	13.477	-30.000	3.000	0.106	0.300	0.760	0.500	90.873
390.643	13.477	-30.000	3.000	0.106	2.000	0.794	0.481	90.873

These lists are outputs of the design code RFQuick and the tracking code Parmteq. The full lists are included for completeness. However, the key parameters to note are: the total RFQ length is around 4 meters, the capture efficiency is ~98% and the beam is fully bunched at 200 keV. The total RF power (to copper and the beam) is ~80 kW. This means that the RFQ can be made of copper and run as a CW device. The power source can be one of the existing RF power vacuum tubes, and the removal of 80 kW of heat from a four meter long object does not seem to be a very challenging task.

MEBT

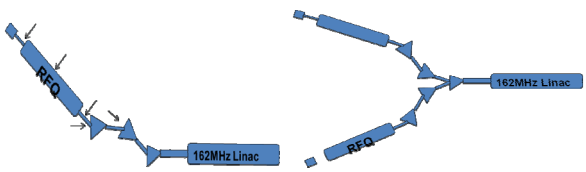

Figure 5: Figure on the left shows a single arm, and the arrows indicate possible laser ports.

Once this configuration of LEBT and MEBT is adopted, there are several options that we can choose from:

- A single arm, with a single 81 MHz RFQ. In this case there is no redundancy, and it must be possible to change the ion source quickly.
- Two identical 81 MHz RFQs, with one in standby for fast switching. This assumes that both systems have H^- sources.
- Two identical 81MHz RFQs, with one arm having an H- source and other a proton source so that the two systems can be switched fast depending on the user's needs.
- Two identical 81 MHz RFQs, with both arms having H^- sources and the last dipole in the MEBT made as a funneling system so that the linac gets 162 MHz structure from the beginning, if there is a need for such a beam.

The dipoles in the MEBT have edge focusing, the straights do not have to be long, and the bending angles can be from 30-70 degrees depending on how much dispersion is needed for momentum collimation. Simulations show that, depending on the focusing channel in the 162-MHz linac, output from the RFQ and the MEBT can be made to match the input to the 162 MHz linac. Figure 6 shows the quadrupole and solenoid matched beam.

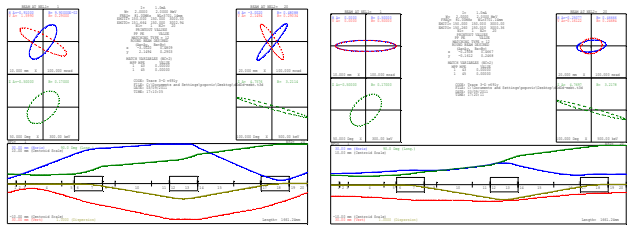

Figure 6: Three dipoles systems with zero dispersion for quad as well as the solenoid based 162 MHz linac. This simulation shows that the bunch structure is preserved and the beam can be injected in the 162 MHz accelerating structure.

1 GeV LINAC

Beam is accelerated from 2 MeV to 1 GeV in structures whose total length is shorter than 240 meters. The acceleration from 2 to ~10 MeV is achieved using superconducting 162 MHz quarter-wave structures. One option is the five-cavity cryomodule with a total length of ~ 5 meters that was suggested by P. Ostroumov as shown in Figure 6.

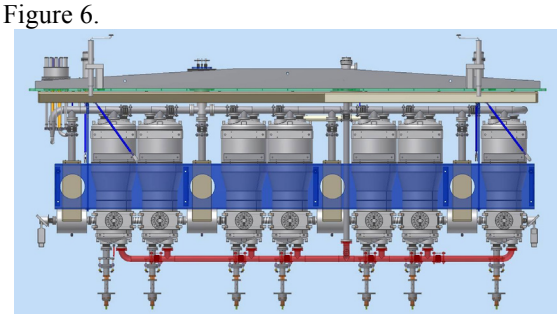

Figure 6: ANL cryomodule with five cavities and focusing solenoids.

Copyright © 2012 by the respective authors — cc Creative Commons Attribution 3.0 (CC BY 3.0)

From 10 MeV up to 1 GeV acceleration is based on the 325 and 650 MHz superconducting cavities as described in the Project X document [ref?].

This structure is to be housed in the existing linac tunnel and is to be built as indicated in Figure 1. One of the ways how this can be staged with minimal interruption of existing High Energy Physics (HEP) program will be described in a separate section.

Table 1. The acceleration options up to 8 GeV.

Section	RF	Energy (MeV)	C/mag/ CM	Type
SSR1(β_G=0.22)	325	10-42	20/20/ 2	SSR, sol.
SSR2(β_G=0.4)	325	42-160	40/20/4	SSR, sol.
LB(β_G=0.61)	650	160-460	36 /24/6	5-cell ell, doublet
HB(β_G=0.9)	650	460-3000	160/40/2 0	5-cell ell, doublet
HB(β_G=0.9)	650	3000-8000	224/56/2 8	5-cell ell, doublet

The next section describes how the existing Booster can use the new linac.

BOOSTER OPERATION

Presently, the 400 MeV H^- beam from the linac is transported along a ~40 meter transfer line to the Booster tunnel, and about $5x10^{12}$ protons are injected per Booster cycle. The peak current of the linac beam is ~30 mA, and injection lasts for twelve Booster turns or 26 μs (total injection time 12*2.2 μs).

The present line has two twelve-degree vertical bending magnets and two ten-degree horizontal bending magnets that would be replaced in order to minimize H^- stripping in the beam at 1GeV.

The new linac would have a peak current of 5 mA, that would require an injection time longer then 180 μs in order to inject more beam in the Booster than is currently possible.

To keep H^- stripping smaller than $5x10^{-5}$, the two vertical dipoles have to be replaced with 3.5 meter long magnets having a magnetic field of 0.35 T. The horizontal magnets would require a field of 0.35 T and length of 2.8 meters.

The rest of the transfer line can be used as is, with the exception of the injection dogleg system. The middle magnet would need to run with 88% more current, alternatively it could be replaced with a 50% longer magnet. Another possibility is to use correctors for additional displacement and painting during injection.

To avoid field swing dB/B bigger than $1x10^{-4}$,the injection time should not be longer than 240 μs. For the linac current of 5mA, this corresponds to $7.5x10^{12}$ protons injected in the Booster. This also insures that space charge tune shift will be half of the value that we have right now at Booster injection. This gives 150 kW of beam power from the Booster at 8 GeV and from the Main Injector, 0.5 MW at 120 GeV without slip stacking.

With the present 400 MeV injection energy of the Booster, the RF frequency swings from 38 MHz to 53 MHz. For injection at 1GeV, this swing is reduced to an interval from 46.5 to 53 MHz. With such a small frequency swing, the cavities can be tuned with just two tuners, and the third tuner can be removed from the cavity, Figure 7. At present, the cavity beam pipe has a diameter of just 2.25 in, the same as the gap in the main magnet. A shorter frequency tuning range will allow the beam pipe to be increased to 3.5 in, thereby significantly decreasing the beam loss on cavities and activation.

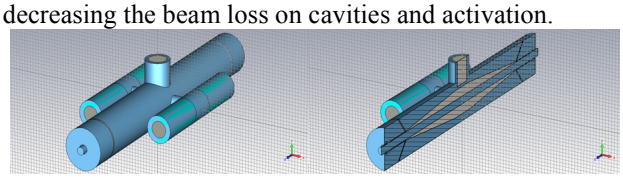

Figure 7: CST model of Booster Cavity with two tuners.

STAGING FROM 400 MeV TO 1GEV

The project can start with the building of 90 meters of tunnel, as indicated with a red line in Figure 2. As soon as a new 400 MeV linac is finished, a transfer line along the present linac tunnel can be built and the present 200 & 800 MHz systems can be decommissioned. Existing linac buildings can be used to house new support equipment, and a new accelerating structure can be installed in the present tunnel. The rest of the linac up to 8 GeV can be built along straight lines (as illustrated in Figure 2) with 8 GeV injection to the Main Injector at MI30. The initial configuration of the 3-8 GeV linac section will be pulsed with a tunnel long enough to accommodate additional RF needed for CW linac.

ACKNOWLEDGMENT

The authors would like to acknowledge useful suggestions and ideas from Charles Ankenbrandt of Muons Inc.

REFERENCES

[1] S. Holmes et al., "Project X Reference Design Report," Project X Document 776-v1 (2010), http://projectx-docdb.fnal.gov

Copyright © 2012 by the respective authors — cc Creative Commons Attribution 3.0 (CC BY 3.0)

ANNULAR-RING COUPLED STRUCTURE FOR THE ENERGY UPGRADE OF THE J-PARC LINAC

H. Ao*, H. Asano, J. Tamura, N. Ouchi, J-PARC, JAEA, Ibaraki, Japan
F. Naito, K. Takata, J-PARC, KEK, Ibaraki, Japan

Abstract

The J-PARC linac is preparing to boost the beam energy from 181 to 400 MeV by using annular-ring coupled structures (ACS) for the 1-MW operation from the 3-GeV rapid cycle synchrotron. The mass-production of the ACS cavities started from March 2009 is proceeding on schedule and most of all the cavities have been fabricated until March 2012. The other cavities will be finished until March 2013. The first mass-produced ACS module was successfully conditioned up to 1.6 MW without any issues. For the installation schedule in 2013, the user operation has to be restarted after six months shutdown due to the strong requests from users. As yet, further work is necessary to arrange the schedule and the required manpower for the installation.

INTRODUCTION

The linac of Japan proton accelerator research complex (J-PARC), which is the injector of the 3-GeV rapid cycle synchrotron (RCS), is preparing to boost the beam energy from 181 to 400 MeV in order to raise the possible output power of the 3-GeV RCS from 0.6 to 1 MW. The output energy of the linac is upgraded by using annular-ring coupled structures (ACS). This energy upgrade will increase the limit on the number of particles due to a space charge effect $\Delta\nu \propto \beta^{-2}\gamma^{-3}$. Here, β and γ are Lorentz factors.

Figure 1 shows the schematic configuration of the linac. The downstream area where the ACS cavities will be installed in the future is used as the beam transport line for 181 MeV at present. The energy upgrade requires 25 ACS modules in total, which include 21 ACS accelerating modules, two ACS bunchers and two ACS debunchers. The two bunchers and three accelerating modules already have been fabricated as a prototype of the common ACS module. All the other cavities have to be mass-produced within a three-year period from March 2009. The cell dimensions of these modules are varied from module to module, which means that the frequencies of many types of cells have to be tuned within a short time. Thus, the iteration of a frequency tuning was reduced to only one step by using the results of the test cell measurement [1]. In the last of 2010, the first mass-produce d ACS module was completed and its high-power test was successfully finished to confirm the stable operation at the required input power.

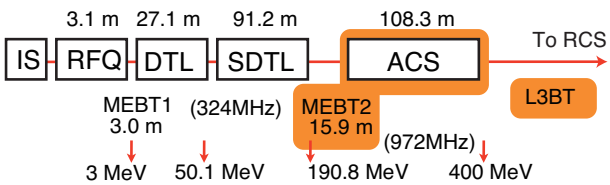

Figure 1: Schematic configuration of the linac.

In the middle of the mass-production, the Great East Japan Earthquake occurred in March 2011 and it severely damaged the linac facility. Fortunately, the factory which were making the ACS cavities is about 1000 km from the epicenter and did not affected.

This paper describes the present status of the ACS cavity fabrication, the measurement result of the first mass-produced ACS module and the installation scenario of the energy upgrade in 2013.

CAVITY FABRICATION STATUS AND INSTALLATION SCHEDULE

Figure 2 shows the progress of the cavity fabrication. At first, all the cavities were schedule to be fabricated until March 2012 and installed in summer of that year. However, the installation was postponed to 2013 due to the earthquake. Most cavities were fabricated until March 2012 according to the first schedule. Of the required 20 ACS modules, 17 modules are completed at present. Of the other three modules, two modules were already brazed and will be finished after assembling an RF window and cooling pipes. The last one module will be done until March 2013[1].

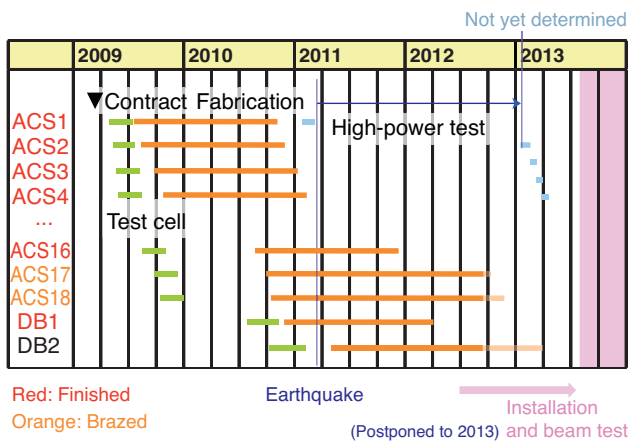

Figure 2: Current progress status of the ACS cavity fabrication.

[1]The schedule of the last three modules is not delayed due to technical issues since it was rearranged after the earthquake.

* hiroyuki.ao@j-parc.jp

Copyright © 2012 by the respective authors — cc Creative Commons Attribution 3.0 (CC BY 3.0)

The damaged overhead cranes are still not available in the linac building. Thus, the modules shipped before the earthquake are stored in the linac building, the ones completed after the earthquake are kept in the factory.

The original plan was to condition all the ACS modules at a high-power test area in the linac building, and then to be installed to the beam line. However, the conditioning has been suspended since the concrete floor of the test area was cracked and broken by the earthquake. Since the repair schedule is not yet determined even now, there is no prospect for restarting the conditioning. Most of the ACS modules, therefore, have to be conditioned after the installation just before the beam test.

Figure 3 shows the preliminary installation schedule in 2013. Due to the strong requests from users, the user operation have to be restarted after six months, which are a usual summer shutdown (3 months) and an extra shutdown (3 months) for the energy upgrade.

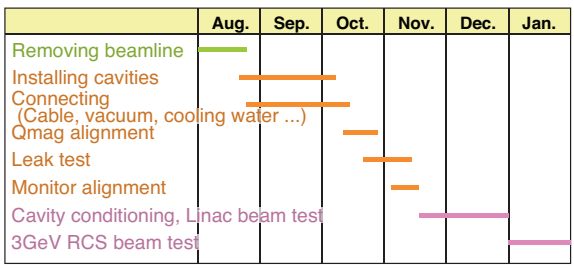

Figure 3: Installation schedule of the energy upgrade in 2013 (preliminary).

In the linac, a 50 mA ion source and an RFQ have to be installed in the same period. Also, existing beam line components require annual maintenance. Thus, further work is necessary to arrange the schedule and the required manpower in order to complete the upgrade installation within 3.5 months.

MASS-PRODUCED ACS MODULES

Low level measurement

Figure 4 shows the configuration of the ACS accelerating module. One ACS module consists of two accelerating tanks and one bridge tank. As an example of the measurements of the mass-produced modules, this section describes the results of the first mass-produced module, which is named as M04 (it includes accelerating tanks T07 and T08[2]).

Table 1 lists the accelerating mode and the coupling mode frequencies after brazing. These frequencies are tuned within the target frequency of 972.04 ± 0.1 MHz. For the accelerating mode, the frequency was tuned only before the brazing. For the coupling mode, the frequency was adjusted by using coupling cell tuners after brazing.

Figure 5 shows the result of the electric field measurement using the bead-pull method (The bead material is

[2]21 ACS modules accelerate H^- beams up to 400 MeV. The accelerating modules are numbered from M01 to M21, and the accelerating tanks are also numbered from T01 to T42, in order of increasing beam energy.

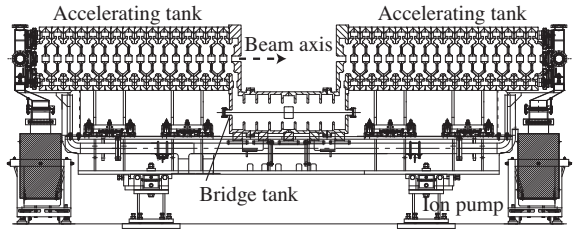

Figure 4: ACS accelerating module. One ACS module consists of two accelerating tanks and one bridge tank.

Table 1: Accelerating mode and coupling mode frequencies after brazing (MHz)

Tank	Accelerating mode	Coupling mode
T07	972.02	972.05
T08	971.98	972.02

SUJ-2[3]. The diameter is 3 mm. The beam bore of the ACS is 40 mm.) This data was measured in normal atmosphere and calibrated so that the frequency shifts at $E_z = 0$ points in the drift space are expressed as zero. The electric field distribution is sufficiently acceptable for beam acceleration.

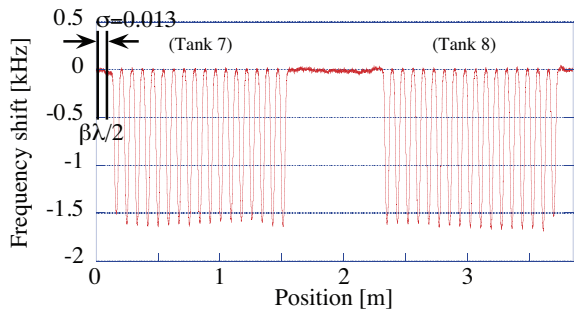

Figure 5: Electric field measurement by the bead-pull method. The frequency shifts were calculated from the measured phase shifts.

Table 2 lists a shunt impedance $Z, Z/Q$. Here, the designed Q-value is calculated by Microwave Studio. This model is only an accelerating tank. Including the bridge tank, the calculated $Z, Z/Q$ values should be smaller according to the ratio of the stored energy of $34/\{34 + 5 \times (24/100)\} = 0.966$. Here, the stored energy ratio between an excited cell in a bridge tank and a accelerating cell was evaluated as 24.0% using the measured coupling factor between an accelerating tank and a bridge tank (Here, the number of the excited cell is five.). The calculated values by Microwave Studio are $Z = 46.9$ MΩ/m and $Z/Q = 2.50 \times 10^3$ Ω/m. Thus, the designed Z and

[3]Provided by Japanese Industrial Standards. It is equivalent to AISI 52100 or DIN 100Cr6.

Copyright © 2012 by the respective authors — cc Creative Commons Attribution 3.0 (CC BY 3.0)

Table 2: Q-value, shunt impedance Z, Z/Q

	Designed	Achieved	%
Q-value	1.78×10^4	1.85×10^4	
Z	45.3 MΩ/m	45.7 ± 2.4 MΩ/m	100.9
Z/Q	2.42×10^3 Ω/m	2.47×10^3 Ω/m	102.1

Z/Q become $Z = 46.9 \times 0.966 \simeq 45.3$ and $Z/Q = 2.50 \times 10^3 \times 0.966 \simeq 2.42 \times 10^3$.

In the table 2, the measurement error of Z was evaluated by shifting the line of $E_z = 0$ ($\Delta f = 0$) to $\sigma = \pm 0.013$ for the electric field integration $\int E_z dz$ (see Fig. 5).

The one of the reasons that the measured Z/Q is slightly higher than 100% is the error of the stored energy ratio. The connecting part between an accelerating tank and a bridge tank is not periodic structure. Thus, it is difficult to evaluate the stored energy ratio only by the coupling factor ratio. To compare the design and the measured value, it is desirable to measure Z and Z/Q for each accelerating tank only, since it does not need the correction for the bridge tank. In the recent modules, the measured Z/Q is in good agreement with the designed one using the measurement for an accelerating tank only.

High-power test

The dissipated power of the cavity inner surface is 1.2 MW, which is evaluated by using $Z = 45.7$ MΩ/m listed in Table 2, the cavity length of 3.083 m, and the accelerating field of 4.2 MV/m. In this power test, the cavity was conditioned up to 1.6 MW including a margin of 15% for the accelerating field. Although the designed pulse length is 600 μs, finally it was extended to 650 μs in order to keep a feedback pulse length. Figure 6 shows the conditioning history of the first mass-produced module (M04). The input power shows the average value of the four pickup antennas attached to both the ends of two accelerating tanks. The vacuum pressure was measured at the center of the bridge tank using Bayard-Alpert gauge.

The conditioning time to reach the target power of 1.6 MW was 60 hours, which is acceptable range for considering future conditioning of the mass-produced modules. Table 3 lists the required conditioning times comparing the short ACS (buncher) module [2]. These cavities were conditioned under the same RF duty (the pulse length of 600 μs, the repetition of 50 Hz). However, the number of accelerating cells of M04 is 3.4 times larger than that of a buncher (5 cells per an accelerating tank). The conditioning time of M04 takes twice longer than that of the buncher module.

The achieved vacuum pressure was 2.0×10^{-6} Pa under the 1.6 MW operation after the 240 hours conditioning. This value is lower than the target vacuum pressure of 4×10^{-6} Pa, which is requirement to reduce the beam loss from residual gas less than 0.1 W/m. However, the residual gas caused beam loss in the SDTL section (see Fig. 1), which is operated at less than this target pressure [3].

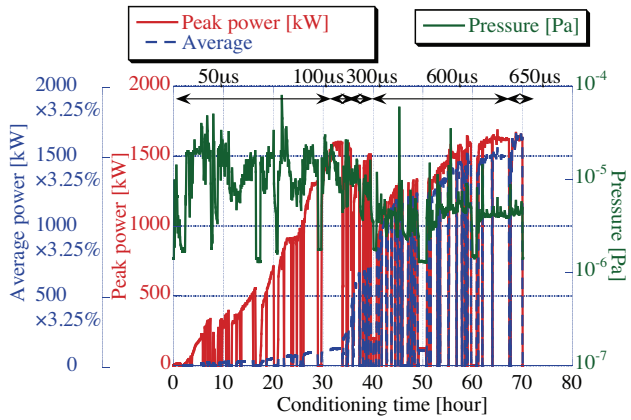

Figure 6: Conditioning history of the first mass-produced module (M04). Red: peak power, Blue: average power, Green: vacuum pressure in the cavity. The repetition is 50 Hz throughout this conditioning.

Table 3: Power level and conditioning time [E_0, E_{sp} (MV/m)]

Time (h)	Power (kW)	E_0	E_{sp}	Kilpatrick
ACS (buncher)				
33	600	5.3	29.6	1.0
ACS (M04)				
60	1600	4.9	26.9	1.0

Thus, the improvement of the vacuum pressure is one of the key issues for future high intensity beam operation. The vacuum pressure distribution on the beam axis in the ACS module and its improvements need to be further examined, for example, by using a completed ACS module until the installation.

SUMMARY

The mass-production of the ACS cavities started from March 2009 is proceeding on schedule and most of all the cavities have been fabricated until March 2012. The other cavities will be finished until March 2013. The first mass-produced ACS module (M04) was successfully conditioned up to 1.6 MW without any issues.

With respect to the cavities, vacuum components and quadrupole magnets will be prepared to be attached to an accelerating module. In addition, the improvement of the achieved vacuum pressure needs to be further examined before the energy upgrade installation. In order to complete the upgrade installation within 3.5 months, further work is necessary to arrange the schedule and the required manpower.

REFERENCES

[1] H. Ao *et al.*, in Proceedings of IPAC'10, 2010, p. 618.

[2] H. Ao *et al.*, Phys. Rev. ST Accel. Beams 15, 2012, 011001.

[3] A. Miura *et al.*, in Proceedings of LINAC10, 2010, p. 587.

Copyright © 2012 by the respective authors — cc Creative Commons Attribution 3.0 (CC BY 3.0)

RECOVERY EFFORTS FROM THE TOHOKU EARTHQUAKE AND ENERGY UPGRADE PREPARATION OF THE BEAM TRANSPORT FROM J-PARC LINAC TO 3-GeV SYNCHROTRON

J. Tamura*, H. Ao, H. Asano, T. Morishita, N. Ouchi, JAEA/J-PARC, Ibaraki, Japan
Y. Sawabe, Mitsubishi Electric System & Service Co., Ltd., Ibaraki, Japan

Abstract

In 2013, the beam energy of the Japan Proton Accelerator Research Complex (J-PARC) linac is going to be increased from 181 to 400 MeV. This energy upgrade is carried out by adding the Annular-ring Coupled Structure (ACS) linac to the beam transport at the downstream of the 191-MeV drift tube linac. To install and condition all the ACS cavities in only five months, we decided to replace and upgrade most of the related components of the beam line (cables, power supplies for magnets and vacuum control systems) for the 400-MeV operation, in the annual maintenance period in summer and the period of the recovery from the 2011 Tohoku Earthquake. The original 181-MeV beam line is operated by using some part of the 400-MeV componets. In this paper, the recovery of the beam transport, the present status of the beam operation, and the future tasks of the beam energy upgrade will be presented.

INTRODUCTION

In the J-PARC linac, H- beams are accelerated by 3-MeV RFQ, 50-MeV DTL, and 181-MeV Separate-type DTL (SDTL). Then, the beams are transported to the 3-GeV synchrotron. To achieve the beam power of 1 MW after the 3-GeV synchrotron, we are planning to increase the injection energy into the synchrotron from 181 to 400 MeV. The beam energy upgrade is scheduled in 2013 and carried out by adding the ACS linac to the beam transport at the downstream of SDTL [1]. Figure 1 shows the diagram of the J-PARC linac. Twenty-one ACS accelerating modules are going to be installed in A0BT. Two ACS buncher modules are going to be installed in MEBT2, which is a matching section for the ACS accelerating section. Two ACS debuncher modules are going be installed in L3BT, which is a beam transport from the linac to the 3-GeV synchrotron.

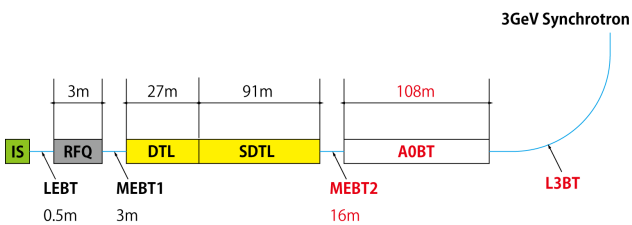

Figure 1: Diagram of the J-PARC linac.

* jtamura@post.j-parc.jp

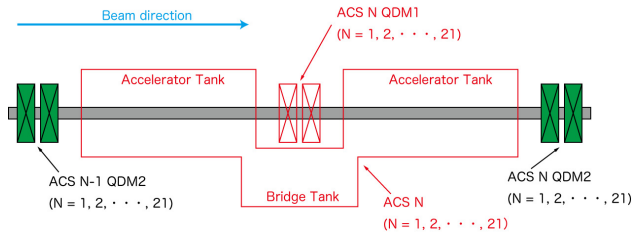

Figure 2: Layout of the quadrupole array in A0BT.

The ACS cavities are operated at 972 MHz, While the RFQ, DTLs and SDTLs are operated at 324 MHz.

MEBT2 and A0BT have 6 and 21 quadrupole doublets, respectively. The drift space length of MEBT2 and A0BT increase gradually from 2.5 to 3.4 m and from 4.6 to 5.7 m, respectively. Figure 2 shows the layout of the quadrupole array in A0BT. ACS accelerating modules and doublets over the ACS bridge tanks, which are drawn by red line in Fig. 2, are going to be installed in the 2013 energy upgrade shutdown.

Before the 2011 Tohoku Earthquake, the beam energy upgrade was scheduled to be completed in 2012. The earthquake caused a tremendous damage to the J-PARC accelerator facility. It made beam operation impossible for nine months and delayed the beam energy upgrade from 2012 to 2013. In this paper, the recovery of the beam transport, the present status of the beam operation, and the future tasks of the beam energy upgrade will be presented.

BEAM LOSS REDUCTION BY BEAM DUCT REALIGNMENT

In the J-PARC linac, almost all the cavities and magnets were precisely realigned because the accelerator tunnel had been deformed by the 2011 Tohoku Earthquake [2]. In MEBT2 and A0BT, the beam ducts have been roughly aligned after the precise alignment of the quadrupole doublets. The beam ducts are made up of titanium pipes with inner radius of 41 mm and branch ducts for vacuum pumps in the center of two doublets.

The beam study operation in the linac has been resumed on 9th of December 2011 [3]. During the first beam operation after the earthquake, remarkable beam loss and residual radiation have been observed at some parts of MEBT2 and A0BT. This beam loss had a strong correlation with the beam orbit. The beam loss has been reduced by adjusting the beam orbit using steering magnets, but it were

Copyright © 2012 by the respective authors — cc Creative Commons Attribution 3.0 (CC BY 3.0)

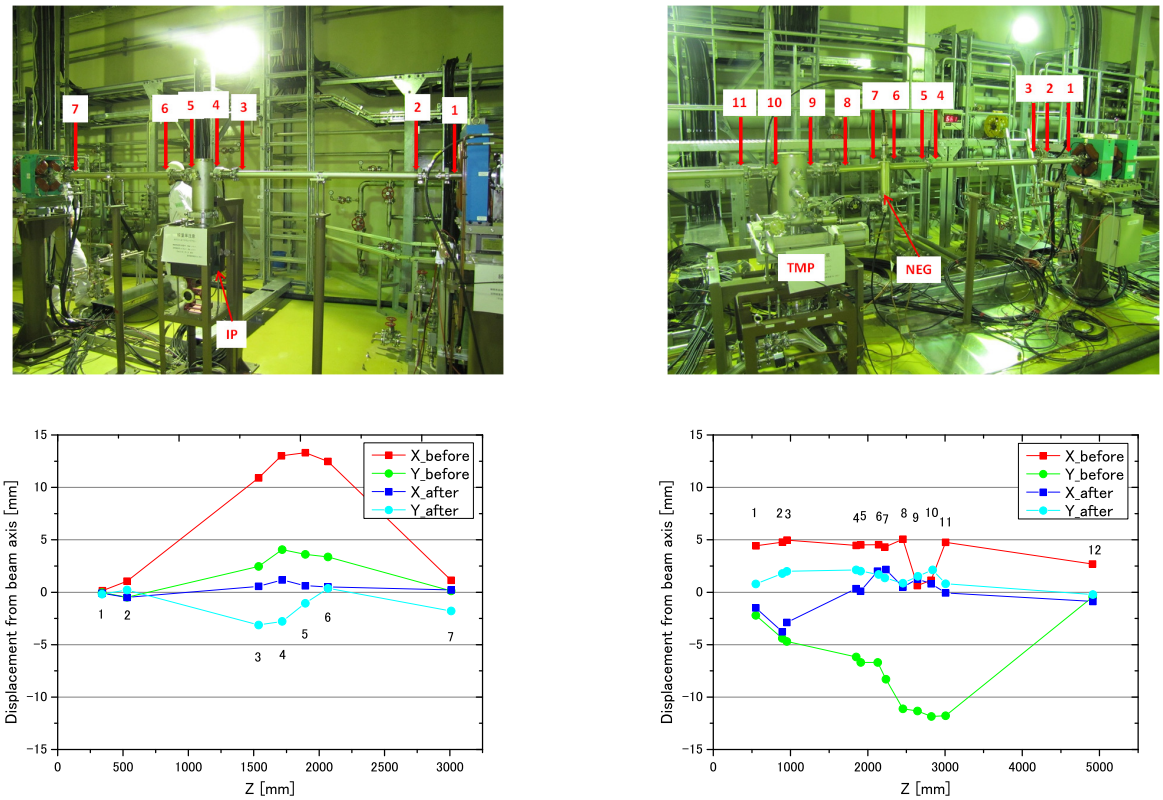

Figure 3: Beam duct realignment in MEBT2 (left) and ACS11 (right). Upper-left figure shows the section between MEBT2-QDM02 and MEBT2-QDM03 which have an IP in its center. Upper-right figure shows the ACS11 section which have a TMP in its center and a NEG Pump just before the TMP. Lower figures show the results of the duct position measurement before and after the duct realignment in MEBT2 (left) and ACS11 (right).

still much bigger than that before the earthquake. The loss and the residual radiation were localized to a branch duct for an ion sputter pump (IP) between MEBT2-QM02 and MEBT2-QM03 of MEBT2 and to a branch duct for a turbo molecular pump (TMP) and a non-evaporable getter (NEG) pump in ACS11 section. Therefore, we decided to check the alignment of the beam ducts with a laser-tracker. As the result of the duct position measurement, the misalignment of over 10 mm displacement from the beam axis were found. Figure 3 shows the displacement of the beam ducts from the beam axis in MEBT2 and ACS11. In MEBT2, there were 13.3 mm of displacement in a horizontal direction at the branch duct while less than 5 mm in a vertical direction. In ACS11, there were 12 mm of displacement in a vertical direction at the branch duct while less than 5 mm in a horizontal direction.

In the maintenance period after the first beam operation called Run#40, the beam ducts between MEBT2-QM02 and MEBT2-QM03, and in ACS02, ACS10, ACS11 and ACS14 have been realigned using a laser level marker [4]. This type of alignment tool based on a laser beam had not been used in the rough alignment before the beam operation. The result of the duct realignment is shown in lower figures of Fig. 3. Although not all the beam ducts in MEBT and A0BT could be realigned due to the limited time, the beam loss and the residual radiation were successfully reduced by the beam duct realignment. Table 2 shows the trend of the residual radiation of the branch ducts in MEBT2 and ACS11.

PREPARATION FOR THE BEAM ENERGY UPGRADE

To install and condition all the ACS cavities in only five months of the energy upgrade shutdown in 2013, we decided to replace and upgrade most of the related components of the beam line (cables, power supplies for magnets and vacuum control systems) for the 400-MeV operation, which are in use in the present 181-MeV operation. Due

Table 1: Trend of the residual radiation (unit: mSv/h). The beam duct realignment has been conducted after the residual radiation measurement on 2/22. The residual radiation listed in this table were measured on the surface of the branch ducts.

	2/22	3/15	3/22	4/11
MEBT2QM02-03	8.0	1.5	1.0	0.7
ACS11	10	2.5	2.5	1.8

Copyright © 2012 by the respective authors — cc Creative Commons Attribution 3.0 (CC BY 3.0)

Table 2: Cable installation and replacement in the beam line. These installation needs to be carried out in annual summer maintenance period. "•" stands for the original configuration for the 181-MeV operation. It is noted that the first SDTL debuncher is operated in ACS03 section for the 181-MeV operation. "○" and "×" stands for the cable installation and the cable removal, respectively.

	MEBT2			ACS																			
	M	B1	B2	1	2	3	4	5	6	7	8	9	10	11	12	13	14	15	16	17	18	19	20	21
Origin	•				•	•			•				•				•				•			•
2010		○	○	○			○	○		○		○		○	○	○		○		○		○	○	
2011	×				×				×				×				×				×			×
	○				○				○		○		○				○		○		○			○
2012																								
2013						×																		
						○																		

to the beam operation, an equipment installation and a facility expansion in the accelerator tunnel are restricted to three months of annual maintenance period in summer. In the beam operation shutdown after the 2011 Tohoku Earthquake, the energy upgrade preparation have been carried out in parallel with the recovery from the Earthquake.

In the original configuration for the 181-MeV operation, equipments such as magnets, vacuum pumps and beam monitors in MEBT2 and A0BT were operated by their power supplies and controllers set in terminal racks of MEBT2M, ACS02, ACS06, ACS10, ACS14, ACS18 and ACS21 in the klystron gallery. The history of the cable installation and replacement is summarized in Table 2. In 2011, the power supplies for quadrupole magnets have been relocated to the regular position of the control terminals corresponding to the ACS module number. And then, the magnets in MEBT and A0BT started to be operated by the corresponding power supplies with the exception of ACS03. ACS03-QDM02 is operated by the power supplies for ACS04-QDM01. Vacuum pumps and beam monitors are operated by using the cables installed in 2010. Cables for ACS-DB1 and ACS-DB2 have been installed in 2011 and 2012, respectively. The length of the cables for ACS-DB2 is about 120 m, while the others are 50 m long.

Rectangular waveguides have been installed from the klystron gallery to the position just before the RF window of the ACS cavities in 2009 and 2010 except for ACS03 and ACS-DB2. In ACS03, a coaxial waveguide is in use for the SDTL-DB1. In 2013, after the removal of the waveguide for SDTL-DB1, waveguide for ACS03 operated in 972 MHz is installed. Installation of the waveguide for ACS-DB2 was started in 2011. This is conducted also in 2012 and is going to be finished in 2013.

In 2013, the cables, waveguide and cooling water system for ACS03 are going to be installed after the removal of the associate equipments for S-DB01.

SUMMARY

We have been preparing for the energy upgrade of J-PARC linac and continuing recovery efforts from the Tohoku Earthquake. We have delivered 181-MeV H- beams to 3-GeV synchrotron mitigating the beam loss in the transport line which had not been observed before the earthquake. In 2012 summer maintenance period, we conducted the beam duct realignment throughout the MEBT2 and A0BT. It will contribute to the beam loss reduction due to the beam duct misalignment. The beam energy upgrade preparation is still going on for the ACS cavity installation in 2013.

REFERENCES

[1] H. Ao et al., "Annular-ring Coupled Structure for the Energy Upgrade of the J-PARC Linac," THPB020, these proceedings.

[2] T. Morishita et al., "Floor Deformation of J-PARC Linac after the Tohoku Earthquake in Japan," IPAC'11, San Sebastián, SEP 2011, WEPS049, p. 2601 (2011).

[3] M. Ikegami et al., "Beam Start-up of J-PARC Linac after the Tohoku Earthquake," IPAC'12, New Orleans, MAY 2012, THPPC010, p. 3293 (2012).

[4] J. Tamura et al., "BEAM LOSS REDUCTION BY THE BEAM DUCT REALIGNMENT IN THE J-PARC LINAC BEAM TRANSPORT LINE," proceedings of the 8th Annual Meeting of Particle Accelerator Society of Japan, Tsukuba, Aug. 1-3, 2011.

Copyright © 2012 by the respective authors — cc Creative Commons Attribution 3.0 (CC BY 3.0)

BEAM PHASE MEASUREMENT FOR PEFP LINEAR ACCELERATOR*

Han-Sung Kim#, Hyeok-Jung Kwon, Jin-Yeong Ryu, Kyung-Tae Seol, Young-Gi Song,
Ji-Ho Jang, Yong-Sub Cho, PEFP/KAERI, Daejeon, Korea

Abstract

According to the commissioning plan of the PEFP proton linac, an accurate measurement of beam phase is essential, especially for setting up the RF operating parameters of DTL. Beam position monitors (BPMs) installed between DTL tanks can provide information about the beam phase as well as about the beam transverse position. By using a BPM as a beam phase monitor, beam phase can be measured without additional devices on the linac or the beam line. The signals from 4 electrodes in the BPM can be summed by using a 4-way RF combiner, by which the effect of the transverse beam offset on the phase measurement can be eliminated. The combined BPM signal (350 MHz) is mixed with LO signal (300 MHz) and down-converted to IF signal (50 MHz), then fed into the signal processing unit, where the phase information is extracted by using IQ demodulation method with a sampling frequency of 40 MHz. In this paper, the beam phase measurement system and signal processing scheme will be presented.

INTRODUCTION

The main facility of the PEFP is 100-MeV proton linac with a high duty factor [1]. Currently the installation of the accelerator is under-going. For the determination of RF set-point during the commissioning of the linac, the beam phase must be measured accurately. A strip-line type beam position monitor (BPM) will be used for the beam phase measurement. Figure 1 shows the layout of beam diagnostic devices along the linac [2]. Note that there is only one BPM between 20-MeV section of linac and MEBT. The 20-MeV section consists of 4 DTL tanks and is driven by single klystron. Therefore, 4 DTL tanks would be considered as single large tank from the view point of RF system [3]. To adjust RF phase of each tank in 20-MeV section, we installed high power RF phase shifter in each RF waveguide branch to each tank.

A 100-MeV section is composed of 7 DTL tanks and one BPM is allocated right after each DTL tanks. One additional BPM is located in front of the beam dump and will be used for RF set-point determination. The initial goal of the linac commissioning is the beam power of 100W with the peak beam current of 20 mA, the pulse width of 50μs in 1 Hz operation [2].

BPM FOR PHASE MEASUREMENT

To measure the beam phase as well as the beam position, we designed and fabricated a strip-line type BPM. The design of the BPM is based on the beam parameters such that the beam energy ranges from 20 MeV to 100 MeV with minimum peak current of 1 mA. The minimum beam pulse width is 50 us, which was determined considering the LLRF control system.

One of the major constraints in BPM design was space limitation. The BPM should be installed between DTL tanks. The shortest gap is between the first and the second DTL tank and is less than 125 mm. The isolation vacuum gate valve and flexible bellows must be installed in that gap as well as the BPM, which leaves only about 50 mm of the net space for the BPM installation.

The electrode aperture is 20 mm in diameter, which is same as the inner diameter of the drift tube. The electrode angular span is 60 degree to increase the output signal amplitude. The electrode is made of stainless steel with thickness of 2 mm to give enough mechanical stability. For the proper operation of the strip-line type BPM, the characteristic impedance should be well matched and the gap was determined to be 3.5 mm based on the POISSON calculation. Figure 2 and 3 show the drawing of the designed BPM and fabricated one, respectively [4].

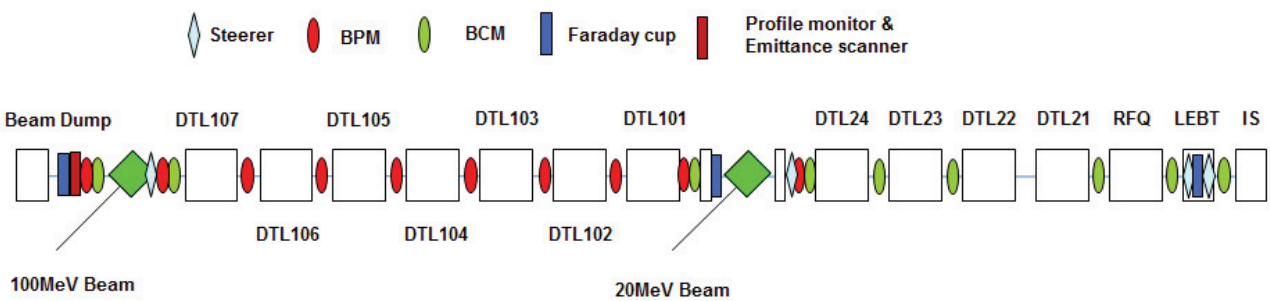

Figure 1: Layout of beam diagnostics in PEFP linac.

*Work supported by Ministry of Education, Science and Technology of the Korean government
kimhs@kaeri.re.kr

Copyright © 2012 by the respective authors — cc Creative Commons Attribution 3.0 (CC BY 3.0)

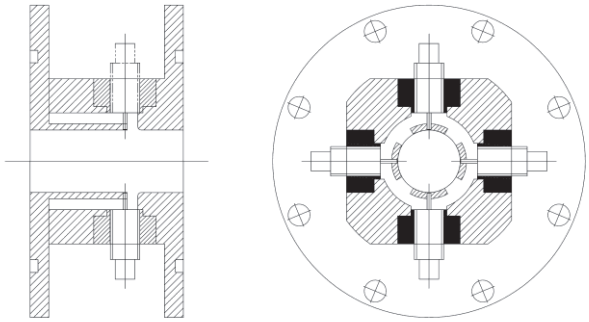

Figure 2: Drawing of the BPM for linac.

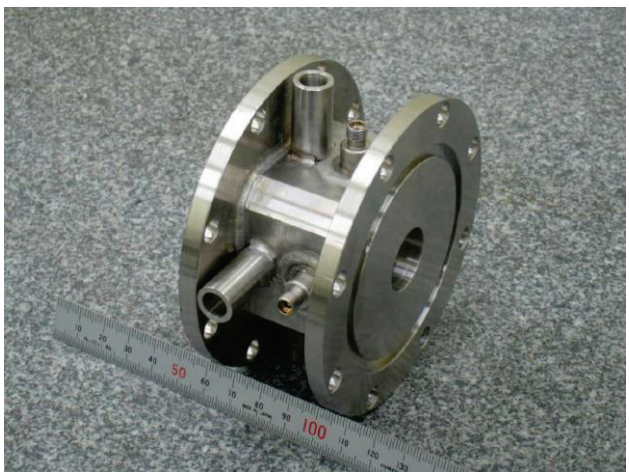

Figure 3: Fabricated BPM for linac.

SIGNAL PROCESSING SCHEME

The signal from the BPM will be processed by using digital IQ demodulation method, which is almost same method used for LLRF system. The output signal contains harmonics of the fundamental frequency of 350 MHz, therefore, we use bandpass filter with a center frequency of 350 MHz. Then each signal is divided into two; one is used for obtaining the position information by using the log-ratio method with a dedicated Bergoz electronics and the other is for phase information. Four signals from a BPM are combined into one by using a RF combiner to remove the dependency of the phase signal on the beam position offset.

To apply the digital IQ demodulation method, the combined signal is mixed with 300 MHz LO signal, which results in 50 MHz IF signal. If we digitize the IF signal with a sampling frequency of 40 MHz, we can obtain IQ data flow as shown in Fig. 4, from which the phase and amplitude information can be calculated.

For digital IQ demodulation, we use a commercial FPGA board (7142 FPGA board, Pentek). It includes 4 ADCs with 125 MHz maximum sampling frequency, 14 bits resolution and 1 DAC with 320 MHz, 16 bits resolution. Xilinx Virtex-4 model FPGA was used for 7142 FPGA PCI mezzanine card. The FPGA board is installed on MVME5100 host board, which includes CPU and memory blocks. For the FPGA core programming, we use VHDL with ISE integrated development tool for FPGA synthesis and implementation. The essential parts of the VHDL code for IQ demodulation is shown in Fig. 5. The application program interface was developed by using Tornado with VxWorks kernel. The signal flow block diagram for the BPM signal processing is shown in Fig. 6.

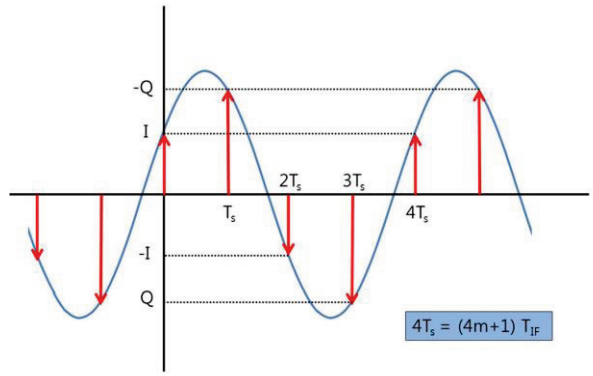

Figure 4: Digital IQ demodulation scheme.

```
process(clk_40MHz)
        begin
        if rising_edge(clk_40MHz) then
                case led_4 is
                        when "00" => data_set(13 downto 0)    <= ADC_IN;
                        when "01" => data_set(27 downto 14)   <= ADC_IN;
                        when "10" => data_set(41 downto 28)   <= ADC_IN;
                        when others => data_set(55 downto 42) <= ADC_IN;
                end case;
        end if;
end process;                                                          MUX

input_data_buffer : infifo56by2048
                port map (
                        clk => clk_10MHz,
                        din => data_set,
                        rd_en => gate_s,
                        rst => gate_s_n,
                        wr_en => gate_s,
                        dout => data_buf,
                        empty => open,
                        full => open);                                Input buffer
                                                                      56 by 2048 FIFO
-- Averaging I and Q ----------------------------------
Q_measure : subtracter14by14
                port map (
                        A => data_buf(27 downto 14), -- data_buf(13 downto 0),
                        B => data_buf(55 downto 42), -- data_buf(41 downto 28),
                        Q => Q_mea_i,
                        CLK => clk_10MHz,
                        SINIT => gate_s_n );
                                                                      Iave=(I-(-I))/2
I_measure : subtracter14by14                                          Qave=(Q-(-Q))/2
                port map (                                            14bit subtracter
                        A => data_buf(13 downto 0), -- data_buf(27 downto 14),
                        B => data_buf(41 downto 28), -- data_buf(55 downto 42),
                        Q => I_mea_i,
                        CLK => clk_10MHz,
                        SINIT => gate_s_n);
-----------------------------------------------------
```

Figure 5: VHDL code for IQ demodulation

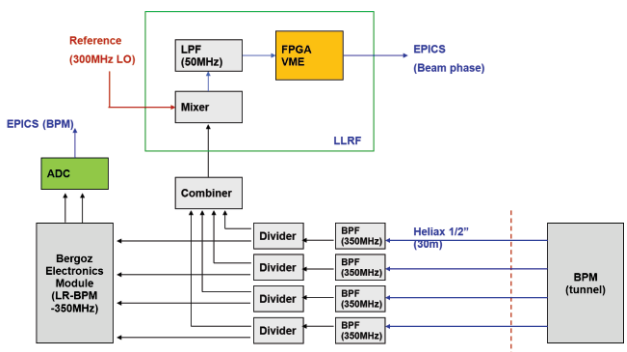

Figure 6: Signal flow block diagram for BPM.

Copyright © 2012 by the respective authors — cc Creative Commons Attribution 3.0 (CC BY 3.0)

PHASE SCAN METHOD

To determine the RF set-point during the commissioning, we will use the phase scan method, which is a well-established technique to set the RF amplitude and phase of the accelerating cavity [5]. The phase scan method is based on the measurement of beam phases at the end of the accelerating cavity under the variation of the input RF amplitude and phase. Then the measured results are compared with the simulation results as shown in Fig. 7, where the RF and beam phases are shifted by a and b to get the best fitting results. Therefore the beam phase and RF phase can be related as following,

$$\phi_{\text{beam}} = b + f(\phi_{\text{rf}} - a).$$

The parameters a and b can be determined by minimizing χ^2 which is defined as follows,

$$\chi^2 = \frac{1}{N}\sum_{i=1}^{N}[f_{\text{ex}}(\phi_i) - (b + f(\phi_i - a)]^2,$$

The number N and function $f_{\text{ex}}(\phi_i)$ represent the number of different RF phase measured during the phase scan experiment and their beam phases, respectively. From the fitting of the χ^2, we can determine the RF amplitude set value.

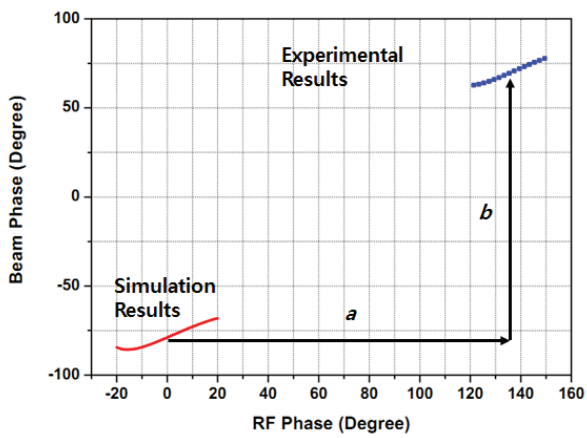

Figure 7: Experimental results compared with the simulation, fitted by shifting RF phase and beam phase.

To facilitate the phase scan procedures, we have developed an RF set-point determination program based on MATLAB GUI with a nonlinear optimization routine, LEVMAR. Figure 8 shows the screen shot of the developed program, which is composed of 4 parts. The first is for input parameters such as DTL tank identification, RF amplitudes of simulation results, the input LLRF (low level RF) value of the RF amplitude, and initial values for shift, a and b. Each parameter has a default value and subjects to be changed to obtain the correct results. The second displays the comparison between the experimental data and simulation results after moving simulation data by the shift parameters, a and b. It calculates the χ value in each case. The fitting results are summarized in the third part of the screen. It includes the determined values of the RF amplitude and phase. The forth part is dedicated to the quadratic fitting of the χ data obtained in the second part. To test the developed program, we generated the artificial experimental data and applied the RF set-point program. It shows that the program works as expected.

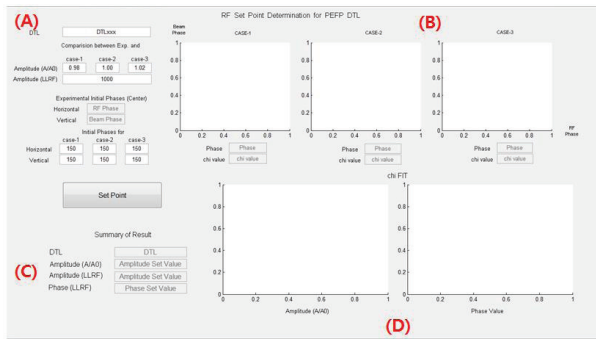

Figure 8: Screen shot of the RF set-point program; (a) input parameters (b) χ^2 calculation by comparing the experiments and simulations (c) determined RF amplitude and phase by quadratic fittings in (d).

CONCLUSION

For the beam phase measurement, which is essential for the RF set-point determination during the commissioning of the PEFP linac, we designed and fabricated strip-line type BPM. The signal processing of the BPM will be performed based on the digital IQ demodulation method by using FPGA. To make it easy to carry out the phase scan procedure, we developed the MATLAB-based GUI program to determine the RF amplitude and phase. Currently the PEFP linac is under installation and the commissioning will be started in early next year.

REFERENCES

[1] K. Y. Kim, Y. S. Cho, J. Y. Kim, K. R. Kim, and B. H. Choi, "The Proton Engineering Frontier Project: Accelerator Development", J. of Korea Phys. Soc., 56 (2010) 1936.

[2] J. H. Jang, H. J. Kwon, and Y. S. Cho, "Beam Commissioning Plan of PEFP 100-MeV Linac", Proceedings of IPAC2011, (2012).

[3] H. S. Kim, Y. S. Cho, S. H. Han, J. H. Jang, Y. H. Kim, and H. J. Kwon, "Initial Test of the PEFP 20 MeV DTL", Proceedings of PAC2005, (2006).

[4] J. Y. Ryu, H. J. Kwon, J. H. Jang, H. S. Kim, K. T. Seol, and Y. S. Cho, "Development of Beam Position Monitor for PEFP Linac and Beam Line", Proceedings of IPAC2011, (2012).

[5] T. L. Owens, M. B. Popovic, E. S. Mccrory, C. W. Schmidt, and L. J. Allen, "Phase Scan Signature Matching for Linac Tuning", Particle Accelerators, Vol.48, p.169, 1994.

Copyright © 2012 by the respective authors — cc Creative Commons Attribution 3.0 (CC BY 3.0)

LINAC CONSTRUCTION FOR CHINA SPALLATION NEUTRON SOURCE

Shinian Fu, Jian Li, Huachang Liu, Huafu Ouyang, Xuejun Yin, IHEP, Beijing 100049, China

Abstract

Construction of China Spallation Neutron Source (CSNS) has been launched in September 2011. CSNS accelerator will provide 100kW proton beam on a target at beam energy of 1.6GeV. It consists of an 80MeV H^- linac and 1.6GeV rapid cycling synchrotron. Based on the prototyping experience, CSNS linac, including the front end and four DTL tanks, has finalized the design and started procurement. In this paper, we will first present an outline of the CSNS accelerator in its design and construction plan. Then the some prototyping results of the linac will be presented. Finally the linac construction progress in recent will be updated.

INTRODUCTION

China Spallation Neutron Source(CSNS) project was approved by the Chinese central government in 2008[1-2]. It has been launched in September 2011. Figure 1 shows the linac tunnel construction status up to now. It is planed to provide neutrons to the users in the first half of 2018. CSNS has a total budget of $260 M for construction of the accelerator, the spallation neutron target and 3 neutron spectrometers. Its site is at Dongguan, south part of China. The local government will support free land, additional budget of $57M, infrastructure, dedicated high-way and power transformer station.

Figure 1: Civil construction status of the linac tunnel.

CSNS accelerator is the first large-scale, high-power accelerator project to be constructed in China. The CSNS is designed to accelerate proton beam pulses to 1.6 GeV kinetic energy at 25 Hz repetition rate, striking a solid metal target to produce spallation neutrons The accelerator provides a beam power of 100 kW on the target in the first phase and then 500 kW in the second phase by increasing the average beam intensity 5 times while raising the linac output energy to 250 MeV. A schematic layout of CSNS phase-I complex is shown in Figure 2. The major design parameters of the CSNS accelerator complex for the two phases are listed in Table 1. In the phase-I, an H^- ion source produces a peak current of 25 mA H^- beam. RFQ linac bunches and accelerates it to 3 MeV. DTL linac raises the beam energy to 80 MeV. After H^- beam is converted to proton beam via a stripping foil, the RCS accumulates and accelerates the proton beam to 1.6 GeV before extracting it to the target.

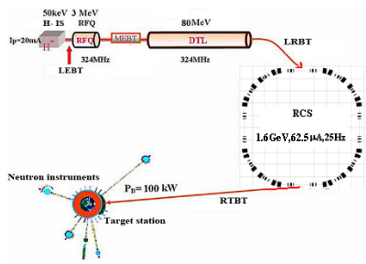

Figure 2: Schematics of the CSNS complex

Table 1: CSNS Design Parameters

Project Phase	**I**	**II**
Beam power on target [kW]	100	500
Proton energy [GeV]	1.6	1.6
Average beam current [μA]	62.5	312.5
Pulse repetition rate [Hz]	25	25
Linac energy [MeV]	80	250
Linac type	DTL	+SC Spoke
Linac RF frequency [MHz]	324	324
Macropulse. ave current [mA]	15	40
Macropulse duty factor	1.0	1.7
RCS circumference [m]	228	228
RCS harmonic number	2	2
RCS acceptance [πmm-mrad]	540	540

LINAC DESIGN AND DEVELOPMENT[3]

Penning H^- ion source is adopted for CSNS linac. The source provides 25 mA peak current, 0.5 ms long, 0.2πμm normalized emittance (rms) pulses at 50 kV and 25 Hz repetition rate for Phase-I.

The LEBT is for matching and transporting the H^- beam from ion source to RFQ accelerator, and pre-chopping the beam according to the requested time structure by the RCS with a chopping rate of 50%. Three-solenoid focusing structure is adopted for space charge neutralization, as shown in Figure 3. An electrostatic deflector is chosen as pre-chopper, positioned at the end of the LEBT. A prototype pre-chopper was installed at the entrance of the 352MHz proton RFQ, and it reached a fast rise time of 15 ns in the beam measurement at the exit of the RFQ[4].

Copyright © 2012 by the respective authors — cc Creative Commons Attribution 3.0 (CC BY 3.0)

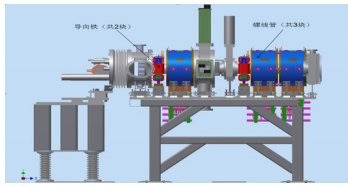

Figure 3: Front end of CSNS linac.

The CSNS RFQ construction is based on our experience of ADS RFQ design and manufacture[5]. A four-vane type RFQ is adopted with RF frequency of 324MHz. It accelerates H- beam from 50 keV to 3 MeV, with duty factor of 1.05%. The inter-vane voltage is 80 kV with Kilpatrick factor of 1.78. It has a total length is 3.62 m and is separated in two segments(Figure4). They are resonantly coupled with the coupling cell in the middle. Each segment technically consists of two modules and each module is composed with two major vanes and two minor vanes, and they are brazed together to form a vacuum cavity. Three sets of 1000 l/s ion pumps and 500 l/s turbo-molecular pumps are designed for an order of 10^{-7} torr dynamic vacuum pressure. Along the RFQ cavity there are 12 tuners in each quadrant for tuning field flatness and minimal dipole component. 20 cooling-water channels are distributed in the cross-section of the cavity for thermal stabilization and frequency tuning during operation. Four RF power couplers feed a pulse power of 510 kW into the cavity.

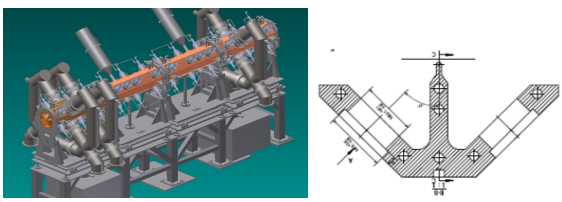

Figure 4: RFQ cavity (right), major vane with cooling-water channels (left).

The total length of MEBT is about 3 m, majorly including 10 qaudrupoles, two bunchers in the first phase. Two J-PARC type RF choppers will be added for the second phase. Beam instruments for beam current, beam position and beam loss are also installed in the MEBT. Figure 5 shows a scheme of the MEBT elements installation. Multi-particle simulation indicates the linac emittance growth majorly occurs in the MEBT. The RMS emittance growths in the x, y, z directions are respectively about 20%, 19% and 16% for 15mA beam in the first phase.

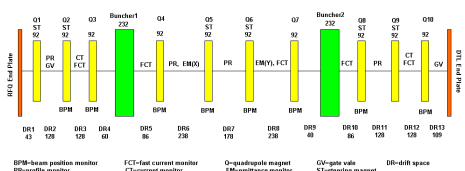

Figure 5: CSNS MEBT elements arrangement.

The DTL accelerates the 3 MeV beam from the RFQ to 80 MeV. The maximum surface field is below 1.3 times the Kilpatrick limit. In the old vision of the DTL design, we used FD lattice with a small drift tube bore radius[4]. It was found the particle losses was more than the limit of 1W/m when all errors were taken into account in the end-to-end multiparticle simulations. So FFDD focusing lattice is used in the new vision of DTL design with a lager bore radius for the drift tubes and lower quadrupole gradient. In this new design, the accelerating field keeps constant in each tank. The major parameters of the DTL tanks are listed in Table 2.

Table 2: The Major Parameters of the DTL Tanks

Tank number	1	2	3	4	total
Output energy (MeV)	21.67	41.41	61.07	80.1	80.1
Length (m)	8.51	8.56	8.78	8.8	
Number of cell	64	37	30	26	157
Cavity power (MW)	1.35	1.32	1.32	1.34	5.33
Total RF power (MW)	1.91	1.92	1.92	1.93	7.68
Accelerating field (MV/m)	2.86	2.96	2.96	3.0	
Synchronous phase (degree)	-35 to -25	-25	-25	-25	

A tank consists of three unit tanks with a length about 2.8 m for fabrication. Drift tubes are mounted on the tank through holes on the top of the tank. DC power supply is used for the focusing quadrupole in the drift tube. Each tank has 12 plug tuners and 2 dynamic tuners. A power coupler with ridged waveguide feed 2 MW RF power to a tank from a klystron. Vacuum of 1×10^{-6} Pa is guaranteed with 6 ion pumps and 3 molecular turbo pumps in each tank. The first tank of the DTL is plotted in Figure 6.

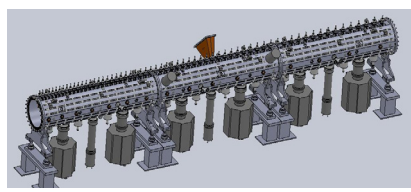

Figure 6: First tank of the CSNS DTL.

A prototype DTL has been fabricated for the technology development and cold measurement[6]. Figure 7 shows the prototype tank and measured alignment result of the drift tubes with error less than 0.03 mm.

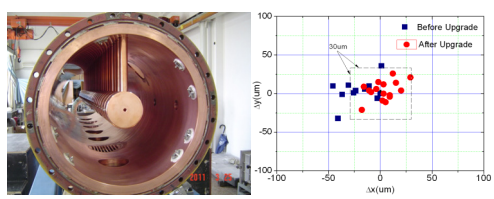

Figure 7: Prototype DTL and the measured center of the drift tubes.

Copyright © 2012 by the respective authors — cc Creative Commons Attribution 3.0 (CC BY 3.0)

LINAC CONSTRUCTION

CSNS linac is planed to start installation at the end of 2013 when the linac tunnel becomes available. Now most of the linac components have started fabrication or procurement.

The ion source has been ready for assembly. Figure 8 shows the major components of the source body. As we have set up a prototype H^- ion source at IHEP with a satisfactory beam current, we can take the advantage of this experience to start beam extraction test and beam transmission tuning in the LEBT in the early of the next year at IHEP before the laboratory at CSNS site becomes available.

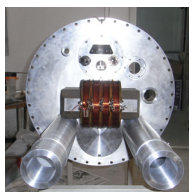

Figure 8: H^- ion source body during assembly.

RFQ cavity is now under fabrication. The 16 major vanes have been drilled the cooling water channels and will start semi-fine machining, while the 16 minor vanes are under fine machining. It is planed to complete the cavity fabrication in the middle of the next year. The RFQ will be powered by two 4616V4 tetrode amplifiers at 324 MHz with an output pulsed power of 350 kW for each. We replaced klystron in the old design with this tetrode just for less cost. Now one of the tetrode power sources has been set up at IHEP, and the test result shows it reached the output power 400 kW with a pulse length of 700㎳ at 25 Hz. Based on this successful experience, another set of the power source will soon start construction. Figure 9 shows the RFQ vanes under fabrication and tetrode power source.

Figure 9: RFQ vanes under fabrication (right) and tetrode power source (left).

For the MEBT, we will not fabricate any magnet and its power supply, as we are going to make use of the existing magnets of the beam line for ADS experiment. Two bunchers will start fabrication in recent and their solid state power sources of 25 kW have been ordered.

The DTL manufacture started in the end of the last year at the workshop of IHEP, at which a prototype DTL has been made. We will basically follow the manufacture technology of the prototype. The tank is made of carbon steel and the inner surface is copper-plated, with a thickness of 0.15mm after polishing. The drift tube is made of full copper and so does the stem. The quadrupole coil is SAKAE type, the same as J-PARC DTL. As the coincident of the mechanical center of the drift tube with the magnetic center of the quadrupole is rather essential requirement beam loss control and the work is very time costing during the manufacture of the drift tube, we built a new rotating-coil measurement system so as to reach a high accuracy of 6㎜ and high efficiency in the measurement of the magnetic center, as well as high-order modes, of the quadrupole. The system is now under test, as shown in Figure 10.

Figure 10: Rotating-coil magnetic measurement system.

Now the first tank is under fabrication, as shown in Figure 11. It is expected the first tank can be installed in the linac tunnel in the January 2014 after the beam commissioning of the RFQ. Then the following three tanks will be installed after the beam commissioning of the MEBT and the first DTL tank in August of 2014.

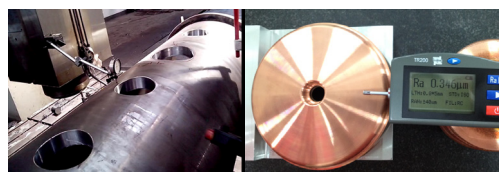

Figure 11: The DTL tank and drift tube under machining.

ACKNOWLEGEMENT

The authors are very grateful to the CSNS linac team members for their great efforts in the design and construction of the linac.

REFERENCES

[1] J. Wei, S.Fu, et al. China Spallation Neutron Source - an overview of application prospects, Chinese Physics C 2009, 33(11): 1033-1042.

[2] Shinian Fu, Hesheng Chen, et al, “Status and Challenges of the Chinese Spallation Neutron Source”, IPAC2011, San Sebastian, Spain, Sept. 2011, TUXA01.

[3] S.N.Fu, H.F.Ouyang, et al., “Status of a High Current Linaer Accelerator at CSNS”, LINAC2008. Victoria, Canada, Sept. 2008, MO202.

[4] H.F.Ouyang, S.N.Fu, J. Li, T. G. Xu, X. J. Yin, “The High Intensity Linac for CSNS”, LINAC2010, Tsukuba, Japan, Sept. 2010, TU202.

[5] S.N.Fu, S.X.Fang, et al., “Construction of a High Current RFQ for ADS Study”, LINAC2006. Knoxville, Tennessee USA, August 2006, MOP053.

[6] H.C. Liu, X.J.Yin, et al, “CSNS DTL Prototyping and RF Tuning”, this proceedings.

Copyright © 2012 by the respective authors — cc Creative Commons Attribution 3.0 (CC BY 3.0)

MAIN LINAC PHYSICS DESIGN STUDY OF THE C-ADS PROJECT*

Fang Yan, Zhihui Li, Cai Meng, Jingyu Tang
Institute of High Energy Physics, Chinese Academy of Science, Beijing, 100049, China

Abstract

The Chinese ADS (C-ADS) project is proposed to build a 1000MW Accelerator Driven sub-critical System before 2032. The accelerator will be operating on CW mode with 10mA average current and the final energy is 1.5GeV. The whole linac are composed of two major sections: the Injector section and the main linac section. There are two different schemes for the Injector section. Injector I is basing on 325MHz RFQ and superconducting spoke cavities and Injector II is basing on 162.5MHz RFQ and superconducting HWR cavities. The main linac design will be different for different Injector choice. If Injector II scheme is adopted, the main linac bunch current will be doubled. In this paper the main linac design basing on Injector II scheme is studied. The design principles and considerations are introduced; the base line design is presented.

INTRODUCTION

Along with the rapid economy growth, China is experiencing an increasing demanding on energy resources and in the mean while is facing an increasing prominent problem of energy resources shortage. In the next two decades, Chinese government will devote major efforts to developing nuclear power, as nuclear power is acknowledged as a clean, safe, economic energy resource in the international society. However the key roadblock to development of additional nuclear power capacity is the concern over management of nuclear waste and it is an open question not only in China. In China, the accumulated waste is estimated to be more than 10k ton in 2020, and it will be doubled in 2030. Worldwide, more than 250,000 tons of spent fuel from reactors currently operating will require disposal.[1,2] In the past two decades, the accelerator driven sub-critical systems (ADS) is raising more and more interest and is actively studied over the world, because it is recognized as the best option for reducing the radioactive toxicity by transmutation the long-life nuclear radioactive waste into short-life radioactive waste and in the mean while getting power production in a controllable way.[3,4] But until now, there are not any large scale ADS accelerator build yet.

The Chinese ADS project is proposed to build a 1000MW Accelerator Driven sub-critical System before 2032. The driven accelerator will be operating in CW mode and the final goal is 1.5GeVwith average current of 10mA. The C-ADS linac includes two major sections: the Injector section and the main linac section. The Injecor accelerate the proton up to 10MeV and the main linac boost the energy from 10MeV up to 1.5GeV. It is staged in three phases. The first phase is aimed to accomplish two different schemes of the Injector designs (IHEP and IMP independently) by 2015 and in the mean time accomplish a part of the main linac up to the energy of 50MeV by 2016. The second phase is planned to extend the main linac energy up to 600MeV with 10mA average current by 2022 and the phase three is to achieve 1.5GeV 10mA final goal by 2032.

The main linac is a critical part of the whole driven accelerator as any design philosophy has to be considered to ensure the beam going through the whole linac and most of the design problems or defects may not appear until the beam is tracked through to the very end of the linac. This paper will present the design considerations of the main linac lattice basing on Injector II scheme.

LATTICE DESIGN AND BEAM DYNAMICS

For ADS applications, it has a rigorous demand on the accelerator stability and reliability. In order to ensure the availability of the ADS reactor and avoiding thermal stress causing damage to the subcritical reactor core, the number of unwanted “beam trips” should not exceed a few per year. This extremely high reliability specification is several orders of magnitude above usual accelerator performance. [5] To fulfill this strict reliability constrains, over-design, redundancy and fault tolerance strategies are implemented in the basic design.

In order to keep the beam in the stable area of Hofmann stability chart [6] and avoid energy change causing emittance growth and beam quality deterioration by thermal equilibrium between transverse and longitudinal planes. The approximately equipartitioning condition is applied on basis of formula (1) [7] and in the mean time to assure a current-independent lattice. According to this formula, once the normalized emittance ratio is fixed the zero current phase advance ratio is fixed accordingly.

$$\sigma_{0t}/\sigma_{0z} = \frac{k_{t0}}{k_{z0}} = \left(\frac{3}{2}\frac{\varepsilon_{nz}}{\varepsilon_{nt}} - \frac{1}{2}\right)^{1/2} \qquad (1)$$

For conservative and especially avoiding any potential reasons which may cause the beam to be unstable such as envelope resonant, the zero current phase advances in all three planes remain below 90 degree.

One of the most critical characters of C-ADS accelerator is keeping the beam loss rate down to 10^{-8}. In order to meet this strict criterion, one has to control the halo growth as small as possible which means the mismatch factor has to be reduced to the maximum extent. Several methods are applied for approaching this goal. The focusing periods of the main linac are designed to have long drifts at both ends to accommodate the cryomodule warm to cold transition without destroying

*Work supported by Advanced Research Project of CAS
#yanfang@ihep.ac.cn

Copyright © 2012 by the respective authors — cc Creative Commons Attribution 3.0 (CC BY 3.0)

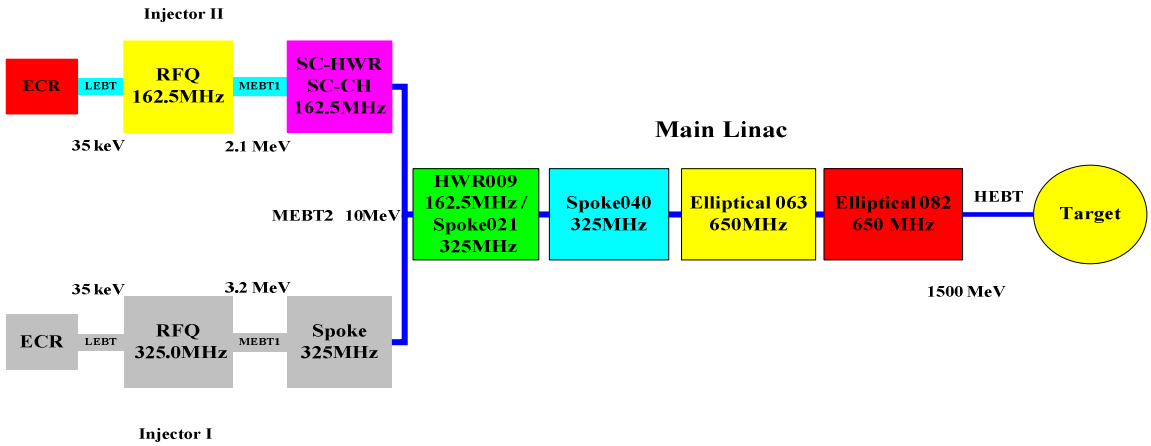

Figure 1: the schematic base line configuration of the C-ADS driver linac.

Table 1: Baseline Design of the C-ADS Superconducting Main Linac Basing on Injector II

	Focusing type	Period length (m)	No. of periods	No. of cavities	Focus devices No.	Eacc* (MV/m)	Nominal Ep (MV/m)	Energy range(MeV)
HWR009	solenoid	2.088	8	16	8	4.1	25	10-17.9
Spoke021	Solenoid	2.168	18	36	18	6.1	25	17.9-49.5
Spoke040	Solenoid	3.856	13	52	13	6.1	25	49.5-139
Ellip063	Triplet	6.074	17	51	17	10.8	30	139-370
Ellip082	Triplet	9.68	21	105	21	12.9	30	370-1500

*The Eacc listed here is corresponding to the nominal design and the effective length used in this paper is $\beta_g \lambda$.

the periodical properties and avoiding possible emittance growth caused by mismatch. The intersection matching is ensured by keeping zero current phase advances per meter smooth along the whole linac. The smoother that the zero current phase advances per meter of the intersection could be designed, the much easier the matching will be. In some cases this is a trade-off because the cavity efficiency may not be fully exploited if the phase advance per meter smooth condition is ensured. The transverse acceptance is ensured by keeping the beam pipe aperture bigger than 8 times of the rms beam size. The longitudinal acceptance is ensured by keeping the synchronous phase bigger than 10 times of the beam rms phase spread. During the intersection matching, the longitudinal acceptance condition must be kept.

Baseline Design

As shown in figure 1, the main linac on basis of Injector II are composed of five sections: two types of two-gap spoke cavities working at 325MHz with geometry beta of 0.21 and 0.40 and two types of 650MHz 5-cell elliptical cavities with geometry beta of 0.63 and 0.82. One additional HWR009 section (the same structure with Injector II cavities) is added in front of spoke021 section. This section is added to meet the longitudinal acceptance condition while keeping the peak gradient of Spoke021 cavity Ep>12.5MV/m to avoid multipacting effects.

The general layout of the main linac base line design is showing in table 1. The total cavity number is 260, the total length is 414 m. For the HWR and spoke section, an additional 117mm space is reserved for the tuner and bellows in each side of the cavity physical length. This number is referenced from the lattice design of the Project-X. The effective length of the solenoid is 150 mm while 75 mm in each side is left for the flange and necessary shielding according to the electromagnetic and mechanical design of the FRIB solenoid. A 100mm is located in between the solenoid and cavity for a cold BPM in case it is needed. At each side of the unit there are two 400mm long drift space, so that 800mm is remained in between the period for accommodating the cryomodule separation. For the ellipse section an inter-cavity distance of 500 mm (100 mm more than the ESS [8] design to ensure there is enough space) nullifies the crosstalk between neighbour cavities, and accommodates both the main power couplers and also higher order mode couplers in case the latter is proven necessary. The relationship between the synchronous phase and 10 times of rms phase spread is shown in figure 2.

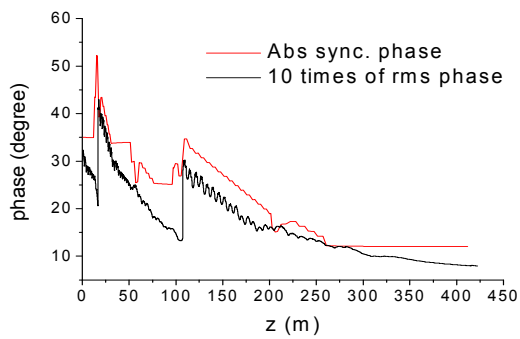

Figure 2: Absolute synchronous phase (red) and 10 times of rms phase spread of the beam (black).

Copyright © 2012 by the respective authors — cc Creative Commons Attribution 3.0 (CC BY 3.0)

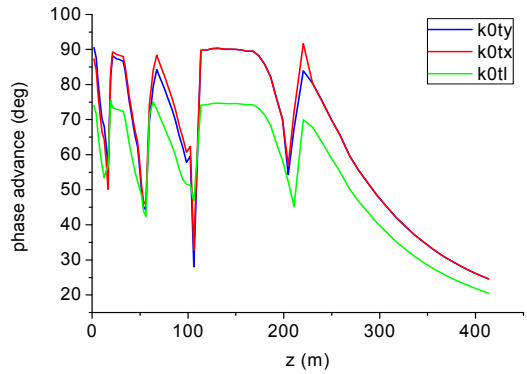

Figure 3: The evolution of transverse (red and blue) and longitudinal (green) phase advances.

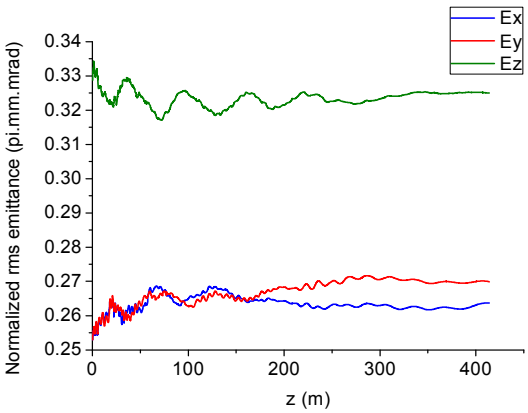

Figure 4: The normalized rms emittance growth along the main linac.

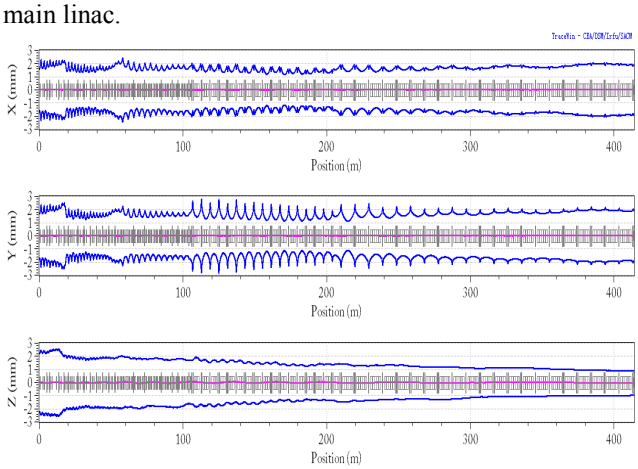

Figure 5: The rms envelope evolution along the main linac

Beam Dynamics Simulations

The beam dynamics programs used for the simulations are TraceWin and Track. The transverse and longitudinal emittance at the exit of RFQ are $0.21\pi mm.mrad$ and $0.273\pi mm.mrad$ respectively. An emittance growth of about 20% is assumed in the injector and MEBT2 section.

Without taking into account all kinds of errors and with an input 6D parabolic distribution of 100000 particles, the multi-particle simulations for the whole main linac section have been carried out. As shown in figure 4, the transverse rms emittance growth are 4.3% and 6.7% for the horizontal and vertical, respectively, the longitudinal emittance growth is -1.1%. From the simulation results, it is find that the rms emittance growth along the linac is under control in all the three phase spaces, e.g. a few percent. The beam halo information is also studied. The 100% emittance growths are under 95%, 120% and 70% for horizontal, vertical and longitudinal directions respectively. These are expected numbers as it is a space charge dominated beam with an average current of 20mA in this design. The envelope evolution is also smooth along the linac as showing in figure 5. The RMS beam size is 2 mm.

SUMMARY AND PERSPECTIVE

A review of the C-ADS main linac basic design and beam dynamics results has been presented. The lattice is designed to be very conservative to meet the reliability and stability specification to the maximum extent. The foot print of the working point in Hoffman Chart is keeping in the stable area to make sure there is no energy change between different freedoms. The error analysis will be processed basing on this design.

REFERENCES

[1] Shinian Fu, Shouxian Fang, Jiuqing Wang, Xialing Guan, Proton linac for ADS application in China, Proceedings of Linear Accelerator Conference LINAC2010, Tsukuba, Japan .

[2] R. L. Sheffield, Utilization of accelerators for transmutation and energy production, Proceedings of HB2010, Morschach, Switzerland.

[3] Shouxian Fang, Xialing Guan, Shinian Fu, Accelerator driven sub-critical research, Proceedings of the 7th Chinese particle accelerator conference 2004:184-190.

[4] Zhixiang Zhao, International research development of the accelerator driven subcritical system. Nuclear Physics Review, 1997, 14 (2): 121-124.

[5] J. L. Biarrotte, Didier Uriot. Dynamic compensation of an rf cavity failure in a superconducting linac, Physical review special topics-Accelerators and beams, 2008, 11 (072803): 1-11.

[6] I. Hofmann Stability of anisotripic beams with space charge. Physical Review E, 1998, 57 (4), 4713-4724.

[7] Martin Reiser, Theory and Design of Charged Particle Beams, Weinheim: Wiely-VCH,208:612.

[8] M. Eshraqi et al, Beam dynamics and design of the ESS linac, Morschach: proceedings of HB2010, 2010:300-303.

Copyright © 2012 by the respective authors — cc Creative Commons Attribution 3.0 (CC BY 3.0)

325 MHz CW ROOM TEMPERATURE HIGH POWER BUNCHING CAVITY FOR THE CHINA ADS MEBT1

S. Pei, H. Ouyang, J. Zhang, X. Li, IHEP, Beijing 100049, P. R. China

Abstract

Two room temperature high power bunching cavities are required to be located in the ADS MEBT1 section. Double re–entrant nose cone geometry has been adopted as the type of the bunching cavity for its simplicity, higher shunt impedance and lower risk of multipacting. SUPERFISH is used to optimize the internal dimensions of the bunching cavity, then the RF–thermal–structural–RF coupled analysis were carried out in ANSYS to obtain the preliminary mechanical design, the layout of the cooling channels is optimized to suppress the frequency shift as much as possible. The cavity was specially designed to have the capability to withstand the 1 atm air pressure effect. In addition, the main dimensions of the coupler and tuner are also estimated.

INTRODUCTION

The ADS pilot project based on the proton linac is being developed at IHEP, Beijing, China [1]. In order to realize the matching in both transversal and longitudinal phase spaces, one Medium Energy Transport Line (MEBT1) is needed in the front end injector—injector–I [2], while bunching cavity is one of the key components. Two 325 MHz bunching cavities with a relatively large aperture of 34 mm and an effective voltage of 120 kV are required. In order to obtain high shunt impedance and low risk of multipacting, the nose–cone geometry shown in Fig. 1 has been selected as the cavity shape.

The China ADS accelerator will operate at the CW mode (100% duty factor), SUPERFISH was used to optimize the internal geometric dimensions of the cavity. The RF–thermal–structural–RF coupled analysis has been done in ANSYS to finalize the layout of the cooling channels, so that the Von Mises stress induced by the high RF heating load can be fairly lower than the yield strength of the cavity material. To suppress the frequency shift caused by the air pressure, the cavity was designed to have double walls consisting of an inner copper wall and an outer stainless steel wall. HFSS and CST Microwave Studio have been used to match the power coupler and estimate the tuner tuning range.

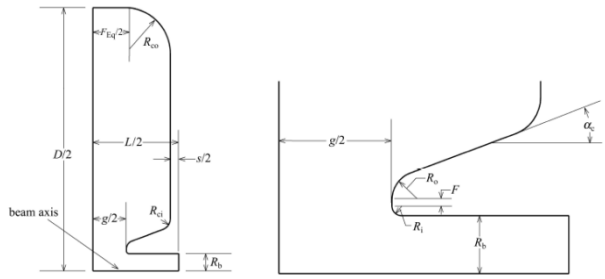

Figure 1: Cavity with nose–cone geometry.

CAVITY INNTERNAL SHAPE OPTIMIZATION

The cavity internal geometric dimensions determine its RF characteristics, such as the shunt impedance *R*, the transit–time factor *T*, the Kilpatrick factor and so on. Cavity with higher *R* and *T* has lower RF heat load, and then the cooling design can be simplified to the largest extent. With the fixed effective cavity voltage, lower Kilpatrick factor will greatly reduce the possibility of electrical discharge (sparking). Fig. 2 shows the relationship between the effective impedance *RTT*, the Kilpatrick factor and the main cavity internal dimensions.

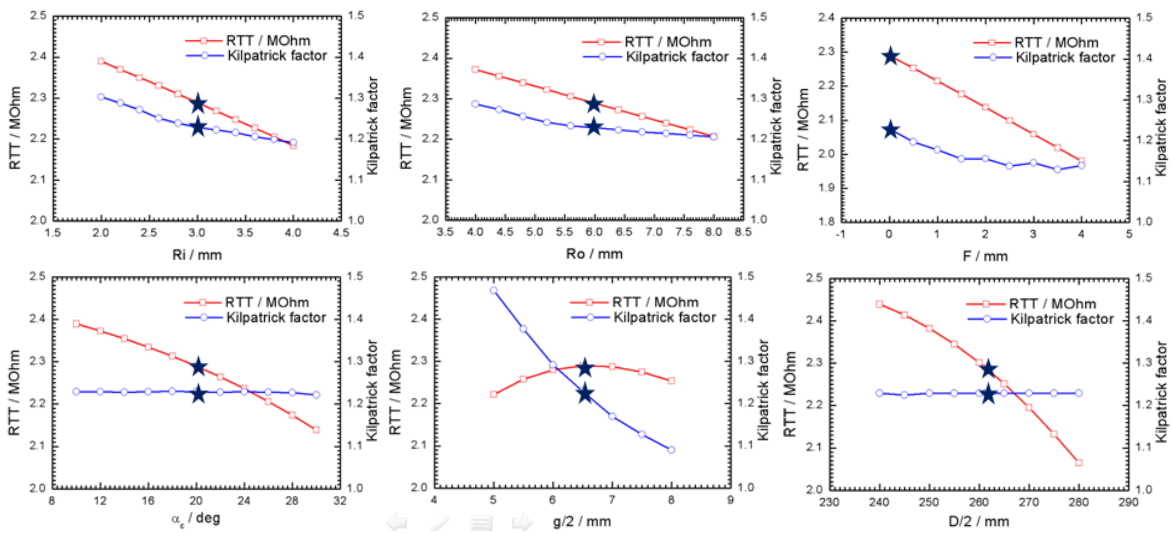

Figure 2: Relationship between the effective shunt impedance *RTT*, the Kilpatrick factor and *Ri*, *Ro*, *F*, α_c, *g*/2, *D*/2.

#peisl@ihep.ac.cn

Copyright © 2012 by the respective authors — cc Creative Commons Attribution 3.0 (CC BY 3.0)

Certain compromise has been made by considering both the RF performance and the mechanical simplicity; the dimensions marked with pentacle were finally selected. Table 1 shows the main specifications of the cavity; Fig. 3 shows the 3D cavity model and the power loss distribution on its inner wall surface.

Table 1: Main specifications of the bunching cavity

Parameter	Value	Unit
Frequency	325	MHz
Particle energy	3.2128	MeV
Effective voltage	120	kV
Q	27159	
Effective shunt impedance *RTT*	2.26	MOhm
Power dissipation (SUPERFISH)	6.3	kW
Peak electric field	21.9	MV/m
RTT/Q	84.3	Ohm
Inner cavity diameter	522.5	mm
Bore diameter	34	mm
Gap	13	mm
Cavity length (wall–to–wall)	170	mm
Tuner tuning range	740	kHz
Kilpatrick factor	1.23	

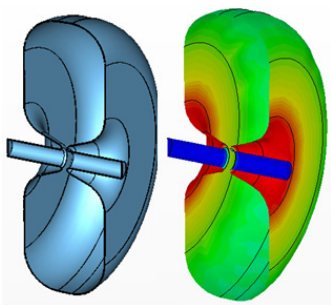

Figure 3: The 3D cavity model and the power loss distribution on the inner cavity wall surface.

RF–THERMAL–STRUCTURAL–RF COUPLED ANALYSIS

The average power dissipation of the two bunching cavities will be ~6.3 kW obtained by SUPERFISH, but real power is generally 1.2–1.4 times of that, here a compromised factor of 1.3 is used in the RF–thermal–structural–RF analysis by ANSYS.

Figure 4 shows the preliminary mechanical design of the cavity. The main body is made of OFE free copper with two separate parts, which will be welded together along the circumference of the 45 mm thick cavity side walls. Due to the internal vacuum, the two end walls was designed to have double plates—25 mm thick inner copper plate and 10 mm outer stainless steel stiffening plate, which are used to suppress the cavity deformation (i.e. frequency shift) induced by the 1 atm air pressure effect. The copper and stainless steel plates are welded together completely before finish machining. Moreover, to reduce the frequency shift caused by the RF heating, 10 rectangular cooling channels (10 mm × 10 mm) with 3 m/s water flowing velocity were applied, of which 8 for the two nose cones/end plates and 2 for the side walls.

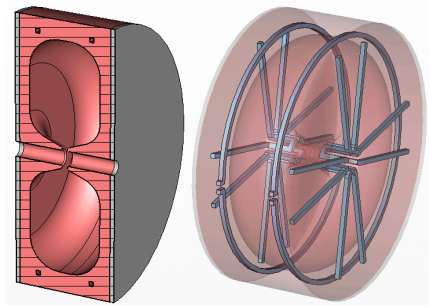

Figure 4: Preliminary mechanical design.

Figure 5 shows the temperature distribution in the cavity body with 20 °C cooling water. The maximum temperature rise is located at the nose cone region, which is 33.5 °C and 12.7 °C higher than the minimum temperature of 20.8 °C. Correspondingly, the cavity body deformation is shown in Fig. 6. Part of the cavity end wall has the largest deformation of 16.3 μm, while the nose cone separation is only reduced by 3.25×2=6.5 μm (~20 kHz frequency decrease [3]). The cavity frequency shift due to the overall deformation is –57 kHz.

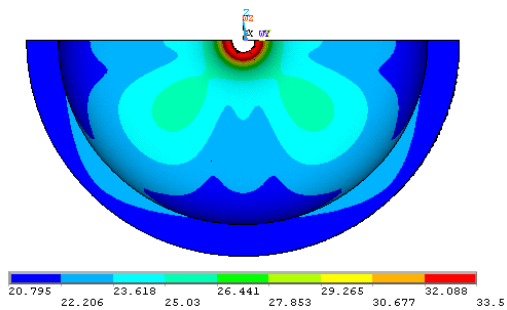

Figure 5: Temperature distribution in the cavity body for 20 °C cooling water.

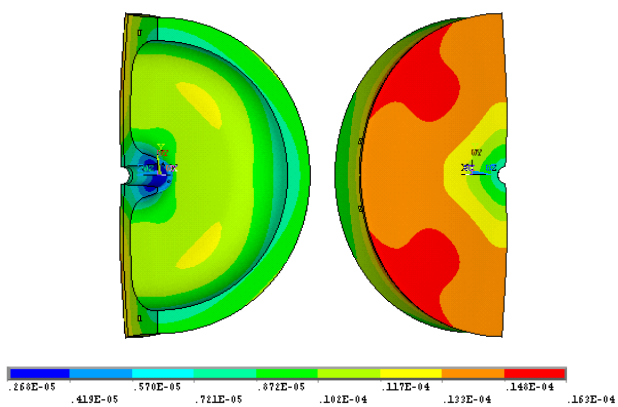

Figure 6: Deformation distribution in the cavity body for 20 °C cooling water.

Copyright © 2012 by the respective authors — cc Creative Commons Attribution 3.0 (CC BY 3.0)

Figure 7 shows the von Mises stress distribution for 20 °C cooling water. It can be seen that the maximum Von Mises stresses are both fairly lower than the yield strengths of the stainless steel (>260 MPa) and copper materials (~33 MPa).

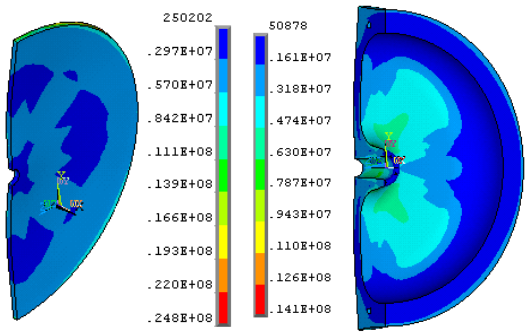

Figure 7: Von Mises stress distribution in the stainless steel plate and the cavity copper part.

If air pressure effect is also considered with the RF heating in the ANSYS coupled analysis, the cavity frequency will be further reduced because the air pressure will put an inward force on the whole cavity body.

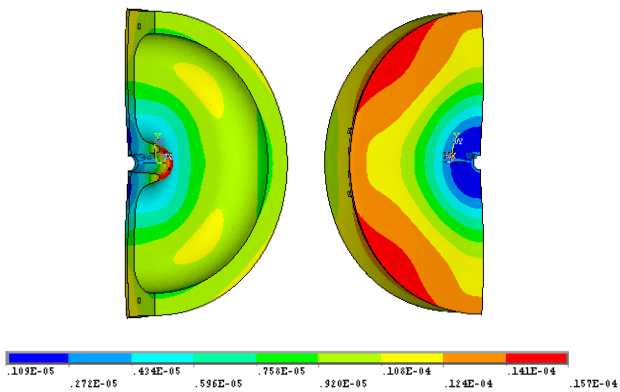

Figure 8: Deformation distribution when both RF heating and air pressure effect are considered.

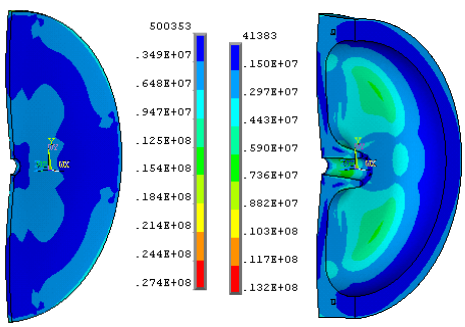

Figure 9: Von Mises stress distribution when both RF heating and air pressure effect are considered.

Fig. 8 shows the cavity deformation caused by both RF heating and air pressure, the resulted frequency shift goes up to –136.5 kHz, which can be adjusted back on resonance by the tuners. Both the nose cone tip and part of the cavity end walls have the largest deformation of 15.7 μm, and the nose cone separation decreases by 13.8×2=27.6 μm (~83 kHz frequency decrease [3]). The cavity deformation at the end wall (also the induced frequency shift) resulted from the RF heating are partially compensated (~40–45%) by the air pressure effect. The corresponding von Mises strength distribution is shown in Fig. 9. Similar to Fig. 7, the connecting edges of the copper side wall and the stainless steel plate have the largest von Mises strengths, which have no big change when air pressure effect is also included in the ANSYS analysis.

TUNER AND COUPLER

Two water cooled tuners will be adopted to tune the cavity frequency back on resonance for CW full power operation (~6.3×1.3=8.2 kW). Each tuner will be remote controlled by a step motor. A total tuning range of 2×370=740 kHz can be obtained by a slug diameter of 50 mm and a maximum penetration of 40 mm into the cavity vacuum region.

Two kinds of power couplers shown in Fig. 10 have been investigated with similar RF characteristics. Due to the relatively bigger inner conductor diameter (~21.4 mm, ~1.5 times of that for the undercut type) at the ceramic window region, the choke type was finally chosen for easy water cooling design. Moreover, for flexible adjustment of the coupling, the coupler will be designed to have a rotatable flange welded to a stainless steel transition to the cavity copper body.

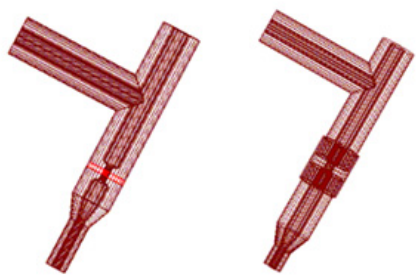

Figure 10: Two investigated power couplers (left—undercut type; right—choke type)

SUMMARY

Two CW bunching cavities with high average power up to couples of kW are needed for the ADS MEBT1 in China. The cavity was optimized to reduce the frequency shift caused by both RF heating and air pressure effects. The tuner and coupler designs were discussed.

REFERENCES

[1] H. Chen et al., “ADS Accelerator Program in China”, IHEP–FNAL Workshop on Proton Accelerator, Beijing, February 15–16, 2011.

[2] H. Geng et al., “The MEBT Design for the China Accelerator Driven System”, WEPS050, Proceedings of IPAC 2011, San Sebastian, Spain.

[3] G. Romanov et al., “CW Room–temperature Bunching Cavity for the Project X MEBT”, WEP221, Proceedings of PAC 2011, New York, USA.

Copyright © 2012 by the respective authors — cc Creative Commons Attribution 3.0 (CC BY 3.0)

THE BEAM COMMISSIONING PLAN OF INJECTOR II IN C-ADS*

Z.J. Wang, Y. He, H. Jia, S.H. Liu, C. Li, X.B. Xu, B. Zhang,
W. Wu, H.W. Zhao IMP, Lanzhou,730000,China

Abstract

The design work of the Injector II, which is 10 MeV proton linac, in C-ADS project is being finished and some key hard wares are being fabricated. Now it is necessary to definite the operation mode of beam commissioning, including the selection of the beam current, pulse length and repetition frequency. Also the beam commissions plan should be specified. The beam commissions procedures is simulated with t-mode code GPT [1]. In this paper, the general beam commissioning plan of Injector II in C-ADS and simulation results of commissions procedures are presented.

INTRODUCTION

Nuclear energy as a kind of clean energy will be widely used in Chinese energy program in the future. But one of the serious problems is how to handle radioactive waste produced by nuclear plants. ADS, which is the effective tool for transmuting the long-lived transuranic radionuclides into shorter-lived radionuclides, is being studied in the Chinese Academy of Sciences. The road map of the project is shown in Fig. 1.

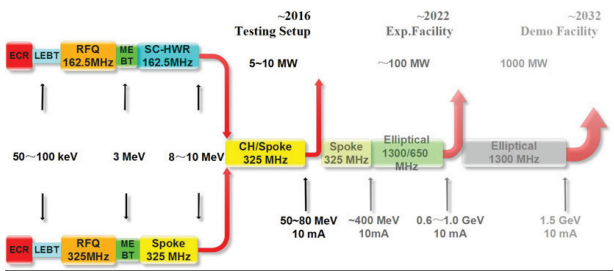

Figure 1: The roadmap of China CAS.

The linac will accelerate the proton with beam current 10mA to about 1.5GeV to produce high flux neutrons for transmutation of nuclear waste.

To ensure technical feasibility in the low energy section, two injectors for the superconduction linac are studded during the first step. One of the injectors, that is Injector II, is been designed and fabricated at Institute of Modern Physics of the Chinese Academy of Sciences.Injector II as part of the ADS is being designed and built at IMP. Injector II is composed of Low Energy Beam transport Line(LEBT), Radio Frequency Quadrupole(RFQ), Medium Energy Beam transport Line(MEBT) and the SC accelerating section. The layout of Injector II is shown in Fig. 2.The LEBT will match the proton beam with 0.035MeV from the ECR source to the RFQ by two solenoids. The RFQ will accelerate and focus the beam from 0.035 MeV to 2.1 MeV simultaneously. The MEBT has two main functions, which are to match the proton beam from the RFQ to the superconducting accelerating section and to place some on line beam diagnostics devices. The superconducting accelerating section will accelerate proton from 2.1 MeV to 10 MeV with 16 superconducting half wave resonator(HWR) cavities. .

The basic parameters of Injector II are listed in Table. 1.

Table 1: The basic parameters of injector II.

Parameters	Value
Particle type	Proton
Operation frequency(MHz)	162.5
Operation mode	CW
Input beam energy(MeV)	0.035
Output beam energy(MeV)	10
Beam current(mA)	10

In this paper, the general beam commissioning plan of Injector II in C-ADS and simulation results of commissions procedures are presented.

THE BEAM DYNAMICS OF INJECTOR II

The MEBT and superconducting section are simulated by TRACK code. The particles distribution out from the RFQ [2] are transported as the initial distribution of the downstream lianc.

The results of the simulation with three-D field map are shown in Fig. 3. The RMS envelopes in both transverse and longitudinal direction are smooth and periodic in the superconducting section. This depicts that there is good matching between MEBT and the superconducting section.

COMMISSIONS BEAMS OF INJECTOR II

The commissions beams will be chopped for the commissioning of RFQ at first stage, then we plan to use unchopped beam for the bulk of the superconducting section commissioning studies. The beam will be consistent with the beam-handing capabilities of the beam diagnostics system in use at the time.

Beam current

The 0.5mA peak current beam will be chosen to be as the initial commissioning study. The reason is we want to reduce the space charge effect as weak as possible to simply the initial commissioning. At the same time the low limitation of measurement dynamics range of the beam diagnostics device should be considered. Also the low current is

* Supported by the National Natural Science Foundation of China (Grant No.11079001)

Copyright © 2012 by the respective authors — cc Creative Commons Attribution 3.0 (CC BY 3.0)

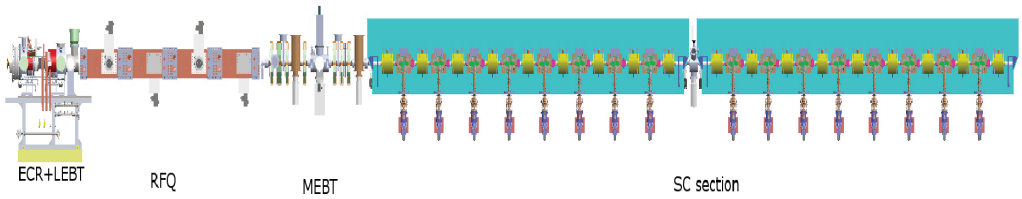

Figure 2: The layout of C-ADS Injector II .

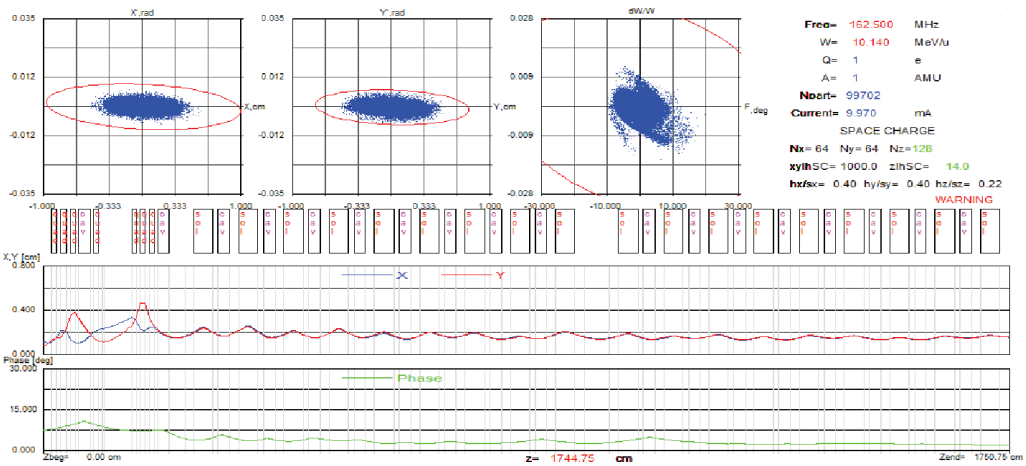

Figure 3: The simulation results of MEBT and the superconducting section.

chosen to minimize dose and activation during initial commissioning. Once the initial linac setup is done, we will increase the current to 1mA, 5mA and finally 10mA.

Pulse length

The pulse length will be set by two factors. One is the limitation of the diagnostics system. The other factor is the machine protect. At the beam commissions stage, the beam will lost on the accelerator element probably. To determine the pulse length, the time dominant code GPT is used to simulated the beam loss in superducting section, which is shown in Fig. 4. . In the Fig.4, the beam loss power distribution is shown supposing the first cavity is broken down. The maximum beam power is 1100W/m. To prevent the quench of superconducting cavity caused by lost beam, the pulse length of commissions at 10mA should be less than 100us.

Repetition rate

The beam commissioning of RFQ will be carried out at repetition rate equal or less that the repetition rate of RFQ RF power supply. Because the energy out from RFQ is 2.1MeV, the radiation activation will be not an issue. For the commissioning of superconducting section, low repetition rate 1Hz will be as initial commissioning beam. ”Beam on demand” mode will be used whenever possible and appropriate in order to minimize activation and thermal damage of the hardware by high energy and high power beam.

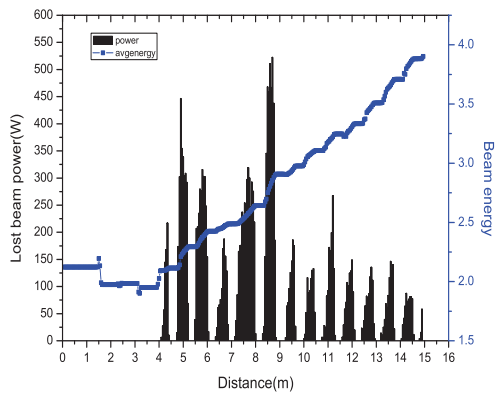

Figure 4: The lost beam power distribution when the first cavity breaks down at 10mA.

THE BEAM COMMISSIONS PLAN OF THE INJECTOR II

In InjectorII, two key sections are RFQ and superducting section. In this paper, the beam commissions plans about this two section are stated. The goal of beam commissions is CW mode at 100KW beam power. An beam dumper will be installed at the end of adjustable HEBT, which will deliver beam with different energy to the beam dumper at different stage.

Copyright © 2012 by the respective authors — cc Creative Commons Attribution 3.0 (CC BY 3.0)

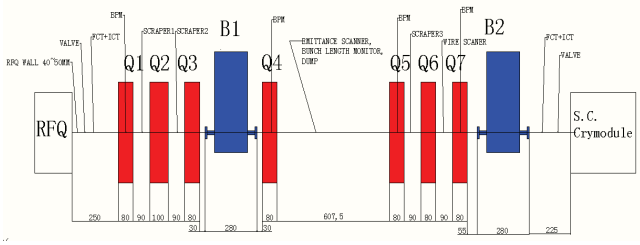

Figure 5: Layout of beam diagnostics in MEBT.

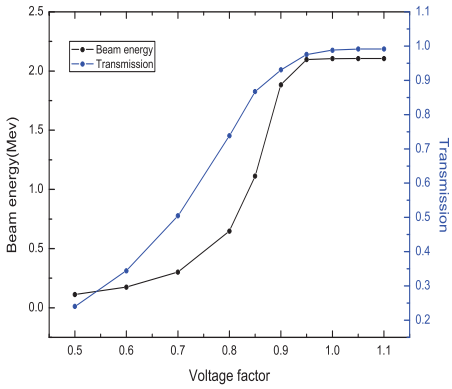

Figure 6: The relation of cavity voltage factor with beam power and transmission.

RFQ and MEBT

The RFQ section will be installed with MEBT at the same time. There are kinds of diagnostics equipments installed at MEBT as shown in Fig. 5. As shown in Fig.5, two sets ICT and FCT are located at the entrance and exit of MEBT to measure the transmission of the RFQ. Also there are other diagnostics equipments to measure the information of beam out from the RFQ, such as emittance, beam halo.

The InjectorII RFQ is designed to accelerated proton beam to 2.1MeV with code PARMTEQ-M [3]. The beam dynamics of RFQ is benchmarked with code TRACK. One of the importance processes of beam commissioning of RFQ is finding the RF operation point by comparing the calculation and experimental results of beam transmission. The simulation results for the beam transmission is given in Fig. 6.

The blue line means the beam transmission rate as a function of the voltage factor, and the black line means output energy evolution with voltage factor. The rehalation can give us an guide in the real beam commissioning experiment.

The superconducting section

For the superconducting section, there are 16 focusing period and one BPM in each period. The BPMs can be used in both transverse orbit correction and RF operation point setting. The RF operation point setting is an main process

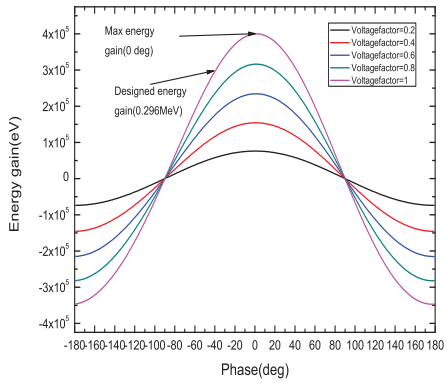

Figure 7: The energy gain of first cavity varying with voltage factor.

in beam commissioning. In the tuning of superconducting cavity, first step is to find the synchronous phase. This can be performed by rotating the phase at low accelerating voltage(150-200KV). Two BPMs down stream are used to find the maximum energy increase, which is correspond to zero degree, and then setting the phase to the designed synchronous phase. Second step is to set the amplitude of field, which can be determined by the beam energy out from the cavity. The beam energy variation with the phase is plotted in the Fig. 7. As shown in Fig.7, maximum energy gain correspond to zero degree, the synchronous phase can be find through this way.

SUMMARY

The installation of Injector II of CADS project will start at the beginning of 2013. the commissioning consists of two main stages, RFQ and superconducting section, is scheduled for 2013. The beam commissioning goal is the proton beam power of 100KW for CW 10MeV out from Injector II. The commissioning beam will begin with peak current 0.5mA, pulse length 100us and repetition rate 1Hz.

REFERENCES

[1] http://www.pulsar.nl/gpt/

[2] P.N. Ostroumov, V.N. Aseev, B. Mustapha, TRACK - a Code for Beam Dynamics Simulation in Accelerators and Transport Lines with 3D Electric and Magnetic Fields, 2007. http://www.phy.anl.gov/atlas/TRACK/Trackv37/Manuals/tv37_man_index.html

[3] K. R. Crandall et al., RFQ Design Codes, Los Alamos National Laboratory report LA-UR-96-1836

Copyright © 2012 by the respective authors — cc Creative Commons Attribution 3.0 (CC BY 3.0)

PROGRESS OF ONE OF 10 MeV SUPERCONDUCTING PROTON LINEAR INJECTORS FOR C-ADS*

Y. He, Z.J. Wang, B. Zhang, S.H. Zhang, Z. XU, W. Wu, J.X. Wu, Z.M. Zhang, J.H. Zhang, J. Meng, A.M. Shi, Z.Z. Zhou, H.W. Zhao, H.S. Xu, Institute of Modern Physics, Lanzhou, China
D. Li, LBNL, Berkeley, California, USA

Abstract

A 10 MeV superconducting proton linac is being design and constructing at Institute of Modern Physics (IMP) of Chinese Academy of Sciences (CAS). This proton linac is one of two injectors for Chinese ADS project. It is to validate one of concepts technical baseline for C-ADS front end, to demonstrate the low beta acceleration, to minimize the risk of key technologies within the Reference Design. It consists of a 2.1 MeV RFQ and two cryomodules hosting 8 HWR cavities. The basic frequency is 162.5 MHz. The physical design of linac and the progress of prototypes for solid-state amplifiers, superconducting solenoids, superconducting HWRs, ion source, and RFQ are presented in the paper.

INTRODUCTION

The China ADS (C-ADS) project [1] is a strategic plan to solve the nuclear waste problem and the resource problem for nuclear power plants in China. The road map is shown in Figure 1. It is a long-term planning till 2032. In the first five years (phase I), the goal of the project is to do the research of key components. The prototypes of high stability proton source, RFQ [2], superconducting cavities and the relative hardware will be developed. A superconducting linac with ~30 MeV proton beam will be demonstrated. The accelerator for C-ADS is a superconducting proton linac. It consists of two injectors with energy of 10 MeV, and a main linac. The two injectors will be identical and hot spare during operation. It is the redundancy of low energy section of accelerator. Due to the technology on low energy superconducting linac is unqualified, the injectors of C-ADS will follow two concept designs. The injector I bases on spoke cavities and frequency of 325 MHz, and the injector II bases on HWR cavities [3] and the frequency of 162.5 MHz. The two injectors will be constructed in parallel by the Institute of High Energy Physics (IHEP) and Institute of Modern Physics (IMP) separately.

Table 1: Main Specifications of C-ADS

Item	Quantity	Unit
Energy	1.5	GeV
Current	10	mA
Beam power	15	MW
RF frequency	(162.5)/325/650	MHz
Duty factor	100	%
Beam loss	< 1	W/m

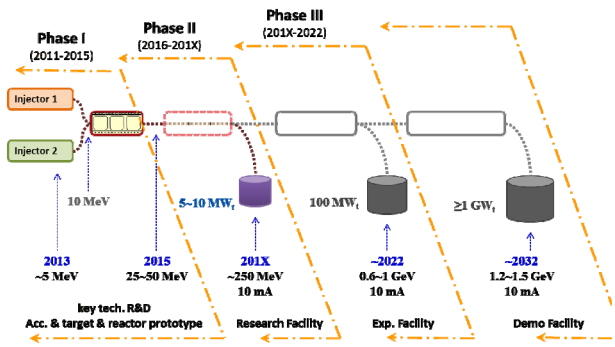

Figure 1: Road map of C-ADS.

PROGRESS OF PROTOTYPES

Conceptual Physics Design

The layout of injector II is shown in Figure 2. The accelerator for C-ADS will operate in CW mode. That is a challenge for RFQ design. Considering the possible thermal-problem of the RFQ, the basic frequency of injector II is selected as 162.5 MHz, the half of frequency of injector I. The main design parameters of injector II for C-ADS proton linear accelerator are listed in Table 2.

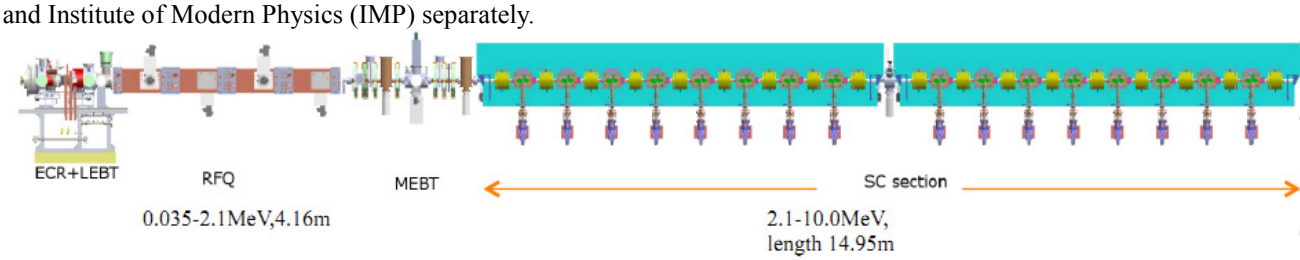

Figure 2: Layout of injector II for C-ADS.

*Work supported by the "Strategic Priority Research Program – Green Nuclear Energy: ADS Transmutation System" of the Chinese Academy of Sciences, Grant No. XDA03020102

Copyright © 2012 by the respective authors — cc Creative Commons Attribution 3.0 (CC BY 3.0)

Table 2: Main Specifications of Injector II

	Energy (MeV)	Focusing elements	RF cavity	Length (m)
ECR	0.035	-	-	-
LEBT	0.035	2 r.t. sols	-	1.6
RFQ	0.035~2.1	-	4-vane	4.2
MEBT	2.1	7 r.t. quads	2 r.t. QWRs	2.5
scDTL	2.1~5~10	18 sc sols	16 sc HWRs	14.95

LEBT

The lattice design of LEBT is upgraded for adding a chopper system. This is because beam chopping is very important for the commissioning of the C-ADS linac, when one increases the beam duty factor from very low to 100% step by step. After having studied the very short pulse length operation mode (down to 10 or 20 us) for commissioning the superconducting cavities and the neutralization effect in the LEBT, we found that a chopper at the LEBT end is necessary, significantly better than just using the pulsing of the ion source. The detail layout of the chopping system is shown in Figure 3.

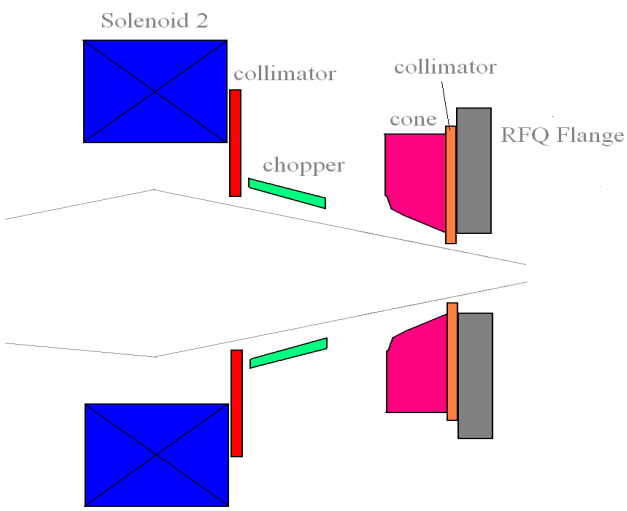

Figure 3: Schematic layout of the fast chopper at LEBT.

The chopping system is located between the second solenoid and the RFQ. The hardware of LEBT has been fabricated. The beam commissioning will be by the end of 2012.

RFQ

The Injector II RFQ is designed to accelerate proton from 0.035MeV to 2.1MeV at 162.5MHz. The main parameters are summarized in Table 3. The mechanical structure is shown in Figure 4.

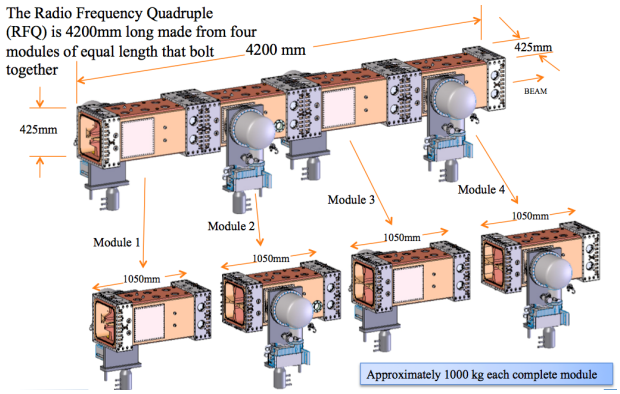

Figure 4: Mechanical structure of RFQ

Table 3: Main Design Parameters for the Injector-II RFQ

Parameter	Value
Inter-vane voltage V (kV)	65
Average bore radius r_0 (cm)	0.5731
Vane tip curvature (cm)	0.4298
ρ / r_0	0.75
Vane length / Total length (cm)	419.2 / 420.8
m_{max}	2.38
Gap1(entrance) (cm)	1.004
Gap2 (exit) (cm)	0.5988
Number of cells	192 (including 2 T cells)
Maximum surface field (MV/m)	15.7791
Synchronous phase	From -90° to -22.7°
a_{min} (cm)	0.3158
Input norm. RMS emittance (x/y, π.mm.mrad)	0.3/0.3
Output norm. RMS emittance (x/y/z, π.mm.mrad, keV.ns)	0.31/0.31/0.92
Overall beam transmission @ 0 /15 mA	99.7% / 99.6%

The RFQ adopts four-vane structure. Considering the dimensions of cavity, four fabrication testing, flying cutter, single vane, 1/4 brazing model, 1/2 full prototype, and an Aluminum model for tuning need to be done in advance. The Al model, 1/4 brazing model, and single vane have been finished. Tuning research on the Al model is on going. The single vane has been machined and the flying cutting tolerance is less than 40 um. 1/4 model brazing has been done in both vacuum and hydrogen finance. The maximum brazing deformation can be controlled less than 100 um. The tolerances are

Copyright © 2012 by the respective authors — cc Creative Commons Attribution 3.0 (CC BY 3.0)

acceptable but still need to be improved. Half size model fabrication is on going. The fabricated testing models are shown in Figure 5. The half model with pi-mode rods, vanes and tuners, also shown in Figure 5, is fabricating in workshops.

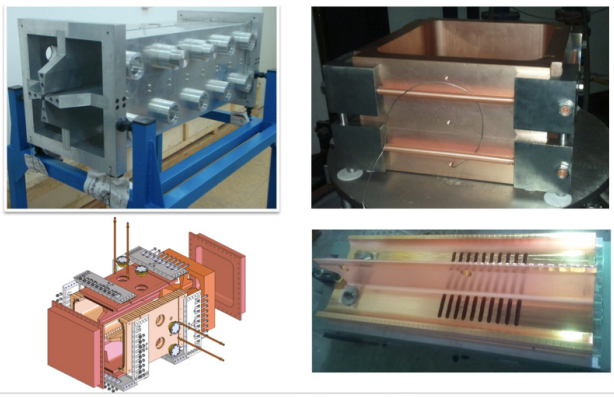

Figure 5: Al and testing models.

Superconducting HWR

The superconducting HWR is designed by IMP. The frequency of cavity is 162.5MHz. The main specifications are shown in Table 4.

Table 4: Main Specifications of HWR

Parameters	Value
F (MHz)	162.0
Gβ	0.09
E_{peak}/E_{acc}	5.34
B_{peak}/E_{acc} (mT/Mv/m)	10.92
R_a/Q_0	148
E_{peak} (MV/m)	25
B_{peak} (mT)	50
E_{acc} (MV/m)	4.7
U_{acc} (MV)	0.78
$G=R_s*Q_0$ (Ω)	28.5
Stored Energy (J)	4
P_{diss} (W)	5.0
Q_0 (4.4K)	1.0E+09

One copper prototype has been fabricated. It was tested in room temperature and liquid nitrogen temperature [2]. The frequency shift 1 atm. and 77 K of liquid nitrogen are 53.59 kHz and 550.6 kHz separately. The tuning sensitive of copper is 150 kHz/mm by calculation and 114 kHz/mm by measurement. The frequency and the field distribution measured by pull-ball are well coincided with the design value. The scissors type tuner works with copper cavity and measured together. The frequency in MHz changes with motor movement in mm is shown in Figure 6.

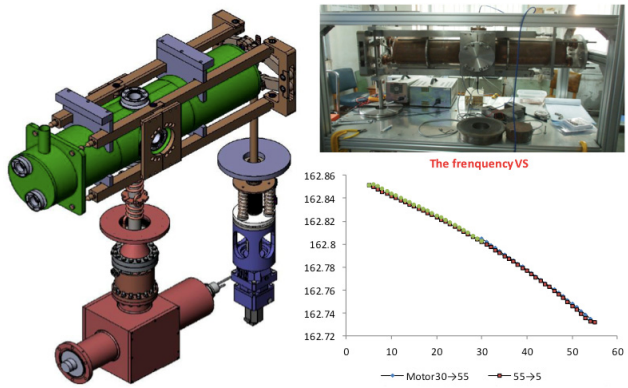

Figure 6: Tuning of copper model.

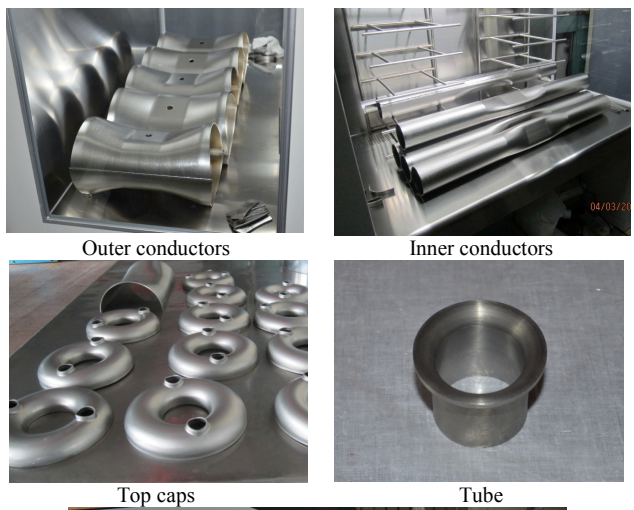

Outer conductors Inner conductors

Top caps Tube

Pre-tuning before assembly of niobium cavity

Figure 7: Prototype of niobium cavity.

The progress of niobium prototype is shown in Figure 7. The parts of cavity were prepared. It was pre-tuned to achieve right frequency. The first batch cavities will be welded by the end of the September 2012. Only BCP and HPR are considered during the surface preparation.

REFERENCES

[1] J.Y. Tang, et al., "Conceptual Physics Design on the C-ADS Accelerators", internal report, 2012

[2] B. Zhang, et al., "Fabrication test for IMP 162.5 MHz RFQ", this proceedings.

[3] W.M Yue, et.al., "R&D of IMP Superconducting HWR for China ADS", this proceedings

Copyright © 2012 by the respective authors — cc Creative Commons Attribution 3.0 (CC BY 3.0)

THE ESS LOW ENERGY BEAM TRANSPORT LINE DESIGN

L. Neri#, L. Celona, S. Gammino, D. Mascali, A. Caruso, A. Longhitano, L. Calabretta, INFN, Laboratori Nazionali del Sud, Catania, Italy
B. Cheymol, A. Ponton, European Spallation Source ESS AB, Lund, Sweden

Abstract

The linear accelerator of the European Spallation Source (ESS) will deliver proton beams of 50 mA and 2.5 GeV onto the 5 MW neutron production target. The Proton Source for ESS (PS-ESS) [1] is based on the experience of TRIPS and VIS developed at LNS Catania [2,3]. A two solenoid Low Energy Beam Transport (LEBT) is foreseen to match the beam into the first acceleration stage, the Radio-Frequency Quadrupole (RFQ) [4]. Beam production means also detailed characterization of produced beam, with this scope the LEBT houses many instrumentation devices and use different techniques that will be described in this work. The LEBT will be also equipped with an electrostatic chopper in order to remove the unwanted part of the beam pulse during the natural rise and fall times of the ion source. Beam dynamics calculations of the LEBT have been carried out considering also the Space Charge Compensation (SCC) produced by the interaction of the beam with the residual gas, and its effect on beam transport and chopping. Particular emphasis has been put on the evaluation of the beam transient behavior, due to the chopping process, at the entrance of the RFQ, results of the study are presented in this paper.

INTRODUCTION

The ESS, to be built in Lund, Sweden, will use a high current proton linac required for generating high flux of pulsed neutrons by the spallation process. The linac layout [5] is made of a warm section and a superconducting section. The warm linac is composed of an ion source (75 keV), a LEBT, a RFQ (3 MeV), a Medium Energy Beam Transport (MEBT) line and a 4-tank Drift Tube Linac (DTL) to accelerate the beam up to 80 MeV. Double-spoke resonators and five cell-elliptical cavities will accelerate the beam in the superconducting linac up to 2.5 GeV. This paper will focus on the LEBT line of the ESS project. The purpose of the LEBT is to transport and adapt the 50 mA beam from the ion source into the RFQ. The beam pulse duration will be 2.86 ms for a repetition rate of 14 Hz; and rise and fall time must be of around 100ns, for that purpose two electrostatic chopper will be used, one located in the LEBT and the other in the MEBT. Beam dynamics investigations have been performed to design the pre-chopper (LEBT) and to evaluate the performances of the latter.

LEBT LAYOUT

The beam focusing in the LEBT is performed by dual solenoid system. The design of the solenoids is similar to the one of the IFMIF LEBT [6]. The deflecting plates of the chopper are inserted between the solenoids. The total length of the line from the plasma electrode to the RFQ entrance is 2.10 m. Two pumping system will be installed in the line, one before the first solenoid and one in between the magnetic elements. The position of the different optical and monitor components are still under discussion and they are subjected to modification. A preliminary layout is shown in Fig. 1.

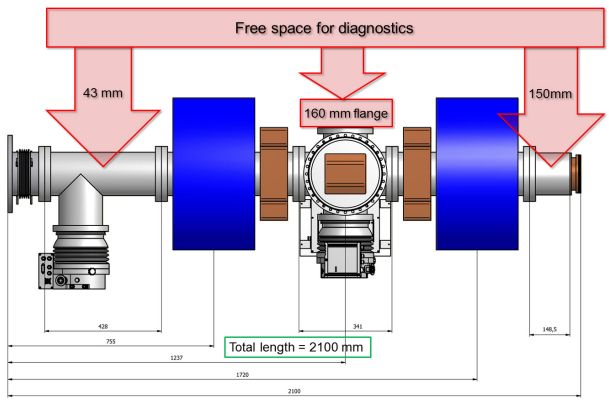

Figure 1: Diagram of the ESS LEBT with beam instrumentation

BEAM INSTRUMENTATION

Beam Profile Measurements

Beam profile measurement will be performed with SEM grids at two locations in the LEBT, between the two solenoids, and after the second solenoid. Each grids will be moved by a stepping motor in order to increase the resolution if it is needed. The profile measurements will be used for the beam steering strategy, and match the beam at the RFQ entrance. In LINAC4, using tungsten wire, the profile measurement was perturbed by thermoionic emission when the beam pulse is longer than 600 μs at a current of 30 mA, the measurable pulse length can be increased by using a carbon wire.

Emittance Measurement

An emittance measurement is foreseen to characterize the ion source and the beam optics in order to optimize the beam injection in the RFQ entrance and provide beam distribution for end to end simulations. The measurements will be performed during commissioning phase and during operation for dedicated beam studies. For operation, the system will be installed between the two solenoid, the slit will be positioned as close as possible to the first solenoid, the SEM grids used for profile measurement will be reused for this measurements. For the commissioning the emittance meter will be positioned

neri@lns.infn.it

Copyright © 2012 by the respective authors — cc Creative Commons Attribution 3.0 (CC BY 3.0)

[7] in different positions: after the source, after the first solenoid, and after the second solenoid. The slit shall be designed in order to stand the full beam power. In order to fit this requirement, the slit will be made in graphite, and its geometry will be made in order to spread the energy deposition in a larger surface [8].

Current measurement

A Faraday cup will be installed after the source; as for the slit, the Faraday cup shall be designed in order to stand the full beam power. This Faraday cup shall be integrated in the Machine Protection System (MPS) and shall be used as a slow mitigation device. In addition, a Beam Current Transformer (BCT) will be installed as close as possible to the RFQ entrance. This BCT shall be integrated in the MPS, the transformer will be used with a second one installed at the RFQ exit in order to measure the beam transmission. This device is relatively slow and for commissioning a Fast Faraday with a time response in the order of the ns or less shall be installed in order to measure the effect of the LEBT chopper on the current rise time.

Optical methods

The emitted light due to the interaction between the beam and the residual gas can be used for different type of measurements, specially the ions species fraction. With a digital camera installed in the focal plane of a monochromator with a few tens of degree angle with respect to the beam propagation axis, the Doppler shift observation of the H_α hydrogen Balmer series allows isolating the fluorescence of each ions species of the beam. The ratio of the different ions is proportional to the light intensity [9].

BEAM TRANSPORT AND CHOPPING

In low energy beam transport of high intensity beams the self-generated repulsion between charged particles can generate a large and irreversible emittance growth, while the optimum matching with the RFQ require high focussing and low emittance. To reduce this negative effect the space charge neutralization of the beam charge can be done by ionizing the residual gas. The generated electrons are captured by the beam potential, while the generated ions are repelled by the beam and lost on the surface of the vacuum chamber. Such SCC regime has many similarity to a plasma but the electric field produced for example by the pre-chopper introduces many significant variations especially in the transition regimes. In order to preserve the SCC from the high electric field located in the extraction system and inside RFQ, a repelling electrode was inserted in the extraction system and in the RFQ collimator, shown in Fig. 2. Then, to reduce the longitudinal dimension of the LEBT and to keep free space for the installation of diagnostics, we designed the chopper chamber coupled to the Turbomolecular Pump (TMP) as shown in Fig. 3. Care was used to locate the high voltage power source as close as possible to the chopper plate to obtain low impedance connection and maintaining high switching speed of the used electronics (15 ns). The measured performances of the chopper power system, already developed for the SPIRAL2 project, are presented in Fig. 4.

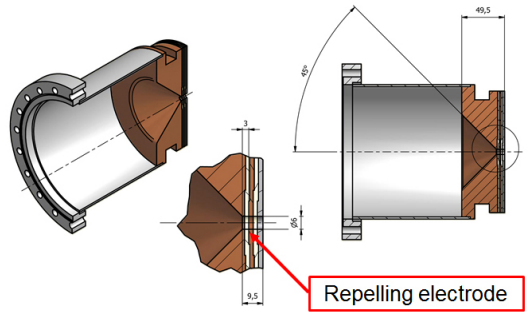

Figure 2: RFQ collimator with integrated repelling electrode.

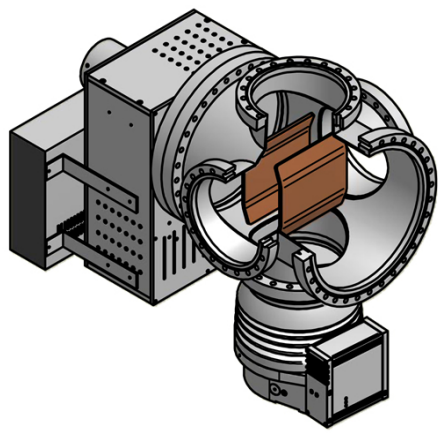

Figure 3: Chopper, TMP, high and low voltage electronics boxes.

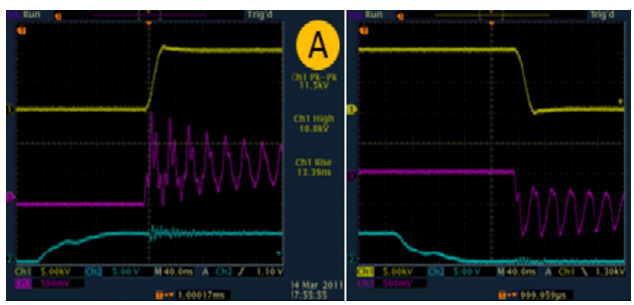

Figure 4: Chopper electronics measured performances.

The extraction system has been simulated with AXCEL and the emittance parameters at the position z = 0.14 m [4] have been used as input for the simulation of the LEBT by using the TraceWin code. This software has been chosen because is able to take into account a SCC map along the LEBT and it is able to perform the optimization of the optical element parameter so that we may achieve the RFQ Twiss parameters ($\alpha x = 1.4464$; $\beta x = 0.0579$; $\alpha y = 1.4847$; $\beta y = 0.0591$). Fig. 5 shows the beam trajectory and the emittance shape obtained at the RFQ entrance by using a SCC value of 98%. At the center of the LEBT, between the two solenoids, the shape of the chopper electrodes can be seen.

Copyright © 2012 by the respective authors — cc Creative Commons Attribution 3.0 (CC BY 3.0)

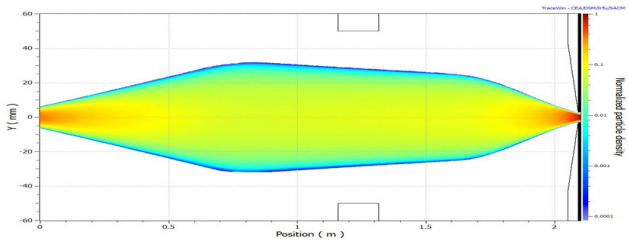

Figure 5: Simulated beam trajectory inside the LEBT.

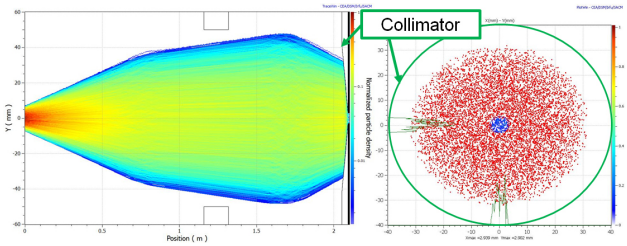

Figure 6: Secondary beam trajectory and its shape inside RFQ collimator.

AXCEL and TraceWin are also able to include in the simulation the secondary beam, that in our case is H_2^+. In sources like VIS and SILHI the proton fraction can reach 90%. As shown in Fig. 6 the RFQ collimator was designed to accept the 10 mA secondary beam shape. The RFQ collimator was also designed to dump the high power transported by the chopped beam (90 mA at 75 keV). Due to the position of the chopper the trajectory of the chopped beam is not trivial because the beam is also deflected by the second solenoid. Fig. 7 shows the radial distribution of the chopped beam and its impact shape over the RFQ collimator. As we can see the chopper deflects the beam out of the center of the collimator while the solenoids rotate of 45° the not centered beam.

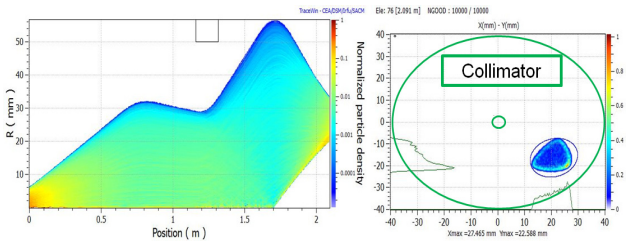

Figure 7: Chopped beam trajectory inside the LEBT; Dump of the beam inside the RFQ collimator.

TIME DEPENDENT BEAM TRANSPORT SIMULATION

The beam longitudinal front at the end of the LEBT is extremely important for the design of the following accelerator cavities of ESS linac. The required rise and fall time is 100 ns while the source modulation is able to perform 2 µs rise time. The chopper was inserted to cut slow edge and fast power electronics with 15 ns transition time was selected. But the chopper electric field and the difference in the two beam trajectories produce a low SCC value during the transport of the first part of the beam. Using the literature result about the SCC creation time [10] and some plasma consideration about the electron gas that neutralizes the beam, we have been able to evaluate the time dependent SCC map along the LEBT, so we have been able to obtain the time shape of the beam at the RFQ entrance.

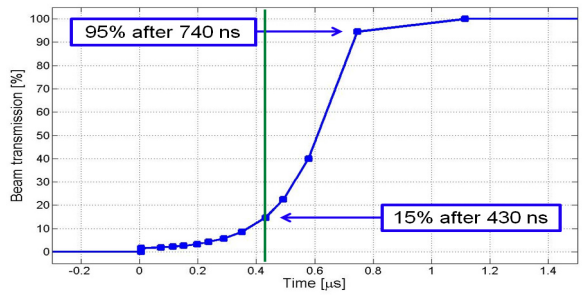

Figure 8: Simulated beam pulse rise time.

The time dependent simulations show that the pulse beam fall time is below 20 ns, while Fig. 8 shows, that 300 ns actually is the limit on the faster possible beam rise time. The time dependent simulations give also the shape, the emittance and the Twiss parameters time dependency. These results are extremely important for the design of the following accelerator cavity and the fast-chopper that must be placed in the MEBT to reach 100 ns pulse rise time. More investigations and a series of measurements are planned within the fall of the year at INFN-LNS and CEA-IRFU to verify this results.

ACKNOWLEDGEMENT

The authors wish to thank D. Campo, L. Allegra for the valuable contribution.

REFERENCES

[1] L. Neri et al., "The Proton Source for European Spallation Source", these proceedings.
[2] L. Celona et al., "TRIPS: The high intensity proton source for the TRASCO project", Rev. Sci. Instrum. 71, 771
[3] S. Gammino et al., "Tests of the Versatile Ion Source (VIS) for high power proton beam production", ECRIS'10, Grenoble, France, MOPOT012.
[4] A. Ponton, "The ESS RFQ beam dynamics design", these proceedings
[5] M. Eshraqi et al., "End-to-end Beam Dynamics of the ESS Linac", IPAC'12, New Orleans, LA, USA
[6] N. Chauvin et al., "Final Design of the IFMIF-EVEDA Low Energy Beam Transport Line", PAC'09, Vancouver, BC, Canada.
[7] B. Cheymol et al., "First Results From Beam Measurements at the 3 MeV Test Stand For CERN LINAC4", DIPAC'11, Hambourg, Germany.
[8] B. Cheymol et al., "Design of the Emittance Meter for the 3 and 12 MeV LINAC4 H- Beam", IPAC'10, Kyoto, Japan.
[9] F. Senee et al., "Diagnostics for High Power Ions Beams with Coherent Optic Fiber for IFMIF-EVEDA Injector", DIPAC' 09, Basel, Switzerland.
[10] A. BenIsmaïl et al., "Space charge compensation in low energy proton beams", CARE Conf-04-025-HIPPI.

Copyright © 2012 by the respective authors — cc Creative Commons Attribution 3.0 (CC BY 3.0)

THE ESS RFQ BEAM DYNAMICS DESIGN

A. Ponton*, European Spallation Source ESS AB, Lund, Sweden

Abstract

The European Spallation Source (ESS), to be built in Lund, Sweden, will use a high current proton linear accelerator (linac) required for generating high flux of pulsed neutrons by the spallation process. The linac will deliver proton beams of 50 mA and 2.5 GeV onto the 5 MW neutron production target. The Radio-Frequency Quadrupole (RFQ) will bunch the continuous beam, coming from the ion souce [1] and transported through the dual solenoid Low Energy Beam Transfer (LEBT) line [2] at 352.21 MHz, focalize and accelerate it from 75 keV to 3 MeV. The current design is a 4-vane RFQ composed of 4 segments of 1 m each. This new RFQ is 1 m shorter than the previous 2011 design. However very similar performances are foreseen. The paper reports the motivations of such a change and presents also the beam dynamics study of the current 4 m RFQ.

MOTIVATIONS FOR A SHORTER RFQ

Previous and current performance requirements

The previous RFQ 2011 design was, in part, based on the following performance requirements:

- initial operation at peak current of 50 mA but upgradable to 75 mA;
- beam loss above 2 MeV is limited to 1 W/m;
- both transverse and longitudinal emittances are minimized to reduce the potential for subsequent halo development;
- there should be no longitudinal tails as they are known to translate into transverse halo.

Beam dynamics studies showed that a long structure was needed to fulfill these requirements. The 2010 RFQ was then composed of 5 one-meter segments [3]. Since the latter design has been achieved, the benefits of having such a long structure and the associated potential risks have been deeply analyzed. In particular, the proton beam induced activation of the linac has been evaluated [4] and the beam loss criterion has been relaxed consequently. Moreover the design intensity has been revised. The reflection has finally led to recommand the following updated requirements:

- peak operational beam current will not exceed 50 mA;
- no limit to allowable beam loss below 3 MeV;
- halo development and beam loss in the high energy linac section traceable to the RFQ are minimized;
- no longitudinal tails as they are known to translate into transverse halo;
- phase advances are matched to adjacent sections.

To reach the requirements a 4 m RFQ has been designed. The latter includes less cells in the bunching section and performs a better rate of acceleration while keeping high performance beam dynamics.

Consequences on the designs

Taking into account the above-mentioned relaxation of the performance requirements, the design study results in a 1 m shorter RFQ. We have shortened the *pure* bunching section [1] from 160 to 55 cells. More losses of high energy protons have then been observed but very similar performances in terms of transmission and emittances are foreseen. Particle tracking have also been performed through the linac from the RFQ output to the end of the superconducting (sc) section and no hazardous losses have occurred. Full integration of the RFQ in the ESS linac has also been improved by matching the phase advances to the subsequent Drift Tube Linac (DTL) [5]. Moreover, the RFQ ouput beam orientation and size have been selected in order to facilitate the transport and matching in the Medium Energy Beam Transport (MEBT) line.

Benefits of a shorter RFQ

Shortening the RFQ has reduced the potential fabrication and operational risks since less tuners and vacuum and RF seals as well as vacuum pumps are required. The construction cost will also be lower as machining and brazing are known to impact significantly the overall cost of the RFQ. Less power dissipated in copper will as well reduce the cost in operation. Removing one segment will finally ease the alignment procedure

BEAM DYNAMICS

Geometry

The main geometry paramaters of the current 4 m RFQ are presented in Fig. 1. It can be observed that the minimal aperture is always greater than 3 mm and the modulation factor stays below 2.4. For more flexibility and in order to reduce sparking problems, the Kilpatrick limit [6] does

* aurelien.ponton@esss.se

[1] Non accelerating section where the synchronous phase is set to zero.

Copyright © 2012 by the respective authors — cc Creative Commons Attribution 3.0 (CC BY 3.0)

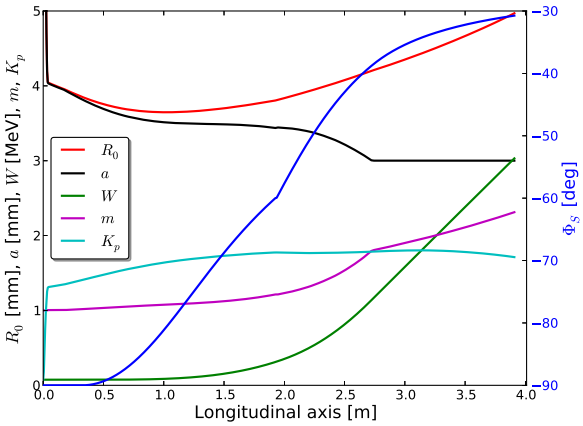

Figure 1: Main geometry parameters.

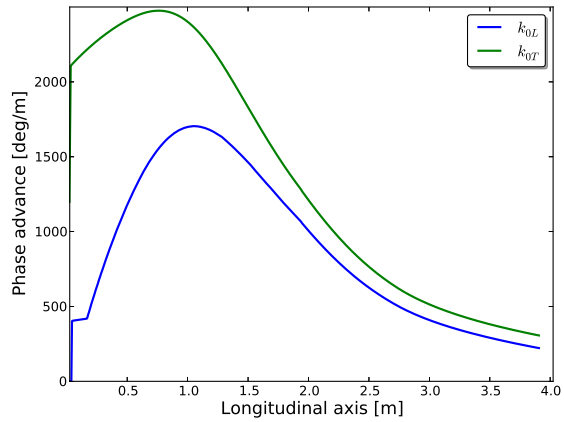

Figure 3: Phase advances.

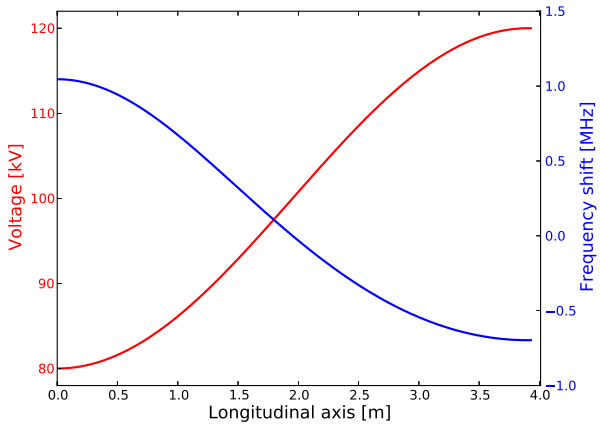

Figure 2: Voltage and 2 D frequency shift.

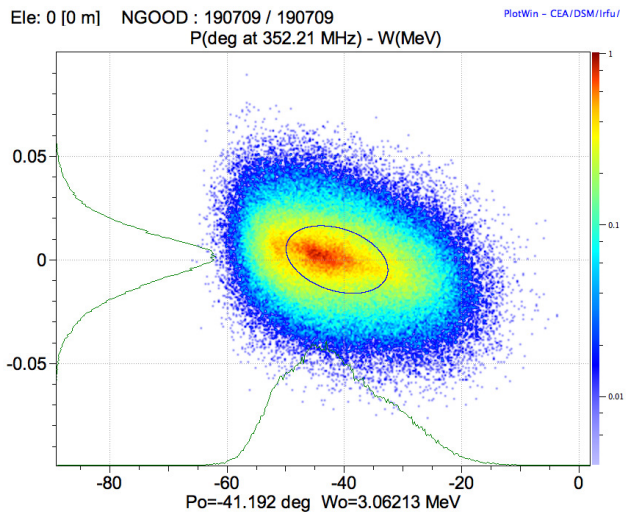

Figure 4: Beam portrait in longitudinal phase space.

not exceed 1.8. The choice of varying the inter-vane voltage ranging from 80 kV to 120 kV has strongly influenced the geometry parameters generation. The voltage follows a sine function which cancells the derivative with respect to z (longidudinal position) at both extremities resulting in the abscence of circulating currents and potential additional losses. The choice of a sine function leads to a small extension range of the 2 D frequency as can be seen in Fig. 2. Finally it is important to mention that the radius of curvature is kept constant ($\rho = 3$ mm) along the z axis due to machining considerations. The latter two points illustrate the fact that the beam dynamics design has integrated in an early stage the mechanical and RF designs.

Matched phase advances to adjacent sections

In order to integrate the RFQ design inside the design of the ESS linac, phases advances at the RFQ exit have been matched to those of the DTL. Moreover, the opening of the has been increased as compared to the previous RFQ version thus facilitating the beam maching into the RFQ.

Evolution of the phase advances along the longitudinal axis can be observed in Fig. 3.

Emittances and transmission

The ESS 4 m RFQ beam dynamics results have been performed with the Toutatis code [7] for 50 mA beams and a gaussian distribution (truncated at $4\,\sigma$) with $0.20\,\pi$.mm.mrad as input RMS transverse emittance. Results are presented in Tab. 1. Resonable transverse emittance growth is experienced and the transmission of the particles inside the longitudinal acceptance is better than 95 %.

Special cares have been taken to produce high quality beams. In particular no longitudinal tails as they may induce losses at high energy if translated into transverse halo have been formed in the RFQ during the bunching and acceleration phases. Figure 4 shows that no longitudinal tails are observed in the output longitudinal phase space.

Copyright © 2012 by the respective authors — cc Creative Commons Attribution 3.0 (CC BY 3.0)

Table 1: Output emittances and transmission.

Current (mA)	Distribution	Output tanvs. em. RMS (π.deg.MeV)	Output long. em. RMS (π.mm.mrad)	Transmission (%)
50	Gaussian	0.13	0.23	> 95

Fringe Field Section (FFS) length optimization

The vanes end with a FFS which makes a smooth transition between the focusing region and the field free region. The choice of the FFS length impacts the orientation of the bunches in the transverse phases spaces as well as their sizes out of the RFQ. Figures 5 and 6 show respectively the evolution at the RFQ ouput of the beam size and the tranverse divergences (in terms of the Twiss parameter α) as functions of the FFS length. A Medium Energy Beam Transport (MEBT) line [8] is foreseen after the RFQ and before the DTL section. The line includes bunching cavities, magnetic quadrupoles, collimator as well as a fast chopper and it is fully equipped by intrumentation for optimal characterization of the beam. The resulting 3.5 m long MEBT line might induce beam degradation as the periodic focusing is broken and the space charge forces are very high at this energy. Halo generation may occur and induce hazardous losses at higher energy. This is why three different output distibutions are being considered: minimal x size, same transverse orientation and same beam size in both transverse planes. First simulations seem to favor the second above-mentioned option [9].

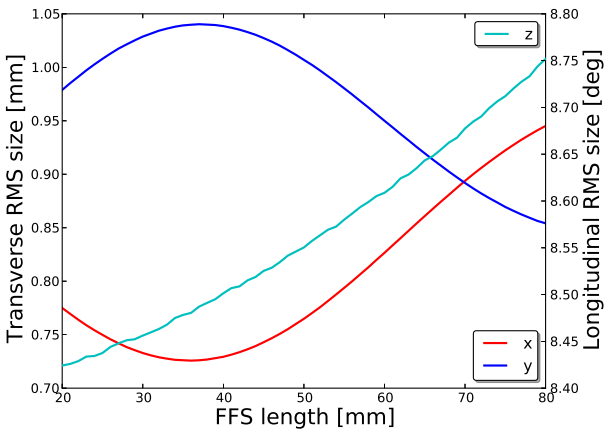

Figure 5: Beam size as a function of the FFS length.

CONCLUSIONS

The current ESS 352.21 MHz 4-vane RFQ is composed of 4 segments of 1 m each. It is one meter shorter than the previous 2011 design. The reduction ine length is, in part, due to the relaxation of the loss criterion and to the limitation of the operational peak current at 50 mA. From a beam dynamics point of view, apart from the losses which remain

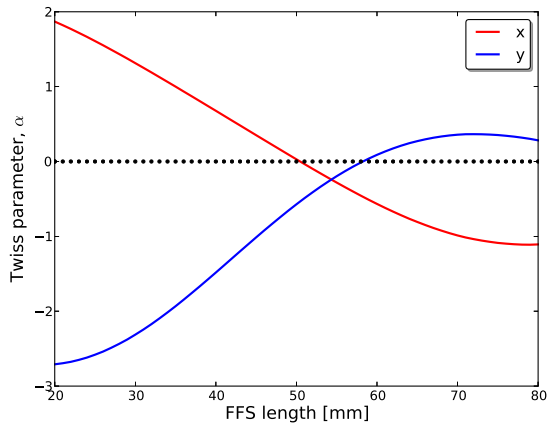

Figure 6: Twiss parameter α as a function of the FFS length.

nonetheless very low, simulations have not indicated any degradation. The transmission is very high and the longitudinal distribution is tailless. Significant improvements in the integration of the RFQ design have also been achieved in parallel with the consolidation of the ESS linac physical design. Not only the new RFQ design is fulfilling all the updated performance requirements but the fabrication and operational risks as well as the cost have also been lowered substantially.

REFERENCES

[1] L. Celona and al., "Design issues of the proton source for the ESS facility", these proceedings.

[2] L. Neri and al., "The ESS Low Energy Beam Transport line design" these proceedings.

[3] A. Ponton, "High power proton linac front-end: beam dynamics investigation and plans for the ESS", Proceedings of IPAC'11, San Sebastián, Spain

[4] J. Stovall and L. Tchelidze, "Estimation of residual dose rates and beam loss limits in the ESS Linac", ESS technical note, revised May 2012.

[5] M. Communian and al., "DTL design for ESS accelerator" these proceedings.

[6] Kilpatrick, W. D., "Criterion for Vacuum Sparking Designed to Include Both rf and dc" , Rev. Sci. Instrum., 1957, 28(824)

[7] R. Duperrier, "TOUTATIS: A radio frequency quadrupole code", Phys. Rev. ST Accel. Beams 3, 124201 (2000).

[8] I. Bustinduy, "Medium Energy Beam Transport Design Update For ESS", in proceedings of HB'2012, to be published

[9] R. Miyamoto, Private communication.

Copyright © 2012 by the respective authors — cc Creative Commons Attribution 3.0 (CC BY 3.0)

DTL DESIGN FOR ESS

M. Comunian, F. Grespan, A. Pisent, INFN/LNL, Legnaro, Italy
M. Eshraqi, ESS, Lund, Sweden
R. De Prisco,ESS Lund University, Lund, Sweden and INFN-LNL, Italy
P. Mereu, INFN Torino, Torino, Italy

Abstract

In the present design of the European Spallation Source (ESS) accelerator, the Drift Tube Linac (DTL) will accelerate a proton beam of 50 mA pulse peak current from 3 to ~80 MeV. It is designed to operate at 352.21 MHz, with a duty cycle of 4% (2.86 ms pulse length, 14 Hz repetition period). Permanent magnet quadrupoles (PMQs) are used as focusing elements in a FODO lattice scheme, which leaves space for steerers and diagnostics. In this paper beam dynamics studies and preliminary RF design are shown, including constraints in terms of quadrupole dimensions, total length, field stability, RF power, and peak electric field.

INTRODUCTION

The ESS, going to be built at Lund, will require a high current linac to accelerate protons for the spallation process on which high flux of pulsed neutrons will be generated. The accelerator is 5 MW superconducting proton linac delivering beams of 2.5 GeV to the target in pulses of 2.86 ms long with a repetition rate of 14 Hz [1]. Beam current is 50 mA, which at 352.21 MHz is equivalent to ~ 9×10^8 protons per bunch.

Both handling on maintenance and machine protection set a strict limit on beam losses and have been a concern in every high power linac: Therefore it is crucial, especially for high power accelerators, to design a linac which does not excite particles to beam halo and also minimizes emittance growth. The ESS linac is carefully designed to minimize such effects all along the linac and transfer lines.

INFN is in charge of the design of this DTL accelerator. This design is based on the mechanical design and prototyping of CERN Linac4 [2], to which INFN has participated in the last years. In this paper the Physical design of ESS DTL is shown.

DTL DESIGN

Table 1: Main DTL Parameters

Parameter	Value
Duty cycle (%)	4
Frequency (MHz)	352.21
Injection Energy (MeV)	3.0 (β=0.008)
Output Energy (MeV)	77.5 (β=0.383)
Accelerated beam current (mA)	50

The design is done by respecting practical technology limits and by avoiding losses along the DTL structure. The maximum RF power per tank is fixed at 2.15 MW. The surface electric field limit is 1.4 Kilpatrick, to avoid sparking, specially at the first DTL cells, due to the contemporaneity presence of electric and static magnetic fields.

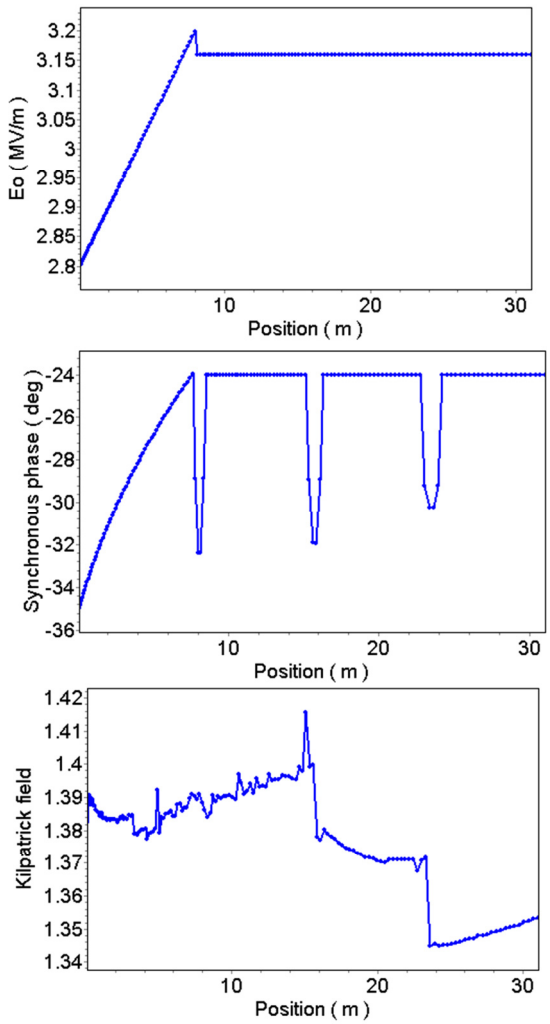

Figure 1: Design E0, synchronous phase and Surface field, along the DTL.

The tank length is limited at 8 meters (9.3 λ), to avoid stability problem on the voltage RF design. The total number of tanks is 4, to reduce the global RF power needed. The DTL beam bore radius is increased along the DTL to avoid losses. The optimized solution has been found by using GenDTL, from the CEA suit of codes.

Copyright © 2012 by the respective authors — cc Creative Commons Attribution 3.0 (CC BY 3.0)

BEAM DYNAMICS

The PMQ law has been selected as a FODO channel, i.e. with half of the drift tubes with empty space, in this way it is possible to allocate diagnostics and steeres inside the DTL. The values of the PMQs permit an equipartitioned beam evolution (Figure 2) and a good phase advance matching with the RFQ at low energy and with the SC linac at high energy: The PMQ range is from 70 to 30 T/m, using permanent magnets (Figure 3).

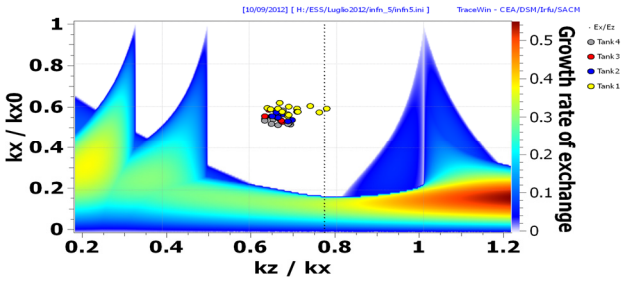

Figure 2: Stability plot for the DTL.

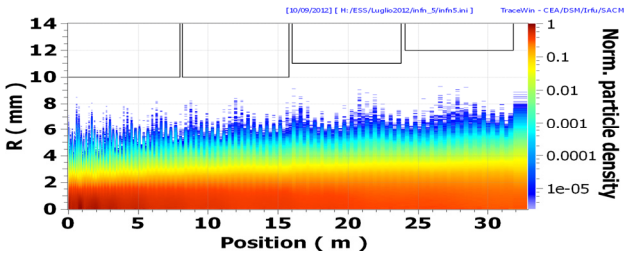

Figure 3: Particles density along the DTL.

RF DESIGN

The presence of DC magnetic field lowers the limit given by Kilpatrick's criterion for electric breakdown [2], [3]. In the first cell of ESS DTL, the maximum surface electric field is on the DT nose at R=12 mm. At that point the PMQ fringe field (B'=70T/m) is 0.092 T. This value of B reduces the maximum E_{surf} to 1.4Kilp (Figure 4).

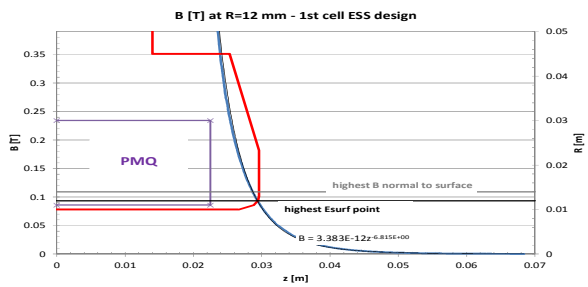

Figure 4: fringe magnetic field in the first cell of tank1.

Beam dynamic and Superfish (GenDTL) runs provide relevant quantities (E0, T, ZTT, Energy gain, Synchronous Phase law, Number of Cells, Cell and Gap lengths). These values, together with other geometric parameters, are inputs for RF design. First of all it is important to evaluate the frequency perturbation induced by stem over each cell. This perturbation can induce a ramped field shape. The stem effect is compensated by an equivalent variation of the face angle. Once all the cells are resonant at the same frequency, they compose the tank. The accelerating field E0 is not yet the nominal one: the final adjusting of E0 law is obtained changing face angles once again. Finally, the mechanical feasibility of the drift tube geometries is checked. A dedicated Matlab routine has been done to run Superfish and obtain a consistent tank design.

This design procedure has been validated with COMSOL 3D simulation, in a representative tank (5.5m, 26 cells) with aggressive ramped field (Figure 5). The mesh of this simulation consists of 1.100,000 tetrahedrons, generated with a revolution sweep, to better reproduction of the Superfish mesh. The error obtained with respect to the nominal design is 4%, located in the 2 end cells, used for ramping.

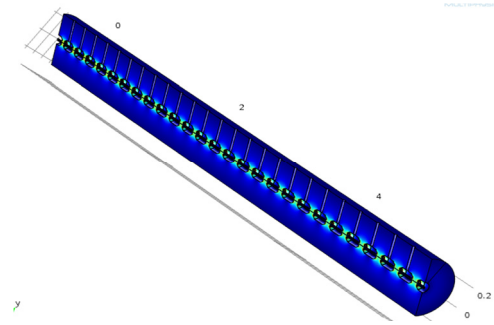

Figure 5: 3D simulation of a tank with ramped field.

The stabilization of the tanks is provided by Post Couplers (PCs). To fix the number of PCs needed in each tank a circuit model of the DTL is used [4]. A reasonable perturbation applied on the end-cells of the circuit induces a tilt on E0. Since the PCs must keep E0 within specifications (±1%) in case of perturbation, the number of PCs per unit length is given by

$$N_{PostCoupler} / m = \frac{|E_{first} - E_{last}|}{E0} \cdot \frac{1}{L_{Tank}} .$$

Slug tuners in a DTL should compensate the frequency effects due to construction errors. The evaluation of the frequency error is done applying realistic tolerances on the important dimension of the cavity (tank diameter, drift-tube lengths, drift tube diameter, face angles). The tuners have diameter of 90 mm, they are located at 45° with respect to the stem axis and are distributed uniformly every 30 cm along the tank. The tuner sensitivity is 3.5 (kHz/mm) × m, linear around 50 mm of penetration.

One klystron of 2.8 MW running at a duty cycle of 4% feeds the required RF power to each tank.

Power available at RF tank input is 2.15MW (30% margin for waveguide losses and LLRF regulation).

Copyright © 2012 by the respective authors — cc Creative Commons Attribution 3.0 (CC BY 3.0)

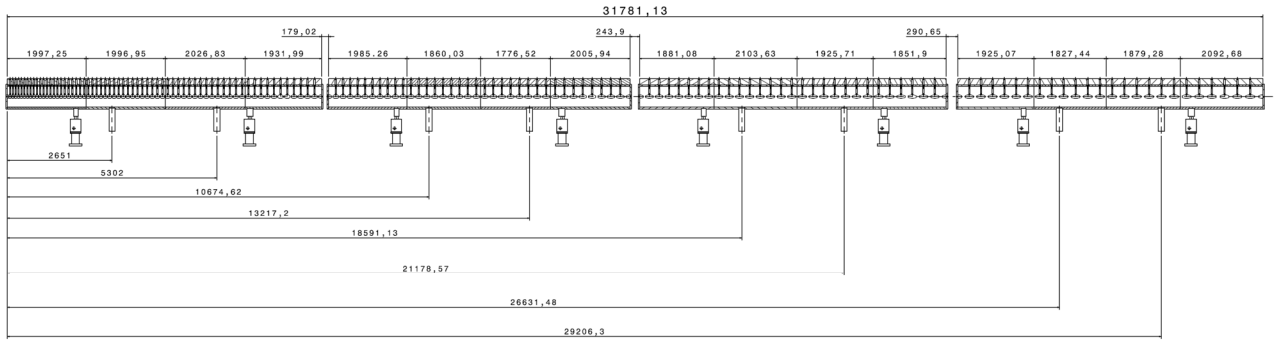

Figure 6: DTL overview.

These 2.15MW should include power dissipated on copper (with 25% margin on Superfish values) and beam power. We foresee 2 iris power couplers per tank [5], designed to have overall coupling factors of $\beta_0=1+P_{beam}/P_{cu}$, see figure 6.

Table 2: Summary of Tank Properties

Parameter/Tank	1	2	3	4
Cells	66	36	29	25
E0 [MV/m]	2.8, 3.2	3.16	3.16	3.16
E_{Max}/Ek	1.4	1.43	1.39	1.37
ϕs [deg]	-35, -24	-24	-24	-24
L_{Tank} [m]	7.95	7.62	7.76	7.72
Bore Radius (mm)	10	10	11	12
Post Couplers	22	23	28	24
Tuning [MHz]	±0.5	±0.5	±0.5	±0.5
Tuners	24	24	24	24
Q0 (SF)	53000	56000	55000	55000
Modules	4	4	4	4
Peak P_{cu} [MW]	0.91	0.91	0.92	0.95
E_{OUT} [MeV]	21.4	41.0	60.0	77.7
P_{TOT} [MW]	2.06	2.12	2.10	2.07

ERROR STUDY

An error study on the parameters sensitivity has been performed, using 100 DTLs and 1.6*10^5 particles (1 W per particle). A uniform input distribution was used with overlapped Gaussian halo distribution. The added halo extends to 3 × σ and the numbers of particles in halo are adjusted to have the equivalent of 1 kW power in the halo. A couple of steeres per axis has been used in each tank, to correct the beam centroid in case of PMQ shaking or input beam error with maximum steerer strength 1.6 mT*m. Figure 7 shows the errors study on PMQ shake, in 10 steps with a maximum of X,Y ±0.2 mm in the centroid position; ±1° on the 3 rotation angles; ±1% on the quadrupole field gradient. The main advantages of the steeres are reduction of the losses by a factor 10 and a reduction of the additional emittance growth by half. The main tolerance results are reported on Table 3.

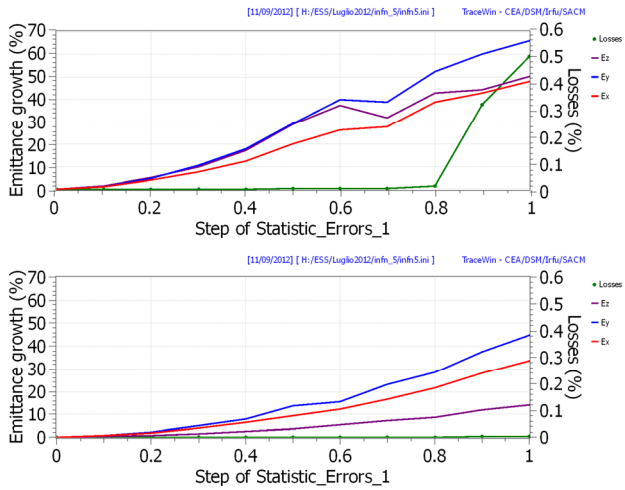

Figure 7: Losses (green) and emittances as a function of applied error on quads, with (bottom) and without (top) steeres.

Table 3: DTL Tolerance Results.

Parameter	Value
Max error on E0 amplitude and phase	+/- 2%; +/- 2°
Max quad error on X,Y position	+/- 0.2 mm
Max quad error on tilting	+/- 1°
Max quad error on amplitude	+/- 1%

REFERENCES

[1] H. Danared, “Design of ESS accelerator”, IPAC12, New Orleans.
[2] S. Ramberger et al., “Drift Tube Linac Design and Prototyping for the CERN Linac4”, linac2008 Proceedings.
[3] A. Moretti et al, Phys. Rev. ST Accel. Beams 8, (2005)
[4] F. Grespan et al., “An Equivalent Circuit for Post Coupler Stabilization in a Drift Tube Linac”, Linac2010 Proceedings.
[5] G. De Michele et al. “Power Coupler Simulations for the Linac4 Drift Tube Linac”, CERN-ATS-Note-2012-002 TECH.

Copyright © 2012 by the respective authors — cc Creative Commons Attribution 3.0 (CC BY 3.0)

STATUS REPORT ON THE FRENCH HIGH-INTENSITY PROTON INJECTOR PROJECT AT SACLAY (IPHI)

B. Pottin, M. Desmons, A. France, R. Gobin and O. Piquet for the CEA and CNRS IPHI team, CEA Saclay, DSM/IRFU, Gif sur Yvette, France

Abstract

The construction of IPHI (High Power Proton Accelerator) is in its final step of installation. The high intensity light ion source (SILHI) has been built first to produce regularly CW high intensity (over 100 mA) proton beams. The low energy front end of IPHI is based on a 352 MHz, 6 m long Radiofrequency Quadrupole (RFQ) cavity. The RFQ will accelerate beam up to 100 mA with energy up to 3 MeV. A diagnostics line has been built to measure all the main characteristics of the beam at the RFQ output. In this paper we will present the status for the main components of the injector, in particularly the RF power facility, the RFQ fabrication, and the RF tuning.

STATUS OF THE INSTALLATION

Source and Diagnostics Line

The ECR source (2.45GHz, 100keV) is for some years producing routinely beam currents of 130 mA. The beam is used to optimize diagnostics for high energy and to develop new non interceptive diagnostics [1]. The beam diagnostics will allow the characterization of the beam accelerated by the RFQ. The diagnostics line is completely assembly and in vacuum. Every diagnostics were tested and operational.

RF Power Facility

The RFQ will be now powered through four RF ports (instead of three in the previous design). This power is provided by two equally loaded 1100kW klystrons. The two klystrons (1100 kW) have been conditioned (CW operation with matched water cooled load). The conditioning duration was two hours for High Voltage only and one day for Radiofrequency.

The four RF windows have been conditioned by pair in standing wave operation (full reflection) at a maximum 550kW 300µs square pulse (10Hz rep. rate) and 250kW CW direct power, the reflected power being dissipated into the circulator load.

RFQ

The IPHI RFQ, 4-vane RFQ, made up of 6, one-meter module assembled in three coupled segments by two coupling plates. Each module is machined in four parts (the vanes) which are brazed together. The final precision (10µm) required is close to the limit of what is possible to manufacture using the technology available today with machining and brazing. After different tests, the brazing in vertical position and in one step was chosen.

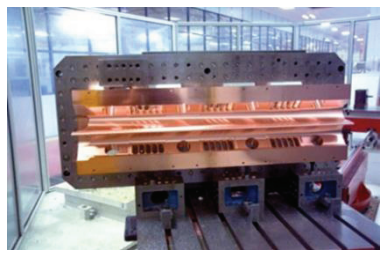

Figure 1 : Final machining of one RFQ's major vane

The method defined is: deep drilling for cooling channels (1 m long with a maximum deviation about 0.4 mm), rough machining (residual skin: 1 mm), annealing, semi-final machining (residual skin: 0.2 mm), RF control, final machining (Fig. 1), cleaning (chemical polishing), assembling, RF checking, brazing, RF control and vacuum test.

The brazing temperature is about 800°C. The required time for brazing is about 36 hours which include warming and cooling time. The RFQ ready for brazing inside the furnace is shown in Figure 2.

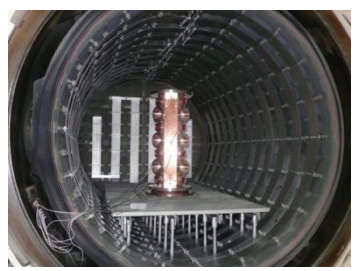

Figure 2: The RFQ in vertical position in the furnace

RF Control of RFQ Modules

RF properties of RFQ modules are carefully controlled after each fabrication step (assembly, 1st braze, etc.). Inter-vane voltages are deduced from bead-pull measurements, and the RFQ 4-wire transmission line model is used to estimate departure of electrical parameters from theoretical values. There are 10 such parameters: 4 parallel inductances, 4 parallel capacitances and 2 diagonal capacitances. However voltage and voltage-slope (the analogue of current for a transmission line) carried by a 4-wire system are dim. 3 vectors (one quadrupole component "Q" and two dipole components "S" and "T"), hence only three parameters may be estimated. Observing that voltage perturbations result primarily from axial region misalignments hence from capacitance errors, and using first-order perturbation analysis, these three parameters are $C_{QQ} = (C_1+C_2+C_3+C_4)/4$, $C_{SQ} = (C_1–C_3)/2$ and $C_{TQ} = (C_4–C_2)/2$ (where the

Copyright © 2012 by the respective authors — cc Creative Commons Attribution 3.0 (CC BY 3.0)

C_i's are inter-vane parallel capacitances). The method is able to discriminate a few 10^{-3} relative errors (Fig. 4).

RF TUNING

Strategy of Tuning

Electrical parameters of end-circuits and coupling-circuits must ensure that the desired voltage profile may be obtained at the end of slug tuning process [2]. Desired values of Q-related coefficients are deduced from accelerating voltage profile V(z). End-circuits should satisfy $(s_{end1})_{QQ} = -(\partial_z V)/V|_{end1}$, $(s_{end2}) = -(\partial_z V)/V|_{end2}$. Each coupling-circuit #i (i = 1, 2) should satisfy tuning condition $(s_{cci})_{\Sigma\Sigma} = (\partial_z V)/V|_{cci}$, matching condition $(s_{cci})_{\Delta\Sigma} = 0$, and coupling capacitance requirement C_c = 1.1 pF (minimizing sensitivity to quadrupole-like perturbations). Q-related coefficients are tuned upon adjusting thicknesses of input plate (e_{end1}), thicknesses on either side of coupling plates (e_{cc1-}, e_{cc1+}, e_{cc2-}, e_{cc2+}), and length of quadrupole rods located on output plate (e_{end2}). Coupling capacitances are determined by gaps separating facing electrodes on either side of coupling-circuits, and cannot be adjusted in significant amounts without compromising beam dynamics.

S/T-related coefficients are determined in order to minimize sensitivity of RFQ voltage to dipole-like perturbations; they are tuned by adjusting lengths L_{end1}, L_{cc1-}, L_{cc1+}, L_{cc2-}, L_{cc2+}, L_{end2} of so-called dipole rods, located on end plates and on either side of coupling plates. The tuning process aims at fitting dipole modes frequencies directly, thus avoiding to consider the complicated variations of boundary conditions vs. dipole rod lengths [3].

Tuning Operations

All the modules are presently brazed and they are assembled to do the tuning (Fig. 3). Tuning operations are detailed in Table 1. Dipole rods modify dipole eigen-frequencies only, while quadrupole devices modify both dipole and quadrupole eigen-frequencies: tuning starts with quadrupole devices (using excitations set method [2]), and proceeds with dipole rods (using spectrum analysis). The excitations set method needs the structure under analysis to be stable, and dipole rods pre-tuning is required. Note that dipole spectrum and quadrupole devices tuning are carefully checked every time a new configuration of segments SG1, SG2, SG3 is assembled.

Figure 3: Modules assembled for tuning

Table 1: Tuning Operations

configuration	operations	method
SG1	dipole rods pre-tuning	spectrum analysis
SG1	end #1 plate tuning	excitations set
SG2	dipole rods pre-tuning	spectrum analysis
SG1-SG2	dipole rods pre-tuning	spectrum analysis
SG1-SG2	coupling plate #1 tuning	excitations set
SG3	dipole rods pre-tuning	spectrum analysis
SG3	end #2 plate tuning	excitations set
SG2-SG3	dipole rods pre-tuning	spectrum analysis
SG2-SG3	coupling plate #2 tuning	excitations set
SG3	dipole rods tuning	spectrum analysis
SG2	dipole rods tuning	spectrum analysis
SG2-SG3	dipole rods tuning	spectrum analysis
SG2-SG3	end #2, coupling #2 check	excitations set
SG1	dipole rods tuning	spectrum analysis
SG1-SG2	dipole rods tuning	spectrum analysis
SG1-SG2	end #1, coupling #1 check	excitations set
SG1-SG2-SG3	dipole rods tuning	spectrum analysis
SG1-SG2-SG3	local modes check	spectrum analysis
SG1-SG2-SG3	slug tuning check	tuning loop

Tuning Report

Tuned devices dimensions and values of Q-related coefficients are reported in Tables 2 and 3 respectively. General accuracy is a few 10^{-2} V/m/V. Coupling capacitances are found to be smaller than expected: stability analysis has been updated accordingly. Sensitivity to quadrupole-like perturbations will be about two time higher than expected (while remaining 1.4 time smaller than for an un-segmented structure).

Table 2: Tuned Devices Dimensions (in mm)

	end1	cc1–	cc1+	cc2–	cc1+	end2
quad. devices	20.00	11.61	6.76	10.12	6.77	41.4
dipole rods	145	150	150	151	140	102

Table 3: Tuned Values of Q-Related Coefficients

		required	achieved		
end1	s_{QQ}	0	$-5.46\ 10^{-3}$	($\sigma = 1.55\ 10^{-2}$)	V/m/V
cc1	$s_{\Sigma\Sigma}$	$+7.91\ 10^{-2}$	$+7.33\ 10^{-2}$		V/m/V
	$s_{\Delta\Sigma}$	0	$+9.29\ 10^{-3}$		V/m/V
	C_c	1.10	0.706	(±0.05)	pF
cc2	$s_{\Sigma\Sigma}$	$+1.304\ 10^{-1}$	$+1.07\ 10^{-1}$		V/m/V
	$s_{\Delta\Sigma}$	0	$+1.82\ 10^{-2}$		V/m/V
	C_c	1.10	0.934	(±0.05)	pF
end2	s_{QQ}	$+2.11\ 10^{-2}$	$+4.48\ 10^{-2}$	($\sigma = 1.24\ 10^{-2}$)	V/m/V

Table 4: Slug Tuning Test Summary

step	tu. pos. (mm)		freq. (MHz)	Q (%)	S (%)	T (%)
0	–4.80	+8.80	350.524 9	84.40	13.03	6.28
1	–1.57	+9.23	351.385 4	12.61	6.04	3.56
2	–0.53	+9.90	351.885 4	8.91	1.78	1.91
3	–0.69	+10.20	352.072 1	3.27	1.10	0.93

This RFQ is tuned to 3% voltage accuracy in 3 steps, with slug tuner positions between –4.8 and +10.2 mm (Table 4, Fig. 5 and 6); additional steps would of course improve accuracy, to the expense of somewhat larger tuner positions.

Copyright © 2012 by the respective authors — cc Creative Commons Attribution 3.0 (CC BY 3.0)

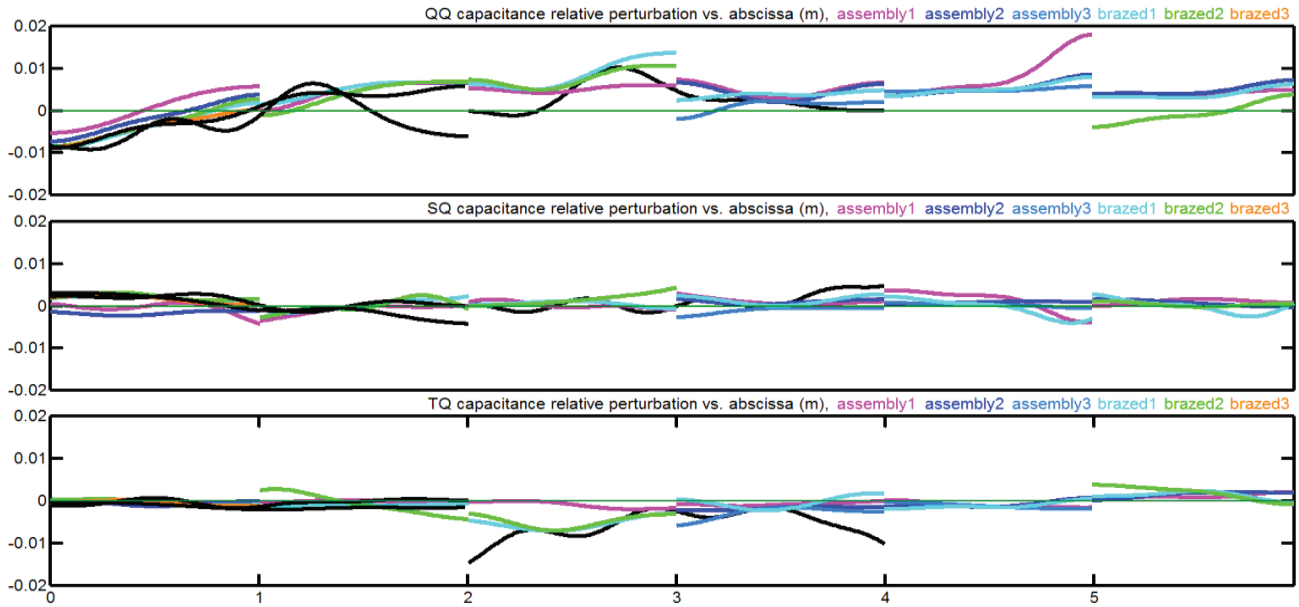

Figure 4: Capacitance relative errors vs. abscissa along RFQ and fabrication step (color code). Black traces apply to segments SG1 and SG2. The wavy shape of curves is due to limited bandwidth of analysis.

Quadrupole and dipole modes frequencies and quadratic frequency shifts (QFS) are reported in Table 5. QFS are seen to be virtually independent of accelerating mode frequency, as expected. QFS of modes closer to accelerating Q_{0+0+0} mode, which have larger impact on stability, are seen to be in good agreement with expected values.

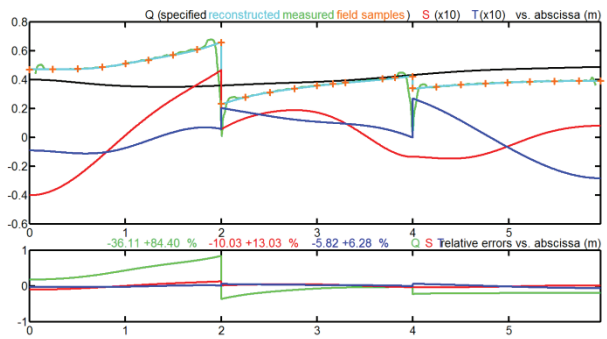

Figure 5: Voltage and voltage error at tuning step 0.

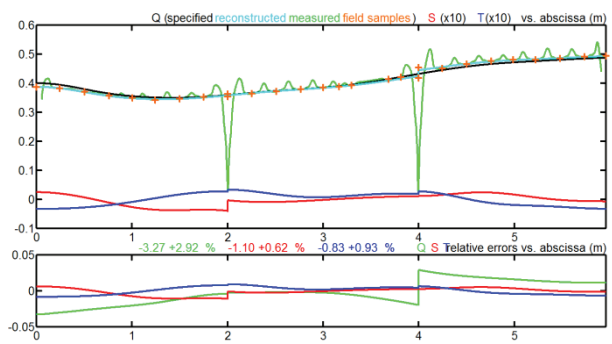

Figure 6: Voltage and voltage error at tuning step 3.

Table 5: Quadrupole and Dipole Modes Frequencies and QFS (Between Brackets). All Values in MHz

mode	model	step0	step2
Q 0–0–0	[–21.03]	347.55 [–22.7]	349.10 [–22.2]
Q 0–1–0	[–27.57]	349.30 [–29.0]	350.60 [–30.2]
Q 0+0+0	[0.00]	350.50 [0.0]	351.90 [0.0]
Q 1–1–1	[+55.07]	354.35 [+52.1]	not observed
Q 1+1–1	[+34.42]	357.25 [+34.6]	358.10 [+33.2]
Q 1+1+1	[+25.18]	358.25 [+24.7]	359.65 [+24.8]
mode	**model**	**step0**	**step2**
D 1–1–1	[–78.49]	342.00 [–76.7]	343.20 [–77.8]
D 1+0+1	[–59.69]	345.75 [–57.5]	346.50 [–61.4]
D 1+1+1	[–46.06]	347.60 [–45.0]	348.60 [–48.1]
Q 0+0+0	[0.00]	350.50 [0.0]	351.90 [0.0]
D 2–2–2	[+102.74]	361.40 [+88.1]	362.65 [+87.6]
D 2+2–2	[+116.40]	366.35 [+106.6]	367.05 [+104.4]
D 2+2+2	[+122.93]	368.50 [+113.8]	not observed

REFERENCES

[1] C. May et al.,"Non-interceptive tomographic reconstruction of the transverse spatial distribution of SILHI ion source beam", BIW 2012, New Port, April 2012

[2] O. Piquet et al., "Tuning Procedure of the 6-meter IPHI RFQ", EPAC'06, Edinburgh, June 2006, MOPCH107.

[3] A.C. France et al., "Unsegmented vs. Segmented 4-Vane RFQ: Theory and Cold Model Experiments", IPAC'10, Kyoto, May 2010, MOPD026

Copyright © 2012 by the respective authors — cc Creative Commons Attribution 3.0 (CC BY 3.0)

BEAM DYNAMICS DESIGN ASPECTS FOR A PROPOSED 800 MEV H- ISIS LINAC

C. Plostinar, C. Prior, G. Rees, STFC/ASTeC, Rutherford Appleton Laboratory, UK

Abstract

Several schemes have been proposed to upgrade the ISIS Spallation Neutron Source at Rutherford Appleton Laboratory (RAL) [1]. One scenario is to develop a new 800 MeV, H- linac and a ~3 GeV synchrotron, opening the possibility of achieving several MW of beam power. In this paper the design of the 800 MeV linac is outlined with an emphasis on the beam dynamics design philosophy. The linac consists of a 3 MeV Front End similar to the one now under construction at RAL (the Front End Test Stand -FETS). Above 3 MeV, a 324 MHz DTL will be used to accelerate the beam up to ~75 MeV. At this stage a novel collimation system will be added to remove the halo and the far off-momentum particles. To achieve the final energy, a 648 MHz superconducting linac will be employed using three families of elliptical cavities with transition energies at ~196 MeV and ~412 MeV.

DESIGN OVERVIEW

The design of the new linac follows the same overall guiding principles as several recent major proton/H- linac projects (ESS, J-PARC, Linac4/SPL, SNS). It consists of a 3 MeV front end copying the FETS project currently under construction at RAL. After 3 MeV, a DTL will accelerate the beam up to 74.8 MeV at which stage an intermediate energy beam transport line (IEBT) with an innovative collimation system will be used to remove the halo and the far off-momentum beam. Although this adds ~7.5 m to the overall linac length, hence increasing its cost, it is imperative to control the beam loss of quality ahead of the superconducting stages. The superconducting linac (SCL) uses 648 MHz cavities to accelerate the beam to 800 MeV with three families of elliptical cavities and transition energies at ~196 and ~412 MeV. A beam line of with achromatic bending sections is used to transport the beam between the linac and the ring. The main linac parameters are presented in Table 1 and a schematic overall layout in Figure 1 [2],[3],[4].

Table 1: General Linac Parameters

Ion Species	H-
Output Energy	800 MeV
Accelerating Structures	DTL/SC Elliptical Cavities
Frequency	324/648 MHz
Beam Current	43 mA
Repetition Rate	30 Hz (Upgradeable to 50)
Pulse Length	0.75 ms
Duty Cycle	2.25 %
Average Beam Power	0.5 MW
Total Linac Length	243 m

THE FRONT END

The linac front end will consist of an H- ion source, a Low Energy Beam Transport Line (LEBT), an RFQ and a Medium Energy Beam Transport Line (MEBT) with a beam chopper [5].

The FETS Penning type surface plasma H- ion source will be adopted for the new linac. This source is already operating at parameters exceeding those required for the new linac having been improved over many years in ISIS and FETS. A beam of 65 keV, 1 ms at 50 Hz with beam currents exceeding 60 mA is routinely extracted.

A three solenoid magnetic LEBT will transport and match the beam from the ion source to the RFQ. A 4 m long, 4-vane RFQ operating at 324 MHz will accelerate the beam up to 3 MeV making use of the available 2.5 MW Toshiba klystron used at J-PARC. An RMS emittance in the region of 0.27 π mm mrad transversally and 0.39 π mm mrad longitudinally is expected at the output of the RFQ.

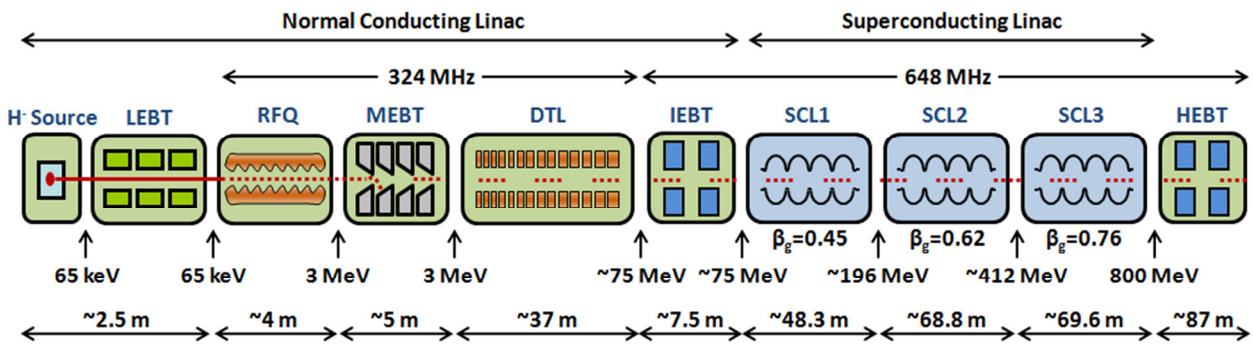

Figure 1: Schematic layout of the new 800 MeV ISIS Linac

Copyright © 2012 by the respective authors — cc Creative Commons Attribution 3.0 (CC BY 3.0)

The RFQ is followed by the MEBT line. It is nearly 5 m long and consists of 11 quadrupoles, 4 re-bunching cavities, a fast beam chopping system with dedicated beam dumps, collimators and a comprehensive set of diagnostics. The last 4 quadrupoles and buncher cavity form the section matching into the DTL.

THE DTL AND IEBT

The DTL section is ~37 m long and accelerates the beam to 74.8 MeV in four tanks. Each tank is fed by a single 2.5 MW peak power Toshiba klystron with output energies of 19.4, 37.7, 56.4 and 74.8 MeV. The average axial electric field is ramped from 2.9 to 3.1 MV/m in the first tank and then kept constant.

A FODO focusing lattice is used throughout the linac. From a beam dynamics point of view, equipartitioning between the transverse and the longitudinal energies is obtained in the first tank after the MEBT matching section and is maintained up to 800 MeV by varying the quadrupole settings while keeping the transverse and longitudinal phase advances per period below 90 degrees. Figure 2 shows the zero current phase advance per period throughout the linac.

A large longitudinal acceptance is needed at the beginning of the DTL and as a result the synchronous phase angle (φ_s) is set to -42 degrees in the first few cells. As the beam becomes more bunched, the phase is slowly increased. Figure 3 shows the evolution of the synchronous phase throughout the linac. Transverse, inter-tank matching is done with six end quadrupoles while longitudinally, this is achieved by offsetting the synchronous phase in selected tank end cells.

A novel addition to the linac design is the inclusion of a collimation section (IEBT) at the end of the DTL. The IEBT is intended to limit the losses further downstream by intercepting halo and far off-momentum particles with stripping foils and loss collectors. Additionally, it facilitates the matching over a double frequency jump and accelerating structure change, providing ample space for diagnostic systems. Beam dynamics simulations indicate that the benefits of adding the IEBT in terms of beam quality outweigh the inherent overall cost increase.

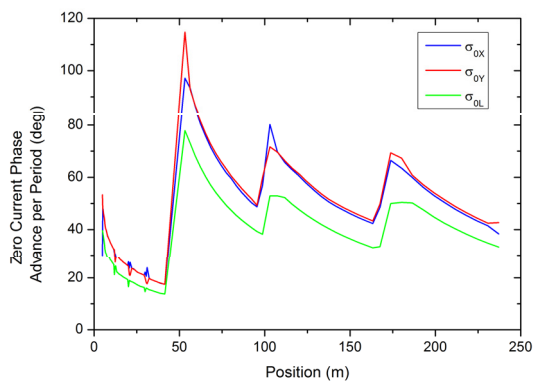

Figure 2: Linac zero current phase advance.

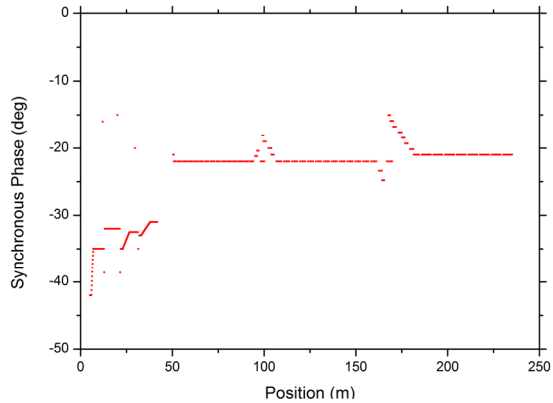

Figure 3: Synchronous phase evolution.

THE SUPERCONDUCTING SECTION

After the IEBT, superconducting cavities are used to accelerate the beam to the final energy. The resonant frequency is doubled to 648 MHz in the SCL, mainly for cryogenic and manufacturing cost reasons. Acceleration is achieved in three stages with three cavity families (β_g=0.45, 0.62, 0.76). Figure 4 shows the energy gain profile throughout the linac. The overall design aim has been to minimize the number of cavities and cryostats without compromising practical and beam dynamics design aspects. A list of parameters of the SCL is given in Table 2, while the configuration of the cryomodules can be seen in Figure 5.

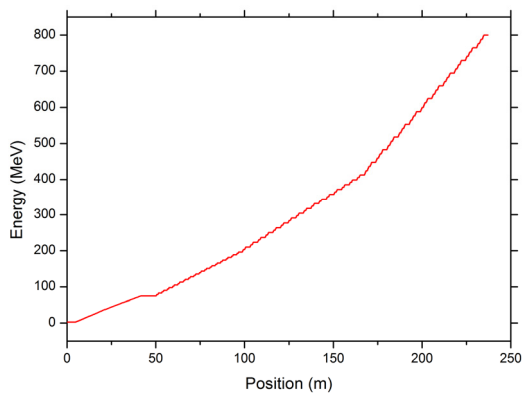

Figure 4: Linac energy profile.

Table 2: Superconducting linac parameters.

	SCL1	SCL2	SCL3
Energy (MeV)	~75-196	~196-412	~412-800
Cavity β_g	0.45	0.62	0.76
Cavity Length ($\beta_g\lambda$)	2	2.5	3
Cells per Cavity	4	5	6
φ_s (deg)	-22	-22	-21
E_{acc} (MV/m)	15.1-19.1	14.1-16.9	16.8-18.7
No. of Cavities	32	32	33
Cavities per Period	2	2	3
Focusing Period ($\beta_g\lambda$)	14.5	15	18
Period Length (m)	3.02	4.30	6.33
No. of Cryostats	16	16	11
Total Length (m)	48.3	68.8	69.6

Copyright © 2012 by the respective authors — cc Creative Commons Attribution 3.0 (CC BY 3.0)

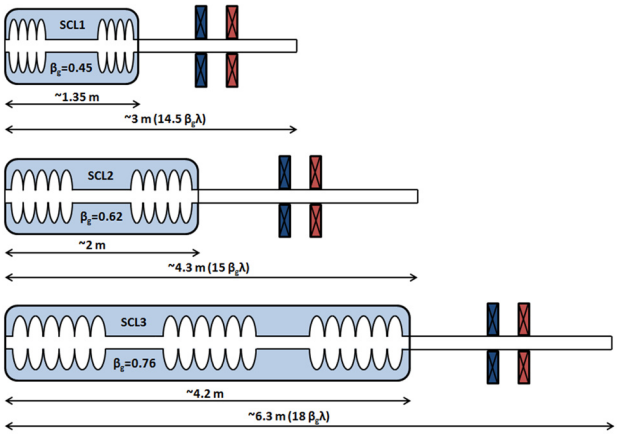

Figure 5: SCL Cryomodules.

The synchronous phase in SCL1 and SCL2 is set to -22 degrees and to -21 degrees in SCL3 (Figure 3). Each cavity family is designed for the same energy gain and beam power per cavity. As a result, the accelerating fields have to vary from cavity to cavity due to phase slips when $\beta \neq \beta_g$.

Transversally, the focusing is done with a doublet quadrupole arrangement located in the room temperature sections at the end of each cell. The six parameter matching between each SCL stage is found by varying six quadrupole gradients and the cavity phases at each transition region. After the SCL, an ~87 m long beam line with a final achromatic section will transport the beam to the ring.

ONGOING STUDIES

Detailed beam dynamics studies are an integral part of the overall linac design development. Tracking simulations of the baseline model performed with Parmila [6] and TraceWin [7] indicate that the choice of tunes is such that the linac operates in the stable area of Hofmann's chart [8], thus avoiding space charge driven resonances, as it can be seen in Figure 6. An example of the beam envelope evolution throughout the linac when using a input waterbag distribution is shown in Figure 7, while Figure 8 shows the emittance evolution for the same input parameters.

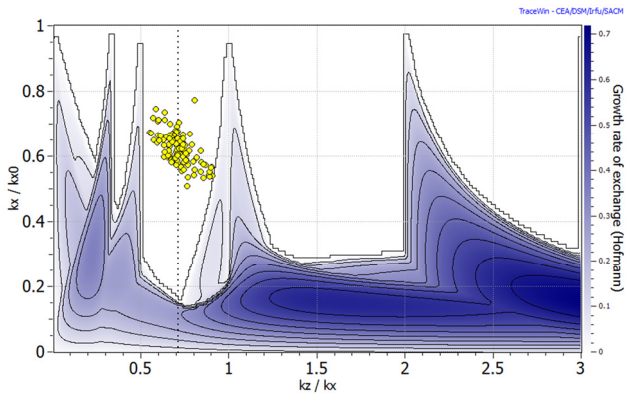

Figure 6: Linac working points on Hofmann's Stability Chart.

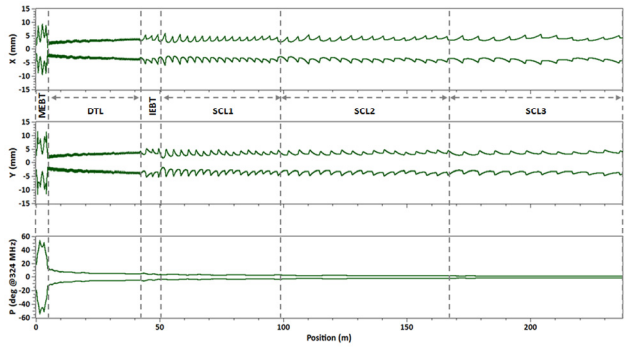

Figure 7: Linac beam envelopes (MEBT to SCL).

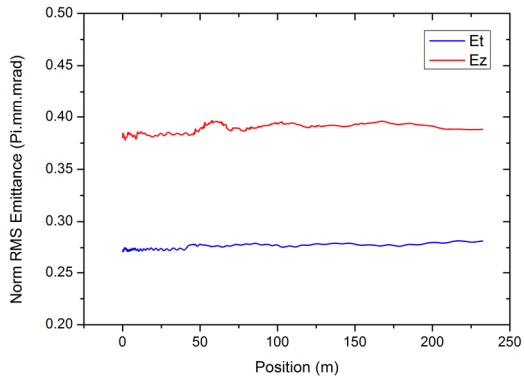

Figure 8: Linac emittance evolution (DTL to SCL).

In preparation for high power operation, one major research direction is understanding the transport of intense beams and the beam behaviour in the space-charge dominated regime, in particular halo formation. Halo is an important source of emittance growth that can eventually lead to beam loss and machine activation, a process that must be avoided in high intensity linacs. The latest advances in computing power will soon make possible simulations with entire particle populations, which is an essential tool in tackling halo formation and beam loss problems [9]. At RAL, current efforts are being put into running detailed end-to-end simulation studies on a local cluster using a parallel version of Impact [10] and 5 million macro-particles.

REFERENCES

[1] J. W. Thomason et al., Proc. of HB'08, WGE15.
[2] G. Rees, "Linac, Beam Line and Ring Studies for an Upgrading of ISIS", RAL Internal Report, 2009.
[3] G. Rees, Proc. of PAC'09, FR5REP086.
[4] C. Plostinar et al., Proc. of IPAC'11, WEPC041.
[5] A. Letchford et al., Proc. of IPAC'12, MOPPR056.
[6] J. Billen et al., Proc. of LINAC'98, MO4047.
[7] R. Duperrier, et al., Proc. of ICCS'02, p. 411.
[8] I. Hofmann et al., Phys. Rev Lett. 86, 2313 (2001).
[9] P. Ostroumov et al., Proc. of LINAC'08, TH301.
[10] J. Qiang et al., Journal of Computational Physics, (163):434–451.

Copyright © 2012 by the respective authors — cc Creative Commons Attribution 3.0 (CC BY 3.0)

STATUS OF THE FAIR 70 MeV PROTON LINAC

L. Groening, W. Barth, R. Berezov, G. Clemente, P. Forck, A. Krämer, C. Mühle, R. Hollinger, J. Pfister, W. Vinzenz, G. Schreiber, J. Trüller, C. Will,
GSI Helmholtzzentrum für Schwerionenforschung, Darmstadt, Germany
B. Launé, J. Lesrel, IPNO, IN2P3, CNRS/Orsay, France
N. Chauvin, O. Delferrière, O. Tuske, C. Simon, IRFU, CEA/Saclay, France
B. Koubek, H. Podlech, U. Ratzinger, A. Schempp, R. Tiede, Goethe Univ., Frankfurt, Germany

Abstract

To provide the primary proton beam for the FAIR anti-proton research program, a 70 MeV, 70 mA linac is currently under design & construction at GSI. The nc machine comprises an ECR source, a 3 MeV RFQ, and a DTL based on CH-cavities. Up to 36 MeV pairs of rf-coupled cavities (CCH) are used. A prototype cavity has been built and is prepared for high power rf-testing. An overview of the status as well as on the perspectives of the project is given.

INTRODUCTION

The FAIR proton linac [1] has to provide the primary proton beam for the production of antiprotons. It will deliver a 70 MeV beam with a repetition rate of 4 Hz. Its conceptual layout is shown in Fig. 3 and its main beam parameters are listed in Tab. 1.

Table 1: FAIR Proton Linac Parameters

Final energy	70 MeV
Pulse current	70 mA
Protons per pulse	$7{\cdot}10^{12}$
Repetition rate	4 Hz
Trans. beam emittance	4.2 µm (tot. norm.)
Rf-frequency	325.224 MHz

DTL-CAVITIES

Acceleration from 3.0 to 70 MeV is accomplished with six H-mode cavities operated in the TE_{211}-mode [2]. Compared to conventional Alvarez cavities these Crossed-bar (CH) cavities feature higher shunt impedance at low energies as shown in Fig. 1. The first three cavities are pairs of two rf-coupled CH-cavities. Rf-coupling is accomplished by merging the first cavity's exit half-drift tube with the second cavity's entrance half-drift tube. This prolonged drift tube of the rf-coupled CHs (CCH) can house a quadrupole triplet. It also provides the rf-coupling cell in the TM_{010}-mode. Such CCHs allow for full exploitations of the available rf-power of up to 3 MW per rf-source. After the CCH-section acceleration from 36 to 70 MeV is done with three single CH-cavities. Tuning of the field flatness is done basically by properly choosing the gap lengths [3]. To this end initially the stems and drift tubes are produced from aluminium. Flatness optimization is done by iterative bead-pull measurements and re-fabrication of the drift tubes. Finally the stems & tubes are drilled from stainless and welded into the cavity. Post fine tuning can just be done by using mobile plungers. The CCH-cavity providing acceleration from 11.6 to 24 MeV (Fig. 2) has been produced and was successfully tuned w.r.t. field flatness. Copper plating is foreseen within this year.

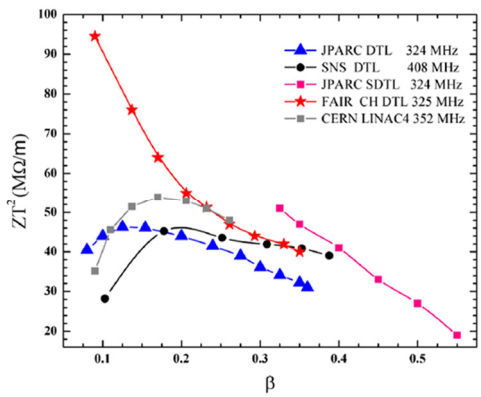

Figure 1: Shunt impedances of several cavity types.

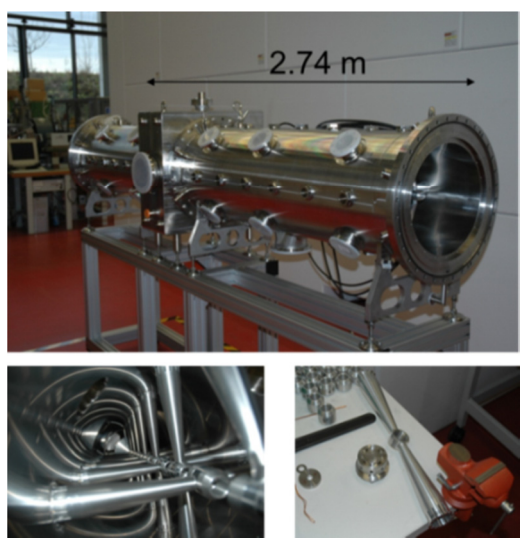

Figure 2: Prototype of CCH-cavity.

Copyright © 2012 by the respective authors — cc Creative Commons Attribution 3.0 (CC BY 3.0)

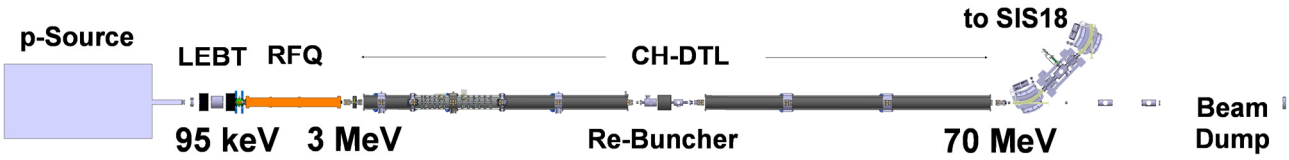

Figure 3: Layout of the FAIR proton linac.

RF-POWER SOURCES

The six DTL cavities and the RFQ will be powered by one klystron each. For the DTL the amount of beam load is up to 50% and the peak rf-power is designed not to exceed 2.2 MW. However, the klystrons are specified to deliver up to 2.7 MW in their linear range. The saturated power is 3.0 MW. Each klystron is fed by an individual modulator. Currently an rf-test stand is under construction at GSI. It will be used for extensive power testing of the prototype CCH-cavity as well as for the SAT procedure of the other cavities. A first TOSHIBA klystron has been delivered and its modulator is expected this year. Along the proton linac three bunchers are used. They require less than 50 kW of rf-power to be provided by solid state amplifiers. The RFQ will require about 800 kW of rf-power. CNRS/Orsay will provide for the procurement of the rf-chain of the proton linac. A considerable amount of equipment for the rf-test has been already delivered as llrf-components, waveguides, scopes etc.

FRONT-END

The proton source & LEBT has to provide a proton current of up to 100 mA within a normalized transverse rms emittance of 0.3 mm mrad. At CEA/Saclay the source & LEBT set-up is currently under construction. Its design is adopted from the IPHI deuteron injector. The beam line magnets are already produced and the terminal is under construction. Commissioning at CEA will start in 2013.

The RFQ is currently foreseen to be a 4-rod type of 3.2 m in length [4] although other types are still under study. Special care has been taken in damping of the dipole modes by extensive parameter scans w.r.t. to its rf-properties [5]. Individual tuning plates between the stems allow for individual tuning of each RFQ-cell thus providing a flat voltage distribution. To verify the simulations a dedicated few-cells copper model was built as shown in the upper part of Fig. 4. Good agreement between low-level rf-measurements and simulations has been obtained [6]. The RFQ beam dynamics layout is based on the New-Four-Section-Procedure which drops the constant-focussing scheme [4]. Figure 4 (lower part) displays the RFQ parameters as functions of the cell number.

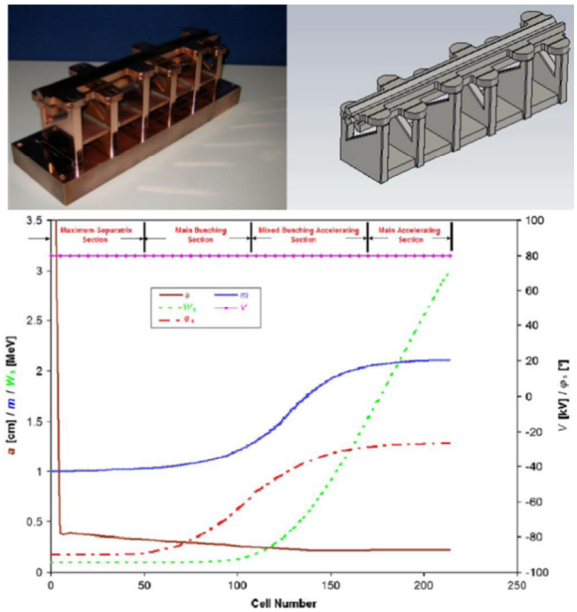

Figure 4: Model of 4-rod RFQ (upper) and beam dynamics parameters (lower).

BEAM DYNAMICS

The beam dynamics of the proton linac has been studied by end-to-end simulations. The linac was split into sections, i.e. source extract, LEBT, RFQ, DTL, and final transportation to the synchrotron. The output of one section served as the input of the following one. Special care was taken in the self-consistent simulation of the space & time dependence of the space charge compensation along the LEBT [7].

Table 2: Linac Sections and Codes for End-to-End Simulations

Section	Code	Features
Source Extract.	AXCEL-INP	2D-PIC, w/o space charge
LEBT	SOLMAX	3D-PIC, res.gas interact.
LEBT	TraceWin	3D-PIC
RFQ	DYNAMION	3D-part-part
DTL	LORASR	3D-PIC
To synchrotron	PARMILA	3D-SCHEFF

The longitudinal dynamic along the CH-DTL is of the KONUS type [8] as sketched in Fig. 5.

Copyright © 2012 by the respective authors — cc Creative Commons Attribution 3.0 (CC BY 3.0)

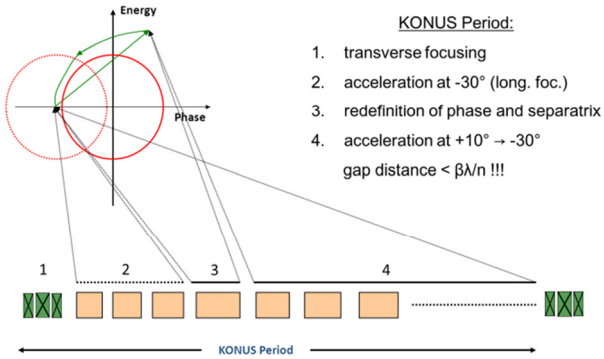

Figure 5: Principle of the KONUS beam dynamics.

Since the most CH-drift tubes do not include focussing quadrupoles, acceleration cannot be performed just at negative phases. The KONUS varies the design phase and even skips the identity of bunch center and synchronous particle. This allows partial acceleration on crest thus increasing the acceleration efficiency. The final distribution obtained at the entrance to the synchrotron [2] fits the requirements listed in Tab. 1. The DTL simulations were extended to error studies. Rf-amplitudes and phases were subject to Gaussian errors of 1° and 1% rms, respectively. As the main source of loss quadrupole translations of 0.1 mm (rms) was identified. However, roll, pitch, and yaw have been included as well. The results revealed loss hot spots (Fig. 6) that went into the layout of the shielding environment.

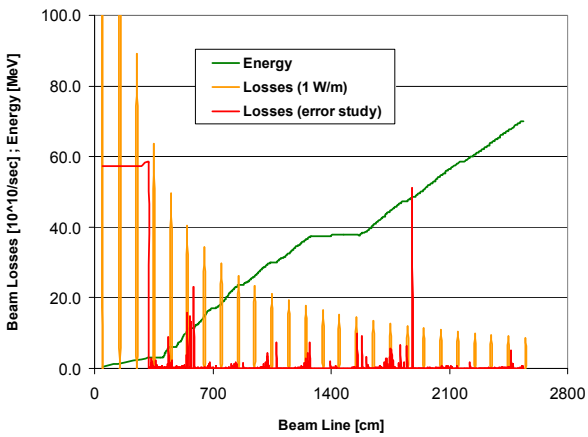

Figure 6: Beam loss profile from DTL error studies.

DIAGNOSTICS

The kind of beam diagnostics and the locations along the beam line are defined as shown in Fig. 7. The layout of the most devices is straight forward. However, the design, mechanical integration, and data acquisition of the phase probes & BPMs is challenging. These 4-bottom BPMs are partially to be integrated into the end drift tubes of the (C)CH-cavities. Special care must be taken for the suppression of primary rf sneeking into the drift tube that holds the BPM bottoms.

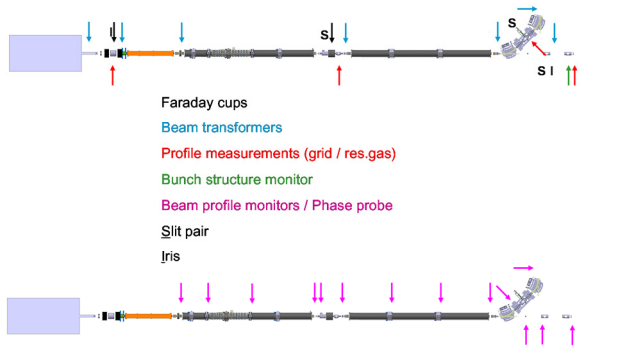

Figure 7: Beam diagnostic devices of the proton linac.

This shielding is accomplished by properly choosing the drift tube diameter being a compromise between reasonable beam tube diameter and sufficient rf cut off. The location of the BPMs represents the interface of many issues as beam dynamics, cavity design, magnets, and diagnostics itself. Extensive MWS-simulations w.r.t. to geometry parameter scans have been performed to this end. Data acquisition is based on evaluation of the second harmonic, i.e. 650.4 MHz. Spatial resolution of the beam center of less than 0.1 mm can be obtained. But there is still work on-going to achieve the required phase resolution of less than 1° for bunch shapes being different from Gaussian. The latter can be expected from the KONUS scheme featuring bunches with extended low energy tails.

SCHEDULE

The parameters of all devices are frozen and the technical specification including mechanical integration is in progress. Major efforts are currently made to finalize the civil construction planning, i.e. provision of load data, cabling lists, specification of rooms, etc. Recent planning assumes the building to be ready in summer of 2016. Commissioning of the linac will be section-wise up to the full design current of 70 mA. After each cavity a mobile diagnostic bench allowing for energy-, current-, and emittance measurement will be installed. We expect commissioning to full performance to last about two years.

REFERENCES

[1] Technical Report "Proton Linac", https://edms.cern.ch/document/994418/1
[2] G. Clemente et al., PRST-AB **14**, 110101 (2011).
[3] G. Clemente et al. these proceedings.
[4] C. Zhang, NIM a 609, p.95, (2009).
[5] B. Koubek et al., Proc. of PAC2011, (2011).
[6] B. Koubek et al., Proc. of IPAC2012, (2012).
[7] N. Chauvin et al., Proc. of LINAC2010, (2010).

Copyright © 2012 by the respective authors — cc Creative Commons Attribution 3.0 (CC BY 3.0)

EXPERIENCE WITH A 4-ROD CW RADIO FREQUENCY QUADRUPOLE

P. Gerhard*, W. Barth, L. Dahl, W. Hartmann, G. Schreiber, W. Vinzenz, H. Vormann
GSI Helmholtzzentrum f. Schwerionenforschung mbH (GSI), 64291 Darmstadt, Germany

Abstract

The High Charge State Injector (HLI) provides heavy ion beams for the linear accelerator UNILAC at GSI [1]. After 20 years of successful operation its four–rod Radio Frequency Quadrupole (RFQ) was replaced in 2010 [2]. Besides higher beam transmission, the principal intention of this upgrade was to raise the duty factor up to 100%. Commissioning and operational experience from the first years revealed that this goal could not be reached easily. After serious problems with melting of rf contacts were overcome, operation is still restricted. There is strong, modulated rf power reflection, most likely due to mechanical instabilities of the structure. In this paper we present the RFQ design, commissioning results, operational experience and future activities.

INTRODUCTION

The HLI is equipped with an ECR ion source and an RFQ-IH linac which accelerates highly charged ion beams with high duty factor of up to 30% to 1.4 MeV/u for further acceleration in the Alvarez DTL of the UNILAC. Since 1991 main user of these beams is the Super Heavy Element (SHE) research, one of the outstanding projects at GSI [3]. Experiments like TASCA and SHIP strongly benefit from the high average beam intensities. A dedicated cw linac for SHE research at GSI is seriously proposed, with the HLI as its injector. The existing HLI is not designed for cw operation. The replacement of the RFQ in 2010 was the first step towards a cw capable injector.

DESIGN & COMMISSIONING

Due to the high average rf power caused by the cw operation, all parts of the new 4-rod RFQ (electrodes, stems, tuning plates, plungers and coupling loop) had to be directly water cooled. This results in 72 connections and vacuum feedthroughs for cooling water, equipped with prevacuum sealing, making the mechanical engineering rather complex. More design properties are given in Tab. 1.

Table 1: Design properties of the new HLI RFQ.

Injection / extraction energy [keV/u]	2.5 / 300
RF frequency [MHz]	108.408
A/q (cw / max.)	6.0 / 8.5
Power (max. avg. / max. pulse) [kW]	60 / 120
Intervane voltage (cw / max.) [kV]	55 / 78
RMS emittance in / out [π mm mrad]	0.1 / 0.1009
Electrode length [m]	2.0

* p.gerhard@gsi.de

The new RFQ was delivered to GSI in autumn 2009. RF and beam commissioning was finished in spring 2010. Achievement of the design beam parameters (transmission, energy, emittance) could be demonstrated (Fig. 1 and [4]). Extensive beam measurements at different locations of the HLI beam line were performed.

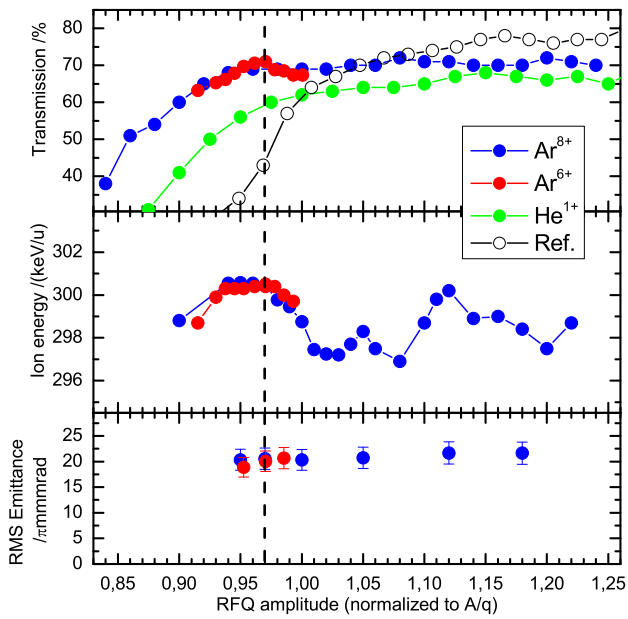

Figure 1: Beam commissioning results (top to bottom): Transmission, ion energy and beam emittance for different ions as a function of the rf amplitude, normalized to the mass-to-charge ratio. Reference data: Old RFQ; dashed line: Derived working point.

THERMAL ASPECTS

During rf commissioning two issues were discovered:

- Insufficient rf contact springs and
- the thermal instability of the 4-rod structure.

Rf contact springs

Several breakdowns of contact springs between the tuning plates and the stems occurred at rf power levels far below the design (s. Fig. 2). The first burning occurred at 16 kW avg. power, possibly due to incorrect mounting of the springs. After two breakdowns, complete renewal with more robust contacts and careful mounting was employed. Nevertheless, damages were found after operation at 24 and 30 kW. Obviously this type of contacts could not handle enough power safely in routine operation. Therefore it was decided to introduce a different contact mechanism using

Copyright © 2012 by the respective authors — cc Creative Commons Attribution 3.0 (CC BY 3.0)

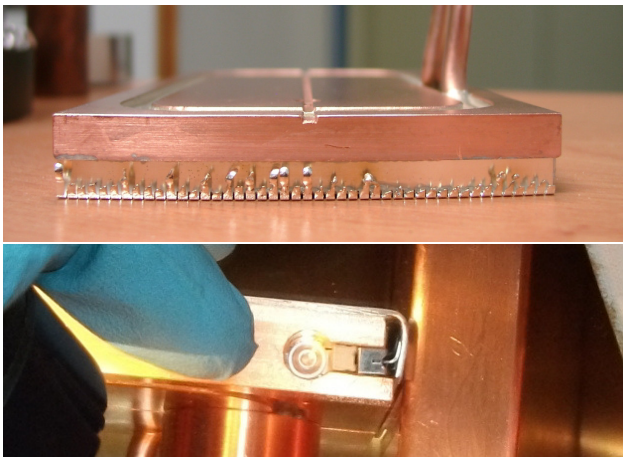

Figure 2: Tuning plate with burnt contact springs (top) and new contacts (bottom). The thick silver foil is pressed against the stem by spring steel foil and steel wedges.

solid silver foils (Fig. 2) [5]. After the new contacts were mounted in November 2010, 30 kW avg. and 110 kW pulse power were reached. Due to other limitations, the avg. design power could not be demonstrated so far.

Thermal instability

Although all relevant parts of the structure are directly water cooled, the structure reacts rapidly to changes of the thermal load. The frequency changes by approx. 200 kHz from rf off to 50% design power; elaborate estimates as well as tests with warm water indicate a temperature change of 10-20 K. Even small changes of the thermal load ($\ll 1\%$) have a significant and almost immediate effect, posing a challenge for the frequency or plunger controller. In normal operation, the average power can only be changed in small steps to allow the controller to follow. After rf breakdowns (sparking), the RFQ immediately cools down and is off resonance. It has to be restarted manually after the plungers have moved to the 'cold' position.

MECHANICAL ASPECTS

Observations

It was known from similar 4-rod RFQs, that the rf power reflected by the cavity can show a modulation [6]. In this case, the magnitude of the modulation turned out to be a major problem (Fig. 3). While the amplitude controller is still able to provide a perfect flattop (at its reference probe), the plunger controller is severely affected, since it relies on the phase difference between forward and reflected rf, which is also modulated. At higher power, it also leads to a significant fraction of the power being reflected. Besides heating up the transmitter, this limits the rf amplitude.

Most probably this modulation originates from mechanical vibrations of the electrode rods or the coupling loop. These vibrations may affect the rf resonance and rf matching. Rf power is then reflected due to the mismatch. The

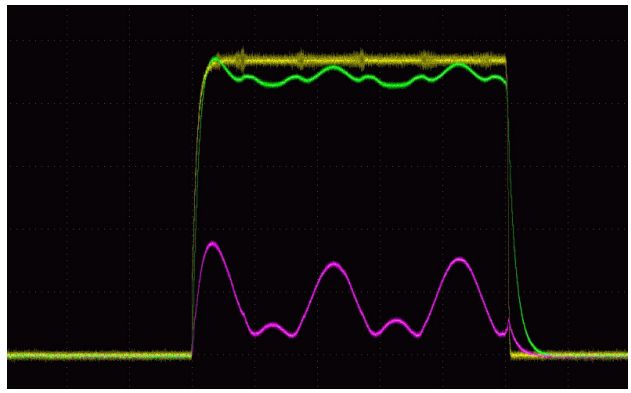

Figure 3: Modulation of the rf tank signals. Magenta: Reflected power; green: Forward power; yellow: Tank amplitude (read out).

modulation has a frequency of about 520 Hz, which is confirmed by simulations considering mechanical vibrations of the rods. A more detailed analysis of the rf signals revealed that the modulation is damped with a time constant between 6 and 10 ms. In order to identify the origin, we tried to increase the damping by putting Vespel clamps on every cell of the RFQ (Fig. 4). Operating the RFQ up to

Figure 4: RFQ structure with mounted Vespel clamps. A plunger is moved in from the top right corner.

moderate rf levels, we found the damping of the modulation to be slightly faster (5–6 ms), but also the modulation frequency slightly higher.

The RFQ is typically operated at 50 Hz pulse repetition rate and pulse lengths of up to 6 ms. During commissioning it turned out, that the RFQ can only be operated at certain pulse lengths, which have to be adjusted carefully in order to minimize the amplitude of the modulation (s. Fig. 5, left, curve 1, 5 and 9 from top). At other values, phase error exceeds the dynamic range of the control loop, rf behavior becomes unstable, reflected power increases and sparking occurs. The behavior changes when the RFQ is operated at 1 Hz. Now every pulse duration is possible and gives the same signal shape. Fig. 5 shows a comparison between the 50 Hz and the 1 Hz operation.

Copyright © 2012 by the respective authors — cc Creative Commons Attribution 3.0 (CC BY 3.0)

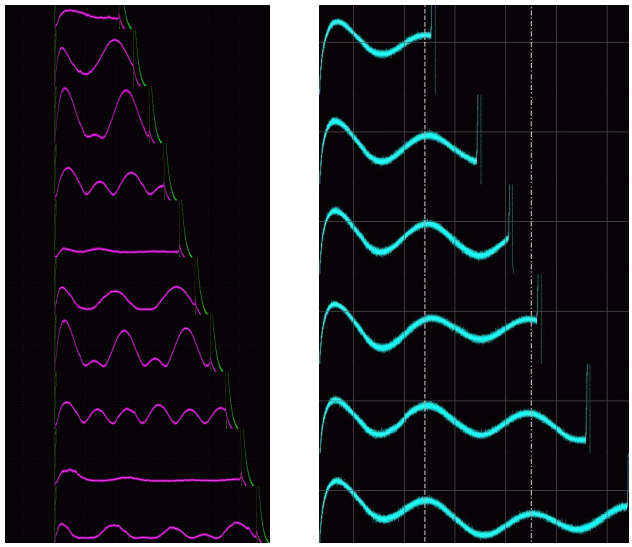

Figure 5: Rf signal modulation at 50 Hz (reflected power, left) and 1 Hz (phase difference forward/reflected, right) pulse repetition rate for pulse lengths of appr. 2-6 ms.

Discussion

The comparison shows, that 15-20 ms after the rf pulse a feedback between successive pulses is observed, while the damping has eliminated the modulation after 1 s. At 50 Hz, the remaining mechanical oscillations interfere with the excitation by the next pulse, leading to different appearances of the modulation for different pulse sequences. This fits nicely to the damping time of 5-10 ms found above. The unexpected rise of the modulation frequency with the Vespel clamps attached can be explained by a raised stiffness of the oscillator, i. e. the electrode rods, when they are pressed by the clamps. The changes induced by the clamps are indicating towards mechanical vibrations of the rods as the origin of the modulation, but they are not significant enough to prove this.

The rf field oscillates 5 orders of magnitude faster than the modulation observed, making it impossible to excite the vibrations. This is supported by the fact, that during the flattop the oscillation is damped. However, the envelope of the rf pulse is of almost rectangular shape. Therefore the rising and falling edges contain a broad frequency spectrum, which could be the origin of excitation. Tests with a trapezoid pulse shape showed a reduction of the modulation, on the cost of rf power used up outside of the flattop.

PULSED & CW OPERATION

After the serious breakdowns in the beginning, beam times with up to 30% duty cycle were conducted successfully in the past years. Handling of the RFQ is complicated due to the fast thermal reactions and the high, modulated power reflection. This also limits the applicable rf amplitude, depending on the duty cycle. A high risk of damage to the rf (pre-)amplifier is obvious. Interruptions like sparking cause long breakdowns, because the rf has to be raised slowly by hand from low levels. Pulsed operation requires absolutely stable repetition of identical pulses (length of pulse and pause, amplitude) at certain pulse lengths, which have to be fine adjusted to the thermal conditions.

So far no cw operation could be established. This is partly due to the low level rf, which is tailored to pulsed operation at 50 Hz rep. rate and 50% duty cycle at most. During a test period, the LLRF was reconfigured to enable cw operation. It turned out that no steady state could be reached. One would have expected that the perturbing modulation was damped out, but this was not the case.

In cw mode the thermal load is much higher than in pulsed mode at the same rf amplitude, hence rf power changes lead to larger thermal and consequently resonance frequency changes. The resonance changes much faster than the reaction time of the frequency controller. This leads to severe fluctuations of the power reflected and, despite the rapid compensation by the amplitude controller, of the power coupled into the cavity, too. The (slow) movement of the plungers also affects the amplitude controller. Finally, the rf amplitude is constantly changing, the system never reaches a steady state and the modulation is excited all the time, in spite of the cw operation.

CONCLUSION AND OUTLOOK

The new RFQ was intended to enable cw operation and enhance operational stability. Both aims could not be reached so far. Pulsed operation is possible with restrictions and special handling instructions. Cw operation has to be established in the framework of the upcoming cw linac.

In order to improve the situation, more tests and simulations are planned concerning the mechanical stability of the rods and the coupling loop. New electrodes with enhanced vibrational resistivity and cooling will be developed and implemented. Tests concerning the thermal stability have to be conducted in order to decide whether the stems and tuning plates have to be redesigned, too.

REFERENCES

[1] N. Angert et al., "Commissioning and First Operation Experience of the New Heavy Ion Injector of the UNILAC", EPAC'92, Berlin, Germany, March 1992, p. 167

[2] L. Dahl et al., "UNILAC Upgrades for Coulomb Barrier Energy Experiments", LINAC'10, Tsukuba, Japan, September 2010, MOP042, p. 148, and references therein

[3] S. Hofmann and G. Münzenberg, The discovery of the heaviest elements, Rev. Mod. Phys. 72, 733 (2000)

[4] P. Gerhard et al., "Commissioning of a new CW Radio Frequency Quadrupole at GSI", IPAC'10, Kyoto, Japan, May 2010, MOPD028, p. 741

[5] This type of contact is similar to and based on contacts implemented at SARAF.

[6] W. Vinzenz, "Resonanzfrequenzanalyse HLI RFQ", GSI internal report, 1997

Copyright © 2012 by the respective authors — cc Creative Commons Attribution 3.0 (CC BY 3.0)

THE NEW OPTION OF FRONT END OF ION LINAC

A. Kovalenko, JINR, Dubna, Russia
A. Kolomiets, ITEP, Moscow, Russia

Abstract

The standard set of elements consisting of RFQ, two tanks of accelerating IH-structures, external matching and focusing sections is modified to achieve better performances. Special insertions corresponding to buncher and quadrupole triplet are combined within the RFQ tank, whereas superconducting focusing elements are install between the DTL - structure tanks. Simulation of the system parameters was performed to provide the output beam energy of 5 MeV/u for the ions with charge – to - mass ratio of $0.33 \leq Z/A \leq 1$. Possible application of the considered scheme for the NICA facility at JINR (Dubna, Russia) is discussed.

INTRODUCTION

The work was motivated by our desire to find optimal way of the constructing linear accelerator chain aimed at injection of light ions and protons for the NICA complex at JINR [1] and also for other applications, in particular for the future carbon/proton superconducting (SC) medical synchrotrons [2].

The physics research program at NICA [3] requests the beams of heavy and light ions, protons, polarized deuterons and protons as well. The facility is based on the existing SC synchrotron - Nuclotron that is in operation since 1993 [4] and that was upgraded in 2008-2010[5]. The accelerator complex will include also two separate injection chains, 25 T·m SC booster synchrotron, the collider SC rings, beam transfer channels. The collider will provide heavy ion collisions of average luminosity of $10^{27}cm^{-2}s^{-1}$ at the energies of $\sqrt{s_{NN}} \sim (4 - 11)$ GeV. The collider detector MPD is scheduled for starting data taken in 2017. The fixed target experiment Baryonic Matter at Nuclotron (BM@N) is planned to start data taking in 2015 in the beam of gold ions extracted from the Nuclotron. The NICA will provide polarized proton and deuteron collisions up to $\sqrt{s}$ = 26 GeV and 12.5 GeV/u, respectively, with the average luminosity of 10^{31} cm^{-2} s^{-1}.

The two injection chains aimed at heavy ions and protons/light ions (including polarized ones) injection contain respectively the following: high charge state heavy ion source → the new heavy ion linac → SC booster → Nuclotron → collider and the sources of protons, deuterons (including polarized) and light ions → upgraded existing linac LU-20 → Nuclotron → Collider.

The Alvarez type proton linac LU-20 was commissioned in 1974. At the present time LU-20 provides proton beam with energy 20 MeV and light ions ($Z/A \geq 1/3$) up to 5 MeV/u. The LU-20 planned upgrade includes, at the first stage, replacement of old high voltage preinjector by the new one having much lower voltage of the ion source platform (U = 100 kV) and the use of RFQ to provide the ion energy required for injection to LU-20.

It is clear, however, that use of LU-20 for acceleration of ions heavier than protons is not very efficient. Moreover it would be very risky to expect reliable operation of the old linac in the coming decades even in the case of complete and very expensive replacement of the drift tubes containing quadrupoles inside.

The main goal of the work is design of compact and efficient linac that can be considered as an option of light ion injector for NICA project.

LIGHT ION INJECTOR

General Layout

Particles that will be accelerated in this device are protons, deuterons (including polarized) and other ions with charge - to - mass ratio of $1/3 \leq Z/A \leq 1/2$, in particular $^{12}C^{6+}$ and $^{12}C^{4+}$ as well. The specified values of the beam currents and the expected transverse emittance define the choice of the injector layout and basic parameters of its accelerating structures. After analysis of different possibilities, the scheme shown in Figure 1 is proposed.

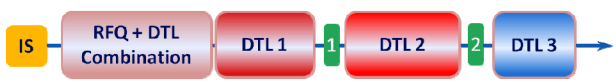

Figure1: Structural scheme of the NICA injector of light and polarized ions. (IS – ion sources)/

Initial part is a combination of RFQ and the DTL that was designed following the idea proposed in [6]. This combination allows to form at output of initial part beam parameters required for injection to DTL 1 and to exclude MEBT with focusing and rf elements for beam matching between RFQ and DTL 1.

DTL 1 and DTL 2 are designed for acceleration of ions with Z/A = 0.33 up to final energy 5 MeV/u. DTL 3 is aimed only for proton acceleration and has to be switched off in the other cases.

Superconducting solenoids are used for beam focusing between DTL sections. It allows reducing drift space between cavities and improving longitudinal beam dynamics. Application of superconducting elements in the proposed new injector is logically follows from the NICA basic technology concept and the advanced level of cryogenics in the Laboratory of High Energy Physics.

RFQ

The RFQ is based on a resonant structure with coupling windows developed in ITEP for TWAC facility injector [7]. The main attention at the design stage was devoted to

Copyright © 2012 by the respective authors — cc Creative Commons Attribution 3.0 (CC BY 3.0)

minimization of the beam longitudinal emittance formed by the RFQ in the case of rather high (> 90%) transmission coefficient. Following to the results obtained in [8], the sinusoidal modulation of the RFQ vanes is used only at the gentle buncher part whereas the trapezoidal one is applied at the main acceleration part with constant modulation coefficient. The trapezoidal modulation provides 15 – 20% higher RFQ accelerating efficiency at the same modulation.

The main feature of the RFQ is the new approach to the beam formation at the RFQ output that provides converging beam in both transverse planes as well as in longitudinal one. It is achieved by adding after regular RFQ vanes several drift tubes connected with opposite vanes with increased distance from axis. Potential difference between tubes is the same as applied to regular vanes.

Drift tube part accelerates ions with higher accelerating efficiency compare with modulated vanes. Due to absence of transverse focusing in this part of structure transverse envelopes amplitude increases approximately by a factor of two. Drift tubes aperture is chosen to exclude the particle losses. Two additional pieces of vanes with quadrupole symmetry βλ long each are installed after the last gap. The distance between the vane sets is βλ also. The model of the front end output is shown in Figure. 2.

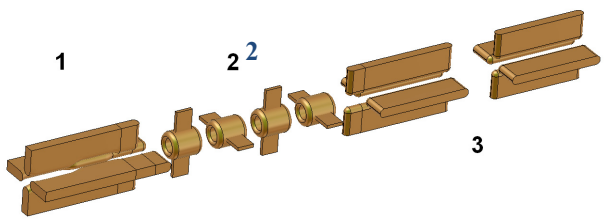

Figure 2: 3D model of the RFQ output part: 1 – the end of regular RFQ vanes, 2 - drift tubes, 3 - rf quadrupoles.

Basic parameters of RFQ + Hybrid combination are given in Table 1.

Table 1: The RFQ Main Design Parameters.

Parameter	Value
Accelerating frequency, MHz	109.0
Voltage between the vanes and tubes, kV	132.0
Average radius, mm	7.50
Thickness of the electrodes, mm	5.25
Maximum modulation coefficient	2.0
Betatron phase advance at the focusing period (minimum), deg.	36
Transverse acceptance (normalized), cm·mrad	0.42
Regular RFQ length, m	3.0
Total combination length, m	3.55
Output beam energy, MeV/u	0.82
Injection energy, MeV/u	0.03
Beam transmission @ I = 10 mA	95%
Maximum electric field at the electrodes surface, kV/cm	227

Hybrid structure consisting of a number of drift tubes without any transverse focusing whereas the focusing is provided by rf quadrupoles placed between the drift tube sections is described in [9]. It is possible to say that described design is a combination of conventional RFQ with a short length hybrid structure. The rf quadrupoles geometry is chosen to provide the bunch enter and exit at the field level closed to zero, i.e. at the accelerating field phase of ±90°. The influence of the output quadrupoles is equivalent to the four static quadrupole lenses forming the FDODF period, i.e. triplet. The distances between the opposite vanes in output quadrupoles are chosen to provide transformation of the beam with quadrupole symmetry at regular RFQ output into converging axially symmetric beam.

Drift Tube Structures

The DTL section is introduced by a crossbar type structure based on the same resonant structure with the coupling windows that has been used for the RFQ. The advantages of such option in compare with the commonly used IH structure are the following: 1) it is possible to equalize gap field level along the section including the first and the last gaps and to exclude dipole component of the field at the system axis and moreover 2) unification of the resonant structures for all cavities leads to lower production and operation cost of the injector. The main design parameters of the DTL sections are presented in Table 2.

Table 2: Design Parameters of DTL Cavities

Parameter	DTL 1	DTL 2	DTL 3
Frequency, MHz	109	109	218
Aperture, mm	10.0	10.0	10.0
Number of acceleration gaps	10	13	11
Electric field at the drift tube surface, kV/cm	230	230	230
Gap length, mm	30.0	50.0	50.0
Gap voltage, kV	600.0	700.0	700.0
Cavity length, mm	830	1605	1200
Output energy, MeV/u	2.58	5.06	10.72

BEAM DYNAMICS SIMULATION

Computer code PreRFQ, ALFIL and TRANSIT, created by the ITEP, were used for the beam dynamics simulation. The first code is aimed for calculations of field distribution in RFQ cell with different types of the vane modulation. ALFIL was used for field calculations in accelerating gap. TRANSIT is the program for multi-particle beam dynamic simulation. The 3D representations of the field are used in TRANSIT for all RFQ cells, accelerating gaps and solenoid. PIC solver is used for calculating particle interactions.

Copyright © 2012 by the respective authors — cc Creative Commons Attribution 3.0 (CC BY 3.0)

The transverse envelopes of the beam of $_{12}C^{4+}$ ions at beam current I = 10 mA calculated by the TRANSIT code are shown in Figure 3.

Twiss parameters of transverse emittances at RFQ output are given in Table 4. It shows that the parameters have very small dependence on beam current. It confirms that the proposed modification of RFQ output provides converged beam with axial symmetry that can be directly injected into DTL 1 cavity for wide range of beam current.

Calculated beam transmission in injector is showed in Figure 4. It shows that in design range of beam current 0 < I < 10 mA it is fully defined by RFQ transmission. Additional particle losses in DTL cavities for higher beam current are explained by increasing phase width of bunch at RFQ output due to space charge.

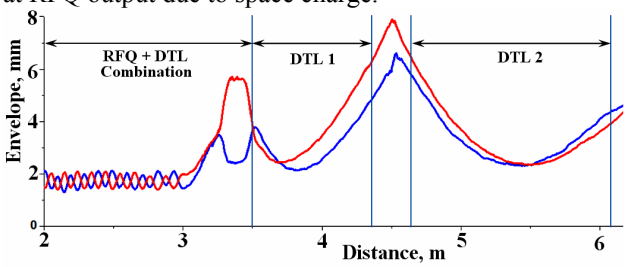

Figure 3: Calculated envelopes of $_{12}C^{4+}$ – ions at 10 мА for x (blue curve) and y (red curve) planes.

Table 3: Twiss Parameters of the Beam at RFQ Output

Beam current, mA	α_x	α_y	β_x m/rad	β_y m/rad
0	-1.82	-1.95	0.468	0.656
5	-2.04	-2.40	0.494	0.767
10	-2.00	-2.63	0.484	0.833
15	-1.96	-2.04	0.477	0.650

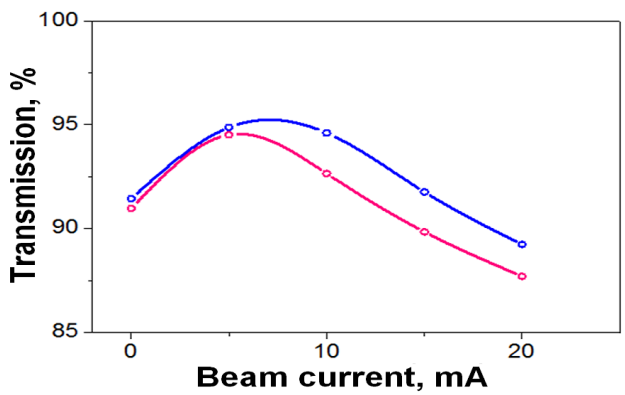

Figure 4: The dependence of $_{12}C^{4+}$ transmission on the beam current. Blue curve represent transmission at RFQ output, red one – at DTL 2 output.

CONCLUSION

Results of development and computer study of light ion injector for NICA project show that proposed combination of RFQ and Hybrid structure provides beam with parameters required for direct injection into following DTL cavity. Beam parameters have only slight dependence on beam current. This approach allows designing injector front end without use of MEBT with additional focusing and rf elements. It can be useful option for design heavy ion linac.

Computer simulations showed that RFQ and DTL cavities can be built using the same type of resonant structure – four vane with coupling windows that reduces manufacture and operation cost of injector.

Injector with total length L_{tot} = 6 m accelerates ions with Z/A = 0.33 up to energy W = 5 MeV/u. Accelerating structures are designed for conservative surface field $E_s \leq 230$ kV/cm to guarantee reliable operation. Injector has only two additional short DTL cavities comparing with structure required for upgrade of LU-20. Nevertheless injector provides higher beam parameters and more efficient and reliable operation. With adding short DTL cavities designed for acceleration of proton injector can completely replace old LU-20 linac for NICA project.

The proposed and considered design is adequate also to carbon ion and proton injector of the future medical synchrotrons.

REFERENCES

[1] Nuclotron-based ion collider facility NICA at JINR, http://nica.jinr.ru/.

[2] A.Kovalenko, N.Agapov et al. “Superconducting Magnet Technologies as basis for Design of Medical Carbon and Proton Synchrotron at Dubna”, Workshop “Physics for Health in Europe”, CERN, February 2-4, 2010. http://cern.ch/physics-for-health

[3] V.Kekelidze et al. Physics Program at NICA@JINR. 35th Int. Conf. on High Energy Physics (ICHEP2010), Paris, France, July 22-28, 2010.

[4] A.D.Kovalenko, “Status of the Nuclotron”, EPAC94, London, June 1994, Proc.v.1, pp.161-164, (1995).

[5] A.Eliseev, N.Agapov et al. “Results of the Nuclotron Upgrade Program”. Proc. IPAC’2011, September 4-11, 2011, San Sebastian, Spain, paper WEPS013.

[6] A. Bechtold, U.Bartz, M. Heilmann, P. Kolb, H. Liebermann, D. Mader, O. Meusel, H. Podlech, U. Ratzinger A. Schempp, C. Zhang, G. Clemente, “A Coupled RFQ – Drift Tube Combination for FRANZ, LINAC 2008, Victoria, 2008, MOP001, p. 46, (2002); http://www.JACoW.org

[7] V.A. Andreev at al., Injector of High Current Multi-charge Heavy Ion Beam for the TWAC Project, EPAC 2000, THP4B06, http://www.JACoW.org

[8] O.K. Belyaev et al., “IHEP Experience on Creation and Opereation of RFQs”,MOD21, LINAC 2000, Monterey, California, http://www.JACoW.org

[9] P.N. Ostroumov and A.A. Kolomiets, “New Concept for Acceleration of Slow, Low-Charge State Heavy Ion Beams”, Proceedings of the 2001 Particle Accelerator Conference, Chicago, p.4077.

Copyright © 2012 by the respective authors — cc Creative Commons Attribution 3.0 (CC BY 3.0)

IRON BEAM ACCELERATION WITH DPIS*

M. Okamura#, BNL, NY, USA / RIKEN, Saitama, Japan
T. Yamamoto, Waseda Univ., Tokyo, Japan
P. Jandovitz, Cornell Univ., NY, USA
T. Kanesue, Frankfurt Univ., Frankfurt am Main, Germany
M. Sekine, TITech, Tokyo, Japan / RIKEN, Saitama, Japan

Abstract

We commissioned an RFQ with a new set of vanes which is for accelerating q/A > 1/7.2 ions. RF power was successfully fed and beam commissioning test was done by using high charge state iron beam supplied by a laser ion source. The obtained current reached 4.3 mA at the peak. Silver beam, design particle, test using solenoid confinement with direct plasma injection scheme will be carried on soon.

BACKGROUND

In 2004, we commissioned a 4 vane RFQ in NIRS, Chiba in Japan. The RFQ was constructed by IAP of Frankfurt University and was designed to accommodate high current carbon beam from a laser ion source using direct plasma injection scheme (DPIS). We could demonstrate very high current heavy ion beam acceleration with the DPIS and the measured current after the RFQ reached more than 60 mA of carbon beam[1]. However, due to the radiation safety limitation in NIRS, output beam energy of the RFQ was restricted to be below 100 keV/u. The entire cavity length was 2.0 m and the beam energy reached the energy limitation at 1.42 m point from injection side. So, in the rest of the section, the vanes had no modulation. By passing through under the transversely confinement RF field without acceleration buckets, the beams were completely de-bunched. To verify the feasibility of the DPIS, this RFQ had worked great, however, it was difficult to examine the beam qualities, since the output energy was too low to transport a high current beam and the transverse emittance of de-bunched beam was affected by the RF cycle.

In 2005, we started to design new replacement vanes. Based on experimentally obtained performances of a laser ion source using a 2.3 J Nd-YAG laser, silver 15+ ion was selected as the design particle[2]. An assembly of the new vanes with supporting stems and a base plate (without outer vessel) was fabricated in 2006 again by IAP.

In 2006, the RFQ and entire experimental equipment was moved from RIKEN in Japan to BNL in USA. In BNL, the study was continued mainly using the old vanes with un-modulated section[3]. Due to a bureaucratic reason, the vane assembly was sent back to Japan after we moved to BNL. However, during the shipment, it was heavily damaged.

*Work supported by US. DOE and RIKEN in Japan.
#okamura@bnl.gov

A photo taken in Japan is shown in Fig. 1. The assembly was sent to Frankfurt directly from Japan and was straightened and aligned again. The repaired new vanes were installed in 2010 and the commissioning was done in 2011 in BNL.

Figure 1: Deformed vanes.

DESIGN PARAMETERS

The vane parameter design was done assuming 15 mA of Ag^{15+} beam (q/A = 7.2) with 0.2 π mm mrad (nor. rms) of injection beam transverse emittance. The operating frequency and vane length were retained as 100 MHz and 2.0 m respectively. The beam extraction column voltage applied to laser plasmas was set to 60 keV which corresponds to 8.3 keV/u for Ag^{15+}. The output beam energy was maximized within the limited length. The final modulation factor reached 3.0. Those values are summarized at Table 1 and Fig. 2.

Table 1: Parameters of the RFQ LINAC

RFQ Type	4rod
Frequency	100.1 MHz
Designed Charge to Mass Ratio	1/7.2
Length	2.0 m
Cell Number	143
Input Energy	8.3 keV/u
Output Energy	270keV/u
Designed Vane Voltage	73 kV
Maximum m	3.0
Q value	4500

Copyright © 2012 by the respective authors — cc Creative Commons Attribution 3.0 (CC BY 3.0)

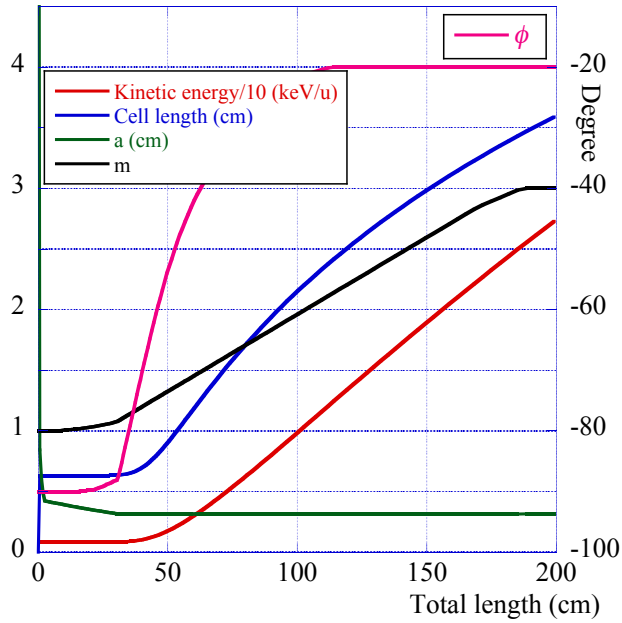

Figure 2: Vane parameters vs. length.

INJECTED BEAM PROPERTY

For the beam commissioning, we used carbon and iron beams. Carbon beam production from the laser ion source had been well established and we focused to examine iron ablation plasma using a plasma analysis beam line as shown in Fig. 3 prior to the beam test.

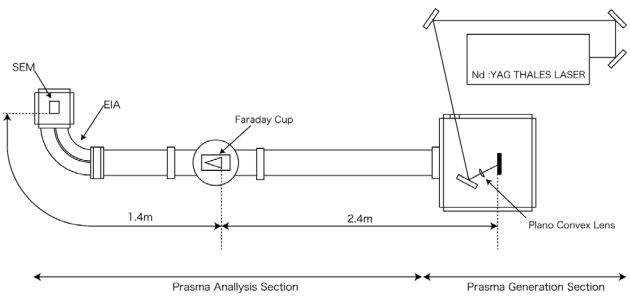

Figure 3: Plasma analysis beam line.

In order to analyze the charge state distribution of the iron plasma, different voltages were applied along a 90 degree electro static bend that ended in a secondary electron multiplier. Particles are bent along a radius of curvature that is determined by the particle's charge to mass ratio and velocity, and the applied voltage. So for a given applied voltage, only particles of a given velocity for a specific charge to mass ratio will reach the detector and produce an electrical signal. Therefore it is possible to determine the charge state that caused a signal simply by looking at the time it occurred. A typical waveform taken in the experiment is shown in Fig. 4. Then, by scanning through a range of voltages, the charge state distribution in a single beam pulse was derived. The integrated charge state distribution is described in Fig. 5.

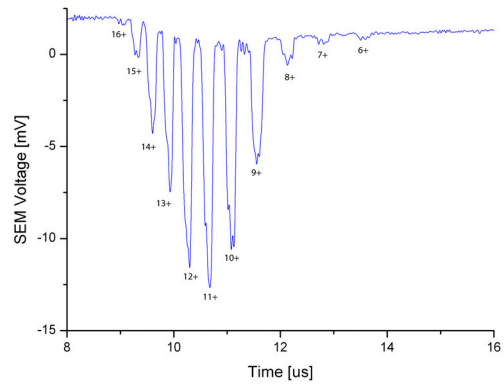

Figure 4: Detected signal by secondary electron multiplier.

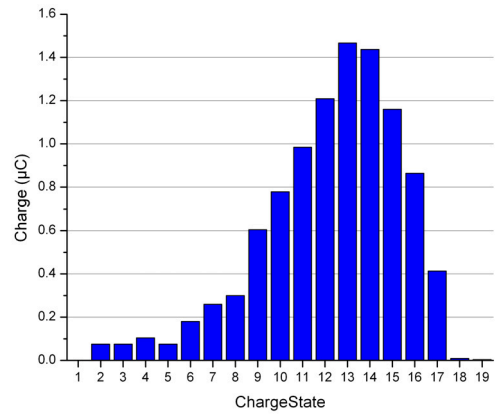

Figure 5: Charge state distribution.

The most abundant charge state was 13+. In this experiment, a Nd-YAG laser (Thales SAGA230) was used. The laser energy and pulse width were 1.5 J and 6 ns respectively. The focal length of the final focusing lens was 100 mm which gave around 10^{12}W/cm^2 on the iron target surface.

BEAM TEST

First, carbon beams were injected into the RFQ to check the all the experimental equipment working properly[4]. And then iron target was installed. The experimental layout is shown in Fig. 6.

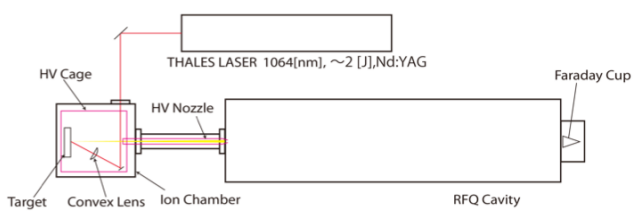

Figure 6: Experimental layout.

The extraction nozzle, facing to the RFQ entrance, has a inner diameter of 4 mm. The peak total current of the

Copyright © 2012 by the respective authors — cc Creative Commons Attribution 3.0 (CC BY 3.0)

injected iron current was 18 mA which was estimated based on the plasma analysis experiment result.

Figure 7 shows the recorded beam current after the RFQ. The injection column voltage was scanned. The blue signal is at 33.3 kV, which corresponds roughly to Ag^{14+} injection beam energy. The accelerated beam comprised 14+ and higher charge states. At the very low injection energy, the beam could not be captured by RF buckets and was not accelerated at all as shown as the red signal. The un-accelerated beam appeared from 3.5 to 6 μs which is slower than the bunched accelerated beam. The green signal shows an intermediate condition. Only the very high charge state ions were accelerated; most of the injected beam was just transported through the RFQ with the plasma extraction beam energy. The RF power was 77 kW.

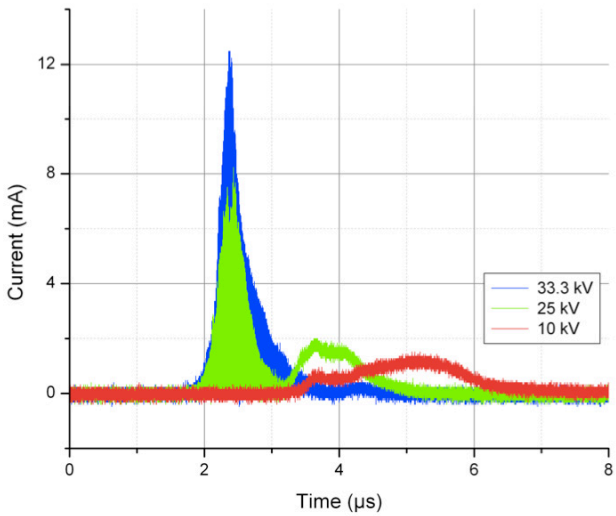

Figure 7: Experimental layout.

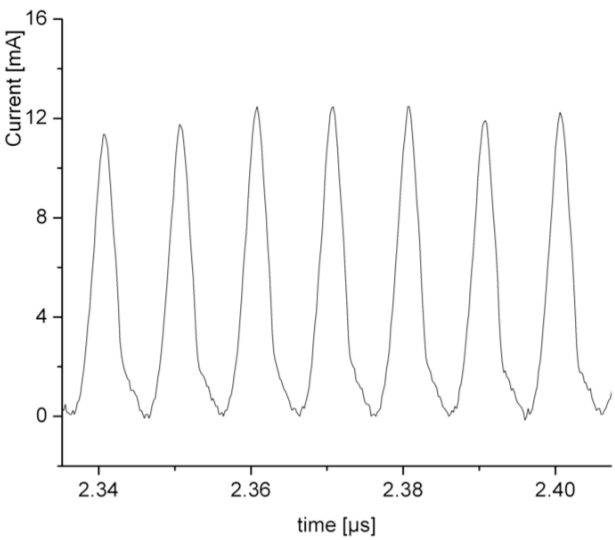

Figure 8: Bunched structure after the RFQ.

Figure 8 shows a magnified version of the accelerated beam peak. The RF bunching expected is readily apparent, with peaks separated by the expected 10 ns. The peak accelerated current reaches about 4 mA with the DC average over 4 periods. The total accelerated charge was plotted as shown in Fig. 9.

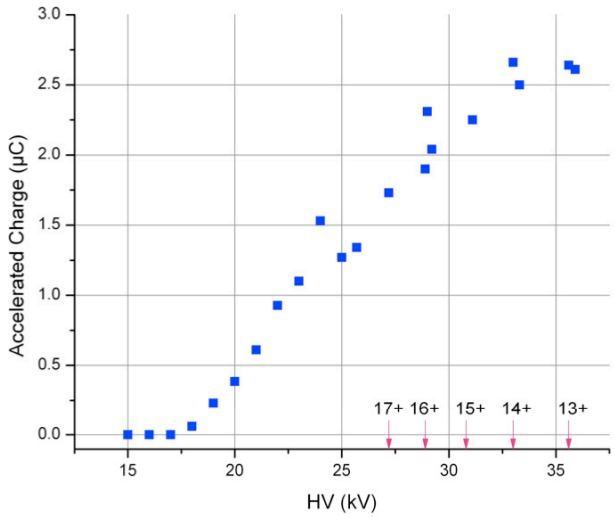

Figure 9: Accelerated charge vs. injection voltage.

We didn't analyze the accelerated beam with a bending magnet yet, however, the bunched structure was clearly observed. This means the beam was accelerated properly with iron beam with DPIS.

SUMMARY AND PLAN

We commissioned the RFQ with replaced new vanes. We confirmed that the entire system is working as we expected. Now we are preparing silver beam acceleration with applying solenoid confinement DPIS. Also analyzing beam lines will be built to measure a current of each charge state ions and transverse beam emittances.

REFERENCES

[1] M. Okamura, H. Kashiwagi, K. Sakakibara, R. A. Jameson, K. Yamamoto, J. Takano, T. Hattori, N. Hayashizaki "High current carbon beam production with DPIS," Rev. Sci. Instrum. 77, 03B303 (2006)

[2] T. Kanesue, K. Ishibashi, M. Okamura, K. Sakakibara, S. Kondrashev "Ag acceleration using direct plasma injection method," EPAC'06, Edinburgh, June 2006, TUPLS093, p. 1720 (2006); http://www.JACoW.org.

[3] M. Okamura, T. Takeuchi, R. A. Jameson, S. Kondrashev, H. Kashiwagi, K. Sakakibara, T. Kanesue, J. Tamura "Direct plasma injection scheme in accelerators," Rev. Sci. Instrum. **79**, 02B314 (2008).

[4] T. Yamamoto, K. Kondo, M. Sekine, M. Okamura, M. WashioD. "RFQ linac commissioning and carbon4+ acceleration for ag15+ acceleration via direct plasma injection scheme," IPAC'12, New orleans, May 2012, TUPPD023, p. 1458 (2012); http://www.JACoW.org.

Copyright © 2012 by the respective authors — cc Creative Commons Attribution 3.0 (CC BY 3.0)

ASSEMBLY AND RF TUNING OF THE LINAC4 RFQ AT CERN

C. Rossi, A. Dallocchio, J. Hansen, J.B. Lallement , A.M. Lombardi, S. Mathot, D. Pugnat, M. Timmins, G. Vandoni, M. Vretenar, CERN, Geneva, Switzerland
M. Desmons, A. France, Y. Le Noa, J. Novo, O. Piquet, CEA, Gif-sur-Yvette, France

Abstract

The fabrication of Linac4 is progressing at CERN with the goal of making a 160 MeV H- beam available to the LHC injection chain as from 2015. In the Linac4 the first stage of beam acceleration, after its extraction from the ion source, is provided by a Radiofrequency Quadrupole accelerator (RFQ), operating at the RF frequency of 352.2 MHz and which accelerates the ion beam to the energy of 3 MeV. The RFQ, made of three modules, one meter each, is of the four-vane kind, has been designed in the frame of a collaboration between CERN and CEA and has been completely machined and assembled at CERN. The paper describes the assembly of the RFQ structure and reports the results of RF low power measurements, in order to achieve the required accelerating field flatness within 1% of the nominal field profile.

INTRODUCTION

The initial conceptual design of a compact 3 MeV RFQ, published at CERN in 2007 [1], was soon after followed by the detailed study of beam dynamics, performed at CERN, and RF design, jointly done by CERN and CEA, [2]. After the mechanical design, the fabrication of the Linac4 RFQ started in 2009 at CERN and was recently completed with the assembly of the three modules that form the accelerating structure. Aiming for maximum reliability, the design choice was for a traditional four-vane structure with a constant section profile; particular attention was given in the design to avoiding the use of dipole mode suppressors by limiting the RFQ length to 3m (3.5 wavelengths) and by carefully compensating local perturbations. In particular, an original solution was to adopt brazed vacuum ports that could precisely compensate for the local field perturbation introduced by the cavity openings. Remaining errors are compensated by slug tuners.

The very tight tolerances imposed by the compact design, in the absence of resonant coupling cells, have put great pressure on the machining and assembly teams and required intense work at the metrology workshop.

The three 1-m long RFQ modules have been assembled at the end of July at the CERN metrology workshop, then the RFQ has been moved and installed at the 3 MeV Test Stand where the last tuning of the accelerating field is presently being performed, with the finalization of the piston tuners and of the RF power coupler, before the start of the RF commissioning foreseen in November.

Figure 1 shows the RFQ cavity installed at the Test Stand and connected to its cooling system.

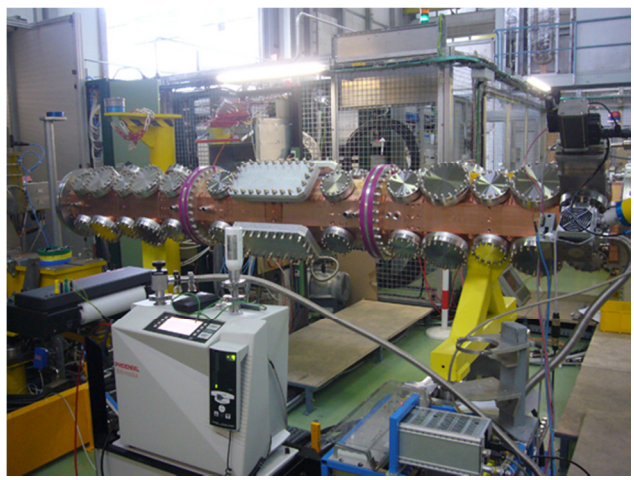

Figure 1: The Linac4 RFQ on its support, installed at the 3 MeV Test Stand.

RFQ MODULE FABRICATION

The fabrication of the RFQ is done through two brazing steps: with the first brazing the four RFQ vanes are assembled to form the RFQ cavity, while the second brazing, at lower temperature, is used to assemble the stainless steel flanges of the piston and vacuum ports and the two end flanges [3]. In the following we report the most relevant aspects of the construction of the three modules that form the RFQ. By convention we have called T1 the first module in the beam direction, followed by T2 and T3; in the fabrication process T1 and T3 were fabricated first, being very similar to each other from the mechanical point of view, while T2 was the last module to be built, due to the additional difficulty presented by the large waveguide openings for the RF power coupler.

T1

The fabrication of T1 started in 2009; it has been in fact the prototype on which all procedures have been tested and the fabrication strategy has been tuned. For that reason a considerable amount of metrology checks has been performed during its fabrication in order to assess that the fabrication was progressing well. For the same reason particular attention has been put into the RF bead-pull measurements, which were performed at each step of the assembly phase: mechanical assembly, first brazing and second brazing.

In table 1 the key dates for the construction of the module T1 are presented.

Copyright © 2012 by the respective authors — cc Creative Commons Attribution 3.0 (CC BY 3.0)

Table 1: Key Dates of the Construction of RFQ Module T1

Status	Date
Start T1 vane machining	June 2009
T1 assembly	March 2010
T1 first brazing	May 2010
T1 second brazing	November 2010

The evolution of the fabrication errors can be traced from the RF bead-pull measurements, in particular by looking at the asymmetries between the four quadrants, which can be referred to capacitance errors associated to the main quadrupole (QQ) and dipole modes (SQ and TQ) in the cavity. In Fig. 2 the vertical scale ranges between -2% and +2%, the error that can still be corrected by the available range of the piston tuners which is ±2.3% for the quadrupole mode and ±3.5% for dipole modes.

Figure 2 shows how, in the case of T1, the measurements performed after the second brazing, green trace, show errors quite below the level of 1%, allowing to assess the conformity of module T1 to the specification.

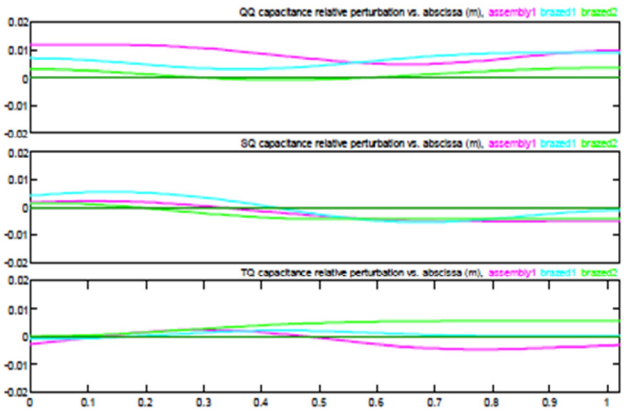

Figure 2: Capacitance errors for quadrupole (QQ) and dipole modes (SQ and TQ) in module T1.

T3

The fabrication of T3 was started at the beginning of 2010, when the construction of T1 was already well advanced. This choice was done in order to profit from the consolidated fabrication procedure coming from the T1 experience. In table 2 the key dates of T3 fabrication are summarized.

Table 2: Key Dates of the Construction of RFQ Module T3

Status	Date
Start T3 vane machining	January 2010
T3 assembly	December 2010
T3 first brazing	February 2011
T3 second brazing	May 2011

After the second brazing, the error associated to the quadrupole mode stays very low and the errors relative to the two polarizations of the dipole mode are lower than 1%, assessing the excellent quality of the fabrication process for this module.

The behavior of the relative error associated respectively to the quadrupole and dipole modes in T3 is represented in figure 3.

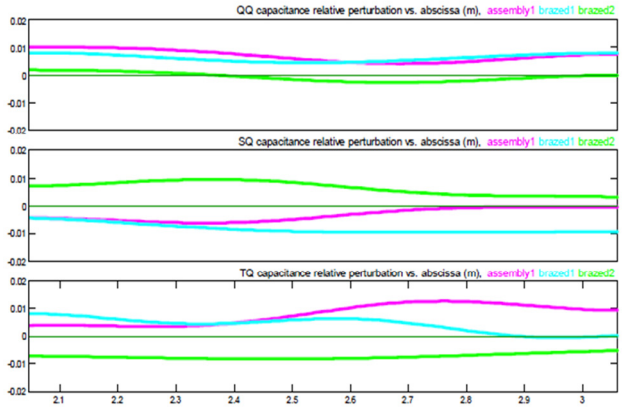

Figure 3: Capacitance errors for quadrupole (QQ) and dipole modes (SQ and TQ) in module T3.

T2

The fabrication procedure of T2 was different because of the presence of the four large stainless steel flanges (one per quadrant) designed to receive the ridged waveguide coupler that feeds the RF power to the RFQ cavity. For symmetry reason, four ports have been machined, but only one is used for the RF power coupler, while rectangular pistons are installed in the remaining three ports in order to make the field locally symmetrical.

The first attempts to braze these flanges were not successful, leading to an important modification to the mechanical design and to the brazing procedure.A traditional brazing of the hippodrome collar was followed by the EBW of the large stainless steel flange, finally permitting the perfect brazing of the ports. A view of the brazed port is presented in Figure 4.

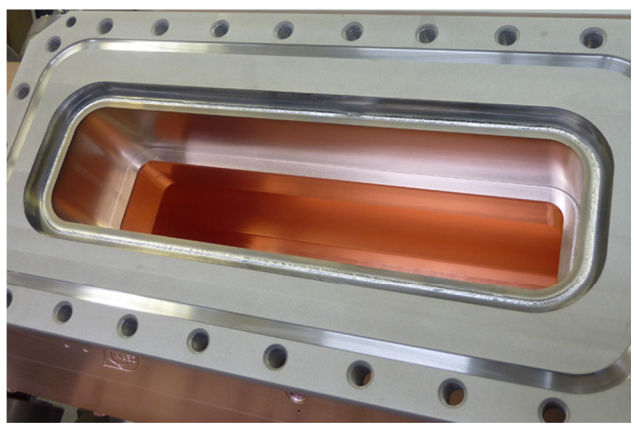

Figure 4: Close view of one of the RF coupler ports.

The realization of T2 has delayed the RFQ completion, initially foreseen for the end of 2011. Several test pieces had to be produced and an accurate preparation work on the RFQ cavity was required. Well controlled procedures allowed preserving the excellent quality of the module construction all the way through this process. In table 3 the key dates for the T2 construction are summarized.

Copyright © 2012 by the respective authors — cc Creative Commons Attribution 3.0 (CC BY 3.0)

Table 3: Key Dates of the Construction of the RFQ Module T2

Status	Date
Start T2 vane machining	June 2010
T2 assembly	June 2011
T2 first brazing	July 2011
T2 second brazing first	September 2011
T2 second brazing last	May 2012

Figure 5 reproduces the behavior of the quadrupole and dipole relative errors after the assembly steps.

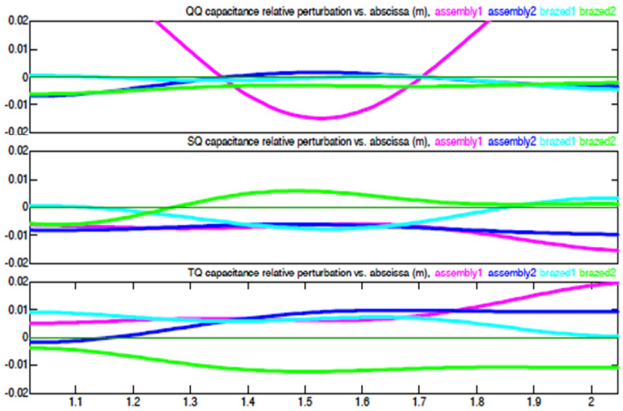

Figure 5: Capacitance errors for quadrupole (QQ) and dipole modes (SQ and TQ) in module T2.

In figure 5 the pink trace (assembly 1) reproduces the effect of a bad compensation of the electromagnetic field penetrating the 1 mm gap between the dummy RF ports and the waveguide openings situated at the middle of this module. The blue trace shows how this effect could be completely compensated by inserting the dummy RF ports by additional 0.7 mm inside the RFQ cavity. The green trace reproducing the error profile after the last brazing step confirms still a good fabrication quality for this module in spite of having passed several times in the brazing furnace.

RFQ MODULE ASSEMBLY

The principle for the final assembly of the three modules was based upon very precise metrology measurements of the reference points located at the entrance and exit of each module. The connection between adjacent modules has been realized by means of centering rings that were machined so to bring the optimized beam axis of the two modules to coincide within ±30 μm when bolted together and a key was used to establish the right azimuthal orientation.

RF Bead-Pull Measurements of the Assembled RFQ

After the RFQ assembly a first series of bead-pull measurements is required to tune the two end cells, thus allowing the fabrication of the end flanges equipped with quadrupole rods. Afterwards, further bead-pulls will allow the fine tuning of the accelerating field and to establish the correct power coupling. Figure 6 documents the result of the first measurements with all pistons in flush position.

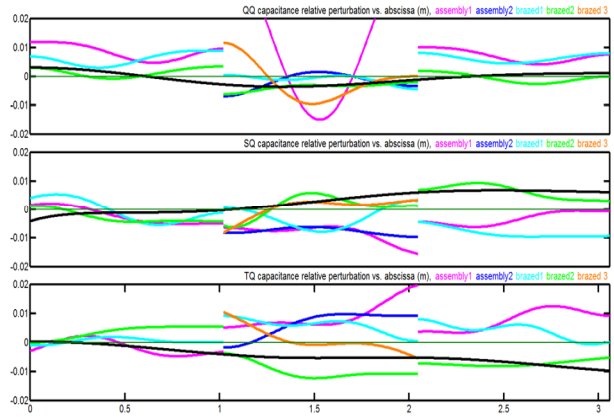

Figure 6: Capacitance errors for quadrupole (QQ) and dipole modes (SQ and TQ) in the assembled RFQ. Lines in colour represent measurements of individual modules, while the black line results from the assembled RFQ measurements, before its final tuning.

The assembled RFQ shows very small errors, within the ±1% range, that confirm the excellent quality of the RFQ machining and assembly.

The RF spectrum shows a separation between the accelerating quadrupole mode and the closer dipole modes of 6 MHz, while the first quadrupole mode is 3 MHz apart.

CONCLUSION

The fabrication of the Linac4 RFQ is approaching its end; within few months we should be able to power the RF cavity and start the commissioning of the accelerator. The first beam tests are foreseen before the end of 2012.

The RF measurements performed until now have confirmed the excellent quality of the mechanical construction, which was able to respect the very tight tolerances imposed by the design.

REFERENCES

[1] C. Rossi et al., "The Radiofrequency Quadrupole Accelerator for the Linac4", Linac08, Victoria BC, Canada.

[2] O. Piquet et al., "The RF Design of the Linac4 RFQ" IPAC10, Kyoto, Japan.

[3] C. Rossi et al., "The Radiofrequency Quadrupole Accelerator for the Linac4", L4-ACRFQ-ES-0001, EDMS 1020166, CERN, Geneva.

[4] S.J. Mathot et al., "Mechanical Design, Brazing and Assembly Procedures of the Linac4 RFQ" IPAC10, Kyoto, Japan.

Copyright © 2012 by the respective authors — cc Creative Commons Attribution 3.0 (CC BY 3.0)

DESIGN OF A FOUR-VANE RFQ FOR CHINA ADS PROJECT*

Zhang Zhouli#, He Yuan, Shi Aimin, Zhang Bin, Liu Yong, Du Xiaonan, Wang Jing, Li Chao,
Jin Xiaofeng, Sun Liepeng, Zhao Hongwei, IMP, Lanzhou 730000,China
D. Li, S. Virostek, M. Hoff, A. Lambert, J. Staples, LBNL, Berkeley, CA 94720, USA
C. Zhang, IAP, J.W. Goethe University Frankfurt, Germany

Abstract

A four-vane RFQ accelerator has been designed for the ADS project which has been launched in China since 2011. As one of the two front ends of C-ADS LINAC, the RFQ works at a frequency of 162.5MHz, accelerating the proton beam from 35keV to 2.1MeV. Due to the CW (continuous wave) operation mode, a small Kilpatric factor of 1.2 was adopted. At the same time, Pi-mode rods are employed to reduce the effect of dipole mode on quadrupole mode, and cavity tuning will be implemented by temperature adjustment of cooling water. Beam dynamics design, RF cavity design and thermal analysis all will be presented in the paper. Some fabrication test of the RFQ cavity will be described, too.

INTRODUCTION

All the countries in the world are confronting energy problems during the process of economic growth and society development nowadays, on one hand more and more energy is required to maintain modernized human life, on the other hand the earth's resources are limited. Although it can help solve the problems, nuclear energy has some drawbacks. First it is not absolutely safe, nuclear radiations caused by accidents happen occasionally; Secondly, management of nuclear waste is difficult [1]. However, the concept of ADS (accelerator driven system) proposed by C. Rubbia and his group has made nuclear energy much more safe and efficient [2]. It makes nuclear reaction controllable and transforms long-lived transuranic elements from conventional nuclear reactors to short-lived ones while producing electricity at the same time. Due to the advantages of ADS and more and more energy demands, China has launched the ADS project in 2011.

There are two front ends of the linear accelerator for the C-ADS project (as shown in Fig. 1), while IMP (Institute of Modern Physics) is responsible for injector2. The RFQ of injector2 will use the four-vane structure because of the CW operation mode. The frequency of injector2 is 162.5MHz, which will lead to a big size of the RFQ cavity and bring some challenges to the fabrication. Here the design of the RFQ will be presented.

BEAM DYNAMICS DESIGN

The RFQ of C-ADS injector2 is designed to accelerate proton beam from 35keV to 2.1MeV which can lead to small neutron production and material activation [3], and main parameters are listed in table 1. The frequency of 162.5MHz is chosen in order to decrease the power loss density of the cavity. The inter-vane voltage is 65kV, which can well reduce the probability of discharge. The twiss parameters and emittances of output beam are required to be less than 1.5, 0.33πmm mrad and 1keV ns respectively, table 1 shows all these requirements are met. Because the cavity is 420.8cm long, it will be equally divided into four modules when fabrication.

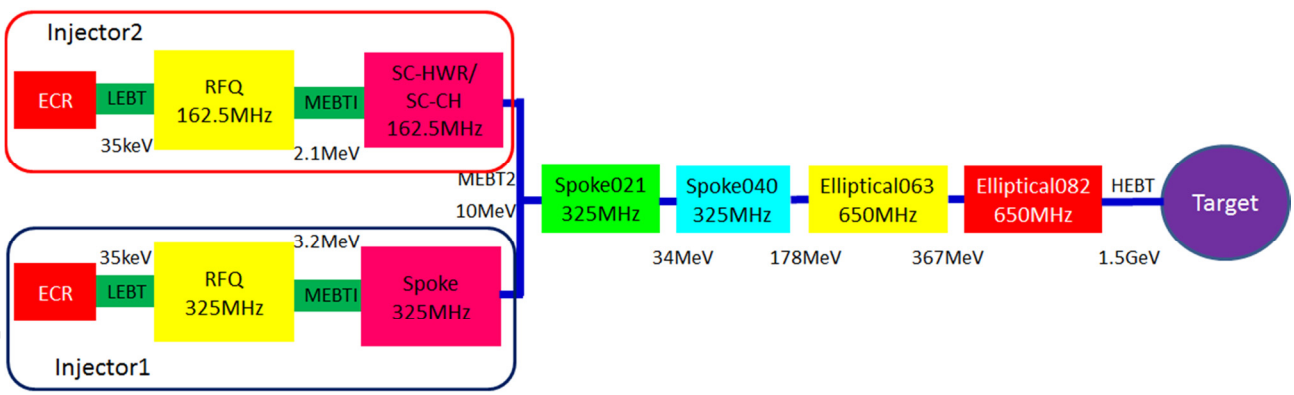

Figure 1: Layout of C-ADS driver accelerator.

* Work supported by NSF under Contract No. 11079001
# jolly@impcas.ac.cn

Copyright © 2012 by the respective authors — cc Creative Commons Attribution 3.0 (CC BY 3.0)

Table 1: Main Parameters of C-ADS Injector2 RFQ

Ion species	Proton
Frequency [MHz]	162.5
Input /Output energy [MeV]	0.035 / 2.1
Current [mA]	15
Input Emittance (nrms) [π mm mrad]	0.3
Output trans. Emittance (nrms) [π mm mrad]	0.31
Output long. Emittance [keV ns]	0.92
αin / α_{xout}, α_{xout}	1.21/0.36,-0.3
Inter-vane voltage [kV]	65
Kp factor	1.2
Minimum aperture [mm]	3.2
Modulation	1-2.38
Synchronous phase [deg]	-90 - -22.7
Cavity length [cm]	420.8
Transmission efficiency [%]	99.6

RF DESIGN AND THERMAL ANALYSIS

The average aperture r_0 of the RFQ is 5.731mm, and the ratio of vane-tip radius ρ to r_0 is 0.75. Four-vane structure is adopted so that cooling channel can be easily configured. A slice of 1mm of the structure (see Fig. 2) was calculated by the CST MWS code [4], and it shows the frequency is 162.31MHz and Q value is 16890 when the distance between cavity wall and beam axis is 177.1mm.

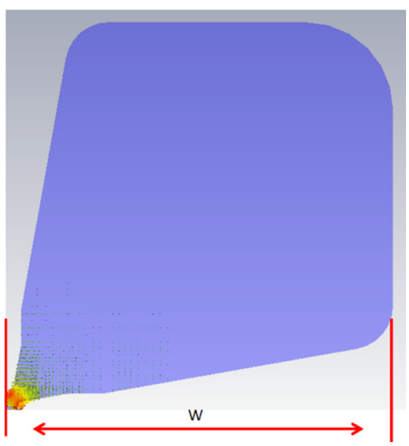

Figure 2: Transverse profile of C-ADS injector2 RFQ.

One feature of the RFQ is that it utilizes pi-mode rods (as shown in Fig. 3) to increase the span between the operation frequency (quadrupole) and adjacent dipole mode frequency, results demonstrate that the dipole mode frequency will shift from 157.6MHz to 181.7MHz when pi-mode rods with interval of 262.5mm are inserted into the RFQ cavity.

Full model of C-ADS injector2 RFQ is shown in Fig. 3, it has 16 pairs of pi-mode rods and 80 tuners. Calculation results reveal that Q value and full power loss of the whole cavity are 13337 and 91kW respectively when its frequency is 162.489MHz.

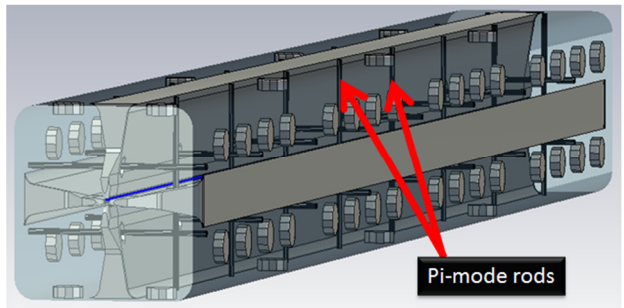

Figure 3: Full model of the C-ADS injector2 RFQ.

Thermal analysis was done with the ANSYS code [5] to study the cavity cooling issues and to know about how to tune the cavity by adjustment of cooling water temperature. Layout of cooling channels is displayed in Fig. 4, there are total eight cooling channels (diameter is 12mm) in the wall and four in vanes for each module. Temperature of the injecting cooling water was assumed 20°C, and velocity of the cooling water was 2.29 meter per second. Basing on the data mentioned above, temperature distribution of the cavity is shown in Fig. 4, and the relationship between cavity shifting frequency and cooling water temperature is -8.7kHz/°C for vane and 6.1kHz/°C for wall respectively.

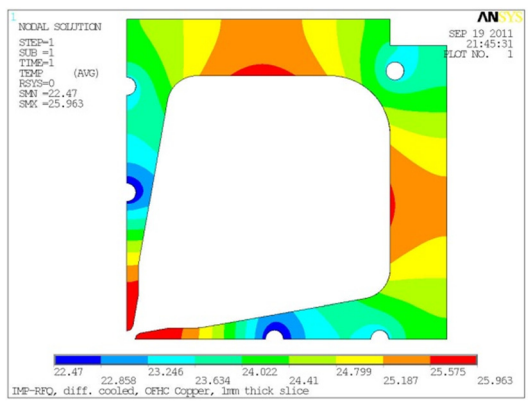

Figure 4: Temperature contour of the C-ADS injector2 RFQ.

FABRICATION TEST

The four-vane C-ADS injector2 RFQ has a big size (length of each side is bigger than 400mm) because of its low frequency. That brings some challenges to the fabrication of the cavity because we do not have any experiences in building such a big bulk. Therefore some fabrication tests are carried out, including flying cutter (as shown in Fig. 5), brazing of the bulk and machining

Copyright © 2012 by the respective authors — cc Creative Commons Attribution 3.0 (CC BY 3.0)

of a single vane (as shown in Fig. 6). Measurement results with CMM demonstrate that machining error of the cutter is controlled within ±11μm, which meets the machining requirement of vanes. Some problems are met during the brazing test, one reason is that the brazing clamp cannot fix the vanes properly, the other is vacuum oven was employed instead of hydrogen oven. Therefore a new hydrogen oven has been purchased, and new clamps are being designed. Besides the above tests, building of a half long module is being underway.

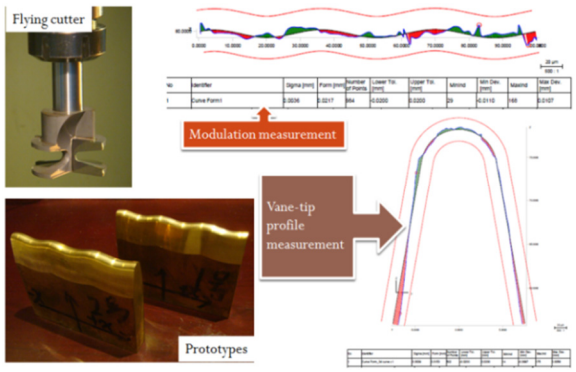

Figure 5: Flying cutter test.

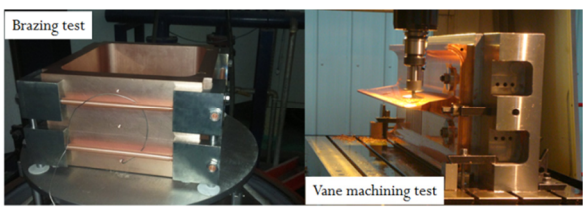

Figure 6: Brazing test and vane machining test.

CONCLUSION

A four-vane RFQ has been carefully designed including beam dynamics design, RF design and thermal analysis. The size of the RFQ is big owing to its low frequency which brings some challenges to the building of the cavity, and some fabrication tests have been done to make sure the real cavity can be built successfully. At present a half long module is being manufactured, and the cooling water system of the cavity is also being built. The real RFQ cavity is expected to be fabricated in next month.

REFERENCES

[1] Y. Kadi, J.P. Revol. Design of an accelerator-driven system for the destruction of nuclear waste, Lectures given at the Workshop on Hybrid Nuclear Systems for Energy Production, Utilisation of Actinides & Transmutation of Long-Lived Radioactive Waste. Trieste, 3 - 7 September 2001

[2] C. Rubbia et al., "Conceptual Design of a Fast Neutron Operated High Power Energy Amplifier", CERN/AT/95-44 (ET), Sept. 29, 1995; see also C. Rubbia, "A High Gain Energy Amplifier Operated with fast Neutrons", AIP Conference Proc. 346, Int. Conf. on ADT Technologies and Applications, Las Vegas, 1994.

[3] C. Baffes, M. Awida, A. Chen,et al. WEPPD035, Proc. of IPAC2012, New Orleans, USA.

[4] http://www.cst.com/Content/Products/MWS/Overview.aspx

[5] http://www.ansys.com/

Copyright © 2012 by the respective authors — cc Creative Commons Attribution 3.0 (CC BY 3.0)

HIGH-POWER RF CONDITIONING OF THE TRASCO RFQ

E. Fagotti, L. Antoniazzi, A. Palmieri, F. Grespan, , INFN-LNL, Legnaro, ITALY
M. Desmons, CEA, Saclay, FRANCE

Abstract

The TRASCO RFQ is designed to accelerate a 40 mA proton beam up to 5 MeV. It is a CW machine which has to show stable operation and provide the requested availability. It is composed of three electromagnetic segment coupled via two coupling cells. Each segment is divided into two 1.2 m long OFE copper modules. The RFQ is fed through eight loop-based power couplers to deliver RF to the cavity from a 352.2 MHZ, 1.3 MW klystron. After couplers conditioning, the first electromagnetic segment was successfully tested at full power. RFQ cavity reached the nominal 68 kV inter-vane voltage (1.8 Kilp.) in CW operation. Moreover, during conditioning in pulsed operation, it was possible to reach 83 kV inter-vane voltage (2.2 Kilp.) with a 0.1% duty cycle. The description of the experimental setup and procedure, as well as the main results of the conditioning procedure will be reported in this paper.

EXPERIMENTAL SETUP

The test was performed at CEA Saclay in January, February and March 2012.

The systems involved in the test are:

- RFQ cavity
- RFQ power system
- Vacuum system
- Cooling system
- Control system

The cavity under test is the first electromagnetic segment of the TRASCO RFQ [1], composed by two 1.2 m long OFE copper modules. The first module accommodates 12 gridded vacuum ports, the second one the 2 coupler ports. The RFQ end plates are equipped with dipole stabilizers [2, 3]. RFQ power level and field flatness are monitored by 16 pick-up loops, located inside the tuners along the 4 quadrants. The preservation of field flatness was verified looking at the pick-up signals, after transportation and positioning inside the CEA tunnel (Figure 1).

The core of the RF power system is the CEA 1.3 MW klystron, protected from the reverse power by a 1 MW circulator. The RF power is led into the RFQ tunnel through full-height WR2300 waveguide and then it is tapered to half-height WR2300 for the final distribution to the RFQ. Just upstream the RFQ, the RF power is split by a magic-TEE: two waveguide arms are coupled into the RFQ through 2 coupling loops, the 4th arm goes to a 100 kW water load. Forward and reverse powers are measured by directional couplers in the two waveguide arms before power couplers.

The vacuum system is composed by a dry primary pump, a turbo pump and two cryogenic pumps. The system was designed to maintain a pressure level $P \leq 1.3 \times 10^{-6}$ mbar under proton gas load. In particular, cryogenic pumps are unnecessary in absence of proton beam and they have not been used for this test. Vacuum gauges are located above couplers and on the vacuum manifold. Gate valves and nitrogen filling channel allow keeping the cavity in inert atmosphere during transports.

Cooling system is designed to remove 300 kW of power and to finely tune the resonant frequency by temperature regulation. For this purpose, it is necessary to have two independent water loops with two regulating temperatures. In the cooling skid, the temperature of each water circuit can be regulated by mixing the cold inlet water with part of the warm water coming from the cavity. Furthermore, the global temperature of the system can be adjusted by regulating the amount of warm water circulating in the heat exchanger. Water flow inside RFQ cooling channel is finely set by flow regulating valves located on each cooling channel. These valves maintain the required flow within ±2% when input pressure varies in the range 1-10 bar. Water flows and input/output temperatures of both water loops are monitored.

Control system [4] is connected to the other subsystems in order to monitor their characteristic parameters (temperature, powers, water flows, pressures), to command their actuators (valves, pumps) and set-up variables (interlock thresholds, water temperatures). In particular, interlocks on temperature, pressure, water flow, forward power are processed by PLC (response time =10 ms), while arc detectors and reflected power are directly sent to klystron to interrupt power in a few μs.

Figure 1: A view of TRASCO RFQ test in the IFMIF tunnel at CEA.

Copyright © 2012 by the respective authors — cc Creative Commons Attribution 3.0 (CC BY 3.0)

RFQ CONDITIONING

The unloaded quality factor Q_0=8460 was measured in the RFQ equipped with two aluminum couplers. Once the copper couplers were installed, the sum of the coupling coefficients ($\beta1+\beta2$) = 1.036 were obtained from the measurement of the cavity filling time τ=3.75 µs, at resonant frequency = 352.329 MHz. The two coupling coefficients are slightly mismatched, then we expect different values of reflected power in the 2 arms of the magic TEE, with less than 1% total reflected power in steady state operation. With that value of Q_0, the nominal voltage of 68 kV corresponds to cavity power P_{cav} = 192 kW (80 kW/m).

The RFQ resonant frequency control loop was not implemented for this conditioning test. The cavity was let free to be detuned, while the master frequency generator followed the RFQ resonant frequency. At low power level, a by-hand frequency control was sufficient. At high power operation (P_{cav} > 100 kW) an automatic frequency feedback control was required.

Three main phases of the RFQ conditioning are distinguishable, as highlighted in Figure 2 and 3.

From 24/01 to 30/01, RFQ was conditioned at very low duty cycle (<0.1%), to reproduce and never exceed Linac4 operating conditions (pulse length = 400 µs, rep.rate = 1.1 Hz, 82 kV), in order to allow the characterization of the X-ray emission at this regime. This phase was completed in 1 week, without any problem from the cavity point of view. In particular no discharges at 2.2 Kilp, no temperature changes or anomalous detuning were observed. Passing through all field levels, an important multipacting zone between 40 kV and 60 kV was noticed, to be treated with longer pulses. The presence of electron loading can be noticed in Figure 2, where the red squares are above the nominal curve, meaning that a large fraction of the power is not converted in accelerating voltage.

The period from 31/01 to 22/02 was dedicated to condition multipacting levels between 40 kV and 60 kV with pulses longer and longer. We adopted the following conditioning strategy:

- Fix a field level, with short pulse and long period;
- Lengthen the pulse length up to the complete conditioning of the level;
- Move on the next working point.

Because of 10 days of stop, the integrated time of this phase was 12 days.

Up to that time, the cavity frequency detuning caused by RF power was followed by changing the frequency of the signal generator by hand. Once the average power passed the 100 kW thresholds, the detuning at the power start was so fast that an electronic circuit was implemented, to give the frequency feedback to the signal generator. From 06/03 the CEA LLRF control was used.

From 23/02 to 14/03 the RFQ voltage was kept above 60 kV, except for the restart after large outgassing activity. In this phase of operations at high power level we noticed the first important discharge phenomena in the couplers, with consequent high vacuum levels (P > 10^{-4} mbar). To avoid long periods of vacuum recovery, interlock threshold of the reflected power was reduced and compensated with a longer blanking time, in order to skip the cavity filling time when the power is fully reflected.

The nominal voltage (68kV – 192 kW) in CW regime was reached in 07/03, and for 6 days the cavity was conditioned at this field with different duty cycles, always higher than 20 %.

Test was considered successfully closed in March 14th, after a continuous running at nominal voltage for 2 h. Temperature monitors did not show anomalous heating in high power steady state operation.

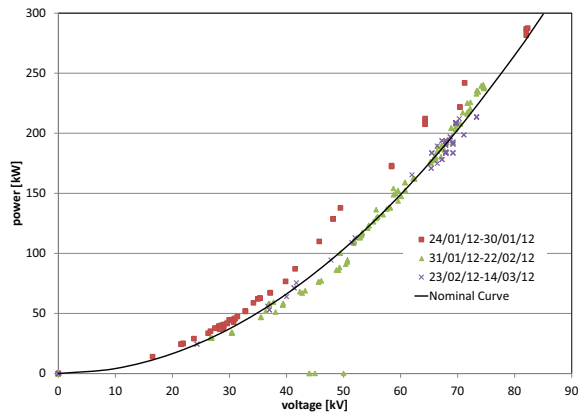

Figure 2: Peak cavity power, obtained as $P_{cav} = P_{forward} - P_{reverse}$, as function of the cavity voltage.

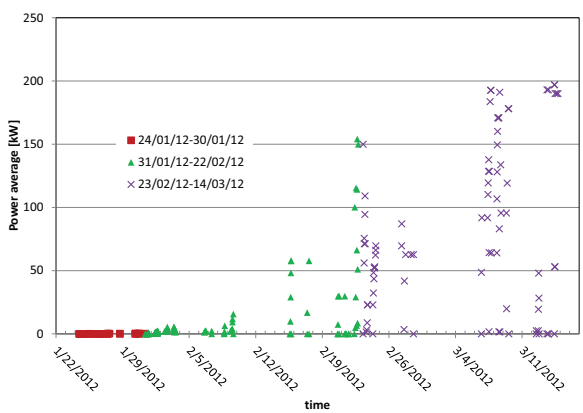

Figure 3: Cavity average power throughout the test.

RESULT ANALYSIS

Once the nominal steady state operation was reached, we observed an anomalous frequency detuning at 192 kW: Δf_{meas}= -238 kHz, to be compared with 2D simulation result Δf_{2D}= -132 kHz. Looking at the pick-up loops, we noticed that this frequency detuning was accompanied by an effect on the field flatness (Figure 4). A detailed simulation of the RFQ end-cells was performed with COMSOL [5], showing an important bending of the vane nose. The frequency perturbation profile obtained from simulation was imported in the

Copyright © 2012 by the respective authors — cc Creative Commons Attribution 3.0 (CC BY 3.0)

transmission line model of the RFQ, to evaluate the induced field and frequency detuning. Figure 5 shows field shape reproduced. The simulated detuning is -245 kHz. The asymmetric field shape, as observed in measurements, is caused by the differences on the end cell geometries. It is important to notice that this is a steady effect, not degenerative.

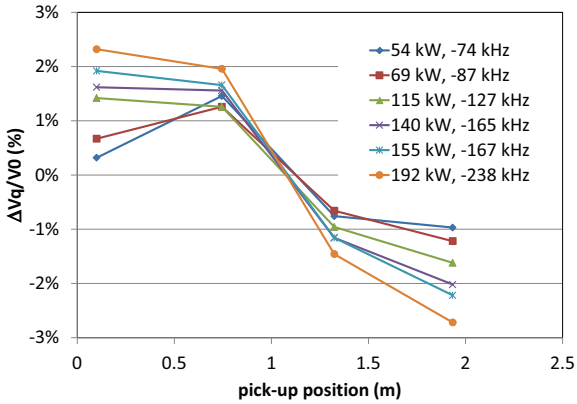

Figure 4: Field perturbation and frequency detuning measured at different power level.

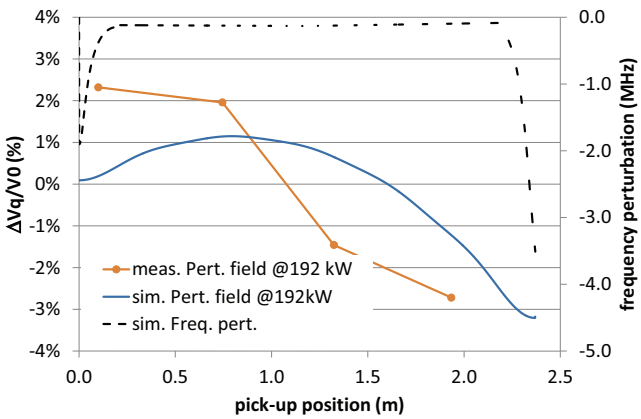

Figure 5: The measured voltage tilt at high power operation is reproduced by a transmission line analysis of the geometry deformation.

At the cavity open after the test, the power couplers showed evident copper sputtering. The RF coupler contacts were damaged and tainted by aluminium during the RF coupler test [6]. The contact degradation and aluminium oxide increase the resistance between hole and coupler wall. This could have generated a voltage difference with consequent discharges and copper sputtering, triggered off by cavity outgassing at high power operation. Sputtering phenomena was also found on the electrodes tip region, near the high energy termination plate. In this zone, R_0 changes and the electric field is a 6 % lower than the maximum value.

Finally, the chemical analysis of the cooling water revealed a copper concentration of 6.65 mg/l, due to the absence of a demineralization station in the cooling skid. In this condition, water conductivity was measured 35.8 μS/cm and PH of the water was measured 6.0.Before the test beginning, the cooling skid was filled with deionized water with 0.4 μS/cm resistivity and neutral PH.

Before removing termination plates (Figure 6), the unloaded quality factor Q_0 and coupling coefficients β_1 and β_2 were measured resulting in agreement with measurements before high power test. The quality of RF joint [7] was tested removing termination plates and then reinstalling them to look for a degradation of the unloaded quality factor. No Q_0 degradation was measured.

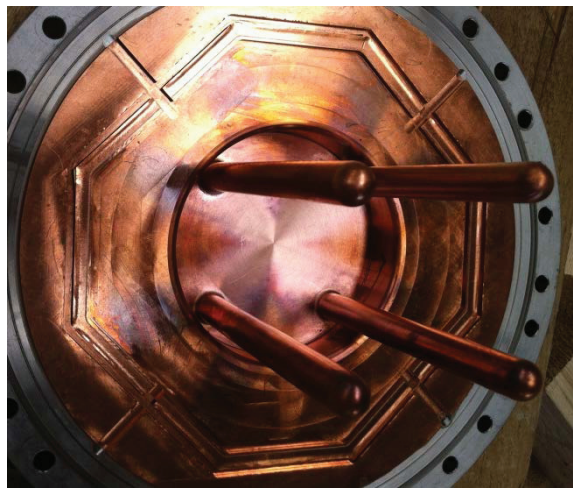

Figure 6: High energy termination plate inspection after high power test. V-shaped violet shadows caused by discharge phenomena are visible around dipole stabilizing rods.

ACKNOWLEDGMENT

We are very grateful to O. Brunasso and R. Panero for their technical support on the test assembly and disassembly. We acknowledge all the CEA team for the availability of people and facilities during the long test period.

REFERENCES

[1] A. Pisent et al., “The TRASCO-SPES RFQ”, LINAC’04, Lübeck, August 2004, MOP16, p.69 (2004); http://www.jacow.org.
[2] F. Grespan et al., “Dipole stabilizing rods system for a four-vane RFQ: Modeling and measurement on the TRASCO RFQ aluminium model at LNL”, EPAC’06, Edinburgh, June 2006, TUPCH123, p.1301 (2010); http://www.jacow.org.
[3] F. Grespan et al., “RF measurements for TRASCO RFQ characterization”, LNL Annual Report, 2010, p. 262; http://www.lnl.infn.it.
[4] L. Antoniazzi et al., “Control System Implementation for TRASCO RFQ High Power Test”, LNL Annual Report, 2012, p. 264; http://www.jacow.org.
[5] http://www.comsol.com/.
[6] E. Fagotti et al., “High Power Tests Bench for the TRASCO RFQ Coupler”, TUPB094, these proceedings.
[7] E.Fagotti et al., “Completion of the fabrication of TRASCO RFQ”, LINAC’10, Tsukuba, September 2012, TUP057, p.536 (2010); http://www.jacow.org.

Copyright © 2012 by the respective authors — cc Creative Commons Attribution 3.0 (CC BY 3.0)

PRODUCTION AND QUALITY CONTROL OF THE FIRST MODULES OF IFMIF-EVEDA RFQ

F. Scantamburlo, A. Pepato, R. Dima, INFN/PD, Padova, Italy,
C. Roncolato INFN/L.N.L., Legnaro, Italy

Abstract

The IFMIF/EVEDA RFQ, designed to accelerate a 125mA D+ beam from 0.1 MeV to 5 MeV at a frequency of 175 MHz, consists of 18 modules with length of ~550 mm each. The production of the modules has been started and 2 prototype modules plus module 16 have undergone all the production steps, including precision milling and brazing. The progress of the construction and especially the fine tuning of the design and engineering phase are reported.

BRAZING PROCEDURE MODIFICATIONS

Once completed the 2 steps brazing of the 1st module prototype, the acquisition of a continuous active scanning measuring machine (Zeiss Accura) allowed a deep and extensive investigation of the internal geometry of the cavity. A wide series of transversal and longitudinal scanning were then performed. The more detailed and reliable measurements showed a lack of symmetry induced by gravitation effect during the 1st step brazing [1]. The final geometry of the cavity resulted still within the acceptable tolerances range for a single module, but not for the complete line, figures 1 and 2. A vertical brazing assembly, which permitted instead a possibility of a single brazing step, has been developed, figure 3. In this respect, the groove geometry, layout and tooling had to be redesigned. We introduced extensive US scanning (destructive test) and inspection (non-destructive) for the qualification of the brazed surfaces (Cu-Cu and Cu-st. steel).

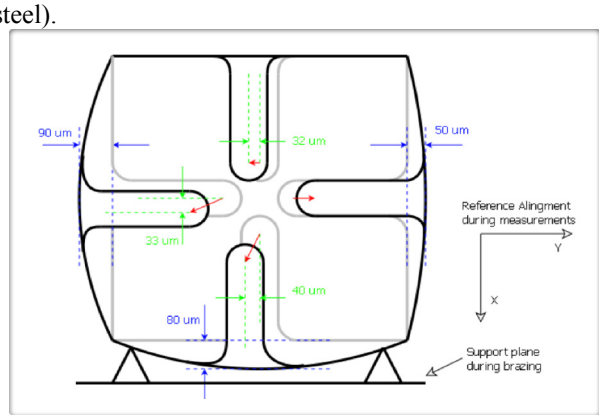

Figure 1: Scheme of the deformation of the cavity of the module 1 prototype after the second brazing

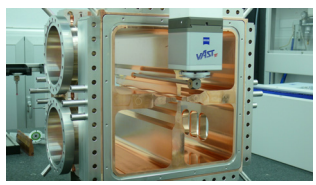

Pole	ΔX [μm]	ΔY [μm]	ΔR_0 [μm]
1	-40	-80	89.44
2	50	0	50.00
3	-32	0	32.00
4	-90	-33	95.86
	mean ΔR_0 [μm]		66.83
	$\partial f/\partial R_0$	[kHz/ μm]	7.60
	Δf	[kHz]	507.87

Figure 2: Module 1 prototype during CMM survey (left) and displacements of the tips (right).

R & D FOR SINGLE BRAZING STEP

With a single brazing step, the number of thermal cycles, reducing the mechanical properties of copper (1 annealing step + 1 final brazing step), is minimized.

The overall precision of the final geometry is optimized.

The cost and the timing of the modules production are also optimized.

Some basic tests on specimens having the same groove design, in order to compare vertical to horizontal brazing, have been performed.

Then two almost full scale tests have been performed finalizing an updated tooling set.

A complete inspection by US scan on slices of the brazed surfaces has been done (destructive). The grooves result always completely empty and no significant voids were detected on the brazing planes, figure 4.

Following these results, the production of the final modules started with SuperModule III-HE section. We adopted the vertical brazing approach but still with 2 brazing steps, until all details were well stated.

We completed the production of the module 16 (April '12), the second prototype module (July '12) and the 1st brazing step of module 17 (July '12).

The 1st single brazing step will be adopted on module 15 by October '12.

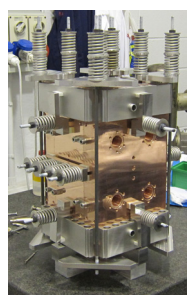

Figure 3: Full scale single brazing test

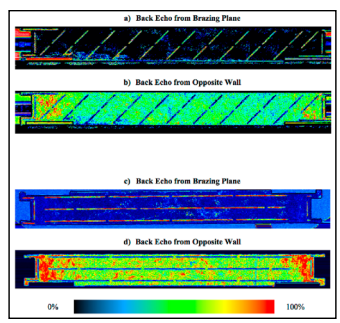

Figure 4: US inspection of two different brazing grooves design

Copyright © 2012 by the respective authors — cc Creative Commons Attribution 3.0 (CC BY 3.0)

THE MODULE 16'S PRODUCTION

The Quality Assurance of the Mechanical Machining

The continuous feedback between the mechanical machining and the measurement results was essential to guarantee the tight design tolerances.

The continuous active scanning survey of the tip geometry is mandatory to check the real geometry with adequate accuracy. The traditional point to point survey measurement (standard approach on CMM's) was attempted, but it failed.

The effectiveness of the active scanning control was essential to adjust and refine the CAM programs and the tooling fine tuning.

A standard procedure for the accurate control of each machining step of all the components and of the assembled module has been established:

- survey and qualification of each component, figure 5 and 6;
- survey and qualification of the dry-assembly of the module before the machining of the common reference planes;
- survey and qualification of the module after each brazing step;
- survey and qualification of the final module compared with the RF measurement.

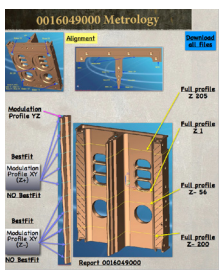

Figure 5: Inspected elements for the qualification of each CuC2 component of the cavity

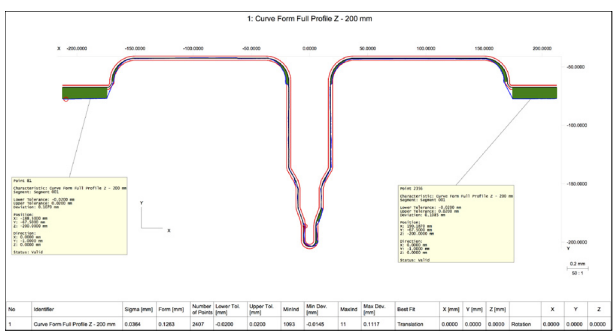

Figure 6: Example of measure of a profile by means active continuous scanning.

The Brazing Procedure, Module Dry Assembly

All the components are aligned to the nominal position and double checked, geometrically and RF.

The assembly is then machined to refine the common planes for the placement of the brazing tooling, figure 7.

The components are then dismantled, chemically cleaned, reassembled in a clean environment by means of the tooling, figure 8.

In this step the 2 sealing st. steel front rings have been mounted in order to provide a relevant constraint, embedding a smooth relative movement of components during the thermal cycle, that could cause an excessive flow down of the brazing material, figure 9.

Figure 7: Module 16 dry assembled before the machining of the common planes

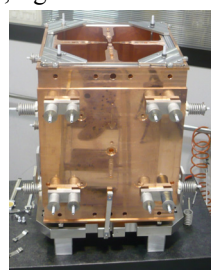

Figure 8: Module 16 assembled with the brazing tooling

The Brazing Procedure, 1st Step

We used Palcusil 10† as brazing material (optimal wetting of the surfaces while allowing for more brazing cycles repairs).

The optical inspection of the brazing joints showed an uniform distribution of the brazing material both on copper-copper and copper-st.steel.

The vacuum tightness of the cavity and of the cooling ducts was well below the specifications (1x10-9 mbar/sec*l).

Nonetheless a relative displacement between the "Ts" and the "Es" profiles was found.

This effect is explained by the relevant different expansion between CuC2 and AISI316LN.

The st. steel ring was not brazed in the first step of the first prototype module. Besides this the structural schemes are slightly different since on the first case the components are separated while in the other they are strictly joined.

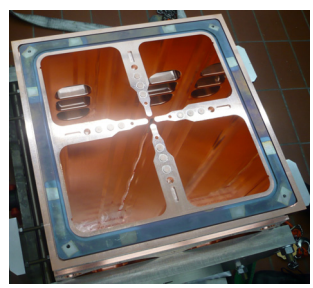

Figure 9: Module 16 after the 1st brazing step.

The Brazing Procedure, 2nd Step

The brazing material used is Cusil‡. During this step all the remaining st. steel components are brazed, figure 10. We encountered 2 problems.

† Palcusil 10 Composition: 59% Ag, 31 % Cu, 10% Pd; liquidus: 854 °C, solidus: 824 °C.

‡ Cusil Composition: 72% Ag, 28% Cu; liquidus : liquidus: 780 °C, solidus: 780 °C.

Copyright © 2012 by the respective authors — cc Creative Commons Attribution 3.0 (CC BY 3.0)

The junctions between the end side flanges and the copper were just partially brazed (as verified by US inspection).

The dimensional check of the cavity showed unexpected deformations.

The reasons:

- we discovered that the heat treatment of the end side flanges was not done following our specifications (the cooling step was too fast thus resulting on an ineffective annealing process);
- again the relevant different expansion between CuC2 and AISI316LN.

Since the brazed connection was too poor, a 3rd brazing step (using Incusil 10*) was performed to join the copper and the st. steel end side flanges by means of a series of pins, figure 11.

Beside all these problems the module 16 fulfills the specifications in terms of geometrical tolerances and vacuum tightness.

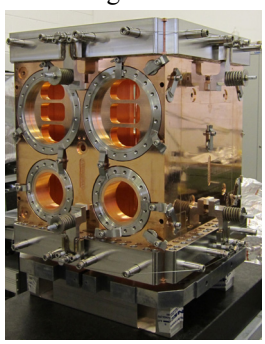

Figure 10: Module 16 before the 2nd brazing step

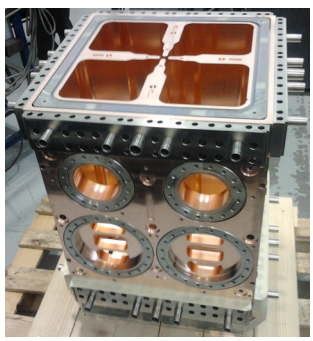

Figure 11: Module 16 after the 3rd repair brazing

Improvements - the results

Keeping in mind the problems found on module 16, a wide range of data for the thermal behaviour of copper and AISI316 were registered in the technical literature [2, 3].

We decided to perform some test with the peculiar material and dimensions to determine the overall relative expansion during our typical brazing cycles.

The tests results were better approximated by the material data as reported in reference [3]. Consequently our design was modified as follows:

- the sealing st. steel ring: any contact between copper and ring on the "Ts" sides (gap about 0.3 - 0.5 mm) was embedded, while the nominal coupling brazing tolerance on the "Es" sides was maintained to ensure a relevant coupling pressure all along the thermal cycle (accepting the residual local deformation at the joint level), figure 12;
- the end side flanges: some almost passing through incisions were introduced, softening the end side flanges stiffness, while ensuring a continuous brazing surface. The local expansion of the cavity was limited to a value around 0.01 mm, figure 13.

All these modifications were introduced and verified on the 1st brazing step of module 17 (sealing st. steel rings) and on the 2nd brazing step of the second prototype module (the incision solution was tested just at one side in order to see the differences).

We developed a more compact and effective constraint fixation made by TZM springs.

This allows for an easier positioning while increasing the contact pressure at high temperature. A more distributed number of constraints are now available.

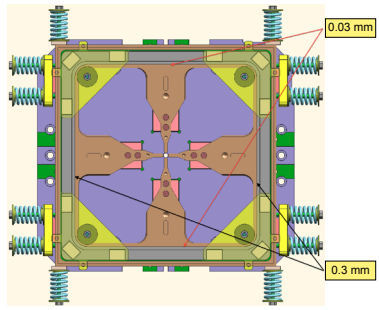

Figure 12: New design of the coupling between copper and sealing st. steel ring avoiding contact with the "Ts"

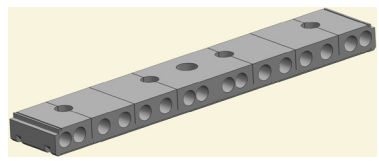

Figure 13: New design of the end side flanges with the incision to reduce the stiffness

WHAT NEXT

The single brazing method will be applied for the first time on the module 15 (October '12).

We assigned a new contract for the production of SuperModule I and the production will start soon.

The production of SuperModule II will be done within INFN. The machining of components is already started.

AKNOWLEDGEMENT

The authors wish to thank the CINEL Scientific Instruments S.r.l. for the active sustaining during R&D phase

REFERENCES

[1] Engineering Design and First Prototype Tests of the IFMIF-EVEDA RFQ, A. Pepato et al, IPAC 2010, Kyoto, Japan.

[2] Thermal expansion of some common LINAC materials, R. Valdiviez, D. Schrage, et al., Linac 2002, Gyeongju, Korea.

[3] N. C. Anderson, Lectures in Ceramic Metal Joining, Amsterdam, 1996.

* Incusil 10 Composition: 63% Ag, 27% Cu, 10% Sn; liquidus : liquidus: 730 °C, solidus: 685 °C

Copyright © 2012 by the respective authors — cc Creative Commons Attribution 3.0 (CC BY 3.0)

THE RFQ INJECTOR FOR THE RADIOACTIVE ION BEAM OF SPES PROJECT

M. Comunian, A. Palmieri, A. Pisent, F. Grespan, INFN/LNL, Legnaro, Italy

Abstract

A Continuous Wave Radio Frequency Quadrupole Accelerator has been designed for the Radioactive Ion Beam of SPES Project to be used as an Injector of the ALPI Linac. The RFQ frequency is 80 MHz for an input energy of 40 keV, with output energy of 5 MeV and ion ratio q/A<= 1/7. Particular care has been put in the design phase to include an internal bunching section able to reduce the longitudinal output emittance. The details of the RF study of such a cavity are included as well.

BEAM DYNAMICS

Within the project SPES laboratory a new injection line will be built at INFN LNL to transport and match the RIB to the existing ALPI superconducting linac [1].

This line includes a new RFQ (see Tab. 1) that will operate in a CW mode (100% duty factor) at a resonant frequency of 80MHz. This frequency is the same of the lowest energy ALPI superconducting structures. The injection energy of ions was set to 5.7 keV/u. This choice is a compromise between the desire to reduce the ion energy to simplify the LEBT and the RFQ bunching section design and the need to increase the injection energy to increase the beam rigidity in the spectrometer and to reduce space charge effects. The extraction energy was set to 727 keV/u (respect to the 588 keV/u of the present SRFQ), to optimize the beam dynamics of the SRF ALPI linac.

Table 1: Principal RFQ Parameters

Parameter (units)	**Value**
Operational mode	CW
Frequency (MHz)	80.
Injection Energy (keV/u)	5.7 (β=0.0035)
Output Energy (keV/u)	727 (β=0.0395)
Accelerated beam current (μA)	100
Charge states of accelerated ions (Q/A)	7 – 3
Internal bunching section	Yes

The design goals were to minimize the longitudinal and transverse emittances growth and to optimize the RF losses and transmission of the RFQ structure. The RFQ cells were created using the program CORTO, used for the design of CERN linac3 RFQ [2,3], PARMTEQ code package and Toutatis in an iterative cell-by-cell procedure. With this design the RF power consumption is minimized, while a variable voltage profile, like the IFMIF RFQ [4], allows accelerating the beam more effectively at higher velocities and achieving higher output energy. A transition cell was used at both the entrance and exit of the RFQ. At the exit side, a radial matching section with an appropriate length after the transition cell was also used so that the output beam has the same Twiss parameters in both the horizontal and vertical planes. Table 2 and Figure 1 show the main parameters of the RFQ. The RFQ transmission is more than 95% of accelerated particles, the final longitudinal RMS emittance is 0.15 nskeV/u. The 99% longitudinal emittance is 1.2 nskeV/u , see Figures 2, 3 and 4.

Table 2: RFQ Design Parameters

Parameter (units)	Design 1
Inter-vane voltage V (kV, A/q=7)	63.8 – 120
Vane length L (m)	5.97
Average radius R_0 (mm)	5.03 – 9.574
Vane radius ρ to average radius ratio	0.8
Modulation factor m	1.0 – 3.16
Total number of cells	303
Synchronous phase (deg.)	-90 – -20
Focusing strength B	5.28 – 2.8
Peak field (Kilpatrick units)	1.7

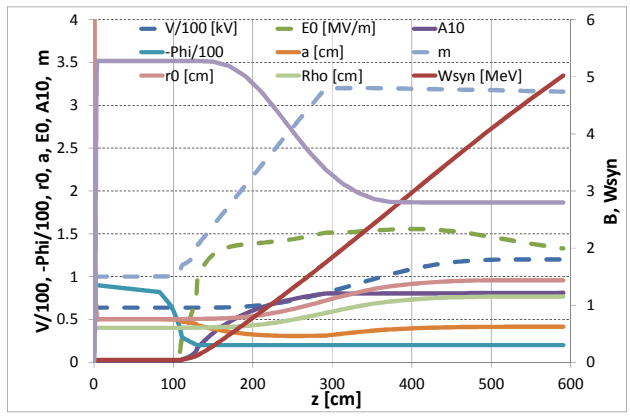

Figure 1: the main RFQ parameters vs. length as for beam dynamics outcomes.

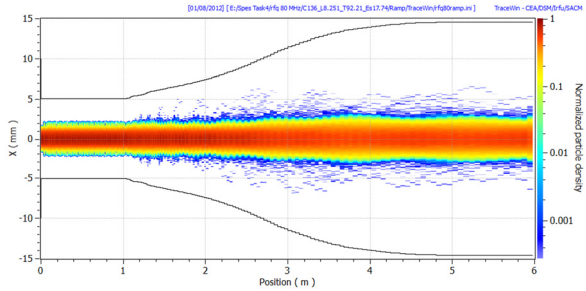

Figure 2: X envelope along the RFQ.

Copyright © 2012 by the respective authors — cc Creative Commons Attribution 3.0 (CC BY 3.0)

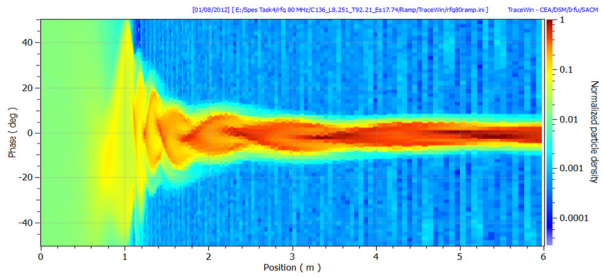

Figure 3: Phase density along the RFQ.

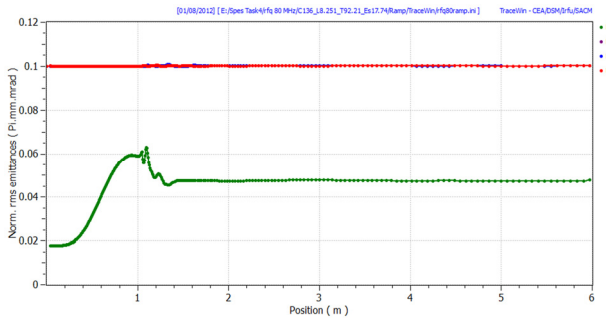

Figure 4: RMS emittance along the RFQ.

CONSTRUCTION CONCEPT

A nc cw four vane RFQ at similar dimensions and is being built for SPIRAL2 project [5].

The construction considered for SPES RFQ is a four vane structure, divided in 6 modules of approximately equal length. The cylindrical tank (800 mm diameter) is in copper plated iron properly annealed. The electrodes are built out of OFE copper and 316LN stainless steel; brazing under vacuum is used to build the cooling channels and the interface reference surfaces between electrode and tank.

The electrode modulation is milled to final value after brazing, and as the last operation the electrodes are positioned, aligned and bolted to their final position in the tank. Vacuum tightness is guaranteed at electrode bases by circular gaskets, that can be inspected and substituted without removing the electrode. The RF joint is at the electrode bases, with a current limited to about 22 A/cm even in the undercut region (see later).

RF STUDY

The choice of a four-vane structure with variable R_0 and voltage profile requires an accurate tuning of the 2D section of the RFQ in order to compensate for local TE_{21} cut-off frequency f(z) variation Δf(z) due both to voltage and aperture variation. In the first case such frequency variation is related to the 2nd derivative of the voltage, according to the relationship

$$\Delta f(z) = \frac{1}{2 f_0}\left(\frac{c}{2\pi}\right)^2 \frac{V''(z)}{V(z)}$$

while, in the second case, the cross section tuning process had to compensate the R_0 variation along the cells. The desired Cross Section Frequency is obtained by varying the Vane Base Width 2•W1 along the RFQ. This first optimization has been accomplished by performing simulations with HFSS (parametric mode) code both and then confirmed by SUPERFISH. The results of the two agree within 0.15%. In particular, in the given range of variation of the parameters, the function $f(W_b, R_0)$ can be approximated as

$$f(W_b, R_0) = (a_1 R_0 + a_0) W_b^{\,2} +$$
$$+ (b_1 R_0 + b_0) W_b + c_2 R_0^{\,2} + c_1 R_0 + c_0$$

where the coefficients were obtained by fitting the simulations data obtained by varying W_b and R_0. From this relationship, given the voltage law and the initial cut-off frequency f(0), it is possible to determine the $W_b(z)$ law directly.

In Figure 5 the variation of the W1 as a function of z and in Figure 6 the cross sections of the cavity corresponding to the Low Energy and High Energy Sides are shown. It is possible to notice that the minimum value of the Wb is about 3.5 cm and the maximum value is 10 cm. It should be noticed that the maximum current density at the RF joint is 22 A/cm

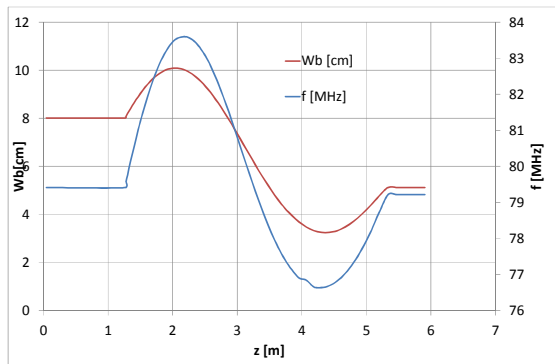

Figure 5: the local cut-off frequency and the Wb as a function of length.

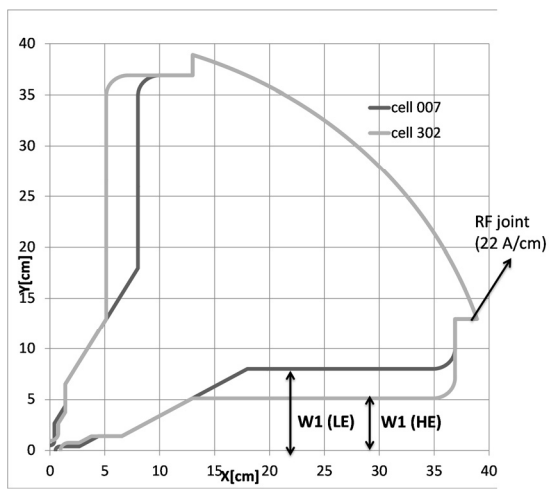

Figure 6: The low energy and High Energy cross sections of the RFQ.

As for power consumption calculations is concerned, it has to be pointed out that the total power P_{RF} is related to

Copyright © 2012 by the respective authors — cc Creative Commons Attribution 3.0 (CC BY 3.0)

the 2D power calculated by SUPERFISH, PSF, by means of the relationship

$$P_{RF} = P_{SF}\alpha_{3D}\alpha_{RF}$$

where α_{3D}=1.3 is a factor that takes into account the 3D losses, α_{RF} = 1.2 takes into account the margins for RF System (losses in the lines and in the circulator, finite bandwidth of the amplifier etc). In the following table the main RF parameters are shown.

Table 3: Main RF Parameters

Shunt Impedance (SF)	400-635	kΩ·m
Q0 (SF)	17500-21500	
Copper power (SF)	100	kW
Stored Energy	3.7	J
Max H field (2D)	2200	A/m
Max Power Density (2D)	0.56	W/cm^2
Max Power Density (3D)	20	W/cm^2
Total Power	156	kW

The RF power will be fed by a single amplifier unit based on a TH535 tube (180 kW max power in CW).

The vane terminations and undercuts correspond to the maximum power density, and have to be properly cooled. Moreover with bolted electrodes one has to be careful about the maximum current across the RF joint at the bases of the electrode. The design proposed (Fig.6) is such to keep the current density always below the value of 2d cross section.

HFSS simulations showed that, actually, on the electrode base, where the RF joint is foreseen to be inserted, the maximum current is equal to 22 A/cm (Figures 7 and 8)

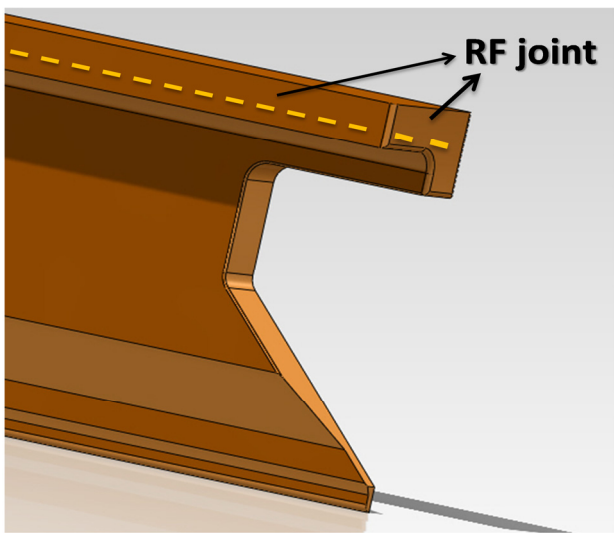

Figure 7: detail of the electrode on the High Energy Side of the RFQ, with the location of the RF joint.

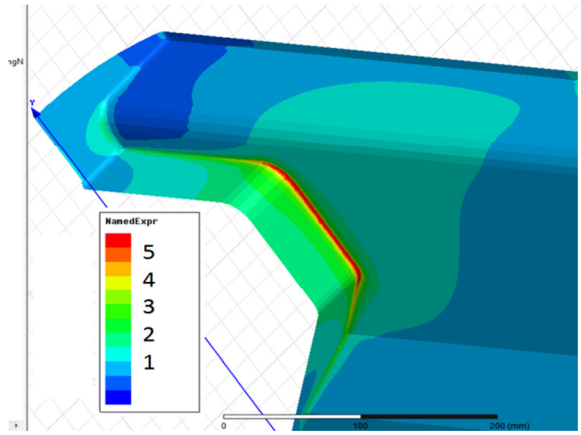

Figure 8: Current density on the undercut normalized to the 2D value (22 A/cm).

Some comments have to be made on the tuning range of the structure, related to the construction and alignment tolerances. The sensitivity with respect to geometrical errors was numerically addressed, and it was found that the maximum [minimum] sensitivity χ_{R0} is located in the initial [final] section of the RFQ, where $\partial f/\partial R0$=3.6 MHz/mm [2.2MHz/mm]. This means that a 0.2 mm misalignment of the electrodes provokes a frequency shift of 720 kHz [440 kHz]. Therefore, in order to allow the positioning of the electrodes with ±0.2 mm precision, an (average) tuning range of ± 600 kHz is needed. For this reason, the frequency f_0 was chosen to be equal to 79.4 MHz. . It has also to be pointed out that, due to the favourable L/λ ratio of this RFQ, the 1st upper quadrupole mode is about 3.8 MHz away from the fundamental one, and the attainment of a dipole-free region of ± 2 MHz is feasible. Therefore in this case the tuning range can be used mainly for compensation of misalignments. In order to allow the tuning of the structure a system of slug tuners has to be foreseen. In the present design, it is foreseen to use 24 tuners of 9 cm diameter. In this way, the working frequency can be reached by inserting all the slugs to a 50 mm penetration inside the cavity. The high value of the shunt impedance*length for such a structure and the power capability of the RF source allows the implementation of such a huge tuning range.

REFERENCES

[1] M. Comunian, et al. "Beam Dynamics of the Linac ALPI-PIAVE in view of possible upgrades scenario for the SPES Project", this conference.
[2] M. Comunian, "DINAMICA DEL FASCIO NELL'RFQ DEL NUOVO INIETTORE DIIONI PIOMBO AL CERN", degree thesis, Padua University, 1994 (in italian)
[3] G. Amendola et al, EPAC 92, p. 973
[4] M. Comunian, et al. "Beam Dynamics of the IFMIF-EVEDA RFQ", EPAC08 Genova.
[5] R. Ferdinand et al, EPAC 2006.

Copyright © 2012 by the respective authors — cc Creative Commons Attribution 3.0 (CC BY 3.0)

PLANS FOR AN INTEGRATED FRONT-END TEST STAND AT THE SPALLATION NEUTRON SOURCE*

Mark S. Champion#, Alexander V. Aleksandrov, Mark Crofford, Dale Heidenreich, Yoon W. Kang, John Moss, Tom Roseberry, James Schubert, Oak Ridge National Laboratory, Oak Ridge, TN, USA

Abstract

A spare Radio-Frequency Quadrupole (RFQ) is presently being fabricated by industry with delivery to Oak Ridge National Laboratory planned in late 2012. The establishment of a test stand at the Spallation Neutron Source site is underway so that complete acceptance testing can be performed during the winter of 2012-2013. This activity is the first step in the establishment of an integrated front-end test stand that will include an ion source, low-energy beam transport (LEBT), RFQ, medium-energy beam transport, diagnostics, and a beam dump. The test stand will be capable of delivering an H- ion beam of up to 50 mA with a pulse length of 1 ms and a repetition rate of 60 Hz or a proton beam of up to 50 mA, 100us, 1Hz. The test stand will enable the following activities: complete ion source characterization; development of a magnetic LEBT chopper; development of a two-source layout; development of beam diagnostics; and study of beam dynamics of high intensity beam.

INTRODUCTION

The Spallation Neutron Source (SNS) Radio-Frequency Quadrupole (RFQ) was commissioned with beam in 2003. The RFQ performance has been sufficient to enable high-reliability neutron production, but there have been two sudden detuning events that required retuning of the structure, and there is evidence that the RFQ is being operated near the limits of thermal stability, i.e., reliable operation at higher average power is uncertain. The SNS accelerator presently delivers a 1 MW proton beam to the neutron production target. It is planned to ramp up the beam power to 1.4 MW over the next few years.

The RFQ structure twice experienced a sudden resonant frequency shift of a few hundred kHz. The first event occurred in October of 2003 during beam operation, the second in February 2009 during a maintenance period with no RF power in the cavity. A thorough examination of the RFQ cavity was conducted after the first event but nothing abnormal was found. The cavity was retuned using available tuners and successfully returned to operation in both cases. The root cause of the detuning has not been determined with certainty, but there is a similarity in both cases. The detuning was coincident with cooling system problems: in the first case a failure in the controls system caused the RFQ to cool down to 8°C; in the second case the cooling water pressure inadvertently increased over 100 psi. It is postulated that these events could create an abnormal stress causing a partial separation of the braze joint between the inner high-purity copper structure and the outer GlidCop exoskeleton.

The RFQ showed resonance control instabilities when operating at a duty factor larger than ~4.2%, and this was one of the limiting factors in reaching 1 MW beam power. The machine downtime due to this RFQ instability was longer than 30 minutes per day, which affected the overall machine availability. The response time (about 5 minutes) of the Resonance Control Cooling System was a major contributing factor. The auto pulse-width adjustment scheme was added to the low level RF control system to provide faster control [1]. With this improvement the SNS RFQ has been confirmed to be stable up to 5.5% RF duty factor at the cost of using up 60 us of available RF pulse width for the temperature control. It is not clear if this solution will work at 7% duty factor required for achieving 1.4 MW beam power.

In order to mitigate the risk of failure of the original RFQ and to prepare for increased beam power, a contract was made for production of a spare RFQ at Research Instruments GmbH near Cologne, Germany. The RFQ is presently in production and delivery to SNS is expected in late 2012. A test stand is being prepared at SNS to support acceptance testing of the RFQ. The test stand will include all infrastructure needed to demonstrate full performance of the RFQ without beam.

It is planned to further develop the test stand thereafter into a fully-integrated front-end test stand that will include an ion source, low-energy beam transport (LEBT), RFQ, medium-energy beam transport (MEBT), diagnostics, and a beam dump. The test stand will be capable of delivering an H- ion beam of up to 50 mA with a pulse length of 1 ms and a repetition rate of 60 Hz or a proton beam of up to 50 mA, 100us, 1Hz. The test stand will enable the following activities: complete ion source characterization; development of a magnetic LEBT chopper; development of a two-source layout; development of beam diagnostics; and study of beam dynamics of high intensity beam.

TEST STAND SITE

The test stand will be installed in the RF Test Facility Annex, building 8320, at the SNS site, as shown in Figure 1. The RF Test Facility, building 8330, is adjacent and presently houses a high-power RF test stand for testing klystrons, RF devices, and cryomodules. Building 8330 also houses infrastructure for superconducting RF development and maintenance activities. This infrastructure includes a clean room, high-purity water system, high-pressure rinsing system, vertical test stand, cryomodule test stand, and cryomodule assembly area.

*ORNL is managed by UT-Battelle, LLC, under contract DE-AC05-00OR22725 for the U.S. Department of Energy.

#championms@ornl.gov

Copyright © 2012 by the respective authors — cc Creative Commons Attribution 3.0 (CC BY 3.0)

Low-conductivity and industrial chilled water is available at the mutual boundary of these buildings. An additional AC power transformer and distribution panels are being installed in the Annex to service the front-end test stand.

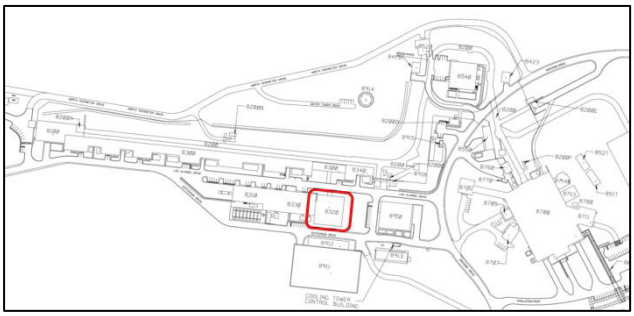

Figure 1: The front-end test stand is being installed in building 8320 across the street from the klystron gallery adjacent to the high-energy end of the superconducting Linac.

TEST STAND LAYOUT AND PROGRESS

The test stand will be installed on the west side of building 8320 under an existing support structure (Figure 2.) This structure was designed to facilitate testing of klystrons and RF components and features cable trays and low-conductivity water distribution on its topside. RF waveguide components will hang from its bottom-side. The waveguide distribution up to the output of the circulator has already been installed. The 2.5 MW, 402.5 MHz klystron and its water cooling skid have been installed as show in Figure 3.

Figure 2: The front-end test stand area as viewed from the position of the beam dump. The RFQ will be to the right of center beneath the blue support structure.

The area where the test stand is being installed will serve several functions in the future. A prototype high-voltage modulator will be installed in the background area of Figure 2 for testing as a collaborative effort with ESS-Bilbao. This modulator was specified to meet SNS superconducting Linac requirements and is presently undergoing factory testing at the Jema company in Spain.

Three 805 MHz, 550 kW klystrons mounted to a single transmitter tank are visible in the Figures 2 and 3. These klystrons are utilized in the superconducting Linac, where 81 klystrons power 81 accelerating cavities. A test stand for these klystrons is being established adjacent to the RFQ test stand. The RF water loads (red) can be seen hanging from the support structure in Figure 2. These klystrons may be powered by the Jema modulator after it passes initial acceptance testing at SNS.

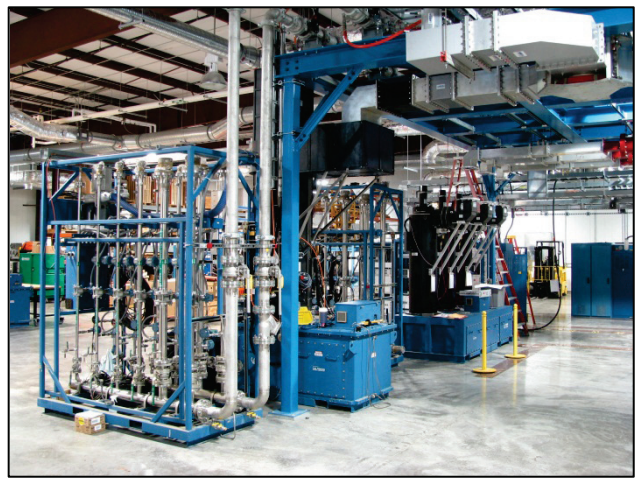

Figure 3: The 402.5 MHz klystron and its cooling cart have already been installed along with a portion of the waveguide system. A trio of 550 kW, 805 MHz klystrons is visible in the background, where a separate klystron testing capability is being established.

The layout of the test stand area is shown in Figure 4. Space has been reserved at the left-end of the RFQ for development of a two-source configuration, which is desirable for high-reliability accelerator operation at SNS. Space has also been reserved immediately beneath the RFQ to support later installation of a MEBT and experimental area for high-intensity beams.

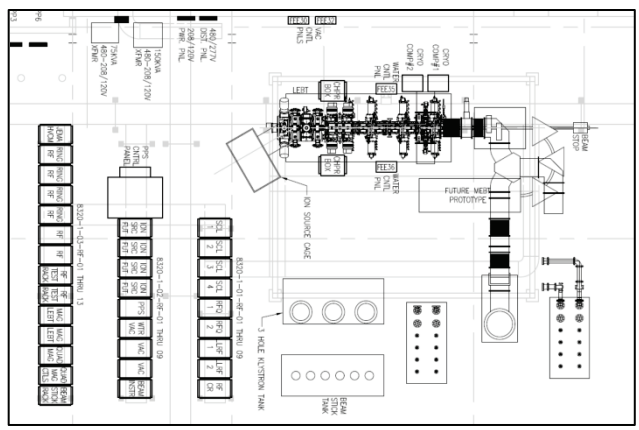

Figure 4: Layout of the front-end test stand. The beam direction is to the right (north).

The 2.5 MW, 402.5 MHz klystron will be powered by an existing high-voltage converter modulator in the RF Test Facility. This modulator is part of a test stand

Copyright © 2012 by the respective authors — cc Creative Commons Attribution 3.0 (CC BY 3.0)

(Figure 5) that is used to test modulators, klystrons, cryomodules, and various RF transmission components. A triaxial high-voltage cable has already been installed from this modulator to the kystron that will power the RFQ.

Figure 5: The existing RF test stand features a high-voltage converter modulator (background) which can be used to operate either 2.5 MW, 402.5 MHz or 5 MW, 805 MHz klystrons (foreground).

RFQ DESIGN AND STATUS

The primary requirement on the spare RFQ is that it be a drop-in replacement for the existing RFQ. This implies compatibility in physical size, RF characteristics, beam dynamics, and interfaces to supporting subsystems such as vacuum, water, and RF. In order to meet this requirement, the vane modulation is unchanged from the original SNS RFQ. Design changes include an octagonal cross section, the use of dipole stabilizer rods in the end plates for mode spacing, and construction of high-purity copper. In contrast, the original RFQ utilizes a square cross section, pi-mode stabilizers, and is constructed of a combination of GlydCop and high-purity copper. The spare RFQ features 64 slug tuner ports, 48 RF pickups ports, 10 vacuum ports, 2 RF input coupler ports, and 2 beam ports [2,3]. The spare RFQ is presently in fabrication at Research Instruments GmbH with delivery to SNS expected later this year. The RFQ will be fully assembled at the vendor facilities, where it will undergo RF tuning and measurements, vacuum integrity testing, and water manifold testing. The fully-assembled RFQ will be shipped to Oak Ridge on a girder as depicted in Figure 6.

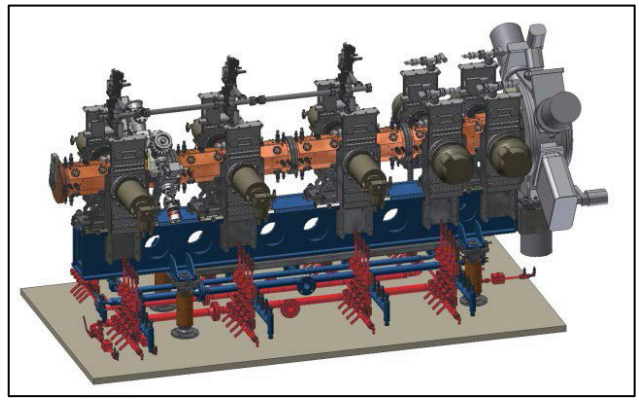

Figure 6: Illustration of the spare RFQ due for delivery to SNS later this year.

EXPERIMENTAL PLANS

Preparations are underway to enable acceptance testing of the spare RFQ during the winter of 2012-1013. Acceptance testing will include verification of the RFQ structure tuning and RF operation up to the design gradient and duty factor. Upon successful completion of this testing, installation of the ion source, LEBT, MEBT, and beam dump will proceed. It is anticipated that this basic configuration will be commissioned with beam in 2013.

The primary initial purpose of the front-end test stand will be complete ion source characterization. Presently this work can be performed only on the SNS accelerator, which is mainly occupied with neutron production.

Other planned experiments include the development of a magnetic LEBT chopper (a prototype exists and awaits testing); development of a two-source configuration that would provide for rapid switchover from one source to the other in case of performance problems; development of beam diagnostics; and study of beam dynamics of high intensity beam.

SUMMARY

The SNS integrated front-end test stand is under construction and will support spare RFQ testing in the upcoming winter. Thereafter it will be outfitted with an ion source, LEBT, MEBT, and beam dump and commissioned with beam in 2013.

REFERENCES

[1] Sang-Ho Kim et al., Physical Review Special Topics – Accelerators and Beams 13, 070101 (2010).

[2] SNS Radio Frequency Quadrupole (RFQ) Spare Structure Specification, SNS-RAD-RF-RF-0001-REV02 (2011).

[3] SNS Spare RFQ Final Design Review Report, 3112-BP-8664-0, Research Instruments GmbH (2011).

Copyright © 2012 by the respective authors — cc Creative Commons Attribution 3.0 (CC BY 3.0)

RF SETUP OF THE MedAustron RFQ*

B. Koubek, J. Schmidt, A. Schempp, IAP, Goethe University, Frankfurt am Main, Germany
J. Haeuser, Kress GmbH, Biebergemuend, Germany

Abstract

A Radio Frequency Quadrupole (RFQ) was built for the injector of the cancer treatment facility MedAuston in Austria [1]. For the RF design simulations were performed using CST Microwave Studio® and the structure was manufactured by Firma Kress in Biebergemuend, Germany. The simulations and the RF setup of the delivered RFQ are presented in this paper.

INTRODUCTION

The 216.8 MHz MedAustron RFQ was designed to accelerate protons and carbon ions from 8 keV to 400 keV [2] on an electrode length of 1.25 m. It is a state of the art 4-Rod RFQ with quite slim electrodes and newly developed connections of the stems to the electrodes. Usually clamps were used to fix the electrodes to the stems (see Fig. 2). The accuracy of the machining allows us to remove the clamps. Simulations have shown that these new connections are causing less capacitance and hence less disturbing electric field than the clamps.
Fig. 1 shows the RFQ during its preparation at the Institute of Applied Physics (IAP) in Frankfurt am Main. More details about the RFQ basic design parameter can be found in Table 1.

Table 1: Design Parameters of the MedAustron RFQ

Parameter	Value	
Frequency	216.612	MHz
Input Energy	8	keV
Output Energy	400	keV
Beam Current (max)	4	mA
Aperture (min)	2	mm
Modulation Factor (max)	2	
Electrode Length	1250	mm
Intervane Voltage	70	kV
RF Cells	15	
Beam Height in Tank	19.5	mm
Stem Thickness	20	mm
Stem Distance	68	mm
Tank Length	1233	mm
Wall Thickness	40	mm

SIMULATIONS

Simulations have been performed using CST Microwave Studio® for the RF design. During this process two different shapes of the backside of the electrodes have been investigated. One is a broad and the other one a more narrow socket of the electrodes backside. A top view of the two different shapes is shown in Fig. 2.

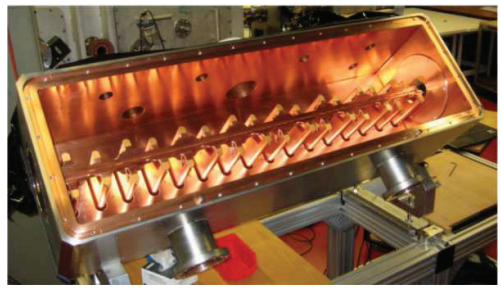

Figure 1: RFQ during preparation at IAP.

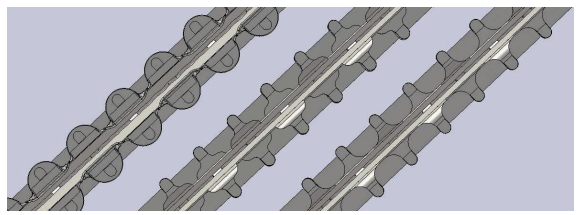

Figure 2: Former clamps (left), new broad (middle) and narrow (right) sockets.

Both shapes are rising the resonance frequency due to less capacitance compared to the old design with clamps. The broad shape increases frequency about one MHz more than the slim one, it shows less inductance and provides a fast and homogenous charge distribution on the electrode tips. Further informations about the RF characteristics of the connections of the electrodes can be found in [3].

MEASUREMENTS AND TUNING

Geometric Measurements

The accuracy of the machining and assembling of the single parts have been checked with a 3-D measurement device. The angle and the distance of the stems, the angle of the electrodes to each other and the position of the beam axis relatively to the reference surfaces have been measured. The measurements have met our expectations. Also no significant longitudinal electrode shift could be measured. Fig. 3 shows the measurement of the angle of the electrodes to each other and the longitudinal shift of the electrodes.

* Work supported by BMBF

Copyright © 2012 by the respective authors — cc Creative Commons Attribution 3.0 (CC BY 3.0)

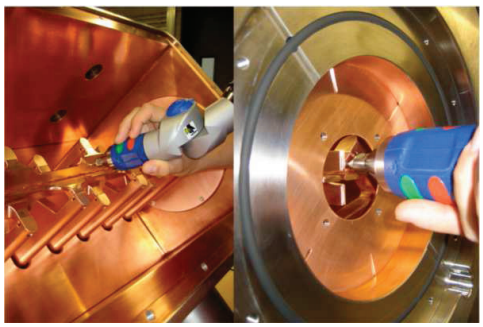

Figure 3: Measurements of the angle and the longitudinal shift of the electrodes using a 3-D measurement device.

RF SETUP

The frequency and flatness tuning have been executed in one procedure. First without the piston tuner to analyse the RF behavior of the RFQ. Later the final tuning was made with the inserted piston tuner on its zero position.
After investigation of the single influence of the tuning blocks, the piston tuner and the input power coupler on frequency and flatness, all the parts together have been adjusted and tuned. The tuning blocks have been fixed with silver screws on individual distance parts made of copper. The whole procedure is very similar to the tuning of the FNAL RFQ described in [4].

Flatness

For operation a homogenous longitudinal voltage distribution (flatness) of the electrodes is required according to the beam dynamics design. By changing the height of the tuning blocks the frequency of the RFQ and the local eigenfrequency of a single cell can be adjusted. Hence an uneven voltage distribution, caused by the modulation of the electrodes or inaccuracies by manufacturing of the RFQ, can be adjusted. The typical banana shaped flatness of the untuned MedAustron RFQ is shown in Fig. 4. It has an unflatness of about ±10 %.

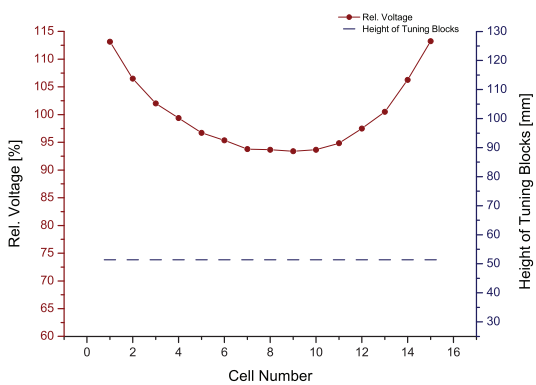

Figure 4: Untuned flatness with equal heights of the tuning blocks.

The flatness tuning is an iterative process to get an equal voltage distribution along the electrodes [5]. Each RF-cell is detuned using a perturbation capacitor (see Fig. 5). From the detuned RF-cell one can calculate the longitudinal voltage distribution of the electrodes. After this a next guess of the tuning block distribution can be made to improve the flatness.

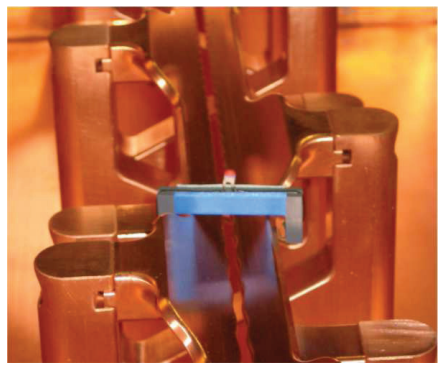

Figure 5: Pertubation capacitor used to detune each cell of the RFQ.

Piston Tuner

The frequency of the RFQ can change under operation due to several reasons. To correct the frequency a piston tuner is used. It has an influence on the resonance frequency by suppressing the magnetic field [6], but it is changing the flatness as well. If the flatness is not adjusted with an inserted tuner it may decrease of about ± 0.8 %. The piston tuner is placed in the middle of the cavity, its influence on the frequency is shown in Fig. 6.

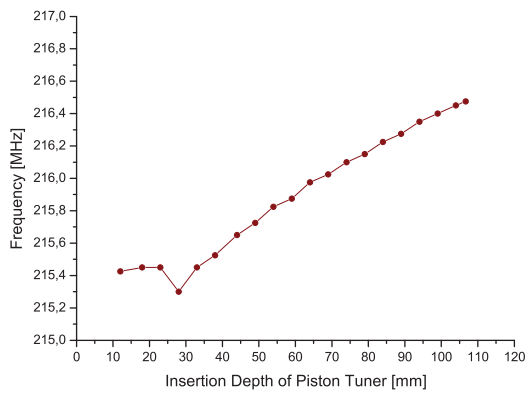

Figure 6: Frequency shift due to the piston tuner.

One can see that the insertion depth of the piston tuner has an almost linear influence on the resonance frequency of the RFQ. Before it enters the RF-cell between the stems it has only weak influence on the frequency. Then there is a small region where it disturbs the resonance of

Copyright © 2012 by the respective authors — cc Creative Commons Attribution 3.0 (CC BY 3.0)

the structure. This means one has to regard a minimum insertion depth of the piston tuner. When it enters the RF-cell between the stems it rises the frequency with its depth with an approximately linear behavior.

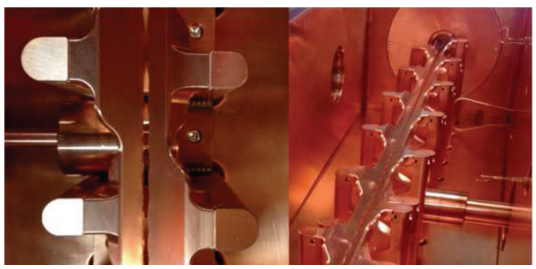

Figure 7: Top and side view of the piston tuner.

RESULTS

After the tuning process the resonance frequency was adjusted to 216.6 MHz with a deviation of the longitudinal voltage distribution of ± 1.7 %. This flatness with its distribution of the tuning blocks is shown in Fig. 8.

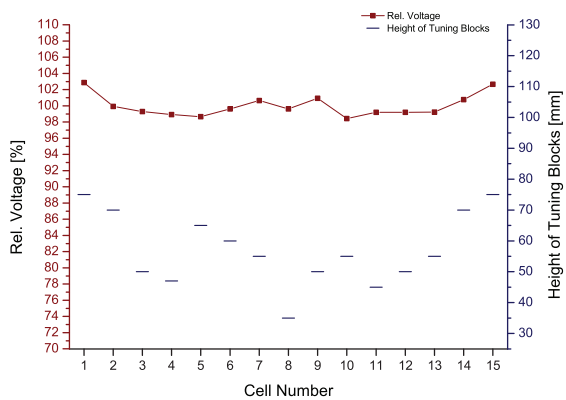

Figure 8: Final flatness and distribution of the tuning blocks.

Finally the piston tuner has been set to be able to adjust the frequency from minimum of 216.4 MHz to maximum 216.9 MHz. This values might rise about 0.1 MHz under vacuum. The overall shift of the piston tuner is about 0.5 MHz. The power coupler has a reflection of -27 dB.
The shuntipedance measured with an perturbation capacitor was 92 kΩm. The RF parameter of the MedAustron RFQ are summerized in Table 2. Overall the tuning process took several weeks and has led to quite satisfactoring results.

Table 2: RF Parameters of the MedAustron RFQ

Parameter	Value	
Frequency	216.612	MHz
Quality Factor Q_0	3600	
Voltage Distribution	± 1.7	%
Shunt Impedance	92.57	kΩm
Reflection Power Coupler	-27	dB
Transmission Pickup 1	-40	dB
Transmission Pickup 2	-39	dB
Transmission Pickup 3	20	dB

OUTLOOK

The MedAustron RFQ has been delivered at the end of July 2012. The ion source, the low energy beam transfer line and the RFQ will be commissioned at the Injector Test Stand (ITS) at CERN [7]. The test stand provides the possibility to prepare the LEBT independently from civil engineering in Austria. As soon as the building is ready the LEBT can move to Wiener Neusadt for commissioning and start of operation [8].

REFERENCES

[1] U. Dorda, A. Fabich, F. Osmic, M. Benedikt, "STATUS OF THE MEDAUSTRON ION BEAM THERAPY CENTRE", IPAC2012, New Orleans, Louisiana, USA

[2] Michael Bededikt, Johannes Gutleber, Marcus Palm, Werner Pirkl, Ulrich Dorda, Adrian Fabich, "OVERVIEW OF THE MedAustron DESIGN AND TECHNOLOGY CHOICES", IPAC2010, Kyoto, Japan

[3] B. Koubek, J. Schmidt, A. Schempp, L. Groening, "RF-DESIGN OF A 325 MHz 4-ROD RFQ", IPAC'11, San Sebastin, Spain

[4] J. Schmidt, B. Koubek, A. Schempp, "TUNING OF THE NEW 4-ROD RFQ FOR FNAL", PAC 2011, NYC, USA

[5] J. Schmidt, B. Koubek, A. Schempp, "TUNING STUDIES ON 4-ROD-RFQs", PAC 2011, NYC, USA

[6] A. Schempp, L. Brendel, B. Hofmann, H. Liebermann, "Tuner Design for High Power 4-Rod-RFQs", LINAC 2004, Luebeck, Germany

[7] F. Osmic, M. Feurstein, A. Gyorgy, A. Kerschbaum, M. Repovz, S. Schwarz, G. Burtin, "OVERVIEW OF THE BEAM DIAGNOSTICS IN THE MEDAUSTRON ACCELERATOR: DESIGN CHOICES AND TEST BEAM COMMISSIONING", IPAC2012, New Orleans, Louisiana, USA

[8] Adrian Fabich on behalf of Michael Benedikt, "MedAustron - the Austrian Ion Therapy and Research Center", CAS lecture 1st June 2012, Senec, Slovakia

Copyright © 2012 by the respective authors — cc Creative Commons Attribution 3.0 (CC BY 3.0)

TEST RFQ FOR THE MAX-PROJECT

M. Vossberg, H. Klein, H. Podlech, A. Schempp, C. Zhang IAP, Univ. Frankfurt, Germany
A. Bechtold, NTG Neue Technologien GmbH und Co KG, Gelnhausen

Abstract

A 17 MeV MHz proton linac is being developed as a front end of the driver accelerator for the MYRRHA facility in Mol. As a part of the MAX (MYRRHA Accelerator Experiment and Development) project a 4-rod Test-RFQ with a resonance frequency of 176 MHz has been designed and built for the MAX-Project. But the RFQ had to be modified to solve the cooling problem at cw-operation, the geometrical precision had to be improved as well as the rf-contacts. The developments led to a new layout and a sophisticated production procedure of the stems and the electrodes. Calculations show an improved Rp-value leading to power losses of <30 kW/m only, which is about 60 % of the power losses which could be achieved safely at cw-operation of the similar Saraf-RFQ. Thermal measurements and simulations with the single components are in progress. The temperature distribution in cw-operation will be measured and the rf-performance checked.

INTRODUCTION

The development of MYRRHA (Multi-purpose hybrid research reactor for high-tech applications) is important to investigate advanced technologies for future power generations. With this test reactor the transmutation of long-lived radioactive waste of nuclear power plants will be studied. Also the reactor will contribute to the present material research and replace the expiring molybdenum reactors, which are essential for the nuclear medicine. An absolutely reliable proton accelerator is required for the operation of the reactor. Breakdowns of the cw proton beam will cause thermal stress in the reactor core and it will also decrease the lifetime of the reactor. This is the reason why the design of the LINAC and the proton injector part has to be very safe [1]. Figure 1 shows an overview of the MYRRHA linac. A short and effective injector section is recommended by a KONUS (combined zero degree structure) beam dynamics design [2].

MYRRHA INJECTOR

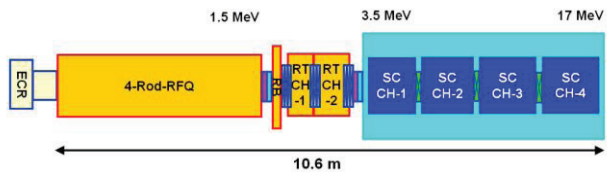

Figure 2: General layout of the MYRRHA injector.

The planned injector (fig. 2) consists of an ECR source, a Radio Frequency Quadrupole (RFQ), two room-temperature CH-cavities and four superconducting CH-cavities. During the EUROTRANS project the RF frequency of the 17 MeV injector part has been set to 352 MHz. The new layout is changed to 176 MHz. The main reason is the possibility to use a flexible and cheap 4-rod-RFQ instead of the 4-vane-RFQ. This 176 MHz RFQ accelerates the particles to 1.5 MeV.

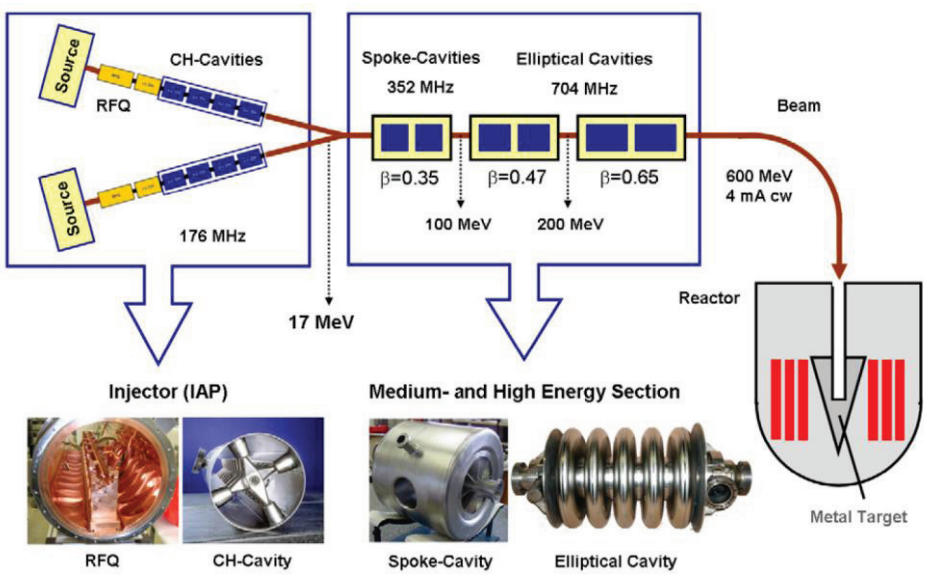

Figure 1: An overview of the MYRRHA driver linac.

Copyright © 2012 by the respective authors — cc Creative Commons Attribution 3.0 (CC BY 3.0)

Between 1.5 MeV end-section of the RFQ and the entrance of the first sc CH-cavity the energy gap is covered by two rt CH-cavities. The main acceleration takes place in the four sc CH-cavities. For the MYRRHA project it is planned to build two identical injectors to fulfil the stringent reliability requirements of the whole project. Good performance of the injector was shown by beam dynamic simulations. [3] [4]

RFQ

By changing the resonant frequency from 352 MHz to 176 MHz it is possible to use a 4-rod RFQ instead of a 4-vane RFQ. Compared to the 4-vane RFQ the 4-rod RFQ has excellent tuning and access capabilities with a significant lower technological risk and capital investigation.

Figure 3: Picture of a typical 4-rod RFQ.

To limit the thermal load of the cavity to 25 kW/m the electrode voltage has been fixed to 40 kV. This is only half the value which has been already shown for a safe operation. A short four stem section of the RFQ is under construction for testing the properties and the behaviour under high average power. Figure 3 shows a typical cw 4-rod RFQ and Table 1 shows the main design parameters.

Table 1: RFQ Beam Dynamics Design Parameters

Operation frequency	176 MHz
Injection energy	30 keV
Operation energy	1.5 MeV
Length	400 cm
Electrode voltage	40 kV
Impedance	67 kΩm
RF power	100 kW
Thermal load	25 kW/m

TEST-RFQ

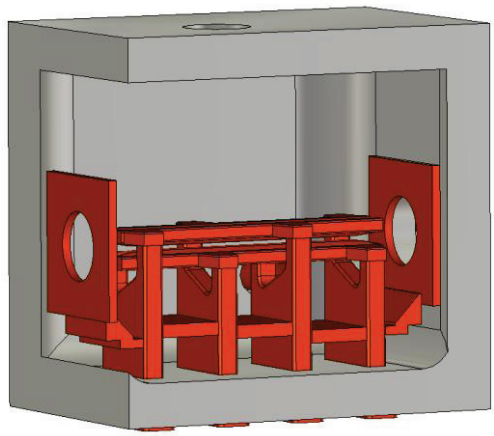

Figure 4: MWS model of the Test-RFQ

The test RFQ-cavity (fig. 4) has of a 5 cm thick tank with a length of about 50 cm and the electrode length is 36.8 cm. Between the stems there are three tuning plates to help the cavity to get the right frequency. By modifying the position of the tuning plates, the frequency can be variabled from 160 MHz to 192 MHz. For a better connection, silver plated tuning plates will be used. During operation a tuner will be used to correct the frequency

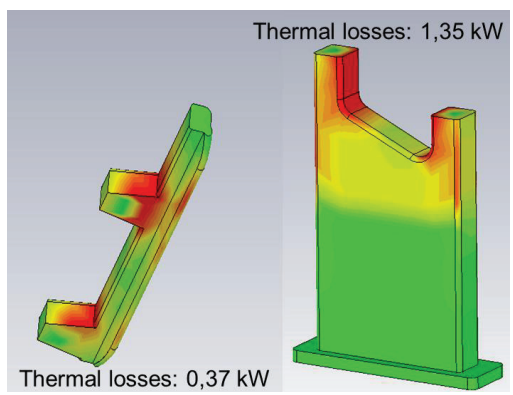

Figure 5: Current distribution and thermal losses.

First simulations with microwave studio shows, that the total thermal losses in this test-RFQ is about 8 kW. In figure 5 the current distribution is shown, the thermal losses are about 1.35 kW for a single stem and 0.4 kW for a single electrode. The highest field is at the connection between the electrodes and the stems [5].

Because of the thermal losses, a very good water cooling system is required to hold the frequency steady during cw operation. A new water cooling system was designed for the stems and the electrodes. Figure 6 shows the cooling channel inside a stem, it is split into two parts so that both sides of the stem are well cooled.

Copyright © 2012 by the respective authors — cc Creative Commons Attribution 3.0 (CC BY 3.0)

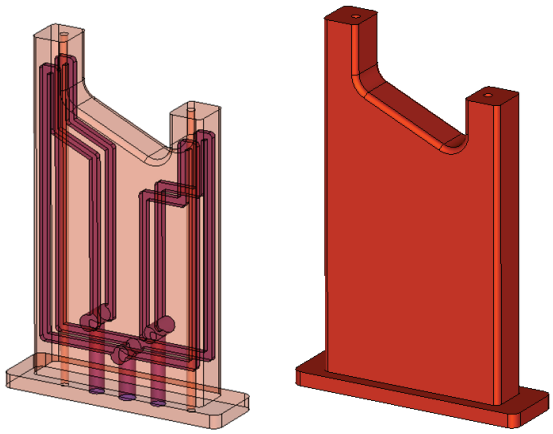

Figure 6: New stem design with the cooling channels.

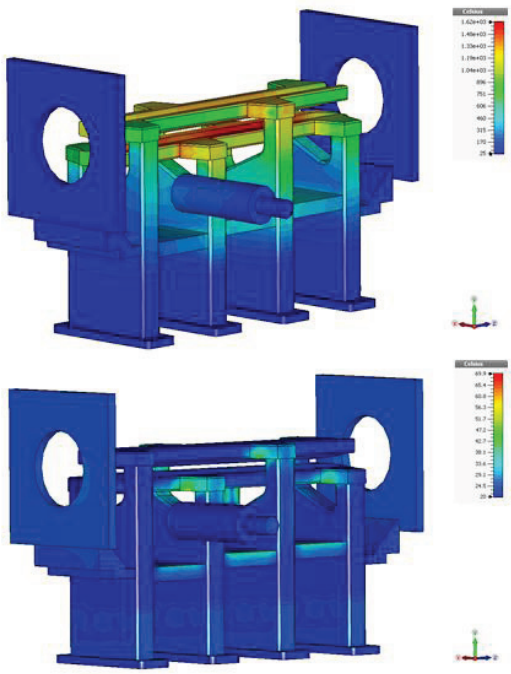

Figure 7: Thermal Microwave Studio simulations with (bottom) and without (top) cooling.

Thermal simulations with this cooling system were done with MWS. Figure 7 shows the difference of the resonant structure without a cooling system and with a water cooled system at 20°C water temperature. In the upper picture there are a very high temperature on the electrodes, with the cooling system there are only a few hotspots with a maximum temperature of about 58 °C. Thermal measurements on a single stem show the temperature distribution on the stem. For this measurement the stem was heated to 90°C, at this temperature the water cooling system was turned on.

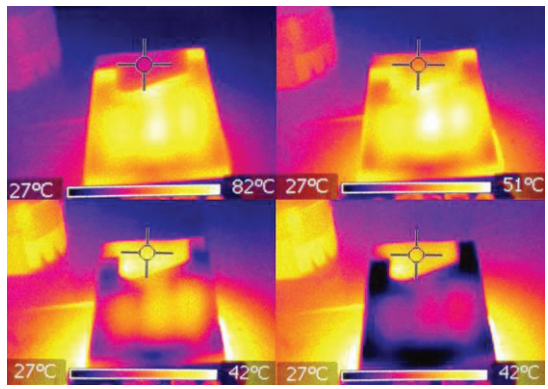

Figure 8: Thermal measurements on a single stem.

Figure 8 shows the different temperatures during the measurement. The stem was cooled down to nearly water temperature after 30 seconds with a water flow rate of only 0.08 l/s at a water pressure of 1 bar.

STATUS

Thermal simulations for the test-RFQ and first thermal measurements on the stems were completed. The stems and the tuning plates were inserted into the cavity. The electrodes will be delivered in September 2012. After the alignment, tuning and vacuum test of the cavity first RF-measurements will be done.

ACKNOWLEDGEMENT

This work has been supported by European Union FP7 MAX Contract No. 269565.

REFERENCES

[1] D. Mäder, H. Klein, H. Podlech, U. Ratzinger, M. Vossberg, C. Zhang, „Developement of CH-Cavaties for the 17 MeV MYRRHA-Injector“, IPAC2011, San Sebastian, Spain, September 2011

[2] R. Tiede, U. Ratzinger, H. Podlech, C. Zhang, G. Clemente, “KONUS beam dynamics design using H-mode cavities” Hadron Beam 2008, Nashville, Tennessee, USA, August 2008

[3] H. Podlech, M. Amberg, H. Klein, D. Mäder, U. Ratzinger, A. Schempp, R. Tiede, M. Vossberg, C. Zhang, “General layout of the 17 MeV injector for MYRRHA” IPAC2011, San Sebastian, Spain, September 2011

[4] C. Zhang, H .Klein, D. Mäder, H. Podlech, U. Ratzinger, A. Schempp, R. Tiede, “From Eurotrans to MAX: New Strategies and Approaches for the injector Development” IPAC2011, San Sebastian, Spain, September 2011

[5] CST Microwave Studio, http://www.cst.com

Copyright © 2012 by the respective authors — cc Creative Commons Attribution 3.0 (CC BY 3.0)

TUNING STUDIES ON 4-ROD RFQs *

J. Schmidt, B. Koubek, A. Schempp, B. Klump, IAP, Univ. Frankfurt, Germany

Abstract

A NI LabVIEW based Tuning Software has been developed to structure the tuning process of 4-rod Radio Frequency Quadrupole s (RFQs). Its results are compared to measurement data of 4-rod RFQs in different frequency ranges. For the optimization of RFQ design parameters, a certain voltage distribution along the electrodes of an RFQ is assumed. Therefore an accurate tuning of the voltage distribution is very important for the beam dynamic properties of an RFQ. A variation can lead to particle losses and reduced beam quality especially at higher frequencies. Our electrode design usually implies a constant longitudinal voltage distribution. For its adjustment tuning plates are used between the stems of the 4-rod-RFQ. These predictions are based, in contrast to other simulations, on measurements to define the characteristics of the RFQ as it was build - not depending on assumptions of the design. This will lead to a totally new structured process of tuning 4-rod-RFQs in a broad range of frequencies by using the predictions of a software. The results of these studies are presented in this paper.

RESONANT CIRCUITS

A simplified model of the 4-rod RFQ resonator is a chain of LC-oscillators where each RF cell has its own resonance frequency. In these RF cells the stems represent the inductance, while the electrodes form the capacitive part of the circuit. A more detailed model is described in [1].

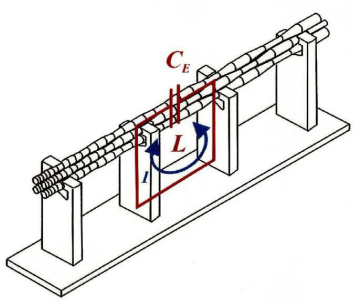

Figure 1: LC Resonator as Equivalent Circuit of a 4-Rod RFQ.

To tune this system, the resonance of each RF cell has to be tuned with tuning plates. They short cut the current path between the stems, to change the inductance of the RF cell. The longitudinal voltage distribution, the so called flatness, is a fundamental parameter in the particle dynamic design of an RFQ. Usually a constant longitudinal voltage along the electrodes is the basis of our design, but other distributions are possible as well [2].

Following the particle dynamics the longitudinal voltage distribution has to be arranged. It is measured using the capacitve perturbation method. A perturbation capacitor sits on a pair of electrodes of one RF cell to cause a frequency shift due to Thomsons law. The resulting frequency shift of the cell is proportional to its voltage (see Eq. 1).

$$U \propto \Delta f_0 = \frac{1}{\sqrt{LC}} - \frac{1}{\sqrt{L(C+\Delta C)}} \qquad (1)$$

THE VOLTAGE TUNING PROCESS

The process of adjusting the flatness is an iterative process of shifting the tuning plates and try to find a set of heights, which results in the desired distribution and total resonance frequency. This process can take some time, especially working on long RFQ structures with a lot of RF cells [3].

Due to several reasons like the changing modulation or differences in the manufacturing, the RFQ has deviations in its characteristics along the electrodes profile [4]. This leads to a different impact of the tuning plates depending on their position in the RFQ.

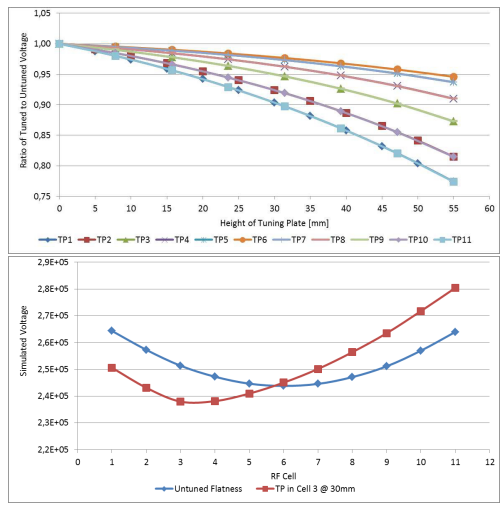

Figure 2: The voltage in z=k from raising tuning plates in all cells (upper graph) and the longitudinal change with a tuning plate in cell k=3 (lower graph).

Raising a tuning plate in cell k $\in [1, n]$ decreases the voltage in cell k and its neighboring cells k$\pm$i with i$<$i$_0$, while the voltage raises in cells k$\pm$i with i$\geq$i$_0$. This behavior is shown in Fig. 2

* Work supported by BMBF

Copyright © 2012 by the respective authors — cc Creative Commons Attribution 3.0 (CC BY 3.0)

In order to quantify this behavior effect functions EC were introduced [5], describing the shift in flatness caused by a change in the position of the tuning plate of each RF cell k. They correspond to the ratio between the tuned and the untuned flatness.

$$U_t(z,h) = U_u(z) + EC(z,h) \times U_U(z) \qquad (2)$$

The single tuning plates all have an individual effect on the RFQ EC_k(z,h). Their superposition describes the total effect of a tuning plate setting with different heights h_k.

$$U_t(z,h) = U_u(z) \times \prod_{k=1}^{n} [EC_k(z,h_k) + 1] \qquad (3)$$

To find the ration $EC_k(z,h_k)$ measurements and simulations of the flatness depending on the longitudinal position z in the RFQ and the heights of the tuning plates have been performed with the aim to find a possibility to split EC(z,h) into two separated functions, one for each k depending just on the z-position and one on the height being valid for all k.

$$EC_k(z,h_k) = EC(h_k) \cdot EC_k(z) \qquad (4)$$

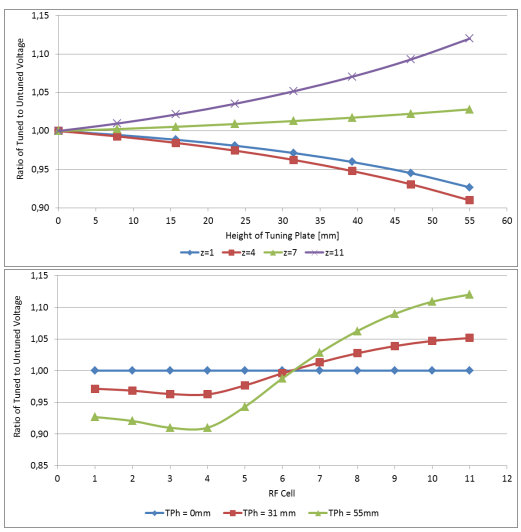

Figure 3: The ratio of the tuned and untuned flatness for a tuning plate in cell k=3 with the height at different z-positions (upper graph) and the corresponding longitudinal change at different heights (lower graph).

STATUS OF THE TUNING PROGRAM

As presented at PAC11 in New York [6] a software has been developed to predict the resulting flatness of an arbitrary tuning plate distribution, which is working well for 4-rod RFQs at 100 MHz. In this version of the program a linear approximation EC(h)=h has been used for the influence of the tuning plates height. Its results in comparison with measurements are presented in Fig. 4

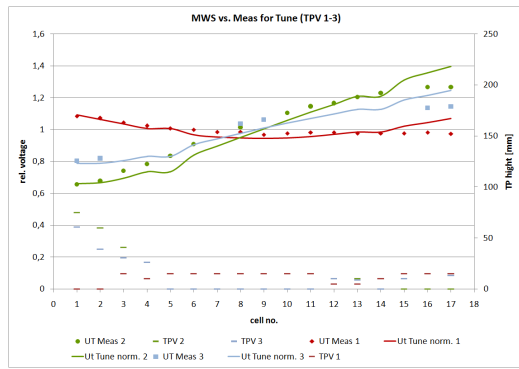

Figure 4: Results of the RFQ tuning program in comparison with three sets of measurements on a 17-cell 100 MHz RFQ [6].

This approximation turns out to be too rough for RFQs with higher frequencies around 200 MHz. Looking at Fig. 3 a square tendency with a - depending on the longitudinal position of measurement z - negative or positive gradient is visible.
To represent this behavior a higher order polynomial fit of the measurement points with different heights was implemented into the software. A comparison of the measured flatness and the simulated predictions with the corresponding tuning plate distribution with a linear and polynomial assumption is shown in Fig. 5.

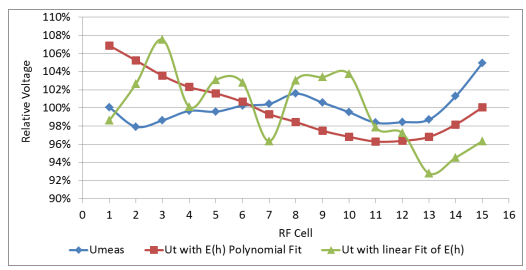

Figure 5: Comparison of the flatness prediction from the RFQ tuning program with linear and polynomial fit in comparison with its corresponding measurement on a 15-cell 200 MHz RFQ.

The measured distribution shows a x^6-like behavior, which is not included in the simulated ones. Even though the fitted version corresponds to the measurement much better, than the linear approximation, it is unfortunately not in a range to work with.

CONCLUSION AND OUTLOOK

Going from 100 to 200 MHz 4-rod RFQs the dependency of the voltage shift to the height of the tuning plate can not be approximated with a linear function anymore. A polynomial fit has been implemented to the simulation software. The results are much better, but are not precise enough to replace the manual iterative process. Other fitting methods have to be tested. Eventually the splitting of

Copyright © 2012 by the respective authors — cc Creative Commons Attribution 3.0 (CC BY 3.0)

the longitudinal and height dependency can not be separated as supposed up to now, because their coupling becomes much stronger in high frequency systems. Fig. 6 shows the change in the data sets due to the scaling process for a raising tuning plate in the middle of a 15-cell RFQ. The symmetric increase and decrease of the voltage around the cell of the tuning plate is pictured in the upper graph. This difference disappears with the scaling to h^2 completely. In the scaled case in the lower graph all curves overlap each other and values of the voltage ratios compared to points at higher tuning plate positions gets much smaller.

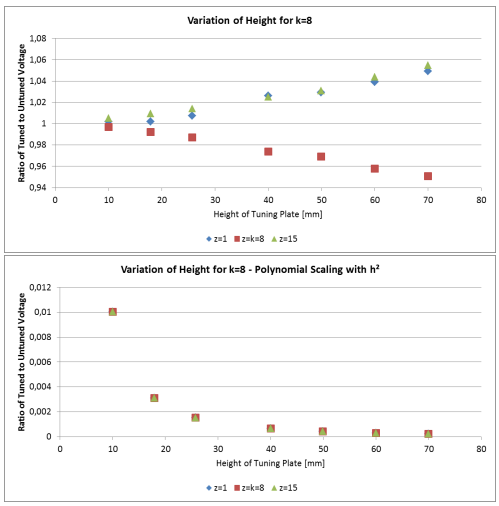

Figure 6: The ratio of the tuned and untuned flatness for a tuning plate in cell k=8 - the middle of the RFQ - with the height at different z-positions before the scaling (upper graph) and the corresponding data after applying a scaling with h^2 (lower graph).

Outlook

The vanishing of the differences in the height dependency at varying z-positions will be analyzed further. It may be an indicator of a strong coupling between the height and z-position dependency. If it is not possible to split them, there need to be another method to make the theory of the effect functions useable.

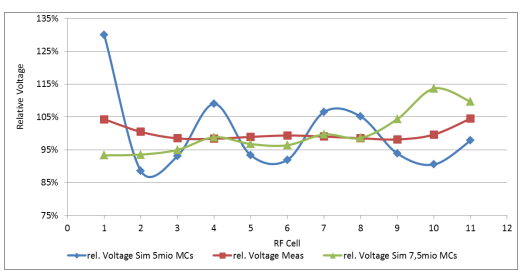

Figure 7: Results of flatness simulations of a 11-cell 200 MHz RFQ with 5 mio. and 7.5 mio. mesh cells in comparison with the corresponding measurement.

In parallel to the development of the simulation software for 4-rod RFQs the simulation of these systems using CST Microwave Studio ® is about to improve, too. As shown in the graph in Fig.7 there is a strong dependency of the flatness simulation results to the meshing of the RFQ.
Both simulation approaches will be followed further, to find a way of predicting the flatness of 4-rod RFQs. At the moment the iterative process is still needed to find the appropriate set up of the tuning plates.

REFERENCES

[1] J.X. Fang and A. Schempp, "Equivalent Circuit of a 4-ROD-RFQ", EPAC 1992, Berlin, Germany.

[2] A. Schempp, "Design of Compact RFQs', LINAC 1996, Geneva, Switzerland.

[3] T. Sieber, "Entwicklung von 4-Rod- und IH- Radio-Frequenz-Quadrupol (RFQ)-Beschleunigern fuer radioaktive Ionenstrahlen bei REX-ISOLDE und MAFF", PhD Thesis, 2001, Munich, Germany.

[4] J. Schmidt, B. Koubek, A. Schempp "Simulations of the Influence of 4-rod RFQ Elements on its Voltage Distribution", IPAC 2012, New Orleans, LA, USA.

[5] P. Fischer, "Ein Hochleistungs-RFQ-Beschleuniger fuer Deuteronen", PhD Thesis, 2007, Frankfurt, Germany.

[6] J. Schmidt, B. Koubek, A. Schempp, "Tuning Studies on 4-rod-RFQs, PAC 2011, New York City, NY, USA.

[7] A. Schempp, "Overview of Recent RFQ Projects", LINAC 2008, Victoria, BC, Canada.

[8] P. Fischer and A. Schempp, "Tuning of a 4-rod CW-Mode RFQ Accelerator", EPAC 2006, Edinburgh, Scotland.

[9] P. Fischer and A. Schempp, "Tuning CW 4-rod RFQ", LINAC 2006, Knoxville, Tennessee, USA.

Copyright © 2012 by the respective authors — cc Creative Commons Attribution 3.0 (CC BY 3.0)

RFQ WITH IMPROVRED ENERGY GAIN

A.S. Plastun, NRNU «MEPhI», Moscow, Russia
A.A. Kolomiets, ITEP, Moscow, Russia

Abstract

RFQ structure is practically only one choice for using in front ends of ion linacs for acceleration up to energy about 3 MeV. This limit is due to its relatively low acceleration efficiency. However it isn't intrinsic feature of RFQ principle. It is defined only by vane geometry of conventional RFQ structure with sinusoidal modulation of vanes. The paper presents results of analysis RFQ with modified vane geometries that allow to reach acceleration efficiency compared with IH DTL structures. RFQ with modified vanes was used for design second section of heavy ion injector of TWAC for acceleration of ions with Z/A=0.33 up to 5 MeV/u.

INTRODUCTION

An RFQ output energy doesn't usually exceed several MeV. Using conventional RFQ structure for acceleration of particles for higher energies is impractical because RFQ energy gain decreases rapidly with energy at constant modulation.

Many DTL structures were proposed for beam acceleration following RFQ that use magnetic or radio frequency focusing. The structures are well studied, they can provide good accelerating efficiency and are realized in a number of linacs. In the framework of heavy ion injector development for TWAC facility [1] several designs of second section based on these structures have been studied. In addition it was considered option that uses conventional RFQ with relatively minor modification of RFQ electrodes and resonant structure.

81 MHz RFQ – front end of TWAC injector has been recently successfully commissioned [2]. It is designed to accelerate beam from laser ion source with Z/A = 0.33 up to energy 1.57 MeV/u.

This paper presents result of study of TWAC injector second section design based on modified RFQ. The main goal of the modification was to provide maximum energy gain at focusing sufficient for acceleration beam with current 30 mA up to 5 MeV/u.

ENERGY GAIN IN RFQ

Vanes with Sinusoidal Modulation

The energy gain of a particle in RFQ is

$$\Delta W = e\frac{Z}{A}UT\cos\varphi_S , \qquad (1)$$

e - electron charge, Z - charge number of the particle, A - mass number of the particle, U - voltage between adjacent vanes, T - accelerating efficiency, φ_s - phase of RF field, when synchronous particle is in a maximum of accelerating field.

Voltage U is usually chosen taking into account many different considerations. However it has to be as high as possible to increase energy gain. Its maximum value in this case is fully defined by acceptable surface electric field $E_{s\ lim}$. Most accurately voltage can be found by numerical simulation for real vane geometry and expressed as

$$U = U_{sim}\frac{E_{s\,\mathrm{lim}}}{E_{s\,sim}} , \qquad (2)$$

Here U_{sim} is voltage between vanes in computer model and $E_{s\ sim}$ is maximum field at vane surface obtained from simulation result.

Figure 1 shows results of field simulation in RFQ cell with code OPERA 3D. Simulated cell length $L_c = \beta\lambda/2$ corresponds particle energy at TWAC RFQ output. Curve 1 presents maximum field at vane surface calculated for sinusoidal modulation in $1 \le m \le 5$ range. Aperture for all modulations was constant a = 8 mm, that is average distance from axis to vane was changed as $R_0 = a(m+1)/2$. Simulation results show that for surface field limit $E_{s\ lim}$ = 250 kV/cm (about 2 Kilpatrick units for frequency f = 81 MHz) maximum voltage can reach according formula (2) $U \cong 500$ kV.

Accelerating efficiency T was calculated from simulated distribution of longitudinal field component E_z on axis. T factor for cell with sinusoidal modulation of vanes is limited by value $T \cong 0.7$. It means that the maximum effective accelerating gain per cell with studied parameters doesn't exceed $UT \cong 350$ kV.

Curve 1 shows that there is no sense to increase modulation factor more than $m = 4 \div 5$ because maximum field $E_{s\ sim}$ reduces very slowly for higher m while focusing efficiency rapidly decreases. Figure 2 shows transverse phase advance calculated with the following expression [3]:

$$\sigma^2 = \frac{2}{\pi^2}K^4 + \frac{\pi eUT}{W_{kin}}\sin\varphi,$$

$$K^2 = \frac{Z}{A}\frac{e\overline{G}}{4W_0}\lambda^2 .$$

Here $\overline{G}$ is mean value of simulated transverse field gradient along RFQ cell, W_0 - rest mass of proton, λ - wavelength of RF field. Estimation shows that transverse motion is very close to stability border at $m \cong 4$. It defines limiting capability of conventional RFQ with sinusoidal modulation for higher energy gain acceleration.

It is possible to improve accelerating efficiency using trapezoidal modulation proposed in [4]. Cell with this modulation type is shown in Figure 3. The trapezoidal

Copyright © 2012 by the respective authors — cc Creative Commons Attribution 3.0 (CC BY 3.0)

modulation allows 15 ÷ 20% higher accelerating efficiency T due to better of longitudinal field component distribution along axis. It is important that this distribution is kept constant along the RFQ so T rises with particle energy at constant voltage.

However maximum surface field for this modulation type in general is close to the value for sinusoidal modulation.

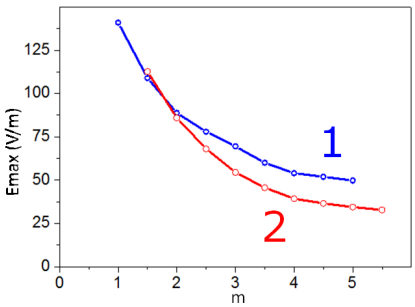

Figure 1: Calculated maximum surface electric field. Curve 1 corresponds to conventional RFQ with sinusoidal modulation, curve 2 – to RFQ with modified vanes.

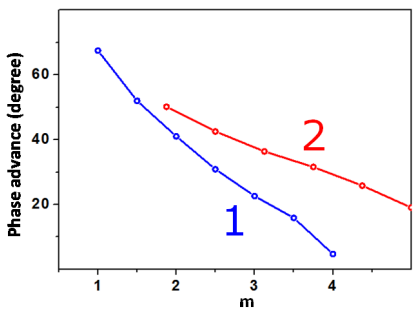

Figure 2: Calculated transverse phase advance. Curve 1 corresponds to RFQ with sinusoidal modulation, curve 2 – to RFQ with improved vanes.

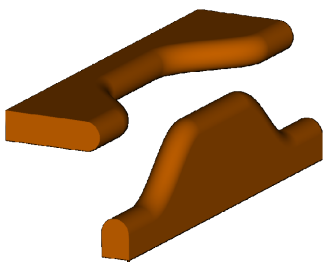

Figure 3: Adjacent vanes with trapezoidal modulation.

Improved Vanes

Whereas trapezoidal modulation considerably improves accelerating efficiency the higher voltage U is required for further energy gain increase. It can be provided if vane geometry allows reducing maximum surface field. Maximum field is reached at vane cross section with exact quadrupole symmetry for RFQ cells with conventional modulation and with parameters corresponding TWAC RFQ output. It was proposed to change vane profile at this cross section to increase distance between adjacent vanes. This can be achieved by transformation of the trapezoidal profile to almost "rectangular" one. Distribution of longitudinal component of field along axis is formed for this profile by "gap" between "rectangles" of adjacent vanes. Vane tips near axis are flat and have about the same curvature radius R_e as the vanes with conventional modulation.

Removing part of vane near axis decreases focusing efficiency. To compensate it more thick flat vanes with curved unmodulated pole are placed at distance from axis $R_q >> a$. Curvature radius of this part of vane is $R_{eq} \cong R_q$. 3D view of improved vanes is shown in Figure 4.

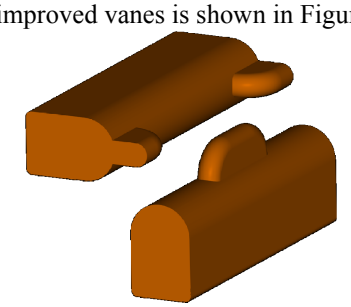

Figure 4: Adjacent vanes with improved profile.

Basic parameters of the improved geometry are shown more detailed in Figure 5. The parameters were optimized to minimize surface field, equalize it on vane surface and to increase focusing efficiency in comparison with conventional vanes with equal modulation.

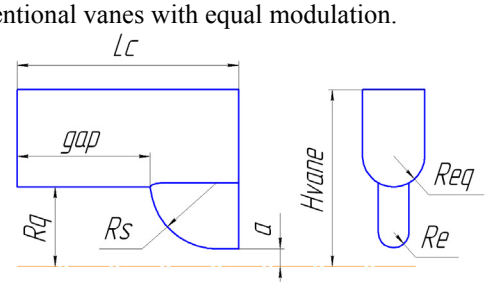

Figure 5: Basic dimensions of improved vanes.

Table 1 allows comparing field simulation results for sinusoidal and improved profiles. The same values for aperture a = 8 mm, cell length L_c = 100 mm, vane tip curvature radius R_e = 5.6 mm and modulation factor m = 4 were used for both cases of simulation.

Table 1: Field Simulation Results

Parameter	Sinus.	Impr.
Limit surface electric field E_{lim}, kV/cm	250	250
Maximum surface electric field $E_{s.max}$ @ 1V intervane voltage, V/cm	0.54	0.39
Voltage U, kV	463	636
Acceleration rate UT, kV	324	513
Transverse phase advance μ, deg	5	26

BEAM DYNAMICS SIMULATION

Improved vane profile was used to design RFQ with parameters corresponds the second section of TWAC injector for detailed computer simulation of beam

Copyright © 2012 by the respective authors — cc Creative Commons Attribution 3.0 (CC BY 3.0)

dynamics. RFQ was designed using 3D field maps calculated by OPERA code. Basic parameters of the RFQ are shown in Table 2.

Table 2: Basic Parameters of Improved RFQ

Operating frequency, MHz	81.36
Z/A of ions	0.33
Input ion energy, MeV/u	1.57
Output energy, MeV/u	5.0
Transverse emittance, norm, π mm·mrad	1.5
Maximum surface field, kV/cm	250.
Voltage, kV	685.
Electrode modulation	4.5
Cell number	20
Total length, m	3.0

Code TRANSIT written in ITEP has been used for the beam dynamics simulation. Longitudinal and transverse field components along section calculated by OPERA 3D code that was used in TRANSIT are shown in Figure 6.

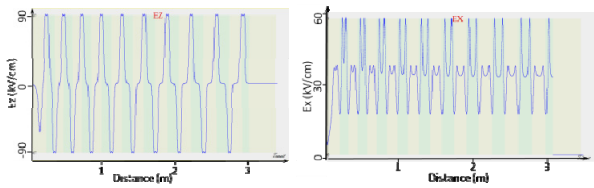

Figure 6: Longitudinal field component on axis (a) and transverse field component at r = 5 mm (b).

Figure 7 shows calculated transverse envelopes that confirm stable transverse particle motion along the section. Simulated envelope size shows that RFQ with improved vanes provides required transverse acceptance.

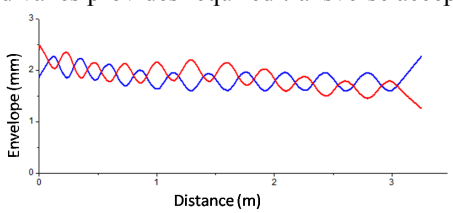

Figure 7: Transverse envelopes calculated with TRANSIT code.

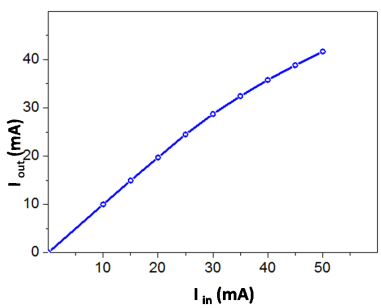

Figure 8: Calculated beam current at RFQ output in dependence on input one.

Simulation results in Figure 8 show that RFQ with improved vanes provides close to 100% beam transmission in required beam current range $0 \le I \le 30$ mA. It is important to say that in spite of complicated vane profile field has good linearity in working area that is evidenced by absence of growth of transverse and longitudinal emittances.

Table 3: Beam Transmission Parameters

Transmission, % (I = 0 / 30 mA)	100 / 98.6
Transverse rms envelope, mm (I = 0 / 30 mA)	2.0 / 3.1
Transverse emittance growth (I = 0 / 30 mA)	1.0 / 1.2
Longitudinal emittance growth (I = 0 / 30 mA)	1.0 / 1.1

CONCLUSION

RFQ structure with improved vane profile is proposed for acceleration following conventional RFQ. Computer simulation showed that new vane profile allows ≈ 30% lower maximum surface field at modulation factor m = 3÷5 comparing with conventional vanes. Accelerating efficiency of new profile is the same as provided by vanes with trapezoidal modulation.

3 m length RFQ has been designed for injector of TWAC facility. It provides about than 3.5 MeV energy gain. Computer simulations confirmed that the structure is capable to accelerate ion beam with current I = 30 mA with transmission about 100% and with only small transverse and longitudinal emittances growth.

ACKNOWLEDGMENT

Authors thank Tatyana Tretiakova for work on adjustment of her codes for RFQ with new vane profile design and beam dynamics simulation.

REFERENCES

[1] N.N.Alexeev, P.N.Alekseev, V.A.Andreev, A.N.Balabaev, V.I.Nikolaev,A.S.Ryabtsev, Yu.A.Satov, V.A.Schegolev, B.Yu.Sharkov, A.V.Shumshurov, V.P. Zavodov, "ITEP-TWAC PROGRESS REPORT", Proceedings of IPAC-2011, p.2193, San Sebastian, Spain

[2] V. Andreev, N.N. Alexeev, A.Kolomiets, V. Koshelev, B. Kondratyev, A. Kozodaev, V. Kuzmichev, Y. Orlov, V. Stolbunov, T. Tretyakova, "FIRST BEAM TEST OF 81.5 MHZ RFQ FOR ITEP-TWAC", Proceedings of IPAC-2011, p.2622, San Sebastian, Spain

[3] I.M. Kapchinskiy, "THEORY OF RESONANCE LINEAR ACCELERATORS", Harwood academic publishers, 1985

[4] O.K. Belyaev, O.V. Ershov, I.G. Maltsev, V.B. Stepanov, S.A. Strekalovskikh, V.A. Teplyakov, A.V. Zherebtsov, "IHEP EXPERIENCE ON CREATION AND OPERATION OF RFQS", Proceedings of the 20th Linac Conference, page 259, Monterey, California.

Copyright © 2012 by the respective authors — cc Creative Commons Attribution 3.0 (CC BY 3.0)

IMPROVEMENTS AT THE BNL 200 MeV LINAC*

D. Raparia, J. Alessi, B. Briscoe, J. Fite, O. Gould, V. LoDestro, M. Okamura, J. Ritter, A. Zelenski
Brookhaven National Laboratory, Upton, NY 11973, USA

Abstract

After reconfiguration of the low energy (35 keV) and the medium energy (750 keV) transport lines in 2009-10, the Brookhaven linac delivered the highest intensity beam since it was built in 1970 (~120 μA average current of H^- to the Brookhaven Linac Isotope Producer). It also delivered lower emittance polarized H- ion beam for the polarized program at RHIC. To increase the intensity further, the match into the RFQ was improved by reducing the distance from the final focusing solenoid to the RFQ and replacing the buncher in the 750 keV line with one with higher Q value, to allow operation at higher power. The transmission efficiencies and beam quality will be discussed in the paper.

INTRODUCTION

The Brookhaven National Laboratory (BNL) 200 MeV drift tube linac (DTL) provides H^- beam at 6.67 Hz, 200 MeV for the polarized proton program for Relativistic Heavy Ion Collider (RHIC) and 66-200 MeV for Brookhaven Linac Isotope Production (BLIP). The RHIC program needs 2 pulses every AGS cycle (~4 sec), one for injection into Booster and other for polarization measurement at the 200 MeV polarimeter located in the High Energy Beam Transport line (HEBT). The rest of the pulses are delivered to BLIP. The requirements for

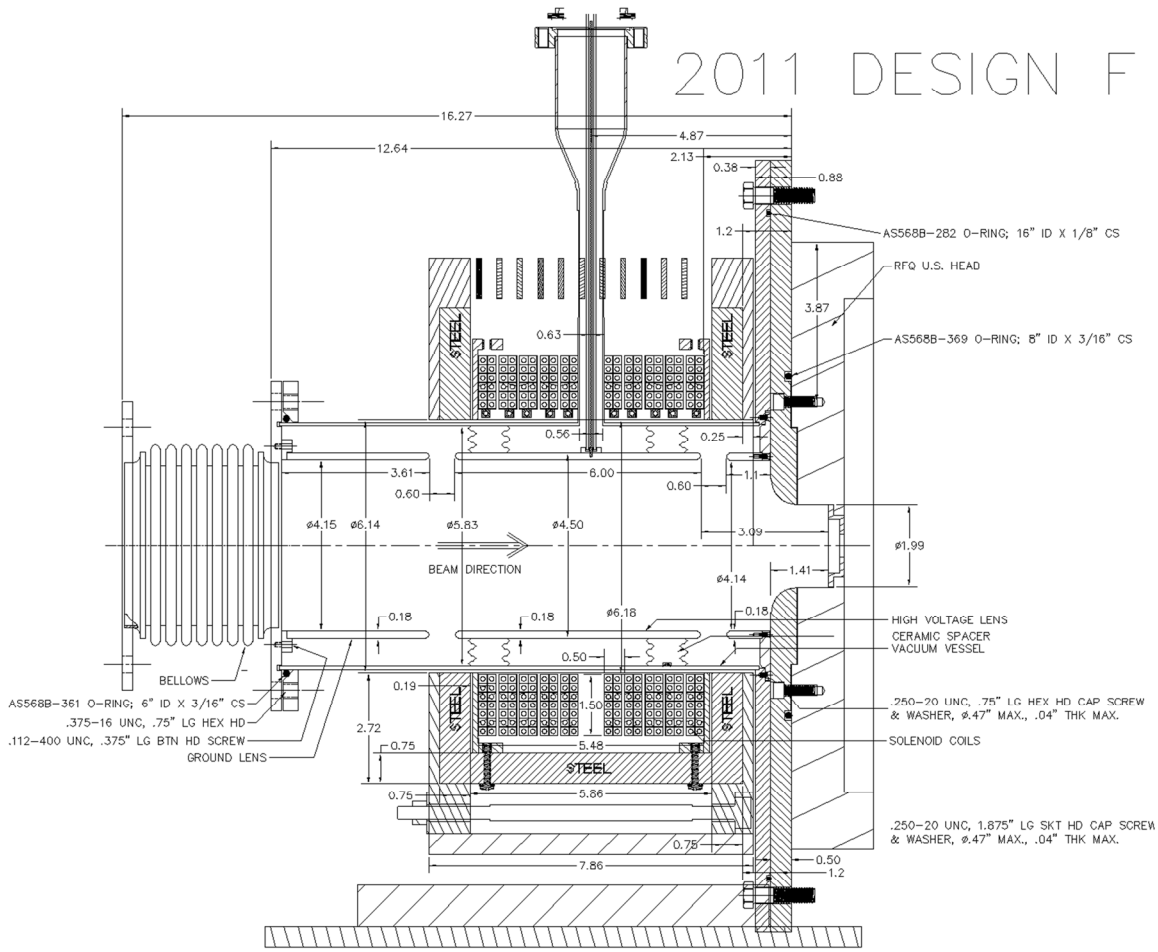

Figure 1: Design of the New Solenoid- and Einzel lens system for the front of the RFQ. The Distance between RFQ and solenoid was decrease by 1.08 inches.

*Work performed under Contract Number DE-AC02-98CH10886 with the auspices of the US Department of Energy
#raparia@bnl.gov

Copyright © 2012 by the respective authors — cc Creative Commons Attribution 3.0 (CC BY 3.0)

these programs are quite different and are the following. (1) RHIC: 200 MeV, 300 μA beam current, up 400 μs pulse length, polarization as high as possible and emittance as low as possible, (2) BLIP: 66-200 MeV, 450 μs pulse length, current as high as possible (~45 mA), uniform beam distribution at the target, and beam losses as low as possible. Prior to the upgrade in 2009, Linac transmission efficiencies from source to tank 9 were about 35% for the high current and 50% for the polarized beams and emittance growth several folds for the both beams. The emittance is one of the most fundamental parameters for any accelerator and in particular for the colliders. To reduce the emittance growth in the linac, low energy and medium energy beam transport lines were reconfigured as proposed in 2004 [1] in 2009 and results were reported in PAC2009, LINAC 2010 and PAC2011 [2,3,4].

CHANGES FOR 2012 RUN

Changes in the Low Energy Beam Transport

As reported in PAC11, the transmission through RFQ was down about 10% due to the increase distance of 1.5 inches between RFQ and solenoid to accommodate high voltage feed through for the Einzel lens. A solenoid and Einzel lens combo was redesign. In this design, solenoid the winding was split in two parts to accommodate the high voltage feed through and system was placed 1.08 inches closer to RFQ than last year. Figure 1 show the new solenoid-Einzel lens system.

The length of the system was reduced by 6 cm compare to 2010 design [4]. The magnetic field components at 5 cm are shown in figure 2.

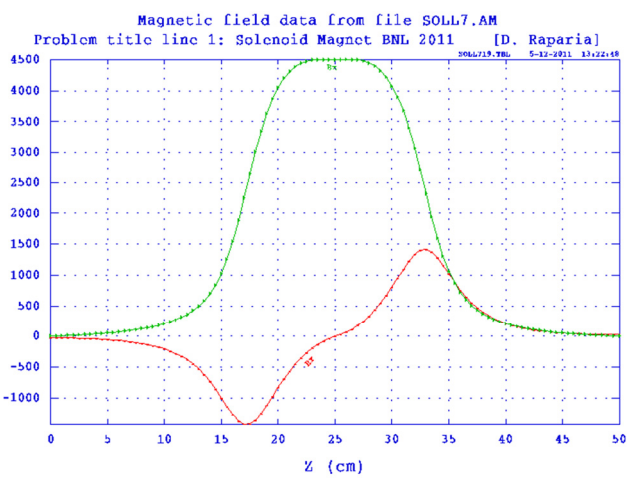

Figure 2: Magnetic field component Br and Bz along the length of the solenoid at 5 cm radius.

There is no depression in the axial magnetic field at 50 mm radius even though there are no winding in the middle due to high voltage feed through. By mistake it had only 120 turn instead of 140. It operated higher current than deign current but performed well and transmission through RFQ was increased by 10% as predicted by the calculations.

We use xenon gas in the low energy beam transport to compensate space charge for high intensity beam. We keep the line pressure about 3.6 x 10^{-6} torr. There is about 5% per meter loss due to stripping of H^- at this pressure. To reduce the pressure in the polarized beam line, we have install aperture in the line just before it meets the high intensity part of the beam line. We were able to keep lower pressure 2x 10^{-7} torr.

Changes in the Medium Energy Beam Transport

As reported in PAC 2011 that buncher performance in the MEBT is limited by the available power even thought the Q value was 10 time higher than the old buncher. For Run 12 we install still new buncher made out of copper instead of aluminium to increase the Q value by 75%. Table 1 shows buncher performance over the years.

Table 1: Buncher performance over the years

Parameters	1970	2009	2011	2012
Loaded Q	300	300	2000	3500
Power (kW)	5	10	5	5
Voltage (kV)	25	35	65	85
Trans. (%)	58	68	80	85

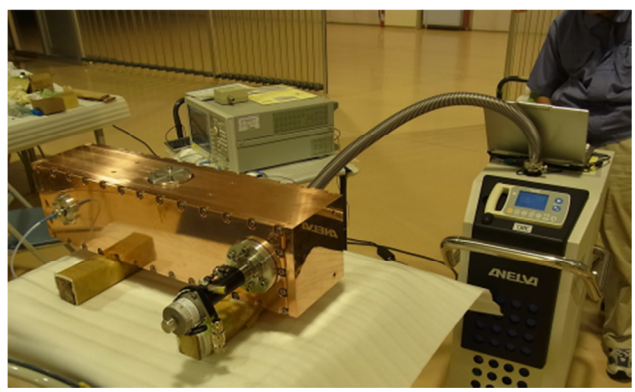

Figure 3: New 201.25 MHz copper buncher for the MEBT with Q (loaded) 3500.

RESULTS

Polarized H^-

For polarized H-, transmission from RFQ to Tank 9 was little better about 73% from 65% and polarization remain same although source current was increased by factor of two. Table 2 show the improvement of linac performance for polarized H- over the years.

Copyright © 2012 by the respective authors — cc Creative Commons Attribution 3.0 (CC BY 3.0)

Table 2: Linac performance for polarized H^-

RUN	ε_x (N,95%) π mm mrad	ε_y (N,95%) π mm mrad	Trans. (%)
2008	10.7	15.9	50
2010	4.5	5.5	65
2012	3.5	4.0	73

High Intensity H^-

The average intensity for the BLIP increased to 48 mA. The modification in the LEBT improved RFQ transmission by 10% and rest of the gain come from the new buncher in the MEBT. Table 3 show the comparison for the transmission for last three years

Table 3: Linac performance for high intensity

Intensity	2010	2011	2012
LEBT(mA)	70	70	70
MEBT (mA)	57	50	56
BLIP Target(mA)	39	41	48
Ave Cur.(μA)	120	125	130

Buncher did not perform as expected, after 3.5 kW, transmission is flat. We are planning to open the buncher and inspect this summer.

Run 12 for the polarized proton was very successful. Ion source (OPPIS) could produce higher current and linac transmission efficiencies are little better than the last year. Due to higher voltage in the buncher emittance for the polarized proton was about 25% better than the last year. In process of optimizing momentum spread out of linac, we discovered that Tank 7 was running about 1 MW lower power than the design.

This year average current delivered to the BLIP was lower than the last year in spite of higher beam current was available for the delivery. BLIP-targets had the problem of survivability.

REFERENCES

[1] D. Raparia, *et. al.,* "Proposal for Reduction of Transverse Emittance of BNL 200 MeV linac", Proceedings of Linac 2004, Lubeck, Germany, 2004

[2] D. Raparia, *et. al.,* "Results of LEBT/MEBT Reconfiguration at BNL 200 MeV Linac", Proceedings of PAC09, Vancouver, Canada.

[3] D. Raparia, *et. al.*, "Low and Medium Energy Beam Transport Upgrade at BNL 200 MeV Linac", Proceeding of Linac 2010, Tsukuba, Japan

[4] D. Raparia, et. al., "Changes in LEBT/MEBT at the BNL 200 MeV Linac" Proceedings of PAC11, New York, USA

Copyright © 2012 by the respective authors — cc Creative Commons Attribution 3.0 (CC BY 3.0)

RECENT PROGRESS WITH THE J-PARC RFQs

Y. Kondo*, T. Morishita, K. Hasegawa, JAEA, Tokai, Naka, Ibaraki, 319-1195, Japan
H. Kawamata, T. Sugimura, F. Naito, KEK, Oho, Tsukuba, 305-0801, Japan

Abstract

In this paper, we will report recent topics about J-PARC RFQs. First, the user operation of the existing RFQ (RFQ I) has been resumed from the long shutdown due to the earthquake. This RFQ has been suffered from a breakdown problem since 2008, therefore we have been developing a back-up RFQ (RFQ II). In April and May 2012, the high power test was successfully performed. Finally, we are fabricating a new RFQ for the beam-current upgrade of the J-PARC linac (RFQ III).

INTRODUCTION

At present, three radio frequency quadrupoles (RFQs) are under operation or development in Japan proton accelerator research complex (J-PARC). The original design energy and peak beam current of the J-PARC linac is 400 MeV and 50 mA, though, at the initial phase, the operation was started with a energy of 181 MeV omitting annular-ring coupled structures[1]. An RFQ built for the Japan hadron facility (JHF) project is used for the initial-phase linac; the design peak beam current of this RFQ is 30 mA[2]. This RFQ is called RFQ I. Because a sparking problem of this RFQ I occurred[3], an RFQ is fabricated as a spare of RFQ I[4]. This is called RFQ II. Moreover, to achieve the original design power of 1 MW (at the neutron target), it is planned to upgrade the linac to the original 400 MeV and 50 mA[5]. To upgrade the beam-current, another RFQ with a design current of 50 mA is newly fabricated and will replace the old one. This 50-mA RFQ is called RFQ III. In Table 1, parameters for each RFQ are listed.

In this paper, the status of each RFQ is described.

RFQ I

Fortunately, there was no damage to the RFQ I due to the Tohoku earthquake. During the period of the linac recovery[6] in 2011, a baking process was applied to desorb the absorbed gases on the surfaces during the operation after the improvement of the vacuum system in 2009[3].

Just after the restart of beam operation, the trip rate was rather high, but it became to be same level (∼20 times / day) as that of just before the earthquake. Figure 1 shows the history of the trip rate from just after the vacuum improvement to the run end before the long shut down of this summer.

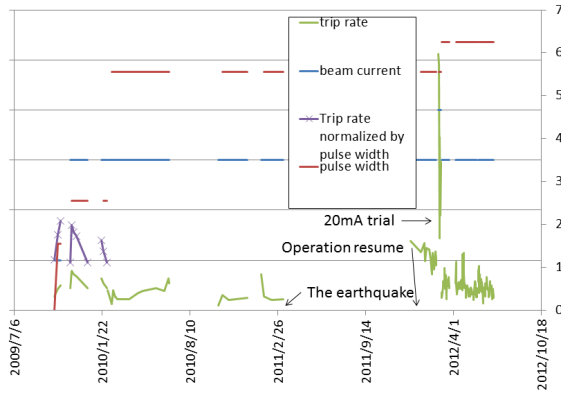

Figure 1: History of the trip rate of RFQ I from just after the vacuum improvement to the last run.

RFQ II

The high-power test of the RFQ II was planed to be completed in March 2011, but it was postponed due to the earthquake till the recovery of the accelerator from the damage of the disaster. After the user operation of the J-PARC was resumed, the high-power test of RFQ II was finally carried out from April to May 2012. Figure 2 is a photograph of RFQ II under high-power test.

Figure 2: High-power testing RFQ II.

After the assembling of high-power tuners, a coupler, and end plates, the measured unloaded Q-value was 9436. This corresponds to the value of 87 % of the SUPERFISH[7] calculation. The coupling factor of the high-power RF-coupler was set to be 1.7. The RFQ II was pumped with one 1700 l/s (for N_2) cryopump and two 400 l/s ion pumps during the high-power test.

In Figure 3, the conditioning history of RFQ II is shown. At first, the pulse height and repetition rate were set to be 30 μs and 25 Hz. After 15 hours conditioning, the peak

* yasuhiro.kondo@j-parc.jp

Copyright © 2012 by the respective authors — cc Creative Commons Attribution 3.0 (CC BY 3.0)

Table 1: Design parameters of the J-PARC RFQs.

	RFQ I	RFQ III	RFQ III
Cavity structure	four vane (monolithic)	← (consist of three units)	← ←
Vane length (mm)	3115	3172	3623
Number of the cells	294	294	317
Inter-vane voltage (kV)	82.9	←	81.0
Maximum surface field (MV/m) (Kilpatrick)	31.6 (1.77)	←	30.7 (1.72)
Average bore radius r_0 (mm)	3.70	3.69	3.49
Vane-tip curvature (mm)	$0.89r_0$ (3.29)	$0.89r_0$ (3.28)	$0.75r_0$ (2.62)
Maximum synchronous phase (deg)	-30	←	-30.6
Transmission (%)	97.7 [1]	← [1]	98.5 [2]
Transverse emittance (π mm mrad, normalized, r.m.s.)	0.18 [1]	← [1]	0.21 [2]
Longitudinal emittance (π MeV deg, normalized, r.m.s.)	0.083 [1]	0.084 [1]	0.11 [2]

[1]PARMTEQM calculation, 1.0 π mm mrad. (100%, normalized, water-bag), 36 mA injection
[2]LINACSrfqSIM calculation, 1.2 π mm mrad. (100%, normalized, water-bag), 60 mA injection

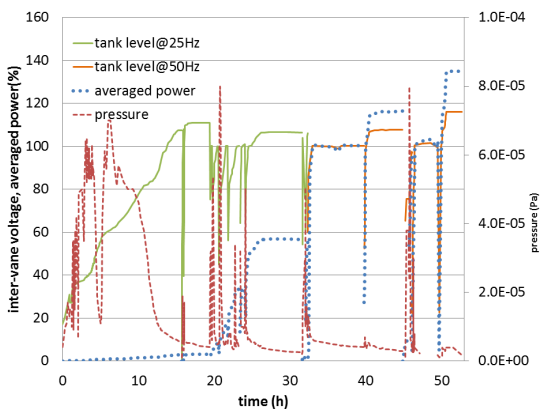

Figure 3: History of the RFQ II aging.

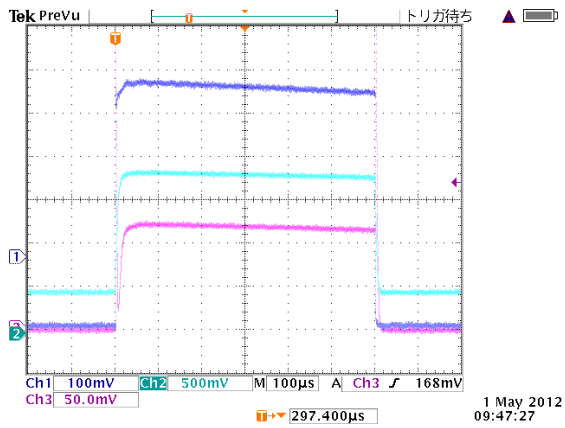

Figure 4: RF waveform of RFQ II. Blue: tank level, Cyan: inputted RF, Magenta: reflected RF.

voltage reached to be 107 % of nominal voltage; nominal voltage corresponds to a power of 333 kW. Next, the pulse width was gradually broaden, then the repetition rate was increased to be 50 Hz. Figure 4 shows the RF-waveform inputted to and reflected from the RFQ II. During a 24-hours operation, the trip occurred only three times.

RFQ III

For the beam-dynamics design of RFQ III, LINACSrfqDES[8][9] was used[10]. LINACSrfqDES is a Mathematica[11] based quite flexible tool. Figure 5 shows the obtained cell parameters as functions of cell number.

The particle simulations were performed by using LINACSrfqSIM[8][9]. LINACSrfqSIM is a time-domain code to treat the space-charge effect correctly. In addition to the conventional multipole-expansion method (mpole mode), a multigrid Poisson solver is implemented in LINACSrfqSIM (Poisson mode). The Poisson solver

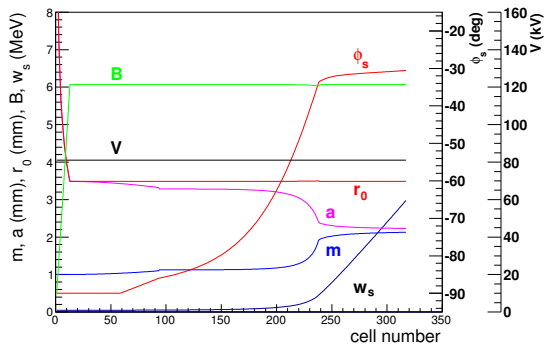

Figure 5: Cell parameters of RFQ III.

calculates the electro-magnetic field more accurately than the mpole method, especially, in the vicinity of the vane tips, and automatically correctly includes the image-charge

Copyright © 2012 by the respective authors — cc Creative Commons Attribution 3.0 (CC BY 3.0)

effect. This feature is important for simulating high intensity RFQs.

In the simulation of RFQ III, the peak current of the input beam is 60 mA, the normalized rms transverse emittance is 0.20π mm mrad, the transverse distribution is water bag, input energy is 50 keV, and the phase distribution is uniform. Figure 6 shows emittance evolution as functions of cell number. The solid line represents the transverse emittance and the dashed line is longitudinal one. The transverse emittance growth to the input emittance is 7 %; this is sufficiently small for the J-PARC purpose.

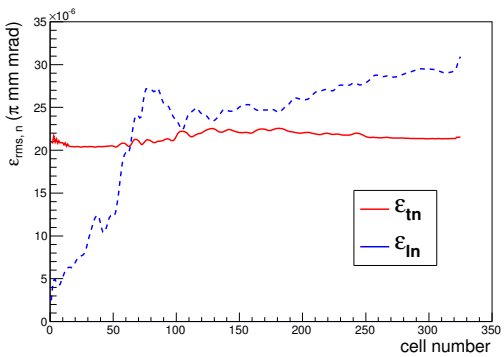

Figure 6: Emittance evolution as functions of cell number. The solid line represents the transverse normalized rms emittance, and the dashed line is the longitudinal one.

Machining of the vanes of the first and second unit cavities has been finished by the end of March 2012[12]. The dimensions of the vane tips were measured on the milling machine with newly developed laser displacement sensor based measuring system[13]. The brazing of the first unit is carried out in September 2012. Figure 7 shows the assembled unit 1 of RFQ III.

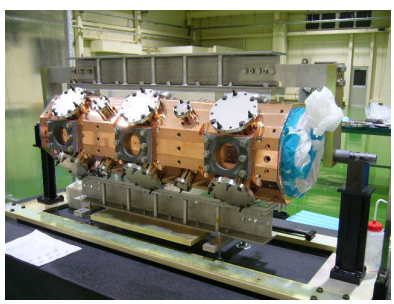

Figure 7: Assembling the RFQ III unit 1.

SCHEDULE

RFQ I will be used until July 2013. A high-power test of RFQ III will be done by the end of March 2013. Beam test will be carried out in the beginning of JPY2013 before the installation to the accelerator tunnel of the linac. RFQ III will replace RFQ I in August 2013.

RFQ II will be re-installed in the test-stand and will be used for various tests of accelerator components, such as ion source and diagnostics.

CONCLUSION

In these few years, remarkable progress has been made with J-PARC RFQs. RFQ I is under user operation with an acceptable trip rate of ∼20 times / day. The high-power test of RFQ II was successfully carried out in the beginning of JPY 2012. The beam dynamics design of RFQ III has been finished and it is now being fabricated. RFQ III will be installed into the accelerator tunnel in August 2013.

ACKNOWLEDGEMENTS

The authors thank the J-PARC linac group for their support for the operation of RFQ I, the high-power test of RFQ II, and so on.

REFERENCES

[1] K. Hasegawa, Commissioning of the J-PARC linac, in: Proceedings of PAC07, Albuquerque, New Mexico, USA, 2007, pp. 2619–2623.

[2] A. Ueno, Y. Kondo, RF-test of a 324-MHz, 3-MeV, H^- RFQ stabilized with PISL's, in: Proceedings of 2000 Linac Conf., Monterey, California, USA, 2000, pp. 545–547.

[3] K. Hasegawa et. al., Status of the J-PARC RFQ, in: Proceedings of IPAC2010, Kyoto, Japan, 2010, pp. 621–623.

[4] T. Morishita et. al, Vacuum brazing of the new RFQ for the J-PARC linac, in: Proceedings of LINAC2010, Tsukuba, 2010, pp. 521–523.

[5] H. Hotchi, J-PARC beam commissioning progress, in: Proceedings of IPAC2011, San Sebastián, Spain, 2011, pp. 6–10.

[6] K. Hasegawa, Recovery of the J-PARC linac from the earthquake, in: these proceedings, Tel-Aviv, Israel, 2012.

[7] J. H. Billen, L. M. Young, POISSON SUPERFISH, Tech. rep., LA-UR-96-1834 (1996).

[8] R. A. Jameson, RFQ designs and beam-loss distributions for IFMIF, Tech. Rep. ORNL/TM-2007/001, Oak Ridge National Laboratory (January 2007).

[9] R. A. Jameson, LINACS design and simulation framework, Tech. Rep. KEK/J-PARC Siminor 6 March 2012, KEK/J-PARC (March 2012).

[10] Y. Kondo et. al., Beam dynamics design of a new radio frequency quadrupole for beam-current upgrade of the japan proton accelerator research complex linac, Phys. Rev. ST Accel. Beams ,to be published.

[11] Mathematica, Wolfram Research Inc.
URL `http://www.wolfram.com`

[12] T. Morishita et. al, Progress of RFQ III fablication in J-PARC LINAC, in: these proceedings, Tel-Aviv, Israel, 2012.

[13] Y. Kondo et. al., On-machine non-contact dimension-measurement system with laser displacement sensor for vane-tip machining of RFQs, Nucl. Instr. and Meth. A 667 (2012) 5–10.

Copyright © 2012 by the respective authors — cc Creative Commons Attribution 3.0 (CC BY 3.0)

NUMERICAL SIMULATION OF PROJECT-X/PXIE RFQ*

J-F. Ostiguy†, N. Solyak, A. Saini
Fermilab, Batavia IL 60510, USA

Abstract

Project-X is a proposed superconducting linac-based high intensity proton source at Fermilab[1]. The machine first stages operate in CW mode from 2.1 to 3 GeV. A high bandwidth chopper is used to produce the required bunch patterns. A 162.5 MHz CW RFQ accelerates the beam from 30 keV to 2.1 MeV. A concern with CW operation is that losses either within the RFQ or in the downstream modules should be well-understood and remain very low to ensure safe and/or reliable operation. In this contribution, we use the code TOUTATIS to perform RFQ simulations.

INTRODUCTION

Project-X is a multi-institutional collaboration. The latter includes LBNL, which in view of its considerable experience, has been assuming the responsibility of designing and delivering the RFQ. The latter is now ready for fabrication; delivery at Fermilab is expected sometime next year. The LBNL design work has been performed using an in-house version of Los Alamos suite of RFQ codes, which includes PARMTEQM. The code is by now well-established and has been used to design numerous successfully operated devices.

The LBNL group has performed extensive numerical studies of its design. In particular, detailed studies of the impact of imperfections on the performance of their RFQ have been reported at a recent Project-X collaboration meeting [3]. In this contribution, we present a first attempt at a similar type of analysis, using TOUTATIS, an alternative RFQ simulation code licensed from CEA/Saclay. This code possesses certain features that are attractive. Among them is the fact that field computations are performed directly from a geometric description of the vanes and are not based on a series expansion. The space charge solver employs a 3D multigrid algorithm and is self-consistent. Integration is performed using time, rather than longitudinal position as an independent variable. Finally, there is, no artificial limitation on the number of particles that can be tracked.

RFQ DESIGN

A set of relevant parameters for the LBNL designed PXIE [2] RFQ is presented in Table 1. It is a conventional device in that it includes the usual radial matcher, gentle buncher and acceleration sections. The downstream termination is of the Crandall type, i.e. it involves one cell where the modulation transitions from $m > 1$ to $m = 1$ followed by another where $m = 1$ whose length is adjusted to control exit beam parameters and to prevent phase dependent exit kicks. The design provides an output beam which is geometrically round with minimal angular divergence. Sections are clearly distinguishable on Figure 1, which shows the vane profile in the horizontal plane. Overall transverse and longitudinal rms beam envelopes are shown in Fig. 2.

Parameter	Value
Vane Length	4.44 m
Energy	30 keV - 2.1 MeV
Input Emittances	0.12,0.12, 0.0 mm-mrad
Output Emittances	0.15 (x),0.15(y), 0.21(z) mm-mrad

Table 1: Some relevant parameters for the Project-X RFQ.

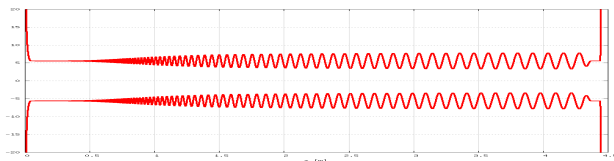

Figure 1: Vane profile in the horizontal plane.

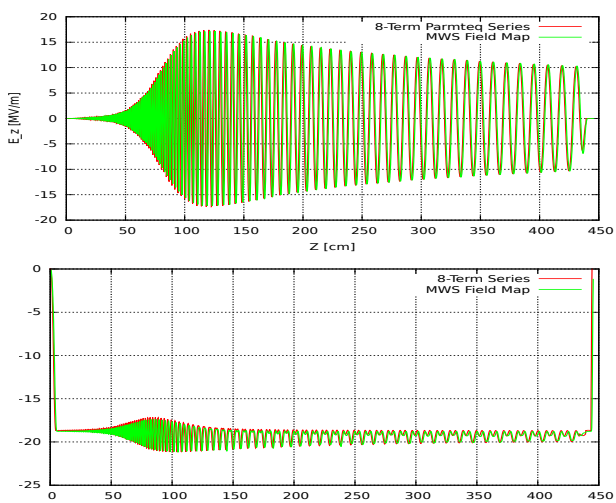

Figure 2: Field profile in the PXIE RFQ.

CODES

The Los Alamos code PARMTEQ is a tracking code where the RFQ field is modelled in the electrostatic approximation between the vanes. The field is obtained from an an 8-term axial expansion solution of Laplace's equation. PARMTEQ does not compute the series coefficients; the latter are interpolated from a parametrized table of pre-computed coefficients extracted from a full so-

* Work performed under US DOE contract DE-AC02-76CH03000.
† ostiguy@fnal.gov, solyak@fnal.gov

Copyright © 2012 by the respective authors — cc Creative Commons Attribution 3.0 (CC BY 3.0)

lution of Laplace equation for cells with different modulation/period ratios. These computations were performed separately with a code based on an integral equation formulation of Laplace's equation. A question that often arises is how accurate is the field obtained from the series compared with the exact solution. Fig. 2 compare the fields obtained from a numerical solution with CSR Microwave Studio to the field obtained from a series using the coefficients used by PARMTEQ. As can be seen, the agreement near the axis is excellent. That said, the accuracy of the series tends to degrade when the radial position approaches the edge of the vanes aperture. Another issue is the the space charge model in PARMTEQ, assumes a beam with azimuthally symmetric geometry while the actual beam is clearly not because of alternating gradient focusing.

The output beam phase space predicted by PARMTEQ was compared to the predictions of two other codes that provide a full-3d space charge model: TRACK (from ANL) and TOUTATIS (from CEA/Saclay). Overall, all three codes agree very well. While the predicted output rms beam parameters are identical, small differences can nevertheless be observed in the "halo" region. As an example, Fig. 3 compares the longitudinal phase space predicted by PARMTEQ and TOUTATIS.

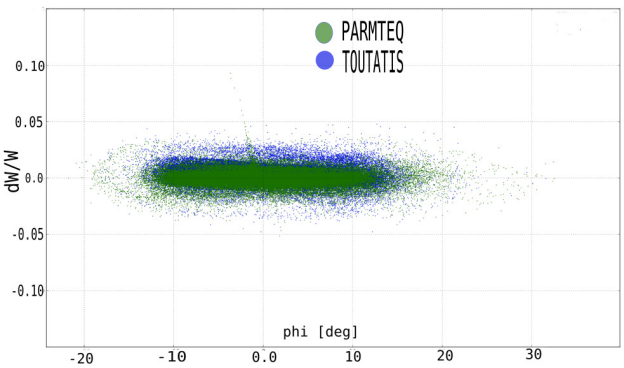

Figure 3: Longitudinal phase space at the rfq output. 100k particles, identical inputs.

LINAC ACCEPTANCE

An important technical challenge for Project-X is to keep losses well below 1 W/m in the CW superconducting linac downstream of the RFQ. A main source of concern is longitudinal phase space, specifically the characteristic "low energy tail" of the beam emerging from the RFQ. While particles populating this tail are transmitted through the RFQ, their phases gradually slip with respect to the synchronous phase because of slightly lower energies,. Eventually synchronism is lost, energy drops significantly below synchronous energy and the halo particles are deflected transversely out of the useful aperture by magnetic Unfortunately, the process of converting a longitudinal "tail" into a transverse one occurs over many betatron periods and collimation cannot be performed inside a cryomodule. In general, rf capture efficiency in an RFQ is not total because the longitudinal vane modulation must be established over a finite length; in other words, the process is not be perfectly adiabatic. Acceptances for the Project-X MEBT and Linac have been estimated by tracking particles initially covering a large area of phase space and determining those which survive. Note that this estimate ignores space charge effects, and is therefore likely to be a modest overestimation. Fig. 4 shows longitudinal acceptance plots for the combined MEBT and linac, about 5π mm-rad. The limiting longitudinal acceptance is the linac. The corresponding transverse acceptance boundaries are not shown, but have a more regular shape. The predicted transverse acceptance is on the order 5π mm-mrad for the MEBT-linac combo. This transverse acceptance is limited by the MEBT, which includes transverse collimation intended to sweep out particles in the "far tail" of the energy distribution; the transverse acceptance of the linac is about twice as large.

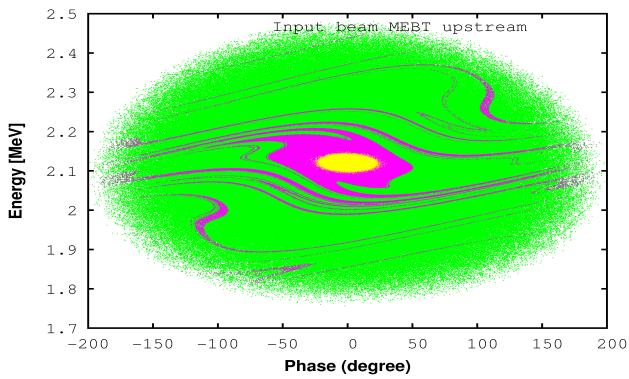

Figure 4: Longitudinal phase space acceptance for the combined MEBT and Linac. The acceptance is the cyan area. The yellow area is a 3σ beam.

IMPERFECTIONS

A real RFQ obviously deviates from the design ideal. Many types of "errors" can be studied. Among relevant ones are voltage profile errors, which may also themselves be a side-effect of mechanical imperfections. Within the vanes region, the RFQ fields are quasi-TEM. The effective longitudinal vane voltage distribution is analogous to that in a transmission line and is determined by the geometry along the device and at both extremities. Tuners are provided correct the voltage profile. The adjustment is however, static. Various effects, in particular thermal effects, or mechanical resonances can still induce dynamic deviations. Fig. 5 shows predicted losses as a function of the voltage on the vanes. The nominal inter-vane voltage is uniform (60 kV). Three curves are presented. The curve labelled RFQ is the fraction lost within the RFQ. The second curve, labelled "MEBT" is the fraction which is more than 0.2 MeV away from the nominal energy and outside a $25\epsilon_t$ transverse acceptance. Those particles are most likely collimated in the MEBT. The third curve, labelled "LINAC" is a fraction outside of $25\epsilon_\ell$ acceptance is likely to be lost in the downstream linac. Fig. 6 illustrates the impact on transmission of a non-uniform voltage profile. The error voltage ramps linearly and goes through 0 half-way into

Copyright © 2012 by the respective authors — cc Creative Commons Attribution 3.0 (CC BY 3.0)

the RFQ. A 1% ramp means that the voltage varies from -0.5% to +0.5%. All computations were performed with TOUTATIS. These results confirm that the design is relatively insensitive to voltage perturbations, comfortably so within a few %.

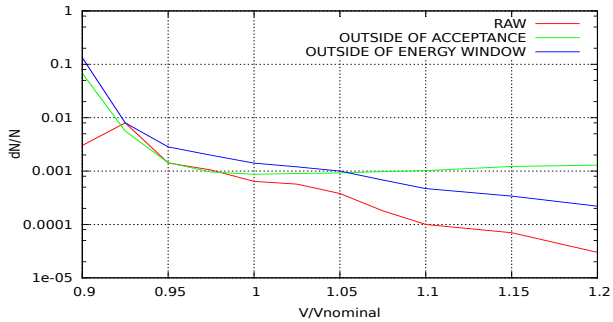

Figure 5: Estimated loss fractions vs relative voltage.

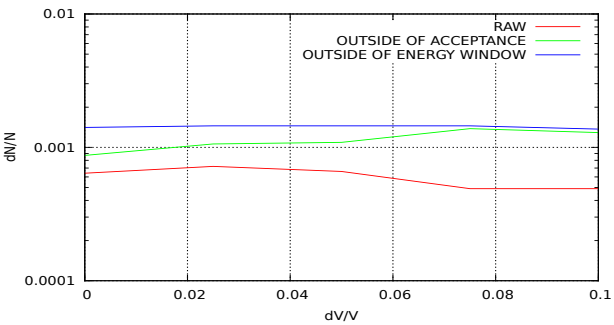

Figure 6: Estimated loss fractions vs linear voltage ramp.

MISMATCH AND INJECTION ERROR

Because the radial matcher section has a finite length, transverse focusing is also not established in a perfectly adiabatic manner. As a consequence, there exists an optimal set of beam parameters, – the matched parameters –, which minimize envelope oscillations within the RFQ. These parameters are close to, but do not correspond exactly to the periodic α, β for the first cell downstream of the radial matcher for the synchronous particle. This is mostly because for each particle, transverse focusing depends on the rf phase upon arriving at the cell. While the LEBT provides some adjustment for matching, vacuum fluctuations and corresponding neutralisation effects are difficult to control and can induce mismatch and injection errors at the RFQ input. Fig. 7 illustrates the impact of a 50% horizontal transverse mismatch on the emittances. Not surprisingly, both transverse emittances are over 20% higher than nominal; the longitudinal one is minimally increased. Fig. 8 illustrates the impact of a vertical injection error of 2 mm and 2mrad. 8.5 % of the beam is lost within the RFQ. In this case, the output transverse emittances are double of nominal while the longitudinal is only 20% higher.

CONCLUSION

The Project-X/PXIE RFQ will be one among few RFQs operating in CW mode. By cross-checking with available

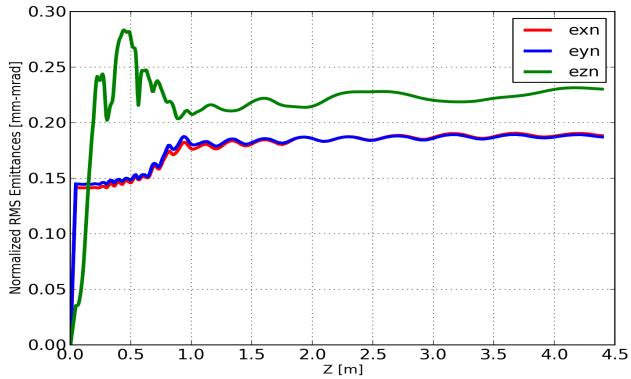

Figure 7: Emittances with a 50 % hor. input mismatch. Losses are not affected.

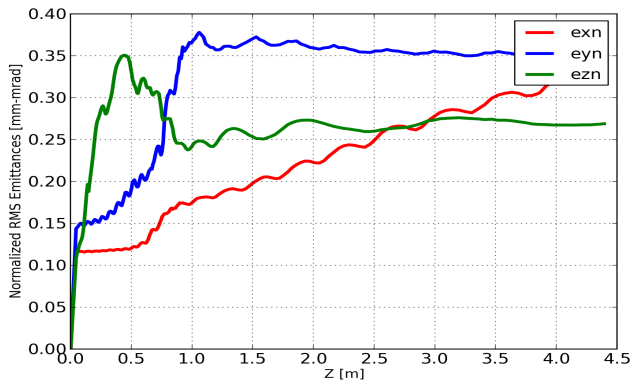

Figure 8: Emittances with 2 mm, 2 mrad vert. input error.

codes and models involving different physics details, our objective is to be well-prepared to better understand and analyse the device performance once it is put in operation. This exercise has allowed us to confirm LBNL results to the effect that that the design is relatively robust with respect to various type of errors. We intend to continue and analyse other types of imperfections; planned future work also includes tracking with a PIC code and a full electromagnetic model based on as-build geometry. Early efforts in that direction have already been described[4].

ACKNOWLEDGEMENTS

The authors would like to express their thanks to J. Staples and D. Li from LBNL for generously providing details of their RFQ design.

REFERENCES

[1] S. Nagaitsev and S. Henderson "Status of FNAL Project-X", LINAC12, TU1A02

[2] V. Lebedev, PXIE Optics and Layout", IPAC12, New Orleans, May 2012

[3] J. Staples, "PXIE RFQ RF Design", Project-X Collaboration Meeting, Apr 10-12 2012

[4] G. Romanov, "Beam Dynamics Simulations in ProjectX with CST Studio Suite', IPAC 2012, New Orleans, MOPPC082

Copyright © 2012 by the respective authors — cc Creative Commons Attribution 3.0 (CC BY 3.0)

EXPERIMENTAL AND SIMULATION STUDY OF THE LONG-PATH-LENGTH DYNAMICS OF A SPACE-CHARGE-DOMINATED BUNCH*

I. Haber, B. L. Beaudoin, S. Bernal, R. A. Kishek, T. W. Koeth, Y. C. Mo
University of Maryland, College Park, MD 20742, USA

Abstract

The University of Maryland Electron Ring (UMER) is a low-energy (10 KeV) electron facility built to study, on a scaled machine, the long-propagation-length evolution of a space-charge-dominated beam. Though constructed in a ring geometry to achieve a long path length at modest cost, UMER has observed important space-charge physics directly relevant to linear machines. Examples are presented that emphasize studies of the longitudinal dynamics and comparisons to axisymmetric simulations. The detailed agreement obtained between axisymmetric simulation and experiment is presented as evidence that the longitudinal physics observed is not strongly influenced by the ring geometry. Novel phenomena such as soliton formation, unimpeded bunch-end interpenetration, and an instability that occurs after this interpenetration, are discussed.

BACKGROUND

The University of Maryland has had a long-standing program, inspired and nurtured by the late Prof. Martin Reiser, of using electron beams to conduct research, on a scaled basis, into the fundamental physics of intense charged particle beams when the beam evolution is dominated by the influence of space charge. An important and continuing element of this research has been its emphasis on comparison of theory and simulation to experiment. The early successes achieved are a strong motivation for the current research.

During the early years, the primary experimental facility was a 240 mA, 5 KeV electron beam injected into a transport system that consisted of 38 discrete iron core solenoid magnets, placed 13.6 cm apart [1]. Particle-in-cell (PIC) simulations [2] that carefully modelled the iron core solenoids [3] were successful in reproducing, in detail, experimentally observed behavior. The influence of space charge on beam characteristics such as emittance growth in the presence of misalignments and small errors in the initial match [4] were quantitatively reproduced and explained.

A significant milestone in simulation/experiment benchmarking [5] was achieved in an experiment where a mask was placed immediately downstream of the electron gun to produce a five beamlet pattern. This experiment was performed to test the theory that a nonuniform transverse current profile will relax to the lowest-potential-energy uniform profile. The excess energy would be converted to kinetic energy, causing the beam emittance to grow [6]. Agreement was obtained on the emittance growth between experiment and simulation and theory.

An unexpected downstream re-emergence of the initial five-beamlet pattern was observed on a series of downstream phosphor screen images. Furthermore, the image evolution was reproduced in striking detail in simulation. The simulations assumed uniform emission from the gun with the intrinsic emittance calculated from the cathode temperature and employed no adjustable free parameters. In addition, evolution of the current cross-section was sufficiently sensitive to the initial emittance that only a few percent variation in the initial emittance assumed in the simulation resulted in a noticeable deviation from the experimentally observed patterns. Comparison between simulation and experiment could therefore be used to deduce beam emittance.

To study conversion of the space charge potential energy in a mismatch to kinetic energy, an additional series of experiments was performed where the beam was purposely mismatched. Theoretical predictions of the energy exchange were verified. However, unlike the matched beamlet case where a final distribution with a uniform cross section was observed, the extra kinetic energy was transferred mostly to a beam halo [7].

Additional experiments were also conducted to test longitudinal beam dynamics. Generally good agreement between theory and experiment was also obtained [8]. In investigating both transverse and longitudinal dynamics, many experiments were conducted that validated both theoretical predictions of the physics of the evolution of space-charge dominated beams, as well as, the ability of simulations to predict the observed behavior. However, because of the limited length of the linear transport line, it was not possible to address many significant questions about the physics of space-charge-dominated beams. For example, what are the characteristic of the equilibrium distribution that is reached after long time relaxation of a space-charge-dominated beam? In addition, many questions concerning the longitudinal dynamics, which have a much slower evolution time than the transverse dynamics are inaccessible in a short linear transport system.

UNIVERSITY OF MARYLAND ELECTRON RING (UMER)

Ring Description

In order to address the long pathlength physics of a space charge dominated beam, while remaining within the available space and budgetary limits, the University of Maryland Electron Ring (UMER) was constructed. A

*Work supported by the United States Department of Energy and the Office of Naval Research.

Copyright © 2012 by the respective authors — cc Creative Commons Attribution 3.0 (CC BY 3.0)

substantial number of simulation studies was first conducted. From these studies it was determined that emittance growth of the propagating bunch would remain within acceptable limits with achievable construction tolerances [9].

UMER is a 11.52m circumference electron ring with 36 alternating-gradient (A-G) quadrupole periods and an approximate 60° phase advance per period. Immediately downstream of the 10KeV electron gun is an aperture wheel that can selectively insert different apertures without breaking vacuum. The apertures allow injected beam currents to be varied from 0.6mA to 100mA. Normalized beam emittances for the range of injected currents range between ~0.3μm and ~3μm. As a result, the beam space charge phase advance can range from moderately to substantially depressed. Under usual operating conditions, a 100ns constant current bunch is injected covering approximately half of the ring. The injection dipole is then switched to recirculate the bunch. Details of the UMER ring as well as performance measured during conditioning are beyond this discussion, but are documented in detail elsewhere [10-12].

Longitudinal Dynamics in UMER

A consequence of employing a ring is the added complexity of the transverse dynamics compared with a linear machine. For example, there are potential distortions of the transverse equilibrium as the beam is bent and the possibility of resonances that are not present in a linear geometry. This is a complex area of space-charge physics currently under study and is beyond the scope of the current discussion. However, because of the separation of time scales between the transverse and longitudinal evolution, the conventional wisdom expects that the longitudinal evolution will be averaged over the more rapid transverse dynamics and the two will be decoupled. Evidence is presented that this is what actually happens.

Bunch-End Expansion and Interpenetration

Because the injected UMER bunch does not fill the entire ring, unless the bunch ends are contained by an applied bunching force, the space charge forces in the bunch will cause the ends to expand [13]. The front of the bunch will eventually overtake the rear end of the previous turn. Because the bunch length is much greater than the pipe radius, the longitudinal electric field is largely shorted-circuited by the conducting pipe. This results in a longitudinal self-electric field that is proportional to the derivative of the line density. Consequently, at the minimum in current that occurs between overtaking bunch ends, the self-electric field vanishes and the ends freely interpenetrate.

This behavior and the consequent evolution of the longitudinal bunch toward uniformly filling the ring, is illustrated in Fig. 1, which is a plot of the time evolution of the beam current passing a resistive wall current monitor about half way around ring circumference downstream of the injection. Also plotted on the same axes is a simulation using a straightened-pipe axisymmetric numerical PIC model with a uniform constant applied solenoid focusing force. The simulated curve is corrected for the measured transverse beam loss and also for the characteristics of the measurement circuit, primarily the inductance that is in parallel with the resistance of the current monitor [14].

Multi-Stream Instability

As the bunch ends overtake and interpenetrate more than once, there are eventually several interpenetrating streams with different longitudinal velocities at any location along the bunch. Owing to the multiple streams, development of space-charge-driven instability is predicted by simulation, and is observed experimentally. There are small differences in details of the instability onset time and the details of the current modulation. However, this can be expected, since instability onset is generally sensitive to fine details of the initial distribution. This instability, which occurs at a wavelength several times larger than the pipe diameter, differs from the usual plasma two-stream instability. The usual two-stream instability is observed in simulations but occurs at a much shorter wavelength and saturates at too low a level to be observed experimentally.

Solitons

Another series of experiments where excellent agreement has been obtained between experiment and simulation, is the propagation of a short large-amplitude perturbation in the initial beam current created by laser excitation of the cathode [15]. In this case also, axisymmetric simulations reproduce, in detail, the measured current evolution, including the breakup of the large-amplitude initial pulse into a soliton train. Several parametric tests have been conducted to verify that the observed behavior reproduces what is expected from soliton propagation.

SUMMARY

Several experiments have been described where the beam evolution is reproduced in detail by “straightened” axisymmetric simulations. These simulations replace the flutter in the alternating-gradient focusing with a constant axisymmetric focusing force. In addition to neglecting the A-G flutter, these simulations also neglect the consequences of beam bending. The major effect that must be included to obtain agreement between simulation and experiment is to account for transverse current loss. This was done by assuming that such loss occurs uniformly along the bunch.

The degree to which agreement is obtained notwithstanding these assumptions argues strongly for the assumption that the transverse and longitudinal dynamics are decoupled. The UMER ring is therefore an excellent vehicle for the general exploration of space-charge-dominated longitudinal beam dynamics, and the results obtained should be directly applicable to linear machines.

Copyright © 2012 by the respective authors — cc Creative Commons Attribution 3.0 (CC BY 3.0)

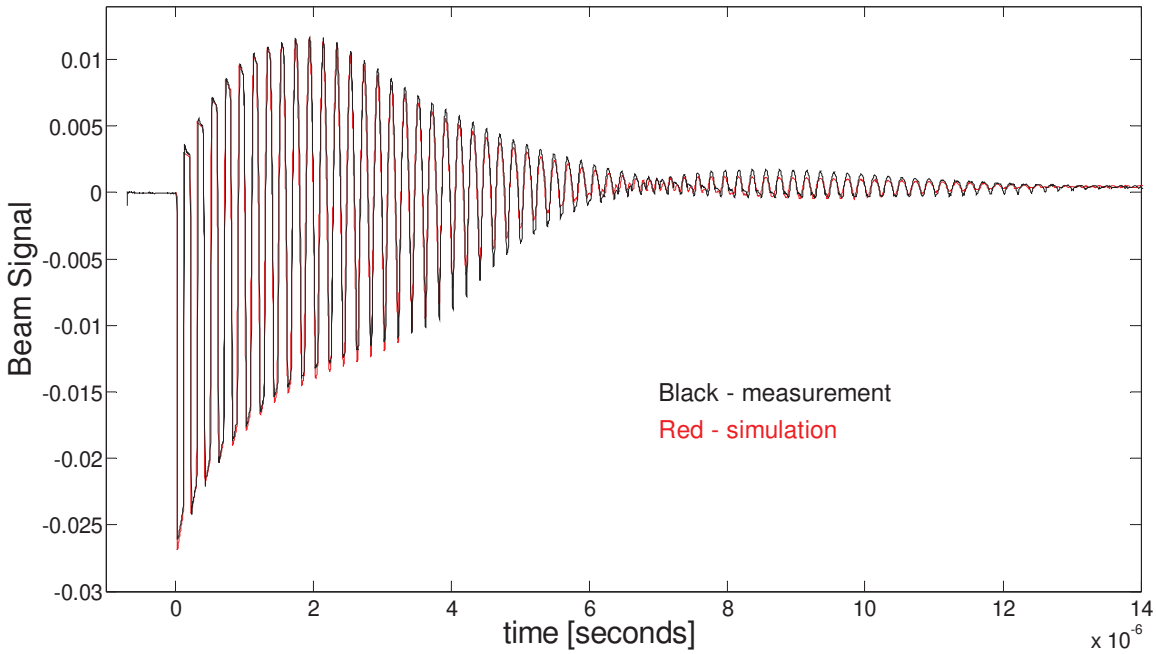

Figure 1: Excellent simulation/experiment agreement is seen in a comparison of the 6 mA wall-current monitor signal with simulated current profile adjusted to include beam loss and the equivalent circuit model of the detector.

REFERENCES

[1] D. Kehne, K. Low, M. Reiser, T. Shea, C.R. Chang, Y. Chen "Experimental studies of electron beam transport in the Maryland periodic solenoid channel," Nucl. Instrum. Methods A **278,** 194 (1989).

[2] David P. Grote, Alex Friedman, Jean-Luc Vay, and Irving Haber, "WARP – A Parallel Framework Combining Features of Plasma (Particle in Cell) and Accelerator Codes," AIP Conf. Proc 749(1) 2005.

[3] P. Loschialpo, W. Namkung, M. Reiser, J. D. Lawson, "Effects of space charge and lens aberrations in the focusing of an electron beam by a solenoid lens," J. Appl. Phys. **57** 10 (1985).

[4] H. Rudd, C. R. Chang, D. Kehne, K. Low, M. Reiser, T. Shea, and I. Haber, "Comparison of Simulation Theory & Measurement for the Maryland Transport Experiment," Nucl. Instr. & Methods in Physics Res. A278, 198 (1989).

[5] I. Haber, D. Kehne, M. Reiser, and H. Rudd "Experimental, Theoretical and Numerical Investigation of the Homogenization of Density Nonuniformities in the Periodic Transport of a Space-Charge Dominated Beam," Phys. Rev. A15, 44, 5194 (Oct. 15, 1991).

[6] T. P. Wangler, K.R. Crandall. R.S. Mills. and M. Reiser, "Relation Between Field Energy and RMS Emittance in Intense Particle Beams," IEEE Trans. Nucl. Sci. NS-32. 2196, 1985.

[7] D. Kehne, M. Reiser, H. Rudd, "Experimental Studies of Emittance Growth Due to Initial Mismatch of a Space Charge Dominated Beam in a Solenoidal Focusing Channel," Proc. of the 1991 Particle Accelerator Conf. http://www.JACoW.org

[8] D. X. Wang, J. G. Wang, D. Kehne, M. Reiser, I. Haber, "Experimental Studies of Longitudinal Beam Dynamics of Space-Charge Dominated Beams,". Proc. of the 1993 Particle Accel. Conf. http://www.JACoW.org

[9] R.A. Kishek, S. Bernal, M. Reiser, M. Venturini, J.G. Wang, I. Haber, and T. Godlove "Beam Dynamics Simulations of the University of Maryland Electron-Ring Project" Nuclear Instruments and Methods **A415**, 417-421 (1998).

[10] I. Haber, S. Bernal, B. Beaudoin, M. Cornacchia, D. Feldman, R.B. Feldman, R. Fiorito, K. Fiuza, T.F. Godlove, R.A. Kishek, P.G. O'Shea, B. Quinn, C. Papadopoulos, M. Reiser, D. Stratakis, D. Sutter, J.C.T. Thangaraj, K. Tian, M. Walter, and C. Wu, "Scaled electron studies at the University of Maryland," Nuclear Instruments and Methods A **606**, 64-68 (2009).

[11] R.A. Kishek, B.L. Beaudoin, S. Bernal, M. Cornacchia, K. Fiuza, I. Haber, T. Koeth, P.G. O'Shea, D.F. Sutter, and H. Zhang, "Advances in Modeling the University of Maryland Electron Ring," PAC 2011, New York, (2011). http://www.JACoW.org

[12] http://www.umer.umd.edu

[13] A. Faltens, E.P. Lee, S.S. Rosenblum, "Beam end erosion," J. of Appl. Phys., Vol. **61**, 12, p.5219, (1987).

[14] T. Koeth, B. Beaudoin, S. Bernal, I. Haber, R.A. Kishek, and P.G. O'Shea, "Longitudinal Relaxation of a Space-Charge Dominated Bunch," Proceedings of the 2011 IEEE Particle Accelerator Conference.http://www.JACoW.org

[15] Y. Mo, B.L. Beaudoin, D. Feldman, I. Haber, R.A. Kishek, P.G. O'Shea, and J.C.T. Thangaraj, "Experimental Observations of Large-amplitude Solitary Waves in Electron Beams," Paper ID TUPPC094, IPAC 2012, New Orleans (2012).

Copyright © 2012 by the respective authors — cc Creative Commons Attribution 3.0 (CC BY 3.0)

MULTIPOLE FIELD EFFECTS FOR THE SUPERCONDUTING PARALLEL-BAR/RF-DIPOLE DEFLECTING/CRABBING CAVITIES*

S. U. De Silva[1,2#], J. R. Delayen[1,2],
[1]Center for Accelerator Science, Old Dominion University, Norfolk, VA 23529, USA.
[2]Thomas Jefferson National Accelerator Facility, Newport News, VA 23606, USA.

Abstract

The superconducting parallel-bar deflecting/crabbing cavity is currently being considered as one of the design options in rf separation for the Jefferson Lab 12 GeV upgrade and for the crabbing cavity for the proposed LHC luminosity upgrade. The knowledge of multipole field effects is important for accurate beam dynamics study of rf structures. The multipole components can be accurately determined numerically using the electromagnetic surface field data in the rf structure. This paper discusses the detailed analysis of those components for the fundamental deflecting/crabbing mode and higher order modes in the parallel-bar deflecting/crabbing cavity.

INTRODUCTION

The parallel-bar/rf-dipole deflecting/crabbing cavity has been optimized from a rectangular-shaped design with cylindrical-shaped parallel bars into a design with a cylindrical-shaped outer conductor with trapezoidal-shaped parallel bars [1,2], named the rf-dipole cavity. The improved rf-dipole deflecting/crabbing cavity design operating in TE_{11}-like mode has attractive properties with low and balanced surface fields, high shunt impedance and well separated higher order modes (HOMs). The deflecting/crabbing mode is the lowest mode in the rf-dipole design.

Currently the rf-dipole design is being considered as one of the rf separator options for the Jefferson Lab 12 GeV upgrade and as one of the crabbing cavity options for proposed LHC luminosity upgrade operating at 499 MHz and 400 MHz respectively. A 750 MHz design is also being considered as a crabbing cavity for the proposed medium energy electron-ion collider (MEIC) at Jefferson Lab [3]. The first prototypes of the cylindrical-shaped 499 MHz and 400 MHz rf-dipole cavities (Fig. 1 (A) and (B)) are being fabricated and are in preparation for rf testing [4].

The 400 MHz crabbing cavity design was further modified into a square-shaped outer conductor (Fig. 1(C)) with fixed transverse dimensions of <295 mm, to meet the dimensional constraints of the LHC crabbing system. The design was further improved by curving the bar geometry at the beam aperture (Fig. 1(D)) to reduce the transverse field variation across the beam aperture.

*Authored by Jefferson Science Associates, LLC under U.S. DOE Contract No. DE-AC05-06OR23177. The U.S. Government retains a non-exclusive, paid-up, irrevocable, world-wide license to publish or reproduce this manuscript for U.S. Government purposes.
Part of this work was done in collaboration with and supported by Niowave Inc. under the DOE STTR program.
#sdesilva@jlab.org

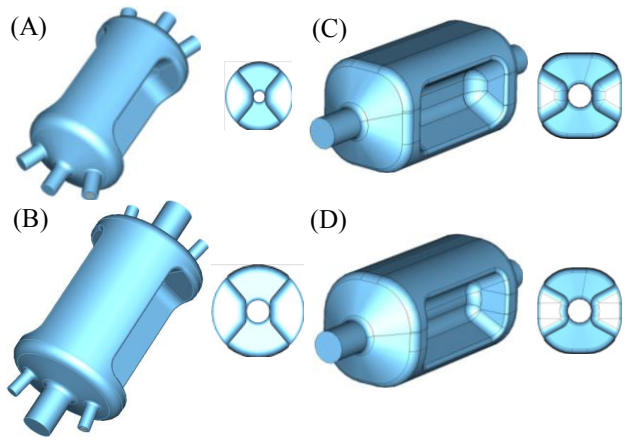

Figure 1: RF-dipole geometries and cross sections of (A) 499 MHz design, (B) cylindrical-shaped 400 MHz design, (C) square-shaped 400 MHz design and (D) square-shaped 400 MHz design with curved inner bar surfaces.

MULTIPOLE FIELD ANALYSIS

In the rf-dipole design, the field varies across the beam aperture off the beam axis generating a non-uniform transverse deflection. The field variation in x and y directions are shown in Fig. 2, for all the rf-dipole designs mentioned in Fig. 1.

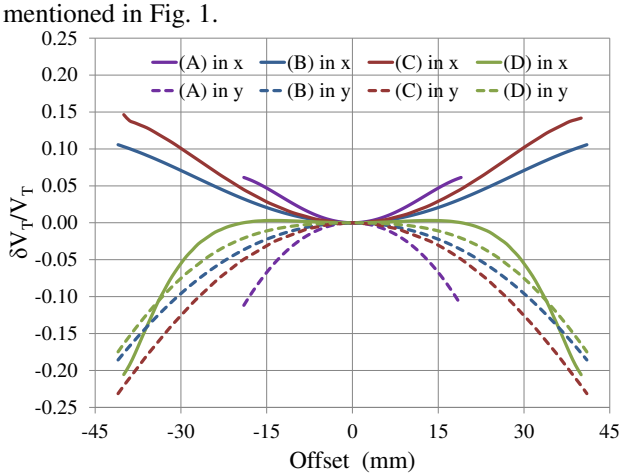

Figure 2: Normalized transverse voltage in x and y directions for designs (A), (B), (C) and (D) in Fig. 1.

The non-uniform transverse fields can generate higher orders of transverse momentum apart from the first order transverse momentum that corresponds to the deflecting or crabbing voltage. These higher order transverse multipole components may lead to perturbations in the beam. This paper presents the higher order multipole components present in the rf-dipole cavity and supressing of those components by modifying the geometry.

Copyright © 2012 by the respective authors — cc Creative Commons Attribution 3.0 (CC BY 3.0)

Calculation of Multipole Components

The fields in magnets are often expressed in terms of multipole components. The standard representation of multipole fields [5] can be expressed as,

$$B(r,\phi) = B_{ref}\sum_{n=1}^{\infty} a_n + ib_n \left(\frac{r}{r_{ref}}\right)^{n-1} e^{i(n-1)\phi} \quad (1)$$

where B_{ref} is the reference magnetic field at a given radius of r_{ref}.

Similarly, close to the beam axis, the electro-magnetic fields in an rf cavity within the beam aperture can be represented as given in Eq. 2. The symmetry in the rf-dipole cavities doesn't produce any skew components; therefore the fields can be represented as in Eq. 3.

$$E_z(r,\phi,z) = \sum_{n=0}^{\infty} E_z^{(n)}(z) r^n e^{jn\phi} \quad (2)$$

$$E_z(r,\phi,z) = \sum_{n=0}^{\infty} E_z^{(n)}(z) r^n \cos(n\phi) \quad (3)$$

The multipole field components $E_z^{(n)}(z)$ along the beam line can be obtained by using the Fourier series expansion of $E_z(r,\phi,z)$ as shown in Eq. 4.

$$E_z^{(n)}(z) = \frac{1}{r^n}\int_0^{2\pi} E_z(r,\phi,z)\cos(n\phi)\,d\phi \quad (4)$$

In rf cavities with time dependent rf fields, the higher order multipole components with time dependence can be given by $E_{acc}^{(n)}(z) = E_z^{(n)}(z)e^{j\omega t}$.

The higher order multipole components can be determined using the method given by A. Grudiev in Ref. [6]. The transverse momentum imparted by the higher order multipole field components (n>0) can be determined using the Panofsky Wenzel Theorem,

$$\begin{aligned} p_t^{(n)}(z) &= \frac{1}{c} r^{n-1}\int_{-\infty}^{\infty} F_t^{(n)} dz = -j\frac{q}{\omega}\int_{-\infty}^{\infty} \nabla_t E_z^{(n)}(z) e^{j\omega t} dz \\ &= -j\frac{q}{\omega} n r^{n-1}\int_{-\infty}^{\infty} E_{acc}^{(n)}(z) dz \end{aligned} \quad (5)$$

or by using the Lorentz Force,

$$\begin{aligned} p_t^{(n)}(z) &= \frac{1}{c} r^{n-1}\int_{-\infty}^{\infty} F_t^{(n)} dz \\ &= \frac{q}{c} r^{n-1}\int_{-\infty}^{\infty}\left[E_t^{(n)}(z)e^{j\omega t} + cB_t^{(n)}(z)e^{j\omega t}\right] dz \end{aligned} \quad (6)$$

The multipole components (b_n) are defined using the standard definition for magnets [6] as,

$$\begin{aligned} B^{(n)}(z) &= \frac{1}{qc} F_t^{(n)}(z) = j\frac{n}{\omega} E_{acc}^{(n)}(z) \left[T/m^{n-1}\right] \\ b_n &= \int_{-\infty}^{\infty} B^{(n)}(z) dz \left[T/m^{n-2}\right] \end{aligned} \quad (7)$$

These coefficients (b_n) can be used to determine the effect of higher order multipole components on beam perturbations [6].

Multipole Components for the RF-Dipole Cavity

The rf-dipole cavity has zero on axis longitudinal electric field, where the transverse deflection is given by both transverse electric and magnetic fields. The higher order multipole components can be determined using both the methods given in Eqs. 5 and 6. The $E_z(r,\phi,z)$ field data are obtained for each rf-dipole geometry using CST Microwave Studio, at three different radii within the beam aperture. A finer mesh as shown in Fig. 3 is used especially at smaller radii with a fixed number of points at each concentric cylinder.

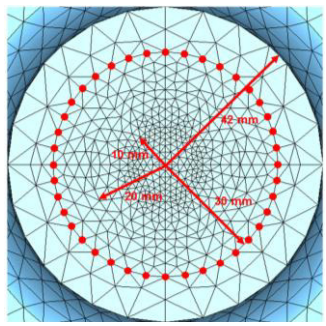

Figure 3: $E_z^{(n)}(z)$ of n = 1, 3 and 5 at r_0 = 1 cm, 2 cm and 3 cm for the cylindrical-shaped 400 MHz rf-dipole cavity.

The Fourier-decomposed field components of $E_z^{(n)}(z)$, $E_x^{(n)}(z)$ and $H_y^{(n)}(z)$ calculated using a MatLAB code at radii of 1 cm, 2 cm and 3 cm normalized to a transverse voltage (V_t) of 1 V are shown in Fig. 4, 5 and 6 for the cylindrical-shaped 400 MHz crabbing cavity. At radii closer to the beam axis the field data has higher noise content. Also, as the order increases, the noise content increases and becomes dominant over the field content. The rf-dipole cavity has components of order 2n for n = 1, 2, 3, etc. In the rf-dipole cavity the $E_z^{(n)}(z)\sin(\omega t)$ components corresponds to that of deflecting cavities and $E_z^{(n)}(z)\cos(\omega t)$ corresponds to the components related to crabbing cavities with a synchronous phase of $\phi_s = 90^0$. The higher order multipole components (b_n) can be determined by either using the Panofsky-Wenzel Theorem (Eq. 5) or using Lorentz Force (Eq. 6).

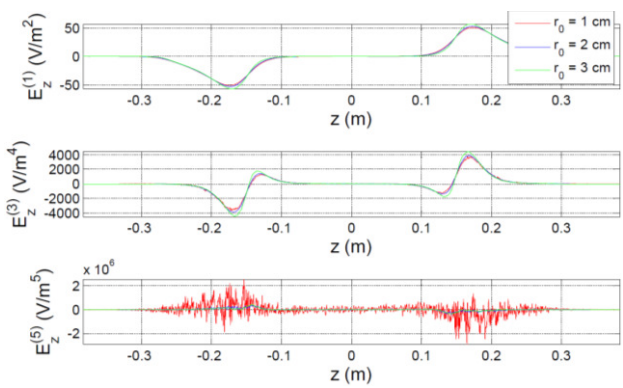

Figure 4: $E_z^{(n)}(z)$ of n = 1, 3 and 5 at r_0 = 1 cm, 2 cm and 3 cm for the cylindrical-shaped 400 MHz rf-dipole cavity.

Copyright © 2012 by the respective authors — cc Creative Commons Attribution 3.0 (CC BY 3.0)

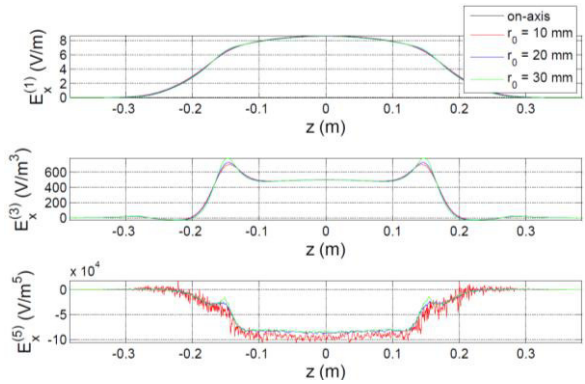

Figure 5: $E_x^{(n)}(z)$ of n = 1, 3 and 5 at r_0 = 1 cm, 2 cm and 3 cm for the cylindrical-shaped 400 MHz rf-dipole cavity.

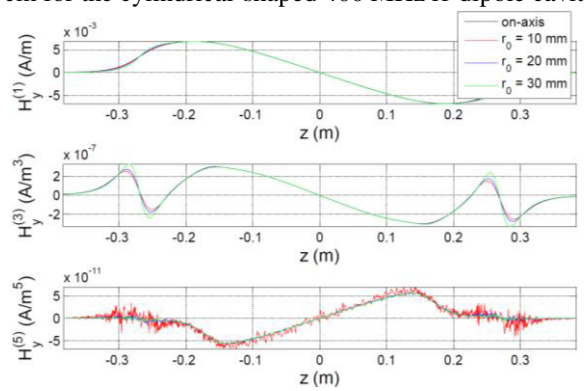

Figure 6: $H_y^{(n)}(z)$ of n = 1, 3 and 5 at r_0 = 1 cm, 2 cm and 3 cm for the cylindrical-shaped 400 MHz rf-dipole cavity.

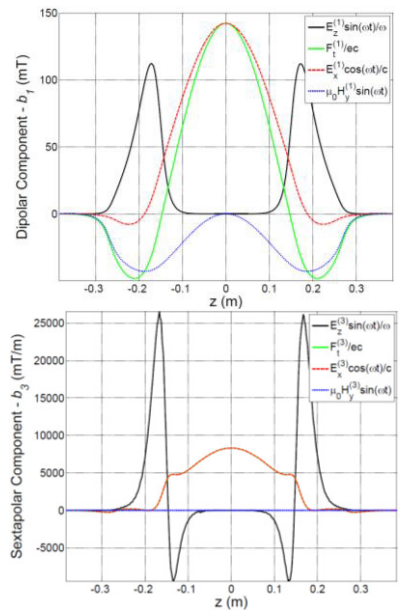

Figure 7: Dipolar and sextapolar field components of the 400 MHz cylindrical-shaped rf-dipole cavity.

The field components of the first two non-zero multipole components are shown in Fig. 7. The components $F_t^{(1)}/c$ and $E_{acc}^{(1)}(z)/\omega = E_z^{(n)}(z)\sin(\omega t)/\omega$ has different dependence on z, however gives the same b_1 when integrated along z, that corresponds to the transverse voltage given by the rf-dipole cavity.

The higher order multipole components of the fundamental deflecting/crabbing mode are shown in Table 1, for the four rf-dipole designs shown in Fig. 1. As seen by the field profiles the b_n for n = 0, 2, 4, 6… are zero. All the higher order multipole components are normalized to a transverse voltage (V_t) of 1.0 MV. Comparing the 400 MHz crabbing cavities of cylindrical-shaped outer conductor, the 400 MHz cavity with a square shaped outer conductor has higher multipole components. The square-shaped 400 MHz rf-dipole cavity with curved bar surfaces has reduced b_3 and b_5, but has higher b_7 compared to the other 400 MHz designs.

Table 1: Multipole components for the rf-dipole cavity designs shown in Fig. 1.

	(A)	(B)	(C)	(D)	Units
V_z	0.0	0.0	0.0	0.0	MV
V_t	1.0	1.0	1.0	1.0	MV
b_1	3.3	3.3	3.3	3.3	mT m
b_2	0.0	0.0	0.0	0.0	mT
b_3	8.3×10^2	3.0×10^2	4.1×10^2	1.0×10^2	mT/m
b_4	0.0	0.0	0.0	0.0	mT/m^2
b_5	$-5..8\times10^5$	-4.6×10^4	-4.1×10^4	-2.2×10^4	mT/m^3
b_6	0.0	0.0	0.0	0.0	mT/m^4
b_7	-7.1×10^8	-1.03×10^7	-2.0×10^7	-6.9×10^7	mT/m^5

CONCLUSION

The higher order multipole components were calculated for the rf-dipole cavity designs of different geometries. The modified square-shaped 400 MHz cavity with curved bar surfaces has improved lower order multipole components. The values of the multipole components are comparable to standard magnets in a beam line. The rf-dipole geometry requires further optimization in suppressing the dominant multipole components, and therefore needs to be considered as a design optimization parameter.

REFERENCES

[1] J.R. Delayen and S.U. De Silva, in Proceedings of the 15th International Conference on RF Superconductivity, Chicago, Illinois (2011), p. 219.
[2] S.U. De Silva and J.R. Delayen, in Proceedings of the 15th International Conference on RF Superconductivity, Chicago, Illinois (2011), p. 135.
[3] A. Castilla et.al., in Proceedings of the 3rd International Particle Accelerator Conference, New Orleans, Louisiana (2012), p. 2447.
[4] S.U. De Silva and J.R. Delayen, in Proceedings of the 3rd International Particle Accelerator Conference, New Orleans, Louisiana (2012), p. 2453.
[5] A.W. Chao and M. Tigner, "Handbook of Accelerator Physics and Engineering", (World Scientific Publishing Co. Pte. Ltd), 1999.
[6] J. Barranco Garcíaorelov et.al., in Proceedings of the 3rd International Particle Accelerator Conference, New Orleans, Louisiana (2012), p. 1873.

Copyright © 2012 by the respective authors — cc Creative Commons Attribution 3.0 (CC BY 3.0)

SIMULATED PERFORMANCE OF THE CARIBU EBIS CHARGE BREEDER TRANSPORT LINE*

C. Dickerson#, S.A. Kondrashev, B. Mustapha, P.N. Ostroumov, ANL, Argonne, IL 60439, U.S.A.

Abstract

An Electron Beam Ion Source (EBIS) has been designed and is being built to charge breed ions from the CAlifornium Rare Isotope Breeder Upgrade (CARIBU) for post acceleration in the Argonne Tandem Linear Accelerator System (ATLAS). The calculated transverse acceptance of the EBIS charge breeder can approach the emittance of the injected ion beam, so beam distortion during transport could lead to incomplete injection and a decrease in the overall system efficiency. The beam quality can be maintained for simulations of the transport line using the ideal ion beam parameters. This paper reports the results of the electrostatic and ion beam transport simulations used to minimize the ion beam distortions by optimizing component designs and configurations.

INTRODUCTION

Acceleration in the Argonne Tandem Linear Accelerator System (ATLAS) requires a $q/A \geq 1/7$, so +1 and +2 fission fragment beams from the CAlifornium Rare Isotope Breeder Upgrade (CARIBU) [1] require charge breeding prior to injection into ATLAS. An Electron Cyclotron Resonance (ECR) ion source is currently used to charge breed the ions, but the contamination of the accelerated beams from plasma-surface interactions within the source obscures the signal of low intensity radioactive ion beams. An Electron Beam Ion Source (EBIS) has been designed [2, 3] and is being built for the CARIBU system, and will improve the purity and intensity of the beams for post acceleration in ATLAS. The CARIBU EBIS is largely based on the Test EBIS developed at Brookhaven National Laboratory [4], and has been designed to operate with a high current, 2 A, and a low current, 0.2 A, electron gun. Ostensibly the high current gun will replicate operating conditions achieved with the Test EBIS, while the low current gun will maximize breeding efficiencies by operating in the closed-shell mode [5]. The low current electron gun was designed to produce 0.2 A to avoid possible virtual cathode formation at the low energies required to match shell closures of the injection ions (~2 keV), and the gun will employ a Ø1.6 mm cathode to maintain a high current density within the trap, ~500 A/cm2.

Ion beams from CARIBU, cooled and bunch in a Radio Frequency Quadrupole (RFQ), will have a full emittance of 3 π·mm·mrad at 50 keV for the expected mass range 80-160 amu [6]. Aside from the general desire to maintain the best possible ion beam quality during transport, the normalized emittance corresponding to mass 80 amu, 0.0035 π·mm·mrad, is only slightly smaller than the calculated EBIS acceptance under nominal operating conditions with the low current electron gun, 0.0037 π·mm·mrad. Another critical function of the transport line is to match the injected ion beam transverse emittance with the EBIS 4D phase space acceptance.

The layout in Fig. 1 indicates the various sections of the system for the offline testing configuration Transport simulations using generalized components were reported previously [7]. This paper reports the results of the electrostatic and ion beam transport simulations used to optimize the specific component designs and configurations for the transport beamlines by minimizing the transverse emittance growth of the ion beam. The ability of the offline diagnostic line to resolve individual charge states is also discussed.

SIMULATIONS

Ion beam transport simulations were performed with TRACK [8] and CST-EM Studio [9]. TRACK integrates the equations of motion for charged particles in 3D fields, but does not incorporate a numerical solver to calculate external electromagnetic fields explicitly. TRACK can use internal expressions for the fields of a number of idealized components, or can incorporate fields mapped from external solvers. TRACK allows the user to easily scale and rearrange the fields to investigate a wide variety of configurations. EM Studio, part of the CST Studio Suite, incorporates a solid modeler and numeric solver to calculate 3D static fields for arbitrary geometries. EM Studio models can be parameterized and programmatically optimized based on user-defined constraints. EM Studio was used to optimize the optical component geometries within the transport line to minimize beam distortion. Typically, the fields calculated in EM Studio were mapped, extracted, and incorporated into TRACK for particle tracking simulations. The space charge of the ion beam for the ion beam transport simulations was neglected since the maximum expected ion current from the CARIBU source will be ~1 nA.

*Work supported by the U.S. Department of Energy, Office of Nuclear Physics, under contract number DE-AC02-06CH11357.

#cdickerson@anl.gov

Copyright © 2012 by the respective authors — cc Creative Commons Attribution 3.0 (CC BY 3.0)

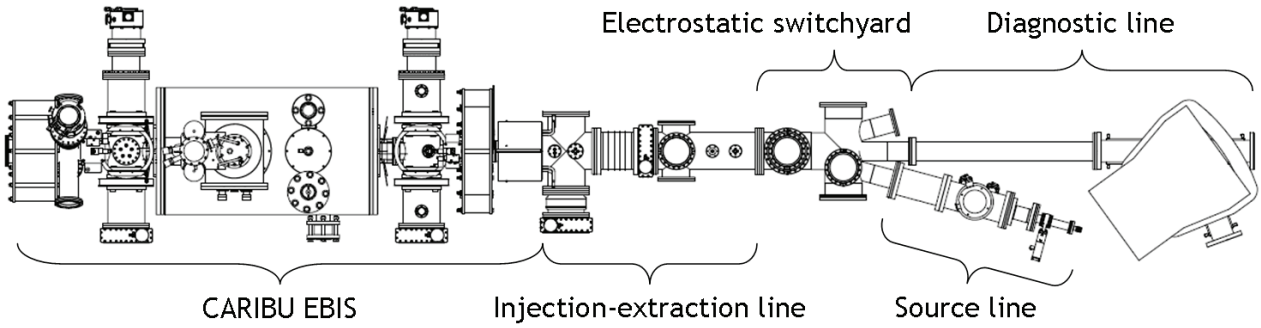

Figure 1: The layout of the EBIS charge breeder and transport lines for offline testing.

RESULTS

Injection-Extraction (I-E) Beamline

The injection-extraction (I-E) section will transport both the injected and extracted beams between the switchyard and the EBIS charge breeder. The optical elements of the I-E line – two lens assemblies, two steerers, and an acceleration tube – are shown in Fig. 2. Each lens assembly incorporates a steerer, and the extractor lens assembly uses the extraction electrode as one of its elements. The Einzel lens assembly geometries were based on the anticipated beam size and the linearity of the focusing fields. The gap and aperture combination had to produce linear focusing fields for the anticipated maximum beam diameter, ~30 mm, to minimize beam distortions. The gap between elements also had to be minimized to mitigate the influence of the grounded vacuum chamber walls on the electric field. The vacuum chambers of the I-E line are not axisymmetric, and initial simulations resulted in non-axisymmetric beams. The gaps between Einzel lens electrodes were adjusted to minimize the influence of the grounded tube, but this reduction in turn reduced the region of the linear portion of the focusing field. A lens configuration with an aperture diameter of 110 mm and gap of 20 mm was chosen for the electrodes in the I-E line to balance the range of the linear focusing fields, the influence from the grounded vacuum chambers, the strength of the lenses, and the physical size of the vacuum chamber.

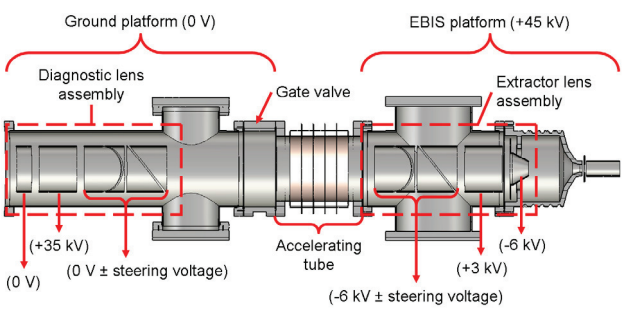

Figure 2: The electrostatic model of the I-E beamline. Nominal component voltages are shown for the injection cycle and are referenced to their respective platforms.

Three steerer configurations, shown in Fig. 3, were investigated to identify the one which maintained the best beam quality. The steerers were modelled as isolated components within a long grounded tube with the same diameter as the I-E beam pipe. A Ø20 mm 50 keV $^{133}Cs^{+1}$ beam with a full normalized emittance of 0.1 π·mm·mrad was transported through the electric field of each configuration and the emittance was monitored. Voltages were applied to the electrodes until a deflection of 13 mrad was achieved in both X and Y planes, and the results are reported in Table 1. The two sets of diagonally halved cylinders distorted the beam the least, only contributing 2% to the full normalized emittance, and were selected as the preferred steerer configuration.

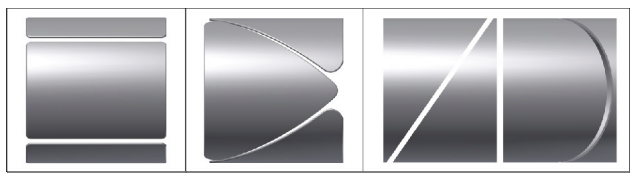

Figure 3: Side views of the three X-Y steerer configurations studied: (left) parallel quartered cylinder, (middle) diagonally quartered cylinder, and (right) two sets of diagonally halved cylinders.

Table 1: Comparison of the Emittance Growth and Strength of the Three Different Steerer Designs

Steerer configuration	Parallel quartered	Diagonally quartered	Two sets diagonally halved
ΔV	1000 V	1000 V	2000 V
Emittance growth	55%	10%	2%

Electrostatic Switchyard

The electrostatic switchyard will consist of a single 15° deflector to direct the injected beam from the source line to the I-E line. Nominally, the deflector will be inactive during extraction allowing the beam to travel straight from the I-E line to the diagnostic line. A schematic of the switch yard is shown in Fig. 4. The diagonally halved cylindrical configuration was chosen for the deflector because this design can maintain the beam quality better than others, as discussed with respect to the investigated steerer designs.

A focus of these simulations was to determine the deflector positioning with respect to the +15° and 0° axes

Copyright © 2012 by the respective authors — cc Creative Commons Attribution 3.0 (CC BY 3.0)

so the injected beam will be deflected directly on the 0° axis. This goal was achieved by shifting the deflector midplane 0.96 cm from the intersection of the +15° and 0° axes. A spare -15° port was included in the switchyard design for the installation of additional analytical if the need arises. The -15° axis offset was investigated and was incorporated into the switchyard chamber construction to enable the on-axis deflection of the extracted beam. The axis offsets are also shown in Fig. 4.

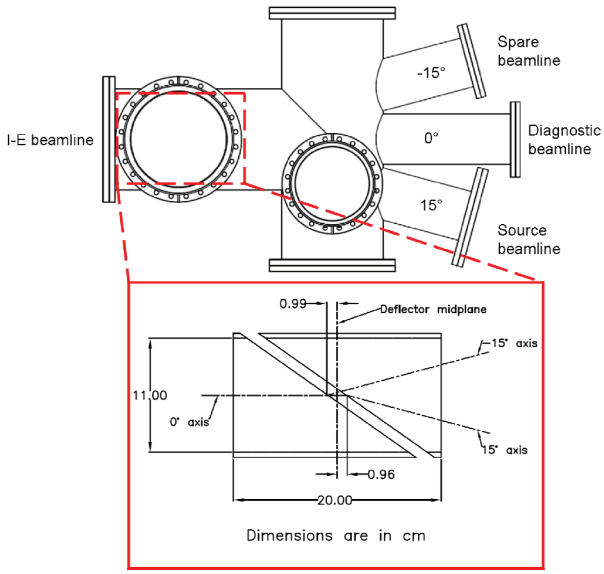

Figure 4: The electrostatic switchyard configuration and deflector positioning necessary to achieve an injected beam on the 0° beamline axis.

Offline Diagnostic Beamline

The ability of the diagnostic beamline to resolve the charge state distribution from the EBIS during the testing phase is critical to ensuring the charge breeder will meet the design specifications. The diagnostic beamline for offline testing will principally consist of a 70° analyzing magnet followed by a set of horizontal slits and a large aperture, Ø83 mm, Faraday cup. While the cup will measure the beam current, the slits should be able to isolate individual charge states if the optics permit. To simulate the resolution of the diagnostic testing beamline a multiple charge state beam was defined based on the anticipated beam parameters for extraction. The focusing required to resolve individual charge states using the 70° analyzing magnet was determined by simulating trajectories through the full I-E and diagnostic lines using TRACK. An energy spread equal to the depth of the electron beam potential well within the EBIS trap, ~370 eV for a 2 A electron beam at nominal operating conditions, was included. Fig. 5 shows the results of the individual x-x' distributions for $^{133}Cs^{+19}$, $^{133}Cs^{+20}$, and $^{133}Cs^{+21}$. The beam diameter of the $^{133}Cs^{+20}$ beam was ~10 mm and separation from the $^{133}Cs^{+19}$ and $^{133}Cs^{+21}$ beams was ~15 mm. Given this separation and the planned use of horizontal slits, accurate analysis of the individual charge state currents will be possible.

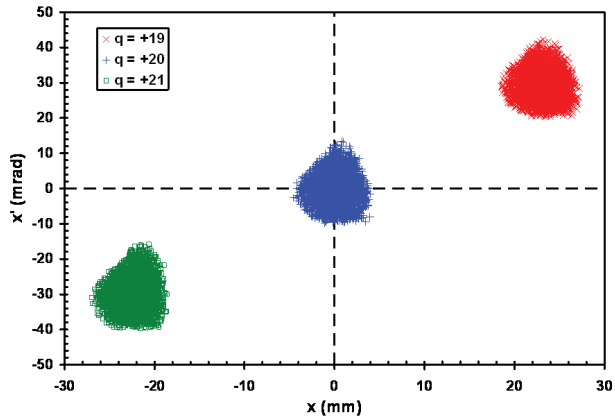

Figure 5: The transverse phase space distributions of $^{133}Cs^{+19}$, $^{133}Cs^{+20}$, and $^{133}Cs^{+21}$ at the entrance to the Faraday cup after the analyzing magnet.

Summary

An EBIS will be built to charge breed radioactive beams from CARIBU. Electrostatic and ion beam transport simulations were used to optimize the optical component designs and configurations to minimize the emittance growth of the transported beam. Designs of the Einzel lens assemblies, steerer, and electrostatic switchyard resulted. Transport simulations also showed the offline diagnostics will be able to adequately evaluate individual charge states of the extracted beam. The accuracy of these simulations will be investigated and reported as the construction of the EBIS and its ancillary systems continues.

REFERENCES

[1] G. Savard et al, Nucl. Instrum. Meth. B 266 (2008) 4086.
[2] P. Ostroumov et al, J. Instrum. 5 (2010) C07004.
[3] S. Kondrashev et al, Rev. Sci. Instrum. 83 (2012) 02A902.
[4] E. N. Beebe et al, J. Phys. Conf. Ser. 2 (2004) 164
[5] F. Wendander, J. Instrum. 5 (2010) C10004.
[6] R.C. Pardo et al, Nucl. Instrum. Meth. B 261 (2007) 965.
[7] C. A. Dickerson et al, Rev. Sci. Instrum. 83 (2012) 02A502.
[8] P. N. Ostroumov, V. Aseev, and B. Mustapha, TRACK – a Code for Beam Dynamics Simulation in Accelerators and Transport Lines with 3D Electric and Magnetic Fields, ANL, Argonne, IL, USA, v. 37 ed. (2007), see http://www.phy.anl.gov/atlas/TRACK
[9] See http://www.cst.com for CST of America, Inc., 492 Old Connecticut Path, Suite 505 Framingham, MA 01701 USA.

Copyright © 2012 by the respective authors — cc Creative Commons Attribution 3.0 (CC BY 3.0)

BEAM DYNAMICS TOOLS FOR LINACS DESIGN

A. Setty, THALES Communications, 160 Bld de Valmy 92 700, Colombes, France

Abstract

In the last 25 years, we have been using our in house 3D code PRODYN [1] for electron beam simulations. We have also been using our in house code SECTION for the design of the travelling wave accelerating structures and the beam loading compensation. PRODYN follows in time, the most complicated electron trajectories with relativistic space-charge effects. This code includes backward as well as forwards movements. This paper will describe those two codes and will give some simulations and measurements results.

INTRODUCTION

The electron dynamics are complicated. Their energies varies from zero to more than one MeV in a length comparable to the prebucket dimension. Velocities are different at the same abscissa. On-axis oscillations occur. RF field phase and amplitude laws must be shaped precisely. Radial behaviour can be analyzed by noting optical effects at the input and output regions of the cells. The equivalent lenses have either a convergent, a divergent or a null effect. It depends on the electron beam to RF electrical field dephasing. Their positions can be modified as long as overall longitudinal acceleration occurs.

BEAM DYNAMICS TOOLS

For the design of a linac we use 5 principal codes:

- Our in house code SECTION, for the design of the travelling wave accelerating structures and the beam loading compensation.
- Our in house code PRODYN, for the beam dynamics simulations.
- The well-known EGUN [2] code written by Dr. Hermannsfeldt from SLAC, for the gun design.
- The also well-known SUPERFISH code written by Ron. F. Holsinger and Klaus Halbach from LOS ALAMOS for the design of cavities and electric field in accelerating structures.
- The also well-known POISSON code written by the same authors from LOS ALAMOS, for the shielded lenses and solenoids.

SECTION code

SECTION code provides along a travelling wave structure the filling time, the group velocity, the circulating power, the shunt impedance, the electric field and the energy gain.

This code uses the beam loading theory, based upon diffusion equation (Beam loading and transient behavior in travelling wave electron linear accelerators", J.E Leiss page 151, linear accelerators edited by P. Lapostolle and A. Septier, 1970 North-Holland publishing company-Amsterdam) and the S band measurements mainly the ALS structures ("Les sections accélératrices" page 1194 D. Tronc et Al, L'onde électrique Vol 49, Fasc 11-n°: 513 Dec 1969).

This code was used recently for the design of the ALBA and BESSY accelerating structures, in particular the beam loading effects.

The accelerating structures met the calculated values at ALBA, 53 MeV for 18.8 MW in the first accelerating structure (16 MeV in the buncher) July 2008 Spain.

PRODYN code

PRODYN code tackles particle dynamics, electrons in our case, according to time and in the presence of an electromagnetic field. The code includes backward as well as forward movements and relativistic space-charge effects. The space to be simulated is divided into several elementary cells. Each cell changes the input beam into an output beam that can then be injected into the next cell. If the simulation covers a large number of cells, one can test a change by taking the beam at the output of the cell that precedes the change, and injecting it into the sequence of new cells.

The particle beam is either generated by the code using the entered settings, or read from the particle file supplied by the user.

An elementary particle is represented by its position, its energy, and its phase. To solve differential equations, one uses the Runge-Kutta method with x, y, z, Vx, Vy and Vz as variables, and time as the integration variable.

The provided elements are: RF accelerating cell, drift, magnetic lens, quadripole, dipole and bending magnet. The accelerating cell may include a magnetic lens and a dipole. Subharmonic frequencies can be used.

Space charge module

When calculating dynamics at low beam currents, we can neglect the space charge effects. But with nominal beam currents, as soon as we want to properly define an accelerating section that is self-focused or provided with external focus, we must take the space charge forces into account.

In particular, in the first cavities of a buncher where the beam energy is low, the charge density becomes significant when modulating the beam. This results in significant radial de-focussing.

To elaborate the space charge calculation, we proceed as follows:

Initially, we change the Coulomb law for macro-particles that are close to each other. In order to eliminate

Copyright © 2012 by the respective authors — cc Creative Commons Attribution 3.0 (CC BY 3.0)

the calculation artefacts due to repulsive forces in the particle field in $1/R^2$ that had nothing in common with physical reality.

We replace the macro-particle with the product of a charge density and the interaction volume, which produced a field in R. However, the whole difficulty lies in the determination of the threshold radius from which the interactive law is modified.

Then, we express the fields applied to particle P at point j by a charge q placed at point i.

This module was validated using drift spaces that are appropriate for the analytical calculation of space charge for continuous beams. We placed ourselves in very unfavorable conditions. In particular, we handled the behavior of a parallel beam with energy equal to 16 keV, current of 1 Ampere and an initial diameter equal to 1 mm. The radius is doubled after 9 mm. We observe a gap of a few % due to the longitudinal limitation of the packet and the finite number of macro charges.

Our 3D modeling of the particle dynamics enabled us to replace the analytical feasibility study with a more detailed step-by-step approach to the behavior and evolution of each beam particle along an accelerating line.

Validation on operating machines

The PRODYN dynamics code enabled us to simulate the beam line of the following accelerators:

- Helios I injection at 200 MeV (IBM - USA).
- ESRF synchrotron accelerator at 200 MeV.
- ELETTRA synchrotron accelerator at 1200 MeV.
- SOLEIL synchrotron at 100 MeV.
- ALBA synchrotron at 100 MeV.
- BESSY II synchrotron at 50 MeV.

This code also enabled us, using adjustment settings only, to improve the ARTEMIS accelerator (Moronvilliers AEC) by reconstructing the computer model of the accelerator, conducting a setting optimization survey, and recovering the corresponding performance results at the experimental level.

SIMULATION RESULTS

Turnkey linacs were manufactured by Thales Communications and Security in order to inject electrons into boosters of SOLEIL [3], ALBA and BESSY II synchrotrons. The figures hereafter represent the beam dynamics simulations for the SOLEIL linac.

Fig. 1 shows the energy histogram at the buncher exit for the 120 mA mode.

Figures 2 and 3 show the phase-energy diagram and the Y-Y' plane emittance at the linac end for the 120 mA mode.

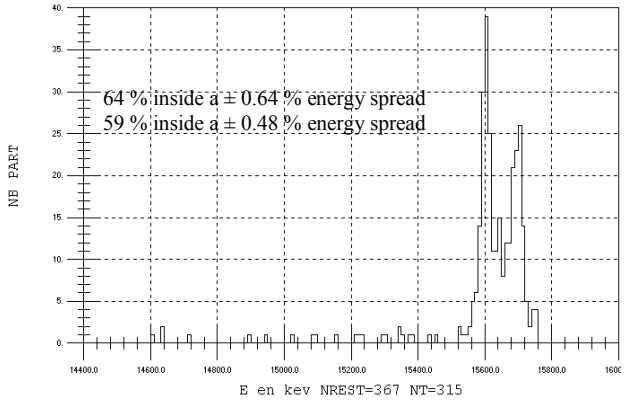

Figure 1: Energy histogram at the buncher exit for the 120 mA mode.

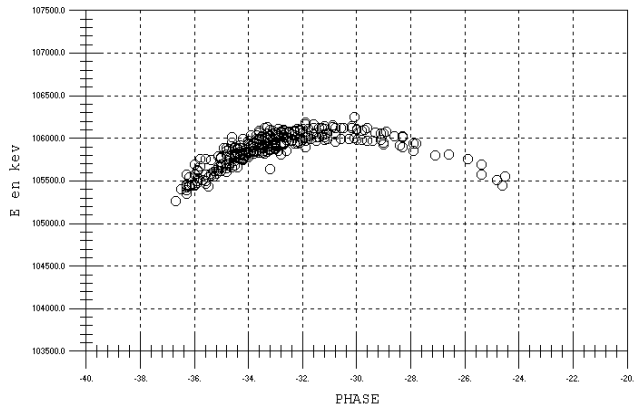

Figure 2: Phase-energy diagram at the linac exit for the 120 mA mode.

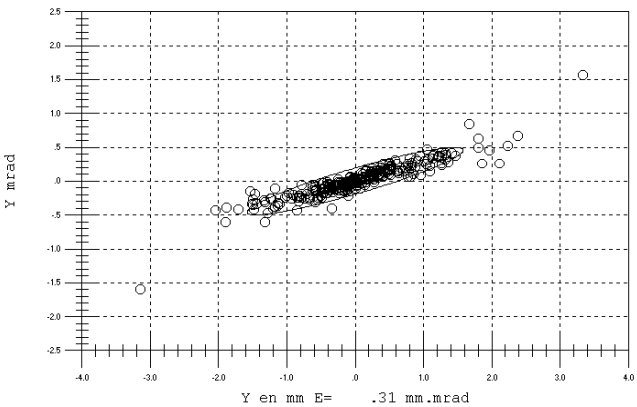

Figure 3: Emittance at the linac end for the 120 mA mode.

Copyright © 2012 by the respective authors — cc Creative Commons Attribution 3.0 (CC BY 3.0)

BEAM LOADING COMPENSATION

Generally, the first electrons of a long pulse have the greatest energy gain while crossing an accelerating section as the stored energy left for the last electrons is reduced. This is what we call the beam loading effect.

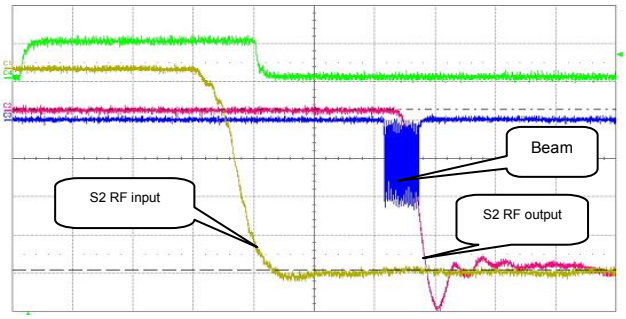

Figure 4: Beam loading compensation

The beam loading compensation is achieved by sending the beam during the filling time of the second accelerating structure. In fact, the first electrons cross the last part of the section without the nominal stored energy in it. The last electrons cross a full stored energy section. In certain conditions of power, charge and pulse length, the beam loading effect can be considerably reduced [3].

Fig. 4 shows the RF input and output signals of the second section of SOLEIL together with the beam pulse.

Fig. 5 shows, for SOLEIL, the 2 measured curves without and with beam loading compensation. The FWHM energy spread has been reduced from 3.75 MeV to 0.77 MeV for the 9.3 nC behind the slit.

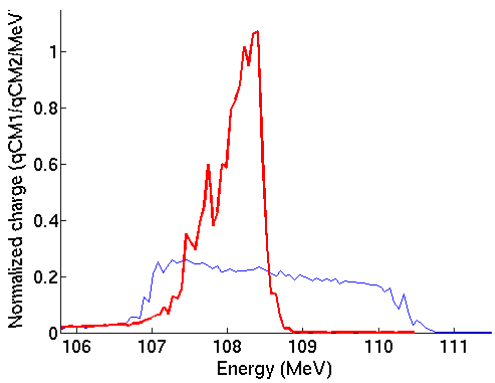

Figure 5: Energy spread for both cases

SIMULATIONS AND MEASUREMENTS

For ALBA, measurements of the beam at 70 MeV were done with and without the prebunching cavities for the Multi Bunch Mode [4]. The measured values met the simulated ones. The results are summarized in table 1.

Table 1: Simulations and measurements (%)

	Buncher exit		AS1 exit	
Beam mode	Simul.	Meas.	Simul.	Meas.
0.5 & 3 GHz	98	96	68	66
3 GHz	84	83	67	58*
0.5 GHz	77-87**	80	47	47
No cavities	59***	64	-	37

* Measurement was done without the phase adjustment of the 3 GHZ prebuncher.
** Simulations show oscillations of some electrons being apart from the main bunch. The main bunch and the first satellite, being 333 picoseconds apart, contain 77% and 5% of the gun current.
*** Simulation has been done without space charge and without magnetic field.

The 500 MHz prebunching cavity allows for only one pulse at 3 GHz, instead of three, from the 1 ns pulse. The energy spread is then reduced. Table 2 gives the summarized results at 70 MeV.

Table 2: Charge and energy spread measurements

	BCM1(nC)	ΔE/E%
Without cavities	0.25	0.6
500 MHz	0.30	0.6
3 GHz	0.45	**0.9**
500 MHz & 3 GHz	0.55	0.6

CONCLUSION

In the last decade, turnkey linacs were manufactured by Thales Communications and Security in order to inject electrons into boosters of SOLEIL, ALBA and BESSY II [5] synchrotrons. The measured linacs parameters fitted well with the beam dynamic simulations.

Our in house codes, SECTION for the design of the travelling wave accelerating structures and the beam loading compensation with PRODYN for the beam dynamics simulations, helped us to obtain those performances.

REFERENCES

[1] D. Tronc and A. Setty, Electrons RF auto-focusing and capture in bunchers, Linear Accelerator Conference 1988, Virginia.
[2] W. B. Herrmannsfeldt, EGUN An electron optics and gun design program, SLAC report 331, 1988.
[3] A. Setty et al., "Commissioning of the 100 MeV preinjector HELIOS for the SOLEIL synchrotron", EPAC06, Scotland, Edinburgh, June 2006.
[4] A. Setty et al., "Commissioning of the 100 MeV preinjector for the ALBA synchrotron", PAC09, Canada, Vancouver, May 2009.
[5] T. Atkinson et al., "Commissioning of the 50 MeV preinjector linac for the BESSY II facility", IPAC11, Spain, San Sebastian, September 2011.

Copyright © 2012 by the respective authors — cc Creative Commons Attribution 3.0 (CC BY 3.0)

STATUS OF THE BEAM DYNAMICS CODE DYNAC*

E. Tanke, W. Ding, J.A. Rodriguez, W. Wittmer, X. Wu, FRIB, East Lansing, MI 48824, USA
S. Valero, Consultant, retired from CEA-Saclay, Paris, France

Abstract

The efficacy of using the beam dynamics code DYNAC [1] as an online beam simulation tool for the Facility for Rare Isotope Beams (FRIB) [2] and its concomitant Reaccelerator (ReA) is discussed. DYNAC was originally developed at CERN, where a set of accurate quasi-Liouvillian beam dynamics equations was introduced for accelerating elements, applicable to protons, heavy ions and non-relativistic electrons.

A numerical method has been added, capable of simulating a multi-charge state ion beam in accelerating elements (i.e. cavities). Beam line devices such as sextupoles, quadrupole-sextupoles as well as electrostatic devices are now also included. Capability of second order calculations for a multi-charge state beam has been implemented. A Radio Frequency Quadrupole (RFQ) model has been added and a preliminary comparison of beam simulation results with beam measurements on the ReA RFQ is reported. Benchmarking of the code for a multi-charge state beam is discussed. The three space charge routines contained in DYNAC, including a 3D version [3], have remained unchanged.

MAGNETIC DIPOLE WITH GRADIENT

The capability of simulating a multi-charge state beam in a magnetic dipole has been added to DYNAC using a computationally efficient matrix formalism. The FRIB Front End (FE) contains two Electron Cyclotron Resonance (ECR) sources, followed by a source and charge state selection line using magnetic dipoles (see Fig. 1).

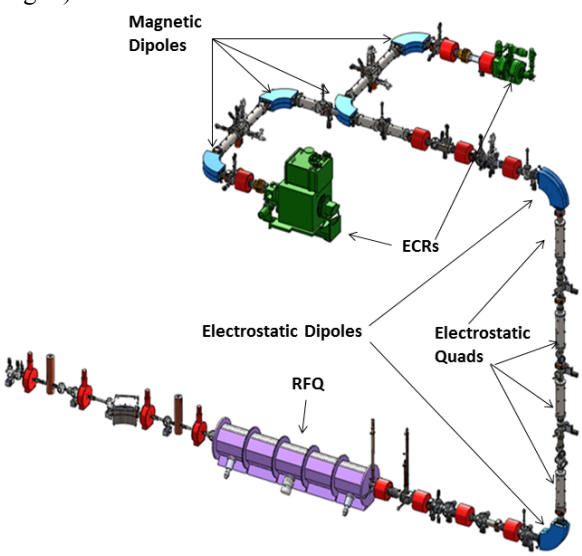

Figure 1: FRIB FE layout.

The DYNAC hard edge model for this dipole, which has an effective field length of 1 m, has been benchmarked against TRACK [4], which used a 3-D representation of the 1.7 m long field. This dipole has a field gradient of about 0.93. The output distributions are shown in Fig. 2 for a 12 keV/u uranium beam with charge states 33+ and 34+. Table 1 shows numerical results based on 4k macro-particles. The differences in the vertical phase plane are smaller than in the horizontal one.

Table 1: DYNAC and TRACK Horizontal Emittance Data for a Multi-Charge State Beam Tracked Through a FE Dipole

Parameter	U^{33+}	U^{34+}
α_x,DYNAC	0.431	0.360
α_x,TRACK	0.465	0.440
β_x,DYNAC	2.586	2.695
β_x,TRACK	2.605	2.551
ε_x,DYNAC	54.03	53.72
ε_x,TRACK	54.28	53.94

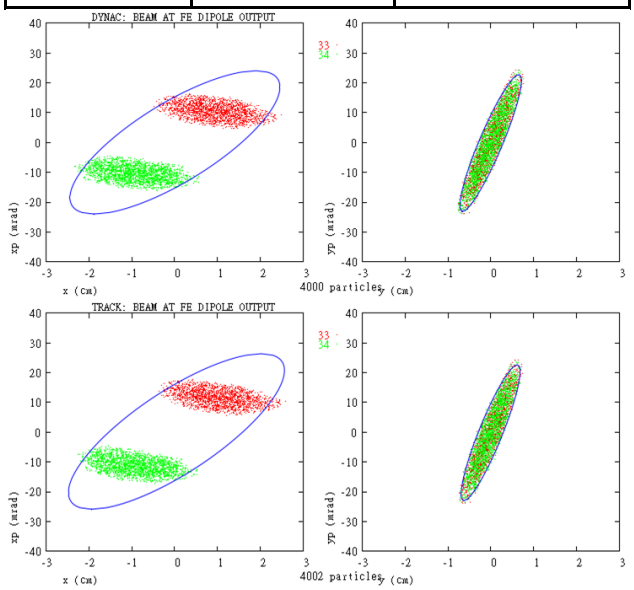

Figure 2: Horizontal emittances (left) and vertical (right) for DYNAC (top) and TRACK (bottom) for a multi-charge state beam tracked through the FE charge selection dipole.

ELECTROSTATIC QUADRUPOLES

To benchmark the electrostatic quadrupole model, a two charge state output beam from the FE charge selection dipole was simulated in a lattice containing six electrostatic quadrupoles. In DYNAC a 20 cm effective length hard edge model was used, whereas TRACK used a 3-D representation of a 30 cm long field. Again, there is good agreement between the two codes (see Table 2).

*This is based upon work supported by the U.S. Department of Energy Office of Science under Cooperative Agreement DE-SC0000661

Copyright © 2012 by the respective authors — cc Creative Commons Attribution 3.0 (CC BY 3.0)

Table 2: DYNAC and TRACK Horizontal Emittance Data for the Electrostatic Quadrupole Benchmark

Parameter	U^{33+}	U^{34+}
α_x,DYNAC	1.762	1.724
α_x,TRACK	1.759	1.679
β_x,DYNAC	5.638	5.500
β_x,TRACK	5.676	5.494
ε_x,DYNAC	54.27	53.96
ε_x,TRACK	54.50	54.12

ACCELERATING CAVITIES

The analytical method in DYNAC for simulating accelerating elements cannot be used for multi-charge state beams. A numerical method has been added to DYNAC, capable of simulating a multi-charge state ion beam in accelerating elements (i.e. cavities). This routine has been benchmarked against the simulation code IMPACT [5]. For this comparison, the case of a uranium beam with charge states 33+ and 34+ passing through the 100 accelerating cavities of the FRIB Linac Segment 1 (LS1) was taken. The FRIB superconducting (SC) driver linac is of a compact design (see Figure 3). The FE delivers a 500 keV/u beam to LS1, which consists of 3 cryomodules with 4 SC β=0.041 cavities each followed by 11 cryomodules with 8 SC β=0.085 cavities each, taking the beam to 16.6 MeV/u. Transverse focusing is achieved with SC solenoids, which are mounted inside the cryomodules.

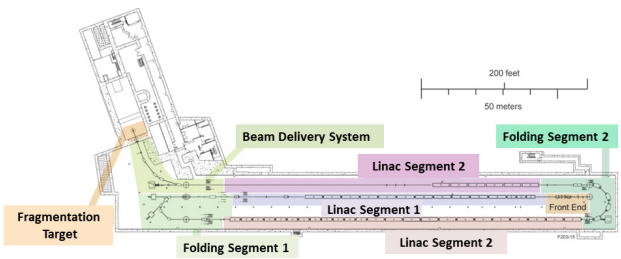

Figure 3: FRIB driver linac layout.

For the DYNAC/IMPACT comparison, the macro-particles were tracked from the FE output through LS1 to the charge stripper in the following Folding Segment 1 (FS1) including a chicane consisting of 4 dipoles with a 5° bend each and 2 matching cryomodules.

Table 3: Emittance Data at the FRIB Charge Stripper Input

	U^{33+}			U^{34+}		
	H	V	L	H	V	L
α_{DYNAC}	0.016	-0.029	0.844	-0.379	-0.095	0.056
α_{IMPACT}	-0.008	0.051	0.813	-0.277	0.012	0.082
β_{DYNAC}	0.396	0.378	1.6E-4	0.248	0.243	2.5E-4
β_{IMPACT}	0.429	0.422	1.6E-4	0.261	0.279	2.6E-4
ε_{DYNAC}	2.284	2.279	2181.1	2.333	2.360	2944.7
ε_{IMPACT}	2.287	2.283	1965.8	2.316	2.348	2580.1

Table 3 shows emittance data for the transverse (H, V) planes (units are mm/mrad (Twiss β) and mm.mrad (ε)) and longitudinal plane (units are deg/keV (Twiss β) and keV.deg (ε)) for each of the two charge states based on simulations with about 20k macro-particles.

Good agreement between the two codes was obtained, except for the longitudinal emittance, which is about 10 to 12 % smaller with IMPACT than with DYNAC for 33+ and 34+ respectively. The corresponding phase space plots are shown in Figure 4. Changing the number of steps (i.e. step size along the z-axis) in either the DYNAC or IMPACT numerical routine can decrease these differences, though they are within the accuracy of longitudinal emittance measurements.

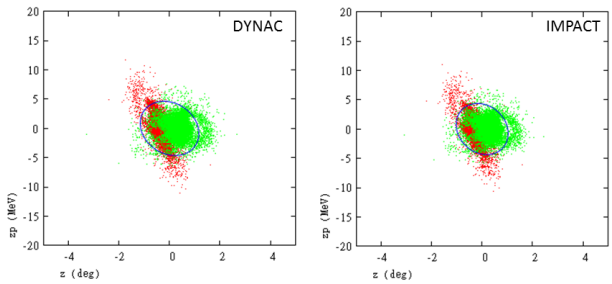

Figure 4: Longitudinal phase space plots for DYNAC (left) and IMPACT (right) at the charge stripper input for U33+ (red) and U34+ (green).

Table 4 shows the output energy for each of the two charge states. The difference on the energy gain through LS1 is less than 0.02%.

Table 4: Beam Energy at the FRIB Charge Stripper Input

	U^{33+}	U^{34+}	Unit
DYNAC	16.7187	16.7197	MeV/u
IMPACT	16.7216	16.7234	MeV/u

QUADRUPOLE-SEXTUPOLE MAGNET

For the purpose of benchmarking combined function quadrupole-sextupole magnets, the transport of a 5 charge state uranium beam from the charge stripper in FS1 to the Linac Segment 2 input (see Figure 3) was taken as this section contains four quadrupole-sextupole magnets. This section also contains two matching cryomodules and another chicane consisting of four dipoles with a 5° bend each as well as a bending section made up of four 45° dipoles. In this second order simulation, DYNAC results for about 20k macro-particles were compared to those obtained with IMPACT (see Table 5). Again, good agreement between the two can be observed.

RFQ

An RFQ model has been added to DYNAC, using as input the relevant parameters from the RFQ cell by cell data listed in a PARMTEQ output file. The case of a uranium beam with charge states 33+ and 34+ passing through an RFQ with an output energy of 500 keV/u was studied and compared with data obtained from RIAPMTQ [6]. The longitudinal emittances are within 12% and the transverse within less than 4%. The difference in output energy is about 0.4%. These differences are in part due to the lack of precision in the table of available external

Copyright © 2012 by the respective authors — cc Creative Commons Attribution 3.0 (CC BY 3.0)

Table 5: Emittance Data at the FRIB LS2 Input. The Units are as for Table 3

	U^{76+}			U^{77+}			U^{78+}			U^{79+}			U^{80+}		
	H	V	L	H	V	L	H	V	L	H	V	L	H	V	L
α_{DYNAC}	0.303	-0.132	-0.707	0.290	-0.108	-0.392	-0.009	-0.128	-0.136	-0.276	0.015	0.112	-0.211	0.361	0.330
α_{IMPACT}	0.207	-0.135	-0.694	0.218	-0.122	-0.386	-0.022	-0.137	-0.131	-0.242	0.015	0.121	-0.203	0.366	0.347
β_{DYNAC}	2.848	3.512	8.1E-5	2.253	2.556	6.5E-5	1.826	2.354	5.9E-5	2.249	2.239	5.9E-5	3.161	1.842	6.6E-5
β_{IMPACT}	2.568	3.453	7.9E-5	2.121	2.548	6.5E-5	1.826	2.377	5.9E-5	2.174	2.266	5.9E-5	2.980	1.857	6.6E-5
ε_{DYNAC}	2.379	2.501	17.32	2.476	2.418	16.84	2.514	2.457	16.60	2.522	2.439	16.81	2.548	2.473	16.52
ε_{IMPACT}	2.399	2.501	17.29	2.485	2.415	16.82	2.510	2.454	16.57	2.502	2.438	16.78	2.515	2.473	16.50

parameters used as input by DYNAC for this particular RFQ.

DYNAC beam simulations for the ReA RFQ have been made for a single charge state beam, accelerated from 12 to 600 keV/u. Preliminary results of transverse emittance measurements at the RFQ output are shown in Figure 5, as well as DYNAC beam simulation results for the nominal RFQ settings.

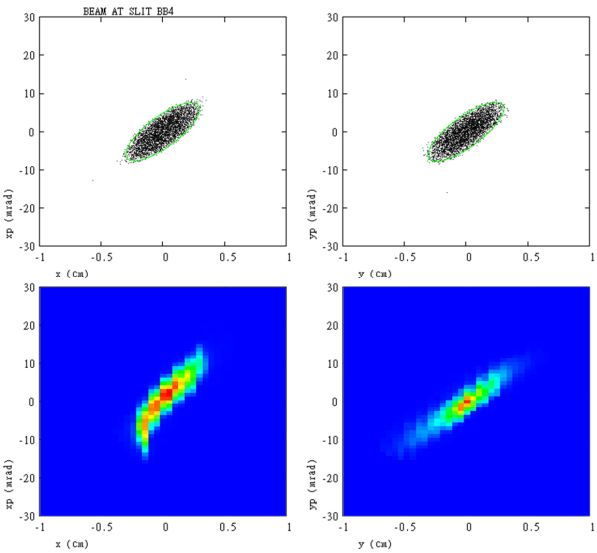

Figure 5: Preliminary results for the horizontal (left) and vertical (right) phase planes at the output of the ReA RFQ for DYNAC (top) and measurement (below).

About up to 10% emittance fluctuation has been observed in results from these measurements. Investigation in possible causes of the differences visible in Figure 5 is under way.

ONLINE MODEL

Online models are necessary for both commissioning and operations. Envelop (matrix) tracking, though computationally efficient, has limitations for treating multi-charge state, heavy ion beam dynamics. DYNAC does not have these limitations and is computationally efficient: simulating a 20k macro-particle two charge state beam through the 100 cavities in LS1 takes about 64 sec on a 2.93 GHz CPU with a 4 GB 1067 MHz RAM. Reducing to 1k macro-particles (see Figure 6) yields an execution time of about 3 sec, which is sufficiently low for online modelling. For a single charge state beam, the analytical model takes about 10.7 seconds for 20k macro-particles and about 0.7 seconds for 1k macro-particles.

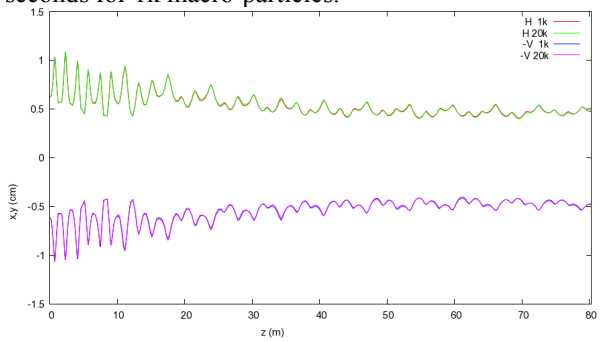

Figure 6: LS1 transverse beam envelopes for 1k and 20k macro-particles.

STATUS AND PLANS

It has been demonstrated that DYNAC is a good candidate for online modelling. Multi-charge state functionality has been added and benchmarked for the various new beam line elements. At ReA the code is used in commissioning. The charge stripper model is being refined, the analytical model for accelerating elements is under further development and a model for electrostatic dipoles is planned.

DYNAC and its graphics post-processor will work on Linux, MAC and MS Windows. The source code is available at http://dynac.web.cern.ch/dynac/dynac.html

REFERENCES

[1] E. Tanke et al, "DYNAC: A Multi-Particle Beam Dynamics Code for Leptons and Hadrons," LINAC02, Gyeongju, TH429, p. 667 (2002).

[2] J.Wei, "Status and challenge of FRIB project," this conference, Tel Aviv, September 2012, MOPCH31.

[3] E. Tanke et al, "HERSC: A New 3 Dimensional Space Charge Routine for High Intensity Bunched Beams," LINAC02, Gyeongju, TH424, p. 658 (2002).

[4] P.N. Ostroumov and K.W. Shepard. Phys. Rev. ST. Accel.Beams 11, 030101 (2001).

[5] J. Qiang, R. D. Ryne, S. Habib, and V. Decyk, J. Comput.Phys. 163 (2000) 434.

[6] T. P. Wangler, et al., "RIAPMTQ/IMPACT: Beam Dynamics Simulation Tool for RIA", LINAC06, Knoxville, TUP079, p. 441 (2006).

Copyright © 2012 by the respective authors — cc Creative Commons Attribution 3.0 (CC BY 3.0)

PHOTOINJECTOR SRF CAVITY DEVELOPMENT FOR B*ERL*inPro *

A. Neumann†, W. Anders, T. Kamps,
J. Knobloch - Helmholtz-Zentrum Berlin, Berlin, Germany
E. Zaplatin - FZJ Jülich, Jülich, Germany

Abstract

In 2010 HZB has received approval to build B*ERL*inPro , an ERL project to demonstrate energy recovery at 100 mA beam current by pertaining a high quality beam. These goals place stringent requirements on the SRF cavity for the photoinjector which has to deliver a small emittance 100 mA beam with at least 1.8 MeV kinetic energy while limited by fundamental power coupler performance to about 230 kW forward power. In oder to achieve these goals the injector cavity is being developed in a three stage approach. The current design studies focus on implementing a normal conducting cathode insert into a newly developed superconducting photoinjector cavity. In this paper the fundamental RF design calculations concerning cell shape for optimized beam dynamics as well as SRF performance will be presented. Further studies concentrate on HOM properties, the field-flatness and tuning mechanism for that design.

REQUIREMENTS TO THE CAVITY DESIGN

The B*ERL*inPro ERL will be a prototype facility demonstrating energy recovery with a 100 mA beam at 50 MeV beam energy while preserving a normalized emittance of better than 1 mm mrad at a pulse length of 2 ps or less [1]. This machine will make fully use of superconducting RF technology operated in continuous wave (CW). The injector has to deliver a high brightness beam at a high repetition rate, filling every RF bucket, a low emittance allowing for emittance compensation and a compression of the longitudinal phase space in the ps regime. At this high average current also higher order mode excitation and damping have to be considered as well as coupling strongly to the fundamental. The high beam brightness will be achieved by inserting a high quantum efficiency normal conducting semi-conductor cathode within the SC environment of the cavity. This cathode insert will mainly rely on the design by HZDR used in the ELBE SC 3.5 cell injector cavity [2]. As these are demanding goals, the injector and cavity are developed in a three stage approach. First results of an all superconducting gun cavity with a SC lead cathode were published in [5][6].

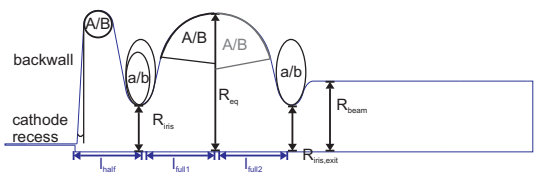

Figure 1: Geometry design parameters used for the cavity optimization scheme.

RF DESIGN STUDIES

The gun cavity has to fulfill several objectives while limited by some fundamental boundary conditions. The available total power will be limited to about 230 kW by using two KEK-style [3] fundamental power couplers (FPC), whereas the maximum electric peak field E_{peak} was recently demonstrated to reach 45 MV/m [4]. To name a few, regarding SRF and beam based properties the injector cavity has to be designed regarding the following aspects:

- Minimize E_{peak}/E_0 with $E_{\text{cathode}} < E_0$: This maximizes the field during beam extraction $E_{\text{launch}} = E_{\text{cathode}} \cdot \sin\Phi$ compared to the field anywhere on the surface E_{peak}, while it might be helpful to have the maximum on-axis field E_0 away from the cathode to reduce the probability of dark current.
- Minimize $H_{\text{peak}}/E_{\text{peak}}$ and maximize R/Q to minimize losses. Consider the cutoff of the beam tube and iris diameter for a compromise between R/Q and HOM propagation and cell-to-cell coupling.
- The resonators length determines the launch phase Φ and field level during emission and thus energy gain and emittance. Thereby it also defines the field level for the field emitted dark current at about $\Phi = 90 \pm 20$ degrees.
- Transverse beam properties are influenced by the field during emission (>10 MV/m [7]) as by the transverse focussing due to e.g. retraction of the cathode, backwall inclination and the transverse field component when the bunch leaves the RF structure.

Figure 1 shows the geometric parameters used in this work to run different optimization steps to converge to a suitable design. The design iteration was done by implementing different optimization schemes, like golden section search and Nead-Melder Simplex algorithms within a MATLAB™ wrapper to run the 2-D RF field solver Superfish [8]. The obtained fields were used in the same loop to perform a first field-phase scan of the longitudinal phase space using a simple self written tracking code. Following, a set of candidates were included in ASTRA-based [9] beam dynamics simulations including the solenoid or the whole injector

* Work supported by Bundesministerium für Bildung und Forschung and Land Berlin
† Axel.Neumann@helmholtz-berlin.de

Copyright © 2012 by the respective authors — cc Creative Commons Attribution 3.0 (CC BY 3.0)

chain of B*ERL*inPro . The outcome of these calculations delivered the feedback for further changes to the cavity's geometry.

Half-cell optimization

In a first iteration the half-cell was optimized to maximize the launch phase via a scan of the half cell's length taking transit time effects into account. Figure 2 shows the launch phase for maximum energy gain for half-cells varying from 0.4-0.6 $\lambda/2$. The 0.4 cell design shows the best performance with respect to launch phase, as all of them after fine tuning achieved comparable RF properties. Going to even shorter half-cells was omitted due to mechanical stability and peak field considerations. As can be seen in Table 1 the resultant E_{launch} of a pure 0.4 design is still rather low. Hence another full cell, starting from a TESLA shape, was added to the design. As can be seen in the energy-field-phase scan presented in Figure 3, a 1.4 cell design features a quite high launch field making full use of the offered 230 kW at $E_0 = 30$ MV/m. The corresponding field distribution is shown in Figure 4. A 1.X cell design has the further advantage, that the dark current emitted at field maximum on the cathode still can propagate out of the cavity which limits the danger of back bombardment.

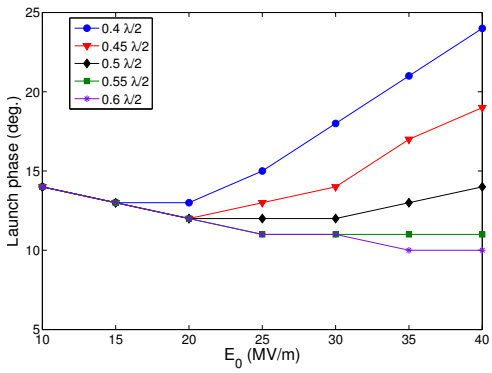

Figure 2: Energy-phase-field scan vs. half-cell length showing the phase with the highest energy gain in the half-cell.

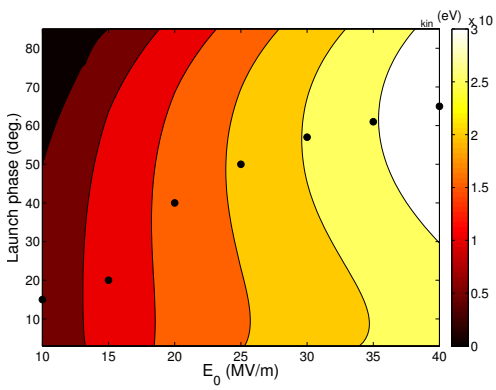

Figure 3: Energy-phase-field scan of a 1.4 cell cavity. The black dots denote the phase with the maximum energy gain at the given maximum on-axis field E_0.

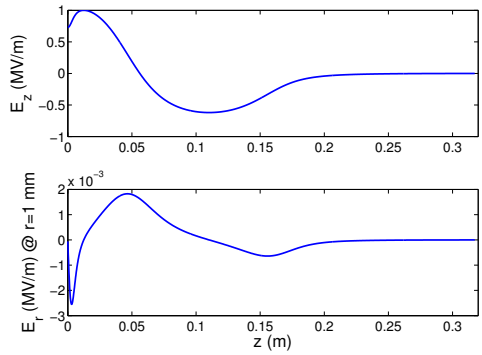

Figure 4: Field distribution (E_z, E_r) of a 1.4 cell gun cavity design with 35 mm exit iris and 53 mm beam tube radius.

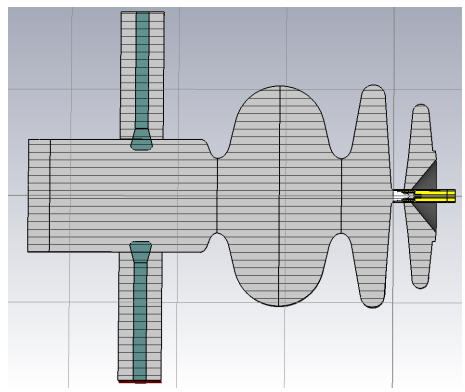

Figure 5: Possible design of the next 1.4 cell gun cavity featuring the HZDR-style choke cell, a modified cathode stock, two TTF-III type FPC having a 35 mm exit iris.

Figure 5 shows the current design for the next gun cavity which should demonstrate a beam of some mA using two modified TTF-III FPCs [10]. This cavity will mainly be used to study the cathode insert mechanism within the SC environment, beam dynamics and the HOM properties.

CELL TUNING

Preliminary investigations of the cell mechanical properties (the structure without helium vessel and any stiffening rings) showed that by simultaneous tuning of both cells E_z along the beam path varies within 2%. At the same time because of the cell deformations under external LHe pressure the field profile in the 0.4-cell changes up to 10%. With an installation of stiffening rings there are possibilities to find ring positions that the total effect of external pressure applied on the whole cavity and liquid helium vessel walls results in nearly complete compensation of the frequency shifts caused by cavity and vessel wall deformations (df/dp is close to zero, Figure 6). For df/dp=0 the field profile change is within 5%, being near the accuracy limit of that calculation.

Copyright © 2012 by the respective authors — cc Creative Commons Attribution 3.0 (CC BY 3.0)

Table 1: Cavity figures of merit for the TM_{010}-π mode of three gun cavity options at E_0= 30 MV/m and cathode retracted by 1.5mm. Note, that Q_{ext} relates to the limit in total forward power of 230 kW. All values are for β =1 as calculated by Superfish.

Parameter	0.4 cell	1.4 cell 35 mm exit iris	1.4 cell 40 mm exit iris
$R/Q(\Omega)$	93	151	146
E_{peak}/E_0	1.5	1.5	1.57
$E_{cathode}/E_0$	0.75	0.75	0.75
H_{peak}/E_{peak} (mT/(MV/m))	1.9	2.2	2.1
$\Phi_{launch}(E_{kin,max})$ (deg.)	18	52	50
E_{launch} (MV/m)	6.9	17.7	17.3
E_{kin} (MeV)	1.2	2.67	2.6
k_{cc} (%)	-	1.6	1.5
Q_{ext} at 100 mA	$1.44 \cdot 10^5$	$1.52 \cdot 10^5$	$1.58 \cdot 10^5$

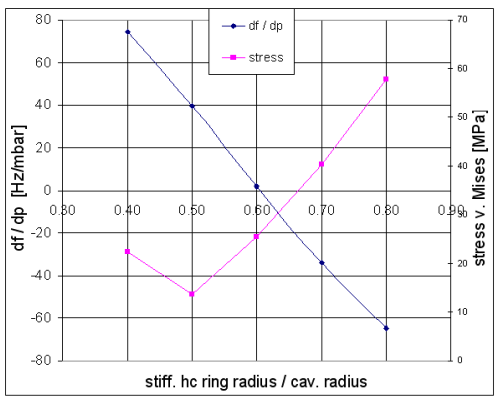

Figure 6: Detuning vs. LHe pressure coefficient and v. Mises stress versus position of a stiffening ring for the 1.4 cell design.

OUTLOOK

The current design work focusses on studying 3-D aspects using CST MWS [11] of the gun cavity design including optimizing the FPC's position and beam tube size for a minimized coupler kick by the fundamental to the beam while preserving the HOM damping capabilities. Further studies aim for calculation of the HOM losses and damping, especially taking the $\beta(z,t)$ dependent loss factor into account as depicted in Table 2. Beam dynamics based tolerance studies have to show how susceptible the beam properties are with respect to field flatness variations with respect to cavity tuning to decide whether two independent tuners for each cell are needed.

ACKNOWLEDGEMENTS

The authors acknowledge the fruitful discussions with J. Sekutowicz (DESY), J. Teichert and A. Arnold (both HZDR).

Table 2: Launch field dependent $R/Q(\Omega)$ of the TM monopole modes

f (MHz)	$R/Q_{\parallel}$ ($\beta = 1$)	$R/Q_{\parallel}$ E_0=16MV/m	$R/Q_{\parallel}$ E_0=30MV/m
1270	59	4.9	0.51
1300	150	125	147
2403	16.1	3.0	14.8
2510	49	24.9	20.8
2663	36.8	3.5	0.9
2750	28.6	3.5	0.04

REFERENCES

[1] J. Knobloch et al., ICFA Beam Dynamics Newsletters, No.58, p. 118, August 2012, http://www-bd.fnal.gov/icfabd/Newsletter58.pdf.

[2] A. Arnold et al., Nuclear Instruments and Methods in Physics Research Section A, Volume 593, Issues 12, 1 August 2008, Pages 57-62, DOI 10.1016/j.nima.2008.04.035.

[3] S. Noguchi et al., IPAC'10, Kyoto, 2010, WEPEC024, p. 2944, http://www.JACoW.org.

[4] P. Kneisel et al., PAC'10, New York, 2010, TUP109, p. 1047, http://www.JACoW.org.

[5] A. Neumann et al., IPAC'11, San-Sebstian, September 2011, MOODA03, p. 41, http://www.JACoW.org

[6] T. Kamps et al., IPAC'11, San-Sebstian, September 2011, THPC109, p. 3143, http://www.JACoW.org

[7] T. Kamps et al., LINAC'12, Tel Aviv, September 2012, THPB069, these proceedings.

[8] K. Halbach and R.F. Holsinger, SUPERFISH - a computer program for evaluation of RF cavities with cylindrical symmetry, Part. Acc., 7:213222, 1976

[9] K. Flöttmann, A Space Charge Tracking Algorithm (ASTRA), http://www.desy.de/~mpyflo/.

[10] O. Kugeler et al., SRF'09, Berlin, Germany, September 2009, THPPO046, p. 683, http://www.JACoW.org

[11] Computer Simulation Technology AG, Microwave Studio®, 64289 Darmstadt, Germany http://www.cst.com

Copyright © 2012 by the respective authors — cc Creative Commons Attribution 3.0 (CC BY 3.0)

FIRST OBSERVATION OF PHOTOEMISSION ENHANCEMENT FROM COPPER CATHODE ILLUMINATED BY Z-POLARIZED LASER PULSE

H. Tomizawa, H. Dewa, A. Mizuno, and T. Taniuchi
Japan Synchrotron Radiation Research Institute (JASRI/SPring-8)
Kouto, Sayo-cho, Sayo-gun, Hyogo 679-5198, Japan

Abstract

Since 2006, we have been developing a novel photocathode gun gated by the laser-induced Schottky-effect. This new type of gun utilizes laser coherency to aim at a compact femtosecond laser oscillator as an IR laser source using Z-polarization on a metal photocathode. This Z-polarization scheme reduces the laser photon energy to excite the cathode with a longer wavelength by reducing its work function due to the Schottky effect. Before this epoch-making scheme emerged, photocathode guns had never utilized a laser's coherency itself. We applied a hollow laser incidence scheme with a hollow convex lens that is focused after passing the beam through a radial polarizer. Based on our calculations (convex lens: NA=0.15; 60% hollow ratio), a Z-field of 1 GV/m needs 1.26 MW at peak power for the fundamental wavelength (792 nm) of a Ti: Sapphire laser. To confirm photoemission enhancement effects due to a Z-field of a few GV/m compared with copper's conventional photoemission, we used third harmonic generation (THG: 264 nm) as a pilot experiment and generated a Bessel beam with a hollow axicon lens in a vacuum to relax the phase matching condition of the wavefront on the cathode's focus point. We observed the first Z-field emission enhancement with a copper cathode at THG (264 nm). The enhancement factor was 1.4 times at 1.6 GV/m of the averaged Z-field of the central laser spot (Bessel beam) on the cathode surface.

INTRODUCTION

A conventional photocathode RF gun needs a UV-laser source (~260 nm) for robust cathodes like metal copper due to their high work functions that exceed 4 eV. Consequently, the laser system becomes larger and more complex. To make the laser source compact and simple, we need a cathode with a lower work function and high QE. However, such a high QE Negative Electron Affinity (NEA) cathode requires an ultra-high vacuum (< 10^{-8}Pa) and does not have a long lifetime in an RF gun.

One solution to reducing the work function is to apply a high field on the cathode surface. In a field of 1~2 GV/m, the copper cathode's work function is reduced by ~2 eV. To achieve such a high field (~1 GV/m) on the photocathode, a tungsten needle (radius: ~1 μm) photocathode with photo-assisted field-emission was tested [1]. The obtained QE of the needle tip was found to be proportional to the >10th power of the electric field over 500 MV/m and reached 3% of QE at about 800 MV/m. This observed field enhancement of QE is qualitatively explained with a field-emission process that includes the Schottky effect, the tunneling effect, and photoexcitation. However, such a needle cathode tip becomes round and broken in the gun cavity during RF conditioning. The dark current is also very large due to a 100-times longer half-cycle of RF than the pulse duration of the illuminating laser.

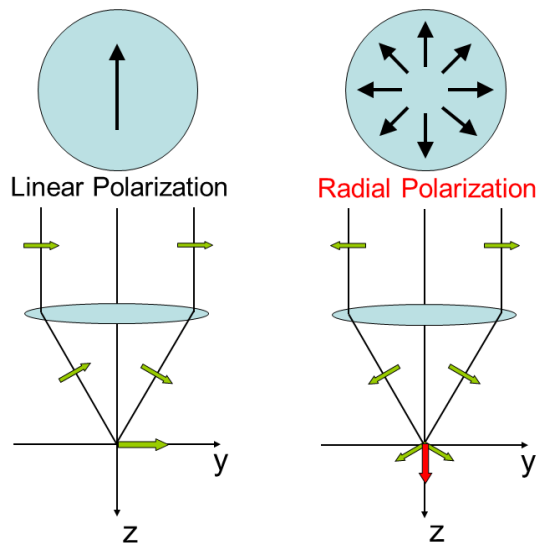

Figure 1: Principle of Z-polarization field on cathode surface generated from radial polarization

Therefore, we started to investigate with a plane-field emitter gated by a laser radiation field by exploiting recent progress in optical technologies to generate radially polarized laser modes. The fundamental mode of radial or azimuthal polarization is the superposition of TEM_{01} and TEM_{10} modes as orthogonal linear polarizations. By focusing a radially polarized laser beam on the photocathode (Fig. 1), the laser's electric field is generated in the laser propagating direction (Z-direction) at the focus point. The generated Z-polarized laser field (Z-field) easily exceeds an electrical field of 1 GV/m with fundamental wavelength from compact femtosecond laser systems. On the other hand, focusing an azimuthally polarized beam on the photocathode results in the zero Z-fields. Comparing the radial and azimuthal polarizations by focusing on metal cathodes, we conducted a feasibility study of Z-field effects on the photocathode [2]. This is also a fundamental study of

Copyright © 2012 by the respective authors — cc Creative Commons Attribution 3.0 (CC BY 3.0)

cathode response and emission mechanisms with a cylindrical vector beam in the femtosecond region.

In our first test run, we focused a radially polarized hollow laser with a hollow convex spherical lens in a vacuum to enhance the electron emission. After comparing the radial and azimuthal polarizations by focusing, we could not observe any significant enhancement differences of electron emission [3]. In our second test run, we prepared a hollow axicon lens that was especially designed to tolerate the constructive phase condition of the wavefront to generate a Z-field in the depth of focus on the cathode. We report the first observation and analysis of the emission enhancements due to the laser Z-field effects on the copper photocathodes by varying from radial to azimuthal polarizations of the incident laser pulses.

PRINCIPLE OF Z-POLARIZATION GUN

Principle of Z-polarization Generation

If the Schottky or tunnelling effect due to the Z-field is dominated, we expect that electrons will emit from the outermost surface of the metal cathode and be extracted with the external electric field of the RF cavity.

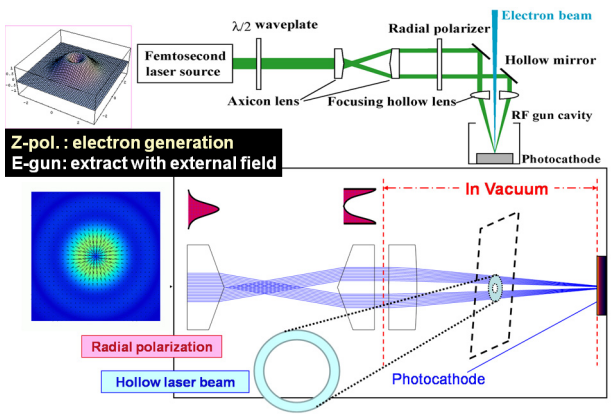

Figure 2: Schematic drawing of Z-polarization gun with novel laser illumination system of hollow laser beam incidence

To effectively utilize Z-polarization, we must develop special hollow optics. A schematic drawing of a Z-polarization gun with the optical systems of hollow laser beam incidence [2] is shown in Fig. 2. The original hollow incidence scheme was designed with a hollow spherical convex lens in a vacuum that focuses the laser pulse that passed through a radial polarizer. The Z-field is proportional to the square of the numerical aperture (NA). To make NA as large as possible, we designed a final focusing lens in a vacuum and a hollow laser beam generator with an axicon lens pair that transforms the Gaussian profile (intensity distribution) from the inside out (anti-Gaussian profile).

UV Radial Polarization Converter for Big Hollow Laser Beam

The radial polarization fundamental mode is generated from a combination of Hermite-Gaussian (HG) modes TEM_{01} and TEM_{10} [4]. Therefore, we chose a simple divided waveplate (see details in ref. [3]) to generate radial polarization from a conventional linearly polarized beam.

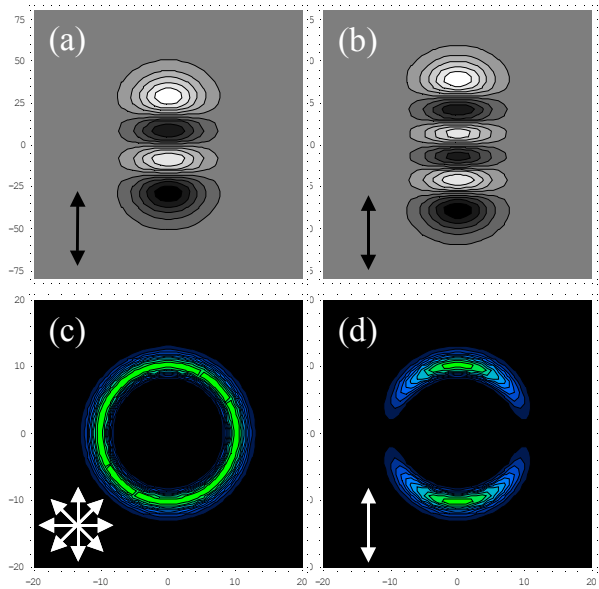

Figure 3: Electric field distribution of Hermite-Gaussian (HG) beam: (a) TEM_{03} and (b) TEM_{05}. Intensity distribution of radially polarized hollow beam expressed by superposition of higher order modes of HG (c), and its vertically polarized component (d). Arrows indicate polarization orientation.

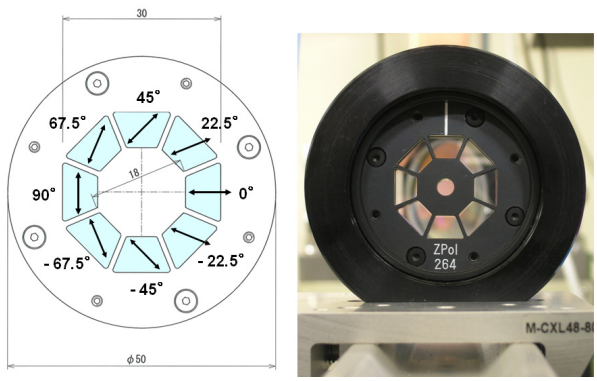

Figure 4: Eight-segment zero-order half waveplate (designed for femtosecond laser incidence; optical-contact) for a hollow beam @ 264 nm: eight-segment waveplate for a hollow beam (right) and orientations of optical axes in each segment (left).

However, a higher order mode of radial polarization is required to make NA larger. For instance, a higher order mode of radially polarized hollow beam is generated

Copyright © 2012 by the respective authors — cc Creative Commons Attribution 3.0 (CC BY 3.0)

from a combination of higher HG modes: TEM_{03}, TEM_{30}, TEM_{05}, and TEM_{50} (Fig. 3). We designed an eight-segment half waveplate especially for a hollow beam (Fig. 4).

FEASIBILITY TEST OF Z-FIELD GUN

Experimental Concept and Setup

We performed experiments in a single-cell RF gun generated laser Z-field at the cathode. For this feasibility test, we chose a combination with a copper cathode illuminated by Ti:Sa THG (264 nm) to compare with the emission at the conventional photocathode RF gun with normal laser incidence. Switching from radial to azimuthal polarizations of incident laser pulse, we measured the difference of the bunch charge of photoemission with a Faraday cup downstream.

The hollow laser incidence with the axicon lens is shown in Fig. 5. It is more complicated than a spherical convex lens to focus at the cathode surface, because the focal length depends on the outer and inner diameters of the incident hollow laser beam. The hollow, copper lens protection ring restricts the inner diameter of the hollow laser beam whose outer diameter is 20 mm. On the other hand, the entrance of the RF gun works as an aperture with a 20-mm diameter to restrict the hollow laser beam's outer diameter. The distance between these two optical obstacles with the inner and outer permissible diameter of 20 mm defines the focal length of this laser incidence system. Due to our single cell RF gun cavity, the working distance between the gun's entrance and cathode is rather short: 88 mm. The hollow laser's outer diameter must be 26~27 mm. In this case, the focal length is between 114.4~118.8 mm. The NA of this final focusing system is around 0.11.

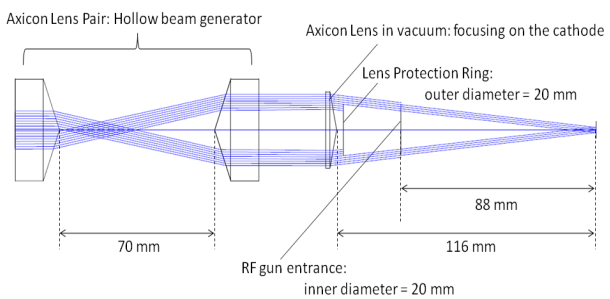

Figure 5: Optical configuration of Z-field RF gun with final focusing of axicon lens

Experimental Result

We focused a radially polarized THG on a copper cathode with an axicon lens (NA=0.11) to generate the Z-field. The maximum cathode surface of the RF gun field was 84 MV/m. We observed the first Z-field emission enhancement with a copper cathode at THG (264 nm) with a pulse duration of 100 fs (Fig. 6). The enhancement factor was 1.4 times at 1.6 GV/m of the Z-field of the averaged peak laser spot on the cathode surface (pulse energy: 25 μJ; central peak spot diameter: 30 μm). During polarization dependency measurements with switching from radial to azimuth, the dark currents were measured individually to observe whether breakdown occurred. We could not observe any significant increase of dark currents.

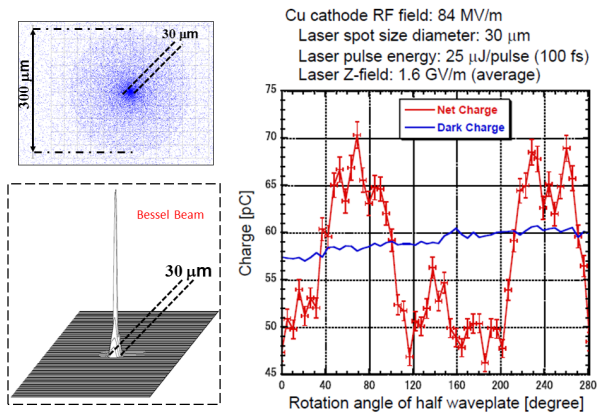

Figure 6: Experimental result of Z-field enhancement with final focusing by axicon lens, varying from radial to azimuthal polarizations of incident laser pulses.

SUMMARY AND DISCUSSION

We reported the first observation on Z-field enhancement in an RF gun cavity and demonstrated a feasible condition of the Z-polarization gun we proposed in 2006. Focusing radially polarized 100-fs THG pulses on the copper cathode with an axicon lens, we observed an enhancement factor of 1.4 at 1.6 GV/m of the Z-field on the cathode surface. This result clarifies the photoemission differences between a Z-field gun (Z-field: 1~2 GV/m) and the conventional photocathode gun with normal incidence (zero Z-field).

The net charge of the Z-field enhancement was 15 pC. As shown in Fig. 6, some significant spike strictures were observed. They can be the results of the Z-field phase mismatching among higher order transverse modes.

We expected the electrons to be mitted just from the outermost atomic layer within the cathode's central laser spot. Based on our calculation with the WKB approximation under the experimental condition, the effective reduction of work function was 1.4 eV.

Next, we are going to prepare backward illumination with half-cycle laser pulses (optical certification) in mid-IR to generate a Z-field on a spin-polarized photocathode without utilizing the NEA surface [2].

REFERENCES

[1] T. Inoue, et al., *JJAP*, **41**, 12, (2002) 7402.
[2] H. Tomizawa, et al., *Proc. of FEL 2007*, Novosibirsk, Russia (2007) 382.
[3] H. Tomizawa, et al., *Proc. of FEL 2010*, Malmo, Sweden (2010) 640.
[4] S. C. Tidwell, et al., *Applied Optics*, **29**, 15, (1990) 2234.

Copyright © 2012 by the respective authors — cc Creative Commons Attribution 3.0 (CC BY 3.0)

BEAM DYNAMICS STUDIES FOR SRF PHOTOINJECTORS*

T. Kamps†, A. Neumann, J. Voelker
Helmholtz-Zentrum Berlin, Germany

Abstract

The SRF photoinjector combines the advantages of photo-assisted production of high brightness, short electron pulses and high gradient, low-loss continuous wave (CW) operation of a superconducting radiofrequency (SRF) cavity. The paper discusses beam dynamics considerations for ERL class applications of SRF photoinjectors. One case of particular interest is the design of the SRF photoinjector for BERLinPro, an ERL test facility demanding a high brightness beam with an emittance better than 1 mm mrad at 77 pC and average current of 100 mA.

MOTIVATION

The primary goal of this study is to design an electron injector within the boundary conditions of B*ERL*inPro [1]. For B*ERL*inPro, the electron injector needs to deliver an electron beam with a normalized emittance of $\varepsilon_{\rm n} = 1$ mm mrad and average current of $I_{avg} = 100$ mA. The rms pulse length must be $\sigma_t \leq 7$ ps in order to reduce emittance growth in the merger, linac and recirculation loop of the ERL. In addition the injector design should be compatible with technical boundary conditions. These translate into rf forward power limits set up by the rf power source and rf input coupler technology of choice. In particular the gun forward power is limited to $P_{\rm fd} = 230$ kW by the rf input coupler.s The secondary goal is to develop guidelines and requirements for the microwave desgin of the SRF cavity.

PRELIMINARIES

The main building blocks for the electron injector of B*ERL*inPro are an SRF gun with drive laser, solenoid and booster section (see Fig. 1). The solenoid and SRF cavity are located in a gun cryomodule. The beam exits the cryomodule and is guided through a short warm section with laser input and diagnostics ports before it enters the booster cryomodule. In this study beam parameters are first evaluated after the gun section at the location of the first booster cavity and finally after the booster section, before the beam enters the merger section. All beam dynamics simulations for this study have been carried out with the ASTRA code [2].

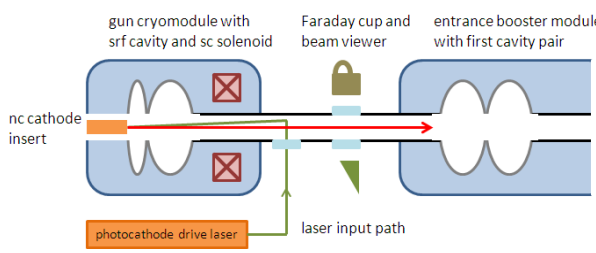

Figure 1: Schematic overview injector system with SRF gun and booster.

EMITTANCE CONTRIBUTIONS

The initial emittance for a beam from a photocathode RF gun is given by the product of initial spot size and the mean transverse energy distribution ($\mathrm{MTE} = (h\nu - \phi_{\rm eff})/3$) of the electron distribution after photoemission from the cathode with effective workfunction $\phi_{\rm eff}$ and single-photon energy $h\nu$ of the drive laser [3]. Low emittance requires a cathode material with a workfunction near the single-photon energy of the drive laser and small initial spot size. The lower limit for the initial spot size is given by the equilibrium between the forces of the image-charge and the accelerating field. This space-charge limited (scl) emission radius is a function of the ratio of bunch charge q_b and launch field E_l the bunch experiences during emission. The resulting thermal (or cathode) emittance and the lower limit for the emission spot size can be expressed by

$$\varepsilon_{\rm th} = \sigma_{\rm in}\sqrt{\frac{\mathrm{MTE}}{m_o c^2}} \quad \text{with} \quad \sigma_{\rm in}|_{\rm scl} = \sqrt{\frac{q_b}{4\pi\epsilon o E_l}} \qquad (1)$$

It is clear from Eq. (1) that a high launch field is required to achieve low thermal emittance for a given target bunch charge. The upper limit for the launch field is given by the cathode-to-peak field ratio (given by cavity design) and the achievable peak field in SRF gun cavity structures of $E_{pk} = 45$ MV/m [4]. For B*ERL*inPro we assume a drive laser running at $\lambda = 532$ nm illuminated a photocathode made of CsK_2Sb ($\phi_{\rm eff} = 1.9$ eV) resulting in a divergence term of $\sqrt{\mathrm{MTE}/m_o c^2} = 0.51$ mrad. The goal for the B*ERL*inPro injector is to deliver a projected emittance of $\varepsilon_{\rm proj} \leq 1$ mm mrad and slice emittance of $\varepsilon_{\rm slice} \leq 0.6$ mm mrad. To allow for some degradation due to non-linear processes, the target for the thermal emittance is $\varepsilon_{\rm th} = 0.3$ mm mrad. This can be achieved with initial spot size of $\sigma_{\rm in} = 0.6$ mm, resulting in a space-charge limited launch field of $E_l|_{\rm scl} = 5$ MV/m. The gun should be operated at least a factor of two away from this limit to allow for acceleration of the complete bunch including the tail particles. Therefore the launch field the cavity has to

* The work is supported by Bundesministerium für Bildung und Forschung and Land Berlin.
† kamps@helmholtz-berlin.de

Copyright © 2012 by the respective authors — cc Creative Commons Attribution 3.0 (CC BY 3.0)

supply is $E_l \geq 10$ MV/m. The ratio of launch-to-peak field in the cavity also wants to be high to reduce the propability of dark current production due to field emission.

The final state of the emittance is the result of a dynamic evolution under the influence of various forces. These forces can be electro-magnetic fields of the solenoid and SRF cavity as well as space-fields due to Coulomb repulsion. The normalized emittance at the injector exit can be summarized as the root-square sum of the individual contributions.

$$\varepsilon_n = \sqrt{\varepsilon_{\mathrm{th}}^2 + \varepsilon_{\mathrm{sol}}^2 + \varepsilon_{\mathrm{sc}}^2 + \varepsilon_{\mathrm{rf},\parallel}^2 + \varepsilon_{\mathrm{rf},\perp}^2} \qquad (2)$$

For now, we neglect the interaction between the beam and the cavity itself and due to higher-order modes and thus all transverse rf contributions to $\varepsilon_{\mathrm{rf},\perp}$. The contribution from space-charges forces $\varepsilon_{\mathrm{sc}}$ scales linearly with the peak beam current and therefore inversely with the laser pulse length. The contribution from longitudinal rf fields $\varepsilon_{\mathrm{rf},\parallel}$, mainly the slope and curvature of the accelerating field, scale quadrically or cubically with the pulse length. Consequently there exists an optimum pulse length at which the emittance is balanced between the two effects. Generally, the optimal pulse length is on the order of 10 degress of rf phase [5]. Projected emittance growth is caused by effects leading to mismatch of the motion in phase space of individual slices of the bunch. This type of emittance groth can be fixed by emittance compensation [6]. In this process, a solenoidal lens is used to remove linear correlations between the transverse and longitudinal phase space. Slice emittance growth, caused by non-linear space-charge forces or aberrations in optical elements, cannot be fixed by emittance compensation and needs to be suppressed by design of the gun cavity and the solenoid. The key is to start with a constant charge distriution, thus motivating complex longitudinal shaping of the drive laser pulse. Emittance growth caused by longitudinal rf effects can be mitigated by a proper field balance and by reduction of the initial pulse length.

Aberrations in the solenoid are a cause for slice emittance growth $\varepsilon_{\mathrm{sol}}$. Emittance growth by spherical aberrations scale quadratically with the transverse spot size. Hence we want to keep the transverse spot size in the solenoid small. This can be achieved by moving the solenoid closer to the SRF gun cavity and by focusing the beam during emission with radial electric field components of the accelerating field. This rf focusing is achieved by retracting the cathode out of the cavity backplane by a distance Δz_{cath}, usually by 1 to 3 mm [7]. By doing so, the electric field has a radial focussing component, which increases linearly in longitudinal direction and supplies the low energy electrons with initial focusing. Obviously this reduces the launch field and the launch-to-peak field ratio.

Conclusion for the cavity design

For the cavity design we can conclude from these considerations that the launch field during electron emission should be $E_l \geq 10$ MV/m with a high launch-to-peak field ratio and that the cathode should be retractable to achieve initial rf focusing.

SRF CAVITY OPTIONS

In this section we will evaluate several cavity options build and under considerations against the criteria setup in the previous section.

The purpose of the SRF gun cavity is to accelerate the electrons from almost zero energy to an energy as high as possible. An SRF gun cavity consits of a half cell with embedded cathode plus a varying number of full cells. Due to technical choices made in the design process, the average power delivered to the beam cannot exceed 230 kW [1]. At 100 mA beam current this means that the exit energy from the gun must be below 2.3 MeV. The launch field depends on the maximum field on axis E_{max}, the cathode-to-maximum field ratio G_{FF} and the launch phase according to $E_l = E_{max} \cdot G_{\mathrm{FF}} \cdot \sin\phi_l$. The maximum-to-peak field ratio is for all cavity designs under consideration $E_{pk}/E_{max} = 1.5$. Complementary studies focused on the RF properties indicate that a SRF gun cavity with a length of $1.n \cdot \lambda_{rf}/2$ with $0.4 < n < 0.6$ offers good performance with regard to field flatness and peak field on the metal surface [13]. In Table 1 launch fields and phases derived from simulations of phase scans are summarized for different design candidates. Listed are entries for the cavity employed at Gun0 [8, 9, 10] with 1.6cells, for the CDR baseline design [11] and three candidates for Gun1 (with 0.4 and 1.4cells [13]). Two entries for different values of cathode surface retraction Δz_{cath} are given for the 1.4cell design. The short cavities with 0.4 and 0.6 cells offer only low launch-to-peak field ratios togther with low absolute launch field levels. Therefore we will concentrate on a cavity design with 1.4 cells to study the effect of longitudinal laser pulse shaping.

Table 1: Cavity field parameters relevant for beam dynamics studies for 2 MeV target exit energy. See text for explanation of the parameters.

No.	Δz_{cath} mm	G_{FF}	E_{max} MV/m	ϕ_l degL	E_l MV/m
Gun0 1.6	0	0.99	21	27	9.4
CDR 0.6	-1.5	0.74	44	15	8.4
Gun1 0.4	-1.0	0.82	48	21	14.0
Gun1 1.4	-1.5	0.79	26	41	13.4
Gun1 1.4	-2.0	0.69	26	39	11.3

ADDING LONGITUDINAL LASER PULSE SHAPING

The beam quality from a photoemission electron gun is strongly dependent upon the transverse and longitudinal shape of the drive laser pulse. For lowest transverse

Copyright © 2012 by the respective authors — cc Creative Commons Attribution 3.0 (CC-BY-3.0)

emittance, the B*ERL*inPro baseline design requires a uniformly filled round transverse distribution and flat-top longitudinally. However since longitudinal laser pulse shaping is a technical challenge, it is important to study with simulations the effect of laser shaping on the transverse beam emittance. Fig. 2 shows the result of optimization runs leading to emittance compensation for Gaussian and Plateau shaped pulses at peak current of $I_{pk} = 5$ A. The

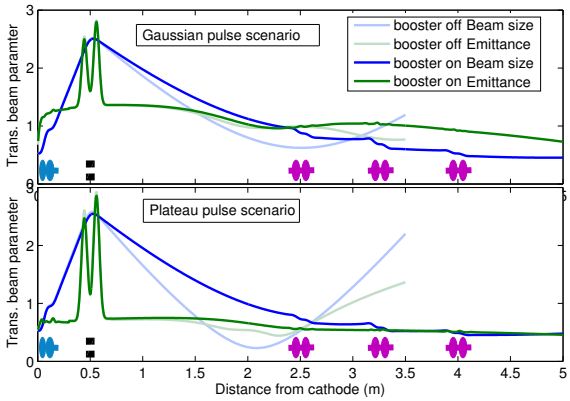

Figure 2: Transverse beam parameters for Gaussian and Plateau shaped drive laser profiles. Results are shown for booster on and off situations. The solenoid focal length has been slightly adjusted to optimize the matching of the beam into the booster.

Gaussian pulse has a rms length of $\sigma_t = 6$ ps, the Plateau shaped pulse has 1.8 ps rise/fall time and 18 ps width. The goal is to keep the rms pulse length constant from the cathode to the merger section of the ERL. The initial transverse spot size is round with 0.5 mm rms radius and the same for the two scenarios. The target beam parameters can be reached with both pulse shapes, the Plateau pulse setup outperforms the Gaussian shaped pulse by 20% with respect to projected emittance and linearity of the longitudinal and transverse phase space distribution.

Complete injector setup

A booster linac is added to gun and solenoid. The booster consits of three 2cell cavities of Cornell design [12]. The first cavity is located at the working point which results from the emittance compensation process. The goal is to effectivly freeze in the slice oscillation by increasing the beam energy to a level where the phase advance of the individual slices is not any more dominated by space-charge forces. The proposed setup may serve as guideline for the construction process of a realistic gun and booster setup. The gradient in the first cavity is set according to the invariant envelope criterion [14] to $E_{\mathrm{bc1}} = 7$ MV/m increasing the beam energy from 2.25 to 3 MeV. The two subsequent cavities each are set to $E_{\mathrm{bc2,3}} = 17.5$ MV/m to add 2 MeV resulting in an injector exit energy of 7 MeV. Here the emittance oscillations are effectively damped as can be seen in Fig. 2 for Gaussian

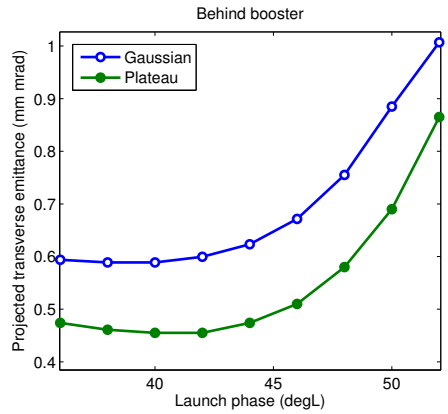

Figure 3: Transverse beam parameters for complete injector setup with initial Gaussian and Flat-top drive laser profile.

and Plateau drive laser profiles. The minium emittance at the end of the injector is a function of the launch phase as can be seen in Fig. 3

SUMMARY AND OUTLOOK

The goals for the B*ERL*inPro baseline beam parameter set can be reached with at 1.4cell cavity with retractable cathode design. With Plateau shaped bunches the performance with respect to the transverse beam emittance improves by more than 20% compared to Gaussian bunches. The next step is to move towards fully 3D simulation including all transverse rf effects from coupler kicks, higher-order modes and wakefields.

ACKNOWLEDGEMENTS

The authors acknoledge many fruitful discussions with M. Abo-Bakr, D. Dowell (SLAC/LBL), J. Sekutowicz (DESY), J. Teichert and A. Arnold (both HZDR).

REFERENCES

[1] The BERLinPro Conceptual Design Report (CDR), Eds.: A. Jankowiak, J. Knobloch, B. Kuske and N. Paulick
[2] K. Flöttmann, ASTRA V3 (2011)
[3] D. Dowell, SLAC-PUB-13535
[4] P. Kneisel, et al., Proc. of PAC 2010
[5] K. J. Kim, NIM A 275 (1989) 201
[6] B. E. Carlsten, NIM A 285 (1989) 313
[7] D. Janssen and V. Volkov, NIM A 452 (2000) 34
[8] A. Neumann, et al., Proc. of IPAC 2011
[9] T. Kamps, et al., Proc. of IPAC 2011
[10] J. Völker, et al., Proc. of IPAC 2012
[11] T. Kamps, Proc. of HBHAP 2009
[12] M. Liepe, et al., Proc. of SRF 2007
[13] A. Neumann, et al., Proc. of Linac 2012
[14] J. Rosenzweig and S. Serafini, Phys. Rev. E 55 6 (1997)

Copyright © 2012 by the respective authors — cc Creative Commons Attribution 3.0 (CC BY 3.0)

INITIAL RF TESTS OF THE DIAMOND S-BAND PHOTOCATHODE GUN

C. Christou and S. A. Pande
Diamond Light Source, Oxfordshire, UK

Abstract

An S-band photocathode electron gun designed to operate at repetition rates up to 1 kHz CW has been designed at Diamond and manufactured at FMB. The first test results of this gun are presented. Low-power RF measurements have been carried out to verify the RF design of the gun, and high-power conditioning and RF test has begun. Initial high power tests have been carried out at 5 Hz repetition rate using the S-band RF plant normally used to power the Diamond linac: the benefits and limitations of this approach are considered, together with plans for further testing.

GUN DESIGN

In recent years, the RF photoinjector gun has been increasingly used as a source of high brightness beams for free electron lasers [1, 2], inverse Compton scattering sources [3] and ultrafast relativistic electron diffraction devices [4]. A programme is underway at Diamond Light Source to develop a high repetition rate S-band photocathode gun [5] using a coaxial RF coupler similar to that used at the DESY PITZ gun [6]. Such an approach preserves the axial symmetry of the gun, ensures coupling takes place in a region of low power dissipation and allows the gun main solenoid to be mounted directly around the gun cavity to achieve minimum transverse emittance [7]. The DLS gun is a 1.6-cell design with a removable cathode plug. The RF electric field distribution of the accelerating π mode is shown in Figure 1: the cathode plug is located at the lower left and the coupler is on the right.

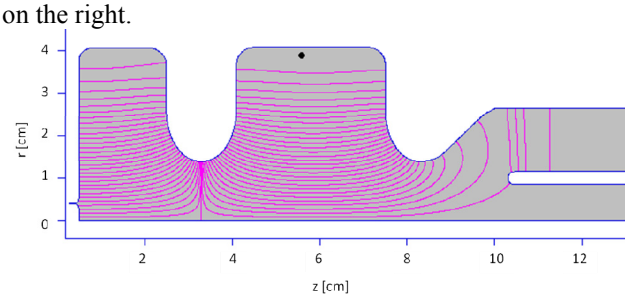

Figure 1: SUPERFISH calculation of π mode

The gun was manufactured at FMB and delivered to Diamond in early 2012: Figure 2 shows the assembled gun and coupler. Gun cavity and coupler are two brazed units connected by a Conflat fitting using one of a range of spacer gaskets of different thickness used to control coupling. The gun includes extensive water cooling channels allowing it to operate at a pulse repetition rate of 1 kHz, and to enable fine tuning of the cavity resonant frequency by control of the water temperature.

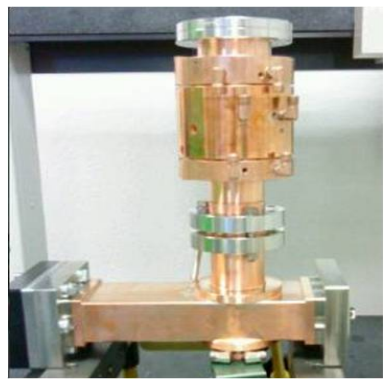

Figure 2: The assembled gun and coupler

LOW POWER TESTS PRIOR TO TUNING

Gun and coupler were probed together at Diamond using a Rohde and Schwarz ZB8 Vector Network Analyzer. Three resonances were measured around 3 GHz: the zero mode (2984 MHz), π mode (3003 MHz) and a small mode at 3021 MHz located at the antenna. The frequency of the π mode at room temperature was designed to be higher than the operating frequency of 2998 MHz in order to compensate for the drop in frequency expected as the cavity warms to its operating temperature when RF power is applied.

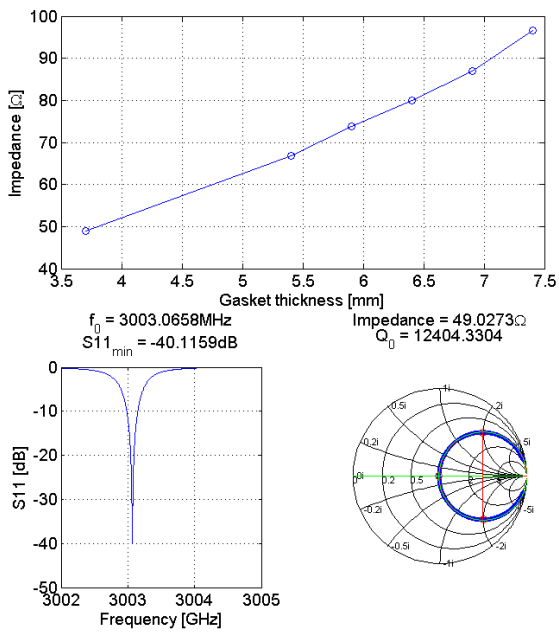

Figure 3: Tuning of gasket thickness for critical coupling (above) and cold test results at critical coupling (below).

A number of coupling gaskets were tested to establish critical coupling. Results are shown in Figure 3, with the

Copyright © 2012 by the respective authors — cc Creative Commons Attribution 3.0 (CC BY 3.0)

full range in the upper plot and the cavity parameters with critical coupling displayed in the lower plot.

A set of cathode pieces were manufactured with holes drilled through their centres to allow a bead-pull measurement to be carried out. In this measurement, the cavity was mounted vertically and a dielectric bead was pulled along the axis while the resonant frequency was monitored with the VNA. For a small spherical bead of radius r, the electric field, E, at the point of the bead can be related to the measured relative frequency shift, $\Delta f/f$ by

$$\left(\frac{\Delta f}{f}\right) = -\left(\frac{\pi r^3}{U}\right)\left[\varepsilon_0\left(\frac{\varepsilon_r - 1}{\varepsilon_r + 2}\right)E^2 + \mu_0\left(\frac{\mu_r - 1}{\mu_r + 2}\right)H^2\right]$$

where ε_r is the relative permittivity of the bead. For a dielectric bead with permeability $\mu_r = 1$, the frequency shift is independent of magnetic field and the measured change in frequency can be used to measure the electric field at a point in the cavity.

Results of a bead pull measurement for the cavity as manufactured with no fine tuning are shown in Figure 4. The peak field of the first (half) cell was found to be 17% greater than the peak field of the second (full) cell.

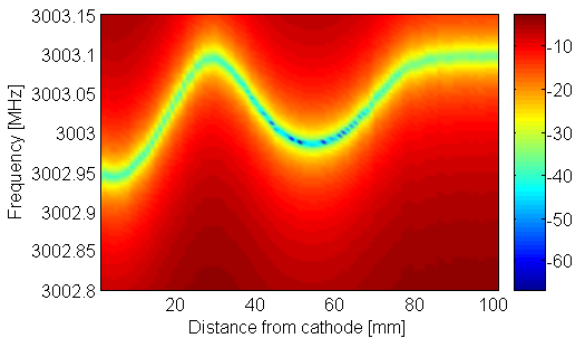

Figure 4: Bead pull results before correction

After evacuation of the cavity, vacuum bake-out tapes were used to control the cavity temperature and investigate the drop in resonant frequency caused by thermal expansion. Resonant frequency rose by approximately 1 MHz on evacuation. The plot in Figure 5 shows that some further tuning was necessary to bring the cavity frequency down to the level such that water temperature control could be used for fine tuning around 2998 MHz.

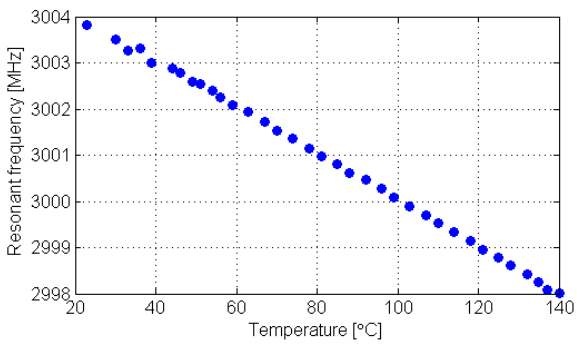

Figure 5: Scaling of resonant frequency with temperature before correction.

TUNING BY CATHODE INSERTION

The only component that is readily accessible for a rework is the cathode, as it is designed to be easily removed and replaced. Tuning by cathode position preserves the axial symmetry of the gun and is completely reversible, requiring no plastic deformation of the cavity walls. Moving the cathode surface info the first (half) cell has the effect of reducing both the resonant frequency and the field imbalance, as shown by the SUPERFISH calculations in Figure 6. Q_0 of the cavity is also increased by approximately 1000 with a 2 mm re-entrant cathode.

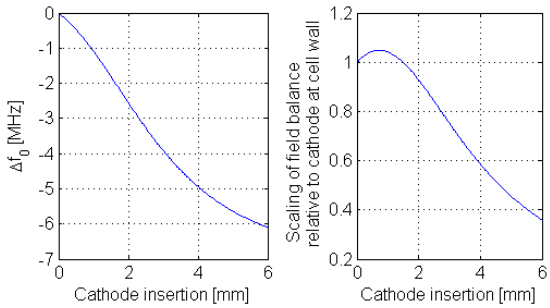

Figure 6: Prediction of cathode tuning

Five new cathode pieces were made up to investigate this approach, with results summarised in Figure 7 and Figure 8, for measurements in air.

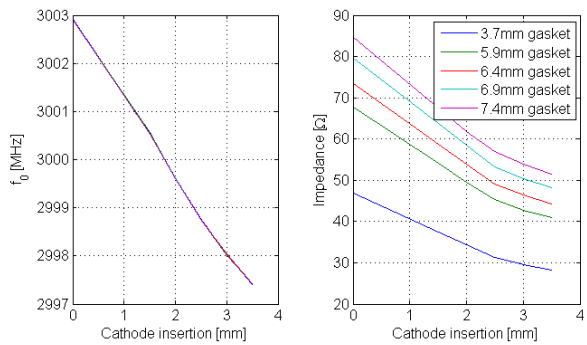

Figure 7: Change of resonant frequency (left) and impedance (right) with re-entrant cathode.

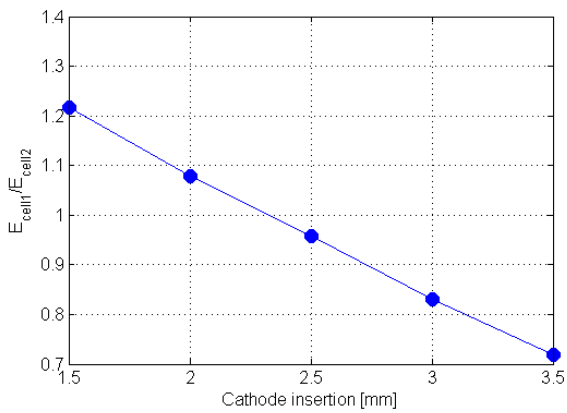

Figure 8: Field balance measurements with re-entrant cathodes.

Copyright © 2012 by the respective authors — cc Creative Commons Attribution 3.0 (CC BY 3.0)

The original design parameters for the gun were a field excess of 4% in the first cell and a resonant frequency of 2998 MHz at an elevated temperature achieved by RF heating and precisely maintained by the water in the cooling channels [5]; tuning of the gun by adjustment of the cathode face positioning has allowed these parameters to be achieved.

HIGH POWER TESTS

RF parameters of the evacuated gun at 20°C after correction by cathode adjustment and choice of appropriate coupling gasket are shown in Figure 9. This gun was mounted on a test bench for high-power RF testing. Prior to the test, the gun was pumped down for four weeks to 5 x 10^{-9} mbar.

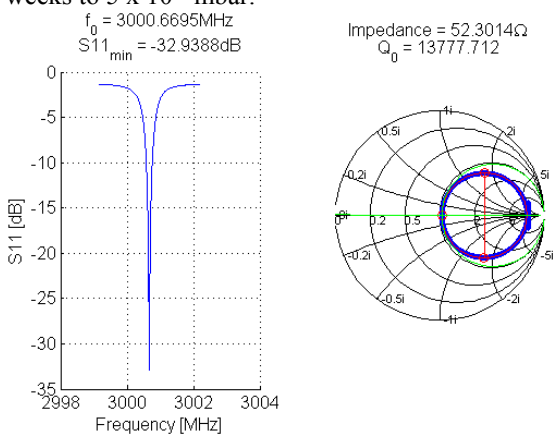

Figure 9: Characterisation of gun with re-entrant cathode

A photograph of the high-power test bench is shown in Figure 10: the gun is wrapped in bake-out foil in this picture. Power is supplied from one of the DLS linac amplifiers, which can provide pulses well in excess of the 3 µs, 6 MW requirement of the gun, although only at a repetition rate of 5 Hz. The bench is connected to a recently installed switch in the waveguide network [8] through a Titan Beta air-cooled circulator and forward and reflected power are monitored with a directional coupler close to the gun window. The waveguide is pressurised to 2 barG with SF_6.

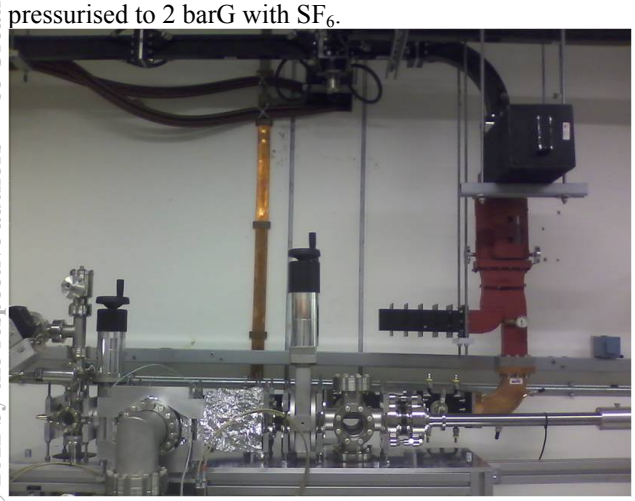

Figure 10: Gun assembly for high-power tests

Initial high-power test results are encouraging: Figure 11 is a record of the first period of conditioning of the corrected gun, showing forward power in the top plot and vacuum activity in the lower plot. A 3 µs RF pulse was used, and the gun conditioned rapidly allowing 2 MW to be applied to the gun within two working days. Initial vacuum activity died away quickly, and towards the end of the conditioning period the conditioning events were all arcs recorded by the arc detector viewing the window.

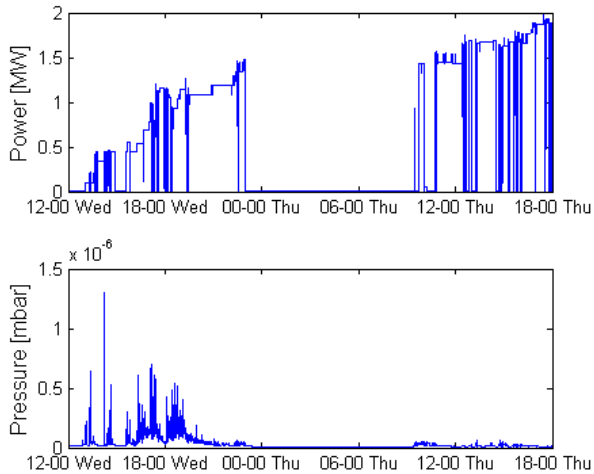

Figure 11: S-band gun conditioning

CONCLUSIONS AND FURTHER WORK

An S-band photoinjector gun has been manufactured and delivered to Diamond Light Source and low-power RF characterisation has been carried out. Reversible frequency and field flatness tuning has been achieved by adjusting the position of the cathode surface, and high power conditioning has begun. The effect on beam of the RF field distortion introduced by the cathode shift must be studied in detail, and work is underway to design and build the solenoid coils required for gun operation. A second gun cavity is also in design that requires a smaller RF correction to reach the target parameters.

ACKNOWLEDGEMENTS

The authors would like to acknowledge the loan of the Titan Beta circulator from CERN.

REFERENCES

[1] J. Arthur et al., SLAC Report SLAC-R-593, 2002.
[2] R. Brinkmann et al., DESY Report TESLA-FEL-2002-09.
[3] W. Brown et al., PRSTAB 7, 060702 (2004).
[4] J. Hastings et al., Appl. Phys. Lett.89, 184109 (2006).
[5] J. H. Han et al., NIM A 647, 17-24 (2004).
[6] B. Dwersteg et al., NIM A 393, 93 (1997).
[7] R. Alley et al., NIM A 429, 324 (1999).
[8] C. Christou, EPAC 2010 p. 82.

Copyright © 2012 by the respective authors — cc Creative Commons Attribution 3.0 (CC BY 3.0)

RF PHOTOINJECTOR AND RADIATING STRUCTURE FOR HIGH-POWER THz RADIATION SOURCE

S.M. Polozov, T.V. Bondarenko,
National Research Nuclear University (MEPhI), Moscow, Russia.
Yu.A. Bashmakov, Lebedev Physical Institute of RAS (LPI), Moscow, Russia

Abstract

Sources of high-power electromagnetic radiation in THz band are becoming promising as a new method of a low activation introscopy. Research and development of accelerating RF photoinjector and radiating system for THz radiation source are reported. The photoinjector is based on disk loaded waveguide (DLW). Two different designs of accelerating structure were modelled: widespread 1.6 cell of DLW structure and travelling wave resonator structure (TWR). The resonant models of these structures and the structures with power ports were designed. Electrodynamics characteristics and electric field distribution for all models were acquired. Results of picoseconds photoelectron beam dynamics in simulated structures are reported. Designs of decelerating structures exciting Cherenkov radiation are based on corrugated metal channel or metal channel coated with dielectric. Analysis of radiation intensity and frequency band are presented.

INTRODUCTION

THz radiation is nowadays becoming promising in solving such vital problems as national security, biomedicine and in manufacturing processes control. In national security issue THz radiation can be used in introscopy systems. The definition of the weapons, explosives, drags and fissionable materials is the main aim of introscopy. The introscopy of cargo transport is much more complicated objective then passenger introscopy issue. The gamma, electron or neutron facilities are used in introscopy system including cargo introscopy at present. The compact electron or ion gun or accelerator is the basic element of such facilities. The main difficulty is the fact that it is necessary to use an electron linear accelerator (LINAC) which can derive the beam with 3-5 times energy variation. LINACs of this type are utterly complex facilities. All of gamma, electron or neutron facilities have a number of disadvantages as needs of environmental shielding and cargo activation.

High-power THz radiation source based on photoinjector and decelerating capillary channel is now one of the most discussable compact facilities providing monochromatic THz radiation of power high enough to be used for cargo introscopy [1].

Facility is based on two main parts: accelerating structure and decelerating radiating channel. Capillary is placed right after the accelerating structures and is made of copper with either dielectric coated inner surface or corrugated surface.

ACCELERATING STRUCTURES

1.6 cell DLW structure

Accelerating structure consists of two accelerators connected sequentially: 1.6 cell DLW and 9 cell TWR structure.First part of facility accelerating system is 1.6 cell standing wave accelerating structure (figure 1). This accelerating structure by itself comes artlessly as a photoinjector part of the accelerating system.

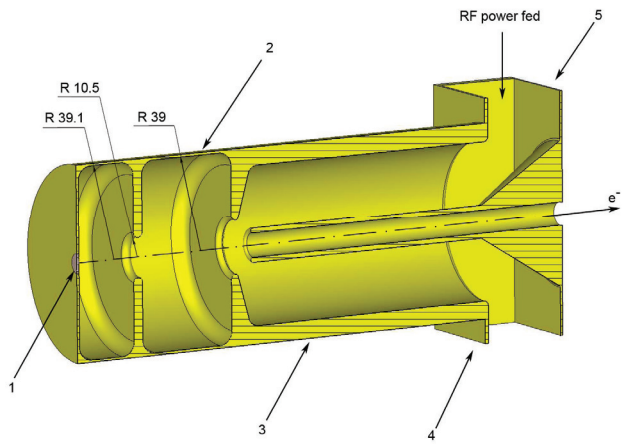

Figure 1. 1.6 accelerating structure: 1 – photocathode, 2 - resonator, 3 – coaxial wave type transformer, 4 – vacuum port, 5 – power input.

This accelerating structure operates on π mode and S-band frequency 2856 MHz (λ=105 mm). Resonant frequency of the structure was tuned to the desired value by means of cell radius variation. Iris profile was made with rounding to eliminate the possibility of breakdown. First cell length is 0.6 of full-sized cell to obtain maximum field amplitude in the center of the photocathode arranged in the cell's sidewall. Performance of the structures was also increased by rounding of shells edges. The rounding radius value was chosen to provide the highest possible shunt impedance and Q-factor.

Structure RF power input in organized by S-band standard rectangular waveguide with the coaxial coupler. RF power is fed into the structure through only one of the connected waveguides; another is used for structure field symmetry and will be applied for vacuum and other accompanying connections. This scheme provides high level of field symmetry in the system that leads to better quality of the accelerated beam.

This type of wave transformer differs from recently used RF power inputs in photoinjectors like ones in BNL Guns [2]. That type was exploiting the scheme of power

Copyright © 2012 by the respective authors — cc Creative Commons Attribution 3.0 (CC BY 3.0)

input through the coupling diaphragm directly into the full-sized cell of the structure in this wise fill cell was a wave transformer.

TWR structure

Travelling wave resonator is a type of ordinary linear accelerator structure with some additions. Basically the accelerating wave propagating in acceleration structure is travelling wave type but the trait that makes this system a resonator is energy recuperation coming out of interlocking RF power input with output and feeding power with directional coupler (figure 2). If the length of the TWR circuit is devisable to the generator wavelength, the magnitude of electromagnetic fields in TWR reaches its maximum and magnitude of the wave incoming to the load from the ring turns to minimum [3].

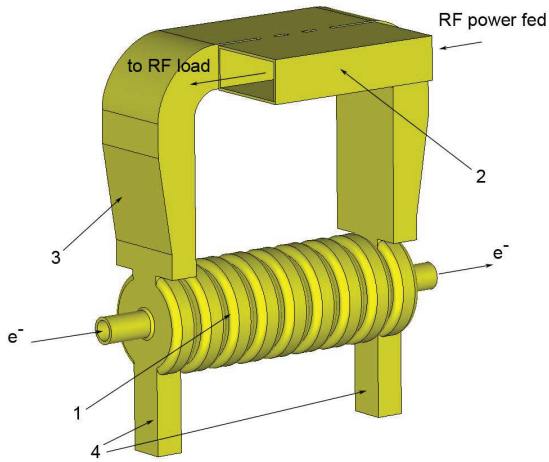

Figure 2. Travelling wave resonator structure: 1 – accelerating structure, 2 – directional coupler, 3 – TWR ring, 4 – vacuum ports.

TWR is based on 9 cell travelling wave S-band structure with $\pi/2$ operating mode. The optimal operation regime of the structure is critical mode. In this regime part of RF power is fed into the accelerating system through the directional coupler and fills in the power resistance losses in the resonators sidewalls. In this case the part of power that is not branched into the TWR ring is summed with the one from generator in the opposite phase and gives the minimal magnitude signal coming to the load. Two main parameters determining efficiency of TWR are the circuit power attenuation factor and the directivity factor of the directional coupler.

Directional coupler with narrow or wide side coupling represents the connection of two waveguides by coupling windows with space shift of quarter wavelength between the windows irradiating in the opposite directions of jointed waveguide. Directional coupler computation included receiving of required transfer coefficient in the forward direction of jointed waveguide C and simultaneously keeping transfer coefficient in the opposite direction of jointed waveguide $|\Gamma|$ below the certain level.

Three coupling window model was applied to provide high directivity level of directional coupler. Enlarging the number of coupling windows doesn't improve the directivity coefficient.

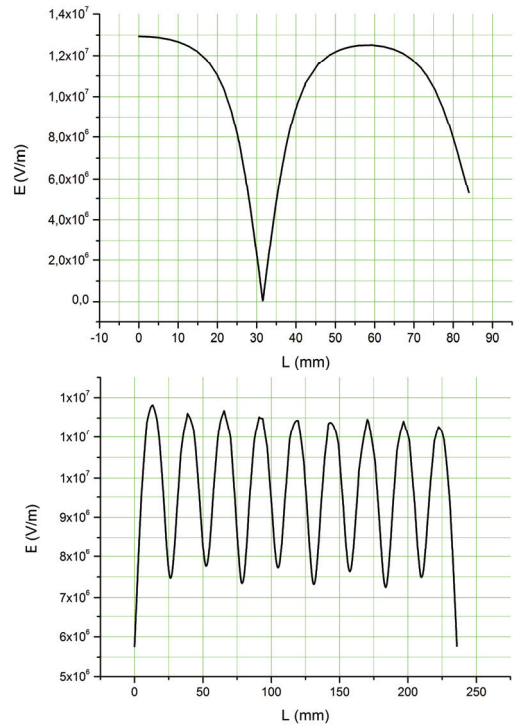

Figure 3. Electrical field magnitude plots at 1 MW power fed for 1.6 cell structure (upper) and for TWR structure (lower)

Taking into account part of the signal branching in the opposite direction and intensity attenuation factor, expression for the magnitude of electrical field spreading in TWR storage ring for critical mode can be written as:

$$A_{TWR} = \pm j \frac{1}{\sqrt{1-e^{-2\alpha_T}}} \frac{C-|\Gamma|}{C} A_{input}, \qquad (1)$$

here A_{TWR} - TWR circuit electrical field intensity magnitude, α_T - TWR ring signal intensity attenuation factor, A_{input} – RF generator signal intensity magnitude.

In considered case transition coefficient of directional coupler C=3.9% that equals to TWR ring decay coefficient at the 14 mm coupling window width, sidewall width between waveguides is 4 mm. Sidewalls width doesn't have much impact on directivity coefficient but ought to be wide enough to provide coupler ruggedness. Transfer coefficient in the opposite direction of TWR ring equals Γ=-48dB. Thus directivity coefficient of directional coupler is D=23dB. Using the formula (1) power in TWR multiplies 9 times vs. input power level.

BEAM DYNAMICS

Beam dynamics simulation in designed accelerating structures was done using BEAMDULAC-BL code

Copyright © 2012 by the respective authors — cc Creative Commons Attribution 3.0 (CC BY 3.0)

designed in laboratory DINUS of NRNU MEPhI [4]. The simulation was done with the following beam parameters: injection energy W_{inj}=5 eV, feeding RF power P=2.5MW, beam pulse current I=5 A, beam pulse charge Q=1 nC. Photoelectron beam initial radius is r=200 μm that corresponds to the laser spot of the same size focused on the cathode surface. This beam parameters values are similar to most of photoinjectors. The first accelerating section is fed by 1.5 MW and the second by 1 MW power.

The results of photoinjector beam dynamics investigation shows that at this value of RF power fed beam bunch can be accelerated to the energy of 1 MeV. The further acceleration of the beam in TWR section resulted in 5 MeV beam energy that meet the requirements for the beam in THz generation process.

Pencil-shaped and high brightness beam is necessary for Cherenkov THz generator to achieve that beam size preservation can be realized in accelerator using longitudinal magnet field focusing.

CHAPILLARY CHANNEL

Two types of channels could be used for generation of Cherenkov radiation: the conducting (metal) capillary coated by dielectric inside (see Fig. 4a) and the corrugated channel or grating surface also (Fig. 4b). The inner channel radius $d/2$ should be comparable to the wavelength, i.e. should be about 0.1 – 1 mm. The structure period t (the distance between of diaphragms) in the second case should also be comparable to the wavelength.

The main idea of using the capillary channel as a source for radiation lies in a principle of Cherenkov radiation. The phase velocity of the wave propagating inside the capillary channel is less than the electron beam velocity. So the beam propagating in such structure would induce the radiation with the frequency dependent on the channel dimensions.

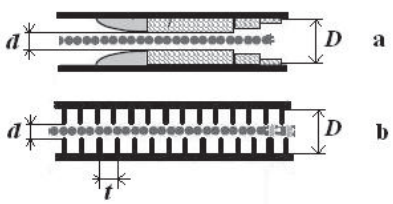

Figure 4. The conducting (metal) capillary coated inside by dielectric (a) and the corrugated channel or grating surface (b).

Different approaches can be estimated for achieving the induced power in the accelerated structures. One of the ideas is based on using the form-factor concept [5]. The decelerating structure parameters such as shunt impedance, Q-factor and group velocity are numerically investigated in terms of TM01 wave excited inside of the capillary. Then radiated power can be founded using the formula for the case of short burst mode when pulse repetition time is much longer than the beam length:

$$P = \frac{\omega}{4}\frac{r}{Q}\left|v_{group}\right| \cdot \left|\frac{q\Phi}{1-\beta_{group}/\beta}\right|^2, \qquad (2)$$

where ω - radiation resonant frequency, r – channel shunt impedance, Q – channel quality factor, q – bunch charge Φ - bunch form-factor, v_{group}, β_{group} - absolute and relative group velocity of the channel. For considered capillary channels Q is about 2000, β_{group} - 0.8 and r is around $3 \cdot 10^4$.

Another concept was discussed by Bolotovsky [6]. In this concept beam energy loss for the Cherenkov radiation is described by the force acting on the moving charge by the induced fields. Electron beam is presented as a point charge because beam sizes are smaller than induced radiation wavelength. The corrugated channel in this concept is presented as a small disk loaded. This method doesn't take in the account beam form factor.

Both cases show alike results for power radiated by the beam propagating in the channels. The goal was to achieve the radiation with 1 THz frequency. Channel length for both designs was 2 cm. Dielectric channel dimensions are: 300 μm channel radius and 30 μm teflon thickness. In case of corrugated channel transverse sizes appears to be smaller: 100 μm cell radius, 80 um diaphragm radius. For the stated above beam parameters the radiated power appears to be around 50 kW in the case of dielectric coated channel and 20 kW in case of corrugated channel in case of 1 nC beam charge and 5 MeV beam energy.

CONCLUSION

RF photoinjector and decelerating system were investigated for high-power THz generator. RF photoinjecr is based on two accelerating sections: 1.6 cell standing wave structure with coaxial power input and travelling wave section based on travelling wave resonator. Both are fed by S-band 2.5 MW magnetron. First is used to emit photoelectrons and to accelerate bunch to 1 MeV. Second is used for further acceleration to 5 MeV.

Decelerating channel can be based on two main concepts: corrugated metal channel and dielectric covered channel. Both are applicable for achieving high radiation power rates.

REFERENCES

[1] Yu.A. Bashmakov, T.V. Bondarenko, S.M. Polozov, et al., Problems of Atomic Science and Technology. Series: Nuclear Physics Investigations, 3 (79), 2012, p. 53-57.
[2] D. T. Palmer, R.H. Miller, X.J. Wang, et al., SLAC–PUB–7420, May 1997.
[3] J. L. Altman, Microwave circuits, Van Nostrand Co., 1964.
[4] T.V. Bondarenko, E.S. Masunov, S.M. Polozov, et al., Proceedings of IPAC 2011, MOPS037.
[5] A.V. Smirnov, Nuclear Instruments and Methods in Physics Research A 480 (2002), 387–397.
[6] K.A. Trukhanov, V.V. Poliektov, V.I. Shvedunov, Proceedings of RuPAC'04, p. 106.

Copyright © 2012 by the respective authors — cc Creative Commons Attribution 3.0 (CC BY 3.0)

DESIGN ISSUES OF THE PROTON SOURCE FOR THE ESS FACILITY

L. Celona, L. Neri#, S. Gammino, G. Ciavola, D. Mascali, G. Castro, L. Allegra, C. Caliri, R. Di Giugno, INFN, Laboratori Nazionali del Sud, Catania, Italy

Abstract

The European Spallation Source facility will be one of the fundamental instruments for science and engineering of the future. A 2.5 GeV proton accelerator is to be built for the neutron production. INFN-LNS is involved in the Design Update for the proton source and Low Energy Beam Transport (LEBT) line. The proton source is required to produce a low emittance 90 mA beam, 2.86 ms pulsed with a repetition rate of 14 Hz. Microwave Discharge Ion Sources (MDIS) enable us to produce such high intensity proton beams characterized by very low emittance (< 0.2 π.mm.mrad). The source design is based on a flexible magnetic system which can be adapted to electrostatic Bernstein waves heating mechanism; this will permit a strong increase in the electron density with an expected boost of the output current. The main features of the source design, including the microwave injection system and beam extraction, will be described hereinafter.

INTRODUCTION

The European Spallation Source (ESS) [1] will be at Lund and it is expected to provide 5MW of protons when completed. The Design Update of the Linac has been started in 2011 and it is to be completed with the Technical Design Report by the end of 2012. INFN is responsible of the WP6-Front End and the Laboratori Nazionali del Sud (LNS) are responsible of the WP6 management, of the Proton Source and LEBT design.

The Proton Source for European Spallation Source (PS-ESS) will be based on the know-how acquired during the design phase, the construction phase and the commissioning of the sources named TRIPS and VIS at INFN-LNS [2,3] operating at 2.45 GHz, and of the SILHI source at CEA-Saclay [4], but some remarkable improvements are to be developed because of the high current needed at a lower extraction voltage and because of the request to operate in pulsed mode. A new and flexible magnetic system was designed using three solenoids. Microwave injection system will be deeply revised according to the recent experience gained with the VIS source. Performance of the extraction system was simulated to produce the starting condition for the end to end beam simulation needed for the accelerator design. This different aspects of the new proton source will be presented hereinafter.

SOURCE REQUIREMENTS

ESS initially requires a proton beam of 50 mA (90 mA in the final configuration), at 75 keV with a maximum emittance of 0.2 π.mm.mrad, a 14 Hz of repetition rate with 2.86 ms pulse length, and 99.9% reliability. In terms of emittance, the VIS source, developed by LNS group, is able to largely fulfil the requirements for ESS in continuous mode and the tests carried out on SILHI [5] confirmed also the capability to fulfil them also in pulsed mode. In fact, it was observed that for a pulse duration of 3 ms, for 10 and 20 Hz repetition rate, the beam emittance is around 0.15 π.mm.mrad. [5].

The current required for the ESS facility in the baseline configuration can be satisfied by means of conventional Microwave Discharge Ion Source (MDIS) like VIS, based on the plasma direct absorption of the pumping electromagnetic waves through the Electron Cyclotron Resonance mechanism. Recent studies performed at INFN-LNS [6] have shown a critical influence of the magnetic field profile on the plasma properties, especially the density. In particular, two innovative plasma heating methods will be attempted. The first is based on non-conventional ways of RF coupling to the plasma which will be depicted in the following, the latter consist of an optimization given by short plasma confinement. In PS-ESS design we merged the best solutions already tested in previous sources with a flexible magnetic system able to produce both standard and new magnetic profiles that will allow us to increase the current, increase the proton fraction, reduce the emittance and take under control the beam formation.

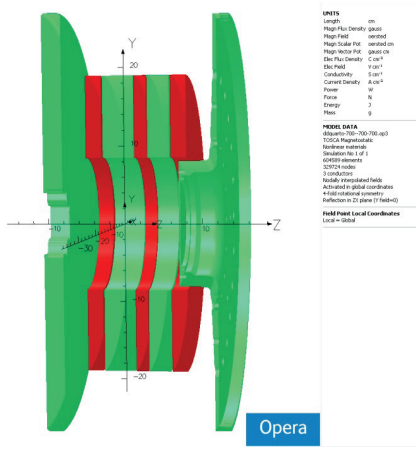

Figure 1: PS-ESS flexible magnetic system.

NEW MAGNETIC SYSTEM

PS-ESS will be similar to the VIS proton source except for the magnetic system that will consists of a set of three solenoids (instead of two). The new magnetic system shown in Fig. 1 was designed to obtain very high flexibility, by using three different coils that can be differently energised and that can be also changed in polarity. Key point of obtained flexibility is the use of

neri@lns.infn.it

Copyright © 2012 by the respective authors — cc Creative Commons Attribution 3.0 (CC BY 3.0)

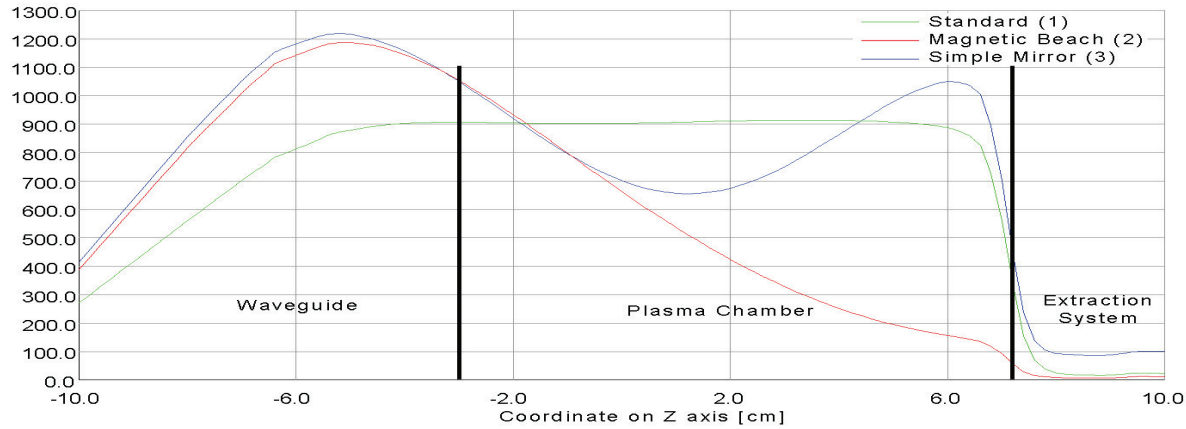

Figure 2: Magnetic profiles generated by three shielded coils.

ARMCO Pure Iron disc between the solenoids to spatially confine the magnetic field produced by each one.

To avoid a Penning discharge inside the extraction column, and to avoid emittance growth due to the stray magnetic field, an adequate shield of ARMCO will be employed. The field is depleted from 1000 to 100 Gs in 1.6 cm regardless the selected magnetic configurations, as shown in Fig. 2.

The typical shape of the magnetic field for MDIS machines is therefore the one labeled by (1) in Fig. 2, i.e. a quasi-flat profile everywhere above the resonance value of 875 Gauss. This ensures electron densities around the cutoff at 2.45 GHz or slightly larger ($n \approx 10^{17}$ m^{-3}), temperatures sufficient for hydrogen ionization (T=15-20 eV) and H_2 molecule lifetimes long enough for complete ionization and proton generation. Such plasma parameters require RF power around 1-1.5 kW and background pressures down to 10^{-5} mbar.

Recently, the possibility to overcome the cutoff density by converting the incoming electromagnetic wave into a plasma wave has been investigated [7]. This study goes in parallel with similar investigations in fusion science, where large plasma densities are needed to fulfill Lawson criterion [8]. At INFN-LNS signs about the occurred conversion mechanism has been observed with the VIS source equipped with a movable permanent magnets and operating at variable frequency [6]. The process is based on the conversion of an oblique (with respect to the applied magnetic field) electromagnetic wave (called extraordinary mode, or X mode) into an electron oscillation (longitudinal wave) propagating across the magnetic lines and called Bernstein Waves (BWs). Plasma waves travel in plasmas of whatever densities and are absorbed at cyclotron harmonics. Since they are sustained by the electron motion, BWs cannot be externally excited, but originate from an X mode interacting with gyro-rotating electrons at the Upper Hybrid Resonance (UHR) [9]. The first experiments have put in evidence the formation of a 10-20 times overdense plasma when operating in second harmonic mode. To be converted into a BWs, the X mode requires a rapidly dropping magnetic field which makes possible either UHR and second harmonic absorption. This configuration is labeled as (2) in Fig. 2, and sometime called "Magnetic Beach". We expect this second way of RF-plasma energy coupling will significantly enhance the output currents, but it can be employed in a second phase, once carefully studied implications on the ion dynamics (possible ion heating as ancillary mechanism) and then on beam emittance.

Finally, a second way to optimize the proton generation of a MDIS will be attempted by designing a simple-mirror-like trap, like the one labeled by (3) in Fig. 2. Studies about balance equations of the different plasma species (H_2, H_2^+, H^+) reveal that their reciprocal abundance is regulated by the relative lifetimes. In a quasi-flat magnetic field, under normal operative pressure conditions, ions lifetime is only governed by collisional diffusion across the magnetic field, which is a rather fast process. The prolongation of H_2^+ molecule lifetime, obtained when using the simple-mirror configuration, should increase the ionization efficiency thus boosting the proton fraction already at moderate RF power, thus improving also the reliability of the source.

MICROWAVE COUPLING

In order to improve the performances of such ion source a detailed electromagnetic study of the plasma chamber as a cavity has been carried out with Ansoft HFSS™ eigenmode solver.

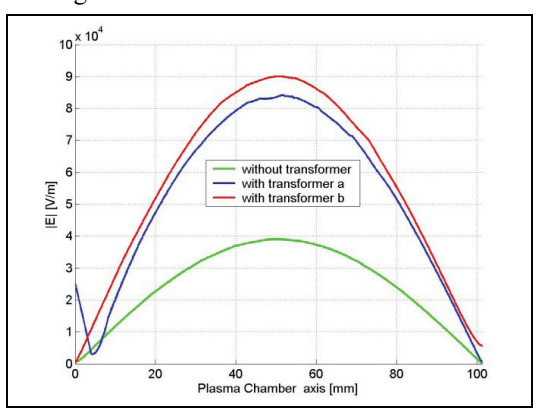

Figure 3: Comparison of electric field amplitude simulated for three different configurations.

Copyright © 2012 by the respective authors — cc Creative Commons Attribution 3.0 (CC BY 3.0)

As a result of this analysis the plasma chamber dimensions has been determined in order to have a TE_{111} dominant mode at the frequency of around 2.5 GHz and the effect of two different matching transformers on the microwave coupling has been fully studied [10]. Fig. 3 shows the electric field distribution concerning the TE_{111} mode inside a cylindrical resonance cavity with 101.2 mm length and 45.3 mm radius. It can be noticed that it is possible to increase the ion source performances by introducing a matching transformer (Fig. 4) that reduce the reflected power.

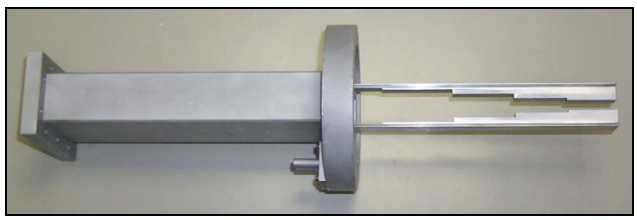

Figure 4: Matching transformer

FOUR ELECTRODE EXTRACTION SYSTEM

The extraction system consists of four electrodes: a plasma electrode placed on the HV platform at a voltage of 75 kV and a set of three electrodes, the first and the last attached to the grounded flange, and between them a repelling electrode placed at few hundred volt to preserve the space charge compensation of the LEBT.

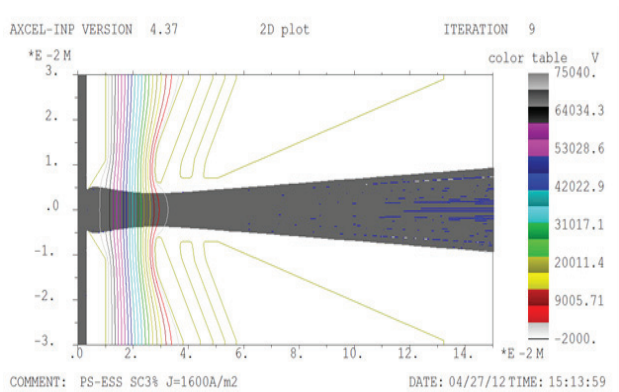

Figure 5: Four electrode extraction system.

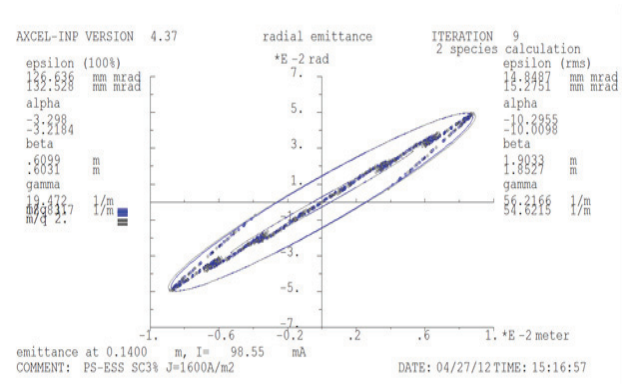

Figure 6: Extracted beam emittance simulated with AXCEL.

The simulations have been made with AXCEL and a typical trajectory plot is shown in Fig. 5, while Fig. 6 shows the rms beam emittance ellipses at z = 0.14 m far from the extraction aperture. The total beam current used in the simulation is 100 mA circa: the proton fraction considered is 90%, while 10% is H_2^+.

CONCLUSION

ESS requirements for proton source are quite restrictive. Considering the experience gained with the already designed and optimized sources at INFN-LNS, the needs of the initial phase of the facility will be fulfilled by using a "conservative" approach, based on a standard MDIS configuration (VIS-like machine). The second phase requirements are more stringent in terms of currents (up to 90 mA or more), but possible solutions for the source upgrading have been considered already in the design phase, by proposing a new flexible magnetic system. More standard solutions for performance optimization (which do not require any ab-initio design modification) will be implemented, as the alumina tubes introduced into the plasma chamber [11]. Therefore we will not only take care about currents, emittance, efficiency and reliability requirements, but also to a continuous MDIS development.

ACKNOWLEDGEMENT

The authors wish to thanks D. Campo and F. Maimone for the valuable contribution.

REFERENCES

[1] M. Lindroos et al., “The European Spallation Source”, NIM B vol.269, issue 24, 3258-3260.
[2] L. Celona et al., “TRIPS: The high intensity proton source for the TRASCO project”, Rev. Sci. Instrum. 71, 771.
[3] S. Gammino et al., “Tests of the Versatile Ion Source (VIS) for high power proton beam production”, ECRIS’10, Grenoble, France.
[4] R. Gobin et al., “Status of the light ion source developments at CEA/Saclay”, Rev. Sci. Instrum. 75, Issue 5, 1414 (2004).
[5] R. Miracoli et al., “Note: Emittance measurements of intense pulsed proton beam for different pulse length and repetition rate”, Rev. Sci. Instrum. 83, Issue 5, 056109.
[6] G. Castro et al., “Comparison between off-resonance and E.B.W. heating regime in a Microwave Discharge Ion Source”, Rev. Sci. Instrum. 83, 02B50.1
[7] D. Mascali et al., “Electrostatic wave heating and possible formation of self-generated high electric fields in a magnetized plasma”, Nucl. Instr. & Meth. A, 653-1, 11-16 (2011).
[8] H.P. Laqua, “Electron Bernstein wave heating and diagnostic”, Plasma Physics and Controlled Fusion, 49, R1 (2007).
[9] F. F. Chen, “Introduction to the Plasma Physics and Controlled Fusion”, U.K., London Press, London, 1986
[10] L. Neri, “RF System Design Report”, ESS internal report ADU_1.6.2.1.6.
[11] S. Gammino et al., “Enhancement of ion current from the TRIPS source by means of different electron donors”, Rev. Sci. Instrum. 77 (3): Art. No. 03B511 Part 2 MAR 2006.

Copyright © 2012 by the respective authors — cc Creative Commons Attribution 3.0 (CC BY 3.0)

DEVELOPMENT OF A SUPERCONDUCTING FOCUSING SOLENOID FOR CADS*

W. Wu, X.L. Yang, Z.J. Wang, B.M. Wu, S.F. Han, D.S. Ni, W.J. Yang, L. Zhu, S.J Zheng, L.Z. Ma, Y. He Institute of Modern Physics, Lanzhou,730000, China

Abstract

A superconducting focusing solenoid has been designed and developed for the China Accelerator Driven System (CADS). In order to meet the requirement of focusing strength and fringe field while minimizing physical size of the solenoid, the novel optimizing design method based on linear programming method was employed. In this report, we will introduce the design of the solenoid including magnetic field optimization, mechanical design and quench protection. The fabrication and the test results of the solenoid will also be introduced in this report.

INTRODUCTION

Accelerator Driven System(ADS) is the effective tool for transmuting the long-lived transuranic radionuclides into shorter-lived radionuclides. A project called CADS is being studied in the Chinese Academy of Sciences. Fig. 1 shows the roadmap of CADS. The linac of CADS will accelerate the proton with beam current 10mA to about 1.5GeV to produce high flux neutrons for transmutation of nuclear waste. The beam dynamics of superconducting linacs operating in the velocity range below 0.4c require a compact accelerating-focusing lattice. Superconducting solenoids together with SC RF resonators within a common cryostat meet this requirement. For its simple design, easily producing and low cost of manufacture, many typical superconducting Linac such as ISAC-II of Canada, Project X of FANL and FRIB of MSU in USA employ solenoid as focusing element[1, 2, 3].

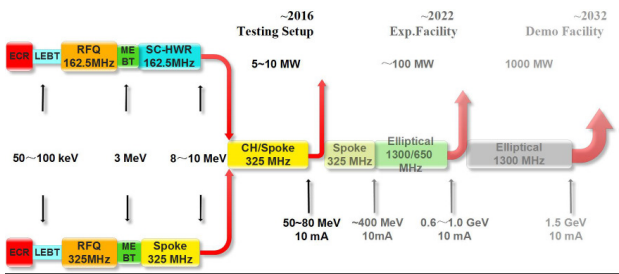

Figure 1: The roadmap of China CADS.

The solenoid will generate stray magnetic field that must be shielded to very low levels at the nearby SRF cavities. Two orthogonal steering dipoles, coaxial to each other and to the solenoid, are required to steer the beam in transverse directions. The specifications of the solenoid are summarized in Table. 1[4].

* Supported by the National Natural Science Foundation of China (Grant No.11079001)

Table 1: Specifications of SC solenoid

Parameters	Value
Center field	7 T
Effective length	150 mm
Stray field 200 Gs line	$\leq 280\ mm$ from the center
Correction of integral	$> 0.01\ T \cdot m$
Bore diameter	44 mm

MAGNETIC DESIGN

The solenoids must have low fringe fields to avoid magnetic-flux capture in the superconducting cavity. Before the SC cavity cooled into superconducting state, the level of the fringe field must be much lower than the earth-s magnetic field 50 μT and according to some estimates should be on the level of 1 μT [5]. This requires that the solenoid should be constructed only of material with low relative magnetic permeability to minimize remnant fields when the magnet is off. Once the cavity is in the superconducting state, the fringe field of the fully energized magnet is to be less than $20 \sim 40\ mT$.

The main goal of the magnetic design is to find a configuration of a solenoid that would meet the major requirements while minimizing the cost. The reverse wound active shielding coils are also used in our design to reduce stray magnetic field as ISAC-II and FRIB did. A two-step method which combines linear programming and a nonlinear optimization algorithm has been employed to design the solenoid[6, 7]. Linear Programming is used to carry out the topology optimization to get the coils' initial location and shape, and then the nonlinear optimizing methods are used as the second step to further simplified the coils' shape.

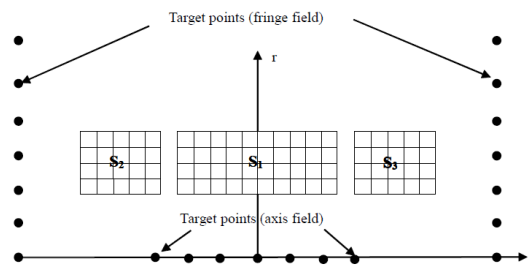

Figure 2: The feasible coil regions with numerical grid.

For a multi-coils magnet the feasible coil space can be divided into several regions and then each section is densely sampled by an array of candidate current loops (Fig. 2). The goal is to determine a set of current loops to create a desired field distribution at the target points while achieving a low fringe field and minimizing the coil volume. This

Copyright © 2012 by the respective authors — cc Creative Commons Attribution 3.0 (CC BY 3.0)

problem can be converted to a standard linear programming problem

$$\begin{aligned} \text{Minimize:} \quad & 2\pi \sum r_n S_n \\ \text{Subject to:} \quad & B_0(1-\epsilon) \le AI \le B_0(1+\epsilon) \\ & |C_z I| \le B_{z,shield} \\ & |C_r I| \le B_{r,shield} \\ & 0 \le I_n \le Ic_n \end{aligned} \tag{1}$$

where S_n and r_n are the cross-sectional area and radii of the current loop n, respectively. After the first step, the coil domains are usually non-rectangular as shown in Fig. 3. It is difficult to fabricate a magnet with non-rectangular coils, so we have to find a solution that can be implemented with only rectangular coils. The non-rectangular domain is then divided into a set of geometrically simple parts. These parts are replaced with rectangular regions whose shape and location parameters can be determined by using the nonlinear optimizing method. Fig. 4 shows the resulting coils configuration and stray field distribution. The fringe field is less than 4 mT in the cavity zone (280 mm from the center). The maximum field in the coil is 7.45 T at the current of 204 A. 30% of the current margin is used.

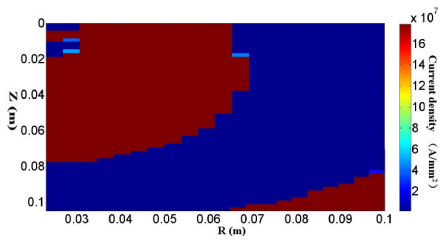

Figure 3: The resulting coil domains after the LP optimization

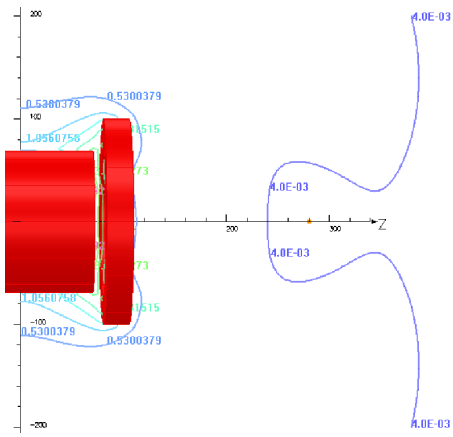

Figure 4: The resulting coil domains with the nonlinear optimizing method

MECHANICAL DESIGN AND ANALYSIS

The final coils configuration of the magnet is shown in Fig. 5. It includes one solenoid, two bulking coils and two pairs of steering dipole coils. All the coils are wound with NbTi/Cu composite superconducting wire and impregnated with epoxy resin to ensure mechanical stability. The integrated design of the bobbin and helium vessel is shown in Fig. 6. Stress analysis of the magnet has been performed. Fig. 7 shows that the maximum stress is only 95 MPa, which is within the allowable limits. The coil formers and helium vessel are fabricated with 316L stainless steel to ensure low relative magnetic permeability and good cryogenic mechanical properties. In order to prevent quench caused by separation of the coils inner layer from the bobbin during excitation, the aluminum alloy overbinding is applied.

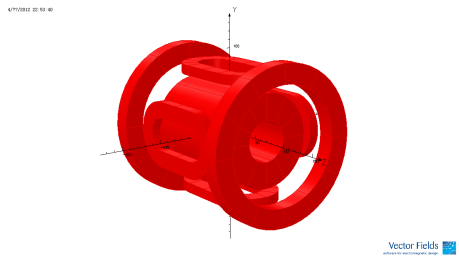

Figure 5: Coils configuration of CADS solenoid

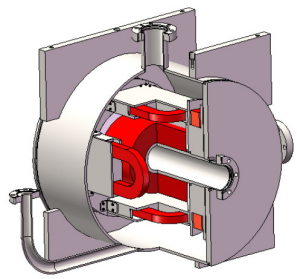

Figure 6: CADS solenoid assembly

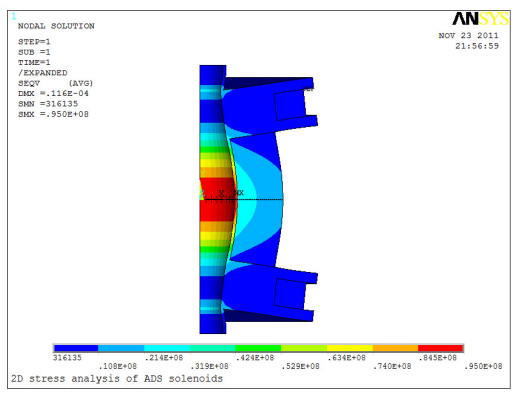

Figure 7: Simulated stress distribution of the solenoid caused by the electromagnetic forces

FABRICATION AND TESTING RESULTS

The solenoid have been built and tested in Institute of Modern Physics (IMP). The solenoid was installed into a

Copyright © 2012 by the respective authors — cc Creative Commons Attribution 3.0 (CC BY 3.0)

vertical experimental testing dewar and Fig. 8 shows the assembly of the test insert for the magnet. Because of the small storage energy (24 kJ), the cold diodes have been used to protect the magnet from quench. Fig. 9 shows the quench protection circuit for the magnet.

Figure 8: Assembly of test insert for CADS solenoid

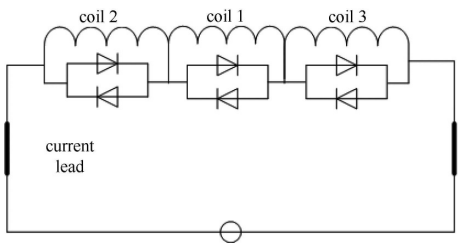

Figure 9: Quench protection circuit

The maximum central field of the solenoid reached 8.2 Tesla. The magnetic field along the axis was measured with hall probe and the result is shown in Fig. 10. When the current is 180 Ampere, the central field is 7.321 Tesla. The measured effective length is about 134mm. The fringe field on the cavity surface was also measured. Fig. 11 draws a comparison between the measured fringe field and the calculated value.

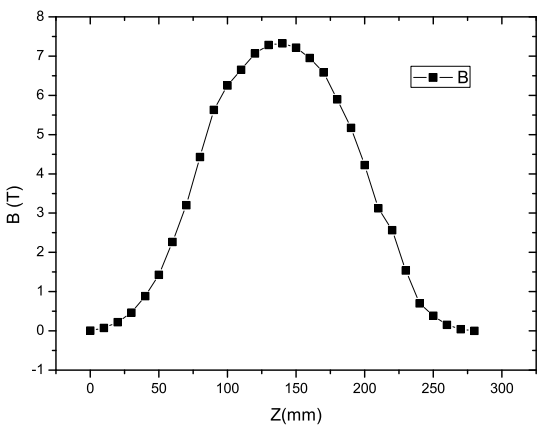

Figure 10: The measured magnetic field distribution along the axis of the solenoid

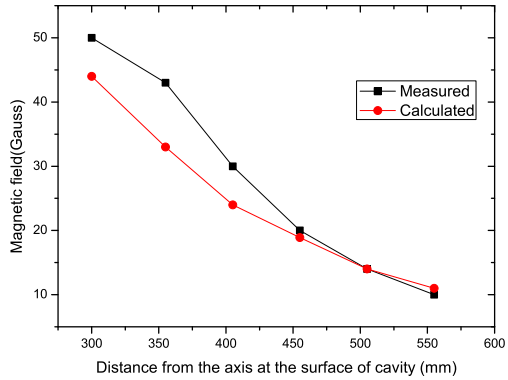

Figure 11: Comparison between the measured fringe field and the calculated value

SUMMARY

In this paper we present the design, fabrication and test of the superconducting solenoid for CADS-linac. A two step method combined Linear Programming and nonlinear optimization method was used to optimize the coils configuration. The fabrication and the test results of the prototype validates the magnetic and mechanical design of the magnet. The steering dipole will be finished and integrated to the solenoid and tested by the end of the year.

REFERENCES

[1] Ostroumov, P. N., S. H. Kim, E. S. Lessner, K. W. Shepard, R. E. Laxdal, and R. Wheatley. A new generation of superconducting solenoids for heavy-ion linac application. LINAC2003, Gyeongiu (2002).

[2] Davis, G., V. V. Kashikhin, T. Page, I. Terechkine, J. Tompkins, and T. Wokas. Designing focusing solenoids for superconducting RF accelerators. Applied Superconductivity, IEEE Transactions on 17, no. 2 (2007): 1221C1224.

[3] Terechkine, I., V. V. Kashikhin, T. Page, M. Tartaglia, and J. Tompkins. Focusing solenoid for the front end of a linear RF accelerator. In Particle Accelerator Conference, 2007. PAC. IEEE, 473C475, 2007.

[4] YANG Xiao-Liang,MA Li-Zhen, WU Wei,ZHENG Shi-Jun, DU Jun-Jie, HAN Shao-Fei, GUAN Ming-Zhil, HE Yuan. "Design of a superconducting magnet for CADS". Chinese Physics C 36 (2012): 886-890.

[5] A. W. Chao and M. Tigner, "Handbook of accelerator physics and engineering", World Scientific Publishing Co.. Pte. Ltd., 1998, p. 531.

[6] Wei, W., H. Yuan, M. Li-Zhen, H. Wen-Xue, and X. Jia-Wen. Optimal design of a 7 T highly homogeneous superconducting magnet for a Penning trap. Chinese Physics C 34 (2010): 978.

[7] H. Xu, S. M. Conolly, G. C. Scoot, and A. Macovski, Homogeneous magnet design using linear programming, IEEE Trans. Magn., vol. 36, pp. 476-483, Mar. 2000.

Copyright © 2012 by the respective authors — cc Creative Commons Attribution 3.0 (CC BY 3.0)

THE DEVELOPMENT OF TIMING CONTROL SYSTEM FOR RFQ

J. Bai, L. Zeng, S. Xiao, T. Xu
Institute of High Energy Physics, CAS, Beijing, 100049, P.R China

Abstract

In order to meet the need of RFQ accelerator, Timing extension hardware based on VME configuration has been developed. In the future, it will be used in the diagnostics system of CSNS. This paper introduces the function of Timing extension hardware, EPICS driver for Timing extension hardware and MEDM operator interface.

BACKGROUND

The core research of intense-proton beam accelerator is mainly concentrated in the field of beam loss control. Based on the intense-beam RFQ accelerator [1] which accelerates proton beam of 46mA pulse current to 35MeV at more than 7% duty factor, a beam line has been built. In order to do beam loss control experiment, many devices have been developed, one of which is Timing extension hardware. Timing extension hardware, as an important device in the running of RFQ accelerator, provides high accuracy and high stability timing trigger signals for the whole system. In the future, it will be used in the CSNS (Chinese Spallation Neutron Source).CSNS adopts EPICS [2] (Experimental Physics and Industrial Control System) as its software environment. So it is necessary to develop EPICS driver [3] for timing extension hardware.

INTRODUCTION OF TIMING EXTENSION HARDWARE

Timing extension hardware uses VME bus of A24 nonpriviledged data access address modifier [6]. It is listed below as fig. 1. Since A24 space is of predicable size 16MB, default window encompassing the full space is always provided. The A24 window is for VME bus address from 0x000000 to 0xffffff, which is usually mapped by VxWorks subroutine sysBusToLocalAdrs to local memory from 0xfa000000 to 0xfaffffff [6].

```
#define VME_AM_STD_USR_DATA     0x39    /* A24, nonpriviledged data access*/
```

Figure 1: Address Modifiers of A24 nonpriviledged data access

Timing extension hardware based on VME configuration is not only consistent with RFQ requirement, it but also avoids the disadvantage of original timing control system, achieving parameters remedy on line. When operators need to remedy parameters of original timing control system, they have to stop the accelerator and calculate the parameters according to the request of experiments, and then use dip switch to change the parameters. The whole process will last almost two hours and affect the efficiency, stability and continuity. Besides, Timing extension hardware based on VME architecture achieves utility of the same hardware to perform different functions by using reconfiguration of the FPGA, which enhances the flexibility of timing extension hardware.

Timing extension hardware has two types of functions [4]. One is providing primary timing signals for RFQ and secondary timing signals which divide frequency of primary timing signals for beam commissioning and RF system. The other is providing delaying or broadening timing signals according to the needs of various devices. In fact, the principle of these two functions is calculating clock signals. For example, primary timing outputs a timing pulse when it calculates the clock signal to the certain amount. Broadening hardware is triggered by timing signal and starts counting program. It will output a TTL pulse with the width of 3us when counting program reaches to the setting value.

Fig. 2 shows timing signals of RFQ, and the timing extension hardware is shown in Fig. 3.

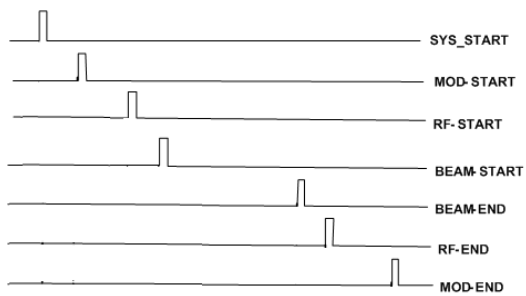

Figure 2: Timing signals of RFQ

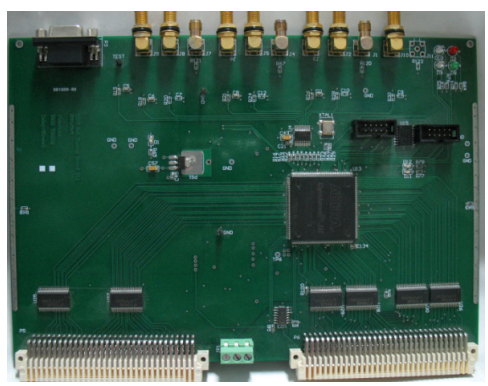

Figure 3: The timing extension hardware

Copyright © 2012 by the respective authors — cc Creative Commons Attribution 3.0 (CC BY 3.0)

Table 1: Timing control system records access registers step by step

Function	db	dbd	Device support	Driver support
Set primary timing/secondary timing value	Time:$(CARD): $(CHAN): TimingValue:set	device(ao,VME_IO, devAoTime, "Time")	devAoTime{ ….. Write_ao, ……}	Write _Val
Set delay/ broaden value	DelayOrBroaden:$(CARD):$(CHAN):Value :set			
Chose clock signal from internal or external	Time:$(CARD):ClockSignal:set	device(bo,VME_IO, devBoTime, "Time")	devBoTime{ ….. Write_bo ……}	Write _CSR
Chose logic of primary timing/secondary timing	Time:$(CARD): $(CHAN):TimingLogic:set			
Chose logic of delay/broaden	DelayOrBroaden:$(CARD): $(CHAN):Logic :set			
Chose delay or broaden	DelayOrBroaden:$(CARD): $(CHAN):Select :set			
Read timing register of card	Time:$(CARD):CSR:read	device(mbbiDirect,VME_IO, devMbbiDirectTime, "Time")	devMbbiDirectTime { ….. Read_ mbbiDirect ……}	Read_CSR
Read delay/broaden register of card	DelayOr Broaden:$(CARD):CSR:read			
Read actual primary timing/secondary timing value	Time:$(CARD): $(CHAN): TimingValue:read	device(ai,VME_IO, devAiTime, "Time")	devAiTime{ ….. Read_ai, ……}	Read_Val
Read actual delay/ broaden value	DelayOrBroaden:$(CARD): $(CHAN): Value:read			

DTYP

DTYP

DTYP

DTYP

EPICS DRIVER FOR TIMING CONTROL SYSTEM

The functions of timing extension hardware achieve by single read or write register [5]. Table 1 is provided to give an outline about how records access registers step by step.

OPERATOR INTERFACE

The operator interface which is under development makes use of MEDM [7] (Motif Editor and Display Manager). With the interface of Timing control system, operator can chose system clock, logic of primary timing and secondary timing, delay or broaden of every channel and logic of every channel. Besides, primary timing, secondary timing, delay or broaden time of each channel can be set through the Interface. Fig. 4 is the operator Interface for Timing control system.

According to the control of interface, timing extension hardware can work normally.

ACKNOWLEDGEMENTS

The authors would like to thank the CSNS Control Group, Accelerator Center, Institute of High Energy Physics, CAS to provide the EPICS platform to work on and technical support.

REFERENCES

[1] Shinian Fu, Xialing Guan. Development of High Intensity RFQ Proton Accelerator. Beijing: Atomic Energy Science and Technology 2009:1-6

[2] Argonne National Laboratory. Experimental Physics and Industrial Control System. [Online]Available: http://www.aps.anl.gov/epics/

[3] Martin R. Kraimer. IOC Application Developer Guide[M]. 1998:1-180

[4] Shuai Xiao. Lei Zeng. Xian Guo. Taoguang Xu. Timing control system of Intense-beam proton accelerator[C]. Beijing： Nuclear Electronics &Detection Technology 2011：1-7

[5] PSI. Writing EPICS Drivers

[6] WindRiver. WTN-56 Going out on the VME bus

[7] Kenneth Evans, Jr. MEDM Reference Manual: http://www.aps.anl.gov/epics/EpicsDocumentation/ExtensionsManuals/MEDM/MEDM.html

Copyright © 2012 by the respective authors — cc Creative Commons Attribution 3.0 (CC BY 3.0)

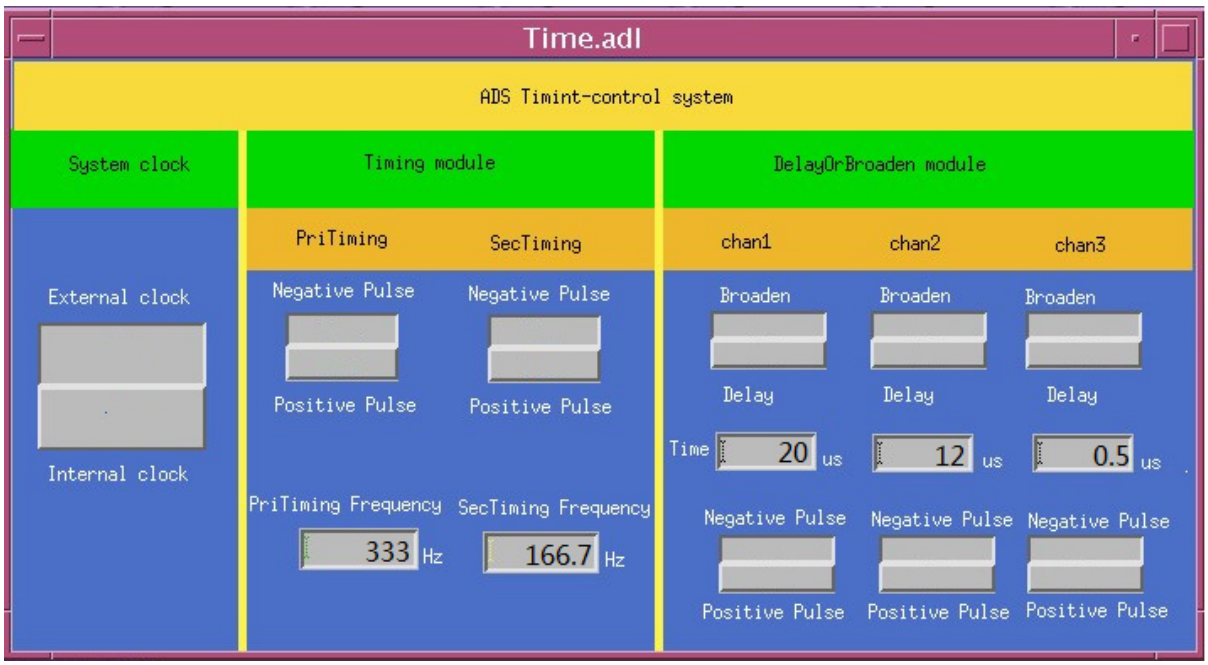

Figure 4: The operator interface

Copyright © 2012 by the respective authors — cc Creative Commons Attribution 3.0 (CC BY 3.0)

STATUS OF E-XFEL STRING AND CRYOMODULE ASSEMBLY AT CEA-SACLAY

C. Madec, S. Berry, P. Charon, J.-P. Charrier, C. Cloué, A. Daël, M. Fontaine, O. Napoly, N. Sacépé, C. Simon, B. Visentin, A. Brasseur, Y. Gasser, S. Langlois, R. Legros, G. Monnereau, J.-L. Perrin, D. Roudier, Y. Sauce, T. Vacher, CEA/Irfu, Gif-sur-Yvette, France

Abstract

As In-Kind contributor to the E-XFEL project, CEA is committed to the integration on the Saclay site of the 100 cryomodules (CM) of the superconducting linac as well as to the procurement of the magnetic shieldings, superinsulation blankets and 31 cold beam position monitors (BPM) of the re-entrant type. The assembly infrastructure has been renovated from the previous Saturne Synchrotron Laboratory facility: it includes a 200 m^2 clean room complex with 112 m^2 under ISO4, 1325 m^2 of assembly platforms and 400 m^2 of storage area. In parallel, CEA has conducted industrial studies and three cryomodule assembly prototyping both aiming at preparing the industrial file, the quality management system and the commissioning of the assembly plant, tooling and control equipment. In 2012, the contract of the integration has been awarded to ALSYOM. The paper will summarize the outputs of the preparation and prototyping phases and the status of the up-coming industrial phase.

INTRODUCTION

The 17.5 GeV superconducting RF linac of the E-XFEL project [1] will comprise 100 cryomodules (cf fig.1), after the injector module. These twelve-meter long cryomodules, deriving from the FLASH technology, include a string of eight 1.3 GHz RF cavities with an average gradient of 24 MV/m, followed by a BPM and a superconducting quadrupole.

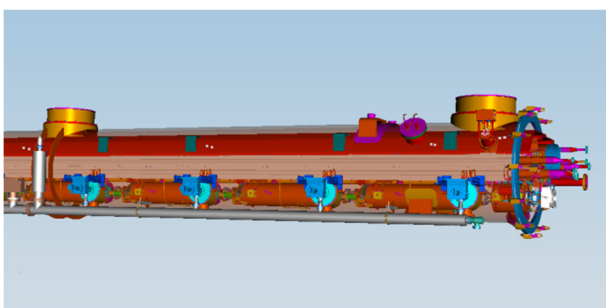

Figure 1: XFEL Cryomodule 3D-model

This string is closed by two gate valves at both ends. Within the Accelerator Consortium (AC), CEA is committed to the assembly of the 103 cryomodules over 2013 to mid-2015 with the goal to deliver one cryomodule per week to DESY for RF acceptance. Strategic decisions, shared by the AC, were taken in 2008 first to host the assembly plant on CEA premises at Saclay, using the former Saturne Synchrotron Laboratory accelerator and experimental halls, second to subcontract the 103 modules, assembly work, including 3 pre-series modules, to an industrial company for. The layout of the assembly plant (see Fig. 2), was optimized by breaking down the assembly work in seven successive blocks of one-week procedures, leading to one clean room complex for coupler and string assembly, and five cryostating workstations for the remaining cryostating work, including alignment and control operations. To allow for a fluid circulation of the cryomodules along the assembly chain even when a repair is needed at one workstation, each workstation, but the vacuum vessel cantilever (see Fig. 3), has been doubled to offer module parking possibilities.

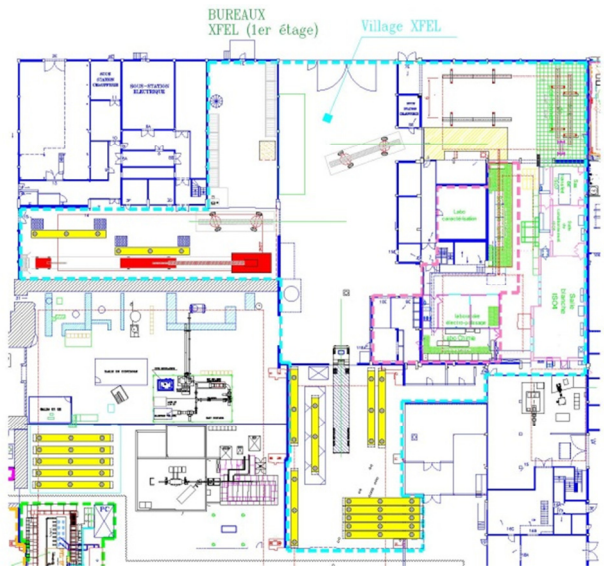

Figure 2: Layout of the XFEL infrastructure

Figure 3: Vacuum vessel and cold mass on the cantilever

OUTPUTS FROM THE PREPARATION PHASE

To ensure the integration of 103 CM at the rate of one cryomodule per week, CEA has set up a program to form

Copyright © 2012 by the respective authors — cc Creative Commons Attribution 3.0 (CC BY 3.0)

an expert team and to commission the facility. This program includes a training phase, a prototyping phase and the industrial phase.

Training phase:

In 2007, CEA and DESY have started the transfer of the knowledge by a period of observation by CEA personnel at DESY (M3 CM for FLASH) followed by a "hands-on" assembly period where CEA personnel participated in the assembly of the FLASH M8-PXFEL1 CM with the DESY team.

Pre-industrial studies:

Meanwhile, CEA has conducted industrialisation studies aiming at defining industrial equipment and methods for the cryomodule assembly. The first study has determined the workflow from the storage to the shipment, with cavity reception, clean room assembly, roll-out, alignment, vessel roll-over and coupler assembly (see Figs.2-7). The areas have been dimensioned accordingly and matched to the infrastructure which was renovated from the previous Saturne Synchrotron Laboratory facility: the 200m2 clean room complex with 112 m2 under ISO4 allows us to assemble the couplers to the cavity and two cavity strings in parallel; the *cryostating* will be held on the 1325 m2 of assembly platforms and 400 m2 are dedicated to storage.

Figure 4: PXFEL2_2 in the ISO4 clean room facility

The first fabrication file included assembly procedures with task description, duration and manpower skills definition. It included also the big tools drawing updates, tasks schedules and risk analysis. The cost estimate of the 103CM integration has been estimated. The outputs of this first study lead CEA to launch the big tool fabrication, speed-up the infrastructure set-up, establish the quality insurance plan and start the prototyping phase where CEA team is training in house on assembling 3 CM using its infrastructure and tools.

The second more detailed study finalized the tools such as the clean room tools specific to CEA infrastructure, the detailed assembly procedures with tools in use, duration of the task, incoming and outcoming parts; the parts flow has been consolidated, the stock needs have been evaluated. This study has defined the product breakdown structure, updated the risk analysis and detailed the schedule in tasks. The outputs of this study were used to place the call for tender for the 103 CM integration.

Prototyping phase:

The prototyping phase consisted of the assembly of 3 CM (namely PXFEL2_1, PXFEL3_1 and PXFEL2_2) at CEA by both CEA and DESY staff allowing qualifying the team, the tools and the infrastructure.

The infrastructure was equipped with the services and fluids for the CM assembly. Big tools such as girders and pillars (cf Fig 5) have been manufactured ahead of time and commissioned along the prototyping phase.

Figure 5: PXFEL2_2 cold mass and string hooked to the girder in the Roll-Out area

Small tools, especially those dedicated to clean room assembly (cf Fig. 6), were manufactured and commissioned during the prototype phase. Ionized gun and particle counters for clean room assembly were ordered and used to insure the required low level of particles on the part to be assembled (less than 10 particles over 1 minutes of 0.3 mm on the part to be assembled).

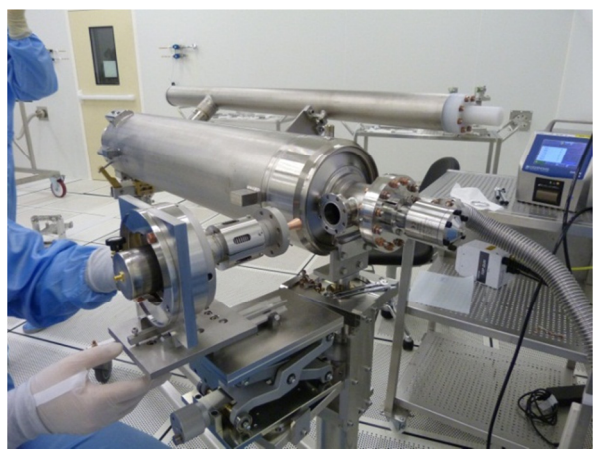

Figure 6 : coupler to cavity assembly in the clean room with tools (elevator table and coupler holding) and particle counter

Vacuum groups, equipped with RGA and slow pumping-venting system, have been installed on the clean room wall and in the coupler hall. Those groups, provided

Copyright © 2012 by the respective authors — cc Creative Commons Attribution 3.0 (CC BY 3.0)

by DESY, are designed to reduce the particles migration when pumping or venting a cavity or a coupler.

CEA has designed specific vacuum groups with a turbo pump and gauge attached to the cavity in the clean room and the primary pumps outside the clean room. Those groups are dedicated to the leak detection and venting of the cavity during the assembly. They have been ordered for the XFEL CM assembly.

The tests and controls have been detailed (RF, mechanical, vacuum, electrical), implemented and validated. The automated RF and tuner test bench have been developed for systematic measurements and recordings as well as the alignment and particle counter software. They have been tested on the prototypes.

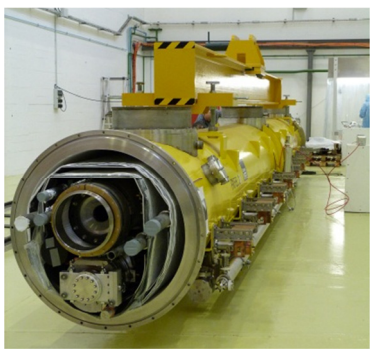

Figure 7 : CM after warm coupler assembly

The assembly procedures have been tested during a first assembly, then modified according to CEA's infrastructure and tools and rechecked on a last assembly for repetitive tasks. The part workflow from the reception to the assembly halls has been validated. Improvements on a few workstations are under evaluation, aiming at saving assembly time.

During the prototype phase, CEA and DESY established the Manufacturing Bill Of Material (MBOM [2]) which is collecting, recording, and archiving the complete mandatory fabrication information. It is focused on the parts that are needed to manufacture a CM at CEA. The MBOM also includes information about how the parts relate to each other, the inspection to be performed, the tests to be recorded, the assembly procedures, the documentation etc... The XFEL cryomodule MBOM contains roughly 500 lines i.e. 500 elements are assembled on a CM at CEA.

PROCUREMENTS

CEA is in charge of the procurement of the 800 cavity magnetic shields. The awarded company proposed some closing improvements as well as a new Cryophy™ material which was qualified on the CM prototypes.

Precut and assembled multilayer blankets for the 2K and 70K superinsulation have been ordered: they facilitate the assembly and reduce its duration. Cryogenic loss measurements on the prototype modules qualified them for the series.

CEA is also in charge of 31 cold re-entrant BPM (cf. figure 8). These BPM have been studied and prototyped at CEA [3], and tested on FLASH. The integration with the cold quadrupole is done at DESY. The electronics developed by CEA in collaboration with PSI will be implemented in the modular BPM unit [4].

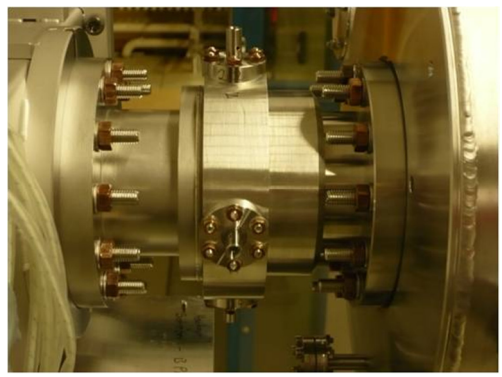

Figure 8 : BPM installed on PXFEL3_1

INDUSTRIAL PHASE

The contract for 103 CM integration has been awarded to ALSYOM in July 2012. The first phase (until Dec 2012), consists of the observation by ALSYOM of the assembly by CEA of the first pre-series cryomodule (XM-3) and the deployment of their industrial method based on the outputs of the prototyping. It also includes the set-up of the storage area, the ERP (entreprise resource planning) parameterization and the consumable parts ordering. The second phase is the training of the company team attended by the CEA team on the assembly of the second and third pre-series modules XM-2 and XM-1. From XM1 on, ALSYOM will be in charge of the series module assembly. A ramp-up period of six months is foreseen to reach the production rate of 1 CM per week. Based on quality assurance and quality control, the Acceptance Data Package (ADP) will support the first step of CM acceptance by CEA. It includes the certificate of conformity, the "as-built" configuration, the traveler, and the test and non-conformities reports. PXFEL2_2 CM ADP was built following our experience and needs, and it was delivered to DESY with the CM on Sept 4th, 2012 for approval. The second CM acceptance stage will be based on the RF test at DESY.

CONCLUSIONS

The CM factory is ready to start the assembly of the XM-3 pre-series XFEL cryomodule on September 17th, 2012.

REFERENCES

[1] E. Vogel et al. , 'Integration of the European XFEL accelerating modules', MOPB017 (this conference)
[2] L. Hagge, et al., "Parts management during fabrication at the European XFEL", IPAC2012, WEPPC005
[3] C. Simon, et al., Physical Review, 11, 082802 (2008)
[4] C. Simon, et al., the European XFEL BPM system, IPAC2010, MOP064

Copyright © 2012 by the respective authors — cc Creative Commons Attribution 3.0 (CC BY 3.0)

A LOW-LEVEL RF CONTROL SYSTEM FOR A QUARTER-WAVE RESONATOR*

J. W. Kim, D. G. Kim Institute for Basic Science, Daejeon, Korea
C. K. Hwang, Korea Atomic Energy Research Institute, Daejeon, Korea

Abstract

A low-level rf control system was designed and built for an rf deflector, which is a quarter wave resonator with a resonance frequency near 88 MHz. Its required phase stability is approximately ±1° and amplitude stability less than ±1%. The control system consists of analog input and output components, and a digital system based on an FPGA for signal processing. It is a cost effective system, while meeting the stability requirements. Some basic properties of the control system were measured. Then the capability of the rf control has been tested using a mechanical vibrator made of a dielectric rod attached to an audio speaker system, which induced regulated perturbation in the electric fields of the resonator. The control system is flexible such that its parameters can be easily configured to compensate for disturbance induced in the resonator.

INTRODUCTION

The low-level rf (LLRF) system is a control device to stabilize electromagnetic fields of the rf resonators used for electron and ion beam applications. A quarter-wave resonator was built to deflect a secondary electron beam to measure the longitudinal beam emittance of a low-energy ion beam [1, 2]. Stability required for the resonator in measuring the charge distribution of a beam bunch is around ±1° in rf phase and ±1% in amplitude, respectively.

The LLRF system is composed of analogue components in the front ends and a digital signal processing board using a field programmable gate array (FPGA), which is controlled by software based on Windows OS. The feedback loop in the FPGA needs a large phase margin to avoid loop instabilities. This kind of approach utilizing both analog and digital devices have successfully been applied to different accelerator systems [3], which often asks for more strict rf stabilities. A major merit of this system is that the rf components are readily available as commercial products employing a simple architecture, and thus curtails its cost. The properties of the LLRF system were first measured with signals generated using an attenuator to replace the pick-up signal of the cavity.

The test of the LLRF was performed using the vibrator and a model rf deflector which has a fundamental resonance frequency at 87.9 MHz in the deflection mode. The frequency of disturbance induced for testing is less than a hundred Hz because this low frequency range corresponds to resonance bandwidth for the mechanical structure similar to that of the rf deflector [4].

Numerical simulations have been performed using MATLAT tools [5] to test control methods such as one using ESO (extended state observer) and simple PID. We plan to adapt this LLRF system to use for superconducting cavities operating around at 80 MHz with further works on simulation and testing.

CHARACTERISTICS OF LLRF SYSTEM

Figure 1 shows a schematic circuit diagram of the LLRF system designed and constructed, and a photo of the components connected. The method that we chose utilizes both digital and analogue components. An analogue IQ demodulator (Analog Device model 8348) is used to convert the pick-up signal into I (in phase) and Q (quadrature phase) signals.

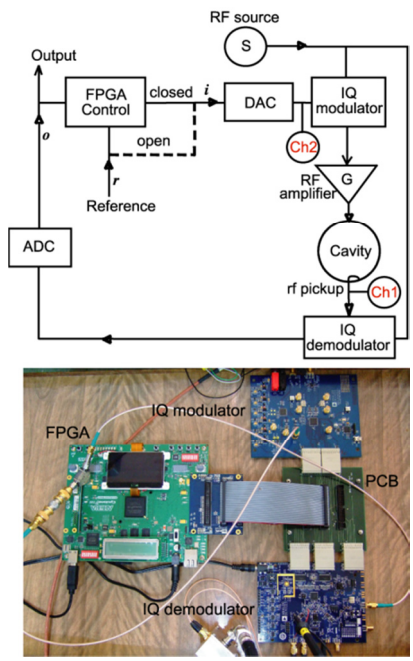

Figure 1: Upper: Schematic diagram of the LLRF system, Lower: Photo of the LLRF system showing major components. A printed circuit board (PCB) used for cable connections is also shown on the photo.

A detailed connection scheme describing the actual components used in the circuit is shown in Fig. 2. The

*Work supported by National Research Foundation Grant No. 20110018946 and by the Rare Isotope Science Project.
jwkim@ibs.re.kr

Copyright © 2012 by the respective authors — cc Creative Commons Attribution 3.0 (CC BY 3.0)

input signals are digitized by using AD 9204 analog to digital converter (ADC), and fed into the FPGA of CYCLONE III evaluation board (Altera Corp.) for signal processing. The processed signal is converted by using a digital to analog converter (DAC) AD9743, and is fed into IQ modulator (Analog Device ADL5385) to generate the control signal for the rf amplifier. The reference signal is provided by the rf source that is used to accelerate an ion beam for its longitudinal emittance to be measured. The maximum IQ gain and phase imbalances of the demodulator in use are ±0.25 dB and ±0.5◦, respectively, while the imbalances for the IQ modulator are lower.

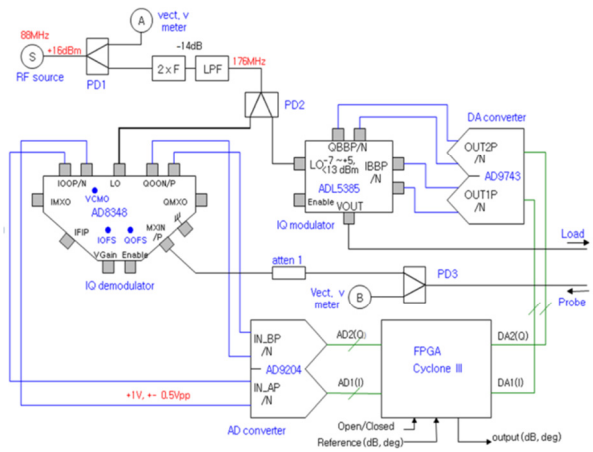

Figure 2: A detailed circuit diagram of the LLRF system.

The response of the LLRF system from the onset of disturbance, which was a change in amplitude, was checked as shown in Fig. 3. The clock of the FPGA is set as 50 MHz, and the time is counted as the number of clock cycle. The total delay for the test unit was roughly 30 cycles, *i.e.*, 0.6 μs. In this delay, about 0.5 μs came from hardware and 0.1 μs from software processing. Also, an additional delay can occur if signal processing is not performed at every clock cycle. The control loop of the amplitude induced some fluctuation at the beginning of the test, which later decayed. This result shows the transient behavior of the resonator at the disturbance. Both the amplitude and the phase change in the transient state even when the amplitude alone is disturbed. The control in steady state kept the phase variation to less than ±1◦. The phase control is independent of the amplitude control. Stabilization of the phase disturbance was also confirmed by inducing a pure phase disturbance. The reponse became smoother with averaging during software processing.

The properties of the LLRF system were first measured using the rf signals obtained with an attenuator to replace the signal from the cavity pick-up. Figure 4 shows the signals on the oscilloscope for the two modes of the loop circuit. The control signal matching the disturbance signal, which is produced by a signal generator, is shown when the loop is closed. Ch. 1 measures the error signal, and the signal shown on the open-loop disappears when the loop is closed. Ch. 2 gives the signal to control the error, which has the same frequency as that of the error signal. Noise shown on Ch. 1 in the closed-loop, which induced fluctuations in the control signal initially, was mainly generated by the mixers in the IQ demodulator. This noise was later reduced when the resonator was connected and can be reduced by installing a low-pass filter on the IQ demodulator.

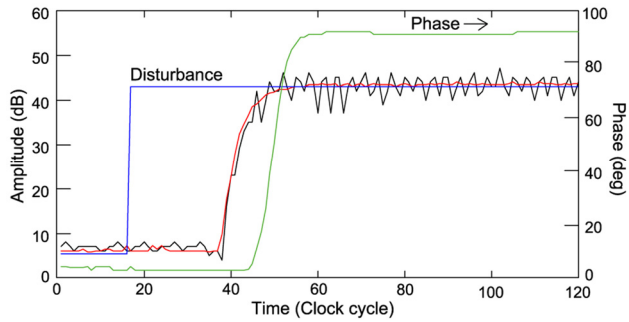

Figure 3: Controls of the amplitude and the phase by the LLRF system against a disturbance versus the time measured as clock cycle of the FPGA.

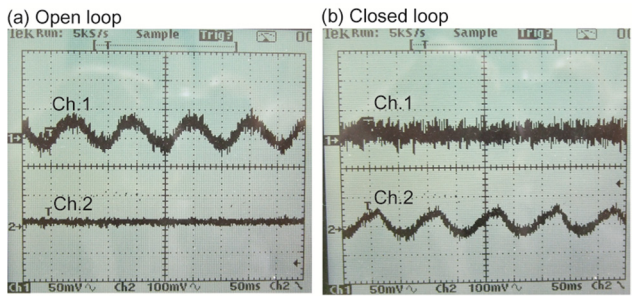

Figure 4: (a) Signals on the oscilloscope measured at two channels denoted in Fig. 1 when the loop is open, (b) when the loop is closed.

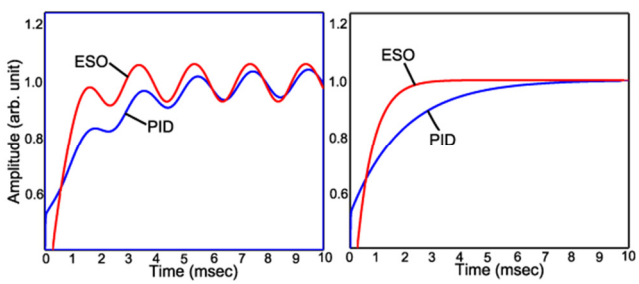

Figure 5: Comparison between ESO and PID methods. (Left) when the resonance frequency is adjusted to see variation on circuit parameters, (Right) when circuit parameters are fixed.

Different control methods have been tested by numerical simulations using MATLAB tools for the ESO and PID methods. Figure 5 shows the responses for the two kinds of disturbances, (1) when the circuit parameters

Copyright © 2012 by the respective authors — cc Creative Commons Attribution 3.0 (CC BY 3.0)

are fixed, and (2) when the resonance frequency is adjusted. It was observed that the response is slower for the PID when disturbance is a step function, but faster with small slow variation on the circuit parameters.

TEST OF THE LLRF USING A VIBRATION DEVICE

The LLRF system was tested using a full-scale model of the rf deflector, which was built prior to constructing the actual unit [1]. The resonance frequency of the lowest out-of-phase mode is 87.9 MHz, and the quality factor (Q value) measured is around 970. For the mechanical structures of the cavity having resonace frequency of around 90 MHz, major part of perturbation energy spectrum lies in the frequency range of less than 100 Hz [4]. In addition, main vibrational frequency of the support system is also expected to be less than 100 Hz. To perturb the system in the range of tens of Hz up to several hundred Hz, we devised a vibrating system driven by an audio speaker and amplifier system. The amplifier system was fed by a frequency generator.

The vibration test has been carried out at different frequencies, which were induced by a dielectric rod with a diameter of 3.0 mm firmly attched to the speaker system. The end of the rod is located between two plates of the deflector. The bead-pull method [6] was used to map the electric fields along the beam path inside the rf deflector. The shift of the frequency measured by using a Network Analyzer was 0.02 MHz when a bead made of Acetal with a diameter of 3.6 mm was inserted to the region between the two deflection plates, where the electric field is nearly uniform and its strength higher than in other region.

The control signals of the phase and amplitude when the purturbing frequencies are 20 Hz, 60 Hz and 100 Hz, are shown in Fig. 6. Noise is greatly reduced as the cavity is connected to the rf circuit as 50-MHz noise of the clock is filtered out by the cavity since its lowest resonance frequency is around 88 MHz. The steps shown in the amplitude signal corresponds to single bit of the DAC, meaning the error is controled to the hardware limit. A larger number of bits is needed for the control with a higher resolution. Also, a lowpass filter can be installed on the IQ demodulator at the cost of signal amplitude. A loss of signal intensity by 10 dB is usual, and thus an addiationl rf amplifier is needed.

The deflector system was well stabilized for the induced disturbances by the LLRF. The tests were performed againt much larger disturbances than usually occuring in the rf deflector system firmly fabricated and supported. There are some spikes appearing in the control signals in continous run, which will be addressed for further stable operation.

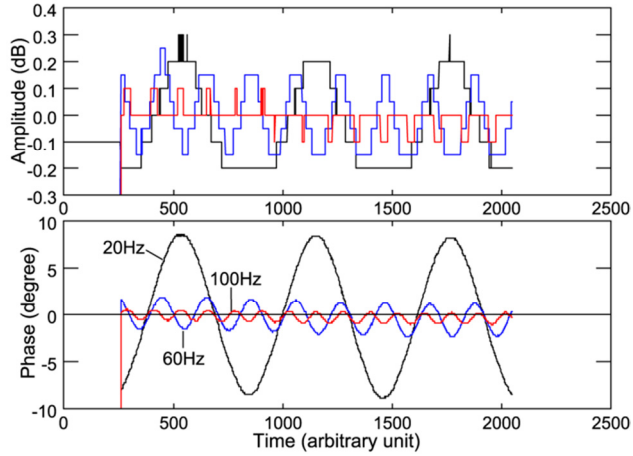

Figure 6: Upper: Amplitude signals needed for the corrections at three different frequencies of disturbance generated by a vibrating rod. Lower: Phase signals for the corrections. The same colors correspond to the same disturbance frequencies.

SUMMARY

An LLRF system has been designed based on analogue front ends and a digital processing board utilizing an FPGA. The system meets stability requirements for the rf deflector constructed for the bunch-length measurement of a low-energy ion beam. The system has been tested using a model rf-deflector cavity and by inducing controlled perturbation using an audio speaker system with a dielectric rod attached in the resonant frequency range of the cavity mechanical structure. Software to adjust the delay time and so forth can be easily configured to effectively control the perturbation, which varies the electric fields inside the cavity. It is a low cost system that can be used to control the rf fields of resonators operating in the frequency range of around 90 MHz.

REFERENCES

[1] J.-Y. Kim, D. Kim, H. Bhang and J. Kim, “A detector system for measurement of the longitudinal bunch shape of a CW ion beam”, J. Korean Phys. Soc. 58, 234 (2011).

[2] J.-Y. Kim et al., “Development of a bunch length detector”, Proc. of the Linac Conf., Tsukuba, Japan, Sep. 12-17, 2010, p. 617 (2010).

[3] H. Hassanzadega et al., “Low level rf system for the European spallation source’s Bilbao linac”, Phys. Rev. ST, 14, 052803 (2011).

[4] A. Facco, ”Mechanical mode damping in superconducting low β resonators” Proc. of 1997 Workshop on RF Superconductivity, Padova, Italy, Oct. 6-10, p. 685 (1997).

[5] MATLAB is a product of MathWorks, Inc.

[6] T. Wangler, Principles of RF Linear Accelerators, John Wiley & Sons, Inc., New York, 1998.

Copyright © 2012 by the respective authors — cc Creative Commons Attribution 3.0 (CC BY 3.0)

LLRF AUTOMATION FOR THE 9mA ILC TESTS AT FLASH

J. Branlard[1]*, V. Ayvazyan[1], G. Cancelo[2], J. Carwardine[3], W. Cichalewski[4], B.C. Chase[2], O. Hensler[1], W. Jałmużna[4], S. Michizono[5], C. Schmidt[1], N.J. Walker[1], M. Walla[1], H. Schlarb[1], [1]DESY, Germany, [2]FNAL, USA, [3]ANL, USA, [4]DMCS-TUL, Poland, [5]KEK, Japan

Abstract

Since 2009 and under the scope of the International Linear Collider (ILC) research and development, a series of studies takes place twice a year at the free electron laser accelerator in Hamburg (FLASH) DESY, in order to investigate technical challenges related to the high-gradient, high-beam-current design of the ILC. Such issues as operating cavities near their quench limit with high beam loading or in klystron saturation regime are investigated. To support these studies, a series of automation algorithms have been developed and implemented at DESY. These include automatic detection of cavity quenches, automatic adjustment of the superconducting cavity quality factor, and automatic compensation of detuning including Lorentz force detuning. This paper explains the functionality of these automation tools and shows the experience acquired during the last 9mA ILC test which took place at DESY in February 2012. The benefits of these algorithms and operation experience with them are discussed.

INTRODUCTION

In pulsed accelerators, like FLASH or the ILC, the electric field inside a cavity is ramped up at the beginning of each pulse and then held constant both in amplitude and phase for the entire duration of the beam train. To meet luminosity goals, the vector sum flat top gradient should be regulated and controlled to better than 0.1% in amplitude and 0.1 degree in phase, according to ILC specifications. At FLASH like in the ILC design, one klystron provides power to several cryomodules. Due to performance disparities among cavities, the klystron RF power is distributed according to the individual cavity gradient limits. At FLASH, this is achieved by fixing the waveguide distribution system so that the spread in power distribution matches the spread among cavity gradients within a cryomodule. As a consequence, the beam loading also differs from cavity to cavity, resulting in positive or negative gradient tilts during the flat top while the vector sum of all cavity gradients remains perfectly flat. While this tilting effect is negligible for low beam currents (below 1 mA), it can induce 10 to 20% tilts on single cavities for high beam currents such as the 9 mA ILC upgrade design, as illustrated in Fig. 1. It was demonstrated that a physical misalignment of cavities combined with a gradient tilt during beam acceleration results in a transverse dispersion of the beam [1], and would force lowering the operational gradient in the machine.

One of the goals of the ILC 9mA runs at FLASH was to demonstrate the flattening of individual beam-induced cavity tilts using loaded quality factor (Q_L) adjustments. The test was carried out on the last two cryomodules of the accelerator (ACC6 and ACC7), which contain the cavities with the highest gradient performance and are equipped with motorized controllers of the cavity Q_L.

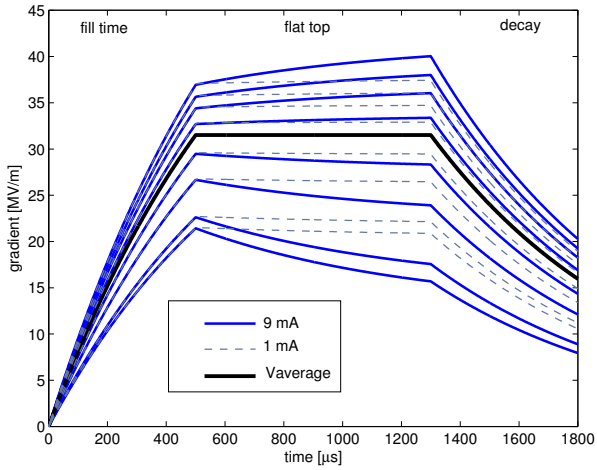

Figure 1: Cavity gradients for one cryomodule (8 cavities) with 1 mA (dotted) and 9 mA (solid) beam currents. The normalized vector-sum gradient is shown in black.

AUTOMATION

Automation for Machine Operation

Automatic Q_L control. Gradient flattening studies require frequent changes of the cavity Q_L, so the automation of these settings was necessary. A middle-layer DOOCS [2] server was implemented for this purpose. When a new Q_L setting is requested, the server compares it to the current Q_L value, which is computed for all cavities and at each RF pulse. The server then moves the coupler motor to modify the position of the coupler antenna, effectively changing the cavity Q_L and bandwidth, until the measured Q_L value matches its setting. A discrete-time feedback control scheme is applied, where the input error is the difference between measured Q_L and setting, and the controller output directly drives the coupler motor. To avoid over exercising the coupler motor, a move is only requested if the Q_L error exceeds a certain threshold. The server robustness was improved by taking into account exceptions such as out-of-range Q_L settings, invalid Q_L measurements or motor reaching the end of its excursion, etc. A complete description of the automatic Q_L server is found in [3].

* julien.branlard@desy.de

Copyright © 2012 by the respective authors — cc Creative Commons Attribution 3.0 (CC BY 3.0)

Automatic cavity tuning with piezo. During normal FLASH operation, coarse cavity tuning is performed using the cavity motorized tuner, while fine tuning and compensation for Lorentz force detuning (LFD) is achieved with the piezos mounted onto each cavity tuner structure [4]. A pulsed sinusoidal excitation of the piezo is used to compensate for LFD. A DOOCS server automates this process by computing the cavity detuning during the pulse, and adjusting the piezo stimulus parameters (DC offset, AC amplitude, frequency and pulse delay) to maintain a minimal detuning over the duration of the flat top. This server includes protective measures to prevent over-stressing the piezos. The frequency and the maximum total amplitude of the excitation are limited. Should the cavity frequency drift outside of the safe piezo tuning range, an alert is given to the operator who can then choose to tune the cavity with the motorized tuner, hence, re-centering the piezo correction in its nominal operating range.

Automation for Machine Protection

Cavity gradient limiters. Gradient limiters are implemented inside the controller board, effectively comparing each cavity gradient to a settable threshold for the entire duration of the RF pulse. The RF drive is truncated should one cavity gradient exceed its limiter value. Typically, these thresholds are set to prevent any cavity gradient from going above its quench gradient. As a compromise between safe operation and performance optimization, the limiters are conservatively set 1-2 MV/m below quench limit for nominal RF pulse length. This action is effective in feedforward and in feedback mode.

Cavity gradient pre-limiters. In addition to the cavity limiter described above, each cavity is also assigned a pre-limiter, typically set 0.5-1 MV/m below the cavity limiter. During the RF pulse, every cavity gradient is also compared to its pre-limiter value. If this threshold value is reached (for any cavity), the vector sum set point is lowered within the pulse, by 1 μsec increments until the cavity gradient falls back into its safe zone, or until a maximum number of steps is reached. The action of cavity limiters and the pre-limiters are depicted in Fig. 2. Because it is acting on the vector sum set point, this action is only effective when operating in feedback mode.

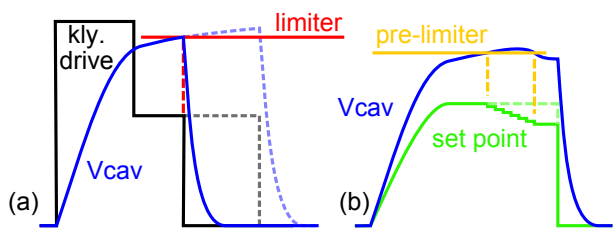

Figure 2: Actions triggered by the cavity limiter (a) and pre-limiter (b).

Quench detection. A quench detection server compares individual cavity Q_L to their previous values averaged over the last N pulses ($N \approx 20$). A sudden drop in Q_L (typically larger than 5×10^5) triggers a quench alert which results in shutting the RF off on the next pulse. Due to server latency, the reaction to a detected quench can be delayed by one RF pulse. The pre-limiters are intended to prevent quenching without tripping off the RF. The limiter and quench server are only triggered if the pre-limiter failed to act.

Tuning Approach

A first attempt at flattening beam-induced gradient tilts was successfully implemented during the 9mA run at FLASH in 2011 [5]. Optimized Q_L values were first calculated for a given beam current using simulations. Setting the predicted optimized Q_L values at FLASH achieved flattening of the gradient tilts to better than 1%. Fig. 3 shows the simulated cavity gradient tilts after Q_L optimization for a nominal beam current of 4.2 mA. Due to their low operating gradients, cavities 5 and 6 of cryomodule ACC6 were not included in the optimization algorithm, however, the net effect of flattening all other cavities combined with the feedback vector sum control contributed to flattening the gradient of these two cavities as well. One set of optimized Q_L values is given in Table 1. When optimized Q_L's converge toward low values, their implemen-

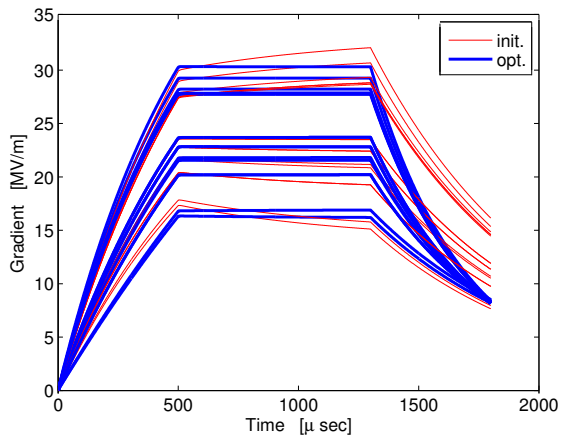

Figure 3: Simulated cavity gradients for ACC6 and 7 before and after Q_L optimization for $I_b = 4.2$ mA.

Table 1: Initial and optimized Q_L values [$\times 10^6$].

ACC6	C1	C2	C3	C4	C5	C6	C7	C8
init	3	3	3	3	3	3	3	3
opt	1.6	1.6	1.7	1.7	3	3	2.1	2.1
ACC7	**C1**	**C2**	**C3**	**C4**	**C5**	**C6**	**C7**	**C8**
init	3	3	3	3	3	3	3	3
opt	2	2	1.9	1.9	1.7	1.7	2.2	2.2

Copyright © 2012 by the respective authors — cc Creative Commons Attribution 3.0 (CC BY 3.0)

tation at FLASH can be troublesome as some cavities have a minimum achievable Q_L value limited to 1.8 to 1.9×10^6. The next step was to implement a simple feedback control on individual Q_L settings, using the corresponding cavity gradient tilt as error signal. Proportional gains were chosen conservatively, resulting in slower Q_L adjustments but avoiding over-exercising the coupler motors. This approach was successfully implemented during the last 9mA test at FLASH.

RESULTS

Fig. 4 shows the three step Q_L optimization sequence for the cavities of ACC6 and ACC7. The gradients are normalized to their beam arrival time value. Also shown in thick is the toroid signal, scaled for comparison with the cavity gradients. Initially, all cavities have their Q_L set to the default 3×10^6 value. The beam train is kept short (400 μsec) and the gradient tilts induced by the beam loading are clearly visible during the first 400 μsec of the flat top, Fig.4(a). The individual cavity Q_L are then optimized automatically so that all gradients are flat with beam, Fig.4(b). While the optimized Q_L values flatten the gradients with beam, they also worsen the tilts in the flat top region where no beam is present. In the last step (c), the beam train is extended to its full 800 μsec. While this Q_L optimization scheme had been previously simulated and its feasibility verified, it is the first time that it was successfully implemented at FLASH. With optimized Q_L, all gradients were kept flat with a 0.2% peak-to-peak accuracy, while accelerating a full 800 μsec beam train. To complete the test, the laser was blocked and later unblocked, to simluate a beam-off / beam-on scenario. This was done keeping all Q_L optimized for full beam conditions. When the beam was switched off, all cavities gradient tilted. The cavities with a positive tilt exceeded their pre-limiter threshold resulting in the automatic lowering of the set point (during the same RF pulse), hence, avoiding any quench scenario. This protective measure is a direct result of the cavity prelimiters, as explained in the previsous section. When the beam was re-enabled, all cavities returned to their flat gradient profile; no beam was lost, no cavity quenched during this exercise.

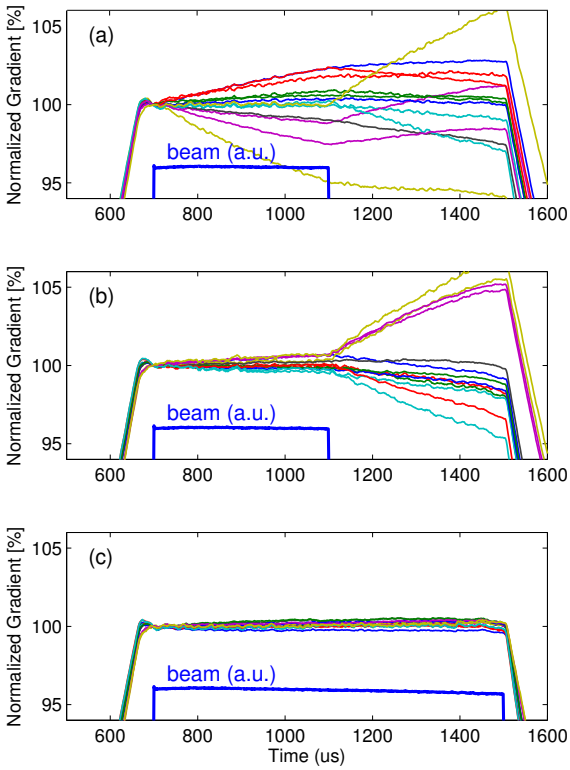

Figure 4: ACC6 and ACC7 normalized cavity gradients with default Q_L values (a), after optimization (b) and with full beam train length (c).

One key lesson from this test is the importance of precedence among automation algorithms. "Run-away" scenarios were experienced during the Q_L optimization phase. Indeed, changing Q_L will affect the cavity gradient, influencing the Lorentz force detuning, which in turn will trigger a counter action from the piezo automation, resulting in a positive feedback situation for the Q_L automation algorithm. To prevent such a situation, careful exception handling needs to be implemented. For example, one can wait until the piezo feedback is finished compensating for Lorentz force detuning, before applying the next iterative step of Q_L optimization. The feedback gains on automatic piezo control and Q_L control are also of crucial importance and should be chosen so as not to make the system unstable. These issues will be investigated during the next 9mA test scheduled for September 2012 at DESY.

SUMMARY AND OUTLOOK

A series of automation tools were developed to support the high-gradient, high-beam current conditions required for the ILC 9mA studies at FLASH. These tools are implemented as a combination of firmware modules and high-level software. The functionality of these automated tools was explained and the results they allowed to achieve were presented. A key conclusion from this study is the importance of arbitrating between these various automation tools, as they can have conflicting actions and jeopardize the machine stability. Priority among automation servers and exception handling are two key topics on the agenda of the next 9mA study scheduled for September 2012.

REFERENCES

[1] K. Kubo, "Effect of Cavity Tilt and RF Fluctuation to Transverse Beam Orbit Change in ILC Main Linac", KEK 2010

[2] `http://doocs.desy.de`

[3] W. Cichalewski *et.al.* "SC Cavities Automatic Loaded Quality Factor Control at FLASH", Real Time conf. 2012

[4] K. Pryzgoda *et.al.* "Piezo Control for Lorentz Force Detuned SC Cavities of DESY FLASH", IPAC 2010

[5] J. Carwardine *et. al*, "Report on the 2^{nd} Workshop on Linac Operations with Long Bunch-trains", ILC report 2011-032

Copyright © 2012 by the respective authors — cc Creative Commons Attribution 3.0 (CC BY 3.0)

PRECISION REGULATION OF RF FIELDS WITH MIMO CONTROLLERS AND CAVITY-BASED NOTCH FILTERS

C. Schmidt*, S. Pfeiffer, J. Branlard, H. Schlarb (DESY, Hamburg),
W. Jalmuzna (TUL-DMCS, Poland)

Abstract

The European XFEL requires a high precision control of the electron beam, generating a specific pulsed laser light demanded by user experiments. The low level radio frequency (LLRF) control system is certainly one of the key players for the regulation of accelerating RF fields. A uTCA standard LLRF system was developed and is currently under test at DESY. Its first experimental results showed the system performance capabilities. Investigation of regulation limiting factors evidenced the need for control over fundamental cavity modes, which is done using complex controller structures and filter techniques. The improvement in measurement accuracy and detection bandwidth increased the regulation performance and contributed to integration of further control subsystems.

INTRODUCTION

The European Free Electron Laser XFEL is a free electron laser generating X-Ray laser light of tunable wavelength by the SASE process, using an electron beam accelerated to about 17.5 GeV, in a pulsed operation mode. Providing its users stable and reproducible photons, requires a very precise control of acceleration fields. Developing and studying LLRF hardware and control strategies for the XFEL benefits from implementing and testing concepts at the Free electron LASer Hamburg FLASH. The latest renovation of the LLRF system is a change of the controller hardware to an uTCA based technology standard. One major impact for the LLRF regulation is the change of field detection, sampling frequency and precision of signal processing. Especially the higher sampling frequency allow for direct measure of further dynamics in the feedback loop.

It is well known that next to the acceleration mode, there exist further fundamental modes in a resonator effecting the closed loop system [1]. Especially the so called $8\pi/9$-mode generating a significant limitation on the maximum loop gain. In this paper a control concept is presented which has been implemented and tested at FLASH. Filtering approaches and measurements for the next fundamental mode are outlined. This allows to keep the relative amplitude and absolute phase error below the XFEL requirements of 0.01 % (rms) and 0.01 degrees (rms).

* christian.schmidt@desy.de

REGULATION LIMITING FUNDAMENTAL CAVITY MODES

The Tesla type cavities used for the XFEL linear accelerator are operated in the so called π-mode. Next to the acceleration mode there exist further fundamental modes hosted by this resonator. Resonance frequencies have been measured and further theoretical background can be found in [1]. A sketch of the on axis electrical field distribution in beam direction for these modes can be found in Fig. 1.

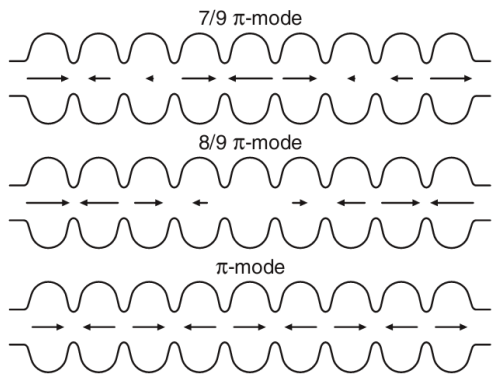

Figure 1: Sketch of electrical field $\vec{E}_z$ distribution along the axis for the acceleration and the two next fundamental modes of Tesla type cavities [1]

Exciting this resonance modes lead to a degradation of the regulation performance up to an unstable loop. Furthermore it is limiting the parameter area which can be used for the controller design. So far only aliased contributions have been measurable due to the lower sampling frequency of $f_s = 1$ MHz, and actively suppressed using a complex feedback controller. Identifying the location has been done by bandwidth sweeping techniques in iterative processes [2]. With the upgrade of the LLRF system the sampling frequency of the LLRF digital processing has been increased to 9 MHz to meet the given intra train bunch repetition frequency of XFEL. This allows to measure directly the next two fundamental modes, $8\pi/9$ and $7\pi/9$, which are located about 800 kHz and 3 MHz below the π-mode carrier frequency of 1.3 GHz. Excitation measurements have been tested at FLASH to identify there exact location.

MEASUREMENT RESULTS

Defining the necessary system control parameters requires knowledge of the particular system dynamics. Be-

Copyright © 2012 by the respective authors — cc Creative Commons Attribution 3.0 (CC BY 3.0)

side deriving the model from physical consideration there exist methods to treat the system as unknown and derive knowledge by exciting it and measuring the response. In addition, when considering a closed loop system, it is necessary to estimate its performance and stability in terms of changing system parameters. The results displayed in the following have been done at the FLASH facility with the uTCA based control system at the first acceleration module.

Resonant mode excitation scans

For the following presented measurement a very simplified approach has been chosen for identifying the location of resonance modes for all cavities within one cryomodule. Since it is known that the $8\pi/9$-mode is located at about 800 kHz, a sinusoidal excitation signal, which is modulated during the RF pulse flattop, is applied on the drive signal. Within one step of this scan, a specific excitation frequency is taken and a couple of pulses are recorded for each cavity. Taking the amplitude response allows to scan through a defined frequency range and record a system frequency response plot, as shown in Fig. 2.

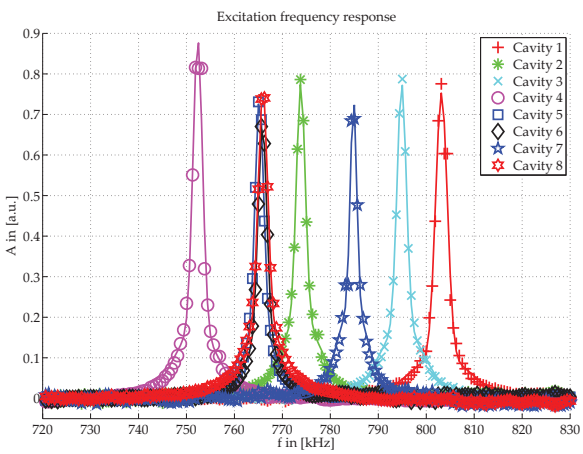

Figure 2: Individual cavity response to a sweeping sinusoidal excitation modulated to drive signal

It can be observed that there exists a spread of resonance frequencies for individual cavities of about 50 kHz, whereas 3 cavities have almost the same resonance frequency. This derives the question which distribution would be more feasible from controls perspective? Assuming all cavities within the vector sum have identical mode frequencies, suppression can be done using a narrow band notch filter. Whereas all modes are equally distributed their contribution would be suppressed by $1/N$, where N defines the number of cavities within this vector sum. Since both cases are hard to realize, individual filtering each cavity is combining both approaches.

Next also the $7\pi/9$-mode can be identified using the same approach which is presented in Fig. 3.

One can observe comparable results in terms of spread of resonance frequencies for this scan. Identifying each cryomodule location of resonance modes is one of the initial LLRF characterization measurement done in the module test stand before installation in the XFEL tunnel.

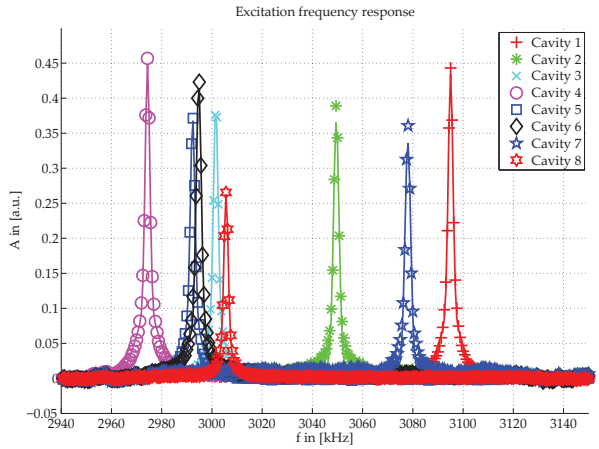

Figure 3: Individual cavity response to a sweeping sinusoidal excitation around 3 MHz, comp. Fig 2

Characterization of feedback loop parameters

From control theory it is known that within digital control loops the processing delay introduces phase lags in the system which reduces the gain margin of the closed loop system. Having additional resonance peaks in the system this effect even leads to stability regions as function of the delay, [1]. To study this effect an additional loop delay has been introduced by shifting the output signal in steps of 81 MHz clock cycles. For each measurement point the proportional gain has been increased and the VS error has been recorded, this is shown in Fig. 4.

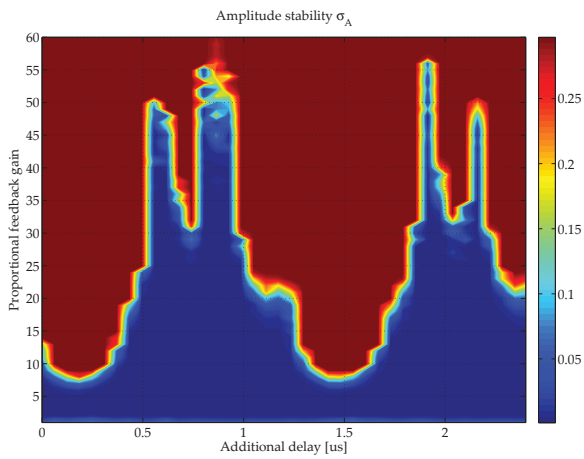

Figure 4: Stability diagram for scanning the amplitude error as function of feedback gain and additional loop delay

It is clearly visible that for the initial system delay this leads to instabilities already for small feedback gains. In addition one can see that the distance between two unstable regions is about 1.25 us which corresponds to 800 kHz

Copyright © 2012 by the respective authors — cc Creative Commons Attribution 3.0 (CC BY 3.0)

resonance frequency. Once applying a notch filter for this particular mode, further instability regions are visible in Fig. 5.

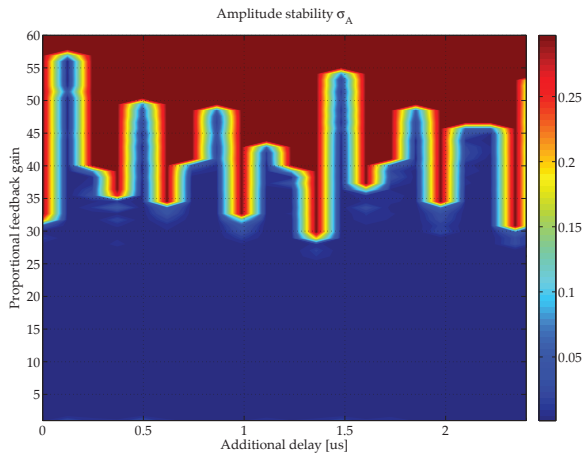

Figure 5: Stability diagram compare Fig. 4 with applied band-stop filters

Comparable to the previous plot one can observe stability regions, which are separated by about 300 ns, fitting to the $7\pi/9$-mode location.

REGULATION STRATEGY

The spread of resonance frequencies within one cryomodule requires a broad band notch filter to sufficiently suppress all individual cavity contributions. First only the $8\pi/9$-mode is considered. With the change of the LLRF system and increased hardware capabilities it turned out to be preferable to introduce individual filters in a preprocessing stage before computing the vector sum. This allows to reduce the bandwidth of the notch filter and individual tuning. Realization is done by a second order IIR filter:

$$\begin{pmatrix} \widetilde{u}_I(k) \\ \widetilde{u}_Q(k) \end{pmatrix} = \begin{bmatrix} F(z) & 0 \\ 0 & F(z) \end{bmatrix} \cdot \begin{pmatrix} u_I(k) \\ u_Q(k) \end{pmatrix},$$

where each controller transfer function is implemented as

$$F(z) = \frac{b_0 + b_1 z^{-1} + b_2 z^{-2}}{1 + a_1 z^{-1} + a_2 z^{-2}}.$$

The filter is designed such that data processing is done internally with a higher clock frequency, allowing usage of the same filter stage for multiple channels, minimizing the implementation costs in terms of FPGA space. Keeping the system most generic, this filter can be used for other applications, by application of a different set of coefficients computed by the control system server.

A comparison of the closed loop regulation with and without applied filters for equal feedback parameters is shown in Fig. 6.

It can be easily observed how the $8\pi/9$-mode oscillations on the signals are filtered such that only pulse to pulse

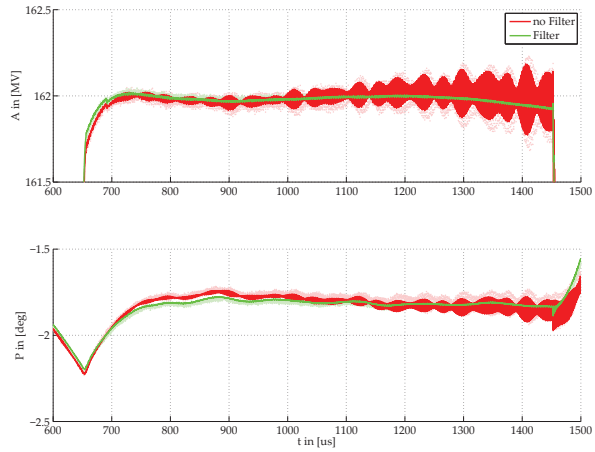

Figure 6: Zoomed flattop region of regulation with proportional feedback, with and without $8\pi/9$-mode filter

fluctuations are visible. A higher feedback gain can be achieved without adjusting the loop delay of the system.

CONCLUSION AND OUTLOOK

With the change of the LLRF control system a strategy for regulation of fundamental modes had to be developed. Recent measurements show the distribution of resonance modes within one cryomodule demanding active suppression strategies to fulfill performance specifications of the XFEL. Implementation of individual narrow band notch filters in the preprocessing stage for each cavity allows to improve the regulation performance of the closed loop system. Suppression of the $7\pi/9$-mode is intended to be done using a complex multiple input/output (MIMO) controller. Since the mode location, measured at about 3 MHz, is far outside the closed loop bandwidth allows to use a broad band notch filter at the output stage of the controller. Further measurements are planned to study the interaction of these modes with the electron beam.

REFERENCES

[1] Elmar Vogel, "High gain proportional rf control stability at TESLA cavities", PHYSICAL REVIEW SPECIAL TOPICS - ACCELERATORS AND BEAMS, 10, 2007, THZCH03

[2] S. Pfeiffer, G. Lichtenberg, C. Schmidt, H. Schlarb, H. Werner, Design of an Optimal and Robust Controller for a Free-Electron Laser Exploiting Symmetries of the RF-System, *51st IEEE Conference on Decision and Control*, Maui, Hawaii, USA, 2012

[3] C. Schmidt, M. K. Bock, S. Pfeiffer, H. Schlarb, W. Koprek, W. Jalmuzna ,"Feedback Strategies for Bunch Arrival Time Stabilization at FLASH Towards 10 fs", FEL'2011, Shaghai, August 2011, THPA12,http://www.JACoW.org

Copyright © 2012 by the respective authors — cc Creative Commons Attribution 3.0 (CC BY 3.0)

MAGNETIC CHARACTERIZATION OF THE PHASE SHIFTER PROTOTYPES BUILT BY CIEMAT FOR E-XFEL*

I. Moya#, J. Calero, J.M. Cela-Ruiz, J. de la Gama, L. García-Tabarés, A. Guirao, J.L. Gutiérrez, L.M. Martínez, T. Martínez de Alvaro, E. Molina Marinas, L. Sanchez, S.Sanz**, F. Toral, C. Vázquez, CIEMAT, Madrid, Spain
J. Campmany, J. Marcos, V. Massana, CELLS, Barcelona, Spain

Abstract

The European X-ray Free Electron Laser (E-XFEL) will be based on a 10 to 17.5 GeV electron linac that will accelerate the beam used in the undulator system to obtain ultra-brilliant X-ray flashes for experimentation. The so-called intersections are the transitions between undulators, where a quadrupole on top of a precision mover, a beam position monitor, two air coils and a phase shifter are allocated. CIEMAT participates in the development of the phase shifters (PS), as part of the Spanish in-kind contribution to the E-XFEL project. The updated design of the phase shifter is presented here to improve its behaviour as a result of the measurements on the first prototype, which did not fulfil the first field integral specification. This paper describes the magnetic measurements carried out on the last two prototypes in the test bench at CELLS, together with the tuning process to decrease the field integral dependence with gap.

INTRODUCTION

The E-XFEL phase shifter will be located at the intersections in-between the undulators (Figure 1). The role of the phase shifter is to adjust the phase of the electron beam and the radiation when entering into an undulator according to different required beam energies and wavelengths. The main specifications [1, 2] that the device must currently satisfy can be found in Table 1.

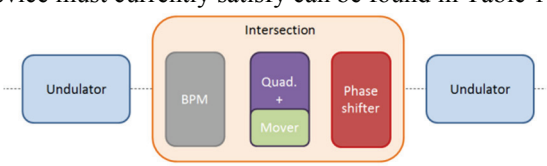

Figure 1: Undulator system intersection layout.

Four magnetic modules in a hybrid Halbach array produce a double sinus magnetic field in the mid-plane. The magnetic modules are surrounded by a pure iron yoke to enhance the phase integral value and weaken the fringe fields at nearby elements (Figure 2). The variation of the magnetic field strength is obtained by approaching or moving further the magnetic modules. Upper and lower modules move simultaneously with a unique spindle.

DEVELOPMENT OVERVIEW

The conceptual design and a first prototype were developed by DESY [1], based on the experience gained from TESLA project [3]. Up to now, CIEMAT has developed three prototypes in collaboration with industry, as part of the Spanish in-kind contribution to the facility. The first CIEMAT prototype design [4] was based on the previous DESY prototype. Some design modifications were already introduced, agreed with the E-XFEL counterparts, in order to ease fabrication and assembly. That prototype fulfilled all the specifications, except the most challenging one, the variation of the first field integral with the gap (DESY prototype had failed as well).

In agreement with the E-XFEL, CIEMAT had developed a magnetic measurement bench based on a moving long coil connected to an analog integrator [5]. However, there are still some problems to get the required accuracy, incompatible with the project timeline.

Table 1: Technical Specifications

Magnetic specifications	
Min. phase integral at gap 10.5 mm (21ºC)	23,400 $T^2 \cdot mm^3$
Max. variation of 1st field integral with gap	± 0.004 T·mm
Max. variation of 2nd field integral with gap	± 67 $T \cdot mm^2$
Mechanical specifications	
Gap	10.5 to 100 mm
Gap repeatability in bidirectional movement	± 50 µm
Gap repeatability in unidirectional movement	± 10 µm
Gap speed	0.01 to 10 mm/s

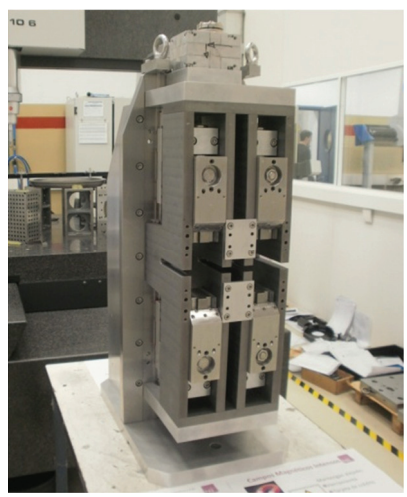

Figure 2: Third CIEMAT prototype

*Work supported by Spanish Ministry of Science and Innovation under SEI Resolution on 17-Sept.-2009 and project ref. AIC-2010-A-000524
**S.Sanz is now with Tecnalia Energy, Spain.
#ivan.moya@ciemat.es

Copyright © 2012 by the respective authors — cc Creative Commons Attribution 3.0 (CC BY 3.0)

As a consequence, in November 2011, the E-XFEL organized an external panel review to assess the problem. The main recommendations of the panel review were: 1) trying to relax by all means the first field integral specification, and 2) the use of standard methods for the magnetic measurements. On the one hand, the E-XFEL revisited the first field integral specification [6]: it can be up to 0.018 T·mm for gaps below 16 mm, but still below 0.004 T·mm for larger gaps. However, the mechanical reproducibility is stricter, only a 10 µm deviation in bidirectional movements is allowed. E-XFEL discarded the possibility to use the nearby air coil correctors to compensate the first field integral variation provided by the phase shifters. On the other hand, CIEMAT decided to characterize the devices at the CELLS test-bench [7, 8], which is based on flipping coil and Hall probe techniques (Table 2), for the field and phase integral measurements, respectively. It is worth to highlight that the flipping coil bench accuracy is the state of the art (the bench is produced by ESRF, Grenoble), but still close to the specification for the E-XFEL phase shifter.

Table 2: Main specifications of the CELLS test-bench

Hall probe test bench main specifications	
Field absolute accuracy	0.5 Gauss
Field integral accuracy	About 0.01 T·mm
Minimum step size	20 µm
Flipping coil main specifications	
Field integral absolute accuracy	0.001 T·mm

Finally, the phase shifter design was reviewed to improve the magnetic behaviour and, at the same time, to correct small mechanical problems. CIEMAT decided to produce two units, in order to check the first field integral variation and to validate the design for the industrial production of 91 units.

MAGNETIC ADJUSTMENT

The design of the phase shifter allows regulating the vertical position of the lateral magnets and also the vertical position and transverse orientation (tilt angle) of each pole by means of screws (Figure 3).

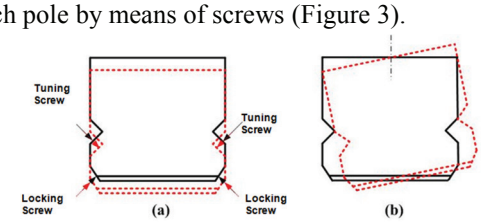

Figure 3: Pole adjustment: height (a) and tilt (b) shifts [9]

The effect of those movements on the first field integral can be noticed as follows:

- Lateral magnet vertical position: the vertical field is enhanced when the magnet is moved towards the middle plane.
- Pole vertical position: the vertical field is enhanced when the pole is moved towards the middle plane.
- Pole tilt: the horizontal field is enhanced in the direction of the tilting.

Besides, shims of different magnetic materials can be used for additional magnetic calibration. They must be placed symmetrically to affect only the horizontal or vertical field component.

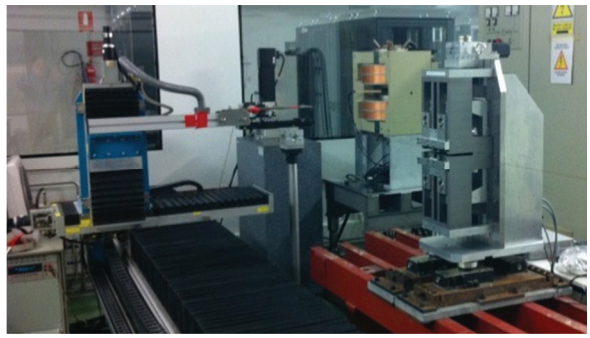

Figure 4: 3rd CIEMAT prototype at CELLS test-bench

MAGNETIC MEASUREMENTS AND ANALYSIS

It is worth to mention that the reproducibility of the flipping coil bench measurement of the first field integral is better than 0.001 T·mm, although there is an uncertainty about the absolute value, because the phase shifter is 200 mm long but the flipping coil length is 4 m. The iron yoke shields partially the ambient field. When no phase shifter is present, the first field integral is -0.018 T·mm in the horizontal direction, and -0.157 T·mm in the vertical one. They are due to the Earth field and the synchrotron storage ring contribution, being constant during the measurements. When the phase shifter is present and open at maximum gap, the first integral of horizontal field is -0.024 T·mm (second prototype) and -0.021 T·mm (third prototype), while -0.153 T·mm and -0.157 T·mm for the vertical component. We have assumed -0.020 (horizontal) and -0.153 (vertical) T·mm as a fair value for the reference value, with a confidence margin of ± 0.002 T·mm. Further studies are ongoing to fix this value with more accuracy.

Second CIEMAT prototype (PS2)

Figure 5 depicts the variation of the first field integral with the gap. The vertical one is within specifications (± 0.004 T·mm for gaps above 16 mm, ± 0.018 T·mm for gaps below 16 mm), but not the horizontal one. It was not possible to decrease the horizontal field integral, neither with shims nor tilting the poles. A weak remnant magnetization is present in the horizontal direction, but it is very difficult to correct it with external coils.

The most likely explanation is coming from the problems found during the assembly of this particular unit. The dowel pins which placed the iron yoke on the support plate were wrongly machined, and hence the iron was finally positioned without dowel pins. Since the magnetic modules have been assembled and disassembled

Copyright © 2012 by the respective authors — cc Creative Commons Attribution 3.0 (CC BY 3.0)

several times, some residual magnetization of the yoke may take place.

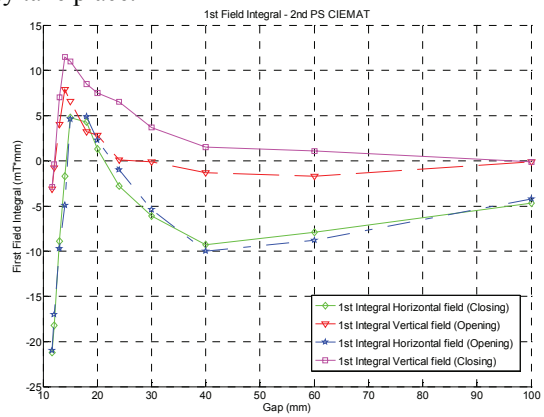

Figure 5: Measured first field integral dependence with gap (second CIEMAT prototype).

On the other hand, a slight hysteresis has been measured in the vertical component, with a maximum of 0.006 T·mm at a gap of 24 mm. A careful study of the operation strategy must be done to conclude if it can be a problem for the undulator performance. It was checked that no mechanical hysteresis (backlash) was present.

The second field integral is well below the requested tolerances (67 T·mm^2) for all gaps: ± 8 T·mm^2 for the vertical component and ± 4 T·mm^2 for the horizontal one.

The phase integral calculated from the measurements of the field profile in the middle plane at 10.5 mm gap is 23,702 T^{2}mm^3 (at 21ºC).

Third CIEMAT prototype (PS3)

Figure 6 depicts the variation of the first field integral with gap. In the opening movement, both field components are within specifications. When a bidirectional movement is considered, in the case of the vertical field, hysteresis is present again, with a maximum of 0.010 T·mm at gap 20 mm. At this point, one can conclude that the hysteresis is inherent to the existing design, because measurements also match numerical simulations with FEM when modelling real materials. No mechanical hysteresis (backlash) is present.

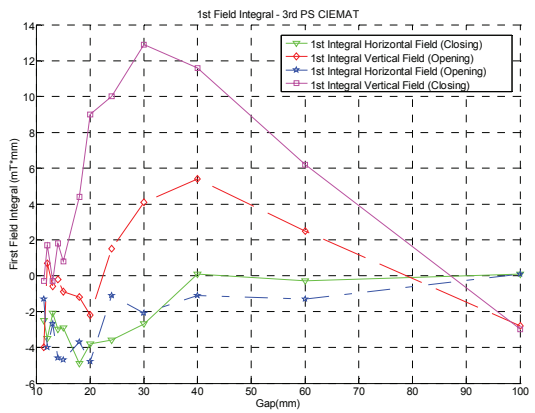

Figure 6: Measured first field integral dependence with gap (third CIEMAT prototype).

The second field integral is well below the requested tolerances (67 T·mm^2): ± 4.4 T·mm^2 for vertical and horizontal components and all gaps.

The phase integral calculated from the measurements of the field profile at 10.5 mm gap is 23,478 T^{2}mm^3 (at 20ºC).

CONCLUSIONS

CIEMAT is contributing to the E-XFEL with the phase shifters for the undulator intersections, among other components. For the PS, the most challenging specification is the variation of the first field integral with gap. The design has been revisited after the first prototype characterization. As consequence, for the next two prototypes, the first field integral variation has been reduced. Specifically, the last one is about the allowed limits. Besides, a small magnetic hysteresis has been measured in the vertical component. That effect is inherent to the existing design and the magnetic materials available in the market for industrial production. CIEMAT prototypes have successfully complied with the rest of specifications.

ACKNOWLEDGMENTS

The authors want to thank valuable discussions with J. Pflueger and S. Karabekyan (E-XFEL), and fruitful suggestions from the Spanish companies (Desarrollos Mecánicos de Precisión, Ingeniería Index, Utillajes Huerta) involved in the fabrication process.

REFERENCES

[1] J. Pflueger, Y. Li, H. H. Lu "The permanent magnet phase shifter for the European X-ray free electron laser", Nucl. Instr. and Meth. A605,(2009) 399-408

[2] M. Altarelli, Editor, "The European X-Ray Free Electron Laser Technical Design Report", ISBN 3-935702-17-5.

[3] J. Pflueger, M. Tischer, "A prototype phase shifter for the undulator system at the TESLA X-ray FEL", TESLA-FEL 2000-08, 2000; http://flash.desy.de/ reports_ publications/

[4] I.Moya, et al, "Manufacturing and testing of the first phase shifter prototypes built by Ciemat for the European-XFEL", IPAC 2011, THPC174.

[5] S. Sanz et al., "Development of a Test Bench for Magnetic Measurements on E-XFEL Phase Shifters", IEEE Trans. App. Superconductivity, Vol. 22, June 2012.

[6] Y. Li, J. Pflüger, "New Assessment of Field Integral Tolerances for the EXFEL Phase Shifters", E-XFEL WP71 Report, WP71/2012/03, February 2012

[7] J. Campmany, J. Marcos, D. Einfeld, "Characterization of ALBA storage ring bending magnets using a high precision hall probe bench", IMMW16, October 2009

[8] D. Beltran, J. Bordas, J. Campmany, A. Molins, J.A. Perlas, M. Traveria, "An instrument for precision magnetic measurements of large magnetic structures", Nuclear Instruments and Methods A, 459 (2001) 285.

[9] H.H. Lu, J. Pflueger, S. Sanz, "First Experience and Magnetic Measurements on the first Phase Shifter Prototype made by CIEMAT", E-XFEL WP71 Report, WP71/2010/13, March 2011.

Copyright © 2012 by the respective authors — cc Creative Commons Attribution 3.0 (CC BY 3.0)

MACHINE PROTECTION ISSUES AND SOLUTIONS FOR LINEAR ACCELERATOR COMPLEXES

M. Jonker, H. Schmickler, R. Schmidt, D. Schulte, CERN, 1211 Genève 23, Switzerland
M. Ross, SLAC, Menlo Park, CA 94025-7015, USA

Abstract

The workshop "Machine Protection focusing on Linear Accelerator Complexes" was held from 6-8 June 2012 at CERN. This workshop brought together experts working on machine protection systems for accelerator facilities with high brilliance or large stored beam energies, with the main focus on linear accelerators and their injectors. An overview of the machine protection systems for several accelerators was given. Beam loss mechanisms and their detection were discussed. Mitigation of failures and protection systems were presented. This paper summarises the workshop and reviews the current state of the art in machine protection systems.

WORKSHOP OBJECTIVES

Machine protection has become a major concern in the design stages of the high power linear accelerators now under construction or being planned (e.g. high intensity protons linacs, XFEL, electron positron colliders). Due to the increased beam power the need for a dependable machine protection system becomes imperative. For this reason we organized this workshop on machine protection with a main focus on Linear Accelerator Complexes.

The objective of this workshop was to bring together for the first time experts on machine protection from various origins and disciplines, and to exchange experience and ideas for machine protection systems. The workshop was organized at CERN and could profit from the recent experience of the LHC collider, an accelerator where the need for a machine protection system was taken into account already during the design phase.

WORKSHOP ORGANISATION

The workshop was attended by 60 participants with a significant number from outside CERN.

Over 30 presentations were made in 6 half day sessions leaving ample time for discussion. The workshop sessions focused on the following topics:

Introduction: The session assessed the objectives for machine protection and reviewed existing solutions and challenges faced by future installations.

Beam loss mechanisms: The experience with beam loss mechanisms in existing installations and the outlook for future accelerator complexes were reviewed.

Failure detection: The session addressed the detection of failures that may lead to uncontrolled beams.

Failure mitigation: The session discussed various failure specific mitigations strategies.

Operational aspects: The session was dedicated to the operational aspects of machine protection (e.g. commissioning, intensity ramp, availability) and to risk management (risk assessment and management tools).

Summing up and closing: These five sessions were followed by a workshop summary session.

It is not in the scope of this paper to make a thorough report of these presentations. Here we highlight key issues and identify new trends and recommendations.

MACHINE PROTECTION

The purpose of machine protection is to protect the accelerator equipment from beam induced damage.

We did not consider equipment protection from other threats, (e.g. overheating of a power supply, protection of super conducting magnets). However, beam induced quenches and the effect of a magnet quench on the beam should be evaluated in the scope of machine protection.

Machine protection must not be confounded with personnel protection. Personnel protection is more stringent and need to fulfil legal requirements while the applied approach and solutions are often more basic.

Machine protection is not limited to the interlock system and its control and surveillance software. There are many more elements within the scope of machine protection ranging from failure studies to spares policies. The following list is non-exhaustive:

1. The passive protection devices (collimators and masks) to limit the damage caused by unmanageable failures.
2. The active beam-abort systems to dispose of any present beam upon detection of instabilities, including beam observation instrumentation, abort kicker-magnets, beam dumps and other beam inhibit systems.
3. A beam interlock system to inhibit the beam in case of equipment failures.
4. A strategy to limit the rate with which magnetic fields and device positions can change.
5. A post cycle beam and equipment quality assessment system to inhibit the next cycle when performance parameters are outside predefined limits.
6. A beam-stop restart system: i.e. an intensity ramp sequence that provides an appropriate protection depending on the machine mode and state.
7. A version control and parameter change authorization system.
8. A fault recording, analysis and playback system.
9. The written procedures to introduce changes in the parameters that control the machine protection system.
10. A set of test procedures to thoroughly test the components of the machine protection system after each change in the system.

Copyright © 2012 by the respective authors — cc Creative Commons Attribution 3.0 (CC BY 3.0)

11. A spares policy to reduce the loss of operational availability caused by unavoidable beam damage to equipment.

RISK NORMALIZATION

The damage potential of a system is given by the total amount of energy that can be released before the system can safely dispose of its energy and shut down the plant. Figure 1 shows that the beams of various accelerators contain enough stored energy to melt between 1 gr and 1 ton of copper. The vertical scales show the charge density of these beams, a measure how easily the beam can damage various materials on direct impact.

The stored beam energy information can be misleading as it does not account for the sensitivity of the equipment. The Fermi@Elletra accelerator in Trieste, presented at the workshop, is an example were very modest beam power of a few Watts still poses a concern due to the high sensitivity of the permanent magnets to beam loss induced radiation.

To compare the importance of machine protection systems of various accelerators and, more important, the individual failure scenario that each machine protection system has to protect for, we propose to normalise the risk with the available resources of the accelerator complex.

In essence, risk is expressed in statistical terms as the expectation value of the impact caused by a given failure scenario:

$$Risk = Impact \times Frequency$$

There are two types of impacts: cost of damage repair and operational downtime. These impacts can be normalized by the yearly available financial resources and the yearly scheduled operational time. As such the risks terms are expressed as the fraction of the available resources.

By normalizing the risks, we can prioritize the need for risk mitigation independent of the actual impact of the failure. Furthermore it indicates where risk reduction pays off: i.e. where the achieved risk reduction is larger than the required investment expressed as a fraction of the available resources.

Yet, great care must be given to risk terms coming from low frequency high impact failure modes as those risks are particularly difficult to estimate. The frequency can be underestimated (e.g. not considering aging, human errors, unanticipated configuration changes or coincidences with other failure modes). The impact can be underestimated by ignoring knock-on effects (e.g. as the worst case potential knock-on effect: lab closure due to lost confidence by the resource providers).

BEAM LOSS SCENARIO

In evaluating failure scenarios, the mechanisms for beam losses play a key role and needs to be studied first. The beam loss mechanisms to be taken into account are:

Operational beam losses: These are the inherent quasi continuous losses that form the loss background. Although not the primary concern of failure studies, the accumulated effect of induced radiation may contribute to long term failure of machine components. Moreover, when the radiation fields are very high, this background may pose a problem to the electronics located in the accelerator environment.

Sources of operational losses are, depending on the accelerator, dark current, un-captured beam, satellite bunches, beam gas induced parasitic beam halo and beam collision debris.

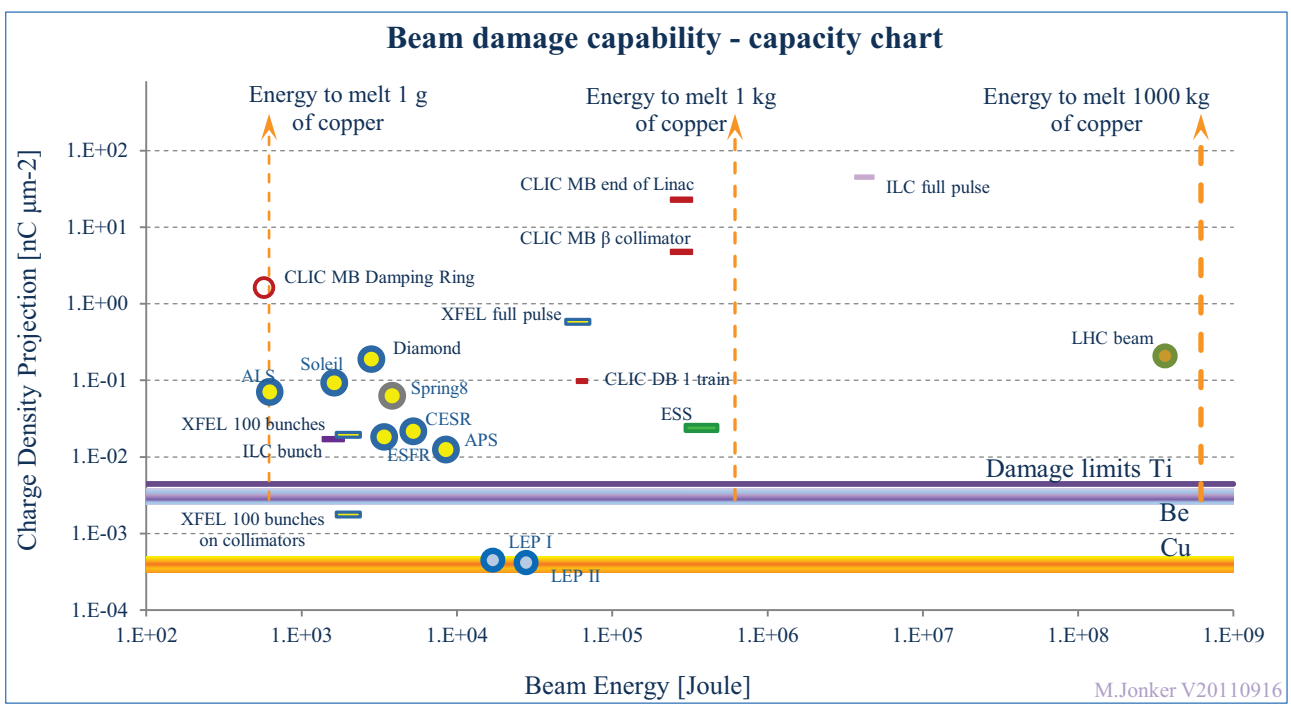

Figure 1: The charge density projection (a measure of the capability for a beam to cause damage) versus the total beam energy (a measure for the amount of damage the beam can cause) of existing and projected accelerators.

Copyright © 2012 by the respective authors — cc Creative Commons Attribution 3.0 (CC BY 3.0)

Equipment failure induced beam losses: losses leading to major damage of the accelerator components.

Transient beam losses: related to changing environment i.e. temperature drift, ground motion, UFOs* and others.

The session reviewed software tools and methods to simulate beam behaviour and beam loss for various failure modes. A presentation on the first measurement of induced beam kicks caused by breakdown in CLIC RF structures was of particular relevance to forecast the effect of these transient beam losses in CLIC.

FAILURE DETECTION

Detection and acting before a failure leads to damage is the most effective measure. Whilst largely used in circular accelerators, beam quality detection is not always applicable for a real-time beam abort system in linear accelerators. The observation of beam quality, however, is still very useful to detect upcoming instabilities and the information is fundamental for a beam permit system. Experience from the LHC transfer line and injection beam permit system gave a good example of the quality checks that can be implemented in linear accelerators.

Various beam diagnostics instruments were presented with emphasis on instrumentation for beam loss detection. Of particular interest were the scintillating fibre detectors which may provide an economic solution for large beam loss observation systems (e.g. for the CLIC drive-beam decelerators).

FAILURE MITIGATION

The basic principle of failure mitigation is to reduce either the frequency or the impact of a failure.

Equipment reliability has a direct impact on the failure frequency. Two presentations, on a kicker pulsing circuit and on a fault-tolerant magnet powering configuration were examples to reduce the frequency of critical equipment failures. It is worth noting that in both cases the solution also contributes to higher system availability.

A beam interlock system that stops the beam when equipment errors are detected or when the beam parameters are outside defined limits will reduce the frequency of dangerous beam failures. Such system relies on an efficient detection, decision and beam abort system.

For '*in-flight*' failures†, one has to rely entirely on passive protection such as masks and collimators. Due to the high brilliance of the beams the collimation systems are often on (or above) the edge of damage level in case of beam failures. Various ideas for improvements were presented during this session: alternative collimator design, nonlinear collimation optics as well as the use of novel material.

An important aspect to reduce the impact in case of damage is the spares policy. Although not explicitly discussed during this session, these points were addressed in the case of collimator spare surface, or in the build-in hot spares of the powering configurations.

IMPLEMENTATION AND OPERATION

The implementation and operation of the machine protection system is key to its success and performance.

The presentation on the operational experience in the SLC showed a case where the machine protection actions were actually a contributing factor to the unstable operation: Stopping beam operation provoked thermal oscillations not properly corrected for, which would subsequently induce new beam instabilities later in time.

Hence, the recovery from a beam stoppage should be considered carefully. Two presentations addressed this issue, one on the recovery of RF breakdowns, and a second on beam intensity ramp up procedures.

Also presented at this session were two tools, one to categorize and evaluate the risks in order to prioritize the mitigation and a second tool to evaluate machine availability. Both tools have similar goals, i.e. both tools have to catalogue failure scenarios, their frequency and impact whilst taking into account possible redundancies in the system and knock-on effects.

The complexity of a system certainly plays a large role in its reliability. This point already came up during various discussions at the workshop. It was further expanded in a dedicated presentation which stressed that the implementation of a machine protection system must follow an overall system approach, e.g. it is incorrect to oversimplify the interlock system at the price of creating extra complexity that is hidden in less controlled components elsewhere in the system.

CONCLUSIONS

Machine protection (MP) plays a crucial role in future high power linear accelerators and poses many new challenges, e.g. robust collimator designs; large scale beam loss detection systems; intensity ramp-up whilst following beam performance and environmental changes; improving equipment reliability and managing system complexity. Some challenges will be addressed through R&D programs, whilst others will need learning in realistic machine environments.

The workshop has shown that MP must be an integral part of the accelerator design stage and include well-planned and engineered instrumentation. Such instrumentation is crucial to understand the dynamics of the machine and will allow the MP to evolve in parallel with the commissioning of the machine at increasing stored beam energies.

The workshop allowed a fruitful exchange of experience and was highly valued by the participants. It is foreseen to repeat the workshop in two or three year. More details will be made available on the workshop website [1] or can be obtained by contacting the authors.

REFERENCES

[1] Conference web site and presentations repository: http://indico.cern.ch/conferenceDisplay.py?confId=185561

*Unidentified Falling Objects: dust particles observed in LHC beam.

† Failures occurring during beam passage.

Copyright © 2012 by the respective authors — cc Creative Commons Attribution 3.0 (CC BY 3.0)

RECENT IMPROVEMENTS IN SPRING-8 LINAC FOR EARLY RECOVERY FROM BEAM INTERRUPTION

S. Suzuki, T. Asaka, H. Dewa, T. Kobayashi, T. Magome, A. Mizuno,
T. Taniuchi, H. Tomizawa, K. Yanagida and H. Hanaki
Japan Synchrotron Radiation Research Institute (JASRI/SPring-8)
Kouto, Sayo-cho, Sayo-gun, Hyogo, 679-5198 Japan

Abstract

The 1GeV SPring-8 linac is an injector for the SPring-8 synchrotron radiation storage ring with 8GeV booster synchrotron. In recent years, backup systems were installed to eliminate long-time interruption of the beam injections. The main gun system is usually operated, and the backup gun is always pre-heated and can inject electron beams into the buncher section at intervals of several minutes if the main gun fails. The first klystron, which feeds the RF powers to the buncher system and the downstream klystrons, can be relieved by the next klystron in about 20 minutes by switching the waveguide circuit. When one of the eleven working klystrons fails, one of the standby klystrons, which are kept on line as hot spares, is automatically activated to accelerate beams instead of the failed one to avoid beam interruption. The total downtime in FY 2011 was 0.11% in the top-up operation user time. The averaged fault frequency was 0.2 times per day.

INRTODUCTION

The SPring-8 accelerator complex is composed of a 1-GeV electron linac, an 8-GeV booster synchrotron, and an 8-GeV storage ring. The linac injects electron beams into the booster synchrotron and the 1.5-GeV storage NewSUBARU ring of the University of Hyogo.

In the early stage of SPring-8 operation, the linac injected beams one or two times a day into each ring. In 2004, the top-up operation of the SR and the NewSUBARU ring (at 1 GeV) started to stabilize the stored currents and realized constant SR lights. At present, SR is being injected every 20 seconds to five minutes depending on the filling pattern, and the stored current stability is 0.03% at 99.5 mA. The NewSUBARU ring runs the injection every six or seven seconds with current stability of 0.01% at 250 mA.

To maintain such frequent injections to both rings without interruptions, injector linacs are strongly required to minimize device failures and the recovery time from such failures. We thus improved various components of linac and enhanced its stability and reliability. Important improvements achieved in recent years include the introduction of a twin gun system, a backup system for the first klystron, and the automatic exchange of a standby klystron. These improvements gradually reduced linac's downtime to 0.11% in FY 2011.

IMPROVEMENT OF ELECTRON GUN SYSTEM

The SPring-8 linac was equipped with only one electron gun system, i.e., a high-voltage inverter type pulse power supply, a pulse transformer, a high-voltage deck, and an electron gun. When any of these parts fail, the linac cannot inject beams into the booster synchrotron until the failure is fixed. In particular, the replacement of a cathode assembly requires at least three days to complete the mounting processes for a new cathode assembly and cathode evacuation and activation. Therefore, the construction of a backup system is an important issue for enhancing the reliability of the electron gun system and to reduce the downtime of the beam injection during gun failures. Thus we made the following improvements:

1) Composition of a twin electron gun system.
2) Development of a reliable high-voltage pulse power supply.

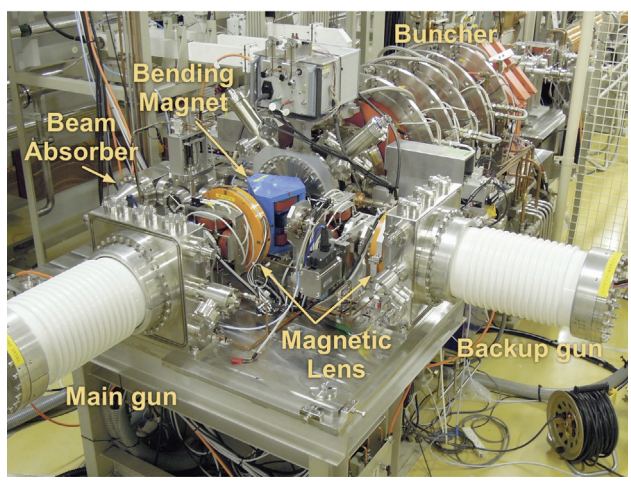

Figure 1 : Twin electron gun.

Twin Electron Gun System

We considered two ideas to realize a twin gun system: duplicating the present electron gun or doubling the present injector part, including the gun and the buncher system, for example. We built a backup gun and its power supply and considered the following issues in our backup gun design.

1) The original performance of the main gun must be maintained after the backup gun's installation, but the backup gun's performance for the backup operation, the

Copyright © 2012 by the respective authors — cc Creative Commons Attribution 3.0 (CC BY 3.0)

beam current, for example, can be inferior to that of the main gun.

2) The backup gun's cathode has to be pre-heated during linac operation to immediately generate electron beams if a main gun failure occurs.

Figure 1 shows the twin electron gun system installed in the accelerator room. A 90° bending magnet was installed to orthogonally inject beams from the backup gun mounted on the main gun, which was relocated upstream to make space for the bending magnet. This bending magnet, which adopts a combined type and holds an n value of 0.5, focuses beams horizontally. We installed a magnetic lens for each gun to reduce the beam divergence caused by the space charge effects. A beam profile monitor and a coaxial type beam absorber to measure beam currents were also installed to diagnose the backup gun's beam. Beam simulation by Parmela from the backup electron gun is shown in Fig. 2.

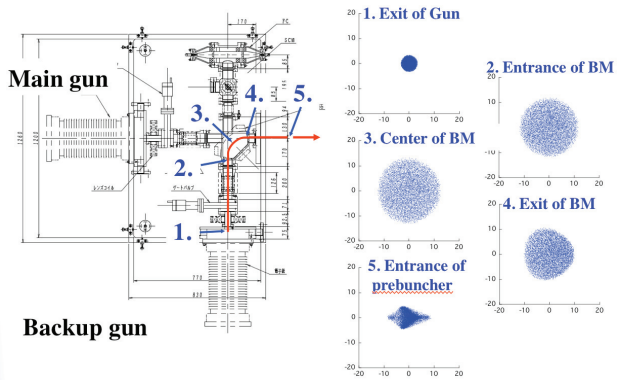

Figure 2 : Beam tracking simulation for backup gun.

The backup gun was tested and operated in September 2008. Since an additional high-voltage power supply system for the backup gun was constructed in 2008, we installed a remote change system to smoothly change the main and backup guns in FY 2010. The backup gun is always in a suspended state for emergencies. We checks its injection to the synchrotron after every long-term maintenance.

New High Voltage Pulse Power Supply

The previous pulse power supply often caused discharges at the high-voltage terminal of the inverter power supply. It was also difficult to maintain the pulse power supply because it was designed so many years ago. The new power supply was completed in 2005 and has been operated in a test stand for almost one year to confirm its performance and reliability. At the end of 2006, we replaced the previous power supply system with the new one.

The new system has the following features:

1) A pulse transformer with a step-up ratio of 1:30 decreases the primary voltage and solves the discharge problem. The inverter power supply now feeds a voltage of only 12 kV to the PFN to generate a pulse voltage of 180 kV at the electron gun's terminal.

2) We installed a larger high-voltage deck to enhance the following: functionality, expandability, and serviceability.

The high-voltage pulse applied to the electron gun has a long rise/fall time of approximately 3 μs because the large step-up ratio enlarges the stray capacitances of the secondary circuit. At first, we used a long pulse beam (1 μs). However, the pulse's short flat top caused by the long rise/fall time does not limit operation since in practice we use short pulse beams with pulse widths less than 40 ns. The voltage stability of the inverter power supply is about 0.05% rms, which is sufficiently stable for the injector linac.

BACKUP OF THE FIRST KLYSTRON

Linac is equipped with thirteen 80-MW pulse klystrons (Toshiba E3712) that feed 10-Hz RF power to the accelerating structures. Two of them are intermittently disabled by the trigger system in synchronization with 1-Hz beam trigger signals to avoid beam accelerations. That is, eleven of the klystrons are usually used to accelerate electron beams to 1 GeV, and the other two are kept as hot spares on line.

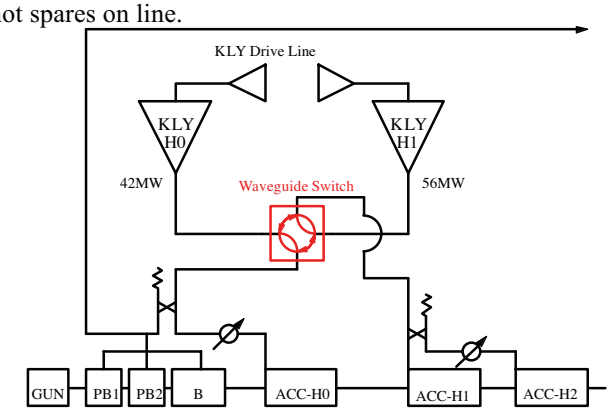

Figure 3 : Circuit using high power waveguide switch.

Except for the first and the Energy Compression System's (ECS) klystrons, when one of the eleven working klystrons fails and cannot be recovered within a few minutes, a standby klystron is activated to accelerate the beams instead of the failed one. But linac operation completely stops for a long time due to the serious failure of the first klystron because it feeds RF power to the linac's injector section and the long drive line for the other eleven klystrons. In 2004, we therefore constructed a backup system for the first klystron to feed RF power from the second klystron to the injector. The backup system is composed of waveguide circuits, a high-power waveguide switch, and its control system [1]. This system's circuit is shown in Fig. 3.

This backup system has worked very efficiently. In 2008, a serious failure of the first klystron occurred and it could not be recovered. We exchanged the first klystron

Copyright © 2012 by the respective authors — cc Creative Commons Attribution 3.0 (CC BY 3.0)

with the second one using this backup system and restarted linac in a few hours. The first was replaced with a new one and its RF conditioning was carefully performed without disturbing the linac operation because the second klystron had completely played the role of the first one for one month.

At that time, the exchanging time was long because a klystron drive system and part of the interlock signals had to be manually reconnected to the second klystron and its local controller. We upgraded this backup system to reduce the linac downtime to 10 minutes.

AUTOMATIC KLYSTRON EXCHANGEING SYSTEM

Faults of the klystron modulators occur about once every three days and interrupt the top-up operation for a few minutes. When one of the normal 11 klystron systems fails (except for the first and ECS's klystrons), one of the standby klystrons can be activated to continue the beam acceleration, as mentioned above.

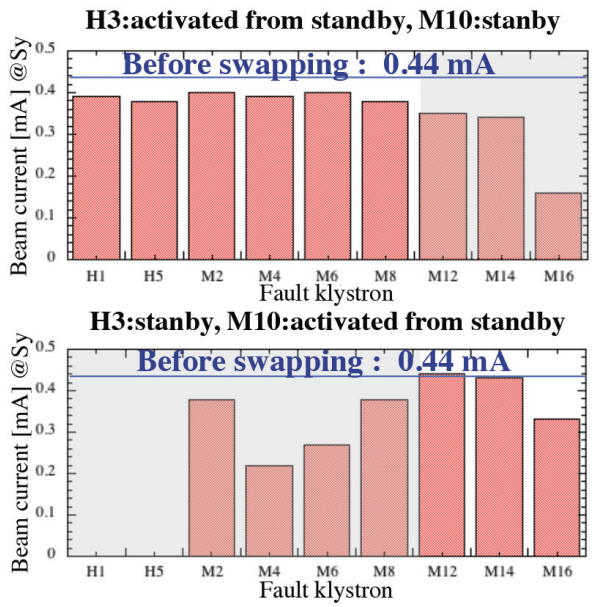

Figure 4 : The synchrotron current depending on a fault klystron.

The standby klystrons are H3(3rd) and M10(9th).

We introduced an automatic klystron exchanging system to shorten the linac downtime caused by the klystron failures. The system automatically controls the trigger system that defines the standby klystrons and can change them within one second. All the RF power of the 11 klystrons is adjusted at the same level to keep the same beam energy after the klystrons are exchanged.

When activating a standby klystron, since the currents of the Q magnets are not adjusted, they remain constant. Orbital variations may occur that reduce the current. We therefore examined the synchrotron currents that depend on every activating pattern (Fig. 4).

In this experiment, the 3rd and 9th klystrons were in standby mode. The current value before the experiment was 0.44 mA. Except for the first and ECS's, every working klystron was deactivated to simulate a klystron fault. If the third klystron were activated instead of the 2nd to 8th klystrons or the 9th klystron were activated instead of one of the 10th to 12th klystrons, the current reduction would probably be less than 20%.

DISCUSSION

Figure 5 shows the operation statistics from 2005 to 2011. The fault rates gradually reduced as a result of improving the components.

Although in 2008 we recognized that long downtime was caused by the trouble of the gun bias circuit, introducing the twin gun and backup systems for failed klystrons considerably suppressed the interruption of the top-up operation caused by linac's failures. Although linac's downtime was 0.59% in FY 2005, it decreased to 0.11% in FY 2011.

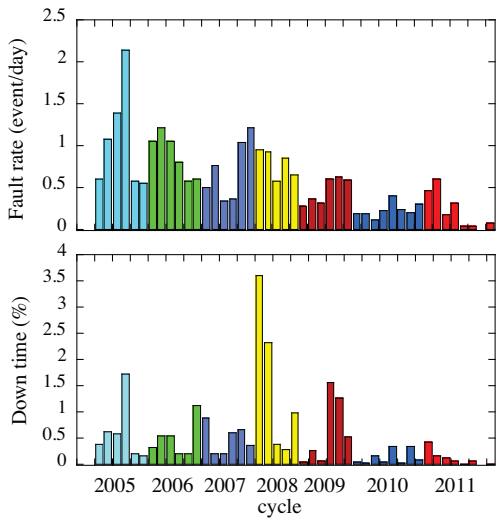

Figure 5 : The history of the fault in 2005 to 2011 fiscal year.

The twin gun system effectively reduced linac's downtimes that were caused by the failures of the cathode assembly and greatly improved reliability.

REFERENCES

[1] T. Taniuchi, "HIGH POWER WAVEGUIDE SWITCHING SYSTEM FOR SPring-8 LINAC" EPAC'06, Edinburgh, Scotland, July 2006, TUPCH159, p. 1397 (2006); http://www.JACoW.org

Copyright © 2012 by the respective authors — cc Creative Commons Attribution 3.0 (CC BY 3.0)

PERFORMANCE OF BEAM CHOPPER AT SARAF VIA RF DEFLECTOR BEFORE THE RFQ

A. Shor, D. Berkovits, I. Fishman, A. Grin, B. Kaiser, L. Weissman
Soreq Nuclear Research Center, Yavne 81800, Israel

Abstract

We describe performance of a beam chopper at the SARAF accelerator consisting of a HV deflector preceding the RFQ. The deflector and electronics, developed at LNS Catania, was designed to provide slow beam chopping for beam testing and diagnostics where low beam power is necessary. The HV deflector sweeps away the low energy beam onto a water-cooled beam catcher, while a fast HV switch momentarily switches off the HV whenever a transmitted beam to the RFQ is desired. We report on measurements with this chopping system, where minimum transmitted beam pulse of 180 ns duration is attained and where individual nano-bunches of the RFQ are visible. Comparisons are made with beam dynamics calculations that simulate the LEBT and the RFQ. The simulations suggest that single RFQ bunch selection can be attained with appropriate alternating positive-negative deflecting HV waveform, where single bunch transmission occurs during the positive-negative crossover.

THE SARAF ACCELERATOR: PHASE I

The SARAF accelerator complex [1] is designed to provide CW proton or deuteron beams of up to 5 mA and 40 MeV. Currently, phase I of SARAF has been installed and has undergone commissioning, and is currently operational for experimental work. SARAF phase I consists of an ECR ion source (EIS), a 176 MHz radio-frequency quadrupole (RFQ), and a prototype superconducting module (PSM). The PSM contains 6 superconducting half-wave resonators (HWR) and 3 superconducting solenoids, and provides acceleration up to about 5 MeV. Figure 1 shows the layout for SARAF phase I, including the EIS ion source and LEBT, the RFQ, MEBT, the PSM and D-plate, and the magnetic beam line transporting the beam either to the beam dump or to target station for experimentation.

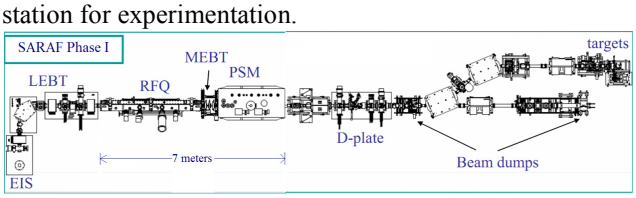

Figure 1: Layout of SARAF phase I showing EIS source, LEBT, RFQ, MEBT, PSM, D- plate, and beam lines.

SLOW CHOPPER AT SARAF

The slow chopper at SARAF consists of deflection plates and electronics developed at LNS Catania within the SPIRAL II program [2] and mounted in SARAF for tests and evaluation. The slow chopper consists of a set of parallel plates on which HV is applied for deflecting a low energy beam at an angle of 20°. For a transmitted beam, a fast switch shuts off the HV for the required beam on-time. The slow chopper was provided to SARAF along with electronics that enable applying a potential of up to 10 kV, and controls for varying the duration, frequency and phase for the off-time. The electronics provided allows for minimum off-time of about 180 ns and maximum switching repetition rate of up to 800 Hz. The slow chopper was installed in the SARAF LEBT between the second and third solenoids. The slow chopper provides a simple mechanism for lowering beam current and/or duty factor without having to pulse the ion source. Pulsing of the beam is especially required in order to tune the high intensity beam when using the downstream beam-destructive diagnostics. Figure 2 shows a schematic diagram of the LEBT and placement of the slow chopper, including the water cooled beam catcher at 20°, and also the RFQ and MEBT.

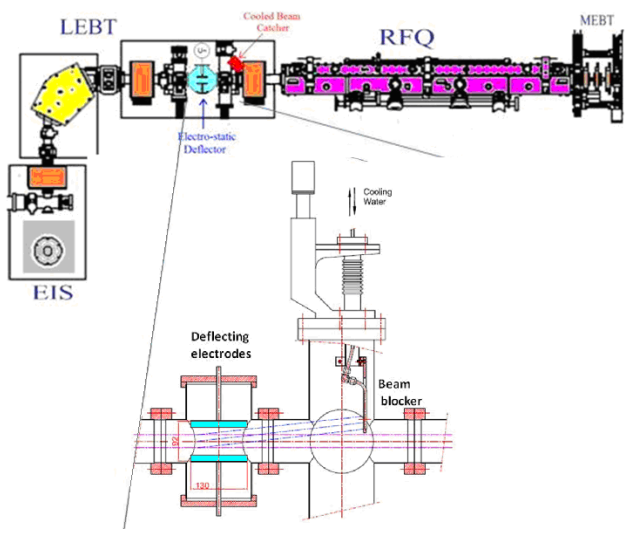

Figure 2: Schematic diagram of the EIS source, LEBT, RFQ and MEBT, with placement of slow chopper and beam catcher in the LEBT. A detailed drawing of the LEBT section containing the chopper and beam blocker is shown in the inset.

Copyright © 2012 by the respective authors — cc Creative Commons Attribution 3.0 (CC BY 3.0)

The slow chopper was tested with a ~0.5 mA and 2.1 MeV proton beam. The beam was deflected onto the movable water cooled beam catcher positioned at ~20°. The chopper HV was switched off at rate of a few Hz for durations of 10 μs down to ~0.2 μs. The accelerated beam was measured with the beam position monitor (BPM) in the MEBT, consisting of 4 button current pick-up devices, and by a fast Farraday cup (FFC) situated in the D-plate [3]. Figure 3 (top panel) shows the signals on a fast digital oscilloscope with 6 GHz bandwidth. The BPM signal is shown in yellow, and the FFC signal in green. The proton TOF and the distance between the BPM in the MEBT and the FFC in the D-plate are reflected by the separation of their waveforms as seen by the scope. The measured transmitted pulse has a pulse width of about 180 ns. Most prominent are the individual RFQ bunches which are resolved very well by the fast scope. Figure 3 (bottom panel) shows a blow-up where the individual bunches are resolved very well by the FFC. Beam dynamics simulations discussed below show the RFQ bunches to have a bunch width of about 0.3 ns FWHM, corresponding to a phase width of $\Delta\phi \sim 20°$, consistent with the measured bunch widths shown in figure 3.

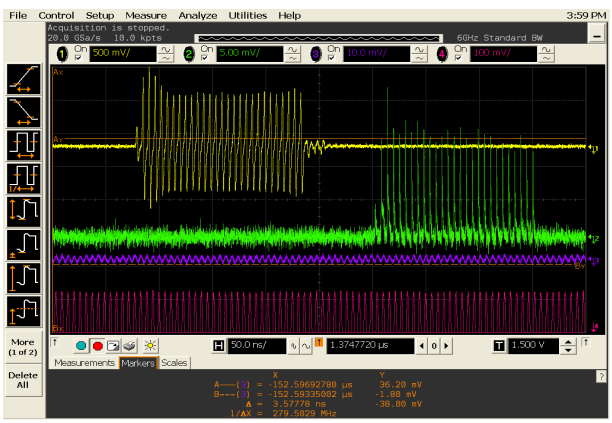

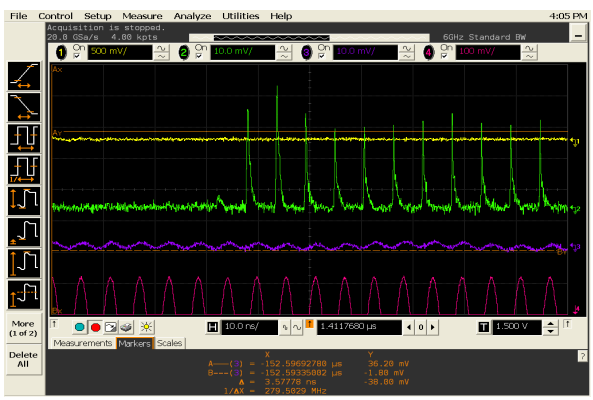

Figure 3: Trace on fast oscilloscope of beam pulse following slow chopper and RFQ. Yellow trace shows BPM (beam position monitor) which is upstream of the FFC (fast Faraday cup) shown in green trace. Red trace is signal from RFQ RF. Beam pulse has width of 180 ns. Individual beam bunches following RFQ are separated by 5.5 ns and have width of about 0.3 ns.

BEAM DYNAMICS SIMULATIONS

Detailed beam dynamics simulations of the SARAF, including the LEBT, RFQ, MEBT, PSM, RF deflector, and beam lines have been preformed to obtain a better understanding of the optics and systematic of SARAF phase I facility. The simulations were performed with the General Particle Tracer (GPT) code from Pulsar Physics, a time-based code includes space charge, an assortment of accelerating and focusing elements, and hooks for providing user supplied elements using c-code based platform. The simulations begin with 20 keV/u proton or deuteron beam from the ion source with normalized transverse emittance of 0.2 π mm-mrad. The RFQ was simulated using a code developed at Soreq [4] and implemented into the GPT simulation package.

Illustration of simulation results are shown in figure 4. To provide a more suitable visualization of the simulations, the SARAF LEBT, RFQ, and MEBT are all displayed along a straight line, where the 90° bend is implied. Figure 4 shows simulated beam entering the RFQ, with the energy development of the beam on the top graph, the transverse development in the bottom graph, and a schematic of the acceleration section in the middle graph for better visualization. Note the transition from DC beam to bunched beam as the beam traverses the RFQ.

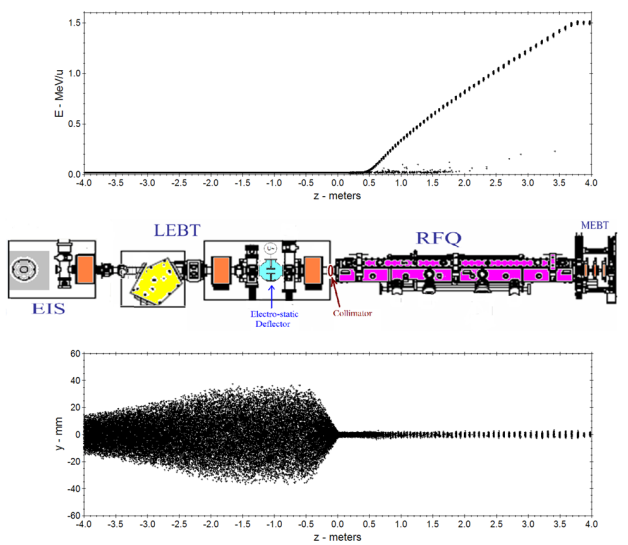

Figure 4: Simulation of CW deuteron beam traversing the LEBT and RFQ. The RFQ bunches and accelerates the beam to 1.5 MeV/u. Top graph shows energy development as a function of longitudinal advance. Bottom graph shows transverse displacement including transverse focusing by solenoids. 90° bend was straightened to facilitate viewing.

SINGLE BUNCH SELECTION

We take advantage of the simulations to investigate possibilities for HV waveforms on the RF deflector that will enable single bunch-selection. RF deflection before the RFQ can be an efficient method for single bunch

Copyright © 2012 by the respective authors — cc Creative Commons Attribution 3.0 (CC BY 3.0)

selection since the beam energy is still low and therefore relatively low electric fields and moment arms are required for adequate deflection, and less problematic cooling requirements are foreseen for the beam catcher. Inherent in any pulse selection scheme is proper synchronization with the RFQ RF phase. With the advent of fast high voltage/ high power switching, various deflector pulsing schemes can be possible.

We have found that effective single bunch selection can be achieved by applying an alternating positive-negative HV waveform with a fast switch that can change deflector polarity with a switching time Δt of 80 ns or less. For deuterons at 20 keV/u, a ΔV of ±6kV is required. The switch can be made at any desired repetition rate, provided the HV source and switch can handle the current. In Figure 5, we show again plots and schematic drawing of the LEBT, RFQ, and MEBT, but this time with a positive-negative HV of ± 5 kV applied to the electric-field deflector, and with a switch that changes polarity over a switching time of 40 ns. The electrostatic deflector deflects the unwanted pre-bunches either left or right, with zero net deflection only for the desired pre-bunch, which is focused and transmitted to the RFQ. In the plots, the simulated switching frequency was 3.524 MHz, and so the bunch separation for the transmitted bunches, as shown in figure 5, is 50 $\beta\lambda$.

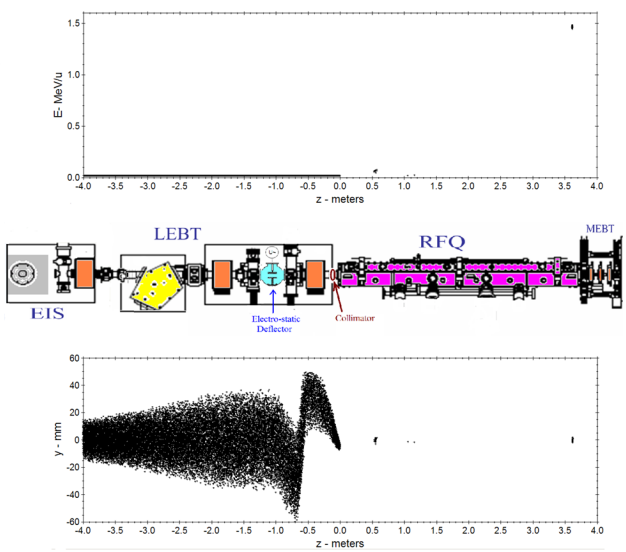

Figure 5: Simulation of a CW beam traversing the LEBT, with alternating positive-negative HV applied on RF deflector, with only non-defleted beam in the HV cross-over surviving to the RFQ. For this simulation, a positive-negative HV of ±5 kV, with a polarity switch of 40 ns at a frequency ot 3.52 MHz. Time snapshot showing beam with two bunches with separation of 50 $\beta\lambda$ successfully traverse the RFQ.

DISCUSSION

We report on a slow chopper developed at LNS Catania and installed at the LEBT in SARAF accelerator just before the RFQ. We have shown experimental data taken with a fast faraday cup and peak pickup electrodes using a fast oscilloscope, showing the transmitted non-deflected beam bunch. The data also shows the mico-bunch structure of the beam exiting the RFQ, with 0.3 ns FWHM bunch width consistent with simulations obtained using the GPT particle simulation code.

We have also explored possible HV waveforms on the existing RF deflector which can provide appropriate deflection patterns to enable single bunch selection in the RFQ. We have found that a scheme for alternating positive-negative HV for deflection of the beam, with fast switching between polarities enabling the desired pre-bunch to enter the RFQ at the HV crossover. Detailed simulations show that for applied HV of ±5 kV, with switching speeds of 40 ns or less, efficient single bunch selection can be achieved with more than 60 % transmission for the selected bunch, and less that 3% transmission for the adjacent bunches.

We are now testing electronics that will give us switching speeds of ~10^5 Hz and also with capabilities for alternating positive-negative polarities to allow us to test our ideas for single-bunch selection with the existing HV deflector..

ACKNOWLEDGEMENT

We would like to thank our colleagues from LNS Catania and SPIRAL II collaboration for developing and loaning to us the slow chopper and electronics used for the measurements presented here.

REFERENCES

[1] I. Mardor et al., "The Saraf CW 40 MeV Proton/Deuteron Accelerator," Part. Acc. Conf. 2009 Vancouver, (2009) 74-80, MOODAU04 and L. Weissman, et al., "The Status of the Saraf Linac Project," in LINAC10 (Tsukuba, Japan, 2010), pp. 679-683.

[2] A. Caruso et al., "Preliminary Design of the Slow Chopper for the Spiral 2 Project," LINAC 2008, Victoria, BC, Canada (2008) 891-893. THP046 Linac2008.

[3] C. Piel, K. Dunkel, M. Pekeler, H. Vogel, and P. vom Stein, "Beam Operation of the Saraf Light Ion Injector,", in PAC2007 (Albuquerque, New Mexico, USA, 2007), pp. 1410-1412.

[4] B. Bazak, et al. , "Simulations of Ion Beam Loss in RF Linacs,", in LINAC10 (Tsukuba, Japan, 2010), pp. 956-958.

Copyright © 2012 by the respective authors — cc Creative Commons Attribution 3.0 (CC BY 3.0)

DESIGNING OF A PHASE-MASK-TYPE LASER DRIVEN DIELECTRIC ACCELERATOR FOR RADIOBIOLOGY*

K. Koyama †, A. Aimidula, Y. Matsumura, M. Uesaka, The University of Tokyo, Tokai, Japan
M. Yoshida, T. Natsui, KEK, Tsukuba, Japan

Abstract

In order to develop a useful tool for the basic investigation of the radiobiology, the laser driven dielectric accelerator is studied. From the viewpoint of the fabrication, our effort is focused on the phase-modulation-mask-type laser-driven dielectric accelerator (PLDA). The required beam energy and bunch charge, which depend on the thickness of the specimen, are in the range of 100 keV to 1 MeV and 0.1 fC to 1 fC, respectively. The simulation results by using the FDTD simulation code, Meep, showed that the minimum grating period, was $L_G/\lambda = 0.5$ for the original type of PLDA provided that the accelerator structure was made of silica. The initial electron speed was $v = 0.5c$ (79 keV) to match the minimum grating period of PLDA. The optimistic value of the required total laser energy is 4 mJ for obtaining 1 MeV electron bunch. The acceleration field was also produced by the inside-out accelerator structure. However, L_G/λ was limited to longer than 0.6 in the preliminary simulation result.

INTRODUCTION

Radiobiologists desire to understand basic radiobiological processes around DNAs in living cells in order to estimate the health risk associated with a low radiation dose. Compact devices which deliver the spatially and temporally defined particle bunches or X-ray pulses serve to accomplish the purpose. The suitable beam size is as small as the resolving power of an optical microscope with a spatial resolution of a few hundred nanometers. The required beam energy and bunch charge, which depend on the thickness of the specimen, are in the range of 100 keV to 1 MeV and 0.1 fC to 1 fC, respectively. Moreover, it is required that one can aim at the target specimen using the optical microscope. Photonic crystal accelerators (PCAs) are capable of delivering nanometer beams of subfemtosecond pulses because the characteristic length and frequency of accelerators are on the order of those of laser light.

A phase-modulation-mask-type laser-driven dielectric accelerator (PLDA) has a simpler structure [1] than other types of PCAs[2,3]. Since the required output energy of the accelerator for the radiobiology is in the non-relativistic or weakly relativistic region the parameters of the PLDA is different from previously published one [1]. The structure and dimensions of the PLDA as well as the required laser power are discussed in this paper.

* This work was supported by KAKENHI, Grant-in-Aid for Scientific Research (C) 24510120.

† koyama@nuclear.jp

DIMENSIONS OF THE ACCELERATOR

The structure of the original type of PLDA is expressed in terms of the grating period L_G, the width of the grating pillar L_p, the height of the pillar H_p, and the distance between opposite pillars D as shown in Fig. 1. The thickness of the base plate can be adopted arbitrary value. The maximum length of the pillar, i.e., the width of the accelerator channel W, is restricted by the suppliable laser power. The accelerator is energized by the face-to-face irradiation of laser pulses in a orthogonal direction to the electron beam. Laser pulses, which are linearly polarized parallel to the axis of the electron beam, pass through the pillar and vacuum depending on their longitudinal position of the accelerator. An electric field along the beam axis behaves similar to a standing wave when the optical path difference between two paths through the pillar and vacuum is tuned to the half-period of the laser light. In order

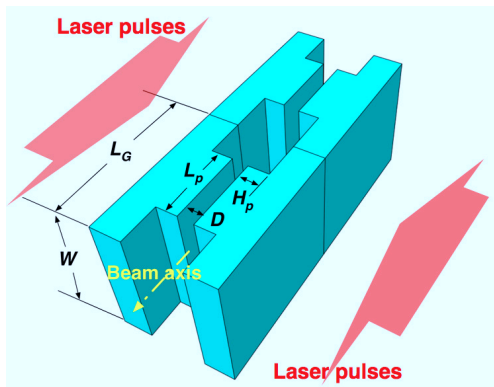

Figure 1: Schematic drawing of two periods of an accelerator unit.

to accelerate the electron, the speed of the injected electron, v_0 must be tuned to satisfy $v_0/c = L_G/\lambda$, where the electric field distribution is approximated by a sine wave and c and λ are the speed of light and the wavelength of the laser, respectively. The normalized pillar height is approximated to be $H_p/\lambda \approx 1/(2(n-1))$ by considering a path difference of π, where n is the refractive index of the pillar material [4]. The distance between opposite pillars is assumed to be $D/\lambda < 1/4$ by considering the diffraction blurring from the pillar edge. According to the reference [1], the acceleration field strength decreases by 20 percent by increasing D/λ from 0.25 to 0.5 in case of silica (SiO_2, $\epsilon = n^2 = 2.07$ for $\lambda = 1\mu$m). Accurate values of these parameters are determined with help of the numerical simulation code.

Copyright © 2012 by the respective authors — cc Creative Commons Attribution 3.0 (CC BY 3.0)

The free finite-difference time-domain (FDTD) simulation software, Meep [5] was used to know electric field distributions in PLDAs. The wavefront of the laser pule is deformed to concave shape as shown in Fig. 2(a). The boundary between the dielectric and the vacuum causes diffraction and reflection of the laser beam. The diffracted and reflected wavefronts interfere each other and make a complex pattern of field intensity. The alternate field distribution is produced if the configuration satisfies the proper condition as seen in Fig.2(b). Since the shorter L_G is desirable to reduce a restriction on designing an electron gun of the PLDA, we studied to find the minimum L_G to produce the alternate field distribution. Contour plots of the electric field in the xt-space along the center of the acceleration channel are shown in Fig.3 with world lines, trajectories in xt-space, of electrons. Electrons can be efficiently accelerated in the parameter region of $1 \geq L_G/\lambda \geq 0.5$ ($L_p = L_g/2$ is assumed), if electrons always feel the electric field of the same direction along their trajectory. In the region of smaller grating period than $L_G/\lambda < 0.48\,(L_p/\lambda < 0.24)$, the acceleration field disappears as shown in Fig.3(c). Electric field distributions along world lines of electron motion in an oscillation period of the laser field are shown in Fig. 4. The positive region and the negative region of the field $E\,(x\,(t)\,,t)$ contribute to the electron acceleration and the deceleration, respectively. The negative component of the field might be due to adopting non-optimal values of L_G, L_p, H_p, W_G, etc. If it is difficult to increase the acceleration field at the short grating period of $L_G/\lambda \approx 0.5$, the required accelerator length become longer than that listed in Table 1.

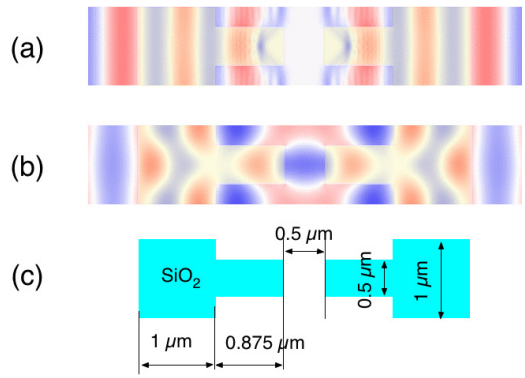

Figure 2: Simulation results of field distributions in the period of the accelerator. (a) The transient feature of the electric field distribution. (b) The steady state field distribution. (c) One unit of the accelerator made of silica. $\lambda = 1\mu$m.

ANOTHER CONFIGURATION; INSIDE-OUT

Since the original configuration of PLDA (Fig. 1) is unfavorable from the view point of the fabrication, we studied an inside-out structure as shown in Fig.5(a). The alternate electric field is also created in the acceleration channel (Fig. 5(b)). Because the structure of the acceleration channel is similar to the Fabre-Pérot etalon, $2D/\lambda = N$ is the optimal condition for producing the intense field in the accelerator gap, where N is the integer. The preliminary result shows that the alternate field disappear in the shorter grating period of $L_G/\lambda < 0.6$. The adoption of the thinner base plate may lead us better results.

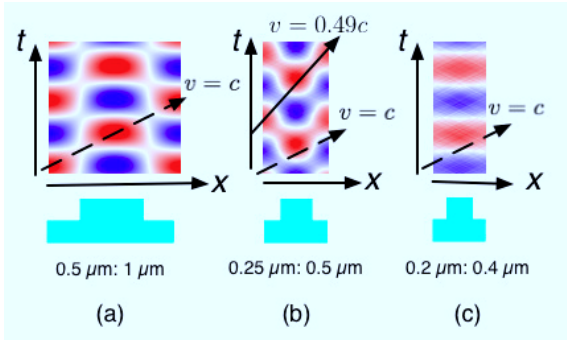

Figure 3: Contour plots of the electric field and world lines in xt-space. Arrows with broken lines and solid line indicate electron trajectorie at the speed of $v = c$ and $v = 0.49c$, respectively. (a) is at $L_G/\lambda = 1$ and $L_p/\lambda = 0.5$. (b) is at $L_G/\lambda = 0.5$ and $L_p/\lambda = 0.25$. (c) is at $L_G/\lambda = 0.4$ and $L_p/\lambda = 0.2$.

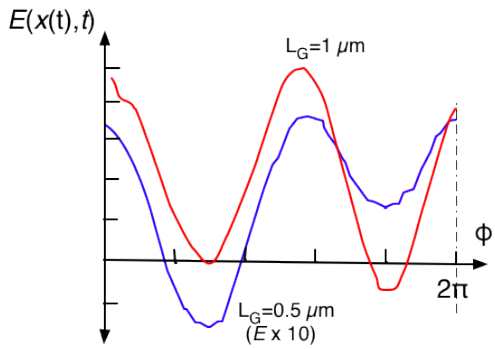

Figure 4: Electric field distributions along world lines of electrons in a period. The field strength of $L_G/\lambda = 0.5$ is expanded ten times.

LASER PARAMETERS

The irradiation intensity of the laser pulse on the surface of the dielectric material must be kept below the damage threshold value I_{th}. The required energy of the laser pulse for one side is expressed to be $E_L = I_{th} L_A^2 W/\langle v \rangle$, where L_A, and $\langle v \rangle$ are the accelerator length and average velocity of the electron, respectively. In order to reduce the required energy of the laser, the illumination area and time of the laser pulse is limited around the electron bunch by

Copyright © 2012 by the respective authors — cc Creative Commons Attribution 3.0 (CC BY 3.0)

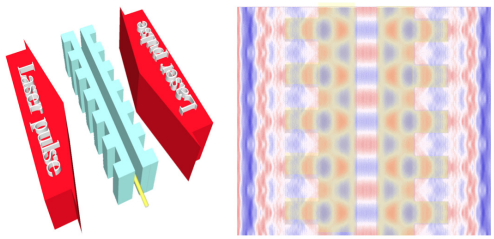

(a) (b)

Figure 5: (a) the sketch of the inside-out structure. (b) the field strength contour map. The dielectric structure of five units is shown by the pale yellow. $L_G/\lambda = 1$, $L_p/\lambda = 0.5$, $D/\lambda = 0.5$, $H_P = 0.875$. The material is silica.

synchronizing the laser pulse with the motion of the electron bunch. If the accelerator is illuminated by sequential N pulses, the energy of each laser pulse is decreased to $E_L(N) = I_{th} L_A^2 W / (\langle v \rangle N^2)$. For producing such an illumination scheme, Plettner [1] proposed that the short laser pulse be divided into many segments by mirrors and that each pulse be introduced into the accelerator through a properly tuned optical delay. However, the use of many optical mounts in a small space is inproper for our purpose. A fiber laser system might increase the freedom of the configuration, as shown in Fig. 6. While there are still uncertainties, parameters of the accelerateor and laser are listed in Table 1 for the ideal case.

Table 1: Parameters of the PLDA and Fiber laser. The wavelength of the laser is 1μm. Both the reflection and diffraction effects are not included.

Grating period L_G	0.5λ to 0.94λ
Initial electron energy	79 keV
Width of the accelerator channel W	0.1 mm
Length of the accelerator L_A	0.48 mm
Area of irradiation (one side) A	4.8×10^{-4} cm^2
Acceleration time τ_A	2 ps
Laser power P_L	4.8 GW
Laser energy (one side)	9.6 mJ
Pulse width τ_L	2 ps
Number of laser pulses (one side) N	5
Power of each laser pulse	950 MW
Laser energy per pulse	0.38 mJ/fiber
Total laser energy (one side)	1.9 mJ
Pulse width	400 fs

SUMMARY AND DISCUSSION

In order to develop a useful tool for the basic investigation of the radiobiology, we are studying the laser driven dielectric accelerator. From the viewpoint of the fabrication, our effort is focused on the phase-modulation-mask-type laser-driven dielectric accelerator (PLDA). The required beam energy and bunch charge, which depend on the thickness of the specimen, are in the range of 100 keV to 1 MeV and 0.1 fC to 1 fC, respectively.

The simulation results by using the FDTD simulation code, Meep, showed that the minimum grating period, was $L_G/\lambda = 0.5$ for the original configuration of PLDA provided that the accelerator structure was made of silica. The acceleration field strength at $L_G/\lambda = 0.5$ was around 10% of the value of $L_G/\lambda = 1$. Since this is the serious problem for realizing the compact accelerator with a small scale laser (see Table. 1), we are conducting the precise simulation study to fix optimal values of the structure and the laser. The optimistic value of the required total laser energy is 4 mJ for obtaining 1 MeV electron bunch.

The acceleration field was also produced by the inside-out accelerator structure. However, L_G/λ was limited to longer than 0.6 in the preliminary simulation result.

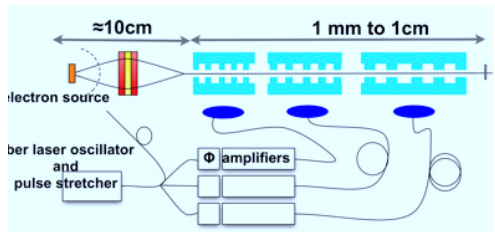

Figure 6: The conceptual drawing of the laser driven dielectric accelerator.

REFERENCES

[1] T. Plettner, P. P. Lu, and R. L. Byer, Phys. Rev. ST Accel. Beams **9** (2006)111301.

[2] X. Lin, Phys. Rev. ST Accel. Beams **4** (2001)051301 and B. Cowan, *et al.*, Phys. Rev. ST Accel. Beams, **11** (2008)011301.

[3] A. -C. Tien, *et al.*, Phys. Rev. Lett. **82** (1999)3883.

[4] K. Koyama, *et al.*, IPAC12, New Orleans, May 2012, THPB095, p. 2763 (2012); http://www.JACoW.org

[5] http://ab-initio.mit.edu/wiki/index.php/Meep

Copyright © 2012 by the respective authors — cc Creative Commons Attribution 3.0 (CC BY 3.0)

HIGH-POWER SOURCES OF RF RADIATION DRIVEN BY PERIODIC LASER PULSES*

S.V. Kuzikov#, IAP RAS, Nizhny Novgorod, Russia and Omega-P Inc., New Haven, USA
A.V. Savilov, IAP RAS, Nizhny Novgorod, Russia.

Abstract

A short, periodic laser pulses can be applied for phase and frequency locking of RF sources operated in a single-mode regime. In particular, these pulses, irradiating GaAs sample, are able to produce fast modulation of Q-factor (due to inserted time dependent losses) with frequency to be close to natural single-mode oscillation frequency. In a steady state regime a phase of oscillations automatically slaves to provide minimum of the losses in GaAs. Another possible principle is to provide electron beam modulation in a cavity excited by periodically modulated current, the resulted beam with modulated density in this case generates RF power in next output cavity. The necessary exciting current can be provided by means of a DC generator those current due to a photoconductivity is externally modulated with definite frequency by laser which irradiates GaAs isolator inserted in-between electrodes. This klystron principle also solves a problem of phase locking.

INTRODUCTION

Because high-gradient accelerators typically have a photoinjector, where electron bunches are born by laser pulses, it is natural to use RF sources those frequency and phase are controllable by the same laser pulses. A possible scheme, showing how to use these new sources, is shown in Fig. 1.

Many well-known RF oscillators acquire new properties, if one modulates a quality factor of its electrodynamic systems [1]. A switch of Q-factor (Q-switch) might be based on GaAs semiconductor which has several unique properties. Laser radiation with photon energy near 1.43 eV, corresponding to GaAs band gap, causes an induced photoconductivity in a penetration depth ~1 μm so that GaAs becomes an absorber for less than 0.1 ns and recovers itself for ~0.6 ns [2]. At 1 GHz for low electron concentration in the conducting zone (N_e<10^{13} cm^{-3}) GaAs is a dielectric, for high N_e (> 10^{17} cm^{-3}) GaAs is similar to metal, good absorber (to be used for Q-switch) takes place for N_e~10^{15} cm^{-3}. Typical necessary laser power is 1-100 nJ/mm^2 using popular Ti:Sa lasers with wavelength λ=870 nm.

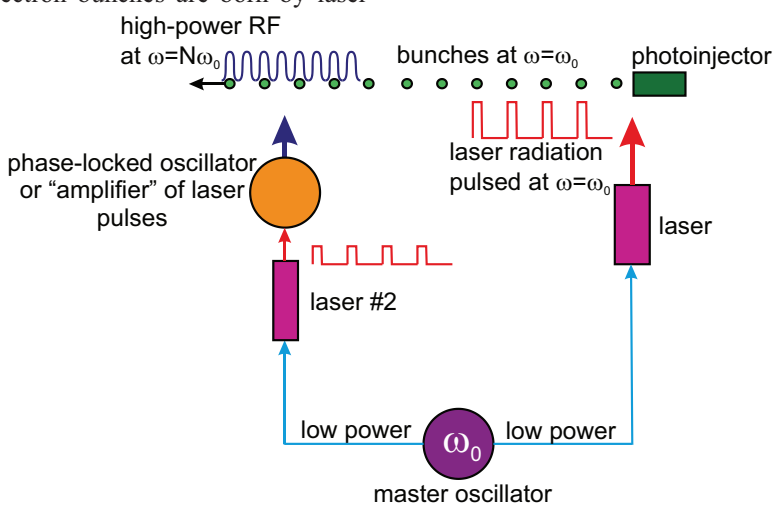

Figure 1: Scheme of accelerator with RF source driven by periodic laser light.

RF OSCILLATORS CONTROLLED BY PERIODIC LASER PULSES

If one irradiates GaAs by pulses cycling with frequency ≤1 GHz and put it in RF cavity, where electrons generate RF power, such a new device might lock frequency and phase (Fig. 2). Indeed, among all possible RF oscillations, which electron beam can excite, only oscillations with a proper frequency and a phase, corresponded to minimum of absorption in GaAs, are able to survive.

This principle was tested in a well known Van Der Pol oscillator, which allows to simulate a non-linear electron device having a threshold of the self-excitation [3]. In Fig. 3 one can see oscillations in dependence on normalized time (x=ω_0t) in the mentioned generator those

* Supported in part by DoE USA.
#kuzikov@appl.sci-nnov.ru

Copyright © 2012 by the respective authors — cc Creative Commons Attribution 3.0 (CC BY 3.0)

dimensionless parameter μ, which is responsible for an excess above threshold of a generation (similar to Pierce parameter), was periodically modulated with frequency close to eigen frequency. Note that resulting steady state oscillations in Fig. 3 (black) are placed so that time intervals with negative μ (corresponded to power absorption) lie near zero oscillation magnitude.

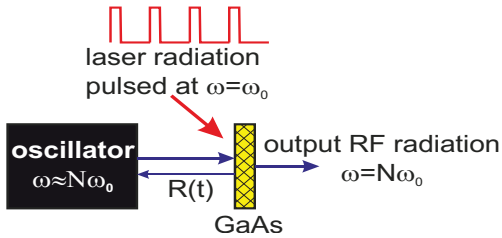

Figure 2: Sketch of RF oscillator locked by periodic laser radiation.

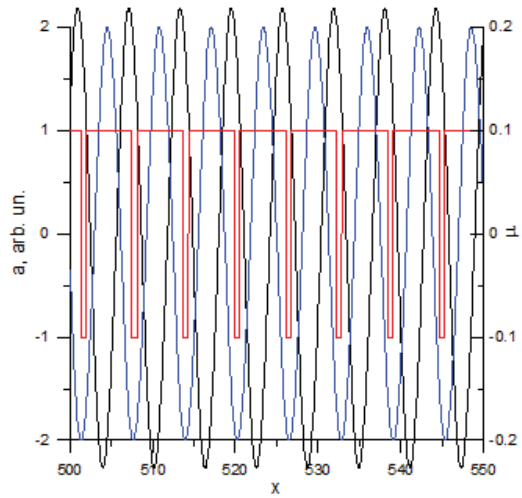

Figure 3: Oscillations in absence of Q- modulation (blue), oscillations in presence of modulation (black), and modulation shape (red).

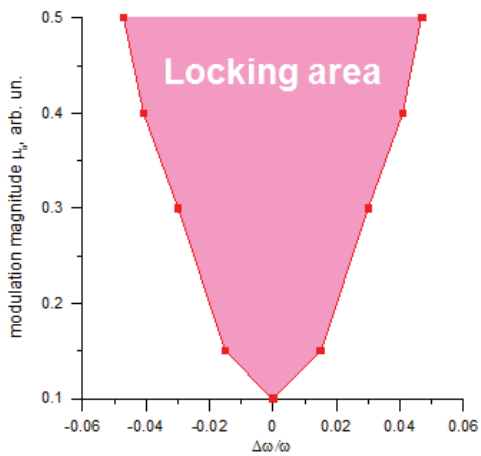

Figure 4: Zone of modulation magnitude which provides locking.

General properties of the described type of phase locking are following:

- Phase locking with accuracy 0/π is possible. 0 or π phase depends on initial conditions and, therefore, might be controlled.
- The far oscillator away a threshold, the deeper modulation is necessary and the longer time to lock (Δt_{min}~1/μ). This is visible in Fig. 4, where locking area is shown in coordinates frequency shift – modulation amplitude.
- The time to obtain phase locking is more for modulation at subharmonics in comparison with modulation at basic frequency (Δt_{min}~N, N – is a number of a subharmonic).

Note that modulation of a conductivity leads to absorption of some RF power in GaAs. These losses do not allow using too powerful and too long pulses. For example, if one takes at f=1 GHz P=100 MW power, τ=1 μs pulse duration, 100 Hz repetition rate and assumes that only 1% of RF power is absorbed in GaAs, average power loss would be 100 W. For GaAs sample of ~1 cm^2 size this value requires intense cooling. Average laser power (10 nJ/micropulse) in this case is not high (~10^{-3} W).

RF AMPLIFIERS DRIVEN BY PERIODIC LASER PULSES

Laser pulses, irradiating GaAs, might also be used for fast periodic commutation of DC voltage or current. The resulted periodic voltage or current are able to excite RF radiation. This allows to modulate beam parameters (density, velocity, etc) in a input low-power cavity of a high-power electron amplifier (Fig. 5).

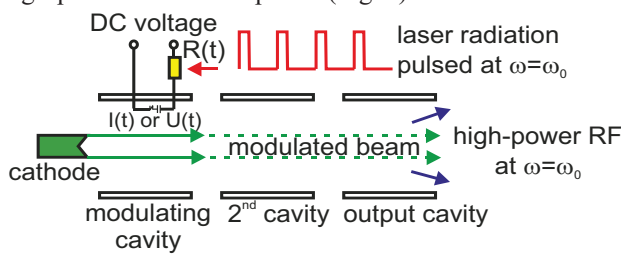

Figure 5: Scheme of klystron those input cavity is controlled and excited by laser pulses switching DC voltage.

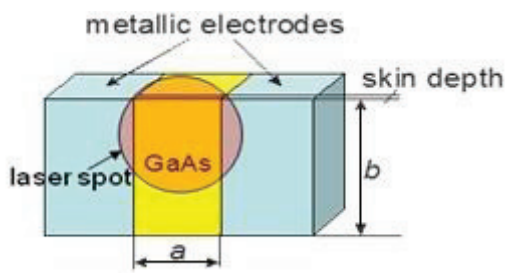

Figure 6: GaAs built-in between two electrodes and irradiated by laser light.

The simplest commutator consists of two electrodes and a piece of GaAs bulk in-between (Fig. 6). If one applies DC voltage to electrodes, the current oscillates in accordance with resistance modulation caused by laser

Copyright © 2012 by the respective authors — cc Creative Commons Attribution 3.0 (CC BY 3.0)

light. A switching laser light should be focused so that it closes electrodes by arisen photoconducting layer.

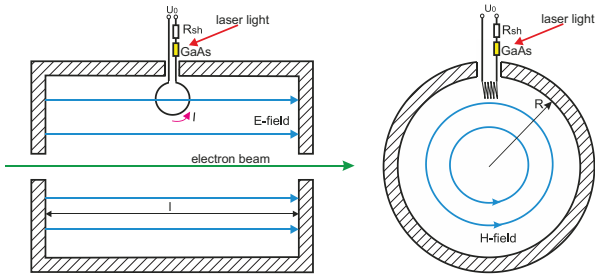

Figure 7: TM_{010} cavity excited by coil with modulated current.

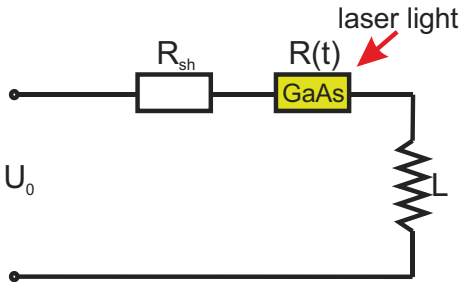

Figure 8: Simple equivalent scheme of current modulator.

Let us consider an example. In Fig. 7 the TM_{010} cavity is shown which is excited by antenna in a form of a coil. The current in antenna is generated by modulation of DC voltage which feeds a time-dependent load (GaAs sample). An equivalent scheme, which can be used in order to calculate current oscillations, is shown in Fig. 8. Let us take DC voltage as high as U=5 kV, modulation frequency f=1 GHz, GaAs size is $a \times b$=2×2 mm^2, radius of coil antenna Rc=25 mm with n=30 wire turns, cavity length is l=100 mm, the Q-factor of cavity is Q=1000 (in a regime without modulation). In accordance with these parameters and laser power W_{las}=10 nJ in each pulse we calculated current for different values of shunt resistance R_{sh} (Fig. 9). As one can see, the less shunt resistance the higher is the achievable peak current. However, the shunt resistance helps to reduce Ohmic losses in GaAs and to avoid a complicated cooling system.

In particular, if shunt resistance is zero, maximum E-field at cavity axis reaches almost 20 kV/cm (W_{las}= 10 nJ), but average power loss in this case is about 10 W. On the other hand, if to take the shunt resistance as high as 30 kOhm, the mentioned power loss reduces down to 1 W. This value equals to average power which laser pulses bring into GaAs. Of course, in this case the E-field becomes less (~4 kV/cm).

In Fig. 10 one can see how electric field on the axis depends on laser pulse energy. One can conclude that 10 nJ energy is enough to obtain a field which is near a possible maximum. At this laser energy GaAs resistivity is varied from ~100 MOhm (no light irradiation) and to ~1 kOhm (in presence of a laser light).

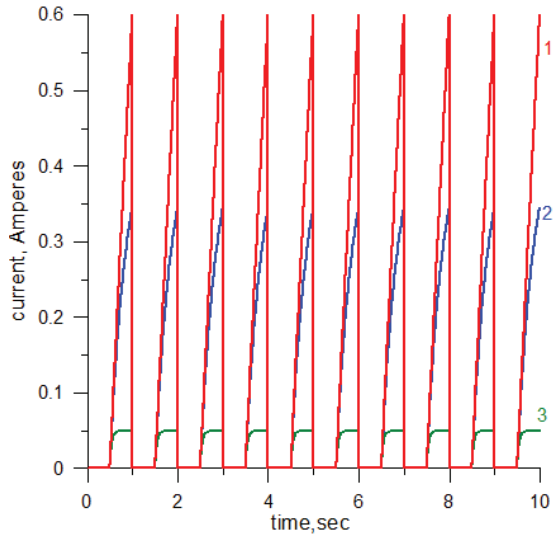

Figure 9: Modulation current in coil antenna: 1 – R_{sh}=0, 2 – R_{sh}=10 kOhm, 3 – R_{sh}=100 kOhm.

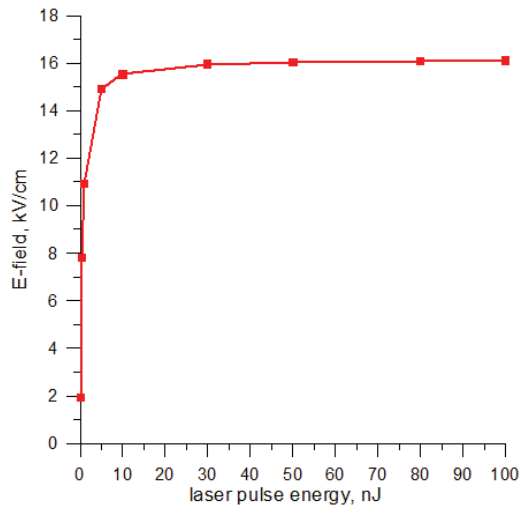

Figure 10: Excited E-field in TM_{010} cavity.

Maximum of fields, which can be excited in the cavity, linearly depends on Q-factor value. So, hundreds of kV/cm can be obtained, if to increase Q-factor up to 10^4. Such a quality seems reasonable at low frequencies (f≤1 GHz).

REFERENCES

[1] G. G. Denisov, S. V. Kuzikov, A. V. Savilov. "Q-switching in the electron backward-wave oscillator", Physics of plasmas 18, 103102 (2011).

[2] G.G. Denisov, et al. "Nanosecond Semiconductor Modulator of MM Waves Controlled by an Optical Laser", IRMMW-THz 2010, Rome, September 5-10, 2010, Mo-P.49.

[3] Van der Pol, B., "On relaxation-oscillations", The London, Edinburgh and Dublin Phil. Mag. & J. of Sci., **2**(7), 978-992 (1927).

Copyright © 2012 by the respective authors — cc Creative Commons Attribution 3.0 (CC BY 3.0)

FRIB FRONT END DESIGN STATUS*

E. Pozdeyev#, N. Bultman, G. Machicoane, G. Morgan, X. Rao, Q. Zhao, FRIB, East Lansing, MI 48824, USA
L.M. Young, LANL, Los Alamos, NM 87545 USA
J. Stovall, CERN, Geneva, Switzerland
V. Smirnov, S. Vorozhtsov, JINR, Dubna, Russia
L. Sun, IMP, Lanzhou, China

Abstract

The Facility for Rare Isotope Beams (FRIB) will provide a wide range of primary ion beams for nuclear physics research with rare isotope beams. The FRIB SRF linac will be capable of accelerating medium and heavy ion beams to energies beyond 200 MeV/u with a power of 400 kW on the fragmentation target. This paper presents the status of the FRIB Front End designed to produce uranium and other medium and heavy mass ion beams at world-record intensities. The paper describes the FRIB high performance superconducting ECR ion source, the beam transport designed to transport two-charge state ion beams and prepare them for the injection in to the SRF linac, and the design of a 4-vane 80.5 MHz RFQ. The paper also describes the integration of the front end with other accelerator and experimental systems.

FRONT END LAYOUT AND PARAMETERS

The FRIB Front End is designed to provide stable ion beams up to uranium with intensity sufficient to achieve 400 kW beam power on the FRIB target [1]. The FRIB Front End includes two ECR ion sources, two charge selection systems, LEBT, RFQ, and MEBT. To enhance availability and maintainability, the ECR sources and their charge selection systems are placed at the ground level in the support building about 10 m above the linac tunnel floor. Table 1 shows principle parameters of the Front End. The Front End layout is shown in Figure 1.

Table 1: FRIB Front End principle parameters

LEBT (before RFQ)	
Energy (keV/u)	12
Nominal beam current (eμA, typ.)	400
Emittance (πμm, 99.5%, norm.)	0.9
MEBT (after RFQ)	
Energy (keV/u)	500
Nominal current (eμA, typ.)	330
Emittance (πμm, 99.5%, norm.)	1.1
Long. Emittance (πkeV/u·ns, 99.5%)	1.5
Bunch repetition rate (MHz)	40.25, 80.5
Beam pulse length (μs)	0.6 – CW

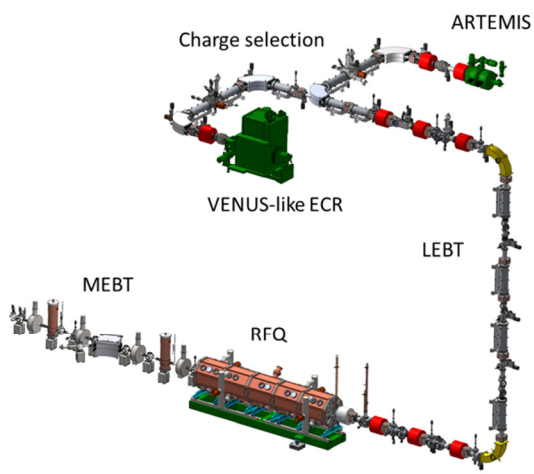

Figure 1: FRIB Front End Layout. Two ECR sources are located at the ground level. The RFQ and MEBT are located in the linac tunnel 10 m below grade.

FRONT END SYSTEMS

Ion Sources

FRIB Front End includes two ion sources: a superconducting high-power source based on the VENUS ECRIS developed at LBNL [2] and, primarily for commissioning, a room-temperature ECR ARTEMIS. The sources are placed on high voltage platforms to match the RFQ injection energy for all beams.

The ARTEMIS ECR source, built at MSU and based on the AECR-U ECR developed at LBNL, operates at 14.5 GHz with room temperature coils. Minimal re-configuration of the source is required to make the source compatible with operation on a high voltage platform.

The superconducting high-performance source will be based on the design of VENUS ECR ion source operating at a maximum frequency of 28 GHz. In 2007, VENUS demonstrated intensity required for FRIB for a 238U beam with the two charges states, 33+ and 34+, combined. Based on this result, FRIB was designed to accelerate two charge states from an ion source to double intensity. Recent beam tests demonstrated that better

*Work supported by the U.S. Department of Energy Office of Science under Cooperative Agreement DE-SC0000661 and grant #DE-FGO2-08ER41553
#pozdeyev@frib.msu.edu

Copyright © 2012 by the respective authors — cc Creative Commons Attribution 3.0 (CC BY 3.0)

performance from VENUS can be obtained by better tuning and coupling of microwave power to the ion source. A new intensity record of 450 eA of U was demonstrated by VENUS at LBNL with a direct participation of the NSCL ECR group. The measured emittance for this charge state showed that 95% of the beam was within the FRIB acceptance. This test demonstrated that VENUS can satisfy the FRIB intensity requirement in a single charge state that can significantly simplify linac tuning. FRIB modifications to the original design of the VENUS cryostat include the cooling capacity at 4.2K been extended from 6 W to 12 W to include the dynamic heat load generated by the plasma Bremsstrahlung electrons.

Beam transport

Beams extracted from the sources are filtered in the charge selection systems. The systems are achromatic, designed to select and transport two charge states simultaneously for beams heavier than xenon.

The LEBT design is achromatic allowing transporting two charge states simultaneously. To facilitate transport of two-charge state beams through LEBT electrostatic quadrupoles and two 90° deflectors are used in the vertical transport line. To reduce losses in the superconducting linac, the beam is collimated by several apertures in the LEBT. To satisfy experimental system requirements and facilitate linac tuning the Front End is able to vary intensity of accelerated beams by several orders of magnitude. A chopper is used to vary the duty cycle controlling the pulse length from several hundreds of ns to CW and the pulse frequency from 0 to 30 kHz. Several mesh screens allow reduction of the beam intensity by several orders of magnitude while keeping the nominal bunch frequency. The two 90° electrostatic deflectors in the vertical transport line are incorporated into the machine protection system. The voltage on the deflector electrodes is controlled by fast switches that receive the inhibit signal from the MPS with shut-off time below 1 μs. Additional details on the beam dynamics in the LEBT can be found in [3].

Downstream of the RFQ, MEBT includes two room-temperature QWR bunchers, four SC solenoids, an energy analyzing dipole, and diagnostics. MEBT matches the beam to the SC linac and removes un-accelerated beam from the RFQ.

Multi-harmonic buncher and velocity equalizer

The CW beam is bunched before injection into the RFQ by a multi-harmonic buncher (MHB) operating at 40.25, 80.5, and 120.75 MHz. The design of the buncher is described in [4]. A second RF cavity conceptually similar to MHB but operating at 40.25 MHz is required upstream of the RFQ for two-charge-state beam injection, acting as a velocity equalizer (VE). The construction and assembly of MHB have been completed (Figure 2). The buncher currently undergoes tuning and testing.

MEBT Bunchers

Two identical FRIB MEBT bunchers are used in MEBT to longitudinally match the beam to the SRF linac. The bunchers are room temperature quarter wave resonators similar in design and dimensions to the PIAVE bunchers developed at Legnaro [5]. Table 2 shows a summary of main parameters of the MEBT bunchers. The RF design of the buncher, including the coupler loop, has been completed. The thermal management analysis and development of mechanical drawings and details are in progress.

Table 2: **M**ain parameters of FRIB MEBT bunchers

Frequency (MHz)	80.5
Voltage (Typical, uranium, kV)	120
Transit time factor	0.82
Power (kW)	1.3

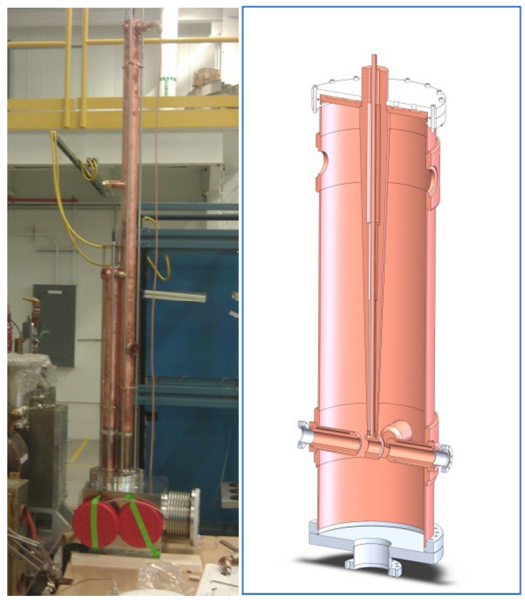

Figure 2: FRIB Front End bunchers. Left: multiharmonic LEBT buncher completed assembly. Right: MEBT 80.5 MHz QWR buncher assembly drawing.

RFQ

The FRIB RFQ utilizes a 4-vane structure to accelerate single and two-charge state beams from 12 to 500 keV/u with estimated transmission efficiency above 80%. Table 3 shows main RFQ parameters, while Figure 3 shows evolution of structure parameters along the RFQ length.

The RFQ beam physics design is optimized to minimize the longitudinal emittance of the accelerated beam as described in [6][7]. To increase the RFQ output energy a linear accelerating voltage ramp is implemented. The linear voltage ramp is accomplished through proper sizing of the vane undercuts. Dipole mode suppression rods attached to the structure endplates are utilized to move dipole mode frequencies away from the accelerating mode frequency. The quadrupole and dipole

Copyright © 2012 by the respective authors — cc Creative Commons Attribution 3.0 (CC BY 3.0)

mode local perturbations are fine-tuned during construction using 27 fixed mechanical slug tuners distributed along the length of the machine. A full 3D model of the RFQ, including undercuts, stabling rods, and the slug tuners, was implemented in the CST Microwave Studio (MWS) [8] to accurately select required parameters and simulate fields and surface losses. Figure 4 shows the design voltage profile used in PARMTEQ and the voltage profile simulated by CST MWS. The difference between the design and simulated voltage profiles is less than 1%.

Mechanical construction of the RFQ will be performed as a brazed structure with dual-circuit cooling water resonance control. Mechanical fabrication is performed in 5 longitudinal sections to optimize machining and handling. Although thermal management of CW RFQs is challenging, given the modest drive power, no significant cooling issue is expected. All components are made of high-conductivity copper and actively water cooled. Additional care is taken in the vane-undercut regions where the local RF heating is increased due to magnetic-field compression in these zones. The power is fed using a single magnetic-field loop-coupler drive.

Table 3: FRIB Front End RFQ design parameters. RF parameters obtained in CST Microwave Studio simulations.

Frequency (MHz)	80.5
Injection/Output energy (keV/u)	12/500
Design charge-to-mass ratio	1/7-1/3
Accelerating voltage ramp (U, kV)	60 – 112
Surface electric field (Kilpatrick)	1.6
Quality factor	16500
Operational RF power (kW, O-U)	15-100
Dipole modes (closest, MHz)	78.3 / 83.2
Length (m)	5.04

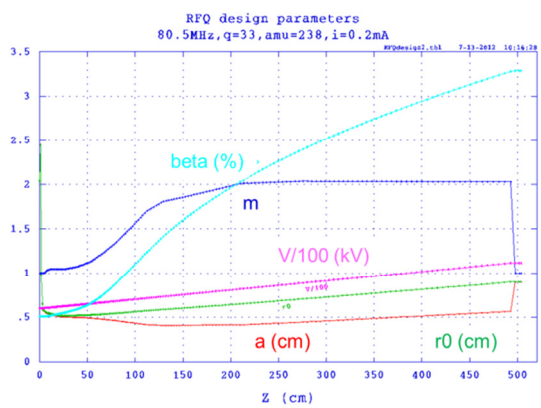

Figure 3: RFQ structure parameters as a function of the longitudinal coordinate (PARMTEQ notations).

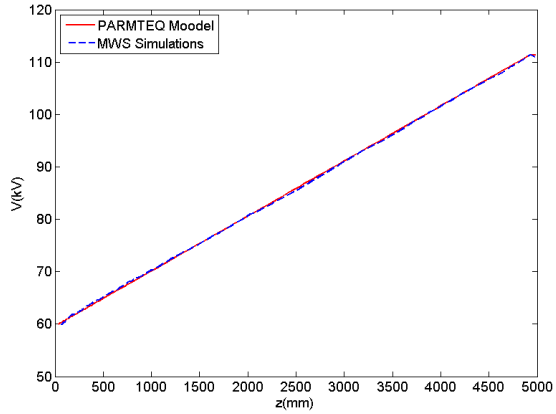

Figure 4: RFQ design voltage profile (red solid line) and the voltage profile simulated by CST MWS.

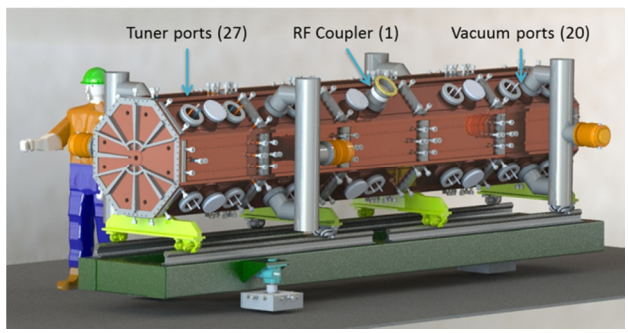

Figure 5: RFQ assembly drawing.

ACKNOWLEDGMENT

Authors would like to express their special gratitude to A. Aleksandrov, J. Benitez, A. Facco, R. Keller, B. Laxdal, D. Leitner, M. Leitner, C. Lyneis, F. Marti, B. Mustafa, P. Ostroumov, R. Pardo, R. Vondrasek, X. Wu, Y. Yamazaki for their input and advice. Also, the authors are thankful to members of FRIB and NSCL teams who participated in this work.

REFERENCES

[1] J. Wei, et al, TU1A04, These proceedings
[2] D. Leitner et al, Rev. Sci. Instru. 79 (2008) 02C710
[3] L. Sun, et al, Rev. Sci. Instru. 83 (2012) 02B705
[4] J.Holzbauer, et al, PAC'11, New York, 2011, TUP091, p. 1000
[5] A. Facco, F. Scarpa, V. Zviagintsev, EPAC 2000, Vienna, Austria, pp.2037-2039
[6] P. Ostroumov, et al, Phys. Rev. ST Accel. Beams 5, 060101 (2002)
[7] Q. Zhao, et al, LINAC 2004, Lübeck, Germany, p. 599
[8] CST Microwave Studio, v.12, CST GmbH (Darmstadt, Germany), 2012. www.cst-world.com

Copyright © 2012 by the respective authors — cc Creative Commons Attribution 3.0 (CC BY 3.0)

HEAVY ION STRIPPERS *

F. Marti, FRIB/MSU, East Lansing, MI 48824, USA

Abstract

Stripping of high current heavy ion beams is a key technology for future accelerators as FAIR (Germany) [1] and FRIB (USA) [2] and current ones as RIBF (RIKEN, Japan) [3]. A small change in the peak charge state produced at the stripper could require a significant expense in additional accelerating stages to obtain the required final energy.

The main challenges are the thermal effects due to the high power deposition (~ 50 kW/mm^3) and the radiation damage due to the high energy deposition. The effects of heavy ion beams are quite different from proton beams because of the much shorter range in matter.

We present an overview considering charge stripping devices like carbon foils and gas cells used worldwide as well as the current research efforts on plasma stripping, liquid metal strippers, etc. The advantages and disadvantages of the different options will be presented.

INTRODUCTION

The use of strippers in heavy ion accelerators provides a way of increasing the final energy without increasing the total accelerating voltage. But there are drawbacks. Usually the stripper efficiency is low, especially when only one charge state can be accelerated like it occurs in cyclotrons, and only a fraction of the incoming particles are in the correct charge state. In the new high beam power regimes proposed for linear accelerators under construction an additional problem occurs because of the high power deposition in the stripping media.

STRIPPER CHALLENGES

Power Deposition and Radiation Damage

The major issue associated with beam strippers for high intensity heavy ion accelerators compared with H- accelerators is the much larger energy deposition per unit length of the heavy ions compared with the protons. Using the code SRIM [4] we can calculate the energy loss. As an example, a U ion at 16.5 MeV/u (FRIB stripper case) deposits 25.7 MeV/μm and has a range of 0.14 mm in a C foil (2.25 g/cm^3), while a 1 GeV proton (i.e. SNS stripper) deposits about 0.44 keV/μm and has a range of 1.62 m; a ratio of close to 60000 in linear energy deposition.

This much higher linear energy deposition produces significantly larger radiation damage effects in solids.

Thermal Effects

Although the beam powers are quite different (40 kW at the FRIB stripper and 1.4 MW at the SNS stripper) the much higher linear energy deposition more than compensates it and the thermal effects are also more severe. These become important when gas or liquid strippers are proposed to avoid the radiation damage to the solid lattice. They could produce density variations that result in large energy spreads of the stripped beam.

EXAMPLES OF STRIPPERS IN USE

Brookhaven National Laboratory

The Relativistic Heavy Ion Collider (RHIC) is the major heavy ion accelerator at Brookhaven National Laboratory (BNL) (see Figure 1). The Au beam was until recently accelerated in a tandem (now an EBIT is being used) with the first stripper in the tandem terminal (S1), a second stripper after the tandem (S2), a third between the Booster and the AGS (S3) and a fourth one between the AGS and the Collider (S4) [5].

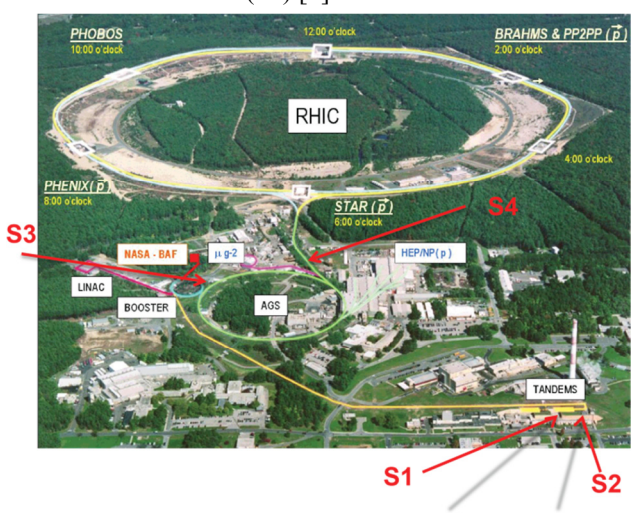

Figure 1: Layout of the RHIC accelerator at BNL showing the location of the four strippers, S1 at the tandem terminal, S2 after the tandem, S3 between the Booster and the AGS and S4 after the AGS.

The two more challenging strippers are S1 and S3. The first stripper (S1) is very thin, just 2 micro grams/cm^2. The Au ions are stripped from Au^{-1} to Au^{+12}. The lifetime of this stripper when using evaporated carbon foils was short. The introduction of foil produced by laser ablation of carbon extended the average lifetime by a factor of three. A ladder with several hundred foils is located at the terminal and oscillates to spread the beam damage over a larger surface.

* This material is based upon work supported by the U.S. Department of Energy Office of Science under Cooperative Agreement DE-SC0000661

Copyright © 2012 by the respective authors — cc Creative Commons Attribution 3.0 (CC BY 3.0)

The third stripper (S3) originally made of carbon has been replaced by a composite stripper of a first layer of aluminum (6.4 mg/cm^2) followed by a glassy carbon layer (9.2 mg/cm^2) [5]. The difference between the two materials is that the ions reach a high charge state faster (thinner stripper thickness) in aluminium than in carbon, but the final charge state is not as high. With the new double layer stripper the total stripper thickness mass is reduced and lower energy loss (important for the matching between the Booster and AGS). In addition a lower energy spread has been obtained than previously because of the non-uniformities in the previous thicker carbon stripper.

GSI Helmholtz Centre for Heavy Ion Research

The GSI accelerator complex includes a low energy section that accelerates the U beam up to energy of 11.4 MeV/u (see Figure 2).

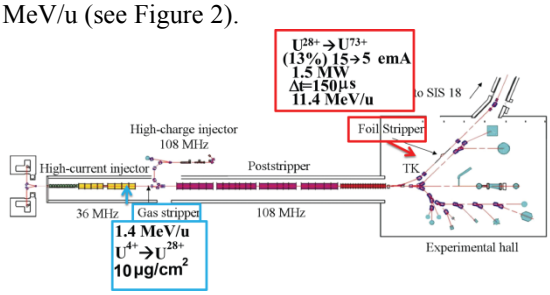

Figure 2: Layout of the low energy section of the GSI accelerator.

In this section two strippers are normally used to bring the U beam to a charge state acceptable for injection into the SIS 18 synchrotron. The first is a gas stripper at energy of 1.4 MeV/u consisting of a N_2 jet with a total thickness of approximately 10 μg/cm^2. The U ions are stripped from a charge of 4+ to a charge of 28+. The second stripper is a carbon foil that takes the 28+ to a 73+ at an a energy of 11.4 MeV/u. The drawback of this scheme for the new facility is the low efficiency associated with the losses inherent in selecting only one charge state from the distribution produced by each stripper. Studies have been performed to replace both strippers with a single foil (20 μg/cm^2) at 1.4 MeV/u. The experiments have shown that U^{39+} can be obtained with a total efficiency of 20 % to be injected in the SIS 18. Intensity significantly higher than what is obtained using the present pair of strippers [6].

A very comprehensive study of the material modifications of these foils is being pursued at GSI by M. Tomut and colleagues [7-8]. It appears that there is a beam-induced graphitization of the amorphous foil that leads to stresses due to the higher density of the crystalline phase. The lifetime of the foils seems to average 0.8 10^{16} ions/cm^2.

The interesting point is that the GSI experiments do not seem to indicate a thinning of the foils, contrary to the experience at RIKEN [9] and at MSU [10]. This last experimental work seems to point toward the "ion hammering" effect described by Klaumunzer and collaborators [11] as the cause of the foil thinning.

RIKEN Nishina Center

The RIKEN accelerator complex is shown in Figure 3. The U beam is first accelerated by a linac and later by four cyclotrons in series, achieving a final energy of 350 MeV/u. The intensity goal is 1 pμA. Two strippers are being used, between the first and second cyclotron and between the second and third. Due to the limitation of selecting a single charge state after each stripping the efficiency is intrinsically low and a high intensity at the first stripper is necessary.

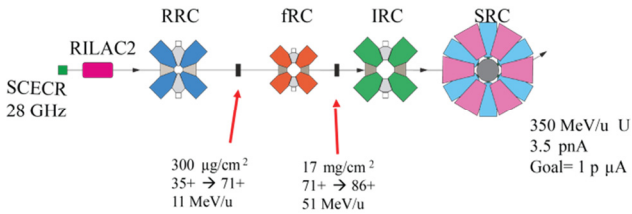

Figure 3: Layout of the RIKEN accelerator showing the linac followed by the four cyclotrons

Extensive development of carbon foils has been performed by H. Hasebe and collaborators for RIKEN [12-13]. The carbon foils, either static or in rotating cylinders do not seem to be able to withstand the higher current needed to achieve the RIKEN RIBF design goals. The present operating point is about 100 times below design.

With the expectation of achieving higher beam intensities the RIKEN team has been pursuing several variations of gas strippers. The first attempt with a nitrogen stripper produced charge states too low to be accepted by the second cyclotron. An important measurement performed at RIKEN by Okuno and collaborators [14] determined the equilibrium charge state for U in a helium gas at three energies between 11 and 15 MeV/u (see Figure 4).

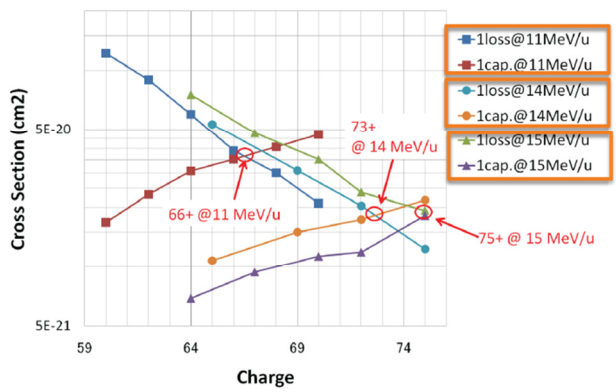

Figure 4: Cross sections for electron loss and electron capture for U in helium at three different energies 11, 14 and 15 MeV/u.

These measurements confirmed that the charge state emerging from a helium stripper is higher than from a nitrogen gas stripper. As described in [14] "The e-capture phenomenon is particularly highly suppressed because of

Copyright © 2012 by the respective authors — cc Creative Commons Attribution 3.0 (CC BY 3.0)

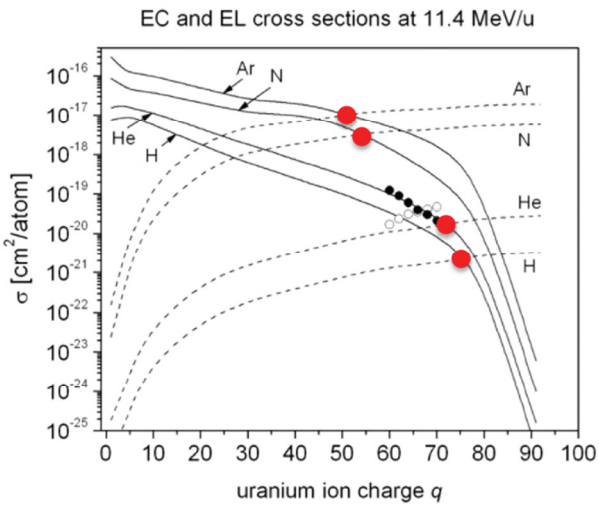

Figure 5: Calculated [15] cross sections of electron capture (EC, dashed curves) and electron loss (EL, solid curves) for Ar, N, He and H for U at 11.4 MeV/u. The red dots indicate the points where both cross sections are equal and determine the equilibrium charge state. The small open and closed circles are the RIKEN measurements at 10.8 MeV/u.

poor kinematical matching when the ion velocity significantly exceeds the velocity of 1s electrons, V_{1s}, which are the fastest target electrons". This mismatch is much higher for helium than for nitrogen, lowering the electron capture cross section and moving the equilibrium charge state to higher charges.

The relative effect can be seen in Figure 5 where the calculated cross sections and the expected equilibrium charges (red dots) are shown for four different gases [15]. Due to the hazards of handling hydrogen, helium is the preferred gas. On the other hand the drawback of helium is the difficulty in pumping it, due to the low efficiency of traditional vacuum pumps.

An extensive development program converged on the construction of a powerful helium gas stripper by Imao and collaborators [16] that has been tested with beam. The new system consists of five stages of differential pumping [9] and 21 pumps. The gas cell has a length of 50 cm at a pressure of 7 kPa to provide a 0.7 mg/cm^2 stripper. On each side of the gas cell four apertures of 10 mm separate the different stages. This system has produced the necessary charge state to inject into the second cyclotron after modifications to its magnetic field. Future work will include the improvement of the gas recycling system due to the large volume of gas circulating. It is also important to study the effect of impurities (oil, water, N2, etc) that could increase the capture cross sections. This is a well-known issue that has affected the gas stopping cell at MSU [17].

The development of this system is a major step in stripper R&D, especially when the beam current is increased and the gas will develop regions of high temperature and low density, increasing the energy spread introduced by the system. With the present beam intensities the RIKEN measurements indicated a lower energy spread than with the carbon foil it replaces due to the thickness non-uniformity of the foils, but an increase in intensity of a factor of 100 will be different territory.

FRIB/MSU- ANL: Liquid Lithium Stripper

The layout of the accelerator proposed for the Facility for Rare Isotope Beams (FRIB) is shown in Figure 6. It consists of a folded linac with the stripper at the end of the first segment [2]. The baseline design has selected a liquid lithium stripper with an alternate design of a helium gas stripper with plasma windows to contain the gas in the cell.

The liquid lithium stripper was proposed by J. Nolen from Argonne National Laboratory (ANL) [18]. It consists of a high pressure liquid lithium jet that impinges on a deflecting plate and produces a thin film (~ 10 μm) of lithium that is traversed by the heavy ion beam (see Figure 7). Lithium becomes liquid at approximately 180 C. An experimental test of a single pass liquid lithium loop has been developed by the ANL team collaborating with FRIB. This single pass loop consists of a reservoir pressurized with argon gas that in the production system will be replaced with an electromagnetic pump. In the test chamber the liquid is pumped back to its original vessel after it has completed one cycle and the process is repeated. The results achieved so far indicate that we can obtain the correct thickness of the liquid film and that it is stable in time. The next steps will be to test if the film is disturbed by depositing power with a proton beam on a beam spot of approximately 3 mm diameter. We expect the FRIB beam to deposit approximately 700 W on the liquid. The high velocity of the film (about 50 m/s) is expected to remove the hot liquid before bubbles can form. Another development will be the endurance tests. Lithium is a very corrosive substance and attacks many common materials like copper. Soft iron on the other hand is compatible with lithium.

The hazards associated with lithium make it necessary to take especial precautions to avoid contact with many substances, concrete, water, nitrogen, etc. For our prototype design (see Figure 8) we are planning to enclose the stripper system in a secondary containment vessel made of iron that will be filled with argon gas to prevent the possibility of starting a fire.

FRIB/MSU- BNL: Helium Gas Stripper

As an alternate solution to the liquid lithium we are developing a helium gas stripper with the ags cell enclosed by plasma windows, in collaboration with BNL. The excellent results obtained by RIKEN encouraged us to consider this alternate solution. The plasma windows sketched in Figure 9 were developed by A. Hershcovitch [19]. The plasma works as a buffer between the high pressure helium (1/3 atmosphere) and the low pressure in the beam line.

The high temperature of the plasma allows a lower

Copyright © 2012 by the respective authors — cc Creative Commons Attribution 3.0 (CC BY 3.0)

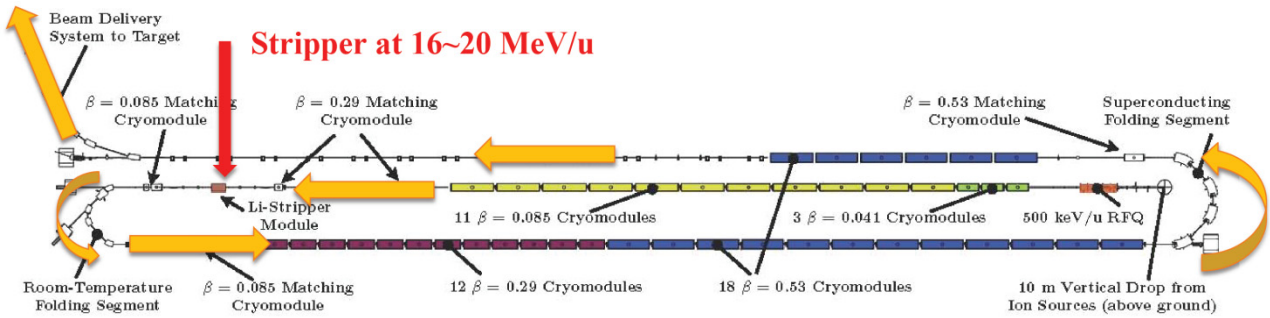

Figure 6: Layout of the Facility for Rare isotopes (FRIB) being designed at Michigan State University for US-DOE. It consists of a SRF linac folded in three sections. After the first section and before the first bend a stripper section is included. Typical stripping energies are between 16 and 20 MeV/u.

density gas to equal the pressure of a denser low temperature gas. Tests at BNL [20] have shown that we can obtain a conductance reduction factor (pressure on the low pressure side with plasma window off divided by pressure with the plasma window on) of 20 and larger in runs lasting many hours.

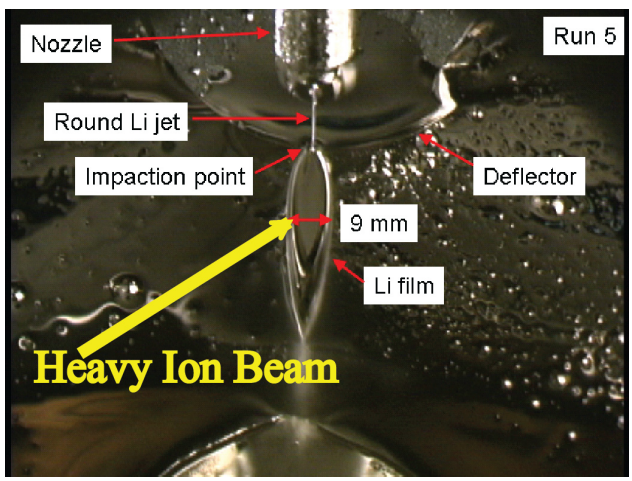

Figure 7: Liquid lithium film produced at ANL. The nozzle is shown at the center top of the photo with the lithium jet hitting the deflector plate. The yellow arrow indicates the direction of the heavy ions traversing the film.

A typical plasma window is shown in Figure 10. A reasonable question is why should we complicate the system with the plasma windows? As we saw from the RIKEN helium stripper it is a very complex system and it is important to be able to circulate the gas at high velocity to decrease the temperature increase. The reduction of the conductance and loss of the helium gas is a very desirable goal specially to reduce the possibility of introducing impurities. As in the case of the liquid lithium the study of the effect of power deposition is necessary to prevent the formation of a low density volume in the beam path.

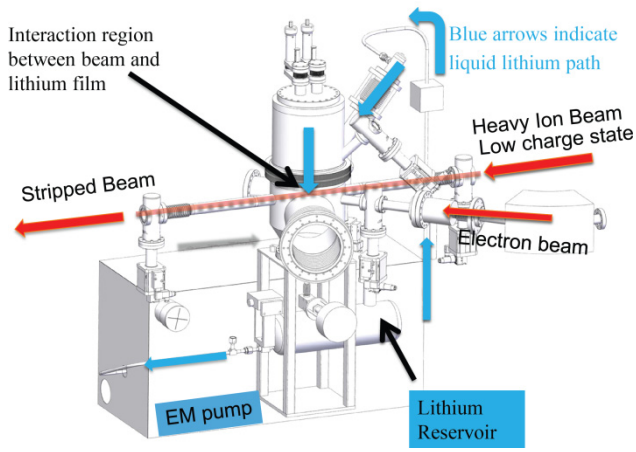

Figure 8: Prototype of the liquid lithium stripper for FRIB. The electron beam will be used to measure the film thickness.

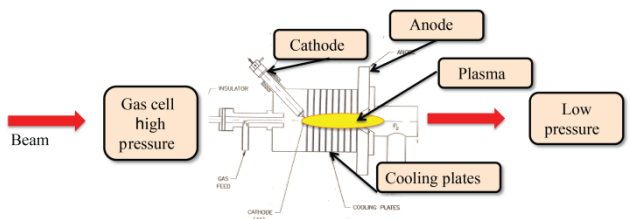

Figure 9: Configuration of a high pressure He gas cell enclosed in plasma windows.

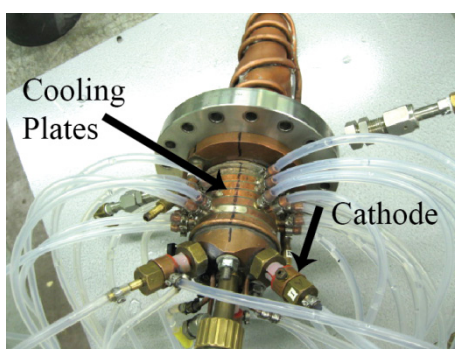

Figure 10: Plasma window developed by A. Hershcovitch [19]

Copyright © 2012 by the respective authors — cc Creative Commons Attribution 3.0 (CC BY 3.0)

Frankfurt/GSI – Plasma Strippers

The use of plasma strippers has not been implemented routinely yet but the Frankfurt group working at GSI is making important steps in that direction. The idea behind a plasma stripper is that direct capture of an electron by a moving ion violates the simultaneous conservation of energy and momentum [21-22]. The excess binding energy must be taken away by radiative recombination, 3-body recombination or dielectronic recombination, all low probability processes. This restriction lowers the electron capture cross section compared to the bound electron case increasing the charge of the ion compared with a cold target. This effect is more important at low energies. At higher energies the high relative velocity also depresses the capture process.

An experiment is scheduled at GSI [23] to test a plasma stripper with a 4 MeV/u U beam. The ions will interact with a θ-pinch plasma (see Figure 11) produced by an induction coil. The process is geared toward low energy beams and in pulsed mode, not continuous beams.

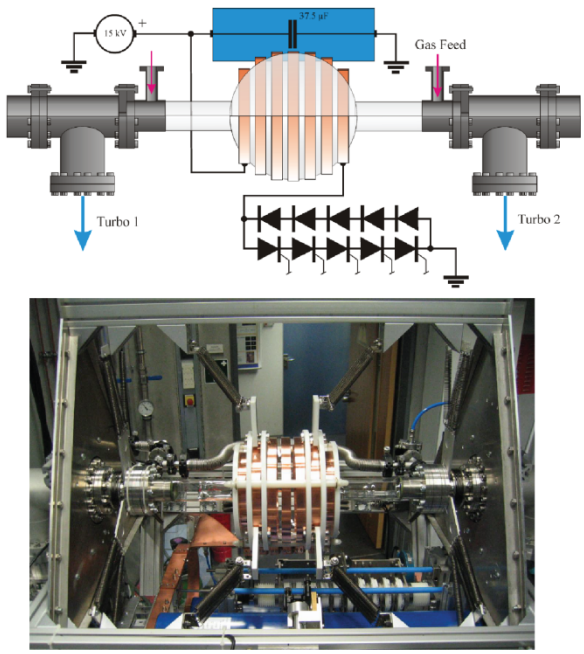

Figure 11: Plasma stripper setup, sketch (above) and equipment (below) showing the induction coil.

CONCLUSIONS

We have recently seen important developments in the field toward new gaseous and liquid metal strippers. The low power tests of helium strippers at RIKEN are very encouraging. The ANL work has shown the stability of the lithium film with the correct thickness. The next steps are to explore how they react to high power deposition by intense beams.

ACKNOWLEDGMENT

I am indebted to many colleagues that provided information for this paper and to those which have been collaborating with the FRIB team exchanging ideas and results about stripper R&D. I must especially recognize D. Chowjnoski, Y. Momozaki, J. A. Nolen and C. B. Reed, J. Specht from ANL; A. Hershcovitch, L. Snydstroup and P. Thieberger from BNL; J. Jacoby from Frankfurt; W. Barth, O. Kester and M. Tomut from GSI; H. Imao, H. Kuboki and H. Okuno from RIKEN; P. Guetschow, W. Mittig and T. Xu from MSU.

REFERENCES

[1] FAIR Baseline Technical Report, Vol. 2 (2006). http://www.fair-center.eu/fair-users/publications/fair-publications.html
[2] J. Wei et al," Status and challenge of FRIB project", TU1A04, these proceedings.
[3] H. Imao et al., "Charge stripping of Uranium-238 ion beam with helium gas stripper", IPAC2012, New Orleans, THPPP084, p. 3930 (2012); http://www.JACoW.org
[4] J. Ziegler, http://www.srim.org
[5] P. Thieberger et al., PRST-AB **11** (2008) 011001.
[6] W. Barth et al., "Carbon stripper foils for high current heavy ion operation", INTDS 2012.
[7] M. Tomut et al., GSI SCIENTIFIC REPORT 2011, p. 412.
[8] M. Tomut, "Failure mode of carbon stripper foils exposed to intense heavy ion beams", INTDS 2012.
[9] H. Okuno, personal communication.
[10] F. Marti et al., "Stripper foil developments at NSCL/MSU", Cyclotrons 2010, Lanzhou, THM2CCO03, p. 373. http://www.JACoW.org
[11] A. Benyagoub and S. Klaumunzer, Radiation Effects and Defects in Solids, **126** (1993) p. 105.
[12] H. Hasebe et al., NIM A **613** (2010) 453.
[13] H. Hasebe et al., NIM A **655** (2011) 57.
[14] H. Okuno et al., PRST-AB **14** (2011) 033503.
[15] V. P. Shevelko et al., NIM B **278** (2012) 63.
[16] H. Imao et al., "Charge stripping of Uranium-238 ion beam with helium gas stripper", THPPP084, Proc. IPAC2012, p. 3930, http://www.JACoW.org
[17] D. J. Morrissey et al., NIM B **266** (2008) 4822.
[18] Y. Momozaki et al., JINST 4 (2009) P04005.
[19] A. Hershcovitch, Phys. of Plasmas **5** (1998) 2130.
[20] A. Hershcovitch, P. Thieberger, L. Snydstroup, personal communication.
[21] E. Nardi and Z. Zinamon, Phys. Rev. Lett., **49** (1982) 1251.
[22] J. Jacoby et al., Phys. Rev. Lett. **74** (1995) 1550.
[23] C. Teske, G. Xu, J. Jacoby, T. Rienecker –Frankfurt, Beam Time Proposal: U275.

Copyright © 2012 by the respective authors — cc Creative Commons Attribution 3.0 (CC BY 3.0)

LIGHT ION ECR SOURCES STATE OF THE ART FOR LINACS

R. Gobin*, N. Chauvin, O. Delferrière, O. Tuske, D. Uriot, Commissariat à l'Energie Atomique et aux Energies Alternatives, CEA/Saclay, DSM/IRFU, 91191 - Gif/Yvette, France

Abstract

Since the middle of the 90's development of high intensity light ion injectors are undertaken at CEA-Saclay. The first 100 mA proton beam has been produced by the SILHI ECR source in the framework of the IPHI project. Ever since, more than 100 mA of protons or deuteron beams, with high purities, have been regularly produced in pulsed or continuous mode, and with very good beam characteristics analyzed in dedicated beam diagnostics. CEA-Saclay is currently involved in several high intensity LINAC projects such as Spiral2, IFMIF-EVEDA and FAIR, and is in charge of their source and LEBT design and construction.

This article reports the latest developments and experimental results carried out at CEA-Saclay for the 3 projects. In addition, a review of the developments and beam results performed in other laboratories worldwide are also presented.

INTRODUCTION

For several decades numerous projects are based on high intensity beam interaction with different targets, either for industrial applications or research facilities. High intensity light ion beam projects are often ranked in the HPPA (High Power Proton Accelerator) family. Table 1 gives a list of worldwide research facility projects based on positive ions. One could note, numerous projects based on negative ion production (mainly H-) also exist and are not listed here.

Table 1: List of several HPPA around the world

	Particles	Intensity	Pulse length	Repetition	Duty Factor	Emittance
	p/d/H⁻	mA	ms	Hz	%	π mm.mad
LEDA	H^+	100	CW	-	100	0.25
IPHI*	H^+	100	CW	-	100	0.25
TRASCO	H^+	30	CW	-	100	0.2
SARAF	H^+, D^+	2	CW	-	100	0.2
IFMIF*	D^+	140	CW	-	100	0.25
Spiral2*	H^+, D^+	5	CW	-	100	0.25
PEFP	H^+	20	2		8-20	
MYRRHA	H^+	10/25	CW	-	100	0.25
Chinese ADS	H^+	10	CW	-	100	
FAIR*	H^+	100	1	4	0.4	0.3
ImPUF	H^+, D^+	5	CW	-	100	
ESS	H^+	60/90	2.9	14	4	0.3

Like for all ion accelerators, the general lay out (fig. 1) shows the first element of such HPPA is the ion source.

email: rjgobin@cea.fr

The ion source has to provide the requested beam with characteristics giving the best conditions to inject the beam into the1st accelerating cavity. Thus the source has to be designed to minimize the beam emittance. The 1st accelerating cavity is generally an RFQ (Radiofrequency Quadrupole) which bunches and accelerates the beam up to few MeV. A LEBT (Low energy Beam Transport), follows the source and allows matching the beam at the entrance of the RFQ. As shown in table 1, the requested rms normalized emittance value turns out to be 0.25 π.mm.mrad at the RFQ entrance. As a consequence, for an HPPA, while designing an injector, one has to consider not only the source but the ion source, the extraction system and the LEBT as a whole[1].

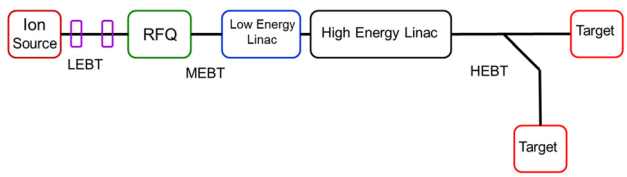

Figure 1: Schematic lay out of a high intensity Linac

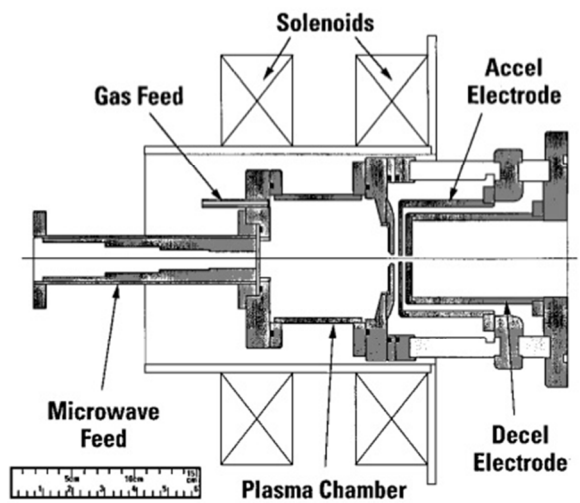

Figure 2: 1st ECR ion source dedicated to HPPA, developed in Chalk River

Then, after the RFQ, the main part of the accelerator consists of a long string of cavities (generally superconducting cavities) separated by matching sections and equipped with well-adapted diagnostics.

Copyright © 2012 by the respective authors — cc Creative Commons Attribution 3.0 (CC BY 3.0)

One of the main requests for the HPPA, mainly for ADS (Accelerator Driven System) is the reliability and the reproducibility. Such demands push injector designers to use well-known reliable sources which are ECRIS (Electron Cyclotron Resonance Ion Source). An ECRIS source has to satisfy the equation:

$$\omega = e B / m$$

where: ω = pulsation, e = electron charge, B = magnetic field and m = electron mass.

The 1st ECR ion source dedicated to high intensity proton facility has been developed in Chalk River by Taylor and Mouris [2] at the beginning of 90's. One can consider now such a source as an "ECR ion source" as it has been demonstrated the plasma density is increased with an ECR zone into the plasma chamber. Few years later, the Chalk River source has been moved to Los Alamos where a new version has been developed for the LEDA project. This new source, equipped with a 4 electrode extraction system, allowed injecting and accelerating a 75 mA - 6.7 MeV beam after the RFQ.

GENERAL ASSESSMENTS

Since then, the Chalk River source has often been taken as reference for the design of the new sources around the world.

The source design is generally based on a 2.45 GHz frequency generator which transfers the RF power to the plasma chamber via waveguides and RF window. For such a frequency, the electron resonance occurs when the magnetic field reaches 875 Gauss in the plasma chamber.

A multi-electrode (3, 4 or 5 electrodes) system (accel – decel) is used for the beam extraction. Different codes allow simulating particles trajectories in the extraction system and minimizing the emittance at the very beginning of the accelerator. For beam transport at low energy, codes have also to take into account the space charge compensation.

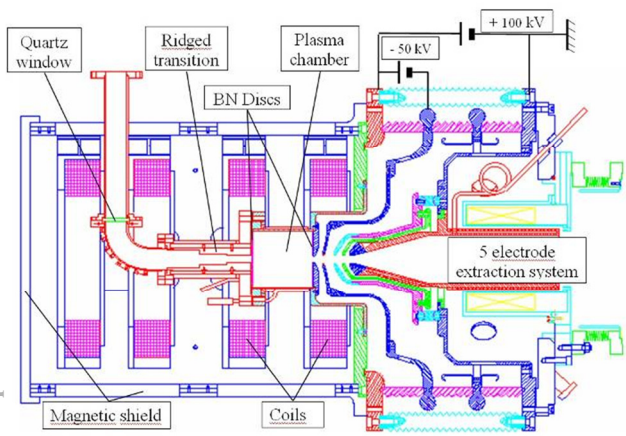

Figure 3: SILHI source design with BN disks, Electron repeller, Window protected by a bend, Ridged waveguide transition

Numerous modifications have been done worldwide by the different groups developing high intensity light ion beam injectors. And now, one can say several key points are of most importance for an injector design.

- Extraction system with electron repeller allows minimizing electron backstreaming from LEBT
- Hardening and/or protection of the RF window (from backstreaming electrons produced in extraction system) is needed for longer lifetime. In order to help thermal dissipation, aluminium nitride window can be used. Other solution for longer window life time is to protect it with some ceramic shielding made of alumina or boron nitride. Finally it is possible to protect the window behind a bend.
- A ridged or tapered transition allows increasing the electromagnetic field at the entrance of the plasma chamber.
- Installing ceramic disks at both extremities of the plasma chamber permits to increase the plasma density resulting from production of secondary ions.
- The localisation of one ECR resonance at the entrance of RF into the plasma chamber (just at the surface of the ceramic disk) greatly improves the plasma density and as a consequence, the extracted beam intensity. Positioning 1 ECR resonance zone on both sides of the plasma chamber allows other performance enhancement [3].
- In the accelerator column, the shielding of the negative triple junction (ceramic, vacuum and flange) is important to minimize the ignition of sparks [4].
- Reducing the length of the LEBT (and first between the source and the first focussing solenoid) helps to minimize the emittance growth in the beam line [5, 6].
- Injecting amount of heavy gas into the beam line also allows reducing the emittance growth by improving the space charge compensation [7].

The SILHI source [3] presents several of these key points (Fig. 3) which allowed obtaining a robust and efficient design. Figure 4 presents the emittance gain while injecting nitrogen gas into the beam line [8].

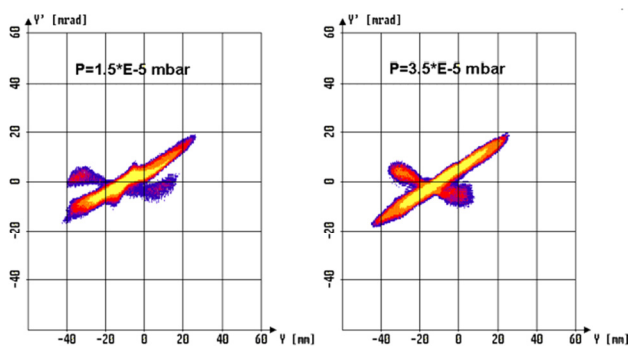

Figure 4: Emittance gain by injecting N_2 gas into the SILHI beam line.

Copyright © 2012 by the respective authors — cc Creative Commons Attribution 3.0 (CC BY 3.0)

WORLWIDE OVERVIEW

Since the beginning of 90's, several laboratories as well as several private companies develop and operate this kind of sources.

After the pioneers already mentioned (in Chalk River (Fig. 2) and Los Alamos), we can report the work done in Europe by CEA/Saclay with SILHI source and INFN/LNS in Catania with TRIPS source and very long high voltage DC break [9]. In parallel, works were carried out in China at IMP Lanzhou and Peking University [10].

Since then, with the large number of facilities demanding high intensity light positive ion beams, such sources are developed and designed all over the world. Important work is done to minimize the source size and also to provide the most efficient magnetic configuration. The magnetic configuration can be provided by pure permanent magnets [5] (Fig. 5a), by a mix of permanent magnets and iron pieces, by permanent magnets associated with coils or by coils and iron pieces [10]. New design is proposed for ESS source; a third coil biased with opposite current will be added in order to obtain a minimum B magnetic configuration into the plasma chamber [11] (Fig. 5b).

Concerning the plasma chamber size, work has been first carried out at the early 90's [2] and then with permanent magnet sources in order to limit the volume of permanent magnets. Other experiments are in progress with variable length of the plasma chamber, in addition with different diameter chamber.

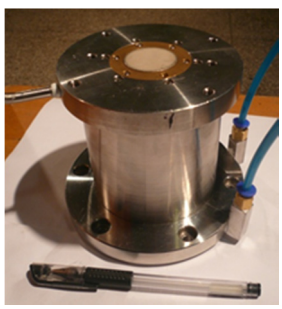

Figure 5a: all permanent magnet PKU source

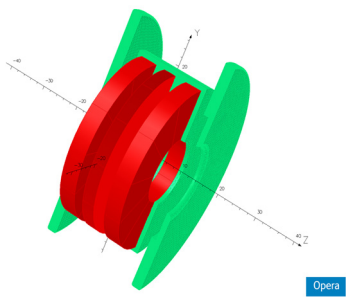

Figure 5b: ESS source design with 1 inversed coil

FOCUS ON SPIRAL 2, IFMIF AND FAIR INJECTORS

For the IPHI (High Intensity Proton Injector) project [13], CEA/Saclay designed the SILHI source in the middle of the 90,s and developed it in order to reach more than 100 mA H^+ continuous beam at 95 keV energy with high reliability. Since then CEA is participating in several HPPA project injectors such as Spiral 2, IFMIF [14] and FAIR.

SPIRAL 2 Injector

For Spiral 2, CEA/Saclay participated first to the design of the proton and deuteron source (Fig. 6). As the requested current of H^+ and D^+ is equal to 5 mA, the source design has been based on permanent magnets. Preliminary source tests were done on the Silhi experimental beam line at 40 keV. Then, in the recent years, the whole light ion Spiral 2 injector has been built and tested at CEA/Saclay [13].

Before moving the whole injector to Ganil at the end of 2O12, beam characterization has been done in several locations along the LEBT. Of course beam intensity and species fractions were checked. The first dipole allows demonstrating the source is producing more than 80 % of H^+ or D^+ depending on the selected gas injected into the plasma chamber. Then emittances have been measured in both plans after both dipoles. Emittance values are 0.22 π mm.mrad for 20 keV H^+ beam and 0.18 π mm.mrad for 40 keV D^+ beam after the second solenoid. Recently, emittances have been analysed just at the entrance of the RFQ location.

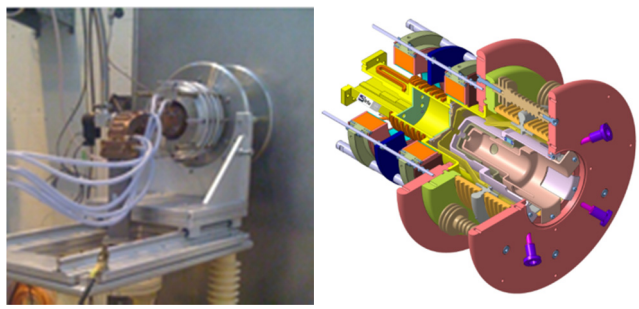

Figure 6: Picture and 3D view of the Spiral 2 ion source with permanent magnets and 5 electrode extraction system.

IFMIF Injector

The IFMIF injector performance is very challenging with a 140 mA of D^+ continuous beam demand at the entrance of the 176 MHz RFQ. To reach such high intensity, it has been decided to keep a magnetic configuration which allows online tuning during conditioning and operation. For this, the magnetic configuration of the source (Fig. 7) is based on 2 coils like the SILHI source. Of course, the extraction system has been initially optimised for such high intensity deuteron beam [15] with 4 electrodes.

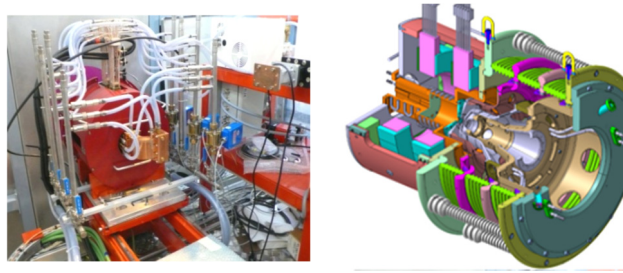

Figure 7: Picture and 3D view of the Spiral 2 ion source with coils and initial 4 electrode extraction system.

The first hydrogen plasma and the first beam were produced in May 2011 in pulsed mode. Then up to 75 keV continuous beam has been extracted with intensity of about 100 mA through a 10 mm diameter aperture. In

Copyright © 2012 by the respective authors — cc Creative Commons Attribution 3.0 (CC BY 3.0)

parallel, diagnostics able to characterize high power beams have been installed and commissioned. An Allison emittance scanner has been especially developed with a highly water cooled entrance slit.

Recently, a pulsed Deuteron beam (125 mA) has been produced at 100 keV with a 1% duty cycle. Up to now, with D^+ beam, the duty cycle is limited for neutron production and activation reasons.

As preliminary results demonstrated a quite high spark rate, the addition of a 5^{th} electrode (as grounded electrode between puller and electron repeller) is presently underway.

FAIR Injector

The FAIR injector demands high intensity (100 mA) pulsed beam at 9 keV, with pulsed as short as few 10 µs. After, preliminary experiments done with the SILHI source several years ago [8], FAIR project asked for a copy of SILHI source. Therefore, CEA is presently designing the FAIR proton injector.

Then, this injector will be installed and tested at Saclay before moving to GSI. A slow chopper will be designed by GSI and installed just before the RFQ entrance in order to get a very short rise time.

CONCLUSION

For more than 20 years, numerous projects of HPPA demand reliable high intensity (from few mA to more than 100 mA) light ion beam, either in pulsed or continuous mode. Such demands pushed the ion source community to develop robust and reproductive ion injectors. Important work has been done worldwide on ion sources based on the ECR principle operating at 2.45 GHz low frequency.

Of course, such sources are not only used for Linear accelerator. They are also used as Cyclotron Injector. For example, this one of these sources is installed on the proton-therapy facility in Bloomington (Indiana University). This example proves the high reliability of the source.

In addition, one can note such sources are also able to produce single-charged heavy ions with high efficiency.

ACKNOWLEDGMENT

The authors would like to especially thank people who gave help with data and pictures for this review (L. Celona, V. Derenchuk, S. Djekic, S. Gammino, S. Peng, D. Vandeplassche, L. Weissman, Z. Zhang, H. Zhao). They also would like to thank people involved in Spiral2, IFMIF and FAIR injector works, either at Saclay or in other institutes.

REFERENCES

[1] S. Gammino et al., Rev. Sci. Instrum.. (2012)
[2] T. Taylor and J. F. Mouris, Nucl. Instrum. Methods Phys. Res. A 336, 1993
[3] J-M. Lagniel et al., Rev. Sci. Instrum. 71, 830 (2000)
[4] J. Sherman et al., Rev. Sci. Instrum. 69 (1998)
[5] S. Peng et al., Rev. Sci. Instrum.
[6] O. Delferrière et al., Rev. Sci. Instrum.. (2012)
[7] N. Chauvin et al., Rev. Sci. Instrum.. 83, 02B320 (2012)
[8] R. Hollinger et al. Proceedings of Linac 2006 conference (TU3001), Knoxville, USA
[9] L. Celona et al., Rev. Sci. Instrum.
[10] R. Gobin et al., Rev. Sci. Instrum. (2006)
[11] L. Celona et al., this conference (TUPB
[12] B. Pottin et al., this conference (THPB031)
[13] O. Tuske et al., Rev. Sci. Instrum. **83**, 02A316
[14] A. Mosnier et al., this conference (TU1A01)
[15] O. Delferrière et al., Rev. Sci. Instrum. **79**. 02B723 (2008)

Copyright © 2012 by the respective authors — cc Creative Commons Attribution 3.0 (CC BY 3.0)

IN FLIGHT ION SEPARATION USING A LINAC CHAIN*

M. Marchetto†,F. Ames, P. Bender, B. Davids, N. Galinski, A. Garnsworthy, G. Hackman,
O. Kirsebom, R.E. Laxdal, D. Miller, A.C. Morton, A. Rojas,
C. Unsworth, TRIUMF, Vancouver, Canada
L. Evitts, C. Nobs, University of Surrey and TRIUMF

Abstract

The ISAC accelerator complex now can accelerate radioactive heavy ion beams to above the Coulomb Barrier. Recently an ECR type charge state booster has been added to allow the acceleration of radioactive beams with masses $A > 30$. A characteristic of the ECR source is the efficient ionization of background species that can overwhelm the low intensity RIB beam. The long linac chain at ISAC can be used to provide some in flight separation both in the time domain and in the spatial domain analogous to fragment separators at in-flight fragmentation facilities. The paper summarizes the work done at TRIUMF to develop tools for the filtration and diagnosis of beam purity in the post acceleration of charge bred beams.

INTRODUCTION

Radioactive ion beams (RIB) are produced and post accelerated at the TRIUMF ISAC facility, represented in Fig. 1, via the isotope separation on line (ISOL) method.

The ISAC RIB production uses protons from the TRIUMF cyclotron. The radioactive species released by the thick target are singly charged and extracted at source potential. The radioactive ions are magnetically separated and can be post accelerated to a variable final energy. The post-accelerator chain is composed of a radio frequency quadrupole (RFQ), a drift tube linac (DTL) and a superconducting (SC) linac.

In order to reach high energies and limit the cost of the post-accelerators the singly charged beam is stripped to a higher charge state. Light masses ($A \leq 30$) are stripped downstream of the RFQ by means of a thin carbon foil. Heavy masses ($A > 30$) are stripped before injection into the RFQ by means of an ECR type charge state booster (CSB).

The charge state booster ionizes both the RIB but also any other element present in its vacuum chamber and immediate surroundings. Such elements belong either to the background residual gas or to the materials that constitute the vacuum chamber itself. The ionization of these contaminants generates a background current of orders of magnitude higher than the radioactive species. This background makes identifying and selecting the RIB extremely challenging. In most of the cases the contaminants to RIB ratio can be improved in favor of radioactive species but the contaminants can not be completely suppressed. Also the necessary cleaning of the beam from contaminants has the side effect of losing part of the produced RIB.

In order to suppress the contaminants a toolkit of separation and filtration techniques as well as software and diagnostic aids to plan and streamline the beam tuning and delivery is in place.

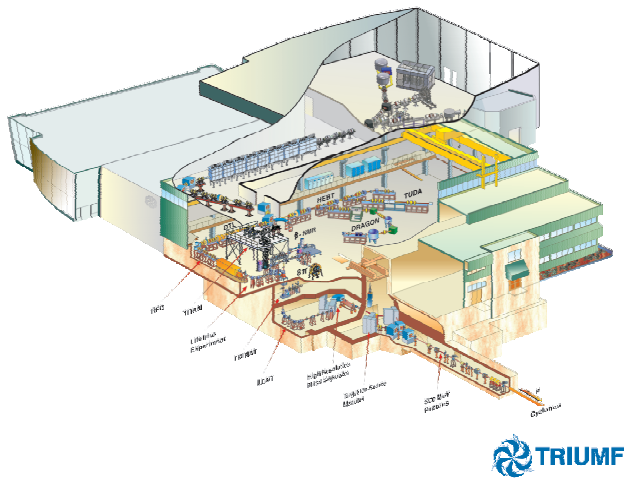

Figure 1: Artistic overview of the ISAC facility at TRIUMF.

THE ISAC FACILITY

The ISAC facility plan view is represented in Fig. 2. The detailed description of the facility can be found in previous proceedings [1].

The RIB production takes place in one of the two underground target stations (ITE and ITW see shaded area in Fig. 2) at a time using 500MeV up to 100μA of current (namely up to 50kW of beam power). Different target materials can be used to produce the neutral beams. Two types of production target containers are available, rated as low and high power relatively to the proton beam current. The production target material and type are chosen based on the experimental needs.

The produced neutral atoms diffuse into the ion source. Different sources are available (surface, LASER, FEBIAD) and others are under development (ECR). Each target is combined with the proper sources to optimized the overall

*TRIUMF receives federal funding via a contribution agreement through the National Research Council of Canada
† marco@triumf.ca

Copyright © 2012 by the respective authors — cc Creative Commons Attribution 3.0 (CC BY 3.0)

RIB production. The beam is singly charged and extracted from the source at a potential up to 60kV.

Before exiting the target hall, the extracted beam is pre-separated using a low resolution ($\Delta M/M \sim 1/500$) spectrometer (pre-separator). This spectrometer is in common between the two target stations. The pre-separation takes place in order to contain most of the radiation inside the target hall.

The beam is then further selected using the main separator that routinely operates with a resolution of $\Delta M/M = 1/3000$.

After selection it is possible to divert the beam through an electron cyclotron resonance ion source (ECRIS) before sending it to ground level. The source, a 14.5GHz PHOENIX by Pantechnik [2], acts as charge state booster (CSB) to further strip electrons from the singly charged beam. The selected charge state at the exit of the booster is such that the mass to charge ratio is ≤ 7 for $A > 30$. This upper limit is dictated from the installed linacs (RFQ and DTL).

A Nier type spectrometer with a resolution of $\Delta M/M = 1/100$ is located downstream of the ECR to select the desired A/q.

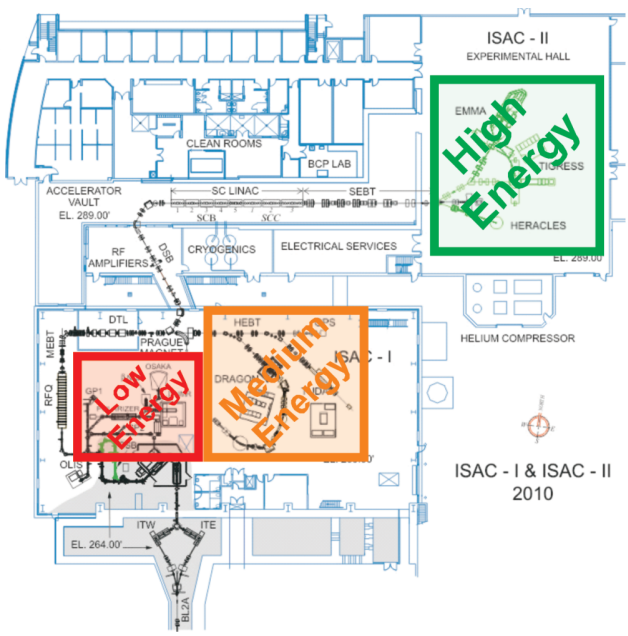

Figure 2: Plane view of the ISAC facility at TRIUMF. The acceleration chain is composed of room temperature RFQ and DTL in ISAC-I and a superconducting linac in ISAC-II.

The RIB can be directed to a low energy area at source potential ($\leq$ 60keV).

In the post-accelerator chain the beam is injected at 2keV/u into the 35.36MHz CW RFQ and accelerated to 150keV/u. The RFQ accepts beam with $3 \leq A/q \leq 30$. The beam is pre-bunched at injection using a three harmonic (quasi saw-tooth) buncher located 5m upstream of the RFQ. The fundamental harmonic of the pre-buncher is 11.78MHz. Since the RFQ operates at the third harmonic, the time structure after acceleration consist of main peaks $\sim$ 86ns apart and smaller satellite peaks spaced $\sim$ 28ns apart. In order to remove the satellite peaks and clean the time structure an 11MHz chopper is located downstream of the RFQ.

The next stage of acceleration is accomplished with a DTL operating at 106.08MHz. The DTL acceptance in terms of mass to charge ratio is $2 \leq A/q \leq 7$. Any beam from the RFQ with $A/q > 7$ is further stripped upstream of the DTL using a 4μg/cm^2 carbon foil. The stripping efficiency to $A/q \leq 7$ is about 30% for ions with $A < 30$. The DTL can provide any energy between 150keV/u to 1.8MeV/u to a medium energy experimental area.

The last stage of acceleration utilizes a SC linac capable of 40MV of acceleration voltage. The SC linac is composed of two main sections (SCB and SCC) operating at 106.08MHz and 141.44MHz respectively. The beam is injected from the DTL at 1.5MeV/u. The final energy is A/q dependent with a peak velocity corresponding to 18MeV/u.

RIB DELIVERY

The ECR charge state booster is instrumental to accelerate high masses ($A > 30$) in ISAC. This type of breeder produces a background of stable species by ionization of residual gasses and vacuum chamber materials. Virtually any multi-charged bred radioactive isotope of interest is accompanied with a few stable isotopes (contaminants) with similar A/q ($(\Delta A/q)/(A/q) < 1/100$) forming a so called cocktail beam . Typical background currents are in the order of only a few pico-Amperes but they are still orders of magnitude higher with respect to the RIB intensity ranging between 10^3 to 10^6 particle/sec.

There are two major challenges in dealing with these cocktail beams. The first is the identification of the RIB component and the consequent optimization of the transport beam lines, including the accelerators, for this component. The second is the filtration of the contaminants. This last one is related to the issue that the RIB's need to be delivered relatively pure (free of contaminants) to the experimental stations.

Both hardware and software diagnostic tools are required to identify the radioactive species. In-flight separation is necessary to reduce the stable component.

THE TOOLKIT

The toolkit is an ensemble of diagnostic tools, stripping/energy degrading carbon foils and filtration techniques that act both in the longitudinal and transverse phase space.

Diagnostic tools

The standard ISAC diagnostics include Faraday cups (FC), rotating (RPM) and linear (LPM) profile monitors, and low intensity monitors (mostly Si detectors) that provide information on the intensity (counts/s), energy, and

Copyright © 2012 by the respective authors — cc Creative Commons Attribution 3.0 (CC BY 3.0)

time profile of the beam. Additional dedicated diagnostics are installed to analyze the cocktail beam and optimize the accelerator tune.

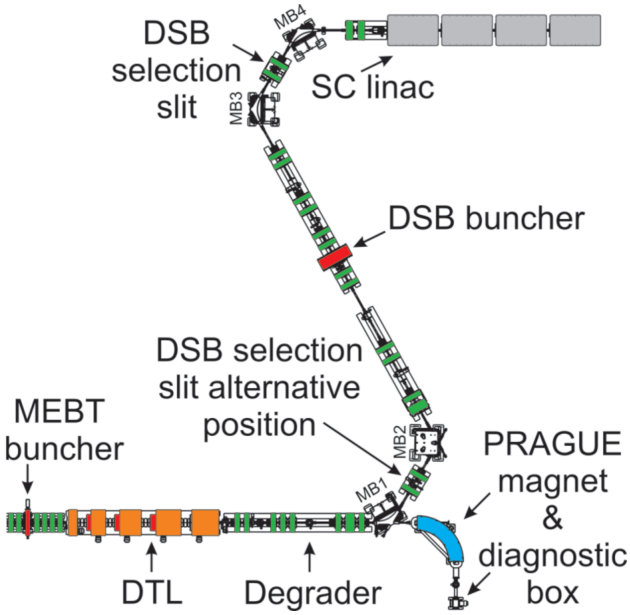

Figure 3: The DTL to SC linac beam (DSB) transport line has an S-shape with two achromatic bending sections. The DSB buncher is needed to match the beam into the SC linac. A stripper-degrader (thick carbon foil) is used to generate velocity differences and therefore selection along the beam line.

A diagnostic station is positioned downstream of the analyzing magnet (PRAGUE) serving the medium energy section after the DTL. The diagnostic station is comprised of a silicon detector to detect total counts and identify total energy (mass of the cocktail constituents), a beta counter to detect activation and a gamma counter to identify the activation. A stripping foil (degrader) upstream of the magnet (see Fig. 3) can be used to strip the ions into a variety of charge states that further enable particle identification after an A/q magnet scan.

Two different detectors located downstream of the SC linac can be used to determine the beam composition before the final delivery (see Fig. 2). A $\Delta E - E$ silicon detector telescope is capable of identifying beam A and Z for total intensities limited to a few 10^3. This detector is extremely valuable but we are limited in the amount of current we can send through it. The second is a $\Delta E - E$ gas Bragg detector capable of handling higher current up to 10^5.

There are two software applications in support of the high mass beam delivery.

The first is a web based application [3] (the so called $CSBAssistant$) that predicts all the possible contaminants based on measured atomic masses (M) for given A/q ranges as defined by the separation techniques including an in-flight charge stripping stage. The tool highlights expected contaminants based on the CSB background scan. The tool is useful in determining the best M/q value and filtering strategy to minimize the level of contamination while optimizing the transport efficiency.

The second application is the scaling routine. This is an EPICS application that scales all optics elements and RF amplitudes base on M/q and beam energy.

Electrostatic elements are scaled by voltage while magnetic components are either scaled by current (steerers and quadrupoles) or by magnetic field (hall probe in dipoles). Studies show that cycling the quadrupole current to a set point gives a field reproducibility of 2.26G over 1240.26G while approaching the field from the same side of the hysteresis curve gives a field reproducibility of < 0.05G over 1240.8G. In order to provide the best reproducibility, the scaling routine has the option of invoking a current set-point ramped from zero to the set-point. The routine also scales the amplitudes of all the RF cavities (RFQ, DTL, SC linac, etc.).

The scaling factors are calculated in each section from the M/q ratio (either from the source or after a stripper-degrader foil) and energy (from the ion source or after a linac). The scaling routine performs precise steps in M/q of the entire acceleration chain starting from a reference tune. The accelerator is tuned with a known stable beam (example $^{12}C^{2+}$) of convenient intensity. This beam is also used to calibrate the various energy detectors.

Pre-buncher and RFQ filtration

It is possible to achieve a longitudinal selection of $(M/q)/\Delta(M/q) \sim 1000$ by exploiting the time of flight separation between the pre-buncher and the RFQ.

At fixed source extraction voltage, different M/q's are extracted with different velocities $v = (2 \cdot q \cdot V_{ext}/M)^{1/2}$. Different velocities generate different times of flight in the 5m between the pre-buncher and the RFQ. The RFQ phase acceptance is 75° (being $-25°$ the synchronous phase of the RFQ [4]) or $\delta t = 5.9$ns. M/q's that are spaced in time by more than $\delta t = 5.9$ns at the RFQ injection can be filtered by adjusting the pre-buncher phase (namely synchronizing the desired M/q with the RFQ accelerating bucket). At 2keV/u (injection energy for the RFQ) the beam velocity is $v = 6 \cdot 10^5$m/s ($\beta = 0.002$) that produces a time of flight $t = 8.3\mu$s. The RFQ relative phase acceptance is then $\delta t/t = 7.1 \cdot 10^{-4}$.

At fixed extraction voltage the following relation holds:

$$\frac{\delta(M/q)}{(M/q)} = -2 \cdot \frac{\delta v}{v} = -2 \cdot \frac{\delta t}{t} \qquad (1)$$

The relative phase acceptance at the entrance of the RFQ becomes then a relative M/q acceptance equal (in absolute value) to $\delta(M/q)/(M/q) = 1.42 \cdot 10^{-3}$ or $(M/q)/\Delta(M/q) \sim 700$.

This resolution was demonstrated [1] using two cocktail beams: $^{116}Sn^{18+}$ and $^{84}Kr^{13+}$ with M/q respectively of 6.439 and 6.455 ($(M/q)/\Delta(M/q) = 408$), and $^{19}F^{3+}$ and $^{38}Ar^{6+}$ with M/q respectively 6.333 and 6.327

Copyright © 2012 by the respective authors — cc Creative Commons Attribution 3.0 (CC BY 3.0)

$((M/q)/\Delta(M/q) = 1115)$. Suppression factors of 100 and 15 respectively were achieved in each case.

Carbon foil stripper-degraders

Beams with different mass but the same M/q ratio are accelerated to the same final velocity by the DTL. A stripper-degrader (thick carbon foil) is installed 3.6m downstream of the DTL (see Fig. 3) to strip the beam to a new charge state and M/q range as well as create a velocity difference depending on the particle Z. Different foil thickness can be selected, the standard one being 44μg/cm^2 in order to reach charge state equilibrium.

The goal is to shift the M/q of the contaminant outside the acceptance of the downstream linac chain that is tuned to the M/q of the RIB.

In order to accelerate the beam through the SClinac it is necessary to compensate the energy loss of the beam going through the degrader. This energy loss is accurately measured at the the PRAGUE magnet. The compensation is done by increasing the beam energy out of the DTL enough to enough to match the velocity of the ion to the unstripped velocity. Such increase in energy, though, leads to a time of flight difference over the 3.6m that separate the DTL from the foil. This difference is compensated by adjusting the downstream RF devices (DSB buncher and SC linac sections) phases by a calculated amount.

Given that the distance from the degrader to the SC linac is equal to 27.9m and that the beam velocity at 1.5MeV/u is $v = 1.71 \cdot 10^7$m/s ($\beta = 0.057$), the time of flight is $t = 1.63\mu$s. Given a 40° phase acceptance for the 106.08MHz SCB cavities we then have a selection $\delta v/v = 6.4 \cdot 10^{-4}$ or $(M/q)/\Delta(M/q) \sim 800$. The velocity difference at this location though is going to be partially compensated by DSB buncher (see Fig. 3) that has the function to match the beam at the entrance of the SC linac by minimizing the time spread.

The DSB filtration

The two achromatic bending section in the DSB beam line (see Fig. 3) have a dispersed focus between dipoles of 1.5m and 1.6m respectively giving resolving power of $(M/q)/\Delta(M/q) \sim 375$ and $(M/q)/\Delta(M/q) \sim 320$ respectively.

A selection slit 2 mm wide is conveniently installed in the center of the second bending section downstream of MB3. The resolution of this magnet is confirmed with simulation and measurement [1] using a cocktail beam composed of $^{40}Ar^{7+}$,$^{63}Cu^{11+}$ and $^{86}K^{15+}$ with M/q values of 5.709, 5.722 and 5.727 respectively.

HIGH MASS DEVELOPMENT RUN

The goal of the development run (August 2012) was to demonstrate the capability of purifying the radioactive isotope ^{94}Rb to an acceptable level for a real experiment. This run takes advantage of previous developments (May 2012 [1]) in particular in terms of the new diagnostic installed in the PRAGUE box, the location of the degrader

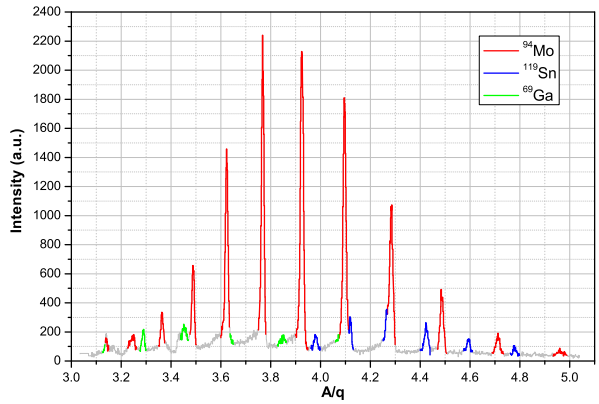

Figure 4: Charge state distribution at the PRAGUE magnets. Three isotopes are identified: ^{69}Ga, ^{94}Mo, ^{119}Sn.

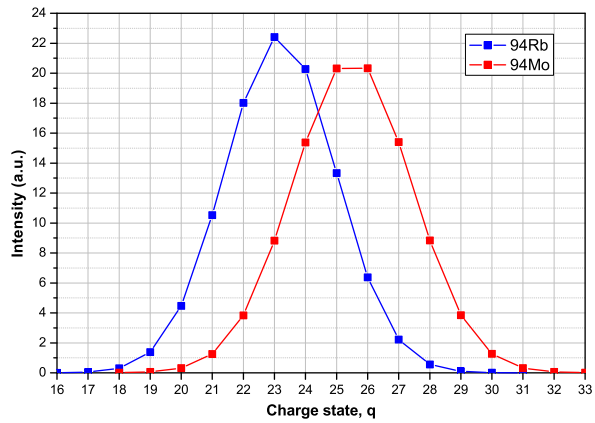

Figure 5: Theoretical charge state distribution of ^{94}Rb and ^{94}Mo. The two isobars are separated by a relative mass difference of $\Delta M/M = 1/4405$.

downstream of the DTL and the installation of the new Bragg detector downstream of the SC linac.

The entire linac chain is initially tuned with $^{12}C^{2+}$ with no stripping foil in place. Once the tune is established the accelerator is scaled from $^{12}C^{2+}$ to the M/q containing the RIB using the scaling routine.

A ^{94}Rb charge state of 15+ ($M/q = 6.260$) is selected in the Neir spectrometer. The selection is based on the prediction from the $CSBAssistant$ where only three low intensity contaminants $^{69}Ga^{11+}$, $^{94}Mo^{15+}$ and $^{119}Sn^{19+}$ are expected after the pre-buncher and RFQ time of flight filtration. The M/q's of these isotopes are respectively 6.265, 6.260 and 6.258.

The stripping foil produces characteristic charge state distributions at the Prague magnet diagnostic station. The charge state distribution measured downstream of the PRAGUE magnet confirms the predicted cocktail compo-

Copyright © 2012 by the respective authors — cc Creative Commons Attribution 3.0 (CC BY 3.0)

sition as represented in Fig. 4.

In this case the DSB is tuned to $^{94}Mo^{22+}$ ($M/q = 4.268$) in order to filter out the contaminants with $A = 69$ and $A = 119$. The charge state choice is a compromise between purity and efficiency of the RIB beam. Figure 5 is the expected charge state distribution of ^{94}Rb and ^{94}Mo ($(M)/\Delta(M) = 4405$). The stripping efficiency ratio between ^{94}Rb and ^{94}Mo at charge state 23+ and 22+ is respectively 2.5 and 4.5.

The DSB buncher and the SC linac sections RF phases were shifted respectively of 26°, 77° (for SCB) and 103° (for SCC) after energy compensation at the stripping foil.

The beam accelerated with the SC linac is analyzed at the Bragg detector. The result is shown in Fig. 6, left picture. The cocktail is dominated by $^{94}Mo^{22+}$ with still a minor component of ^{69}Ga and ^{119}Sn plus other contaminants that are in the noise of the charge state distribution. The ^{119}Sn is in the tail of the charge state distribution of $^{94}Mo^{22+}$ (see Fig. 4). The result is also compatible with the $CSBAssistant$ calculation as shown in Fig. 7. Even though nuclides like ^{107}Ag, ^{113}In or ^{132}Xe are theoretically cut out by the pre-buncher and RFQ filtration (represented in Fig. 7 by the cyan vertical band), it's possible that these ions have extended distribution tails that are eventually accelerated.

In fact the accelerator can be optimized on these extra elements (with respect to ^{94}Mo) by changing the pre-buncher phase. For example a shift of $-12°$ highlights ^{69}Ga, while 20° phase shift increases the ^{119}Sn and 71° shift increases ^{100}Mo.

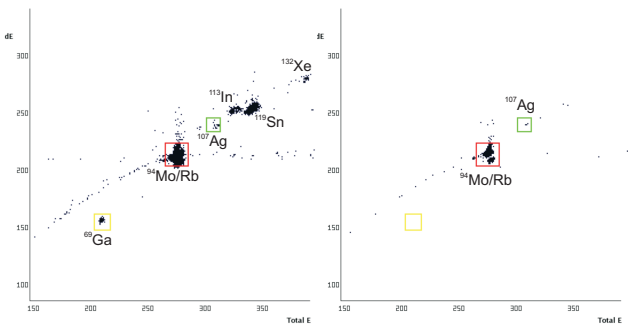

Figure 6: Effect of the DSB filtration measured at the Bragg detector: the left picture correspond to the unfiltered cocktail beam from the DTL

Virtually all contaminants are finally suppressed using the DSB slit filtration as represented in Fig. 6 right picture. This result is also in agreement with the $CSBAssistant$ calculation. The final filtered cocktail beam is optimized on the radioactive beam $^{94}Rb^{22+}$, noting that the final distribution is still dominated by the $^{94}Mo^{22+}$ contaminant.

CONCLUSION

ISAC is now in a position to deliver its first high mass charge bred radioactive beam to an experiment. A set of

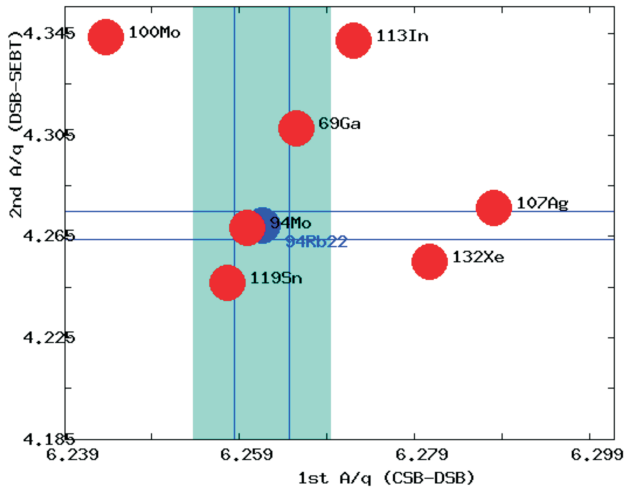

Figure 7: Filtration prediction of the$CSBAssistant$. The cyan vertical band represent the pre-buncher and RFQ filtration while the horizontal band represent the DSB filtration.

tools is available to address the contamination of the delivered beam. It remains clear that the delivery of such beams is not going to be effortless. Every new RIB delivery has to be planned in advance and will require development time.

ACKNOWLEDGMENT

The authors belong to the High Mass Task Force, a collaboration between Accelerator and Science division. We want to aknowledge: Lia Merminga (Accelerator Division head), Reiner Kruecken (Science Division head), ISAC operators for their support, Victor Verzilov and Josef Holek (diagnostic group), Robert Openshaw (gas-handling system on the TBragg), Corina Andreoiu, Carmen Wong, Mustafa Rajabali, and Gordon Ball for their assistance in running and analyzing data from the TBragg.

REFERENCES

[1] M. Marchetto,"Progress and Plans for the High Mass Beam Delivery at TRIUMF", HIAT 2012, Chicago, Illinois, USA, June 2012.

[2] F. Ames et Al.,"Commissioning of the ECRIS Charge State Breeder at TRIUMF", ECRIS2010, Grenoble, France, August 2010, p. 178

[3] A. Garnsworthy, http://trshare.triumf.ca/ garns/CSB

[4] S. Koscielniak et al., "Beam Dynamics Studies on the ISAC RFQ at TRIUMF", PAC'97, Vancouver, British Columbia, CANADA, May 1997, p. 1102.

Copyright © 2012 by the respective authors — cc Creative Commons Attribution 3.0 (CC BY 3.0)

SARAF PHASE II P/D 40 MeV LINAC DESIGN STUDIES*

P.N. Ostroumov, Z.A. Conway, M.P. Kelly, A.A. Kolomiets, S.V. Kutsaev and B. Mustapha
Argonne National Laboratory, Argonne, IL 60441, USA
J. Rodnizki#, Soreq NRC, Yavne, Israel

Abstract

The Soreq NRC initiated the establishment of SARAF – Soreq Applied Research Accelerator Facility [1]. SARAF will be a multi-user facility for basic research, e.g., nuclear astrophysics, radioactive beams, medical and biological research; neutron based non-destructive testing (using a thermal neutron camera and a neutron diffractometer) and radio-pharmaceuticals research, development and production. The SARAF continuous wave (CW) accelerator is planned to produce variable energy (5-40 MeV) proton and deuteron beam currents (0.04-5 mA). Phase I of SARAF (ion source, radio-frequency quadrupole (RFQ), and one cryomodule housing 6 half-wave resonators (HWR)) was installed and is operating at Soreq NRC delivering CW 1mA 3.5 MeV proton beams and low-duty cycle (10^{-4}) 0.3 mA 4.7 MeV deuteron beams [2]. SARAF is designed to enable hands-on maintenance, which implies very low beam losses for the entire accelerator. This paper presents the physics design of two options to subsequently develop a conceptual design for extending the SARAF Phase I linac to its planned Phase-II beam parameters (40 MeV, 5 mA protons and deuterons).

INTRODUCTION

We present the physics design of two options for a CW linac capable of delivering 200-kW beams of 40-MeV, 5-mA protons and deuterons [3, 4]. The two options analyzed are (1) a linac based on superconducting (SC) halfwave resonators (HWRs) operating at a fundamental frequency of 176 MHz; and (2) a linac based on SC quarter-wave resonators (QWRs) operating at a fundamental frequency of 109 MHz. Both options include a CW radio frequency quadrupole (RFQ) designed for acceleration of protons or deuterons from 20 keV/u to 1.3 MeV/u.

The main SC cavity parameters are based on recent Argonne National Laboratory (ANL) experience with a performance margin. These parameters are used to develop baseline designs of the SC linacs. The ANL approach for CW RFQs for both options is described. Significant effort was devoted to the electromagnetic (EM) optimization of both QWRs and HWRs. The concepts for the engineering and beam physics design of the linac and its cryomodules are discussed. The results of detailed beam dynamics simulations with realistic fields and machine errors are presented.

#jacob@soreq.gov.il
* This work was supported by the ANL WFO No. 85Y47

CHOICE OF SC CAVITY PARAMETERS

The choice of SC cavity parameters for SARAF Phase II is based on the demonstrated performance of TEM-class cavities at ANL. The horizontal bands in Fig. 1 show the proposed operating regions for each of the two pairs of 109-MHz QWRs and 176-MHz HWRs. The critical point is that in all cases there is a performance margin with respect to demonstrated Argonne cavity performance in the ATLAS energy upgrade cryomodule [5]. Overall, the choice of operating parameters is weighted toward maintaining E_{PEAK} at or below 36 MV/m because the performance margin with respect to B_{PEAK} is relatively larger. Based on the most recent ANL experience with the development of new 72 MHz QWRs for the ATLAS efficiency and intensity upgrade [6], it is most likely that the margin in both electric and magnetic fields will be increased up to 100% [7].

Generally, the proposed quarter-wave option has a modestly larger margin due to the lower value of B_{PEAK} for a given value of E_{PEAK} in QWR geometries versus HWR geometries.

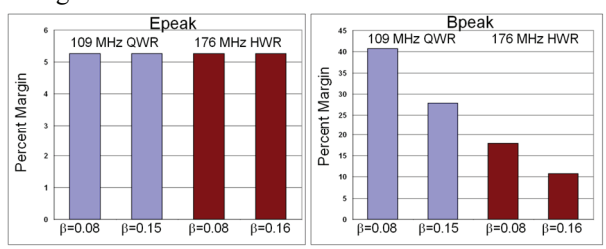

Figure 1: Operating margin with respect to already demonstrated performance in ATLAS.

RFQ BEAM AND EM DESIGN

To maintain a high level of operational reliability, we recommend the development and fabrication of a new 1.3-MeV/u RFQ with reduced RF power losses relative to the existing SARAF Phase-I 4-rod RFQ. The new RFQ would be based on a 4-vane structure. The main requirements for the RFQ for the high-intensity SARAF linac are as follows:

- Absolutely reliable CW operation for both protons and deuterons.
- Formation of a beam with extremely low halo in the longitudinal phase space.
- Moderate peak fields to avoid any possible breakdowns and avoid long conditioning of the resonator. In particular, the peak electric fields should be below 1.8EK where EK is the Kilpatrick limiting field.

Copyright © 2012 by the respective authors — cc Creative Commons Attribution 3.0 (CC BY 3.0)

- High acceleration efficiency (>97%) for the design beam current of 5 mA.
- No transverse rms emittance growth through the RFQ.

The output beam energy of the RFQ is a compromise between the complexity and cost of the RFQ resonator and the low-beta SC cavities. As a result of past experience and a detailed analysis of both the RFQ and the SC structures, a 1.3-MeV/u transition energy is adequate for the SARAF proton and deuteron accelerator. A beam energy that is too high increases the RFQ length and the required RF power.

A conventional 4-vane structure is proposed for the 176-MHz RFQ to provide the highest possible shunt impedance and to keep the required RF power below 120 kW. The main parameters of the RFQ are listed in Table 1. High transverse phase advance per period (>33°) along the RFQ provides strong transverse focusing that maintains a low transverse emittance and a low sensitivity to possible fabrication and tuning errors. Appropriate variation of RFQ parameters such as synchronous phase and modulation factor along the RFQ are applied in order to form the low longitudinal emittance of the halo-less beam in the longitudinal phase space. The transmission through the RFQ is very high, greater than 99.9% for both protons and deuterons. The acceleration efficiency is 98.5%. Relative losses of the deuteron beam inside the RFQ are below 10^{-4}, while the similar value for protons is higher, 1.5×10^{-3} due to the stronger space charge effects.

Fig. 2 shows the relative number of particles located outside a given longitudinal emittance obtained by simulation of 200k particles with an input current of 5.5 mA. The total longitudinal emittance is well below the acceptance of the SC linac.

An exploded view of the 4-segment 4-vane RFQ is shown in Fig. 3. The main advantage of the 4-vane structure over a 4-rod structure is a significantly lower RF power consumption, just 110 kW for deuterons based on MWS [8] simulations.

It is well known that in a long 4-vane structure the frequencies of neighbouring dipole modes are close to the operational frequency. The length of the proposed 176 MHz RFQ is just 2.2 λ, where λ is the wavelength of the operational mode, and frequencies of dipole modes are more than 3 MHz away from the operational frequency. Simple techniques have been developed and used in the past to control the frequencies of the non-operational modes. In particular, the frequency spectrum of the non-operational modes can be efficiently adjusted using four plug tuners installed on the end-plates of the RFQ.

The success of a CW RFQ and long-term reliable performance is primarily defined by the fabrication technology. Past experience confirms that highly reliable, high duty cycle normal conducting accelerating structures can be built using 100% oxygen free electronic (OFE) copper structures brazed in a high-temperature hydrogen atmosphere furnace. Usually, a brazed copper cavity is an integral vacuum and structural vessel.

The SARAF RFQ will be fabricated from OFE copper. Each part of the segments will be machined to the required tolerances, ~25 μm, and brazed in a high-temperature furnace in a hydrogen atmosphere. This technology has been successfully applied to CW RFQs such as the RIA prototype RFQ [9] and the ANL ATLAS Upgrade RFQ [6] which was successfully commissioned with beam recently. The dimensions of the 176-MHz RFQ segments are similar to those for the ATLAS Upgrade RFQ. This ensures that the fabrication technology developed for this RFQ can be directly applied to the SARAF RFQ.

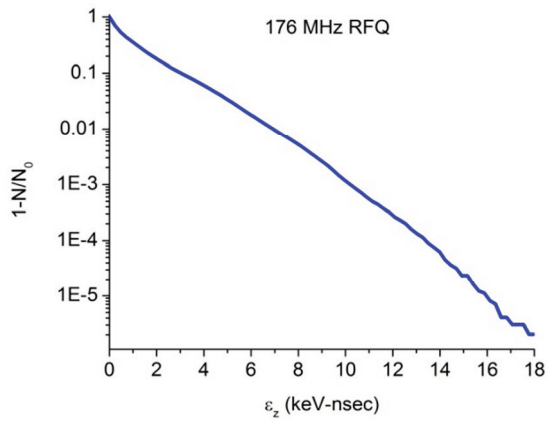

Figure 2: The relative number of particles located outside a given longitudinal emittance obtained by simulation of 200k particles with an input current of 5.5 mA.

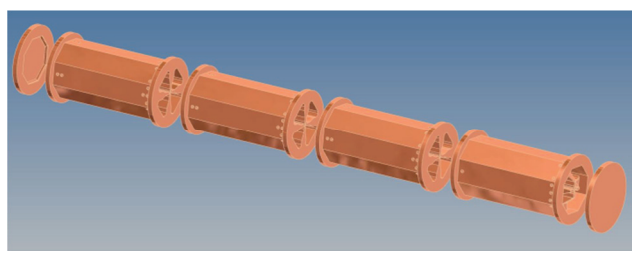

Figure 3: Engineering model of the 4-segment 4-vane RFQ.

The main parameters of the 176 MHz and 109 MHz RFQs are listed in Table 1. The 109 MHz RFQ provides very similar beam properties as the 176 MHz RFQ.

Two possible electromagnetic structures for the 109-MHz RFQ have been investigated: (1) a 4-vane structure with windows similar to the 60-MHz RFQ developed at Argonne for the ATLAS upgrade and (2) a conventional 4-vane structure. The smaller transverse dimension of the 4-vane structure with windows compared to the conventional 4-vane structure is an advantage. Indeed, the transverse dimension of the 109-MHz structure can be matched to the exact dimensions of the Argonne 60-MHz RFQ so that the fabrication technology (fixtures and tooling) of the Argonne RFQ structure can be directly applied to the SARAF RFQ. However, the introduction of windows increases the RF power losses to 145 kW versus 79 kW for the 4-vane structure. Therefore, we propose to

Copyright © 2012 by the respective authors — cc Creative Commons Attribution 3.0 (CC BY 3.0)

use the conventional 4-vane structure for the 109-MHz SARAF RFQ.

Table 1: Main Parameters of the 176 & 109MHz RFQs

Parameter	Value	Value
Frequency, MHz	176	109
Charge to mass ratio	1, ½	1, ½
Input energy, keV/u	20	20
Output energy, keV/u	1318	1314
Design beam current, mA	5.0	5.0
Inter-vane voltage, kV	75	85
Maximum field at vane surface, kV/cm	232	209
Maximum field at vane surface, Kilpatrick units	1.57	1.79
Average radius, mm	4.4	6.0
Modulation factor, max	2.0	2.0
Minimal aperture, mm	2.93	3.93
Minimal transverse phase advance, degree	33.0	40.3
Transverse acceptance, normalized, mm-mrad	2.5	4.3
Number of cells	257	195/50
RFQ length, m	3.8	4.5
Deuteron beam (I = 0 mA) longitudinal rms emittance, keV/u deg	56	58
Deuteron beam (I = 5 mA) longitudinal rms emittance, keV/u deg	36	35.3
RF power losses in the RFQ (MWS data), kW	110	79

LEBT AND MEBT

The existing LEBT is able to deliver and match both proton and deuteron beams into the RFQ acceptance. The RFQ consists of a conventional entrance radial matching section and a short output matching section that transforms the transverse phase space into a double-waist beam at the exit of the RFQ and facilitates matching to the MEBT. The MEBT's primary functions are as follows:

- Match either a proton or a deuteron beam into the 6D acceptance of the SC linac;
- Avoid emittance growth and formation of beam halo;
- Provide a space for beam diagnostic devices;
- Provide efficient isolation of cold vacuum from warm vacuum by using a short cold trap upstream of the cryomodule.

Several options for MEBTs have been studied to satisfy these requirements. Matching of the RFQ beam to the SC linac acceptance is not a trivial task for the following reasons:

- The available accelerating gradient of the SC structures is appreciably higher than that of the RFQs;
- The MEBT must form an axially symmetric beam for injection into the SC linac;
- Emittance growth in the transverse and longitudinal phase space planes must be avoided.

Focusing in the SC section is provided by SC solenoids. We have explored several options of MEBTs differentiated by the number of focusing quadrupoles and re-bunchers. The best option for the MEBT that satisfies all mentioned requirements is the MEBT shown in Fig. 4. Extensive studies of beam dynamics for both frequency options and for both proton and deuteron beams showed that the proposed version of the MEBT is capable of matching proton and deuteron beams into the SC linac for a wide range of beam currents from 0 to 5 mA without any emittance growth.

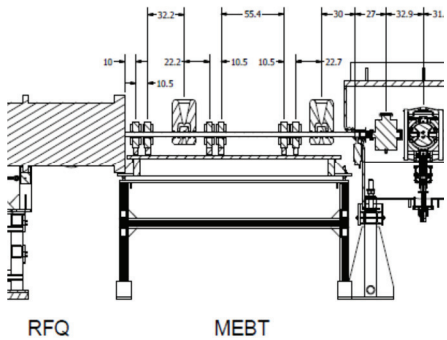

Figure 4: Medium energy beam transport (MEBT).

SC LINAC LAYOUT

A linac lattice design has been iterated between the beam dynamics and engineering designs [10,11]. The main goal of the beam dynamics design is to minimize emittance growth and halo formation within the constraints defined by the mechanical arrangement of cavities, SC solenoids, beam diagnostics and cryomodules. The concept of the physics design of high-intensity linacs based on RFQ and SC cavities is well established (see, for example, ref. [12]). One of the most important general concepts for high-intensity linac design is that the transverse and longitudinal wave numbers, κ_{T0} and κ_{L0}, for zero beam current must change adiabatically along the linac. This feature minimizes potential mismatches and helps assure a current-independent lattice and its tune. The wave numbers of particle oscillations are expressed as $\kappa_{T0}=\sigma_{T0}/L_f$, $\kappa_{l0}=\sigma_{l0}/L_f$, where σ_{T0} and σ_{L0} are the zero-current transverse and longitudinal phase advances per focusing period of length L_f. An adiabatic change of the real-estate accelerating gradients and focusing fields is required to fulfil these conditions which results in a current-independent tune of the SC linac section. In the proposed lattice design for both frequency options we follow this concept very closely with a focus on minimizing the number of cavities and solenoids for cost effectiveness.

The beam dynamics design and optimization starts with the proton beam for which the beam dynamics is more sensitive to high accelerating gradients than the deuteron beam dynamics due to the higher accelerating voltage per

Copyright © 2012 by the respective authors — cc Creative Commons Attribution 3.0 (CC BY 3.0)

nucleon. In addition, space charge effects for the proton beam are stronger than for deuterons. The most critical part of the linac is the initial section downstream of the RFQ, which provides acceleration to 5–8 MeV. In the SARAF linac, this section consists of low-β SC cavities and solenoids in both frequency options. As it follows from the detailed proton beam dynamics simulations, the highest available voltages of low-β SC cavities cannot be applied for acceleration in the first several periods of the accelerating and focusing structure. High accelerating gradients in the low-velocity range produce strong nonlinear motion in the longitudinal phase space along with notable emittance growth and halo formation. These studies resulted in a better beam quality in a focusing period composed of a cavity and a solenoid in contrast to the current SARAF Prototype Superconducting Module (PSM), which has two cavities per focusing period.

176-MHz OPTION LAYOUT AND BEAM DYNAMICS

The 176-MHz SC linac is composed of four cryomodules: one low-β and three high-β cryomodules. The low-β cryomodule contains seven SC cavities and seven solenoid-steering magnet packages. The high-β cryomodules each contain seven SC cavities and four SC solenoid-steering magnet packages. Fig. 5 shows the low-β cryomodule layout.

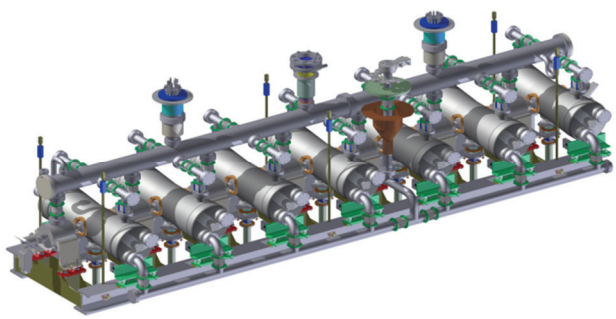

Figure 5: 3D engineering model of the cavity-solenoid string attached to the cryostat lid. 176 HWR option.

The HWR lattice beam dynamics study shows that a 5 mA proton/deuteron beam reaches 40 MeV with 28 HWRs. The rms emittance growth along the linac for a nominal run is a few percent. In the simulations with the TRACK code [13], no losses were found for 100 runs including errors based on realistic dynamic and static error ranges, and using 100k macro particles each (Fig. 6).

A COMPACT HWR LATTICE

The real-estate gradient of the 176-MHz baseline lattice [3] may be increased further by reducing the solenoid magnet length used therein. In the pre conceptual design study we used, for simplicity, the same solenoids for both the low-β and the high-β cryomodules for both accelerator options: the 176-MHz HWRs and the 109-MHz QWRs. In both options the low-β cryomodule solenoid length may be reduced which will result in shorter focusing periods in the low-β cryomodules thus allowing higher real-estate accelerating gradients. Table 2 compares the compact solenoid option for the entire SC section to the baseline option. These results demonstrate that the shorter solenoids improve the beam dynamics relative to the original lattice design. Notice that the shorter solenoids reduce the emittance growth and enable an energy gain that is slightly larger than the energy gain in the baseline lattice.

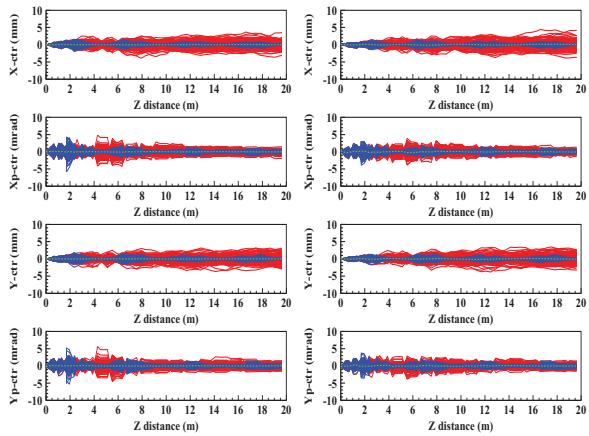

Figure 6: 176-MHz linac beam centroid motion- x,x',y,y' along the linac for 100 error simulations of 5-mA proton (left) and deuteron (right) beams simulated with 10^5 particles each, blue curves- with monitors and corrections scheme.

Table 2: 176 MHz Linac Parameters for the Compact Solenoid Compared to the Long Solenoid Lattices

Emittance growth	**Protons**		**Deuterons**	
Lattice	Compact	Baseline	Compact	Baseline
Energy, MeV	37.9	37.7	40.5	40.1
x_rms, %	4	7	1	3
x_0.99, %	30	40	12	22
y_rms, %	5	7	2	3
y_0.99, %	27	30	9	12
z_rms, %	8	12	3	3
z_0.99, %	2	23	10	14

109-MHz OPTION LAYOUT AND BEAM DYNAMICS

The 109-MHz SC linac consists of three cryomodules: one low-β cryomodule and two high-β cryomodules. The low-β cryomodule contains six SC cavities and solenoid-steering magnet packages. The high-β cryomodules each contain seven SC cavities and four SC solenoid-steering magnet packages. Fig. 7 shows the low-β cryomodule and the high-β cryomodules layout. The effect of QWR non-symmetric magnetic field component on beam center

Copyright © 2012 by the respective authors — cc Creative Commons Attribution 3.0 (CC BY 3.0)

steering is compensated to the order of 0.1 mrad by a drift tube face tilt angle [14].

Beam dynamics studies for 5 mA proton and deuteron beams were carried out in the QWR's lattice. The rms emittance growth along the linac for a nominal run is a few percent. Beam dynamics simulations of 100k macro particles each in 100 runs with errors showed no losses. In general, beam parameters in the 109 MHz option are less sensitive to the errors than in the 176 MHz option.

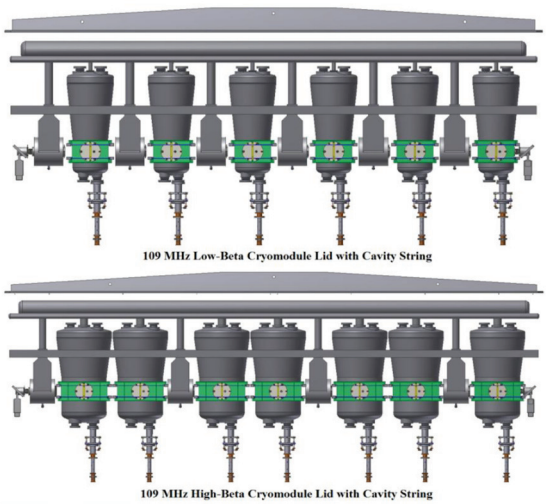

Figure 7: The 109 MHz superconducting modules, low-β (top) and high β (bottom) lattice design.

INTEGRATING SARAF PSM INTO SARAF PHASE II LATTICE

The existing SARAF Phase-I prototype SC module (PSM) can be used as a second cryostat in Phase II. To verify the beam dynamics of the Phase II with the PSM, we have performed simulations for a 5 mA deuteron beam. The integrated beam dynamics lattice includes the required space around the PSM for beam diagnostics boxes. The PSM cavities were set at 600 kV, 70% of its nominal original design voltage. The result is an additional 5 MeV deuteron energy gain (3 MeV are gained at the PSM and 2 additional MeV are a result of a better velocity matching downstream of the PSM, table 3). Modifications of the PSM cavity stiffness to reduce df/dP (now it is 50 Hz/mBar) and the RF input couplers to transmit 4kW are desirable for integration into Phase II.

Table 3: Phase II Beam Energies Before and After Including the PSM.

	Phase II [MeV/u]	Phase II with the PSM [MeV/u]
RFQ	1.32	1.32
Module 1	3.92	3.92
PSM		5.59
Module 2	8.51	11.10
Module 3	14.70	17.31
Module 4	20.65	23.09

SUMMARY

Two linac options based on 109 MHz QWRs and 176 HWRs capable of delivering 5 mA, 40 MeV proton and deuteron beams have been studied. Extensive end-to-end beam dynamics simulations iterated with the engineering design show that both options can hold the hands-on maintenance criterion which is vital for a high intensity machine. As there are only slight differences between both options, the SARAF project adopted the 176 MHz HWR linac since it will be a smooth transition from phase I. With some modifications, the current SARAF PSM can be included in the Phase II lattice.

REFERENCES

[1] A. Nagler, I. Mardor, D. Berkovits, Soreq NRC, K. Dunkel, M. Pekeler, C. Piel, P. vom Stein, H. Vogel, Status of the SARAF project, Proceedings of the LINAC'06, Knoxville, TN, p. 168.

[2] D. Berkovits et al, Operational experience and future goals of the SARAF Linac at SOREQ, these proceedings.

[3] P. N. Ostroumov et al, Intermediate Report on WFO 85Y47, Conceptual Design of a 40 MeV Proton & Deuteron Accelerator for SARAF, ANL, Jan. 2012.

[4] B. Mustapha et al, New Design for the SARAF Phase II Linac, Talk at the HIAT-2012 Conference, June 18-21, 2012, Chicago, IL USA.

[5] M.P. Kelly, High-Performance SC Cryomodule for CW Ion Accelerators, proc. of LINAC'10, p. 387.

[6] P.N. Ostroumov et al., ATLAS Upgrade, Proceedings of the PAC'11, New York, NY, p. 2110.

[7] M.P. Kelly, Z. A. Conway, S. Gerbick, M. Kedzie, R. Murphy, P.N. Ostroumov, T. Reid, Cold Testing of Superconducting 72 MHz Quarter-wave Cavities for ATLAS, Paper MOPB073, these proceedings.

[8] CST – Computer Simulation Technology AG. Darmstadt, Germany.

[9] P.N. Ostroumov et al., High-Power Test of a 57-MHz CW RFQ, Proceedings of the LINAC'06, Knoxville, TN, p. 767.

[10] B. Mustapha Z.A. Conway, P.N. Ostroumov, A Ring-shaped Center Conductor Geometry for a Half-wave Resonator, IPAC 2012.

[11] Z. Conway et al., Cryomodule Designs for Superconducting Half-Wave Resonators, Paper TUPB068, in these proceedings.

[12] P.N. Ostroumov (2006), "Physics Design of the 8-GeV H-minus Linac." New Journal of Physics, 8:281. http://stacks.iop.org/1367-2630/8/281.

[13] P.N. Ostroumov, V.N. Aseev and B. Mustapha, TRACK Beam dynamics simulation code, TrackV37, (2007)

[14] B. Mustapha and P.N. Ostroumov, Electro-magnetic Optimization of a QWR, LINAC'10, Tsukuba (2010), p.169.

Copyright © 2012 by the respective authors — cc Creative Commons Attribution 3.0 (CC BY 3.0)

RECOVERY OF THE J-PARC LINAC FROM THE EARTHQUAKE

K. Hasegawa#
Accelerator Division of J-PARC, KEK/JAEA, Tokai, Ibaraki, 319-1195, Japan

Abstract

J-PARC was severely damaged by the March 11 Great East Japan Earthquake in 2011. When the earthquake struck, we had a beam study operation of the linac, and the machine automatically stopped immediately. The damages to the facilities and infrastructure were very serious over the entire site. Thanks to the significant effort of restoration, we resumed beam operation in December 2011 and user operation in January 2012. We learnt many lessons from the earthquake.

INTRODUCTION

J-PARC, which stands for Japan Proton Accelerator Research Complex, consists of the linac, the 3 GeV rapid cycling synchrotron (RCS), the 30 GeV Main Ring synchrotron (MR) and three experimental facilities[1]. The linac consists of a negative hydrogen ion source, a 3 MeV RFQ (Radio Frequency Quadrupole linac), a 50 MeV DTL (Drift Tube Linac) and a 191 MeV SDTL (Separated-type DTL) as shown in Fig. 1. But currently, the last 2 SDTL cavities are used as debunchers with no acceleration, and then the injection energy to the RCS is 181 MeV. Construction of superconducting linac (SCL) from 400 to 600 MeV and experimental facilities for the Accelerator Driven Transmutation System (ADS) are planned in the next construction phase of J-PARC. A proton beam from the RCS is injected to Materials and Life Science Experimental Facility (MLF) for neutron and muon experiments. The MR has two beam extraction systems. One is a fast extraction for the neutrino beam line for the Tokai-to-Kamioka (T2K) experiment, and the other is a slow extraction for Hadron Experimental Facility.

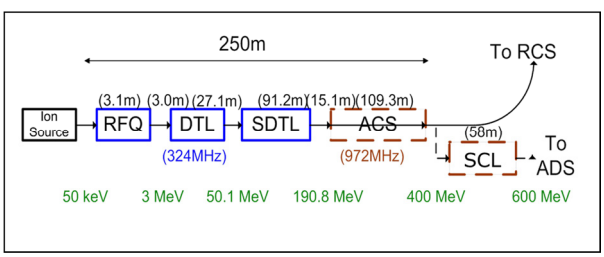

Figure 1: The structure of the J-PARC linac.

Coincidentally no user services were scheduled in the daytime of March 11, 2011. Beam study at the linac, and radiation survey work at the RCS and MR tunnels were carried out. The earthquake occurred when we suspended a beam for changing a beam destination from the linac to the RCS. The earthquake intensity was 6 lower at Tokai, which is the third highest intensity of the ten-ranked Japanese seismic scale. Whereas we prepared up to 8 m tsunami, the actual level was much lower at 3 m. It was extremely fortunate that no one was injured or missing.

STATUS BEFORE THE EARTHQUAKE

Commissioning of the linac started in 2006 and entire accelerators started operation in 2009. We had a discharge trouble at the RFQ, but this was settled during the summer shutdown of 2009 by improving the vacuum system. Since then, we had kept stable operation for users, concretely 90 to 95% availability. We ramped up the beam power from the RCS to the MLF to 120 kW in the 2009 fall and then to 200 kW in November 2010. Corresponding linac beam power is simply calculated by the ratio of energy, 0.060=(181/3,000), e.g. 200 kW RCS power corresponds 12.0 kW linac power. At the MLF, many neutron beam lines were in operation and numerous data had been accumulated before the earthquake. We also performed 400 kW (equivalent current beam) acceleration for higher power demonstration in January 2011.

The MR had been increased beam power steadily and had delivered beam at 145 kW to the neutrino beam line. Muon neutrinos may convert to electron neutrinos while travelling J-PARC to the Super-Kamiokande detector in 295 km distance. Detailed study results before the earthquake revealed that there were 6 possible events of the appearance of electron neutrinos.

The MR slow extracted beam to the Hadron Facility was 3 kW. Many experiment just started and the first data of the penta quark search were obtained.

THE EARTHQUAKE DISASTER

The big earthquake with magnitude of 9.0 hit the northeastern Japan on March 11, 2011. The J-PARC is located at about 200 km from the epicenter and had significant damage. Because the status of the J-PARC facility in general is described in some references[2,3], this paper mainly focus on that of the linac.

Linac

The linac building had the most seriously damages among all other buildings. A wide area at the entrance of the linac building subsided about 1.5 m, and almost all water supply and drainage pipes were broken as shown in Fig. 2. We could not get into the building until March 17 due to many strong aftershocks. It was found that there were fortunately no severe damages on the accelerator components themselves, but found that water was accumulated by 1 cm in depth on the linac tunnel floor. When we entered the tunnel again a week later on the 24th, the water level increased to approximately 10 cm. The leakage speed in this week was much faster than that of the first week from the earthquake. Therefore, we

#hasegawa.kazuo@jaea.go.jp

Copyright © 2012 by the respective authors — cc Creative Commons Attribution 3.0 (CC BY 3.0)

decided to pump it out immediately. Because the electricity for the building had yet not been restored for the building, we used a diesel engine generator. In addition, because the leaked water that went through the

Figure 2: Subsidence near the entrance of the linac building. Water supply and drainage pipes were broken.

concrete wall was highly alkaline, we had to neutralize it by acids before draining it. It took two days to drain approximately 150 m^3 of water. When the floor exposed, numerous lateral cracks were recognized on the floor and the walls.

Thereafter our main concern was the damage from the flooding and high humidity. One was damage on vacuum pumps placed on the floor. We rinsed and dried the pumps first, and then turned them on after tested their insulation resistance. It turned out that eight pumps and four controllers out of 36 pumps were broken down. Small aluminium boxes for diagnostics pre-amplifiers on the floor also had been submerged, and had been corroded by strong alkaline water. Several beam monitors and bellows welded to beam transport pipes between the SDTL cavities were also damaged, due to strong vibration[4]. Consequently many cavities were exposed by air with high humidity.

Vertical and horizontal displacement of the tunnel floor was measured. It turned out that there was a deformation of 4 cm in vertical and 2.5 cm in horizontal directions.

The acceleration cavities, such as the RFQ, the DTL and the SDTL were checked through visual inspection, vacuum test, and measurement of resonant frequencies and Q factors. As a result, small vacuum leaks at some flanges were found but no RF property changes were recognized. Displacement of the drift tubes in the DTL and SDTL cavities was observed by an alignment telescope.

The building floor on the ground was also displaced in both vertical and horizontal directions. Some pillars inclined due to the damage of their bases. So we could not use most of the cranes.

RCS and MR

The damages of the RCS were mainly outside of the building. The surrounding road became wavy and we had to repair it first to access to the yard. There were many high power devices to be restored in the yard, such as chilling refrigerators, cooling towers, capacitors, transformers, and power distribution boards, etc. Because the yard subsided about 0.3 - 1 m at many places, we first jacked up the devices and put concrete underneath to be levelled the base. In contrast, we fortunately had few significant damages in the RCS building.

For the MR, groundwater leaked from cracks into the main tunnel, but the tunnel, except for a part of the sub-tunnel, did not flood. We had a detailed test throughout the ring, and fortunately, there were no leaks in the beam ducts. Inspection of main electromagnets was also performed. It appeared that there was significant displacement by 2 to 3 cm at the maximum in some places. All 400 magnets were realigned to the original positions. It was time-consuming work to restore the MR.

Experimental Facilities

The most serious problem was displacement of shield blocks at the MLF. We had to move out 2,800 tons of ion blocks near the neutron target and restacked piece by piece. It was time-consuming. The attached building for a long baseline of the neutron spectrometer sank approximately 30 cm compared to the main MLF building. We had to jack up this building to the same level as the main building.

There were many subsidence spots around the building of Neutrino Experimental Facility but fortunately very little damage was found in the main components.

Subsidence also occurred around Hadron Experimental Facility. Although serious damage was not found in the main components, there were many gaps between shielding blocks. We reloaded over 3,000 tons of blocks and restacked.

RESTORATION

We surveyed the total scale of the damage on the entire J-PARC facilities and investigated the technical possibility of early recovery. As a result, the J-PARC Center announced the restoration schedule in May 2011. The main points are as follows:

- We would start test operation with using beams in December 2011.
- We would restart the user program in January 2012 and would provide beams for users for two months in JFY2011.

To meet the schedule, we selected the higher priority items that were necessary for operation, experiments and safety, such as water sealing in the tunnel, realignment work, firewalls repair, etc. Not only hardware experts, but also beam simulation experts did their utmost to shorten the restoration period.

Figure 3 shows the displacement of the linac components such as cavities and magnets. There were about 40 mm and 25 mm displacements in vertical and horizontal directions, respectively. It is time-consuming work to move DTLs by several centimeters because a

Copyright © 2012 by the respective authors — cc Creative Commons Attribution 3.0 (CC BY 3.0)

large number of heavy cables for electromagnets are connected. The estimated time for the realignment was about 6 months. We discussed a better scenario for the realignment of DTLs and also SDTLs to meet the restoration schedule with minimizing an effect on the beam degradation[5]. We decided to steer the beam at the downstream of the DTL section horizontally and vertically as shown as the dotted lines in Fig. 3. In the beam simulation, it appeared that this deflection of the alignment axis showed no effects on beam transmission and emittance degradation, because the steering angle was small in the order of 1 mrad or less.

Based on the measurement of displacement of the drift tubes, it appeared that there was 0.1 mm or 0.2 mm maximum misalignment for some drift tubes[6]. The particle simulation results also showed that the tolerable limit of the misalignment was ±0.2 mm. Therefore, we concluded that the observed drift tube misalignment would not be critical and decided we would not realign the drift tubes at this time.

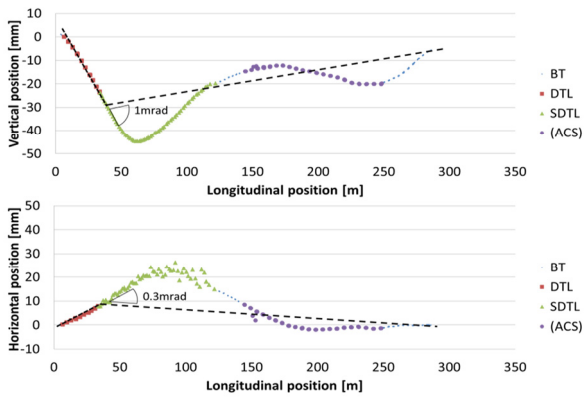

Figure 3: Displacement of the accelerator components after the earthquake (dots) and target realignment line (dashed lines).

BEAM OPERATION

Thanks to the effort of staff members and the support, the restoration work was accomplished on schedule. Before beam operation, the accelerating cavities were conditioned at high power RF for 24 hours a day from October 17 for the RFQ and from November 7 for the DTLs and SDTLs, respectively. It took a longer time than usual because some cavities were exposed to high humidity air. We started beam tuning at the linac on December 9, which was three days ahead of the detailed schedule established in September. Although many damaged things such as roads, cranes, doors, pillars, etc., had not been repaired yet, we could safely turn on the beam.

The purpose of the December's tuning was to check the operation processes from linac to the downstream facilities with low duty factor beam. At the linac, the beam was accelerated to 181 MeV on the 10th of December, and then the beam was injected to the RCS on the 17th. At the RCS the beam energy reached to 3 GeV on the 20th. The beams were extracted to the MLF successfully and also to the MR on the 22nd. On that day, the acceleration to 30 GeV in the MR was achieved. And eventually, the beam was extracted to the neutrino area on December 24 and all the tuning work was safely completed on time on December 27.

We successfully accelerated the beam current almost the same as before the earthquake: the peak current of 15 mA and the pulse length of 500 μs at the linac, while the repletion was lower.

At the beginning of January 2012, we started beam tuning at the full repetition of 25 Hz at the linac and the RCS. During the tuning, we conducted the 300 kW test from the RCS (the corresponding linac power was 18.1 kW) and confirmed that we could increase the power when the neutron target was ready. In February, the beam current from the linac was increased from 15 to 20 mA and a 420 kW tuning with the RCS was carried out. When we tested this condition, we examined the effect of the misalignment of the RCS magnets due to the earthquake. It appeared that, by adjusting the operating parameters of the RCS, we could reduce beam loss in the RCS and also in the downstream beam transport line. Although the beam loss was still higher than that before the earthquake, the loss-amount was reasonably agreed with that from simulations and was at an acceptable level. Therefore, we decided to perform the realignment of the RCS magnets, which will take several months, in the summer of 2013.

Figure 4 shows the beam power history for MLF. We started user operation to the MLF on January 24 at the RCS power of 120 kW (the linac power of 7.2 kW), then increased the power as it was before the earthquake of 220 kW (the linac power of 13.3 kW) on March 15. In the last three days of the run before the summer shutdown, the stable operation of 275 kW at 3GeV (the linac power of 16.6 kW) was successfully demonstrated. Based on this result, we are going to increase the power to 300 kW from this fall.

Regarding the MR fast extraction, we started beam delivery at about 100 kW in January. As a result of faster repetition operation and parameter tunings, beam power to the neutrino increased from 160 to 200 kW while it had been 145 kW before the earthquake. Regarding the MR slow extraction to hadron users, we delivered the beam at 3 kW as it was before the earthquake in February, and increased to 6 kW in June.

The J-PARC accelerator facilities had been operating successfully until March 22, however, the operation stopped due to the trouble of the linac klystron power supply. This trouble was caused by the diode breakdown in the high voltage transformation unit. We first suspected that a cause of this trouble might have been also related to the earthquake damage or the following poor atmospheric condition. However, it was turned out that an underlying cause would be electrical damages that accumulated during the long-years operation. We could not recover the operation time anymore because the trouble occurred in

Copyright © 2012 by the respective authors — cc Creative Commons Attribution 3.0 (CC BY 3.0)

March, at the end of fiscal year. As a consequence, the availability to users was down to 73% for JFY2011.

The user operation time of JFY 2012 (April 2012 - March 2013) is about 200 days. After resuming the beam operation from the klystron power supply trouble, we did not have any big troubles, and ended user operation in the morning of July 2 as scheduled. The total operating hours so far (from April 5 to July 2) are 2,104 hours. The deliverable beam times to the MLF, NU and HD were 1,646, 1058 and 376 hours, respectively, and the availabilities were approximately 94%, 90% and 94%, respectively.

The performance of the J-PARC accelerators is similar to or even better than before the earthquake in terms of beam power and availability.

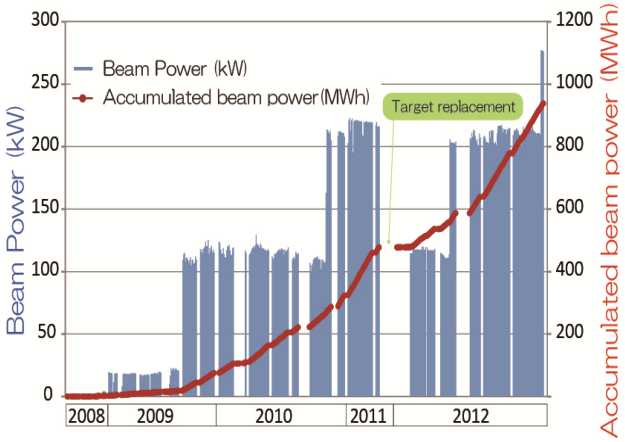

Figure 4: Beam power and accumulated beam power for the MLF users.

ISSUES OF THE LINAC IN BEAM OPERATON

The following two issues have been revealed in the beam operation after the earthquake: (1) the beam loss level became higher; (2) one of SDTL cavity units did not work at design RF amplitude. Beam loss mitigation is discussed in elsewhere[7].

There was a recognizable beam loss after the beam restoration, in particular after the SDTL straight beam transport section. Through a beam study, we found that beam loss was affected by beam trajectory, and to reduce beam losses, we had to adjust the beam trajectories at +5 mm and -5 mm as shown in Fig. 5. We found that high radiation dose points existed at vacuum pump boxes in the transport line, and there was a larger displacement than expected[8] as shown in Fig. 6.

After realignment of the boxes and ducts, the amount of beam loss declined to that before the earthquake. Through this problem, we learnt that we should have considered not only precise alignment of magnets and cavities, but also that of the other components, such as the ducts and vacuum boxes.

The second issue is on the SDTL section. One of the SDTL units, No.5, does not work properly within the designed RF amplitude region after the restoration. Therefore, we operate the SDTL at higher amplitude that is 109-116% of the designed value.

We tried to investigate a cause of this issue. Many peaks of hydrocarbon components in origin (e.g. mass of 12, 28, 44, etc.) are observed in the Q-mass data. We suspect if the cause is multipacting by hydrocarbons.

Before the earthquake, we used only ion pumps for the routine operation and we had seldom problems. But during the restoration, we purged the vacuum condition several times, and to recover the vacuum we used the rough vacuum system including an oil rotary pump. We suspect if oil vapor might have got back into the cavities. Therefore, we have already replaced oil rotary pumps with oil-free ones in the summer shutdown of 2012.

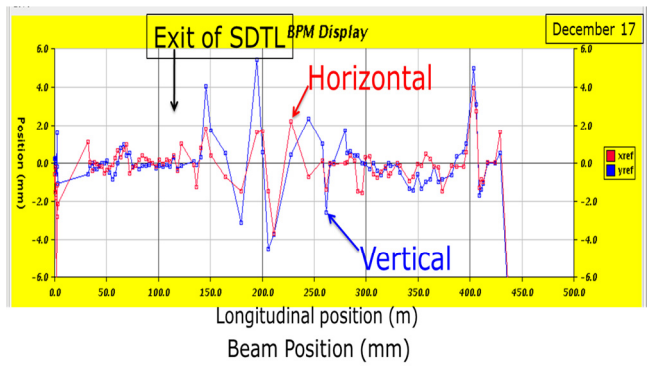

Figure 5: Beam position at the minimum beam loss condition on December 17, 2011.

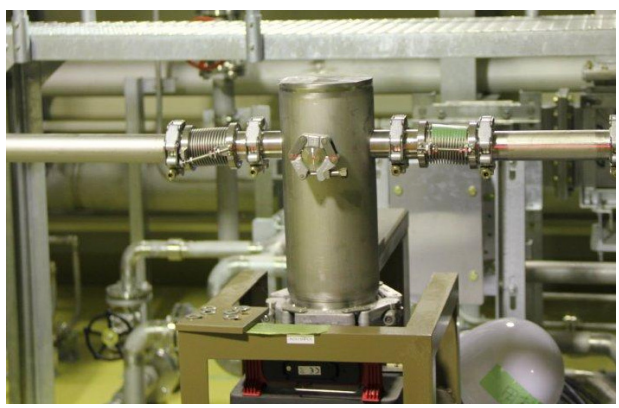

Figure 6: Displacement of the box. Deformed bellows with a red laser level marker line are shown.

LESSONS LEARNT FROM THE EARTHQUAKE

We have many learnt lessons from the earthquake.

Earthquake Proof System

An earthquake proof system is equipped to the DTL and SDTL tank support[9]. The system gives flexibility to the movement in X- and Z-axes. Thanks to the system, we thought, we didn't have significant displacement of the

Copyright © 2012 by the respective authors — cc Creative Commons Attribution 3.0 (CC BY 3.0)

drift tubes. A mechanical flexibility (in the range of 25 mm) helped to avoid having DT displacement. But bellows and monitors between the cavities could not stand for these flexibilities and broken. In this case, because the time of "DT realignment" is much longer than the time of "bellows and monitor rebuild", the earthquake proof system contributed to short restoration time. Through this problem, we learnt that we should consider side effects in advance to mitigate the total damage.

Also we had to clear in the movable area to secure the earthquake proof system. But we can see some materials such as a bolt, a hose or a cable, after the earthquake. The reason why that we did not investigate this area was because we assumed that we would not have big earthquakes like as the 3.11 earthquake in the near future. To cope with the disasters, we have to recall the famous Japanese saying "A natural disaster will happen when we least expect it." (by Dr. Torahiko Terada, physicist, 1878-1935).

High Humidity

Because the air conditioning system was broken and not available for several months, we used several dehumidifiers in the tunnel during the restoration work. But we could not maintain the normal humidity for instruments, and had to leave them under a very high humidity (> 70 %) condition. This caused many troubles such as a discharge at ion pump connectors, bad electricity connection and poor insulation, etc., even after the beam operation. Lessons Learnt: We should keep off high humidity. (We know, but in realistic, it is not easy to maintain low humidity because the volume of the tunnel is huge for several small dehumidifiers.)

Loose Connection of Coaxial Line

After the user operation, we had troubles several times due to a loose connection of coaxial lines, WX-203D. Although we checked the connection or tighten screws during the restoration, the screws became loose. We found that these troubles were caused by frequent aftershocks. We had no spring mechanisms in the screw. Lessons Learnt: We should consider occasional movement of aftershocks in mechanical design.

FUTURE SCOPE OF LINAC

The full energy (400 MeV) linac is necessary for the J-PARC facility to reach the nominal performance of 1 MW at RCS and 0.75 MW at MR. For beam energy upgrade from 181 to 400 MeV, we plan to install a new accelerating structure ACS (Annular-ring Coupled Structure)[10] and a 400 MeV RCS injection system. And also we need to upgrade the peak beam current from 30 to 50 mA. The development of new ion source[11] and RFQ[12,13] are underway.

Due to the users request to run fully during JFY2012, the installation of 400 MeV linac is postponed from 2012 to summer of 2013. After the installation and beam tuning, we will ramp up the beam power towards 1 MW at 3 GeV.

SUMMARY

J-PARC had severe damage by the earthquake, but it has been fixed in 9 months. User operation was resumed in January 2012. But some repairs are still temporal and permanent measure is needed. We are still working to recover from the damage.

The performance of the J-PARC accelerators is good as before the earthquake or better than before in terms of the beam power and the availability. Users accumulate data and many fruitful results are published.

Regarding the linac performance upgrade, the construction of the 200-400 MeV linac and the development of higher current ion source and RFQ are underway. They will be installed in summer 2013 and we will ramp up the beam power.

We have many lessons learnt from the earthquake. Some of them are trivial and/or specific to the earthquake. But in case of disaster, I would like to emphasize that not only the hardware preparation, but also software-like preparation such as "occasional evacuation drill" is quite important.

We didn't expect tsunami before the earthquake. Now we have in mind of the height above the sea level, and we prepared gears to save our lives.

We don't hope big earthquakes again, but next time, we could be able to manage better.

In the remark, we received encouragement, offers, donations, support, etc. from the world after the earthquake. We deeply appreciate your kindness and support that we received from all over the world.

ACKNOWLEDGEMENT

The author gratefully acknowledges the hard work of the J-PARC members and support for restoration from the earthquake. The author also would like to thank the linac group members to provide many data, in particular, Drs. H. Oguri, F. Naito and M. Ikegami.

REFERENCES

[1] Y. Yamazaki ed., JAERI-Tech 2003-044, KEK Report 2002-13 (2003).
[2] S. Nagamiya, IPAC2012, TUXA01, p1005.
[3] K. Hasegawa, et al., IPAC2011, WEPS095, p2727.
[4] A. Miura, et al., IPAC2011, WEPC144, p.2328.
[5] T. Morishita, et al., IPAC2011, MOOCB01, p44.
[6] T. Ito, et al., in these proceedings, TUPB100.
[7] M. Ikegami, in these proceedings, MOPB096.
[8] J. Tamura, in these proceedings, THPB021.
[9] F. Naito, et al., LINAC 2006, THP069, p. 743.
[10] H. Ao, et al, in these proceedings, THPB020.
[11] A. Ueno, et al., "Over 60mA RF-driven H^- ion source for the J-PARC", NIBS2012, 3-7 Sept 2012, Jyväskylä, Finland, to be published.
[12] Y. Kondo, et al., in these proceedings, THPB052.
[13] T. Morishita, et al., in these proceeding, TUPB042.

Copyright © 2012 by the respective authors — cc Creative Commons Attribution 3.0 (CC BY 3.0)

Copyright © 2012 by the respective authors — cc Creative Commons Attribution 3.0 (CC BY 3.0)

List of Authors

Bold papercodes indicate primary authors

— A —

Abernathy, J.M. MOPB026,TUPB081
Abram, T.N. MOPB004
Adli, E. TH3A04
Adolphsen, C. MOPB029,TH1A01
Adonev, O.A. TUPB023
Ahammed, M. MOPB091
Ahuja, R. TUPB033
Aimidura, A. THPB095
Ainsworth, R. **SUPB018**,TUPB048,**TUPB052**
Akemoto, M. MOPLB02,MOPB002,TH1A01
Alberty Vieira, L. TUPB047
Aleksandrov, A.V. MO2A02,THPB012,**THPB013**, THPB044
Alesini, D. MOPLB09,MOPB080
Alessi, J.G. **TUPB105**,THPB051
Alex, J. TUPB009
Allegra, L. THPB076
Almomani, A. **THPB006**
Alsari, S.M.H. THPB004
Altinbas, Z. MOPB064
Ambattu, P.K. MOPLB08,MOPB004,MOPB079
Amberg, M. SUPB022,TUPB071,SUPB023, TUPB072
Ames, F. MOPB024,MOPB026,WE1A04, FR1A04
Anders, W. MOPB067,THPLB12,THPB066
Andersson, A. SUPB008,MOPB045
André, T. TUPB029
Ang, Z.T. MOPB033
Angal-Kalinin, D. MOPB011
Antipov, S.P. MOPLB03,MOPLB05,MOPLB11, MOPB041,MOPB047,MOPB093
Antoniazzi, L. TUPB094,THPLB08,THPB040
Ao, H. **THPB020**,THPB021
Aoyama, M. TUPLB10,TUPB080
Arai, S. TUPB095
Arakawa, D.A. MOPLB02,MOPB002
Arakida, Y. MOPLB02,MOPB002
Arenius, D. TU1A04
Arenshtam, A. MO1A01
Arimoto, Y. MO3A04
Arkan, T.T. TH1A01
Arnaudon, L. THPB010
Asaka, T. THPB092,**TUPB006**
Asano, H. THPB020,THPB021
Aslaninejad, M. THPB004
Atkinson, T. **SUPB003**,SUPB004,**MOPB036**, MOPB037
Aulenbacher, K. SUPB023,TUPB072
Ayvazyan, V. TUPB019,THPB085
Ayzatskiy, M.I. MOPB023

— B —

Baartman, R.A. MOPB024,WE1A04
Back, J.J. THPB004
Baffes, C.M. MOPB095
Bai, J.N. **SUPB037**,**THPB081**
Barbanotti, S. MOPB017,TH1A01
Barcikowski, A. TUPLB08,TUPB046
Barnes, B.W. THPLB02,THPB015
Barnyakov, A.M. SUPB009,MOPB048
Barth, W.A. SUPB022,SUPB023,MO3A01, TUPB035,TUPB071,TUPB072, **TUPB074**,**THPLB07**,**THPB034**, THPB035,**TUPB074**
Bashmakov, Y.A. SUPB035,THPB074
Bathe, B.N. MOPB032
Battistoni, M.A. TH1A01
Baudrenghien, P. THPB010
Bazin, N. **MOPB074**
Beard, K.B. MOPB014
Beaudoin, B.L. THPLB11,THPB061
Bechtold, A. THPB047
Beebe, E.N. TUPB105
Bellaveglia, M. MOPLB09,MOPB080
Bellodi, G. THPB010,**THPB011**
Belomestnykh, S.A. **MOPB063**,**MOPB064**,**MOPB063**, **MOPB064**
Ben Aliz, Y. MO1A01
Ben-Naim, M. TH1A05
Ben-Zvi, I. MOPB063,MOPB064,**TU2A04**
Berezov, R. THPB034
Berkovits, D. **MO1A01**,THPB094
Bernal, S. THPLB11,THPB061
Bernard, E.C. MOPLB10,MOPB090,TU1A04, TUPB040
Berry, S. MOPB017,THPLB09,THPB083
Bertone, C. THPB010
Bertrand, P. **TH2A02**
Binkowski, J. TUPB040
Binyukov, P.V. TUPB023
Bird, B. TUPB040
Birney, P.S. TUPB081
Bishofberger, K. **TH1A05**
Bliss, N. MOPB011
Blokland, W. THPB013
Blot, F. MOPB013
Blumer, H. TUPB009
Body, Y. THPB010
Bogacz, S.A. **MOPB014**
Bondarenko, A.V. SUPB003,SUPB004,MOPB036, MOPB037
Bondarenko, T.V. SUPB035,THPB074
Boni, R. **MOPLB09**,**MOPB080**
Boorman, G.E. THPB004

Bopp, M. TUPLB01,TUPB009,TUPB010, TUPB012
Borowiec, P.B. MOPB012,MOPB017
Bosco, A. THPB004
Bosland, P. MOPB074
Bosotti, A. MOPB017,TUPB020,TH1A01
Boulware, C.H. MOPB064
Brackebusch, K. MOPB067
Branlard, J. MOPB017,TUPB019,**THPB085**, THPB086
Brasseur, A. THPLB09,THPB083
Bricker, S. MOPLB10,MOPB090,TUPB040
Briscoe, B. THPB051
Brodhage, R. M. MO3A01
Broere, J.C. THPB010
Brossard, J. MOPB013
Brueck, H. MOPB017
Brunasso Cattarello, O. TUPB094
Bruni, C. MOPB013
Brunner, O. THPB010
Brutus, J.C. MOPB063,MOPB064
Buckley, S.R. MOPLB08,MOPB079
Bultman, N.K. TU1A04,THPB097
Burandt, C. SUPB010,TUPB026
Burrill, A. MOPB030,MOPB064
Burrows, I. MOPB004
Burrows, P. SUPB008,MOPB045
Burt, G. **MOPLB08**,**MOPB004**,**MOPB079**
Busch, M. **SUPB022**,SUPB023,MO3A01, **TUPB071**,**TUPB072**
Butkowski, L. TUPLB04,TUPB004
Butler, J.E. MOPLB03,MOPB041
Buzaglo, Y. MO1A01
Buzio, M.C.L. THPB010
Bylinskii, I.V. WE1A04

— C —

Calabretta, L. THPB028
Calaga, R. MOPB064
Calatroni, S. TUPB047
Calero, J. THPB089
Calic, S. MOPB033
Caliri, C. THPB076
Cameron, D.P. TUPB081
Campmany, J. THPB089
Cancelo, G.I. MOPB077,**TUPB062**,THPB085
Cao, J. MOPB023
Capatina, O. TUPB047
Carli, C. THPB010
Carlson, K. MOPB054
Carlsten, B.E. TH1A05
Carneiro, J.-P. THPB014
Carter, H. TH1A01
Caruso, A.C. THPB028
Carwardine, J. THPB085
Casagrande, F. TU1A04
Castro, G. THPB076
Cavalier, S. MOPB013
Cayla, J-N. MOPB013
Cela-Ruiz, J.M. THPB089
Celona, L. THPB028,**THPB076**
Chakrabarti, A. **MOPB024**,MOPB026
Chalykh, B.B. TUPB032
Champion, M.S. TH1A01,TUPB053,**THPB044**
Chao, Y.-C. MOPB024,MOPB026,WE1A04
Charon, P. THPLB09,THPB083
Charrier, J.-P. THPLB09,THPB083
Chase, B. MOPB054,MOPB077,TUPB062, THPLB02,THPB015,THPB085
Chau, L.P. MO3A03
Chaumat, V. MOPB013
Chauvin, N. FR1A02,THPB034
Cheban, S. TUPB053
Chel, S. MOPB074
Chen, A.Z. MOPB095
Chen, J. TUPB034
Chen, J.E. TUPB034
Chen, Q. TUPB103
Chen, S. THPLB04,THPB002
Cheng, P. TUPB075
Cherepenko, A. TUPLB04,TUPB004
Chernousov, Y.D. SUPB009,MOPB048
Cherry, G.L. TUPB068
Chevallay, E. TUPB041
Cheymol, B. TUPB041,THPB028
Chi, Y.L. MOPLB04,MOPB023,MOPB046, **TU1A03**
Chiba, Y. TUPB095
Cho, M.-H. MOPB049
Cho, Y.-S. TU1A05,THPB022
Choi, C. TUPB030
Choroba, S. MOPB017,TUPLB04,TUPB004
Chouhan, S. MOPLB10,MOPB090,TU1A04, TUPB040
Chowdhury, G.K. TUPB033
Christou, C. **MOPB016**,**THPB073**
Ciavola, G. THPB076
Cichalewski, W. TUPB019,THPB085
Citterio, A. TUPLB01,TUPB009,TUPB010
Clarke, C.I. **TH3A04**
Clarke-Gayther, M.A. THPB004
Clayton, C.E. TH3A04
Clemente, G. **MO3A01**,TUPB035,THPB034
Cloué, C. THPLB09,THPB083
Cole, M.D. MOPB064
Collaboration, A.C. FR2A02
Colocho, W.S. MOPLB01,MOPB001
Compton, C. MOPLB10,MOPB071,MOPB090, TU1A04,TUPB040
Comunian, M. **TUPB032**,**THPB030**,**THPB043**
Conde, M.E. MOPLB05,**MOPLB11**,MOPB047, **MOPB093**

Constance, B. **MOPB003**
Conway, Z.A. MOPB073,**TUPLB07**,TUPLB08, TUPB046,**TUPB066**,**TUPB067**, **TUPB068**,**TUPB093**,**FR1A05**
Corde, S. TH3A04
Corlett, J.N. **TU2A01**
Corlett, P.A. MOPB004
Corsini, R. MOPB003,**WE1A02**
Corso, J.-P. THPB010
Coupard, J. THPB010
Crawford, D.J. MOPB054,MOPB077
Crisp, J.L. TUPB093
Crofford, M.T. THPB044
Cullerton, E. MOPB054,THPLB02,THPB015
Curry, D. TUPB084
Cuvet, Y. TH2A03
Cywinski, R. TUPB077
Czuba, K. TUPB019

— D —

Daël, A. THPLB09,THPB083
Dahl, L.A. TUPB035,THPLB07,THPB035
Dai, J. MOPB064
Dai, M.H. MOPLB04,MOPB046
Dale, D. WE1A04
Dallocchio, A. TH2A03,THPB038,THPB010
Danared, H. TH2A01
Dancila, D.S. TUPB108
Darve, C. TH2A01
D'Auria, G. **WE1A03**
Davids, B. FR1A04
Davidson, K.D. TU1A04
Davis, G.K. MOPB030,**MOPB031**
Dawson, R.J. WE1A04
de la Gama, J.G.S. THPB089
De Prisco, R. THPB030
De Silva, S.U. **SUPB038**,**SUPB039**,**TH1A02**, **THPB062**,**SUPB038**,**SUPB039**, **TH1A02**,**THPB062**
Dechoudhury, S. MOPB024
Decker, F.-J. **MOPLB01**,**MOPB001**,MOPB087, TH3A04
Decking, W. **MO1A02**
Deibele, C. **TUPB084**
Delaup, B. TUPB047
Delayen, J.R. SUPB026,SUPB038,MOPB056, MOPB072,**TH1A03**,THPB062
Delferrière, O. FR1A02,THPB034
Delgiusto, P. MOPB083
D'Elia, A. TUPB047
Deng, B. MOPB023
Deng, C.D. MOPB023
Deng, J. THPLB04,THPB002
Desmons, M. TUPB094,THPLB08,THPB031, THPB038,THPB040
Devanz, G. MOPB074
Dewa, H. THPB068,THPB092
Dexter, A.C. MOPLB08,MOPB079
Di Giugno, R. THPB076
Di Pirro, G. MOPLB09,MOPB080
Dickerson, C. **THPB063**
Dickson, R. TUPB084
Dima, R. SUPB015,THPB042
Dimov, V.A. THPB011
Dolgashev, V.A. MOPLB08,MOPB079
Doran, D.S. MOPLB11,MOPB093
Dos Santos, N. THPB010
Doutresssoulles, C. TUPB029
Droba, M. THPB006
Drury, M.A. **MOPB030**
Du, X. TUPB036,THPB039
Du, Y.-C. **MOPLB12**,**MOPB089**
Dubbs, L.J. MOPB071
Dubrovskiy, A. **MOPB032**
Ducoudret, B. TUPB029
Dudovich, O. MO1A01
Duffy, L.D. TH1A05
Dunning, M.P. MOPB029
Duraffourg, M. TUPB041
Dutt, R.N. TUPB033
Dwivedi, J. THPLB05,THPB003
Dyubkov, V.S. **TUPB031**
Dziuba, F.D. SUPB022,**SUPB023**,MO3A01, TUPB071,**TUPB072**

— E —

Ebert, M. TUPB019
Edstrom, Jr, D.R. MOPB054,MOPB077
Ego, H. MOPB084
Eichhorn, R. SUPB010,TUPB026
Eidelman, Y.I. MOPB095,TUPB062
Eisen, Y. MO1A01
Ekelöf, T.J.C. TUPB108
El Khaldi, M. MOPB013
Eliyahu, I. MO1A01
Elliott, K. MOPB070,MOPB071,TUPB040
England, R.J. TH3A04
Enkhbat, B. TUPB040
Enomoto, A. MOPLB02,MOPB002
Eremeev, G.V. MOPB060
Erickson, R.A. TH3A04
Eschke, J. TUPB019
Eshraqi, M. THPB030

— F —

Fabris, A. **MOPB083**
Facco, A. MOPLB10,MOPB070,MOPB071, MOPB090,TU1A04,TUPB060, TUPB040
Fagotti, E. **TUPB094**,**THPLB08**,**THPB040**
Faircloth, D.C. THPB004
Fang, W. **SUPB031**,**MOPB086**

Fang, Z. MOPB096
Favale, A.J. MOPB064
Favre, G. TH2A03
Feinberg, G. MO1A01
Feng, Y. MOPLB04,MOPB046
Ferdinand, R. TH2A02
Ferrario, M. MOPLB09,MOPB080
Fila, A. MOPLB10,MOPB090
Fischer, R.L. TUPB067,TUPB068
Fisher, A.S. TH3A04
Fishman, I. MO1A01,TUPB092,THPB094
Fite, J.M. THPB051
Flisgen, T. MOPB067
Flöttmann, K. MOPB082
Focker, G.J. TUPB041
Fong, K. MOPB026
Fontaine, M. THPLB09,THPB083
Forck, P. THPB034
Fox, A.D. TUPB040
France, A. THPB031,THPB038
Fraser, M.A. TUPB047
Fu, S. TU1A03,TUPB103,**THPLB01**,
THPB023
Fuchs, J.-F. THPB010
Fujimaki, M. MO3A02
Fukuda, S. SUPB024,MOPLB02,MOPB002,
TUPLB12,TUPB090,TH1A01
Funken, A. THPB010
Furukawa, K. MOPLB02,MOPB002
Futatsukawa, K. MOPB096
Fuwa, Y. **SUPB024**,MOPLB07,MOPB053,
TUPLB12,**TUPB090**

— G —

Gabor, C. THPB004
Gai, W. MOPLB03,MOPLB05,MOPLB11,
MOPB041,MOPB047,MOPB093
Gajewski, K.J. TUPB108
Galambos, J. **MO2A02**
Galek, T. MOPB067
Gallo, A. MOPLB09,MOPB080
Gamba, D. MOPB003
Gammino, S. THPB028,THPB076
Ganni, V. TU1A04
Gao, S.L. TUPB034
García-Tabarés, L. THPB089
Garoby, R. THPB010
Gasser, Y. THPLB09,THPB083
Gassner, D.M. MOPB064
Gavish, I. MO1A01
Geisser, J.-M. TH2A03
Gelmetti, F. MOPB083
Geltenbort, P.W. MO3A04
Geng, H. TUPB075
Gentini, L. TH2A03
Gerbershagen, A. **SUPB008**,**MOPB045**
Gerbick, S.M. MOPB073,TUPLB07,TUPLB08,
TUPB046,TUPB066,TUPB067,
TUPB068
Gerhard, P. **THPLB07**,**THPB035**,TUPB074
Gerigk, F. **TH2A03**,THPB010
Gertz, I.G. MO1A01,TUPB092
Gessner, S.J. TH3A04
Gettmann, V. TUPB035,TUPB074
Ghosh, S. TUPB033
Gibson, P.E. TU1A04
Giguet, J.-M. TH2A03
Gilevich, S. MOPB029
Ginsburg, C.M. MO1A03,**MOPLB06**,**MOPB052**
Glasmacher, T . TU1A04
Gobin, R. THPB031,**FR1A02**
Gössel, A. TUPB019
Goh, G. MOPB024
Gohar, Y. MOPB023
Gong, C. MOPB026
Gong, K.Y. TUPB103
Gonin, I.V. TUPB054,TUPB067
Gonnin, A. MOPB013
Goryashko, V.A. **TUPB107**,TUPB108
Goudket, P. MOPLB08,MOPB079
Gould, O. THPB051
Goulden, A.R. MOPB004
Gover, A. SUPB011,**TUPLB05**,**TUPB005**,
TH2A004
Grespan, F. TUPB094,THPLB08,THPB030,
THPB040,THPB043
Grimm, T.L. MOPB064
Grin, A. MO1A01,THPB094
Groening, L. MO3A01,MOPB098,**THPB034**
Grouas, N. MOPB074
Grudiev, A. MOPLB08,MOPB043,MOPB079
Gu, D. **SUPB006**,**TUPB018**
Gu, Q. SUPB006,SUPB031,SUPB032,
MOPB007,MOPB086,TUPB018,
TUPB021,**TUPB022**,TUPB097
Gubarev, V. MOPB012
Guetre, E.R. WE1A04
Guirao, A. THPB089
Guo, H.S. MOPB023
Guo, X.H. **TUPB044**
Guo, X.L. TUPB055
Guo, Z. TUPB075
Guo, Z.Y. TUPB034
Gupta, P.D. THPLB05,THPB003
Gutiérrez, J.L. THPB089

— H —

Haber, I. **THPLB11**,**THPB061**
Haeuser, J. SUPB014,THPB046
Hagen, U. THPB007
Hagge, L. MOPB017
Hahn, H. MOPB063,MOPB064

Hajima, R. **WE1A05**
Halfon, S. MO1A01
Hammons, L.R. MOPB064
Hammouti, L. THPB010
Han, S.F. THPB079
Han, Y.N. TUPB044
Hanaki, H. TUPLB09,TUPB079,THPB092
Hanke, K. THPB010
Hanna, B.M. MOPB095
Hannurkar, P.R. THPLB05,THPB003
Hansen, J. THPB038,THPB010
Hara, K. TH1A01
Harders, I. TUPLB04,TUPB004
Hardy, P. MOPB074
Har-Even, D. MO1A01
Harle, L.L. MOPLB10,MOPB071,MOPB090, TUPB093,TUPB040
Harmer, P.R. MOPB033
Harms, E.R. **MOPB054**,MOPB077,TUPB020
Hartmann, W. THPLB07,THPB035
Hartnett, T. MOPB004
Hartung, J. TUPLB04,TUPB004
Haruvy, Y.F. MO1A01
Hasebe, H. MO3A02
Hasegawa, K. TUPB042,THPB052,**FR2A01**
Hasegawa, T. TUPB006
Hashida, M. MOPLB07,MOPB053
Hast, C. MOPB029,TH3A04
Hayano, H. MOPLB07,MOPB025,MOPB053, MOPB069,**TH1A01**
He, D.Y. MOPLB04,MOPB023,MOPB046
He, S. SUPB019,SUPB020,**SUPB027**, SUPB028,**MOPB057**,MOPB059, TUPB055,TUPB056,TUPB057
He, X. MOPLB04,MOPB023,MOPB046
He, Y. SUPB013,SUPB019,SUPB020, SUPB027,SUPB028,MOPB057, MOPB059,TUPB036,TUPB039, TUPB055,TUPB056,TUPB057, THPB026,**THPB027**,THPB039, THPB079
He, Z.Q. **TUPB058**,**TUPB058**
Heid, O. TUPB091,THPB007
Heidenreich, D. THPB044
Heilmann, M. MO3A03,**THPB008**
Hein, L.M. THPB011
Henderson, S. TU1A02
Hensler, O. THPB085
Herfurth, F. TUPB035
Hermansson, L. TUPB108
Heßler, C. TUPB041
Higashi, N. TH1A01
Higashi, Y. MOPLB02,MOPB002
Higo, T. MOPLB02,MOPB002
Higurashi, Y. MO3A02
Hill, C. MOPLB08,MOPB011,MOPB079
Hindley, J.P. MOPB004
Hirano, K. TUPB099,TUPB101,TUPB100
Hirsch, T. MO1A01
Hirschmann, D. MO1A01
Hocker, A. MOPB054,TH1A01
Hodek, M. MOPLB10,MOPB070,MOPB090, TUPB040
Hodges, L. MOPLB10,MOPB090
Hoeltermann, H. THPB007
Hoff, M.D. THPB039
Hofmann, I. THPB006
Hogan, J. MOPB030
Hogan, M.J. TH3A04
Holek, J.V. TUPB081
Holland, K. TU1A04
Hollinger, R. THPB034
Holmes, D. MOPB064
Holzbauer, J.P. **SUPB025**,**MOPB055**
Hong, Y. MOPB035
Honma, H. MOPLB02,MOPB002
Hopper, C.S. **SUPB026**,**MOPB056**,MOPB072
Horvitz, Z. MO1A01
Hosoda, S. MOPB025
Hou, M. MOPB022,MOPB023
Hua, J.F. MOPLB12,MOPB089
Huang, D. SUPB006,**MOPB007**,TUPB018, **TUPB021**
Huang, G. **MOPB020**,**MOPB021**,MOPB035
Huang, H. MOPLB04,MOPB046
Huang, S.C. SUPB019,SUPB020,SUPB027, SUPB028,MOPB057,MOPB059, TUPB056,TUPB057
Huang, W.-H. MOPLB12,MOPB089
Huang, Y.L. SUPB019,SUPB020,SUPB028, MOPB059,TUPB056,TUPB057
Hüning, M. **TUPB015**
Hug, F. **SUPB010**,**TUPB026**
Hughes, T.J.S. TUPB091,THPB007
Hwang, C.K. THPB084
Hwang, J.G. TUPB104

— I —

Igarashi, Z. TUPB102
Iida, N. MOPLB02,MOPB002
Iijima, H. MOPB025
Ikeda, M. MOPLB02,MOPB002
Ikegami, M. MOPB094,TUPB101,**MOPB096**
Ilday, F.Ö. SUPB008,MOPB045
Imajo, S. MO3A04
Inagaki, T. **MOPB005**,MOPB084,TUPB006
Isoyama, G. MOPB025
Ito, T. TUPB099,TUPB101,**TUPB100**
Ivannikov, V. SUPB009,MOPB048
Ivanov, E.V. TUPB091
Iversen, J. MOPB012
Iwasaki, A. TUPLB10,TUPB080

Iwashita, Y. SUPB024,MO3A04,**MOPLB07**, **MOPB053**,**TUPLB12**,**TUPB090**

— J —

Jałmużna, W. TUPB019,THPB085,THPB086
Jamet, C. **TUPB029**
Jamilkowski, J.P. MOPB064
Jamison, S.P. MOPB011
Jandovitz, P.J. THPB037
Jang, J.-H. TU1A05,THPB022
Jecklin, N.M. TUPB047
Jensch, K. MOPB017,TH1A01
Jeon, D. **TUPB030**,TUPB104
Jia, D. MOPB020,MOPB021,MOPB035
Jia, H. SUPB013,TUPB039,THPB026
Jiang, T.C. SUPB019,SUPB020,SUPB028, MOPB059,TUPB056,TUPB057
Jin, K. MOPB020,MOPB021,**MOPB035**
Jin, T. TUPB044
Jin, X. THPB039
Jing, C.-J. MOPLB03,**MOPLB05**,MOPLB11, MOPB041,**MOPB047**,MOPB093
Jobe, R.K. MOPB029
Johnson, M.J. TU1A04,TUPB040
Jolly, S. THPB004
Jones, J.K. MOPB011
Jones, R.M. MOPLB08,MOPB079
Jones, S. MOPLB10,MOPB090,TU1A04
Jonker, M. **THPB091**
Joo, J.D. TUPB030
Joshi, C. TH3A04
Joshi, S.C. **THPLB05**,**THPB003**
Jung, H.C. TUPB030

— K —

Kaabi, W. MOPB017
Kadi, Y. TUPB047
Kadokura, E. MOPLB02,MOPB002
Käfer, D. MOPB017
Kaiser, M. TUPB035
Kaizer, B. MO1A01,**TUPB092**,THPB094
Kajioka, S.Y. TUPB081
Kakihara, K. MOPLB02,MOPB002
Kako, E. TH1A01
Kamigaito, O. MO3A02,TUPB073,TUPB095
Kamitani, T. **MOPLB02**,**MOPB002**
Kamps, T. THPLB12,THPB066,**THPB069**
Kanareykin, A. **MOPLB03**,MOPLB05,**MOPB041**, MOPB047
Kanesue, T. THPB037
Kang, Y.W. THPB044
Kanjilal, D. TUPB033
Karlen, D. MOPB026,TUPB081,WE1A04
Karmakar, J. TUPB033
Karnaukhov, I.M. MOPB023
Kase, M. TUPB095
Kashiwagi, S. MOPB025
Katagiri, H. MOPLB02,MOPB002,TH1A01
Katalev, V.V. MOPB017
Kato, R. MOPB025
Kato, S. MOPB069
Kawamata, H. TUPB042,THPB052
Kawase, K. MOPB025
Kayran, D. MOPB063,MOPB064
Kazakov, S. **TUPB053**
Kedzie, M. MOPB073,TUPLB07,TUPLB08, TUPB046,TUPB066,TUPB067, TUPB068,TUPB093
Kelley, M.J. MOPB018,SUPB001,MOPB060
Kellogg, S. TUPB081
Kelly, M.P. **MOPB073**,TUPLB07,TUPLB08, TUPB046,TUPB066,TUPB067, TUPB068,**TUPB093**,FR1A05
Kemp, M.A. **WE2A02**
Kendjebulatov, E. TH2A03
Kephart, R.D. TH1A01
Kerby, J.S. TH1A01
Kester, O.K. MOPB098
Kewisch, J. MOPB064
Khabiboulline, T.N. TUPB053,TUPB054
Khan, N. WE1A04
Khan, V.F. **MOPB043**
Khare, P. THPLB05,THPB003
Kijel, D. MO1A01
Kim, D.G. THPB084
Kim, D.I. TU1A05
Kim, H.J. TUPB030
Kim, H.J. TUPB030,**TUPB104**
Kim, H.S. TU1A05,**THPB022**
Kim, J.-W. **TUPLB06**,**TUPB028**,**THPB084**
Kim, S.H. MOPB049
Kim, S.H. TUPB068
Kim, S.K. TUPB030
Kim, Y.H. TUPB030
King, L.K. MOPB030
Kishek, R.A. THPLB11,THPB061
Kitaguchi, M. **MO3A04**
Klaus, M. MOPLB10,MOPB090
Kleeb, T. TUPB009
Klein, H. SUPB012,THPLB03,THPB005, THPB009,THPB047
Klump, B. SUPB017,THPB049
Knobloch, J. SUPB029,MOPB065,MOPB067, THPLB12,THPB066
Kobayashi, T. THPB092
Kobayashi, Y. **WE1A01**
Koeth, T.W. THPLB11,THPB061
Kojima, Y. TH1A01
Kolomiets, A. FR1A05,**SUPB016**,THPLB06, THPB036,**THPB050**
Kondo, C. MOPB005
Kondo, Y. TUPB042,**THPB052**

Kondo, Y. TH1A01
Kondrashev, S.A. THPB063
Konecny, R. MOPLB11,MOPB093
Kong, X.C. MOPB023
Konrad, M. SUPB010,TUPB026
Koscielniak, S.R. MOPB033,**WE1A04**
Kostin, D. MOPB012,MOPB017,TUPB019, TH1A01
Koubek, B. **SUPB014**,SUPB017,THPB034, **THPB046**,**THPB049**
Kovalenko, A.D. **THPLB06**,**THPB036**
Koveshnikov, A. MOPB091,WE1A04
Koyama, K. **THPB095**
Koyama, R. MO3A02
Kozsar, I. THPB010
Krämer, A. THPB034
Krafft, G.A. MOPB014
Kramp, M. TUPB053
Krasnov, A.A. TUPB091
Krasnykh, A. **MOPB087**
Kravchuk, L.V. MOPB082
Kreisel, A. MO1A01
Kreps, G. MOPB012
Kruchkov, Ya.G. TH2A03
Krzysik, K. MOPB012
Kucera, M.J. MOPB054
Kudla, I.M. TUPB019
Kugeler, O. SUPB029,MOPB065
Kumar, M. TUPB033
Kumar, R. TUPB033
Kuramoto, A. MOPB025
Kurashina, M. MOPLB02,MOPB002
Kuriki, M. **MOPB025**
Kurup, A. THPB004
Kush, P.K. THPLB05,THPB003
Kushnir, V.A. MOPB023
Kutsaev, S.V. TUPLB08,TUPB046,TUPB067, TUPB093,FR1A05
Kuzikov, S.V. **THPB096**,**THPB096**
Kwon, H.-J. **TU1A05**,THPB022

— L —

Laface, E. MO2A02
Lallement, J.-B. THPB011,THPB038,THPB010
Lambert, A.R. THPB039
Langlois, S. THPLB09,THPB083
Langstaff, R.R. WE1A04
Launé, B. THPB034
Lawrie, S.R. THPB004
Laxdal, A. MOPB026,WE1A04
Laxdal, R.E. MOPB024,**MOPB026**,MOPB033, **MOPB091**,**FR1A04**,**WE1A04**
Le, Q. MOPB023
Le Coz, W. TUPB029
Le Noa, Y. THPB038
Lebedev, V.A. MO2A02,MOPB095,THPB014
LeClair, R.W. MOPB087
Ledu, G. TUPB029
Lee, J.H. TUPB030
Lee, Y.Y. TUPB030
Leibfritz, J.R. MOPB054
Leitner, D. TU1A04
Leitner, M. MOPLB10,**TUPB040**,MOPB090, TU1A04
Leloir, S.L. TUPB029
Lempert, G. MO1A01
Lenckowski, M. TUPB081
Lepercq, P. MOPB013
Lesrel, J. THPB034
Letchford, A.P. THPB004
Lettry, J. THPB010
Levichev, A.E. **SUPB009**,**MOPB048**
Li, A.H. TUPB103
Li, C. SUPB013,TUPB039,THPB026, THPB039
Li, D. THPB027,THPB039
Li, J. THPLB01,THPB023
Li, S.Z. TH3A04
Li, X. MOPLB04
Li, X. MOPB022
Li, X. MOPB046
Li, X. MOPB023,THPB025
Li, Z. **TUPB075**,THPB024
Li, Z. MOPLB04,MOPB046
Liang, X. MOPB064
Lilje, L. MOPB017,TH1A01
Limborg-Deprey, C. **MOPB029**
Lin, H. MOPB020,MOPB021
Lindroos, M. **TH2A01**
Lingwood, C. MOPLB08,MOPB004,MOPB079
Lipkowitz, N. MOPLB01,MOPB001,TH3A04
Litos, M.D. TH3A04
Litvinenko, V. **MOPB034**,MOPB063,MOPB064
Liu, H.C. **TUPB103**,THPLB01,THPB023
Liu, J. MOPLB04,MOPB046
Liu, J. MOPB023
Liu, L.Q. TUPB044
Liu, R.L. MOPB023
Liu, S.H. SUPB013,TUPB039,THPB026
Liu, W. MOPLB11,MOPB093
Liu, W.B. MOPB023
Liu, Y. THPB039
Liu, Y. THPB002
Liu, Y. MOPB096
Liu, Y. THPB013
Liu, Y. MOPB020,MOPB021
Liu, Z. TUPB058,TUPB060,TUPB061
LoDestro, V. THPB051
Lofnes, T. TUPB108
Lombardi, A.M. THPB011,THPB038,THPB010
Long, C.D. THPB013
Longhitano, A. THPB028

Lopez Hernandez, L.A. THPB010
Loret, S. TUPB029
Lu, L. **TUPB073**
Lu, P.N. TUPB034
Lu, W. TH3A04
Luner, J. MO1A01
Lunin, A. TUPB054,TUPB067
Lurie, Yu. **TUPB014**
Lv, K. MOPB023

— M —

Ma, C. MOPLB04,MOPB023,MOPB046
Ma, H.Z. MOPB023
Ma, L.Z. THPB079
Machicoane, G. THPB097,TU1A04
Madec, C. **THPLB09**,**THPB083**,MOPB017
Mäder, D. **SUPB012**,THPLB03,THPB005, THPB008,**THPB009**
Maesaka, H. TUPB006
Maesen, P. TUPB047
Maglioni, C. THPB010
Magome, T. THPB092
Mahler, G.J. MOPB063,MOPB064
Maier, M.T. TUPB035
Malka, V. **MO2A01**
Malloch, I.M. MOPB070,MOPB071,TUPB040
Mammarella, F. WE1A04
Mandag, E.N. MOPB013
Marchetto, M. MOPB024,MOPB026,**FR1A04**, WE1A04
Marcos, J. THPB089
Mardor, I. MO1A01
Marhauser, F. MOPB030
Marsh, K.A. TH3A04
Marti, F. **FR1A01**,TU1A04
Martinez, L.M. THPB089
Martínez de Alvaro, T. THPB089
Maruta, T. **MOPB094**,MOPB096,TUPB082, TUPB101
Mascali, D. THPB028,THPB076
Massana, V. THPB089
Matalevich, J. MOPB031
Matheisen, A. MOPB012,MOPB017,TH1A01
Mathot, S.J. TH2A03,THPB038,THPB010
Mathuria, D.S. TUPB033
Matsubara, S. TUPLB10,TUPB080
Matsukawa, T. TUPLB10,TUPB080
Matsumoto, S. MOPLB02,MOPB002
Matsumoto, T. MOPLB02,MOPB002,TH1A01
Matsumura, Y. THPB095
Matsushita, H. MOPLB02,MOPB002
Matveenko, A.N. SUPB003,SUPB004,MOPB036, MOPB037
McCormick, D.J. MOPB029
McCrady, R.C. TH1A05
McGinnis, D.P. TH2A01
McIntosh, P.A. MOPB004,MOPLB08,MOPB079
McIntyre, G.T. MOPB063,MOPB064
McKenzie, J.W. MOPB011,MOPLB08,MOPB079
Meng, C. TUPB075,THPB024
Meng, J. THPB027
Mercier, B. MOPB013
Mereu, P. THPB030
Merminga, L. MOPB024,WE1A04
Merz, W. TUPB019
Meusel, O. **MO3A03**,THPB008
Miahnahri, A. MOPB029
Michelato, P. MOPB017,TUPB020
Michizono, S. SUPB024,MOPLB02,MOPB002, TUPLB12,TUPB090,THPB085, TH1A01
Mickat, S. SUPB022,SUPB023,MO3A01, TUPB071,TUPB072,TUPB074
Middleman, K.J. MOPB011,MOPB004
Midttun, O. THPB011
Migne, J. MOPB074
Mikawa, K. MOPLB02,MOPB002
Mikulec, B. THPB010
Militsyn, B.L. **MOPB011**
Miller, D. R. MOPLB10,MOPB090,TUPB040
Miller, S.J. MOPLB10,MOPB090,TUPB040
Milloch, M.M. MOPB083
Milocco, A. MOPB083
Minamide, H. TUPLB10,TUPB080
Minato, M. TUPB081
Mistri, K.K. TUPB049
Mitchell, D.V. TH1A01
Mitra, A.K. **MOPB033**,WE1A04
Mittag, F. TUPB019
Miura, A. MOPB096,TUPB082,**TUPB101**, **TUPB102**
Miura, T. MOPLB02,MOPB002,TH1A01
Miyahara, F. MOPLB02,MOPB002
Miyao, T. MOPB096,TUPB101,TUPB102
Mizuno, A. THPB068,THPB092
Mo, Y. THPLB11,THPB061
Möller, W.-D. MOPB012,MOPB017,TH1A01
Molina Marinas, E. THPB089
Molloy, S. SUPB018,**TUPB048**,TUPB052, TH2A01
Monaco, L. TUPB020
Monard, H. MOPB013
Mondino, I. TUPB047
Mondrel, M. MOPB091
Monnereau, G. THPLB09,THPB083
Montesinos, E. TUPB047
Moody, N.A. **TU3A03**
Morgan, G. THPB097
Morgan, J.W. TUPLB07,TUPLB08,TUPB046, TUPB066,TUPB068
Mori, T. MOPLB02,MOPB002
Morishita, T. THPB021,THPB052,**TUPB042**

Morozov, V.S. MOPB014
Morris, D. MOPLB10,MOPB090,TU1A04
Morton, A.C. FR1A04
Mosnier, A. **TU1A01**
Moss, J. THPB044
Mostacci, A. MOPLB09,MOPB080
Moya, I. **THPB089**
Mühle, C. THPB034
Muller, N. MOPB091
Mundra, G. THPLB05,THPB003
Murphy, R.C. MOPB073,TUPLB07,TUPLB08, TUPB046,TUPB066
Mustapha, B. TUPLB08,TUPB046,TUPB067, THPB063,FR1A05
Mytrochenko, V.V. MOPB023

— N —

Nagaitsev, S. MOPB095,**TU1A02**,TUPB062
Naik, V. MOPB024,MOPB026
Naito, F. TUPB042,**TUPB099**,TUPB100, TUPB101,THPB020,THPB052
Nakai, H. TH1A01
Nakajima, H. MOPLB02
Nakajima, H. TH1A01
Nakanishi, K. TH1A01
Nakao, K. MOPLB02,MOPB002
Namkung, W. MOPB049
Nanmo, K. TUPB099,TUPB100,TUPB101
Nantista, C.D. TH1A01
Napoly, O. MOPB017,THPLB09,THPB083
Nassiri, A. SUPB025,MOPB055
Natsui, T. MOPLB02,MOPB002,THPB095
Naumenko, M.Y. TH2A03
Nause, A. TUPLB05,TUPB005,TH2A004, **SUPB011**
Neidherr, D. TUPB035
Neilson, J. **WE2A03**
Nellis, T. TUPB040
Neri, L. **THPB028**,THPB076
Neumann, A. MOPB066,**MOPB067**,**THPLB12**, **THPB066**,**THPB069**
Nezhevenko, O.A. MOPB054
Ng, K.Y. TUPB021
Ni, D.S. THPB079
Nicklaus, D.J. MOPB054
Nikolskiy, K.I. TUPB091
Nisbet, D. THPB010
Niu, X.F. TUPB044
Nölle, D. MOPB017
Noguchi, S. TH1A01
Nolen, J.A. TU1A04
Noor, M. TUPB108
Norton, D. TUPB040
Nosochkov, Y. MOPLB01,MOPB001,TH3A04
Novo, J. THPB038

— O —

Ogawa, K. TUPLB10,TUPB080
Ogawa, Y. MOPLB02,MOPB002
Oh, J.-S. MOPB049
Ohsawa, S. MOPLB02,MOPB002
Ohshima, T. TUPB006
Ohuchi, N. TH1A01
Okamura, M. **THPB037**,THPB051
Okayasu, Y. TUPLB10,TUPB080
Okuno, H. MO3A02,TUPB095
Olave, R.G. **MOPB072**
Onken, R. TUPB019
Orlov, Y. TUPB053
Orsini, F. MOPB074
Orzhekhovskaya, A. TUPB035
Ostiguy, J.-F. MOPB095,THPB014,THPB017, **THPB055**
Ostroumov, P.N. MOPB073,TUPLB07,**TUPLB08**, **TUPB046**,**TUPB066**,**TUPB067**, TUPB068,THPB063,**FR1A05**
Otake, Y. MOPB005,MOPB084,**TU2A02**, TUPB006
Otani, K. MOPLB07,MOPB053
Ouchi, N. THPB020,THPB021
Ouyang, H.F. THPLB01,THPB023,THPB025
Owada, S. TUPLB10,TUPB080
Oweiss, R. MOPLB10,**MOPB070**,MOPB071, MOPB090,TUPB040
Ozelis, J.P. MOPLB10,MOPB071,MOPB090, TU1A04,TUPB040

— P —

Pagani, C. TUPB020,TH1A01
Palczewski, A.D. MOPB062
Palmieri, A. TUPB094,THPLB08,THPB040, THPB043
Palumbo, L. MOPLB09,MOPB080
Paly, L. TUPB009
Pan, W.M. TU1A03
Pande, S.A. THPB073
Pandey, A. TUPB033
Panero, R. TUPB094
Paoluzzi, M.M. THPB010
Paparella, R. TUPB020,TH1A01
Papke, K. MOPB067
Paramonov, V.V. **MOPB081**,**MOPB082**,**TUPLB02**, **TUPB001**,**TUPB002**
Park, B.-S. TU1A05
Park, G.-T. TUPB030
Park, H. MOPB030
Paskvan, D.R. TUPLB08,TUPB046
Pasquinelli, R.J. MOPB095
Pate, D. MOPB064
Patra, P. TUPB033
Pavlov, V.M. SUPB009,MOPB048
Peauger, F. MOPB074

Peggs, S. **TUPB077**,**TUPB077**
Pei, G. **MOPLB04**,**MOPB046**,MOPB023
Pei, S. **MOPB022**,**MOPB023**,**THPB025**
Pekeler, M. SUPB022,TUPB071
Peng, J. TUPB103
Peng, N. TUPB044
Peng, S. TU1A04
Peng, S.X. **TUPB034**
Pepato, A. SUPB015,THPB042
Perrin, J.L. THPLB09,THPB083
Perry, A. MO1A01
Petenev, Y. SUPB003,**SUPB004**,MOPB036, **MOPB037**
Petersen, B. MOPB017
Peterson, D.W. MOPB095
Peterson, T.J. TH1A01
Pfeiffer, S. THPB086
Pfingstner, J. **SUPB007**,**MOPB042**
Pfister, J. THPB034
Phillips, D. MOPB064
Phillips, H.L. MOPB060
Pierini, P. TUPB020,TH1A01
Pietralla, N. SUPB010,TUPB026
Pikin, A.I. TUPB105
Pilat, F.C. **TH3A02**
Pinhasi, Y. TUPB014
Piotrowski, A. TUPB019
Piquet, O. THPB031,THPB038
Pischalnikov, Y.M. MOPB054,MOPB077,TH1A01
Pisent, A. THPB030,THPB043
Planche, T. WE1A04
Plastun, A.S. SUPB016,TUPB031,THPB050
Plawski, E.P. MOPB017
Plostinar, D.C. **THPB004**,**THPB032**
Plum, M.A. MO2A02
Podlech, H. SUPB012,SUPB022,SUPB023, MO3A01,MO3A03,TUPB071, TUPB072,THPLB03,THPB005, THPB007,THPB009,THPB047, THPB034
Polini, M. TH2A03
Poloubotko, V. TUPB053
Polozov, S.M. **SUPB035**,TUPB070,**THPB074**
Ponton, A. THPB028,**THPB029**
Popielarski, J. **MOPLB10**,MOPB070,MOPB071, **MOPB090**,**TUPB060**,**TU1A04**, TUPB040
Popielarski, L. MOPLB10,MOPB070,**MOPB071**, MOPB090,TU1A04,TUPB040
Popovic, M. **THPB016**,**THPB017**
Posocco, P.A. THPB011
Pottin, B. **THPB031**
Power, J.G. MOPLB05,MOPLB11,MOPB047, MOPB093
Powers, T. MOPB031
Pozdeyev, E. **THPB097**,TU1A04
Pozimski, J.K. THPB004
Prakash, P.N. **TUPB049**
Preble, J.P. MOPB030
Prenting, J. MOPB017
Prevost, C. MOPB013
Pribaz, F. MOPB083
Prieto, P.S. MOPB054
Prior, C.R. THPB032
Pronitchev, O. TUPB053
Prost, L.R. MOPB095
Przygoda, K.P. TUPB019
Ptitsyn, V. MOPB063
Puccio, B. THPB010
Pugnat, D. THPB038
Puntambekar, A. THPLB05,THPB003

— R —

Raguin, J.-Y. **TUPLB01**,TUPB009,**TUPB010**, **TUPB011**,**TUPB012**
Rai, A. TUPB033
Raich, U. TUPB041,THPB010
Ramberger, S. TH2A03,THPB010
Rao, T. MOPB064
Rao, X. THPB097
Rao, Y.-N. WE1A04
Raparia, D. TUPB105,**THPB051**
Rathke, J. MOPB064
Ratzinger, U. SUPB012,SUPB022,SUPB023, MO3A01,MO3A03,TUPB071, TUPB072,THPLB03,THPB005, THPB006,**THPB007**,THPB008, THPB009,THPB034
Raubenheimer, T.O. MOPB029,**TU2A03**
Rawnsley, W.R. MOPB033,MOPB026,MOPB091, TUPB081
Reece, C.E. SUPB001,MOPB018,MOPB030, MOPB060,**MOPB061**,**MOPB062**
Rees, G.H. THPB032
Reid, J. MOPB054
Reid, T. MOPB073,TUPLB07,TUPB066, TUPLB08,TUPB046
Reilly, A.V. MOPB030,MOPB061
Reinfeld, E. MO1A01
Ren, H.T. TUPB034
Repnow, R. TUPB035
Reschke, D. MOPB012,MOPB017
Riemann, B. **MOPB066**,MOPB067
Riffaud, B. TH2A03
Rimmer, R.A. MOPB030
Ritter, J. THPB051
Roblin, Y. MOPB014
Rodnizki, J. MO1A01,FR1A05
Rodriguez, J.A. THPB065
Roncarolo, F. **TUPB041**,THPB010
Roncolato, C. SUPB015,TUPB032,THPB042
Roper, M.D. MOPB011

Roseberry, R.T. THPB044
Ross, M.C. TH1A01,TH3A01,THPB091
Rossi, C. **THPB038**,TH2A03,THPB010
Roudier, D. THPLB09,THPB083
Roux, R. **MOPB013**
Roy, A. TUPB049,**TH1A04**,TUPB033
Roy, S.B. THPLB05,THPB003
Ruber, R.J.M.Y. TUPB108,TUPB107
Ruiz-Osés, M. MOPB064
Russo, T. TU1A04
Rydberg, A. TUPB108
Ryu, J.Y. TU1A05,THPB022

— S —

Sacépé, N. THPLB09,THPB083
Sacharias, J. TUPB049
Saeki, T. MOPB069,TH1A01
Saewert, G.W. MOPB095
Sahu, B.K. **TUPB033**
Saini, A. TUPB054,THPB014,THPB055
Saito, K. MOPLB10,MOPB070,MOPB071, TUPB060,MOPB090,TU1A04, TUPB040
Sakabe, S. MOPLB07,MOPB053
Sakamoto, N. **MO3A02**,TUPB073,TUPB095
Sakaue, K. MOPB025
Sako, H. MOPB096,**TUPB082**
Sakurai, T. MOPB005,**MOPB084**
Saminathan, S. MOPB026
Samoshin, A.V. **TUPB069**,**TUPB070**
Sanchez, L. THPB089
Santiago Kern, R. TUPB108
Sanz, S. THPB089
Sarid, E. **FR2A02**
Sato, T. TUPLB10,TUPB080
Satoh, D. MOPLB02,MOPB002
Satoh, M. MOPLB02
Sauce, Y. THPLB09,THPB083
Savage, P. THPB004
Savard, G. **FR1A03**
Saveliev, Y.M. MOPB004
Savilov, A.V. THPB096
Sawabe, M. MOPB069
Sawabe, Y. THPB021
Scantamburlo, F. **SUPB015**,**THPB042**
Scarpa, F. TUPB094
Scarpine, V.E. MOPB095
Schappert, W. MOPB054,MOPB077,TH1A01
Schempp, A. SUPB014,SUPB017,THPLB03, THPB005,THPB007,THPB008, THPB046,THPB047,THPB049, THPB034
Scherer, A. TUPLB01,TUPB010
Schietinger, T. **TUPB013**
Schilling, P. TH1A01
Schlarb, H. MOPB017,**TU3A01**,THPB085, THPB086
Schlitt, B. MO3A01
Schmickler, H. THPB091
Schmidt, Ch. **THPB086**,THPB085
Schmidt, J.S. SUPB014,**SUPB017**,THPB046, **THPB049**
Schmidt, R. THPB091
Schmökel, M. MOPB017,TH1A01
Schoessow, P. MOPLB05,MOPB047
Schrage, D.L. TUPLB08,TUPB046
Schreiber, G. THPLB07,THPB035,THPB034
Schubert, J.P. THPB044
Schulte, D. SUPB007,SUPB008,MOPB042, MOPB045,THPB091
Schultheiss, T. MOPB064
Schwarz, M. THPB008
Schwerg, N. THPB010
Scrivens, R. THPB011,THPB010
Seberg, S.K. MOPB064
Seda, T. MOPB064
Seeman, J.T. TH3A04
Seki, Y. MO3A04
Sekine, M. THPB037
Sekutowicz, J.K. MOPB017,**TUPB019**
Seol, K.T. TU1A05,THPB022
Serpico, C. MOPB083
Sertore, D. TUPB020
Setty, A.S. **THPB064**
Seviour, R. **TU3A02**,TUPB077
Sha, P. TU1A03
Shanks, R.W. MOPB033
Sharamentov, S.I. TUPLB08,TUPB046
Shebolaev, I.V. SUPB009,MOPB048
Sheehy, B. MOPB064
Shemyakin, A.V. **MOPB095**
Shen, Y. THPLB04,THPB002
Shepard, K.W. TUPB068,TUPLB08,TUPB046, TUPB067
Shepherd, B.J.A. MOPB011
Sheppard, J. MOPLB01,MOPB001,TH3A04
Shi, A. TUPB036,THPB027,THPB039
Shi, J. THPLB04,THPB002
Shi, S. MOPLB04,MOPB046
Shidara, T. MOPLB02,MOPB002,TH1A01
Shimel, G. MO1A01
Shimizu, H.M. MO3A04
Shirakawa, A. MOPLB02,MOPB002
Shishido, T. TH1A01
Shishlo, A.P. MO2A02
Shoji, Y. **MOPB038**
Shor, A. MO1A01,**THPB094**
Shrivastava, P. THPLB05,THPB003
Shteynas, B.G. MOPB095
Shuptar, M. TUPB040
Silverman, I. MO1A01
Simon, C.S. THPLB09,THPB034,THPB083

Singer, W. MOPB012,MOPB017
Sitnikov, A. WE1A04
Skaritka, J. MOPB064
Skowroński, P. MOPB003
Smirnov, A.Yu. **TUPB023**,**TUPB091**
Smirnov, V.L. THPB097
Smith, B.E. TH1A01
Smith, H. MOPLB01,MOPB001
Smith, K.S. MOPB064
Smith, R.J. MOPB004,MOPB011
Sobenin, N.P. TUPB023
Socol, Y. **MOPB051**
Sodomaco, N. MOPB083
Solyak, N. **MOPB077**,TUPB054,TUPB062,
THPB014,**THPB055**,**MOPB095**
Song, H. MOPB023
Song, J. TUPB030
Song, Y.-G. TU1A05,THPB022
Sonti, S.S. TUPB049
Soskov, V. MOPB013
Spataro, B. MOPLB09,MOPB080
Srivastava, S. MOPB032
Stanford, G. MOPB091
Staples, J.W. THPB039
Storey, D.W. MOPB026,TUPB081
Stovall, J. THPB097
Su, H.L. TUPB044
Suda, K. MO3A02,TUPB073,**TUPB095**
Sugimoto, H. MOPLB02,MOPB002
Sugimura, T. TUPB042,THPB052
Sukhanov, A.I. **TUPB054**
Sulimov, A.A. **MOPB012**
Suman, S.K. TUPB033
Sun, B. TUPB075
Sun, D. MOPB095
Sun, L.P. **TUPB036**,THPB039
Sun, L.T. THPB097
Sun, Y. MOPLB01,MOPB001
Sun, Y.-E. **TU3A04**
Suwada, T. MOPLB02,MOPB002
Suzuki, S. TUPLB09,TUPB079,**THPB092**
Świerbleski, J. MOPB017
Syratchev, I. **WE2A01**
Szewiński, J. TUPB019

— T —

Takahashi, E. TUPLB10,TUPB080
Takahashi, S. TUPB006
Takata, K. THPB020
Takatomi, T. MOPLB02,MOPB002
Takeda, K. MOPB038
Takenaka, T. MOPLB02,MOPB002,TH1A01
Tamura, J. MOPB096,THPB020,**THPB021**
Tan, C.C. THPLB02,THPB015
Tanaka, H. TUPB099
Tang, C.-X. MOPLB12,MOPB089
Tang, E. MOPLB04,MOPB046
Tang, J.Y. TUPB075,THPB024
Tang, T. MOPB095
Taniuchi, T. THPB068,THPB092
Tanke, E. **THPB065**
Tecker, F. MOPB032
Terashima, A. TH1A01
Than, R. MOPB063,MOPB064
Therasse, M. TUPB047
Tian, H. MOPB062
Tiede, R. THPLB03,THPB005,THPB034
Tikhomirova, N.V. TUPB091
Timmins, M.A. THPB038
Todd, A.M.M. MOPB064
Togashi, T. TUPLB10,TUPB080
Togawa, K. TUPB006
Toge, N. TH1A01
Tokita, S. MOPLB07,MOPB053
Tomizawa, H. **THPB068**,THPB092,**TUPLB10**,
TUPB080
Tong, D.C. SUPB031,MOPB086
Tongu, H. SUPB024,MOPLB07,MOPB053,
TUPLB12,TUPB090
Toral, F. MOPB017,THPB089
Tribendis, A.G. TH2A03
Trüller, J. THPB034
Tsuchiya, K. TH1A01
Tudosa, I. TH3A04
Tuozzolo, J.E. MOPB063,MOPB064
Tuske, O. FR1A02,THPB034
Tyagi, P.V. **MOPB069**

— U —

Uesaka, M. THPB095
Ugena Tirado, P. TH2A03
Umer, R. MOPB083
Urakawa, J. MOPB025
Uriot, D. FR1A02
Usher, N.R. MOPLB10,MOPB090

— V —

Vacher, T.V. THPLB09,THPB083
Vafaei, N. TH3A04
Valero, S. THPB065
Valizadeh, R. MOPB011
Valuch, D. TUPB047
van Rienen, U. MOPB067
Vandoni, G. THPB010,THPB038
Varghese, P. MOPB054,**THPLB02**,**THPB015**
Variola, A. MOPB013
Vázquez, C. THPB089
Velianoff, G.J. TUPB040
Veljak, L. MOPB083
Venturini Delsolaro, W. **TUPB047**
Verzilov, V.A. MOPB026,**TUPB081**,WE1A04
Vinzenz, W. MO3A01,THPLB07,THPB035,

	THPB034
Virostek, S.P.	THPB039
Visentin, B.	MOPB017,THPLB09,THPB083
Vlieks, A.E.	MOPB029
Völker, J.	THPB069
Vogel, E.	**MOPB017,TUPB020**
Vogel, V.	**TUPLB04,TUPB004**
Vogt, J.M.	**SUPB029,MOPB065**
Volk, K.	MO3A03,THPB007
Vollaire, J.	THPB010
Vormann, H.	THPLB07,THPB035,TUPB035
Vorobjev, G.	TUPB035
Vorozhtsov, S.B.	THPB097
Vossberg, M.	THPLB03,THPB005,**THPB047**
Vostrikov, A.	TUPB054
Vretenar, M.	**THPB010**,TH2A03,THPB038
Vuitton, VC.	TUPB041

— W —

Waldschmidt, G.J.	SUPB025,MOPB055
Walker, N.J.	TH3A01,TH1A01,THPB085
Walla, M.	THPB085
Walz, D.R.	MOPB029
Wang, B.L.	MOPB022
Wang, C.P.	**SUPB032,TUPB097**
Wang, D.	THPB065
Wang, E.	MOPB064
Wang, F.F.	SUPB027,MOPB057
Wang, H.	MOPB030
Wang, J.	THPB039
Wang, L.	MOPB023
Wang, M.-H.	MOPLB01,MOPB001
Wang, R.X.	SUPB019,SUPB020,SUPB027, SUPB028,MOPB057,MOPB059, TUPB055,TUPB056,TUPB057
Wang, S.H.	MOPB023
Wang, W.D.	THPLB04,THPB002
Wang, X.	MOPLB04
Wang, X.	MOPB023
Wang, X.	MOPB046
Wang, Z.	TUPB034
Wang, Z.J.	**SUPB013**,SUPB028,MOPB059, **TUPB039,THPB026,THPB027**, THPB079
Watanabe, K.	MOPLB07,MOPB053,MOPB025, TH1A01
Watanabe, T.	MO3A02
Watanabe, Y.	TUPB095
Weathersby, S.P.	MOPB029
Webber, R.C.	TU1A04
Wedberg, R.	TUPB108
Wegner, R.	TH2A03,THPB010
Wei, G.H.	MOPB096
Wei, J.	**TU1A04**,TUPB058,TUPB060, TUPB061,TUPB040
Weis, T.	MOPB066,MOPB067
Weise, H.	MOPB017,TH1A01
Weisend, J.	MOPLB10,MOPB090
Weissman, L.	MO1A01,THPB094
Weisz, S.	THPB010
Wendt, M.	MOPB095
Wheelhouse, A.E.	MOPLB08,MOPB011,MOPB079
White, C.J.	MOPB004
White, G.R.	MOPLB01,MOPB001,TH3A04
Wienands, U.	MOPLB01,MOPB001,TH3A04
Wiesner, C.	MO3A03
Will, C.	THPB034
Williams, M.	TU1A04,TUPB040
Wiseman, M.	MOPB031,MOPB030
Wisniewski, E.E.	MOPLB11,MOPB093
Witgen, K.	TUPB040
Wittmer, W.	THPB065
Woodley, M.	MOPLB01,MOPB001,TH3A04
Woolley, B.J.	MOPLB08,MOPB079
Wu, B.M.	THPB079
Wu, G.	SUPB025,MOPB055
Wu, J.X.	THPB027
Wu, Q.	MOPB064
Wu, W.	SUPB013,TUPB039,THPB026, THPB027,**THPB079**
Wu, X.	THPB065
Wu, Z.	TH3A04

— X —

Xia, J.W.	SUPB028,MOPB059,TUPB043
Xia, L.S.	THPLB04,THPB002
Xiao, B. P.	**MOPB060,MOPB060**
Xiao, C.	**MOPB098**
Xiao, S.	SUPB037,THPB081
Xiao, Y.C.	TUPB103
Xin, T.	MOPB064
Xing, Q.Z.	TU1A03
Xiong, L.-Y.	TUPB044
Xiong, P.R.	TUPB055
Xu, C.	**SUPB001,MOPB018**
Xu, H.S.	THPB027
Xu, M.H.	SUPB020
Xu, M.X.	SUPB019,SUPB027,**SUPB028**, MOPB057,**MOPB059**,TUPB055, TUPB056,TUPB057
Xu, T.G.	SUPB037,THPB081
Xu, W.	MOPB063,MOPB064
Xu, X.B.	SUPB013,TUPB039,THPB026
Xu, Y.	TUPB060,TUPB040
Xu, Y.	TUPB034
Xu, Z.	THPB027

— Y —

Yabashi, M.	TUPLB10,TUPB080
Yakimenko, V.	MOPLB03,MOPB041
Yakovlev, V.P.	**MO1A03**,TUPB053,TUPB054, MOPB095,TUPB067

Yamada, K. MO3A02,TUPB073,TUPB095
Yamaguchi, S. TH1A01
Yamamoto, A. **TH3A01**,TH1A01
Yamamoto, T. THPB037
Yamamoto, Y. MOPLB07,MOPB053,TH1A01
Yamazaki, Y. TU1A04,TUPB040
Yampolsky, N.A. TH1A05
Yan, F. TUPB075,**THPB024**,MOPB024
Yan, L.X. MOPLB12,MOPB089
Yanagida, K. **TUPLB09**,**TUPB079**,THPB092
Yang, H. **MOPB049**
Yang, Q. MOPB023
Yang, W.J. THPB079
Yang, X. MOPLB04,MOPB046
Yang, X.L. THPB079
Yang, X.W. MOPB046
Yang, Y.Z. SUPB019,SUPB020,SUPB027, SUPB028,MOPB057,MOPB059, TUPB056,TUPB057
Yano, Y. MOPLB02,MOPB002
Yaramyshev, S.G. **TUPB035**
Yin, X. TUPB103,THPLB01,THPB023
Yocky, G. MOPLB01,MOPB001,TH3A04
Yogi, R.A. TUPB107,**TUPB108**
Yokoya, K. TH1A01
Yokoyama, K. MOPLB02,MOPB002
Yoshida, M. MOPLB02,MOPB002,THPB095
Yoshioka, T. MO3A04
Yosifov, D. WE1A04
Young, L.M. THPB097
Yu, C.H. MOPLB04,MOPB046
Yuan, Q. MOPLB04,MOPB046
Yuan, Y.J. TUPB043
Yue, J. MOPB023
Yue, W.M. SUPB019,SUPB020,SUPB027, MOPB057,SUPB028,MOPB059, **TUPB055**,**TUPB056**,**TUPB057**
Yun, S.P. TU1A05
Yusof, Z.M. MOPLB11,MOPB093

— Z —

Zaltsman, A. MOPB063,MOPB064
Zang, L. MOPLB02,MOPB002
Zaplatin, E.N. THPLB12,THPB066
Zelenski, A. THPB051
Zelinsky, A.Y. MOPB023
Zeller, A. TU1A04
Zemach, E. MO1A01
Zembala, Ł. TUPB019
Zeng, L. SUPB037,THPB081
Zennaro, R. **TUPB009**
Zha, H. MOPLB12,MOPB089
Zhang, B. SUPB013,**MOPB088**,TUPB039, TUPB055,THPB026,THPB027, THPB039
Zhang, C. SUPB012,**THPLB03**,**THPB005**, THPB009,THPB047,THPB039
Zhang, C. **SUPB019**,**SUPB020**,SUPB027, MOPB057,SUPB028,MOPB059, TUPB036,TUPB055,**TUPB056**, **TUPB057**
Zhang, H. THPLB04,THPB002
Zhang, J.H. TUPB044,THPB027
Zhang, J.R. MOPB022,MOPB023,THPB025
Zhang, L.W. THPLB04,THPB002
Zhang, M. SUPB006,MOPB007,TUPB018, TUPB022
Zhang, S.C. MOPB035
Zhang, S.H. SUPB019,SUPB020,SUPB027, MOPB057,SUPB028,MOPB059, TUPB055,TUPB056,TUPB057, THPB027
Zhang, S.X. SUPB019,SUPB020,SUPB027, SUPB028,MOPB057,MOPB059, TUPB055,TUPB056,TUPB057
Zhang, X. MOPLB04,MOPB046
Zhang, X.H. **TUPB043**
Zhang, Y. MOPLB10,TUPB058,TUPB060, TUPB061,MOPB090,TU1A04, TUPB040
Zhang, Z. MOPLB12,MOPB089
Zhang, Z.L. TUPB036,**THPB039**
Zhang, Z.M. THPB027
Zhao, F. MOPLB04,MOPB023,MOPB046
Zhao, H.W. SUPB013,SUPB019,SUPB020, SUPB027,SUPB028,MOPB057, MOPB059,TUPB039,THPB026, TUPB055,TUPB056,TUPB057, THPB027,THPB039
Zhao, J. MOPLB04,MOPB046
Zhao, J. TUPB034
Zhao, J.B. MOPB023
Zhao, J.X. MOPB023
Zhao, M.H. SUPB006,TUPB018,TUPB022
Zhao, Q. TU1A04,THPB097
Zhao, S. MOPLB10,TUPB061,MOPB090
Zhao, Z.T. SUPB031,SUPB032,MOPB086, TUPB097
Zheng, Q. MOPB026
Zheng, S.J. THPB079
Zheng, Z. MOPLB10,**TUPB060**,**TUPB061**, MOPB090,TUPB058,**TUPB060**, **TUPB061**
Zholents, A. **TUPB008**
Zhou, Weishi„Zhou. MOPB020,MOPB021
Zhou, X. MOPLB02,MOPB002
Zhou, Z.S. MOPLB04,MOPB023,MOPB046
Zhou, Z.Z. THPB027
Zhu, J. **THPLB04**,**THPB002**
Zhu, L. THPB079
Zhu, Z. MOPLB04,MOPB046
Zhukov, A.P. **THPB012**,THPB013

Zickler, Th.	THPB010	Zocca, F.	TUPB041
Ziemann, V.G.	TUPB107,TUPB108	Zvyagintsev, V.	MOPB026,MOPB091,WE1A04
Zimmermann, F.	**TH3A03**		
Zinkann, G.P.	TUPLB08,TUPB046		

Institutes List

AES
Medford, NY, USA
- Cole, M.D.
- Favale, A.J.
- Holmes, D.
- Rathke, J.
- Schultheiss, T.
- Todd, A.M.M.

ANL
Argonne, USA
- Barcikowski, A.
- Carwardine, J.
- Cherry, G.L.
- Conde, M.E.
- Conway, Z.A.
- Dickerson, C.
- Doran, D.S.
- Fischer, R.L.
- Gai, W.
- Gerbick, S.M.
- Gohar, Y.
- Holzbauer, J.P.
- Kedzie, M.
- Kelly, M.P.
- Kim, S.H.
- Kolomiets, A.
- Kondrashev, S.A.
- Konecny, R.
- Kutsaev, S.V.
- Liu, W.
- Morgan, J.W.
- Murphy, R.C.
- Mustapha, B.
- Nassiri, A.
- Nolen, J.A.
- Ostroumov, P.N.
- Paskvan, D.R.
- Power, J.G.
- Reid, T.
- Savard, G.
- Schrage, D.L.
- Sharamentov, S.I.
- Shepard, K.W.
- Waldschmidt, G.J.
- Wu, G.
- Yusof, Z.M.
- Zholents, A.
- Zinkann, G.P.

Ariel University Center of Samaria, Faculty of Engineering
Ariel, Israel
- Lurie, Yu.
- Pinhasi, Y.

BARC
Mumbai, India
- Bathe, B.N.
- Srivastava, S.

BEVATECH OHG
Offenbach/Main, Germany
- Hoeltermann, H.

Bilkent University
Bilkent, Ankara, Turkey
- Ilday, F.Ö.

BINP SB RAS
Novosibirsk, Russia
- Barnyakov, A.M.
- Kendjebulatov, E.
- Kruchkov, Ya.G.
- Levichev, A.E.
- Pavlov, V.M.
- Tribendis, A.G.

BNL
Upton, Long Island, New York, USA
- Alessi, J.G.
- Altinbas, Z.
- Beebe, E.N.
- Belomestnykh, S.A.
- Ben-Zvi, I.
- Briscoe, B.
- Brutus, J.C.
- Fite, J.M.
- Gassner, D.M.
- Gould, O.
- Hahn, H.
- Hammons, L.R.
- Jamilkowski, J.P.
- Kayran, D.
- Kewisch, J.
- Litvinenko, V.
- LoDestro, V.
- Mahler, G.J.
- McIntyre, G.T.
- Okamura, M.
- Pate, D.
- Peggs, S.
- Phillips, D.
- Pikin, A.I.
- Ptitsyn, V.
- Rao, T.
- Raparia, D.
- Ritter, J.
- Seberg, S.K.
- Seda, T.
- Sheehy, B.
- Skaritka, J.
- Smith, K.S.
- Than, R.
- Tuozzolo, J.E.

- Wang, E.
- Wu, Q.
- Xu, W.
- Yakimenko, V.
- Zaltsman, A.
- Zelenski, A.

CAEP/IFP
Mainyang, Sichuan, People's Republic of China
- Chen, S.
- Deng, J.
- Shen, Y.
- Shi, J.
- Wang, W.D.
- Xia, L.S.
- Zhang, H.
- Zhang, L.W.
- Zhu, J.

CEA/DSM/IRFU
France
- Bazin, N.
- Berry, S.
- Bosland, P.
- Charrier, J.-P.
- Chauvin, N.
- Chel, S.
- Daël, A.
- Delferrière, O.
- Desmons, M.
- Devanz, G.
- Fontaine, M.
- France, A.
- Gasser, Y.
- Gobin, R.
- Grouas, N.
- Hardy, P.
- Le Noa, Y.
- Migne, J.
- Napoly, O.
- Novo, J.
- Orsini, F.
- Peauger, F.
- Piquet, O.
- Pottin, B.
- Sauce, Y.
- Simon, C.S.
- Tuske, O.
- Uriot, D.
- Vacher, T.V.
- Visentin, B.

CEA/IRFU
Gif-sur-Yvette, France
- Brasseur, A.
- Charon, P.
- Chauvin, N.
- Cloué, C.
- Delferrière, O.
- Gobin, R.
- Langlois, S.
- Madec, C.
- Monnereau, G.
- Perrin, J.L.
- Roudier, D.
- Sacépé, N.
- Tuske, O.

CEA
Gif-sur-Yvette, France
- Madec, C.
- Valero, S.

CELLS-ALBA Synchrotron
Cerdanyola del Vallès, Spain
- Campmany, J.
- Marcos, J.
- Massana, V.

CERN
Geneva, Switzerland
- Alberty Vieira, L.
- Andersson, A.
- Arnaudon, L.
- Baudrenghien, P.
- Bellodi, G.
- Bertone, C.
- Body, Y.
- Broere, J.C.
- Brunner, O.
- Buzio, M.C.L.
- Calaga, R.
- Calatroni, S.
- Capatina, O.
- Carli, C.
- Chevallay, E.
- Collaboration, A.C.
- Constance, B.
- Corsini, R.
- Corso, J.-P.
- Coupard, J.
- Cuvet, Y.
- D'Elia, A.
- Dallocchio, A.
- Delaup, B.
- Dimov, V.A.
- Dos Santos, N.
- Duraffourg, M.
- Favre, G.
- Focker, G.J.
- Fraser, M.A.
- Fuchs, J.-F.
- Funken, A.
- Gamba, D.
- Garoby, R.
- Geisser, J.-M.
- Gentini, L.
- Gerbershagen, A.

- Gerigk, F.
- Giguet, J.-M.
- Grudiev, A.
- Hammouti, L.
- Hanke, K.
- Hansen, J.
- Hein, L.M.
- Heßler, C.
- Jecklin, N.M.
- Jonker, M.
- Kadi, Y.
- Khan, V.F.
- Kozsar, I.
- Lallement, J.-B.
- Lettry, J.
- Lombardi, A.M.
- Lopez Hernandez, L.A.
- Maesen, P.
- Maglioni, C.
- Mathot, S.J.
- Midttun, O.
- Mikulec, B.
- Mondino, I.
- Montesinos, E.
- Nisbet, D.
- Paoluzzi, M.M.
- Pfingstner, J.
- Polini, M.
- Puccio, B.
- Pugnat, D.
- Raich, U.
- Ramberger, S.
- Riffaud, B.
- Roncarolo, F.
- Rossi, C.
- Ruber, R.J.M.Y.
- Schmickler, H.
- Schmidt, R.
- Schulte, D.
- Schwerg, N.
- Scrivens, R.
- Skowroński, P.
- Stovall, J.
- Syratchev, I.
- Tecker, F.
- Therasse, M.
- Timmins, M.A.
- Ugena Tirado, P.
- Valuch, D.
- Vandoni, G.
- Venturini Delsolaro, W.
- Vollaire, J.
- Vretenar, M.
- Vuitton, VC.
- Wegner, R.
- Weisz, S.
- Zickler, Th.
- Zimmermann, F.
- Zocca, F.

CIEMAT

Madrid, Spain

- Calero, J.
- Cela-Ruiz, J.M.
- de la Gama, J.G.S.
- García-Tabarés, L.
- Guirao, A.
- Gutiérrez, J.L.
- Martinez, L.M.
- Martínez de Alvaro, T.
- Molina Marinas, E.
- Moya, I.
- Sanchez, L.
- Sanz, S.
- Toral, F.
- Vázquez, C.

Cockcroft Institute, Lancaster University

Lancaster, United Kingdom

- Abram, T.N.
- Ambattu, P.K.
- Burt, G.
- Dexter, A.C.
- Lingwood, C.
- Woolley, B.J.

Cornell University

Ithaca, New York, USA

- Eichhorn, R.
- Jandovitz, P.J.

DELTA

Dortmund, Germany

- Riemann, B.
- Weis, T.

DESY

Hamburg, Germany

- Ayvazyan, V.
- Barbanotti, S.
- Borowiec, P.B.
- Branlard, J.
- Brueck, H.
- Butkowski, L.
- Cherepenko, A.
- Choroba, S.
- Decking, W.
- Ebert, M.
- Eschke, J.
- Flöttmann, K.
- Gössel, A.
- Gubarev, V.
- Hagge, L.
- Harders, I.
- Hartung, J.
- Hensler, O.
- Hüning, M.
- Iversen, J.
- Jensch, K.
- Katalev, V.V.
- Kostin, D.

- Kreps, G.
- Krzysik, K.
- Käfer, D.
- Lilje, L.
- Matheisen, A.
- Merz, W.
- Mittag, F.
- Möller, W.-D.
- Nölle, D.
- Onken, R.
- Petersen, B.
- Pfeiffer, S.
- Prenting, J.
- Reschke, D.
- Schilling, P.
- Schlarb, H.
- Schmidt, Ch.
- Schmökel, M.
- Sekutowicz, J.K.
- Singer, W.
- Sulimov, A.A.
- Vogel, E.
- Vogel, V.
- Walker, N.J.
- Walla, M.
- Weise, H.

Diamond
Oxfordshire, United Kingdom
- Christou, C.
- Pande, S.A.

ELETTRA
Basovizza, Italy
- D'Auria, G.
- Delgiusto, P.
- Fabris, A.
- Gelmetti, F.
- Milloch, M.M.
- Milocco, A.
- Pribaz, F.
- Serpico, C.
- Sodomaco, N.
- Umer, R.
- Veljak, L.

ESS
Lund, Sweden
- Cheymol, B.
- Danared, H.
- Darve, C.
- Eshraqi, M.
- Laface, E.
- Lindroos, M.
- McGinnis, D.P.
- Molloy, S.
- Peggs, S.
- Ponton, A.

Euclid TechLabs, LLC
Solon, Ohio, USA
- Antipov, S.P.
- Butler, J.E.
- Jing, C.-J.
- Kanareykin, A.
- Schoessow, P.

Falcon Analytics
Netanya, Israel
- Socol, Y.

Fermilab
Batavia, USA
- Arkan, T.T.
- Baffes, C.M.
- Barbanotti, S.
- Barnes, B.W.
- Battistoni, M.A.
- Cancelo, G.I.
- Carlson, K.
- Carneiro, J.-P.
- Carter, H.
- Champion, M.S.
- Chase, B.
- Cheban, S.
- Chen, A.Z.
- Crawford, D.J.
- Cullerton, E.
- Edstrom, Jr, D.R.
- Eidelman, Y.I.
- Ginsburg, C.M.
- Gonin, I.V.
- Hanna, B.M.
- Harms, E.R.
- Henderson, S.
- Hocker, A.
- Kazakov, S.
- Kephart, R.D.
- Kerby, J.S.
- Khabiboulline, T.N.
- Kramp, M.
- Kucera, M.J.
- Lebedev, V.A.
- Leibfritz, J.R.
- Lunin, A.
- Mitchell, D.V.
- Nagaitsev, S.
- Nezhevenko, O.A.
- Ng, K.Y.
- Nicklaus, D.J.
- Orlov, Y.
- Ostiguy, J.-F.
- Pasquinelli, R.J.
- Peterson, D.W.
- Peterson, T.J.
- Pischalnikov, Y.M.
- Poloubotko, V.
- Popovic, M.
- Prieto, P.S.
- Pronitchev, O.

- Prost, L.R.
- Reid, J.
- Ross, M.C.
- Saewert, G.W.
- Saini, A.
- Scarpine, V.E.
- Schappert, W.
- Shemyakin, A.V.
- Shteynas, B.G.
- Smith, B.E.
- Solyak, N.
- Sukhanov, A.I.
- Sun, D.
- Sun, Y.-E.
- Tan, C.C.
- Varghese, P.
- Vostrikov, A.
- Wendt, M.
- Yakovlev, V.P.

FRIB
East Lansing, USA

- Bernard, E.C.
- Binkowski, J.
- Bird, B.
- Bricker, S.
- Bultman, N.K.
- Casagrande, F.
- Chouhan, S.
- Compton, C.
- Crisp, J.L.
- Davidson, K.D.
- Dubbs, L.J.
- Elliott, K.
- Enkhbat, B.
- Facco, A.
- Fila, A.
- Fox, A.D.
- Gibson, P.E.
- Glasmacher, T .
- Harle, L.L.
- He, Z.Q.
- Hodek, M.
- Hodges, L.
- Holland, K.
- Johnson, M.J.
- Jones, S.
- Leitner, D.
- Leitner, M.
- Liu, Z.
- Machicoane, G.
- Malloch, I.M.
- Marti, F.
- Miller, D. R.
- Miller, S.J.
- Morgan, G.
- Morris, D.
- Nellis, T.
- Norton, D.
- Oweiss, R.
- Ozelis, J.P.
- Peng, S.
- Popielarski, J.
- Popielarski, L.
- Pozdeyev, E.
- Rao, X.
- Rodriguez, J.A.
- Russo, T.
- Saito, K.
- Shuptar, M.
- Tanke, E.
- Usher, N.R.
- Velianoff, G.J.
- Webber, R.C.
- Wei, J.
- Weisend, J.
- Williams, M.
- Witgen, K.
- Wittmer, W.
- Wu, X.
- Xu, Y.
- Yamazaki, Y.
- Zeller, A.
- Zhang, Y.
- Zhao, Q.
- Zhao, S.
- Zheng, Z.

Fusion for Energy
Garching, Germany

- Mosnier, A.

FZJ
Jülich, Germany

- Zaplatin, E.N.

GANIL
Caen, France

- André, T.
- Bertrand, P.
- Doutresssoulles, C.
- Ducoudret, B.
- Ferdinand, R.
- Jamet, C.
- Le Coz, W.
- Ledu, G.
- Leloir, S.L.
- Loret, S.

GSI
Darmstadt, Germany

- Barth, W.A.
- Berezov, R.
- Clemente, G.
- Dahl, L.A.
- Forck, P.
- Gerhard, P.
- Gettmann, V.
- Groening, L.
- Hartmann, W.
- Herfurth, F.

- Hollinger, R.
- Kaiser, M.
- Krämer, A.
- Maier, M.T.
- Mickat, S.
- Mühle, C.
- Neidherr, D.
- Orzhekhovskaya, A.
- Pfister, J.
- Schlitt, B.
- Schreiber, G.
- Trüller, J.
- Vinzenz, W.
- Vormann, H.
- Vorobjev, G.
- Will, C.
- Yaramyshev, S.G.

HIM
Mainz, Germany
- Amberg, M.
- Barth, W.A.
- Gerhard, P.

HU/AdSM
Higashi-Hiroshima, Japan
- Hosoda, S.
- Iijima, H.
- Kuriki, M.

HZB
Berlin, Germany
- Anders, W.
- Atkinson, T.
- Bondarenko, A.V.
- Kamps, T.
- Knobloch, J.
- Kugeler, O.
- Matveenko, A.N.
- Neumann, A.
- Petenev, Y.
- Völker, J.
- Vogt, J.M.

IAP/RAS
Nizhny Novgorod, Russia
- Kuzikov, S.V.
- Savilov, A.V.

IAP
Frankfurt am Main, Germany
- Almomani, A.
- Amberg, M.
- Brodhage, R. M.
- Busch, M.
- Chau, L.P.
- Droba, M.
- Dziuba, F.D.
- Heilmann, M.
- Hofmann, I.
- Kanesue, T.
- Kester, O.K.
- Klein, H.
- Klump, B.
- Koubek, B.
- Meusel, O.
- Mäder, D.
- Podlech, H.
- Ratzinger, U.
- Schempp, A.
- Schmidt, J.S.
- Schwarz, M.
- Tiede, R.
- Volk, K.
- Vossberg, M.
- Wiesner, C.
- Xiao, C.
- Zhang, C.

IBS
Daejeon, Republic of Korea
- Choi, C.
- Hwang, J.G.
- Jeon, D.
- Joo, J.D.
- Jung, H.C.
- Kim, D.G.
- Kim, H.J.
- Kim, J.-W.
- Kim, S.K.
- Kim, Y.H.
- Lee, J.H.
- Park, G.-T.
- Song, J.

ICKC SB RAS
Novosibirsk, Russia
- Ivannikov, V.
- Shebolaev, I.V.

ICKC
Novosibirsk, Russia
- Chernousov, Y.D.

IFJ-PAN
Kraków, Poland
- Borowiec, P.B.
- Świerbleski, J.

IHEP
Beijing, People's Republic of China
- Bai, J.N.
- Cao, J.
- Chen, Q.

- Cheng, P.
- Chi, Y.L.
- Dai, M.H.
- Deng, B.
- Deng, C.D.
- Fu, S.
- Geng, H.
- Gong, K.Y.
- Guo, H.S.
- Guo, Z.
- He, D.Y.
- He, X.
- Hou, M.
- Kong, X.C.
- Le, Q.
- Li, A.H.
- Li, J.
- Li, X.
- Li, Z.
- Liu, H.C.
- Liu, J.
- Liu, R.L.
- Liu, W.B.
- Lv, K.
- Ma, C.
- Ma, H.Z.
- Meng, C.
- Ouyang, H.F.
- Pan, W.M.
- Pei, G.
- Pei, S.
- Peng, J.
- Sha, P.
- Song, H.
- Sun, B.
- Tang, J.Y.
- Wang, L.
- Wang, S.H.
- Wang, X.
- Xiao, S.
- Xiao, Y.C.
- Xu, M.H.
- Xu, T.G.
- Yan, F.
- Yang, Q.
- Yang, X.W.
- Yin, X.
- Yu, C.H.
- Yue, J.
- Zeng, L.
- Zhang, J.R.
- Zhao, F.
- Zhao, J.B.
- Zhao, J.X.
- Zhao, J.
- Zhou, Z.S.

IKP
Mainz, Germany
- Aulenbacher, K.

Illinois Institute of Technology
Chicago, Illinois, USA
- Wisniewski, E.E.

ILL
Grenoble, France
- Geltenbort, P.W.

Imperial College of Science and Technology, Department of Physics
London, United Kingdom
- Alsari, S.M.H.
- Aslaninejad, M.
- Kurup, A.
- Posocco, P.A.
- Pozimski, J.K.
- Savage, P.

IMP
Lanzhou, People's Republic of China
- Du, X.
- Guo, X.H.
- Guo, X.L.
- Han, S.F.
- Han, Y.N.
- He, S.
- He, Y.
- Huang, S.C.
- Huang, Y.L.
- Jia, H.
- Jiang, T.C.
- Jin, T.
- Jin, X.
- Li, C.
- Liu, S.H.
- Liu, Y.
- Ma, L.Z.
- Meng, J.
- Ni, D.S.
- Niu, X.F.
- Shi, A.
- Su, H.L.
- Sun, L.P.
- Sun, L.T.
- Wang, F.F.
- Wang, R.X.
- Wang, Z.J.
- Wu, B.M.
- Wu, J.X.
- Wu, W.
- Xia, J.W.
- Xiong, P.R.
- Xu, H.S.
- Xu, M.X.
- Xu, X.B.
- Xu, Z.
- Yang, W.J.
- Yang, X.L.
- Yang, Y.Z.
- Yuan, Y.J.

- Yue, W.M.
- Zhang, B.
- Zhang, C.
- Zhang, J.H.
- Zhang, S.H.
- Zhang, S.X.
- Zhang, X.H.
- Zhang, Z.L.
- Zhang, Z.M.
- Zhao, H.W.
- Zheng, S.J.
- Zhou, Z.Z.
- Zhu, L.

INFN- Sez. di Padova
Padova, Italy
- Dima, R.
- Pepato, A.
- Scantamburlo, F.

INFN-Torino
Torino, Italy
- Brunasso Cattarello, O.
- Mereu, P.
- Panero, R.

INFN/LASA
Segrate (MI), Italy
- Bosotti, A.
- Michelato, P.
- Monaco, L.
- Pagani, C.
- Paparella, R.
- Pierini, P.
- Sertore, D.

INFN/LNF
Frascati (Roma), Italy
- Alesini, D.
- Bellaveglia, M.
- Boni, R.
- Di Pirro, G.
- Ferrario, M.
- Gallo, A.
- Spataro, B.

INFN/LNL
Legnaro (PD), Italy
- Antoniazzi, L.
- Comunian, M.
- Facco, A.
- Fagotti, E.
- Grespan, F.
- Palmieri, A.
- Pisent, A.
- Roncolato, C.
- Scarpa, F.

INFN/LNS
Catania, Italy
- Allegra, L.
- Calabretta, L.
- Caliri, C.
- Caruso, A.C.
- Castro, G.
- Celona, L.
- Ciavola, G.
- Di Giugno, R.
- Gammino, S.
- Longhitano, A.
- Mascali, D.
- Neri, L.

Institute of Fluid Physics, China Academy of Engineering Physics
Mianyang„Sichuan, People's Republic of China
- Liu, Y.

Institute of High Energy Physics (IHEP)
People's Republic of China
- Feng, Y.
- Huang, H.
- Shi, S.
- Tang, E.
- Yang, X.
- Yuan, Q.
- Zhu, Z.

INTA
Santa Clara, USA
- LeClair, R.W.

IPN
Orsay, France
- Launé, B.
- Lesrel, J.

ISIR
Osaka, Japan
- Isoyama, G.
- Kato, R.
- Kawase, K.

ITEP
Moscow, Russia
- Chalykh, B.B.
- Kolomiets, A.

IUAC
New Delhi, India
- Ahuja, R.
- Chowdhury, G.K.
- Dutt, R.N.
- Ghosh, S.
- Kanjilal, D.

- Karmakar, J.
- Kumar, M.
- Kumar, R.
- Mathuria, D.S.
- Mistri, K.K.
- Pandey, A.
- Patra, P.
- Prakash, P.N.
- Rai, A.
- Roy, A.
- Sacharias, J.
- Sahu, B.K.
- Sonti, S.S.
- Suman, S.K.

J-PARC, KEK & JAEA
Ibaraki-ken, Japan
- Hasegawa, K.
- Ikegami, M.

JAEA/J-PARC
Tokai-mura, Japan
- Ao, H.
- Asano, H.
- Hasegawa, K.
- Hirano, K.
- Ito, T.
- Kondo, Y.
- Maruta, T.
- Miura, A.
- Morishita, T.
- Ouchi, N.
- Sako, H.
- Tamura, J.
- Wei, G.H.

JAEA/Kansai
Kyoto, Japan
- Aoyama, M.

JAEA/LINAC
Ibaraki-ken, Japan
- Hirano, K.
- Ito, T.
- Morishita, T.

JAEA
Ibaraki-ken, Japan
- Hajima, R.
- Hasegawa, K.
- Kondo, Y.
- Sako, H.

JAI
Oxford, United Kingdom
- Burrows, P.

JASRI/SPring-8
Hyogo-ken, Japan
- Asaka, T.
- Dewa, H.
- Ego, H.
- Hanaki, H.
- Kobayashi, T.
- Magome, T.
- Matsubara, S.
- Mizuno, A.
- Okayasu, Y.
- Suzuki, S.
- Taniuchi, T.
- Togashi, T.
- Tomizawa, H.
- Yanagida, K.

JINR
Dubna, Moscow Region, Russia
- Dubrovskiy, A.
- Kovalenko, A.D.
- Smirnov, V.L.
- Vorozhtsov, S.B.

JLAB
Newport News, Virginia, USA
- Arenius, D.
- Bogacz, S.A.
- Burrill, A.
- Davis, G.K.
- De Silva, S.U.
- Drury, M.A.
- Eremeev, G.V.
- Ganni, V.
- Hogan, J.
- Kelley, M.J.
- King, L.K.
- Krafft, G.A.
- Marhauser, F.
- Matalevich, J.
- Morozov, V.S.
- Palczewski, A.D.
- Park, H.
- Phillips, H.L.
- Pilat, F.C.
- Powers, T.
- Preble, J.P.
- Reece, C.E.
- Reilly, A.V.
- Rimmer, R.A.
- Roblin, Y.
- Tian, H.
- Wang, H.
- Wiseman, M.
- Xiao, B. P.

KAERI
Daejon, Republic of Korea
- Cho, Y.-S.
- Hwang, C.K.

- Jang, J.-H.
- Kim, D.I.
- Kim, H.S.
- Kwon, H.-J.
- Lee, Y.Y.
- Park, B.-S.
- Ryu, J.Y.
- Seol, K.T.
- Song, Y.-G.
- Yun, S.P.

KEK/JAEA
Ibaraki-Ken, Japan
- Liu, Y.

KEK
Ibaraki, Japan
- Akemoto, M.
- Arakawa, D.A.
- Arakida, Y.
- Arimoto, Y.
- Enomoto, A.
- Fang, Z.
- Fukuda, S.
- Furukawa, K.
- Futatsukawa, K.
- Hara, K.
- Hayano, H.
- Higashi, N.
- Higashi, Y.
- Higo, T.
- Honma, H.
- Igarashi, Z.
- Iida, N.
- Ikeda, M.
- Ikegami, M.
- Kadokura, E.
- Kakihara, K.
- Kako, E.
- Kamitani, T.
- Katagiri, H.
- Kato, S.
- Kawamata, H.
- Kobayashi, Y.
- Kojima, Y.
- Kondo, Y.
- Kurashina, M.
- Matsumoto, S.
- Matsumoto, T.
- Matsushita, H.
- Michizono, S.
- Mikawa, K.
- Miura, T.
- Miyahara, F.
- Miyao, T.
- Mori, T.
- Naito, F.
- Nakai, H.
- Nakajima, H.
- Nakanishi, K.
- Nakao, K.
- Nanmo, K.
- Natsui, T.
- Noguchi, S.
- Ogawa, Y.
- Ohsawa, S.
- Ohuchi, N.
- Saeki, T.
- Satoh, M.
- Sawabe, M.
- Shidara, T.
- Shimizu, H.M.
- Shirakawa, A.
- Shishido, T.
- Sugimoto, H.
- Sugimura, T.
- Suwada, T.
- Takata, K.
- Takatomi, T.
- Takenaka, T.
- Tanaka, H.
- Terashima, A.
- Toge, N.
- Tsuchiya, K.
- Urakawa, J.
- Watanabe, K.
- Yamaguchi, S.
- Yamamoto, A.
- Yamamoto, Y.
- Yano, Y.
- Yokoya, K.
- Yokoyama, K.
- Yoshida, M.
- Zang, L.
- Zhou, X.

Kress GmbH
Biebergemuend, Germany
- Haeuser, J.

Kyoto ICR
Uji, Kyoto, Japan
- Fuwa, Y.
- Hashida, M.
- Iwashita, Y.
- Otani, K.
- Sakabe, S.
- Tokita, S.
- Tongu, H.

Kyoto University, Research Reactor Institute
Osaka, Japan
- Kitaguchi, M.

Kyoto University
Kyoto, Japan
- Imajo, S.

Kyushu University
Fukuoka, Japan
- Yoshioka, T.

LAL
Orsay, France
- Blot, F.
- Brossard, J.
- Bruni, C.
- Cavalier, S.
- Cayla, J-N.
- Chaumat, V.
- El Khaldi, M.
- Gonnin, A.
- Kaabi, W.
- Lepercq, P.
- Mandag, E.N.
- Mercier, B.
- Monard, H.
- Prevost, C.
- Roux, R.
- Soskov, V.
- Variola, A.

LANL
Los Alamos, New Mexico, USA
- Ben-Naim, M.
- Bishofberger, K.
- Carlsten, B.E.
- Duffy, L.D.
- McCrady, R.C.
- Moody, N.A.
- Yampolsky, N.A.
- Young, L.M.

Lanzhou University of Technology
People's Republic of China
- Wang, J.

LASTI
Hyogo, Japan
- Shoji, Y.
- Takeda, K.

LBNL
Berkeley, California, USA
- Corlett, J.N.
- Hoff, M.D.
- Lambert, A.R.
- Li, D.
- Staples, J.W.
- Virostek, S.P.

LOA
Palaiseau, France
- Malka, V.

LPI
Moscow, Russia
- Bashmakov, Y.A.

Lund University
Lund, Sweden
- De Prisco, R.

MELCO SC
Tsukuba, Japan
- Sawabe, Y.

MEPhI
Moscow, Russia
- Adonev, O.A.
- Binyukov, P.V.
- Bondarenko, T.V.
- Dyubkov, V.S.
- Plastun, A.S.
- Polozov, S.M.
- Samoshin, A.V.
- Smirnov, A.Yu.
- Sobenin, N.P.

MPI-K
Heidelberg, Germany
- Repnow, R.

Muons. Inc.
USA
- Beard, K.B.

NCBJ
Świerk/Otwock, Poland
- Kudla, I.M.
- Plawski, E.P.
- Szewiński, J.

NFRI
Daejon, Republic of Korea
- Oh, J.-S.

Niowave, Inc.
Lansing, Michigan, USA
- Boulware, C.H.
- Grimm, T.L.

NRCN
Beer-Sheva, Israel
- Sarid, E.

NSC/KIPT
Kharkov, Ukraine
- Ayzatskiy, M.I.
- Karnaukhov, I.M.
- Kushnir, V.A.
- Mytrochenko, V.V.
- Zelinsky, A.Y.

NSCL
East Lansing, Michigan, USA
- Wang, D.

NTG Neue Technologien GmbH & Co KG
Gelnhausen, Germany
- Bechtold, A.

ODU
Norfolk, Virginia, USA
- De Silva, S.U.
- Delayen, J.R.
- Hopper, C.S.
- Olave, R.G.

Omega-P, Inc.
New Haven, USA
- Kuzikov, S.V.

ORNL RAD
Oak Ridge, Tennessee, USA
- Curry, D.
- Dickson, R.

ORNL
Oak Ridge, Tennessee, USA
- Aleksandrov, A.V.
- Blokland, W.
- Champion, M.S.
- Crofford, M.T.
- Deibele, C.
- Galambos, J.
- Heidenreich, D.
- Kang, Y.W.
- Liu, Y.
- Long, C.D.
- Moss, J.
- Plum, M.A.
- Roseberry, R.T.
- Schubert, J.P.
- Shishlo, A.P.
- Zhukov, A.P.

PKU/IHIP
Beijing, People's Republic of China
- Chen, J.E.
- Chen, J.
- Gao, S.L.
- Guo, Z.Y.
- Lu, P.N.
- Peng, S.X.
- Ren, H.T.
- Wang, Z.
- Xu, Y.
- Zhao, J.

POSTECH
Pohang, Kyungbuk, Republic of Korea
- Cho, M.-H.
- Namkung, W.
- Yang, H.

PSI
Villigen, Switzerland
- Alex, J.
- Blumer, H.
- Bopp, M.
- Citterio, A.
- Kleeb, T.
- Paly, L.
- Raguin, J.-Y.
- Scherer, A.
- Schietinger, T.
- Zennaro, R.

RAS/INR
Moscow, Russia
- Kravchuk, L.V.
- Paramonov, V.V.

RFNC-VNIITF
Snezhinsk, Chelyabinsk region, Russia
- Naumenko, M.Y.

RI Research Instruments GmbH
Bergisch Gladbach, Germany
- Pekeler, M.

RIKEN ASI
Sendai, Miyagi, Japan
- Matsukawa, T.
- Minamide, H.

RIKEN Nishina Center
Wako, Japan
- Arai, S.
- Chiba, Y.
- Fujimaki, M.
- Hasebe, H.
- Higurashi, Y.
- Kamigaito, O.
- Kase, M.
- Okuno, H.
- Sakamoto, N.

- Seki, Y.
- Suda, K.
- Watanabe, T.
- Watanabe, Y.
- Yamada, K.

RIKEN SPring-8 Center
Sayo-cho, Sayo-gun, Hyogo, Japan
- Asaka, T.
- Hasegawa, T.
- Inagaki, T.
- Kondo, C.
- Maesaka, H.
- Ogawa, K.
- Ohshima, T.
- Otake, Y.
- Sakurai, T.
- Sato, T.
- Takahashi, S.
- Togawa, K.
- Tomizawa, H.
- Yabashi, M.

RIKEN
Saitama, Japan
- Lu, L.
- Takahashi, E.

RISE
Tokyo, Japan
- Sakaue, K.
- Yamamoto, T.

RLNR
Tokyo, Japan
- Sekine, M.

Rostock University, Faculty of Computer Science and Electrical Engineering
Rostock, Germany
- Brackebusch, K.
- Flisgen, T.
- Galek, T.
- Papke, K.
- van Rienen, U.

Royal Holloway, University of London
Surrey, United Kingdom
- Ainsworth, R.
- Boorman, G.E.
- Bosco, A.

RRCAT
Indore (M.P.), India
- Dwivedi, J.
- Gupta, P.D.
- Hannurkar, P.R.
- Joshi, S.C.
- Khare, P.
- Kush, P.K.
- Mundra, G.
- Puntambekar, A.
- Roy, S.B.
- Shrivastava, P.

SBU
Stony Brook, New York, USA
- Liang, X.

SFU
Burnaby, BC, Canada
- Goh, G.

SHI Accelerator Service Ltd.
Tokyo, Japan
- Koyama, R.

Siemens AG
Erlangen, Germany
- Hagen, U.
- Heid, O.
- Hughes, T.J.S.

Siemens Research Center
Moscow,, Russia
- Ivanov, E.V.
- Krasnov, A.A.
- Nikolskiy, K.I.
- Smirnov, A.Yu.
- Tikhomirova, N.V.

SINAP
Shanghai, People's Republic of China
- Fang, W.
- Gu, D.
- Gu, Q.
- Huang, D.
- Wang, B.L.
- Wang, C.P.
- Zhang, M.
- Zhao, M.H.
- Zhao, Z.T.

SLAC
Menlo Park, California, USA
- Adli, E.
- Adolphsen, C.
- Clarke, C.I.
- Colocho, W.S.
- Corde, S.
- Decker, F.-J.
- Dolgashev, V.A.
- Dunning, M.P.
- England, R.J.

- Erickson, R.A.
- Fisher, A.S.
- Gessner, S.J.
- Gilevich, S.
- Hast, C.
- Hogan, M.J.
- Jobe, R.K.
- Kemp, M.A.
- Krasnykh, A.
- Li, S.Z.
- Limborg-Deprey, C.
- Lipkowitz, N.
- Litos, M.D.
- McCormick, D.J.
- Miahnahri, A.
- Nantista, C.D.
- Neilson, J.
- Nosochkov, Y.
- Raubenheimer, T.O.
- Ross, M.C.
- Seeman, J.T.
- Sheppard, J.
- Smith, H.
- Sun, Y.
- Tang, T.
- Tudosa, I.
- Vlieks, A.E.
- Walz, D.R.
- Wang, M.-H.
- Weathersby, S.P.
- White, G.R.
- Wienands, U.
- Woodley, M.
- Wu, Z.
- Yocky, G.

Sokendai
Ibaraki, Japan
- Kuramoto, A.
- Tyagi, P.V.

Soreq NRC
Yavne, Israel
- Arenshtam, A.
- Ben Aliz, Y.
- Berkovits, D.
- Buzaglo, Y.
- Dudovich, O.
- Eisen, Y.
- Eliyahu, I.
- Feinberg, G.
- Fishman, I.
- Gavish, I.
- Gertz, I.G.
- Grin, A.
- Halfon, S.
- Har-Even, D.
- Haruvy, Y.F.
- Hirsch, T.
- Hirschmann, D.
- Horvitz, Z.
- Kaizer, B.
- Kijel, D.
- Kreisel, A.
- Lempert, G.
- Luner, J.
- Mardor, I.
- Perry, A.
- Reinfeld, E.
- Rodnizki, J.
- Shimel, G.
- Shor, A.
- Silverman, I.
- Weissman, L.
- Zemach, E.

STFC/DL/ASTeC
Daresbury, Warrington, Cheshire, United Kingdom
- Angal-Kalinin, D.
- Buckley, S.R.
- Corlett, P.A.
- Goudket, P.
- Goulden, A.R.
- Hill, C.
- Jamison, S.P.
- Jones, J.K.
- McIntosh, P.A.
- McKenzie, J.W.
- Middleman, K.J.
- Militsyn, B.L.
- Saveliev, Y.M.
- Shepherd, B.J.A.
- Smith, R.J.
- Valizadeh, R.
- Wheelhouse, A.E.

STFC/DL
Daresbury, Warrington, Cheshire, United Kingdom
- Bliss, N.
- Burrows, I.
- Hartnett, T.
- Hindley, J.P.
- Roper, M.D.
- White, C.J.

STFC/RAL/ASTeC
Chilton, Didcot, Oxon, United Kingdom
- Gabor, C.
- Plostinar, D.C.
- Prior, C.R.
- Rees, G.H.

STFC/RAL/ISIS
Chilton, Didcot, Oxon, United Kingdom
- Clarke-Gayther, M.A.
- Faircloth, D.C.
- Lawrie, S.R.
- Letchford, A.P.

Stony Brook University
Stony Brook, USA
- Belomestnykh, S.A.
- Dai, J.
- Ruiz-Osés, M.
- Xin, T.

Technische Universität Dresden
Dresden, Germany
- Klaus, M.

THALES
Colombes, France
- Setty, A.S.

The College of William and Mary
Williamsburg, USA
- Kelley, M.J.
- Xiao, B. P.
- Xu, C.

The University of Tokyo, Nuclear Professional School
Ibaraki-ken, Japan
- Aimidura, A.
- Uesaka, M.

The University of Tokyo
Tokyo, Japan
- Iwasaki, A.
- Owada, S.

TIPC
BeiJing, People's Republic of China
- Liu, L.Q.
- Peng, N.
- Xiong, L.-Y.

TIT
Tokyo, Japan
- Satoh, D.

Tohoku University, Research Center for Electron Photon Science
Sendai, Japan
- Kashiwagi, S.

TRIUMF
Vancouver, Canada
- Ames, F.
- Ang, Z.T.
- Baartman, R.A.
- Birney, P.S.
- Bylinskii, I.V.
- Calic, S.
- Cameron, D.P.
- Chao, Y.-C.
- Dale, D.
- Davids, B.
- Dawson, R.J.
- Fong, K.
- Gong, C.
- Guetre, E.R.
- Harmer, P.R.
- Holek, J.V.
- Kajioka, S.Y.
- Kellogg, S.
- Khan, N.
- Koscielniak, S.R.
- Koveshnikov, A.
- Laxdal, A.
- Laxdal, R.E.
- Lenckowski, M.
- Mammarella, F.
- Marchetto, M.
- Merminga, L.
- Minato, M.
- Mitra, A.K.
- Morton, A.C.
- Muller, N.
- Planche, T.
- Rao, Y.-N.
- Rawnsley, W.R.
- Saminathan, S.
- Shanks, R.W.
- Sitnikov, A.
- Stanford, G.
- Verzilov, V.A.
- Yan, F.
- Yosifov, D.
- Zheng, Q.
- Zvyagintsev, V.

TSL
Uppsala, Sweden
- Gajewski, K.J.
- Lofnes, T.
- Wedberg, R.

TU Darmstadt
Darmstadt, Germany
- Burandt, C.
- Hug, F.
- Konrad, M.
- Pietralla, N.

TUB
Beijing, People's Republic of China
- Du, Y.-C.
- He, Z.Q.
- Hua, J.F.
- Huang, W.-H.
- Tang, C.-X.
- Tong, D.C.

- Xing, Q.Z.
- Yan, L.X.
- Zha, H.
- Zhang, Z.
- Zheng, Z.

TUL-DMCS
Łódź, Poland
- Cichalewski, W.
- Jałmużna, W.
- Piotrowski, A.
- Przygoda, K.P.

UCLA
Los Angeles, California, USA
- Clayton, C.E.
- Joshi, C.
- Lu, W.
- Marsh, K.A.
- Vafaei, N.

UCL
London, United Kingdom
- Jolly, S.

UMAN
Manchester, United Kingdom
- Jones, R.M.

UMD
College Park, Maryland, USA
- Beaudoin, B.L.
- Bernal, S.
- Haber, I.
- Kishek, R.A.
- Koeth, T.W.
- Mo, Y.

University of Huddersfield
Huddersfield, United Kingdom
- Cywinski, R.
- Seviour, R.

University of Tel Aviv
Tel Aviv, Israel
- Nause, A.

University of Tel-Aviv, Faculty of Engineering
Tel-Aviv, Israel
- Gover, A.
- Nause, A.

University of Tokyo
Tokyo, Japan
- Matsumura, Y.

University of Warwick
Coventry, United Kingdom
- Back, J.J.

Università degli Studi di Milano & INFN
Segrate, Italy
- Pagani, C.

Uppsala University, Department of Engineering Sciences
Uppsala, Sweden
- Dancila, D.S.
- Rydberg, A.

Uppsala University
Uppsala, Sweden
- Ekelöf, T.J.C.
- Goryashko, V.A.
- Hermansson, L.
- Noor, M.
- Ruber, R.J.M.Y.
- Santiago Kern, R.
- Yogi, R.A.
- Ziemann, V.G.

URLS
Rome, Italy
- Mostacci, A.
- Palumbo, L.

USTC/NSRL
Hefei, Anhui, People's Republic of China
- Hong, Y.
- Huang, G.
- Jia, D.
- Jin, K.
- Lin, H.
- Zhang, S.C.
- Zhou, Weishi„Zhou.

USTC
Hefei, Anhui, People's Republic of China
- Liu, Y.

UTNL
Ibaraki, Japan
- Koyama, K.

VECC
Kolkata, India
- Ahammed, M.
- Chakrabarti, A.
- Dechoudhury, S.
- Mondrel, M.
- Naik, V.

Victoria University
Victoria, B.C., Canada
- Abernathy, J.M.
- Karlen, D.
- Langstaff, R.R.
- Storey, D.W.

Warsaw University of Technology, Institute of Electronic Systems
Warsaw, Poland
- Czuba, K.
- Zembala, Ł.

Wuxi EL PONT Radiation Technology Ltd
Wuxi, People's Republic of China
- Li, Z.
- Zhang, X.